

EACWE 2025 Trondheim

Proceedings of the 9th European African Conference on Wind Engineering

Organized by the Norwegian University of Science and Technology (NTNU) and the Norwegian Society for Wind Engineering

Trondheim, Norway

June 2025

NTNU

Edited by:
Ole Øiseth, NTNU
Aksel Fenerci, NTNU
Øyvind Wiig Petersen, NTNU

Preface

These proceedings contain the extended abstracts presented at the 9th European–African Conference on Wind Engineering (EACWE2025), held in Trondheim, Norway, from June 16–19, 2025.

EACWE2025 is organized by the Norwegian University of Science and Technology (NTNU) and the Norwegian Society for Wind Engineering, with support from the International Association for Wind Engineering (IAWE). This marks the 9th edition in the series, following previous conferences held in Guernsey (1993), Genoa (1997), Eindhoven (2001), Prague (2005), Florence (2009), Cambridge (2013), Liège (2017), and Bucharest (2022). As part of a long-standing tradition, the conference continues to serve as a key platform for researchers, engineers, and industry professionals engaged in all aspects of wind engineering.

We thank all authors for their valuable contributions. Special recognition is due to the local staff, session organizers, and reviewers. Their efforts help ensure that EACWE remains a vital meeting point for dialogue across the scientific and technical wind engineering community.

We hope you have enjoyed the conference and that it has been both insightful and rewarding. We look forward to seeing you again at future events.



Ole Øiseth
Chair of EACWE2025

Contents

Preface **1**

Sponsors **13**

Keynote speakers **18**

Theme: Bluff body aerodynamics **19**

Dynamic Mode Decomposition: what can be and should be done . . . 19
Peizhen Yang, Zhuangyi Yuan, Yunlong Wang, Cruz Y Li

Impact of microcylinders cross-section geometry on wake characteristics . . . 24
Renata Gnatowska

Wind force coefficients for designing open-type structures with flat roofs . . . 28
Yuki Takadate, Yasushi Uematsu

Identify and visualize energy-wise and evolution-wise significant nonlinear flow features . . . 32
Xisheng Lin, Yixiang Wang, Cruz Y Li, Tim K.T. Tse, Bingchao Zhang, Bingchao Zhang, Peizhen Yang

Application of wind tunnel blockage correction to force measurements of U-beams with different flange porosity . . . 36
Stanislav Hračov, Petr Michálek, Blanka Ledvinková, Michael Macháček

Numerical evaluation of internal pressure in a low-rise building model in tornado-like vortex . . . 40
Qiang Chen, Jiping Kang, Delong Zuo

Study on the vortex-induced vibration and aerodynamic characteristics of two tandem 4:1 rectangular cylinders . . . 44
Jing Zhu

A refined surface roughness method to simulate the transcritical flow regime past a circular cylinder . . . 48
Claudio Mannini, Tommaso Massai, Niccolò Barni

Cladding pressure amplitudes and their variation rates . . . 52
Richard Brand, Frank Kemper

Sensitivity of cycling aerodynamics in crosswinds to turbulence modelling and CFD approaches . . . 56
Jose Matias Arbelo Romero, Hassan Hemida, Mark Sterling, Bert Blocken

Theme: Aeroelasticity **60**

Instability of solar trackers in turbulent wind flow . . . 60
Juan Ignacio Zaracho, John Ginger, David Henderson

Experimental 2D analysis of the wake speed profile of a flat plate solar tracker in a defence position . . . 64
José Luis Ruiz Moral, Raúl Manzanares , Omar Gómez-Ortega, Carlos Rodríguez-Casado, Carlos Carbajosa, Adriana Carolina Hernández-Badillo

Enhancing solar tracker stability using machine learning techniques and numerical methods . . . 69
Carlos Carbajosa, Rongshen Wang, Alejandro Martínez-Cava, Juan Andrés Cárdenas-Rondón, Raúl Manzanares-Bercial

Portable wind tunnel for single-degree-of-freedom flutter representation in single-axis solar trackers . . . 73
Carlos Rodríguez-Casado, Claudia González-Gutiérrez, Eduardo Blanco Marigorta, Maria E. Moreyra Garlock, Antonio Navarro-Manso

Essential considerations when comparing unsteady time and frequency domain responses of structures . . . 77
Romain Plasseraud, Aymeric Perret du Cray

Investigating the effect of vegetation on PV trackers design and operation . . . 81
Tiziano Leone, Giorgio Frontini, Sara Muggiasca

Evolutionary shape against vortex shedding . . . 85
Olivier Flamand, Pedrazzini Andrea, Elsa Caetano

An aerodynamic mitigation measure for wind-induced vibration of a cable-supported photovoltaic farm . . . 88
Haiwei Xu, Linyuan Shao, Wenjuan Lou

Investigation of transient vortex-induced vibrations on a 2D square cylinder under accelerating flow conditions . . . 92
Hao-Yu Bin, Gianmarco Lunghi, Mario Morello, Alessandro Mariotti, Maria Vittoria Salvetti, Stefano Brusco, Giuseppe Piccardo

Experimental Analysis of Vortex-Induced Second-Order Vibration Modes in Highly Slender Aeroelastic Models . . . 96
Luisa Pagnini, Giuseppe Piccardo, Stefano Torre, Edoardo Ruffini, Akihito Yoshida, Stefano Cammelli

Theme: Bridge aerodynamics **100**

A simplified formulations for free vibration and flutter analysis of simple suspension bridges . . . 100
Tuan-Kiet La, SeungHo Lee, ByeongCheol Won, SoonDuck Kwon

Deep learning emulation of forced vibration flows for accurate prediction of shape-dependent self-excited forces . . . 104

Omar A Mures, Miguel Cid Montoya, Sumit Verma, Ashutosh Mishra

Buffeting analysis on the Miguelturra footbridge . . . 108
Alfredo Cámara, Gia Khanh Nguyen, Mikel Ogueta, Juan Andrés Cárdenas-Rondón, Sebastián Franchini

Wind tunnel investigations of the aerodynamic interference of two independent bridge decks . . . 112
Tor Martin Lystad, Ingrid Masdal, Stian Nilsen, Ole Andre Øiseth

RANS CFD simulations to complement skew wind tunnel tests in bridge design . . . 116
Trond-Ola Hågbo, Bernardo Morais da Costa

Estimating bridge downtime from wind hazards considering comfort criterion . . . 120
Zubair Zahoor Banday, Aksel Fenerci, Torodd Nord, Ole Andre Øiseth

Application of reliability based design optimization to twin-box girder shape and gap for suspension bridges considering flutter constraint . . . 124
Ibuki Kusano, Juan Quintela, Miguel Cid Montoya, José Ángel Jurado, Santiago Hernandez

Reliability analysis of long-span suspension bridges against buffeting considering uncertainty in flutter derivatives . . . 128
Juan Quintela, José Ángel Jurado Albarracín Martinón, Miguel Cid Montoya, Ibuki Kusano, Santiago Hernández Ibáñez

Aeroelastic analysis of a pedestrian suspension bridge with a span of 648 m . . . 132
Juan Quintela, Arturo Fontán Pérez, Aitor Baldomir García, José Ángel Jurado Albarracín Martinón, Miguel Cid Montoya, Ibuki Kusano, Santiago Hernández Ibáñez

Aerodynamic investigation of twin-deck long-span bridges for vortex-induced vibrations . . . 137
Samir Chawdhury, Gledson Rodrigo Tondo, Guido Morgenthal

Dynamic excitation of long-span bridges to downburst wind loading . . . 141
Antonino Maria Marra, Luca Salvatori, Mario De Stefano, Paolo Spinelli

Stochastic wind load model for the reliability assessment and partial factor calibration of movable bridges in the Netherlands using local wind speed measurements . . . 145
Liesette Cornelia La Gasse, Franka Elisa Maria Swaalf

Design of a wind tunnel sectional model for skew wind buffeting analysis . . . 150
Lorenzo Rosa, Tommaso Argentini, Giulia Pomaranzi, Bernardo Morais Da Costa, Bernardo Morais da Costa, Jungao Wang

The influence of along-span variation of static rotation angle in multi-mode flutter calculations . . . 154
Sanne Poulin, Allan Larsen

An Open-Source Python Package for Stochastic Dynamic Analysis of Structures under Wind and Wave Loads . . . 158
Aksel Fenerci, Knut Andreas Kvåle, Øyvind Wiig Petersen, Ole Andre Øiseth

Interaction of wind barrier and deck overhang on the vortex induced vibration response of slender bridge decks . . . 162
Marko Duranovic, Craig Meskell

Consideration of buffeting and vortex-induced vibration in wind-resistant design of a balanced cantilever bridge in construction stage . . . 166
Juel Petter Bergseth, Aja Anta Tønnessen , Aksel Fenerci, Per Norum Larsen

Theme: Computational wind engineering **170**

Enhancing OpenFOAM with EnKF for Efficient State and Parameter Optimization in Atmospheric Flows . . . 170
Emanuele Bombardi, Alessandro Gambale, Alessandro Parente

Reproducing the atmospheric boundary layer for wind engineering using Mann and TurbSim inflow generation methods from wind energy . . . 174
Sophie Christine Breitkopf, Christian Hartz, Girma Bitsuamlak

Simulating building-induced windshear at airports . . . 178
Nick Pedersen, Bård Venås, Olai R. Hjetland

LES simulation study of wind turbine aerodynamic characteristics with fluid-structure interaction analysis considering blade and tower flexibility 182
Li Weipeng

Computational conditions for Large-Eddy Simulation to predict wind pressure acting on building walls with sufficient numerical stability and accuracy186
Yu Inaba, Yuta Yamane, Yasuyuki Ishida

A novel eddy current tuned rolling cylinder damper for vibration control of wind turbine . . . 190
Chao Wang, Zhenqing Liu

Large urban CFD simulations for wind and air quality analysis over Antwerp . . . 194
Rober Mamani, Jorge Sousa, Stijn Vranckx

Application and Limitations of URANS Simulations to determine the Aeroelasticity of Bridge Decks . . . 199
Yuanchao Ding, Cong Chen, Julian Unglaub, Klaus Thiele

High performance computing resources and workflows on DesignSafe . . . 203
Fred Haan, Jean-Paul Pinelli, Ahsan Kareem

Enhancing Darrieus H-Rotor Performance by Integration of J-Shaped and Microcylinder . . . 205
Dishant Sharma, Rahul Goyal

Understanding the effect of large-scale forcing on small-scale flow response using canonical flows. 209
Akshay Patil, Clara Garcia-Sanchez

Towards the development of the extreme temperature map of Genoa using OpenFoam 213
Alessia Piazza, Massimiliano Burlando, Girma Bitsuamlak, Maria Pia Repetto

Towards a database for validation of urban ventilation and pollution dispersion models 217
Petar Ognyanov Hristov, Radostin Mitkov, Mariya Pantusheva, Vasilis Naserentin, Anders Logg, Anjali Radhakrishnan Jayakumari, Stefanie Gillmeier

Measurements and simulation of internal fan-driven airflow in a commercial greenhouse 221
Peter Sutherland Sharpe, William David Lubitz

Simulation of helicopter downwash during take-off and landing in urban environments 225
Knut Erik Teigen Giljarhus, Olli-Kerstan Baricako

Theme: Codes and standards **229**

Non-uniform risk in ASCE 7 wind load reliability analyses: investigation and design recommendations 229
Brian Nielsen Skourup, Tushar Guha

Code Provisions and Wind Tunnel Tests on Ground-Mounted Solar Structures 233
Francesco Dorigatti, Matthew T.L. Browne, Zachary Taylor

Reliability-based Load-resistance Factors for the Correlated Wind-wave Loads-governed Limit States in Floating Structures 237
Jeong-Gon Kim, Hae Sung Lee, Ho-Kyung Kim

Theme: Wind tunnel testing **241**

Wind Tunnel Measurement of Aerodynamic Characteristics of Trains Passing each other on a Simply Supported Bridge 241
Haonan He, Xiaozhen Li, Ming Wang

Wind tunnel study of the drag coefficient of Mediterranean urban trees 245
Vasiliki Pappa, Demetri Bouris, Stella Tsoka, Nikos Markos

Experimental analysis of wind effects on moored container ships in harbour environments 250
Thomas Arnoult, Gertjan Glabeke, Luca Donatini, Jeroen Van Beeck

Estimation of mean value and variance of velocity from pressure measured by a pressure transducer 254
Carlos Carbajosa, Sergio Marín-Coca, Alejandro Martínez-Cava, Carolina Hernández-Badillo, Omar Gómez-Ortega

Influence of PV panel Sizes on Wind-Induced Loads: A Comparative Study on Flat Roofs 258
Ioannis Zisis, Mahmoud Abdallah

Development of a simple experimental method for wind and fire interaction problems 262
Hiroshi Hasebe, Yusuke Nakamura

Experimental aerodynamic study of three-dimensional solar tracker plant model 266
Adrián Iglesias Sánchez, Mikel Ogueta, Jose Luis Ruiz-Moral, Adriana Carolina Hernández-Badillo, Sergio Marín-Coca

Simulating super- and trans-critical Regimes on curved Surfaces in Atmospheric-Boundary-Layer Wind Tunnels: Evidences from Surface Pressure Studies on a Hemisphere and Quarter-Calotte Roof of a Biogas Plant 270
Christof Gromke, Oliver Lippert, Olivier Eiff, Rosemarie Wagner

Round-Robin Wind Tunnel Testing for High-Rise Buildings: Impact of Approach Flow Variations on Aerodynamics and Structural Response . . 274
DongHun Yeo, Adam Pintar, Girma Bitsuamlak, Arindam Gan Chowdhary, Tsinuel Geleta, Kurtis Gurley, Stéphanie Hartlin, Un Yong Jeong, Sukjun Joo, Sunho Kim, Soon Duck Kwon, Seungho Lee, Jens Møller-Madsen , Claudio Mannini, Tommaso Massai, Søren Østbirk, Brian Phillips, Ioannis Zisis

Investigation of the impact of roof ancillary structure on the wind load distribution of high-support photovoltaic array 278
Linyuan Shao, Tianzhu Wu, Haiwei Xu

Real-Time Hybrid Simulation on Wind and Wave Load Responses of Floating Structures 282
Giheon You, Yunbyeong Chae

Terrain Effects on Wind Loads of Ground-Mount PV Systems 286
Daniel Markus, André Stollenwerk

Wind load assessment of urban trees: A study of drag coefficients using wind tunnel testing 288
Fouad Elazaka, Haitham Ibrahim, Amal Elawady

Twin Wind Tunnel investigation of the scale effects on a street canyon flow 292
Nikolaos Petros Pallas, Brian Dsouza, Demetri Bouris, Andrea Sciacchitano, Christof Gromke

Effects of model scale and surroundings on surface pressures of a mid-rise building 296
Vincenzo Picozzi, Antonio Malasomma, Fabio Rizzo, Aleksander Pistol, Renata Klaput, Alberto Maria Avossa, Francesco Ricciardelli

Wind tunnel testing of U-shaped and rectangular prisms at two turbulence levels of incoming flow 300
Michael Macháček, Stanislav Hračov, Karel Dejmal

Advancements underway in designing a national full-scale testing infrastructure for community hardening in extreme wind, surge, and wave events (NICHE) . . . 304
Arindam Gan Chowdhury, Amal Elawady, Hermann Fritz, Catherine Gorle, Kurtis Gurley, Tracy Kijewski-Correa, Frank Lombardo, Pedro Lomonaco, Forrest Masters, Jack Puleo, Kristin Taylor, John van de Lindt, Paul Vasilescu, Ioannis Zisis

Theme: Building aerodynamics **308**

Discussion of design wind loads on mullions installed at the corners of rectangular buildings . . . 308
Tomoko Aihara, Yuji Isshiki, Yasushi Uematsu

Aerodynamic oscillations of high-rise buildings using building mass damper . . . 312
Jiarui Wu, Tsuyoshi Nozu, Kiyoshi Sasaki, Yuta Tomiyoshi

The mechanism behind VIV onset on rectangular cylinders with porous coverings: an experimental and numerical study . . . 316
Marcello Catania, Giulia Pomaranzi, Alberto Zasso

Full-scale vs. wind tunnel pressure measurements on a mid-rise building . . . 320
Antonio Malasomma, Vincenzo Picozzi, Luca Caracoglia, Alberto Maria Avossa, Francesco Ricciardelli

Theme: Cables and transmission lines **324**

Selected results of experimental studies on the effect of icing on the aerodynamics of bridge cables . . . 324
Piotr Górski, Marcin Tatara, Stanislav Pospíšil, Arsenii Trush

Effects of conductors on wind-induced vibration of multi span transmission towers under various wind directions . . . 328
Yongfei Zhao, Yang Yang, Ruwei Ma, Mingshui Li

Cross-sectional variations and their impact on drag and vortex-induced vibrations in bridge hangers . . . 332
Alessandro Galimberti, Federico Zanelli, Sara Muggiasca, Tommaso Argentini, Alberto Zasso, Jungao Wang

Enhanced Atmospheric Icing Modelling of High-Voltage Transmission Lines . . . 336
Erick Ulloa Jimenez , Stefan Steevens, Norbert Hoelscher , Susanne Diburg Hoelscher

Theme: Towers and chimneys **340**

Vortex-induced vibrations measured on a full scale chimney . . . 340
Pascal Hémon

An estimation of the unsteady lateral force on two full scale large vertical cylinders submitted to natural wind . . . 344
Pascal Hémon, Ika Kurniawati, Francesca Lupi, Marc Seidel, Rüdiger Höffer

Vortex-induced vibrations of wind turbine towers: Sensitivity analysis of prediction models for first and second mode . . . 348
Ika Kurniawati, Francesca Lupi, Marc Seidel, Rüdiger Höffer, Hans-Jürgen Niemann

Wind tunnel investigation of aerodynamic loads of circular cylinders from subcritical to supercritical Reynolds number regime . . . 352
Alessandro Giusti, Andi Xhelaj, Andrea Orlando, Alessio Torrielli, Olivier Flamand

Inverse calculation of aerodynamic coefficients of a polygonal cylinder from full-scale monitoring data . . . 356
Mekdes Tadesse Mengsitu, Andrea Orlando, Maria Pia Repetto

Fatigue assessment of pedestals for wind assisted propulsion systems on merchant ships . . . 360
Gaute Storhaug, Jens Petter Turøy, Bernt Leira, Dag Myrhaug

Sensitivity of tower cranes to autorotation . . . 364
Frank Kemper, Lin Hao, Johannes Duelli, Simon Kley

Aerodynamic loads on groups of offshore wind turbine towers during the pre-assembly phase on port quaysides . . . 368
Claudio Mannini, Tommaso Massai, Niccolò Barni, Alessandro Giusti

Theme: Performance-based wind engineering **372**

Assessing seismically damaged buildings in wind environments: a comprehensive framework . . . 372
Aniket Panchal , Anastasia Athanasiou

Risk-targeted design wind speeds for performance-based design of long-span bridges . . . 376
Zihang Liu, Genshen Fang, Yaojun Ge

Wind-driven considerations for tall RC building design in seismic environments . . . 380
Morewe Mall, Aniket Panchal, Anastasia Athanasiou

Cost-based optimization of a tall building subjected to wind action . . . 384
Alessandro Giovani, Mattia Francioli, Francesco Petrini

Comparative Study on Wind-Induced Response of High-Rise Core-Wall Buildings through Wind Spectral and Time History Analyses . . . 388
Sol-Gi Eun, Thomas Kang

Calibration Algorithm for FNA Nonlinear Analysis in Wind-Resistant Design Using the Biaxial Bouc-Wen Model . . . 392
Seonhyeong Kim, Thomas Kang

Theme: Wind field simulation **396**

Using WRF-CFD simulation to reproduce the environmental wind field during a helicopter crash accident . . . 396
Yong-Ming Yang, Mei-Jiau Huang, Brian C. Kuo

Prediction of hurricane wind field with sparse observational data . . . 400
Feng Hu, Bin Lu, Junyi He, Qiusheng Li

Development of multi-region Reduced-order Modeling framework: application in Atmospheric Boundary Layer flows over urban areas . . . 404
Haoyan Li

Field measurements and numerical analysis of downslope winds in port areas . . . 408
Ivana Ivančić, Alessio Ricci, Massimiliano Burlando, Djordje Romanic, Branko Grisogono, Hrvoje Kozmar

Comparison between LIDAR measurements and reanalysis wind velocities: a case study. . . . 412
Vincenzo Sepe, Francesco Ricciardelli, Sergio Montelpare, Alberto M. Avossa

Theme: Wind energy **416**

Vibration characteristics of multiple flat plates based on flow visualization . . . 416
Nozomi Suzuki, Hiroshi Hasebe

Torsional flutter harvester in non-stationary outflows, exploiting negative stiffness element for energy conversion . . . 420
Luca Caracoglia

Vortex methods for wind turbine rotors on floating substructures . . . 424
Tor Anders Nygaard, Carlos Renan Santos, Lars Einar Sørensen Stieng, Mathias Huuse Marley

Fluid-structure simulation and structural design analysis of a 5-MW wind turbine blade at different wind speeds . . . 428
Chun-Ying Lee, Chun-Chi Chang, Cheng-Han Zhuang, Jinsiang Shaw

Wind power estimations of staggered high-rise building arrays with voids at varied plan area densities . . . 432
Yee-Ting Lee, An-Shik Yang, Men-Shen Tsai

Comparative study of aerodynamic characteristics on urban high-rise vertical farms . . . 436
Simeng Xie, Pedro Martinez-Vazquez , Charalampos Baniotopoulos

Wind Power Forecast confidence interval based in LSTM combination of GFS-ECMWF-WRF ensembles. . . . 440
Victor Matheus Silveira, Sofia Orteli, Alejandro Gutierrez

About fatigue in wind turbines and the use of HSFD to enhance structural durability . . . 444
Ettore Sorge, Carlos Riascos, Nicola Caterino

Wind speed and turbulence recovery from SCADA data . . . 448
Lasse Svenningsen, Troels Juul Pedersen

Dynamic stall control of wind-turbine blades equipped with vortex generators and Gurney flaps . . . 452
Marin Ivanković, Marvin Jentzsch, Anna Friederike Rahel Großmann , Vladimir Zimmermann, Marinos Manolesos, Christian Navid Nayeri, Hrvoje Kozmar

Hierarchical dynamic wake modeling of wind turbine based on physics-informed generative deep learning . . . 456
Q. Wang, Z. Ti, S. Yang, K. Yang, J. Wang, X. Deng

Theme: Pollutant dispersion **460**

A quick atmospheric dispersion simulation based on a coupling LES-database with on-site meteorological data . . . 460
hiromasa Nakayama, Takuto Sato

Establishing correlations between wind and air pollutant fields around isolated buildings . . . 464
Yaojia Guo, Xuelin Zhang, Asiri Umenga Weerasuriya

Comparison of dynamic mesh and source term methods in simulating vehicle emission dispersion in a street canyon . . . 468
Wen Lin, Wenbing Liu, Xuelin Zhang, Asiri Umenga Weerasuriya

A Dynamic Overset Mesh Approach for Large-Eddy Simulation of Vehicle-Induced Turbulence and Pollutant Dispersion . . . 472
Bingchao Zhang, Xuelin Zhang, Yunfei Fu, Tim K.T. Tse, Peizhen Yang

Analysis of air pollutant transport near a real urban canyon depending on daily traffic patterns . . . 476
Ursula Voss, Svetlana Valger

Experimental Assessment of the Pollutant Dispersion of Ship Emissions . . . 480
Stefanie Gillmeier, Anjali Krishnan Radhakrishnan Jayakumari, Eric Roosenboom, João Muralha, Guilherme Beleza Vaz, Felipe Sánchez Castro

Measuring a Pollutant Plume over a 3D printed City Model . . . 484
Tomos Rich, Christina Vanderwel

Indoor-outdoor pollutant transport through a hollow cube with a cross-ventilating flow . . . 488
Subhajit Biswas, Matteo Carpentieri, Christina Vanderwel

Evaluation of steady and unsteady-RANS simulations for pollutant dispersion in a realistic urban configuration . . . 492

Xinyi Li, Mohammadreza Shirzadi, Yoshihide Tominaga, Tsubasa Okaze

Evaluating turbulence model reliability for near-field pollutant dispersion in a realistic urban scenario. . . . 496
Apostolos Krassas, Stefano Capra, Salvatore Renda, Eugene De Villiers

Pollutant removal mechanisms of fetch effects in street canyons with different aspect ratios . . . 500
Daniel Ziyue Peng, Bingchao Zhang, Yunfei Fu, Cruz Y Li, Yixiang Wang, Tim K.T. Tse

Rooftop emissions and dispersion into near-building flow fields in suburban areas . . . 504
Cornelia Kalender, Mohammad Norouzi , Frank Harms, Ulf Winkelmann, Bernd Leitl, Rüdiger Höffer

Theme: Train/vehicle aerodynamics **508**

Assessment framework of bridge VIV on running performance of high-speed trains . . . 508
Ming Wang, Xiaozhen Li , Shihao Zhao, Mingfang Yang

Wind loading on a moving train due to a downburst . . . 512
Aleksander Pistol, Mark Sterling, Chris Baker

Measurement of aerodynamic forces acting on a model train passing through a swirling flow using a tornado vortex generator . . . 516
Masahiro Suzuki, Nobuyuki Okura

Effects of multi vehicles on aerodynamic forces of running vehicle on bridge against crosswind . . . 520
Hiroshi Katsuchi, Jiaqi Wang

Investigation of perceived precipitation and accumulation characteristics on different surfaces of a moving vehicle . . . 524
Mohammadsadegh Moradi Ghareghani, Farimah Hosseinnouri, Kiran Keshavan, Eric Villeneuve, Ismail Gultepe, John Komar, Martin Agelin-Chaab, Horia Hangan

Interference Effects between High-Sided Road Vehicles: Aerodynamic Interactions under Crosswinds . . . 528
Muhammad Ahmad Siddique, Partha Sarkar, Omar Smadi

Crosswind stability of road vehicles under thunderstorm downburst winds . . . 532
Carlos Esteban Araya Reyes, Antonio Cioffi, Gisella Tomasini

Full-scale measurements of freight train aerodynamics . . . 536
Mike Jesson, David Soper, Chris Baker

Comprehensive Risk Assessment of Vehicle Stability on Sea-Crossing Bridges : Joint Effects of Wind and Precipitation Data . . . 540
Hyeong Yun Cheon, Sejin Kim, Ho-Kyung Kim

Effect of static pitch angle on the upwind aerodynamics of yachts. . . . 544
Craig Meskell, Andrew Coyle

Extreme value distributions of vehicle lateral lane deviation using frequency-domain models and real-world data . . . 548
Sebastian Reymert, Øyvind Wiig Petersen, Ole Andre Øiseth

Theme: Ventilation **552**

Defining geometric level of detail of furniture for indoor ventilation . . . 552
Nadine Hobeika, Philomena M. Bluyssen, Clara Garcia-Sanchez

Evaluating the Impact of Horizontal Louvers on Natural Ventilation and Thermal Comfort in Polish Multi-Family Homes: A CFD Analysis . . . 556
Mohammad Mahdi Mohammadi, Maciej Janowski

Wind-driven natural ventilation of airport terminals . . . 561
Matko Jelašić, Christoph Irrenfried, Guenter Brenn, Hrvoje Kozmar

Theme: Vibration mitigation and control **565**

Study on the Active Aerodynamic Countermeasure for Vortex-Induced Vibration of the Π-shaped box girder . . . 565
Han Xiao, Zhiwen Liu, Klaus Thiele, Zhengqing Chen

Wind-induced vibration control of high-rise buildings with double-skin facades using distributed multiple tuned facade-dampers-inerters . . . 569
Chengxi Pan, lingfeng Su, haiwei Xu

Experimental study of an asymmetric Stockbridge damper . . . 573
Giacomo Bacci, Ole Andre Øiseth, Øyvind Wiig Petersen, Vincent Denoël

Equivalent damping in structures subjected to vortex induced vibrations and damped with tuned mass dampers . . . 577
Anass Mayou, Vincent Denoël

Theme: Machine learning and artificial intelligence **581**

Extreme compression of URANS flow data . . . 581
Omar A. Mures, Miguel Cid Montoya, Sumit Verma, Ashutosh Mishra

Learning weakly nonlinear Vortex-induced Vibration governing equations from experimental data . . . 585
Teng Ma, Wei Cui, Lin Zhao

An initiative for consolidating a universal aerodynamic coefficients database using LLM-driven web scraping . . . 589
Dario Fernandez Castellon

A Novel Hybrid Machine Learning Approach for Wind Pressure Reconstruction Around Buildings with Limited Sensors . . . 593
Foad Mohajeri Nav, Seyedeh Fatemeh Mirfakhar, Reda Snaiki

High-resolution mean flow and Reynolds stress reconstruction in a two-dimensional urban street canyon using physics-informed neural networks 597
Yichen Wang, Bingchao Zhang, Chaoyi Hu, Hideki Kikumoto

Prediction of Wind Pressure on Rectangular Buildings Using Diffusion Model . . . 601
Yeong In Lee, Thomas Kang

Efficient analysis of mean flow around three-dimensional isolated building under multiple wind directions using physics-informed neural network 605
Chaoyi Hu, Hongyuan Jia, Yichen Wang, Hideki Kikumoto

Anomaly detection for mooring failure in pontoon-supported floating bridges . . . 609
Jihun Song, Jonghyeok Lee, Seungjun Kim

Theme: Aerodynamic aspects in extreme crossings **613**

Bridge buffeting in skew winds – experimental aerodynamic coefficients and numerical analysis . . . 613
Bernardo Morais da Costa, Jungao Wang

Aerodynamic stability of a single span suspension bridge for crossing of Sulafjord. . . . 617
Allan Larsen, Ketil Aas-Jakobsen, Mads B Eriksen

Aerodynamic performance of the Julsund bridge deck . . . 621
Jungao Wang, Ketil Aas-Jakobsen, Tommaso Argentini, Giulia Pomaranzi, Alberto Zasso, Bjørn Isaksen , Johannes Veie

Insights into the nose-up effect on the Çanakkale twin-box bridge deck based on CFD simulations . . . 625
Nicola Cortellazzi, Federico Di Lenardo, Maja Rønne, Daniele Rocchi, Tommaso Argentini

Wind engineering aspects of the Gordie Howe International Bridge between Canada and the United States . . . 629
Pierre-Olivier Dallaire, Zachary Taylor, Mark Istvan, Stoyan Stoyanoff

Aero-hydrodynamic coupled analysis of a floating long-span bridge . . . 633
Soomin Kim, Youchan Hwang, Jeong-Gon Kim, Chungkuk Jin, Ho-Kyung Kim

Internal Resonance during nonlinear flutter response of long-span bridges . . . 637
Lin Zhao, Wei Cui

An overview of the aerodynamic design of the Julsundet bridge towers . . . 641
Giulia Pomaranzi, Jungao Wang, Tommaso Argentini, Alberto Zasso

Long-term analysis of the Halsafjorden Bridge accounting for parametric effects of turbulence . . . 645
Niccolò Barni, Ole Andre Øiseth, Øyvind Wiig Petersen, Claudio Mannini

Modelling of nonlinear aerodynamic self-excited forces on bridge decks – Going forward . . . 649
Henrik Skyvulstad, Øyvind Wiig Petersen, Ole Andre Øiseth

Sensitivity analysis of numerical modelling approaches for curved floating bridge buffeting response . . . 653
Zihao Wang, Jasna Bogunović Jakobsen, Yanyan Sha

Theme: Roof systems and cladding performance **657**

A wind tunnel-based approach for evaluating wind loads simultaneity in photovoltaic park design . . . 657
Giorgio Frontini, Stefano Giappino, Sara Muggiasca

Aeroelastic Response of a Large Suspension Roof: Wind Tunnel Tests and Numerical Simulations . . . 661
Tommaso Argentini, Filippo Calamelli, Umberto Spinelli, Lorenzo Rosa, Alberto Zasso

Influence of turbulence of oncoming flow on the admittance function of local pressures on a building roof . . . 665
Vincent Denoël, Mattia Ciarlatini, Catherine Gorle

Cable net stiffness fluctuation under wind flow . . . 669
Fabio Rizzo, Aleksander Pistol, Renata Kaput , Francesco Ricciardelli, Maria Francesca Sabbà, Dora Foti , Luca Caracoglia

Theme: The second generation Eurocode wind actions **673**

Evaluation of the provisions for wind induced vibrations in the second generation Eurocode EN 1991-1-4 . . . 673
Chris Geurts, Okke Bronkhorst

The second generation Eurocode 1 Part 1-4 on wind actions . . . 677
Francesco Ricciardelli

Accounting for the incomplete correlation of windward and leeward pressures in EN 1991-1-4 . . . 681
Frank Kemper, Richard Brand, Chris Geurts

Computational wind engineering for structural design: the Annex K of the new Eurocode 1 part 1-4 . . . 685
Luca Bruno, Nicolas Coste, Claudio Mannini, Alessandro Mariotti, Luca Patruno, Paolo Schito, Giuseppe Vairo

Modernizing wind load standards for Ireland: A comparative analysis of first and second generation Eurocodes . . . 689
David Cunningham, Jennifer Keenahan, Rubina Ramponi, Reamonn MacReamoinn

Along-wind dynamic response in Eurocode . . . 693
Svend Ole Hansen, Marie Louise Pedersen, Robin George Srouji, Nicolo Daniotti

Theme: Wind-particle-structure interaction **697**

Impact of climate change for blowing snow in Hokkaido assessed by a large ensemble dataset . . . 697
Kuniyasu Sugawara, Masaru Inatsu, Yusuke Harada

CFD simulation of aeolian sand erosion and deposition around a bluff body . . . 701
Zitao Jiang, Yoshihide Tominaga, Xin Zhang

Optimalization of PV plants in snow rich areas . . . 705
Thomas Thiis, Arnkell J. Petersen, Jan Potac, Matthias Henkies, Iver Frimannslund

Considerations in replicating In-cloud Ice Accretion on Power Lines in Climatic Wind Tunnel Testing . . . 709
Francesca Lupi, Erick Ulloa Jimenez , Lubomir Matejicka , Norbert Hoelscher , Holger Hundborg Koss

Field Observations of Snowdrift Formation Process Under Blowing Snow Using a Portable LiDAR Device . . . 713
Tsubasa Okaze, Horofumi Niiya, Satoshi Omiya, Sojiro Sunako, Takahiro Tanabe, Kouichi Nishimura

Theme: ERIES: Advancing frontier knowledge in wind engineering through laboratory testing **717**

The aerodynamic impact of overtaking manoeuvres on platooning vehicles . . . 717
David Soper, Samuel Marshall, Mark Sterling, Stefanie Gillmeier

Pollutant re-introduction investigation for occupational risk reduction (PRIORR) . . . 721
Romain Guichard, Anjali Krishnan Radhakrishnan Jayakumari, Stefanie Gillmeier, Ali Bahloul

Vortex shedding of circular cylinders mounted on a rolling support at different Reynolds number regimes . . . 725
Alessio Torrielli, Andrea Orlando, Andi Xhelaj, Alessandro Giusti, Olivier Flamand

Experimental evaluation of wind effects on non-standard shapes and structures . . . 729
Anoop Kodakkal, Rodrigo Castedo-Hernandez, Guillermo Martinez-Lopez, Ann-Kathrin Goldbach, Kai-Uwe Bletzinger, Kimberly Adamek, Tibebu Birhane, Girma Bitsuamlak

Wet Snow Accretion on Transmission Lines in Climatic Wind Tunnel . . . 733
Erick Ulloa Jimenez, Francesca Lupi, Norbert Hoelscher , Susanne Diburg Hoelscher, Jean Paul Bouchet , Bruno Gauducheau, Thomas Batmalle , Philippe Delpech , Olivier Flamand

Wind impacts on vertiport design . . . 737
Mohammad Amir Neshat, Edoardo Ruffini, Stefano Torre, Giuseppe Piccardo, Maria Pia Repetto, Yana Gorbachova, Dario Milani

CLIMATHUNDERR: A first attempt to combine impinging jet and gravity current techniques to simulate downburst winds at large scale . . . 741
Federico Canepa, Anthony Guibert, Andi Xhelaj, Josip Žužul, Djordje Romanic, Alessio Ricci, Horia Hangan, Olivier Flamand, Jean-Paul Bouchet, Philippe Delpech, Massimiliano Burlando

ERIES-SOLAR: The assessment of downburst actions on solar panels at the WindEEE Dome . . . 745
Antonio J. Alvarez, Felix Nieto, Petar Škvorc, Hrvoje Kozmar, Jeroen Van Beeck, Tibebu Birhane, Kimberley Adamek, Girma Bitsuamlak

ERIES-TLTB: Thunderstorm Loading on Tall Buildings . . . 749
Camila Aldereguía Sánchez, Stefano Torre, Anna Bagnara, Frederica Tubino, Maria Pia Repetto

Evaluation of aerodynamic coefficients on a lattice structure by experimental wind tunnel tests . . . 753
Bruno Jorge Clavelo, Kristof Maes, Patricia Martín, Vivian Elena, Frederica Tubino, Giuseppe Piccardo, Maria Pia Repetto, Geert Lombaert

Vortex-induced vibrations of the flexible bridge cable model . . . 757
Arsenii Trush, Stanislav Pospíšil, Olivier Flamand, Armando Carusone

Rain-wind induced vibration of stay cables: several recommendations for wind tunnel testing . . . 761
Vitor Diniz Pinto, Christos T. Georgakis, Allan Larsen, Cristoforo Demartino, Werner Brand , Jasna Bogunovic Jakobsen, Francesco Ricciardelli, Don Bergman, Robert Soltys

Costal Urban-BOundary Layer Dynamics (CU-BOLD) . . . 765
Djordje Romanic, Alessio Ricci, Masoud Meoini, Priyadarshi Maurya, Massimiliano Burlando

The ERIES BOLT Project: Behavior of Telecommunication Lattice Towers to Thunderstorms Winds . . . 769
Ileana Calotescu, Coșoiu Costin-Ioan , Horia Hangan, Kim Adamek, Tibebu Birhane, Girma Bitsuamlak

Data-driven Monte Carlo simulations of tornado-like-vortex-induced loads on low-rise buildings . . . 773
Edmundo Gabriel Narancio, Han Ping Hong, Horia Hangan

Numerical simulation of the flow around a sectional scale model of a lattice tower . . . 777
Costin Ioan Coșoiu, Ileana Calotescu, Kim Adamek, Tibebu Birhane, Girma Bitsuamlak

Does tornado vortex wandering really exist? . . . 781

Aleksander Pistol, Mark Sterling, Mike Jesson, Girma Bitsuamlak, Fred L. Haan, Tibebu Birhane, Yealemnegus Waktola, Gregory A. Kopp

Theme: Recommendations for best practice in CFD **785**

Effects of the inflow turbulence on the force and pressure characteristics of a three-dimensional square cylinder by LES . . . 785
Yoshiyuki Ono, Hiroto Kataoka

Application of lattice Boltzmann method-based large-eddy simulation in flow around an isolated building . . . 789
Mengtao Han, Hideki Kikumoto, Ryozo Ooka

CFD Analysis of louvre blade designs on rooftop for enhancing wind energy potential . . . 793
Wan-Yi Chen, Ting-Yu Wei, Yu-Hsuan Juan

Quality control of CFD analysis of virus-laden droplet transmission in indoor environments . . . 797
Xuelin Zhang, Xiaodan Fan, Asiri Umenga Weerasuriya

Numerical study of wind effects on moored container ships in harbour environments . . . 801
Andrea P. C. Bresciani, Matilde Fiore, Thomas Arnoult, Julien Christophe, Gertjan Glabeke, Jeroen Van Beeck

Speeding Up Wind Load Predictions on Cargo Ships through Multi-Fidelity Modeling . . . 805
Matilde Fiore, Miguel Alfonso Mendez, Jeroen Van Beeck

The importance of details during the development of CFD simulations: an example in sports aerodynamics . . . 809
Fabio Malizia, Bert Blocken

Recommendations on practical applications of inflow turbulence generation for large eddy simulation in wind engineering . . . 813
Bowen Yan, Yangjin Yuan, Qingshan Yang, Jiawei Wan

Complementary use of CFD simulations and wind tunnel tests in the built environment . . . 817
Yoshihide Tominaga, Zitao Jiang

Linkage between spatial resolution and accuracy in 3D LES: three examples in bluff body aerodynamics . . . 821
Felix Nieto, Antonio J. Alvarez, Kenny C.S. Kwok, Luca Patruno

LES for solar tracker wind loads: A benchmark experiment and validation study . . . 825
Tsigereda Getachew Eshete, Tsinuel Geleta, Girma Bitsuamlak

Challenges and developments in CFD modeling of urban microclimate at neighborhood scale . . . 829
Aytac Kubilay, Dominique Derome, Jan Carmeliet

Reflecting on the wind direction effects: how many degrees are enough? . . . 833
Clara Garcia-Sanchez, Akshay Patil

Recommendations for CFD best practice guidelines and requirements for wind loads on buildings . . . 837
Tsinuel Geleta, Girma Bitsuamlak

Implementing surface roughness in OpenFOAM using the CORINE database for mesoscale CFD simulations . . . 841
Alessio Ricci

Some observations on LES vs RANS in predicting pedestrian wind comfort . . . 845
Knut Erik Teigen Giljarhus, Usman Shaukat

Automatic 3D geometry reconstruction of a large-scale city on complex topography for CFD simulations . . . 849
Josip Žužul, Alessio Ricci, Massimiliano Burlando

Uncertainties by surface roughness specification in RANS CFD simulations of wind flow in urban areas . . . 853
Bert Blocken

An inflow turbulence over rough terrain generated with a digital filter method . . . 857
Tsubasa Okaze, Akashi Mochida

CFD simulation for urban canyon flow under surface heating: Comparison between wall-resolved versus wall-modeled Large Eddy Simulation . 861
Pu Gong, Weiheng Liang, Xing Zheng

Theme: Wind hazards assessment and climate change **865**

A framework to assess the risk of windthrow in Irish forests. . . . 865
Emmanuel Chukwudi Ekeoma, Mark Sterling, Nicole Metje, John Spink, Niall Farrelly, Owen Fenton

Wind vulnerability of industrial facilities equipment . . . 869
Nahuel Bonfante, Jean-Paul Pinelli

Observed wind characteristics causing building damage during severe thunderstorms in a temperate coastal region . . . 873
Matthew John Glanville

A novel framework to assess multiscale wind hazard on structures and infrastructures: an application to Italy . . . 877
Lorenzo Raffaele, Luca Bruno, Elisabetta Colucci, Nicolas Coste

Stow regime considerations for single axis tracker solar structures . . . 881
Mike Gibbons, Zachary Taylor, Julia Veerman, David Horrocks

Integrated Risk Assessment of Tree-Induced and Wind-Induced Damage to Low-Rise Buildings in Hurricane Scenarios . . . 884
Mohammad Bakhshandeh, Jean-Paul Pinelli, Amal Elawady

Effects of climate change on future winds and wind engineering practice in the UK . . . 888
David Hankin, Anna Bagnara, Daniel Hackett, Stefano Cammelli, Rubina Ramponi

Theme: Urban wind climate and pedestrian comfort **890**

Investigating the impacts of urban microclimate on energy consumption of residential high-rise buildings . . . 890
Wenbing Liu, Xuelin Zhang, Asiri Umenga Weerasuriya

Reducing the double corner effect in orthogonal building layout to improve pedestrian wind comfort . . . 894
Hakan Baş

Predicting probability distributions of pedestrian-level wind speeds in realistic urban environments using mean and standard deviation . . . 898
Wei Wang, NAOKI IKEGAYA

Wind microclimate studies in the UK: subtleties, discrepancies and on-going challenges . . . 902
Stefano Cammelli, Andrew Nicoli

Comprehensive study of pedestrian wind comfort in large city centre . . . 906
Agnieszka Kocoń

Urban ventilation dynamics assessment of opening geometry and vertical configuration in permeable buildings . . . 910
yingming su, Yu-cheng Fang

Fast short-term forecasting of wind field using meteorological reanalysis data and near-surface observations . . . 914
Xiang Wang, Hongyuan Jia, Chaoyi Hu, Keisuke Naoka, Hideki Kikumoto

Urban planning at Nyhavna using CFD . . . 918
Ken-Robert Gjelstad Jakobsen, Jacob Hudtwalcker, Ralph Bertram, Sarah Falbe Hansen

Characterising the velocity field in the pedestrian zone under the influence of landscaping elements. . . . 922
Jeremy Sacco, Daniel Micallef, Sudarshan Babu, Simon Paul Borg, Christopher Micallef

POD study of Bristol CFD simulations with different levels of detail . . . 927
Álvaro Manzano Sevillano, Clara Garcia-Sanchez, Soledad Le Clainche Martínez, Dani Fernández Comesaña

Method for Visualizing Wind Corridors Using Persistent Homology . . . 931
Yuta Honda

Windbreak effects of Igune as traditional homestead trees in a clustered settlement at Osaki Koudo, Japan . . . 935
Kento Minami, Eito Mizuta, Chinatsu Yonezawa, Tsubasa Okaze

Theme: Field measurements and wind characteristics **939**

SAMURAI-S: A novel drone-mounted sonic anemometer for turbulence analysis . . . 939
Mauro Ghirardelli, Stephan Kral, Etienne Cheynet, Joachim Reuder

Comparative analysis of gust factor for offshore monsoon, tropical cyclone, and thunderstorm winds . . . 944
Yucheng Xue, Junyi He, Pakwai Chan, Qiusheng Li

Vortex-induced force estimation in long-span bridges using latent force model . . . 948
Shengyi Xu, Øyvind Wiig Petersen, Genshen Fang, Ole Andre Øiseth, Yaojun Ge

Drone swarm wind measurements within the shear layer of a nominally cuboid building . . . 952
Sebastian James Kean, Mathew Marino, Abdulghani Mohamed, Simon Watkins

Outdoor Particle-Tracking Velocimetry of Wind Above a Full-Scale Nominally Cuboid Building . . . 956
Finn Sutherland, Abdulghani Mohamed, Mathew Marino, Simon Watkins

The Flow Field over a Cuboid Building: Full-Scale and Model-Scale Comparison . . . 960
Finn Sutherland, Simon Watkins, Abdulghani Mohamed, Matthew Marino

Aerodynamic forces on novel tetra-shaped solar panels mounted on flat roof: first insights from field measurements . . . 964
Anjali Krishnan Radhakrishnan Jayakumari, Stefanie Gillmeier

Wind conditions monitoring for solar collector array design: the case of Nevada Solar One . . . 968
Yuanchen Wan, Etienne Cheynet, Yan Li, Ulrike Egerer

Wind-induced vibration of traffic signal structures: Health monitoring and vibration mitigation . . . 972
Partha Sarkar, Nayan Tiwari, Alice Alipour

Offshore vertical wind shear with WRF simulation and ERA5 reanalysis in Atlantic Ocean coast location . . . 976
Victor Matheus Silveira, Ignacio Franco, Alejandro Gutierrez

A dataset for studying the impact of heat waves on the built environment in a humid continental climate . . . 980
Miguel Martin Fehlmann, Clara Garcia-Sanchez, Jantien Stoter, Mario Berges

Field Observations of Buffeting Loads on a Suspension Bridge Girder . . . 983
Nicolo Daniotti, Jasna Bogunovic Jakobsen, Jonas Thor Snæbjörnsson, Etienne Cheynet

Urban flow observations using lidars on a university campus . . . 987
Jonas Thor Snæbjörnsson, Jasna Bogunovic Jakobsen

Theme: Non-synoptic and extreme wind events **991**

Hazard Maps of Typhoon-induced Wind, Wave and Surge along Southeast China . . . 991
Xiaonong Hu, Genshen Fang, Yaojun Ge

Scaling of a full-scale thunderstorm for laboratory simulations . . . 995
Ileana Calotescu, Horia Hangan

Extreme gust trees damage in Montevideo city, operational alarm forecast with WRF ensemble simulation. . . . 999
Alejandro Gutierrez, Mariana Molinari, German Vazquez, Sofia Orteli, Victor Silveira

Torsional instabilities of single-axis solar trackers: a benchmark for wind tunnel testing . . . 1004
Carlos Rodríguez-Casado, Eduardo Blanco Marigorta, Sebastián Franchini Longhi, Juan A. Cárdernas-Rondón, Antonio Navarro-Manso

Reconstructing thunderstorm wind speed time series from observed damage . . . 1008
Djordje Romanic

Experimental investigation of building openings effect on internal and external pressures induced by tornadic flows . . . 1012
Shirin Barkhordari, Elena Dragomirescu, Matthieu Hancock-LeFebour

Maximum dynamic response of a monitored structure subjected to thunderstorm outflows: comparison between closed-form solutions and full-scale data . . . 1016
Luca Roncallo, Frederica Tubino, Mekdes Tadesse Mengistu, Maria Pia Repetto

Large-eddy simulation of downburst wind interaction with a mid-rise building . . . 1020
Mohammad Hadavi, Djordje Romanic, Alessio Ricci

Simulation of high-translation-speed tornado-like vortex effects on building aerodynamics through a rapid traversing system . . . 1024
Stefano Brusco, Adrian Costache, Timothy J. Acosta, Gregory A. Kopp

Comprehensive Framework for Scaling and Analyzing Downburst-like Outflows in Wind Tunnels— methodology and case study . . . 1028
Mohamed Eissa, Amal Elawady

3D wind field retrieval within the thunderstorm cloud that occurred on September 23, 2023 in Piedmont (Italy) . . . 1032
Priya Kumari, Massimiliano Burlando, Renzo Bechini, Djordje Romanic, Alessandro Battaglia

Thermal effects on large-scale experimental downbursts . . . 1036
Federico Canepa, Anthony Guibert, Andi Xhelaj, Josip Žužul, Djordje Romanic, Alessio Ricci, Horia Hangan, Olivier Flamand, Jean-Paul Bouchet, Philippe Delpech, Massimiliano Burlando

Challenges in simulating the wind field for full bridge buffeting response to non-synoptic winds . . . 1040
Maria Antonietta Pace, Filippo Calamelli, Tommaso Argentini

Identification of non-synoptic wind events from historical meteorological data . . . 1044
Adriana Chitez, Ileana Calotescu

Combined use of mast and lidar measurements for improved mapping of the wind climate in complex topography . . . 1048
Hálfdán Ágústsson, Martin Grønsleth, Ola Eriksen

Dynamic response of the Hålogaland Bridge subject to non-stationary wind . . . 1052
Sebastian Knedahl Hansen, Aksel Fenerci, Øyvind Wiig Petersen, Ole Andre Øiseth

Simulating a Downburst Turbulent Outflow Velocity Field on a Moving Vehicle . . . 1056
Andi Xhelaj, Massimiliano Burlando, Luisa Pagnini, Maria Pia Repetto

Climate Change and Structural Damage Sensitivity in Extreme Storm Events: The Case of Storm Anatol. . . . 1060
Johanne Kristine Øelund, Holger Hundborg Koss, Jens Hesselbjerg Christensen, Rune Zeitzen, Henrik Vedel

Experimental modeling of gusty bora windstorms . . . 1064
Petar Škvorc, Hrvoje Kozmar, Branko Grisogono, Antonio Jose Alvarez, Felix Nieto, Jeroen Van Beeck, Tibebu Birhane, Girma Bitsuamlak

Equivalent Synoptic Wind: a tool for assessing non-synoptic wind effects on slender structures . . . 1068
Andrea Orlando, Luisa Pagnini, Maria Pia Repetto

Experimental testing of bridge decks in downburst-like winds . . . 1072
Øyvind Wiig Petersen, Aksel Fenerci, Sebastian Knedahl Hansen, Ole Øiseth, Tibebu Birhane, Girma Bitsuamlak

Statens vegvesen

Norwegian Public Roads Administration

The Norwegian Public Roads Administration (NPRA) is a national agency under the Ministry of Transport, responsible for the planning, construction, operation, and maintenance of the national and European road networks in Norway. Established in 1864, the NPRA plays a central role in ensuring a safe, efficient, and environmentally sustainable transport system across the country.

With a workforce of approximately 5,000 employees, the NPRA manages over 10,000 kilometres of roads, including more than 600 tunnels and nearly 5,600 bridges. In addition to infrastructure management, the agency oversees vehicle inspections, driver licensing, and provides subsidies for ferry operations, ensuring comprehensive support for Norway's transport ecosystem.

As a leading authority in infrastructure development, the NPRA is deeply committed to integrating cutting-edge research and innovation into its practices, particularly in areas such as wind engineering, where it collaborates with academic institutions, research bodies, and industry partners to better understand wind effects on long-span bridges. This research is vital for the design and maintenance of Norway's extensive bridge network, especially in regions with complex topography and harsh weather conditions.

Flagship initiatives like the Fjord X project—which aims to replace ferry crossings with fixed links along the 1100 kilometres' E39 Coastal Highway Route in the west coast of Norway—and the adoption of digital twin technology for real-time infrastructure monitoring, highlight the NPRA's commitment to innovation, safety, and sustainability.

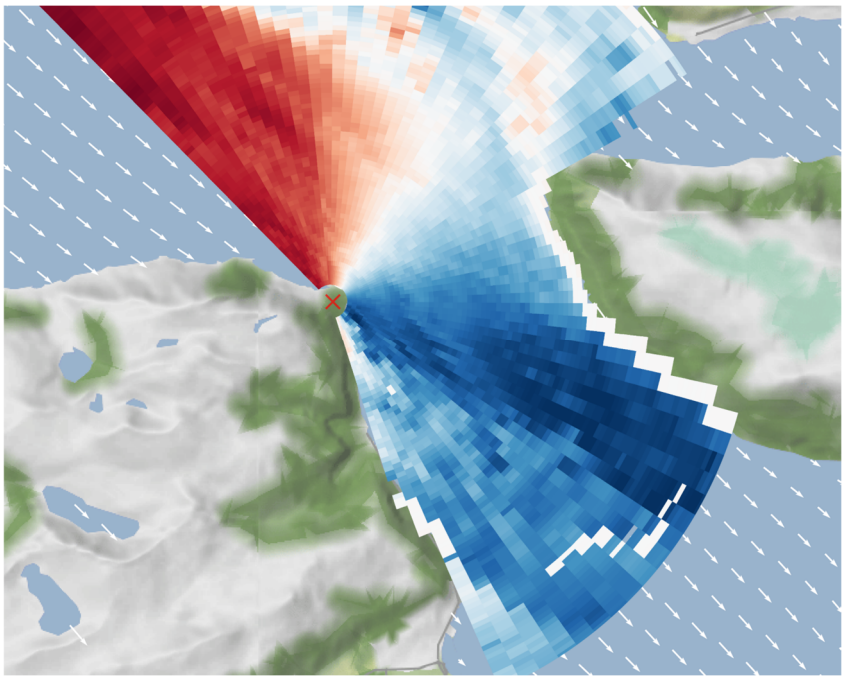
By integrating advanced research, emerging technologies, and sustainable practices, the NPRA continues to enhance the resilience and efficiency of Norway's transport infrastructure, contributing to national economic development and environmental goals.

Learn more: www.vegvesen.no

At the forefront of wind engineering in the Nordics

Norconsult

Norconsult is a leading pan-Nordic interdisciplinary consulting firm. We combine engineering, architecture, and digital expertise across projects of all sizes, for private and public customers. Through innovation and creativity, we are constantly seeking more sustainable, efficient, and socially useful solutions.





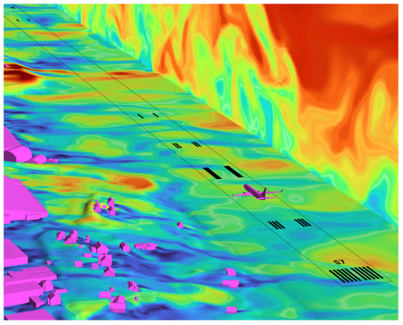


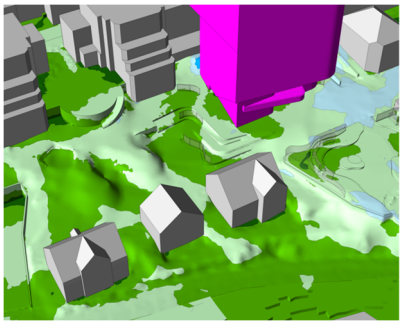
Our diverse consultants within wind engineering collaborate to deliver a complete A-to-Z scope of services across markets and industries

We have specialists within meteorology, aerodynamics, CFD and FEA simulation, wind and ice field-measurement, structural dynamics, pollution dispersion, aviation turbulence and more.

Our services include:

- Meteorological analysis
- Wind measurement and instrumentation
- Mesoscale and microscale climate modelling
- Icing measurements, modelling, and analysis
- Computational Fluid Dynamics
- Long-span bridge design
- Full scale bridge wind and strain measurement
- Static and dynamic wind loading
- Dynamic structural response
- Wind turbine micro-siting and yield assessments
- Aviation turbulence and windshear prediction
- Airport and helipad development and analysis
- Pedestrian wind comfort (PWC)
- Atmospheric dispersion and pollution analysis
- Simulation of natural and forced ventilation
- Tunnel ventilation and train induced pressure wave analysis





6 600
Employees

140
Offices

+30 000
Assignments yearly

www.norconsult.com



Bridges

Multiconsult is one of Norway's most experienced consultants with broad expertise in bridge design across all types of bridges.

Multiconsult has unique expertise in large complex bridge structures.

Through the design consortium AMC (Aas-Jakobsen, Multiconsult, and Cowi), Multiconsult is responsible for the design of a floating bridge over Bjørnafjorden (2019 – 2024), where our combined expertise is world-leading.

Dewesoft Structural Health Monitoring Group

Dewesoft® – Advancing Structural Health Monitoring with Precision and Innovation
Dewesoft is a globally trusted leader in data acquisition (DAQ) systems, renowned for delivering robust, high-accuracy solutions for dynamic and long-term monitoring across industries. At the heart of Dewesoft's offerings is its Structural Health Monitoring (SHM) technology — enabling real-time insights and predictive diagnostics for critical infrastructure like bridges, dams, buildings, and concrete, steel, and timber structures.

Why Choose Dewesoft SHM Solutions?

✅ All-in-One Monitoring System
Dewesoft provides an integrated SHM solution combining hardware, software, and cloud connectivity. Our systems measure vibrations, strain, displacement, tilt, temperature, humidity, and more — all synchronized to microsecond accuracy with GPS or PTP timing.

✅ Real-Time Data with Cloud Access
With Dewesoft Historian, all measured data is logged locally and optionally streamed to a cloud-based database, accessible from anywhere via intuitive web dashboards for live monitoring and alerting.

✅ Durability & Reliability
Built for harsh environments, Dewesoft hardware operates 24/7 in extreme weather conditions, ensuring long-term durability and minimal maintenance — critical for remote or high-risk locations like bridges and dams.

✅ Scalable & Flexible Architecture
From a single structure to nationwide infrastructure networks, Dewesoft systems scale effortlessly. Modular design supports both wired and wireless nodes, and integrates seamlessly with legacy or third-party sensors.

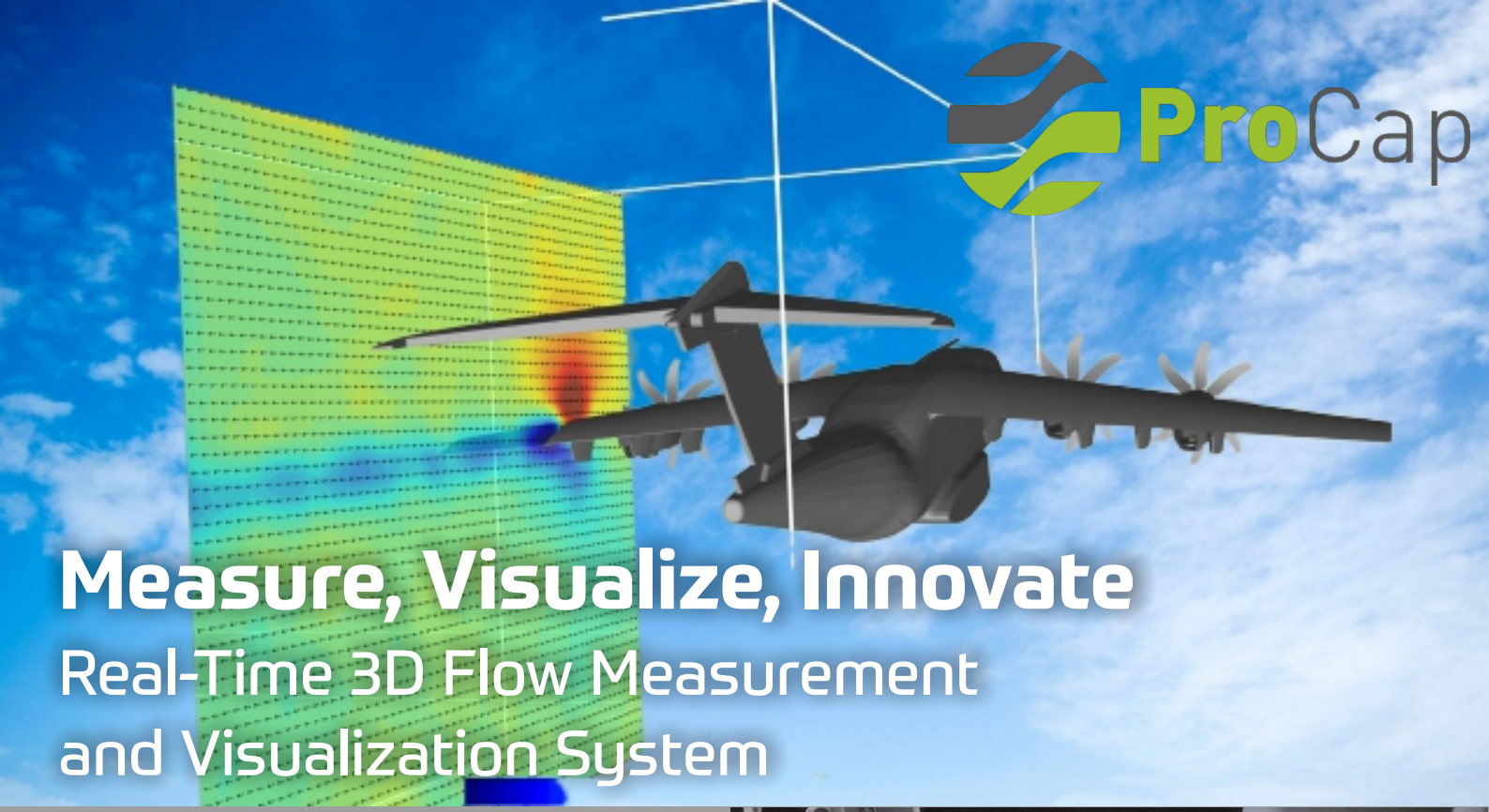
Applications: Proven Across All Structural Types

Bridges: Long-span, cable-stayed, arch, and suspension bridges worldwide benefit from real-time vibration, tilt, and strain monitoring using Dewesoft DAQ systems.

Dams: Monitor seepage, pressure, temperature, and structural movements in concrete and earth dams for regulatory compliance and risk prevention.

Buildings: Track dynamic responses to wind, traffic, and seismic activity in high-rises and heritage buildings.

Concrete & Steel Structures: Understand stress distribution, fatigue cycles, and joint behavior under varying loads.
Timber Structures: Ensure longevity and safety in modern engineered timber structures with humidity, deformation, and stress monitoring



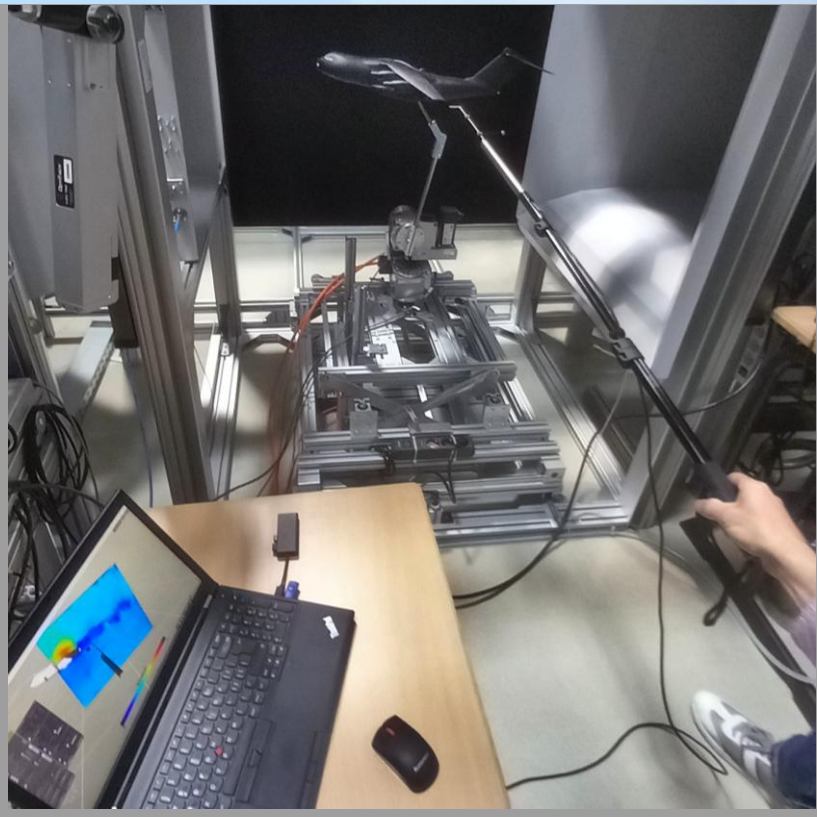
ProCap

Measure, Visualize, Innovate

Real-Time 3D Flow Measurement and Visualization System

ProCap is the first commercially available real-time Sensor Tracking Velocimetry (STV) system.

The real-time GPU rendered visualization of the complete 3D flow and pressure field provides instantaneous understanding of the aerodynamics and the data quality.



Key Features

- GPU powered processing and rendering for analysis and visualization of the flow field during acquisition
- Real-time processing of probe data and tracking position including spatial interpolation, correction for probe movement, data storage and import/export
- Fully quantitative 3D data output compatible with CFD post processors for validation
- Interactive user interface for intuitive operation
- CAD geometry import for model visualization
- Transportable, fast and easy to install

For more details or to request a demonstration:

Call: **+44 (0)1264 316470**

Email: **enquiries@evolutionmeasurement.com**
Web: **www.EvolutionMeasurement.com**

EVOLUTION
MEASUREMENT

Keynote speakers



Girma Bitsuamlak
Professor
Western University
Canada

Title: New Approaches for Assessing Synoptic and Non-Synoptic Wind Loading on Structures

Abstract: Designing for wind effects is crucial for ensuring the safety and sustainability of buildings and civil structures. Accurate modeling of wind and its interactions with the built environment is essential. The presentation will focus on the intricacies of generating various wind systems, including multi-scale synoptic wind systems like hurricanes, and non-synoptic winds like downbursts and tornadoes, within a controlled environment. This exploration is facilitated by physical testing of scaled models at the WindEEE Research Facilities located at Western University, capable of generating both stationary and non-stationary wind systems with varying levels of turbulence. Recent collaborative research projects focusing on assessing the effects of downbursts and tornadoes on buildings and other structures will be presented as case studies. The aerodynamic data obtained from the WindEEE serves dual purposes: direct utilization in wind-resilient design practices and the codification process. Additionally, it is used to validate numerical models, which, in turn, enables the exploration of multi-physics and multi-scale simulations that may extend beyond the capabilities of experimental facilities.



Bert Blocken
Professor
Heriot-Watt University/KU Leuven
Scotland/Belgium

Title: CFD in wind engineering: on successes and failures in large case studies

Abstract: Over the past two decades, CFD has transitioned from a tool in basic research and some simplified case studies to a tool that is frequently used for complex case studies in research and engineering practice. These studies range from pedestrian-level wind comfort and air pollutant dispersion in actual urban areas, over wind forces on buildings and ships in complex topography to urban thermal microclimate including heat waves in urban areas and their amplification by the urban heat island effect. However, not all of these case studies have been successful. It appears that in some cases, this application of CFD for complex case studies has gone too fast compared to the required basic research achievements, in terms of wall function development and basic recommendations and best practice guidelines that should ensure a minimum level of accuracy and reliability of the case studies. This presentation presents some successes but also some failures in large case studies that were due to these problems. The presentation indicates which basic developments are missing and suggests venues for future basic research to alleviate the present hurdles towards successful large case studies.



Jasna B. Jakobsen
Professor
University of Stavanger
Norway

Title: Field observations of bridge deck aerodynamics

Abstract: The lecture will give an overview of ongoing studies into the interaction between the natural wind and a suspension bridge, utilizing an advanced monitoring system that has been in operation on the Lysefjord bridge in Norway since 2013. Initially, the system comprised a conventional set of sonic anemometers, weather station and accelerometers, but has since been expanded by deploying several novel measurement systems, designed to capture the nature of the wind-bridge interaction. This includes a dedicated anemometry in the proximity of the bride deck trailing and leading edge, detachable strips for non-invasive surface pressure measurements, and several campaigns with dual and triple optical wind sensors (lidars). The lecture will offer a synthesis of the data acquired by the complementary measurement systems, as well as the analysis undertaken, with focus on the generation of the buffeting loading and the vortex shedding process, in the local wind field.

Dynamic Mode Decomposition: what can be and should be done

Peizhen Yang [1], Zhuangyi Yuan [2], Yunlong Wang [3], Cruz Y. Li [4]

[1] *Imperial College London, London, United Kindom, ny222@ic.ac.uk*
[2] *University of Connecticut, Storrs, United States, hkris9161@gmail.com*
[3] *Liaoning Technical University, Fuxin, China, 47211035@stu.lntu.edu.cn*
[4] *Chongqing University, Chongqing, China, yliht@connect.ust.hk*

SUMMARY:
The linear-time-invariance notion to the Koopman Analysis (**Part I** - Li et al., 2022, *Phys. Fluids* 34(12) 125136; **Part II** - Li et al., 2023, *J. Fluid Mech.* 959, A15) and the derived augmented algorithm (Fu et al., 2023, *Phys. Fluids* 35(2) 025112) are recent advances in fluid mechanics, addressing the challenge of correlating nonlinear excitation and response in fluid-structure interactions (FSI). Continuing the serial research, this work presents a data-driven, Koopman-inspired approach integrated with the "Proper Orthogonal Decomposition-Dynamic Mode Decomposition-Discrete Fourier Transform Augmented Analysis (POD-DMD-DFT)" to decouple nonlinear FSI. This innovative approach first isolates significant nonlinear flow features in terms of energy and evolution, subsequently establishing cause-and-effect correspondences between these flow features and structural surface pressure. Dynamic visualizations of in-sync fluid-structure-coupled Koopman modes are then implemented for phenomenological analysis. Finally, FSI energy transfers are statistically quantified via spatiotemporal contributions and probability density distributions. Demonstrated based on high-fidelity direct numerical simulations and large eddy simulations of flow over typical rigid obstacles, our method offers insightful descriptions and interpretations of phenomena occurring in the flow and on the boundaries (walls) of an FSI domain, and readily applies to various engineering problems given its data-driven nature.

Keywords: Fluid-structure Interaction, Dynamic Mode Decomposition, Direct Numerical Simulation

1. INTRODUCTION

The dealing of nonlinear fluid dynamics around bluff bodies, such as cylinders, is pivotal for various engineering applications. The systemic scientific issue lies in establishing a framework for characterizing the correlation features between nonlinear excitations and response phenomena within FSI. The linear-time-invariance notion to the Koopman Analysis and its derived augmented algorithm [1,2] are recent advances in fluid mechanics, addressing the challenge of correlating nonlinear excitation and response in FSI. Studying FSI requires a comprehensive understanding of the dynamic interplay between fluid and structural behavior. To this end, the linear-time-invariance notion of the Koopman analysis (Koopman-LTI) has been proposed by the serial research of Li et al [1,2]. POD-DMD-DFT, an augmented algorithm rooted in Applied Koopmanism, identifies three types of modes—energetically and dynamically significant, energetically significant & dynamically insignificant, and energetically insignificant & dynamically significant—facilitating the assessment of the impact on the system's energy distribution and temporal dynamics. This work proposes a Koopman-inspired approach that leverages data-driven insights, integrating the aforementioned theories to decouple nonlinear FSI.

Specifically, our study has two main objectives. One is to conduct a comprehensive evaluation of the coherent structures of the flow past circular cylinder in the subcritical regime using the POD-DMD-DFT procedure based on DNS data. This helps to isolate and visualize all important mechanisms and unveil their clear spectral information. The second is to test the applicability and the necessity of the procedure in a more fundamental case across different Reynolds numbers.

2. METHODOLOGY

2.1. Title, author and affiliation

The wake of a circular cylinder at three Reynolds numbers—350, 1350, and 4000—was selected as the test subject. The Reynolds number of 350 falls within the beginning range of the lower subcritical range (TrSL1). The Reynolds number of 1350 is at the beginning range of the intermediate subcritical range (TrSL2), slightly higher than 1250, where Couregelongue noted the onset of transition eddies. Finally, the Reynolds number of 4000 is at the upper end of TrSL2, close to one of the most widely investigated Reynolds numbers, 3900. All computational cases were scrutinized through DNS-IBM study, and rigorous validation was performed.

2.2. POD-DMD-DFT AUGMENTED ANALYSIS PROCEDURE

In this study of the circular cylinder wake, we introduce the POD-DMD-DFT procedure proposed by Fu et al. [3] This method has been further refined and adapted for this specific case, which contains some differences in applicability compared to the original street canyon case.
This procedure is delineated into three steps, as illustrated in **Figure 1**.

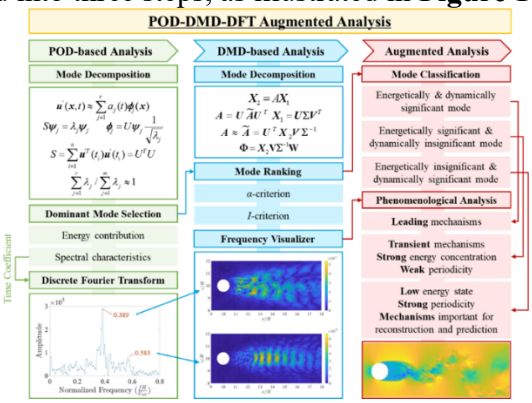


Figure 1. The proposed POD-DMD-DFT augmented analysis procedure.

1) POD-based analysis: POD is first to conducted, after the dataset has been validated and sampling convergence has been thoroughly tested based on the Koopman-LTI framework proposed by Li et al. [1]. Then, critical POD modes are selected based on eigenvalue and mode uniqueness. DFT is then performed on the temporal coefficients of these selected modes to extract their spectral information. These identified dominant frequencies represent the coherent structures in the flow field with significant energy contributions.
2) DMD-based analysis: Generally, the DFT results of a POD mode may include multiple dominant frequencies, complicating the association with specific flow structures. Therefore, DMD is then conducted on the same dataset. The specific coherent structures can be visualized by identifying DMD modes whose frequencies match the dominant frequencies determined in Step 1. Additionally, DMD modes are ranked using the α-criterion and I-criterion [2] to provide a global evaluation of the energetic and dynamic influences of these flow field structures.

a) Augmented analysis: Based on the rankings from POD and DMD, and using a process of

elimination, three types of modes are identified: **Type 1:** energetically & dynamically significant mode; **Type 2:** energetically significant & dynamically insignificant mode; **Type 3:** energetically insignificant & dynamically significant mode.

3. RESULTS AND DISCUSSION

3.1. POD-based modal analysis

Figures 2 illustrate the primary lower-rank POD mode patterns of normalized velocity U in the x-z plane at y = 2D under various Re scenarios. The aggregate energy contribution of the initial six POD modes to the flow field is almost 90% of the total energy, exhibiting distinct mode structures and spectral information. Notably, in this low Reynolds number scenario, the first several dominant POD modes manifest in pairs, exhibiting analogous patterns, energy contributions, and frequencies. POD analysis reveals that the first two modes at all three Reynolds numbers dominate the energy contribution, corresponding to the Bérnard-Kármán vortex shedding, with a frequency of 0.192, which governs the fundamental dynamics of fluid flow around a cylinder. Furthermore, the low-order modes continuously exhibit low-frequency structures and harmonic patterns that may be associated with the generation of turbulence. However, the DFT results indicate frequency mixing, making it challenging to distinguish between harmonic and low-frequency structures.

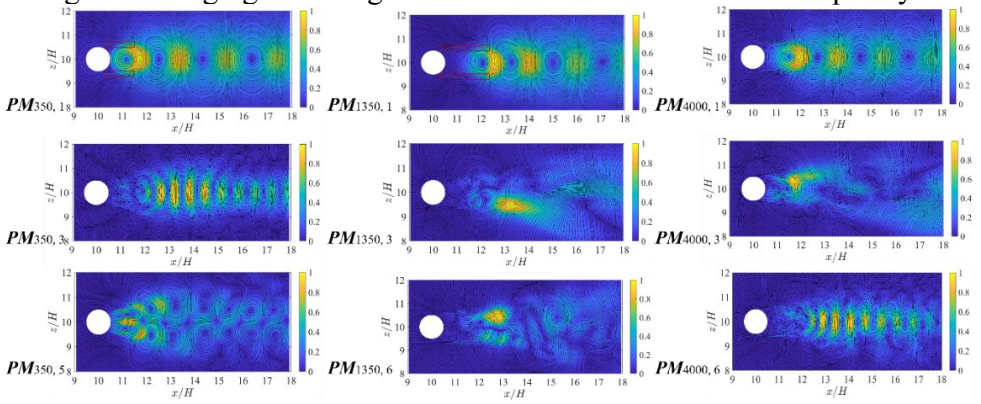


Figure 2. Lower-rank POD modes patterns of case Re = 350, 1350 and 4000 (The subscript's first term denotes the Reynolds number, and the second term indicates the POD mode's rank).

3.2. DMD-based modal analysis

In this step, DMD is conducted based on the same dataset, serving as a visualizer and supplementing mode evaluation. **Figure 3** depicts the DMD velocity spectrum, with each point representing a DMD mode for the three scenarios. DMD mode structures clearly exhibit the Bérnard–Kármán vortex shedding, transition vortices, and harmonic structures.

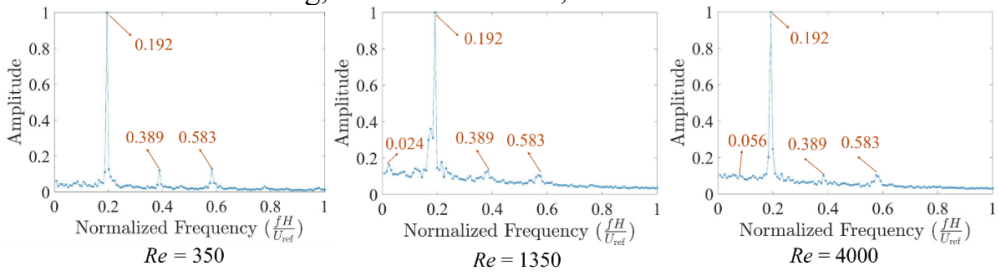


Figure 3. α vs fH/U_{ref} of the flow field U of case Re = 350, 1350 and 4000..

DMD mode frequencies align with the dominant frequencies identified in the POD analysis, further corroborating the POD results and providing a visualization of the low-frequency structures. DMD mode frequencies for the three cases of Re are consistent with the dominant frequencies identified in the POD analysis, including the frequency of the Bérnard–Kármán vortex shedding (0.192), as well as the second (0.389) and third (0.583) harmonics. In the cases of Re = 1350 and 4000, the DMD mode structures have revealed low-frequency structures that are likely associated with turbulence generation, with frequencies of 0.024 and 0.056, respectively.

3.2. Augmented analysis and further discussions

Overall, the analysis of the POD and DMD results indicates that at low Reynolds number, Re = 350, both the energy contribution and dynamic impact are maximized by the Bérnard-Kármán vortex shedding and its harmonic structures. As the Re increases, the spectral characteristics of the higher-order POD modes exhibit pronounced frequency mixing, making it difficult to conduct effectively analyze of flow phenomena. POD-DMD-DFT analysis has elucidated the mechanisms of transition vortices and turbulence generation, with the energy contribution from turbulence being slightly higher than that from harmonic structures. The intensity of transition vortices and turbulence generation diminishes with the increase in Reynolds number. At Re = 4000, the intensity of transition vortices and turbulence generation further diminishes, suggesting that the turbulence generation mode may become one with significant energy contribution but a relatively minor dynamic impact.

4. CONCLUSIONS

A significant extension of the “POD-DMD-DFT augmented procedure” is proposed to assess its applicability and necessity in analyzing the flow past a circular cylinder across varying Reynolds numbers (350, 1350, and 4000). Based on the DNS data, the augmented analysis procedure consistently identifies Bérnard–Kármán vortex shedding and its associated secondary and third harmonic structures across all test scenarios. The Bérnard–Kármán shedding emerges as the most prominent feature in terms of energy contribution and dynamic influence, accounting for at least 60% of the total energy in all cases. As the Reynolds number increases to the intermediate subcritical range, low-frequency modes indicative of turbulence production become more pronounced, albeit with a slightly greater energy contribution than that of harmonic structures. While the dynamic influence of turbulence production slightly decreases with higher Reynolds numbers, the energy contribution of the third harmonic slightly increases. Besides, no obvious energetically insignificant but dynamically significant mode is detected in the circular cylinder cases.

REFERENCES

[1] C.Y. Li, Z. Chen, X. Lin, A.U. Weerasuriya, X. Zhang, Y. Fu, T.K.T. Tse, The linear-time-invariance notion to the Koopman analysis: The architecture, pedagogical rendering, and fluid–structure association, *Physics of Fluids* 34(12), 125136 (2022).

[2] C.Y. Li, Z. Chen, T.K.T. Tse, A.U. Weerasuriya, X. Zhang, Y. Fu, X. Lin, The linear-time-invariance notion of the Koopman analysis. Part 2. Dynamic Koopman modes, physics interpretations and phenomenological analysis of the prism wake, *Journal of Fluid Mechanics* 959, A15 (2023).

[3] Y. Fu, X. Lin, L. Li, Q. Chu, H. Liu, X. Zheng, C.-H. Liu, Z. Chen, C. Lin, T.K.T. Tse, C.Y. Li, A POD-DMD augmented procedure to isolating dominant flow field features in a street canyon, *Physics of Fluids* 35(2), 025112 (2023).Scanlan, R. H., Béliveau, J.-G., and Budlong, K. S., 1974. Indicial aerodynamic functions for bridge decks.

Impact of microcylinders cross-section geometry on wake characteristics

Renata Gnatowska [1], Karolina Gajewska [1], Paweł Niegodajew [1]

[1]*Czestochowa University of Technology, Faculty of Mechanical Engineering and Computer Science, POLAND, renata.gnatowska@pcz.pl*

SUMMARY:
This study investigates the impact of cross-sectional shapes (circular, square, and triangular with varying apex angles) of microcylinders on flow patterns and wake characteristics. Using Particle Image Velocimetry (PIV) at a Reynolds number of Re = 5000, the research provides insights into vortex shedding, turbulence phenomena, and flow separation. The contour maps of normalized longitudinal velocity, transverse velocity, and turbulent kinetic energy show that the shape of the microcylinder significantly influences the wake structure. Circular shapes generate more uniform wakes, while square and triangular shapes exhibit deviations from uniformity, with stronger flow separation occurring near sharp edges. Triangles with larger apex angles result in broader and less intense wakes, while sharper triangles lead to higher turbulence and stronger lateral flow components. These findings enhance the understanding of wake behaviors in various bluff body geometries, with implications for flow control and energy dissipation in engineering design. This research contributes to the broader understanding of micro-scale dynamics and their applications in engineering.

Keywords: microcylinders, flow patterns, Strouhal number, wake characteristics, turbulence

1. INTRODUCTION

Bluff bodies (BBs) are commonly utilized in various engineering applications, including flow control, electronic cooling, mixing processes, vehicle platooning, and urban flow management. Their simple geometries exhibit intriguing flow features relevant across many fields. Consequently, the flow around BBs has been extensively studied through both experimental and numerical approaches. When the flow encounters a circular or square cylinder, the most commonly studied shapes of bluff bodies (BBs), large vortical structures are generated on either side of the object. The aerodynamic characteristics of BBs are significantly influenced by the behavior of shear layers that separate from the leading edge. Even subtle changes in BB geometry, such as altering the corner shape of a square cylinder, can substantially affect the shear layers and, consequently, the drag forces.

However, as highlighted by Derakhshandeh and Alam (2019), limited attention has been paid to the triangular cylinder, which produces significantly higher vorticity compared to circular or square cylinders. Existing research focuses on the flow around a single triangular cylinder, investigating factors like apex angle, Reynolds number, and the cylinder's orientation relative to the flow (Agrwal et al., 2016, Yagmur et al., 2017). The most studies have concentrated on triangular prisms at very high or very low Reynolds numbers, with a lack of detailed flow field information for this geometry. The computational analysis of flow around a triangular cylinder at low Reynolds numbers, highlighting the unique flow features and vortex dynamics (Manzoor et

al. 2023, 2024). Despite the extensive studies on circular and square bluff bodies, the influence of triangular shapes, particularly at moderate Reynolds numbers, remains less explored. Previous research has focused primarily on extreme Reynolds numbers, creating a knowledge gap that this study addresses through systematic PIV measurements.
This work presents systematic experimental studies utilizing the PIV technique to analyze the flow around different shapes of bluff bodies. The present study aims to enhance existing knowledge on the impact of the cross-section geometry of microcylinders on wake characteristics, flow structure, and the dynamics of the vortices.

2. THE EXPERIMENT DESCRIPTION

The PIV measurements were conducted at the Environmental Aerodynamics Laboratory at the Czestochowa University of Technology. The light source used was a Nd:YLF double-pulsed laser (Litron) with a wavelength of 527 nm, a maximum repetition frequency of 10 kHz, a pulse energy of 10 mJ (tuned to 1 kHz), and a corresponding power of 10 W per single laser beam. To capture the illuminated area, a CMOS SpeedSense VEO340 camera equipped with a Nikon Nikkor 50 mm lens was used. The tracer particles employed were DEHS oil droplets, approximately 1 μm in size. The experiment involved various cylinder cross-sections: circular, square, and triangular. The triangular cross-section cylinders had different apex angles of 30°, 45°, and 60° (Fig. 1). Each cylinder's flow was examined at a Reynolds number of 5000 [-]. The micro-cylinders, made of PLA (polylactide) plastic using 3D printing technology, had a diameter of 0.02 mm. The cylinders were placed in the wind tunnel such that their axes were oriented parallel to the airflow direction. The laser beam was directed upwards, perpendicular to the surface of the object. A movable traverse positioned the camera in front of the cylinders to facilitate precise alignment and measurement. The schematic of the experimental setup for analyzing the flow around the cylinders is shown in Fig. 1. The green lines represent the laser beam illuminating the object, while the dark grey area indicates the region captured by the camera. The cylinders were always positioned in the same location, with the zero point set at the rear edge of each object. PIV measurements of the flow around the bluff bodies were performed at a frequency of 600 Hz for a recording time of 10 s, providing 6000 pairs of images with a resolution of 1920×500 pixels. This allowed for the precise evaluation of statistical quantities.

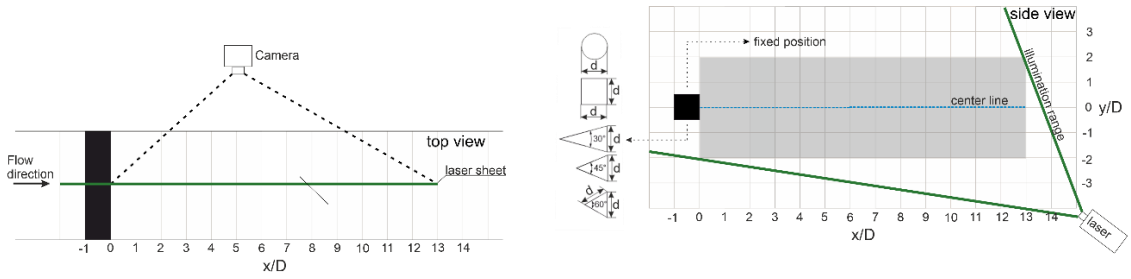


Figure 1. Sketch of the experimental setup; top view, and side view.

3. RESULTS

This chapter presents the results of the wake generated by microcylinders with different cross-sections: circular, square, and triangular with apex angles of 30° (T30), 45° (T45), and 60° (T60). Contour maps show normalized longitudinal velocity U_x/U_∞ [-], transverse velocity U_y/U_∞ [-],

turbulence kinetic energy TKE/$(U_\infty)^2$ [-] are presented in Figure 2.

3.1 Longitudinal Velocity Analysis

The contour maps for the longitudinal velocity highlight the wake regions directly behind the microcylinders, where the flow velocity decreases relative to the free-stream velocity. Each shape of the microcylinder causes a distinct wake pattern. Circular shapes tend to produce a more uniform wake, while square and triangular shapes exhibit deviations from this uniformity, particularly around sharp edges. These variations are caused by differences in flow separation, with sharp corners influencing how the flow detaches from the surface. Although the flow is along the axis of symmetry, the sharpness of edges in square and triangular geometries can lead to subtle deviations from idealized symmetric flow patterns. These effects might also be attributed to small positional inaccuracies in the model, such as slight misalignments in the angle of attack or geometric imperfections, which can influence the flow separation. Triangles with larger apex angles (T45, T60) result in a broader and less intense wake, with flow separation occurring at a less acute angle. This leads to a smoother transition in the flow and a slightly shorter wake compared to the triangle T30.

3.2 Transverse Velocity Analysis

The transverse velocity maps capture the flow movement perpendicular to the primary flow direction, emphasizing lateral flow behavior, which is typically strongest near the edges where flow separation occurs. Square and triangular shapes, particularly those with sharper angles, generate stronger transverse components, with distinct regions of positive and negative velocity values, indicating recirculation zones. Circular shapes show a more diffused transverse profile due to smoother separation. For the triangle with a 45° apex angle (T45), the transverse velocity is strong but more diffused compared to the triangle T30, suggesting a more gradual separation. The triangle T60 exhibits the least intense transverse velocities, with more gradual flow separation and less pronounced lateral movement.

3.3 Turbulent Kinetic Energy (TKE) Analysis

The TKE contour maps reveal regions of high turbulence in the wake. Sharp-edged shapes, such as the square, induce higher levels of turbulence directly in the wake due to abrupt flow separation, resulting in a more chaotic wake compared to the circular cross-section. The triangular cross-section, particularly with smaller apex angles, exhibits less intense turbulence than initially expected. For example, the triangle T30, with a larger apex angle, allows for a smoother flow separation, reducing the intensity of turbulent eddies and resulting in a more stable, less turbulent wake. This is in contrast to the square, which demonstrates a higher level of turbulent kinetic energy due to its sharper corners, generating stronger vortex shedding and turbulence in the wake.

This abstract presents only the main findings; however, the analysis was broader. Additionally, the evolution of vorticity over time ($\omega c/U_\infty$) was examined, and the Strouhal number was calculated and compared with results available in the literature.

7. CONCLUSIONS

The study presents an experimental analysis of wake characteristics for bluff bodies with circular, square, and triangular cross-sections (30°, 45°, and 60° apex angles). Using PIV measurements, detailed contour maps for normalized longitudinal and transverse velocities and turbulent kinetic energy (TKE) were obtained. Results show that circular bodies tend to produce more uniform wake structures, while square and triangular shapes generate deviations from this uniformity, particularly around sharp edges. These shapes experience stronger flow separation, which is more pronounced for triangles with sharper apex angles.

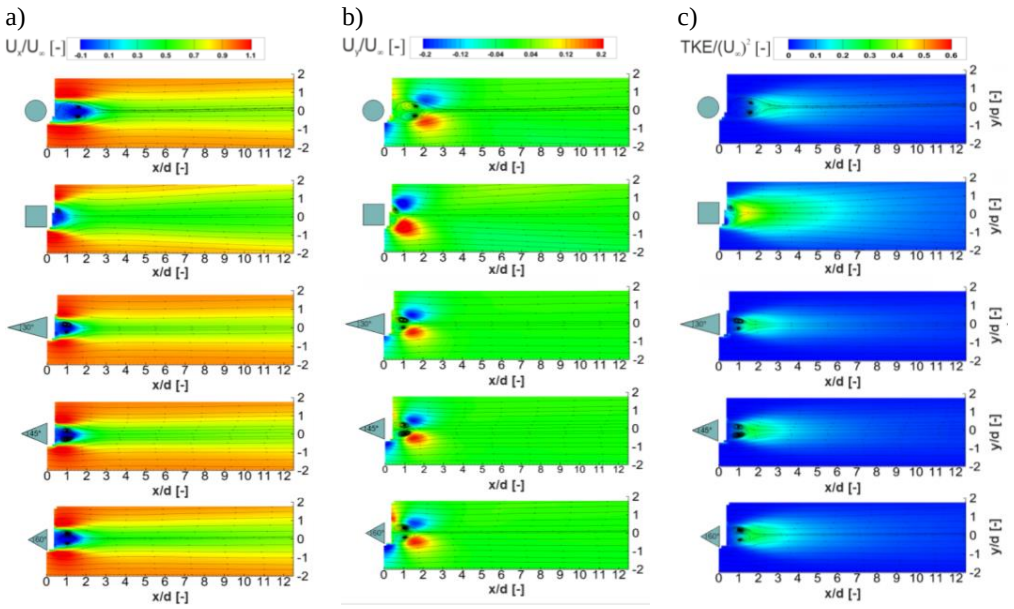


Figure 1. Contour maps illustrating normalized longitudinal velocity component U_x/U_∞ [-], transverse velocity component U_y/U_∞ [-], turbulent kinetic energy $TKE/(U_\infty)^2$ [-] for square and triangular shapes with various apex angles.

Triangular bodies with larger angles (T45, T60) exhibit broader and less intense wakes compared to the smaller angle (T30), where flow separation is more abrupt, leading to higher turbulence and stronger vortex dynamics. The transverse velocity maps reveal that square and sharp-angled triangular shapes generate more pronounced recirculation zones compared to circular shapes, particularly near the separation points. TKE analysis highlights higher turbulence levels around sharp-edged bodies, with the triangle T30 displaying the most intense turbulence due to its abrupt flow separation.

ACKNOWLEDGEMENTS

This research was funded in party by Ministry of Education and Science of Poland under scientific research funds No. BS-PB-1-100-3011/2024/P.

REFERENCES

Derakhshandeh, J. F., & Alam, M. M. 2019. A review of bluff body wakes. Ocean Engineering, 182, 475-488.

Manzoor, R., Mushtaq, S., Nadeem, N., Perveen, S., Kalsoom, S., Naeem, A., & Akbar, R. 2023. Numerical investigation of flow past a triangular cylinder at various Reynolds numbers. Physics of Fluids, 35(12).

Manzoor, R., Habib, R., Nadeem, N., & Kalsoom, S. 2024. Numerical analysis of flow past over a triangular rod through passive control method. Physics of Fluids, 36(3).

Agrwal, N., Dutta, S., & Gandhi, B. K. 2016. Experimental investigation of flow field behind triangular prisms at intermediate Reynolds number with different apex angles. Experimental Thermal and Fluid Science, 72, 97-111.

Yagmur, S., Dogan, S., Aksoy, M. H., Goktepeli, I., & Ozgoren, M. 2017. Comparison of flow characteristics around an equilateral triangular cylinder via PIV and Large Eddy Simulation methods. Flow Measurement and Instrumentation, 55, 23-36.

Wind force coefficients for designing open-type structures with flat roofs

Yuki Takadate [1], Yasushi Uematsu [2]

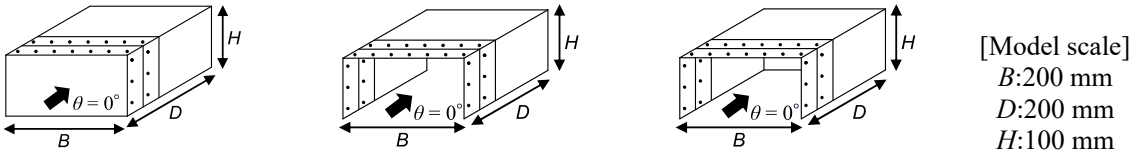
[1]*Buildling Research Institute, Tsukuba, Japan, takadate@kenken.go.jp*
[2]*Tohoku University, Sendai, Japan, yasushi.uematsu.d8@tohoku.ac.jp*

SUMMARY:
Wind loads on open-type structures with flat roofs are investigated based on a wind tunnel experiment. Three types of gable wall configurations (i.e., enclosed, open, and semi-open) are examined. The structure consists of parallel moment frames with hinged or clamped supports. The load effect of interest is selected based on the response of the frame subjected to the mean wind forces. In practice, focus is on the bending moments at the beam-column joint and the column base for the frames with hinged and clamped bases, respectively. Then, the maximum load effect on the frame is detected from the time-history response analysis. It is found that the largest load effect occurs at windward frame in an oblique wind. Finally, the distribution of wind force coefficients providing the maximum load effect is estimated using the load response correlation (LRC) method.

Keywords: Open-type structure, Wind tunnel experiment, Wind force coefficient, LRC method, Low-rise building

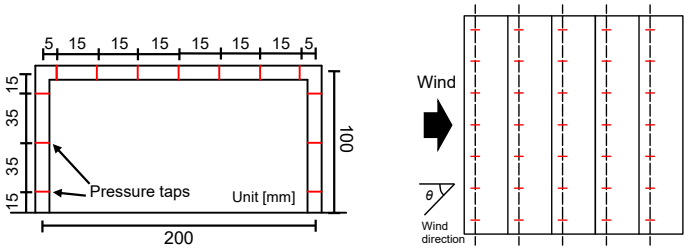
1. INTRODUCTION

Open-type structures are commonly used for temporary buildings, sports facilities, and welfare facilities. In Japan, the AIJ Recommendations for Loads on Buildings (Architectural Institute of Japan, 2015) and the Building Standard Law (BSL) of Japan specify wind loads for the main wind force resisting systems and cladding/components. However, these codes and standards do not address wind loads for open-type structures with two sides open. In our previous study (Takadate and Uematsu, 2019), wind force coefficients on open-type structures with gable roofs were investigated. For these structures, the magnitude and distributions of internal pressure change significantly with wind direction. Furthermore, the net wind forces provided by the difference between external and internal pressures become rather complicated. Considering that wind pressure distribution on a building is highly sensitive to roof shape, the focus is on flat-roofed low-rise buildings in the present paper. Three types of gable-end configurations, i.e., enclosed, open, and semi-open types, are examined. Wind pressure distributions on these structures are measured in a turbulent boundary layer. It is assumed that the structure consists of parallel moment frames with either hinged or clamped supports. Focus is on the bending moment at the column base for the frames with clamped supports and at the beam-column joint for the frames with hinged supports, which is critical for designing these structures. Then, a response analysis is carried out to identify the maximum load effects. The distribution of wind force coefficients providing the maximum load effect is estimated using the load-response correlation (LRC) method, as proposed by Kasperski (1992).



(a) Enclosed type (b) Open type (c) Semi-open type

Figure 1. Wind tunnel models used in the present study



(a) Section view (b) Top view

Figure 2. Section and top view of wind tunnel model

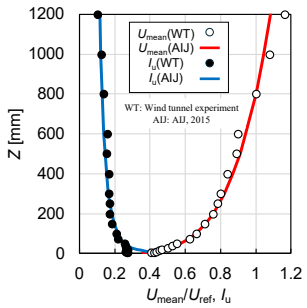


Figure 3. Wind speed and turbulence intensity profiles

2. EXPERIMENTAL APPARATUS AND PROCEDURES

The model building investigated in the present study has a flat roof. The width B, depth D, and height H are 30 m, 30 m, and 15 m at full scale, respectively. The wind tunnel model is made with a geometric scale of 1/150. Fig. 1 shows three types of building models used in the present study: an open type with open gable sides, a semi-open type with one open gable side, and an enclosed type fully enclosed one. The model consists of active frames equipped with pressure taps, as well as several dummy frames without pressure taps. Fig. 2 shows a section and top view of the wind tunnel model. The pressure taps are installed on both external and internal surfaces of the active frames, positioned at almost the same location 10 mm from the edges. The number of pressure taps on each surface of the active frame is 13. Wind pressure distributions on Frames 1 to 5 (as shown in Fig. 2b) can be measured by changing the positions of active and dummy frames.

The wind tunnel experiment is carried out in a turbulent boundary layer wind tunnel at the Building Research Institute. The width, height, and length of the wind tunnel are 3 m, 2.5 m, and 25 m, respectively. Wind tunnel flow is generated using spires and roughness blocks. Fig. 3 shows the velocity profiles, which correspond to suburban terrain specified in the AIJ Recommendations for Loads on Buildings (AIJ, 2015). The power-law exponent α for the mean wind speed profile is approximately 0.20. The mean wind speed U_{mean} and turbulence intensity I_{uH} at the model height are 6.6 m/s and 23 %, respectively.

3. EXPERIMENTAL RESULT

3.1. Load effects on a framed structure

Surface pressures are normalized to the wind pressure coefficients by using the static pressure and the velocity pressure q_H at the model height. In the present paper, the external and internal pressure coefficients are denoted as C_{pe} and C_{pi}, respectively. The wind force coefficient C_f is defined by the difference between C_{pe} and C_{pi}. The time-history of the bending moment induced in the frame

can be obtained using the following equation (Holmes, 1988):

$$M(t)=q_H \sum_{i=1}^{n} \alpha_i C_{fi}(t) A_i \quad (1)$$

where n is the number of measurement points (n = 13); α_i is the influence factor at Point i determined through a finite element analysis; C_{fi} is the wind force coefficient at Point i; and A_i is the tributary area of Point i. The bending moment is normalized as follows:

$$M^*(t)=\frac{M(t)}{q_H BHd} \quad (2)$$

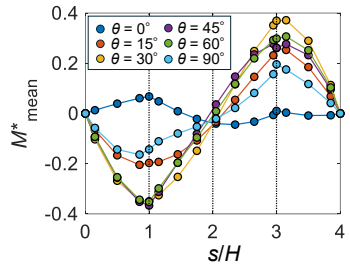
where d is column spacing in the depth direction (3.5 m at full scale). Fig. 4 represents the distributions of the mean non-dimensional bending moments M^* induced in the frames with hinged and clamped supports for the open-type structures. The horizontal axis indicates the distance s from the windward column base along the frame, normalized by the model height H. The bending moments at the windward beam-column joint (s/H = 1) and the windward base (s/H = 0) are selected as the load effects for the frames with hinged and clamped bases, respectively. Fig. 5 shows the maximum non-dimensional bending moment induced in the clamped-base frame of open type at various wind directions. It is found that oblique wind causes the largest bending moments. Table 1 summarizes the wind direction, frame number, and gust effect factor that induces the maximum load effect. The gust effect factor G_f is defined as the ratio of the maximum load effect to the mean load effect. In general, the maximum load effect is induced in the windward frame in an oblique wind, irrespective of the column-base condition and wall configuration.

3.2 Wind force coefficients and load effects on open and semi-open type structures

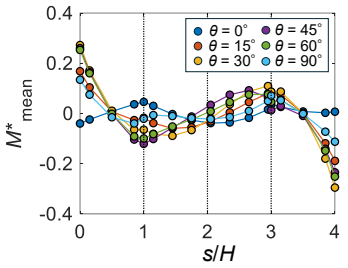
The wind force coefficients C_f generating the maximum load effects are estimated using the LRC method proposed by Kasperski (1992). The C_f values are provided by the following equation:

$$C_f = \overline{C}_f + g_r C_f' \rho_{rp} \quad (3)$$

where $\overline{C}_f$ is the mean wind force coefficient; C_f' is the RMS fluctuating wind force coefficient; g_r is the peak factor of load effect; and ρ_{rp} is the correlation coefficient between load and response. The peak factor of the load effect is provided by the difference between the maximum (or minimum) and mean load effects divided by the standard deviation of the load effect. Fig. 6 shows the distribution of wind force coefficients generating the maximum load effects. In these figures, C_{f_cond}, C_{f_Gust}, and C_{f_LRC} represent the results of the conditional sampling technique, the gust effect factor approach, and the LRC method, respectively. The C_{f_cond} distribution is based on the instantaneous distribution of C_f that generates the maximum load effect. The C_{f_gust} distribution is derived from the $\overline{C}_f$ distribution multiplied by G_f that is defined by M^*_{max}/M^*_{mean}. In Fig. 6b, the distribution based on the BSL is also plotted as C_{f_BSL} for comparison. It is found that the C_{f_cond} and C_{f_LRC} distributions are in good agreement with each other, while C_{f_gust} are generally large in magnitude compared with C_{f_LRC} and C_{f_cond}, especially in the case of semi-open type. The LRC method appears to accurately capture the instantaneous distribution of wind force coefficients that generates the maximum load effect. Fig. 7 shows the M^* distributions estimated from the C_{f_Gust}, C_{f_cond}, C_{f_LRC}, and C_{f_BSL} distributions for the semi-open type with clamped bases. It is interesting



(a) Hinged support



(a) Clamped support

Figure 4. Distribution of mean bending moment

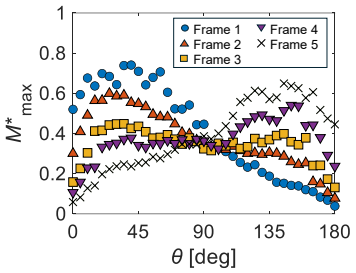
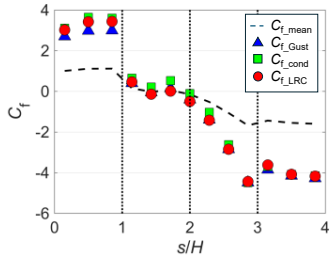


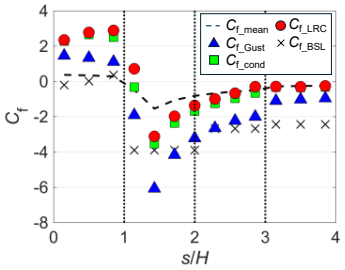
Figure 5. Maximum bending moment for the open type

Table 1. Critical conditions that induces the maximum load effect

Hinged-base	θ [deg]	Frame	G_f	Clamped-base	θ [deg]	Frame	G_f
Enclosed type	40°	1	2.43	Enclosed type	45°	1	2.63
Open type	40°	1	2.42	Open type	40°	1	2.68
Semi open type	25°	1	2.79	Semi open type	30°	1	3.93



(a) Open type



(b) Semi-open type

Figure 6. Distribution of wind force coefficients

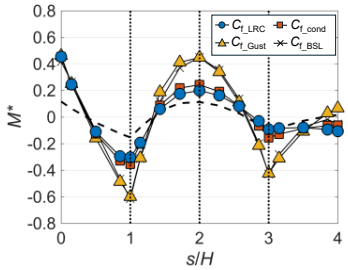


Figure 7. Distribution of M^* estimated by various C_f distributions

to note that all of the C_f distributions provide almost the same M^* values at the windward column base. However, the M^* values at $s/H = 1$ for the C_{f_Gust} and C_{f_BSL} distributions are larger in magnitude than those for the C_{f_LRC} and C_{f_cond} distributions.

4. CONCLUDING REMARKS

Wind loads for designing open-type structures with flat roofs have been investigated through a wind tunnel experiment, response analysis, and the LRC methods. The distributions of wind force coefficients which provide the maximum load effect are obtained. The correlation between external and internal pressures and their impact on load effects will be examined in future studies.

ACKNOWLEDGEMENTS

This work was financially supported by the Nohmura Foundation for Membrane Structure's Technology, Japan.

REFERENCES

Architectural Institute of Japan (AIJ). 2015. AIJ Recommendations for Loads on Buildings (2015).

Holmes, J. D. 1988) Distribution of peak wind loads on a low-rise building, Journal of Wind Engineering and Industrial Aerodynamics, 29, 59–67.

Kasperski, M. 1992. Extreme wind load distributions for linear and non-linear design, Engineering Structures, 14(1), 27–34

Takadate, Y., Uematsu, Y. 2019. Design wind force coefficients for the main wind force resisting systems of open- and semi-open-type framed membrane structures with gable roofs, Journal of Wind Engineering and Industrial Aerodynamics, 184, 265 – 276

Identify and visualize energy-wise and evolution-wise significant nonlinear flow features

Xisheng Lin [a], Yixiang Wang [b], Cruz Y. Li [c], Tim K.T. Tse [d], Bingchao Zhang [e], Peizhen Yang [f]

[a]*The Hong Kong University of Science and Technology, Hong Kong, China, xlinbl@connect.ust.hk*
[b]*The Hong Kong University of Science and Technology, Hong Kong, China, yixiangwang@ust.hk*
[c]*Chongqing University, Chongqing, China, cruzli@cqu.edu.cn*
[d]*The Hong Kong University of Science and Technology, Hong Kong, China, timkttse@ust.hk*
[e]*The Hong Kong University of Science and Technology, Hong Kong, China, zhangbc@ust.hk*
[f]*Imperial College London, London, United Kingdom, ny222@ic.ac.uk*

SUMMARY:
This study builds upon the framework developed by Fu et al. (*Phys. Fluids*, vol. 35, no. 2, p. 025112), the "Proper Orthogonal Decomposition (POD)-Dynamic Mode Decomposition (DMD)-Discreate Fourier Transform (DFT) augmented analysis procedure", to further evaluate its necessity and applicability in analyzing flow patterns around a circular cylinder at varied Reynolds numbers (*Re* = 350, 1350, and 4000). Results show that at lower *Re*, POD effectively visualize coherent structures with clean spectral information. When *Re* increases to the intermediate subcritical range (TrSL2), the flow complexity obscures the higher-order POD results, necessitating applications of the augmented analysis procedure. Based on Direct Numerical Simulation (DNS) data, the procedure consistently identifies Bérnard–Kármán vortex shedding and the associated harmonic structures. The former accounts for at least 60% of the energy and dynamic influence in all cases. As *Re* increased to TrSL2, low-frequency modes indicative of turbulence production are isolated, showing a slightly higher energy contribution than the harmonic structures. Energetically insignificant yet dynamically significant modes are not detected in this scenario. This preliminary study serves as a foundational effort for establishing constitutive relationships between wind loads and wind-induced phenomena, which is essential for developing strategies to fundamentally mitigate wind-induced vibrations.

Keywords: Proper orthogonal decomposition, Dynamic mode decomposition, Direct numerical simulation

1. INTRODUCTION

Understanding nonlinear coherent flow structures around bluff bodies, like cylinders, is essential for engineering applications. To gain a deeper understanding, most studies use Computational Fluid Dynamics (CFD) simulations that offer high-fidelity flow visualizations. However, CFD simulations require effective post-analysis methods to identify and visualize clear coherent flow structures, subsequently establishing constitutive relationships between these flow patterns and extreme surface pressures.

Reduced-Order Modeling (ROM) techniques, capable of identifying spatiotemporal features of vortex structures, are proposed as solutions. Among the existing ROM techniques, Proper

Orthogonal Decomposition (POD) is most widely applied in fluid dynamics analysis. However, POD has limitations, providing modes mixed in frequencies and neglecting low-energy modes with significant dynamical effects. This complicates correlating flow patterns with specific frequencies and the subsequent in-sync fluid-structure correlation (Rowley and Dawson, 2017).

On the other hand, Dynamic Mode Decomposition (DMD), another popular ROM technique, generates each mode at a distinct frequency (Schimid, 2010). While DMD modes are ranked by both energy contribution and dynamical importance, DMD has difficulties in ranking the eigenvalue significance of modes, making it less effective than POD in identifying highly physically relevant modes.

To overcome the limitations of POD and DMD, the authors proposed a POD-DMD-DFT augmented analysis procedure. This approach clearly visualizes flow patterns with clear spectral information and quantifies the contribution of these structures to energy distribution and temporal evolution. Previously applied to an urban canyon setting (Fu et al., 2023), this approach successfully identified energetically insignificant but dynamically significant mechanisms. However, its general applicability requires further validation, especially in low Reynolds number scenarios.

Therefore, this work proposes two main objectives. One is to evaluate coherent structures of flow past a circular cylinder in the subcritical regime using POD-DMD-DFT with DNS data. The second is to test the applicability and the necessity of the procedure in a more fundamental case.

2. METHODOLOGIES

2.1. Computational Domain

Fig. 1 depicts the computational domain for the direct numerical simulation (DNS) incorporating an immersed boundary method (IBM) of flow around an infinite circular cylinder with a diameter of D. The inflow features a uniform free-stream velocity, U_{ref} = 16.07 m/s, without initial perturbations. The boundary conditions include symmetry on the lateral sides and periodic conditions at the top and bottom, with a no-slip condition at the cylinder surface. A confined sampling area R are set within the domain for ROM analysis. The study evaluates three cases with Reynolds numbers Re = 350, 1350, and 4000. After achieving statistical flow stability, 1875 snapshots are collected for each case at a 15Hz frequency, covering 25 oscillation cycles.

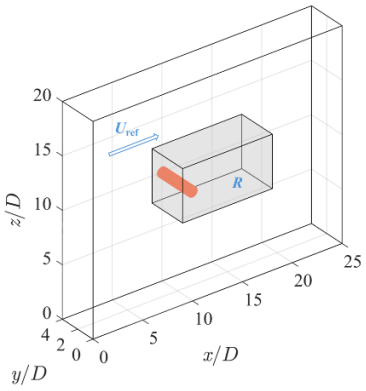


Figure 1. Computational domain.

2.2. POD-DMD-DFT Augmented Analysis

The POD-DMD-DFT procedure (see Fig. 2), initially developed for street canyon scenarios, has been adapted to analyze flow around a circular cylinder. It begins with a POD-based analysis, which identifies key modes and their spectral characteristics using Discrete Fourier Transform (DFT). If multiple dominant frequencies are found, a DMD-based analysis is performed to visualize and assess the coherent structures and their impacts on the flow field. Lastly, an augmented analysis integrates findings from both POD and DMD, classifying modes based on their energy and dynamic significance.

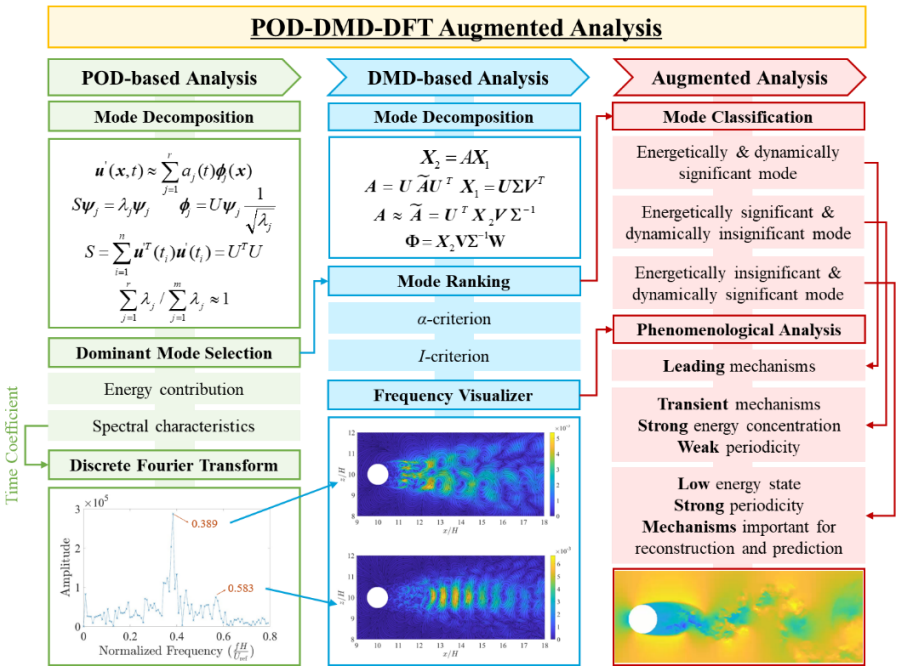
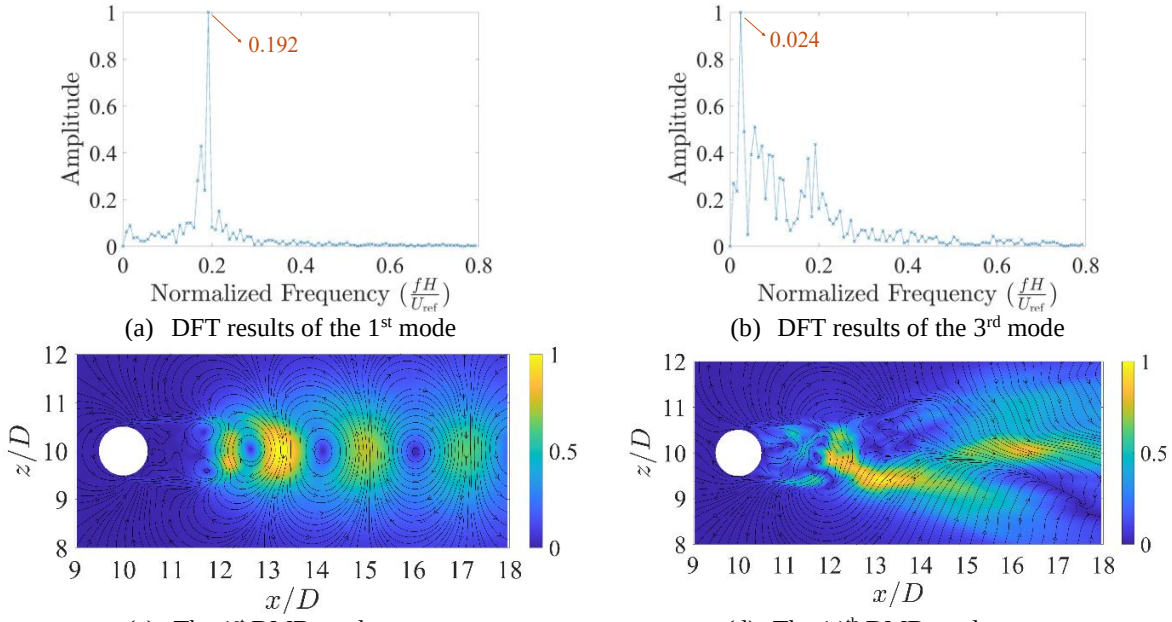


Figure 2. The proposed POD-DMD-DFT augmented analysis procedure.

3. RESULTS AND DISCUSSIONS

Due to page limit, this section shows the third step, augmented analysis and further discussions, for case *Re* = 1350 as an example. In this case, the results of POD and DMD only align in the identification of the most dominant mode (Fig. 3a). The spectra of the higher-order POD modes reveal a substantial blending of frequencies (Fig. 3b). The POD-DMD-DFT augmented analysis has elucidated the role of transition eddies and turbulence production (Fig. 3d), where the latter imparts a more significant energy contribution to the flow field compared to the harmonic structures. As the Reynolds number increases from 350 to 1350, both the Bérnard-Kármán vortex shedding (Figure 3c), and its harmonic frequencies exhibit a reduced level of dominance within the flow domain. The energy of the second and third harmonics shows some entanglement, but the energy contribution of the second harmonic is slightly higher than the third. Additionally, the results confirmed that when transition waves begin to evolve into transition vortices, the vortex formation length reaches its maximum value.



(a) DFT results of the 1st mode

(b) DFT results of the 3rd mode

(c) The 1st DMD mode pattern

(d) The 11th DMD mode pattern

Figure 3. DFT results and mode pattern for case *Re* = 1350.

4. CONCLUSIONS

In the intermediate subcritical range, where flow complexity heightens, POD alone is inadequate as it can only associates the most dominant flow pattern with a unique frequency. This limitation underscores the need for the comprehensive POD-DMD-DFT procedure to identify all dynamically significant and energetically contributing modes. The insights are foundational for establishing constitutive relationships between structural and flow-field phenomena. This understanding is vital for developing strategies to fundamentally mitigate wind-induced vibrations, enhancing structural safety and performance in engineering applications.

REFERENCES

Fu, Y., Lin, X., Li, L., Chu, Q., Liu, H., Zheng, X., Liu, C.-H., Chen, Z., Lin, C., Tse, T. K. T., and Li, C. Y., 2023. A POD-DMD augmented procedure to isolating dominant flow field features in a street canyon. *Physics of Fluids* 35(2), 025112.

Rowley, C. W. and Dawson, S. T. M., 2017. Model reduction for flow analysis and control. *Annual Review of Fluid Mechanics* 49(1), 387-418.

Schmid, P. J., 2010. Dynamic mode decomposition of numerical and experimental data. *Journal of Fluid Mechanics* 656, 5–28.

Application of wind tunnel blockage correction to force measurements of U-beams with different flange porosity

Stanislav Hračov [1a], Petr Michálek [1b], Blanka Ledvinková [1c], Michael Macháček [1d]

[1]*Institute of Theoretical and Applied Mechanics, The Czech Academy of Sciences, Prague, Czech Republic,* [1a] *hracov@itam.cas.cz,* [1b] *michalek@itam.cas.cz,* [1c] *ledvinkova@itam.cas.cz,* [1d]*machacek@itam.cas.cz*

SUMMARY:
The abstract presents results from aerodynamic wind tunnel testing on a set of slender, porous and non-porous U-beams. All tested beams share identical U-shaped cross-sections with a side ratio of two. The impact of two different blockage conditions on aerodynamic coefficients is analysed under smooth flow conditions across various wind attack angles. The blockage correction method proposed in the ESDU document was successfully applied to the experimental drag coefficient data, with differences in the corrected results highlighted and examined in detail.

Keywords: U-beam, flange porosity, blockage corrections

1. INTRODUCTION

The size of the wind tunnel testing section limits the flow compared to free-flow conditions. A model installed in the wind tunnel introduces blockage, which can cause inaccuracies in measured forces, moments, and pressures if the blockage ratio exceeds a certain threshold. This blockage ratio is defined as the ratio of the model's projected frontal area to the wind tunnel's cross-sectional area. Typically, blockage corrections are applied if the blockage ratio surpasses 5%. The presence of the model in the tunnel induces both a solid blockage effect on the model itself and a wake blockage effect in the flow behind it. The UK Standard (ESDU 80024, 1998) outlines several blockage corrections for confined wind tunnel flows around bluff and "quasi-streamlined" bodies. Bluff body flow occurs when flow separation happens at or before the body's maximum cross-sectional area, whereas quasi-streamlined flow occurs when separation happens after this point. The U-shaped beams analysed here meet the conditions for bluff body flow, so blockage corrections for this flow type were applied.

The impact of blockage on the mean aerodynamic drag coefficient and its correction based on the actual blockage ratio is presented for a set of porous and non-porous U-shaped beams and rectangular prisms. This study was inspired by prior tests conducted by the authors on similar bodies (Hračov and Macháček, 2023), where higher blockage ratios were necessary due to limitations in modelling high flange porosity at a smaller scale. For this study, a new, more robust flange design was implemented, allowing for testing at both larger and smaller scales in the wind tunnel, even for porous cases.

2. DESCRIPTION OF THE EXPERIMENTAL CAMPAING

Two sets of wooden experimental beams, each 160 cm in length, were tested to simulate two different blockage conditions. Both sets include prisms with U-shaped or rectangular cross-sections, all with a width-to-depth ratio of 2:1. The difference between the sets lies in the cross-sectional dimensions: the first set (larger models) has dimensions of 300 mm x 150 mm (B x H), while the second set (smaller models) is scaled down by half, with dimensions of 150 mm x 75 mm. This results in the cross-section of the second set being at half the scale of the first. The basic U-shaped cross-sectional geometry and dimensions of the beams are shown schematically in Fig. 1a. The U-beams were constructed using a wooden rectangular prism with a width-to-depth ratio (B/Dr) of 6:1, combined with a pair of wooden flanges with a height (Db) equal to one-third of the width (B). Within each set, the U-beams differed only in the porosity level of the flanges, simulating both nonporous and 50% porous configurations, as shown in Fig. 1. The flanges were manufactured from wooden boards, 6 mm thick for the first set and 3 mm thick for the second. Square holes, measuring 5 mm in the first set and 2.5 mm in the second, were laser-cut into the boards to create the desired porosity. The blockage ratio for the first set ranges from 7.9% to 11.7%, while for the second set it ranges from 3.9% to 5.9%, depending on the rotation angle (α) of the models. For comparison, rectangular prisms with side ratios of B/D = 2:1 and 6:1 were also tested.

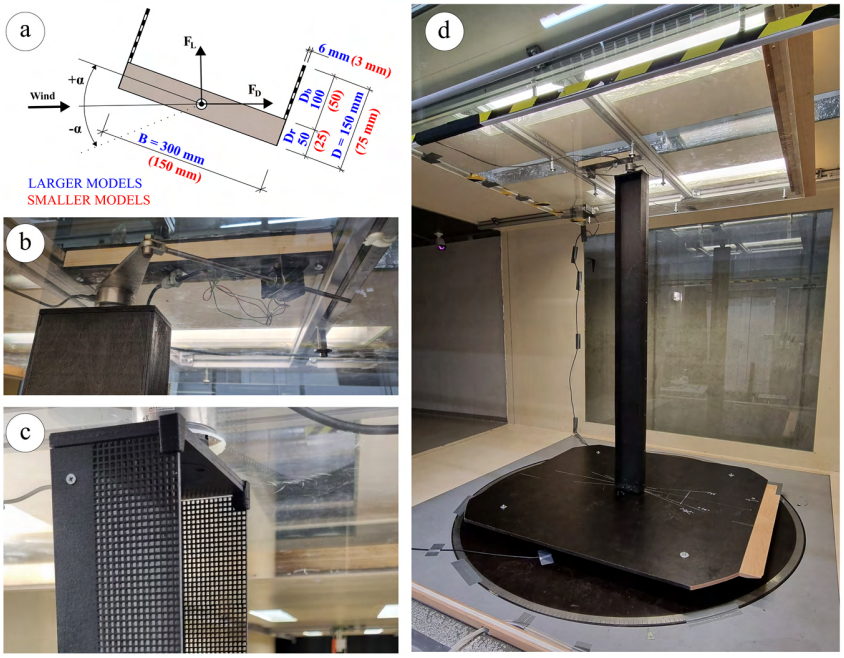


Figure 1. (a) Outline of the U-profiles; (b) Rotation mechanism; (c) Detail of the porous flange of the smaller model; (d) Photo of the non-porous smaller U-shaped beam installed in the wind tunnel.

Each model was positioned vertically in the test section of the wind tunnel, which measures 1.9 m in width and 1.8 m in height. The models were enclosed between wooden and plastic end-plates to maintain bidimensional flow conditions, as shown in Fig. 1d. Two ATI Industrial Automation Mini 40 load cells were used to measure the aerodynamic forces exerted on the specimens at angles of attack (α) ranging from -14° to +14°. These sensors were attached to the top and bottom of the specimens and connected to a synchronized rotation mechanism, allowing precise adjustments with an angular increment of $\Delta\alpha = 0.5°$. Data from the sensors was recorded over 60 seconds at a sampling frequency of fs = 1000 Hz, sufficient for ensuring both ergodicity and stationarity of the

process. The wind tunnel tests were conducted under nominally smooth flow with low turbulence intensity (approximately 1%). Tests on the larger models were conducted at two wind speeds, approximately 7 and 14 m/s, corresponding to Reynolds numbers of Re = 7.2e4 and Re = 1.4e5, normalized by the along-wind dimension, D. The smaller models were tested at a wind speed of 14 m/s to achieve the same Re = 7.2e4 as for the larger models.

3. BLOCKAGE CORRECTION APPLIED TO WIND TUNNEL MEASUREMENTS

ESDU 80024 recommends using the bluff body flow correction method when the Reynolds number is below 10^6 and the uncorrected drag coefficient, C_D, is greater than 0.8. Both conditions are satisfied for all tested U-profiles and rectangular prisms. The uncorrected drag coefficient as a function of the angle of attack, α, for these bodies is shown in Fig. 2 by the solid lines. In all cases, the drag coefficient is normalized to the profile height, D.

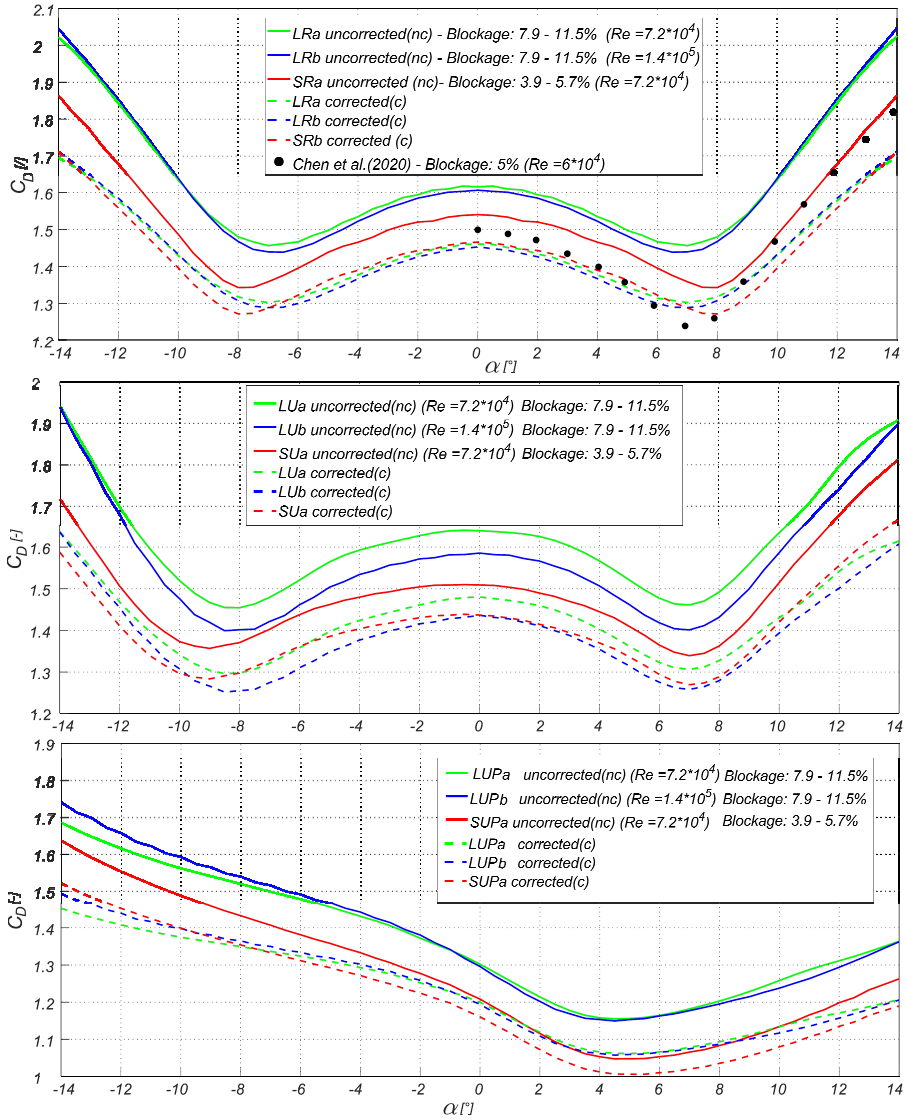


Figure 2. Uncorrected and corrected drag coefficients for rectangular prisms and U-beams (nonporous and porous) as a function of angle of attack (α). Abbreviations: LR and SR—large and small rectangular prisms; LU and SU—large and small nonporous U-profiles; LUP and SUP—large and small porous U-profiles.

The correction method recommended by Maskell (Maskell, 1965) calculates the blockage correction ratio as follows:

$$\frac{C_{Ff}}{C_F} = \frac{1}{1+\varepsilon C_D S/A} \quad (1)$$

where C_{Ff} is the corrected force (drag C_D or lift C_L) coefficient, C_F is uncorrected force coefficient, C_D is uncorrected drag coefficient, S is frontal blockage area of the body and A is the cross section area of the wind tunnel. The blockage correction parameter ε =0.83, specified in ESDU 80024 Table 10.1 for rectangular prisms with a side ratio of two, is applied to all models analysed. For porous profiles, the calculation of frontal blockage area includes the area of the holes. The corrected drag coefficient curves, calculated using Eq. (1), are shown as dashed lines for the rectangular prism and U-beams in Fig. 2.

4. CONCLUSIONS

The analysis of drag coefficients at various angles of attack confirms that values associated with higher blockage ratios are greater than those for lower blockage levels across all tested bodies. The precision of the measurements was validated using rectangular prisms, where the data closely aligns with the literature (Chen et al., 2020). The bluff body flow correction method outlined in ESDU 80024 was successfully applied to correct the drag coefficients for both rectangular prisms and porous and non-porous U-beams across two blockage ratios. Generally, the corrected values for the two analysed blockage levels were found to be closer to each other than the uncorrected values. The results demonstrated a similar trend in drag coefficient relative to the angle of attack for both blockage ratios across all analysed cases of porous and non-porous models. Notably, a significant decrease in drag was observed at positive angles of attack for all porous U-beams.

ACKNOWLEDGEMENTS

The kind support of Czech Scientific Foundation project No. 24-13061S is gratefully acknowledged.

REFERENCES

Chen, C., Mannini, C., Bartoli, G., Thiele, K., 2020. Experimental study and mathematical modeling on the unsteady galloping of a bridge deck with open cross section, Journal of Wind Engineering and Industrial Aerodynamics, 203, 104170.

ESDU 80024, 1998. Blockage corrections for bluff bodies in confined flows, Engineering Science Data Unit, The Royal Aeronautical Society, March 1998.

Hračov S., Macháček M., 2023. Experimental Investigation of Galloping Susceptibility of U Beams with Different Flange Porosity, Lecture Notes in Civil Engineering, 224, 183 – 193.

Maskell, E.C., 1965. A theory of the blockage effect on bluff bodies and stalled wings in a closed wind tunnel. ARC R&M 3400, Aeronautical Research Council, UK, Nov. 1965

Numerical evaluation of internal pressure in a low-rise building model in a tornado-like vortex

Qiang Chen [1], Jiping Kang [2], Delong Zuo [3]

[1]*Texas Tech University, Lubbock, USA, qiang.chen@ttu.edu*
[2]*Texas Tech University, Lubbock, USA, jiping.kang@ttu.edu*
[3]*Texas Tech University, Lubbock, USA, delong.zuo@ttu.edu*

SUMMARY
This paper presents a study in which the internal pressure inside a building model subjected to tornado-like loading is evaluated based on measured external pressure. The relationship between the internal pressure and external pressure is modelled by discharge equations. The discharge coefficient and flow exponent in the discharge equations are identified using unscented Kalman filter (UKF). The internal pressure is estimated by solving the discharge equations with measured external pressure near the opening on the building model as the input. The effectiveness of the numerical approach is illustrated using the pressure measurements from an experiment in which a low-rise building model is tested in a tornado-like vortex.

Keywords: tornadic loading, internal pressure, discharge equation

1. INSTRUCTIONS

Internal pressure inside a building depends critically on the openings in the building envelope. Because internal pressure can account for a large portion of the overall wind loading, many studies have been conducted to study how openings affected the internal pressure. Holmes (1979) modeled the internal pressure as a Helmholtz resonator and showed that this model can effectively capture the major characteristics of the internal pressure based on given external pressure. Subequently, many more studies were conducted to model internal pressure (e.g., Ginger, 2000; Sharma, 2003; Vickery, 1986) in a building with a large opening. In addition, Oh et al. (2007) proposed a method to determine the internal pressure in a building with multiple openings using discharge equartions. Regardless of the model, the key for effective application of these models is the determination of the model parameters. In this study, the unscented Kalman filter is used to identify the discharge coefficient and flow exponent in the discharge equations that are used to model the internal pressure inside a low-rise building with a large opening. The effectiveness of the method is illustrated by comparing the measured internal pressure inside a low-rise building model translating through a tornado-like vortex with the numerically determined internal pressure based on measured external pressure. In addition, a parametric study is used to show the influence of the discharge coefficient and flow exponent in the accuracy in determining the internal pressure through discharge equations.

2. METHODOLOGY

For a building with a single dominant opening, the relationship between the external and internal

pressures can be modeled by the discharge equations (Oh et al. 2007):

$$\rho l_e \ddot{x} + (\frac{1}{k})^{1/n} (\frac{\rho}{2})^{1/2n} \dot{x}|\dot{x}|^{(1/n)-1} + \frac{32\mu l_0}{d^2}\dot{x} = p_e - p_i \quad (1)$$

$$\rho A x = \frac{\rho V_0}{\gamma P_{ref}} p_i \quad (2)$$

where p_e is the external pressure at the opening; p_i is the internal pressure. ρ is the density of air; A is the area of the opening. l_e is the effective length of the opening (taken as $l_0 + 0.89\sqrt{A}$, l_0 being the thickness of the wall); d is the opening diameter; μ is the dynamic viscosity of air; k is the orifice discharge coefficient; n is the flow exponent; x, $\dot{x}$ and $\ddot{x}$ are the moving distance, velocity and acceleration that the "air slug", respectively; V_0 is the internal volume; $\gamma = 1.4$ is the polytropic gas constant of the air; P_{ref} is atmospheric pressure. Discharge coefficient k and flow exponent n are the parameters that need to be determined, and previous studies suggested various values for different turbulence intensities and opening conditions. However, since those previous studies are for boundary-layer type winds, those values may not be applicable for tornado-like flow. In this study, the UKF (Wan et al. 1999) is used to identify k and n in the discharge equations that are used to model the relationship between the external and internal pressures of a building model in a tornado-like flow.

3. ILLUSTRATIVE APPLICATION

3.1 Experimental Configuration

To facilitate an illustration of the application of the method, a 1:100 model of a building with a nominally flat roof that is 13.8 m in length, 9.3 m in depth and 3.9 m in height was tested in a tornado simulator at Texas Tech University (Chen et al. 2023). In the tests, the model was mounted on the center section of the simulator floor and translated with the floor at a speed of 1.25 m/s along a path through the center of a two-celled tornado-like vortex. The pressures acting on the external and internal surfaces of the model were measured while it translated. Table 1 summarizes the major characteristic of the vortex when the floor was stationary. Here, the swirl ratio and radial Reynolds number as defined by Church et al. (1979) are estimated based on the velocity of the flow along a vertical line at the edge of the updraft hole of the simulator, and the internal aspect ratio is defined as the ratio of the height of the confluent region to the radius of the updraft hole. The core radius of the vortex is taken as the radial distance between the location of the maximum mean tangential velocity and the nominal time-averaged vertical axis of the vortex. More details of the vortex can be found in Chen et al. (2023). Figure 1 (a) shows an exploded view of the building model with a rectangle representing a dominant opening on one of its walls and small circles indicating the locations of the pressure taps on the external surfaces of the model. The opening ratio, which is defined the area of the opening cross section to the total external surface area of the model, is 0.63%. To satisfy dynamic similarity between the internal pressures in the full-scale building and the building model, a sealed box was attached to the bottom of the model. The total volume enclosed by the model and the box were determined according to the volume scale suggested by Holmes (1979), $V_m/V_f = (L_m/L_f)/(U_m/U_f)$, where V, L and U represent volume, length and wind speed, respectively, and subscripts m and f indicate model and full scales, respectively. The velocity scale, U_m/U_f is chosen to be 1:4. Figure 1 (b) shows the orientation of the translating model relative to the rotating direction of the vortex, represented by the arrows along the circle of radius r_c, for a typical experimental configuration. A fixed coordinate system, x-o-y, with its origin at the center of the vortex at the floor level and the x axis aligned with the direction of model translation is defined to locate the model. For each configuration, the test was

repeated 115 times to enable a good estimation of the loading statistics. The parameters k and n in the discharge equations were identified based on measurements from each test run. The mean values of k and n from the 115 runs are 0.27 and 0.74, respectively.

Table 1. Characteristics of simulated tornado-like vortex.

Swirl ratio	Internal aspect ratio	Radial Reynolds number	Maximum mean tangential velocity (m/s)	Core radius r_c (cm)	Height of maximum mean tangential velocity z_c (cm)
0.83	0.5	6.1×10^5	11.5	46	6

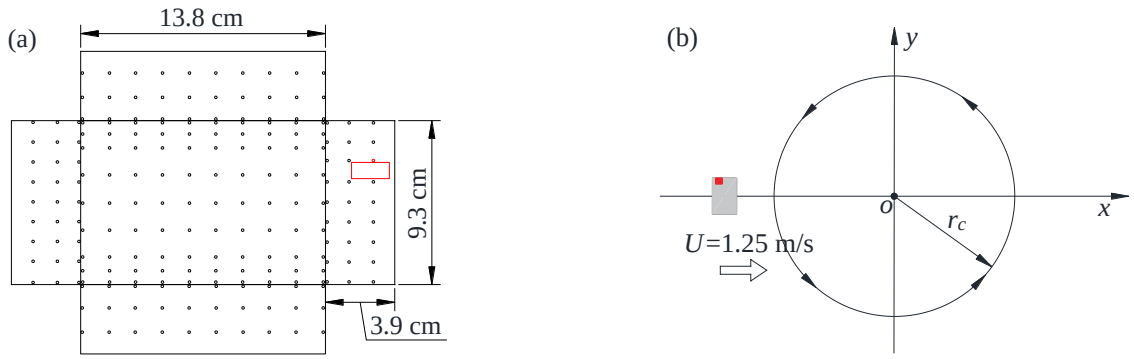


Figure 1. (a) Building model and (b) test configuration.

3.2 Illustrative results

Figure 2 shows a comparison of the internal pressure coefficient, C_{Pi}, estimated based on an example measurement and numerical solution. It is seen that the numerical result closely matches the measurement. In addition, according to the evolutionary power spectral density (EPSD, 1/Hz) functions of C_{Pi} shown in Figure 3 from experimental and numerical results shown in the numerical solution is able to effectively reproduce the frequency composition of the internal pressure as the model translates through the vortex. In particular, the numerical solution successfully captures the narrowband component with a characteristic frequency of 2.73 Hz and the resonance with a Helmholtz frequency of about 55 Hz in the internal pressure.

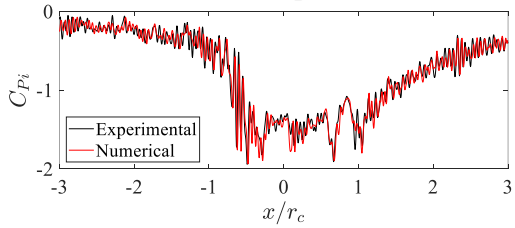


Figure 2. Comparison of C_{Pi} from experimental and numerical results.

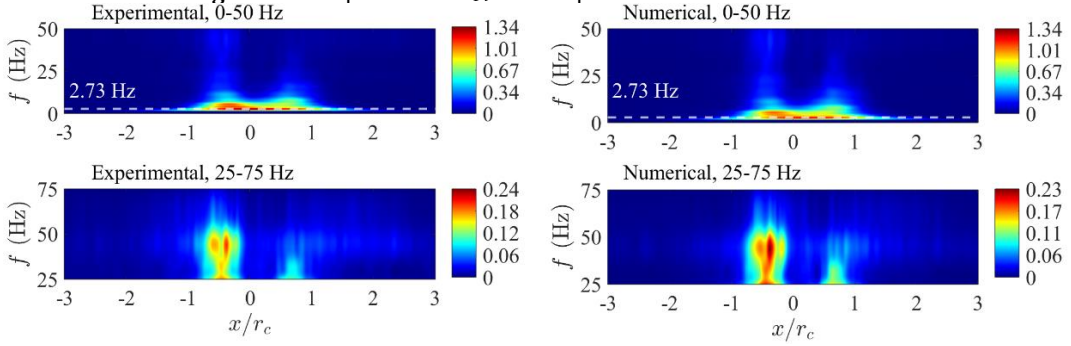


Figure 3. EPSD of internal pressures from experimental and numerical results.

Figure 4 shows the first four moments of estimated C_{Pi} based on the measurements and numerical results. Good agreements are again observed.

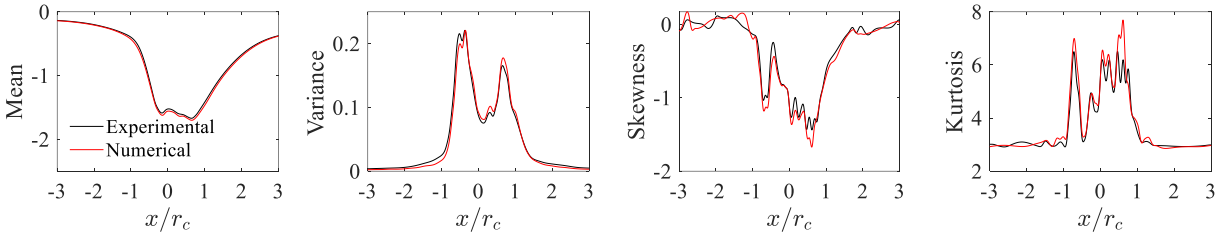


Figure 4. Comparison of first four moments of C_{Pi} from experimental and numerical results.

Figure 5 shows the error of numerically estimated internal pressure as compared to the measurements, which is defined as $(\breve{C}_{Pi_numerical} - \breve{C}_{Pi_experimental})/\breve{C}_{Pi_experimental}$. It is seen that the discharge coefficient, *k*, critically controls the accuracy of the numerical solution. As long as this coefficient is effectively identified, the influence of the flow exponent, *n*, is not significant.

More details of the results will be presented in the full paper.

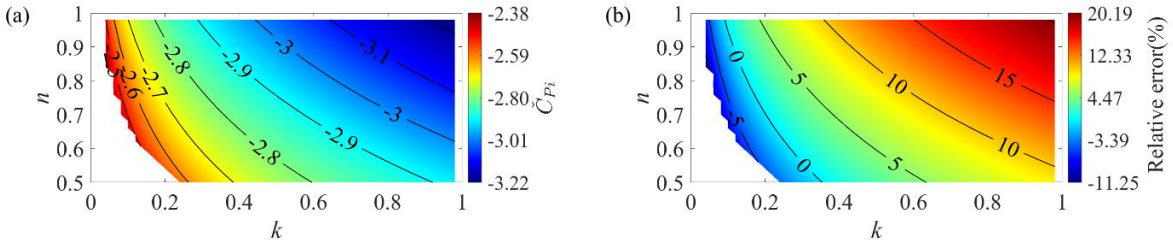


Figure 5. Error of numerical solutions for various combinations of *k* and *n* values.

REFERENCES

Chen, Q., Tang, Z., Wu, X., Zuo, D., and James, D., 2023. Laboratory study of tornado-like loading on a low-rise building model. Journal of Wind Engineering and Industrial Aerodynamics, 238, 105443.

Church, C.R., Snow, J.T., Baker, G.L., Agee, E.M., 1979. Characteristics of tornado-like vortices as a function of swirl ratio: a laboratory investigation. Journal of Atmospheric Sciences, 36, 1755-1776.

Ginger, J. D., 2000. Internal pressures and cladding net wind loads on full-scale low-rise building . Journal of structural engineering, 126(4), 538-543.

Holmes, J. D., 1979. Mean and fluctuating internal pressures induced by wind. Proceedings of the Fifth international Conference on Wind Engineering. July, Fort Collins, Colorado, USA, 435-440.

Oh, J. H., Kopp, G. A., and Inculet, D. R., 2007. The UWO contribution to the NIST aerodynamic database for wind loads on low buildings: Part 3. Internal pressures. Journal of Wind Engineering and Industrial Aerodynamics, 95(8), 755-779.

Sharma, R. N., 2003. Internal pressure dynamics with internal partitioning. Proceedings of the 11th International Conference on Wind Engineering, 705-712.

Vickery, B. J., 1986. Gust-factors for internal-pressures in low rise buildings. Journal of Wind Engineering and Industrial Aerodynamics, 23(C), 259-271.

Wan, E., Van Der Merwe, R., and Nelson, A., 1999. Dual estimation and the unscented transformation. Advances in neural information processing systems, 12.

Study on the vortex-induced vibration and aerodynamic characteristics of two tandem 4:1 rectangular cylinders

Jing Zhu [1], Hanfeng Wang [1,2]

[1]*School of Civil Engineering, Central South University, Changsha, 410075, China*
[2]*National Engineering Research Center for High-speed Railway Construction, Central South University, Changsha, 410075, China, email: zhujing@csu.edu.cn*

SUMMARY:
The present paper investigates the distribution of surface pressure and the formation and development of motion-induced vortices of two tandem 4:1 rectangular cylinders. Results show that the two heaving VIV lock-in regions exist as the wind velocity increases, where the reduced velocity at the amplitude extreme point of the latter is exactly twice that of the former. The evolution properties of surface pressure during different stages of VIV highly depend on the vibration amplitude, especially during the ascent stage. Furthermore, phase-averaged results indicate that the interaction between the cyclic induction of vortices and the model motion repeats in each vibration cycle, thereby maintaining a stable VIV response. In the future, it is necessary to compare these results with those of a single 4:1 rectangular cylinder to further reveal the VIV mechanisms under the influence of tandem rectangular cylinders.

Keywords: Separated box girders, Vortex-induced vibration, Phase-averaged method

1. INTRODUCTION

As the main spans and slenderness of long-span bridges increase, the structures become more sensitive to wind loads, especially the issue of flutter. Recently, separated-box girders (SBGs) have been widely used in long-span bridges due to their excellent flutter stability. However, with the complex aerodynamic interference between the upstream and downstream box girders and the gap, SBGs are more susceptible to the effects of vortex-induced vibration (VIV) (Ge et al., 2019). Currently, research on SBGs mainly focuses on the influence of gap ratio and Reynolds number, as well as aerodynamic vibration suppression measures (Laima & Li, 2015). There is still a lack of comprehensive explanations for the spatiotemporal evolution of aerodynamic forces on SBG surfaces, as well as the contributions of upstream and downstream box girders to VIV. In this study, the synchronized pressure and vibration measurement experiments were conducted in a wind tunnel, systematically comparing the aerodynamic characteristics at different VIV development stages. Using the phase-averaging method, the formation and development of surface pressure fluctuations and motion-induced vortices within one VIV cycle were analyzed.

2. EXPERIMENTAL DETAILS

The experiments were conducted in CSU-WT2, which was a closed-loop wind tunnel with a test section of 1.5 m (length) × 0.8 m (width) × 1.2 m (height), and the wind speed could be adjusted

continuously from 2 to 30 m/s. The spanwise length (L) of the tested model was 0.78 m, and the width B and height D were 0.28 m, and 0.07 m, respectively, resulting in an aspect ratio B/D = 4. Two tandem rectangular cylinders were made of carbon fiber and fixed on the plate spring system outside the wind tunnel by T-shaped brackets. Structurally, these cylinders were interconnected rather than independent. The experimental layout of the vibration system is shown in Fig. 1(a). An array of 52 pressure taps was arranged at the central cross-sections of both the upstream and downstream cylinders, as shown in Fig. 1(b). A DTC Initium pressure scanner was used to record the pressure distribution on the model's surface at a sampling frequency of 333 Hz. Hot-wire probes were placed at the 1D position in the gap between the models and at the 3D position in the wake. Additionally, two laser sensors were installed to monitor the VIV amplitude. The vibration amplitude and the gap velocity were synchronously recorded by an INV3062 at a sampling frequency of 2000 Hz. In this experiment, the pressure scanner and INV3062 acquisition instrument were synchronized through an external synchronous trigger signal, with the sampling mode set to external triggering and a sampling duration of 60 s.

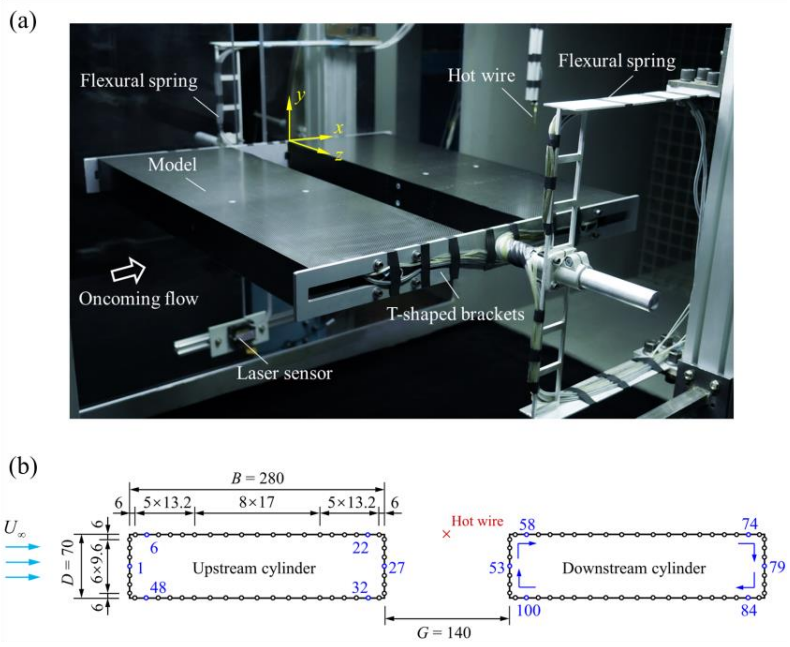


Figure 1. Experimental setup: (a) experimental layout of the vibration system; (b) distribution of pressure tabs.

3. RESULTS AND DISCUSSIONS

3.1. VIV responses

Figure 2(a) shows the relationship between the non-dimensional amplitude and the reduced velocity for a 4:1 rectangular cylinder and two tandem rectangular cylinders, where the blue and yellow lines represent the results for the 4:1 rectangular cylinder. For both structural systems, the primary lock-in oscillations start at U_r = 7.23, and the response amplitude gradually increases with the increase of U_r. After exceeding the peak response, a sharp decline in the response is observed and exits the lock-in region at U_r = 9.81. Notably, the tandem dual rectangular cylinder exhibits two fluctuating VIV lock-in regions, with a secondary resonance occurring at U_r = 4.23. Figure 2(b) shows the non-dimensional vortex shedding frequency in the gap and wake. Within the two

VIV lock-in oscillations, the dominant frequency in the gap and wake deviates significantly from the line representing the Strouhal number (*St*), and the vortex shedding frequency within lock-in closely approaches the natural frequency of the model.

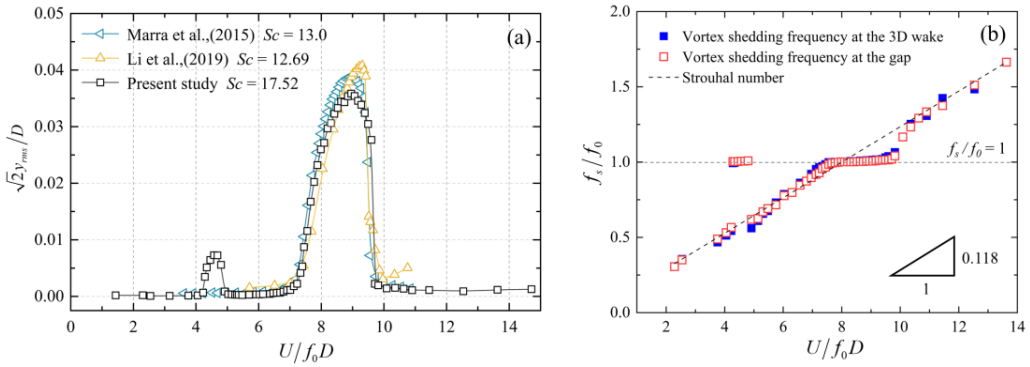


Figure 2. (a) non-dimensional amplitude of vibration at different reduced velocities; (b) non-dimensional vortex shedding frequency in the gap and wake.

3.2. Aerodynamic characteristics

Figure 3 shows the distribution of the mean pressure coefficient ($\overline{C_p}$) and the fluctuating pressure coefficient (C'_p) for the rectangular cylinder at the maximum y_{rms}/D. By comparing the wind pressure on the upper surface of the upstream cylinder of the SBGs with that of the 4:1 rectangular cylinder, it is found that they exhibition similar pressure distribution characteristics at the maximum VIV response [Fig. 3(a) & (b)]. Specifically, when the shear flow separates from the leading edge and reattaches to the surface, $\overline{C_p}$ initially decreases slightly, then gradually increases along the flow direction, and finally undergoes a sharp change on the leeward side. Compared to $\overline{C_p}$, a small hump at $\Delta x/D = 2.73$ is observed, which is caused by the shear flow reattachment. For the downstream cylinder of the tandem rectangular cylinders, the development of $\overline{C_p}$ is relatively smooth, attributed to the dissipation of large-scale vortices as they move downstream. Meanwhile, the strong fluctuations in C'_p for the downstream cylinder are primarily concentrated in the gap and the leading edge.

Figure 4 shows the distribution of surface pressure fluctuations and the formation and development of motion-induced vortices within a VIV cycle of tandem rectangular cylinders at the maximum y_{rms}/D. At the highest position (t = 0T), the motion-induced vortex *A* at the leading edge forms synchronously with the model vibration, resulting in negative pressure on the upper surface of the leading edge. Vortex *A* continues to grow throughout one vibration cycle, and eventually shedding from the trailing edge *E*. At the equilibrium positions (t = T/4 and 3T/4), vortices *D* and *D*' induce a suction effect in the negative pressure regions, and the direction of the dynamic lift *y*' aligns with the downward movement of the model, contributing positively to VIV and reaching the maximum motion speed. The cyclic induction of vortices and the interaction with model motion repeat in each vibration cycle. Thus, the cylinder is subjected to an in-phase exciting force produced by the vortices and the VIV is maintained steadily. In future studies, the contributions of the upstream and downstream cylinders to vortex shedding will be further analyzed through lift time history, work loops, and phase differences between pressure and displacement.

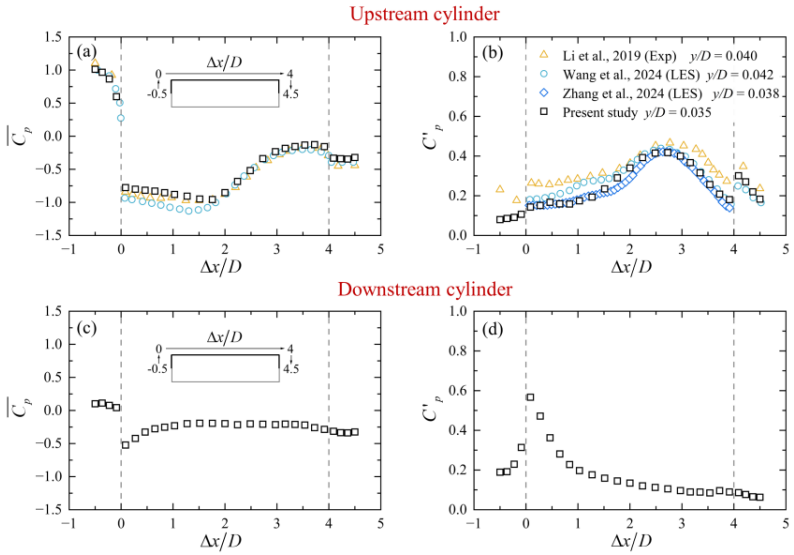


Figure 3. Pressure distribution around the 4:1 rectangular cylinder and the tandem rectangular cylinders at the maximum y_{rms}/D.

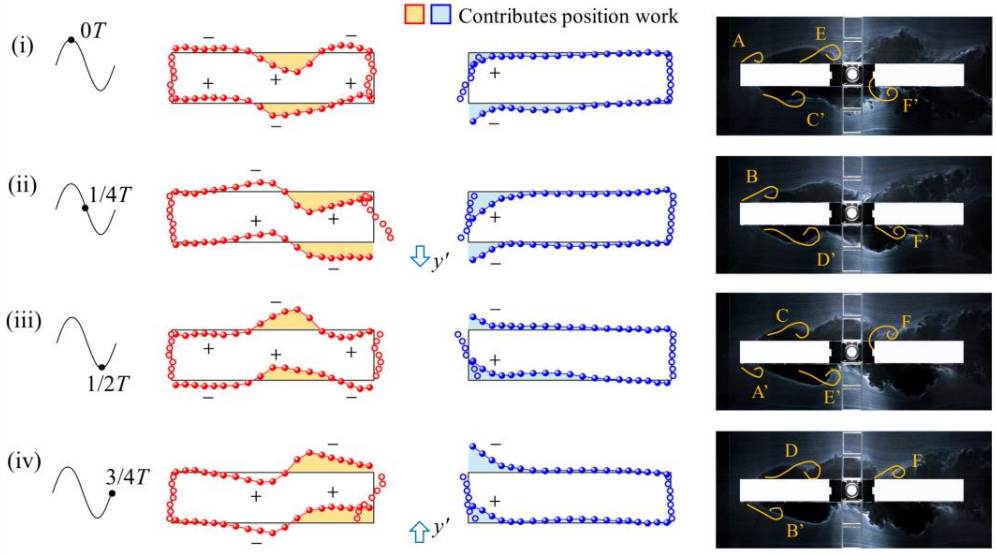


Figure 4. The formation and development of surface pressure fluctuations, and motion-induced vortices on a tandem rectangular cylinder within one VIV cycle.

ACKNOWLEDGEMENTS

The authors wish to acknowledge the grants from the National Natural Science Foundation of China (52078505).

REFERENCES

Ge, Y., Zhao, L., & Xu, K. (2019). Review and Reflection on Vortex-induced Vibration of Main Girders of Long-span Bridges. China Journal of Highway and Transport, 32(10), 1-18.

Laima, S., & Li, H. (2015). Effects of gap width on flow motions around twin-box girders and vortex-induced vibrations. Journal of wind engineering and industrial aerodynamics, 139, 37-49.

A refined surface roughness method to simulate the transcritical flow regime past a circular cylinder

Claudio Mannini[1], Tommaso Massai[1], Niccolò Barni[1]

[1]*CRIACIV/University of Florence, Florence, Italy, claudio.mannini@unifi.it*

SUMMARY:
The simulation in the wind tunnel of the high Reynolds number (transcritical) regime for a circular cylinder is of great interest for many civil engineering structures, but it is still a challenging task. The problem is further complicated by the free-stream turbulence investing the structures and by the need in some practical applications to adopt strategies that work independently of the wind direction. Having this in mind, a solution with staggered discontinuous ribs has previously been proposed by the authors and is refined and carefully studied in the present work with specific experiments. Two types of sandpaper strips are employed, and the less rough strips reveal to be very promising to trigger the transcritical regime at relatively low Reynolds number, in terms of mean drag coefficient, root-mean-square of the lift coefficient and Strouhal number. The experimental results also highlight the possibly misleading local behaviour of pressures in the sections of strip discontinuity.

Keywords: Circular cylinder, Reynolds number, wind tunnel

1. INTRODUCTION

Despite the long track of research, the simulation in the wind tunnel of the high Reynolds number behaviour of a circular cylinder, in particular the so-called transcritical (or postcritical) regime, is still an open issue, although it is crucial for load and vibration assessment of large structures such as chimneys and wind turbine towers. This task is made even more complicated by the uncertainty in the target statistics of force and pressure coefficients, demonstrated by the large spread of results collected from the literature (see, e.g., Mannini et al., 2023). Wind tunnel tests have shown that diffused surface roughness allows achieving a transcritical regime, but with earlier separation and significantly higher drag compared to a smooth cylinder due to the excessive subtraction of momentum to the attached turbulent boundary layers (e.g., Buresti, 1981; Nakamura and Tomonari, 1982). In contrast, localized spanwise ribs or trip wires are more successful in just triggering the laminar-to-turbulent transition of the boundary layers and in simulating the behaviour of smooth cylinders at high Reynolds number (e.g., Nakamura and Tomonari, 1982). An additional parameter that makes the problem even more intricate is the free-stream turbulence, which is always present in practical wind engineering problems and which is known to strongly affect the Reynolds number transitions (see Mannini et al., 2023 for a collection of references).

Moreover, studies of groups of cylinders (e.g., offshore wind turbine towers without rotor and nacelle during the pre-assembly phase at the port quayside; see Mannini et al., 2023) highlight the need for an omnidirectional behaviour of surface roughness on wind tunnel models. To this end, a promising solution was proposed in Mannini et al. (2023) based on staggered discontinuous ribs. The goal of the current work is to explore in-depth this idea through a refined experimental setup.

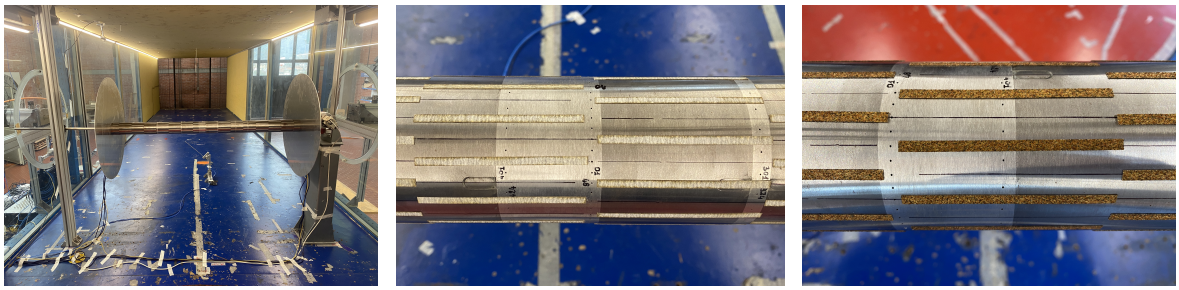


Figure 1. Cylinder model in the wind tunnel (left); sandpaper strips for roughness 1 (middle) and roughness 2 (right).

2. EXPERIMENTS

The experimental tests are carried out in the CRIACIV wind tunnel, featuring a test section of 2.4 m $\times$ 1.6 m and a maximum flow speed of about 30 m/s. The cylinder model is made of stainless steel and is mounted horizontally in the wind tunnel (Fig. 1-left). It is 1220 mm long and has a diameter D of 80 mm. Circular end-plates with a diameter of 660 mm are placed at both ends of the model to confine the flow. The blockage ratio is 5%.

The model is equipped with 190 pressure taps, distributed between seven arrays (48 taps in the midspan array), and the measurements are carried with the PSI DTC Initium system at a sampling rate of 650 Hz. The sensor accuracy is ± 1.24 Pa. 500 mm-long Teflon tubes with an internal diameter of 0.8 mm are employed to connect the pressure taps with the miniaturized sensors. Measurement results are corrected to account for the transfer function of the tubes. Rough cylinder configurations are tested covering the model surface with sandpaper strips having a length of 80 mm (D) and a width of 4 mm ($0.05D$). The strips are spaced 30 deg apart and present a staggered arrangement, as shown in the middle and right pictures of Fig. 1. Sandpaper P220 with a total thickness k of 0.25 mm ($k/D = 3.1 \cdot 10^{-3}$) and P80 with a total thickness of 0.45 mm ($k/D = 5.6 \cdot 10^{-3}$) are employed for so-called "roughness 1" and "roughness 2", respectively.

Tests are performed in both smooth and turbulent flows. In the first case, the turbulence intensity is below 1%. In contrast, homogeneous isotropic turbulence is generated through a grid made of 140 mm-wide slats assembled according to a 550 mm square mesh. For turbulent flow 1 the grid is placed 7.56 m upstream of the model, producing a longitudinal turbulence intensity I_u in the range 8.3-11% and a longitudinal integral length scale L_u^x between 220 mm and 280 mm, depending on the mean wind speed. Instead, the grid is located 5.65 m upstream of the model for turbulent flow 2, and I_u is between 11.5% and 13.2%, while 175 mm $\leq L_u^x \leq$ 240 mm. The grid also reduces the maximum wind tunnel flow speed.

3. RESULTS

Fig. 2 shows the cylinder mean drag coefficient obtained by pressure integration as a function of the nominal Reynolds number ($\mathrm{Re} = UD/\nu$, where U is the mean wind speed and ν the air kinematic viscosity). Without roughness, the cylinder is always in the subcritical regime in smooth flow, while the drag crisis is reached in turbulent flow. For the less rough cylinder (roughness 1), a nearly constant drag coefficient of about 0.6 is achieved for $\mathrm{Re} \gtrsim 1.3 \times 10^5$ in smooth flow and for

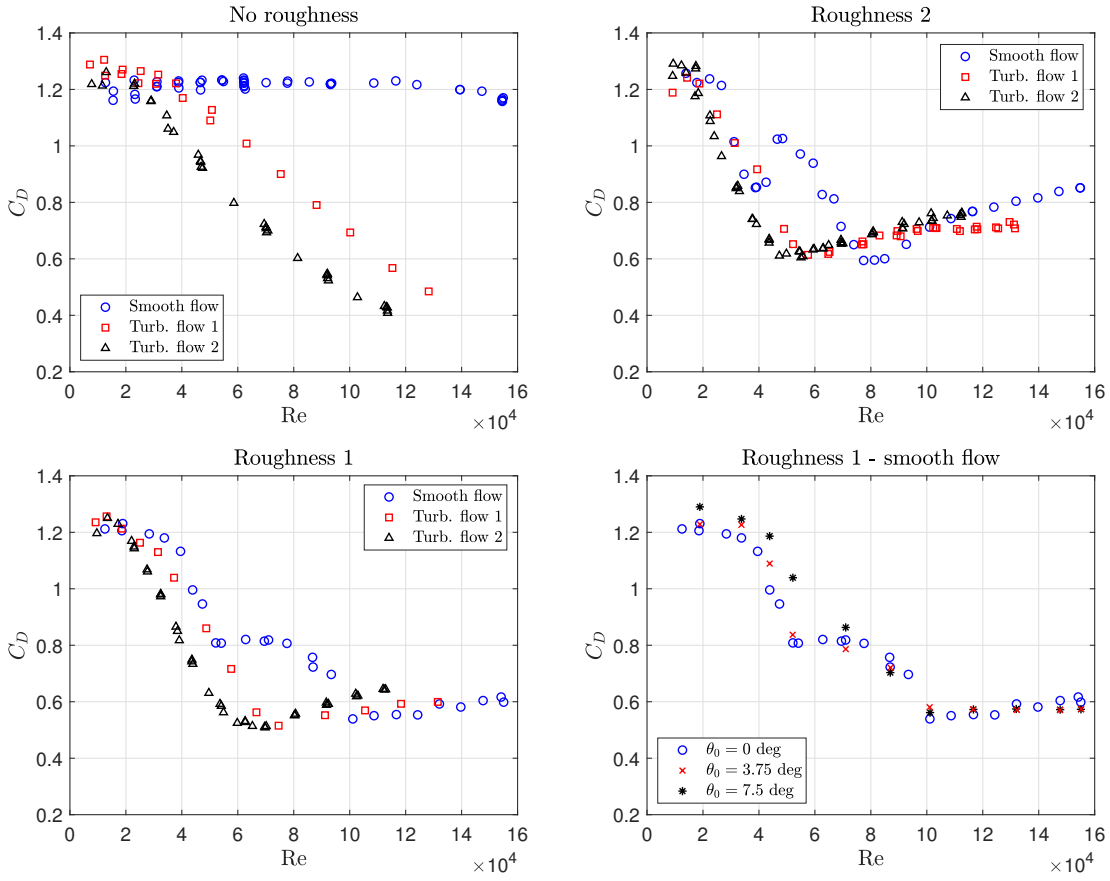


Figure 2. Drag coefficient vs. Reynolds number for various roughness solutions and turbulence intensities.

$\mathrm{Re} \gtrsim 1.1 \times 10^5$ in turbulent flow. Such a drag value is only slightly higher than that measured by Schewe (1983) in a high-pressure wind tunnel for a smooth cylinder at $\mathrm{Re} \gtrsim 6 \times 10^6$. In contrast, for the rougher cylinder (roughness 2), a higher drag coefficient is obtained, and no saturation of the C_D-curve with Re is attained. Moreover, though not shown here, the root-mean-square of the lift coefficient in smooth flow changes from about 0.55 in the subcritical regime to about 0.06 in the transcritical regime simulated with roughness 1, a result that well complies with those reported in Schewe (1983). A much higher value is got, instead, with roughness 2. The Strouhal number is equal to about 0.19 in the subcritical regime, and it increases to 0.26-0.27 in the transcritical regime with roughness 1, where it is apparent even in turbulent flow. In contrast, a value around 0.23 is measured with roughness 2. The bottom-right frame of Fig. 2 also demonstrates that the results are substantially independent of the wind direction (θ_0 denotes the model rotation).

Finally, Fig. 3 compares the mean pressure coefficient C_p for roughness 1 solution in case of smooth flow and turbulent flow 1. The left frames in the figure refer to the finely instrumented central array #1, while the right frames correspond to array #2, spaced $D/2$ apart. The difference is that all roughness strips start or end in correspondence of array #1, while they all cross array #2. It is apparent that the interruption of the roughness strips affects the local flow field, reflecting on the minimum value of the pressure coefficient, while the base pressure remains nearly unchanged.

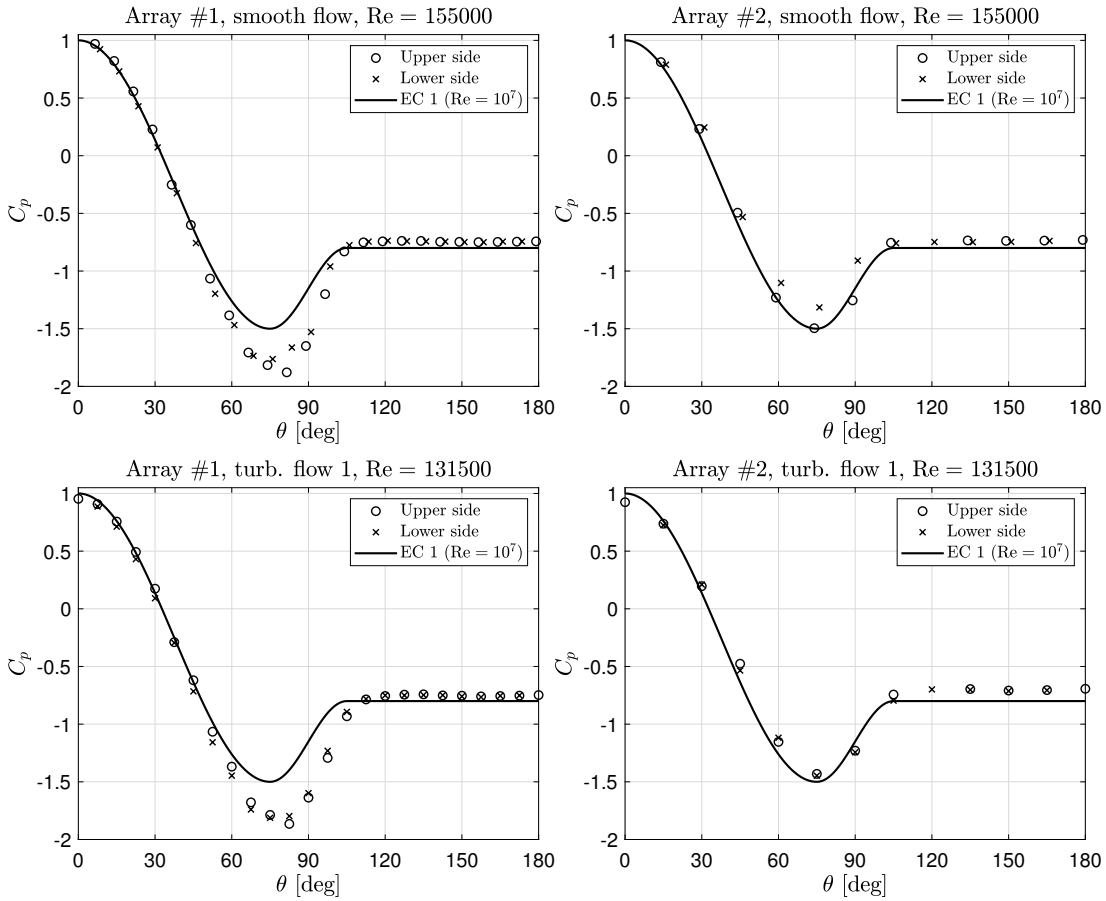


Figure 3. Pressure coefficient distribution as a function of the latitude θ for roughness 1 solution.

4. CONCLUSION

Staggered discontinuous ribs represent a promising strategy for simulating the transcritical flow regime past a circular cylinder under both smooth and turbulent wind, independently of the flow direction. The less rough solution is clearly preferable, but additional tests with narrower roughness strips are underway, so to cross also the densely instrumented midspan pressure tap array.

REFERENCES

Buresti, G., 1981. The effect of surface roughness on the flow regime around circular cylinders. Journal of Wind Engineering and Industrial Aerodynamics 8, 105–114.

Mannini, C., Massai, T., Giachetti, A., and Giusti, A., 2023. Aerodynamic loads on groups of offshore wind turbine towers stored on quaysides during the pre-assembly phase. Journal of Wind Engineering and Industrial Aerodynamics 242, 105569.

Nakamura, Y. and Tomonari, Y., 1982. The effects of surface roughness on the flow past circular cylinders at high Reynolds numbers. Journal of Fluid Mechanics 123, 363–378.

Schewe, G., 1983. On the force fluctuations acting on a circular cylinder in crossflow from subcritical up to transcritical Reynolds numbers. Journal of Fluid Mechanics 133, 265–285.

Cladding pressure amplitudes and their variation rates

Richard Brand[1] and Frank Kemper[1]

[1]*Center for Wind and Earthquake Engineering, RWTH Aachen University, Germany,*
brand@cwe.rwth-aachen.de

SUMMARY:
A deeper understanding of wind loading is essential for designing bonded connections in facade elements. This construction type is currently prohibited for load-bearing connections due to unclear safety aspects, including the time-dependent resistance of adhesives, which, like metals, can experience fatigue failure from repeated loading. Fatigue resistance depends on loading amplitude and factors such as loading rate, requiring precise modeling of loads. For cladding elements, wind loads and the building's aerodynamic behavior are primary forces. Wind tunnel investigations provided pressure time series, which were analyzed to create histograms of pressure amplitudes and rates across building positions and wind directions. These histograms were normalized to pressure coefficients and plotted as double-sided histograms to preserve amplitude-rate relationships.

Keywords: cladding load, external pressure, pressure rates, adhesives

1. INTRODUCTION

Façades, as part of a building's exterior, are regularly exposed to environmental elements such as weather, sunlight, and wind forces. This exposure subjects adhesives used in such applications to temperature variations, UV light, and mechanical forces. Fatigue resistance in adhesives is typically evaluated through cyclic loading tests, where fatigue resistance can be influenced by environmental conditions. Recent studies have examined these effects on the fatigue resistance of adhesive connections, with a focus on a 2K-Polyurethane adhesive (Ciupack et al., 2016). Fig. 1 shows the results of fatigue tests conducted under varying environmental conditions. In addition to an impact on mean stress amplitude and temperature, an influence of load frequency was also identified. The latter finding was also confirmed in a study focusing on butt-bonded joints for another adhesive (Pederbelli et al., 2023). Despite the different elastic behaviors both adhesives, it is evident that test frequency plays a role in fatigue resistance.

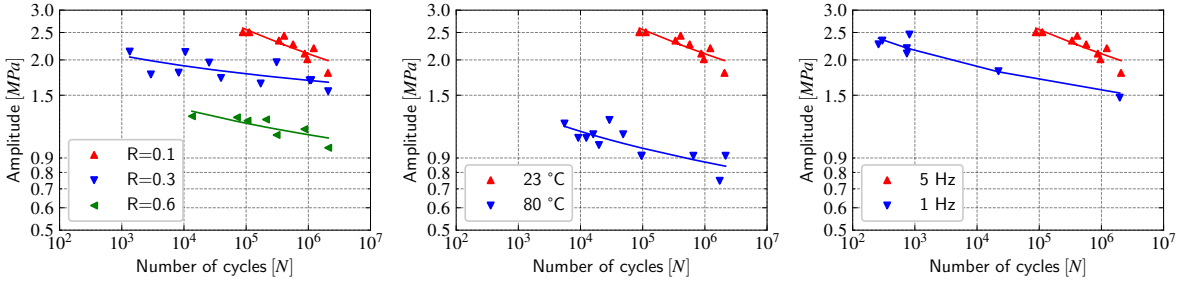


Figure 1. Exemplary influencing parameter on fatigue for adhesives (Ciupack et al., 2016)

In structural glazing façade systems (SSG), adhesives with hyper-elastic behavior are widely used. However, their response to varying amplitude rates has yet to be studied. To accurately analyze their fatigue behavior in realistic conditions, an effective approach is also needed to estimate the amplitudes and rates under wind force exposure.

Information on mean and extreme values of wind pressure on facades for various structures is widely available (e.g. Cook, 1990; Kemper and Feldmann, 2012). A few studies have assessed the fatigue impact of facade pressures. Suresh Kumar and Stathopoulos, 1998 analyzed stresses on roof components using descriptive statistical parameters from wind tunnel tests and "level-crossing" approaches for normally distributed processes (Wirsching and Light, 1980). This study was limited to two roof measuring points for a single building geometry and considered cycles but not cycle rates. A similar study by Xu, 1995b focused only on roof measuring points and used the "Rainflow method" to classify frequency for measured pressure amplitudes, without addressing pressure change rates. In Xu, 1995a, original pressure time series measurements were examined for fatigue behavior and compared to models.

Hence, there is still a lack of knowledge with respect to the frequency of pressure amplitudes and the frequency of pressure changes (histograms), which is important to address the load rate dependence of the fatigue resistance.

2. WIND TUNNEL MODELS

Extensive measurement data for 60 different shapes with typical geometries used in modular and industrial construction is available (Kemper and Feldmann, 2010). The data includes buildings with various roof shapes (flat roofs with and without parapets, pitched roofs, and gabled roofs with different inclinations) and provides detailed dimensions. The raw data, available as pressure time series in the time domain for these model structures, will serve as the foundation for planned evaluations. Measurements were taken fully synchronously in a boundary layer with a roughness length of z_0 = 0.05m and a geometry scale of 1:250.

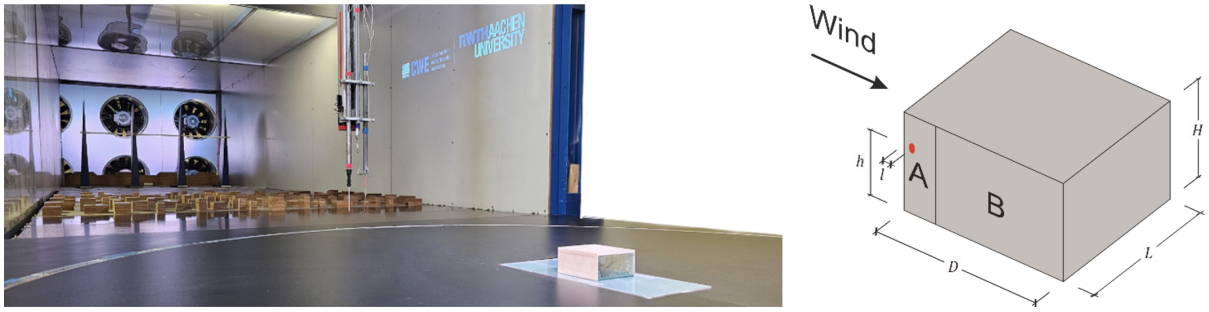


Figure 2. Flat roof model without parapets in the boundary layer wind tunnel. (H:D:L=1:2:2 , h/H=0.65 , l/D=0.04)

3. PRESSURE FLUCTUATIONS

For the application of cladding elements, the main driving force is the natural wind load and the aerodynamic behavior of the building. Based on various wind tunnel investigations, time series of pressure have been analyzed regarding the histograms of pressure amplitudes and pressure rates

at different building positions and for different wind directions. For the purpose to visualize the different amplitude rate characteristics the basic flat roof without parapets is shown in Fig. 2.

Unlike a global static perspective, the pressure on façade elements is less significant because most adhesives used in these systems are nearly incompressible and have high pressure resistance. Instead, tensile stress is the critical factor, making suction forces particularly important. To illustrate the impact of wind direction on the building, a point near the corner edge was selected, where strong suction forces with varying distribution characteristics, as shown in Fig. 3 (Gaussian and non-Gaussian), were observed.

The histograms have been evaluated with three different angles 0°, 90° and 180° and for a tributary area of A=1m^2. The amplitude has been normalized to pressure coefficients and therefore the rates and plotted as double-side histograms to maintain the relationship between amplitude and variation rate, as shown in Fig. 3.

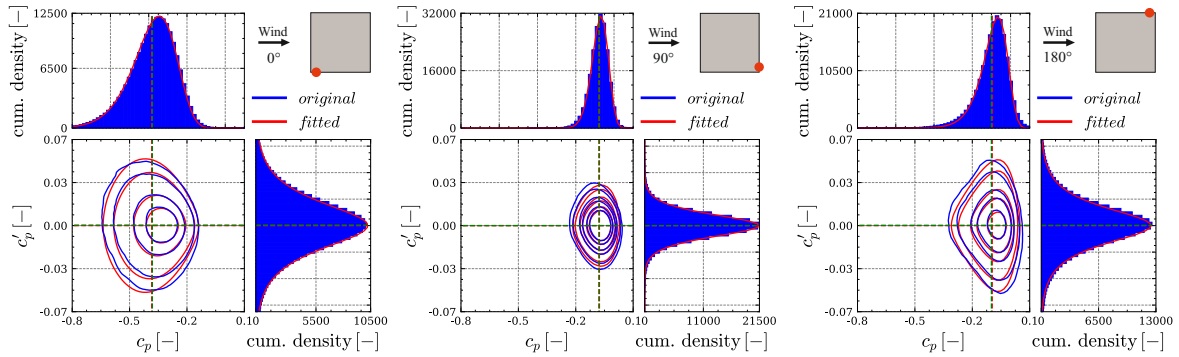


Figure 3. Double-sided histograms of pressure c_p and rate c_p' at the same location for various wind directions.

The analysis revealed an expected extreme distribution for the pressure amplitudes at the investigated locations, while a mixed distribution was identified for the pressure rate distributions. Each wind direction exhibits distinct characteristics. Specifically, the combination of pressure rates and pressure coefficients indicates that, at a 0° wind direction, the distribution of pressure rates spans more widely across the c_p spectrum. In contrast, at 90° and 180°, the pressure rates concentrate more densely around the mean cp value. Additionally, the pressure rates are approximately doubled in the outer regions, where they exhibit a more pronounced fluctuating component for this angle. It has been found that the distributions of c_p and c_p' are highly dependent the wind direction, and the mean and fluctuating pressure coefficients.

$$
\begin{aligned}
n_1(c_{p,\theta}) &= \exp\left[-\gamma\cdot(c_{p,\theta}-\delta)-\zeta\cdot(c_{p,\theta}-\delta)^2-\exp\left\{-\gamma\cdot(c_{p,\theta}-\delta)\right]\right\} \\
n_2(c'_{p,\theta}) &= \exp\left[-(\beta\cdot\eta\cdot c'_{p,\theta})^2\right]\cdot\left\{\varepsilon\cdot\left[1+\left(\frac{\eta\cdot c'_{p,\theta}}{\varepsilon}\right)^2\right]\right\}^{-1} \\
n\left(c_p,c'_p\right)_\theta &= \alpha\cdot n_1(c_{p,\theta})\cdot n_2(c'_{p,\theta})
\end{aligned}
\tag{1}
$$

To support future design approaches for safety-critical glued connections in cladding, spatial fitting

functions were used to develop parameterization concepts. The evaluated test data was fitted to a 7-parameter function using the least squares method. Since both amplitude and rate distributions deviate from typical Gaussian behavior, non-Gaussian parameters were incorporated, including a Cauchy distribution specifically for the rates (see Fig. 3 in red color).

The presented methodology defines a parameter set to describe precise load and speed conditions on a facade under short-term extreme wind loads, considering both direction and position. To account for the lifetime load spectrum, prevalent wind speeds are incorporated using the Weibull distribution with respect to direction and building-location. The cumulative classification is obtained by summing across all wind speed and direction bins.

Such a generalized approach, using fitting parameters dependent on building shape as introduced in Eq. (1), enables the design of material fatigue testing schemes. The classification of c_p and c'_p can be adjusted with as much detail as desired, based on the needs for accuracy, repeatability, and reduction of the data sets.

4. CONCLUSIONS

The load process on building envelopes due to natural wind flow and turbulence is complex in both time and space. Wind tunnel experiments have shown that double-sided histograms of pressure coefficients and pressure rates can be used to evaluate load rates on bonded connections. Establishing these relationships is essential for addressing the fatigue behavior of adhesives under realistic loading conditions. A general approach is under development to describe and maintain the dependency between load and load rate, enabling the formulation of representative load scenarios and their frequencies. Further research aims to establish a broader set of descriptive parameters for a wider range of building shapes.

REFERENCES

Ciupack, Y., Ledecky, L., Pasternak, H., Stammen, E., Mette, C., and Dilger, K., 2016. *Untersuchungen zum Tragverhalten und der Lebensdauer von Klebverbindungen im Stahlbau unter zyklischen Belastungen (LebKleb)*. Abschlussbericht. TU Braunschweig und Brandenburgische TU Cottbus-Senftenberg.

Cook, N., 1990. The Designer's Guide to Wind Loading of Building Structures. Building Research Establishment report. Butterworths.

Kemper, F. H. and Feldmann, M., 2010. *Optimierte Windlastansätze auf der Basis einer realistischen und praxisorientierten Erfassung flächen- und längenkorrelierter Effekte infolge dynamischer Lastanteile: Abschlussbericht*. Abschlussbericht. RWTH Aachen University.

— 2012. Vereinfachte Windlastansätze für Industriehallen aus Stahl durch transiente Berücksichtigung des Korrelationseffektes. Bauingenieur, S2–S8.

Pederbelli, D., Goglio, L., Paolino, D., Rossetto, M., and Tridello, A., 2023. Effect of Loading Frequency on the Fatigue Response of Adhesive Joints up to the VHCF Range. Applied Sciences 13.

Suresh Kumar, K. and Stathopoulos, T., 1998. Fatigue analysis of roof cladding under simulated wind loading. Journal of Wind Engineering and Industrial Aerodynamics 77-78, 171–183.

Wirsching, P. H. and Light, M. C., 1980. Fatigue under Wide Band Random Stresses. Journal of the Structural Division 106, 1593–1607.

Xu, Y., 1995a. Model- and full-scale comparison of fatigue-related characteristics of wind pressures on the Texas Tech Building. Journal of Wind Engineering and Industrial Aerodynamics 58, 147–173.

Xu, Y., Jan. 1995b. Determination of wind-induced fatigue loading on roof cladding. English. Journal of Engineering Mechanics 121, 956–963.

Sensitivity of cycling aerodynamics in crosswinds to turbulence modelling and CFD approaches

Jose Matias Arbelo Romero [1], Hassan Hemida [2], Mark Sterling [3], Bert Blocken [4,5]

[1]*University of Birmingham, Birmingham, United Kingdom, JMA337@student.bham.ac.uk*
[2]*University of Birmingham, Birmingham, United Kingdom, h.hemida@bham.ac.uk*
[3]*Manchester Metropolitan University, Manchester, United Kingdom, m.sterling@mmu.ac.uk*
[4]*Heriot-Watt University, Edinburgh, United Kingdom, b.blocken@hw.ac.uk*
[5]*KU Leuven, Leuven, Belgium, bert.blocken@kuleuven.be*

This research investigates the sensitivity of aerodynamic drag to different turbulence models and CFD approaches in cross-wind studies of an isolated cyclist. Specifically yaw angles of 0° and 15° are investigated. Amongst the turbulence models considered for the steady RANS equations, transition-SST performed best in terms of C_DA. The unsteady RANS approach to the transition-SST closure was the only to agree with wind tunnel results within a 2% difference for both yaw, and therefore arrive at an accurate C_DA prediction in yaw conditions.

Keywords: Computational fluid dynamics (CFD), turbulence models, sports aerodynamics, cross-wind

1. INTRODUCTION

In the past three decades, the 3D steady Reynolds-Averaged Navier-Stokes (RANS) approach has traditionally been used for most of wind engineering applications, including cycling aerodynamics. However, this has started to change and other approaches including Scale-adaptive simulations (SAS) coupled with the SST *k-ω* model (Blocken et al., 2020) or even Large Eddy Simulation (LES) (Fintelman et al., 2015) have started to be used more frequently. Other approaches such as the classical Unsteady 3D RANS (URANS) have seen sparse use so far (Javadi, 2022). For clarification, in this work a turbulence model is referred to the set of equations used as a closure for the 3D RANS equations. Whereas approaches are differentiated by the scale resolving ability.

Some research groups have addressed the challenge in selecting a turbulence model and approach by evaluating the mean drag force on a cyclist as a function of each model/approach. However, these studies focused on a fixed yaw angle (Druenen and Blocken, 2024), typically zero yaw in most cases. Other studies considered non-zero yaw cases and various turbulence approaches (Fintelman et al., 2015), yet the range of turbulence models considered within the steady RANS formulation were limited to standard *k–ε* and *k-ω*.

The current research work examines the sensitivity of CFD simulations to different turbulence models and approaches in cross-wind cases of an isolated cyclist. Amongst the approaches, namely steady RANS, URANS and SAS approaches are considered. The focus is on the drag force area coefficients (C_DA).

2. NUMERICAL CASE DESCRIPTION

The computational geometry of the cyclist and bicycle was similar to that of Fintelman et al., (2015) and extends over a region of $21h \times 11h \times 6h$, where $h = 1.52$ m is the cyclist's height. The cyclist and bicycle were elevated from the ground plane by 10 mm, as per guidelines for cross-wind applications (Malizia and Blocken, 2020). The combined frontal area (A) of the bicycle and cyclist was 0.55 m^2. The computational grid was discretised following a hybrid topology consisting of tetrahedral and hexahedral cells. The near-wall grid for the surfaces of the cyclist and the bicycle consisted of a total of 20 prismatic layers down to the viscous sublayer. The ratio between the height of the cells in the last prism layer and the size of the local surface-cell where the prisms are being grown from, was set to 30% of the local surface-cell size. To ensure that the average y+ was around 1, the distance from the wall-adjacent cell centre to the wall was 10 μm. Due to flow acceleration, the y+ reached values as large as 5 at few locations. On the ground wall-surface, 8 prismatic layers were used. Tetrahedral cells were employed to transition from the near-surface region surrounding the cyclist and bicycle, to the far-field, where hexahedral cells were used. The maximum cell size inside the refinement box around the cyclist was 10 mm. A cylindrical interface allows for the rotation of the cyclist. The total cell count was 73.3×10^6.

The 3D steady RANS equations were closed with the standard k–ω turbulence model, baseline (BSL) k-ω , shear stress transport (SST) k-ω, transition SST (T-SST), Generalised (GEKO) k-ω, k-kl-w model, realizable k-ε (RLZ), RNG k–ε model and Spalart-Allmaras (SA) turbulence model and the Unsteady-RANS (URANS) approach was used with the T-SST turbulence model. For the turbulence models based on the ε-framework, enhanced wall treatment was applied utilizing Wolfshtein's one-equation model in the viscous sublayer. For the SA model, vorticity-based production was applied. Whereas for the SA-B model, a strain-vorticity based production was applied. Curvature corrections were included in all settings except the k-kl-w model. Production limiters with clip factor 10 were included in all settings but the SA and k-kl-w models.

The approaching flow was with a free streamwise velocity (U) of 9.91 m/s, and turbulence intensity (TI = 0.67%) was applied to the inlet boundary condition, in line with the wind tunnel (WT) setup described in Fintelman et al, (2014). The experimental measurement conducted at the open wind-tunnel facility at the University of Birmingham, serves as validation of the numerical results. Symmetry boundary conditions are imposed on the side walls and roof. At the outlet, zero static gauge pressure was assumed. The ground, bicycle and helmet wall surfaces were treated as smooth walls, whereas the rough no-slip condition was set to the cyclist using the equivalent sand-grain roughness height k_s= 0.1 mm (Blocken et al., 2017) and a roughness constant of 0.5. Figure 1 schematically summarizes the computational grid and boundary conditions. The Coupled algorithm was used for the pressure-velocity coupling together with the pseudo-transient solver. The pseudo time-step was set to 0.01s. Gradient interpolation was taken care of by the Green-Gauss cell based method, and second order schemes were used for spatial discretisation. The simulation was first initialised for 2000 pseudo time steps, and the simulation was stopped once the moving average of the drag force converged to a statistically steady average (<0.05%). Reaching this state typically required 8,000 pseudo time steps. For the unsteady simulations, the spatial discretisation schemes were second order upwind and the time discretisation used a second-order backward Euler scheme. A constant time of 8×10^{-4} ensures the Courant-Friedrichs-Lewy (CFL) was around 1 to balance the temporal and spatial scales. Because of the thin prism layer and flow acceleration around the cyclist body, the CFL violated such condition at few locations.

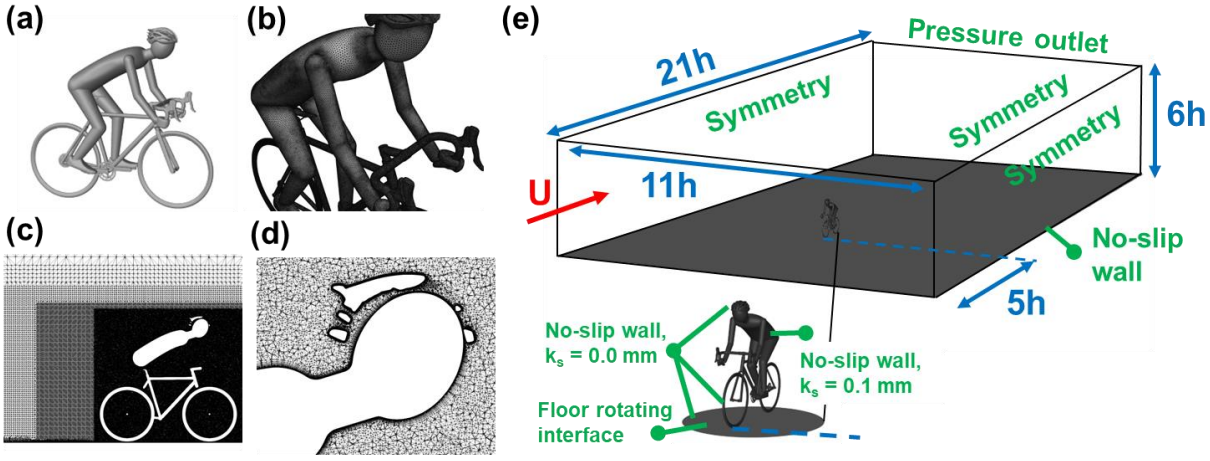


Figure 1. (a) Digital model of cyclist (Fintelman et al., 2015); (b) Surface mesh; (c) Volume mesh in vertical centreplane; (d) Prismatic and tetrahedral cells on volume around cyclist in vertical centreplane; (e) Computational domain and boundary conditions

3. RESULTS

The results were evaluated in terms of the drag area $C_D A$, as illustrated in Figure 2 for the no cross-wind condition. The whisker accounts for the WT measurement uncertainty, approximately 2%. In general, those turbulence models which use the specific dissipation rate for closure, perform best. Interestingly, the SA model has a relative error with respect to the WT of 1.3%, in contrast to the 14.2% discrepancy in Druenen and Blocken (2024). But the TSST closure model for the 3D RANS equations showed the best agreement with WT measurements, both for the steady and unsteady approach (1.3% and 0.7% respectively). A similar agreement was observed by Druenen and Blocken (2024).

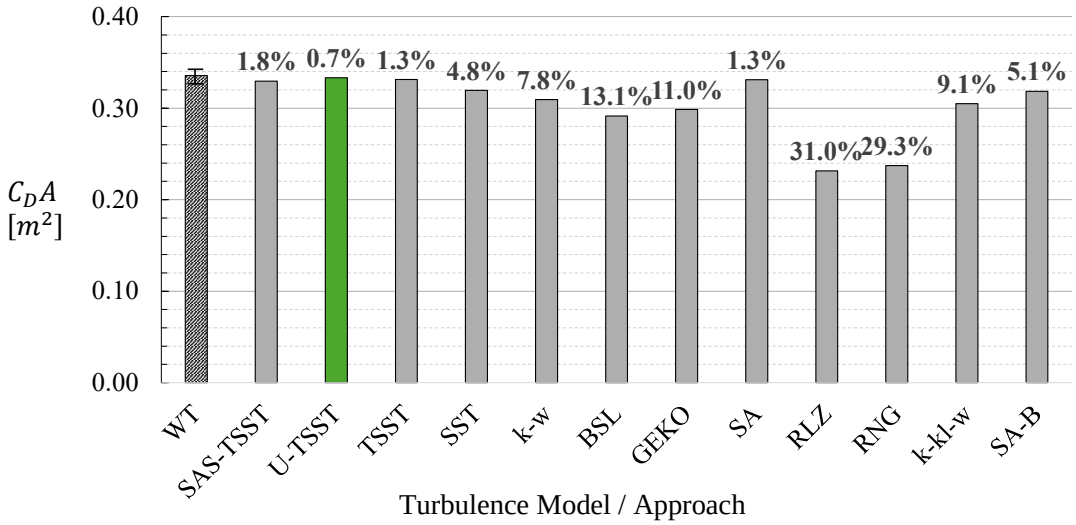


Figure 2. Wind tunnel measurements and CFD simulations evaluated in terms of $C_D A$ for 0° yaw

For a yaw angle of 15° (Figure 3) a similar trend is observed. Those turbulence models which use the specific dissipation rate for closure, perform best. The SA provides results comparable to the

TSST and SST. However, only the U-TSST exhibits an acceptable agreement (ie within 2%). The reason behind is yet unclear, and further work is required to address this.

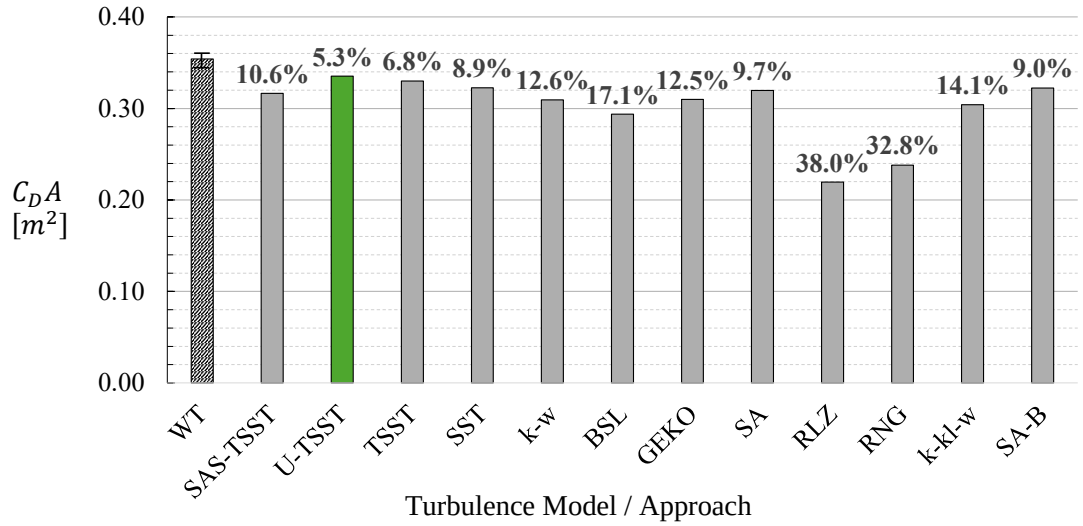


Figure 3. Wind tunnel measurements and CFD simulations evaluated in terms of C_DA for 15° yaw

4. CONCLUSION AND LIMITATIONS

Using the TSST turbulence model for closure of the steady 3D RANS equations provided the best performance in terms of C_DA. Though the URANS approach outperformed that of the steady at the yaw angles considered, 0° and 15°. Further work will follow to address the reasoning behind the enhanced performance of the URANS approach in predicting C_DA results of cycling aerodynamics in crosswind.

ACKNOWLEDGEMENTS

All simulations performed on the Birmingham Environment for Academic Research (BEAR) computational facility. The contribution of Dr. Fabio Malizia is acknowledged, for helping with meshing the cyclist model.

REFERENCES

Blocken, B., Stathopoulos, T. & Carmeliet, J., 2007. CFD simulation of the atmospheric boundary layer: wall function problems. Atmospheric Environment, January, 41, 238-252

Blocken, B., Malizia, F., van Druenen, T. and Gillmeier, S., 2020. Aerodynamic benefits for a cyclist by drafting behind a motorcycle. *Sports engineering*, *23*, 1-11.

Druenen, Thijs & Blocken, Bert., 2024. CFD simulations of cyclist aerodynamics: Impact of computational parameters. Journal of Wind Engineering and Industrial Aerodynamics 249, 105714

Fintelman, D., Sterling, M., Hemida, H., Li, F., 2014. The Effect of Crosswinds on Cyclists: An Experimental Study. Procedia Engineering. 72. 720-725.

Fintelman, D, Hemida, H, Sterling, M & Li, F-X 2015, 'CFD simulations of the flow around a cyclist subjected to crosswinds', Journal of Wind Engineering and Industrial Aerodynamics 144, 31-41

Javadi, Ardalan, 2022. Aerodynamic Study of the Pedalling of a Cyclist with a Transitional Hybrid RANS-LES Turbulence model. Flow Turbulence and Combustion, 108, 717-738

Malizia, F. and Blocken, B., 2020. CFD simulations of an isolated cycling spoked wheel: The impact of wheel/ground contact modeling in crosswind conditions. European Journal of Mechanics-B/Fluids, 84, 487-495.

Instability of solar trackers in turbulent wind flow

Juan Zaracho [1,2], John Ginger[1], David Henderson[1]

[1]*Cyclone Testing Station, James Cook University, Townsville, Australia,*

[2] *juanginacio.zaracho@jcu.edu.au*

SUMMARY:
A 1/20 scale aeroelastic model was tested in the wind tunnel for various tilt angles and wind directions. Time-varying moments were measured using a moment transducer at the fixed end of the model across different wind speeds, identifying the critical velocity at which the system became unstable. The response of the model was analysed utilizing Blevins' theory. The instability curve of the tracker was determined, and the variation in effective damping and stiffness was calculated and analysed.

Keywords: Solar tracker, wind loading, effective damping, effective stiffness, torsional galloping, divergence

1. INTRODUCTION

The large surface area and slender structure of single-axis solar trackers make them susceptible to aeroelastic instabilities induced by wind loading. These instabilities, divergence and galloping can potentially compromise structural integrity and disrupt the operations of these systems. This paper presents the results of an experimental investigation conducted on an aeroelastic model of a single-axis solar tracker in the boundary layer wind tunnel of the Cyclone Testing Station in Australia. The study focuses on identifying critical wind speeds at which instabilities occur for several wind directions. By employing the equation of motion in torsion proposed by Blevins (1990), the change of effective damping and effective stiffness in the structure is examined to characterize divergence and torsional galloping.

2. LITERATURE REVIEW

The response of a plate of breadth b, and thickness t, supported axially by a tube, fixed at one end and free to rotate at the other end is shown in Fig. 1. The response can be described using the equation of motion in torsion; $I_0\, d^2\gamma/dt^2 + c_0\, d\gamma/dt + k_0\gamma = M(t)$, where γ is the angle of twist, I_0 is the polar mass moment of inertia about the centre of the tube. The structural damping is, $c_0 = 2I_0\zeta_0(2\pi f_0)$, where ζ_0 is the damping ratio and f_0 is the torsional natural frequency. The torsional stiffness of the tube is $k_0 = GJ_0/l$. Here G is the shear modulus, J_0 is the polar second moment of area of the tube, and l is the total length of the plate.

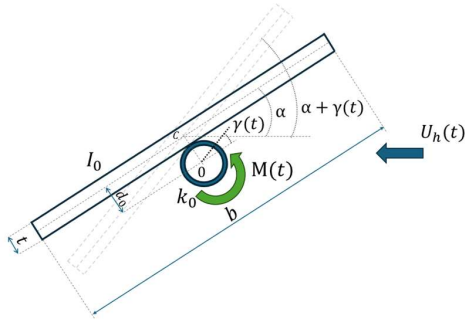


Figure 1. Response of an axially supported plate

Torsional galloping is a form of single-degree-of-freedom structural aerodynamic instability, which can occur on systems like solar trackers. In torsional galloping, the tilt angle α changes with the angle of twist, γ and with the angular velocity $d\gamma/dt$. According to Blevins (1990) for α <<< 1, the relationship between tilt angle and angular velocity of the tube is given by, $\alpha \simeq -(d\gamma/dt)b/4\bar{U}_h$, where $\bar{U}_h$ is the mean wind speed at a reference height.

The moment is then, $M(t) \cong -(\partial C_M/\partial\alpha)\frac{1}{2}\rho\bar{U}_h{}^2 b^2\, \alpha l$. Where $C_M(t) = M(t)/\frac{1}{2}\rho\bar{U}_h{}^2 b^2 l$, is the moment coefficient. Replacing α in the expression gives, $M(t) = -(\partial C_M/\partial\alpha)\frac{1}{8}\rho\bar{U}_{ref} b^3 (d\gamma/dt) l$. Then, applying this to the equation of motion, gives:

$$I_0\frac{d^2\gamma}{dt^2} + c_0\frac{d\gamma}{dt} + k_0\gamma = -\frac{\partial C_M}{\partial\alpha}\frac{1}{8}\rho\bar{U}_{ref} b^3\frac{d\gamma}{dt} l \tag{1}$$

This equation can be rearranged as shown by Blevins (1990),

$$I_0\frac{d^2\gamma}{dt^2} + \left(c_0 + \frac{\partial C_M}{\partial\alpha}\frac{1}{8}\rho\bar{U}_{ref} b^3 l\right)\frac{d\gamma}{dt} + \left(k_0 - \frac{\partial C_M}{\partial\alpha}\frac{1}{2}\rho\bar{U}_{ref}{}^2 b^2 l\right)\gamma = 0 \tag{2}$$

Here, $\left(c_0 + \frac{\partial C_M}{\partial\alpha}\frac{1}{8}\rho\bar{U}_{ref} b^3 l\right)$ is the "effective damping" comprising structural damping, c_0 and the aerodynamic damping. The onset of torsional galloping occurs when the effective damping is negative. This is only possible if $\partial C_M/\partial\alpha < 0$.

$\left(k_0 - \frac{\partial C_M}{\partial\alpha}\frac{1}{2}\rho\bar{U}_{ref}{}^2 b^2 l\right)$ is the "effective stiffness" comprising structural stiffness k_0 and the aerodynamic stiffness. A form of instability that can be derived from that term, is called torsional divergence. This form of instability occurs when the effective stiffness falls to zero, which is only possible if $\partial C_M/\partial\alpha > 0$. Divergence is associated with tilt angles α ≈ 0°.

3. METHODOLOGY

An aeroelastic model of a solar tracker was constructed at length scale 1/20 (Zaracho et al., 2023) and tested in the 22m long wind tunnel at the Cyclone Testing Station. The turbulence intensity at the height *h* was about 22%, in accordance with open approach terrain in AS-NZS 1170 (2021). The parameters of interest of the model are b = 0.20 m, l = 1.65 m, $I_0 = 0.0013$ kgm^2, f_0= 7.65 Hz, c_0= 0.057 Nm/s, k_0=3.63 Nm, and ζ_0= 0.28. The model was tested at range of tilt angles α, from 0° to 50°, and wind directions θ, ranging between 0° and 180°. The wind

speed in the tunnel was increased progressively until the instability was observed. The critical mean wind speed $\overline{U}_{cr}$ was defined as the 10-second mean wind speed preceding the onset of instability. Fig. 2. Shows the model in the wind tunnel.

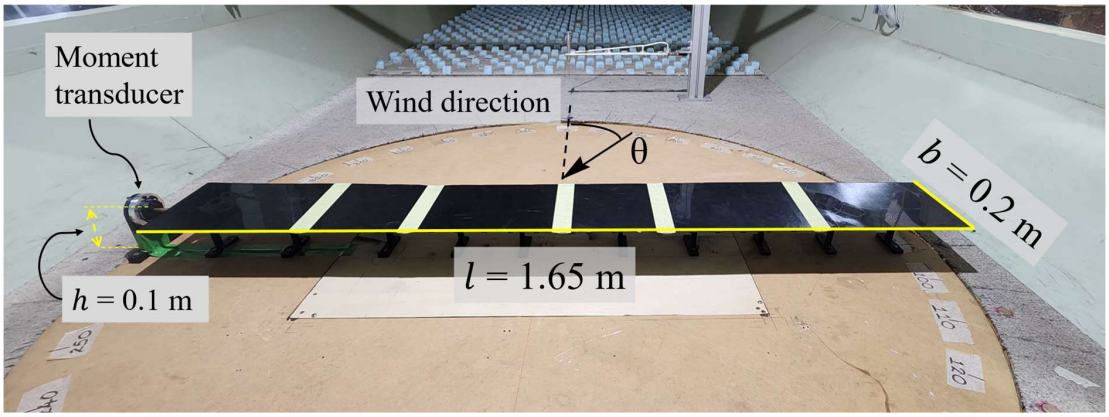


Figure 2. Aeroelastic model of the solar tracker in the wind tunnel at stow position (α = 0°)

4. RESULTS

The critical mean wind speed $\overline{U}_{cr}$ was normalised as a reduced critical wind speed $U_{red} = \overline{U}_{cr}/bf_0$. Fig. 3 shows the critical wind speed vs tilt angle and approach wind direction.

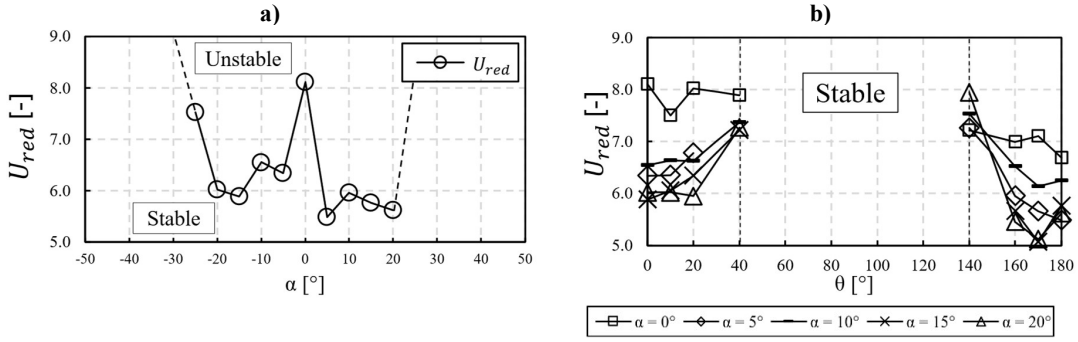


Figure 3. a) U_{red} vs tilt angle. b) U_{red} vs approach wind direction θ

Fig. 3a shows that the reduced wind speed for tilt angle (α = 0°), is about 8 and decreases as the tilt increases up to 25°. In general, positive tilt angles (i.e. θ = 180°) resulted in lower reduced wind speed compared to negative tilt angles (i.e. θ = 0°) similar to that observed by Martínez-García et al., (2021). The wind direction also influenced the model's stability. Fig. 3b shows that the reduced wind speed for instability remained relatively constant within each configuration as the wind direction deviated by ±40° from the principal directions (0° and 180°). Beyond this range, the model was stable even at higher wind speeds. This is attributed to the reduced wind loading on solar panels for oblique approach winds as found by Ginger et al., (2019).

The effective damping and the effective stiffness were calculated using Eq. 2. The variation in terms of the reduced wind speed is shown in Fig. 4.

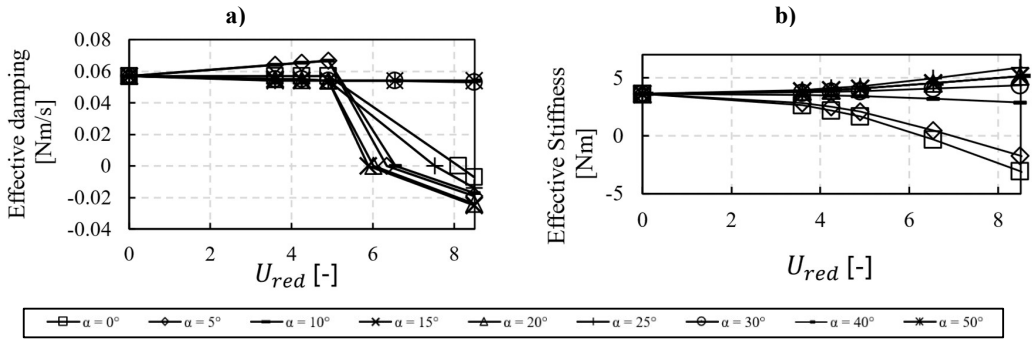


Figure 4. a) Effective damping variation. B) Effective stiffness variation.

Fig. 4a shows that the aerodynamic damping increases with increasing wind speed for tilt angles (α) between 0° and 25°. This increased aerodynamic damping, reducing the effective damping, which after falling to zero allowed the onset of torsional galloping. Tilt angles from 30° to 50° remained stable within the tested wind speed range. The effective damping for these configurations remained almost constant. Fig. 4b shows that the effective stiffness slightly increases for all tilt angles except for α = 0° and 5°. For these configurations, the aerodynamic stiffness became increasingly negative with increasing wind speed, counteracting the structural stiffness of the model. This reduction in overall stiffness eventually led to divergence. It is important to note that for α = 0°, the model's effective stiffness falls to zero before its effective damping. This suggests that the model likely experienced divergence first, followed by torsional galloping. The initial static increase in deflection (tilt) due to divergence could have changed the effective aerodynamics, leading to a reduction in effective damping and favouring the onset of torsional galloping.

5. CONCLUSIONS

The solar tracker model exhibited aeroelastic instabilities across a wide range of wind directions, including oblique winds. The critical wind speed required to trigger instability remained relatively consistent despite variations in wind direction, indicating that even oblique winds can pose a significant risk. For tilt angles between 5° and 25°, torsional galloping was the primary instability mechanism observed. However, at near-zero tilt angles (α ≈ 0°), the model exhibited divergence, which could subsequently trigger torsional galloping due to the altered aerodynamic loading caused by the increased deflection. This finding indicates the relationship between different instability mechanisms and the need to consider both divergence and galloping in the design of solar trackers, especially at low tilt angles.

REFERENCES

Blevins, R. D. (1990). Flow-induced vibration, K. P. Company, Ed. 2nd ed.

Ginger, J. D., Bodhinayake, G. G., & Ingham, S. (2019). Wind loads for designing ground-mounted solar-panel arrays. Australian Journal of Structural Engineering, 20(3), 204-218.

Martínez-García, E., Blanco-Marigorta, E., Gayo, J. P., & Navarro-Manso, A. (2021). Influence of inertia and aspect ratio on the torsional galloping of single-axis solar trackers. Engineering Structures, 243, 112682.

Standards Australia. (2021). Structural design actions. Part 2: Wind Actions Sydney, New South Wales, Australia, Australian/New Zealand Standard, AS-NZS 1170.2:2021.

Zaracho, J.I., Ginger, J.D., Parackal K.I., Henderson, D.J., (2023, August 27-31). Aeroelastic modelling of solar trackers. 16th International Conference on Wind Engineering, Florence, Italy.

Experimental 2D simplified analysis of the wake velocity profile of a flat plate solar tracker in a defence position immersed in a uniform flow

José Luis Ruiz-Moral [1,3], Omar Gómez-Ortega [1], Raúl Manzanares-Bercial [1], Carlos Carbajosa [1], Adriana Carolina Hernández-Badillo [1], Carlos Rodríguez-Casado [2]

[1] *Instituto Universitario de Microgravedad "Ignacio Da Riva" (IDR/UPM), Universidad Politécnica de Madrid, Plaza Cardenal Cisneros, 3, E.28040, Madrid, Spain,*
[2]*Universidad de Oviedo, Oviedo, Asturias, Spain,*
[3]*joseluis.ruiz.moral@upm.es*

SUMMARY:
The wake speed profile of a solar tracker is studied by analysing the wake deflection and dynamic pressure loss in the streamlines at a fixed distance downwind from the axis of the solar tracker. The defence angle is modified to analyse its influence on the tracker wake speed profile.

Keywords: Solar tracker, wake deflection, dynamic pressure loss.

1. INTRODUCTION

Satisfying the growing demand for electricity requires the development of new energy sources, such as solar energy. A solar tracker has 10 to 30% higher efficiency than a fixed solar panel (Zhang et al 2023). The structures that support these trackers are becoming less rigid and lighter to save cost. Therefore, they are more sensitive to aeroelastic instabilities whose effects lead to structural deterioration (Rodríguez-Casado et al 2024, Cárdenas-Rondón et al 2024).

Solar trackers are installed in multiple rows of trackers fields. For this reason, upstream trackers influence the aeroelastic behaviour of others downstream. The incoming flow of a tracker is the wake of another one upstream (Wang et al 2021).

The objective of this work is to experimentally characterise the wake of a solar tracker modelled as a flat plate for different defence angle positions at a certain position downstream. The selection of this position is based on the most popular distance between tracker rows in the industry.

2. EXPERIMENTAL SETUP

The model consists of a wooden flat plate with a chord $B = 40$ cm, set at a fixed angle, with a wooden false floor. The height between the model axis and the floor is $H/B = 0.5$. Tests have been performed in the IDR/UPM AB6 wind tunnel, located in Montegancedo campus premises of the Universidad Politécnica de Madrid. It is a two-dimensional closed-circuit wind tunnel, which has a 2.5m × 0.5m closed test section, 4m length, with a 4.5:1 contraction ratio. The maximum wind speed inside the test chamber is 35 ms^{-1}. For the instrumentation, a two-component hot-wire

probe Dantec 55P61 has been used to measure the velocity at different heights z. To change the height of the hot wire, a Zaber guide has been placed under the false floor of the wind tunnel, attached to the tunnel wall, which moved an "L"-shaped metal support structure probe holder holding the hot wire probe on top of it, as shown in Figure 1. This velocity has been characterised with its both components: horizontal u and vertical w.

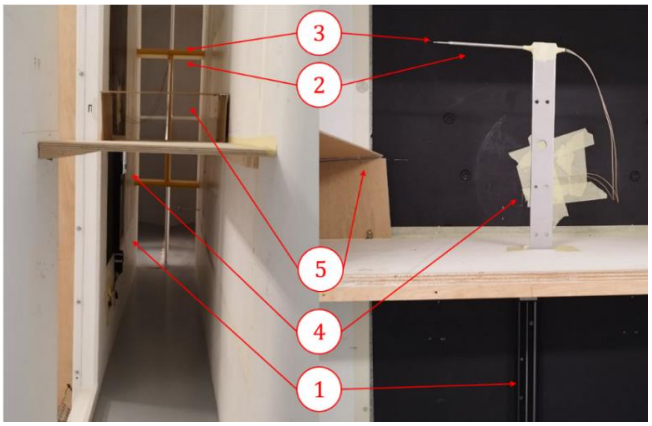


Figure 1. Experimental set-up inside the test chamber. Labels: (1) ZABER Guide (2) Probe holder; (3) Wire probe; (4) Metallic structure; (5) Solar tracker model.

The tests have been repeated for several values of the defence angle α_d = 5°, 10°, 15°, 20° and 30°. For each configuration, the flow velocity has been U_∞ = 5 ms^{-1}, 10 ms^{-1} and 15 ms^{-1}. Finally, in each test the height where wind speed has been measured between $z/B = 0.1$ and $z/B = 1$, in 40 evenly spaced points at a position $d/B = 0.75$. The height between the model axis and the floor is $H/B = 0.5$. A sketch of this experimental set-up is shown in Figure 2.

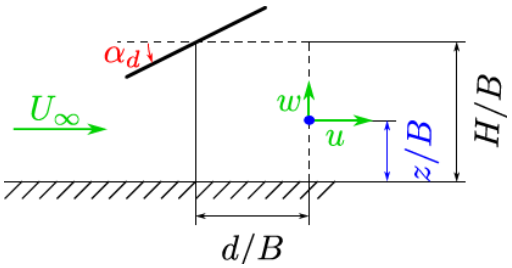


Figure 2. Sketch of the studied parameters: the defence angle α_d, flow velocity U_∞, measurement points height z/B, distance between the measurement position and the tracker axis d/B, axis tracker height H/B, horizontal u and vertical w wake speed components.

3. RESULTS

The behaviour of the streamlines in the wake is analysed: their modulus (dynamic pressure loss $\eta = (u^2 + w^2)/U_\infty^2 = |\vec{v}|^2/U_\infty^2$) and direction (wake deflection ε), vary with α_d. The mean non-dimensional wake velocity profile for each α_d is shown in Figure 3. It has been calculated with the mean for all tested U_∞ for each α_d, since it is almost identical for each U_∞. In each graph, there is a continuous line at $z/B = 0.5$, corresponding to the tracker axis height, and two dashed lines, one at a lower and one at a higher height, corresponding to the model leading and trailing edge height, respectively. The medium wake height is called wake axis (red dotted line in Figure 3).

For α_d = 5°, the streamlines show hardly any deflection, and a slight dynamic pressure loss. The maximum pressure loss is $\eta = 0.74$ and the maximum deflection is $\varepsilon = 0.80°$. In this case, the wake axis height is practically coincident with the leading edge height.

For α_d = 10°, the streamlines show more deflection than for α_d = 5°, and the dynamic pressure loss is also higher. The maximum dynamic pressure loss is $\eta = 0.53$ and the maximum deflection is $\varepsilon = 4°$. In this case, the wake axis height is close to the leading edge height, but closer to the tracker axis height than the wake axis height for α_d = 5°.

For α_d = 15°, the streamlines show a similar deflection as for α_d = 10°, and the dynamic pressure loss is also higher. The maximum dynamic pressure loss is $\eta = 0.29$ and the maximum deflection is $\varepsilon = 6°$. In this case, the wake axis height is approximately at the midpoint between the tracker axis height and the leading edge height.

For α_d = 20°, the streamlines show a behaviour analogous to that of α_d = 15°, with a slightly higher dynamic pressure loss. The maximum dynamic pressure loss is $\eta = 0.23$ and the maximum deflection is $\varepsilon = 7°$. In this case, the wake axis height is closer to the wake axis height than to the leading edge height.

For α_d = 30°, the streamlines show the highest dynamic pressure loss of the cases studied although they do not show a higher deflection, but lower. The maximum dynamic pressure loss is $\eta = 0.16$ and the maximum deflection is $\varepsilon = 5°$. In this case, the wake axis height practically corresponds to the height of the tracker axis. The wake is similar to a bluff body wake (Wang et al 2021).

It should be noted that in all cases, the streamlines above those of the wake show an increase in velocity, especially appreciable for α_d = 30°.

4. CONCLUSIONS

The wake axis height moves closer to the tracker axis height and away from the leading edge height if the defence angle increases.

The streamlines deflection and the dynamic pressure loss increase with defence angle. It occurs if the defence angle is smaller than a value between 20° and 30°.

The dynamic pressure loss is bigger than 1 above the wake height if α_d > 20°.

ACKNOWLEDGEMENTS

This work is part of the project TED2021-130541B-C21 funded by MCIN/AEI/10.13039/501100011033, the European Union ‘‘NextGenerationEU’’/PRTR and project PID2022-137630OB-C21 financed by MCIN/AEI/10.13039/501100011033/FEDER, UE. The work of Carlos Carbajosa has been supported by Programa Propio de I+D+i de la Universidad Politécnica de Madrid. The authors would like to thank Javier Pascual Alonso, Carlos Pascual Alonso, Manuel Ortega Hidalgo, Alberto Escribano Baeza, Guillermo Banús and Camilo Zomeño López for their participation in the construction of the model and the performing of the test campaign.

REFERENCES

Zhang, Xiaobin, Wenyong Ma, Xiaohan Kang et al. 2023. Parametric Analysis of Self-Excited Aeroelastic Instability of An Isolated Single-Axis Two-Dimensional Flat Solar Tracker. Journal of Wind Engineering and Industrial Aerodynamics 240, page 105.486.

Juan A. Cárdenas-Rondón, Mikel Ogueta-Gutiérrez, Sebastián Franchini, Raul Manzanares-Bercial 2024. Stability analysis of two-dimensional flat solar trackers using aerodynamic derivatives at different heights above ground. Journal of Wind Engineering and Industrial Aerodynamics 243, page 105.606.

Carlos Rodríguez-Casado, Eva Martínez-García, Raúl Manzanares-Bercial, José Luis Ruiz-Moral, Eduardo Blanco-Miragorta and Atonio Navarro-Manso. Journal of Wind Engineering and Industrial Aerodynamics 253, page 105.838.

Chaoqun Wang, Xugang Hua, Zhiwen Huang and Qing Wen 2021. Aerodynamic Characteristics of Coupled Twin Circular Bridge Hangers with Near Wake Interference. Applied Sciences 11, page 4.189.

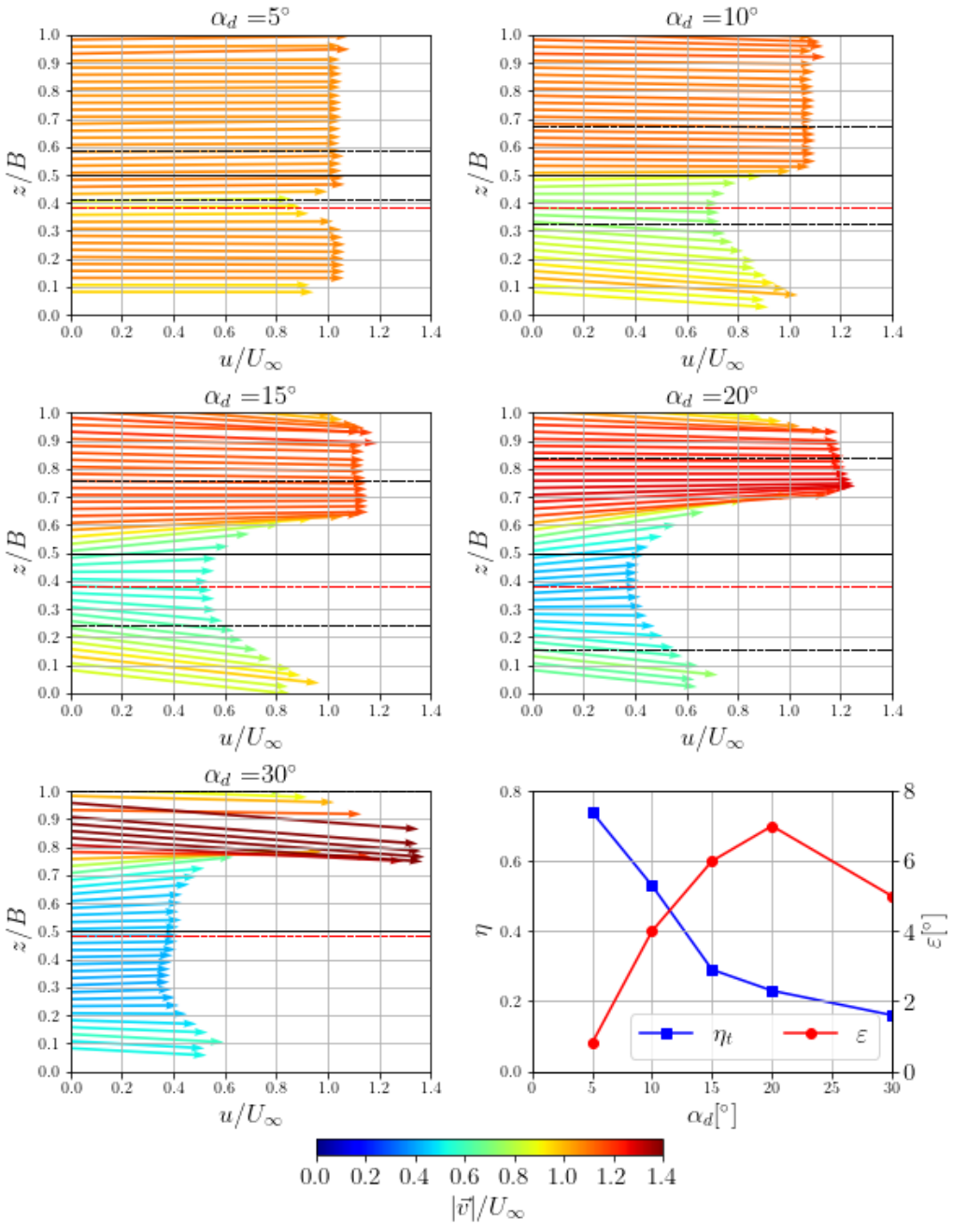


Figure 3. Mean non dimensional tracker wake velocity profile.

Enhancing solar tracker stability using machine learning techniques and numerical methods

Rongshen Wang[1], Alejandro Martínez-Cava [1], Juan Andrés Cárdenas-Rondón[1], Carlos Carbajosa[1], Raúl Manzanares-Bercial[1]

[1]*Instituto Universitario de Microgravedad "Ignacio Da Riva" (IDR/UPM), Universidad Politécnica de Madrid, Plaza Cardenal Cisneros, 3, E.28040, Madrid, Spain,*
rongshen.wang@alumnos.upm.es

SUMMARY:
Aeroelastic instability presents a significant challenge in photovoltaic solar trackers, primarily due to the reduction in structural stiffness, which can lead to structural failures. This study aims to enhance prediction methods for such instabilities by utilizing aerodynamic derivatives and machine learning techniques. A synthetic database is generated through regression models and subsequently used to train an artificial neural network (ANN) to predict the stability of two-dimensional isolated solar trackers based on their structural properties and operational conditions. The training dataset (input) includes geometric and physical characteristics of the trackers, along with a wide range of wind speeds and tilt angles. The ANN's prediction results, which include both a synthetic expanded database and aeroelastic performance prediction, are promising, demonstrating a high detection rate, although the model tends to be conservative in its classification.

Keywords: machine learning, solar tracker, aerodynamic derivatives, aeroelasticity

1. INTRODUCTION

In the past decade, there has been a substantial increase in the adoption of solar photovoltaic (PV) systems for clean electricity generation. A notable trend is the growing use of single-axis solar trackers (PST), which can adjust their tilt and orientation to maximize energy production. However, as PSTs become more commonly employed, there is an increasing drive to reduce manufacturing costs. Often, this involves lowering the stiffness around the tracker's rotation axis, which makes PSTs more vulnerable to aeroelastic instabilities. Recent discussions have highlighted that both the tilt angle of the tracker and the wind flow characteristics significantly influence the onset of these instabilities (Taylor et al., 2024; Zhang et al., 2023). Despite this, limited data is available to establish a robust prediction model, due to the large number of geometrical and physical parameters involved.

The study of self-excited instabilities in trackers is typically conducted using Scanlan's sectional formulation (Scanlan and Tomko, 1971), where aerodynamic forces and moments are analyzed through aerodynamic derivatives. These parameters can be experimentally determined by exploring the design space of solar trackers to calculate the critical wind speed at which instability occurs (Cárdenas-Rondón et al., 2023). In this work, we explore the use of regression models and machine learning techniques to calculate aerodynamic derivatives and develop a predictive model for

critical wind speed of two-dimensional isolated solar trackers. A synthetic database, generated using regression models, is employed to train an artificial neural network (ANN) that estimates the stability of a tracker based on its structural properties and operational conditions.

2. METHODOLOGY

The aerodynamic derivatives used to predict the onset of aeroelastic instability are influenced by three key input variables: the tracker's chord-height aspect ratio, the reduced wind speed, and the mean effective angle of attack. For brevity, the process of experimentally determining these aerodynamic derivatives through sectional models release tests, as well as a detailed explanation of the flow physics behind the instability, are not discussed here. The reader is referred to previous works by the authors for further information (Cárdenas-Rondón et al., 2023). To predict the stability of a tracker, a synthetic database was first generated using regression models, which was then combined with a deep learning model incorporating the tracker's mechanical properties. The overall process is illustrated in Fig. 1.

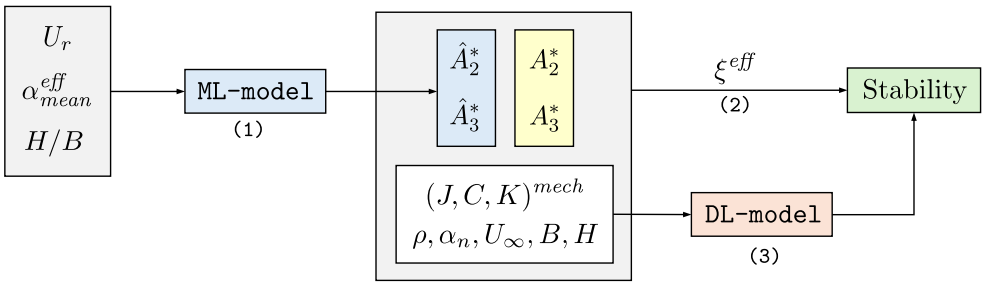


Figure 1. Workflow for the aeroelastic stability prediction.

2.1. Generation of synthetic database

The creation of an accurate ANN model requires a large and diverse database. To estimate aerodynamic derivatives for configurations not included in the experimental dataset, a piecewise linear interpolation method was applied. The synthetic database consists of data from 20 different commercial trackers, obtained from experimental testing (Martínez-García et al., 2021), resulting in 121800 data entries. This dataset includes the trackers' physical properties, reduced wind speed, tilt angle, and geometric ratio. For each case, the output is the effective damping coefficient, which is computed using an iterative approach and applies Steffensen's method for faster convergence. For the purpose of this study, the natural oscillation frequency of each tracker model was assumed to be 2.19 Hz, due to the unavailability of specific data.

2.2. Artificial Neural Network (ANN)

The synthetic database was used to train a pseudoclassifier ANN, with an 80-20 training-test split. The ANN architecture consisted of three hidden layers in a 5-4-3 configuration, with each layer using a Swish activation function. The structural properties and operational conditions of each tracker were represented by five input variables. However, after performing principal component analysis (PCA), it was determined that only four variables were necessary for the model. The ANN was trained over 100 epochs with a batch size of 32. The performance of the trained network was evaluated using a receiver operating characteristic (ROC) curve.

3. RESULTS

3.1. Iterative method accuracy

The critical wind speed is typically represented by the W-curve, which plots the reduced wind speed ($U_r = 2\pi U_\infty / B\omega$, where B is the tracker length and ω is the system's oscillation frequency) against the tracker's tilt angle. Fig. 2 shows the superimposition of two different methods. The blue line with error bars represents the averaged stability curve for seven experimentally tested tracker models, extracted from (Martínez-García et al., 2021). Using the properties of the same seven models (Id 1 to 7 in Fig. 2), the iterative method was applied, resulting in the different curves shown. The agreement between the two approaches is excellent, demonstrating the accuracy of the iterative method.

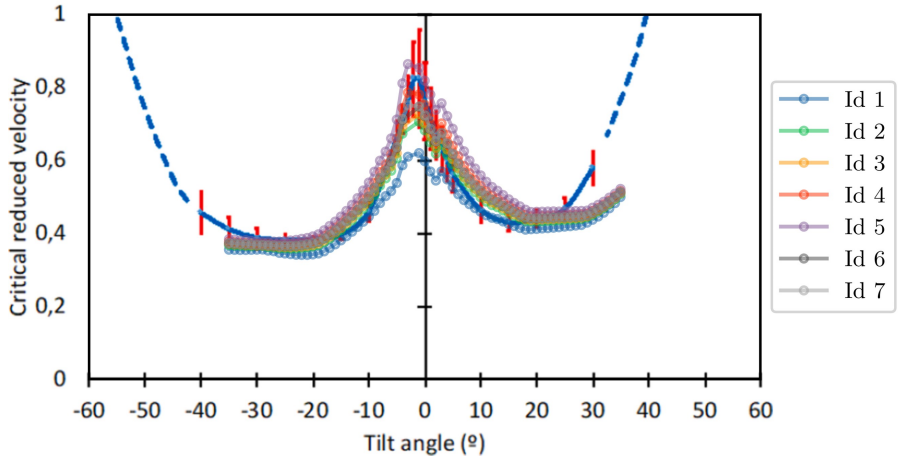


Figure 2. Comparison between the stability curves obtained with the iterative method (marked lines) and the experimental data (dashed line with error bars) (Martínez-García et al., 2021).

3.2. Classification method analysis

The ANN was trained and validated using the synthetic database and configured for binary classification. A threshold value is required to determine whether a tracker is stable or unstable. To identify the optimal threshold, the ROC curve was constructed by iteratively adjusting the threshold and plotting the true positive rate (TPR) and false positive rate (FPR). The results, shown in Fig. 3, are compared to the ROC curve of a random classifier.

The area under the curve (AUC), which reflects the model's accuracy, was calculated to be 0.892, which is considered acceptable for a simple ANN. The point on the curve that is farthest from the random classifier (indicated by a red marker) corresponds to TPR and FPR values of 95.91% and 32.03%, respectively. This indicates that the ANN successfully detects the majority of unstable cases, though it tends to be conservative, often classifying stable cases as unstable.

4. CONCLUSIONS

A regression model utilizing piecewise linear interpolation was employed to generate a synthetic database containing aerodynamic derivatives, which are essential for predicting the aeroelastic stability of photovoltaic solar trackers. The database encompasses the geometric and physical characteristics of the trackers, along with a wide range of wind speeds and tilt angles. The data

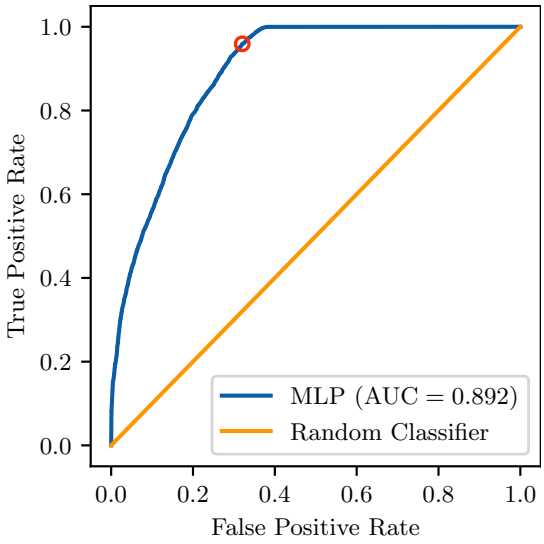


Figure 3. ROC of the ANN classification results.

obtained from this approach shows good agreement with experimental reference data, and it was subsequently used to train a deep learning model based on a relatively simple artificial neural network (ANN). When combined with the mechanical properties of the tracker, this model can classify the configuration as either stable or unstable from an aeroelastic perspective.

The results from the ANN indicate a high detection rate; however, the model tends to be conservative, as evidenced by a moderate false positive rate. Given the complex nature of neural networks, further improvements in the architecture and configuration of the ANN could enhance its performance and predictive accuracy.

ACKNOWLEDGEMENTS

This work is part of the project TED2021-130541B-C21, funded by MCIN/AEI/10.13039/ 501100011033, the European Union "NextGenerationEU"/PRTR and project PID 2022-137630OB-C21 financed by MCIN/AEI/10.13039/ 501100011033/FEDER, UE. The work of Carlos Carbajosa has been supported by the FPU grant FPU23/00716 from the Spanish Ministry of Science and Innovation (Ministerio de Ciencia, Innovación y Universidades).

REFERENCES

Cárdenas-Rondón, J. A., Ogueta-Gutiérrez, M., Franchini, S., and Manzanares-Bercial, R., 2023. Stability analysis of two-dimensional flat solar trackers using aerodynamic derivatives at different heights above ground. Journal of Wind Engineering and Industrial Aerodynamics 243.

Martínez-García, E., Blanco-Marigorta, E., Gayo, J. P., and Navarro-Manso, A., 2021. Influence of inertia and aspect ratio on the torsional galloping of single-axis solar trackers. Engineering Structures 15.

Scanlan, R. H. and Tomko, J. J., 1971. Airfoil and bridge deck flutter derivatives. Journal of Engineering Mechanics 97, 1717–1737.

Taylor, Z. J., Feero, M. A., and Browne, M. T., 2024. Aeroelastic instability mechanisms of single-axis solar trackers. Journal of Wind Engineering and Industrial Aerodynamics 244.

Zhang, X., Ma, W., Kang, X., Shao, Q., and Tang, Z., 2023. Experimental study of the torsional aeroelastic instability of single-axis solar trackers under different turbulence intensities. Journal of Wind Engineering and Industrial Aerodynamics 240.

Portable wind tunnel for single-degree-of-freedom flutter representation in single-axis solar trackers

Carlos Rodríguez-Casado [1], Claudia González-Gutiérrez [2], Eduardo Blanco Marigorta [3], Maria E. Moreyra Garlock [4], Antonio Navarro-Manso [5]

[1]*Energy Department, University of Oviedo, Gijón, Spain, rodriguezccarlos@uniovi.es*
[2] *Energy Department, University of Oviedo, Gijón, Spain, UO288902@uniovi.es*
[3] *Energy Department, University of Oviedo, Gijón, Spain, eblanco@uniovi.es*
[4]*CEE Princeton University, Princeton, NJ, USA, mgarlock@princeton.edu*
[5] *Energy Department, University of Oviedo, Gijón, Spain, navarroantonio@uniovi.es*

SUMMARY:
"DEMO-TRACK^{FW}" is the first portable device designed to demonstrate the impact of wind on single-axis solar trackers (SAT). It is made of five fans, a 24V power supply, honeycomb, contraction, and a 1/60 full aeroelastic scale model of a benchmark tracker made from PLA 3D printing and carbon fiber. The design is intended to control both wind speed (up to 5 m/s) and tilt angles. Several testing configurations are allowed: stand-alone and multi-row. The maxima outer dimensions are 0.7 x 0.5 x 0.2 m. This device is easy to use for educational purposes and for conducting preliminary research in Civil Aerodynamics and Aeroalasticity, regarding SAT torsional instabilities.

Keywords: aeroelastic model, teaching and learning, design of experiments, torsional instability

1. MOTIVATION

In education, a distinction is often made between theoretical and practical classes. However, both approaches combine to form the concept of "learning by doing," (Hayne, 2011) which emphasizes learning through direct experience (Rodríguez García et al., 2014). Theoretical models developed by scholars like Lewin, Dewey, and Piaget have shaped this methodology, showing that true learning stems from practical action, followed by reflection (Kolb, 1984). For instance, in Civil Engineering, this method is applied through experiments such as airflow visualization around objects in wind tunnels (Trinder and Jabbal, 2013) or the development of scale models to study structural stability (Navarro-Manso et al., 2018).

Experimentation plays a key role in Aeroelasticity, a branch of Civil and Aeronautical Aerodynamics, which studies the interaction between aerodynamic, elastic, and inertial forces acting on objects under wind loads. Its complexity relies on the variety of phenomena and cases that can be analyzed. Wind tunnel tests are usually required to measure variables and calculate structural design values, for solving Navier-Stokes equations analytically is often impossible. A prime example of aeroelasticity in teaching and research is the single-axis solar tracker (SAT). This structure consists of solar panels mounted on a horizontal torsion tube, rotated by a motor to track the sun from east to west, optimizing energy capture. These systems have one degree of freedom (1DOF), with torsional vibrations as their primary mode of instability (Rohr et al., 2015). However, as industry competition drives the design of thinner torsion tubes, SAT become more susceptible to aeroelastic instability (Martínez-García et al., 2021; Cárdenas-Rondón et al., 2023).

Despite decades of research on flexible structures, the destructive aeroelastic phenomena, such as torsional galloping and vortex-induced vibrations, have only recently been observed in SAT (Valentin et al., 2022). Understanding these phenomena and their interactions, as well as improving damping and structural design, is critical for enhancing tracker performance (Gross et al., 2020). Research on these systems is ongoing worldwide (Bruner et al., 2022).

This article presents the design and construction of a portable device, the DEMO-TRACK^{FW} (see Fig 1), based on a benchmark model model (Rodríguez-Casado et al. 2024). Following similarity laws, the device is intended for preliminary research and teaching, allowing the identification and visualization of critical aeroelastic instability speeds. Using a 3D-printed full aeroelastic SAT model (either isolated or in multi-row configurations), basic measurements can be taken to provide preliminary insights into aerodynamic behavior. The device facilitates explaining complex wind tunnel tests and planning future research. It was designed and built for use by the University of Oviedo (FW), the Polytechnic University of Madrid (IDR), and Princeton University (CEE).

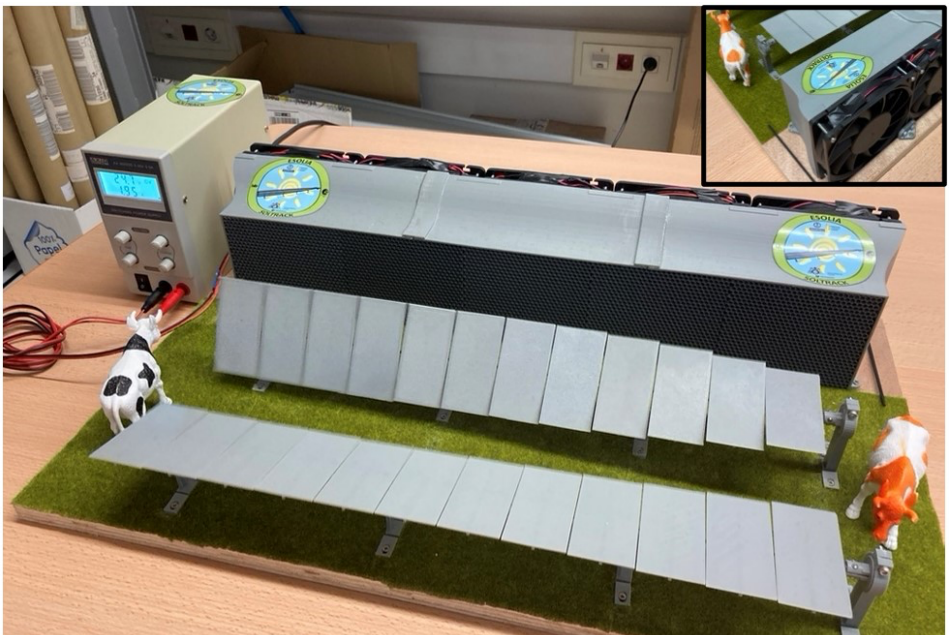


Figure 1. DEMO-TRACK^{FW}, exhibited in an International Forum (GENERA, Madrid, February 2024).

2. METHODS

Applying Buckingham's π theorem with a total of n = 8 variables and s = 3 independent dimensional variables, 5 dimensionless numbers are obtained:

Eu (Euler number): Represents the force on the structure due to wind, which physically depends on Re and the shape of the object. Generally, it is the ratio between pressure energy (force on the object) and the kinetic energy of the air.

St (Strouhal number): Describes the vortex shedding frequency due to the fluid, also dependent on Re and the shape of the object. It relates fluid oscillations to the mean velocity, indicating the residence time of a phenomenon.

Re (Reynolds number): Represents the importance of viscous forces relative to inertial forces. In this case, inertial forces dominate.

fr (reduced frequency): Describes the structural vibration frequency, which depends on the structure's inertia (mass) and stiffness.

Ck (stiffness coefficient): Represents the stiffness or flexibility (deformation) of the structure, which also depends on Re and the object's shape.

3. RESULTS

Figure 2 shows the DEMO-TRACK^{FW} data for the first row of trackers. As can be seen, the trends are captured well (and the values are better for the negative angles of inclination), in comparison to the data obtained in a wind tunnel (Martínez-García et al., 2021). This suggests that the proposed model allows sufficiently reliable results to be obtained, with a clear potential for teaching and used in preliminary research phases. The Stability Diagram of the tracker is depicted in terms of reduced variables (rad/s for the frequency).

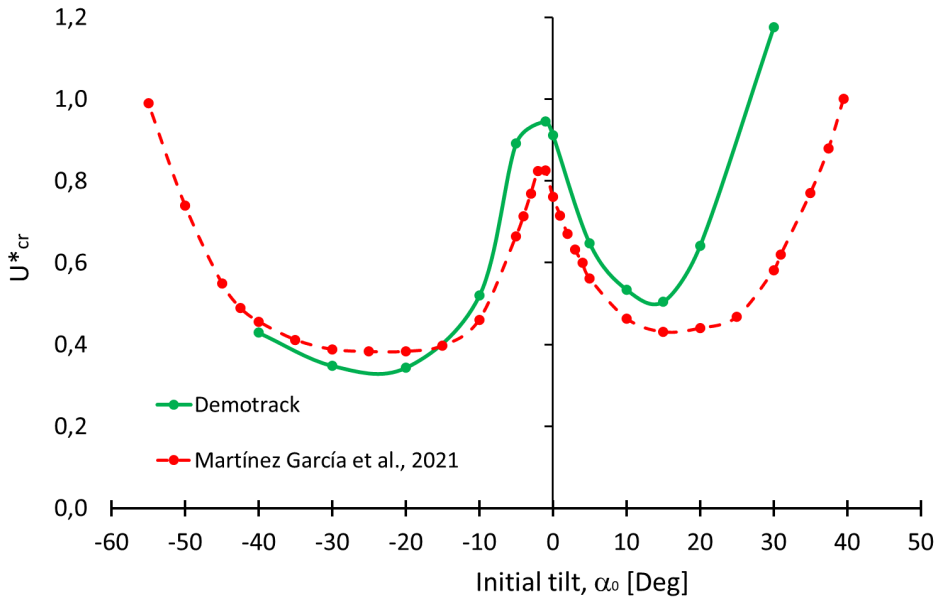


Figure 2. Comparison between the Stability Diagram of a SAT (Martínez-García et al., 2021) and the test performed with the DEMO-TRACK^{FW}.

The device has been designed to keep the cost as low as possible in order to facilitate its academic use. The budget required for its construction is divided into four main items: materials (1.41%), power equipment (11.42%), printing of elements and assembly (87.17%) and an item for instrumentation (optional and mainly focused on the research part) (about 7% additional). Thinking about a possible commercialisation of the product, to determine the price, it is necessary to add the design and know-how of the research team, as well as the % of profit to be obtained.

4. CONCLUSIONS:

The benefits of the DEMO-TRACK^{FW}'s design, construction, and use can be summarized as follows:

4.1. Teaching and Learning

The "Learning by Doing" methodology emphasizes experiential learning. Its application involved: **1) Problem Statement:** A real case in Civil Aerodynamics where a commonly used structure for solar energy generation faces stability issues. **2) Idea Proposal:** Students individually propose solutions while reviewing relevant literature to identify fundamental concepts. **3) Sharing Ideas:** Group discussion and debate facilitated by the instructor. **4) Solution Development:** the practical approach includes dimensional analysis of the fluid-structural problem, design and construction of a simplified wind tunnel, scale model construction of the tracker and conducting tests and obtaining results. This approach enhances individual skills such as critical thinking, self-assessment, communication, and leadership while promoting teamwork and holistic problem-solving.

4.2. Research

The careful design, backed by years of wind tunnel experimentation, yields excellent results in determining critical flame speeds, enabling ambitious research campaigns. The DEMO-TRACK^{FW} also facilitates the use of advanced instrumentation, like laser distance meters, and introduces programming routines for data acquisition. A minor modification allows testing of non-perpendicular wind directions to the tracker.

ACKNOWLEDGEMENTS

This work is part of the project TED2021-130541B-C21 funded by MCIN/AEI/10.13039/501100011033, the European Union "NextGenerationEU"/PRTR and project PID2022-137630OB-C21 financed by MCIN/AEI /10.13039/501100011033/FEDER, UE.

REFERENCES

Bruner, J., Navarro, A., Maas, A., Reed, B., 2022. Locking Solar Tracker Bushing. San Luis Obispo.

Cárdenas-Rondón, J.A., Ogueta-Gutiérrez, M., Franchini, S., Manzanares-Bercial, R., 2023. Stability analysis of two-dimensional flat solar trackers using aerodynamic derivatives at different heights above ground. Journal of Wind Engineering and Industrial Aerodynamics 243. https://doi.org/10.1016/j.jweia.2023.105606

Gross, F., Luengo, M.R., Hennings, L., Landman, W., Balz, M., 2020. The impact of tracker structure on bifacial PV performance.

Hayne W. Reese, 2011. The Learning by Doing Principle 17, 1–19.

Kolb, D.A., 1984. Experiential Learning: Experience As The Source Of Learning And Development.

Martínez-García, E., Blanco-Marigorta, E., Parrondo Gayo, J., Navarro-Manso, A., 2021. Influence of inertia and aspect ratio on the torsional galloping of single-axis solar trackers. Engineering Structures 243. https://doi.org/10.1016/j.engstruct.2021.112682

Navarro-Manso, A. et al., Design become reality: the power of scale model experimentation, IV Int. Conference on Structural Engineering Education, Structural Engineering Education Without Borders, June 20-22, 2018, Madrid, Spain.

Rodríguez-Casado, C. et al., 2024. Experimental Benchmark for the 3D wind tunnel testing of torsional aeroelastic instabilities in single-axis solar trackers. Journal of Wind Engineering and Industrial Aerodynamics 253. https://doi.org/10.1016/J.JWEIA.2024.105838.

Rodríguez García, A.B., De Chile, S., López, L.J.R., 2014. Aprender Haciendo-Investigar Reflexionando: Caso De Estudio Paralelo En Colombia Y Chile, Revista Academia y Virtualidad.

Rohr, C., Bourke, P.A., Banks, D., 2015. Torsional Instability of Single-Axis Solar Tracking Systems, in:14th International Conference on Wind Engineering

Trinder, M., Jabbal, M., 2013. Development of a smoke visualization system for wind tunnel laboratory experiments. International Journal of Mechanical Engineering Education 41, 27–43. https://doi.org/10.7227/IJMEE.41.1.5

Valentín, D., Valero, C., Egusquiza, M., Presas, A., Egusquiza, E., 2022. Failure investigation of a solar tracker due to wind-induced torsional galloping induced torsional galloping. Engineering Failure Analysis 135.

Essential considerations when comparing unsteady time and frequency domain responses of structures

Romain Plasseraud[1] and Aymeric Perret du Cray[2]

[1]*setec tpi, Paris, France, romain.plasseraud@setec.com*
[2]*setec tpi, Paris, France, aymeric.perret-du-cray@setec.com*

SUMMARY:
This study offers an engineering perspective on comparing the unsteady response of structures evaluated in both time and frequency domains. It outlines key considerations to keep in mind when performing such comparisons. First, the validity of Davenport's peak factor is examined, emphasizing the impact of damping on the peak factor and the standard deviation of maximum displacement. Subsequently, the evolution of result accuracy relative to the number of simulations in the time domain is analyzed. Lastly, the assumptions underlying the frequency and time methods are contrasted by examining the spectral density curves of the generalized forces. The along-wind response of the Normandie bridge serves as an illustrative example.

Keywords: turbulent wind, fluid-structure coupling, indicial functions

1. MODEL

1.1. Frequency method

In order to calculate aeroelastic forces in the frequency domain, Scanlan's coefficient functions H_i^*, P_i^* and A_i^*, whose values are measured in wind tunnels, are widely used (Caracoglia and Jones, 2003; Scanlan, 1993). The steady-state aeroelastic forces per unit length are given by equations 1, 2 and 3. L is the lift, D the drag, M the bending moment, ρ the density, U the mean velocity, $K = \frac{B\omega}{U}$ the reduced frequency, B the deck width, h and p the deck vertical and horizontal displacements and α the section rotation. These expressions are only valid for sinusoidal movements. The notation $\dot{()}$ designates the first time derivative.

$$L^{aero} = \tfrac{1}{2}\rho U^2 B\left(KH_1^*(K)\tfrac{\dot{h}}{U} + KH_2^*(K)\tfrac{B\dot{\alpha}}{U} + K^2H_3^*(K)\alpha + K^2H_4^*(K)\tfrac{h}{B}\right) \tag{1}$$

$$D^{aero} = \tfrac{1}{2}\rho U^2 B\left(KP_1^*(K)\tfrac{\dot{p}}{U} + KP_2^*(K)\tfrac{B\dot{\alpha}}{U} + K^2P_3^*(K)\alpha + K^2P_4^*(K)\tfrac{p}{B}\right) \tag{2}$$

$$M^{aero} = \tfrac{1}{2}\rho U^2 B^2\left(KA_1^*(K)\tfrac{\dot{h}}{U} + KA_2^*(K)\tfrac{B\dot{\alpha}}{U} + K^2A_3^*(K)\alpha + K^2A_4^*(K)\tfrac{h}{B}\right) \tag{3}$$

1.2. Time method

In the time domain, Scanlan suggests the use of indicial functions to describe the response of the structure (Scanlan, 1993). These indicial functions φ link forces to displacements by means of a convolution product (see equations 4, 5 and 6) (Caracoglia and Jones, 2003; Zhang et al., 2011). Forces are given as a function of dimensionless time $s = \frac{Ut}{B}$. Note that the derivatives $()'$ are given with respect to the dimensionless time s.

$$L^{aero}(s) = \tfrac{1}{2}\rho U^2 B\left[\int_0^s \varphi_{L\alpha}(s-\sigma)\,\alpha'(\sigma)\,d\sigma + \int_0^s \varphi_{Lh}(s-\sigma)\,\tfrac{h''(\sigma)}{B}d\sigma\right] \tag{4}$$

$$D^{aero}(s) = \tfrac{1}{2}\rho U^2 B\left[\int_0^s \varphi_{D\alpha}(s-\sigma)\,\alpha'(\sigma)\,d\sigma + \int_0^s \varphi_{Dp}(s-\sigma)\,\tfrac{p''(\sigma)}{B}d\sigma\right] \tag{5}$$

$$M^{aero}(s) = \tfrac{1}{2}\rho U^2 B^2\left[\int_0^s \varphi_{M\alpha}(s-\sigma)\,\alpha'(\sigma)\,d\sigma + \int_0^s \varphi_{Mh}(s-\sigma)\,\tfrac{h''(\sigma)}{B}d\sigma\right] \tag{6}$$

Different approximations have been suggested for these indicial functions (Bucher and Lin, 1988; Patron Solares, 1998; Zhang et al., 2011). Jones approximation is used here (see equation 7) because it simplifies inverse Fourier transforms by using exponential functions.

$$\varphi_k(s) = a_{0,k} - \sum_{i=1}^{n} a_{i,k} e^{-b_{i,k} s} \tag{7}$$

Some authors (Patron Solares, 1998; Zhang et al., 2011) have developed methods for avoiding the storage of the memorial terms of equation 4 to 6 by using a recursive formulation. For the sake of simplicity, only α's contribution to aeroelastic lift is considered in equation 8. It is then possible to isolate the memorial terms (superscript *). An approximation of the integral then allows these memorial terms to be calculated recursively (see equation 9).

$$L_\alpha(s) = \tfrac{1}{2}\rho U^2 B \times a_{0,L_\alpha}\alpha(s) - \sum_{i=1}^{n} L^*_{\alpha,i}(s) \; ; \; L^*_{\alpha,i}(s) = \tfrac{1}{2}\rho U^2 B \times \int_0^s a_{i,L_\alpha} e^{-b_{i,L_\alpha}(s-\sigma)} \alpha'(\sigma) d\sigma \tag{8}$$

$$L^*_{\alpha,i}(s + \Delta s) \approx L^*_{\alpha,i}(s) \times e^{-b_{i,L\alpha}\Delta s} + \tfrac{1}{2}\rho U^2 B \times \Delta s \times \left[a_{i,L_\alpha} e^{-b_{i,L_\alpha}(\frac{\Delta s}{2})} \alpha'(s + \tfrac{\Delta s}{2}) \right] \tag{9}$$

To determine the values of the indicial functions as a function of the scaled time, the coefficients a_i,b_i are optimized on the Scanlan coefficient curves, using the least-squares method (see figure 1) (Caracoglia and Jones, 2003). The final step is to generate a turbulent wind signal from a statistical model. The harmonic wave superposition method (Guillin and Cremona, 1997; Shinozuka, 1972) is used to make a Monte Carlo simulation of turbulence.

2. CASE STUDY

To highlight key considerations when comparing unsteady time and frequency domain responses of structures, the case study of the central steel section of the deck Normandie bridge is adopted[1]. This example is noteworthy as it involves a flexible structure with low damping, for which the designers were particularly concerned about the effects induced by transverse displacement.

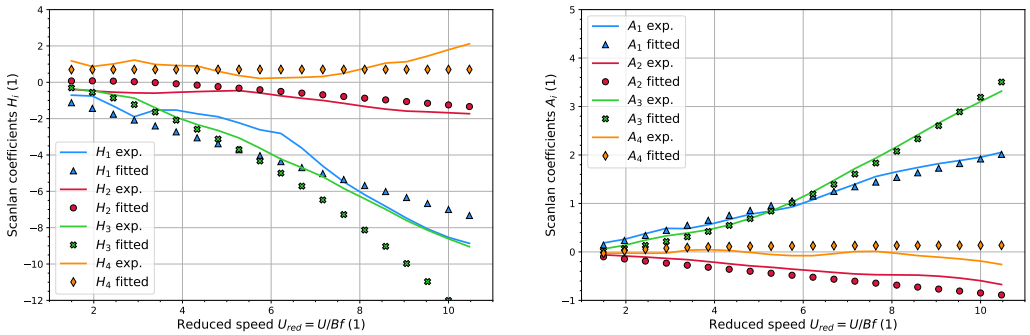


Figure 1. Optimization of indicial functions parameters on Scanlan coefficient curves

2.1. Validity of the Davenport peak factor expression for low dampening rate

Some authors (Guillin and Cremona, 1997) have identified significant discrepancies between the amplitude values derived using the Davenport peak factor and the maximum temporal amplitude, highlighting the limitations of this peak factor for narrow-band processes (Huang et al., 2013).

[1]This part of the deck is 624m long and 21.2m wide. Sinusoidal modal deformation, perfectly correlated wind (adopted here to simplify the analysis) are assumed. The parameters of the Von Kármán turbulence model are the following : $U_{moy} = 44$ m/s, $\sigma_u = 3.96$ m/s and L_u = 200 m. Mode 1 characteristics: $f_1 = 0.151Hz$, $m_1^* = 4706$ T, $\xi_1 = 0.3$ %, $C_X = 0.08$ (Patron Solares, 1998).

To evaluate the expression of the Davenport peak factor, a single-degree-of-freedom damped harmonic oscillator subjected to a horizontal turbulent wind force is analyzed. Only the horizontal component u of the turbulence is considered. The harmonic oscillator's characteristics are selected to match to the first mode of the Normandy bridge deck. A Monte Carlo simulation is conducted with 10000 samples of 600s each, using a time step of 0.1s (see figure 2).

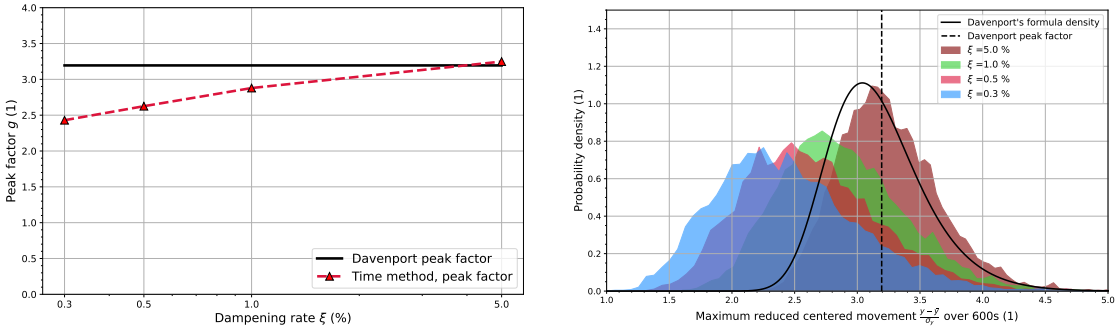


Figure 2. Comparison of the maximum displacement computed with the Davenport peak factor and the time method

In the case of a narrow-band process, the Poisson approximation for the threshold crossing frequency is no longer valid (Huang et al., 2013). At low damping, both a significantly lower peak factor and a significantly larger standard deviation of the response maximum than predicted by Daveport's probability density (Davenport, 1964) are observed. The effect is all the more pronounced when the response is dominated by the resonant component (the quasi-static component being broadband).

2.2. Study of the accuracy of results in relation to simulation time

The choice of simulation time is crucial in computations employing the time method. Let n_{95} represent the value such that $\mathbb{P}(\mu < \bar{y}_{max,N} + n_{95,N} \times \sigma_{y_{max,N}}) = 0.95$, with μ the expectation of the maximum displacement and $\bar{y}_{max,N}$ and $\sigma_{y_{max,N}}$ estimators on N samples. To determine the minimum number of simulations required, the variation of n_{95} as a function of the number of samples of $T_0 = 600$ s used for the estimator is illustrated in figure 3. For a given accuracy, the lower the damping, the greater the number of simulations required.

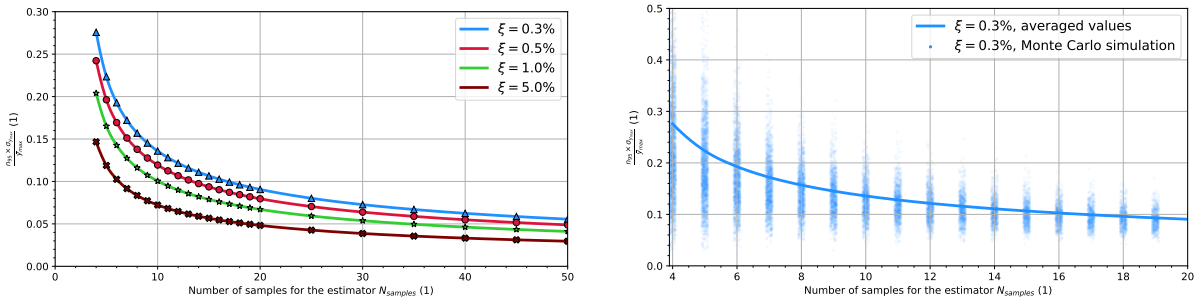


Figure 3. Evolution of $\frac{n_{95} \times \sigma_{ymax}}{\bar{y}_{max}}$ with the number of 600s samples $N_{samples}$

2.3. Comparison of generalized force spectral density for the time and frequency method

In this section, the 3-degree-of-freedom model of the Normandie bridge is employed. The turbulence and unsteady contribution on the generalized force p_j can be separated. For vertical displacement h, the generalized force p_h^{aero} can be written as equation 10, with $\psi_h(x)$ as the modal deformation. Aeroelastic lift L^{aero} is defined by equation 4 for the time method and equation 11 for the frequency method[2].

[2]Coupling terms are neglected in relation to equation 1, an approximation usually done.

Figure 4 compares the power spectral densities[3] of the generalized forces associated with vertical displacement h and rotation α. Neglecting coupling terms in the frequency method's aeroelastic force expression alters the spectral density curves (figure 4).

$$\ddot{y}_j(t) + 2\xi_j\omega_j\dot{y}_j(t) + \omega_j^2 y_j(t) = \frac{p_j(t)}{m_j^*} = \frac{p_j^{turb}(t)+p_j^{aero}(t)}{m_j^*} \quad ; \quad p_h^{aero}(t) = \int_0^L L^{aero}(x,t)\psi_h(x)dx \tag{10}$$

$$L_{lin}^{aero} = \frac{1}{2}\rho U^2 B\left(KH_1^*\frac{\dot{h}}{U} + K^2H_4^*\frac{h}{B}\right) \tag{11}$$

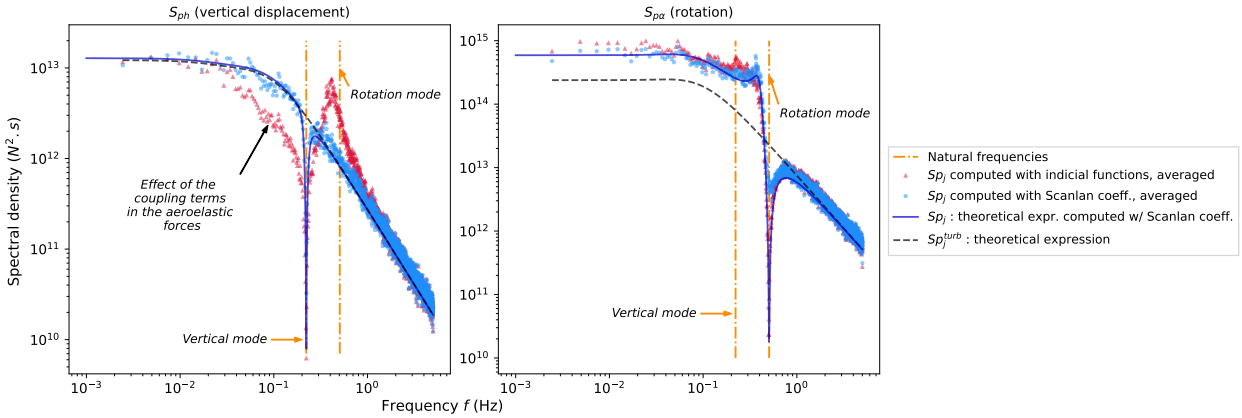


Figure 4. Power spectral density of generalized forces S_{ph} and $S_{p\alpha}$

3. CONCLUSIONS

For narrow-band processes, Davenport's peak factor, as used in EN 1991-1-4 (Appendix B, §B.2), notably overestimates the maximum response. Secondly, it has been shown that for the temporal method, the simulation time to be adopted depends on the structural damping. Finally, the influence of the frequency method's assumptions not to consider coupling terms in unsteady forces and to take $H_k(\omega) = H_k(\omega_j)$ has been highlighted. However, despite these simplifications, the frequency method remains significantly faster than the time method, making it a compelling approach for practical applications.

REFERENCES

Bucher, C. G. and Lin, Y. K., 1988. Stochastic stability of bridges considering coupled modes. Journal of Engineering Mechanics 114, 2055–2059.

Caracoglia, L. and Jones, N. P., 2003. Time domain vs. frequency domain characterization of aeroelastic forces for bridge deck sections. Journal of Wind Engineering and Industrial Aerodynamics 91, 371–402.

Davenport, A. G., 1964. Note on the distribution of the largest value of a random function with application to gust loading. Proceedings of the Institution of Civil Engineers 28, 187–190.

Guillin, A. and Cremona, C., 1997. Développement d'algorithmes de simulation de champs de vitesse au vent. OA27, LCPC :1–43, 61–107.

Harris, C. M., 2010. Shock and vibration handbook. McGraw-Hill :22.1–22.22.

Huang, G., Chen, X., Li, M., and Peng, L., 2013. Extreme value of wind-excited response considering influence of bandwidth. Journal of Modern Transportation 21, 125–134.

Patron Solares, A., 1998. Modélisation numérique de la tenue au vent des ponts souples. phdthesis, Marne-la-vallée, ENPC :1–49, 72–162.

Scanlan, R. H., 1993. Problematics in formulation of wind-force models for bridge decks. Journal of engineering mechanics 119, 1353–1375.

Shinozuka, M., 1972. Monte Carlo solution of structural dynamics. Computers & Structures 2, 1–23.

Zhang, Z., Chen, Z., Cai, Y., and Ge, Y., 2011. Indicial functions for bridge aeroelastic forces and time-domain flutter analysis. Journal of Bridge Engineering 16, 546–557.

[3]The power spectral density was computed using the ensemble averaging procedure (Harris, 2010).

Investigating the effect of vegetation on PV trackers design and operation

Tiziano Leone[1], Federico di Lenardo[1], Giorgio Frontini[1], Sara Muggiasca[1]

[1]*Department of Mechanical Engineering, Politecnico di Milano, Milan, Italy,*
tiziano.leone@polimi.it, federico.dilenardo@polimi.it, giorgio.frontini@polimi.it,
sara.muggiasca@polimi.it

SUMMARY:
The study explores the aeroelastic stability of photovoltaic (PV) trackers, in particular when installed above crops in agricultural settings. The primary issue addressed is the stiffness-driven instability occurring at low angles of attack due to wind loads on PV panels which are mounted on torque tubes. The study employs a Computational Fluid Dynamics (CFD) model based on the URANS (Unsteady Reynolds-Averaged Navier-Stokes) approach, developing a low-cost method to investigate aerodynamic coefficients at low angles of attack in a variety of different configurations such as torque tube geometry and positioning, ground proximity, and crop typology, validating the method against wind tunnel experiments. The research offers insights into optimizing PV tracker designs to improve their structural performance, contributing to better engineering practices for these systems.

Keywords: PV Trackers, Aeroelastic instablity, RANS

1. INTRODUCTION

Due to the increase in demand for sustainable solutions for energy production, photovoltaic (PV) panels are experiencing a surge in interest over the last decades. In dense areas, however, the land space needed to install large solar farms is expensive, thus the industry is moving towards exploring solutions that can transform land that is currently being used only for agricultural purposes in a dual-use configuration, by installing PV panels above the crops. The PV panels must then be installed at higher height than in typical solar farms, thus experiencing higher loads due to the wind action. Moreover, to take full advantage of the solar energy all throughout the day these panels make use of tracking systems instead of the more standard ground-mounted configuration. The different mean of constraining the system, by using a torque tube, leads to a mechanical system prone to aeroelastic instabilities (Frontini et al., 2022; Taylor et al., 2024): stiffness-driven at low static angles of attack and damping-driven for angles between 10° and 30°. At low angles of attack, which are usually chosen as stow position during high winds (Young et al., 2020), it is critical to assess correctly the slope of the moment coefficient C_M due to its leading role in the onset of stiffness-driven instability, since the critical velocity can be expressed as: $U_{crit} = \sqrt{k_\theta/(1/2\rho L^2 K_M)}$, where k_θ is the torsional stiffness of the system, ρ the density of air, L the length of the panel and K_M the derivative of the moment coefficient. As a last remark, these systems present a wide range of possible designs and are operated in different conditions. Some examples are the large variations we can observe in sizing, geometry and positioning of the torque tube, ground proximity, spacing between panel rows, angle of attack, wind condition, type of crops cultivated underneath. Regarding the geometry and positioning of the torque tube, the available literature is lacking, and for assessing the

stiffness-driven instability its effect cannot be discounted (Young et al., 2020). In any case effort is still needed in coming up with standard practices for testing both from the experimental (Aly and Bitsuamlak, 2013) and the computational point of view (Eshete et al., 2024).

In this study we come up with a CFD model inspired by wind tunnel practice to explore the dependency of aerodynamic coefficients of the panel at low angles of attack on a wide range of possible configurations for torque tube placement and geometry, ground proximity, vegetation. This model is based on the URANS formulation validated through wind tunnel testing, allowing to test a wide range of cases. An attempt is also proposed in assessing the occurrence of damping-driven instability for higher stow angle configurations, still with a target of low computational cost, to assess quickly different designs and operational conditions.

2. METHODOLOGY

Since the aim of the work is to come up with a method suitable for current engineering practice the choice was to employ a CFD model based on the URANS formulation, which allows to test in reasonable time a wide range of parameters. The analysis focused on the angles of attack between -10° and 10°, a situation in which the URANS formulation still shows satisfactory performances. For higher angles of attack the presence of large detachments and recirculation zones would make such a formulation less suited (Güemes et al., 2021). The presence of the vegetation is modelled through a Darcy-Forchheimer porosity model, tuned to represent the blockage effect of various crops, validated for a particular configuration with experimental data, and expanded to other crop typologies with coefficients found in literature.

2.1. Experimental Setup

Experiments have been carried out in two major configurations. Pressure coefficients have been examined in the park model immersed in the ABL, while the static and dynamic stability has been studied on a sectional model in the low-turbulence test section inside the wind tunnel at Politecnico di Milano (GVPM). For the park model, the pressure loads have been studied at different panel heights and stow angles, and the effect of the vegetation has been modelled through the addition of porous metal sheets underneath the photovoltaic panels.



Figure 1. Pictures from the experimental tests. From left to right: high panel height park model; medium panel height with vegetation modeled with a metal sheet; sectional model.

2.2. CFD Method

The simulations are mainly carried out on the 2D geometry of the panel-torque tube assembly. The method employed for resolving the fluid flow is the URANS k-omega SST model implemented in

the software OpenFOAM. The mesh is discretized with a mix of tetrahedral and hexahedral ele-

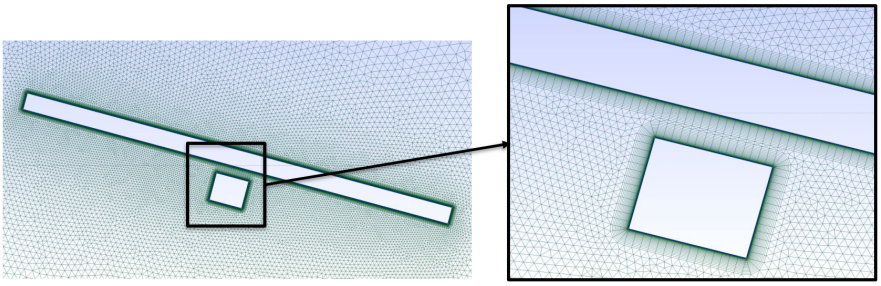


Figure 2. Mesh detail of the panel-torque tube assembly

ments, with the boundary layer on the object resolved up to $y^+ = 1$. An image of the mesh around the panel and a detail of the torque tube is show in Fig. 2. The inflow conditions vary depending on which experimental setup is object of the comparison, thus by imposing an atmospheric boundary layer profile when studying the effect of the vegetation or the distance from the ground, while imposing a free-stream velocity when comparing with the sectional model. The vegetation effect is modelled using a Darcy-Forchheimer porosity model in which the coefficients are validated using the corresponding experiments and extrapolated to represent different sizes and types of vegetation, based on their Leaf Area Density (*LAD*) and drag (Tamimi and Kacira, 2013), focusing on typical crops such as tomato plants (S. Sase et al., 2012), or trees (Buccolieri et al., 2018). The momentum sink term in the Navier-Stokes equation on the i-th component is defined as in Eq. (1):

$$S_i = -\rho LADC_d U u_i \tag{1}$$

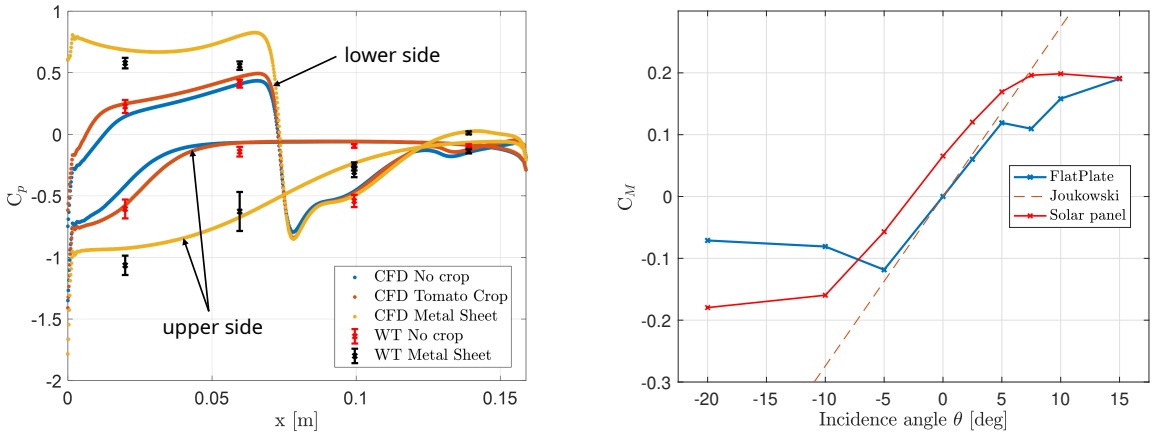
where ρ is the fluid's density, C_d is the drag coefficient depending on the type of crop, U is the wind velocity in the along-wind direction and u_i the instantaneous velocity in the i-th direction.

3. RESULTS

The results will be shown in terms of integral aerodynamic coefficients and local pressure measurements on the panel varying the angle of attack depending on design and the configuration. In Fig. 3a you can see an example of the results obtained for the pressure coefficients on the panels varying the blockage due to the crops. We can see that a high blockage changes completely the behavior of the pressure coefficients, as shown both in the experimental and numerical model. Moreover, carefully reviewing the slope of the momentum coefficient is key for a correct dimensioning of the torque tube. For example, you can see in Fig. 3b how the torque tube presence shifts the moment coefficient C_M around the 0° angle of attack (α) and changes its slope with respect to the flat plate geometry, compared also to Jouwkowski theorem.

4. CONCLUSIONS

Overall, the CFD model seems promising in evaluating the aerodynamic coefficients and stability around small angles of attack with a very reduced cost, allowing to explore a wide range of possible designs an setups. The preliminary results show that the vegetation presence creates a



(a) **(b)**

Figure 3. Two examples of results: **(a)**: dependency of the pressure coefficients on the presence of the blockage for a panel with torque tube at $\alpha = 0°$; **(b)**: impact of the torque tube on the momentum coefficient around $\alpha = 0°$

non negligible pressure gradient which impacts the coefficients. Moreover, for low angles of attack the geometry and positioning of the torque tube must be taken into account for assessing the aeroelastic stability of the system.

REFERENCES

Aly, A. M. and Bitsuamlak, G., Dec. 2013. Aerodynamics of ground-mounted solar panels: Test model scale effects. en. Journal of Wind Engineering and Industrial Aerodynamics 123, 250–260.

Buccolieri, R., Santiago, J.-L., Rivas, E., and Sanchez, B., Apr. 2018. Review on urban tree modelling in CFD simulations: Aerodynamic, deposition and thermal effects. en. Urban Forestry & Urban Greening 31, 212–220.

Eshete, T., Geleta, T., and Bitsuamlak, G., Oct. 2024. Towards benchmark validation of LES for ground-mounted solar panel wind loads. en. Journal of Wind Engineering and Industrial Aerodynamics 253, 105843.

Frontini, G., Calamelli, F., Muggiasca, S., Argentini, T., and Belloli, M., 2022. Solar trackers analysis: a parametric study to evaluate aeroelastic effects inside a photovoltaic park array. Proceedings of 8th EUROPEAN-AFRICAN CONFERENCE ON WIND ENGINEERING (8EACWE).

Güemes, A., Fajardo, P., and Raiola, M., Mar. 2021. Experimental Assessment of RANS Models for Wind Load Estimation over Solar-Panel Arrays. en. Applied Sciences 11, 2496.

S. Sase, M. Kacira, T. Boulard, and L. Okushima, 2012. Wind Tunnel Measurement of Aerodynamic Properties of a Tomato Canopy. en. Transactions of the ASABE 55, 1921–1927.

Tamimi, E. and Kacira, M., Oct. 2013. Analysis of climate uniformity in a naturally ventilated greenhouse equipped with high pressure fogging system using computational fluid dynamics. en. Acta Horticulturae, 177–183.

Taylor, Z. J., Feero, M. A., and Browne, M. T., 2024. Aeroelastic instability mechanisms of single-axis solar trackers. Journal of Wind Engineering and Industrial Aerodynamics 244, 105626.

Young, E., He, X., King, R., and Corbus, D., Nov. 2020. A fluid-structure interaction solver for investigating torsional galloping in solar-tracking photovoltaic panel arrays. en. Journal of Renewable and Sustainable Energy 12, 063503.

Evolutionary shape against vortex shedding

Olivier Flamand [1], Andrea Pedrazzini [2], Elsa Caetano [3]

[1]*CSTB, Nantes, France, olivier.flamand@cstb.fr*
[2] *ingegneri pedrazzini guidotti sagl, Lugano, Switzerland, andrea.pedrazzini@ing-ppg.ch*
[3]*FEUP, Porto, Portugal, ecaetano@fe.up.pt*

SUMMARY:
A slender footbridge over the river Limmat, north-west of Zürich, was designed to span 123m above still water. To minimize material usage, it was imagined as one single beam with section increasing from side to middle span, following the increase of bending moment. Wind can be quite uniform above this surface of small roughness, promoting the possibility of excitation by vortex shedding but, on the other hand, the height of the structure opaque to wind evolves from one side to the other making ViV excitation inhomogeneous along the span. It was not possible at the design stage to assess if vortex shedding was due to happen or not on this evolutionary shape. To resolve this important feature a boundary layer wind tunnel test with a full aeroelastic model was made at a scale 1/65, with different levels of wind turbulence.
With this model it was possible to assess that no vortex shedding excitation was forming on the footbridge for moderate wind speeds thanks to the evolutionary shape. A study was subsequently undertaken, using the same aeroelastic model with incremental modification of the shape, to verify which ratio of shape evolution was necessary to desynchronize ViV on such a structure.

Keywords: vortex shedding, bluff body, shape evolution, tappering

1. OVERVIEW OF THE AEROELASTIC MODEL

The model was built at a scale 1/65 from a rectangular aluminum central beam 14.91mm wide and 12.80mm high of constant section and a length 1898 mm. It was made of alloy 1017 T6, carefully machined. It was completed by 35 cladding elements made of polyamide sintered powder by 3D printing, reproducing the outside shape of the footbridge, respecting the weight of the footbridge at the reduced scale 1/65 with a 1mm gap between two adjacent parts.

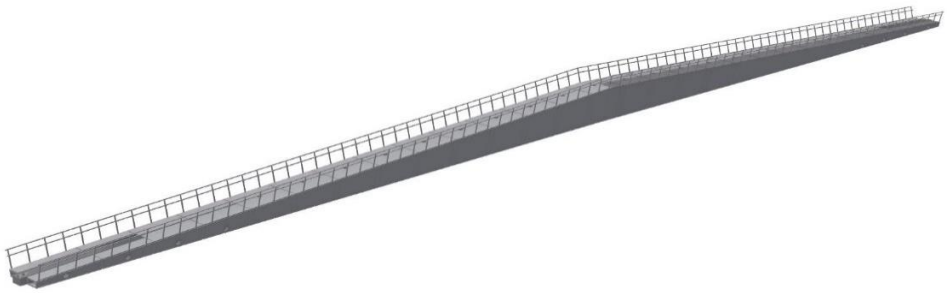


Figure 1. shape of the overall model.

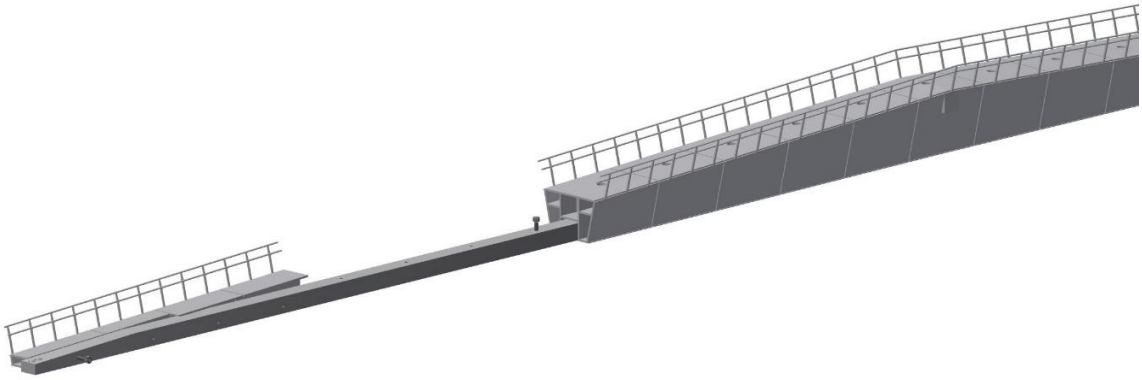


Figure 2. Principle of the cladding elements added on the continuous metallic spine.

The model was carefully designed to reproduce the mode shapes of the 3 first modes of the structure, with a reduced structural damping. The initial structural damping obtained for the 3 first modes was as low as ξ =0.04% of critical, what is much lower than the natural structural damping of such structure. This damping was kept low for a first series of tests to check the possibility of occurrence of vortex shedding, it was tuned to the value ξ =0.3% of critical in a second stage, to fairly reproduce the nominal damping of the bridge. The modal form of the three first modes was close to the one provided by the FE model of the real footbridge.

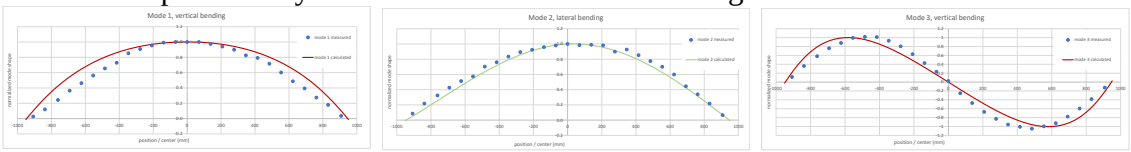


Figure 3. Mode shapes on the model (dots) compared with the calculated ones of the real footbridge.

The mode with the lowest frequency, vertical bending with one wave, is the most relevant one considering the excitation by vortex shedding.

2. WIND TUNNEL TESTS

The initial wind tunnel series of tests was performed with a complete representation of surroundings including orography and vegetation and real wind turbulence characteristics. In this case no vortex shedding was observed, even when the structural damping of the model was minimum and the turbulence intensity reduced to its lowest value, corresponding to a category 0 terrain in the Eurocode (wind coming from sea or large lake). Few wind incidences have been reproduced.

For the second series of wind tunnel tests the model will be settled 1m above ground without any turbulence generator upstream, to recreate a uniform and not turbulent flow. The aim is not to recreate a peculiar location for a peculiar bridge, but to make a theoretical case of a slender beam with a shape that can be changed step by step, to look for the boundary in shape evolution. Only wind normal to the beam axis will be reproduced. Results are not available yet, but will be presented at the conference.

The aim is to find which rate of evolution of the shape of the bridge is sufficient to decorrelate the vortex shedding excitation along the span. This case is quite new, as the existing references of

similar studies all refer to vertically standing structures (as chimneys or towers), all subject to a mean wind speed varying with height, due to the boundary layer above ground. In the case of a bridge, the span being horizontal, there is no such variation of the mean wind speed along the length. Practical application of this research results by bridge designers can be of main importance.



Figure 4. Model in the BLWT for the first series of tests.

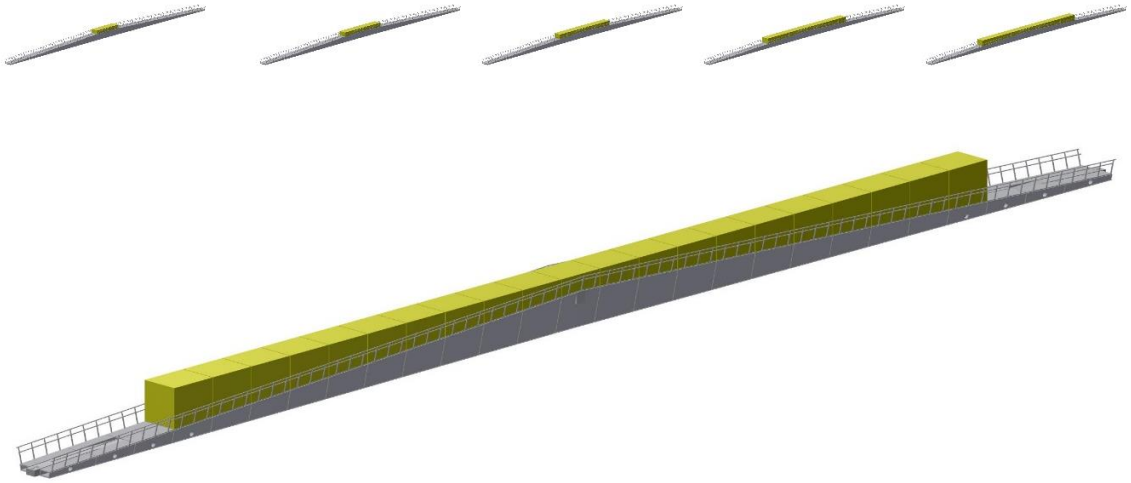


Figure 5. Successive additions on the model to look for the limit in shape evolution prone to vortex shedding.

REFERENCES

Li Y., Zhu Y., Chen F. B., Li Q.-S, 2023. Aerodynamic loads of tapered tall buildings: Insights from wind tunnel test and CFD. Structures, Volume 56, 104975.

Amerio L., Argentini T., Bernini L., Perotti F., Zasso A. , 2017. Wind induced vibrations of a high tapered obelisk: wind tunnel tests, numerical analysis and design of countermeasures. Procedia Engineering, Volume 199

Kima Y.M. , Youa K.P., Kob N.H., 2008. Across-wind responses of an aeroelastic tapered tall building. Journal of Wind Engineering and Industrial Aerodynamics 96, 1307–1319

Brusco S., Bagnara A., Cammelli S., Piccardo G., 2023. Experimental investigations on the vortex-shedding from a highly tapered circular cylinder in smooth flow. In Journal of Fluids and Structures 122.

An aerodynamic mitigation measure for wind-induced vibration of a cable-supported photovoltaic farm

Haiwei Xu [1], Linyuan Shao [2], Wenjuan Lou[3]

[1] *College of Civil Engineering and Architecture, Zhejiang University, Hangzhou, China, Email: haiweix@zju.edu.cn*
[2] *College of Civil Engineering and Architecture, Zhejiang University, Hangzhou, China, Email: shaoly@zju.edu.cn*
[3] *College of Civil Engineering and Architecture, Zhejiang University, Hangzhou, China, Email: louwj@zju.edu.cn*

SUMMARY
To deal with the global energy crisis, photovoltaic (PV) power generation has become increasingly popular in recent years. The cable-suspended PV structure was proposed and quickly attracted market attention, due to its large span and good site adaptability. However, these flexible structures are vulnerable to wind loading. Most of previous attempts at vibration control may increase the construction cost and affect the competitiveness of a solar farm. Therefore, an innovative aerodynamic measure involving a spoiler to mitigate the excessive vibration of a cable-supported PV array under wind action was proposed. An aeroelastic wind tunnel test was conducted on a PV array with and without spoilers. The wind-induced vibration (WIV) characteristics of the PV array were demonstrated and effects of the parameters of spoilers on mitigation of WIV were investigated. The study results show that large WIV is prone to occur at the windward midspan PV module. Setting a spoiler with a large tilt angle will be conducive to WIV suppression of a cable-supported flexible PV farm, while increasing the tilt angle could, in general, improve the WIV performance.

Keywords: Cable-suspended photovoltaic array, Spoiler, Aeroelastic model

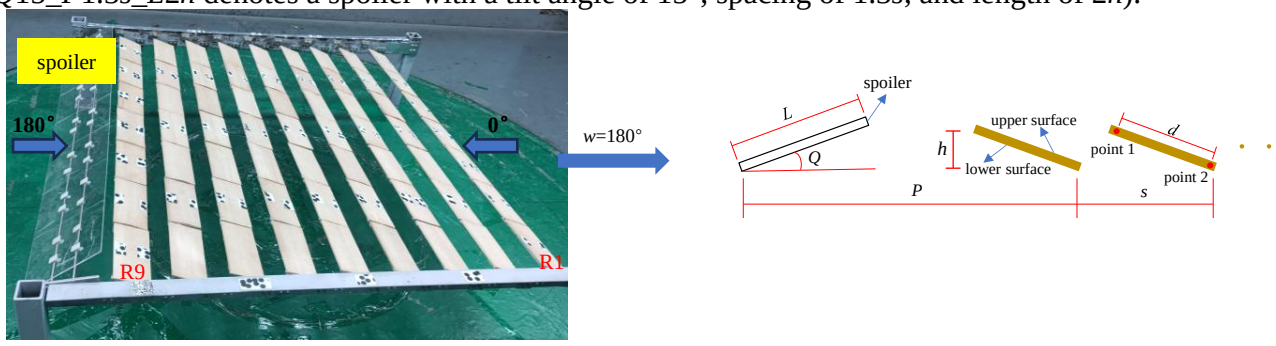
1. INTRODUCTION

To cope with the challenging of global climate change and energy crisis, solar power as a clean and renewable source of energy has been widely used in power generation, leading to a boom in the number of photovoltaic (PV) power plants in recent years. To meet construction needs in complex sites where a traditional beam-supported structure is difficult to fit in, a cable-suspended structure has been increasingly applied to PV power plants, due to its large span and efficient space utilization. This flexible structure has a nature of light weight and low damping, which is therefore vulnerable to wind loading. Wind-induced excessive vibration of cable-suspended PV modules has been reported frequently during strong winds, which is the main reason for the failure and cracking of PV modules. Therefore, suppression measures should be taken to reduce the wind-induced vibration (WIV) of cable-suspended PV systems. most of existent studies rely on strengthening the structure stiffness by adding additional stable cables or lateral connectors(Jiaqi Liu et al., 2023; Xu-Hui He et al., 2021). Although these methods of suppression are effective, they will increase the construction cost. Except for enhancing support structure, using aerodynamic optimization to reduce wind action is a simpler and more cost-

effective way for WIV mitigation of PV structure. which was widely applied in wind-resistant design of high-rise buildings (Bernardini et al., 2015; Elshaer et al., 2017)and bridge(Hu et al., 2019; Rui Wang et al., 2019). For WIV mitigation of PV structure, aerodynamic measures were rarely studied, Thus, the WIV suppression measure was proposed based on an aerodynamic mitigation device (*i.e*. a spoiler). Aero-elastic wind tunnel testing was conducted on a large cable-supported PV array to show the WIV characteristic with and without spoiler, aiming to providing references for the vibration mitigation design of cable-supported PV structures.

2. AEROELASTIC WIND TUNNEL TEST OF A PV ARRAY

A cable-supported PV array (9 rows by 7 columns) measuring 15.3 m (span) × 3.6 m (height) ×13 m (length) was adopted to study the WIV characteristics. The aeroelastic test was conducted in the ZD-1 boundary layer wind tunnel at Zhejiang University. An aeroelastic model with a geometric scale of 1:10 was designed, as shown in Figure 1(a). The PV module had a tilt angle of 20° and was made from light wood so that the model measured 200 mm (length) × 100 mm (width) ×4 mm (thickness). The row and column spacings of the PV arrays were 150 mm(*s*) and 5 mm in the model, respectively, as shown in Figure 1(b). Aeroelastic wind tunnel tests were conducted for the spoiler with different tilt angles (*Q*), lengths (*L*), and spacings (*P*). The spacing(*P*) is the distance between the spoiler and the first row of the PV modules, where *h* is the vertical height of the PV modules, and *s* represents the row spacing of the PV array. Each PV module was fixed to the cable at four corners. The scaled cable was manufactured by steel wire and supported by rigid frames at each of the two ends. The initial cable pretension force (about 27 N) giving a sag ratio of 1/174 was applied by connecting each cable to a weight through a pulley. Once the pretension was applied, the two ends of a cable would be fixed at the frame. (For ease of discussion, the test cases are indicated by symbolic abbreviations. For example, *Q*15_*P*1.3*s*_*L*2*h* denotes a spoiler with a tilt angle of 15°, spacing of 1.3*s*, and length of 2*h*).



(a) Spoiler parameters (b) Spoiler equipment

Figure 1. The setting and specific parameters of the spoiler

The wind-induced three-dimensional displacements of PV modules at typical location of the array were recorded by visual displacement analyzer (VDA) to acquire the displacements at 70 monitoring points on the PV modules synchronously. Additionally, a uniform inflow with a mean wind speed of 9 m/s and a turbulence intensity of 10 % was used. Considering the array symmetry, typical and unfavorable wind directions (i.e. w = 0°~45° and w = 135°~180°) were tested with an increment of 15°. To study the aerodynamic mitigation effect of the spoiler, aeroelastic wind tunnel tests were conducted for the spoiler with different parameters.

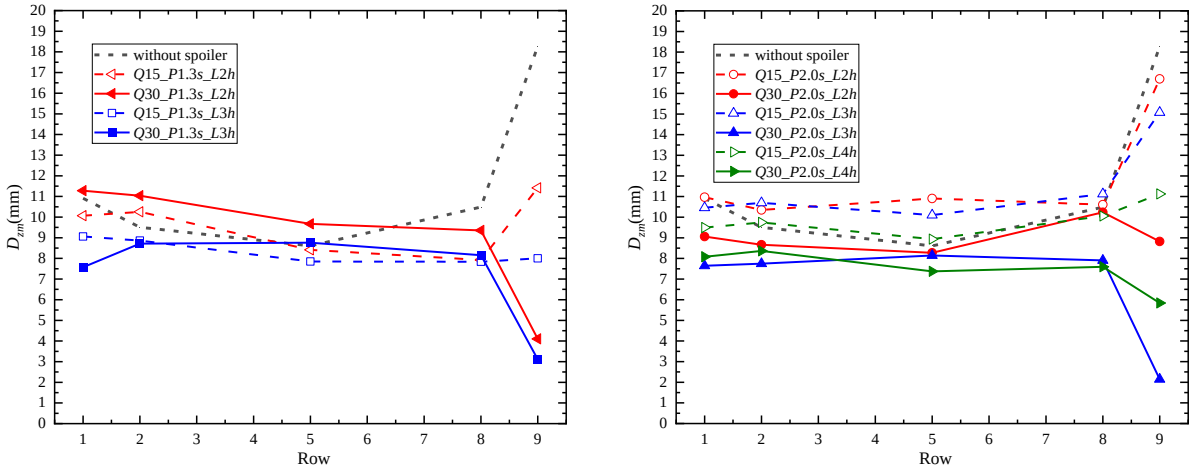
3. WIV CHARACTERISTICS OF A CABLE-SUSPENDED PV ARRAY

For all tested wind directions, Table 1 lists the maximum mean vertical displacements of the PV arrays without spoiler, and its locations as well as the corresponding mean torsional displacements. The most unfavorable positive and negative vertical responses occur in the middle span of the first and ninth rows of the PV arrays, respectively. Compared to the vertical vibration, the torsional response is minor and has an insignificant contribution to the WIV behaviour of the studied PV structure.

Table 1. The maximum displacement of PV arrays without spoiler under different wind directions

Wind direction w (°)	Maximum mean vertical displacement $D_{zm\text{-}max}$(mm)	Current location	Mean torsional displacement D_{tm}(°)
0	-14.4	middle span, R1	-1.0
15	-12.5	middle span, R1	-0.8
30	-13.3	middle span, R1	-0.8
45	-8.7	middle span, R1	-0.8
135	12.3	middle span, R1	1.0
150	16.8	middle span, R9	1.3
165	17.3	middle span, R9	1.3
180	18.3	middle span, R9	1.3

To investigate the effects of spoiler tilt angles on aerodynamic optimization, Figure 2 plots D_{zm} of the PV array at five typical rows (R1, R3, R5, R7, R9) under different tilt angles and two spacings (P = 1.3s and 2.0s). The corresponding results of PV modules without a spoiler are also given in Figure 2 (dashed line). It can be observed that the maximum WIV (in R9) of the PV array reduced by using different spoilers. This is because that for a pure PV array, wind pressure and wind suction on the lower and upper surfaces of the windward first PV row will be combined to produce a large net wind load; however, the presence of the spoiler alters the separation characteristics of the approaching flow so that both surfaces of the windward PV module are subjected to wind suction, leading to a neutralized net wind load.



(a) P = 1.3s (b) P = 2.0s

Figure 2. Effect of the spoiler tilt angle on the mean vertical wind vibration displacement

Compared to the tilt angle Q = 15°, the mitigation effect on the maximum WIV is much better at Q = 30° for both spacing cases, as shown in Figure 2. This could be attributed to the enhanced separation vortex or re-attachment flow generated by a spoiler with a large tilt angle, which will in turn increase the suction on the lower surface of the windward module and thereby reduce the total suction on the PV module. However, it is worth noting that the spoiler caused different flow separation patterns at the windward PV row, which may cause a slight increase in the vibration response of the rear rows (*e.g.* *Q*30_*P*1.3*s*_*L*2*h*), but it still remains relatively small compared to the maximum vibration amplitude of the original PV array.

4. CONCLUSIONS

The WIV characteristics of a cable-supported PV array at different array zones were studied by aero-elastic wind tunnel test. The effects of spoiler parameters in WIV reduction were investigated. The main conclusions are as follows:

1) Both vertical and torsional vibrations of a cable-suspended PV array show a decreasing trend from upstream to downstream PV modules. Large WIV is prone to occur at the mid-span and the maximum vertical response of the PV array appears at a wind direction of 180°.
2) The maximum WIV of the PV array reduced by using spoilers. Compared with the spoiler with small tilt angle, the WIV mitigation effect is improved by applying a spoiler with a large tilt angle.
3) Further studies should address real-world challenges, including detailed CFD simulations to analyse aerodynamic performance and long-term durability tests to assess material fatigue and environmental impacts, ensuring the practical viability of the proposed spoiler design.

ACKNOWLEDGEMENTS

The work described in this paper was partially supported by the National Natural Science Foundation of China (Project No. 51978614) and Zhejiang Provincial Natural Science Foundation of China (Project No. LY19E080026). This support is much appreciated.

REFERENCES

Bernardini, E., Spence, S.M.J., Wei, D., Kareem, A., 2015. Aerodynamic shape optimization of civil structures: A CFD-enabled Kriging-based approach. J. Wind Eng. Ind. Aerodyn., Selected papers from the 6th International Symposium on Computational Wind Engineering CWE 2014 144, 154–164.

Elshaer, A., Bitsuamlak, G., El Damatty, A., 2017. Enhancing wind performance of tall buildings using corner aerodynamic optimization. Eng. Struct. 136, 133–148.

Hu, C., Zhao, L., Ge, Y., 2019. Mechanism of suppression of vortex-induced vibrations of a streamlined closed-box girder using additional small-scale components. J. Wind Eng. Ind. Aerodyn. 189, 314–331.

Jiaqi Liu, Shouying Li, Jing Luo, Zhengqing Chen, 2023. Experimental study on critical wind velocity of a 33-meter-span flexible photovoltaic support structure and its mitigation. J. Wind Eng. Ind. Aerodyn. 236, 105355.

Kim, Y.-M., You, K.-P., Ko, N.-H., 2008. Across-wind responses of an aeroelastic tapered tall building. J. Wind Eng. Ind. Aerodyn. 96, 1307–1319. https://doi.org/10.1016/j.jweia.2008.02.038

Rui Wang, Dabo Xin, Jinping Ou, 2019. Experimental investigation on suppressing circular cylinder VIV by a flow control method based on passive vortex generators. J. Wind Eng. Ind. Aerodyn. 187, 36–47.

Xu-Hui He, Hao Ding, Hai-Quan Jing, Xiao-Ping Wu, Xiao-Jun Weng, 2021. Mechanical characteristics of a new type of cable-supported photovoltaic module system. Sol. Energy 226, 408–420.

Investigation of transient vortex-induced vibrations on a 2D square cylinder under accelerating flow conditions

Hao-Yu Bin[1], Gianmarco Lunghi[2], Mario Morello[2], Alessandro Mariotti[2], Maria Vittoria Salvetti[2], Stefano Brusco[3], Giuseppe Piccardo[1]

[1]*DICCA, University of Genoa, Genoa, Italy, hao-yu.bin@edu.unige.it, giuseppe.piccardo@unige.it*
[2]*DICI, University of Pisa, Pisa, Italy, gianmarco.lunghi@phd.unipi.it, mario.morello@phd.unipi.it, alessandro.mariotti@unipi.it, maria.vittoria.salvetti@unipi.it*
[3]*Faculty of Engineering, Western University, London, Canada, sbrusco@uwo.ca*

SUMMARY:
Full-scale records of thunderstorm outflows, such as those gathered by the anemometric network in the High Tyrrhenian Sea, coordinated by Giovanni Solari Wind Engineering and Structural Dynamics Research Group (GS-WinDyn), reveal that abrupt changes in mean wind velocity are a defining characteristic of non-synoptic events. Experimental simulations were performed in the Goettingen-type wind tunnel at the University of Pisa to investigate the effects of these accelerating flows on the transient aeroelasticity of a two-dimensional square cylinder with appropriate selected dynamic system setups. The study analyzes vortex-induced vibrations (VIVs) under both steady and transient flow conditions. Initially, a fundamental identification process was conducted to verify the system parameters, confirming that the estimated Scruton number is sufficiently high to ensure a clear separation between VIVs and galloping phenomena. Preliminary findings suggest that significant VIVs can occur even during transient events, with the magnitude of flow acceleration playing a crucial role in influencing the vortex-shedding response.

Keywords: Accelerating flow, Transient vortex-induced vibration, Thunderstorm outflows

1. INTRODUCTION

Since 2007, the Giovanni Solari Wind Engineering and Structural Dynamics Research Group (GS-WinDyn) at the University of Genoa has registered hundreds of non-stationary wind records in the High Tyrrhenian Sea through a comprehensive monitoring network (see, e.g., Solari et al., 2012; Burlando et al., 2018). This database now supports a line of research focused on thunderstorms, involving site detection, physical and numerical simulations, and analytical modeling of the aerodynamic loading and the structural response. At the same time, several novel ideas have been proposed to simulate specific aspects of thunderstorm phenomena in laboratories all around the world. Traditional wind tunnels have been updated with new functionalities such as multi-blade devices (e.g., Le and Caracoglia, 2019; Yuan et al., 2024) and passive grids with adjustable sizes (e.g., Aldereguía Sánchez et al., 2023) to reproduce nose-like vertical wind profiles. In addition, innovative wind simulators such as multi-fan wind tunnels, first introduced in Asia in the late 20th century, can generate accelerating flows in straight channels by using small fans positioned at the inlet section. These facilities enable the study of bluff-body aerodynamics under transient flow conditions (e.g., Brusco et al., 2024). To further explore the effects induced by transient conditions

on the structural aeroelasticity, a topic that is under-researched in wind engineering, this paper proposes an experimental campaign that aims to investigate the transient vortex-induced vibrations (VIVs) of a 2D square cylinder under accelerating and decelerating flow conditions.

2. TRANSIENT FLOW REPRODUCTIONS

The experimental campaign was conducted in the closed-return Goettingen-type wind tunnel at the University of Pisa (Fig. 1a), which is characterized by a free-stream velocity 0-35 m/s and by a turbulence intensity level of 0.9%. Its newly equipped fan motor enables instantaneous changes in wind velocity (U), achieving the desired peak flow acceleration (a_U) by adjusting three key parameters: the initial velocity (U_i), the target velocity (U_t), and the time interval (Δt), as shown in Fig. 1b.

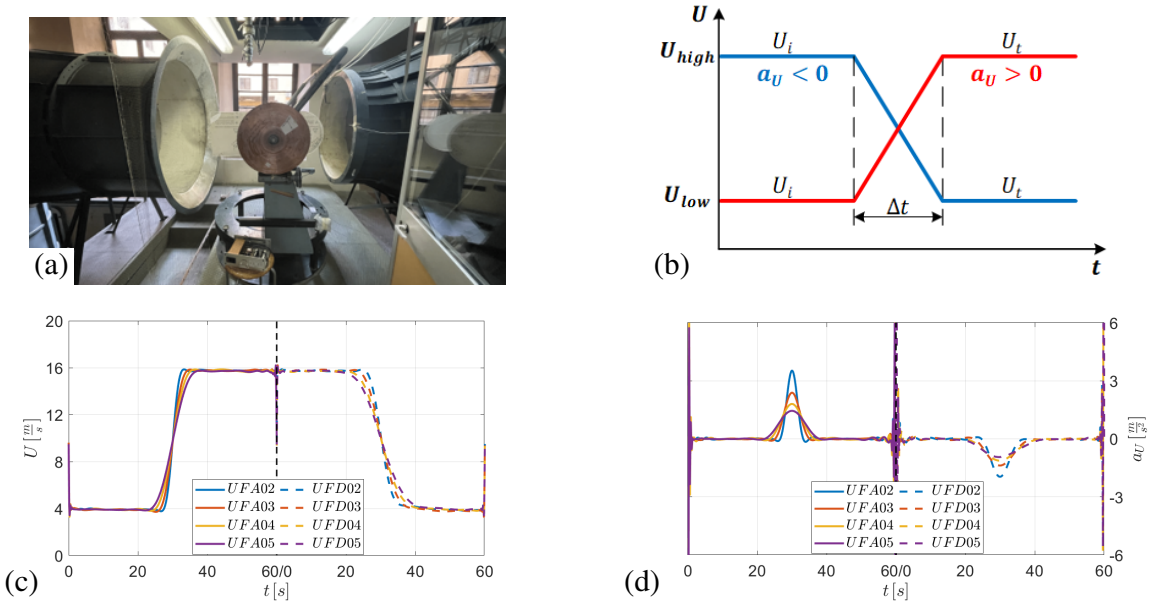


Figure 1. (a) The DICI wind tunnel at UniPi; (b) schematic representation of a single cycle of accelerating/decelerating flow conditions. Sample time histories of flow reproduction: (c) wind velocity (U); (d) wind acceleration (a_U).

In this study, the benchmark accelerating flow replicates the UF1 case from Brusco et al. (2024), where the wind velocity rapidly increased from 4.3 m/s to 15.9 m/s in approximately 2 seconds with a Gaussian-type acceleration. While maintaining the same U_i and U_t values, only Δt is varied to simulate a range of flow conditions. The velocity and acceleration time histories for these conditions are shown in Fig. 1c and Fig. 1d. The notation "A/D" refers to accelerating or decelerating flow, while the numbers indicate the multiple ratios of Δt relative to the benchmark case.

3. AEROELASTIC TEST SET-UP

The test model features a square cross-section with sides measuring 6 cm (i.e., B = D = 6 cm), and its natural frequency is controlled using a suitable spring-set system (Fig. 2a). The primary objec-

tive of this study is to explore the potential for significant transverse VIV responses in the presence of accelerating flow. Additionally, it aims at comparing the VIV behavior at a specific steady wind velocity with the response at the same velocity during the acceleration phase of a varying flow. To achieve this, two system frequency configurations were developed, corresponding to vortex-shedding frequencies at wind velocities of approximately 5.7 m/s (close to the start of acceleration phase, Spring-01) and 7.7 m/s (in the middle of acceleration phase, Spring-02), respectively. This was possible by preliminary considering a Strouhal number of 0.13, which corresponds a typical value for square sections.

Fig. 2b shows the system identification results, with the blue line representing Spring-01 and the red line representing Spring-02. In both cases, the damping ratio is about 0.3% ($\xi_{y1} = \xi_{y2}$), which is estimated from the decay curve of the normalized displacement response ($\tilde{Y}$). The measured natural frequencies align with the design setup, at approximately 12.3 Hz (n_{y1}) and 16.6 Hz (n_{y2}), respectively. The total mass per unit length of the system is about 3.5 Kg/m, leading to an estimated Scruton number of 36, which is well above the typical VIV-galloping separation threshold of approximately 20 (see Scruton, 1965; Miyata et al., 1983). Therefore, both of these configurations appear able to ensure a clear separation between VIV and galloping within the test flow range.

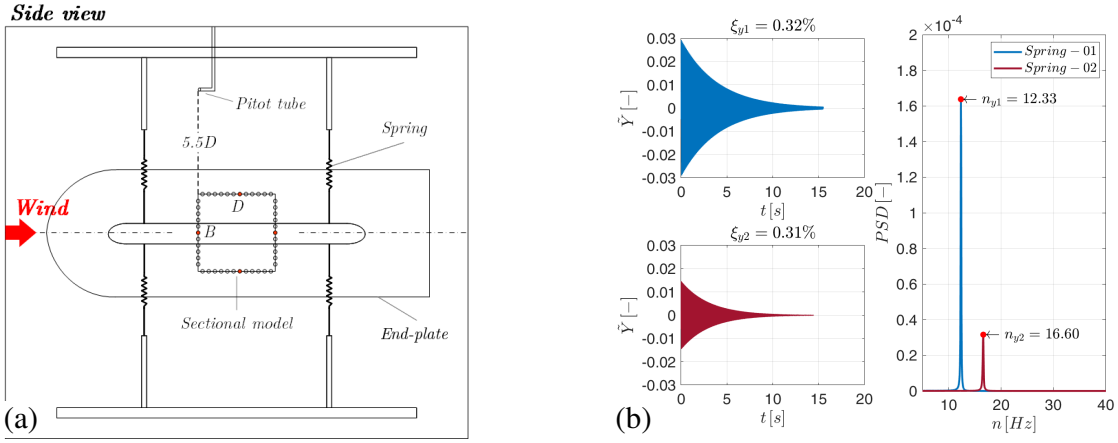


Figure 2. (a) Schematic diagram of the aeroelastic test setup; (b) identification of the basic parameters of the two systems.

4. PRELIMINARY RESULTS

Preliminary results for VIVs observed in the model equipped with Spring-01, under both steady and unsteady conditions, are presented in Fig. 3. In steady flow conditions, Fig. 3a shows the curve of the standard deviation (SD) of normalized displacement ($\sigma_{\tilde{Y}_s}$) plotted against the wind velocity, revealing a single distinct peak that confirms the separation between VIVs and galloping phenomena. For this setup, the maximum VIV response occurs at a wind velocity of approximately 6.2 m/s, which serves as a reference point for transient flow cases. In accelerating flow cases, an ensemble SD ($\langle\sigma\rangle_{\tilde{Y}_t}$) across 10 repetitions is applied to evaluate vibration levels at different temporal instants. Two accelerating flow cases were selected for presenting the preliminary results, UFA02 and UFA04, which corresponding Δt values are 4 and 16 seconds, respectively. Fig. 3b and 3c display the time histories of the ensemble mean of the wind velocity and the SD of normalized

displacements in these cases. In these plots, the green dot indicates the time at which the peak of $\langle\sigma\rangle_{\tilde{Y}_t}$ occurs under unsteady conditions, while the red line marks the reference velocity value from the steady flow results. Notably, in both accelerating flow cases, the peak values show a delay compared to the steady condition. For the lower acceleration case, UFA04, the peak occurs closer to the steady reference value and exhibits a significantly higher magnitude compared to the higher acceleration case, UFA02, while still remaining well below the peak value observed under steady conditions.

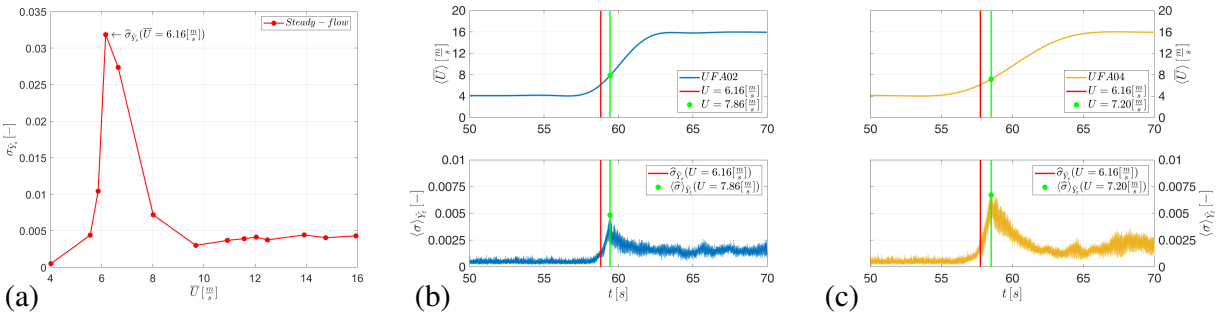


Figure 3. Preliminary results of Spring-01: (a) steady flow; ensemble evaluations across 10 repetitions of accelerating flow: (b) UFA02; (c) UFA04.

To enhance understanding of the experimental dataset, time-frequency analyses are deemed essential due to the high non-stationarity of the signals measured under accelerating flow conditions. These are based on the continuous wavelet transform, and their results will be presented in the final paper.

ACKNOWLEDGEMENTS

Special thanks to the laboratory staff at the University of Pisa and the University of Genoa for their technical support with the model, dynamic rig, and instrumentation.

REFERENCES

Aldereguía Sánchez, C., Tubino, F., Bagnara, A., and Piccardo, G., 2023. Experimental Simulation of Thunderstorm Profiles in an Atmospheric Boundary Layer Wind Tunnel. Applied Sciences 13, 8064.

Brusco, S., Bin, H.-Y., Lo, Y.-L., and Piccardo, G., 2024. Transient aerodynamics of a square cylinder under downburst-like accelerating flows reproduced in a multiple-fan wind tunnel. Journal of Fluids and Structures 124, 104038.

Burlando, M., Zhang, S., and Solari, G., 2018. Monitoring, cataloguing, and weather scenarios of thunderstorm outflows in the northern Mediterranean. Natural Hazards and Earth System Sciences 18, 2309–2330.

Le, V. and Caracoglia, L., 2019. Generation and characterization of a non-stationary flow field in a small-scale wind tunnel using a multi-blade flow device. Journal of Wind Engineering and Industrial Aerodynamics 186, 1–16.

Miyata, T., Miyazaki, M., and Yamada, H., 1983. Pressure distribution measurements for wind induced vibrations of box girder bridges. Journal of Wind Engineering and Industrial Aerodynamics 14, 223–234.

Scruton, C., 1965. On the wind excited oscillations of stacks, towers and masts. Proceedings of International Conference on Wind Effects on Buildings and Structures. Vol. II. HMSO, London, 798–832.

Solari, G., Repetto, M. P., Burlando, M., De Gaetano, P., Pizzo, M., Tizzi, M., and Parodi, M., 2012. The wind forecast for safety management of port areas. Journal of Wind Engineering and Industrial Aerodynamics 104, 266–277.

Yuan, Y., Yan, B., Zhou, X., Li, X., Yang, Q., Zhou, X., and Shu, Z., 2024. An active-controlled multi-blade facility to generate 2-D downburst-like outflows in the boundary layer wind tunnel. Journal of Wind Engineering and Industrial Aerodynamics 248, 105713.

Experimental Analysis of Vortex-Induced Second-Order Vibration Modes in Highly Slender Aeroelastic Models

Luisa Pagnini [1], Stefano Cammelli [2], Edoardo Ruffini [3], Stefano Torre [1], Akihito Yoshida [4], Giuseppe Piccardo [1]

[1]*DICCA, University of Genoa, Genoa, Italy, luisa.pagnini@unige.it, stefano.torre@edu.unige.it, giuseppe.piccardo@unige.it*
[2]*WSP, London, UK, stefano.cammelli@wsp.com*
[3]*NOVA Fluid Mechanics, Teddington, UK, Edoardo.Ruffini@novafluidmechanics.com*
[4]*Tokyo Polytechnic University, Tokyo, Japan, yoshida@arch.t-kougei.ac.jp*

SUMMARY:
This paper presents an experimental study to evaluate vortex-induced vibrations, focusing specifically on second-order vibration modes. The literature provides limited experimental data on this phenomenon, both for full-scale structures and scaled models. However, these dynamical features have clear technical relevance for highly slender structures, such as tapered light poles and lightning rods in industrial settings, and even for advanced super-tall buildings that may be susceptible to aeroelastic excitation. Starting from select case studies involving wind tunnel testing of aeroelastic models, this research aims at clarifying the complexities associated with the assessment of the vortex shedding response on second-order modes in highly slender structures with a square cross-section. The investigation utilizes a purposely built aeroelastic wind tunnel model, equipped with pressure taps, accelerometers, and base force measurement capabilities, to provide a comprehensive analysis of the dynamic response.

Keywords: Vortex-induced vibrations, Second-order vibration modes, Wind tunnel testing

1. INTRODUCTION

Vortex-Induced Vibrations (VIVs) are a critical concern for wind-excited slender structures. In wind engineering, the key parameters used to characterize VIV are the Strouhal number and the Scruton number. The Strouhal number, an aerodynamic parameter influenced by the shape of the structure, dictates the vortex shedding frequency and it is typically Reynolds number dependent. The Scruton number, a mass-damping parameter, governs the synchronization region during lock-in, when the oscillations of the structure align with the vortex shedding frequency. Structures undergoing VIVs can oscillate at remarkable amplitudes, which can lead to serviceability (e.g., wind-induced accelerations for comfort assessments) and ultimate limit states (e.g., fatigue failure of structures). At the same time, slender structures can be subjected to other aeroelastic phenomena such as galloping, which can induce large-amplitude oscillations leading to ultimate limit state conditions. Also in this case, the Scruton parameter can be used to provide preliminary indications on the sensitivity to this instability phenomenon. A classical case study concerning these phenomena is the square section. In the literature, a significant number of researches are related to the galloping oscillations of a square cylinder with sharp corners (e.g., Païdoussis et al. 2011; Hu et al., 2015) and its VIV behaviour is thoroughly investigated as well (e.g., Amandolèse and

Hémon, 2010). Also, the square cross-section with modified corners has been widely investigated from an aerodynamic point of view in static conditions, both experimentally (e.g., Tamura and Miyagi 1999; Carassale et al. 2013) and numerically (e.g., Cao and Tamura, 2018). However, to the best of the authors' knowledge, the studies involving wind tunnel tests on a full-aeroelastic model of square cylinders in boundary-layer flow with various corner shapes are exceedingly limited. On the other hand, in the last decade there has been great interest in optimizing the response of tall buildings to the wind action and one possible approach is to modify the corners or the façade. The square with rounded corners is perhaps the more common section examined in numerous numerical (e.g., Elshaer et al. 2017), experimental (e.g., Tamura et al. 2017, Liu et al. 2021) and numerical-experimental studies (e.g., Tanaka et al. 2013). In the experimental tests, rigid scale models of buildings equipped with rings of pressure taps or placed on a high-frequency force balance are commonly used.

The proposed research aims at addressing a gap in literature by conducting comprehensive full-aeroelastic tests on finite-length square cylinders in boundary-layer flow, designed to model the dynamic response of idealized super-slender tall buildings. The study specifically aims to investigate the influence of second-order vibration modes on VIVs. Additionally, there can also be interest in comparing the 3D dynamic response of these structural typologies with results from 2D sectional models, providing deeper insights into the behavior under VIV excitation.

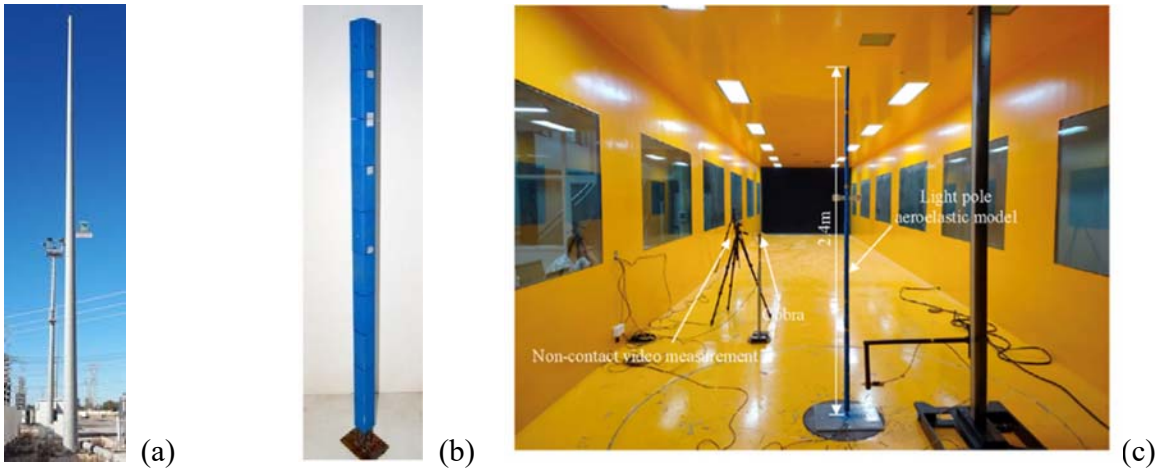
2. CASE STUDIES ON THE SECOND-ORDER VIBRATION MODES

Experimental data on VIVs in higher-order vibration modes are exceedingly rare in the literature, with limited examples primarily from wind tunnel studies (Cammelli and Sinh, 2016; Han et al., 2021). However, such oscillations can occur in real cases represented by slender structures in which the first mode of vibration is excited by vortex shedding at low wind speeds, as it happens for tapered light pole and lightning rods (Figure 1a). For these slender structures featuring circular or multi-sided polygonal sections, collapse may occur due to fatigue induced by frequent oscillations in the second-order vibration mode. Unfortunately, to the authors' knowledge, no full-scale experimental data on these vibrations exists, and insights are largely evidence-based.

Cammelli and Sinh (2016) conducted a wind tunnel testing campaign to investigate the wind-induced response of an exceptionally slender tall building, featuring an aspect ratio of 20:1. The selected model represented an idealized structure standing at 400 m in height, with a 20 m square cross-section and rounded corners (radius of curvature of 2 m, approximately). Given the non-linear aeroelastic behavior inherent in super-slender structures, a 1:400 full-aeroelastic wind tunnel model was designed and constructed to investigate deeply such topic (Figure 1b). The model was characterized by a Scruton number approximately of 15.4 for the second order vibration mode. The wind tunnel tests were conducted under smooth and boundary-layer turbulent flow. Experimental results highlight a pronounced vortex-induced response on the second-order vibration mode, surpassing the significance of the response associated with the first mode.

Han et al. (2021) investigated VIVs in a tapered light pole using a simplified aeroelastic model and a static sectional model in wind-tunnel experiments. The study explored the VIV characteristics and aerodynamic performance of an actual light pole, considering the presence or the absence of the weld on the surface. The model used in the experiments was 2.4 m in height, with a geometrical scale of 1:5 compared to the prototype (Figure 1c). The model scale diameter gradually decreased from 0.04 m to 0.02 m along the height of the model. The findings revealed

that the light pole model could experience second-order mode VIV and multi-mode vibrations at different incoming wind speeds. The estimated Scruton number was around 1.6 for the aeroelastic model. In the case of second-order mode VIV, the crosswind vibration amplitudes were approximately twice those observed in the along-wind direction, with the motion trajectory exhibiting a steady ellipse shape.



(a) (b) (c)

Figure 1. Case studies: (a) full-scale lightning rod, (b) 1:400 full aeroelastic wind tunnel model of a super-slender tall building (Cammelli and Sinh, 2016), (c) 1:5 aeroelastic model of a light pole (Han et al., 2021).

3. OVERVIEW OF CURRENT TEST CAMPAIGN

Building on the work of Cammelli and Sinh (2016), this research plan outlines a testing campaign using a 1:400 model of a super-slender tall building featuring an aspect ratio of 20:1 (as the model in Figure 1b). The idealized structure stands 400 m tall, with a square cross-section measuring 20 m by 20 m (i.e., square side b=5 cm in the scaled model) and a bulk density of approximately 300 kg/m³. The stiffness of the model will be provided by an internal tapered lattice brass spine, properly crafted to replicate the balance between flexural and shear deformation of the full-scale structure. An approximate ratio of 3 between the frequencies of the first- and second-order modes is expected. The model outer cladding will comprise 10 shell sections with small air gaps of 1 mm in between, each point-connected to the inner spine and 3D printed using rapid-prototyping techniques. A few accelerometers will be located inside the model itself (both at the top and at the second-order antinode), whilst its base will be rigidly connected to a High-Frequency Force Balance. A distinctive feature of the proposed experimentation lies in the incorporation of approximately 40 pressure taps within the full-aeroelastic model itself spread along the height of the model. To focus on the VIV response while minimizing the potential for galloping (as observed in Hu et al. 2015, for square-section 3D rigid models pivoted at the base by a gimbal system with an aspect ratio of 18:1), a cross-section shape with rounded corners having r/b= 2/15 (r being the corner radius) has been designed. Nevertheless, a comparison with a sharp-corner square cross-section is also planned. The tests are anticipated to be conducted in both smooth flow conditions and turbulent atmospheric boundary layer flow, simulating an urban area, in the Tokyo Polytechnic University (TPU) large-size turbulent boundary layer wind tunnel. Additionally, capturing flow measurements in the wake of the model using probes, smoke flow visualization, or advanced tools such as PIV, are expected to enhance the overall value of the project.

Preliminary tests are set to be conducted at the Giovanni Solari Wind Tunnel on a model with *r*/*b*= 1/10 in smooth flow conditions only. The system exhibits a transverse frequency and damping ratio of approximately 12 Hz and 0.5 % for the first vibration mode, and 30 Hz and 1% for the second vibration mode. Figure 2, derived from a preliminary analysis of the raw data collected from the accelerometer at the top of the model, indicates the potential for a distinct VIV peak associated with the second-order vibration mode, particularly under smooth flow conditions.

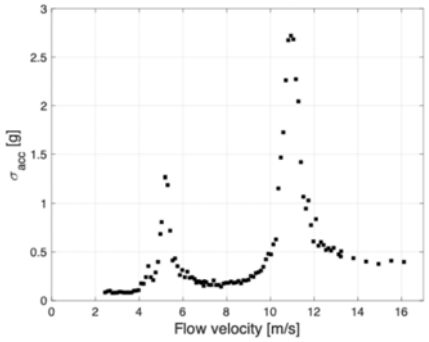


Figure 2. RMS acceleration at the top of the model (*r*/*b*=1/10, smooth flow; raw data)

ACKNOWLEDGEMENTS

This research has been selected as Joint-Usage/Research Projects in 2024 fiscal year by the Wind Engineering Research Center of the Tokyo Polytechnic University (Japan). The authors warmly thank the TPU Wind Engineering Research Center for the scientific and financial support.

REFERENCES

Amandolèse, X. and Hémon, P., 2010. Vortex-induced vibration of a square cylinder in wind tunnel. C. R. Mecanique 338, 12–17.

Cammelli, S. and Sinh, H.N., 2016. The aerodynamics of super-slender tall buildings. Proc..IN-VENTO 2016, XIV Conference of the Italian Association for Wind Engineering, Terni, Italy.

Cao, Y., Tamura, T. (2018). Aerodynamic characteristics of a rounded-corner square cylinder in shear flow at subcritical and supercritical Reynolds numbers. J Fluids Struct 82, 473–491.

Carassale, L., Freda, A., Marrè-Brunenghi, M. (2013). Effects of free-stream turbulence and corner shape on the galloping instability of square cylinders. J Wind Eng Ind Aerodyn 123, 274–280.

Elshaer, A., Bitsuamlak, G., El Damatty, A. (2017). Enhancing wind performance of tall buildings using corner aerodynamic optimization. Eng Struct 136, 133–148.

Han, Y., Zhou, X., Wang, L., Cai, C.S., Yan, H., Hu, P., 2021. Experimental investigation of the vortex-induced vibration of tapered light poles. J. Wind Eng. Ind. Aerod. 211, 104555.

Hu, G., Tse, K.T., Kwok, K.C.S. (2015). Galloping of forward and backward inclined slender square cylinders. J Wind Eng Ind Aerodyn 142, 232–245.

Liu, J., Hui, Y., Yang, Q., Tamura, Y. (2021). Flow field investigation for aerodynamic effects of surface mounted ribs on square-sectioned high-rise buildings. J Wind Eng Ind Aerodyn 211, 104551.

Païdoussis, M.P., Price, S.J., de Langre, E. (2011). Fluid-structure interactions: cross-flow-induced instabilities. Cambridge Univ. Press, NY.

Tamura, T., Miyagi, T. (1999). The effect of turbulence on aerodynamic forces on a square cylinder with various corner shapes. J Wind Eng Ind Aerodyn 83, 135–145.

Tamura, Y., Xua, X., Tanaka, H., Kima, Y.C., Yoshida, A., Yang, Q. (2017). Aerodynamic and Pedestrian-Level Wind Characteristics of Super-Tall Buildings with Various Configurations. Procedia Engineering 199, 28–37.

Tanaka, H., Tamura, Y., Ohtake, K., Nakai, M., Kim, Y.C., Bandi, E.K. (2013). Aerodynamic and flow characteristics of tall buildings with various unconventional configurations. Int J High-Rise Build 2(3), 213–228.

A simplified formulations for free vibration and flutter analysis of simple suspension bridges

Tuan-Kiet La [1], Seungho Lee [2], Byeongcheol Won [3], Soon-Duck Kwon [4]

[1]*Department of Civil and Environmental Engineering, Northeastern University, Boston, MA, USA, kiet.latuann@gmail.com (former graduate student at Jeonbuk National University)*
[2]*KOCED Wind Tunnel Center, Department of Civil Engineering, Jeonbuk National University, Jeonju, Jeonbuk 54896 Korea, guide1th@jbnu.ac.kr*
[3]*KOCED Wind Tunnel Center, Department of Civil Engineering, Jeonbuk National University, Jeonju, Jeonbuk 54896 Korea, bcwon.wind @jbnu.ac.kr*
[4]*KOCED Wind Tunnel Center, Department of Civil Engineering, Jeonbuk National University, Jeonju, Jeonbuk 54896 Korea, sdkwon@jbnu.ac.kr*

SUMMARY
This study introduces a simplified method for estimating the fundamental frequencies and flutter velocity of simple suspension bridges in the preliminary design. For three types of simple suspension bridges, the two closed-form equations exhibit good agreement in the fundamental frequencies and flutter velocities. Differences between the proposed closed-form equations and those reported in the literature are maximum 13.5% for frequencies and 15.3% for flutter velocity. Present simplified approach is not intended to replace the well-established conventional methods but rather to provide rapid predictions that help engineers optimize bridge properties for better design in the preliminary stage.

Keywords: Bridge dynamics, aeroelastic instability, natural frequency

1. INSTRUCTIONS

The preliminary assessment of aerodynamic stability is a critical aspect of the overall design process for suspension bridges. Since this issue involves the interaction between wind and the structure, understanding the dynamic characteristics of suspension bridges in free vibration is essential for evaluating aerodynamic instability.

Research on free vibration frequency analysis of suspension bridges began with Bleich et al. (1950), who provided exact solutions for natural frequencies and mode shapes based on bridge girder stiffness, and subsequently studied by Abdel-Ghaffar (1979) and many other researchers. Banerjee (2003) introduced a simplified method using coupled bending-torsion beam theory for free vibration and flutter analysis but overlooked cable effects. Wu et al. (2022) improved predictions by incorporating cable effects for vertical frequencies, though their method lacks a simplified approach for torsional frequencies.

Aeroelastic instability in suspension bridges is typically assessed by integrating structural and aerodynamic properties, often using complex eigenvalue or time-domain analyses involving

experimental flutter derivatives. These methods can require specialized software, unfamiliar to many engineers. To simplify critical flutter velocity calculations, various studies, including works by Selberg (1961), Chen (2007), Bartoli and Manini (2008), Vu et al. (2011), and others, have proposed alternative approaches for easier evaluation.

This study introduces a closed-form frequency equation for predicting the first vertical and torsional frequencies of simple suspension bridges. This equation is directly integrated into the closed-form critical flutter equation for bimodal coupled flutter, proposed by Chen (2007), resulting in a simplified scheme that allows engineers to swiftly predict the flutter performance of simple suspension bridges without rigorous analysis. The proposed procedure is not intended to replace conventional methods but rather to serve as a tool for evaluating flutter performance at the early stages of bridge design.

2. METHODOLOGY

To propose a simplified frequency equation, this study focuses on an analytical approach based on the coupled bending-torsion beam explicit theory, utilizing Hamilton's principle. The governing differential equations can be solved using standard mathematical approaches, resulting in a transcendental frequency equation from which the "exact" natural symmetric frequencies and mode shapes of the bridge can be determined. However, the complexity of the nonlinear transcendental equation requires iterative numerical approach to get solution.

To further simplify the calculations, Ritz method can be applied to the energy representation of the bridge system. By extending the work of Bleich et al. (1950), the smallest solution corresponds to the the first symmetric vertical and torsional frequencies is expressed in the following standard form:

$$f_{h,\alpha} = \frac{1}{2\pi}\sqrt{\frac{5}{9}\delta + 5\beta + 41\chi - \sqrt{\frac{25}{81}\delta^2 - \frac{32}{9}\delta\beta - \frac{320}{9}\delta\chi + 16\beta^2 + 320\beta\chi + 1600\chi^2}} \quad (1)$$

For vertical motion: $\delta = \frac{512s^2g}{\pi^2 wL^3}\frac{EA}{L_E}, \qquad \beta = \frac{\pi^2 g}{8s}, \qquad \chi = \frac{\pi^4 EIg}{wL^4}$ (2a)

For torsional motion: $\delta = \frac{256s^2B^2}{\pi^2 L^3 I_m}\frac{EA}{L_E}, \qquad \beta = \left(GJ + \frac{wL^2B^2}{16s}\right)\frac{\pi^2}{I_m L^2}, \qquad \chi = E\Gamma\frac{2\pi^4}{I_m L^4}$ (2b)

where I_m is the mass moment of inertia of the bridge per unit span length (including effects of cables); EI is the flexural stiffness of the girder; $E\Gamma$ and GJ denote the warping and torsional stiffness of the girder, respectively; B is the deck width; L is the span length and g is the gravitational acceleration.

For asymmetric vertical and torsional modes, the simplicity of the analysis allows for the direct application of previous results from Bleich et al. (1950), as the vibration does not result in an increase in additional horizontal tension

A closed form solution for coupled flutter by Chen (2007) is sued in this study. The flutter solution can be viewed as a theoretical basis for Selberg's equation, extending its applicability to other bridges with slender deck sections beyond flat plates. It is important to note that the flutter equation is a function of the structural properties of bridge, flutter derivatives, and fundamental frequencies

in both vertical and torsional modes. Thus, by combining the closed-form equations for free vibration, one can easily estimate the flutter speed of a simple suspension bridge through straightforward calculations without the need for complex programming steps.

3. NUMERICAL EXAMPLES AND DISCUSSION

As shown in Fig. 1, numerical examples were conducted on three bridges that are currently in operation: (a) the Majang Lake Bridge in Korea (a rope pedestrian bridge), (b) the Jinyanomori Bridge in Japan (a stress-ribbon bridge), and (c) the Runyang Yangtze River Bridge (a single-span box girder bridge).



(a) Majang Lake Bridge in Korea (b) Jinyanomori Bridge in Japan (c) Runyang Yangtze River Bridge in China

Figure 1. Example of figure.

Tables 1 and 2 show good agreement between the present simplified equation and those in the references obtained from the conventional analysis. Maximum difference was 13.5% for natural frequencies and 15.3% for flutter velocity.

Table 1. Natural frequencies of example bridges.

Mode		Majang Lake Bridge			Runyang Yangtze River Bridge		
		Present	Reference	Difference	Present	Reference	Difference
Symmetric	Vertical	0.453	0.460	-1.6 %	0.127	0.126	0.8 %
	Torsional	0.795	0.802	-0.9 %	0.266	0.241	9.4 %
Asymmetric	Vertical	0.334	0.338	-1.2 %	0.092	0.087	5.4 %
	Torsional	1.173	1.205	-2.7 %	0.279	0.292	-4.7 %

Table 2. Flutter velocities of example bridges.

Bridge	γ	Closed-form (m/s)	Conventional (m/s)	Wind tunnel (m/s)	Difference (with conventional)
Majang Lake	0.446	15.4	13.4	14.0	-15.3 %
Jinyanomori	0.498	100.5	115.1	-	12.7 %
Runyang	0.537	60.8	56.2	67.4	-8.3 %

4. CONCLUSIONS

This paper introduces a simplified procedure for estimating the fundamental vertical and torsional frequencies, along with the onset flutter velocity, of simple suspension bridges. This method relies on only two closed-form equations, one for fundamental frequencies and the other for bimodal coupled flutter velocity. Numerical examples were carried out on three types of simple suspension bridges to validate the accuracy of the present approach. The results exhibit good agreement in the

fundamental frequencies between the proposed closed-form equations and those reported in the literature. The disparities between computed and documented frequencies for all bridges in both vertical and torsional motions were observed to be less than 13.5%. Regarding flutter velocity, the simplified approach yielded results with a maximum difference of 15.3% compared to the conventional approach. It is noted that present simplified approach is not intended to replace the well-established conventional methods but rather to provide rapid predictions that help engineers optimize bridge properties for better design in the preliminary stage.

ACKNOWLEDGEMENTS

This research was supported by Basic Science Research Program through the National Research Foundation of Korea (NRF) funded by the Ministry of Education (NRF-2021R1I1A3055677).

REFERENCES

Abdel-Ghaffar, A.M. 1979. Free torsional vibrations of suspension bridges. J. Struct. Div., 105 (4).

Banerjee, J.R. 2003. A simplified method for the free vibration and flutter analysis of bridge decks. J. of Sound and Vibration, 206 (5).

Bartoli, G., Mannini, C. 2008. A simplified approach to bridge deck flutter. J. Wind Eng. Ind. Aerodyn., 96 (2).

Bleich, F., et al. 1950. The mathematical theory of vibration in suspension bridges. US: Bureau of Public Roads.

Chen, X.Z. 2007. Improved understanding of bimodal coupled bridge flutter based on closed-form solutions. J. of Structural Engineering, 133 (1).

Hayashikawa, T., et al. 1984. Vertical vibration in Timoshenko beam suspension bridges. J. of Engineering Mechanics, 110 (3).

Kim, M.Y., Kwon, S.D., and Kim, N.I., 2000. Analytical and numerical study on free vertical vibration of shear-flexible suspension bridges. J. of Sound and Vibration, 238 (1).

Selberg, A. 1961. Oscillation and aerodynamic stability of suspension bridge. Acta Polytech. Scand., 13.

Wu, Y., and Ma, K. 2022. New formula for calculating the vertical natural frequency of a suspension bridge. Practice Periodical on Structural Design and Construction 27(4).

Deep learning emulation of forced vibration flows for accurate prediction of shape-dependent self-excited forces

Omar A. Mures[1], Miguel Cid Montoya[2], Sumit Verma[3], Ashutosh Mishra[4]

[1]*XLab, Dept. of Civil Eng., University of A Coruña, Spain, omar.alvarez@udc.es*
[2]*ASTRO Lab, Glenn Dept. of Civil Eng., Clemson University, USA, mcidmon@clemson.edu*
[3]*ASTRO Lab, Glenn Dept. of Civil Eng., Clemson University, USA, sumitv@clemson.edu*
[4]*Dept. of Eng., Texas A&M Univ.-Corpus Christi, USA, amishra1@islander.tamucc.edu*

SUMMARY:

Accurate prediction of aeroelastic behavior is crucial in the wind-resistant design of bridges. Hence, developing robust workflows is pivotal for determining nonlinear fluid-structure interaction parameters, particularly flutter derivatives, across varying deck shapes and reduced velocities within the chosen design domain. Traditional interpolation methods usually work in the frequency and design domains. While convenient, this approach omits useful information in the self-excited forces time series or the forced vibration flows. This investigation proposes an emulation in the space-time domain by training a deep learning (DL) model with flow fields to build a prediction workflow with enhanced accuracy. A custom auto encoder (AE) architecture is trained on flow field data, incorporating deck shape and physical constraints as inputs. To enhance performance, SDF-biased sampling prioritizes critical flow features near the bridge deck surface when obtaining flow field images. The model leverages attention mechanisms and recurrent layers to capture the complex temporal and spatial dynamics of flow fields. Skip connections further improve the resolution and accuracy of the predicted flow fields. Preliminary results show that this method can surpass the accuracy of existing image-based flow field prediction techniques, and consequently improve flutter derivative emulation.

Keywords: Flow fields, Deep Learning, Deck shape

1. INTRODUCTION

Emulating bridge aeroelastic responses is a fundamental step in several wind engineering iterative workflows, such as aero-structural design optimization. While streamlined geometries may be designed to some extend by taking advantage of the quasi-steady theory (QST) assumptions and relying on the emulation of the force coefficients and their slopes (Cid Montoya, Hernández, et al., 2022), other deck typologies, such as truss, multi-box, and bluff box decks require the direct calculation of the fluid-structure interaction parameters, such as flutter derivatives, as a function of the deck shape and reduced velocity (Verma et al., 2024). The highly nonlinear nature of these parameters within shape design domains makes their prediction a challenge. However, as discussed in Argentini et al. (2012), there is rich information in the surface pressures and flow fields to understand the fluid-structure interaction phenomenology that is missed in the integrated flutter derivatives. This information can be leveraged to enhance prediction workflows.

Figure 1 shows the bridge evaluation process that is conducted during a CFD-based design process and compares potential emulation strategies based on their level of depth into the fluid-structure

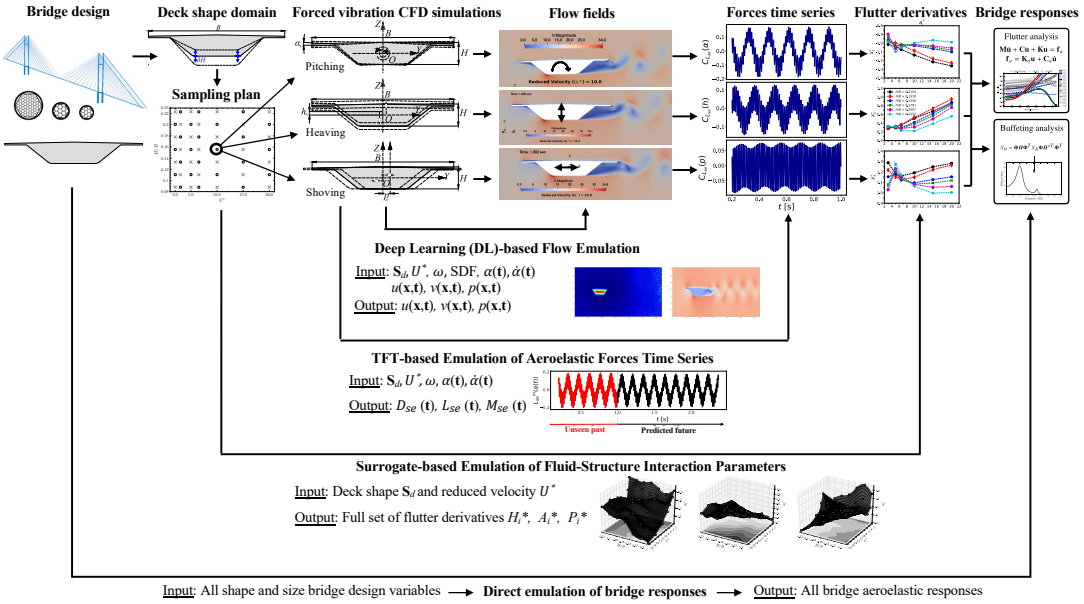


Figure 1. Metamodeling schemes for the shape-dependent aeroelastic response of bridges depending on their depth

interaction problem. A straightforward alternative is the direct emulation of the bridge responses as a function of all design variables, as proposed by Rizzo and Caracoglia (2020). This may be effective when the most relevant design variables have been identified, but can lead to dimensionality issues. Alternatively, the emulation can be done at the fluid-structure interaction parameters level, as they only depend on the shape design variables S_d and the reduced velocity U^*. This approach was successfully implemented by Verma et al. (2024), clearing the way for the aero-structural design of bridges considering the nonlinear effects of flutter derivatives. However, the quality of the emulation heavily depends on the sampling quality and the emulation worsens as candidate designs are far from training sample neighborhoods. On the other hand, DL techniques, and specially flow based ones, permit the development of deeper interpolation/extrapolation strategies taking advantage of all the information available in the simulations. A first alternative in this direction is the emulation of the self-excited forces in the time domain and then extracting the flutter derivatives after the prediction is done, as proposed by Cid Montoya, Mishra, et al. (2024) harnessing temporal fusion transformers (TFT) (Wen et al., 2023). An alternative, more comprehensive approach is conducting the emulation directly in flow space-time domain and decoupling flutter derivative calculation from the prediction process. This strategy focuses on predicting the complete flow field behaviour over time, capturing non-linear interactions that influence aeroelastic behavior.

Flow emulation for deck shape design exploration was previous studied by Yu and Wu (2023) focusing on static simulation flows for predicting the deck force coefficients using ANN. However, the methodology relies on training a prediction model per each time step, which limits its applicability when dealing with simulations involving thousands of time steps as required for forced-vibration simulations to properly capture all nonlinear aerodynamic effects. Alternatively, image-based flow prediction models offer a promising path to enhance self-excited forces prediction. By leveraging the information embedded within these flow-based image representations, these models can capture complex nonlinear aerodynamic behaviors and provide more accurate predictions.

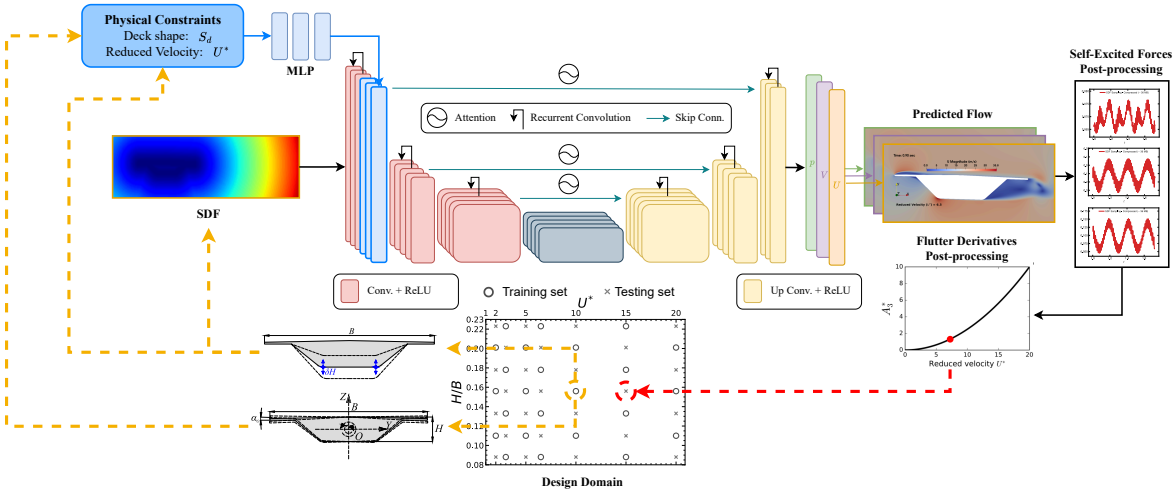


Figure 2. Proposed framework for flow prediction and design domain exploration. The model is fed an SDF function to ascertain bluff body geometry characteristics and physical constraints (S_d and U^*). The auto encoder contains several embedding layers comprising recurrent convolutions, upsampling layers with recurrent up convolutions to reconstruct output fields, and skip connections with attention to focus on the relevant parts of the input. Finally, the decoder produces the output flow fields p, U, and V, which are post-processed to yield the flutter derivatives.

2. PROPOSED IMAGE-BASED FLOW PREDICTION FRAMEWORK

We propose an ad hoc image-based flow prediction model capable of predicting flow fields for new bluff body shapes and reduced velocities. This task requires transforming CFD data, typically represented as values for each mesh cell center, into a format suitable for image-based deep learning models. We consider that the data can be discretized for each time step t in the form of an image $\psi \in \mathbb{R}^{w \times h}$. Our goal is to interpolate the image series for all desired simulation time steps ψ_t, $\forall t = 1, \ldots, T$, being T the total number of time steps. To effectively capture critical flow features, particularly around the bluff body surface with variable shape, we employ SDF-biased sampling. This method prioritizes mesh cells near the boundary layer during the discretization process, ensuring high-fidelity representation of the flow field in these regions.

The resulting image sequence, along with the signed distance function (SDF) (Osher et al., 2003) of the mesh boundary shape, physical constraints, and time step information, forms the input to our deep learning model. Our proposed model architecture (see Figure 2) draws inspiration from the U-Net (Ronneberger et al., 2015) architecture, incorporating attention mechanisms for skip connections and recurrent layers to enhance performance (Zuo et al., 2021). Additionally, we incorporate relevant physical parameters into the model through a small multi-layer perceptron (MLP) that yields a physical constraint vector, which is then transformed to a suitable format and added to the first set of convolutional layers in the encoder. This architecture is further adapted to output the desired flow field prediction outputs (p, U, and V), to enable post-processing.

3. PRELIMINARY RESULTS AND CONCLUDING REMARKS

A deck cross-section similar to the Sunshine Skyway Bridge in Tampa, FL, subject to shape modifications in the deck depth of up to $\pm 43.5\%$ (Verma et al. (2024)), leading to variations in the width to dept ratio B/H from 0.0879 to 0.2232, is used as test case. Forced vibration

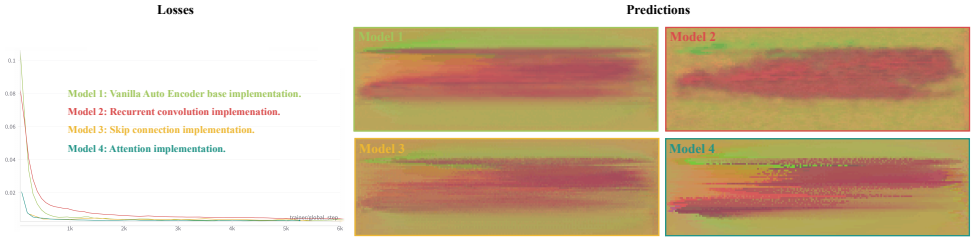


Figure 3. Model predictions and convergence graph in terms of the SDF-biased sampling during the architecture development and hyperparameter tuning process. The SDF-biased sampling enables shape adaptation of predicted flows. Deck shape and flow patterns are distorted before their reorganization into the original space coordinates.

CFD simulations using the $k-\omega$ SSK turbulence model were conducted at reduced velocities $U^* = [3.0, 5.0, 6.5, 10.0, 15.0, 20.0]$ with Reynolds numbers around $Re = 6 \cdot 10^5$. Flow fields, self-excited forces time series, and flutter derivative values were verified and validated using the experimental data reported in Mannini et al. (2016). Figure 3 shows some preliminary results plotted using the proposed SDF-biased sampling with a mean average percentage error (MAPE) of the image pixels of $\sim$5 %. A more comprehensive set of results will be reported in the oral presentation.

ACKNOWLEDGEMENTS

Investigation funded by the NSF (Grant No. CMMI-2301824). Omar A. Mures thanks the Galician Supercomputing Center (CESGA), funded by the Spanish Ministry of Science and Innovation, the Galician Government, and the European Regional Development Fund (ERDF). Miguel Cid Montoya thanks the start-up funds by Clemson University.

REFERENCES

Argentini, T., Rocchi, D., Muggiasca, S., and Zasso, A., 2012. Cross-sectional distributions versus integrated coefficients of flutter derivatives and aerodynamic admittances identified with surface pressure measurement. J Wind Eng Ind Aerodyn 104-106, 152–158.

Cid Montoya, M., Hernández, S., and Kareem, A., 2022. Aero-structural optimization-based tailoring of bridge deck geometry. Eng Str 270, 114067.

Cid Montoya, M., Mishra, A., Verma, S., Mures, O. A., and Rubio-Medrano, C. E., 2024. Predicting aeroelastic forces via temporal fusion transformers. Under Review.

Mannini, C., Sbragi, G., and Schewe, G., 2016. Analysis of self-excited forces for a box-girder bridge deck through unsteady RANS simulations. Journal of Fluids and Structures 63, 57–76.

Osher, S., Fedkiw, R., Osher, S., and Fedkiw, R., 2003. Constructing signed distance functions. Level set methods and dynamic implicit surfaces, 63–74.

Rizzo, F. and Caracoglia, L., 2020. Artificial Neural Network Model to Predict the Flutter Velocity of Suspension Bridges. Comput. Structures 233, 106236.

Ronneberger, O., Fischer, P., and Brox, T., 2015. U-net: Convolutional networks for biomedical image segmentation. Proceedings of Medical image computing and computer-assisted intervention–MICCAI 2015: 18th international conference, Munich, Germany, October 5-9, 2015, proceedings, part III 18. Springer, 234–241.

Verma, S., Cid Montoya, M., and Mishra, A., 2024. Shape- and frequency-dependent self-excited forces emulation for the aero-structural design of bluff deck bridges. J. Wind Eng. Ind. Aerod. 252, 105769.

Wen, Q., Zhou, T., Zhang, C., Chen, W., Ma, Z., Yan, J., and Sun, L., 2023. Transformers in Time Series: A Survey. Proceedings of the Thirty-Second International Joint Conference on Artificial Intelligence (IJCAI-23).

Yu, X. and Wu, T., 2023. Simulation of unsteady flow around bluff bodies using knowledge-enhanced convolutional neural network. J Wind Eng Ind Aerodyn 236, 105405.

Zuo, Q., Chen, S., and Wang, Z., 2021. R2AU-Net: attention recurrent residual convolutional neural network for multimodal medical image segmentation. Security and Communication Networks 2021, 6625688.

Buffeting analysis on the Miguelturra footbridge

Alfredo Cámara [1], Gia Khanh Nguyen [2,3], Mikel Ogueta-Gutiérrez [2,4], Juan Andrés Cárdenas-Rondón [2,5], Sebastián Franchini [2,6]

[1]*Department of Continuum Mechanics and Theory of Structures, Universidad Politécnica de Madrid, Madrid, Spain, alfredo.camara@upm.es*
[2]*Instituto Universitario de Microgravedad "Ignacio da Riva", ETSI Aeronáutica y del Espacio, Universidad Politécnica de Madrid, Madrid, Spain*
[3]*khanhnguyen.gia@upm.es*
[4]*mikel.ogueta@upm.es*
[5]*ja.cardenas@upm.es*
[6]*s.franchini@upm.es*

SUMMARY:
Wind tunnel tests have been performed on the Miguelturra footbridge (Spain), which has span of 124 m, to study its buffeting response. With the static coefficients, buffeting analysis has been performed on a full footbridge FEM model. Deflections are within limits, but accelerations may be regarded as uncomfortable. Other instabilities such as VIV, flutter and torsional divergence have been studied but the footbridge has shown no to be prone to them.

Keywords: wind tunnel, footbridge, buffeting.

1. INTRODUCTION

Bridges are known to suffer from several instabilities. Amongst them, footbridges are also sensitive to those phenomena. Both wind and pedestrians can trigger instabilities in footbridges. In the case of wind, flutter, VIV and buffeting are the most common instabilities in slender structures. Even though buffeting is not destructive, it can lead to unacceptable fatigue loads and discomfort for the users (Simiu and Scanlan 1996).

2. EXPERIMENTAL SETUP

Wind tunnel tests have been performed in a two dimensional wind tunnel in the facilities of the Instituto Universitario de Microgravedad "Ignacio da Riva", in Madrid. The wind tunnel has a rectangular test chamber of 2.5x0.5 m^2. The maximum velocity is 32 m/s. A model of a footbridge has been manufactured using carpentry and milling. The sectional shape of the footbridge is shown in Fig. 1. The model has been installed linked to two strain gauges, which measure the forces and moments in three axes.

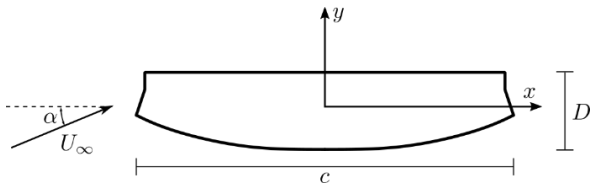


Figure 1. Shape of the footbridge and definition of the axes. Barriers are not included in the image.

The mean value of the vertical and horizontal forces and torsional moments are displayed in Fig. 2. Vertical force coefficient is negative for almost every angle of attack. The reason for this is that the lower part of the deck is curved, so the flow is attached, and high suction is created in that part.

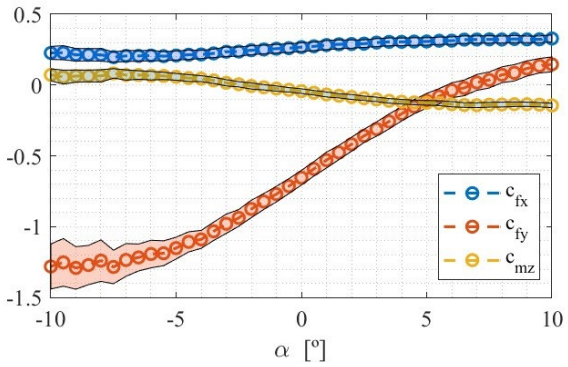


Figure 2. Force and moment coefficients per unit length of the sectional model

A dynamic modal analysis using MDyn has been performed to study its behavior under turbulent wind (Cámara 2021). For that, 10 different sets of turbulent wind records have been generated synthetically in the time domain. A sample of the wind generated can be seen in Fig. 3.

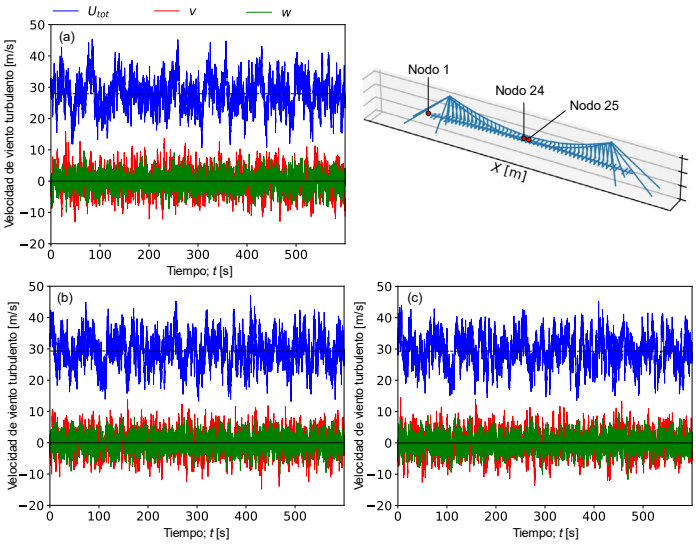


Figure 3. Time series generated on several different nodes of the FEM model (node 1, top left; node 24, bottom left; node 25, bottom right).

With this wind and the modal superposition analysis using a linear quasi-steady wind load model that accounts for quasi-steady, buffeting and aeroelastic effects, deformations and accelerations on all nodes of the footbridge have been calculated. The maximum vertical displacement for each node for each one of the 10 different simulations is displayed in Fig. 4. The thicker line represents the average value for all 10 repetitions and the shaded area, the standard deviation of those repetitions.

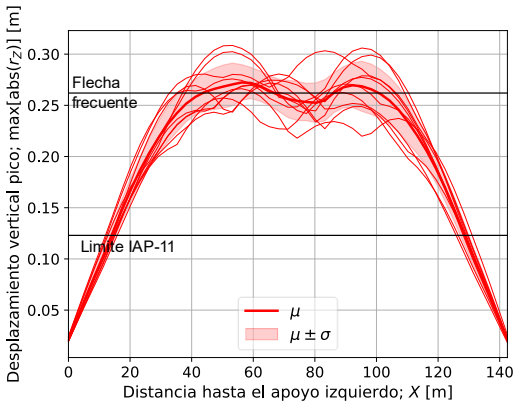


Figure 4. Maximum vertical displacement of each node of the footbridge for each of the repetitions.

From that image, the average displacement is beyond the Spanish standard limits (IAP-11 limit line in the graph) and near the 40% threshold of the use load. However, that deflection limit refers to the serviceability of the bridge subject to pedestrians walking in resonant frequencies, not to wind actions.

The vertical discomfort factor can be seen in Fig. 5. Two different criteria have been used, one using the Spanish standard IAP-11, $\eta(x) = \frac{\max|a(x,t)|}{a_{lim}}$, where $a_{lim} = 2.5\ \mathrm{m/s^2}$ and the other one using the Irwin criteria for storms, $\eta(x) = \max\frac{a_{RMS}(x,f)}{a_{lim}(f)}$, where $a_{lim}(f)$ is a value that depends on the frequency (Irwin, 1978).

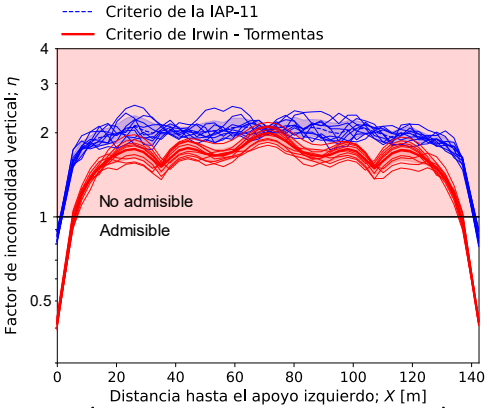


Figure 5. Vertical discomfort factor for each node for each repetition using both Eurocode criteria and Irwin storm

criteria.

In that figure, the thicker line is the average value of the 10 repetitions and the shaded area is the standard deviation. Both under the Spanish standard criterium or the Irwin storm criterium, most parts of the footbridge undergo uncomfortable accelerations.

In that figure, the thicker line is the average value of the 10 repetitions and the shaded area is the standard deviation. Both under the Spanish standard criterium or the Irwin storm criterium, most parts of the footbridge undergo uncomfortable accelerations.
For better understanding the origin of the discomfort, the frequencies that contribute most to the discomfort are identified and displayed in Fig. 6. In that figure, Irwin's storm limit is also displayed. Modes 2, 4 and 7 are identified as the modes that generate discomfort, trespassing Irwin's storm threshold. Their modal shapes are also displayed in the right part of Fig. 6.

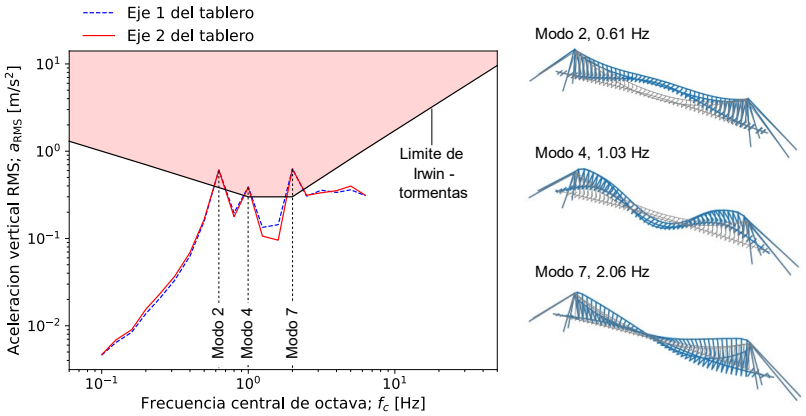


Figure 6. Vertical RMS accelerations for each frequency of the footbridge.

The modes have different shapes. For example, mode 7 has a node in the mid-span, so a damper in that position would not contribute significantly to the reduction of the discomfort.

7. CONCLUSIONS

The stability of the footbridge has been studied. Even though the deformations on the footbridge are not critical, vertical accelerations on pedestrians may be uncomfortable. The modes contributing to these accelerations have been identified. The frequency analysis of these modes can help design and place dampers along the footbridge span to try to minimize them.

ACKNOWLEDGEMENTS

The authors would like to thank Seranco A.A.U., Azul Construcción Repair S.A. and Estudio A.I.A. Arquitectos e Ingenieros Asociados, S.A.

REFERENCES

Camara, A., 2021. A fast mode superposition algorithm and its application to the analysis of bridges under moving loads. Advances in Engineering Software, 151, 102934.

Irwin, A. W., 1978. Human response to dynamic motion of structures. Structural Engineer, 56A (9), 237-244.

Simiu, E. and Scanlan, R. H., 1996. Wind effects on structures: fundamentals and applications to design. 3rd ed. John Wiley & Sons, New York, USA.

Wind tunnel investigations of the aerodynamic interference of two independent bridge decks

Tor Martin Lystad [1,2], Ingrid Masdal [2], Stian Nilsen [2], Ole Øiseth [2]

[1]*Norconsult ASA, Sandvika, Norway, tor.martin.lystad@norconsult.com*
[2]*Norwegian University of Science and Technology, Trondheim, Norway*

SUMMARY:
When a new bridge is built next to an existing bridge, the aerodynamic interference of the two independent bridge decks can cause a complex challenge. In this study the interaction between two bridge decks considering vortex induced vibrations as well as aerodynamic stability is investigated through wind tunnel testing. The findings indicate important effects that should be closely considered when designing adjacent structurally independent long-span bridges.

Keywords: Aerodynamic interference, Vortex-induced vibrations, Aerodynamic stability

1. INTRODUCTION

When the traffic capacity at an already existing bridge crossing is exceeded, an interesting solution often considered is to build a new bridge in parallel with the existing bridge. For long-span bridges this will increase the aerodynamic complexity since the two independent bridge decks will interact with each other through being embedded in the same fluid. In such cases, the static coefficients will be influenced, but perhaps more interestingly, effects such as vortex-induced vibrations (VIV) and aeroelastic stability can also be significantly affected.

Previous studies have shown that interference of two adjacent bridge decks can cause an increase of the VIV amplitudes when compared to a single deck alone (Park et al., 2017; Park & Kim, 2017; Seo et al., 2013). This is interesting since it will require careful considerations for both bridges if two independently suspended adjacent bridges are designed, or a new bridge is being planned next to an existing bridge. Some studies also indicate that the aerodynamic stability limit of the bridges may be affected by such interference effects as well (Boonyapinyo & Junruang, 2017), displaying that these phenomena also have a more dramatic consequence potential.

In this study, the aerodynamic interference effects on both VIV and aerodynamic stability of two independently suspended bridge decks are investigated through free vibration wind tunnel tests. Effects of gap widths between the two decks, as well as differences in eigenfrequencies are considered. Further, the efficiency of some simplified experimental setups, where one deck is statically suspended in the tests, were also considered. The findings show important effects both on the VIV amplitudes as well as the aerodynamic stability limit of the system.

2. EXPERIMENTAL WIND TUNNEL SETUP

Two identical section models were independently suspended in the wind tunnel at NTNU. The tunnel is a closed loop wind tunnel with a cross section of 2.7m x 1.8m. The 1:50 scale section models replicated the shape of the Hardanger Bridge girder, and no railings or other aerodynamic measures was included in the tests. The distance between the section models could be adjusted in the setup, and the frequency ratios between the decks could be changed through introducing additional masses to the models. The test setup is shown in Figure 1.



Figure 1. Wind tunnel test setup.

The vertical vibrations were the focus for the VIV considerations, and the vertical frequency was either 4.3 Hz or 4.0 Hz, depending on if the additional mass was included or not. The damping ratio in the test setup varied between 0.21-0.35% of critical damping.

For the aerodynamic stability investigations, another set of springs was used to replicate slower motions. The vertical frequencies were either 1.4 Hz or 1.3 Hz depending on the inclusion of additional masses. The torsional frequency was almost unchanged at 2.7-2.8 Hz regardless of the introduced masses.

3. RESULTS

3.1. Vortex induced vibrations

The effect of gap width between the two decks and the effect of the frequency ratio between the two vibrating section models were both studied. When considering the gap width, the frequency ratio between the models was kept as 1.0, and the gap width ratios of L/D = {2,3,4,5} was considered. Here, L is the free gap width between the bridge decks and D is the height of the section models. In Figure 2, the largest VIV amplitudes found in the tests are shown and compared with the single deck reference test. It becomes evident that the interference VIV significantly increased vibration amplitudes, especially for the downstream bridge deck. The amplitudes are also dependent on the gap widths, which was traced back to the connection between the gap width, the wind speed and the phase difference between the vibrations of the two decks.

The effect of the frequency ratio is found to be significant, with an observed change in behaviour when the frequency ratio deviates from 1.0 as shown in Figure 1. The change in frequency ratio is achieved by adding mass to either of the section models. This also affects the Scruton number slightly, so to indicate the effect, a datapoint for frequency ratio of 1.0 from a test with added mass in both models is indicated in the plot. When there is a difference in frequency ratio, the vibration amplitudes of the upstream deck are similar to the single deck reference case, whereas the downstream deck have a lower amplitude. Actually, it is observed that the downstream deck experiences a wake buffeting from the correlated narrow-banded vortices shed from the upstream deck vibrations. The amplitude of the downstream deck systematically follows a fraction of the amplitude of the upstream deck vibrations, indicating that the intensity of the buffeting actions increases with increased upstream vibrations. It should however be noted that the literature shows varying sensitivity to frequency ratio (Kimura et al., 2008; Xiao et al., 2023).

To reduce the complexity of the wind tunnel test setup it can be appealing to include one section model statically suspended and one deck free to vibrate in a simplified setup. In the investigations done herein, such a simplified test setup was found unable to reproduce the important interference effects seen when the frequency ratio is 1.0, as shown in Figure 2. When the static deck was located downstream of the suspended deck, the found behaviour was similar to the single deck reference. However, when the static deck was held upstream of the suspended deck, the chaotic turbulence shed form the upstream static deck kept the downstream deck from locking-in to VIV and only small amplitudes was observed.

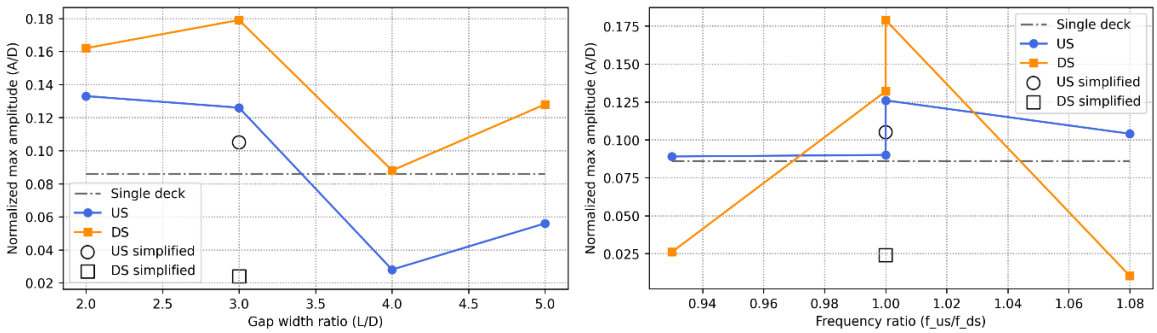


Figure 2. Effect of gap width- and frequency ratio on the VIV amplitudes. (US: Upstream, DS: Downstream)

3.2. Aerodynamic stability

The aerodynamic stability was investigated by direct observations in the tunnel, where the instability was identified when the system had zero-, or negative damping. The resulting critical wind speeds read from the wind tunnel are shown in Table 1. It was found that the interference system could show lower critical wind speeds than the single deck reference. The flutter motion that was observed for the two decks was a combination of a classical flutter like motion for the upstream deck, with a coupling of the vertical and torsional motions, whereas the downstream deck displayed more of a pure torsional vibration, with less contribution from the vertical degree-of-freedom. When the eigenfrequencies of the interference system was adjusted, the resulting critical wind speed changed as well, indicating a coupling of all four degrees-of-freedom in the system. The double dynamic test setups did however show a soft flutter

behaviour, where the system self-stabilized with zero damping, although at rather large vibration amplitudes. When a static deck was included upstream of the free deck, a similar critical wind speed and classical flutter behaviour was found.

Table 1. Identified aerodynamic stability limits

Test setup	fv1/fv2	fv1/ft1	fv2/ft2	ft1/ft2	v_{crit} [m/s]	Instability type
Single deck	-	0.511	-	-	9	Hard
Static upstream	-	-	0.511	-	9.2	Hard
Double dynamic 1	0.996	0.485	0.510	1.048	6.2	Soft
Double dynamic 2	1.080	0.469	0.478	1.099	8.5	Soft

4. CONCLUSIONS

The complex aerodynamic behaviour of two closely spaced independent long-span bridge decks has been investigated. Both the VIV interference phenomena as well as the aerodynamic stability was studied. A significant increase in the VIV amplitudes was found when the frequency ratios between the decks was close to 1.0. This was the case for all considered gap width ratios, although some gap width ratios where more critical than others. The behaviour dramatically changed when a slight change in the frequency ratio of approximately +/- 7-8% was introduced. Further, the independently suspended bridge decks were able to reduce the stability limit of the system dramatically when compared with the single deck reference case. These observations highlight the importance of addressing the complexity of such aerodynamically interacting systems through thorough wind tunnel testing.

ACKNOWLEDGEMENTS

Parts of the research presented in this paper has been financed by Norconsult Norge AS. The authors greatly appreciate the contribution.

REFERENCES

Boonyapinyo, V., and Junruang, J. 2017. Aerodynamic Response of Two Parallel Cable-Stayed Bridges. “9th Asia-Pacific Conference on Wind Engineering”, 3-7 December 2017. Auckland, New Zealand

Kimura, K., Shima, K., Sano, K., Kubo, Y., Kato, K., and Ukon, H. 2008. Effects of separation distance on wind-induced response of parallel box girders. Journal of Wind Engineering and Industrial Aerodynamics, 96, 954–962.

Park, J., and Kim, H. K. 2017. Effect of the relative differences in the natural frequencies of parallel cable-stayed bridges during interactive vortex-induced vibration. Journal of Wind Engineering and Industrial Aerodynamics, 171, 330–341.

Park, J., Kim, S., and Kim, H. K. 2017. Effect of gap distance on vortex-induced vibration in two parallel cable-stayed bridges. Journal of Wind Engineering and Industrial Aerodynamics, 162, 35–44.

Seo, J. W., Kim, H. K., Park, J., Kim, K. T., and Kim, G. N. 2013. Interference effect on vortex-induced vibration in a parallel twin cable-stayed bridge. Journal of Wind Engineering and Industrial Aerodynamics, 116, 7–20.

Xiao, H., Liu, Z., He, F., Chen, Z., Liu, Z., and Yan, A. 2023. Aerodynamic Interference Effects on Vortex-Induced Vibration of Two Parallel Railway– and Highway–Cable-Stayed Bridges with Triple-Separated Decks. Journal of Bridge Engineering, 29(2).

RANS CFD simulations to complement skew wind tunnel tests in bridge design

Trond-Ola Hågbo[1] and Bernardo Morais da Costa[2]

[1]*NablaFlow, Stavanger, Norway, toh@nablaflow.io*
[2]*Statens Vegvesen, Stavanger, Norway, bercos@vegvesen.no*

SUMMARY:
A case-study combining Reynolds-Averaged Navier-Stokes (RANS) Computational Fluid Dynamics (CFD) simulations with wind tunnel tests for the aerodynamic design of the Bjørnafjord Bridge is presented. During the Front-End Engineering Design (FEED) phase of the 5.5 km long floating bridge, preliminary wind tunnel test results were available, but only for a limited range of skew wind angles due to physical wind tunnel constraints. Efficient 3D RANS CFD simulations were performed to better understand, fit, and extrapolate the two-angle-dependent aerodynamic coefficients, in six degrees of freedom, onto a wider range of yaw and inclination angles. The combined wind tunnel and CFD results enabled more accurate predictions of the vertical buffeting response.

Keywords: CFD, wind tunnel testing, bridge design

1. INTRODUCTION

The prediction of the aerodynamic response of bridges is critical for ensuring structural stability and safety under various wind conditions. While traditional wind tunnel tests are effective, they have limitations. Scaling issues in wind tunnels make precise replication of real-world conditions challenging. The presence of sensors in the tunnel can disrupt airflow, leading to inaccuracies. Moreover, small-scale models may inadequately capture boundary layer effects, causing discrepancies in aerodynamic force predictions, particularly for long-span bridges (Zhang et al., 2021).

Computational Fluid Dynamics (CFD) simulations offer several advantages and can serve as an effective alternative. They provide detailed flow field data at any point in the domain, are better suited for iterative aerodynamic design optimizations, deliver results in shorter and predictable time frames, and can simulate otherwise unfeasible or costly scenarios, such as long bridge decks at large yaw angles, angle-dependent boundary conditions, or complex wind conditions.

This extended abstract presents a methodology that integrates RANS CFD simulations with wind tunnel testing, leveraging the strengths of both approaches. This study focuses on the planned Bjørnafjord bridge, a curved floating bridge spanning 5.5 km across a 500 m deep fjord.

2. METHODOLOGY

RANS CFD simulations were conducted using the AeroCloud platform. These were first validated against wind tunnel data obtained by Svend Ole Hansen (SOH) in 2018, using identical geometries

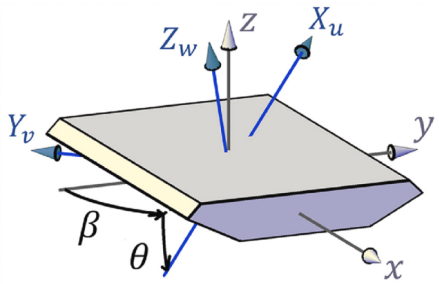


Figure 1. Global wind (X_u, Y_v, Z_w) and local structural (x, y, z) coordinate systems. Yaw angle β and inclination angle θ. (Morais da Costa, 2022).

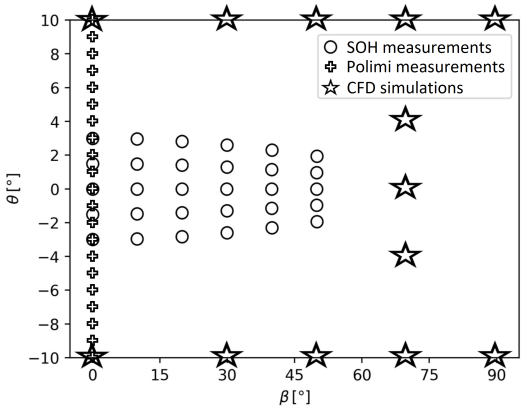


Figure 2. Wind tunnel vs CFD simulation angles.

and skew wind conditions. Subsequent small changes to the Bjørnafjord cross-section made it similar to the Julsund Bridge cross-section. For the Julsund Bridge, wind tunnel data from Politecnico di Milano (Polimi) was also available for a wide range of inclination angles, but under normal (perpendicular) wind only. The Bjørnafjord aerodynamic coefficients were obtained by fitting the SOH and CFD data with constrained bi-variate polynomials, as described in (Morais da Costa, 2022). The data was then scaled to the Polimi results under normal wind, according to the empirical expression: $C(\beta,\theta) = C^{SOH+CFD}(\beta,\theta) + \left(C^{Polimi}(0,\theta) - C^{SOH+CFD}(0,\theta)\right)\cos\beta$. The axes and angle definitions are shown in Figure 1. The angles of the measured and simulated datapoints are illustrated in Figure 2.

The numerical setup for the RANS CFD simulations followed the approaches outlined in previous studies on aerodynamic simulations, such as those by (Giljarhus, Liland, Bardal, et al., 2024; Giljarhus, Liland, and Oggiano, 2023; Giljarhus, Reid, et al., 2022; Schaffarczyk et al., 2022). The simulations were conducted using the web-based CFD platform AeroCloud (NablaFlow, 2023), which automates mesh generation, simulation, and post-processing. AeroCloud leverages the open-source CFD tool OpenFOAM (Jasak et al., 2007; Weller et al., 1998) and the Amazon AWS infrastructure (Amazon Web Services, 2023) to enable extensive parallelization, resulting in a total simulation and post-processing time of approximately 2 hours per case.

The aerodynamic coefficients necessary to estimate wind loads were computed for all six degrees of freedom (DOF) of the bridge deck. The coefficients, normalized by the bridge width (B or B^2), include the forces (C_x, C_y, C_z) and moments (C_{rx}, C_{ry}, C_{rz}) along the local structural coordinate system (x, y, z).

The yaw angles, β, and inclination angles, θ, used in the CFD simulations were chosen to complement the wind tunnel data and to address the knowledge gaps in this case study and in the literature.

3. RESULTS

A comparison between the original skew wind coefficients from SOH wind tunnel data and the newly proposed coefficients combining SOH and CFD data scaled to Polimi data is shown in

Figure 3. The resulting coefficients are continuous and differentiable functions over the β and θ domain of interest. At normal wind angles ($\beta = 0$), the functions closely fit the Polimi data. As yaw angles increase, a cosine rule transition between the Polimi and the SOH data occurs. For even larger yaw angles or combinations of large yaw and inclination angles, the CFD data fills the information gap.

An aspect of interest was the slope of the vertical coefficient C_z at larger yaw angles, which could govern the vertical response of the curved floating bridge over a wide range of wind directions. The CFD results indicated a significant reduction of this slope with increasing yaw angle, which was not apparent from the limited SOH data. Recent comprehensive wind tunnel tests at Polimi under skew winds (Morais da Costa and Wang, 2025) have also supported this trend.

4. CONCLUSIONS

This extended abstract documents the simultaneous use of CFD simulations and wind tunnel tests in the FEED phase of a major bridge project. The CFD simulations provided useful data at large skew wind angles, otherwise difficult to assess in a wind tunnel. These new insights into the bridge's aerodynamic behavior led to more reliable extrapolations of the aerodynamic coefficients. A reduced slope of the vertical coefficient at large yaw angles was observed, which is relevant for predicting vertical buffeting responses of the curved floating bridge over a wide range of wind directions. While wind tunnel testing remains a standard, CFD offers a complementary tool that can augment traditional methods, allowing for more efficient, cost-effective, and reliable design processes.

REFERENCES

Amazon Web Services, 2023. *Amazon Web Services Free Tier*.

Giljarhus, K. E. T., Liland, F. F., Bardal, L. M., and Oggiano, L., 2024. Aerodynamic optimization of athlete posture using virtual skeleton methodology and computational fluid dynamics. Journal of Biomechanics 176, 112303.

Giljarhus, K. E. T., Liland, F. F., and Oggiano, L., 2023. Virtual skeleton methodology for athlete posture modification in CFD simulations. Sports Engineering 26, 39.

Giljarhus, K. E. T., Reid, R., Liland, F. F., Oggiano, L., and Elfmark, O., 2022. Aerodynamic influence of an alpine skier's arms. Sports Engineering 25, 20.

Jasak, H., Jemcov, A., Tukovic, Z., et al., 2007. OpenFOAM: A C++ library for complex physics simulations. Proceedings of International workshop on coupled methods in numerical dynamics. Vol. 1000. Dubrovnik, Croatia), 1–20.

Morais da Costa, B., 2022. Bridge aerodynamics in skew winds: Generalized buffeting load modelling and response analysis. PhD Thesis, University of Stavanger, Norway.

Morais da Costa, B. and Wang, J., 2025. Bridge buffeting in skew winds – experimental aerodynamic coefficients and numerical analysis. Submitted to the 9th European-African Conference on Wind Engineering.

NablaFlow, 2023. *AeroCloud Platform for Aerodynamic CFD Simulations*.

Schaffarczyk, A., Koehn, S., Oggiano, L., and Schaffarczyk, K., 2022. Aerodynamic Benefits by Optimizing Cycling Posture. Applied Sciences 12.

Weller, H. G., Tabor, G., Jasak, H., and Fureby, C., 1998. A tensorial approach to computational continuum mechanics using object-oriented techniques. Computers in physics 12, 620–631.

Zhang, Y., Cardiff, P., and Keenahan, J., 2021. Wind-induced phenomena in long-span cable-supported bridges: a comparative review of wind tunnel tests and computational fluid dynamics modelling. Applied Sciences 11, 1642.

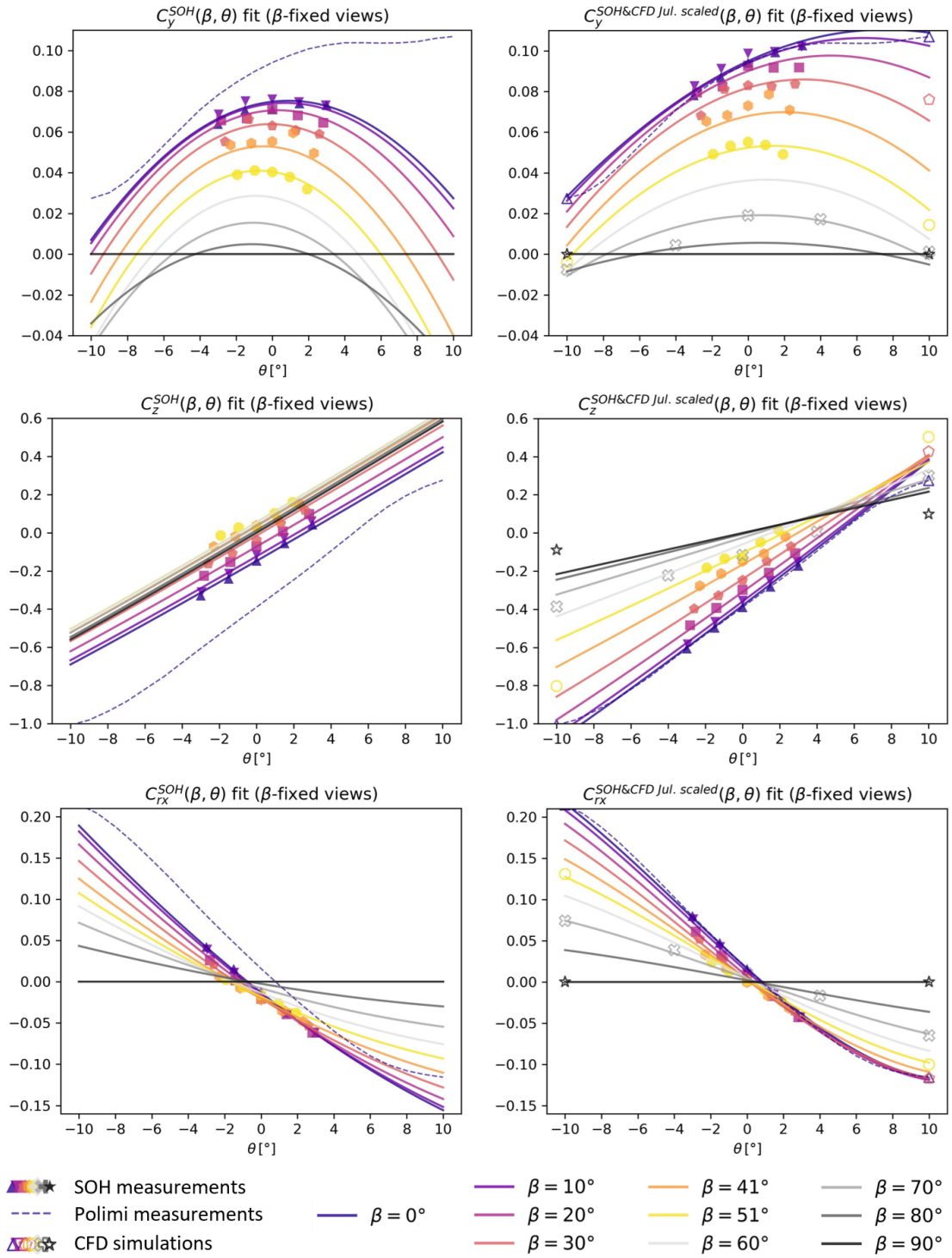


Figure 3. Comparison of the horizontal, vertical, and torsional aerodynamic coefficients (C_y, C_z, C_{r_x}) between the original SOH data only and the hybrid SOH + CFD + Polimi approach, for various yaw (β) and inclination angles (θ). In the hybrid approach, the datapoints are scaled to the Julsund bridge results.

Estimating bridge downtime from wind hazards considering comfort criterion

Zubair Zahoor Banday[1], Aksel Fenerci[2], Torodd Skjerve Nord[3], Ole Andre Øiseth[4]

[1]*Norwegian University of Science and Technology, Ålesund, Norway, zubair.z.banday@ntnu.no*
[2]*Norwegian University of Science and Technology, Trondheim, Norway, aksel.fenerci@ntnu.no*
[3]*Norwegian University of Science and Technology, Ålesund, Norway, torodd.nord@ntnu.no*
[4]*Norwegian University of Science and Technology, Trondheim, Norway, ole.oiseth@ntnu.no*

SUMMARY:
This paper presents an approach to estimating long-span bridge downtime caused by wind hazards, incorporating site-specific turbulence characteristics into the assessment. The comfort criterion is established based on a threshold for vertical deck acceleration, estimated from the bridge's stochastic buffeting response. Fragility analysis is conducted using the extreme value distribution of peak buffeting responses, leading to the development of fragility functions. These functions are then used to estimate the bridge's annual downtime. Unlike traditional methods that often treat wind speed as the sole uncertain parameter, this study investigates the influence of uncertain wind speed and turbulence intensity on bridge performance, focusing on downtime estimation as a metric for operational resilience. By leveraging a joint probabilistic model that reflects local turbulence conditions, this work enables a more accurate assessment of expected closures and associated disruptions. The methodology is applied to a case study, demonstrating how site-specific turbulence modelling can refine downtime predictions.

Keywords: buffeting theory, fragility analysis, serviceability

1. INTRODUCTION

Exposure to whole-body vibration in vehicles has been shown to affect drivers, ranging from temporary discomfort and reduced performance to lasting physiological harm. Although determining precise user comfort levels remains challenging due to individual variability in vibration sensitivity, codal provisions provide substantial insights into the impacts of whole-body vibration and established ride comfort thresholds (*Mechanical Vibration and Shock – Evaluation of Human Exposure to Whole-Body Vibration – Part 1: General Requirements* 1997). In recent years, numerous long-span cable-stayed and suspension bridges have been constructed, and more are planned. When such wind-sensitive structures are situated in wind-prone areas, they are subject to significant wind-induced vibrations, driven mainly by the buffeting forces from wind turbulence.

This work is focused on developing a framework for calculating the probability of failure of user comfort criterion based on the vertical acceleration of the bridge deck as a function of the mean wind speeds as well as turbulence field parameters. The framework proposed is finally applied to a real suspension bridge in Norway for which a site-specific turbulence model is available. Annual downtime is computed using the traditional deterministic as well as probabilistic turbulence

models. Results indicate that deterministic turbulence leads to an underestimation of the failure probability associated with comfort serviceability limit state. In contrast, the proposed probabilistic framework provides a more accurate assessment of expected closures, thereby supporting informed maintenance and operational strategies as well as accurate life cycle cost evaluations.

1.1. Risk analysis based on fragility functions

The objective of calculating the annual downtime is achieved by calculating the probability that the structural response exceeds a threshold T for varying wind intensity measures. For a stationary wind condition over a period $T_{st} = 600s$, the average upcrossing rate of threshold T over T_{st} can be expressed as:

$$\nu_R^+(T|\boldsymbol{w}) = \frac{1}{2\pi}\frac{\sigma_{\dot{R}}(\boldsymbol{w})}{\sigma_R(\boldsymbol{w})}\exp\left\{-\frac{1}{2}\left(\frac{T}{\sigma_R(\boldsymbol{w})}\right)^2\right\} \tag{1}$$

where σ_R denotes the standard deviation of R, and $\sigma_{\dot{R}}$ represents the time derivative. The response and its derivative's statistical moments are determined by integrating the response spectrum. Using the mean upcrossing rate, the probability that R remains below T can be computed if the individual up-crossings are assumed to be independent, resulting in an exponential distribution. The fragility functions are obtained as:

$$P\left[R(\boldsymbol{w}) > T \mid \boldsymbol{w}\right] = 1 - \exp\left\{-\nu_R^+(T,\boldsymbol{w})T_{st}\right\} \tag{2}$$

Fragility functions estimate bridge serviceability by calculating the probabilities of exceeding the specified performance limits. The expected failure probability is:

$$P_f = \int_0^\infty P\left[R(\mathbf{w}) > T \mid \mathbf{w}\right] f_w \, d\mathbf{w} \tag{3}$$

where P_f accounts for the joint PDF f_w of wind parameters, thus integrating frequency of occurrence. The probability of failure finally allows for estimating annual bridge downtime t_d considering N_{tst} number of stationary time intervals in a year.

$$t_d = N_{tst}P_f \tag{4}$$

2. RESULTS

The Hardanger bridge in Norway is used as a case study for which the long-term anemometry data was used to fit a correlated joint log-normal distribution of the turbulence parameters conditional

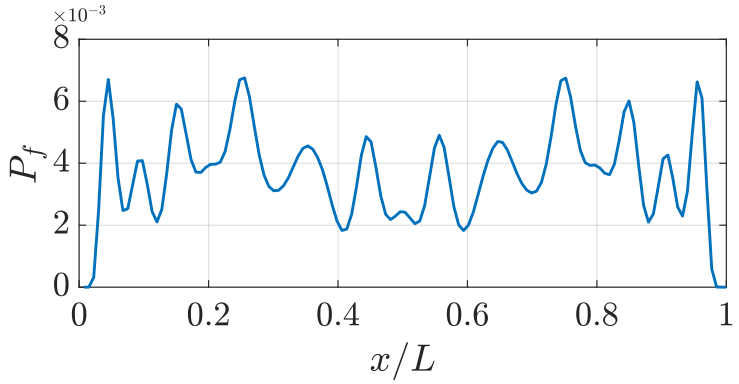


Figure 1. Probability of failure of the comfort criterion evaluated across the bridge span for the easterly winds.

to the mean wind velocity. Both cross-wind directions are considered, while skew winds are not treated. The easterly and the westerly winds conform to two Weibull distributions. The details of the model can be found in Fenerci and Øiseth, 2018 and Lystad et al., 2020.

The threshold T can be located in the range of "annoying disturbances" for user comfort, defined between 15 and 50 milli-g for vibration at frequencies below $1\,Hz$ (Simiu and Scanlan, 1996). In our analysis, we set a conservative threshold of $T = 0.15\,m/s^2$ and incorporated the combined effects of the vertical and torsional modes to determine the net vertical response. Fig. (1) illustrates the resulting failure probability distribution along the bridge deck, highlighting that the critical regions occur at the quarter-span sections. This observation can be attributed to the significant contribution of the first vertical mode at these locations, as shown in the mode shape in Fig. (2a). Consequently, the failure probabilities are computed at the quarter span for computing the downtime. Fig. (2) shows the PSD of the two responses at the quarter span obtained using the multi-mode buffeting calculations in the frequency domain.

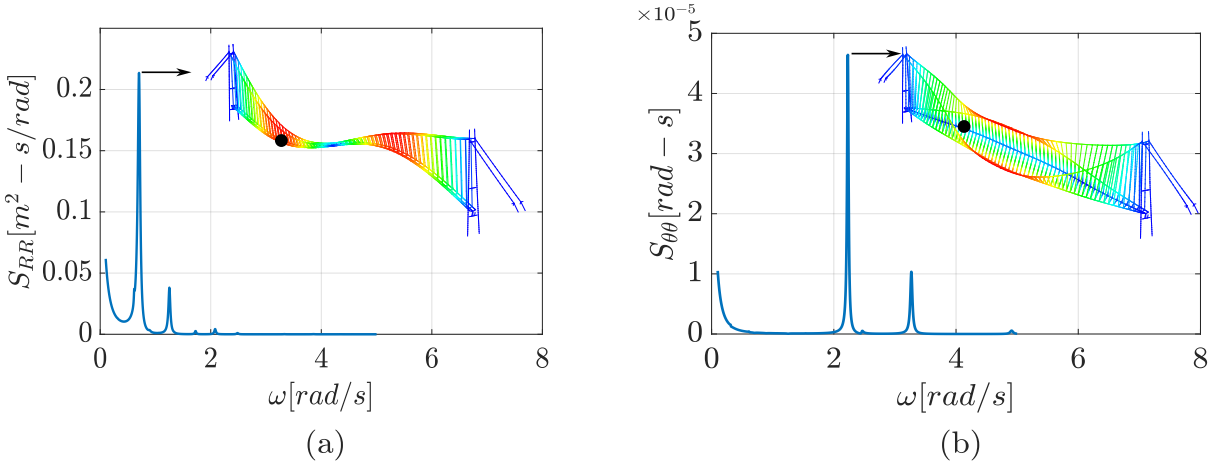


Figure 2. Power spectral density of (a) vertical and (b) torsional buffeting responses, evaluated under identical wind conditions at the quarter span, illustrating the minimal contribution of torsional response to the vertical deck acceleration.

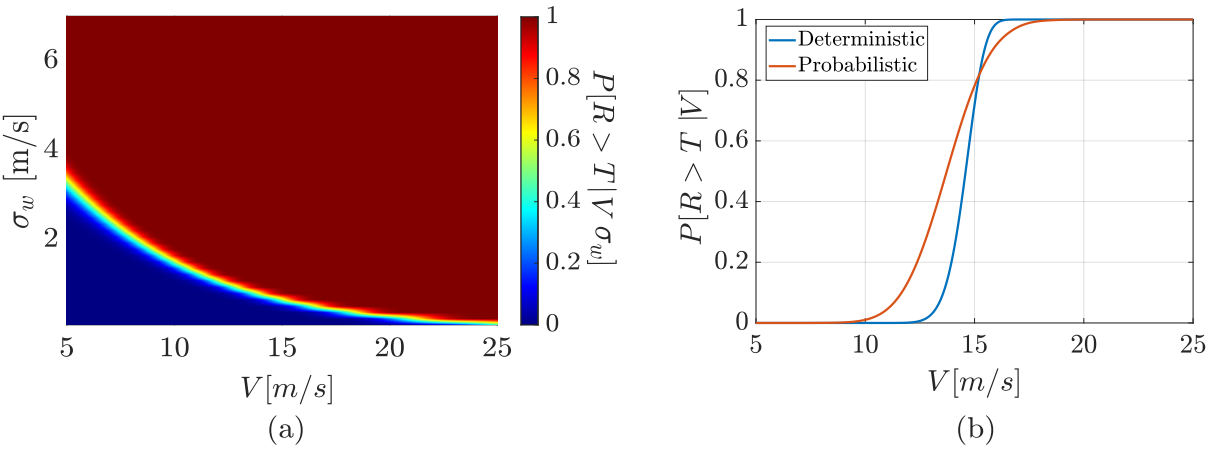


Figure 3. The fragility function shown in (a) is utilized to develop the probabilistic fragility curve depicted in (b), incorporating the joint PDF of V and σ_w.

Considering the mean wind velocity V and the standard deviation of vertical turbulence σ_w as uncertain parameters, Eq. (2) can be utilized to construct the fragility function, illustrated in Fig. (3a). The joint probability distribution of these wind parameters is then applied to reduce the dimensionality of the fragility function, as depicted in Fig. (3b).

Table 1. Comparison of failure probabilities for the comfort criterion under deterministic and uncertain across-wind turbulence intensity, including the estimated annual downtime.

	$P_f(East)$	$P_f(West)$	Downtime
Deterministic σ_w	2.00×10^{-3}	5.78×10^{-4}	11 hours and 16 minutes
Probabilistic σ_w	5.30×10^{-3}	1.01×10^{-3}	1 day 3 hours 40 minutes

Table (1) presents the failure probabilities for the driver comfort criterion under both wind directions. Assuming equal likelihood for each wind direction, the annual downtime is calculated using Eq. 4 by averaging the two P_f values. A comparison with the deterministic approach reveals that the deterministic method estimates an annual downtime of around 11 hours, whereas the probabilistic method indicates a significantly higher downtime of almost 28 hours. This substantial difference highlights the significant impact of accounting for variability in the turbulence field.

REFERENCES

Fenerci, A. and Øiseth, O., 2018. Site-specific data-driven probabilistic wind field modeling for the wind-induced response prediction of cable-supported bridges. Journal of Wind Engineering and Industrial Aerodynamics 181, 161–179.

Lystad, T. M., Fenerci, A., and Øiseth, O., 2020. Buffeting response of long-span bridges considering uncertain turbulence parameters using the environmental contour method. Engineering Structures 213, 110575.

Mechanical Vibration and Shock – Evaluation of Human Exposure to Whole-Body Vibration – Part 1: General Requirements, July 1997. Revised version. Geneva, Switzerland: International Organization for Standardization.

Simiu, E. and Scanlan, R. H., 1996. Wind effects on structures: fundamentals and applications to design. Vol. 688. John Wiley New York.

Application of reliability based design optimization to twin-box girder shape and gap for suspension bridges considering flutter constraint

Ibuki Kusano [1], Juan Quintela [2], Miguel Cid Montoya [3], José Ángel Jurado [2], Santiago Hernández [2]

[1]*IQS Ramon Llull University, Barcelona, Spain, ibuki.kusano@iqs.url.edu*
[2]*Universidade da Coruña, Coruña, Spain, juan.quintela.suarez@udc.es*
[3]*Clemson University, Clemson, South Carolina, USA, mcidmon@clemson.edu*

SUMMARY:
The reliability based design optimization (RBDO) was performed on a suspension bridge deck featuring a twin-box girder considering a probabilistic flutter constraint. Extensive Computational Fluid Dynamics (CFD) simulations were conducted at 15 sample points, utilizing forced oscillation simulations to acquire flutter derivatives within the design domain. Subsequently, surrogate models were generated to provide flutter derivatives for diverse deck designs during the optimization process. The twin-box section was characterized by three design variables, and flutter derivatives and wind speed were considered to contain uncertainty. The RBDO for the deck shape looking for a minimum material was then carried out considering probabilistic flutter constraints along with other deterministic structural constraints.

Keywords: reliability-based design optimization, twin-box girder, surrogate model, flutter

1. RBDO FUNDAMENTALS AND DEFINITION OF TWIN BOX DESIGN DOMAIN

Designing suspension bridges requires thoroughly assessing structural performance, particularly regarding wind-induced vibrations like flutter. Among various design parameters, the shape of the deck is crucial in assessing aeroelastic behavior. In recent years, twin-box girders have gained significant attention for long-span suspension bridges, as they offer improved performance against flutter compared to mono-box girders. The aeroelastic response of twin-box girders is known to be sensitive to the gap width between the boxes.

Optimizing a structure is crucial for material conservation, which plays a key role in reducing overall construction costs. Reliability-based design optimization (RBDO) incorporates system uncertainties into the design process, making it more robust and reliable than traditional deterministic optimization methods. The RBDO approach has been successfully used to optimize the size and shape of single box-girder decks (Kusano et al., 2014, 2020). To extend this method to twin-box sections, an extensive study was conducted at the University of Coruña, where forced-vibration simulations were used to obtain flutter derivatives, complemented by experimental validation of various designs (Badhurshah et al., 2023).

In this study, reliability-based design optimization was applied to the shape of a twin-box section of a suspension bridge, taking into account flutter constraints. Therefore, the objective function is the minimum area of the section. This analysis included uncertainties related to extreme wind

velocity and flutter derivatives.
To define a specific section of the twin-box girder, three design variables were selected: the depth (D) and width (C) of each box section and the gap (D) between them as shown in Figure 1. The section is symmetrical around the central vertical axis. The width (C) can range ±5% of the nominal value of 14 m, while the depth (D) can vary from -10% to +25% of the nominal value of 2 m. The gap ranges from -25% to 60% of the nominal value of 8 m.

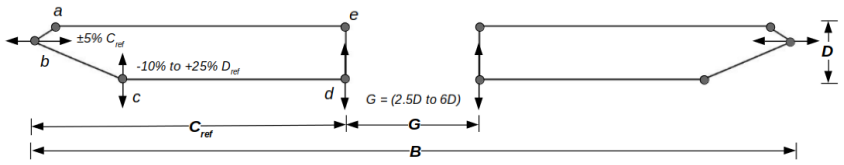
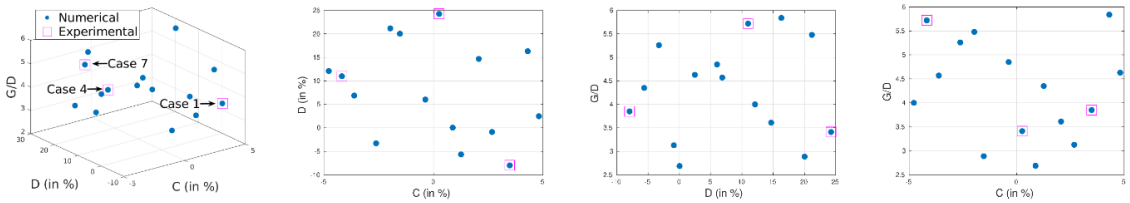


Figure 1. Definition of the twin-box section with 3 design variables

To cover the entire design domain, 15 sample sets were generated using the Latin Hypercube Sampling method, with each set representing a unique combination of the three design variables. To evaluate aeroelastic performance, forced vibration simulations were conducted at five reduced velocities, focusing on pitch and heave degrees of freedom. This resulted in a total of 45 aerodynamic simulations and 150 forced vibration analyses. Additionally, to validate the simulation results, three sections were selected for wind tunnel experiments.



(a) 3-D view **(b)** C vs D **(c)** G/D vs D **(d)** G/D vs C

Figure 2. Sampling plan in the design domain

Once all CFD results were obtained, surrogate hyperspaces were established across the entire design domain. The input variables for the surrogate models, width (C), depth (D), and gap (G), were transformed into non-dimensional forms. The surrogate models then provided flutter derivatives over a range of reduced velocities.

3. RELIABILITY AND RBSO OF SUSPENSION BRIDGES

Reliability analyses provide insights into the probability of failure concerning structural limit states while accounting for system uncertainties. In this study, we considered uncertainties in the extreme wind velocity at the bridge location, as well as in the flutter derivatives obtained from CFD simulations. Some of the flutter derivative isosurfaces from surrogate models at V^*=20 are represented in Figure 5. Each flutter derivative value at a given reduced velocity is assumed to follow a normal distribution, with its computed value as the mean value. We introduced a linearly increasing standard deviation to model increasing uncertainty with larger wind velocity. This

standard deviation was set to 0 at V^*=0 and σ_{max}=0.15μ at V^*=30 (Baldomir et al., 2013).

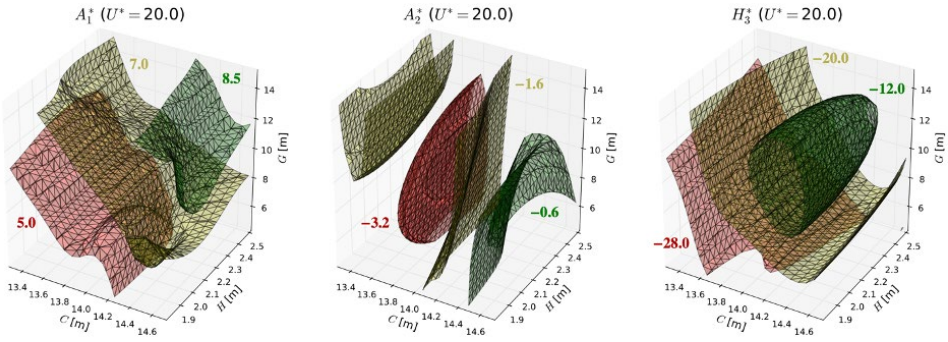


Figure 3. Isosurface of some flutter derivatives for the design variables at V^*=20

The limit state function that defines the structural failure under flutter can be written as:

$$G(\mathbf{x}) = V_f(x_i) - x_w \qquad i = 1,...,n \tag{3}$$

where V_f is the flutter wind speed, x_i are n random variables representing a set of points of flutter derivatives and x_w is the random variable of the extreme wind velocity at the bridge location. The total number of random variables is expressed as vector **x** of n+1 dimension.
The First Order Reliability Method (FORM) is used in this study to compute the reliability index, β of the bridge structure due to flutter failure. This method calculates the minimum distance from the mean value of the random variables to the failure surface G(**U**)=0. The resulting optimization problem is:

$$\beta = \sqrt{\mathbf{U}^{\mathrm{T}} \cdot \mathbf{U}} \text{ subject to: } \; G(\mathbf{U}) = 0 \tag{4}$$

The solution $\mathbf{U}^*$ is denoted as the Most Probable Point of Failure (MPP). The Hasofer-Lind method (Hasofer and Lind, 1974) was used to solve the problem among different algorithms.

A reliability-based design optimization (RBDO) was conducted on a long-span suspension bridge with characteristics similar to the Great Belt East Bridge. The baseline geometry of the deck section is shown in Figure 1. A 3D finite element model using Abaqus was employed to perform both static and modal analysis of the bridge during the optimization process. The initial design's natural frequencies and mode shapes were calculated, and several relevant modes were selected for flutter analysis. The random variables and the limit state function were defined earlier in Section 3. The mean and standard deviation of the extreme wind speed were based on the Danish Wind Code DS410 (1998).
The RBDO for shape optimization was performed considering three design variables: the depth (D), width (C), and gap (G) of the box section. The objective was to minimize the girder volume of the twin-box.

The RBDO problem is formulated as follows:
Minimize: *Girder volume* (**d**)

subject to:
$$g_1 : P\left[V_f(\mathbf{x}) - x_w \le 0\right] \le P_f \qquad P_f = \Phi(-\beta) \text{ where } \beta=4.0$$
$$g_2 : -5\% \le \Delta C \le 5\%;\ -10\% \le \Delta D \le 10\%;\ -25\% \le \Delta G \le 60\% \tag{5}$$
$$g_4 : z_d / z_{\max} - 1 \le 0 \qquad \text{where } z_{max}=L/500;\ L=1624 \text{ m}$$
$$g_5 : \sigma_c = 565 \text{ MPa}$$

g_1 is the probabilistic flutter constraint while g_2 sets the design limits. g_4 and g_5 are deterministic constraints restricting the maximum girder vertical displacement, and the cable stress obtained from static analyses. Figure 4 shows an example of the evolution of the girder volume during optimization.

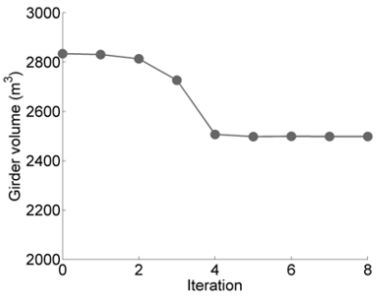


Figure 4. Evolution of the girder volume during optimization

7. CONCLUSIONS

The RBDO was performed on a twin-box deck section shape of a long-span suspension bridge considering uncertainty in the extreme wind velocity as well as the flutter derivatives obtained from surrogate models based on CFD simulations. The RBDO can provide the optimum design considering uncertainties associated with wind-induced phenomena of suspension bridges, which is more robust than conventional deterministic designs.

ACKNOWLEDGEMENTS

This research has been funded by the National Research Agency (AEI) of the Spanish Ministry for Science and Innovation, in the frame of the research project PID2022-138069OB-I00.

REFERENCES

Badhurshah, R., Álvarez, A.J., Nieto, F., Jurado, J.A., Hernández, S., 2023. Experimental and numerical results on evaluation of flutter, 16th Int'l Conference on Wind Engineering, Florence, Italy

Baldomir, A., Kusano, I. Jurado, J.A., Hernández, S. 2013. "A reliability study for the Messina Bridge with respect to flutter phenomena considering uncertainties in experimental and numerical data" Computers and Structures 128 91-100

DS 410 (1998). Danish Wind Code DS 410, Danish Standard Association, Copenhagen, Denmark.

Hasofer, A. M., Lind, N. (1974) An exact and invariant first-order reliability format. Journal of the Engineering Mechanics Division, 100(EM1) 111–121

Kusano, I., Baldomir, A., Jurado, J.A., Hernández, S. 2015. "Probabilistic optimization of the main cable and bridge deck of long-span suspension bridges under flutter constraint", J. Wind Engineering and Industrial Aerodynamics 146 59-70

Kusano, I., Cid Montoya, M., Baldomir, A., Nieto, F., Jurado, J.A., Hernández, S. 2020. "Reliability based design optimization for bridge girder shape and plate thicknesses of long-span suspension bridges considering aeroelastic constraint" J. Wind Engineering and Industrial Aerodynamics, 202 104176

Reliability analysis of long-span suspension bridges against buffeting considering uncertainty in flutter derivatives

J. Quintela [1], J.Á. Jurado [2], M. Cid Montoya [3], I. Kusano [4], S. Hernández [5]

[1]*School of Civil Engineering, Universidade da Coruña, Spain, juan.quintela.suarez@udc.es*
[2]*School of Civil Engineering, Universidade da Coruña, Spain, jose.angel.jurado@udc.es*
[3]*Glenn Department of Civil Engineering, Clemson University, USA, mcidmon@clemson.edu*
[4]*Departament Industrial Engineering, Universitat Ramon Llull, Spain, ibuki.kusano@iqs.url.edu*
[5]*School of Civil Engineering, Universidade da Coruña, Spain santiago.hernandez@udc.es*

SUMMARY:
The flutter derivatives relate the displacements of a bridge deck to aeroelastic forces and are a key parameter in the analysis of different aeroelastic phenomena in bridges, particularly in buffeting. These functions have inherent uncertainties associated with them. In this work, a probabilistic analysis of a long-span suspension bridge has been conducted, introducing the flutter derivatives as well as wind turbulence parameters and aerodynamic coefficients as random variables and obtaining the bridge's failure probability using the First Order Reliability Method (FORM) for different limit states. Additionally, a parallel computation method has been implemented to reduce computational cost, simultaneously solving the buffeting problem across various frequency ranges.

Keywords: buffeting, reliability studies, uncertainties, bridge aeroelasticity, random variables

1. BUFFETING FORMULATION

Buffeting is a phenomenon in which turbulent wind exerts dynamic, repetitive forces on a structure. For bridges, it describes the oscillations or vibrations caused by fluctuating wind forces impacting the bridge's components.

The buffeting response of a bridge is obtained from the global dynamic equilibrium equation, considering the buffeting forces exerted on the deck. This can be expressed as

$$\mathbf{M}\ddot{\mathbf{u}} + \mathbf{C}\dot{\mathbf{u}} + \mathbf{K}\mathbf{u} = \mathbf{f_a} + \mathbf{f_b} \tag{1}$$

where **M**, **C** and **K** are, respectively, the global mass, damping and stiffness matrices of the system, $\mathbf{f_a} = \mathbf{C_a}\dot{\mathbf{u}} + \mathbf{K_a}\mathbf{u}$ is the vector of aeroelastic forces and f_b the vector of the buffeting forces. Rearranging terms Eq. (1) can be expressed as:

$$\mathbf{M}\ddot{\mathbf{u}} + (\mathbf{C} - \mathbf{C_a})\dot{\mathbf{u}} + (\mathbf{K} - \mathbf{K_a})\mathbf{u} = \mathbf{f_b} \tag{2}$$

Using a frequency domain approach, the multi-modal buffeting analysis can be solved. The buffeting responses of the bridge defined by the matrix of Power Spectral Density (PSD) of the displacements, $\mathbf{S_u}$, can be obtained through manipulation of Eq. (2) as:

$$\mathbf{S_u} = \mathbf{\Phi H} \Phi^T \mathbf{S_{fb}} \mathbf{\Phi H}^{*T} \mathbf{\Phi}^T \tag{3}$$

where **Φ** is the modal matrix normalized to the mass, **H** is the impedance matrix, and $\mathbf{S_u}$ is the matrix of PSDs of the buffeting forces, defined as:

$$\mathbf{S_u} = \chi_A^*(U^*)\mathbf{S}_{\text{wind}}(f^*)\chi_A^{*T}(U^*) = \left(\frac{1}{2}\rho U B l_e\right)^2 \begin{vmatrix} \chi_{Du}^* & \chi_{Dw}^* \\ \chi_{Lu}^* & \chi_{Lw}^* \\ B\chi_{Mu}^* & B\chi_{Mw}^* \end{vmatrix} \begin{vmatrix} S_{uu} & S_{uw} \\ S_{uw} & S_{ww} \end{vmatrix} \begin{vmatrix} \chi_{Du}^* & \chi_{Lu}^* & B\chi_{Mu}^* \\ \chi_{Dw}^* & \chi_{Lw}^* & B\chi_{Mw}^* \end{vmatrix} \quad (4)$$

where χ_A^* are the admittance functions, and $\mathbf{S}_{\text{wind}}(f^*)$ is the cross-power spectrum matrix of the incoming turbulence, and S_{uu}, S_{uw} and S_{ww} are the different components of the wind spectrum. By integrating the resulting matrix of the PSD, $\mathbf{S_u}$, for each node of the deck and wind velocity, the buffeting responses are obtained as the root mean square (RMS).

$$\mathrm{u}_{RMS} = \sqrt{\int_0^\infty S_{u_i u_i}\, df}, \quad \dot{u}_{RMS} = \sqrt{\int_0^\infty 4\,\pi^2 f^2 S_{u_i u_i}\, df} \quad \text{and} \quad \ddot{u}_{RMS} = \sqrt{\int_0^\infty 16\,\pi^4 f^4 S_{u_i u_i}\, df} \quad (5)$$

This methodology has been implemented in custom Python code to obtain buffeting responses at specified wind speeds. The code computes the PSD values for each frequency considered in the analysis and derives the RMS values through the integration of these PSDs.

2. RELIABILITY ANALYSIS CONSIDERING BUFFETING PHENOMENA

In buffeting analysis, various parameters, each with inherent uncertainties, play a critical role in influencing the structural response. Key factors include flutter derivatives, aerodynamic coefficients and wind turbulence parameters, which can vary significantly. A probabilistic approach to buffeting analysis is therefore essential, representing these parameters with random distributions to capture their variability.

The buffeting responses of a structure must remain below a predefined limit, typically established in accordance with the project's criteria, which often involves setting maximum accelerations at a specific point on the deck. Considering the uncertainty in the aforementioned parameters and characterizing them through random distributions, the limit state can be expressed using a probabilistic approach, as follows:

$$G(\mathbf{x}) = \mathrm{RMS}_{max} - \mathrm{RMS}_{buff}(x_i) \qquad i = 1, \ldots\ldots, n \quad (6)$$

where x_i are the random variables considered in the buffeting analysis. After defining the random variables and establishing the limit state function, structural reliability can be determined using the First Order Reliability Method (FORM). This method defines the reliability index, denoted as β, as the minimum distance between the origin in the normalized **u**-space and the limit state function $G(\mathbf{u}) = 0$.

The iterative process for determining the reliability index requires evaluating the limit state function, $G(\mathbf{u}) = 0$, along with its gradients at each iteration. This necessitates calculating the buffeting response in every iteration, resulting in significant computational expense due to the high number of random variables and the extensive frequency range analyzed in each buffeting calculation. To address this, a parallelization strategy using a High-Performance Computing

Cluster (HPCC) was implemented. In this approach, the frequency range is divided into smaller intervals, enabling concurrent buffeting analyses for each interval. Once completed, the results are combined to provide the overall response across the full frequency range.

3. APPLICATION CASE: GREAT BELT BRIDGE

The method described in the previous section was applied to assess the structural reliability of the Great Belt Bridge. Fig. 1 illustrates the bridge's general layout. The structural model used for the modal analysis was developed in the open-source software OpenSees, with the deck and towers modelled as beam-column elements that account for large displacements.

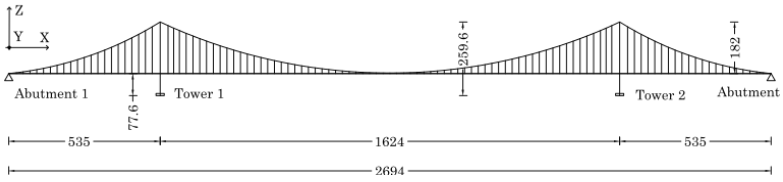
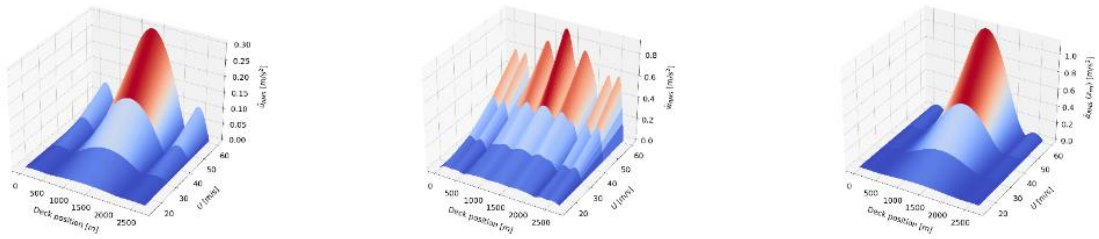


Figure 1. Great Belt Bridge general layout

The random variables considered in the reliability analysis are the experimental values that define the flutter derivatives, the wind speed, the structural damping, the aerodynamic coefficients and their slopes, as well as the intensity of turbulence and the integral length scales, both horizontal and vertical, of the incoming turbulent wind. The wind speed has been characterized by a Gumbel distribution with a mean of 25 m/s and a standard deviation of 1.5 m/s, derived from extreme wind in the region. The rest of the random variables considered were characterized with normal and log-normal distributions, where the mean value is the deterministic value obtained in experimental tests (Kusano et al., 2018). The standard deviation considered was a 10% of the mean values for the incoming turbulent wind parameters and a 15% of the mean values for the flutter derivatives, respectively.

Two cases have been considered with limits for RMS of vertical and equivalent torsional accelerations of 0.25 m/s^2 at the midpoint. These values were defined based on studies from various publications and the deterministic buffeting response displayed in Fig. 2. While different acceptance criteria can be adopted for vehicle drivability (Isyumov 2012) and ride comfort (Zhu et al. 2021), similar thresholds are imposed in the project specifications of many bridges, such as in the Messina Bridge project (Stretto di Messina 2004).



(a) RMS of lateral acc. (b) RMS of vertical acc. (c) RMS of torsional acc.

Figure 2. RMS of the accelerations along the span of the deck for an increasing wind speed

The first case considered for reliability analysis involves treating each of the points defining a flutter derivative, in addition to the wind speed, as random variables, which is particularly interesting for determining which functions have the greatest impact on the buffeting response.

Table 1. Reliability results considering the flutter derivatives as random variables

Random variables	Nº of RV	Vertical limit state		Torsional limit state	
		β	P_f	β	P_f
$x_u,\ A^*_{1.1}, \dots, A^*_{1.n}$	5	4.616	1.94e-06	4.075	3.36e-05
$x_u,\ A^*_{2.1}, \dots, A^*_{2.n}$	7	4.613	1.98e-06	3.839	6.16e-05
$x_u,\ A^*_{3.1}, \dots, A^*_{3.n}$	7	4.618	1.92e-06	4.179	1.47e-05
$x_u,\ A^*_{4.1}, \dots, A^*_{4.n}$	7	4.618	1.93e-06	4.170	1.52e-05
$x_u,\ H^*_{1.1}, \dots, H^*_{1.n}$	5	4.498	3.42e-06	4.181	1.44e-05
$x_u,\ H^*_{2.1}, \dots, H^*_{2.n}$	7	4.619	1.92e-06	4.181	1.44e-05
$x_u,\ H^*_{3.1}, \dots, H^*_{3.n}$	7	4.607	2.03e-06	4.133	1.78e-05
$x_u,\ H^*_{4.1}, \dots, H^*_{4.n}$	7	4.617	1.94e-06	4.181	1.44e-05

Table 1 shows the results considering only the uncertainty of each flutter derivative individually. The most influential functions are A^*_1, which relates the moment force with the velocity of vertical displacement, A^*_2, which relates the moment force with the velocity of rotation, H^*_1, which relates the lift force with the velocity of vertical displacement, and H^*_3, which relates the lift force with the rotation. Once the flutter derivatives with the most impact have been identified, the probability of failure has been calculated by including the wind turbulence parameters as random variables, in addition to these functions, increasing the number of random variables up to 56. The results are shown in Table 2.

Table 2. Reliability results considering the flutter derivatives and turbulence parameters as random variables

Random variables	Nº of RV	Vertical limit state		Torsional limit state	
		β	P_f	β	P_f
x_u, ζ, C_D, C_L, C_M, $\hat{C}_D$, $\hat{C}_L$, $\hat{C}_M$, I_u, I_w, L_u, L_w $A^*_1, A^*_2, A^*_3, A^*_4, H^*_1, H^*_2, H^*_3, H^*_4$	56	4.112	1.96e-05	3.561	1.84e-04

4. CONCLUSIONS

A reliability analysis of the Great Belt has been conducted, taking into consideration the buffeting phenomenon and incorporating the flutter derivatives as random variables. The probability of failure is heavily affected by the uncertainty of the A^*_1, A^*_2, H^*_1, and H^*_3 flutter derivatives.

ACKNOWLEDGEMENTS

This research has been funded by the Spanish Ministry for Science and Innovation, in the frame of the research project PID2022-138069OB-I00.

REFERENCES

Isyumov N., 2012. Alan G. Davenport's mark on wind engineering. Journal of Wind Engineering & Industrial Aerodynamics, 104:12–24.

Kusano, I., Baldomir, A., Jurado, J.Á., Hernández, S., 2018. The importance of correlation among flutter derivatives for the reliability based optimum design of suspension bridges. Engineering Structures, 173, pp. 416 - 428.

Stretto di Messina. Messina Strait Bridge, 2004. Basis of design and expected performance (italian: Ponte sullo Stretto di Messina: Fondamenti progettuali e prestazioni attese per l'opera di attraversamento). Technical report, Stretto di Messina Report GCG.F.04.01.

Zhu J., Xiong Z., Xiang H., Huang X., and Li Y., 2021. Ride comfort evaluation of stochastic traffic flow crossing long-span suspension bridge experiencing vortex-induced vibration. Journal of Wind Engineering & Industrial Aerodynamics, 219:104794.

Aeroelastic analysis of a pedestrian suspension bridge with a span of 648 m

A. Fontán [1], J. Quintela [2], J.Á. Jurado [3], A. Baldomir [4], M. Cid Montoya [5], I. Kusano [6], S. Hernández [7]

[1]*School of Civil Engineering, Universidade da Coruña, Spain, arturo.fontan@udc.es*
[2]*School of Civil Engineering, Universidade da Coruña, Spain, juan.quintela.suarez@udc.es*
[3]*School of Civil Engineering, Universidade da Coruña, Spain, jose.angel.jurado@udc.es*
[4]*School of Civil Engineering, Universidade da Coruña, Spain, aitor.baldomir@udc.es*
[5]*Glenn Department of Civil Engineering, Clemson University, USA, mcidmon@clemson.edu*
[6]*Departament Industrial Engineering, Universitat Ramon Llull, Spain, ibuki.kusano@iqs.url.edu*
[7]*School of Civil Engineering, Universidade da Coruña, Spain, santiago.hernandez@udc.es*

SUMMARY:
Aeroelastic studies on suspension pedestrian bridges with lightweight decks are limited. The flexible and slender cable structures of these bridges are susceptible to wind-induced vibrations and instabilities. This paper presents an analysis of a footbridge with a span of 648 m using the multi-modal flutter and buffeting aeroelastic analysis software developed by the Universidade da Coruña for long-span bridges. The analysis relies on a suitable number of vibration modes derived from a finite element structural model, complemented by aerodynamic coefficients and flutter derivatives of the deck, which can be preliminarily estimated through the quasi-steady theory using the aerodynamic coefficients or be obtained from experimental tests in wind tunnel.

Keywords: flutter, pedestrian suspension bridges, buffeting

1. AEROELASTIC ANALYSIS OF PEDESTRIAN SUSPENSION BRIDGES

Cable-supported pedestrian bridges have seen significant growth in recent years. This bridge type is very slender, with a positive visual impact, minimal environmental impact at their location, and they effectively facilitate crossing geographic obstacles in mountainous areas or deep valleys. They enable hiking activities that would otherwise be impossible, and often become a tourist attraction, drawing new visitors who can appreciate the beauty of the areas where they are situated.

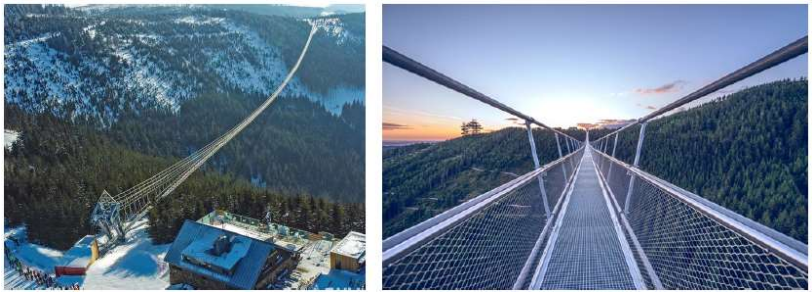


Figure 1. Ski Bridge 721 in Czech Republic.

Examples of studies on this topic include those by Faridani and Barghian, 2012 and Tadeu et al., 2022. The Universidade da Coruña developed two multi-modal analysis software designed to assess the wind flutter speed and the buffeting response of long-span bridges, respectively. Both software have since been utilized in numerous studies aimed at optimizing long-span bridges, as seen in the works of Kusano et al., 2014. The functionality of the flutter software can be understood by starting with the dynamic equilibrium equation:

$$\mathbf{M}\ddot{\mathbf{u}} + \mathbf{C}\dot{\mathbf{u}} + \mathbf{K}\mathbf{u} = \mathbf{f}_a \tag{1}$$

where **M**, **C**, and **K** are global mass, damping, and stiffness matrices respectively, $\mathbf{u}$, $\dot{\mathbf{u}}$, $\ddot{\mathbf{u}}$ are displacement, velocity and acceleration vector of the structure. $\mathbf{f}_a$ can be expressed as the product of an aeroelastic stiffness matrix $\mathbf{K}_a$ by the displacements plus an aeroelastic damping matrix $\mathbf{C}_a$ multiplied by the velocities. The forces acting on deck structural nodes *i* are related to its movements and velocities through the flutter derivatives, which are used to define the previous matrices $\mathbf{K}_a$ and $\mathbf{C}_a$. By multi-modal analysis Eq. (1) leads to a non-linear eigenvalue problem as follows:

$$(\mathbf{A} - \mu\mathbf{I})\mathbf{w}_\mu e^{\mu t} = 0 \tag{2}$$

where matrix **A** depends on **K**, **C**, $\mathbf{K}_a$ and $\mathbf{C}_a$ matrices. This equation is solved as an eigenvalue problem using a multi-modal formulation (Jurado et al., 2011) where the critical flutter speed is obtained when the real part of one of the eigenvalues becomes null, indicating that the instability appears.

For the buffeting analysis a new term of buffeting forces, $\mathbf{f_b}$, is added to Eq. (1). Using a frequency domain approach, the multi-modal buffeting analysis can be solved. The buffeting responses of the bridge defined by the matrix of Power Spectral Density (PSD) of the displacements, $\mathbf{S_u}$, can be obtained through manipulation of Eq. (1) as:

$$\mathbf{S_u} = \mathbf{\Phi H}\Phi^T\mathbf{S_{fb}}\mathbf{\Phi H}^{*T}\mathbf{\Phi}^T \tag{3}$$

where $\mathbf{\Phi}$ is the modal matrix normalized to the mass, **H** is the impedance matrix, and $\mathbf{S_u}$ is the matrix of PSDs of the buffeting forces, defined as:

$$\mathbf{S_u} = \chi_A^*(U^*)\mathbf{S}_{\text{wind}}(f^*)\chi_A^{*T}(U^*) = \left(\frac{1}{2}\rho U B l_e\right)^2 \begin{vmatrix} \chi_{Du}^* & \chi_{Dw}^* \\ \chi_{Lu}^* & \chi_{Lw}^* \\ B\chi_{Mu}^* & B\chi_{Mw}^* \end{vmatrix} \begin{vmatrix} S_{uu} & S_{uw} \\ S_{uw} & S_{ww} \end{vmatrix} \begin{vmatrix} \chi_{Du}^* & \chi_{Lu}^* & B\chi_{Mu}^* \\ \chi_{Dw}^* & \chi_{Lw}^* & B\chi_{Mw}^* \end{vmatrix} \tag{4}$$

where χ_A^* are the admittance functions, and $\mathbf{S}_{\text{wind}}(f^*)$ is the cross-power spectrum matrix of the incoming turbulence, and S_{uu}, S_{uu} and S_{ww} are the different components of the wind spectrum. By integrating the resulting matrix of the PSD, $\mathbf{S_u}$, for each node of the deck and wind velocity, the buffeting responses are obtained as the root mean square (RMS).

This methodology has been implemented in custom Python code to obtain buffeting responses at specified wind speeds. The code computes the PSD values for each frequency considered in the

analysis and derives the RMS values through the integration of these PSDs.

2. STRUCTURAL MODEL

The main feature of the adopted solution is that it was decided to not build towers for aesthetic and environmental reasons, which posed a technical challenge in designing this unique structure. The main supporting element of the 648 m span deck consists of two spatial catenaries with a cable length of 828 m between anchors, which is a world record for its typology. The deck is made up of 162 metal modules, each 4 meters long, and is suspended from the main catenaries by two sets of hangers, one upper and one lower. A cable system has been installed to provide lateral bracing for the deck and to ensure overall rigidity of the structure, comprising other two spatial catenaries and a series of hangers that connect the deck to these catenaries at intervals of 16 meters. The general dimensions of the pedestrian bridge are shown on Fig. 2.

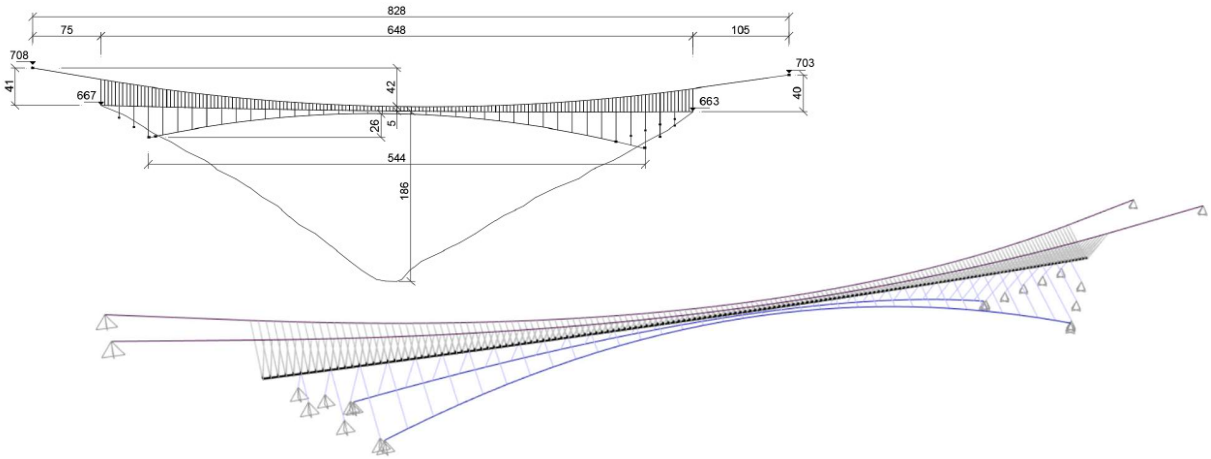


Figure 2. Lateral view of the suspension footbridge and 3D view of the structural model

The structural behavior of the footbridge was determined by creating a finite element model using the SAP2000 software (Fig.2). It is a highly flexible structure, supported by cables, requiring that the analysis account for changes in stiffness as loads are applied. Unlike more conventional structures, the stiffness of this structure constantly depends on the loads it is subjected to, making it necessary to conduct the analysis considering geometric nonlinearity with large displacements. Cable elements are used to model the catenaries, hangers, and wind cables, while frame elements are used for the metal modules of the deck. To generate the model, a Python script was created to produce a fully parameterized model of this bridge type with the desired deck geometry defined as a starting point.

3. AEROELASTIC ANALYSIS RESULTS

The flutter analysis of the pedestrian bridge was carried out for two different damping factors, 1% and 4%. For both cases two different sets of flutter derivatives were considered. In a first preliminary case, analytical expressions defined by Theodorsen for a flat plate were used, allowing for an approximation of the critical flutter speed without the need for wind tunnel testing. In a second case considered, the flutter derivatives were obtained through a quasi-static theory approximation using the aerodynamic coefficients of a similar footbridge (Tadeu et al. 2022).

Table 1 presents preliminary results of the critical flutter speed obtained for all the cases.

Table 1. Preliminary critical flutter speed results

Damping factor	Flutter derivatives	U_{crit} (m/s)
0.01	Theodorsen	31.21
	QST-Theory	71.36
0.04	Theodorsen	48.71
	QST-Theory	85.70

Currently aeroelastic wind tunnel tests are being carried out in order to obtain the experimental flutter derivatives (Fig. 3). This will allow to compare the critical flutter speed with the experimental flutter derivatives to the quasi-steady theory case. Additionally, once the experimental flutter derivatives are obtained, a buffeting analysis of the footbridge will be carried out to obtain the RMS of the accelerations along the deck.

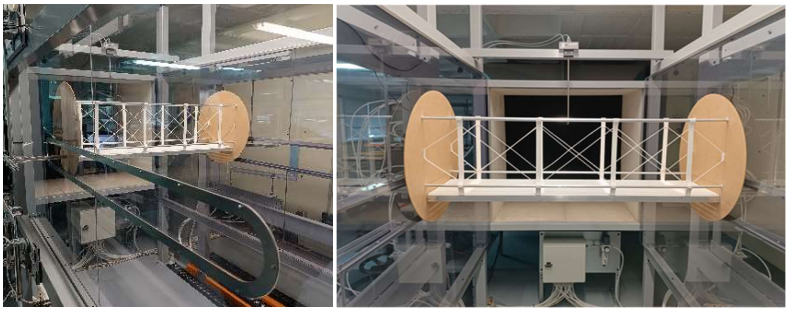


Figure 3. Wind tunnel experiment of a sectional model

4. CONCLUSIONS

Aeroelastic analyses of a suspension footbridge have been carried out to investigate flutter phenomena in these structures. The critical flutter speed results for suspension footbridges help engineers assess whether additional stiffness is needed for the structure, such as by adding stabilizing cables beneath the deck. Future work will include aeroelastic wind tunnel test to obtain the flutter derivatives experimentally and the assessment of the buffeting response of the pedestrian bridge.

ACKNOWLEDGEMENTS

This research has been funded by the Spanish Ministry for Science and Innovation, in the frame of the research project PID2022-138069OB-I00.

REFERENCES

Faridani H.M., Barghian M., 2012. Improvement of dynamic performances of suspension footbridges by modifying the hanger systems, Engineering Structures, Volume 34, 2012, pp. 52-68, ISSN 0141-0296.

Jurado J.A., Hernández S., Nieto F., Mosquera A., 2011. Bridge Aeroelasticity. Sensitivity Analysis and Optimal Design, Wit Press, 2011, Ashurst Lodge, Ashurst, Southampton, SO40 7AA, UK.

Kusano I., Baldomir A, Jurado J.Á., Hernández S., 2014. Reliability Based Design Optimization of long-span bridges considering flutter, Journal of Wind Engineering & Industrial Aerodynamics, 2014, Vol. 135, pp. 149–162.

Tadeu A., Marques da Silva F., Ramezani B., Romero A., Škerget L., Bandeira F., 2022. Experimental and numerical evaluation of the wind load on the 516 Arouca pedestrian suspension bridge, Journal of Wind Engineering & Industrial Aerodynamics, 2022, Vol. 220.

Aerodynamic investigation of twin-deck long-span bridges for vortex-induced vibrations

Samir Chawdhury[1], Gledson Rodrigo Tondo[2], Guido Morgenthal[3]

[1]*Bauhaus University, Weimar, Germany, samir.chawdhury@uni-weimar.de*
[2]*Bauhaus University, Weimar, Germany, gledson.rodrigo.tondo@uni-weimar.de*
[3]*Bauhaus University, Weimar, Germany, guido.morgenthal@uni-weimar.de*

SUMMARY:
Modern long-span bridges are highly flexible and susceptible to aeroelastic phenomena caused by wind action. Twin-deck bridges have recently attracted interest due to their aerodynamic benefits in reducing flutter instability and enhancing traffic capacity. However, the aeroelastic response of these bridges is complex, as the gap between two decks affects the aerodynamic coupling between upstream and downstream sections. This interaction complicates predictions of aerodynamic and aeroelastic behavior, especially when seeking an optimal, cost-effective deck geometry. This paper presents a numerical study on the vortex-induced vibration (VIV) behavior of long-span twin-deck bridges, emphasizing the impact of different gap configurations. A reference cross-section is chosen and validated against static wind coefficients from previous studies, followed by an analysis of six modified configurations. Flow simulations are performed on static bridge cross-sections to investigate the vortex shedding pattern and identify the resonance wind speed. Subsequently, coupled dynamic simulations are performed over a range of wind speeds to investigate the VIV behavior. Results reveal complex coupled response mechanisms influenced by gap configuration, where the spectral similarity of lift forces and the correlation between upstream and downstream forces play a key role. These findings highlight the importance of parametric studies in optimizing twin-deck bridge configurations for improved aerodynamic performance.

Keywords: Aerodynamic investigation, Vortex-induced vibrations, Numerical simulations, Long-span twin-deck bridges.

1. INTRODUCTION

The design of super long-span bridges presents significant challenges, as these structures are highly susceptible to wind-induced vibrations due to their flexibility, large spans, and low damping. With growing demand for efficient and sustainable infrastructure, managing these aerodynamic effects is essential to ensure the safety, durability, and serviceability of such bridges. In recent years, twin-deck long-span bridges have gained attention for their aerodynamic advantages, particularly in reducing flutter instability, allowing engineers to push the boundaries of long-span bridge design. However, their aerodynamic performance is complex due to interference effects, necessitating detailed studies to understand their behavior under varying gap widths and wind conditions. The observed vortex-induced vibrations (VIV) in the Xihoumen Bridge (Zhu et al., 2018) across several vibration modes underscore the need for careful consideration of the aeroelastic interaction between the upstream and downstream decks, as well as the influence of the gap width and depth.

This study investigates the wind-induced vibration behavior of twin-deck bridge sections (as shown schematically in Fig. 1) through computational analyses, focusing on parameters such as the gap-to-depth ratio and its impact on the coupled response. The following sections provide an overview of the numerical methods used and present key findings from the parametric studies.

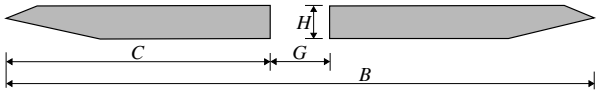


Figure 1. Schematic of twin-deck bridge cross-section, with B as total deck width, H as deck height, and G as gap.

2. METHODOLOGY

A computational fluid dynamics (CFD) solver, which is fundamentally based on vortex particle methods (VPM), is used to perform the numerical analysis of bridge sections. VPM relies on a simplified vorticity formulation of the fundamental Navier–Stokes equations for inviscid, incompressible flow. This approach is advantageous for developing fluid-structure interaction (FSI) models, as it is primarily a grid-free method and requires no conforming mesh at the interface. The use of the immersed interface technique allows to discretize the geometry assuming piecewise linear panels of approximately uniform length. In each time step, the vorticity distribution is calculated and the system thus integrated forward in time. More details regarding the particle-based vortex methods and several applications with validation can be found in (Morgenthal and Walther, 2007; Morgenthal, 2002) while extended implementations in (Morgenthal, Corriols, et al., 2014).

3. RESULTS

A reference twin-deck bridge section is selected from Nieto et al. (2020), and a comparison of the numerically analyzed static wind coefficients with wind tunnel test results shows good agreement, despite the limited range of angles of attack available in the reference data (see Fig. 2). The section is modified for six gap-to-height (G/H) ratios, and static simulations are performed for each section under free-stream flow U_∞ to identify the shedding frequency f_s and calculate the Strouhal number ($St = f_s H/U_\infty$). For six considered G/H of 1, 2, 3, 4, 5 and 6, the corresponding resonant wind speeds are determined as 7.5 m/s, 9.0 m/s, 7.2 m/s, 7.0 m/s, 7.0 m/s and 6.5 m/s, respectively. With an adaptation from Nieto et al. (2020), the dynamic properties are set as follows: bending mass $m = 28{,}200$ kg/m, damping ratio $\zeta_h = 0.5\%$, and bending frequency $f_1 = 0.5$ Hz.

From the coupled dynamic analysis, the root mean square (RMS) and maximum absolute displacements are compared in Fig. 3. The configuration with a G/H of 3 shows the most significant response, and time histories at various wind speeds are compared in Fig. 4 along with response and force spectra. To investigate the reasons behind varying response patterns, Fig. 5 presents the RMS lift forces on individual sections and the total.

To explain why G/H ratios of 4, 5, and 6 exhibit lower response than 3, the correlation of lift forces on upstream and downstream sections is compared in Fig. 6, revealing a negative correlation. Additionally, Fig. 7 compares the lift force spectra on upstream and downstream sections, showing

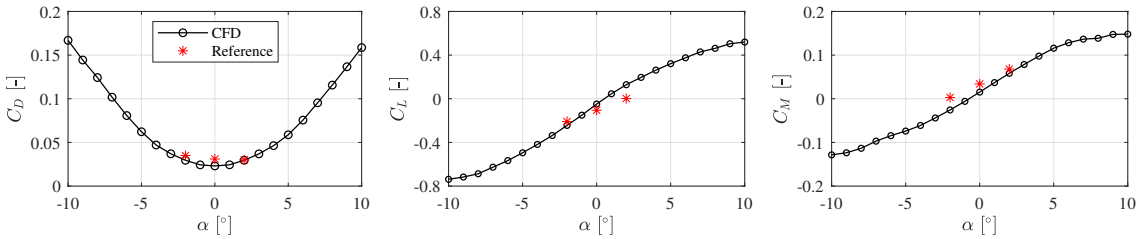


Figure 2. Comparison of static wind coefficients at different angle of attacks.

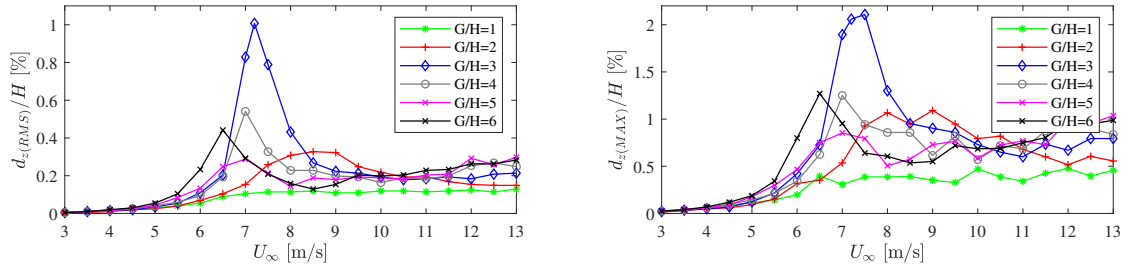


Figure 3. Root mean square (RMS) and maximum absolute displacement of bridge sections with different gap ratios.

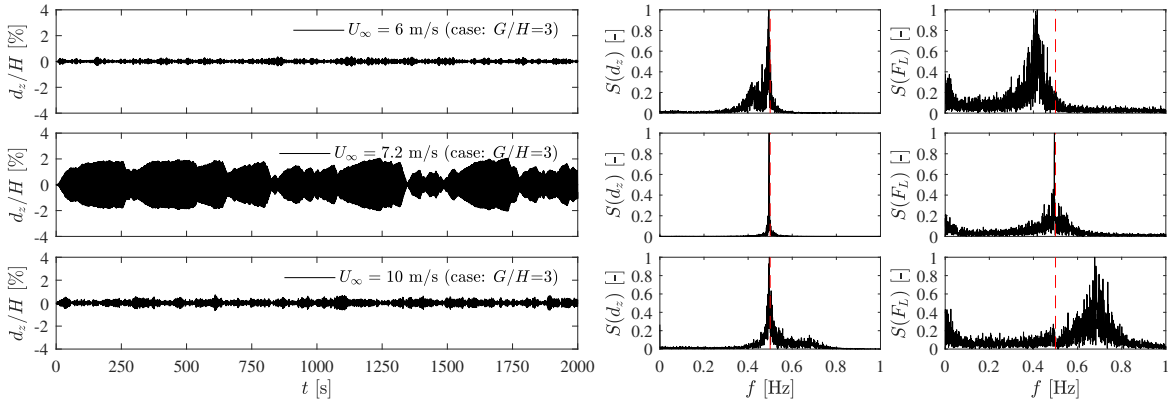


Figure 4. Coupled motion of twin-deck bridge with $G/H = 3$ at various wind speeds: normalized response (left), vertical displacement spectra (middle), and lift force spectra (right). Red dashed lines indicate first natural frequency.

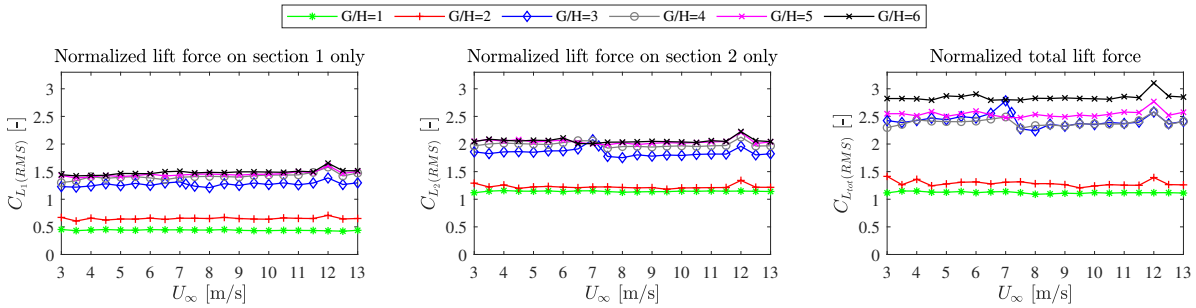


Figure 5. Comparison of RMS lift forces at different wind speeds considering various gap ratios.



Figure 6. Correlation of section forces: particle map at resonance for $G/H = 3$ and $G/H = 5$ (left), and correlation of section forces across studied G/H values and wind speeds (right), with legends as shown in Fig. 5.

spectral similarities for G/H ratios of 3 and 4, which contributes to increased response. In contrast, the presence of lower-frequency wakes for G/H ratios of 5 and 6 disrupts the synchronization of shedding forces, resulting in reduced response. A summary of the outcome is shown in Fig. 8.

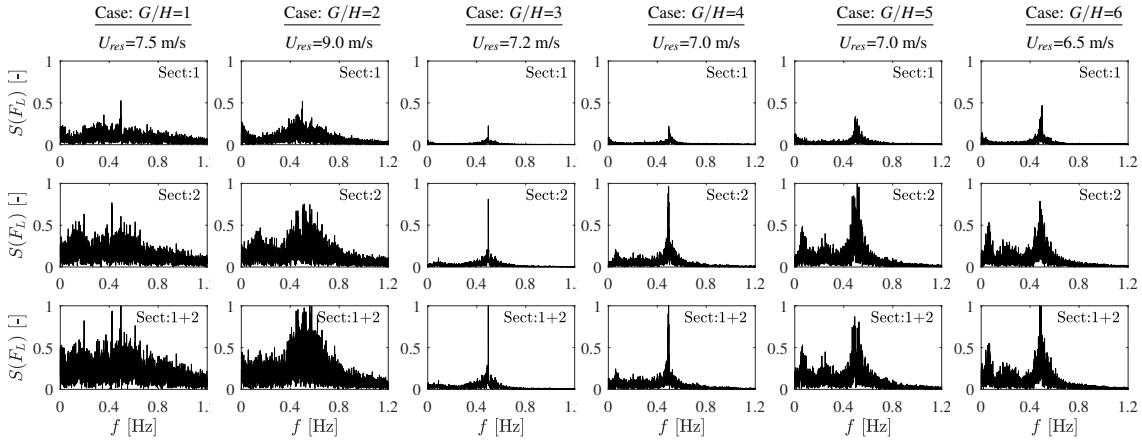


Figure 7. Comparison of normalized lift force frequency spectra for upstream (Section 1), downstream (Section 2), and combined bridge sections at resonance wind speeds, considering each gap-to-height ratio (G/H) case.

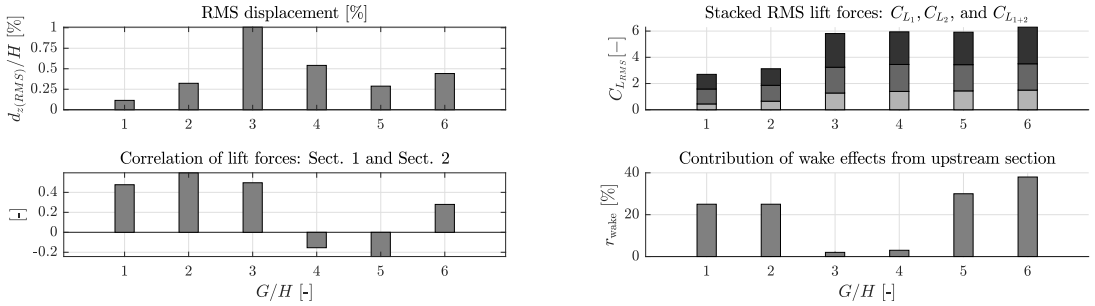


Figure 8. Summary of the effects of the resonance wind speed on twin-deck bridges with different gap ratios.

4. CONCLUSIONS

This study numerically investigated twin-deck long-span bridges, focusing on the impact of the gap-to-height (G/H) ratio on aerodynamic behavior. Vortex Particle Method (VPM) simulations were performed for a reference twin-deck bridge section and validated against experimental data. Subsequently, the aerodynamic behavior of six G/H cases of twin-deck bridge sections was analyzed. The results showed that certain configurations are highly susceptible to VIV, particularly when the shedding forces from the upstream and downstream sections are synchronized in frequency and phase. These findings highlight the importance of thorough parametric studies to optimize twin-deck bridge designs for stability and safety.

REFERENCES

Morgenthal, G. and Walther, J. H., 2007. An immersed interface method for the Vortex-In-Cell algorithm. Computers & structures 85, 712–726.

Morgenthal, G., 2002. Aerodynamic analysis of structures using high-resolution vortex particle methods. Ph.D. Dissertation, University of Cambridge, England.

Morgenthal, G., Corriols, A. S., and Bendig, B., 2014. A GPU-accelerated pseudo-3D vortex method for aerodynamic analysis. Journal of Wind Engineering and Industrial Aerodynamics 125, 69–80.

Nieto, F., Montoya, M. C., Hernández, S., Kusano, I., Casteleiro, A., Álvarez, A. J., Jurado, J. Á., and Fontán, A., 2020. Aerodynamic and aeroelastic responses of short gap twin-box decks: Box geometry and gap distance dependent surrogate based design. Journal of Wind Engineering and Industrial Aerodynamics 201, 104147.

Zhu, Q., Xu, Y. L., Zhu, L., and Li, H., 2018. Vortex-induced vibration analysis of long-span bridges with twin-box decks under non-uniformly distributed turbulent winds. Journal of Wind Engineering and Industrial Aerodynamics 172, 31–41.

Dynamic excitation of long-span bridges to downburst wind loading

A. M. Marra[1], L. Salvatori[2], M. De Stefano[1], P. Spinelli[2]

[1]*Dept. of Architecture, University of Florence, Italy, antoninomaria.marra@unifi.it*
[2]*Dept. of Civil and Environmental Engineering, University of Florence, Italy*

SUMMARY:
The effects of non-synoptic winds have been mainly investigated for low-rise buildings and vertically-developed structures (e.g., towers, antenna). In comparison, little attention has been paid to suspension bridges despite full-scale tests have shown that their response to non-synoptic winds can exceed that of synoptic winds. This work aims to address this gap in the literature, simulating the dynamic response of super-long span bridges during the passage of various downbursts. In particular, a three-dimensional analytical model, recently proposed in the literature, has been used for reproducing the downburst flow-field. The model reproduces the vertical components of downburst wind fields, which, combined with the horizontal component, generate significant angles of attack not observed during synoptic events. The downburst model has been implemented in an ad hoc finite element code for predicting the dynamic response of suspended bridges under wind loads.

Keywords: Long-span bridges, Downburst wind loading, Dynamic response

1. INTRODUCTION

The effects of downbursts on structures have been investigated by considering mainly low-rise buildings (Jesson et al., 2015) and vertically-developed structures, such as towers and antenna masts (Chen and Letchford, 2004b; Savory et al., 2001; Solari, 2016), lighting poles (Solari et al., 2017) and high-rise buildings (Chen and Letchford, 2004a). Transmission lines are the horizontally-developed structures mainly considered in the scientific literature (Elawady et al., 2017; Holmes and Oliver, 2000).

Despite non-synoptic winds have demonstrated their ability to produce responses on long-span bridges exceeding the ones of stationary winds (Owen et al., 2020), the research on this topic are very limited. Spinelli et al. (2023) raised the issue of the significant angles of attack observed during the passage of a downburst through a bridge. As a matter of fact, the vertical component of the velocity combined with the horizontal one results in significant changes in the angle of attack, which plays a key role in the estimation of both wind loads and dynamic response. Salvatori et al. (2024) develop an analytical model to estimate the wind loads on bridges during the passage of a downburst. The model allows investigating the wind field at different deck levels for small/medium-diameter downbursts revealing the presence of non-negligible time intervals in which the angle of attack is over 10 degrees with high wind velocities. Force simulations confirm that the wind loads correspond to the maximum ones in these time intervals, which are not predictable through the existing approaches.

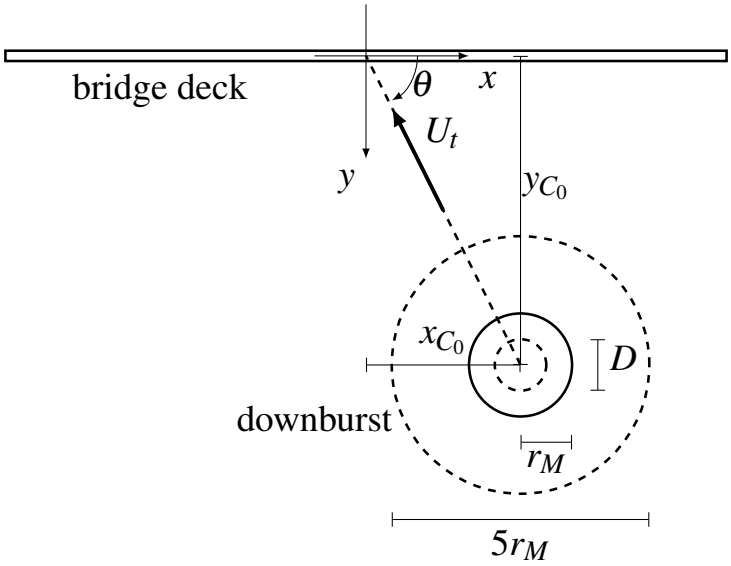


Figure 1. Reference sketch with dimensions and position of the downburst with respect to the bridge deck.

In this work, we proceed from assessing the wind loads produced by the passage of a downburst (Salvatori et al., 2024) to estimating the dynamic response induced on a super long-span bridge. The analytical model has been implemented in a finite element code for suspended bridges developed in Matlab environment (Salvatori and Spinelli, 2007).

The next section reports a brief outline of the analytical model. The structural and aerodynamic modelling of the bridge is described in section 3. Some preliminary results are reported in the last section.

2. DOWNBURST WIND MODEL

The analytical model for simulating downburst wind loading proposed by Salvatori et al. (2024) is used in this study to compute the dynamic of the entire bridge. A brief outline of the model is provided here, more details can be found in the original paper.

A three-dimensional field is provided by the model, which is constituted by a vertical jet dragged by the environmental wind. In particular, the environmental velocity is horizontal and directed at an angle θ with respect to the x-axis (Fig. 1), it represents the mean wind and is also responsible for the 'transport' of the downburst. The environmental velocity is considered constant with height and equal to the velocity of the moving downburst U_t, i.e. $U(z) = U_t$. The velocity field of the vertical jet (stationary downburst) is modelled by considering the radial and vertical downburst velocity components given by

$$\begin{aligned} \mathscr{V}_r(r,z) &= \mathscr{U}_{\max} \upsilon_\rho(r/r_{\max}) \upsilon_\zeta(z/z_{\max}), \\ \mathscr{V}_z(r,z) &= -\mathscr{W}_{\max} \omega_\rho(r/r_{\max}) \omega_\zeta(z/z_{\max}), \end{aligned} \tag{1}$$

where υ_ρ and υ_ζ are modulating functions of the radial velocity as a function of the dimensionless radial and vertical coordinates $\rho = r/r_{\max}$ and $\zeta = z/z_{\max}$, ω_ρ and ω_ζ are modulating

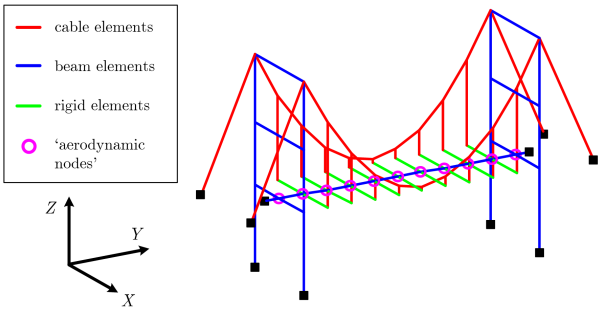


Figure 2. Finite element model of the suspended bridge.

functions of the vertical velocity, $r_{\max}$ and $z_{\max}$ are the radial and vertical positions at which the maximum downburst horizontal velocity $\mathscr{U}_{\max}$ is achieved, $\mathscr{W}_{\max}$ is the maximum downburst vertical downward velocity; the latter is achieved at the downburst centre and can be obtained as $\mathscr{W}_{\max} = c\frac{z_{\max}}{r_{\max}}\mathscr{U}_{\max}$, where the coefficient c depends on the downburst model. The relationships of the shaping functions reported in Eq. 1 can be found in the original paper (Salvatori et al., 2024).

3. BRIDGE AND AERODYNAMIC MODELLING

Fig. 2 shows the finite element model of the bridge characterized by a fishbone deck (Salvatori and Spinelli, 2007). Beam and cable elements employ a corotational approach to account for geometrical nonlinearities, while cable elements incorporate a no-compression behavior. Rigid cross-sections are represented through a penalty approach. Aerodynamic forces are applied to specific nodes where the wind velocity field is assessed and converted into aerodynamic forces using a quasi-steady aerodynamic sectional model.

4. SIMULATIONS

Fig. 3 shows a frame of the velocity vectors at the deck level during the passage of a small diameter environmental-driven downburst.

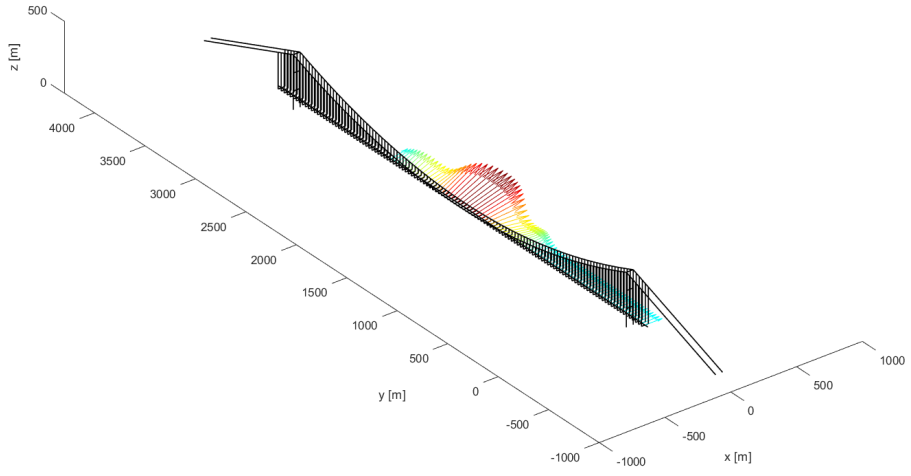


Figure 3. Frame of the wind velocity vectors at the deck level during the passage of a downburst through the bridge.

5. CONCLUSIONS

In this work, the dynamic responses of super-long span bridges during the passage of various downbursts have been simulated. A three-dimensional analytical model, which also reproduces the vertical components of downburst wind fields, generated significant angles of attack not observed during synoptic events. Consequently, the aerodynamic behavior of bridge deck sections for angles of attack close to zero is no longer guaranteed under these conditions. The downburst model has been implemented in an ad hoc finite element code for predicting the dynamic response of suspended bridges under wind loads. Due to the lack of space, only the initial results of this study are presented here, while the complete findings will be available in the full paper.

ACKNOWLEDGEMENTS

The studies presented here were carried out as part of the activities envisaged by the Agreement between the High Council of Public Works (CSLLPP) and the ReLUIS Consortium implementing Ministerial Decree 578/2020 and Ministerial Decree 240/2022. The contents of this paper represent the authors' ideas and do not necessarily correspond to the official opinion and policies of CSLLPP.

REFERENCES

Chen, L. and Letchford, C. W., 2004a. Parametric study on the along-wind response of the CAARC building to downbursts in the time domain. Journal of wind engineering and industrial aerodynamics 92, 703–724.

Chen, L. and Letchford, C. W., 2004b. A deterministic–stochastic hybrid model of downbursts and its impact on a cantilevered structure. Engineering structures 26, 619–629.

Elawady, A., Aboshosha, H., El Damatty, A., Bitsuamlak, G., Hangan, H., and Elatar, A., 2017. Aero-elastic testing of multi-spanned transmission line subjected to downbursts. Journal of Wind Engineering and Industrial Aerodynamics 169, 194–216.

Holmes, J. D. and Oliver, S., 2000. An empirical model of a downburst. Engineering structures 22, 1167–1172.

Jesson, M., Sterling, M., Letchford, C., and Haines, M., 2015. Aerodynamic forces on generic buildings subject to transient, downburst-type winds. Journal of wind engineering and industrial aerodynamics 137, 58–68.

Owen, J. S., Nguyen, D. T., Meng, X., Psimoulis, P., and Xie, Y., 2020. An observation of non-stationary response to non-synoptic wind on the Forth Road Bridge. Journal of Wind Engineering and Industrial Aerodynamics 206, 104389.

Salvatori, L., Marra, A. M., De Stefano, M., and Spinelli, P., 2024. Downburst wind loading on bridge decks through an analytical model. Engineering Structures 319, 118802.

Salvatori, L. and Spinelli, P., 2007. A discrete 3D model for bridge aerodynamics and aeroelasticity: nonlinearities and linearizations. Meccanica 42, 31–46.

Savory, E., Parke, G. A., Zeinoddini, M., Toy, N., and Disney, P., 2001. Modelling of tornado and microburst-induced wind loading and failure of a lattice transmission tower. Engineering Structures 23, 365–375.

Solari, G., 2016. Thunderstorm response spectrum technique: theory and applications. Engineering Structures 108, 28–46.

Solari, G., Rainisio, D., and De Gaetano, P., 2017. Hybrid simulation of thunderstorm outflows and wind-excited response of structures. Meccanica 52, 3197–3220.

Spinelli, P., Marra, A. M., and Salvatori, L., 2023. Super-long-span bridges: wind-resistant design developments and open issues. Proceedings of the Institution of Civil Engineers-Bridge Engineering. Emerald Publishing Limited, 1–20.

Stochastic wind load model for the reliability assessment and partial factor calibration of movable bridges in the Netherlands using local wind speed measurements

Liesette la Gasse [1], Lisa Swaalf [1], Okke Bronkhorst[1]

[1]*TNO, Delft, The Netherlands, liesette.lagasse@tno.nl*

SUMMARY: (10 pt)
The Netherlands has many movable bridges which are exposed to wind loading during their opening cycle. The question is whether using the partial safety factor of 1.8 specified in NEN6786 (NEN, 2021) for wind loading on existing operating mechanisms in movable bridges potentially leads to uneconomical decisions. This research focusses on a specific type of movable bridge: an electromechanically driven bascule bridge with a panama wheel. To calibrate the partial safety factor by a full probabilistic analysis, the physical model as well as the actual stochastic distribution of the wind load effect on the operating mechanism during opening are required. For the stochastic description of the wind speeds, measurements from KNMI (KNMI Data Platform, 2024) are used and applied to different opening regimes. Other parameters in the wind loading chain, the terrain factor, aerodynamic or force coefficients and structural factor including dynamic and size effects, are studied and stochastic variables are proposed.

Keywords: wind loading chain, existing movable bridges, wind speeds measurements

1. INTRODUCTION

The Netherlands, located in a low-lying delta region, has more than 1500 movable bridges. There are several types of movable bridges; the focus of this paper is an electromechanically driven bascule bridge, with a panama wheel as operating mechanism. According to the Dutch standard for movable bridges (NEN6786, 2021) waterways are categorized into four types with different requirements of maximum non-availability due to high wind loads. Meaning that above a certain critical wind speed the bridge operator leaves the bridge deck closed. This influences the amount of openings and the duration of the openings, which is called the ‘opening regime’ in this paper. The aim of this paper is to examine the occurring wind speeds during different opening regimes, and to research the other parameters which determine the wind loading on the bridge during opening, closing and the open situation. For a closed bridge configuration EN 1991-1-4 (CEN, 2011) applies; this configuration is not considered in this work.

Many movable bridges in the Netherlands were built between 1950-1970 and are approaching the end of their design lifetime. To determine whether a bridge and its operating mechanism require renovation or replacement, a reassessment of structural safety is needed. In Swaalf et al. (2024) the wind loading was found dominant when assessing the reliability of the opening mechanism of the bridge. According to NEN-EN 1990 (NEN, 2019), a structure in consequence class 2 (CC2) has to satisfy a reliability index of 3.8 for a reference period of 50 years. NEN6786 is currently used for design and assessment of movable bridges. A partial factor of 1.8 is specified in this code for CC2 wind loading on both new and existing operating mechanisms in movable bridges, which

is inconsistent with the partial factor of 1.5 defined in NEN-EN 1990 which is used for the fixed elements of the bridge. The question is whether using the partial safety factor of 1.8 potentially leads to uneconomical decisions, both in design and assessment of the operating mechanisms. Therefore, partial safety factors are calibrated using a full probabilistic assessment. This abstract presents the proposed (stochastic) wind model used in this calibration.

2. WIND MODEL

Wind load effects in standards and codes are based on the wind loading chain model by Davenport (1965), which gives a physical description of the stochastic wind load. Practical considerations often lead to simplified choices in this model to prevent unnecessary complexity in the design or assessment process. To derive a new standard, parameters and corresponding characteristic values have to be selected. Furthermore, to determine the partial factor, also the actual stochastic description of the wind load effect is required.

2.1. Physical model

In this research, Eq. 1 is used for the wind load model, which aligns with EN 1991-1-4 (CEN, 2011), ensuring that the same principles are applied as much as possible in the design and assessment of the mechanical operating systems as for the fixed part of the bridge:

$$F_{w,d;bridge} = \gamma_w \, 1.05 c_s \, c_d \, C_t \, q_p \, (z_e \,) A_{val} \tag{1}$$

$$q_p \, (z_e \,) = \frac{1}{2} \, \rho \left(c_{dir} \, c_{prob} \, c_o \, (z_e \,) v_{ref,k} \, 0{,}19 \left(\frac{z_0}{0{,}05} \right)^{0{,}07} \, ln \left(\frac{z_e}{z_0} \right) \right)^2 \times \left(1 + \frac{7 k_l}{c_o \, (z_e \,) ln \left(\frac{z_e}{z_0} \right)} \right) \tag{2}$$

in which γ_w is defined as the partial factor of the wind, c_s the size factor, c_d the dynamic factor, C_t the force coefficient, q_p the velocity pressure $[N/m^2]$, z_e the reference height $[m]$ and A_{val} the area loaded by wind $[m^2]$, ρ_{air} the density of air $[kg/m^3]$, z_o the roughness length $[m]$, $v_{k,ref}$ the 10-minute average wind speed at a height of 10 m above ground level, c_o the orography factor, c_{dir} the wind directionality factor, c_{prob} the probability factor, k_l the turbulence factor, and z_0 the roughness length. The value 1.05 is used to take into account the inaccuracy in the measurement of wind speed at which the bridge may be opened according to (NEN6786, 2021). This physical model will be implemented in the currently developed version of NEN6786-1.

2.2. Stochastic model

The following stochastic model is proposed, applying the force coefficients method (JCSS, 2011):

$$F_{w;bridge} = \theta_{model} \, c_s \, c_d \, C_t \sum q_p \, (z_e \,) A_{ref} \tag{3}$$

$$q_p \, (z_e \,) = \frac{1}{2} \, \rho (c_r \, v_{max})^2 \, \, c_g \tag{4}$$

The values for the different parameters are provided in Table 1. The stochastic properties of the roughness factor c_r^2, the gust factor c_g and the dynamic factor c_d are based on the definitions in

the Probabilistic Model Code (JCSS, 2001); additional studies have been performed for the wind speed v_{max}, the gust factor c_g, the force coefficient C_t and the dynamic factor c_d.

The force coefficient defined in NEN6786-1 (NEN, 2021) for movable bridges is derived from wind tunnel measurements (Allaart, 1949; Bouma and Rem, 1950). The force coefficients depend on the opening angle of the bridge deck and whether the wind force acts in the opening or closing direction of the movable bridge (opening or closing wind). Since (Allaart, 1949; Bouma and Rem, 1950) only provide mean values, the other stochastic properties of the force coefficient were determined from an analysis of other wind tunnel studies (Bronkhorst et al., 2023) that were found representative.

For the roughness factor, gust factor and structural factor the definitions according to the EN 1991-1-4 (CEN, 2011) were found appropriate for movable bridges as well. Additionally a sensitivity study was performed on the natural frequency and damping of the bridge. From this sensitivity study the coefficient of variation for the dynamic factor was derived.

This stochastic wind load model is used in the calibration of the partial factor for wind loads on movable bridges. This will be included in the currently developed version of the Dutch design code for movable bridges NEN6786-1.

Table 1. Stochastic parameters for wind load model

Parameter	Description	Distribution type	Mean/ specified	V	Characteristic fractile	Source
c_r^2	Roughness factor	Lognormal	0,8	15 %	$F_{C_r}\left(\mu_{C_r}\right)$	JCSS/ Davenport, 1987
c_g	Gust factor	Lognormal	1,00	10 %	$F_{C_g}\left(\mu_{C_g}\right)$	JCSS/ Davenport, 1987
v_{max}	Distribution of maximum 10-minute average wind speeds during opening	Empirical	1,00	From data of wind speed measurements	$F_{vmax,year} = 1 - 0.02$ per year	Data KNMI (KNMI Data Platform, 2024)
C_t	Force coefficient	Gumbel	1,00	10 %	$F_{C_t}\left(\mu_{C_t}\right)$	Wind tunnel research/ JCSS
c_d	Dynamic factor	Lognormal	1,00	10 %	$F_{C_d}\left(\mu_{C_d}\right)$	JCSS and sensitivity study
θ_{model}	Model uncertainty	Lognormal	1,00	10 %		JCSS

3. WIND SPEED DISTRIBUTIONS

In the National Annex to EN 1991-1-4 (NEN, 2019) the Netherlands is divided into three wind areas for which a different basic wind velocity is defined. At different locations throughout the country, KNMI has installed wind stations measuring wind speeds at a certain reference height with a certain terrain roughness (KNMI Data Portal, 2024). For this research, the 10 minute mean wind speeds measured at Schiphol and Cabauw are used, both found representative for wind area 2 (see Fig. 1).

To derive the distributions of maximum wind speeds during different opening regimes of a

movable bridge a simulation procedure is used. Mean wind speeds of 10 minutes are randomly sampled from the distribution of 10 minute mean wind speeds fitted to the measurement data. Since the wind speeds are correlated in time, this correlation is taken into account. Consequently, events of opening of the bridge are simulated. These events are assumed equidistantly distributed over the year and correlated in time when they are less than 24 hours apart. The bridge only opens when the current (10 minute mean) wind speed is below the critical wind speed. The maximum wind speed during bridge opening is recorded, resulting in the distribution of the maximum wind speeds during an opening event. The distribution of the yearly maximum wind speeds during the bridge's opening events is derived assuming independence of individual events.



Figure 1. Wind areas in the Netherlands with wind station locations Schiphol (top star) and Cabauw (bottom star)

The final results for the stochastic wind load model will be discussed in the presentation.

ACKNOWLEDGEMENTS

The authors wish to acknowledge the participation of the partners in this research: Rijkswaterstaat and Ingenieursbureau Gemeente Rotterdam.

REFERENCES

Allaart, P., 1949. Een onderzoek naar de winddruk op beweegbare bruggen met horizontale draaiingsas. De Ingenieur 61-8, 11-18.

Bouma, A.L. and Rem, H.J., 1950. Winddruk op klapbruggen. De Ingenieur 62-17, 45-52.

Bronkhorst, A.J., Geurts, C.P.W., Akhnoukh, J.T., van Uffelen, M., Mooijweer, R., 2023. Wind tunnel measurement of overall wind loads on a swing bridge, Proceedings of ICWE 2023.

Davenport, A.G., 1965, The buffeting of structures by gusts, Proc. of Conference on'Wind Effects on Structures', NPL, 1965 (ICWE-1), HMSO, 357.

Davenport A.G., 1987. Proposed new international (ISO) wind load standard. High winds and building codes. Proceedings of the WERC/NSF Wind engineering symposium. Kansas City, Missouri, Nov., p.373-388

JCSS, 2001. JCSS Probabilistic Model Code. European Convention for Constructional Steelwork.

KNMI Data Platform, 2024, https://dataplatform.knmi.nl/dataset/windgegevens-1-0, d.d. 13-3-2024

NEN/CEN, 2019. Eurocode: Basis of structural design, NEN-EN 1990+A1+A1/C2:2019.

NEN/CEN, 2011. Eurocode 1: Actions on structures – part 1-4: General actions – Wind actions, NEN-EN 1991-1-4+A1+C2:2011.

NEN/CEN, 2019. National Annex to Eurocode 1: Actions on structures – part 1-4: General actions – Wind actions, NEN-EN 1991-1-4+A1+C2:2011/NB+C1:2019

NEN, 2021. Rules for the design of movable parts of civil structures - Part 1: Movable bridges, NEN 6786-1:2017+C1.

Swaalf, F., van Battum, C., Courage, W., and Steenbergen, R., 2024. Reliability Assessment of the Operating Mechanism of a Movable Bridge. In International Probabilistic Workshop (pp. 452-458). Cham: Springer Nature Switzerland.

Design of a wind tunnel sectional model for skew wind buffeting analysis

L. Rosa[1], T. Argentini[2], G. Pomaranzi[2], B. M. Costa[3], J. Wang[3]

[1]*Politecnico di Milano, Wind tunnel lab, Milano, Italy, lorenzo.rosa@polimi.it*
[2]*Politecnico di Milano, Department of Mechanical Engineering, Milano, Italy*
[3]*Norwegian Public Roads Administration, Stavanger, Norway*

SUMMARY:
The design of the Bjørnafjord Bridge, part of the E39 fjord crossing project in Norway, is dictated by its curved structure and the complex wind conditions resulting from the surrounding terrain. Even under uniform flow conditions, the bridge's curvature introduces a significant variation in the local mean wind yaw angle, reaching up to 60° along its length. To accurately evaluate the aerodynamic properties of the bridge's cross-section, vertical columns, and pontoons in skew turbulent boundary layer flow, an experimental campaign was conducted in the Politecnico di Milano wind tunnel, employing a 1:35 scale sectional model, designed to measure force coefficients in skew wind conditions. This abstract presents the design of the sectional model and the strategic design decisions made to address the unique challenges posed by the bridge's curvature and wind conditions, finally allowing the application of refined 3D buffeting response theories.

Keywords: wind tunnel tests, bridge aerodynamics, skewed wind

1. INTRODUCTION

Evaluating bridge buffeting response relies on aerodynamic coefficients typically obtained from wind tunnel tests on sectional models. Traditional buffeting theory applies to straight decks subject to 2D flow-structure interactions, where the mean wind vector lies in the plane normal to the deck axis (Strømmen, 2010). For more complex wind scenarios, these theories extend to skew wind conditions, where the mean wind direction is not normal to the bridge's longitudinal axis. A common approach in such cases is the "cosine rule," which simplifies the problem by decomposing wind into normal and longitudinal components, discarding the latter, and proceeding with a 2D interaction analysis (Xie et al., 1991). However, as noted by (Costa, Wang, Jakobsen, Øiseth, et al., 2022b), skew winds significantly impact bridge responses, and 2D simplified analyses can underestimate buffeting effects. To address these limitations, Morais da Costa (Costa, Wang, Jakobsen, Øiseth, et al., 2022a,b) proposed (2D+1D) and 3D frameworks, which add an independent axial component (+1D) or fully incorporate three-dimensional wind flow (3D). While the 3D approach provides a comprehensive buffeting response, it requires wind tunnel data for aerodynamic coefficients across varying yaw and inclination angles.

The scope of this paper is to present the design of the setup for wind tunnel sectional model tests in skew wind conditions. Specifically, using the Bjørnafjord Bridge as a case study, we employ this setup to obtain the full set of aerodynamic coefficients in skew turbulent boundary layer flow

necessary for 3D buffeting theory.

1.1. Bjørnafjord bridge

The planned Bjørnafjord Bridge is a single-curvature, side-anchored floating bridge with a length of 5.5 km and a horizontal curvature radius of 5000 m. It consists of two main sections: a high cable-stayed bridge with a 380 m, and a low floating bridge supported by pontoons with a 125 m span. The high bridge reaches an elevation of 55 m, while the center of the low bridge is 16 m above the average water level. Both bridge decks are designed as asymmetrical closed steel box sections, as shown in Fig. 1. The wind conditions at Bjørnafjord were studied using a weather research and forecasting model (WRF) (Costa, Wang, Jakobsen, Snæbjörnsson, et al., 2023).

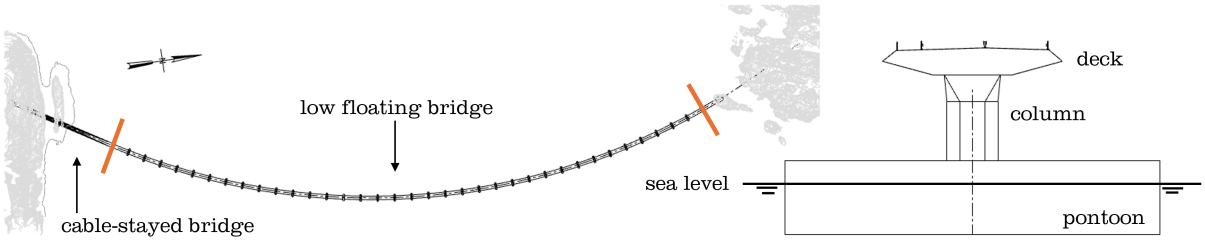


Figure 1. The planned floating bridge for the Bjørnafjord.

2. METHODOLOGY

Due to the complexity of the curved floating bridge project and the challenging wind conditions at the site, the 3D skew buffeting formulation was applied in the aerodynamic design (Costa, Wang, Jakobsen, Snæbjörnsson, et al., 2023). To obtain the aerodynamic coefficients of the floating bridge in skew wind conditions, a set of wind tunnel tests was conducted. These tests used a sectional model designed to rotate around its global vertical axis Z and its longitudinal axis x, as shown in Fig. 2.

The sectional model consisted of three segments of the low bridge, where each segment represented the span between two columns. The central part was equipped with a dynamometric balance for the force measurements. Given the bridge's curvature radius (5000 m) and segment length (125 m), each span segment's curvature was negligible, making the sectional model with a straight longitudinal axis suitable for accurately assessing aerodynamic coefficients.

This setup allowed for the simulation of key skew wind conditions, providing aerodynamic coefficients for the entire bridge length. Additionally, it enabled the measurement of aerodynamic forces on a column and a pontoon as a function of exposure angle as well.

2.1. Rotation angles

To simulate various skew wind conditions (yaw angle β and inclination angle θ, Fig.2(b)) using a sectional model — and given the fixed flow direction in the wind tunnel — the bridge model was rotated around its global vertical axis z and its longitudinal axis x, as shown in Fig.2(c). The relationship between the model rotation angles α and γ and the skew wind angles is defined as

follows:

$$\alpha = -arctan\left(\frac{tan\theta}{cos\beta}\right), \quad \gamma = -arccos\left(\frac{cos\theta \cdot cos\beta}{cos\alpha}\right) \tag{1}$$

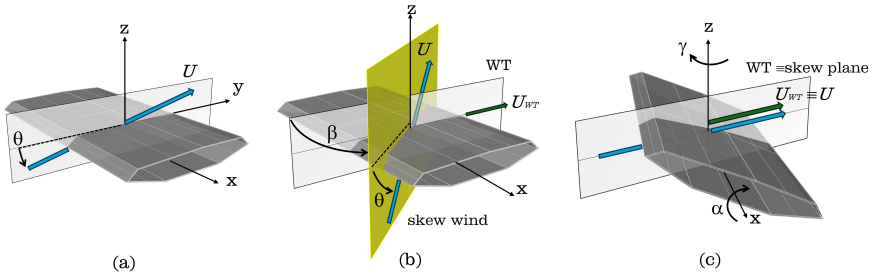


Figure 2. Definition of skew wind and its simulation in the wind tunnel.

Flow conditions in the area, combined with the curvature of the low bridge, predict skew winds with yaw angles $\beta \in [0°, +180°]$ and inclination angles $\theta \in [-10°, +10°]$. However, based on the relationships in (1), certain angle combinations lead to an impractically close distance between the deck nose and the floor surface. Consequently, the model's rotation around its longitudinal axis x was restricted to the range $\alpha \in [-12.5°, +12.5°]$. This limitation excludes only skew wind combinations that are less critical to bridge aerodynamics, such as large θ values when the yaw angle approaches 90°.



Figure 3. Sectional model in the boundary layer test section.

3. MODEL DESIGN

The model was built at a scale of 1:35 to cover all available space on the wind tunnel turntable, equal to 13 m, Fig. 3. According to this scale the outer measure B of the deck (chord) was equal to 767 mm and the distance between the bottom of the deck and the floor was 400 mm. Using this scale it was also possible to simulate an accurate boundary layer at the height of the deck.

The model consists of two dummy parts (A1 and A2) to establish appropriate boundary conditions, along with a central segment made up of two independent dynamometric sections (B1 and B2, each 1500 mm long) (Fig. 4). Each dynamometric section is attached to the model using a single dynamometric balance, which avoids creating a hyperstatic system that would require two balances for a continuous 3-meter section, thus improving measurement sensitivity. A gap of 5 mm is

maintained between the different model parts to accommodate construction tolerances, and tape is used to partially cover these gaps to minimize their effects.

Each dynamometric section consists of a rigid carbon shell (c6) connected to a steel C-beam (c5) via a RUAG192 six-component balance (f3). The dummy parts consist of a shell (c1) and a rigid aluminum beam (c2). The three segments are connected through a 30 mm diameter steel shaft supported by two pivoting bearings (c4). The model rests on four columns, each mounted on a pontoon, and can rotate along its longitudinal axis (c4) using two linear actuators (c3) positioned beside the inner columns. One column (c7) and one pontoon (c8) were constructed as separate rigid shells and connected to the model's structure with ATI-MINI45 dynamometric balances (f1 for the pontoon and f2 for the column) to estimate their aerodynamic loads, as shown in Fig.5. The model's rotation around the global vertical axis Z is achieved by rotating the wind tunnel turntable by an angle γ, while the rotation α around the longitudinal axis x is facilitated by the two linear actuators (c3) (Fig.5(b)).

This newly proposed wind tunnel setup allows for practical and accurate measurement of force coefficients in skew wind conditions, allowing the application of the refined 3D buffeting response theory.

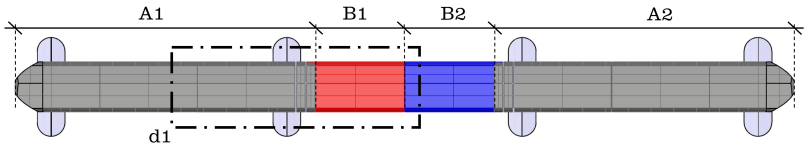


Figure 4. Top view of the model. A1 and A2 are the dummy parts, B1 and B2 the dynamometric sections.

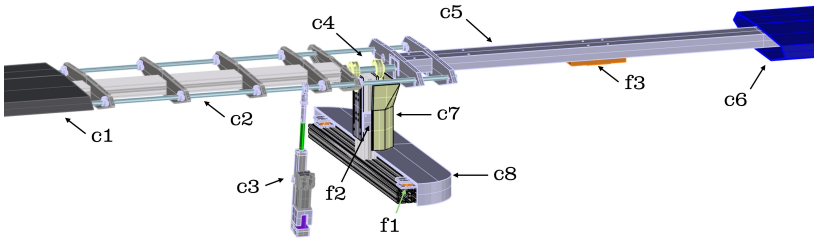


Figure 5. Detail of the realization of the model (area d1 in previous Figure).

REFERENCES

Costa, B. M., Wang, J., Jakobsen, J. B., Øiseth, O. A., and Snæbjörnsson, J. þór, 2022a. Bridge buffeting by skew winds: A quasi-steady case study. Journal of Wind Engineering and Industrial Aerodynamics 227, 105068.

— 2022b. Bridge buffeting by skew winds: A revised theory. Journal of Wind Engineering and Industrial Aerodynamics 220, 104806.

Costa, B. M., Wang, J., Jakobsen, J. B., Snæbjörnsson, J. þór, and Øiseth, O. A., 2023. Long-term response of a curved floating bridge to inhomogeneous wind fields. Journal of Wind Engineering and Industrial Aerodynamics 240, 105488.

Strømmen, E. N., 2010. Theory of Bridge Aerodynamics. Springer, Heidelberg, Berlin.

Xie, J., Tanaka, H., Wardlaw, R., and Savage, M., 1991. Buffeting analysis of long span bridges to turbulent wind with yaw angle. Journal of Wind Engineering and Industrial Aerodynamics 37, 65–77.

The influence of along-span variation of static rotation angle in multi-mode flutter calculations

Sanne Poulin [1], Allan Larsen [2]

[1]*COWI, Lyngby, Denmark, sami@cowi.com*
[2]*COWI, Lyngby, Denmark, aln@cowi.com*

SUMMARY:
For some bridge deck sections, the variation of the static deck rotation angle at or near the critical flutter wind speed can be significant. The aerodynamic derivatives may therefore not be very well represented by one set of derivatives for one rotation angle. The present analyses show how the flutter wind speed changes when the aerodynamic derivatives are allowed to vary along the span according to the local static rotation angle.

Keywords: multi-mode flutter, aerodynamic derivatives, static rotation angle

1. INTRODUCTION

The static deck rotations for flexible, long-span suspension bridges at high wind speeds can be significant. In numerical flutter analyses, for which measured aerodynamic derivatives from wind tunnel tests are important input, the applied aerodynamic derivatives must correspond to the actual static rotation of the deck at or near the critical flutter wind speed. Because the static rotation varies along the span, the aerodynamic derivatives are often selected corresponding to a representative static rotation angle, e.g. the average value for the central part of the span. Another option is to select and apply the derivatives corresponding to the actual rotation at each span-wise point of the bridge deck in the analyses, thereby applying different derivatives along the bridge.

A comparison of flutter wind speeds calculated with and without taking these along-span variations of static rotation angle and aerodynamic derivatives into account is presented in the following for two long-span suspension bridge designs.

2. BRIDGE CASES

Two bridge cases used to illustrate the influence of varying static rotation along the bridge. One is the Çanakkale Bridge in Turkey and the other is the 2011 Progetto Definitivo design for Messina Strait Bridge in Italy (not built yet). Both are long-span multi-box suspension bridges. The deck cross sections are presented in Fig. 1.

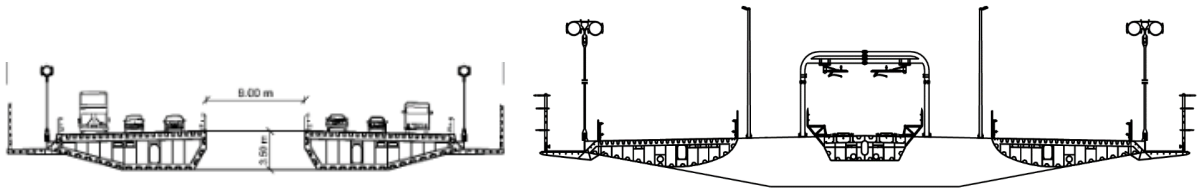


Figure 1. Deck cross sections for the Çanakkale bridge (left) and the Messina Strait Bridge (right).

Some key properties are given in Table 1 along with the rotation angles where aerodynamic derivatives were available for the analyses.

Table 1. Some key properties.

Case	Main span length m	Deck width B m	Number of ADs	Angles of attack for ADs deg
Çanakkale	2023	45.1	8	-2, 0, 1, 2, 3, 5
Messina	3300	60.4	18	--2, 0, 2, 4, 6

3. OUTLINE OF FLUTTER ANALYSIS METHOD

The calculation method for determining the flutter wind speed for the deck is based on solving the eigenvalue problem of the complex flutter determinant. It is a multi-mode flutter model including all three components of the mode shapes included in the analysis (vertical, horizontal and rotation). The classical two-degree-of-freedom flutter analysis can be selected as a sub-set in this model. The variation of the static rotation angle and thereby the variation of the aerodynamic derivatives along the span is included through the modal coupling coefficients as illustrated below for the coupling between rotation and vertical component for the H_2^*-derivative:

$$CH2_{ij} = \int_{x=0}^{xmax} \{H_2^*(\alpha(x)) \cdot uz_i(x) \cdot rot_j(x)\} dx$$

where $\alpha(x)$ is the static rotation angle, x is the spanwise coordinate, u_z the vertical component of a mode and *rot* the rotational component. Indices i and j run over the included modes. Similar expressions apply to the remaining H^*, A^* and P^* derivatives.

4. EFFECT OF STATIC DECK ROTATION

The flutter wind speeds obtained with and without including the dependence on the local static rotation angle is presented below for the two cases.

4.1. Çanakkale Bridge

Fig. 2 shows the variation of the static rotation angle at the relative wind speed U_r = 20 (81 m/s). It is seen that the variation of the rotation angle is significant.

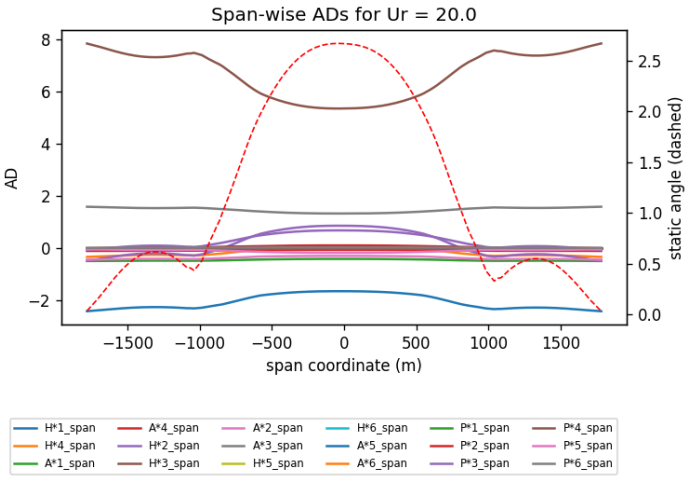


Figure 2. Variation of the static rotation angle (dashed) and aerodynamic derivatives along the bridge. Çanakkale.

The results of the three-degrees-of-freedom flutter analyses including the lowest 25 global modes are presented in Table 2. The differences in the calculated flutter wind speeds are significant. Disregarding the static rotation entirely (the 0° degree case) leads to a low flutter wind speed. Using derivatives for a rotation angle of 2.5°, which represents the average value over the central 1000 m or so of the span fairly well, leads to an overestimation of the flutter wind speed while an angle of 2° leads to a result close to the flutter wind speed including the angle variation. Selecting one representative rotation angle may not be straight forward as this example shows and it is also unnecessary when inclusion of the rotation angle variation is relatively easy to do.

It shall be noted that the results correspond to a fixed mean wind speed of 81 m/s. As the flutter wind speed is higher than this and the static rotations increase with wind speed, the calculation can include one or two iterative steps to obtain the best estimate of the flutter wind speed.

Table 2. Flutter wind speeds with and without static rotation considerations, U = 81 m/s.

Case	Including angle variation	Constant ADs corresponding to 2°	Constant ADs corresponding to 2.5°	Constant ADs corresponding to 0°
Çanakkale	90.6 m/s	90.3 m/s	92.1 m/s	84.5 m/s

4.2. Messina Strait Bridge

Fig. 3 shows the static angle variation and the corresponding variations of the aerodynamic derivatives for the Messina case for a relative wind speed U_r = 21 (86 m/s). As it is seen from this figure, the static rotation angle, and therefore the aerodynamic derivatives, do not vary much along the bridge.

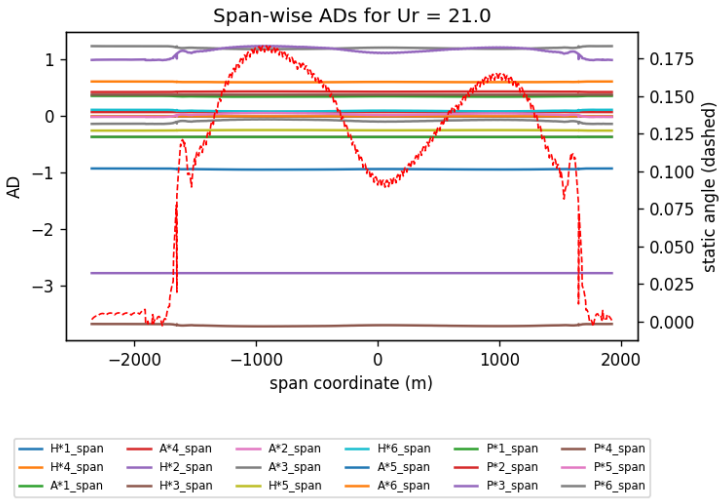


Figure 3. Variation of the static rotation angle (dashed) and aerodynamic derivatives along the span. Messina.

The results of the three-degrees-of-freedom flutter analyses including the lowest 50 global modes are presented in Table 3. The difference with and without including the static angle variation is not large but still notable. As the static rotation angles are small it could be the obvious choice to use the aerodynamic derivatives for 0°, but that appears to under-estimate the flutter wind speed.

Table 3. Flutter wind speeds with and without static rotation considerations, U = 86 m/s.

Case	Including angle variation	Including angle variation and no horizontal components (8 ADs)	Constant ADs corresponding to 0°
Messina	84.0 m/s	84.0 m/s	82.7 m/s

5. CONCLUSION

The two examined cases have shown that including the variation of the static rotation angle and thus the aerodynamic derivatives along the bridge span in numerical flutter calculations may have a significant influence on the resulting flutter wind speeds. It is also indicated that selecting an average value when selecting which set of measured aerodynamic derivatives to use may not always be representative for the case where the rotation angle along the span varies as determined by the mean wind loading.

An Open-Source Python Package for Stochastic Dynamic Analysis of Structures under Wind and Wave Loads

Aksel Fenerci [1,2], Knut Andreas Kvåle [1,3], Øyvind Wiig Petersen [1], Ole Øiseth [1]

[1]*Norwegian University of Science and Technology, Trondheim, Norway, aksel.fenerci@ntnu.no, knut.a.kvale@ntnu.no, oyvind.w.petersen@ntnu.no, ole.oiseth@ntnu.no*
[2]*Multiconsult, Oslo, Norway*
[3]*Dr.Ing. A. Aas-Jakobsen AS, Oslo, Norway*

SUMMARY:
This paper presents WAWI, an open-source Python package designed for the stochastic dynamic analysis of structures subjected to wind and wave loads. Operating in the frequency domain, WAWI offers a fast and accurate solution for calculating the power spectral density (PSD) of structural responses due to stationary stochastic loading, with a focus on applications on long-span bridges. The package integrates with finite element analysis (FEA) software by using modal properties (e.g., mass, stiffness, frequencies, and mode shapes) as input. WAWI has been verified using the IABSE Task Group 3.1 benchmark results. Additionally, the library incorporates standard Python unit testing to ensure reliability and consistent results. In our humble opinion, WAWI addresses an important need in the wind engineering community for stochastic dynamic wind analysis and promotes broader access to advanced computational methods.

Keywords: Wind-induced response, stochastic dynamics, frequency-domain analysis

1. INTRODUCTION & MOTIVATION

The accurate analysis of wind-induced response of flexible structures such as long-span bridges is a critical aspect of modern engineering, especially for structures exposed to extreme environmental conditions. The stochastic dynamic response is commonly calculated in the frequency domain in the absence of nonlinear effects, which is rather efficient. However, despite the increasing need for tools that can handle such complex calculations, there is a surprising shortage of accessible and reliable software capable of performing stochastic dynamic analyses in a rigorous and validated manner. Most of the commercial FE software options used in bridge design do not offer methods for calculation of stochastic dynamic response due to wind and waves. Therefore, one is often required to do such calculations in separate software or in-house solutions, which commonly lack verification. Additionally, they frequently suffer from inadequate documentation, making it difficult for engineers and researchers to fully understand or modify the underlying models and assumptions. In response to this need, we have developed WAWI, an open-access Python library designed to fill the gap left by existing solutions. WAWI provides a comprehensive platform for performing stochastic dynamic analysis of structures subjected to wind and wave-induced forces in the frequency domain. The package's primary focus is on long-span floating or land-based bridges. However, its modular and flexible architecture allows it to be easily applied to any structure where dynamic responses to wind and wave forces are important, including tall buildings, wind turbines, and other large-scale civil engineering structures. WAWI's versatility is one of its

key strengths, making it suitable for a wide range of structural engineering applications.

One of the main motivations behind the development of WAWI was to provide an open-access solution that could be freely used and adapted by both the engineering and academic communities. By making the software open-source, we aim to foster greater collaboration and transparency in the field of dynamic analysis of wind and wave-exposed structures. Practicing structural and wind engineers will benefit from a fast and reliable tool that can be easily integrated with widely used finite element analysis (FEA) software, streamlining the workflow for complex dynamic analyses. On the other hand, researchers in the wind engineering community will have access to a tool that is both flexible and transparent. Another key advantage of WAWI is its focus on verification and validation. From the outset, we have prioritized ensuring that the algorithms and models implemented in WAWI are rigorously tested and verified against real-world data and benchmark problems. This provides users with confidence in the reliability of the results produced by the library, addressing one of the major concerns with existing commercial solutions.

In the following, we describe the theoretical foundations that WAWI in built on, introduce the structure and capabilities of the package and describe our strategy for verification and testing that will ensure a sustainable environment for further development. Here, in the spirit of the conference, we limit our discussions to wind excitation. However, it is worth noting that WAWI does support complex wave excitation scenarios, including inhomogeneous sea states, hydrodynamic interaction, and wave-current interaction modifications.

2. THEORETICAL CONSIDERATIONS

WAWI is built over the years at NTNU, where it has been used for research on stochastic dynamic response calculations of bridges that are excited by wind. Buffeting response due to turbulence is calculated by the multimode buffeting theory, as described in (Øiseth et al., 2010), where turbulent wind fields are treated as stationary stochastic processes. Vortex-induced vibration response can be calculated in the case where calculations can be carried out using a spectral method, as described in the Eurocodes (Hansen, 2013). Aerodynamic stability is calculated using an iterative modal approach, as described in (Øiseth et al., 2010). According to random vibration theory, the spectral density matrix of the dynamic response, including the auto- and cross-spectra, can be written in generalized coordinates of the still-air vibration modes as:

$$\tilde{\mathbf{S}}_{\mathbf{r}}(\boldsymbol{\omega}) = \tilde{\mathbf{H}}(\boldsymbol{\omega})\left(\widetilde{\mathbf{S}_{\mathbf{Q}}}(\boldsymbol{\omega})\right)\tilde{\mathbf{H}}(\boldsymbol{\omega})^{*},\ \ \tilde{\mathbf{H}}(\boldsymbol{\omega}) = \left[-\widetilde{\boldsymbol{M}} + \left(\widetilde{\boldsymbol{C}} - \widetilde{\boldsymbol{C}}_{\boldsymbol{ae}}(\boldsymbol{\omega})\right)i\boldsymbol{\omega} + \left(\widetilde{\boldsymbol{K}} - \widetilde{\boldsymbol{K}}_{\boldsymbol{ae}}(\boldsymbol{\omega})\right)\right]^{-\mathbf{1}} \quad (1)$$

Essentially, WAWI establishes and solves the above equation. Further postprocessing can also be done in WAWI to obtain engineering response quantities, such as RMS or peak displacements or sections forces at the nodes or integration points of the finite element (FE) model. WAWI relies on a FE model of the structure where the system matrices $\widetilde{\boldsymbol{M}}, \widetilde{\boldsymbol{K}}, \widetilde{\boldsymbol{C}}$ and the still-air vibration modes are calculated. The aerodynamic matrices $\widetilde{\boldsymbol{C}}_{\boldsymbol{ae}}(\boldsymbol{\omega}), \widetilde{\boldsymbol{K}}_{\boldsymbol{ae}}(\boldsymbol{\omega})$ and the load spectra $\widetilde{\mathbf{S}_{\mathbf{Q}}}(\boldsymbol{\omega})$ are assembled and transformed to generalized coordinates in WAWI, using the nodes and beam element formulation of the FE model. A spectral wind field model (such as von Karman, Kaimal, Davenport, etc) and aerodynamic coefficients and derivatives are input to WAWI. If frequency-dependent aerodynamic derivatives are not available, quasi-steady theory is adopted.

3. WAWI – STRUCTURE AND WORKFLOW

Here, we summarize the key features of WAWI for wind-induced response to show its working principle and describe the step-by-step workflow that a user should adopt.

3.1. Key features

- *Model object:* WAWI operates on a model object that includes required analysis settings and the following main sub-objects:
    - Modal representation of the dry in-vacuum model (vibration frequencies, mode shapes, damping definitions)
    - Hydrodynamic definition and sea state definition
    - Aerodynamic definition wind state definition
- *Aerodynamic elements:* The elements of the model that are subjected to wind loading are assigned aerodynamic properties such as static force coefficients and aerodynamic derivatives. Aerodynamic system matrices are calculated based on a FE beam formulation, based on provided definitions of nodes, elements and connectivity.
- *Analysis:* The model object includes a method for running a frequency-domain analysis. The method requires input of a frequency axis, and which actions and motion-induced effect would be included in the analysis.
- *Post-processing:* WAWI model object also includes a set of tools for post-processing the analysis results. Different results (RMS values, cross-spectral densities) could be extracted and visualized at both generalized and physical (FE) coordinates of the structure.

3.2. User workflow

A typical workflow of a buffeting analysis of a long-span bridge will look like below:

- Prepare input files containing FE, modal and aerodynamic properties
- Define wind field (wind profile, wind spectrum, coherence, etc.)
- Establish the model object
- Run frequency-domain analysis
- Post-process using the model object

4. VERIFICATION AND TESTING

4.1. Verification (IABSE benchmark)

The verification of the wind response module of WAWI was conducted by comparing its results against established benchmark results of the IABSE Task Group 3.1 benchmark study (Diana et al., 2023). The benchmark offers a reliable standard for assessing the performance of dynamic analysis tools, as it includes results from the foremost experts in the field. Some results of comparison of RMS values of displacement response (typical response for a long-span bridge) are given in Fig 1. In general, a very good agreement is obtained. Some discrepancy is present compared to the reference values, but in the margin of uncertainty and restricted to high wind speeds. The complete details of the verification cases, along with a comprehensive comparison of the results, will be made available in the library's documentation.

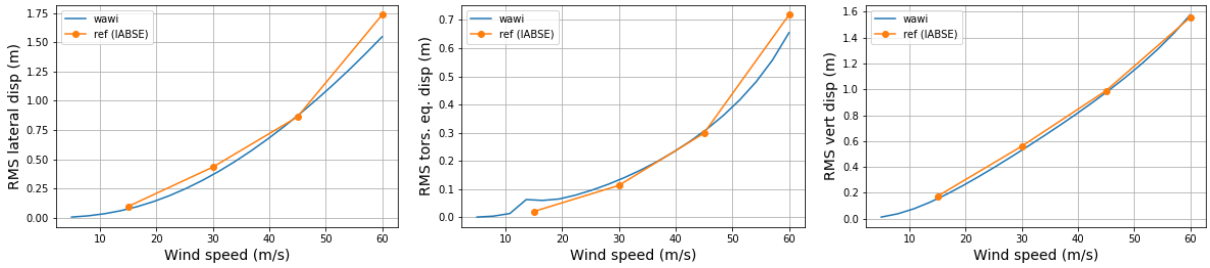


Figure 1. Comparison of results: WAWI vs. IABSE Task Group 3.1 reference values for benchmark study 1.1c using experimental aerodynamic data

4.1. Testing

In addition to external verification, WAWI employs rigorous internal testing using the pytest framework. The key functions are covered by unit tests that ensure their reliability and accuracy. The tests validate that each function operates correctly and produces consistent results when handling different modal properties, wind field configurations, and stochastic inputs. This systematic testing framework enables quick identification of any potential errors in the codebase and supports future updates and developments in the library. The combination of external verification with well-documented benchmarks and internal testing using unit tests ensures that WAWI provides reliable and accurate results for both research and practical applications.

5. CONCLUSIONS

WAWI is a powerful and versatile Python package designed for the stochastic dynamic analysis of structures under wind and wave loads in the frequency domain. Its capabilities have been verified against established benchmarks such as the IABSE Task Group 3.1 results. WAWI can be easily integrated with external finite element analysis software, which brings flexibility in application. Its open access nature ensures that the structural engineering community can benefit from its advanced capabilities, fostering both research and practical applications in wind engineering and beyond. As more users adopt WAWI, ongoing feedback and updates will help it evolve to meet future demands.

ACKNOWLEDGEMENTS

The authors acknowledge all the members of the Structural Dynamics group at NTNU who contributed to development of the package.

REFERENCES

Diana, G., Stoyanoff, S., Allsop, A., Amerio, L., Andersen, M.S., Argentini, T., Calamelli, F., Montoya, M.C., de Ville de Goyet, V., Hernández, S., Jurado, J.Á., Kavrakov, I., Larose, G., Larsen, A., Morgenthal, G., Rocchi, D., Svendsen, M.N., Wu, T., 2023. IABSE Task Group 3.1 Benchmark Results. Numerical Full Bridge Stability and Buffeting Simulations. Struct. Eng. Int. 33, 623–634. https://doi.org/10.1080/10168664.2022.2104188

Hansen, S., 2013. Vortex-induced vibrations – the Scruton number revisited. Proc. ICE - Struct. Build. 166, 560–571. https://doi.org/10.1680/stbu.11.00018

Øiseth, O., Rönnquist, A., Sigbjörnsson, R., 2010. Simplified prediction of wind-induced response and stability limit of slender long-span suspension bridges, based on modified quasi-steady theory: A case study. J. Wind Eng. Ind. Aerodyn. https://doi.org/10.1016/j.jweia.2010.06.009

Interaction of wind barrier and deck overhang on the vortex induced vibration response of slender bridge decks

Marko Đuranovic[1] and Craig Meskell[2]

[1]*Roughan & O'Donovan Consulting Engineers, Dublin, Ireland marko.duranovic@rod.ie*
[2]*Trinity College, Dublin, Ireland cmeskell@tcd.ie*

SUMMARY:
A simplified geometry for a slender bridge deck is defined and the position of the box girders is varied to modify the overhang at the leading and trailing edge. Each section is modelled with and without a 20% blockage wind barrier on the upper deck. The flow is modelled using 2D unsteady RANS with a prescribed structural motion. An energy balance approach is then used to assess the impact of geometric variations and damping on the maximum amplitude response due vortex induced vibration (VIV) and the associated lockin range. It is found that overhang tends to reduce both the VIV response amplitude and the lockin range. However, when the barrier is present, the amplitude tends to increase with increased overhang.

Keywords: Vortex induced vibration, Overhang, Prescribed motion

1. INTRODUCTION

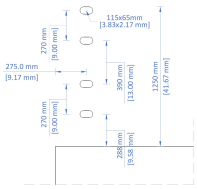
It is well known that like other slender bluff bodies, flexible bridge decks, typical of suspension bridges, may experience vortex induced vibration (VIV). For example, design codes in Ireland and UK (based on PD 6688-1-4 (2015)) and Japan (Japan Road Association, 2007) provide semi-empirical formulae to estimate response amplitudes for VIV. This can can lead to operartional problems after construction (e.g. (Fujino and Yoshida, 2002); (Benicke and Butz, 2015)). For bluff bodies generally, it has long been recognized that a splitter plate in the near downstream wake can substantially suppress periodic vortex shedding (e.g. Matsumoto et al. (1993)), but the effect can be sensitively dependent on the geometry of the section. In the context of bridge decks, if the deck slab extends past the girders it will act as a splitter plate. Thus, the VIV excitation and response will be modified by this overhang length. This effect is partially and implicitly included in both design codes referred to above as an addition factor, although the value of this factor is based on sparse data and limited geometric variation.

In this study, the effect of an installed wind barrier on the capacity of the overhang to modify the vortex induced vibration is investigated.

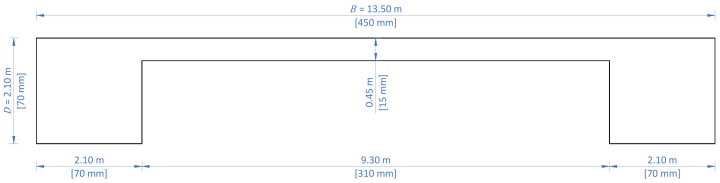
2. GEOMETRY

A simplified bridge deck section with two rectangular box girders has been defined. The position of the girders is varied to achieve different lengths of overhang. The overhang length is defined as a percentage of half the deck width. Figure 1(b) shows no overhang, labeled S0, while Figure 1(c) depicts the 50% overhang section, labeled S50. This geometry is indicative of bridges already

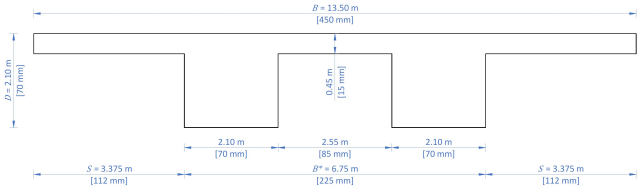
commissioned (e.g. Clyde Bridge) or in development (e.g. Narrow Water Bridge). A barrier with a blockage ratio of 20% and is shown in Figure 1(a). In what follows, the sections with a barrier are designated "SBxx" while without a barrier are labeled "Sxx", where "xx" is the percentage overhang. These geometries are defined at a scale typical of wind tunnel models to allow direct comparison in the future.



(a) Barrier geometry



(b) Bare deck with no overhang (S0)

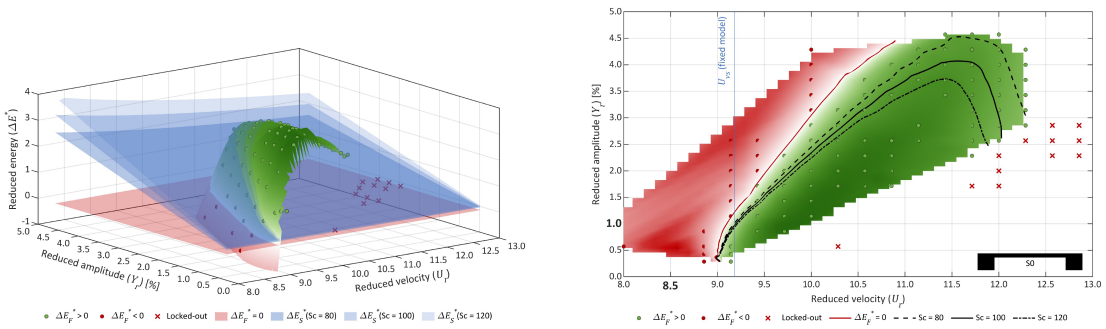


(c) Bare deck with 50% overhang (S50)

Figure 1. Schematic of deck geometry

3. METHODOLOGY

The airflow around the 2D bridge deck was simulated using unsteady RANS with the SST turbulence model in ANSYS-Fluent R2021. The modeling strategy and mesh size was developed initially with the Cylde Bridge geometry (similar to SB0) for which wind tunnel data was available. While it is possible to execute a free response model with full fluid-structure interaction including an elastic bridge deck mount, this would be computationally expensive and time consuming for two reasons. Firstly, each damping level and initial condition would represent a separate simulation. Secondly, and more importantly, as the system approaches lockin, the net system damping tends towards zero which means the number of oscillations periods required to achieve the limit cycle amplitude will be very large. In order avoid this, each deck geometry is simulated undergoing prescribed sinusoidal motion (Meskell and Pellegrino, 2019). An energy balance method sinilar to that used by Grinderslev et al. (2022) is then used to extract the maximum amplitude response for different Scruton numbers (i.e. different damping levels). In this approach, for a given oscillation amplitude and flow velocity, the energy transferred to the structure by the fluid force (ΔE_F) is balanced with the energy dissipated by the structural damping ΔE_S). A positive net energy ($\Delta E_F > \Delta E_S$) indicates vortex shedding lockin. This can be visualized as the intersection of two surfaces. Figure 2(a) depicts the fluid force energy surface in green and the structural energy surfaces for three levels of damping in blue. The plan view of this space is shown in figure 2(b) with the colours indicating positive (green) or negative (red) net energy. The oscillation amplitude necessary for net energy balance represents the limit cycle amplitude. Individual simulation results are indicated with markers and the redcued velocity for Karman vortex shedding observed with the fixed bridge deck (i.e. zero amplitude oscillation) is indicated for reference.

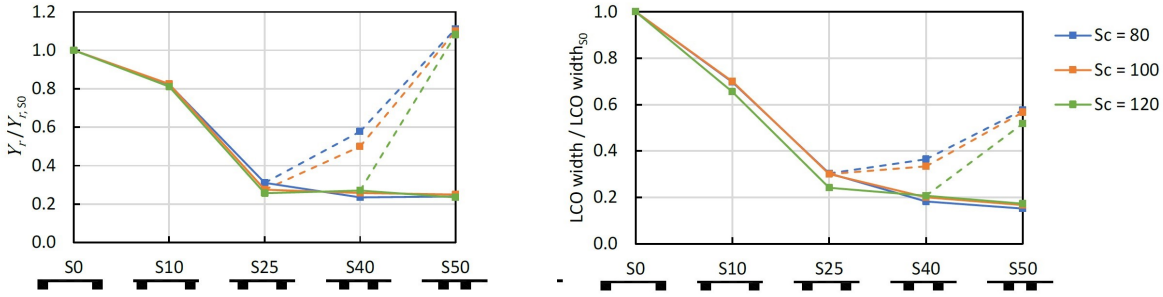


(a) Isometric view of energy surfaces (b) Net energy balance indicating lockin region.

Figure 2. Energy balance for geometry S0 based on CFD simulations.

4. RESULTS AND DISCUSSION

Five levels of overhang were investigated both with and without a barrier. Figure 3(a) shows the variation of the maximum limit cycle amplitude (i.e. the expected maximum response amplitude). These have been normalized by the amplitude for the zero overhang case (S0). As can be seen, even a small overhang of 10% yields a reduction in amplitude (S10) and a overhang of 25% produces a reduction of 70% for all damping levels examined. With a larger overhang, the wake exhibits both Karman vortex shedding (at low amplitudes) and motion induced vortex shedding (at higher amplitudes). The limit cycle amplitude motion induced vortex shedding is more or less constant, but the equilibrium amplitude associated with Karman vortex shedding increases (shown with dashed lines). This suggests that there is an optimal overhang length to minimize response to vortex shedding, but this is likely to be geometry dependent. Nonetheless, even at 50% overhang (S50), the response amplitude is only marginally greater than the S0 case, suggesting that overhang is nearly always beneficial. Furthermore, Figure 3(b) in all cases the the width of the veolcity range which will exhibit lockin is reduced with overhang, though again , there may be an optimal.

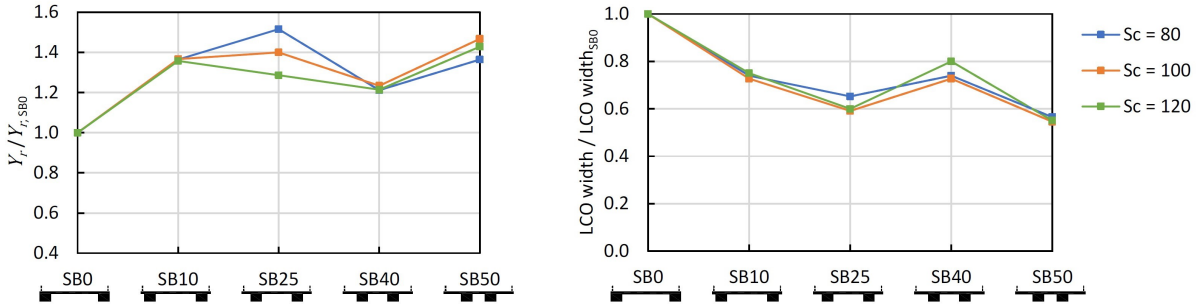


(a) Normalized maximum displacement amplitude (b) Normalized lockin velocity range

Figure 3. Behaviour of the bridge deck with overhang no barrier, normalized by the zero overhang case (S0).

The situation is signifcantly different when the barrier is added. Figure 4(a) shows the maximum limit cycle amplitude again normalized by the zero overhang case (SB0). The presence of the barrier eliminates the apparent benefit of overhang, with the response amplitude actually increasing with increased overhang. The lockin velcoity range still reduces, but to a smaller degree as shown

in Figure 4(b).



(a) Normalized maximum displacement amplitude (b) Normalized lockin velocity range

Figure 4. Behaviour of the bridge deck with overhang and barrier, normalized by the zero overhang case (SB0).

5. CONCLUSIONS

Increasing the deck overhang in the presence of a barrier generally tends to increase the maximum displacement amplitude associated with vortex excited vibration. For the lowest Scruton number considered this could be upto 40% larger. However, the overhang does tend to reduce the lock-in range and this reduction is relatively insensitive to Scruton number. Further work is need to examine the effect of barrier porosity, but it can already be seen that the benefit of a large overhang in terms of VIV response is ambiguous.

6. ACKNOWLEDGEMENTS

The research conducted in this publication was funded by the Irish Research Council under grant number EBPPG/2020/96 and Roughan & O'Donovan Consulting Engineers. The authors would like to acknowledge the Irish Centre for High-End Computing (ICHEC) for the provision of computational facilities and support.

REFERENCES

Benicke, O. and Butz, C., 2015. Volgograd-bridge: Efficiency of passive and adaptive tuned mass dampers. Proceedings of IABSE Conference, Geneva 2015: Structural Engineering: Providing Solutions to Global Challenges - Report. Geneva, Switzerland, 1428–1435.

Fujino, Y. and Yoshida, Y., 2002. Wind-Induced Vibration and Control of Trans-Tokyo Bay Crossing Bridge. Journal of Structural Engineering 128, 1012–1025.

Grinderslev, C., Normark Sørensen, N., and Raimund Pirrung G.and González Horcas, S., 2022. Multiple limit cycle amplitudes in high-fidelity predictions of standstill wind turbine blade vibrations. aWind Energy Science 7, 2201–2213.

Japan Road Association, 2007. Wind resistant design manual for highway bridges (in Japanese).

Matsumoto, M., Shiraishi, N., Shirato, H., Stoyanoff, S., and Yagi, T., 1993. Reynolds number effects in the flow around a bluff bridge deck cross section. Journal of Wind Engineering and Industrial Aerodynamics 49, 467–476.

Meskell, C. and Pellegrino, A., 2019. Vortex Shedding Lock-In due to Pitching Oscillation of a Wind Turbine Blade Section at High Angles of Attack. International Journal of Aerospace Engineering, 6919505 (12 pp.)

PD 6688-1-4, 2015. Background information to the National Annex to BS EN 1991-1-4 and additional guidance. The British Standards Institution.

Consideration of buffeting and vortex-induced vibration in wind-resistant design of a balanced cantilever bridge in construction stage

Aja Anta Tønnessen [1], Juel Petter Bergseth [1], Aksel Fenerci [1], Per Norum Larsen[1]

[1]*Multiconsult, Oslo, Norway, aja.anta.m.tonnessen@multiconsult.no, juelpetter.bergseth@multiconsult.no, aksel.fenerci@multiconsult.no*

SUMMARY: (10 pt)
This paper presents results from the wind-induced response calculations in the construction stage of the Ytre Steinsund Bridge, a prestressed concrete bridge that will be built by the balanced cantilever method in Norway. Referring to earlier wind-tunnel tests and full-scale observations, we point out that the dynamic response is likely to be affected by both buffeting and vortex shedding actions. The need for a standardized analytical procedure for prediction of dynamic response in such bridges are discussed considering the results of the case study.

Keywords: balanced cantilever bridge, buffeting response, vortex-induced vibration

1. INTRODUCTION

Prestressed concrete bridges with rectangular box-girders are commonly constructed using the balanced cantilever method. Several such bridges exist that span over 300 meters. In the construction phase, just before connecting of the cantilevers, the structure is a T-shaped column with cantilever beams on either side, and it is highly susceptible to wind-induced vibrations due to buffeting actions of the turbulent wind and vortex-induced vibrations that arise due to shedding of vortices downstream of the girder. The forces in the bridge pillar at this stage can govern the design. The cantilever structure is therefore commonly stiffened against such actions using support columns or tendons at this vulnerable stage, which brings additional costs and practical difficulties. Decisions on whether to use such measures or when and where they should be placed require accurate calculation of the wind-induced response.

Extensive wind-tunnel campaigns in the early 1990s (Bogunović Jakobsen and Hjorth-Hansen, 1998; Hjorth-Hansen et al., 1992; Strømmen et al., 2001) in relation to the design of the first long-span prestressed concrete bridges in Norway such as the Raftsundet Bridge revealed that the lift response in this stage was severely affected by vortex-induced vibrations (VIV), even in relatively high wind velocities and turbulent wind. It was reported that the drag response could be predicted with good accuracy by the buffeting theory, where the lift response could be severely underestimated if vortex-induced response was not considered. This observation was further confirmed by full-scale measurements of wind speed and acceleration of the Raftsundet (298 m span, opened 1998) and Sandsfjord (290 m, opened 2015) Bridges. The observed vertical acceleration response was about 2-4 times what was calculated by the buffeting theory (Hole et

al., 2016) at high wind velocities where the buffeting response is expected to be considerable. It was also shown that galloping might be important for these types of sections, and the interference of galloping with VIV might govern the response (Mannini et al., 2016). In the case where VIV occur at a velocity much smaller than the design wind speed, the two responses can be calculated separately according to the design regulations (Standard Norge, 2005). However, the broad-banded nature of the vortex shedding induced forcing on the cantilever might lead to significant excitation in a wide range of wind velocities, including high wind speeds close to the design wind condition. In that case, the effects of buffeting and VIV should be considered in tandem. To the authors' knowledge, no well-established analytical tools are available to tackle this problem.

The designers of the constructed bridges tackled this problem by superposing the excitation spectra of the two processes in the calculation of the wind-induced response, assuming that the total response is narrow-banded and small in amplitude. Here, we adopt the same methodology to predict the response of the Ytre Steinsund Bridge (YSB), currently under construction in Norway. We report the results, their importance in structural design, and highlight the need for a standardized and reliable procedure for estimation of the wind-induced effects of such bridges. In the following, we briefly present the bridge, adopted methodology and obtained results.

2. YTRE STEINSUND BRIDGE (YSB)

2.1. General

Ytre Steinsund bridge is a five span prestressed concrete box-girder bridge on the west coast of Norway. It is a design-build contract planned with limited time for both design and construction. The variable-height cross-section of the bridge (varying between 3.0 – 13.5 meters) is shapewise similar to two previously constructed bridges in Norway, Raftsundet Sandsfjord bridges where wind tunnel tests have been performed.

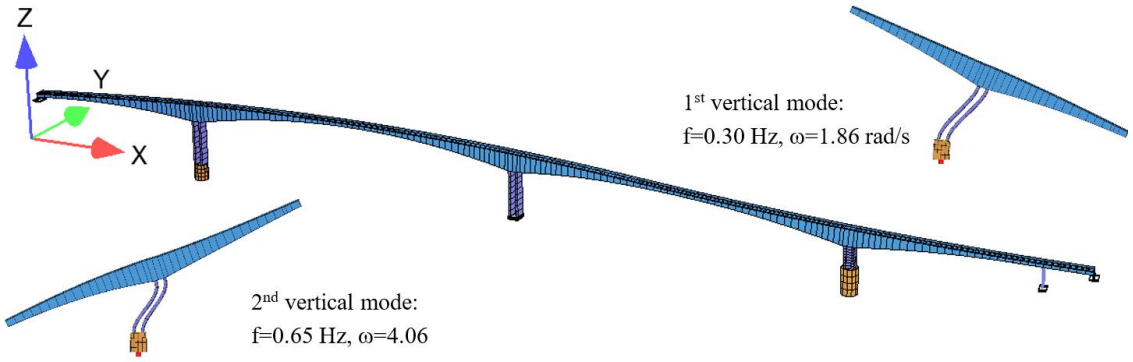


Figure 1. FE model and the two first vertical vibration modes

2.2. Structural and modal properties

The bridge was modelled in SOFISTIK and NovaFrame with all construction stages. The construction stage presented in this report is of axis 3 before connection to the auxiliary column, where the cantilever has a length of 68m. The columns are in this case assumed uncracked. An eigenvalue analysis was run and the most important mode shape with the corresponding vibration frequencies are given in (Figure 1).

2.3. Aerodynamic properties

Static force coefficients are taken from the wind tunnels test for the Raftsundet bridge and the parameters regarding vortex shedding are taken from Sandsfjord bridge in accordance with the Vickery & Basu model. The Strouhal number is around 0.14 for most of the span.

3. WIND-INDUCED RESPONSE OF YSB IN THE CONSTRUCTION STAGE

3.1. Methodology

For the case of the YSB, it is assumed that the aeroelastic response of the cantilever structure due to turbulence action can be modelled using linear quasi-steady buffeting theory in the considered range of displacements and wind angles-of-attack. It is further assumed and confirmed by multimode calculations that coupling between vibration modes can be ignored owing to well-separated modes. Under these assumptions, the spectral density of the dynamic response in generalized coordinates of i-th mode is written based on the random vibration theory:

$$\tilde{S}_{r,i}(\omega) = \left|\tilde{H}_i(\omega)\right|^2 * \left(\widetilde{S_{Q,i}}(\omega)\right), \quad \tilde{H}_i(\omega) = -\tilde{M}_i + \left(\tilde{C}_i - \tilde{C}_{ae,i}(\omega)\right)i\omega + \left(\tilde{K}_i - \tilde{K}_{ae,i}(\omega)\right) \qquad (1)$$

where $\widetilde{S_{Q,i}}(\omega)$ is the spectral density of the buffeting loading and M, C and K denotes the system matrices in generalized coordinates of the mode shape and the subscript "ae" denotes the aerodynamic counterparts. A Kaimal-type spectra along with a Davenport coherence function is adopted for turbulence. According to Vickery and Basu (Hansen, 2013) formulation which is adopted also in the Eurocodes, vortex shedding forcing can be described in a similar manner, i.e. in terms of a power spectral density. The lift spectrum is given:

$$S_V = \frac{\left(\frac{1}{2}\rho U^2\right)^2}{\sqrt{\pi\omega_{crit}}}\left[\frac{(B\breve{\sigma}_z)^2}{b_z}\exp\left(-\left(\frac{\left(1-\frac{\omega}{\omega_{cr}}\right)}{b_z}\right)^2\right)\right]\cos\left(\frac{2\Delta x}{3\lambda_m D}\right)\exp\left[-\left(\frac{\Delta x}{3b_z D}\right)^2\right] \qquad (2)$$

where ω_{crit} is the vortex shedding frequency, determined by the Strouhal number and $\breve{\sigma}_z, b_z, \lambda_m$ are parameters dependent on the cross-sectional shape and D is a characteristic depth. It was shown that for the box-sections considered here, the theory by Vickery and Basu gives reasonable estimates of the VIV response, adopting a linearized aerodynamic damping model (Hansen, 2013). Here, the dynamic response of the YSB is calculated by Eqn. (1) and superposing the load spectra due to buffeting and vortex shedding.

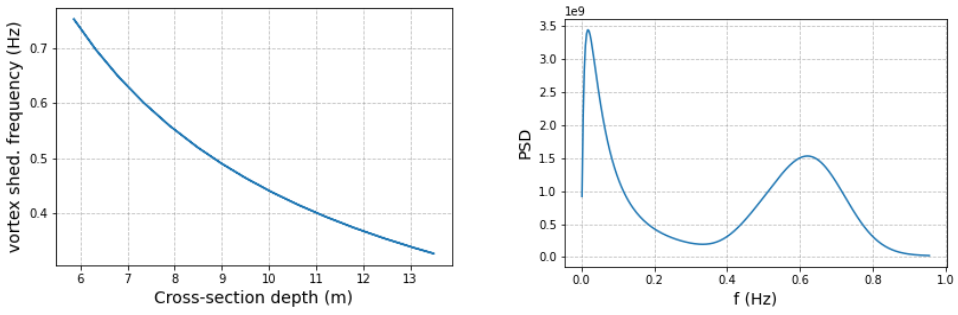


Figure 2. Vortex shedding frequency range (left) and generalized power spectral density of the loading (right)

It is assumed that the interference between the two processes is minimal due to small amplitude

response and that superposition will give a conservative approximation of the actual loading.

3.2. Results

The dynamic response of the YSB was calculated in frequency domain using the described methodology. The aerodynamic properties were based on previous data and varied along the span, depending on the section height to width ratio. Comparisons with a multimode analysis showed negligible modal coupling. Two sets of analyses were carried out: 1) a pure buffeting analysis 2) a buffeting analysis with vortex-induced effects included. Fig. 3 below shows the amplification due to vortex-induced effects for the 2nd vertical mode (Fig. 1). It is seen that the response is dominated by VIV despite the high wind speed.

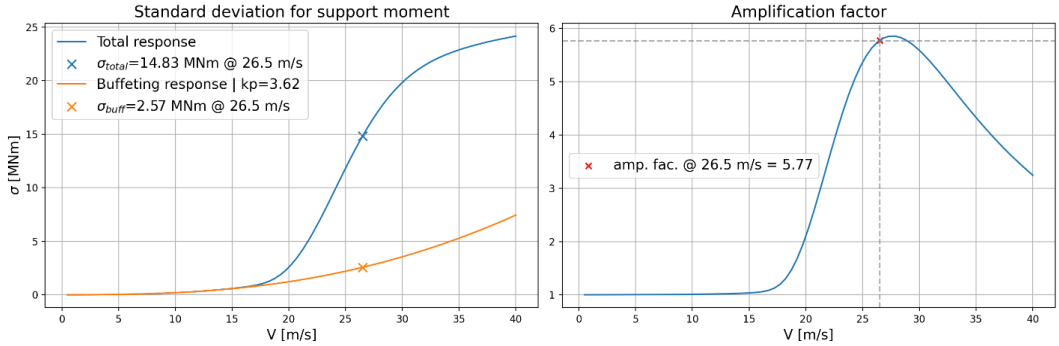


Figure 3. RMS bending moment due to deflection in the vertical direction (across-wind) vs. the mean wind speed (left). Amplification factor (total response / buffeting response)

7. CONCLUSIONS

Previous work on balanced cantilever bridges in construction stage (both wind tunnel and full-scale) showed increased wind-induced response due to VIV effects, even in higher wind speeds in the vicinity of design values. Due to the lack of reliable and established analytical tools in our disposal, we used a conservative approach to calculate the resulting load effects. The findings highlight the importance of the effects and the need for the development of analytical methodology to address this problem.

REFERENCES

Bogunović Jakobsen, J., Hjorth-Hansen, E., 1998. Aeroelastic effects on a rectangular box-girder bridge. J. Wind Eng. Ind. Aerodyn. 74–76, 819–827. https://doi.org/10.1016/S0167-6105(98)00074-9

Hansen, S., 2013. Vortex-induced vibrations – the Scruton number revisited. Proc. ICE - Struct. Build. 166, 560–571. https://doi.org/10.1680/stbu.11.00018

Hjorth-Hansen, E., Jakobsen, A., Strømmen, E., 1992. Wind buffeting of a rectangular box girder bridge. J. Wind Eng. Ind. Aerodyn. 42, 1215–1226. https://doi.org/10.1016/0167-6105(92)90128-W

Hole, K.D., Fergestad, S., Aas-Jakobsen, K., 2016. Wind induced response of the Sandsfjord Bridge - a balanced cantilever bridge at the western coast of Norway. Presented at the IABSE Congress: Challenges in Design and Construction of an Innovative and Sustainable Built Environment, Stockholm, Sweden. https://doi.org/10.2749/stockholm.2016.0173

Mannini, C., Marra, A.M., Massai, T., Bartoli, G., 2016. Interference of vortex-induced vibration and transverse galloping for a rectangular cylinder. J. Fluids Struct. 66, 403–423. https://doi.org/10.1016/j.jfluidstructs.2016.08.002

Standard Norge, 2005. Eurocode 1: Actions on structures - Part 1-4: General actions - Wind actions.

Strømmen, E., Hjorth-Hansen, E., Kaspersen, J.H., 2001. Dynamic loading effects of a rectangular box girder bridge. J. Wind Eng. Ind. Aerodyn. 89, 1607–1618. https://doi.org/10.1016/S0167-6105(01)00138-6

Enhancing OpenFOAM with EnKF for Efficient State and Parameter Optimization in Atmospheric Flows

Emanuele Bombardi[1], Alessandro Gambale[2], Alessandro Parente [1,3]

[1]*Université Libre de Bruxelles, École polytechnique de Bruxelles, Brussels, 1050, Belgium*
[2]*BuildWind SPRL, Brussels, 1070, Belgium*
[3]*WEL Research Institute, Wavre, 1300, Belgium*

SUMMARY:
This work introduces an efficient urban flow modeling framework integrating Ensemble Kalman Filter with OpenFOAM. Key innovations include a Building Influence Area technique reducing computational costs by 60%, a physics-aware data assimilation approach balancing observations with physical constraints, and parameter optimization showing robust transferability from simple to complex urban environments. The framework demonstrates 25% error reduction in Tokyo's Shinjuku district model, significantly advancing urban CFD simulation capabilities.

Keywords: Ensemble Kalman Filter, Building Influence Area, Urban Flow CFD Simulation

1. INTRODUCTION

Urban flow modeling presents significant computational challenges due to the complexity of urban geometries and the need for high-resolution simulations. Computational Fluid Dynamics (CFD) offers a cost-effective alternative to full-scale measurements and wind tunnel experiments but faces limitations in accuracy and computational efficiency. Data assimilation techniques such as the Ensemble Kalman Filter (EnKF) show promise for improving simulation accuracy by incorporating observational data. However, their application to large-scale urban environments has been constrained by computational demands. This study introduces innovative approaches to implement EnKF efficiently in OpenFOAM for urban flow simulations.

2. CORE INNOVATION: BIA-BASED DOMAIN REDUCTION

The cornerstone of our methodology is a dynamic physical clipping technique based on the Building Influence Area (BIA) concept (Parente, 2011). The BIA identifies regions where flow is significantly affected by building presence, typically comprising only 10% of the global domain. By dynamically isolating this critical area and focusing EnKF operations exclusively within it, we achieve substantial computational savings without compromising solution accuracy. Our implementation extends the BIA-based localization to the propagation step—typically the most resource-intensive simulation component—by operating on a subdomain of the full simulation. This approach employs homogeneous boundary conditions to ensure consistency between flows

inside the subdomain and the outer regions, preserving physical integrity throughout the entire domain while dramatically reducing computational demands.
Our implementation demonstrates exceptional efficiency gains, consistently achieving over 60% reduction in computational time per iteration compared to conventional EnKF approaches without physical clipping. This significant performance improvement results from strategically concentrating computational resources on dynamically identified regions of interest, effectively reducing the domain size for EnKF operations while maintaining solution accuracy to the third decimal place.

3. ENKF IMPLEMENTATION IN OPENFOAM

We have fully integrated the EnKF algorithm within OpenFOAM version 7, leveraging its native parallel computing capabilities. This integration eliminates external data exchanges, creating a cohesive system that efficiently handles data assimilation, flow solving, and turbulence modeling within a single computational environment. Our steady-state simulation approach implements EnKF as an iterative process rather than time-stepping, with three key phases: (1) EnKF update, where flow fields are adjusted based on EnKF innovation; (2) Propagation, allowing updated fields to adapt to physical constraints imposed by Navier-Stokes equations; and (3) Iteration, repeating steps 1-2 until convergence balances data assimilation with physical consistency.

4. PHYSICS-AWARE ENKF METHODOLOGY

uilding upon this foundation, we introduce a physics-aware EnKF assimilation approach addressing challenges in steady-state simulations. Traditional EnKF implementations often compromise physical consistency when fitting observations. Our novel approach monitors solution physicalness by comparing velocity divergence between EnKF and CFD solutions. The physicalness metric ϕ is defined as 1 minus the error admitted with respect to the CFD divergence velocity value.

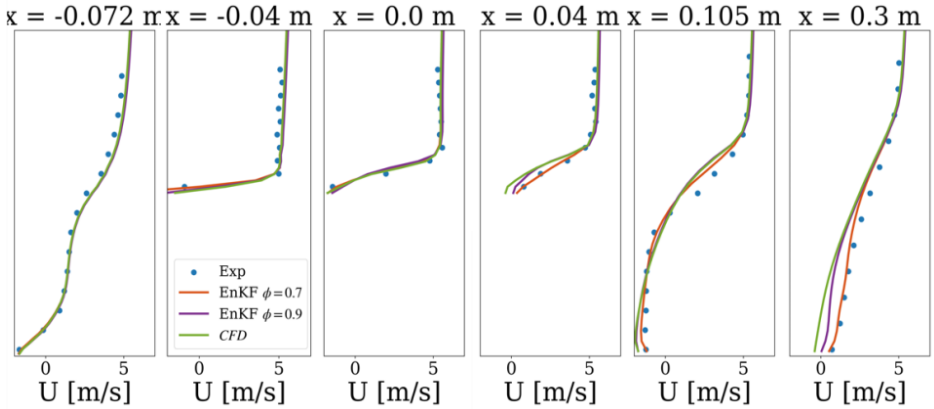


Figure 1. Experimental and numerical profiles of velocity. Blue dot: experimental data. Green line: CFD simulation. Orange line: EnKF solution with phisicalness $\phi = 0.7$. Purple line: EnKF solution with phisicalness $\phi = 0.9$.

Updates occur only when physicalness meets predefined threshold criteria, creating a controlled balance between data assimilation and physical constraint adherence. This methodology introduces a strategic trade-off: more frequent updates improve alignment with experimental data

but may reduce physicalness, while less frequent updates maintain higher physical consistency but potentially capture fewer observed dynamics.

We validated our physics-aware EnKF implementation using the well-documented CEDVAL A1-1 single-building test case (Leitl, 1998), featuring a rectangular building within an atmospheric boundary layer flow. Six velocity measurement locations provided data for assimilation and validation, covering upstream, roof-top, downstream regions, and a wake measurement point. Results demonstrate significant improvements in flow prediction accuracy, particularly in wake regions where our assimilated solution achieves smooth, physically consistent wake structures while maintaining 90% physicalness.

5. REGULARISED AUGMENTED STATE ENKF

To further enhance the capabilities of the EnKF framework, an augmented state approach is introduced for simultaneous state and parameter optimisation. The state vector ψ is expanded to include both physical states ϕ and model parameters α, allowing for their simultaneous update through observations d. To prevent parameter estimates from deviating excessively from their prior p values and maintain physical consistency, a regularization term is incorporated into the EnKF cost function. This modification enables the computation of a regularized Kalman gain that is employed in the update equation, ensuring a Bayesian-consistent framework that balances observational fit with physical constraints.

The augmented cost function is formulated as:

$$\mathcal{J}(\boldsymbol{\psi}) = \|\boldsymbol{\psi}^{\mathrm{f}} - \boldsymbol{\psi}\|^2_{\mathbf{C}^{f^{-1}}_{\psi\psi}} + \|\boldsymbol{d} - \mathbf{M}_q\psi\|^2_{\mathbf{C}^{-1}_{dd}} + \|\boldsymbol{p} - \mathbf{M}_\alpha\boldsymbol{\psi}\|^2_{\mathbf{C}^{-1}_{pp}} \quad (1)$$

where $C^f_{\psi\psi}, C_{dd}, C_{pp}$ are the state, observations, and prior term's covariance matrices respectively. ψ^f represents the forecast state vector, while M_q and M_α are the state-to-observable and state-to-parameters mapping matrices respectively.

A diverse set of parameters is selected for optimization, stratified by their influence on the turbulence model. Highly influential parameters—including a_1, β^*, and $\alpha_{\omega 2}$—directly affect the core SST $k-\omega$ turbulence model dynamics (Bellegoni, 2023), while secondary parameters such as limiters. This strategic parameter selection evaluates the framework's capability to precisely identify and optimize critical parameters while maintaining less influential ones near their prior values. The parameters are optimized on the simple well-documented CEDVAL A1-1 single-building test case (Leitl, 1998), providing a controlled environment for validation. The convergence results (Table 1) demonstrate clear correlation with parameter significance, validating the effectiveness of the augmented state regularized EnKF approach. Specifically, highly influential parameters (a_1 β^*, $\alpha_{\omega 2}$) exhibit robust, stable convergence patterns, while less influential parameters appropriately remain near their prior values with expected larger variance.

blank line before table heading and one blank line after the table, as in Table 1 shown below.

Table 1. Prior and Optimized parameter values with prior, assigned, and final, obtained, standard deviation.

Parameter	$\beta^* \pm \sigma$	$a_1 \pm \sigma$	$b_1 \pm \sigma$	$c_1 \pm \sigma$	$\omega_{\alpha_2} \pm \sigma$
Prior Value	$0.09 \pm 9e-3$	0.31 ± 0.03	1 ± 0.1	10 ± 1	0.85 ± 0.08
Optimized Value	$0.09 \pm 3e-3$	0.51 ± 0.09	0.9 ± 0.16	9.78 ± 1.3	0.30 ± 0.06

To demonstrate transferability and validate the effectiveness of the optimized parameters obtained from the augmented state EnKF, we applied them to increasingly complex test cases, culminating in the Shinjuku district domain—a highly intricate urban environment modeling Tokyo's business district with 54 million mesh cells. Comparing the normalized velocities against experimental measurements (Figure 2) reveals a substantial reduction in mean square error of over 25% across 25 experimental locations, confirming robust transferability to real-world urban environments. This successful transfer to a real-world urban environment highlights the robustness and effectiveness of the optimized parameters obtained through the augmented state regularized EnKF approach.

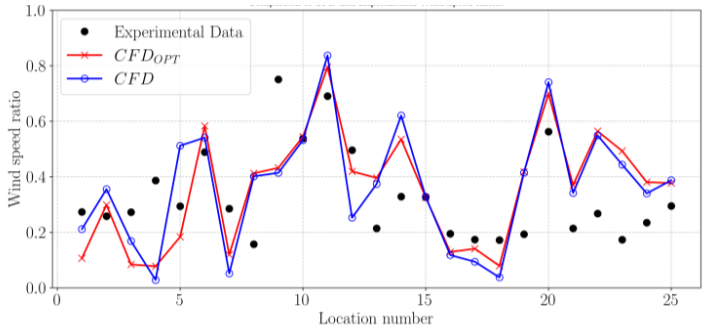


Figure 2. Experimental and numerical normalized velocity values. Black dot: experimental data. Blue line: baseline CFD simulation. Red line: EnKF parameters optimized CFD simulation

6. CONCLUSIONS

In conclusion, this study presents a comprehensive framework enhancing OpenFOAM with efficient, physics-aware Ensemble Kalman Filter implementations for urban flow simulations. Our key contributions include a 60% reduction in computational costs through BIA-based domain optimization; a physics-aware EnKF assimilation approach balancing data incorporation with physical constraints; and successful regularized parameter optimization using augmented state EnKF with demonstrated transferability from simple test cases to complex urban applications. This framework bridges computational efficiency and physics-aware modeling gaps, enabling accurate, reliable simulations of complex urban environments.

REFERENCES

Parente, A., Gorlé, C., van Beeck, J., and Benocci, C., 2011. A comprehensive modelling approach for the neutral atmospheric boundary layer: Consistent inflow conditions, wall function and turbulence model. Boundary-Layer Meteorology 140, 411–428.

Bellegoni, M., Cotteleer, L., Srikumar, S.K.R., Mosca, G., Gambale, A., Tognotti, L., Galletti, C., and Parente, A., 2023. An extended SST k−ω framework for the RANS simulation of the neutral Atmospheric Boundary Layer. Environmental Modelling & Software 160, 105583.

Leitl, B., 1998. CEDVAL at Hamburg University.

Reproducing the atmospheric boundary layer for wind engineering using Mann and TurbSim inflow generation methods from wind energy

Sophie Breitkopf[1], Christian Hartz[2], Girma Bitsuamlak[3]

[1]*Chair of Structural Design, TU Dortmund University, Dortmund, Germany Email address*
[2]*Chair of Structural Design, TU Dortmund University, Dortmund, Germany Email address*
[3]*WindEEE Research Institute, Western University of Ontario, London, Canada, Email address*

SUMMARY:
This study focuses on calibrating and adapting the Mann and TurbSim synthetic inflow generation methods from wind energy for application in wind engineering. The calibration process enhanced the Mann method to include a mean velocity profile and achieve higher turbulence intensities. In terms of adaptation, the resulting tensors were integrated into the OpenFOAM framework. Comparisons with wind tunnel measurements revealed initial discrepancies in turbulence levels and height developments; however, subsequent calibration improved the results. This work lays the foundation for future comparisons of synthetic inflow generation methods, ensuring that wind energy techniques are utilized effectively to adjust for various terrains.

Keywords: synthetic inflow, LES, comparison

1. INTRODUCTION

In wind engineering, accurately reproducing the atmospheric boundary layer (ABL) for specific terrain is crucial for assessing wind loads on structures. Synthetic inflow generation methods offer an efficient approach to introduce turbulence at the inlet of computational domains based on statistical characteristics. However, achieving all target turbulence properties simultaneously can be challenging. The synthetic turbulent vortices always require some adaptation length for the target flow to develop fully (Tabor and Baba-Ahmadi, 2010). Additionally, the propagation of the turbulent flow through the computational domain can lead to deviations from the intended target properties (Blocken et al., 2007), potentially impacting the accuracy of the simulation results. In the absence of specific guidelines for synthetic inflow generation in computational wind engineering, the inflow thus requires elaborate a priori studies. To gain insight into the state of the art, it is important to examine adjacent disciplines. In the field of wind energy, synthetic inflow generation methods such as Mann (Guo and Mann, n.d.; Mann, 1994) and TurbSim (Laboratory, 2012; Veers, 1988) are common practice recommended in the codes (DIN EN IEC 61400-1, 2019). With wind turbines reaching heights comparable to those of average high-rise buildings (Global Wind Energy Council, 2024), the height of the ABL that must be considered is also quite similar. This raises the question of whether the guidelines for computational fluid dynamics (CFD) in wind energy can be applied to wind engineering. In open or offshore terrain, the turbulence intensity required for wind energy applications is typically low. Therefore, it must be tested whether the methods can produce increased turbulence levels that accurately represent suburban or urban terrain. In wind energy

applications, inflow generation often considers atmospheric stability, including unstable or stable stratification. However, neutral stratification is commonly used in wind engineering (ASCE-49, 2021; ESDU 82026, 2003).
This study focuses on the calibration process of Mann and TurbSim inflow generation methods to reproduce the atmospheric boundary layer (ABL) for different terrains. It highlights the steps necessary for calibration and the adaptation of these wind energy methods for wind engineering applications in large eddy simulations (LES) using OpenFOAM. This work is part of a larger interdisciplinary comparison of synthetic inflow generation methods, validated through wind tunnel tests. While the broader study will showcase the suitability of different methods, this paper focuses on the calibration process.

2. METHODOLOGY

The Mann and TurbSim models were calibrated to adapt their inflow generation to the ESDU profiles for the open, suburban and urban terrain. Both methods belong to the group of spectral representation methods, where the flow is represented by sinusoidal waves. Their amplitude and phase shift is determined based on the decomposition of a target spectrum. The resulting inflow tensor, which already represents the full turbulence characteristics over the cross-section and duration, can be analysed independently before entering the domain.
Starting with the default settings described in the handbooks, the calibration process involved adjusting the available parameters to understand their influence on the model's output. For the Mann simulation, initial values were also sourced from literature and existing code (DIN EN IEC 61400-1, 2019; Nybø et al., 2021). This iterative calibration aimed to refine the parameters to achieve the desired mean velocity profile and higher turbulence intensities.
The Mann tensor provides the fluctuating components that are rather constant over the height. The mean velocity profile was included by adding it at every time step in the alongwind direction. The turbulence intensity can only be adjusted by setting the turbulent energy according to Eq. (1) and (2) from Mann (1994) and thus the Kolmogorov spectrum. Longer simulation durations naturally introduce larger turbulence length scales, as more energy accumulates across scales in the inertial subrange. The calibration was therefore mainly based on the final duration of the simulation and the relationship between length scale and energy was investigated. Another crucial parameter was the anisotropy factor that affected the distribution throughout the three directions. By nature, the Mann tensor has to match 2^n for the elements in x, y and z direction. This creates a restriction for the discretization and different resolutions mapped onto the mesh are investigated.

$$E(k) = \alpha \varepsilon^{2/3} k^{5/3} \tag{1}$$

$$\alpha \varepsilon^{2/3} \approx \frac{\sigma_{iso}^2}{0.688 L^{2/3}} \tag{2}$$

TurbSim provides parameters comparable to those used in wind engineering, which were utilized to establish the longitudinal direction. They define the properties at a reference point in the upper part of the domain. For the alongwind velocity a profile can be selected (power law, log law, yet or based on IEC). The turbulence intensity is derived from the terrain characteristics in DIN EN

IEC 61400-1 (2019). However, even the roughest terrain leads to rather low turbulence intensities. With the normal turbulence model (NTM), the turbulence intensity can be defined explicitly at the reference height. The spectral model can be selected explicitly; in this case, the von Kármán model was chosen over the Kaimal spectrum or other wind energy-specific models. Even though coherent turbulent scales can be adjusted, the length scales remain relatively low.
The parameters to determine the flow for both methods are summarized in Table 1.

Table 1. parameters to target inflow with Mann and TurbSim inflow generation

parameter	Mann	TurbSim
U_{ref}	at definable H_{ref}	at H_{ref} in upper half
$U(z)$	not incl., but α_{shear}	profile choice, u^*, z_0 and PLExp
T_i	not explicitly, $\alpha\varepsilon^{2/3}$	IECturbc [%] at ref. height
L_u^x	at ref. height, γ evolution (alongwind)	not provided directly
spectral model	Kolmogorov, factors f_1, f_2 slope eddy life time	sprectra choice
$u\prime w\prime$	not explicitly	at reference height
anisotropy	Γ factor	not specified

After analyzing and calibrating the inflow tensor to match the open, suburban, and urban terrain ESDU flows, the next step is to investigate the effect of mapping the flow onto the mesh, which requires interpolation, followed by verifying its propagation through the computational domain. The tensors, produced through executables, have to be split appropriately for use as inflow conditions in OpenFOAM per time step in suitable spatial resolution. The flow can then be compared to the wind tunnel measurements from the Boundary Layer Wind Tunnel II of the BLWTL taken at Western University of Ontario, to account for the influence of a confided domain. Similarly, the numerical simulations are scaled to 1:400 with the same cross-section of 3.4 m x 2.5 m as the mentioned wind tunnel. The ground roughness is modelled explicitly through roughness elements based on the layout of the BLWT II.

3. RESULTS

During the calibration of the Mann method, it was found that the energy control parameter $\alpha\varepsilon^{2/3}$ including the length scale as well as the anisotropy constant Γ had the largest influence. The required increase of the turbulence intensity was achieved through balance of the parameters with a reduced length scale and slightly adjusted turbulent variance. The resulting length scale profiles matches the ESDU profiles of all terrains reasonable well with a slight underestimate in the vertical direction for the duration corresponding to 1 hour at full-scale. The turbulence intensity was closely matched for the reference height in alongwind, crosswind and vertical direction due to fitting the factor Γ. A smaller Γ lead to better fit of the Reynolds shear stresses while the turbulence intensities in the crosswind and vertical direction increased in relation to the alongwind diretion.
For the TurbSim method, the turbulence intensity and the length scales were underestimated. This could be improved by adjusting the available settings to directly enter the intensity. For the alongwind and crosswind direction, the turbulence intensity profiles matched the target very well, while the vertical direction showed a slight overestimate. The coherence parameters didn't significantly increase the obtained length scales.
The propagation of inflow through the domain revealed that an initial overestimation of turbulence at the inlet resulted in faster convergence to the target properties, proving more effective than relying solely on the turbulence generated by the roughness elements. Similarly, in wind tunnel ex-

periments, sufficient energy levels are introduced before the roughness elements to ensure optimal flow characteristics.

4. CONCLUSIONS

This study calibrated and adapted two state-of-the-art synthetic inflow generation methods from wind energy, Mann and TurbSim, for use in open, suburban, and urban terrains in wind engineering. The Mann method was modified to include the mean velocity profile. Both methods were calibrated for higher turbulence intensities and integrated into the OpenFOAM framework.
Comparisons of the generated inflow with wind tunnel measurements revealed initial discrepancies in turbulence levels, height developments, and spectra. Calibration improved the results, highlighting their full potential. Ultimately, this initial work establishes a foundation for broader comparisons of synthetic inflow generation methods.

ACKNOWLEDGEMENTS

The authors would like to express their gratitude to the WindEEE Research Institute for their invaluable support in facilitating knowledge transfer and conducting the wind tunnel tests. We also acknowledge the Heinrich Hertz Foundation and the German Research Foundation (DFG) for providing the scholarships and financial assistance that enabled travel and the establishment of international collaborations, which were essential to this research.

REFERENCES

ASCE-49, 2021. *Wind Tunnel Testing for Buildings and Other Structures*. Code.

Blocken, B., Stathopoulos, T., and Carmeliet, J., 2007. CFD simulation of the atmospheric boundary layer: wall function problems. Atmospheric environment 41, 238–252.

DIN EN IEC 61400-1, Dec. 2019. *Wind energy generation systems - Part 1: Design requirements (IEC 61400-1:2019); German version EN IEC 61400-1:2019*. Norm.

ESDU 82026, Mar. 2003. *Strong winds in the atmospheric boundary layer. Part 1: hourly-mean wind speeds*. Norm. [Amendement (E)].

Global Wind Energy Council, 2024. *GLOBAL WIND REPORT 2024*. https://gwec.net/. [Online; accessed 07.06.2024, 17:00]. Brussels, Belgium.

Guo, F. and Mann, J., n.d. *Initial release of the 4D Mann Turbulence Generator: MannTurb4D (Version v1.0)*.

Laboratory, N., 2012. *TurbSim Simulation Tool*. https://www.nrel.gov/wind/nwtc/turbsim.html.

Mann, J., 1994. The spatial structure of neutral atmospheric surface-layer turbulence. Journal of fluid mechanics 273, 141–168.

Nybø, A., Nielsen, F. G., and Godvik, M., 2021. Analysis of turbulence models fitted to site, and their impact on the response of a bottom-fixed wind turbine. Proceedings of Journal of Physics: Conference Series. Vol. 2018. IOP Publishing, 012028.

Tabor, G. and Baba-Ahmadi, M., 2010. Inlet conditions for large eddy simulation: A review. Computers & Fluids 39, 553–567.

Veers, P. S., 1988. *Three-dimensional wind simulation*. Tech. rep. Sandia National Labs., Albuquerque, NM (USA).

Simulating building-induced windshear at airports

N. Pedersen[1], B. Venås[2], O. R. Hjetland[3]

[1]*Norconsult Norge AS, Sandvika, Norway, nick.pedersen@norconsult.com*
[2]*Norconsult Norge AS, Sandvika, Norway, bard.venas@norconsult.com*
[3]*Avinor AS, Oslo, Norway, olai.rune.hjetland@avinor.no*

SUMMARY:
The study uses CFD to simulate building-induced windshear at airports, crucial for crosswind operations where building wakes may cross runways or glide paths. Traditional RANS models are inadequate for accurate wake predictions, leading to the use of LES models despite higher costs. The New Bodø Airport project serves as an example using CFD and LES to assess terminal building designs. The study finds current acceptance criteria for wind speed deficits challenging to apply in complex scenarios and suggests developing new criteria based on transient wind data from advanced CFD and real-world measurements.

Keywords: CFD, LES, Windshear

1. AIRCRAFT OPERATIONS IN CROSSWIND

Landing is typically the most vulnerable phase of flight as aircraft are near the ground and at low airspeeds. Standard procedure for commercial operations is for aircraft to be in a stabilized approach by a set altitude above the airport elevation. Any major deviations away from the glide slope in heading, roll, pitch, or speed may require a “go-around.” In the final approach and during the flare, the worst-case outcome is a loss of control. Airports are laid out such that runway headings are, as far as practically possible, aligned with the prevailing wind directions. Landings and take-offs normally occur into the wind, but operations during crosswinds, where the incoming wind is at an angle to the runway, are inevitable. In such cases, buildings and other obstructions in the vicinity of the airport will generate aerodynamic wakes that may cross

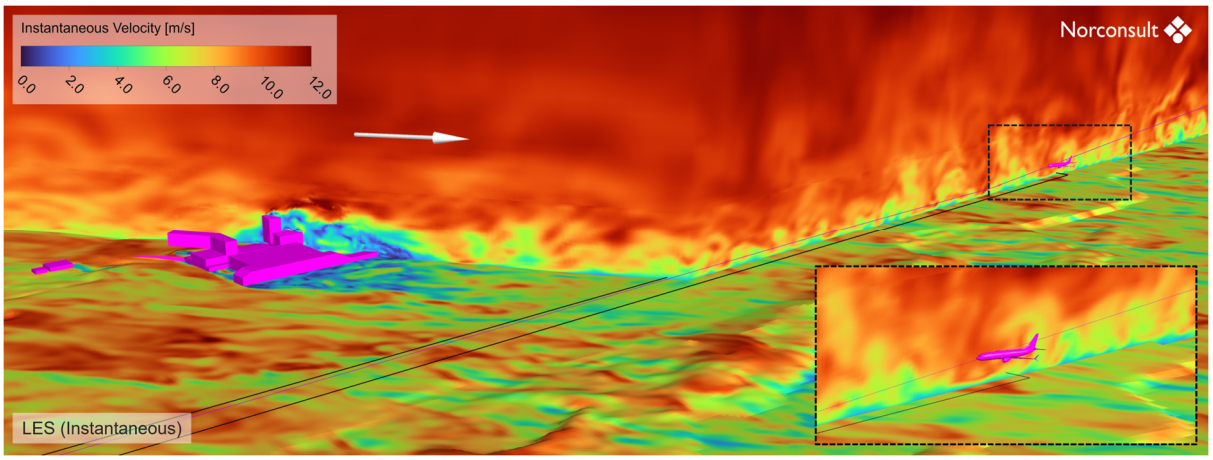


Figure 1. Example of CFD (LES) simulation of the wind over the New Bodø Airport in Norway.

the runway or the glide slope. These wakes represent wind speed deficits, shear regions, and areas of turbulence that may greatly interfere with aircraft stability. To predict the way such building wakes travel and impact aircraft operations, 3D wind simulations using Computational Fluid Dynamics (CFD) are performed (see Fig. 1 as an example).

2. WIND DEFICIT CRITERIA IN THE VICINITY OF AIRPORTS

The Royal NLR have developed a set of recommended threshold values for the allowable mean wind speed deficit downwind of a free-standing structure through rigorous flight simulator testing (Nieuwpoort et al., 2010). Their recommendations were that, below an aircraft altitude of 200 ft, the permissible variation in mean wind speed across the glide path ought to be limited to 7 knots in the "along aircraft trajectory" and 6 knots in the "across aircraft trajectory." These speed deficits must endure for at least 100 m, in order for the threshold values to be applicable.

3. CFD SIMULATION OF WIND AROUND BUILDINGS

The simulation of the lower portion of the Atmospheric Boundary Layer (ABL) with wind over buildings and terrain using CFD is a well-established area of research. The way in which turbulence in the flow field is modelled is essential to the quality of the result. RANS-based turbulence models ("Reynolds Averaged Navier-Stokes") have historically been the most used for microscale wind simulation, due to their relatively low computational cost. However, in many applications where the modelling of shear regions in the free stream is the primary interest, RANS models do not produce satisfactory results. Instead, scale resolving models such as Large Eddy Simulation (LES) approaches are necessary. These are orders of magnitude more costly compared with RANS, but the growth in computational power over the past decade mean that they are now often practical to use.

Specifically speaking, for the purposes of simulating wind around buildings, RANS-models overpredict the length of the downstream wake. LES-based models predict the wake length much more accurately. This is depicted in Fig. 2. The increased accuracy for wake lengths when using LES also holds true when using coarser simulation models, where perhaps not all the theoretical recommendations for LES are stringently met.

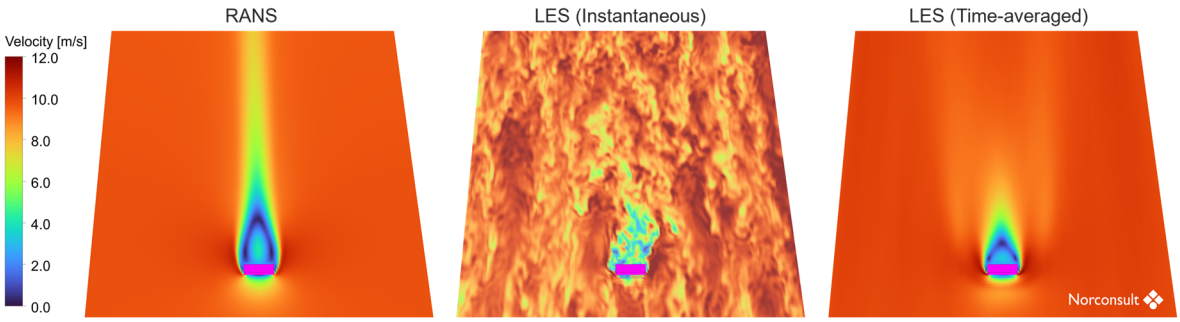


Figure 2. Comparison of wake lengths predicted by RANS and LES behind a rectangular building.

4. EXAMPLE: THE NEW BODØ AIRPORT

Avinor AS plans, develops, and operates the state-owned airports and the air navigation service in Norway. They are currently developing the New Bodø Airport (project acronym "NLBO"), a new regional hub in Nordland County. For construction projects in the vicinity of their airports, where the construction height exceeds 1/35th the perpendicular distance to the runway centreline (or the extended centreline), Avinor assesses the expected consequences and may require CFD-analysis of the building-induced windshear and turbulence. Avinor may deny planning permission to ensure that new construction does not interfere with flight safety.

Norconsult Norge AS performed CFD analysis using ANSYS CFX (2019 R3) throughout the feasibility study of NLBO, to assess different airport building layouts and designs. CFD models were constructed based on BIM-data of the airport buildings, as well as neighbouring buildings and terrain. The overall model dimensions were 5.0 x 2.6 x 0.5 km (L x W x H), and the geometry fitted mesh was primarily hexahedral cells in a structured arrangement. The mesh resolution away from buildings was 5 x 5 m horizontally, with a vertical resolution ranging from 1 m along the terrain to 25 m at the top of the domain. In the zones near the buildings themselves, unstructured tetrahedra with extruded prisms were used to represent the complex building surfaces, with a resolution of down to 1 m. Standard ABL velocity and turbulence profiles were generated and applied at the inlet (Jacobsen, 2005), based on appropriate terrain roughness lengths z_0 and corrected for far-field upstream fetch length. Zero relative pressure entrainment openings were used for the top, side and outlet boundaries of the model.

Initially RANS-based analysis was performed using the SST k-omega model, but it became clear that LES was required to give satisfactory results. The "Zonal LES" function of CFX was used to activate WMLES in the domain and to generate resolved turbulence at the inlet from the k-omega based inlet profiles. A verification study was performed, to confirm that the chosen methodology was able to recreate the wake length from available model scale ABL wind tunnel data from (Woo et al., 1977). A comparison of the wake lengths with RANS and LES for the new airport is shown in Fig. 3. A wide range of wind directions and building designs were simulated as part of the feasibility study.

The primary strength of the NLR-criteria is that they give concise and quantitative threshold values. However, their conciseness is also their primary weakness; they are difficult to evaluate under real-world conditions. The criteria are based on a single free-standing building, and they only consider the mean wind. When developing a new airport with terminal buildings, hangars, maintenance facilities, and other structures, or when erecting new construction amidst existing

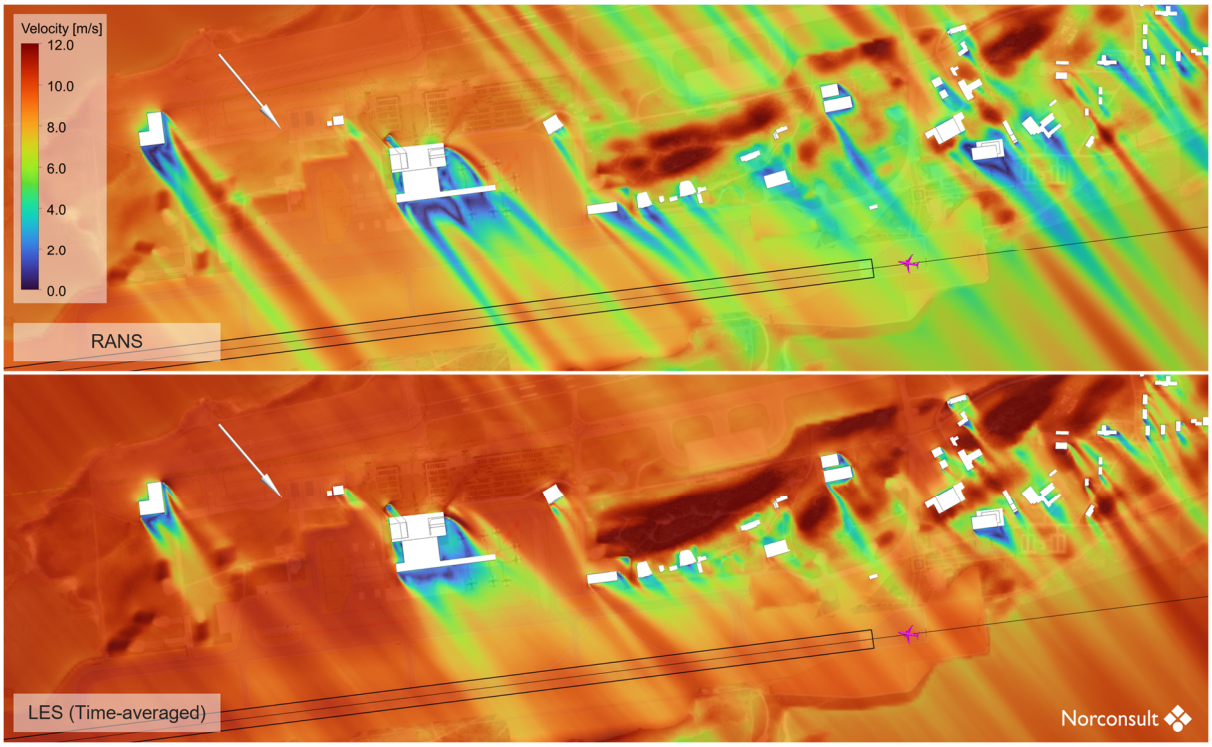


Figure 3. Building wake comparison for NLBO with RANS and LES, with velocity plotted on a 10 m terrain-offset surface. White arrow shows wind direction. The runway and its extended centreline are shown in black.

buildings, the flow field with multiple interacting building wakes becomes complex and highly transient. It can be difficult to judge the wind deficit contributions from specific buildings, or to identify which wind changes are relevant. An aircraft does not experience a mean wind field, but instead flies quickly through an unsteady and gusty flow field at more than 70 m/s.

Norconsult, in collaboration with Avinor and with support from the main operators at the airport (SAS, Widerøe, and Norwegian), developed an approach to analyse the CFD-results. The LES simulations were time-averaged over a period of 60 minutes, after which running means over lengths of 1000 m (to represent the background wind) and 100 m (to represent the building wind deficit) were taken. The difference between the two running means became the delta for comparison with the criteria. The analysis still requires a degree of subjective evaluation. When buildings are placed next to each other, the wind field is both accelerated and decelerated, the result of which is a complicated set of peaks and troughs in wind speed along the glide slope and runway. This is depicted in Fig. 4, where the dashed black lines indicate, for a specific building of interest, the positive and negative wind delta above and below the background wind. The NLR-criteria do not suggest how to interpret this in practice.

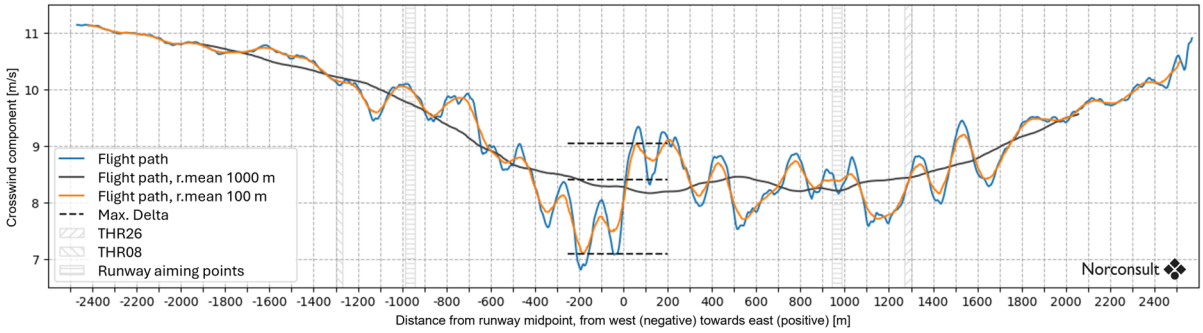


Figure 4. Analysis of the time-averaged LES results. Wind speed is plotted against distance from the runway midpoint in both directions. The time-averaged value is in blue, and the two running means in black and orange. The maximum delta above and below the 1000 m mean for a particular building wake shown with dashed lines.

5. CONCLUSIONS AND RECOMMENDED FURTHER WORK

A CFD based method for simulating and analysing building-induced windshear at airports has been developed. Due to the overprediction of building wakes when using RANS, scale-resolving turbulence models such as LES must be employed to accurately predict downstream wake lengths. The NLR-criteria give concise and quantitative threshold values for wind speed deficits in the vicinity of airports, but they are not trivial to utilize in more complicated real-world scenarios. After the NLR-criteria were developed, there have been significant advances in the fidelity of both CFD modelling and wind measurements. As a result, Norconsult sees potential for the development of a new set of acceptance criteria, based not on the mean wind flow downstream of a single free-standing building, but instead on transient wind data from more complex cases, with a combination of advanced CFD such as LES and real-world measurements using e.g. ground based LiDAR and air data computer logs from onboard landing aircraft.

REFERENCES

Jacobsen, Mark Z., 2005. Fundamentals of Atmospheric Modeling, 2nd Edition, Stanford University, California.

Nieuwpoort, A. M. H., Gooden, J. H. M., and de Prins, J. L., 2010. Wind criteria due to obstacles at and around airports. Report no. NLR-TP-2010-312, National Aerospace Laboratory NLR.

Woo, H. G. C., Cermak, J. E., and Peterka, J. A., 1977. Wind tunnel measurements in the wakes of structures. NASA contractor report NASA CR-2806, National Aeronautics and Space Administration.

LES simulation study of wind turbine aerodynamic characteristics with fluid-structure interaction analysis considering blade and tower flexibility

Weipeng Li[1], Zhengqing Liu[2], Dongqin Zhang[3]

[1]*School of Civil and Hydraulic Engineering, Huazhong University of Science and Technology, Wuhan, Hubei, China, li_weipeng@hust.edu.cn*
[2]*School of Civil and Hydraulic Engineering, Huazhong University of Science and Technology, Wuhan, Hubei, China, liuzhengqin@hust.edu.cn*
[3]*School of Civil and Environment Engineering, Harbin Institution of Technology, Shenzhen, China, zhangdongqin@hit.edu.cn*

SUMMARY:
With the trend toward longer and more flexible wind turbine blades, aerodynamic behavior has grown increasingly complex, necessitating comprehensive analysis. This study introduces a two-way fluid-structure interaction (FSI) model to examine how inflow conditions—specifically, uniform and atmospheric boundary layer (ABL) winds—and the flexibility of both blades and towers impact the aerodynamic performance of turbine blades. A real 4.5 MW wind turbine, featuring a 152 m rotor diameter and a 94 m hub height, serves as the model for this analysis. Findings indicate that edgewise blade motion is negligible, whereas the tower movement and flap-wise blade motion have a significant impact on blade aerodynamics. Separation flow on the suction side of the blade root is pronounced, diminishing with spanwise distance, and stagnation points are concentrated along the flow separation boundary from 0.45L to 0.95L. The blade's three-dimensional rotational effect causes substantial fluctuations in the pulsating pressure coefficient, particularly in this region, with a notable peak around 0.65L. Consequently, special attention to this area is advised to reduce potential fatigue loads.
Keywords: LES simulation, wind turbine, fluid-structure interaction

1. INSTRUCTIONS

Wind turbines mainly consist of a rotating blade system and a generator, and the blades play a crucial role in converting wind energy to the electrical energy. The increase in blade size and tower height has been identified as a favourable trend for the wind turbine industry in recent years (GWEC, 2022**)**, as it boosts power generation efficiency and capacity. It is essential to investigate the aerodynamic characteristics of blades as they become longer, slenderer, and flexible, which can help to improve the overall efficiency and reliability of wind turbines.

This study aims to achieve two primary objectives. Firstly, it proposes a FSI framework to explore the aerodynamic characteristics of wind turbines. In order to enhance computational efficiency, an investigation is conducted into the effects of blade and tower flexibility. This analysis allows for the elimination of unnecessary degrees of freedom during FSI simulations. The second objective focuses on investigating the aerodynamic characteristics of a practical 4.5 MW wind turbine, featuring a rotor diameter of 152 m and a hub height of 94 m. The findings of this investigation

aim to provide valuable insights and suggestions for optimizing blade design. Additionally, a comprehensive examination of the impact of inflow conditions on wind turbine aerodynamics is conducted, encompassing the study of limiting streamlines, average wind pressure, and wind pressure fluctuation on the blades under varying operational conditions.

2. THEORIES AND NUMERICAL METHODS

As illustrated Fig. 1, the left is the configurations of the computational domain and the right is the numerical grids. The rectangular computational domain is 1700m (length) × 456m (width) × 398m (height). The wind turbine is 500m from the inlet and 1200m from the outlet, with a 300m - long wake refinement zone. The dynamic domain, a 100m (length) × 240m (width) × 188m (height) cuboid, is at the center. The rotation domain has a 170m diameter, extends 5m forward and backward (10m thick). The tower is 94m tall, with the hub and blades in the rotation domain, and the tower, nacelle, and rotation domain in the dynamic domain.

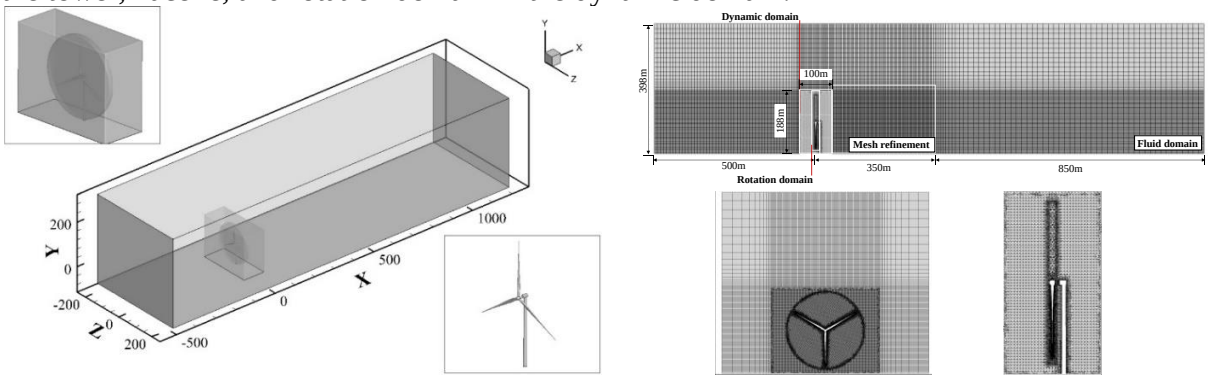


Fig. 1. Configurations of the computational domain (left) and the numerical grids (right)

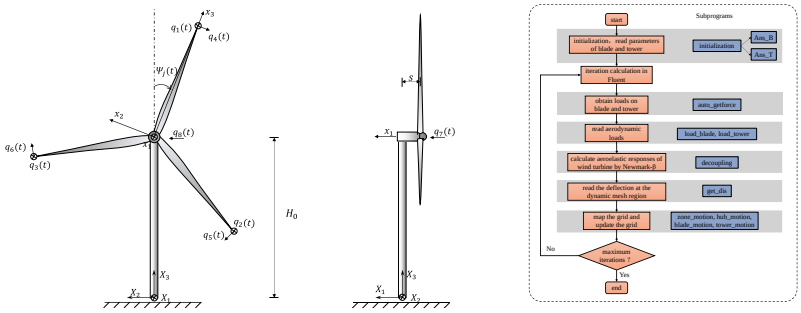


Fig. 2. The local coordinate system and degrees of freedom (left) and the framework of this FSI model (right)

The eight-degree of freedom (DoFs) wind turbine structural dynamics model proposed by Liu et al. (2021). is used in the structural calculation, as shown in Fig. 2, the right side presents the framework of this calculation model. The FSI model includes blade flutter direction motion, blade motion along blade direction, forward and backward movement of tower and left and right movement of tower. To ascertain the ABL wind velocity at the inlet boundary of the computational domain, a numerical model is established based on wind tunnel experiments conducted by Ishihara et al. (2004). The numerical wind tunnel features a spire located at the front, generating an ABL wind field. And the results were compared with those calculated by the commercial software GH-

Bladed. A scatter plot as shown in Fig.3 was drawn, where the red line represents a 10% error, demonstrating the good performance of this FSI calculation model.

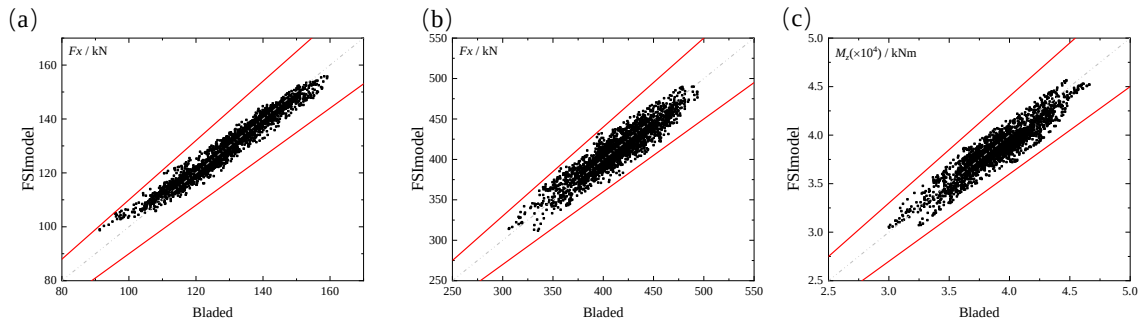


Fig. 3. Comparisons of aerodynamic loads calculated by the FSI model and the commercial software Bladed: (a) the thrust force at the blade root; (b) the thrust force at the tower base; (c) the bending moment at the tower base

3. CASE SETTING AND REUSLTS

In order to investigate the influence of inflow condition and blade and tower flexibility on the aerodynamic performance of wind turbines, a total of 16 cases are examined and detailed in Table 1. The first eight cases are studied under uniform wind conditions, while the subsequent eight cases are conducted under ABL wind conditions. The influence of blade and tower flexibility is analyzed where the flap-wise and edgewise motions of the blades, as well as the tower motion, are considered.

Table 1. Case settings.

Case	Uniform inflow	ABL inflow	Tower motion	Flap-wise motions of blades	Edgewise motions of blades	Index
1	●	○	○	○	○	W0T0B0b0
2	●	○	○	○	●	W0T0B0b1
3	●	○	○	●	○	W0T0B1b0
4	●	○	○	●	●	W0T0B1b1
5	●	○	●	○	○	W0T1B0b0
6	●	○	●	○	●	W0T1B0b1
7	●	○	●	●	○	W0T1B1b0
8	●	○	●	●	●	W0T1B1b1
9	○	●	○	○	○	W1T0B0b0
10	○	●	○	○	●	W1T0B0b1
11	○	●	○	●	○	W1T0B1b0
12	○	●	○	●	●	W1T0B1b1
13	○	●	●	○	○	W1T1B0b0
14	○	●	●	○	●	W1T1B0b1
15	○	●	●	●	○	W1T1B1b0
16	○	●	●	●	●	W1T1B1b1

●: adopt this inflow condition or consider the corresponding DoFs

○: do not adopt this inflow condition or neglect the corresponding DoFs

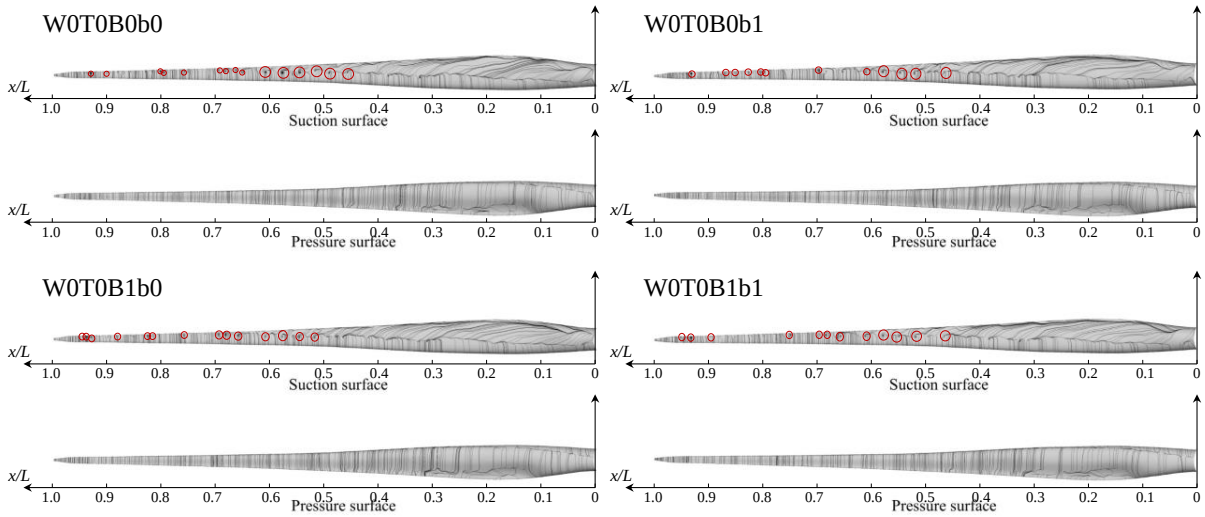


Fig. 4. The limiting streamlines on the blade surface under uniform winds

The Fig. 4 illustrate the distribution of limiting streamlines on the wind turbine blade surface under some cases. The normalized blade length is employed to facilitate comparisons, and a Cartesian coordinate system is established with the blade divided into ten sections from the root, and the detailed conclusion will be given in the next section.

4. CONCLUSION

This research proposes a FSI framework to study wind turbine aerodynamics, analyses a 4.5 MW wind turbine's aerodynamics under various conditions for blade optimization, and obtains several key findings: This research explores tower and blade flexibility's impact, finding edgewise blade motion negligible while tower and flap - wise blade motion matter. For inflow conditions, ABL winds lower the average pressure coefficient, and tower - blade flexibility can be ignored under ABL winds. Stagnation points are at 0.45 - 0.95L on the suction side, with 3D rotation causing pressure fluctuations and a peak at 0.65L, so this region needs more attention for fatigue load reduction.

REFERENCES

GWEC. 2022. Global wind report 2022.

Liu, Z., Wang, Y., Nyangi, P., Zhu, Z. and Hua, X., 2021. Proposal of a novel GPU-accelerated lifetime optimization method for onshore wind turbine dampers under real wind distribution. Renewable Energy, 168, 516–43.

Ishihara, T., Yamaguchi, A. and Fujino, Y., 2004. Development of a new wake model based on a wind tunnel experiment. Global Wind Power, 105, 33-45.

Computational conditions for Large-Eddy Simulation to predict wind pressure acting on building walls with sufficient numerical stability and accuracy

Yu Inaba [1], Yuta Yamane [2], Yasuyuki Ishida [3]

[1] *Institute of Science Tokyo, Yokohama, Japan, inaba.y.fd40@m.isct.ac.jp*
[2] *Shimizu Corporation, Tokyo, Japan, yamane_y@shimz.co.jp*
[3] *Tohoku University, Sendai, Japan, yasuyuki.ishida.e1@tohoku.ac.jp*

SUMMARY:
The accurate prediction of wind pressure acting on building walls via large-eddy simulation (LES) requires a high grid resolution near the walls and difference schemes with a low discretization error, which generally tend to be numerically unstable. OpenFOAM, which is a widely used CFD solver, specifies that the static pressure in all cells at the outlet boundary of a domain must be a constant value. In our previous studies, we confirmed that this specification causes excessive static pressure fluctuations that do not occur in real phenomena when turbulent velocity fluctuations with fluctuating flow rates are imposed as the inflow boundary condition. Thus, we first attempt to fix the inflow rate constant to suppress the excessive fluctuations. Subsequently, the effect of the grid resolution on the computational stability and accuracy is investigated for LES computations of wind pressure acting on a cubic model.

Keywords: LES, pressure fluctuation, grid resolution

1. INTRODUCTION

High-rise buildings generate strong winds around them. Ishida et al. (2023) conducted wind tunnel tests to investigate the impact of a high-rise building on the wind pressure acting on the surrounding low-rise buildings. They reported that when the wind direction was around 25°, the absolute value of negative peak pressure on the roof of a low-rise building, which was located directly behind a high-rise building, became extremely high. Further, a large-eddy simulation (LES) was performed to analyze the flow field under the high negative peak pressure (Ishida et al., 2024). However, the results indicated that the absolute value of the negative peak wind pressure coefficient tended to be overestimated as compared with the experimental results. This is attributable to the use of a mixed scheme with 25% first-order upwind differencing, which presents significant numerical viscosity effects, to discretize the advection term. A guidebook for CFD simulation (Architectural Institute of Japan, 2020) states that the blending rate of first-order upwind differencing should be maintained below 5%. In the LES by Ishida et al. (2024), the reduction ratio of grid size near building walls was set to a high value, thus requiring a high percentage of the first-order upwind differencing scheme to avoid computational instability. Consequently, the turbulence was significantly damped, and the accuracy was reduced. Based on the above, this study examines the computational conditions for LES to predict wind pressure acting on building walls with sufficient numerical stability and accuracy.

2. SUPPRESSION OF EXCESSIVE STATIC PRESSURE FLUCTUATIONS

In this study, LES was performed using OpenFOAM v8. OpenFOAM sets the static pressure in all cells at the outlet boundary of the computational domain to a constant value. This specification is assumed to generate excessive static pressure fluctuations, which do not occur in real phenomena, when turbulent velocity fluctuations with fluctuating flow rates are imposed as the inflow boundary condition. To suppress these fluctuations, this study first attempted to keep the fluctuating inflow rate constant.

2.1. Control for Constant Inflow Rate

In this study, the inflow rate was fixed as a constant by multiplying the three components of the generated instantaneous wind velocity vector (u_0, v_0, and w_0) with the ratio of the target mean inflow rate Q_{mean} to the instantaneous inflow rate Q_{inst} of the inflow turbulence (Eq. (1)). Here, x, y, and z denote the spatial coordinates in the streamwise, lateral, and vertical directions, respectively; t represents time; u, v, and w represent the three components of the instantaneous wind speed of the inflow fixed to a constant.

$$(u, v, w)_{(y,z,t)} = (u_0 \frac{Q_{mean}}{Q_{inst}}, v_0 \frac{Q_{mean}}{Q_{inst}}, w_0 \frac{Q_{mean}}{Q_{inst}})_{(y,z,t)} \quad (1)$$

2.2. Outlines of LES in Section 2

The computational domain and inflow conditions are illustrated in Figs. 1 and 2, respectively. A length scale of 1/200, velocity scale of 1/6 and time scale of 3/100 were assumed. In the experiment, the wind velocity was measured only in the streamwise direction. No buildings were modeled in the computational domain. Turbulent fluctuations in the inflow were generated using a Cholesky decomposition–based artificial method (Okaze and Mochida, 2017; Xie and Castro, 2008). The WALE model was applied as a subgrid-scale model ($C_w = 0.325$). For the outlet boundary conditions, an advective condition was applied to the velocity, and the pressure was fixed at zero. The other surfaces were set as solid walls, and Spalding's law was used for the wall function. The time-derivative term was discretized using the two-step Adams–Morton method. For the discretization of the advection and diffusion terms, second-order central differencing with a 5% mixture of first-order upwind differencing and second-order central differencing schemes was used, respectively. The PISO method was applied as a pressure–velocity coupling calculation procedure. The time interval was set as 6.25×10^{-5} s, and the data were obtained and averaged over 20 s.

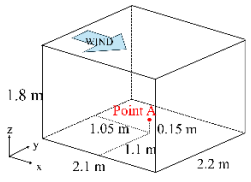
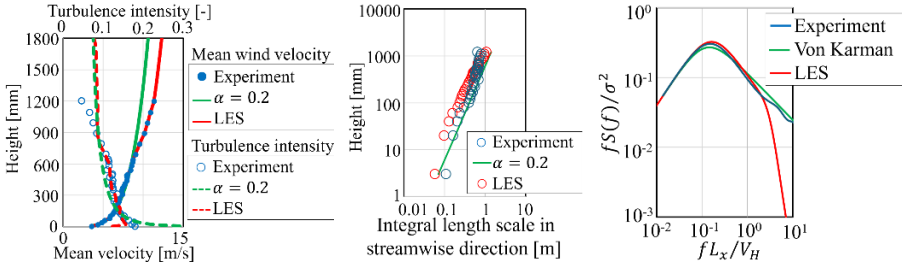


Figure 1. Computational domain.



(a) Mean wind velocity and turbulence intensity

(b) Integral length scale

(c) Power spectrum of wind velocity

Figure 2. Characteristics of inflow.

2.3. Results

Figs. 3 and 4 show the time histories of the inflow rate at the inlet boundary and the static pressure at point A in Fig. 1, respectively. Fig. 5 presents the mean wind velocity and turbulence intensity at x =1.05 m. The results confirmed that fixing the inflow rate to a constant suppressed excessive fluctuations in the static pressure without altering the characteristics of the approaching flow. Two-point statistics were not conducted.

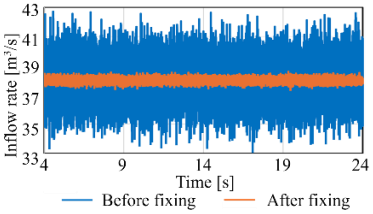


Figure 3. Time histories of inflow rate.

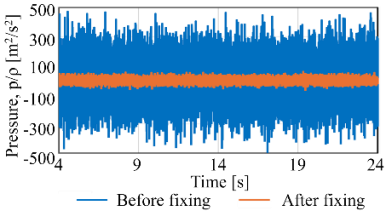


Figure 4. Time histories of static pressure.

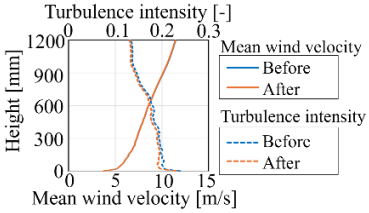


Figure 5. Characteristics of approach flow (x=1.05 m).

3. INVESTIGATION ON GRID RESOLUTION

Wind tunnel tests were simulated via LES using a single cube (Ishida et al., 2023), and the effect of the grid resolution was analyzed. Fig. 6 shows the computational domain. The single cube comprised 356 pressure taps: 10×10 on the roof and 8×8 on other surfaces (Fig. 7).

The wind pressure coefficients were calculated using Eqs. (2)–(5). $C_{p_{wind}}(t)$ [-] is the instantaneous wind pressure coefficient for each tap. The reference velocity pressure $\langle q_H \rangle$ was the mean wind velocity at the roof height of the cube, $\langle u_H \rangle$. $\langle C_{p_{wind}} \rangle$ [-] is the mean wind pressure coefficient and $minC_{p_{wind}}$ [-] is the minimum wind pressure coefficient at each tap.

$$C_{p_{wind}}(t) = \frac{p_{wind}(t)}{\langle q_H \rangle} \quad (2)$$

$$\langle q_H \rangle = \frac{1}{2}\rho \langle u_H \rangle^2 \quad (3)$$

$$\langle C_{p_{wind}} \rangle = \frac{\langle p_{wind} \rangle}{\langle q_H \rangle} \quad (4)$$

$$minC_{p_{wind}} = \frac{p_{wind_Min}}{\langle q_H \rangle} \quad (5)$$

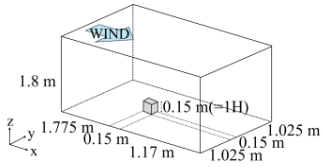


Figure 6. Computational domain.

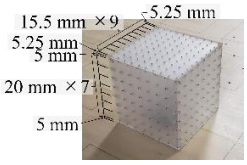


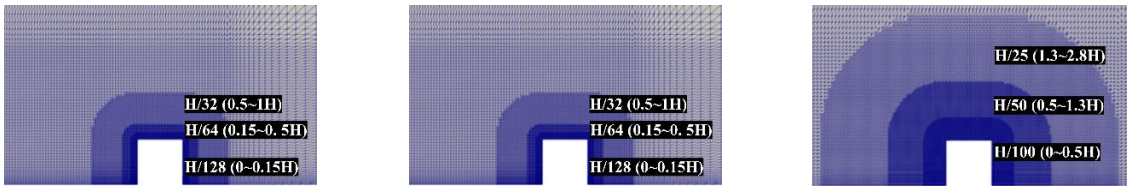
Figure 7. Pressure taps.

3.1. Setting of Grid Resolution and Outlines of LES in Section 3

Three grid resolutions were set around the cube (Fig. 8). Case_previous featured the same grid resolution as that of Ishida et al. (2024). The grid discretization of Case_coarse and Case_fine was set based on previous studies (Tamura, et al., 2021; Ricci, et al., 2018). The computational conditions were the same as those described in section 2, and the inflow rate was fixed.

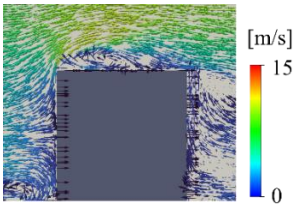
3.2. Results

Fig. 9 shows the mean wind velocity distribution in the central cross-section of the cube. Case_previous did not yield results because of computational instability. As shown in Fig. 9, no significant difference was indicated between the two cases. Figs. 10 and 11 present $\langle C_{p_{wind}} \rangle$ and $minC_{p_{wind}}$ compared with the wind tunnel test results, respectively. The $\langle C_{p_{wind}} \rangle$ of both cases agreed well with the experimental values. For $minC_{p_{wind}}$, in Case_coarse, several error points relative to the test exceeded 20%, whereas in Case_fine, only two error points were indicated.

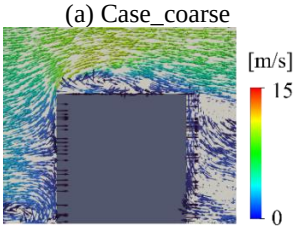


(a) Case_previous (b) Case_coarse (c) Case_fine

Figure 8. Grid arrangement around a cube.

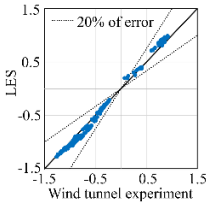


(a) Case_coarse

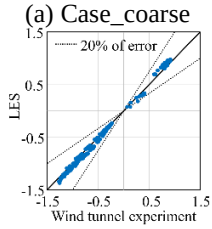


(b) Case_fine

Figure 9. Mean wind vector around a cube.

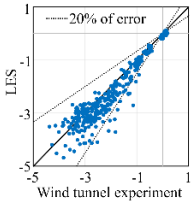


(a) Case_coarse

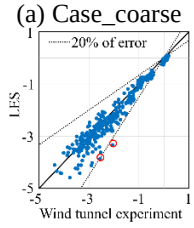


(b) Case_fine

Figure 10. $\langle C_{p_{wind}} \rangle$.



(a) Case_coarse



(b) Case_fine

Figure 11. $minC_{p_{wind}}$.

4. CONCLUSIONS

Excessive static pressure fluctuations caused by the boundary condition of zero static pressure at the outlet boundary can be suppressed by maintaining a constant inflow rate. Subsequently, in LES the for the flow field around a single cube, a grid resolution that can adequately predict the negative peak wind pressure acting on the cube was obtained by applying a scheme with few numerical viscous effects.

ACKNOWLEDGEMENTS

This work was supported by the JSPS Grant-in-Aid for Scientific Research (B), Grant Numbers JP21H01486 and JP24K01035 supercomputing resources at the Cyberscience Center at Tohoku University.

REFERENCES

Ishida, et al., 2023. Wind Tunnel Experiments on Interference Effects of a High-Rise Building on the Surrounding Low-Rise Buildings in an Urban Block, Wind, 3, 97-114

Ishida, et al., 2024. Impact of a single high-rise building on the wind pressure acting on the surrounding low-rise buildings, Journal of Wind Engineering and Industrial Aerodynamics, 250.

Architectural Institute of Japan, 2020. Guidebook for CFD predictions of urban wind environment.

Okaze and Mochida, 2017. Cholesky decomposition–based generation of artificial inflow turbulence including scalar fluctuation, Computers & Fulids, 159, pp. 23-32.

Xie, Z.-T., Castro, I. P.: Efficient Generation of Inflow Conditions for Large Eddy Simulation of Street-Scale Flows, Flow, Turbulence and Combustion, 81(3), pp.449–470, 2008.

Ricci, et al., 2018. Towards LES as a design tool: Wind loads assessment on a high-rise building, journal of Wind Engineering &Industrial Aerodynamics, 180, pp.1-18.

Tamura, et al., 2021. Introduction of CFD for Wind Resistant Design of Buildings, Wind Engineers, JAWE, Vol.46, No.4(No.169). (in Japanese)

A novel eddy current tuned rolling cylinder damper for vibration control of wind turbine

Chao Wang [1], Zhenqing Liu [2]

[1] *School of Civil and Hydraulic Engineering, Huazhong University of Science and Technology, Wuhan, China, wangchao_wch@hust.edu.cn*
[2] *School of Civil and Hydraulic Engineering, Huazhong University of Science and Technology, Wuhan, China, liuzhenqing@hust.edu.cn*

SUMMARY:
As the size and capacity of wind turbine continue to increase, so does the demand for effective vibration control. Traditional tuned mass damper (TMD) is prone to leakage and damage, which can lead to a rapid decline or even total loss of vibration reduction performance. To address this issue, the tuned rolling cylinder damper (TRCD) is considered as a potential replacement. This study integrates eddy current damping into the TRCD to create an eddy current tuned rolling cylinder damper (ECTRCD). A wind turbine model is constructed in Simpack and validated against results from the GH-Bladed model. The optimization results indicate that the damping performance of the ECTRCD is influenced by the radius ratio of the roller disc to the shaft. As this radius ratio increases, the ECTRCD's damping performance decreases, the moment of inertia of the roller grows, and the radius of the guide rail arc contracts. When the radius ratio varies from 6 to 1/6, the optimal damping performance improves from 5.3% to 17.7%, representing a 3.34-fold increase. Furthermore, the vibration reduction effect of the ECTRCD exhibits a pronounced nonlinear relationship with variations in damper mass, frequency, and damping levels.

Keywords: Wind turbine vibration reduction, TRCD, eddy current damping

1. GENERAL INSTRUCTIONS

Around the turn of the 21st century, as the global energy industry advanced, research on renewable energy sources such as wind energy began to replace traditional fossil fuels in addressing issues like environmental pollution. As the primary structure for wind power generation, the development and refinement of wind turbine technology are crucial for the sustainable growth of the entire wind power industry.

With the rapid growth of the wind power industry, the increasing size and capacity of wind turbines have made the control of vibration and fatigue loads a key issue. As wind turbine technology has advanced, research on dampers has increasingly diversified to accommodate different turbine capacities through varied oscillator designs. One such approach is the tuned mass damper, with its simple geometry and direct vibration control mechanism. Zhang (2020) pioneered the use of TMD for controlling blade vibration in wind turbines. However, the spring stiffness and oil damping systems in TMD have shown significant limitations, with potential leakage posing risks of secondary damage to the whole turbine. To address these issues, alternative damper designs such as TRCD have been introduced. Zhang et al. (2014) and Singh et al. (2015) proposed using rolling cylinders instead of rolling balls to construct the TRCD. Saeki et al. (2019) further explored TRCD

parameters, identifying relationships between damper structural parameters and vibration reduction performance. Although the TRCD offers certain advantages in terms of maintenance, further experimental studies and theoretical analyses are essential to fully realize its potential.

Therefore, this study introduces eddy current damping force into the TRCD, utilizing the TRCD's and eddy current's damping characteristics, and conducts a numerical simulation of vibration reduction performance using a Simpack wind turbine model. After verifying the turbine model against the GH-Bladed model, we optimized the eddy current TRCD damping parameters, using the equivalent fatigue load of the lateral bending moment at the base of the wind turbine tower as the objective function. The study also analyzes the effects of the eddy current TRCD on load and dynamic response across various parts of the wind turbine under different operating conditions.

2. NUMERICAL MODELS AND VERIFICATION

This study selected the specific H155-4.5MW unit and modeled various components of the wind turbine, including the blades, tower, yaw system, generator, and foundation, before assembling the complete model. The GH-Bladed commercial simulation software was then used to provide a corresponding model for validating the Simpack model.

2.1. Wind turbine model

Before modeling the tower in Simpack, the material properties of the tower must first be defined. Then, based on the geometric data of the tower from the GH-Bladed model, the section properties at each height are specified. The Linear SIMBEAM tool is used to create the tower structure, with each section's height and sequence defined. For blade modeling in Simpack, an RBL file is generated according to the blade properties specified in GH-Bladed. The Utilities function page is used to automate the blade modeling process. Finally, all the wind turbine substructure models are assembled to create the complete wind turbine model, as shown in Fig. 1.

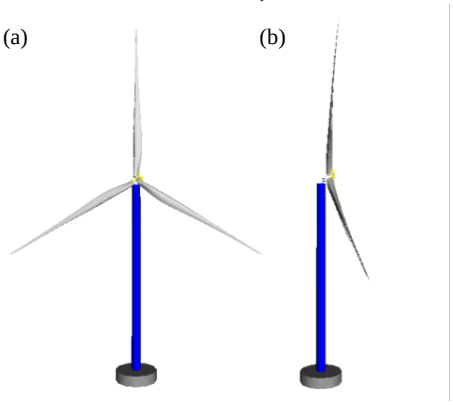


Figure 1. Simpack wind turbine model. (a) Front view. (b) Side view.

2.2. Model verification

To verify the accuracy of the model, key structural parameters, including the various modes of the tower and blades, were calculated, and the final results were compared with those from the GH-Bladed model in Table 1. The comparison of parameters for the wind turbine model is presented in Table 3-3, with calculation errors referenced against the GH-Bladed model. In Simpack, the frequencies corresponding to the first two modes of the full assembly are 0.261 and 0.266 Hz,

respectively, while in GH-Bladed, the first two mode frequencies are 0.260 and 0.262 Hz, with errors of 0.14% and 0.27%, respectively. This alignment in dynamic characteristics between the two models provides a reliable foundation for subsequent calculations.

Table 1. Comparisons of calculations by Simpack and GH-Bladed.

Parameters	Simpack	GH-Bladed	Relative error (%)
Balde mass	19743.2kg	19743kg	0.001
Rotor mass	102229kg	102253kg	0.023
Tower mass	352366kg	352363kg	0.0008
Total mass	619596kg	619617kg	0.003
Blade 1st order mode	0.428Hz	0.427Hz	0.2
Blade 2nd order mode	0.696Hz	0.695Hz	0.5
Tower 1st order mode	0.261Hz	0.260Hz	0.4
Tower 2nd order mode	0.266Hz	0.262Hz	1.6

3. RESULTS AND DISCUSSION

Considering the multi-body dynamics characteristics in Simpack modeling, the normal contact force between the support shaft and the track is first modeled using the 18th force element (Unilateral Spring-Damper Cmp), restricting the motion of the rollers to the guide rail. Next, the friction force at the contact point between the roller and the track is modeled using the 100th force element (Non-linear Friction Cmp). To account for the effect on the rotational degrees of freedom of the roller around its own axis in the theoretical derivation, an additional support frame structure is introduced with a mass and moment of inertia of 0.001. Releasing the degrees of freedom allows the roller to rotate around the guide rail center. The damping force is constructed between the reference point of the roller axis and the reference point of the support frame using the 43rd damping force element (Bushing Cmp), as illustrated in Fig. 2.

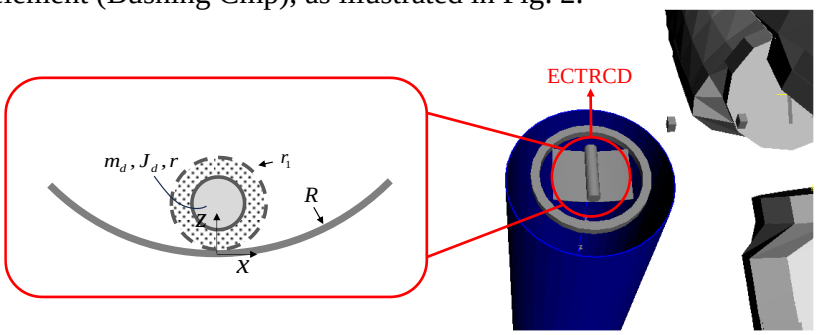


Figure 2. ECTRCD installation diagram.

A statistical analysis was conducted on the vibration reduction effects across all optimized parameter combinations of the eddy current damper as shown in Fig. 3. For each parameter set, the optimal values for vibration reduction performance were selected via neural network predictions: when the radius ratio is 1/6, the mass ratio is 1.2%, the frequency ratio is 0.943, and the damping ratio is 0.059, achieving an optimal vibration reduction effect of 17.7% for the eddy current TRCD. The trend of vibration reduction performance aligns with changes in the parameters, showing a clear nonlinear relationship—generally increasing initially with both parameters before declining as they further increase. Notably, the optimal frequency ratio fluctuates widely between 0.9 and 1.1, while the damping ratio remains more variable.

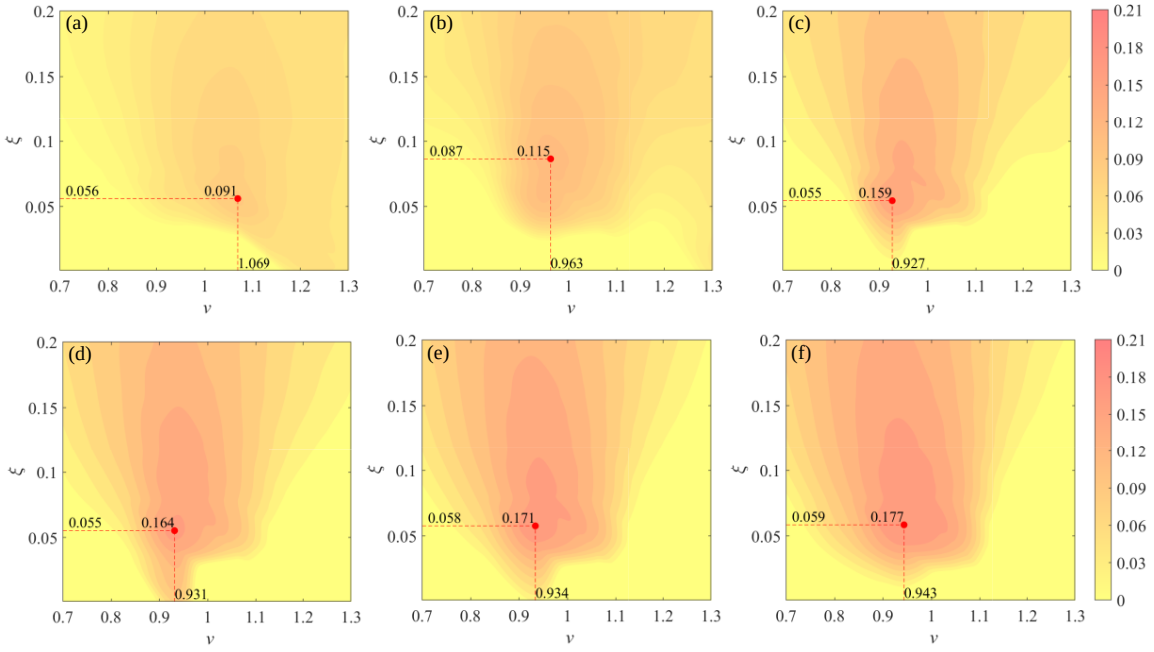


Figure 3. Reduction rate of equivalent fatigue load under different parameter combinations of ECTRCD when the radius ratio is 1/6.

4. CONCLUSION

Based on the TRCD structure and eddy current damping characteristics, this study combines a disc type rotating eddy current damper with TRCD, and introduces basic electromagnetic theory to analyze the damper parameters. The Simpack fan model is used for numerical simulation research on the damping performance of the damper. And compared and calculated with the commercial wind turbine simulation software GH Blade from three aspects: wind turbine modal analysis, swept wind state quantity verification, and load comparison of key parts of blades and towers. The final results verified the reliability of the model. The final results indicate that the vibration reduction performance of the eddy current TRCD in this study is related to the radius ratio of the roller disc to the shaft. As the radius ratio increases, the vibration reduction performance of the eddy current TRCD deteriorates, and the corresponding moment of inertia of the roller increases. The arc radius of the guide rail decreases, and the radius ratio varies from 6 to 1/6. The optimal parameter vibration reduction performance changes from 5.3% to 17.7%, with an improvement of 3.34 times.

REFERENCES

Zhang, Z., 2020. Optimal tuning of the tuned mass damper (TMD) for rotating wind turbine blades. Engineering Structures 207, 110209.

Zhang, Z., Li, J., Nielsen, S. R. K., Basu, B., 2014. Mitigation of edgewise vibrations in wind turbine blades by means of roller dampers. Journal of Sound and Vibration 333, 5283–5298.

Singh, K. V., Li, S., Fu, L., Kong, F., 2015. Seismic response reduction of structures equipped with a voided biaxial slab-based tuned rolling mass damper. Shock and Vibration 2015, 1070–9622.

Tsuda, R. and Saeki, M., 1974. Efficiency of vibrational energy dissipation by tuned rolling-cylinder dampers. Journal of Sound and Vibration 463, 114977.

Large urban CFD simulations for wind and air quality analysis over Antwerp

Jorge Sousa[1], Rober Mamani[1], Stijn Vranckx[1]

[1]*Flemish Institute for Technological Research (VITO), Mol, Belgium, Jorge Sousa, Rober Mamani, Stijn Vranckx*

SUMMARY:
Computational Fluid Dynamics (CFD) has become an essential tool to investigate various environmental parameters, including wind comfort, wind hazard, urban ventilation, air quality, heat stress and wind energy. There is a growing request by policy makers and urban planners for high resolution wind flow analysis. In this study, several CFD simulations were computed for the full city of Antwerp. The main findings are related to the quantification of the wind flows in the city, the wind comfort assessment, air quality and wind energy.

Keywords: CFD, Air Quality, Wind Comfort

1. INTRODUCTION

CFD has become a powerful tool to compute urban wind flows and quantify their direct impacts on city air quality, wind comfort, and heat stress (Martinez et al., 2018). To ensure sustainable urban developments CFD has become a useful approach to assess wind comfort, wind hazard, air quality, wind energy, during the development of new built areas (Blocken, 2015). In this paper we computed several of these variables for the city of Antwerp. The city is located is in the northern part of Belgium alongside of the Scheldt River, at low elevation (7-9 meters above sea level), relatively flat topography, and complex urban structure due to its combination of old non-structured streets, and modern grid structured urban designs. The city is surrounded by big green areas, some parks in city centre, and a diverse trees collection along its streets.

Although, CFD has been widely used for wind comfort assessment of new high-rises buildings, simulations of full cities have been scarcely pursued due to the computational demand and the difficulty to generate suitable building geometries for CFD analysis.

This study tackles the complexity of computing CFD simulations for a full city. Beside the large computational demand several challenges had top be overcome. Specifically, the inclusion of different surfaces types, the inclusion of green areas, the topography changes and the integration of existing and future buildings.

2. METHODOLOGY

The domain consisted of a quadrangular shape with 9 km from East to West, and 10 km South to North. The Reynolds Average Navier Stokes equations were solved using OpenFOAM libraries

and k-e turbulence closure following the best practices guideline for urban CFD (Franke et al., 2007). The city geometry was constructed using City4CFD (Pađen et al., 2024) based on building footprints and heights. The number of cells were 21.4M per km^2 of surface, which reached to 1.7 billon cells in total, and the residuals for wind speed are used to judge convergence; they are set at $1x10^{-6}$. The sensitivity analysis was performed with three different mesh resolutions, and few detectable differences were found. Trees were simulated as porous zones and different terrain roughness length were considered. Different scenarios were simulated to investigate the impact of new high rise buildings and vegetation layouts.

The wind flows in the city were computed for 12 inflow wind directions, and meteorological observations measured at 30 meters from the ground between 2007 and 2019. To manage this extensive domain, it has been divided into nine overlapping zones, each approximately 3.5 by 3.5 km, and later integrated through post-processing. Finally, the wind comfort index processing was made according the Dutch Wind Nuisance Standard NEN8100 (NEN, 2006). Additionally, annual average indicators have been extracted NO_2 concentrations following the methodology in (Martín et al., 2024). Figure 1 depicts the inputs used for to setup the 3D geometry model and an example of the average wind output over the city of Antwerp.

3. MAIN FINDINGS

The main wind direction over the city of Antwerp is 240 degrees (from southwest to northeast) with a mean wind speed of 1.89 m/s at 1.75 meters above the ground. The main wind direction follows the course of the Scheldt River, as shown in Fig. 1, generating the highest wind speeds in the North side of the city. The wind comfort index relies mostly in the A quality class. However, there are areas nearby high buildings with C and D quality class showed in Figure 2. The Antwerp Opera area has high wind speed due to the combination of high-rise, a wide street, and the predominant wind direction is parallel to that street. The vegetation was included in the simulations. Their major tree impact on wind flows can be seen in areas with high-tree density; this effect is noticeable in the big parks in the surroundings of the city. In terms of air quality, hot spots have been identified at tunnels outlets and at street canyons. The annual average concentration results have been validate with NO_2 passive samplers over different locations in the city.

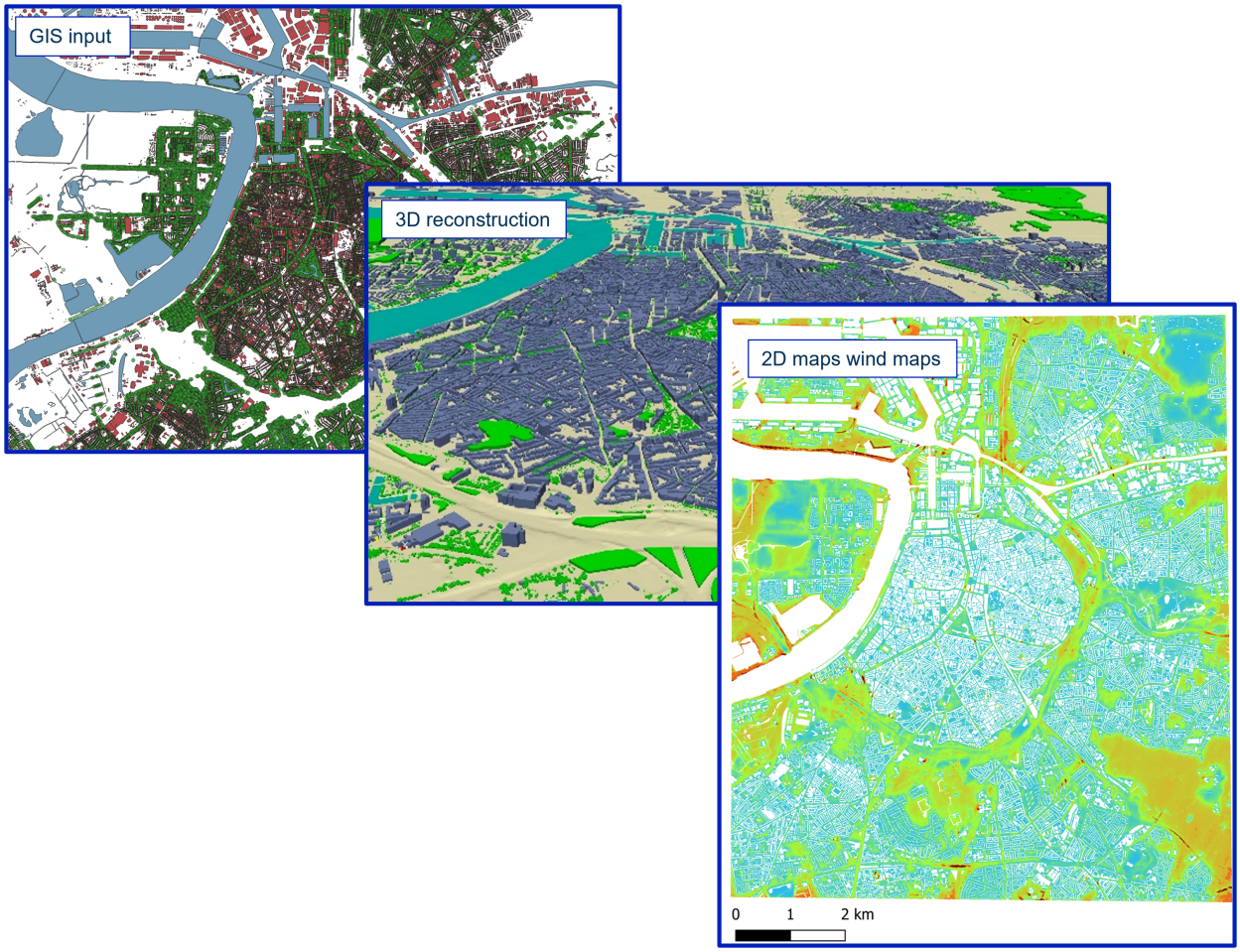


Figure 1. Wind study framework, from GIS input to wind maps.

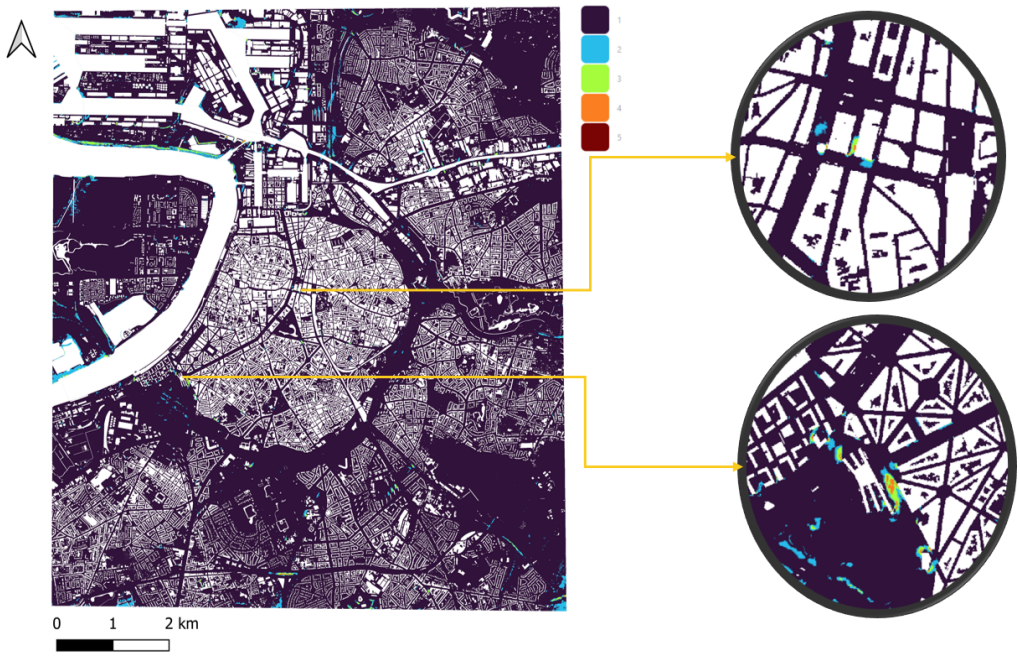


Figure 2. Wind comfort in Antwerp city with a close-up at Antwerp Opera (Up), and Justice Palace (Down).

In summary, this study has the following outputs:

- The wind comfort assessment.
- Wind ventilation potential.
- Wind energy potential and roof and pedestrian level.
- Annual NO2 concentration predictions and validation with available reference stations in Antwerp.
- Compare different design scenarios, where new buildings, bridges, and vegetation are planned to be constructed.

4. CONCLUSIONS

In this study a large 3D CFD simulation was computed for the entire city of Antwerp. The objective of the study was to evaluate the wind comfort in the full city, quantify the potential for wind energy at roof and pedestrian level, and identify NO_2 hot spots concentrations due to tunnel outlets and street canyons. The 3D geometry, included the terrain topography, all the detectable trees, and new large development projects with high rise buildings. High wind speed areas were identified in the northern side, around high buildings in the city centre, and wind comfort is predominantly

classified as Class A. Additionally, NO_2 concentration was validated along the city for air quality assessments.

The CFD simulations in Antwerp have demonstrated various applications to support a sustainable urban planning which including assessments of wind comfort, air quality, wind energy potential, wind flow changes due to new urban developments, and enable to assess other parameters directly affected by wind dynamics.

ACKNOWLEDGEMENTS

The authors would like to thank to the Flemish Supercomputer Center (Vlaams Supercomputer Centrum - VSC) for their cluster usage and support, and the city of Antwerp for supporting this project.

REFERENCES

Blocken, B., 2015. Computational Fluid Dynamics for urban physics: Importance, scales, possibilities, limitations and ten tips and tricks towards accurate and reliable simulations. Building and Environment 91, 219–245.

Franke, J., Hellsten, A., Schlünzen, H., and Carissimo, B., May 2007. *Best Practice Guideline for the CFD Simulation of Flows in the Urban Environment*. Tech. rep. COST European Cooperation in Science and Technology.

Martín, F., Janssen, S., Rodrigues, V., Sousa, J., Santiago, J., Rivas, E., Stocker, J., Jackson, R., Russo, F., Villani, M., Tinarelli, G., Barbero, D., José, R. S., Pérez-Camanyo, J., Santos, G. S., Bartzis, J., Sakellaris, I., Horváth, Z., Környei, L., Liszkai, B., Kovács, Á., Jurado, X., Reiminger, N., Thunis, P., and Cuvelier, C., 2024. Using dispersion models at microscale to assess long-term air pollution in urban hot spots: A FAIRMODE joint intercomparison exercise for a case study in Antwerp. Environment International 925.

Martinez, G. S., Diaz, J., Hooyberghs, H., Lauwaet, D., Ridder, K. D., Linares, C., Carmona, R., Ortiz, C., Kendrovski, V., Aerts, R., Nieuwenhuyse, A. V., and Dunbar, M. B.-N., 2018. Heat and health in Antwerp under climate change: Projected impacts and implications for prevention. Environment International 111, 135–143.

NEN, 2006. *Wind comfort and wind danger in the built environment - NEN 8100*.

Pađen, I., Peters, R., García-Sánchez, C., and Ledoux, H., 2024. Automatic high-detailed building reconstruction workflow for urban microscale simulations. Building and Environment 265, 111978.

Application and Limitations of URANS Simulations to determine the Aeroelasticity of Bridge Decks

Yuanchao Ding [1], Cong Chen [2], Julian Unglaub [1], Klaus Thiele [1]

[1]*Institute of Steel Structures, Technische Universität Braunschweig, Braunschweig, Germany, yuanchao.ding@tu-braunschweig.de*
[2]*State Key Laboratory of Featured Metal Materials and Life-cycle Safety for Composite Structures, Guangxi University, Nanning, China*

SUMMARY:
In the preliminary design stage, the Unsteady Reynolds Averaged Navier-Stokes (URANS) technique, due to its low computational cost, may be used by bridge engineers to assess the aeroelasticity of a bridge deck cross section. For bridge decks of small side ratios, the evaluation of galloping instability according to the quasi-steady theory requests the aerodynamic drag and lift coefficients involving the rather large wind angle of attacks. The Institute of Steel Structures, TU-Braunschweig, has investigated a bridge deck open cross section with a side ratio of two at Re = 20000, by means of wind tunnel tests. Interests arise to what extent can the 2D-URANS simulation replicate the results observed in the wind tunnel tests. The simulation was carried out with the open-source software OpenFOAM, adopting the k-ω-SST turbulence model. Numerical results show reasonable agreement with the wind tunnel test results at the small wind angles of attack of the bridge deck. However, starting from about -8.0° angle of attack, the numerical results show increased discrepancies. Possible reasons for this deviation, such as the influence of the computational model setup, the choice of turbulence model, and the necessity for 3D simulation, are also discussed in this paper.

Keywords: URANS-simulation, open cross section, galloping instability

1. INTRODUCTION

1.1. Engineering background

Wind-induced aeroelasticity, such as galloping and flutter, is characterized by unrestricted oscillations once a critical wind speed is exceeded. This can lead to damage or even collapse of the bridge. The critical wind speed of an aeroinstability depends on the shape of the bridge deck. This condition should be considered in the design of bridge decks to avoid at least 1.25 of the design wind speed for galloping and 2.0 for flutter according to the Eurocode (DIN EN 1991-1-4, 2010).

The critical wind speed of galloping can be determined by aeroelastic wind tunnel tests using a scaled model with the same Scruton number as the real bridge. Alternatively, it can be calculated according to the quasi-steady theory with using aerodynamic coefficients, which can be obtained from aerodynamic wind tunnel tests. The critical wind speed for flutter can be estimated by aeroelastic wind tunnel tests using a wind tunnel model with all dimensionless parameters scaled. Alternatively, it can be calculated using Scanlan's semi-empirical model (Scanlan and Tomko, 1971) with eight flutter derivatives that can be identified from aeroelastic wind tunnel tests.

At the preliminary design stage, wind tunnel testing is time consuming and expensive. The draft of the new Eurocode for wind loads (prEN 1991-1-4, 2024) recommends that computational simulations can be used instead of wind tunnel tests at this design stage for both galloping and fluttering. The applicability and limitations of the use of computational simulations, in particular URANS simulations due to its low computational cost, to predict the galloping behavior have been investigated in this work.

1.2. Wind tunnel tests

For galloping, all the wind tunnel tests of a 2:1 rectangular cylinder and a 2:1 open cross bridge section were carried out in the boundary layer wind tunnel at the Institute of Steel Structures of Technische Universität Braunschweig, Germany. The results of the wind tunnel tests have been published (Chen, et al., 2020). All CFD simulations in this work were based on the wind tunnel models.

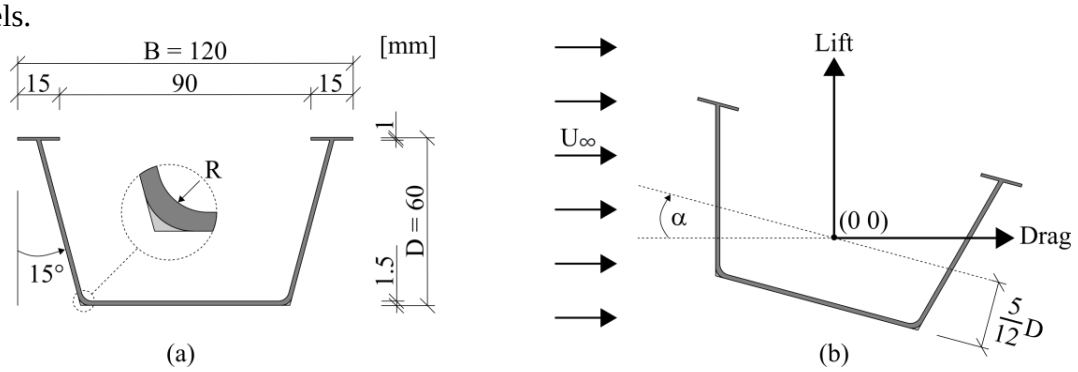


Figure 1. geometry of the open cross section.

The part of the work on flutter, both in wind tunnel tests and CFD simulations, is currently in progress, and further additions are expected to follow.

2. URANS SIMULATIONS

At the beginning of all simulations, the computational model was carefully studied with the main numerical parameters described in the following figure to ensure that the numerical setup was correctly chosen.

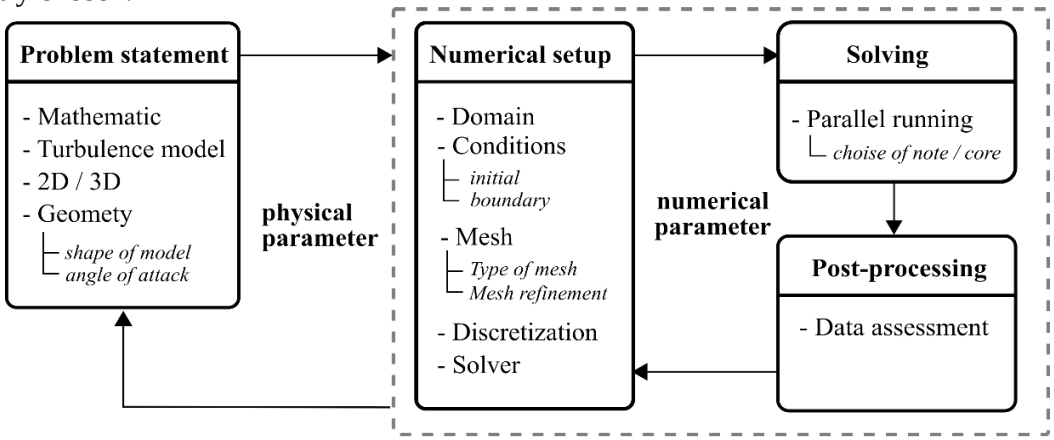


Figure 2. Workflow with the passage of two loops.

A rectangular computational domain in Figure 3 was used in this work, as this shape corresponds to the cross-section of the wind tunnel and is more sensible for defining the boundary conditions. The corresponding boundary conditions are also shown in Figure 3. A Courant number of 1.0 was used in all simulations for the independence study of the meshing, and the 2-order scheme was used for all discretisations in the work. The *backward* scheme is used for the temporal terms, the *cellMDLLimited least squares* scheme for the gradient terms and the *linear upwind* scheme for the convective terms. All other terms are *Gaussian linear*.

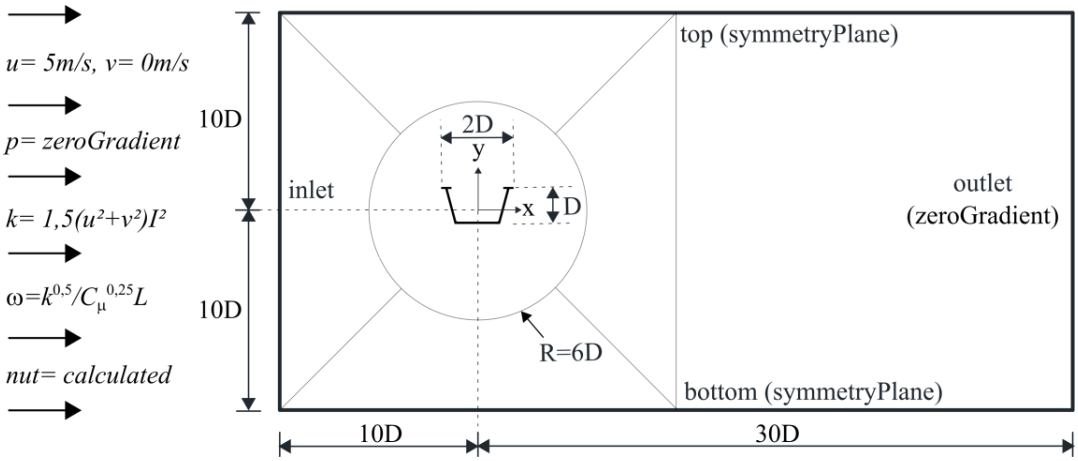


Figure 3. computational domain and the boundary conditions.

3. RESULTS AND DISSCUTION

Figure 4 shows the aerodynamic coefficients C_D and C_L. It can be seen that the coefficient C_D in the range from -6° to approx. 12° agrees very well with the test results. Beyond that, especially at angles of attack less than -6°, the C_D coefficient deviates significantly, with the largest deviation being 46 % at an angle of attack of -16°. The lift curve generally agrees with the test results. However, there are small deviations in the intervals from -6° to 0° and from 10° to 14°.

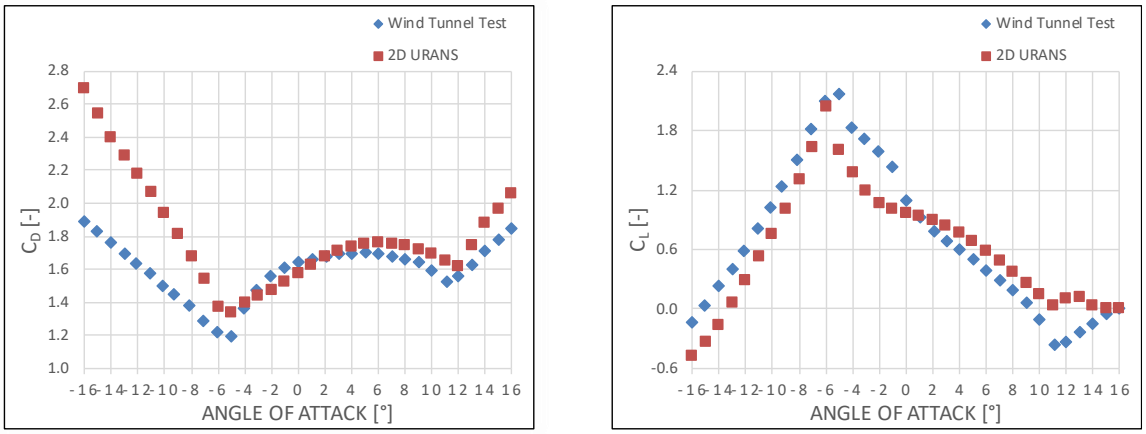


Figure 4. aerodynamic coefficients at different angles of attack.

Figure 5 shows that the time-history drag coefficient curve from the 3D-URANS simulation with a 1D span (D is the model height) is almost identical to the curve from the 2D URANS calculation. However, the 3D-URANS simulation with a span of 5D shows a strong instationarity of the drag coefficient curve. It can also be seen that the mean C_D value of 2.28 from 3D-URANS with a 5D span is smaller than the results of the other two simulations, which is more consistent with the experimental results.

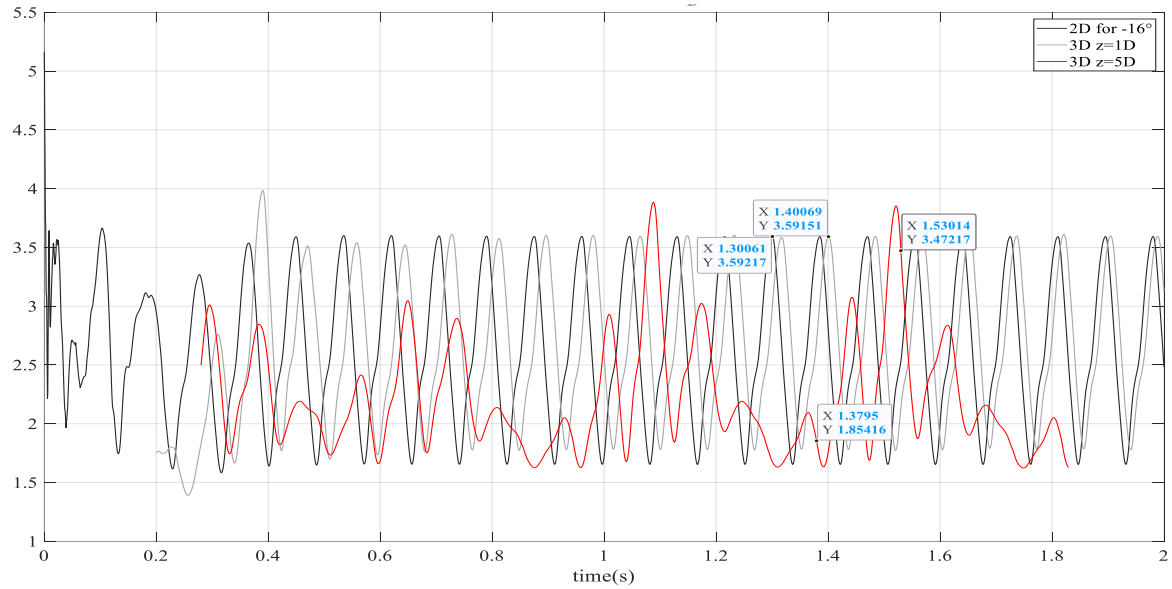


Figure 5. time-history drag coefficients in simulations for 2D and 3D with a span of 1D and 5D at -16°.

4. CONCLUSION

It was found that the 2D-URANS method for mean aerodynamic coefficients such as C_D and C_L is only applicable within a certain range of angles of attack. At large angles of attack, e.g. -16°, the calculation results of 2D-URANS deviate considerably from the wind tunnel results.

In this work, a 3D-URANS simulation was carried out with an angle of attack of -16°. The simulation results are in better agreement with the wind tunnel results and show that the results clearly depend on the 3D effect. At the same time, the work shows that a sufficient span must be considered in the 3D simulation in order to improve the calculation results.

REFERENCES

DIN EN 1991-1-4, 2010. Eurocode 1. Einwirkungen auf Tragwerke – Teil 1-4: Allgemeine Einwirkungen – Windlasten. December 2010.

R.H. Scanlan and J.J. Tomko, Airfoil and bridge deck flutter derivatives, ASCE Journal of the Engineering Mechanics Division, 97 (6) (1971), pp. 1717-1737.

prEN 1991-1-4, 2024. Eurocode 1. Actions on structures – Part 1-4: General actions - Wind actions. March 2024.

C. Chen, C. Mannini, G. Bartoli, and K. Thiele, Experimental study and mathematical modeling on the unsteady galloping of a bridge deck with open cross section, Journal of Wind Engineering and Industrial Aerodynamics, vol. 203, p. 104170, August 2020.

High performance computing resources and workflows on DesignSafe

Fred Haan [1], Jean-Paul Pinelli [2], Ahsan Kareem [3]

[1]*Calvin University, Grand Rapids, USA, frederick.haan@calvin.edu*
[2]*Florida Institute of Technology, Melbourne, USA, pinelli@fit.edu*
[3]*University of Notre Dame, Notre Dame, USA, kareem@nd.edu*

SUMMARY:
The DesignSafe cyberinfrastructure makes high-performance computing resources and workflows available to natural hazards researchers from around the world. This presentation will describe the resources available and will demonstrate an OpenFOAM workflow to illustrate one particular wind engineering tool that is available.

Keywords: HPC, cyberinfrastructure, DesignSafe

1. OVERVIEW OF THE DESIGNSAFE CYBERINFRASTRUCTURE

The first portion of this presentation provides an overview of the different components of the DesignSafe cyberinfrastructure as they relate to wind engineering and the resources available. This will include a review of specific use cases of research for wind hazards. These examples include electronic data reports that use Jupyter notebooks to allow researchers to interrogate data interactively within the web portal, computational workflows that integrate ensembles of HPC-based simulations and surrogate modelling, and the publication of field research data after natural hazard events that utilize a variety of DesignSafe tools.

DesignSafe (www.designsafe-ci.org, Rathje et al., 2020) is the cyberinfrastructure component of the Natural Hazards Engineering Research Infrastructure (NHERI) of the US National Science Foundation (NSF). It is available to hazard researchers from around the world and provides cloud-based tools to manage, analyze, understand, and publish critical data for research to understand the impacts of natural hazards, including wind.

DesignSafe accounts are free to acquire and come with initial high-performance computing (HPC) allocations. All the resources are intended for open science research. The intent of the presentation is to promote the use of the platform and to lower the barriers of entry for using simulation tools, HPC resources, and AI and machine learning (ML) workflows. This includes portal apps that use HPC on the backend (including some NHERI SimCenter tools) but also JupyterLab with Jupyter notebook access to machines at the Texas Advanced Computing Center (TACC) with CPU and GPU resources on HPC machines. DesignSafe is the primary access point for all these resources.

Figure 1 illustrates the different constitutive parts of DesignSafe-ci. The DesignSafe Data Depot

provides private and public disk space to support research collaboration and data publishing through a web interface. Researchers can explore published datasets (there are over 1000), connect to a network of people, reuse datasets that have been published, and curate/publish their own data. The DesignSafe Recon Portal uses a map interface to provide easy access to data collected from damage investigations of a broad range of natural hazards including tornadoes and hurricanes. The DesignSafe Workspace provides cloud-based tools for simulation, data analytics, and visualization as well as access to high performance computing (HPC).

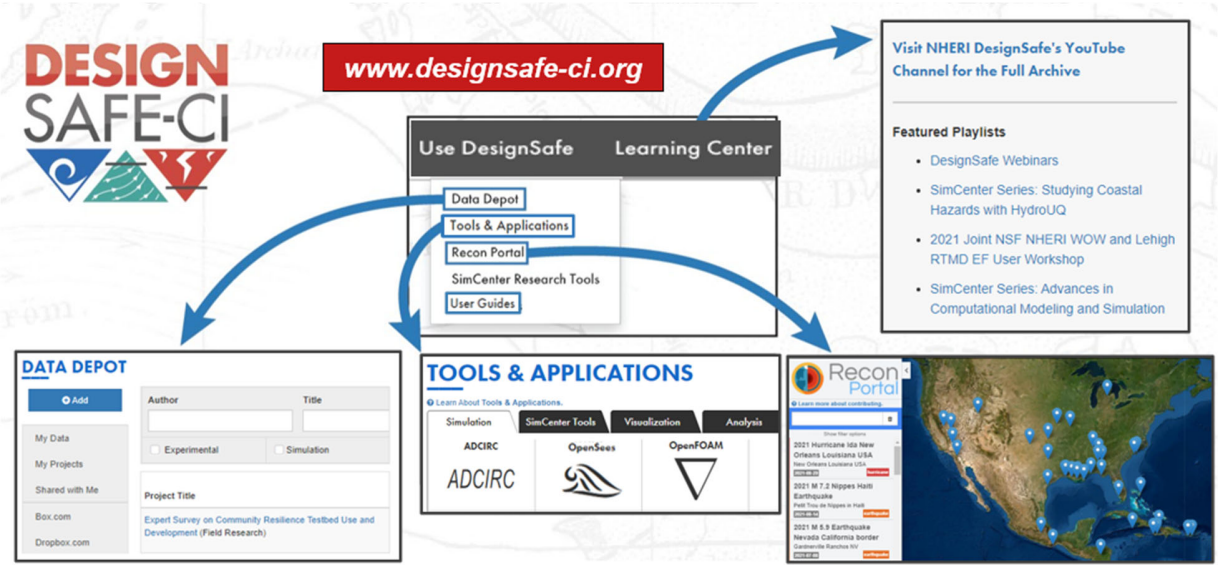


Figure 1. DesignSafe cyberinfrastructure components

2. OPENFOAM WORKFLOW

The second half of the presentation will demonstrate an OpenFOAM workflow to illustrate one particular tool that is available. Jupyter notebooks are a widely used tool in science and engineering to combine text, images, and videos with computational codes that streamline the sharing and reproducing of research. The open-source software OpenFOAM is a widely used computational fluid dynamics tool for wind engineering research. Combining these tools with the HPC resources on DesignSafe constitutes a powerful tool for wind engineering research. The DesignSafe portal itself has more details and more specific use cases that new users can use for learning and can modify for their own uses.

ACKNOWLEDGEMENTS

The support of the US National Science Foundation under award 2022469 NHERI Cyberinfrastructure (DesignSafe) is gratefully acknowledged.

REFERENCES

Rathje, E.M., Dawson, C., Padgett, J.E., Pinelli, J.P., Stanzione, D., Haan, F., Kareem, A., et al., 2020. Enhancing Research in Natural Hazards Engineering Through the DesignSafe Cyberinfrastructure, Frontiers in Built Environment, v. 6, https://doi.org/10.3389/fbuil.2020.547706.

Enhancing Darrieus H-Rotor Performance by Integration of J-Shaped and Microcylinder

Dishant Sharma [1], Rahul Goyal [1]

[1]*Indian Institute of Technology Delhi, New Delhi, India, Dishant.Sharma@ces.iitd.ac.in*
[1]*Indian Institute of Technology Delhi, New Delhi, India, rahulgoyal@dese.iitd.ac.in*

ABSTRACT:
Vertical-axis wind turbines are effective for urban wind energy extraction, yet aerodynamic losses from negative torque, and dynamic stall considerably restrict their efficiency. To address these challenges, the current study numerically investigates a novel combined passive flow control technique to enhance performance of a two-dimensional model of a VAWT. The proposed technique incorporates a J-shaped configuration featuring a 90% opening ratio, alongside leading-edge microcylinders having diameter-to-chord and spacing-to-chord ratios of 0.01 and 0.015, respectively. Simulations are performed at a low tip speed ratio, where deep dynamic stall significantly impacts the aerodynamic performance and torque stability of H-rotors. The results indicate that the optimised arrangement enhances the power coefficient by 2.4 times compared to a conventional H-rotor, underscoring the efficacy of this integrated flow-control strategy in reducing aerodynamic losses and augmenting VAWT performance in urban environments.

Keywords: VAWT, J-Shaped, Microcylinder

1. INTRODUCTION

The role of renewable energy in alleviating climate change, bolstering energy security, and fostering sustainable economic growth is crucial. It is becoming increasingly necessary to have renewable sources that are both scalable and reliable as global policies strive to limit the increase in temperature to below 2ºC. In this transition, wind energy is a key factor due to availability of mature technology for its harness (Celik et al., 2022). Due to a growing demand for decentralised and urban-compatible energy solutions, wind energy systems such as VAWTs have gained attention. VAWTs provide several advantages for distributed generation in urban and offshore settings; for example, they are omni-directional, are more scalable, have lower centre of gravity, and require less maintenance compared to horizontal axis wind turbines (HAWTs). However, VAWTs are aerodynamically more challenging to operate. For instance, flow instability resulting from blade wake interactions and rapid cyclical fluctuations in the angle of attack (AoA) may potentially induce a dynamic stall. The dynamic stall effect is severe and most significant at low tip speed ratios (TSRs, λ), where it substantially impacts the turbine's self-starting capability, lowers the power coefficient (C_p), amplifies torque fluctuations, reduces stability and eventually affects the overall performance of the VAWT.

One method to reduce the problem of self-starting at low TSR is to use a J-shaped profile of the turbine blade. This method effectively reduces the torque amplitude, decreases fatigue stress, augments self-starting, and enhances C_p at low TSR. The numerical investigation of Zamani *et al.*

(Zamani et al., 2016) has shown that the employment of J-shaped profile reduces the torque amplitude with reduction in vibrations and fatigue stresses acting on the rotor and shaft. It has been shown that the modified profile improved the power efficiency by 3.41%. Naik *et al.* (Naik and Sahoo, 2023) determined that the performance of the airfoil with an upper cut surpassed that of the one with a lower cut. The moment coefficient (C_m) increased as the opening ratio reduced from 0.9 to 0.2 for elevated TSRs, whereas it decreased with a reduction in opening ratio at lower TSRs. Luo *et al*. (Luo et al., 2017) employed an off-surface flow control technique, i.e., a leading edge microcylinder to mitigate stalling. The performance was seen to be more sensitive to spacing than to diameter. Prior to stall, specifically at angles of attack below 18º, significant separation was noted for *s/c* of 0.005. When the *s/c* ratio was elevated to 0.015, the lift coefficient was augmented to correspond with the original, but drag coefficient also increased. Post stall, specifically at angles of attack above 18º, for *s/c* greater than 0.01, the lift coefficient exhibited a substantial rise.
Following the findings of the cited literature, a J-shaped profile with 0.9 opening ratio is combined with a microcylinder (*d/c*=0.01, *s/c*=0.015) in the present study to assess the improvement offered by implementing a hybrid mitigation technique. The transition SST *k-ω* model is utilized for the present study and a quantitative comparison is drawn between the conventional and modified H-rotor's aerodynamic performance. Also, a qualitative flow behaviour around the surface of airfoil is projected for better understanding the flow physics involved in a deep dynamic stall.

2. NUMERICAL METHODOLOGY

The current study simulates the VAWT model using turbine parameters (as shown in Table 1) obtained from the experimental work conducted by Tescione *et al.* (Tescione et al., 2014). The computational domain is comprised of a rectangular area surrounding the rotor, as depicted in Fig. 1(a), with length and breadth set at 35 and 20 times the rotor diameter, respectively. The domain size is carefully chosen to reduce boundary-induced artefacts, ensuring that the results are independent of the dimensions of the computational region. The computational domain is partitioned into a rotating and a stationary zone, and the rotor's motion is simulated using a sliding mesh model to precisely capture the rotor's dynamic behavior.

Table1. Conventional H-rotor parameters

Parameter	**Value**	**Parameter**	**Value**
Number of blades	2	Rotor and Shaft diameter, D and D_s [m]	1, 0.04
Blade airfoil	NACA 0018	Blade solidity [-]	0.12
Blade chord, c [m]	0.06	Wind speed, V [m/s]	9.3
Chord based Reynolds number, Re_C ($\times 10^5$)	0.85 to 1.95	Turbulence intensity [%]	5

This study conducts 2D simulations utilizing the commercial CFD software ANSYS FLUENT (ANSYS Inc, 2015). The SIMPLE method is utilized to control the pressure-velocity coupling. Together with the second order pressure configuration, gradients of solution variables are computed using a least-squares cell-based method. Momentum, turbulent kinetic energy, and specific dissipation rate are discretized using a second-order upwind method. A non-uniform structured grid (Fig. 1(b)) has been generated within the computational area, with a refined mesh close to the blade surfaces. The average dimensionless wall distance $y+$ was maintained below 1, whereas the maximum $y+$ value is kept under 5 for all blade surfaces.

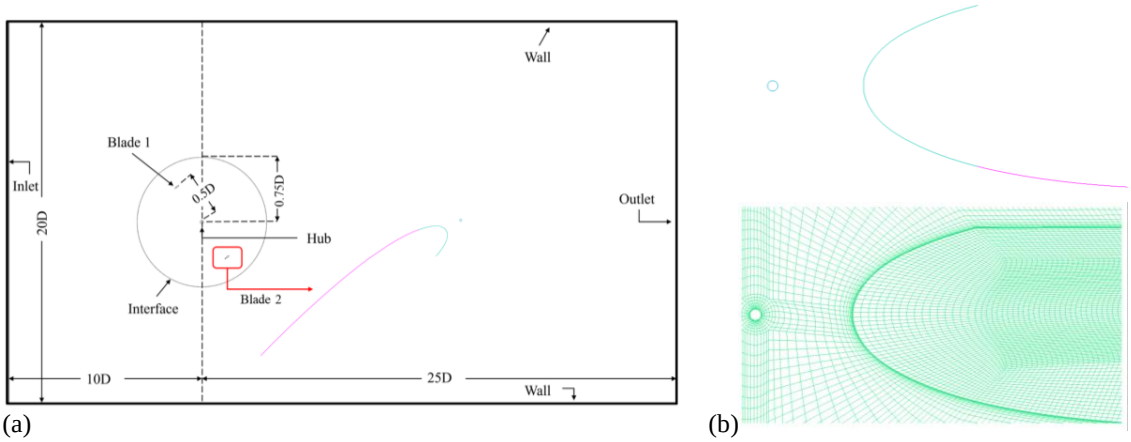


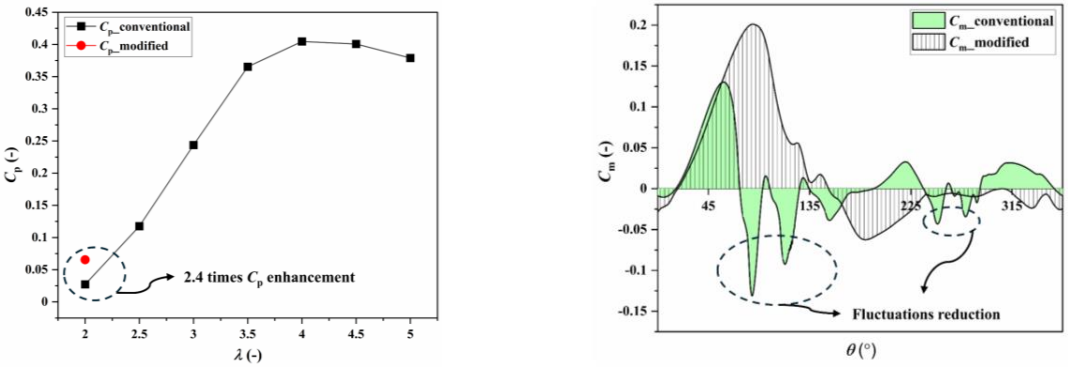
Figure 1. (a) Computational domain, and (b) Modified airfoil profile with non-structured mesh

Based on grid and temporal independence studies, a mesh density of 679952 elements and a time step size of 2.345872651e-5 s are selected for the simulation. The experimental data reported by Tescione et al. at 4.5 TSR is used to validate the numerical results. The transition SST *k-ω* turbulence model is used for the simulation and a deviation of 0.18% from experimental data is observed for the conventional rotor. The simulations are further carried out to analyze the deep dynamic stall condition at low TSR value of 2. Implementation of hybrid mitigation technique is conducted to improve the performance and reduce the torque fluctuations observed at low TSR.

3. PRELIMINARY RESULTS

The simulation of the H-rotor was conducted at a TSR = 2 for both conventional and modified H-rotor VAWT. The results show the enhancement in power coefficient of modified rotor by 2.4 times the conventional rotor as depicted in Fig. 1. The negative torque reduction for most of the upwind region, and an enhanced amplitude, provide the same conventional 2 bladed H-rotor a better self-start and improved its working range. Thus, the reduction in fluctuations for both upwind and downwind region of modified H-rotor confirm the improvement in self-starting ability and delay in stall events.

For both conventional and modified H-rotors, the flow is initially attached over both airfoil surfaces in the rotor's upwind zone, as seen in Figure 3. As the azimuthal angle increases, the trailing edge generates a smaller anticlockwise vortex. The modified rotor successfully reduces the strength of the trailing edge vortex, and the flow remains attached to the surface, as seen at 65° azimuthal position. These vortices at the trailing edge induce a pressure wave to move over the suction airfoil surface, where the laminar to turbulent transition occurs, in the direction of the leading edge. During this transition, laminar separation bubbles form, causing the leading-edge vortex to grow over the airfoil's suction surface. The flow is firmly adhered to the surface, and there is an increase in moment amplitude as illustrated in Fig. 2a. These contours confirm the reduced fluctuations and stable performance of the modified H-rotor VAWT, as indicated by the moment coefficient curve (Fig. 2a).



(a) (b)

Figure 2. (a) Variation of C_p with λ, and (b) Comparison of conventional and modified H-rotor's C_m with θ for λ=2

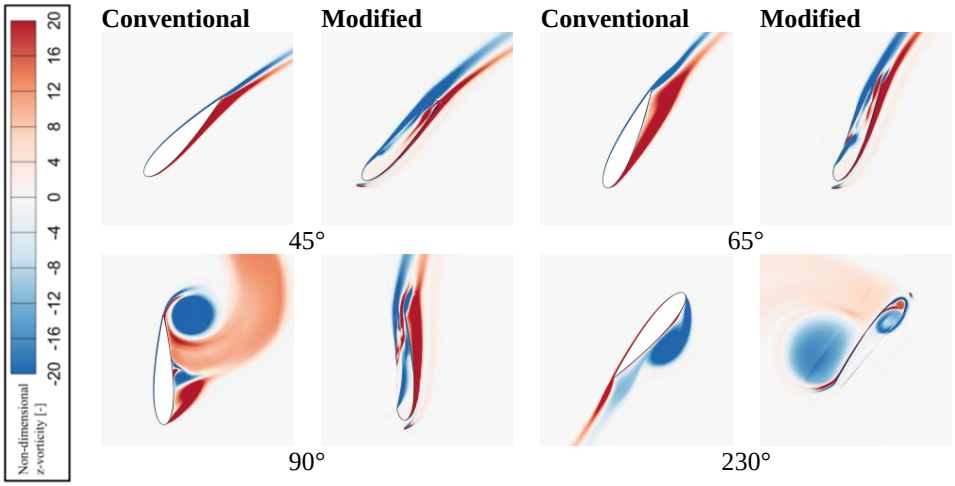


Figure 3. Non-dimensional z-vorticity contours of conventional and modified profile

ACKNOWLEDGEMENTS

Dishant Sharma and Rahul Goyal are thankful to the Ministry of Education, India, and the IIT Delhi HPC facility for computational resources.

REFERENCES

ANSYS Inc, 2015. ANSYS Fluent Theory Guide 12.0.

Celik, Y., Ingham, D., Ma, L., Pourkashanian, M., 2022. Design and aerodynamic performance analyses of the self-starting H-type VAWT having J-shaped aerofoils considering various design parameters using CFD. Energy 251, 123881. https://doi.org/10.1016/j.energy.2022.123881

Luo, D., Huang, D., Sun, X., 2017. Passive flow control of a stalled airfoil using a microcylinder. J. Wind Eng. Ind. Aerodyn. 170, 256–273. https://doi.org/10.1016/j.jweia.2017.08.020

Naik, K., Sahoo, N., 2023. Synergistic Effect of J-Shape Airfoil on the Performance of Darrieus-Type Straight-Bladed Vertical Axis Wind Turbine. J. Energy Resour. Technol. 145, 1–13. https://doi.org/10.1115/1.4062082

Tescione, G., Ragni, D., He, C., Simão Ferreira, C.J., van Bussel, G.J.W., 2014. Near wake flow analysis of a vertical axis wind turbine by stereoscopic particle image velocimetry. Renew. Energy 70, 47–61. https://doi.org/10.1016/j.renene.2014.02.042

Zamani, M., Maghrebi, M.J., Varedi, S.R., 2016. Starting torque improvement using J-shaped straight-bladed Darrieus vertical axis wind turbine by means of numerical simulation. Renew. Energy 95, 109–126. https://doi.org/10.1016/j.renene.2016.03.069

Understanding the effect of large-scale forcing on small-scale flow response using canonical flows.

Akshay Patil[1] and Clara García-Sánchez[1]

[1]*3DGeoinformation Research Group, Delft University of Technology, Delft, The Netherlands.*
a.l.patil@tudelft.nl

SUMMARY:
Most environmental flows are subject to time-varying large-scale forcing such that the flow is rarely in a statistically stationary flow condition. Consequently, understanding the effect of time-varying large-scale forcing and its impact on the flow response can provide crucial insights into the overall dynamics involved in such environmental flows. This is especially true for the atmospheric flows that experience gusts as a response to varying large-scale forcing and can have a large local impact. This study uses a canonical flow setup to simulate turbulent flow in a channel geometry subject to time-varying forcing conditions and naturally rough walls to understand the flow dynamics using a scale-resolving computational framework.

Keywords: Unsteady Flows, Turbulence, Computational Fluid Dynamics

1. INTRODUCTION

Environmental flows, such as those in atmospheric systems, are inherently complex due to their susceptibility to external, time-varying, large-scale forces that disrupt statistical stationarity (Jayaraman and Brasseur, 2021). These forces introduce dynamic changes in flow behaviour, which can propagate through the system and significantly influence local and global flow response. In the atmosphere, such phenomena often manifest as gusts—sudden, short-lived increases in wind speed that can have a large local impact on air quality, dispersion of pollutants, and wind loading, to list a few (Ciarlatani et al., 2023; Liu et al., 2023). The variability imposed by these changes underscores the importance of studying how transient forcing impacts turbulent flow structures.

To address this challenge, our study employs a canonical computational setup that simulates turbulent flow within a channel geometry with scaled versions of complex urban-like geometries, mirroring real-world conditions. This configuration is subjected to time-dependent forcing to observe and analyze the intricate response mechanisms at different scales. By leveraging a scale-resolving computational framework, we aim to capture detailed flow dynamics, including the interaction between roughness-induced turbulence and the temporal variability of the imposed forcing. These insights contribute to a deeper understanding of the turbulence characteristics and energy transfer processes within environmental flows under non-stationary conditions.

2. METHODOLOGY

In this work, we solve the non-dimensional incompressible Navier-Stokes equations given by

$$\partial_t u_i + \partial_j u_j u_i = -\partial_i p + \frac{1}{Re_\tau}\partial_j \partial_j u_i + \Pi_c(t)\delta_{1j} + F_{\text{IBM}}, \tag{1}$$

subject to incompressible continuity equation given by

$$\partial_i u_i = 0, \tag{2}$$

where t is time, u_i is the velocity vector, p is pressure, $Re_\tau \equiv u_\tau H/\nu$ is the friction Reynolds number, u_τ is the friction velocity, H is the characteristic length scale (channel height), and ν is the kinematic viscosity of the fluid, $\Pi_c(t)$ is the time-varying pressure gradient, and F_{IBM} is the immersed boundary force used to represent the urban-like geometry. The governing equations are discredited using second-order accurate finite differences over a Cartesian grid, while the equations are integrated in time using a Runge-Kutta three-step method based on the fractional step algorithm (Moin and Verzicco, 2016; Orlandi, 2000). The urban-like roughness geometry is introduced using a volume-penalization immersed boundary method (*VIBM*) as introduced by Scotti, 2006. Using the signed distance field (SDF), the flow is forced to satisfy the no-slip and no-penetration condition at the interface of the geometry (SDF equals 0). Due to the nature of the volume penalisation introduced in this methodology, if care is not taken along the boundary of the solid, large dispersive errors can be observed as the geometry is merely voxelised over the grid. In this work, we use the Delft University of Technology campus as a test model scaled down using a geometric factor of $S = 760$ to limit the computational resources required to simulate the flow. Figure 1 shows the streamwise velocity in the domain that is designed using the best practice guidelines as detailed by Franke et al., 2011 such that the boundary conditions do not affect the inference in the region of interest.

3. PRELIMINARY RESULTS

As shown in figure 1, the computational framework has been developed to simulate flow around complex obstacles using an efficient simulation framework to better understand the small-scale dynamics. Additionally, as seen in figure 2, the time-varying pressure gradient can be supplied as a user input where the model uses linear interpolation to map the driving pressure gradient. Figure 1 shows the instantaneous flow field results obtained from one such simulation which shows the local zone of acceleration due to the high-rise building located centrally within the campus. These observations are consistent with previous Reynolds-Averaged simulations carried out by García-Sánchez et al., 2021 thus providing further support to explore the effect of varying the driving pressure gradient and its effect on small scale statistics.

4. CONCLUSION & FUTURE WORK

As illustrated in this very simple snapshot, the flow field around such complex geometries is sensitive to the kind of driving forces and provide an effective testing bed for understanding complex flow patters. The goal here would be to connect the time-varying driving force with the small scale flow response that could enable parameterisation of highly spatio-temporally local phenomenon

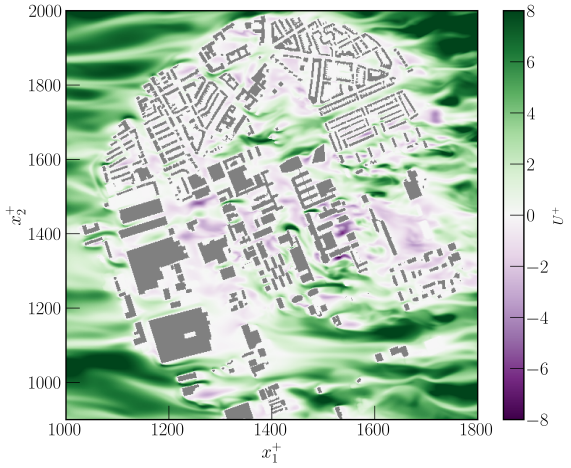


Figure 1. Instantaneous snapshot of the streamwise velocity around the Delft University of Technology campus where the gray color denotes the built environment while the green and purple color denotes the streamwise velocity. All parameters non-dimensionalised using wall units.

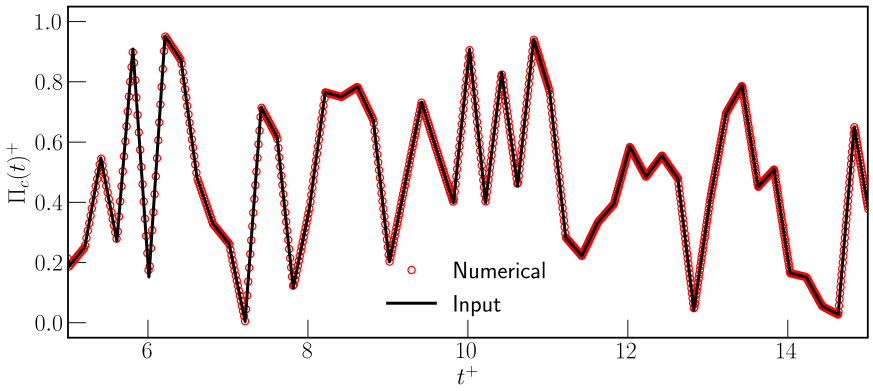


Figure 2. Comparison of the input driving force (solid black) against the computationally interpolated (circles red) algorithm implemented within the numerical solver to accurately and efficiently obtain the driving force.

such as gusts. Additionally, this scale resolving simulation framework can also provide a means to compare the steady state simulations and understand the similarities and differences.

ACKNOWLEDGEMENTS

This research was carried out as a part of the EU-Project RefMAP. RefMAP has received funding from the Horizon Europe program under grant agreement No 101096698. The opinions expressed herein reflect the authors' views only. Under no circumstances shall the Horizon Europe program be responsible for any use that may be made of the information contained herein.

REFERENCES

Ciarlatani, M. F., Huang, Z., Philips, D., and Gorlé, C., 2023. Investigation of peak wind loading on a high-rise building in the atmospheric boundary layer using large-eddy simulations. Journal of Wind Engineering and Industrial Aerodynamics 236, 105408.

Franke, J., Hellsten, A., Schlunzen, K. H., and Carissimo, B., 2011. The COST 732 Best Practice Guideline for CFD simulation of flows in the urban environment: a summary. International Journal of Environment and Pollution 44, 419–427.

García-Sánchez, C., Vitalis, S., Paden, I., and Stoter, J., 2021. The impact of level of detail in 3d city models for cfd-based wind flow simulations. English. International Archives of the Photogrammetry, Remote Sensing and Spatial Information Sciences - ISPRS Archives 46. 16th 3D GeoInfo Conference 2021 ; Conference date: 11-10-2021 Through 14-10-2021, 67–72.

Jayaraman, B. and Brasseur, J. G., 2021. Transition in atmospheric boundary layer turbulence structure from neutral to convective, and large-scale rolls. Journal of Fluid Mechanics 913, A42.

Liu, G., Wang, X., Wu, Q., Fang, D., Wu, Z., Liu, H., and Lyu, M., 2023. Effect of urbanization on gust wind speed in summer over an urban area in Eastern China. Environmental Research Letters 18, 074025.

Moin, P. and Verzicco, R., Jan. 2016. On the suitability of second-order accurate discretizations for turbulent flow simulations. European Journal of Mechanics - B/Fluids 55, 242–245.

Orlandi, P., 2000. Fluid Flow Phenomena, Volume 55 of Fluid Mechanics and Its Applications. Springer Netherlands, Dordrecht.

Scotti, A., 2006. Direct numerical simulation of turbulent channel flows with boundary roughened with virtual sandpaper. Physics of Fluids 18, 031701.

Towards the development of the extreme temperature map of Genoa using OpenFOAM.

A. Piazza[1,2], M. Burlando[3], G.T. Bitsuamlak[4], M.P. Repetto[5]

[1]*University of Genoa, Genoa, Italy, alessia.piazza@edu.unige.it*
[2]*Western University, London ON, Canada, apiazz2@uwo.ca*
[3]*University of Genoa, Genoa, Italy, massimiliano.burlando@unige.it*
[4]*Western University, London ON, Canada, gbitsuam@uwo.ca*
[5]*University of Genoa, Genoa, Italy, maria.pia.repetto@unige.it*

SUMMARY:
Urban Heat Island (UHI) effect and heat waves are significant phenomena that affect urban environments, exacerbating temperatures and compromising the pedestrian comfort from June to September. Therefore it is vital to understand the spatio-temporal variation of the temperature in urban environment realizing an accurate map of extreme temperatures in order to improve the well-being of population through proper city planning and the application of mitigation strategies. In order to achieve this, Computational Fluid Dynamics (CFD) offers the possibility to obtain data from a multi-physics simulation of the urban microclimate. The city of Genoa, an Italian coastal city that had recently experienced a rapid growth and urban sprawl, has been used as a case study. The simulations were run using the open source software OpenFOAM integrated with the data collected by the Meteorological Agency for Environmental Protection (ARPAL).

Keywords: Extreme temperature hazard, UHI effect, Long-term temperature measurements, CFD, OpenFoam

1. INTRODUCTION

It has been projected that by 2050 the 70% of the world population will be living in urban areas (Kadakia and Galea, 2023). Urban Heat Island (UHI) effect and heat waves are significant phenomena that affect urban environments, exacerbating the already elevated temperatures in cities and leading to an increase in illness and mortality (Beniston et al., 2007). While the UHI effect phenomenon is one of the most prominent consequences of urbanization and climate change (Jamei et al., 2005), heat waves are an extreme and unpredictable weather event that can have severe impact, such as causing between 25,000 to 70,000 deaths across Europe during the summer of 2003 (Zuo et al., 2015). Particularly from June to September, pedestrian thermal comfort is significantly compromised due to climate change (Sarrat et al., 2006). Therefore, understanding the complex spatio-temporal variation of temperature in a complex urban environment is vital to put mitigation measures in place and issue warnings, if needed, for general well-being of the public. To achieve this, the mapping of extreme temperatures is the first step to investigate and detect the most critical and dangerous part of urban areas. Extreme temperature maps are usually realized using long-term data taken at given locations and interpolated through a linear or non-linear model (Menna and Waktola, 2022). Unfortunately, the available data from meteorological stations are often not enough to obtain an accurate representation of the reality, leading to an inaccurate estimation of the temperatures, especially in complex urban areas.

2. METHODOLOGY

Computational Fluid Dynamics (CFD) offers a unique opportunity to apply a physically-based interpolation to measured data by providing a multi-physics simulations of the urban microclimate. Therefore, the objective of this study is to create a framework to develop extreme temperature map at the city-scale using numerical simulations conducted on OpenFOAM. The city of Genoa in Italy has been used as a case study for a proof of concept.

2.1. Genoa case study

Genoa, Italy, serves as an illustrative case of a coastal city that has experienced rapid growth and urban sprawl, resulting in significant modifications to its urban climate. Like many other coastal cities, Genoa is particularly vulnerable to the effects of climate change (Rosenzweig et al., 2011) due to its proximity to the sea. In recent years, there has been an increasing need for detailed investigations of extreme weather patterns in the Mediterranean region, as it is identified as one of the two most susceptible regions to predicted climate changes (Giorgi, 2006). Genoa, which is characterized by extensive concrete infrastructure similar to many other cities in Europe, serves as a major example in this context. Moreover, in this area the long-term data of the meteorological network of ARPAL area available to establish a database of spatially distributed temperature parameters in different climatological scenarios within the city and can be used to set up a realistic CFD simulations.

2.2. Test case description

An accurate model of the city of Genoa developed and used by (Žužul et al., 2024) is now utilized in the present study. The geometry, due to the large scale, has been divided into three sub-domains and the topography was still present in all of them. The simulations have been performed using the CFD software open source OpenFOAM-v2212. The domain was considered closed and the flow confined, without the introduction of wind at the inlet. At the top of the domain a fixed shear stress condition has been applied. The temperature used inside the domain is associated to different return periods calculated conducting a statistical analysis on the data acquired by the meteorological stations. In order to perform the simulation, the solver Buoyant Boussinesq PimpleFoam based on the Boussinesq approximation has been used. In Figure 1, as an example, the geometry of the computational domain is shown considering a small subset of buildings in the western part of Genoa.

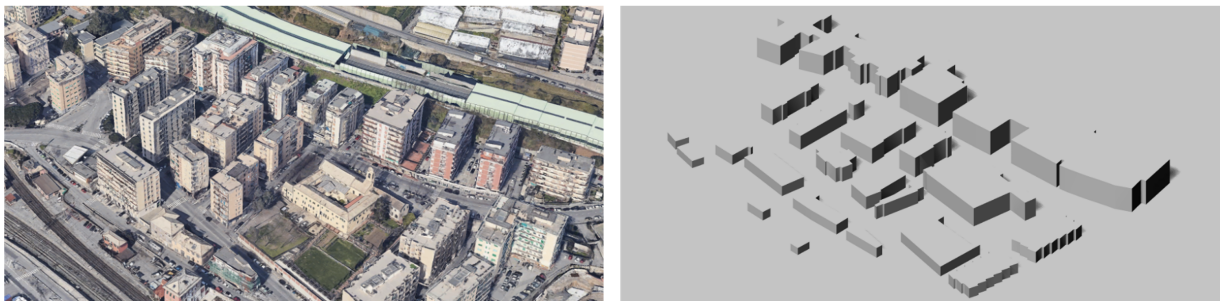


Figure 1. Part of the Voltri neighbourhood 3D model (right) and comparison with the real urban texture (left, credits Google Earth)

3. PRELIMINARY RESULTS

The dominant mechanism of heat transfer in our simulations is the natural convection. Accordingly, any wind flows are generated by temperature differences within the simulation domain, which in turn are due to the heating of the external facades of the buildings, warmed homogeneously. It is possible to notice that where the airflow due to the movement of heat from a warmer area to a colder one is weaker, the temperature increases. These outcomes will be used to identify and flag risk areas for the population.

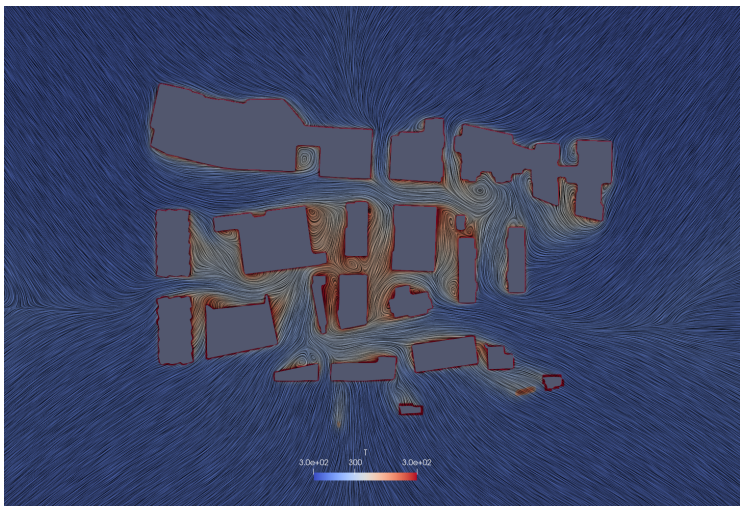


Figure 2. Contours plot of the temperature at 2m height with surface LIC around the domain shown in Figure 1.

4. CONCLUSIONS

The ability of CFD to analyze heat transfer due to convection induced by temperature gradients, i.e. natural convection, in a complex urban environment is presented. Elevated temperature is noticed in stagnant flow areas such as the wake region behind buildings or in confined areas. Therefore, urban geometry plays a crucial role in locally augmenting or inhibiting heat transfer depending on the contribution of mainly convection or conduction. Such observations can potentially be used to design mitigation strategies for improving local pedestrian comfort, enhance thermal performance of building facades and early stage urban planning. A more detailed analysis of the date is currently underway. The details of the methodology, including the numerical set up, and results from simulations conducted on a larger scale will also be presented.

ACKNOWLEDGEMENTS

This study was partially funded by ADAPTNOW Project – "ADAPTation Capacity Strengthening for Highly Affected and Exposed Territories in the Alps NOW" (Grant No. ASP0100048). ADAPTNOW is co-financed by the European Regional Development Fund through the Interreg Alpine Space programme.

REFERENCES

Beniston, M., Stephenson, D., and Christensen, O. e. a., 2007. Future extreme events in European climate: an exploration of regional climate model projections. JClimatic Change 81, 71–95.

Giorgi, F., 2006. Climate change hot-spots. Geophysical research letters 33.

Jamei, E., Rajagopalan, P., Seyedmahmoudian, M., and Jamei, Y., 2005. Review on the impact of urban geometry and pedestrian level greening on outdoor thermal comfort. Renewable and Sustainable Energy Reviews 54, 1002–1017.

Kadakia, K. and Galea, S., 2023. Urbanization and the Future of Population Health. The Milbank Quarterly 14, 153–175.

Menna, B. and Waktola, D., 2022. Extreme temperature trend and return period mapping in a changing climate in Upper Tekeze river basin, Northern Ethiopia. Physics and Chemistry of the Earth.

Rosenzweig, C., Solecki, W. D., Hammer, S. A., and Mehrotra, S., eds., 2011. *Climate Change and Cities: First Assessment Report of the Urban Climate Change Research Network*. Cambridge, U.K.

Sarrat, C., Lemonsu, A., Masson, V., and Guedalia, D., 2006. Impact of urban heat island on regional atmospheric pollution. Atmospheric Environment 40, 1743–1756.

Zuo, J., Pullen, S., Palmer, J., Bennetts, H., Chileshe, N., and Ma, T., 2015. Impacts of heat waves and corresponding measures: a reviews. Journal of Cleaner Production 92, 1–12.

Žužul, J., Ricci, A., and Burlando, M., 2024. An automated geometry generation procedure for CWE applications in OpenFOAM: the case study of a thunderstorm downburst moving over Genoa city. Meccanica, 1–18.

Towards a database for validation of urban ventilation and pollution dispersion models

P. O. Hristov[1], R. Mitkov[1], M. Pantusheva[1], V. Naserentin[2], A. Logg[2], A.K.R. Jayakumari[3], S. Gillmeier[3]

[1]*GATE Institute, Sofia University, Bulgaria, peter.hristov@gate-ai.eu*
[2]*Digital Twin Cities Center, Chalmers University of Technology, Gothenburg, Sweden*
[3]*Eindhoven University of Technology, Eindhoven, the Netherlands*

SUMMARY:
Digital twins present a virtual replica of an asset, which allows decisions about the life cycle of that asset to be tested in a virtual sandbox before being effected in reality. Using digital twins in the context of urban development facilitates the transformation of urban areas into the cities of the future. For urban environments, digital twins offer the opportunity to recreate many features and monitor important indicators, such as air quality.
The complexity and costs of full-scale pollution dispersion experiments, have made computational fluid dynamics popular in understanding air quality at the street level. To use any model as a scientific decision-support tool, its reliability must be quantified against representative experimental data. The model, can then be used as part of the digital twin to investigate air pollution and to evaluate the efficacy of measures to alleviate air quality problems.
This paper presents the ValUr project, which aims to carry out an experimental wind tunnel campaign to collect high-quality validation data to be used for studying air pollution dispersion in an urban environment via computational modelling. The motivation, setup, plan and results of ValUr available to date are presented.

Keywords: urban air quality, computer model validation, pollution dispersion experiments

1. INTRODUCTION

ValUr is a project funded under the Engineering Research Infrastructures for European Synergies (ERIES) programme for transnational access to research infrastructure. Under ERIES, ValUr proposes to develop a ventilation and air pollution dispersion testing campaign in the atmospheric boundary layer (ABL) wind tunnel at the Eindhoven University of Technology (TU/e), to collect high-quality validation data and to use this data to assess the accuracy and estimate the predictive capability of dispersion CFD models of an urban area in the city of Sofia, Bulgaria.

The project features several phases including the selection of a suitable test region, extensive geometry preparation, pre-test computational modelling, experimental test campaign and subsequent numerical experiments which aim at verification, validation and predictive capability estimation for the dispersion models. Despite the fact that the core of the project and the ERIES programme as a whole is the experimental campaign, described in this paper, the outcomes of ValUr are planned to extend far beyond the temporal duration of the wind tunnel tests themselves.

1.1. Motivation

Air pollution has been named one of the major health problems of our time by the World Health Organization (WHO). The problem with air pollution is particularly prominent in the city of Sofia, where the yearly average concentration for particulate matter and gaseous pollutants regularly exceeds several times the WHO guidelines[1]. Pollution is mainly due to the usage rate and average age of the vehicle fleet, industrial and domestic energy sources, and the lack of focused efforts and regulations in the field of urban ventilation planning.

The choice of testing area has been motivated by the fact that Sofia suffers from high levels of both fine particulate matter and gaseous pollution all year round. The impact poor air quality has on both the population health and the environment has prompted the European Commission to choose Sofia among the 100 European cities to become climate-neutral by the year 2030. To help achieve this goal, there is an extensive effort for the creation of a digital twin of Sofia. To ensure their trustworthiness and utility for informed urban decision-making, the digital twins need to be based upon models validated on relevant data.

1.2. State-of-the-art

As discussed in a recent review of the use of CFD in air pollution dispersion (Pantusheva et al., 2022), neither urban physics-based pollution dispersion modelling, nor validation are new disciplines. However, based on the analysis of 74 publications focused on using CFD in an urban setting and published in the last decade, the authors of the paper determined that verification, validation, and predictive capability estimation are the least well-understood and applied aspects of pollution dispersion modelling and simulation. At the same time the authors of different models aim to include physics of ever-increasing sophistication and complexity. These two observations demonstrate that the community equates model prediction trustworthiness with model sophistication, an assumption that clearly violates scientific reasoning. This trend persists despite the existence of large-scale urban applications of CFD and the importance of high-quality verification, validation, and uncertainty quantification in urban fluid modelling having been repeatedly stated over the years (Blocken et al., 2016; Dauxois et al., 2021; Jakeman et al., 2006; Schatzmann et al., 2010).

Despite the existence of several prominent validation databases (*e.g.*, AIJ, CEDVAL, CODASC), a relevant validation data for Sofia is needed, because existing experiments are carried out on geometries very different from the one under consideration. The primary reason behind the necessity of having a relevant validation data is the estimation of the predictive capability of the model, which is, ultimately the best measure of whether the model's predictions can be trusted.

2. VALIDATION CAMPAIGN

The project is split into four general stages as follows.

2.1. Model Making

This stage includes the selection of a suitable region in Sofia. Ten candidate zones were shortlisted for consideration. A region close to the city's Court House was chosen due to the presence of a

[1] See for example the factsheet on http://unmaskmycity.org/wp-content/uploads/2018/05/City_Factsheet_Sofia-English.pdf.

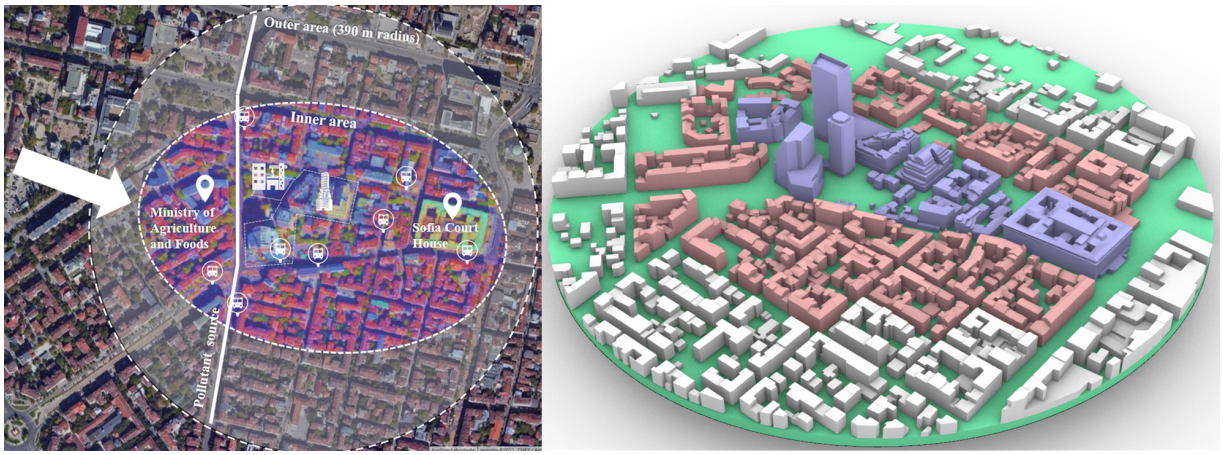


Figure 1. A satellite view of the region selected for testing, along with key landmarks, predominant wind direction and main pollution source (left); a perspective over the final model geometry, showing the three level-of-detail zones in different colours (right).

main road, oriented perpendicular to the predominant wind direction, good heterogeneity of the building landscape within the measurement area and good homogeneity outside of it, as well as a relatively low proportion of greenery. The region is shown on the left of Fig. 1. There, some of the landmark buildings are shown, along with the main road in the region (white polyline) and the direction of the predominant, west-northwesterly winds (white arrow). Considering the size of the region morphology, the wind tunnel's test section size, and blockage ratio guidelines, the model scale was selected as 1:300. This translates to region with a 390 m radius.

The model geometry, shown on the right of Fig. 1, was split into three zones of detail (colors) and was created by augmenting existing cadastre information about building footprints and height, with roof geometry from satellite imagery. The geometry itself was created in Rhinoceros®, Blender and Ansys SpaceClaim®.

2.2. Wind tunnel testing

The experimental measurement campaign will be carried out in the ABL wind tunnel of Eindhoven University of Technology, the Netherlands. All tests will be conducted for the determined prevailing wind direction (WNW). The pollutant dispersion of a passive scalar will be investigated for two possible source locations along the selected street of interest. Fast-flame ionization detectors (Fast-FID) will be used to measure concentrations at several relevant locations within the inner area (see left pane of Fig. 1). At a number of such measurement locations, the Reynolds number sensitivity and source strength independence will be assessed. Repeated measurements will be performed at these locations to create a comprehensive data set suitable for the purposes of the analysis and uncertainty quantification.

2.3. Data analysis

The raw data of pollutant concentrations will be analysed and cast into a format suitable for validation work. Throughout ValUr particular focus is placed on quantifying both aleatory and epistemic uncertainty from different sources to ensure the effect of potential errors and various unknowns is adequately accounted for.

2.4. Validation

Consultations with urban development experts, along with preliminary numerical experiments to determine some of the measurement locations were carried out using the Reynods-averaged Navier-Stokes (RANS) solver Ansys Fluent. However these types of models can serve as screening tools only and cannot be used during the detailed validation stage which will rely on large-eddy simulations (LES).

3. CONCLUSIONS

This paper presents the ValUr project, which aims to produce a state-of-the-art, open validation dataset of air quality measurements for a region in the city of Sofia as part of the ongoing effort to create a digital twin of the city. The work in ValUr is focused on delivering a best-practices validation protocol for urban CFD models and to raise awareness about the practical importance of validation and uncertainty quantification to the computational wind engineering community.
The final paper will include greater detail in each of the validation campaign stages and results from the wind tunnel tests, simulation work and preliminary outcomes of the validation activities.

ACKNOWLEDGEMENTS

This work is part of the transnational access project "ERIES – ValUr", supported by the Engineering Research Infrastructures for European Synergies (ERIES) project (www.eries.eu), which has received funding from the European Union's Horizon Europe Framework Programme under Grant Agreement No. 101058684. This is ERIES publication number C39.

Research has been supported by the GATE project - Horizon 2020 WIDESPREAD-2018-2020 TEAMING Phase 2 programme, no. 857155, and the Swedish Research Council for Sustainable Development Formas - 2019-01169 and 2019-01885.

REFERENCES

Blocken, B., Stathopoulos, T., and van Beeck, J. P. A. J., 2016. Pedestrian-level wind conditions around buildings: Review of wind-tunnel and CFD techniques and their accuracy for wind comfort assessment. Building and Environment 100, 50–81.

Dauxois, T., Peacock, T., Bauer, P., Caulfield, C. P., Cenedese, C., Gorlé, C., Haller, G., Ivey, G. N., Linden, P. F., Meiburg, E., Pinardi, N., Vriend, N. M., and Woods, A. W., 2021. Confronting Grand Challenges in environmental fluid mechanics. Phys. Rev. Fluids 6 (2), 020501.

Jakeman, A., Letcher, R., and Norton, J., 2006. Ten iterative steps in development and evaluation of environmental models. Environmental Modelling & Software 21, 602–614.

Pantusheva, M., Mitkov, R., Hristov, P. O., and Petrova-Antonova, D., 2022. Air Pollution Dispersion Modelling in Urban Environment Using CFD: A Systematic Review. Atmosphere (Basel) 13, 1640.

Schatzmann, M., Olesen, H., and Franke, J., 2010. *Cost 732 Model Evaluation Case Studies: Approach and Results*. Tech. rep. European Cooperation in Science and Technology (COST) Office, Brussels, Belgium.

Measurements and simulation of internal fan-driven airflow in a commercial greenhouse

Peter Sharpe [1], William Lubitz [2]

[1]*University of Guelph, Guelph, Canada, sharpep@uoguelph.ca*
[2]*University of Guelph, Guelph, Canada, wlubitz@uoguelph.ca*

SUMMARY:
Increasingly in greenhouses and controlled environment agriculture (CEA), internal circulation fans are deployed as a tool to help optimize growing conditions. Fans are typically mounted near the ceiling in a grid pattern with the flow direction parallel to crop rows. Fans are typically run at a constant speed, full time. The resulting airflow helps regulate temperature, and humidity, distribute carbon dioxide, and aid in plant transpiration. This study examines a specific fan type and spatial configuration in a seven-meter-tall 2.6-hectare Venlo style greenhouse, with a mature crop of vertically grown vine tomatoes. Ultrasonic air velocity measurements in three dimensions were taken at prescribed locations surrounding a fan. A CFD model is in development to simulate the airflow, using a domain representing a repeating zone of the greenhouse. The simulation results are compared with measurements, and conclusions for future research will be presented.

Keywords: greenhouse, fan-driven airflow, CFD simulation

1. INTRODUCTION

Controlled environment agriculture (CEA) aims to optimize environmental conditions for crop growth. A continuous circulation of low-speed air in and around the crop is thought to be beneficial as a tool to help control temperature, humidity and transpiration rate. Increasingly, commercial scale growers are installing fans that circulate air within the greenhouse to accomplish this. This study aims to model the airflow resulting from a network of internal fans in a large 2.6-hectare greenhouse. The greenhouse in this study and its fan layout is shown in Fig. 1.

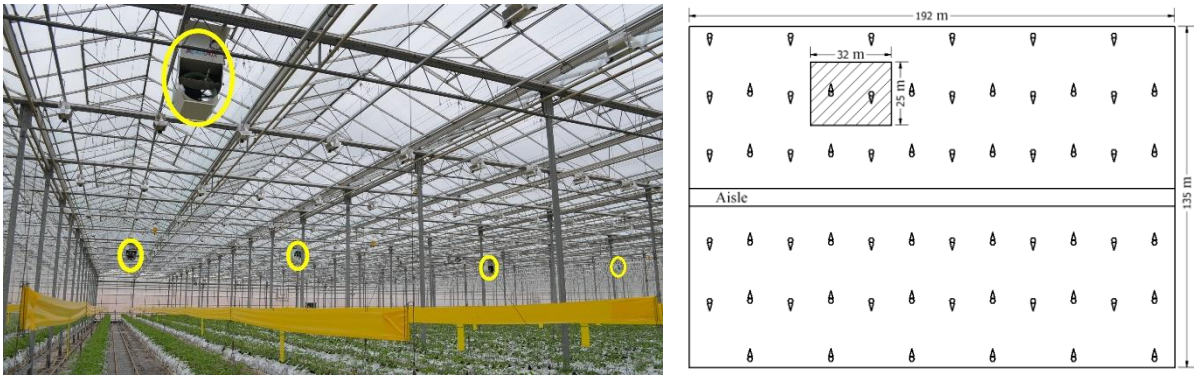


Figure 1. Greenhouse with fans and top view schematic with fan layout, and hatched area of simulation domain.

CFD has been used extensively to model airflow in greenhouses, particularly airflow

resulting from external wind. Bournet and Boulard summarized the methods of fifteen studies of naturally ventilated greenhouses (Bournet and Boulard, 2010). These studies treat smaller domains (maximum length 80 meters) and employed the κ-ε or the Re-Normalisation Group (RNG) method. They didn't however treat internal circulation with internal fans. Bassiouny et al. (2011), and Gao et al. (2017) successfully modeled a simple cuboid room with a ceiling fan using the RANS κ-ε methodology and observed qualitatively that predicted air velocity magnitudes correlated well with measured data. Limane et al. (2017) simulated the air movement, temperature and humidity in an indoor swimming pool using RANS methods with different turbulence treatments. They compared four different turbulence models (κ-ε, RNG κ-ε, κ-ε Launder Sharma, and κ-w SST) and found good correlation with all, though the κ-ε Launder Sharma performed slightly better.

2. MEASUREMENTS

Airflow measurements in the greenhouse were taken using three-dimensional ultrasonic anemometers (RM Young 81000) in two discrete modes. First, high spatial resolution measurements were taken to characterize the fan output flow, which is an important input parameter to the simulation. The anemometers were also used to measure airflow at a range of locations within the greenhouse, corresponding to a domain representing a repeating zone in the larger greenhouse layout. Three-dimensional wind velocity measurements were recorded at a frequency of 32 Hz to also capture turbulent characteristics of the airflow.

2.1. Fan Characterization Measurements

Measurements were made in a grid pattern at the outlet of the fan to. At each grid location data was recorded for one minute and the middle thirty seconds was averaged. The results are shown graphically in Fig. 2. From these measurements, average axial and rotational velocities were determined to be 7.0 m/s and 200 rpm respectively (the radial velocity component was found to be negligible). These values were used as input parameters in the simulation, described in section 3.

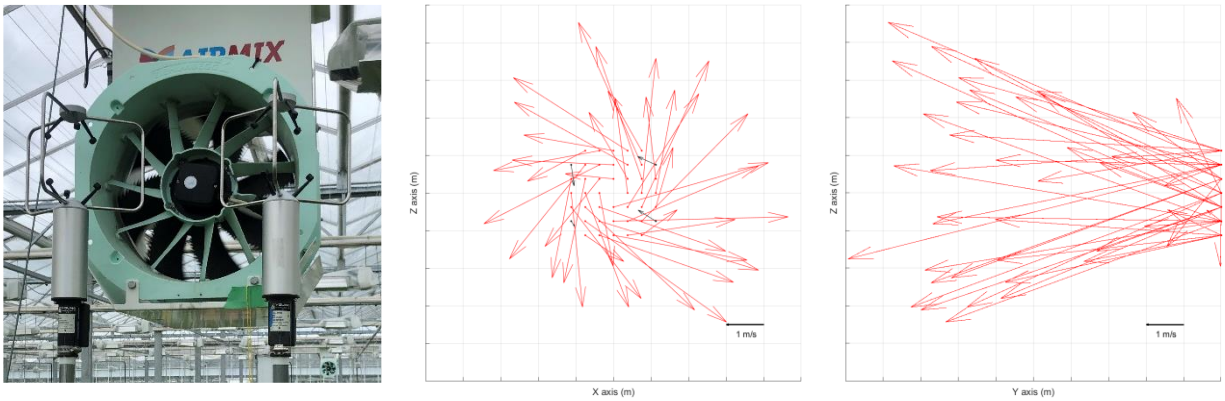


Figure 2. Fan output measurements.

2.2. Airflow Movement Measurements

Measurements in the crop rows were made at locations in the vicinity of one fan. A telescoping tower supported the anemometers at prescribed heights. The telescoping tower, and measurement locations are shown in Fig. 3. Airspeed data was recorded for ten minutes at each location. Readings were averaged over a ninety second period after seven minutes elapsed. The time delay was used to minimize any external effects.

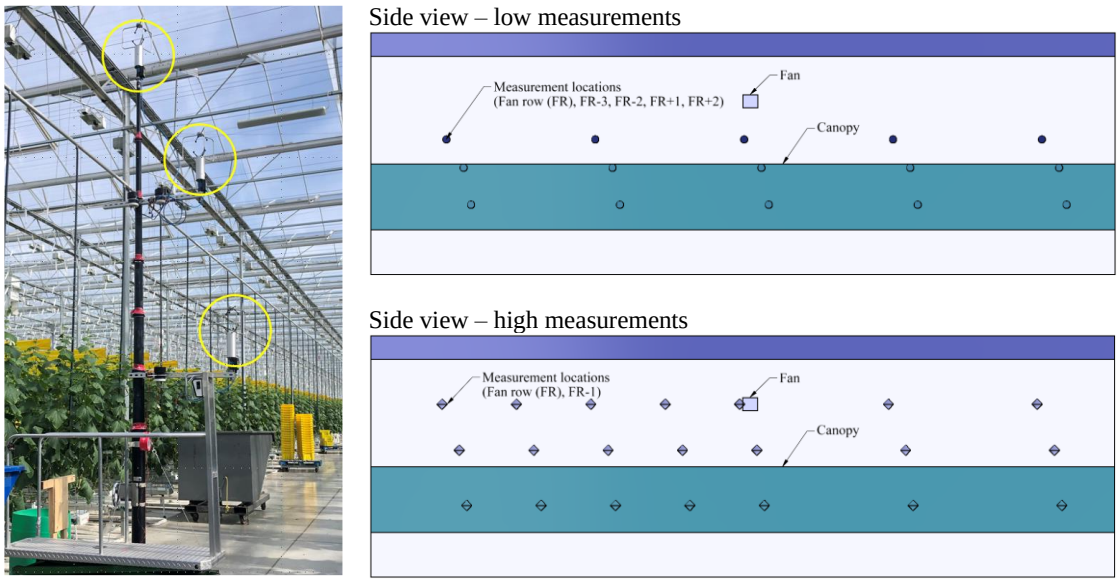


Figure 3. Telescoping tower and measurement locations.

3. SIMULATION

One purpose of the experiments was to provide validation data for CFD modelling of fan-driven airflow within the greenhouse, with the ultimate goal of using the validated CFD model to investigate optimal distributions of fans and air handling equipment. Reynolds Average Navier Stokes (RANS) CFD simulations were completed using classical κ-ε turbulence closure. The tool used for the simulation is OpenFOAM, with the simpleFoam solver. The domain is taken as a 25 m by 32 m section of the greenhouse, with cyclic repeating vertical boundaries. Inside this domain are two equally spaced fans pointed in opposite directions, replicating the actual greenhouse (Fig. 1). An example of this domain is shown in Fig. 4. Meshing is accomplished using snappyhexmesh, and the crop canopy is treated as a porous media, providing resistance to airflow. The fan outlet (domain inlet) boundary condition used the cylindrical inlet velocity field with the axial and rotational components determined experimentally (section 2). The fan inlet (domain outlet) was treated as a zero-pressure gradient condition. The floor and ceiling were treated as no-slip boundaries. The remaining left, right, front and back walls of the domain were treated as cyclic boundaries to emulate the repeated section of a much larger greenhouse.

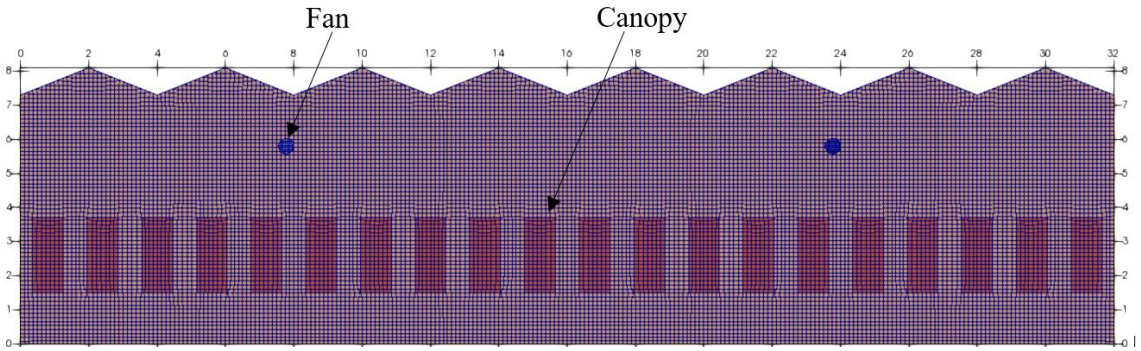


Figure 4. Front view of simulation domain showing boundary mesh, crop canopy and fans.

4. RESULTS

A comparison of measurements and corresponding initial simulation results is shown in Fig. 5 for three different rows. The simulation predicts higher airflow velocities than what was

measured. Further simulation refinement is currently underway to achieve results more aligned with the measurements. Such refinement should include structural components which act as a barrier to flow, and gravity and buoyancy forces, all of which will act to absorb the flow's energy. After further model refinement and improved correlation, error will be quantified and compared to related studies in the literature. Recommendations for further CFD simulation of fan-driven air movement in large-extent greenhouses will be provided.

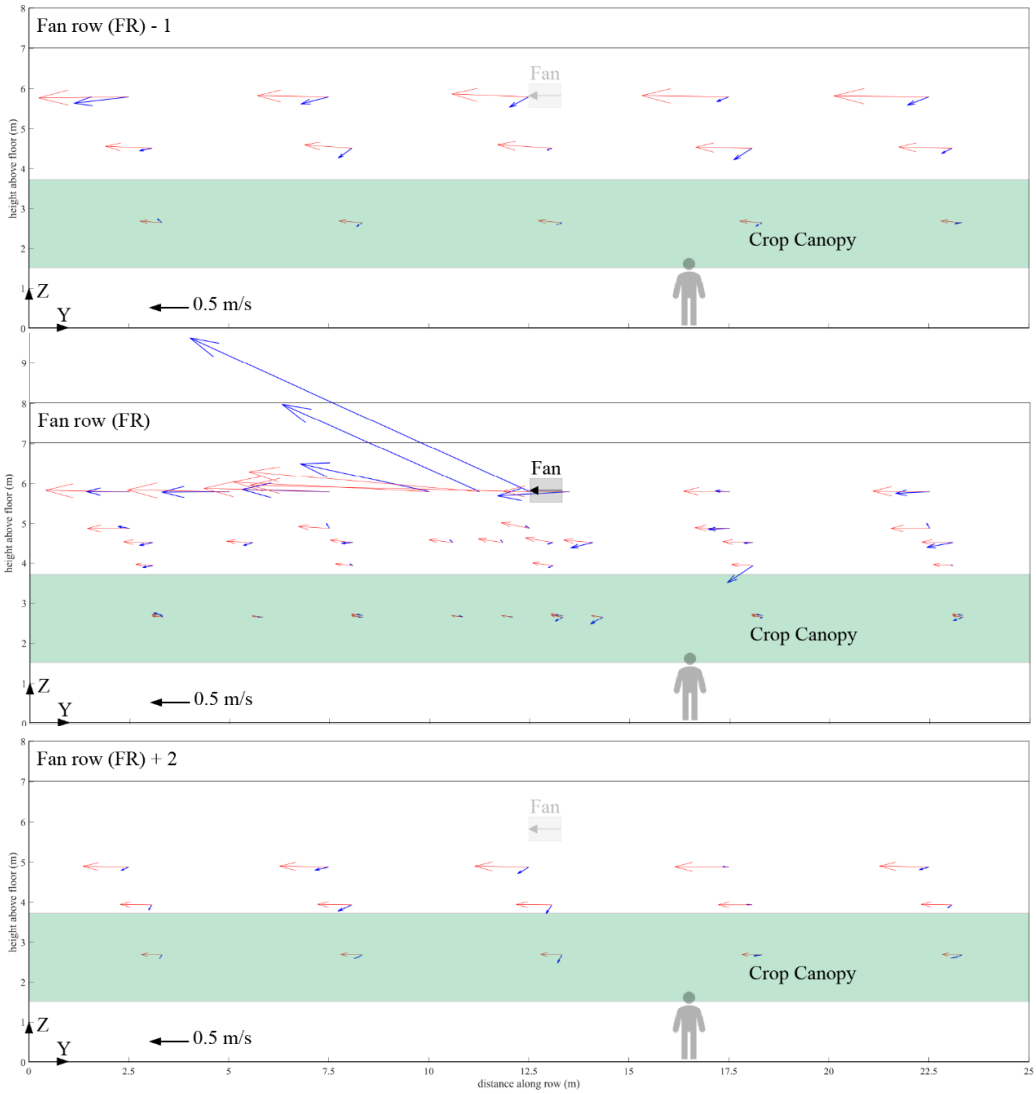


Figure 5. Comparison of air velocity measurement (in blue) and simulation (in red) for three crop rows.

ACKNOWLEDGEMENTS

This research project is funded by the Ontario Ministry of Agriculture, Food and Agribusiness (OMAFA), through the Ontario Agri-Food Innovation Alliance, grant UG-T1-2022-101640.

REFERENCES

Bournet, P-E., and Boulard,T., 2010. Effect of ventilator configuration on the distributed climate of greenhouses: A review of experimental and CFD studies. Computers and Electronics in Agriculture 74, 195–217.

Bassiouny, R., and Korah, N. S., 2011. Studying the features of air flow induced by a room ceiling-fan. Energy and Buildings, vol. 43, no. 8, 1913–1918.

Gao, Y., et al., 2017. Ceiling fan air speeds around desks and office partitions. Building and Environment, vol. 124, 412–440.

Limane, A., et al., 2017. Simulation of airflow with heat and mass transfer in an indoor swimming pool by OpenFOAM. International Journal of Heat and Mass Transfer 104. 862-878.

Simulation of helicopter downwash during take-off and landing in urban environments

Knut Erik Teigen Giljarhus[1,2] and Olli-Kerstan Baricako[1]

[1]*University of Stavanger, Stavanger, Norway, knut.e.giljarhus@uis.no*
[2]*NablaFlow, Stavanger, Norway*

SUMMARY:
During helicopter take-off and landing, the downwash induced by the helicopter rotor can cause high wind speeds in the surrounding environment. The interaction with surrounding buildings can cause further acceleration, potentially presenting a risk for pedestrians. These interactions are challenging to predict, making it difficult to mitigate the risks during the building design phase. Computational fluid dynamics simulations is an attractive alternative to enable identification of risks, and to design efficient mitigation measures. This work presents a methodology to perform such simulations using OpenFOAM. The rotor is represented as a momentum source, and the motion of the helicopter is handled using overset meshing. The simulation results are compared with experiments of a hovering helicopter, and then applied to a realistic urban environment.

Keywords: Helicopter downwash, Overset meshing, Pedestrian wind comfort

1. INTRODUCTION

In 2007, the Norwegian All Weather Search And Rescue Helicopter (NAWSARH) project was initiated in Norway, with the purpose of replacing the existing fleet of rescue helicopters. The selected new helicopter, Augusta Westland AW101, is around 35 % heavier than the previous model, the Westland Sea King Mk.43. This requires higher thrust during take-off and landing, thereby creating higher induced wind speeds by the rotor downwash. During testing, this was found to create in worst-case scenarios. This illustrates the need to sufficiently understand the wind flow in the surrounding environment and be able to design efficient mitigation measures.

While there are some studies ship-helicopter interaction in a marine environment (Crozon et al., 2018; Kääriä et al., 2013; Lu et al., 2020; Sharma et al., 2019), there are few studies in an urban setting. Caprace et al. (2023) used a fully-resolved rotor model to investigate the downwash from a quad-rotor urban air taxi. This is computationally demanding, and detailed information about the rotor configuration and blade design is often not available. Bernardo et al. (2019) studied the effect of downwash in an urban environment using a simplified rotor model. However, they did not include the effect of a moving helicopter.

This work presents a methodology to enable efficient simulation of a moving helicopter to investigate the effect of rotor downwash on the surrounding environment. The rotor is modeled using a virtual blade model (VBM), and the helicopter motion is treated using overset meshing.

2. METHODS

2.1. Simulation methodology

In this study, the VBM method was used to simulate the rotor of the helicopter Wahono, 2013. This method is available in OpenFOAM as the `rotorDiskSource` source object. The VBM approximates the rotor forces by applying momentum sources across a virtual disc representing the rotor's swept area, allowing accurate modeling of the aerodynamic forces generated by the rotor without needing to model individual blades. This approach is computationally efficient while effectively capturing the impact of the rotor on the surrounding airflow. The thrust used as input to the model is based on the design weight of the helicopter.

An overset mesh strategy was used to enable motion of the helicopter. Overset meshing involves mapping between a set of disconnected, overlapping meshes, allowing complex interactions. In this work, the background mesh consists of the buildings and the terrain, while a single overset block is created around the helicopter, rotor and immediate downwash region. An excerpt of the overset mesh block and the background mesh is shown in Fig. 2b.

2.2. Computational setup

Two different configurations are considered. First, a validation test of the rotor model is performed. Simulations of the AW101 helicopter hovering 27 m above the ground are compared to full-scale experimental results Camporeale, 2013. In the experiment, an array of sonic anemometers was placed 1.2 m above ground level, 0.6 m away from the helicopter axis. During the experiment, a 2 m/s cross-wind was measured, hence this is applied to the simulation, using a logarithmic velocity profile. For the helicopter fuselage, a simplified model of the AW101 was created in Autodesk Inventor.

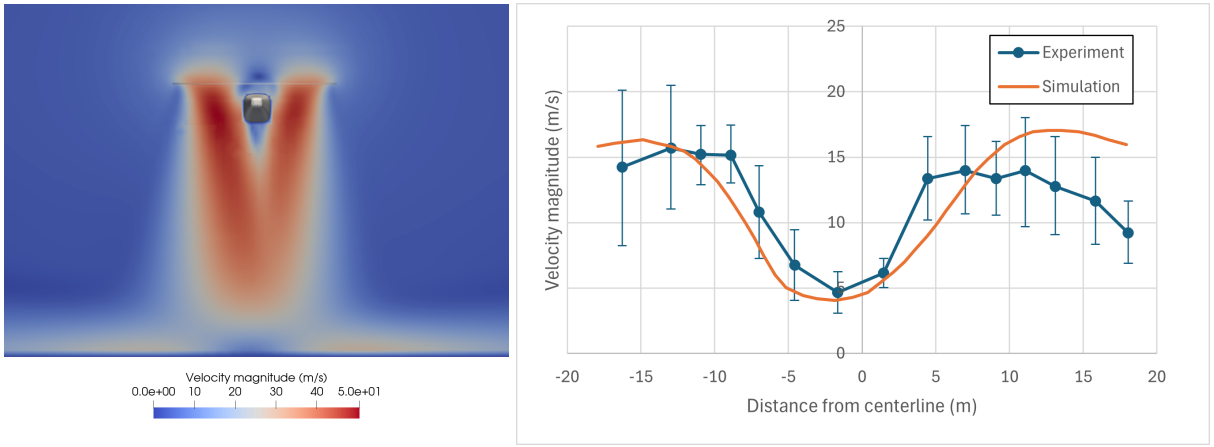
Next, a test of simulating a complete landing in a complex environment was performed. The geometry used for the test was the new hospital building in Stavanger, Norway, where a helicopter landing site is designed for the new helicopter. For the hospital, a simplified geometry model was created from the building information model as well as pictures from the construction site. The terrain was created from elevation data obtained from the Norwegian Mapping Authority. The hospital building, together with the surrounding terrain and the helicopter landing trajectory is shown in Fig. 2a.

3. RESULTS

3.1. Validation of rotor model

Fig. 1a shows contours of velocity magnitude in a slice through the rotor midplane. The rotor downwash, as well as the redirection of the induced wind to a horizontal jet near the ground, can be clearly seen. There is a slight asymmetry in the wake due to the atmospheric crosswind.

Fig. 1b compares the simulation with the experiment. There is good agreement considering the complexities of full-scale measurements. The slight overprediction in the far-field is also conservative in terms of designing mitigation measures.



(a) Velocity magnitude contours

(b) Comparison against experiment

Figure 1. Results from the helicopter hover test, validating the virtual blade model used for the rotor.

3.2. Simulation of helicopter landing

Fig. 2c shows the velocity magnitude as a function of time extracted at the blue point shown in Fig. 2a. There is an initial rise in the velocity as the helicopter approaches the helideck. This is followed by a sharp peak in the velocity just as the helicopter passes the measurement point.

4. CONCLUSIONS

In this work, a methodology to simulate. A successful simulation of a full helicopter landing in a complex environment with terrain and buildings was demonstrated. The method is promising with respect to analyzing whether mitigation measures are needed in the vicinity of the landing site, and in the design of such measures.

Analysis of data from a full-scale measurements during the landing with the real helicopter trajectory and wind measurements is ongoing and will be presented in future work.

ACKNOWLEDGEMENTS

We acknowledge the support of the NAWSARH project in sharing experimental data.

REFERENCES

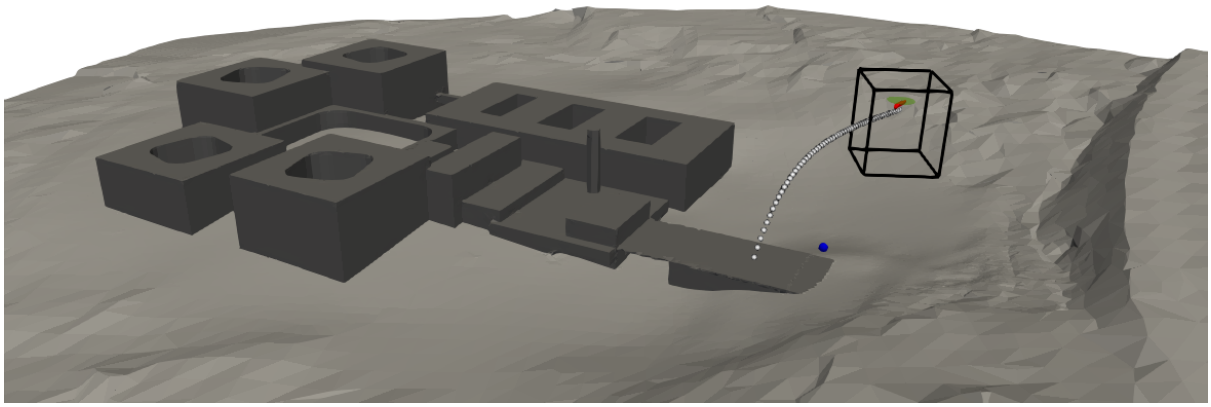
Bernardo, P., Mac Réamoinn, R., Young, P., Brennan, D., Cardiff, P., and Keenahan, J., 2019. Investigation of the helicopter downwash effect on pedestrian comfort using CFD. Infrastructure Asset Management 8, 133–140.

Camporeale, S., 2013. *Downwash Assessment of the NAWSARH Evaluation Agusta Westland AW101*. Tech. rep. Royal Norwegian Ministry of Justice and Public Security.

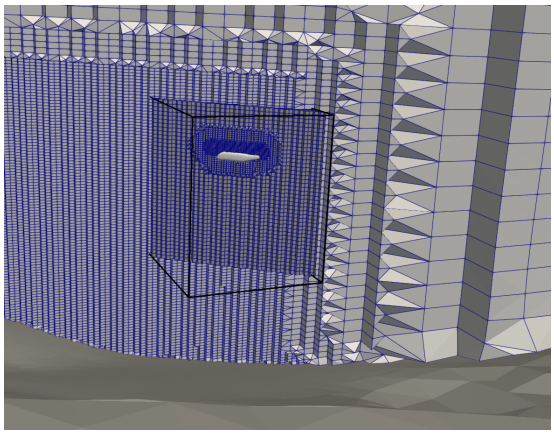
Caprace, D.-G., Diaz, P. V., and Yoon, S., 2023. Simulation of the Rotorwash Induced by a Quadrotor Urban Air Taxi in Ground Effect. Proceedings of Vertical Flight Society's 79th Annual Forum & Technology Display.

Crozon, C., Steijl, R., and Barakos, G., 2018. Coupled flight dynamics and CFD–demonstration for helicopters in shipborne environment. The Aeronautical Journal 122, 42–82.

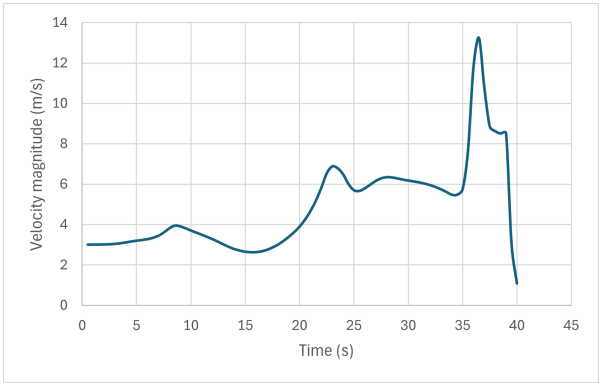
Kääriä, C., Forrest, J., and Owen, I., 2013. The virtual AirDyn: a simulation technique for evaluating the aerodynamic impact of ship superstructures on helicopter operations. The Aeronautical Journal 117, 1233–1248.



(a) Simulation domain with terrain and buildings. The black block indicates the moving overset mesh box. The fuselage is given in red and the domain for the rotor model is shown in transparent green. The white dots illustrate the helicopter trajectory.



(b) Slice of background mesh and overset mesh.



(c) Velocity magnitude over time in a single point (shown in blue above).

Figure 2. Domain, mesh and result for the helicopter landing simulation.

Lu, Y., Chang, X., Chuang, Z., Xing, J., Zhou, Z., and Zhang, X., 2020. Numerical investigation of the unsteady coupling airflow impact of a full-scale warship with a helicopter during shipboard landing. Engineering Applications of Computational Fluid Mechanics 14, 954–979.

Sharma, A., Xu, J., Padthe, A. K., Friedmann, P. P., and Duraisamy, K., 2019. Simulation of maritime helicopter dynamics during approach to landing with time-accurate wind-over-deck. Proceedings of AIAA SciTech 2019 forum, 0861.

Wahono, S., 2013. *Development of Virtual Blade Model for Modelling Helicopter Rotor Downwash in OpenFOAM.* Tech. rep. Aerospace Division, Defence Science and Technology Organisation, Department of Defence, Australian Government.

Non-uniform risk in ASCE 7 wind load reliability analyses: investigation and design recommendations

Brian N. Skourup [1], Tushar K. Guha [2]

[1]*Nextracker, Inc., Fremont, CA USA, bskourup@nextracker.com*
[2]*Nextracker, Inc., Fremont, CA USA, tguha@nextracker.com*

SUMMARY:
The North American ASCE 7 standard promotes uniform risk wind loads to support reliability-based structural safety (ASCE, 2022). Ellingwood's (1981) original study of wind load statistics recommended a composite for reliability analyses but neglected reliability variation between the composite and its constituents. Subsequent updates to the composite statistics (Ellingwood and Tekie, 1999; McAllister, et al. 2018) have not addressed the variation inherent to this approach. Consequently, ASCE 7 reliability targets are only achieved on average over the entire inventory resulting in non-uniform, geographically concentrated risk. For occupied structures, significant gravity loads, stiffness-controlled limit states, and other factors may conceal deficient reliability in the strength-controlled limit states. However, structures without these ameliorating factors remain exposed to significant risk. As shown in this study, site-specific reliability often falls below the composite target. Additionally, we show that a shift to longer return periods to minimize this variation also fails to achieve uniform risk. Corrective approaches that adjust wind load bias cannot offset large statistical variance and are therefore inadequate. Pragmatic risk control is possible using site specific wind load statistics and reliability analyses. This approach eliminates the problematic reliability variation to achieve the ASCE 7 uniform risk objective.

Keywords: Performance-based wind engineering, reliability, codes and standards

1. INTRODUCTION

The North American ASCE 7 standard promotes uniform risk wind loads to support reliability-based structural safety. According to the standard (ASCE, 2022), "A strength-level design wind speed map brings the wind loading approach in line with that used for seismic loads, in that they both are aimed at achieving uniform risk rather than uniform hazard, thus eliminating the use of a load factor for strength design." However, the original study of wind load statistics (Ellingwood, 1981) recommended a composite for reliability analyses, but neglected to calculate either the composite or the constituent reliabilities for comparison. The composite approach necessarily includes variation in design reliability, which remains unaccounted for in the current specified reliability targets. If the variation is small, the uniform risk objective of the ASCE 7 standard may be achieved. However, if the variation is large, structural risk is not only non-uniform but will be geographically concentrated in the locations where constituent wind climates are less conservative than the composite used for reliability analysis. This study aims to quantify this variation, estimate its effect on structural safety, and recommend alternative approaches as required to achieve the ASCE 7 uniform risk objective.

2. BACKGROUND

The composite wind load statistics first derived by Ellingwood (1981) are used to provide target reliability indices and to calibrate partial factors for load combinations including wind load. This calibration process provides assurance that target reliability is achieved in the prescriptive design approach. If the ensuing factors and calculations are correct, the resulting design should have reliability consistent with the target. However, the composite statistics are not used on a site-specific basis; thus, they are also not used in any project-specific capacity. Variance between the composite and site-specific statistics should be expected. Controlling the magnitude of this variation is critical to achieving the uniform risk objective. Over time, the composite statistics have been modified due to changes in accounting for wind directionality. Originally, the wind directionality factor, K_d, was inherent to the statistical model (Ellingwood, 1981). Based on later research (Ellingwood and Tekie, 1999), K_d appeared as a separate factor in the prescriptive wind load calculations resulting in an adjustment to the composite wind load bias. Recent research conducted by McAllister, et al. (2018) once again revised the composite bias to account for new information affecting the directionality factor.

In each of these studies the composite wind load bias was adjusted, however the coefficient of variation remained essentially constant. In the context of wind loads, bias is a measure of accuracy between the predicted wind load and the nominal, or code-specified, wind load. However, the coefficient of variation is a measure of precision between the composite and site-specific wind load statistics. Clearly, uniform risk is associated with precision, or low variation in site-to-site reliability. Therefore, satisfying the ASCE 7 uniform risk objective requires high precision or low variance in the comparative reliabilities. A clear omission from Ellingwood's original study (1981) and the subsequent updates is *any* comparison of site-specific reliability to composite reliability. Quantifying the precision of the composite wind load statistics is therefore required to ensure the ASCE 7 standard objective is met.

3. RELIABILITY STUDY

There is no current measure comparing site-specific reliability to the composite statistics used to define acceptable reliability according to ASCE 7. The motivation for conducting a reliability study is to ensure that the resulting site-specific reliability is acceptable. Or, if it is not, to suggest an improved approach. Following Ellingwood's (1981) approach and using the original data, site-specific location (U) and scale (a) parameters for a Gumbel fit to the wind load effect are computed from $5x10^4$ trials using Monte Carlo simulation. The composite Gumbel parameters are simply the average values across the seven sites considered in the original study. A bias and coefficient of variation are derived from the Gumbel parameters. These values are used in a Monte Carlo reliability simulation to arrive at site-specific reliability indices and failure probabilities. The reliability simulation models a combination including dead load and wind load consistent with McAllister, et al. (2018) and returns a failure probability corresponding to a 50-year reference period from $1x10^6$ trials. Although the assumed inputs to the simulation were meant to be realistic, the results should be understood as notional, or for comparison purposes only. This is consistent with interpretation of reliability targets in the ASCE 7 standard (2022) and the reliability literature (Ellingwood, et al. 1980). We are interested in how the notional reliability for each site compares to that for the composite.

3.1 Reliabilities for 50-yr mean recurrence interval wind speeds

The reliability study results are presented in Table 1 for wind speeds with a 50-yr Mean Recurrence Interval (MRI), consistent with practice at the time the research was performed. The average failure

probability from seven sites is 6.0×10^{-2}, approximately three times greater than that for the composite model. The ensemble coefficient of variation for the failure probability is 130%. Note that four of the seven constituent site reliability indices (β) fall below the composite reliability index of 2.01 although perhaps one or two of those sites remain generally consistent with the composite target. There is significant variation in reliability between constituent locations and the composite wind load model used for general reliability analysis.

Table 1. Wind load statistics and corresponding reliabilities for 50-yr MRI.

Site	U	a	Bias	CoV	β	p_{fail}
Baltimore	0.81	4.27	0.95	0.32	1.85	0.0322
Detroit	0.59	5.55	0.69	0.33	2.70	0.0035
St. Louis	0.78	3.78	0.93	0.36	1.78	0.0375
Austin	0.46	7.46	0.54	0.32	3.45	0.0003
Tucson	0.96	3.02	1.15	0.37	1.18	0.1190
Rochester	0.77	4.95	0.89	0.29	2.16	0.0154
Sacramento	1.07	2.45	1.31	0.40	0.80	0.2119
Composite	0.78	4.50	0.91	0.31	2.01	0.0222

3.2 Reliabilities for 700-yr mean recurrence interval wind speeds

A natural question arises regarding the effects of a transition to ultimate wind speeds and unity load factors in modern versions of the ASCE 7 standard. The previously described procedure was repeated for wind loads with a 700-year MRI, consistent with the default, or most common, class of structures controlled by the current ASCE 7 standard. The results are presented in Table 2.

Table 2. Wind load statistics and corresponding reliabilities for 700-yr MRI.

Site	U	a	Bias	CoV	β	p_{fail}
Baltimore	0.66	5.79	0.76	0.29	3.22	0.0006
Detroit	0.63	5.74	0.73	0.31	3.21	0.0007
St. Louis	0.67	4.89	0.79	0.33	2.88	0.0020
Austin	0.51	7.52	0.59	0.29	4.01	0.0000
Tucson	0.93	3.73	1.08	0.32	2.03	0.0212
Rochester	0.58	6.99	0.66	0.28	3.73	0.0001
Sacramento	1.15	2.66	1.37	0.35	1.27	0.1020
Composite	0.73	5.33	0.84	0.29	2.91	0.0018

The average failure probability from seven sites is 1.8×10^{-2}, ten times greater than the composite result. The ensemble coefficient of variation for the failure probability is 210%. Note that three of the seven constituent site reliability indices (β) fall below the composite reliability index of 2.91 although perhaps one of those sites remains generally consistent with the composite target. The transition to ultimate wind speeds apparently reduces structural risk but does not improve the reliability variation inherent to this approach. Uniform risk is not achieved for *any* MRI.

3.3 Non-uniform risk in the ASCE 7 wind load reliability analysis

Target reliability for wind-controlled members in ASCE 7 is only provided “on-average” across the entire inventory because the composite wind load statistics used for the reliability analysis result in low precision when compared to site-specific wind load statistics. This lack of precision results in non-uniform risk that is concentrated geographically in areas where the local wind climate statistics diverge from the composite statistics supporting the ASCE 7 target reliability.

4. CONSEQUENCES

Empirically, interacting with the built environment is the lowest risk activity in which we regularly engage (Melchers and Beck, 2018). On the capacity side, many structures are controlled by combinations of load effects rather than a single, dominant effect. Additionally, for occupied structures, stiffness-controlled limit states ensuring occupancy comfort are often more robust than strength-controlled limit states. This is especially true for structural steel, which features lower self-weights and greater flexibility than reinforced concrete or masonry systems.

On the demand side, design events are associated with return periods that are many multiples of the structural service life. Accordingly, most structures will never be subject to events corresponding to the hazards for which they are designed. When structures are exposed to these events, combined load effects provide some additional margin against failures. Finally, additional design conservatism due to stakeholder decisions will reduce the real risk associated with reliability variation inherent to the current prescriptive provisions. However, structures without these ameliorating factors remain exposed to significant risk.

5. CONCLUSIONS AND RECOMMENDATIONS

The wind load reliability analysis supporting ASCE 7 is demonstrably imprecise, resulting in non-uniform risk across the inventory and failure to achieve the ASCE 7 uniform risk objective. Additionally, it should be clear that attempts to address the resulting non-uniform risk through bias adjustments have been, and will continue to be, ineffective as this approach does not address the large coefficient of variation in reliability inherent to the method and therefore does not reconcile imprecise reliability.

However, uniform risk can be achieved by an approach that does address the large coefficient of variation in reliability. Very simply, the coefficient of variation inherent to a composite reliability model vanishes when site-specific wind load statistics are used for the structural design. This approach is particularly effective for structures primarily composed of strength-controlled members that are sensitive to wind loading. Project-specific reliability analyses, like a Monte Carlo reliability simulation, can demonstrate design correspondence to any target reliability, including those specified by the ASCE 7 standard. Thus, uniform risk may be achieved for every location, satisfying the ASCE 7 objective.

REFERENCES

ASCE (American Society of Civil Engineers)., 2022. Minimum Design Loads and Associated Criteria for Buildings and Other Structures, Standard ASCE/SEI 7-22. ASCE, Reston, VA.

Ellingwood, B., Galambos, T. V., MacGregor, J. G., and Cornell, C. A., 1980. Development of a probability-based load criterion for American National Standard A58. NBS Special Publication 577, National Bureau of Standards, Gaithersburg, MD.

Ellingwood, B., 1981. Wind and Snow Load Statistics for Probabilistic Design. Journal of the Structural Division, Proceedings of the American Society of Civil Engineers, ASCE 107(7), 1345-1350.

Ellingwood, B. R., Tekie, P. B., 1999. Wind Load Statistics for Probability-Based Structural Design. Journal of Structural Engineering, ASCE 125(4), 453–463.

McAllister, T. P., Wang, N., and Ellingwood, B. R., 2018. Risk-Informed Mean Recurrence Intervals for Updated Wind Maps in ASCE 7-16. Journal of Structural Engineering, ASCE 144(5), 06018001.

Melchers, R. E., and Beck, A. T., 2018. Structural reliability-analysis and prediction, 3rd Ed., Wiley, New York, NY.

Code Provisions and Wind Tunnel Tests on Ground-Mounted Solar Structures

Francesco Dorigatti [1], Matthew T.L. Browne [2], Zachary J. Taylor [3]

[1]*Rowan, Williams, Davies & Irwin (RWDI), Milan, Italy, francesco.dorigatti@rwdi.com*
[2]*Rowan, Willaims, Davies & Irwin (RWDI), Guelph, Canada, matthew.browne@rwdi.com*
[3]*Rowan, Willaims, Davies & Irwin (RWDI), Guelph, Canada, zachary.taylor@rwdi.com*

SUMMARY
The deployment of solar photovoltaics (PV) around the world continues to increase as it is an attractive source of renewable energy. The sheer size of the arrays of solar panels has led to them being properly referred to as utility scale plants. These large utility scale arrays represent significant financial investment implying the importance to stakeholders as well as to the general public that rely on the energy produced. Therefore, reliability of these structures is of obvious importance. The forces of the natural environment must be resisted by these structures with one of the most significant natural forces being the potential for high wind loads. The standard of practice in the industry continues to evolve and provisions are being incorporated into various codes and standards for the proper wind design of these solar PV structures. The current study compares wind tunnel data and provisions in ASCE 7 with the available provisions in the Eurocode. This comparison aims to highlight the benefit of leveraging code provisions derived specifically for solar PV structures and helps identifying instances where particular attention from the designers is warranted.

Keywords: wind tunnel testing, ASCE 7, Eurocode EN 1991-1-4

1. INTRODUCTION

Both fixed-tilt systems and single-axis ground-mounted solar trackers are increasingly being deployed at utility scales for power production. These sites range in power production capacity from 1 MW to greater than 2 GW. There is a significant amount of financial investment in the power production of these arrays, which carries with it a strong desire for reliability. Therefore, the attention to the accurate determination of the wind loading on these solar PV structures continues to increase with their deployment around the world.

Building codes and standards were not developed to predict wind responses of small flexible structures near the ground, with the historical focus being on large low-rise and high-rise buildings. Therefore, design methodologies have had to be developed for solar PV structures (Browne et al., 2020). The methodology and dataset proposed by Browne et al. (2020) was adopted by the ASCE 7 standard in the 2022 edition (ASCE/SEI, 2022). There are also provisions for wind loading on ground-mounted solar PV structures in the Australian/New Zealand Standard (AS/NZS, 2021), which was informed by the work of Ginger et al. (2019). Both the American and Australian/New Zealand standards have recognized the need for specific design guidance for the wind loads on these solar PV structures. However, neither the National Building Code of Canada nor the Eurocode have adopted similar provisions for ground-mounted solar. The lack of specific provisions requires manufacturers to invest in system-specific wind tunnel research. However,

this approach may not be economically viable for small-sized projects and leaves designers to rely on the coefficients provided for 'monoslope free roofs' and/or 'monopitch canopy roofs'. The focus of the current study will be to compare the design approaches for ground-mounted solar PV structures that rely on wind tunnel data, guidelines from ASCE 7 and provisions from Eurocode EN 1991-1-4.

2. BACKGROUND

When carrying out a wind tunnel test, the peak pressure is estimated from the time series and converted to a peak pressure coefficient normalized to the mean speed at nominal panel height as follows.

$$\widehat{C_{p}}_{WT} = \frac{\hat{p}_{WT}}{\frac{1}{2}\rho\overline{U}^2} = \frac{\hat{p}_{WT}}{\overline{q}_{WT}} \tag{1}$$

These results are then converted to a wind load through establishing the appropriate mean reference pressure, $\overline{q}$. This process is not always straightforward since each regional code or standard has different approaches to codifying extreme wind speeds, effects of wind directionality, and overall reliability. All codes and standards around the world employ the concept of quasi-steady theory to derive the design wind loads. In its simplest form, the quasi-steady theory for wind loading is given by:

$$\hat{p} = \hat{q}\overline{C}_p \tag{2}$$

which relates the peak pressure to the peak velocity pressure. The peak velocity pressure occurs due to fluctuations in the turbulent flow, which have been shown to be Gaussian in both wind tunnel and full-scale field data. This quasi-steady theory approach is well suited to code applications since the effects of different exposures can be directly accounted for in $\hat{q}$ without providing different aerodynamic coefficients. However, the validity of quasi-steady theory should not be taken for granted and the potential shortfalls in ground-mounted solar PV structures is the focus of the current study. The quasi-steady implementation in Eurocode (EN, 2010) provisions relates the mean pressure coefficients c_p to the peak pressures, $\hat{p}_{EN}$, as follows:

$$\hat{p}_{EN} = \left(1 + 7 \cdot I_v(z)\right) \cdot \frac{1}{2} \cdot \rho \cdot v_m^2(z) \cdot c_p = c_e(z) \cdot q_b \cdot c_p \tag{3}$$

$$\overline{q}_{EN} = \frac{1}{2}\rho\left(\frac{v_m(z)}{1.065}\right)^2 \tag{4}$$

$$\widehat{C_{p}}_{EN} = \left(1 + 7 \cdot \left(\frac{1}{\ln\left(\frac{z}{z_0}\right)}\right)\right) \cdot 1.065^2 \cdot c_p \tag{5}$$

The relationship between a 10-minute mean wind speed v_m and the mean-hourly wind dynamic pressure $\overline{q}_{EN}$ in open terrain (i.e., terrain category II) is applied in Eq. (4) as estimated from Durst (1960) at 10 m elevation. The peak pressure coefficient normalized by the mean-hourly reference dynamic pressure $\widehat{C_{p}}_{EN}$ is then given by Eq. (5). The ASCE 7 provisions (ASCE/SEI, 2022) summarized in Eq. (6) differ from the Eurocode provisions in the use of a 3-second gust wind speed V in contrast to the 10-minute mean speed. Furthermore, the relationship in Eq. (7) is

directly given to convert a 3-second gust speed to a mean-hourly reference wind dynamic pressure $\overline{q}_{ASCE}$. This relationship allows for the peak pressure coefficient normalized by the mean-hourly reference $\widehat{C_p}_{ASCE}$ to be provided in Eq. (8).

$$\hat{p}_{ASCE} = \frac{1}{2}\rho K_z K_{zt} K_e V^2 \cdot GC_p \tag{6}$$

$$\overline{q}_{ASCE} = \frac{1}{2}\rho\left(\overline{b}\left(\frac{z}{10\text{ m}}\right)^{\overline{\alpha}} V\right)^2 \tag{7}$$

$$\widehat{C_p}_{ASCE} = \frac{K_z K_{zt} K_e}{\left(\overline{b}\left(\frac{z}{10\text{ m}}\right)^{\overline{\alpha}}\right)^2} GC_p \tag{8}$$

For open terrain (Exposure C), the following values are substituted in Eq. (9).

$$\widehat{C_p}_{ASCE} = \frac{2.41\left(\frac{z}{750\text{ m}}\right)^{\frac{2}{9.8}}}{\left(0.66\left(\frac{z}{10\text{ m}}\right)^{\frac{1}{6.4}}\right)^2} GC_p = 2.942 \cdot \left(\frac{z}{1\text{ m}}\right)^{-0.108} GC_p \tag{9}$$

Note that in both the Eurocode and ASCE 7 cases the minimum cutoffs on elevation (z) have not been applied at this point. These minimum elevations add an extra point of comparison that will be addressed in the full conference paper.

3. RESULTS

The data presented in this paper are enveloped over many different systems with broadly similar parameters. A similar dataset was used in Browne et al. (2020) which informed the ASCE 7 provisions for Ground-Mounted Fixed-Tilt Solar Panel Systems (GMFTSPS). Typical scales for the wind tunnel tests were approximately 1:30 with a photo of a typical model shown in Figure 1.



Figure 1. Example of a wind tunnel test of a solar PV structure array.

The canopy roof coefficients are typically used in Eurocode designs in the absence of specific provisions. Therefore, the enveloped coefficients from the wind tunnel studies are compared to

overall force coefficients and net pressure coefficients provided in the Eurocode for canopy roofs with no blockage underneath, as a function of averaging area in Figure 2. ASCE 7 monoslope free roof coefficients for Main Wind Force Resisting System (MWFRS) and for Components and Cladding (C&C) are also included for comparison.

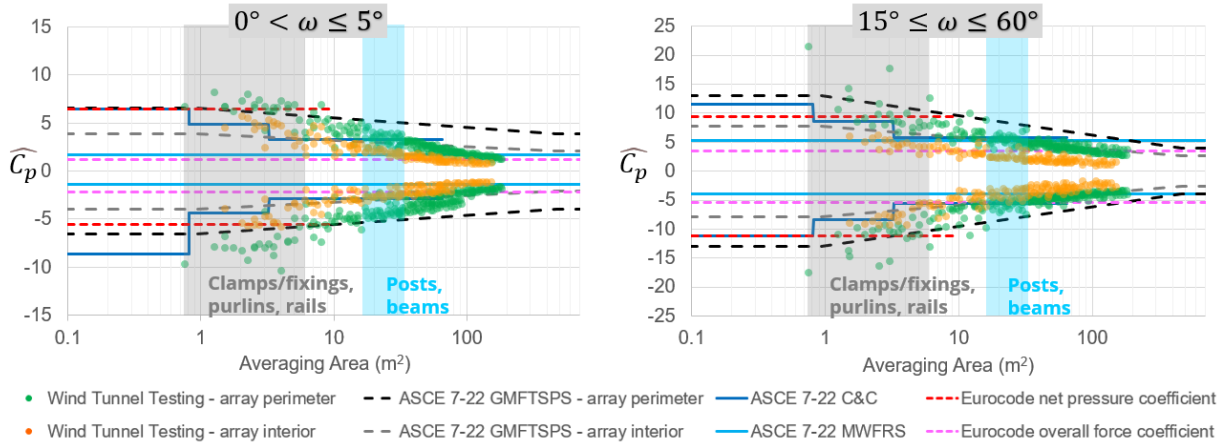


Figure 2. Normal peak pressure coefficients $\widehat{C_p}$ for uplift (negative) and downforce (positive), normalized by the mean hourly reference wind dynamic pressure (with no minimum cutoffs on elevation applied). Comparison of wind tunnel, Eurocode and ASCE 7-22 code provisions as a function of area for a nominal tracker (highlights indicate area ranges for design of typical structural elements/components). ω: tilt angle from horizontal (Left: 0°<ω≤5°; Right: WT and ASCE 7-22 GMFTSPS: 15°<ω≤60°; ASCE 7-22 MWFRS and C&C: 15°<ω≤45°; Eurocode: 15°<ω≤30)

4. DISCUSSION AND CONCLUSIONS

The wind engineering codes and standards were developed long before the advent of utility scale solar PV arrays. At present, some of these codes and standards are being updated to deal with important wind engineering aspects of these structures. The data provided in this abstract have demonstrated that the monoslope free roof / canopy roof coefficients reasonably envelope the data for larger averaging areas. However, greater differences are observed for smaller averaging areas especially in the perimeter of the array. The peak factors observed for these smaller averaging areas indicate the behaviour is not quasi-steady. The full conference paper will provide further discussion on these differences, the effect of considering a minimum cutoff on elevation, comparisons of the moment coefficients, and on inertial forces.

REFERENCES

ASCE/SEI, 2022. Minimum Design Loads and Associated Criteria for Buildings and Other Structures. ASCE/SEI 7-22.

AS/NZS, 2021. Australian/New Zealand Standard – Structural design actions – Part 2: Wind actions, AS/NZS 1170.2:2021.

Browne, M. T., Taylor, Z. J., Li, S. and Gamble, S., 2020. A wind load design method for ground-mounted multi-row solar arrays based on a compilation of wind tunnel experiments, J. Wind Eng. and Ind. Aerodyn. 205, 104294.

Durst, C. S., 1960. Wind Speeds over Short Periods of Time, Meteorological Magazine 89, 181-186.

EN, 2010. Eurocode 1: Actions on structures – Part 1-4: General actions – Wind actions, EN 1991-1-4:2005+A1:2010.

Ginger, J. D., Bodhinayake, G. G. and Ingham, S., 2019. Wind loads for designing ground-mounted solar-panel arrays, Aus. J. Struct. Eng. 20, 204-218.

Reliability-based Load-resistance Factors for the Correlated Wind-wave Loads-governed Limit States in Floating Structures

Jeong-Gon Kim [1], Hae Sung Lee [2], Ho-Kyung Kim [3]

[1]*Seoul National University, Seoul, South Korea, rhsl13@snu.ac.kr*
[2]*Seoul National University, Seoul, South Korea, chslee@snu.ac.kr*
[3]*Seoul National University, Seoul, South Korea, hokyungk@snu.ac.kr*

SUMMARY
This study presents load-resistance factors for the ultimate limit state governed by wind-wave loads in floating structures. Reliability and inverse reliability analyses, as well as optimization, were conducted, considering the marine environmental conditions in which floating structures are deployed. Since buoyancy in floating structures is dependently influenced by imposed loads, it cannot be considered using linear load combinations. Instead of treating buoyancy as a separate load, the variability of buoyancy was incorporated into the gravitational load effects. Additionally, as waves are generated and propagated by wind, the wind and wave loads acting on the structure exhibit high correlation. The correlation of wind-wave load effects was derived from the correlation between wind speed and wave height, and a reliability analysis methodology that considers this correlation was formalized. To standardize the limit state function, the concept of load (effect) ratio was applied to define the wind-wave load-dominant limit state. The load breakpoints distinguishing the dominant regions of each load were determined to minimize the objective function for three structural members (RC, ST, PC). As a result, load factors for each dominant region were provided according to the correlation coefficient of the load effects.

Keywords: Buoyancy, Wind-wave correlation, Optimization

1. INTRODUCTION

Studies on floating structures, widely applied in marine structures, are actively being pursued internationally. Although various structural types for floating structures are under development, reliability-based design standards encompassing these structures have yet to reach a satisfactory level. Such design standards should ensure uniform safety across all structural members and clearly represent this safety probabilistically. However, current reliability-based design standards lack a clear logical basis for establishing target reliability indices. Although each limit state should reflect the statistical characteristics of variable loads and resistance strength, the same resistance factor is applied across all limit states. This issue also leads to calculated nominal resistance strengths that do not satisfy the prescribed target reliability indices. DNV-CS 30.6 (Structural reliability analysis of marine structures) mentions a limitation in that target reliability indices cannot generally be specified and must be set case by case (DNV, 1992). However, Lee (2019) proposed a generalized method for determining load-resistance factors that standardizes the limit state based on total nominal load effects and expresses each load effect as a load (effect) ratio, independent of structural type. This study aims to define a wind-wave load-governed limit state

by optimizing load-resistance factors while considering the key characteristics for floating structures: buoyancy and the wind-wave correlation.

2. STATISTICAL CHARACTERISTICS OF LOAD EFFECTS

2.1. Gravitational load effects considering buoyancy

For civil structures constructed directly on the ground, buoyancy is determined by the water depth and acts independently of other loads. Therefore, in the limit state design, buoyancy load effects can be considered through linear combinations with other loads. In contrast, for floating structures, buoyancy achieves equilibrium by adjusting draft according to the magnitude of applied loads. Since buoyancy does not act independently of other gravitational loads, it cannot be considered through a linear load combination. Ultimately, the load effect is defined as shown in Eq. (1), with the load induced by buoyancy—expected to exhibit significant variability—considered as the main load.

$$\bar{Q}_{i+Bi} \leq CB_i\bar{q}_{Bi} = CB_i\bar{q}_B\bar{q}_i \tag{1}$$

In this equation, $\bar{Q}_{i+Bi}$ represents the standardized load effect, C is an influence coefficient indicating the uncertainty of the analysis, B_i is a modeling coefficient representing the uncertainty in load modelling, and $\bar{q}_{Bi}$ is the buoyancy variable. Here, $\bar{q}_i$ denotes the original load variable, and $\bar{q}_B$ refers to the load variable related to hydrostatic pressure. When Monte Carlo Simulation (MCS) is performed using the statistical characteristics of each variable (Lee, 2019; Assakkaf, 2000), the coefficient of variation for each load effect increases compared to cases where buoyancy is not considered.

2.2. Wind-wave load effects

In previous studies (Lee, 2019), the statistical characteristics of wind pressure were assumed to be identical to those of the wind load effect. In this study, the statistical characteristics of the wind load effect were derived through MCS, additionally considering uncertainties of the analysis.

Wave pressure was modeled using the representative wave load equation provided in design standards (BSI, 2003), and the relationship between maximum wave height and significant wave height was applied to the MCS by modeling Goda's (2010) probabilistic model with a Gumbel distribution. The statistical characteristics of the wind and wave load effects, based on design life and return period, are represented in Eqs. (2)-(3). Here, R represents the return period, t_d is the design life, and $\delta_{V_{10}}$ and δ_{H_s} are the coefficients of variation for the maximum 10-minute average wind speed and significant wave height, respectively, corresponding to the design life.

$$\lambda_{WS} = \frac{0.986+0.242\delta_{V_{10}}}{\left(1+\sqrt{6}\delta_{V_{10}}(\ln R/t_d-\kappa)/\pi\right)^2},\ \delta_{WS} = 0.091 + 1.845\delta_{V_{10}} \tag{2}$$

$$\lambda_{WP} = \frac{1}{1+\sqrt{6}\delta_{H_S}(\ln R/t_d-\kappa)/\pi},\ \delta_{WP} = 0.084 + 0.752\delta_{H_s} \tag{3}$$

3. OPTIMIZATION OF LOAD-RESISTANCE FACOTRS

3.1. Reliability analysis considering correlation between wind and wave

This study performs reliability analysis in the standard normal variable space using equivalent normal variables obtained through the Rackwitz-Fiessler transformation. When correlations exist between variables, it is necessary not only to standardize the variables but also to transform the correlation coefficient matrix into a form suitable through eigenvalue analysis or Cholesky decomposition. This process allows for the conversion of the limit state function into uncorrelated variables, thereby enabling the identification of the failure point of the original variables through reliability analysis. In this study, the transformed negative unit normal vector, which converts the original variables into their equivalent standardized forms, was applied to the failure point function and equivalent standard deviation function defined by Lee (2019) to perform reliability analysis that considers correlations.

3.2. Optimization

In order to obtain the load-resistance factors for each limit state, optimization is performed to minimize the error between the nominal resistance strength ($\bar{\mathbf{S}}_0$) and the target resistance strength ($\bar{\mathbf{S}}_T$) according to the load (effect) ratio as shown in Eq. (4).

$$\underset{\boldsymbol{\phi},\boldsymbol{\gamma}}{\text{Min}}\ \Pi = \frac{1}{2}\iiint \|\bar{\mathbf{S}}_0 - \bar{\mathbf{S}}_T\|^2\, d\xi d\eta d\chi \tag{4}$$

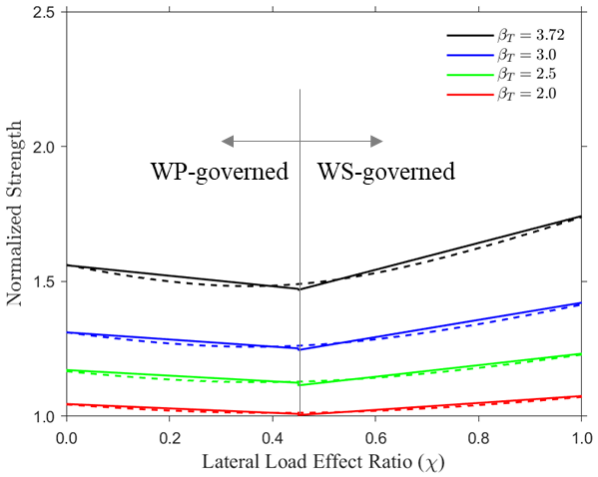


Figure 1. Load-governed regions based on the breakpoint

Table 1. Proposed load-resistance factors for each target reliability index.

β_T	Governing Load	ϕ_{RC}	ϕ_{ST}	ϕ_{PC}	γ_{DC}	γ_{DW}	γ_{WS}	γ_{WP}
2.0	WP	0.9	0.90	0.82	0.90	0.90	0.70+0.3ρ	1.00
	WS	0.9	0.90	0.82	0.90	0.90	1.00	0.70+0.3ρ
2.5	WP	0.9	0.91	0.83	0.95	0.90	0.70+0.5ρ	1.10
	WS	0.9	0.90	0.83	0.95	0.90	1.20	0.70+0.4ρ
3.0	WP	0.9	0.92	0.84	1.00	0.95	0.75+0.7ρ	1.25
	WS	0.9	0.91	0.83	0.95	0.90	1.45	0.75+0.5ρ
3.72	WP	0.9	0.93	0.85	1.05	0.95	0.80+1.0ρ	1.55
	WS	0.9	0.92	0.85	1.00	0.95	1.80	0.75+0.8ρ

As shown in Figure 1, the breakpoint was introduced to minimize the error in approximating the curve with a straight line. Objective function values for various breakpoints were calculated for three structural members (RC, ST, PC) and for each correlation coefficient of the wind-wave load effect, with 0.45—most frequently selected as the point minimizing the objective function—defined as the optimal load breakpoint (Lee et al., 2019). Optimization results indicated that, with changes in the correlation coefficient, the load factor for the non-dominant load varied linearly, while other load-resistance factors remained constant. The load-resistance factors for each target reliability index obtained by considering these findings are shown in Table 1.

4. CONCLUSION

Reliability-based design standards require a load-resistance factor system that satisfies the target reliability index. Additionally, generalization is necessary to ensure applicability across various structural types, and to achieve uniform safety across materials, the standards must consider the relative statistical characteristics of member resistance within the same limit state. To satisfy these criteria, this study conducted optimization by applying load (effect) ratios. Each load-resistance factor satisfies the target reliability index within 5% error, as shown in Figure 2.

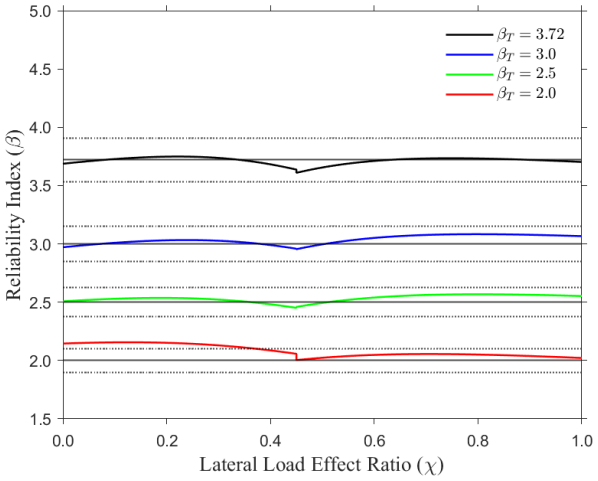


Figure 2. Reliability indices secured by proposed factors (RC member)

ACKNOWLEDGEMENTS

This work is supported by the Korea Agency for Infrastructure Technology Advancement (KAIA) grant funded by the Ministry of Land, Infrastructure and Transport (Grant RS-2023-00250727) through the Korea Floating Infrastructure Research Center at Seoul National University.

REFERENCES

Assakkaf, I. A., Ayyub, B. M., & Mattei, N. J. (2000). Reliability-based load and resistance factor design (LRFD) of hull structural components of surface ships. *Naval Engineers Journal, 114*.

BSI. (2003). Maritime structures - Part1: Code of practice for general criteria (BS 6349-1:2000). The British Standards Institution

DNV. (1992). Structural reliability analysis of marine structures (DNV-CS 30.6). Det Norske Veritas.

Goda, Y. (2010). *Random seas and design of maritime structures*. World scientific.

Lee, H. S. (2019). *Reliability-based Load-resistance Factors*. Kimoondang.

Lee, H. S., Song, S. W., & Kim, J. H. (2019). Determination of optimal load-resistance factors for gravitational loads-governed limit state of korean bridge design code. *KSCE Journal of Civil Engineering, 23*, 3451-3463.

Wind Tunnel Measurement of Aerodynamic Characteristics of Trains Passing each other on a Simply Supported Bridge

Haonan He [1], Xiaozhen Li [2], Ming Wang [3]

[1]*Southwest Jiaotong University, Chengdu, China, hhn@my.swjtu.edu.cn*
[2]*Southwest Jiaotong University, Chengdu, China, xzhli@swjtu.edu.cn*
[3]*Southwest Jiaotong University, Chengdu, China, ming.wang@swjtu.edu.cn*

SUMMARY:
To investigate the aerodynamic performance of high-speed trains during their passing each other on the bridge structure under crosswinds, a simply supported box girder bridge with span of 32m was selected. The bridge and train models modelled at a geometric scale ratio of 1:30 were used to test the aerodynamic force of train with the help of a detailed designed moving test rig in the XNJD-3 wind tunnel. The effects of wind speed, train speed and yaw angle on the aerodynamic coefficients of train were analysed. Comparison between the static and moving model tests were investigated to show the influence of movement of train model on its aerodynamic characteristics. The results show that the sheltering effect introduced by trains' passing each other can cause a sudden changed force on the leeward train, which will be furtherly influenced by the wind speed and running speed. The detailed analyses related to the effect of wind speed and train speed on the aerodynamic coefficients were conducted. The relationship between the change of aerodynamic coefficients and yaw angle was finally confirmed by proposing a series of certain fitting formulas.

Keywords: aerodynamic coefficient, two trains passing each other, wind tunnel test

1. GENERAL INSTRUCTIONS

With the rapid development of high-speed railway construction in China, a widely distributed bridge structures are adopted due to its ability to cross the river and uneven terrain. Most of the bridges are higher from the ground, the inevitable strong wind will weaken the probability of train running on the bridge. Interaction effect between the crosswind, train and bridge systems constitutes a current research topic, et al., the wind-vehicle-bridge coupled system. The effect of crosswind is usually treated as the additional side force acting on the train-bridge system (Diana, 1989). When two trains pass each other, an adverse effect will be introduced due to the shielding effect between two trains under crosswinds (Wang, 2016), which will affect the operation stability and riding comfort of the train system.

The wind tunnel test is widely used to measure the aerodynamic characteristics of train under complex wind environment. A wind tunnel moving test system is developed to study the aerodynamic characteristics of two trains crossing each other. The influences of train speed, wind speed and yaw angle on the aerodynamic coefficient of the train are discussed. In addition, the comparison between the static and dynamic train model testes are carried out.

2. WIND TUNNEL TEST

2.1. Description of the wind tunnel moving test system

The wind tunnel test was carried out in XNJD-3 measured at Southwest Jiaotong University in China. As seen in Fig. 1, the moving train wind tunnel test system was composed by bridge model, train model, and the driving system.

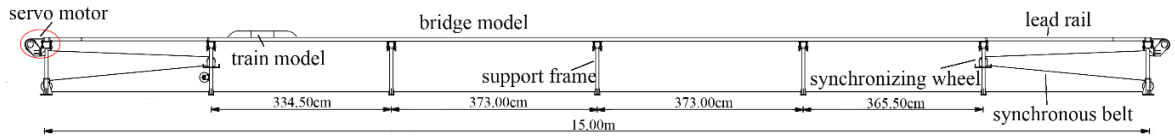


Figure 1. General schematic diagram of test system.

2.2. Train and bridge models

The test model is manufactured by 1:30 geometric scale to achieve the model simulation and test accuracy as much as possible. As seen in Fig. 2, the train is simplified as a three-section train model composed of the head car, the middle car and the rear car. The bridge model is set according to the 32m precast ballastless track post tensioned prestressed concrete simply supported box girder for 350 km/h high-speed railway, shown in Fig. 3.

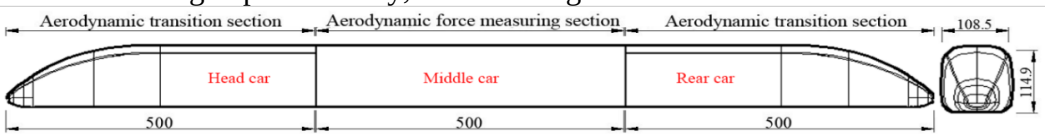


Figure 2. Fig. 2. Train model (mm).

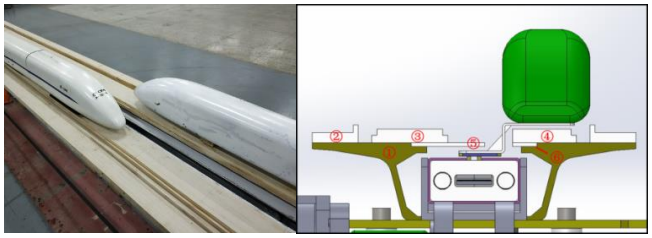


Figure 3. Bridge model.

2.3. Test cases

The wind direction angle of natural wind is set for the wind tunnel test. In order to reduce the error of dynamic test, the test is repeated for three times for each working condition, taking the average value as the final test value. The test conditions of moving trains under cross wind are shown in Table 1.

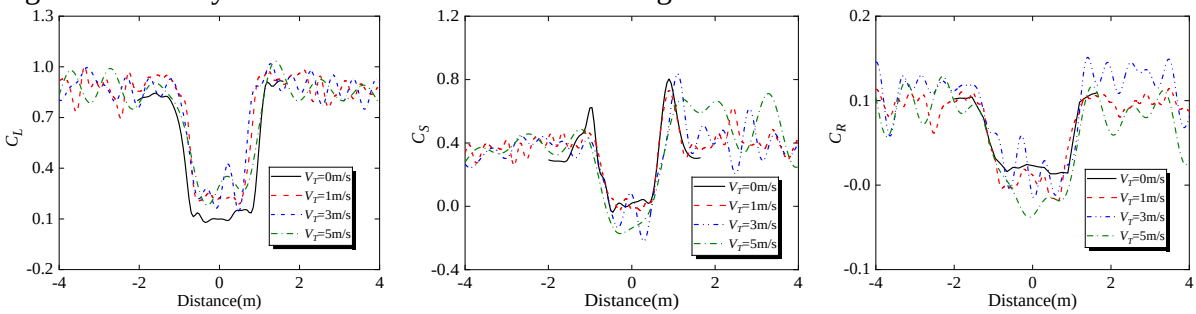
Table 1. Test cases.

Train speed / $(m \cdot s^{-1})$	Wind speed / $(m \cdot s^{-1})$	α / (°)	Track position of moving train
1 ~ 7	5 ~ 10	90	Leeward side

3. RESULTS AND DISCUSSION

3.1. Comparison between static and moving model tests

In order to compare and analyse the difference of aerodynamic coefficients of train in the moving state and the static state when the test train passes through the intersection region, the wind speed of 8 m/s, and the train speed of 1,3,5m/s are chosen to be dynamic test cases. The time history diagrams of aerodynamic coefficients are shown in Fig.4.

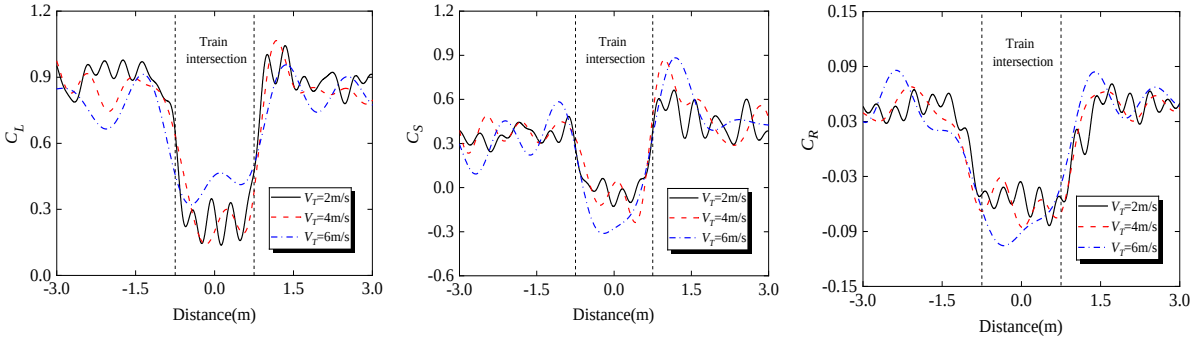


(a) Lift force coefficient (b) Side force coefficient (c) Rolling moment coefficient

Figure 4. The static and dynamic comparison of train aerodynamic coefficients (U =8m/s)

3.2. Effect of train speed on shielding effect

According to the test conditions that the wind speed is 8m/s and the train speed is 2m/s, 4m/s, 6m/s separately to explore the effect of the train on aerodynamic coefficient of moving trains. The aerodynamic coefficient of train on the leeward side at different speed is shown in Fig. 5

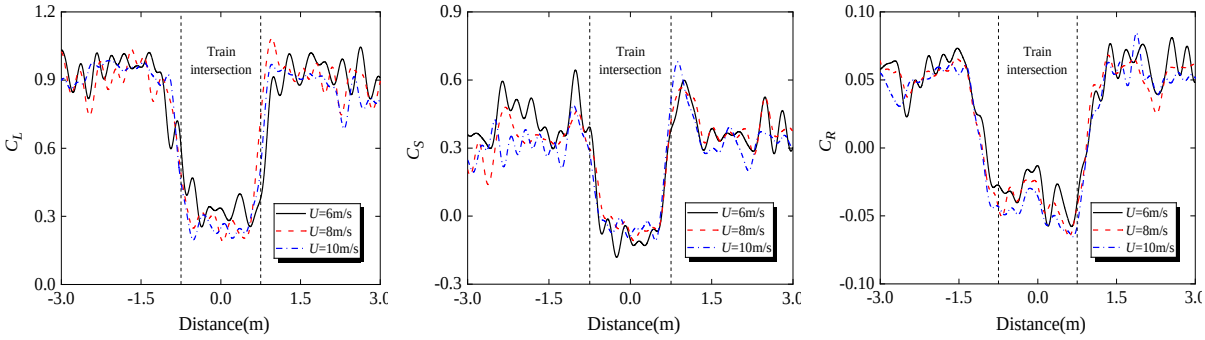


(a) Lift force coefficient (b) Side force coefficient (c) Rolling moment coefficient

Figure 5. Train aerodynamic coefficients on leeward side with different train speeds (U=8m/s)

3.3. Effect of crosswind speed on aerodynamic coefficients

According to the test conditions that the train speed is 1m/s and the wind speed is 6m/s, 8m/s, 10m/s separately to explore the influence of the crosswind on aerodynamic coefficient of moving trains, the aerodynamic coefficient of trains on the leeward side at different wind speed is shown in Fig.6.

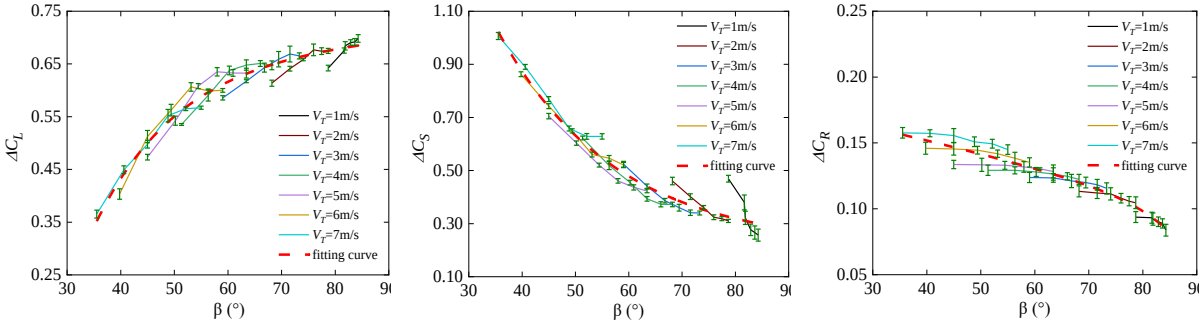


(a) Lift force coefficient (b) Side force coefficient (c) Rolling moment coefficient

Figure 6. Train aerodynamic coefficients on leeward side with different wind speeds (V_T =1m/s)

3.4. Relationship between the sudden force coefficients and yaw angle

From Fig.7, we can see that the three-component aerodynamic coefficients are affected both by the train speed and wind speed. For the convenience of practical engineering applications, we obtained the fitting curve and the certain formula of the three-component aerodynamic coefficient changing with the yaw angle through curve fitting in Table 2.



(a) Lift force coefficient (b) Side force coefficient (c) Rolling moment coefficient

Figure 6. Sudden change of train aerodynamic coefficients with different yaw angle

Table 2. Fitting curve formulas.

Coefficient	Formula
ΔC_L	$y=-2.36461+1.53145(1-e^{-x/16.44945})+1.53145(1-e^{-x/16.44945})$
ΔC_S	$y=4.2802-2.03459(1-e^{-x/22.0424})-2.0342(1-e^{-x/22.02464})$
ΔC_R	$y=0.39768-0.17763e^{(x+39.6007)/245.07037}-5.05354\times10^{-10}e^{(x+39.6007)/7.11375}$

7. CONCLUSIONS

In this paper, we have studied the aerodynamic characteristics of two train passing by each other in the wind tunnel test. The following conclusions can be drawn: (1) Compared with the aerodynamic characteristics of static and dynamic train model, C_S of static state is smaller than that of dynamic state, C_L and C_R of static state is bigger than that of dynamic state.(2) the sudden change area is greatly affected by the train speed, while the wind speed has little effect on the sudden change area; (3) For the convenience of practical engineering applications, we obtained the fitting curve and the certain formula of the three-component aerodynamic coefficient changing with the yaw angle through curve fitting.

ACKNOWLEDGEMENTS

This work was financially supported by the National Natural Science Foundation of China (U1434205, 51708645).

REFERENCES

Diana,G., Cheli, F., 1989. Dynamic interaction of railway systems with large bridges. Vehicle System Dynamics, 18 (1),71-106.

Wang, M., 2018. An experimental analysis of the aerodynamic characteristics of a high-speed train on a bridge under crosswinds. Journal of Wind Engineering and Industrial Aerodynamics. 177, 92-100.

Wind tunnel study of the drag coefficient of Mediterranean urban trees

Vasiliki Pappa[1], Demetri Bouris [1], Stella Tsoka [2], Nikos Markos[3]

[1]*School of Mechanical Engineering, National Technical University of Athens, Greece, vaspappa@mail.ntua.gr, dbouris@fluid.mech.ntua.gr*
[2]*School of Civil Engineering, University of Patras, Greece, stsoka@upatras.gr*
[3]*Hellenic Agricultural Organization Dimitra, Thessaloniki, Greece, nmarkos@elgo.gr*

SUMMARY
This study presents the results of wind tunnel measurements of the aerodynamic drag force of Mediterranean tree species, within the framework of the research project Re.Nature Cities. The study involves measurements on real tree specimens of 4 different species that are commonly encountered in the urban areas of Greek cities. Drag coefficients have been calculated for different wind speed velocities, ranging from 1.4 m/s to 10 m/s, while the optical and aerodynamic porosity of each examined tree have also been measured.

Keywords: natural Mediterranean trees, drag coefficient, wind tunnel study

1. INTRODUCTION

This study has been conducted within the framework of the research project "Re.Nature Cities" that aims to evaluate via experimental and simulation means the ability of street trees as nature-based solution (NBS), to act as an effective measure against the consequences of climate change on the built environment. Despite the undeniable effect of urban greenery on the regulation of the outdoor thermal environment, (Reis et al., 2019), street trees also impact urban ventilation as they act as barriers, disturbing the wind flow and affecting buildings' energy needs, thermal comfort and air quality; the positive effect of wind sheltering during the cold winter period, can be significantly counterbalanced during the warmer periods of the year, with the existing evidence revealing that the green elements' implementation in the built environment without holistically account all the vegetation-air-buildings interactions, can even exacerbate human discomfort and deteriorate indoor natural ventilation (Zheng et al., 2020). It becomes thus obvious that the accurate evaluation of the street trees' effect as a NBS towards the resilience of the built environment would impose a precise determination of the heat and mass exchange between the vegetation elements and the environment, strongly correlated with trees' aerodynamical, geometrical and thermal properties.

2. EXPERIMENTAL SET UP

One of the main objectives of this experimental work was to determine the drag coefficient (C_d) of natural trees/shrubs with different geometric properties (height, H_{tree} and width, W_{tree}) and porosities. The natural trees/shrubs selected for the experimental study are representative Mediterranean deciduous and evergreen species i.e. i) *Clementine,* ii) *Magnolia*, iii) *Oleander* and

iv) *Tilia*. For repeatability and sensitivity analysis purposes, three different samples of each tree/shrub were tested at two different orientations (0^o and 90^o degrees) with respect to the direction of the wind flow. The drag coefficient, C_d , of the tree species, for a given reference velocity, U_{ref} (m/s) is given as:

$$C_d = \frac{2F}{\rho\ U_{ref}^2\ A_{frontal}} \tag{1}$$

where F is the measured drag force (N) in the direction of the wind speed, ρ is the air density (kg/m^3) and $A_{frontal}$ is the projected frontal area of the tree crown (m^2). The three-dimensional forces acting on each tree sample were measured simultaneously using a three-dimensional load cell (Kistler, multi-component force plate, Type 9253B) with a sampling frequency, f_s , of 100 Hz for an acquisition time, t_{ac} , of 120 sec. The mean load force acting in the flow direction (F_x) was used in eq. (1). The effect of the incoming wind speed was tested for ten reference velocities U_{ref} (m/s), in the range from 1.4 m/s to 10 m/s , with a step of 1 m/s. The reference velocity was measured with a Prandtl pitot tube, while the air density, ρ was calculated based on barometric pressure, relative humidity and temperature measurements, recorded simultaneously with the force measurements. Hot wire measurements verified that upstream mean velocity profiles were uniform across the test section and turbulence levels were below 1.5%. The calculation of the projected frontal area $A_{frontal}$ was based on an image processing workflow of the photographs taken before drag force measurements, when the trees/shrubs were at rest. The original image was captured (see Fig. 2a), a white background was added (see Fig. 2b) and thresholding was used to classify tree and non-tree pixels (see Fig. 2c). After thresholding, the surface area for the enclosed frontal area ($A_{frontal}$) within the periphery of the crown was determined, ignoring the empty spaces among leaves in the crown (see Fig. 2d).

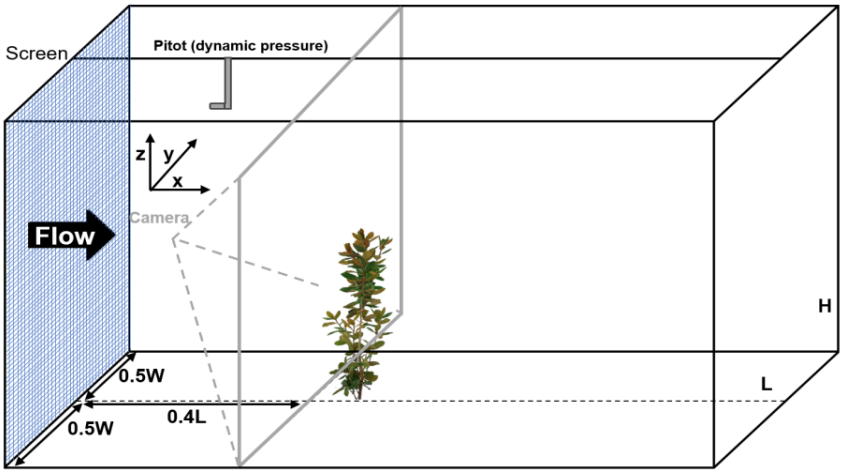
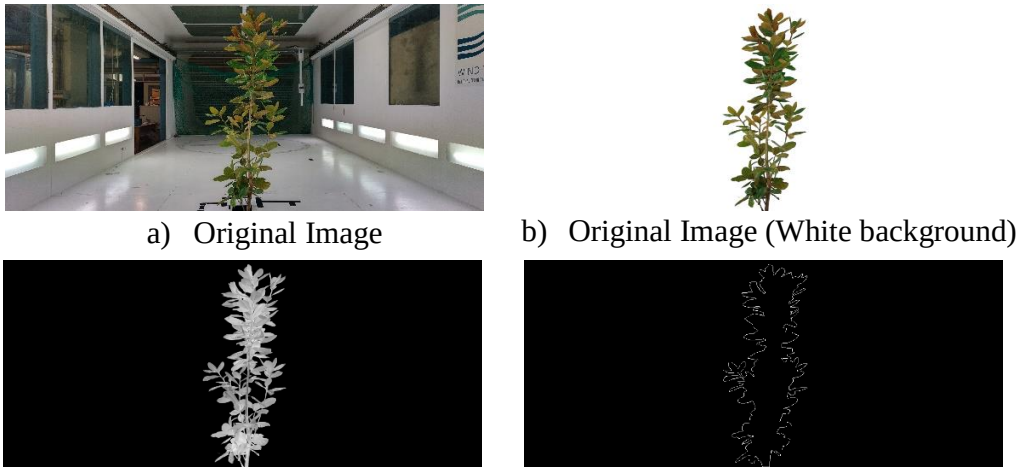


Figure 1. Wind tunnel set-up of the drag force measurements.

In addition, the optical porosity, β , and the aerodynamic porosity, α, were calculated and their values are listed in Table 1. Optical porosity is defined as the ratio between the number of white pixels and the total number of pixels within the silhouette of the tree (Kenney,1987). The empirical relationship relating optical porosity to aerodynamic porosity (Guan et al.,2003) is as follows as:

$$\alpha = \beta^{0.4} \quad (2)$$

Fellini et al.(2022) has calculated the aerodynamic porosity based on velocity measurements upstream and downstream of a single tree and based on the empirical relationship. She concluded that the aerodynamic porosity α based on eq. (2) can be calculated correctly, even if the velocity measurements are not always possible to perform.
All conversions from pixel units to metres were based on the measurement of the H_{tree} dimension.



a) Original Image b) Original Image (White background)

c) Thresholded Image d) Frontal area (below white contour)

Figure 2. An example of the image processing workflow for the natural tree *Magnolia* (Sample 1, 0º orientation): a) original image, b) original image with white background, c) thresholded image and d) frontal area, in white contour.

Table 1. Specifications of the species, samples, and indicative values of the geometric characteristics (H_{tree}, $A_{frontal}$), optical porosities, β, aerodynamic porosities, α.

Species	Sample	Orientation	H_{tree} (m)	$A_{frontal}$ (m^2)	β	α
Clementine	1	0º	1.30	0.77	0.0280	0.2391
Clementine	1	90º	1.29	0.68	0.0413	0.2796
Magnolia	1	0º	1.52	0.43	0.0827	0.3690
Magnolia	1	90º	1.56	0.51	0.1158	0.4221
Oleander	2	0º	1.10	0.40	0.1220	0.4311
Oleander	2	90º	1.07	0.35	0.2129	0.5386
Tilia	2	0º	2.02	0.27	0.0540	0.3112
Tilia	2	90º	2.03	0.29	0.2082	0.5338

3. RESULTS

Figure 3 shows the mean drag coefficient, C_d as a function of the mean wind speed U (m/s) for the four species tested: *Clementine, Magnolia, Oleander and Tilia*. The values of the drag coefficient for a given wind speed, are between 0.55 and 0.95 for the four species. These values are within the range measured for other tree species, according to (Vollsinger et al.,2005; Manickathan et al., 2018). Error bars in the figure include sample and orientation variations but the mean trend for all species is that, at low velocities (< 5 m/s) the C_d values increase with increasing velocity until they reach a maximum value and then decrease sharply as the velocity further increases. This is probably related to the high foliage of the trees and the reconfiguration of the tree, as also observed in (Manickathan et al., 2018). Further analysis of the data sets on the

effects of reconfiguration, including analysis of the Vogel exponent (Vogel, 1989) are ongoing and are expected to provide more information on the effects of foliage during reconfiguration and how reconfiguration dynamically affects the drag coefficient. The results will be presented in the full paper and at the conference.

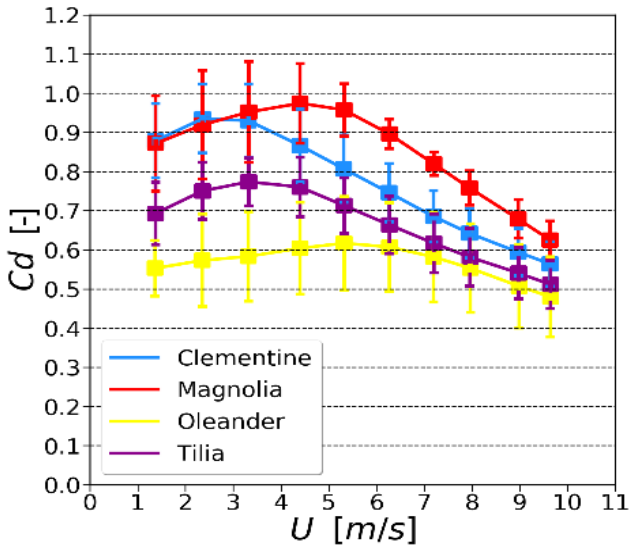


Figure 3. Estimates of the mean drag coefficient, C_d as a function of the mean wind speed, U (m/s) for *Clementine* (blue), *Magnolia* (red), *Oleander* (yellow) and *Tilia* (purple) trees/shrubs. Error bars represent the standard deviation of C_d values attributed to sample and orientation effects.

4. CONCLUSIONS

A wind tunnel test has been performed to determine the drag coefficient of four representative urban Mediterranean species for the same wind speed range. Initial observations showed that with increasing wind speed, the drag coefficient increases at low wind speeds and then decays at high wind speeds. This is expected to be related to the reconfiguration of the tree foliage.

ACKNOWLEDGEMENTS

The authors would like to acknowledge that the Re.Nature Cities research project is implemented in the framework of H.F.R.I call “Basic research Financing (Horizontal support of all Sciences)” under the National Recovery and Resilience Plan “Greece 2.0” funded by the European Union – Next Generation EU (H.F.R.I. Project Number:15566).

REFERENCES

Fellini S., Marro M., Del Ponte A. V., Barulli M., Soulhac L., Ridolfi L., and Salizzoni P. (2022). High resolution wind-tunnel investigation about the effect of street trees on pollutant concentration and street canyon ventilation. Building and Environment 226. issn: 03601323. doi: 10.1016/j.buildenv.2022.109763.

Guan, D., Zhang, Y., Zhu, T., 2003. A wind-tunnel study of windbreak drag. Agricultural and Forest Meteorology 118, 75–84.

Kenney,W.A.,1987. A method for estimating windbreak porosity using digitized photographic silhouettes. Agricultural and Forest Meteorology, 39, 91-94.

Manickathan, L., Defraeye, T., Allegrini, J., Derome, D., Carmeliet, J., 2018. Comparative study of flow field and drag coefficient of model and small natural trees in a wind tunnel. Urban Forestry & Urban Greening 35, 230–239.

Reis, C., & Lopes, A., 2019. Evaluating the cooling potential of urban green spaces to tackle urban climate change in Lisbon. Sustainability, 11(9), 2480.

Vogel, S., 1989. Drag and reconfiguration of broadleaves in high winds. Journal of Experimental Botany, Vol. 40, No. 217, 941-948.

Vollsinger, S., Mitchell, S.J., Byrne, K.E., Novak, M.D., Rudnicki, M., 2005. Wind tunnel measurements of crown streamlining and drag relationships for several hardwood species. Canadian Journal of Forest Research 35, 1238–1249.

Zheng, S., Guldmann, J. M., Liu, Z., Zhao, L., Wang, J., Pan, X., & Zhao, D. 2020. Predicting the influence of subtropical trees on urban wind through wind tunnel tests and numerical simulations. Sustainable Cities and Society, 57, 102116.

Experimental analysis of wind effects on moored container ships in harbour environments

Thomas Arnoult[1], Gertjan Glabeke[1], Luca Donatini[2], Jeroen van Beeck[1]

[1]*Environmental and Applied Fluid Dynamics Department - von Karman Institute for Fluid Dynamics, Sint-Genesius-Rode, Belgium, thomas.arnoult@vki.ac.be*
[2]*Faculty of Engineering and Architecture - Department of Civil Engineering - Ships and Marine Technology Division - Ghent University, Ghent, Belgium*

SUMMARY:
This study examines the influence of wind loads on modern, large container vessels, which have undergone a notable increase in both size and capacity. The von Karman Institute conducted wind tunnel experiments to quantify wind forces on a scaled model of a container ship in various harbour environments. The results underscore the shortcomings of traditional wind load calculations and emphasise the necessity for updated methodologies that account for local environmental effects. The findings offer valuable data for improving numerical models and enhancing the safety of moored vessels.

Keywords: wind loads, container ship, harbour environment, wind tunnel tests

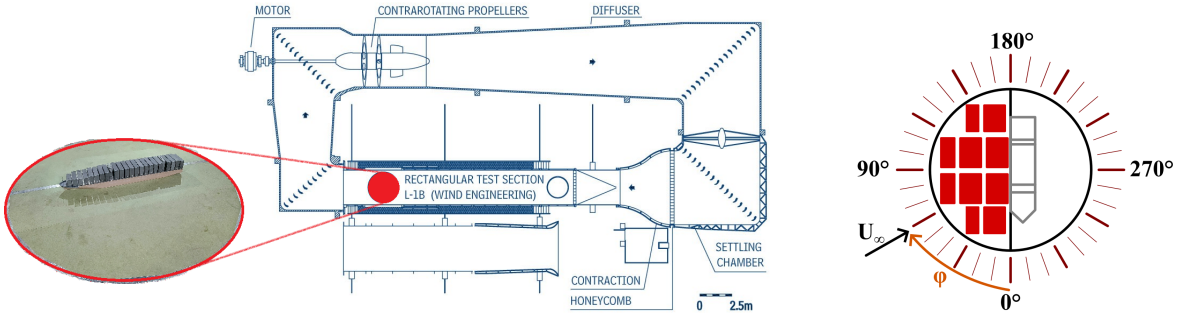
1. INTRODUCTION

In recent decades, container ships have significantly increased in size and capacity, with many now carrying over 20 000 TEUs (Rodrigue, 2024). Most containers are stored above deck, increasing windage and air drafts, making these ships more susceptible to stronger winds at higher altitudes. As a result, modern vessels face greater wind loads, exacerbated by more frequent severe weather events. Mooring infrastructure, both shore-based and onboard, has not kept pace with this growth. Traditional wind load calculations, developed when wind forces were less critical, are oversimplified (Van Zwijnsvoorde et al., 2019). Furthermore, local effects, such as sheltering and channelling, are often neglected but can significantly influence wind-induced forces and mooring loads (Ricci, Janssen, et al., 2020). This has contributed to incidents of moored vessels breaking loose in strong winds (SAFETY4SEA, 2019). A deeper understanding of wind flow and improved prediction tools are crucial for ensuring moored vessel safety (Ricci, Vasaturo, et al., 2023).

To address this issue, the von Karman Institute (VKI) conducted experiments on wind loads acting on a moored ship in a complex environment. Although scale models cannot fully replicate all physical phenomena, they provide controlled conditions and valuable data on wind forces and moments for validating numerical models. Current methodologies rely on outdated designs that do not account for the larger size of modern vessels. Furthermore, previous wind tunnel studies have used open sea Atmospheric Boundary Layer profiles, ignoring environmental disturbances that affect wind loads (Andersen, 2013). This project will investigate how different geographical settings and quay configurations impact wind loads on moored ships.

2. METHODOLOGY

The experimental tests were conducted in the VKI L1-B wind tunnel, with a test section of 3 m width and 2 m height. The model, placed on a 1.8 m diameter turntable (Figure 1a), was scaled 1:250, enabling measurements across various wind directions φ, defined as the angle between the freestream velocity U_∞ and the ship centerline (Figure 1b). This scale effectively replicates full-scale flow characteristics while keeping blockage below 5% (Barlow et al., 1999) and the facility's flow and turbulence profiles correspond to different roughness classes, from marine to suburban (VDI-guidelines, 2019).



(a) (b)

Figure 1. Illustration of the VKI L1-B wind tunnel (red circle: test location) (**a**) and sketch of the turntable including the wind direction φ definition (**b**).

The ship model was based on a representative example of a modern large container vessel characterized by substantial size, though not extreme for its class. The reference vessel has an overall length of 366 m, a breadth of 48 m and a cargo capacity exceeding 14 000 TEUs (Twenty Foot Equivalent Unit). A 3D model was developed to accurately reflect this ship, including the arrangement of all deck containers in 22 rows. This model was constructed using general arrangement plans provided by the Ships and Marine Technology Division at Ghent University, yielding a model with a Length On Waterline (LWL) of ≈ 1.4 m and three different container stacks as illustrated on Figure 2. The study presents three compositions of the harbour environment, each representing a different scenario: a bare terminal, i.e. an empty quay (Figure 2c); a terminal with container stacks (Figure 2a); and a terminal with storage tanks (Figure 2b). In addition, an open sea case is included for comparison with existing literature.



(a) (b) (c)

Figure 2. The figure illustrates, for a wind direction $\varphi = 90°$, the different harbour environments and ship loading configurations tested in the VKI L1-B wind tunnel: (**a**) container environment with intermediate stack, (**b**) tank environment with no-stack and (**c**) empty quay environment with full stack.

In order to obtain load measurements, a balance system is integrated within the model, thereby enabling the precise determination of the global forces and moments acting on the stationary ULCS model. The system comprises four ATI Nano25 sensors (SI-125-3), which are positioned symmetrically around the model's geometrical centre. Furthermore, 72 pressure taps have been integrated into the surface of the model, thus enabling a comparison between the experimental and numerical pressure distributions. To this end, an in-house-built acquisition system facilitates the simultaneous acquisition of multiple AMS5812-pressure sensors (AMS5812-0000-D-B).

3. RESULTS AND DISCUSSION

Measurements in various harbour environments, open sea condition and ship loading configurations (Figure 2) were conducted for 13 relative wind directions, φ (Figure 1b), and two reference velocities, $U_{ref} = 6\,\mathrm{m\,s^{-1}}$ and $10\,\mathrm{m\,s^{-1}}$. For the sake of concision, only the pressure measurements are discussed in the present paper. Indeed, the trend and conclusions drawn from these results are similar to the one observed with the PIV and balance measurements. Furthermore, since no Reynolds number effects were observed in the measurements, the subsequent results are presented for $U_{ref} = 6\,\mathrm{m\,s^{-1}}$ only. The time averaged pressure coefficient, $C_{p,\mathrm{mean}}$, was calculated using the standard formula, based on data acquired over 60 seconds at a sampling rate of 200 Hz.

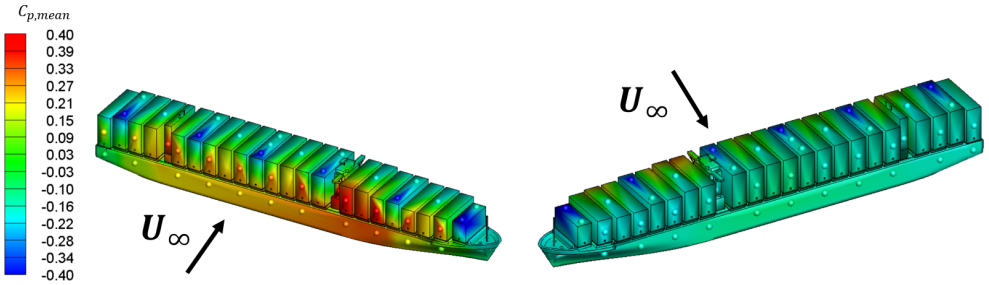
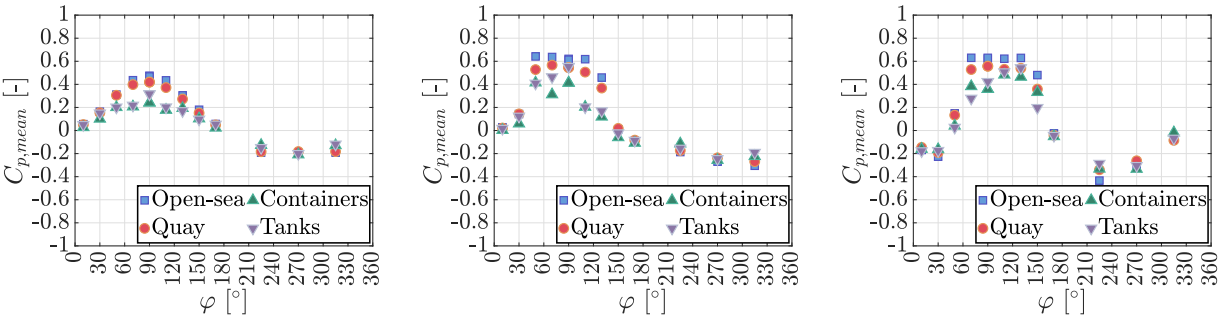


Figure 3. The interpolation of $C_{p,\mathrm{mean}}$ over the ship's surface in the full-stack configuration, within the container harbour environment ($\varphi = 90°$), is presented. Each coloured sphere represents the location of a pressure tap.

Figure 3 shows the mean pressure distribution over the ship for $\varphi = 90°$ in the full stack ship configuration within the container harbour environment. Maximum $C_{p,\mathrm{mean}}$ values are observed on the starboard side, though the pressure distribution across this surface is non-uniform due to the impact of the modelled harbour environment. Recirculating flow regions above the ship are detected via pressure taps installed on the top of the ship containers, with the minimum $C_{p,\mathrm{mean}} = -0.4$ recorded at these locations. The recirculation zone also extends downstream of the ship, where the port side experiences increased static pressure compared to the container tops, resulting in $C_{p,\mathrm{mean}} \approx -0.15$ over the port side surface. While Figure 3 provides an overall view of the pressure distribution across the ship, a more detailed understanding of the effects of different harbour environments and loading configurations can be obtained by analysing the variation of $C_{p,\mathrm{mean}}$ as a function of φ at various pressure tap locations, as illustrated in Figure 4.

Figure 4 illustrates the evolution of the mean pressure coefficient, $C_{p,\mathrm{mean}}$, as a function of the wind direction, φ, for the fully loaded ship and the different environments. As expected, for $0° < \varphi < 180°$, the highest values of $C_{p,\mathrm{mean}}$ are observed with both the open sea and quay environments, where the ship is directly exposed to the incoming wind. In this same range of wind directions, the surrounding containers yield lower $C_{p,\mathrm{mean}}$ values compared to the tank environment, with the exception of $\varphi = 70°$ and $150°$ at the aft superstructure pressure tap. This discrepancy can be

attributed to the fact that the container environment is denser than the tank environment, thereby providing better shielding of the ship from the incoming wind. For $180° < \varphi < 360°$, the influence of the different environments on the pressure distribution at the various pressure tap locations is consistent across all cases.



(a) Ship starboard shell. **(b)** Ship front superstructure. **(c)** Ship aft superstructure.

Figure 4. The evolution of the mean pressure coefficient, $C_{p,\text{mean}}$, as a function of the wind direction, φ, is presented for the three harbour environments in the fully loaded case across different pressure tap location.

4. CONCLUSIONS

The study conducted by the VKI highlights the significant impact of wind loads on modern large container vessels, particularly within the context of complex harbour environments, which present a considerable challenge. The experimental findings demonstrate that traditional wind load calculations are inadequate for addressing the demands posed by the increased size and capacity of modern ships. Significant variations in pressure distribution, observed across different harbour settings and wind directions, emphasise the necessity to account for local environmental factors in wind load predictions. The data obtained from wind tunnel experiments provide valuable insights for the refinement of numerical models and the enhancement of the safety and stability of moored vessels.

ACKNOWLEDGMENTS

We would like to express our gratitude to the dedicated technical team of VKI for their help with the wind tunnel tests. This work was made possible by the financial support of The Flemish Agency for Innovation and Entrepreneurship (VLAIO) for the Everblue project (HBC.2022.0663).

REFERENCES

Andersen, I. M. V., Jan. 2013. Wind loads on post-panamax container ship. en. Ocean Engineering 58, 115–134.

Barlow, J. B., Rae, W. H., and Pope, A., 1999. Low-speed wind tunnel testing. en. 3. ed. Wiley, New York Weinheim.

Ricci, A., Janssen, W., Van Wijhe, H., and Blocken, B., Oct. 2020. CFD simulation of wind forces on ships in ports: Case study for the Rotterdam Cruise Terminal. en. Journal of Wind Engineering and Industrial Aerodynamics 205, 104315.

Ricci, A., Vasaturo, R., and Blocken, B., Mar. 2023. An integrated tool to improve the safety of seaports and waterways under strong wind conditions. en. Journal of Wind Engineering and Industrial Aerodynamics 234, 105327.

Rodrigue, J.-P., Mar. 26, 2024. The Geography of Transport Systems. 6th ed. Routledge, London.

SAFETY4SEA, Dec. 3, 2019. Case study: Mooring line failure onboard. SAFETY4SEA.

Van Zwijnsvoorde, T., Donatini, L., Van Hoydonck, W., and Lataire, E., Oct. 17, 2019. Wind modeling for large container vessels: A critical review of the calculation proce dure. International Journal of Transport Development and Integration 3, 369–381.

VDI-guidelines, 2019. *VDI 3783 Blatt 12: Environmental Meteorology - Physical Modelling of Flow and Dispersion Processes in the Atmospheric Boundary Layer - Application of Wind Tunnels*. Accessed: 2024-09-24. VDI (Verein Deutscher Ingenieure).

Estimation of mean value and variance of velocity from pressure measured by a pressure transducer

Carlos Carbajosa[1], Sergio Marín-Coca[1], Alejandro Martínez-Cava[1], Carolina Hernández-Badillo[1], Omar Gómez-Ortega[1]

[1]*Instituto Universitario de Microgravedad "Ignacio Da Riva" (IDR/UPM), Universidad Politécnica de Madrid, Plaza Cardenal Cisneros, 3, E.28040, Madrid, Spain,*
c.carbajosa@upm.es

SUMMARY:
Pressure measurements are commonly used to determine mean velocity in Pitot tubes and surface pressure in pressure taps. However, it is often assumed that the temporal variations recorded by pressure transducers directly reflect those at the measurement point, without accounting for the attenuation and phase shift introduced by the tube. This study has two main objectives: first, to propose a simplified analytically derived formulation for obtaining the transfer function of tubes; and second, to develop a methodology for calculating the mean value and variance of velocity based on the statistical properties of the measured pressure. These formulations aim to improve the accuracy of experimental measurements in pressure systems, addressing the limitations of current techniques.

Keywords: pressure measurement, experimental aerodynamics, transfer function, mean velocity calculation

1. INTRODUCTION

There are several experimental techniques for determining fluid variables, such as velocity or pressure at specific points in the flow field. Among these, pressure measurements using pressure transducers are one of the most widely used methods. This technique is employed not only to measure pressure (via pressure taps) but also to calculate mean wind velocity using Pitot tubes. In both cases, the measurement point is connected by a pneumatic soft tube with a pressure transducer. However, it is often assumed that the temporal variations recorded by the transducers precisely reflect the conditions at the measurement point, which is located at the opposite end of the pneumatic tube. This assumption overlooks important details of the pressure's unsteady behavior, such as its variance. In reality, the tube introduces both attenuation and phase shifts effects that depend on the frequency of the disturbances, together with the consequences of friction effects and the presence of the tube end. Several authors have attempted to derive the transfer function that relates the real and measured pressures in tubes under different assumptions. In 1950, Iberall proposed a theoretical formulation that accounts for various effects, such as fluid compressibility, modeling pressure transducers as air-filled reservoirs (Iberall, 1950). Later studies built on this formulation, extending it to systems where multiple tubes are interconnected through reservoirs (Bergh and Tijdeman, 1965; Davies, 1988). Classical texts on acoustics also address the propagation of acoustic waves in ducts (Morse and Ingard, 1968). Recent contributions and technical notes, consolidated much of the current knowledge regarding the transfer function in tubes (Kovarek et al., 2018).

When calculating mean flow velocity from pressure measurements, several approaches are available. The most accurate method involves deriving the velocity time series at the tube's end from the pressure time series measured by the transducer using the aforementioned transfer function. However, implementing this method can be challenging. Factors such as tube attenuation (leading to a lack of signal) or harmonic amplification (resulting in excess noise) can introduce significant deviations from the actual values. This study has two main objectives: first, to propose a simplified alternative formulation for obtaining the transfer function of the pressure signals across the pneumatic lines; and second, to develop a methodology for calculating the mean and variance of velocity based on the mean and variance of pressure. These developments aim to improve the accuracy of determining the pressure time series and, consequently, the mean and variance of velocity at the tube's end based on the pressure measurements recorded by the transducer.

2. MATHEMATICAL FORMULATION AND METHODOLOGY

Depending on the required outcome of the pressure measurements, alternative formulations may be used, of decreasing complexity as the outcomes simplifies. If the complete time series are required, the so-called *exact method* should be used. However, if the temporal variations are not needed, but the variance of the data is of relevance, the here denominated *theoretical method* may be employed. Finally, if only mean values are required, a simplified method can be used.

2.1. Exact Method: Provides the complete time series

Pressure transducers typically provide the time series of the pressure difference, $\Delta p(t) = p_t - p(t)$, between the reference pressure, which is typically the total pressure, p_t, and the static pressure, $p(t)$. From this difference, the *scaled pressure* measured by the transducer can be calculated as $\alpha_{trans}(t) = 2\Delta p(t)/\rho$, where ρ is the air density. The tube's transfer function, assumed to be known, is defined as $\mathrm{TF}(\omega) = \tilde{\alpha}_r(\omega)/\tilde{\alpha}_{trans}(\omega)$, where $\tilde{\alpha}(\omega)$ represents the Fourier Transform of the scaled pressure time series in the frequency domain, evaluated at the transducer and at the opposite end of the tube (*i.e.*, $\tilde{\alpha}_{trans}(\omega)$ and $\tilde{\alpha}_r(\omega)$, respectively). For the transfer function, the classic expressions may be used (Kovarek et al., 2018), or alternatively:

$$\mathrm{TF}(\omega) = \frac{\tilde{\alpha}_r(\omega)}{\tilde{\alpha}_{trans}(\omega)} = \cosh\phi, \;\; \text{with} \;\; \phi = \mathrm{i}\tilde{\omega}\sqrt{\frac{1 - \mathrm{i}\frac{8\Lambda^2}{\tilde{\omega}\mathrm{Re}_L}}{1 + \mathrm{i}\frac{N\tilde{\omega}}{\mathrm{Re}_L}}}, \tag{1}$$

which is a novel expression analytically derived by neglecting the volume inside the transducer compared to the volume within the tube, and assuming there are no joints along the tube. In Eq. (1), $\tilde{\omega} = \omega L/c$, $\mathrm{Re}_L = cL/\nu$, $\Lambda = L/R$, and $N = \tilde{\nu}/\nu$, where L is the tube length, c the speed of sound in the tube, ν the kinematic viscosity, $\tilde{\nu}$ the volumetric kinematic viscosity, and R the tube radius. Using the chosen expression for the transfer function, the scaled pressure at the tube's end can be expressed as $\tilde{\alpha}_r(\omega) = \mathrm{TF}(\omega)\tilde{\alpha}_{trans}(\omega)$. By applying the inverse Fourier Transform, the time-domain pressure $\alpha_r(t)$ can be obtained. Finally, the velocity may be calculated as $u_r(t) = \sqrt{\alpha_r(t)}$, assuming steady, inviscid, incompressible flow. Based on these definitions, the mean values of both variables are defined as $\overline{\alpha}_r = \overline{\alpha_r(t)}$ and $\overline{u}_r = \overline{u_r(t)}$, while their deviations from the mean are given by $\alpha_r'(t) = \alpha_r(t) - \overline{\alpha}_r$ and $u_r'(t) = u_r(t) - \overline{u}_r$. The standard deviations can then be calculated as $\sigma_{\alpha,r} = \sqrt{\overline{\alpha_r'(t)}}$ and $\sigma_{u,r} = \sqrt{\overline{u_r'(t)}}$. In order to characterize the signal variance, the turbulence intensities, defined as $I_{\alpha,r} = \sigma_{\alpha,r}/\overline{\alpha}_r$ and $I_{u,r} = \sigma_{u,r}/\overline{u}_r$, may be used.

2.2. Theoretical Method: Provides mean values and variances

If only the standard deviations and mean values of the pressure at the measurement position (and velocity, if applicable) are required, an alternative formulation may be employed. This approach is more robust than the exact method, as it eliminates the need for transformations between the time and frequency domains, thereby reducing the potential introduction of numerical noise. Consequently, a more robust formulation is proposed, based solely on the mean values and variances of the variables α and u. From the transducer's time series $\alpha_{trans}(t)$, the mean value $\overline{\alpha}_{trans}$, variance $\sigma^2_{\alpha,trans}$, and power spectral density $\mathrm{PSD}_{\alpha,trans}(\omega)$ are determined. Using the transfer function, the mean value at the tube's end (where $\overline{\alpha}_r$ is shown to be equivalent to $\overline{\alpha}_{trans}$) and the power spectral density $\mathrm{PSD}_{\alpha,r}(\omega) = |\mathrm{TF}(\omega)|^2 \mathrm{PSD}_{\alpha,trans}(\omega)$ are derived. Finally, the variance at the tube's end can be calculated as follows:

$$\sigma^2_{\alpha,r} = \frac{1}{2\pi}\int_{-\infty}^{+\infty} \mathrm{PSD}_{\alpha,r}(\omega)\mathrm{d}\omega - \overline{\alpha}^2_r. \tag{2}$$

Once the mean value and variance of α at the tube's end are determined, the mean value and variance of u can be calculated using the following expressions:

$$\overline{u}_{r,theo} = \sqrt{\overline{\alpha}_r}\left(1 - \frac{1}{8}I^2_{\alpha,r}\right), \text{ and } I^2_{u,theo} = \frac{1}{4}I^2_{\alpha,r}. \tag{3}$$

2.3. Approximated Method: Only provides mean values

Finally, when only the mean values are of interest, from Eq. (1), it can be noted that the mean pressure values at both ends of the tube are identical (since $\mathrm{TF}(\omega = 0) = 1$). Additionally, for calculating the mean velocity, one can refer to:

$$\overline{u}_{r,approx} = \sqrt{\overline{\alpha}_{trans}}. \tag{4}$$

3. RESULTS

For each of the three methods presented in Section 2, the amount of information obtained from the measurement point decreases with the simplicity of the calculations. This raises the question of how reliable the simpler methods are compared to the more complex ones. Although simpler methods may lead to some loss of information, one would expect their results to closely approximate those obtained using more sophisticated approaches. Regarding the transfer function calculation, Figures 1-(a) and (b) compare the transfer functions from Kovarek et al., 2018 with Eq. (1), highlighting the influence of the geometric relation $\Lambda = L/R$ on the transfer function's magnitude. For long tubes, friction effects dominate and cause attenuation, while for short tubes, the tube's end amplifies certain frequencies. The results from both methods are quite similar, although the expression given by Eq. (1) is much simpler than that provided in Kovarek et al., 2018. The error in the mean velocity is defined as $\varepsilon_{\overline{u},i} = |\overline{u}_{r,i}/\overline{u}_r - 1|$, where i refers to either the theoretical ($i = theo$) or approximate ($i = approx$) method. Similarly, the error in the variance is defined as $\varepsilon_{I^2_u} = \left|I^2_{u,theo} - \sigma^2_{u,r}\right|$. In the conducted research, it has been confirmed that, although both errors increase with I_α, their values remain below 0.1% ($\varepsilon_{\overline{u},i}$) and 1% ($\varepsilon_{I^2_u}$) for turbulence intensities, I_α, less than 10%. Therefore, the differences between the three methods are negligible for most applications. For this reason, using more sophisticated methods over simpler ones is only justified when additional information is required, such as when measuring unsteady flows where the full time series (or at least variances) of both pressure and velocity may be needed.

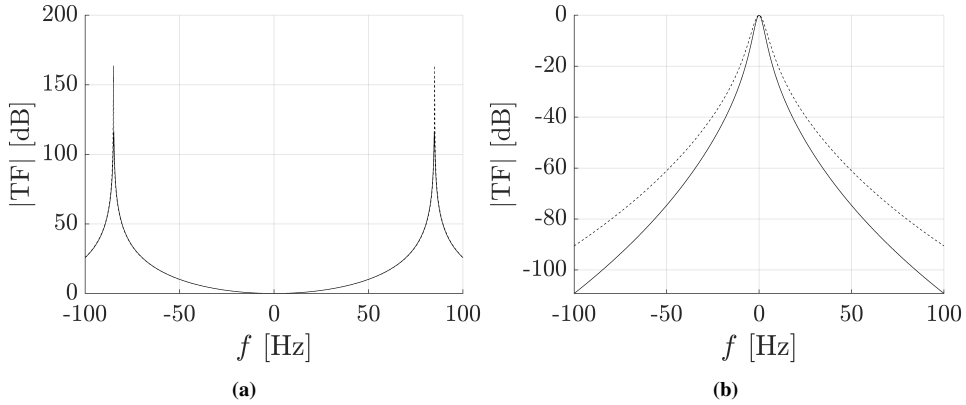


Figure 1. Transfer function module, |TF|, as a function of the frequency, f, given by Kovarek et al., 2018 (continuous lines) and by Eq. (1) (dashed lines) for $\Lambda = 10^1$ (a) and $\Lambda = 10^4$ (b).

4. CONCLUSIONS

Pressure measurements are utilized not only to determine pressure values via pressure taps but also to calculate mean wind velocity using Pitot tubes. A new, simplified formulation for the transfer function has been introduced to derive the pressure at the tube's end from transducer readings. Three methods for calculating mean flow velocity from the measured pressure time series have been presented. The results show that as the signal variance decreases, all three methods yield similar outcomes; however, the simpler methods offer less detail compared to the more sophisticated approaches. This indicates the importance of considering which variables—such as full time series data, variances, or only mean values—are relevant to the specific test. Notably, the exact method requires applying the inverse Fourier Transform to recover the time series, which can introduce significant errors influenced by signal characteristics. Consequently, when only mean values and variances are needed, the theoretical method might be more robust and reliable than the exact method.

ACKNOWLEDGEMENTS

This work is part of the project TED2021-130541B-C21, funded by MCIN/AEI/10.13039/ 501100011033, the European Union "NextGenerationEU"/PRTR and project PID 2022-137630OB-C21 financed by MCIN/AEI/10.13039/ 501100011033/FEDER, UE. The work of Carlos Carbajosa has been supported by the FPU grant FPU23/00716 from the Spanish Ministry of Science and Innovation (Ministerio de Ciencia, Innovación y Universidades).

REFERENCES

Bergh, H. and Tijdeman, H., 1965. *Theoretical and experimental results for the dynamic response of pressure measuring systems*. Tech. rep. Nationaal Lucht-en Ruimtevaartlaboratorium. National Aero- and Astronautical Research Institute Amsterdam.

Davies, P. O., 1988. Practical flow duct acoustics. Journal of Sound and Vibration 124 (1), 91–115.

Iberall, A. S., 1950. Attenuation of Oscillatory Pressures in Instrument Lines 1. Journal of Research of the National Bureau of Standards 45.

Kovarek, M., Amatucci, L., Gillis, K. A., Potra, F. A., Ratino, J., Levitan, M., and Yeo, D., June 2018. *Calibration of dynamic pressure in a tubing system and optimized design of tube configuration: a numerical and experimental study*. Tech. rep. National Institute of Standards and Technology.

Morse, P. M. and Ingard, K. U., 1968. Theoretical acoustics. McGraw-Hill.

Influence of PV panel Sizes on Wind-Induced Loads: A Comparative Study on Flat Roofs

Ioannis Zisis [1], Mahmoud Abdallah [2]

[1]*Department of Civil and Environmental Engineering, International Hurricane Research Center, Extreme Events Institute, Florida International University, Miami, USA, izisis@fiu.edu*
[2]*Department of Civil and Environmental Engineering, Florida International University, Miami, USA, mabda014@fiu.edu*

SUMMARY:
This study investigates the aerodynamic effects of photovoltaic (PV) panel sizes on wind-induced loads for installations on flat roofs. As the industry moves toward producing larger PV panels, often exceeding the chord length limit specified in the US wind standards, there is a growing need to evaluate their feasibility in residential and commercial rooftop applications and their impact on wind-induced loads. This research is aiming to determine whether the panel size and different installation configurations will intensify or mitigate wind-induced loads and consequently alter current design practices. The study uses 1:20 scale flat roof models tested at the NSF NHERI Wall of Wind Experimental Facility, with three distinct PV panel sizes in various commonly used installation configurations. The primary objective is to understand how panel size influences wind-induced peak pressure coefficients (Cp) and force coefficients (Cf) on these roof types. The analysis will provide insights into how roof geometry and PV panel size affect aerodynamic behaviour, with implications for improving the safety of rooftop PV installations. The study's results are expected to guide the refinement of wind load provisions in standards such as ASCE 7, contributing to safer and more efficient PV panel installations.

Keywords: PV panel sizes, Wind loads, Flat roofs.

BACKGROUND AND MOTIVATION

As larger PV panels become more common, understanding how their increased dimensions affect wind pressures and structural performance is crucial. This study focuses on the aerodynamic behavior of flat roofs with PV panel sizes exceeding the chord length limit of 6.7 ft (2.05 m) set by ASCE 7 standards (ASCE 7, 2022). Previous research on sloped roofs, particularly gable configurations, has highlighted the effects of panel size, orientation, and roof coverage scenarios on wind-induced loads. Additionally, ongoing research is investigating the performance of hipped roofs. Together, these studies will provide a comprehensive understanding of how larger PV panels influence wind loads across different roof types. For flat roofs, factors such as panel arrangement, tilt angles, and edge distances are particularly critical in shaping pressure distribution (Kopp et al., 2012; Stenabaugh & Kopp, 2012; Kopp, 2014; Warsido et al., 2014; Stenabaugh et al., 2015). This research will offer key insights into the behavior of larger panels, aiding the development of more robust design standards for flat-roof PV installations.

METHODOLOGY

The study has been conducted at the NSF NHERI Wall of Wind (WOW) Experimental Facility using 1:20 scale models of a flat-roof building with plan dimensions of 110 × 110 ft and a roof height of 15 ft. Three distinct PV panel sizes were evaluated under twelve different test cases, considering variations in panel size, orientation (portrait vs. landscape), and the presence of a parapet. The test matrix included arrays consisting of 21 and 24 instrumented PV panels, strategically placed to measure aerodynamic loads. The panel sizes tested are summarized in Table 1, with the largest panel reaching a length of 98.5 in (250 cm).

Wind directions were tested incrementally from 0° to 345° in 15-degree steps to simulate various real-world environmental conditions. The heights of the PV modules above the roof surface and the gaps between them were carefully controlled to reflect common installation practices. Tests were conducted under a simulated open terrain roughness condition to ensure consistency with real-world exposure categories.

Figure 1 provides an overview of the twelve PV configurations tested at the WOW facility, highlighting the different array arrangements and parapet conditions.

This study builds on previous experiments involving sloped roofs, providing a comparative analysis across roof types. By examining different installation configurations on flat roofs, the research aims to enhance the understanding of wind loads on PV systems, particularly for larger panel sizes.

Table 1. PV panel sizes

Panel Description	Panel Width Inches (cm)	Panel Length Inches (cm)
Standard large PV panel		78.8” (200 cm)
Larger panel	42.25” (115 cm)	88.6” (225 cm)
Largest panel tested		98.5” (250 cm)

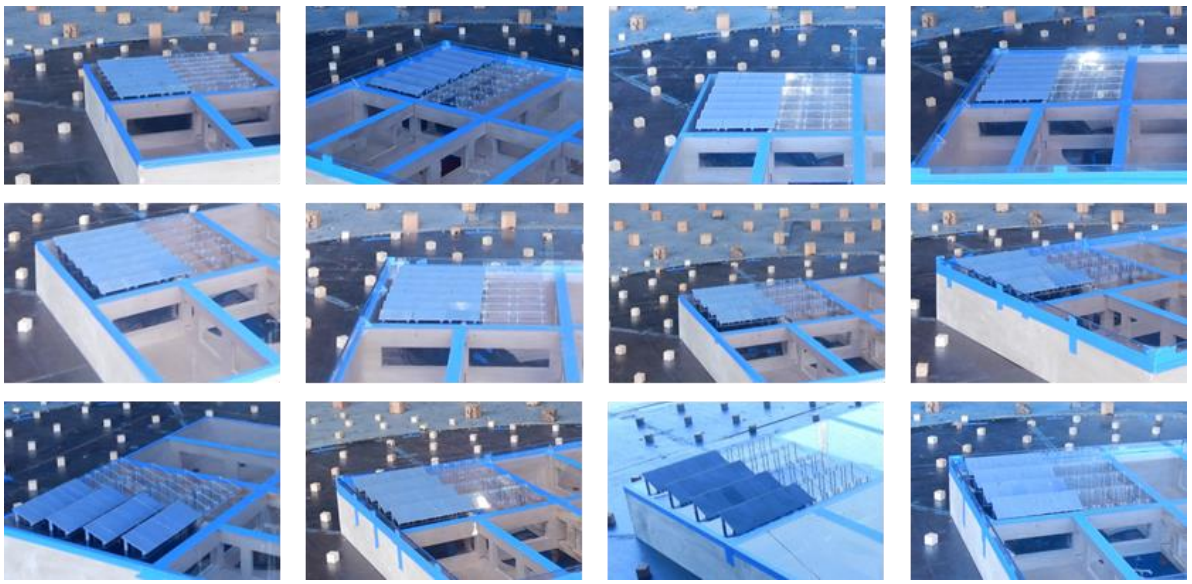


Figure 1. Overview of the twelve PV configurations tested at the WOW facility, showing different array arrangements and parapet conditions.

EXPECTED OUTCOMES

The study has now completed the wind tunnel experiments, and the analysis is providing valuable insights into the effects of PV panel size and configuration on wind-induced loads. The results demonstrate how larger panel sizes impact peak pressure coefficients (Cp) and force coefficients (Cf), with indications of reduced local peak negative pressure coefficients due to increased panel surface area. Variations between portrait and landscape orientations are being examined to determine optimal installation configurations for mitigating wind effects.

A previous study on gable roofs, which has been submitted for publication and is pending review, demonstrated the influence of PV panel size on peak critical minimum pressure coefficients (Cp). Figure 2 presents findings from that study, showing that larger PV panels reduce peak negative Cp values by approximately 10-15% compared to standard-sized panels. Note that the axes represent measurements in millimeters, corresponding to the model-scale panels. A similar analysis on flat roofs is revealing whether this trend applies to low-slope configurations.

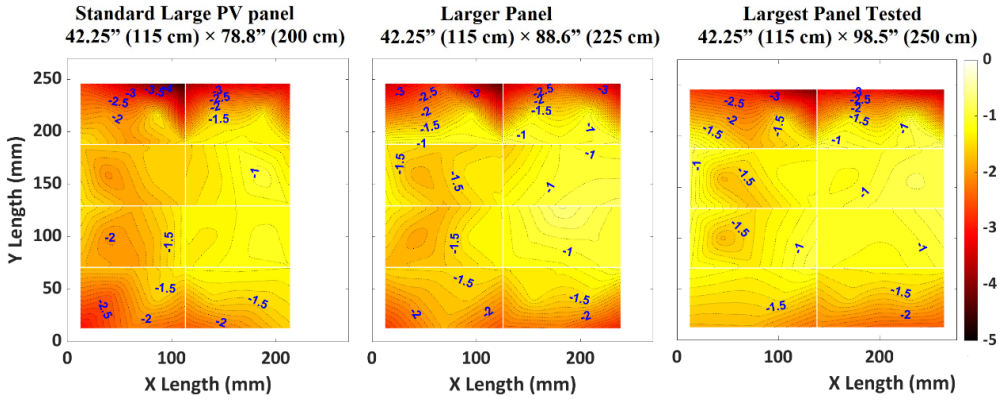


Figure 2. Peak Critical Minimum Cp on Three PV Panel Sizes for Gable Roofs

These findings will inform future revisions to wind load provisions in standards such as ASCE 7, ensuring that they account for the growing use of larger PV panels on flat roofs. The study's results will be presented in full at the conference, providing actionable insights for safer and more efficient PV system designs.

CONCLUSION

This ongoing research will provide crucial data on the aerodynamic effects of different PV panel sizes on flat roofs. By addressing how panel dimensions and configurations influence wind-induced loads, this study will help refine current design practices, improving the safety and performance of PV installations. The findings will support future revisions to ASCE 7 standards, ensuring that they reflect the latest industry trends and promote resilience in residential solar energy systems.

ACKNOWLEDGEMENTS

This ongoing research is supported by the industry-University Cooperative Research Center (IUCRC), the National Science Foundation (NSF), and WHIP-C – Wind Hazard and Infrastructure Performance Center. Their financial support is instrumental in facilitating the experimental work conducted at the NSF NHERI Wall of Wind Experimental

Facility. The opinions, findings, conclusions, or recommendations expressed in this article are solely those of the authors and do not represent the opinions of the funding agencies.

REFERENCES

ASCE 7. (2022). Minimum Design Loads and Associated Criteria for Buildings and Other Structures. American Society of Civil Engineers. https://doi.org/10.1061/9780784415788

Kopp, G. A. (2014). Wind Loads on Low-Profile, Tilted, Solar Arrays Placed on Large, Flat, Low-Rise Building Roofs. Journal of Structural Engineering, 140(2), 04013057. https://doi.org/10.1061/(ASCE)ST.1943-541X.0000825

Kopp, G. A., Farquhar, S., & Morrison, M. J. (2012). Aerodynamic mechanisms for wind loads on tilted, roof-mounted, solar arrays. Journal of Wind Engineering and Industrial Aerodynamics, 111, 40–52. https://doi.org/10.1016/j.jweia.2012.08.004

Stenabaugh, S. E., Iida, Y., Kopp, G. A., & Karava, P. (2015). Wind loads on photovoltaic arrays mounted parallel to sloped roofs on low-rise buildings. Journal of Wind Engineering and Industrial Aerodynamics, 139, 16–26. https://doi.org/10.1016/j.jweia.2015.01.007

Stenabaugh, S. E., & Kopp, G. A. (2012). Failure vs. Flight: An Experimental Study of Wind Speeds Associated with Roof Failures of Houses. Forensic Engineering 2012, 851–860. https://doi.org/10.1061/9780784412640.090

Warsido, W. P., Bitsuamlak, G. T., Barata, J., & Gan Chowdhury, A. (2014). Influence of spacing parameters on the wind loading of solar array. Journal of Fluids and Structures, 48, 295–315. https://doi.org/10.1016/j.jfluidstructs.2014.03.005

Development of a simple experimental method for wind and fire interaction problems

Hiroshi Hasebe [1], Yusuke Nakamura [2]

[1] *Nihon University, Tokyo, Japan, hasebe.hiroshi@nihon-u.ac.jp*
[2] *Wind Engineering Institute Co., Ltd., Tokyo, Japan, yusuke@wei.co.jp*

SUMMARY:
Wind and fire interaction problems, such as urban fires, wildfires, etc., are one of the research targets that wind engineers should work on. However, general wind tunnels cannot be used for fire experiments due to building codes and the lack of smoke control systems. Therefore, we have developed a simple experimental method for wind and fire interaction problems outside of the wind tunnel facility which we normally use. In the present study, we focused on wildfires. First, we developed a portable wind tunnel which could be easily disassembled and transported. Subsequently, we used a training facility for firefighters and the wind tunnel was brought in there. In this facility, an experiment was conducted to measure the rate of fire spread on fallen dry leaves in the context of a surface fire of a wildfire. The rates of fire spread of dry leaves were measured below a wind speed of 7 m/s.

Keywords: wind and fire interaction problem, portable wind tunnel, fire spread rate

1. INTRODUCTION

Recently, the increase of temperature and drying air due to the climate change affects the occurrence of wind and fire interaction problems. In August 2023, a destructive bushfire caused by low humidity and strong winds in Maui Island of Hawaii resulted in the devastation of the town and the loss of numerous lives (Roy et al., 2024; Downs et al., 2024). As a result of the fire reaching the town, the damage of the fire was extensive. It is therefore imperative that the area and the rate of the fire spread be rapidly predicted in the event of fires. The accurate predictions need many cases of experiments and simulations. Nevertheless, wind and fire experiments are difficult to conduct because of building codes and the lack of smoke control systems in the wind tunnel room which we normally used. A fire wind tunnel is one of the options to conduct wind and fire interaction experiments, but there are not many of these facilities. Following this issue, we have developed a simple experimental method for wind and fire interaction problems. Especially, we focused on wildfire problems.

First, we developed a portable wind tunnel which could be easily disassembled and transported. The portable wind tunnel was constructed using personal computer (PC) fans, a 3D modelling technique and a 3D printer. Using a 3D printer, a contraction section was easily designed. The connecting parts were also flexibly manufactured. As a result, it is now possible to transport the wind tunnel in a private car, as it can be easily disassembled.

Subsequently, the problem of not having a facility where fire experiments could be conducted was solved by using a training facility for firefighters. We brought the portable wind tunnel and reassembled it in the facility. Then, an experiment on wind and fire interaction problems was

conducted to measure the rate of fire spread on fallen dry leaves in the context of a surface fire of a wildfire. The rates of fire spread of dry leaves were measured below a wind speed of 7 m/s.

2. DEVELOPMENT OF A PORTABLE WIND TUNNEL

In order to conduct wind and fire interaction experiments at a facility that does not have a wind tunnel, we developed a portable wind tunnel. The wind tunnel had the following concepts: portable, easy to disassemble and reassemble, flexible design, inexpensive.

Fig. 1 and Fig. 2 show a developed our portable wind tunnel. The type of the wind tunnel was selected as an open jet for easy of transport. For the design of the wind tunnel, we developed a script for 3D modelling of the entire wind tunnel. Because the script could parametrically change the length of several parts, we were able to design wind tunnels flexibly. The wind tunnel was disassembled into four parts, a contraction, a honeycomb and screens, a chamber and a diffuser. This made the wind tunnel easy to transport.

Total horizontal length of the wind tunnel was about 1.3 m. The section of the outlet had a square section with a length of 0.25 m on one side. The contraction and diffuser frames, as well as the connecting parts were made with a 3D printer using PLA (Poly-Lactic Acid). The curve of the contraction frame was based on three degrees of polynomial function, 3D printer could easily manufacture it. For the wind tunnel fan, computer fans spinning at 3800 rpm were used to reduce costs. These multiple PC fans were arranged in a grid pattern (9 fans were arranged in a 3 by 3 grid). The power supply and the speed controller were made by us. It worked not only on household power supply, but also on 12 V batteries. As a result, we were able to use the portable wind tunnel in a location without an electrical outlet.

In order to evaluate the performance of the wind tunnel, we measured the velocity using a hot-wire anemometer with an I-type probe. We set the sampling rate to 1 kHz and the recording duration to 30 seconds. Measurement points in the cross-section were set at the center of the section. The distances of measurement point were set to 0, 0.3, 0.6, 0.9 m from the outlet. Fig. 3 shows the results of the mean wind speed and the turbulence intensity at each point. An open-type test section was used for this measurement because the fire experiment described later was conducted with the top open.

The mean wind speed measured at each point was over 6 m/s. The speed did not change much at the downstream measurement points. The minimum turbulence intensity was about 0.5%. It increased downstream and reached about 5%, due to the use of the open-type measurement section. Rothermel et al. conducted a fire spread experiment with fallen leaves in a range of wind speeds up to about 3 m/s and developed a predicting formula of the fire spread speed (Rothermel et al., 1964). We have constructed a wind tunnel that could conduct wind and fire experiments.

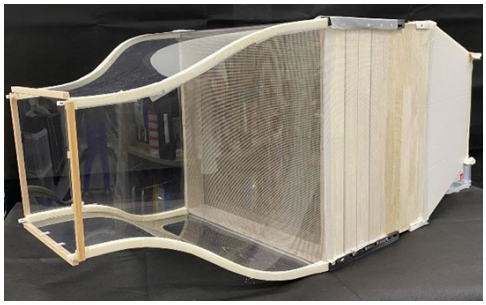


Figure 1. Overview of the portable wind tunnel

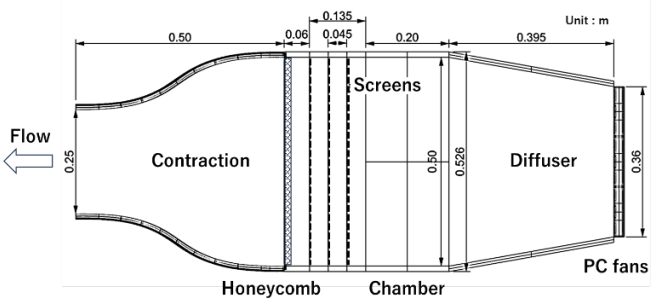


Figure 2. Side view and lengths of the portable wind tunnel

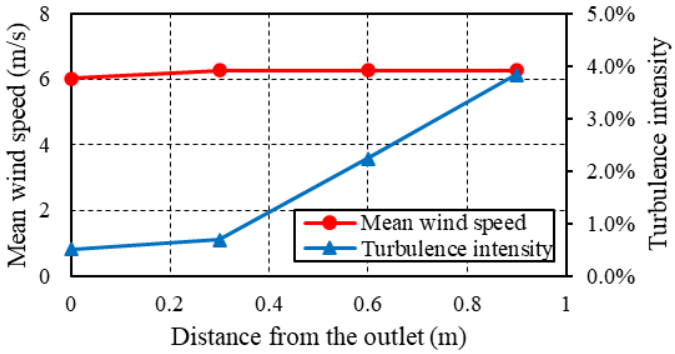


Figure 3. Mean wind speed and turbulent intensity of the portable wind tunnel

3. MEASURING THE RATE OF FIRE SPREAD IN THE WIND

Fig. 4 shows the setup of a wind and fire interaction experiment. Using our portable wind tunnel, we created a fuel bed 0.25 m width and 0.73 m long with a sediment density of 1.0 kg/m^2. Japanese zelkova was used to make the fuel bed. Since the flame height was expected to get higher, the upper boundary of the test section was left open. On the other hand, heat-resistant glasses were installed on the sides to prevent the wind from spreading. The temperature was measured by thermocouples (K type). They were installed at equal 0.1 m intervals, starting 0.15 m downstream of the wind tunnel outlet. Wind speeds of the experiment were set to 0, 2.0, 4.0, 6.5 m/s at the centre of the test section. Because the test section had side walls and a floor, the maximum wind speed increased slightly compared to the result shown in the previous chapter.

Fig. 5 shows the shape of frames at each wind speed. As the wind speed increased, the frame became stronger, and the tilt angle increased. However, there was no significant difference in the tilt angles between wind speed of 4 and 6.5 m/s. Fig. 6 shows measured results. The result by Rothermel et al. (Rothermel et al., 1964) was also plotted. The results showed that the rate of fire spread increased with the change in wind speed. Compared to the result of Rothermel et al., our result was low. This may be due to the difference in fuel bed material and water content.

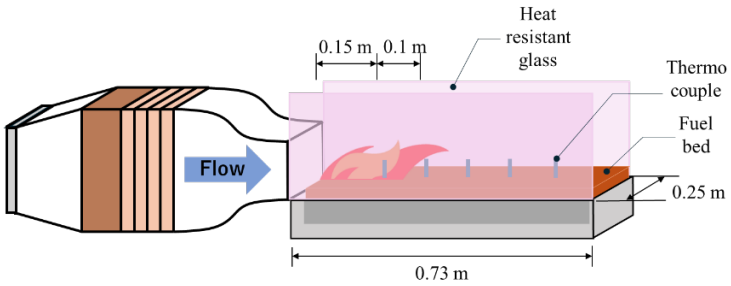
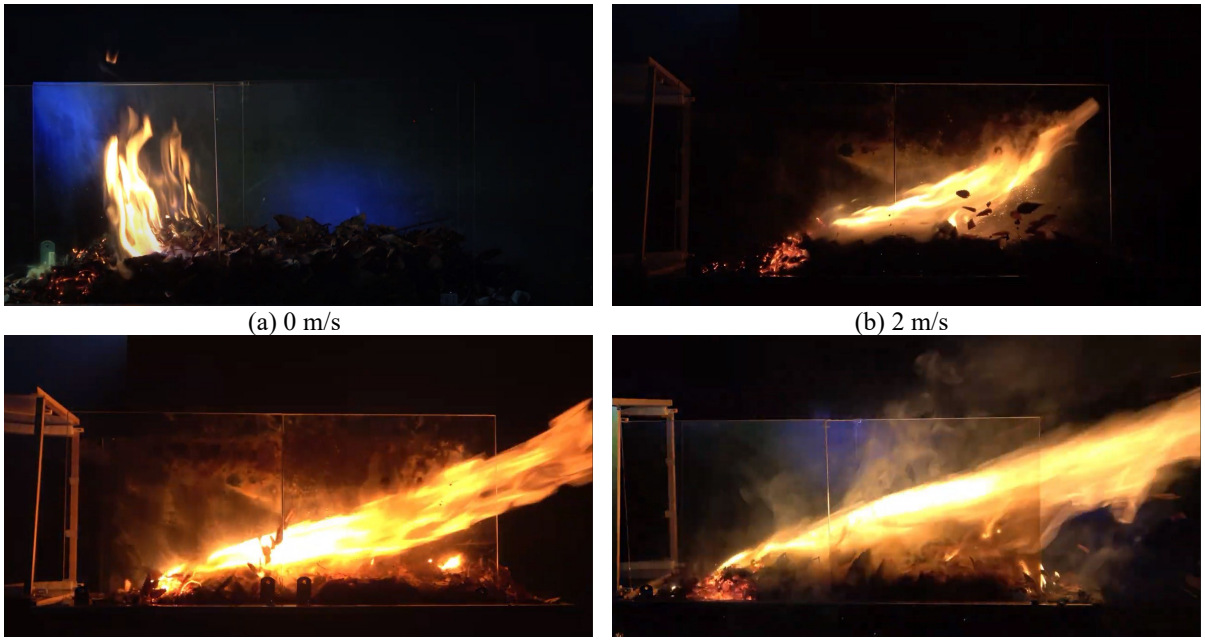


Figure 4. Setup of the wind and fire interaction experiment

4. CONCLUSIONS

In the present study, we developed a simple experimental method for wind and fire interaction problems using a portable wind tunnel and a training facility for firefighters. We confirmed that the frame became stronger, and the tilt angle increased as the wind speed increased. The rate of fire spread also increased with the change in wind speed. We plan to conduct larger-scale experiments.



(a) 0 m/s (b) 2 m/s

(c) 4 m/s (d) 6.5 m/s

Figure 5. Flame shapes at each wind speed

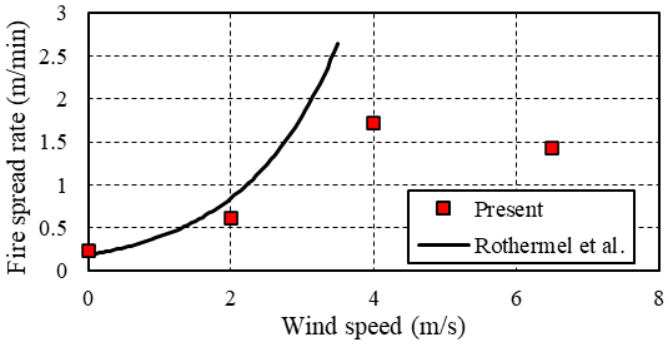


Figure 6. Measured fire spread rates in the wind

ACKNOWLEDGEMENTS

The experiment was conducted using the training room at the Kanagawa Fire Academy, Kanagawa Prefecture Disaster Prevention Center. We would like to express our gratitude to all those involved with the facility.

REFERENCES

Roy, D. P., De Lemos, H., Huang, H., Giglio, L., Houborg, R., Miura, T., 2024. Multi-resolution monitoring of the 2023 maui wildfires, implications and needs for satellite-based wildfire disaster monitoring, Science of Remote Sensing 10, 100142.

Downs, C.A., Doust, S. N., Haghshenas, S. A., Woodley, C. M., Shirzad, B., McDonald, E. M., Nazarpour, A., Farhangmehr, A., Zhao, H., Bishop, E. E., Risk, M. J., 2024. Potential impact of the 2023 Lahaina wildfire on the marine environment: Modeling the transport of ash-laden benzo[a]pyrene and pentachlorophenol, Science of The Total Environment 954, 176346.

Rothermel, C. and Anderson, H. E., 1966. Fire spread characteristics determined in the laboratory, U.S. Forest Service Research Paper, INT-30.

Experimental aerodynamic study of three-dimensional solar tracker plant model

Adrián Iglesias Sánchez [1,2], Mikel Ogueta-Gutiérrez [1,3], José Luis Ruiz-Moral [1,4], Adriana Carolina Hernández-Badillo [1,5], Sergio Marín-Coca [1,6]

[1]*Instituto Universitario de Microgravedad "Ignacio da Riva", Universidad Politécnica de Madrid, Madrid, Spain,*
[2]*adrian.iglesias@alumnos.upm.es*
[3]*mikel.ogueta@upm.es*
[4]*joseluis.ruiz.moral@upm.es*
[5]*carolina.hernandez.badillo@upm.es*
[6]*sergio.marin.coca@upm.es*

SUMMARY
Aerodynamic instabilities in solar trackers, especially flutter, may occur during their operation under noncritical wind loads, triggering a catastrophic result (Martínez-García et al., 2021) . A full aeroelastic test has been conducted to analyse the behaviour of a certain solar tracker prototype. Different angles of attack and the interference between several rows are to be tested within wind tunnel tests in a model which reproduces geometrical and mass characteristics of the real prototype.

Keywords: solar tracker, wind tunnel, flutter.

1. INTRODUCTION

Solar energy is undoubtedly increasing its importance for generating electricity nowadays, and there has been thorough study to maximize the amount of energy produced. (Martínez-García et al., 2021, Cárdenas-Rondón et al., 2023) Currently, solar trackers, which can follow the sun during the day maximizing the energy generated, are the most used technique in solar energy production. The purpose of this study is to determine the effects of wind loads in a solar tracker prototype with a novel design, engineered to minimise dynamic effects, with two fixed points in its span, leading to a configuration with a central part with two embedments and the side parts with a single one.

2. METHODS

Geometrical and mass characteristics of the prototype were given to build a model and test it in a full three-dimensional aeroelastic test.

2.1. Design of the Model

The model should reproduce the behaviour of the real prototype. To achieve this, inertia and torsional stiffness of the prototype also had to be properly scaled (Enshaei et al., 2023), apart from its dimensions.

The panels were made with ABS 3D printing. A scale of 1/25 was used. The most influent parameter affecting the inertia given by the panels was their thickness, which was set to 0.4 mm. Regarding torsional stiffness, the real prototype had two sections with different stiffnesses. This situation was modelled by using two different carbon torque tubes in the model for each section. They were firmly attached with each other in the fixed point to minimize perturbations in the dynamic behaviour of the model.

Natural frequencies for the first torsion mode of the model were determined with a simple free vibration test for the double-fixed section (middle) and the fixed-free section (end), as shown in Fig.2. The relation between both was 1.20, with this value being 1.13 for the real prototype. This showed an accurate reproduction of the dynamics and mass distribution of the prototype.



Figure 2. Frequency test for the model

2.2. Wind Tunnel Tests

Once the first model was completed, four more models were made following the same procedure to obtain a solar tracker plant, shown in Fig. 3. It was tested in the wind tunnel ACLA16 at IDR facilities.

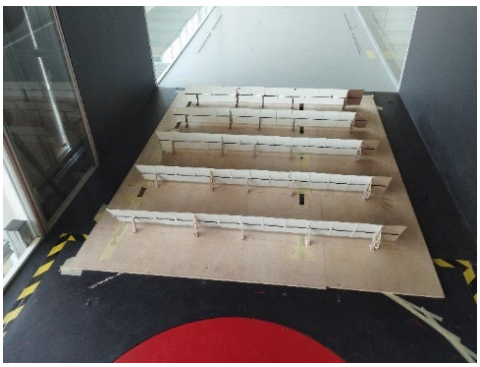


Figure 3. Solar tracker plant

3. RESULTS

The tests consisted in measuring the displacement of the solar trackers as a function of wind velocity in the tunnel for each angle of attack of the trackers.

To analyse each test, standard deviation of the temporal series of displacement (in essence, a means of measuring displacement) was registered as a function of wind velocity. When the standard deviation reaches a certain threshold value, it is considered that the whole plant enters in an instable condition. The velocity at which this situation occurs is used for calculating the critical reduced velocity of the plant, shown in Eq. (3).

$$U^*_{reduced} = \frac{U^*}{b\, f_0} \tag{1}$$

With U^* being wind tunnel velocity, b being the model chord and f_0 is the natural frequency for the first mode of vibration (without wind). The value of f_0 depends on whether the section which triggers the instability of the plant is a middle section or a row end section. The information is gathered from all tests and then summarized in the stability diagram of Fig. 4.

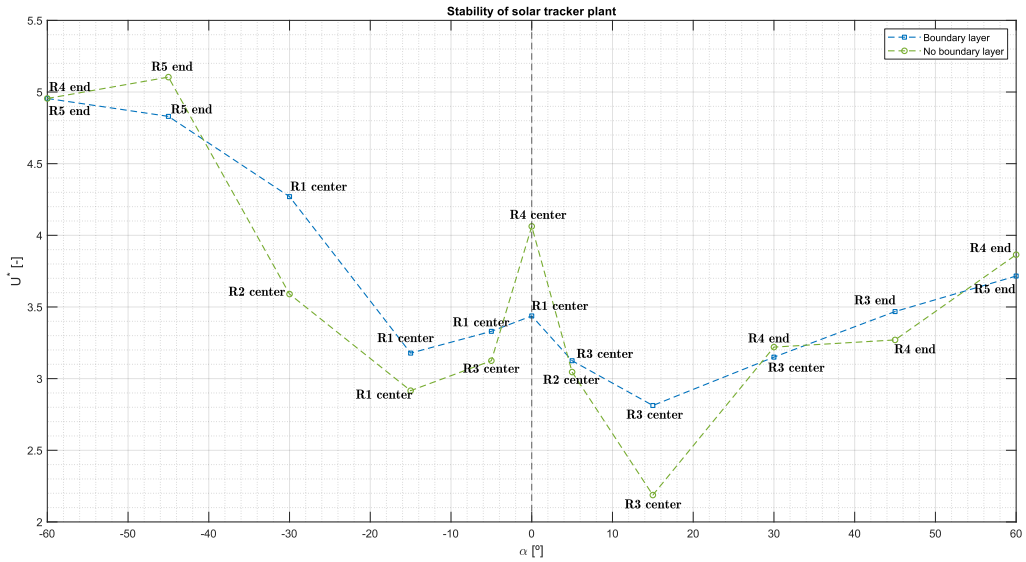


Figure 4. Stability diagram of the plant

4. DISCUSSION

The main result of the tests is the stability diagram of Fig. 4. It shows that the stability of the plant increases with the angle of attack, but it also has a peak when there is no angle of attack, which is consistent with the behavior of a single solar tracker. It can also be seen that, the higher the stability of the plant, the more probable is that the beginning of instabilities is triggered in the outer span of the last rows of the plant (4^{th} and 5^{th} row).

The tests were repeated after installing a boundary layer in the wind tunnel. Results are prompted in Fig. 4, and it can be seen there is a slight difference between both cases, but no clear trend has been found.

5. CONCLUSIONS AND FUTURE WORK

The stability of the plant has proven to increase with the angle of attack of the trackers. The interference between rows seems to become highly important at big angles of attack, as a higher threshold value for standard deviation was needed in these cases. It is believed that this is caused by a major importance of buffeting in these cases due to the turbulence induced downstream by the first rows. With small angles of attack, this phenomenon appears to be far less important than traditional flutter (See Fig. 5). However, this situation needs further study and a proper Fourier analysis of vibration frequencies in panels to determine the main mechanism of instability - traditional flutter or induced buffeting- in each case.

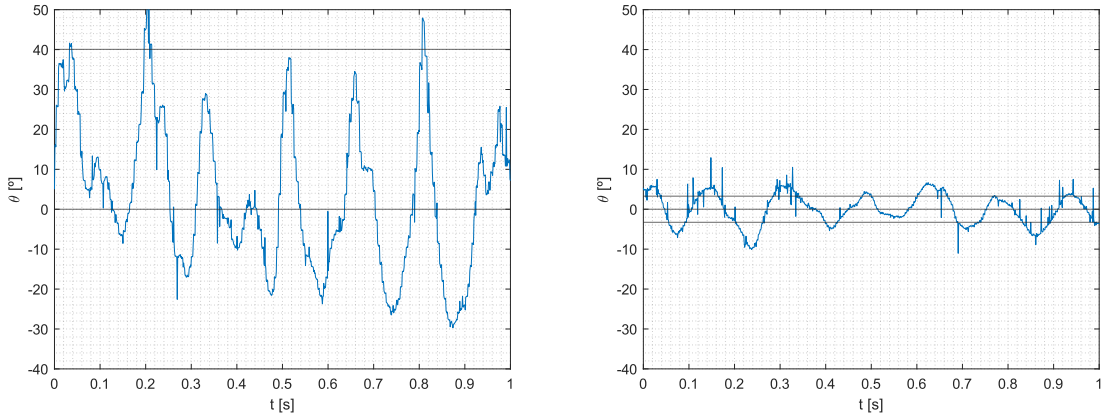


Figure 5. Temporal series for the same section of solar tracker: left; 5 degrees; right; 60 degrees.

ACKNOWLEDGEMENTS

This work is part of the project TED2021-130541B-C21, funded by MCIN/AEI/10.13039/ 501100011033, the European Union "NextGenerationEU"/PRTR and project PID 2022-137630OB-C21 financed by MCIN/AEI/10.13039/ 501100011033/FEDER, UE.

This research was carried out at IDR/UPM facilities in Montegancedo, Madrid. The work described above would have been impossible without the help of Javier Pascual, Carlos Pascual, Alberto Escribano and Manuel Ortega. Especially, CNC operator Guillermo Banús was extremely helpful at manufacturing several pieces for trial before final designs, which made the design process much easier.

REFERENCES

Cárdenas-Rondón, J. A., Ogueta-Gutiérrez, M., Franchini, S., Manzanares-Bercial, R., (2023). Stability análisis of two-dimensional flat solar trackers using aerodynamic derivatives at different heights above ground. Journal of Wind Engineering and Industrial Aerodynamics, 243, 105606. https://doi.org/10.1016/j.jweia.2023.105606

Enshaei, P., Chowdhury, J., Sauder, H., & Banks, D. (2023). Wind Tunnel Testing of Torsional Instability in Single-Axis Solar Trackers: Summary of Methodologies and Results.

Martínez-García, E., Blanco-Marigorta, E., Parrondo Gayo, J., & Navarro-Manso, A. (2021). Influence of inertia and aspect ratio on the torsional galloping of single-axis solar trackers. Engineering Structures, 243, 112682. https://doi.org/10.1016/j.engstruct.2021.112682

Simulating super- and trans-critical Regimes on curved Surfaces in Atmospheric-Boundary-Layer Wind Tunnels: Evidences from Surface Pressure Studies on a Hemisphere and Quarter-Calotte Roof of a Biogas Plant

Christof Gromke [1], Oliver Lippert [1], Olivier Eiff [1], Rosemarie Wagner [2]

[1] *Institute for Water and Environment, Karlsruhe Institute of Technology, Karlsruhe, Germany, gromke@kit.edu*
[2] *Institute for Building Design and Technology, Karlsruhe Institute of Technology, Karlsruhe*

SUMMARY:
Surface pressure measurements at reduced-scale models of biogas plants with hemisphere and quarter-calotte roof were performed in an atmospheric-boundary-layer wind tunnel. To explore whether or not the commonly prevalent super- or trans-critical flow regimes ($Re > 10^6$) at full-scale biogas plants can be replicated at the reduced scale models, tests were done for wind tunnel Reynolds numbers ($4 \cdot 10^4 < Re < 2.7 \cdot 10^5$) at models with smooth and rough surface. The acquired mean pressure and drag coefficients suggest the realization of the super-critical regime at the models with smooth surface and of the trans-critical regime at the models with rough surface, although the wind tunnel Reynolds numbers are one order of magnitude smaller than the corresponding full-scale ones. The replication of the super-critical regime is attributed to the high turbulent approach flow and its boundary layer profile. In addition, roughening of the model surface then results in the replication of the trans-critical regime.

Keywords: Reynolds number sensitivity, non-sharp edged bodies, sand grain roughness

1. INTRODUCTION

The replica of wind loads at reduced-scale wind tunnel models of non-sharp edged bluff or semi-bluff geometries with reliable transferability to their full-scale correspondences is a critical matter in Wind Engineering. This is because typical model Reynolds numbers in wind tunnel tests are two to three orders of magnitude smaller than in full-scale and due to the lack of sharp edges at which flow separates. The flow field and surface pressure distribution remain sensitive with increasing Reynolds number and no threshold value beyond which kinematic and dynamic similarity are deemed to be satisfactorily achieved as with sharp-edged geometries, can be manifested.

The present work investigates the Reynolds number sensitivity of wind tunnel models of biogas plants with hemisphere and quarter-calotte roof (Fig. 1). Both structures consist entirely of curved shapes, whereby the one with the hemisphere roof has no sharp edge at the ring-wall roof interface and the one with the quarter-calotte roof has a 'weak-sharp' edge with an outer reflex angle of 216.9°. The models were subjected to a simulated atmospheric boundary layer and the effects of wind speed and surface roughness on the Reynolds number sensitivity of the surface pressure and drag were analysed.

2. MATERIALS AND METHODS

Two reduced-scale models (M = 1:100) of low-pressure biogas plants consisting of a bottom ring-wall covered by a hemisphere or a quarter-calotte roof were investigated in an atmospheric-boundary-layer wind tunnel (Figure 1). The models were realized with either 'smooth' or 'rough' ring-wall and roof surface whereby in the latter case sand grains with diameter $0.75 < k < 1.20$ mm were clued to the surface (Lippert, 2023). The sand grains were randomly distributed on the surfaces with an approximate average packing density of 0.08 grains/mm^2. The models were subjected to a simulated atmospheric-boundary-layer approach flow with power law profile exponents $\alpha_U = 0.26$ for the streamwise mean velocity $U(z)$ and $\alpha_I = -0.19$ for the streamwise turbulence intensity $I_U(z)$ according to $\Phi(z)/\Phi_\delta = (z/z_\delta)^{\alpha_\Phi}$ with Φ either U or I_U, z the height above ground, z_δ the boundary layer height, and θ_δ either the mean freestream velocity or the streamwise turbulence intensity at z_δ. The wind tunnel was operated at freestream velocities $5 \text{ m/s} \leq U_\delta \leq 33 \text{ m/s}$ providing a Reynolds number range of $4 \cdot 10^4 < Re < 2.7 \cdot 10^5$ where $Re = U_{crest} \cdot d_{rw}/\nu$ with U_{crest} the undisturbed approach flow velocity at crest height ($h + f$), d_{rw} the ring-wall diameter, and ν the kinematic viscosity of air. The turbulence intensity $I_U(z)$ decreased from ≈ 40% at the ground to 15 - 20% at the models' crest. Both roof types were equipped with 62 taps at which pressures were simultaneously acquired. Miniature pressure scanners (type ESP-32HD) were employed to record the pressures. Signals were sampled at a frequency f_s = 1,000 Hz for a duration of 120 s. Transfer functions presented in Bergh and Tijdeman (1965) were applied to correct for frequency-dependent amplitude gain / damping and phase shift.

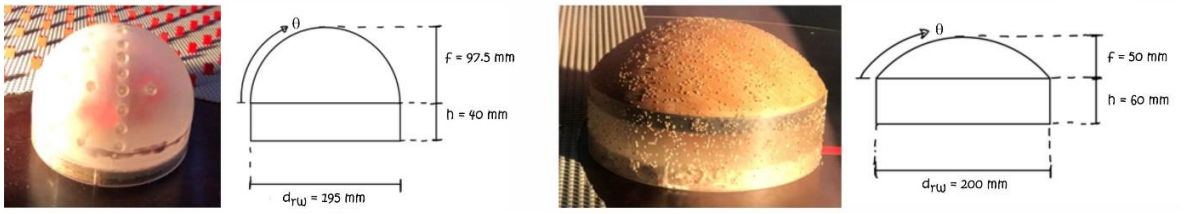


Figure 1. Models of biogas plant with 'smooth' surface and hemisphere roof (left) and 'rough' surface and quarter-calotte roof (right), including model dimensions and altitude angle θ.

3. RESULTS AND DISCUSSION

3.1. Roof surface pressure

Figure 2 presents $c_{p,mean}$-values calculated as $c_p = p/(1/2 \cdot \rho \cdot U_{crest}^2)$ along the central streamwise arch line. For the smooth roofs (a,c) marked differences at the two lowest Re in comparison to the flows at higher Reynolds numbers can be identified, whereas for the rough roofs (b,d) only at the lowest Re differences are present. Calculating the roughness element Reynolds number as $Re_k = U_{crest} \cdot k/\nu$ with k = 1.20 mm for the lowest wind speed tested results in Re_k = 260 for the hemisphere and Re_k = 240 for the quarter-calotte. The corresponding values for the second lowest wind speed are Re_k = 500 and 480, respectively, hence satisfying the relation $Re_k > 400$ required for the establishment of a turbulent boundary layer on curved surfaces as reported in Gandemer et al. (1975). The $c_{p,mean}$-curves exhibit characteristic differences between the smooth and rough surface for both roof types with the largest quantitative and qualitative differences at the crest and in base region. The minimum $c_{p,mean}$-values (maximum suction) at the crest are around 40% lower at the rough surfaces compared to the smooth surfaces whereas the $c_{p,mean}$-values in the base region exhibit stronger suction at the rough surfaces. Furthermore, the rough roof surfaces reveal a more extended base pressure region indicating an earlier separation of the boundary layer as is observed

in the trans-critical flow regime at spheres, e.g. Achenbach (1972), and cylinders with circular cross section, e.g. Ruscheweyh (1982).

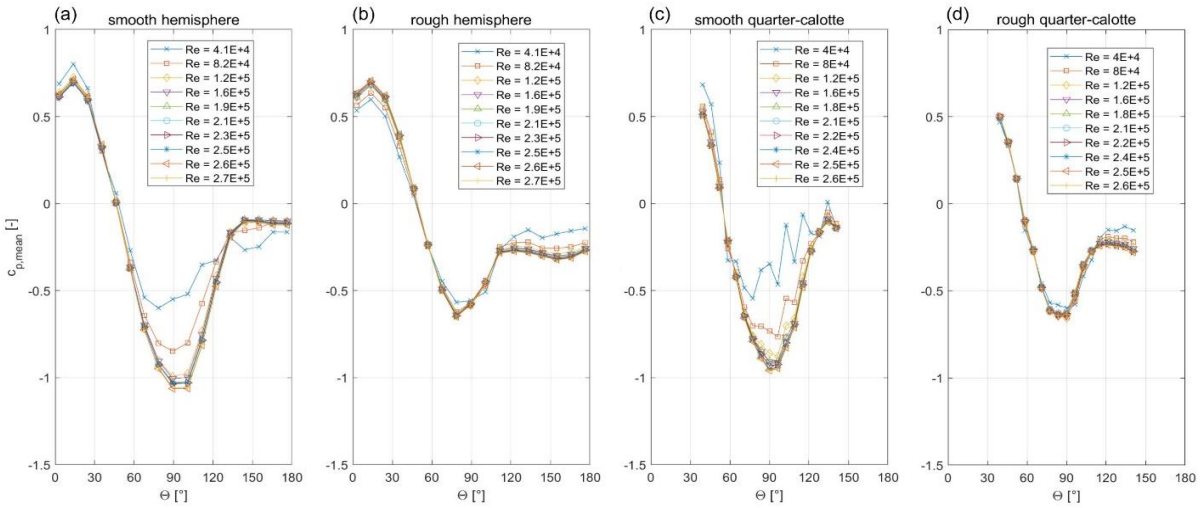


Figure 2. Distribution of pressure coefficient $c_{p,mean}$ along the central streamwise arch line on the smooth hemisphere roof (a), rough hemisphere roof (b), smooth quarter-calotte roof (c), and rough quarter-calotte roof (d).

3.2. Roof drag

The drag coefficients c_d of the roofs in dependence on the Reynolds number as obtained by integration over the surface pressure distribution are provided in Figure 3(a,b). At the smooth hemisphere roof (a), a decrease in c_d for $Re < 8 \cdot 10^4$ followed by a fairly constant course for larger Reynolds numbers can be seen. In contrary, at the rough hemisphere roof, the drag coefficient continuously increases for increasing Re with a stronger increase at lower Reynolds numbers ($Re < 1.2 \cdot 10^5$). A different picture emerges for the quarter-calotte roof. Here, at both the smooth and rough surface, the drag coefficients are virtually insensitive to the Reynolds number, whereby the c_d-values of the rough surface are around 10% higher than those of the smooth surface. Figure 3c replicates drag coefficients of spheres with smooth surface subjected to uniform flows of very low turbulence intensity in the sub-critical, critical, super-critical, and trans-critical flow regime taken from Achenbach (1972) and references therein. It is noted that the drag coefficients from panel (c) are not straightforwardly comparable in a quantitative manner to those from (a) and (b) as the latter were obtained in boundary layer flows with U_{crest} taken as the reference velocity.

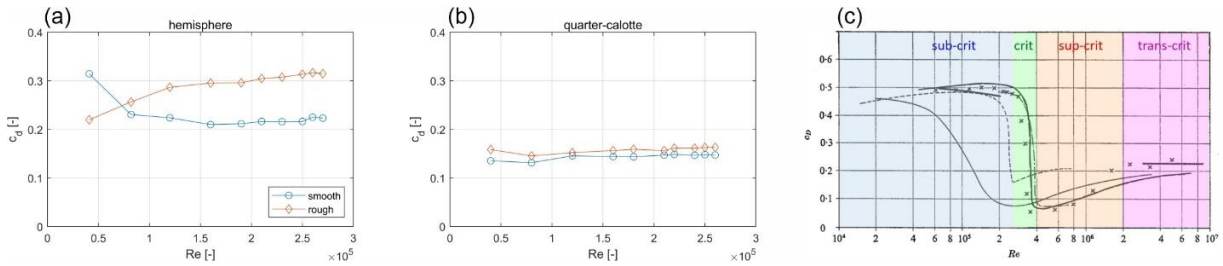


Figure 3. Drag coefficient c_d versus Reynolds number Re for the hemisphere roof (a), the quarter-calotte roof (b), and for spheres with smooth surface in uniform, very low turbulence flows (c) (Achenbach, 1972).

A qualitative comparison between panels (a) and (c) of Figure 3 shows that at the model with smooth hemisphere, the course of the c_d-values resembles that in the upper range of the critical

and the lower range of the super-critical flow regime in panel (c). At the rough hemisphere, the course of the c_d-values resembles that in the upper range of the super-critical and in the trans-critical flow regime in panel (c). Based on these observations it is hypothesized that at the model with hemisphere roof the upper critical and lower super-critical flow regime with a transition at $Re_{crit/sup\text{-}crit} \approx 8 \cdot 10^4$ are replicated in the case of the smooth surface and the upper super-critical and trans-critical flow regime with a transition at $Re_{sup\text{-}crit/trans\text{-}crit} \approx 1.2 \cdot 10^5$ in the case of the rough surface. The occurrence of the critical and super-critical regime at the smooth hemisphere at lower Reynolds numbers than in other studies (e.g. Achenbach, 1972; Ruscheweyh, 1982) is attributed to the highly turbulent boundary layer approach flow and to the supposedly turbulent boundary layer at the roof surface right from the windward eave. In the above mentioned studies, in contrast, the approach flow is uniform and of low turbulence and the transition from a laminar to a turbulent surface boundary layer occurs at the object. Notably increasing the surface roughness, e.g. by sand grains as was done in this work, then results in an enhanced energy extraction from the surface boundary layer and the occurrence of the trans-critical flow regime.

At the quarter-calotte roof, the drag coefficients for the smooth and rough surface appear insensitive to the Reynolds numbers realized in the current study (Figure 3b). This does not allow for an attribution to any flow regime. However, the distinct $c_{p,mean}$-courses in Figure 2 in panels (c) and (d) clearly indicate the presence of different flow regimes and suggest that the 'weak-sharp' edge at the ring-wall roof interface is not sharp enough to trigger flow separation. The lower suction $c_{p,mean}$-values at the crest and the extended base pressure region with larger suction in panel (d) compared to panel (c) suggest the presence of the trans-critical regime at the rough surface and of the super-critical regime at the smooth surface, which is further substantiated by the approximately 10% higher drag coefficients at the rough surface (Figure 3b).

4. CONCLUSIONS

The obtained mean pressure and drag coefficients provide evidence for the simulation of the super- and trans-critical flow regimes at biogas plants with hemisphere or quarter-calotte roof at scaled models (M in the order of magnitude 1/100) in atmospheric-boundary-layer wind tunnels. The present investigation suggests that the highly turbulent boundary layer approach flow in this type of wind tunnel and the supposedly turbulent boundary layer on the entire model surface result in a super-critical regime. By further roughening the model surface, e.g. by sand grains, a trans-critical regime is realized.

ACKNOWLEDGEMENTS

Funding was provided by the EU under (PR 101079125) TWEET-IE: Twin Wind tunnels for Energy and the Environmen T - Innovations and Excellence.

REFERENCES

Achenbach, E., 1972. Experiments on the flow past spheres at very high Reynolds numbers. Journal of Fluid Mechanics 54, 565–575.

Bergh, H., Tijdeman, H., 1965. Theoretical and experimental results for the dynamic response of pressure measuring systems. National Lucht- en Ruimtevaartlaboratorium (NL), report number: NLR-TR F.238.

Lippert, O., 2023. Untersuchungen zur Winddruckverteilung auf Abdeckungen von Niederdruckspeichern für Biogas. Karlsruhe Institute of Technology KIT, Institute for Hydromechanics, Laboratory of Building and Environmental Aerodynamics, BSc thesis.

Gandemer, J., Barnaud, G., and Biétry, J., 1975. Études de la tour D.M.A. Partie I, Étude des efforts dûs au vent sur les façades. Centre Scientifique et Technique du Bâtiment, Nantes, France.

Ruscheweyh, H., 1982. Dynamische Windwirkung an Bauwerken - Band 1: Grundlagen. Bauverlag GmbH, Wiesbaden and Berlin, Germany.

Round-Robin Wind Tunnel Testing for High-Rise Buildings: Impact of Approach Flow Variations on Aerodynamics and Structural Response

DongHun Yeo [1], Adam L. Pintar [2], Girma Bitsuamlak [3], Arindam Gan Chowdhary [4], Tsinuel Geleta [5], Kurtis R. Gurley [6], Stéphanie Hartlin [7], Un Yong Jeong [8], Sukjun Joo [9], Sunho Kim [10], Soon Duck Kwon [11], Seungho Lee [12], Jens Møller-Madsen [13], Claudio Mannini [14], Tommaso Massai [15], Søren F. Østbirk [16], Brian M. Phillips [17], and Ioannis Zisis [18]

[1,2] *National Institute of Standards and Technology, Gaithersburg, Maryland, USA, donghun.yeo@nist.gov / adam.pintar@nist.gov*
[3,5] *Univ. of Western Ontario, London, Ontario, Canada, gbitsuam@uwo.ca / tgeleta@uwo.ca*
[4,18] *Florida International Univ., Miami, Florida, USA, chowdhur@fiu.edu / izisis@fiu.edu*
[6,17] *Univ. of Florida, Gainesville, Florida, USA, kgurley@ufl.edu / brian.phillips@essie.ufl.edu*
[7,8] *Gradient Wind, Ottawa, Ontario, Canada, stephanie.hartlin@gradientwind.com / unyong.jeong@gradientwind.com*
[9,10] *TE Solution, Anseong, Gyeonggi, South Korea, sjjoo@tesolution.com / ksh@tesolution.com*
[11,12] *KOCED Wind Tunnel Center, Jeonbuk National University, Jeonju, Jeonbuk, South Korea, sdkwon@jbnu.ac.kr / guide1th@jbnu.ac.kr*
[13,16] *SOH Wind Engineering, Copenhagen, Denmark, jmm@sohwind.com / sfo@sohansen.dk*
[14,15] *Interuniversity Research Centre on Building Aerodynamics and Wind Engineering (CRIACIV), Firenze, Italy, claudio.mannini@unifi.it / tommaso.massai@unifi.it*

SUMMARY:
Previous studies suggest that variations in experimental approach flows are a significant factor contributing to differences in pressure measurements between wind tunnels, especially when experimental and measurement errors are managed within acceptable limits. To investigate the impact of approach flow variations on the total uncertainties in pressure measurements and structural response estimates of buildings across wind tunnel tests, approximately ten research and commercial laboratories are conducting a round-robin comparison study. This study involves rigorous measurement and analysis of their experimental approach flows and aerodynamic pressures on a high-rise building. The findings will be used to enhance the provisions for experimental approach flows in standards for wind tunnel testing procedures, ensuring compliance with the total uncertainty budget for structural design. Additionally, this study will provide valuable insights for developing consensus-based validation case studies for Computational Fluid Dynamics (CFD) simulation procedures in structural wind engineering applications. Preliminary findings from this ongoing round-robin project will be presented.

Keywords: Approach flow, High-rise buildings, Structural response, Uncertainty, Urban environment, Wind tunnel testing.

1. INTRODUCTION

In the early 2000s, National Institute of Standards and Technology (NIST) undertook a study to examine variations in pressure measurements for low-rise building models across six wind tunnels (Fritz et al. 2008). The study revealed significant variations in peak pressure coefficients and structural response, up to 40 %, which could be attributed to differences in approach flow, characteristics of instrumentation frequency response, reference pressure measurements, and the ratio of model dimension to integral length scale. These factors have also been explored in the context of wind tunnel measurements for high-rise building models by various researchers (Melbourne 1980; Goliger and Milford 1988). While some inconsistencies were found in their contributions, the majority of studies identified the variation in approach flow for a given target exposure as a key factor contributing to differences between wind tunnels. This could be particularly the case when wind tunnel laboratories are able to manage experimental errors, other than those associated with the generated approach flow, within an acceptable budget. These errors include measurement errors related to, e.g., transducer drift, dynamic pressure calibration, and the reference wind speed and static pressure, and experimental model errors related to e.g., the layout and density of pressure taps on a building model as well as the edge curvatures of the building model.

To achieve a comprehensive understanding of the impact of approach flow, this research aims to explore the relationship between variations in experimental approach flow and the resulting aerodynamic pressure measurements and structural response estimates of buildings. This examination is conducted through a round-robin test comparison across multiple wind tunnel laboratories while minimizing the influence of other factors in the tests.

2. PROCEDURE FOR ROUND-ROBIN COMPARISON STUDY

This round-robin study brings together approximately 10 research and commercial wind tunnels to enhance our understanding of how approach flow variations affect wind tunnel pressure measurements and subsequently impact building response estimates. It investigates the variations in approach flow across wind tunnels and their propagation into pressure measurements on building envelopes and pressure-based structural response estimates for a high-rise building, known as the CAARC (Commonwealth Advisory Aeronautical Research Council) building (Melbourne 1980), in both isolated and urban environments. Figure 1 depicts the proximity model used for the testing in the urban environment. The building outlined with white lines at the center of the testing section is the CAARC building, where pressure measurements on its envelope will be taken from various wind directions.

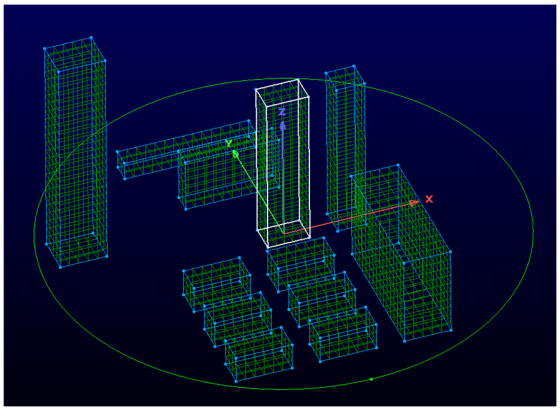


Figure 1. The proximity model for surrounding buildings around the testing building.

To isolate the impact of experimental and measurement errors, the study also collects data on aspects such as tubing responses, tap locations, and the referencing measurement system. In addition, the study conducts a comprehensive assessment of both individual and total uncertainties in the measurements and building response estimates. This rigorous approach ensures a more accurate understanding of the factors influencing wind tunnel pressure measurements and their implications for building response estimates.

Figure 2 shows the procedure for this round-robin comparison study, which comprises four stages. The project has completed the planning phase and is currently in the "measurement" and "analysis" phases.

1. Planning	2. Measurement	3. Analysis	4. Publication
Recruitment of participants Detailed testing procedures Targeted profiles of approach flow Requirements of - Reference speed measurement - Density of pressure taps - Curvature of model edges - Measurement duration - Minimum sampling rate	Approach flow in: - An empty domain - An urban environment Pressures on: - An isolated building in the empty domain - A building in the urban environment	Variations in - Approach flow - Tubing response - Environmental conditions - Pressures - Structural response Propagation of variations	Journals / Conferences Data (through a website) Proposal for updates to standard provisions Benchmark case for CFD validation

Figure 2. Procedure for the round-robin project.

3. EXPECTED CONTRIBUTIONS FROM FINDINGS

The findings of this study will be utilized to improve the provision regarding experimental approach flows in wind tunnel testing procedure standards, such as ASCE (American Society of Civil Engineers) 49 Standard (ASCE 2021), ensuring they comply with the total uncertainty budget for wind tunnel experiments in the context of structural design.

Additionally, the study is poised to offer invaluable insights that can be utilized for the validation of Computational Fluid Dynamics (CFD) simulation results. The experimental datasets will be employed to develop consensus-based validation case studies based on reliable wind tunnel data. This process will ultimately culminate in the development of guidelines for the application of CFD procedures to structural wind engineering. These specific areas were highlighted as the second and highest priority research needs during the workshop on "Advancements in Computational Wind Engineering" held at the ASCE headquarters on May 18 and 19, 2023 (Scott et al. 2023).

4. CONCLUDING REMARKS

The presentation aims to introduce the round-robin project and its preliminary results to the structural wind engineering community. By detailing the methodology, initial findings, and insights gained from this collaboration effort, this study will shed light on how variations in the characteristics of experimental approach flows result in differences in the aerodynamic pressure measurements and the structural response estimates of buildings.

ACKNOWLEDGEMENTS
The authors express their sincere gratitude to all the participating groups in this study for their invaluable cooperation in providing feedback on the plan and supplying data in a timely fashion. Their dedicated efforts in enhancing wind tunnel testing techniques and procedures, as well as advancing CFD methods in wind engineering applications, are greatly appreciated.

REFERENCES
ASCE (2021). *Wind tunnel testing for buildings and other structures (ASCE/SEI 49-21)*, ASCE Standard ASCE/SEI 49-21, American Society of Civil Engineers, Reston, VA.

Fritz, W. P., Bienkiewicz, B., Cui, B., Flamand, O., Ho, T. C. E., Kikitsu, H., Letchford, C. W., and Simiu, E. (2008). "International comparison of wind tunnel estimates of wind effects on low-rise buildings: test-related uncertainties." *Journal of Structural Engineering*, 134(12), 1887-1890.

Goliger, A. M. and Milford, R. V. (1988). "Sensitivity of the CAARC standard building model to geometric scale and turbulence." *Journal of Wind Engineering and Industrial Aerodynamics*, 31(1), 105-123.

Melbourne, W. H. (1980). "Comparison of measurements on the CAARC standard tall building model in simulated model wind flows." *Journal of Wind Engineering and Industrial Aerodynamics*, 6(1-2), 73-88.

Scott, D., Goupil, J., Burton, M., Gorlé, C., Kareem, A., Stathopoulos, T., and Young, B. (2023). *Advancements in Computational Wind Engineering: Workshop Report*. National Institute of Standards and Technology, Gaithersburg, MD.

Investigation of the impact of roof ancillary structure on the wind load distribution of high-support photovoltaic array

Linyuan SHAO [1], Tianzhu WU [2], Haiwei XU [3]

[1] *College of Civil Engineering and Architecture, Zhejiang University, Hangzhou, China, Email: shaoly@zju.edu.cn*
[2] *College of Civil Engineering and Architecture, Zhejiang University, Hangzhou, China, Email: 22312213@zju.edu.cn*
[3] *College of Civil Engineering and Architecture, Zhejiang University, Hangzhou, China, Email: haiweix@zju.edu.cn*

SUMMARY
To make full use of space, the application of high support in roof PV power station is becoming more and more extensive, and the roof auxiliary structure will produce significant aerodynamic interference effect on the incoming flow, increasing the complexity of wind load design.
However, most of the existing research focus on the ideal roof low-support power station without interference. Thus, this study carried out the wind tunnel pressure test on the high-support PV array with auxiliary structure interference under a typical real roof, aiming to explore the influence of auxiliary structure interference on the wind pressure distribution of PV power station, and compared with the current specifications. It was found that compared with the low support on the ideal flat roof, the negative wind suction of the high support photovoltaic array in the windward area near the eaves is significantly increased. In addition, the aerodynamic interference of the auxiliary structure will lead to a large positive wind pressure in the local area of the photovoltaic array, which needs to be paid attention to in the design.

Keywords: High Support, Roof Ancillary Facilities, Wind Tunnel Test

1. INTRODUCTION

In recent years, Photovoltaic (PV) power generation has garnered significant attention and experienced rapid growth. The successive introduction of distributed PV policies has significantly promoted the robust development of roof PV power stations. Compared to ground-mounted PV systems, roof PV systems offer several advantages, including minimal land occupation, proximity to load centers, and the convenience of localized energy consumption. However, they are particularly sensitive to wind loads, and incidents of wind-related damage occur frequently, posing adverse effects on both personal safety and property security. Many researchers have conducted studies on the wind effects of roof PV power stations, contributing to the development of wind resistance standards(Dai et al., 2022; Giorges et al., 2014; Stenabaugh et al., 2015; Warsido et al., 2014).

Most previous studies had focused on ideal roofs, without considering the various ancillary structures present on actual roofs. However, real roofs often contain equipment rooms, stairwells, water tanks, and other ancillary structures, which undoubtedly increase the complexity of the aerodynamic forces acting on roof PV power stations. The wind load distribution characteristics

can differ significantly from those on typical roofs. On the other hand, in order to make full use of roof space, high mounting systems have been increasingly employed in the construction of roof PV power stations in recent years. These high mounts typically stand 2.5 to 3 m above the roof, extending beyond the parapet to effectively utilize the space beneath the mounts. Compared to traditional low supports that are positioned close to the roof (e.g., 0.5 m above), high supports are taller and receive less obstruction from parapets, resulting in notable differences in wind effects and wind resistance risks. Currently, there have been no reports on the wind effects of high mounting structures on real roofs with interference. Therefore, it is essential to conduct targeted analyses in this area.

In this study, a typical distributed roof PV power station located in a typhoon-prone industrial park in the southeastern coastal region of China was examined. The wind tunnel test was conducted to investigate the wind load characteristics of high-mounted PV structures, particularly focusing on the adverse effects of roof ancillary structures on the wind load distribution and compared with existing standards. The aim is to provide valuable insights for the wind resistance design of similar roof systems.

2. MODEL AND EXPERIMENTAL SETUP

The distributed roof PV power generation project is situated on a typical building with dimensions of 80.0 m (length) × 50.0 m (width) × 20.2 m (height). The PV modules are installed on the roof of the factory building. The flat roof features several ancillary structures. To optimize the use of roof space, a frame-type steel structure with high support has been employed. These supports are positioned 2.6 m above the roof surface, extending 1.05 m above the designed parapet height. The PV modules are tilted southward at an angle of 2° (Figure 1).

The test was conducted in the ZD-1 Boundary Layer Wind Tunnel at Zhejiang University, which has a test cross-section of 4 m (width) × 3 m (height), with a scale ratio of 1:60, as shown in Figure 1. The model has a maximum blockage ratio of 3.7%, meeting the requirements of wind tunnel tests, and the turbulence profile simulated by wind tunnel is shown in Figure 2. The actual PV supports extend significantly above the parapet height. Additionally, the wind direction angles for the experimental tests ranged from 0° to 345° in 15° increments (Figure 3).

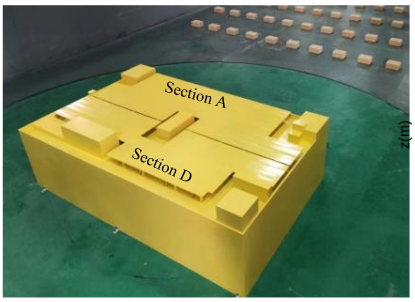


Figure 1. Test model

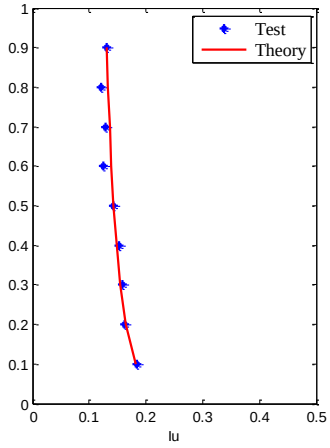


Figure 2. Turbulence profile simulated by wind tunnel

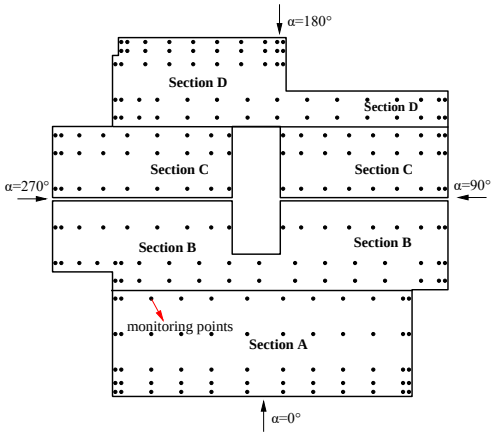


Figure 3. Area division and wind direction angle diagram

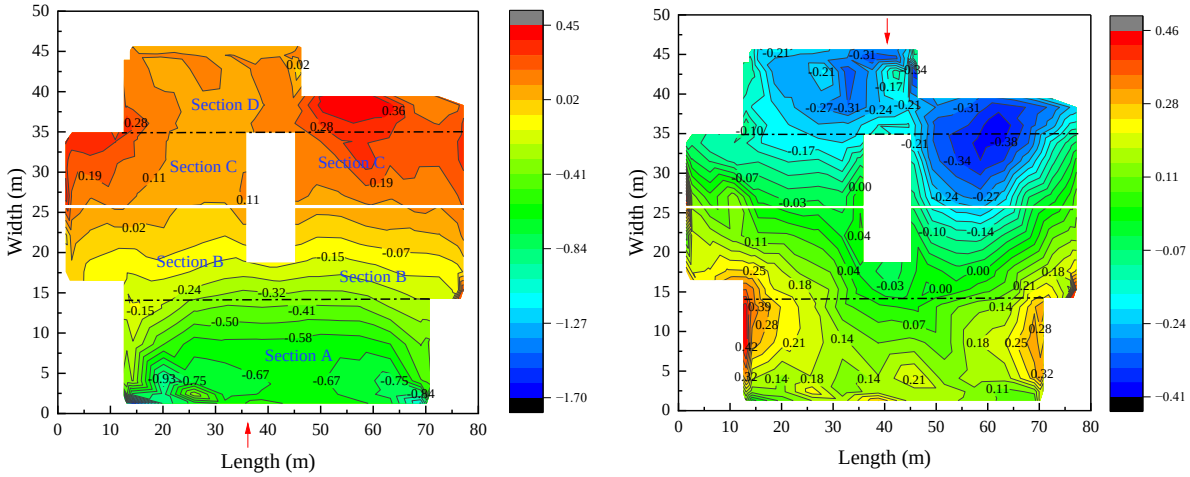
3. ANALYSIS OF WIND LOAD CHARACTERISTICS FOR ROOF PV SYSTEMYS

Numerous research studies have been conducted on the wind load characteristics of ideal flat roofs with low-support PV array, excluding other ancillary facilities. Table 1 presents the distribution results of wind pressure shape coefficients for ideal flat roofs at wind direction angles of α=0° and 180° (Kopp et al., 2012b; Yao et al., 2022b). The definition of wind direction angles is aligned with that used in this study, where the upper surface of the PV panel is oriented toward the wind at α=0° and the lower surface is oriented toward the wind at α=180°. The wind load shape coefficients reported in various studies are generally found to fall within the range of -0.25 to 0.2, for ideal flat roofs with low-slope components. This is attributed to the fact that, for nearly flat-mounted modules, the wind pressures acting on the upper and lower surfaces largely cancel each other out, resulting in a minimal net wind load effect.

Table 1. Research results of wind pressure on ideal flat roof PV array under typical wind direction

Data sources	Model	Wind pressure shape coefficients (α=0°)	Wind pressure shape coefficients (α=180°)
(Kopp et al., 2012)	Flat roofs: 2° module inclination	-0.05~0.05	-0.12~0.1
(Yao et al., 2022)	Flat roofs: 5° module inclination	-0.2~0.1	-0.1~0.2

For the high-support PV station with roof interferences, Figure 4(a) and (b) present the wind load shape coefficient distributions for wind directions of α=0° and 180°, respectively. The windward end modules (Section A) exhibit corner and middle region coefficients of -1.10 and -0.7 to -0.6, respectively at α=0°. These coefficients rapidly decay along the flow direction, and in the wake sections (such as Sections C and D), a relatively large positive wind load shape coefficient of around 0.3 is formed.



(a) α=0° (b) α=180°

Figure 4. The shape coefficients for typical wind directions (h=1.55 m)

Compared to the ideal roof low-support PV in Table 1, the adverse suction at the windward end of the high-support PV array is significantly enhanced. This enhancement is attributed to the intensified columnar separation vortices at the windward leading edge caused by the interference of ancillary structures, which result in greater suction on the upper surface of the PV modules. At

the wind direction of 180°, the modules in the windward end section (Section D) are still positioned some distance from the eave parapet, thus remaining outside the airflow separation zone. This results in less significant negative wind load shape coefficients, mostly ranging from -0.2 to -0.3, while the positive wind load shape coefficients in the wake sections (such as Section A) are around 0.2. Under these conditions, the values are close to the overall range of values for the ideal flat roof scenario presented in Table 1. Regardless of whether the wind direction is $\alpha=0°$ or $\alpha=180°$, the wind loads on the PV modules located in the middle sections of the roof are not significant. Furthermore, the maximum negative suction primarily occurs at the two corner sections on the southern side of section A, with the minimum shape coefficient values reaching below -1.0, according to the distribution of the most unfavorable negative shape coefficients for distributed high-support PV systems on roofs across wind directions ranging from 0° to 345°. This value exceeds -0.95 set by the relevant specifications of China.

4. CONCLUSIONS

The wind tunnel test is conducted to investigate the wind load on a high-support PV array installed on a real flat roof. The main conclusions are as follows:

1) Compared to low-support arrays on an ideal flat roof, the negative wind suction on high-support PV array near the eaves in the windward zone is significantly increased. The interference from roof auxiliary structures causes the negative wind pressure in local areas of the PV array to disappear, resulting in relatively large positive wind pressure.
2) The use of current standards in design may result in the underestimation of adverse wind suction on high-support PV stations on roofs as discussed in this study. Consequently, the complex aerodynamic phenomena generated by the roof and its interfering structures may not be adequately captured.

ACKNOWLEDGEMENTS

The work described in this paper was partially supported by the National Natural Science Foundation of China (Project No. 51978614). This support is much appreciated.

REFERENCES

Dai, S.F., Liu, H.J., Yang, J.H., Peng, H.Y., 2022. Wind loads on roof-mounted isolated solar panels of tall buildings through wind tunnel testing. Sol. Energy 231, 607–622.

Giorges, A.T.G., Amador, G.J., Goodman, J., 2014. Numerical Study of Wind Loads on Residential Roof-Mounted Solar Photovoltaic Arrays, in: Volume 6B: Energy. Presented at the ASME 2014 International Mechanical Engineering Congress and Exposition, American Society of Mechanical Engineers Digital Collection.

Kopp, G.A., Farquhar, S., Morrison, M.J., 2012. Aerodynamic mechanisms for wind loads on tilted, roof-mounted, solar arrays. J. Wind Eng. Ind. Aerodyn. 111, 40–52.

Stenabaugh, S.E., Iida, Y., Kopp, G.A., Karava, P., 2015. Wind loads on photovoltaic arrays mounted parallel to sloped roofs on low-rise buildings. J. Wind Eng. Ind. Aerodyn. 139, 16–26.

Warsido, W.P., Bitsuamlak, G.T., Barata, J., Gan Chowdhury, A., 2014. Influence of spacing parameters on the wind loading of solar array. J. Fluids Struct. 48, 295–315.

Yao, J., Tu, Z., Wang, D., Shen, G., Lou, W., 2022. Experimental Investigation of Wind Loads on Roof-Mounted Solar Arrays. Sustainability 14, 8477.

Real-Time Hybrid Simulation on Wind and Wave Load Responses of Floating Structures

Giheon You [1], Yunbyeong Chae [2]

[1]*Seoul National University, Seoul, Republic of Korea, yugihun0628@snu.ac.kr*
[2]*Seoul National University, Seoul, Republic of Korea, ybchae@snu.ac.kr*

SUMMARY:
The determination of the response of a floating structure is a crucial issue for its design and operation. The floating structure is subject to loads from both water and wind, but there are limitations to obtaining both through analysis alone. Due to limitations in equipment and facilities, conducting model tests on the entire structure is also challenging. In this study, a Real-Time Hybrid Simulation (RTHS) is suggested, combining analytically modeled hydrodynamic loads with wind tunnel experiments. The motion of the floating body is simulated based on the Cummins equation, a time-domain equation of motion, with additional nonlinear fluid forces. The wind loads measured through a 6-axis load cell in the wind tunnel experiment are reflected in real-time on the displacement response of the analytical floating body. The determined displacement of the floating body is applied to the model in real-time through a 6-DOF actuating system. To achieve this, the analytical modeling and verification of the floating body were conducted, and a 6-DOF actuating system was developed which has low time delay and high accuracy on displacement control for RTHS.

Keywords: Real-Time Hybrid Simulation, Floating Structures, 6-DOF Actuating System

1. INTRODUCTION

Innovative floating bridge designs, like cable-stayed bridges with TLP pylons, are proposed for crossing deep, wide waters where conventional bridges face limitations. These structures are significantly influenced by wave and wind forces, making it challenging to accurately assess performance through analysis alone. Experimental validation through scaled model tests in wave tanks or wind tunnels is thus necessary. However, due to equipment and similarity law limitations, accurately simulating both wave and wind loads simultaneously remains difficult. In this study, a Real-Time Hybrid Simulation (RTHS) of floating structures is proposed for floating structures, where the superstructure affected by wind loads is tested in a wind tunnel using a scaled model, and the substructure affected by wave loads is analytically modeled. For this purpose, the analytical model of the floating structure was developed to calculate the displacement response of the floating body, along with the construction of a 6-DOF actuating system to apply real-time displacements.

2. ANALYTICAL FLOATING STRUCTURE MODEL

2.1. Modeling of Analytical Floating Structure

The floating body is assumed to behave as a rigid body with 6-DOF. In the time domain, the motion of the floating body is governed by the Cummins equation which is presented as Eq. (1) (Cummins,

1962);

$$[\mathbf{M} + \mathbf{A}^{\infty}]\ddot{\mathbf{x}}(t) + \int_0^t \mathbf{R}(t-\tau)\dot{\mathbf{x}}(\tau)d\tau + \mathbf{C}\mathbf{x}(t) = \mathbf{F}(t) \quad (1)$$

where $\mathbf{x}$, $\mathbf{M}$, $\mathbf{A}^{\infty}$, $\mathbf{R}$, $\mathbf{C}$, and $\mathbf{F}$ denote 6-DOF displacement of floating body, inertia matrix, added mass matrix at infinite frequency, retardation function, hydrostatic restoring matrix, and external force vector, respectively. The first-order wave load can be represented using a frequency-domain transfer function that describes the amplitude ($P_j(\omega)$) and phase lag ($\varphi_j(\omega)$) of the wave force. When the wave with amplitude A and frequency ω incomes, the first-order wave load is given by Eq. (2) (Ansys Inc., 2022).

$$F_j(t) = P_j(\omega)A\cos\left(\omega t + \varphi_j(\omega)\right) \quad (2)$$

The second-order wave load is proportional to the product of the amplitudes of two waves. This can also be expressed using a quadratic transfer function (QTF) for the amplitude and phase, which is represented in matrix form. The Morison drag represents the resistive force exerted on an object moving through the water and can be expressed by Eq. (3);

$$d\mathbf{F}_D = \frac{1}{2}C_D\rho dA(\mathbf{u}-\mathbf{v})|\mathbf{u}-\mathbf{v}| \quad (3)$$

where $d\mathbf{F}_D$, C_D, ρ, dA, $\mathbf{u}$, and $\mathbf{v}$ denote drag force, drag coefficient, fluid density, small cross-sectional area of Morison member, velocity of fluid, and velocity of Morison member.

2.2. Verification of Analytical Floating Structure

The verification of the analytical floating structure model was conducted using the OC4, a benchmark model for floating offshore wind turbine (Robertson et al., 2014). By using Ansys AQWA, the added mass, radiation damping, and wave load transfer functions in the frequency domain were obtained and then converted to time-domain coefficients

The response amplitude operator (RAO) was derived from the structure's steady-state response to regular waves and compared with frequency domain analysis results. For irregular waves, the response spectrum was verified by comparing the product of the wave spectrum and the square of RAO with the power spectrum of analysis results. Verification results for heave and pitch responses are shown in Fig. 1. The modeling of Morison drag was verified through free decay test. The results were compared by applying the same parameters in OrcaFlex, and the comparison is shown in Fig. 2.

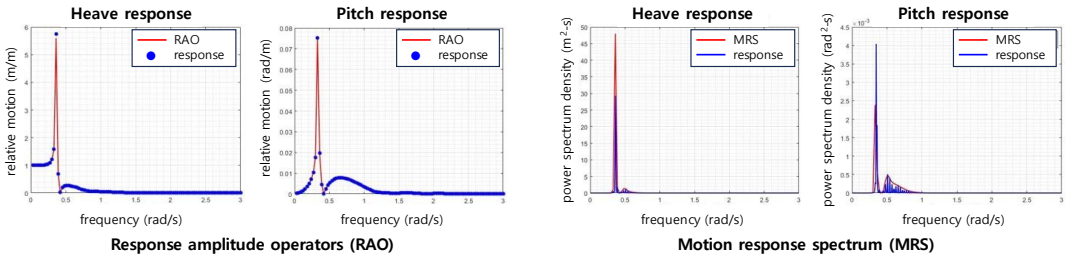


Figure 1. Verification results for regular wave results (left) and irregular wave response (right)

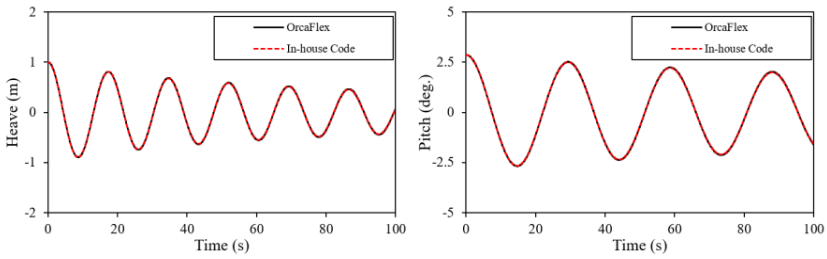


Figure 2. Time-displacement results of the heave and pitch free decay test

3. EXPERIMENTAL SETUP AND 6-DOF ACTUATING SYSTEM

3.1. Experimental Setup

The experimental setup includes a 6-DOF actuating system, a 6-axis load cell, a target PC, a test model, and a wind tunnel. Wind loads generated in the tunnel are measured with the load cell and input into the target PC, where they are applied to the analytical structure and used for numerical integration and real-time control of the 6-DOF actuating system.

3.3. 6-DOF Actuating System

The 6-DOF actuating system, consisting of an upper and base plate connected by six linear motors, adjusts the upper plate's displacement through motor length adjustments, allowing for 6-DOF movement. Inverse kinematics calculates the motor lengths from the 6-DOF displacements, while forward kinematics computes the 6-DOF displacements from the motor lengths. The system uses reference configuration coordinates to determine the coordinates of the upper joint $\mathbf{U}_i$ and the length of each motor L_i by calculating the distance between the joints on the upper and lower plates. The equations are given as Eq. (4);

$$\mathbf{U}_i = \mathbf{R}(\mathbf{U}_i^r - \mathbf{H}) + \mathbf{T} + \mathbf{H},\ L_i = \|\mathbf{U}_i - \mathbf{B}_i\| \tag{4}$$

where $\mathbf{R}$ is 3-dimensional rotation matrix due to the rotation of the upper plate, $\mathbf{T}$ is the translational displacement vector, $\mathbf{U}_i^r$ and $\mathbf{B}_i$ are the coordinates of the upper and lower joints of the i-th motor in the reference configuration.

Determining the 6-DOF displacement from measured motor lengths requires an iterative calculation using gradient descent for forward kinematics. In the n-th iteration, the object function $F_n(\mathbf{u})$ is calculated between the estimated length l_{jn} of the j-th motor for an assumed displacement in i-th DOF u_{in} and the measured length L_j. To minimize $F_n(\mathbf{u}_n)$, the gradient ∇F_{ni} is used to update the estimate of $u_{i(n+1)}$. When $F(\mathbf{u}_n)$ converges to a small value, $\mathbf{u}_n$ is taken as the 6-DOF displacement at that time step. This process is described by Eq. (5);

$$F_n(\mathbf{u}_n) = \sqrt{\sum_{j=1}^{6}(L_j - l_{jn})^2},\ \nabla F_{ni} = \frac{\partial F_n}{\partial u_{ni}},\ u_{i(n+1)} = u_{in} - k_i F_n \nabla F_{ni} \tag{5}$$

where k_i is the learning rate, which controls the speed and stability of the iterative process.

Minimizing time delay is essential for high-accuracy RTHS. The adaptive time series (ATS)

compensator was applied as the time delay compensation algorithm with one ATS compensator applied to each motor (Chae et al., 2013). Fig. 3 compares the z-direction displacement over time with and without the ATS compensator for a sinusoidal input of 10mm amplitude and 1Hz frequency. Applying the ATS compensator significantly reduced both time delay and amplitude errors. Without the ATS compensator, the time delay was around 20ms with an amplitude error of about 1.55mm. with the ATS compensator, the time delay was reduced to under 2ms, and the amplitude error was reduced to approximately 0.03mm.

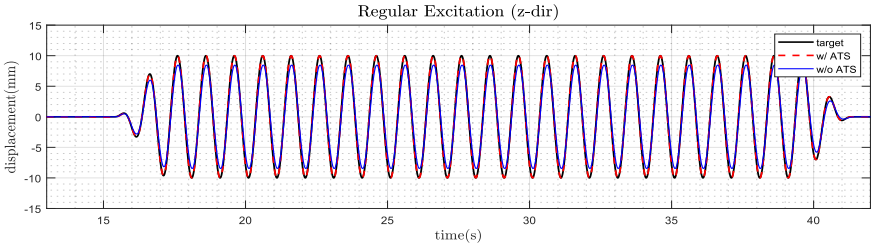


Figure 3. Comparison of the measured displacement with the target displacement

4. CONCLUSIONS

This study developed and verified analytical floating structure and 6-DOF actuating system for RTHS on a floating structure subjected to wind and wave loads. The analytical modeling of the substructure, subjected to wave loads, used the Cummins equation, with coefficients transformed from frequency domain values obtained from Ansys AQWA. The Morison drag was calculated using the Morison equation by defining elements. The experimental setup for simulating 6-DOF response of the floating system included a target PC for control, a wind tunnel, a 6-axis load cell, and a 6-DOF actuating system. Inverse kinematics controlled the system, while the ATS compensator minimized time delay and amplitude errors.

ACKNOWLEDGEMENTS

This work is supported by the Korea Agency for Infrastructure Technology Advancement (KAIA) grant funded by the Ministry of Land, Infrastructure and Transport (Grant RS-2023-00250727) through the Korea Floating Infrastructure Research Center at Seoul National University.

REFERENCES

Ansys Inc., 2022. Aqwa Theory Manual. Canonsburg, PA, USA.

Chae, Y., Kazemibidokhti, K., Ricles, J. M., 2013. Adaptive time series compensator for delay compensation of servo-hydraulic actuator systems for real-time hybrid simulation. Earthquake Engineering & Structural Dynamics, 42(11), 1697–1715.

Cummins, W. E., 1962. The impulse response function and ship motions. Schiffstechnik, 9, 101–109.

Robertson, A., Jonkman, J., Masciola, M., Song, H., Couppee, A., Coulling, A., Luan, C., 2014. Definition of the semisubmersible floating system for phase II of OC4 (No. NREL/TP-5000-60601). National Renewable Energy Lab. (NREL), Golden, CO, USA.

Terrain Effects on Wind Loads of Ground-Mount PV Systems

Daniel Markus [1], André Stollenwerk [2]

[1]*I.F.I. Institut für Industrieaerodynamik GmbH, Aachen, Germany, markus@ifi-ac.com*
[2]*stollenwerk@ifi-ac.com*

SUMMARY:
Boundary layer wind tunnel tests will be conducted with a scaled model of a PV ground-mount system in different topographic settings. First, individual rows will be placed at a larger height to investigate the effects on leeward rows. Second, the array will be installed on a large slope. The tests aim at a better understanding of topographic effects in the wind load of PV ground-mount systems.

Keywords: topography, PV ground-mount, wind load

1. GENERAL INSTRUCTIONS

Wind loads on photovoltaic ground-mount systems are usually determined based on wind tunnel testing. As the sizes of the projects are often on a utility scale covering areas of several hectares or more, even small changes in cost have a significant impact and the precise knowledge of wind loads as the governing parameter for design and cost is essential.

As wind tunnel studies aim at universal applicability the ground floor is usually modelled as uniformly even and flat, whereas in real applications the ground may show significant changes in terrain over an area of several hectares or more. While the effects of an overall increased ground clearance of a whole array have already been addressed (Markus & Weihbrecht, 2023), the effect on individual rows and vertical offsets remains unclear. Changes in terrain affect the wind loads in different ways: change in velocity pressure due to speed ups, higher exposition and loss of wind shelter due to vertical offsets, change in effective tilt angle of tables etc.

In addition to undulating terrain, the above questions are even more important in case of installations on mountain slopes, which feature inclines over a larger scale. This becomes more important as more land might be suitable to solar installations in this case.

2. PLANNED TESTING

As the first major building code to cover ground-mount PV systems in detail, ASCE 7-22 does not directly give a tolerance on vertical offsets between consecutive rows, but it states that results are applicable if the ratio of mean height to chord length is between $0.5 \leq (h/L_c) \leq 0.8$, thus implicitly allowing a tolerance of $\Delta h = 0.3\, L_c$ which amounts to 0.6m for $L_c = 2.0\text{m}$.

Moreover, ASCE 7-22 states that if the topographic factor $K_{zt} > 1.0$ then all rows within the array need to be treated as perimeter or edge rows, eliminating any shielding and reduction in wind loads for interior rows.

In order to quantify the above given aspects and questions a series of wind tunnel tests was planned and testing has commenced in the beginning of November 2024. Based on a previous testing campaign for a ground-mount system (Kray & Markus, 2019), which provides the baseline reference for the current campaign, different scenarios shall be investigated in which height differences between consecutive rows shall be looked upon via measurements of the surface pressure distribution in a boundary layer wind tunnel.

First, a vertical offset of a single row within an otherwise even and flat array is examined to quantify a threshold height, above which wind load characteristics fundamentally change for the row in question and leeward rows. Second, the installation of rows on a large-scale slope shall be modelled to further investigate the influence of effective tilt angle, i.e. the angle between the solar module and the ground. Both scenarios are depicted in Figure 1 and shall be investigated for different tilt angles.

These measurements of pressure coefficients shall finally be complemented with measurements of local velocity at the above-mentioned topographic features to identify and separate contributions from velocity exposure as well as shape and bluff body aerodynamics.

(a) Individual rows on a small topograpic feature (b) All rows on a large topograpic feature

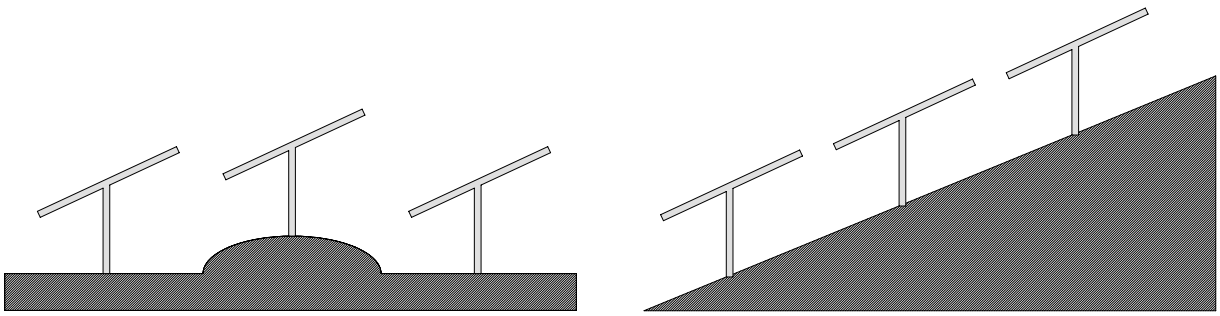


Figure 1. Scenarios modelled in the wind tunnel

REFERENCES

American Society of Civil Engineers, 2022. ASCE Standard ASCE/SEI 7-22 – Minimum Design Loads for Buildings and Other Structures, Reston, Virginia, USA.

Kray, T., and Markus, D., 2019. Peak Wind Loads on Single-axis PV Tracking Systems. Proc. 15th International Conference on Wind Engineering, Beijing, China.

Markus, D., Weihbrecht, T., 2023. The Effect of an Increased Ground-Clearance on Peak Wind Loads on a Single-Axis Solar Tracking System. Proc. 16th International Conference on Wind Engineering, Florence, Italy.

Wind load assessment of urban trees: A study of drag coefficients using wind tunnel testing

Fouad Elazaka[1], Haitham A. Ibrahim[2], Amal Elawady[3,4]

[1]F Florida International University, Miami, Florida, USA, email: felaz001@fiu.edu
[2]Florida International University, Miami, Florida, USA, email: hmoha026@fiu.edu
[3]Florida International University, Miami, FL, USA, email: aelawady@fiu.edu
[4]Extreme Events Institute, Florida International University, Miami, FL, USA

SUMMARY:
The existence of trees in the proximity of structures during extreme wind events can either mitigate wind effects or increase the risk of damage or collapse if they fail. This highlights the critical need to accurately assess the failure probability of urban trees. The drag coefficient (C_D) of urban trees is a key factor in estimating the wind loads acting on trees, yet its estimation is challenging because of the inherent uncertainties in factors such as tree species and canopy typology. This study aimed to estimate the drag coefficient of common urban trees in Florida, USA, through testing two full-scale natural oak trees and two full-scale natural mahogany trees. Results show that natural trees streamlined, reducing static drag as wind speed increased, with C_D values dropping from 0.67 to 0.24, representing a reduction of approximately 64% for one of the oak trees. Additionally, the dynamic drag coefficient of both species decreased as wind speeds increased up to 56.58 m/s, with dynamic C_D values ranging from 0.67 at low speeds to 0.54 at high speeds for the same tree, representing a reduction of around 20%. This study contributes to the understanding of tree aerodynamics under extreme wind conditions.

Keywords: urban trees, static and dynamic drag coefficient, extreme wind conditions, Wall of Wind.

1. INTRODUCTION

Urban trees can become hazardous during extreme weather events such as hurricanes, potentially causing damage to property and posing risks to human lives. During high-intensity winds, trees or large branches may fall onto buildings, automobiles, electricity lines, and highways, causing significant damage and disrupting essential services. Assessing the structural response of trees requires estimating the drag forces produced by wind pressure, which are frequently considered the cause of mechanical failure in trees. The drag coefficient is essential for estimating the wind-induced drag forces on trees, which often lead to tree failures. The drag coefficient of trees is not constant and can vary based on several factors such as wind speed, tree species, and tree size and maturity (Bekkers et al., 2022). Because of the tree's reconfiguration in response to wind forces, drag coefficients tend to decrease with increasing wind speed (Manickathan et al., 2018).

The accurate estimation of drag coefficients for trees is challenging due to their complex geometry and dynamic response to wind forces. For this purpose, several methods have been used, including field observations (Bekkers et al., 2022), numerical modelling, and wind tunnel testing (Gromke & Ruck, 2008). According to the existing studies, trees' drag coefficients range from around 0.20

at high wind speeds (e.g., 20 m/s) to 1.20 at low wind speeds (e.g., 3 m/s) (Bekkers et al., 2022). However, these studies primarily focused on small-scale trees, limiting their applicability to full-scale scenarios. Additionally, potential scaling effects due to Reynolds number mismatch must be considered, as they can influence aerodynamic behaviour and the accuracy of drag coefficient estimations at larger scales.

Existing studies provide no information on the drag coefficient of full-scale trees exposed to extreme winds. Therefore, this study aims to assess the wind loads on two of the most common urban trees in Florida (oak and mahogany) under realistic dynamic wind loading conditions, simulating hurricane scenarios, and using full-scale wind tunnel testing. The assessment of wind loads includes specifically estimating both the static and dynamic drag coefficients, providing a comprehensive understanding of how these trees respond to varying wind intensities. Reporting the dynamic drag coefficients accurately represents the tree's real-world behaviour in wind, as it considers the tree's ability to change its shape and frontal area as wind speed increases.

2. METHODOLOGY

The aerodynamic tests were conducted at the NHERI Wall of Wind (WOW) experimental facility, a large open-jet wind testing facility. The WOW flow management box measures 4.3 m in height and 6.1 m in width and is equipped with spires and automated roughness elements to simulate Atmospheric Boundary Layer flow for different terrains. Natural near-grown trees have been used to represent a scale of 1:1. This scale includes two different species, with two trees for each species. Each tree has a different height and diameter in the crown region to assess the effect of geometry variation on the estimation of drag coefficients. Table 1 lists the dimensions of the trees used for the drag coefficient measurements.

Table 1. Dimensions of the tested trees.

Tree Name	Tree Height (m)	Crown Dia. (m)	Crown Height (m)	Trunk Height (m)
Oak - O1	3.05	1.90	2.19	0.87
Oak - O2	2.60	1.78	1.53	1.07
Mahogany - M1	2.75	1.45	1.99	0.77
Mahogany - M2	3.05	1.90	2.14	0.92

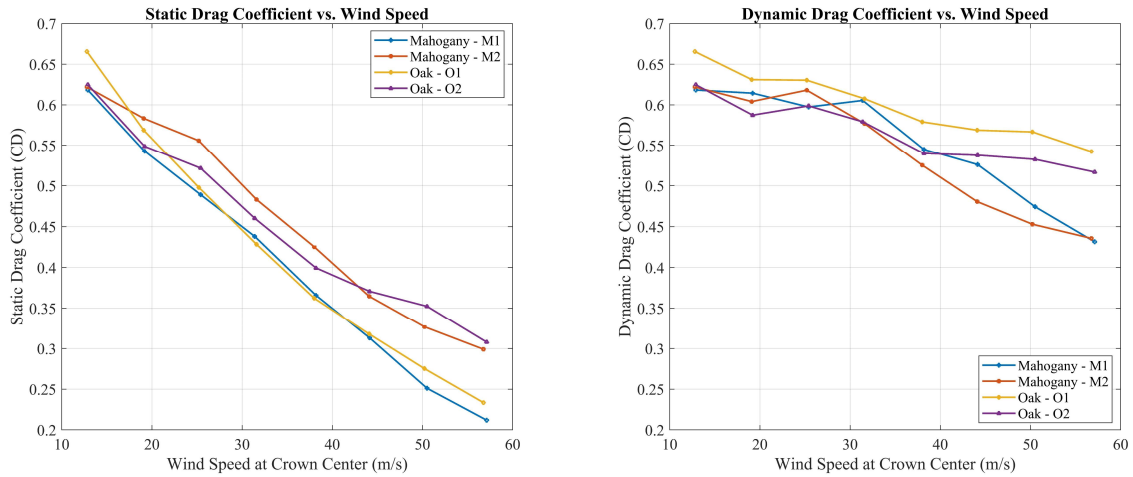
The drag force acting on the natural trees is recorded using a single-range load cell with six-axis force-torque sensors. The load cell has a capacity of 2500 lb-force for horizontal force and a moment capacity of 20,000 ft-lbs. The mean drag force acting on the tree is determined based on the average over a period of two minutes. Additionally, the baseline force at zero wind speed is recorded for 30 seconds. The impact of varying wind speeds is investigated by measuring the drag coefficients at eight different wind speeds. The tested wind speeds at the average height of the crown centre were 12.87, 19.19, 25.40, 31.40, 38.10, 44.00, 50.18, and 56.58 m/s. The wind speeds and drag force data are collected at a sampling rate of 1000 Hz. Based on the collected data, the mean static drag coefficient, and the mean dynamic drag coefficient were calculated using Eq. (1) and Eq. (2), respectively.

$$C_{d-static} = \frac{F_d}{0.5\,\rho V_z^2\,A_s} \quad (1) \qquad C_{d-dynamic} = \frac{F_d}{0.5\,\rho V_z^2\,A_d} \quad (2)$$

where F_d is the measured mean drag force in the direction of the wind speed, ρ is the air density (1.225 kg/m^3), V_z is the mean wind speed at the height of the crown center, A_s is the static projected frontal area at rest, and A_d is the dynamic projected frontal area of the crown at the specific wind speed. The dynamic projected frontal area was measured at each wind speed using images captured during testing.

3. RESULTS

The estimated static and dynamic drag coefficients of the tested trees as a function of wind speeds are displayed in Figure 1. It is clearly observed that the four natural trees appear to respond to changes in wind speed in a similar way, with a decreasing drag coefficient as the wind speed increases. This implies that the natural trees' static drag coefficient appears to depend on wind speed, with an approximate linear relationship. The significant reduction in static drag coefficient at high wind speeds could be attributed to the critical role of the reconfiguring leaves, which are not taken into consideration in the calculation of the static drag. These observations are in agreement with those of existing studies by (Manickathan et al., 2018) and (Gromke & Ruck, 2008). Considering the various sizes of the trees listed in Table 1, the static drag coefficient varied for a given wind speed within the same species. This finding is clear at both lower and higher wind speeds. For instance, for the mahogany tree (M1 and M2), at a wind speed of 25.20 m/s, the observed static drag coefficient ranges from 0.48 to 0.56 which represent a difference of around 14%. This observation might be due to the variation in crown shape, branch arrangement, and leaves amount, which affect how wind interacts with the tree, leading to differences in the drag coefficient. The same observation applies to the dynamic drag coefficient across the different trees. Moreover, looking at Figure 1.b, it can be observed that the dynamic drag coefficient of both species decreased as wind speeds increased. For example, the dynamic drag coefficient decreased by around 20% for the oak tree (O1). The reduction in the dynamic drag coefficient is likely due to the tree's crown streamlining at higher wind speeds, which resulted in a decrease in the crown frontal areas for both species.



(a) Static drag coefficient (b) Dynamic drag coefficient

Figure 1. Drag Coefficient C_d vs. wind speed V_z for the tested trees.

Moreover, due to high wind speeds, the loss of leaves is observed to increase, resulting in a lower drag force through increased crown porosity, which leads to lower drag coefficients. Furthermore, despite being subjected to wind speeds as high as 56.58 m/s, no significant structural failure occurred in the trees. The leaves amount at low and high wind speeds is shown in Figure 2.



(a) (b) (c) (d)

Figure 2. Leaves amount: (a) O1 at 12.87 m/s, (b) O1 at 56.58 m/s, (c) M2 at 12.87 m/s, and (d) M2 at 56.58 m/s.

4. CONCLUSION

This study evaluated the wind effects on full-scale natural urban trees under realistic wind conditions using wind tunnel testing. The findings reveal that the tested species exhibited similar aerodynamic properties, resulting in a lower drag coefficient at high wind speeds. The results provide a dataset on the drag coefficients of common urban tree species, which could enhance the existing frameworks for estimating the failure probability of urban trees. Given that oak and mahogany trees share structural similarities with other common urban species, these findings can be leveraged to assess the vulnerability of various trees in urban environments. For the estimation of failure probability of trees under wind loading, the dynamic drag coefficient is generally more practical than the static drag coefficient as it accounts for the tree's reconfiguration.

ACKNOWLEDGEMENTS

The authors would like to acknowledge the financial support from the State of Florida Division of Emergency Management (FDEM) and the Wind Hazard and Infrastructure Performance (WHIP) centre. The experiments at the National Science Foundation (NSF) Natural Hazards Engineering Research Infrastructure (NHERI) Wall of Wind (WOW) experimental facility were greatly facilitated by the collaborative work of WOW staff members.

REFERENCES

Bekkers, C. C. A., Angelou, N., & Dellwik, E. (2022, 2022/01/01/). Drag coefficient and frontal area of a solitary mature tree. *Journal of Wind Engineering and Industrial Aerodynamics, 220*, 104854. https://doi.org/https://doi.org/10.1016/j.jweia.2021.104854

Gromke, C., & Ruck, B. (2008). Aerodynamic modelling of trees for small-scale wind tunnel studies. *Forestry: An International Journal of Forest Research, 81*(3), 243-258. https://doi.org/10.1093/forestry/cpn027

Manickathan, L., Defraeye, T., Allegrini, J., Derome, D., & Carmeliet, J. (2018). Comparative study of flow field and drag coefficient of model and small natural trees in a wind tunnel. *Urban Forestry & Urban Greening, 35*, 230-239.

Twin wind tunnel investigation of the scale effects on a street canyon flow

Nikolaos Petros Pallas[1], Brian Dsouza[2], Demetri Bouris[3], Andrea Sciacchitano[4], Christof Gromke[5]

[1]*National Technical University of Athens, Greece, npallas@mail.ntua.gr*
[2]*Technische Universiteit Delft, The Netherlands B.S.Dsouza@tudelft.nl*
[3]*National Technical University of Athens, Greece, dbouris@fluid.mech.ntua.gr*
[4]*Technische Universiteit Delft, The Netherlands A.Sciacchitano@tudelft.nl*
[5]*Karlsruhe Institute of Technology, Germany gromke@kit.edu*

SUMMARY:
An investigation of the scale effects when studying urban street canyon flows is carried out in two wind tunnels. The examined model is a series of five identical street canyons, perpendicular to the approaching flow, simulating an urban environment. The study focuses on the fourth canyon with respect to the direction of the flow. The height-to-width and the length-to-width aspect ratios of the street canyons are 1 and 8, respectively. Three-dimensional particle tracking velocimetry (3D-PTV) and pressure measurements were conducted in the closed-loop wind tunnel of the National Technical University of Athens (NTUA) as well as the open jet facility (OJF) of TU Delft. Comparative results for the velocity indicate that Reynolds number independence (RNI) is satisfied for $Re = 30000$. However, the surface pressure results indicate that Reynolds numbers within the range (60000, 100000) may be necessary to achieve RNI.

Keywords: Urban Street Canyon, 3D Particle Tracking Velocimetry, Scaling Effects

1. INTRODUCTION

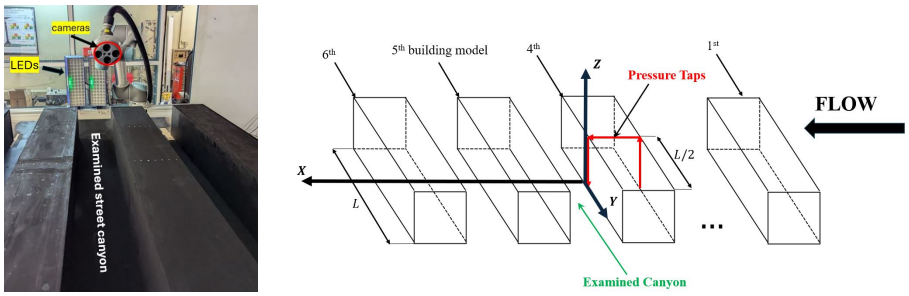
The street canyon geometry is one of the basic structural components of contemporary cities. This geometry is linked to an increased pollutant entrapment (Li et al., 2006) at the pedestrian level, a situation which is more pronounced when the wind direction is perpendicular to the canyon. For this orientation, three distinct flow regimes, depending on the height-to-width (H/W) ratio of the canyon, are distinguished: (i) skimming flow, (ii) wake interference and (iii) isolated roughness regime (Li et al., 2006). A case in the skimming flow regime ($H/W = 1 > 0.65$) is investigated here mainly for two reasons: (a) it corresponds to the worst-case scenario regarding the pollution at pedestrian level (Li et al., 2006), and (b) most of the research involving street canyons focuses on this kind of geometry, commonly with an aspect ratio $AR = 1$ (e.g. Dsouza et al., 2024; Gromke and Ruck, 2009). The length-to-width ratio was chosen as $L/H = 8 > 7$ ensuring the development of a 2D region around the plane of symmetry (Hunter et al., 1990). The series of five canyons (six building blocks) ensures that the flow is in the urban roughness regime (Meroney et al., 1996).

It is often difficult to attain the value of the full-scale Reynolds number in wind tunnel testing (reduced-scale). To circumvent this, Reynolds Number Independence (RNI) has to be established at lower, achievable Reynolds numbers in wind tunnels. Although Chew et al. (2018) found that a

Reynolds number of $Re = 12000$ establishes RNI for urban street canyons with $AR = 1$, Shu et al. (2020) found that RNI is more difficult to achieve for regions close to the walls of the canyon. Dsouza et al. (2024) also examined scaling effects in both three-dimensional (near the one end of the canyon) and two-dimensional regions of a street canyon geometry, by employing 3D Particle Tracking Velocimetry (3D-PTV). They observed RNI within the range Re=13000, 17000 for the mean quantities but not for turbulence quantities. Following previous works and the suggestion of locally varying RNI (Shu et al., 2020), the present study examines a wide range of Reynolds numbers (i.e. $24000 \leq Re \leq 100000$) and aims to complement existing data and observations. Measurements in two wind tunnels provide localised information on 2D and 3D mean and higher order statistics of velocity. Surface pressure distributions on the center plane are also measured, being of interest in building air exchange rate and wind force calculations.

2. EXPERIMENTAL CONFIGURATION

3D-PTV and pressure measurements were conducted in the closed-loop wind tunnel (WT) facility of the National Technical University of Athens (NTUA). The dimensions of the test section were $3.5 \times 2.5 \times 12.1$ m, with minimum attainable turbulence intensity $\sim 2\%$.



(a) (b)

Figure 1. (a) Experimental setup using TU Delft's Coaxial Volumetric Velocimetry (CVV) probe mounted on a Universal Robots UR5 robotic arm at NTUA's facilities. (b) Schematic illustration of the utilised model, its orientation and geometry (not all canyons are shown).

A Universal Robots UR5 robotic arm with six degrees of freedom was used for the PTV measurements. A coaxial volumetric velocimetry (CVV) probe (Schneiders et al., 2018) consisting of four CMOS cameras with 4 mm objectives, had been mounted on the UR5 robotic arm. The specifications of the CVV system, can be found in (Dsouza et al., 2024). For the illumination, two LaVision LED Flashlight 300s were utilised while neutrally-buoyant Helium-filled soap bubbles (HFSB) were used as tracer particles (Faleiros et al., 2019). The acquisition frequency, the number of acquisitions and their duration were adjusted in order to capture at least 80 turnovers of the canyon vortex. The maximum acquisition frequency was $f = 727$ Hz. The equipment had been provided by TU Delft and had been already successfully used for experiments of the same geometry by Dsouza et al. (2024). A photograph of the experimental setup is given in Fig. 1a.

The model was mounted onto a splitter plate elevated from the wind tunnel floor to avoid boundary layer effects. A schematic illustration of the model is given in Fig. 1b. Pressure taps were installed on the fourth building model along the red line of the same figure ($Y = 0$), following the direction of the flow. A 60-channel FCS421 (Furness Controls Ltd) pressure scanner was used to connect the

tubing to a DP103 low pressure Validyne sensor (see Pallas et al., 2024, for details of the system).

The same configuration was also studied at the open jet facility (OJF) of TU Delft (cross section: 2.85×2.85, minimum turbulence intensity: ∼1%). 3D-PTV measurements are still being processed and will be presented at the conference. A DSA3217/3218 Series Scanivalve Pressure Scanner (600 Pa pressure module, accuracy 0.1%) was used for the pressure measurements.

3. RESULTS

Contours of the normalised mean streamwise velocity component and velocity vectors are given for $Re = 30000$ and $Re = 60000$, in Fig. 2 for the centre-plane of the examined canyon at NTUA. The Reynolds number is defined as $Re = U_{Ref}H/\nu$ where U_{Ref} is the free-stream velocity, H is the height of the canyon and $\nu = 1.5 \times 10^{-5}$ m^2/s is the kinematic viscosity of air at 20° C. Overall, no significant differences are obvious between the results of $Re = 30000$ and $Re = 60000$, in Fig. 2, except some small differences in the lower left corner where the secondary vortex is observed. This was also corroborated by examining velocity and turbulent kinetic energy profiles along the centre-line of the plane of symmetry (i.e. for $X = 0.5$ and $Y = 0.5$), which are not shown here.

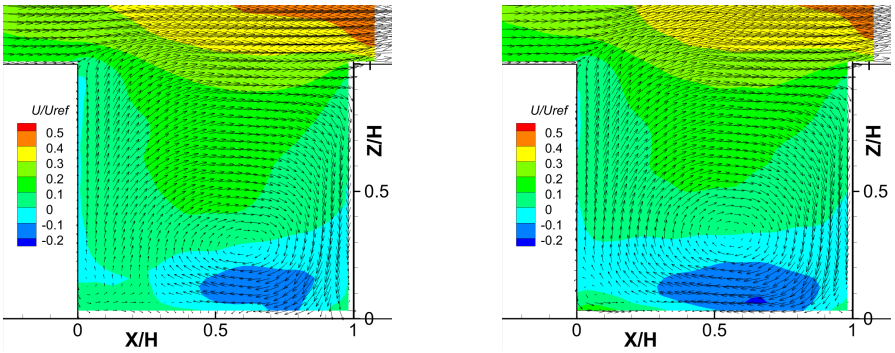


Figure 2. (a) Contours and velocity vectors of the normalised mean streamwise velocity component U/U_{Ref} for: (a) $Re = 30000$ and (b) $Re = 60000$, in the centre-plane.

Finally, surface pressures are shown in Fig. 3, measured along the red line of Fig. 1b. S/H accounts for the non-dimensional distance along the line, in the direction of the flow. The value located at $S/H = 1.04$ (first pressure tap on the roof) is used as a reference pressure for both measurement sets (NTUA and TU Delft). The differences in roof pressure values among the different Reynolds numbers are small for both of these sets. There is some small spread in the results within the canyon ($S/H = 0-1$ and $S/H = 2-3$) between $Re = 30000$ and $Re = 60000$ but for $Re > 60000$ a distinct group of curves arises in Fig. 3b, indicating that there are differences in surface pressures between $Re = 60000$ and $Re = 100000$ while for $Re = 80000$ and $Re = 100000$ the results coincide.

4. CONCLUSIONS

A twin experimental campaign investigating the scale effects in an urban street canyon has been carried out in the closed loop wind tunnel of NTUA and the open jet facility of TU Delft. Initial results presented here indicate that the non-dimensional velocities do not demonstrate significant

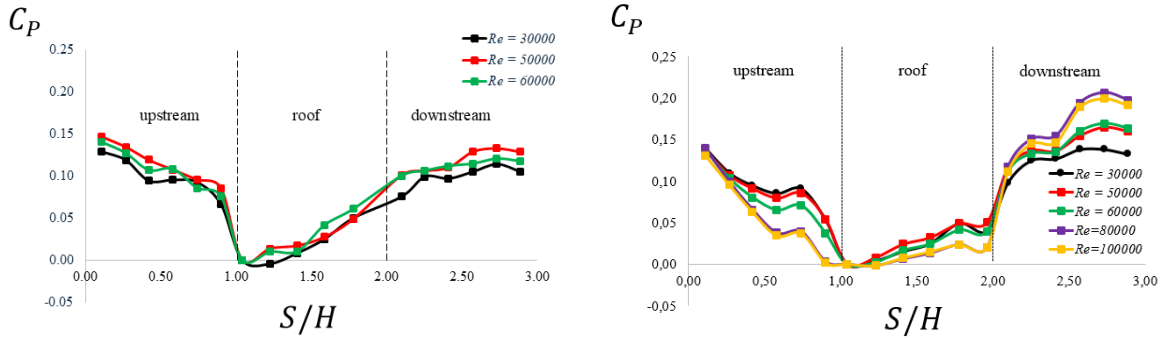


Figure 3. Surface pressure coeffcient profiles for different Reynolds numbers within the range: (a) [30000, 60000] (NTUA experiment) and (b) [30000, 100000] (TU Delft experiment).

differences for Reynolds numbers in the range [30000, 60000]. However, surface pressures show a tendency of satisfying Reynolds number independence (RNI) at a higher Re, namely $Re = 60000 - 100000$. This could also be an indication of local variability of RNI. Further results of velocity measurements at TU Delft and higher order statistics will be presented in at the conference.

ACKNOWLEDGEMENTS

Funding was provided by the EU under (PR 101079125) TWEET-IE: Twin Wind tunnels for Energy and the Environ-menT - Innovations and Excellence

REFERENCES

Chew, L. W., Aliabadi, A. A., and Norford, L. K., 2018. Flows across high aspect ratio street canyons: Reynolds number independence revisited. Environmental Fluid Mechanics 18, 1275–1291.

Dsouza, B., Sciacchitano, A., and Yu, W., 2024. Reynolds Number Independence In An Urban Street Canyon Using 3D Robotic Particle Tracking Velocimetry. Proceedings of 21st International Symposium on the Application of Laser and Imaging Techniques to Fluid Mechanics. LISBON Simposia, 171.

Faleiros, D. E., Tuinstra, M., Sciacchitano, A., and Scarano, F., 2019. Generation and control of helium-filled soap bubbles for PIV. Experiments in Fluids 60, 1–17.

Gromke, C. and Ruck, B., 2009. On the impact of trees on dispersion processes of traffic emissions in street canyons. Boundary-Layer Meteorology 131, 19–34.

Hunter, L. J., Watson, I., and Johnson, G., 1990. Modelling air flow regimes in urban canyons. Energy and Buildings 15, 315–324.

Li, X.-X., Liu, C.-H., Leung, D. Y., and Lam, K. M., 2006. Recent progress in CFD modelling of wind field and pollutant transport in street canyons. Atmospheric Environment 40, 5640–5658.

Meroney, R. N., Pavageau, M., Rafailidis, S., and Schatzmann, M., 1996. Study of line source characteristics for 2-D physical modelling of pollutant dispersion in street canyons. Journal of wind Engineering and industrial Aerodynamics 62, 37–56.

Pallas, N.-P., Kellaris, K., and Bouris, D., 2024. Dynamic calibration of complex tubing systems using a single pressure measurement device. Journal of Wind Engineering and Industrial Aerodynamics 249, 105715.

Schneiders, J. F., Scarano, F., Jux, C., and Sciacchitano, A., 2018. Coaxial volumetric velocimetry. Measurement Science and Technology 29, 065201.

Shu, C., Wang, L. L., and Mortezazadeh, M., 2020. Dimensional analysis of Reynolds independence and regional critical Reynolds numbers for urban aerodynamics. Journal of Wind Engineering and Industrial Aerodynamics 203, 104232.

Effects of model scale and surroundings on surface pressures of a mid-rise building

Vincenzo Picozzi[1,*], Antonio Malasomma[1], Fabio Rizzo[2], Aleksander Pistol[3], Renata Kłaput[4], Alberto Maria Avossa[1], Francesco Ricciardelli[1]

[1]*University of Campania "Luigi Vanvitelli", Aversa, Italy*
[2]*Polytechnic University of Bari, Bari, Italy*
[3]*Manchester Metropolitan University, Manchester, United Kingdom*
[4] *Cracow University of Technology, Cracow, Poland*
**vincenzo.picozzi@unicampania.it*

SUMMARY:
Wind tunnel testing is worldwide used to assess wind loads on buildings featuring a non-conventional shape, where procedures and data provided by codes and guidelines fail. With reference to a mid-rise building for which full-scale monitoring is ongoing, the main aim of this work is to show the effects of model scale and of surroundings (including orography and aerodynamic interference of neighbouring buildings) on wind tunnel pressure measurements. To the aim, three configurations of wind tunnel tests are considered, including (*a*) the isolated 1:200 scaled model of the building, (*b*) the 1:200 scaled model of building with surrounding, and (*c*) the isolated 1:100 scaled model of the building.

Keywords: Wind tunnel testing, Building aerodynamic, Orography, Roughness.

1. INTRODUCTION

Wind loads on mid-rise buildings are commonly assessed using Code procedures (e.g. CEN, 2005). These rely on pressure coefficients measured on simple shapes, usually rectangular plan and uniform height. Furthermore, the influence of surrounding constructions and of orography are accounted for only in a simplistic way. Indeed, actual building geometries, surrounding conditions and orography very much differ from the ideal ones referred to by Codes. Therefore, as an alternative to purely code-based calculations, more accurate analyses relying on results from wind tunnel testing are a valid option. These provide a better description of both the building aerodynamics and the effects of the interaction of the wind field with the surrounding environment.

In this framework, current work aims at investigating the pressure characteristics of a mid-rise building, object of an ongoing full-scale experimental measurement campaign (Malasomma et al., 2025). In detail, results of wind tunnel tests are discussed, showing the effects of the model size and of surrounding orography and constructions on wind loads.

2. MATERIAL AND METHODS

The building is 78 m high, with a 25.10×29.90 m non-rectangular plan oriented 15° with respect to the North (see Figure 1). It is located about 4 km Nort-West of the Naples city centre. The surrounding is characterized by buildings with an average height of about 15 m, resulting in terrain Category III to IV according to EN 1991-1-4. The orography is characterized by a hilly terrain, with an upward slope in the western direction.

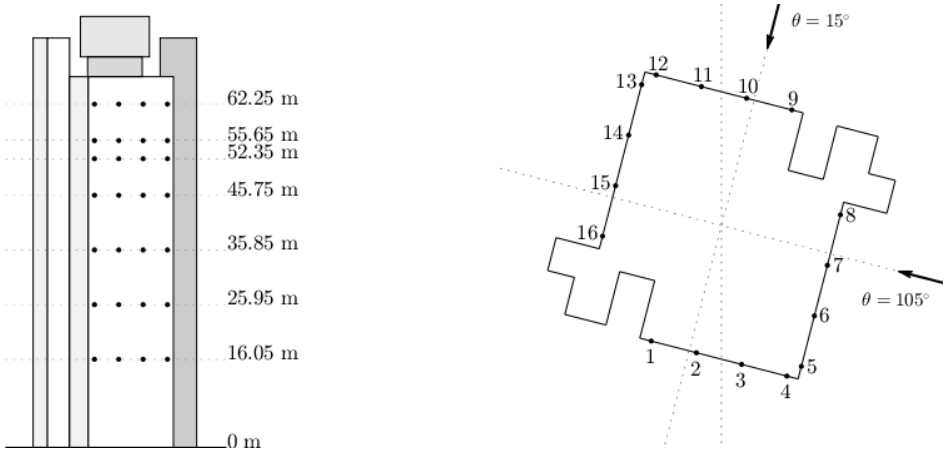


Figure 1. Elevation and plan views of the building model with indication of pressure taps location.

Wind pressures on the building were measured in the wind tunnel of the Laboratory of Environmental Aerodynamics of the Cracow University of Technology, Poland, having a working section of 2.20×1.60 m (width × height). To evaluate the influence of the surroundings with respect to the isolated building, two test configurations are considered: Test #1 is performed on the isolated 1:200 scaled model, and Test #2 is performed on the 1:200 scaled model with surroundings within a radius of 180 m full scale, including both orography and nearby buildings. Furthermore, an additional Test #3 is carried out on the isolated 1:100 scaled model to assess the effects of scaling on the measured pressures. For all tests, a wind profile corresponding to the Category III according to EN 1991-1-4 is generated. The relevant characteristics of the three tests are reported in Table 1, where the reference wind speed v_{ref} and turbulence intensity $I_{v,ref}$ correspond to the building height, H.

Table 1. Relevant characteristics of the wind tunnel tests.

		Test #1	Test #2	Test #3
Length Scale	λ_L	1:200	1:200	1:100
Velocity Scale	λ_V	1:2	1:2	1:2
Reference wind speed	v_{ref}	17.4 m/s	16.8 m/s	18.6 m/s
Turbulence Intensity	$I_{v.ref}$	6%	6%	9%
Sampling Frequency	f_s	250 Hz	250 Hz	250 Hz
Number of runs	-	30	30	20
Single run length	T_a	6 s	6 s	12 s
Total record length	T	180 s	180 s	240 s
Number of runs	-	30	30	20
Wind direction	θ	0° to 360°	0° to 360°	0° to 180°
Wind direction step	$\Delta\theta$	15°	15°	15°

Acquired data are first processed deriving mean ($\bar{c}_p$) and peak ($\hat{c}_p$) values of pressure coefficients within a full-scale reference period $T_a = 10\,\text{min}$ and different averaging periods τ. After performing an Extreme Value (EV) analysis consisting in the calibration of Gumbel distribution parameters of maximum pressure coefficients, $\hat{c}_p$ is derived as the 78% fractile according to the Cook and Mayne method and the current practice (Picozzi et al., 2022; Cook and Mayne, 1979). Comparisons are made for 140 measurement points arranged in 7 arrays along the building height (see Figure 1). They consist in a comparison between the results obtained from Test #1 and from Test #3, so to evaluate the effects of the model scale, and between Test #1 and Test #3 to assess the effect of surroundings.

3. RESULTS

Some results of the analyses of wind tunnel data are shown in Figure 2 in terms of mean pressure coefficients $\bar{c}_p$. In the figure, the regression line calibrated on positive and negative pressure coefficients is reported. This is an indication of the bias between the results of Test #2 and Test #3 with respect to those of Test #1. On the other hand, the standard deviation σ_ε of residuals ε of regression is used to quantify the scatter of results.

Overall, it is found that the influence of surroundings mainly results in biased values of pressure coefficients, while the effect of model scale mainly shows a large scatter. In detail, analysing the effects of surrounding, it is found that:

- Positive values of pressure coefficients are systematically lower in Test #2 than in Test #1, with an additive bias equal to -0.11 when $\theta = 15°$ and to -0.07 when $\theta = 105°$, and a multiplicative bias equal to 1.02 when $\theta = 15°$ and to 0.94 when $\theta = 105°$. The scatter of data is quantified with $\sigma_\varepsilon = 0.07$ and $\sigma_\varepsilon = 0.04$ for $\theta = 15°$ and $\theta = 105°$, respectively.
- Negative values of pressure coefficients are affected by a bias that decreases as suction increases. In detail, it is composed of an additive part equal to -0.08 when $\theta = 15°$ and to -0.17 when $\theta = 105°$, and of a multiplicative part that takes values of 0.84 when $\theta = 15°$ and of 0.79 when $\theta = 105°$. The scatter of data is quantified with $\sigma_\varepsilon = 0.06$ and $\sigma_\varepsilon = 0.09$ for $\theta = 15°$ and $\theta = 105°$, respectively.

On the other hand, analyzing the model scale effects, it is found that:

- Positive values of pressure coefficients in Test #3 are on average larger than Test #1 when $\theta = 15°$, while they are lower when $\theta = 105°$. The residuals are quantified by $\sigma_\varepsilon = 0.12$ when $\theta = 15°$ and by $\sigma_\varepsilon = 0.16$ when $\theta = 105°$.
- Negative values of pressure coefficients are affected by a bias that decreases as suction increases. The additive component of bias is close to 0, while the multiplicative bias is larger when $\theta = 105°$.

The larger scatter observed when assessing model scale effects can be attributed to the different characteristics of freestream flow, i.e. different turbulence intensity and slight deviations in the mean wind speed profile.

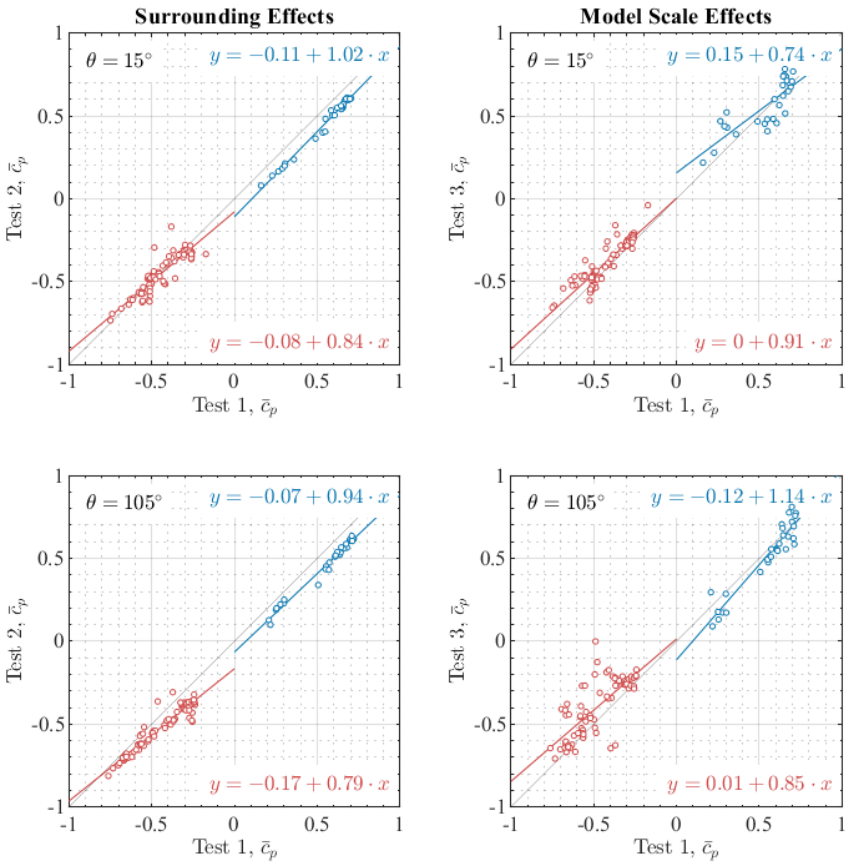


Figure 2. Scatter plot of the mean pressure coefficients: effects of surrounding (left column) for $\theta = 15°$ (top) and $\theta = 105°$ (bottom); effects of model scale (right column) for $\theta = 15°$ (top) and for $\theta = 105°$ (bottom).

REFERENCES

CEN, 2005. EN 1991-1-4. Eurocode 1: Actions on Structures – Part 1-4: General Actions – Wind Actions. European Committee for Standardization (CEN), Brussels, Belgium.

Cook, N.J., Mayne, J.R., 1979. A Novel Working Approach to the Assessment of Wind Loads for Equivalent Static Design. Journal of Wind Engineering and Industrial Aerodynamics, 4, 149-164.

Malasomma, A., Picozzi, V., Caracoglia, L., Avossa, A.M., Ricciardelli, F. 2025. Full-scale vs wind tunnel pressure measurements on a mid-rise building. In: Abstract Proc. of the 9th European and African Conference on Wind Engineering, EACWE2025, 16-19 June 2025, Trondheim, Norway.

Picozzi, V., Malasomma, A., Avossa, A.M., Ricciardelli, F., 2022. The Relationship between Wind Pressure and Pressure Coefficients for the Definition of Wind Loads on Buildings. Buildings, 12 (225).

Wind tunnel testing of U-shaped and rectangular prisms at two turbulence levels of incoming flow

Michael Macháček [1], Stanislav Hračov [2], Karel Dejmal[3]

[1] *Theoretical and Applied Mechanics, The Czech Academy of Sciences, Prague, Czech Republic, machacek@itam.cas.cz*
[2]*Theoretical and Applied Mechanics, The Czech Academy of Sciences, Prague, Czech Republic, hracov@itam.cas.cz*
[3]*Theoretical and Applied Mechanics, The Czech Academy of Sciences, Prague, Czech Republic, dejmal@itam.cas.cz*

SUMMARY:
The paper presents the results of experimental wind tunnel testing of rectangular and U-shaped beams. The aerodynamic coefficients of drag and lift were measured together with the pressure coefficients on the surface test bodies of the beams in section. The results were compared for two intensities of turbulence of the incoming flow. Our observations generally indicate that the pressure distribution and aerodynamic forces are affected by the turbulence intensity of the incoming flow. Maximum lift forces are reduced by turbulent flow, and the drag coefficient is reduced when the flow direction is close to zero. However, turbulence can increase drag forces at higher angles of attack. The pressure distribution over the cross sections is drastically altered by turbulent flow. The mean suction pressure can increase by 83% at certain pressure taps. Turbulence intensity has little effect on windward pressure.

Keywords: Aerodynamics coefficients rectangle, U-shaped beam, wind tunnel testing, pressure coefficients, turbulence intensity

1. INTRODUCTION

The manuscript presents the results of experimental aerodynamic assessments carried out on the slender rectangular beam alongside the beam and the U-shaped beam, which are typically found in structures such as bridge decks with wind barriers or pedestrian bridges with railings. Rectangular beams and U-beams have the same aspect ratio (B/D = 2:1). The test model placed in the wind tunnel is shown in Figure 1 a). The tests were carried out in the closed climatic wind tunnel of ITAM AS CR in Telč, Czech Republic. The wind tunnel tests were carried out in two flow conditions, a smooth flow with a minimum turbulence intensity of less than 1% and a turbulent flow with a turbulence intensity of 6% and an integral turbulence length of 0.1m. The turbulent flow condition was created by placing a grid as a turbulence generator 4.6 m in front of the test model. A detailed description of the flow characteristics can be found in (Trush, 2020). A wooden rectangular prism and two plywood flanges were used to assemble the experimental U-beam specimen. A unique component of the flanges was made of 3D printed plastic, which allowed for the potential addition of pressure taps on both sides of the 6mm thin flanges, as shown in Figure 1b. Figure 1d shows a schematic of the basic geometry and dimensions of their U-shaped cross section. The test specimen was positioned vertically within the 1,9 m wide by 1,8 m high

measurement area of the aerodynamic test section of the wind tunnel. To create two-dimensional flow conditions, the models were enclosed in plastic and wooden end plates (see Figure 1a). The aerodynamic drag and lift coefficients *Cd* and *Cl* that the wind load induced on the specimen bodies for the angles of wind attack, α, between -14° and +14° were measured using two load cells, ATI Industrial Automation sensors Mini 40. These sensors were attached to the top and bottom of the specimens, as well as to custom-built synchronised rotation mechanisms (see Figure 1c), which allowed the specimens to rotate with an angular step of 0,1°. This makes, it is possible to determine the precise change in aerodynamic forces as the angle, α, changes. With a sample frequency of *fs* = 1000 Hz, the sensors' data was recorded for 60 seconds, which was found to be adequate in terms of the process's ergodicity and stationarity. With a sampling frequency of *fs* = 500 Hz, the MPS4264 64-channel miniature pressure scanner was used to measure the pressure coefficients. 52 pressure taps were found in a single section for a rectangular prism, 54 pressure taps in a single section for a U-beam, and the remaining scanner pressure valves were utilized as control pressure taps for other sections. The experiments were carried out at a wind speed of approximately 14 m/s. This corresponds to Re = $2{,}8 \cdot 10^5$, normalized using the along-wind dimension, B. Wind tunnel blockage that ranges from 7.9 to 11.7% depending on simulated angle of the wind attack. There has been no correction of the blockage effect in the calculation of mean values of aerodynamics forces and pressure coefficients. These graphs display all of the data standardized to the same height, D = 150 mm.

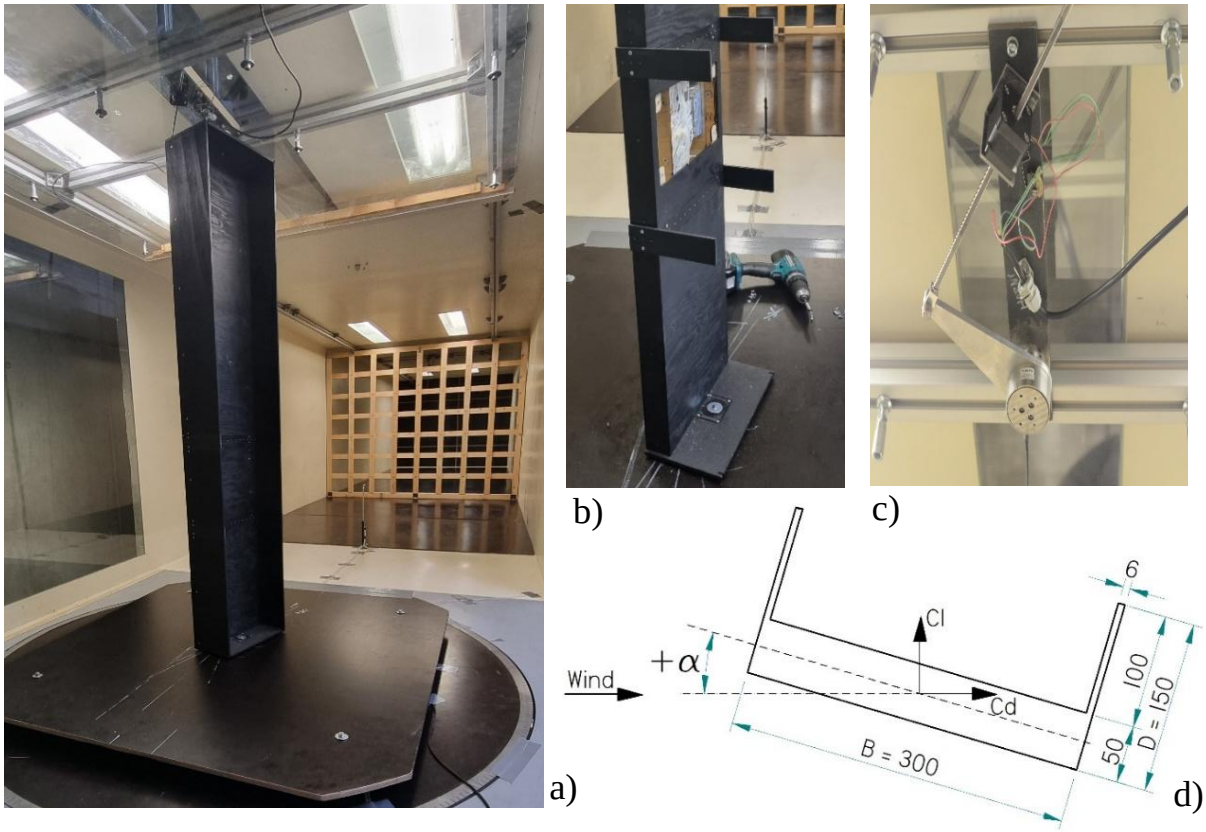


Figure 1. Experimental setup of specimen in wind tunnel a), b), rotational device c) and used sign convention d)

2. RESULTS

The aerodynamic coefficients are shown in Figure 2, where the solid line shows the rectangular cross section and the dashed line shows the U-beam results. The blue colour is used for smooth flow conditions and the red colour is used for turbulent inflow conditions. The slope of the lift coefficient near the zero angle is the same for smooth and turbulent flow for the rectangle, but the range of negative slope is much larger for smooth flow. This phenomenon can lead to a greater response to galloping instability in smooth flow, but the critical wind speed of galloping is calculated from the slope, so the rectangular prism can have the same value of galloping critical wind speed for smooth and turbulent flow. The reduction in drag around zero angle of attack is noticeable in turbulent flow. The results of the measurements were compared with the literature (Chen, 2020 and Santosham, 1966). The mean values of the aerodynamic lift coefficients are in good agreement. The drag coefficients in this study give higher values than in the literature (Chen, 2020), but the characteristic shape of the drag forces in the angle of attack is the same. The differences are most likely due to the blockage effect.

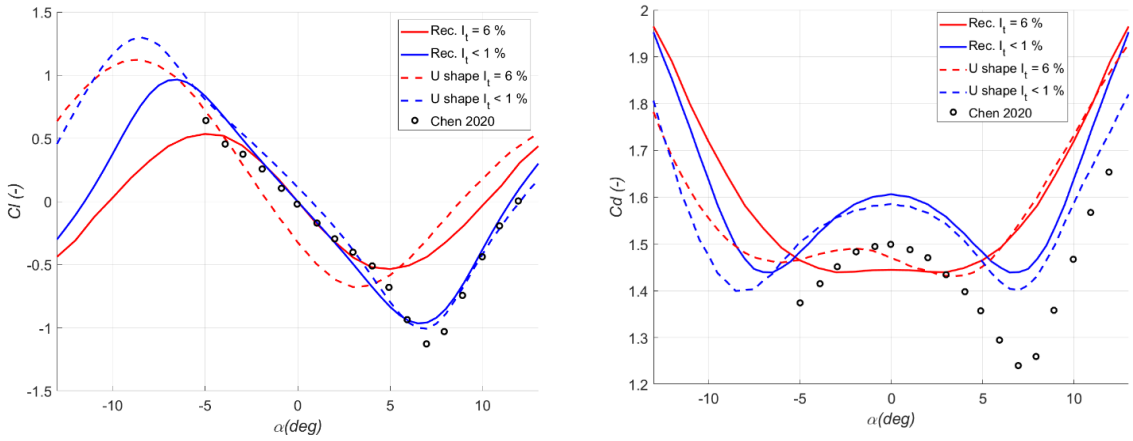


Figure 2. Mean aerodynamics coefficients of lift (left) and drag (right).

The distribution of aerodynamic pressure around the rectangular cross section is shown in Figure 3 for 0° angle of wind attack on the left and for 7.5° angle of wind attack on the right. The red colour represents turbulent flow and the blue colour represents smooth flow. Measured pressure taps are marked by a small black dot on the rectangle.

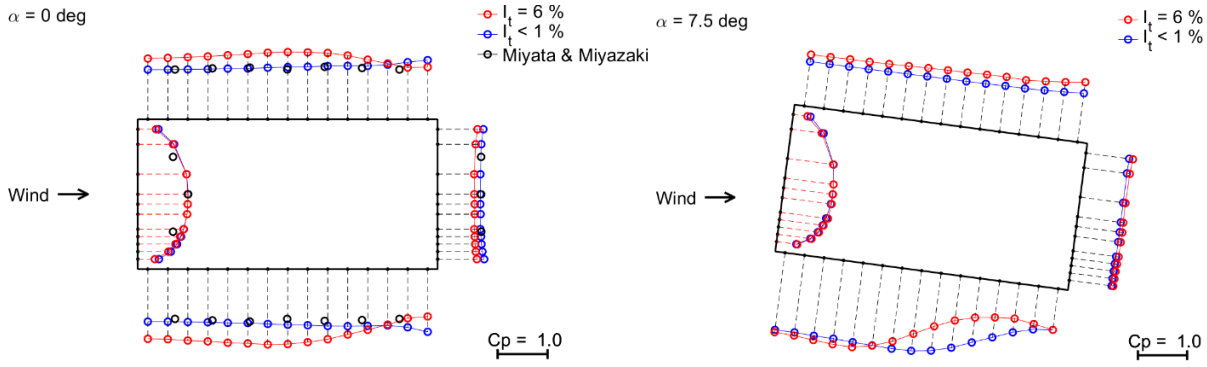


Figure 3. Mean pressure coefficient around rectangular prism for angle of wind attack α=0°(left) and α=7,5° (right).

For comparison with other authors, the results of (Miyata, 1979) have been plotted at zero angle of attack, marked by the black circle (Figure 3, left). Different pressure coefficients can be observed for different turbulence intensities. In general, for turbulent flow there is a reattachment of the flow to a rectangular body closer to the leading edge, especially for an angle of attack of 7.5°. The distribution of aerodynamic pressure around the cross section of the U-beam is shown in Figure 4 for an angle of attack of 0° on the left and 7.5° on the right. These angles were chosen because the most different results of the aerodynamic coefficient from the force balance measurement occur at these angles. For turbulent flow, there is a noticeable increase in suction in the inner cavity of the U-beam at an angle of 7.5 degrees. On the opposite side, the suction decreases significantly. At some points the reduction is almost 50%.

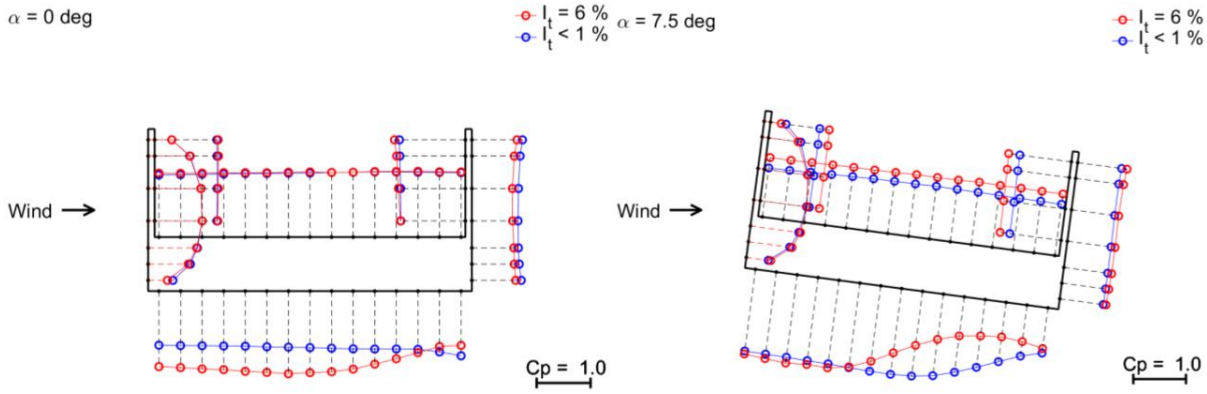


Figure 4. Mean pressure coefficient around U-beam for angle of wind attack α=0°(left) and α=7,5° (right).

3. CONCLUSIONS

In general, our measurements show that the turbulence intensity of the incoming flow has an influence on the pressure distribution and the aerodynamic forces. Turbulent flow reduces the maximum lift forces and near zero reduces the drag coefficient. On the other hand, at higher angles of attack, turbulence can increase drag forces. Turbulent flow significantly changes the distribution of pressure around the cross sections. In some pressure taps, the increase in the average suction can reach 83%, in the lower part of the U-shaped prism at 7,5°. The positive pressure on the windward side is not much affected by the intensity of the turbulence.

ACKNOWLEDGEMENTS

The kind support of Czech Scientific Foundation project No. 24-13061S is gratefully acknowledged.

REFERENCES

Chen, C., Mannini, C., Bartoli, G., Thiele, K., 2020. Experimental study and mathematical modeling on the unsteady galloping of a bridge deck with open cross section, Journal of Wind Engineering and Industrial Aerodynamics, 203, 104170.

Miyata, T., and Miyazaki, M., 1979. Turbulence effects on aerodynamic response of rectangular bluff cylinders, in: J.E. Cermak (Ed.), Wind Engineering, Proc. Fifth Int. Conf., Fort Collins, Colorado, USA, pp. 631—642

Santosham, T. V., 1966. Force measurements on bluff cylinders and aeroelastic galloping of a rectangular cylinder (Doctoral dissertation, University of British Columbia).

Trush, A., Pospisil, S., Hrvoje, K., 2020. Comparison of turbulence integral length scale determination methods. WIT transactions on engineering sciences,128, 113-123.

Advancements underway in designing a national full-scale testing infrastructure for community hardening in extreme wind, surge, and wave events (NICHE)

Arindam Gan Chowdhury [1], Amal Elawady [2], Hermann Fritz [3], Catherine Gorle [4], Kurtis Gurley [5], Tracy Kijewski-Correa [6], Frank Lombardo [7], Pedro Lomonaco [8], Forrest Masters [9], Jack Puleo [10], Kristin Taylor [11], John van de Lindt [12], Paul Vasilescu [13], Ioannis Zisis [14]

[1]*Florida International University, Miami, USA, chowdhur@fiu.edu*
[2]*Florida International University, Miami, USA, aelawady@fiu.edu*
[3]*Georgia Institute of Technology, Atlanta, USA, fritz@gatech.edu*
[4]*Standford University, Stanford, USA, gorle@stanford.edu*
[5]*University of Florida, Gainesville, USA, kgurl@ce.ufl.edu*
[6]*University of Notre Dame, Notre Dame, USA, tkijewsk@nd.edu*
[7]*University of Illinois at Urbana-Champaign Champaign, USA, lombaf@illinois.edu*
[8]*Oregon State University, Corvallis, USA, pedro.lomonaco@oregonstate.edu*
[9]*University of Florida, Gainesville, USA, masters@eng.ufl.edu*
[10]*University of Delaware, Newark, USA, jpuleo@udel.edu*
[11]*Wayne State University, Detroit, USA, kristin.taylor@wayne.edu*
[12]*Colorado State University, Fort Collins, USA, jwv@colostate.edu*
[13]*Aerolab, Jessup, USA, paul@aerolab.com*
[14]*Florida International University, Miami, USA, izisis@fiu.edu*

SUMMARY:
Extreme windstorm events (e.g., hurricanes, downbursts, tornadoes, derechos) occur annually causing damage to civil infrastructure, resulting in population dislocation, economic losses, and community disruption. Every year in the U.S., windstorms alone kill hundreds of people and, on average, cause more than $80B in losses. Along the Atlantic and Gulf coasts, hurricanes and associated storm surge, waves, and flooding increasingly impact infrastructure and communities. In 2022, the U.S. National Science Foundation (NSF) awarded a $12.8M planning grant, through the Mid-Scale Research Infrastructure (MsRI) program, to design a facility called the National Full-Scale Testing Infrastructure for Community Hardening in Extreme Wind, Surge, and Wave Events (NICHE). NICHE addresses a national research need for high-intensity and up to full-scale simulation of extreme winds combined with wave action and storm surge to examine their impacts on natural and built environments. The envisioned NICHE is expected to achieve more resilient communities by reducing losses and disruptions due to climate-driven hazards, helping the U.S. and the world become more sustainable while enhancing the quality of life. The advancements underway in designing NICHE are briefly presented.

Keywords: Community Resilince, Full-scale Testing, Convergence Research

1. INTRODUCITON

Extreme windstorm events (e.g., hurricanes, downbursts, tornadoes, derechos) occur annually causing damage to hazard prone communities, resulting in population dislocation, economic losses, and disruption (National Academies of Sciences, Engineering, and Medicine, 2019). To help protect the United States against losses from extreme windstorm events, a multi-disciplinary team is designing a National Full-Scale Testing Infrastructure for Community Hardening in Extreme Wind, Surge, and Wave Events (NICHE). NICHE responds directly to the pressing national imperative to promote more resilient and sustainable communities by reducing losses, population dislocation, outmigration, and economic impacts due to climate-driven hazards. NICHE will provide a unique, national, multi-user facility with convergence research capabilities to evaluate the impact of extreme winds combined with storm surge and wave actions on different types of civil infrastructure, including full-scale low-rise structures, large-scale infrastructure systems, and communities as scaled models. NICHE is expected to directly respond to one of the biggest societally driven challenges of the 21st Century: achieving more resilient, sustainable, and climate adaptive communities (National Institute of Building Sciences, Multi-Hazard Mitigation Council,2019; ASCE's Policy Statement, 2021). The design of the NICHE is funded through the National Science Foundation's (NSF's) Mid-Scale Research Infrastructure (MsRI) program.

2. METHODOLOGY

The NICHE team is using a robust design process that positions NICHE to converge traditionally siloed disciplines and methodologies for the delivery of novel research, workforce development, and research translation capabilities. This will be accomplished by operationalizing multiple dimensions of strategic integration depicted in Figure 1:

- Disciplinary Convergence: understanding that seminal discovery operates at the intersection of engineering, behavioral, social, and economic sciences.
- Methodological Convergence: optimally leveraging the strengths of computational simulations, physical testing, and field observations.
- Institutional Convergence: contextualizing research within disaster-affected communities to accelerate impacts on policy and practice.

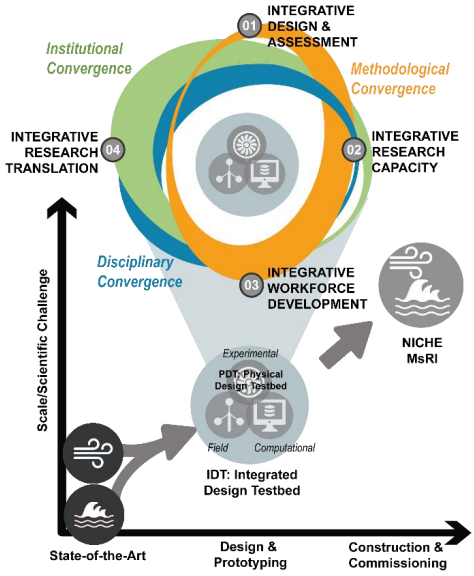


Figure 1. NICHE's evolution over time and convergence framework

The NICHE is being designed for researchers to conduct high-fidelity investigations in three key areas:

- Community Hazard Modeling and Resilience under Combined Hazards
- Coastal Processes Modeling and Mitigation under Interacting Hazards
- Preparing for Tomorrow – Adaptation for a Changing Climate

Data used for designing the full-scale NICHE is obtained from physical testing taking place at multiple physical design testbeds, called PDTs. PDT testing is essential to address and formulate the outstanding scientific and technical requirements associated with constructing this massive new wind-wave research facility. Several PDTs are located at existing facilities, including the wind tunnel at University of Florida (UF) and the wind-wave labs at Oregon State University (OSU), University of Miami (UM), and University of California San Diego (UCSD). In addition, a wind-only physical design testbed (WOPDT) is under construction at Florida International University (FIU). Computational Fluid Dynamics simulations are underway to complement the physical tests.

3. RESULTS AND DISCUSSION

The PDTs are critical in informing NICHE design parameters; for example, the tests at UM helped to determine the effect of seawater versus freshwater spray on structures, while the OSU and UCSD tests are answering important practical questions about design parameters for simulating wind and wave interactions. The UF boundary layer wind tunnel (BLWT) physical tests (Khaled et al., 2025) focused on creating vortices in the straight-line wind tunnel using two methods: (1) a partial blockage vertical wall, and (2) a set of actuated louvers. The resulting data analysis will inform the full-scale NICHE design for generating transient winds. The UF physical tests were complemented by computational models to determine the capability of generating translating

vortices. These models were able to predict the behavior of generated vortices for both boundary conditions. Characteristics of generated vortices (Fig. 2) were in good agreement with field observations and benchmark analytical models.



Figure 2. Flow visualization (video still frame) of a vortex created in the UF BLWT with the louver system.

4. CONCLUSION AND FUTURE WORK

A multi-disciplinary team is designing a National Full-Scale Testing Infrastructure for Community Hardening in Extreme Wind, Surge, and Wave Events (NICHE) that responds directly to the pressing national imperative to promote more resilient and sustainable communities by reducing losses, population dislocation, outmigration, and economic impacts due to climate-driven hazards.

When the design team completes its test-bed experiments and computational simulations by 2025, work begins to outline in detail the specifications for the NICHE facility. When the NICHE planning award is finished in January 2026, the project team will present a robust plan for building the full-scale NICHE, an unprecedented multi-hazard experimental facility with the support of the Major Research Equipment and Facilities Construction (MREFC) program at NSF.

With the NICHE facility, future natural hazards researchers will have the capability to address the complex problems posed by increasingly severe wind-and-water hazards in the U.S. Another aspect of NICHE is its plan for dedicated research-translation pathways, channels for moving a research project beyond the experimentation phase into real-world usage.

REFERENCES

National Academies of Sciences, Engineering, and Medicine (2019). Building and Measuring Community Resilience: Actions for Communities and the Gulf Research Program. Washington, DC: The National Academies Press. doi.org/10.17226/25383

ASCE's Policy Statement, 2021 (Policy statement 360 - Climate change | ASCE)

Khaled, F. Lombardo, F, Gurley, K. (2025). Modeling of vortices in straight-line wind simulators, Journal of Wind Engineering and Industrial Aerodynamics, Volume 257, February 2025, 105992, https://doi.org/10.1016/j.jweia.2024.105992

Discussion of design wind loads on mullions installed at the corners of rectangular buildings

Tomoko Aihara [1], Yuji Isshiki [2], Yasushi Uematsu [3]

[1] *TAISEI Corporation, Yokohama, Japan, tomoko.aihara@sakura.taisei.co.jp*
[2] *TAISEI Corporation, Tokyo, Japan, isshiki@arch.taisei.co.jp*
[3] *Tohoku University, Sendai, Japan, yasushi.uematsu.d8@tohoku.ac.jp*

SUMMARY:
This paper investigates the design wind loads on mullions installed at the corners of rectangular buildings based on a wind tunnel experiment. Since the mullion supports corner curtain walls, it is subjected to two mutually orthogonal wind loads simultaneously. Building codes usually specify positive and negative wind pressure coefficients for designing cladding/components of buildings based on the most critical maximum and minimum peak wind pressure coefficients irrespective of wind direction. Thus, the combinations of these wind pressure coefficients may overestimate the design wind loads on corner mullions. This paper discusses the combination of wind pressure coefficients on the two adjacent walls, which predicts the maximum load effects on the mullions appropriately.

Keywords: Mullion, Wind tunnel experiment, Peak external pressure coefficient, Load combination

1. INTRODUCTION

Wind pressure coefficients for designing cladding/components of buildings are specified in building codes and standards, e.g., Building Standard Law of Japan. They are usually determined based on the most critical maximum and minimum peak wind pressure coefficients irrespective of wind direction. A mullion placed at a corner of rectangular building supports two curtain walls which are perpendicular to each other. Thus, it is subjected to two orthogonal wind loads simultaneously. If these loads are calculated using the wind pressure coefficients specified in the building codes and standards, it may result in an overestimation of wind loads on the mullions. The present paper proposes the equivalent wind pressure coefficients on the corner walls providing the maximum load effects on the mullion based on a wind tunnel experiment, in which the side and aspect ratios of building are varied over a wide range.

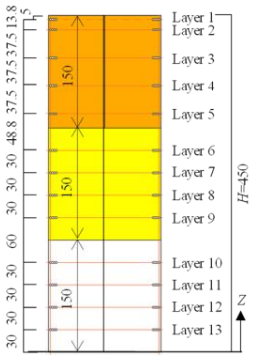
2. EXPERIMENTAL PROCEDURE

2.1. Experimental model

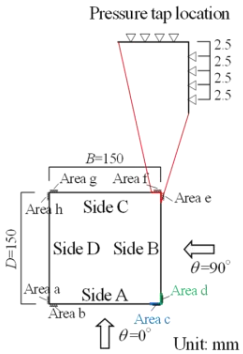
Fig. 1a shows the dimensions of the experimental models which are made by combining cubes with side lengths of 150 mm. The width/depth (or side) ratio, B/D, ranges from 1 to 4 and the height/depth (or aspect) ratio, H/D, ranges from 0.25 to 3. The model has 8 pressure taps (4 taps on each side) near each of four corners at several heights (layers). The geometric scale λ_L is assumed to be 1/200. Fig. 1b-1d show the dimensions and pressure tap arrangement for Model 9.

Model	*B*	*D*	*H*
1	150	150	150
2	200	300	150
3	600	600	150
4	300	150	150
5	600	150	150
6	150	150	300
7	300	150	300
8	600	150	300
9	150	150	450
10	300	150	450
11	600	150	450

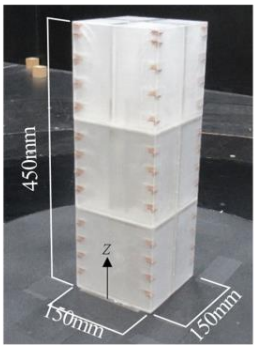
(a) Dimensions (mm)



(b) Elevation



(c) Plan



(d) Picture

Fig. 1. Experimental models: (b) - (d) for Model 9.

2.2 Wind tunnel flow

The wind tunnel flow is a turbulent boundary layer with a power-law exponent of α = 0.2 for the mean wind speed profile. The mean wind speed U_Z, the turbulence intensity I_Z and the integral scale of turbulence L_Z are as follows; that is, U_Z = 8 m/s, I_Z = 0.20 and L_Z = 699 mm at Z = 150 mm; U_Z = 9 m/s, I_Z = 0.12 and L_Z = 999 mm at Z = 300 mm; and U_Z = 10 m/s, I_Z = 0.16 and L_Z = 817 mm at Z = 450 mm. The geometric scale of this flow is approximately 1/200. The velocity scale λ_V is assumed to be 1/4.2, resulting in the time scale of λ_T = 1/48.

2.3 Experimental procedure

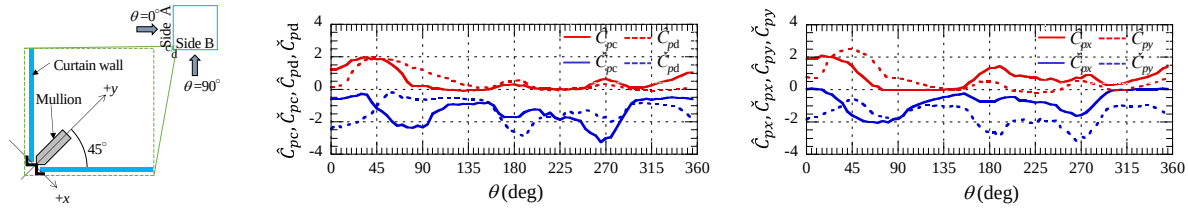
The wind pressures at all pressure taps are sampled simultaneously at a sampling frequency of 1,000 Hz for a period of about 131 s, from which we obtain 10 sets of time histories for 10 min at full scale. A low-pass filter with a cut-off frequency of 300 Hz is used to eliminate electric noise. The wind pressure distortion due to tubing is compensated by using the frequency response function of the tubing system. The wind pressures are reduced to wind pressure coefficients C_p, defined in terms of the mean velocity pressure q_H of the approch flow at the model height H. The maximum and minimum peak wind pressure coefficients, $\hat{C}_p$ and $\check{C}_p$, during a period of 10 min at full scale are evaluated by applying ensemble averaging to the results obtained from the consecutive 10 runs. The wind direction θ, defined as shown in Fig. 1c, is varied from 0° to 90° at an increment of 5°. In the present study, assuming that the load bearing width l_{M} of the corner mullion is 1 m on the safer side and the wind pressure fluctuations are perfectly correlated in the vertical direction at each floor, the area-averaged wind pressures over the tributary area are computed using the measured C_p data. In the case of l_{M} = 1 m, the wind pressures at two pressure taps near the corner on each side are used for calculating the area-averaged wind pressures.

3. Experimental results and discussion

3.1 Wind pressures on the walls and the resultant wind forces on the corner mullions

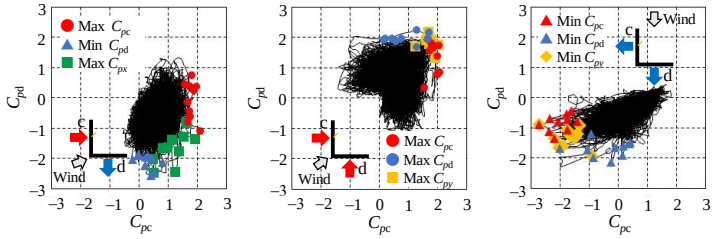
Our previous study (Aihara et al., 2023) indicated that the instantaneous wind pressure distribution on a curtain wall supported by a corner mullion was nearly uniform. Therefore, it is assumed that the area-averaged wind pressure acts on the whole tributary area of the wall at any time. The area-averaged wind pressure coefficients, C_{pc} and C_{pd}, on the two orthogonal walls (referred to as Areas ‘c’ and ‘d’, see Fig. 1c), are converted to the equivalent wind pressure coefficients, C_{px} and C_{py}, in the x and y directions (see Fig. 2a).

Fig. 2b shows the variation of the maximum and minimum peak values of C_{pc} ($\hat{C}_{pc}$ and $\check{C}_{pc}$) and C_{pd} ($\hat{C}_{pd}$ and $\check{C}_{pd}$) with θ at Layer 4 in Case 9. Similarly, Fig. 2c shows the results on the maximum and minimum peak values of C_{px} ($\hat{C}_{px}$ and $\check{C}_{px}$) and C_{py} ($\hat{C}_{py}$ and $\check{C}_{py}$). The $\hat{C}_{px}$ value becomes the maximum at $\theta \approx 20°$; $\hat{C}_{pc}$ and $|\check{C}_{pd}|$ are both large. The value of $\check{C}_{px}$ becomes the minimum at $\theta \approx 70°$; $|\check{C}_{pc}|$ and $\hat{C}_{pd}$ are both large. Thus, the most critical maximum and minimum peak values of C_{px} occur when a large positive C_p value acts on one side and a large negative C_p value acts on the other side simultaneously (Load case 1). The $\hat{C}_{py}$ value becomes the maximum at $\theta \approx 45°$; $\hat{C}_{pc}$ and $\hat{C}_{pd}$ are both large. This, the most critical maximum peak value of C_{py} occurs when large positive C_p values act on both sides (Load case 2). The $\check{C}_{py}$ value becomes the minimum (maximum in magnitude) at $\theta \approx 180°$ or $270°$; $|\check{C}_{pc}|$ and $|\check{C}_{pd}|$ are both large. Thus, the most critical minimum peak value of C_{py} occurs when large negative C_p values act on both sides (Load case 3).



(a) Local coordinates (b) Peak pressure coefficient (c) Peak equivalent pressure coefficient

Fig. 2. Maximum and minimum peak wind pressure coefficients.



(a) Load case 1 (θ= 20°) (b) Load case 2 (θ= 45°) (c) Load case 3 (θ= 270°)

Fig. 3. Phase plane representation of the C_{pd} and C_{pc} relation (Case 9).

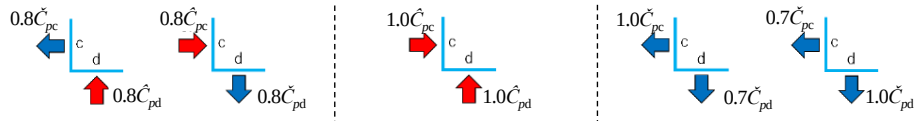
3.2. Equivalent wind pressure coefficients for designing the corner mullions

Combination of peak wind pressure coefficients on two orthogonal walls near a corner may overestimate the wind loads on corner mullions, because these peak values do not necessarily occur simultaneously. Therefore, we focus on the equivalent wind pressure coefficients providing the maximum wind loads on the corner mullion in the x and y directions.

Fig. 3 shows the phase plane representation of the $C_{pd} - C_{pc}$ relation for a period of 100 min at full scale at Layer 4 in Case 9. The wind directions of 20°, 45° and 270° correspond to Load cases 1, 2 and 3, respectively. In the figure, each symbol represents a combination of C_{pd} and C_{pc} that provides the maximum or minimum peak value of the designated wind pressure coefficient during 10 min at full scale. For example, ● represents the state when C_{pc} is at the maximum peak value $\hat{C}_{pc}$. According to Fig. 3a (Load case 1), the maximum peak C_{px} generally occurs when both C_{pd}

and C_{pc} are large in magnitude. It does not necessarily occur neither at the moment when C_{pc} is at its maximum peak value nor at the moment when C_{pd} is at its minimum peak value. Fig. 3b (Load case 2) shows that the maximum peak C_{py} generally occurs when either C_{pc} or C_{pd} is at its maximum peak value. When one coefficient is at its maximum peak value, the value of the other coefficient is also large. It is found from Fig. 3c (Load case 3) that the minimum peak C_{py} occurs when larger absolute value of C_{pc} and C_{pd} takes its minimum peak values. Regarding the peak values of C_{px} and C_{py}, similar features were observed for the other models.

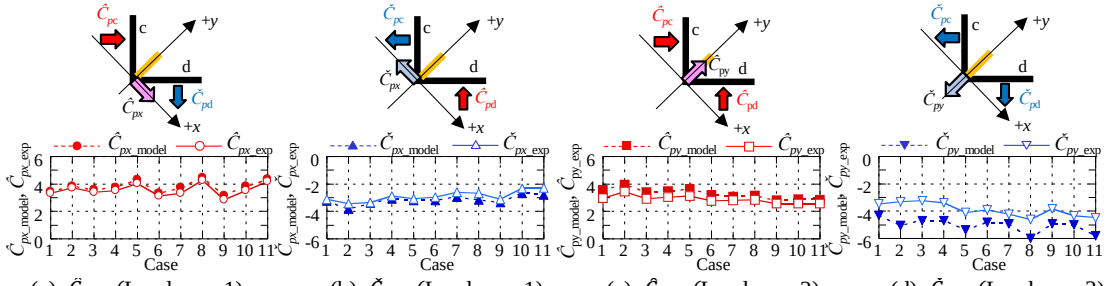
Based on the above-mentioned results, we propose the wind pressure coefficients on two orthogonal walls as shown in Fig. 4 for designing corner mullions. In the figure, $\hat{C}_{pc}$. and $\hat{C}_{pd}$ represent the most critical maximum peak wind pressure coefficients irrespective of wind direction on Areas 'c' and 'd', respectively. Similarly, $\check{C}_{pc}$ and $\check{C}_{pd}$ represent the most critical minimim peak wind pressure coefficients irrespective of wind direction on Areas 'c' and 'd', respectively.



(a) Load case 1 (b) Load case 2 (c) Load case 3

Fig. 4. Wind pressure coefficients on the orthogonal walls for designing corner mullions.

Fig. 5 shows comparisons between 'experiment' and 'model' for the maximum and minimum peak values of C_{px} and C_{py} among all layers and all wind directions. Note that 'experiment' indicates that the values are obtained from the time histories of C_{pc} and C_{pd}, while 'model' indicates that the values are estimated from the models of wind pressure coefficients shown in Fig. 4. It is found that the agreement is generally good for Load cases 1 and 2. On the other hand, the agreement is relatively poor for Load case 3. The 'model' values are generally larger in magnitude than the 'experiment' values. In other words, the 'model' estimates the design wind loads on the safer side. Therefore, they can be applied to practical structures.



(a) $\hat{C}_{px}$ (Load case 1) (b) $\check{C}_{px}$ (Load case 1) (c) $\hat{C}_{py}$ (Load case 2) (d) $\check{C}_{py}$ (Load case 3)

Fig. 5. Comparison between 'experiment' and 'model' for the maximum and minimum peak values of C_{px} and C_{py} among all layers and all wind directions.

REFERENCES

Aihara, T., Fushihara, K., Isshiki, Y., Uematsu, Y., Experimental study of wind loads acting on the mullions placed at the corner of the orthogonal walls of a high-rise building, Part 4 Wind loads for designing mullions, Summaries of Technical Papers of Annual Meeting, Architectural Institute of Japan, Structure I, 101-102. (in Japanese)

Aerodynamic oscillations of high-rise buildings using building mass damper

Jiarui Wu [1], Tsuyoshi Nozu [1], Kiyoshi Sasaki [1], Yuta Tomiyoshi [1]

[1] *Shimizu Corporation, Tokyo, Japan, wu-jiarui@shimz.co.jp*

SUMMARY: (10 pt)
This study investigates the aerodynamic vibration characteristics of high-rise buildings equipped with a building mass damper, considering various shapes and dynamic characteristics. This study conducted an experiment, and investigated the influence of the mass ratio, damping coefficient, and cross-sectional shape on aerodynamic vibrations. The elastic model used in this experiment was designed based on a model that condenses the structural characteristics into a four-degree-of-freedom system. The wind tunnel experiments were conducted under conditions that satisfy the similarity laws. The experimental results showed that a higher mass ratio results in greater vibration reduction effects in the across-wind direction. Increasing the damping coefficient significantly improves the control performance. Moreover, regarding damping, a higher reduction rate was also observed in the across-wind direction. As for cross-sectional shape, it was confirmed that using a chamfered shape helps suppress the rapid increase in inter-story deformation at high wind speeds.

Keywords: Aerodynamic oscillations, building mass dampers, wind tunnel testing

1. INTRODUCTION.

In recent years, with the increasing demand for seismic performance in buildings, many high-rise buildings employ passive-control devices such as tuned mass damper (TMD). A TMD uses a mass located on the top story of a building to decrease vibration. The control performance of a TMD improves if the mass is increased; however, this results in a burden for the structure. To solve this problem, a building mass damper (BMD) has been devised. This method assumes that part of the building acts as a TMD, achieving greater control performance than a traditional TMD for earthquake (Wang, S.J., 2018). On the other hand, the aerodynamic vibration of super high-rise buildings with BMD needs to be elucidated. Therefore, this study assesses the influence of building shape and its dynamic characteristics on aerodynamic vibrations in control performance. In this report, wind tunnel experiments using elastic models are conducted to examine the influence of building shape and mechanical structural characteristics on aerodynamic vibration properties.

2. DESIGN OF ELASTIC MODELS

2.1. About Building Mass Damper

BMD is used to suppress the seismic responses of high-rise buildings. As shown in Figure 1., which shows a building equipped with BMD, the upper and lower structures are connected by a “connecting layer,” and the BMD utilizes the upper structure as a TMD. Consequently, the BMD

achieves much larger mass ratios (10–50%) compared to conventional TMD and is expected to have a significant seismic damping effect against large earthquakes.

2.2. Overview of the Wind Tunnel Test Model

This paper uses a building with a height of 250m, a square horizontal cross-section of 50m × 50m, a slenderness ratio of 5, and a side length ratio of 1. The mass ratio between the mass of upper structure (MU) and the mass of lower structure (ML) is set at 0.2 and 0.4. Table 1. shows the design natural periods for each configuration.The stiffness distribution is assumed to be trapezoidal one, resulting in vibration modes with discontinuous deformations at the connection points. The internal damping is assumed to be proportional to stiffness.

To replicate the discontinuous vibration modes, a multi-degree-of-freedom elastic model condensed into a 4degree-of-freedom system is used for the wind tunnel testing (Wu, J., 2023 & 2024). The scale of the model is set to 1/400. The damping constants of the model are set to 2%, 6%, and 0.6% using silicone oil and viscoelastic sheets. The cross-sectional shapes used are a square and a chamfered shape, where 5% of the length from each end of one side is cut diagonally.

3. OVERVIEW OF WIND TUNNEL TESTING

The wind tunnel used is the wind resistance testing facility at the Institute of Technology of Shimizu Corporation. The wind tunnel airflow simulates surface roughness category III. The response displacement of the model is measured using a non-contact laser displacement meter. The study considers a real wind speed of 31.8 m/s (with a recurrence period of 50 years) and a design wind speed of approximately 90.8 m/s, which is about 1.5 times the recurrence period of 500 years. The wind tunnel speeds measured range from 3 m/s to 9 m/s. The vortex-induced vibration onset wind speed is 52.5 m/s in real wind conditions. The response displacement is measured at a sampling frequency of 1000 Hz, and an ensemble average equivalent to 10 waves over a real-time duration of 10 minutes is performed. Figure 2. shows a photo of the model.

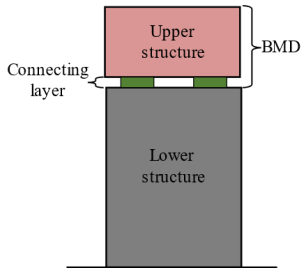


Fig. 1. Building using building mass damper

Tab. 1. Natural period

degree	0.2 model [s]	0.4 model [s]
	MU / ML	MU / ML
1	7.56	7.84
2	4.07	3.50
3	1.66	1.43
4	1.01	0.91
5	0.73	0.87

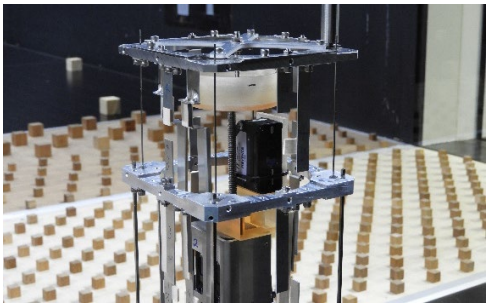


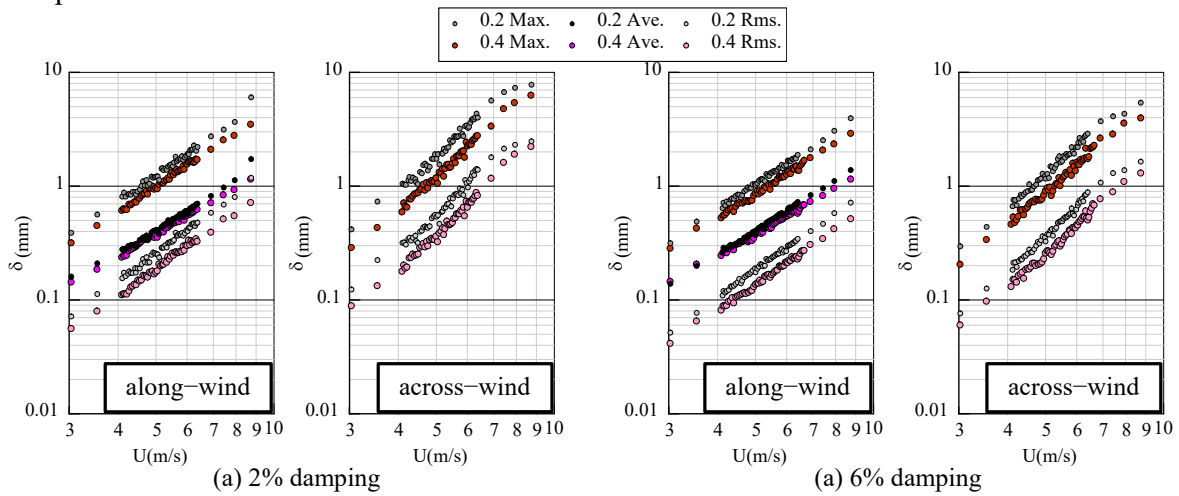
Fig. 2. Photo of the model

4. ANALYSIS OF WIND TUNNEL TESTING RESULTS

4.1. Influence of Mass Ratio

This section investigates the influence of a mass ratio. Figure 3. illustrates the relationship between wind speed and inter-story deformation δ (mean, standard deviation, and maximum displacement) for the third and fourth layers at damping constants of 2% and 6%. In all cases, it is observed that in the wind direction, the response displacement increases monotonically with increasing wind

speed. Conversely, in the across-wind direction, the rate of increase in response decreases in the high wind speed range. Additionally, compared to a mass ratio of 0.2, the inter-story deformation for a mass ratio of 0.4 shows a reduction in the maximum value by 20% and the standard deviation by 28% in the wind direction, and a reduction in the maximum value by 34% and the standard deviation by 34% in the across-wind direction. This confirms that the influence of mass ratio is more pronounced in the across-wind direction.

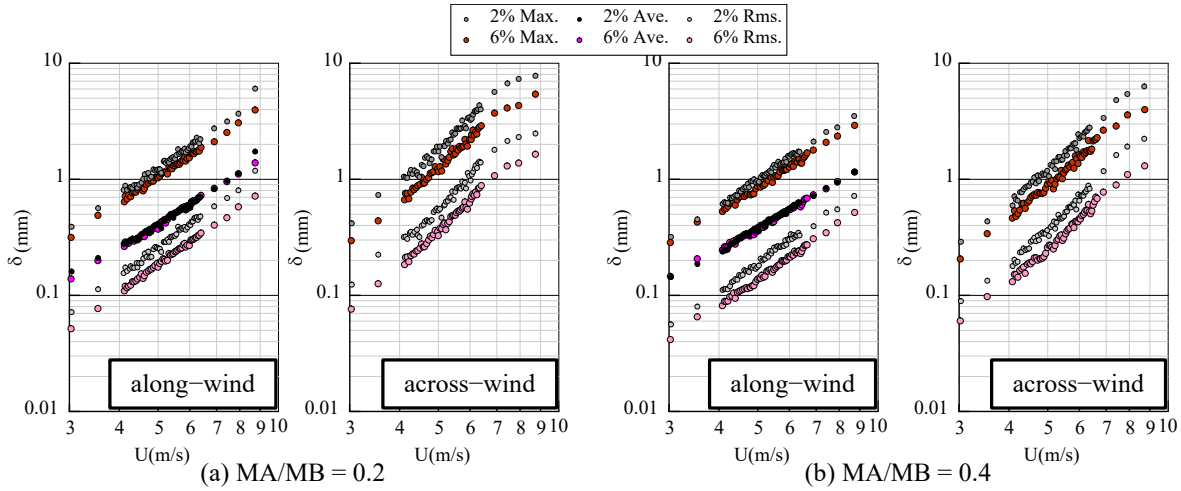


(a) 2% damping (a) 6% damping

Fig. 3. variations in response characteristics due to differences in mass ratio

4.2. Influence of Damping Ratio

This section investigates the influence of a damping ratio. Figure 4. shows the relationship between wind speed and inter-story deformation for the fourth layer at mass ratios of 0.2 and 0.4. For both models, regardless of the mass ratio, there is no difference in the mean component of inter-story deformation in the wind direction due to damping. However, increasing the damping from 2% to 6% reduces the maximum value by 16% and the standard deviation by 29%. In contrast, in the across-wind direction, increasing the damping from 2% to 6% reduces the maximum value by 31% and the standard deviation by 36%. This confirms that the influence of the damping constant is more pronounced in the inter-story deformation in the across-wind direction.



(a) MA/MB = 0.2 (b) MA/MB = 0.4

Fig. 4. variations in response characteristics due to differences in damping

4.3. Difference in Cross-Sectional Shape

This section investigates the influence of a cross-sectional shape. Figure 5. shows the relationship between wind speed and inter-story deformation for the fourth layer in both square and chamfered shapes. It was observed that, at all wind speed levels, the chamfered shape results in smaller deformation in the wind direction. When examining the response displacement in the across-wind direction, it appears that the inter-story deformation for the square shape increases beyond the vortex-induced vibration onset wind speed of 5 m/s. Particularly at a damping of 0.6%, the inter-story deformation for the square shape increases sharply beyond 6 m/s, whereas the chamfered shape effectively suppresses the inter-story deformation.

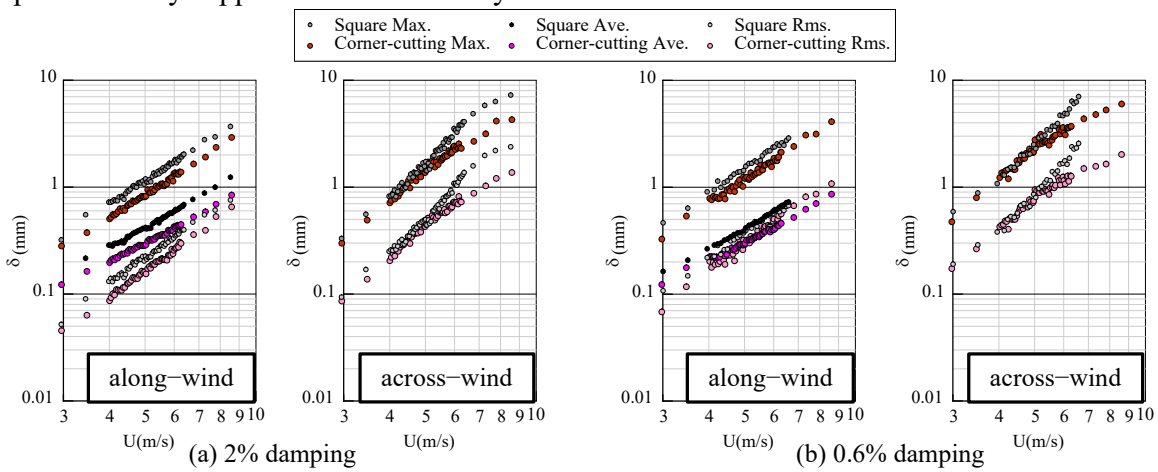


Fig. 5. variations in response characteristics due to differences in cross-sectional shape

5. CONCLUSIONS

In this report, elastic model experiments were conducted on high-rise buildings equipped with BMD to examine the influence of structural characteristics on aerodynamic vibration properties. The findings are summarized as follows:

・Increasing the mass ratio is expected to reduce the response, with a particularly higher reduction rate observed in the across-wind direction.

・Regarding damping, a higher reduction rate was also observed in the across-wind direction.

・As for cross-sectional shape, it was confirmed that using a chamfered shape helps suppress the rapid increase in inter-story deformation at high wind speeds.

REFERENCES

Wang, S.J., Lee, B.H., Chuang, W.C., Chang, K.C., 2018. Optimum dynamic characteristic control approach for building mass damper design. Earthq. Eng. Struct. Dyn. 47(4), 872–888

Sato, D., Tamura, T., Fugo, Y., Nakamura, O., Katsumura, A., Kasai, K., Kitamura, H., 2015. Wind-induced Response Characteristic Evaluation of High-rise Seismic Isolated Building Based on Observed Records. 14th International Conference on Wind Eng.

Wu, J., Nozu, T., Sasaki, K., Tomiyoshi, Y., and Imai, K., 2023. Study on aerodynamic vibrations in high-rise buildings with seismic isolation and damping devices. Summaries of technical papers of annual meeting, 20061, 121-122. (In Japanese)

Wu, J., Nozu, T., Sasaki, K., Tomiyoshi, Y., and Imai, K., 2024. Study on aerodynamic vibrations in high-rise buildings with seismic isolation and damping devices. Summaries of technical papers of annual meeting, 20049, 97-98. (In Japanese)

The mechanism behind VIV onset on rectangular cylinders with porous coverings: an experimental and numerical study

Marcello Catania[1], Giulia Pomaranzi[2], Alberto Zasso[3]

[1]*Politecnico di Milano, Milan, Italy, marcello.catania@polimi.it*
[2]*Politecnico di Milano, Milan, Italy, giulia.pomaranzi@polimi.it*
[3]*Politecnico di Milano, Milan, Italy, alberto.zasso@polimi.it*

SUMMARY:
This study investigates the aeroelastic effects of a porous envelope on an elongated rectangular cylinder with an aspect ratio of 3.33. The addition of a porous covering to a solid structure allows airflow into the gap between the two surfaces, altering the dynamics of the separated shear layer, with potential for vortex-shedding (VS) suppression. An experimental campaign, complemented by 3D CFD simulations, was conducted to examine the role of the porous covering in VS behavior and the vortex-induced vibrations (VIV) of the structure. Specifically, large eddy simulation (LES) was employed to capture the evolution of the flow field and to assess how the permeable covering affects the forcing mechanisms induced by VS. Results highlight that the onset of VIV is governed by the spatial correlation of the instantaneous pressure field, reaffirming the state-dependent nature of this phenomenon.

Keywords: Porous covering, Vortex Shedding, Vortex-Induced Vibration, Wind Tunnel, LES

1. INTRODUCTION

Vortex-induced vibration (VIV) is an aeroelastic phenomenon that occurs when aerodynamic forces resonate with one of the natural frequencies of the structure, leading to stable, high-amplitude oscillations. Slender structures such as long-span bridges and high-rise buildings could incur in comfort issues and even severe fatigue damages if the problem is not controlled. Various VIV mitigation solutions have been explored, including the application of porous elements (A. Teimourian and H. Teimourian, 2021). Permeable wind barriers on bridge decks or shrouds installed on chimneys and towers are an example of aerodynamic modifications that can damp oscillations by affecting the separated shear layer and the force correlation along the height. In recent years, porous envelopes have found new applications in the civil sector, in the form of permeable double-skin façades (PDSFs). The porous medium modifies the pressure distribution on the underneath structure due to the presence of air circulating in the gap and the formation of a new recirculation zone from the windward edges of the envelope. The interaction between these vorticose structures completely changes the aerodynamics of the system, leading to a wind loads reduction on the inner façade (Pomaranzi et al., 2020). Numerous studies on elongated rectangular cylinders confirm that the aerodynamic forcing causing VIV is generated by vortex shedding from the leading edges' permanent separation points. Small structural displacements can synchronize motion and vortex shedding, promoting the onset of self-excited forces that will ultimately result in large-amplitude oscillations (Li et al., 2016; Wang et al., 2024). How this complex aeroelastic interaction is affected by the presence of a porous covering applied over a solid cylinder is still unclear. In particular, how

the pressure field is modified by the presence of the porous envelope and how the motion of the system is affected by this modification are crucial questions that need to be answered to understand the VIV onset mechanism (Catania et al., 2024). This study proposes investigating these aspects and defining the applicability of porous envelopes as a VIV control strategy. The aeroelastic behavior of an elongated rectangular cylinder in the presence of a porous cover will be studied through a high-fidelity computational fluid-dynamic (CFD) simulation. A 3D free-to-oscillate prism of aspect ratio 3.33 has been chosen as a model that could be representative of the aerodynamics of a bridge deck or a high-rise buildings. Large-eddy simulations (LES) will be employed to accurately reproduce the evolution of the flow field and to assess how the shroud affects the spatial correlation of forces on the structure.

2. METHODOLOGY

The geometry chosen for this study is a rectangular cylinder of aspect ratio 3.33 with fixed mechanical properties. It has been tested under different wind conditions without and with the porous envelope to characterize VIV. The phenomenon has been observed experimentally and numerically, focusing on the evolution of the correlation between displacement and the pressure field.



(a) Experimental model. (b) Numerical model.

Figure 1. Tested model with focus on the porous envelope.

2.1. Experimental setup

The model is a rigid rectangular cylinder mounted on an elastic base that allows low-frequency oscillations in the cross-wind direction. The setup includes four accelerometers and 208 pressure taps distributed across eight levels to capture displacement and pressure variations. Two façade configurations were tested: a "naked" single-glazed cladding and a "porous" double-skin façade. The porous configuration involves a perforated mesh with 55% porosity, placed 20 mm from the solid façade, with a measured pressure loss coefficient of $k = 1.8$ (Figure 1a). The geometric, mechanical and aerodynamic properties of the system are reported in Table 1. The tests were carried out in the atmospheric boundary layer section of the Politecnico di Milano wind tunnel, under smooth flow conditions with turbulence intensity $I_u \approx 2\%$.

Table 1. From the left: along-wind and cross-wind dimensions, height, natural frequency in still-air, equivalent modal mass per unit length and non-dimensional structural damping (cross-wind vibration mode) and Strouhal number of the model in different configurations

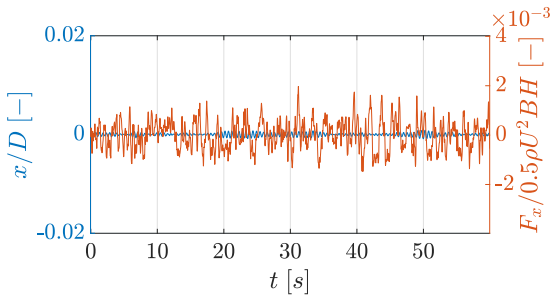
Configuration	$B\ [m]$	$D\ [m]$	$H\ [m]$	$f_1\ [Hz]$	$m_1\ [kg/m]$	$\xi\ [\%]$	$St\ [-]$
Naked	1.00	0.30	2.00	1.95	45.2	1.0	0.13
Porous	1.04	0.34	2.00	1.88	48.6	1.0	0.15

2.2. CFD setup

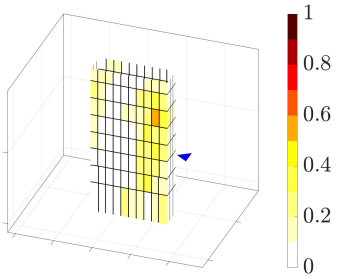
A set of LES simulations have been employed to relate the evolution of the measured quantities to the flow field around the structure. The CFD model is characterized by the same mechanical properties as its experimental counterpart. To allow cross-wind oscillations, a deforming mesh has been implemented. Regarding the porous covering, a macroscopic representation is adopted through a set of cells where the momentum-conservation equation is modified with a tensorial sink term defined according to the Darcy-Forchheimer model. The tensor describing the resistance term has been derived with experimental measurements and numerical simulations on explicitly modelled geometry (Marykovskiy et al., 2024). Figure 1b shows the set of cells representing the porous covering.

3. RESULTS AND DISCUSSION

Referring to the porous configuration, Fig. 2a and 3a show the displacement recorded at the top of the cylinder (blue curve) along with the cross-wind force (red line) when the wind velocity reaches the critical vortex shedding velocity. Specifically, Fig. 2a refers to null initial conditions, while Fig.3a refers to a perturbed initial state of the structure. In the former case (null ICs), the system does not exhibit VIV. As demonstrated by the the magnitude-square coherence (MSC) between pressure signals on the façades and displacement (Figure 2b), the porous covering affect the spatial coherence of the pressure field on the façade preventing effective forcing.



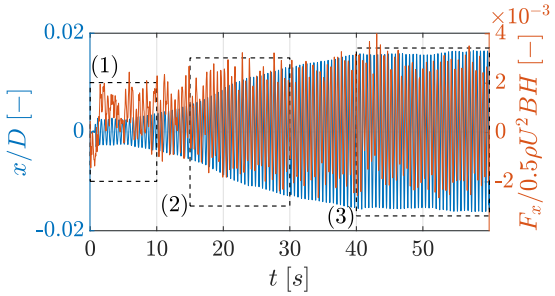
(a) Non-dimensional displacement (left axis) and total force in the cross-wind direction (right axis).



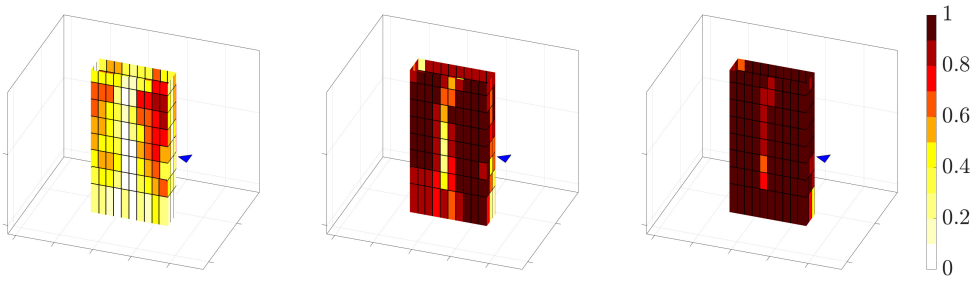
(b) MSC between each pressure tap and displacement.

Figure 2. Build-up, steady initial conditions.

However, if the initial state is perturbed, significant oscillations arise (Figure 3a). To understand the onset of the VIV, we can refer to the spatial correlation between force and structure response: at low oscillation amplitudes, pressure signals exhibit weak correlation in most areas of the façade, except at the leading edge, where $MSC > 0.7$ indicates that motion-induced vortices start to drive



(a) Non-dimensional displacement (left axis) and total force in the cross-wind direction (right axis).



(1) $t = [0-10]s$ (2) $t = [15-30]s$ (3) $t = [40-60]s$

Figure 3. Build-up with perturbed initial conditions. Up: displacement and force time history, down: MSC between each pressure tap and displacement at different time frames. The blue arrow indicates the wind direction.

VIV (Figure 3.1). As oscillation amplitude increases, spatial coherence also rises, particularly at the leading and trailing edges (Figure 3.2). When the system reaches steady state, a strong correlation with $MSC > 0.9$ is observed over the entire façade (Figure 3.3). These observations suggest that the increase in coherence responsible for effective forcing originates at the leading edges due to motion-induced vortices, underscoring the state-dependent nature of the phenomenon. In the full paper, results here shown will be complemented with the CFD ones, allowing to visualize flow field behaviour and the correlation of the pressure field, with particular focus on the vortex-shedding mechanism.

References

Catania, M., Pomaranzi, G., and Zasso, A., 2024. The role of Permeable Double Skin Façades on the onset of VIV on high-rise buildings. Journal of Wind Engineering and Industrial Aerodynamics 253, 105831.

Li, M., Li, S., Liao, H., Zeng, J., and Wang, Q., 2016. Spanwise correlation of aerodynamic forces on oscillating rectangular cylinder. Journal of Wind Engineering and Industrial Aerodynamics 154, 47–57.

Marykovskiy, Y., Pomaranzi, G., Schito, P., and Zasso, A., 2024. A Method to Evaluate Forchheimer Resistance Coefficients for Permeable Screens and Air Louvers Modelled as a Porous Medium. Fluids 9.

Pomaranzi, G., Daniotti, N., Schito, P., Rosa, L., and Zasso, A., 2020. Experimental assessment of the effects of a porous double skin façade system on cladding loads. Journal of Wind Engineering and Industrial Aerodynamics 196, 104019.

Teimourian, A. and Teimourian, H., 2021. Vortex Shedding Suppression: A Review on Modified Bluff Bodies. Eng 2, 325–339.

Wang, X., Xu, F., Zhang, Z., and Wang, Y., 2024. 3D LES numerical investigation of vertical vortex-induced vibrations of a 4:1 rectangular cylinder. Advances in Wind Engineering 1, 100008.

Full-scale vs. wind tunnel pressure measurements on a mid-rise building

A. Malasomma [1,*], V. Picozzi [1], L. Caracoglia [2],
A. M. Avossa[1], F. Ricciardelli[1]

[1]*University of Campania "Luigi Vanvitelli", Aversa, IT*
[2]*Northeastern University, Boston, MA, USA*
[*]*antonio.malasomma@unicampania.it*

SUMMARY
Wind pressures on a 78 m high building are being monitored by a system including 16 pressure transducers mounted on the 15th and 18th floors. At the same time, wind tunnel pressure measurements have been taken on a 1:200 scaled model with and without surroundings, as well as on a 1:100 model without surroundings of the same building. Comparisons will be carried out between the pressures measured at full scale and those measured in the three experimental setups, in terms of mean, RMS, peak pressures and power spectral densities (PSDs) of the pressure fluctuations. Finally, pressure correlation and coherence functions within the same floor and between the two floors, mentioned above, will be compared.

Keywords: Mid-rise building, Full-scale monitoring, Wind tunnel testing, Wind pressures, Reliability

1. INTRODUCTION

The understanding of how wind fields translate into wind actions on civil structures has always been a theme of wide interest in Wind Engineering (Davenport, 1961). Wind-induced pressures on buildings have a complicated spatiotemporal fluctuating nature; their investigation is possible mainly via three methods: wind tunnel tests, field measurements and numerical simulations. Wind tunnel tests are performed at the design stage, and they are considered a relatively inexpensive and reliable way of reproducing both wind conditions and wind actions on structures. On the other hand, full-scale monitoring of civil structures, especially wind-sensitive structures (e.g. long-span suspension bridges and high-rise buildings) has become essential in validating and improving wind tunnel testing procedures (Cermak, 2003). The most relevant aspect of a full-scale monitoring campaign is its time- and cost-intensive nature (Caracoglia and Jones, 2009). Choosing the appropriate measurement equipment that best describe the building characteristics, including geometry, structural typology and use, and establishing contacts with the building owners and getting necessary permissions (Kijewski-Correa et al., 2006) are among the main technical issues associated with full-scale experiments. This paper presents a new installation of a full-scale monitoring system, designed for a 19-story building, in Napoli, Italy (Figure 1). The experimental campaign has the broader aim of validating the available design procedures for high-rise buildings though comparison with full-scale data. Some preliminary results will be presented on the

comparison between pressures measured in full-scale and in the wind tunnel.

2. METHODOLOGY

The monitored building is part of the "Federico II" University Hospital Campus located in the northern area of Naples (Italy); it is commonly referred to as *Torre Biologica* (Figure 1). It is 78 m high, with floor plan dimensions $B \times D = 25.10 \times 29.90\ m$, and features a composite concrete-steel structure with three reinforced concrete cores: a large $10.00 \times 10.00\ m$ central core is made by four walls intersecting each other in the shape of "a hashtag"; two L-shaped smaller cores are located on opposite corners of the building. The building is located in a hilly area and stands out compared to surrounding constructions.

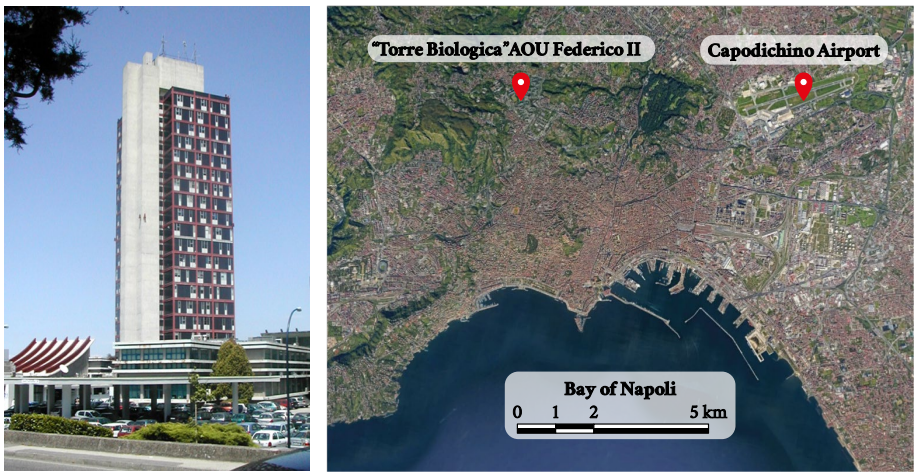


Figure 1. Monitored building and its geographical location.

The monitoring system consists of:

- 2 Gill Wind Master 3D, 20Hz sonic anemometers
- 16 Setra 264 differential pressure transducers
- 1 Quad static pressure probe
- 22 PCB Piezotronics accelerometers (model 393A03 and model 393C)
- 1 National Instruments compact DAQ-9137data logger

The two sonic anemometers are placed about 2 m above the rooftop, using two rigid antenna poles. The 15th and 18th floors are equipped with eight pressure transducers each (Figure 2). These instruments measure the differential pressures, i.e., the difference of the surface pressure with respect to a static reference value; the latter is taken with a static pressure probe installed near one of the anemometers placed on the rooftop. To establish the same static reference pressure for all transducers, a dedicated pneumatic line is installed connecting the static probe with the 16 anemometers. This pneumatic line allows taking into account time-fluctuations in the reference pressure due to varying meteorological conditions. Measurements started at the end of October 2024.

Wind tunnel testing is a valuable method for assessing the impact on structural and cladding elements (Xiang W., 2022). However, an accurate reconstruction of field conditions, including

incident turbulence and terrain characteristics, can be challenging in wind tunnel experiments. Therefore, it is crucial to validate wind tunnel predictions against full-scale measurements to quantify the accuracy of the model test results and assess the effectiveness of the wind tunnel testing techniques.

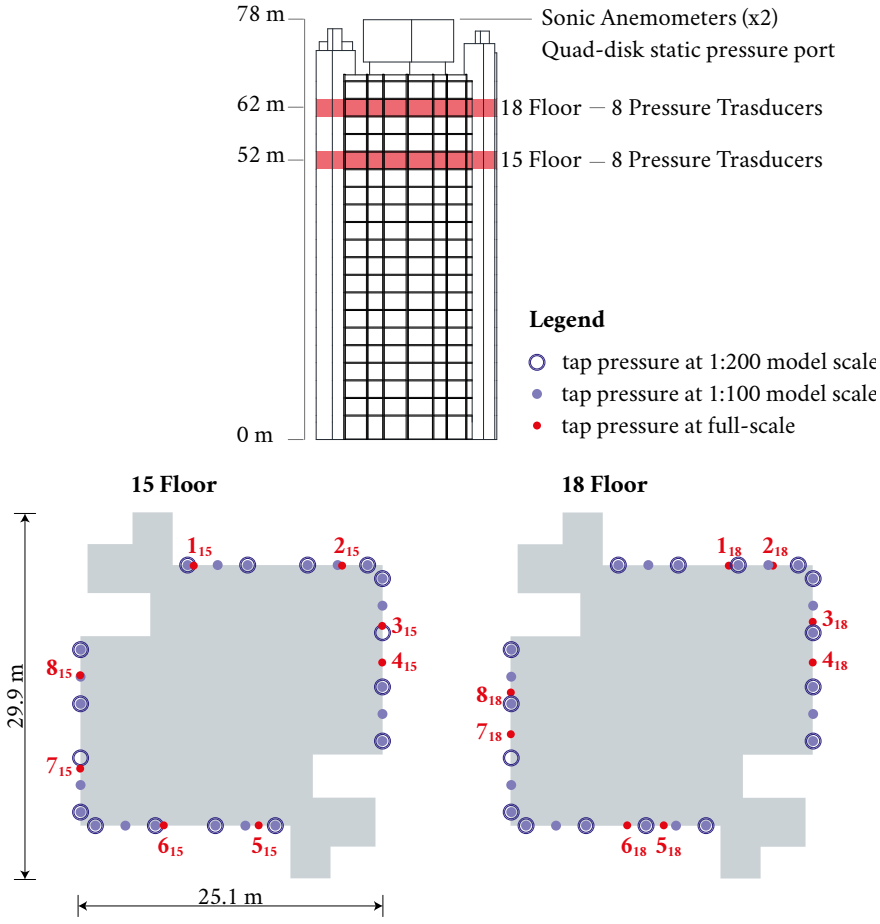


Figure 2. Pressure port configuration.

To achieve these aims, given the non-conventional shape of the building as well as the complexity of the surrounding architecture, four different wind tunnel tests were carried out at the Laboratory of Environmental Aerodynamics of the University of Cracow, Poland. Wind profiles are measured on a 1:200 scaled orography model, and pressure measurements are made on a 1:200 scaled model with and without surroundings as well as on a 1:100 model without surroundings. A step of 15° was used when varying the angle of attack.

For the 1:200 model, pressure coefficients were measured for 180 s corresponding to a duration of 5 hrs full-scale at a time scale of 1:100, i.e. 30 runs of 10 min each. For the 1:100 model, pressure coefficients were measured for 240 s corresponding to a duration of 200 min at a time scale of 1:50, i.e. 20 runs each of 10 min each. Pressure coefficients for both wind tunnel tests and full-scale measurements can be defined as follows:

$$c_p(M,t) = \frac{p(M,t) - p_0}{\frac{1}{2}\rho V_H^2}$$

where $\mathrm{p}(M,t)$ is the external absolute surface pressure at point M and time t; p_0 is the static reference air pressure (barometric pressure), and V_H is the wind speed at the reference height, corresponding to the building height.

3. EXPECTED RESULTS

The characteristics of pressures at the 16 instrumented points of the full-scale building will be investigated by means of their mean, RMS, and peak values, as well as of the energy distribution using power spectral densities (Davenport, 1963). Correlations between pressure fluctuations in instrumented locations on the same side and between different side of the building are investigated (Jia-hui Yuan et al.,2023). Several wind directions will be considered, depending on the available data.

Comparisons will be carried out between the pressures statistics, spectra and correlations as evaluated from full-scale measurements and in the three experimental setups. So doing, we expect to be able to quantify the discrepancy between the full-scale values and those coming from scaled model tests, and an attempt will be made to relate those to the characteristics of the three WT setups.

Furthermore, the study will examine instantaneous measurements of the static p_0 (i.e., static pressure value may drift during a measurement). The issues of pressure data stationarity, instrumental fidelity and resolution for low differential pressure values will also be considered. Given the large amount of data that will likely become available during the full-scale experimental campaign, and that is already available from the wind tunnel tests, this paper aims at providing a summary of the main preliminary findings.

ACKNOWLEDGEMENTS

The wind tunnel tests used for comparison in this paper were conducted at the Laboratory of Environmental Aerodynamics of the University of Cracow. Support received from the Laboratory and help received from Prof. Fabio Rizzo, Dr. Aleksander Pistol, and Dr. Renata Kłaput in conceiving and performing the tests are acknowledged.

REFERENCES

Davenport, A.G., (1961). The application of statistical concepts to the wind loading of structures. Institution of Civil Engineers. Proceedings., 1961, Vol. 19, pp. 449–472.

Cermak, J.E. (2003). Wind-tunnel development and trends in applications to civil engineering. Journal of Wind Engineering and Industrial Aerodynamics 91 (2003) 355–370.

Kijewski-Correa, T. et al. (2006). Validating Wind-Induced Response of Tall Buildings: Synopsis of the Chicago Full-Scale Monitoring Program. Journal of Structural Engineering 132(10):1509-1523.

Caracoglia, L., Jones, N. P., (2009). Analysis of full-scale wind and pressure measurements on a low-rise building. Journal of Wind Engineering and Industrial Aerodynamics Volume 97, Issues 5–6, 2009: 157-173.

Davenport, A.G. (1963). The relationship of wind structure to wind loading. Proceedings of Symposium No. 16 -Wind Effects on Buildings and Structures; Her Majesty's Stationery Office: London, 1963; pp. 53–111.

Jia-hui, Y. et. al. (2023). Non Gaussian feature of fluctuating wind pressures on rectangular high rise buildings with different side ratios. Wind and Structures, Vol. 37, No. 3 (2023) 211-227.

Xiang, W. et. al. (2022). Study on the size reduction factor of extreme wind pressure of façade cladding of high-rise buildings with square section. Wind and Structures, Vol. 36, No. 1 (2023) 41-60.

Selected results of experimental studies on the effect of icing on the aerodynamics of bridge cables

Marcin Tatara [1], Piotr Górski [2], Stanislav Pospíšil [3], Arsenii Trush [4]

[1] *Opole University of Technology, Opole, Poland, m.tatara@po.edu.pl*
[2] *Opole University of Technology, Opole, Poland, p.gorski@po.edu.pl*
[3] *Institute of Theoretical and Applied Mechanics of the Czech Academy of Sciences, Prague, Czech Republic, pospisil@itam.cas.cz*
[4] *Institute of Theoretical and Applied Mechanics of the Czech Academy of Sciences, Prague, Czech Republic, trush@itam.cas.cz*

SUMMARY:
This paper presents an outline of the results of experimental studies on the effect of icing on the aerodynamics of cables of cable-supported bridges. The following were carried out in the framework of these studies: (1) the experimental icing process of the bridge cable model with a circular cross-section in the climatic chamber of the wind tunnel, (2) the optical visualization PIV (*Particle Image Velocimetry*) in the near-wake behind the ice-accreted cable model, (3) the *Strouhal* number investigations, and (4) the investigations of the mean aerodynamic force coefficients. Aerodynamic tests were carried out at average free stream velocities within the range of 3–25 m/s, corresponding to the *Reynolds* number values within the range of $2 \cdot 10^4$–$17 \cdot 10^4$. The average turbulence intensity during the investigations was about 3% and 12%. The test results for the ice-accreted bridge cable model were compared with those obtained for a circular smooth cylinder in similar flow conditions.

Keywords: bridge cable, ice accretion, aerodynamic investigations

1. INTRODUCTION

In certain weather conditions, the circular cross-section of bridge cables can change due to icing. This can have a significant effect on the aerodynamics of the cables and can lead to serious damage due to the wind. The presented study aims to expand knowledge on the phenomena occurring during the airflow around an iced bridge cable and to determine its essential aerodynamic parameters, such as the *Strouhal* (*St*) number and the mean aerodynamic force coefficients. Research on this topic is still insufficient to fully describe the problem, e.g. Demartino et al, 2015 and Koss et al, 2012. Therefore, there is a need for continued research in this area.

2. EXPERIMENTAL ICE ACCRETION PROCESS AND REPRODUCTION ICE-ACCRETED CABLE MODEL FOR AERODYNAMIC INVESTIGATIONS

An experimental icing process was conducted on a yawed/inclined cable section model. The 2.5 m long test model (a polyvinylchloride pipe) with a circular cross-section of 0.16 m in diameter was fixed to a special frame at an angle of 30° to the horizontal plane and yawed at an angle of 60° with respect to the wind velocity direction. The icing process was carried out in the climatic

chamber of the Climatic Wind Tunnel Laboratory in Telč. Immediately after the icing process, the shape of the ice was registered using the digital photogrammetry technique. For further aerodynamic investigations, a new sectional ice-accreted cable model was made at a scale of 1:1.6 using a 3D printing method. The outer dimensions of the ice cover were 0.12 m in height and 0.113 m in width, while the length of the test model was 0.43 m. The reproduced iced model is shown in Fig. 1.

The aerodynamic investigations were carried out at an average free stream velocity within the range of 3–25 m/s, which corresponds to the *Reynolds* (*Re*) number values in the range of $2 \cdot 10^4$–$17 \cdot 10^4$. The average turbulence intensity during the tests was about 3% and 12%. Thus, the two flow states were defined as low and moderately turbulent flow, respectively. The iced cable model was fixed crosswise to the airflow in a special frame. To demonstrate the effect of icing on the bridge cable aerodynamics, the results obtained for the iced model were compared with those obtained for a circular smooth cylinder under the same flow conditions. The presented results refer to the model configuration with ice ribs at the bottom of the model, as obtained in the icing process.

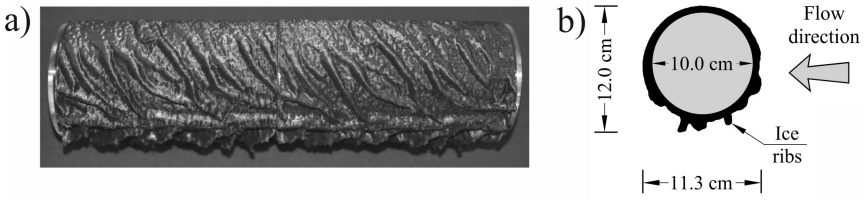


Figure 1. a) Reproduced ice-accreted cable model for aerodynamic investigations and b) cross-section of the model.

3. PIV FLOW VISUALIZATION OF THE NEAR-WAKE OF THE ICED CABLE MODEL

The optical visualization PIV (*Particle Image Velocimetry*) technique was carried out to better understand the nature of the near-wake behind the ice-accreted cable. Fig. 2 shows representative snapshots of instantaneous streamline patterns in the near-wake behind the smooth cylinder and the ice-accreted model in the low and moderately turbulent flow conditions at a free stream velocity of 3.6 m/s. As can be seen, despite the significant change in the shape of the cable surface caused by the irregular ice accretion, the vortex excitation phenomenon similar to that existed for the circular cylinder can be observed. However, under the same flow conditions, the geometric features of this phenomenon are different.

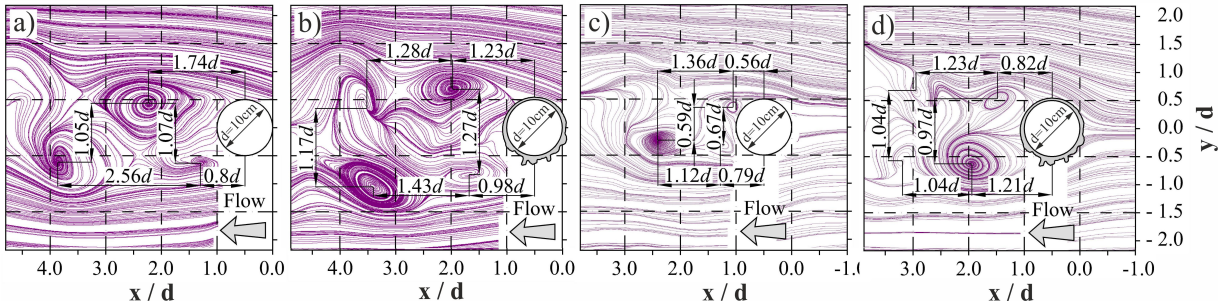


Figure 2. Representative streamline patterns of the instantaneous flow field in the near-wake behind (a,c) the smooth cylinder and (b,d) the ice-accreted cable model in the (a,b) low and (c,d) moderately turbulent flow.

4. *STROUHAL* NUMBER TEST RESULTS

The *St* values were determined based on the dominant vortex-shedding frequencies f_s extracted from the Power Spectral Densities of the airflow velocities in the near-wake behind the model:

$$St = \frac{f_s \cdot d}{\overline{u}} \tag{1}$$

where: f_s is the vortex-shedding frequency, d is the external reference dimension of the iced model, and $\overline{u}$ is the averaged free stream velocity in front of the model.

The measurements were carried out using two hot-wire anemometers CTA (*Constant Temperature Anemometry*), whose locations were determined based on PIV visualization. Fig. 3 shows the variation of the *St* number with the *Re* number for the circular smooth cylinder and the ice-accreted cable model in low and moderate turbulent flow. In the low turbulent flow, the *St* values obtained for the iced cable model were approximately 5–13% higher than those obtained for the smooth cylinder. At moderate turbulence intensity, the analyzed range of the *Re* number values corresponded to the critical range for the smooth cylinder, characterized by a significant increase in the *St* value. Such a relationship was not observed for the iced cable model.

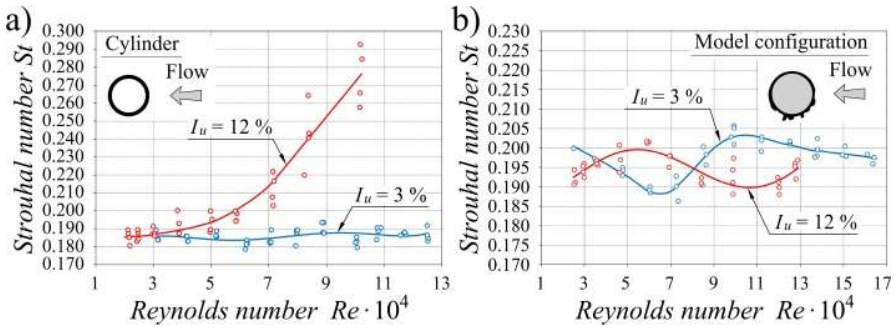


Figure 3. Variation of *St* with *Re* for: a) the circular smooth cylinder and b) the ice-accreted cable model in the low and moderately turbulent flow conditions.

5. RESULTS OF THE STUDY OF MEAN AERODYNAMIC FORCE COEFFICIENTS

The mean aerodynamic coefficients, i.e. drag C_D, lift C_L and moment C_M coefficients of the iced cable model were calculated according to the following formulas:

$$C_D = \frac{\overline{F}_D}{0.5 \cdot \rho \cdot \overline{u}^2 \cdot d \cdot l}, \quad C_L = \frac{\overline{F}_L}{0.5 \cdot \rho \cdot \overline{u}^2 \cdot d \cdot l}, \quad C_M = \frac{\overline{F}_M}{0.5 \cdot \rho \cdot \overline{u}^2 \cdot d^2 \cdot l} \tag{2}$$

where: $\overline{F}_D$, $\overline{F}_L$ i $\overline{F}_M$ are the averaged aerodynamic drag, lift and moment forces, respectively, ρ is the air density, and l is the length of the model.

Representative dependencies between the C_D, C_L and C_M coefficients for the cylinder and the iced cable model versus *Re* are shown in Fig. 4. The C_D values of the iced model were higher than those for the smooth circular cylinder under similar flow conditions. In low-turbulence flow conditions, the C_D values ranged from 1.32 to 1.50, while in moderate-turbulence flow conditions, they ranged

from 0.93 to 1.16. The obtained C_L and C_M values in low-turbulence flow conditions ranged from -0.06 to -0.44 and from -0.02 to -0.13, respectively. In moderate-turbulent flow conditions, these coefficients ranged from -0.21 to -0.54 and from -0.05 to -0.15, respectively.

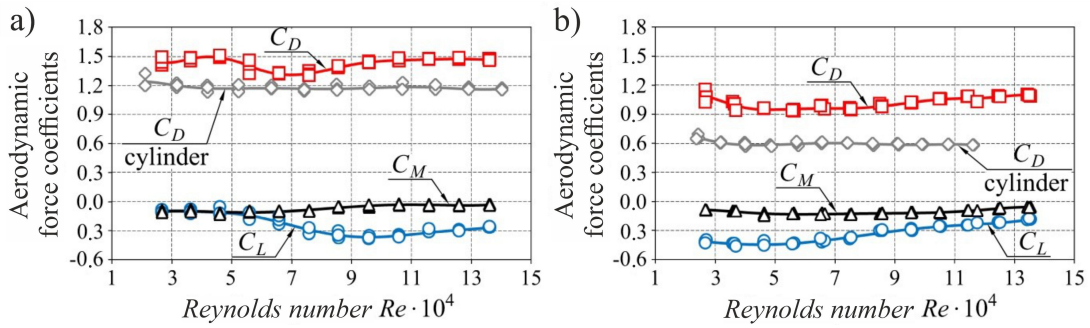


Figure 4. C_D, C_L and C_M coefficients versus Re for the cylinder and the ice-accreted model a) in the low and b) moderately turbulent flow conditions.

6. CONCLUSIONS

The test results showed that icing of cables of cable-supported bridges can significantly affect the phenomena occurring during the airflow around these cables and their aerodynamics, leading to changes in the studied aerodynamic parameters. This was confirmed by the following observations. In the case of the iced model in the low turbulent flow conditions, a 20–30% wider vortex street and a 30–40% wider cross-stream spacing between two free shear layers were created in comparison with the case of the moderately turbulent flow or the dry cylinder in the low turbulent flow. In the case of the moderately turbulent flow, a clear weakening of vortex excitation was observed, which was associated with an increase in free stream turbulence. The vortex street became narrower and the vortices became smaller. In the low turbulent flow, the St values determined for the iced model in the tested Re range are greater than those obtained for the smooth cylinder by 5% to 13%. In the moderately turbulent flow, for $Re < 6.0 \cdot 10^4$, the St values obtained for the iced cable are greater than for the dry cable, with a maximum difference of about 6%. In turn, for $Re > 6.0 \cdot 10^4$, the St values for the smooth cylinder are significantly greater than for the ice-accreted model. The C_D coefficient of the iced model obtained experimentally in the low turbulent flow was 26% higher than 1.2, used as a reference for the circular cylinder, while in the moderately turbulent flow, C_D in relation to a value of 0.6, as a reference value, was higher up to 93%. The flow turbulence significantly reduces the C_D coefficient of the ice-accreted model by about 23–38%, depending on the Re number. No specific influence of the flow turbulence on the C_L and C_M coefficients of the test model was found.

Due to the random nature of icing, conducting further aerodynamic studies for different shapes of ice covers accreted on bridge cables is reasonable.

REFERENCES

Demartino, C., Koss, H. H., Georgakis, C. T., Ricciardelli, F., 2015. Effects of ice accretion on the aerodynamics of bridge cables. Journal of Wind Engineering and Industrial Aerodynamics 138, 98–119.

Koss, H., Gjelstrup, H., Georgakis, C. T., 2012. Experimental study of ice accretion on circular cylinders at moderate low temperatures. Journal of Wind Engineering and Industrial Aerodynamics 104–106, 540–546.

Effects of conductors on wind-induced vibration of multi span transmission towers under various wind directions

Yongfei Zhao[1,2], Yang Yang[1,2], Ruwei Ma[3], Mingshui Li[1,2]

[1]*Research Center for Wind Engineering, Southwest Jiaotong University, Chengdu 610031, China*
[2]*Key Laboratory for Wind Engineering of Sichuan Province, Chengdu 610031, China*
[3]*School of Civil Engineering, Shanghai Normal University, Shanghai, 201418, China*

SUMMARY:
The present wind load and wind-induced vibration assessment for transmission towers is often based on characteristics calculated for an individual tower structure, neglecting the influence of conductors in the service condition of multi-towers. The wind load exerted by transmission tower conductors is significant and cannot be overlooked in comparison to the wind load experienced by the transmission tower itself, thereby complicating the structural vibration of the tower and complicating the estimation of the tower's top displacement. To accurately apply the specified wind load to actual transmission towers, it is essential to perform wind tunnel tests on the composite structures of multi-span transmission with conductors. This study presents the results of wind-induced vibrations of multi-span transmission towers, both with and without conductors, derived from an aeroelastic model wind tunnel test. It systematically examines the impact of conductors on the wind-induced vibrations of these towers under varying wind direction angles. The findings demonstrate that turbulent flow substantially influences the average displacement along the conductor's span, varying systematically with the wind deflection angle. Nonetheless, the RMS of vibration displacement is reduced.

Keywords: transmission towers, wind-induced vibration, wind tunnel testing

1. INTRODUCTIONS

As the demand for renewable and green energy rises to combat the climate change challenge, power transmission has emerged as a critical infrastructure element. In coastal regions characterized by strong winds, transmission tower damage incidents routinely occur, with an increasing frequency that results in significant economic losses and disruptions to national life (Li et al., 2018; Mohammadi Darestani et al., 2020).

The wind-resistant construction of transmission towers and line systems is a significant challenge that has not been completely addressed in structural wind engineering. The results of full-scale measurements (Bai et al., 2012; Momomura et al., 1997) and aeroelastic model wind tunnel tests (Liang et al., 2015; Zhang et al., 2021) indicate that multi-span transmission towers with conductors are not only typical wind-sensitive structures but also exhibit complicated wind-induced vibrations in contrast to independent single towers.

This research performed aeroelastic model wind tunnel experiments on a multi-span transmission tower system within a turbulent flow field of the atmospheric boundary layer, utilizing a real transmission line situated in a coastal region as the technical context. The outcomes of the wind-induced displacement at the tower top were acquired for various wind angles, both with and with-

out conductor installation. The impact of conductors on wind-induced vibrations of multi-span transmission towers under turbulent flow was extensively analyzed and compared.

2. EXPERIMENTAL DESCRIPTIONS

The wind tunnel tests were carried out in the XNJD-3 closed-loop wind tunnel at Southwest Jiaotong University, details of which are given in Zhao et al. (2024). To satisfy the requirement of blocking ratio, the geometric scale of the wind field and the model was selected as $\lambda_L = 1:70$.

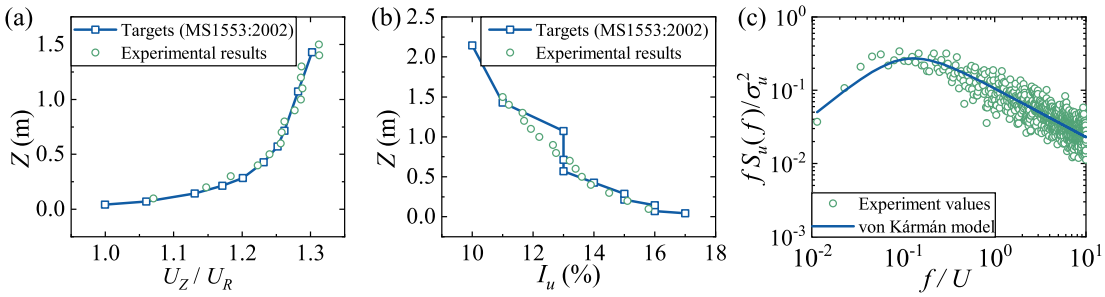


Figure 1. Characteristics of the turbulent flow field (a): Mean wind speed profile; (b): Turbulence intensities profile; (c): Spectra of streamwise fluctuating velocities at reference point.

Based on the codes of MS 1553:2002 (Standard, 2002), suitable rough elements and spires were selected to simulate the turbulent flow field. Fig. 1 shows the simulated results. It can be seen that the experimental results could agree well with the targets.

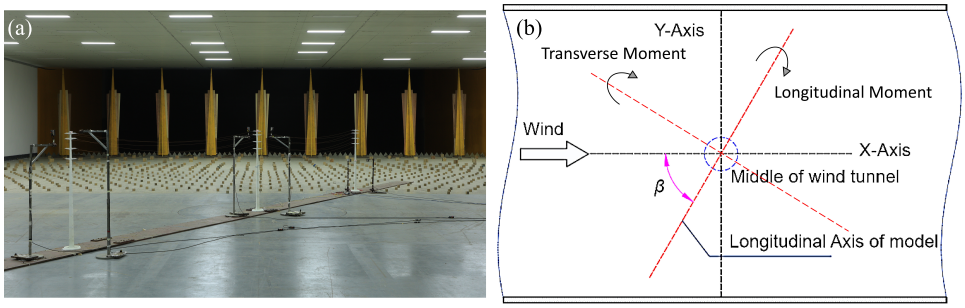


Figure 2. (a): Models tested in the wind tunnel (wind direction angle $\beta = 30°$); (b): Definition of directions.

Fig. 2 (a) shows the tested model of conductors and transmission towers in the simulated atmospheric boundary layer. Laser displacement sensors were used to measure the top displacement of the transmission tower. The wind tunnel test conditions are set at intervals of 15° according to the wind direction angle, varying from 0° to 90°. The definition of directions are shown in Fig. 2 (b), T represents the transverse direction of the transmission tower axis, which is perpendicular to the direction of conductors, while L represents the longitudinal direction of the transmission tower axis, which is the direction of conductors.

3. EXPERIMENTAL RESULS AND DISCUSSIONS

By processing the time history data, the mean and root mean square (RMS) values can be obtained respectively. The peak factor $g = 3.5$ based on Gaussian distribution is selected.

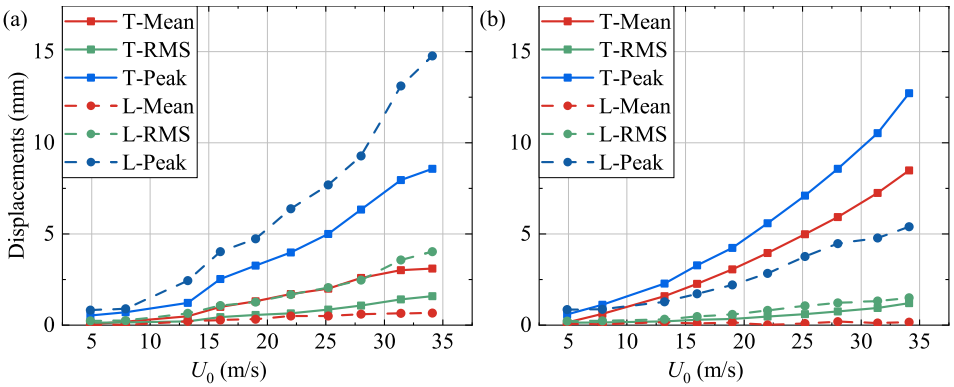


Figure 3. Displacements of transmission tower top ($\beta = 0°$). (a): Without the effects of conductors; (b): With the effects of conductors.

As shown in Fig. 3, after the installation of the conductors, the longitudinal mean value did not change significantly, but the RMS value was significantly suppressed, resulting in a decrease in the longitudinal peak value. This may be because the transmission tower is limited by the tension of the conductors in the longitudinal direction, which suppresses the lateral effect of turbulence and reduces the amplitude of longitudinal vibration of the transmission tower body. After the installation of the conductors, the tower is subjected to greater lateral forces, with a displacement mean increase of about 50% under the maximum U_0, and the RMS value remains basically unchanged. It can be seen that the peak displacement at the top of the transmission tower is increased due to the wind load on the conductors. This indicates that when the incoming wind direction is perpendicular to the span direction, that is, when the direction of conductors' tension is perpendicular to the incoming wind, the transmission tower bears a large amount of mean wind load transmitted by the conductors, resulting in a significant increase in the mean displacement of the tower top. This is because the conductors are mainly subjected to the mean wind load in the wind direction, and an approximate concentrated force is applied to the almost cantilevered top of the transmission tower, significantly increasing the average displacement of the tower top.

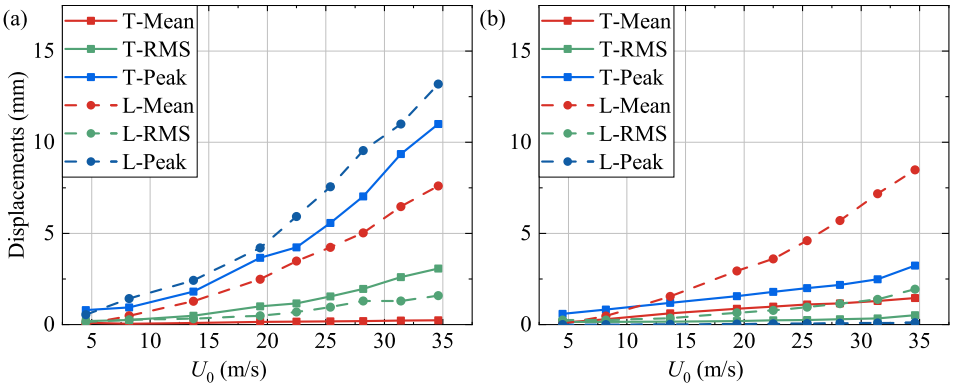


Figure 4. Displacements of transmission tower top ($\beta = 90°$). (a): Without the effects of conductors; (b): With the effects of conductors.

Fig. 4 shows the displacement results of the tower top when $\beta = 90°$. Similar to the results obtained when $\beta = 0°$, the average displacement perpendicular to the incoming direction (in this case, the T

direction) is almost zero when there are no conductors installed, while the average displacement in the windward direction is larger. This is consistent with the results in Fig. 3, which confirms that when there are no conductors installed, the mean displacement is mainly in the forward direction, and the mean displacement perpendicular to the incoming direction can be ignored. But unlike when $\beta = 0^{\circ}$, the wind direction at this time is consistent with the direction of conductors' tension, so after the conductors is installed, the mean displacement does not significantly increase, which is almost consistent with the results of a single tower.

In contrast, as shown in Fig. 4 the RMS perpendicular to the incoming flow direction is significantly reduced due to the installation of the conductors, indicating that conductors have a very significant inhibitory effect on vibration in the vertical incoming flow direction. This may be because conductors limit the effect of turbulent lateral pulsation, or it may be because the conductors are affected by the turbulent lateral pulsation value, causing their own vibration to dissipate, thereby reducing the vibration of the transmission tower itself.

4. CONCLUSIONS

Under turbulent flow, the conductor has an amplifying effect on the mean displacement parallel to the incoming flow direction, but the influence of the mean displacement in the orthogonal incoming flow direction can be almost negligible. And for the displacement pulsation value at the top of the transmission tower, it has a suppressing effect in any direction. This is mainly caused by the mean wind load applied to the top of the transmission tower by the conductors. Overall, the change in maximum peak displacement in the direction that is perpendicular to the wind direction will be increased when conductors are perpendicular to the wind direction but be limited in the orthogonal direction.

ACKNOWLEDGEMENTS

This work is supported by the National Natural Science Foundation of China under Grant Nos. 52008357, 52408550 and the Natural Science Foundation of Sichuan Province under Grant No. 2022NSFSC1044.

REFERENCES

Bai, H.-F., Yi, T.-H., Li, H.-N., and Ren, L., 2012. Multisensors on-site monitoring and characteristic analysis of UHV transmission tower. International Journal of Distributed Sensor Networks 8, 545148.

Li, X., Zhang, W., Niu, H., and Wu, Z. Y., 2018. Probabilistic capacity assessment of single circuit transmission tower-line system subjected to strong winds. Engineering Structures 175, 517–530.

Liang, S., Zou, L., Wang, D., and Cao, H., 2015. Investigation on wind tunnel tests of a full aeroelastic model of electrical transmission tower-line system. Engineering Structures 85, 63–72.

Mohammadi Darestani, Y., Shafieezadeh, A., and Cha, K., 2020. Effect of modelling complexities on extreme wind hazard performance of steel lattice transmission towers. Structure and Infrastructure Engineering 16, 898–915.

Momomura, Y., Marukawa, H., Okamura, T., Hongo, E., and Ohkuma, T., 1997. Full-scale measurements of wind-induced vibration of a transmission line system in a mountainous area. Journal of Wind Engineering and Industrial Aerodynamics 72, 241–252.

Standard, M., 2002. Code of Practice On Wind Loading For Building Structure. MS 1553, 2002.

Zhang, Z., Wang, D., Wang, T., Yu, Z., Huang, Z., and Zhang, D., 2021. Aeroelastic wind tunnel testing on the wind-induced dynamic reaction response of transmission line. Journal of Aerospace Engineering 34, 04020105.

Zhao, Y., Yang, Y., and Li, M., 2024. Wind pressure distribution and non-Gaussian characteristics of a building complex with tree-inspired structures. Journal of Building Engineering 84, 108660.

Cross-sectional variations and their impact on drag and vortex-induced vibrations in bridge hangers

Alessandro Galimberti[1], Federico Zanelli[1], Sara Muggiasca[1], Tommaso Argentini[1], Alberto Zasso[1], Jungao Wang[2]

[1]*Department of Mechanical Engineering, Politecnico di Milano, Milan, Italy,*
alessandro.galimberti@polimi.it, federico.zanelli@polimi.it, sara.muggiasca@polimi.it, tommaso.argentini@polimi.it, alberto.zasso@polimi.it
[2]*Norwegian Public Roads Administration, Norway*
Jungao.wang@vegvesen.no

SUMMARY:
Hanger cables are very important structural elements in suspension bridges that transfer the dead load of the bridge deck to the main cable. Their cylindrical structure, light mass, flexibility and low structural damping, make the hangers prone to vortex induced vibration (VIV). Wind tunnel tests in Politecnico di Milano have been performed to evaluate the aerodynamic behavior of the Julsundet bridge hangers in Norway, through the realization of six models with different coverings: traditional full locked coil (FLC) hanger, high density polyethylene (HDPE) smooth pipe surface, HDPE with double helical fillet, HDPE with triple helical fillet, FLC hanger with anti-vibration grooves and cactus shaped pipe surface. Both static forces and dynamic VIV tests have been employed to characterize the hanger's behavior. The wind tunnel campaign was finalized at characterizing the aerodynamic behavior of the different hanger typologies and at providing a comprehensive set of data allowing for a dimensioning of a reliable damping system, making the bridge hangers safer with respect to wind-induced vibrations issues.

Keywords: hangers, vortex induced vibration, wind tunnel tests, aerodynamic coefficient, damping

1. INTRODUCTION

In the last decades, newer hanger typologies have been designed with locked coil cables and wire strands in the inner part coated with high density polyethylene (HDPE) for corrosion protection. Owing to their light mass, line-like structure and low structural damping, hanger cables are subject to vortex induced vibration (VIV). This behavior is widely described in literature, as example, by the case of the Hålogaland bridge (Larsen et al., 2022) in Norway, the Hardanger bridge (Cantero et al., 2017) in Norway and the Canakkale bridge (Larsen, 2024) in Türkiye that experienced severe VIV excitation on a very similar cable system.

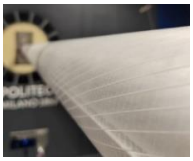
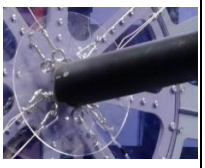
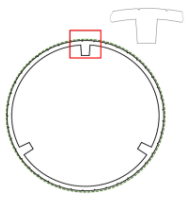
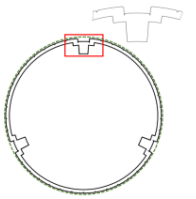
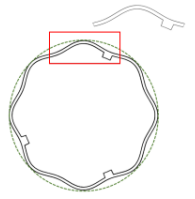
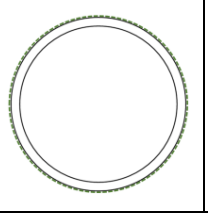
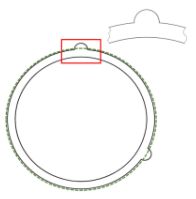
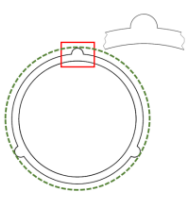
One effective passive method for controlling VIV is altering the aerodynamic shape of the hangers. In (Liu et al., 2021), double and triple helical fillets with a diameter of 10 mm and 15 mm can effectively control VIV responses of horizontal stay cable with a diameter of 140 mm. In (Wang et al., 2019), a peculiar shape named "Cactus configuration" with a grooved cross-section is shown to survive in high wind thanks to a less abrupt drag coefficient reduction with Reynolds number and a smaller fluctuating side force compared to a basic circular shape.

In this paper, different hanger configurations have been investigated to evaluate the effects of the coverings on the aerodynamic performances of the hanger in terms of drag resistance and VIV levels.

2. HANGER VARIATIONS

The hanger models are composed by an inner aluminum tube approximately 4 meters long with six different coverings mounted on them to represent the cross-sectional variations. The models are realized at full scale geometry (1:1). In Table 1 the different configurations are presented.

Table 1. Hanger models description

Tested configurations					
FLC100	FLC100G	CACTUS	HDPE	HDPE-HF	HDPE-HFR
Full locked cable	Grooved full locked cable	Cactus cable cover	HDPE cable cover	HDPE cable cover	HDPE cable cover
Pitch = 9D	Pitch = 9D	8 ridges and 8 throughs	-	Helical fillet (2 mm thick, 130°)	Helical fillet (12 mm thick, 120°)
-	Groove size = 2 x 7.3 mm	Groove depth = 5 mm	-	Double helix	Triple helix
3D printed	3D printed	3D printed	Plastic cover	Plastic cover	Plastic cover
Ref. diameter = 100 mm	Ref. diameter = 100 mm	Ref. diameter = 120 mm	Ref. diameter = 110 mm	Ref. diameter = 110 mm	Ref. diameter = 134 mm
					
					

3. METHODOLOGY

Two different wind tunnel tests have been performed on each model to completely characterize the phenomenon of vortex induced vibration: static force tests and dynamic VIV tests.

Both testing typologies have been performed in the 4 x 4 m high-speed test section of the Politecnico di Milano Wind Tunnel. In the first case, the hanger models were rigidly suspended, and force transducers were used to measure drag and lift forces. The tests have been performed both in smooth (0.2% turbulence intensity) and turbulent flow (5% turbulence intensity) as suggested in (Zasso et al., 2005). Tests with different wind velocity ranging from 5 m/s to 40 m/s with different cable angular positions (0°,30°,60° and 90° around the model axis) have been performed to verify the symmetric behavior of the cylinder. The chosen wind speed interval has allowed to investigate cable aerodynamics behavior in relation with a Reynold number ranging from 10^4 (sub-critical region) to 10^5 (critical region).

Concerning the dynamic VIV tests, a proper set-up was designed by suspending models through springs and by appropriately adopting wall constraints to allow rigid body motions in crossflow and inline directions and reduce the wake tridimensional effect. The VIV tests have been carried out in smooth condition and different levels of Scruton number were tested thanks to the usage of

eddy current dampers which allowed to increase the structural damping of the different models.

4. RESULTS

Static force coefficients (drag and lift) were measured as a function of the mean wind speed to check the trend for increasing values of the Reynolds number and to identify the critical region where the drag crisis is expected. The tests were repeated also in turbulent flow conditions to check the influence of turbulence on the critical region which is expected at lower Reynolds numbers. Looking at Fig. 1 it can be observed that the configurations characterized by low drag coefficient values already at low speed are the FLC100G and the HDPE-HF, while the one denoting the most significant drag crisis is the FLC100. With respect to the drag change rate, the HDPE appears as the fastest configuration, while the Cactus and HDPE-HF are the slowest ones. In case of turbulent condition all the configurations show that the drag crisis is shifted towards lower Reynolds number. Results related to lift coefficients will be included in the presentation too.

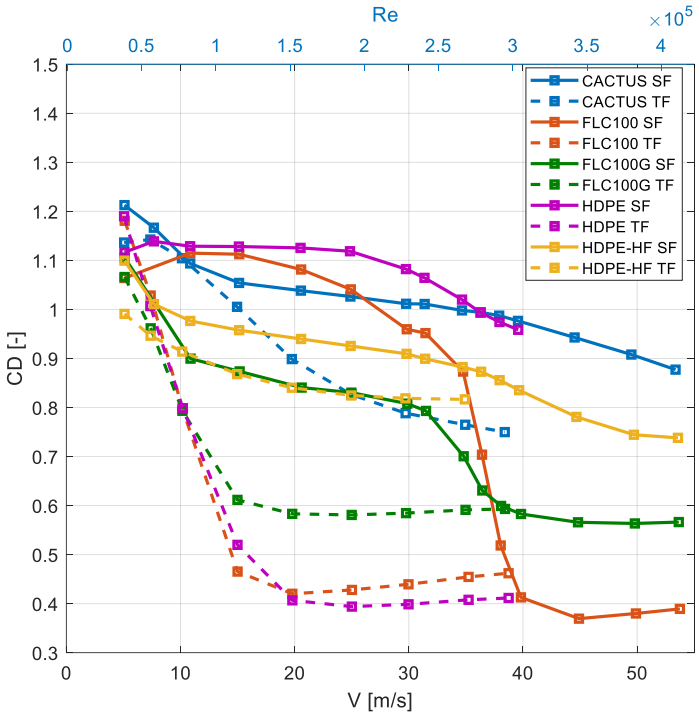


Figure 1. Drag coefficient trends in smooth (SF) and turbulent (TF) flow for the different configurations.

Concerning VIV tests, the non-dimensional standard deviation of free vibration displacements in the cross-wind direction are plotted against the ratio between the wind speed and the Strouhal speed for the different configurations. The two quantities were made non-dimensional using the reference diameter (highlighted in Table 1 with dotted line) for each configuration. The Strouhal number was evaluated for each configuration tested from the spectrum of the lift force. Fig. 2 shows that the trends are very similar for each configuration tested. Configuration FLC100 denotes a shift in the peak of the curve towards lower reduced velocities and a lower peak value with respect to the other models. It is important to note that the presence of the helical fillet of configuration HDPE-HF seems to not play a significant role in suppressing VIV. To investigate deeper this aspect, a new configuration with a thicker helical fillet (12 mm) was realized (configuration HDPE-HFR). It is evident that this configuration is able to completely suppress

vortex induced vibration on hanger, resulting in a completely flat curve in Figure 2. In the presentation, the VIV response of the different hanger configurations will be investigated at different level of Scruton number.

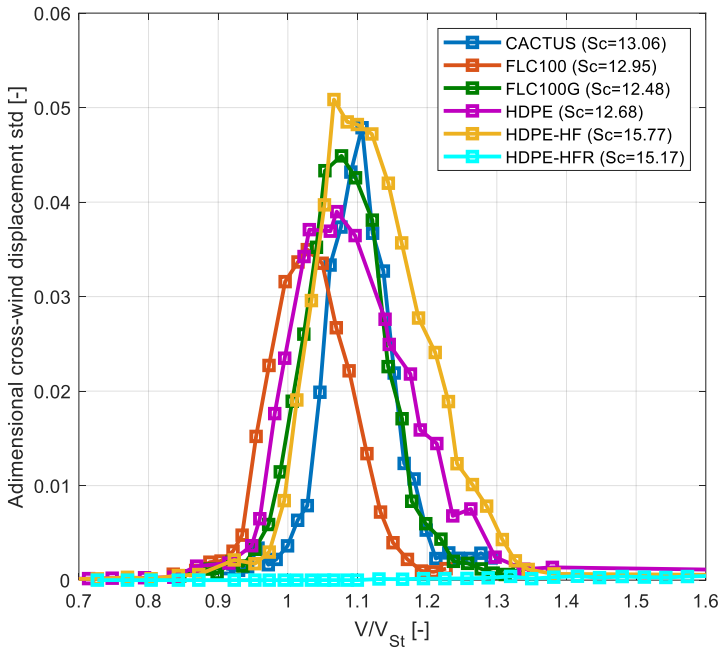


Figure 2. Standard deviation of adimensionalized free vibration displacements in the cross-wind direction against the ratio V/V_{st} for the different configurations.

5. CONCLUSIONS

The paper aim is to present the experimental campaign performed in the Politecnico di Milano Wind Tunnel to characterize the aerodynamic behavior of the Julsundet hangers, both in terms of static force tests and dynamic VIV tests. Six hanger models with different geometries have been tested. The wind tunnel results will be useful to understand what are pro and cons of the different typologies of hanger shapes from the aerodynamic point of view and to eventually drive the design of a suitable additional damping system useful to mitigate vibrations affecting the bridge hangers.

REFERENCES

Larsen, A., Gronne, A. K., and Jamal, A., 2022. Wind Induced Hanger Vibrations - the Halogaland Suspension Bridge. Structural Engineering International 2022.

Cantero, D., Oiseth, O., and Ronnquist, A., 2017. Indirect monitoring of vortex-induced vibration of suspension bridge hangers. Structural Health Monitoring 2017.

Larsen, A., 2024. Vibration Excitation and Damping of Suspension Bridge Hanger Cable. Dynamics and Aerodynamics of Cables (2024).

Liu, Z., Shen, J., Li, S., Chen, Z., Ou, Q., and Xin, D., 2021. Experimental study on high vortex-induced vibration of stay cable and its aerodynamic countermeasures. Journal of Fluids and Structures 100 (2021) 103195

Wang, J., Jakobsen, J. B., McTavish, S., and Larose, G. L., 2019. Aerodynamic performance of a grooved cylinder in flow conditions encountered by bridge stay cables in service. Journal of Wind Engineering & Industrial Aerodynamics 188 (2019) 80-89.

Zasso, A., Larose, G. L., Giappino, S., and Muggiasca, S., 2005. Effects of turbulence intensity and surface roughness on stays of cable-stayed bridge. International Symposium on Cable Dynamics 2005.

Enhanced Atmospheric Icing Modelling of High-Voltage Transmission Lines

Erick Ulloa Jimenez [1], Stefan Steevens [1],
Norbert Hoelscher [2], Susanne Diburg [2]

[1]*Amprion GmbH, Dortmund, Germany, erick.ulloajimenez@amprion.net*
[2]*Niemann Ingenieure GbR, Bochum, Germany, hoelscher@niemann-ing.de*

SUMMARY
In cold and windy weather with high humidity, low-level clouds, and falling snow or rain, severe atmospheric icing can jeopardize the structural reliability of overhead transmission lines. Appropriate icing simulation tools correlate the amount of assembled ice mass with the flux of water particles in the approaching flow. These particles hit the structure, adhere to it, and freeze on the impacted surfaces. A crucial aspect of simulation is incorporating all relevant meteorological parameters, which are considered with high temporal resolution. Certain weather conditions are defined as boundary conditions for initiating or ending the icing process in the numerical code. Additionally, the orientation of the transmission line and other system-dependent parameters are introduced into the calculation. Each icing event is evaluated, and a sample of annual extremes is collected to predict the attached ice mass with respect to their probability of occurrence.
Further improvements are intended for the well-known Makkonen model. Recent experiments on "In-Cloud Icing," "Wet Snow Ice Accretion," and "Freezing Rain" were performed, varying environmental properties such as air temperature below freezing, wind velocity, and the ejected spray of either supercooled droplets, a mock-up of atmospheric snow, or larger rain droplets. Both the quantity of ice accretion and the type of ice attachment were observed. The tests are part of an ongoing study that also cross-validates experimental findings with full-scale data from in-situ ice accretion measurements currently being conducted at several locations within German medium-altitude mountains.

Keywords: Ice loads, transmission line pylons, weather parameters, ice formation, simulation models

1. INTRODUCTION

Atmospheric icing can hamper the operation of overhead transmission lines (OHL), and in extreme cases, their structural integrity may be at risk. Therefore, icing models for OHL must consider all site-specific and system-dependent parameters that significantly affect the impact of icing on these structures. For the structural design of transmission towers and attached conductors, the action of ice must be defined on a probabilistic basis to meet the reliability requirements of the supports according to given codes of practice.
A general calculation model for determining ice loads is provided in [1]. This model depends on particle density, particle velocity, and the surface area where particles collide. Reduction factors are included to account for the efficiency of the ice formation process, such as collision efficiency α_1, sticking efficiency α_2, and accretion efficiency α_3.
Numerous empirical models in the literature link meteorological parameters (e.g., wind speed, wind direction, air temperature, relative humidity, and precipitation) to ice formation, providing a

basis for applying the Makkonen calculation approach. Considerable advancements have been re-evaluated using long-term weather data, adapting power line engineering calculation procedures accordingly.
To improve existing icing calculation tools, experiments have been initiated in two climatic wind tunnels to investigate various types of ice formation on certain conductor specimens, including in-cloud icing and precipitation icing (wet snow or freezing rain). In-cloud icing has been simulated across a range of air temperatures just below freezing and at significantly lower temperatures with moderate wind speeds. Glaze ice, which is transparent with a smooth, compact structure, and rime ice, characterized by its granular, white, opaque appearance and prismatic shape oriented into the wind, have been observed. Tests on freezing rain are in the design phase, focusing on evaluating the impact of droplet size on ice accretion, considering both smaller droplets (diameter < 500 µm, drizzle) and larger particles.
An icing simulation tool has been developed based on a comprehensive understanding of the physical processes governing ice initiation, accumulation, and detachment on surfaces. The model has been validated against historical icing events and their effects on OHL structures. A statistical methodology is utilized to derive annual extreme values from simulated time series, enabling the prediction of future icing scenarios with associated probabilities.

2. ICE ACCRETION MODEL FOR PROBABILISTIC RISK ANALYSIS

Basic Considerations

The initial conditions of the different icing processes, determining when a particular type of ice begins to grow and how long it continues to grow until the attached ice either breaks off or melts, significantly alter the calculated ice mass.
In-cloud icing occurs in fog or if the cloud base is lower than the altitude of the area of interest, with air temperature below 0°C [2]. The calculation proceeds based on a simple correlation with wind speed.
"Wet snow accretion" occurs only in the presence of snow or sleet, with conditions linked to relative humidity (RH) and air temperature [3]. The criteria are: $96 \cdot e^{-0.2 \cdot Ta} \leq RH$, $39 \cdot \sqrt{7.2 - Ta} \geq RH$ and air temperature $T_a < 2°C$. Others also use the wet bulb temperature as boundary conditions [4], though this parameter is only occasionally measured at standard weather stations, making it less practical.
Finally, "freezing rain" occurs when rain or drizzle is observed, and the wet-bulb temperature is below 0°C [5]. In this case, no alternative method is available; the wet-bulb temperature must be derived from other routinely available weather parameters, and the calculation is then correlated with precipitation.
All adaptations of Makkonen's model, as evaluated from literature, apply reduction factors in a simplified manner. For instance, collision efficiency is assumed to be less than 1 for small particles, as they tend to be dragged along by the airflow around the conductor. For water droplets in clouds, fog, or rain, full sticking efficiency is assumed. The accretion efficiency is taken to be 1 during dry ice growth but decreases if particles are removed from the ice surface by a thin water film.

Line-Specific Influencing Factors

In the context of overhead power lines, numerous additional factors significantly influence ice accretion and should be incorporated into calculation models for a more accurate prediction of ice loads. The angle between the overhead line and the prevailing wind direction is a key determinant

of ice load during icing events. Furthermore, the freedom of rotation of the conductor is essential, as rotating surfaces tend to accumulate thicker ice layers. Conductor temperature is another critical variable; energized overhead lines typically have elevated temperatures, reducing the likelihood of ice formation. The influence of these line-specific parameters on the calculation model varies depending on the specific type of ice accretion being considered.

Weather Specific Influencing Factors

For reliable ice load simulations at the mast location, precise site-specific weather parameters are required. Multiple sources are used for this purpose. The German Weather Service maintains an extensive network of weather stations with publicly accessible data. These data are integrated into mesoscale numerical models, from which grid data for key meteorological parameters are derived. In addition, operators monitor weather data at several OHLs (Overhead Lines). Using extrapolation methods such as Kriging, weather data from areas surrounding the OHL can also be applied to simulations.

Based on site investigations, the duration of icing events is observed to depend on altitude, with higher elevations experiencing longer periods of ice accumulation. At higher altitudes, in-cloud icing predominates, while at lower elevations, wet-snow icing is more common. Freezing rain is generally less significant compared to these other icing phenomena. Additionally, it has been shown that the annual extremes of atmospheric icing can be described by a Gumbel probability distribution. An upper limit has been estimated, allowing for a bounded Gumbel-III modelling of the probability of extreme ice loads. In-cloud icing remains the dominant phenomenon, and there are indications that the upper limit of icing is lower in northern Germany compared to medium-altitude mountain regions.

3. EXPERIMENTS AND MEASUREMENTS IN EXISTING INFRASTRUCTURE

Laboratory investigations into ice accretion under in-cloud conditions on power lines were conducted in the climate wind tunnel at Force Technology in Denmark. The investigated and varied parameters included liquid water content (LWC), air temperature (T), wind speed (V), mechanical boundary conditions (fixed, free, rotating), wind direction, sample types, and conductor temperature. These experiments provided significant insights into line-specific parameters, such as conductor temperature and the angle between the overhead line and wind direction (Figure 1). Furthermore, distinct differences were observed between rime ice and glaze ice, including the formation of icicles during glaze ice formation (Figure 1).

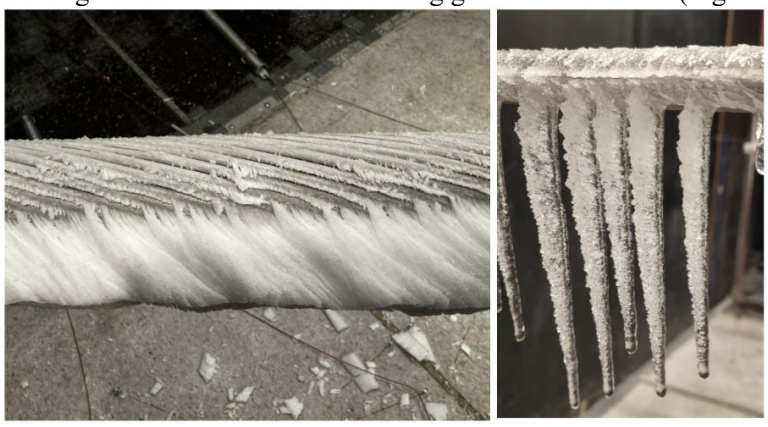


Figure 1. Left: Influence of the angle between the overhead line and the wind, Right: Icicles formation during the glaze experiments

Further tests on wet snow are being conducted at the CSTB wind tunnel. These tests are performed at a constant wind speed of 10 m/s and varying air temperatures between -10°C and -2°C to investigate the effect of temperature on the freezing process. A snow gun is used to create artificial snow by mixing water and air under high pressure. The main focus of these tests is on the influence of conductor rotation and line

angle. Initial results indicate that ice accumulation varies significantly with air temperature.
To further understand the influence of the rotational ability of the conductor during ice formation, additional tests were carried out using different conductor cables. This allowed the rotational capacity to be measured under real-world conditions in the field.
Additional laboratory investigations under freezing rain conditions are also required to capture the full spectrum of ice formation scenarios.
Weather stations and ice sensors are being installed in the existing network. The ice sensors are mounted directly on the conductor cables, while the weather stations are installed on power line towers. These weather stations are also equipped with ice sensors, enabling comparison of field measurements with laboratory data. The goal is to compare these field measurements with lab results to ultimately develop a consistent calculation model.

4. CONCLUSION

A modern design of overhead transmission lines, which ensures a reliable and cost-effective structure capable of sustainable operation and maintenance, must consider all relevant factors that affect structural integrity throughout its intended service life. Of particular significance are climatic factors, including wind, flooding, and icing. This study focuses on enhancing an engineering model for atmospheric icing. Ice formation on masts and conductors is influenced by a variety of meteorological parameters whose effects are often correlated and thus difficult to model. While icing can occur during precipitation or even in dry conditions with high ambient humidity, the amount of ice accreted is determined by a complex interaction of site-specific and line-specific parameters.
The aim is to develop an accurate model that realistically represents the icing of overhead lines. To achieve this, experiments are being conducted in various climatic wind tunnels to replicate different types of icing as realistically as possible. The results indicate that icing is highly dependent on factors such as conductor temperature, the angle of attack of atmospheric wind, and the conductor's ability to rotate. These findings contribute to the refinement of existing empirical models and support the development of reliable probabilistic calculations for different types of ice accretion. The data obtained improve understanding of past icing events and facilitate more accurate predictions of future scenarios, thereby enhancing the safety and efficiency of power line infrastructure.

ACKNOWLEDGEMENTS

This wind tunnel investigation was initiated and kindly supported by Amprion GmbH. It is thanks to their vision and foresight that such a far-reaching research project could be launched. The authors sincerely acknowledge this valuable inspiration for the present study.
Special gratitude is honoured to Prof. Dr. H. Koss and Dr. L. Matejicka for their very precious cooperation performing the wind tunnel tests at Force Technology in Denmark.

REFERENCES

[1] Makkonen, Lasse. "Models for the Growth of Rime, Glaze, Icicles, and Wet Snow on Structures." Philosophical Transactions of the Royal Society of London. Series A: Mathematical, Physical and Engineering Sciences 358, no. 1776 (2000): 2913–39.

[2] Ahti K., & Makkonen L. Observations on rime formation in relation to routinely measured.

[3] Ducloux, H., & Nygaard, B. E. (2014). 50-year return-period wet-snow load estimation based on weather station data for overhead line design in France. Natural Hazards and Earth System Sciences, 14(11), 3031–3041..

[4] Makkonen, L. (1989). Estimation of wet snow accretion on structures. Cold Regions Science and Technology, 17, 83–88..

[5] Makkonen, L. (1998). Modeling power line icing in freezing precipitation. Atmospheric Research, 46(1-2), 131-142.

Vortex-induced vibrations measured on a full scale chimney

Agathe Schmider[1] & Pascal Hémon[2]

[1]*LadHyX, CNRS-Ecole Polytechnique, IP Paris, France, agathe.schmider@polytechnique.edu*
[2]*LadHyX, CNRS-Ecole Polytechnique, IP Paris, France, pascal.hemon@polytechnique.edu*

SUMMARY:
We present the measurements performed on a full scale flexible chimney with a height of 35.5 m and a diameter of 2 m in its main part. The chimney is designed to have a low first frequency of bending and a small Scruton number. The site of the setup is supposed to be of type II of the Eurocode and wind measurements are also performed with four anemometers on a 40 m mast. At moderate wind the velocity gradient and the turbulence intensity are lower than expected.
VIV events were observed and measured during a short term campaign. At lock-in the amplitude at the top reaches 36 % of the diameter while the amplitude is much lower when the velocity deviates from the lock-in speed. The lock-in is obtained with a Strouhal number of 0.225. These data are useful for the study and the validation of prediction models of VIV in natural wind conditions.

Keywords: vortex shedding, full scale measurements, circular cylinder

1. PRESENTATION OF THE FULL SCALE EXPERIMENT

The goal of the paper is to report the measurements performed on a full scale vertical cylinder subject to natural wind. The setup shown in Figure 1 is an experimental chimney erected at Bouin (France) near the Atlantic seashore, in order to measure vortex shedding excitation (Manal & Hémon, 2024). Typical Reynolds number is around 1.1 million. The chimney is 35.5 m high steel tube with an external diameter of 1 m in the lower part, from 0 to 12 m, and 2 m in the upper part above 15 m. From 12 to 15 m the diameter linearly increases from 1 to 2 m. The upper part has an aspect ratio L/D equal to 10. The chimney is clamped at the bottom in a concrete mass properly designed. Structural properties of the chimney are given in Table 1. The Scruton number $Sc = \frac{4\pi m\eta}{\rho D^2}$ is 1.53.

Table 1. Structural parameters of the chimney

Parameters	Symbol	Value	Unit
Linear mass	m	322.6	kg/m
Reduced damping	η	0.185	%
First bending frequency	f	0.848	Hz

Four single component accelerometers are mounted to measure the chimney motion (type PCB 3741). They can measure in the frequency range [0-70 Hz] up to ±2 g with an accuracy better than ±0.04 g. Accelerometers #1 and #2 are fixed at a height of 20.4 meters and #3 and #4 at the top, ie 35.5 meters. The record is continuous with a sampling frequency of 16 Hz. In the

following, only the top accelerometers are used, providing the amplitude of the motion which is based on the first bending mode.

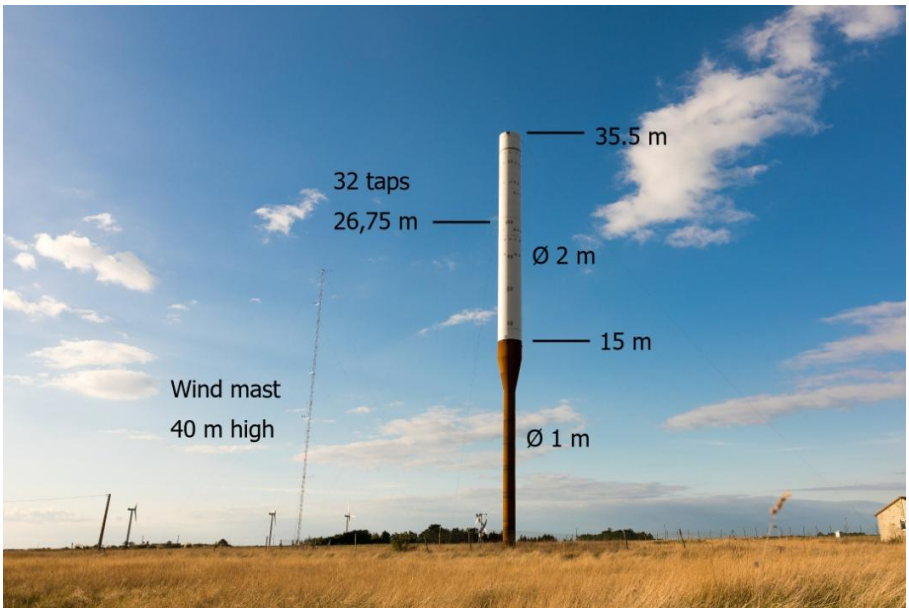


Figure 1. Photo of the Bouin chimney with its dimensions.

2. MEASUREMENTS OF WIND CONDITIONS

A 40 meters high mast is erected 55 meters west from the chimney. It is equipped with 4 anemometers at heights of 10 (cup), 18 (propeller), 25 (3D sonic) and 35 (propeller). Three wind vanes complement the cup and the propeller anemometers. All records are organized in sequences of 10 minutes.

Table 2. Measured wind characteristics

Date	Time	Wind data from sonic anemometer at 25.5 m					Data from cup anemometers		
		Mean velocity	Turbulence intensity	Wind direction	RMS of wind direction	Integral Scale Lu	Mean velocity at 10 m	Mean velocity at 20 m	Mean velocity at 35 m
		m/s	%	° ref MN	°	m	m/s	m/s	m/s
19-juil.-21	16h50	7.70	16.30	72.1	6.3	34	7.21	7.67	8.32
	17h00	7.65	16.20	66.5	7.6	60	6.80	7.55	7.78
	17h10	7.77	14.20	58.9	8.9	35	6.94	7.19	7.81
	17h20	7.36	16.50	59.7	7.3	33	7.00	7.26	7.87
20-juil.-21	14H00	10.09	13.50	76.3	8.0	45	7.70	8.40	9.12
	14h10	9.97	12.96	69.3	8.9	44	8.90	9.60	10.14
	14h20	10.25	13.50	73.0	7.0	46	8.93	9.50	9.85
	14h30	9.22	15.05	82.9	6.89	41	9.11	9.69	10.29
	14h40	8.79	13.42	85.4	9.14	39	8.05	8.69	9.42
	12h40	9.96	13.17	67.5	8.1	50	9.47	9.95	10.58
	12h50	9.72	10.57	73.09	7.55	50	8.43	9.31	9.98

The wind characteristics of the selected sequences are given in Table 2. Overall, while the site is supposed to be of type II in the Eurocode, the measurements show a lower velocity gradient and a lower turbulent intensity than expected. Preliminary results were presented in (Ellingsen et al. 2022, Manal & Hémon 2022).

3. MEASURED OSCILLATIONS

The statistical results are given in Table 3 and plotted in Figure 2 as a function of the reduced frequency $f_r = \frac{f\ D}{\bar{U}}$. Four sequences approach a "perfect" lock-in, with an amplitude that reaches 36 % of the diameter. The corresponding Strouhal number is 0.225.

The other sequences present much lower amplitudes, lower than 10 % of the diameter. In these cases, the chimney response is certainly due to the turbulent excitation with a small participation of the vortex shedding.

Table 3. Measured top amplitude

Date	Time	Reduced frequency f_r	Maximum top displacement Y_{max}/D	RMS top displacement Y_{RMS}/D	Peak factor g
19-juil.-21	16h50	0.2203	0.2418	0.0543	4.45
	17h00	0.2216	0.3630	0.0961	3.78
	17h10	0.2183	0.3372	0.1006	3.35
	17h20	0.2304	0.2516	0.0630	3.99
20-juil.-21	14H00	0.1681	0.0431	0.01337	3.22
	14h10	0.1700	0.0788	0.02210	3.59
	14h20	0.1654	0.0638	0.02463	2.60
	14h30	0.1840	0.0874	0.03430	2.56
	14h40	0.1930	0.0256	0.00380	6.76
	12h40	0.1703	0.0641	0.02638	2.43
	12h50	0.1745	0.0537	0.01724	3.12

The measured amplitudes are compared to amplitudes estimations obtained from the two methods of Eurocode, using Ruscheweyh's model (method 1) or Vickery-Basu model (method 2), which are plotted at resonance in Figure 2. The Vickery-Basu model overestimates the field observations (0.53 against 0.36), while Ruscheweyh's model underestimates them (0.29 against 0.36).

Surprisingly the linear model based on a harmonic lift force gives an amplitude close to the one given by Ruscheweyh's model. This model reads

$$\frac{Y_{max}}{D} = \frac{1}{8\,\pi^2\,{f_r}^2\,M^*}\,\frac{\sqrt{2}\,C_{lat}}{\sqrt{(1-{f^*}^2)^2+4\,\eta^2\,{f^*}^2}} \tag{1}$$

where the mass ratio is $M^* = \frac{m}{\rho\,D^2}$ and the frequency ratio $f^* = \frac{St}{f_r}$. Here, we use the same lift force coefficient value as in Eurocode, $C_{lat} = 0.2$.

Moreover, the measured peak factors are close to the result obtained with Davenport's formula

$$g = \sqrt{2\ ln(\nu\ T)} + \frac{0.577}{\sqrt{2\ ln(\nu\ T)}} = 3.69 \quad (2)$$

where the frequency ν=0.848 Hz and the observation time is T=600 s.

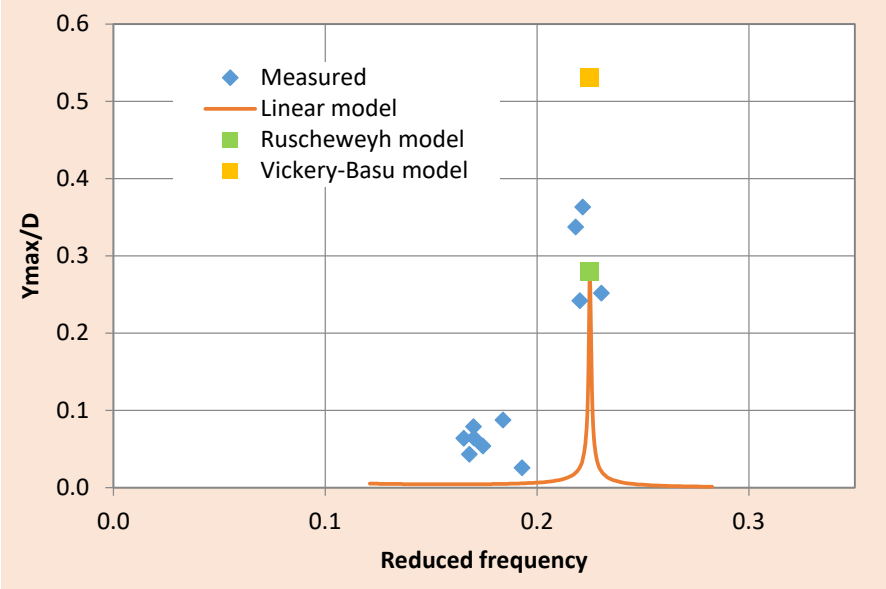


Figure 2. Measured maximum top amplitude versus reduced velocity.

4. CONCLUSION

Wind-induced vortex shedding has been measured on a full scale flexible chimney at Reynolds number of 1.1 million. The upcoming wind at moderate value is turbulent with intensity around 13-16 %. Wind-induced vibrations were observed during a short term campaign with lock-in at the reduced frequency (or Strouhal number) of 0.225. The maximum amplitude at the top was 36 % of the diameter. The presented data are useful for the study and the validation of prediction models of VIV in natural wind conditions.

ACKNOWLEDGEMENTS

This experiment was included in a partnership co-funded by Beirens (Poujoulat Group), Centre Scientifique et Technique du Bâtiment (CSTB), Centre National d'Etudes Spatiales (CNES) and LadHyX, CNRS-Ecole Polytechnique.

REFERENCES

Ellingsen Ø., Flamand O., Amandolese X., Coiffet F., Hémon P., 2022. Field tests on a full-scale steel chimney subjected to vortex-induced vibrations. Structural Engineering International, 32, 55-61.

Manal, Y., Hémon, P., 2024. Unsteady loads on circular cylinder in cross-flow: an observation in natural wind and comparison with wind tunnel experiments. Journal of Fluids and Structures 124, 104019.

Manal Y. & Hémon P., 2022. Unsteady wall pressure measurements on a full scale flexible chimney subject to natural wind. Flow-Induced Vibrations 2022, Paris-Saclay, July 2022.

An estimation of the unsteady lateral force on two full scale large vertical cylinders submitted to natural wind

Pascal Hémon[1], Ika Kurniawati[2], Francesca Lupi[3],
Marc Seidel[4], Rüdiger Höffer[2,3]

[1] *LadHyX, CNRS-Ecole Polytechnique, IP Paris, France, pascal.hemon@polytechnique.edu*
[2] *Ruhr-Universität Bochum, Bochum, Germany*
[3] *Niemann Ingenieure GbR, Bochum, Germany*
[4] *Siemens Gamesa Renewable Energy GmbH & Co. KG, Hamburg, Germany*

SUMMARY:
The paper deals with full scale measurements performed on two vertical cylinders submitted to natural wind, one chimney of 35 m with a Reynolds number around 1.1 million, and a wind turbine tower of 155 m with a Reynolds number around 5 millions. In both cases, unsteady wall pressure measurements are performed which are processed in order to obtain an estimation of the unsteady lateral force coefficient which is of great importance in the prediction models used to determine the motion amplitude due to vortex shedding in a turbulent wind.

Keywords: vortex shedding, full scale measurements, circular cylinder

1. INTRODUCTION

The goal of the paper is to report the measurements and their post-processing performed on two full scale vertical cylinders submitted to natural wind. The first one shown in Figure 1 is an experimental chimney erected at Bouin, close to the Atlantic seashore, France, in order to measure vortex shedding excitation (Manal & Hémon, 2024). Typical Reynolds number is around 1.1 million. The second cylinder presented in Figure 2 is a large wind turbine tower, named SG14, erected in the Test Centre Østerild in North Jutland, Denmark (Kurniawati *et al.*, 2024). Reynolds number is larger, around 5 millions.

This paper focuses on the synchronized unsteady wall pressure measurements around the cylinders which are analysed using the bi-orthogonal decomposition (BOD) technique (Hémon & Santi 2003). The principle of the BOD is to decompose the signal $Cp(\theta,t)$ in a series of spatial functions $\phi_i(\theta)$ named further as "topos", coupled with a series of temporal functions $\psi_i(t)$ named "chronos". The BOD can be written as

$$Cp(\theta,t) = \sum_{i=1}^{N} \alpha_i \, \phi_i(\theta) \, \psi_i(t) \qquad (1)$$

where ${\alpha_i}^2$ are the eigenvalues of the spatial or the temporal covariance matrix of the signal $Cp(\theta,t)$. N is the number of terms retained for the decomposition. The azimuth angle θ is set with the wind coming at $\theta = 0°$. The idea is to determine the unsteady pressure distribution that is generating the lateral force due to the vortex shedding induced by the wind.

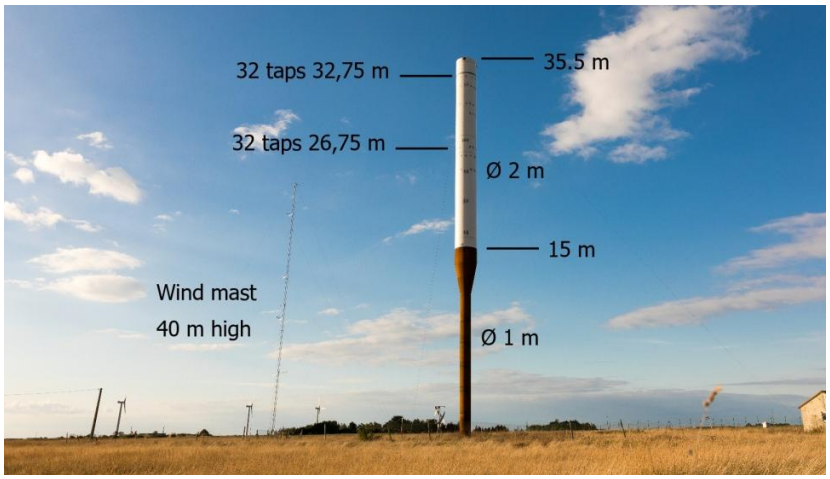


Figure 1. Photo of the Bouin chimney with its dimensions.

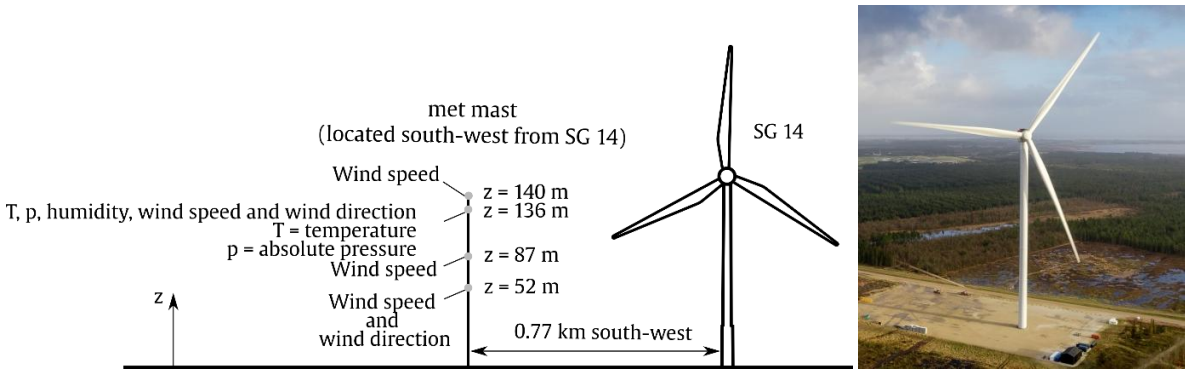


Figure 2. Sketch and picture of the wind turbine tower SG14

2. RESULTS OBTAINED WITH THE BOUIN CHIMNEY

There are 32 pressure taps mounted at the altitude 26.75 m and 32.75 m where the diameter D is 2 meters. More details on this setup can be found in (Ellingsen *et al.*, 2022; Manal & Hémon, 2024). Here we present two cases, one recorded when the chimney is at rest thanks to stay cables, and another one recorded when small oscillations occur with the maximum non dimensional amplitude Y_{max}/D = 0.064 at the top.

The wind characteristics are obtained thanks to a wind mast located 55 m to the west direction. They are resumed in Table 1. Thanks to the BOD, the term which is generating an unsteady lift can be identified and reconstructed in terms of an unsteady pressure coefficient Cp_u,

$$Cp_u(\theta) = \alpha_i \, \phi_i(\theta) \sqrt{\overline{\psi_i(t)^2}}. \qquad (2)$$

This unsteady pressure distribution is plotted in Figure 3 and complemented by the corresponding power spectral densities. The reduced frequency is defined using the diameter D of the chimney and the mean wind speed at 26.75 m, $f_r = f\ D/U$. The first natural bending frequency of the chimney is $f = 0.848$ Hz, on which the chimney motion occurs in the second

case, leading to the peak at $f_r = 0.17$ and its harmonics.
By performing a proper integration over θ of the unsteady pressure distribution $Cp_u(\theta)$, we obtain the unsteady lateral force coefficient C_{lat} which is of great importance in the prediction of the motion amplitude. For case 1, $C_{lat} = 0.153$ at 26.75 m, $C_{lat} = 0.155$ at 32.75 m, and for case 2, $C_{lat} = 0.165$ at 26.75 m, $C_{lat} = 0.143$ at 32.75 m.

Table 1. Wind characteristics of the two selected records

Record	Data from sonic anemometer at 26.75 m					DATA from cup anemometers		
	Mean velocity m/s	Turbulence intensity %	Wind direction ° ref MN	RMS of wind direction °	Integral Scale Lu m	Mean velocity at 10 m m/s	Mean velocity at 20 m m/s	Mean velocity at 35 m m/s
1: chimney at rest	8.49	15.10	67.0	4.5	168	7.21	7.35	8.09
2: small oscillations	9.96	13.17	67.5	8.1	50	9.47	9.95	10.58

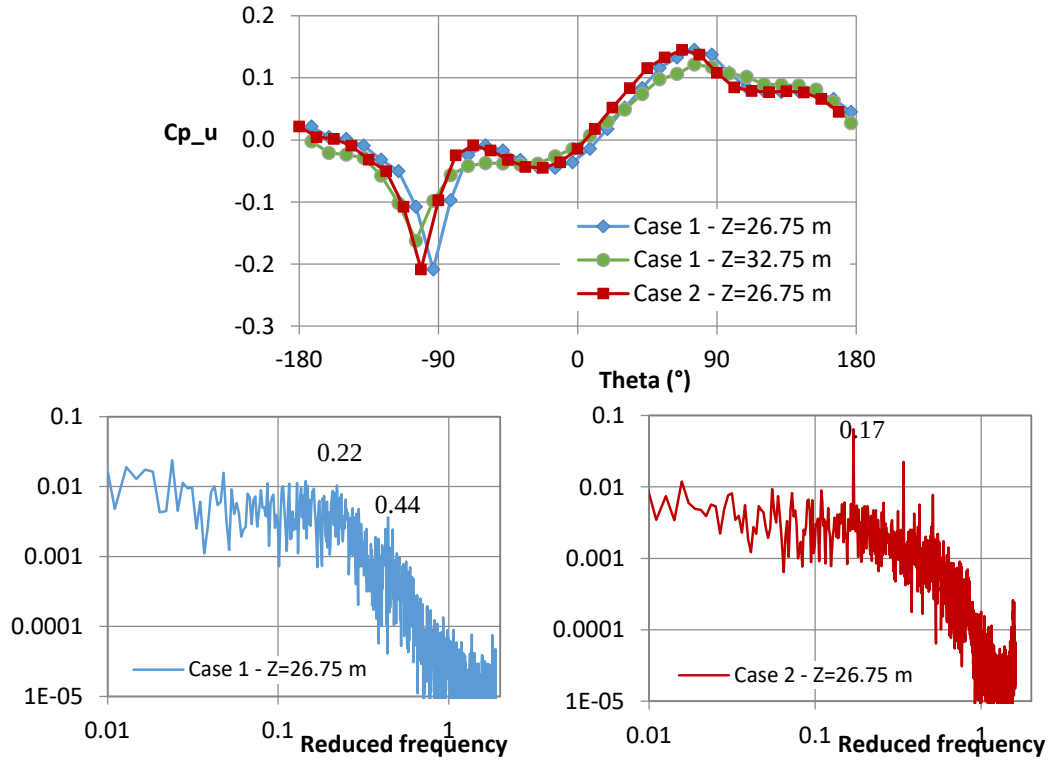


Figure 3. Unsteady pressure coefficient from term 4 of the BOD and corresponding power spectral densities.

3. RESULTS OBTAINED WITH THE TOWER SG14

The tower is equipped with two sets of 24 pressure taps at the altitude 98 and 128 m. The oscillation of the tower at the same time of the evaluated data is estimated around $Y_{max}/D = 0.01$ at around the tower top (149.6 m).
The same BOD technique is applied to one record of 10 minutes at 100 Hz. Once again a term generating the lift can be identified for the two sets of taps. For this 10-minute record, the wind direction comes from north-west around 290°. The resulting unsteady pressure coefficient

distribution is shown in Figure 4, with the corresponding power spectral densities.
The reduced frequency is calculated using the diameter $D = 6.5$ m and the mean wind velocities are 10.25 and 10.88 m/s for the two altitudes of measurements.
Using the pressure distribution at $z = 98$ m and $z = 128$ m respectively, the integration gives $C_{lat} = 0.148$ and $C_{lat} = 0.098$, showing in particular the effect of the top end.

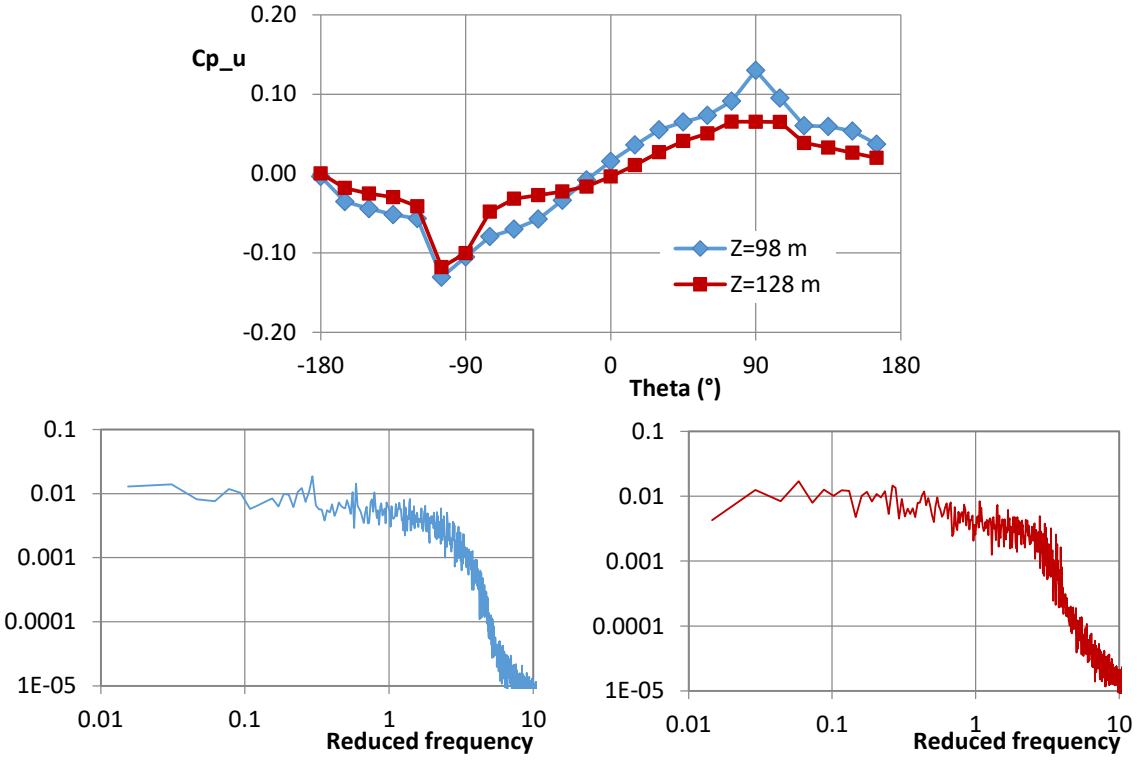


Figure 4. Unsteady pressure coefficient from term 4 of the BOD and corresponding power spectral densities.

ACKNOWLEDGEMENTS

The Bouin experiment was included in a partnership co-funded by Beirens (Poujoulat Group), Centre Scientifique et Technique du Bâtiment (CSTB), Centre National d'Etudes Spatiales (CNES) and LadHyX, CNRS-Ecole Polytechnique. The measurement and evaluation on SG 14 tower is a part of Deutsche Forschungsgemeinschaft (DFG, German Research Foundation) research transfer project Nr. 493357786 with Siemens Gamesa Renewable Energy, the support from DFG is gratefully acknowledged.

REFERENCES

Ellingsen Ø., Flamand O., Amandolese X., Coiffet F., Hémon P., 2022. Field tests on a full-scale steel chimney subjected to vortex-induced vibrations. Structural Engineering International, 32, 55-61.

Hémon, P., Santi, F., 2003. Applications of biorthogonal decompositions in fluid-structure interactions. Journal of Fluids & Structures 17.8, 1123–1143

Kurniawati, I., Lupi, F., Seidel, M., Niemann, H-J, and Hoffer, R., 2024. Vortex shedding load on a full-scale wind turbine tower at transcritical Reynolds numbers. Journal of Wind Engineering & Industrial Aerodynamics 252, 105821.

Manal, Y., Hémon, P., 2024. Unsteady loads on circular cylinder in cross-flow: an observation in natural wind and comparison with wind tunnel experiments. Journal of Fluids and Structures 124, 104019

Vortex-induced vibrations of wind turbine towers: Sensitivity analysis of prediction models for first and second mode

Ika Kurniawati[1], Francesca Lupi[2], Marc Seidel[3], Rüdiger Höffer[1,2]

[1]*Ruhr-Universität Bochum, Bochum, Germany, ika.kurniawati@ruhr-uni-bochum.de*
[2]*Niemann Ingenieure GbR, Bochum, Germany*
[3]*Siemens Gamesa Renewable Energy GmbH & Co. KG, Hamburg, Germany*

SUMMARY:
This paper presents a sensitivity analysis of a prediction model for vortex induced vibrations (VIV) on wind turbine tower. The analysis examines the output variation of the model under varying input parameters such as wind profile, turbulence intensity, lift coefficient, Strouhal numbers, and structural damping. The random distribution of input parameters is developed from field measurements data, including tower response, wind conditions, and surface pressure data to obtain aerodynamic coefficients and vortex shedding parameters. Sensitivity analysis is performed using Monte Carlo simulations. The work will also discuss the updated findings from the field measurements including the observation of second mode VIV and the discussion of post-lock-in cross-wind oscillations.

Keywords: Wind turbine tower, Sensitivity analysis, Vortex-Induced Vibration, Second-mode

1. INTRODUCTION

Full-scale measurements were conducted on two offshore wind turbine towers in Østerild, Denmark, to investigate Vortex-Induced Vibration (VIV). Two wind turbine towers are D8 Tower and SG 14-222 DD (SG 14) from Siemens Gamesa Renewable Energy. In addition to response measurement, the full-scale test also consists of the surface pressure measurement on two levels of the tower exclusively for SG 14. The details of the full-scale pressure measurement are reported in detail in Kurniawati et al. (2024a), where aerodynamic parameters and vortex shedding load are obtained. Tower's cross-wind vibrations and the initial formulation of VIV data sets are documented in Kurniawati et al. (2024b) and Kurniawati et al. (2024c). A VIV prediction model is proposed and validated on the D8 Tower case in Livanos et al. (2024), which is then evaluated for sensitivity analysis in this work.

To test the model's sensitivity, random input parameters are generated based on the distribution concluded from the full-scale measurement data. A Monte Carlo simulation is performed to generate the response, considering the variation of the input parameters.

Many interesting observations have been found in the measurements, such as the large cross-wind oscillation after lock-in (post-lock-in oscillation) and the 2nd mode VIV. The 2nd mode VIV response shows complex vibration characteristics, with high intermittency (instantaneous increase

in vibration amplitude), even during resonance to the 2nd mode. The 2nd mode VIV case can provide further insight into high-mode vibration.

2. METHODS AND RESULTS

The tower response is measured using accelerometers placed along the height from Micro Epsilon inertial Sensor ACC5703 and base bending moment measured using strain gauges four-bridge strain gauges from Micro Measurements type CEA-06-W250C-350. Surface pressure measurements were conducted on the SG 14 tower using JUMO Midas S06 pressure transmitters. Wind conditions are evaluated using the 10-minute wind speed and direction data, with turbulence intensity calculated as the standard deviation divided by the mean wind speed. Power-law wind profile with shear exponent α are used to estimate the wind profile under neutral atmospheric conditions. Curated cross-wind response data sets of D8 tower for the period July 2021 to April 2022 are used as the case study in this paper.

Figure 1 shows a four-by-four plot illustrating the D8 tower's response (in standard deviation, σ_y) to wind speed $\bar{u}$, turbulence intensity I_u, and wind shear exponent α from the same curated data sets. Scatter in the data is guessed due to varying input conditions and structural damping uncertainties. This data cluster is used to validate whether the suggested VIV prediction model can simulate the same level of scatter given varying inputs.

The proposed VIV prediction model by Livanos et al. (2024) predicts the standard deviation of VIV response while considering 3-D negative aerodynamic damping model where its values are calculated using contour map model considering both displacement response (in σ_y/D) and the velocity (in its ratio to the critical velocity, $\bar{u}/u_{cr}$). u_{cr} is calculated using equation (1) with Strouhal number St = 0.21, and the tower effective diameter D_{eff} and the tower's natural frequency f_n.

$$u_{cr} = f_n \cdot D_{eff}/St \tag{1}$$

The effect of both displacement and velocity ratio defined varying along the height, models the aeroelastic effect considering wind profile and mode shape of displacement.

The model calculates the displacement response for any given wind speed $\bar{u}$, at reference height $\bar{u}$, and for the n^{th} mode of vibration, as described in equation (2).

$$\sigma_{y,n}^2(\bar{u}, z_r) = \frac{\lambda \cdot D_{eff} \cdot \int_0^h g_n^2(f_n, z) \cdot dz}{4 \cdot \omega_n^3 \cdot M_n^2 \cdot [\zeta_s + \zeta_a]} \tag{2}$$

where λ is the correlation length, g_n is the modal spectral load function due to vortex shedding (equation (3)), integrated along height z. ω_n is the n^{th} radial frequency, M_n is the modal mass, ζ_s is the structural damping ratio and ζ_a is the negative aerodynamic damping defined in equation (4).

$$g_n(f,z) = \frac{1}{2}\rho\bar{u}(z)^2 \cdot D(z) \cdot \frac{c_L(z)}{\sqrt{\sqrt{\pi}\cdot St(z)\cdot\frac{\bar{u}(z)}{D(z)}\cdot B(z)}} \cdot exp\left(-\frac{1}{2}\left(\frac{1-\frac{f}{St(z)\cdot\frac{\bar{u}(z)}{D(z)}}}{B(z)}\right)^2\right) \cdot \Phi_n(z) \quad (3)$$

where ρ is the air density, $D(z)$ is tower's diameter profile, c_L is the lift coefficient, B is the bandwidth parameter and Φ is the mode shape.

$$\zeta_a = -\frac{\rho\cdot D_{eff}^2(z)}{M_n}\int_0^H \Phi_n(z)\cdot K_a\left(\frac{\bar{u}(z)}{u_{cr}(z)}, \frac{\sigma_y(z)}{D(z)}\right)\cdot\left(1-3I_u(z)\right)\cdot\Phi_n(z)\cdot dz \quad (4)$$

K_a is the nondimensional maximum aerodynamic damping for infinitely cylinder and the value can be calculated using a contour map. The contour map is an empirical matrix of K_a developed from the forced-vibration measurements.

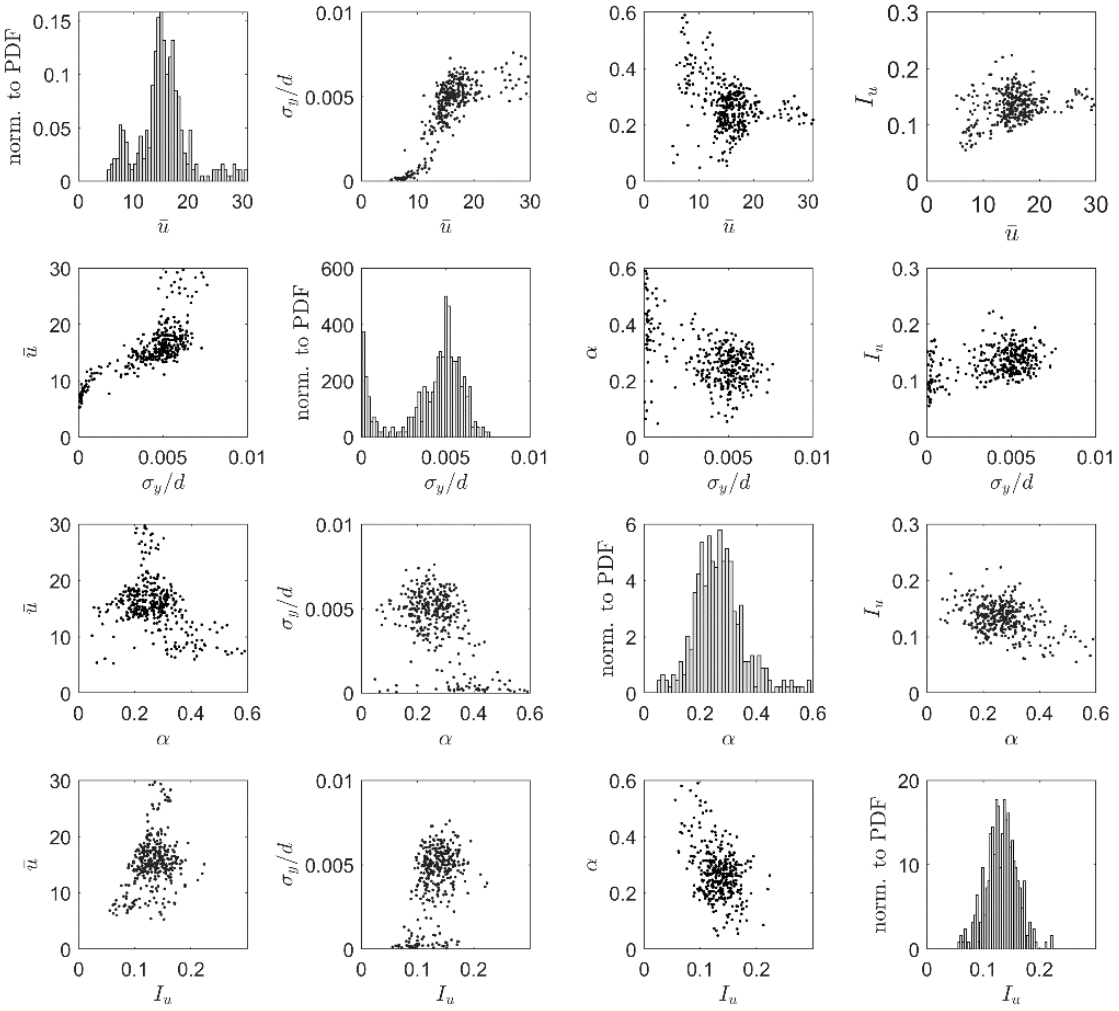


Figure 1. The distribution of related parameters from all curated VIV events. Diagonal subplots are the histogram of each parameter.

To perform sensitivity analysis, random values of input parameters are generated based on field-measured distributions, assuming a normal distribution with calculated mean (mu) and standard deviation (sigma) values. For example, a multivariate correlation is considered to describe the distribution of turbulence intensity and wind shear exponent (Figure 2a). The random values are generated as shown in Figure 2b. Monte Carlo simulations are conducted given random input values set for the seven parameters to analyze the variation of calculated VIV response. The sensitivity analysis also identifies the most significant parameter and assesses the effect of various types of input wind profile.



(a) (b)

Figure 2. Distribution of turbulence intensity I_u and wind profile exponent α (a) measured from met mast; (b) random generated distribution for calculation compared with the measured values

Not shown in this abstract, is the measured 2nd mode VIV occurrence on fully-built SG 14 tower (with nacelle). The 2nd mode VIV occurrences were at the high critical wind speed with high turbulence. The full-scale measurements showed that the 2nd mode VIV has a complex cross-wind oscillation, with the 2nd mode dominating the middle section of the tower, while the top of the tower oscillates predominantly in the 1st mode.

ACKNOWLEDGEMENTS

This research project is supported by the Deutsche Forschungsgemeinschaft (DFG, German Research Foundation) for the support through the projects Nr. 493357786. The authors would like to thank Siemens Gamesa Renewable Energy for providing the measurement data and measurement system.

REFERENCES

Kurniawati, I., Lupi, F., Seidel, M., Niemann, H.-J., Höffer, R., 2024a. Vortex shedding load on a full-scale wind turbine tower at transcritical Reynolds numbers. Journal of Wind Engineering and Industrial Aerodynamics 252, 105821. https://doi.org/10.1016/j.jweia.2024.105821

Kurniawati, I., Lupi, F., Seidel, M., Höffer, R., Niemann, H.-J., 2024b. Field measurement data set of wind turbine tower for enhanced calculation of vortex-induced vibration. Journal of Physics: Conference Series. Volume 2647, Issue 11. 10.1088/1742-6596/2647/11/112003

Kurniawati, I., Lupi, F., Seidel, M., Höffer, R., Niemann, H.-J., 2024c. Vortex-induced vibrations and post-lock-in cross-wind oscillations of wind turbine towers based on field measurements. Journal of Wind Engineering and Industrial Aerodynamics. Volume 258, 106010. https://doi.org/10.1016/j.jweia.2025.106010

Livanos, D., Kurniawati, I., Seidel, M., Daamen, J., Wennecker, F., Lupi, F., Höffer, R., 2024. An enhanced analytical calculation model based on sectional calculation using a 3D contour map of aerodynamic damping for vortex induced vibrations of wind turbine towers. Wind And Structures. https://doi.org/10.12989/was.2024.38.6.445

Wind tunnel investigation of aerodynamic loads of circular cylinders from subcritical to supercritical Reynolds number regime

Alessandro Giusti[1], Andi Xhelaj[2], Andrea Orlando[3], Alessio Torrielli[4], Olivier Flamand[5]

[1]*Siemens Gamesa Renewable Energy A/S, Brande, Denmark,* *alessandro.giusti@siemensgamesa.com*
[2]*Department of Civil, Chemical and Environmental Engineering, University of Genoa, Italy,* *andi.xhelaj@edu.unige.it*
[3]*Department of Civil, Chemical and Environmental Engineering, University of Genoa, Italy,* *andrea.orlando@edu.unige.it*
[4]*Siemens Gamesa Renewable Energy A/S, Brande, Denmark,* *alessio.torrielli.ext@siemensgamesa.com*
[5]*Centre Scientifique et Technique du Bâtiment, Nantes, France,* *olivier.flamand@cstb.fr*

SUMMARY:
The wind-structure interaction around circular cylinders has recently captured the attention of the wind energy industry, due to the peculiarities of the installation process of an offshore wind turbine. Indeed, towers without rotor-nacelle assembly are temporarily erected at the harbor quayside in different group arrangements and then transported on the installation vessel. This paper focuses on the aerodynamic loads of finite-length circular cylinders at different Reynolds number regimes, from subcritical (about 2.6×10^5) to supercritical (about 1.7×10^6). The study is conducted by means of wind tunnel tests on a cylinder having an aspect ratio (height to diameter) similar to a real half tower and equipped with eight rings of pressures taps, distributed along the height. The mean pressure distributions and the corresponding drag and lift (standard deviation) coefficients are calculated for the different Reynolds numbers. Moreover, data are analyzed using the Proper Orthogonal Decomposition (POD) method to identify the modes associated with the pressure distribution and, in combination with machine learning, to develop a robust technique for data correction.

Keywords: finite-length circular cylinders, aerodynamic coefficients, high Reynolds number regime

1. INTRODUCTION

The installation of an offshore wind turbine includes some preparatory phases aimed at setting up the components (nacelle, blades and tower sections) prior to the load out onto special vessels, which will complete the assembly of the wind turbine on the offshore foundation. Towers are usually erected and transported in different group arrangements (e.g., Mannini et al., 2023) driven by the capabilities of the harbor quayside, cranes and vessels. The wind-structure interaction of finite-length circular cylinders is therefore a topic also relevant to the wind energy industry. Recent works on gust buffeting (e.g., Mannini et al., 2023) and vortex shedding (e.g., Kurniawati et al., 2024) aimed to fill the gap of design standards, but a clear understanding of how the aerodynamic loads evolve from subcritical to supercritical Reynolds number regimes is still missing. Moreover,

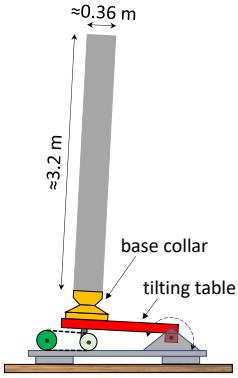


Figure 1. Sketch of the wind tunnel setup.

Table 1. Details on the pressure measurements in the different phases of the wind tunnel campaign. d_i/D is the ratio of distance from the top of the i-th ring to cylinder diameter.

Ring	d_i/D	N° of pressure taps connected		
		phase 1	phase 2	phase 3
1	0.0845	25	0	0
2	0.1690	25	0	21
3	0.3380	25	0	0
4	0.6761	25	0	21
5	0.9859	25	0	0
6	1.9718	25	25	21
7	2.9577	25	25	0
8	5.9155	25	0	0

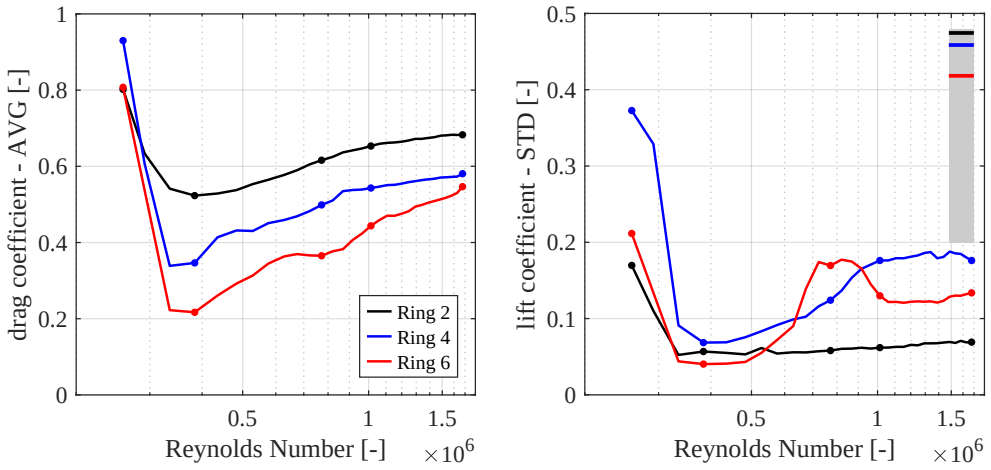
the influence of the movement of the base of the tower associated with the motion of the vessel during navigation needs to be clarified. This paper aims to shed light on the aerodynamic loads of circular cylinders from subcritical to supercritical Reynolds number regime by means of wind tunnel tests performed on smooth cylinders, and it is part of a more comprehensive study, which also includes the movement of the base (see Torrielli et al., 2025).

2. EXPERIMENTAL TESTS

The study is conducted by wind tunnel tests carried out at the Centre Scientifique et Technique du Bâtiment (CSTB), Jules Verne facility. The model used for measurements (see Fig. 1) consists of an aluminum tube connected by means of a base collar to a tilting table and equipped with 200 pressure taps, distributed along 8 rings (see Tab. 1). Three phases of measurements are carried out to cover different Reynolds number regimes. High-velocity measurements of phase 2 and phase 3 require scanners with high-pressure range, reducing to 63 the number of active pressure taps due to the limited availability of such scanners. All tests are performed in uniform flow, low turbulence intensity and with the tilting table turned either off or on, the latter to introduce a vessel-like motion. For more details on the test setup see Torrielli et al., 2025.

3. RESULTS

Pressure measurements are integrated to identify the mean drag coefficient and the lift coefficient's standard deviation across different Reynolds numbers, ranging from the end of subcritical to supercritical regime (see Fig. 2). The mean drag coefficient (see Fig. 2(a)) increases moving towards the top of the cylinder, following a trend similar to that reported by Mannini et al., 2023, although in that study cylinders were more slender. Ring 6, located about two cylinder diameters from the top (see Tab. 1), shows values that align with those available in the literature for sectional models (e.g., Adachi, 1997, Delany and Sorensen, 1953). Furthermore, the proximity to the top of the cylinder (see Fig. 2(b)) seems to reduce the variability of the lift coefficient's standard deviation with the Reynolds number, especially after the critical region. Finally, the average lift coefficient (not reported here for the sake of brevity), regardless of the position of the ring, is not zero in the entire critical region, where evidence of bi-stable flow phenomena and separation bubbles is found, as documented in the literature (e.g., Buresti, 2012).



(a) mean drag coefficient (b) lift coefficient's standard deviation

Figure 2. Aerodynamic coefficients at different heights of the cylinder and for different Reynolds numbers.

The mean pressure distribution from phase 3, in the case of tilting table turned off, is shown in Fig. 3 for different rings and different Reynolds numbers. It is apparent that the proximity to the top of the cylinder influences the pressure distribution, which becomes only slightly affected by the Reynolds number at the very top. By contrast, at Ring 6, pressures develop differently with Reynolds number, following a trend similar to that reported by Achenbach, 1968. It is worth mentioning that the preliminary results presented in this abstract are based on a direct post-process of that data from wind tunnel tests without applying any correction to missing or anomalous measurements. For this reason, the measurements will be further processed, and additional analyses will be performed. Moreover, a suitable technique combining machine learning and Proper Orthogonal Decomposition (POD) will be employed to predict and correct missing pressure tap data, enhancing the reliability of the results.

4. CONCLUSIONS

The results of this study aim to provide a clear understanding of the aerodynamic loads experienced by a finite-length circular cylinder along its height under different Reynolds number regimes. Preliminary findings confirm that the free-end of the cylinder significantly influences the pressure distributions. Pressures in the upper part of the cylinder, where the free-end effect is more significant, seem to slowly change with Reynolds numbers larger than 10^6. In contrast, pressures further down the cylinder, such as those measured at Ring 6, align well with established literature. The use of Proper Orthogonal Decomposition (POD) and machine learning techniques to correct missing data are expected to provide greater accuracy and more reliable results. These findings will provide important insights for optimizing the design of vertically developed cylindrical structures, such as chimneys and wind turbine towers, by improving the understanding of wind-structure interactions under vortex shedding conditions. More insights will be presented at the conference.

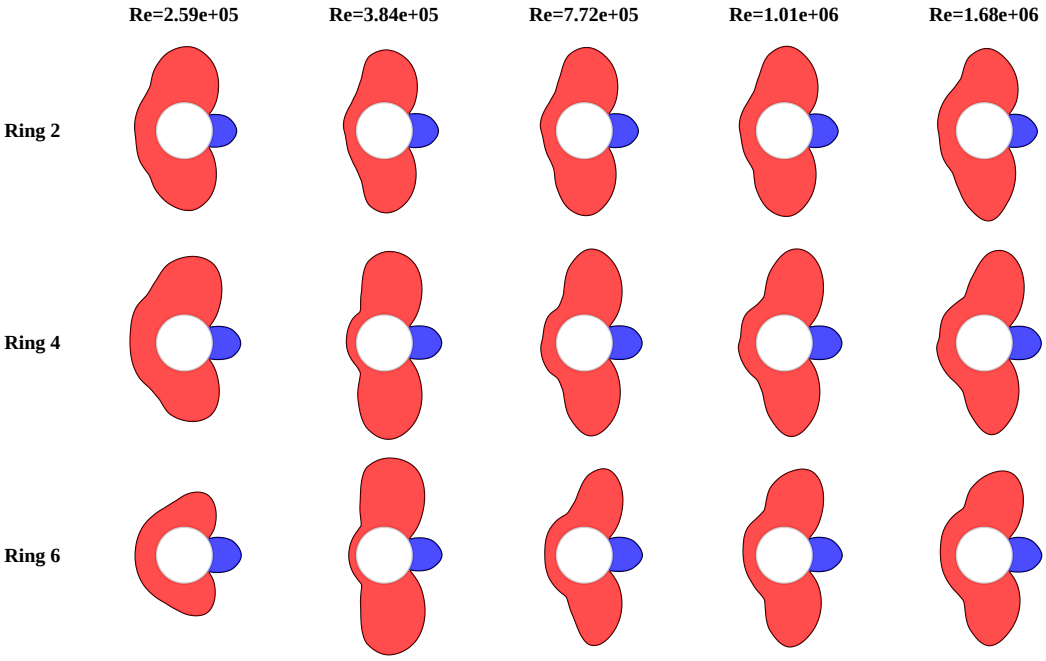


Figure 3. Mean pressure distribution at different heights and for different Reynolds numbers.

ACKNOWLEDGEMENTS

This work is part of the transnational access project "ERIES – VORSEA", supported by the Engineering Research Infrastructures for European Synergies (ERIES) project (www.eries.eu), which has received funding from the European Union's Horizon Europe Framework Programme under Grant Agreement No. 101058684. This is ERIES publication number C27.

REFERENCES

Achenbach, E., 1968. Distribution of local pressure and skin friction around a circular cylinder in cross-flow up to $Re = 5 \times 10^6$. Journal of Fluid Mechanics 34, 625–639.

Adachi, T., 1997. Effects of surface roughness on the universal Strouhal number over the wide Reynolds number range. Journal of Wind Engineering and Industrial Aerodynamics 69-71, 399–412.

Buresti, G., 2012. Elements of Fluid Dynamics. Imperial College Press.

Delany, N. K. and Sorensen, N. E., 1953. *Low-speed drag of cylinders of various shapes*. Tech. rep. National Advisory Committee for Aeronautics (NACA).

Kurniawati, I., Lupi, F., Seidel, M., Niemann, H.-J., and Höffer, R., 2024. Vortex shedding load on a full-scale wind turbine tower at transcritical Reynolds numbers. Journal of Wind Engineering and Industrial Aerodynamics 252, 105821.

Mannini, C., Massai, T., Giachetti, A., and Giusti, A., 2023. Aerodynamic loads on groups of offshore wind turbine towers stored on quaysides during the pre-assembly phase. Journal of Wind Engineering and Industrial Aerodynamics 242, 105569.

Torrielli, A., Orlando, A., Xhelaj, A., Giusti, A., and Flamand, O., 2025. Vortex shedding of circular cylinders mounted on a rolling support at different Reynolds number regimes. Proceedings of the 9th European-African Conference on Wind Engineering (EACWE 2025). Trondheim, Norway (extended abstract).

Inverse calculation of aerodynamic coefficients of a polygonal cylinder from full-scale monitoring data

Mekdes T. Mengistu[1], Andrea Orlando[2], Maria Pia Repetto[3]

[1]*University of Genova, Genova, Italy, mekdestadesse.mengistu@edu.unige.it*
[2]*University of Genova, Genova, Italy, andrea.orlando@edu.unige.it*
[3]*University of Genova, Genova, Italy, maria.pia.repetto@unige.it*

SUMMARY:
A novel approach is applied to calculate the aerodynamic coefficients of a 16-sided cylindrical pole from full-scale monitoring data. The simultaneous monitoring data of wind speed and strain recordings during selected wind events were used to inverse-calculate the mean drag and lift coefficients. The calculated coefficients were then compared with the results of wind tunnel tests. The comparison between the results of full-scale monitoring and wind tunnel tests showed that the general pattern of the drag coefficient variability with the angle of attack is closely similar. Although the lift coefficients obtained in the wind tunnel were shown to be highly variable with small changes in the angle of attack, this variability was not evident from the full-scale monitoring results. The study introduced a simplified inverse calculation approach that can be applied to vibration-based monitoring data to validate wind tunnel test results.

Keywords: Aerodynamic coefficients, Full-scale monitoring, Wind tunnel investigation

1. INTRODUCTION

Aerodynamic pressure has been monitored by many researchers, on the facades and walls of many low-rise to super-tall buildings, to validate aerodynamic coefficients obtained through wind tunnel tests. This approach of monitoring pressure on the structure's surface can not be directly applied to slender structures such as cylindrical/polygonal poles, lattice structures, and bridge components. Rather, the full-scale monitoring of such slender structures usually involves vibration measurement through strain, acceleration, and displacement sensors. Although wind force identification from vibration measurements is widely studied in the field of structural monitoring, Kazemi Amiri and Bucher, 2017; Law et al., 2005, the output is usually the fluctuating component of the wind force excluding the mean. This hinders the calculation of the mean aerodynamic coefficients using the input wind force identification. One exception where a full-scale vibration record measured with accelerometers is used to calculate aerodynamic coefficients is in Acampora et al. (2014) in which the estimated aerodynamic damping from ambient vibration data is used to calculate the drag coefficients using quasi-steady theory. Although this is a novel approach to obtain the drag coefficients from vibration monitoring, the uncertainty usually observed in damping estimation from ambient vibration data could be propagated to the calculated drag coefficient. An exemplary work on the inverse calculation of aerodynamic coefficients from vibration measurement through strain sensors and the fusion of multiple sensors data can be found in Azzi et al. (2021) and Jeddi et al. (2023). The drag and moment coefficients were calculated for a scaled aeroelastic model of a lattice tower subjected to wind load in a boundary layer wind tunnel. However, a similar

application in a full-scale monitored structure is not available and the difficulties arising from full-scale long-term monitoring remain to be investigated.

This study proposes a novel approach for calculating aerodynamic coefficients inversely from full-scale structural response data. Simultaneous measurements of wind speed and strain are used to calculate the aerodynamic coefficients of a 16-sided cylindrical section. The results are compared with the aerodynamic coefficients obtained through wind tunnel tests of a scaled sectional model.

2. DESCRIPTION OF THE STRUCTURE AND THE MONITORING SYSTEM

The monitored structure is a 16.6 m high steel lighting pole made of a 16-sided polygonal shaft with a tapered cross-section that decreases its maximum cross-sectional dimension from 528 mm at the base of the pole to 254 mm at the top. The structure supports an intermediate platform at 10 m and a lighting fixture housed in a rectangular platform at the top. A circular ladder is attached to one of the faces of the polygonal shaft and it runs from the bottom to the top of the pole.

The monitoring system consists of an ultrasonic anemometer installed at 21.7 m for the wind speed and direction measurement, 2 bi-axial accelerometers installed at 11 m and the top of the structure, and 8 uni-axial strain gauges installed at 0.5 m and 1.5 m. So far, the monitoring system has registered 4230 hrs of data (Mengistu et al., 2023).

3. INVERSE CALCULATION OF MEAN AERODYNAMIC COEFFICIENTS

The mean drag and lift forces on the monitored structure are defined using the quasi-steady theory:

$$\bar{F}_d(z) = 0.5\rho b(z)\bar{u}^2(z)C_d \qquad \textit{and} \qquad \bar{F}_l(z) = 0.5\rho b(z)\bar{u}^2(z)C_l \tag{1}$$

where $\bar{F}_d(z)$ and $\bar{F}_l(z)$ are the mean drag and lift forces respectively; ρ is the air density; $b(z)$ is the windward breadth of the structure; $\bar{u}(z)$ is the mean wind speed; and C_d and C_l are equivalent height-invariant mean drag and lift coefficients, respectively.

The principal axes of the structure X and Y are rotated 44.5 degrees counterclockwise from the global East and North directions, respectively (Fig. 1). Thus, the mean drag and lift coefficients can be projected on the principal axes of the structure $X-Y$ to obtain the mean aerodynamic forces $\bar{F}_X(z)$ and $\bar{F}_Y(z)$.

$$\bar{F}_X(z) = \bar{F}_d(z)\cos\theta + \bar{F}_l(z)\sin\theta \qquad \textit{and} \qquad \bar{F}_Y(z) = \bar{F}_l(z)\cos\theta - \bar{F}_d(z)\sin\theta \tag{2}$$

where $\theta = 44.5 - \beta$ and β is the angle the mean wind speed makes with the horizontal East and West axes (Fig. 1).

Considering the complexity of the geometry to apply the influence line approach, the mean displacement at the top of the structure is:

$$\bar{d}_X = \frac{\int_0^H \bar{F}_X(z)\psi_X(z)dz}{K_X} \qquad \textit{and} \qquad \bar{d}_Y = \frac{\int_0^H \bar{F}_Y(z)\psi_Y(z)dz}{K_Y} \tag{3}$$

where ψ_X and ψ_Y are the mode shapes in the X and Y directions, respectively normalized to one at the top of the tower; and K_X and K_Y are the stiffnesses corresponding to the vibration modes in the X and Y direction.

The dynamic properties of the structure were obtained using operational modal analysis. Consequently, the stiffnesses corresponding to the first vibration modes in the X and Y directions, K_X and K_Y, were obtained using the circular frequencies and modal masses in the X and Y directions. The mean quasi-static displacements at the top of the structure, $\bar{d}_X$ and $\bar{d}_Y$, were obtained from the strain registrations. The mean wind speed was generated along the height of the structure, considering the logarithmic law for the vertical profile of mean wind speed. Substituting Eq. (2) in Eq. (3), the only unknowns are the aerodynamic coefficients C_d and C_l. Thus, the mean aerodynamic coefficients are obtained by solving Eq. (3) simultaneously.

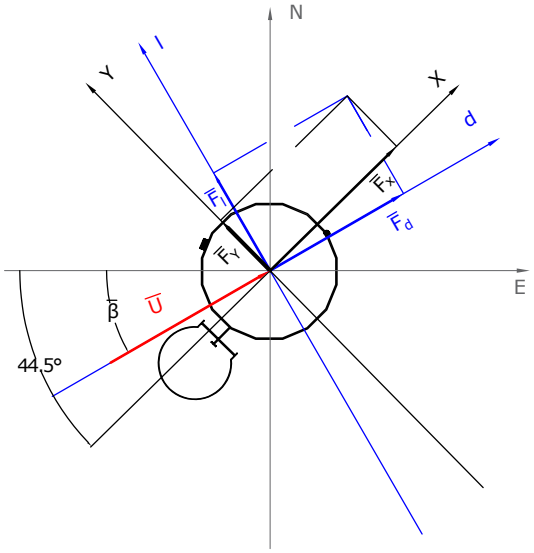


Figure 1. Orientation of the drag and lift forces relative to the principal axes

4. COMPARISON OF AERODYNAMIC COEFFICIENTS OBTAINED FROM WIND TUNNEL TESTING AND FULL-SCALE MONITORING

The wind tunnel investigation previously done for the monitored structure at the boundary layer wind tunnel of the University of Genova is considered for this comparison (Orlando et al., 2023). Two scaled sectional models were tested, representing the largest and smallest cross-sections, respectively, at the base and top of the pole. The test considered the presence of the steel ladder and also the longitudinal welding.

The equivalent height-invariant mean aerodynamic coefficients obtained from inverse calculation are compared with those obtained from wind tunnel tests. Fig. 2 shows the mean drag and lift coefficients of the largest and the smallest sections in blue continuous lines and the equivalent mean drag and lift coefficients of the polygonal shaft obtained through inverse calculation in gray points. The mean value obtained at the center of each 5-degree bin is also shown with a black line. Although there is a clear scatter in the results of the inverse calculation, the general pattern of the variability of the calculated mean drag coefficients with angles of attack is in close agreement with that obtained from the wind tunnel testing. Although the mean lift coefficients are closer to those obtained through wind tunnel tests for some wind directions, in general, the variability with the angle of attack is not comparable.

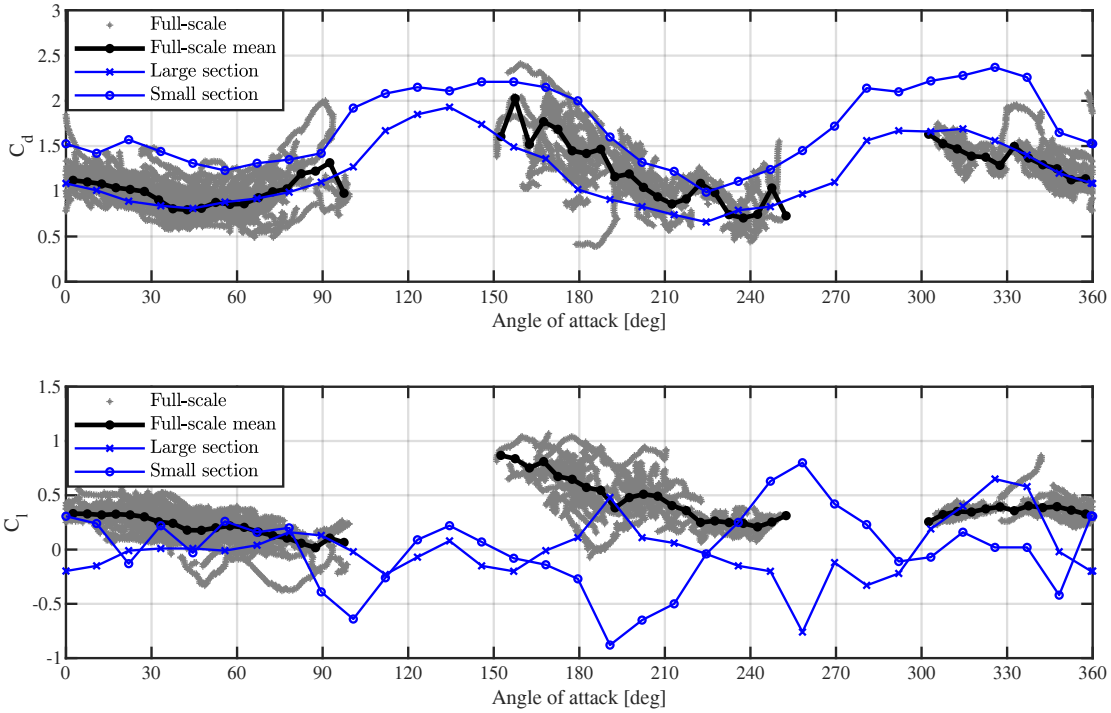


Figure 2. Comparison of results of wind tunnel test and inverse calculation approach

ACKNOWLEDGEMENTS

The contribution of the third author is funded by the European Research Council (ERC) under the European Union's Horizon 2020 research and innovation program (grant agreement No. 741273) for the project "THUNDERR - Detection, simulation, modeling and loading of thunderstorm outflows to design wind-safer and cost-efficient structures" – through an Advanced Grant 2016. The monitoring system is co-funded by the Italian Ministry of Instruction and Scientific Research (MIUR), Prot. 2015TTJN95 in the framework of the Research Project of Relevant National Interest (PRIN 2015).

REFERENCES

Acampora, A., Macdonald, J. H., Georgakis, C. T., and Nikitas, N., 2014. Identification of aeroelastic forces and static drag coefficients of a twin cable bridge stay from full-scale ambient vibration measurements. Journal of Wind Engineering and Industrial Aerodynamics 124, 90–98.

Azzi, Z., Elawady, A., Irwin, P., Chowdhury, A. G., and Shdid, C. A., 2021. Aeroelastic modeling to study the wind-induced response of a self-supported lattice tower. Engineering Structures 245, 112885.

Jeddi, A. B., Azzi, Z., Shafieezadeh, A., Elawady, A., Gan Chowdhury, A., and Irwin, P., 2023. Revisit of underestimated wind drag coefficients and gust response factors of lattice transmission towers based on aeroelastic wind tunnel testing and multi-sensor data fusion. Engineering Structures 278, 115486.

Kazemi Amiri, A. and Bucher, C., 2017. A procedure for in situ wind load reconstruction from structural response only based on field testing data. Journal of Wind Engineering and Industrial Aerodynamics 167, 75–86.

Law, S. S., Bu, J. Q., and Zhu, X. Q., 2005. Time-varying wind load identification from structural responses. Engineering Structures 27, 1586–1598.

Mengistu, M. T., Orlando, A., and Repetto, M. P., 2023. Wind and structural response monitoring of a lighting pole for the study of downburst effects on structures. Journal of Wind Engineering and Industrial Aerodynamics 240.

Orlando, A., Pagnini, L., and Pia Repetto, M., 2023. Wind tunnel tests of a hexadecagonal cylinder with imperfections and ancillaries: aerodynamic characterization and technical discussion. Engineering Structures 274, 115114.

Fatigue assessment of pedestals for wind assisted propulsion systems on merchant ships

Gaute Storhaug [1], Jens Petter Turøy [2], Bernt Leira [2], Dag Myrhaug[2]

[1]*DNV, Høvik, Norway, gaute.storhaug@dnv.com*
[2]*NTNU, Dept. Marine Technology, Trondheim, Norway, jensptu@stud.ntnu.no*
[2]*NTNU, Dept. Marine Technology, Trondheim, Norway, bernt.leira@ntnu.no*
[2]*NTNU, Dept. Marine Technology, Trondheim, Norway, dag.myrhaug@ntu.no*

SUMMARY:
Wind assisted propulsion systems (WAPS) represent sails in a new wrapping installed on merchant ships. The main intention is to supplement the conventional propulsion system in favourable conditions. Each WAPS needs to be properly designed to meet extreme and operational loads to be safe with limited maintenance needs. The foundation of the sail needs to be tailored to each specific ship. This involves design against collapse (yielding and buckling) and fatigue cracking. It turns out that the latter is frequently the most critical one. The main foundation loads are related to inertia and wind. The inertia may follow the equivalent design wave (EDW) approach by the ship rules. However, those are related basically to 6 directions for fatigue but extended to 8 directions including extreme EDWs for bow quartering. The question is whether these direction intervals give convergent results when applied also for the wind loads. This is studied in the following considering resolution of the wind heading, as well as resolution of the wind speed and resolution of the vertical wind speed profile. An academic sail profile is applied for calculation of the wind induced fatigue with simplified formulation for the wind gust process based on previous research.

Keywords: WAPS, fatigue, discretization

1. INTRODUCTION

The present paper focuses on fatigue and resolution effects of wind heading, as well as wind speed and vertical wind shear on fatigue damage calculation for an academic pedestal and academic and non-optimized sail shape. The fatigue damage is calculated based on the wind gust process from Storhaug et al. (2022) and without inertia load effects included, which is much simplified. It may, however, serve as technical background for reducing the calculation efforts related to fatigue.

2. INPUT PARAMETERS

2.1 Vessel speed

The vessel speed for wave-induced loads is specified by IACS (IACS, 2022) to be 75% of the vessel design speed. Vessels that may have a significant benefit of WAPS are vessels with low speed such as blunt vessels like oil tankers, bulk carriers and ore carriers. Blunt vessels have typically a maximum service speed of 15 knots. The vessel forward speed is therefore assumed to be $15 \cdot 0.75 = 11.25$ knots, i.e. 5.79 m/s rounded up to 6 m/s.

2.2 Sail location, size and profile

Since blunt vessels are chosen it is assumed that the freeboard is 5 meters, and that the distance from deck to bottom of the sail is 5 m. The sail height is assumed to be 40 m, with equal chord length of 15 m over the height of the sail. These are approximative sizes that resemble realistic ones.

The sail profile from rigid sail suppliers should be optimized to produce maximum forward thrust at any given angle of attack. For simplicity, an available NACA profile with the associated drag and lift coefficients has been applied.

2.3 Distribution of heading angles

The heading distribution is selected to be evenly distributed with the same heading step in most cases, but this is not necessarily desirable for loading application: (i)1 heading, true beam wind: 90º (ii)2 headings, true beam wind and head wind: 0, 90º (iii)3 headings, head, beam, stern: 0, 90, 180º (iv)4 headings: 0, 90, 180, 270º (v)8 headings: 0, 45, 90, 135, 180, 225, 270, 315º (vi)16 headings: 22.5º step (vii)36 headings: 10º step (viii)72 headings: 5º step

2.4 Wind speed distribution

The wind speed is normally specified by the global wind speed probability but in this case it is specified by data provided by DNV. It is specified by 0.25 m/s resolution, see Fig.1, and it contains wind speed probabilities above 30 m/s although these probabilities are very small. The reference height is 10 m above the sea surface.

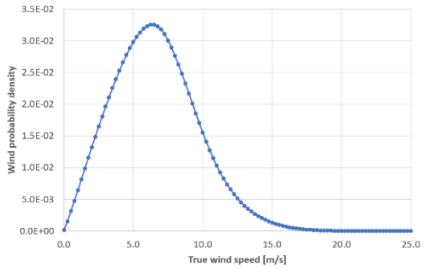


Figure 1. Wind speed prob. density function.

Different resolutions are applied for the wind speed probability distribution. The initial data is provided at bin midpoints so the intervals for the first bins for the six different resolutions becomes:

(i)0.25m/s (initial data) :0-0.125,0.125-0.375,…
(ii)0.5m/s: 0-0.25, 0.25-0.75, …
(iii)0.75m/s: 0-0.375, 0.375-1.125, …
(iv)1.0m/s: 0-0.5, 0.5-1.5, …
(v)1.25m/s: 0-0.625, 0.625-1.875, …
(vi)1.5m/s: 0-0.75, 0.75-2.25, …

2.5 Wind speed profile and vertical resolution

The wind speed profile represented by the power law from DNV (2021) with a base case value of $\alpha = 0.12$ for wind conditions above open sea with waves and at a reference height of H = 10 m above the sea surface.

The wind shear affects the vertical resolution of the sails. The sail is divided into strips in the vertical direction such as: (i)1.0 m: 40 strips with 1st mid interval at 10.5 m (ii)2.0 m: 20 strips with 1st mid interval at 11.0 m (iii)4.0 m: 10 strips with 1st mid interval at 12.0 m (iv)8.0 m: 5 strips with 1st mid interval at 14.0 m (vi)10.0 m: 4 strips with 1st mid interval at 15.0 m (vii)20.0 m: 2 strips with 1st mid interval at 20.0 m (viii)40.0 m: 1 strip with 1st mid interval at 30.0 m.

The area center represented by the last case may not be adequate, as the focus is on calculation of the overturning moment. This may be a better basis for comparison of such a simple formulation with more elaborate procedures.

The sensitivity of the computed results to the exponent α is also considered. Furthermore, this sensitivity is seen on the background of comparison with logarithmic velocity profiles, see e.g. Myrhaug (2024).

2.6 Gust factor

Romar's gust factor (Storhaug et al. 2022) has been used to define the load cycle appropriate for fatigue. This is based on the wind speed and the roll period. The roll period for inertia is taken at 15 seconds, which is regarded realistic. A larger and smaller roll period may have been chosen but the gust factor and the roll period are counter acting, so a larger roll period gives less fatigue cycles but a larger gust factor and vice versa, so this is not a critical assumption. The gust factor is independent of the vessel speed as it is related to the true wind speed.

2.7 Pedestal and stress concentration factor

For convenience an academic pedestal has been chosen. There is a slewing bearing up on the pedestal to make sure that the sail can rotate, and at this point the pedestal is circular. It is therefore assumed that the pedestal in way of the support point at the deck level is also circular and with an outer diameter of 1.0 m and with a thickness of 40 mm. It is further assumed that the pedestal continues below deck and that the foundation is premade, so that the pedestal above deck is welded from the outside with a single side butt weld with a stress concentration factor of 2.48 (DNV, 2021b). This is not a good factor, but the thickness of the pedestal is chosen to have a fatigue life which is around the target fatigue life of 25 years, regarded to be the acceptance criteria (DNV, 2023).

2.8 Hot spots and fatigue strength

The hot spots are distributed around the pedestal. For many codes dealing with pipes the number of hot spots may be 8, one at each 45-degree step. This is, however, not regarded as a good starting point in this case because of the resolution of the wind headings, the change of the apparent wind and the stall angle of the sail, so better resolution is needed. It is decided to use 72 points at 5-degree steps reflecting the finest resolution of the wind headings. This makes it possible not only to track the maximum fatigue damage of the pedestal, but also to see if the worst hot spot shifts to another location when the resolution changes.

The fatigue strength is given by the S-N curve FAT 90 D curve for hot spot stress range of welded details (DNV, 2021b). This is a two-slope S-N curve. The nominal stress at the pedestal is calculated from bending, and then the nominal stress is multiplied with the stress concentration factors of 2.48.

3. FATIGUE CALCULATIONS

The fatigue procedure is as follows: (1)Consider a true wind heading β and a true wind speed U at height 10 m (2)Consider a vertical height z (3)Calculate the true wind speed at height z (4)Calculate the gust factor at height z (5)Calculate the apparent wind angle at height z based on the true wind speed, the true wind angle and the vessel speed (the gust is disregarded here, so it is kind of an average apparent wind angle during the gust process) (6)Calculate the apparent wind speed plus gust based on the true wind speed plus gust factor, true wind angle and the vessel speed (7)Calculate the apparent wind speed minus gust based on the true wind speed minus gust factor, true wind angle and the vessel speed (8)Calculate the force on the sail strip from drag and lift (9)Calculate the thrust and side force component (10)Calculate the moment about the y-axis from thrust (11)Calculate the moment about the x-axis for side force (12)Repeat for all z to find the total moment about x and y (the apparent angle changes in vertical direction so the resultant component of drag and lift rotates upwards) (13)Calculate the stress range for all hot spots (14)Calculate the number of cycles dependent on the heading and wind speed probability (15)Calculate the partial fatigue damage for all hot spots (16)Repeat for all headings and all wind speeds and sum up.

This approach is based on considering each z, U and β cell and performing a summation, which is practical in numerical calculations. A more pragmatic approach may be required when applying

load cases in relation o a finite element model in order to limit the number of load cases. This provides a strong motivation to limit the number of headings and wind speed levels. The decomposition into x- and y-moments may, however, be more convenient for load applications, which in principle could be represented by unit load cases in the FE model. For each wind speed and heading, a bending moment around the x- and y- axis could then be provided.

Based on the original heading distribution, or original wind speed distribution it is possible to identify which headings or wind speeds that dominate the fatigue damage for the most important hot spot.

4. CONCLUSIONS

The convergence study suggests that 8 segments in the vertical direction is sufficient, but the calculated results are not very sensitive to this. Further the wind probability distribution should be based on a true wind speed step of 1.0 m/s or less, but the result is also not very sensitive to this because of the forward speed effect and nonlinear nature of the wind force. The number of headings is regarded to converge only at 36 headings, i.e. for each 10º. This is not convenient and does not fit well with the ship rules that apply 8 equivalent design waves. In that case there should be a penalty factor on the wind force of the order of 1.6, for the wind damage. This implies about a 15% increase of the stress range due to wind.

While the true wind probability distribution has the highest probability at about 7.0 m/s, the true wind speed that dominates the wind-induced fatigue damage is around 17 m/s due to vessel speed and wind force being nonlinear and as a function of apparent wind speed. For apparent wind, a velocity of 22.5 m/s dominates. This suggest that operational restrictions may significantly reduce the fatigue damage.

The most important hot spot is at 90 and -90º because of the side force, while the trust force and drag force with wind from the stern direction gives a symmetric damage at 0 and 180º, which is much lower. The side force is apparently important for fatigue of the pedestal. However, with only 8 headings there are four peaks, shifting the maximum away from 90º with the risk of identifying the wrong hot spots. The most contributing wind directions are from beam to head wind with 10º being dominant.

5. REFERENCES

DNV, 2021a, Environmental conditions and environmental loads, recommended practice, DNV-RP-C205, September 2019, amended September 2021.

DNV, 2021b, Fatigue assessment of ship structures, class guideline, DNV-CG-0129, edition October 2021.

DNV, 2023, Wind assisted propulsion systems, Standard, DNV-ST-0511, edition December 2023.

DNV, 2024. Wind assisted propulsion systems – WAPS, Rules for classification: DNV-RU-SHIP Pt.6 Ch.2 Sec.12, July 2024

DNV, 2025, Performance of wind assisted propulsion systems, recommended practice DNV-RP-0686, January 2025.

IACS, 2022, Standard wave data, IACS Rec. no. 34, rev. 2 December 2022 complete revision.

Myrhaug, D., 2024, Wind Speed Shear Exponent: Effects of Sea Surface Roughness in Terms of Spectral Bandwidth, JOMAE, Vol. 147/024501-1.

Storhaug, G., Borzacchiello, G.R. & Hoffmeister, H., 2022, Fatigue assessment of wind assisted propulsion systems, Int. conf. on offshore mech. and arctic eng., OMAE2022,OMAE2022-80511, V002T02A037; https://doi.org/10.1115/OMAE2022-80511.

Sensitivity of tower cranes to autorotation

Frank Kemper[1], Hao Lin[1], Johannes Duelli[2], Simon Kley[2]

[1]*Center for Wind and Earthquake Engineering, RWTH Aachen University, Germany,*
kemper@cwe.rwth-aachen.de
[2]*Liebherr-Werk Biberach GmbH, Germany*

SUMMARY:
This study investigates the sensitivity of tower cranes to autorotation in complex wind conditions. Through numerical modeling, this analysis introduces geometric parameters to characterize these disturbed wind patterns and predicts autorotation risk by balancing aerodynamic and structural factors. The aim is to generalize these findings, enabling predictions in complex flow environments without needing detailed transient analyses in all cases.

Keywords: autorotation, tower crane, wind field

1. INTRODUCTION

Tower cranes are set to be torque-free when strong winds are expected, using an electrical or mechanical switch on the slewing motor that leaves only frictional torques to dampen rotation. Beyond a certain wind speed, these torques become negligible, allowing the crane to align itself with the wind, minimizing lateral wind loads, enhancing stability, and reducing structural risk. Opposing wind forces on the jib and counter-jib aid in balancing the crane's alignment; however, disturbances from nearby structures can disrupt this alignment, complicating wind load dynamics on the crane. In disturbed wind conditions, cranes may experience autorotation instability (continuous rotation caused by imbalanced wind forces) leading to increased wear and safety risks. Predicting autorotation risk requires modeling wind moments with factors like inertia and friction. Our analysis introduces geometric parameters that characterize disturbed wind patterns, improving autorotation predictions in complex flow environments.

While the phenomenon of autorotation is well-known in principle (see e.g. Voisin et al., 2004), our analysis focused on the impact of various local flow fields and their associated risks of inducing autorotation. To better summarize these findings, we introduced a set of relevant geometrical parameters that characterize the local flow's vector field. These parameters help to quantify aspects of the disturbed wind patterns, such as directional gradients and velocity variations, and allow us to correlate them with the likelihood of autorotation occurring. By systematically analyzing the relationship between these geometric characteristics and the crane's response, we can more accurately predict the conditions under which autorotation becomes a significant risk, offering a deeper understanding of the phenomenon in complex flow environments.

2. CRANE DYNAMICS

Autorotation of eccentric rotor structures result from a asymmetrical in-plane flow field, leading to a predominant orientation of the induced external wind moment. The general behavior can be described by a differential equation of motion for a 1 DOF rotor:

$$\Theta_{\text{Crane}} \cdot \ddot{\psi}(t) - \mathrm{M}_{\text{Friction}}\left(\dot{\psi}(t)\right) = \mathrm{M}_{\text{Wind}}\left(\psi(t)\right) \tag{1}$$

where Θ_{Crane} is the mass moment of inertia of the rotational crane system. $\mathrm{M}_{\text{Friction}}$ is a function of the rotational velocity and represents the system dependent rotational friction, including static and sliding components. M_{Wind} is the angular position dependent function of the wind force moment, considering the relative wind force distribution and the individual angles of attack over the jib and counter-jib length. The wind force moment is significantly influenced by the local flow field, which is described by a matrix of speed-up factors $\beta(x,y)$ in the crane swept area (see section 3).

As the wind and friction moment are functions of motion, Eq. (1) represents a non-linear second-order differential equation. Therefore, we employ a full transient scheme for the numerical analysis of the crane's dynamic behavior. The method offers a comprehensive and accurate prediction of autorotation risk by continuously updating the crane's position, rotational velocity, and acceleration.

Friction in crane bearings increases the onset wind velocity for autorotation, while inertia reduces it by resisting rotational movement. The balance between these forces determines the autorotation threshold. Neglecting friction is conservative, but neglecting inertia is not. The inertia has an influence on the duration of the onset of autorotation, but not on the final rotational speed. Another aspect for a precise prediction of the crane behavior and the onset velocity is the initial position of the crane jib in the wind field.

3. FLOW FIELD CHARACTERISTICS

In realistic, complex flow situations, the local flow field within the crane-swept area is highly dependent on the wind direction and can vary significantly from a uniform or homogeneous flow. Wind flow around buildings or other obstacles leads to disturbances, creating areas of acceleration, deceleration, and flow separation. These disturbances introduce localized variations in both wind speed and direction, resulting in a non-uniform flow pattern.

Assuming simplified flow fields aligned with the undisturbed flow direction u_∞ and neglecting the superposition with the rotational velocity of the jib (relative velocity), the wind moment for each angular position ψ within A_{cs} is determined by integration of the crane axis $\widetilde{x}$ and results to:

$$M_{\text{Wind}}(\psi) = -\frac{\rho}{2} \cdot u_\infty^2 \cdot \int_{-l_{\text{cjib}}}^{l_{\text{jib}}} \widetilde{x} \cdot c_{\text{f}}A(\widetilde{x}) \cdot sin(\psi) \cdot \left\{\beta\left[x(\widetilde{x}), y(\widetilde{x})\right]\right\}^2 \, d\widetilde{x} \tag{2}$$

We introduce the following simplifications and normalizations: $c_{\text{f}}A(\widetilde{x})$ is constant over both the jib and the cjib. Their ratio is $\varepsilon = (c_{\text{f}}A)_{\text{cjib}}/(c_{\text{f}}A)_{\text{jib}}$. The length ratio of jib and cjib is $\lambda = l_{\text{cjib}}/l_{\text{jib}}$. An aerodynamically unstable situation arises when the disturbance of the wind field results in uniformly directed wind moments. The main parameters influencing this balance are the crane lengths l_{jib} and l_{cjib}, the relative wind forces over the crane axis $c_f A(\widetilde{x})$, and the shielding factors

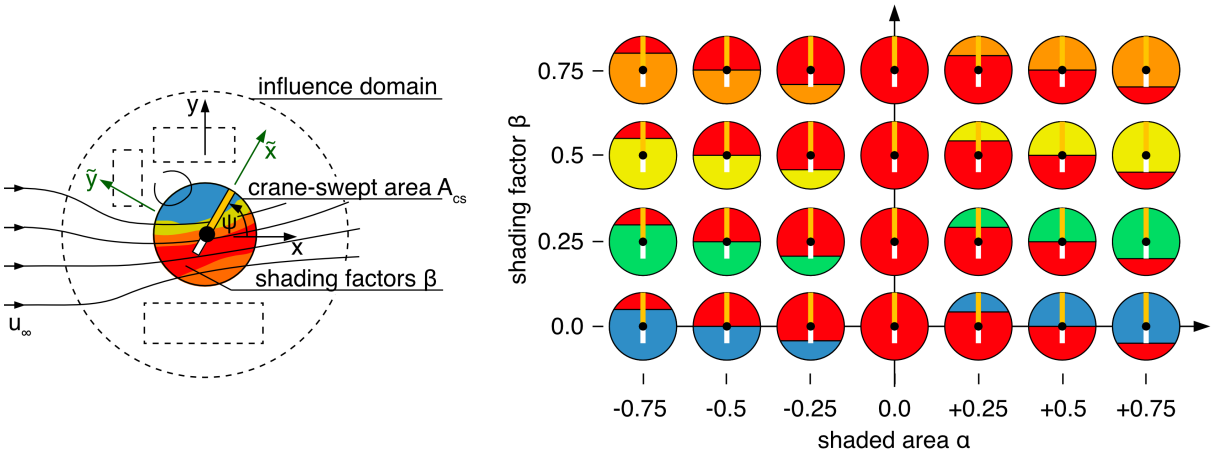


Figure 1. Left: Plan view of a tower crane in a built environment, showing the flow field and key definitions. Right: Abstract flow field with shaded areas, where geometric factor α represents the shaded area, and shading factor $\beta \leq 1$ (color-coded) indicates reduced flow velocity. Red denotes unshaded areas with inlet velocity ($\beta = 1$).

.

$\beta\,[x(\tilde{x}), y(\tilde{x})]$ within the crane's swept area. For a shaded area of $\alpha = -0.5$ (see Figure 1) with arbitrary shading factor β for the shaded area, the wind moments M_{Wind} for both perpendicular orientations $\psi = \pm 90°$ derive to:

$$M_{\mathrm{Wind}}(+90) = \frac{\rho}{2} \cdot u_{\infty}^2 \cdot \frac{1}{2} \cdot l_{jib}^2 \cdot (\lambda^2 \varepsilon \cdot \beta^2 - 1)\ ;\ M_{\mathrm{Wind}}(-90) = \frac{\rho}{2} \cdot u_{\infty}^2 \cdot \frac{1}{2} \cdot l_{jib}^2 \cdot (\beta^2 - \lambda^2 \varepsilon) \tag{3}$$

As for $\alpha = -0.5$, autorotation is only possible for negative wind moments, as the undisturbed flow is in the upper sector of the crane system for this case (see Figure 2, left). The wind moment contribution of both, jib and cjib are negative for this case:

$$\beta^2 < \min\left(\frac{1}{\lambda^2 \varepsilon}, \lambda^2 \varepsilon\right) \tag{4}$$

A stability factor κ can be introduced, which allows a better understanding of the crane stability dependent on the influencing parameters. To avoid singularities, it is formulated case sensitive:

$$\kappa = \frac{M_{\mathrm{Wind}}(-90°)}{M_{\mathrm{Wind}}(+90)} = \frac{\beta^2 - \lambda^2 \varepsilon}{\lambda^2 \varepsilon \beta^2 - 1} \text{ for } \lambda^2 \varepsilon < 1\ ;\ \kappa = \frac{M_{\mathrm{Wind}}(+90°)}{M_{\mathrm{Wind}}(-90)} = \frac{\lambda^2 \varepsilon \beta^2 - 1}{\beta^2 - \lambda^2 \varepsilon} \text{ for } \lambda^2 \varepsilon \geq 1 \tag{5}$$

A value of $\kappa > 0$ (indicating a unique direction of rotation) shows a situation which is considered as "aerodynamically unstable". Figure 2 shows the solution of Eq. (5) for $\varepsilon = 2$ and $\lambda = 0.5$, as a function of the shading factor β. The aerodynamic flow field introduces unidirectional moments for $\beta < 0.7$, which form a significant precondition for autorotation. However, this simplification according to Eq. (5) describes only the aerodynamic aspects of instability, and only for simplified wind fields. It does not account for the influences of mass inertia and friction, which can be either beneficial or detrimental. Furthermore, predicting the onset wind velocity is not possible without considering these influencing factors.

Figure 3 (left) shows the results for the onset wind velocity for autorotation obtained by the detailed transient approach, see Eq. (1) for the same parameters $\varepsilon = 2$, $\lambda = 0.5$, and for the variety of

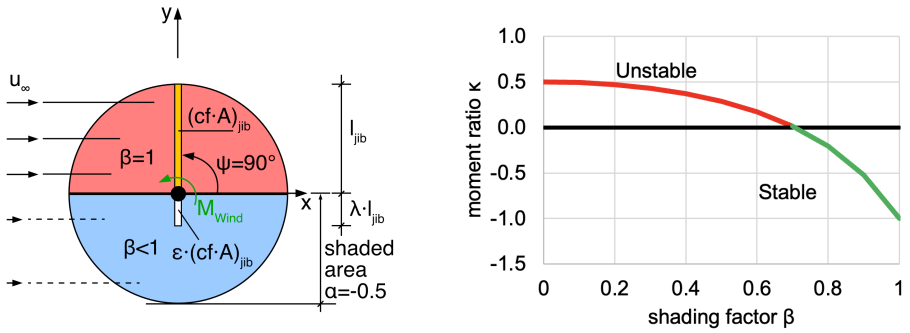


Figure 2. Left: Normalization of aerodynamic and geometrical properties for a crane in a simplified wind field with $\alpha = -0.5$, Right: Result of Eq. 4 for different β-values for a normalized situation with $\varepsilon = 2$ and $\lambda = 0.5$

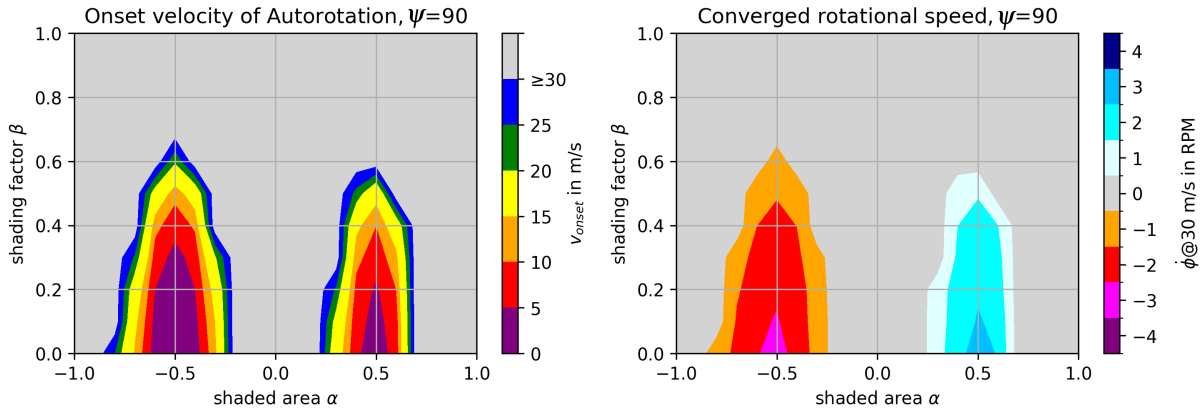


Figure 3. Left: Onset wind velocities for a crane $\varepsilon = 2$ and $\lambda = 0.5$ based on transient approach
Right: Corresponding rotational velocities for at a wind speed of $u_\infty < 30$ m/s.

α and β parameters as shown in Figure 1 (right). For a shaded area $\alpha = -0.5$, we found an aerodynamic instability ($u_\infty < 30$ m/s) for $\beta \leq 0.65$. Figure 3 (right) shows the corresponding rotational velocities for an assumed wind speed of $u_\infty = 30$ m/s.

4. CONCLUSIONS

Our analysis reveals that the stability of tower cranes in strong and disturbed wind conditions relies heavily on the balance of aerodynamic and geometric factors. By introducing normalized parameters, we provide a framework for predicting autorotation risks, especially in complex environments. The aim is to develop a further generalization for complex flow fields that renders a detailed transient analysis unnecessary in certain cases.

REFERENCES

Voisin, D., Grillaud, G., Solliec, C., Beley-Sayettat, A., Berlaud, J.-L., and Miton, A., 2004. Wind tunnel test method to study out-of-service tower crane behaviour in storm winds. Journal of Wind Engineering and Industrial Aerodynamics 92. A selection of papers derived from those presented at the 11th International Conference on Wind Engineering, 687–697.

Aerodynamic loads on groups of offshore wind turbine towers during the pre-assembly phase on port quaysides

Claudio Mannini[1], Tommaso Massai[1], Niccolò Barni[1], Alessandro Giusti[2]

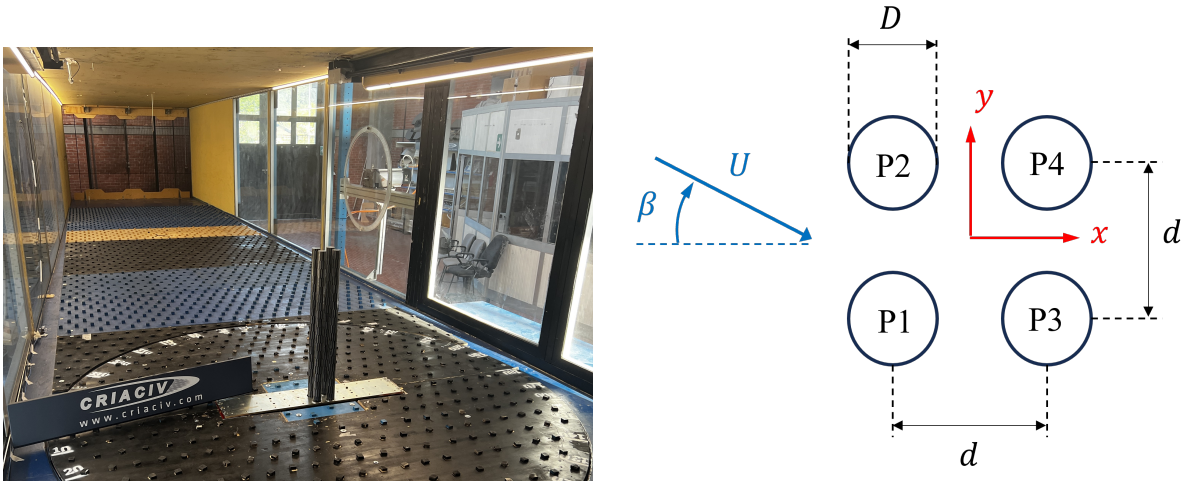
[1]*CRIACIV/University of Florence, Florence, Italy, claudio.mannini@unifi.it*
tommaso.massai@unifi.it, niccolo.barni@unifi.it
[2]*Siemens Gamesa Renewable Energy A/S, Brande, Denmark,*
alessandro.giusti@siemensgamesa.com

SUMMARY:
Offshore wind turbine towers, without rotor-nacelle assembly, are usually erected at the harbor quaysides with different possible layouts and at small center-to-center distance. Then, the towers are loaded out onto special vessels, which complete the installation of the wind turbines in the final offshore position. The activities at the harbor quayside usually last 6 to 12 months. The accurate knowledge of the dynamic wind loads in the different group configurations is essential for a safe and economic design of the substructures. In this work, the results of a wide campaign of wind tunnel tests on towers with a height greater than 125 m are discussed. Force and pressure measurements are carried out, focusing on the loads both at the base of each tower in a group and on the overall group for every possible wind direction. The possibility of narrow-band excitation phenomena is also carefully inspected, especially for the back towers in a group. The common pack of 2×2 towers is taken into account as a paradigmatic case study for this engineering problem.

Keywords: Wind-turbine tower groups, high Reynolds number, wind loads

1. INTRODUCTION

The installation of an offshore wind turbine is typically carried out by special vessels equipped with legs (for the jack-up) and a massive crane able to lift more than 1000 t. The components (blades, nacelles, tower sections) are prepared for loading onto the vessel at the harbor quayside where the so-called pre-assembly activities take place. The aim is to shorten as much as possible marine operations, which are typically one of the current main cost drivers. Towers without rotor-nacelle assembly are therefore erected at the quayside on dedicated freestanding (gravity based) foundations, and then transported vertically on the vessel. This pre-assembly phase usually lasts between 6 and 12 months. Towers on the quayside foundations are typically arranged in groups, with a square mesh (groups of $2 \times n$ towers, with $n = 2, \ldots, 6$), at small center-to-center distance to ease crane operations. Such a peculiar system with towers taller than 100 m placed at close distance has recently been the subject of some research works (Lupi et al., 2024; Mannini et al., 2023), and it is further developed in this work by addressing a study of the aerodynamic coefficients with a different ratio of the center-to-center distance to the diameter with focus on a group of 2×2 towers (named G4), and providing some insights on the interferences between neighboring 2×2 groups. The latter turns out to be useful when more than one group is placed at the harbor quayside. Indeed, the number of groups and the number of towers within the group, i.e., the harbor layout, is



(a) (b)

Figure 1. View of a four-towers group (G4) model in the wind tunnel (a); schematic of tower arrangement (b).

usually project specific and depends, among others, on the crane capabilities, number of vessels, and number of jack-up positions at the harbor.

2. WIND TUNNEL STUDY

The large variety of possible tower group configurations during the pre-assembly phase makes wind tunnel tests necessary. The last-generation towers considered in the current study have a height H above 125 m and a variable diameter, increasing from the bottom to the top of tower. However, finite-length cylinders with an equivalent constant diameter D are mostly studied for the sake of generality (Mannini et al., 2023). The ratio of center-to-center distance between the towers to tower equivalent diameter is $d/D = 1.84$. The tests are performed at a geometric scale 1:210.

The experimental campaign is carried out in the CRIACIV[1] boundary layer wind tunnel (Fig. 1(a)). The turbulent wind profile provided by Eurocode 1 (EN 1991-1-4, 2010) for terrain category I is assumed as a target. Models of the towers are constructed in carbon-fibre (Fig. 1(a)). Moreover, a model made of stainless steel and aluminum is also produced and equipped with 190 pressure taps distributed over eight rings. Either the measuring model or a steel circular plate supporting the entire group of towers is connected to a strain-gauge high-frequency force balance placed below the wind tunnel floor.

The very high target Reynolds number ($\mathrm{Re} \sim 2 \cdot 10^7$) represents a serious challenge in wind tunnel tests. An original discontinuous and staggered surface roughness solution is employed to trigger the transcritical Reynolds number regime, as explained in detail in Mannini et al. (2023). A further study on this issue is reported in Mannini et al. (2025).

[1] Inter-University Research Centre on Building Aerodynamics and Wind Engineering

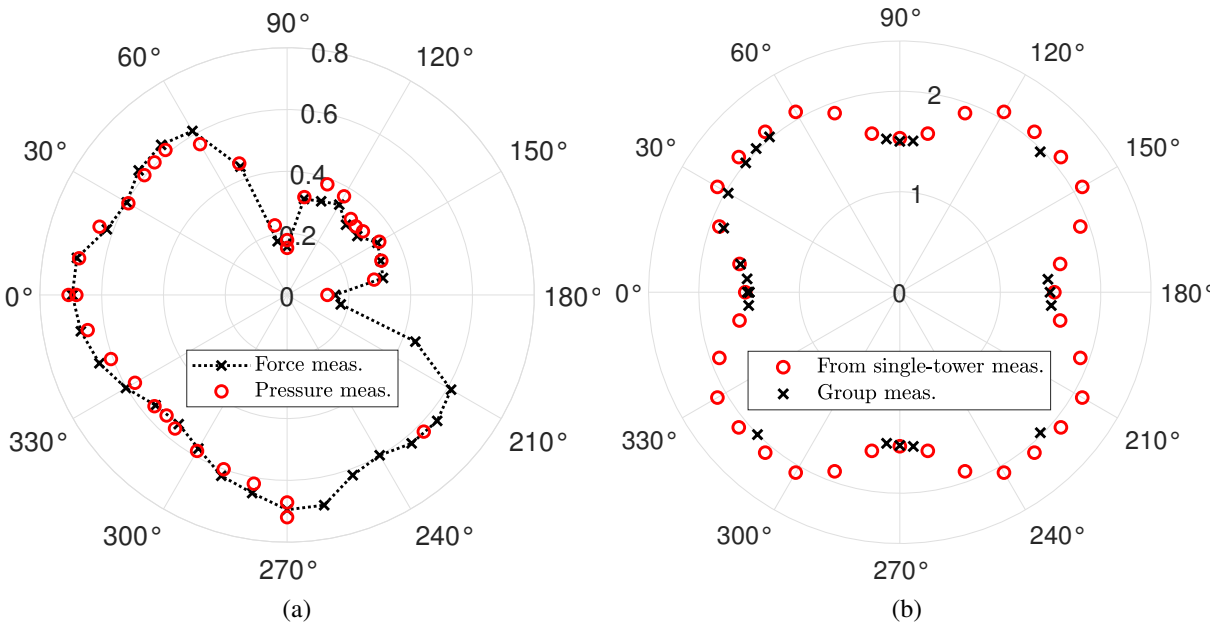


Figure 2. Mean resultant of bending moment coefficient at the base of tower G4-P1 (a) and of the whole group (b).

3. RESULTS

Based on what explained in Section 1, the resultant shear force and, even more, the bending moment at the base of both each tower within the group and the group as a whole are of great engineering interest. Examples of measured wind loads (mean moment coefficients normalized with the mean velocity pressure at the height of the tower top times $0.5HD^2$) are shown in Fig. 2. The measurements for the single tower in the group for different wind directions (Fig. 2(a)) highlight an increase in the maximum mean moment coefficient (for $\beta = 0°$ and 270°) of about 13% compared to the isolated tower. Moreover, one can notice the good agreement between the results of force measurements and the integration of pressures. Fig. 2(b) reports the mean resultant moment coefficient for the overall group of towers. The experimental data are compared with the estimates based on single-tower measurements. Given the relatively low level of fluctuation in the quasi-steady wind forces, the agreement between the two sets of data is excellent. In contrast, the same procedure cannot be followed for the peak loads, since the composition of single-tower measurement results cannot properly account for the partial correlation of the wind action on different towers in the group. Therefore, direct force measurements are very important.

Given the relatively low natural frequency of the system tower + high-frequency force balance (about 37.5 Hz for the single-tower measurement set-up), pressure measurements at a sampling rate of 650 Hz are essential to highlight possible narrow-band wake excitation phenomena, such as vortex shedding and wake impingement from upstream towers. The lateral force spectra reported in the left frame of Fig. 3 show that tower G4-P1 (Fig. 1(b)) does not exhibit any narrow-band excitation for a wind direction $\beta = 0°$. In contrast, the level of narrow-band excitation is similar to the case of the isolated tower when tower P1 is in the wake of tower P2 ($\beta = 90°$) or tower P3 ($\beta = 180°$). Nevertheless, the highest spectral peaks can be observed for wind directions in the range $110° \lesssim \beta \lesssim 160°$, where the narrow-band spectral peak is significantly more pronounced

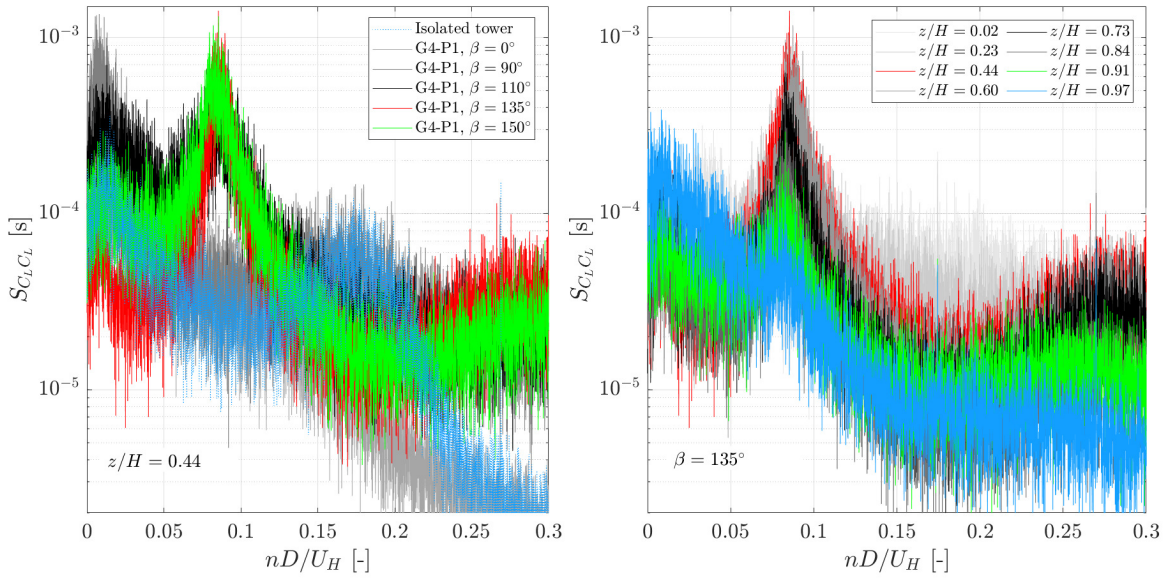


Figure 3. Power spectral density of the lateral force coefficient C_L at various heights along the tower obtained from pressure integration (tower G4-P1, see Fig. 1(b)). The blue dotted line on the left is associated with the isolated tower and is reported as a reference. n denotes the frequency in Hz, while nD/U_H is a nondimensional frequency.

than for the isolated tower. Additionally, one can notice that, while for $\beta = 90°$ or 270° the nondimensional excitation frequency is around 0.15, just slightly lower than for the isolated tower, for $110° \lesssim \beta \lesssim 160°$ the dominant nondimensional frequency drops below 0.1. Finally, the right frame of Fig. 3 shows that, for an angle in that range (e.g., $\beta = 135°$), the narrow-band excitation is present at any height except close to the bottom and close to the tip of the tower.

4. CONCLUSION

This study shows the complexity of aerodynamic loads acting on offshore wind turbine towers during the pre-assembly phase on the quaysides of harbors. We also stress the importance of advanced wind tunnel tests, providing mean and fluctuating loads, and warning about possible narrow-band dynamic excitation phenomena, for achieving not only a safe but also an economic design of the expensive tower substructures.

REFERENCES

EN 1991-1-4, 2010. *Eurocode 1 - Actions on structures - Part 1-4: General actions - Wind actions*.

Lupi, F., Seidel, M., Höffer, R., Hölscher, N., and Niemann, H.-J., 2024. Mitigation of interference-induced vibrations for towers in group arrangements. Proceedings of the XVII Conference of the Italian Association for Wind Engineering (IN VENTO 2022), Milan, Italy, 4-7 September, 2022. Springer, 102–113.

Mannini, C., Massai, T., and Barni, N., 2025. A refined surface roughness method to simulate the transcritical flow regime past a circular cylinder. Proceedings of the 9th European and African Conference on Wind Engineering (EACWE 2025), Trodheim, Norway, 16-19 June 2025. (submitted).

Mannini, C., Massai, T., Giachetti, A., and Giusti, A., 2023. Aerodynamic loads on groups of offshore wind turbine towers stored on quaysides during the pre-assembly phase. Journal of Wind Engineering and Industrial Aerodynamics 242, 105569.

Assessing seismically damaged buildings in wind environments: a comprehensive framework

Aniket Panchal [1], Anastasia Athanasiou [2]

[1]*PhD Candidate, Indian Institute of Technology Gandhinagar,India, panchal_aniket@iitgn.ac.in*
[2]*Ass.Professor, Bauhaus University Weimar, Germany, anastasia.athanasiou@uni-weimar.de*

SUMMARY
The persistent focus of modern building codes on the single-hazard, inadequately addresses the complexities of real-world situations where multiple hazards often occur. This work proposes a comprehensive performance-based framework for the assessment of the overall damage in buildings sited in combined earthquake and wind environments. The framework comprises independent hazard analyses, predictions of the dynamic wind and earthquake responses at distinct damage states, but also sequential wind simulations on buildings affected by the design-level earthquake. Focus is given in the realistic representation of dynamic lateral loading, accurate modelling of the 3D lateral force resistance system, deterministic evaluation and statistical assessment of the multi-hazard response under single- and multi-hazard scenarios. The methodology is demonstrated on a code-complaint, 25-story reinforced concrete hospital, sited in a high seismic and high wind zone of the Indian subcontinent. A 3D, nonlinear model of the structural system is used for seismic simulations at the design level. Dynamic wind simulations of the intact and seismically damaged buildings are performed at the occupant comfort, operational, and continuous occupancy performance levels. Results show the detrimental effect of wind on the overall performance of the damaged building, and highlight the knowledge gap in current multi-hazard research and practice.

Keywords: Multi-hazard assessment, wind hazard, seismic hazard

1. INTRODUCTION

The average annual economic losses due to seismic hazards is estimated to be millions of dollars (Silva et al., 2023). Experience from recent earthquakes indicates that seismically damaged buildings face extended periods of downtime, which can exacerbate their vulnerability to future hazards. Major international design codes are single hazard-oriented, overlooking the impact of multiple hazard events on structural integrity and performance. Roy et al. (2021) investigated the effect of wind and strong motion excitation on tall buildings, isolated at their base, and showed how the single hazard approach underestimates damage. Athanasiou et al. (2023) studied the effect of wind hazards on intact and earthquake-damaged steel buildings. Their findings confirmed that subsequent wind hazards can affect severely structures already compromised by rare earthquakes. Song et al. (2023) found that ductility demands on seismically damaged tall buildings may increase by three to four times, if such buildings are subjected to thunderstorm downbursts prior to their retrofitting. Research on multi-hazard effects on structures is limited but underscores a critical gap in existing design codes, which often fail to account for multi-hazard scenarios.

In this light, the present study proposes a performance-based framework for the comprehensive assessment of buildings in seismic and wind environments. Focus is given to the realistic

representation of the dynamic nature of the hazards, and possible occurrence of wind events within the downtime period of seismically affected buildings. The method is demonstrated through the quantification of the multi-hazard performance of a 25-story reinforced concrete (RC) building, sited in a high seismic and high wind zone of the Indian subcontinent.

2. METHODOLOGY

Figure 1 briefly illustrates our new performance-based framework for the assessment of code-complaint buildings, sited in multi-hazard environments. Once the initial section design is completed, the seismic and wind performance assessments for the intact building are performed independently (Case I). Each assessment includes hazard characterization, selection/generation of strong motion/wind data, and nonlinear response simulations at distinct limit states. In Case II, the wind assessment is performed on the seismically damaged building, post-earthquake (DBE). Case II scenario is crucial for understanding how residual seismic damage can influence the building's response to subsequent wind loads.

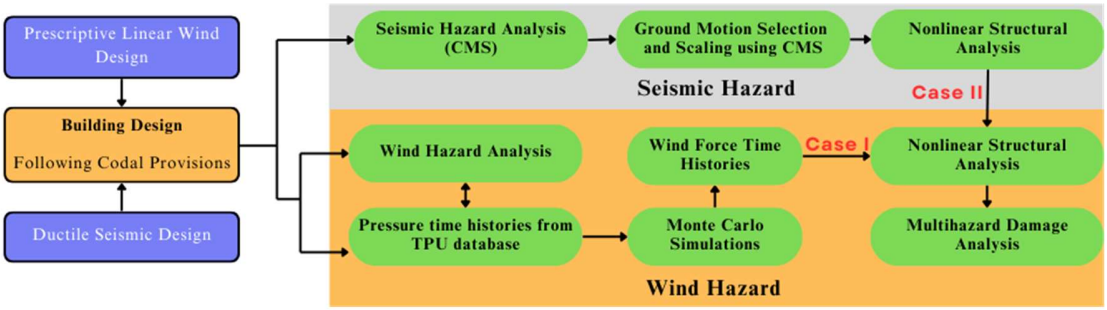


Figure 1 Multi-hazard Performance-Based Assessment Framework

3. NUMERICAL APPLICATION

3.1. Case study

The case study is a 25-story RC hospital, sited on medium soil and urban environment, in Guwahati, India. This is a high seismicity site (peak ground acceleration of 0.36g), exposed to strong winds (basic wind speed at 10m of 50m/s). The building is regular in plan and height, and has a *Height-Breadth-Depth* ratio *H-B-D* = 8.25-2-2. The lateral force resisting system (LFRS) comprises 4 shear walls, working together with 4 moment-resisting frames, in the N-S and E-W directions. The building is designed for seismic (IS: 1893 (Part 1), 2016) and wind hazards (IS: 875 (Part 3), 2015) using the Indian RC design code (IS: 456, 2000) and the Indian mandate for ductile seismic detailing (IS: 13920, 2016). As per all major building codes, seismic design benefits from the capacity and ductility concepts, whereas wind design is linear prescriptive. Earthquake loads dominate the design, since the inelastic seismic base shear is much higher than the linear wind base shear: $V_{in,E}$ = 8252kN > $V_{el,W(N\text{-}S)}$ = 5728kN, and $V_{in,E}$ =8252kN> $V_{el,W(E\text{-}W)}$ =4793kN in the N-S (along-wind) and E-W (across-wind) directions respectively. The building plan and LFRS sections are shown in Figure 2. The first two modes of the building are purely translational, i.e., occur along the N-S and E-W directions, and have a period of 2.5sec. The third mode is torsional and has a period of 2.0sec.

The seismic hazard analysis at DBE (MRI=475 years) provides us with a Conditional Mean Spectrum (CMS) at T_1=2.5sec (Gurjar and Basu 2022a, 2022b). The CMS, shown in Figure 3a, is then used to select and scale 11 sets of CMS-compatible ground motions from the PEER ground motion database. Figure 3b shows the normalized gust spectra for a typical realization of along-, across- and torsional-wind loads, lumped at the 20th story of the hospital. The across- and torsional-

wind gust spectra have significant energy content quite far from the fundamental frequency. In total, 11 wind sets are generated through Monte Carlo simulations (Shinozuka, 1971), and scaled at the Occupant Comfort (OC), Operational (OP) and Continuous Occupancy (CO) limit states (ASCE, 2023). The OC, OP and CO limit states refer to events with MRI=10, 50, and 3000 (post-disaster buildings) years, and mean wind speed at the roof U_H = 38, 43 and 57m/s.

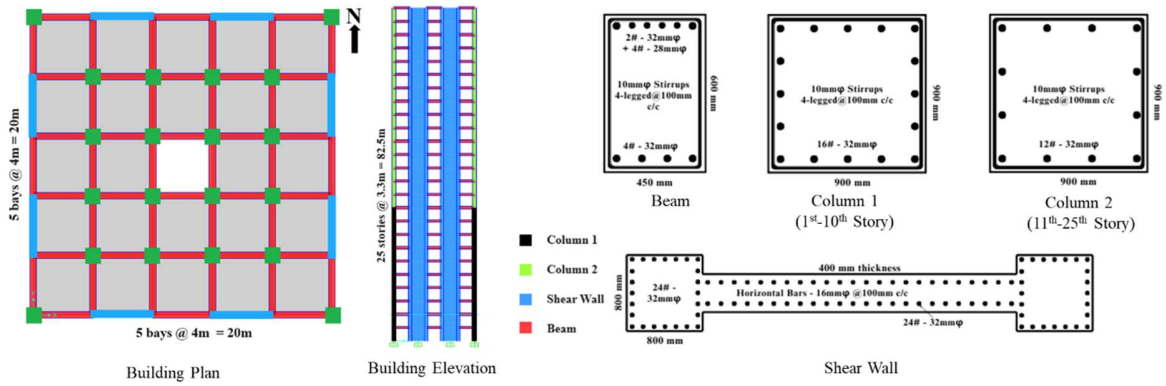
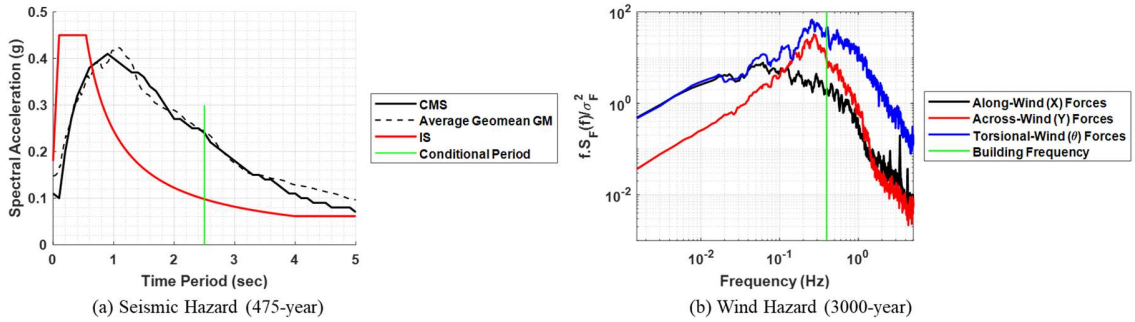


Figure 2 Building plan, elevation and section dimensions



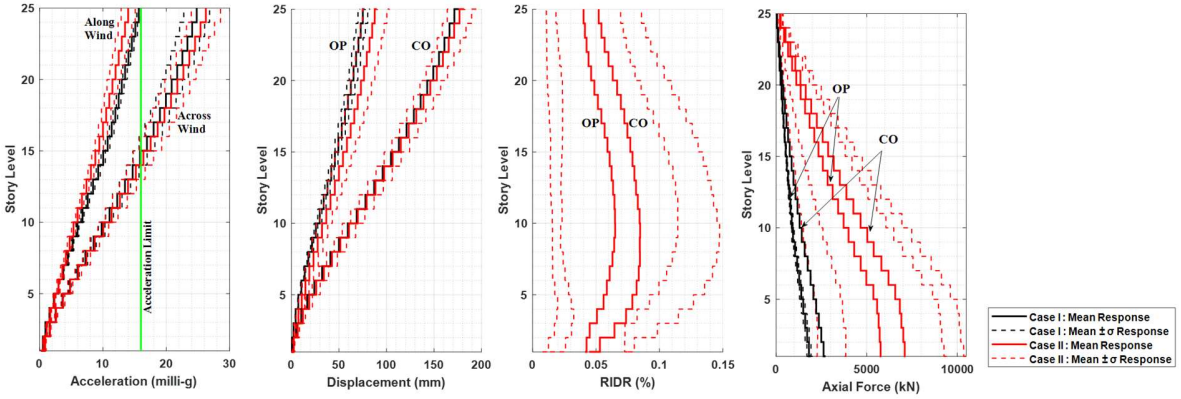
(a) Seismic Hazard (475-year) (b) Wind Hazard (3000-year)

Figure 3 Seismic design and wind pressure gust spectra

3.2. Multi-hazard response of intact and seismically-damaged building

A 3D finite element model of the LFRS is constructed in CSI SAP2000. Such model accounts for material and geometrical nonlinearities. The model of the intact building is subjected to the 11 strong motions scaled at DBE, and the 11 wind sets scaled at OC, OP and CO (Case I). Then the wind analyses are repeated on the seismically-damaged building (Case II). The typical response in the critical across-wind direction is summarised in Figure 4. Due to the building's regularity, the N-S and E-W seismic responses are similar. The findings confirm the initial hypothesis that the effect of wind on seismically-damaged building is always detrimental. Moreover:

i. the wind record-to-record variability is more pronounced in Case II;
ii. the across-wind accelerations at the upper building half, fail to meet the ASCE OC criteria (16 milli-g), suggesting that the floors of the damaged and undamaged hospital are uninhabitable;
iii. the OP and CO peak roof drifts are well within the ASCE acceptance criteria (H/500=165mm and H/300=275mm) for both Case I and II;
iv. mean residual inter-story drifts (RIDR) at OP and CO, occur only in Case II and are less than the ASCE 0.1% threshold for undamaged buildings, and the empirical demolition 0.5% limit;
v. uniform distribution of IDR and RIDR along the building height points to uniform ductility demands among the superstructure floors, and essentially validates the initial design;
vi. residual stresses increase significantly axial demands on the column.



(a) Peak Acceleration (OC) (b) Peak Displacement (OP and CO) (c) Residual IDR (OP and CO) (d) Peak Column Axial Force (OP and CO)

Figure 4 Undamaged and damaged building response under OC, OP, and CO winds

5. CONCLUSIONS

This study advocates for the establishment of a comprehensive, multi-hazard performance assessment framework. The framework is implemented for the damage quantification of an Indian code-complaint, tall RC building, subjected to single and sequential earthquakes and winds. Realistic representation of dynamic strong motion and wind excitation, sophisticated modelling of the LFRS, and nonlinear simulations of the system response at distinct limit states demonstrate that the current, single-hazard code concept underestimates losses due to multiple hazards. The study highlights a significant gap in current research and practice regarding the assessment of multi-hazard performance. The persistent focus on single-hazard assessments inadequately addresses the complexities of real-world situations where multiple hazards occur.

ACKNOWLEDGEMENTS

We would like to thank Dr. Basu from IIT Gandhinagar for his invaluable contributions to the seismic assessment of our case study. Moreover, we are indebted to the Carl-Zeiss-Stiftung foundation for its generous financial support.

REFERENCES

ASCE, 2019. Prestandard for Performance-Based Wind Design. American Society of Civil Engineers, Reston, VA.

Athanasiou, A., Dakour, M., Tirca, L., Stathopoulos, T., 2023. Wind hazard on earthquake damaged buildings. ce papers 6, 2394–2399.

Gurjar, N., Basu, D., 2022a. Epistemic Uncertainty in PSHA and Seismic Hazard Characterization Using the Logic Tree Approach: Part II, Implementation over North-East India. Pure and Applied Geophysics 179,4341–4370

Gurjar, N., Basu, D., 2022b. Epistemic Uncertainty in PSHA and Seismic Hazard Characterization Using the Logic Tree Approach: Part I, Developing the Framework. Pure and Applied Geophysics 179, 3647–3676.

IS: 456, 2000. Plain and Reinforced Concrete - Code of Practice.

IS: 875, 2015. Code of practice for design loads (Other than Earthquake) for Buildings and Structures–Part 3: Wind.

IS: 1893, 2016. Criteria for Earthquake Resistant Design of Structures Part 1: General Provisions and Building.

IS: 13920, 2016. Ductile Design and Detailing of Reinforced Concrete Structures Subjected to Seismic Forces - Code of Practice.

Roy, T., Saito, T., Matsagar, V., 2021. Multihazard framework for investigating high-rise base-isolated buildings under earthquakes and long-duration winds. Earthq Engng Struct Dyn 50, 1334–1357.

Shinozuka, M., 1971. Simulation of Multivariate and Multidimensional Random Processes. The Journal of the Acoustical Society of America 49, 357–368.

Silva, V., Calderon, A., Caruso, M., Costa, C., Dabbeek, J., Hoyos, M.C., Karimzadeh, Z., Martins, L., Paul, N., Rao, A., Simionato, M., Yepes-Estrada, C., Crowley, H., Jaiswal, K., 2023. Global Seismic Risk Map.

Song, J., Skalomenos, K., Martinez-Vazquez, P., 2023. A multi-hazard analysis framework for earthquake-damaged tall buildings subject to thunderstorm downbursts. Earthq Engng Struct Dyn 52, 1463–1485.

Risk-targeted design wind speeds for performance-based design of long-span bridges

Zihang Liu [1], Genshen Fang [2], Yaojun Ge [3]

[1]*Tongji University, Shanghai, China, liuzihang@tongji.edu.cn*
[2] *Tongji University, Shanghai, China, 2222tjfgs@tongji.edu.cn*
[3] *Tongji University, Shanghai, China, yaojunge@tongji.edu.cn*

SUMMARY:
To achieve the controllability and consistency in failure levels of long-span bridges under wind load, this study introduces the "uniform risk" analysis method into the bridge wind engineering to determine the performance-based and risk-targeted design wind speeds. Four performance objectives (occupant comfort, operational, continuous occupancy and instability), associated with the annual failure probability, are summarized. To implement this method, fragility curves for the Xihoumen Bridge are analyzed, and the failure risks with respect to four performance objectives are estimated. Subsequently, the risk-targeted multi-level performance design wind speeds are calculated through the risk integral method.

Keywords: Uniform-risk, Performance-based design, Structural reliability

1. INTRODUCTION

Currently, most wind-resistant design standards adopt the notion of "uniform hazard", defining design wind speeds based on the annual extreme mean or gust wind speed at a reference height corresponding to a 100-year (or 50-year) return period. This can lead to varying risk levels among structures, influenced by uncertainties in materials and construction. The Federal Emergency Management Agency (FEMA) aimed to achieve a total failure probability of 2% over 50 years, considering all potential levels of earthquake. This concept was termed "uniform risk", which means that within the specified structural service life, the failure probability of structures built in regions with different hazard intensities should be equivalent and lower than a socially and economically acceptable level. While risk-targeted seismic maps have developed in various regions (Luco et al.2007), research on risk-targeted wind loads, particularly for bridges, is scarce. This study seeks to incorporate the "uniform risk" concept into long-span bridge wind design, serving the uptake of performance-based wind engineering design from the community.

2. PERFORMANCE-BASED AND RISK-TARGETED DESIGN IN BRIDGE WIND ENGINEERING

The fundamental aspect of performance-based and risk-targeted design involves determining the performance objectives and acceptable failure probabilities, followed by deriving the risk-targeted design wind speeds according to these multi-level performances.

2.1. Performance objectives and acceptable probabilities of failure

With reference to what is commonly accepted for the performance-based wind design of buildings and the performance-based seismic design of long-span bridges, a long-span bridge's performance objectives for wind design can be categorized into four levels, namely, *occupant comfort*, *operational*, *continuous occupancy* and *instability*. The first three objectives primarily focus on the service performances of the bridge, whereas the last one aligns with the ultimate limit state (ULS) of the bridge. A comprehensive description of the performance objectives, coupled with their associated acceptable probabilities and recurrence periods, is provided in Table 1.

Table 1. The description of the performance objectives, acceptable probability and recurrence period.

Performance objectives	Description	Acceptable annual probabilities	Recurrence periods
Occupant comport	Interruption to service not expected; a few people may experience discomfort	$3 \times 10^{-2} \sim 6.7 \times 10^{-1}$	15~30 years
Operational	Short interruption to service, and all bridge components retain elastic performance with no damage; maintenance workers may experience fear and panic	$8.3 \times 10^{-3} \sim 1.25 \times 10^{-2}$	80~120 years
Continuous occupancy	Weeks to months interruption to service; fatigue problems will emerge without controlling; maintenance workers will experience strong fear and panic	$3 \times 10^{-3} \sim 6.7 \times 10^{-3}$	150~300 years
Instability	The bridge may experience divergent instability, leading to the possibility of collapse	$7 \times 10^{-7} \sim 5 \times 10^{-6}$	200~1400 thousand years

2.2. Method for determining the risk-targeted design wind speed

The failure risk of a structure within a specific design period T can be determined by the following equation:

$$\upsilon_T = \int_0^\infty -F_R(U)\mathrm{d}H_T(U) = \int_0^\infty H_T(U)\mathrm{d}F_R(U) \tag{1}$$

in which, υ_T refers to the failure risk of the structure within T years; $H_T(U)$ is the exceeding probability of mean wind speed U within T years; $F_R(U)$ is the structural vulnerability function, or else fragility curve, and it usually assumed to follow the lognormal distribution, as:

$$F_R(U) = \Phi\left[\frac{\ln(U/U_R)}{\beta_R}\right] \tag{2}$$

where U_R and is defined as the risk-targeted design wind speed; β_R is the standard deviation of the distribution in lognormal space. Rather than using the derivative of the hazard curve, the derivation of the structural vulnerability function is adopted herein. Thus, the failure risk of the structure within T years can be rewritten as:

$$\upsilon_T = \int_0^\infty H_T(U) f_R(U)\,\mathrm{d}U \tag{3}$$

Given the predetermined failure risk υ_T, the risk-targeted design wind speed U_R can be computed through iteration.

3. WIND-INDUCED PERFORMANCE EVALUATION OF XIHOUMEN BRIDE

This bridge is often attacked by typhoons and as such a mixed wind climate composed of typhoon and non-typhoon wind hazards should be considered. For buffeting analysis and serviceability limit states (SLS), it is more suitable to choose the parent distribution of wind speed to establish the hazard curve (daily hazard curve); while extreme wind speed is usually employed to form extreme hazard curve for the ULS (Ciampoli et al, 2011). Herein, four thresholds are defined, as listed in Table 2, corresponding to the four performance objectives. Notably, these thresholds are commonly considered deterministic, neglecting the subjective judgment and variability in sensitivity. However, this paper employs lognormal distributions to describe the thresholds, accounting for these uncertainties.

Table 2. Thresholds corresponding to four performance objectives.

Thresholds	Vertical		Torsional	
	mean	CoV	mean	CoV
T1	$0.19\mathrm{m/s^2}$	0.3	$1.27\times10^{-2}\mathrm{rad/s^2}$	0.3
T2	$0.49\mathrm{m/s^2}$	0.2	$3.27\times10^{-2}\mathrm{rad/s^2}$	0.2
T3	2.75m	0.05	0.18rad	0.05
T4	Flutter			

To derive the fragility curves, the scattered vibration needs to be quantified. For buffeting vibration, the wind-induced vibration data measured by Structural Health Monitoring System of Xihoumen Bridge is utilized to establish a mean wind speed-dependent probabilistic model, as shown in Figure 1. For flutter instability, 10^5 Monte Carlo simulations are conducted to account for the uncertainty in flutter derivatives, structural damping ratios and angle of attack. The fragility curves of the four thresholds in Table 2 are illustrated in Figure 2. After combining with the wind hazard curves, the annual failure probabilities corresponding to the four thresholds are 9.21×10^{-2}, 9.00×10^{-3}, 7.93×10^{-6} and 1.84×10^{-9}.

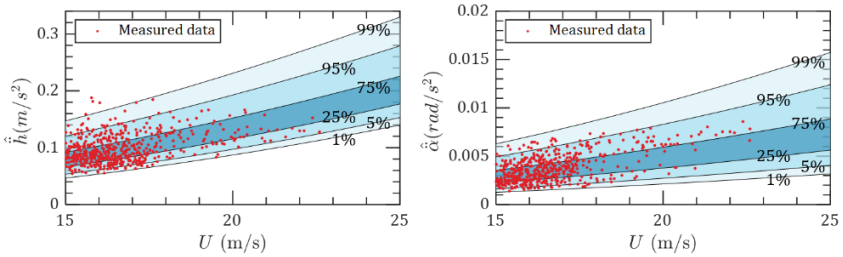


Figure 1. Evolution of the probability distributions of the peak response.

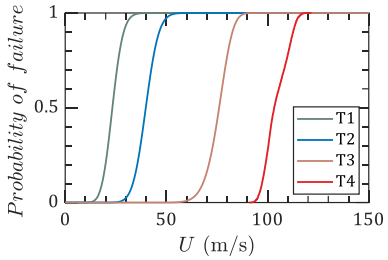


Figure 2. Fragility curves corresponding to different thresholds.

4. RISK-TARGETED DESIGN WIND SPEEDS

By fitting the fragility curves through Eq. (2), the values of U_R and β_R can be obtained, and the exponential function is adopted to fit the relationship between β_R and U_R. Then, according to the iteration in section 2.2, the risk-targeted design wind speeds corresponding to different performance objectives can be calculated, as listed in Table 3.

Table 3. Rik-targeted design wind speeds U_R and β_R corresponding to different performance objectives.

Performance objectives	Acceptable annual probabilities v_1	U_R (m/s)	β_R (m/s)	95% confidence band	
				U_R (m/s)	β_R (m/s)
Occupant comport	3×10^{-2}	31.23	0.16	30.44~32.84	0.10~0.24
Operational	8.3×10^{-3}	39.32	0.14	38.10~42.00	0.08~0.22
Continuous occupancy	3×10^{-3}	45.24	0.13	43.72~48.81	0.07~0.20
Instability	7×10^{-7}	92.59	0.06	88.21~106.57	0.03~0.12

Besides, a sensitivity analysis of v_1 and β_R is conducted, which can be further used to optimize wind resistance design under the impact and consideration of economic costs.

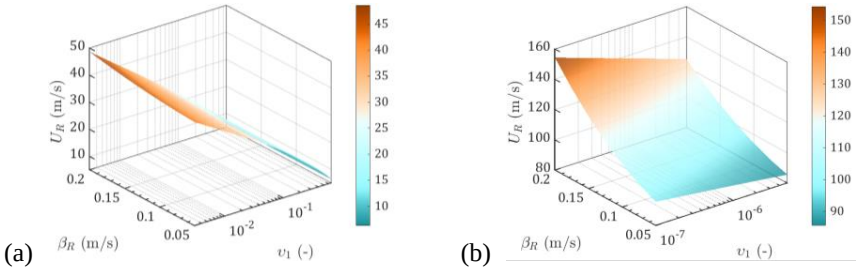


Figure 4. The impact of changes in v_1 and β_R on U_R: (a) SLS; (b) ULS.

5. CONCLUSIONS

This paper presents a method for calculating failure risk and determining risk-targeted design wind speeds. Four performance objectives for long-span bridges are defined, along with their corresponding acceptable annual failure probabilities. Taking the Xihoumen Bridge as an indicative example, the fragility curves corresponding to different performance objectives are developed and examined. By integrating these fragility curves with wind hazard curves, the failure probabilities corresponding to multi-level performances are estimated. Besides, the vulnerability parameter, β_R, decreases with risk targeted wind speed, U_R, and this relationship can be represented as an exponential function. Leveraging this exponential relationship, the risk-targeted multi-level performance design wind speeds can be calculated using the risk integral method.

ACKNOWLEDGEMENTS

The authors gratefully acknowledge the support of the National Natural Science Foundation of China (52108469, 52278520), the Fundamental Research Funds for the Central Universities (22120220577).

REFERENCES

Ciampoli, M., Petrini, F., Augusti, G., 2011. Performance-Based Wind Engineering: Towards a general procedure. Structural Safety 33, 367-378.

Luco, N., Ellingwood, B.R., Hamburger, R.O., Hooper, J.D., Kimball, J.K., Kircher, C.A., 2007. Risk-targeted versus current seismic design maps for the conterminous United States.

Wind-driven considerations for tall RC building design in seismic environments

Morewe Mall[1], Aniket Panchal [2], Anastasia Athanasiou [3]

[1]*MSc student, Bauhaus-University Weimar, Germany, morewe.mall@uni-weimar.de*
[2] *PhD Candidate,Indian Institute of Technology Gandhinagar,India, panchal_aniket@iitgn.ac.in*
[3]*Ass.Professor, Bauhaus-University Weimar, Germany, anastasia.athanasiou@uni-weimar.de*

SUMMARY:
The integration of wind and seismic design principles is increasingly critical in the engineering of tall buildings, as urban environments evolve. Current design practice for lateral loads, focuses on the most dominant hazard, and often misestimates the building performance in multi-hazard environments. For instance, buildings designed for high wind loads may exhibit different behaviour during seismic events, compared to buildings designed with a primary focus on seismic resistance. Herein, we present preliminary findings from the design of four 25-story office buildings, sited in various combined wind and seismic environments of the Indian peninsula. Our results show that the identification of the dominant hazard in design is not always straightforward, and that the non-consideration of the less dominant hazard misevaluates the actual system response. They also stress the need to use realistic representations of 3D wind loadings, along with advanced numerical tools and performance-based assessment schemes, for meaningful dynamic wind simulations. We are currently developing nonlinear finite element models of the buildings in SAP2000, and assessing their multi-hazard performance through nonlinear static (pushover) and dynamic simulations.

Keywords: Multi-hazard performance assessment, wind, earthquake

1. INTRODUCTION

Windstorms and earthquakes are typically independent events with a low probability of occurring simultaneously; however, their combined impacts on a building should be accounted for throughout its lifespan (Bruneau et al, 2017). Wind and earthquake loads dominate the design of tall buildings, both in terms of capacity and admissible deflections. Earthquake practitioners design structures that can withstand seismic events, while ensuring life safety and economic viability. This is achieved by integrating the inherent system overstrength and ductility in the capacity-based seismic design. On the counterpart, wind design remains linear and prescriptive. In combined environments, the inconsistency between the two approaches may be critical. Increasing the size of Lateral Force Resisting System (LFRS) sections to meet wind strength criteria, can significantly impact the seismic load distribution within the building. This is particularly relevant in the context of displacement-controlled (ductile) and force-controlled (brittle) members. Recently, Athanasiou et al. (2022) showed that the sole consideration the dominant hazard in design, may mislead life-cycle loss estimations. Integration of wind hazard in seismic design requires the understanding of the dynamic nature of wind, along with the use of advanced numerical tools and performance-based methods (ASCE,2023) for the accurate quantification of multi-hazard effects on structures.

This study starts with the code-compliant design of 4 identical 25-story office buildings, sited in 4 combined high-speed wind, and low- to very high-seismic environments of the Indian subcontinent. The reinforce concrete (RC) buildings are designed for the dominant hazard. Focus

is given on the case study for which both seismic and wind loads are critical. Preliminary simulations of the LFRS response to lateral loads indicate that relying solely on single-hazard assessments can lead to significant misestimations of the actual, multi-hazard performance.

2. CASE STUDY

2.1. Building design

The case studies include four 25-story office buildings, with identical geometry, but sited in four different regions of the Indian subcontinent, characterized by low- to very high-seismicity (zone 2 to 5) and high wind speeds. The building rests on medium soil and suburban environment. The building is doubly symmetric in plan, and its LFRS consists in a dual system of RC shear walls and moment resisting frames, as shown in Figure 1. The design parameters for earthquake (IS: 1893 (Part 1), 2016), and wind loads (IS: 875 (Part 3), 2015) are shown in Table 1. In zones 2,3 and 4, the elastic, along- and across-wind base shear demands are higher than the corresponding inelastic, seismic demands. In the highest seismic zone 5, earthquake effects are dominant.

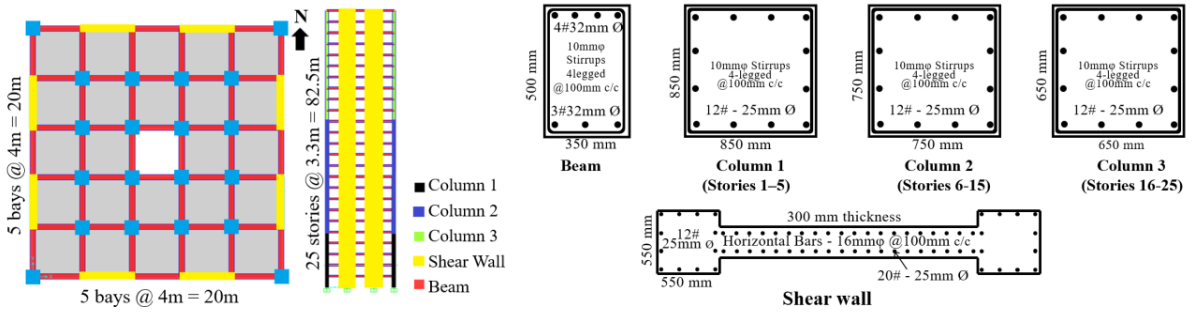


Figure 1. Plan, elevation, and LFRS sections for office building in high wind and high seismic zone 4.

Table 1. Design parameters for seismic and wind loads as per IS:1893 and IS:875.

Seismic Design Parameters		**Wind Design Parameters**	
PGA (Zone 2-3-4-5)	0.10g-0.16g-0.24g-0.36g	Basic Wind Speed, U_{10m}	50m/s
Reduction factor, R	5.0	Risk factor, k_1	1.0
Importance factor, I	1.0	Terrain category	2
Fundamental period, T_1	1.65s (N-S and E-W)	Roughness height, z_o	0.05m
$S_a(T_1,5\%)$	0.82g	Force coefficient, C_F	1.4
Seismic base shear, V_E (Zone 2-3-4-5)	1692 kN -2707 kN-4060 kN-6091 kN	Along- and across-wind base shear, V_W	4770 kN -4351 kN

Figure 2a compares the cumulative shear demands in the four combined seismic and wind sites considered. Thereafter, focus is given to the building in zone 4, for which both hazards are critical, at least in terms of base shear demands. Initially, the LFRS is designed for earthquake loads (DBE, 1-in-475 years), as per the Indian code of RC practice (IS 456, 2000), and detailed for seismic ductility (IS 13920, 2016), see Figure 1. Then, the gust approach is used for the distribution of the design level (1-in-50 years), along- and across-wind forces along the building height (IS: 875, 2015). Response spectrum analysis at DBE, and equivalent static analyses under winds scaled at the operational (1-in-10years) and design limit states, provide the inter-story drift (IDR) and story shear demands, illustrated in Figures 2b and c. Inelastic seismic IDR at DBE are within the IS 0.40% threshold. Operational roof drifts satisfy the 0.25% (206mm) ASCE (2023) criterion, however, the same is not true for floor accelerations. Across-wind response is generally higher than the along-wind response. The story shear distribution, provided in Figure 2c, shows how

earthquake effects are dominant in the lowest and highest levels, whereas wind effects are critical in stories 6-21. However, a close look into the axial force-bending moment (P-M) interaction curves of the vertical members, in Figure 3, reveals that earthquake loads are critical for column and shear wall detailing. This is a simple example on how the dominant hazard approach may complicate the design process in combined environments.

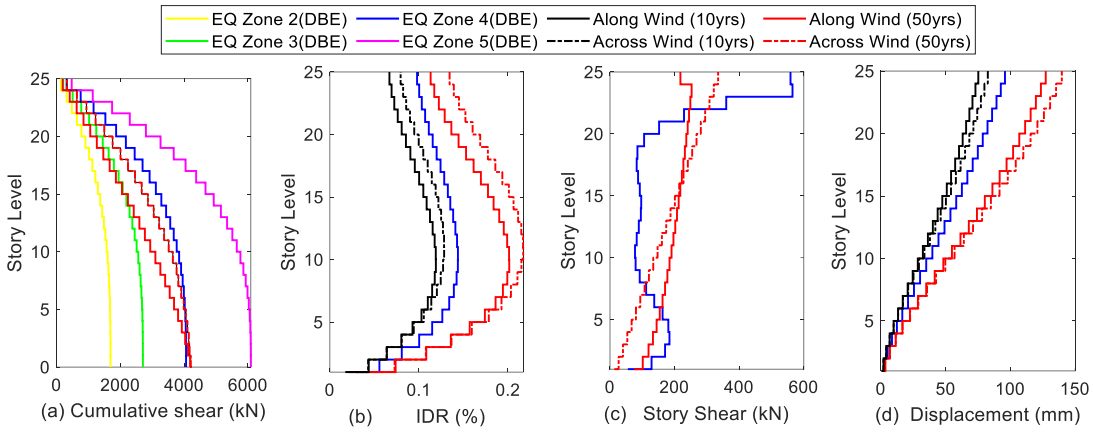


Figure 2. Wind and seismic demands for office buildings at various combined environments.

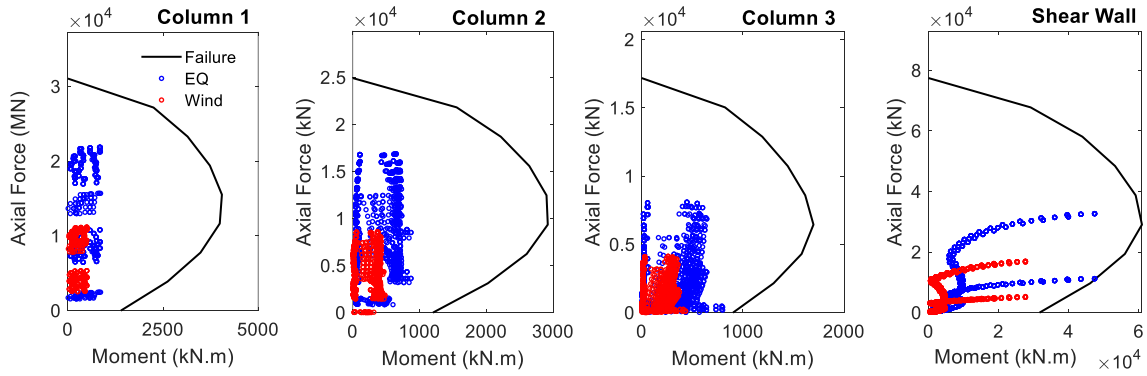


Figure 3. Axial force-bending moment interaction curve for vertical LFRS members under wind and earthquake.

2.2. Multi-hazard performance assessment

Standard design practice cannot account for the potential detrimental effect of the less dominant hazard. Herein, we quantify the misestimation of the actual multi-hazard performance, by implementing the comprehensive performance assessment framework, shown in Figure 4. Such scheme allows us to obtain accurate predictions of the dynamic system response, under realistic multi-hazard scenarios. For structural analyses, we use finite models of the LFRS, comprising geometrical and material nonlinearities, and accounting for the inherent system overstrength. We subject the models to a minimum of 11 sets of 3D ground motions, and 11 sets of along-, across- and torsional winds, scaled at distinct limit states. Seismic and wind analyses are run in parallel, since the two hazards can be considered independent. The consideration of the vertical seismic component is not a standard practice, but is necessary for the correct prediction of axial demands on the vertical components. Each limit state is associated to an event that occurs once in MRI years, and mapped to predefined performance objectives. Acceptance criteria take the form of

admissible ductility (equal or higher than 1), capacity ratio, peak floor acceleration, roof and inter-story drifts. The ground motions are retrieved from the PEER database, whereas the wind sequencies are generated through Monte Carlo simulations, based on available wind tunnel data.

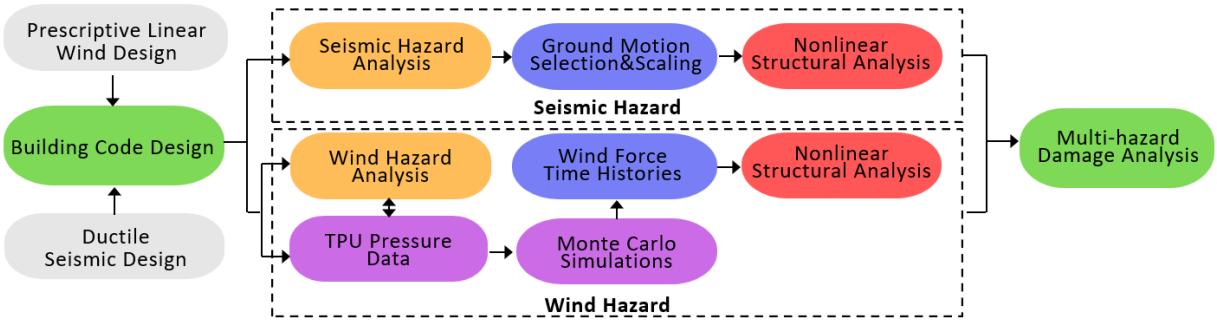


Figure 4. Multi-hazard performance assessment framework.

4. CONCLUSIONS

This study highlights the limitations of the single-hazard approach, used in all major international codes for lateral force design. While the single-hazard approach simplifies the design process, it often overlooks the cumulative effects of multiple hazards on the overall building performance. Preliminary results from the design of four 25-storey office buildings located in various combined wind and seismic environments on the Indian Peninsula, together with anticipated future results, highlight that: (*i*) the identification of the dominant hazard is not always straightforward, (*ii*) the non-consideration of the less dominant hazard misevaluates the building performance, (*iii*) accurate wind simulations require realistic representations of along-, across-, and torsional-wind force histories, (*iv*) equivalent static procedures provide overly conservative estimates of the along-wind response, and may be inappropriate for quantifying across-wind performance. This research work reinforces the belief that the design process should integrate all potential hazards. Available nonlinear modelling and analysis techniques for structures under earthquake excitation, are implemented for wind response simulations through collapse. Such methods are updated to account for the unique characteristics of wind loads, and their effects on structures at the design level and beyond.

ACKNOWLEDGEMENTS

We are all very thankful to the Carl-Zeiss Foundation and Bauhaus-University Weimar for their trust in our research work, and provided funding.

REFERENCES

ASCE, 2023. Prestandard for Performance-Based Wind Design. American Society of Civil Engineers, Reston, VA.

Athanasiou, A., Dakour, M., Pejmanfar, S., Tirca, L., Stathopoulos, T., 2022. Multihazard performance-based assessment framework for multi-story steel buildings. J. Struct. Eng., 148(6), 04022054.

Bruneau, M, Barbato, M, Padgett, A, Zaghi, A, Mitrani-Reiser, J, Li, Y. 2017. State of the Art of Multihazard Design. J. Struct. Eng., 143(10): 03117002.

IS: 456, 2000. Plain and Reinforced Concrete - Code of Practice.

IS: 875, 2015. Code of practice for design loads (Other than Earthquake) for Buildings and Structures–Part 3: Wind Loads.

IS: 1893, 2016. Criteria for Earthquake Resistant Design of Structures Part 1: General Provisions and Building.

IS: 13920, 2016. Ductile Design and Detailing of Reinforced Concrete Structures Subjected to Seismic Forces - Code of Practice.

Cost-based optimization of a tall building subjected to wind action

Alessandro Giovani [1], Mattia Francioli [2], Francesco Petrini [3]

[1]*Sapienza University of Rome, Rome, Italy, alessandro.giovani@uniroma1.it*
[2]*Sapienza University of Rome, Rome, Italy, mattia.francioli@uniroma1.it*
[3]*Sapienza University of Rome, Rome, Italy, francesco.petrini@uniroma1.it*

SUMMARY
The construction of tall buildings addresses the demands of modern society: with the increase of population in large cities and migration to urban centres, available space has become scarce and precious. Building tall allows to make the most of limited land, accommodating more people or activities on a reduced surface (thus optimizing the available space). High-rise buildings are valuable structures that entail significant construction costs due to their complexity, and a correct design must necessarily take into account also the economic and environmental impact. In this work, the topic of structural optimization is addressed with specific regard to the development of a procedure that considers as alternative objective functions the total steel volume, the total structural cost or total CO_2 emissions produced by steel production, having as a case-study a high rise building subjected to wind load. A detailed study is conducted exploring how structural optimization can be applied in an automated manner.

Keywords: Tall Building, Wind, Automation, Optimization.

1. STRUCTURAL OPTIMIZATION

The optimization problem can be defined as that process of minimization/maximization of an objective function through the exploration of the values that it assumes when design variables vary, checking the acceptability of the values assumed by state variables (Pardalos et al, 2002). The optimization problem is defined by three elements: (i) Design Variables (DVs), (ii) Objective Function(s) (OF) and (iii) Constraints (State Variables SVs). In civil engineering, structural optimization is an iterative process aimed at obtaining the best configuration of a structure by minimizing (or maximizing) an objective function while simultaneously adhering to imposed constraints. Depending on the objective function to be optimized, structural optimization can be divided into different types: size-optimization (micro-scale); shape-optimization (meso-scale); topology-optimization which combines features from both size and shape optimization (macro-scale optimization); multi-objective optimization (Mei et al, 2021). Moreover, in civil engineering, there are different objectives that are argument of structural optimization (minimize or maximize) (Mei et al, 2021), such as cost, structural performance and environmental impact. In this work, the focus is on the structural optimization of a tall steel building under wind loads, using as objective function OF the total steel volume, the total structural cost or total CO2 emissions produced by steel production.

2. DESCRIPTION OF THE PROCEDURE

The optimization process starts with the selection of a combination of design variables (which are 24: size of structural elements and location of outriggers); once all design variables are fixed, a modal analysis is performed to obtain the dynamic characteristics (vibration frequencies). Based on the structure's frequencies, it is possible to calculate the equivalent static wind forces and peak accelerations induced by the wind; then, having obtained the equivalent static wind forces in both the longitudinal and transverse directions relative to the wind direction, these two directions are combined, and static analyses are conducted for each combination. As a result of the static analyses, nodal displacements and the stresses to which the elements are subjected are extracted; peak wind accelerations, nodal displacements, and stresses represent the constraints for the optimization process, determining whether the configuration of design variables is feasible or infeasible. Starting from the choice of design variables, particularly column selection, it is possible to design column - column connections. Based on the stresses extracted from static analysis, connections involving beams and braces can be designed; once all connections are designed, the values of objective functions can be calculated: total steel volume, total structural cost, and total CO_2 emissions produced during steel production. To have all elements are in place for the optimization algorithm, it is necessary to choose which objective function to minimize and to match it with constraints. This process is repeated for a certain number of iterations (50 times the number of design variables, 50 × 24 = 1200) and at the end of the 50 * number of design variables iterations, the optimal combination of design variables that minimizes the chosen objective function is obtained.

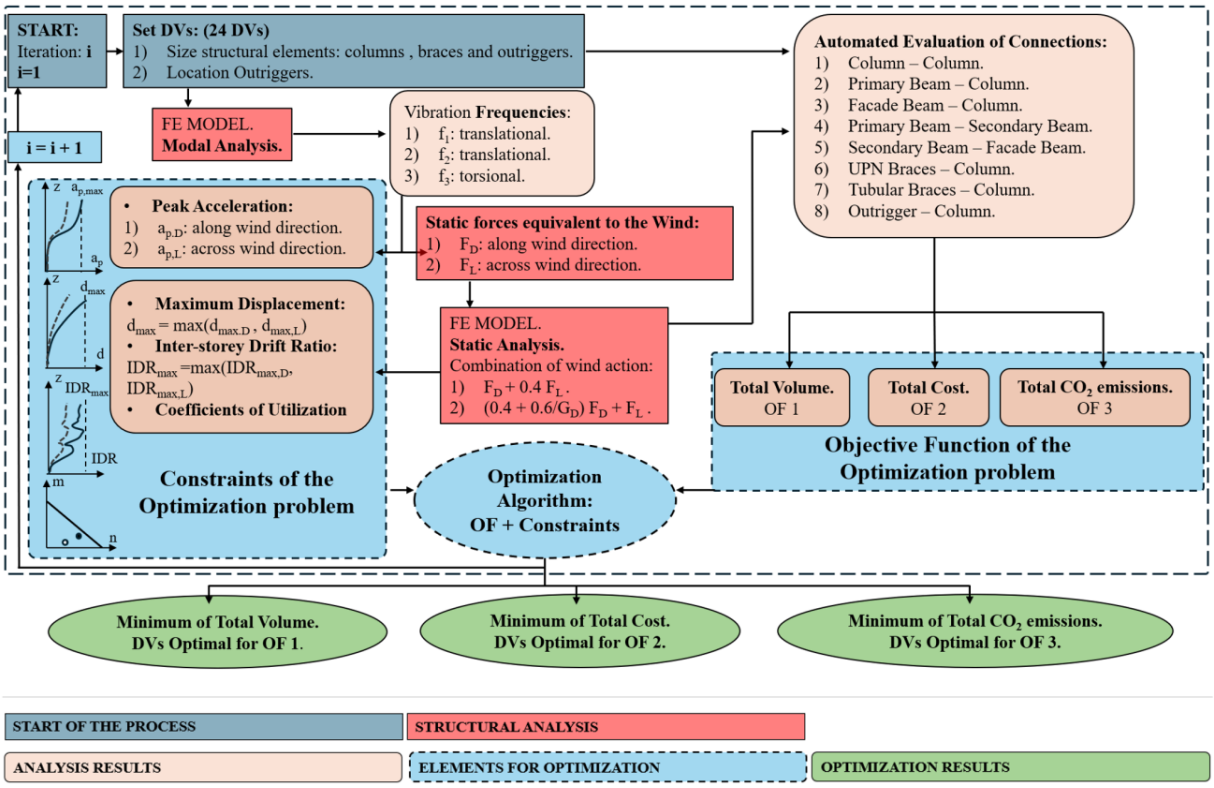
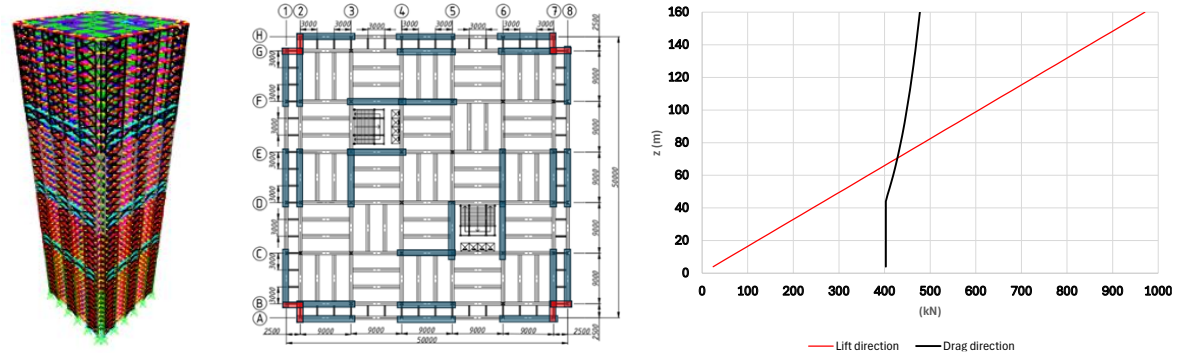


Figure 1. Flowchart of the proposed procedure.

3. DESCRIPTION OF THE CASE STUDY AND RESULTS

The case stud is a steel, consisting of 40 floors, with an inter-floor height of 4 meters (total height of 160 m). The dimensions of the building's layout are 50×50 m^2; the building is composed of a square core with frames in both directions. The internal core has 5 bays on each of its 4 outermost sides (each span is 9 meters wide). The structural system chosen for the vertical elevation consists of a system with vertical continuous columns. There are 28 X-bracing members using U-profiles, of which 12 are located in the outer bays of the building (3 on each facade) and 8 K-bracing using tubular 'O' profiles members located in the corner bays of the building. To limit relative inter-floor displacements and stiffen the structure, 3 outriggers are used, exclusively applied to the bays that form the building's facades.



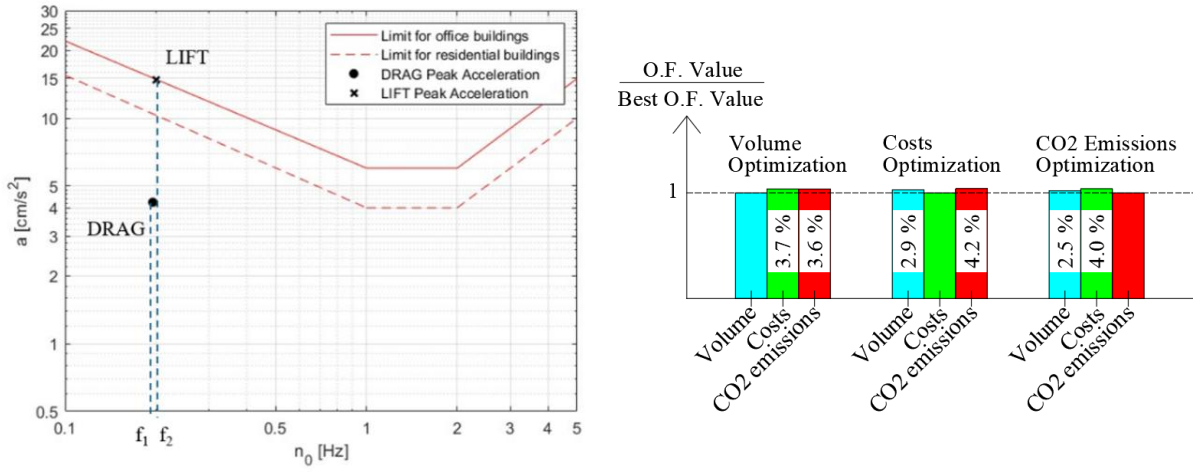
(a) (b) (c)

Figure 2. 3D structure (a); floor-scheme of the location of the braces: X-braces in blue, K-braces in red (b); Equivalent static forces to the wind action: along wind direction (black), across wind direction (red) (c).

The construction site is located in Genoa, Italy, and wind data are obtained from the current Italian regulations (CNR-DT 207 R1/2018, 2018). Liguria region falls into Zone 7 of the Italian zoning, characterized by a base wind velocity at sea level of $v_{b,0}$=28 m/s (site roughness class is defined as category A), given the low seismicity of the region where the building is located, and given the high-rise an relatively low-frequency of the building, the wind is the driving design action. A detailed procedure was conducted to determine the longitudinal and transverse dynamic coefficients, resulting in a value of c_{dD} = 0.83 and c_{dL} = 5.12 (for the pre-optimization configuration). To obtain the equivalent static action (external pressure acting on the faces of the structure), the peak aerodynamic action is multiplied by the dynamic coefficient in the relevant direction; the resulting static forces equivalent to the action of the wind both in the along wind direction and in the across wind direction are shown in figure 2c. From the results, it can be said that, for all three different optimizations, the oscillations that the building experiences in the transverse direction (with respect to the wind's one) represent the predominant constraint for the building's design. Therefore, the most critical combination is one in which the lift forces are maximized (CNR-DT 207 R1/2018, 2018). Table 1 reports the sections as obtained from the different optimizations (for sake of brevity, only bracing elements and outriggers are listed). It must be recalled that one of the major concern in high-rise buildings design is the comfort of the occupant (Tamura et al., 2015); the results in terms of acceleration values causing discomfort is presented in figure 3a.

Since there are minor differences in terms of frequencies obtained, just one case is presented here (total volume optimization). It is shown in figure 4b the percentage by which the values of the other two objective functions exceed their minimum values found in the other configuration. These

results open the way to the multi-objective optimization problem, which are characterized not by a single solution but by a set of optimal solutions for the different objective functions (i.e., compromise could be the best solution).



(a) (b)

Figure 3. Limit value for peak acceleration for comfort analysis (a); Percentage of exceeding the best OF value (b).

Table 1. Sections of the elements obtained from the optimization process.

Element Type	Group	Total Volume	Total Cost	Total CO_2 Emissions
UPN Braces	Storey 1 to 10	2x UPN 260	2x UPN 240	2x UPN 240
	Storey 11 to 20	2x UPN 220	2x UPN 240	2x UPN 220
	Storey 21 to 30	2x UPN 200	2x UPN 200	2x UPN 180
	Storey 31 to 40	2x UPN 160	2x UPN 140	2x UPN 140
Tubular Braces	Storey 1 to 10	TUB 168.3x7.1	TUB 244.5x16	TUB 406.4x16
	Storey 11 to 20	TUB 168.3x7.1	TUB 244.5x16	TUB 219.1x20
	Storey 21 to 30	TUB 168.3x7.1	TUB 114.3x10	TUB 193.7x8
	Storey 31 to 40	TUB 114.3x5	TUB 114.3x8	TUB 193.7x8
Outrigger (Storey of outriggers)	All	HE 700B 19; 24; 30	HE 550B 18; 24; 25	HE450B 16; 17; 29
Total Volume of Steel [m^3]		2033	2092	2083
Total Structural Cost [million €]		36.2	34.9	36.3
Total CO_2 Emissions [ton]		31936	32095	30816

ACKNOWLEDGEMENTS

The Financial support of the Research Project No. CN1221844D08208F from Sapienza University of Rome under the umbrella of the national program PNRR – CN1 – Spoke 5 (Directorial Decretation no. 1031 of June, 17th, 2022) is gratefully acknowledged.

REFERENCES

Pardalos, P. M.; Romeijn, E. H. Handbook of global optimization. Volume 2. Kluwer Academic Publishers. 2002. DOI: 10.1007/978-1-4757-5362-2.

Mei, L.; Wang, Q. Structural Optimization in Civil Engineering: A Literature Review. Buildings 2021, 11, 66. https://doi.org/10.3390/buildings11020066.

CNR, Istruzioni per la valutazione delle azioni e degli effetti del vento sulle costruzioni, CNR-DT 207 R1/2018, 2018.

Tamura, Y. et al. Response characteristics of super-tall buildings – Effects of number of sides and helical angle. Elsevier Ltd. 2015. http://dx.doi.org/10.1016/j.jweia.2015.07.001

Comparative Study on Wind-Induced Response of High-Rise Core-Wall Buildings through Wind Spectral and Time History Analyses

Sol-Gi Eun [1], Thomas Kang [2]

[1]*Seoul National University, Seoul, Korea, solgi@snu.ac.kr*
[2] *Seoul National University, Seoul, Korea, tkang@snu.ac.kr*

SUMMARY
With the increasing prevalence of high-rise buildings, research on analytical methods for wind-resistant design has been actively conducted. Despite the growing emphasis on considering nonlinearity to more accurately capture the structural behavior under dynamic loads, linear analyses such as spectral analysis (SA) and time history analysis (THA) remain widely utilized in both research and practice due to their computational efficiency and ease of implementation. Thus, this study aims to optimize design approaches by selecting the most appropriate analytical method based on building characteristics and wind load conditions, through understanding the differences in responses. A comparative analysis was conducted between SA and THA, which consider both linearity and nonlinearity of time history analyses, which serves as the foundation for performance-based design. Through this comparison, the study aims to enhance the understanding of the accuracy of these analytical methods, validate simplified models, and identify their limitations. Consequently, this research seeks to provide fundamental data on wind-resistant design and analysis for engineers.

Keywords: spectral analysis, time history analysis, aerodynamic wind load.

1. INTRODUCTION

With the increasing prevalence of high-rise buildings, research on analytical methods for wind-resistant design has been actively conducted. Recognizing the strengths and limitations of various analytical methods allows engineers to optimize the safety and performance of high-rise structures, ensuring precise wind load predictions when computational efficiency and design timelines are critical. The comparison between spectral analysis (SA), linear and nonlinear time history analyses (LTHA and NLTHA) holds both theoretical significance and practical applicability.

2. ANALYSIS MODELS

2.1. Design parameters

The core wall is crucial for resisting lateral loads like wind and provides significant stiffness to the building, which is vital for limiting lateral movements and ensuring stability. This stiffness plays a significant role in determining a building's natural frequencies, which influence the structure's dynamic response and are closely tied to both stiffness and mass. Therefore, developing an accurate model that reflects the distribution of stiffness and mass is essential for precise structural

analysis (Mohammadnejad and Haji Kazemi, 2017). In this study, a lateral load-resisting system incorporating a core-wall system and coupling beams was utilized.

Fig. 1 shows the structural plan of the analysis models. To closely emulate the layout of an actual building, a dual-core wall system was incorporated into the design. Table 1 displays the dimensions of the building models and their corresponding structural components, organized into Model 1 through Model 9.

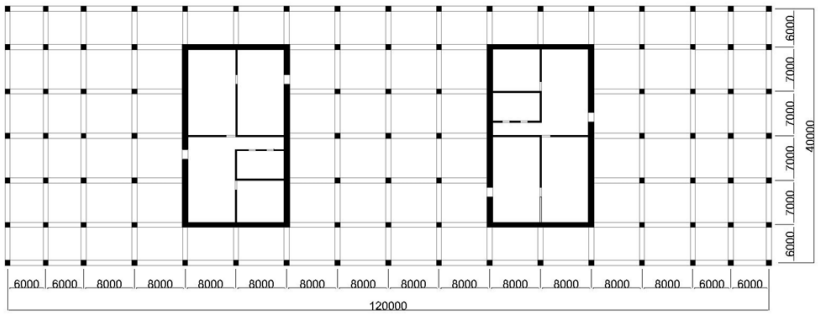


Figure 1. Structural plan view of model with aspect ratio 3.

Table 1. Dimensions of building models and structural elements.

	B (m)	*D* (m)	*H* (m)	Column (mm)	Core Wall (mm)	Beam (mm)
Model 1	40	40	120	1st-18th stories: 1000 x 1000 19th-30th stories: 800 x 800	Inner: 150 Outer: 650	Beam: 400 x 500 Coupling Beam: 650 x 650
Model 2	80					
Model 3	120					
Model 4	40	40	160	1st-18th stories: 1200 x 1200 19th-34th stories: 1000 x 1000 35th-40th stories: 800 x 800	Inner: 150 Outer: 700	Beam: 500 x 700 Coupling Beam: 700 x 700
Model 5	80					
Model 6	120					
Model 7	40	40	200	1st-18th stories: 1200 x 1200 19th-34th stories: 1000 x 1000 35th-50th stories: 800 x 800	Inner: 250 Outer: 900	Beam: 600 x 800 Coupling Beam: 900 x 900
Model 8	80					
Model 9	120					

1.2. Wind Loads

This research employed the open-access aerodynamic database provided by Tokyo Polytechnic University (Tamura, 2012), which contains results from high-frequency pressure integration (HFPI) tests conducted on 1/400 scale prism models. The analytical models vary in terms of height, side ratios (*B*/*D*), exposure conditions, and wind attack angles. A damping ratio of 1.2% was implemented following the guidelines of ISO 4354-09 (ISO, 2009).

2. SPECTRAL ANALYSIS

Structural responses to wind loads are typically evaluated using SA, which is based on the principles of random vibration theory (Tsukagoshi et al., 1993). This method estimates the responses of structures subjected to aerodynamic wind forces through a simplified approach that leverages the wind force power spectral density (PSD) and the dynamic characteristics of the structure. The SA approach focuses solely on the first mode and assumes elastic behavior in the

frequency domain. While high-rise buildings exhibit responses across several vibration modes, their overall behavior is primarily influenced by the first mode of vibration (Ryu et al. 2019). Consequently, SA is an effective technique that simplifies the analysis by concentrating on the dominant first mode. The method involves integrating the aerodynamic wind force PSD with the mechanical admittance to derive the structural responses and determine the building's overall behavior.

3. LINEAR AND NONLINEAR TIME HISTORY ANALYSES

Unlike SA, THA models these loads as a time series, reflecting real-time fluctuations in wind speed and direction. This enables THA to capture the influence of multiple vibrational modes within the system while assuming a linear structural response. LTHA is advantageous because it efficiently incorporates dynamic wind loads and provides insights into the contribution of higher modes to the overall response, which SA cannot capture accurately.

LTHA is particularly beneficial when analyzing structures with well-behaved elastic behavior and when computational efficiency and clarity of results are prioritized. NTHA extends this approach by considering nonlinearities in material behavior, geometric deformations, and other factors that can influence the actual response of structures under wind loads. NTHA can simulate more realistic conditions, making it suitable for cases where material yielding, stiffness degradation, or geometric nonlinearities play a significant role.

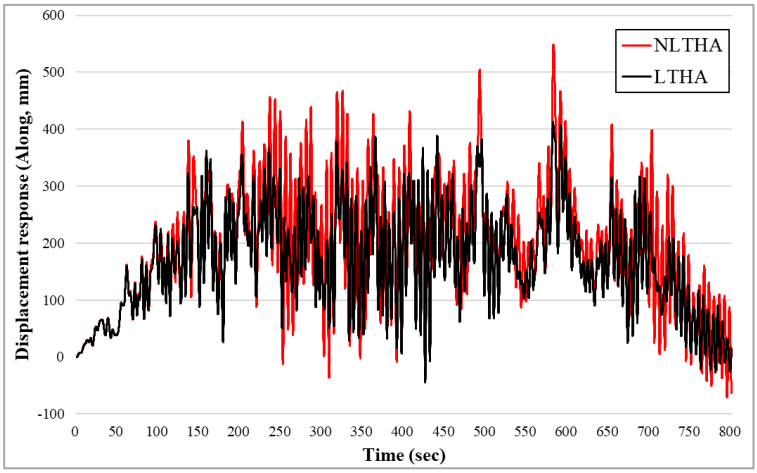


Figure 2. Displacement responses of LTHA and NLTHA for along-direction.

The comparison between LTHA and NTHA is crucial for determining the applicability and reliability of linear assumptions in different scenarios. Such a comparison highlights the conditions under which linear assumptions may be insufficient and identifies cases where nonlinear effects must be considered to achieve accurate predictions. By contrasting LTHA and NTHA, engineers can select the most appropriate analysis method based on the structure’s characteristics and design requirements, ensuring a balance between computational efficiency and analysis accuracy.

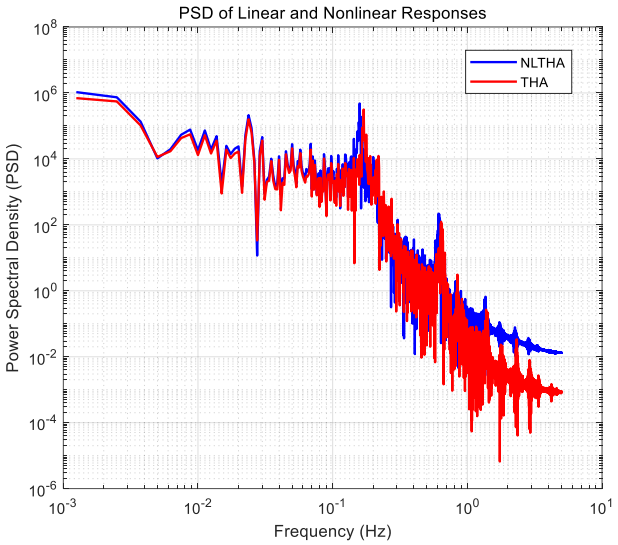


Figure 3 Displacement response PSDs of LTHA and NLTHA.

4. CONCLUSIONS

This study compared the responses of models with varying aspect ratios, side ratios, and wind angles based on wind tunnel experiment results. Using the calculated wind loads, SA with single-degree-of-freedom system, time-history analysis with multi-degree-of-freedom system, and nonlinear analysis were performed to compare responses. The findings indicate the necessity for further research on efficient performance-based wind design that satisfies computational efficiency and ease of implementation, providing foundational data for such efforts.

ACKNOWLEDGEMENTS

This work was supported by the National Research Foundation of Korea (NRF) grant (NRF-2021R1A1A5A1032433), the Institute of Information & Communications Technology Planning & Evaluation (IITP) grant funded by the Korean government (MSIT) (No. 2021-0-01343), and by the Institute of Engineering Research at Seoul National University. The views expressed are those of authors, and do not necessarily represent those of the sponsors.

REFERENCES

ISO 4354:2009, 2009. Wind actions on structures. International Standardization, Geneva, Switzerland, 68.

Mohammadnejad, M. and Haji Kazemi, H., 2017. Dynamic response analysis of a combined system of framed tubed, shear core and outrigger-belt truss. *Asian Journal of Civil Engineering*, 18, 1211-1228.

Ryu, H.-J., Shin, D.-H., and Ha, Y.-C., 2019. The wind load evaluation on building considering vertical profile of fluctuating wind force. *Journal of the Architectural Institute of Korea - Structure & Construction*, 35, 157-164. (in Korean)

Tamura, Y., 2012. Aerodynamic Database of Highrise Buildings, Tokyo Polytechnic Univ., Global Center of Excellence Program.

Tsukagoshi, H., Tamura, Y., Sasaki, A., and Kanai, H., 1993. Response analyses on along-wind and across-wind vibrations of tall buildings in time domain. *Journal of Wind Engineering and Industrual Aerodynamics*, 46-47, 497-506.

Calibration Algorithm for FNA Nonlinear Analysis in Wind-Resistant Design Using the Biaxial Bouc-Wen Model

Seonhyeong Kim [1], Thomas Kang [2]

[1]*Seoul National University, Seoul, Korea, linearkim@snu.ac.kr*
[2]*Seoul National University, Seoul, Korea, tkang@snu.ac.kr*

SUMMARY
This study improves nonlinear wind-resistant analysis for high-rise buildings by calibrating fast nonlinear analysis (FNA) to align with the direct integration method (DIM), incorporating P-delta effects and nonlinear behavior to derive accurate displacement responses. While DIM offers high accuracy, it has high computational costs, whereas FNA is faster but less precise. To address this, FNA and DIM results were compared to identify discrepancies, and a biaxial Bouc-Wen model-based optimization algorithm was applied to calibrate FNA.

Keywords: direct integration method, fast nonlinear analysis, wind-resistant design, p-delta effects

1. INTRODUCTION
High-rise buildings are significantly affected by wind loads, which amplify the dynamic response of long-period structures, impacting safety and serviceability. As height increases, wind pressure intensifies and structural flexibility grows, complicating lateral load behavior. Traditional wind-resistant design assumes elasticity but may not capture actual responses, leading to reduced ductility under seismic conditions (Jeong et al., 2021). Performance-based wind design (PBWD) addresses these limitations by incorporating nonlinear structural responses for more accurate wind resistance evaluation. While nonlinear time history analysis (NTHA) is effective in assessing inelastic behavior under extreme wind, its high computational cost limits practical use. To improve efficiency and accuracy, advanced analytical methods are being developed, and this study explores a refined approach for high-rise building wind resistance evaluation.

2. NONLINEAR TIME HISTORY ANALYSIS
Linear analysis considers only elastic behavior, while nonlinear analysis accounts for geometric and material nonlinearities like P-delta effects and material yielding, which are critical for high-rise buildings. Direct integration method (DIM) provides accurate nonlinear analysis but is computationally expensive. To improve efficiency, fast nonlinear analysis (FNA) (Wilson, 2002) simplifies the process by focusing on key nonlinear components and using Ritz vectors. However, FNA does not fully capture geometric nonlinearities like P-delta effects, leading to potential inaccuracies, especially in ETABS-based high-rise building analysis.

3. MODELING
This study models a 50-story, 200 m-high reinforced concrete (RC) structure using ETABS v19. The building, with a 40 m × 40 m floor plan and a 20 m × 20 m core wall, resists lateral loads from

dead, live, seismic (KDS 41-17-00), and wind (KDS 41-12-00) loads. Wind loads were derived from TPU (Tamura, 2012) database pressure coefficients, dividing the envelope into four regions for along-wind, across-wind, and torsional loads. Nonlinear modeling, based on AIK (2021) seismic guidelines, incorporated concrete C40 and rebar SD500. Beams were assigned Takeda and Pivot model hinges, columns used Fiber-P-M2-M3 hinges for axial and moment interactions, and shear walls applied Fiber-P-M3 hinges for M3 moment and axial force behavior.

4. LINEAR ANALYSIS

4.1. Damping Effect

The linear analysis evaluated the effect of damping settings on structural response. In ETABS, FNA allows only modal damping, while DIM can incorporate Rayleigh damping. To compare with FNA, two DIM analyses were performed: one with only modal damping and another with a 9:1 modal-to-Rayleigh ratio. The combined damping (9:1) reduced RMSE from 3.83 mm to 3.72 mm (along-wind), improving alignment with FNA.

4.2. P-delta Effect

The linear analysis evaluated the P-delta effect by comparing FNA and DIM. When included in DIM but not in FNA, DIM showed significantly larger displacements, especially in the across-wind direction. Applying only the initial gravity load P-delta effect in FNA improved alignment, increasing the FNA-DIM along-wind correlation from 0.539 to 0.989 and reducing RMSE from 85.1 mm to 13.55 mm. This confirms that considering the initial gravity load P-delta effect enhances FNA accuracy and reduces discrepancies with DIM.

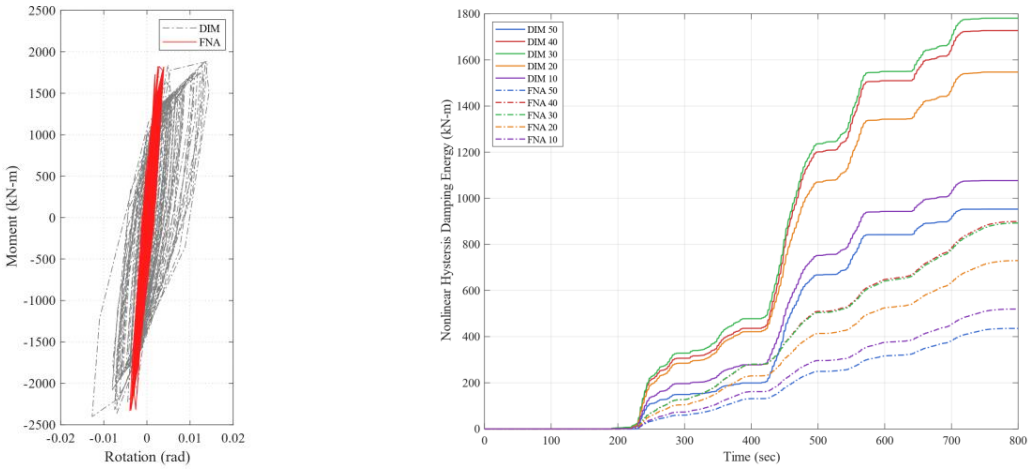
5. NONLINEAR ANALYSIS

5.1. Building Level Analysis

The nonlinear analysis was performed with the same combined damping and initial gravity load P-delta settings as the linear analysis. Wind loads were increased to induce nonlinear behavior, and top-floor displacements were compared. The results showed that DIM with the P-delta effect had smaller displacements than FNA in both along-wind and across-wind directions. A comparison of maximum story displacements revealed that FNA generally showed larger values, with DIM exceeding FNA in the lower stories but FNA surpassing DIM in the upper stories along the Y direction. These differences are attributed to energy dissipation and nonlinear behavior variations, highlighting key factors in the discrepancies between linear and nonlinear analysis.

5.2. Member Level Analysis

Nonlinear behavior was observed in the coupling beams connecting the shear walls, initially occurring in the upper stories and gradually propagating downward over time. According to **Fig. 1**, FNA exhibits a narrower hysteresis range than DIM, and DIM's energy dissipation is approximately twice as high as that of FNA. Consequently, the overall structural displacement in DIM is expected to be smaller than in FNA. Story displacement analysis shows that DIM has greater displacement in the lower stories, while FNA exhibits larger displacement in the upper stories. This is attributed to higher energy dissipation in the upper stories of DIM, leading to reduced displacement, whereas insufficient dissipation in the lower stories results in relatively higher displacement. Finally, correlation analysis between energy dissipation and inter-story displacement differences (FNA - DIM) shows a high correlation coefficient of 0.903, confirming that differences in hysteresis loops are the primary cause of displacement variations.



a) Nonlinear Behavior Graph b) Nonlinear Hysteresis Damping Energy Graph

Figure 1. Nonlinear Analysis of Structural Members

6. CALIBRATION ANALYSIS

6.1. Calibration Algorithm

The displacement response and hinge behavior differences between FNA and DIM arise because FNA does not fully account for the P-delta effect and simplifies hinge behavior. To address this while maintaining FNA's computational efficiency, this study develops a calibration algorithm that relies solely on FNA results to produce DIM-consistent displacements. A 2DOF Bouc-Wen model (**Fig. 2**) is introduced to incorporate P-delta effects and nonlinear behavior, with displacement calculations performed using the Newmark-Beta numerical integration method. The calibration process consists of two steps. In the first step, the eight key parameters of the Bouc-Wen model are optimized based on FNA displacements. The Newmark-Beta method is applied to compute displacement, velocity, and acceleration, while iterative optimization adjusts the parameters, including hysteresis variables, to accurately capture nonlinear behavior. In the second step, a new equation of motion incorporating the P-delta effect is formulated, and final corrected displacements are obtained using the Newmark-Beta method.

6.2. Calibration Results

The calibration results show that FNA displacement responses were effectively aligned with DIM in both along-wind and across-wind directions. **Fig. 3** illustrates that DIM-FNA differences are more concentrated around zero with fewer large deviations, confirming the calibration's success. RMSE comparisons across floors showed an average reduction of 30%, indicating improved FNA accuracy. Notably, the largest error reduction occurred near coupling beams, demonstrating that the calibration model effectively captured nonlinear structural responses.

6.3. Deep Learning-based Calibration Model

Both FNA and DIM results were used to identify an optimized parameter dataset for effective calibration, which was then used to develop and train a deep learning model. This model automatically generates optimized parameters from FNA results of other structural models, enabling easy calibration. As shown in **Fig. 4**, applying the model to different cases resulted in successful corrections, effectively aligning FNA with DIM.

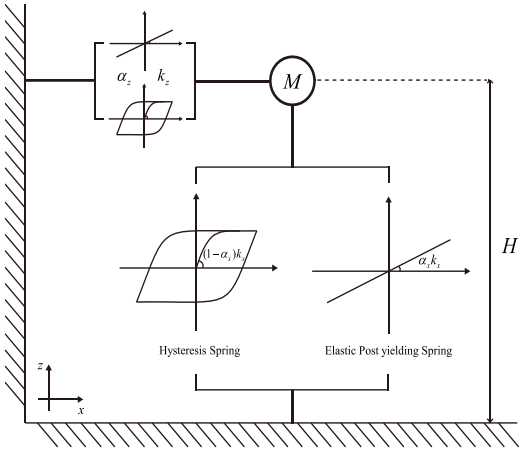


Figure 2. Biaxial Bouc-Wen Model

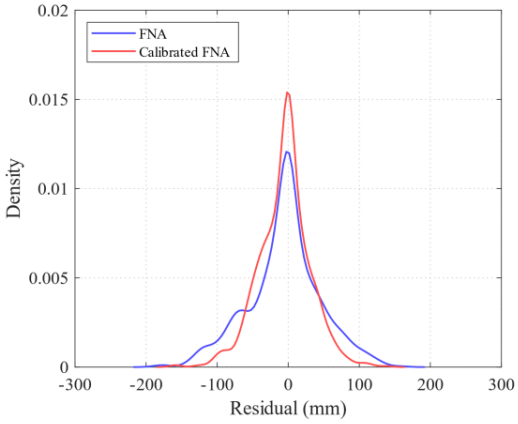


Figure 3. Residual Density Graph

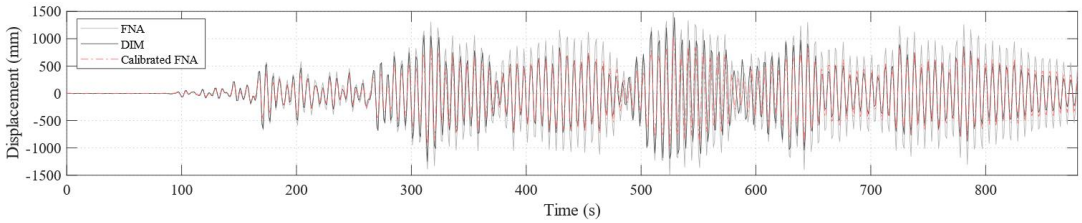


Figure 4. Calibration Result Graph

7. CONCLUSIONS

This study developed a calibration algorithm by comparing FNA and DIM nonlinear analysis results, improving the efficiency and accuracy of wind-resistant analysis. Elastic analysis showed that applying initial gravity load settings and combined damping made FNA responses similar to DIM. However, in nonlinear analysis, differences in P-delta effects and nonlinear behavior were identified as the primary causes of discrepancies. To address this, a biaxial Bouc-Wen model-based calibration algorithm was developed, allowing FNA results alone to estimate DIM outcomes. Additionally, a deep learning model was introduced to generate DIM-level results without the calibration process, and testing confirmed its effectiveness across different structural models.

ACKNOWLEDGEMENTS

This work was supported by the National Research Foundation of Korea (NRF) grant (NRF-2021R1A1A5A1032433). The views expressed are those of authors, and do not necessarily represent those of the sponsors.

REFERENCES

Jeong, S. Y., Alinejad, H., and Kang, T. H.-K. (2021), “Performance-based wind design of high-rise buildings using generated time-history wind loads”, J. Struct. Eng., 147(9).

Tamura, Y., 2012. Aerodynamic Database of Highrise Buildings, Tokyo Polytechnic Univ., Global Center of Excellence Program.

Using WRF-CFD simulation to reproduce the environmental wind field during a helicopter crash accident

Yong-Ming Yang [1], Mei-Jiau Huang[2], Brian C. Kuo[3]

[1]*Mechanical Engineering Department, National Taiwan University, Taipei, ROC, R11522105@ntu.edu.tw*
[2] *Mechanical Engineering Department, National Taiwan University, Taipei, ROC, mjhuang@ntu.edu.tw*
[3]*Taiwan Transportation Safety Board, Taipei, ROC, chiawei@ttsb.gov.tw*

SUMMARY:
The Emerald Pacific Airlines B-31118 crashed in the mountainous area of eastern Taiwan in 2017. In order to explore whether the complex environmental wind field in the valley posed a threat to flight, the computational fluid dynamics (CFD) is employed to reproduce the wind field by taking advantage of the large-scale data from the Weather Research and Forecasting (WRF) simulation and measurements from a nearby weather observation station. The RANS simulation result shows that the wind speed encountered by the helicopter was not large, but the wind direction changes significantly. Along the flight route, no severe wind shear or turbulence intensity is found. However, the velocity vector diagram at different flight altitudes shows that there were multiple airflows coming from different directions and merged near the crash site. This might threaten the helicopter which was in circling flight.

Keywords: Computational fluid dynamics, Weather research and forecasting, Environmental wind field

1. INTRODUCTION

The Emerald Pacific Airlines B-31118 crashed in the mountainous area of eastern Taiwan in June, 2017. All three people on board died unfortunately. The eastern region of Taiwan is famous for its beautiful coastal mountainous terrain. The southwest monsoon in summer and the northeast monsoon in winter often form complex wind fields. In order to understand whether complex wind fields ever posed a threat to helicopter flight, it is necessary to recreate the wind field at that time. The Weather Research and Forecasting (WRF) and the Computational Fluid Dynamics (CFD) are chosen to reconstruct the wind field.

WRF is a meteorological simulation system whose applications include short-term and medium-term weather forecasting, climate, atmospheric dynamics, pollution diffusion, etc. (Skamarock et al., 2019). It has a highly flexible architecture that can adapt to a variety of application requirements and provides a variety of physical solutions. It takes into consideration of cumulus effect, atmospheric radiation, planetary boundary layer, surface physics (including vegetation, soil moisture, snow cover, sea ice, and so on). However, WRF grid resolution range from tens of meters to hundreds of kilometres, which is not sufficiently fine to provide the details of the wind field in the mountains. Computational fluid dynamics (CFD) solves the Navier-Stokes equations with grid resolution ranging from a few millimetres to tens of meters. It can therefore capture more details

of the rugged terrain and provide a more accurate low-altitude wind field.

In this study, we intend to use these simulation tools to reproduce the wind field to which the helicopter was exposed during the accident. A numerical terrain model for the complex coastal mountain topography of eastern Taiwan is constructed first. This terrain model covers an area several kilometres near the accident site. The WRF wind field which has considered mesoscale atmospheric factors provides the required boundary conditions for CFD. The steady RANS solution with k-ω SST turbulent model is solved. In addition to exploring the complex wind field, flight safety standards about the wind shear and turbulence intensity are also examined.

2. TERRAIN MODEL AND SIMULATION METHOD

2.1. Terrain Model

In Fig. 1, the red pushpin indicates the crash site which locates in a valley surrounded by mountains with a river running through. At the outlet of the Xiuguluan River, there is an alluvial fan beach and a small island called Shiqiu Island. The nearest weather observation station is in Jeongpo, marked with a yellow pushpin. The blue box is the simulation domain (D05) of WRF, which area is about 6km×6km. To enhance the resolution, the CFD domain is further shrunk to be 5.22km×5.28km, covering the helicopter's flight path within two minutes before the crash as indicated by the purple curve in Fig. 1(c). To reduce the difficulty of building the terrain model and meshing, a Gaussian filter is employed to smooth the terrain. Because the wind direction at the crash time is south-south west (blue arrow), a smaller filter window (0.5m) is adopted in the middle region right upstream and downstream of the crash site (between two parallel red lines) and a larger one (2m) for the outer regions (outside the blue lines); a linear transition is made in between. On the other hand, the height of the CFD simulation domain is 5km, resulting in a blockage ratio less than 10% (Badshah et al., 2019) and at least 5 times higher than the highest mountain (741m) (Franke, 2004).



(a) (b) (c)

Figure 1. (a) The red pushpin indicates the crash site in the mountainous region. (b) The simulation domain D05 of WRF. (c) The terrain model for CFD simulation. (source: google earth)

Because the helicopter's flight altitude in the last two minutes was below 400 meters, the flow field under 400m should be well resolved. After grid testing, the resolution of the grid system finally adopted is summarized in Table 1, compared with that used by WRF. The resolution decreases with increasing altitude. All elements are tetrahedral and the total number of elements is about 90

million, of which 77 million are below 1200m.

Table 1. The resolution of the grid systems employed by WRF and CFD.

altitude	WRF (m)	CFD (m)
<100m	46.6	1.5~4
100~500m	46.6~100	4~16
500~900m	100~132	16~28
900~1200m	132~151	28~36
1200~1600m	151~185	36~40
1600~5000m	185~343	40

2.2 Boundary Conditions

The boundary conditions required for CFD simulation are extracted from the WRF simulation results which were performed by the research team at the Department of Atmospheric Science, National Taiwan University. Because the WRF grid is much coarser than the CFD one, the inverse-distance-weighting interpolation is used for velocities at all boundary surfaces of the CFD simulation domain excluding the ground on which no-slip boundary condition is applied. The normal velocity component on the top boundary surface is slightly modified in order to retain the global mass conservation (Luo and Cao, 2021). The inlet turbulent kinetic energy (k) and dissipation rate (ω) are specified according to the suggestion of Zhao et al., 2021 with one parameter so adjusted that the computed turbulent kinetic energy matches with the measured value at the Jeongpo weather observation station.

3. SIMULATION RESULTS AND DISCUSSION

The streamlines are shown in Fig. 2. As seen, the overall airflow is from southwest to northeast; southwest airflow also exhibited upwelling characteristics. The 10min-average horizontal wind speed measured at Jeongpo observation station is 5.5m/s. The simulated values by WRF and CFD are 2.83m/s and 5.15m/s respectively. This confirms that CFD possesses a much better near-ground accuracy because it can better capture the terrain effects.

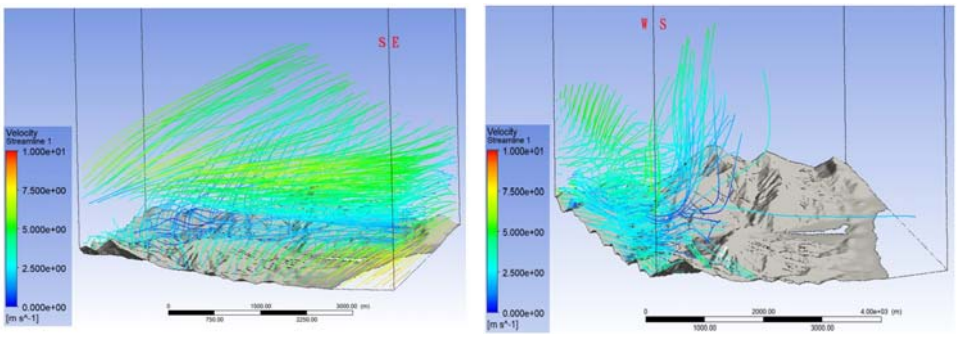


Figure 2. The streamlines of particles released from the southern (left) and western (right) boundaries.

The velocity vector diagram of the helicopter at different flight altitudes is presented in Fig. 3., in which the yellow sphere indicates the location of the helicopter at the corresponding altitude. The crash site happened to be in the valley surrounded by mountains. The video recordings from the

helicopter shows that the helicopter was in normal flight at the altitude 420m, slightly vibrating at 320m, in continuous decline at 270m, and significantly shaking at 180m. Air currents from both the west and south flew to the northeast. A large circulation formed in the area south of the valley. When flying in such a complex wind field, the wind direction encountered by the helicopter changed quite a lot. However, the turbulent intensity and wind shear along the flight path are found to be small, much less than the noticeable level (Standards Norway, 2013; Wilson and Riley, 1989).

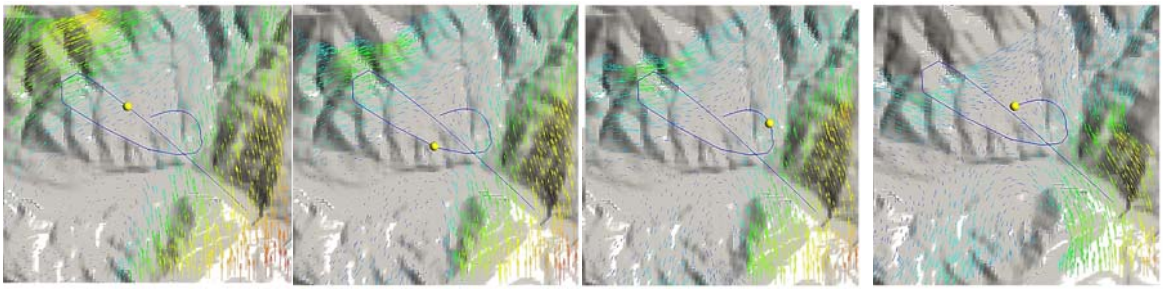


Figure 3. Velocity vector diagram of the helicopter at different flight altitudes, where the yellow sphere represents the location.

4. CONCLUSIONS

The wind field in the mountainous area of eastern Taiwan was reproduced in order to investigate the cause of a helicopter crash accident. The study uses the simulation results from the mesoscale WRF weather forecast model as the boundary conditions for the small-scale CFD simulation, which provides better resolution in low-altitude areas. The CFD simulation did not find serious wind shear or turbulence intensity along the flight path, but it did reveal that the helicopter flew through a complex wind field, which may have safety concerns.

ACKNOWLEDGEMENTS

This research was supported by NSTC 113-2221-E-002 -189 -MY2 and Government Science and Technology Project 113-3801-04-28-01. The authors would like to express our sincere gratitude for the support of the research team led by Professor Po-Hsiung Lin at the Department of Atmospheric Science, National Taiwan University.

REFERENCES

Badshah, M., VanZwieten, J., Badshah, S., and Jan S., 2019. A CFD study of blockage ratio and boundary proximity effects on the performance of a tidal turbine. IET Renewable Power Generation 13, 744-749.

Franke, J., 2006. Recommendations on the use of CFD in predicting pedestrian wind environment. The fourth International symposium on computational wind engineering, Yokohama, Japan.

Luo, X. and Cao, Y., 2021. Simulation of the wind fields over complex terrain with coupling of CFD and WRF. Journal of Computational Methods in Sciences and Engineering 21, 1155-1166.

Skamarock, W.C., Klemp, J.B., Dudhia, J., Gill, D.O., Liu, Z., Berner, J., Wang, W., Powers, J.G., Duda, M.G., Barker, D.M., and Huang, X.Y., 2019. A Description of the Advanced Research WRF Version 4. National Center for Atmospheric Research, P. O. Box 3000 Boulder, Colorado 80307-3000, USA.

Standards Norway, 2013. Norsok Standard C-004: Helicopter deck on offshore installations. 2nd ed. Norway.

Wilson, D. and Riley, D., 1989. Cooper-harper pilot rating variability. 16th Atmospheric Flight Mechanics Conference.

Zhao, Z., Li, C., Xiao, Y., Wang, J., Hu, G., and Xiao, K., 2021. Multiscale modelling of planetary boundary layer fow over complex terrain: implementation under near neutral conditions. Environmental Fluid Mechanics 21, 759–790.

Prediction of hurricane wind field with sparse observational data

Feng Hu [1], Bin Lu [1], Junyi He [1], Qiusheng Li [2,3]

[1]*Department of Architecture and Civil Engineering, City University of Hong Kong, Hong Kong, China*
[2]*Department of Architecture and Civil Engineering, City University of Hong Kong, Hong Kong, China, Email address: bcqsli@cityu.edu.hk*
[3]*Architecture and Civil Engineering Research Center, City University of Hong Kong Shenzhen Research Institute, Shenzhen, China*

SUMMARY:
In this paper, the hurricane boundary layer wind field is predicted based on physics-informed neural networks with sparse observational data. The governing equations of the wind field, which incorporate a spatially varying eddy diffusivity coefficient, are embedded within the loss function. This integration allows the model to learn the underlying physics of the boundary layer wind field. The model is applied to predict the wind field of Hurricane Lee (2023) in the Atlantic. Observational data from satellite, dropsonde, and Doppler radar records are assimilated into the model. And the model's performance is evaluated by comparing its results with observations. The proposed model does not require strict boundary conditions to reconstruct the wind field, offering greater flexibility compared to traditional numerical models. With sparse observational data, the proposed model accurately predicts the horizontal, radial, and vertical distributions of the hurricane wind fields.

Keywords: hurricane, boundary layer, physics-informed neural networks

1. INTRODUCTION

Hurricanes are recognized as mesoscale circulation systems with low-pressure cores. Dynamics in the hurricane boundary layer are extremely complicated due to surface interactions and turbulence. To date, it is still challenging to model the full three-dimensional wind field of hurricanes in the boundary layer. However, high-fidelity wind field models are crucial for hurricane intensity forecasting and risk assessment given the fact that hurricanes make recurrent landfalls in some coastal regions every year and have caused significant losses globally.

The challenge lies in utilizing sparse observational data from satellites, radars, dropsondes and aircrafts to accurately predict the boundary layer winds of hurricanes. The rapid development of physics-informed machine learning sheds light on this issue (Cuomo et al., 2022; Raissi et al., 2019). Physics-informed neural networks (PINNs) facilitate the neural networks to approximate solutions with minimal data by embedding prior physical knowledge into the loss function. For hurricane winds, Snaiki & Wu (2019) first proposed to reconstruct the three-dimensional hurricane wind field based on PINNs though hard boundary constrains were required in their model. Eusebi et al. (2024) successfully reconstructed realistic hurricane winds using PINNs, but their focus was

not on the boundary layer where the inviscid assumption may not hold true.

This work aims to predict the three-dimensional hurricane boundary layer wind field using PINNs with limited observations. The proposed method does not require strict boundary conditions, and atmospheric turbulence is estimated by introducing a spatially varying eddy diffusivity coefficient.

2. METHODOLOGY

2.1. Governing equations

According to the Boussinesq approximation, the momentum equation of the atmosphere on an f-plane in Cartesian coordinates can be written as (Holton & Hakim, 2013)

$$\frac{\partial \bar{u}}{\partial t} + \bar{u}\frac{\partial \bar{u}}{\partial x} + \bar{v}\frac{\partial \bar{u}}{\partial y} + \bar{w}\frac{\partial \bar{u}}{\partial z} = -\frac{1}{\rho_0}\frac{\partial \bar{p}}{\partial x} + f\bar{v} + \frac{\partial}{\partial z}\left(K\frac{\partial \bar{u}}{\partial z}\right) \tag{1}$$

$$\frac{\partial \bar{v}}{\partial t} + \bar{u}\frac{\partial \bar{v}}{\partial x} + \bar{v}\frac{\partial \bar{v}}{\partial y} + \bar{w}\frac{\partial \bar{v}}{\partial z} = -\frac{1}{\rho_0}\frac{\partial \bar{p}}{\partial y} - f\bar{u} + \frac{\partial}{\partial z}\left(K\frac{\partial \bar{v}}{\partial z}\right) \tag{2}$$

$$\frac{\partial \bar{\theta}}{\partial t} + \bar{u}\frac{\partial \bar{\theta}}{\partial x} + \bar{v}\frac{\partial \bar{\theta}}{\partial y} + \bar{w}\frac{\partial \bar{\theta}}{\partial z} = -\bar{w}\frac{d\theta_0}{dz} + \frac{\partial}{\partial z}\left(K\frac{\partial \bar{\theta}}{\partial z}\right) \tag{3}$$

where u, v, and w are zonal, meridional and vertical winds; p is the pressure; t is the time; ρ_0 is the reference air density; x and y have positive directions of east and north, respectively; z is pointing vertically up from the sea level; f is the Coriolis parameter; θ is the potential temperature; K is the eddy diffusivity.

The eddy diffusivity coefficient must be determined empirically, and the accuracy of hurricane boundary layer modeling is sensitive to the parameterization of the eddy diffusivity (Kepert, 2012). He et al. (2021) recommended to use the K-profile parameterization (KPP) scheme (Troen & Mahrt, 1986) to parameterize the hurricane boundary layer based on observations from a 356 meters high meteorological tower. The KPP scheme is in the form of

$$K(z) = \kappa z \frac{u_*}{\varphi_m}\left[\alpha\left(1 - \frac{z}{h}\right)^p\right] \tag{4}$$

where $\kappa = 0.4$ is the von Kármán constant; z is the height above the sea surface; $u_* = 0.5$ m/s is the surface friction velocity (Vickers et al., 2015); $\varphi_m = 1$ is the nondimensional wind shear for neutral stability; $\alpha = 1.0$ is an empirical coefficient; $h = 2000$ m is the boundary layer height; $p = 2$ is the shape parameter.

2.2. PINN Architecture

The architecture of the PINNs applied to reconstruct the hurricane boundary layer wind field is shown in Fig. 1. The inputs of the model are storm-relative coordinates of the winds, which are passed through a network consisting of 8 hidden layers, each with 100 neurons. The tanh (hyperbolic tangent) activation function is employed for each hidden neuron. The outputs of the model are wind, pressure and temperature field at a given time. All parameters of the model are initialized via Xavier initialization technique. In the process of backpropagation, the model is trained using the Adaptive Moment Estimation (Adam) optimizer for the first 5,000 iterations, and

then using the L-BFGS optimizer until convergence.

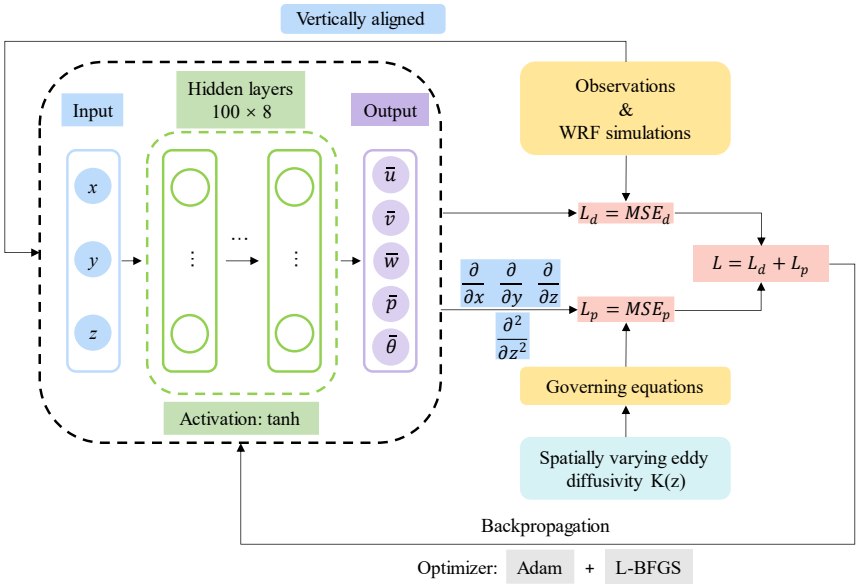


Figure 1. The architecture of PINNs for hurricane wind field predictions.

3. RESULTS

Taking Hurricane Lee (2023) as an example, the training data are obtained from Tail-Doppler Radar (TDR) and dropsondes. PINN predictions that assimilate the observational data are shown in Fig. 2. The eye size of Hurricane Lee is well captured by the proposed model. Besides, the maximum winds in the PINN model are concentrated in front of the track motion, which aligns with the satellite observations. More intense winds are located to the north of the center in the PINN predictions. Additional investigation indicates that the PINN model provides accurate predictions of the horizontal and vertical wind field distribution. With the increase in the availability of real data, the accuracy of the proposed model will be further improved.

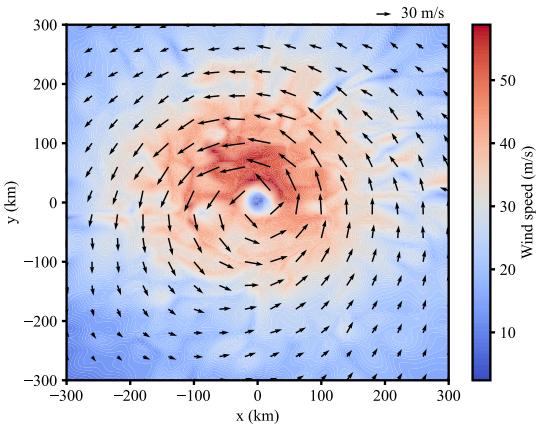


Figure 2. Wind field at 1500 m predicted by the PINN model.

4. CONCLUSIONS

In this paper, a PINN model was proposed to predict the hurricane boundary layer wind field using sparse observational data. Prior physical knowledge was embedded into the training loss of the PINN model, enabling the model to learn the dynamics of the boundary layer. Unlike numerical methods, the PINN model does not require hard boundary conditions. The model presents satisfactory performance in predicting the 3D wind field of hurricanes. With the growing availability of the observational data collected by the meteorological flights, satellites and other instruments, wide applications of the proposed PINN framework in weather forecasting and engineering risk assessments are promising.

ACKNOWLEDGEMENTS

This study is supported by grants from the Research Grants Council of Hong Kong (GRF: CityU 11206922 and CityU 11213523; RIF: R1006-23), the Science, Technology and Innovation Commission of Shenzhen Municipality (Project No.: JCYJ20220818101201003), and the National Natural Science Foundation of China (Project No.: 52278538).

REFERENCES

Cuomo, S., Di Cola, V. S., Giampaolo, F., Rozza, G., Raissi, M., & Piccialli, F. (2022). Scientific machine learning through physics–informed neural networks: Where we are and what's next. *Journal of Scientific Computing*, *92*(3), 88.

Eusebi, R., Vecchi, G. A., Lai, C.-Y., & Tong, M. (2024). Realistic tropical cyclone wind and pressure fields can be reconstructed from sparse data using deep learning. *Communications Earth & Environment*, *5*(1), 8.

He, J. Y., Chan, P. W., Li, Q. S., Li, L., Zhang, L., & Yang, H. L. (2021). Observation of vertical eddy diffusivity and mixing length during landfalling Super Typhoons. *Journal of Wind Engineering and Industrial Aerodynamics*, *219*, 104816.

Holton, J. R., & Hakim, G. J. (2013). *An introduction to dynamic meteorology*. Elsevier.

Kepert, J. D. (2012). Choosing a boundary layer parameterization for tropical cyclone modeling. *Monthly Weather Review*, *140*(5), 1427–1445.

Raissi, M., Perdikaris, P., & Karniadakis, G. E. (2019). Physics-informed neural networks: A deep learning framework for solving forward and inverse problems involving nonlinear partial differential equations. *Journal of Computational Physics*, *378*, 686–707.

Snaiki, R., & Wu, T. (2019). Knowledge-enhanced deep learning for simulation of tropical cyclone boundary-layer winds. *Journal of Wind Engineering and Industrial Aerodynamics*, *194*, 103983.

Troen, I. B., & Mahrt, L. (1986). A simple model of the atmospheric boundary layer; sensitivity to surface evaporation. *Boundary-Layer Meteorology*, *37*(1–2), 129–148.

Vickers, D., Mahrt, L., & Andreas, E. L. (2015). Formulation of the sea surface friction velocity in terms of the mean wind and bulk stability. *Journal of Applied Meteorology and Climatology*, *54*(3), 691–703.

Development of multi-region Reduced-order Modeling framework: application in Atmospheric Boundary Layer flows over urban areas

Haoyan Li[1], Ruggiero Signoriello[4], Alessandro Gambale[2], Alessandro Parente [1,3]

[1]*Université Libre de Bruxelles, École polytechnique de Bruxelles, Brussels, 1050, Belgium*
[2]*BuildWind SPRL, Brussels, 1070, Belgium*
[3]*WEL Research Institute, Wavre, 1300, Belgium*
[4]*Politecnico di Milano, Dept. of Energy (DENG), Milan, 20156, Italy*

SUMMARY:
Computational Fluid Dynamics (CFD) is a powerful tool for simulating Atmospheric Boundary Layer (ABL) flows in urban environments, enabling detailed analysis of wind patterns, pollutant dispersion, and more. However, its high computational cost makes it impractical for widespread use, particularly when dealing with complex geometries like cityscapes filled with buildings. Traditional Reduced-Order Models (ROMs) offer a solution by reducing this computational burden, but their global application of dimensionality reduction—treating the entire domain uniformly—fails to account for local flow variations, such as those caused by structures.
To overcome this limitation, this study proposes a novel multi-region ROM framework designed to improve both the accuracy and efficiency of predicting ABL flows over urban areas. The methodology leverages K-means clustering to divide the computational domain into distinct regions, separating areas influenced by buildings from those unaffected by obstructions. Within each region, Principal Component Analysis (PCA) is applied to reduce dimensionality by identifying the most significant flow features, while Gaussian Process Regression (GPR) constructs a predictive mapping to estimate flow fields efficiently.
The framework was validated using a case study involving flow over an array of buildings, tested across 64 different operating conditions (40 for the training and 24 for the testing). Results show that an optimal configuration with 2 clusters significantly outperforms traditional Global ROMs, reducing the mean Root Mean Square Error (RMSE) by 9.5% for stream-wise velocity and by 18.2% for turbulent kinetic energy (TKE). This improvement underscores the framework's ability to capture localized flow phenomena more effectively, offering a promising advancement for urban flow modeling while keeping computational demands manageable.

Keywords: Atmospheric Boundary Layer flows, Reduced-order model, Building-influenced regions

1. INTRODUCTION

Machine Learning (ML) techniques are now widely used across various fields, from computer vision to physics modelling. This paper specifically examines ROMs, a class of ML algorithms known for their effectiveness in both exploratory data analysis and predictive tasks. We introduce an innovative approach to enhance ROMs for ABL flows by integrating clustering and dimensionality reduction techniques. The proposed framework starts by employing clustering methods, specifically K-means, to divide the computational domain into distinct local regions: those influenced by obstacles like buildings and those dominated by unobstructed ABL flows. This partitioning ensures that subsequent dimensionality reduction captures the unique flow structures

within each region effectively. PCA is then applied individually to each region, extracting local flow patterns, and generating corresponding PCA coefficients that represent the latent flow dynamics. Following this, GPR is utilized to create a predictive mapping between these local PCA coefficients and the input parameters defining the boundary conditions. This mapping enables the ROM to accurately predict flow behaviour under new or varying operating conditions.

This multi-region ROM framework was developed and validated for ABL flows over an array of buildings from the CEDVAL database (Leitl et al.,1998). A series of simulations were conducted by defining a realistic range of input parameters, including friction velocity and surface roughness. Numerical simulations were performed using the ABL k-omega SST turbulence model (Bellegoni et al.,2023).

The results demonstrate that the multi-region ROMs significantly out-performs the traditional ROM in terms of prediction accuracy, particularly for velocity and turbulent kinetic energy (TKE) fields. By leveraging localized dimensionality reduction and regression, the multi-region ROMs effectively capture the complex flow dynamics influenced by obstacles, offering a more precise and reliable tool for simulating ABL flows in urban environments.

2. METHODOLOGY

Different from the traditional ROM framework, the current study introduces an additional step: domain partitioning to clustering the domain according to the flow properties. Figure 1 shows the workflow of traditional Global ROM which applies dimensionality reduction to the whole domain and multi-region ROM.

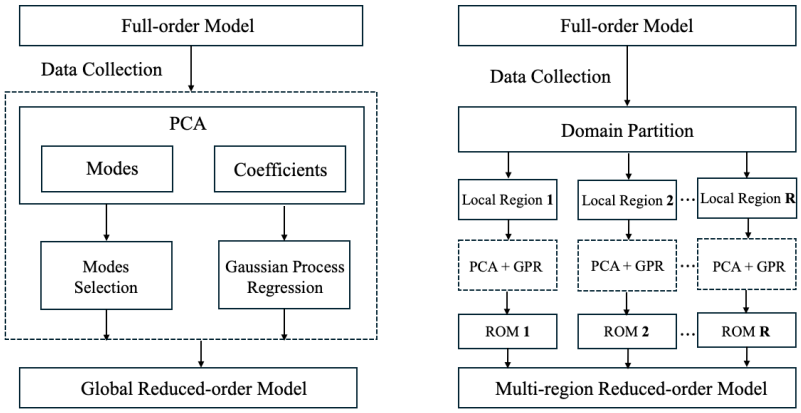


Figure 1. The framework of Global ROM and multi-region ROM.

To effectively partition the domain based on its intricate flow properties, variables that capture flow structures are required. Specifically, velocities and TKE are essential for this purpose. The matrix used for clustering is structured as $\widehat{\boldsymbol{Y}} = [\widehat{\boldsymbol{y}}_{\boldsymbol{1}}, \widehat{\boldsymbol{y}}_{\boldsymbol{2}}, \ldots, \widehat{\boldsymbol{y}}_{\boldsymbol{c}}]$, each $\widehat{\boldsymbol{y}}_{\boldsymbol{1}}$ is a matrix containing the rescaled velocities and TKE vectors, stacked in each column of $\widehat{\boldsymbol{y}}_{\boldsymbol{i}}$. The number of rows in the clustering matrix represents the spatial point, the number of columns of the matrix is the product of number of variables and operating conditions. This arrangement ensures that the clustering algorithm operates directly in the spatial domain, grouping points in all simulations. The global domain can be divided into R local regions using clustering methods: $\boldsymbol{\Omega} = \bigcup_{\boldsymbol{r=1}}^{\boldsymbol{R}} \boldsymbol{\Omega}^{(\boldsymbol{r})}$. As the domain is partitioned locally by means of clustering method, the dimensionality reduction can be implemented in each local region to extract the latent

variables. The matrix $\mathbf{Y}$ used for developing ROM is the collection of the CFD simulations dataset with size $(m \times n)$, where n is the total number of simulations and m is the number of grid-points $\times$ the number of chosen variables. For the clustered domain, the matrix $\mathbf{Y} = \bigcup_{r=1}^{R} \mathbf{Y}^{(r)}$ and each $\mathbf{Y}^{(r)}$ has different number of the spatial points. By computing the eigen-value decomposition for the covariance matrix of $\mathbf{Y}^{(r)}$ the principal components $\mathbf{A}^{(r)}$ (PCs) with size $(n \times n)$ are identified from: $\mathbf{C}^{(r)} = \frac{1}{\mathbf{n-1}} \mathbf{Y}^{(r)^{\mathbf{T}}} \mathbf{Y}^{(r)} = \mathbf{A}^{(r)} \mathbf{L}^{(\mathrm{r})} \mathbf{A}^{(r)^{\mathbf{T}}}$. $\mathbf{L}^{(\mathrm{r})}$ is the diagonal matrix of the eigen-values with size $(n \times n)$ and $\mathbf{A}^{(r)}$ is the orthogonal matrix. By projecting the original data $\mathbf{Y}^{(r)}$ to the PCs $\mathbf{A}^{(r)}$, the PCA modes of the local region is obtained: $\mathbf{Z}^{(r)} = \mathbf{Y}^{(r)} \mathbf{A}^{(r)}$. Then the original data can be reconstructed by only keeping important $\mathbf{q}$ PCs as follows: $\mathbf{Y}^{(r)} = \mathbf{Z}^{(r)} \mathbf{A}^{(r)^{\mathbf{T}}} \approx \boldsymbol{Z}_{\boldsymbol{q}} \mathbf{A}_{\boldsymbol{q}}^{(r)T}$. Subsequently, the GPR is used to regress the $\mathbf{A}_{\boldsymbol{q}}^{(r)}$ and input parameters $\boldsymbol{x}$ of the operating conditions through developing the prior distribution: $\boldsymbol{p}\left(\mathbf{A}_{\boldsymbol{q}}^{(r)} | \boldsymbol{x}\right) \sim \boldsymbol{N}(\mathbf{A}_{\boldsymbol{q}}^{(r)T} | \boldsymbol{\mu}, \mathbf{K})$, and the prediction can be made by the posterior distribution: $\boldsymbol{p}\left(\mathbf{A}_{\boldsymbol{q}}^{*(r)} | \boldsymbol{x}^{*}, \boldsymbol{x}, \mathbf{A}_{\boldsymbol{q}}^{(r)}\right) \sim \boldsymbol{N}(\mathbf{A}_{\boldsymbol{q}}^{*(r)} | \boldsymbol{\mu}^{*}, \mathbf{K}^{*})$ when giving the new operating conditions $\boldsymbol{x}^{*}$.

3. DESIGN OF THE INPUT DATASET

The effectiveness of data-driven approaches, such as ROMs, heavily relies on the quality of data used during the training phase. In this study, we created a dataset parameterized by two variables, allowing us to design a process that ensures controlled coverage of the solution space. This approach enables us to assess the impact of ML techniques on tasks involving interpolation as well as extrapolation. The input data used in ROMs consist of fluid flow characteristics of ABL when the friction velocity (m/s) $u^{*}$and roughness length (m) z_0 are changed. Specifically, we adopted flow over an array of building blocks, see Figure 2, with $u^{*} \in [0.26, 0.58]$, $z_0 \in [0.0001, 0.003]$. The simulations are executed using the simpleFoam solver in OpenFOAM v7, a steady-state, incompressible solver and ABL k-omega SST model.

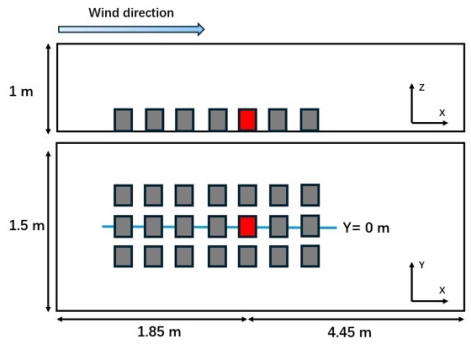


Figure 2. The computational domain is depicted with dimension indicators provided for the central lateral view at y=0 and for the top view.

4. RESULTS

The multi-region ROMs for ABL flows over an array of building blocks have been developed. The K-means is implemented to cluster the domain, see Figure 3. Results show that an optimal configuration with 2 clusters significantly outperforms traditional global ROMs, reducing the mean Root Mean Square Error (RMSE) by 9.5% (from 0.336 to 0.304) for stream-wise velocity

and by 18.2% (from 0.077 to 0.064) for turbulent kinetic energy (TKE), see Figure 4. The more detailed results will be shared during the oral presentation.

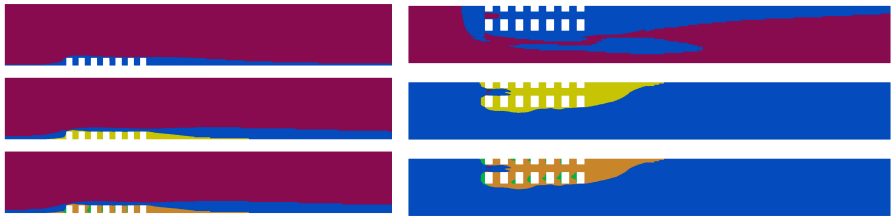


Figure 3. The central lateral view at $y = 0m$ and top review at $z = 0.025m$ from 2 clusters to 4 clusters (top to bottom.

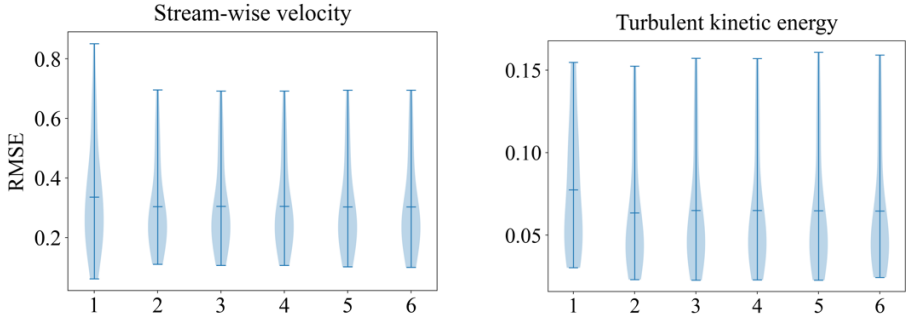


Figure 4. The RMSE of stream-wise velocity and TKE of Global ROM (1 cluster) and multi-region ROMs (2 to 6 clusters). Ticks inside represent the Max, Mean and Min.

5. Application in Real-life urban flows

The future case study focuses on the ULB Solbosch campus, located at 1050 Brussels, as shown in Figure 5. The multi-region ROMs will be developed on this case in the future several months.

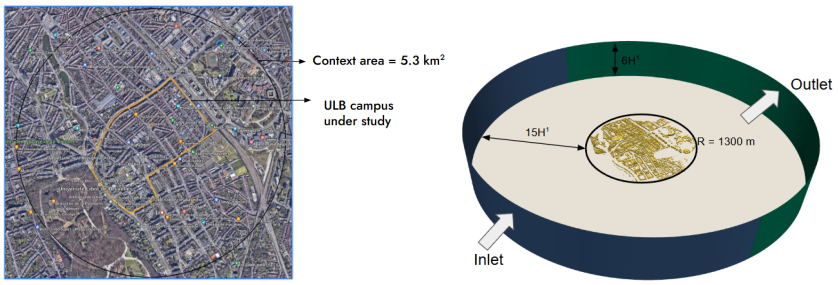


Figure 5. ULB campus under study and context area for simulation.

ACKNOWLEDGEMENTS

The study has received funding from the European Union's Horizon Europe research and innovation programme under grant agreement No 101072559.

REFERENCES

Leitl B, Schatzmann M, 2010. CEDVAL at Hamburg University. URL: https://mi- pub.cen.uni-hamburg.de/index.php?id=433.

Bellegoni, M., Cotteleer, L., Raghunathan Srikumar, S. K., Mosca, G., Gambale, A., Tognotti, L., Galletti, C., Parente, A. (2023). An extended $k - \omega$ SST framework for the RANS simulation of the neutral Atmospheric Boundary Layer. Environ. Model. Softw. 160, 105583.

Field measurements and numerical analysis of downslope winds in port areas

Ivana Ivančić[1], Alessio Ricci[1], Massimiliano Burlando[2], Djordje Romanic[3], Branko Grisogono[4], Hrvoje Kozmar[4]

[1]*University School for Advanced Studies, IUSS, Pavia, Italy, ivana.ivancic@iusspavia.it, alessio.ricci@iusspavia.it*
[2]*University of Genoa, Genoa, Italy, massimiliano.burlando@unige.it*
[3]*McGill University, Montreal, Canada, djordje.romanic@mcgill.ca*
[4]*University of Zagreb, Zagreb, Croatia, branko.grisogono@gfz.hr, hrvoje.kozmar@fsb.hr*

SUMMARY:
Severe weather conditions can impact the structural integrity of buildings and infrastructures, and pose risk to human safety. Strong wind is one of the most destructive natural phenomena and primary cause of the accidents occurring in coastal areas. International codes and standards commonly used to design wind-resistant structures are based on neutrally stratified atmospheric boundary layer (ABL). ABL winds during neutral stratification are often characterized by lower mean velocities near the ground compared to other types of winds as thunderstorm downbursts, tornadoes and downslope winds (DW). A particular type of DW frequently occurs in the main valleys of Liguria, Italy, impacting the Port of Genoa on the coastline at the end of Turchino Valley. In some cases, port operations need to be suspended to prevent accidents involving ships, infrastructures, and workers. Thus, assessing the nature of DW is mandatory to improve existing standards and codes for wind design of buildings, port infrastructures and safety management of port operations. This is the goal of the preliminary field measurements and numerical simulations (i.e., Computational Fluid Dynamics, CFD) presented in this study.

Keywords: Downslope wind, LiDAR measurements, CFD simulations

1. INTRODUCTION

Ports play a crucial role in economic growth as they serve as hubs for international trade and key points. However, coastal areas, in particular port areas, are highly vulnerable to extreme meteorological phenomena. Severe wind is one of the most destructive natural phenomena and a major cause of the accidents in ports (Solari et al., 2012). International codes and standards for wind design of structures are commonly based on neutrally stratified ABL winds. However, these ABL winds are typically characterized by lower mean wind velocities near the ground compared to other types of wind systems, such as thunderstorm downbursts, tornadoes, and downslope winds (DW). DW develop for air flows over high mountain ridge with a steep lee slope (Figure 1). Those winds are well-known to occur all over the world with different local names, e.g., Alpine Foehn, Rocky Mountain Chinook, Croatian Bora, e.g., Kozmar et al., 2012; Durran, 2014; Lepri et al., 2015. In particular, specific DW occur in Liguria valleys, Italy, when the wind from north of the Maritime Alps and Apennines mountains blows down the sloping terrain towards the sea. This phenomenon is driven by large-scale pressure gradients directed from the cold continental air towards warmer maritime air over the Mediterranean Sea (Burlando et al., 2017); mountain wave

breaking is often related to such flows as an additional wind enhancement (e.g. Durran, 2014). During strong windstorms, which could last several days, port operations and activities are usually suspended to avoid accidents. Thus, assessing the nature of DW is imperative to provide analytical formulations for wind load provision on structures and for the safety management of port operations. This research is also the goal of a PhD project that started early 2024 and organized in three work packages (WP): (1) field measurements using a Light Detection and Ranging (LiDAR) scanner in the Port of Genoa will be performed to characterize the DW (2) Computational Fluid Dynamics (CFD) simulations will be used to calibrate DW in an empty computational domain; (3) CFD simulations will be used in the complex built environment of the Port of Genoa for wind load analysis of port infrastructure. It is worth noting that, while DWs have been typically simulated by means of mesoscale numerical weather forecast models, the CFD has never been used to the best of authors' knowledge. The application of CFD methodology represents the innovative aspect of the present project. In the presentation, the preliminary results of the ongoing analyses related to WP1 and WP2 will be discussed.

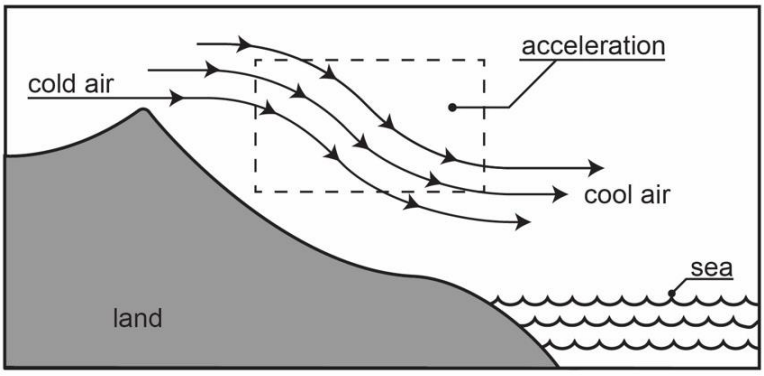


Figure 1. Schematic view of downslope winds.

2. METHODOLOGY

2.1. Field measurements

During the winter period, DW occurring in the Turchino Valley (Western part of the Genoa city) are stronger than the ones occurring during other seasons. The reason is twofold: stronger synoptic activity moves generally southward, and the air-sea temperature contrast enhances and prolongs mountain wave breaking (Enger and Grisogono, 1998). Therefore, field measurements will be performed during the winter using the LiDAR station WindCube 400S in the port area (Figure 2a). The station is managed by the University of Genoa and operates in a range of 14 km and a gate resolution set to 75 m. This location has been selected because it is suitable to measure DW developing from the outlet of Turchino Valley toward the open sea. The measurement campaign is aimed to assess the main characteristics of DW occurring in Liguria. The wind velocity and turbulence characteristics, e.g., turbulence intensity, turbulence length scales, power spectral density, will be analysed to their respective vertical profiles for wind load provisions. The data obtained during this field measurement campaign will be used to validate CFD simulations of WP2

and WP3.

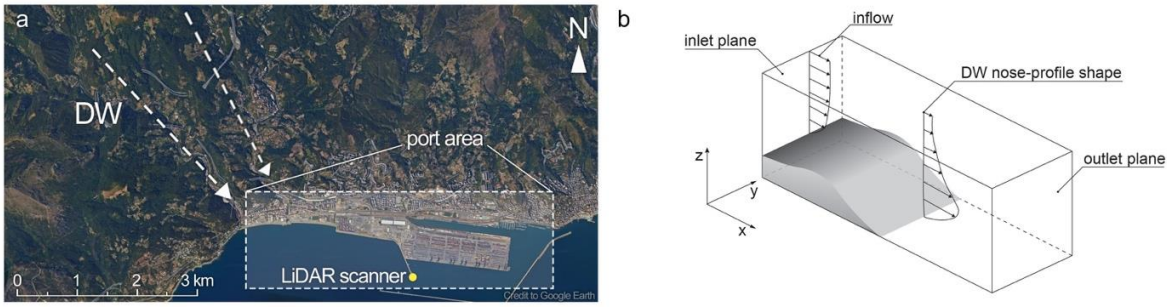


Figure 2. a) Aerial view of the Port of Genoa with the LiDAR scanner position and DW direction. b) Schematic view of CFD simulations to be carried out on an empty domain for the calibration of DW.

2.2. CFD simulations

In WP2, the CFD technique will be used to calibrate the vertical profile of DW in terms of velocity and turbulence characteristics. The steady-state Reynolds-averaged Navier-Stokes (RANS) approach coupled to various turbulence models, e.g., standard k-ε, realizable k-ε, standard k-ω, and SST k-ω will be used to investigate the effect of inflow conditions, grid resolution, surface roughness on the DW nose-profile shape (Figure 2b). Unsteady RANS, scale-adapted simulation (SAS) and large-eddy simulation (LES) will be carried out next on the same empty domain to understand the dynamics and transient nature of DW. Numerical simulation results will be further compared to measured data from the LiDAR scanner (Figure 2a). In WP3, the calibrated DW will be applied to the simulation of the real built environment of the Port of Genoa including complex structures such as buildings and port infrastructure. Here, two levels of complexity will be simulated: (1) the real topography of the area of interest (Port of Genoa) with the implicit modeling of buildings and small-scale obstacles surrounding the port infrastructures (explicitly modeled); (2) the real topography with explicitly modeled obstacles and port infrastructure. The computational domain will be designed using the digital terrain model and digital elevation model by using the automatic reconstruction approach by Žužul et al. (2024).

3. CONCLUDING REMARKS

This study assesses preliminary field measurements and CFD simulations of downslope windstorms commonly occurring in Liguria, Italy. The LiDAR data will elucidate physical mechanisms that contribute to the formation of DW from the top of hills/mountains to the coastline. The same phenomenon will be reproduced by CFD using steady and transient approaches. In the presentation, the preliminary results of the ongoing analyses related to WP1 and WP2 will be discussed.

ACKNOWLEDGEMENTS

This study was developed while attending the PhD programme in PhD in Sustainable Development And Climate Change at the University School for Advanced Studies IUSS Pavia, Cycle XXXIX, with the support of a scholarship financed by the Ministerial Decree no. 351 of 9th April 2022, based on the NRRP - funded by the European Union -

NextGenerationEU - Mission 4 "Education and Research", Component 1 "Enhancement of the offer of educational services: from nurseries to universities"- Investment 4.1 "Extension of the number of research doctorates and innovative doctorates for public administration and cultural heritage". This work is part of the transnational access project "ERIES–LIDAR", supported by the Engineering Research Infrastructures for European Synergies (ERIES) project (www.eries.eu), which has received funding from the European Union's Horizon Europe Framework Programme under Grant Agreement No. 101058684. The authors gratefully acknowledge the funding of the Croatian Science Foundation IP-2022-10-9434.

REFERENCES

Burlando, M., Tizzi, M., Solari, G., 2017. Characteristics of downslope winds in the Liguria Region. Wind and Structures 24, 613-635.

Durran, D.R., 2014. Encyclopaedia of Atmospheric Sciences. 2nd ed., Academic press, 69-74.

Enger, L., Grisogono, B., 1998. The response of bora-type flow to sea surface temperature. Quarterly Journal of the Royal Meteorological Society 124, 1227-1244.

Kozmar, H., Butler, K., Kareem, A., 2012. Transient cross-wind aerodynamic loads on a generic vehicle due to bora gusts. Journal of Wind Engineering and Industrial Aerodynamics 73-84.

Lepri, P., Večenaj, Ž., Kozmar, H., Grisogono, B., 2015. Near-ground turbulence of the Bora wind in summertime. Journal of Wind Engineering and Industrial Aerodynamics 345-357.

Solari, G., Repetto, M.P., Burlando, M., De Gaetano, P., Pizzo, M., Tizzi, M., Parodi, M., 2012. The wind forecast for safety management of port areas. Journal of Wind Engineering and Industrial Aerodynamics 104-106, 266-277.

Žužul, J., Ricci, A., Burlando, M., 2024. An automated geometry generation procedure for CWE applications in OpenFOAM: the case study of a thunderstorm downburst moving over Genoa city. Meccanica. https://doi.org/10.1007/s11012-024-01816-z.

Comparison between LIDAR measurements and reanalysis wind velocities: a case study

Vincenzo Sepe [1], Francesco Ricciardelli [2], Sergio Montelpare [1], Alberto M. Avossa [2]

[1]Department of Engineering and Geology, University "G. d'Annunzio", Pescara, Italy, {vincenzo.sepe; sergio.montelpare}@unich.it
[2]Department of Engineering, University of Campania "Luigi Vanvitelli", Aversa, Italy, {friccia; albertomaria.avossa}@unicampania.it

SUMMARY
This paper brings a comparison between wind velocities measured by a LIDAR anemometer and the corresponding values obtained at the mesoscale by means of reanalysis of meteorological data. The results show how numerical techniques can reproduce the general evolution of the mean wind velocity, capturing the main features of the onset and development of intense wind events. They also show discrepancies occurring between measured and calculated values, thus indicating that the downscaling procedure needs to be adjusted in order to achieve the desired degree of accuracy, depending on the target use of the data. For example, when it comes to the assessment of the extreme wind velocities, it has to be assured that all mechanisms giving rise to strong winds are properly reproduced, and that local circulation characteristics are also.

Keywords: wind Lidar, reanalysis, design wind maps

1. INTRODUCTION

In the last decades, numerical techniques are becoming more and more widespread, thanks to which it is potentially possible to reconstruct, at the mesoscale, the wind field at any point on the Earth's surface starting from the data available at the macroscale (Montelpare *et al.*, 2019; Germano *et al.*, 2020a; Germano *et al.*, 2020b). These data are in turn obtained by means of numerical procedures for the reanalysis of measurements at meteorological stations located over a large part of the Earth's surface, for time intervals that can extend for many decades.
Thanks to the increased reliability of the numerical models, and to the increased computational capacity, a detailed reconstruction of the wind field consistent with the available measurements can so be obtained at sites and/or time periods different from those of the measurements.
This may significantly contribute to the definition of national or regional mean and extreme wind velocity maps, for use in the fields of wind energy and structural design. To the latter aim, the reference wind velocity for evaluating the wind actions associated with a given return period must in fact necessarily refer to long-term data for the specific site under consideration, seldom available in real cases.

A numerical procedure is therefore needed, able to reconstruct the local wind field including the effects of surface roughness distribution and of the presence of orographic features.
Most of the available experimental data used for the validation of reanalysis procedures, however, consist of anemometric measurements at low elevations above the ground, as those collected in airport sites. The calibration of theoretical models describing the variation of wind field as a function of the elevation, instead, would require experimental data at different altitudes, up to hundred meters above the ground, for a wide area upstream the specific site of interest.
Nowadays (Sepe *et al.*, 2023), wind velocity measurements at medium and high elevations above the ground can be obtained by means of LIDAR (LIght Detection And Ranging), increasingly widespread in recent decades, more easily than traditional technologies (e.g. weather balloons). Comparison of LIDAR measurements with the wind field reconstructed by means of reanalysis can therefore contribute to the validation and calibration of numerical procedures.
To this aim, this paper describes the comparison between data measured by a LIDAR in the city of Aversa in southern Italy and the corresponding numerical data reconstructed at the mesoscale, for an observation period of about one year.

2. CASE STUDY

The experimental data discussed in this paper have been obtained with a wind LIDAR over a period of about one year, from October 2015 to December 2016 (Sepe *et al.*, 2019).
The LIDAR device was located (40°58'00''N, 14°12'00''E) on the roof of a 2-story building belonging to the University of Campania "Luigi Vanvitelli" in Aversa, a city 15 km North of Napoli, at an elevation of 50 m above sea level and at a distance from sea of about 15 km.
The device consists of a WindCube® V2 wind LIDAR manufactured by Leosphere, which operates as a pulsed Doppler anemometer and allowed to measure the wind velocity at 12 different elevations above the ground (50, 60, 70, 80, 90, 100, 110, 120, 150, 200, 220 and 250 m), with a sampling rate of about 1 Hz.
The adopted numerical procedure is based on a modified version of the MM5v3 code (Grell *et al.* 1994) and utilizes, as input initialization condition, the DS083.2 dataset; these data are available on 1° x 1° grids with a time step of six hours. These NCEP FNL (Final) Operational Global Analysis data are derived from the Global Data Assimilation System (GDAS), which continuously collects experimental observational data from different facilities. The numerical procedure adopted in this work is based on a two-way nesting procedure, over five nested domains, in order to span from synoptic scales to local regional ones (Silvero *et al.*, 2019). The numerical output is more refined both in terms of spatial- (down to 300 meters) and time-resolution (with a sampling period of 4 minutes).
An example of comparison between the numerically-evaluated wind speeds at an elevation of 50 m above the ground (red line) and the corresponding value measured by the LIDAR (green line) is shown in Fig. 1 for the month of February 2016. For the LIDAR data, an average over four minutes of the signal sampled at about 1 Hz is reported.
Comparison over a shorter time interval of two days is also reported in Fig. 2.

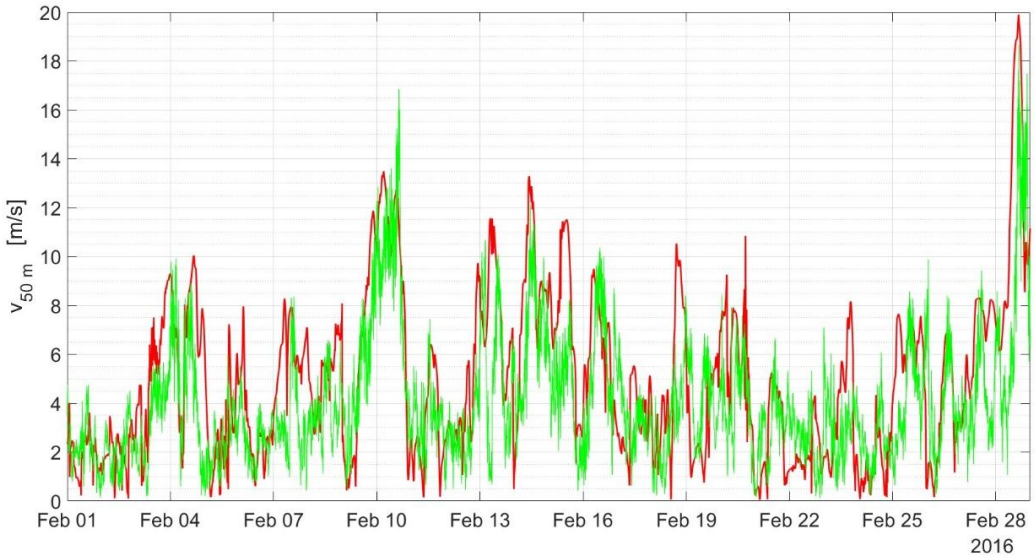


Figure 1. Time-history (time-step 4 minutes) of the wind speed at an elevation of 50 m above the ground: LIDAR (green line) and reanalysis (red line) data between first and 29 of February 2016.

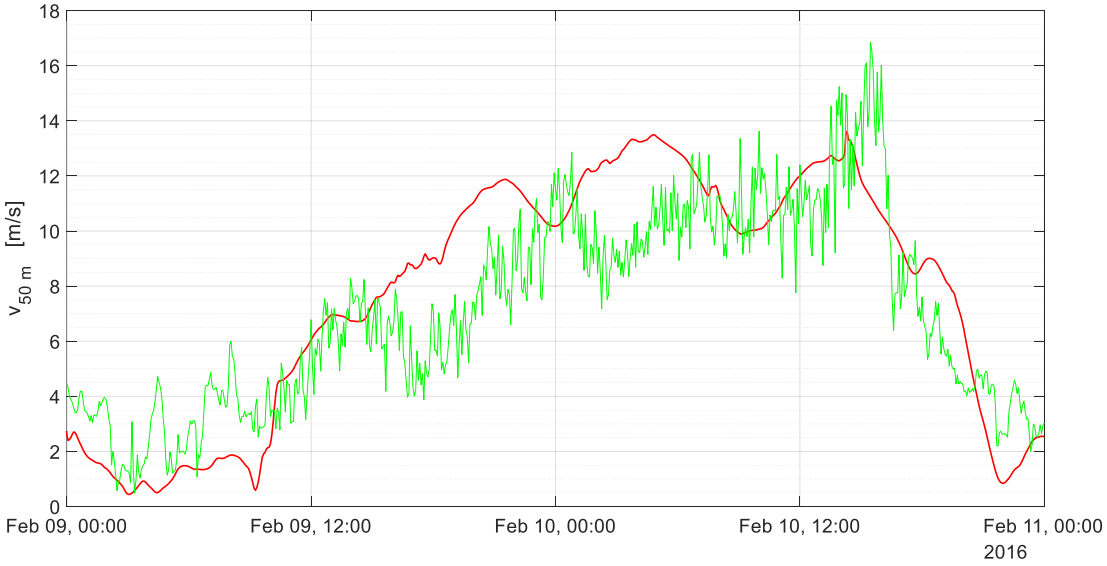


Figure 2. Time-history (time-step 4 minutes) of the wind speed at an elevation of 50 m above the ground: Lidar (green line) and reanalysis (red line) data, 9-10 February 2016.

The first results so far available show that numerically simulated and measured data have similar trends (Fig. 1), with the numerical simulation able to capture the onset and development of intense wind events, including large wind speed values (Fig. 2). It is also recognized, however, peak values as well as instantaneous values are not always in agreement, with discrepancies in the order of up to 3 m/s for the events analysed.

This stimulates further analyses and comparisons, to be extended for example to the entire vertical profile of the mean wind speed (e.g of the 10-minutes averaged wind speed used for the purpose

of structural design) and to the statistical distribution of such mean speed along the whole time-interval of available LIDAR data, but also to the spectra of the experimental and numerical wind speeds.

3. CONCLUDING REMARKS

This work describes the comparison between the average wind speed, at various elevations, measured by a LIDAR in an urban area characterized by medium-to-low buildings and the corresponding time histories numerically reconstructed by a MM5v3 modified numerical procedure, for an observation period of about one year.

The results of this comparison show how numerical procedures available today can reproduce with a rather good approximation the time evolution of the wind speed averaged over some minutes, capturing in particular the onset and development of intense wind events; single and peak values seem at the moment harder to capture.

Further analyses, now in progress, will explore the reliability of the numerical procedures to reconstruct the vertical profile of the mean wind speed and the statistical distribution of the wind speed (mean and maximum values, as well as frequency content) along the whole time-interval of available LIDAR data.

ACKNOWLEDGEMENTS

This research was partially funded by the Italian Ministry of University and Research within the PRIN (Research Projects of Relevant National Interest) 2022 "WIZARD - Criteria and Guidelines for Wind Hazard Analysis.

REFERENCES

Germano, N., Lops, C., Matera, S., Montelpare, S., Camata, G., 2020a. A multiscale approach for creating boundary conditions for building energy analysis. TECNICA ITALIANA-Italian Journal of Engineering Science, 64(2-4): 298-302. https://doi.org/10.18280/ti-ijes.642-426

Germano N., Lops C., Montelpare S., Camata G., Ricci R., 2020b. Determination of Wind Pattern Inside an Urban Area Through a Mesoscale-Microscale Approach, Mathematical Modelling of Engineering Problems , Vol. 7, No. 4, pp. 515-519

Grell, G.A., Dudhia, J., Stauffer, D., 1994. A description of the fifth-generation Penn State/NCAR Mesoscale Model (MM5) (No. NCAR/TN-398+STR). University Corporation for Atmospheric Research. https://doi.org/10.5065/D60Z716B

Montelpare, S., D'Alessandro, V., Lops, C., Costanzo, E., Ricci, R., 2019. A Mesoscale-Microscale approach for the energy analysis of buildings. Journal of Physics: Conference Series, 1224(1). https://doi.org/10.1088/1742-6596/1224/1/012022

Sepe, V., Rizzo, F., Ricciardelli, F., Avossa, A. M., 2019. Characterization of Mean Wind Profiles and Surface Roughness Assessment from Wind LIDAR Measurements, In: Ricciardelli, F., Avossa, A. (eds) Proceedings of the XV Conference of the Italian Association for Wind Engineering. IN VENTO 2018. Lecture Notes in Civil Engineering, vol 27. Springer, Cham. https://doi.org/10.1007/978-3-030-12815-9_52.

Sepe, V., Avossa, A. M., Rizzo, F., Ricciardelli, F., 2023. Calibration of Mean Wind Profiles Using Wind LIDAR Measurements, Applied Sciences 13, 5077, https://doi.org/10.3390/app13085077.

Silvero, F., Lops, C., Montelpare, S., Rodrigues, F., 2019.Generation and assessment of local climatic data from numerical meteorological codes for calibration of building energy models, Energy and Buildings, Volumes 188–189, Pages 25-45, ISSN 0378-7788, https://doi.org/10.1016/j.enbuild.2019.02.001.

Vibration characteristics of multiple flat plates based on flow visualization

Nozomi Suzuki [1], Hiroshi Hasebe [2,]

[1]*Nihon University, Tokyo, Japan, csno21114@g.nihon-u.ac.jp*
[2] *Nihon University, Tokyo, Japan, hasebe.hiroshi@nihon-u.ac.jp*

SUMMARY
Flutter is an unstable aeroelastic vibration that increases in amplitude with small changes in wind speed. If the energy of flutter vibration could be corrected, it would become a new system for wind power generation. Therefore, we have developed a flutter-based wind power generation system. In the preliminary work, we found that multiple flat plates placed in a wake flow showed flutter vibrations on each plate. According to the preliminary result, we constructed a wind power generation system which corrected power the energy of flutter vibration on multiple flat plates using piezoelectric elements. When there three plates were arranged in series, the torsional amplitude of the third flat plate was smaller than that of the first and second flat plates. Therefore, in this study, smoke flow visualization around multiple flat plates occurring flutter vibrations were conducted. According to the flow visualization, we confirmed that a large vortex formed above the second plate intensified the torsional amplitude of the second plate. Furthermore, the vortex was rapidly dissipated in the wake of the second plate. As a result, the torsional amplitude of the third place was decreased.

Keywords: flat plate, flutter, wake, flow visualization

1. INTORODUCTION

Conventional propeller wind turbines create a strong turbulent wake as the blades rotate. The turbulent wake prevents the installation of another wind turbines in the downstream area unless there is sufficient distance between them (Uchida and Gagnon, 2022; Bayron et al., 2024). On the other hands, there are many locations in urban areas that generate wind, such as highway sides and subway platforms, most of this wind energy has been not corrected. Under these circumstances, the development of compact wind power systems that can be installed in limited spaces and operate flexibly even within wakes would greatly promote wind energy harvesting in urban areas. From this perspective, our research group has been working on the development of a wind power generation system that utilizes aeroelastic vibration phenomena within wake flows. Previously, we focused on the construction of tried to construct a system using the wake galloping of multiple cylinders (Nomura et al., 2017). However, we encountered a problem in constructing a power generation system under high wind speeds due to complex vibration modes.

We then focused on the flutter vibration (Matsumoto, 2010) of multiple flat plates. In preliminary studies using one flat plate as an oscillator, we found that the vibration modes could be controlled, which opened up the prospect of constructing a novel wind power generation system. Furthermore, when multiple flat plates using as oscillators for power generation were arranged in series in the wake, flutter vibration occurred in each plate. In addition, the torsional amplitude of the second

plate was larger than that of the first plate. Based on these findings, we predicted that additional flat plates could be installed in the downstream area for the power generation. When three flat plates were arranged in series, the third plate also vibrated, but its amplitude was about half that of the first and second plates. Therefore, we investigated the factors contributing to the decrease in amplitude of the third plate using flow visualization methods. **Figure 3** shows an arrangement of the piezoelectric element. As illustrated in **Figure 3**, the power generation device was installed in accordance with the prescribed specifications. In this experimental procedure, the power generation device was deliberately excluded to facilitate a clearer understanding of the flow mechanism.

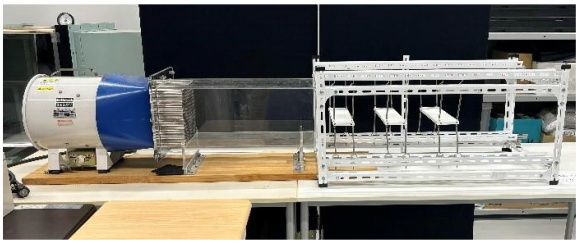


Figure 1. Experimental setup.

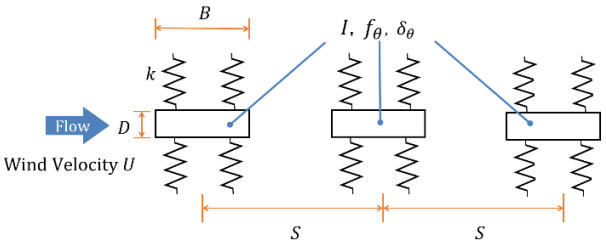


Figure 2. Experimental parameters.

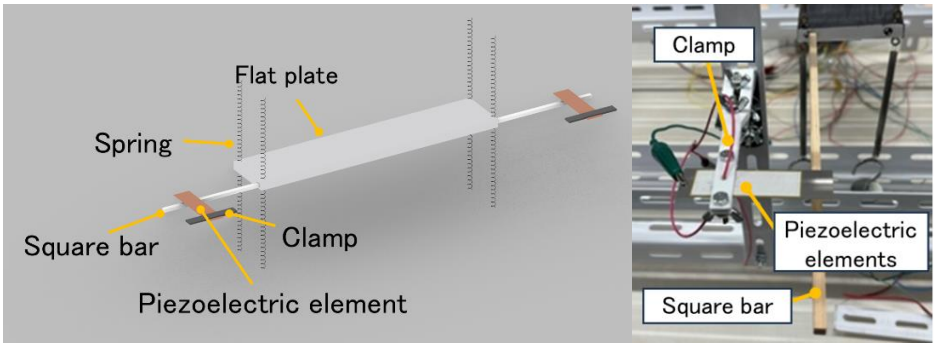


Figure 3. Arrangement of piezoelectric elements

Table 1. Flat plate specification.

Depth D	10 mm
Breadth B	80 mm
Length L	300 mm
Spring constant k	0.007 N/mm
Moment of inertia I	20583 g · mm^2
Frequency of torsion f_θ	7.8 Hz
Wind speed U	2 ~7 m/s
Distance between the center of flat plates S	200 mm
Logarithmic damping δ_θ	0.123

2. OVERVIEW OF WIND TUNNEL TESTS

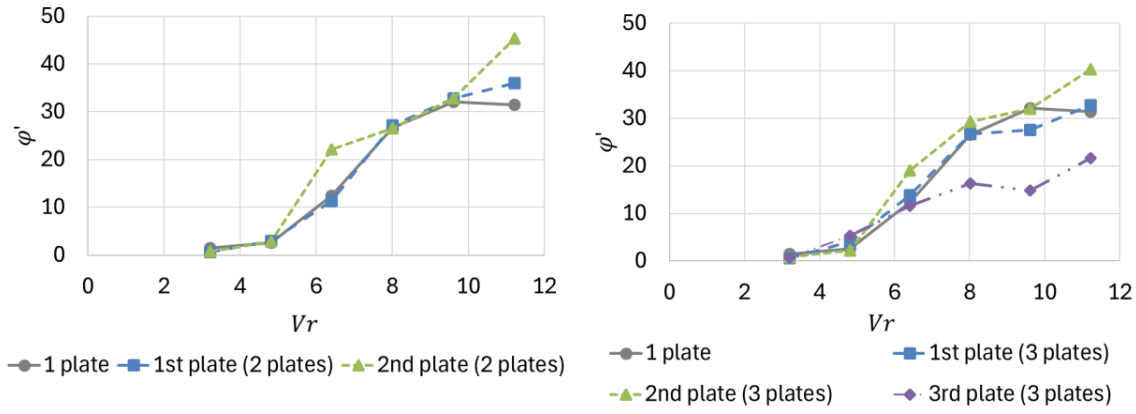
2.1. EXPERIMENTAL DEVICE

Figure 1 shows the wind tunnel apparatus used in this study. An open type wind tunnel with a 225 mm × 225 mm square outlet was used. A frame with adjustable spacing of flat plates was attached to the outlet. **Figure 2** and **Table 1** show the model specifications and experimental parameters. The flat plate had a breadth of $B = 80$ mm, a depth of $D = 10$ mm, and a length

of $L = 300$ mm. The aspect ratio, B/D, was 8. The flat plate was supported at eight points by coil springs with a spring constant of $k = 0.007$ N/mm. The moment of inertia $I = 20583\ \mathrm{g \cdot mm^2}$, the frequency of torsional vibration f_θ=7.8 Hz, and the logarithmic damping of torsional vibration δ_θ was 0.123. The center of the first flat plate was installed 100 mm from the wind tunnel outlet. Subsequently, flat plates with the same aspect ratio were installed in series in the downstream direction. The center-to-center distance between the two flat plates is denoted as S was get at 200 mm. The dimensionless wind speed $V_r = U/f_\theta B$ was used as a parameter to organize the experimental results.

2.2. PRELIMINARY EXPERIMENT

Preliminary, the vibration characteristics of several flat plates were investigated. In this paper, we show the case of two and three flat plates. **Figure 4** shows the results of measured torsional amplitudes of two and three flat plates. **Figure 4**(a) shows the case of two plates. At the nondimensional velocity $V_r = 6.4, 11.2$, it was found that the amplitude of the second plate was larger than that of the first plate. We confirmed that multiple flat plates in the wake can independently exhibit flutter vibration. There is a potential to increase the power output of our system by exploiting this phenomenon. **Figure 4**(b) shows the three plates case. Similar to the two plates case, it was confirmed that multiple flat plates in the wake can independently flutter vibration even with three flat plates. In this case, the torsional amplitudes of the first and second plates were equal to or larger than those of a single flat plate. Furthermore, by comparing the cases of two and three flat plates in **Figure 4** (a), (b), it was found that there was no significant difference in the amplitudes of the first and second plates. On the other hand, at high wind speeds, the amplitude of the third plate was found to be smaller than that of the first and second plates. Therefore, we decided to investigate the factors that cause the amplitude of the third flat plate to be smaller using smoke flow visualization.



(a) Two flat plates case (b) Three flat plates case

Figure 4. Torsional amplitudes of two and three flat plates .

3. INVESTIGATION OF VIBRATION MECHANISM USING SMOKE FLOW VISUALIZATION AND ITS EVALUATION

Figure 5 shows a snapshot of the smoke flow visualization in the three flat plates configuration. In the wake of the first plate, cross flows from upper/lower region to lower/upper region of the plate were clearly observed. Additionally, a large vortex formed by the cross flow was observed

above the second flat plate. As a result, the torsional amplitude of the second flat plate was increased. However, the vortex was rapidly dissipated in the wake of the second plate. Flow fluctuations seemed to be small compared to that in the wake of the first plate. As a result, the formation of a large-scale vortex was not observed above the third flat plate and the torsional amplitude of the third plate was about half of that of the first and second plates.

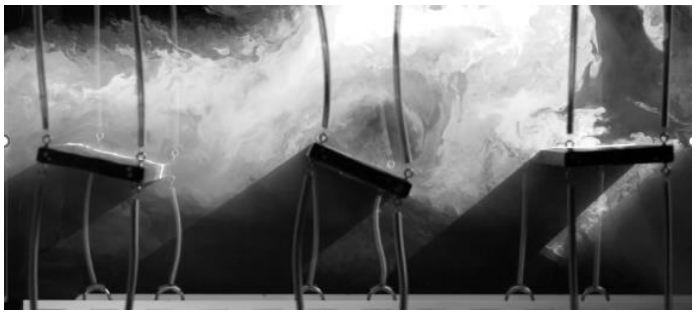


Figure 5. A snapshot of smoke flow visualization

4. CONCLUSION

The objective of the present study was the develop a novel wind power generation system. The system employed flutter vibrations of multiple flat plates in the wake region. It was observed that the multiple flat plates exhibited flutter independently in the wake region. In the case of two flat plates, both the first and second plates exhibited flutter vibrations, with torsional amplitudes comparable to those observed in a single plate. In the case of three flat plates, all plates exhibited flutter vibrations, and the amplitudes of the first and second plates were comparable to those of a single plate. However, the amplitude of the third plate was approximately half that of a single plate. Accordingly, smoke flow visualization was conducted to clarify the factors responsible for the reduction in the amplitude of the third plate. Consequently, the following results were obtained.

(1) Visualization experiments conducted to observe the flow of smoke revealed the formation of large-scale vortices above and below the second flat plate. It is postulated that this phenomenon has served to amplify the vibration amplitude of the second flat plate.

(2) The large-scale vortex that had above and below the second flat plate collapsed rapidly as soon as the vortex flowed down. As a result, the wake behind the second plate exhibited minimal fluctuations, which led to a reduction in the amplitude of the third plate.

In the future, we will conduct the particle image velocimetry (PIV) to evaluate the flow fluctuations quantitatively.

REFERENCES

Bayron, P., Kelso, R. and Chin, R., 2024. Experimental analysis of co-rotating and counter-rotating tandem horizontal-axis wind turbine performance and wake dynamics, Journal of Wind Engineering and Industrial Aerodynamics 253, 105840

Matsumoto, M., 2013. Flutter and its application - Flutter mode and ship navigation， Journal of Wind Engineering and Industrial Aerodynamics 122, 10-20.

Nomura, T., Saegusa, N. and Hasebe, H., 2017. Vibration of Multiple Circular Cylinders in Tandem Alignment, Proceedings of the First International Symposium on Flutter and its Application –ISFA2016-, 385-392.

Uchida, T. and Gagnon, Y., 2022. Effects of continuously changing inlet wind direction on near-to-far wake characteristics behind wind turbines over flat terrain, Journal of Wind Engineering and Industrial Aerodynamics 220, 104869.

Torsional flutter harvester in non-stationary outflows, exploiting negative stiffness element for energy conversion

Luca Caracoglia[1]

[1]*Department of Civil and Environmental Engineering, Northeastern University, 360 Huntington Avenue, Boston, Massachusetts, 02115 (USA), orcID: 0000-0002-4783-2600, lucac@coe.neu.edu*

SUMMARY:
This work continues recent studies on flutter-based energy harvesting. The work quantifies the output power of a harvesting device in non-ideal, non-stationary wind conditions, typical of a moderate-intensity thunderstorm outflows. Stochastic calculus methods are employed to examine the post-critical behavior and the propensity to energy conversion. A negative-stiffness apparatus is designed to enhance energy conversion by exploiting stochastic resonance.

Keywords: energy harvesting, torsional flutter, non-stationary turbulent outflows

1. INTRODUCTION

Several wind-based energy harvesters, exploiting bending-torsion "classical" flutter instability have been proposed (e.g., Shimizu et al., 2008). Analogously, torsional flutter can be used for energy conversion. Although a purely rotational mechanism is simple and, therefore, appealing, torsional flutter usually entails low-performing energy conversion compared to classical flutter.

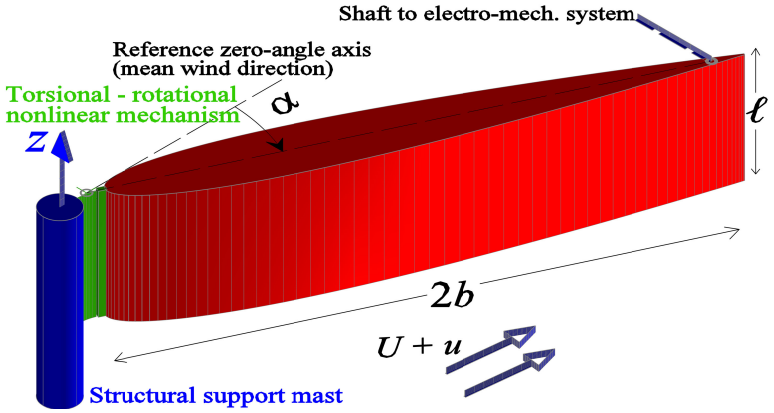


Figure 1. Torsional flutter harvester: three-dimensional view.

The author has explored such an an apparatus (Fig. 1), composed of a rigid blade-airfoil of chord-wise length $2b$ ($0 < b \leq 1$ m) and span-wise length ℓ. The blade-airfoil is a NACA0012 streamlined profile of aspect ratio $\mathrm{AR} = \ell/b = 4$. The blade-airfoil is connected to a support mast by a flexible plate-like interface, indicated as "torsional-rotational mechanism" in Fig. 1. This interface enables transmission of nonlinear, elastic restoring torque about pivot "O".

Recent work (Caracoglia, 2024) has explored the performance of the harvester in non-ideal winds. These non-ideal flows are, for example, non-stationary gusts, moderate-intensity thunderstorms and gust fronts associated with a downburst (Solari, 2015; Solari et al., 2015). They can be often observed in urban settings (Burlando et al., 2017) and on building roofs.

The work continues herein by examining a harvester equipped with a negative-stiffness element to enhance energy conversion, as shown in Fig. 2. The negative stiffness mechanism is installed at equally spaced supports [Fig. 2(b)] and it is used to enhance the amplitude of transverse, post-critical vibration of a shaft connected to a permanent magnet within the "power system". Conversion to electrical power is inspired by a similar vibration device (Kwon et al., 2013); it is possible by eddy currents, generated with a multi-loop magnetic coil and the translating permanent magnet.

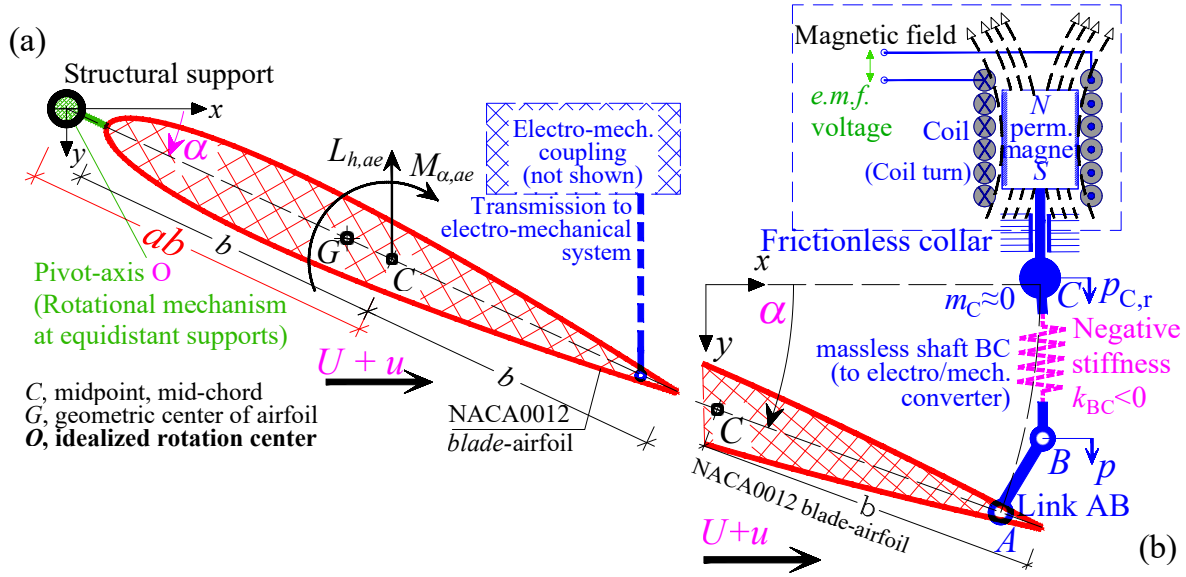


Figure 2. Harvester schematics - cross sectional views on XY horizontal plane: (a) flapping blade-airfoil, (b) eddy-current conversion apparatus (not to scale).

2. THEORETICAL BACKGROUND

2.1. Non-stationary Outflow Properties

The mean wind speed is slowly-varying, $U(\tau) = \Pi(\tau)U_{\max}$ with dimensionless time $\tau = \omega_\alpha t$, normalized with respect to the angular frequency of the linear dynamic system (ω_α, Section 2.2). Quantity $0 \leq \Pi(\tau) \leq 1$ is the intensification/decay function, which is main transitory feature of the non-stationary outflow, and $U_{\max}$ is the maximum velocity of the non-stationary flow. The intensification (intensity factor) is derived from Le and Caracoglia (2017); derivation of $\Pi(\tau) = {}^{U(\tau)}/_{U_{\max}}$ is also explained in Caracoglia (2024). The maximum mean flow intensification occurs at time $\tau_{\max}$, where $200 < \tau_{\max} < 500$; $\tau_{\max}$ is found from $t_{\max} = \tau_{\max}/\omega_\alpha \approx 300\,\mathrm{s}$ according to full-scale data presented by Solari (2015).

Moreover, the non-stationary ("ns") turbulence is described as $u_{\mathrm{ns}}(\tau) = \varphi_{\mathrm{mf}}(\tau)\hat{u}(\tau)U_{\max}$; $\hat{u}(\tau)$, normalized with respect to $U_{\max}$, is a stationary Gaussian white noise, acceptable for output power estimation; $0 < \varphi_{\mathrm{mf}}(\tau) \leq 1$ is a uniform modulation function ("mf") (Solari, 2015), found as

$\varphi_{\mathtt{mf}}(\tau) = \mathrm{e}^{\left(\tau_{\max}-\tau/\omega_\alpha\right)}\left(\tau/\tau_{\max}\right)^{\tau_{\max}/\omega_\alpha}$. Dimensionless time $\tau_{\max} > 0$ designates the instant of maximum turbulence intensity; it is the same quantity used for $\Pi(\tau)$. Due to small $(\sqrt{2b\ell})$ dimension compared to integral turbulence length scales, the gusty wind field is coherent across the blade-airfoil of the apparatus.

2.2. Dynamic Flapping and Electro-mechanical Models

First, the equilibrium equation at node C of the transmission shaft BC is briefly examined. In Fig. 2(b) p is the absolute translation at the massless link AB; $p_{\mathtt{C,r}}$ is the relative displacement between B and C. The non-rigid connector between nodes "B" and "C" of the transmission shaft connects the linkage AB to the electro-magnetic induction converter, and it is composed of a negative-stiffness "soft" element. If the mass $m_{\mathtt{C}} \approx 0$ is negligible, the equilibrium equation at C is quasi-static, and can be simplified as $k_{\mathtt{C}} p_{\mathtt{C,r}}(t) = f_{(\mathtt{e.m.})}(t) = F_{\mathtt{AB}}$ with t time. $F_{\mathtt{AB}}$ is also the internal constraint force transferred to the primary system through AB rigid link; $F_{\mathtt{AB}}$ and p are primarily in the y direction for small flapping angles, i.e., $p(t) \approx (1-a)b\alpha(t)$.

Second, the dynamic equilibrium equation of the primary, vibrating flapping foil is studied. The physical variables are torsional rotation α and derivative $\mathrm{d}\alpha/\mathrm{d}\tau$ with respect to τ. The equation is:

$$\frac{\mathrm{d}^2\alpha}{\mathrm{d}\tau^2} + 2\zeta_\alpha \frac{\mathrm{d}\alpha}{\mathrm{d}\tau} + \alpha + \mathrm{H}_{\mathrm{NL}}\left(\alpha, \frac{\mathrm{d}\alpha}{\mathrm{d}\tau}\right) = \frac{M_{0z}(\tau) + M_{(\mathtt{e.m.})}(\tau)}{\omega_\alpha^2 I_{0\alpha}} \tag{1}$$

In Eq. (1), the external aeroelastic torque $M_{0z}(\tau)$ is about the pivot O; modeling of $M_{0z}(\tau)$ is described in previous works (Caracoglia, 2024). The dimensionless quantity $a < 0$ measures the position of pivot O from the geometric center of the airfoil [Fig. 2(a)]; $a = -1$ coincides with the windward edge. $I_{0\alpha}$ is the total polar mass moment of inertia about O. Linear structural damping is simulated by term ζ_α in Eq. (1). The function $\mathrm{H}_{\mathrm{NL}}\left(\alpha, \mathrm{d}\alpha/\mathrm{d}\tau\right)$ is explained in Section 2.3.

In Eq. (1), the electro-motive torque about O, transmitted through the negative-stiffness element is $M_{(\mathtt{e.m.})}(\tau) = (1-a)bF_{\mathtt{AB}} = -(1-a)b\Phi_{(\mathtt{e.m.c.})}\imath(\tau)i_0$; $\imath(\tau)$, is a dimensionless current, i_0 is a reference current intensity. $M_{(\mathtt{e.m.})}(\tau)$ is found through Faraday's law (Caracoglia, 2024), with $\Phi_{(\mathtt{e.m.c.})}$ being the electro-mechanical coupling coefficient. Specifically, Eq. (2) couples the flapping foil and electro-mechanical system, with impedance $\lambda_{\mathtt{RL}} = R_C/(\omega_\alpha L_C)$ (R_C resistance, L_C inductance):

$$\mathrm{d}\imath/\mathrm{d}\tau = \Delta_{\mathtt{BC}}\lambda_{\mathtt{RL}}(\mathrm{d}\alpha/\mathrm{d}\tau - \imath) \tag{2}$$

The "soft" coupling parameter $\Delta_{\mathtt{BC}}$ is found from $\Delta_{\mathtt{BC}}^{-1} = (1 + \lambda_{RL}\Psi/4\chi_{\mathtt{BC}})$; it is designated after normalizing the negative stiffness coefficient of the BC link as $k_{\mathtt{BC}} = \chi_{\mathtt{BC}} k_\alpha b^{-2}$ with $\chi_{\mathtt{BC}} < 0$ and torsional stiffness $k_\alpha = \omega_\alpha^2 I_{0\alpha}$. Ψ is a dimensionless electro-mechanical coupling coefficient. For a rigid link BC, we note $\chi_{\mathtt{BC}} \to +\infty$, $\Delta_{\mathtt{BC}} \to 1$.

2.3. $\mathrm{H}_{\mathrm{NL}}\left(\alpha, \mathrm{d}\alpha/\mathrm{d}\tau\right)$ Function

This function replicates the nonlinear restoring and damping torque mechanism at the pivot O, which enables limit-cycle oscillation. Two models are employed. The *Duffing Model* simulates a nonlinear restoring torsional effect with $\mathrm{H}_{\mathrm{NL}}\left(\alpha, \mathrm{d}\alpha/\mathrm{d}\tau\right) = \kappa\alpha^3$, with $\kappa > 0$ suitable dimensionless constant. In the *Hybrid Duffing–Van-Der-Pol Model*, the nonlinear function incorporates both Duffing and van der Pol (Nayfeh and Mook, 1995) mechanisms: $\mathrm{H}_{\mathrm{NL}}\left(\alpha, \mathrm{d}\alpha/\mathrm{d}\tau\right) = \left[\kappa\alpha^3 - 2\zeta_\alpha\gamma\alpha^2 \mathrm{d}\alpha/\mathrm{d}\tau\right]$. Besides κ, the nonlinear damping coefficient $\gamma > 0$ models the self-limiting, negative damping effects. Design of either mechanism will be considered in future studies.

3. PRELIMINARY RESULTS, DISCUSSION AND CONCLUSIONS

The simulations analyze post-critical flutter under non-stationary turbulence outflows with variable geometry, dynamic properties and accounting for aeroelastic load variability. Three Duffing-type nonlinear harvesters are considered: "Ty.0", "Ty.1", "Ty.2" (Caracoglia, 2024). For example, the main properties of type-2 ("Ty.2") harvester are: mid-chord length $b = 0.5\,\mathrm{m}$, frequency $\omega_\alpha/2\pi = 0.1\,\mathrm{Hz}$, $\zeta_\alpha = 0.3$ and $\Psi = 0.1$. All the base units are modified by a negative-stiffness "soft link" with $\chi_{\mathtt{BC}} = -0.1$. Stochastic calculus methods are used to numerically solve the equations. Fig. 3 examines a "frozen" gust front with $\Pi(\tau) \equiv 1$, $\varphi_{\mathtt{mf}}(\tau) \equiv 1$ and variable $U_{\mathtt{max}}$.

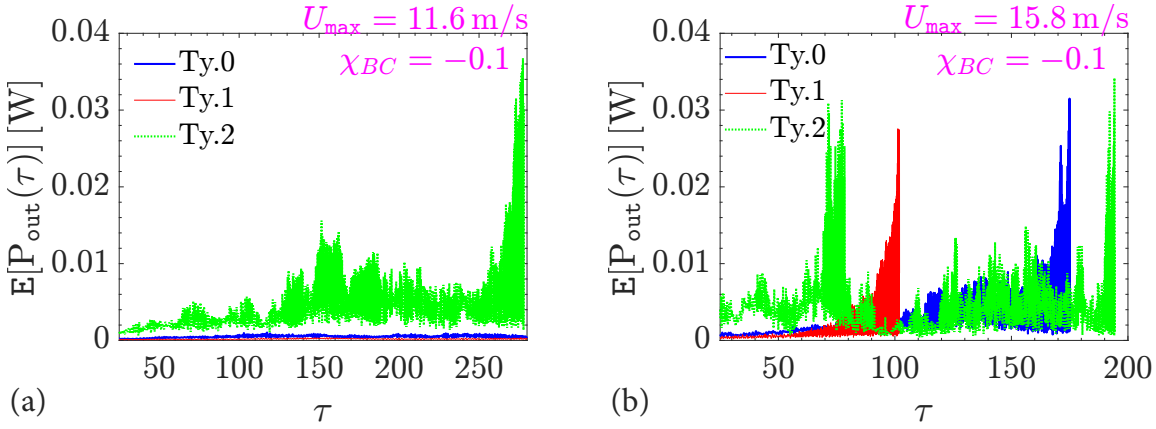


Figure 3. Mean output power of the Duffing nonlinear harvester under the effects of moderate-turbulence, non-stationary "frozen" gust front: (a) $U_{\mathtt{max}} = 11.6\,\mathrm{m/s}$, (b) $U_{\mathtt{max}} = 15.8\,\mathrm{m/s}$.

Examination of the figure suggests that the negative-stiffness soft link is efficient, , instigating the operational regime at low wind speeds for type-2 ("Ty.2") harvester. The link also triggers the other two harvester types at a higher $U_{\mathtt{max}}$. These result are encouraging. Additional studies and comparisons will be discussed in the final presentation.

ACKNOWLEDGMENTS

This material is based upon work supported by the National Science Foundation of the USA, Award CMMI-2020063.

REFERENCES

Burlando, M., Romanić, D., Solari, G., Hangan, H., and Zhang, S., 2017. Field Data Analysis and Weather Scenario of a Downburst Event in Livorno, Italy, on 1 October 2012. Mon. Weather Rev. 145, 3507–3527.

Caracoglia, L., 2024. Stochastic performance of a torsional-flutter harvester in non-stationary, turbulent thunderstorm outflows. J. Fluids Struct. 124, 104050.

Kwon, S.-D., Park, J., and Law, K., 2013. Electromagnetic energy harvester with repulsively stacked multilayer magnets for low frequency vibrations. Smart Mater. Struct. 22.5, 055007.

Le, T.-H. and Caracoglia, L., 2017. Computer-based model for the transient dynamics of a tall building during digitally simulated Andrews AFB Thunderstorm. Comput. Struct. 193, 44–72.

Nayfeh, A. H. and Mook, D. T., 1995. Nonlinear Oscillations. Wiley-VCH Verlag GmbH & Co., Weinhein, Germany.

Shimizu, E., Isogai, K., and Obayashi, S., 2008. Multiobjective design study of a flapping wind power generator. J. Fluids Eng.-ASME 130.2, 021104.

Solari, G., 2015. Characteristics of thunderstorms relevant to the wind loading of structures. Wind Struct. 20.6, 763–791.

Solari, G., De Gaetano, P., and Repetto, M. P., 2015. Thunderstorm response spectrum: fundamentals and case study. J. Wind Eng. Ind. Aerodyn. 143, 62–77.

Vortex methods for wind turbine rotors on floating substructures

Carlos Renan dos Santos [1], Lars Einar Sørensen Stieng [1], Mathias Huuse Marley[2]
Tor Anders Nygaard [1]

[1]*Institute for Energy Technology (IFE), Kjeller, Norway, Carlos.Santos@ife.no*
[2]*Equinor ASA, Fornebu, Norway*

SUMMARY
This work compares different vortex methods for wind turbine rotor aerodynamics with the commonly used Blade Element/Momentum theory method (BEM) and experimental results for forced nacelle motion. The implications of the different rotor models on the aero-servo-hydro-elastic response of floating substructures are examined for spar-buoys and free-yaw semisubmersible platforms. We get the best results with the Free Vortex Wake method (FVW) with a fully deforming wake, but at a considerable computational cost. A substantial reduction of computational cost is obtained by several assumptions for the far and near wake, without significant loss of accuracy. Ongoing work examines computational costs for rotor models within the perspective of aero-servo-hydro-elastic computations of a complete floating wind turbine, and the potential for further speedup.

Keywords: rotor aerodynamics, vortex methods, floating wind turbines

1. INTRODUCTION

Loads, motions, deflections and control systems interact for floating wind turbines. Analyses are therefore usually carried out in the time domain with nonlinear aero-servo-hydro-elastic simulation tools. The most common model for rotor aerodynamics is the Blade Element/Momentum Theory (BEM). BEM provides a reasonable balance between accuracy and computational speed but has shortcomings for configurations with unsteadiness, large motions and skewed inflow. The mooring system for a spar-buoy has low stiffness towards platform yaw motion, and details of the aerodynamic rotor yaw moment and aerodynamic damping may play a role in the dynamic response. Several floating substructure conceptual designs under development utilize self-alignment of the platform towards the wind, where the rotor is placed downwind of a turret mooring. Yaw-drift and fishtailing has been observed for such platforms, indicating that the response is sensitive to details of the aerodynamic model. We have implemented several versions of vortex and lifting line models in 3DFloat (Nygaard et al., 2016). The aim of this work is to assess the differences in aerodynamic forcing, stiffness and damping, and the response on spar-buoys and free-yaw platforms due to the different aerodynamic models.

2. MODEL DESCRIPTION

BEM combines the lift and drag characteristics of two-dimensional (2D) airfoils with continuity and

momentum balances for a thin annulus through each radial position, and corrections for tip losses, dynamic inflow, unsteady airfoil aerodynamics, and yaw misalignment. The Unsteady Vortex Lattice Method, or Free Vortex Wake method (FVW) also uses lift- and drag characteristics for the airfoil aerodynamics, combined with a state-space model for circulation and lift dynamics for airfoil aerodynamics (Santos and Marques, 2022). FVW computes the wake and retardation of the velocity (induced velocity) at the rotor by releasing vortex particles from the rotor at each time step corresponding to the radial lift distribution (Katz and Plotkin, 2001). It has been implemented with an optional "far wake" region, in which all particles in that region are updated according to a constant wake velocity proportional to the ambient freestream, and a downwind cutoff distance after which particles are discarded. Further speedup can be obtained by assuming that the entire wake moves with a constant wake velocity.

The Unsteady Lifting Line Theory (ULLT) uses the same state-space model for circulation and lift dynamics as FVW. The wake and induced velocity are based on the works of Okulov (Fukumoto and Okulov, 2005) (Okulov and Fukumoto, 2020) (Okulov, 2021) (Wood, Okulov and Vaz, 2021), where analytical solutions are found for the induced velocity from vortex rings extending to infinity. We have implemented both the monopole and dipole terms of the expansion. Since this wake model is essentially quasi-static, it benefits from some of the same corrections as BEM, such as the Øye model for dynamic inflow. The models for BEM, FVW, ULLT and the Øye model are summarized in (Santos et al., 2023).

3. SAMPLE RESULTS

The following results are derived from our participation in the IEA OC6 project (OC6) (Bergua et al., 2023), with further analyses in (Santos et al., 2023). In OC6, a model rotor undergoing motions similar to what is experienced on a semisubmersible floater was tested in a wind tunnel. A total of 29 academic and industrial partners from 10 different countries participated with codes of different fidelity ranging from BEM to CFD. Table 1 presents comparisons of thrust and torque computed by IFE for the complete FVW (with a completely deforming wake), ULLT and BEM in relation to the experimental measurements. The complete FVW approach holds the highest accuracy among the methodologies employed in this work.

Table 1: Comparison between numerical methods (Santos et al., 2023) and OC6 data (Bergua et al., 2023)

	Experiment	FVW	ULLT	BEM
Thrust [N]	35.91	35.99	35.34	34.59
Torque [Nm]	3.32	3.22	3.04	2.99

Figure 1 compares the resulting distributions of effective angle of attack α, and normal and tangential forces over the blade. BEM and ULLT have very similar results, which show good agreement with the loading distributions obtained through the complete FVW method (with a deforming wake). Meanwhile, Figure 1 also compares three different FVW approaches: the complete method, and two solutions where the wake is shed with velocity proportional to the wind speed (fraction $\epsilon = 0.8$ and 1.0). The results show almost indistinguishable distributions for the complete FVW and the case where $\epsilon = 0.8$. On the other hand, the application of $\epsilon = 1.0$ in the method leads to higher values of angle of attack over the blade and overestimates normal and tangential forces, as a consequence. Therefore, differently from analyses of fixed wings, where several authors concluded that the use of the freestream velocity to shed wake vortices retains the accuracy of the resulting loads; in the case of wind turbines this simplification fails.

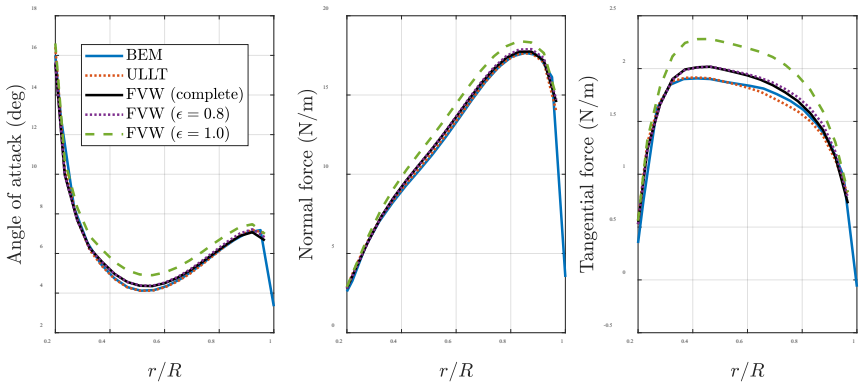


Figure 1: Distribution of aerodynamic properties along the blade (ω = 240 RPM and V = 4.19 m/s).

Figure 2 repeats the same exercise in an above-rated condition. The wind turbine rotates with rotational speed ω = 265 RPM at wind speed V = 6.03 m/s. In this case, the blades are pitched 12.5◦. As for the case in rated condition, BEM and ULLT have very similar results. The main difference comes from the comparisons between the three FVW approaches: the complete FVW and the case where ϵ = 0.8 still hold good agreement among them, although the FVW with ϵ = 0.8 tends to underestimate the normal and tangential forces; however, now the complete FVW and the case where ϵ = 1.0 show a better similarity. This is in agreement with the findings by (Keck et al., 2014), where lower induction factors associated with above-rated wind speeds lead to higher ϵ values due to the higher spatial mean velocities in the wake relative to the ambient wind for these cases.

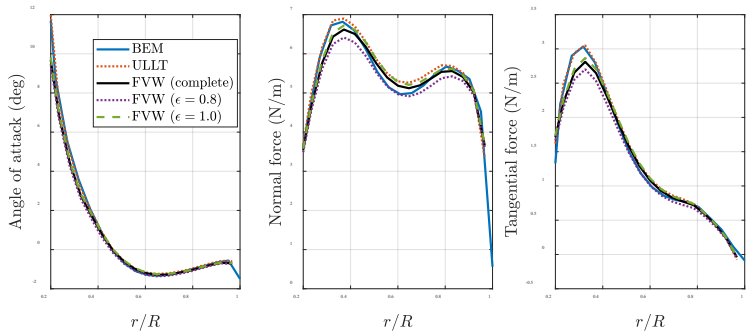


Figure 2: Distribution of aerodynamic properties along the blade (ω = 265 RPM and V = 6.03 m/s).

The methods are also validated for unsteady cases considering surging oscillations of the platform. The wind turbine undergoes surge oscillations with amplitude of 35 mm and frequency 1 Hz around its rated condition. As shown in Figure 3, the FVW method with a complete free and deforming wake and the FVW method with prescribed wake and ϵ = 0.8 have the better agreement in relation to experimental results. BEM tends to underestimate the unsteady torque. ULLT results are closer than BEM to the FVW methods. The final paper and presentation will also include cases with more unsteadiness for a 25MW rotor, highlighting the need for higher-fidelity models such as the FVW.

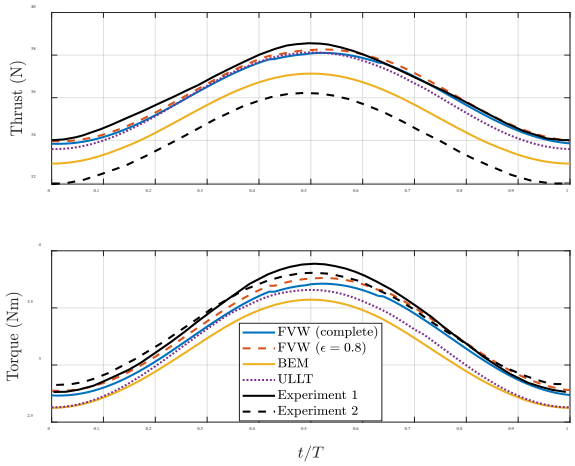


Figure 3: Surge oscillations of the wind turbine (amplitude 35 mm and frequency 1 Hz).

4. CONCLUSIONS AND ONGOING WORK

In line with the results in OC6, FVW delivers consistently results with better agreement with experiments than BEM, but at a considerable computational cost. Computational cost can be reduced significantly with various assumptions for the wake and parallel computing. Ongoing work with complete floating wind turbines assesses the implications for response and overall computational costs for aero-servo-hydro-elastic computations.

REFERENCES

Bergua, R., Robertson, A., Jonkman, J., Branlard, E., Fontanella, A., Belloli, M. , .. Nygaard, T. A., Santos, C. R. et al. (2022). OC6 Project Phase III: Validation of the Aerodynamic Loading on a Wind Turbine Rotor Undergoing Large Motion Caused by a Floating Support Structure. Wind Energy Science. Vol. 8, April 2023, pp. 465-485; DOI: 10.5194/wes-8-465-2023.

Fukumoto, Y. and Okulov, V. L., 2005. The velocity field induced by a helical vortex tube. Physics of Fluids 17, 107101

Katz, J., and Plotkin, A., 2001. Low-speed aerodynamics, Vol. 13, Cambridge university press, 2001

Keck, R.-E., Mikkelsen, R., Troldborg, N., de Maré, M., and Hansen, K. S., (2014). Synthetic atmospheric turbulence and wind shear in large eddy simulations of wind turbine wakes. Wind Energy, Vol. 17, No. 8, 2014, pp. 1247–1267.

Nygaard, T. A., De Vaal, J., Pierella, F., Oggiano, L. and Stenbro, R. (2016). Development, Verification and Validation of 3DFloat; Aero-Servo-Hydro-Elastic Computations of Offshore Structures. Energy procedia 2016, Vol. 94, pg. 425-433

Okulov, V. L. and Fukumoto, Y., 2020. Analytical solution for self-induced motion of a helical vortex with a Gaussian core. Thermophysics and Aeromechanics, 2020, Vol. 27, No. 4. DOI: 10.1134/S0869864320040022

Okulov, V. L. and Fukumoto, Y., 2021. Singular approximations for calculating vortex filaments. Journal of Applied Mechanics and Technical Physics, Vol. 62, No. 3, pp. 519–524.

Santos, C. R., Hanssen-Bauer, Ø. W. and Stenbro, R., 2023. Considerations on vortex methods for aerodynamic analyses of wind turbines. AIAA 2023-0971.

Santos, C. R., and Marques, F. D., 2022. Finite wing effects on the energy harvesting from stall-induced oscillations. Journal of Vibration and Control, 2022, p. 10775463221089732.

Wood, D. H., Okulov, V. L. and Vaz, J. R. P., 2021. Calculation of the induced velocities in lifting line analyses of propellers and turbines. Ocean Engineering Vol 235,109337, ISSN 0029-8018

Fluid-structure simulation and structural design analysis of a 5-MW wind turbine blade at different wind speeds

Chun-Chi Chang[1], Cheng-Han Zhuang[1], Jinsiang Shaw[2], Chun-Ying Lee[1,2]

[1]*Graduate Institute of Manufacturing Technology, National Taipei University of Technology, Taipei, Taiwan, t109568030@ntut.org.tw & t111408077@ntut.org.tw*
[2] *Department of Mechanical Engineering, National Taipei University of Technology, Taipei, Taiwan, jshaw@ntut.edu.tw & leech@ntut.edu.tw*

SUMMARY:
In this study, a 5 MW reference blade model from NREL was used to analyse the loading on blade structure at different wind speeds. In the beginning, rated wind speed, cut-out wind speed and extreme wind speed, beside the adjustment in the blade's pitch angle, were set as boundary conditions of flow field analysis using a finite element software. In terms of structural analysis, this 5 MW turbine blade was divided into five layup areas, such as leading edge, trailing edge, spar cap, blade root, and shear web. Composite laminates and stacking sequences were defined based on different layup areas. The FEM results show that modifying the shape of blade could reduce the influence of stress concentration when blade was under rated wind speed. In addition, weight reduction of blade was achieved greatly by reducing the layers of spar cap and blade root. Although less layers might cause insufficient structure rigidity, it was found that changing the stacking configuration could avoid this problem. After design modification, the blade was eventually 12% lighter than its NREL counterpart. Besides, Tsai-Wu index of the composite layup from the fluid-structure interaction analysis at different wind speeds were within safe range. In addition, the maximum tip deflection was also within safe range and the natural frequency of blade was away from the blade pass frequency to avoid resonance.

Keywords: Wind turbine blade, fluid-structure loading analysis, composite laminate

1. INTRODUCTION

Carbon neutral is an urgent subject to mitigate the climate change worldwide. Fortunately, wind energy has provided an opportunity for Taiwan in energy transition due to the quality wind environment around the island. Theoretically speaking, the electricity output from a wind turbine is proportional to diameter squared and wind speed cubic. Therefore, the development of larger turbine is the inevitable trend for the industry. However, longer turbine blade poses challenging issues in weight, strength, and safety in operation. Subsequently, the use of composite materials for their high specific stiffness and strength is a reasonable choice. The complicated loading stresses of bending and torsion from wind load and others could cause different failure modes, such as shear fracture of shear web, breakaway of spar cap, etc. which undermine the function of the wind turbine. In this study, 5 MW reference blade model from National Renewable Energy Laboratory (NREL), which allows the adjustment in pitch angle of blade (Jonkman, 2009), was used to analyse the loading on blade structure at different wind speeds. This reference model has been a popular subject in the research society. The potential design modification to improve its operational safety and weight reduction could be beneficial to the relevant societies. In the early stage of research, rated wind speed, cut-out wind speed and extreme wind speed were set as boundary condition of flow field analysis, which was calculated by a finite element software. The

consideration of loading from the extreme wind speed and the influence of the pitch angle would be readily applicable to the weather pattern near Taiwan. Moreover, the design improvement from the composite laminate configuration could reduce the blade's weight while maintains the structural safety.

2. PROCESS OF NUMERICAL ANALYSIS

2.1. Design of Wind Turbine Blade

A typical blade can be classified into three regions: root, mid-span, and tip. Root contains the transition from circular cross-section to the first aerofoil section. High loading stress and low relative wind speed and lift are its characteristics. Mid-span, considering its aerodynamic efficiency, possesses thin aerofoil section. Aerodynamic efficiency in the tip region dominates the performance and provides the source of most propulsion. Therefore, the aerofoil profile in tip region has the thinnest dimension and largest lift/drag ratio. In summary, the NREL blade has 17 defined cross-sections, starting from the root with circular section, DU series sections, and lastly NACA sections near the tip. The NACA sections have reduced size toward the very tip end. The span of the 17th aerofoil section becomes 1.419 m, the minimum among 17 cross-sections.

2.2. Modelling of Turbine Blade

To avoid the model distortion in format transfer, the blade model was built by using the Spaceclaim CAD module in ANSYS. The aerofoil profiles at 17 cross-sections were inputted from the corresponding coordinates of the data points listed in the NREL report. These aerofoil sections were deployed along the pitch axis sequentially by referring to the approaches of Bazilevs et al. (Bazilevs, et al., 2010) and Sandia National Lab (SNL) for the 5 MW turbine. Fig. 1(a) presents the blade model built in this study.

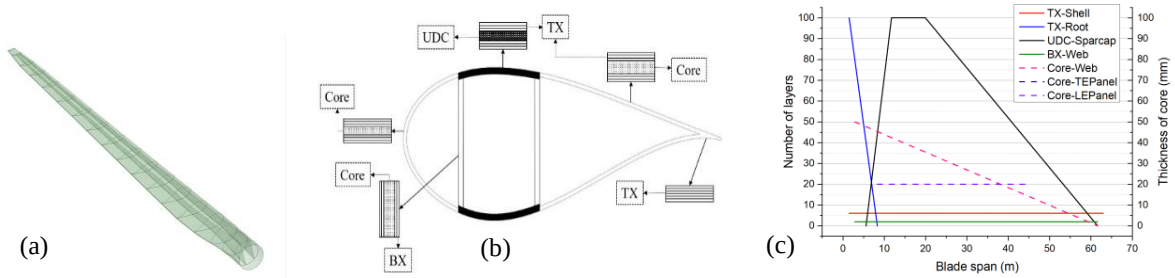


Figure 1. The blade model, the cross-section of the aerofoil blade and the associated stacking configuration of the original design.

2.3. Flow Field Analysis

ANSYS Fluent module was adopted in this flow field analysis. The domain for this flow field analysis was a one third frustum of cone with an inner circular sector encompassing one turbine blade. A multiple reference frame (MRF) method was employed in this rotating field simulation with the reference coordinate rotating in the rotor speed. The k-ω SST turbulence model was used in both domains. The following conditions were set in the simulation: ambient temperature 15^{o}C, air density 1.225 kg/m^{3}, viscosity 1.780×10^{-5} kg/m-s; velocity inlet on the small circular section and conical surface of the frustum with velocities of 11.4 m/s and 25 m/s as the rated wind speed and cut-off wind speed, respectively; nominal rotation speed 12.1 rpm of the rotating domain; extreme wind speed 70 m/s with turbine blade locked at zero speed and pitch angle 90^{o}; pressure outlet of 1 atm on the large circular section of the frustum; axially periodic conditions on the 120^{o} boundary which allowed the fluid crossing to account for three rotating blades; non-slip wall condition on the blade surfaces.

2.4. Structural Analysis

The Composite PrepPost ACP module was employed in the definition of the composite laminate stacking sequence and the material properties. The main composites used in the blade construction were glass fibre, carbon fibre and foam (core), which included triaxial (TX) and bi-axial (BX) woven fabrics in addition to the uniaxial (UDC) laminates. In the design of the stacking sequence of the laminate, the aerofoil cross-section, as presented in Fig. 1, can be divided into seven parts: leading edge, trailing edge, trailing edge panel, top and bottom spar caps, leading web, and trailing web. Moreover, the outer profile of the aerofoil was set as shell structure, i.e. the layup covered the whole blade.

3. RESULTS AND DISCUSSION

3.1. Fluid Pressure Loading

Figure 2 presents the pressure coefficients on the surface near the tip (95% of the blade length) of the blade design. The coefficient was calculated based on the following formula: $C_p = \frac{(P-P_O)}{0.5P_O[{V_O}^2+(\omega r)^2]}$, in which the variables used are: the pressure on blade surface P, the free stream pressure P_0, the free stream velocity V_0, the blade angular velocity ω, the radial coordinate of location where C_p is calculated. Comparing to the results from other studies in the literature, our simulated pressure distribution showed fairly good consistency.

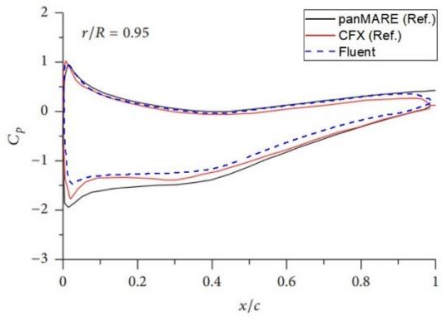


Figure 2. the pressure coefficients at blade tip

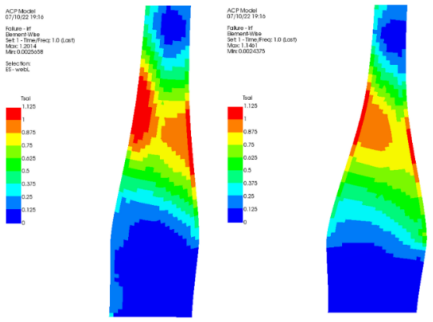


Figure 3. The calculate Tsai-Wu index near the spar cap

3.2. Structural Performances

The weight of the original design presented in Fig. 1 was 26309 kg, close to 28028 kg reported in (Ha, et al., 2014). However, the structural analysis revealed that the maximum Tsai-Wu index at outer shell of the blade was 0.88 while the index reached 1.2 at location near the junction between shear web and outer shell, as shown in the red region of Fig. 3. The Tsai-Wu index larger than 1 denotes the failure of composite in loading. Therefore, the design modification had to be undertaken. Figure 4 presents the composite stacking configuration of the modified design. By properly reducing the number of layups and their distributions, the total weight of the blade became 15580 kg which was 12% lighter than its NREL counterpart. The performances of this modified blade design are shown in Fig. 5, which not only demonstrate its satisfactory rigidity to pass the clearance between the blade and the monopole but also its structural safety under all three operating wind speeds.

3.3. Modal Analysis

Blade pass frequency is the frequency which the blade passes the same position in rotation

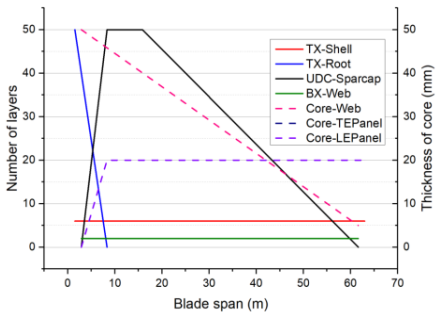


Figure 4. The composite stacking configuration of the modified design

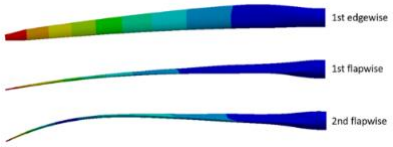


Figure 5. The performances of the modified design

periodically. It is calculated based on the product of rotor angular speed and number of blades. This frequency denotes the forcing frequency of the vibration excitation. Based on the rated rotor speed of 12.1 rpm and three blades, the blade pass frequency is 0.60 Hz in this 5 MW turbine. Table 1 lists the first six natural vibration modes of the SNL and modified designs. The natural frequencies of these modes are higher than those of SNL design and well above the blade pass frequency. Therefore, the vibrational characteristics are also satisfactory in design.

Table 1. The comparison of modal characteristics between SNL and the proposed modified design.

Mode	Frequency (Hz)	
	SNL design	This study
1 (1st flapwise)	0.87	1.24
2 (1st edgewise)	1.06	1.39
3 (2nd flapwise)	2.68	3.42



4. CONCLUSION

Based on the pressure loadings in three different wind speed: rated wind speed, cut-off wind speed, and extreme wind speed, the design of a 5 MW wind turbine blade using the fabrication composite laminates demonstrated the feasibility in modification of stacking configuration to reduce the structural weight while maintaining proper rigidity and strength. The outer profile modification of the NREL design near the root according to SNL approach can reduce the stress concentration in the shear webs and retain the safe Tsai-Wu index. Moreover, by reducing the number of layups in the spar cap can effectively lower the weight. But this has to accompany with the reconfiguration in stacking sequence and the improvement of its continuity in order to reduce the Tsai-Wu index. This study only concentrates on the quasi-static analyses of the composite turbine blade, the fatigue performance can be the subject for further study in terms of its long-term durability.

ACKNOWLEDGEMENTS

The partial financial supports from National Science and Technology Council, Metal Industries Research & Development Centre, Taiwan, are gratefully acknowledged.

REFERENCES

Bazilevs, Y., et al., 2010. 3D simulation of wind turbine rotors at full scale. Part I: Geometry modeling and aerodynamics. International Journal for Numerical Methods in Fluids 65, 207-235.

Ha, S., Hayat, K. and Xu, L., 2014. Effect of shallow-angled skins on the structural performance of the large-scale wind turbine blade. Renewable Energy 71, 100-112.

Jonkman, J., 2009. Definition of a 5-MW reference wind turbine for offshore system development. Golden, Colo.: National Renewable Energy Laboratory.

Wind power estimations of staggered high-rise building arrays with voids at varied plan area densities

Yee-Ting Lee [1], An-Shik Yang [2,3], Men-Shen Tsai [4]

[1] *Department of Greenergy, National University of Tainan, Tainan 700, Taiwan, ytlee@mail.nutn.edu.tw*
[2] *Department of Energy and Refrigerating Air-Conditioning Engineering, National Taipei University of Technology, Taipei 106, Taiwan, asyang@ntut.edu.tw*
[3] *Research Center of Energy Conservation for New Generation of Residential, Commercial, and Industrial Sectors, National Taipei University of Technology, Taipei 106, Taiwan*
[4] *Graduate Institute of Automation Technology, National Taipei University of Technology, Taipei, Taiwan, mstsai@ntut.edu.tw*

SUMMARY:
The placement of wind turbines on buildings is gaining more attention for on-site urban wind power generation to realize a net zero carbon-built environment. High-rise buildings with configured voids can enhance the airflows across building complexes, and thereby take the advantages of urban wind resources for power production. Using the wind tunnel experiments to validate the computational model, this study probes the measured mean velocity and turbulence intensity distributions around reduced-scale models of towering void buildings in the 6×6 cube arrays. The Reynolds stress model (RSM) also demonstrates the good accuracy in predicting the wind velocities and turbulent intensities, as compared to other common Reynolds-averaged Navier-Stokes (RANS) turbulent models. This study then analyses the impact of plan area density on the wind power density and turbulence intensity over the full-scale high-rise 6×6 building arrays with the openings. The CFD results pinpoint the suitable arrangement of a plan area density of 0.33, causing the smooth permeation of airflows through void channels to yield the satisfactory wind energy potentials and turbulence intensities on the roofs, beside the buildings and over the void channels in the void building array.

Keywords: Wind resource, Urban wind power, High-rise building with void space, CFD simulation

The incorporation of voids into high-rise buildings can augment the breathability of airflows over densely populated areas, and hence strengthen the aeration outcomes of urban canopy layer (UCL), which is of great significance to the realization of sustainable development goals (SDGs). Because of its sustainable, environmental-friendly, free and versatile features, renewable energy is the best alternative towards abandoning fossil fuels. As one of major renewable energy supplies, the wind energy has been speedily growing in the current century. The implementation of building openings can be considered as one of the effective measures to enhance elevated wind speeds and decreased turbulence intensities for attaining desirable wind characteristics (Fan et al., 2017). The void buildings facing the wind tend to generate the pressure difference between the inlet and outlet of designed openings, developing a high-speed region over the through-building passage suitable for more economically feasible deployment of wind turbines in the urban environment (Lee, et al., 2023). Mostly, urban wind energy harvesting systems present a decentralized power production form close to where generated power is needed, reducing transmission losses by eliminating long distances from end-users. This can be essential for the implementation of sustainable development goals to realize the smart grid systems and carbon emissions reduction. In practice, the power

performance of wind turbines in the urban environment is greatly affected by the complicated wind flows characterized by low mean wind speeds and high turbulence intensities. Hence, it is crucial to pinpoint the proper turbine installation sites in and around buildings to facilitate urban wind power generation. This paper proposes the utilization of void configurations on compact high-rise buildings to improve the urban microclimate environment and maximize the exploitation of urban wind energy. Considering the wind over a 6×6 compact high-rise building array with the openings, the associated wind power potential outcomes were analysed by varying urban patterns. The wind tunnel measurements of airflow velocity and turbulence intensity were conducted to validate the computational model. The Reynolds stress model (RSM) has demonstrated the best prediction accuracy, as compared to the Reynolds-averaged Navier-Stokes (RANS) calculations using other four turbulence models. This study then examines the effect of plan area density on the predictions of wind velocity, power density, and turbulence intensity over the full-scale high-rise 6×6 building arrays with the openings for resolving the suitable locations for turbine installation.

The measurements are performed by a boundary layer wind tunnel at the Wind Engineering Research Center, Tamkang University, Taiwan (in Fig. 1(a)). Figure 1(b) shows the normalized velocity and turbulent intensity profiles of the incident airflow in this study. There is an in-line building model involving 36 square-shaped plastic prisms arranged in a 6×6 array at a scale of 1:300. The sizes of the square prism models are 0.067 m long× 0.067 m wide× 0.30 m high, characterizing the dimensions of 20 m× 20 m× 90 m at the full scale. The square voids of 0.042 m on each side are located at two upstream void buildings in the central 2×2 array, with the openings located at one-half of the building height (= 0.5*H*).

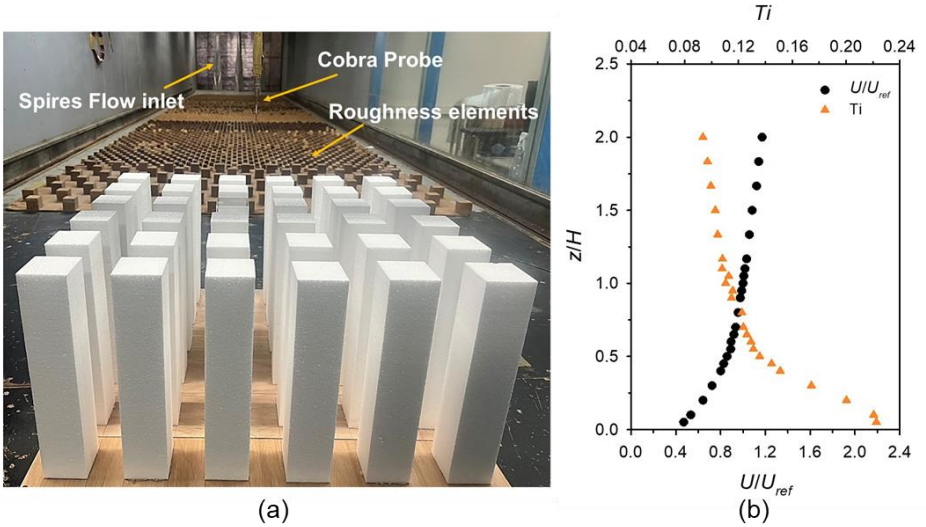


Figure 1 (a) Experimental setup in the wind tunnel and (b) normalized velocity and turbulent intensity profiles of incident airflow

Figure 2 demonstrates the full-scale building array model in urban street canyons. Having 36 generic high-rise buildings to construct a 6×6 array, the building model is a cuboid with the dimensions of 20 m in length (*L*), 20 m in breadth (*B*), and 90 m in height (*H*), respectively. This study then proposes a square void with the extent of 12.5 m×12.5 m to probe the impacts of urban morphology in terms of the plan area density (λ_p) ranging 0.09 to 0.59 on the urban wind power outcomes.

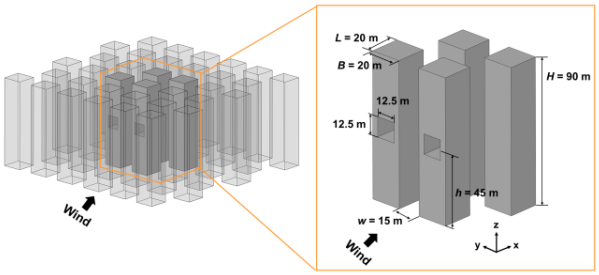


Figure 2 Building array model in CFD simulations

The steady three-dimensional Reynolds-averaged Navier–Stokes equations of mass and momentum for the incompressible isothermal turbulent flow are applied to resolve the airflow field around and inside a 6×6 high-rise void building array. The Reynolds Stress Model (RSM) (Launder et al., 1975) is chosen as the turbulence model. The u_{ref} for full-scale simulations at 90 m is 9.4 m/s. Figure 3 presents a comparison of the predictions of normalized streamwise mean velocity (U/U_{ref}) and turbulence intensity (Ti) profiles over different vertical lines (at x/L= -1.7, 0, 1.7) along the main street at y/B= 0 for the 6×6 cube array with the wind-tunnel measurements. The predicted U/U_{ref} results by five turbulence models agree reasonably well with the wind-tunnel measurements in general. In practice, the associated mean absolute percentage deviations (MAPDs) range from 2.3%−4.9% and 5.1%−13.2% at x/L = -1.7 to 1.7. Consequently, the validation study pinpoints the RSM model as the recommended baseline selection for further CFD calculations.

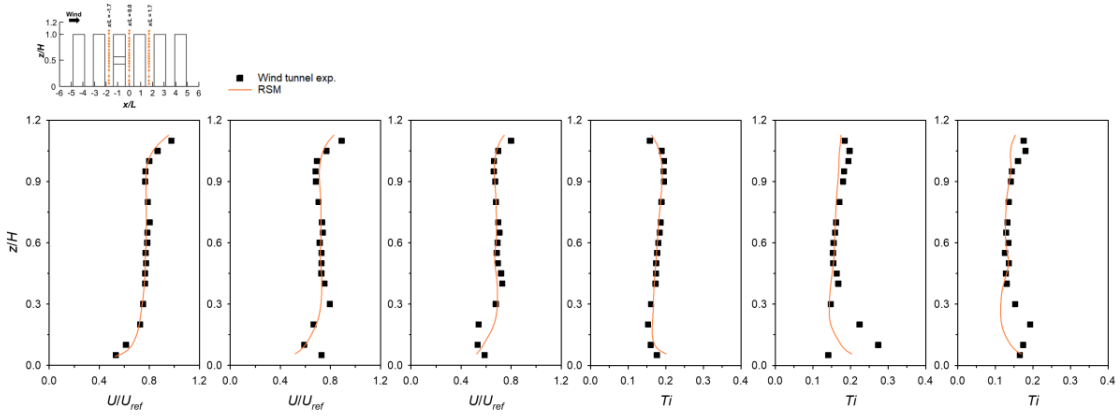


Figure 3 Comparison of CFD predictions of normalized streamwise mean velocity (U/U_{ref}) and turbulence intensity (Ti) profiles over vertical lines (at x/L = −1.7, 0, 1.7) along main street at y/B = 0 for 6×6 cube array

Figure 4 illustrates the calculated contours of (a) u/u_{ref}, (b) PD/PD_{ref} and (c) I_{ref} over the horizontal x-y plane at z/H= 0.5 for λ_p = 0.59, 0.33 and 0.09 (from the compact to sparse city forms). The predicted u/u_{ref} distribution over the middle horizontal plane pinpoint relatively greater airflow velocities through the void channels at λ_p = 0.09. The intense shear flows with escalated u/u_{ref} of 1.2 emerge above the rooftops at the first row (row-1) of buildings, and serially extend over the entries of staggered street passages to the third row for λ_p = 0.59. Instead, the reduction in λ_p from 0.59 to 0.33 or even to 0.09 can facilitate the infiltration of the wind into street canyons through the downstream (i.e., row-6 buildings), revealing escalated wind velocities of u/u_{ref} > 1.0 along the main streets because of the channeling effect between parallel buildings. For λ_p= 0.59, the airflows are difficult to penetrate into the building array, and the regions with $PD/PD_{ref} \geq 0.4$ are limited in the first two rows of buildings in a staggered building array. For λ_p= 0.33 and 0.09, the sparse

urban configuration achieves the maximum PD/PD_{ref} of 0.9 in the row-2 street canyons and void space, suggesting a significant increase in the extent of the region with the prominent potential wind energy harvesting. Considering λ_p= 0.59, the airflows are clearly impeded by upstream void buildings with $I_{ref} \leq 0.12$ in these downstream main streets. At λ_p= 0.33 and 0.09, the void space of upstream void buildings can allow for the smooth infiltration of airflows through void channels, leading to a substantial reduction in I_{ref} within the void channels. This study considers λ_p=0.33 as a preferable choice to promote land use for further sustainable development.

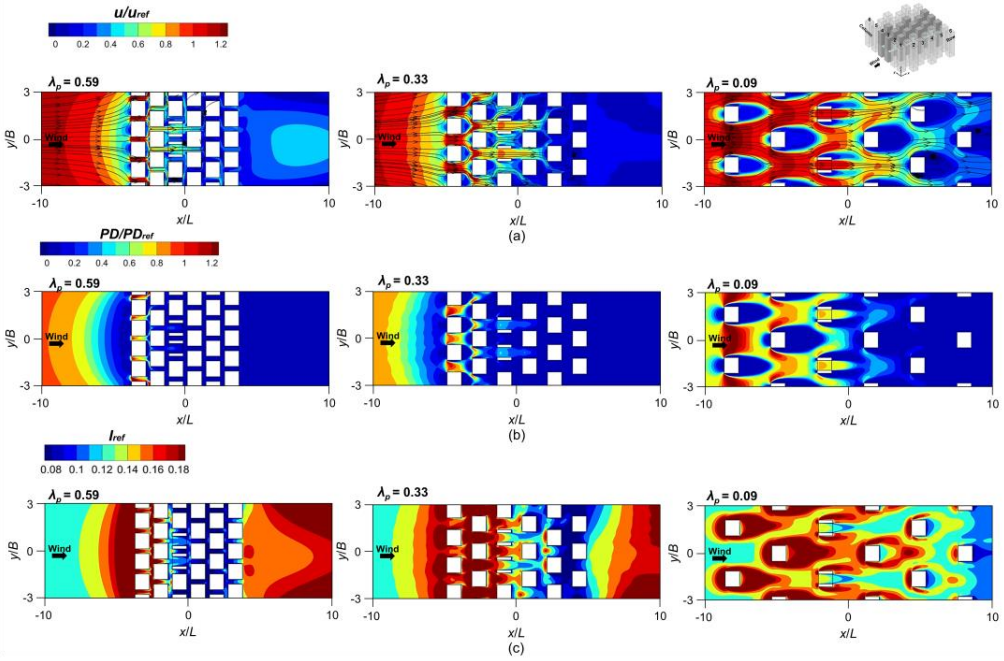


Figure 4 Predicted contours of (a) u/u_{ref}, (b) PD/PD_{ref} and (c) I_{ref} over horizontal x-y plane at z/H= 0.5 for λ_p = 0.59, 0.33 and 0.09

The CFD simulations and wind-tunnel experiments were conducted to systematically appraise the wind power potentials at different plan area densities, staggered dispositions, and void shapes, around staggered 6×6 compact high-rise building arrays. The conclusions are summarized below:

1. The calculated U/U_{ref} and Ti profiles agree reasonably with the wind tunnel measurement data of the void buildings in a 6×6 cube array over the main street with MADs of 2.3%−4.9% and 5.1%−13.2%.
2. The sparse urban configuration can enhance the wind power density and lessen the unacceptable turbulence level over the void channel. The suggested λ_p setting is 0.33 to achieve the auspicious wind power densities and reference turbulence intensities.

REFERENCES

Fan, M, Chau, C.K., Chan, E., Jia, J., 2017. A decision support tool for evaluating the air quality and wind comfort induced by different opening configurations for buildings in canyons. Science of the Total Environment 574, 569-582.

Lee, Y. T., Lo. Y. L., Juan, Y. H., Li, Z., Wen, C. Y., Yang, A. S., 2023. Effect of void space arrangement on wind power potential and pressure coefficient distributions for high-rise void buildings, J. Build. Eng. 75, 107061.

Launder B. E., Reece G. J., Rodi W., 1975. Progress in the development of a Reynolds-stress turbulence closure. J. Fluid Mech.68, 537-66.

Comparative study of aerodynamic characteristics on urban high-rise vertical farms

Simeng Xie, Pedro Martinez-Vazquez, Charalampos Baniotopoulos

Department of Civil Engineering, School of Engineering,
University of Birmingham, Birmingham, UK, sxx366@student.bham.ac.uk
p.vazquez@bham.ac.uk
c.baniotopoulos@bham.ac.uk

SUMMARY:
Urban vertical farms can effectively manage soil and climate conditions, in addition to mitigating transport issues related to the growth of crops. However, the problems around high operating costs and energy consumption during production ensue. To address these drawbacks, this study investigates an urban high-rise vertical farm's wind aerodynamics and energy potential, using results obtained via wind tunnel testing and CFD simulations. The study scrutinises the influence of height, wind speed, and turbulence intensity, on the operation of wind turbines installed on the building's façade and roof, respectively. The results demonstrate that a wind turbine operating at heights equal to or above z/h=0.725 reaches the cut-in speed when the wind speed is greater than 7 m/s, while we observe that the turbulence intensity does not affect the start-up of wind turbines. On the other hand, a wind turbine whose hub operates at z/h = 1.185 achieves rated power at wind speeds above 9 m/s. Wind energy harvesting is better off on the roof since turbine hubs operating at z/h = 0.725 (façade) do not reach the rated power when the wind speed reaches 12 m/s, which also represents a threshold value for pedestrian comfort inside the vertical farm.

Keywords: vertical farm, CFD, wind tunnel test.

1. INTRODUCTION

Urban farms are vertically stacked, automated, and utilise recycled energy and greenhouse technology to produce continuously, regardless of the region, season, or climate. The economic and social benefits of these facilities contribute to industrial growth, although that comes together with increased operating and maintenance costs in addition to high energy consumption, which hinders their fast development (Al-Kodmany et al., 2018). For this reason, the development of clean energy generation systems for vertical farming lies at the top of the sustainability agenda. To mitigate the problem of high energy consumption of vertical farms, we seek to further reduce energy costs through capturing renewable energy e.g., wind energy, with a suitable aerodynamic design (Arabzadeh et al., 2023). Hence, this study investigates the wind flow characteristics and wind energy potential of a high-rise vertical farm located in an urban area.

2. METHODOLOGY

This study was conducted with CFD modelling and wind tunnel testing (WTT) of an elliptical vertical farm prototype with a height of 108m, major and minor axis of 80 m and 60 m, respectively. We designed two separate wind turbine layouts as shown in Figure 1 and simulated horizontal axis

wind turbines with 15 m diameter, rated power of 55 kw. A single wind turbine was installed at z/h=1.185 in Model A and at z/h=0.725 in Model B. The results obtained with the CFD simulations and experimental models helped to compare the wind speed at the building envelope, together with the turbulence intensity, and establish the corresponding wind energy potential. The pedestrian wind comfort within the building's 5 m wide ventilation corridors located at heights z/h=0.125, 0.275, 0.425, 0.575, 0.725, 0.875, is also discussed.

The WTT was carried out in the boundary layer wind tunnel at the University of Birmingham, UK. The scale-down ratio of the model was 1:300, and the experimental wind speed collection device was a Cobra probe. The CFD simulations were carried out in ANSYS Fluent, where the vertical farm was modelled in full size. This model was developed using the basic grid, with a residual of 10^{-4} as the criterion for convergence of iterative runs. The specific setup of the CFD test is described in detail in (Xie et al., 2024). The wind speed profile, turbulence intensity, and wind velocity spectrum were verified before the start of the numerical and experimental simulations to ensure these were in good agreement with the theoretical values.

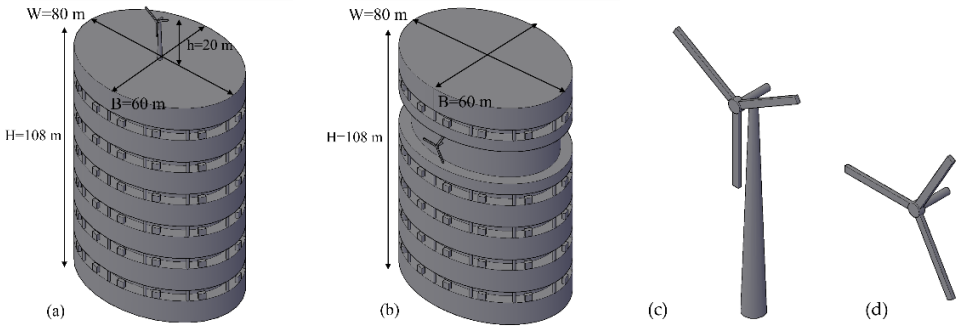


Figure 1. Overview of the (a) Model A, (b) Model B, (c) turbine on the roof (hub height z/h=1.185), and (d) turbine on the façade (hub height z/h=0.725).

3. RESULTS

3.1. Wind speed and pedestrian wind comfort

The wind speed in the 5 m outdoor corridors was analysed and compared at each level, with the results obtained shown in Figure 2. According to this, when the inlet velocity exceeds 7 m/s, the wind speed in the critical corridor reaches 4 m/s which matches the wind turbine's cut-in velocity expected at height of z/h=0.725 (location of the wind turbine installed in Model B) or at higher up points. This implies that the wind turbine would start operating at this speed if located anywhere within the established height range. At the same inflow speed, both the wind tunnel tests and the CFD results show that the wind speed of Model A measured at a height z/h=1.185 is 1.6~1.9 times higher than that of Model B with the referred measuring position z/h=0.725. As we know, the wind energy conversion is directly proportional to the air density, the area swept by the wind turbine, and the third power of the wind speed. It indicates that for model, wind turbines located on the roof would harvest more wind energy when subject to the same incoming wind speed.

On the other hand, according to the Lawson wind comfort criteria (Lawson, 1978), people's activities are hindered if the wind speed is above 10 m/s. According to our study, people's activities within the six lower corridors in the vertical farm prototype do not have a significant impact when

the wind speed reaches 12 m/s.

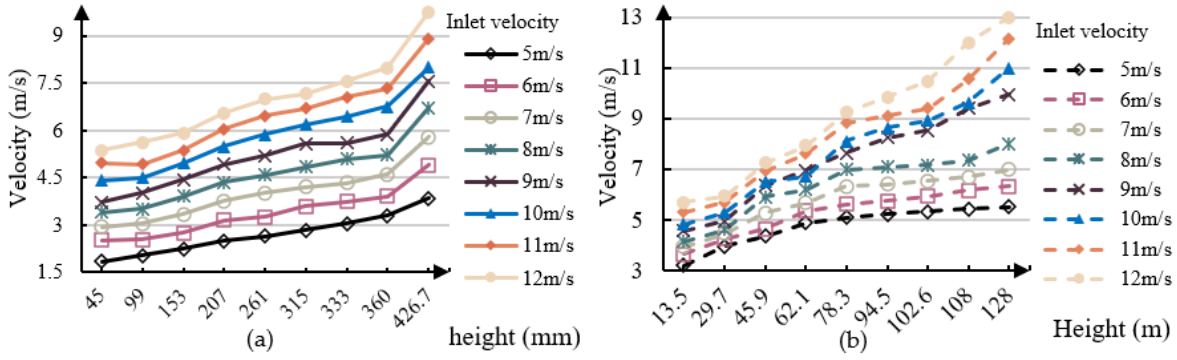


Figure 2. Wind speed at different inlet velocities of each test layer in (a) WTT and (b) CFD.

3.2. Turbulence intensity and power generation potential

In CFD simulation, we observe flow separation on the upwind edge of the roof of Model A. And based on the wind tunnel test results, we compared the turbulence intensity recorded at the two heights z/h=1.185 and z/h=0.725 both, for free flow conditions, and when the model was placed in the tunnel. The results show that the presence of the building increases turbulence significantly. Although, such increase does not undermine the performance of the wind turbines, in fact past research has been demonstrated that wind turbines can still operate properly provided the turbulence intensity is lower than 25% (Han et al., 2022). In Figure 3 we can see that the turbulence intensity at the position of the wind turbines in implemented in Model A and B does not exceed 20%, therefore, the building's aerodynamic performance seems fine.

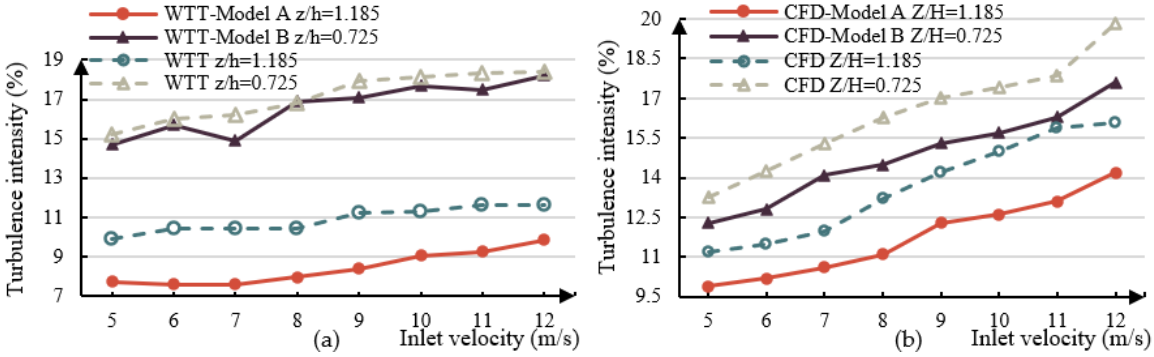


Figure 3. Turbulence intensities at z/h=1.185 and z/h=0.725 heights when the model placed in (a) WTT and the free flow domain, and (b) CFD and the free flow domain.

Finally, Table 1 shows the wind energy captured by the wind turbine at two heights for either simulation technique, when the inlet speed is varied from 5-12 m/s. Both the WTT and CFD simulations indicate that the wind turbine at the height of Model A, z/h=1.185, has a higher wind potential, capturing 2-4 times more energy than the wind turbine placed at the height z/h=0.725 in Model B, under the same exterior wind speed. Notably, when the wind speed around the building exceeds 9 m/s, the wind turbine on the roof can reach the rated power of 55 kw. Notwithstanding the value of these results, we see some discrepancies in Table 1. The possible explanation is that the turbulence caused by the scaled-down wind tunnel test model is larger than that in the CFD

simulations. Since the wind speed is greatly affected by the shape of the bluff building, the wind speed and wind speed growth are suppressed, resulting in a decrease in the captured wind energy.

Table 1. The maximum wind energy of each wind turbine of Model A at z/h=1.185 and Model B at z/h=1.185.

Inlet Velocity (m/s)	Wind Energy (KW)			
	WTT		CFD	
	Model A, z/h=1.185	Model B, z/h=0.725	Model A, Z/H=1.185	Model B, Z/H=0.725
5	7.27	1.48	10.67	8.51
6	13.15	2.98	16.19	11.45
7	20.15	4.79	21.82	16.24
8	29.46	7.24	33.03	21.78
9	46.95	11.21	55	28.62
10	55	15.24	55	34.09
11	55	19.34	55	43.88
12	55	23.64	55	50.41

4. CONCLUSIONS AND DISCUSSION

The simulation methods considered wind flowing in an urban environment at speeds above 7 m/s. In these conditions, a wind turbine placed in the building prototype at z/h=0.725 or above, can reach the cut-in velocity and start running, If the energy harvest devise is placed at the roof with the hub positioned at z/h=1.185, the wind turbine operating efficiency increases 2-4 times. This is mainly because turbulence at the facades of vertical farm attenuates the speed of the wind flowing through the wind turbine. Meanwhile, the prospect of installing wind turbines on roofs is superior to that of building facades, in terms of up-front investment and energy-saving potential of wind turbines.

The results obtained also highlight some research gaps in terms of experimental and numerical simulations. The possible reasons of the mismatch of some results relate to the interference of the scaled-down model in the WWT, constrained by the tunnel walls, the influence of the bracket and the testing equipment, as well as the small size of the model which reinforces the effect of turbulence on the wind speed. The instantaneous fluctuations in wind direction, angle of incidence, and wind speed can dramatically affect the performance of wind turbines. These phenomena can be discussed with more details in future experiments.

ACKNOWLEDGEMENTS

The financial support by the China Scholarship Council (Grant number: 202308360083) for the research stay of the first author, Simeng Xie, at the University of Birmingham, United Kingdom, is gratefully acknowledged.

REFERENCES

Al-Kodmany K. The vertical farm: A review of developments and implications for the vertical city. Buildings, 2018, 8(2): 24.

Arabzadeh V, Miettinen P, Kotilainen T, et al. Urban vertical farming with a large wind power share and optimised electricity costs. Applied Energy, 2023, 331, 120416.

Xie S, Martinez-Vazquez P, Baniotopoulos C. Wind Flow Characteristics on a Vertical Farm with Potential Use of Energy Harvesting. Buildings, 2024, 14(5), 1278.

Lawson T V. The wind content of the built environment. Journal of Wind Engineering and Industrial Aerodynamics 1978, 3(2-3), 93-105.

Han X L, Li Q S, Zhou K, et al. Comparative study between field measurements of wind pressures on a 600-m-high sky-scraper during Super Typhoon Mangkhut and wind tunnel test. Engineering Structures 2022, 272, 114958.

Wind Power Forecast confidence interval based in LSTM combination of GFS-ECMWF-WRF ensembles.

Victor Silveira[1], Sofia Orteli[2], Alejandro Gutiérrez[3]

[1]*IMFIA FING UdelaR, Montevideo, Uruguay, vsilveira@fing.edu.uy*
[2]*IMFIA FING UdelaR, Montevideo, Uruguay, sofiao@fing.edu.uy*
[3]*IMFIA FING UdelaR, Montevideo, Uruguay, aguti@fing.edu.uy*

SUMMARY:
Forecast dispersion and development of confidence interval are crucial aspects in wind energy forecasts. Different strategies have been proposed to address this challenge. In the present work, we propose a methodology for wind power forecasting with a confidence interval, based on a combination of GFS-ECMWF-WRF ensembles and ANN-LSTM neural Networks. The model is developed for each of the 36 wind farms of Uruguay, and is employed for forecasting the full wind energy production of the country, with 1516.5 MW of wind power installed capacity.

Keywords: Wind energy forecast, WRF, LSTM neural Networks

1. INTRODUCTION

Forecasting wind power involves predicting atmospheric variables that influence wind energy production, such as wind speed and air density at the turbine hub heights, along with other factors that may have a significant impact, such as wind direction and atmospheric stability or instability conditions. It is important to emphasize that each time horizon requires specific forecasting techniques for optimal accuracy (Widén et al., 2015). For efficient electrical energy dispatch, it is essential to have forecasts covering different time horizon. Wind power forecasts can be implemented using global atmospheric circulation models, such as the European Centre for Medium-Range Weather Forecasts (ECMWF) or the Global Forecast System (GFS). Additionally, it is possible to integrate mesoscale numerical models, such as the Weather Research and Forecasting (WRF) (Skamarock et al., 2019). These models aim to predict future atmospheric conditions based on initial conditions provided by global circulation models, focusing on specific geographical areas. Identifying the most suitable parameterizations in numerical simulations for local mesoscale wind conditions is essential to improve forecasting accuracy (Gutiérrez and Fovell, 2018). It is possible to develop a probabilistic forecast, performing multiple runs of the WRF mesoscale model with ensemble members (perturbed initial conditions) (Gutiérrez Arce et al., 2018), followed by post-processing with ANNs, is proposed (Almeida L. et al., 2020). This approach can be more effectively in addressing the inherent variability in the atmosphere. This work introduces a methodology for wind power forecasting, along with a confidence interval for the predictions, based on a combination of GFS-ECMWF-WRF ensembles. The model is implemented for each of the 36 wind farms of Uruguay, related to the full wind power production of the country, with 1516.5 MW of wind power installed capacity.

2. DATA DESCRIPTION

WRF 4.3 simulation data uses a domain of 12km horizontal resolution, Lambert projection. Extracted variables were wind velocity, and air density at 100m over the period 01/09/2020 to 31/03/2024. All the parametrization employed on the simulation, are the same used in (Gutiérrez and Fovell, 2018). There are employed artificial variables that add information about the day of the year and hour of the day. Observational data, used as target variable, is the hourly power output from 36 wind farms installed across Uruguay, for the same period (01/09/2020 to 31/03/2024).

3. COMBINED FORECASTING MODEL

The scheme of forecast model used is shown in figure 1. It consists of the combination of three power forecasting models, which employ different numerical weather prediction data: GFS, ECMWF and GFS-WRF. Each of them were calibrated using the conceptual model outlined in (Almeida L. et al., 2020) with artificial neural networks (ANN). The combined forecasting model uses an LSTM (Long Short Term Memory) architecture (Hochreiter, 1997), which is trained also for each wind farm. Each simulation provides a daily forecast with a time horizon of 72 hours. The training period spans from 01/09/2020 to 30/06/2022, while the testing period covers 01/07/2022 to 30/06/2023.

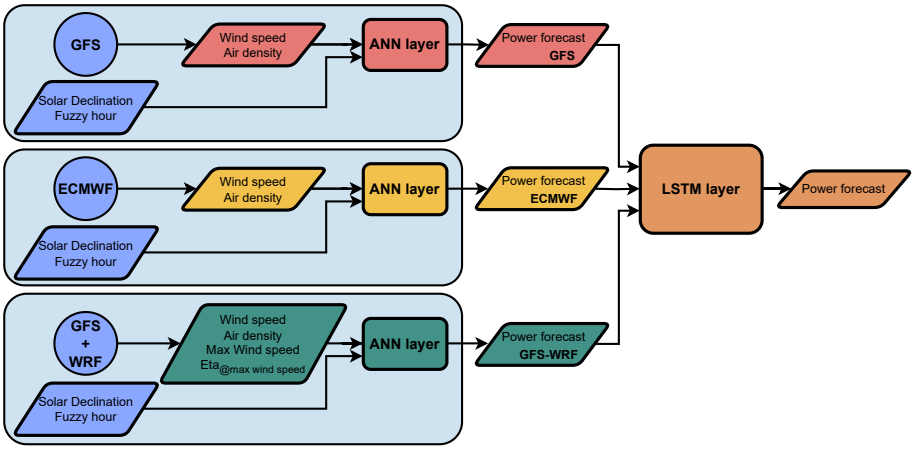


Figure 1. Scheme of combined forecasting model

3.1. Ensemble forecasting

It is possible to obtain a forecast of uncertainty using the input data from atmospheric forecasts through the ensemble forecasting technique. This is achieved employing the GFS control run and ensembles from ECMWF (50 members) and GFS-WRF (30 members), resulting in a total of 1500 forecast scenarios for each wind farm at every time step. The maximum and minimum power forecasts define a "interval", as indicated in Figure 2. Each ensemble is represented with blue lines, and the minimum - maximum "interval" is represented with red lines.

4. CONFIDENCE INTERVAL CALIBRATION

The prediction interval coverage probability (PICP) of the interval, Equation 1, is defined as the ratio between the number of cases inside the interval C_{Inside} and the total number of cases C_{Total}.

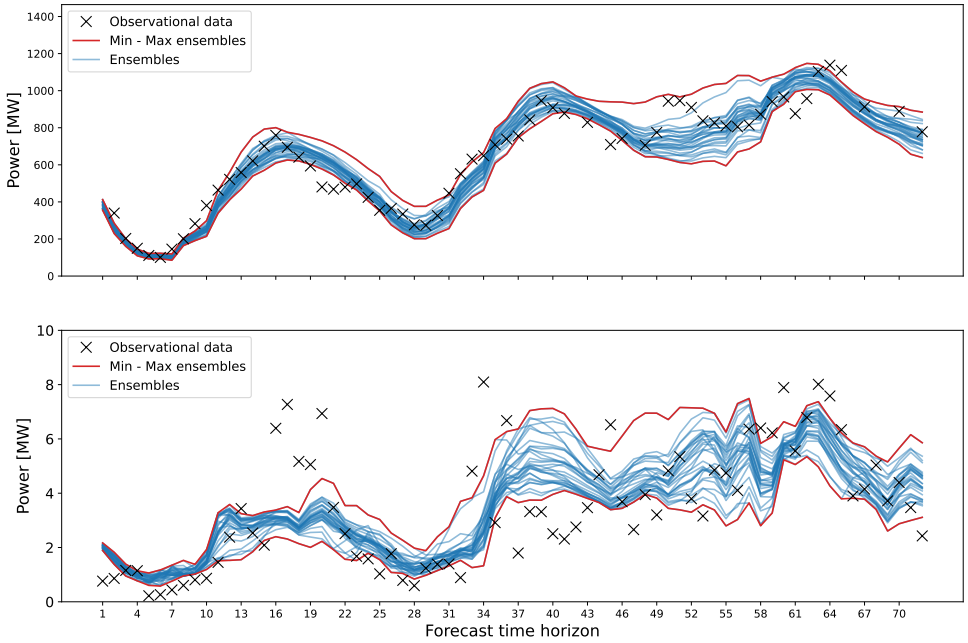


Figure 2. a) National wind power forecast. b) A single wind farm power forecast. Both presented for 01/01/2024, identifying four zones by power and three forecasting horizons. Each blue line represents a single combination of the 50×30 ensembles. Red lines represent Min - Max Band.

The goal is to obtain a confidence interval where 80% of the real power cases are within the interval. Therefore, a corrected value C^*_{Inside} must be found that guarantees a $PICP^*$ of 80%.

$$PICP = \frac{C_{Inside}}{C_{Total}} \qquad (1)$$

$$C^*_{Inside} = C_{Inside}\frac{PICP^*}{PICP} \qquad (2)$$

Since the confidence interval is not symmetric with respect to the forecasted value, it is proposed to work with the cases outside the interval: $C_{Outside}B$ (cases below the interval) and $C_{Outside}A$ (cases above the band), respectively. Therefore, once the interval is corrected, the detailed values should be obtained as shown in equation 3. From this point, there are several possible ways to adjust the interval. A simplifying assumption is used, which consists of adjusting the cases that fall above and below the band in equal proportions. Such proportion is called F, presented in equation 4.

$$C_{Outside}B^* + C_{Outside}A^* = C_{Total} - C_{Inside}\frac{PICP^*}{PICP} \qquad (3)$$

$$F = 1 + \left(1 - \frac{PICP}{PICP^*}\right)\frac{C_{Inside}}{C_{Total} - C_{Inside}} \qquad (4)$$

The F factor is computed for three different forecast horizons namely 00hs-24hs, 24hs-48hs, and 48hs-72hs. Four categories are defined by fractions of the nominal power, dividing the interval between 0% and 25%, 25% and 50%, 50% and 75%, and finally 75% to 100%. The interval is then corrected with this factor on each of the four zones, in order to obtain the "confidence interval".

5. DISCUSSION AND RESULTS

The performance of the confidence interval is evaluated using data between the dates 01/01/2024 to 30/03/2024. The PICP index values obtained are presented in Table 1 for different forecast horizons 00-24 hours, 24-48 hours, and 48-72 hours, respectively. When observing the PICP values obtained, it is noted that they range between 75% and 85%. While it is expected that they may differ from 80% for datasets other than the calibration set, it is considered that with a longer data period and with real data covering all seasons of the year, the PICP index should reach values closer to 80%. Similar results are obtained for each of the 35 of the 36 wind farms evaluated for the same period.

Table 1. PICP evaluated for the national wind power forecast. Evaluation period: 01/01/2024 - 30/03/2024

Forecast Horizon	00hs - 24hs	24hs - 48hs	48hs - 72hs
PICP [%]	74.91	83.91	84.07

6. CONCLUSIONS: FINAL CHECKS AND SUBMISSION

The present work proposes a combined forecasting model for wind power generation, calibrated for the 36 wind farms across Uruguay. This model employs a combination of GFS-ECMWF-WRF prediction variables as input data for a ANN-LSTM model.

A methodology for computing a confidence interval of wind power forecast with a combination of 1500 ensembles members for each wind farm is presented. The model uses a full year of data (01/01/2023 to 31/12/2023) for train and the period 01/01/2024 to 31/03/2024 for verification. With maximum and minimum values of 1500 ensembles members, it is computed a preliminary interval, which is then adjusted based on performance during the calibration period. The calibration is done for different forecasting horizons: 00-24 hours, 24-48 hours, and 48-72 hours, with four power categories defined by percentages of the nominal power. Satisfactory test results show PICP values between 75% and 85%. Seasonal effects may influence the corrections. Future work could explore alternative calibration methods, such as seasonal adjustments, techniques for weighting minimum and maximum ensemble member values, and the use of artificial intelligence tools.

REFERENCES

Almeida L., E. de, Gutiérrez Arce, A., and Camargo, S., 2020. Pronóstico de energía eólica en Uruguay para horizontes temporales de corto plazo en base a modelo numérico de mesoescala y redes neuronales artificiales. ENERLAC. Revista De Energía De Latinoamérica Y El Caribe 4, 32–43.

Gutiérrez, A. and Fovell, R. G., 2018. A new gust parameterization for weather prediction models. Journal of Wind Engineering and Industrial Aerodynamics 177, 45–59.

Gutiérrez Arce, A. M., Almeida, E. de, Porrini, C., Romero, M., Ortelli, S., Cazes, G., Bandeira, A. A., Moreira, D., and Cataldo, J., 2018. Pronósticos operativos de energía eólica, para la gestión de los sistemas eléctricos en la Región. ENERLAC. Revista De Energía De Latinoamérica Y El Caribe 2, 28–41.

Hochreiter, S., 1997. Long Short-term Memory. Neural Computation MIT-Press.

Skamarock, W. C., Klemp, J. B., Dudhia, J., Gill, D. O., Liu, Z., Berner, J., Wang, W., Powers, J. G., Duda, M. G., Barker, D. M., et al., 2019. A description of the advanced research WRF model version 4. National Center for Atmospheric Research: Boulder, CO, USA 145, 145.

Widén, J., Carpman, N., Castellucci, V., Lingfors, D., Olauson, J., Remouit, F., Bergkvist, M., Grabbe, M., and Waters, R., 2015. Variability assessment and forecasting of renewables: A review for solar, wind, wave and tidal resources. Renewable and Sustainable Energy Reviews 44, 356–375.

About fatigue in wind turbines and the use of HSFD to enhance structural durability

Ettore Sorge [1], Carlos Riascos [2], Nicola Caterino [1,3]

[1]*Department of Engineering, University of Naples "Parthenope", Napoli, Italy,*
ettore.sorge@collaboratore.uniparthenope.it, nicola.caterino@uniparthenope.it
[2]*Department of Mechanics of Continuous Media and Theory of Structures, Universitá Politécnica de Valencia, 46022, Spain*
[3]*Construction Technologies Institute, Italian National Research Council, Napoli, 80146, Italy*

SUMMARY:

Wind turbines, essential for renewable energy production, are continuously exposed to fluctuating wind-induced loads that generate significant stresses, leading to progressive fatigue damage. These loads compromise the structural lifespan, particularly in the turbine tower, and result in frequent maintenance needs with substantial economic impacts on the overall wind farm. Given the increasing size and power of modern turbines, the need to accurately predict long-term fatigue damage from short-term data has become crucial to ensure structural reliability and reduce operational costs. This study provides an overview of current long-term fatigue prediction models and introduces an approach to extrapolate 10-minute fatigue damage calculations to represent the entire turbine lifecycle. Furthermore, this methodology is applied to the case study of a hinge-spring-friction device (HSFD) as a passive control device to reduce dynamic loads, thus extending structural life and mitigating fatigue.

Keywords: wind turbine, vibration reduction, fatigue.

1. INTRODUCTION

The demand for wind energy continues to grow as turbines become larger and more powerful, making them increasingly susceptible to fatigue-related structural issues, particularly in the tower base (Chou et al., 2019). These turbines experience highly variable, continuous wind stresses that accumulate as fatigue damage over time, gradually reducing their lifespan and increasing maintenance demands. Accurate life-cycle fatigue predictions often rely on short-term data, typically 10-minute wind load histories, which must then be scaled to estimate cumulative damage over the entire operational life. Table 1 provides an overview of recent papers dealing with the phenomenon of fatigue in wind turbines and the estimation of fatigue life.

This study presents an advanced methodology for calculating fatigue life, applied to a specific case study involving a wind turbine equipped with a Hinge-Spring-Friction Device (HSFD), described in Sorge et al. (2024). This device, developed to extend the operating life of the turbine, acts directly on the structure, reducing the cyclic stresses resulting from the operating conditions to which it is constantly exposed. The main objective of this analysis is therefore to verify the effectiveness of the HSFD in mitigating fatigue damage, with a consequent increase in the durability and overall reliability of the turbine. The proposed methodology allows the fatigue life

of the turbine to be accurately estimated by considering specific load histories based on 10-minute intervals, which realistically reflect the load fluctuations to which a wind turbine is subjected during its operation. This calculation approach, based on short but frequent load sequences, allows a detailed evaluation of the effect of the HSFD, comparing two scenarios: one in which the turbine operates without the use of the device and one in which it is used. The results of the comparison show how the integration of the HSFD contributes to a significant reduction in cyclic stresses, with a possible positive impact on the life of structural components. The proposed methodology represents an advancement in analysis and optimization techniques to improve sustainability and efficiency in the renewable energy industry.

Table 1. State of the Art paper on fatigue life estimation in wind turbines. OFF=Offshore, ON=Onshore.

Year	Authors	Type	short description
2022	Rincón-Casado et al.	ON-OFF	Experimental residual life assessment of bolts
2022	Sadeghi et al.	OFF	LFFD integration in time domain analysis
2022	Zheng and Chen	OFF	Blade-rotor bolt analysis
2023	Bai et al.	ON-OFF	Fatigue estimation using Neural Network
2023	de N Santos et al.	OFF	Fatigue estimation using Neural Network
2023	Lee et al.	OFF	Fatigue on offshore support structure
2023	Li et al.	OFF	Fatigue analysis on an offshore foundation
2023	Zha et al.	OFF	Fatigue analysis on an offshore foundation
2023	Zhang et al.	ON-OFF	Review methods for fatigue life estimation
2023	Zhao et al.	ON-OFF	Fatigue analysis based on monitored data
2023	Zhu et al.	ON	Fatigue estimation with probabilistic framework
2024	Ren, Xing, and Patel	OFF	Fatigue on mooring lines
2024	Tao et al.	OFF	Yaw influence on bolt fatigue life
2024	Xi et al.	OFF	Fatigue analysis based on monitored data
2024	Zhang et al.	OFF	Fatigue analysis with different accumulation models

2. METHODOLOGY FOR ESTIMATING FATIGUE LIFE

This section describes the method of calculating the fatigue life from 10-minute stress histories on the tower, calculated for different wind speed scenarios at the hub. For each scenario, 10-minute stress histories were considered and, through the application of the rainflow method (Bai et al. 2023) the fatigue damage (D) was estimated using the Miner equation (Miner 1945).
The damage calculated for a 10-minute period at a given wind speed (v) was then extended on an annual basis. To determine the average annual damage value, the damage estimate over the individual 10-minute intervals was combined with the frequency distribution of wind speeds, $f(v)$, which represents the number of annual hours corresponding to each speed interval.
To adequately represent the wind speed behavior at a given site, the Weibull distribution (IEC61400-1, 2019) was used as a probabilistic model, with its probability density function accurately describing the frequency of the various wind speed intervals. Considering the number of 10-minute periods constituting a year and the frequency distribution and f(v), it is possible to estimate the annual damage of each scenario. This calculation is equivalent to estimating the annual damage considering its frequency on an annual basis in terms of ten-minute periods. The fatigue life of the detail considered was evaluated by again applying the theory of linear damage accumulation, thus allowing an accurate estimate of the fatigue life.

3. CASE STUDY AND RESULTS

The methodology described was applied to the case study of a 5WM wind turbine (Sorge et al. 2024), equipped with a passive Hinge-Spring-Friction Device (HSFD), installed near to Lecce, Italy. The site in question has specific wind speed conditions, represented by a Weibull distribution curve. The objective of the study was to assess the fatigue damage suffered by the turbine structure under its operating conditions. Two conditions were considered: a base in which the turbine tower is rigidly fixed to the base (Fixed Base - FB) and a second condition with the tower equipped with the HSFD (Rotating Base - RB). For each scenario, the fatigue damage was calculated using a normal wind model, in line with IEC61400-1 (2019) standards. Fatigue damage was estimated for 10-minute intervals and the influence of the HSFD on cyclic stress reduction was then estimated for both conditions. This comparison is represented graphically in Fig. 1, where the damage curve for the FB scenario without the device is compared with that of the RB scenario equipped with the HSFD.

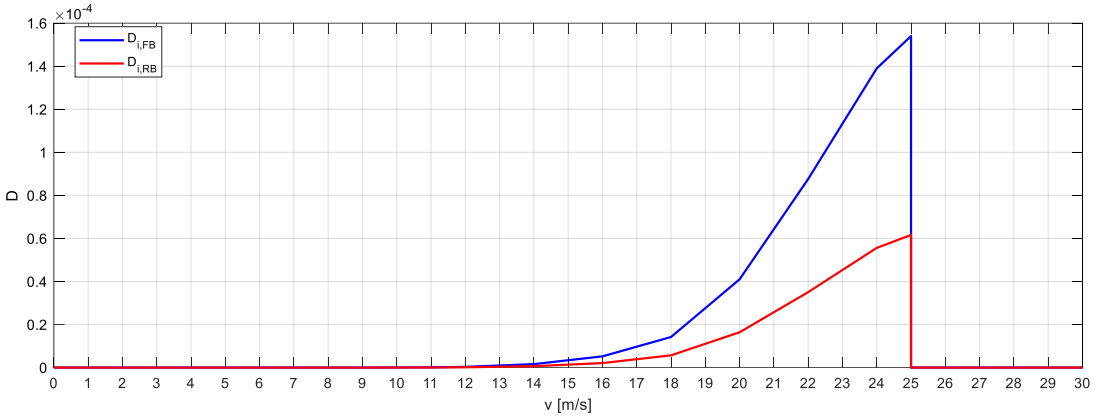


Figure 1. Fringe fatigue damage at the base of the tower in any wind scenario.

The results of the analysis show a significant reduction in fatigue damage in the RB scenario with HSFD compared to the FB scenario without the device. This reduction can be expressed in terms of an increase in the fatigue life of the structure and its structural components.

4. CONCLUSION

In conclusion, this work presented an advanced methodology for calculating the fatigue life of wind turbines, based on the analysis of short-term stress histories in 10-minute intervals. This approach provides accurate estimates of long-term damage, which is crucial for assessing the structural durability of turbines under varying and intense wind loads. Subsequently, the methodology was applied to a specific case study of a NEREL5WM turbine equipped with an HSFD device, showing how this passive control system can significantly reduce cyclic stresses and, consequently, cumulative damage over time. The results obtained from the case study confirm the effectiveness of the methodology and HSFD in extending turbine life, reducing maintenance costs and improving overall reliability. These two central contributions make the work relevant to improving the sustainability and efficiency of wind turbines, and also suggest possibilities for future application and optimization under different operating conditions.

REFERENCES

Bai, H., Shi, L., Aoues, Y., Huang, C., and Lemosse, D. 2023. Estimation of probability distribution of long-term fatigue damage on wind turbine tower using residual neural network. Mechanical Systems and Signal Processing, **190**: 110101. Elsevier.

Chou, J.-S., Ou, Y.-C., and Lin, K.-Y. 2019. Collapse mechanism and risk management of wind turbine tower in strong wind. Journal of Wind Engineering and Industrial Aerodynamics, **193**: 103962. Elsevier.

IEC, I.E.C. 2019. 61400-1: 2019 Wind Energy Generation Systems—Part 1: Design Requirements. IEC: Geneva, Switzerland,.

Lee, G.-N., Ngo, D.-V., Lee, S.-I., and Kim, D.-H. 2023. Fatigue Life Convergence of Offshore Wind Turbine Support Structure According to Wind Measurement Period. Energies, **16**: 3199. MDPI.

Li, B., Shi, H., Rong, K., Geng, W., and Wu, Y. 2023. Fatigue life analysis of offshore wind turbine under the combined wind and wave loadings considering full-directional wind inflow. Ocean Engineering, **281**: 114719. Elsevier.

Miner, M.A. 1945. Cumulative damage in fatigue. American Society of Mechanical Engineers.

de N Santos, F., D'Antuono, P., Robbelein, K., Noppe, N., Weijtjens, W., and Devriendt, C. 2023. Long-term fatigue estimation on offshore wind turbines interface loads through loss function physics-guided learning of neural networks. Renewable Energy, **205**: 461–474. Elsevier.

Ren, C., Xing, Y., and Patel, K.S. 2024. Application of an active learning method for cumulative fatigue damage assessment of floating wind turbine mooring lines. Results in Engineering, **22**: 102122. Elsevier.

Rincón-Casado, A., Juliá-Lerma, J.M., García-Vallejo, D., and Domínguez, J. 2022. Experimental estimation of the residual fatigue life of in-service wind turbine bolts. Engineering Failure Analysis, **141**: 106658. Elsevier.

Sadeghi, N., Robbelein, K., D'Antuono, P., Noppe, N., Weijtjens, W., and Devriendt, C. 2022. Fatigue damage calculation of offshore wind turbines' long-term data considering the low-frequency fatigue dynamics. *In* Journal of Physics: Conference Series. IOP Publishing. p. 32063.

Sorge, E., Riascos, C., Caterino, N., Demartino, C., and Georgakis, C.T. 2024. Optimal design of a hinge-spring-friction device for enhancing wind induced structural response of onshore wind turbines. Engineering Structures,.

Tao, T., Yang, Y., Yang, T., Liu, S., Guo, X., Wang, H., Liu, Z., Chen, W., Liang, C., and Long, K. 2024. Time-domain fatigue damage assessment for wind turbine tower bolts under yaw optimization control at offshore wind farm. Ocean Engineering, **303**: 117706. Elsevier.

Xi, Y., Li, H., Sun, L., and Wang, Z. 2024. Extreme load extrapolation and long-term fatigue assessment of offshore wind turbine tower based on monitoring data. Ocean Engineering, **300**: 117180. Elsevier.

Zha, X., Lai, Y., Rui, S., and Guo, Z. 2023. Fatigue life analysis of monopile-supported offshore wind turbines based on hyperplastic ratcheting model. Applied Ocean Research, **136**: 103595. Elsevier.

Zhang, L., Jiang, B., Zhang, P., Yan, H., Xu, X., Liu, R., Tang, J., and Ren, C. 2023. Methods for fatigue-life estimation: A review of the current status and future trends. Nanotechnology and Precision Engineering (NPE), **6**. AIP Publishing.

Zhang, X.-L., Zhang, B., Wang, D., and Xu, C. 2024. Fatigue damage analysis method of offshore wind turbine foundation. Ocean Engineering, **302**: 117618. Elsevier.

Zhao, Y., Li, X., Wang, X., Jiang, J., and Wang, Z. 2023. Fatigue Life Evaluation of Wind Turbine Tower Based on Measured Data. Advances in Civil Engineering, **2023**. Hindawi.

Zheng, T., and Chen, N.-Z. 2022. Time-domain fatigue assessment for blade root bolts of floating offshore wind turbine (FOWT). Ocean Engineering, **262**: 112201. Elsevier.

Zhu, D., Ding, Z., Huang, X., and Li, X. 2023. Probabilistic modeling for long-term fatigue reliability of wind turbines based on Markov model and subset simulation. International Journal of Fatigue, **173**: 107685. Elsevier.

Wind speed and turbulence recovery from SCADA data

Lasse Svenningsen [1], Troels Juul Pedersen [1]

[1]*EMD International A/S, Aalborg, Denmark, ls@emd.dk, tjp@emd.dk*

SUMMARY:
Most wind turbines are designed for 20 years of operation. Extended turbine operation beyond design lifetime significantly improves both the return of investment and the climate benefit. Most national guidelines and standards on wind turbine lifetime extension require both theoretical calculations and practical inspections. Theoretical calculations compare fatigue accumulation, incurred during the operation period relative to the original design limits. Fatigue accumulation is chiefly driven by wind speed and turbulence. Hence, accurate data for wind speed and turbulence form an important basis for potential lifetime assessments. Here, we present a method to accurately recover wind speed and turbulence data from time series of typical 10-minute wind turbine SCADA operational data. The proposed method does not rely on the notoriously inaccurate nacelle mounted anemometers, nor does it require mounting of new sensors. Instead, the method relies on an improved model for the interaction between a turbine rotor and a turbulent wind field akin to the background factor approach for wind loads. The proposed method makes it possible to recover reliable wind speed and turbulence from turbine SCADA data.

Keywords: Fatigue loads, Turbine lifetime, SCADA data

1. INTRODUCTION - DATA & CHALLENGES

In Europe, 22 GW of the 272 GW of existing wind farm capacity has operated for more than 20 years, and by 2030, 52 GW will be more than 20 years old (European Wind Energy Association, 2024). These data illustrate the important potential in lifetime extension of wind turbines, to generate more renewable energy with no significant use of additional depletable resources.

Most national guidelines and standards on wind turbine lifetime extension require both theoretical calculations and practical inspections. The theoretical calculations concern fatigue accumulation, during the operational period of a wind turbine, relative to its original design limits. This is a cheap first step to quantify the potential for operation beyond design life before investing in expensive on-site inspections. Lifetime calculations require data of the operational history, as wind turbines typically have no dedicated load sensors to monitor the components. As the main drivers of fatigue loads are wind speed and turbulence, knowing these data for the operational history is valuable input. The question is whether these quantities can be retrieved with sufficient accuracy from the data typically recorded and stored by a standard SCADA (supervisory control and data acquisition) system of a wind turbine. The obvious go-to for such data is measurements from the anemometers, mounted on the turbine nacelle, downwind of the rotor, used by the turbine controller. Fig. 1 illustrates such 10-minute data of wind speed mean and standard deviation (turbulence) for the Vestas V52 turbine, operating at the Risø campus of Danish Technical University (DTU). The graphs show errors of the nacelle wind speed measurements, compared to undisturbed wind measurements at an upstream meteorological mast.

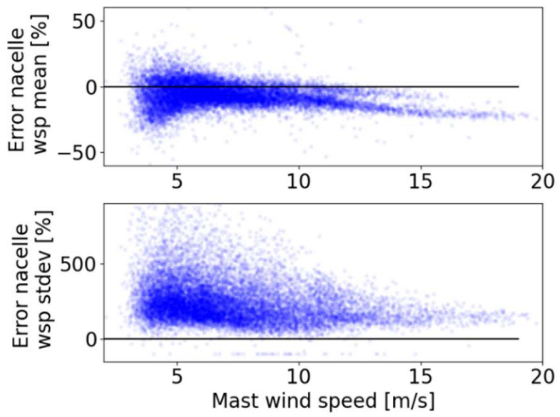


Figure 1. Plot showing errors of 10-minute wind speed mean (upper) and standard deviation (lower) measured by the V52 nacelle anemometer relative to the accurate mean and standard deviation data measured at the mast.

Upper plot of Fig. 1 shows that errors in mean wind speed from the nacelle data mostly varies between ±25% across the 10-minute samples. An increasingly negative systematic deviation, exceeding -15% is evident above ca. 8 m/s. Lower plot in Fig. 1 shows that 10-minute standard deviations (turbulence) from the nacelle anemometer, on average, have a severe positive bias of several hundred percent combined a very large scatter. From the V52 data we conclude that wind speed recordings from nacelle anemometers appear unfit for any meaningful lifetime calculations. The main cause of these errors is expected to be the nacelle anemometers position in the wake of the rotor and very close to the large nacelle structure.

2. METHOD & SOLUTION

The alternative to measurements from the nacelle anemometer is outputs from the turbine itself. Here, the wind field has been filtered through the rotor, and then converted to electrical energy in the generator. Information of past wind speed variations is therefore stored in the 10-minute data of mean and standard deviation of power. Unfortunately, the power data loses sensitivity at higher wind speeds due to the pitch control of modern turbines. This control levels off power output to the constant rated power for wind speeds above 10-12 m/s. However, in this high wind speed regime the turbine pitch data takes over the sensitivity to wind speed. The 10-minute mean and standard deviation of pitch angle reflects the controller's adaptation to variations in wind speed and turbulence seen by the turbine rotor. Fig. 2 illustrates the 10-minute data of power and pitch mean and standard deviation corresponding to the nacelle data shown in Fig. 1.

Note how the 10-minute mean power levels-off above ca. 12 m/s (upper plot). Similarly, above 12 m/s, the mean pitch angle starts increasing significantly from a relatively constant level close to zero degrees at lower wind speeds. These data clearly show that the variations in wind speed and turbulence are directly reflected in the corresponding data of mean and standard deviation of power and pitch angle. The question is if, and how, the mean and standard deviation of the original wind field can be recovered from such operational SCADA data.

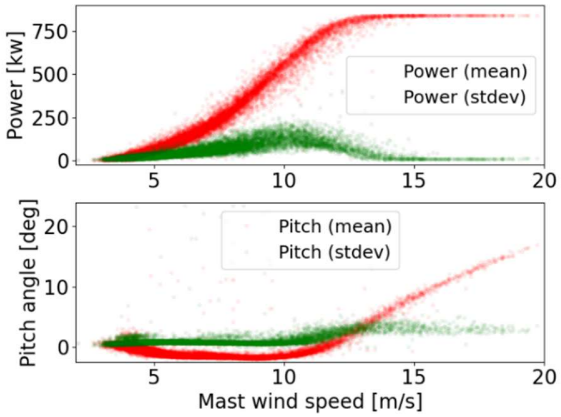


Figure 2. Plot showing 10-minute wind mean and standard deviations of power (upper plot) and pitch (lower plot) measured for the V52 wind turbine versus wind speed measured at the up-stream mast.

2.2. Forward problem & solution to inverse problem

First step to retrieve wind speed and turbulence from power and pitch data is to establish a forward model, predicting how the rotor interacts with the wind field and results in the turbine power and pitch outputs. The proposed method relies on the IEC61400-12-1, 2022, methodology for power curve corrections, that is based on establishing a power curve representing zero turbulence. Power output at other turbulence levels is predicted by integrating this power curve with a gaussian wind speed distribution, with mean and standard deviation representing 10-minute wind speed data. Several important improvements to the IEC method have been included in this work:

1) An improved zero-turbulence power curve model, based on Saint-Drenan et al., 2022.
2) Including the low-pass filter-effect of the turbine rotor (Svenningsen and Slot, 2023).
3) An equivalent model for pitch is developed, based on similar methods and principles.

In (2), the low-pass filter-effect is based on the back-ground factor approach (e.g. EN1991-1-4, 2005), modelling the rotor as a disc. As a result, a rotor of 52m, as the V52, filters out ca. 25% of the turbulence seen by a cup anemometer. A rotor of 200m filters out close 50% of turbulence.
With the forward model established, the inverse problem of recovering mean wind speed and turbulence from mean and standard deviations of power and pitch may be addressed. In the proposed method of this study, the inverse problem has been solved by establishing an elaborate data set of forward calculations, which may then be used as a look-up table for very fast predictions. This process of the forward problem and inverse solution are illustrated in Fig. 3.

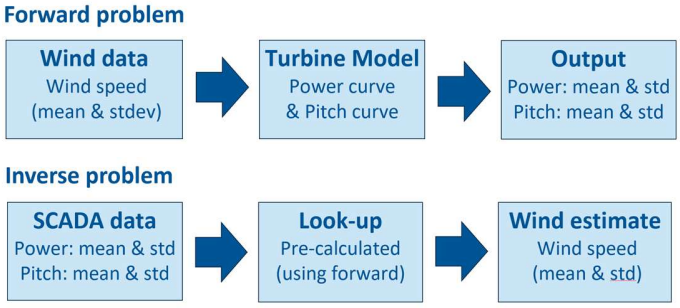


Figure 3. Diagram illustrating the forward problem and the solution to the inverse problem.

3. RESULTS & CONCLUSION

Fatigue lifetime calculations, according to IEC61400-1, 2019, are based on the 90-percentile of turbulence (TI90%) conditioned on wind speed. This means that calculation of accurate lifetimes require, as a minimum, accurate TI90%, which in turn requires both accurate wind speeds and accurate an turbulence distribution (or at least 90-percentile).

Fig. 4 shows the TI90% resulting from the mast measurements, from the nacelle anemometer and finally recovered using the proposed method from the power and pitch data. The two latter cover wind speeds below 12 m/s and above 12 m/s, respectively, together covering the full wind speed range.

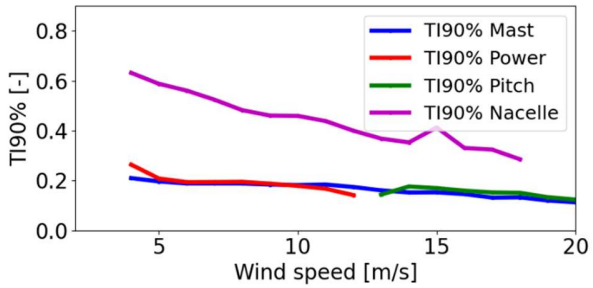


Figure 4. Plot showing the resulting 90-percentile of turbulence based on the accurate mast measurements, the nacelle measurements and for the proposed method using power and pitch data for the Risø V52.

The results show that the nacelle TI90% data have errors of 100 to 300%, severely overestimating turbulence. Results for the proposed method, based on power and pitch data, show errors of the order of 5-10%, a drastic improvement relative to nacelle wind speed measurements, making it useful for lifetime calculations. A further benefit from the proposed method is that it includes the full turbulent wind field, including both ambient and wake effects from neighbouring wind turbines for both wind speed and turbulence as seen by the turbine rotor.

ACKNOWLEDGEMENTS

This work was supported by the EUDP (Danish Energy, Development & Demonstration Program) as part of the IEA Wind Task 42 – Lifetime extension. Special thanks to DTU (Danish Technical University) for giving access to the V52 operational and mast data as part of IEA task 42.

REFERENCES

EN1991-1-4, 2005. European Standard: Eurocode 1: Actions on structures – General actions – Part 1-4: Wind actions. European Committee for Standardization.

European Wind Energy Association, 2024. Wind energy in Europe: 2023 Statistics and the outlook for 2024-2030.

IEC61400-1, 2019. International Standard: Wind energy generation systems – Part 1: Design requirements. International Electrotechnical Commission.

IEC61400-12-1, 2022. International Standard: Wind energy generation systems – Part 12-1: Power performance measurements of electricity producing wind turbines. International Electrotechnical Commission.

Saint-Drenan, Y.M., Bessau, R., Jensen, M., Staffell, I., Troccoli, A., Dubus, L., Schmidt, K. Gruber, K., Simões, S. G. and Heier, S., 2020. A parametric model for wind turbine pow-er curves incorporating environmental conditions. Renewable Energy 157, Elsevier.

Svenningsen, L. and Slot, R. M. M., 2023, Does wind turbine rotor size impact the effect of turbulence on power production?, ICWE16 - 16th International Conference on Wind Engineering, Florence, Italy.

Dynamic stall control of wind-turbine blades equipped with vortex generators and Gurney flaps

Marin Ivanković [1,2], Marvin Jentzsch [2], Anna Friederike Rahel Großmann [2], Vladimir Zimmermann [2], Marinos Manolesos [3], Christian Navid Nayeri [2], Hrvoje Kozmar [1]

[1] *Faculty of Mechanical Engineering and Naval Architecture, University of Zagreb, Ivana Lučića 5, 10000 Zagreb, Croatia, marin.ivankovic@fsb.unizg.hr, hrvoje.kozmar@fsb.unizg.hr*

[2] *Hermann-Föttinger-Institut, Technische Universität Berlin, Straße des 17. Juni 135, 10623 Berlin, Germany, marvin.jentzsch@tu-berlin.de, a.grossmann.1@tu-berlin.de, vladimir.zimmermann@campus.tu-berlin.de, christian.nayeri@tu-berlin.de*

[3] *School of Mechanical Engineering, National Technical University of Athens, Heroon Polytechniou 9, 15780 Zografou, Greece, marinos@fluid.mech.ntua.gr*

SUMMARY:
Dynamic stall increases unsteady aerodynamic loading of airfoils and wind turbine blades, thus reducing the lifetime of wind turbines. These adverse aerodynamic load fluctuations can be mitigated using passive flow control devices such as vortex generators (VGs) and Gurney flaps (GFs) attached to wind turbine blades. While some relevant work was previously carried out on the effects of these devices acting alone, further work is still required to fully elucidate the performance of airfoils concurrently equipped with VGs and GFs. For this purpose, the Clark Y airfoil equipped with VGs and GFs was studied in dynamic stall conditions. Wind tunnel experiments were performed at Reynolds number (*Re*) and reduced frequencies (*k*) typical for small wind turbines. The results indicate that VGs and GFs enhance aerodynamic airfoil performance. Concurrent application of VGs and GFs yields enhancement in lift, delay of stall, and reduction of load fluctuation due to dynamic stall vortex. The effects of VGs and GFs on wind turbine blades are considered to explore the possibility of reducing fatigue loads on wind turbines with these passive flow control devices.

Keywords: Airfoil, Dynamic stall, Vortex generators, Gurney flaps, Wind-tunnel experiments.

1. INTRODUCTION

Dynamic stall occurs when flow separates from airfoils that experience a dynamic change in angle of attack (*AoA*), that extends beyond critical *AoA*. This is characterized by the formation and convection of the dynamic stall vortex (DSV) over the airfoil suction side. Horizontal-axis wind turbine blades usually experience cyclic changes in the effective AoA due to various issues including misalignment of the rotational axis with wind direction, atmospheric boundary layer, and turbulence. Dynamic stall is a major cause of increased fatigue loading and reduced lifetime, power production and the efficiency of wind turbines.

Adverse effects of dynamic stall can be mitigated by increasing the maximum achievable lift force, and delaying stall to a larger *AoA*. However, enhanced lift force results in a larger amplitude of

force oscillations when a dynamic stall occurs, which has an adverse effect on structural integrity. Demirci et al. (2023) achieved lift enhancement and stall delay of the Clark Y airfoil by employing tubercles on the airfoil leading edge (LE). A similar outcome can be achieved using vortex generators (VGs) and Gurney flaps (GFs).

VGs are typically placed on the suction side of the airfoil near its LE to reduce the risk of flow separation. VGs postpone the occurrence of dynamic stall to higher *AoA*s, increase the maximum lift force, and enhance flow reattachment, according to Zhu et al. (2022). Furthermore, VGs proved to increase the power production of wind turbines, Bak et al. (2016). GFs applied on the pressure side at the trailing edge (TE) increase c_L/c_D in the pre-stall regime, especially for very small GFs, (Chng et al. (2022)). GFs proved to enhance the aerodynamic performance of rotating blades of wind turbines, Yang et al. (2024).

While VGs and GFs on airfoils have been abundantly studied individually as passive flow control methods, the characteristics of airfoils concurrently equipped with both devices are still not sufficiently explored. There is evidence that the combined application of both devices may enhance the flow around airfoils, e.g., Chen et al. (2023) and Alber et al. (2022). Some benefits include larger c_L/c_D ratios in the pre-stall region and a shift of flow separation to larger *AoA*s.

The main objective of this study is the effect of concurrent application of VGs and GF on airfoil and wind turbine blades subjected to dynamic *AoA* oscillations. Results regarding dynamic stall characteristics are expected to advance the understanding of this phenomenon and to enable improvements in the power production of future and already existing wind turbines.

2. METHODOLOGY

Two test setups were used: the first includes an oscillating Clark Y airfoil and the other a research wind turbine blade.
Experiments on the Clark Y airfoil were performed in a closed-return wind tunnel featuring an open test section at the Technische Universität Berlin. This approach was adopted to allow for an undisturbed wake development in the case of the dynamic stall, a procedure suggested by Du et al. (2015). The flow is characterized by a turbulence intensity lower than 1%. A wing with a constant chord c = 0.14m and aspect ratio AR = 2 was placed in the test section.

Measurements were performed at Reynolds number of Re = 180,000, i.e., typical for small wind turbines commonly used in urban environments. Aerodynamic phenomena on the oscillating airfoil with and without passive flow control devices (PFCDs) were studied in the $0° < AoA < 30°$ and $0.00 < k < 0.15$ ranges, conditions that are typical for the blade AoA oscillations in the case of wind-turbine yaw misalignment. Reduced frequency is defined as $k = \pi fc/U_\infty$, where f, c and U_∞ denote the airfoil oscillation frequency, the airfoil chord length and free stream velocity, respectively.

VGs and GFs were studied on the airfoil and wind turbine blades. VGs with height (h) in the $0.011c$

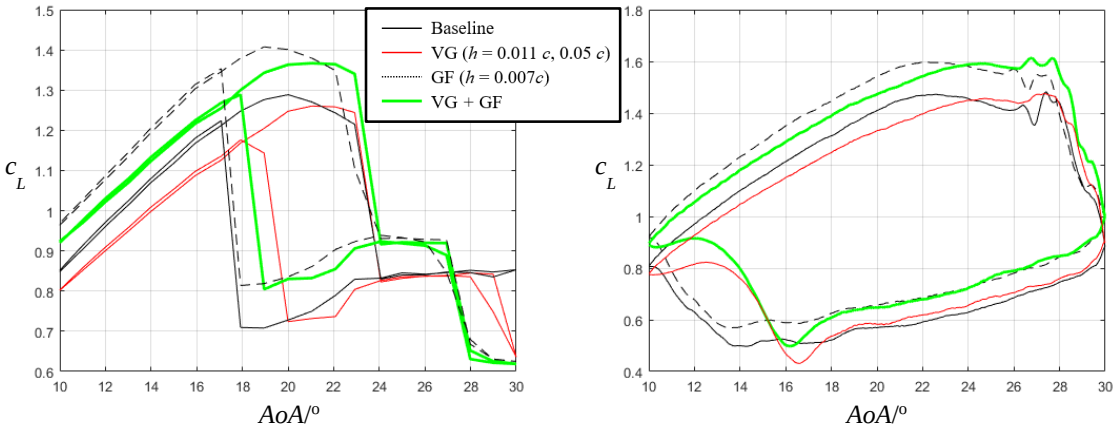
$< h < 0.037c$ range were placed on the suction side between $0.05c$ and $0.15c$ downstream of the LE, while GFs with height of $0.0014c < h < 0.0143c$ were placed along the entire wingspan on the pressure side at the TE. The effects of VGs and GFs were studied separately and concurrently.

Experiments on a scaled wind turbine were performed on the 3-meter diameter Berlin Research Turbine (BeRT) in a closed return wind tunnel with a closed test section of 4,2 m x 4,2 m x 5 m (width x height x length), for more details see Bartholomay et al. (2023). The wind turbine model was rotated around its vertical axis to simulate yaw misalignment.

Lift, drag and moment were determined from the surface pressure distribution on the Clark Y airfoil. Drag is based on the pressure drag only, while the friction drag was not considered. The effect of VGs and GFs on the airfoil was studied based on aerodynamic force, power and torque coefficients.

3. RESULTS

The results of the Clark Y airfoil with VGs and GF are presented here, while the BeRT results will be published in the scope of the full conference paper. It was found that maximal improvements in airfoil performance were achieved by employing VGs with a height of $0.011c$ at $0.05c$ and GF with a height of $0.007c$. Figure 1 presents c_L dependence on *AoA* for $10° < AoA < 30°$ and four configurations: baseline (black), optimal VGs (red), optimal GF (dashed black), and a combination of optimal VGs and GF (green). While Figure 1. a) is for the statical pitching of the airfoil, Figure 1. b) is for dynamic pitching with $k = 0.05$.



a) b)

Figure 1. Lift polar of Clark Y airfoil: a) static $k = 0.0$, b) dynamic $k = 0.05$.

Proposed VGs (red curve) have similar effects on static and dynamic change in *AoA*: they reduce c_L in the pre-stall region, delay the occurrence of maximal c_L to a larger *AoA*, and promote flow reattachment when the airfoil is in pitching down motion. VGs suppress c_L oscillations due to DSV, which are present for dynamic *AoA* oscillations for $26^o < AoA < 28^o$. The only significant

effect of GF (dashed curve) is the offset of the lift coefficient in a positive direction, both for static and dynamic change in *AoA*. The concurrent application of VGs and GF (green line) yields a superposition of aerodynamic enhancements of two devices: a 9% increase in dynamic stall *AoA*, a 15% increase in reattachment *AoA*, a 6% increase in the maximum c_L while maintaining the same c_L/c_D ratio, and a 68% decrease in c_L oscillation due to DSV. Reasons for the described behavior of proposed VGs, GF and their combination will be provided in the full conference paper.

4. CONCLUDING REMARKS

Wind tunnel experiments were performed to study the performance of an airfoil and a wind turbine equipped with vortex generators and Gurney flaps in dynamic stall conditions. The oscillating Clark Y airfoil was studied at various reduced frequencies k in terms of aerodynamic force coefficients. The results indicate that VGs and GF enhance airfoil performance when used alone and concurrently. Concurrent application of VGs and GF yields enhancement in lift, delay of stall, and reduction of load fluctuation related to dynamic stall vortex. The effects of VG and GF on wind turbine blades are considered in order to explore the possibility of reducing fatigue loads on wind turbines equipped with these passive flow control devices.

ACKNOWLEDGEMENTS

The support of Deutsche Forschungsgemeinschaft (DFG) Project #446073296, Deutscher Akademischer Austauschdienst (DAAD), the Erasmus+ program, COST Action CA20109 (MODENERLANDS) is gratefully acknowledged. This work was supported by the Croatian Science Foundation under the project number HRZZ-IP-2022-10-9434.

REFERENCES

Alber, J., Manolesos, M., Weinzierl-Dlugosch, G., Fischer, J., Schönmeier, A., Nayeri, C. N., Paschereit, C. O., Twele, J., Fortmann, J., Melani, P. F., Bianchini, A. 2022. Experimental investigation of mini Gurney flaps in combination with vortex generators for improved wind turbine blade performance. Wind Energy Science, 7, 943-965.

Bak, C., Skrzypiński, W., Gaunaa, M., Villanueva, H., Brønnum, N.F. and Kruse, E.K., 2016, September. Full scale wind turbine test of vortex generators mounted on the entire blade. In: *Journal of Physics: Conference Series* (Vol. 753, No. 2, p. 022001). IOP Publishing.

Bartholomay, S., Krumbein, S., Perez-Becker, S., Soto-Valle, R., Nayeri, C.N., Paschereit, C.O. and Oberleithner, K., 2023. Experimental assessment of a blended fatigue-extreme controller employing trailing edge flaps. *Wind Energy*, *26*(2), pp.201-227.

Chen, H., Du, S. L., Chen, Z. 2023. Lift Augmentation on a Tiltrotor Wing Using the Combination of Vortex Generators and Gurney's Flap. International Journal of Aerospace Engineering, 2023, 6646817.

Chng, L., Alber, J., Ntouras, D., Papadakis, G., Kaufmann, N., Ouro, P., Manolesos M. 2022. On the combined use of Vortex Generators and Gurney Flaps for turbine airfoils. Journal of Physics: Conference Series, 2265, 032040.

Demirci, V., Seyhan, M., Sarioglu, M. 2023. Investigation of aerodynamic performance of Clark-Y airfoil with more realistic tubercle model and internal slots. Physics of Fluids, 35, 087109.

Du, L. H., Berson, A., Dominy, R. G. 2015. Aerofoil behaviour at high angles of attack and at Reynolds numbers appropriate for small wind turbines. Proceedings of the Institution of Mechanical Engineers Part C-Journal of Mechanical Engineering Science, 229, 2007-2022.

Yang, J., Yang, H. and Wang, X., 2024. Experimental study of turbulent inflow on the aerodynamic performance of a wind turbine with Gurney flaps. *Journal of Renewable and Sustainable Energy*, *16*(3).

Zhu, C. Y., Qiu, Y. N., Feng, Y. H., Wang, T. G., Li, H. 2022. Combined effect of passive vortex generators and leading-edge roughness on dynamic stall of the wind turbine airfoil. Energy Conversion and Management, 251, 115015.

Hierarchical dynamic wake modeling of wind turbine based on physics-informed generative deep learning

Q. Wang[1], Z. Ti[2], S. Yang[1], K. Yang[1], J. Wang[1], X. Deng[1, *]

[1]*Department of Civil Engineering, The University of Hong Kong, Hong Kong, China*
[2]*State Key Laboratory of Bridge Intelligent and Green Construction, Southwest Jiaotong University, Chengdu, Sichuan, China*

SUMMARY:
With the increasing demand for electric power, the size of wind farms is becoming much larger than ever before. Power and load prediction are two of the most essential topics in wind farm layout optimization. Traditional wake modeling methods, such as analytic models and CFD simulations, struggle to handle such large-scale problems accurately and efficiently. In this study, a novel hierarchical dynamic wake modeling approach for wind turbines using generative deep learning, `PHOENIX` (PHysics-infOrmed gEnerative deep learniNg for hIerarchical dynamic wake modeling eXploration), is proposed to capture the spatial-temporal features of the unsteady wake field in wind turbine clusters. The dynamic wake meandering (DWM) model is employed to generate the corresponding datasets for training, testing, and validating the deep learning-based wake prediction framework. This research is expected to accelerate the prediction process and improve accuracy, and it can be further applied to wind turbine design and wind farm layout optimization.

Keywords: Hierarchical temporal aggregation, Generative deep learning, Wind farm wake modeling

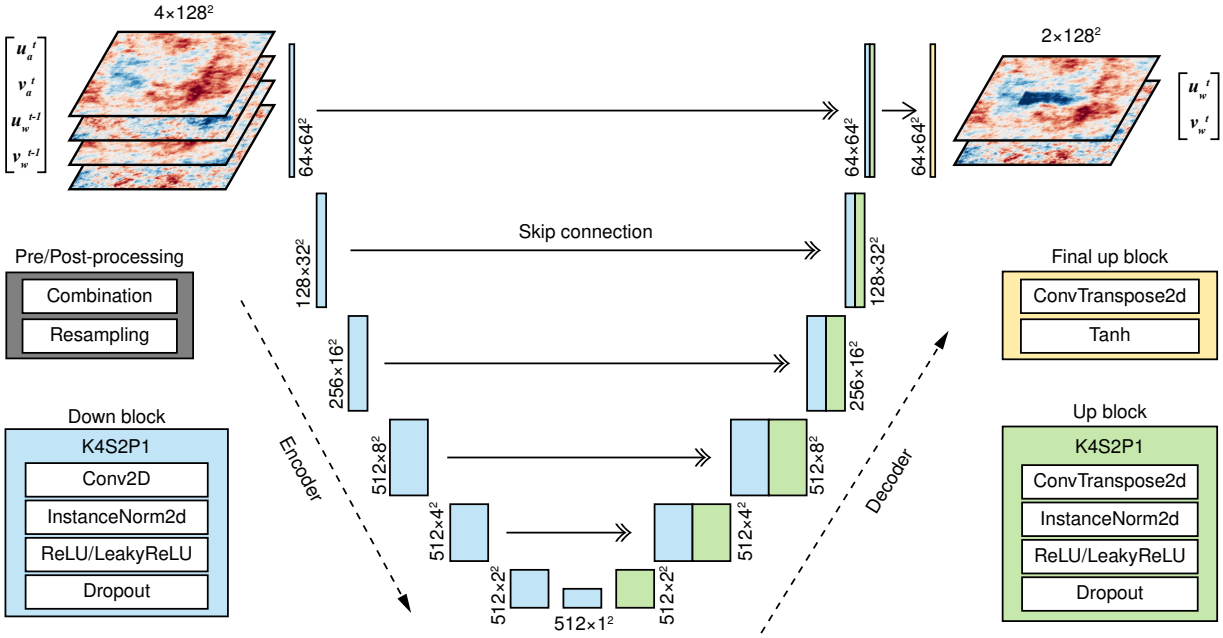
1. MOTIVATIONS

The increasing importance of energy issues in human society has accelerated the adoption of renewable energy sources, particularly wind power, which plays a vital role in the generation of electricity. However, wake interactions between nearby wind turbines are a primary cause of energy losses in operational wind farms, with wake-induced power reductions reaching up to 45% (Hasager et al., 2013) in some cases. These effects are especially critical for offshore wind farms, where compact layouts are necessary to reduce Operation and Maintenance (O&M) costs but can lead to substantial energy losses. The complexity of wake effects, including near-wake and far-wake phenomena, highlights the need for advanced wake modeling techniques that balance computational efficiency and accuracy. Given the limitations of traditional analytical and numerical models, data-driven methods, particularly those leveraging AI advancements, offer a promising solution to improve the prediction and mitigation of wake losses in wind farms.

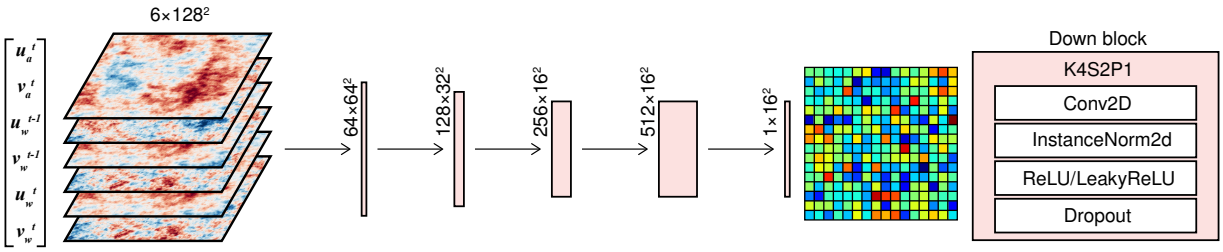
2. METHODS

2.1. Physics-Based Wake Modeling

This study uses the National Renewable Energy Laboratory's (NREL) DWM implementation via the FAST.Farm modules for physics-based wake modeling. To model ambient wind conditions, statistical methods are employed to define velocity spectra and spatial coherence. Wind speed time



(a) U-Net generator



(b) Markovian discriminator (PatchGAN)

Figure 1. Generative adversarial network architecture with (a) U-Net generator and (b) Markovian discriminator model. The corresponding kernel size (K), stride (S), and number of padding (P). Different colored blocks indicate specific functions: gray for preprocessing and post-processing, blue for encoding, green for decoding, yellow for output, and pink for downsampling modules of discriminator.

series are generated using the inverse Fourier transform and interpolated based on Taylor's frozen turbulence hypothesis.

Wind turbine aerodynamics are modeled using Blade Element Momentum (BEM) theory to estimate aerodynamic forces and predict power output, thrust, and torque. Wake dynamics, including advection, deflection, and meandering, evolve under a shear-layer approximation, with near-wake corrections and the Root Sum Square (RSS) method ensuring energy conservation and improving wake interaction predictions.

2.2. Generative Deep Learning-Based Wake Prediction

This study introduces a deep learning framework based on conditional generative adversarial networks (cGANs) (Mirza and Osindero, 2014) for wake field prediction, addressing the limitations of traditional physics-based models (Meng et al., 2024). By formulating wake evolution as a sequential image generation task, the model leverages past wake data and ambient wind conditions to im-

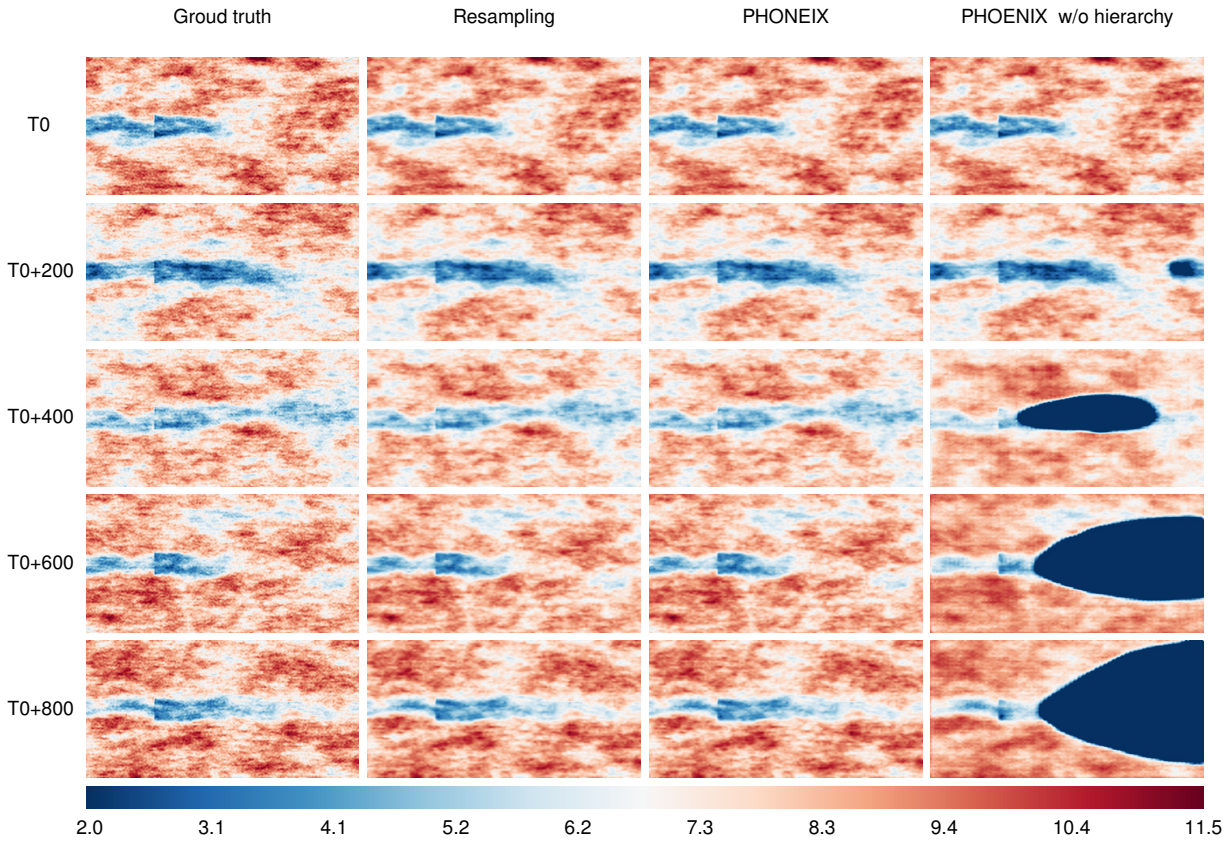


Figure 2. Randomly selected time-series flow snapshot under waked inflow. The color bar at the bottom of the figure represents the wind speed magnitude, ranging from 2.0 to 11.5, with cooler colors indicating lower speeds and warmer colors indicating higher speeds.

prove predictive accuracy and capture complex wake interactions. The dataset, generated using the TurbSim simulator within OpenFAST, includes turbulence data for three hub-height wind speeds (8 m/s, 9 m/s, and 10 m/s) with simulations covering upstream and downstream turbine conditions. A U-Net-based generator analyzes wake field inputs, while a PatchGAN-based discriminator ensures realistic wake dynamics, as depicted in Fig. 1. To maintain physical consistency, a hybrid loss function combines adversarial loss, L1 prediction loss, and a physical term to enforce conservation laws. Additionally, a hierarchical temporal aggregation strategy, training across multiple time scales, mitigates error accumulation and enhances long-term prediction stability while significantly reducing computational costs, making the model well-suited for large-scale wind farm simulations.

The `PHOENIX` model demonstrates high accuracy in wake field prediction across various wind conditions, with R^2 values for streamwise (u) and spanwise (v) velocity components approaching 1, indicating strong agreement with actual values. It maintains a low mean absolute percentage error (MAPE) of 0.9%, reducing prediction errors by 4.8% compared to the dynamic wake meandering (DWM) model. The hierarchical approach significantly improves stability, preventing error accumulation over time, whereas the non-hierarchical model degrades after $400 \sim 600$ seconds and fails beyond 800 seconds. Additionally, `PHOENIX` achieves a computational acceleration of up to

$\sim \times 4890$ on an NVIDIA RTX 3090 GPU and $\sim \times 274$ on a Intel Xeon Gold 6258R CPU, making it highly scalable for large-scale simulations. Fig. 2 presents a comparison of four different methodologies for predicting time series snapshots under waked inflow conditions.

A wind farm evaluation using a 3×3 turbine array under an 8 m/s freestream wind speed shows that wake effects reduce downstream turbine power by over 50%, significantly impacting Annual Energy Production (AEP). PHOENIX maintains a MAPE of 5.03% in power predictions, demonstrating its reliability for real-world applications. By integrating a hierarchical cGAN-based framework, PHOENIX enables accurate long-term wake modeling, crucial for wind farm layout optimization and fatigue load assessments. Unlike conventional data-driven methods prone to error accumulation, PHOENIX sustains accuracy over extended periods, providing a robust and efficient solution that outperforms traditional physics-based and non-hierarchical deep learning approaches.

3. CONCLUSIONS

As global energy demand continues to rise, wind power plays a crucial role in the energy transition due to its renewable and sustainable nature. However, the wake regions created by wind turbines, characterized by reduced wind speed and increased turbulence, pose challenges for downstream turbines. To optimize power generation and reduce mechanical stress, it is essential to position turbines strategically to minimize the impact of wake regions. While traditional analytical wake models are computationally efficient, they often fall short in accurately capturing the complex dynamics of wake interactions. This leads to less reliable predictions of power output and turbine loads. Therefore, a more accurate and dynamic modeling approach is needed to optimize wind farm design and performance.

To address this, we propose PHOENIX, a hierarchical deep learning-based wake model that significantly advances dynamic wake prediction. Compared to existing methods, it offers several key improvements: (i) Higher prediction accuracy: The prediction error has been reduced from 4.8% concerning the freestream wind speed to a maximum mean of 0.9% over the entire time dimension. (ii) Extended time-series stability: Unlike traditional models prone to cumulative errors, PHOENIX maintains accurate predictions for at least 800 seconds, meeting IEC requirements for power and fatigue analysis. (iii) More stable model performance: With a maximum standard deviation of 0.002, the model demonstrates robustness in long-term predictions, an aspect often overlooked in prior studies. (iv) Integration of physical information: By embedding domain-specific knowledge into loss function and incorporating ambient wind conditions, PHOENIX aligns more closely with physical laws, unlike purely data-driven models.

REFERENCES

Hasager, C. B., Rasmussen, L., Peña, A., Jensen, L. E., and Réthoré, P.-E., Feb. 2013. Wind Farm Wake: The Horns Rev Photo Case. Energies 6, 696–716.

Meng, D., Yang, S., Yang, H., De Jesus, A. M., Correia, J., and Zhu, S.-P., Sept. 2024. Intelligent-Inspired Framework for Fatigue Reliability Evaluation of Offshore Wind Turbine Support Structures under Hybrid Uncertainty. en. Ocean Engineering 307, 118213.

Mirza, M. and Osindero, S., 2014. *Conditional Generative Adversarial Nets*. preprint.

A quick atmospheric dispersion simulation based on a coupling LES-database with on-site meteorological data

Hiromasa Nakayama [1], Takuto Sato [2]

[1] *Japan Atomic Energy Agency, Ibaraki, Japan, nakayama.hiromasa@jaea.go.jp*
[2] *Japan Atomic Energy Agency, Ibaraki, Japan, sato.takuto@jaea.go.jp*

SUMMARY
An accurate analysis of local-scale atmospheric dispersion of radioactive materials is important for safety and consequence assessments of nuclear facilities at short distances from an emission source under normal operation or accident conditions. We developed a framework for prediction system of local-scale atmospheric dispersion based on a coupling of large-eddy simulation (LES) database and on-site meteorological data. The LES-database was created by pre-calculating high-resolution turbulent flows in the target site at mean wind directions of class interval 10°. We provided the meteorological observed data with the LES-database in consideration of building conditions and calculated the three-dimensional distribution of the plume with a Lagrangian dispersion model. First, we conducted LESs on turbulent flows in the vicinity of Rokkasho Reprocessing Plant during the test operations of reprocessing, the nuclear fuel reprocessing plant in Rokkasho, Japan. Then, we compared with the air dose rates obtained from the monitoring posts (MP). The time variation patterns and the magnitude of the fluctuations of the calculated air dose rates were generally similar to the MP data. It is concluded that a quick atmospheric dispersion simulation based on a coupling LES-database with on-site meteorological data is effective.

Keywords: A quick atmospheric dispersion simulation, LES-database, on-site meteorological data

1. INTRODUCTION

In safety and consequence assessment of nuclear facilities at short distances (i.e. up to several kilometres) from an emission source under normal operation or accident conditions, it is important to accurately predict air concentrations at the evaluation point for internal doses and the three-dimensional and surface distributions for external doses in consideration of individual buildings and meteorological conditions. For predicting plume dispersion over complex surface geometry, large-eddy simulation (LES)-based computational fluid dynamics (CFD) models are useful. The advantage of the LES models is that they can well capture plume dispersion behaviours in complex turbulent flows such as impinging, separated, and recirculating flows around buildings. However, a serious issue is encountered because they have a significant disadvantage of calculation time for real-time plume monitoring because of unsteady calculations with a time step usually less than 0.1 seconds.

To solve the problem of calculation time, we proposed a framework for a real-time atmospheric dispersion simulation using a Lagrangian particle dispersion model based on a coupling of LES-database of wind flows within roughness sublayer and on-site meteorological observation (OBS) above it that takes into account both individual buildings and real meteorological conditions (Nakayama et al., 2021). We conducted with meteorological observations by a Doppler LiDAR and simple dispersion experiments using a mist-spraying system for representing a plume at the

site of Japan Atomic Energy Agency (JAEA). The dispersion behaviours of the water mist plume were observed using a digital camera. Compared to instantaneous shots of dispersion behaviours of the real mist plume, it was shown that the transport direction of the simulated plume is reproduced well by the Doppler LiDAR-derived wind velocities. However, our approach was limited to the evaluation of the qualitative behaviour of plume dispersion.

In this study, we conduct atmospheric dispersion simulation based on a coupling the LES-database with on-site meteorological data and estimate the air dose rates produced by a radioactive plume of actual radionuclides released from a stack in the nuclear facility. Our objective is to evaluate the basic performance of estimating air dose rates by coupling the LES-database with on-site meteorological data under the influence of buildings and meteorological conditions in comparison with the MP data in the vicinity of the nuclear facility.

2. THE METEOROLOGICAL OBSERVATION DATA

The target site is Rokkasho Reprocessing Plant (RRP), the nuclear fuel reprocessing plant in Japan Nuclear Fuel Limited (JNFL), Japan. There are many structures and nine monitoring posts in the vicinity of the RRP site. The stack height is 150 m above ground level. The 10-minute averaged wind velocities were obtained at heights of 50 m, 75 m, 150 m, 250 m, and 300 m in the one-dimensional vertical direction with a 10-minute time interval by the Doppler sodar (Kaijo, monostatic type, AR-410) located about 700 m west side of the stack. The target period is from 0900 JST to 1930 JST on 17 June 2008.

3. LOCAL-SCALE HIGH-RESOLUTION ATMOSPHERIC DISPERSION AND DOSE ASSESSMENT SYSTEM (LHADDAS)

The LHADDAS was developed to utilize for safety and consequence assessment of nuclear facilities and emergency response to nuclear accidents or deliberate releases of radioactive materials in built-up urban areas (Nakayama et al., 2022). This system comprises three parts: preprocessing of input files, and main calculation by a local-scale high-resolution atmospheric dispersion model using large-eddy simulation (LOHDIM-LES) and a real-time urban dispersion simulation model based on a lattice Boltzmann method (CityLBM) (Onodera et al., 2021), and postprocessing of dose calculation by a simulation code powered by lattice dose-response functions (SIBYL) (Satoh et al., 2021).

4. A QUICK ATMOSPHERIC DISPERSION SIMULATION SETTINGS

4.1. Coupling of the LES-database and on-site meteorological data

In our proposed framework, air flow fields are created by coupling LES-database of wind flows and on-site meteorological OBS. The wind flows over a target site under an assumption of a neutral atmospheric stability condition are pre-calculated by LOHDIM-LES code (Nakayama et al., 2022). The dataset of 3-dimensional distributions of mean and turbulent components is created for 36 mean wind directions at 10°class interval. The wind velocities above roughness sublayer are measured by meteorological instruments. The formulation is as follows:

$$U_{coup}(x,y,z) = U_{OBS}(x,y,h_{OBS}) \text{ for } z > h_{OBS} \quad (1)$$

$$U_{coup}(x,y,z) = U_{LES}(x,y,z)\,\frac{U_{OBS}(x,y,h_{OBS})}{U_{LES}(x,y,h_{OBS})} \text{ for } z \le h_{OBS} \quad (2)$$

Where U_{coup}, U_{OBS}, U_{LES}, and h_{OBS} are the mean wind velocity estimated by coupling the LES-database with on-site OBS data, the OBS wind velocities, the LES database of mean wind velocity, and the lowest measurement height of the meteorological device, respectively. U_{LES} is extracted from the LES-database pre-calculated for 36 different mean wind directions at class interval 10 degrees in accordance with the target meteorological condition.

Each component of the turbulence standard deviations σ_u is estimated by the Normal Turbulence Model (NTM) proposed by the International Electrotechnical Commission (IEC) in the international standard IEC61400-1 (2005).

4.2. Lagrangian particle dispersion model

We used a lagrangian particle dispersion model which allows for quick simulation (Yamada and Bunker, 1988).

$$x_i(t + \Delta t) = x_i(t) + u_{pi}\Delta t \quad (3)$$

$$u_{pi} = U_i + u_i' \quad (4)$$

$$u_i'(t + \Delta t) = au_i'(t) + b\sigma_{ui}\xi + \delta_{i3}(1 - a)t_{Lxi}\frac{\partial \sigma_{ui}^2}{\partial x_i} \quad (5)$$

where x_i, u_{pi}, U_i, u_i', σ_{ui}, ξ, t_{Lxi}, δ_i, t, and Δt are the particle position in the *i*-direction (east-west direction, i = 1; north-south direction, i = 2; vertical direction, i = 3), velocity of the particle, mean wind velocity, turbulence velocity, standard deviation of the velocity fluctuation, a random number from a Gaussian distribution with zero mean and unit variance, the Lagrangian integral time, the Dirac delta function, time, and calculation time step interval, respectively.

The mean wind velocities and the standard deviations of the velocity fluctuation are given by coupling the LES-database and on-site meteorological data as shown in the section 4.1.

4.3. Computational conditions

The size of the computational domain is 3 km × 3 km in the horizontal directions at 600 m height. The grid spacing is 5.0 m in the horizontal direction and 2.5–30 m stretched in the vertical direction. The plume is released from the stack in consideration of the plum rise. The particles are assumed to be reflected at the solid boundaries. The calculation time step interval is 0.05 s. In the lagrangian dispersion model, the number of the particles is 60000 for each 10-minute and the mean air concentrations are estimated at a 10-minute time interval during the target period.

5. RESULTS

Figure 1 shows time series of the air dose rates produced by ^{85}Kr in the air at the MP in the main transport direction of the plume. Here, the air kerma free-in-air rates calculated by the SIBYL module from the 10-minute mean air concentrations were compared with the MP data of the air absorbed dose rates. The background values at each MP were assumed to be time-averaged values during the period that time variations of the air dose rates were not significantly observed, and those were excluded from the MP data. Here, the air dose rates estimated from the mean concentrations of the LES unsteady calculations are also compared. In this case, the Doppler sodar data of the 10-minute averaged wind velocities obtained at a stationary point were prescribed at the inflow boundary conditions under the assumption of horizontal homogeneity (Nakayama et al., 2021).

Although the time variation patterns of the LES unsteady calculation case are basically simulated, the peak at 16:40 is highly overestimated. On the other hand, the time variation patterns and the magnitude of the peaks of the LES-database case are generally similar to the MP data. It is shown

that the LES-database approach is also effective to quickly predicting plume dispersion under the influences of both individual buildings and real meteorological conditions.

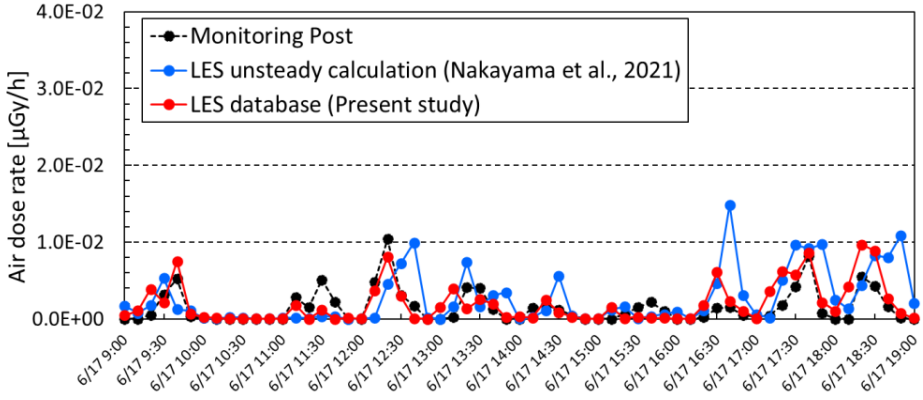


Figure 1. Time series of the air dose rate.

6. CONCLUSION

We demonstrated a framework for a quick atmospheric dispersion based on a coupling of LES-database and on-site meteorological observation that takes into account both individual buildings and real meteorological conditions. We then compared with the air dose rates produced by the 10-minute mean air concentrations of ^{85}Kr at the MP in the vicinity of the nuclear facility. The time variation patterns and the magnitude of the fluctuations of the calculated air dose rates were generally similar to the MP data.

It is shown that the LES-database approach is effective to quickly predicting plume dispersion under the influences of both individual buildings and real meteorological conditions.

ACKNOWLEDGEMENTS

The authors thank JNFL for providing the meteorological measurement data, etc. This work was also partially supported by JSPS KAKENHI Grant Number JP23H00220.

REFERENCES

IEC61400-1. Wind Turbines Part 1: Design Requirements, 3rd ed.; International Electrotechnical Commission: Geneva, Switzerland, 2005.

Nakayama H., Yoshida T., Terada H., Kadowaki M, 2021: Toward Development of a Framework for Prediction System of Local-Scale Atmospheric Dispersion Based on a Coupling of LES-Database and On-Site Meteorological Observation, Atmosphere, 12, 899.

Nakayama H., Satoh T., Nagai H., Terada H, 2021: Development of local-scale high-resolution atmospheric dispersion model using large-eddy simulation part 6: introduction of detailed dose calculation method, 58, 949-969.

Nakayama H., Onodera N., Satoh D., Nagai H., Hasegawa Y., Idomura Y, 2022: Development of local-scale high-resolution atmospheric dispersion and dose assessment system, Journal of Nuclear Science and Technology, 59, 2022, 1314–1329.

Onodera N, Idomura Y, Hasegawa Y, Nakayama H, Shimokawabe T, Aoki T. Real-time tracer dispersion simulations in Oklahoma City using the locally mesh-refined Lattice Boltzmann method. Bound.-Layer Meteorol. 2021, 179, 187–208.

Satoh D, Nakayama H, Furuta T, Yoshihiro T and Sakamoto K. Simulation code for estimating external gamma-ray doses from a radioactive plume and contaminated ground using a local-scale atmospheric dispersion model, PLOS ONE, doi: 10.1371/journal.pone.0245932.g011, 2021.

Yamada, T.; Bunker, S. Development of a nested grid, second moment turbulence closure model and application to the 1982 ASCOT Brush Creek data simulation. J. Appl. Meteorol. Climatol. 1988, 562–578.

Establishing correlations between wind and air pollutant fields around isolated buildings

YaoJia Guo [1], Xuelin Zhang [1], A. U. Weerasuriya [2]

[1] *School of Atmospheric Sciences, Sun Yat-sen University, Southern Marine Science and Engineering Guangdong Laboratory (Zhuhai), Zhuhai, PR China, guoyj9@mail2.sysu.edu.cn, zhangxlin25@mail.sysu.edu.cn*

[2] *Department of Construction and Quality Management, School of Science and Technology, Hong Kong Metropolitan University, Ho Man Tin, Hong Kong, auweeras@hkmu.edu.hk*

SUMMARY: (10 pt)

Air pollutant dispersion around buildings is a highly complex process due to the interactions between turbulent wind flows and air pollutants. Therefore, predicting air pollutant concentrations in built-up areas depends on an accurate estimation of the impacts of turbulent wind on air pollutant dispersion. This study revealed the correlations between turbulent wind and pollutant fields around isolated buildings with height-to-width ratios (*AR*) ranging from 4 to 0.33 by using large eddy simulation (LES), proper orthogonal decomposition (POD), extended proper orthogonal decomposition (EPOD), and contribution analyses. POD and EPOD identified the pollutant dispersion patterns synchronized with dominant wind flow features. The contribution analysis estimated the impact of dominant flow features on pollutant dispersion. The analyses revealed that the staggered and symmetrically arranged spanwise vortices dispersed air pollutants in the building wake in spanwise and streamwise directions, respectively. The contribution of the symmetrically arranged spanwise vortices to air pollutant dispersion reached a maximum of 98% for the tall building with $AR = 4$ because of the intense and large vortices in its wake.

Keywords: Air pollution dispersion, Building aspect ratio, Correlation analysis

1. INTRODUCTION

Air pollutant dispersion in built-up areas is a complex process that consists of intrinsic interactions of wind and pollutant fields around buildings. The turbulent wind field near buildings has nonlinear flow dynamics, of which some flow features enhance pollutant dispersion while others resist the process. Because of this duality, the current air pollutant modeling is limited to estimating pollutant concentrations and proposing remedial measures without revealing the driven flow mechanisms of pollutant dispersion. The common air pollution modelling techniques, such as wind tunnel testing and computational fluid dynamics (CFD) simulations (Blocken et al., 2008) seem acutely impossible to establish correlations between wind and pollutant fields because both systems are infinite-dimensional and nonlinear (Fiedler, 1988).

Mode decomposition is a fitting technique to identify dominant coherent structures in nonlinear systems. It has been widely used in various wind engineering applications, such as natural ventilation and wind load analysis (Zhang et al., 2022). However, it is challenging to establish direct correlations between wind and pollutant fields due to misalignments in the dominant flow

features and pollutant dispersion patterns. As a solution, correlation analyses, such as the co-spectrum (Zhang et al., 2022) and extended proper orthogonal decomposition (EPOD) (Borée, 2003), are often combined with mode decomposition.

Following the cues of previous studies, this study used EPOD and contribution analyses to link dominant wind flow features and pollutant dispersion patterns near isolated buildings to elucidate the correlations between turbulent wind and pollutant fields in built-up areas. To explore the full capacity of the proposed method, this study modeled pollutant dispersion near five isolated buildings with *AR* ranging from 4 to 0.33. This study chose *AR* as a building design parameter because previous studies revealed significant impacts of *AR* on the wind field (Sumner et al., 2017) and pollutant dispersion (Aristodemou et al., 2018). Understanding how turbulent wind affects air pollutant dispersion is crucial to devising pollutant mitigation measures, such as promoting advantageous wind circulations by altering building geometries in the surroundings.

2. METHODOLOGY

Fig.1 shows the conceptual framework of the current study. The framework started with conducting large eddy simulation (LES) to estimate instantaneous wind velocity and pollutant concentrations around buildings. A validation study evaluated the quality and accuracy of LES before conducting further analyses. Then, proper orthogonal decomposition (POD) decomposed the high-quality LES data of fluctuating wind speeds into spatial modes and temporal coefficients to identify the dominant wind circulations. Next, EPOD extracted the pollutant field's modes that were correlated with the wind field's modes. Finally, the contributions of these dominant wind circulations to pollutant dispersion were estimated by conducting a contribution analysis.

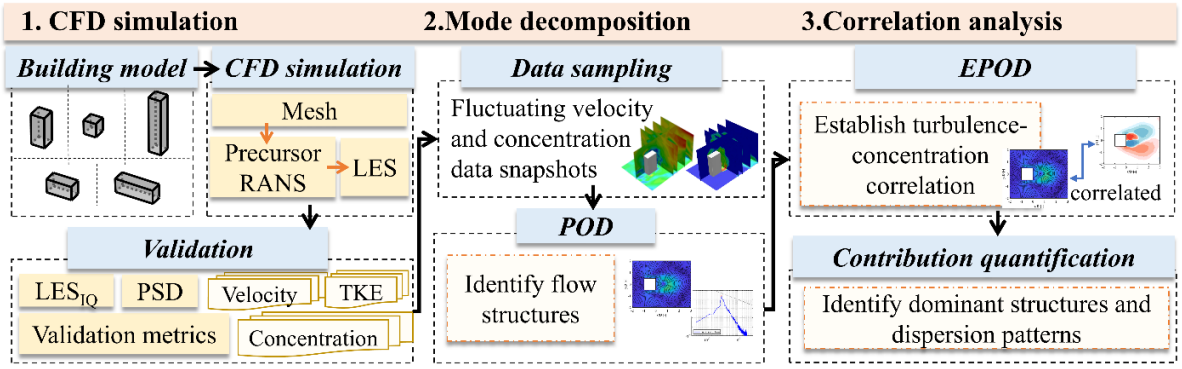


Figure 1. The current study's framework for identifying the relationships between the wind and pollutant fields around buildings using CFD simulation, mode decomposition, and correlation analysis.

3. RESULTS AND DISCUSSION

3.1. Identification of wind circulations and correlated dispersion patterns

Two dominant flow structures in the wake of the isolated building with $AR = 2$ were the staggered and the symmetrically arranged spanwise vortices. As shown in Fig.2, Mode A, i.e., staggered vortices, was the most energetic mode in the wind field, with an energy portion of 8.86% and a dominant reduced frequency of $fB/U_H = 0.085$. Mode A was governed by two distinct vortices in the building wake – one adjacent to the building leeward rotating counterclockwise, while the other

rotating clockwise. The antisymmetric wind field of Mode A, referred to as the staggered spanwise vortices, promoted lateral pollutant dispersion, with an increase at $y > 0$ and a decrease at $y < 0$.

Mode S represented the most energetic modes in the symmetric wind field. In Mode S, two vortices formed approximately symmetric about the centerline in the building wake. A clockwise vortex formed at a distance $y > 0$, while a counterclockwise vortex was at $y < 0$. The counter-rotating vortices carried pollutants toward the building, leading to an increase in pollutant concentration next to the building's leeward wall. The symmetrically arranged spanwise vortices promoted the pollutant dispersing in the streamwise direction.

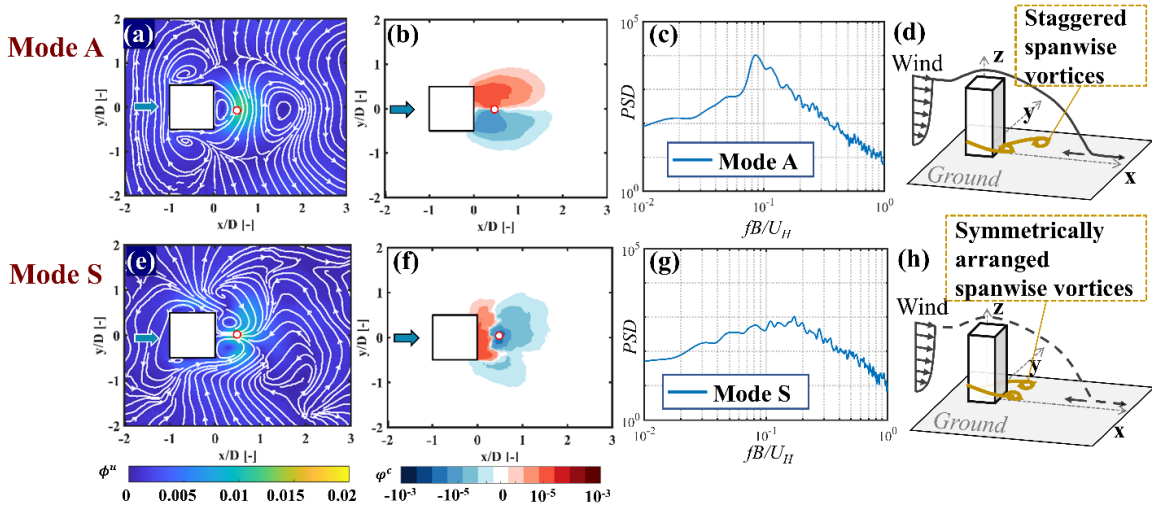


Figure 2. Modes A and Mode S: (a, e) the velocity modes and (b, f) the correlated concentration modes; (c, g) the power spectral density of temporal coefficients; and (d, h) the schematics of spanwise vortices around the building.

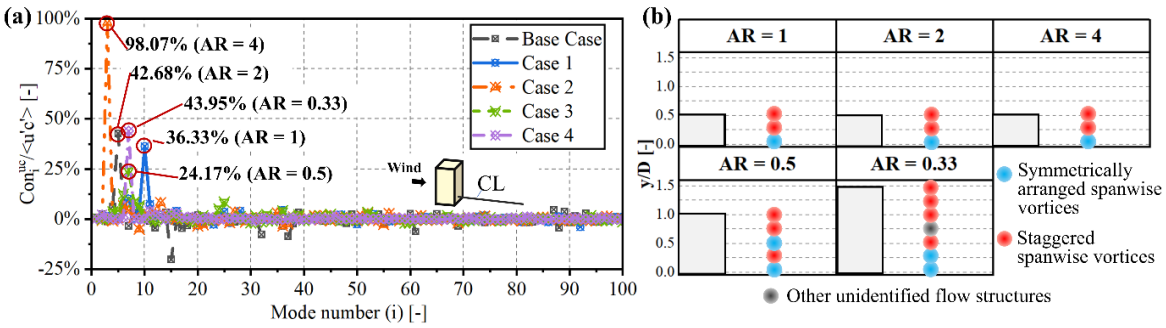


Figure 3. (a) The velocity mode contribution to the streamwise pollutant dispersion along Line CL; (b) the dominant flow structures along lines at $y/D = 0$ to 1.5 in the building wake.

3.2. The effect of the aspect ratio (*AR*)

Fig.3a shows how each velocity mode contributed to the streamwise pollutant dispersion along Line CL with the modes of largest contributions marked. The most significant modes, referred to as the symmetrically arranged spanwise vortices, contributed 43.95%, 24.17%, 36.33%, 42.68%, and 98.07% for the streamwise pollutant dispersion near the buildings with $AR = 0.33$, 0.5, 1, 2, and 4. Interestingly, the largest contribution increased with AR, such that the largest contribution increased by 6.35% for $AR = 2$ and 61.74% for $AR = 4$ compared to $AR = 1$. In contrast, the largest

contribution displayed no trend when *AR* decreased to 0.5 and 0.33 but the contribution decreased by 12.16% for *AR* = 0.5 and increased by 6.35% for *AR* = 0.33. Fig.3b shows that the symmetrically arranged spanwise vortices were the dominant turbulent flow features in the building wake, and the staggered spanwise vortices prevailed in the areas closer to the buildings' lateral sides. However, the influence of the symmetrically arranged spanwise vortices grew as *AR* decreased from 1 to 0.33, as the flow dynamics became increasingly complex and transient from the wake center to the building's sides. These findings indicate the significant impacts of building *AR* on the turbulent wind and pollutant fields.

4. CONCLUDING REMARKS

This study attempted to combine EPOD and contribution analyses to reveal the relationships between dominant turbulent wind flow patterns and pollutant dispersion near buildings. The concluding remarks are as follows:

Two dominant wake flow structures, the staggered and symmetrically arranged spanwise vortices, contribute differently to air pollutant dispersion downstream of buildings. While the staggered spanwise vortices enhance the lateral mixing of air pollutants and prevail in the area closer to the building's lateral side, the symmetrically arranged spanwise vortices promote pollutants mixing in streamwise directions and dominate the building wake center.

The building aspect ratio significantly modifies turbulent wind around buildings and influences pollutant dispersion in buildings' wakes. The taller a building becomes, such as when *AR* increases from 1 to 4, the more symmetrically arranged spanwise vortices dominate at the wake center. For buildings with *AR* = 4, the symmetrically arranged spanwise vortices contribute about 98% to streamwise air pollutant dispersion. For *AR* less than 1, the dominant area of the symmetrically arranged spanwise vortices grows compared with the building of *AR* = 1, exhibiting an increase in the complexity of air exchange and pollutant dispersion.

ACKNOWLEDGEMENTS

This study is partly supported by the National Natural Science Foundation of China (No. 42175180, 42475185, and 21EAA00654). The CFD simulations of this research were conducted on the Tianhe II supercomputer at the National Supercomputer Center, Guangzhou, P. R. China.

REFERENCES

Aristodemou, E., Boganegra, L. M., Mottet, L., Pavlidis, D., Constantinou, A., Pain, C., Robins, A., & ApSimon, H., 2018. How tall buildings affect turbulent air flows and dispersion of pollution within a neighbourhood. Environmental Pollution, 233, 782–796.

Blocken, B., Stathopoulos, T., Saathoff, P., & Wang, X., 2008. Numerical evaluation of pollutant dispersion in the built environment: Comparisons between models and experiments. Journal of Wind Engineering and Industrial Aerodynamics, 96(10–11), 1817–1831.

Borée, J., 2003. Extended proper orthogonal decomposition: A tool to analyse correlated events in turbulent flows. Experiments in Fluids, 35(2), 188–192.

Fiedler, H. E., 1988. Coherent structures in turbulent flows. Progress in Aerospace Sciences, 25(3), 231–269.

Sumner, D., Rostamy, N., Bergstrom, D. J., & Bugg, J. D., 2017. Influence of aspect ratio on the mean flow field of a surface-mounted finite-height square prism. International Journal of Heat and Fluid Flow, 65, 1–20.

Zhang, B., Hu, H., Kikumoto, H., & Ooka, R., 2022. Turbulence-induced ventilation of an isolated building: Ventilation route identification using spectral proper orthogonal decomposition. Building and Environment, 223, 109471.

Comparison of dynamic mesh and source term methods in simulating vehicle emission dispersion in a street canyon

Lin Wen[1*], Xuelin Zhang[1], Wenbing Liu[1], A. U. Weerasuriya [2]

[1]*School of Atmospheric Sciences, Sun Yat-sen University, Zhuhai, PR China, wenlin5@mail2.sysu.edu.cn, zhangxlin25@mail.sysu.edu.cn, guoyj9@mail2.sysu.edu.cn*
[2]*Hong Kong Metropolitan University, Ho Man Tin, Hong Kong, auweeras@hkmu.edu.hk*

SUMMARY:
The source term (STM) and dynamic mesh (DMM) methods are two main techniques used in CFD simulation to model air pollution dispersion in street canyons. STM modifies the governing equations of CFD simulation using several source terms to implicitly model the effect of vehicle motions on air pollutant dispersion. In contrast, the dynamic mesh method explicitly models vehicle movements in street canyons. This study modeled one-way and two-way traffic in an idealized 3D street canyon using steady and unsteady Reynolds-averaged Navier-Stokes equations-based CFD simulations. The comparison of wind speed, turbulence, and pollution concentrations in the street canyon revealed that STM tended to generate higher turbulence up to a greater height due to the use of the source terms. In contrast, DMM generates higher wind speeds and turbulence around explicitly modeled moving vehicles. STM and DMM modeled higher pollutant concentrations in the middle of the street canyon for two-way traffic than one-way traffic. However, STM modeled highly asymmetric pollutant dispersion in one-way traffic because of dissimilar source terms' magnitudes at the two ends of the street canyon.

Keywords: Air pollution modeling, Source term method, Dynamic mesh method, CFD simulation

1. GENERAL INSTRUCTIONS

CFD simulation uses two main techniques, the source term method (STM) and dynamic mesh method (DMM), to simulate air pollutant dispersion in street canyons (Zhao et al., 2021). STM implicitly models the effects of vehicle motions on air pollutant dispersion by adding extra terms, namely source terms, to the governing equations of CFD simulations (Katolický et al., 2005). The source term added to the conservation of momentum equation accounts for the effects of vehicle motions on wind speeds, while the source terms added to the transportation of turbulence kinetic energy and its dissipation include vehicle-induced turbulence to the wind field in the street canyon (Jicha et al., 2000). In contrast, DMM explicitly simulates vehicle motions by moving the computational grids around vehicles, mimicking vehicle movements (Cai et al., 2020). By doing so, DMM explicitly models the wind speed and turbulence modifications based on vehicle geometries and velocities, traffic conditions, and tailpipe emissions (Wang et al., 2019).

Researchers justify using STM for modeling air pollutant dispersion in street canyons using the simplicity and ease of using the method and DMM based on its ability to model the wind field perturbed by moving vehicles. However, previous studies sparsely assessed these two methods to elucidate the differences in modeled wind speed, turbulence, and pollutant concentrations in street canyons. This study evaluated these two methods for modeling vehicular emission in an idealized

two-dimensional street canyon with two-way and one-way traffic. By comparing the differences in wind speed, turbulence, and pollutant concentration, this study aims to highlight the impact of explicit and implicit modeling of vehicle movements on air pollutant dispersion in street canyons.

2. METHODOLOGY

2.1. The turbulence source term method (STM)

This study modeled a 2D street canyon with dimensions of = 18 m × 18 m × 180 m (height (H) × width (W) × length (L)). The street canyon has two 9 m wide lanes, in which 12 vehicles with a frontal area of 1.5 m × 0.9 m and a length of 3.75 m move as one-way or two-way traffic. Each lane has a fluid region with a cross-section area of 1.5 m × 0.9 m, in which the source terms are applied. The moment source (S_m) (Eq.1) and turbulent kinetic energy source (S_K) (Eq. 2) were defined as in Jicha et al. (2000):

$$S_m = \frac{NF_{D,i}}{A_{cel}} \tag{1}$$

where $F_{D,i} = \frac{1}{2}\rho_\infty C_D A_{veh} |U_{veh,i} - U_i| (U_{veh,i} - U_i)$

$$S_k = 0.5 * C_d \rho_\infty (U_{veh} - U_i)^2 Q_{car} \tag{2}$$

where $F_{D,i}$ $F_{D,i}$ is the drag force in *i* direction, ρ_∞ is the density of the ambient air, C_D is the drag coefficient, A_{veh} is the cross-section of the vehicles in i direction, $U_{veh,i}$ and U_i are the vehicle speed and ambient wind velocity in the *i* direction. *N* is the number of vehicles per unit length, A_{cel} is the cross-section of control volumes. Q_{veh} (veh/s) is the traffic rate equal to 0.067 veh moving at 11.1 m/s. Sulfur hexafluoride (SF6) gas was emitted from two line sources with a diameter of 100 mm at 0.5 m above the ground, equivalent to the emission of 12 vehicles in the street canyon. STM was implemented on steady Reynolds-averaged Navier-Stokes (RANS) equation-based simulations with the Realizable k-ε model.

This study implemented DMM on the commercial CFD software ANSYS Fluent 19.2, using the dynamic layering method. DMM used unsteady RANS simulations with the Realizable k-ε model and 40 iterations for a 0.005 s time step. The explicitly modeled 40 mm diameter tailpipes emitted SF6 at an exit velocity of 4.8 m/s (Shi et al., 2020).

3. RESULTS AND DISCUSSION

3.1. Comparison of wind speed and turbulence

The distributions of normalized wind speed (U/U_{ref}) and normalized turbulent kinetic energy (k/U_{ref}^2) in a vertical plane near the leeward side of the street for one-way and two-way traffic are shown in Figure 1. The STM method predicted significantly larger k/U_{ref}^2 spanned to a greater height in both traffic scenarios than the dynamic mesh method, which modeled high k/U_{ref}^2 around the moving vehicles (Fig.1 (a)-(b)). In contrast, STM estimated smaller wind speeds, especially near the street canyon's bottom, than DMM (Fig.1 (c)-(d)). The higher wind speeds and turbulence near vehicles modeled by DMM resulted from explicit modeling of the perturbed wind field, which could not be accurately modeled using source terms by STM.

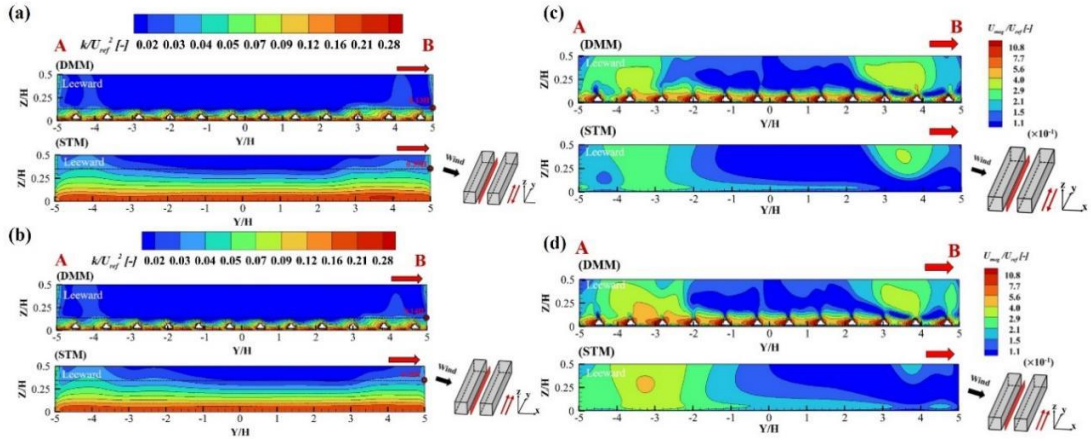


Fig.1. Distribution of normalized TKE fields along the leeward lane for (a) two-way traffic and (b) one-way traffic. (c)-(d) Same as (a)-(b) but for distribution of normalized velocity

The vertical distributions of U/U_{ref} and k/U_{ref}^2 in the street canyon were summarized along two vertical lines near the leeward (Line L1) and windward walls (Line W1). STM estimated about 90% larger k/U_{ref}^2 up to z/H = 0.6 than DMM (Fig. 2(a) and (b)). Larger k/U_{ref}^2on a broader region of STM was a result of the source terms applied in 1.5 m taller fluid regions in the street canyon. In contrast, DMM modeled higher U/U_{ref} up to z/H = 0.13 with peak values at about z/H = 0.05 (Fig 2 (c) and (d)). In fact, DMM modeled 36% and 29% higher volume-average wind speeds at a height below z/H = 0.13 for two-way and one-way traffic than STM.

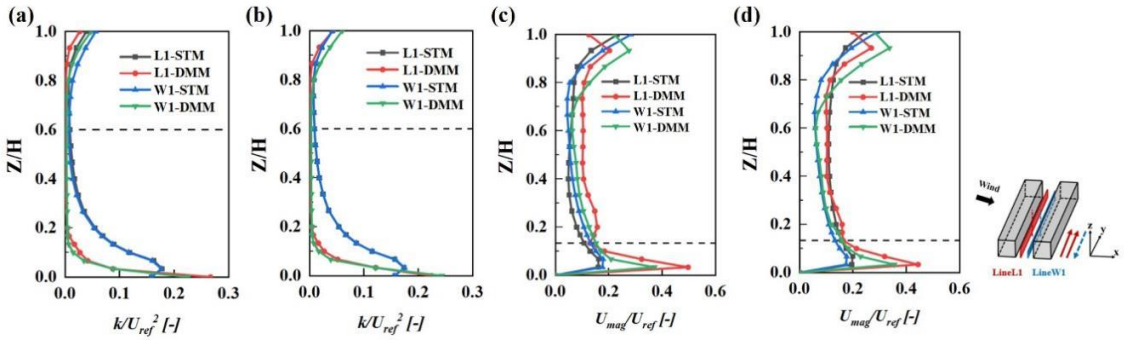


Fig.2. Vertical distribution of normalized TKE along the lingL1 and lineW1 for (a) two-way traffic and (b) one-way traffic. (c)-(d) Same as (a)-(b) but for distribution of normalized velocity

3.2. Comparison of pollutant dispersion

Fig. 3(a) and (b) shows the distribution of normalized pollutant concentration ($C^+ = CU_{ref}H/Q^*$, where C is the mean pollutant concentration and Q* is gas source strength) in a horizontal plane along the street canyon with one-way and two-way traffic. In general, pollutant distribution was symmetrical, with high concentrations found in the middle of the canyon for two-way traffic. High pollutant concentrations are mainly found in the lanes in DMM but spread throughout the canyon width in STM. In one-way traffic, the pollutant accumulation in the middle of the street canyon is less. However, STM predicted highly asymmetric pollutant distribution due to the dissimilar values generated by the term (U_{veh} - U_i) in Eq. (1) and (2) at the two ends of the street canyon.

STM estimated 62.44% and 60.58% higher volume average C^+ in the canyon (z/H ≤ 1) for two-way traffic and one-way traffic than DMM.

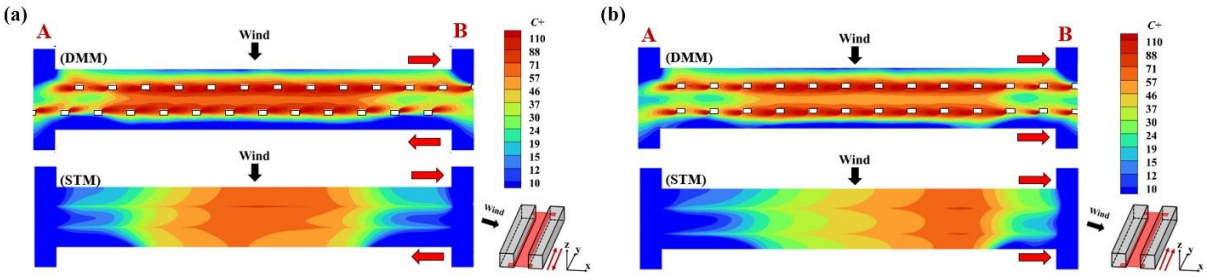


Fig.3. Distribution of pollutant concentration for DMM and STM at plane z/H = 0.5 m for (a) two-way traffic and (b) one-way traffic

4. CONCLUDING REMARKS

STM and DMM generated significantly different TKE in the lower part of the canyon (z/H ≤ 0.6), where STM estimated approximately 90% higher k/U_{ref}^2 than DMM, both for two-way traffic and one-way traffic. STM tends to predict higher k/U_{ref}^2 in the whole fluid region where the source terms are applied, whereas DMM generates higher k/U_{ref}^2 around moving vehicles. On the other hand, DMM modeled 36% and 28% higher U/U_{ref} near the street canyon's bottom than STM because the former explicitly modeled the wind field perturbed by moving vehicles rather than implicitly adding momentum changes to the wind field in the street canyon. In general, STM and DMM predicted higher C+ in the middle of the street canyon with two-way traffic. However, STM predicts a highly asymmetric C+ distribution due to the dissimilar values of (U_{veh} - U_i) at the two ends of the street canyon.

ACKNOWLEDGEMENTS

This study is partly supported by the National Natural Science Foundation of China (No. 42175180, 42475185 and 21EAA00654). The CFD simulations of this research were conducted on the Tianhe II supercomputer at the National Supercomputer Center, Guangzhou, P. R. China.

REFERENCES

Cai, C., Ming, T., Fang, W., De Richter, R., & Peng, C. (2020). The effect of turbulence induced by different kinds of moving vehicles in street canyons. Sustainable Cities and Society, 54, 102015.

Jicha, M., Pospisil, J., & Katolicky, J., 2000. Dispersion of pollutants in street canyon under traffic induced flow and turbulence. Environmental Monitoring & Assessment, 65(1-2), 343-351.

Katolický, J., & Jicha, M., 2005. Eulerian–Lagrangian model for traffic dynamics and its impact on operational ventilation of road tunnels. Journal of Wind Engineering and Industrial Aerodynamics, 93(1), 61-77.

Shi, T., Ming, T., Wu, Y., Peng, C., & Richter, R. D.,2020. The effect of exhaust emissions from a group of moving vehicles on pollutant dispersion in the street canyons. Building and Environment, 181, 107120.

Wang, Q., Fang, W., de Richter, R., Peng, C., & Ming, T. (2019). Effect of moving vehicles on pollutant dispersion in street canyon by using dynamic mesh updating method. Journal of Wind Engineering and Industrial Aerodynamics, 187, 15-25.

Zhao, Y., Jiang, C., & Song, X., 2021. Numerical evaluation of turbulence induced by wind and traffic, and its impact on pollutant dispersion in street canyons. Sustainable Cities and Society, 103142.

A Dynamic Overset Mesh Approach for Large-Eddy Simulation of Vehicle-Induced Turbulence and Pollutant Dispersion

Bingchao Zhang [1], Xuelin Zhang [2], Yunfei Fu [3], Tim K.T. Tse [4], Peizhen Yang[5]

[1]*The Hong Kong University of Science and Technology, Hong Kong, China, zhangbc@ust.hk*
[2] *Sun Yat-sen University, Zhuhai, China, zhangxlin25@mail.sysu.edu.cn*
[3]*The Hong Kong Polytechnic University, Hong Kong, China, timkttse@ust.hk*
[4]*The Hong Kong University of Science and Technology, Hong Kong, China, timkttse@ust.hk*
[5]*Imperial College London, London, United Kingdom, ny222@ic.ac.uk*

SUMMARY:
This study applied large-eddy simulation (LES) with a dynamic overset mesh approach to model vehicle-induced turbulence in a two-dimensional street canyon. The simulation included two-way traffic, with vehicles modeled as moving objects within the flow field, each equipped with a pollutant source. Statistical analyses compared the simulated turbulence with results from conventional and quasi-steady methods. The findings showed that moving vehicles significantly distorted the primary circulation, altering the transport pathways of lateral momentum and air pollutants. Vehicle motion also induced substantial turbulence. Ensemble-average analysis revealed a downwash followed by an upwash within each vehicle movement cycle, contributing to momentum and pollutant transport. These results highlight the need for accurate modeling of moving vehicles in LES to improve turbulence modeling.

Keywords: Vehicle-induced turbulence, Pollutant dispersion, Large-eddy simulation

1. INSTRUCTION

Vehicle-induced turbulence significantly affects pollutant dispersion in street canyons. Traditional studies often overlook moving vehicles, modeling traffic as a line source. Over the past twenty years, studies have attempted to account for traffic-induced turbulence, typically using simplified models due to the challenges of modeling moving objects. For example, the quasi-steady method, commonly used in ensemble average modeling like Reynolds-averaged Navier–Stokes simulations, does not directly incorporate vehicle geometry but adds equivalent drag force and turbulence quantities as uniform source terms in the governing equations (Katolický & Jícha, 2005). While computationally efficient, this method can be overly simplified for large-eddy simulation (LES), leading to inaccuracies in local turbulence within the canyon. This issue is more pronounced in two-way traffic scenarios, where intense and complex turbulence arises from opposing flows. Hence, this study aims to directly simulate vehicle-induced turbulence in LES by treating vehicles as moving objects, using a dynamic overset mesh approach. The results are compared with those from conventional and quasi-steady methods, aiming to guide more accurate and reliable turbulence modeling in urban environments.

2. LARGE-EDDY SIMULATION

The simulation geometry is shown in Figure 1. The street canyon dimensions are $H \times H$ (width ×

height), with H = 12 m. The domain spans $2H \times 6.5H \times 6H$ in the streamwise (x), spanwise (y), and vertical (z) directions. External wind flows from the inlet to the outlet at a volume-averaged speed of U_{avg} = 4 m/s, achieved using periodic boundary conditions with specified pressure differences. The vehicles, modeled to resemble SUVs, move in two-way traffic at U_{car} = 10 m/s, maintaining a vehicle distance of D = 15 m. Each vehicle has a moving pollutant source at the rear. The vehicles execute U-turns at the end of the street, running in a loop (Figure 2).

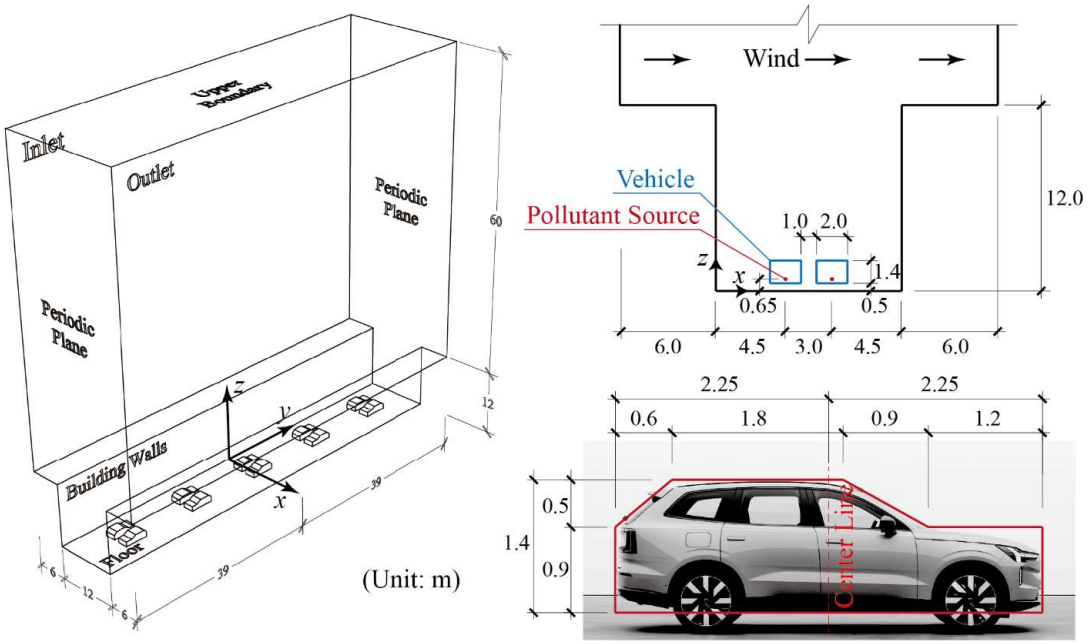


Figure 1. Geometry of the simulation domain, the street canyon, and the vehicle model.

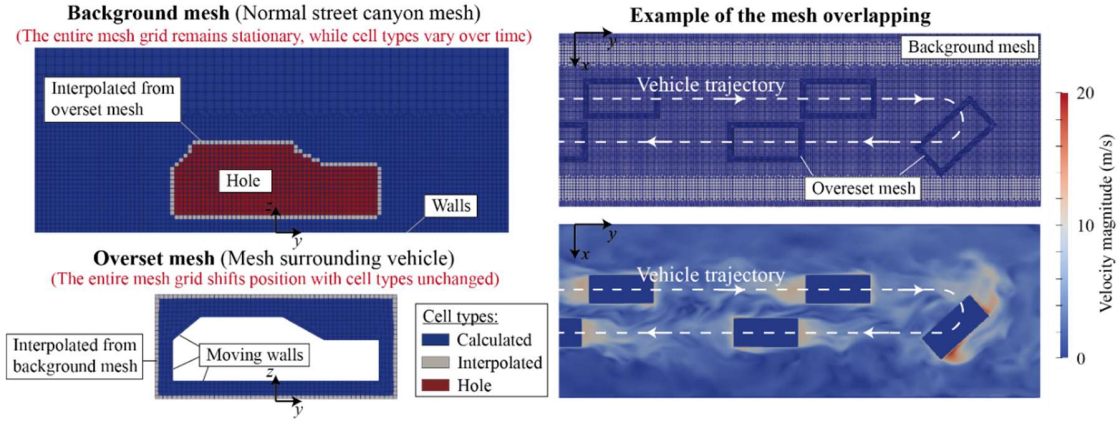


Figure 2. Cross-sections of the background and overset meshes and example of mesh overlapping.

In the dynamic overset mesh approach, a composite domain is created by overlapping several disconnected mesh regions, as illustrated in Figure 2. The background mesh is a conventional mesh of an empty two-dimensional street canyon, while each overset mesh conforms to the geometry of a single moving vehicle. The positions of the overset meshes are updated at each timestep to follow the vehicle's trajectory. In this study, the combined meshes contain 5.1 million cells, with an average cell size of 0.1 m in the refined zones.

All cells within both meshes are categorized into three types, as shown in Figure 2: (i) “Calculated” cells, where the governing equations are solved conventionally; (ii) “Interpolated” cells, where values are computed by interpolating between overlapping meshes; and (iii) “Hole” cells, where no solution is computed. The cell types change at each timestep due to vehicle movements.

The velocity and concentration fields were calculated using the LES approach in OpenFOAM. Mesh velocity was included in all convective terms of the governing equations, being zero in the background mesh and matching vehicle velocity in the overset meshes. In each overset mesh, a pollutant source was placed in a specific cell and moved with the mesh. The simulation ran for 900 s ($tU_{avg}/H = 300$), with data sampled only in the last 300 s ($tU_{avg}/H = 100$) to achieve statistically stationary time series. The mean flow and second-order turbulent statistics were validated against multiple experimental datasets. For more details, see Zhang et al. (2024).

3. RESULTS AND DISCUSSION

Figure 3 shows the simulated mean velocity, turbulent kinetic energy (TKE), and concentration fields at $y = 0$, compared with conventional and quasi-steady methods. The conventional simulation models an empty street canyon with two line pollutant sources, while the quasi-steady method adds equivalent drag force and turbulence quantities along vehicle paths. The sampled velocity and TKE are normalized by the reference speed at $z/H = 1.2$ in the conventional case, and the sampled concentration is further normalized by the total emission rate.

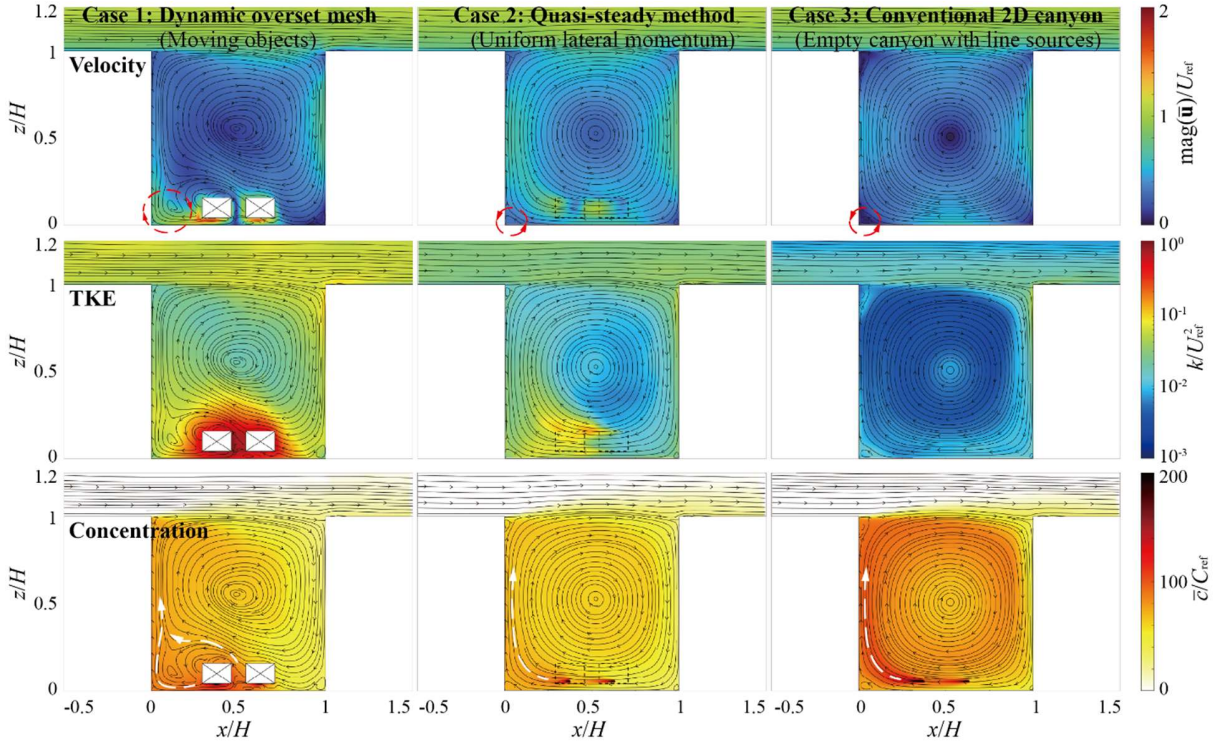


Figure 3. Normalized mean velocity, TKE, and concentration fields at the plane $y = 0$.

The comparison shows that moving vehicles significantly distort the primary circulation within the canyon. The additional momentum sources in the quasi-steady method, however, are insufficient to replicate this distortion. This change in primary circulation alters the transport

pathways of lateral momentum and air pollutants at the canyon's bottom, as shown by the dashed arrows in Figure 3.

Furthermore, vehicle motion induces substantial turbulence, with TKE at the canyon's bottom being much higher than in the quasi-steady and conventional approaches. The large spatial gradient in the TKE field causes its transport to be primarily through diffusion rather than advection by the primary circulation. In the quasi-steady method, however, TKE is mainly induced by shear instability due to the speed difference between source regions and ambient air.

Figure 4 provides an ensemble-average analysis on the velocity fields, showing the variation of the surrounding flow within a cycle of vehicular movement (D/U_{car}), providing a general observation on in-canyon dispersion mechanisms. After a vehicle passes, the lateral momentum or air pollutant produced is forced to remain at the base of the canyon due to a downwash that occurs at the rear of the vehicle. Subsequently, an upwash occurs, which propels the lateral momentum or air pollutant upward, where they merge with the primary circulation within the canyon.

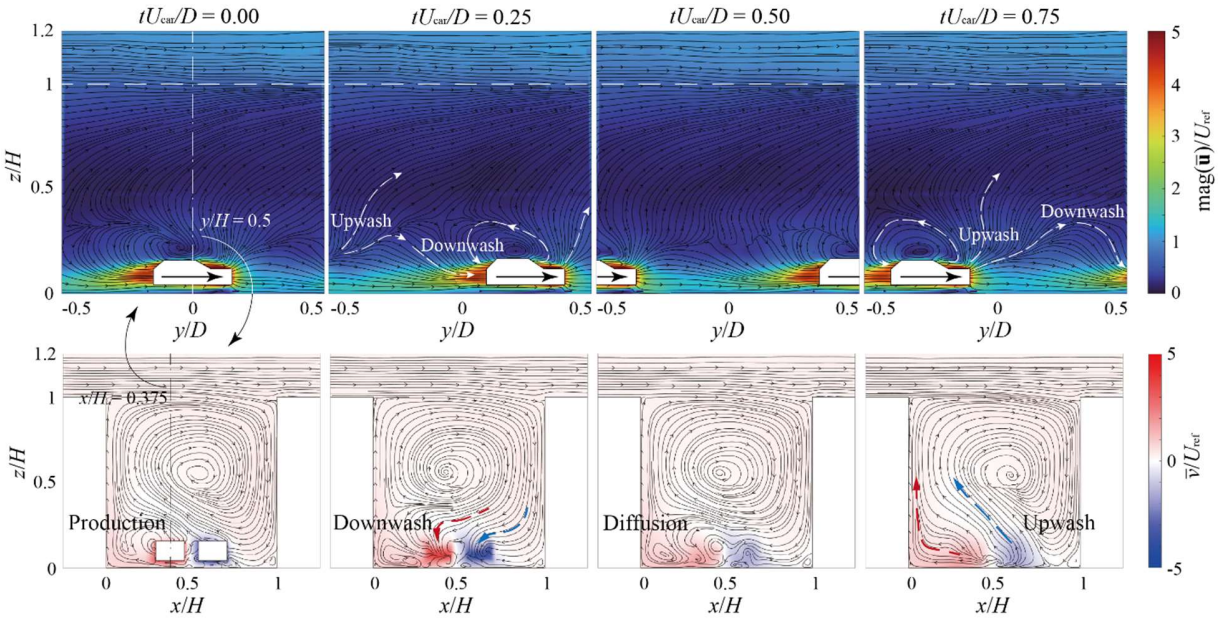


Figure 4. Ensemble average of the velocity field and lateral (y-directional) velocity component.

4. CONLUSIONS

This study used LES with a dynamic overset mesh to simulate vehicle-induced turbulence in street canyon, directly modeling vehicles as moving objects. Differences in mean flow and turbulence patterns were observed, and ensemble-average analysis revealed a periodic process in scalar transport. These results underscore the need for accurate modeling of moving vehicles in LES.

REFERENCES

Katolický, J., & Jícha, M., 2005. Eulerian-Lagrangian model for traffic dynamics and its impact on operational ventilation of road tunnels. Journal of Wind Engineering and Industrial Aerodynamics 93(1), 61–77.

Zhang, B., Wen, L., Zhang, X., Fu, Y., Tse, K. T., & Mak, C. M., 2024. Enhanced modeling of vehicle-induced turbulence and pollutant dispersion in urban street canyon: Large-eddy simulation via dynamic overset mesh approach. Available at SSRN: https://doi.org/10.2139/SSRN.4899965

Analysis of air pollutant transport near a real urban canyon depending on daily traffic patterns

Svetlana Valger and Ursula Voss

Hochschule für Technik Stuttgart, Stuttgart, Germany,
Svetlana.Valger@hft-stuttgart.de, Ursula.Voss@hft-stuttgart.de

SUMMARY:
Air pollution caused by road traffic is still an actual problem in many cities around the world. Therefore, there is a great need to analyse the pollutant concentrations in cities in different scenarios. The paper presents the development and application of a CFD model for the dispersion of particulate matter, CO and NOx from traffic in a real urban area with the topology of a street canyon. Daily statistics of traffic data along the considered road, collected as a result of measurements in 2024, are used to describe the boundary conditions for the pollutant sources. The CFD model is based on a 3D city model of the urban environment under consideration together with meteorological data from a nearby station. The combination of numerical methods and in-situ measurements allows us to analyse scenarios of pollution dispersion in an urban canyon as a function of time of day and the associated traffic volume.

Keywords: Vehicle pollution, Urban Wind Environment, Computational Fluid Dynamics

1. INTRODUCTION

Air pollution caused by road traffic is still an actual problem in many cities around the world. Computational fluid dynamics (CFD) methods, based on geospatial data describing the building geometry and landscape of a city combined with meteorological data of the considered area, are actively used today to analyse the transport processes of harmful gases and particles in urban air (Di Sabatino et al., 2013). Studies comparing wind tunnel experiments for a street canyon with CFD calculations show that RANS (Reynold-averaged Navier-Stokes) simulations can achieve qualitatively good results for pollutant transport, while RANS has the advantage of keeping the computational effort for realistic city models within reasonable limits (Salim et al., 2011). Currently, the simulation of urban micro-climate and human health during the course of the day on an hourly basis is gaining importance, requiring regional input data with an appropriate resolution (Antoniou et al., 2024). Although pollutant dispersion is numerically investigated in numerous studies, only a few studies deal with the temporal course or at least with different traffic situations such as congestion, slow-moving and dense traffic (Amorim et al., 2013; Blocken et al., 2016; Ioannidis et al., 2024). In this study, we combine the simulation of a real urban environment with hourly recorded traffic data, which allows us to analyse scenarios of pollution dispersion in an urban canyon as a function of time of day and the associated traffic volume.

2. CASE STUDY DESCRIPTION

A section of Schloss-Strasse, an important collector road in the city centre of Stuttgart, Germany, adjacent to building 7 of the HFT Stuttgart campus, is used as a case study to study the effect of

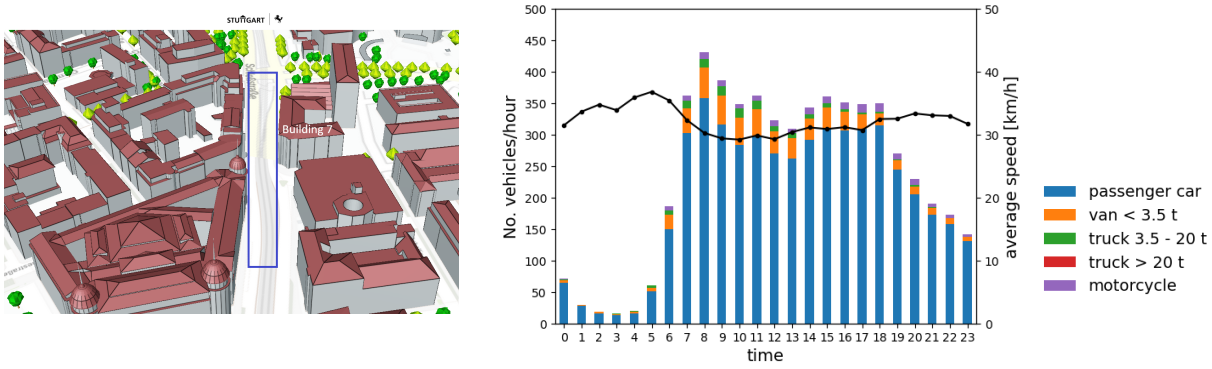


Figure 1. 3D model of the area near the HFT Stuttgart campus in Stuttgart along Schloss-Strasse (left) and average number of vehicles per hour by category on working days, recorded in front of building 7 (right)

road traffic on the air quality around the HFT Stuttgart campus and in particular in the street canyon near building 7 (Fig. 1, left). In 2024/25, traffic data (number of vehicles per hour, divided into 11 vehicle classes, and speed statistics) were recorded on both sides of the road in front of building 7 using two so-called TOPO boxes (RTB, 2024). Fig. 1, right, shows the number of vehicles over an average working day, whereby the vehicles were assigned to five classes, together with the average speed.

3. NUMERICAL MODEL AND METHODS

The CFD simulation was carried out using a geometric model obtained from a 3D model of Stuttgart in CityGML format. The CFD domain shown in Fig. 2, left, consists of two parts with radius R_1 and $R_2 = 1.5R_1$ and height H_d. The "inner" domain contains the considered case study environment and is covered by a high resolution grid. The "outer" domain represents the zone with a coarser grid needed to ensure that the flow near the buildings is not influenced by the external boundary conditions. The mean height of the domain is $H_d = 20H_b$, where H_b is the height of building 7. The test case shown in Fig. 2 corresponds to the case where the inflow velocity is perpendicular to the front facade of the building 7. The air pollution sources are described as two sections located at the bottom of the domain, corresponding to the location of the lanes on the road (Fig. 2, right). In addition to the commonly used boundary conditions, a "mass-flow" boundary

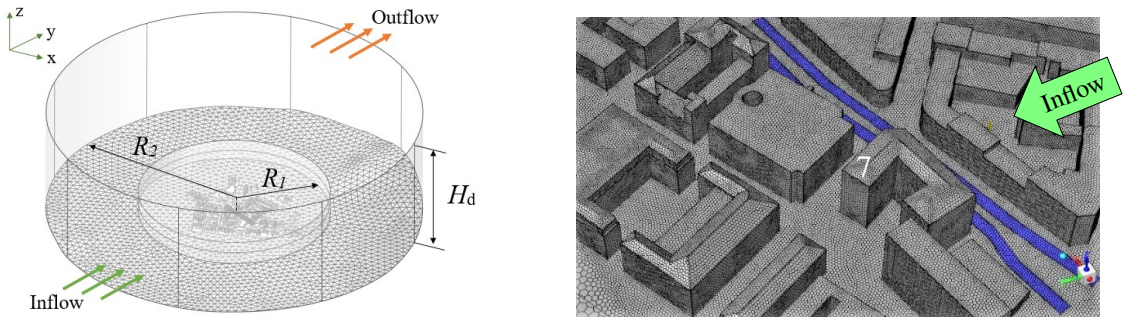


Figure 2. CFD Domain for the simulation (left), and the computational grid on the walls of the building, on the ground and at the lanes (right)

condition represents the pollutant sources along the ground boundaries adjacent to the road. The composition of vehicle exhaust pollutants includes carbon monoxide CO, nitrogen oxides NO_x, sulphur dioxide SO_2, hydrocarbons (HC) and benz(a)pyrene (BAP). Emission of the i-th pollutant [g/s] by a moving vehicle stream on a road section of fixed length L_r [km] is given by

$$M_{L_i} = \frac{L_r}{1200} \sum_{n=1}^{x} M_{k,i}^{L} G_k r_i, \tag{1}$$

where $M_{k,i}^{L}$ [g/km] is the specific emissions per kilometre of the i-th pollutant of the k-th vehicle category, x is the number of vehicle categories, G_k [1/hour] is the actual maximum intensity of traffic of k-th vehicle category passing through a section of the road in both directions on all lanes, and r_i is the correction factor for the average speed of traffic. The specific pollutant emissions of different vehicle types can be estimated using the local emission standards or the COPERT software (COPERT, 2024).

The CFD simulation is performed using the 3D RANS equations with k-ε turbulence model and convection-diffusion equations for the pollutants in Ansys Fluent 2023R3. The numerical model was validated in advance against wind tunnel experiments (Abbasi et al., 2023).

4. RESULTS AND DISCUSSION

The base airflow scenario is characterised by the inflow direction being almost perpendicular to the main road. In the results, the expected vortex that moves the air volume from the "windward" wall to the "leeward" wall of the canyon can be clearly seen (Fig. 3). The highest concentrations of pollutants for the case are observed on the leeward side of the canyon (Fig. 4). The results shown depict a special temporal situation. In case of simulations for lower wind speeds, the effects of traffic-induced turbulence should also be taken into account (Di Sabatino et al., 2013), e.g. using additional source terms (Abbasi et al., 2023), as well as buoyancy effects. As shown by Zheng and Yang, 2021, RANS produces qualitatively good results also when traffic-induced turbulence is included in the model.

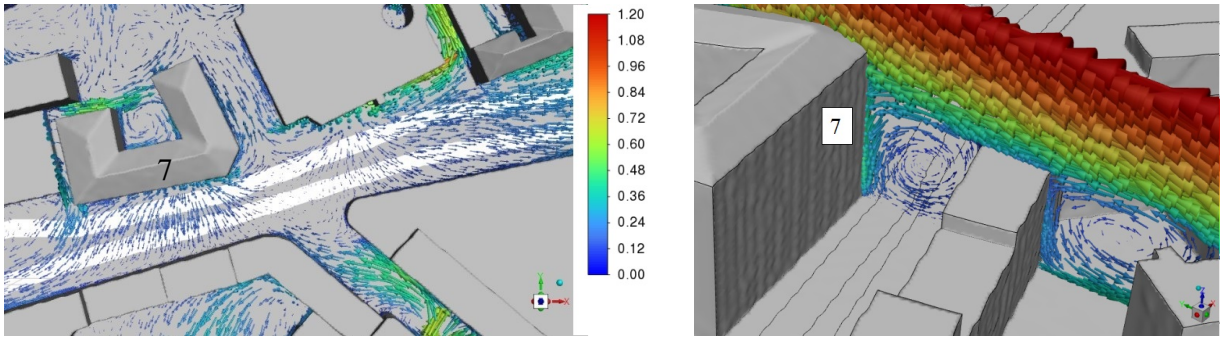


Figure 3. Vector velocity fields coloured by velocity U/U_{ref} in the horizontal x-y-plane, at $h = 5$m (left) and in a cross section of the canyon (right). Inflow in positive y-direction (green)

5. CONCLUSIONS

A pollutant dispersion model (gas emissions and PM) has been implemented, parameterized with traffic data specific for the site and applied to the simulation of building complex in Stuttgart.

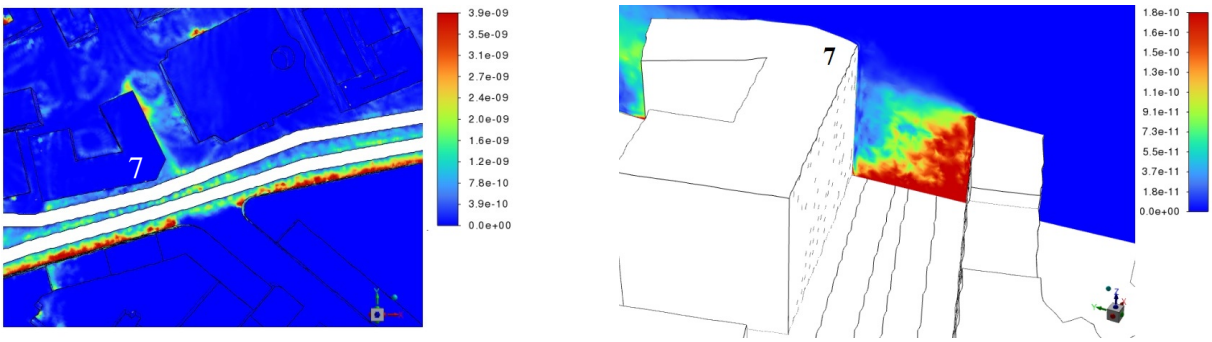


Figure 4. Distribution of the PM mass concentration $[\mathrm{kg/m^3}]$ at the walls of buildings and at the ground (left) and in a cross section plane of the canyon (right). Inflow in positive y-direction (green)

The simulation reproduced the expected flow characteristics within the densely built-up area and and a next step to take into account the different traffic situations throughout the day when simulating pollutant concentrations.

FUNDING AND ACKNOWLEDGEMENTS

This research was funded by the German Federal Ministry of Education and Research (BMBF) within the funding program "Forschung an Fachhochschulen" as part of the SenSim4iCity project under contract no. 13FH9I09IA. The responsibility for the content of this publication lies with the authors. The authors thank RTB for providing the measuring devices and Steffi Reinhold, HFT Stuttgart, for carrying out the measurements. The authors further and acknowledge the support by the state of Baden-Württemberg through bwHPC and by Stadtmessungsamt Landeshauptstadt Stuttgart through providing the 3D city model of Stuttgart.

REFERENCES

Abbasi, M., Valger, S., and Voss, U., 2023. Evaluation of a model for vehicle induced turbulence for urban wind simulation. Proceedings of ICWE 16, August 27 -31, 2023, Florence, Italy. (under review).

Amorim, J., Rodrigues, V., Tavares, R., Valente, J., and Borrego, C., 2013. CFD modelling of the aerodynamic effect of trees on urban air pollution dispersion. Science of The Total Environment 461-462, 541–551.

Antoniou, N., Montazeri, H., Blocken, B., and Neophytou, M., 2024. On the impact of climate change on urban microclimate, thermal comfort, and human health: Multiscale numerical simulations. Building and Environment 260, 111690.

Blocken, B., Vervoort, R., and Van Hooff, T., 2016. Reduction of outdoor particulate matter concentrations by local removal in semi-enclosed parking garages: A preliminary case study for Eindhoven city center. Journal of Wind Engineering and Industrial Aerodynamics 159, 80–98.

COPERT, 2024. https://copert.emisia.com/.

Di Sabatino, S., Buccolieri, R., and Salizzoni, P., 2013. Recent advancements in numerical modelling of flow and dispersion in urban areas: A short review. International Journal of Environment and Pollution 52, 172–191.

Ioannidis, G., Li, C., Tremper, P., Riedel, T., and Ntziachristos, L., 2024. Application of CFD Modelling for Pollutant Dispersion at an Urban Traffic Hotspot. Atmosphere 15, 113.

RTB, 2024. https://www.rtb-bl.de/detektion/verkehrszaehlung/.

Salim, S. M., Buccolieri, R., Chan, A., and Di Sabatino, S., 2011. Numerical simulation of atmospheric pollutant dispersion in an urban street canyon: Comparison between RANS and LES. Journal of Wind Engineering and Industrial Aerodynamics 99, 103–113.

Zheng, X. and Yang, J., Dec. 2021. CFD simulations of wind flow and pollutant dispersion in a street canyon with traffic flow: Comparison between RANS and LES. en. Sustainable Cities and Society 75, 103307.

Experimental Assessment of the Pollutant Dispersion of Ship Emissions

S. Gillmeier[1], A. Krishnan Radhakrishnan Jayakumari[1],
E.W.M. Roosenboom[2], J. Muralha[3], G. Beleza Vaz[3], L.F. Sánchez Castro[4]

[1] *Eindhoven University of Technology, Eindhoven, The Netherlands, s.g.gillmeier@tue.nl, a.k.radhakrishnan.jayakumari@tue.nl*
[2] *Damen Naval, Vlissingen, The Netherlands, e.roosenboom@damennaval.com*
[3] *blueOASIS, Ericeira, Portugal, jmuralha@blueoasis.pt, gvaz@blueoasis.pt*
[4] *Knud E. Hansen, Elsinore, Denmark, fec@knudehansen.com*

SUMMARY:
The dispersion of pollutants exhausted from a generic service offshore vessel are investigated in an atmospheric boundary layer wind tunnel. The vessel is replicated at a geometric scaling ratio of 1:100 and exposed to maritime neutral atmospheric flow conditions. Conducted measurements relate to 25% of maximum continuous rating (MCR) engine load and a full-scale approach flow velocity of 10 m/s at exhaust height. To match the densimetric Froude number in experiments, and reality, a velocity scaling ratio of 1:10 is chosen. Focus of pollutant concentration measurements is set on locations at 1.5 m height on the vessel's deck to assess the possibility of workers' exposure to emitted pollutants. It is found that due to turbulent dispersion, several locations experience relatively high percentage concentrations of emitted pollutants. For headwind conditions, the highest time-averaged pollutant concentrations are found in negative pressure and re-circulation zones, relatively close to the exhaust, where pollutants are trapped.

Keywords: pollutant dispersion, ship emissions, buoyant release

1. BACKGROUND

Air pollution is recognized by the WHO as one of the greatest health risks. Although emissions of key air pollutants have decreased over the past decades, air quality remains poor in many areas (European Environment Agency, 2022). Among others this concerns the shipping industry and port areas. In situations where vessels operate in open sea or manoeuvre in harbours, various wind conditions might occur, possibly resulting in the exposure of crew or passengers on deck to noxious pollutants (e.g., Kennedy, 2019). For harbour operation, not only particulate matter remaining on deck is critical, but emitted pollutants can also be transported into the urban environment, resulting in locally increased concentrations of hazardous pollutants (e.g., Toscano et al., 2021). There is overall consensus for development into green(er) alternatives for fossil fuels and zero emission shipping within the shipping industry. This, however, is a long-term ambition (International Maritime Organization, 2022) and until then emissions will still need to be critically assessed. The presented work is part of a larger ongoing research project that deals with the effect of neutral maritime-like atmospheric boundary layer (ABL) wind conditions on the exhaust gas dispersion of a vessel under realistic operational conditions: (i) in isolation, (ii) in proximity to a second vessel and (iii) nearby harbour infrastructure. For the sake of brevity, focus is here laid on the isolated

vessel.

2. METHODOLOGY

The vessel under investigation is a generic version of a representative service offshore vessel (length: 84 m; beam: 17 m), typically used for the construction and maintenance of wind farms in open sea. Pollutants are released from one circular exhaust pipe of 0.76 m inner diameter (full-scale), located on the wheelhouse in 20.2 m height (full-scale). The model hull is milled while other more complex parts on deck are 3D powder printed. The railings are cut from aluminium to guarantee sharp edges and flow separation. Figure 1 shows an illustration of the vessel model.

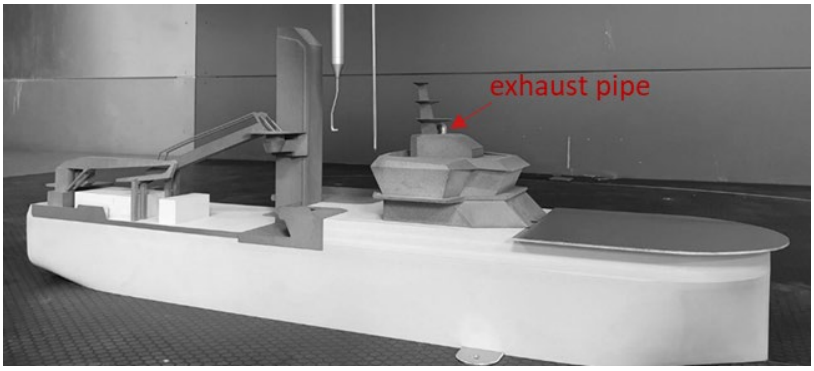


Figure 1. Illustration of the model vessel and highlighted location of exhaust pipe.

Measurements are conducted in the closed-circuit Atmospheric Boundary Layer Wind Tunnel at Eindhoven University of Technology at a reduced geometric scaling ratio of 1:100. With this geometric scale, neutral atmospheric flow conditions over sea can be replicated in the wind tunnel while keeping the densimetric Froude number in experiments and reality similar, following VDI-3783 (2000) guidelines. To guarantee Froude number similitude, a velocity scale of 1:10 is chosen.

Pollutants are released at a reduced-scale velocity of 0.88 m/s which corresponds to 25% of Maximum Continuous Rating (MCR) engine load. With an assumed full-scale wind velocity of about 10 m/s at 20 m height above water (Dutch Offshore Wind Atlas, 2019), relatively low approach flow velocities of about 1 m/s at exhaust height are required for the experiments. The resulting Reynolds number is about 11,200 based on the vessel's beam (0.17 m - reduced-scale).

For the isolated vessel, pollutant concentrations (in ppm) are measured at a height of 1.5 m (full-scale) at 25 locations on deck of the vessel using an HFR400 fast flame ionisation detector from Cambustion Ltd. At each location, a 300-second-long time series of pollutant concentrations is recorded at a frequency of 85 Hz. The effect of changing approach flow directions on the pollutant dispersion is assessed for headwind ($\gamma = 0°$), sidewind ($\gamma = 90°$), tailwind ($\gamma = 180°$) and $\gamma = \pm 15°$. In what follows, measured concentrations at individual locations are presented in percentage of the released concentration.

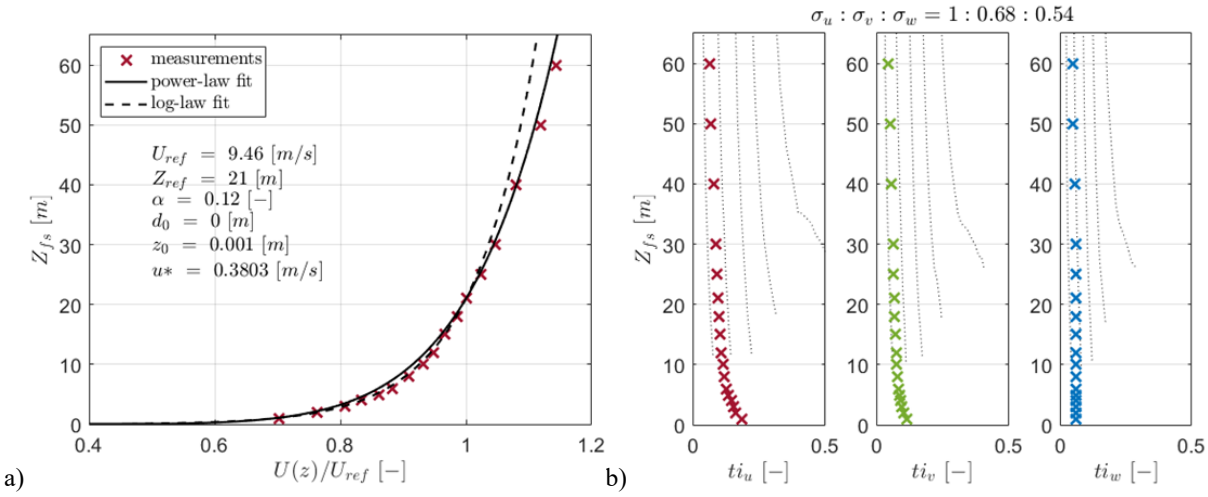
Atmospheric approach flow conditions are measured every 0.001 second for 60 seconds with a 4-hole Cobra probe positioned with a 3-axis traverse system inside the wind tunnel.

3. RESULTS

This section presents the flow characteristics of the approaching atmospheric boundary layer and time-averaged pollutant concentrations on deck.

3.1. Atmospheric approach flow conditions

Maritime atmospheric boundary layer approach flow conditions are simulated by means of vortex generators and surface roughness elements. The height profile of time-averaged streamwise velocities is presented in Figure 2a. By means of the logarithmic law of the wall, a corresponding aerodynamic roughness length of z_0 = 0.001 m (full-scale) is obtained, and consistent with this, the profile exponent law with α = 0.12 matches the approach flow well (VDI-3783, 2000). Also, turbulence intensities (Figure 2b) fall within the maritime roughness category, with streamwise turbulence intensities (ti_u) of about 20% close to the surface and a decrease to about 10% with height, lateral turbulence intensities (ti_v) of about 10% and vertical turbulence intensities (ti_w) of below 10%. Corresponding, energy spectral densities for the three velocity components and turbulent integral lengths scales have also been assessed.



a) b)

Figure 2. (a) Height profile of time-averaged streamwise velocities and logarithmic law and profile exponent law (power-law) fit. (b) Height profile of streamwise (ti_u), lateral (ti_v) and vertical (ti_w) turbulence intensities.

3.2. Pollutant concentrations on deck

Figure 3 illustrates time-averaged percentages of emitted pollutant concentrations observed at indicated locations for $\gamma = 0°$. At all locations downstream of the exhaust, pollutant concentrations are measured. The negative pressure region behind the wheelhouse seems responsible for highest measured concentrations. The presence of the tower seems to trap pollutants between wheelhouse and tower in a possible re-circulation zone. Also further downstream, at the lower deck, averaged percentage concentrations from 0.19 % to 0.2% are measured. As expected, a change in approach flow direction significantly affects the pollutant concentration distribution on deck of the vessel. For the sake of brevity, results obtained for other wind directions are not shown here.

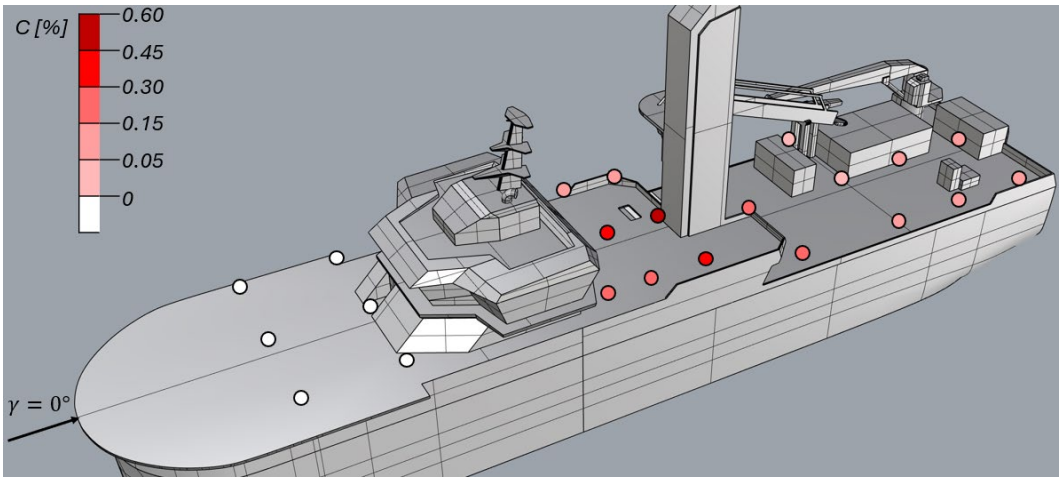


Figure 3. Time-averaged pollutant concentrations in percentage of released concentrations at 1.5 m height on deck of the vessel for headwind ($\gamma = 0°$).

7. CONCLUSIONS

The dispersion of pollutants originating from a generic service offshore vessel are investigated for realistic operating conditions (neutral maritime atmospheric boundary layer flow, 25% of MCR engine load and 10 m/s velocities at exhaust height). In this short abstract, percentages of time-averaged concentration in relation to the emitted concentration are presented for an isolated vessel exposed to headwind conditions. It is relevant to highlight that (1) a detailed analysis of exposure to pollutants should not rely on time-averaged parameters, instead the assessment of higher percentiles is relevant and (2) several parameters are expected to affect the distribution and quantities of obtained concentrations on the isolated vessel, e.g., the approach flow direction, the engine load, the approach flow velocity. All of the aforementioned points have been analyzed in the current work.

ACKNOWLEDGEMENTS

This work is supported by the Engineering Research Infrastructures for European Synergies (ERIES) project (www.eries.eu), which has received funding from the European Union's Horizon Europe Framework Programme under Grant Agreement No. 101058684. This is ERIES publication number C24.

REFERENCES

Dutch Offshore Wind Atlas, (2019). 10 year average wind speed for different heights – 20m. Available: https://www.dutchoffshorewindatlas.nl/atlas/image-library/image-library/wind-speed-parameter-f.

European Environment Agency, (2022). Air Quality in Europe. Available: https://www.eea.europa.eu//publications/air-quality-in-europe-2022.

International Maritime Organization, (2022). Next steps to deliver IMO GHG strategy. Available: https://www.imo.org/en/MediaCentre/PressBriefings/Pages/18-MEPCGHGprogramme.aspx.

Kennedy, R.D. (2019). An investigation of air pollution on the decks of 4 cruise ships. A Report for Stand.earth.

Toscano, D., Marro, M., Mele, B., Murena, F., Salizzoni, P., (2021). Assessment of the impact of gaseous ship emissions in ports using physical and numerical models: The case of Naples, Building and Environment, 196.

VDI-3783, (2000). Verein Deutscher Ingenieure. Environmental Meteorology – Physical modelling of flow and dispersion Processes in the atmospheric boundary layer – Application of wind tunnels.

Measuring a Pollutant Plume over a 3D printed City Model

Tomos Rich[1] and Christina Vanderwel[2]

[1]*University of Southampton, Southampton, United Kingdom, tjr1u19@soton.ac.uk*
[2]*University of Southampton, Southampton, United Kingdom, C.M.Vanderwel@soton.ac.uk*

SUMMARY:
The modelling of urban air pollution requires an understanding of the turbulent processes involved. This projects aims to provide direct measurements of turbulent dispersion over urban terrain with a high-fidelity experimental study. An investigation into scalar dispersion over a 3D-printed model of the City of Southampton, which is a medium-size coastal city in the south of England, was carried out. This 1000:1 scale model was created to represent 1 km^2 of Southampton's city centre experiencing an onshore south-south-westerly wind. Experimentally measuring turbulent scalar fluxes is challenging as it requires both concentration and velocity measurements in the same place, and at the same time. Particle image velocimetry (PIV) and planar laser induced fluorescence (PLIF) were used to measure full fields of these turbulent scalar fluxes. Measurements were carried out in streamwise-vertical and wall-parallel planes to create a detailed map of concentration and velocity data for a case in which a plume from an offshore point source was introduced upstream of this model.

Keywords: Urban wind climate, Building aerodynamics, Pollutant dispersion

1. INTRODUCTION

The risk to public health posed by air pollution is significant (Dziubanek et al., 2017), and living in an urban environment is a risk factor that increases exposure. The world's population is still growing and is also gravitating more towards these urban environments. This means that a larger proportion of this population will be directly exposed to urban air pollution (United Nations Department of Economic and Social Affairs, 2018). Due to this, there is an increasing need for more accurate predictions of urban air pollution. Computational models for urban air flow and air pollution are popular because of their speed and convenience. However, realistic data remains crucial for the development and calibration of the mathematical models required for simulations. Acquiring realistic data for this purpose can only be done through either sensor data in real world scenarios, or through scaled experiments in wind or water tunnels.

Experimentally measuring pollutant dispersion can be done through several methods, both intrusive and non-intrusive. In wind tunnels, the most common methods are to use a fast flame ionisation detector (FFID) (Carpentieri et al., 2012) or photo-ionisation detector (PID) (Talluru et al., 2018). These measurement techniques acquire concentration data at a single location at the head of a probe. Doing experiments in a water flume allows for the use of the planar laser induced fluorescence (PLIF) technique. This technique is a non-intrusive technique that quantitatively measures the fluorescence response of a dye in planar slices and calibrates this response to known dye concentration values.

There is a very limited amount of existing experimental data that includes both concentration and velocity measurements over realistic city models. The majority of existing experimental studies use either idealized urban roughness or fully randomized roughness (Fuka et al., 2018). While idealized roughness can prove somewhat representative in highly ordered cities, such as Barcelona; most cities are built in a pseudo random form with neighbourhood scale order. Out of the existing aerodynamic studies into realistic city models, most are carried out in wind tunnels, in which acquiring full fields of concentration data is much more difficult than it is in water (Lim et al., 2022; Nironi et al., 2015). We aim to fill this gap by collecting full fields of concentration and velocity data above a realistic city, in order to characterise the spatial distribution of pollutant dispersive fluxes.

2. METHODOLOGY

Experimental measurements were made in the University of Southampton's Recirculating Water Tunnel. The city model is submerged in the water tunnel during the experimental campaign. This model was created to represent 1 km^2 of Southampton's city centre and the full to model scale is 1000:1. In this model, both terrain elevation and building height are represented, and the flow direction corresponds to the predominant wind direction of an onshore south-south-westerly.

The incoming flow was conditioned to have a boundary layer depth of approximately 300 mm and a free-stream flow velocity of 0.6 m/s. Using the maximum building height of 45 mm as the length-scale, the Reynolds number was 27,000. Using the mean building height across the central section of the model of 20 mm gives a Reynolds number of 12,000. All data in this paper has been made dimensionless using a characteristic building height of $H = 20$ mm. In order to experimentally simulate an onshore pollutant plume from the docks, a scalar source was introduced 50 mm upstream of the model. The scalar used was Rhodamine 6G fluorescent dye, which was illuminated using a Nd-YAG laser with an emission wavelength of 532 nm. This scalar was introduced with a low enough velocity that it did not measurably affect the velocity field, and was introduced at ground level through the use of a non-intrusive tube underneath the experimental setup.

3. RESULTS

Figure 1 presents a map of the upper limit of the plume as defined as the isocontour of 0.002 percent of the source concentration. This plot was generated through the use of the seven streamwise-vertical slices. The isocontour heights were then extrapolated and interpolated in the cross-stream direction between the seven points assuming a Gaussian. This avoided any assumption of the streamwise development but did result in cross-stream bands in the image. Using the peaks of the plume height, it was calculated that the plume deflects from the mean flow direction by 4.2 degrees. This deflection can be attributed to the influence of the mean street canyon orientation being aligned towards the left side of the model.

The vertical advective and turbulent fluxes are displayed in figures 2 and 3 respectively. We focus on the vertical fluxes as these are the most relevant for weather and pollution modelling. This data is taken from the centre plane of the flow. The turbulent flux field has a constant upwards direction at nearly all points in the flow, as is shown by the predominant red colour visible in figure 3. The sign of the advective flux field varies across the city model. As the scalar field has a constant

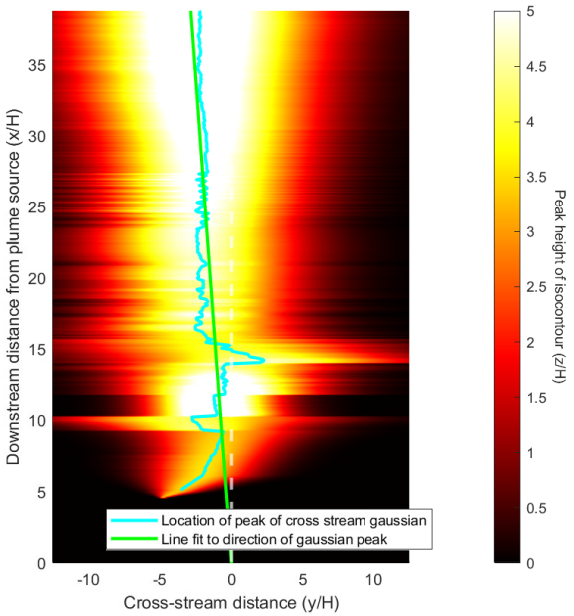


Figure 1. A map of the upper limit of the plume as defined as the isocontour of 0.002 percent of the source concentration. The displacement of the centre of the mean plume is shown in blue. The best-fit line in green shows the centre follows a mean direction of 4.2 degrees to the left of the mean flow direction.

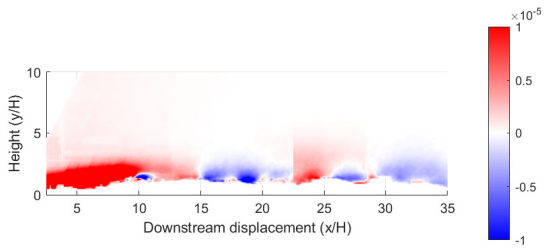


Figure 2. The vertical advective scalar flux ($\frac{CV}{C_s U_\infty}$) measured along the centreline of the city model.

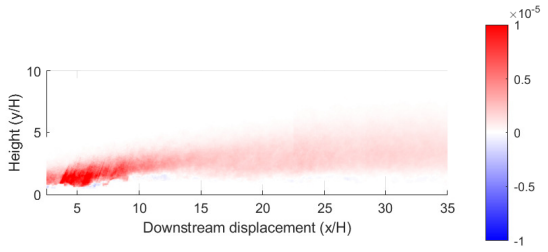


Figure 3. The vertical turbulent scalar flux ($\frac{\overline{c'v'}}{C_s U_\infty}$) measured along the centreline of the city model.

positive sign, this is reflecting the varying sign of the vertical velocity component. This is most visible at $x/H = 22.5$ in figure 2 where the sign change happens close to a camera stitch line. It is noteworthy that both components of vertical transport are of similar average magnitudes.

4. CONCLUSION

This study has shown that across most areas of an urban flow, the magnitude of the vertical turbulent flux is very similar to the magnitude of the vertical advective flux. The vertical turbulent and advective fluxes also share no correlation in sign or strength, making the prediction of one using the other impossible. This demonstrates the difficulty in modelling the turbulent fluxes accurately, while also showing the importance of this modelling to simulating accurate results of scalar dispersion. This study is one of very few to measure full fields of simultaneous concentration and velocity data over a realistic city model.

The mean concentration data and plume shape indicate that the buildings are strongly influencing the shape of the plume away from what you would expect over regular or random roughness. Instead, the plume still seems mostly Gaussian, but is diverted from its expected direction. The current hypothesis is that the plume is being influenced to follow the mean street canyon direction of the large street canyons.

The conclusion that can be drawn from these measurements is that in most areas the city is acting as uniform roughness increasing the general turbulent mixing. The key exceptions to this rule are the neighbourhood scale order that is created due to street canyon alignment and the few particularly large buildings.

Acknowledgements We gratefully acknowledge funding from Christina Vanderwel's UKRI Future Leaders Fellowship (MR/S015566/1)

REFERENCES

Carpentieri, M., Hayden, P., and Robins, A. G., Jan. 2012. Wind tunnel measurements of pollutant turbulent fluxes in urban intersections. Atmospheric Environment 46, 669–674.

Dziubanek, G., Spychała, A., Marchwińska-Wyrwał, E., Rusin, M., Hajok, I., Ćwielag-Drabek, M., and Piekut, A., 2017. Long-term exposure to urban air pollution and the relationship with life expectancy in cohort of 3.5 million people in Silesia. Science of the Total Environment 580, 1–8.

Fuka, V., Xie, Z. T., Castro, I. P., Hayden, P., Carpentieri, M., and Robins, A. G., 2018. Scalar Fluxes Near a Tall Building in an Aligned Array of Rectangular Buildings. Boundary-Layer Meteorology 167, 53–76.

Lim, H. D., Hertwig, D., Grylls, T., Gough, H., Reeuwijk, M. V., Grimmond, S., and Vanderwel, C., June 2022. Pollutant dispersion by tall buildings: laboratory experiments and Large-Eddy Simulation. Experiments in Fluids 63 (6).

Nironi, C., Salizzoni, P., Marro, M., Mejean, P., Grosjean, N., and Soulhac, L., 2015. Dispersion of a Passive Scalar Fluctuating Plume in a Turbulent Boundary Layer. Part I: Velocity and Concentration Measurements. Boundary-Layer Meteorology 156, 415–446.

Talluru, K. M., Philip, J., and Chauhan, K. A., 2018. Local transport of passive scalar released from a point source in a turbulent boundary layer. Journal of Fluid Mechanics 846, 292–317.

United Nations Department of Economic and Social Affairs, 2018. *68% of the world population projected to live in urban areas by 2050, says UN*. https://www.un.org/development/desa/en/news/population/2018-revision-of-world-urbanization-prospects.html.

Indoor-outdoor pollutant transport through a hollow cube with a cross-ventilating flow

Subhajit Biswas[1], Matteo Carpentieri[2], Christina Vanderwel[1]

[1]*Dept. of Aeronautics and Astronautics, University of Southampton, UK, s.biswas@soton.ac.uk*
[2]*Centre for Aerodynamics and Environmental Flow, School of Mechanical Engineering Sciences, University of Surrey, UK*

SUMMARY:
Cross-ventilation plays a critical role in dispersing indoor pollutants by promoting the exchange of indoor and outdoor air. To investigate pollutant transport in such scenarios, we experimentally investigate the flow through a hollow cube immersed in an atmospheric boundary layer as an idealized representation, with a ground-level passive scalar (pollutant) source placed at the centre of the building. The focus is on characterizing the velocity and concentration fields to understand the scalar transport mechanisms within and outside the cube. Two different experiments are conducted comparing results from the University of Surrey EnFlo wind tunnel and the University of Southampton water tunnel. The wind tunnel experiments used a laser Doppler anemometer (LDA) and a Fast flame ionization detector (FFID) to collect point measurements of the velocity and concentration, respectively. The water tunnel experiments used Planar Laser-Induced Fluorescence (PLIF) and Particle Image Velocimetry (PIV) to obtain simultaneous measurements of scalar and flow fields. The insights gained from this study can potentially improve our understanding and help model pollutant exchange between indoor and outdoor environments, especially in complex atmospheric boundary layer conditions.

Keywords: Air pollution, Outdoor dispersion, Scalar dispersion, Cross-ventilation.

1. INTRODUCTION

In urban environments, pollutants can originate from both indoor and outdoor sources. Consequently, when it comes to modelling pollutant dispersion, numerous studies have concentrated on scalar dispersion in outdoor environments (e.g., Lim et al. (2022)) as well as indoor environments (e.g., Biswas and Vanderwel (2024a), Biswas and Vanderwel (2024b), and Tominaga and Blocken (2016)). The indoor environment poses health challenges due to various sources of pollutants, such as volatile organic compounds and particulate matter and could be life-threatening in cases such as potential gas leaks and airborne transmission of infectious diseases. Since humans spend most of their time indoors, maintaining a healthy and sustainable indoor environment would be very critical for human health. In such scenarios, cross-ventilation could help to keep a healthy indoor environment (Finnegan et al., 1984).

To date, most experimental studies on flow and pollutant dispersion for outdoor and indoor environments predominantly utilize wind tunnel facilities, while the use of water tunnels for similar studies remains relatively limited. Drawing motivation from this, we perform a series of experiments examining pollutant transport in a cross-ventilating flow through a scaled-down hollow building (a hollow cube) in a water tunnel with an indoor scalar (Rhodamine dye) source (Fig. 1(a)). Subsequently, the findings are compared with sets of analogous experiments performed in

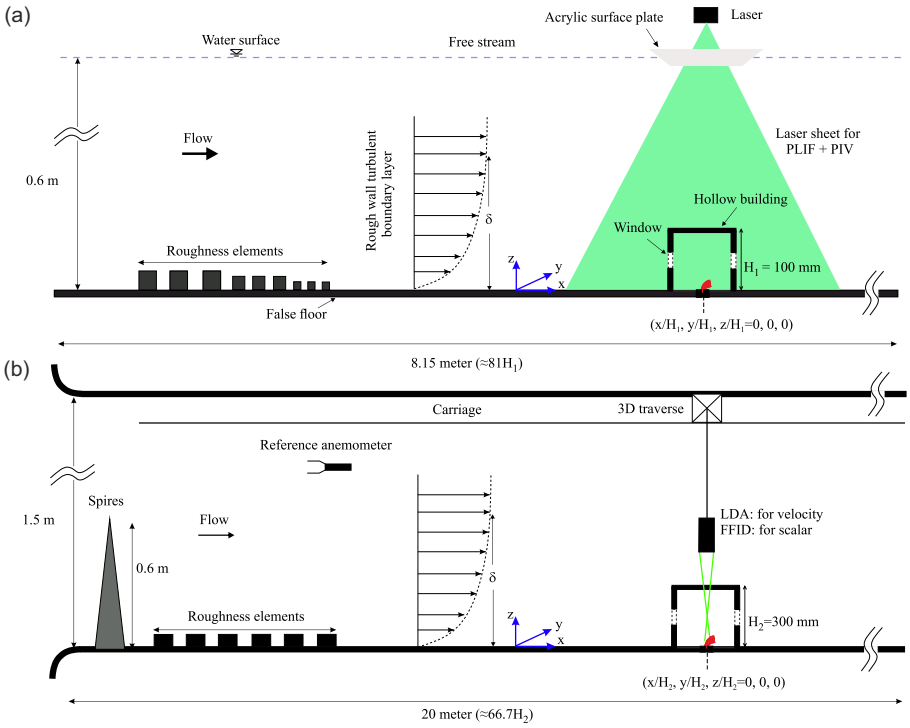


Figure 1. Schematic of the experimental setups showing the hollow building inside the turbulent boundary layer inside (a) water flume facility and (b) wind tunnel facility.

a wind tunnel, with the model building being equipped with an indoor gaseous (Propane) scalar source (Fig. 1(b)). Our comparative approach aims to establish the consistency and reliability of dispersion measurements across two experimental arrangements by evaluating and comparing the flow dynamics and scalar dispersion.

2. EXPERIMENTAL METHODOLOGY

Two different experiments were conducted and then compared results from the University of Southampton water tunnel (see Fig. 1(a)) and the University of Surrey EnFlo wind tunnel (Fig. 1(b)). The condition of a turbulent atmospheric boundary layer was created using a series of roughness elements placed upstream as shown in Fig. 1 (for details, see Biswas, Hayden, et al. (2024) and Biswas and Vanderwel (2024b)).

The water tunnel experiments involved a cube of height H_1 = 100 mm (approximately 40:1 to full scale) with a reference water speed at the cube height of $U_{Ref,1}$ = 0.45 m/s, resulting in a Reynolds number of $Re = U_{Ref,1}H_1/\nu_{water} \approx$ 50,000. The wind tunnel experiments were performed using a cube of height H_2 = 300 mm (approximately 13:1 scale to full-scale) with a reference wind speed at the cube height of $U_{Ref,2}$ = 2.5 m/s, resulting in the $Re(= U_{Ref,2}H_2/\nu_{air})$ being the same as in the water tunnel. Both setups benefited from spires and roughness to condition the oncoming boundary layer to have a depth of $\delta/H \approx 3$ (H=cube height). The hollow (acrylic) cubes had two opposite openings ($0.35H \times 0.35H$) in the windward and leeward façade, with about 10% area-based porosity (as in Biswas and Vanderwel (2024a)).

2.1. Water tunnel setup

In the water tunnel, Rhodamine 6G dye is injected from a ground-level source at the centre of the model, with negligible effects on the flow (similar to Biswas and Vanderwel (2024a)). The aqueous solution of the dye with concentrations (C_S) of 1 mg/L was injected at a constant flow rate of Q_S=7 mL min^{-1} (see Fig. 1(a)). The two-dimensional maps of the velocity (U) and the scalar concentration (C), within the cube were captured simultaneously through Particle Image Velocimetry (PIV) and Planar Laser-Induced Fluorescence (PLIF), in the streamwise plane (x-z) along the centreline of the building. For the PIV measurements, the flow was seeded with 50 μm polyamide seeding particles. For both the PIV and PLIF measurements, the illumination was provided by a 100 mJ Nd:YAG double-pulsed laser with an emission wavelength of 532 nm, and appropriate filters were used in two cameras to separate the PIV and PLIF signals.

2.2. Wind tunnel setup

The EnFlo wind tunnel facility (see Fig. 1(b)) at the University of Surrey (Placidi et al., 2023) is a suction tunnel with a large working section measuring 20m in length, 3.5m in width, and 1.5m in height. The flow was seeded with micron-sized sugar particles, and the flow velocity was measured using a Dantec two-component laser Doppler anemometer (LDA). For scalar, a mixture of Propane gas and air was used as the tracer, released from ground level. The flow rate of the gas mixture (Q_S) was about 0.021 l min^{-1}, at a concentration (C_S) of about 15,000 ppm. Tracer concentration measurements were performed using a Cambustion Fast Flame Ionization Detector (FFID) with a frequency response of 200 Hz.

3. RESULTS AND DISCUSSIONS

The results from the water tunnel measurements are compared with the wind tunnel (Figs. 2(b,c,d)), in terms of the wall-normal (z/H) profiles for the mean velocity, scalar and variance at different locations as illustrated in Fig. 2(a). The magnitude and the wall-normal variation in velocity and the scalar measured at these locations along the streamwise centre plane are found to be substantially similar [Figs. 2(b,c,d)] across the water tunnel and wind tunnel, thus establishing universality in the methodologies and measured quantities. To help quantify the out-of-plane variations in $\overline{C}$, the wind-tunnel measurements performed at two out-of-plane locations clearly show [Figure 2(c(ii))] a lower scalar buildup than the centre plane and the nearly uniform wall-normal (z/H) scalar concentration implies a relatively well-mixed scalar in these regions in comparison with the centre plane.

4. CONCLUSION

To summarise, the present work experimentally investigated a cross-ventilating flow through a hollow cube with an indoor scalar source, immersed in a rough-wall turbulent boundary layer. The primary focus was on comparing the water tunnel PIV and PLIF measurements for indoor velocity and velocity, with the wind tunnel measurements using LDA and FFID. The in-plane scalar (dye) field from the water tunnel shows scalar accumulation in re-circulation regions, with the peak concentration being around the source and the upstream near-ground corner. These magnitudes of water velocity and scalar concentration and their spatial variations are considerably close to the air velocity and gas concentration from wind tunnel experiments.

The substantial similarities in the results obtained from both water tunnel and wind tunnel experiments affirm the validity and reliability of both experimental setups in simulating the scalar

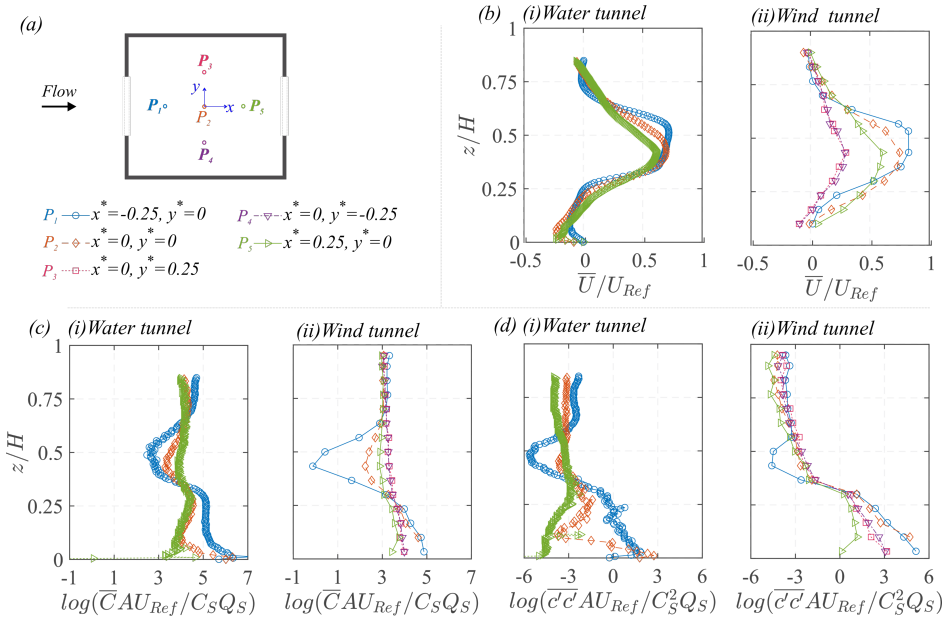


Figure 2. (a) A top-view schematic (x-y plane) showing the x-y coordinates of the different indoor locations (P_1 to P_5) where the wall-normal (z/H) profiles for indoor velocity and concentration are obtained; here, $x^* = x/H$, $y^* = y/H$ and $z^* = z/H$. (b,c,d) Wall-normal (z/H) profiles of the indoor mean stream-wise velocity ($\overline{U}/U_{Ref}$), mean concentration ($\overline{C}AU_{Ref}/C_SQ_S$) and concentration variance ($\overline{c'^2}/C_S^2$), at different locations, as illustrated in 'a'. In 'b, c & d', the water tunnel and wind tunnel measurements are shown in 'i' and 'ii', respectively.

dispersion in such urban flows with reasonable accuracy. This gives us confidence in the use of both wind tunnel and water tunnel methodologies as complimentary experimental approaches for studying pollutant dispersion in complex atmospheric boundary layer conditions.

ACKNOWLEDGEMENTS

Many thanks to Youssef Elashmawi, Tomos Rich and Dominic Clements for helping with the water tunnel experiments and to Paul Hayden for helping with the wind tunnel experiments. We gratefully acknowledge the funding from CV's UKRI Future Leaders Fellowship (MR/S015566/1).

REFERENCES

Biswas, S. and Vanderwel, C., 2024a. Indoor-outdoor pollutant exchange in a flow through a hollow cube submerged in a turbulent boundary layer. Proceedings of Thirteenth International Symposium on Turbulence and Shear Flow Phenomena (TSFP13), 1–6.

Biswas, S., Hayden, P., Carpentieri, M., and Vanderwel, C., 2024. Pollutant dispersion in a cross-ventilating flow through a scaled building: Wind and water measurements. Proceedings of Fourteenth UK Conference on Wind Engineering.

Biswas, S. and Vanderwel, C., 2024b. Flow through a hollow cube in a turbulent boundary layer: Towards understanding indoor pollutant dispersion. Flow. In Press.

Finnegan, M., Pickering, C., and Burge, P., 1984. The sick building syndrome: prevalence studies. British medical journal (Clinical research ed.) 289, 1573.

Lim, H., Hertwig, D., Grylls, T., Gough, H., Reeuwijk, M. van, Grimmond, S., and Vanderwel, C., 2022. Pollutant dispersion by tall buildings: laboratory experiments and Large-Eddy Simulation. Experiments in Fluids 63, 92.

Placidi, M., Hancock, P. E., and Hayden, P., 2023. Wind turbine wakes: experimental investigation of two-point correlations and the effect of stable thermal stability. Journal of Fluid Mechanics 970, A30.

Tominaga, Y. and Blocken, B., 2016. Wind tunnel analysis of flow and dispersion in cross-ventilated isolated buildings: Impact of opening positions. Journal of Wind Engineering and Industrial Aerodynamics 155, 74–88.

Evaluation of steady and unsteady-RANS simulations for pollutant dispersion in a realistic urban configuration

Xinyi Li[1,2], Mohammadreza Shirzadi[3], Yoshihide Tominaga[4], Tsubasa Okaze[5]

[1]*School of Environment and Society, Institute of Science Tokyo, Tokyo, Japan, li.x.3347@m.isct.ac.jp*

[2]*Wind and Fluid Engineering Research Center, Niigata Institute of Technology, Niigata, Japan, li.x@niit.ac.jp*

[3]*Graduate School of Advanced Science and Engineering , Hiroshima University, Hiroshima, Japan, shirzadihiroshima-u.ac.jp*

[4]*Wind and Fluid Engineering Research Center, Niigata Institute of Technology, Niigata, Japan, tominaga@abe.niit.ac.jp*

[5]*School of Environment and Society, Institute of Science Tokyo, Tokyo, Japan, okaze.t.f356@m.isct.ac.jp*

SUMMARY:
Reynolds-averaged Navier–Stokes equations (RANS) approaches are widely applied to pedestrian wind and wind-related problems. In this study, an unsteady-RANS (URANS) involving time-scale modification in $\varepsilon-$equation of the standard $k-\varepsilon$ model was applied to a three-dimensional air pollutant dispersion problem in a realistic urban configuration. A scaled wind tunnel experiment (WTE) was conducted to validate the URANS simulation. Section 2 details the WTE setup, including the wind tunnel, the target model, the measurement apparatus, and the experimental procedure for both concentration and velocity measurements. In Section 3, a URANS simulation based on the WTE setup, was performed. The results of the mean concentration and time-dependent fluctuations were compared with those from a steady-RANS (SRANS) simulation and validated using the WTE data. It indicates that the URANS method provides superior predictive capability for concentration dispersion. Specifically, large-scale periodic fluctuations were successfully captured by the URANS, and the concentration distribution around high-rise buildings on the upwind side was better reproduced compared to the SRANS simulation, consistent with the WTE observations. Furthermore, the URANS improved lateral and downwind, yielding more accurately results over the SRANS simulation.

Keywords: Urban air pollutant dispersion, Unsteady-RANS (URANS), Wind tunnel experiment

1. INTRODUCTION

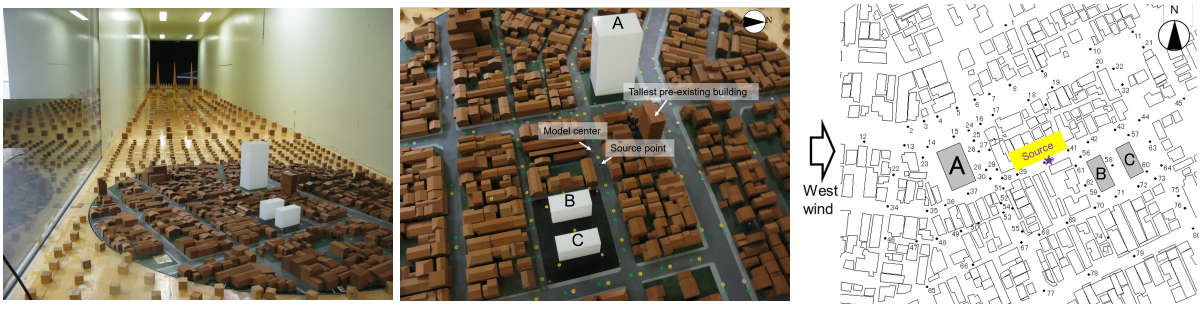
The dispersion of air pollutants in urban areas poses significant environmental hazard to human health and constitutes a pervasive challenge for densely populated region in recent years. Numerical simulations employing computational fluid dynamics (CFD) are widely used for evaluating pollutant dispersion in urban environments. It offers comprehensive data on the flow and concentration fields within the computational domain. The steady-state Reynolds-averaged Navier–Stokes (SRANS) method remains the most widely used. However, the dispersion of plumes around an isolated obstacles in the lateral direction was notably underestimated when using the SRANS approach (Blocken et al., 2008). A similar finding was observed in a study on the concentration dispersion within a simplified building array model (Tominaga and Stathopoulos, 2013). It

is because SRANS methods based on isotropic assumptions and steady-state conditions cannot correctly capture flow characteristics such as periodic fluctuations and transient vortices. However, RANS models, derived by ensemble averaging, can reproduce large-scale fluctuations distinguished from turbulent fluctuations in building wakes through a phase-averaged approach by applying unsteady simulation. Younis and Zhou (Younis and Przulj, 2006) introduced a time-scale modification to the standard $k-\varepsilon$ (SKE) (Launder and Spalding, 1974) model, which accounted for interactions between the large-scale organized periodicity of the mean flow and the random small-scale high-frequency turbulent motions and successfully reproduce the periodic fluctuation behind a 2D square cylinder. This method was also applied by the authors (Li and Okaze, 2024) in 3D simulations of an isolated building, where the large-scale fluctuations were successfully reproduced. In this study, we aim to apply the modified $k-\varepsilon$ equation in URANS simulations of air pollutant dispersion in a realistic urban configuration and evaluate its performance through comparisons with SRANS results and wind tunnel experiment (WTE) data.

2. WIND TUNNEL EXPERIMENT

2.1. Target model

The WTE for air pollutant dispersion was conducted at the Wind and Fluid Engineering Research Center in Niigata Institute of Technology. The closed-circuit atmosphere boundary layer (ABL) wind tunnel, with a cross section of 1800 $\times$ 1800 mm^2 and a total length of 16,000 mm, was used (see Figure 1a). The target model area was set on a 1600 mm diameter turntable that are same urban configurations introduced a benchmark case as Case E by Architectural Institute of Japan (AIJ, 2020). The target area (see Figure 1b) represents a downtown in Niigata city, Japan, which features dense low-rise buildings (under 2 stories), one high-rise building (Building A, 60 m tall) and two smaller buildings (Buildings B and C, 16 m tall). The urban model was scaled down by 1:250.



(a) Inside view **(b)** Target model **(c)** Wind direction and sampling point

Figure 1. Inside view of the wind tunnel and the target model.

2.2. WTE setup

The inlet profiles of time-averaged streamwise velocity $\bar{u_1}$ and standard deviations of wind velocity fluctuations in three components u_i' were measured. The reference velocity U_H at a height of 1000 mm was 2.2 m/s, with a power-law exponent of 0.21 for the mean streamwise velocity. The source point had a diameter of 5 mm, and the gas flow rate was 4.91 $\times$ 10^{-6} m^3/s, corresponding to an exhaust velocity of 0.25 m/s. The WTE was conducted under west wind direction (see Figure

1c). Concentration measurements were taken at 76 points at pedestrian height (8 mm, equivalent to 2 m in real scale). Ethylene (C_2H_4) was used as the source gas, with a mass flow controller regulating its flow rate. A flame ionization detector (FID) measured concentrations, converting ionized hydrocarbons into electric signals. Sampling was conducted at 1 kHz for 90 seconds per point, with 90,000 data points collected.

3. CFD SIMULATIONS

3.1. Computational setups

Based on the analysis of the WTE, the west wind case was used to estimated the CFD simulations. The computational domain measures $2.4H \times 1.8H \times 1.8H$ where H is the reference height of 1000 mm, and the simulation scale corresponds to that of the wind tunnel. Building A is $0.24H$ tall, while buildings B and C are each $0.072H$. The ABL inflow profiles for velocity and turbulent kinetic energy were interpolated from the WTE. A same polyhedral mesh was used for both SRANS and URANS simulations. The simulations were conducted by OpenFOAM-v2006. The QUICK scheme was applied for the divergence schemes of velocity, while the TVD scheme was used for the divergence schemes of turbulent kinetic energy, dissipation rate, and concentration. The turbulent Schmidt number Sc_t was 0.7 for both URANS and SRANS simulations.

3.2. Outline of turbulence models for URANS

In SRANS simulation, the SKE model was used for the turbulent modelling. To reproduce large-scale periodic fluctuations in URANS simulation, a modified turbulence model based on the ε–equation in the SKE model was utilized. The transport equation of ε modified with an additional production term by direct energy input are shown in Equation 1:

$$\frac{\partial \varepsilon}{\partial t} + \langle u_j \rangle \frac{\partial \varepsilon}{\partial x_j} = C_{\varepsilon 1} P_k \left(\frac{1}{T_t} + C_t \frac{1}{T_p}\right) - C_{\varepsilon 2} \frac{\varepsilon^2}{k_t} + \frac{\partial}{\partial x_j}\left[\left(\nu + \frac{\nu_t}{\sigma_\varepsilon}\right)\frac{\partial \varepsilon}{\partial x_j}\right] \tag{1}$$

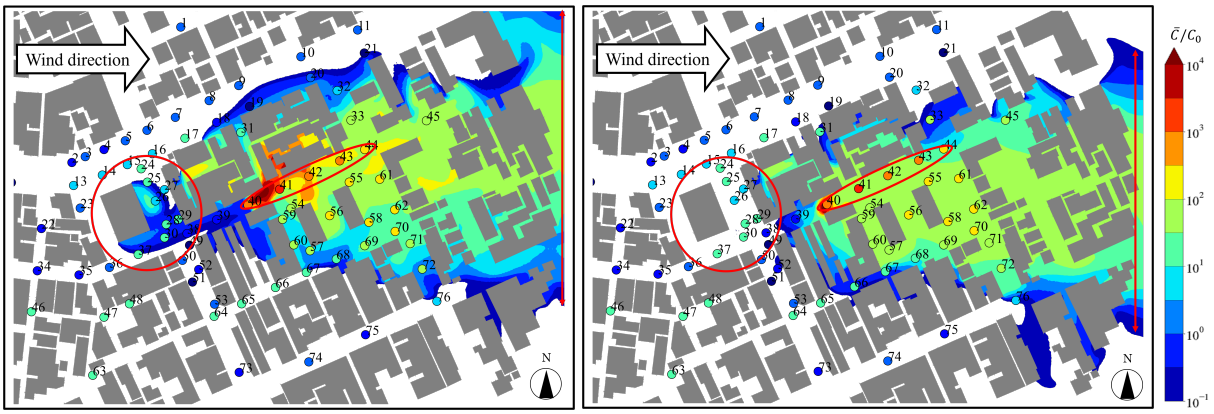
where T_t is the conventional turbulent characteristic time scale taken as k_t/ε. k_t is the turbulent kinetic energy. In the modified model, the same coefficients as those in the SKE model were used. Numerical optimal constant C_t is equal to 0.38. The time scale of the periodic large-scale motion T_p is defined as shown in Equation 2:

$$T_p = \frac{q + k_t}{|D(q + k_t)/Dt|} \tag{2}$$

where the $K(= 1/2\langle u_i \rangle^2)$ is the local ensemble-mean value of the mean kinetic energy.

3.3. Results and discussions

Figure 2 shows time-averaged concentration at pedestrian height, with contours representing simulation results and colored points indicating WTE results. The dispersion of concentrations predicted by the URANS primarily extends downwind. The lateral dispersion width was also quite close to that observed in the WTE. Additionally, the URANS successfully reproduced the windward concentrations, such as those on the south and leeward sides of high-rise building A, which closely agreed with the WTE observations although the concentration around the high-rise building A could not be reproduced in the SRANS simulation. The lateral dispersion of concentration in URANS was also broader than in SRANS, suggesting the unsteady large-scale periodic motion



(a) URANS **(b)** SRANS

Figure 2. Contour of the time-averaged concentration on pedestrian level (Contours: simulations; Points:WTE).

in URANS enhanced spatial dispersion. However, the accuracy of URANS was limited in certain areas. For example, it failed to accurately predict concentration at probe points 13–17 on the north side of building A, indicating an underestimation of the reverse flow in the upwind region.

4. CONCLUSIONS

The URANS method demonstrated superior predictive capability for concentration dispersion. Specifically, large-scale periodic fluctuations were successfully captured by the URANS, and the concentration distribution around high-rise buildings on the upwind side was better reproduced compared to the SRANS simulation, consistent with the WTE observations. Furthermore, the URANS improved lateral and downwind, yielding more accurately results over the SRANS simulation.

ACKNOWLEDGEMENTS

This work was supported by the Japan Society for the Promotion of Science (JSPS) KAKENHI (Grant number: 21H01489, 24K01037) and the Environment Research and Technology Development Fund JPMEERF20232003 of the Environmental Restoration and Conservation Agency provided by Ministry of the Environment of Japan.

REFERENCES

AIJ, 2020. Guidebook for CFD Predictions of Urban Wind Environment. Architectural Institute of Japan.

Blocken, B., Stathopoulos, T., Saathoff, P., and Wang, X., 2008. Numerical evaluation of pollutant dispersion in the built environment: Comparisons between models and experiments. Journal of Wind Engineering and Industrial Aerodynamics 96, 1817–1831.

Launder, B. and Spalding, D., 1974. The numerical computation of turbulent flows. Computer Methods in Applied Mechanics and Engineering 3 (2), 269–289.

Li, X. and Okaze, T., 2024. URANS simulation reproducing large-scale periodic fluctuations and their impact on pollutant dispersion around an isolated 1:1:2 building. Building and Environment 265, 111872.

Tominaga, Y. and Stathopoulos, T., 2013. CFD simulation of near-field pollutant dispersion in the urban environment: A review of current modeling techniques. Atmospheric Environment 79, 716–730.

Younis, B. A. and Przulj, V. P., 2006. Computation of turbulent vortex shedding. Computational Mechanics 37, 408–425.

Evaluating turbulence model reliability for near-field pollutant dispersion in a realistic urban scenario.

Apostolos Krassas [1], Stefano Capra [2], Salvatore M. Renda [1], Eugene de Villiers [1]

[1]*ENGYS UK, London, United Kingdom, a.krassas@engys.com*
[2]*Ramboll Denmark, Copenhagen, Denmark, sca@ramboll.dk*

SUMMARY
This study aims to evaluate the suitability of various Computational Fluid Dynamics (CFD) models for accurately simulating near-field pollutant dispersion. More specifically, the results of scale-resolving Large Eddy Simulation (LES), are compared with the widely used Reynolds Averaged Navier Stokes (RANS) approach in predicting contaminant dispersion over Tokyo Polytechnic University's Atsugi campus. Numerical results are benchmarked against wind tunnel experimental data available in the literature (Tachibana et al.). Preliminary analyses reveal that, for this specific urban area geometry and flow conditions, the results of steady-state RANS are highly sensitive to the choice of the turbulence model, with the significant discrepancies observed between the realizable k-ε and the standard k-ω SST models, indicating a fundamental uncertainty in the predictions. Conversely, LES computations are in good agreement with the experimental measurements, even at decreased temporal resolution, which might be a solid underlining that the employment of scale-resolving approaches is necessary for sufficiently modelling near-field pollutant dispersion.

Keywords: RANS, LES, pollutant dispersion,

1. INTRODUCTION

With urbanization and industrial activity on the rise, air pollution poses a critical threat to public health and environmental sustainability. Contaminants released into the atmosphere, particularly in dense urban areas, can have a significant impact on air quality and human well-being. Understanding and predicting the dispersion of pollutants in proximity to the source, especially around complex urban geometries, is essential for effective urban planning and the mitigation of health risks. In this context, CFD has become a vital tool in the field of wind engineering, offering insight into pollutant transport mechanisms under various atmospheric and structural conditions.

Reliable numerical modeling of dispersion, however, can be challenging, as flow characteristics around urban landscapes are highly turbulent, hence complex. Selecting appropriate CFD models for simulating near-field pollutant dispersion is critical to achieving accurate predictions. The industry workhorse RANS models have been extensively used due to their reduced computational cost and, in many cases, reliable results, but, despite their undoubted advantages, their accuracy can vary significantly depending on the specifics of the flow environment and the geometry involved. On the other hand, through resolving the most important part of the turbulence spectrum, LES constitutes an advanced, high-fidelity approach, but the historically prohibitive, computational cost entailed renders it impractical for many industrial applications, where fast

turnaround times are a key. However, the outcomes of a recent study in this context (Renda et al.), demonstrate that the computational burden of LES can be alleviated through the employment of an implicit pressure velocity block-coupled solver, which allows for running with larger time-steps with limited impact on the accuracy in terms of mean results.

Given the ever-increasing reliance on CFD in urban wind engineering, there is a growing need to assess the suitability of different models and to establish best practices for pollutant dispersion modelling. Through evaluating the accuracy of RANS and LES simulations, the objective of this comparative research is to further advance the understanding of model reliability in near-field pollutant transport through adding an additional data point to the list of dispersion studies in realistic urban geometries.

2. METHODOLOGY

2.1. Numerical Setup & data organizing

The study was aimed at replicating the wind tunnel experiment (Tachibana et al.). In terms of spatial discretization, different approaches were adopted for the RANS and LES simulations, with two hex-dominant meshes comprising 20 and 14 million cells respectively being created using HELYX, an open-source CFD simulation software. The Finite Volume Method (FVM) was used for solving the governing equations. An implicit pressure-velocity block-coupled solver was employed for solving the momentum equations. A time-dependent inflow velocity profile, obtained by performing a precursor simulation of the actual wind tunnel geometry was used as inlet boundary condition for the LES simulation and the time-step was set to 0.003s. For the steady RANS simulations, tabulated velocity profiles were applied at the inlet and the turbulent kinetic energy and dissipation rate were calculated based on the Richards-Hoxey equations. More details concerning spatial discretization, numerical setup and data organizing methodology can be found in a previous publication (Krassas et al.).

2.2. Measured quantities

The main quantity of interest, as defined in the original experiment (Tachibana et al.), was the dimensionless concentration C/C_0, with C denoting the local concentration, and C_0 the reference concentration defined according to Eq. (1), where q denotes the gas emission rate and U_H and H denote the reference velocity and reference height respectively. This quantity was measured at 15 probe locations. The predictions of these values were monitored at the corresponding locations inside the computational domain and were used for evaluating the accuracy of the simulations.

$$C_0 = \frac{q}{U_H H^2} \tag{1}$$

The Normalized Mean Square Error (NMSE) as defined in Eq. (2) was used as a metric for quantifying model accuracy, where C_o denotes the observed value, C_p the numerically predicted value and the overbar symbol '-' denotes the average over the entire dataset.

$$\mathrm{NMSE} = \frac{\overline{(C_o - C_p)^2}}{\overline{C_o}\,\overline{C_p}} \tag{2}$$

3. PRELIMINARY RESULTS

The outcomes of the preliminary simulations are presented in Figure 1 and Figure 2.

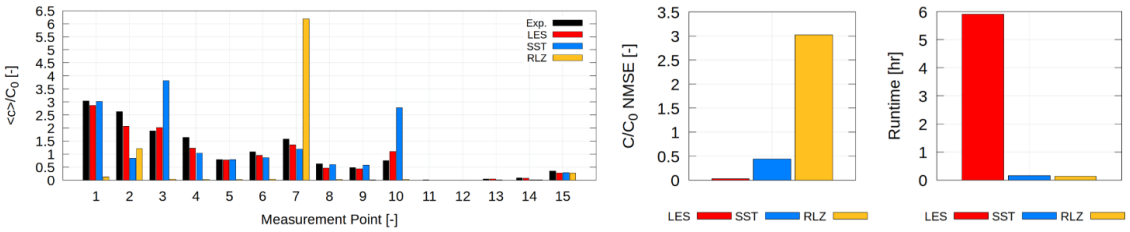


Figure 1. Computed mean dimensionless concentration for all 15 measurement points (left), normalized mean square error comparison (center), computational time (right).

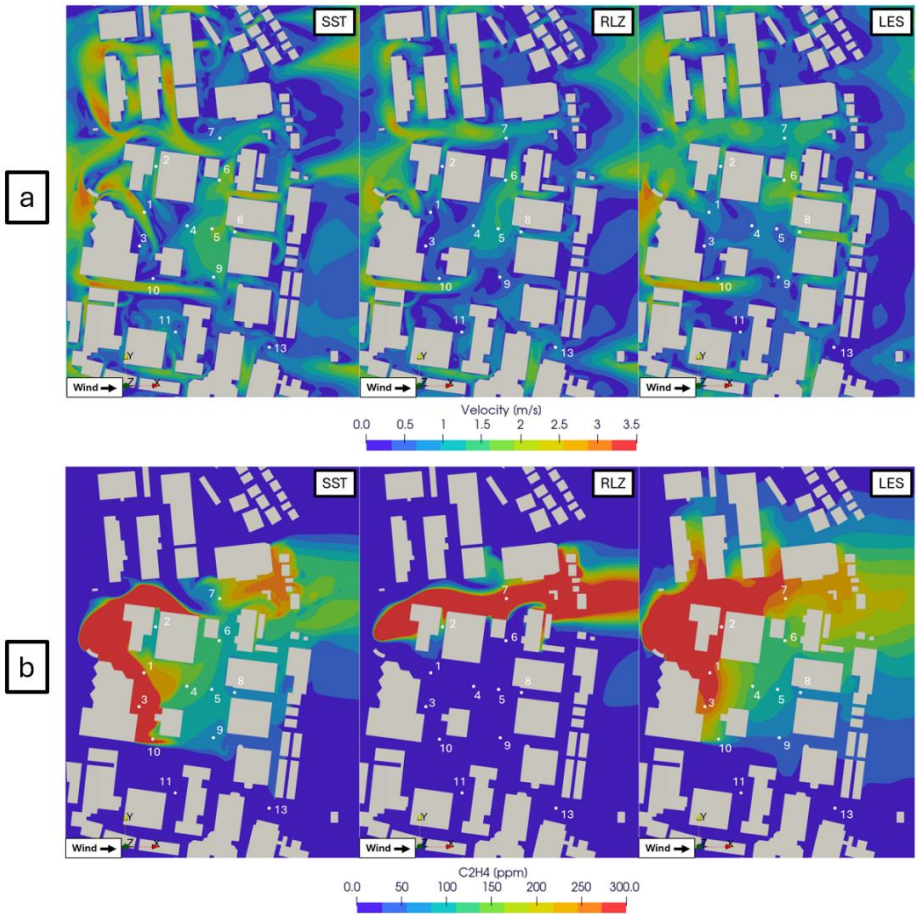


Figure 2. Contours of the mean velocity (a) and the mean C2H4 concentration (b) at a z-normal plane located at 0.059 m above ground level (model scale).

Results obtained so far indicate that under these flow conditions and for this particular urban environment, characterized by low to mid-raise buildings, sparce planning and a tracer source that is flush to the ground, within the urban canopy layer, the capability of steady-state RANS models to accurately predict mean concentration transport is highly uncertain. As illustrated in Figure 2, the realizable k-ε RANS model produces a solution substantially different from that of the k-ω SST model. More specifically, the realizable k-ε model predicts tracer gas transport predominantly towards measuring point 7, resulting in near-zero concentrations across most other measuring points situated at the centre of the campus, a behaviour that diverges from experimental data. Conversely, the k-ω SST model aligns more closely with wind tunnel measurements, yielding mean concentration contours that better match the accurate results obtained from the LES simulation. However, even this improved performance falls short in the vicinity of measuring points 3 and 10, where concentration is significantly overpredicted. The large wake regions that are present in both steady RANS solutions seem to act as secondary tracer sources which, together with the jet-like regions, have a severe impact on the pollutant's transport.

4. CONCLUSIONS & FURTHER WORK

Through capturing the transient, highly turbulent nature of the flow, LES performs remarkably well in predicting the mean concentration at all measuring points, even at reduced temporal resolution, which allows completing the run within 6 hours. It should be noted that steady RANS models require 0.1 hours to converge on the same computational resources. Despite the difference in computational cost still being substantial, running an LES simulation in less than one workday is still viable and given its demonstrated accuracy, it might constitute an overall better option when it comes to modelling near field pollutant dispersion.

The observations that emerge from these preliminary computations provide a good lead in favour of the previous statement, but a more in-depth investigation is necessary before drawing any concrete conclusions regarding the suitability of each modelling approach. As part of the further work, the authors deem it appropriate to include different turbulence models in their assessment, including the Reynolds Stress Tensor (RST) model to determine how accounting for turbulence anisotropy can impact results. Additionally, within the scope of this study is also a wind direction sensitivity study for determining how slight changes in external flow conditions affect model performance.

REFERENCES

Krassas, A., Renda, S., Mijorski, S., De Villiers, E., and Capra, S., 2024. Evaluating numerical models for the prediction of pollutant dispersion over Tokyo's Polytechnic University campus. Journal of Wind Engineering and Industrial Aerodynamics 251.

Renda, S., Krassas, A., De Villiers, E., and Capra, S., 2024. Towards efficient scale resolving simulation for the prediction of industrial pollutant dispersion applications, Proceedings of 14th UK Conference on Wind Engineering, 4-6th September 2024, Southampton United Kingdom, 72-75

Tachibana, T., Yoshie R., Nakayama, S., Kishida, S., Miyashita, K., and Sasaki, R., 2022. Comparison between field measurement and wind tunnel experiments of gas dispersion in an urban area and verification of similarity law. Journal of Wind Engineering and Industrial Aerodynamics 47(3), 238-252.

Pollutant removal mechanisms of fetch effects in street canyons with different aspect ratios

Daniel Ziyue Peng[1], Bingchao Zhang [1], Cruz Y. Li [2], Yunfei Fu [1], Tim K.T. Tse [1]

[1] *The Hong Kong University of Science and Technology, Hong Kong, China, daniel.z.peng@connect.ust.hk; zhangbc@ust.hk; yfuar@connect.ust.hk; timkttse@ust.hk*
[2] *Chongqing University, Chongqing, China, cruzli@cqu.edu.cn*

SUMMARY:
Existing literature reports differences between isolated and fully developed street canyon flows due to variations in upstream fetch length. To date, unresolved questions include the impact of fetch on street canyon flow fields and pollutant dispersion, the fetch length required for fully developed flows, and whether fetch should be regarded as an essential factor in street canyon models. This study examines the influence of fetch on flow mechanics and pollutant dispersion within 50 consecutive street canyons, with aspect ratios (*H/W*) ranging from 1 to 5. Results indicate that fetch significantly alters the velocity field, causing the primary recirculation to elevate and decelerate in the first canyon. Deep canyons (*H/W* = 3–5) generate multiple vortices in the initial building row, which amalgamate into a single primary vortex for fully developed flow with sufficient fetch length. Higher aspect ratios produce a stronger fetch effect. Moreover, fully developed flows demonstrate more efficient pollutant mixing and uniform distribution, reducing air pollution within deep street canyons. For *H/W* = 5, the average pollutant concentration in the first canyon reaches 42 times that of the fully developed state. Finally, this work introduces a new index, the *marginal rate of change*, which quantifies proximity to the fully developed state, occurring at approximately canyon 30 (fetch length = 60*W*) for *H*/*W* = 1-5. The findings demonstrate significant distinctions between isolated, intermediate, and fully developed street canyon flows. Real-world urban canyon flows often exist in intermediate states, making fetch a critical factor for urban design, operation, and management.

Keywords: Street canyon, Pollutant dispersion, Fetch, Computational fluid dynamics

1. INTRODUCTION

Urban air pollution, driven by traffic and industrial emissions, accumulates in street canyons, especially with high aspect ratios (*H/W* > 0.65), due to restricted airflow. While fully developed and isolated canyon flows are well-studied, transitional states in deep canyons (*H/W* ≥ 2) remain underexplored. This research investigates intermediate street canyon flows, fetch length required to reach a fully developed state, and pollutant dispersion to improve urban air quality strategies.

2. METHODOLOGY AND VALIDATION

This study used Reynolds-averaged Navier-Stokes (RANS) simulations on 50 consecutively placed street canyons with aspect ratios (*H*/*W*) ranging from 1 to 5. The simulated flow and pollutant dispersion are validated by the data of wind tunnel tests conducted by Meroney et al. (1996) and Gromke and Ruck (2009) for single and fully developed flow, respectively.

3. RESULTS AND DISCUSSION

In street canyons with *H/W* = 1(See **Figure 1**), a clockwise single-vortex flow is observed. The

vortex center drops from 0.6*H* in canyon 1 to 0.5*H* by canyon 5, stabilizing thereafter. Circulation speed peaks at 0.5 m/s in canyon 20. Pollutant concentrations in canyon 50 are nearly double those in canyon 1, as elevated recirculation in canyon 1 enhances pollutant removal, unlike canyon 50 where pollutants remain trapped.

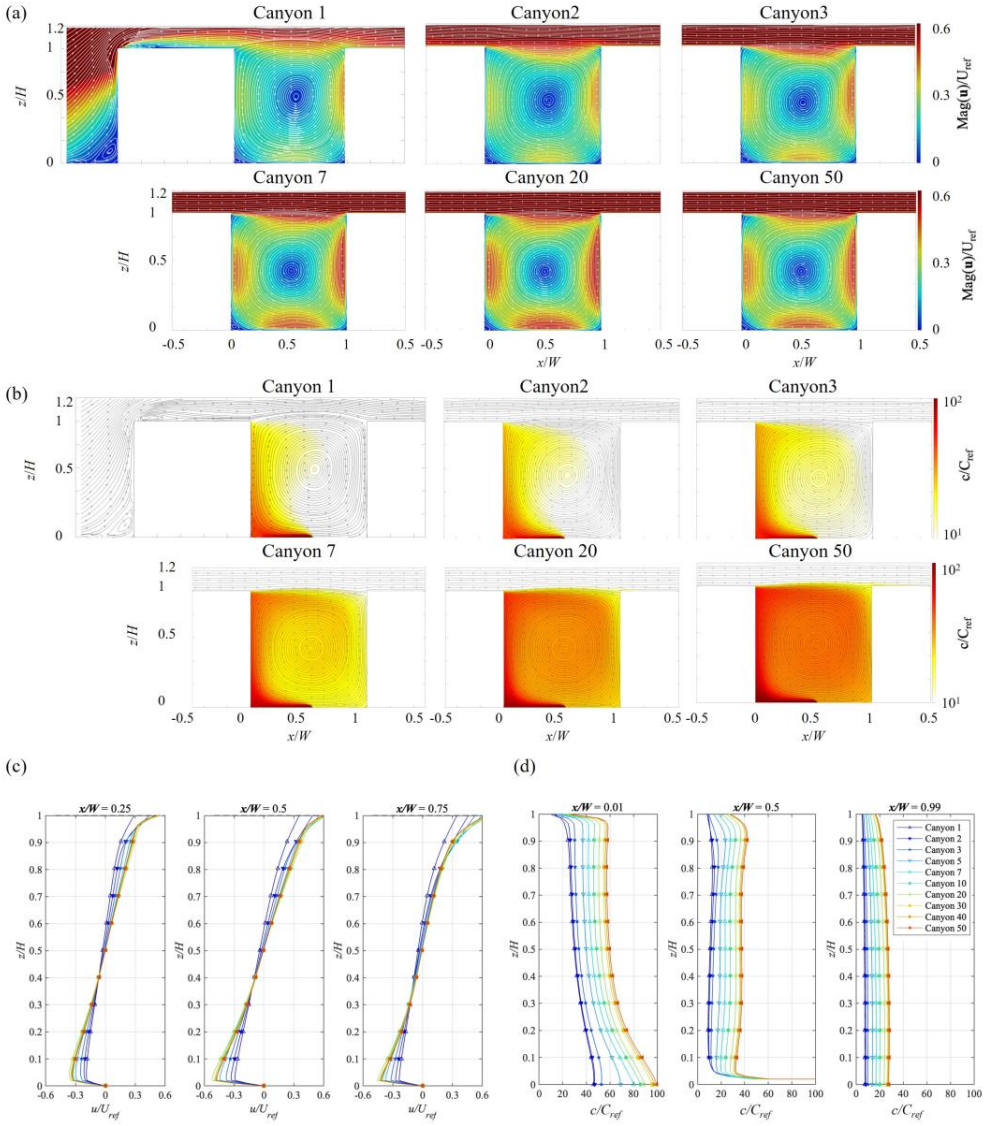


Figure 1. Flow and pollutant dispersion in street canyon of Case A (H/W = 1): (a) Velocity fields within the selected representative canyons; (b) Distributions of the velocity component in the streamwise direction at x/W = 0.25, 0.5, and 0.75; (c) Pollutant concentration fields within the selected representative canyons; (d) Profiles of pollutant concentration at x/W = 0.01, 0.5, and 0.99.

In high-aspect-ratio street canyons (*H/W* = 4 and 5), canyon 1 exhibits multiple vertically stacked vortices—three for *H/W* = 4 and four for *H/W* = 5 (See **Figure 2**). Downstream of canyon 3, flow transitions to a single clockwise vortex, with the recirculation center descending from 0.9*H* to 0.8*H* by canyon 30. Near-ground wind speeds, initially near-zero, increase and stabilize after canyon 20. Pollutant concentrations are significantly higher in lower vortices of initial canyons, decreasing downstream due to single-vortex flow.

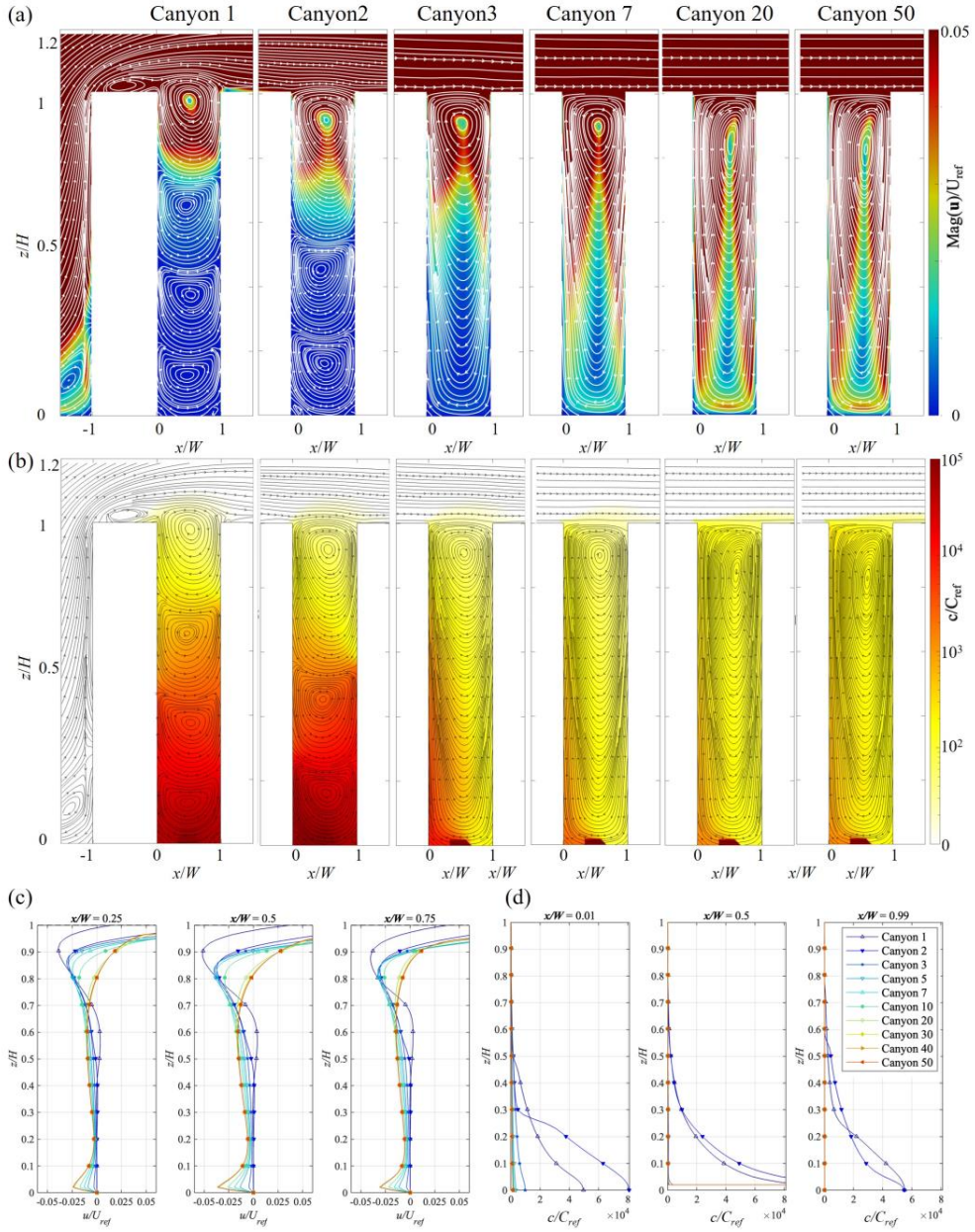


Figure 2. Flow and pollutant dispersion in street canyon of Case E (H/W = 5): (a) Velocity fields within the selected representative canyons; (b) Distributions of the velocity component in the streamwise direction at x/W = 0.25, 0.5, and 0.75; (c) Pollutant concentration fields within the selected representative canyons; (d) Profiles of pollutant concentration at x/W = 0.01, 0.5, and 0.99.

$$MRC_V = \frac{\frac{1}{HW}\int_0^H \int_0^W |\mathbf{u}_{i2}(z) - \mathbf{u}_{i1}(z)| dx\, dz}{\overline{u_{50}} \cdot (i_2 - i_1)}. \quad \textbf{(1)}$$

$$MRC_C = \frac{\frac{1}{HW}\int_0^H \int_0^W |c_{i2}(x,z) - c_{i1}(x,z)| dx dz}{\overline{c_{50}} \cdot (i_2 - i_1)}. \quad \textbf{(2)}$$

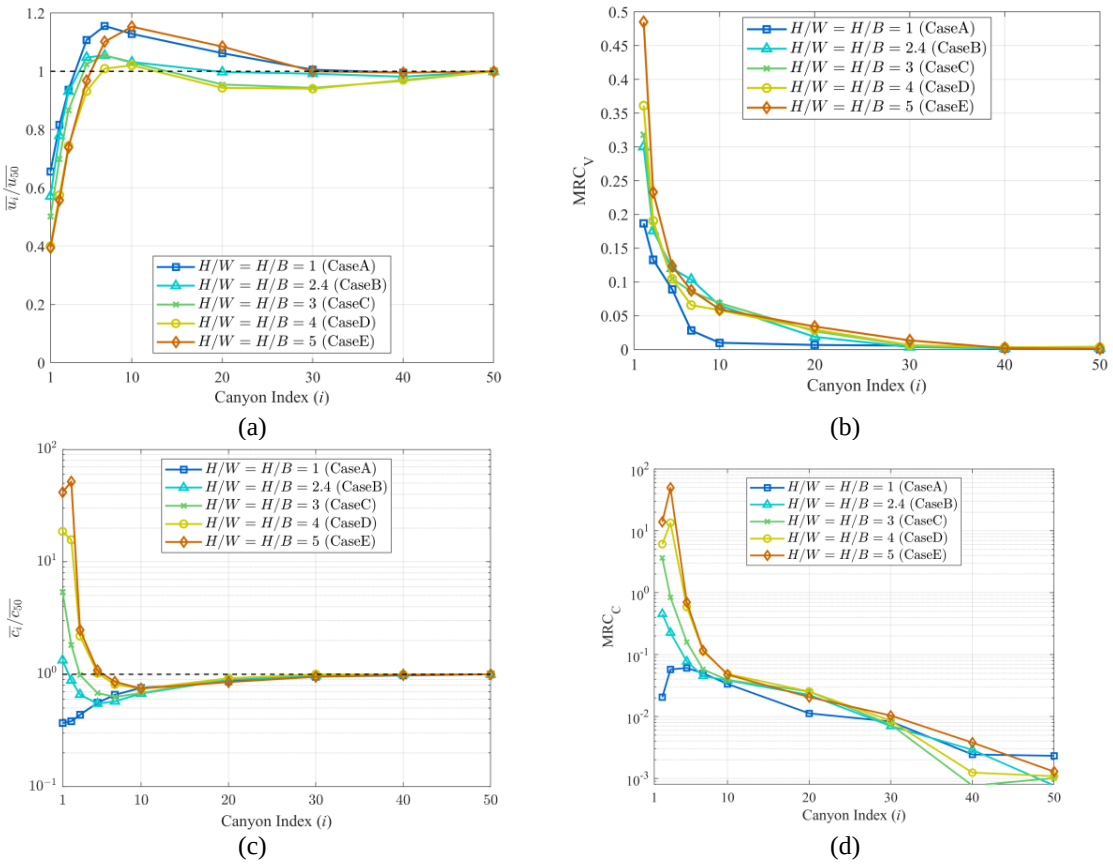


Figure 3. (a) Spatially average flow speed, normalized by the value in canyon 50. (b) *MRC* on the velocity field. (c) Spatially averaged concentration within the canyons, normalized by the value in canyon 50. (d) *MRC* on the pollutant concentration field.

To quantify the fetch effect on street canyon flow and pollutant dispersion, the spatially average flow speed is normalized by that in canyon 50, $\overline{u_i}/\overline{u_{50}}$. Results show that in canyon 1, the normalized speed drops from 0.65 at H/W = 1 to 0.39 at H/W = 5, then increases, peaking at canyon 7 or 10, before converging to 1 (See **Figure 3 (a)**). Differences in flow speed between canyons 30 and 50 are <5%, and <2% between canyons 40 and 50, indicating 30–40 upstream rows (fetch length 60W–80W) are needed for near-fully developed flow. The marginal rate of change (*MRC*, **Equation 1**) quantifies flow field changes with fetch, showing negligible changes after canyon 30 for all cases, as shown in **Figure 3 (b)**. The fetch significantly impacts pollutant concentration, quantified by spatially averaged concentration and its *MRC* (See **Equation 2**). Normalized $\overline{c_i}/\overline{c_{50}}$ shows higher initial concentrations in deep canyons (H/W = 2.4–5), e.g., 42× higher in canyon 1 at H/W = 5, converging downstream (See **Figure 3 (c)**). *MRC* values drop below 1% by canyon 30, indicating convergence to fully developed states, with higher aspect ratios showing faster changes (See **Figure 3 (d)**).

REFERENCES

Gromke, C., Ruck, B., 2009. Effects of trees on the dilution of vehicle exhaust emissions in urban street canyons. Int. J. Environ. Waste Manag. 4 (3–4), 225–242.

Meroney, R.N., Pavageau, M., Rafailidis, S., Schatzmann, M., 1996. Wind engineering study of line source characteristics for 2-D physical modeling of pollutant dispersion in street canyons. J. Wind Eng. Ind. Aerodyn. 62 (1), 37–56.

Rooftop emissions and dispersion into near-building flow fields in suburban areas

Cornelia Kalender [1], Mohammad Norouzi [1], Frank Harms[2], Ulf Winkelmann [1],Bernd Leitl [2], Rüdiger Höffer [1]

[1]*Wind Engineering and Flow Mechanics, Ruhr-University Bochum, Germany, cornelia.kalender@rub.de, mohammad.norouzi@ruhr-uni-bochum.de, ulf.winkelmann@rub.de; ruediger.hoeffer@rub.de*
[2]*Environmental Wind Tunnel Laboratory, University of Hamburg, Germany, frank.harms@uni-hamburg.de, bernd.leitl@uni-hamburg.de*

SUMMARY:
In this project, the dispersion from chimneys at various particularly unfavourable positions and heights under different conditions and configurations is observed systematically and compared with a more favourable emission from 40 cm above the roof ridge. The aim is to obtain a precise picture of the problematic situations that arise in existing, typically German suburban residential areas and to develop recommendations for new buildings and conversions. For the investigation, both wind tunnel tests and numerical flow simulations are used, which, after validation, will carry out the parameter studies as effectively and extensively as possible synergistically for different configurations.

Keywords: pollution dispersion, suburban, rooftop chimney

1. INTRODUCTION AND MOTIVATION

The current challenges with air pollution and air quality in residential areas dealing very often with direct emissions from small solid fuel combustion systems. Particularly in suburban areas, as shown in Fig. 1, unfavourable dispersion conditions, such as a particular arrangement and density of buildings, unfavourable positioning of chimneys on the roofs or certain local wind patterns, can lead to poor local air quality, even if the emissions from the chimneys are within the legal limits in Germany. For new installations (from 2022), the chimneys must be installed with: a) The outlet is located near the roof ridge, or b) The outlet must be at least 40 cm above the ridge.



Figure 1. Exhaust from a rooftop chimney with unfavourable plum dispersion in a typical suburban area

For existing installations (before 2022): The chimney outlet must fulfil certain requirements depending on the roof pitch and the total heat output. At present, it is not yet fully analysed for such configurations what effect the release of emissions into the recirculation area of this type of house will have in unfavourable situations and how it will affect the immediate neighbourhood.

2. METHODOLOGY

The building configuration analysed for the validation here shown corresponds to a real suburban situation in Germany. The source building is equipped with three chimneys for the investigation, one at the side along the front (Q1), one in the center of the roof close to the ridge (reference position Q2) and one in the center halfway up the roof (Q3), as seen in Fig. 2. The building dimensions are width : length : height of W : L : H = 10m : 9m : 9m in real scale.

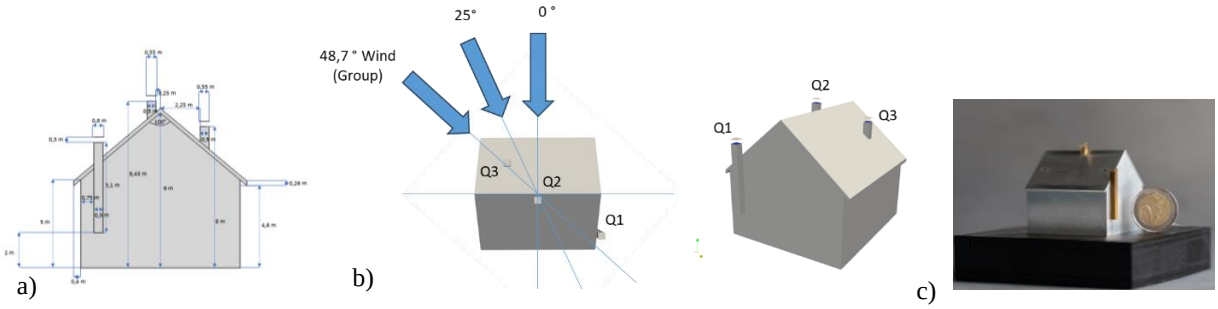


Figure 2. Details of the geometrical model: a) dimensions of the source-building, b) the three different chimney positions and definition of the used wind directions, c) scaled wind tunnel model

The used wind tunnel “Wotan” of the Environmental Wind Tunnel Laboratory, University of Hamburg, is 25m long, 4m wide and 2.75m to 3.25m high. The boundary layer characteristics are carefully set and documented in accordance with VDI Guideline 3783 Part 12, 2022 for a geometrical scale of 1:200 and corresponds to an ABL profile for a moderately rough terrain with $\alpha = 0.17 \pm 0.01$ resp. $z_0 = 0.05 \pm 0.02$. In Fig. 3. shows the wind tunnel model with view against wind direction (left) and exemplary the measurement positions in the leeward zone (right).

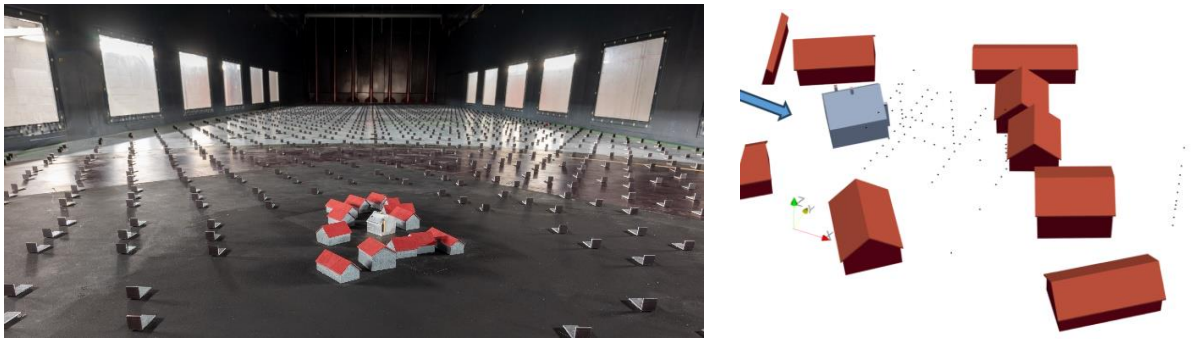


Figure 3. Left: wind tunnel model of the group arrangement, right: exemplary visualisation of measurement positions

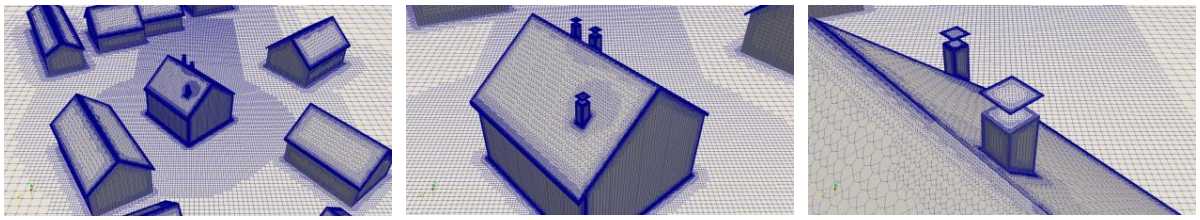


Figure 4. Used numerical mesh (hierarchical structured) with refinements around the main building

The shown simulations were performed in real scale with OpenFoam and the Realizable k-eps turbulence model. The quality assurance, regarding e.g. domain size, mesh refinement zones, inlet conditions etc., was done according to the current state of the art (Blocken, 2015; Richards et al., 2019; Tominaga, Yoshihide, 2024). A mesh sensitivity study was carried out and the final mesh (see in Fig. 4.) consists of 11.1Mio volumes. All simulations run until 6000 iterations for max residuals of 1e-6 and the convergence of the variables were checked in all measurement points.

3. FIRST RESULTS

The comparison of the velocity components and the concentration are plotted in Fig. 5 and Fig. 6.. The agreement for the flow field is very convincing, only very low velocities were slightly over predicted numerically. For the normalized concentrations the calculated values lie mostly within FAC2, except for the very low concentrations. This result matches the known properties of RANS modelling of dispersion and again shows the model-related underestimation of turbulent diffusion.

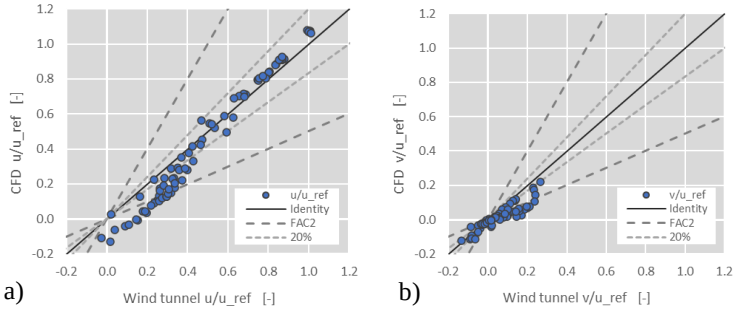


Figure 5. Scatter plots for the comparison between wind tunnel (x-axis) and numerical simulations (y-axis), a) normalised u velocity component, b) a) normalised v velocity component

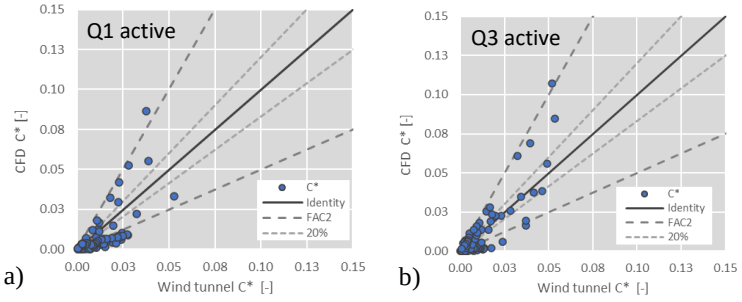


Figure 6. Scatter plots for the comparison between wind tunnel (x-axis) and numerical simulations (y-axis), a) normalised concentration with chimney Q1 is active, b) normalised concentration with chimney Q3

4. CONCLUSIONS

The project aims to develop approaches for more effectively controlling pollutant dispersion from roof chimneys in unfavorable situations. This includes the application of numerical simulations in combinations with wind tunnel experiments, which allow for detailed analysis of dispersion conditions and prediction of pollution levels under various geometrical scenarios. The results shown here are the first steps in the project and primarily serve to validate and harmonise the methods presented. A hit rate was explicitly not calculated, as this depends heavily on the number and position of the selected measuring points. In the future, numerical simulations and wind tunnel investigations will be used together with the aim to address the issue of particulate matter and other air pollutants from small combustion systems in situations with challenging dispersion conditions.

ACKNOWLEDGEMENTS

Funded by the German Environment Agency under the grant number 3722 19 301 0

REFERENCES

Blocken, Bert (2015): Computational Fluid Dynamics for urban physics: Importance, scales, possibilities, limitations and ten tips and tricks towards accurate and reliable simulations. In: Building and Environment 91, S. 219–245. DOI: 10.1016/j.buildenv.2015.02.015.

Richards, Peter J.; Norris, Stuart E. (2019): Appropriate boundary conditions for computational wind engineering: Still an issue after 25 years. In: Journal of Wind Engineering and Industrial Aerodynamics 190, S. 245–255. DOI: 10.1016/j.jweia.2019.05.012.

Tominaga, Yoshihide (2024): CFD simulations of turbulent flow and dispersion in built environment: A perspective review. In: Journal of Wind Engineering and Industrial Aerodynamics 249, S. 105741. DOI: 10.1016/j.jweia.2024.105741.

VDI Guideline 3783 Part 12, 2022. Environmental meteorology Physical modelling of flow and dispersion processes in the atmospheric boundary layer Application of wind tunnels, Association of German Engineers, Verein Deutscher Ingenieure, VDI/DIN-Kommission Reinhaltung der Luft (KRdL) – Normenausschuss Fachbereich Umweltmeteorologie, July 2022

Assessment framework of bridge VIV on running performance of high-speed trains

Ming Wang [1], Xiaozhen Li [2], Shihao Zhao [3,] Mingfang Yang [4]

[1] *Southwest Jiaotong University, Chengdu, China, Ming.wang@swjtu.edu.cn*
[2] *Southwest Jiaotong University, Chengdu, China, xzhli@swjtu.edu.cn*
[3] *China Railway Major Bridge Reconnaissance & Design Group Co., Ltd., Wuhan, 2549241989@qq.com*
[4] *State key laboratory of bridge intelligent and green construction, Wuhan, mingfang_yang@163.com*

SUMMARY:
This work introduces how to analyze the influence of bridge vortex-induced vibration (VIV), which is the most concerned in blunt body aerodynamics, on the running stability of high-speed trains. The analysis of this problem involves three aspects: bridge engineering, track engineering and vehicle engineering, so an efficient evaluation framework will be put forward from two aspects: track smoothness evaluation and system dynamic simulation. Track smoothness evaluation is mainly used to identify which VIV forms and driving conditions will affect train operation. System dynamic simulation focuses on how to take into account the influence of VIV on train operation. The premise of the preface work is to establish the relationship between the known VIV form and the unknown track dynamic irregularity in the process of VIV. The purpose of the above analysis framework is to guide the allowable limit of bridge VIV amplitude from the aspect of train running performance.

Keywords: Bridge VIV, running performance of high-speed train, evaluation framework

1. GENERAL INSTRUCTIONS

VIV is a wind-induced oscillation phenomenon, which occurs in the range of train operating wind speed. For railway bridges, the periodic oscillation of bridge caused by VIV will not only cause structural fatigue, but also affect the running stability of trains on the bridge. The design of railway bridge needs to determine the allowable limit of VIV. The purpose of this study is to establish the evaluation framework of long-span bridge VIV on the running performance of high-speed train, and combine the evaluation technology of track irregularity and the dynamic simulation technology of vehicle-bridge system to realize the identification of unfavorable VIV irregularity and the accurate evaluation of train dynamic response.

2. DETERMINE OF VIV-INDUCE TRACK IRREGULARITY

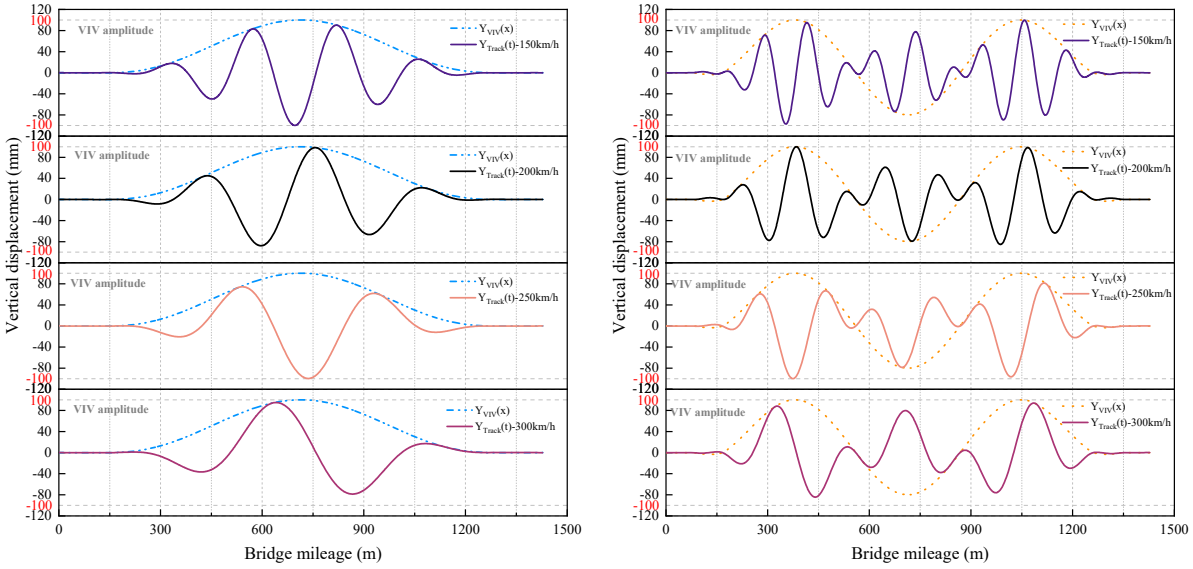
When the train runs on a bridge experiencing VIV at a certain speed, the maximum vertical spatial displacement at the wheelset of the train at a certain mileage is the VIV value of the bridge here.

When the train passes through the whole bridge mileage range, the spatial irregularity of wheelsets during the occurrence of VIV can be obtained. Temporarily ignore the contribution of track irregularity, Equation (1) establishes the relationship between the elevation of the track irregularity at the wheelsets on the bridge at time *t* (named $Y_{Track}(t)$) and $Y_{VIV}(x)$.

$$Y_{Track}(t) = \sin\left(\frac{t}{T_{Mode}} \cdot 2\pi\right) \times Y_{VIV}(x) \tag{1}$$

where the time *t* for the train to travel on the bridge can be determined by $t = x/v$, v is the train speed, T_{Mode} is the modal period corresponding to the VIV line shape.

Taking a long-span suspension bridge as the engineering background, and considering that the train speed ranges from 150 km/h to 300 km/h, Figure 1 provides the track irregularity experienced by the first wheelset in various VIV modes. It can be seen that the higher the speed of the train on the bridge, the shorter the running time on the bridge, making the track irregularity relatively simple at the corresponding speed. Conversely, the lower the speed, the longer the train runs on the bridge, and the track irregularity is relatively complex.



(a) mode 3 (b) mode 10

Figure 1. Track dynamic irregularities under VIV

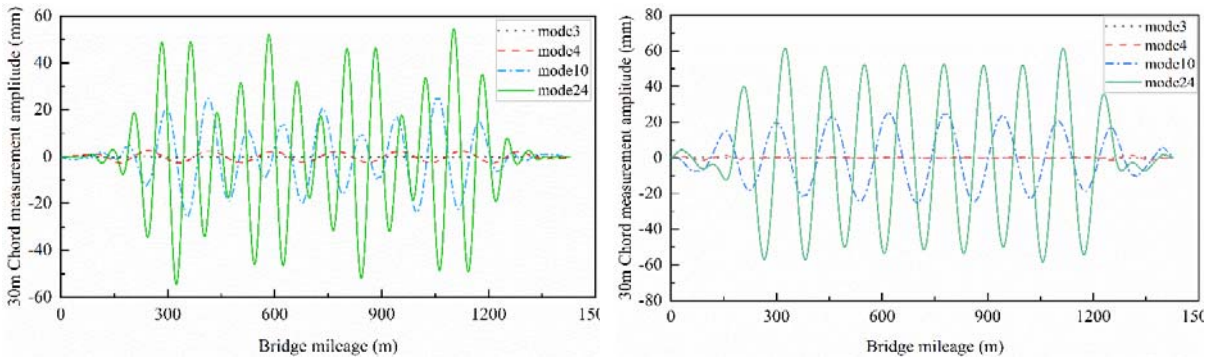
3. ASSESSMENT RAMEWORK

There are two tasks in this part, the first is to determine which ones will affect the driving from many VIV forms, and the second is to determine how to analyze the dynamic response.

3.1. Identification of VIV-induced Track Irregularity

The train running stability mainly depends on the long-wave irregularity of the track irregularity, and the irregularity can be quantitatively analyzed by midpoint chord measurement. It can be

observed from Figure 2 that the higher the order of VIV mode, the greater the amplitude of chord measurement of track irregularity under the same speed. It is inferred that when the train travels on a bridge with high-order VIV mode at the same speed, the train running stability will be worse than that of the low-order VIV mode. From the results of the midpoint chord measurement, it can be preliminarily inferred that within the analyzed train speed range, the VIV-induce track irregularities in high-order modes (mode 10 and mode 24) are more unfavorable for the running stability of high-speed train, so they can be subjected to subsequent dynamic simulation analysis.



(a) Track irregularities at 150 km/h (b) Track irregularities at 250 km/h

Figure 2. Dynamic track irregularities chord measurement results

3.2. Train-bridge Coupling Analysis with VIV

The wind-resistant performance of trains on bridges needs to be evaluated with the help of mature wind-train-rail-bridge (WTTB) coupling vibration simulation technology. By taking into account the VIV of bridge and the dynamic coupling between structures, the system constitutes a large-scale system with significant time-varying characteristics. The improved train-bridge coupling system with accounting the influence of VIV-induce track irregularity is shown by Figure 3.

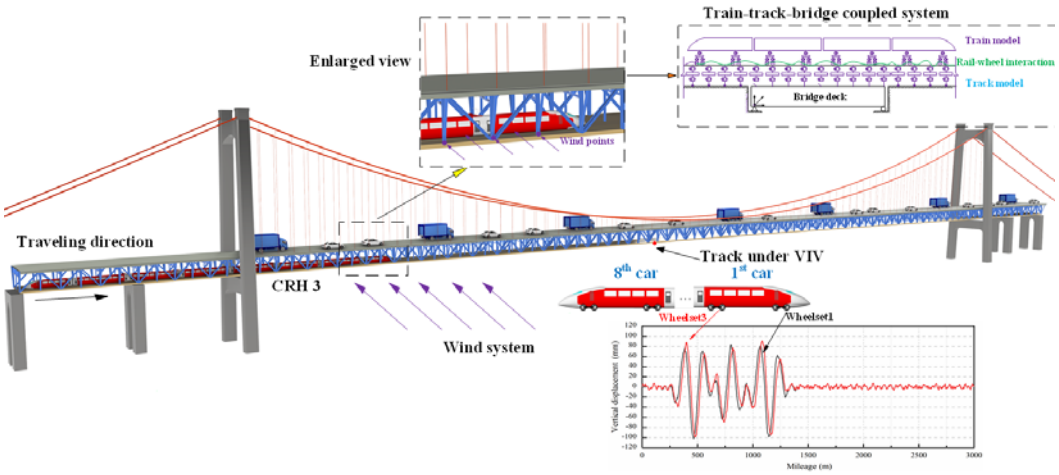


Figure 3. WTTB system under VIV

3.3. Assessment Framework

In view of the characteristic sensitive wavelength of train's running stability, the track irregularity

evaluation technology can be used to preliminarily identify the unfavorable VIV shapes. Combined with the train-bridge coupling vibration analysis considering the influence of VIV, the framework for assessing the influence of bridge VIV on train' running stability can be established. The detailed flow chart of the evaluation framework is shown below, which can be used to determine the allowable limit of VIV of the specified bridge.

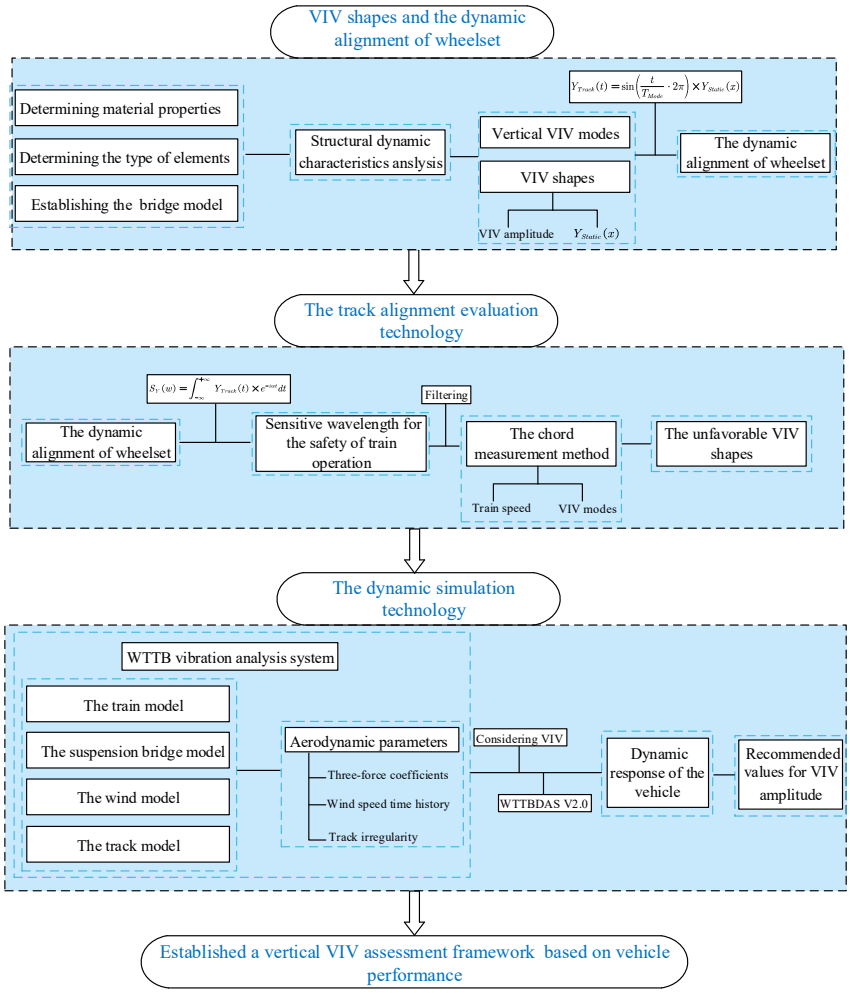


Figure 4. Flow chart of the assessment framework

ACKNOWLEDGEMENTS

The research reported in this paper was supported in part by the National Natural Science Foundation of China under Grant No. 52208505.

REFERENCES

Larsen A., Esdahl S., Andersen J., Vejrum T., 2022. Storebælt suspension bridge – vortex shedding excitation and mitigation by guide vanes. Journal of Wind Engineering and Industrial Aerodynamics. 88(2): 283-96.

Liu D., Li X., Mei F., Xin L., Zhou Z., 2023. Effect of vertical vortex-induced vibration of bridge on railway vehicle's running performance. Vehicle System Dynamics. 61(5): 1432-47

Wang M., Wang X., Li X., Wang P., 2023. Influence of spatial track alignment of long-span arch bridge on train operational stability. Vehicle System Dynamics. 61(12): 3161-80.

Wind loading on a moving train due to a downburst

Aleksander Pistol [1], Mark Sterling [2], Chris Baker [3]

[1]*Manchester Metropolitan University, Manchester, UK, a.pistol@mmu.ac.uk*
[2]*Manchester Metropolitan University, Manchester, UK, m.sterling@mmu.ac.uk*
[3]*Emeritus Professor, University of Birmingham, Birmingham, UK, c.j.baker@bham.ac.uk*

SUMMARY:
The paper describes a novel analytical method for calculating train stability in downburst-type winds. The first section briefly outlines the aims and motivation behind the research. Section 2 summarizes the previously established methodology of calculating the train overturning moments, while section 3 describes the applied model of a downburst wind field. Section 4 presents the results of a parametric study around the values of downburst translation speed, train speed, distance between the downburst and the train and angle between the train and downburst paths. Finally, section 5 encapsulates the main findings of the study.

Keywords: non-synoptic winds, downbursts, train stability

1. INTRODUCTION

Interest in non-synoptic winds has grown noticeably over the past 10 years. In North America, considerable attention has been directed towards understanding tornadoes and their impact on engineering structures whilst in Europe, downbursts have been shown to be of particular importance and occur more frequently than was initially envisaged. Despite the increased interest in these storms, relatively little is still known about the impact of both types of winds on transport systems. The current research will devise a novel analytical method for calculating train stability in downburst-type winds.

2. TRAIN STABILITY

Baker (2013) illustrated that the overturning moment coefficients for a variety of vehicles tend to follow similar trends, i.e., at low yaw angles ψ (angle between the train path and the acting side force in the horizontal plane, see Fig. 2a) the overturning moment coefficients typically exhibited a variation up to a maximum value between 50-60 degrees and then decreased. Using an extended database, Baker obtained the expressions given in Eq. (1) and (2) for low and high yaw angles respectively. For the purpose of this paper, these expressions have been modified to take into account the normalized wind velocity relative to the train $\overline{\Omega}$ (defined in Section 3).

$$\overline{C_{RL}(\psi)} = C_{RL}(30)\left(\frac{sin(\psi)}{\sin(30)}\right)^{1.5}\overline{\Omega}^2 \quad (1)$$

$$\overline{C_{RL}(\psi)} = C_{RL}(90)\left(\frac{sin(\psi)}{\sin(90)}\right)^{-1.9}\overline{\Omega}^2 \quad (2)$$

In the following, the values of $C_{RL}(30)$ and $C_{RL}(90)$ are adopted at 3.63 and 4.60, respectively.

3. AN ANALYTICAL MODEL OF A DOWNBURST

The downburst wind field model begins with the assumption that the radial velocity has a 'nose' profile (Fig. 1a) and is given by Eq. (3) where $\bar{U}= U/U_m$, U is the radial velocity, U_m represents the maximum value of U, $\bar{r}= r/r_m$, r is the radial distance from the centre of the impingement, r_m corresponds to radial distance at which U_m is located, $\bar{z}= z/z_m$, z represents a height above the ground and z_m is the height at which U_m occurs. Assuming that the circumferential flow is zero (which is consistent with measurements – Jesson et al., 2015), then normalized vertical velocity ($\bar{W}$) can be obtained from the radial continuity equation and is given in Eq. (4) and Fig. 1b, where $\bar{W}= W/U_m$ and $\delta = z_m/r_m$. It should be noted that its impact on the train stability can be neglected. For a full derivation and discussion of the model see Sterling et al. (2023).

$$\bar{U} = \frac{2\bar{r}}{(1+\bar{r}^2)}\frac{4\bar{z}}{(3+\bar{z}^4)} \tag{3}$$

$$\bar{W} = \frac{8\delta}{(1+\bar{r}^2)^2}\frac{tan^{-1}(\bar{z}/\sqrt{3})}{\sqrt{3}} \tag{4}$$

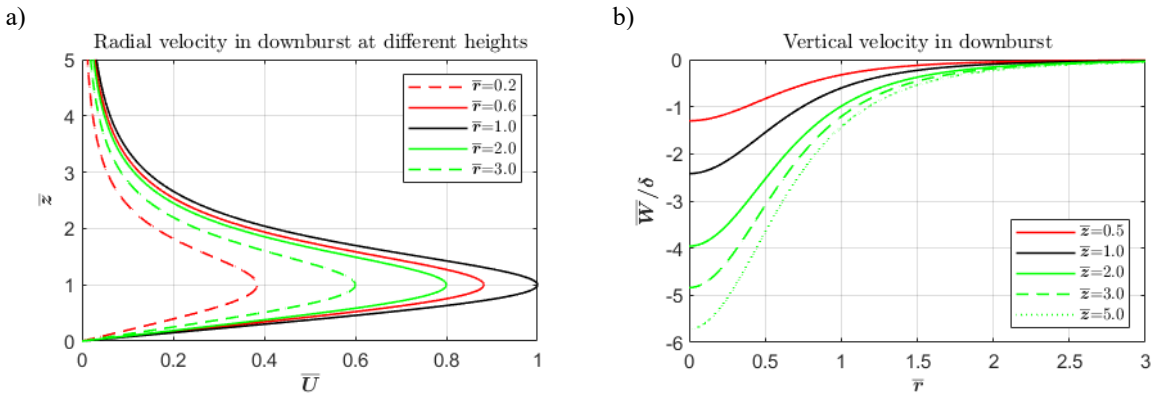


Figure 1. Radial (a) and vertical (b) velocities in a downburst

In the following, we are considering the wind field at a constant train reference height, which is taken as $z_v = 3$ m. This allows us to simplify the expression for the radial downburst velocity at train height $\overline{U_v}$ and use this in further considerations as our normalization velocity:

$$\overline{U_v} = \frac{U_v}{U_{mv}} = \frac{2\bar{r}}{(1+\bar{r}^2)};\ U_{mv} = U_m\frac{4(z_v/z_m)}{(3+(z_v/z_m)^4)} \tag{5}$$

Assuming that the downburst maintains its nose profile as the parent storm translates (a highly questionable assumption) while moving at speed Q_{db}, the train moves at a constant speed Q_v (Fig. 2a), then we can calculate the wind field relative to the train. Eq. (6) and Eq. (7) give expressions for the normalized relative wind speed of the train ($\bar{\Omega}$) and the yaw angle (ψ) respectively.

$$\bar{\Omega} = ((\overline{Q_v}\cos(\varepsilon) - \overline{Q_{db}} - \bar{U}\cos(\theta))^2 + (\overline{Q_v}\sin(\varepsilon) - \bar{U}\sin(\theta))^2)^{0.5} \tag{6}$$

$$\psi = \text{atan}\left(\frac{\overline{Q_v}\sin(\varepsilon)-\bar{U}\sin(\theta)}{\overline{Q_v}\cos(\varepsilon)-\overline{Q_{db}}-\bar{U}\cos(\theta)}\right) - \varepsilon \tag{7}$$

Where ε is the angle between the downburst's translation path and the train's direction of travel and θ is the angle at which the downburst radial velocity acts on the train along its route (Fig. 2a).

4. RESULTS

As a base case, we consider a train moving at a normalised speed of $\overline{Q_v} = Q_v/U_{mv}$ of 2, at a dimensionless distance of $\bar{Y} = Y/r_m$ of 1 from a stationary downburst ($\overline{Q_{db}} = Q_{db}/U_{mv} = 0$) located at the origin. Fig. 2a shows the velocities acting on a moving train and Fig. 2b shows the time histories of the normalized wind velocity relative to the train ($\bar{\Omega}$) and the yaw angle (ψ).

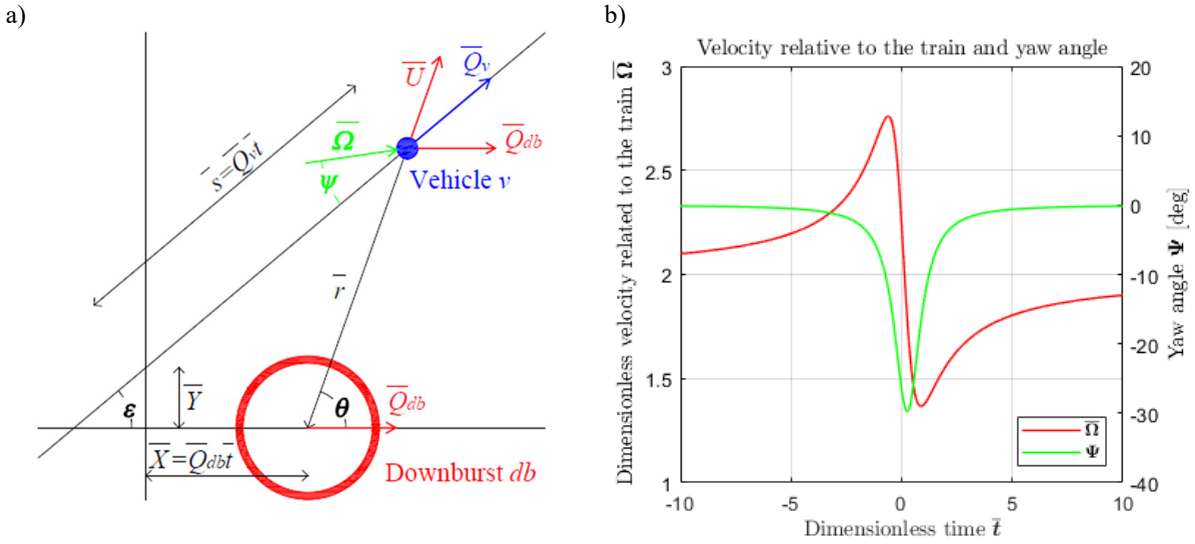
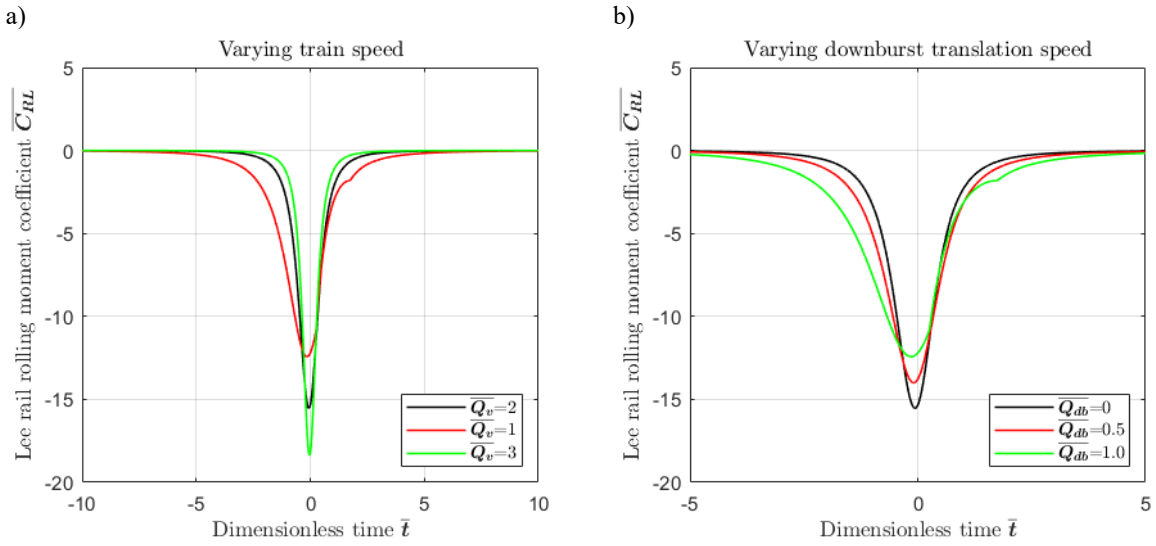


Figure 2. Schematic of a vehicle moving through downburst (a) and normalized wind velocity $\bar{\Omega}$ related to the train and yaw angle ψ related to the train path (b)

A parametric study was carried out around these base values to see how altering each of them affects the lee rail rolling moment coefficient: downburst translation speed $\overline{Q_{db}} \in \{0,0.5,1.0\}$; train speed $\overline{Q_v} \in \{1.0,2.0,3.0\}$; distance $\bar{Y} \in \{0.5,1.0,2.0\}$. In addition, the angle between the downburst and train paths (ε; see Fig. 2a) is also considered in the cases of non-stationary downburst, varying between 0° and 45° with a step of 15°. The results are presented in Fig. 3.



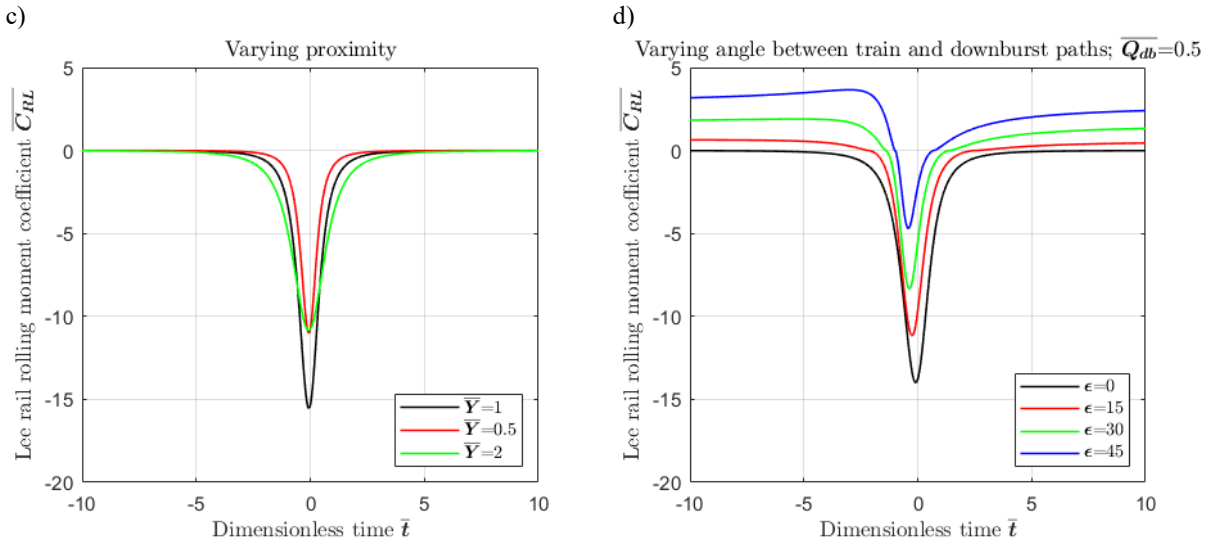


Figure 3. Parametric study around the base parameters: effects of varying train speed (a), effects of varying the downburst translation speed (b), effects of varying proximity (c) and effects of varying angle between the train and downburst paths (note the change of $\overline{Q_{db}}$ to 0.5 from the base case) (d)

Increasing the train speed results in larger peak values of C_{RL}, but with a sharper, narrower peak, thus limiting the time when the train is at risk of higher wind loads. A similar effect is observed when decreasing the downburst translation speed, as both changes fundamentally lead to an increase in the train speed relative to the downburst in our base case. As can be expected, when varying proximity of the train path to the downburst, the largest values are observed for $\bar{Y} = 1.0$ when the train passes directly through the high outflow region. The peak reduces notably to similar levels when this distance is either doubled or halved. Increasing the angle ε for moving downburst results in a decrease of peak C_{RL} and more complex time histories without any symmetry.

5. CONCLUSIONS

A novel method was used to calculate the downburst-type wind action on moving vehicles. A brief parametric study was performed to examine the influence of different parameters on the wind action and the resulting lee rail rolling moment coefficients. There is considerably more to unpack using this model, but it is always worth noting that the model contains several assumptions and therefore the analysis should not be taken too far without appreciating its limitations.

REFERENCES

Baker, C. J. 2013. A framework for the consideration of the effects of crosswinds on trains. Journal of Wind Engineering and Industrial Aerodynamics. 123, 130 – 142.

Baker, C. J., and Sterling, M. 2018. The calculation of train stability in tornado winds. Journal of Wind Engineering and Industrial Aerodynamics. 176, 158-165.

Jesson, M., Sterling, M., Letchford, C. and Haines, M. 2015. Aerodynamic forces on generic buildings subject to transient downburst-type winds. Journal of Wind Engineering and Industrial Aerodynamics. 137, 58-68.

Sterling, M., Huo, S., and Baker, C. J. 2023. Using crop fall patterns to provide an insight into thunderstorm downbursts. Journal of Wind Engineering and Industrial Aerodynamics. 238, 105431.

Measurement of aerodynamic forces acting on a model train passing through a swirling flow using a tornado vortex generator

Masahiro Suzuki [1], Nobuyuki Okura [1]

[1]*Meijo university, Nagoya, Japan, msuzuki@meijo-u.ac.jp*

SUMMARY:
While encounters between trains and tornadoes are rare, they can result in significant damage. Estimating the aerodynamic forces that tornadoes exert on moving vehicles is crucial for improving safety. However, the localized and sudden nature of tornadoes makes real-world testing challenging and hazardous, prompting researchers to explore model experiments using tornado vortex generators. Inuzuka et al. developed a method using a tornado vortex generator and a moving model rig, examining the effects of core radius, vehicle position, and speed on aerodynamic forces. On the other hand, Baker et al. proposed a similarity law that a tornado vortex generator should satisfy. It was found that the device used by Izunuzka et al. only partially satisfied this similarity law. Therefore, the purpose of this study was to develop a new tornado vortex generator that satisfies more similar conditions and to measure the aerodynamic forces on a model vehicle traveling in a swirling flow. The new generator, featuring a larger fan and motor, generates stronger swirling flows, and wind velocity distribution measurements confirmed that more similarity parameters were satisfied. Aerodynamic forces acting on a model train were measured during its passage through the swirling flow, revealing changes in aerodynamic forces.

Keywords: tornado, train, aerodynamic force

1. INTRODUNCTION

The occurrence of a train encountering a tornado is rare, but once an accident occurs, it can cause significant damage. In fact, there have been railway accidents in Japan and the United States in the past that were caused by or possibly related to tornadoes (Aircraft and Railway Accidents Investigation Commission, 2008；McClurg, 1931). To advance the investigation of railway accidents caused by tornadoes and the development of countermeasures, it is essential first to estimate the aerodynamic forces that tornadoes exert on moving vehicles. However, because tornadoes are highly localized and occur suddenly, predicting their occurrence is extremely difficult, and conducting tests using actual tornadoes is not only challenging but also dangerous. Therefore, model experiments conducted in laboratory environments are considered one of the most promising methods. Inuzuka et al. (2022) developed an experimental method using a tornado vortex generator and a moving model rig. They assumed small tornadoes, which frequently occur in Japan, and modified an electric fan to create an Iowa State University-type tornado vortex generator (Hann, 2008). The aerodynamic forces acting on model vehicles moving through the swirling flow generated by this device were measured. As a result, the effects of the core radius and vortex structure of the swirling flow on the aerodynamic forces, as well as the influence of the

vehicle's travel path, speed, and position within the train consist on the aerodynamic forces, were clarified.

On the other hand, Baker et al. (2019) proposed the geometric, dynamic, and kinematic similarities that a tornado vortex generator, used in wind resistance studies for various structures, should satisfy. They suggested the range of these values based on real-world data. They reported that while it is difficult for large tornado vortex generators to satisfy dynamic similarity, they can fulfill geometric similarity for small to medium-sized tornadoes. Upon examining the swirling flow generated by the tornado vortex generator developed by Inuzuka et al., it was found that only some aspects of geometric similarity were achieved (Okuda, 2024). Therefore, although it is impossible to satisfy all forms of similarity, a new tornado vortex generator was developed to meet as many similarity conditions as possible in this study. This new device, combined with the moving model apparatus, was used to re-investigate the aerodynamic forces acting on the vehicle.

2. TORNADO VORTEX GENERATOR

2.1. Overview of the device

The basic structure is similar to the device developed by Inuzuka et al., but a larger fan and more powerful motor were used to design and construct a system that generates a larger and stronger swirling flow. The tornado vortex generator consists of an inner duct, outer duct, motor, fan, guide vanes, and stage (Fig. 1). The fan, installed inside the inner duct, generates an upward airflow, which passes through the guide vanes positioned at the top of the device. These guide vanes are angled relative to the radial direction, creating a swirling airflow component. This causes a helical airflow to descend through the outer duct, producing a tornado-like swirling flow on the stage. The fan has a diameter of 1,250 mm, and the motor has an output of 1.5 kW. Although the angle of the guide vanes is adjustable, it was set to 70 degrees for the subsequent experiments.

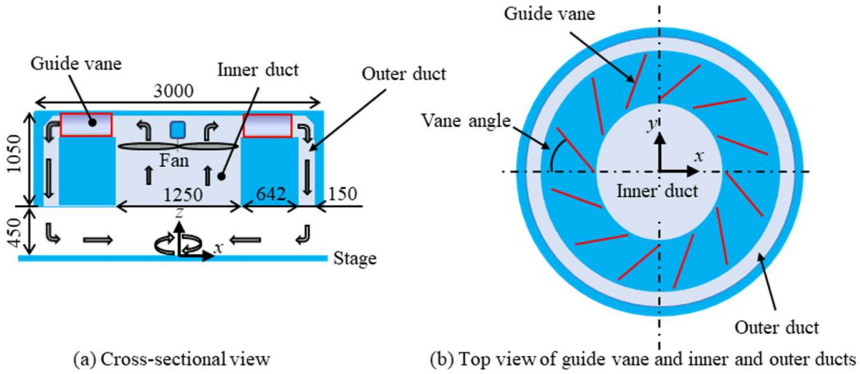


Figure 1. Tornado vortex generator (unit: mm).

2.2. Wind velocity measurement

The wind velocity of the flow field generated by the tornado vortex generator was measured using a five-hole pitot tube. A descending airflow was observed near the center, confirming the presence of a two-cell vortex. Based on this results, Baker et al.'s parameters were calculated (Table 1). In this context, G1, G2, and G3 represent the geometric scale ratios of the tornado, K is the kinematic parameter, and D is the dynamic parameter (Reynolds number). The value of D is based on the height of the model vehicle, which will be discussed in the next section. Additionally, *Vm*

represents the maximum tangential wind speed, Um is the maximum central wind speed, *r_Vm* is the radius at which *Vm* occurs, *r_Um* is the radius where Um occurs, *z_Vm* is the height at which *Vm* occurs, and *z_Um* is the height at which *Um* occurs. The new tornado vortex generator does not satisfy K, but it satisfies all the geometric parameters; the value of D does not yet reach the value proposed by Baker et al. but shows some improvement.

Table 1. Geometric, kinematic and dynamic parameters.

Parameters	G1 (r_Vm/z_Vm)	G2 (r_Um/r_Vm)	G3 (z_Um/z_Vm)	K (Vm/Um)	D ($Vm \cdot H/v$)
The range of values proposed by Baker et al.	5 to 20	1 to 4	0.5 to 1.5	4 to 7	$> 5\times10^5$
Present study	5.0	1.0	0.6	1.7	7×10^4

3. MODEL RUNNING EXPERIMENT

3.1. Method

The tornado vortex generator was combined with the moving model rig (Fig. 2). The moving system consists of a straight track, a launch mechanism, and a braking device. The track was arranged so that the model vehicle would pass through the center of the tornado simulator. The launch mechanism utilized the elasticity of rubber to give the model vehicle an initial speed of 4.5 m/s. Additionally, lasers were projected at the entrance, center, and exit of the tornado simulator, and the passage of the vehicle was detected using photodiodes mounted on the vehicle. The running speed was calculated based on the time taken to travel from the entrance to the exit. After passing through the tornado simulator, the vehicle was safely brought to a stop by the braking device, which used sponges to hold the vehicle from both sides.

A 1/40 scale model of a single-car train was used. A total of 96 pressure ports were installed on the top, bottom, and sides of the vehicle. The vehicle was equipped with pressure sensors, a data logger, and batteries. The differential pressure between the symmetric pressure ports on the top and bottom, as well as on the left and right sides, was measured. For each pressure measurement point, 10 test runs were conducted to obtain an ensemble average. Side and lift forces and rolling moments were calculated from the ensemble-averaged pressure values.

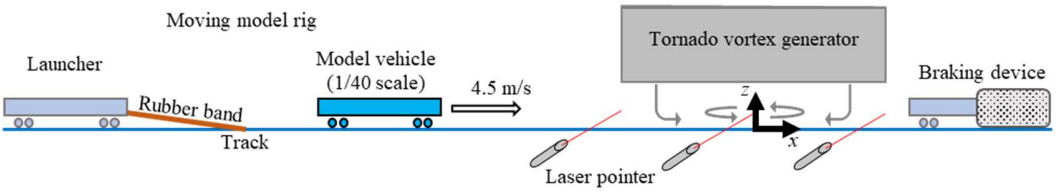


Figure 2. Moving model rig and tornado vortex generator.

3.2. Results

As an example, Fig. 3 illustrates the changes in lateral forces acting on the model vehicle while it travels through the swirling flow. The horizontal axis represents the distance from the center of the vortex to the center of the vehicle, nondimensionalized by the core radius *R*. The vehicle moves

from the negative to the positive side. The vertical axis shows the non-dimensionalized value (side force coefficient Cs), which is derived from the magnitude of the vector sum of the train speed and the maximum tangential wind speed, and the vehicle's side area and air density. The lateral force reaches its maximum value around $x/R \approx -2$ decreases to a minimum around $x/R \approx 1.5$, and then recovers. Notably, the absolute value of the minimum is nearly twice that of the maximum. A simple comparison cannot be made between this experiment and Inuzuka et al.'s because the ratio of core radius to vehicle length and the ratio of maximum swirling wind speed to vehicle speed are different, but the results are qualitatively consistent with theirs.

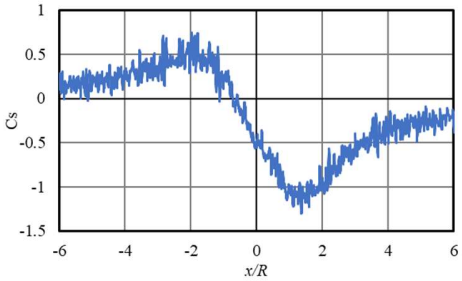


Figure 3. Side force acting on the vehicle.

4. CONCLUDING REMARKS

A tornado vortex generator was developed to satisfy the similarity laws as much as possible, and the aerodynamic forces acting on a model vehicle during its motion through the swirling flow were measured. Although the constructed device could not satisfy all similarity laws, it succeeded in increasing the number of similarity parameters that could be fulfilled compared to the device by Inuzuka et al. By combining this device with the running apparatus, the aerodynamic forces obtained were qualitatively consistent with those reported by Inuzuka et al.

In the future, there are plans to use a larger vehicle model and increase the vehicle speed to achieve the same ratios of core radius to vehicle length and maximum tangential wind speed to vehicle speed as those of Inuzuka et al., allowing for a quantitative comparison with their results. Additionally, strategies will be considered to address the unsatisfactory kinematic parameter.

ACKNOWLEDGEMENTS

The authors thank Ryuichi Nagai and Hiroki Takesawa for their help in conducting the experiments. This work was supported by JSPS KAKENHI Grant Number JP23K04352.

REFERENCES

Aircraft and railway accidents investigation commission, 2008. Railway accident analysis report RA2008-4. (in Japanese)

Baker, C., and Sterling, M., 2019. Are tornado vortex generators fit for purpose? Journal of Wind Engineering and Industrial Aerodynamics 190, 297-292.

Hann, F. L., Sarkar, P. P., and Gallus, W. A., 2008. Design, construction and performance of a large tornado simulator for wind engineering applications. Engineering Structures 30, 1146-1159.

Inuzuka, F., Feng, Y., Okura, N., and Suzuki, M., 2022. Experimental study on aerodynamic forces acting on train passing through a tornado-like swirling flow. Transactions of the JSME (in Japanese), Vol. 88, No. 911, 1-18.

McClurg, R. J., 1931. Tornado strikes swiftly-moving train. Monthly Weather Review, 198-199.

Okuda, T., 2024. Estimation of aerodynamic forces acting on a train moving through a tornado-like swirling flow using wind tunnel experiment. Master's thesis, Meijo University, Nagoya, JAPAN.

Effects of multi vehicles on aerodynamic forces of running vehicle on bridge against crosswind

Hiroshi Katsuchi [1], Jiaqi Wang [2]

[1] *Yokohama National University, Yokohama, Japan, katsuchi@ynu.ac.jp*
[2] *Yokohama National University, Yokohama, Japan, wang-jiaqi-nf@ynu.ac.jp*

SUMMARY:
Running vehicles on a bridge are vulnerable to crosswinds, which result in steering difficulty and an overturning accident. These events are serious on strait-crossing bridges and particularly around bridge towers. In addition, it is recently reported that running vehicle instability by strong crosswinds is induced by overtaking vehicles in the adjacent lane. This study investigates effects of multi-vehicle aerodynamic interference on aerodynamic forces acting on a running vehicle on a bridge by using a specially developed test equipment in a wind tunnel. It was found that a windward vehicle largely changes aerodynamic forces on a leeward vehicle by aerodynamic interference. In particular, an overshoot phenomenon in the side force and yawning moment was observed just after vehicle passing.

Keywords: crosswind, aerodynamic forces, vehicle interference

1. INTRODUCTION

Strong crosswinds often induce vehicle running instability and accidents on a bridge. In order to understand the mechanism and take effective countermeasures, many studies (Shiraishi et al., 1982; Baker, 1986; Charuvisit, 2004; Zhu, 2012; Chen, 2015; Tachibana, 2016; Kim, 2021) on crosswind-vehicle interaction, running vehicle stability and preventive measures have been carried out. Practically, traffic regulations such as driving speed reduction and bridge closure are enforced to prevent these problems for many existing bridges. In addition, some bridges successfully install wind screens around bridge towers and even on the entire bridge span to reduce crosswinds.

Recently, running vehicle instability during strong crosswind events was reported when one vehicle was overtaken by another vehicle (see Fig. 1). This is a similar phenomenon when a vehicle passes a bridge tower section. Sudden change of crosswind due to overlapping of two vehicles induced the vehicle running instability.

In this study, multi-vehicle aerodynamic interference effects on aerodynamic forces of a running vehicle on a bridge deck were investigated by using a specially developed model vehicle driving test equipment and an aerodynamic force measurement devise in a wind tunnel.

2. AERODYNAMICALLY INTERFERENCED FORCE MEASUREMENT

2.1. Measurement System

Aerodynamic forces of a running vehicle under multi-vehicle aerodynamic interference were

measured by a specially developed test equipment as shown in Fig. 2. A running vehicle model was driven with a constant speed of up to 800 mm/s. The test equipment was placed in a wind tunnel of Yokohama National University (width and height of the test section are 1,800 mm and 1,800 mm, respectively). A small 6-component force transducer was equipped inside the running vehicle model and force signals were transmitted to a computer at 1,200 Hz sampling with Wifi. Fig. 3 shows the layout of vehicles on a bridge deck model. A dummy static model was placed on a lane and a force measurement vehicle model was driven on the other lanes. The running vehicle model can travel at the constant speed in the middle section of 800 mm. 1/45-scale truck models (H×W×L: 45×52×200 mm [2×2.3×9 m in full scale]) were used in this study.



Figure 1. Aerodynamic interferences

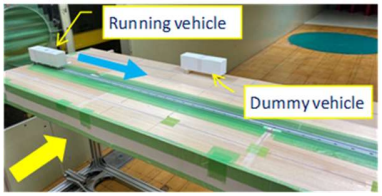


Figure 2. Measurement system

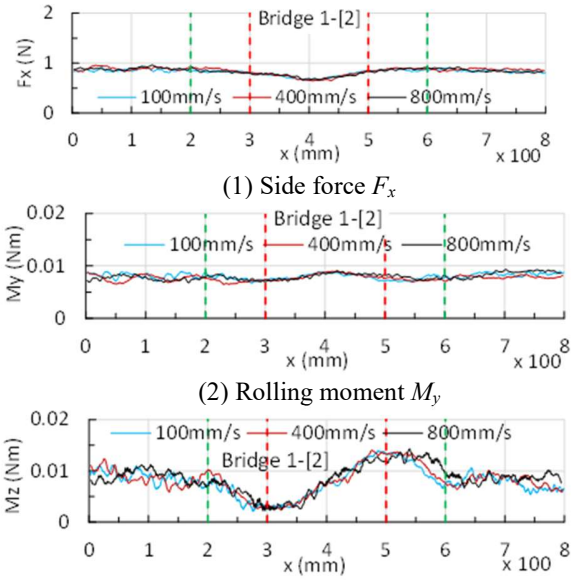


Figure 3. Vehicle layout

2.2. Transient Aerodynamic Forces by Muti-vehicle Aerodynamic Interference

Running a force measurement vehicle model on a leeward lane of a dummy static model, effects of the distance between two vehicles and the running speed on transient aerodynamic forces were investigated. Figs. 4 -7 show transient aerodynamic forces of the running vehicle model at the running speed of 100, 400 and 800 mm/s [16, 65 and 130 km/h in full scale] ((1) side force F_x, (2) rolling moment M_y and (3) yawing moment M_z). Since the figures compare the forces at different running speeds, the abscissa was taken running distance in mm. Red broken lines show the range of the windward vehicle length, and green broken lines show the starting and ending of the overlapping of two vehicles.

Side forces decreased gradually with the progress of the overlapping of two vehicles, reached the minimum at the complete overlapping and gradually recovered to the original magnitude. There is no significant difference among different running speeds. Different transient trend in the large distant case (Lanes 1-3) was observed. Rolling (overturning) moments did not change significantly with the vehicle interference and the running speed, however it slightly increased at the complete overlapping. Yawing moments decreased (vehicle front turned to windward) when the running vehicle went into behind the windward dummy vehicle and reached the maximum (vehicle front turned to leeward) when the front half of the running vehicle went out of the windward dummy vehicle. Significant difference among the running speed is not seen, however different trend in the large distant case (Lanes 1-3) is observed. It might be due to the flowfields behind the windward vehicle. Unlike the side force and the rolling moment, yawing moment showed an overshoot phenomenon before returning to the original magnitude. In particular, about 1.5 times change (increase) in the yawing moment after the overlapping is induced compared with the change (decrease) before the overlapping. It should be noted that the same magnitude change in the yawing moment occurs within the different time duration. In other word, a faster running speed induces larger unit-time variation of the yawing moment.

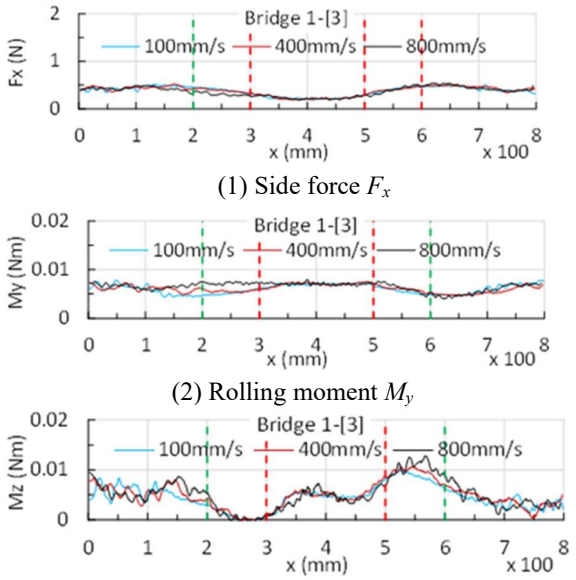


(1) Side force F_x

(2) Rolling moment M_y

(3) Yawing moment M_z

Figure 4. Transient aerodynamic forces with running vehicle on lane 2 and dummy vehicle on lane 1

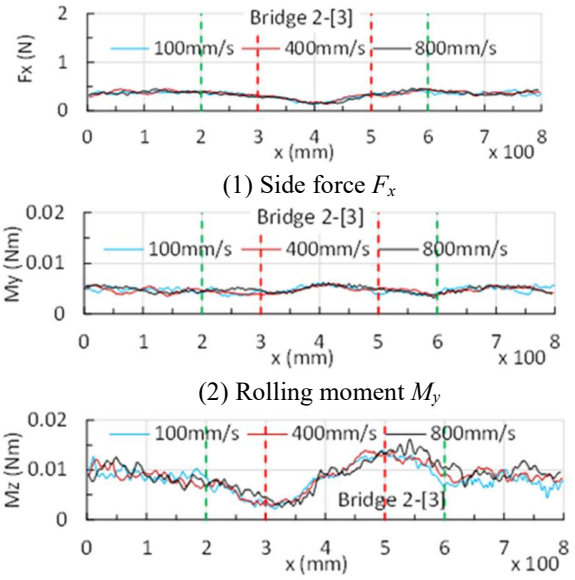


(1) Side force F_x

(2) Rolling moment M_y

(3) Yawing moment M_z

Figure 5. Transient aerodynamic forces with running vehicle on lane 3 and dummy vehicle on lane 1

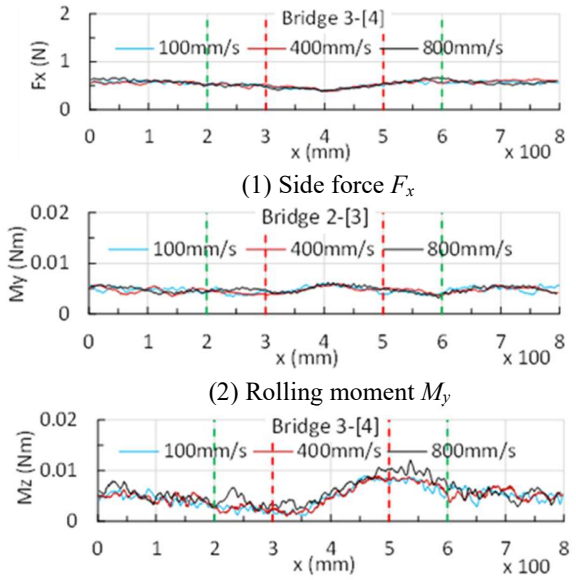


(1) Side force F_x

(2) Rolling moment M_y

(3) Yawing moment M_z

Figure 6. Transient aerodynamic forces with running vehicle on lane 3 and dummy vehicle on lane 2



(1) Side force F_x

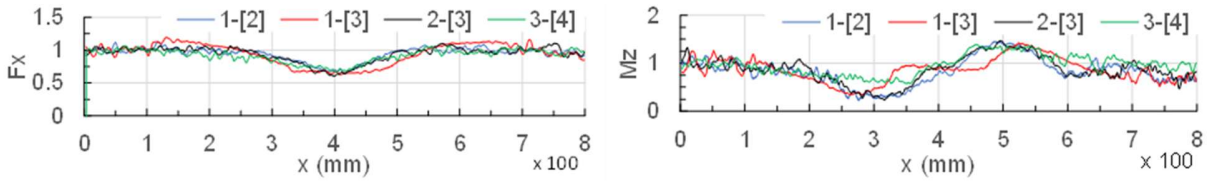
(2) Rolling moment M_y

(3) Yawing moment M_z

Figure 7. Transient aerodynamic forces with running vehicle on lane 4 and dummy vehicle on lane 3

Fig. 8 shows transient side forces and yawing moments with different vehicle distances at the running speed of 100 mm/s [16 km/h in full scale]. The figures show the ensemble average of 30 times measurements and the magnitude ratios normalized by the average value in the first 1s period in each case. More clear trends discussed above can be seen. Based on the result, the change ratios of the side force and yawing moment before and after the overlapping of two vehicles are shown in Table 1. In particular, different trends in the larger distance (aerodynamic force on lane 3 with

the dummy on lane 1) and the most leeward lane case (aerodynamic force on lane 4 with the dummy on lane 3) are observed.



(1) Side force ratio (2) Yawing moment ratio

Figure 8. Transient aerodynamic forces with muti-vehicle interference (100 mm/s)

Table 1. Change ratios of transient aerodynamic forces by multi-vehicle interference in Figure 8

	Lane 2 [lane 1]		Lane 3 [lane 1]		Lane 3 [lane 2]		Lane 4 [lane 3]	
	F_x	M_z	F_x	M_z	F_x	M_z	F_x	M_z
Min.: *a*	0.650	0.221	0.627	0.337	0.600	0.230	0.663	0.573
Max. [1-3s]: *b*	1.124	1.023	1.191	1.189	1.068	1.087	1.023	0.986
Max. [5-7s]: *c*	1.090	1.423	1.133	1.426	1.101	1.423	1.061	1.358
(*c* - *a*)/(*b* - *a*)	0.928	1.499	0.897	1.278	1.070	1.391	1.107	1.901

3. CONCLUSIONS

Multi-vehicle aerodynamic interference effects on aerodynamic forces of a running vehicle on a bridge deck due to crosswinds were investigated. The change in the transient aerodynamic forces was affected by the wind-directional distance of two vehicles. A large overshoot phenomenon in the transient yawing moment was observed. The magnitude of transient aerodynamic forces was not affected by the running speed, however faster running speed induces larger unit-time variation of the yawing moment.

ACKNOWLEDGEMENTS

This work was supported by JSPS KAKENHI Grant Numbers JP22H01574. The authors would also like to appreciate their contributions to the aerodynamic force measurement experiment of former students, Mr. Shusuke Inada, Mr. Kyohei Nashimoto and Mr. Kazuma Onodera.

REFERENCES

Shiraishi, N., Matsumoto, M. and Shirato, N., 1982. A fundamental study about unsteady aerodynamic characteristics of structures due to fluctuating wind, Proc. of JSCE, No. 328, 19-30. (in Jqapanese)

Baker, C. J., 1986. A simplified analysis of various types of wind-induced road vehicle accidents, J. of Wind Engineering and Industrial Aerodynamics, 22, 69-85.

Charuvisit, S., Kimura, K. and Fujino, Y., 2004. Effects of wind barrier on a vehicle passing in the wake of a bridge tower in cross wind and its response, J. of Wind Engineering and Industrial Aerodynamics, 92, 609–639.

Zhu, L. D., Lia, L., Xu, Y. L., Zhu, Q., 2012. Wind tunnel investigations of aerodynamic coefficients of road vehicles on bridge deck, Journal of Fluids and Structures, 30, 35–50.

Chen, N., Li, Y., Wang, B., Su, Y., Xiang, H., 2015. Effects of wind barrier on the safety of vehicles driven on bridges, J. of Wind Engineering and Industrial Aerodynamics, 143, 113–127.

Tachibana, T., Shirato, H., et al., 2016. Consideration of overturning risk for running vehicles due to crosswinds, J. of Structural Mechanics and Earthquake Engineering, A1, Vol. 72, No.1, 220-233. (in Japanese)

Kim, H., Fujino, Y., Katsuchi, H., Siringoringo, D. M., Yamada, H. and Okoshi, S., 2021. Computational fluid dynamics simulation and stability analysis of vehicle on bridge under strong winds, J. of Structural Mechanics and Earthquake Engineering, A1, Vol. 77, No.1, 107-120. (in Japanese)

Investigation of perceived precipitation and accumulation characteristics on different surfaces of a moving vehicle

Mohammadsadegh Moradi Ghareghani[1], Farimah Hosseinnouri[1], Kiran Keshavan[1], Eric Villeneuve[2], Ismail Gultepe[2], John Komar[2], Martin Agelin-Chaab[1], Horia Hangan[1]

[1]*Department of Mechanical and Manufacturing Engineering, Ontario Tech University, Oshawa, Canada. Email address*

[2]*Automotive Centre of Excellence (ACE), Ontario Tech University, Oshawa, Canada. Email address*

SUMMARY:
Precipitation and accumulation on a moving vehicle pose significant road safety risks and can negatively affect the performance of sensors. Therefore, it is essential to accurately estimate precipitation and accumulation patterns across various surfaces of the vehicle. Theoretically, the amount of precipitation encountered by a moving surface is influenced by its orientation and travel speed. However, various external factors, including wind, turbulence, and Particle Size Distribution (PSD), can further impact the perceived intensity of precipitation on the vehicle. In this study, full-scale field measurements were conducted to analyze precipitation distribution across various surfaces of a moving vehicle. The collected data were then utilized in a numerical model to simulate additional scenarios and investigate the correlation between natural precipitation and the precipitation perceived by the vehicle in motion. The findings show that variations in vehicle speed and direction alter perceived precipitation due to relative velocity changes. This allows for the estimation of perceived precipitation based on natural precipitation data, along with vehicle speed and direction.

Keywords: Adverse weather, Perceived precipitation, Field observations

1. INTRODUCTION

A moving object may experience varying amounts of precipitation compared to measurements taken from a stationary tower, influenced by factors such as precipitation type, speed of movement, and surface orientation. Correlating dynamic and static observations serves two primary practical purposes. First, this correlation helps to define simulation targets for indoor testing within climatic wind tunnels, which is essential for studying new autonomous vehicle (AV) technologies (Pao and Agelin-Chaab, 2021). This is particularly important for optical sensors like LiDARs and cameras, as they are highly sensitive to hydrometeors (e.g., rain, snow, fog) due to the significant attenuation of transmitted radiation, driving conditions, and surface material characteristics (Walker et al., 2020; Zang et al., 2019). Second, with advances in connectivity and artificial intelligence, it becomes possible to enhance weather networks and leverage data from dynamic observations of moving vehicles for broader applications (Treis et al., 2019).

Most existing research on the effects of precipitation, such as rain and snow, on vehicles and autonomous vehicle (AV) sensors has been conducted in indoor environments. However, these

studies often overlook the concept of perceived precipitation, which may result in conclusions that do not fully reflect real-world conditions. To the best of the authors' knowledge, while several physical models have been developed to estimate perceived precipitation for objects, these models typically rely on simplified assumptions and lack comprehensive validation through observational data (Bocci, 2012; Lanza and Barbera, 2016; Stern, 1983). This gap in the literature is likely due to the absence of standardized and controlled testing methodologies. Conducting outdoor experiments presents significant challenges, including the influence of various uncontrolled environmental parameters and the need to wait for natural precipitation events. As a result, acquiring reliable, full-scale data on perceived precipitation remains a difficult yet critical step in improving the accuracy of simulations and predictions, especially for the testing and validation of AV sensor technologies in real-world scenarios. Addressing these challenges could enable more realistic assessments of precipitation impacts on vehicle performance and sensor functionality, ultimately enhancing the reliability and safety of AV systems under diverse weather conditions.

2. METHODOLOGY

2.1. Field measurements

The experimental setup is composed of two primary modules designed for full-scale measurements. The first module includes a test vehicle equipped with a Vaisala WXT530 Weather Transmitter, an Airmar WX220 Weather Station, and two Theis LPM (Laser Precipitation Monitor) optical disdrometers, oriented at 0° and 90°, as shown in figure 1.



Figure 1. The research vehicle for outdoor experiment.

This vehicle records weather data while traveling along a designated track at the Weather Farm, a facility provided by Ontario Tech University in northern Oshawa, Ontario. Adjacent to this track, two meteorological towers are positioned, each equipped with Vaisala WXT530 transmitters and Theis LPM disdrometers mounted at a 0° orientation. These towers act as static reference points, enabling comparisons and correlations between their measurements and those collected by the moving vehicle.

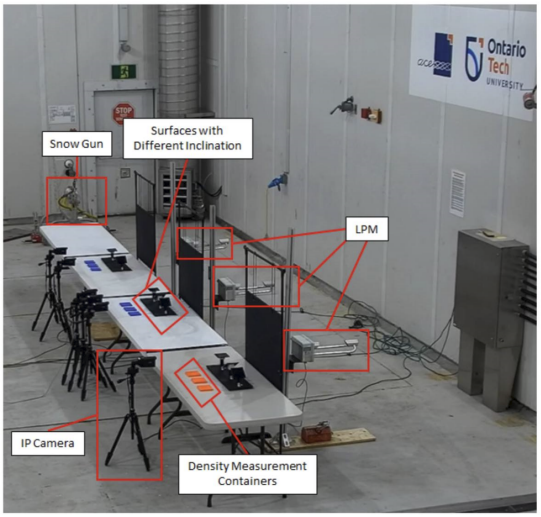
2.2. Climatic chamber experiments

To examine the accumulation on an object under diverse environmental conditions, a series of experiments was designed and executed within the Automotive Center of Excellence (ACE) Large Climatic Chamber, specifically under wind-free conditions to isolate the effects of temperature and artificial snowfall. The experimental protocol was meticulously developed to focus on observ-

ing artificial snow accumulation on a horizontal surface (0 degrees) while varying the chamber's internal temperature and the snow gun's flow rate. High-resolution IP cameras were strategically placed to capture the sample, allowing real-time monitoring of snow deposition under different test conditions. Figure 2 illustrates the experimental setup used during this study. The findings from this research are anticipated to contribute to advancements in replicating realistic indoor snowfall conditions.



(a)



(b)

Figure 2. (a) The accumulation on 0°, +30°, and -50° inclined surfaces, (b) Indoor experiment setup at ACE climatic chamber.

2.3. Numerical simulation

Field measurements of natural and perceived precipitation inform a numerical model, which incorporates parameters like particle size distribution, wind speed, and particle velocity. This model simulates wind-driven particle flow, while a User Defined Function (UDF) collects data on particles at sensor boundaries for analysis. The model's outputs are validated against field data and refined by adjusting parameters, enabling the creation of a predictive model for perceived precipitation under different conditions.

3. RESULTS

The results demonstrate the influence of various factors, including vehicle speed, direction, and particle size distribution, on perceived precipitation. For instance, Figure 3 illustrates the perceived precipitation on a horizontal surface of the moving vehicle at a constant speed in opposite directions characterized by different car speeds.

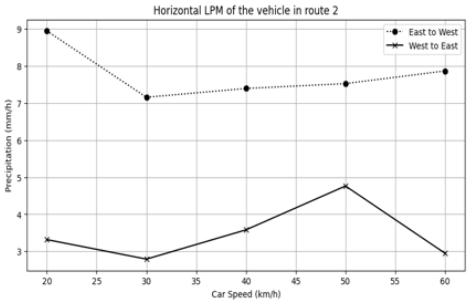


Figure 3. Comparison of the impact of vehicle direction on perceived precipitation for a horizontal surface.

4. CONCLUSIONS

Field measurements were conducted for outdoor conditions to assess perceived precipitation to evaluate both natural and perceived precipitation on a moving vehicle. Various factors influencing perceived precipitation, including wind speed, particle size distribution, and wind direction, have been analyzed. The results indicate that for a horizontally oriented sensor, the perceived precipitation closely aligns with natural precipitation. However, for a vertically oriented sensor, the perceived precipitation increases with higher vehicle speeds due to the larger swept area. The results will be further detailed and comparison will be provided with the preliminary model developed by Carvalho and Hangan, 2023.

ACKNOWLEDGEMENTS

The author gratefully acknowledges the support of the Canada Research Chair Tier 1 Program in Adaptive Aerodynamics and the Canada Foundation for Innovation.

REFERENCES

Bocci, F., 2012. Whether or not to run in the rain. European Journal of Physics 33, 1321.

Carvalho, M. and Hangan, H., 2023. Modelling Weather Precipitation Intensity on Surfaces in Motion with Application to Autonomous Vehicles. Sensors 23, 8034.

Lanza, L. and Barbera, P., 2016. “Method for the determination of the precipitation intensity from a moving vehicle/boat, and system for the space-time characterization of a precipitation field on wide territory areas”. Patent.

Pao, W. Y. and Agelin-Chaab, M., 2021. Fundamental and parametric considerations for numerical rain simulation in a wind tunnel. Progress in Canadian Mech. Eng 4.

Stern, S., 1983. An optimal speed for traversing a constant rain. American Journal of Physics 51, 815–818.

Treis, A., Pfister, A., Falk, D., Kutschera, G., Braun, M., Pätsch, M., and Eckardt, D., 2019. Improving the short-term forecast of precipitation events using vehicle sensor data–research project mobile VIEW. Proceedings of Rainfall Monitoring, Modelling and Forecasting in Urban Environment. UrbanRain18: 11th International Workshop on Precipitation in Urban Areas. Conference Proceedings. ETH Zurich, Institute of Environmental Engineering, 121–126.

Walker, C. L., Boyce, B., Albrecht, C. P., and Siems-Anderson, A., 2020. Will weather dampen self-driving vehicles? Bulletin of the American Meteorological Society 101, E1914–E1923.

Zang, S., Ding, M., Smith, D., Tyler, P., Rakotoarivelo, T., and Kaafar, M. A., 2019. The impact of adverse weather conditions on autonomous vehicles: How rain, snow, fog, and hail affect the performance of a self-driving car. IEEE vehicular technology magazine 14, 103–111.

Interference Effects between High-Sided Road Vehicles: Aerodynamic Interactions under Crosswinds

Muhammad A. Siddique[1], Partha Sarkar[2*], Omar Smadi[3]

[1]*Graduate Research Assistant, Iowa State University, Ames, USA, ahmadsid@iastate.edu*
[2]*Professor, Iowa State University, Ames, USA, ppsarkar@iastate.edu*
[3]*Professor, Iowa State University, Ames, USA, smadi@iastate.edu*

SUMMARY:
High-sided Road Vehicles are vulnerable to strong crosswinds. To better understand the effects of crosswinds on the safety of these vehicles, a realistic experimental setup is developed in the boundary layer wind tunnel using scaled models of a Truck, SUV and highway section. Crosswind effects on these vehicles along with interference effects between multiple vehicles are studied in detail at various yaw angles and relative positions of the vehicles. Drag, lift and side force coefficients are validated and then studied in detail with changing yaw angles. Pressure distribution on the vehicle surfaces is also measured for each case. Static stability analysis is conducted and critical wind speeds are determined. The results show that with increasing yaw angle, the drag coefficient decreases for both types of vehicles. The side force increases with increasing yaw angle, becoming maximum at 90 degrees. Lift coefficient initially increases to a maximum at 30° yaw and then decreases before again rising with yaw angle.

Keywords: High-sided road vehicles, Semi-truck aerodynamics, Crosswinds, Interference effects, Wind tunnel

1. INTRODUCTION

Ground transportation remains the most popular mode of moving people and goods around the world. It is influenced by various factors such as fuel economy, weather conditions, and driver behaviour, etc. As population around the world grows, so does the demand on the transportation system. Therefore, it is an ever-evolving field in terms of technology and requires overcoming unique challenges to help meet evolving transportation needs.

With increasing amount of traffic on the roads, safety must be ensured first. To make transportation safer, various hazards must be considered. Weather is one of the top hazards on highways for moving vehicles and one that is not necessarily in human control. Rain, snow, ice, low visibility and strong winds can make driving conditions dangerous. Crosswinds frequently affect larger vehicles with bluff body shapes that have a significantly exposed surface area.

There are several studies in the literature that have studied simplified high-sided vehicles such as semi-truck using numerical or CFD techniques. Very few studies have experimentally studied these vehicles under realistic wind conditions. For this reason, this research is conducted experimentally on high-sided road vehicles that are affected by crosswinds on highways. Based on literature survey, a class 8 commercial vehicle like an articulated semi-trailer truck is extremely common on highways as it forms the backbone of the freight industry across the world. In addition, an SUV (Sport Utility Vehicle) is a frequently used type of personal family transport on highways.

It is found that Freightliner Cascadia is the most common semi-truck in North America and Jeep Grand Cherokee is a commonly used SUV model (Picone, 2024). For the purposes of this experimental research study, it is decided to build realistic wind tunnel models of these vehicles.

Kwon et al. (2011) used simulation software to study the design criteria required for wind barriers to protect vehicles driving on an expressway. Alrejjal et al. (2022) studied roll stability of trucks under curved paths using high-fidelity vehicle dynamics simulation modelling. Kim et al. (2016) studied sideslip and overturning vulnerability of vehicles due to crosswinds over bridge decks using a probabilistic approach through cumulative distribution function that used long-term wind data. Bridge aerodynamic data was used to study the effects over a bridge. Critical wind speeds were recommended based on the static analysis. Batista et al. (2014) used a static stability model to determine the critical wind speed for overturn-, sideslip- and rotation-type of accidents. Haan et al. (2017) studied the sliding, flipping and lofting behaviours of vehicles using tornado simulator. Tornadic winds of different categories were investigated to find critical wind speeds required to move parked vehicles during a full-scale tornado. The study was conducted on scaled models of minivans and an agricultural harvester. This study aims to recreate the complex wind characteristics experienced by high-sided vehicles under different situations in real life and to study the effects in further detail by developing wind tunnel models.

2. EXPERIMENTAL SETUP

In this research presented here, all experiments were performed in the Aerodynamic and Atmospheric Boundary Layer (AABL) Wind and Gust Tunnel (2.44m W×1.83m H) located at Iowa State University. The maximum wind speed during the experiments in the closed-circuit wind tunnel did not exceed 15.7m/s for safety reasons, and the overall turbulence intensity was approximately 10.9%, both referenced at the vehicle height, mimicking the open terrain turbulence and boundary layer profile. This was achieved using a combination of roughness blocks, spires and chains. Since high-sided road vehicles are prone to wind related incidents and are potentially a safety risk to other vehicles, they are chosen to be studied in detail in this experimental setup. One of the main effects of a passing vehicle is the aerodynamic interference caused by it to other vehicles. In most cases, it is expected that a larger passing vehicle's aerodynamics affects the smaller vehicle (such as an SUV) more significantly. Therefore, the setup included the two types of vehicles in vicinity of each other in the parallel lanes on the highway model.

2.1. SUV and Truck model

In this study, an SUV and Semi-truck wind tunnel model was designed and manufactured at the $1/16^{th}$ scale. Highway sections with an embankment angle of 45 degrees were also created at this scale level. The $1/16^{th}$ scale was determined based on the blockage effects in the wind tunnel test section. Blockage ratio was kept under 5%, particularly for the 90-degree crosswind setup case when the truck is closest to the walls of the tunnel. Fig. 1 shows the SUV and Semi Truck models on the highway at 60-degree yaw angle, one of the several cases studied. To study the interference effect on the SUV, it is fully instrumented with pressure taps and load transducer. The dummy semi-truck (non-instrumented) is used to modify the flow that the SUV will sense and is placed on the right-side parallel lane to the SUV. Three locations of the SUV were chosen, staggered aft (Fig. 1) and staggered ahead of the semi-truck, and parallel to the semi-truck during overtaking.

The semi-truck and SUV were fixed on top of a realistically developed highway section model in

the wind tunnel. Data was collected at wind yaw angle of 0, 30, 45, 60 and 90 degrees (Fig. 1). SUV and Semi-Truck were first positioned individually on the highway to study baseline data without any vehicle interference. Then the SUV and Semi-Truck were placed in various positions relative to each other in parallel lanes. The procedure was standardized and repeated for all yaw (wind direction) angles. Data was collected at multiple wind speeds to verify and validate that the force and pressure coefficients that were measured matched closely at various speeds and followed a trend. After validation, coefficients obtained at three different wind speeds were averaged. For the rest of the study, only averaged coefficients are plotted and discussed. Data were sampled over 2.5 minutes and then time averaged. After cleaning and analysing the data, results were plotted.

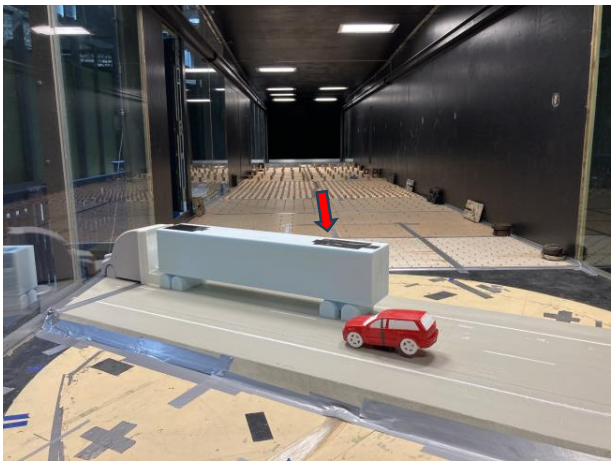


Figure 1. SUV and Semi-Truck models on the Highway in AABL Wind Tunnel.

3. PRELIMINARY RESULTS

First, the baseline SUV coefficients were validated with data from the literature. Next, the load coefficients data were validated with pressure data calculated coefficients, manufacturer provided coefficient and CFD. Fig. 2 shows the validation results of the drag coefficient of the SUV. At Yaw 0, the load cell-based Cd value is 0.33 and pressure-based Cd is 0.37. It is noted that the manufacturer supplied Cd is 0.35, which is between the two experimentally obtained Cd values.

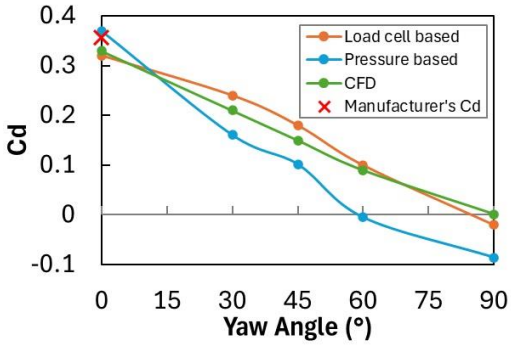


Figure 2. Validation of SUV Drag Coefficient.

Baseline coefficients for SUV and Truck, i.e. for individual vehicles, are then compared for drag, side force and lift as shown in Fig. 3. More detailed analysis and results are further worked on.

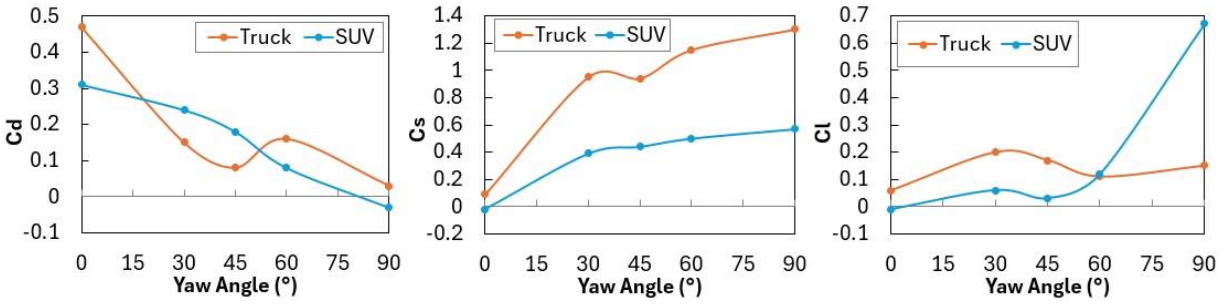


Figure 3. Drag, Side Force and Lift Coefficient comparison of the Baseline SUV and Truck.

For the Yaw 90 crosswind case, when the SUV passes the truck in a parallel lane, the SUV experiences increase in negative pressure (suction) on its windward or truck side (Fig. 4).

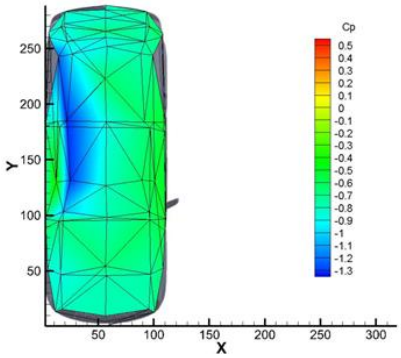


Figure 4. Pressure contour plot of SUV under 90-degree crosswind during interference effect when passing a Truck.

4. CONCLUSIONS

It is seen that with increasing yaw angle, the drag coefficient decreases for both types of vehicles. The side force coefficient increases with increasing yaw angle, becoming maximum at yaw 90°. Lift coefficient initially increases to a maximum at 30° yaw and then decreases before again increasing with yaw angle. While the overall trend is similar, there are some dissimilarities between SUV and Truck baseline data. Interference effects are further analyzed for further discussions. Moreover, static stability analysis is performed on the SUV to determine critical wind speeds for different modes and types of accidents and hazards.

REFERENCES

Alrejjal, A. and Ksaibati, K., 2022. Impact of crosswinds and truck weight on rollover propensity when negotiating combined curves. International Journal of Transportation Science and Technology 12, 86-102.

Batista, M., and Perkovic, M., 2014. A simple static analysis of moving road vehicle under crosswind. Journal of Wind Engineering and Industrial Aerodynamics 128, 105–113.

Haan, F., Sarkar, P. P., Kopp, G. A., and Stedman, D. A., 2017. Critical wind speeds for tornado-induced vehicle movements. Journal of Wind Engineering and Industrial Aerodynamics 168, 1-8.

Kim, S. -J., Yoo, C. -H., and Kim, H. -K., 2016. Vulnerability assessment for the hazards of crosswinds when vehicles cross a bridge deck. Journal of Wind Engineering and Industrial Aerodynamics 156, 62-71.

Kwon, S.-D., Kim, H. D., Lee, S. H., and Song, H., 2011. Design criteria of wind barriers for traffic. Part 1: Wind barrier performance. Wind and Structures: An International Journal 14, 55-70.

Picone, J., 2024. Slash Gear. https://www.slashgear.com/1670414/semi-trucks-most-popular-america/.

Crosswind stability of road vehicles under thunderstorm downburst winds

Araya Reyes C E [1*], Cioffi A[1], Tomasini G[1]

[1]*Department of Mechanical Engineering, Politecnico di Milano, Milan, Italy*
**Corresponding author: carlosesteban.araya@polimi.it*

SUMMARY:
Because thunderstorm winds can have severe consequences on the risk of accident of road vehicles, this study aims at developing a comprehensive methodology to assess vehicle stability considering also the effect of the driver. The methodology proposed consider three parts: the simulation of the wind field encountered by a car while traveling across a downburst event, the calculation of the aerodynamic forces due to the winds and the evaluation of the dynamic response of the vehicle by means of some risk indexes. In this work an overview of the methodology is presented and preliminary result for a small lorry travelling across a thunderstorm are shown as an example. This work is part of the on-going CROSS-STORM project.

Keywords: crosswind, thunderstorm, vehicle stability.

1. INTRODUCTION

The intense nonstationary winds generated during a thunderstorm may represent a significant risk for road vehicles. In fact, some studies have reported that intense storm conditions and situations in which sudden changes in wind intensity and direction occur are well correlated with the occurrence of accidents (Baker et al., 2009; Zhang et al. 2018) and some hybrid procedures have been developed to study the behaviour of ground vehicles under crosswinds (Cioffi et al., 2022). Even so, in general the studies regarding vehicle stability are made considering just generic synoptic wind conditions.

In this context, the CROSS-STORM aims at developing a numerical experimental procedure to study the stability of a road vehicle travelling across the strong winds generated during a thunderstorm downburst event. The methodology is articulated in three main steps:

1. Definition of the wind velocity field during a thunderstorm downburst,
2. Calculation of the aerodynamic loads acting on the road vehicle.
3. Evaluation of the dynamic response of the vehicle-driver system.

Given the critical role of driver response to storm-induced winds (Cioffi et al., 2023), the most critical scenarios will be analysed in a driving simulator to study the behaviour of the vehicle-driver system.

In this abstract an overview of the methodology is presented and some preliminary result for a small camion travelling across a thunderstorm are shown as an example.

2. SIMULATION STRATEGY

A simulation framework was developed to reproduce the effect of crosswind in thunderstorm conditions on a vehicle. The key elements composing it are:

- A wind model.
- A vehicle model.
- A driver model (if the simulations are performed without a driver in the loop).

At each simulation time-step, the outputs coming from the vehicle model are used to evaluate the crosswind forces and moments acting on the vehicle. This set of aerodynamic forces is then fed as input to the vehicle model, together with the driver's input. Two indexes are computed in post-processing to assess the effective stability of the vehicle under consideration.

2.1. Wind model and aerodynamic loas calculation

The wind velocity field that a vehicle encounters when traveling across a thunderstorm downburst was simulated following the approach developed under the CROSS-STORM project. At first, the horizontal slowly varying mean wind velocity filed of a traveling downburst is modelled by using a semi empirical analytical model (Xhelaj et al., 2020) that integrates the stationary radial velocity, storm motion, and boundary layer background wind. Then, the downburst turbulence field, a non-stationary, non-Gaussian, bi-variate and partially coherent random process, is calculated. Finally, the non-stationary outflow wind velocity field generated by the thunderstorm downburst is reconstructed by adding all the wind field components (Xhelaj et al., 2024). Considering the trajectory of the vehicle, wind speed and direction time histories are computed (Xhelaj et al., 2025) and serve as the input to evaluate the aerodynamic forces acting on the vehicle during simulation.

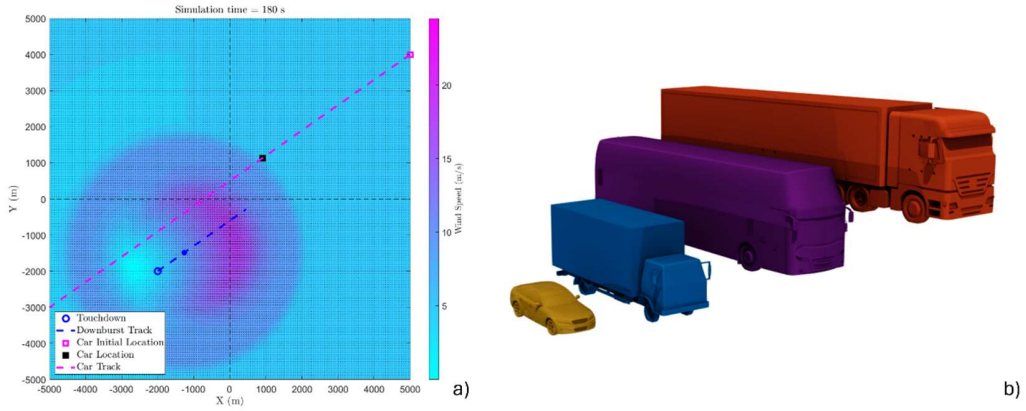


Figure 1. a) Simulated wind field. b) Road vehicles to be studied.

The aerodynamic forces acting on the vehicle are calculated considering the wind velocity along experience by the vehicle along the trajectory, the vehicle speed and vehicle orientation using a quasi-static approach. From the wind velocity and vehicle velocity, it is possible to calculate the relative wind speed and angle of attack of the wind with respect to the vehicle. The aerodynamic loads, it is, forces and moments referred to centre of gravity of the vehicle, are obtained for each time step, considering the corresponding wind relative speed and the aerodynamic coefficients that characterise the vehicle. The aerodynamic coefficients, that depends on the vehicle orientation with respect to the wind, are obtained from wind tunnel test on scale models for the four vehicles considered and shown in Fig 1b).

2.3. Vehicle model and driver

The vehicle dynamics is reproduced using the commercial software VI-CarRealTime. A 14 degrees of freedom multibody model was used to reproduce the dynamics of a given four-wheel vehicle. The particular vehicle can be modelled by defining: the main geometrical and inertial parameters (i.e.: wheelbase, track, mass, moments of inertia, etc.) of the modelled vehicle; the powertrain and brakes characteristics; the tire model (for all the vehicles, Pacejka's Magic Formula with combined friction and relaxation length was used); the suspension and steering system characteristics.

User defined control logics can be introduced directly in Matlab/Simulink thanks to the VI-CarRealTime model interface. The interface defines several channels that can be read and written at simulation time during each time-step. In Fig. 2 it is reported a schematic Simulink model used to perform co-simulation with VI-CarRealTime.

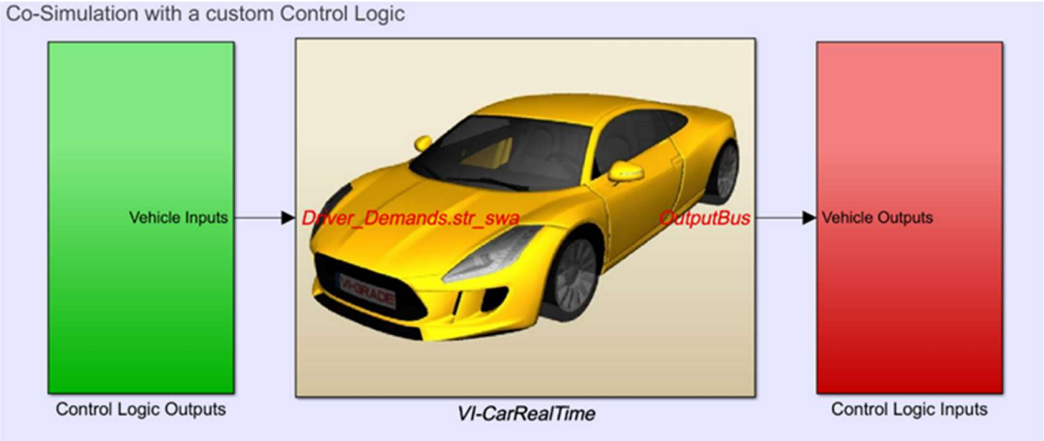


Figure 2. Co-Simulation with Simulink and VI-CarRealTime.

As mentioned in Section 2, it is possible to perform simulations off-line, using Matlab/Simulink and using a Driver-in-the-Loop approach, thanks to the VI-Grade DiM 400 simulator available at the Dri.S.Mi. Laboratory. When simulating off-line, the driver model used is a multiple preview distance one, configured to work with three different weighted preview times. The steering wheel is then controlled in angle by directly imposing the output of the controller.

2.5. Accident indexes

When exposed to a downburst wind, there are two principal kind of events that may occur: the vehicle moves laterally veering out of the lane, producing a lane invasion, or the vehicle rollover. Therefore, to determine the behaviour of the vehicle under thunderstorm winds, two indexes that quantifies the vehicle condition have been defined. The Lane Invasion (LI), consist of computing the remanent lane width considering the lateral displacement of the vehicle. The second index, Normalised Load Transfer (NLT), regarding the rollover risk, and related to the lateral load transfer, is computed as the difference in vertical load between left and right wheel, divided by the total steady state vertical load of the axle, the worst axle is considered.

4. RESULTS

The procedure has been used to simulate the case of an unladen small lorry that travels across the thunderstorm following the trajectory defined in Fig 1.a) at 80 km/h, while the downburst moves at 5 m/s in the opposite direction. The atmospheric boundary wind was set at 5 m/s. In this case the simulation was performed off-line. In Fig. 3 the time histories of the two indexes are shown. LI index overcome the threshold, meaning the lorry goes out of the lane which represent a severe risk of accident, while from the NLT index values a low risk of rollover is obtained.

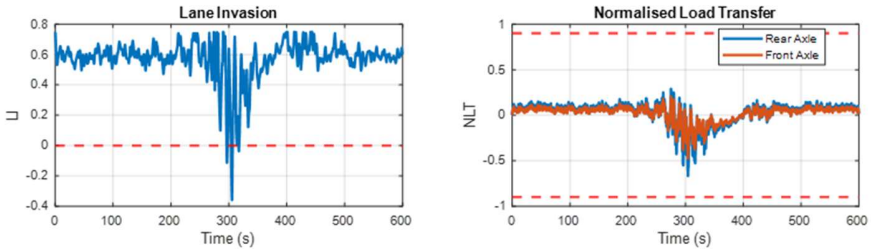


Figure 3. Simulation of an unladen small lorry at 80 km/h under thunderstorm downburst winds. Lane Invasion (LI) and Normalised Load Transfer (LTI) indexes.

7. CONCLUSIONS

In this work an overview of a methodology for the evaluation of vehicle stability under strong nonstationary cross winds generated by a thunderstorm downburst was presented. The procedure is composed by three main steps: the definition of the wind velocity field during a thunderstorm downburst, the calculation of the aerodynamic loads acting on the road vehicle and the evaluation of the dynamic response of the vehicle-driver system.

Future developments of this project include the wind tunnel test to characterise diverse kind of vehicle that are representative of the vehicle universe: saloon car, small lorry, double-decker bus and an articulated lorry.

ACKNOWLEDGEMENTS

The project CROSS-STORM has been funded by EU, NextGenerationEU, M4C2I1.1, Project PRIN 2022 PNRR "CROSS-STORM", Prot. 202284ZER9 – CUP D53D23003170006

REFERENCES

Baker, C., Cheli, F., Orellano, A., Paradot, N., Rocchi, D., 2009. Cross-wind effects on road and rail vehicles. Vehicle System Dynamics 47(8), 983–1022.

Cioffi A., Semeraro F., Dellavedova A., Schito P., Vignati, M., 2022. A numerical methodology to assess the rollover risk of a generic car-caravan system in different driving conditions. International Journal of Automotive Engineering 13(3), 103–113.

Cioffi, A., Prakash, A.R., Sabbioni, E., Vignati, M., Cheli, F., 2023. Heavy-Vehicle Response to Crosswind: Evaluation of Driver Reactions Using a Dynamic Driving Simulator. Vehicles 5, 344–366.

Xhelaj, A., Burlando, M., Solari, G., 2020. A general-purpose analytical model for reconstructing the thunderstorm outflows of travelling downbursts immersed in ABL flows. Journal of Wind Engineering and Industrial Aerodynamics 207, 104373.

Xhelaj, A., Araya Reyes, C. E., Repetto, M. P., Pagnini, L., Tomasini, G., 2024. CROSS-STORM project: Developing a numerical-experimental procedure for evaluating the risk of accident on road vehicles due to the strong crosswinds generated by a thunderstorm. 14th UK Conferencon Wind Engineering, Southampton, UK.

Xhelaj, A, Burlando, M, Pagnini, L, Repetto, M.P,2025. Simulating the downburst turbulent outflow velocity field on a moving vehicle. 9th European-African Conference on Wind Engineering (EACWE2025), Trondheim, Norway.

Zhang, Z., Li, J., Guo, W., 2018. Combined simulation of heavy truck stability under sudden and discontinuous direction change of crosswind with computational fluid dynamics and multi-body system vehicle dynamics software. Advances in Mechanical Engineering 10(7).

Full-scale measurements of freight train aerodynamics

Mike Jesson [1], David Soper [2], Chris Baker[3]

Dept. of Civil Engineering, University of Birmingham, Birmingham, UK.
[1]m.a.jesson@bham.ac.uk
[2]d.soper@bham.ac.uk
[3]c.j.baker@bham.ac.uk

SUMMARY:
In many countries, freight train speeds are limited to significantly below the speeds of passenger services. In the UK, for example, freight is limited to 75mph (120km/h) compared to the 125mph (200km/h) of high-speed passenger trains. This difference leads to challenges when running freight and passenger services on the same network, with freight services being looped while passenger services pass, and large intervals required between freight and passenger services using the same line. These inefficiencies add additional carbon costs to rail freight and limit the amount of rail freight which the network can carry. One means of addressing this issue is to increase freight train speeds. However, this has inherent risk through a resulting increase in slipstream velocities and pressures, with potential safety implications for passengers on platforms and trackside workers. This paper presents results from a long-term study in which freight train aerodynamic parameters (slipstream velocity and pressure) have been measured at full-scale at a live railway, the UK West Coast Main Line. Sonic anemometers and static pressure tubes were installed in accordance with EN14067-4, while CCTV was used to record train passes to provide consist and loading information.

Keywords: Vehicle aerodynamics, full-scale testing, freight train slipstreams

1. INTRODUCTION

As trains travel, they create changes in both local pressures and velocities. Pressure changes are important in terms of loading on trackside structures and passing trains, while velocity changes (the train's slipstream, caused by air being dragged by the train due to friction between the train and the air (Baker et al., 2019)) may be experienced by objects and people as gusts, with potentially detrimental effects. To-date, slipstream research has mainly focused on passenger trains in line with development of faster, more aerodynamically efficient trains and network upgrades (Schulte-Werning, 2002) , although some freight slipstream studies have been conducted by rail authorities following incidents (RAIB, 2017) and there is a very limited set of full-scale data (e.g. Soper and Baker, 2020).

There is a push towards increasing freight train speeds above the 75mph (120km/h) limit in place in many countries. Doing so will not only facilitate an increase in freight capacity but will also significantly reduce the routing/timetabling issues which arise when running freight and passenger services on the same lines. This is an important development to enable efficient use of existing infrastructure and the encourage a move towards rail freight and away from road freight, with a corresponding reduction in freight carbon emissions. This forms a vital part of the UK (and global) move towards Net Zero. Clearly, this move to faster freight must be done in a safe manner and

with due consideration of impacts on infrastructure. Freight train aerodynamics plays an important part in this, with the need to ensure that air speeds in train-generated slipstreams do not cause gusts which are dangerous to station users and trackside workers, and that increased slipstream forces on infrastructure do not cause significant wear and potential failure.

This paper presents a unique, long-term full-scale study run by the University of Birmingham (UoB) as part of a project for the UK Railway Standards and Safety Board (RSSB) with the aim of quantifying the slipstreams generated by freight trains under real operating conditions. Trackside wind velocities and pressures were measured over a 3-month+ period (measurements are ongoing at the time of writing), allowing ensemble averaging of large numbers of freight train slipstreams, aggregated by train configuration to ensure statistical convergence of the results. This work will feed into complementary moving model tests, allowing extrapolation to higher train speeds.

2. SITE LOCATION AND METHODOLOLGY



Figure 1 Anemometer and static pressure rakes on-site

The site used for these tests was just north of Acton Bridge station on the UK West Coast Main Line (WCML). The WCML is one of the main freight routes in the UK, with the section chosen being a full line speed section (freight speeds up to 75mph, passenger speeds up to 125mph). Access to the site was possible through a Network Rail maintenance yard approximately 400m south of the test site, allowing relatively easy access for installation and maintenance. Due to the necessity to install apparatus at height, installation was coordinated with Network Rail scheduled maintenance, allowing track access. Data were recorded using eight Gill R3 sonic anemometers (two rakes of four) and seven static pressure probes (two rakes of three plus one additional probe

for additional train speed calculations), as shown in Figure 1. Instrumentation was installed at the positions relative to centre of track (CoT) and top of rail (ToR) as specified in the relevant standards (EN14067-4). All apparatus was installed on two existing OLE stanchions, approximately 50m apart, with a rake of anemometers and a rake of static pressure probes on each. Anemometers A1, A2, A3 and A4 were co-located with static pressure tubes P1, P2 and P3, with anemometers A5, A6, A7 and A8 co-located with P4, P5 and P6. The additional static pressure measurement tube was recorded along with P4-6.

3-D velocities were recorded at 20Hz and pressures were recorded at 200Hz, both exceeding the minimum sampling frequencies required by the standards. Data were logged locally using Raspberry Pi microcomputers running bespoke software developed at the UoB, with automated upload of data to UoB servers. Information about passing trains was extracted from www.realtimetrains.co.uk, providing route information, time at which the train passed Acton Bridge and (for passenger trains) train consists information. Due to the lack of detailed freight train data available, a CCTV system was installed to record trains passing the test site. As data analysis progresses, this will be used to classify trains by type and consist, enabling aggregation of data from trains with the same configuration and thus the ensemble averaging necessary for a statistical analysis of the train aerodynamics, which can vary considerably between nominally identical trains.

Data capture has been ongoing since late August 2024 and continues at the time of writing.

3. RESULTS

Over 700 freight train passings have been recorded by the system, along with passenger services such as Pendolinos. Data analysis is on-going and more detailed analysis will be presented at the conference, including ensemble-averaging and statistical analysis of maximum wind speeds. Example results for freight and a Pendolino service are shown in Figure 2 and Figure 3 respectively. The larger slipstream velocities for the freight train, despite its slower speed, and the repeated pressure spikes along the train length are evident.

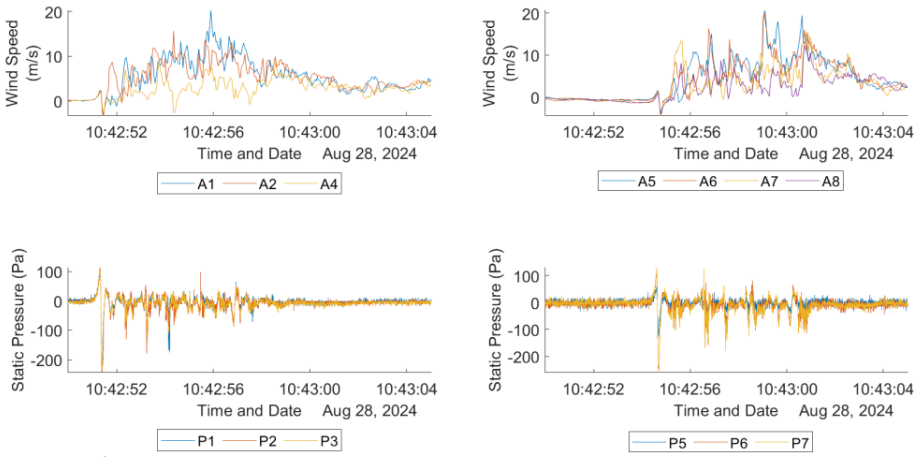


Figure 2 Example freight train slipstream data - wind speed and static pressure at each measured point

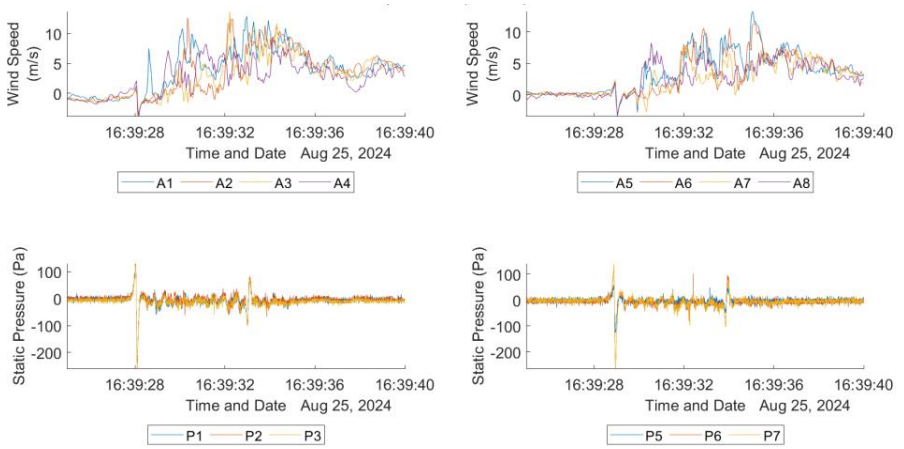


Figure 3 Example freight train slipstream data - wind speed and static pressure at each measured point

ACKNOWLEDGEMENTS

The authors would like to thank RSSB for funding the project. We gratefully acknowledge the assistance of Network Rail for their help with facilitating trackside access for installation and maintenance of the apparatus, in particular the numerous COSSs who have accompanied us on site visits.

REFERENCES

Baker, C., Johnson, T., Flynn, D., Hemida, H., Quinn, A., Soper, D., Sterling, M., 2019. Train Aerodynamics: Fundamentals and Applications, 1st ed. Elsevier.

RAIB, 2017. Occupied wheelchair contacting a passing train at Twyford station 7 April 2016. Rail Accident Investigation Branch Report.

Schulte-Werning, B., 2002. The TRANSAERO Project, in: Schulte-Werning, B., Grégoire, R., Malfatti, A., Matschke, G. (Eds.), *TRANSAERO — A European Initiative on Transient Aerodynamics for Railway System Optimisation*. Springer Berlin Heidelberg, Berlin, Heidelberg, pp. 11–24.

Soper, D., Baker, C., 2020. A full-scale experimental investigation of passenger and freight train aerodynamics. *Proceedings of the Institution of Mechanical Engineers, Part F: Journal of Rail and Rapid Transit* 234, 482–497. doi:10.1177/0954409719844431

Comprehensive Risk Assessment of Vehicle Stability on Sea-Crossing Bridges : Joint Effects of Wind and Precipitation Data

Hyeong-Yun Cheon [1], Sejin Kim [2], Ho-Kyung Kim [3]

[1]*Seoul National University, Seoul, South Korea, jeonhysnu@snu.ac.kr*
[2]*Chungbuk National University, Cheongju, South Korea, sejinkim@chungbuk.ac.kr*
[3] *Seoul National University, Seoul, South Korea, hokyungk@snu.ac.kr*

SUMMARY
Long-span sea-crossing bridges are highly vulnerable to strong winds due to their elevated structure and exposure to open areas. The wind speed on these bridges varies significantly because of unpredictable wind flows, posing a substantial risk to driving safety. Another critical factor is the friction between vehicle tires and the wet road surface, which can be drastically reduced during severe weather conditions like heavy rain. Such adverse conditions frequently lead to dangerous accidents. In this study, we focus on a specific sea-crossing bridge where a major vehicle accident occurred and analyze wind tunnel testing data from scaled vehicle and bridge models. Additionally, field data collected from the bridge, such as wind, water film depths (WFD) and friction coefficients provide an accurate assessment of vehicle stability under severe weather conditions. A new accident criterion for vehicles is introduced, and the correlation between wind and rainfall intensities is examined. By incorporating these elements, the study offers a more comprehensive and differentiated risk assessment model, allowing for the prediction of accident probabilities based on wind speed and road conditions, thereby enhancing the accuracy of risk assessment for vehicles driving in extreme weather conditions on sea-crossing bridges.

Keywords: Long-span sea-crossing bridges, Severe weather conditions, risk assessment,

1. INTRODUCTIONS

Global warming and climate change have led to an increase in unpredictable weather patterns worldwide, including frequent occurrences of strong winds accompanied by heavy rainfall. These severe weather conditions pose significant risks to vehicles traveling on long-span sea-crossing bridges, which are particularly vulnerable due to their elevated structure and exposure to open areas (Kim et al., 2020). Rainfall also critically affects vehicle safety by reducing the friction between tires and the road surface, increasing the likelihood of accidents. However, in Korea, traffic control on bridges is implemented based on general guidance, as shown in Table 1, without fully considering the localized meteorological conditions surrounding the bridge. These adverse conditions, particularly on-site, often lead to accidents for traveling vehicles (Figure 1).

While previous studies, such as Kim et al. (2022), have primarily focused on the effects of wind on vehicle stability, this study expands the scope by incorporating road conditions influenced by rainfall, including water film depths (WFD) and friction coefficients. According to Luo et al. (2019), field data indicated that water film depths (WFD) respond to rainfall with a certain time

delay, and some models have been developed to predict WFD. By analyzing on-site data, this study investigates the correlation between friction coefficients and specific rainfall events, offering a more comprehensive understanding of vehicle stability under severe weather conditions.
To assess the driving stability of vehicles under these combined wind and rainfall conditions, an empty truck was selected as a representative vehicle. The study uses the Critical Wind Curve (CWC) to evaluate wind impacts, and incorporates an enhanced risk assessment approach that accounts for varying levels of rainfall intensity (RI), providing a more differentiated and accurate evaluation of vehicle stability on sea-crossing bridges.

Table 1. Current traffic control according to wind speed

	Response	Wind speed (m/s)
Level 1	Limit vehicle speed up to 80 km/h	15
Level 2	Limit vehicle speed up to 50 km/h	20
Level 3	Bridege closure	25



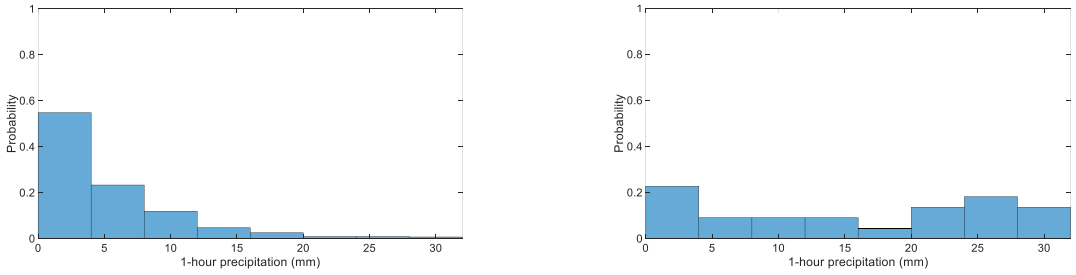
(a) (b)

Figure 1. Vehicle accident caused by (a) Typhoon on Gwangan bridge (2020)
(b) Severe weather condition on the Golden Gate Bridge (2023)

2. FIELD DATA ANALYSIS

2.1. Wind & Precipitation data

The probability of precipitation under wind conditions is shown in Figure 2. Figures 2(a) and 2(b) show the probability density of 4-minute cumulative rainfall for wind speeds over 15 m/s and 25 m/s, respectively. In Figure 2(a), the precipitation is mostly concentrated at 0 mm, indicating low rainfall probability. However, in Figure 2(b), there is a higher probability of increased rainfall intensity, suggesting a stronger likelihood of precipitation under higher wind speeds. This figure suggests a correlation between wind speed and rainfall, leading to an analysis of their joint distribution. Both figure show that rainfall intensity tends to increase during strong winds, which, considering the bridge service, could significantly threaten vehicle stability.

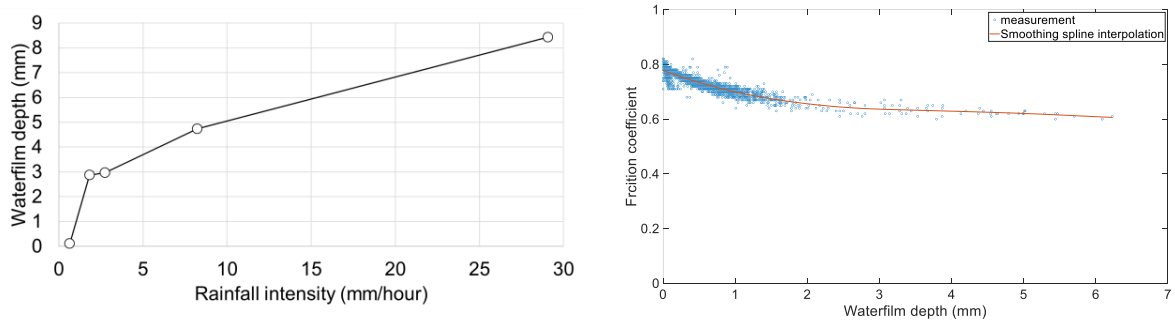


(a) (b)

Figure 2. Probability of precipitation for wind speeds (a) over 15 m/s, (b) over 20 m/s

2.2. Waterfilm Depth – Friction Coefficient

Six years of precipitation data from an AWS located near the bridge were analyzed and categorized into five rainfall intensity levels, RI0~RI5. And water film depth (WFD) and friction coefficient data were collected simultaneously during rainfall using a low-speed vehicle device operated by the Meteorological Administration. Intensity Figure 3(a) shows how water film depth (WFD), an important variable affecting road-tire friction, varies with rainfall intensity. Figure 3(b) presents the relationship between WFD and the friction coefficient, showing how friction decreases as WFD increases. The red line represents interpolated values, providing a continuous estimation of friction loss as a function of WFD, essential for assessing vehicle safety on wet surfaces.



(a) (b)

Figure 3. (a) WFD according to a hour precipitation (b) Friction coefficient correponding to WFD

3. RISK ASSESSMENT OF VEHICLE STABILITY

For a risk assessment, it is essential to acquire both the critical wind curves (CWC) and the vehicle's fragility curves, which are based on the friction coefficient that changes with different RI levels. As noted by Kim et al. (2022), the accident probability and risk index are calculated in Equations (1) and (2).

$$P_E = \sum_{k=0}^{N_{RI}} \sum_{i=1}^{16} P_{E|RI_k,\theta_i} \, P(\theta_i) \, P(RI_k) \tag{1}$$

$$N_E = 365 \, Q_d \, R_L \, R_v \, P_E \tag{2}$$

Where $P_{E|RI_k,\theta_i}$ represents the probability of an accident occurring under rainfall intensity levels RI_k and wind direction θ_i. $P(\theta_i)$ is probability of the wind coming from θ_i, and $P(RI_k)$ is the probability of rainfall intensity at level k. This approach allows for the integration of changing road conditions due to rainfall, which can significantly impact vehicle stability. The calculated accident probability enables the calculation of the risk index, as shown in Equation (2). Q_d represents the AADT (Average Annual Daily Traffic) of the examined bridge, R_L is the ratio of traffic volume occupied by the lane of interest and R_v is the composition ratio of the vehicle type

of interest. Figure4 illustrates the annual accident frequency for different rainfall intensity levels (RI0 to RI4). Notably, the combined accident frequency for RI1 through RI4 is approximately 16% of the accident frequency observed under RI0 (no rain condition), indicating that although the accident frequency is lower during rainfall than in non-rain conditions, the occurrence of accidents under rainfall conditions remains significant and should not be disregarded.

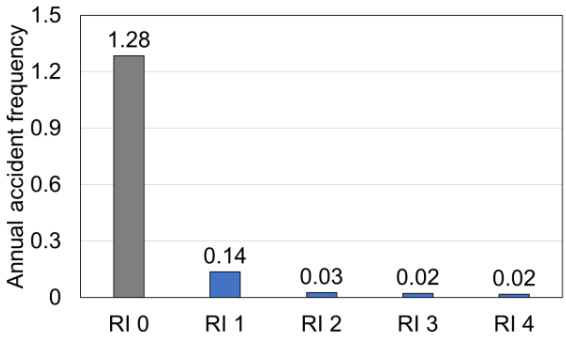


Figure 4. Risk index according to RI

4. CONCLUSIONS

This study presents a comprehensive risk assessment model for vehicle stability on sea-crossing bridges under severe weather conditions by integrating both wind and rainfall data. The findings emphasize that strong winds, coupled with reduced tire-road friction during rainfall, significantly increase accident risks on these bridges. By using critical wind curves (CWC) and vehicle fragility curves that account for various rainfall intensity (RI) levels, the tool offers a more precise prediction of accident probabilities. The results indicate that although accident frequency is higher under dry conditions (RI0), the combined accident frequency for rainfall conditions (RI1~RI4) still constitutes a substantial portion (approximately 16%) of the dry condition frequency. This highlights the importance of addressing both wind and rain impacts to enhance safety protocols on sea-crossing bridges, particularly under changing climate conditions that can lead to more frequent and intense severe weather events. This approach provides a valuable tool for developing traffic management and vehicle safety guidelines for such vulnerable infrastructure.

ACKNOWLEDGEMENTS

This work was supported by the National Research Foundation of Korea(NRF) grant funded by the Korea government(Ministry of Science and ICT) (RS-2024-00351592)

REFERENCES

Kim, S. J., Shim, J. H., & Kim, H. K. (2020). How wind affects vehicles crossing a double-deck suspension bridge. Journal of Wind Engineering and Industrial Aerodynamics, 206, 104329.

Kim, S., Seyedi, M., & Kim, H. K. (2022). Risk assessment of wind-induced vehicle accidents on long-span bridges using onsite wind and traffic data. Journal of Structural Engineering, 148(10), 04022155.

Luo, W., Wang, K. C., & Li, L. (2019). Field test validation of water film depth (WFD) prediction models for pavement surface drainage. International Journal of Pavement Engineering, 20(10), 1170-1181.

Photo by Matt LaFever. "Golden Gate Bridge closed in both directions after big-rig crash," Redheaded Blackbelt, Jan 14, 2023, https://kymkemp.com/2023/01/14/golden-gate-bridge-closed-in-both-directions-after-big-rig-crash/.

Effect of static pitch on upwind aerodynamics of yachts.

Craig Meskell[1] and Andrew Coyle[1]

[1]*Trinity College, Dublin, Ireland cmeskell@tcd.ie*

SUMMARY:
The effect of a constant, static pitch angle on the performance of the sails of the AC33 1/15 scale racing yacht rig has been modelled in an upwind condition at an apparent wind angle of 19° with the sail trim configuration associated with maximum drive. The airflow is simulated using RANS with the SST turbulence model. A rudimentary representation of the hull is included in the model and the wind shear associated with the atmospheric boundary layer is included in the inflow conditions. The airflow and sail performance has been assessed for four heel angles (0°, 5°, 10°, 15°) and a range of static pitch angles (-5° to +5°). The drive and side forces are renormalized with reference to the zero heel, zero pitch condition and it is found that negative pitch (i.e. bow downwards) does not significantly effect the drive force, but does increase the side force. Conversely even a small positive pitch (bow upwards) can reduce the drive force by as much as 8% caused by the secondary vortex formed at the foot of the genoa streaming across the mainsail.

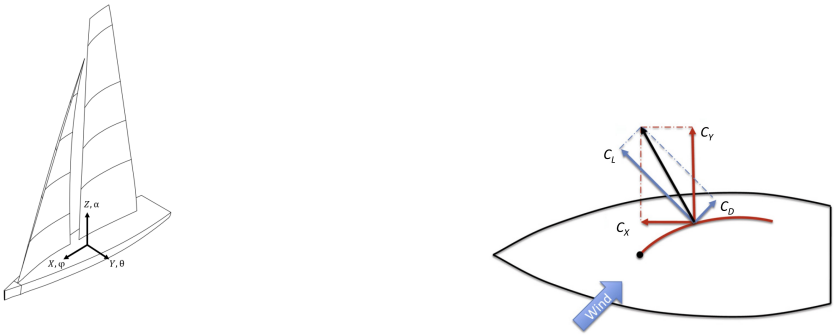
Keywords: Upwind sail, Secondary flow

1. INTRODUCTION

The so-called Bermuda rigged sloop has become very common for leisure and racing sail boats ranging in size from small dinghies (e.g. RS-200) to large ocean going yachts (e.g. IMOCA60). Viola et al. (2013) have measured the sail shape and performance in a wind tunnel at 1/15 scale and executed simulations to determine the flow field. They found that a significant proportion of the drive force is associated with the leading edge region of the jib (i.e. the front sail). The mast was vertical (i.e. no heel) and at zero pitch. Persson et al. (2017) have numerically examined the effect of dynamic pitching on the air flow around the sails. They found the flow at the head of the sail is significantly modified because of the relatively high additional local velocity. Furthermore, Augier et al. (2014) have demonstrated that the effect of dynamic pitching cannot simply be modeled as a series of quasi-steady conditions. They note that further work is required to understand the effect of pitch. In these studies the sails are not studied integrated with the hull. Nava et al. (2017) have experimentally measured and numerically modeled the effect of interaction between a sail rig and a flat plate, generally representative of the deck, finding that the jib exhibited a leading edge vortex. Viola et al. (2013) found RANS was sufficient to accurately resolve the mean pressure field around the sails. In this study, the effect of static pitch angle on the upwind performance of the sails is assessed and a simple representation of the hull and deck is included.

2. METHODOLOGY

The local coordinate system fixed to the hull is shown in Fig. 1(a). The apparent angle of attack of the wind to the boat is α which is defined as positive for wind in the positive quadrant of the $X-Y$ plane. Note that a positive pitch, θ, corresponds to a displacement of the bow upwards, while a



(a) Coordinate system and sign convention (b) Aerodynamic force system relative to hull.

Figure 1. Force definition

positive heel (or roll) angle, ψ leads to the sails leaning away from the wind.

By convention, the lift (F_L) and drag (F_D) forces on a lifting surface (in this case the sails) are perpendicular and parallel to the air flow direction. However, the components of the aerodynamic forces relevant to the operation of the boat are the drive force (F_X) and the side force (F_Y) which are aligned with and perpendicular to the hull, respectively. The drive force propels the boat forward, while the side force is unwanted and creates a tendency for the boat to slip sideways (i.e. drift) and to heel (i.e. roll). The relationship between the two sets of aerodynamic forces is shown in Figure 1(b).

The aerodynamic forces can be non-dimesnionalised in the usual way.

$$C_i = \frac{F_i}{\frac{1}{2}\rho_{air} U_{REF}^2 a} \tag{1}$$

where U_{REF} is taken from an upstream point at the height of the main sail. The reference length used is the indicative chord, $a = 0.4$m, defined as $a = \frac{S}{2h}$ where h is the distance from the deck to the top of the mainsail and S is the projected sail area of the entire rig (jib and mainsail).

Since the objective in this study is to assess the effect of heel and pitch angles, the force coefficients can be further normalized to yield a relative drive force using a reference configuration:

$$C_i^* = \frac{C_i}{C_{i_{REF}}} \tag{2}$$

For both drive force coefficient, C_X and side force coefficient, C_Y, the reference value $C_{i_{REF}}$ is the respective values obtained for the zero pitch, zero heel case.

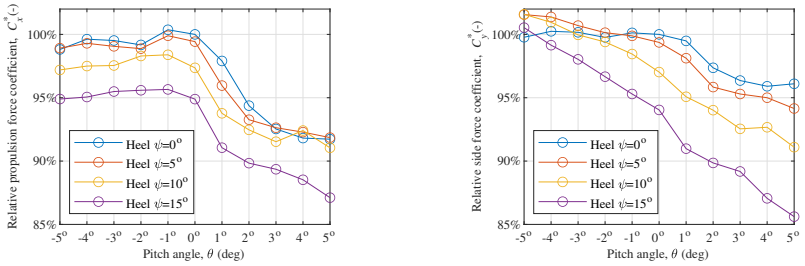
The sail shape used for this analysis was the Emirates Team New Zealand's AC33 challenger. The sail geometry under wind load was determined and pressure distribution measured on a 1/15th scale model at the Yacht Research Unit, University of Auckland Viola et al. (2013) and the sail trim chosen corresponds to the maximum drive force referred to trim position G3M2.

The sail rig and hull assembly were situated at an angle of incidence, α, of 19° within a rectangular domain which was orthogonally aligned with the wind direction and was $40a$ long in the streamwise direction, $70a$ wide and $7.5a$ high. The floor of the domain representing the sea surface was flat. Unlike the simulations previously conducted by Viola et al. in which the sails were mounted on a flat plate flush with the nominal water surface, in the current study a rudimentary representation of the hull was included based on the gross dimensions of the AC33. This facilitates the application of static pitch and heel to the sails as it is only the geometry near the intersection of the hull with the flat domain boundary that changes.

The simulations were conducted at model scale with a Reynolds number of 2×10^5 to allow direct comparison with experimental data. ANSYS Fluent R2023 was used to execute RANS simulations using the SST turbulence model and the second order coupled solver. The mesh was a poly hexcore mesh with 2.6×10^6 cells. The near wall (sail and deck surfaces) had local mesh refinement to achieve y^+ less than 1. With a uniform inflow, the current simulation model has been found to be in good agreement with the available experimental surface pressure data (Viola et al., 2013). Inflow conditions were modified to include a vertical shear to model the atmospheric boundary layer (Richards and Hoxey, 1993).

3. RESULTS AND DISCUSSION

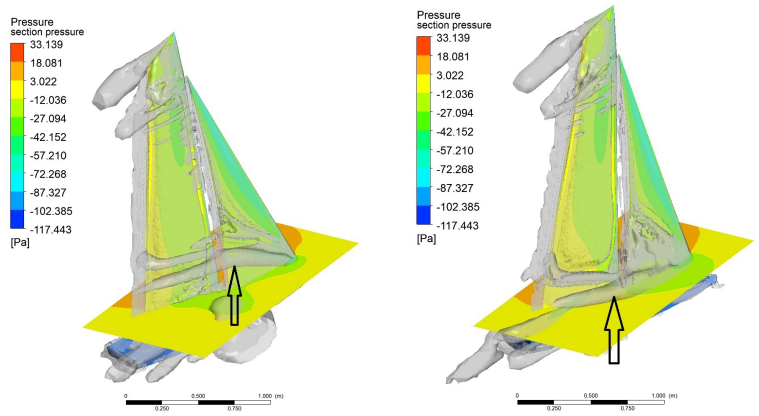
Figure 2 shows the variation of force coefficients with pitch angle for four heel angles. The zero pitch, zero heel condition is used as the reference in eqn. 2 so this condition has a value of 100%. Figure 2(a) shows that even a small positive (i.e. bow up) pitch angle can decrease the drive force coefficient by as much as 8% compared to zero pitch. Similar trends can be seen for different heel angles. Conversely, negative pitch does not yield increased propulsion force, but does increase the side force, with the effect less significant at smaller heel angles (fig 2(b)). This suggests that trimming the boat to have slightly negative pitch will yield improved propulsion.



(a) Relative drive force coefficient, C_x^*. (b) Relative side force coefficient, C_y^*.

Figure 2. Force coefficients on sails as pitch angle changes for various heel angles relative to the zero heel (ψ), zero pitch (θ) condition .

Figure 3 shows the downwind (leeward) side of the rig for two pitch angles at zero heel ($\psi = 0$). The sails are rendered by static pressure and a static pressure is also shown on a slice plane close to the deck. An isosurfaces of the Q-criterion is also shown as a transparent surface. The relevant flow feature in the current study is the secondary flow which arises due to interaction of the leading edge of the genoa and flow over deck. This causes a large vortex structure, substantially aligned in the streamwise direction, at the bottom (foot) of the jib starting from the intersection of the sail



(a) Pitch angle $\theta = +5°$ (b) Pitch angle $\theta = -5°$

Figure 3. Visualization of the Q criterion and pressure field around the sails at two pitch angles for zero heel ($\psi = 0$)

and the deck (the tack). This flow feature is indicated by an arrow in Figure 3. As can be seen in Figure 3(a), at positive pitch angles, this vortex streams higher on both mailsail and jib, modifying the flow and causing a reduction in the extent and intensity of the low pressure on the suction side of the genoa, thus reducing the drive force. Conversely, Figure 3(b) shows that at negative pitch angles the vortex is guided down towards the deck and away from the sails.

4. CONCLUSIONS

It has found that the drive force obtained when sailing upwind is reduced when even a small static upward pitch is applied, suggesting that trimming the boat so that the bow is deflected downwards may yield improved performance. However, negative pitch also increases sideforce, which will tend to increase heel angle and leeway. So whether negative pitch will actually improve overall boat speed can only be assessed with a comprehensive Velocity Prediction Programme (VPP), which is beyond the scope of this study. Further work is also needed to assess whether the effect reported here persists in a more common scenario of dynamic pitching. Nonetheless, the current results indicate that pitch angle may be important in evaluating the sail performance in upwind operation.

REFERENCES

Augier, B., Hauville, F., Bot, P., Aubin, N., and Durand, M., 2014. Numerical study of a flexible sail plan submitted to pitching: Hysteresis phenomenon and effect of rig adjustments. Ocean Engineering 90. Innovation in High Performance Sailing Yachts - INNOVSAIL, 119–128.

Nava, S., Cater, J., and Norris, S., 2017. Modelling leading edge separation on a flat plate and yacht sails using LES. International Journal of Heat and Fluid Flow 65, 299–308.

Persson, A., Lindstrand, R., Muggiasca, S., and Larsson, L., 2017. CFD prediction of steady and unsteady upwind sail aerodynamics. Ocean Engineering 141, 543–554.

Richards, P. and Hoxey, R., 1993. Appropriate boundary conditions for computational wind engineering models using the k-ε turbulence model. Journal of Wind Engineering and Industrial Aerodynamics 46-47, 145–153.

Viola, I., Bot, P., and Riotte, M., 2013. Upwind sail aerodynamics: A RANS numerical investigation validated with wind tunnel pressure measurements. International Journal of Heat and Fluid Flow 39, 90–101.

Extreme value distributions of vehicle lateral lane deviation using frequency-domain models and real-world data

Sebastian Reymert[1], Øyvind Wiig Petersen[2], Ole Øiseth[3]

[1]*Norwegian University of Science and Technology (NTNU), Trondheim, Norway,* *sebastian.reymert@ntnu.no*
[2]*Norwegian University of Science and Technology (NTNU), Trondheim, Norway,* *oyvind.w.petersen@ntnu.no*
[3]*Norwegian University of Science and Technology (NTNU), Trondheim, Norway,* *ole.oiseth@ntnu.no*

SUMMARY:
Theoretical frameworks have been proposed to describe the dynamic lateral motion of vehicles in their lanes under the action of crosswinds before. In some such works, the concept of a gust factor is used based on the assumption that the extreme value distribution is a Type I Generalised Extreme Value distribution (GEV Type 1, or Gumbel). In this work, a frequency-domain method is used to model the Power Spectral Density (PSD) of the vehicle's lateral motions and is compared to spectra measured in the field with a test vehicle. Due to the high bandwidth of the response PSD and the short time interval relevant to vehicle safety assessments – i.e. the time interval of the order of minutes during which vehicles are typically exposed to strong crosswinds on public roads – it is found that it may be more appropriate to model the extreme values with a Gaussian distribution rather than a Gumbel.

Keywords: field experiment, vehicle safety, driver

1. INTRODUCTION

Crosswinds can pose a safety risk to motorists and lead to serviceability issues as a result of wind-related traffic regulations. Consequently, it is important to have an accurate and precise understanding of road vehicle accident risk under strong crosswinds. The objective of this work is to compare a model of a vehicle-driver-wind system to field measurements collected using a test vehicle in strong crosswinds. The appraised model is then used to study the extreme value distribution of lane deviation.

2. METHOD

The model was composed of: 1) a description of the turbulence spectrum for a moving point in a stationary wind field, 2) a single-track vehicle model (describing vehicle motion in the plane of the road), 3) a path-following driver model and 4) a quasi-steady aerodynamic force model.

The turbulence spectrum was calculated using the closed-form expressions derived by Hu et al. (2019), using a Kaimal spectrum and a Davenport coherence model. The single-track model was the one presented by Abe (2015) expressed relative to a global frame of reference. The path-following driver model was also presented by Abe (2015) and is a proportional gain on the vehicle's



(a) *Test vehicle*



(b) *Dolmsund bridge*

Figure 1. Field experiment

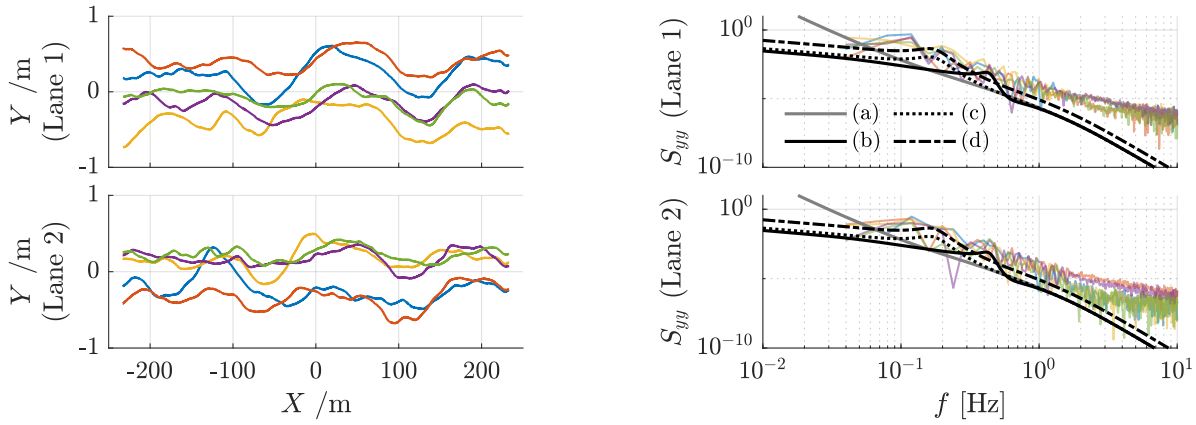
position error at a look-ahead distance L with driver reaction delay time $\tau_l = 0.3$ s. The quasi-steady aerodynamic force model applied was the one presented by Baker, 1986. The PSD of the lateral position of the vehicle can be expressed,

$$S_{\mathbf{zz}}(\omega) = \mathbf{HB}S_{uM}(\omega)\mathbf{B}^*\mathbf{H}^*, \tag{1}$$

as demonstrated by Yan et al. (2018), where $\mathbf{z}$ is the state vector containing the lateral position of the vehicle relative to the centreline of the road lane y, $\mathbf{H}$ describes the vehicle-driver dynamics and $\mathbf{B}$ is the input matrix of the system dynamics. The only input that was considered is the longitudinal component of turbulence u. $S_{\mathbf{uM}}$ is the PSD of u from the point of reference of a point moving through the wind field.

The test vehicle was the one pictured in Figure 1a and the field experiments were performed on the Dolmsund bridge (pictured in Figure 1b). The test vehicle was driven at 80 km/h repeatedly in each lane/direction across the bridge 5 times under an almost perfectly – on average – perpendicular crosswind with a mean wind speed – relative to a non-moving point – of 16 m/s. The test vehicle was equipped with a dual-antenna Global Navigation Satellite System (GNSS) measurement system with Real-Time Kinematic (RTK) base-station corrections to give 2 cm position accuracy, a steering angle sensor and an Inertial Measurement Unit (IMU).

The single-track model parameters were calibrated using controlled manoeuvres on a flat surface under zero wind conditions. The driver model steering gain was calibrated using the field data by first estimating the aerodynamic loads through an inverse method. The obtained loads were then used to identify the gain h and look-ahead distance that minimised the difference between the model and measured steering angle (h = 0.03 deg/m and $L = 19$ m). This is a rough estimate that will be discussed further next. The shear velocity of the flow $u_* = 0.99$ was calculated using the semi-empirical log wind vertical profile (Hu et al., 2019), taking $z_0 = 0.05$ m (surface roughness, first guess) and $z_d = 3$ m (average height of obstacles, first guess) at a height of $z = 35$ m (the average height of the bridge deck over sea level).



***(a)** Measured time series* ***(b)** PSD*

Figure 2. Measured and modelled lateral vehicle position, measured repetitions in different colours (a) single-track model w/o driver (b) w/ driver (c) $h = 0.01$ (d) $h = 0.01$ and $u_* = 1.98$

3. RESULTS

Time series of the vehicle deviation from the centreline of the lane measured by the GNSS antenna can be seen in Figure 2a in each of lanes 1 and 2. Figure 2b shows the PSD of these time series compared to various modelled spectra (discussed next).

4. DISCUSSION & CONCLUSION

The modelled spectra without (a) and with a driver (b) in Figure 2b generally show a good match in shape with the measurements up to about 2 Hz. Clearly, the driver has the biggest impact at the lower frequencies (below $\approx 10^{-1}$) and this is where the model with a driver (b) matches the shape of the measured spectra better than the model without a driver (a) which continues to rise with descreasing f. The model with a driver has a peak-trough feature at ≈ 0.3 Hz that is not evident in the measured data. The driver parameters h and L were only indirectly approximated and may contain significant errors and even vary in time and/or with driving conditions. A model with a lower gain $h = 0.01$ deg/m (line c) shows a better match with the measurements suggesting that the driver may on average be less aggressive in their response to crosswinds than originally estimated.

Line (c) appears offset from the measurement data by a negative constant up to about 1 Hz. Above this frequency, the measured and modelled spectra diverge, possibly due to noise in the GNSS position measurements – sensor noise or local vibrations of the roof rack on which the antennae are mounted are possible explanations. An explanation for the offset may be that the shear velocity (turbulence intensity) is underestimated by the log vertical wind profile model. It is known that the high depth of the concrete arch girder increases the turbulence intensity in the airspace above the bridge deck in which the vehicle is driving. The line (d) where the turbulence intensity is doubled shows a better match with the measurements. These results suggest that the model – given correct input parameters – has the potential to accurately model the real-world response of a vehicle to crosswinds.

S_{yy} is very widely banded (the shape factor ε for the modelled spectrum is 0.91), suggesting that the distribution of peaks is more likely to look like a Guassian than a Rayleigh distribution (Moe and Niedzwecki, 2005). Regardless, if the time interval is long enough, then the extreme value distribution – the peak distribution taken to the power N, the number of peaks – does approach the Gumbel shape. Figure 3 shows histograms of 5,000 extreme values from the same number of Monte Carlo simulations from the modelled spectrum S_{yy}. For a long interval (10,000 s or 2.7 hours), a Gumbel distribution fits well, though the same cannot be said of a 3 minute period (120 s), which is the approximate period taken by the vehicle to cross the bridge. A Normal distribution has been fitted, where the fit matches the histogram nicely on the right side of the distribution and in the upper tail. The Normal distribution is therefore a better model for the extreme value distribution – at least for the percentiles above the 70-80th.

In conclusion, it has been shown that the model is a good approximation of the measurements made in the field in real operating conditions on a bridge. Further study is needed to appraise the accuracy of the driver model and the moving point wind spectrum. Key parameters are the turbulence intensity of the oncoming wind and the driver's steering gain. The vehicle's lateral lane deviation response spectrum is highly wideband ($\varepsilon = 0.91$) and for the short period interval that is relevant in the practical case of a vehicle crossing a bridge (3 min), the extreme value distribution is closer to a Normal distribution rather than the Gumbel form that has previously been assumed in the literature.

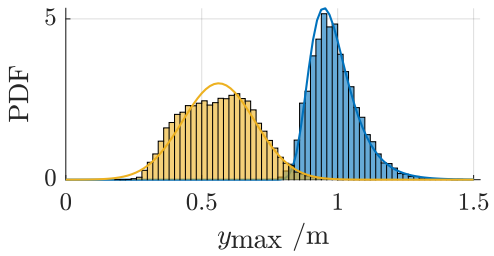


Figure 3. Extreme value PDFs of lateral deviation y for time intervals of 10,000 s (blue) and 120 s (yellow)

ACKNOWLEDGEMENTS

The work was funded by the Norwegian Public Roads Administration (NPRA)

REFERENCES

Abe, M., 2015. Vehicle Handling Dynamics. Second. Butterworth-Heinemann.

Baker, C., Apr. 1986. A simplified analysis of various types of wind-induced road vehicle accidents. Journal of Wind Engineering and Industrial Aerodynamics 22, 69–85.

Hu, P., Han, Y., Cai, C., Cheng, W., and Lin, W., May 2019. New analytical models for power spectral density and coherence function of wind turbulence relative to a moving vehicle under crosswinds. Journal of Wind Engineering and Industrial Aerodynamics 188, 384–396.

Moe, G. and Niedzwecki, J. M., Dec. 2005. Frequency of maxima of non-narrow banded stochastic processes. Applied Ocean Research 27, 265–272.

Yan, N., Chen, X., and Li, Y., Mar. 2018. Assessment of overturning risk of high-speed trains in strong crosswinds using spectral analysis approach. Journal of Wind Engineering and Industrial Aerodynamics 174, 103–118.

Defining geometric level of detail of furniture for indoor ventilation

Nadine Hobeika[1], Philomena M. Bluyssen[2], Clara García-Sánchez[3]

[1]*Delft University of Technology, Delft, the Netherlands, N.Hobeika@tudelft.nl*
[2]*Delft University of Technology, Delft, the Netherlands, P.M.Bluyssen@tudelft.nl*
[3]*Delft University of Technology, Delft, the Netherlands, C.Garcia-Sanchez@tudelft.nl*

SUMMARY:
When simulating indoor airflows with computational fluid dynamic (CFD) simulations, researchers often assume varying levels of geometric detail for different surfaces and objects in the room. These choices stem from lacking certain geometrical data, simplifying mesh generation, or neglecting certain geometry effects. For the modelled furniture in a room, the literature ranges from basic box models to detailed representations of furniture. However, to the best of our knowledge, no study has systematically examined how furniture detail affects indoor airflow predictions and how to classify that level of detail for CFD simulations. This paper addresses this gap, using CFD simulations to explore how the level of furniture detail influences airflow in a room with a breathing occupant, using steady, incompressible RANS simulations with OpenFOAM. The results show a difference between different levels of detail of furniture. Depending on the application, this can help engineers make more informed decisions on the geometry of the furniture in their simulations.

Keywords: level of detail, indoor ventilation, computational fluid dynamics

1. INTRODUCTION

The rapid spread of the severe acute respiratory syndrome coronavirus 2 (SARS-CoV-2) initiated extensive research on ventilation and aerosol transmission within the indoor environment, emphasising the need for computational fluid dynamics (CFD) simulations to predict airflow patterns and contaminant distribution. These simulations incorporate varying levels of geometric detail (the degree of geometric simplification employed) to model indoor spaces; however, no standardised framework exists to guide when and how different indoor levels of detail (ILoD) should be used, particularly for objects such as furniture that could significantly influence the airflow. Previous studies have demonstrated the impact of the ILoD of a manikin on the convective flow and the concentration distribution of pollutant in a room, both numerically (Topp, Hesselholt, et al., 2003) and experimentally (Topp, Nielsen, et al., 2002). However, the role of furniture ILoD in CFD simulations has not been thoroughly investigated. Standards such as IndoorGML (OGC, 2020) provide frameworks for modelling indoor furniture and topology for navigation and location-based applications. Still, these are not tailored for airflow simulations. Additionally, some recent studies have proposed frameworks for energy (Penn, 2018) and daylighting applications (Forouzandeh et al., 2024), yet no similar approach for furniture has been defined for ventilation analysis. This work proposes an initial framework for defining the ILoD of furniture specifically for CFD-based indoor ventilation simulations. This allows us to systematically determine which components to retain or omit at different ILoDs. By establishing a structured approach to ILoDs, we aim to enhance

the comparability of ventilation studies and help researchers choose appropriate ILoD based on its advantages and limitations.

2. METHODS

2.1. ILoD specification

The room's geometry (ceiling, floor, interior walls) in all ILoDs is defined by simple surfaces deprived of protrusions or details. The input and output of the ventilation system are reduced to one patch integrated into the closest room surface. A manikin head placed in the room behind the furniture includes an inlet mouth patch.

For the furniture, we first model the geometry based on our measurements using the modelling software Rhinoceros 3D® and Grasshopper. Based on that geometry, we define the following ILoDs. ILoD0 is the base level and contains no furniture (see Fig. 1 a). ILoD1 models the furniture using the bounding box of the original geometry (see Fig. 1 b). For the higher ILoDs, we first decompose the furniture into different parts, similar to the medial axis transform structure (Blum, 1967). This results in two types of parts: planar features, such as the tabletop, the seat of the chair and the backrest, and linear features, such as the legs of the tables and chairs. Then, we find the largest disc that fits completely inside the decomposed parts and filter the parts based on the diameter of those discs. Based on that, ILoD2 includes all furniture parts that fit the largest disc with a diameter of 10 cm and higher (see Fig. 1 c). ILoD3 includes all furniture parts that can fit a disc with a diameter of 1 cm and higher. We define the filtering thresholds to get geometry differences between the ILoDs based on the available furniture measurements.

2.2. Case setup

The geometry of the room and furniture with the highest level of detail presented in this study is a replicate of the Experience room in the Senselab at the Delft University of Technology (Bluyssen et al., 2018). The studied ventilation regime is mixing ventilation with four inlet grilles distributed evenly across the room's ceiling and two exhausts in the plinth on the two short sides of the room. The manikin head in the room acts as a source of pollutants in the space (see Fig. 1).

2.3. CFD simulation setup

We use OpenFOAM ESI to solve the Reynolds-Averaged Navier-Stokes equations with the RNG k-ε turbulence model (Yakhot et al., 1992). The equations are solved in the steady state with a pollutant modelled as a passive scalar at the mouth of the manikin. We apply a uniform velocity profile at the inlets (0.17 m/s) and the mouth of the manikin (1.85 m/s). We use an unstructured mesh for all three cases, ranging from 58 million cells for ILoD0 to 59 million cells for ILoD3.

3. RESULTS

Fig. 2 shows a longitudinal cross-section of the velocity magnitude at the mouth for the four levels of detail of furniture. The general airflow around the chairs and tables is affected by the furniture's level of detail. Fig. 2 a shows two jets from the inlet that hit the floor, creating a large upward vortex in the room. That pattern is disrupted by the presence of furniture regardless of their ILoD (Fig. 2 b, c, and d). ILoD1 shows lower velocity magnitudes between the tables than in all other ILoDs since the boxes create a larger obstacle for airflow. The biggest difference in velocity magnitudes is

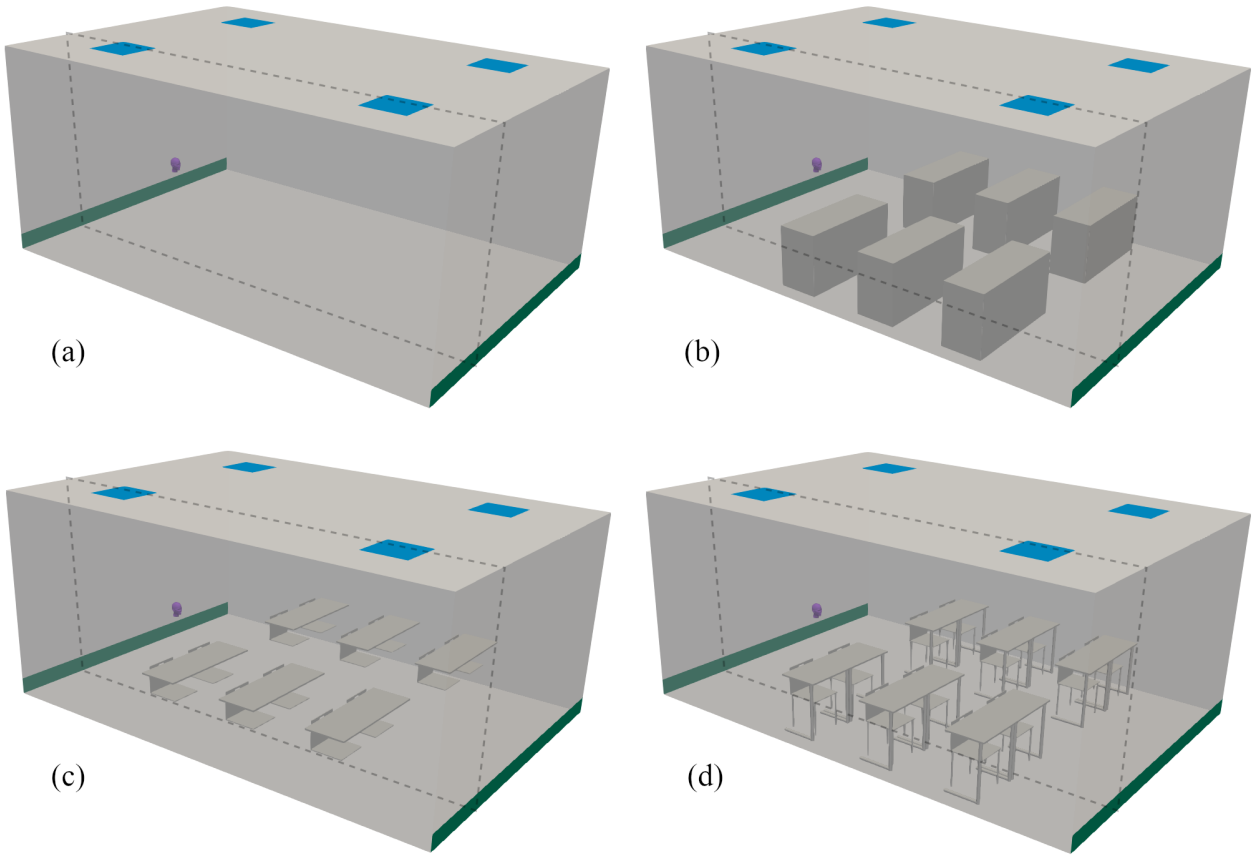


Figure 1. The four levels of detail of furniture - (a) ILoD0, (b) ILoD1, (c) ILoD2, (d) ILoD3 - The blue squares on top are the mixing ventilation inlets, the green rectangles are the mixing ventilation outlets, the head with a mouth patch is in purple, and furniture and geometry of the room is in grey, the dashed rectangle is the location of the cross-section for the results.

between ILoD1 and ILoD2, with a maximum difference value of 0.25 m/s around the table area. The difference in velocity magnitudes is the smallest between ILoD2 and ILoD3, with a maximum difference value of 0.06 m/s below the furniture. The lower support of the furniture in ILoD 3 seems to have a local impact on the airflow below the table that propagates to the airflow above the furniture. The jet of the mouth is also affected by the different ILoDs. With the absence of the upward vortex from ILoD0, the mouth's jet seems to break into two more prominent vortices than in ILoD0. In ILoD1, the jet of the mouth breaks into the biggest 2 vortices compared to the other ILoDs. ILoD2 and ILoD3 show the same two vortices with a smaller lower vortex near the furniture.

4. CONCLUSION

This study aims to understand the impact of the geometric level of detail of furniture in a room on the airflow. The results show that the ILoD impacts both the background airflow in the room and the jet coming from the mouth. However, the transition from ILoD2 to ILoD3 shows more local changes in the airflow compared to the other transitions between successive ILoDs. This is

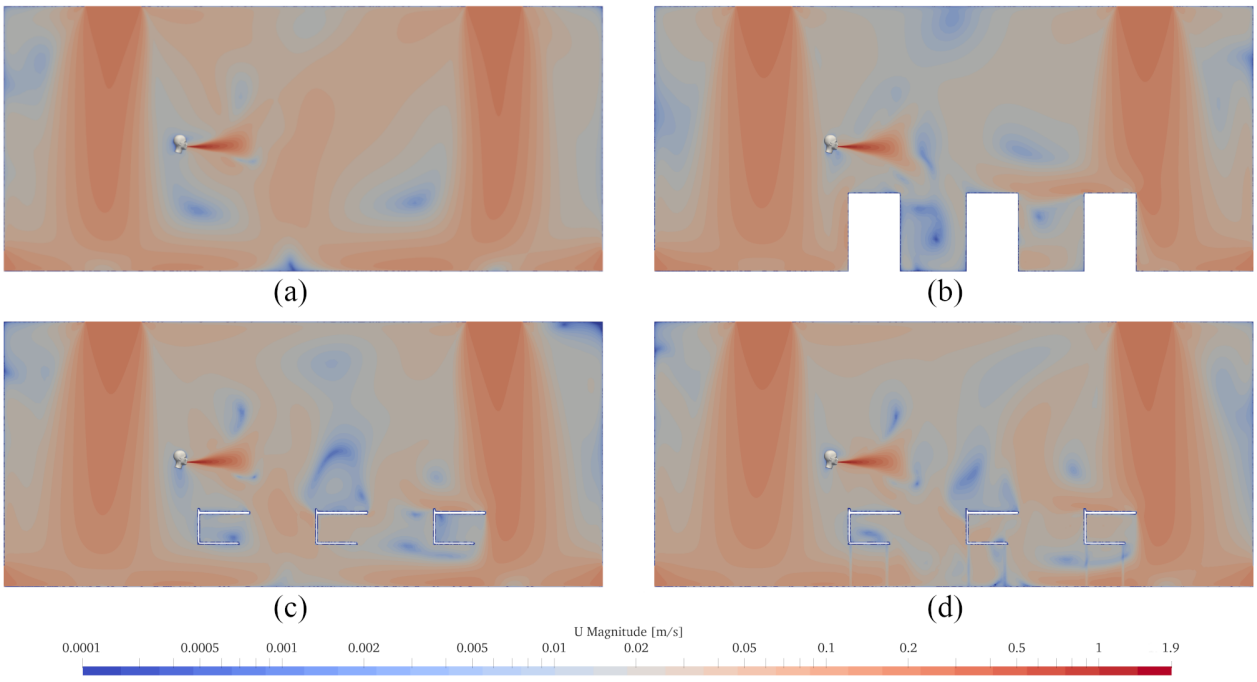


Figure 2. A longitudinal cross-section at the mouth of the velocity magnitude field of ILoD0 (a), ILoD1 (b), ILoD2 (c), ILoD3 (d).

beneficial for reducing the computational cost of indoor CFD simulations while ensuring that the most airflow-relevant furniture features are included in the computational domain. For future work, we aim to formalise the framework of ILoDs to provide guidelines for ventilation simulations that include manikins, furniture and the room's geometric level of detail.

REFERENCES

Blum, H., 1967. A transformation for extracting new descriptions of shape. Models for the perception of speech and visual form, 362–380.

Bluyssen, P. M., Zeist, F. van, Kurvers, S., Tenpierik, M., Pont, S., Wolters, B., Hulst, L. van, and Meertins, D., 2018. The creation of SenseLab: a laboratory for testing and experiencing single and combinations of indoor environmental conditions. Intelligent Buildings International 10, 5–18.

Forouzandeh, N., Brembilla, E., Nan, L., Stoter, J., and Jakubiec, A., 2024. Influence of geometrical levels of detail and inaccurate material optical properties on daylight simulation. Energy and Buildings 306, 113924.

OGC, 2020. OGC IndoorGML. Open Geospatial Consortium inc. Document 19-011r4, version 1.1.

Penn, P., 2018. Adequate BIM level of detail for LCA energy simulation. phdthesis, Open Access Te Herenga Waka-Victoria University of Wellington.

Topp, C., Hesselholt, P., Trier, M. R., and Nielsen, P. V., 2003. Influence of geometry of thermal manikins on concentration distribution and personal exposure. Proceedings of Healthy Buildings 2003.

Topp, C., Nielsen, P. V., and Sorensen, D., 2002. Application of computer simulated persons in indoor environmental modeling/Discussion. ASHRAE transactions 108, 1084.

Yakhot, V., Orszag, S. A., Thangam, S., Gatski, T., and Speziale, C., 1992. Development of turbulence models for shear flows by a double expansion technique. Physics of Fluids A: Fluid Dynamics 4, 1510–1520.

Evaluating the Impact of Horizontal Louvers on Natural Ventilation and Thermal Comfort in Polish Multi-Family Homes: A CFD Analysis

Mohammad Mahdi Mohammadi [1], Maciej Janowski [2]

[1]*Poznan University of Technology, Poznan, Poland,*
mohammad.mohammadi@doctorate.put.poznan.pl
[2] *Poznan University of Technology, Poznan, Poland, maciej.janowski@put.poznan.pl*

SUMMARY:
Climate change is intensifying summer overheating issues in buildings across cold regions like Poland, where designs have focused mainly on winter heat retention. This study evaluates the effectiveness of horizontal louvers as a passive heat-rejection strategy in Polish multi-family residential buildings, using computational fluid dynamics (CFD) to analyse thermal and ventilation performance. Over 300 residential building models were examined, categorized by fenestration and shading configurations, and 2 cases were chosen as prototypes. CFD simulations focused on horizontal louvers on sun-exposed facades, particularly in south-facing windows. Contrary to expectations, results indicate that horizontal louvers can increase indoor overheating. Louvers on sun-facing facades absorbed solar radiation, which caused heated air to enter the building—particularly with winds from the southeast, south, or southwest—increasing indoor temperatures. These findings suggest that while horizontal louvers may provide cooling benefits under specific conditions, they require careful design, material selection, color, and placement to avoid unintended heating effects. Alternative shading solutions or adaptive design strategies may offer more reliable summer comfort in cold-climate buildings facing climate-induced temperature extremes.

Keywords: Natural Ventilation, horizontal louvers, multi-family residential buildings

1. BACKGROUND AND MOTIVATIONS

With climate change bringing hotter summers, countries with cold winters, like Poland, are increasingly experiencing indoor overheating challenges. Buildings in these regions, historically designed for winter heat retention, now face summer discomfort for occupants, as their designs often lack adequate summer cooling strategies (Bugenings & Kamari, 2022; Konstantinou & Prieto, 2018). In this context, shading solutions like horizontal louvers are widely promoted to mitigate solar heat gain in warm seasons (Bugenings & Kamari, 2022; Nazari et al., 2023). However, this study provides an in-depth evaluation of horizontal louvers in 2 Polish residential buildings, specifically examining their impact on thermal comfort and airflow in naturally ventilated homes. Using computational fluid dynamics (CFD), this research investigates the conditions under which louvers may exacerbate rather than mitigate overheating and offers insights into optimizing their use.

The residential building sector in Poland consumes approximately 38% of the nation's total energy (Anna Dworakowska, 2016; Tao et al., 2021), primarily for heating (Attia et al., 2022). Yet, as summer temperatures increase, the demand for cooling is growing. With recent studies highlighting the need for passive cooling strategies in multi-family housing (van Hooff et al., 2014; van Hooff et al., 2016), it is crucial to understand how shading devices interact with natural ventilation to influence indoor thermal environments. Horizontal louvers are a common solution intended to block direct solar radiation (Li et al., 2016) while allowing airflow. However, their performance in reducing indoor temperatures during hot summers remains largely unverified under Polish climatic conditions. This research fills this gap by focusing on the performance of horizontal louvers on sun-facing facades, especially for south-located spaces where solar exposure is the highest. By integrating CFD simulations with solar radiation analysis, this study evaluates the efficacy of louvers in cooling indoor spaces and determines under which conditions they might counterintuitively contribute to overheating.

2. METHODOLOGY

This study is structured in three stages, beginning with an extensive overview of over 300 multi-family residential blueprints across Poland. These blueprints were categorized based on size, ventilation type, façade orientation (ventilation type), and window and shading configurations (Mohammadi & Janowski, 2023). This categorization established a foundation for selecting 2 typical residential units that could serve as accurate models for the CFD analysis (table 1).

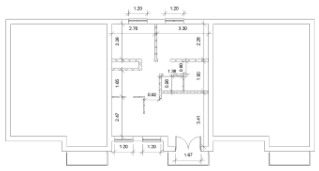
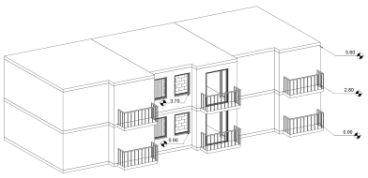
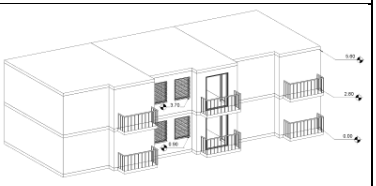
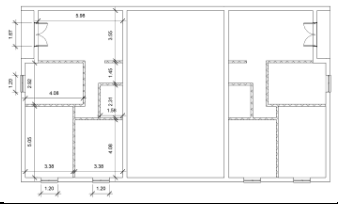
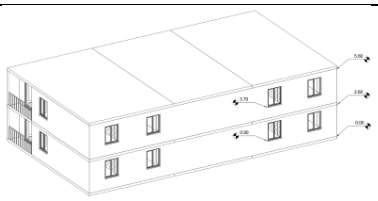
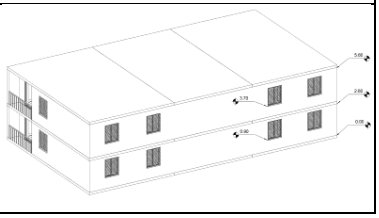
	Plan view	**Base Model**	**Louvered Windows**
Model 1			
Model 2			

Table 1: Demonstration of two prototypes for chosen for this study.

In the second phase, 2 cased and boundary conditions were developed in Autodesk CFD (Mohammadi & Janowski, 2023) using the best practices of previous studies regarding the Computational domain and grid and urban densities (Ramponi et al., 2015; Tominaga et al., 2023). Each simulation has fixed condition except for shading devices (Horizontal Louvers), resulting air permeability of the building envelope. This approach enabled a nuanced analysis of how different louver configurations influence indoor airflow velocities and temperatures.

The third step, CFD simulations were conducted on representative models by Autodesk CFD. It involved a coupled thermal and airflow CFD simulation, for 2 cases with and without louvers. The models were analysed under several scenarios, including fully open windows, louver exposure and

in 8 different directions. As the main study considered multiple wind directions—southeast, south, and southwest—to understand how wind direction interacts with louvers on sun-facing facades; here because of the limitations we only provide results for the scenario of wind blowing from the south (table 1 and table 2).

3. KEY FINDINGS AND RESULTS

The simulations offer significant insights into the effects of horizontal louvers on indoor condition:

3.1. Effectiveness of Louvers in Blocking Solar Radiation

The simulations confirmed that louvers effectively reduce direct solar radiation when oriented appropriately. However, in cases where the louvered facades face the south or southwest, the louvers absorbed considerable amounts of solar heat. This heating effect becomes pronounced when outdoor air flows through the louvers into the building.

3.2. Unintended Heating Effect

In contrast to the intended cooling benefit, the study found that louvers on sun-facing facades could inadvertently increase indoor temperatures. In cases with wind flowing from the southeast, south, or southwest, the louvers absorbed sun radiation and heated the air entering the building. This effect was especially strong when wind-driven ventilation carried warm air between the heated louvers into the interior space, raising indoor temperatures by up to 2-3°C above those of models without louvers (Base Model).

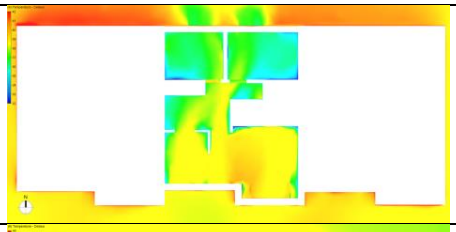
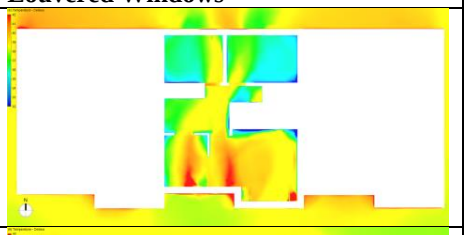
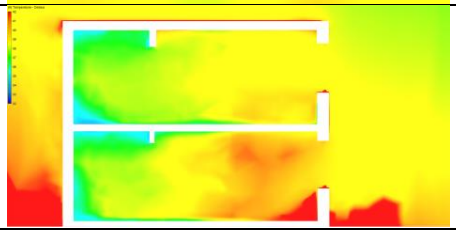
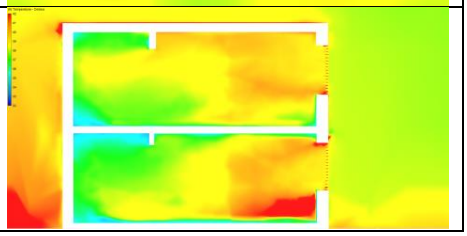
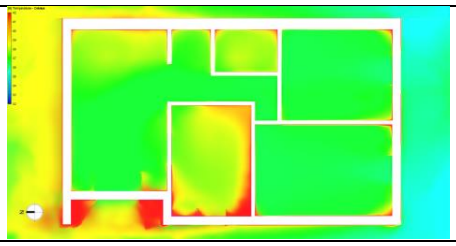
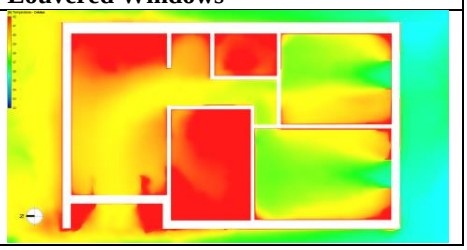
Model 1	**Base Model**	**Louvered Windows**
Plan View Wind direction: ↑ (S) Ref. velocity: 4.0 m/s Ref. temperature: 35°C Temperature range: 32-42°C		
Sections View Wind direction: ← (S) Ref. velocity: 4.0 m/s Ref. temperature: 35°C Temperature range: 32-42°C		

Table 2: Results regarding plan and section view for the model 1.

Model 2	**Base Model**	**Louvered Windows**
Plan View Wind direction: ← (S) Ref. velocity: 4.0 m/s Ref. temperature: 35°C Temperature range: 32-42°C		

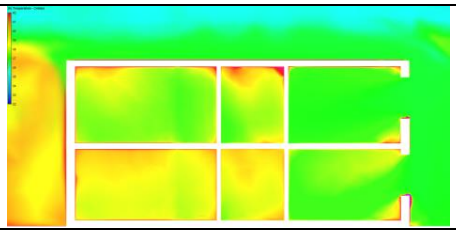
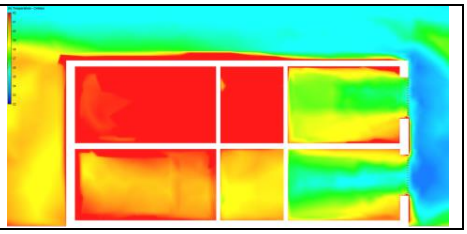
Sections View Wind direction: ← (S) Ref. velocity: 4.0 m/s Ref. temperature: 35°C Temperature range: 32-42°C		

Table 3: Results regarding plan and section view for the model 1.

3.3. Optimal Design Considerations for Louver Efficiency

The findings indicate that certain design configurations like the louvers' placement, material, and especially orientation could mitigate the unwanted heating effect. For instance, adjusting louver material to reduce heat absorption, modifying the louver depth and angle (self-shading), or pairing louvers with other shading mechanisms (e.g., overhangs) can improve thermal comfort and prevent overheating effect. Additionally, louvers perform better when positioned away from direct sun exposure or on non-southern facades. In cases where they are used on sun-exposed sides, louvers with reflective coatings or low thermal conductivity materials may enhance their performance in reducing indoor temperatures.

4. DISCUSSION AND FUTURE RESEARCH DIRECTIONS

This research highlights the potential and limitations of horizontal louvers as a passive strategy in Polish multi-family housing, where summer overheating is becoming a critical issue. The findings reveal that while louvers can mitigate solar heat gain under some conditions, they may also introduce unanticipated heating effects. This study recommends that future architectural designs in Poland and similar climates consider adaptive or hybrid shading solutions that respond dynamically to solar exposure and wind direction.

5. CONCLUSION

The analysis demonstrates that horizontal louvers, while promising as a passive strategy, require precise design and placement to effectively mitigate summer overheating during heat waves in summer. The coupled CFD simulations integrated with solar radiation in a dense urban area (to include urban heat island, or UHI effect) revealed that louver systems on south-facing facades can unintentionally increase indoor temperatures when exposed to direct solar radiation, especially under south wind driven conditions. These findings underscore the need for careful consideration of orientation, wind direction, and material choice when implementing louver-based shading solutions. The results also suggest that alternative shading options, such as overhangs, vertical fins or dynamic shading systems, might better support natural ventilation goals under Polish summer conditions. For architects and engineers working in climates like Poland, these insights provide a valuable framework for designing climate-resilient buildings that balance winter heating demand with summer cooling demands, enhancing occupant comfort and energy efficiency in an era of climate change.

REFERENCES

Anna Dworakowska, M. Z., Łukasz Pytliński, Edyta Walczak, Piotr Pawlak and Piotr Siergiej. (2016). *Energy Efficiency in Poland. 2015 Review*.

Attia, S., Kosiński, P., Wójcik, R., Węglarz, A., Koc, D., & Laurent, O. (2022). Energy efficiency in the polish residential building stock: A literature review. *Journal of Building Engineering*, *45*, 103461. https://doi.org/https://doi.org/10.1016/j.jobe.2021.103461

Bugenings, L. A., & Kamari, A. (2022). Bioclimatic Architecture Strategies in Denmark: A Review of Current and Future Directions. *Buildings*, *12*(2).

Konstantinou, T., & Prieto, A. (2018). Environmental Design Principles for the Building Envelope and More: Passive and Active Measures. In *Energy Resources and Building Performance* (pp. 147-180). TU Delft.

Li, L., Qu, M., & Peng, S. (2016). Performance evaluation of building integrated solar thermal shading system: Building energy consumption and daylight provision. *Energy and Buildings*, *113*, 189-201. https://doi.org/https://doi.org/10.1016/j.enbuild.2015.12.040

Mohammadi, M., & Janowski, M. (2023). The impact of size in fenestration design on the airflow and temperature in natural cross ventilation, case study: A two-bedroom Polish multifamily home. *BUILDER*, *315(10)*, 74-83. https://doi.org/https://doi.org/10.5604/01.3001.0053.8994.

Nazari, S., Keshavarz Mirza Mohammadi, P., & Sareh, P. (2023). A multi-objective optimization approach to designing window and shading systems considering building energy consumption and occupant comfort. *Engineering Reports*, *5*(10), e12726. https://doi.org/https://doi.org/10.1002/eng2.12726

Ramponi, R., Blocken, B., de Coo, L. B., & Janssen, W. D. (2015). CFD simulation of outdoor ventilation of generic urban configurations with different urban densities and equal and unequal street widths. *Building and Environment*, *92*, 152-166. https://doi.org/https://doi.org/10.1016/j.buildenv.2015.04.018

Tao, Y., Zhang, H., Zhang, L., Zhang, G., Tu, J., & Shi, L. (2021). Ventilation performance of a naturally ventilated double-skin façade in buildings. *Renewable Energy*, *167*, 184-198. https://doi.org/https://doi.org/10.1016/j.renene.2020.11.073

Tominaga, Y., Wang, L., Zhai, Z., & Stathopoulos, T. (2023). Accuracy of CFD simulations in urban aerodynamics and microclimate: Progress and challenges. *Building and Environment*, *243*, 110723. https://doi.org/https://doi.org/10.1016/j.buildenv.2023.110723

van Hooff, T., Blocken, B., Hensen, J. L. M., & Timmermans, H. J. P. (2014). On the predicted effectiveness of climate adaptation measures for residential buildings. *Building and Environment*, *82*, 300-316. https://doi.org/https://doi.org/10.1016/j.buildenv.2014.08.027

van Hooff, T., Blocken, B., Timmermans, H. J. P., & Hensen, J. L. M. (2016). Analysis of the predicted effect of passive climate adaptation measures on energy demand for cooling and heating in a residential building. *Energy*, *94*, 811-820. https://doi.org/https://doi.org/10.1016/j.energy.2015.11.036

Wind-driven natural ventilation of airport terminals

Matko Jelašić[1], Christoph Irrenfried[2], Günter Brenn[2], Hrvoje Kozmar[1]

[1]*Faculty of Mechanical Engineering and Naval Architecture, University of Zagreb, Zagreb, Croatia, matko.jelasic@fsb.unizg.hr, hrvoje.kozmar@fsb.unizg.hr*
[2]*Institute of Fluid Mechanics and Heat Transfer, Graz University of Technology, Graz, Austria, c.irrenfried@tugraz.at, guenter.brenn@tugraz.at*

SUMMARY:
Wind-driven natural ventilation of airport terminals is an important approach, given the current efforts to conserve energy, protect the environment, and protect human health from airborne diseases and respiratory hazards. To learn more about the effects of airport terminal size, wind incidence angle, and ventilation type on the wind-driven natural ventilation of airport terminals, laboratory experiments were performed in a boundary layer wind tunnel of the Institute of Fluid Mechanics and Heat Transfer at the Graz University of Technology, Austria. In these experiments, the air change rate (ACH), which is the volume flow rate divided by the internal volume of a building model, was determined using a tracer gas method to quantify the effects of various parameters. The studied parameters are mean freestream flow velocity u, flow incidence angle β, airport terminal model length L, and windows opening angle γ. Impact of various building lengths in the buildings with roof windows was not studied yet. The results indicate some important findings. In particular, the ACH increases with an increase in u and γ whereas the maximum ACH was obtained for $0° < \beta < 90°$.

Keywords: Wind-driven natural ventilation, airport buildings, air change rate, laboratory experiments

1. INTRODUCTION

Natural ventilation is a method of ventilating space without the use of mechanically powered devices like fans and ventilation chambers, but only by the means of natural forces. It is important given the current efforts to save energy and the environment, and to protect human health regarding indoor air quality (Bernstein et al.,2008). Approximately 20 % of the total energy in developed countries is used for HVAC (Chua et al., 2013), so applying natural building ventilation is likely to result in significant energy savings.

Airport terminals are particularly important to be addressed in this regard given their substantial size and large numbers of travelers, so this type of structure is analyzed in the present study. Wind-driven type of ventilation was assessed as more effective than the buoyancy-driven type of ventilation.

The effects of size, wind incidence angle, and ventilation type on the wind-driven natural ventilation of airport terminals were studied in a boundary layer wind tunnel. The studied parameters are mean freestream flow velocity u, flow incidence angle β, model length L, and windows opening angle γ.

2. EXPERIMENTS

2.1. Atmospheric boundary layer simulation

The experiments were performed at the Institute of Fluid Mechanics and Heat Transfer at the Graz University of Technology, Austria. A boundary layer wind tunnel was used for this purpose. Its test section is 2 m wide, 1 m high and 8.6 m long. The investigated model is placed on the turntable at the end of the test section. Turbulence generating devices (variable spacing rods, serrated barrier, and small surface roughness elements) were used for the atmospheric boundary layer (ABL) simulation.

2.2. Experimental technique

The characteristics of the created ABL simulation were determined based on the flow velocity measurements. These experiments were carried out using hot-wire anemometry. The velocity profile was assessed from the ground surface of the wind-tunnel test section up to a height of 700 mm in the lateral center of the test section, i.e., y = 0 m.

The air change rate (ACH) was determined by employing a tracer gas method. The exchanged volume of the gas was calculated based on two concentrations measured at two different time points, with full details of this approach provided in Golubić et al. (2020). ACH is provided in Eq. (1), where $\dot{V}$ is the volume flow rate, V is the internal volume of the building model, Δt is the time step between two measurements, and ΔC is the concentration difference between two measurements.

$$ACH = \frac{\dot{V}}{\mathrm{V}} = \frac{1}{\Delta t} \ln \frac{\Delta C\ (t)}{\Delta C\ (t+\Delta t)} \tag{1}$$

2.3. Building models

The ACH was first measured on a cubic building model characterized by the edge length of L=200 mm for both the single-sided (one window) and cross ventilation (two windows on opposite walls). This way the obtained ACH was assessed against previous relevant studies to validate the experimental approach.

The ACH was measured next on three generic airport building models with roof windows. These models represent a very simplified airport-terminal-like building, while future work will be performed on more precisely designed airport building models. All three models have the same cross-section as the cubic building model (200 mm wide and 200 mm high) with three lengths of L=200 mm, L=400 mm, and L=600 mm in the main flow direction. In these models, there is one roof window on every 200 mm of the airport model length. This way the smallest model has one window, the middle-size model has two and the largest model has three roof windows. These models are analyzed for various flow velocities, windows opening angles, and flow incidence angles. The largest model (L = 3H) and analyzed parameters (flow incidence angle β, airport model length L, and windows opening angle γ) are shown in Fig. 1.

3. RESULTS

The ABL simulation agrees well with wind conditions above a rural terrain type including the power-law exponent and the aerodynamic surface roughness length. Single-sided and cross ventilation of a cubic building model exhibits the expected results and agree well with the results of Golubić et al. (2020) and Miše et al. (2024).

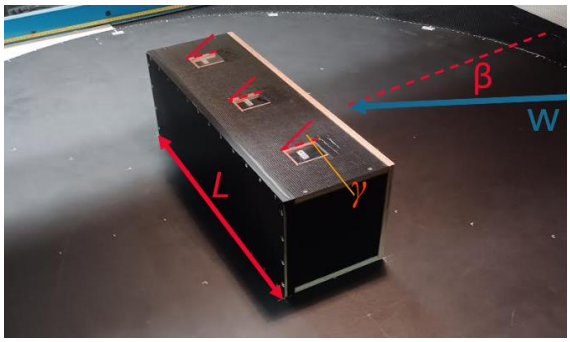


Figure 1. The largest airport building model ($L = 3H$)

In general, for all airport building models, an increase in the mean flow velocity and an increase in the window opening angle yields larger ACH, as seen in Figs. 2a and 2b.

In Fig. 3, the ACH is shown for the three airport building models. The smallest building ($L = H$) exhibits a lower ACH than the other two building models ($L = 2H$ and $L = 3H$). The smallest building is characterized by the lowest ACH, likely due to only one window. The other two building models have more windows, which enhances the ventilation and yields a higher ACH. In addition, the middle-sized building model ($L = 2H$) has a slightly higher ACH than the largest building model ($L = 3H$). This indicates that an increase in the building length and number of windows does not necessarily enhance the natural building ventilation.

a) b)

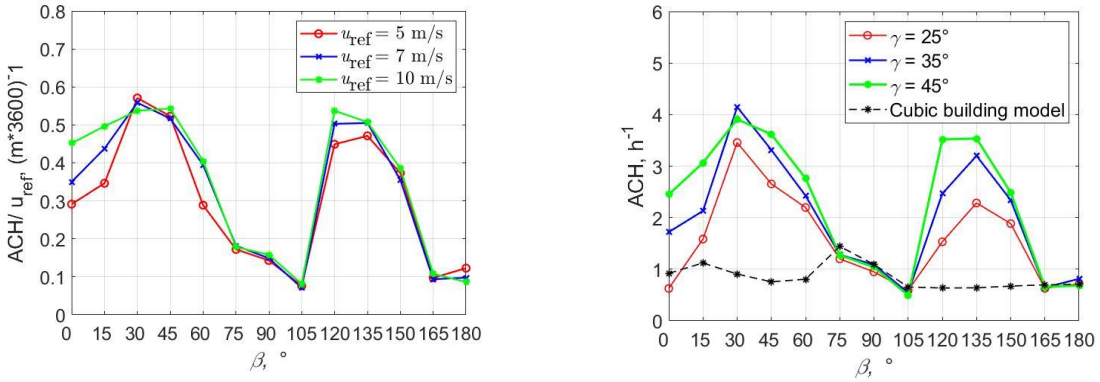


Figure 2. a) Normalized ACH of an airport building model ($L = H$) for various flow velocities and a window opening angle of $\gamma = 45°$ b) ACH of an airport building model ($L = H$) for various window opening angles and the mean flow velocity $u = 7$ m/s

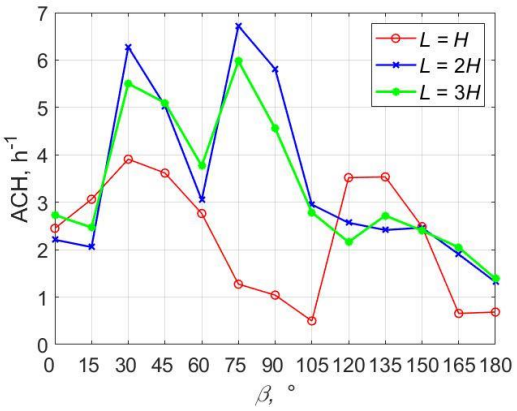


Figure 3. ACH of airport building models for three building lengths in the main flow direction, the window opening angle $\gamma = 45°$ and mean flow velocity $u = 7$ m/s

3. CONCLUDING REMARKS

Three airport terminal models were studied in a boundary layer wind tunnel to investigate the effects of terminal size, wind incidence angle, and ventilation type on the wind-driven natural ventilation of airport terminals. The terminal building models were subjected to the rural-type ABL simulation. The results indicate some notable findings. The ACH increases with higher mean flow velocities and larger window opening angles. An increase in the airport model length is not characterized by a one-way increase in ACH. Further work is required to assess in detail all the aspects of wind-driven natural ventilation of airport terminals.

ACKNOWLEDGEMENTS

This work was supported by the Croatian Science Foundation under the project number HRZZ-IP-2022-10-9434. The work of doctoral student Matko Jelašić has been fully supported by the "Young researchers' career development project – training of doctoral students" of the Croatian Science Foundation.

REFERENCES

Bernstein, J. A., Alexis, N., Bacchus, H., Bernstein, I. L., Fritz, P., Horner, E., Li, N., Mason, S., Nel, A., Oullette, J., Reijula, K., Reponen, T., Seltzer, J., Smith, A., Tarlo, S. M., 2008. The health effects of nonindustrial indoor air pollution. Journal of Allergy and Clinical Immunology 121(3), 585-591.

Chua, K. J., Chou, S. K., Yang, W. M., Yan, J., 2013. Achieving better energy-efficient air conditioning–a review of technologies and strategies. Applied Energy 104, 87-104.

Golubić, D., Meile, W., Brenn, G., Kozmar, H., 2020. Wind-tunnel analysis of natural ventilation in a generic building in sheltered and unsheltered conditions: Impact of Reynolds number and wind direction. Journal of Wind Engineering and Industrial Aerodynamics 207, 104388, 1-17.

Miše, D., Irrenfried, C., Meile, W., Brenn, G., Kozmar, H., 2024. Wind-driven natural ventilation of cubic buildings in rural and suburban areas. Journal of Building Engineering 87, 1-27.

Study on the Active Aerodynamic Countermeasure for Vortex-Induced Vibration of the Π-shaped box girder

Han Xiao [1,2,3], Zhiwen Liu [1,2], Klaus Thiele [3], Zhengqing Chen [1,2]

[1]*College of Civil Eng., Hunan Univ., Changsha, China, zhiwenliu@hnu.edu.cn*
[2]*Hunan Prov. Key Lab for Wind & Bridge Eng., Hunan Univ., Changsha, China*
[3] *Institute of Steel Structures, Technische Universität Braunschweig, Braunschweig, Germany*

SUMMARY:
In this study, wind tunnel tests on a cable-stayed bridge with a Π-shaped box girder showed that passive aerodynamic countermeasures cannot completely suppress vortex-induced vibrations (VIV) of the main girder. Consequently, an active aerodynamic control method was proposed and the feasibility and VIV suppression effects were studied by numerical simulation methods. Combined with the User Defined Function (UDF) and moving-mesh technology in ANSYS Fluent, the numerical simulation method for the active aerodynamic countermeasure of VIV was established. Based on the passive aerodynamic countermeasures, the reduced-size deflectors at the railings were used as the active aerodynamic countermeasure, and it can effectively suppress the VIV response when the plate width is 0.35m, the rotation angle is 5°, and the rotation frequency is 2.38Hz. According to the flow field distribution, the active aerodynamic countermeasure makes the phenomenon of alternating vortex shedding away from the tail of the section, and the periodic force of alternating shedding has no effect on the section, so the vibration response is suppressed.

Keywords: Π-shaped box girder, vortex-induced vibration, active aerodynamic countermeasure

1. INTRODUCTION

1.1. Engineering Background

A railway bridge under construction in China is used as the engineering background, and the main span of the bridge is 408m. As shown in Fig. 1 (a), the Π-shaped steel concrete composite girder is 20.0 m wide and 4.0 m high. Liu et al. 2023 studied the wind-induced vibration response of this bridge by the small-scale (1:60) sectional model, as shown in Fig. 1(b). In the wind tunnel test, the length, width, and height of the sectional model are L=1733mm, B=333mm, and D=67mm, respectively. Moreover, the vertical and torsional frequencies are f_v=4.64 Hz and f_α=9.52 Hz, respectively, and the vertical and torsional damping ratios are both 0.65%.

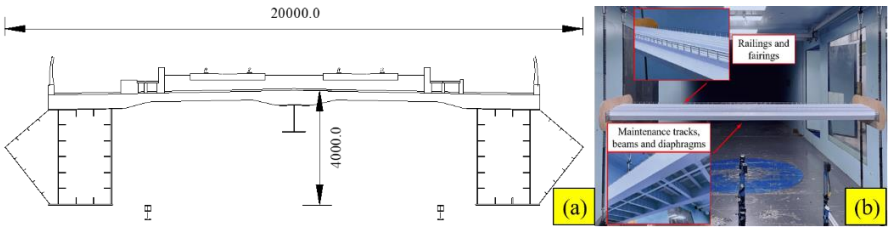


Figure 1. Main girder section and experimental setup of the Π-shaped girder.

1.2. Numerical Method for Active Aerodynamic Control

In recent years, many researchers have explored various active aerodynamic control methods to enhance flutter stability (Li et al., 2017a and 2017b) and suppress vortex-induced vibration (VIV) (Chen et al., 2019; Deng et al., 2024). In this study, the active control parameters are combined with the VIV mechanism of the wind tunnel tests, the passive aerodynamic countermeasures and the torsional frequency of the main girder to determine the layout, width, rotation angle and rotation frequency of the movable deflector. As shown in Figure 2, Flow chart of the active aerodynamic control calculation of the main girder is illustrated. The synchronous movement of the main girder and the active movable deflector is achieved through the dynamic mesh macro and dynamic mesh setting. When the amplitude of the main girder reaches a limit value, the active movable deflector starts to move. Under the aerodynamic interference of the active movable deflector, the amplitude of the main girder changes and finally reaches stability. The active movable deflector rotates around the connection point with the main girder, and the corresponding rotation angle is: $\beta_p(t)=\beta_0\sin(2\pi/f_p)t$ (β_0 and f_p are the maximum rotation angle and the rotation frequency of the active movable deflector, respectively). Moreover, the active movable deflector performs relative torsional vibration compared to the main girder, so its two-degree motion equation are $h_p(t)=h(t)$, and $\alpha_p(t)=\beta_p(t)+\alpha$ ($h_p(t)$ and $\alpha_p(t)$ are the vertical and torsional amplitudes of the active movable deflector, respectively and h and α are the vertical and torsional amplitude of the main girder, respectively).

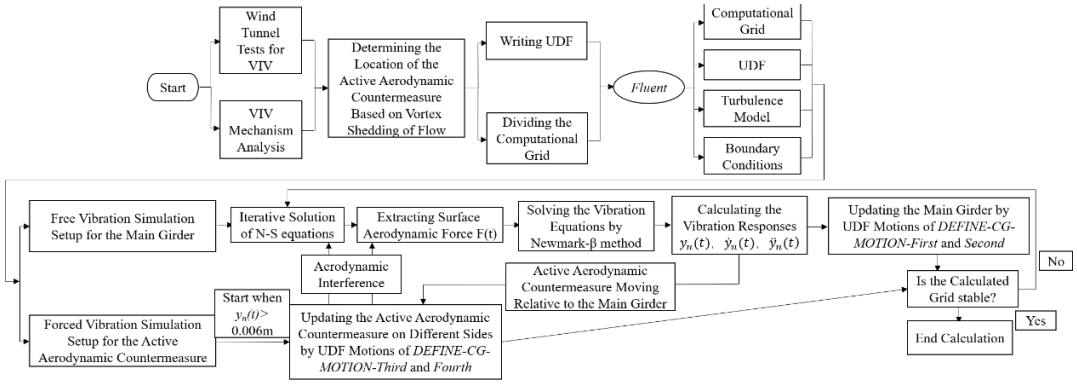


Figure 2. Flow chart of the active aerodynamic control calculation of the main girder.

2. RESULTS

2.1. Wind Tunnel Tests

Liu et al. 2023 studied the wind-induced vibration of the original main girder by the small-scale (1:60) sectional model. The results showed that the VIV occurred in the original main girder at different angles of attack (AOA), and the VIV amplitude reaches the largest at the AOA of +3°. The suppression effect of a large number of passive aerodynamic countermeasures was tested through wind tunnel tests. The results showed that the combined aerodynamic countermeasures of increasing the angle of wind fairing and adding inclined deflectors can effectively reduce the VIV amplitude, but cannot completely suppress it.

2.2. Numerical Simulations

2.2.1. Numerical setup

The numerical simulation parameters are consistent with the studies in Liu et al. 2023. As shown in Fig. 3(a), for the dynamic grid setting, the blue area is the fixed grid, the dark red area is the dynamic grid, and the light red area is the rigid grid. Fig 3(b) shows the numerical simulation results of the passive aerodynamic countermeasures in this study are in good agreement with the results in Liu et al. 2023, and the Fig. 3(c) shows the detail of the active movable deflector.

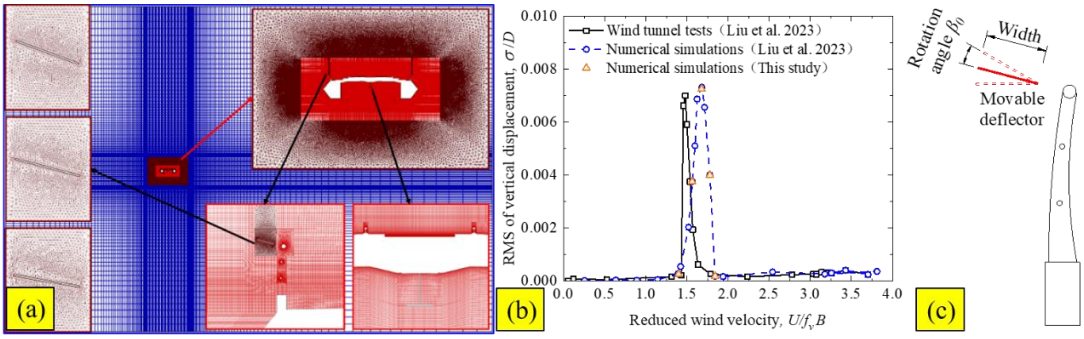


Figure 3. Setup of the numerical simulations.

2.2.2. Results of numerical simulations

Fig. 4 (a) and (b) show that at AOA of +3° and V_{red}=2.49, the vibration responses of the main girder with different width of static deflectors still exist. Based on results of the static deflectors, the amplitude limit of the main girder is set to 0.06m for active aerodynamic control. Fig. 4 (c) and (d) show that when the 0.35m and 0.4m wide movable deflectors move at β_0=5° and f_p=4.76Hz, the vibration responses of the main girder are suppressed. Considering that 0.35m wide deflector costs less, the simulations for different β_0 and f_p are carried out for 0.35m wide movable deflector. Fig. 4 (e) and (f) show that for f_p=4.76Hz and β_0=1°, the vibration responses of the main girder still exist, while for f_p=4.76Hz and β_0=5°, the vibration responses are suppressed and reach the minimum value. Fig. 4 (g) and (h) show that for β_0=5°, the vibration responses of the main girder are suppressed under different rotation frequencies, and reach the minimum value at f_p=2.38Hz.

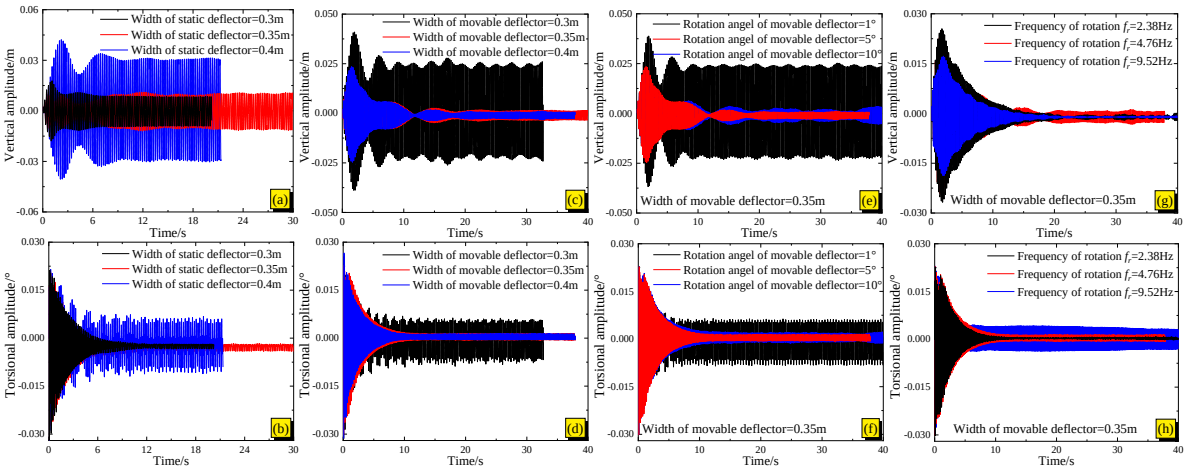


Figure 4. Results of the numerical simulation.

2.2.3. Aerodynamic Mechanism

Fig. 5(a) shows that after taking passive combined aerodynamic countermeasures, the flow on the lower surface forms a vortex at the tail and then approaches the vortex shed on the upper surface. forming a "guiding" effect, generating alternating vortices, which in turn leads to vortex-induced vibration. The vortex on the lower surface forms a “guiding” effect, which leads to the alternating vortex shedding and further causes VIV. Fig. 5(b) shows that after taking movable deflectors as the active aerodynamic countermeasure, the alternating vortex is moved away from the tail of the girder, so that the influence of the alternating shedding force on the main girder is weakened and the vibration response is suppressed.

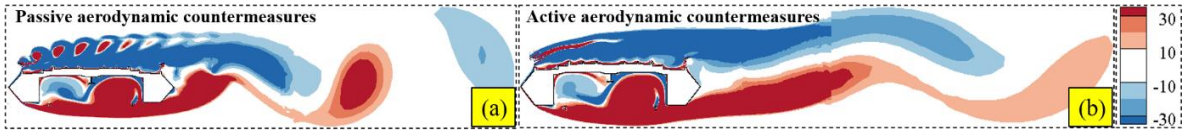


Figure 5. Vorticity contours of the main deck with the passive and active aerodynamic countermeasure.

7. CONCLUSIONS: FINAL CHECKS AND SUBMISSION

This study established a numerical simulation method for active aerodynamic control method for VIV based on the movable deflector, and calculated the vibration suppression effect under different motion parameters. The specific conclusions are as follows: (1) Combining dynamic mesh technology and UDF secondary development function, the free vibration of the main girder and the forced vibration of the movable deflector relative to the main girder are realized simultaneously. (2) For Π-shaped box girder, static movable deflector cannot effectively suppress the vibration of the main girder. The suppression effect of the 0.35m wide movable deflector at β_0=5° and f_p=2.38Hz is the best. (3) The active movable deflector moves the alternating shed vortices away from the tail of the girder, thereby weakening the influence of the periodic force of the alternating shedding and suppressing the VIV.

ACKNOWLEDGEMENTS

This research was financially supported by the National Natural Science Foundation of China (grant numbers 52178475 and 51778225) and Postgraduate Scientific Research Innovation Project of Hunan Province (grant number CX20240036, for which the authors are grateful. The authors also gratefully acknowledge China Railway Siyuan Survey and Design Group Co., Ltd., China, for its financial support.

REFERENCES

Liu Z. W., He F. W., Yan A. G., et al., 2023. Mechanism and aerodynamic countermeasures of vortex-induced vibration of a cable-stayed bridge with narrow Π-Shaped girder sections. Journal of Bridge Engineering, 2023, 28(12): 04023090.

Li K., Ge Y. J., Zhao L., et al., 2017a. Numerical simulation of feedback flutter control for a single-box-girder suspension bridge by twin-winglet system. Journal of Wind Engineering and Industrial Aerodynamics, 169:77-93.

Li K., Zhao L., Ge Y. J., et al., 2017b. Flutter suppression of a suspension bridge sectional model by the feedback controlled twin-winglet system. Journal of Wind Engineering and Industrial Aerodynamics, 168:101-9.

Chen W. L., Yang W. H., Li H., 2019. Self-issuing jets for suppression of vortex-induced vibration of a single box girder. Journal of Fluids and Structures, 86: 213-235.

Deng X. L., Hu G., Chen W. L., 2024. Intelligent active flow control of long-span bridge deck using deep reinforcement learning integrated transfer learning. Journal of Wind Engineering and Industrial Aerodynamics, 44: 105632.

Wind-induced vibration control of high-rise buildings with double-skin facades using distributed multiple tuned facade-dampers-inerters

Chengxi PAN [1], Lingfeng SU [2], Haiwei XU [3]

[1] *College of Civil Engineering and Architecture, Zhejiang University, Hangzhou, China, Email: 12212077@zju.edu.cn*
[2] *College of Civil Engineering and Architecture, Zhejiang University, Hangzhou, China, Email: slfjob1@163.com*
[3] *College of Civil Engineering and Architecture, Zhejiang University, Hangzhou, China, Email: haiweix@zju.edu.cn*

SUMMARY
To address the shortcomings of tuned mass dampers (TMD), such as excessive internal space occupation and overlarge physical mass, this paper proposes a tuned façade damper-inerter (TFDI) that utilizes parts of the outer façades of double-skin façades (DSF) as damping mass, capitalizing on the lightweight and efficient characteristics of inerters. The TFDI effectively re-solves the challenge of multi-layer connections of inerters in high-rise buildings by utilizing cor-ridor space. By vertically distributing TFDIs, a distributed multiple TFDI (d-MTFDI) system is formed. The configuration and motion of equations of this system are presented, and the control effectiveness is validated using wind tunnel test data. Two tuning modes are further proposed: unified tuning mode and distributed tuning mode. For the unified tuning mode, analytical ex-pressions for optimal tuning frequency and damping ratio are derived; for the distributed tuning mode, numerical optimization methods are employed to determine the optimal tuning frequency range and damping ratio. Comparative results indicate that the distributed tuning mode achieves higher control efficiency than the unified tuning mode, with a significant reduction in the re-quired optimal damping ratio. Furthermore, comparisons with d-MTMD demonstrate that d-MTFDI significantly enhances wind-induced vibration control performance

Keywords: distributed multiple tuned façade-dampers-inerters (d-MTFDI); high-rise building; double-skin façade (DSF); vibration control; tuning optimization

1. INTRODUCTION

The rapid growth of urban populations and limited space in metropolitan areas has driven the increase in high-rise buildings. At the same time, concerns about the global energy crisis have led to a demand for environmentally sustainable and energy-efficient designs. Double-skin façades (DSF), known for their excellent acoustic insulation and thermal performance, are widely used in high-rise buildings like The Shanghai Tower, The Shard, and The Central Park Tower. However, the low stiffness and damping of super high-rise buildings often result in excessive wind-induced vibration (WIV) responses(Kwok et al., 2009), causing discomfort and limiting the usability of upper floors.

To mitigate building vibrations, three main strategies are employed: (a) structural modifications of stiffness and mass, (b) aerodynamic optimization of building shape, and (c) the use of

auxiliary dampers to increase structural damping (Wang et al., 2023). Structural alterations are costly, and aerodynamic changes may conflict with architectural design. Recently, passive dampers have become a popular solution due to their cost-effectiveness. Tuned mass dampers (TMDs), effective in some high-rise buildings (Bhattacharya et al., 2022), can reduce vibrations by tuning to the building's natural frequency. However, TMDs struggle with off-tuning and multimodal vibrations, and they require considerable internal space. To address these limitations, multiple tuned mass dampers (MTMDs) were introduced, offering flexibility with smaller dampers tuned to different modes or distributed across multiple floors (Asami et al., 2020). However, MTMDs still require significant physical mass. The introduction of the inerter, a device that generates a virtual mass far greater than its physical mass, has revolutionized passive vibration control (Malcolm et al., 2020). Despite their advantages, inerter-enhanced devices require space and remain limited in high-rise applications.

This paper proposes a novel inerter-enhanced damper, the tuned façade damper-inerter (TFDI), which combines movable outer skins (MOS) with inerters. A method for wind-induced vibration suppression using distributed multiple TFDIs (d-MTFDI) is presented, with verification from wind tunnel tests. The paper compares two tuning modes for the d-MTFDI and demonstrates its advantages over traditional d-MTMD systems.

2. CONCEPT OF D-MTFDI SYSTEM

This study focuses on incorporating movable outer skins (MOS) in the double-skin façade (DSF) of high-rise buildings to absorb vibration energy generated by wind excitation. Figure 1 illustrates the parallel motion mode of MOS under wind action. Wind-induced vibrations (WIV) in buildings can be divided into X and Y components. For Y-direction vibrations, mitigation is achieved through the spontaneous movement of MOS along this direction, while X-direction vibrations are reduced by MOS moving in the X-direction.

A Tuned Façade Damper-Inerter (TFDI) consists of four key components: mass, spring, damper, and inerter. The mass element is represented by two MOS that move in parallel. Figure 2 shows the TFDI configuration, which includes: 1) Two parallel MOS supported by a guide rail system (blue), allowing for parallel movement. The spring element is provided by spring sets connecting MOS to the fixed inner skin, and the damper element comes from inherent mechanical damping and motion-induced friction. 2) Two inerters connected by cables (red) within the DSF's lower floors, linked to MOS across multiple floors. 3) Safety limiters and guide rails (green) at building corners to prevent MOS collisions and facilitate multi-layer connections between the inerters and MOS.

Figure 3 shows that for a single TFDI, the total mass of two MOS is defined as m_{di}, stiffness as k_{di}, damping as c_{di}, and inertance produced by the inerters as b_{di}.Figure 4 demonstrates the vertical distribution of a distributed-MTFDI (d-MTFDI) system under wind load $P(t)$. The system consists of R TFDIs, with each TFDI's MOS located on the ai-th floor and its corresponding inerters on the bi-th floor. The cables connecting the MOS and inerters cross p_i floors ($p_i = |a_i - b_i|$). The d-MTFDI system allows for variable inerter topologies between different TFDIs, which provides the potential for multi-mode response control, particularly for wind-induced and seismic responses. The main objective of this paper is to reduce the basic modal response of high-rise buildings under wind excitation.

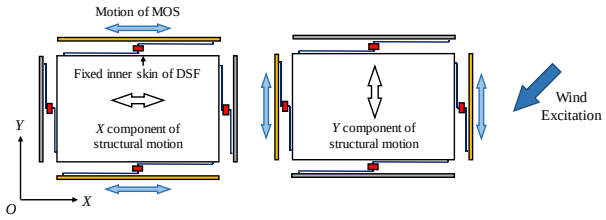


Figure 1. Parallel motion mode of MOS.

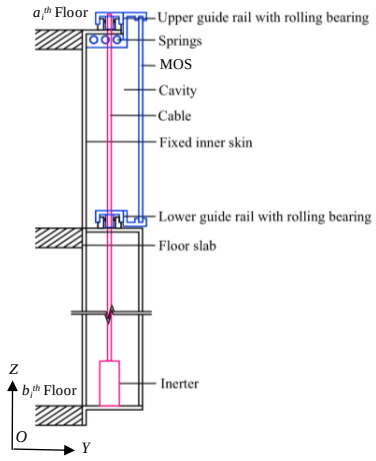


Figure 2. Cross-section view of TFDI confiIguration.

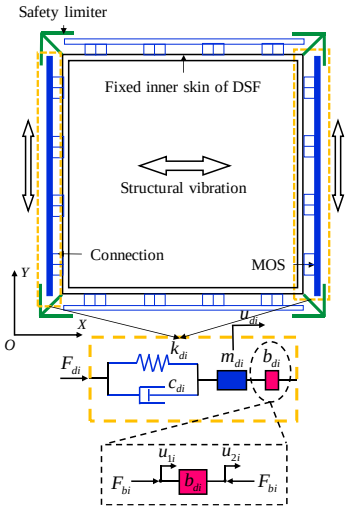


Figure 3. Plan view of the TFDI configuration

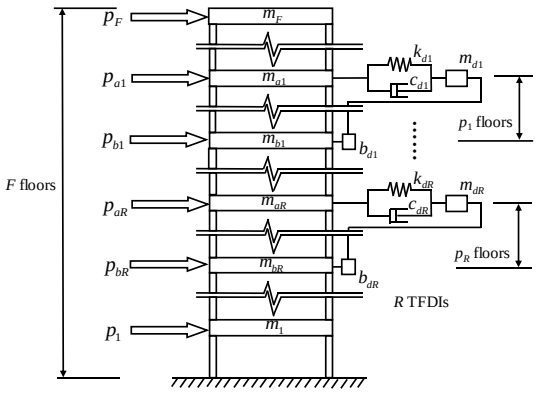


Figure 4. Elevation view of a super high-rise building with a d-MTFDI system

3. TWO DIFFERENT TUNING MODE OF D-MTFDI

In order to accurately assess the transverse wind forces, wind tunnel tests were conducted on a 76-floor benchmark building (Yang et al., 2004) proposed by ASCE specifically to evaluate the performance of WIV control using dampers. This section will show the differences of d-MTFDI with two tuning modes with respect to the WIV control performance and optimal damping ratio. Taking combination [R, p, the inertance ratio β] = [10, 8, 0.25] as an example, the optimal parameters of d-MTFDI with two tuning modes are shown in Table 1. As can be seen in the table, the damping ratio ξ_d^{opt} of distributed tuning mode is only about 25% of that with unified frequency, but the WIV control efficiency J^{opt} is higher by 1.9%. The corresponding two NTFs

are plotted in Figure 5, the NTF of unified tuning mode exhibits two peaks, while that of distributed tuning mode is flattened, resulting in a broader frequency range being controlled and an improved WIV control performance.

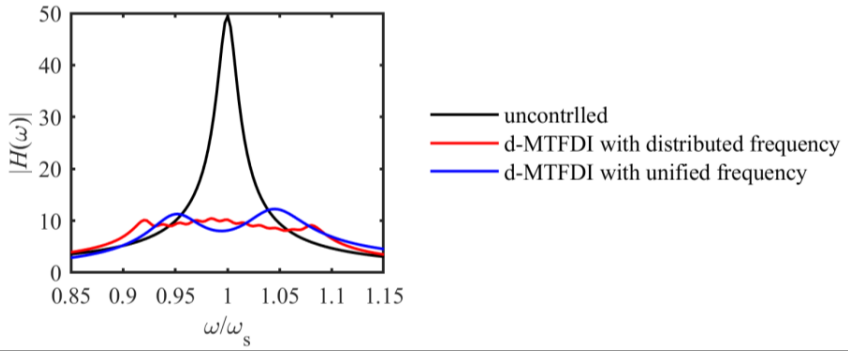


Figure 5. Comparison of modulus of NTF with two different tuning frequency (R = 10, p = 10, β = 0.25)

Table 1. Optimal tuning parameters and J^{opt} for d-MTFDI with two tuning modes.

Tuning mode	unified optimal frequency ratio ν_d^{opt} or normalized frequency range Δ^{opt}	damping ratio ξ_d^{opt}	WIV control efficiency J^{opt}
Unified	0.993	0.048	41.6%
Distributed	0.144	0.011	43.7%

4. CONCLUSIONS

This study proposed a new inerter enhanced damping system, namely d-MTFDI, by using part of the outer skins of DSF and combining inerters. Based on a 76-floor benchmark building with wind tunnel test data, the WIV control effectiveness is verified, and the performance with two tuning mode are studied and compared.The main conclusions are as follows:

1) By utilizing the DSF system, the d-MTFDI not only addresses the challenge of space limitations for multi-layer inerter installations in high-rise buildings but also signifi-cantly reduces the additional mass required for the tuned damping system.
2) For the unified tuning mode, the formulas of optimal tuning frequency ratio and damping ratio are derived. The WIV mitigation ratio J typically increases with p and β, but in cases of small β, introducing inerters to MOS may negatively impact WIV con-trol effect.

REFERENCES

Wang, L.K., Zhou. Y., Nagarajaiah, S., Shi, W.X. Bi-directional semi-active tuned mass damper for torsional asymmetric structural seismic response control. Eng Struct 2023, 294, 116744.

Bhattacharya, S, Dalui, S. K. Effect of tuned mass damper in wind-induced response of "V" plan-shaped tall building[J]. The Structural Design of Tall and Special Buildings, 2022, 31(9): e1931.

Asami, T.; Mizukawa, Y.; Yamada, K. Optimal design of a hysterically damped dynamic vibration absorber. Mech Eng J 2020, 7(2), 19–00482.

Malcolm, C. S. The Inerter: A Retrospective. Annual Review of Control, Robotics, and Autonomous Systems 2020, 3, 361-391.

Kwok, K. C. S.; Hitchcock, P. A.; Burton, M. D. 2009, Perception of vibration and occupant comfort in wind-excited tall buildings. J Wind Eng Ind Aerodyn. 97(7-8), 368-80.

Yang, J. N.; Agrawal, A. K.; Samali, B. 2004, Benchmark Problem for Response Control of Wind-Excited Tall Buildings. Journal of Engineering Mechanics. 130(4), 437-446.

Experimental study of an asymmetric Stockbridge damper

Giacomo Bacci[1], Ole Øiseth[1], Øyvind W. Petersen[1], Vincent Denoël[2]

[1]*NTNU, Trondheim, Norway, giacomo.bacci@ntnu.no*
[2]*ULiège, University of Liège, Liège, Belgium*

SUMMARY:
Hanger vibrations are a known issue in many modern suspension bridges, often linked to innovative hanger designs. To address these vibrations, Stockbridge dampers—originally used in high-voltage cables—have been adapted for structural engineering. However, frequent cases of damper failure have been reported globally, with the root causes still undetermined. This study investigates an asymmetric Stockbridge damper installed on the hangers of a long-span suspension bridge in northern Norway. Experimental testing was conducted on the complete damper as well as on its separated top and bottom masses to assess its performance across various vibration frequencies and amplitudes. The findings provide insights into the damper's behavior, which can support numerical modeling and inform future design strategies for Stockbridge dampers in structural applications. This work contributes to optimizing damper installation and enhancing the effectiveness of vibration mitigation in bridge structures.

Keywords: Stockbridge, experimental setup, nonlinear device

1. SETUP DESCRIPTION

A Stockbridge damper comprises two flexible messenger cables connecting weighted masses to a central clamp attached to the vibrating structure. When the structure vibrates, the masses oscillate, deforming the messenger cables. Damping arises from static hysteresis due to Coulomb (dry) friction between the cable's individual wires undergoing bending deformation (N. Barbieri and R. Barbieri, 2012). In this study, the damper was designed to mitigate vortex-induced vibrations on the Hålogaland Bridge in northern Norway. To resemble the field installation position, in the experimental setup the damper is positioned vertically, supported by two bending load cells, and connected to a horizontal slider, as illustrated in Fig. 1. Each mass is equipped with two IEPE accelerometers to capture lateral and rotational motion, while an additional accelerometer on the slider records the clamp motion. The damper is excited using a modal vibration shaker (APS 420), which provides monoharmonic excitation at constant and sweep frequencies between 3 and 35 Hz. Following IEEE 664-1993 (IEEE Standards Committee, 1993), the velocity amplitude of the clamp motion was maintained constant during experiments. Field measurements on the Hålogaland Bridge indicated velocity amplitudes between 0.01 m/s and 0.05 m/s, while the IEEE guide recommends 0.1 m/s. Numerical models for Stockbridge dampers in the literature (N. Barbieri and R. Barbieri, 2012; Foti and Martinelli, 2018) were identified for half-dampers and then applied to symmetric dampers by doubling the output force for a given input clamp motion. With this modeling approach in mind, the damper is tested in halves, with the top half shown in Fig. 5a and the bottom half in Fig. 5b. The sensor layout remains consistent with the full damper configuration. The main geometric characteristics of the damper are summarized in Table 1.

Table 1. Geometric parameters of the Hålogaland Stockbridge dampers.

Upper mass [kg]	**Lower mass** [kg]	**Total mass** [kg]	**Length messenger cable** [mm]	**Diameter messenger cable** [mm]
4.9	8.0	14	250	16



Figure 1. Experimental setup for the whole damper configuration.

2. EXPERIMENTAL DATA

2.1. Impedance function

The impedance function is defined as $Z(\omega) = \frac{F_c(\omega)}{\dot{Y}_c(\omega)}$, where $F_c(\omega)$ is the Fourier transform of the force at the clamp and $\dot{Y}_c(\omega)$ is the Fourier transform of the velocity of the clamp $\dot{y}_c(t)$. Fig. 2 shows impedance functions for the entire damper configuration at various vibration amplitudes. Since the damper dissipates energy through the deformation of the messenger cable, its performance depends on the vibration amplitude. The plot reveals four resonance peaks, which correspond to two degrees of freedom for each mass: lateral oscillation and rotation. Due to the damper's asymmetry, these peaks appear at four distinct frequencies. The wider the amplitude of vibration the more the resonance peaks get sharper and move to lower frequencies.

2.2. Modes of vibration

By analyzing the time history of the mass displacements, it is possible to better understand the two primary vibration modes and the transitions between them. Note that, although these are referred to as "modes of vibration," unique vibration modes cannot be clearly identified due to the system's highly nonlinear nature. To visualize the kind of motion in function of frequency a frequency response function (FRF) can be defined as $H(\omega) = Y_a(\omega)/Y_c(\omega)$, where $Y_a(\omega)$ and $Y_c(\omega)$ are respectively the Fourier transforms of the displacement of a measurement point on the mass and of the clamp displacement. Fig. 4 shows the magnitude of $H(\omega)$ in function of frequency for two points on each mass. The points analyzed are the tip of the messenger cable, measured by sensor $A03$ in Fig. 5b and $A01$ in Fig. 5a, and the outermost point of the mass, measured by sensor $A04$ in

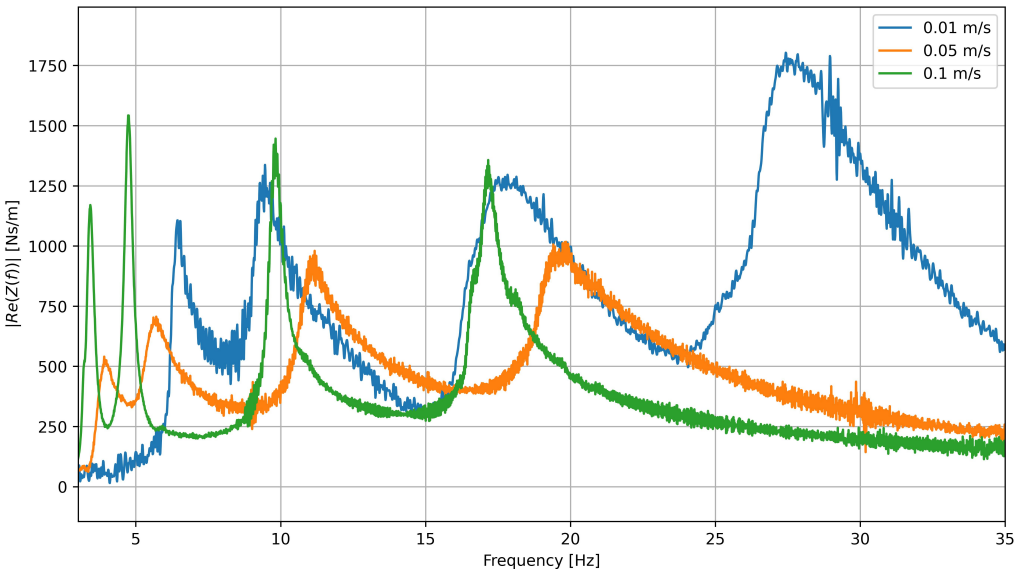


Figure 2. Impedance function of the whole damper for different velocity amplitudes.

Fig. 5b and *A*02 in Fig. 5a. As shown in the plot, for both cases the top sensor moves more at lower frequencies, with the second sensor closely following. In this frequency range, the mass primarily undergoes lateral movement with minimal rotation. A qualitative representation of this mode is given on the left of Fig. 3. At higher frequency, however, there is a reversal: the motion of the outer sensor decreases significantly, while the second sensor registers a peak. This second mode is characterized by minimal lateral translation and a pronounced rotation of the mass about its center of mass, as shown on the right of Fig. 3. Furthermore, it can be noticed how the lower mass (bigger mass) is characterized bby higher and sharper peaks, while the top mass (smaller mass) has lower and wider peaks that cover the entire tested frequency range.

3. CONCLUSIONS

These preliminary results provide insight into the dynamic behavior of the damper. The damper's asymmetry produces three distinct peaks in the system's impedance function. Testing each half separately clarifies the vibration modes, showing that the mass and weight orientation affect not only the resonance frequencies but also the width of the peaks. Notably, the rotational mode peaks differ between the half-damper and whole-damper tests.

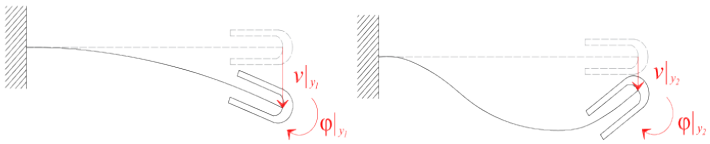
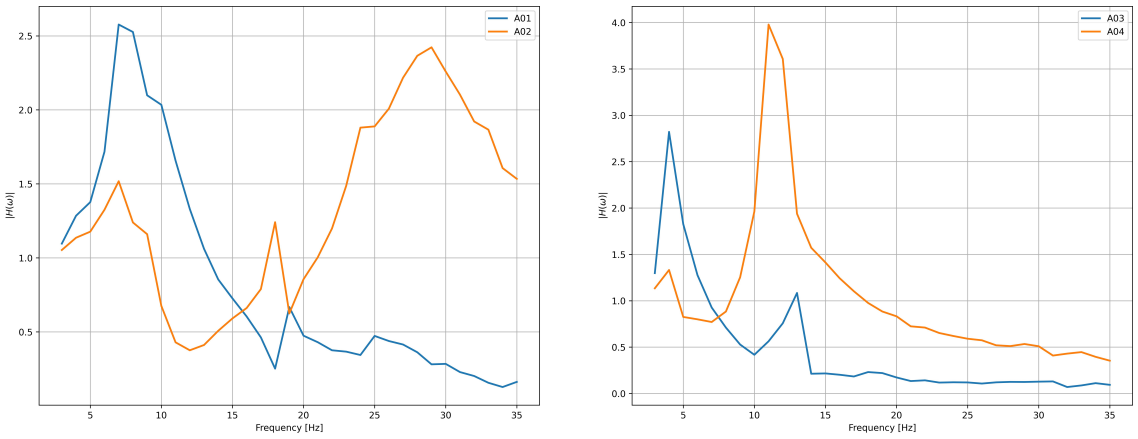
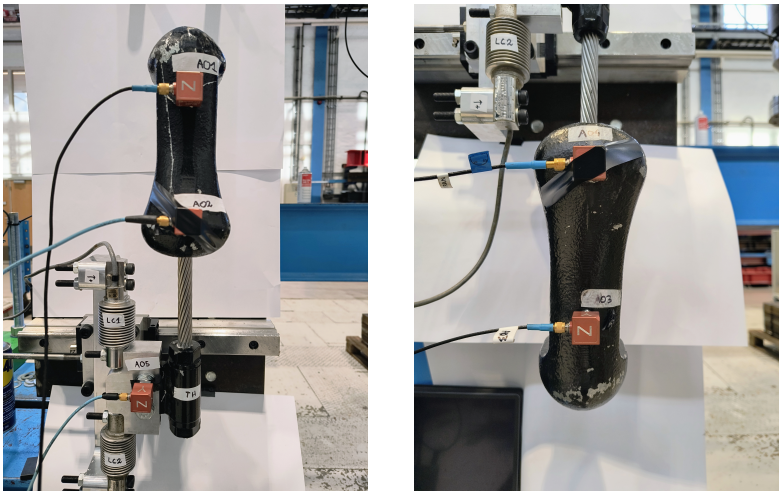


Figure 3. Qualitative representation of the two main modal deformation of half damper (Bogani and Alex, 2021).



(a) **(b)**

Figure 4. Magnitude of displacement transfer function $H(\omega)$ for damper's a) top half, b) bottom half. Velocity amplitude 0.05m/s.



(a) **(b)**

Figure 5. a) Top half of the damper (smaller mass) tested separately. b) Bottom half of the damper (bigger mass) tested separately.

REFERENCES

Barbieri, N. and Barbieri, R., 2012. Dynamic analysis of stockbridge damper. Advances in Acoustics and Vibration 2012.

Bogani, F. and Alex, S., 2021. Modellazione di dissipatori stockbridge per la mitigazione delle vibrazioni eoliche dei cavi sospesi. mathesis, Politecnico di Milano, p. 140.

Foti, F. and Martinelli, L., 2018. Hysteretic Behaviour of Stockbridge Dampers: Modelling and Parameter Identification. Mathematical Problems in Engineering 2018.

IEEE Standards Committee, 1993. IEEE Guide for Laboratory Measurement of the Power Dissipation Characteristics of Aeolian Vibration Dampers for Single Conductors.

Equivalent damping in structures subjected to vortex induced vibrations and damped with tuned mass dampers

Anass Mayou[1] and Vincent Denoël[2]

[1]*Structural & Stochastic Dynamics, University of Liège, Belgium, anass.mayou@uliege.be*
[2]*Structural & Stochastic Dynamics, University of Liège, Belgium, v.denoel@uliege.be*

SUMMARY:
This paper discusses methods for deriving equivalent damping for vortex-induced vibrations. Here, equivalence is defined as the structural damping ratio that would produce the same maximum displacement as a structure equipped with a Tuned Mass Damper. Given that the wind loads resulting from VIV are neither perfectly narrowband nor wide band, the equivalence presented in this paper is unique. Based on Tamura's 2-D wake oscillator model, the three governing differential equations of the damped wake oscillator are analyzed and illustrated numerically.

Keywords: VIV, TMD, damping ratio, equivalence, multiple scales.

1. CONTEXT

Vortex-Induced Vibration (VIV) poses significant challenges in structural engineering, particularly for slender structures like bridges and towers. Effective control methods are crucial for maintaining structural integrity. There are several ways to model VIV, spanning from the simplest passive harmonic loading, to more complex wake-oscillator models (Hartlen and Currie, 1970), passing through nonlinear models and their statistical equivalent forms (Simiu and Scanlan, 1996). Based on physical concepts and principles of mechanics, Tamura and Matsui's original 2-D wake oscillator model (Tamura and Matsui, 1980) is able to capture many of the features of the problem, among which synchronization. It treats the structure as a single-degree-of-freedom oscillator, and the wake (lamina) as another degree-of-freedom, emphasizing the intricate dynamics essential for predicting lock-in conditions. Although their model has been refined multiple times to account for multi-degree-of-freedom systems, or specific sheared wind profiles or aerodynamic cross sections, the original version is studied in this work, in view of providing a simple understanding of the response of structures equipped with tuned mass dampers (TMDs).

Very few experimental studies have been reported on the use of TMDs for VIV. However, doughnut and tuned liquid dampers are regularly installed on tall chimneys to tame their daily vibrations (Kareem et al., 1999; Rahman et al., 2024). Also (Gerges and Vickery, 2003) demonstrated the substantial response reduction achieved by TMDs during wind tunnel tests, suggesting that these systems offer improved equivalent damping compared to linear designs. Otherwise, many authors have focused on the wind response to VIV of structures equipped with TMDs, by means of numerical analysis (Andersen et al., 2001; Ricciardelli, 2001).

2. METHODS AND MODEL

2.1. Governing equations

A structure damped with a TMD is represented with two degrees-of-freedom, y and z, representing the motion of the structure and the motion of the tuned mass in a fixed reference frame. The governing equations read

$$\begin{pmatrix} m_\mathrm{s} & 0 \\ 0 & m_\mathrm{t} \end{pmatrix}\begin{pmatrix} \ddot{y} \\ \ddot{z} \end{pmatrix}+\begin{pmatrix} c_\mathrm{s}+c_\mathrm{t} & -c_\mathrm{t} \\ -c_\mathrm{t} & c_\mathrm{t} \end{pmatrix}\begin{pmatrix} \dot{y} \\ \dot{z} \end{pmatrix}+\begin{pmatrix} k_\mathrm{s}+k_\mathrm{t} & -k_\mathrm{t} \\ -k_\mathrm{t} & k_\mathrm{t} \end{pmatrix}\begin{pmatrix} y \\ z \end{pmatrix}=\begin{pmatrix} F_\mathrm{L} \\ 0 \end{pmatrix} \tag{1}$$

where m_s and m_t are the structural mass and the tuned mass, c_s and c_t are the structural viscosity and the damper's viscosity, k_s and k_t are the structural stiffness and the damper's stiffness, and F_L represents the lift force resulting from vortex shedding. The mass ratio $\mu = m_\mathrm{t}/m_\mathrm{s}$ (usually fixed to values around 1% to 3%), the frequency ratio $\alpha = \omega_\mathrm{t}/\omega_\mathrm{s}$ and the damping ratio $\xi_\mathrm{t} = c_\mathrm{t}/\left(2\sqrt{k_\mathrm{t}m_\mathrm{t}}\right)$ are adjusted to provide optimal performances (Fujino and Abé, 1993; Mayou and Denoël, 2022).

In Tamura and Matsui's model, the total structural damping ratio ξ is the sum of the inherent structural damping $\xi_\mathrm{s} = c_\mathrm{s}/\left(2\sqrt{k_\mathrm{s}m_\mathrm{s}}\right)$ and an aerodynamic damping proportional to the wind velocity $\xi_\mathrm{a} = n(f+C_D)\frac{\Omega}{2S^\star}$. The lift force is expressed by means of the angular position of the lamina q, which oscillates in the wake of the cylinder following

$$q'' - 2\zeta\Omega\left(1-\frac{4f^2}{C_{L0}^2}q^2\right)q' + \Omega^2 q = -m^\star Y'' - \Omega S^\star Y' \tag{2}$$

where $Y = y/D$ is the dimensionless crossflow displacement obtained by normalizing through the crossflow dimension D. The drag coefficient C_D, the standard deviation of the lift coefficient C_{L0}, the fluid/structure mass ratio n, the radial Strouhal $S^\star = 2\pi St$, the dimensionless half length of wake-oscillator $m^\star$, the damping ratio of the wake-oscillator ζ and the lift coefficient of the equivalent wake f are model parameters. The reduced wind velocity $\Omega = \frac{VS^\star}{\omega D}$, is the control parameter in VIV analyses. In the following illustrations, they are chosen as indicated in Table 1.

2.2. Dimensionless equations

The nonlinearity in the wake equation is responsible for a limit cycle and, when coupling with the structural motion takes place ($m^\star \neq 0$ or $\Omega \neq 0$), this limit cycle can include the structural degree(s)-of-freedom. In the absence of additional loading, this phenomenon is semantically not a synchronization (Denoël, 2020). The set of equations (1)-(2) is cast into a dimensionless formulation, with dimensionless time $\tau = \omega t$, similar to that employed in (Rigo et al., 2022)

$$\begin{pmatrix} 1 & 0 \\ 0 & \mu \end{pmatrix}\begin{pmatrix} Y'' \\ Z'' \end{pmatrix}+2\begin{pmatrix} \xi+\alpha\mu\xi_t & -\alpha\mu\xi_t \\ -\alpha\mu\xi_t & \alpha\mu\xi_t \end{pmatrix}\begin{pmatrix} Y' \\ Z' \end{pmatrix}+\begin{pmatrix} 1+\alpha^2\mu & -\alpha^2\mu \\ -\alpha^2\mu & \alpha^2\mu \end{pmatrix}\begin{pmatrix} Y \\ Z \end{pmatrix}=\begin{pmatrix} -\frac{fn\Omega^2}{S^{\star 2}}q \\ 0 \end{pmatrix} \tag{3}$$

so that a multiple scale analysis of the resulting set of equations can be derived. These two governing equations are combined with (2) to form the simplest version of the problem, expressed as a function of the states $Y = y/D$, $Z = z/D$ and q. The full version of the article will develop the multiple timescale analysis of the problem, and analyze the amplitude of the structural response in the entire lock-in range.

3. DEFINITION OF EQUIVALENT DAMPING RATIO

A practical and straightforward approach would be to employ an equivalent damping value, which allows for a simplified analysis of the system's behavior under VIV conditions. This equivalent damping can be defined as the H_∞ norm of the frequency response function (FRF), effectively consolidating the dynamic effects into a single parameter. The equivalent damping $\xi_{\text{eq}}^{\text{FRF}}$ can be expressed mathematically as $\|H(j\omega)\|_\infty := 1/\left(2\xi_{\text{eq}}^{\text{FRF}}\right)$, which engages a simpler and resource-light approach for practitioners. This formulation enables designers to access the response of the damped structure without resolving the specific characteristics of the wind loading. In the article, we show that this approach is not accurate, sometimes significantly unconservative. Alternatively, a more rigorous definition of the equivalent damping ξ_{eq} is given in this paper as the value of total structural damping ξ to be chosen in the analysis of the undamped system ($\mu = 0$), so that the maximum structural response in this case corresponds to the baseline results of the 3-DOF problem: $x^{\text{3-DOF}}(\xi, \Omega) = x^{\text{2-DOF}}\left(\xi_{\text{eq}}, \Omega\right)$.

4. ILLUSTRATIONS AND DISCUSSION

Table 1 provides the numerical values chosen for the illustrations of Test Case #1. They correspond to the values adjusted in (Tamura and Matsui, 1980) to the experimental results of Feng. Additionally, the mass ratio μ of the TMD is varied across several values, while its relative frequency ratio α and damping ratio ξ_{t} are fixed to 0.99 and 5% irrespective of the mass ratio (this choice is made to make Test Case #1 simple, but is in fact suboptimal with respect to several existing tuning strategies (Fujino and Abé, 1993; Mayou and Denoël, 2022)).

Figure 1-a shows the maximum structural displacement $Y_{\max}$ obtained in Test Case #1 while varying the total structural damping ξ from 10^{-3} to 10^{-1}. These responses have been obtained by simulating the 3-DOF problem with $\mu = 0$, which degenerates into the 2-DOF problem (without TMD). These values of the structural response will serve as a reference to define the equivalent damping ξ_{eq}. Figure 1-b shows the maximum structural response for various values of the mass ratio μ. It is noted that under nearly ideal tuning conditions, the TMD demonstrates remarkable efficiency, likely surpassing that observed with other VIV loading models (Andersen et al., 2001). This is understood as a strength of the Tamura model in effectively capturing the rapid variations of $Y_{\max}$ with respect to the Scrouton value (more detailed illustrations will follow in the full paper).

The equivalent damping ξ_{eq} is defined independently for each value of the reduced wind velocity Ω, as the value of the structural damping ξ (in 1-a) that provides the same $Y_{\max}$ as the considered case. This yields the results shown in Figure 1-d. Since the equivalent damping is determined independently for each wind velocity, the primary result of this study is $\xi_{\text{eq}}(\Omega)$. This definition yields results that vary significantly with wind velocity, reaching up to 7.5% for a TMD mass ratio of only 1.5%. However, to provide a conservative estimate of the equivalent damping ratio across the entire range of wind velocities within the lock-in range, one should consider the minimum value, which is approximately 1.5% in this case. These values are visually compared to the equivalent damping $\xi_{\text{eq}}^{\text{FRF}}$, derived solely from the infinite norm of the FRF. While for lower mass ratios, i.e. smaller equivalent damping, $\xi_{\text{eq}}^{\text{FRF}}$ tends to be an upper bound of $\xi_{\text{eq}}(\Omega)$ across the lock-in range, for larger mass ratios such as $\mu = 1.5\%$, $\xi_{\text{eq}}^{\text{FRF}}$ only agrees well on average with $\xi_{\text{eq}}(\Omega)$, yielding therefore to significant over- and under-estimations in the structural response.

Table 1. Numerical values used for the illustrations (with $\mu \in [0\%; 1.5\%]$).

Param.:	α	η	ξ_t	f	C_{L0}	C_D	n	$m^\star$	$S^\star$	ζ
Case #1 :	0.99	0.00181	0.05	1.16	0.4	1.2	0.00257	0.625	$2\pi \cdot 0.2$	0.038

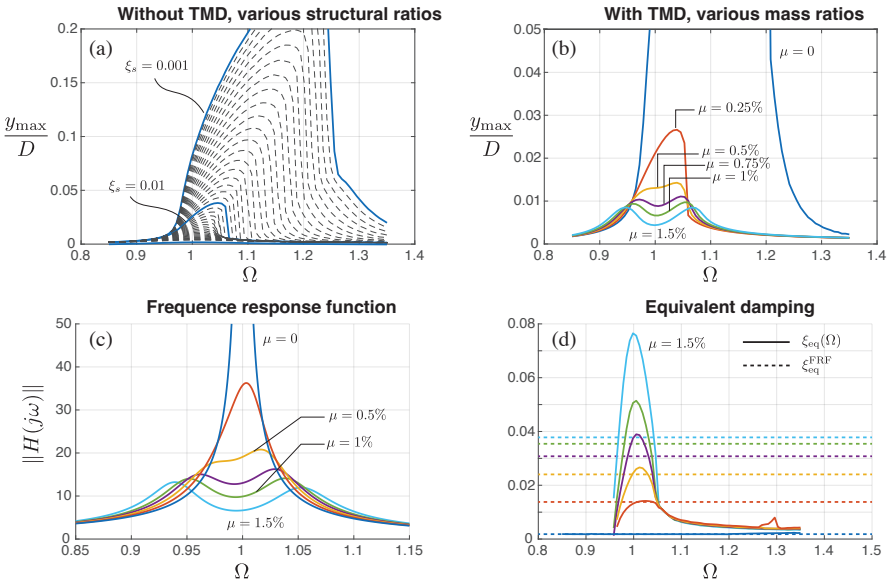


Figure 1. (a) Structural response obtained without TMD and for various structural damping ratios, (b) Structural response obtained with variousTMDs and with $\xi_s = 1.8\%$, (c) FRFs of the damped structure for various mass ratios, (d) equivalent damping: solid lines=current definition; dashed lines, definition based on H_∞ norm of the FRF.

REFERENCES

Andersen, L., Birch, N., Hansen, A., and Skibelund, J.-O., 2001. Response analysis of tuned mass dampers to structures exposed to vortex loading of Simiu-Scanlan type. Journal of Sound and Vibration 239. Cited by: 16, 217–231.

Denoël, V., 2020. Derivation of a slow phase model of vortex-induced vibrations for smooth and turbulent oncoming flows. Journal of Fluids and Structures 99. Cited by: 5; All Open Access, Green Open Access.

Fujino, Y. and Abé, M., 1993. Design formulas for tuned mass dampers based on A perturbation technique. Earthquake Engineering & Structural Dynamics 22. cited By 230, 833–854.

Gerges, R. R. and Vickery, B. J., 2003. Wind tunnel study of the across-wind response of a slender tower with a nonlinear tuned mass damper. Journal of Wind Engineering and Industrial Aerodynamics 91. Cited by: 27, 1069–1092.

Hartlen, R. and Currie, I., 1970. Lift-oscillator model of vortex-induced vibration. ASCE Journal of Engineering Mechanics 96. cited By 516, 577–591.

Kareem, A., Kijewski, T., and Tamura, Y., 1999. Mitigation of motions of tall buildings with specific examples of recent applications. Wind and structures 2, 201–251.

Mayou, A. and Denoël, V., 2022. Asymptotic analysis of multiple mode structures equipped with multiple tuned mass dampers. Journal of Sound and Vibration 535. cited By 6.

Rahman, S., Jain, A., Jha, K., Bharti, S., and Datta, T., 2024. Response control of chimneys using tuned mass damper, multi-tuned mass damper and tuned mass inerter system. Structures 69. Cited by: 0.

Ricciardelli, F., 2001. On the amount of tuned mass to be added for the reduction of the shedding-induced response of chimneys. Journal of Wind Engineering and Industrial Aerodynamics 89. cited By 17, 1539–1551.

Rigo, F., Andrianne, T., and Denoël, V., 2022. Parameter identification of wake-oscillator from wind tunnel data. Journal of Fluids and Structures 109. cited By 8.

Simiu, E. and Scanlan, R., 1996. Wind Effects on Structures. cited By 3277.

Tamura, Y. and Matsui, G., 1980. "Wake-oscillator model of vortex-induced oscillations of circular cylinder". Proceedings of *Wind Engineering*. Ed. by J. Cermak. Pergamon, pp. 1085–1094.

Extreme compression of URANS flow data

Omar A. Mures[1], Miguel Cid Montoya[2], Sumit Verma[3], Ashutosh Mishra[4]

[1]*XLab, Dept. of Civil Eng., University of A Coruña, Spain, omar.alvarez@udc.es*
[2]*ASTRO Lab, Glenn Dept. of Civil Eng., Clemson University, USA, mcidmon@clemson.edu*
[3]*ASTRO Lab, Glenn Dept. of Civil Eng., Clemson University, USA, sumitv@clemson.edu*
[4]*Dept. of Eng., Texas A&M Univ.-Corpus Christi, USA, amishra1@islander.tamucc.edu*

SUMMARY:

The rise of exascale supercomputing has motivated an increase in high-fidelity CFD simulations, yielding massive datasets that can pose a problem for conventional data management and analysis pipelines. The detail in these simulations, often involving complex, non-linear turbulent flows, is essential for fueling innovations in fields like wind or aerospace engineering. The amount of data these simulations produce can overwhelm storage systems and negatively affect post-processing workflows, including iterative procedures such as design space exploration, optimization, and uncertainty quantification. This work proposes a novel sampling method harnessing the Signed Distance Function (SDF) concept and implicit compression based on neural networks for URANS CFD simulation data compression. Designed to alleviate the abovementioned problems, our approach achieves compression ratios of approximately 17 000:1, reducing simulation data size from roughly 600 GB to ∼36 MB while maintaining low reproduction errors (in most cases below 0.5 %). Given that image sampling is a fundamental step for any image-based flow field prediction model, the proposed SDF-based sampling method can significantly improve the accuracy and efficiency of such models, helping any application that relies on precise flow field predictions.

Keywords: compression, neural networks, CFD simulations

1. INTRODUCTION

Current exascale computing trends (Bergman et al., 2008) point to data storage and analysis becoming major bottlenecks in the near future. Computational Fluid Dynamics (CFD) simulations are no stranger to this trend, with current simulation outputs already reaching terabytes of data. Precise simulations are essential for many wind engineering workflows, particularly for wind-resistant design and optimization. Examples of large-scale CFD simulations can be found in several wind and civil engineering applications (Blocken, 2014; Melaku and Bitsuamlak, 2024). In bridge engineering, 2D URANS is one of the most widely used simulation types given its ability to extract fluid-structure interaction parameters for bridge decks (Mannini et al., 2016). While the number of mesh cells is typically more contained, e.g. below 1 M, shape design applications require handling flow data from multiple simulations involving different deck shape designs and reduced velocity values (Verma et al., 2024). State-of-the-art compression techniques usually do not leverage domain information, testing general compression algorithms like LZMA, bzip2, PPMd, or even more domain-specific algorithms like tensor-tensor (Kilmer et al., 2021), resulted in compression ratios ranging from ∼5:1 to ∼50:1. Our approach, an evolution of (Tancik et al., 2020) combined with a new image sampling method, obtains orders of magnitude higher compression ratios and

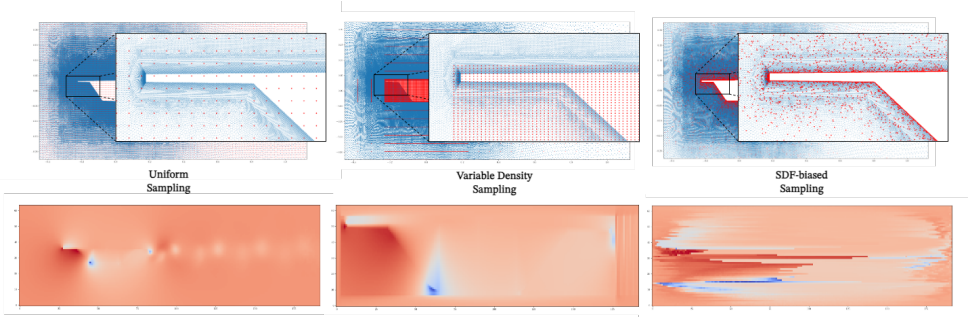


Figure 1. Comparison of different sampling strategies for a common complex geometry modeling scenario using a 192×64 image. While uniform sampling is probably the optimal representation for visualization, it lacks the required precision in relevant regions for accurate post-processing. Conversely, the proposed SDF-biased sampling preserves the required surface information perfectly by tailoring the density distribution to the influential flow regions such as the boundary layer of the bluff body. Variable density sampling presents a middle ground by increasing the density in the neighbourhoods of the boundary layers but, as a consequence, wasting samples outside the flow domain.

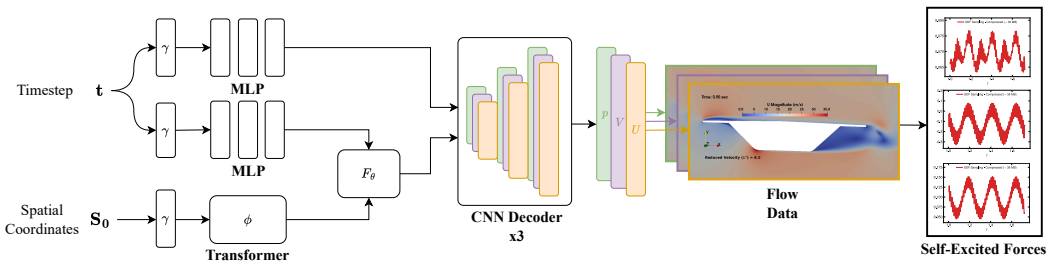


Figure 2. Proposed neural network architecture for flow compression. The required input is the simulation timestep value $\mathbf{t}$ that the neural network will use to produce the corresponding p, U, and V. The architecture is composed by two big MLPs, a small F_θ MLP, a small transformer ϕ, and three convolutional decoders.

greater scalability, i.e., up to $\sim$17 000:1 in the current example. The proposed methodology offers an alternative that removes the need to select subsets of data and discard massive parts of datasets, opening the door to systematically saving all relevant data available.

2. PROPOSED FRAMEWORK FOR COMPRESSION OF FLOW DATA

Our goal is to compress the data output of a CFD simulation for visualization, analysis, and training of deep learning flow prediction models. We consider that the data can be discretized for each time step t in the form of an image $\psi \in \mathbb{R}^{w \times h}$. Our goal is to reconstruct the image series for the full simulation ψ_t, $\forall t = 1, \ldots, T$. Being T the total number of time steps that the simulation encompasses. Since initially we do not have images but mesh data for each simulation cell center, a scheme for discretizing said information losing minimal fidelity is required. Conventional image sampling methods (uniform or variable density) typically fail to capture critical flow features in complex CFD simulations. Our work introduces SDF-biased sampling (see Figure 1), a novel technique motivated by (Osher et al., 2003), leveraging mesh data to favor preserving information in essential regions. By incorporating the Signed Distance Function (SDF), our method preferentially samples cell centers near deck surfaces or user-defined regions of interest. This strategy ensures that critical regions are reproduced with high fidelity while less important ones are sampled

more sparsely. In addition, motivated by image-wise implicit neural representations (Tancik et al., 2020) we propose leveraging a similar architecture to E-NeRV (Li et al., 2022), to encode fluid information representing the simulation as a mapping function $f_\theta : \mathbb{R} \rightarrow \mathbb{R}^{3\times h\times w}$ (see Figure 2), being θ trainable weights. We disentangle time and spatial representations with the use of F_θ, a small Multi-layer Perceptron (MLP). ϕ represents a small transformer (Vaswani, 2017) for parameterizing spatial information. Features generated by neural network blocks are finally processed by three convolutional decoders that produce the desired output flow variables p, U, and V.

3. REPRESENTATIVE RESULTS

To test the fidelity of our compressed simulations, we applied common simulation post-processing steps to the generated images, computing the non-dimensional drag, lift, and moment time series for a representative deck shape under forced vibrations (Verma et al., 2024) using both original and compressed simulation data. As shown in Figure 3, our compression scheme accurately captures turbulent flow effects on aerodynamic forces, even with a low input resolution of 192×64 pixels. Mean Absolute Error (MAE) and Mean Relative Error (MRE) values are compared in Table 1. Notably, using SDF-biased sampling alone yields near-lossless reproduction of drag, lift, and moment (all under 0.35 % error). Incorporating implicit compression introduces minor errors in the lift and moment forces, but always remaining below 0.5 %. While the drag exhibits slightly higher errors, our method still outperforms traditional uniform and variable density sampling. Regarding data size reduction our method attains a 17 000:1 compression ratio, which if applied to the full simulation space yields the following size: $49 \times 36\,\text{MB} = 1.7\,\text{GB}$, while the uncompressed simulations yield: $49 \times 600\,\text{GB} = 28.71\,\text{TB}$. The total data space savings would amount to 28.7 TB.

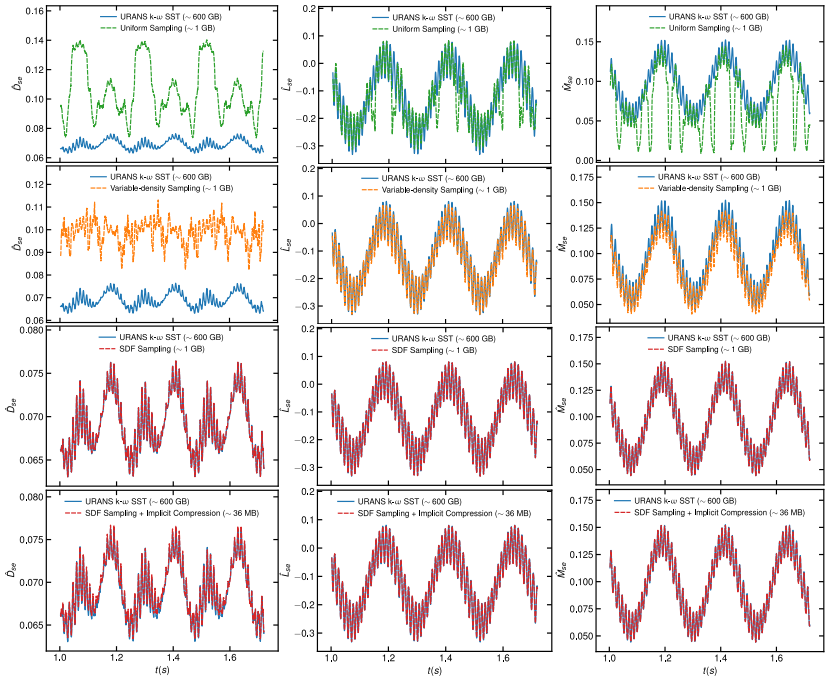


Figure 3. Non-dimensional self-excited drag, lift, and moment extracted from 192×64 flow images. Uniform and variable density sampling methods present clear problems in drag, conversely our method yields better results with orders of magnitude higher compression ratios, while for an equivalent compression ratio it is close to lossless.

Table 1. Absolute and relative errors for non-dimensional self-excited drag, lift, and moment extracted from 192×64 flow images. The proposed sampling and compression method outperforms all others by a wide margin in terms of accuracy (highly apparent in drag) while maintaining much higher compression ratios. Original simulation size is ~ 600 GB. **Bold** represents lowest error and underlined represents the second lowest.

Sampling	Size	Compression Ratio	$\hat{D}_{se}(t)$		$\hat{L}_{se}(t)$		$\hat{M}_{se}(t)$	
			MAE	MRE	MAE	MRE	MAE	MRE
Uniform	1 GB	600:1	0.03660	273.895%	0.03130	7.591%	0.02585	23.878%
Variable	1 GB	600:1	0.02971	222.306%	0.00816	1.980%	0.00726	6.705%
SDF	1 GB	600:1	**0.00005**	**0.351%**	**0.00001**	**0.002%**	**0.00012**	**0.110%**
SDF	36 MB	17 000:1	0.00027	2.024%	0.00136	0.330%	0.00047	0.436%

4. CONCLUDING REMARKS AND ONGOING RESEARCH

Our compression method achieves compression ratios in the order of 10^4 at the negligible cost of relative errors of 2.024 %, 0.330 %, and 0.436 %, for the drag, lift, and moment, respectively. This ability to efficiently manage and analyze massive flow fields has exponential benefits in modern engineering applications. The developed scheme allows researchers to tackle problems that otherwise would be impossible due to data size limitations, such as large dataset storage and computational applications involving iterative processes, such as AI training, optimization, UQ, RA, or RBDO. While this paper focuses on 2D URANS, the method proposed can be recast for compressing any kind of flow data, including massive wind tunnel testing and full case monitoring data.

ACKNOWLEDGEMENTS

Investigation funded by the NSF (Grant No. CMMI-2301824). Omar A. Mures thanks the Galician Supercomputing Center (CESGA), funded by the Spanish Ministry of Science and Innovation, the Galician Government, and the European Regional Development Fund (ERDF). Miguel Cid Montoya thanks the start-up funds by Clemson University.

REFERENCES

Bergman, K., Borkar, S., Campbell, D., Carlson, W., Dally, W., Denneau, M., Franzon, P., Harrod, W., Hill, K., Hiller, J., et al., 2008. Exascale computing study: Technology challenges in achieving exascale systems. Defense Advanced Research Projects Agency Information Processing Techniques Office (DARPA IPTO), Tech. Rep 15, 181.

Blocken, B., 2014. 50 years of Computational Wind Engineering: Past, present and future. J. Wind Eng. Ind. Aerod. 129, 69–102.

Kilmer, M. E., Horesh, L., Avron, H., and Newman, E., 2021. Tensor-tensor algebra for optimal representation and compression of multiway data. PNAS 118, e2015851118.

Li, Z., Wang, M., Pi, H., Xu, K., Mei, J., and Liu, Y., 2022. E-nerv: Expedite neural video representation with disentangled spatial-temporal context. Proceedings of European Conference on Computer Vision. Springer, 267–284.

Mannini, C., Sbragi, G., and Schewe, G., 2016. Analysis of self-excited forces for a box-girder bridge deck through unsteady RANS simulations. Journal of Fluids and Structures 63, 57–76.

Melaku, A. F. and Bitsuamlak, G. T., 2024. Prospect of LES for predicting wind loads and responses of tall buildings: A validation study. J Wind Eng Ind Aerodyn 244, 105613.

Osher, S., Fedkiw, R., Osher, S., and Fedkiw, R., 2003. Constructing signed distance functions. Level set methods and dynamic implicit surfaces, 63–74.

Tancik, M., Srinivasan, P., Mildenhall, B., Fridovich-Keil, S., Raghavan, N., Singhal, U., Ramamoorthi, R., Barron, J., and Ng, R., 2020. Fourier features let networks learn high frequency functions in low dimensional domains. Advances in neural information processing systems 33, 7537–7547.

Vaswani, A., 2017. Attention is all you need. Advances in Neural Information Processing Systems.

Verma, S., Cid Montoya, M., and Mishra, A., 2024. Shape- and frequency-dependent self-excited forces emulation for the aero-structural design of bluff deck bridges. J. Wind Eng. Ind. Aerod. 252, 105769.

Learning weakly nonlinear Vortex-induced Vibration governing equations from experimental data

Teng Ma [1,2], Wei Cui [1], Lin Zhao [1,3]

[1]*State Key Lab of Disaster Reduction in Civil Engineering, Tongji University, Shanghai 200092, China*
[2]*Department of Civil and Environmental Engineering, Politecnico di Milano, Milan 20133, Italy*
[3]*Key Laboratory of Disaster Prevention and Structural Safety of China Ministry of Education, Guangxi University, Nanning 530004, China*

SUMMARY:
While the behaviours of vortex-induced vibrations can be observed in experiments, simulations and field measurements, their underlying dynamics remain elusive until now. We proposed an evolutionary learning approach to autonomously discover the weakly nonlinear governing equation of vortex-induced vibrations. A 1:20 scaled wind tunnel test of Xihoumen Bridge is conducted to validate our approach. From the experimental data, we inferred a concise ODE which can capture the amplitude and phase evolutions accurately.

Keywords: Vortex-indeuced vibration, Data-driven inferring method, weakly nonlinear oscillator

1. GENERAL INSTRUCTIONS

Vortex-induced Vibrations (VIVs) have widely applications in many fields of engineering, such as wind, ocean and aeronautical engineering. In past several decades, the effects of VIVs on long-span bridges are often reported around the world and caused lots of economic loses and traffic issues. While the behaviours of vortex-induced vibrations can be observed in experiments, simulations and field measurements, their underlying dynamics remain elusive until now. Ordinary differential equations (ODEs) have been widely used to model VIVs, like van der pol equations (Cui et al., 2024) and weak oscillator model (Facchinetti et al., 2004). However, these models have certain limitations on describing real-world phenomena, such as pre-defined forms and simplified physics, and lead to biased fitting or predicting results. Fortunately, the increasing available of experiment data and advances of machine learning theories provide an opportunity to update the modelling paradigm of VIV (Zhang et al., 2024). Instead of modelling the dynamics of VIV using a pre-defined equation (like ODE), it becomes possible to "learn" the hidden governing equations from experiment data.

Pioneering contributions by Schmidt and Lipson (2009) and Brunton et al. (2016) leveraged stratified symbolic regression and sparse identification of nonlinear dynamics (SINDy) to successfully distil the underlying differential equations that govern nonlinear system dynamics from data. Recently, data-driven aerodynamics force formula identification methods are also developed in wind engineering (Ma et al., 2023; Laima et al. 2024). However, these methods may not effectively address the real systems exhibit weakly effects, like VIV. The mass of an

individual vortex is very small relative to the mass of structure and the force of vortex exerting is also very small relative to the stiffness of structure. The nonlinearities caused by vortex is super small than oscillatory frequency of structure itself. The previous method will ignore the weakly effect naturally.

Here, the evolutionary learning method is proposed, which can overcome this challenge and infer the governing equation of vortex-induced vibration. The proposed approach utilizes method of averaging to transfer the second-order oscillating ODE to first-order evolutionary ODEs, which capture the effects from weakly nonlinearities accurately. To validate the effectiveness of our approach, we conducted a wind tunnel tests on a 1:20 scaled sectional model of the Xihoumen Bridge. From the experimental data of wind tunnel test, our method successfully discovers the ODEs of free vibrations and vortex-induced vibrations. We found that the non-linearity does not only exist due to vortex shedding, but also in free vibration at zero wind velocity, which is usually ignored in vortex-induced vibration research.

2. EVOLUTIONARY LEARNING METHOD

The governing equation of 1DOF vortex-induced vibration can be generally described as a second-order ODE:

$$\ddot{x} + \omega_0^2 x + \epsilon f(x, \dot{x}) = 0 \quad (1)$$

Where x is the displacement of bridge deck, $\dot{x}$ and $\ddot{x}$ are the velocity and acceleration of bridge deck respectively, ω_0 is the oscillating frequency of bridge deck, ϵ is a small coefficient and $f(x, \dot{x})$ is the unknown function representing the weakly nonlinearity from structure or vortex.

Without the prior knowledge of weakly nonlinear function Eq. (1), it can be approximately expressed as the summation of several basis functions $\boldsymbol{\Theta}(x, \dot{x}) = \{x, \dot{x}, x^2, x\dot{x}, \dot{x}^2, \cdots\}$. Then the equation learning problem can be recast to the selection of appropriate subset of $\boldsymbol{\Theta}(x, \dot{x})$ that best match ODE function $\ddot{x} = \boldsymbol{\Theta}(x, \dot{x})\Xi$. Because of small coefficient ϵ, linear frequency term $\omega_0^2 x$ almost dominate the ODE function and weakly nonlinearity will be ignored naturally.

Utilizing the method of averaging, the original ODE function can be transferred into evolutionary ODEs involving amplitude A function (Eq. (2)) and phase β function (Eq. (3)). The method of averaging is an approximate theory for weakly nonlinear oscillator (Volosov, 1962). By integrating each basis function over a period of vibration, their contribution to the dynamic evolution can be determined, naturally distinguishing terms of different orders of magnitude in the oscillatory equation. Then the sparse regression method can used to find the best subset to match Eq.(2) and Eq.(3) at the same time.

$$\dot{A} - \frac{\epsilon}{2\pi\omega_0}\int_0^{2\pi} f(x, \dot{x}) \cos(\phi)\, d\phi = 0 \quad (2)$$

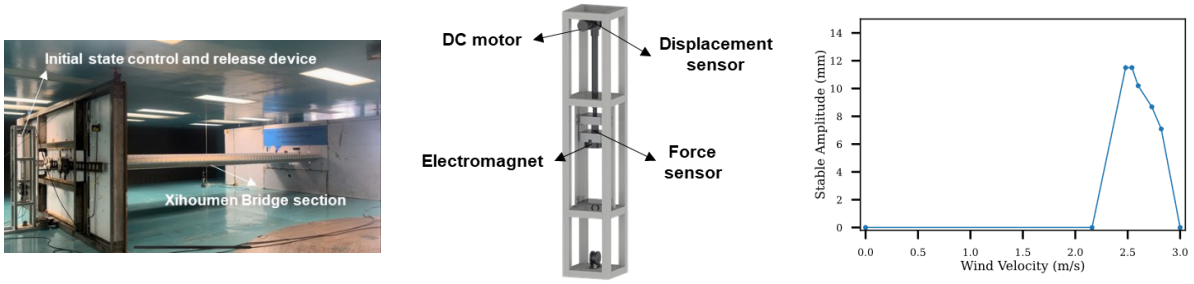
$$\dot{\beta} + \frac{\epsilon}{2\pi A\omega_0}\int_0^{2\pi} f(x, \dot{x}) \sin(\phi) d\phi = 0 \quad (3)$$

Where $\phi = \omega_0 t + \beta$ and $\dot{A}, \dot{\beta}$ are the evolutionary variables about amplitude and phase respectively.

3. LARGE-SCALE SECTIONAL WIND TUNNEL TEST

The 1:20 scaled Xihoumen bridge sectional model testing (Figure 1 a.) in this study were implemented in TJ-3 boundary layer wind tunnel, which is a vertical arranged circuit-flow wind tunnel with a test section of 15m wide, 14m long and 2m high. The width, height, and length of the sectional model are 1800mm, 163mm and 6000m, respectively. The total mass including the model, boom and spring is 417.81kg, the vertical vibration frequency of the suspension system is 2.014Hz. Because only vertical VIVs occur in experiments, the torsional inertia and frequency are not reported in this study. The stable limit-cycle oscillation of VIV amplitudes for different wind speeds was obtained by experiments, and the amplitudes versus wind speeds are shown in Figure 1 c.

Vortex-induced vibration perform the sensitization to the initial states because of the weakly nonlinearities. However, it's difficult to control quantificationally the initial state of oscillation in wind tunnel test. We invent a novel initial state control and release device (Figure 1 b.), which composed by DC motor, displacement sensor, force sensor and electromagnet. The DC motor drives the model to generate displacement, the force sensor is used to eliminate static wind displacement interference, the displacement sensor is used to quantify the initial displacement, and the electromagnet can release the model into free vibration. In this research, we test two initial states (0mm and 14mm) to validate the inferred governing equation.



a. Wind tunnel test

b. Initial state control and release device

c. VIV amplitudes

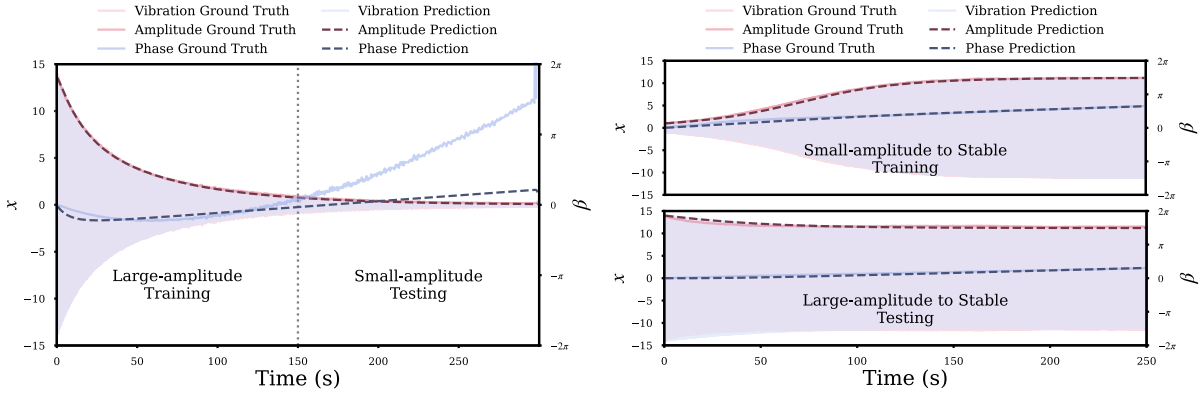
Figure 1. Large-scale sectional wind tunnel test.

4. INFERRED VIV EQUATIONS

Based on these experimental data, our approach successfully infers a concise effective governing equation with different weakly magnitude effects (Eq. (4)). As Figure 2 shown, inferred weakly nonlinearities accurately describe the evolutions of free vibration and vortex-induced vibration. Because empirical systems lack ground truths, we verify the inferred equation by testing its generalizability to different initial states. For vortex-induced vibration cases, the small displacement initial state is used to train and large displacement is for testing. For free vibration cases, large amplitude is used to train and small amplitude is for testing. It's interesting that we found that the non-linearity does not only exist due to vortex shedding, but also in free vibration at zero wind velocity, which is usually ignored in vortex-induced vibration research. Remarkably, these equations are autonomously inferred from the observation data, devoid of preconceived assumptions about its structure.

$$\ddot{x} + \omega_0^2 x + 2\omega_0 \zeta \dot{x} + N_1 \dot{x}^3 - N_2 \dot{x}^4 x - N_3 \dot{x}^5 = 0 \tag{4}$$

Where ζ is the linear damping coefficient and N_1, N_2, N_3 are the small coefficients of weakly nonlinear terms. The magnitude difference between weakly nonlinear terms and oscillating frequency is 8-12.



a. Free vibration at $U = 0m/s$ b. Vortex-induced vibration at $U = 2.54m/s$

Figure 2. Comparison between the wind tunnel test results and inferred equation reconstruction

5. CONCLUSIONS

The evolutionary learning approach is proposed in order to infer the dynamic equations of vortex-induced vibration. To obtained the oscillatory data, we conducted a wind tunnel tests on a 1:20 scaled sectional model of the Xihoumen Bridge, whose prototype frequently experiences VIVs in the real world. From the experimental data of wind tunnel test, our method successfully discovers the ODEs of free vibrations and vortex-induced vibrations. We found that the non-linearity does not only exist due to vortex shedding, but also in free vibration at zero wind velocity, which is usually ignored in vortex-induced vibration research.

ACKNOWLEDGEMENTS

The authors gratefully acknowledge the support of National Natural Science Foundation of China (52078383, 52008314, 51978527).

REFERENCES

Brunton, S. L., Proctor, J. L., & Kutz, J. N., 2016. Discovering governing equations from data by sparse identification of nonlinear dynamical systems. Proceedings of the national academy of sciences, 113(15), 3932-3937.

Cui, W., Zhao, L., Ge, Y., & Xu, K., 2024. A generalized van der Pol nonlinear model of vortex-induced vibrations of bridge decks with multistability. Nonlinear Dynamics, 112(1), 259-272.

Facchinetti, M. L., De Langre, E., & Biolley, F., 2004. Coupling of structure and wake oscillators in vortex-induced vibrations. Journal of Fluids and structures, 19(2), 123-140.

Laima, S., Zhang, Z., Jin, X., Li, W., & Li, H., 2024. Identification of the form of self-excited aerodynamic force of bridge deck based on machine learning. Physics of Fluids, 36(1).

Ma, T., Cui, W., Gao, T., Liu, S., Zhao, L., & Ge, Y., 2023. Data-based autonomously discovering method for nonlinear aerodynamic force of quasi-flat plate. Physics of Fluids, 35(2).

Schmidt, M., & Lipson, H., 2009. Distilling free-form natural laws from experimental data. science, 324(5923), 81-85.

Volosov, V. M., 1962. Averaging in systems of ordinary differential equations. Russian Mathematical Surveys, 17(6), 1.

Zhang, Z., Li, S., Feng, H., Zhou, X., Xu, N., Li, H., ... & Chen, W., 2024. Machine learning for bridge wind engineering. Advances in Wind Engineering, 100002.

An initiative for consolidating a universal aerodynamic coefficients database using LLM-driven web scraping

Dario Castellon [1,2]

[1]*NTNU, Trondheim, Norway, dario.r.f.castellon@ntnu.no*
[2]*AFRY Norway AS, Oslo, Norway, dario.castellon@afry.com*

SUMMARY:
This research proposal aims to leverage a Large Language Model (LLM)-based AI agent to automate the extraction of aerodynamic coefficients (drag, lift, and moment) from scientific publications. The objective is to develop a web-scraping tool integrated with natural language processing (NLP) techniques to gather relevant aerodynamic data from open-access scientific papers and repositories. By analyzing the text, tables, and figures within these publications, the AI will isolate and extract information such as the aerodynamic force coefficients required for bridge aerodynamics and structural engineering applications.
The project will focus on overcoming challenges related to the diverse formatting of scientific data, ensuring accurate parsing of aerodynamic coefficients across various sources. Ethical considerations, including adherence to web-scraping regulations and copyright policies, will be strictly maintained by focusing on open-access journals and publicly available datasets. The outcome will be a structured database of aerodynamic coefficients, potentially streamlining research in bridge aerodynamics and enabling more efficient access to crucial data for future studies.
This approach holds the potential to significantly accelerate literature reviews and data acquisition in aerodynamics research, offering an innovative solution for extracting key scientific metrics.

Keywords: Large Language Models LLM, Web scraping, Aerodynamic force coefficients

1. DATABASES FOR AERODYNAMICS

Several existing databases provide aerodynamic information from wind tunnel testing, yet they primarily focus on specific domains like buildings and airfoils. One prominent resource is the Database-Assisted Design (DAD) tool from NIST, which offers wind force data for building structures (Yeo, 2011). The advantage of DAD is that it allows users to make well-informed decisions based on a wide range of experimental data, improving wind engineering design. However, a major disadvantage is that DAD is limited to buildings and does not extend to other structures like bridges.

In addition, the University of Tokyo offers a wind pressure estimation tool and database for buildings with simple shapes, facilitating quick analyses of wind forces on building structures (Quan et al., 2007). Similarly, the UIUC Low-Speed Airfoil Tests project has compiled aerodynamic data for airfoils, providing insights into their performance under various flow conditions (Selig et al., 2012). Table 1 shows a list of some databases available together with the data format provided.

Despite these efforts, each study is limited to local data acquisition, with researchers often

consolidating their own data without integrating results from a broad range of sources. There has been no significant research effort to consolidate data from multiple wind tunnel tests or across diverse studies, resulting in fragmented datasets. To the best of the author's knowledge, no comprehensive or unified database exists for aerodynamic force coefficients, especially one tailored specifically to bridge design. This lack of a consolidated resource highlights a critical gap in the field, underscoring the need for a universal database that compiles data from multiple studies.

Therefore, this research seeks to address this gap by using advanced technologies to compile a universal database of aerodynamic force coefficients, extending findings from buildings and airfoils to the bridge design domain.

Table 1. Databases available

Database	Provider	Structure type	Content
D.A.D.	NIST	Buildings	Pressure coefficients
UIUC Low-Speed Airfoil Tests	University of Illinois	Airfoil	Force coefficients
TPU Aerodynamic database	Tokyo Polytechnic University	Buildings	Pressure coefficients

2. LEVERING WEB SCRAPING WITH LARGE LANGUAGE MODELS

Web scraping, combined with Large Language Models (LLMs), offers a powerful tool to automate data extraction from scientific publications (Ahulawalia et al., 2024). Traditional web scraping collects data from structured sources like HTML tables, but LLMs go further by processing unstructured text, interpreting complex tables, and extracting figures from PDFs or scanned documents (Gill et al., 2024). This research proposes using an LLM-based agent to scrape and extract aerodynamic coefficients (drag, lift, moment) from open-access scientific literature. Previous studies (Han et al., 2024; Shamsabadi et al., 2024) have demonstrated the capabilities of LLM-based web scraping tools for enhancing literature reviews and compiling scientific data. However, due to the emerging characteristic of this technology, its application in bridge aerodynamics remains unexplored. The goal of this approach is to streamline the literature review process, providing efficient access to critical aerodynamic data that can be applied to bridge design and other structural engineering challenges.

By leveraging NLP techniques, the LLM will not only identify and extract relevant aerodynamic data but also understand the context in which these coefficients are presented. For example, LLMs can be prompted to locate specific keywords like "drag coefficient" or "moment coefficient" within the text and return relevant data in a structured format. A web-scraping pipeline integrated with an LLM might parse the following sentence: "The drag coefficient for the bridge model was found to be 0.45 for an angle of attack of 12 degrees", automatically extracting the numeric value along with the corresponding conditions. Figure 1 shows a schematic flowchart of the architecture of the web scraping tool.

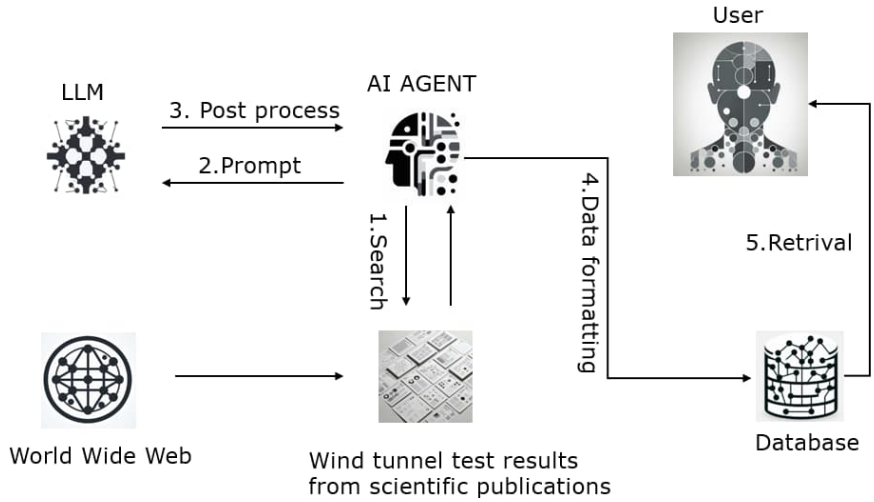


Figure 1. Flowchart architecture.

3. ETHICAL CONSIDERATIONS IN AI AND DATA MANAGEMENT

The use of LLMs and AI agents for data extraction raises ethical concerns, particularly regarding data management, legal rights, and transparency. Strict adherence to copyright laws and web-scraping policies is essential, especially when accessing scientific publications. Data used in this project will be sourced from open-access repositories, ensuring compliance with legal frameworks. Transparency in data collection and algorithmic decision-making will be maintained to avoid biases or misuse of information. Proper data handling protocols will be followed to respect intellectual property rights, ensuring that the research aligns with ethical standards in AI and data management.

4. PREELIMINAR RESULTS

In this chapter, it is presented a proof-of-concept aimed at building the initial model and to explore potential challenges associated with scaling and deployment. The materials used included four open-access papers from the NTNU research group, which contained information on aerodynamic coefficients: (Lystad et al. 2020), (Castellon et al. 2022) (Kildal et al. 2025) and (Kildal et al. 2023). The method involved utilizing an LLM-enhanced web scrapping model to extract and store all tables and images referencing aerodynamic coefficients in the papers. The source code and retrieved data was placed in public online repository (https://github.com/dfernand90/WindScrapper).

The proof-of-concept results are promising, achieving a 100% retrieval rate for assets. However, a false positive rate of approximately 20% suggests the need for further noise reduction. Table 2 shows an overview of the retrieved assets.

Table 2. Summary of results

	Image	Table
Total assets to retrieve	21	4
True positive assets retrieved	21	4
False positives	6	1
Retrieve score	100%	100%
Retrieve noise score	22%	20%

Beyond accuracy, the test revealed additional qualitative challenges. Accessing the articles requires API keys and access permissions, which can hinder data collection. Moreover, correctly identifying and naming relevant papers remains a manual, time-consuming task. A practical approach is to involve researchers and professionals in submitting DOIs or URLs of relevant papers directly to the repository.

Addressing these challenges also requires significant efforts in science communication and dissemination. This highlights the value of conferences like EACWE 2025, which provide a vital platform for networking and collaboration.

5. EXPECTED OUTCOMES

This research is expected to develop a comprehensive database of aerodynamic force coefficients, specifically for bridges, filling a critical gap in the current body of knowledge. By utilizing LLM-based web scraping, the project will automate the extraction of drag, lift, and moment coefficients from scientific literature, streamlining the data collection process. The resulting database will provide structural engineers and researchers with easy access to key aerodynamic data, facilitating more accurate wind load assessments in bridge design. This tool will also create a foundation for the development of future data-driven models, potentially extending the applications of emerging digital technologies like machine learning for bridge aerodynamic assessment.

REFERENCES

DongHun Yeo, 2011. Database-Assisted Design for Wind: Multiple Points-in-Time Approach. NIST TECHNICAL NOTE 1711.

Quan, Yinggeer & Tamura, Yukio & Matsui, M. & Cao, S.Y. & Yoshida, A., 2007. TPU aerodynamic database for low-rise buildings. Proceedings of 12th International Conference on Wind Engineering. 1615-1622.

Michael Selig, Robert Deters and Gregory Wiliamson, 2012. Wind Tunnel Testing Airfoils at Low Reynolds Numbers. 49th AIAA Aerospace Sciences Meeting including the New Horizons Forum and Aerospace Exposition.

Aman Ahluwalia and Suhrud Wani, 2024. Leveraging Large Language Models for Web Scraping. arXiv:2406.08246 [cs.CL].

Gill JK, Chetty M, Lim S, Hallinan J, 2024. Large language model based framework for automated extraction of genetic interactions from unstructured data. PLOS ONE 19(5): e0303231.

Mahsa Shamsabadi and Jennifer D'Souza and Sören Auer, 2024. Large Language Models for Scientific Information Extraction: An Empirical Study for Virology. arXiv 2401.10040 [cs.CL]

Han, Binglan, Teo Susnjak, and Anuradha Mathrani, 2024. Automating Systematic Literature Reviews with Retrieval-Augmented Generation: A Comprehensive Overview. *Applied Sciences* 14, no. 19: 9103. https://doi.org/10.3390/app14199103

Tor Lystad, Aksel Fenerci, and Ole Øiseth, 2020. Buffeting response of long-span bridges considering uncertain turbulence parameters using the environmental contour method. *Engineering Structures*, no. 213: 110575. https://doi.org/10.1016/j.engstruct.2020.110575

Dario Castellon, Aksel Fenerci, and Ole Øiseth, 2022. Investigations of the long-term extreme buffeting response of long-span bridges using importance sampling Monte Carlo simulations. *Engineering Structures*, no. 273: 114986. https://doi.org/10.1016/j.engstruct.2022.114986

Oddbjørn Kildal, Øyvind Petersen, and Ole Øiseth, 2025. On the uncertainty of aerodynamic derivatives obtained using forced vibration tests in active grid generated turbulent flow. *Journal of Wind Engineering and Industrial Aerodynamics*, no. 257: 106005. https://doi.org/10.1016/j.jweia.2025.106005

Oddbjørn Kildal, Leon li, Jason Hearst, Øyvind Petersen, and Ole Øiseth, 2023. On the use of an active turbulence grid in wind tunnel testing of bridge decks. *Journal of Wind Engineering and Industrial Aerodynamics*, no. 233: 105331. https://doi.org/10.1016/j.jweia.2023.105331

A Novel Hybrid Machine Learning Approach for Wind Pressure Reconstruction Around Buildings with Limited Sensors

Foad Mohajeri Nav [1], Seyedeh Fatemeh Mirfakhar[2], Reda Snaiki [3]

[1] *Department of Construction Engineering, École de Technologie Supérieure, Université du Québec, Montréal, QC, H3C 1K3, Canada, foad.mohajeri-nav.1@ens.etsmtl.ca*
[2] *Department of Construction Engineering, École de Technologie Supérieure, Université du Québec, Montréal, QC, H3C 1K3, Canada, seyedeh-fatemeh.mirfakhar.1@ens.etsmtl.ca*
[3] *Department of Construction Engineering, École de Technologie Supérieure, Université du Québec, Montréal, QC, H3C 1K3, Canada, reda.snaiki@etsmtl.ca*

SUMMARY:

Accurate and rapid wind pressure predictions on high-rise buildings are essential for mitigating the risks associated with strong winds in rapidly evolving urban landscapes. This study presents a novel hybrid machine learning (ML) method for predicting wind pressure distributions across the entire façade of high-rise buildings using a limited set of sensor measurements. The proposed framework integrates proper orthogonal decomposition (POD) for dimensionality reduction and long short-term memory (LSTM) neural networks to establish an end-to-end mapping between limited sensor data and the full wind pressure distribution for various wind directions. A comprehensive dataset, obtained from wind tunnel experiments on a scaled high-rise building at Tokyo Polytechnic University, was used to train and evaluate the ML-based surrogate model. The results demonstrate the framework's efficiency and accuracy in capturing the essential features of wind pressure distributions while significantly reducing computational costs. This approach offers a promising solution for efficient wind pressure prediction, particularly in urban environments where rapid and reliable assessments are crucial.

Keywords: Wind pressure prediction, Machine learning, Dimensionality reduction, Limited sensors

1. INTRODUCTION

Accurately predicting wind loads on buildings is essential for ensuring structural integrity and optimizing building design, particularly in urban environments characterized by complex airflow interactions (Hu et al., 2024; Zhang et al., 2022; Zhang et al., 2021). Traditional methods often rely on extensive sensor networks to capture wind pressure distributions across entire building façades, which can be both costly and impractical (Abdelaziz et al., 2024). This study addresses these challenges by proposing a hybrid machine learning approach that enables efficient prediction of wind pressure distributions using a limited number of strategically placed sensors. By leveraging the power of machine learning, the proposed method offers a practical and cost-effective solution for wind load estimation, even in scenarios with varying wind directions.

2. METHODOLOGY

The proposed framework integrates advanced dimensionality reduction techniques and machine learning to predict wind pressure distributions using a minimal set of sensor data. The process starts by selecting a few sensor locations using the QR method. Proper Orthogonal Decomposition (POD) is then employed to reduce the dimensionality of the data and identify its underlying dynamics. A Long Short-Term Memory (LSTM) network is subsequently trained to establish a direct mapping between the reduced-dimensional dynamics corresponding to the limited sensor data and the full wind pressure distribution dynamics across the entire building façade for various wind directions. Table 1 outlines the step-by-step algorithm.

Table 1. Pseudo- code for predictive hybrid wind pressure distribution

Inputs: A limited set of sensor data containing m snapshots for each direction**;** *t*: time steps**;** *α:* angles of attack; p: number of sensors

Output: Wind pressure distribution across the entire building façade

1. Sensor placement

1.1 Snapshot matrix: Wind pressure distribution, $X \in \mathbb{C}^{n_1 \times m}$

1.2 Proper orthogonal decomposition (POD):

- Construct matrix X_{input} by subtracting X_{mean} from X
- Perform singular value decomposition (SVD) on X_{input} : $X_{input} = U\Sigma V^*$; where $U \in \mathbb{C}^{n_1 \times n_1}$, $\Sigma \in \mathbb{C}^{n_1 \times m}$, and $V^* \in \mathbb{C}^{m \times m}$
- Truncate the SVD to retain the top r singular values and corresponding columns of $U_r \in \mathbb{C}^{n_1 \times r}$, $\Sigma_r \in \mathbb{C}^{r \times r}$, and $V^* \in \mathbb{C}^{r \times m}$. Choose r based on capturing at least the desired amount of total variance in the data is favorable: $min\{r: \sum_{i=1}^{r} \Sigma_i^2 / \sum_{i=1}^{n_1} \Sigma_i^2 \}$ $(p \geq r)$.

1.3 QR decomposition: implement QR for U_r to obtain sensors' locations

1.4 Reconstructed dynamic: Reconstruct the dynamics at any time t using POD model:

$$X_{new} = U_r\left(U_r^{\dagger}[sensor - loc\ :] \times X[sensor - loc\ :]\right)$$
$$X_{LF} = X_{new} + X_{mean}$$

2. Dimensionality Reduction via POD

2.1 Snapshot matrices: Prepare and rearrange the dataset (X_{LF} and X_{HF}); Use almost 80% (8 scenarios) for training (X_{LF}^{train}, X_{HF}^{train}) and the remaining for testing (X_{LF}^{test}, X_{HF}^{test});

2.2 SVD: Perform SVD on both X_{LF}^{train}, X_{HF}^{train}:

$$X_{LF}^{train} = U_{LF}^{train} S_{LF} V_{LF}^{T}$$
$$X_{HF}^{train} = U_{HF}^{train} S_{HF} V_{HF}^{T}$$

2.3 Truncate SVD: Truncate the SVD to retain the top k singular values and corresponding columns of U_{LF}^{train} and U_{HF}^{train}:

$$k = min\{k: \sum_{i=1}^{k} S_i^2 / \sum_{i=1}^{N} S_i^2 \}$$
$$U_{LF,k} = U_{LF}^{train}[1:k]$$
$$U_{HF,k} = U_{HF}^{train}[1:k]$$

2.4 Obtain the Reduced Space (POD Coefficients)

Project both X_{LF}^{train} and X_{HF}^{train} onto the reduced subspace to obtain the corresponding POD coefficients:

$$c_{LF}^{train} = U_{LF}^{train} \times X_{LF}^{train}$$
$$c_{HF}^{train} = U_{HF}^{train} \times X_{HF}^{train}$$

3. Surrogate model to predict the reduced space dynamics:

3.1 Use c_{LF}^{train}, t, and α as inputs, and the corresponding c_{HF}, as the output to train an LSTM network (f_θ):

$$f_\theta(t\ \alpha\ c_{LF}^{train}) = c_{HF}^{train}$$

3.2 Compute the reduced space for the testing set by projecting the data onto the POD basis obtained from the training set:

$$c_{LF}^{test} = U_{LF}^{train} \times P_{LF}^{test}$$
$$c_{HF}^{test} = U_{HF}^{train} \times P_{HF}^{test}$$

3.3 Prediction of HF coefficients for the testing set:

Use the trained LSTM model to predict the high-fidelity POD coefficients of the testing set:

$$c_{HF}^{predict} = f_\theta(c_{LF}^{test})$$

4 Reconstruct HF data:

Reconstruct the predicted wind pressure distributions for the scenarios included in the testing set with the POD modes obtained from the training set:

$$P_{HF}^{predict} = U_{HF\,k} \times c_{HF}^{predict}$$

3. CASE STUDY

3.1. Data generation

Wind pressure data for a high-rise building was acquired from the aerodynamic database of Tokyo Polytechnic University. The data was collected through controlled experiments conducted in an open-circuit wind tunnel with a test section measuring 1.2 meters by 1.0 meters. A scale model of the building, at a scale of 1:400, was exposed to a simulated wind flow that followed a power-law profile with a 1/4 exponent. The peak wind speed was set at 11 meters per second, and turbulence levels were calibrated to represent category III (suburban terrain) conditions. To monitor pressure distributions on the model, 500 pressure taps were strategically placed across the building's exterior, evenly distributed among the four sides. These taps were arranged in a grid of 5 by 25 along the horizontal and vertical axes. Pressure readings were captured at a frequency of 1000 Hz over a period of 32.768 seconds for 11 distinct wind directions, ranging from 0 degrees to 50 degrees.

3.2. Results

The dataset consists of 11 distinct wind directions. To train the model, 8 of these directions were randomly selected, representing approximately 80% of the total data. The remaining 3 directions were set aside for testing purposes. The proposed model is noteworthy for its ability to predict the complete wind pressure distribution on the building's façade using data from only 25 sensors as input. Figure 1 provides a visual comparison between the predicted wind pressure distributions and the corresponding ground truth data for two different testing scenarios at two distinct time steps. This visualization highlights the model's accuracy in capturing the spatial and temporal variations of wind pressure.

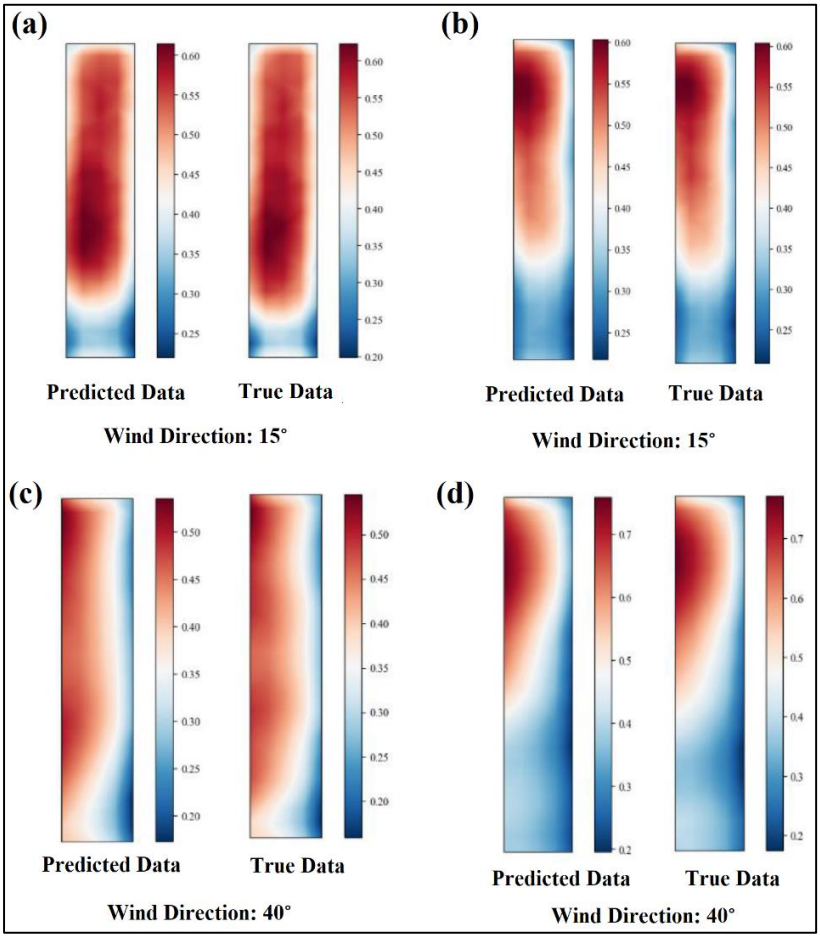


Figure 1. Comparison of predicted wind pressure distribution vs. true data, (a) t = 5 sec and wind direction 15°, (b) t = 20 sec and wind direction 15°, (c) t = 5 sec and wind direction 40°, (d) t = 20 sec and wind direction 40°.

4. CONCLUSIONS

This study introduces a novel hybrid methodology for predicting wind pressure distributions on high-rise buildings using a limited number of sensor measurements. By effectively reducing measurement costs without compromising accuracy, the proposed approach offers a practical and efficient solution for wind engineering applications.

REFERENCES

Abdelaziz, K.M., Alipour, A. and Hobeck, J.D., 2021. A smart façade system controller for optimized wind-induced vibration mitigation in tall buildings. Journal of Wind Engineering and Industrial Aerodynamics, 212, p.104601.

Hu, C., Kikumoto, H., Zhang, B. and Jia, H., 2024. Fast estimation of airflow distribution in an urban model using generative adversarial networks with limited sensing data. Building and Environment, 249, p.111120.

Zhang, B., Ooka, R., Kikumoto, H., Hu, C. and Tim, K.T., 2022. Towards real-time prediction of velocity field around a building using generative adversarial networks based on the surface pressure from sparse sensor networks. Journal of Wind Engineering and Industrial Aerodynamics, 231, p.105243.

Zhang, S., Kwok, K.C., Liu, H., Jiang, Y., Dong, K. and Wang, B., 2021. A CFD study of wind assessment in urban topology with complex wind flow. Sustainable Cities and Society, 71, p.103006.

High-resolution mean flow and Reynolds stress reconstruction in a two-dimensional urban street canyon using physics-informed neural networks

Yichen Wang [1], Bingchao Zhang [2], Chaoyi Hu [3], Hideki Kikumoto [4]

[1]*The University of Tokyo, Tokyo, Japan, wyc23@iis.u-tokyo.ac.jp*
[2]*The Hong Kong University of Science and Technology, Hong Kong, China, zhangbc@ust.hk*
[3]*The University of Tokyo, Tokyo, Japan, hu-cy123@iis.u-tokyo.ac.jp*
[4]*The University of Tokyo, Tokyo, Japan, kkmt@iis.u-tokyo.ac.jp*

SUMMARY:
In this study, a physics-informed neural network (PINN) is used to reconstruct the mean flow field and Reynolds stress distribution from sparse sensor data within a two-dimensional urban street canyon. A high-resolution dataset generated by a large-eddy simulation is used to provide the mean and standard deviation of the airflow velocities at selected sensor locations and validate the prediction accuracy. In addition, a two-step reconstruction process using PINNs is proposed to improve the performance across multiple output quantities, particularly for high-order moments. In the first step, the high-resolution mean flow field and wind pressure on building surfaces are predicted. In the second step, the reconstructed velocity and pressure are incorporated into the training to further estimate the pressure field and Reynolds stress. The results demonstrated that the proposed method accurately reconstructs the mean velocity field and normal stress distributions and successfully estimates the pressure field and shear stress without direct sensor data. This approach shows promise for effectively evaluating mean and turbulent flow statistics in urban street canyons, thus providing a valuable method for capturing high-resolution data to address the limitations of wind tunnel experiments.

Keywords: High-resolution flow field, Reynolds stress, Physics-informed neural network

1. INTRODUCTION

Numerous wind tunnel experiments have been conducted to better understand the wind characteristics in urban environments, focusing on urban street canyons with distinctive flow patterns. Wind tunnel experiments are widely regarded as reliable for predicting airflow and wind pressure. However, they face limitations in measuring a large number of points using velocity and pressure sensors, making detailed spatial measurements time-consuming and limiting the capture of high-resolution data. Recently, data-driven machine learning methods have been explored for reconstructing wind flow patterns to offer an alternative to simulation-based approaches (Brunton et al., 2020). However, these methods require large amounts of data. In contrast, Raissi et al. (2019) introduced physics-informed neural networks (PINNs) to solve partial differential equations (PDEs), such as the Navier–Stokes equations. Although PINNs have shown strong predictive potential for fluid flows with minimal data, challenges remain regarding their accuracy and computational cost, particularly for high-Reynolds number turbulent flows in urban environments.

In a previous study (Kikumoto et al., 2024), the authors used PINNs to reconstruct a high-resolution mean flow field and wind pressure on building surfaces from sparse mean velocity data in a two-dimensional urban street canyon. However, for reasons of prediction accuracy, fluctuation statistics, such as Reynolds stress, were not considered. In this study, a two-step reconstruction approach using PINNs was proposed to further estimate the Reynolds stress distribution to accurately represent the complex nature of turbulence. The sparse mean velocity and velocity variance data from a large-eddy simulation (LES) were used at select sensor locations.

2. METHODOLOGY

Figure 1 shows the target domain of a two-dimensional urban street canyon. The dimensions of the buildings and the canyons between them were $H \times H$, where H = 0.12 m. The wind flowed along the x-direction and was assumed to be cyclic. The target domain, measuring $2H \times 2H$, includes one canyon and two building cubes. The black points within the domain indicate the sensor locations where the mean velocity and velocity variance data from the LES dataset (Zhang et al., 2022) were used. A total of 45 data points were positioned within the canyon and spaced at approximately $H/6$, and 49 data points were placed above the canyon. More sensors were concentrated in regions with large velocity gradients in the shear layer and at building corners to ensure accurate predictions.

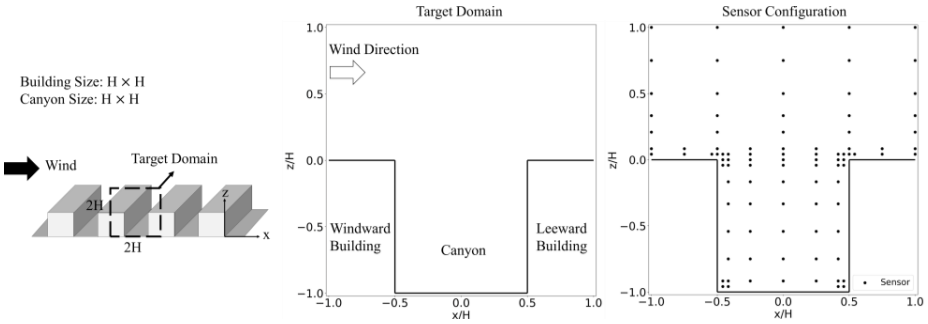


Figure 1. Target domain of urban street canyon and sensor configuration.

Figure 2 illustrates the framework of the proposed PINNs. We employed the continuity and Reynolds-averaged Navier–Stokes (RANS) equations (Eq. (1)) as the physical laws. In the first step (Step 1), the forcing vector method (Foures et al., 2014) is applied to replace the Reynolds stress ($\overline{\boldsymbol{u}'\boldsymbol{u}'}$) with a solenoid vector $\boldsymbol{f}_s$, as shown in Eq. (2). The total loss is calculated using the physics loss $\mathcal{L}_{PDE}$, boundary loss $\mathcal{L}_{BC}$, and sensor data loss $\mathcal{L}_{Data(s1)}$. In the second step (Step 2), the original RANS equations (Eq. (1)) are solved for $\mathcal{L}_{PDE}$, and the sensor data of the standard deviation are used for the data loss $\mathcal{L}_{Data(s2)}$. Then, the predicted $\bar{u}$ and $\bar{w}$ values are used along with $\bar{p}$ on the building surfaces from Step 1 for the data loss $\mathcal{L}_{Data(p)}$. The open-source library DeepXDE (Lu et al., 2021) was used to train the model. Both steps employed the Adam optimizer for initial training over 30,000 epochs with a learning rate of 10^{-3}, and this was followed by the L-BFGS optimizer for an additional 20,000 epochs to further minimize the total loss.

$$\bar{\boldsymbol{u}} \cdot \nabla \bar{\boldsymbol{u}} = -\nabla \bar{p} + \frac{1}{Re} \nabla^2 \bar{\boldsymbol{u}} - \nabla \cdot \overline{\boldsymbol{u}'\boldsymbol{u}'} \tag{1}$$

$$\bar{\boldsymbol{u}} \cdot \nabla \bar{\boldsymbol{u}} = -\nabla (\bar{p} - \phi) + \frac{1}{Re} \nabla^2 \bar{\boldsymbol{u}} + \boldsymbol{f}_s \tag{2}$$

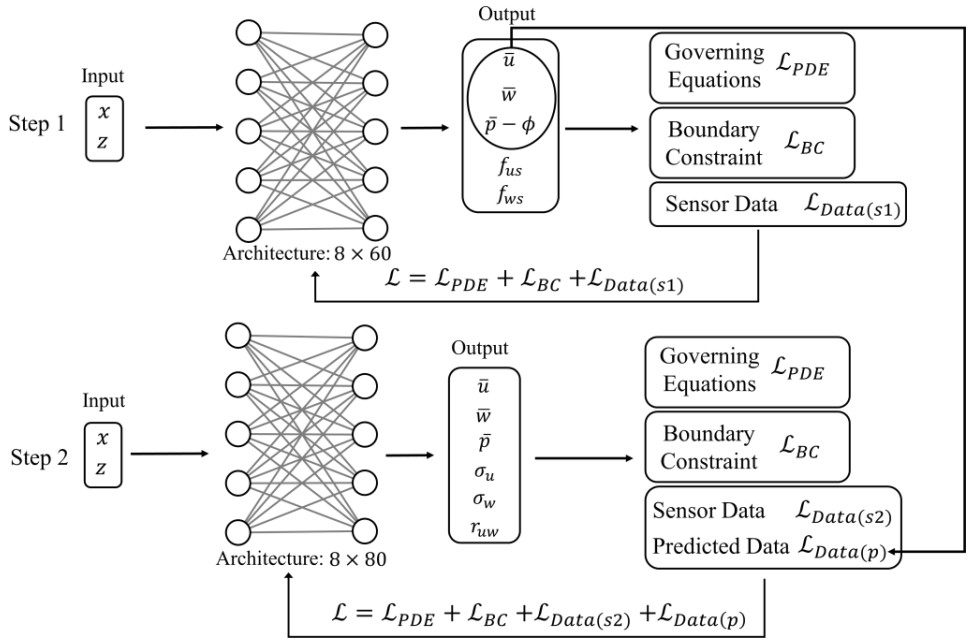


Figure 2. Framework of PINNs with a two-step reconstruction process.

3. RESULTS

Figure 3 shows the reconstructed mean flow, pressure field, Reynolds stress distributions, and corresponding errors compared with the truth (LES) values after the two-step reconstruction process. The PINN model demonstrated favorable predictions of the mean wind speed ($\sqrt{\bar{u}^2 + \bar{w}^2}$) and streamline throughout the entire domain and successfully captured the principal recirculating cell inside the canyon as well as the small counter-rotating vortices in the corners. However, the errors were primarily concentrated near the building walls, particularly at the top surfaces, as the sharp velocity gradients near the building surfaces are more challenging. Moreover, the wind pressure field ($\bar{p}$) was accurately estimated using the two-step reconstruction process. Larger errors were observed near the corner of the leeward building, where the model struggled to precisely predict regions of negative pressure created by the wind flow conflict.

The normal stresses ($\overline{u'u'}$ and $\overline{w'w'}$) were reconstructed with high accuracy across the entire domain with some errors concentrated in the shear layer at the canyon top and around the leeward building wall. For the shear stress ($\overline{u'w'}$), the general pattern was captured, despite the absence of direct sensor data. However, the errors were notably larger than those for the other quantities. These results are likely due to the smaller scale of the shear stress, relative to the other outputs, which makes it inherently more challenging to minimize the associated physics-based losses.

4. CONCLUSION

In this study, a physics-informed neural network method was introduced to capture high-resolution airflow fields using sparse data in a two-dimensional urban street canyon. The model effectively reconstructed key mean flow features, including recirculating cells and small vortices, although it struggled in regions with large velocity gradients near building surfaces. The pressure field was

accurately estimated without sensor data, although predicting negative pressure in high-conflict areas remains challenging. The proposed two-step reconstruction provided accurate predictions for the Reynolds stress components, particularly for the normal stress, whereas the shear stress predictions were less precise due to scale discrepancies. Overall, this approach shows a strong potential for reconstructing complex urban flows of turbulent fluctuation components while addressing data limitations in wind tunnel experiments.

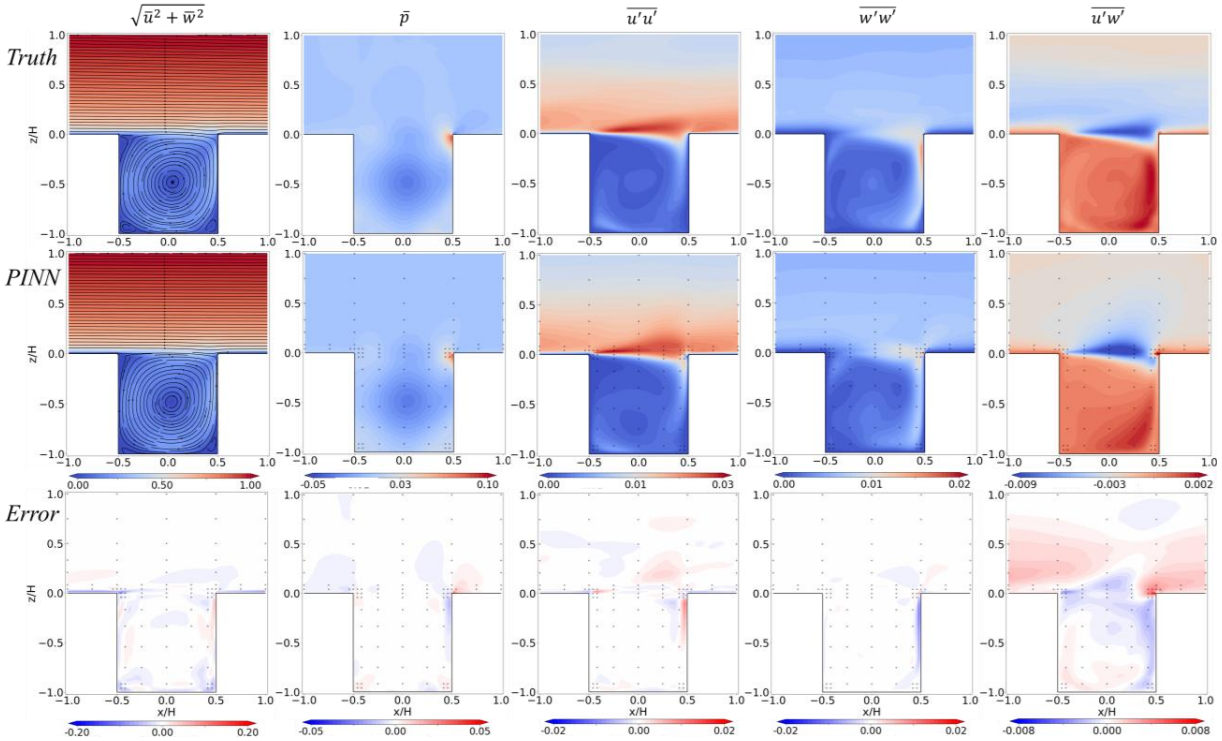


Figure 3. True and reconstructed (PINN) flow fields and Reynolds stress distributions. From left to right: streamline with wind speed, pressure field, normal stresses of the *x* and *z* components, and shear stress distributions. The error distribution is calculated as PINN value – Truth value. The gray dots in the PINN and error graphics indicate sensor position.

ACKNOWLEDGEMENTS

This work was partly supported by the Japan Society for the Promotion of Science (JSPS) KAKENHI Grant Number 23H01563 and 24K21642.

REFERENCES

Brunton, SL., et al., 2020: Machine learning for fluid mechanics. Annual Reviews, 52, 477-508.

Raissi, M., et al., 2019: Physics-informed neural networks: A deep learning framework for solving forward and inverse problems involving nonlinear partial differential equations. Journal of Computational Physics 378, 686–707.

Kikumoto, H., et al., 2024: Enhanced wind velocity and pressure measurement around buildings using physics-informed neural networks: A case study with a two-dimensional urban street canyon. 9th International Buildings Physics Conference, Toronto, Canada.

Zhang, B., et al., 2022: Spectral proper orthogonal decomposition analysis of turbulent flow in a two-dimensional street canyon and its role in pollutant removal. Boundary-Layer Meteorology 183, 97–123.

Foures, D. P. G., et al., 2014: A data-assimilation method for Reynolds-averaged Navier–Stokes-driven mean flow reconstruction. Journal of Fluid Mechanics, 759, 404–431.

Lu, L., et al., 2021: A deep learning library for solving differential equations. SIAM Review 63(1), 208–228.

Prediction of Wind Pressure on Rectangular Buildings Using Diffusion Model

Yeong In Lee [1], Thomas Kang [2]

[1]*Interdisciplinary Program in Artificial Intelligence, Seoul National University, Seoul, Korea, happyleeyi@snu.ac.kr*
[2]*Department of Architecture and Architectural Engineering & Interdisciplinary Program in Artificial Intelligence, Seoul National University, Seoul, Korea, tkang@snu.ac.kr*

SUMMARY:
Wind tunnel test is one of the most effective methods for accurately assessing the impact of wind on buildings. It is therefore essential in designing high-rise structures significantly affected by wind forces. Among various wind tunnel tests, the wind pressure test measures the pressure exerted on building surfaces due to wind. This process involves attaching wind pressure sensors to building surfaces; however, malfunctioning of several sensors frequently occurs. Data from faulty sensors cannot be used, and rerunning the test each time a sensor fails is highly labor-intensive and costly ineffective. Thus, estimating the results of faulty sensors using data from surrounding sensors has emerged as a key challenge. This study aims to generate data for faulty sensors by leveraging a diffusion model, an AI approach widely used in the vision AI field for image generation. This research offers a method for acquiring reliable data for faulty sensors, potentially mitigating the need for extensive and costly experimental repetitions. By exploiting the inherent flexibility of conditioning within diffusion models, a single trained model can effectively address the restoration of wind pressure data across a spectrum of building aspect ratios. Furthermore, this framework offers the potential to generate approximate, yet plausible, wind pressure data for aspect ratios not explicitly represented within the training dataset, leveraging the model's inherent interpolation capacity.

Keywords: wind tunnel test, wind pressure, diffusion model

1. MOTIVATION

Advances in structural engineering technology have enabled the construction of increasingly taller buildings, with a growing number of high-rise structures emerging globally. High-rise buildings are significantly affected by wind, making wind-sensitive design essential in their development. Among methods to assess wind effects during the design phase, wind tunnel test stands out as one of the most realistic and effective approaches. Wind pressure test, in particular, measures the pressure exerted on building surfaces by wind.

1.1. Wind pressure test

In wind pressure test, multiple wind pressure sensors are attached to the surface of a scaled-down building model to measure pressure variations across different locations. These sensors record real-time pressure applied to each surface as wind speed and direction change. This data enables precise understanding of the distribution of forces exerted on the building by wind, allowing for structural reinforcements or designs that reduce pressure on specific areas to enhance wind resistance. Wind pressure testing is thus essential for designing high-rise buildings highly

susceptible to wind impact.

During wind pressure test, hundreds of sensors are attached to the model's surface to collect data. However, sensor malfunctions frequently occur during testing (Kim et al., 2021). Data collected from faulty sensors becomes inaccurate and unusable, compromising the overall accuracy and reliability of the test. In such cases, re-testing the whole test or correcting data from faulty sensors is required. This issue highlights the need for research to correct the values of faulty sensors using data from surrounding functional sensors.

1.2. Diffusion model

The diffusion model is an AI model widely applied in the field of Vision AI for image generation which creates images by generating them from noise (Ho et al., 2020). This model comprises two primary components. The first component gradually adds noise to a given image, making it progressively random, starting from the initial image until it becomes pure white noise. The second component operates in the reverse direction, utilizing a trained network that begins with pure noise and progressively restores the image. Through this process, the model ultimately generates the desired image. This model has found recent applications in a variety of image-related tasks, including text-to-image synthesis, super-resolution, and masked image restoration.

This study draws inspiration from the diffusion model's capability to accurately restore masked images after training on various image datasets. If masked data, formatted as an image, is input into the model for restoration, it is anticipated that the desired data can be reconstructed. Accordingly, this research proposes a method for utilizing the diffusion model with wind pressure experiment data as input, rather than images, to recover data lost due to sensor malfunctions within the experimental dataset.

2. METHOD

The proposed method consists of three stages: data preprocessing, model training, and model evaluation. Data utilized for this study comes from the TPU Aerodynamic Database of Tokyo Polytechnic University, specifically the wind pressure experiment data for high-rise buildings with rectangular or square plans.

2.1. Data preprocessing

The dataset comprises wind pressure data for rectangular buildings with varying width, depth, and height aspect ratios. Each building is equipped with wind pressure sensors positioned at consistent intervals. In this study, the wind pressure data recorded on the four faces of each rectangular building were visualized as fixed-size contour plots, which were then concatenated into a single, larger contour plot. Although each dataset represents a rectangular building with a different aspect ratio, sensor arrangement, and number of sensors, converting the wind pressure data from each dataset into a contour plot of uniform size allowed for standardization of the data shape used for training. The generated contour plots are 120 pixels wide and 120 pixels high. A total of 81,920 data points were used for training, consisting of 8,192 data points for each of 10 different rectangular building aspect ratios.

2.2. Model training

The contour plot data obtained from the preprocessing stage was utilized to train a diffusion model. The diffusion model employed in this study integrates key elements of both the Latent Diffusion Model (LDM) (Rombach et al., 2022) and Diffusion Transformers (DiT) (Peebles and Xie, 2023). Specifically, a Variational Autoencoder (VAE) was used to compress the input data into a latent representation. Within this latent space, data generation was subsequently carried out using the DiT. Finally, the generated data was decoded back into the original data space via the VAE, producing the final reconstructed representation.

To implement this framework, the VAE was pre-trained as an initial step, followed by the training of the DiT model. Additionally, the aspect ratio of the input building data was incorporated as a conditioning factor within the diffusion model. This conditioning allows the model to generate contour plots that more closely correspond to the specified aspect ratio during the regeneration process.

2.3. Model evaluation

The evaluation process was conducted according to the following procedure. First, for each data instance, a single sensor was randomly selected, and the surrounding region of that sensor's location was masked using a rectangular area. The previously trained diffusion model was then employed to regenerate the masked region. The reconstructed data was subsequently compared against the corresponding ground truth data.

Furthermore, the data corresponding to the randomly selected "faulty" sensor location was extracted from both the ground truth and the regenerated data. Finally, a quantitative error metric was computed between these extracted values to assess the accuracy of the model's reconstruction.

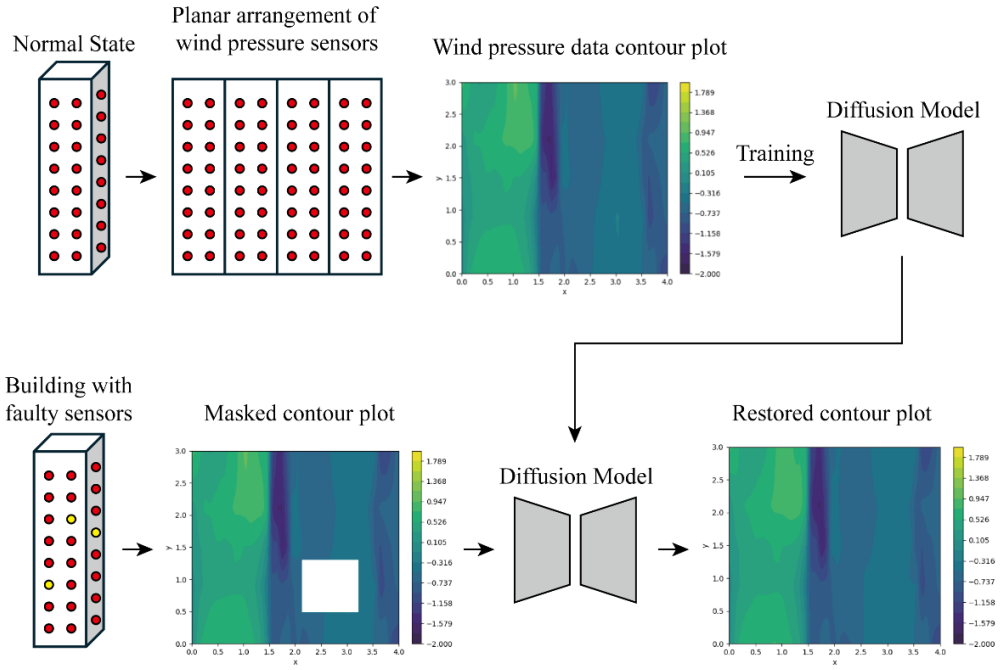


Figure 1. Overall process of predicting wind pressure using diffusion model.

3. RESULT

The experiments compared the proposed diffusion model with restoration methods based on classical interpolation, as well as other AI-driven data generation techniques, including Autoencoders, U-Nets, and Generative Adversarial Networks (GANs). The results demonstrated that the diffusion model outperformed the alternative approaches in terms of restoration accuracy, although its performance closely aligned with that of the GAN-based method.

However, unlike GANs, the diffusion model offers the distinct advantage of effectively incorporating conditioning, enabling the generation of results across a range of aspect ratios within a single model. This feature enhances user convenience by eliminating the need for multiple separately trained models for different aspect ratios. Furthermore, if the aspect ratio condition is introduced as a continuous variable rather than a discrete label during training, the model may generalize to unseen, yet similar, aspect ratios to some extent. Consequently, a diffusion model trained on experimental results from existing, similar aspect ratios could potentially be leveraged for restoration tasks, even in cases where the specific aspect ratio has not been explicitly included in the training data.

ACKNOWLEDGEMENTS

This work was supported by Institute of Information & communications Technology Planning & Evaluation (IITP) grant funded by the Korea government(MSIT) [NO.RS-2021-II211343, Artificial Intelligence Graduate School Program (Seoul National University)].

REFERENCES

Kim, B., Yuvaraj, N., Sri Preethaa, K. R., Hu, G., and Lee, D. E., 2021. Wind-induced pressure prediction on tall buildings using generative adversarial imputation networks. *Sensors*, 21(7), 2515.

Ho, J., Jain, A., and Abbeel, P., 2020. Denoising diffusion probabilistic models. *Advances in Neural Information Processing Systems*, 33, 6840-6851.

Rombach, R., Blattmann, A., Lorenz, D., Esser, P., and Ommer, B., 2022. High-resolution image synthesis with latent diffusion models. *Proceedings of the IEEE/CVF conference on computer vision and pattern recognition*, 10684-10695.

Peebles, W., and Xie, S., 2023. Scalable diffusion models with transformers. *Proceedings of the IEEE/CVF international conference on computer vision*, 4195-4205.

Tamura, Y., 2012. Aerodynamic Database of Highrise Buildings, Tokyo Polytechnic Univ., Global Center of Excellence Program.

Efficient analysis of mean flow around three-dimensional isolated building under multiple wind directions using physics-informed neural network

Chaoyi Hu [1], Hongyuan Jia [2], Yichen Wang [3], Hideki Kikumoto [4]

[1]*The University of Tokyo, Tokyo, Japan, hu-cy123@iis.u-tokyo.ac.jp*
[2]*The University of Tokyo, Tokyo, Japan, jhy@iis.u-tokyo.ac.jp*
[3]*The University of Tokyo, Tokyo, Japan, wyc23@iis.u-tokyo.ac.jp*
[4]*The University of Tokyo, Tokyo, Japan, kkmt@iis.u-tokyo.ac.jp*

SUMMARY:
To ensure the safety of pedestrians, it is critical to assess the wind environment under various wind directions. In this study, a physics-informed neural network (PINN) is developed for efficient analysis of mean flow around a three-dimensional isolated building under various wind directions. The input of PINN is information on position and wind direction. The PINN model employs the continuity and Reynolds-averaged Navier–Stokes (RANS) equation as the physical equation. Airflow distribution under four wind directions (0°, 30°, 60°, and 90°) within the 90° range due to the symmetric building geometry is obtained by computational fluid dynamics (CFD) in advance and is used in the PINN training data. In addition, a loss balance strategy is used to calculate the weight of each loss term. The results demonstrate that PINN can estimate mean flow around a 3D isolated building under multiple wind directions. In addition, coefficient of determination (R^2) of velocity across wind directions ranging from 0° to 90° at intervals of 7.5° is calculated, and R^2 of velocity is over 0.9.

Keywords: Physics-informed neural network, mean flow, wind direction

1. INTRODUCTION

With population growth and urbanization, urban densification poses many significant environmental challenges. Accurate assessment of wind environments is essential to meet the complex environmental and safety challenges posed by urbanization. Wind environment assessments usually require the analysis of airflow distributions under multi-wind directions. Some studies usually use 16 wind directions to assess the wind environment (Yoshie et al., 2007). However, recent research suggests that 24-36 wind directions should be analyzed for high-accuracy and safety-focused assessments (Hågbo and Giljarhus, 2024). Despite the development of computational fluid dynamics (CFD) techniques, the assessment of 24-36 wind directions still gives rise to a considerable computational burden. Thus, it is necessary to develop an effective method for estimating airflow distributions under other wind directions from airflow distribution under limited wind direction.

In recent years, deep-learning models have exhibited significant potential for estimating airflow distributions. However, the performance of a deep learning model is strongly dependent on the amount of data used during the training process. If the data is insufficient, the model may not

capture the airflow distribution modes, thereby affecting the estimation performance.

Fortunately, Physics-Informed Neural Network (PINN) can be employed to address this issue. In contrast to traditional data-driven deep learning, PINN integrates physical equations, enabling the utilization of physical equations to fill the insufficiency in the training data set. Several studies have been conducted for estimating airflow using the PINN method (Rui et al., 2023;). However, Rui et al. (2023) research focused on the outdoor airflow around an isolated building and considered the flow only in one wind direction. There are no PINN applications for the estimation of airflow distribution under multiple wind directions based on limited data. To fill this gap, in this study, we applied PINN to estimate the airflow distribution under multi-wind directions based on the limited wind-direction flow field data obtained from CFD.

2. METHODOLOGY

In this study, the airflow distribution around a 1:1:2 scale building model is selected as the object of investigation. The analysis domain is defined as an area with the center of the building as the center, a radius of $3H$, and a height of $2H$. The side of the building length b is 100 mm, and the building height $H = 2b = 200$ mm (Figure 1a). The velocity components in the x_1-, x_2-, and x_3 -directions were denoted by u_1, u_2, and u_3, respectively.

The PINN model was developed to estimate the mean velocity (u_1, u_2, u_3) at arbitrary position (x_1, x_2, x_3) for arbitrary wind-direction angle θ (Figure 1b). The variation of the airflow distribution for the range of θ from 0° to 90° was considered owing to the symmetric property of the building model. The inlet velocity was projected to obtain a projection of the inlet wind velocity on the x_1, x_2 axis (Figure 1c. In addition, the corresponding $\cos\theta$ and $-\sin\theta$ during projection were used as inputs to represent the wind direction information in the PINN model. The inlet velocity $U_{inlet}(x_3)$ is shown in Figure 2.

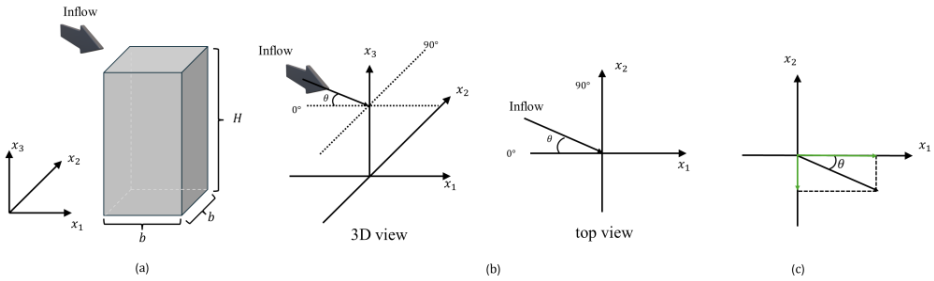


Figure 1. isolated building model information, the definition of wind direction angle θ, and decomposition of velocity in the x_1, x_2 axis

The schematic of the PINN model is shown in (Figure 3). The physical equation was the continuity and Reynolds-averaged Navier–Stokes (RANS) equations (Eq. (1)). Since virtual boundary conditions are used in this study (detailed in Section 3), the loss of boundary conditions is part of the velocity loss $\mathcal{L}_{u_i}$. Thus, the loss is calculated using the physical loss $\mathcal{L}_{PDE}$, $\mathcal{L}_{u_i}$, pressure loss $\mathcal{L}_p$, and viscosity loss $\mathcal{L}_{\nu_t}$ (Eq. (2)). An algorithm (Rui et al., 2023) is used that automatically adjusts the weight of loss. The network weights were initialized using the Xavier initialization method. The training configuration specified 70,000 epochs. The tanh function was selected as the

activation function. We used the Adam optimizer with the learning rate set to 0.0003. The model with the lowest training loss was eventually saved.

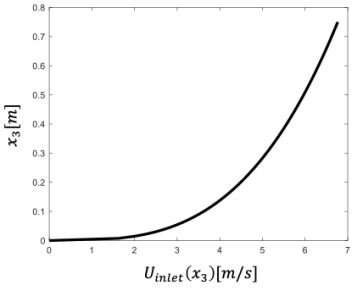


Figure 2. Vertical inlet velocity profile.

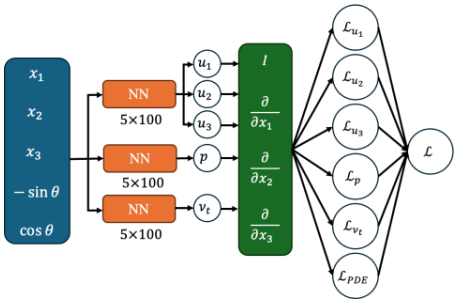


Figure 3. Schematic of the PINN.

$$u_j \frac{\partial u_i}{\partial x_j} = -\frac{\partial p}{\partial x_i} + \frac{\partial}{\partial x_j}\left\{(\nu + \nu_t)\left(\frac{\partial u_i}{\partial x_j} + \frac{\partial u_j}{\partial x_i}\right)\right\} \quad (1)$$

$$\mathcal{L} = \lambda_{u_1}\mathcal{L}_{u_1} + \lambda_{u_2}\mathcal{L}_{u_2} + \lambda_{u_3}\mathcal{L}_{u_3} + \lambda_p\mathcal{L}_p + \lambda_{\nu_t}\mathcal{L}_{\nu_t} + \mathcal{L}_{PDE} \quad (2)$$

3. CFD AND VIRTUAL BOUNDARY TO GENERATE TRAINING DATA

Figure 4 depicts the computational domain of the side and top views. Simcenter STAR-CCM+ 12.02.010 (Siemens) was used to simulate the airflow distribution. For the Turbulence model, we used the realizable $k-\varepsilon$ two-layer model, and the cell in the mesh is 2.2 million. Based on previous studies (Hu et al., 2024), the performance of PINN is significantly reduced when CFD data is not incorporated, thus the airflow distribution data under four wind directions (0°, 30°, 60°, and 90°) were calculated and utilized as PINN training data.

A virtual boundary is introduced to address the varying boundary conditions under different wind directions in PINN. This boundary is defined as a cylindrical region with a radius of $6H$ and a height of $3H$, situated in a central position relative to the building. It is assumed that the velocity components on virtual boundary were set to $u_1 = U_{inlet}(x_3)\cos\theta$ and $u_2 = -U_{inlet}(x_3)\sin\theta$. Figure 5 depicts the top view of sampling points for PDE.

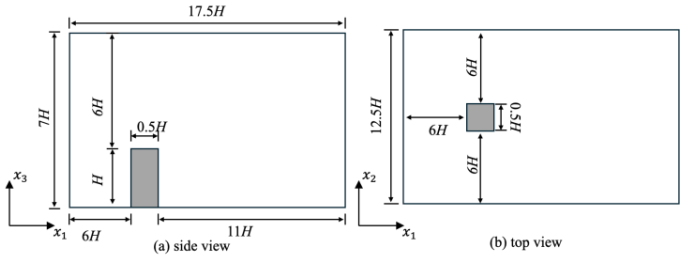


Figure 4. Computational domain in CFD: side view and top view.

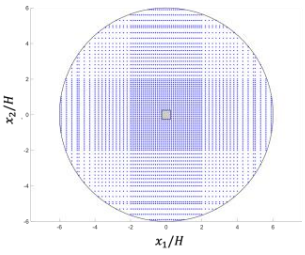


Figure 5. The sampling points for PDE: top view.

4. RESULTS

Figure 5 shows the estimated flow field under a representative wind direction of $\theta = 15°$ in the horizontal plane at a height of $1/2H$ (a, b) and the vertical plane at $x_2 = 0$ (c, d). The accelerated

flow due to the building and wake flow (u_1 and u_2) is successfully estimated by PINN, although there is some underestimation for u_1 on the sides of the building (Fig. 5a, b, c). The upward and downward flow around building (u_3) is also successfully estimated (Fig. 5d). To understand the estimation results at different angle, Coefficient of determination (R^2) of velocity across wind directions ranging from 0° to 90° at intervals of 7.5° is calculated. R^2 of u_1 and u_2 is over 0.9 in the horizontal plane at a height of 1/2H and in the vertical plane at $x_2 = 0$.

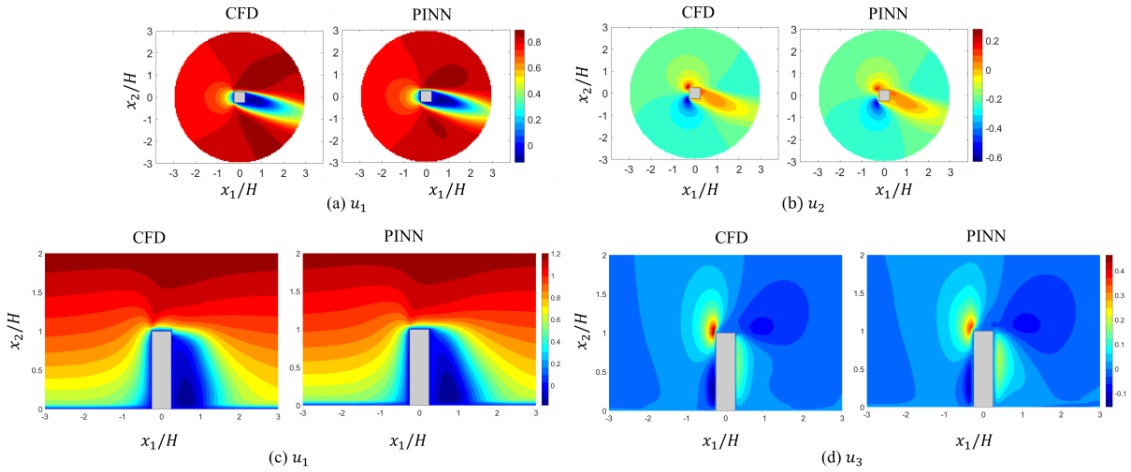


Figure 5. Estimated flow field under $\theta = 15°$ in the horizontal plane at a height of 1/2H and in the vertical plane at $x_2 = 0$.

5. CONCLUSION

This study introduced a PINN method to estimate mean flow around a 3D isolated building under multiple wind directions. Airflow distribution under four wind directions (0°, 30°, 60°, and 90°) is obtained in advance and is used in the PINN training data. The results demonstrate that PINN can estimate mean flow with high accuracy around a 3D isolated building under multiple wind directions. R^2 of velocity is over 0.9 in the horizontal plane at a height of 1/2H and in the vertical plane at $x_2 = 0$.

ACKNOWLEDGEMENTS

This work was partly supported by the Japan Society for the Promotion of Science (JSPS) KAKENHI Grant Number 23H01563 and 24K21642.

REFERENCES

Hågbo, T.O., Giljarhus, K.E.T., 2024. Sensitivity of urban morphology and the number of CFD simulated wind directions on pedestrian wind comfort and safety assessments. Build Environ 253.

Rui, E.Z., Chen, Z.W., Ni, Y.Q., Yuan, L., Zeng, G.Z., 2023. Reconstruction of 3D flow field around a building model in wind tunnel: a novel physics-informed neural network framework adopting dynamic prioritization self-adaptive loss balance strategy. Engineering Applications of Computational Fluid Mechanics 17.

Yoshie, R., Mochida, A., Tominaga, Y., Kataoka, H., Harimoto, K., Nozu, T., Shirasawa, T., 2007. Cooperative project for CFD prediction of pedestrian wind environment in the Architectural Institute of Japan. Journal of Wind Engineering and Industrial Aerodynamics 95, 1551–1578.

Hu, C., Jia, H., Lin, C., Wei, C., Wang, Y., Kikumoto, H., 2024. Efficient Analysis of Airflow Distribution Under Multiple Wind Directions Using a Physics-Informed Neural Network: Mean Flow Around Two-Dimensional Isolated Building.

Anomaly detection for mooring failure in pontoon-supported floating bridges

Jihun Song [1], Jonghyeok Lee [1], Seungjun Kim [1]

[1]*School of Civil, Environmental and Architectural Engineering, Korea University, Seoul, Korea, 2016170334@korea.ac.kr; whsur123@korea.ac.kr; rocksmell@korea.ac.kr*

SUMMARY
The floating bridge is exposed to various combinations of environmental loads and possibly experiences unexpected damages such as mooring failures, which can lead to progressive collapse through the load distribution in structural components. To ensure the structural integrity of the floating bridge, an anomaly detection method based on a continuous monitoring system using AI techniques is required for immediate response and maintenance. This study proposes a mooring failure detecting algorithm for the straight floating bridge based on unsupervised learning. The proposed method employs a response pattern recognition model using convolutional autoencoder (CAE) to amplify the reconstruction error of structural responses in abnormal conditions. The dataset, consisting of structural responses from the floating bridge, was obtained through a global response analysis based on aero-hydrodynamics. The target model was a straight, 4.6-km-long pontoon-supported girder bridge designed for the Bjørnafjord, with a semi-taut mooring system comprising four clusters.

Keywords: Floating bridge, Unsupervised learning, Damage detection

1. INTRODUCTION

This study is a preliminary investigation into damage detection and localization for critical structural components of floating bridges. Floating bridges are highly reliant on their mooring systems to maintain stability, and any failure in these systems can alter load distribution, potentially leading to progressive collapse. For this reason, detecting damage within the mooring system is essential. Although recent trends in floating bridge design often lean toward curved structures that lessen mooring dependency, this study focuses on a straight bridge model with high mooring dependency to better investigate damage detection methods. This highlights the need for robust damage detection algorithms tailored for floating bridge systems that rely fundamentally on mooring stability.

In recent years, artificial intelligence (AI)-based pattern recognition has gained attention as a method for structural health monitoring, offering capabilities for early detection of structural anomalies by identifying complex response patterns of offshore floating structures (Min et al., 2022; Min et al., 2023a, 2023b, and 2023c; Min et al., 2024; Ryu et al., 2024). In this study, we propose an unsupervised learning algorithm to detect mooring failures in floating bridges. The algorithm uses a convolutional autoencoder (CAE) to amplify reconstruction errors when abnormal structural responses are present. To validate this approach, we applied it to a 4.6-km pontoon-supported girder bridge model, designed for the Bjørnafjord, with response data obtained from a global aero-hydrodynamic analysis. This approach provides a promising framework for

early detection of mooring failures, contributing to the resilience and safety of floating bridge structures.

2. PROPOSED METHOD

Anomalies in the floating bridge can be defined as any alteration in structural characteristics, primarily due to a reduction in the stiffness of specific structural components. This leads to alteration of dynamic behaviors of the floating system, and capturing this altered behavioral pattern is the key for anomaly detection. To capture changes in the behavioral patterns of the floating bridge, this study employed a CAE-based pattern recognition model. The model processes the time-series responses of the floating bridge through a stack of 1D-CNN layers, which are combined with encoding and decoding compartments. The fundamental formula is given in Eqs. (1) and (2), and the model optimizes its parameters to minimize the loss function defined in Eq. (3).

$$E = \delta_{encoding}(z) = \delta(W * z + b) \tag{1}$$

$$D = \delta_{decoding}(E) = \delta(E * W^T + b^T) \tag{2}$$

$$L(z, \hat{z}) = \frac{1}{n}\sum_{j=1}^{n}\left(z_j - \hat{z}_j\right)^2 \tag{3}$$

The parameter z represents time-series motion, $\hat{z}$ represents reconstructed motion, $*$ denotes one-dimensional convolution, W denotes filters, b denotes bias, and δ denotes the activation function.

The NN-based model trains dynamic responses of an intact structure under various environmental conditions to accurately reconstruct the given signals. The performance for reconstruction should be reliable for signals from untrained load conditions to demonstrate that the model recognizes the behavioral patterns of the structure. When the model receives signals from a damaged structure, which exhibits entirely different behavioral patterns, it fails to reconstruct the given signals and amplifies the errors. The threshold follows the 3-sigma rule for the reconstruction errors in the intact structure case, and the detection performance can be evaluated by the percentage ratio of off-boundary data for given signals.

3. FLOATING BRIDGE MODEL

The proposed damage detection method is intended for application to the floating bridge model designed for Bjørnafjord, which incorporates a stay-cable tower and a pontoon-supported girder bridge with varying heights (Multiconsult, 2017). This study adopted a simplified side-anchored pontoon bridge model by replicating the numerical framework used by Dai et al. (Dai et al., 2020). The numerical model was constructed in OrcaFlex as demonstrated in Fig. 1. The coupled model consists of lumped mass and beam elements, representing the pontoon's hydrodynamic behavior through diffraction and radiation analysis, and effectively capturing the referenced model's behavior.

The dataset was constructed using the accelerations in vertical and horizontal directions with respect to the longitudinal axis of the bridge. The measurement points were selected at the two

ends of the moored pontoons, to account for rotation caused by torsion, and a specific girder section, comprising a total of 13 points. Based on the design basis, various wave and wind loads at the site were simulated to build the dataset (Norwegian Public Roads Administration, 2017). Additionally, under the same conditions, a damaged case dataset was obtained by simulating scenarios with a single mooring line failure in each mooring cluster.

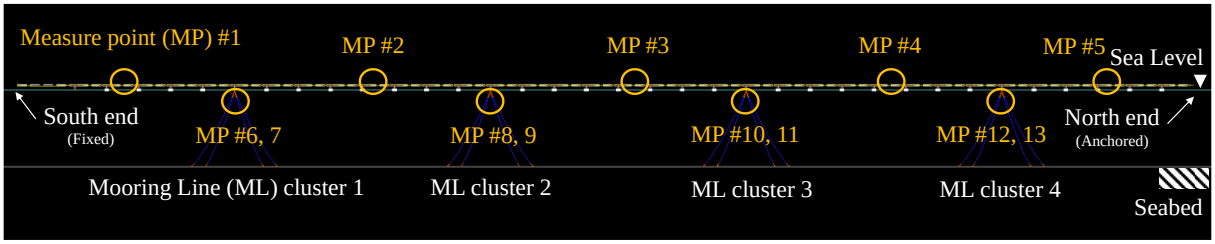


Figure 1. Floating bridge model in OrcaFlex.

4. DAMAGE DETECTION BASED ON PATTERN RECOGNITION

The signals were preprocessed into sequential data before being fed into the machine learning model, which augmented the dataset's dimensionality. This approach also helped capture inherent patterns within the signals. The NN-based model was trained to reproduce signals as closely as possible to the originals. On the other hand, the trained model had difficulty reproducing the given signals when they were obtained from the structure with one of the mooring lines removed. Fig. 2 shows an example of reconstruction error within the sequences, represented by root mean squared error (RMSE) at measured point 3. The damaged cases 1, 2, and 3 represent single line failures in different mooring clusters. These results indicate that the behavioral pattern of the structure changed due to the mooring line failure, causing the trained model to fail in reproducing signals with response patterns differing from the intact condition as intended. Furthermore, it was observed that the statistical characteristics of reconstruction errors vary depending on the damage location, suggesting that the pattern recognition model could potentially be used not only for simple anomaly detection but also for identifying the location of damage.

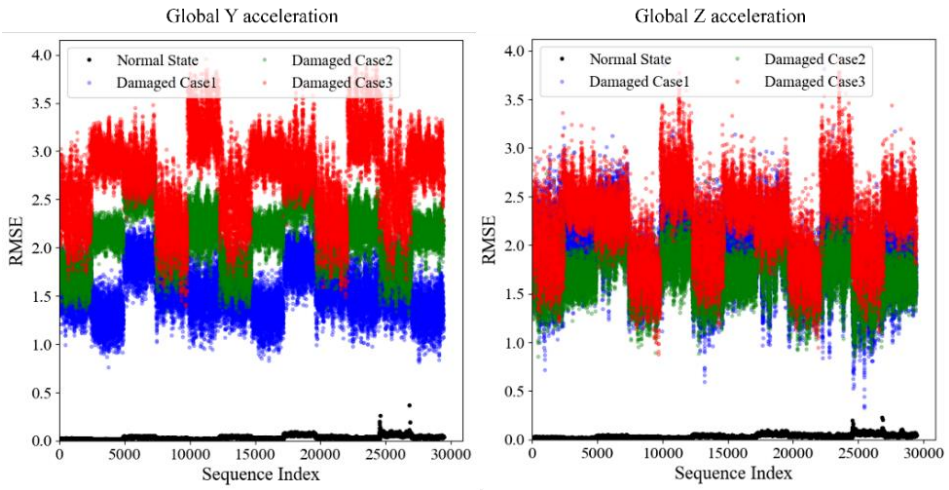


Figure 2. Reconstruction errors at measured point 3.

5. CONCLUDING REMARKS

This study proposed a methodology for identifying mooring failures in a floating bridge using a 1D CAE algorithm, with its applicability validated through simulation-based data from a global response analysis of a straight, side-anchored floating bridge. The proposed method effectively recognized the response patterns of the floating bridge and was unable to reconstruct the original signals when provided with damaged signals, demonstrating its potential for damage detection. However, further investigation into the detection performance across various damage scenarios, considering feasibility, remains necessary. Additionally, optimization of sensor arrangement and quantity could enhance performance. Despite these needs, this methodology offers promising applications for the early detection of mooring failures during operation.

ACKNOWLEDGEMENTS

This work was supported by a Korea Agency for Infrastructure Technology Advancement (KAIA) grant funded by the Ministry of Land, Infrastructure, and Transport (Grant RS-2023-00250727) through the Korea Floating Infrastructure Research Center at Seoul National University.

REFERENCES

Dai, J., Leira, B.J., Moan, T. and Kvittem, M.I., 2020. Inhomogeneous wave load effects on a long, straight and side-anchored floating pontoon bridge. Marine Structures 72, 102763.

Min, S., Jeong, K., Lee, Y., and Kim, S., 2023a. Estimation of unmeasured structural responses of submerged floating tunnels using pattern model trained via long short-term memory. Ocean Engineering 277, 114284.

Min, S., Jeong, K., Lee, Y., Jung, D., and Kim, S., 2023b. Estimation of reaction forces at the seabed anchor of the submerged floating tunnel using structural pattern recognition. Computers and Concrete 31(5), 405-417.

Min, S., Jeong, K., and Kim, S., 2024. Detecting failed tethers in submerged floating tunnels using an LSTM autoencoder and DNN algorithms. Ocean Engineering 312, 119105.

Min, S., Jeong, K., Noh, Y., Kim, S., and Won, D., 2023c. Convolutional neural network-based damage detection of the tethers of submerged floating tunnels using structural response data under various incident waves. Bridge Safety, Maintenance, Management, Life-Cycle, Resilience and Sustainability - Proceedings of the 11th International Conference on Bridge Maintenance, Safety and Management, IABMAS 2022, 1170-1177.

Min, S., Jeong, K., Noh, Y., Won, D., and Kim, S., 2022. Damage detection for tethers of submerged floating tunnels based on convolutional neural networks. Ocean Engineering 250, 111048.

Multiconsult, 2017. Document: Bjørnafjorden, straight floating bridge phase 3 Analysis and design (Base Case). Document no.: SBJ-31-C3-MUL-22-RE-100.

Norwegian Public Roads Administration, 2017. Document: Design basis Metocean. Document no.: SBJ-01-C3-SVV-01-BA-001.

Ryu, S., Min, S., Kang, Y. J., and Kim, S., 2024. LSTM-based structural pattern recognition for floating bridges. In Bridge Maintenance, Safety, Management, Digitalization and Sustainability, 726-734.

Bridge buffeting in skew winds – experimental aerodynamic coefficients and numerical analysis

Bernardo Morais da Costa[1], Jungao Wang[2]

[1]*Norwegian Public Roads Administration, Stavanger, Norway, bercos@vegvesen.no*
[2]*Norwegian Public Roads Administration, Stavanger, Norway, junwan@vegvesen.no*

SUMMARY:
A static section model of the Bjørnafjord bridge was tested in a wind tunnel to estimate aerodynamic coefficients in skew winds. The two-angle-dependent coefficients are fitted and discussed. Numerical buffeting analyses of three simplified bridge models are performed and a response comparison is made between a traditional approach that only considers wind normal to the bridge and a preferred three-dimensional skew wind buffeting approach.

Keywords: bridge aerodynamics, skew wind buffeting, wind tunnel

1. INTRODUCTION

In bridge aerodynamics, the governing wind speed, turbulence intensity, and aerodynamic coefficients might occur for wind directions that are not perpendicular to the bridge girder, i.e., in skew winds. The proposed Bjørnafjord crossing in Norway features a continuous 5000 m long curved floating bridge. Given its length, curvature and relatively wide and gentle topography, strong winds are expected from multiple directions. A traditional approach to estimate the bridge response is to project the skew wind onto a plane that is normal to the bridge girder and to proceed with the 2D bridge buffeting theory in that normal plane, as in e.g., (Davenport, 1962). The so-called cosine rule is commonly used as a simplified planar projection of the wind, as in e.g., (Xie, et al., 1991). A more comprehensive approach to skew winds considers the complex three-dimensionality of the wind-structure interaction and uses the 3D bridge buffeting theory, described in (Zhu, 2002) and (Costa, 2022). Such a 3D approach to bridge buffeting requires the estimation of aerodynamic coefficients that depend on two angles instead of one, namely the yaw angle β (related to the wind direction) and the inclination angle θ (related to the angle of attack).

2. WIND TUNNEL TESTS

The wind tunnel at Politecnico di Milano was used to test a short static section model of the bridge, illustrated in Figure 1. The tunnel is 13.84 m wide, 3.84 m high and 35 m long. The bridge model length scale is 1:35. In full-scale dimensions, the steel box cross-section of the bridge girder is 4 m high and 26.8 m wide. The span between columns is 126.7 m. Two identic dynamometric parts are assembled in the centre span, each corresponding to 52.5 m. The dummy parts on both side spans are 149 m long each and are intended to fully develop the boundary layer at the girder, model the 3D interaction with columns and pontoons, and suppress undesired girder end effects.



Figure 1. Left: Section model of the Bjørnafjord bridge on a rotating table, in skew wind. The dynamometric parts are in the centre span and dummy parts are used in the side spans. Right: Close-up view of the deck and railings.

The measured aerodynamic coefficients are represented by the data points shown in Figure 2. The cosine rule method uses only the data points at $\beta = 0$ (under normal wind), where it accurately fits the data, and then extrapolates the fitted coefficients to other β values through the relationship $C(\beta, \theta) = C(0, \theta)\cos^2\beta$. The 3D method directly fits all the experimental data points with bivariate constrained polynomials, following the procedure described in (Costa, et al., 2022). Their differences are further compared in Figure 3. The coefficients are conveniently represented in a structure-oriented coordinate system and denoted lateral, vertical, and moment (torsional) coefficients. Only when $\beta = \theta = 0$ do "lateral" and "vertical" correspond to drag and lift.

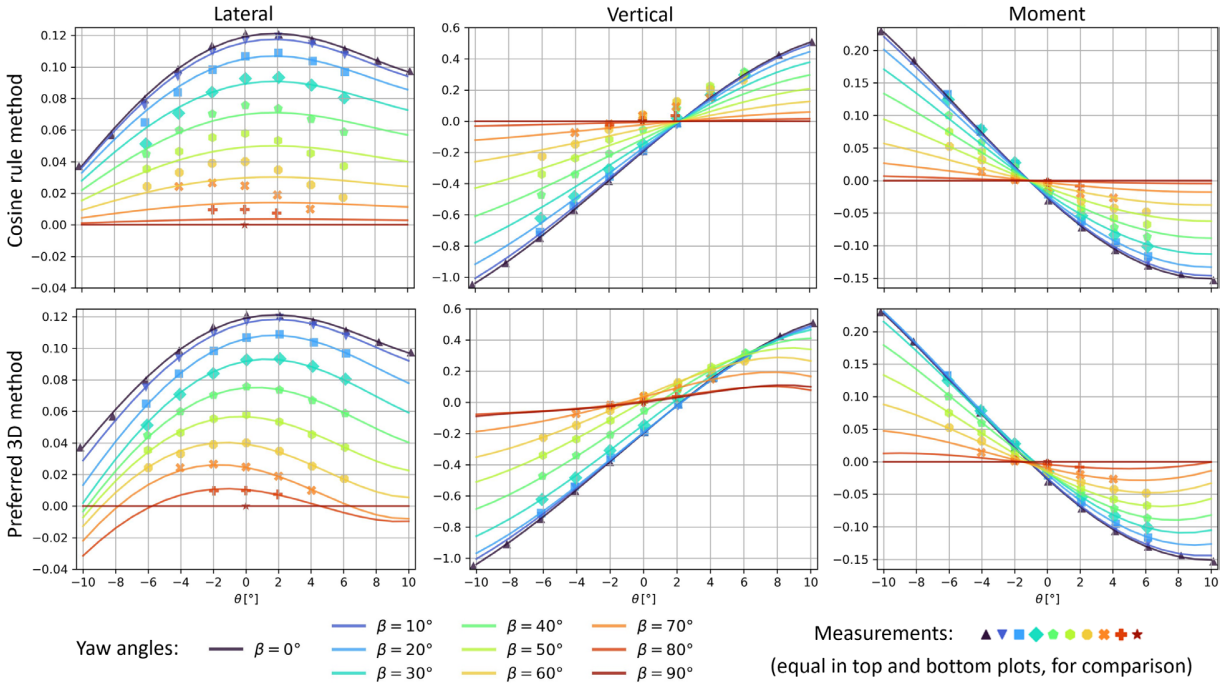


Figure 2. Comparison of the implicit coefficients of the cosine rule approximation, with the experimentally measured and fitted coefficients (w.r.t. β and θ) that are used in a 3D buffeting approach.

Absolute values

β [deg]	C_y	C_z	C_{rx}
0	0%	0%	0%
10	0%	-2%	2%
20	1%	-10%	17%
30	3%	3%	19%
40	7%	45%	-6%
50	15%	105%	-51%
60	32%	178%	-112%
70	76%	248%	-214%
80	190%	222%	-440%
90	∞	∞	∞
	Lateral	Vertical	Moment

Partial derivatives ∂_θ

β [deg]	$C_y'^{\theta}$	$\lvert C_z'^{\theta}\rvert$	$\lvert C_{rx}'^{\theta}\rvert$
0	0%	0%	0%
10	12%	1%	2%
20	23%	9%	9%
30	11%	21%	18%
40	-38%	34%	28%
50	-141%	58%	42%
60	-356%	103%	67%
70	-807%	175%	119%
80	-1517%	442%	236%
90	∞	∞	∞
	Lateral	Vertical	Moment

Partial derivatives ∂_β

β [deg]	$C_y'^{\beta}$	$C_z'^{\beta}$	$C_{rx}'^{\beta}$
0	N/A	N/A	N/A
10	5%	-156%	184%
20	6%	2%	89%
30	13%	141%	-77%
40	13%	135%	-121%
50	11%	55%	-74%
60	11%	-51%	-10%
70	-4%	-195%	63%
80	-102%	-299%	271%
90	429%	∞	881%
	Lateral	Vertical	Moment

Figure 3. Relative change [%] from cosine rule to 3D method coefficients. Less relevant derivatives are greyed out.

While the cosine rule seems to adequately model the lateral coefficient for $\beta < 50°$, it does significantly misestimate the vertical and moment coefficients for $\beta \geq 40°$ and $\beta \geq 20°$ respectively, which will affect the respective static responses. Regarding the θ-derivatives, larger differences for the vertical and moment derivatives are seen from $\beta \geq 30°$, which will affect the respective buffeting response.

3. NUMERICAL ANALYSIS

Three finite element method (FEM) models of simplified floating bridges are established, with 1000 m in length, a constant height above the water, and without mooring lines. The spans, cross-section and all other properties are taken from the planned Bjørnafjord bridge. The three models represent a straight bridge, a slightly curved bridge (R=1000 m), and a markedly curved bridge (R=500 m). These models help to clarify how the differences in the aerodynamic coefficients, between the cosine rule and 3D buffeting methods, translate into differences in bridge response, in terms of displacements, when the bridge curvature is also at play affecting local yaw angles β. Static and buffeting analyses are performed on each model, for each wind direction. The wind is assumed to be homogeneous, with uniform properties across all wind directions. The maximum response along the bridge is recorded for each degree-of-freedom, first using the cosine rule method, and then using the 3D buffeting method and the corresponding aerodynamic coefficients. The differences in maximum response between the two methods are summarized in Figure 4. The wind direction is represented in the figure by the local yaw angle at the bridge midpoint, β^{centre}. The top row shows the difference in the maximum responses, regardless of wind direction.

It can be observed that the bridge response differences between the cosine rule and the 3D buffeting method generally increase with the yaw angles, as expected. With regards to the static response, non-monotonic differences are seen for the different response components, because of the same differences in the coefficients. Significant differences can be seen as early as for $\beta^{centre} = 20°$ for the vertical and torsional responses. Regarding the buffeting response, the cosine rule consistently underestimated the bridge response for all response components for the three bridge curvatures. This underestimation was up to 10% at 20° and rapidly increased with β^{centre}. Regarding the effect of the bridge curvature, on one hand, it seems to smoothen out the coefficient differences across larger ranges of yaw angles. This improves the otherwise poor response comparison under more skewed wind directions. On the other hand, the response differences

increased by up to 8% under near perpendicular wind due to the same effect. Despite this being a modest difference, this is where the maximum responses are observed, which may impact the bridge design.

		Straight bridge			$R = 1000\ m$			$R = 500\ m$		
	β^{centre}	Lateral	Vertical	Torsional	Lateral	Vertical	Torsional	Lateral	Vertical	Torsional
Static	At max. resp.	0%	0%	0%	2%	1%	-3%	9%	1%	-5%
	0°	0%	0%	0%	1%	4%	-3%	3%	2%	-6%
	20°	1%	10%	-17%	2%	0%	-10%	3%	2%	-7%
	40°	7%	-45%	6%	4%	8%	5%	6%	4%	6%
	60°	32%	-22%	112%	16%	-47%	73%	19%	6%	37%
	80°	190%	22%	440%	89%	-8%	208%	51%	-44%	100%
	β^{centre}	Lateral	Vertical	Torsional	Lateral	Vertical	Torsional	Lateral	Vertical	Torsional
Buffeting	At max. resp.	0%	0%	0%	2%	1%	2%	8%	2%	6%
	0°	0%	0%	0%	3%	1%	2%	8%	2%	7%
	20°	1%	6%	10%	8%	2%	8%	10%	2%	10%
	40°	8%	24%	26%	21%	12%	23%	17%	3%	18%
	60°	42%	69%	55%	56%	34%	46%	26%	16%	30%
	80°	162%	336%	181%	132%	100%	91%	65%	38%	45%

Figure 4. Relative change [%] in the displacement response of the three simplified bridge models (one straight, one slightly curved, one markedly curved), from using the cosine rule to the preferred 3D buffeting method.

4. CONCLUSIONS

This study compares the use of a traditional 2D buffeting approach with the preferred 3D buffeting approach, for all wind directions. The 3D approach uses two-angle-dependent aerodynamic coefficients, experimentally obtained. The case study is a simplified 1000 m long floating bridge, and three bridge curvature alternatives are assessed. A numerical analysis is performed, and the bridge displacement responses are compared. Significant response differences were obtained between the two approaches. The difference strongly increased with the yaw angle for most cases. For the static response, the 2D approach was shown to both under- and overestimate the response, depending on the wind direction and the response component. For the buffeting response, the 2D approach consistently underestimated the response predicted by the 3D approach. An increased bridge curvature appeared to improve the comparisons at large yaw angles but resulted in a poorer comparison when the wind was perpendicular to the bridge at its midpoint. These results provide a reference for preliminary assessments of the applicability of the 2D buffeting theory in skew winds, for bridges with similar geometries and cross-sections.

REFERENCES

Costa, B. M., 2022. Bridge aerodynamics in skew winds: Generalized buffeting load modelling and response analysis. Ph.D. Dissertation, University of Stavanger

Costa, B. M. et al., 2022. Bridge buffeting by skew winds: A quasi-steady case study. Journal of Wind Engineering and Industrial Aerodynamics 227, 105068.

Davenport, A. G., 1962. The response of slender line-like structures to a gusty wind. Proceedings of the Institution of Civil Engineers 23, 389-408.

Xie, J. et al., 1991. Buffeting analysis of long span bridges to turbulent wind with yaw angle. Journal of Wind Engineering and Industrial Aerodynamics, 37(1), 65–77.

Zhu, L., 2002. Buffeting response of long span cable-supported bridges under skew winds: field measurement and analysis. Ph.D. Dissertation, The Hong Kong Polytechnic University.

Aerodynamic stability of a single span suspension bridge for crossing of Sulafjord

Allan Larsen [1], Ketil Aas-Jakobsen [2], Mads B. Eriksen [3]

[1]*COWI Consulting Engineers, Kgs. Lyngby, Denmark, aln@cowi.com*
[2]*Aas-Jakobsen, Oslo, Norway, kaa@aaj.no*
[3]*FORCE Technology, Kgs. Lyngby, Denmark, mabe@forcetechnology.com*

SUMMARY:
The present abstract summarizes wind tunnel testing and dynamic analyses carried out for verification of the flutter stability of a 2707 m single span suspension bridge designed for crossing of Sulafjord, Norway. It is demonstrated that the aeroelastic properties of a long span flexible twin box bridge develops favourably at increasing angles of incidence relative to the oncoming wind yielding sufficient stability to meet the requirements specified for the North Atlantic costal wind climate.

Keywords: Suspension bridge twin box bridge deck, wind tunnel testing, multi-mode flutter analysis.

1. INTRODUCTION

The fixed link crossing of Sulafjord is an essential part of Norway's E39 project connecting Kristiansand in the south to Trondheim in the north by road. Several bridge schemes have been considered for crossing of the 3.1 km wide and 400 m deep Sulafjord. Among them a 2707 m single span suspension bridge. A major engineering challenge of this bridge scheme is to achieve sufficient aerodynamic stability to meet the minimum critical wind speed of 72 m/s for onset of flutter set by the requirements of the Norwegian Road Directorate (Hb-N400, 2015).

Experience from the design of the 2023 m main span 1915 Çanakkale suspension bridge, Türkiye, suggests that the twin box bridge girder concept have desirable aerodynamic properties to meet the stability requirement for onset of two degree of freedom flutter. However, the increased span length and the reduced girder torsion stiffness of the Sulafjord bridge compared to the 1915 Çanakkale bridge may compromise the flutter stability.

The present paper outlines the dynamic analyses and wind tunnel testing carried out to verify the flutter stability of the single span suspension bridge for crossing of Sulafjord.

2. AERODYNAMIC FLUTTER STABILITY OF THE TWIN BOX BRIDGE GIRDER

The superior flutter stability of the twin box girder compared to the classical trapezoidal mono box girder derives from the development of the aerodynamic moment acting on the bridge girder as function of the inflow angle of the wind (angle of attack, AOA). A well-designed twin box girder shall have a positive aerodynamic moment coefficient for horizontal inflow (AOA = 0 deg.) and

increasing with increasing inflow angles but with a decreasing slope. This property ensures and increased aerodynamic stability compared to bridge girders having linear slopes, (Larsen and Sørensen, 2022) and is referred to as the "nose-up" effect. The progress of the moment coefficient is a function of the girder section geometry as well as wind screens and external rails for inspection gantries (Rønne et. al., 2024).

2.1. Sulafjord twin box girder

Based on the experience gain from the 1915 Çanakkale bridge the Sulafjord twin box deck was designed with two 12 m wide, and 3.5 m deep trapezoidal road girders separated by a 12 m wide central gap. 3.15 m wide foot / bicycle paths carrying 5 m tall wind screens of 50% open area ratio are cantilevered from the tips of the roadway girders. Gantry rails are fitted to the lower bottom plates of the box girders. A photo of the 1:70 model of the deck section is shown in Fig. 1.



Figure 1. 1:70 scale wind tunnel section model of the Sulafjord bridge deck at FORCE Technology.

2.2. Wind tunnel tests

Static wind tunnel section model tests were carried out to obtain the wind load coefficients (lift, drag and moment) whereas aerodynamic derivatives were measured by the forced motion technique for fixed inflow angles ranging from -2 deg to +8 deg at 2 deg intervals. An excerpt of the wind tunnel test results presenting the moment C_M coefficient as function of angle of attack and the A_3^*, A_2^* aerodynamic derivatives as function of the non-dimensional wind speed U/fB and smoothed by polynomial expansions are shown in Fig. 2.

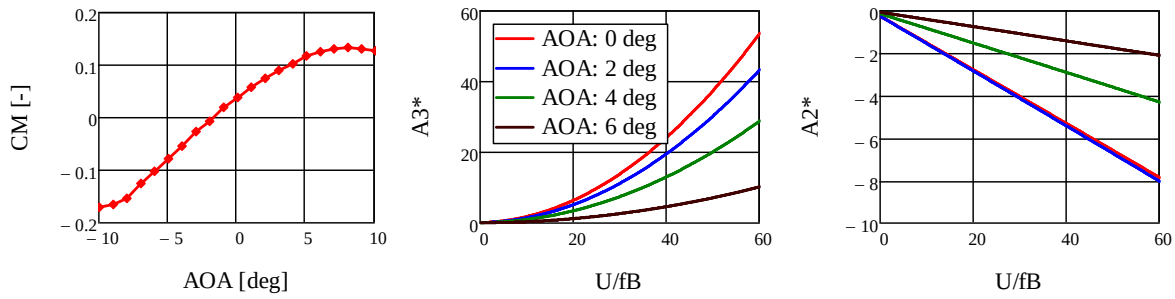


Figure 2. Moment coefficient (left) and A_3^* (middle), A_2^* (right) aerodynamic derivatives measured for the Sulafjord section model.

From Fig. 2 it is noted that the moment displays the desired progression being positive C_M = 0.038

at AOA = 0 deg while the moment slope decreases from 1.2 at AOA = 0 deg to 0 at 8 deg. The A_3^* aerodynamic derivative is seen to decrease with increasing AOA showing that the loss of aerodynamic stiffness is less at higher angles of attack indicating an increase of the flutter wind speed at high AOA. The decrease of A_2^* with increasing AOA may in part counterbalance the beneficial effect of the decreasing A_3^* on the critical wind speed for onset of flutter.

3. STRUCTURAL ANALYSES

The critical wind speed for onset of flutter of a flexible long span suspension bridge depends on the dynamic properties of the structure as well as the twist of the bridge girder due to mean wind loading as indicated in the previous section. This information is provided by a global finite element model of the bridge.

Fig. 3 displays the bending and torsion modes governing flutter. The modal analysis is performed for the deflected shape of the structure corresponding to a mean wind of 72 m/s. It is noted that the modes are asymmetric due to the large mass of the main cables. The torsion frequency is roughly 25% lower than the lowest torsion frequency governing the aerodynamic stability of the 1915 Çanakkale bridge emphasizing the importance of the flutter issue for the Sulafjord bridge.



Vertical mode: Modal mass $M = 5.310 \cdot 10^7$ kg
Eigenfrequency $f = 0.059$ Hz

Torsion mode: Modal mass $M = 2.932 \cdot 10^7$ kg
Eigenfrequency $f = 0.114$ Hz

Figure 3. Asymmetric vertical and torsion modes governing aerodynamic stability of the Sulafjord bridge.

The stationary rotation of the bridge girder due to the mean wind loading is important for the flutter performance as indicated by the dependency of the A_3^*, A_2^* aerodynamic derivatives on the angle of attack shown in Fig. 2 above. The mean rotation of the bridge girder obtained from the global FE model observing the non-linearity of the moment coefficient is shown in Fig. 4 for wind speeds of 45 m/s (design wind speed) and 72 m/s (flutter criterion).

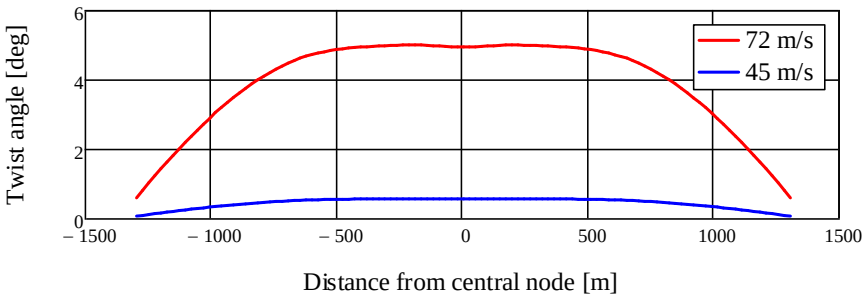


Figure 4. Twist angle along the main span for wind speed of 45 m/s and 72 (m/s).

From Fig.4 it is noted that the maximum twist of the bridge girder is about 0.6 deg at mid span for a wind speed of 45 m/s being less than the 3% (1.7 deg) cross fall of the roadway and thus not of concern for the traffic which is expected to be stopped at lower wind speeds of 25 m/s. At a wind speed of 72 m/s the maximum twist angle increases to 5.5 deg for the central 1000 m of the span.

3. FLUTTER ANALYSIS

The critical wind speed of the Sulafjord bridge is obtained by a multimode flutter analysis procedure combining modal properties and measured aerodynamic derivatives observing their dependency on the twist of the bridge girder due to mean wind loading. The multimode flutter analysis combined all vertical and torsion modes up to the first symmetric torsion mode at 0.137 Hz. Horizontal modes were excluded from the analysis as previous experience has demonstrated that inclusion of measured horizontal P^* aerodynamic derivatives yield slightly higher critical wind speeds for onset of flutter as compared to omitting them, (Larsen, 2014). The result of the multimode flutter analysis yielded a critical wind speed 74 m/s and thus above the requirement of 72 m/s.

It is interesting to note that if the twist of the main span had not been considered a critical wind speed of 56 m/s would have resulted clearly not fulfilling the requirement. The "nose-up" effect for twin box girders is thus very important to consider when evaluating the aerodynamic stability for very long and flexible suspension bridges featuring this type of bridge girder.

4. FULL PAPER

The full paper will discuss further details of the multimode flutter analyses carried out for the Sulafjord suspension bridge including the effect of gap width, wind screens and simulated ice accumulations. Further, comparisons between direct measurements of the flutter wind speeds of the elastically suspended section model and critical wind speeds obtained applying the measured the aerodynamic derivatives will be discussed.

ACKNOWLEDGEMENTS

The authors acknowledge the dedication of the FORCE Technology wind tunnel crew in carrying out the wind tunnel tests and the permission of the Norwegian Road Directorate (SVV) to publish the results of the analyses and tests.

REFERENCES

Hb-N400, Bruprosjektering. Statens Vegvesen (SVV), 2015.

Larsen, A., Sørensen, J. W., 2022. Benefits and challenges of the twin-box girder, 2022. IABSE Congress Nanjing.

Rønne, M., Larsen, A., Argentini, T., Rocchi, D., Walther. J. H. 2024. The influence of gantry rails on twin-box deck aerodynamics. Paper submitted to Journal of Wind Engineering and Industrial Aerodynamics.

Larsen A., 2014. Horizontal aerodynamic derivatives in bridge flutter analysis. PVP2014-28251. *Proceedings of the 8th ASME International symposium on fluid-structure interaction.* Anaheim, California, USA.

Aerodynamic performance of the Julsund bridge deck

Jungao Wang [1], Ketil Aas-Jakobsen [2], Tommaso Argentini [3], Giulia Pomaranzi [4], Alberto Zasso [5], Bjørn Isaksen [6], Johannes Veie [7]

[1] *Norwegian Public Roads Administration, Stavanger, Norway, jungao.wang@vegvesen.no*
[2] *Aas-Jakobsen AS, Oslo, Norway, kaa@aaj.no*
[3] *Politecnico di Milano, Milan, Italy, tommaso.argentini@polimi.it*
[4] *Politecnico di Milano, Milan, Italy, giulia.pomaranzi@polimi.it*
[5] *Politecnico di Milano, Milan, Italy, alberto.zasso@polimi.it*
[6] *Norwegian Public Roads Administration, Oslo, Norway, bjorn.isaksen@vegvesen.no*
[7] *Norwegian Public Roads Administration, Hamar, Norway, johannes.veie@vegvesen.no*

SUMMARY:
Various aerodynamic countermeasures including the use of upper and lower central stabilizers, different gantry rail configurations, the impact of snow accumulation and various traffic scenarios were experimentally investigated for a suspension bridge with the main span of 1625m. The results highlight both the effectiveness and drawbacks of various countermeasures in influencing the critical wind speed (CWS) associated with wind-induced instability, as well as their impact on vortex-induced vibrations (VIV), and the snow accumulation significantly reduces the aerodynamic performance.

Keywords: critical wind speed, vortex-induced vibration, central stabilizer, wind tunnel tests

1. INTRODUCTION

For long-span bridges that are sensitive to wind loads, wind-bridge interactions cause several design challenges such as stability and VIV. Aerodynamic countermeasures such as using twin/triple-box deck instead single box deck, optimizing wind nose, adding stability plates (upper and/or lower vertical plates), adding flow separation plates (horizontal and/or inclined plates at wind nose tip, guided vanes), optimizing gantry rail dimension and location, optimizing porosity of the traffic/wind barriers, using gratings as part of the deck to control the flow around the deck, as well as some active control measures have been investigated [1]. These countermeasures may have opposite effects on performance related to stability and VIV, and their effectiveness varies with different angles of attack. Therefore, it is often necessary to combine several countermeasures to achieve an overall good aerodynamic performance. The aerodynamic behavior of the bridge deck is sensitive to snow/ ice accumulation at railings [2]. For the Julsund suspension bridge with a main span of 1625 meters, wind tunnel tests were carried out to evaluate different aerodynamic countermeasures, as well as the snow accumulation impact and traffic scenarios, aiming to secure the design from wind induced instability and VIV.

2. WIND TUNNEL TESTING AND METHODOLOGY

A comprehensive wind tunnel test campaign was carried out in the Politecnico di Milano wind tunnel, and Figure 1 illustrates the base deck configuration and the 2D free-vibration setup. The base bridge deck geometry is shown in Figure 1(a) and is not symmetric in terms of the upper road surface and traffic barrier arrangement due to the one-sided pedestrian lane. The deck has a width/height dimension of 27.5m/ 4m, and the bottom plate is 13m wide. The wind nose has a lower inclination angle of 15 degrees and upper inclination angle of 40 degrees which results in the wind nose tip locates at half of the deck height. The tested deck model has a geometric scaling ratio of 1:35.

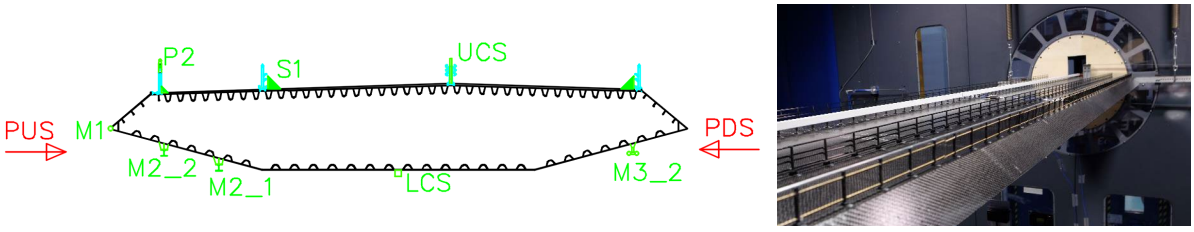


Figure 1. Bridge deck drawing with various testing details and a bridge deck model in the wind tunnel.

3. AERODYNAMIC PERFORMANCE OF THE DECK

Table 1 summarizes the CWS results from 2D free-vibration tests, considering the first vertical and torsional symmetric modes. Comparison of configurations Jul_G_R0 to Jul_G_R4 shows that the lower central stabilizer (LCS) improves CWS at negative angle of attack (AoA) but worsens at positive AoAs, while the upper stabilizer has the opposite effect. The combination of both stabilizers improves CWS only at positive AoA, suggesting that a larger lower stabilizer might be necessary to increase CWS at both negative and positive AoAs [3]. The effect of vertical stabilizers on VIV performance remains unclear and could potentially worsen it for this cross section, while also adding material and maintenance costs. Among the three gantry rail configurations, the rounded nose (used in the Hardanger Bridge) performs comparably or better than the base case, whereas the I-beam and twin-pipe solutions decrease CWS at positive AoAs. Notably, snow accumulation on the guard rails (0.6 m high) causes a significant CWS drop (40% at AoA = 0° and 60% at AoA = +3°), associated with negative aeroelastic torsional damping, revealed from forced vibration tests [4].

Table 1. Summary of the CWS from 2D free-vibration tests considering mode VS1 (0.118Hz) and TS1 (0.28Hz).

Configuration	Note	Wind dir.	Flow	CWS (w.r.t Jul_G_R0/ PUS/ SF*)		
				AoA = -3	AoA = 0	AoA = +3
Jul_G_R0	Base Config. (default railings)	PUS	SF	61.4 m/s	71.3 m/s	62.9 m/s
		PDS		2.28%	0.98%	-2.23%
		PUS	TF	6.84%	0.70%	5.56%
Jul_G_R1	Base Config. + LCS h_{low}/H=7.5%	PUS	SF	8.35%	-1.59%	-5.42%
Jul_G_R2	Base Config. + UCS h_{up}/H=22.5%	PUS	SF	-6.46%	-1.46%	21.54%
Jul_G_R4	Base Config. + LCS h_{low}/H=7.5% + UCS h_{up}/H=22.5%	PUS	SF	-1.26%	0.93%	20.78%
Jul_G_M1	Base Config. + gantry rail 1 (rounded nose)	PUS	SF	1.47%	1.12%	1.59%
		PDS		4.56%	1.96%	-1.43%
		PUS	TF	6.51%	3.23%	5.41%
		PDS		7.98%	2.95%	5.88%
Jul_G_M2_1	Base Config. + gantry rail 2 (I beams, lower position)	PUS	SF	9.45%	1.98%	-21.08%

Jul_G_M2_2	Base Config. + gantry rail 2 (I beams, upper position)	PUS	SF	5.98%	1.59%	-13.40%
Jul_G_M3_2	Base Config. + gantry rail 3 (twin pipes, upper position)	PUS	SF	1.79%	1.82%	-2.70%
Jul_G_B	Bare deck	PUS	SF	2.77%	0.42%	-5.88%
		PDS		7.33%	0.98%	-11.29%
		PUS	TF	9.12%	0.28%	1.59%
		PDS		10.59%	1.40%	-1.75%
Jul_G_P2	Base Config. + alternative pedestrian barrier (1.6m)	PUS	SF		-3.37%	
		PDS			-0.56%	
Jul_G_S1	Base Config. + snow S1 (30, 60, 60cm snow)	PUS	SF	-3.26%	-1.54%	-22.73%
		PDS		2.28%	-42.08%	-56.44%
		PDS	TF	9.12%	-17.95%	-47.06%
Jul_G_S2	Base Config. + snow S2 (half snow of S1)	PUS	SF	-1.47%	-0.98%	-7.95%
		PDS		4.56%	-4.91%	-40.38%
Jul_G_S3	Base Config. + snow S3 (PDS snow 1m away from wind nose, compared to S1)	PDS	SF	2.61%	-2.66%	-22.42%

*PUS: pedestrian lane upstream; PDS: pedestrian lane downstream; SF: smooth flow; TF: turbulent flow.

Table 2 summarizes the predicted CWS of the full bridge indicating robust stability performance with minimal variation in CWS.

Table 2. Sensitivity study on the predicted CWS for Jul_G_R0, PUS.

Item	Default choice /value	Sensitivity study	CWS (m/s)	Note
Number of modes	All 50 modes	2 – All 50 modes	64.42 – 94.76	GAM.4.0.0
Number of AD terms	18	8 - 18	65.36 – 66.08	GAM.4.0.0
Fitting of ADs	Rational function	Rational /Polynomials	66.08/ 65.34	GAM.4.0.0
Static wind effect	No	No/ Yes	67.72/ 68.52	GAM.2.0.0
Aero damping from cables	Yes	Yes/ No	66.08/ 65.18	GAM.4.0.0
Air density ρ	1.25 kg/m^3	1.3943 – 1.1455	62.24 – 69.15	GAM.4.0.0
Structural damping ratio ξ	0.5%	0.1% - 1.5%	64.29 – 70.94	GAM.4.0.0
Main cable drag coefficient/ Main cable roughness parameter κ	Reynolds dependent/ $\kappa = 0.2mm$	C_D=0.8-1.0/ $\kappa = 0.006$ - 0.2	65.89 – 66.24	GAM.4.0.0
Considered AoA	0	-3/ 0/ +3	63.92/ 66.08/ 60.08	GAM.4.0.0
GAM iteration	GAM4.0.0	GAM1 – GAM4	68.57 - 66.08	

Table 3 and Table 4 presents the vertical and torsional VIV test results, showing that decks without vertical stabilizers experience insignificant VIV at low Scruton numbers, with full suppression at target Scruton numbers. However, the deck with snow experiencing low CWS also exhibits considerable VIV, with three distinct vertical 'lock-in' peaks at different reduced velocities (Strouhal numbers), further highlighting the impact of snow on deck aerodynamic performance.

Table 3. Summary of the vertical VIV response for different deck configurations (blanks are not tested, percentage of the Scruton number to target value: VIV1: 28%, VIV2: 31%, VIV3: 62%, VIV4: 99%, VIV5: 155%.).

Deck config.	Wind dir.	Setup	std. of vertical disp./ deck height (St)		
			AoA = -3	AoA = 0	AoA = +3
Jul_G_R0	PUS	VIV 1	No VIV	0.32% (0.10)	No VIV

	PUS	VIV 3		No VIV	
	PDS	VIV 3		No VIV	
Jul_G_B	PUS	VIV 3		0.45% (0.06)	
	PDS			0.46% (0.06)	
Jul_G_M1	PUS	VIV 1	0.11% (0.11)	0.34% (0.09)	0.40% (0.07)
		VIV 2		0.14% (0.08)	
		VIV 3	No VIV	No VIV	No VIV
	PDS	VIV 3	No VIV	No VIV	No VIV
Jul_G_T1	PUS	VIV 3		No VIV	
	PDS	VIV 3		No VIV	
Jul_G_S1	PUS	VIV 3		0.70% (0.09)	
	PDS			0.47% (0.08)/ 1.65% (0.13)/ 1.67% (0.27)	
		VIV 4		0.35% (0.08)/ 1.50% (0.12)/ 2.20% (0.26)	
		VIV 4 TF		No VIV	
		VIV 5		0.22% (0.08)/ 0.43% (0.11)/ 1.43% (0.26)	
Jul_G_S2	PUS	VIV3		0.17% (0.08)	
	PDS			0.40% (0.08)/ 0.21% (0.13)	

Table 4. Summary of the torsional VIV response for different deck configurations (blanks are not tested, percentage of the Scruton number to target value: VIV3: 62%, VIV4: 99%.).

Deck Config.	**Wind dir.**	**Setup**	**std. of torsional rotation in degrees (St)**		
			AoA = -3	**AoA = 0**	**AoA = +3**
Jul_G_R0	PUS	VIV 3		No VIV	
	PDS			No VIV	
Jul_G_B	PUS	VIV 3		0.034 (0.06)	
	PDS			0.053 (0.06)	
Jul_G_M1	PUS	VIV 3	No VIV	No VIV	No VIV
	PDS		0.007 (0.07)	No VIV	No VIV
Jul_G_T1	PUS	VIV 3		No VIV	
	PDS			No VIV	
Jul_G_S1	PUS	VIV 3		0.010 (0.07)	
	PDS			0.159 (0.09)	
	PDS	VIV 4		0.102 (0.09)	
	PDS	VIV 4 TF		No VIV	
Jul_G_S2	PUS	VIV3		No VIV	
	PDS			0.013 (0.07)	

REFERENCES

[1] L. Zhao, K. LI, C. Wang, G. Liu, T. Liu, S. Song og Y. Ge, «Review on Passive Aerodynamic Countermeasures on Main Girders Aiming at Wind-induced Stabilities of Long-span Bridges,» *Journal of Highway and Transport,* vol. 32, nr. 10, pp. 34-48, 2019.

[2] A. Larsen, «Aerodynamic aspects of the final design of the 1624 m suspension bridge across the Great Belt,» *Journal of Wind Engineering and Industrial Aerodynamics,* vol. 48, nr. 2-3, pp. 261-285, 1993.

[3] S. Xu, G. Fang, L. Zhao, Y. Ge og J. Zhang, «Aerodynamic and Aerostatic Performance of a Long-Span Bridge with Wide Single Box Girder Installed with Vertical and Horizontal Stabilizers,» *Journal of Structural Engineering,* vol. 149, nr. 8, 2023.

[4] T. Argentini, F. Calamelli, A. Zasso og J. Wang, «Flutter stability of a single-box deck: effect of geometry details and external factors on the critical wind speed,» i *9th BBAA*, Birmingham, 2024.

Insights into the nose-up effect on the Çanakkale twin-box bridge deck based on CFD simulations

Nicola Cortellazzi[1], Federico Di Lenardo[1], Maja Rønne[2,3], Daniele Rocchi[1], Tommaso Argentini[1]

[1]*Politecnico di Milano, Department of Mechanical Engineering, Milano, Italy,*
tommaso.argentini@polimi.it
[2]*COWI A/S, Kgs. Lyngby, Denmark*
[3]*Technical University of Denmark, Kgs. Lyngby, Denmark*

SUMMARY:
This study explores the nose-up effect on the 1915 Çanakkale twin-box bridge deck, using CFD simulations to analyze the role of gantry rails. Previous work established that gantry rails influence the aeroelastic stability of the bridge by altering the pitching moment from negative to positive at a 0° angle of attack, which encourages a nose-up rotation of the deck and enhances flutter stability. This research investigates why aerodynamic derivatives decrease with increasing angle of attack and how specific flow patterns contribute to this behavior. 2D stationary CFD simulations were conducted for two configurations – with gantry rails (C1) and without (C2) – using URANS and the k-ω SST turbulence model. The simulations were validated against experimental lift and moment coefficients within an angle-of-attack range from -3° to +4°. Key findings reveal that, in C1, gantry rails impact flow separation and vortex behavior, contributing to lower local lift derivative at higher angles. In C2, where gantry rails are absent, these changes are reduced. Ultimately, the gantry rails contribute to a reduction in lift and moment coefficient slopes, and during the conference, a detailed comparison of C1 and C2 will be presented to further clarify these effects.

Keywords: Nose-up effect, Aeroelastic stability, Gantry rails, Twin-box deck

1. BACKGROUND AND OBJECTIVE

It is well established that small geometric details and ancillary elements can play a major role in the overall aerodynamics of bridge deck sections, and therefore affect the aeroelastic behavior of the bridge (e.g., Argentini et al., 2022; Zasso et al., 2019). Recently, Rønne et al., 2024 demonstrated that, for the twin-box deck section of the 1915 Çanakkale Bridge, gantry rails placed on the bottom of the deck (see Figure 1) have a beneficial effect on aeroelastic performance of the structure. This effect, known as the "nose-up effect", occurs because the presence of the gantry rails – particularly the inner ones – modifies the pitching moment of the section at 0° angle of attack, changing its value from negative to positive. Consequently, as wind speed increases, the deck rotates nose-up (up to 5° at 80 m/s), resulting in a weaker aeroelastic coupling and increased flutter stability, compared to 0° or negative angles of attack. This weaker aeroelastic coupling is evident, according to quasi-steady theory, from the reduced slopes of the lift and moment coefficients, as well as in their corresponding flutter derivatives, in particular H_3^*, A_1^*, A_3^* (Rønne et al., 2021).

Although the nose-up effect is apparent, it is not straightforward to explain why the aerodynamic derivatives decrease with increasing angle of attack, or what changes in the aerodynamics lead to

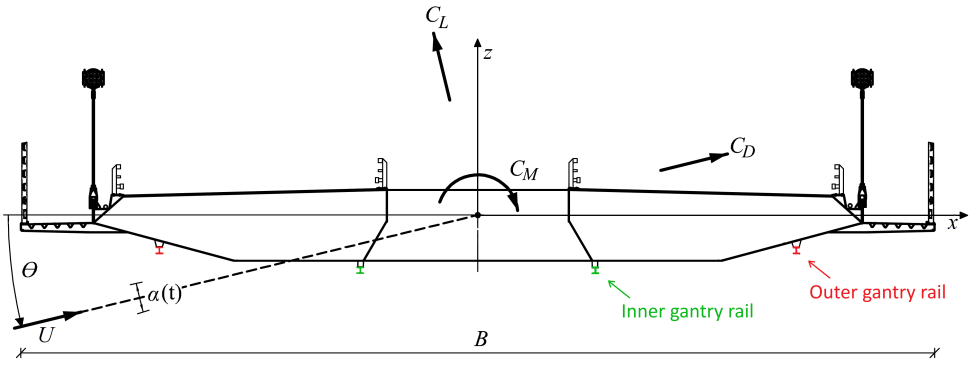


Figure 1. The Çanakkale twin-box deck section, with highlighted the inner and outer gantry rails (I-beam cross-section). Original figure from (Rønne et al., 2021, 2024)

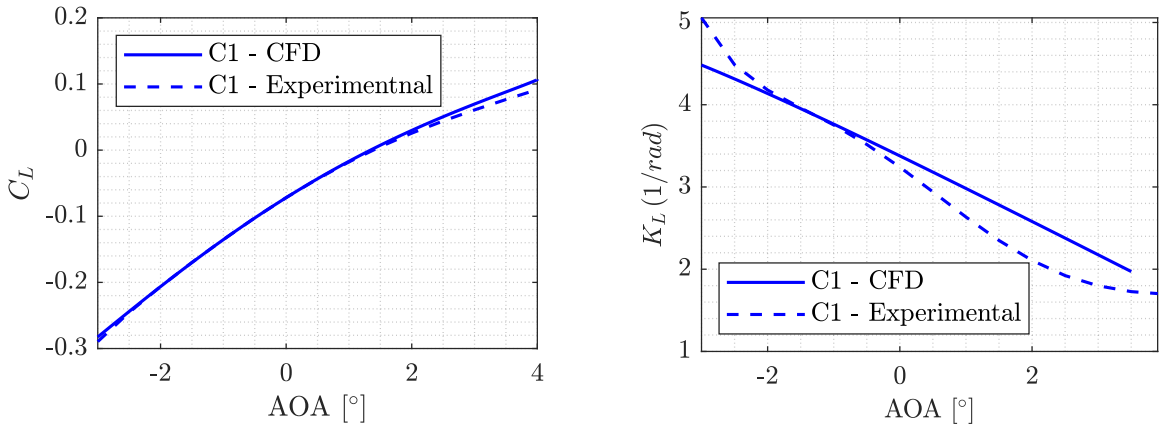
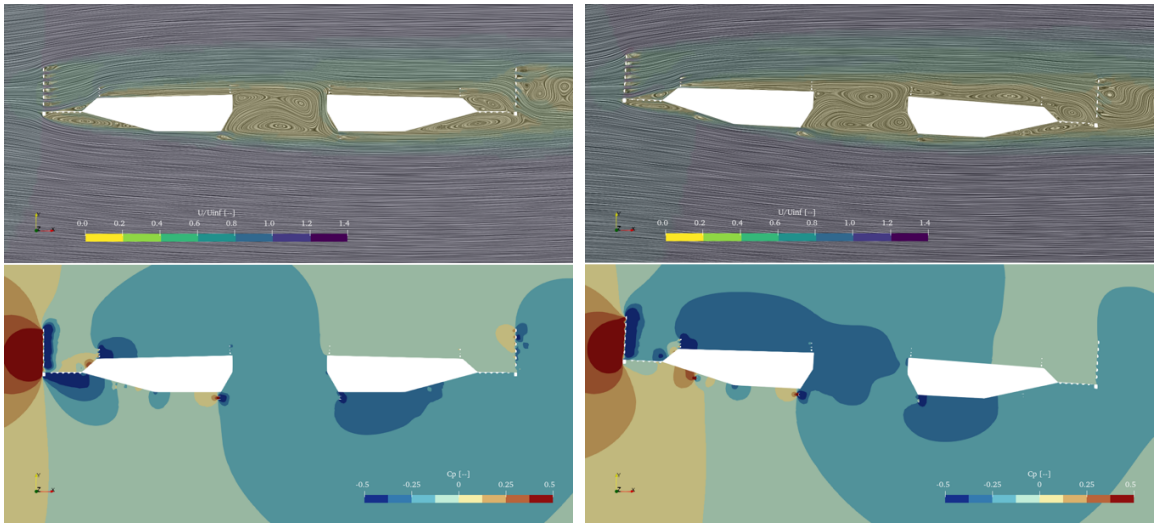


Figure 2. Lift and its slope as a function of the angle of attack, for C1, experimental vs. CFD

this effect. Therefore, the objective of this study is to provide insights into these questions. To this end, a CFD simulation tool based on steady coefficients has been developed to investigate the factors driving this change, with an additional aim of determining whether gantry rails also play a role in this aspect.

2. METHODOLOGY

A series of CFD simulations were conducted to model the flow and the aerodynamic force coefficients as functions of the quasi-steady angle of attack for configurations both with and without gantry rails, referred to as C1 and C2, respectively. The simulations employed URANS with the k-ω SST turbulence model and incorporated mesh morphing. Standard CFD procedures, including grid convergence and time-step verification, were followed to ensure accuracy in the simulation setup. The 2D model demonstrated a satisfactory degree of accuracy for angles of attack within the range $-3°$ to $4°$, quite matching wind tunnel results, particularly for C1. For example, Figure 2 shows the experimental and CFD lift coefficient, C_L, and its slope, K_L, for C1.



(a) AoA 0° **(b)** AoA 3°

Figure 3. Nose-up effect on C1: Scaled velocity field (with LIC) and pressure coefficient.

3. KEY FINDINGS ON NOSE-UP EFFECT

Comparing the mean wind field at 0° and 3° for C1, reported as velocity and pressure fields in Figure 3, the following observations can be made at 3°:

- A lower pressure develops due to intensified flow separation on the upper surface of both decks.
- The strong vortex below the leeward walkway diminishes in size.
- A vortex above the windward walkway enlarges, resulting from separation at the front edge.
- The suction effect below the upwind walkway is partially countered by an extended stagnation region ahead of the external gantry rail, which becomes increasingly exposed to the free stream.

The assessment of the coefficient derivatives is, therefore, based on variations around these two conditions. Focusing on the lift derivative, K_L, the distributions around the deck at 0° and 3° are shown in Figure 4-a) and b). These plots are computed from the difference of C_p between a variation of $\pm 0.5°$ about the reference angle of attack. The difference of distributions between the two mean angles is shown in Figure 4-c). From this, we can conclude the following:

- For the downwind deck, the vortex intensity on the walkway appears to decrease around 0°, which increases the pressure and the local lift derivative. However, at 3°, the vortex intensifies, enhancing suction and consequently reducing the local lift derivative. This reduction is counterbalanced by a net increase in the lift derivative on the upper deck surface due to flow separation. As a result, the overall variation in K_L associated with the downwind deck is minimal (approximately -4%).
- For the upwind deck, the most significant differences are observed near the walkway, particularly on its lower surface. Here, the pressure variation is more pronounced around 0° than at 3°. This occurs due to the different exposure levels of the external gantry rail to the free stream: at 0°, the rail begins to exit the low-pressure region beneath the walkway, reducing

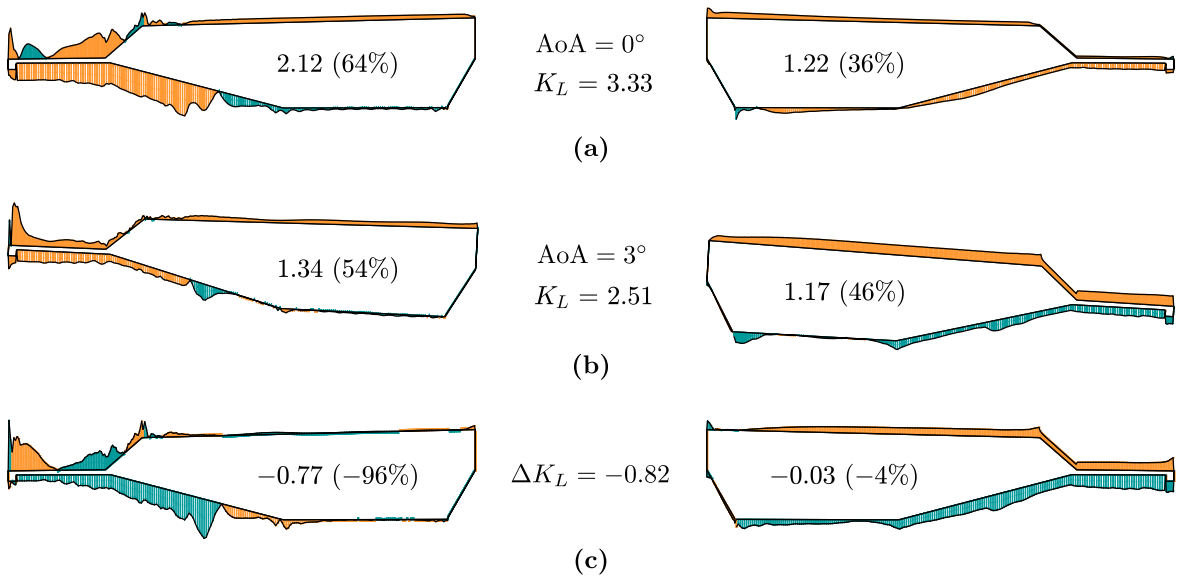


Figure 4. Lift derivative distribution for C1: (a) at AOA = 0°, (b) at 3°, (c) difference (3° - 0°). Orange = positive contribution to total K_L; Green = negative contribution to total K_L. The numbers in the deck refer to the upwind vs. downwind contribution to the total K_L

the strength of the recirculation zone and increasing local pressure. Near 3°, the outer gantry rail is already exposed, resulting in minimal changes to the surface pressure distribution.

4. CONCLUSION

This investigation offers valuable insights into the nose-up effect through CFD simulations. During the conference, configuration C2 (without gantry rails) and the moment slopes for both configurations will also be discussed. The comparison between C2 and C1 will highlight how gantry rails contribute not only to the sign of the moment coefficients at a 0° angle of attack, but also influence the reduction of the slope of lift and moment coefficients.

ACKNOWLEDGEMENTS

The authors would like to thank COWI A/S for funding the experimental wind tunnel testing, the results of which inspired this study.

REFERENCES

Argentini, T., Rocchi, D., Somaschini, C., Spinelli, U., Zanelli, F., and Larsen, A., 2022. Aeroelastic stability of a twin-box deck: Comparision of different procedures to assess the effect of geometric details. J. Wind Eng. Ind. Aerodyn. 220, 104878.

Rønne, M., Larsen, A., and Walther, J. H., 2021. The nose-up effect in twin-box bridge deck flutter: Experimental observations and theoretical model. Wind and Structures 32, 293–308.

Rønne, M., Larsen, A., Walther, J. H., Argentini, T., and Rocchi, D., July 2024. The influence of gantry rails on twin-box deck aerodynamics. Proceedings of 9th International Colloquium on Bluff Body Aerodynamics and Applications. Full-paper submitted for special issue of JWEIA. University of Birmingham, Birmingham.

Zasso, A., Argentini, T., Omarini, S., Rocchi, D., and Øiseth, O., 2019. Peculiar aerodynamic advantages and problem of twin-box girder decks for long span crossings. J. Bridge Structures 15, 111–120.

Wind engineering aspects of the Gordie Howe International Bridge between Canada and the United States

Pierre-Olivier Dallaire[1], Zachary Taylor[2], Mark Istvan[3], Stoyan Stoyanoff[4]

[1]*Rowan Williams Davies & Irwin, Inc. (RWDI), Bromont, Canada, pod@rwdi.com*
[2]*Rowan Williams Davies & Irwin, Inc. (RWDI), Guelph, Canada, zjt@rwdi.com*
[3]*Rowan Williams Davies & Irwin, Inc. (RWDI), Guelph, Canada, msi@rwdi.com*
[4]*Rowan Williams Davies & Irwin, Inc. (RWDI), Bromont, Canada, sts@rwdi.com*

SUMMARY:
The Gordie Howe International Bridge spans between Windsor, Ontario, Canada and Detroit, Michigan, United States. It is located at the eastern end of Ontario's 401 highway which is North America's busiest highway. Existing border crossings between Windsor and Detroit are already the busiest between the two nations. Therefore, it is expected that this bridge will be the busiest border crossing between Canada and the United States. It will also be the longest cable-stayed bridge in North America when it opens. The expected use and scale of the bridge brought some unique wind engineering challenges. Aspects of the wind engineering of the bridge are discussed in the current study including sectional model testing, aeroelastic model testing, derivation of design wind loads, mitigation of wind-induced cable vibration, and vehicle blow-over.

Keywords: Long-span bridge, bridge aerodynamics, cable vibration

1. INTRODUCTION

The Gordie Howe International Bridge (GHIB) is nearing completion and – once open to traffic – will allow for cross-border traffic between Windsor, Ontario, Canada and Detroit, Michigan, United States. When completed it will be the longest cable-stayed bridge in North America with a main span length of 853 m with side spans of 357 m for a total suspended span of 1567 m. The two towers have elevations of approximately 220 m and the total length of cables on supporting the bridge exceeds 57 km. The bridge will be operated by the Windsor-Detroit Bridge Authority and the design of the bridge was carried out by AECOM.

A cross-border bridge has some unique characteristics that had to be considered from a wind engineering perspective. The most practical implication is the dual application of national bridge codes and standards to the job. In this case the design had to be carried out in both a Canadian track and a US track. The Canadian design track was generally governed by the CAN/CSA-S6 standard (CAN/CSA, 2014) while the US design track was governed by the AASHTO LRFD Bridge Design Specifications (AASHTO, 2017). However, there were also specific project requirements outside of these standards defined by the Windsor-Detroit Bridge Authority. The current study outlines some of the wind engineering assessments performed on the bridge.

2. AERODYNAMIC STABILITY

A photograph of the bridge deck sectional model is shown in Figure 1a. The bridge will initially carry 7 lanes of traffic with an additional configuration allowing for 8 lanes of traffic. The deck is 37.5 m wide and 3.17 m deep. One of the significant implications of an international border crossing is the potential for lining up of tractor-trailer trucks. The presence of a line of tractor-trailer trucks at the leading and trailing edge of a bridge deck can substantially alter the aerodynamics of the cross-section. This situation does not pose an ultimate loading case since the bridge will be closed to high-sided vehicles during high winds. However, it was necessary to assess the serviceability of the bridge due to this likely traffic scenario (Figure 1b).

Sectional model testing was the primary method for assessing the aerodynamic stability of the bridge. The full conference paper will show sample results of the free-vibration sectional model testing to demonstrate the aerodynamic performance of the bridge. These tests assessed the potential for vortex-induced oscillations and flutter of the bridge.

In addition to the sectional model testing, aeroelastic model testing was carried out for different construction stages and the completed bridge in service. These tests were used to validate the findings of aerodynamic stability from the sectional model in addition to assessing the aerodynamic stability of the three-dimensional construction stages (Figure 2) that are not as suited to sectional model evaluation.

3. WIND LOADING

As discussed above, the aeroelastic model tests were used to validate the aerodynamic stability of the bridge in various construction and service stages. However, it was also instrumental in the derivation of validation of design wind loads. The state-of-the-art approach to the derivation of design wind loads for long-span bridges remains time domain buffeting response analysis. This approach relies on static aerodynamic coefficients and aerodynamic derivatives measured from the sectional model test. Several hours of windstorms are generated numerically and the response of the bridge to the fluctuating wind is estimated. The aeroelastic model responses can be predicted using the same numerical approach and the buffeting response analysis model was verified through comparison to the physical measurements. From the buffeting responses of the bridge, the equivalent static wind load cases are provided.

Flexible long-span bridges are increasingly incorporating longitudinal restraining devices or “lock-up devices” (LUDs) to restrain both seismic and wind-induced longitudinal motions of the bridge. As a result, these LUDs must resist a significant level of force and are expected to undergo many load cycles due to the wind since a flexible structure will respond in some degree to any wind. The time domain approach that was considered in this study allowed for a direct modelling of the LUD behaviour in terms of geometric non-linearities and the anticipated force vs. velocity relationship of the damper-like devices.

4. WIND-INDUCED CABLE VIBRATION

Being the longest cable-stayed bridge in North America implies that the cables on the bridge will also be the longest in North America. The potential for wind-induced cable vibration is

significant on most cable-stayed bridges and is increasingly important with increasing cable length. An arrangement of external viscous dampers was designed by the design team to control the anticipated wind-induced cable vibrations. The sources of wind-induced cable vibrations include vortex-induced oscillations, rain-wind induced oscillations, parametric excitation, and iced galloping.

In addition to ensuring the damper system had sufficient damping it was also necessary to estimate the expected cyclical loading for the fatigue design of the damper frames. Time domain simulations of the combined bridge and cable responses were carried out to predict the tension/compression cycles in the dampers. These time domain simulations were carried out over a range of wind speeds and wind azimuths and cycles were counted using a rainflow algorithm. These cycles over wind speeds and directions were combined with the local wind climatology to determine average annual cycles.

5. VEHICLE BLOW-OVER

The potential aerodynamic stability influence of high-sided vehicles was discussed above. However, it is also important to ensure the safety of high-sided vehicles during operational conditions. Therefore, wind tunnel tests were carried out on scaled vehicles mounted to six degree-of-freedom load cells in each lane of traffic on the bridge. These wind tunnel measurements were combined with an analytical assessment incorporating the forward speed of the vehicles and the potential for lane manoeuvring. This analytical assessment based on wind tunnel measurements was used to determine the critical blow-over speed as the point at which the over-turning moments acting on these vehicles exceeded the assumed restoring moment.

5. CONCLUSIONS

Extensive wind engineering studies have been carried out on the Gordie Howe International Bridge between Canada and the United States. The full conference paper and presentation will provide details on some of the wind engineering studies that have been carried out. These will focus on the sectional model and aeroelastic model testing to determine aerodynamic stability. The buffeting response analysis for wind load derivation and the calibration through aeroelastic model testing. Furthermore, important details on the longitudinal wind loading and the modelling of lock-up devices will be discussed. In addition to these studies, details of the wind-induced cable vibration mitigation will be discussed along with the determination of the critical blow-over wind speed for high-sided vehicles.

ACKNOWLEDGEMENTS

The authors are grateful for the design team at AECOM as the designer of record and the Windsor-Detroit Bridge Authority. Furthermore, this work would not have been possible without the model builders and wind tunnel staff at RWDI.

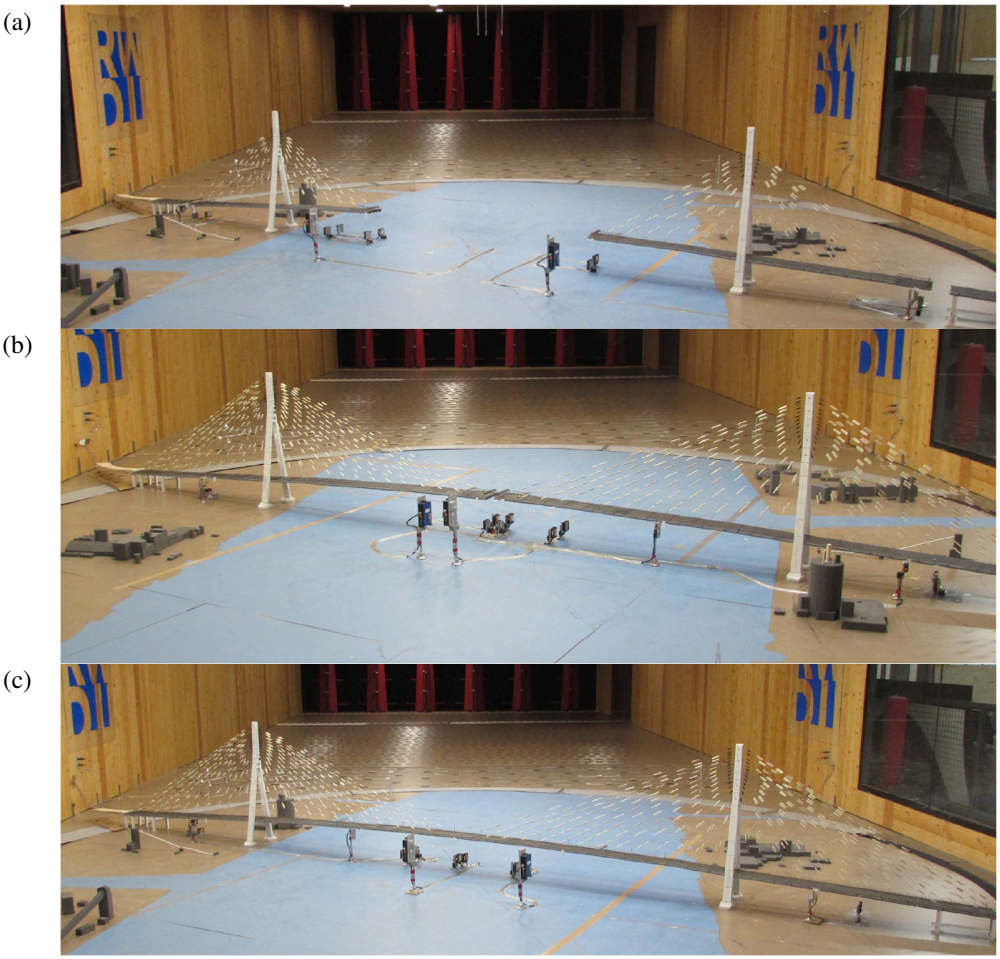
REFERENCES

AASHTO (2017) AASHTO LRFD Bridge Design Specifications, Customary U.S. Units, 8th Edition.
CAN/CSA (2014) Canadian Highway Bridge Design Code, CSA Group, CAN/CSA S6-14.



(a) (b)

Figure 1. Photographs of the sectional model in RWDI's wind tunnel (a) No traffic, and (b) Tractor trailer traffic pattern.



(a)

(b)

(c)

Figure 2. Photographs of the aeroelastic model in RWDI's wind tunnel (a) cantilever construction stage, (b) just prior to main span closure, and (c) completed bridge in service.

Aero-hydrodynamic coupled analysis of a floating long-span bridge

Soomin Kim [1], Youchan Hwang [2], Jeong-Gon Kim[3], Chungkuk Jin[4], Ho-Kyung Kim [5]

[1]*Seoul National University, Seoul, South Korea, ssominkim@snu.ac.kr*
[2]*Seoul National University, Seoul, South Korea, lum4u2526@snu.ac.kr*
[3]*Seoul National University, Seoul, South Korea, rhsl13@snu.ac.kr*
[4]*Florida Institute of Technology, Florida, USA, cjin@fit.edu*
[5]*Seoul National University, Seoul, South Korea, hokyungk@snu.ac.kr*

SUMMARY
A floating long-span bridge differs from conventional bridges in that both wind and wave loads act as primary dynamic forces. The nonlinear interaction between the floating body's hydrodynamic response and the bridge deck's aeroelastic response can significantly affect the entire system. However, existing commercial software lacks the capability to perform fully coupled aero-hydrodynamic analysis. Therefore, this study introduces a time-domain aero-hydrodynamic coupled analysis method for floating bridges. The static wind load and buffeting force were calculated using the aerodynamic force coefficient and quasi-static buffeting theory. Additionally, the aeroelastic self-exciting force was determined using a truncated Fourier series approximation that satisfies the causality condition of the aerodynamic impulse response function. The wave load was considered by converting the frequency-dependent hydrodynamic force coefficients to the time-domain using Cummins equation. Wind and wave loads were simultaneously applied through the ABAQUS User Subroutine. Validation of the developed method was achieved by comparing the response spectrum and RMS values obtained from frequency-domain analysis. Finally, the aero-hydrodynamic coupling effect on the dynamic response was evaluated for the Bjørnafjorden Floating Bridge in Norway.

Keywords: Floating long-span bridge, aerodynamic analysis, hydrodynamic analysis

1. INTRODUCTION

Floating bridges have been introduced worldwide as an economical alternative for crossing wide and deep straits (Wang et al., 2024). Unlike conventional bridges, wind and wave loads significantly affect floating long-span bridges. Additionally, the nonlinear wind-wave impact on the entire system is challenging to evaluate using frequency-domain analysis. Therefore, fully coupled aero-hydrodynamic time-domain analysis must be considered during the design of floating bridges. However, existing commercial analysis software is limited in performing complex analyses, such as coupled wind-wave interaction (Wang et al., 2018; Xu et al., 2018). Previous studies have conducted time-domain wind-wave coupled analyses using in-house developed codes; however, these have limitations, such as not accounting for frequency-dependent flutter coefficients, second-order wave effects, and nonlinearity due to large displacements of the entire structural system (Moe et al., 2017; Cheng et al., 2019). Consequently, this study developed a nonlinear time-domain aero-hydrodynamic analysis module for floating long-span bridges using

the User Subroutine in the commercial structural analysis software ABAQUS. This study focuses on the development and validation of the analysis tool, with future research aimed at performing wind-wave coupled nonlinear analysis of a long-span floating bridge utilizing the developed tool.

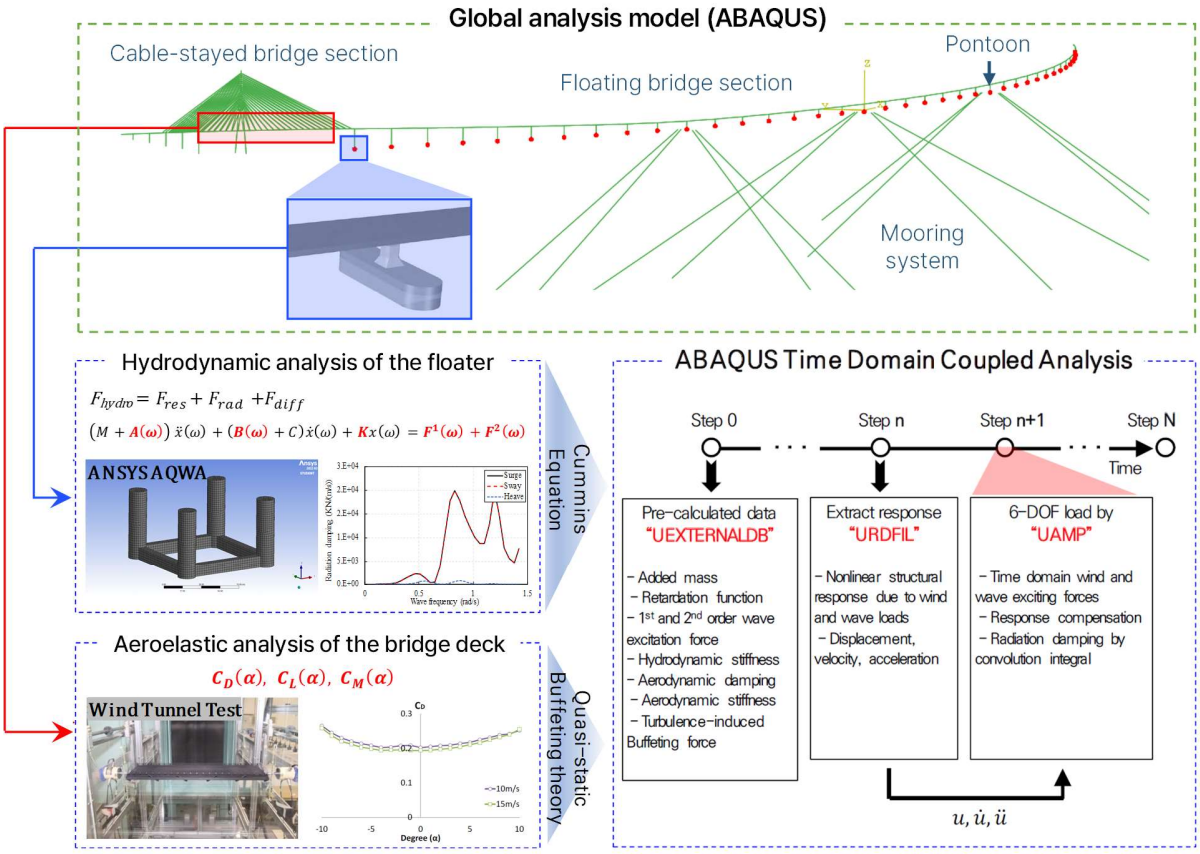


Figure 1. Outline of the aero-hydrodynamic coupled analysis procedure.

2. METHODOLOGY FOR NUMERICAL SIMULATION

2.1. Dynamic equation of coupled analysis

The coupled effect of aero-hydrodynamic loading can be reflected by solving the governing equations directly in the time-domain. When both wind and wave loads are applied, the dynamic equation of motion is expressed as Eq. (1-2).

$$M_s\ddot{x}(t) + C_s\dot{x}(t) + K_s x(t) = F_{hydro} + F_{aero} \tag{1}$$

$$F_{hydro} = F_{res} + F_{rad} + F_{ex}^{(1)} + F_{ex}^{(2)},\ F_{aero} = F_{mean} + F_{Buff} + F_{self} \tag{2}$$

In this equation, $x(t)$ is structure displacement, M_s is structure mass, C_s is structure damping, K_s is structure stiffness. F_{hydro} represents the total hydrodynamic and hydrostatic load, while F_{aero}

is the total aerodynamic load. Here, F_{res} is the hydrodynamic restoring force, F_{rad} is the hydrodynamic radiation force, $F_{ex}^{(1)}$ and $F_{ex}^{(2)}$ are the first and second wave exciting forces, F_{mean} is the mean wind force, F_{Buff} is the turbulence-induced buffeting force, and F_{self} is the motion-induced self-exciting force. To date, no commercial structural analysis software can fully account for hydrodynamic and aeroelastic loads in the time domain. Therefore, the aero-hydrodynamic analysis code was developed using ABAQUS User Subroutine to calculate the response-dependent dynamic forces at each analysis time step, as shown in Fig. 1.

2.2. Hydrodynamic analysis

The procedure for time-domain hydrodynamic analysis using ABAQUS User Subroutine is illustrated. Frequency-dependent parameters based on potential theory—added mass, radiation damping, and first/second-order wave excitation force coefficients—was extracted using ANSYS AQWA Diffraction analysis. The dynamic equations in the time-domain based on the Cummins Equation (Journee and Massie, 2000) can be derived as follows: Eqs. (2-3).

$$[M_s + A^{\infty}]\ddot{x}(t) + \int_0^{\infty} B(\tau) \cdot \dot{x}(t-\tau) \cdot d\tau + \left[K_s + K_{hydro}\right]x(t) = F_{ex}^{(1)}(t) + F_{ex}^{(2)}(t) \tag{2}$$

$$A^{\infty} = A(\omega) + \frac{1}{\omega}\int_0^{\infty} B(\tau) \cdot \sin(\omega\tau) \cdot d\tau\,, \quad B(\tau) = \frac{2}{\pi}\int_0^{\infty} C(\omega) \cdot \cos(\omega\tau) \cdot d\omega \tag{3}$$

where $A(\omega)$ is the added mass, $C(\omega)$ is the radiation damping, and $B(\tau)$ is the retardation function. The ABAQUS User Subroutine is employed to extract the structural response at each time step and perform the convolution integral for calculating radiation damping. Additionally, it is used to apply wave excitation forces at each time step. By utilizing the User Subroutines "UEXTERNALDB", "URDFIL", and "UAMP", the extraction of structural response and the convolution integral are carried out to perform the hydrodynamics analysis.

2.3. Aerodynamic analysis

The static wind load and buffeting force were calculated using the aerodynamic force coefficient and quasi-static buffeting theory (Strømmen, 2010). Additionally, the aeroelastic self-exciting force was determined using a truncated FSA(Fourier series approximation) that satisfies the causality of the aerodynamic impulse response function (Park et al., 2014). The total aeroelastic force is calculated as Eq. (4).

$$q_{tot}(x,t) = \bar{q} + B_q \cdot v(x,t) + C_{ae} \cdot \dot{x} + K_{ae} \cdot x \tag{4}$$

Here, $\bar{q}$ is the time-invariant mean load vector, B_q is the dynamic loading matrix associated with turbulence, $v(x,t)$ is the turbulence wind velocity vector, C_{ae} is the aerodynamic damping matrix, and K_{ae} is the aerodynamic stiffness matrix.

In the structural analysis program ABAQUS, there is no module that directly calculates time-domain aeroelastic responses. Therefore, these calculations were performed using User Subroutines. When using buffeting theory to calculate static wind load and buffeting force, it is necessary to read and apply the buffeting load at each time step. Also, the structure response at each time step must be known during the time-domain analysis to calculate the self-exciting force using FSA method. Therefore, the analysis procedure for calculating aeroelastic responses was established by using the User Subroutines similar to the hydrodynamic analysis module.

3. CONCLUSION

In this study, the time-domain aero-hydrodynamic analysis module for floating long-span bridges was developed using the ABAQUS User Subroutine. The hydrodynamic coefficients by the potential theory were transferred in the time domain based on the Cummins Equation. Also, the aerodynamic coefficients were considered in the time domain based on the buffeting theory. The dynamic equation was solved simultaneously to consider the coupling effect. Each analysis was validated by comparing it with the results of frequency-domain analysis. In future research, a floating long-span bridge will be considered for conducting wind-wave coupled analysis using the developed aero-hydrodynamic module.

ACKNOWLEDGEMENTS

This work is supported by the Korea Agency for Infrastructure Technology Advancement (KAIA) grant funded by the Ministry of Land, Infrastructure and Transport (Grant RS-2023-00250727) through the Korea Floating Infrastructure Research Center at Seoul National University.

REFERENCES

Wang, J., Cheynet, E., Snæbjörnsson, J. Þ., & Jakobsen, J. B., 2018. Coupled aerodynamic and hydrodynamic response of a long span bridge suspended from floating towers. Journal of Wind Engineering and Industrial Aerodynamics, 177, 19-31.

Xu, Y., Øiseth, O., & Moan, T., 2018. Time domain simulations of wind-and wave-induced load effects on a three-span suspension bridge with two floating pylons. Marine Structures, 58, 434-452.

Moe, O. H., Aas-Jakobsen, K., & Amdahl, J., 2017. Analysis of tether anchored floating suspension bridge subjected to extreme environmental loads. Procedia engineering, 199, 3033-3038.

Cheng, Z., Gao, Z., & Moan, T., 2019. Numerical modeling and dynamic analysis of a floating bridge subjected to wind, wave, and current loads. Journal of Offshore Mechanics and Arctic Engineering, 141(1), 011601.

Journee, J. M., & Massie, W. W., 2000. Offshore hydromechanics

Strømmen, E., 2010. Theory of bridge aerodynamics. Springer Science & Business Media.

Park, J., Jung, K., Hong, Y. H., Kim, H. K., & Lee, H. S., 2014. Exact enforcement of the causality condition on the aerodynamic impulse response function using a truncated Fourier series. Journal of Engineering Mechanics, 140(5), 04014017.

Internal Resonance during nonlinear flutter response of long-span bridges

Wei Cui[1] and Lin Zhao[2]

[1]*Tongji University, Shanghai, China, cuiwei@tongji.edu.cn*
[2]*Tongji University, Shanghai, China, zhaolin@tongji.edu.c*

SUMMARY:
Wind-induced flutter instability is the most destructive wind hazards for long-span bridges since the collapse of Tacoma Narrow Bridge. Flutter response is normally characterized as torsional-vertical two modes coupled responses. However, as the bridge span increase, dynamic frequency decreases and modal frequencies are most closely spaced. The higher order modes with same the modal shape symmetricity are likely incorporated into during responses when frequency of one higher order mode is close to flutter frequency. Internal resonance among multiple modes occurs during flutter. When amplitudes increase and aerodynamics enters nonlinear stage, it is difficult the evaluate the flutter response due to multi-modes coupling. This study proposes an analytical formula to estimate the nonlinear flutter response based on complexification-averaging method, which reduce the original 2nd order differential equation of 1st order differential equation about amplitudes and phase differences.

Keywords: Long span bridge, Nonlinear flutter, Flutter Derivatives, internal Resonance

1. GENERAL INSTRUCTIONS

Flutter is the most destructive wind-induced vibration of long-span bridges. Since the collapse of Narrow Tacoma Bridge. Adopted from the airfoil flutter theoryTheodorsen, 1935, the aeroelastic force of bridge deck during flutter is modelled as the flutter derivatives Scanlan, 1978 with respect to motion states, i.e. displacements and velocity. However, as the development of flutter theory of long-span bridges, it is noticed that the original linear flutter derivatives is only able to predict the critical wind speed. Once flutter occurs on-site, the responses grows rapidly. The fluid-structures interaction subjecting to large amplitudes response exhibits nonlinear phenomenon , such as limit-cycle oscillation and frequency multiplication in aeroelastic force. The flutter response simulated by linear flutter derivatives will grow continuously, which is not compatible with nonlinear dynamic phenomenon mentioned above. Therefore, several nonlinear aeroelastic models are proposed in recent decades to simulate the nonlinear flutter responses.

This study will firstly provide an autonomous inference method is employed to find out the polynomial type model of nonlinear aerodynamic. Next, a nonlinear multi-mode coupled flutter analysis was carried out on a 1,688 m span suspension bridge. This study employs complexification-averaging method reducing the 2-nd order dynamic differential equation to 1-st order differential equation about response amplitudes and phase.

1.1. Aerodynamic modelling

A scale model of Nansha bridge deck with length scale ratio as 1:150 (Figure 1) is tested in TJ-7 wind tunnel. The forced motion equipment is employed to measured the aerodynamic force.

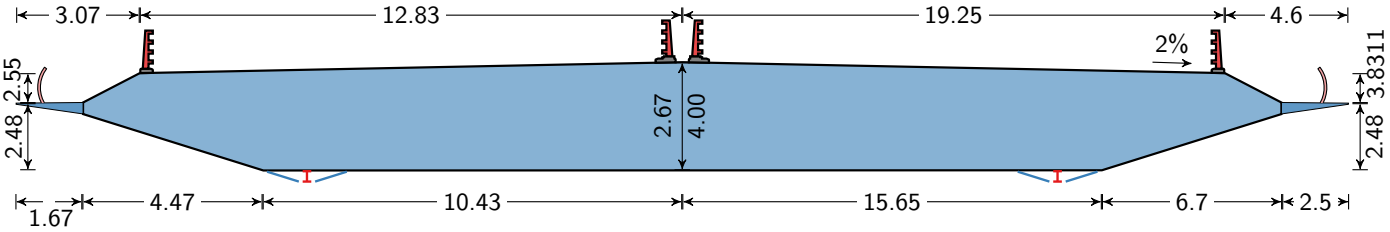


Figure 1. Bridge deck section (left: model scale, unit: cm; right: full scale, unit: m)

Based on the method in Ma et al. (2023), the nonlinear aeroelastic force is identified as:

$$N_{yL}(y,\dot{y}) = 0 \tag{1a}$$

$$N_{\theta L}(\theta,\dot{\theta}) = b_1K^2\theta\dot{\theta} + b_2K^2\theta\dot{\theta}^2 + b_3K^4\theta^3 \tag{1b}$$

$$N_{yM}(y,\dot{y}) = 0 \tag{1c}$$

$$N_{\theta M}(\theta,\dot{\theta}) = c_1K\dot{\theta}^3 + c_2K^2\theta\dot{\theta}^2 \tag{1d}$$

2. MATHEMATICAL FORMULATION OF MULTI-MODES COUPLED FLUTTER WITH INTERNAL RESONANCE

2.1. Vibration governing equation

If only one vertical mode and one torsional mode involved in flutter, the vertical and torsional motion is expressed in modal coordinates:

$$h = B\phi_h y \quad q = \phi_q\theta \tag{2}$$

The dimensionless flutter vibration formula is

$$\ddot{y} + 2\xi_y K_y\dot{y} + K_y^2 y = \frac{m_y^*}{\phi_{hh}}\left(\phi_{hh}KH_1^*\dot{y} + \phi_{hq}KH_2^*\dot{\theta} + \phi_{hq}K^2H_3^*\theta + \phi_{hh}K^2H_4^*y\right) \tag{3a}$$

$$\ddot{\theta} + 2\xi_\theta K_\theta\dot{\theta} + K_\theta^2\theta = \frac{m_\theta^*}{\phi_{qq}}\left(\phi_{hq}KA_1^*\dot{y} + \phi_{qq}KA_2^*\dot{\theta} + \phi_{qq}K^2A_3^*\theta + \phi_{hq}K^2A_4^*y\right) \tag{3b}$$

where ξ_y, K_y, ξ_θ, K_θ are damping coefficients and reduced structural frequencies for vertical and torsional motion, $\dot{}$ indicates the differentiation respect with dimensionless time τ and m_y^* and m_θ^* are mass ratios for vertical and torsional motion. ϕ_{hh}, ϕ_{hh} and ϕ_{hh} are the modal shape parameters for the aerodynamic force, where $\phi_{hh} = \int_0^L \phi_h^2(x)dx/L$, $\phi_{hq} = \int_0^L \phi_h(x)\phi_q(x)dx/L$ and $\phi_{qq} = \int_0^L \phi_q^2(x)dx/L$. The coupling aerodynamic force between vertical and torsional motion are affected by their modal shape. Therefore, the vertical and torsional modes should be the same order, such as both are first order symmetric shape or first order asymmetric shape. If the vertical and torsional modes has different shape, for example symmetric is coupled with asymmetric, there is no coupling effect because of $\phi_{hq} = \int_0^L \phi_h(x)\phi_q(x)dx/L = 0$.

If there is a high order vertical mode (denoted as z with shape function as $\hbar$), whose fundamental frequency K_z is close to the flutter frequency K, the internal resonance may be excited between flutter and high order vertical motion. The vertical motion is expressed as:

$$h = B\left(\phi_h y + \phi_\hbar z\right) \tag{4}$$

Then the three modes coupled motion equation is

$$\begin{aligned}\ddot{y} + 2\xi_y K_y \dot{y} + K_y^2 y = \frac{m_y^*}{\phi_{hh}}[&\phi_{hh} K H_1^* \dot{y} + \phi_{hq} K H_2^* \dot{\theta} + \phi_{hq} K^2 H_3^* \theta + \phi_{hh} K^2 H_4^* y + \\ &\phi_{q^2 h} b_1 K^2 \theta\dot{\theta} + \phi_{q^3 h} b_2 K^2 \theta\dot{\theta}^2 + \phi_{q^3 h} b_3 K^4 \theta^3]\end{aligned} \tag{5a}$$

$$\begin{aligned}\ddot{z} + 2\xi_z K_z \dot{z} + K_z^2 z = \frac{m_z^*}{\phi_{\hbar\hbar}}[&\phi_{\hbar\hbar} K H_1^* \dot{z} + \phi_{\hbar q} K H_2^* \dot{\theta} + \phi_{\hbar q} K^2 H_3^* \theta + \phi_{\hbar\hbar} K^2 H_4^* z + \\ &\phi_{q^2\hbar} b_1 K^2 \theta\dot{\theta} + \phi_{q^3\hbar} b_2 K^2 \theta\dot{\theta}^2 + \phi_{q^3\hbar} b_3 K^4 \theta^3]\end{aligned} \tag{5b}$$

$$\begin{aligned}\ddot{\theta} + 2\xi_\theta K_\theta \dot{\theta} + K_\theta^2 \theta = \frac{m_\theta^*}{\phi_{qq}}[&\phi_{hq} K A_1^* \dot{y} + \phi_{\hbar q} K A_1^* \dot{z} + \phi_{qq} K A_2^* \dot{\theta} + \phi_{qq} K^2 A_3^* \theta + \\ &\phi_{hq} K^2 A_4^* y + \phi_{\hbar q} K^2 A_4^* z + \phi_{q^4} c_1 K \dot{\theta}^3 + \phi_{q^4} c_2 K^2 \theta\dot{\theta}^2]\end{aligned} \tag{5c}$$

In the above equation, z expresses the high-order vertical motion, $\phi_{\hbar q}$ denotes the modes coupling between torsional and high-order vertical motion caused by the linear components of aerodynamic force, but the linear coupling is close to 0 because of the modes orthogonality $\phi_{\hbar q} = 0$. For the nonlinear part, the coupling effect may be different.

Through complexification-averaging method, the differential equations of amplitudes are

$$\begin{aligned}\dot{A}_y + \xi_y K_y A_y = &\frac{m_y^*}{\phi_{hh}} K \left[\phi_{hh} \frac{A_y}{2} H_1^* + \phi_{hq} \frac{A_\theta}{2} H_2^* \cos\beta_{\theta y} - \phi_{hq} \frac{A_\theta}{2} H_3^* \sin\beta_{\theta y} - \right. \\ &\left. \phi_{q^3 h} b_2 \frac{A_\theta^3}{8} \sin\beta_{\theta y} - \phi_{q^3 h} b_3 \frac{3A_\theta^3}{8} \sin\beta_{\theta y}\right]\end{aligned} \tag{6a}$$

$$\begin{aligned}\dot{A}_z + \xi_z K_z A_z = &\frac{m_z^*}{\phi_{\hbar\hbar}} K \phi_{\hbar\hbar} \frac{A_z}{2} H_1^* + \frac{m_z^*}{\phi_{\hbar\hbar}} K \phi_{\hbar q} \frac{A_\theta}{2} \left[H_2^* \cos\beta_{\theta z} - H_3^* \sin\beta_{\theta z}\right] - \\ &\frac{m_z^*}{\phi_{\hbar\hbar}} K \phi_{q^3\hbar} \frac{A_\theta^3}{8} \left[b_2 \sin\beta_{\theta z} + 3b_3 \sin\beta_{\theta z}\right]\end{aligned} \tag{6b}$$

$$\begin{aligned}\dot{A}_\theta + \xi_\theta K_\theta A_\theta = &\frac{m_\theta^*}{\phi_{qq}} K \phi_{hq} \frac{A_y}{2} \left[A_1^* \cos\beta_{\theta y} + A_4^* \sin\beta_{\theta y}\right] + \frac{m_\theta^*}{\phi_{qq}} K \left[\phi_{qq} A_2^* \frac{A_\theta}{2} + \phi_{q^4} c_1 \frac{3A_\theta^3}{8}\right] + \\ &\frac{m_\theta^*}{\phi_{qq}} K \phi_{\hbar q} \frac{A_z}{2} \left[A_1^* \cos\beta_{\theta z} + A_4^* \sin\beta_{\theta z}\right]\end{aligned} \tag{6c}$$

The amplitudes and phase evolution derived by the above formula is derived based on the above formula, and are compared with vibration simulation to demonstrate its

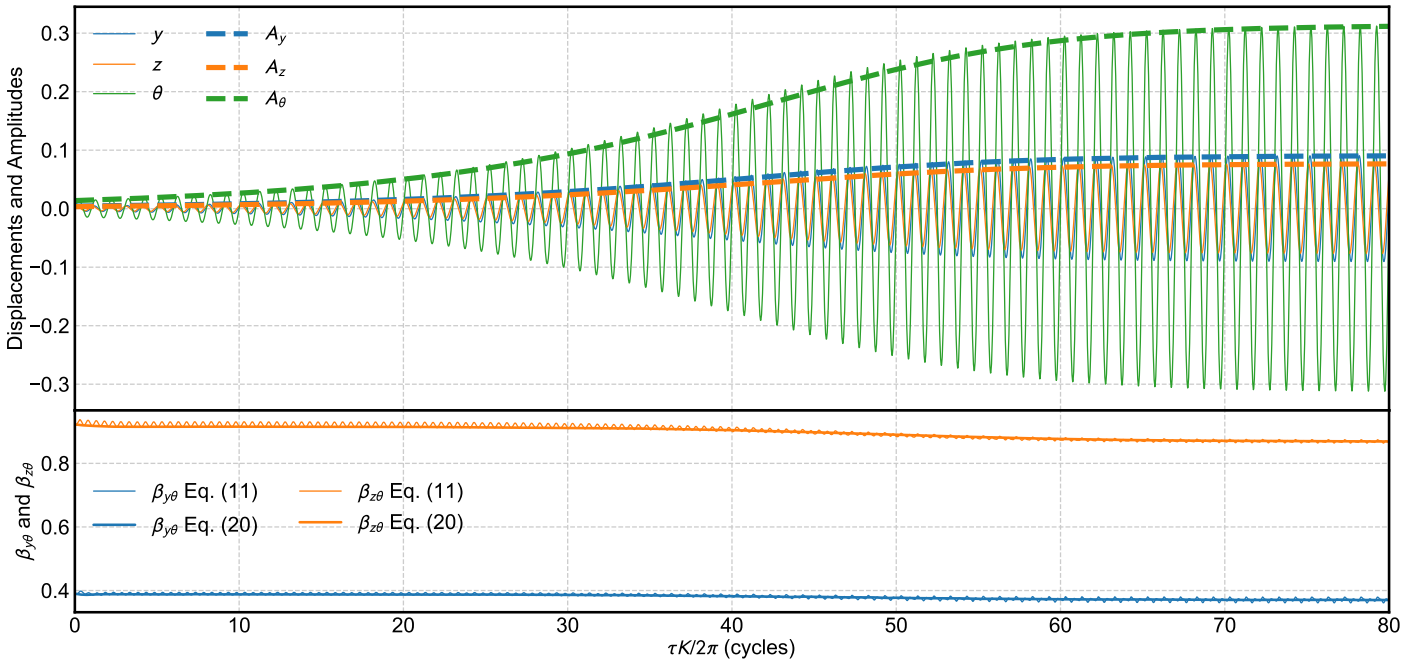


Figure 2. Comparison of displacement evaluated and amplitudes/phase evaluated for multi-modes coupled flutter when $U = 83$ m/s

3. CONCLUSIONS

The amplitudes evolution formula is approved to be effective to derive the multimode flutter response. In further study, the flutter amplitudes between multimode coupling and two-mode coupling will be compared.

ACKNOWLEDGEMENTS

The authors gratefully acknowledge the support of the National Natural Science Foundation of China (52478552)

REFERENCES

Ma, T., Cui, W., Gao, T., Liu, S., Zhao, L., and Ge, Y., 2023. Data-based autonomously discovering method for nonlinear aerodynamic force of quasi-flat plate. Physics of Fluids 35.

Scanlan, R., 1978. The action of flexible bridges under wind, I: flutter theory. Journal of Sound and Vibration 60, 187–199.

Theodorsen, T., 1935. *General theory of aerodynamic instability and the mechanism of flutter*. Tech. rep. National Aeronautics and Space Administration.

An overview of the aerodynamic design of the Julsundet bridge towers

Giulia Pomaranzi[1], Jungao Wang[2], Tommaso Argentini[1], Alberto Zasso[1]

[1]*Politecnico di Milano, Department of Mechanical Engineering, Milano, Italy,*
giulia.pomaranzi@polimi.it
[2]*Norwegian Public Roads Administration, Stavanger, Norway*

SUMMARY:
This paper focuses on the aerodynamic design of the 271-meter-high towers for the Julsund long-span bridge in a fjord-crossing project in Norway. The complex topography of the fjords introduces unique wind conditions, potentially affecting the aerodynamic behaviour of the towers. To investigate these effects, a multi-stage experimental campaign was conducted at the Politecnico di Milano wind tunnel. First, topographic tests using a 1:1000 scale terrain model were performed to assess wind conditions at the tower location and observe variations in wind features with height. Subsequently, sectional model tests measured static force coefficients, evaluated vortex-induced vibrations, and assessed aeroelastic stability across various mean angles of attack. Finally, aeroelastic model tests were also carried out to verify the overall performance of the tower. This paper presents the experimental methodologies and preliminary findings, emphasizing key aerodynamic considerations for the towers' design and stability under challenging wind conditions.

Keywords: wind tunnel tests, topographic effects, tower design

1. INTRODUCTION

In recent years, bridge towers have been built progressively taller as the spans of long-span bridges extend to increasing lengths. As key load-bearing elements, these towers must sustain considerable wind-induced forces, especially during the construction stages when they stand as slender, free-standing structures. During these stages, the towers exhibit lower structural damping and natural frequencies, leaving them more vulnerable to dynamic wind effects, particularly across-wind responses resulting from wind-structure interactions (Belloli et al., 2011; Ma et al., 2019). If the bridge location is characterized by relevant mountain peaks, the tower design could be further complicated being the wind conditions expected to experience substantial changes in speed, direction, and turbulence intensity, potentially affecting the structure stability (Castellon et al., 2022).

Regarding the Julsundet bridge in Norway, an overview of the aerodynamic design of the 271m high towers is here proposed. A multi-stage experimental campaign was conducted in the Politecnico di Milano wind tunnel. First, a topographic model was used to assess site-specific wind conditions and capture wind variations with height. Then, sectional model tests were performed to measure static force coefficients, evaluate vortex-induced vibrations (VIV), and investigate aeroelastic stability at various angles of attack. Finally, aeroelastic model tests were conducted to validate the tower's performance under representative wind conditions.

This paper presents the methodology and main findings, providing some insights into the aerodynamic design required to ensure the stability and safety of the Julsundet Bridge towers.

1.1. The Julsundet bridge towers

The Julsundet bridge towers are 271 meters high, with a H-shaped layout in elevation and varying irregular hexagon shapes in cross sections. A sketch of the towers is shown in Figure 1, along with the cross-section characteristics at 100m (JUL-T1) and 200m (JUL-T2).

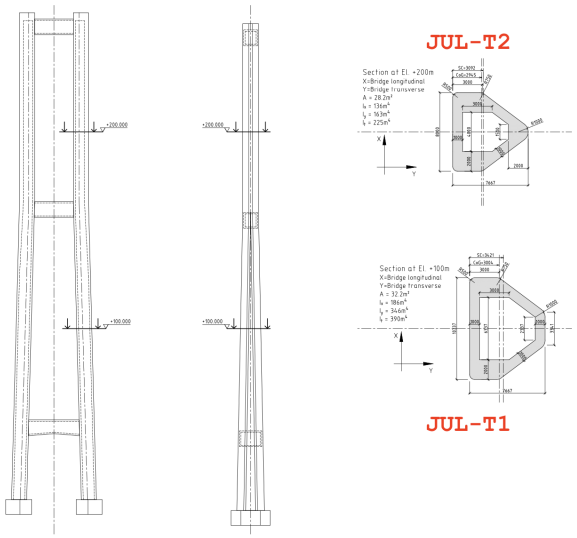


Figure 1. Tower geometry and sections considered for the sectional tests.

2. METHODOLOGY

A multi-stage experimental campaign was conducted at Politecnico di Milano wind tunnel with multiple objectives, including the assessment of the terrain effects on wind flow characteristics at the tower site, the identification and quantification of the vortex shedding effects and the evaluation of the aerodynamic properties of the tower's cross sections under different wind conditions.

2.1. Topogaphic tests

To measure local wind properties due to terrain effects at Julsundet (Norway), a dedicated topographic study has been performed; a 10 km diameter surround area is reproduced in the wind tunnel test section, assuming a length scale of 1:1000, allowing a proper representation of the elevations closest to the site of the Julsund bridge. The flow field over the tower development was measured. Specifically, for each wind direction, the mean wind speed, mean wind direction and turbulence intensities are measured at 50-meter intervals along the axis of both bridge towers. Figure 2 shows the topographic model in the boundary layer test section.

2.2. Sectional model test

Two sectional models, representative of the JUL-T1 and JUL-T2 cross sections, were realized assuming a length scale 1:60 and a total length of 2m at model scale. The setup shown in Figure 3a was used to measure aerodynamic coefficients through a load cell for each leg. To investigate the stability, the model has been then suspended using vertical linear springs (Fig. 3b), anchored



Figure 2. The topographic model in the boundary layer test section.

both to the floor and to the roof of the wind tunnel, tuned to simulate the first two flexural modes and the first torsional one.

2.3. Aeroelastic test

The tower aeroelastic model was designed following the Froude similitude, assuming a length scale equal to 1:200. Aeroelastic response (VIV, buffeting and stability) of the free-standing tower under various wind directions and conditions (smooth and turbulent) was investigated.



(a) Tower sectional model **(b)** Suspended model for torsional mode **(c)** Tower aeroelastic model

Figure 3. Sectional and aeroelastic model of the tower

3. RESULTS AND DISCUSSION

As an example of the results from the topographic test, Figure 4 shows flow measures performed at Nautneset Tower for 317° wind direction. Specifically, the first subplot shows the magnitude of the velocity vector normalized with respect to the reference velocity measured by a Pitot tube placed at the beginning of the turning table at top tower height. Second subplot shows the turbulence intensities variation along the tower and the third reports the yaw and pitch angles. Such angles are defined with respect to the inlet wind direction: yaw angle is in the horizontal plane, and it is positive if counterclockwise with respect to inlet wind; pitch angle is in the vertical plane and it is positive if upward with respect to inlet wind. Effects induced by the orography result in a quite strong deflection in the horizontal plane, that reduces with the height, together with a downwash

effects induced by the upwind fjords.

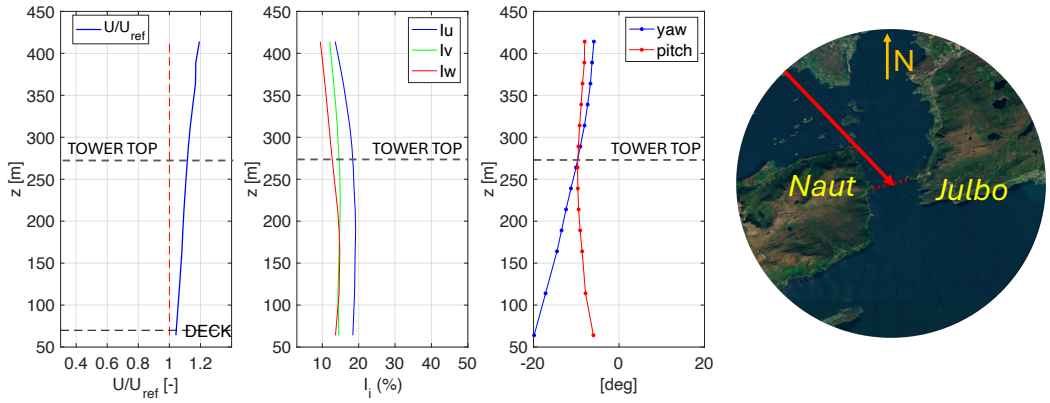


Figure 4. Results from velocity measurements along the tower axis. The incoming wind direction is depicted in the right figure.

Regarding results from other test stages, it is to note first that the tested tower design exhibited no instability across the entire tested velocity range. Additionally, a summary of the VIV analysis from full aeroelastic model tests is provided in Table 1, which shows the maximum accelerations at the tower top (expressed as standard deviation) for modes experiencing VIV in smooth flow conditions. Notably, all identified modes exhibited a damping ratio below the target full-scale value, as reflected in the lower than target Scruton number. The second flexural mode along the weak axis (mode 3) and the first torsional mode (mode 4) entered lock-in conditions, confirming susceptibility to VIV. These findings are aligned with earlier observations from sectional model tests. Additional tests conducted in turbulent flow conditions, representative of the ones measured during the topographic study, revealed a reduction in vortex-induced vibrations across the previously identified lock-in ranges. This demonstrates an improvement in the aerodynamic robustness of the towers under realistic turbulent high winds.

Table 1. Full-scale maximum recorded level of standard deviations due to VIV in smooth flow conditions

	Exp.	Wind speed (m/s)	Scruton (w.r.t. target)	Tower top std value
Mode 3 (2nd weak axis bending)	0°	22.6	0.58	1.07 m/s^2
	0°	46.0		0.64 m/s^2
Mode 4 (1st torsional)	0°	38.0	0.3	0.66 rad/s^2

ACKNOWLEDGEMENTS

Authors gratefully acknowledge the staff at Politecnico di Milano Wind Tunnel who made the experiments possible.

REFERENCES

Belloli, M., Fossati, F., Giappino, S., Muggiasca, S., and Villani, M., 2011. On the aerodynamic and aeroelastic response of a bridge tower. Journal of wind engineering and industrial aerodynamics 99, 729–733.

Castellon, D. F., Fenerci, A., and Øiseth, O., 2022. Environmental contours for wind-resistant bridge design in complex terrain. Journal of Wind Engineering and Industrial Aerodynamics 224, 104943.

Ma, C., Liu, Y., Yeung, N., and Li, Q., 2019. Experimental study of across-wind aerodynamic behavior of a bridge tower. Journal of Bridge Engineering 24, 04018116.

Long-term analysis of the Halsafjorden Bridge accounting for parametric effects of turbulence

Niccolò Barni[a], Ole A. Øiseth[b], Øyvind W. Petersen[b], Claudio Mannini[a]

[a]*CRIACIV/Department of Civil and Environmental Engineering, University of Florence, Via S. Marta 3, 50139 Florence, Italy, niccolo.barni@unifi.it, claudio.mannini@unifi.it*
[b]*Norwegian University of Science and Technology, Trondheim, Norway. ole.oiseth@ntnu.no, oyvind.w.petersen@ntnu.no*

SUMMARY:
This study aims to account for the parametric effects of turbulence on the long-term extreme response of a long-span bridge. Recent contributions by the authors allow most turbulence parametric effects to be incorporated through an equivalent linear system in a frequency-domain approach. A Gaussian Process Regression surrogate model is also used to refine long-term predictions efficiently. The methodology, applied on the Halsafjorden Bridge, highlights the significant impact of turbulence effects on extreme response estimates under varying wind conditions.

Keywords: Long-term extremes, parametric effects, buffeting response

1. INTRODUCTION

Davenport's pioneering work (Davenport, 1961) introduced the gust factor, linking the peak structural response to the mean value under the wind load. This approach has widely been adopted, particularly in building design. However, for highly flexible structures like long-span bridges, the low-frequency nature of the response broadens the probability distribution of response extremes, with tails that can significantly deviate from the mean value. Additionally, variability in environmental conditions significantly influences the structural response. Field measurements (Castellon et al., 2022; Fenerci and Øiseth, 2017) demonstrated that even moderate wind speeds, when combined with high turbulence, can lead to a significant bridge response. Both these effects can be accounted for by studying long-term extremes, a well-known method in offshore structure design (Næss and Moan, 2013).

Variability in turbulence parameters, particularly vertical turbulence intensity, can also influence the parametric effects induced by variations in the angle of attack (Barni et al., 2022; Chen and Kareem, 2003; Diana et al., 2013). These effects alter the self-excited forces, potentially inducing transient low-damped conditions or even phenomena like random flutter (Barni et al., 2024). In long-term analyses, parametric effects of turbulence may strongly influence the average upcrossing frequency, particularly during rare high-turbulence events. However, account for these effects generally requires time-domain approaches, which add substantial computational burden to an already demanding long-term analysis.

This work focuses on incorporating in a simplified and cost-efficient way the parametric effects of

turbulence into long-term extreme response analysis. Furthermore, to address the high computational cost of long-term analyses, a Gaussian Process Regression (GPR) surrogate model is employed, improving several steps of previously proposed algorithms for calculating the long-term extremes (Castellon et al., 2023). The proposed approach is applied to the Halsafjorden Bridge, where results with and without turbulence parametric effects are compared, demonstrating their significant influence on extreme response estimates under various wind conditions.

2. EXTREME RESPONSE

Short-term and long-term approaches are both viable for extreme response calculation; however, while the former assumes predefined design conditions associated with a given return period, only the latter rigorously accounts for the range of wind scenarios a structure may encounter over its lifetime. For short-term extremes, the bridge response $R(t)$ is assumed to be a stationary stochastic process over a brief period T, falling within the wind spectral gap. Under the assumption that upcrossings of high response levels are statistically independent events, the probability that the maximum response does not exceed a threshold r during T can be described by a Poisson distribution (Næss and Moan, 2013):

$$F_{\hat{R}(T)}(r) = \exp\left[-\nu_R^+(r) \cdot T\right] \tag{1}$$

where $\nu_R^+(r)$ is the mean upcrossing rate of the threshold r. For a Gaussian process, $\nu_R^+(r)$ can be expressed as:

$$\nu_R^+(r) = \frac{1}{2\pi}\frac{\sigma_{\dot{R}}}{\sigma_R}\exp\left[-\frac{1}{2}\left(\frac{r-\mu_R}{\sigma_R}\right)^2\right] \tag{2}$$

where μ_R is the mean response, and σ_R and $\sigma_{\dot{R}}$ are the standard deviations of $R(t)$ and its derivative, respectively. According to Davenport, the extreme response for a given return period can be determined by the expected maximum response under a mean wind speed with the same return period.

For long-term extremes, the assumption of stationarity no longer holds as wind conditions vary over time. Assuming stationary response over short-term intervals and ergodic environmental parameters $\mathbf{W}(t)$ (mean wind speed, turbulence intensities, etc.), Næss (1984) derived a relation for the probability of long-term extremes:

$$F_{\hat{R}(T_{LT})}(r) = \exp\left[-T_{LT}\int_{\mathbf{W}} \nu_R^+(r|\mathbf{w}) f_{\mathbf{W}}(\mathbf{w}) d\mathbf{w}\right] \tag{3}$$

where T_{LT} is the long-term period, $\nu_R^+(r|\mathbf{w})$ is the short-term upcrossing rate for a given environmental state $\mathbf{w}$, and $f_{\mathbf{W}}(\mathbf{w})$ is the probability density function of the environmental parameters.

3. AVERAGE PARAMETRIC EFFECTS

Over the past thirty years, models have been developed to capture the impact of turbulence-induced angle-of-attack variations on unsteady self-excited forces (Barni et al., 2022; Chen and Kareem, 2003; Diana et al., 2013). These variations lead to stochastic changes in aerodynamic damping

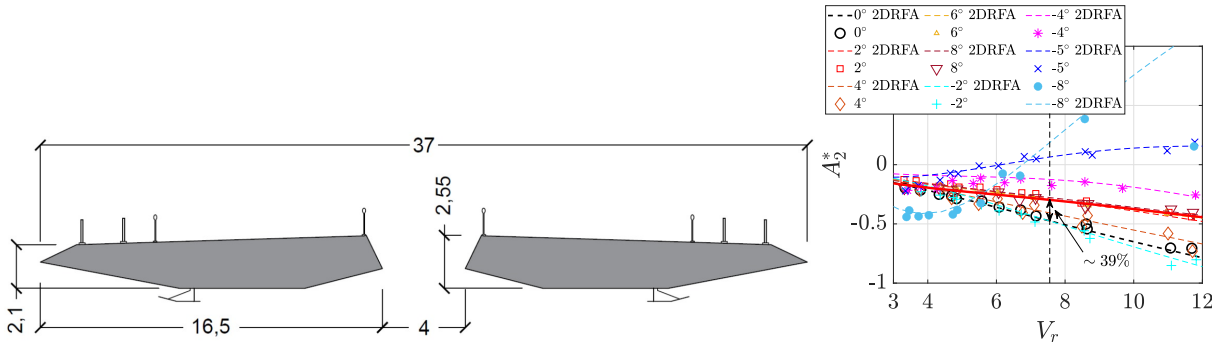


Figure 1. Sketch of the Halsafjorden Bridge deck section with units in meters (left); aerodynamic derivative A_2^* measured in the wind tunnel for various angles of attack (right). The red solid line denotes the average A_2^* for a vertical turbulence intensity of 7.5%.

and stiffness over time. Recent studies (Barni et al., 2024; Barni and Mannini, 2024) demonstrated that turbulence can destabilize structures like the Hardanger Bridge primarily through the so-called "average parametric effect" due to the difference between the average aerodynamic derivatives over a fluctuating angle of attack and the coefficients calculated for the steady mean angle, α_m. This effect depends on the probability density function of the angle of attack, $\alpha(t) = \arctan[w(t)/(V_m + u(t))]$, where u and w are the longitudinal and vertical turbulent velocities, and V_m is the mean wind speed. To account for it in a frequency-domain buffeting calculation, one can consider an average set of aerodynamic derivatives, $\bar{C}$, determined through an ensemble average:

$$\bar{C} = \mathrm{E}[C(\alpha, \alpha_m)] = \int C(\alpha) p(\alpha, \alpha_m)\, d\alpha \tag{4}$$

where $C(\alpha)$ represents the aerodynamic derivatives as functions of α, and $p(\alpha, \alpha_m)$ is the angle of attack probability distribution, which can be expressed in a simplified way as a function of vertical turbulence intensity Barni and Mannini, 2024. For the Halsafjorden Bridge cross section, which shows an aerodynamic derivative A_2^* highly sensitive to angle of attack variations (see Fig. 1), using the average coefficients obtained for a vertical turbulence intensity of 7.5% reduces torsional aerodynamic damping by approximately 39% at 43 m/s (the 100-year return period mean wind speed for a similar bridge site). This average set of aerodynamic derivatives is then used to calculate the upcrossing rate $\nu_R^+(r)$ for different environmental conditions, **W**.

4. PRELIMINARY RESULTS

The Halsafjorden Bridge (Fig. 1), a 2000-m main span structure planned for the Norway's E39 project, serves as the case study for this investigation. The long-term integral in Eq. (3) is calculated based on sequential Gaussian Process Regression modeling (GPR) similarly to a previous work (Castellon et al., 2023). The conference presentation will further detail how the proposed algorithm addresses previous shortcomings in integrating Eq. (3) and selecting the threshold r to train the GPR model. The algorithm's iterations, aimed at identifying the 100-year return period extreme response threshold r, are shown and numbered in Fig. 2

Using the wind probabilistic model developed for the Sulafjorden Bridge (Castellon et al., 2022),

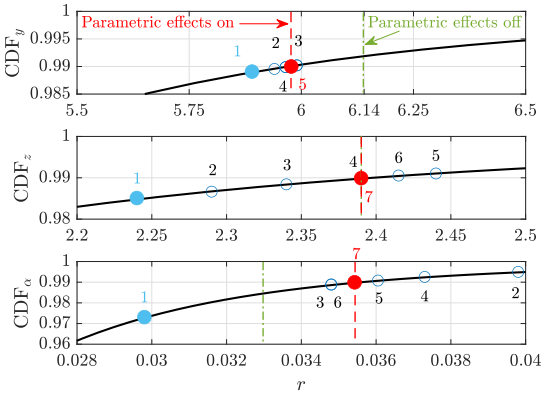


Figure 2. Probability distribution of mid-span lateral, vertical, and torsional extreme bridge response, calculated using a brute-force approach based on a Cartesian grid (thick black line) and the GPR model (circles). The initial trial threshold (point 1) is set to Davenport's extreme response for a 100-year return period mean wind speed.

whose site shows similar conditions, the long-term extreme response of the Halsafjorden Bridge is evaluated considering mean wind speed and vertical turbulence intensity as environmental random variables. Fig. 1 shows that the GPR model predictions (circles) of bridge response probability closely match the converged brute-force long-term calculations based on a Cartesian grid, which serve as a reference. The parametric effect of turbulence slightly stabilizes the lateral response, reducing it by approximately 3%, while it increases the torsional response by about 8%. Overall, in case of two random variables in $\mathbf{W}$, the proposed algorithm reduces the computational time to 1/32 compared to a brute-force Monte Carlo calculation. The results for more environmental random variables and more severe wind conditions will also be discussed.

REFERENCES

Barni, N., Bartoli, G., and Mannini, C., 2024. Lyapunov stability of suspension bridges in turbulent flow. Nonlinear Dynamics 112, 16711–16732.

Barni, N. and Mannini, C., 2024. Parametric effects of turbulence on the flutter stability of suspension bridges. Journal of Wind Engineering and Industrial Aerodynamics 245, 105615.

Barni, N., Øiseth, O. A., and Mannini, C., 2022. Buffeting response of a suspension bridge based on the 2D rational function approximation model for self-excited forces. Engineering Structures 261, 114267.

Castellon, D. F., Fenerci, A., and Øiseth, O. A., 2022. Environmental contours for wind-resistant bridge design in complex terrain. Journal of Wind Engineering and Industrial Aerodynamics 224, 104943.

Castellon, D. F., Fenerci, A., Petersen, Ø. W., and Øiseth, O. A., 2023. Full long-term buffeting analysis of suspension bridges using Gaussian process surrogate modelling and importance sampling Monte Carlo simulations. Reliability Engineering & System Safety 235, 109211.

Chen, X. and Kareem, A., 2003. Aeroelastic analysis of bridges: effects of turbulence and aerodynamic nonlinearities. Journal of Engineering Mechanics 129, 885–895.

Davenport, A. G., 1961. The application of statistical concepts to the wind loading of structures. Proceedings of the Institution of Civil Engineers 19, 449–472.

Diana, G., Fiammenghi, G., Belloli, M., and Rocchi, D., 2013. Wind tunnel tests and numerical approach for long span bridges: The Messina bridge. Journal of Wind Engineering and Industrial Aerodynamics 122, 38–49.

Fenerci, A. and Øiseth, O. A., 2017. The Hardanger Bridge monitoring project: Long-term monitoring results and implications on bridge design. Procedia engineering 199, 3115–3120.

Næss, A., 1984. On the long-term statistics of extremes. Applied Ocean Research 6, 227–228.

Næss, A. and Moan, T., 2013. Stochastic Dynamics of Marine Structures. Cambridge University Press.

Modelling of nonlinear aerodynamic self-excited forces on bridge decks – Going forward

Henrik Skyvulstad [1,2], Øyvind Wiig Petersen[2], Ole Øiseth [2]

[1]*Norconsult AS, Sandvika, Norway, Henrik.skyvulstad@ntnu.no*
[2]*Department of Structural Engineering, Norwegian University of Science and Technology, Trondheim, Norway*

SUMMARY:
In this work we are presenting major finding of the PhD-thesis conducted by Henrik Skyvulstad at NTNU. The thesis identifies experimental nonlinear self-excited forces, makes model predictions of the experimental self-excited forces and uses the trained models is response predictions for dynamic systems. The goal of this work is to draw conclusions going forward in the realm of nonlinear self-excited forces, without going into the details on the method and results.

Keywords: Nonlinear aerodynamics, Volterra models, bridge aerodynamics, flutter

1. INTRODUCTION

Exploring aerodynamic nonlinearities has been a hot topic in the research community in the last 10-years. The introduction of multi-deck sections has further spiked discussion of the validity of the linearity in the load models used for bridge aerodynamic design (Skyvulstad et al., 2021a).

This paper presents the PhD-thesis of Henrik Skyvulstad. The thesis is called "Nonlinear modelling of self-excited forces on bridge decks"(Skyvulstad, 2024). The thesis has 3 main parts:

i. Wind tunnel testing: Wind tunnel testing of single- and double cross-section. The aim of this part was to investigate nonlinearities in the self-excited force data and find methods for identifying nonlinearities in the experimental data.
ii. Nonlinear modelling: The experimental data is used a basis for training nonlinear self-excited force models. The nonlinear models used is based on the Volterra-model description, and the Volterra-model description has been further developed to overcome weaknesses of the model description
iii. Response prediction: The Volterra-model descriptions has been used to predict experimental results of a nonlinear flutter phenomena.

The concluding work gives recommendation from the experience gained during the project. What should one search for when one suspect nonlinear behaviour in the cross-section? What load-models should be explored when trying to model nonlinear self-excited forces? How can one use these nonlinear load models? And is it important to use these load models? Will nonlinear self-excited forces affect the bridge design in the future?

2. OBJECTIVE 1: EXPERIMENTAL INVESTIGATION

Several wind-tunnel campaigns, with the forced vibration rig has been conducted at NTNU. Single and double cross-sections have been tested with different types of motion. Typical motions used is quasi-static

motion, single harmonic motion, biharmonic motions, harmonic sweeps, amplitude sweeps, time-series realization of various types of spectrums. Figure 1 shows a picture from the wind tunnel.



Figure 1: Picture of a section model in the wind tunnel at NTNU

3. OBJECTIVE 2: NONLINEAR MODELLING

The objective this objective is to find suitable mathematical models to predict nonlinear self-excited data. Data-driven identification of the models is employed, and both synthetic and experimental data is used. The nonlinear model is trying to model the transfer-function between the input(motions) and outputs(force). This relation is shown in Figure 2.

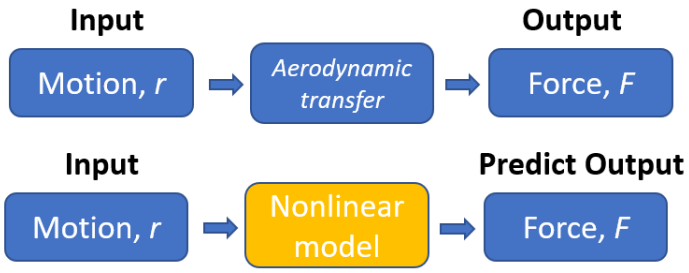


Figure 2: Data driven identification. The yellow box indicates the nonlinear load model to be identified

Laguerrian expansion basis

The nonlinear models used in the thesis is based on the Volterra series models. A single-input-single-output p^{th}-order Volterra model with memory M can be given as follows (Westwick, Kearney, 2003):

$$F[n] = h_0 + \sum_{k=0}^{M} h_1[k] r[n-k] + \sum_{k_1}^{M} \dots \sum_{k_p}^{M} h_p[k_1, \dots, k_p] r[n-k_1] \dots r[n-k_p] \quad (1)$$

Where h_p represents the p^{th}-order unknown Volterra kernels to be determined. The kernels to be identified will typically have a lot of unknowns further leading to large computational effort needed in the identification. A parameterization of the kernel with a Laguarrian filter basis is therefore introduced (Skyvulstad et al., 2021b):

$$h_1[k] = \sum_{l=0}^{J} c_l g_l[k] \quad (2)$$

$$h_P[k_1,\dots,k_p] = \sum_{l_1=0}^{J} \dots \sum_{l_p=0}^{J} c_{l_1\dots l_p}\left(g_{l_1}[k_1]\dots g_{l_p}[k_p]\right), \quad p>1 \tag{3}$$

$$g_l[k] = \alpha^{(k-l)/2}(1-\alpha)^{(1/2)} \sum_{i=0}^{l} (-1)^i \binom{k}{i}\binom{l}{i} \alpha^{l-i}(1-\alpha)^i, \quad k \geq 0 \tag{4}$$

Where c denotes the unknown filter coefficients, l denotes the filter number and $0<\alpha<1$ denotes the decay factor, also to de determined.

Regularization of the Volterra identification

A drawback of the full Volterra model description is that the model is prone to overfitting. A regularization of the identification is introduced to make the identified models more robust. Identification of the full model Volterra description can be conducted with a least-squares identification (Skyvulstad et al., 2021c):

$$\min\left(\left\|\mathbf{F}-\mathbf{rH}\right\|_2^2\right) \tag{5}$$

Regularization is introduced in the least-squares identification:

$$\min\left(\left\|\mathbf{F}-\mathbf{rH}\right\|_2^2 + \lambda^2\left\|\mathbf{LH}\right\|_2^2\right) \tag{6}$$

Where the L-Matrix is the regularization matrix, that can be modified dependent on the regularization goal. The λ is the regularization constant that decides the weighting of the regularization. The optimal choice of λ finds a sweet spot between experimental noise suppression and training accuracy. The L-curve criterion has been employed to find the value of the regularization constant, λ.

4. OBJECTIVE 3: NONLINEAR RESPONSE PREDICTION

There is no use in having a trained nonlinear self-excited force model without being able to use it in response prediction of dynamic systems. The recursive relation of the Laguerrian basis type Volterra model can be leveraged to transform the dynamic system into a state-space formulation. For the 1st-order Laguerrian model, the state-space model is also linear, as expected. For higher order models a Wiener type of nonlinearity unfolds, meaning that one can solve the linear states then transfer the linear states through a nonlinear filter providing the nonlinear self-excited forces, as shown on Figure 3.

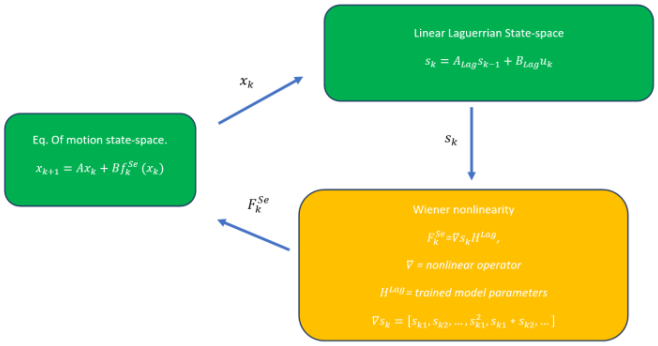


Figure 3: Scheme for the response prediction of nonlinear self-excited forces in a state-space formulation (Skyvulstad, 2024)

5. CONCLUSIONS, FURTHER WORK AND GUIDELINES

The final and most important part of this work will be the guidelines, conclusions and further work:

Wind tunnel testing – Its observed that the twin deck type of cross-sections tends to trigger self-excited forces that are more nonlinear than single streamlined deck solution. It is recommended to specifically check for nonlinearities when designing bridges with twin decks. It is also recommended to avoid cross-sections that experience strong nonlinearities, due to the high uncertainty and complexity. Static tests and single harmonic motions will provide good experimental basis for assessing nonlinearities. A systematic approach in finding, evaluating and drawing conclusions for the nonlinearities present for twin decks should be done in the future. Hopefully, the most common nonlinearities seen can be generalized for understanding and modelling.

Nonlinear self-excited force models – There exists several suggested nonlinear models. The models vary in complexity, need for training data and the generality in possible phenomena they can model. In the authors opinion, a model that clearly outperforms the others is still not found. The research community should push for making the models available for the bridge designers, as available toolboxes, with appended training data.

Response prediction – Response prediction of nonlinear self-excited force models vary both in accuracy and the phenomena modelled. We believe that benchmarking should be conducted to assess the model capabilities, both for modelling the self-excited forces and the response prediction.

Widening the scope – We believe that further work should be placed into generalizing the models, including other effects as nonstationary and turbulence. Hopefully one can find a model or combination of model that outshines the others in accuracy and user friendliness.

ACKNOWLEDGEMENTS

The research presented in this paper was financed by Norconsult AS, The Norwegian Public Roads Administration (NPRA), and The Research Council of Norway grant nr. 263483.

REFERENCES

Skyvulstad, H., Argentini, T., Zasso, A., Øiseth, O.: Nonlinear modelling of aerodynamic self-excited forces: an experimental study. J. Wind Eng. Ind. Aerodyn. 209 (2021).

Skyvulstad, H., Petersen, Ø.W., Argentini, T., Zasso, A.,Øiseth, O.: The use of a Laguerrian expansion basis as Volterra kernels for the efficient modelling of nonlinear self-excited forces on bridge decks. J. Wind Eng. Ind. Aerodyn. 219 (2021).

Skyvulstad, H., Petersen, Ø.W., Argentini, T., Zasso, A.,Øiseth, O.: Regularised Volterra series models for modelling of nonlinear self-excited forces on bridge decks. Nonlinear Dyn 2023;111:12699-12731.

Skyvulstad, H., Petersen, Ø.W., Argentini, T., Zasso, A.,Øiseth, O.: Modelling of nonlinear torsional flutter using Volterra models trained on experimental data. The 16th International Conference on Wind Engineering (ICWE 16), Florence, Italy, 2023.

Skyvulstad, H.: Modelling of nonlinear aerodynamic self-excited forces on bridge decks. Thesis for Degree of Philosophiae Doctor, Trondheim 2024

Westwick, D., Kearney, R., 2003. Identification of Nonlinear physiological systems.

Sensitivity analysis of numerical modelling approaches for curved floating bridge buffeting response

Zihao Wang [1], Jasna Bogunović Jakobsen [2], Yanyan Sha [3]

[1] *University of Stavanger, Stavanger, Norway, zihao.wang@uis.no*
[2] *University of Stavanger, Stavanger, Norway, jasna.b.jakobsen@uis.no*
[3] *University of Stavanger, Stavanger, Norway, yanyan.sha@uis.no*

SUMMARY: (10 pt)
Floating bridges provide a feasible and economical solution for spanning vast and deep waterways. Wind-induced response analysis of such structures has received considerable attention in recent years. This study numerically investigates the buffeting response of a 5.5 km curved floating bridge with a supplementary side-mooring system, where skew wind effects are relevant. The effects of various numerical modelling approaches and parameters on the bridge response are evaluated. Results show that the vertical and rotational responses, which are primarily due to vertical turbulence, are more sensitive to the choice of wind velocity interpolation schemes than the selection of wind field generation tools, such as *TurbSim* and *WindSim4D*. Regarding the wind load modelling in the presence of skew winds, the simplified cosine rule and the 2D (+1D) load formulations tend to underestimate the vertical response compared to the 3D model. Wind evolution in the along-wind direction and the modelling of the *uw* co-spectrum have marginal effects on the bridge response. The effect of the translational and rotational self-excited forces on reducing the overall response at the design wind speed is notable for the cable-stayed section of the bridge but limited for the floating bridge part due to the involved hydrodynamic damping.

Keywords: curved floating bridges, skew wind, unfrozen turbulence

1. INTRODUCTION

Recent bridge failures underscore the importance of thorough studies on the aerodynamic forces acting on floating bridges due to wind-bridge interactions (Zhang et al., 2022). Costa et al. (2022) developed a three-dimensional (3D) buffeting load formulation for curved floating bridges, based on the load model proposed by Zhu et al. (2002). When dealing with curved bridges with large separations, the eddies not only undergo a phase difference but also lose correlation along the streamwise direction. This study provides a framework for systematic analysis of floating bridges, incorporating skew winds, 3D buffeting load formulation, and relevant hydrodynamic effects. The impact of wind evolution, the contributions of different aerodynamic coefficients, and the effects of self-excited forces are also analysed.

2. CASE STUDY BRIDGE AND NUMERICAL MODELS

The Norwegian Public Roads Administration plans to construct an end-anchored floating bridge with a side-mooring system across the Bjørnafjord. A finite element model of this floating bridge was developed in *OrcaFlex*, as presented in a preliminary study (Wang et al., 2023). Figure 1 provides an overview of the main structural components. The model includes rigid vessel objects

for the pontoons, and deformable line elements for the bridge girder, stay cables, piers, pylon, columns, and mooring lines.

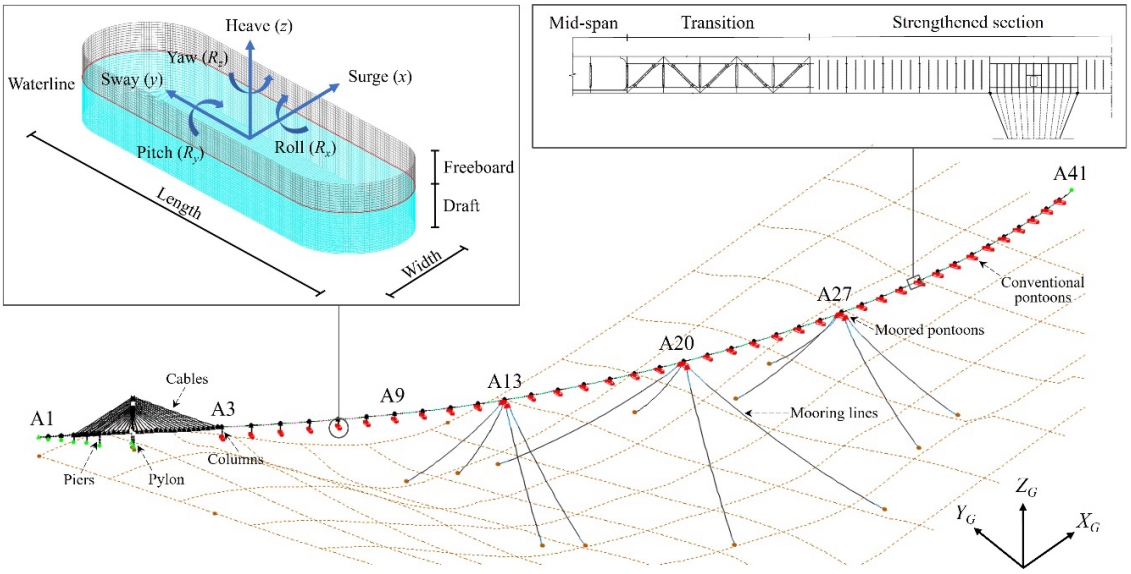


Figure 1. Finite element model of the floating bridge and panel model of the pontoons

3. SIMULATION OF TURBULENT WIND FIELD

TurbSim generates wind vectors on a fixed two-dimensional vertical grid, as illustrated in Figure 2. The rectangular grid in *TurbSim*, commonly applied in wind energy applications, includes many redundant points that do not correspond directly to structural nodes. On the other hand, a *MATLAB*-based algorithm *WindSim4D*, originally developed for bridge applications by Cheynet et al. (2022), is much more computationally efficient, which generates wind component time series directly at the structural nodes using an irregular grid tailored to the bridge's static equilibrium position under gravity and buoyancy.

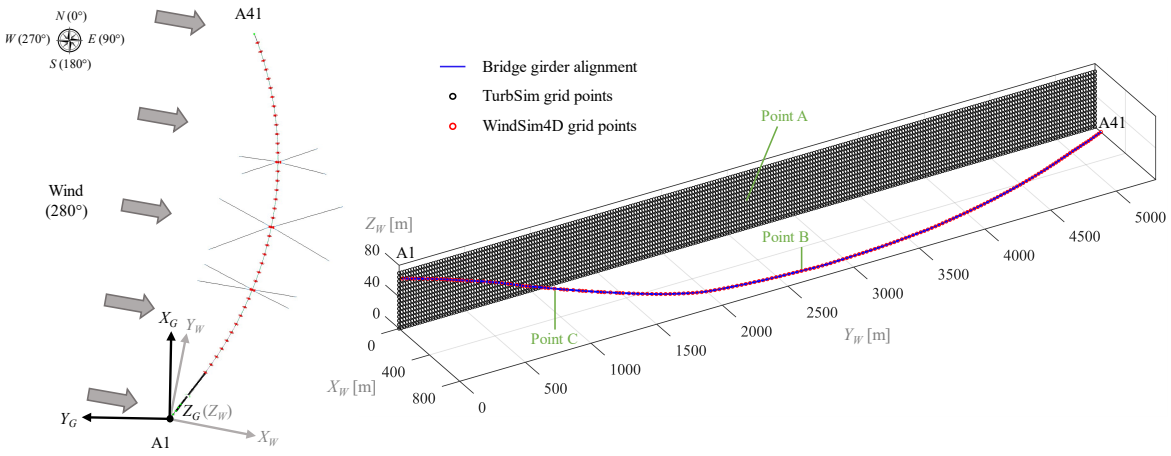
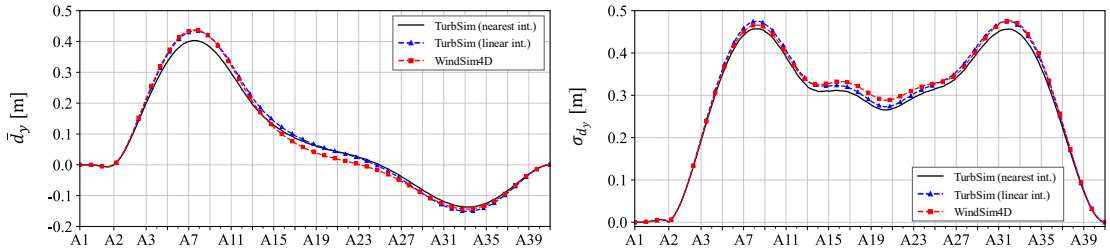


Figure 2. Comparison of the two-dimensional vertical grid in *TurbSim* and the irregular grid used in *WindSim4D*

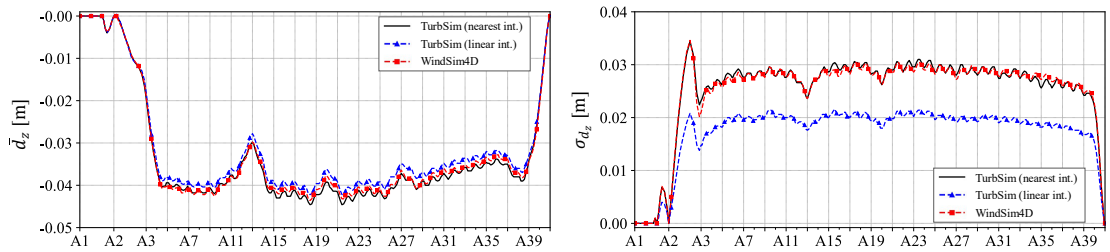
4. BUFFETING RESPONSE OF THE FLOATING BRIDGE

Time-domain simulations were conducted to investigate the sensitivity of aerodynamic response of the studied floating bridge to the selection of wind field generators and interpolation schemes. Figure 3 displays the mean values and standard deviations of horizontal displacement d_y, vertical displacement d_z, and rotational displacement about the longitudinal bridge axis d_{rx}. The standard deviation of the vertical displacement σ_{d_z} is nearly 30 % lower in the *TurbSim* results with linear velocity interpolation for most part of the bridge span, while the *TurbSim* with nearest-neighbour approximation is in good agreement with the *WindSim4D* results.

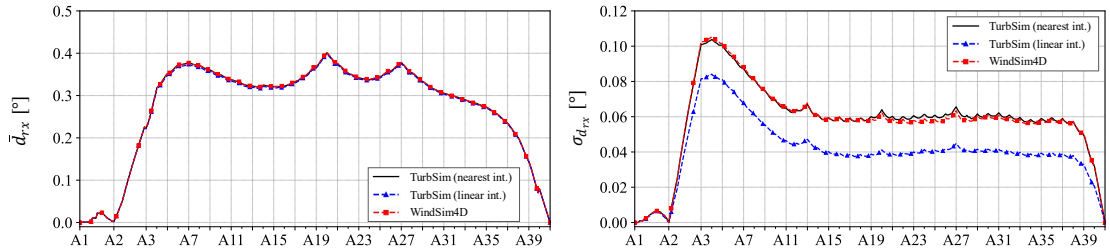
Figure 4 (left) shows the target auto-spectra together with the spectra of turbulence generated in one of the regularly spaced *TurbSim* grid points, adopted as the nearest neighbour of a structural node, for the wind load calculation. As opposed to the good agreement between the two, the right-hand part of the figure demonstrates a smoothing effect of turbulence interpolation between the grid points data. The spectral values are reduced at higher frequencies for the *u*-component and across all frequencies for the *v*- and *w*-components, with an underestimation of wind loads on the bridge structure as a result.



(a) Horizontal displacement



(b) Vertical displacement



(c) Rotational displacement

Figure 3. Displacement response of the bridge girder subjected to wind fields generated by *TurbSim* and *WindSim4D* (left column: the mean values; right column: the standard deviations). Nearest-neighbour and linear interpolation schemes were used for *TurbSim* to approximate the wind velocities at the structural nodes. $\bar{U}_{mid}$ = 29.8 m/s at z_{mid} = 35.0 m, with I_u = 0.140, I_v = 0.112, and I_w = 0.070

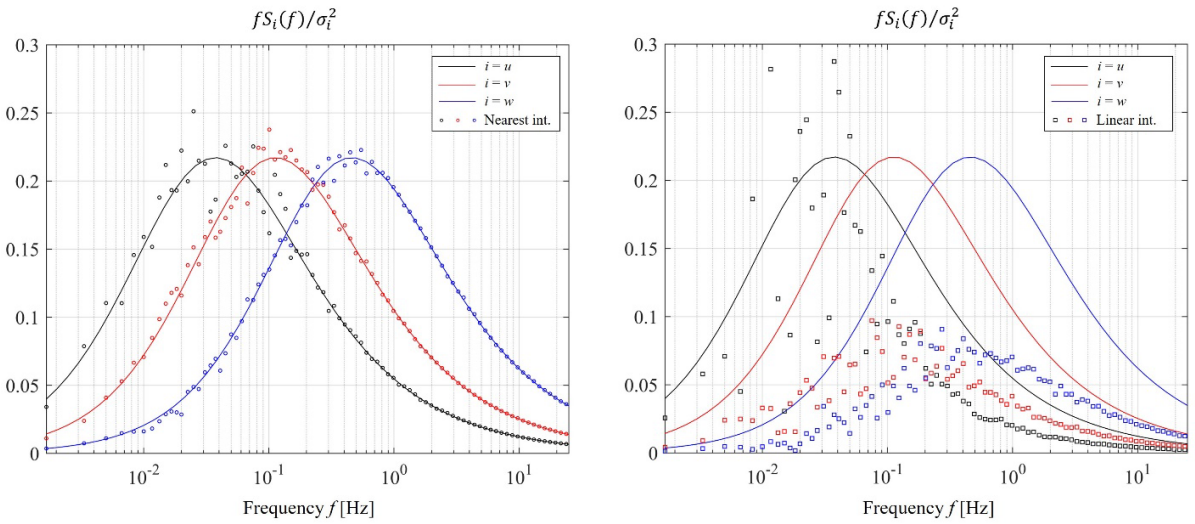


Figure 4. Comparison of target and computed normalized turbulence auto-spectra at a structural node following the nearest-neighbour approximation (left panel) and linear interpolation (right panel) of wind velocities generated by *TurbSim* on a regular 2D grid

Further details regarding different aerodynamic load formulations, the comparative effects of frozen versus unfrozen turbulence, the contributions of aerodynamic coefficients to the bridge's response, and the influence of quasi-steady self-excited will be provided in the full-length paper.

5. CONCLUSIONS

Sensitivity analyses of the buffeting response of a curved floating bridge supported by discrete pontoons and side mooring lines were conducted. Time-domain simulations were performed using *Python* external functions in *OrcaFlex*, applying quasi-steady buffeting theory to account for wind loads. Several key aspects were investigated, including the choice of wind field generators, wind velocity interpolation schemes within a simulation grid, aerodynamic load formulations, wind evolution effects, contributions from different aerodynamic coefficients, and the influence of self-excited forces. In the case of *TurbSim,* the linear interpolation of the grid turbulence has the effect of a low-pass filter and reduces the standard deviations of wind velocities applied to the bridge nodes, leading to decreased aerodynamic loads. Therefore, when utilizing turbulence data simulated in a regular grid, the nearest-neighbour approximation of turbulence in structural nodes should be adopted for response analysis of a curved floating bridge.

REFERENCES

Cheynet, E., Daniotti, N., Jakobsen, J. B., Snæbjörnsson, J., and Wang, J., 2022. Unfrozen skewed turbulence for wind loading on structures. Applied Sciences 12(19), 9537.

Costa, B. M. D., Wang, J., Jakobsen, J. B., Øiseth, O. A., and Snæbjörnsson, J., 2022. Bridge buffeting by skew winds: A revised theory. Journal of Wind Engineering and Industrial Aerodynamics 220, 104806.

Zhang, G., Liu, Y., Liu, J., Lan, S., and Yang, J., 2022. Causes and statistical characteristics of bridge failures: A review. Journal of Traffic and Transportation Engineering 9(3), 388–406.

Zhu, L. D., Xu, Y. L., Zhang, F., and Xiang, H. F., 2002. Tsing Ma bridge deck under skew winds - Part I: Aerodynamic coefficients. Journal of Wind Engineering and Industrial Aerodynamics 90(7), 781–805.

A wind tunnel-based approach for evaluating wind loads simultaneity in photovoltaic plant design

Giorgio Frontini[1*], Stefano Giappino[1], Sara Muggiasca[1]

[1]*Department of Mechanical Engineering, Politecnico di Milano, Milan, Italy*
[*]*giorgio.frontini@polimi.it*

SUMMARY:
In current design practice, the structural evaluation of photovoltaic plants is performed by means of equivalent static wind loading approaches. Among the methods proposed in literature, the dynamic amplification factor (DAF) approach provides a tool for computing the two main wind-induced contributions acting on photovoltaic panel systems: the sectional normal force and moment. While the computation of individual design values is well documented, guidelines for combining these two quantities remain scarce. This aspect may lead designer to combine both components without reductions, potentially resulting in inefficient design strategies, as the two acting loads are not necessarily correlated. The presented article proposes an approach that can provide insights on the expected simultaneity between these load contributions. The advantage of the proposed method is its straightforward application in wind tunnel campaigns, utilizing existing experimental measurements of pressure distributions on a rigid model of the photovoltaic plant. The work will present the methodology applied to the computation of the simultaneity between static coefficients for a simple example case.

Keywords: Wind tunnel, Photovoltaic plants, Equivalent static wind loads

1. INTRODUCTION

In the design stage, the structural assessment is typically performed by means of equivalent static wind loads (Chen and Kareem, 2001; Holmes, 1988) and, more specifically, the acting forces and moment are derived directly by the coefficients computed through the dynamic amplification factors (DAF) method (Browne et al., 2020; Kopp et al., 2012). Focusing on the static coefficients for photovoltaic plants, to account for the most unfavorable loading condition, designers can identify up to four equivalent loads: maximum and minimum for both force and moment contributions. In addition, considering also the combinations of the two terms, if all possible permutations are accounted, the number increases by eight. This scenario, in which loads are combined without reductions, represents the worst-case condition and assumes that all extreme peak events occur simultaneously.

Force and moment however are not necessarily correlated, and some reduction in their combination can lead to a less stringent design verification. The method proposed in this research takes as inputs the force and moment coefficients, processed from wind tunnel pressure measurements, and by accounting for their simultaneity, it aims to evaluate a set of reduction factors.

2. EXPERIMENTAL ACQUISITIONS

The core of the presented activity is based on wind tunnel experimental campaigns carried out on rigid models of photovoltaic plants. The reference dataset has been acquired during experimental investigations carried out in *Politecnico di Milano* wind tunnel. The facility's atmospheric boundary layer test section -measuring $14m$ in width, $4m$ in height, and $35m$ in length- was employed to accurately reproduce the wind speed and turbulence profiles of a typical installation site. Regarding the wind tunnel model, the research is developed on a case study involving one degree of freedom solar trackers, modeled at a 1:15 scale; though the procedure can be extended to fixed-tilt systems. The model represents the corner region of a photovoltaic plant arranged in a rectangular grid, and consists of four rows with a ground cover ratio of 60%, with each row extending $90m$ full-scale. Pressure taps are installed on the model's surfaces to measure the wind pressure distribution: four acquisition points per side are installed at evenly spaced cross-sections to ensure a sufficient resolution of the acting net pressure. The collected data is integrated to obtain a normal force acting on the panel surface and a torsional moment about the tracker's longitudinal axis -both expressed as normalized coefficients. For the presented case, an integration length equal to the width of a single panel along the tracker axis has been assumed.

3. SIMULTANEITY ESTIMATION

This section presents the methodology for assessing the simultaneity coefficients, focusing on peak static components. The force and moment coefficient time histories from experimental tests are processed. In particular, since the distribution fitting the underlying signal peak population will be referenced later, it is noteworthy to remark that the Gumbel's method has been employed to estimate the design peak values. Specifically, the mean value of the distribution (43% risk of exceedance) is used in this study. This statistical procedure yields four set of static coefficients, related to the positive and minimum peak value of the force ($\hat{C}_n$ and $\check{C}_n$) and moment ($\hat{C}_m$ and $\check{C}_m$). Given that only two load components are computed for solar trackers, the dataset can be visualized in a $2D$ plane. For any instrumented model cross-sections, the C_n and C_m signals can be used to produce a scatter plot where each point $\{C_n(\bar{t});C_m(\bar{t})\}$ represents the load coefficients observed at a given time $\bar{t}$. As a reference case, Figure 1a) and b) show the time histories of the two acting components $C_m(t)$ and $C_n(t)$ respectively, while Figure 1c) shows the associated scatter plot.

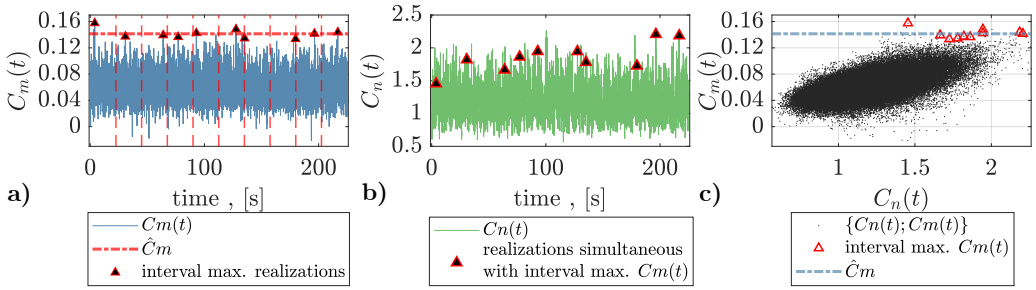


Figure 1. C_n and C_m signals, with the associated scatter plot. Pitch angle 60° nose-down, exposure 30°, leading row. **a)** moment coefficient, **b)** force coefficient, **c)** scatter plot.

In the following, the process for estimating the two design values for $C_n(t)$ (positive and negative), that are expected to occur simultaneously with the realization of the design peak moment $\hat{C}_m$, is presented. In this context, the coefficient assumed equal to the design peak ($\hat{C}_m$) is referred to as

the *primary coefficient*, while the simultaneous term is identified as the *secondary coefficient* and adopts the notation $C^{+}_{n|\hat{C}_m}$ and $C^{-}_{n|\hat{C}_m}$, reminiscing of the concept of conditional probability. Figure 1a) illustrates the implementation of the Gumbel's method for estimating the positive moment peak coefficient $\hat{C}_m$. The time history has been divided into ten intervals and, in each one, the extreme peak to occur has been marked; the horizontal line denotes the expected peak value. Figure 1b) shows, on top of the force time history, the ten measurements recorded simultaneously with the recorded C_m peaks: each instantaneous pair $\{C_n; C_m\}$ is then reported in Figure 1c). As can be observed, the force occurring simultaneously with the maximum moment peak does not fully represent the actual force peak.

Taking as a reference the same time histories depicted in Figure 1, the proposed method identifies a threshold value $C_{m,\text{threshold}}$ for the primary component $C_m(t)$. This value has been arbitrarily set to correspond to a 95% probability of exceedance in the Gumbel probability density function fitting the ten peak realizations, and represents a level above which a signal reading can be considered a relevant peak. Figure 2a) depicts the recorded instances in which the threshold was exceeded, while Figure 2b) reports the force coefficients observed at the time instants in which $C_m(t) > C_{m,\text{threshold}}$. In each of the 10 sub-intervals, the maximum and minimum values of the filtered dataset are marked. These extreme values are also shown also in Figure 2c) providing a clearer plot. Since the mean value was selected as the reference parameter for the design primary component, the design secondary component coefficients $C^{+}_{n|\hat{C}_m}$ and $C^{-}_{n|\hat{C}_m}$ are also inferred by computing the mean value: the results are shown in Figure 2c) with the two horizontal lines.

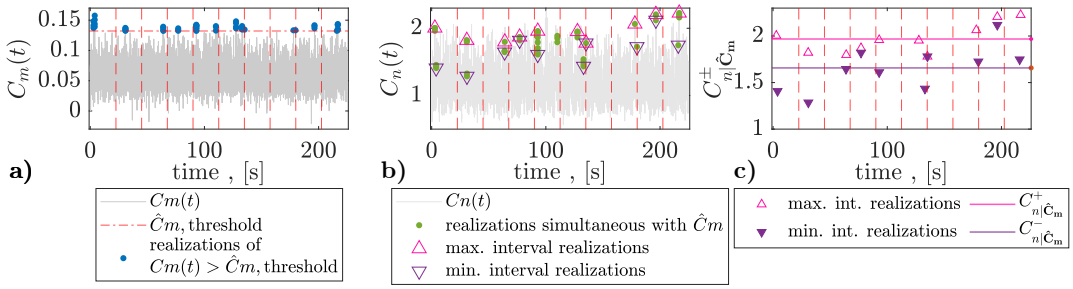


Figure 2. Secondary coefficients identification. **a)** Primary components exceeding the minimum peak threshold. **b)** Secondary components concurrent with the primary peak events. **c)** Secondary coefficients estimation.

Repeating the procedure to compute the pair of secondary coefficients associated with the other three primary components ($\hat{C}_n$, $\check{C}_n$ and $\check{C}_m$), a total of eight combinations are obtained. These values can be used on the $C_n - C_m$ plane to define the vertices of an octagonal shape that bounds the acquisition scatter plot, as depicted in Figure 3a). The *simultaneity combination factors* are then introduced by normalizing the secondary coefficients with respect to the value that the same force or moment component would have when it is a primary component: relationship (1) shows, as an example, the normalization for the previously demonstrated case.

$$\begin{cases} SCF^{\pm}_{n|\hat{C}_m} = +(C^{\pm}_{n|\hat{C}_m}/\hat{C}_n) & \text{for} \quad C^{\pm}_{n|\hat{C}_m} > 0 \\ SCF^{\pm}_{n|\hat{C}_m} = -(C^{\pm}_{n|\hat{C}_m}/\check{C}_n) & \text{for} \quad C^{\pm}_{n|\hat{C}_m} < 0 \end{cases} \tag{1}$$

The resulting normalized coefficients define combination factors that can be used in structural

design. Similar to Figure 3a), the normalized dataset can be conceptually represented in a $2D$ plane to define an octagonal region as depicted in Figure 3b): in this plot, the coordinates of the vertices correspond to the combination factors for the two components C_n and C_m.

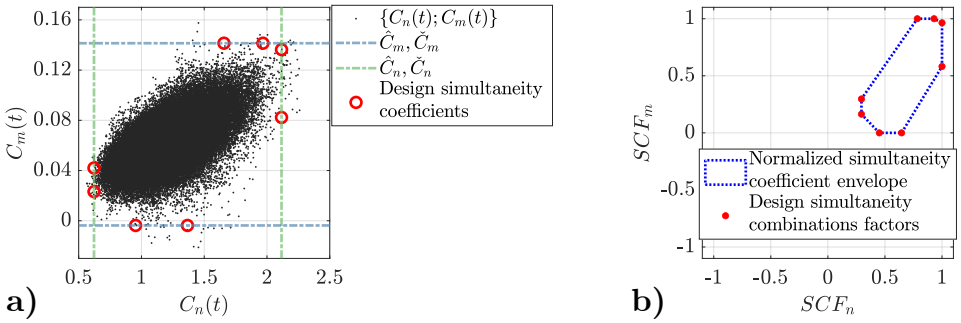


Figure 3. Representation of the simultaneity for a single acquisition case: **a)** as an envelope of the acquisition dataset, **b)** as a $2D$ graphical representation of the simultaneity combination factors.

4. EXTENSION TO ENVELOPED DATA

Since in current practice the resulting data is typically provided as enveloped dataset to summarize critical wind condition, the proposed method has to be extended to multiple time histories. The complete procedure will be discussed in the full paper of the work, presenting the developed methodology and highlighting how the enveloping for multiple exposure angles and acquisition points is performed by leveraging the threshold value introduced in previous section.

5. CONCLUSIONS

The presented procedure demonstrates the application of a method to compute the coefficients simultaneous to the typical four primary components ($\hat{C}_n$, $\check{C}_n$, $\hat{C}_m$ and $\check{C}_m$) commonly used in the design of solar tracker systems. By analyzing the time-domain signals, a threshold value is identified using the Gumbel extreme peak distribution: this limit provides a reference that can be used to identify the time instants in which signal readings can be considered relevant peaks. The assessment of the secondary coefficients is then performed by analyzing the largest occurrences simultaneous to the primary peak events. The eight points obtained by considering all possible permutations are used to bound the scatter plot, providing a valuable tool for quick dataset comparisons. Moreover, the same set of coefficients, when normalized with respect to their design value, are also used to provide simultaneity combination factors: this information is essential for performing analyses that more accurately represent the observed physical phenomenon.

REFERENCES

Browne, M. T., Taylor, Z. J., Li, S., and Gamble, S., Oct. 2020. A wind load design method for ground-mounted multi-row solar arrays based on a compilation of wind tunnel experiments. en. Journal of Wind Engineering and Industrial Aerodynamics 205, 104294.

Chen, X. and Kareem, A., 2001. Equivalent static wind loads for buffeting response of bridges. Journal of Structural Engineering 127, 1467–1475.

Holmes, J., 1988. Distribution of peak wind loads on a low-rise building. Journal of Wind Engineering and Industrial Aerodynamics 29, 59–67.

Kopp, G., Farquhar, S., and Morrison, M., 2012. Aerodynamic mechanisms for wind loads on tilted, roof-mounted, solar arrays. Journal of Wind Engineering and Industrial Aerodynamics 111, 40–52.

Aeroelastic Response of a Large Suspension Roof: Wind Tunnel Tests and Numerical Simulations

Tommaso Argentini[1], Filippo Calamelli[1], Umberto Spinelli[2], Lorenzo Rosa[2], Alberto Zasso[1]

[1]*Politecnico di Milano, Department of Mechanical Engineering, Milano, Italy,*
tommaso.argentini@polimi.it
[2]*Politecnico di Milano, Wind Tunnel Lab, Milano, Italy*

SUMMARY:
This study examines the aeroelastic behavior of "The Wave," a lightweight, suspended canopy structure spanning 120 meters between two buildings in Milan. Given its unique geometry, lightweight construction, and exposure to the wind-altering influence of nearby skyscrapers, predicting the canopy's dynamic response to wind is challenging. To address this, researchers conducted a three-step analysis involving wind tunnel tests on a rigid scale model, numerical simulations of the canopy's dynamic response, and aeroelastic testing on a 1:70 scale model. The rigid model tests provided pressure data, while the numerical simulations helped assess vibration sensitivity and static wind loads. Aeroelastic tests confirmed the canopy's susceptibility to resonant effects, setting an optimal damping ratio near 10%. These tests also validated the structure's stability up to 1.2 times the design wind speed, with a return period of 1,000 years. Findings demonstrate the critical role of aeroelastic testing and simulation in ensuring stability for large-scale, lightweight structures, with implications for similar future designs.

Keywords: Aeroelastic response, Wind tunnel testing, long-span roof

1. BACKGROUND AND OBJECTIVE

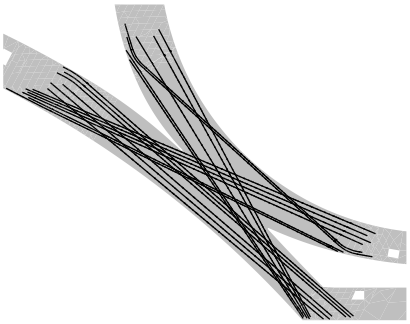
The structure examined in this study, named "The Wave," consists of two buildings, one 110 meters and the other 50 meters in height, connected by a 120-meter-long canopy (Figure 1-a), currently under construction. The canopy is a lightweight wooden suspension roof with a bent "X" shape, supported by a complex network of tensioned cables (Figure 1-b), each composed of a set of parallel cables. Atop the wooden layer, the roof will host the largest photovoltaic park in Milan. The total thickness of the canopy will be approximately 1 m, with an average mass of 250 $\mathrm{kg/m^2}$.

A series of 102 circular extendable tubes hang down from the roof with dual purposes: 38 are designed for water drainage, while 64 house dampers that enhance structural damping, mitigating the canopy's dynamic susceptibility to wind forces. The building is situated in a residential and commercial area, surrounded by three skyscrapers (Figure 1-a) that significantly affect local wind flow and the wind pressure distribution across the canopy.

Due to the unique characteristics of this structure (lightweight with a large and unusual geometry) and the complex surroundings, predicting the aeroelastic response is not trivial (e.g. Chen et al., 2012). Therefore, a wind tunnel study was conducted at Politecnico di Milano.

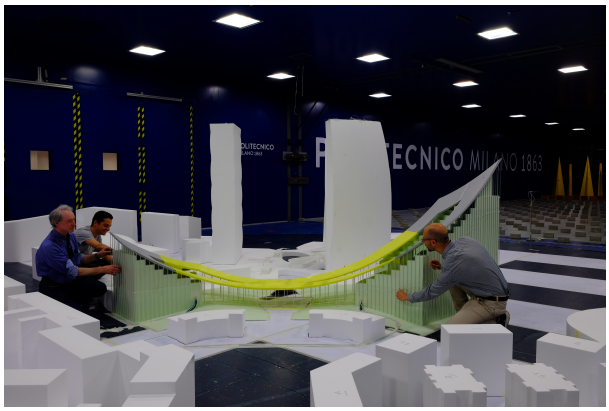


(a)

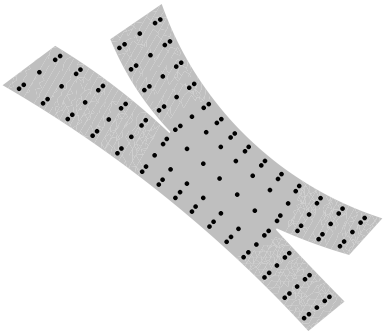


(b)

Figure 1. a) Render of "The Wave" **b)** Top view of the suspension roof with the "X" shape, with the complex network of tensioned cables (in black)



(a)



(b)

Figure 2. a) The rigid model in the wind tunnel **b)** Top view of the roof with location of the 130 net pressure measurement points

2. METHODOLOGY

The investigation was divided into three main steps: pressure measurements on a rigid scale model, numerical assessment of the dynamic response via finite element (FE) simulations, and dynamic response assessment using an aeroelastic scale model.

2.1. Wind Tunnel Tests on Rigid Model

A rigid 1:70 scale model, including surrounding buildings, was used to measure time-history net pressure distributions at 130 measurement points (Figure 2), with wind directions ranging from 0° to 360° relative to North, in 10° increments. Due to the relatively high blockage ratio, corrections were applied to account for this effect in the pressure measurements (ESDU, 1980).

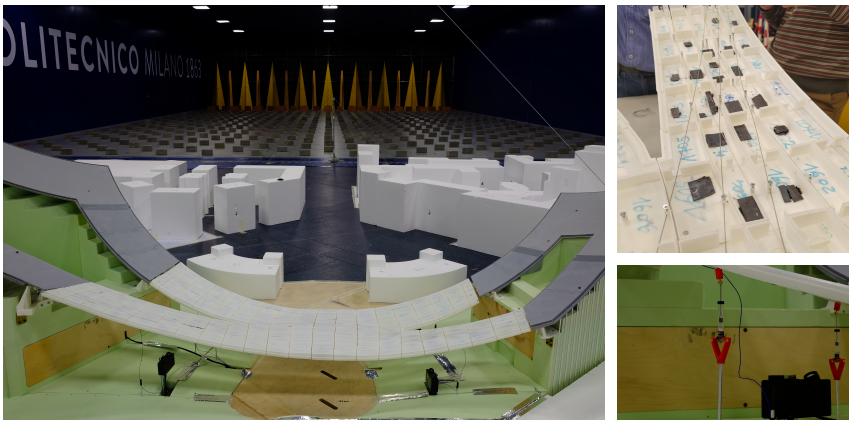


Figure 3. a) The aeroelastic model in the wind tunnel **b)** Detail of the aeroelastic roof **c)** Detail of the air dashpot

2.2. Numerical Simulations

The dynamic response of the structure was simulated by applying the recorded pressure distributions to an FE model of the canopy, evaluating the sensitivity of vibration levels and equivalent static wind loads to structural damping and wind speed (e.g., Denoël, 2024; Frontini et al., 2022; Patruno et al., 2017).

2.3. Wind Tunnel Tests on Aeroelastic Model

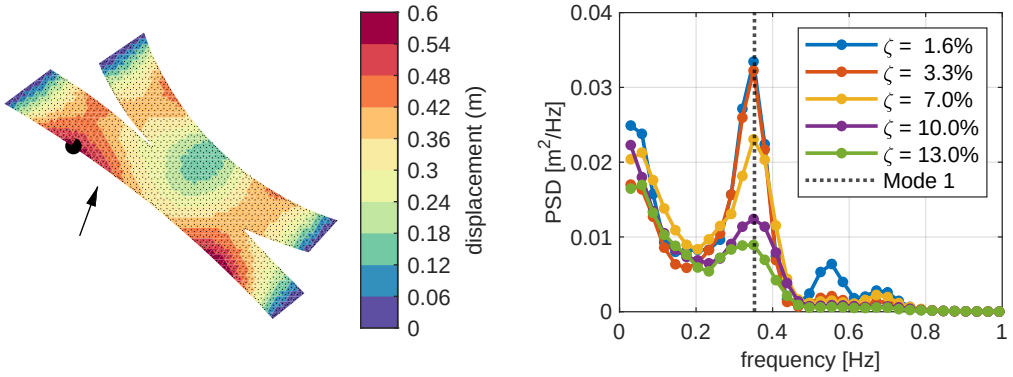
An aeroelastic model, also at a 1:70 scale, was tested to capture aeroelastic effects not observed with the rigid model (Figure 3). Designed according to Froude scaling, the model discretized the canopy into 200 rigid volumes connected by an airtight membrane and supported by a simplified cable system. Distributed, tunable air dashpots were used to adjust modal damping values. The model was instrumented with 7 laser and 7 piezoelectric accelerometers. Modal analysis was conducted using a laser scanner vibrometer to accurately measure mode shapes.

Tests were conducted with wind directions again ranging from 0° to 360° relative to North, and for different damping settings. Again, blockage correction was applied. Results from the aeroelastic tests were subsequently used to validate and refine the numerical simulations, providing data to support structural design verification.

3. KEY FINDINGS

Pressure measurements showed low mean net pressure distributions across all wind directions. However, significant dynamic pressure fluctuations were recorded for wind directions where the canopy is downwind of surrounding skyscrapers, whose wake impacts the canopy. Numerical simulations confirmed that the largest peak vibrations were expected with the wind blowing from those directions. For example, Figure 4-a shows the envelope of simulated peak vertical displacements along the canopy for a wind direction of $-160°$, at the design speed corresponding to a return period of 100 years.

Aeroelastic tests confirmed these characteristics and allowed the definition of a target damping ratio of approximately 10% to suppress resonant contributions. This is illustrated in Figure 4-b,



(a) **(b)**

Figure 4. a) Numerical peak displacement in vertical direction at design wind speed (T=100y) **b)** PSD of experimental displacement, at the point highlighted with a black marker in a), as a function of the damping ratio

where the experimental power spectral density of the vertical displacement at one of the most excited points is shown as a function of different damping values.

In comparison to numerical simulations, experimental responses resulted in lower amplitudes, suggesting that aeroelastic effects, in the considered wind speed range, contribute additional aeroelastic damping. The aeroelastic tests also verified the stability of the structure up to 1.2 times the wind speed with return period of 1000 years.

4. CONCLUSION

This investigation underscores the importance of comprehensive wind tunnel testing and numerical modeling for large, lightweight structures with complex geometries. The study's outcomes contribute valuable insights for optimizing the design of similar architectural structures to ensure stability and performance under dynamic wind loads.

ACKNOWLEDGEMENTS

The authors would like to acknowledge Holzner-Bertagnolli Engineering for providing structural design input data, which was instrumental to the success of this study. Additionally, we thank CityLife S.p.A. and The Wave s.c.a.r.l. for funding this project.

REFERENCES

Chen, B., Yang, Q., and Wu, Y., 2012. Wind-induced response and equivalent static wind loads of long span roofs. Advances in Structural Engineering 15. cited By 29, 1099–1114.

Denoël, V., 2024. Quantifying complexity in the envelope reconstruction problem: Review, comparison and a detailed illustration. Journal of Wind Engineering and Industrial Aerodynamics 254.

ESDU, 1980. Blockage Corrections for Bluff Bodies in Confined Flows. Item 80024. Engineering Sciences Data Unit.

Frontini, G., Argentini, T., Rosa, L., and Rocchi, D., 2022. Advances in the application of the Principal Static Wind Loads: A large-span roof case. Engineering Structures 262, 114314.

Patruno, L., Ricci, M., Miranda, S. de, and Ubertini, F., 2017. Equivalent Static Wind Loads: recent developments and analysis of a suspended roof. Engineering Structures 148, 1–10.

Influence of turbulence of oncoming flow on the admittance function of local pressures on a building roof

Vincent Denoël[1], Mattia Ciarlatini[2], Catherine Gorlé[3]

[1]*Structural & Stochastic Dynamics, University of Liège, Belgium, v.denoel@uliege.be*
[2]*Civil and Environmental Engineering, Stanford University, U.S.A., mattiafc@stanford.edu*
[3]*Civil and Environmental Engineering, Stanford University, U.S.A., gorle@stanford.edu*

SUMMARY:
This paper investigates the influence of turbulence intensity in the oncoming flow on the admittance function of local pressures on a building roof. Using Large-Eddy Simulations (LES), the study analyzes the power spectral densities of wind pressure at selected points on the roof of a model building and their relationship to wind turbulence. The results show that while the overall pressure distribution scales with the turbulence intensity of the oncoming flow, and that the pressure spectra on the roof, near the leading edge, although being affected by level of turbulence, yield very similar admittance functions in the bubble near the leading edge.

Keywords: Wind pressure, large eddy simulation, velocity–pressure admittance.

1. INTRODUCTION

In wind engineering, aerodynamic admittance functions are essential for modeling how structures, such as buildings and bridges, respond to fluctuating turbulence components. These functions typically quantify the resultant pressure in relation to the wind spectrum, which characterizes turbulence across a range of frequencies. Admittance can be understood in several contexts. One key interpretation is related to the size effect, also known as aerodynamic admittance (Vickery, 1968). This concept reflects how the resultant pressure on a surface is reduced due to its finite size and the imperfect correlation of wind pressures across the surface. It is also applied in bridge engineering, where the fluctuations of pressures around a bridge deck are modeled by multiplying an admittance function by the wind spectrum. Davenport introduced six admittance functions for drag, lift, and moment, as well as for two components of turbulence (Davenport, 1962). Furthermore, aerodynamic admittance is used to estimate the base moment and shear force in buildings with various aspect ratios (Kareem, 1982), as specified in various international codes and standards (ASCE7, AS1170.2, NRCC, EN1991-1.4, AIJ). In a different context, admittance functions are useful in numerical implementations of spectral analysis methods, especially when discretizing random fields, such as turbulence (Denoël and Maquoi, 2012). Within Davenport's wind loading framework, the term "mechanical admittance" refers to the frequency response function of the structure.

Aerodynamic admittance functions can also find applications in the determination of local wind pressures on buildings. Early works have shown that the quasi-steady theory can predict average loads well and pressure near the stagnation point, while it struggles in areas of flow separation, necessitating refined models (Letchford et al., 1993). Several empirical studies (Snæbjörnsson and

Geurts, 2006) , like those by Kawai (1996), Sharma (1996), Geurts (1997), and Snæbjörnsson (2002) have correlated pressure spectra with upstream wind velocity, suggesting the potential for generalized models across building types for the windward faces of mid- and high-rise buildings. In these works, the admittance function on the windward face of a building takes the general form

$$|\chi(f_r)|^2 = \frac{S_p(f)}{(\rho C_p U_\infty)^2 S_u(f)} = (1 + n f_r^\alpha)^{-\beta}$$

where n, α and β vary across models, and where f_r is a reduced frequency. This expression indicates how the power spectral density of the actual pressure $S_p(f)$ relates to the pressure that would be obtained with the quasi-steady approach (ρ, C_p, U_∞ are respectively the air density, the mean pressure coefficient and the average wind velocity at considered height above ground). In a review paper, Hunt et al., 1990 indicates that understanding how incident turbulence interacts with the turbulence and vortex shedding in the wake of a bluff body was understood through some of the mechanisms only. Computational methods, such as large-eddy simulations (Lamberti and Gorlé, 2020; Li et al., 2021), have further enhanced understanding of aerodynamic behavior under turbulence. Integrating aerodynamic admittance functions into design practices improves the accuracy of peak load estimations (Pomaranzi et al., 2022).

2. MATERIALS AND METHODS

2.1. Governing equations

The experimental model consists of a building with rectangular floor plan and dimensions of 2000 x 1000 x 300 mm (H x W x b), as illustrated in Figure 1, inside a 8 x 35 x 15 m (H x W x b) domain. To predict wind loading on the building facades, LESs are performed using Cadence's CharLES finite volume solver, which employs a low-Mach isentropic formulation. The solver has previously been used for wind loading simulations of the same building (Ciarlatani et al., 2023). We generate the incoming ABL with a synthetic turbulence generator (Xie and Castro, 2008) for two different turbulence intensities corresponding to streamwise turbulence intensities of 3% (ABL 1) and 4% (ABL 2) at the building location roof height. Pressure and velocity are sampled both on the building surface and in its vicinity over a period of 300s, with sampling frequency 2500 Hz.

In this short abstract, focus is set on the 300 x 280 mm area located on the roof of the building, near the leading edge, under a wind incidence of $\alpha = 10^\circ$ and $U_\infty = 7.73$ m/s, see Figure 1. Among other quantities, the longitudinal component of the wind velocity is analyzed at point P (see Figure 1), located at roof level, 80 mm ahead of the building. It is used to define the admittance functions of the pressure on the roof, at 10 selected points located a distances (in mm) 5, 12.3, 26.9, 48.3, 75.9, 109.2, 147.3, 189.2, 234, 280 from the leading edge of the building. These points are labeled $1, \cdots, 10$. The admittance functions are determined with the H_2 estimator for SISO systems, i.e. as the ratio of the Power Spectral Densities (PSDs) of the pressures on the roof and of the wind velocity at point P. These PSDs are calculated with Welch's periodogram method, on windows of 1024 data points, without overlapping, which corresponds to a frequency resolution of 2.44 Hz.

3. RESULTS AND DISCUSSION

Figure 1 shows the maps of the average pressure coefficient on the roof as well as the RMS values. The contour maps are very similar for the two ABLs. A cut along the centerline of the building,

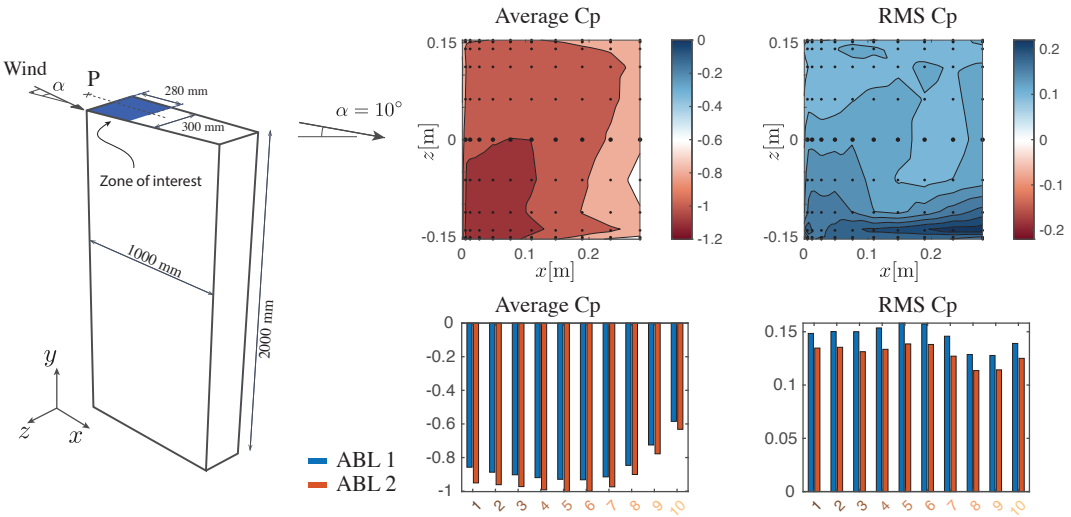


Figure 1. Illustration of the modeled building. The considered zone on the roof is represented by the dark blue tile. Right: maps of average and RMS (top view) and cut line for 12 selected taps along the centerline of the building

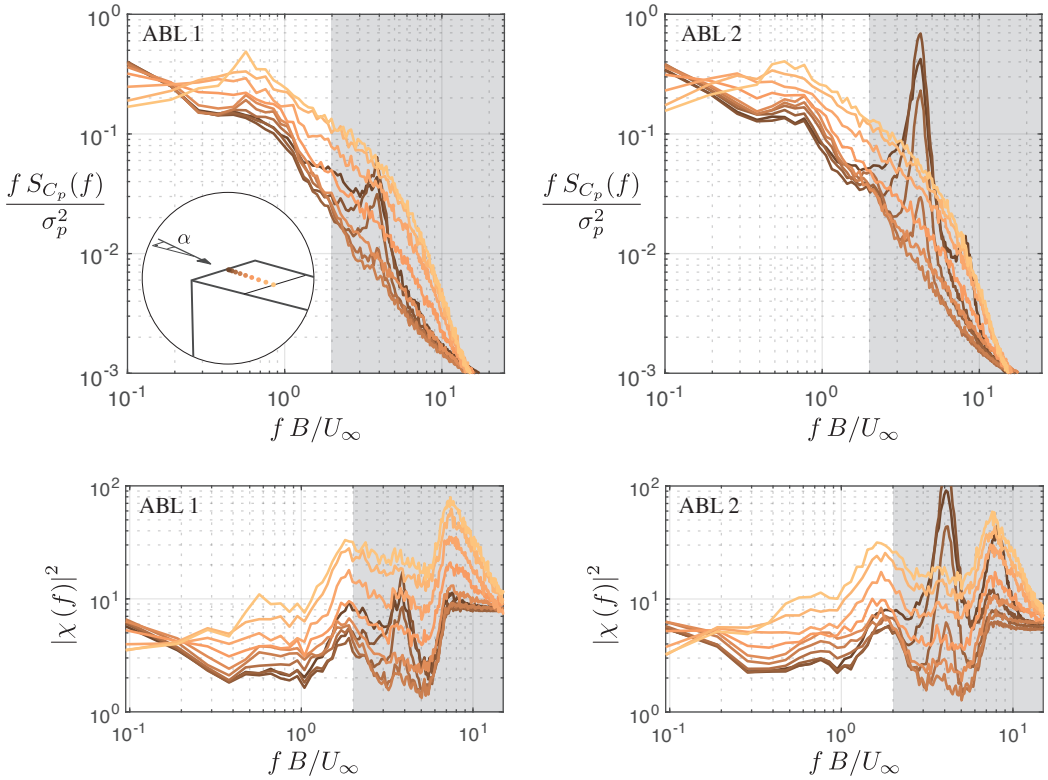


Figure 2. Top: PSDs of the pressure on the roof for the two ABLs. Bottom: Velocity-pressure admittances. Results are shown as a function of the reduced frequency $f_r = fB/U_\infty$, where $B = 0.3$m and $U_\infty = 7.73$m/s.

$z = 0$, shows that the average and RMS pressure coefficients are indeed very similar, in trends, with a consistently smaller RMS for ABL 2, with a reduction of about 10%.

Figure 2 shows the normalized PSDs of the wind pressure $fS_{C_p}(f)/\sigma_p^2$ for the 10 selected points on the roof. The PSDs in the rear part of the considered area are represented with lighter yellow tones (points 8, 9, 10). These PSDs are very similar for the two ABLs. The darker lines, associated with the pressure taps closer to the leading edge, also have a similar trend in the frequency range $fB/U_\infty \in [0;2]$. However, for $fB/U_\infty 2$ (greyed background), they show a significantly different behavior. The flow in the primary bubble (Buresti, 1998) located very near the leading edge, a phenomenon that is difficult to capture near the singularity, is recirculating in a rather narrow frequency band $fB/U_\infty \in [3;5]$. This process is seemingly more regular when the ABL is less turbulent, which favors the regular detachment of eddies from the leading edge. The secondary recirculation bubble is less affected by the turbulence of the oncoming flow. Consequently the admittance functions of the pressures along the roof, have very similar patterns, as shown in the bottom part of Figure 2. The full paper will cover additional cases and extend the analysis of the influence of the ABL on the pressures at other places of the building, including the leeward faces.

REFERENCES

Buresti, G., 1998. Vortex shedding from bluff bodies. Wind effects on buildings and structures, 61–95.

Ciarlatani, M. F., Huang, Z., Philips, D., and Gorlé, C., 2023. Investigation of peak wind loading on a high-rise building in the atmospheric boundary layer using large-eddy simulations. Journal of Wind Engineering and Industrial Aerodynamics 236, 105408.

Davenport, A. G., 1962. Buffetting of a suspension bridge by storm winds. Journal of the Structural Division 88, 233–270.

Denoël, V. and Maquoi, R., 2012. The concept of numerical admittance. Archive of Applied Mechanics 82, 1337–1354.

Hunt, J., Kawai, H., Ramsey, S., Pedrizetti, G., and Perkins, R., 1990. A review of velocity and pressure fluctuations in turbulent flows around bluff bodies. Journal of Wind Engineering and Industrial Aerodynamics 35, 49–85.

Kareem, A., 1982. Fluctuating wind loads on buildings. Journal of the Engineering Mechanics Division 108, 1086–1102.

Lamberti, G. and Gorlé, C., 2020. Sensitivity of LES predictions of wind loading on a high-rise building to the inflow boundary condition. Journal of Wind Engineering and Industrial Aerodynamics 206, 104370.

Letchford, C., Iverson, R., and McDonald, J., 1993. The application of the Quasi-steady Theory to full scale measurements on the Texas Tech building. Journal of Wind Engineering and Industrial Aerodynamics 48, 111–132.

Li, W., Patruno, L., Niu, H., de Miranda, S., and Hua, X., 2021. Aerodynamic admittance of a 6:1 rectangular cylinder: A computational study on the role of turbulence intensity and integral length scale. Journal of Wind Engineering and Industrial Aerodynamics 218, 104738.

Pomaranzi, G., Amerio, L., Schito, P., Lamberti, G., Gorlé, C., and Zasso, A., 2022. Wind tunnel pressure data analysis for peak cladding load estimation on a high-rise building. Journal of Wind Engineering and Industrial Aerodynamics 220, 104855.

Snæbjörnsson, J. T. and Geurts, C. P., 2006. Modelling surface pressure fluctuations on medium-rise buildings. Journal of Wind Engineering and Industrial Aerodynamics 94. Urban Civil Engineering (UCE), Impact of wind and storms on city life and built environment., 845–858.

Vickery, B. J., 1968. Load Fluctuations in Turbulent Flow. Journal of Engineering Mechanics-asce 94, 31–46.

Xie, Z.-T. and Castro, I. P., 2008. Efficient generation of inflow conditions for large eddy simulation of street-scale flows. Flow, turbulence and combustion 81, 449–470.

Cable net stiffness fluctuation under wind flow

Fabio Rizzo [1], Aleksander Pistol [2], Renata Kaput [3], Francesco Ricciardelli [4], Maria Francesca Sabbà [1], Dora Foti [1], Luca Caracoglia[5]

[1]*Polytechnic University of Bari, Bari, Italy, fabio.izzo@poliba.it, mariafrancesca.sabba@poliba.it, dora.foti@poliba.it*
[2]*Manchester Metropolitan University, Manchester, England, a.pistol@mmu.ac.uk*
[3]*Cracow University of Technology, Cracow, Poland, renata.klaput@pk.edu.pl*
[4] *Università della Campania "Luigi Vanvitelli", Aversa, Italy, friccia@unicampania.it*
[5]*Northeastern University, Boston, U.S.A., lucac@coe.neu.edu*

SUMMARY:
Tensile structures are sensitive to wind loads because of their lightness, and their response may depend on geometrical nonlinearity. Cables nets, specifically, are made of two series of cables (i.e. load bearing and stabilizing) that respectively drop and increase their initial pre-tensioning force (i.e. strain and stress) under uplift loads (i.e. suction wind pressures). Therefore, the cables stiffness varies instantaneously under fluctuating wind loads. This paper investigates the time-dependent fluctuations of the cable stiffness due to wind loads. A square-plan cable net is considered. Wind-induced displacements are measured by aeroelastic tests in the wind tunnel.

Keywords: Tensile structures, Aeroelasticity, wind induced effects.

1. INTRODUCTION

Cable net roofs are composed of two orders of cables (i.e. upward and downward oriented) whose dynamic behaviour is very sensitive to wind-induced deformations. Wind loads may change the dynamic properties of the structure, as they produce additional mass and damping. This paper examines the fluctuations in cable stiffnesses under the wind loads. A square-plan cable net is considered. Deformations are measured from an aeroelastic test in wind tunnel.

2. EXPERIMENTAL SETUP

Aeroelastic tests were carried out for the structure illustrated in Figure 1a; l_1 and l_2 respectively designate the span lengths of load bearing (i.e. upward) cables and stabilizing (i.e. downward) cables. The undeformed cable sags $f_{0,1}$ and $f_{0,2}$ can be defined as $f_{0,1} = h_1 - h_2$ and $f_{0,2} = h_3 - h_1$. For the investigated case study, $f_{0,1}$ = 4.44 m, $f_{0,2}$ = 8.89 m, l_1= l_2= 80.00 m (Rizzo et *al*. 2024) at full scale. Subscript "0" means the initial geometry. The initial geometry ('i.e. status 0") is the roof geometry under dead and permanent loads and initial pre-tensioning ($G_P + P_{0,1}$ and $P_{0,2}$).



(a) (b) (c)

Figure 1. Model geometry (a), scale model in the wind tunnel (b), and example of mean wind-indued vertical roof displacements at full scale (U=34.95 m/s), dimensions in cm (c).

The experimental model roof is made of prestressed steel ropes and a silk fabric, stitched to the rope net, but not connected to the steel sub-structure (i.e., the side structural envelope) to avoid any interactions that could increase internal friction, dissipation and, in turn, influence the structural damping. The rope pre-tensioning force is obtained by clockwise tightening a steel screw that is connected to an "ad-hoc" steel coupling. The prestressing force imparted to the steel ropes is estimated empirically, i.e., it is found as the required force that achieves the desired geometry of the net. Once the cable net model is constructed, the roof surface is covered by silk fabric, sewed to the nodes of the net. Figure 1b shows the scale model in the test chamber. Table 1 lists the dynamic similarity scaling ratios, calibrated on the first natural frequency of the roof, f_{m1}: ζ is the model structural damping, λ_L is the geometric scale, λ_m is the mass scale, λ_η is the frequency scale, λ_V is the velocity scale. The model was tested in the Cracow University of Technology's wind tunnel with seven values of the wind speed ranging between 11.7 m/s and 45.1 m/s at the prototype scale. At the prototype scale, the cable cross section is equal to 0.013m^2 (a_1 and a_2) and the initial pre-tensioning force ($P_{0,1}$ and $P_{0,2}$) found by Eq. (1) after imposing an axial deformation by screw tightening equal to 5 milli-strain ($\varepsilon_{0,1}$, cable 1, upward) and 2.6 milli-strain ($\varepsilon_{0,2}$, cable 2 downward). The cable Young's Modulus is equal to 165000 MPa.

$$P_{0,1} = \varepsilon_{0,1} \cdot E \cdot a_1;\ P_{0,2} = \varepsilon_{0,2} \cdot E \cdot a_2 \tag{1}$$

TABLE 1: Dynamic similarity scaling

Model	f_{m1} [Hz]	ζ [%]	λ_L	λ_m	λ_η	λ_V
DMS02	10.35	4.82	0.005	1.25·10-7	58.81	0.29

3. STRUCTURAL BEHVIOUR AND METHODOLOGY

Purpose of this paper is to analyse the time-dependent stiffness of the cable value under wind loads, obtained from the results of the aeroelastic tests. Figure 1c shows an example of the mean wind-induced displacements across the roof. Figure 2 illustrates the simplified static model of a cable net and its deformation under mean uplift forces due to suction wind pressures. Horizontal displacements are assumed equal to zero. It represents two sets of orthogonal cables, intersecting at the centre of the roof. T is the internal cable tension induced by combined dead and permanent loads (G_P), initial pre-tensioning force ($P_{0,1}$and $P_{0,2}$) and wind action (F_W); H and V are the corresponding horizontal and vertical components of T. The initial forces are calculated by Eqs.

(2) to (4).

$$H_{0,1} = \frac{(G_P + P_{0,1}){l_1}^2}{8f_{0,1}};\ H_{0,2} = \frac{(P_{0,2}){l_2}^2}{8f_{0,2}} \tag{2}$$

$$V_{0,1} = \frac{(G_P + P_{0,1})l_1}{2};\ V_{0,2} = \frac{(P_{0,2})l_2}{2} \tag{3}$$

$$T_{0,1} = \sqrt{{H_{0,1}}^2 + {V_{0,1}}^2};\ T_{0,2} = \sqrt{{H_{0,2}}^2 + {V_{0,2}}^2} \tag{4}$$

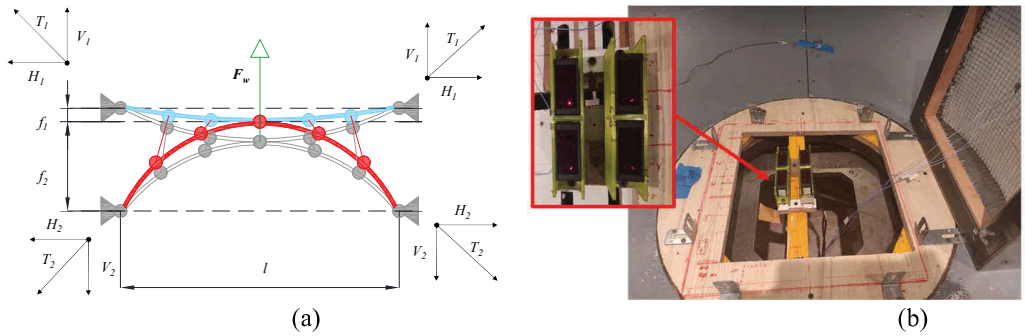
The deformed cable length ($l_{g,1}$ and $l_{g,2}$) is calculated by Eq. (5) and the initial cable deformations ($\Delta l_{0,1} = \varepsilon_{0,1}$ and $\Delta l_{0,2} = \varepsilon_{0,2}$) are estimated according to Eq. (6) below. The corresponding initial cable net stiffnesses ($k_{0,1}$ and $k_{0,2}$) are defined by Eq. (7) below. The load distribution coefficients based on the initial geometry ($c_{0,1}$ and $c_{0,2}$) are given by Eq. (8). The wind flow induces vertical displacements on the roof and, consequently, a time-dependent cable sag variation. For each cable net node, the relative vertical displacements are equal to zero (absolute value $|\Delta f_1(t)|$ equal to $|\Delta f_2(t)|$).

$$l_{g,1} = l_1 \cdot \left(1 + \frac{8}{3}\left(\frac{f_{0,1}}{l_1}\right)^2 - \frac{32}{5}\left(\frac{f_{0,1}}{l_1}\right)^4\right);\ l_{g,2} = l_2 \cdot \left(1 + \frac{8}{3}\left(\frac{f_{0,2}}{l_2}\right)^2 - \frac{32}{5}\left(\frac{f_{0,2}}{l_2}\right)^4\right) \tag{5}$$

$$\Delta l_{0,1} = \frac{l_{g,1} - l_1}{l_1} = \varepsilon_{0,1};\ \Delta l_{0,2} = \frac{l_{g,2} - l_2}{l_2} = \varepsilon_{0,2} \tag{6}$$

$$k_{0,1} = \frac{E \cdot a_1 \cdot {f_{0,1}}^2}{{l_1}^4};\ k_{0,2} = \frac{E \cdot a_2 \cdot {f_{0,2}}^2}{{l_2}^4} \tag{7}$$

$$c_{0,1} = \frac{k_{0,1}}{k_{0,1} + k_{0,2}};\ c_{0,2} = \frac{k_{0,2}}{k_{0,1} + k_{0,2}} \tag{8}$$



(a) (b)

Figure 2. Cable net model (a) and wind tunnel acquisition sensor setup (b).

The dynamic (turbulence induced), variable time-dependent cable sags are given by Eq. (9). The corresponding dynamic, time-dependent cable lengths ($l_{g,1}(t)$ and $l_{g,2}(t)$) are defined in Eq. (10).

$$f_1(t) = f_{0,1} - |\Delta f_1(t)|;\ f_2(t) = f_{0,2} - |\Delta f_2(t)| \tag{9}$$

$$l_{g,1}(t) = l_1 \cdot \left(1 + \frac{8}{3}\left(\frac{f_1(t)}{l_1}\right)^2 - \frac{32}{5}\left(\frac{f_1(t)}{l_1}\right)^4\right);\ l_{g,2}(t) = l_2 \cdot \left(1 + \frac{8}{3}\left(\frac{f_2(t)}{l_2}\right)^2 - \frac{32}{5}\left(\frac{f_2(t)}{l_2}\right)^4\right) \tag{10}$$

The wind induced cable deformation variations ($\Delta\varepsilon_1$ and $\Delta\varepsilon_2$) are given by Eq(11) from which the cable internal traction variation is estimated according to Eq. (12). Eqs. (13) and (14) also give the time-depending horizontal and vertical components of the cable wind-induced axial force

$(T(t))$.

$$\Delta l_1(t) = \frac{l_{g,1}(t) - l_1}{l_1} = \Delta\varepsilon_1(t);\ \Delta l_2(t) = \frac{l_{g,2}(t) - l_2}{l_2} = \Delta\varepsilon_2(t) \tag{11}$$

$$\Delta T_1(t) = \Delta\varepsilon_1(t) \cdot E \cdot a_1;\ \Delta T_2(t) = \Delta\varepsilon_2(t) \cdot E \cdot a_2 \tag{12}$$

$$H_1(t) = \frac{(G_P + P_{0,1} + q_1(t) \cdot c_1(t)) {l_1}^2}{8 f_1(t)};\ H_2(t) = \frac{(P_{0,2} - q_2(t) \cdot c_2(t)) {l_2}^2}{8 f_2(t)} \tag{13}$$

$$V_1(t) = \frac{(G_P + P_{0,1} + q_1(t) \cdot c_1(t)) l_1}{2};\ V_2(t) = \frac{(P_{0,2} - q_2(t) \cdot c_2(t)) l_2}{2} \tag{14}$$

The estimated wind loads action (i.e. concentrated nodal force) on the load bearing cable (i.e. cable 1, upward), $F_{W,1}(t)$, is given by Eq. (15) below and the time-depending load distribution coefficients ($c_1(t)$and $c_2(t)$) and stiffnesses ($k_1(t)$ and $k_2(t)$) are defined by Eqs. (16) and (17). Examples of cable stiffness fluctuation are illustrated in Fig. 3, corresponding to a mean wind velocity equal to 45.1 m/s at the prototype scale.

$$F_{W,1}(t) = \left(\frac{\Delta T_1(t)}{c_1(t)}\right)\left[\frac{l_1\left(1 + 8\left(\frac{f_1(t)}{l_1}\right)^2\right)}{8\left(\frac{f_1(t)}{l_1}\right)}\right] \tag{15}$$

$$c_1(t) = \frac{k_1(t)}{k_1(t) + k_2(t)};\ c_2(t) = \frac{k_2(t)}{k_1(t) + k_{2(t)}} \tag{16}$$

$$k_1(t) = \frac{E \cdot a_1 \cdot f_1(t)^2}{{l_1}^4};\ k_2(t) = \frac{E \cdot a_2 \cdot f_2(t)^2}{{l_2}^4} \tag{17}$$

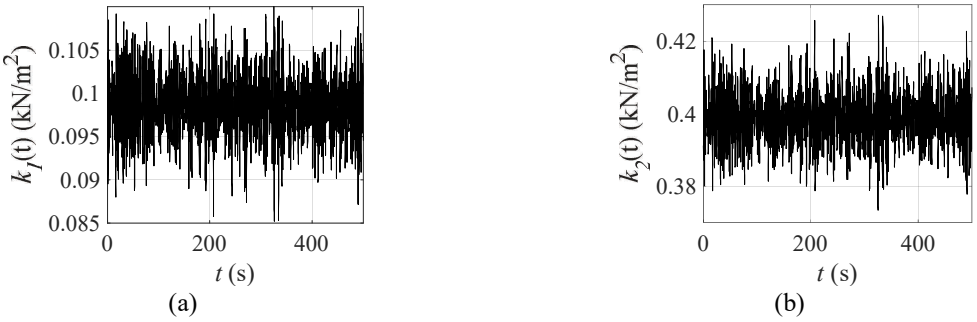


Figure 3. Cables stiffness variation: (a) $k_1(t)$, and (b) $k_2(t)$.

4. RESULTS AND CONCLUSIONS

The dynamic, wind-induced fluctuations of cable nets stiffness are investigated in this study through aeroelastic tests in the wind tunnel. The stiffness standard deviation for the two sets of load bearing and stabilizing cables ranges from 0.0038 ($k_1(t)$) and 0.0075 kN/m^2 for $k_2(t)$. The difference between the observed maximum and the minimum values ranges from 0.02 kN/m^2 ($k_1(t)$). and 0.04 kN/m^2 ($k_2(t)$). The standard deviation of dimensionless load distribution coefficients ($c_1(t)$) and $c_2(t)$) (Eq. (16)) is equal to 0.009. It is suggested that this fluctuation contributes to the roof's natural frequency variations, geometrically influenced by the cable sag magnitudes, under wind loads.

REFERENCES

Rizzo F., Pistol A., Caracoglia L., 2024. Estimating nonlinear wind-induced response of roof cable nets by aeroelastic experiments and ML modeling. Reliability Engineering and System Safety, 2024, 248, 110183.

Evaluation of the provisions for wind induced vibrations in the second generation Eurocode EN 1991-1-4

C.P.W. Geurts[1], A.J. Bronkhorst

[1]*TNO, Department of Reliable Structures, Delft, the Netherlands, chris.geurts@tno.nl*

SUMMARY:
The new Eurocode for wind loads on structures includes adjusted provisions to take the dynamic effects into account. This contribution describes a study of these provisions where practicing engineers have applied the new methods on 3 predefined case studies. Results have been compared afterwards, which lead to a number of recommendations for improvement of the code as well as for the practicing engineers.

Keywords: Wind Loads, Dynamic effects, Eurocode

1. INTRODUCTION

Structural engineering and design in Europe is based on the provisions in the Eurocodes (EN 1990 series). Part 1 of the Eurocode specifies the loads on structures, and more specifically, part 1-4 specifies the wind loads. The second generation of Eurocodes is scheduled to replace the current versions of 2005, ultimately in 2028. An overview of the comparison between the new and existing Eurocode on wind loads is presented by Ricciardelli (2023). Here, the rules to incorporate the dynamic response on buildings is discussed.

The draft version of the new Eurocode on wind loads, prEN 1991-1-4:2024 (CEN, 2023), includes an adjusted model to account for the in-wind dynamic response which replaces the two methods now given in EN 1991-1-4:2005 (CEN, 2005). Although based on the same concepts, this new procedure is different from the previous two, leading to different results.

New is the inclusion of rules to assess cross-wind and torsional vibrations, which are absent in the version that is now being used. These provisions are new to end users of the code. For that reason, an initiative was started to define some case studies and to invite future end users of this code to apply these new rules. In total, 12 structural engineers from different consultant firms from the Netherlands have joined our initiative. Independently, the authors of this paper worked through the procedures. The results of all parties have been discussed within the group, comments to the Eurocode provisions have been addressed, and taken into account in the current draft of the Eurocode, the so-called formal vote version (CEN, 2024).

1. BACKGROUND

1.1. In-wind vibrations

In EN 1991-1-4:2005, a structural factor $c_s c_d$ was introduced to account for the effects of

incomplete correlation of the wind loads and the effect of resonance of the building with the fluctuating load. This factor $c_s c_d$ is a function of the background response factor B and the resonance response factor R, for which two calculation procedures are provided in the current code in annexes B and C. EN 1991-1-4:2005 also gives provisions to calculate the maximum acceleration for serviceability assessments. Both methods in annex B and C are based on the same principles and differ only slightly in terms of $c_s c_d$.
Application of either annex B or C to calculate B and R is a Nationally Determined Parameter (NDP). The project team for the new EN 1991-1-4 has been requested to include a single method, for which calculation rules are provided in the new annex F. These rules, although based on the same principles, differ from the current annexes B and C.
The factor $c_s c_d$ has been replaced by a factor c_{sd}, although these are defined similarly, depending on the background response factor B, the resonance response factor R, the turbulence intensity I (denoted as I_v and I_u in the 2005 and 2024 version respectively) and one or two peak factors (k_p, k_B and/or k_R). Equations 1 and 2 give the current and the new definition.

$$c_s c_d = \frac{1+2\,k_p\;I_v(z_s)\sqrt{(B)^2+(R)^2}}{1+7\,I_v(z_s)} \tag{1}$$

$$c_{sd} = \frac{1+2I_u(z_s)\sqrt{(k_B\,B)^2+(k_R\,R)^2}}{1+2k_B\,I_u(z_s)} \tag{2}$$

Both factors can be split into a factor c_s and a factor c_d, which respectively account for the effects of incomplete correlation and the effect of resonance. For c_{sd} the following factors c_s and c_d apply:

$$c_s = \frac{1+2\cdot k_B\cdot I_u(z_s)\sqrt{B^2}}{1+2\cdot k_B\cdot I_u(z_s)} \tag{3}$$

$$c_d = \frac{1+2\cdot I_u(z_s)\sqrt{(k_B\cdot B)^2+(k_R\cdot R)^2}}{1+2\cdot k_B\cdot I_u(z_s)\sqrt{B^2}} \tag{4}$$

Although the symbols B and R remain unchanged, the underlying equations differ between the two versions. In the current Eurocode, both for B and R other equations have been given, and the new Eurocode differs from both current values. For the background response factor B, the different provisions are:

EN 1991-1-4, annex B:

$$B^2 = \frac{1}{1+0.9\cdot\left(\frac{b+h}{L(z_s)}\right)^{0,63}} \tag{5}$$

EN 1991-1-4, annex C:

$$B^2 = \frac{1}{1+\frac{3}{2}\cdot\sqrt{\left(\frac{b}{L(z_s)}\right)^2+\left(\frac{h}{L(z_s)}\right)^2+\left(\frac{b}{L(z_s)}\cdot\frac{h}{L(z_s)}\right)^2}} \tag{6}$$

prEN 1991-1-4, annex F:

$$B^2 = \chi_U^2(\varphi_{B,C}) \cdot \chi_U^2(\varphi_{B,L}) \quad (7)$$

$$\varphi_{B,C} = 3{,}0 \cdot b / L_u^x(z_s) \quad (8)$$

$$\varphi_{B,L} = 3{,}0 \cdot l / L_u^x(z_s) \quad (9)$$

All three models depend on the height and width of the loaded area (b and h, or b and l), and the integral length scale of the oncoming flow (noted as L in the 2005 version and L_u^x in the 2024 version).
For the resonance response factor R, also three different provisions are given, which will be included in an extended paper. The models of EN 1991-1-4:2005 have been discussed by (Steenbergen et. al, 2012). This paper only deals with the new provisions.

1.2. Cross-wind and torsional vibrations

In the current Eurocode, no provisions for cross-wind and torsional response are given; these were explicitly excluded.
In prEN 1991-1-4, it is specified that these actions should be taken into account. Rules to account for these vibrations are given in annex G and H. The rules are based on the guidelines of the Architectural Institute of Japan (AIJ), as adopted and translated in (Tamura et al, 1996).
The first step is to check whether these calculations are necessary. prEN 1991-1-4 states that no check for these vibrations is needed if the ratio between building height h, width b and depth d fulfils the criterion for the slenderness of the structure:

$$\frac{\mathrm{h}}{\sqrt{\mathrm{b} \cdot \mathrm{d}}} < 3 \quad (10)$$

Annex G in the new Eurocode gives provisions, which can be used when:

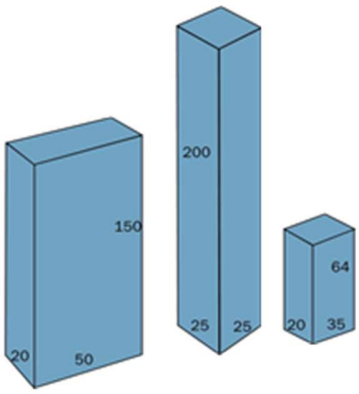
$$3 \leq \frac{\mathrm{h}}{\sqrt{\mathrm{b} \cdot \mathrm{d}}} < 6 \quad (11)$$

Annex H gives additional rules for cross-wind vibrations in more slender structures, primarily derived for structures such as bridge decks. For buildings with a slenderness ratio greater than 6, annex H does not yield accurate answers and has not been part of the study discussed here.

2. CASE STUDIES

Three cases have been selected for which the provisions of prEN 1991-1-4 have been applied. For these buildings, the in-wind, cross-wind and torsional effects have all been assessed. The input variables for wind climate were taken from the current national Annex of EN 1991-1-4.
In a first round of calculations, 7 structural engineers from different firms participated, and all calculations have been done blindly. After delivering the results, these were discussed among the participants. leading to the identification of errors and causes for misunderstanding of the rules. Where necessary, the CEN TC250 working group has been informed of any identified errors or inconsistencies.
This first round led to a common understanding of the choices to be made, and a second round of calculations was defined, based on a fourth case, which was based on the CAARC standard tall

building (Melbourne, 1980).
Additionally, a call for participation was published in a national magazine for structural engineers, to invite other structural engineers to do the same calculations. A total of 5 engineers from different consultant firms responded by carrying out these calculations for the three cases, in a third round. This group was already aware of the lessons from the first round, as these were published in (Bronkhorst, Geurts, 2023). The outcomes of the calculations, as well as the lessons learnt by the participating engineers, will be discussed in our presentation and an extended paper.



	Case 1	Case 2	Case 3
Height h (m)	150	200	64
Width b (m)	50	25	35
Depth d (m)	20	25	20
Roughness length z_0		0.2 m	
Basic Wind Velocity v_b		27 m/s	
First natural frequency n_1	0.31 Hz	0.23 Hz	0.72
Damping δ	0.1	0.05	0.1
k_I, c_0		value = 1	

Figure 1. Definition of case studies

ACKNOWLEDGEMENTS
The calculations have been organised and conducted within the framework of the HiViBe Project. This work was performed as part of the research project "HiViBe". The authors wish to acknowledge the participation of the partners in this research: ABT, Aronsohn, BAM, Besix, Fugro, Geobest, IMd, Peutz, SCIA Engineer, SKW, Structure Portante Grimaud, and Zonneveld Ingenieurs. The "HIVIBE" project is financially supported by the Ministry of Economic Affairs and falls under the Topsector Water & Maritime, contract number T-DEL/2021/024.

REFERENCES
Bronkhorst, Geurts, 2023, Nieuwe Eurocode voor windbelastingen, windtrillingen van hoogbouw, Cement 5/23, pg 52-58
CEN, 2005. EN 1991-1-4, Eurocode Actions on Structures, part 1-4 Wind actions.
CEN, 2023. prEN 1991-1-4, Eurocode Actions on Structures, part 1-4 Wind Actions, version 30-03-2023.
Geurts, C.P.W., Bronkhorst, A.J., 2023. Benchmark study on the guidelines for wind-induced vibrations in the new EN 1991-1-4. 18. Dreiländertagung D-A-CH 2023 der WTG e. V. am 18. und 19. September 2023, Aachen.
Melbourne, W.H., 1980, Comparison of measurements on the CAARC standard tall building model in simulated model wind flows, JWEIA, volume 6, pg 73-88
Ricciardelli, F., 2023. prEN1991-1-4:2021: the draft Second Generation Eurocode on wind actions on structures – a personal view, Wind and Structures, 37(2), 79-84
Steenbergen, R.D.J.M., Vrouwenvelder, A.C.W.M., Geurts, C.P.W., 2012. The use of Eurocode EN 1991-1-4 procedures 1 and 2 for building dynamics, a comparative study (2012) Journal of Wind Engineering and Industrial Aerodynamics 107: pg. 299-306.
Tamura, Y., Kawai, H., Uematsu, Y., Marukawa, H., Fujii,K., Taniike, Y., 1996. Wind load and wind-induced response estimations in the Recommendations for Loads on Buildings, AIJ 1993, Engineering Structures, vol 18, no 6.

The second generation Eurocode 1 Part 1-4 on wind actions

Francesco Ricciardelli

University of Campania "Luigi Vanvitelli", Aversa, Italy, friccia@unicampania.it

SUMMARY:
In 2012, Mandate M/515 of the European Commission to CEN started the transition towards the Second Generation of the EN Eurocodes, a long process now approaching its end. The redrafting of EN 1991-1-4 on wind actions started in august 2017, and the document is now being finalised for submission to formal vote in October 2025. This paper gives a brief overview of the process that brought the document to the current stage, of the changes it brings with respect to the 2005 version, and of the needs that emerged during its drafting and amendment.

Keywords: wind loading codes, Eurocodes, European Committee for Standardization.

1. TOWARDS THE SECOND GENERATION EUROCODE ON WIND ACTIONS

In December 2012, the European Commission issued Mandate M/515, inviting CEN to develop a work programme aimed at the drafting of the Second Generation of the EN Eurocodes. The work programme was approved by CEN TC250 in May 2013, and was divided into four phases, the second of which was to include the revision of EN 1991-1-4 Eurocode 1 – Actions on structures - Part 1-4: General actions - Wind actions. A Project Team (PT) was appointed in June 2017 and started his activities in August the same year. It included S.O. Hansen, R. Höffer, J. Rees., P. Spehl and the author of this paper (Hansen et al. 2019), and was supervised by N. Malakatas, Chairman of TC250/SC1.

The mandate received from CEN TC250 by the PT included four general tasks, having common roots with those given to PTs in charge of redrafting other Eurocode parts:

1. improvement of consistency of the basis for calculations and new basis for calculations;
2. harmonization of the different approaches used in the Eurocodes with the National Annexes;
3. potential harmonization of different Eurocode Parts and CENELEC standards for overhead electric lines, as well as other CEN or ISO standards;
4. possibly reduction of global wind loads leading to more economical structures.

The following seven subtasks were also identified:

a. reduction in number of National Choices (Nationally Determined Parameters, NDPs);
b. enhancement of ease of use;
c. drafting of a design wind map, based on basic wind velocities coming from existing national values and emphasizing differences across borders;
d. improvement of wind models for calculation of wind velocities and peak velocity pressures including roughness categories and transition between roughness categories;

e. systematic review of force and pressure coefficients, including influence areas, based on the state of the art; in doing this basis is considered to be the current version of EN 1991-1-4, other Eurocodes Parts (e.g. for towers and masts, chimneys and other structures together with the wind response of such structures), CENELEC standards and other International codes;
f. revision of the procedures for the evaluation of the dynamic response including vortex induced vibrations, aeroelastic effects, wind loads on bridges and response of structures including mode shapes with changing signs, use of influence lines;
g. editorial improvements aimed at a more user friendly document.

Subtasks *a*, *b* and *g* are very general and common to those given to other PTs, whereas subtasks *c*, *d*, *e* and *f* are specific to wind actions and to EN 1991-1-4.

Four intermediate drafts were submitted to CEN TC250 by the PT between May 2018 and October 2019, which received more than one thousand comments in total from National Standardization Bodies (NSBs), which the PT was requested to systematically respond to. In April 2020, the final draft of the document was submitted to CEN TC250, and the PT ended its activities (Ricciardelli, 2023).

In May 2021 an edited version of the document was provided to Working Group 1 (WG1) - Climatic Actions - of TC250/SC1 for it to prepare the draft to be sent to public enquiry. Between June 2021 and September 2022 Task Group 2 (TG2) - Wind actions - under WG1 amended the document, which was put to a vote of NSBs and approved for public enquiry (CEN, 2024). This started in March 2024 and ended on July 4, 2024, with 1183 comments placed by the NSBs.

At the time of the writing of this abstract, TG2 is handling the comments received in view of the deadline of December 2024 for submission of the amended version of the document to CEN TC250. After final editing and translation into French and German, the document is expected to be submitted to formal vote in October 2025, and will eventually supersede the current version EN 1991-1-4:2005 (CEN, 2005) early in 2026.

2. NOVELTIES IN EN 1991-1-4

With the aim of improving the ease of use, the new document has been organized into a rather small main body of 35 pages in total, containing general information and referring to detailed information given in a set of thirteen annexes.

Annex A was to contain an extreme wind map of Europe, obtained as the merge of the fundamental values of the basic wind velocities provided by the National Annexes (NAs) to EN 1991-1-4:2005, and was produced in response to subtask *c* received by the PT; in fact, CEN TC250 requested to withdraw this Annex, which will therefore not be part of the document that will be sent to formal vote. Annex B contains provisions concerning the effects of terrain; Annexes C, D and E contain aerodynamic coefficients; Annexes F, G and H contain procedures for the inclusion of the dynamic response effects into wind actions; Annex H contain also criteria for the assessment of the aeroelastic response of slender structures; Annex I brings information about the dynamic characteristics of wind-exposed structures; Annex J, borrowed from EN 1993-3-1:2006 (CEN, 2006), contains criteria for the evaluation of the response of steel lattice towers and guyed masts;

Annexes K and L bring guidance on derivation of design parameters from wind tunnel tests and numerical simulations, and of wind speeds from measurements at meteorological stations, respectively; finally, Annex M contains information on the probabilistic description of wind actions, and is meant to represent the link between EN 1991-1-4 and EN 1990 (CEN, 2022). Among these, only annexes C, D and E are normative, the remaining ones being informative.

Main differences with respect to the existing EN 1991-1-4:2005 are as follows (Ricciardelli, 2023).

In addition to the logarithmic wind model, applicable to all structures up to 200 m of height, the use of the linearised Deaves and Harris model is allowed for slender structures up 300 m of height. Furthermore, the linearised approach to the evaluation of peak velocity pressures has been replaced by the quadratic one, and in doing so the peak factor for pressures of 3.5 has been replaced by the peak factor for speeds, for which a value of 2.9 is given.

To the already available $c_{pe,10}$ and $c_{pe,1}$ external pressure coefficients for buildings, a third set of coefficients, called global external pressure coefficients, $c_{pe,G}$, has been added. Criteria are also given for use of the pressure coefficients given for rectangular plan buildings with uniform height to the case of irregular buildings. Pressure coefficients for hyperbolic cooling towers, as well as net pressure coefficients for balconies and porches, were added. Criteria for determining the force coefficients for lattice structures and scaffoldings currently available in EN 1993-3-1:2006 were moved to EN 1991-1-4, and criteria are also given for the evaluation of force coefficients of ice-accreted lattice members based on the value applicable to the bare member and on the ice class.

The ambiguity deriving from the existence of two alternative procedures for the evaluation of the structural factor of EN 1991-1-4:2005 was solved, and only one procedure is given. This applies also to cases in which the vibration mode changes sign. Due to their different nature, the background and the resonant components of the response are combined using two different peak factors, and a general form of the admittance function is defined for the case of vibration modes with uniform sign. For structures featuring vibration modes with changing sign, general expressions of the admittance function are again defined. New provisions have been introduced for acrosswind and torsional actions on buildings with a slenderness $h/\sqrt{b \cdot d}$ in the range of 3 to 6, aspect ratios d/b in the range of 0.2 to 5, and for values of the reduced mean wind velocity $v_m(h)/\left(n \cdot \sqrt{b \cdot d}\right)$ not exceeding 10. Equations for acrosswind and torsional accelerations are also given, as well as combination rules for alongwind, acrosswind and torsional actions. A general procedure is given for the evaluation of equivalent static acrosswind actions on slender structures and structural members due to atmospheric buffeting and due to vortex shedding. As to the latter, only the spectral approach is retained from EN 1991-1-4:2005, and a generalised version of the Scruton number is used to establish the susceptibility to vibration, in which normalization is made with respect to $b \cdot d$ instead of being made with respect to b^2, therefore accounting for two characteristic dimensions of the cross-section.

New material to EN 1991-1-4 is that contained in annexes J through M. Annex J contains criteria formerly contained in EN 1993-3-1:2006 for the evaluation of the response of steel lattice towers and guyed masts. Annex L sets some requirements for the statistical treatment of historical wind records for the assessment of the basic wind speed. Annex K contains provisions for the use of design parameters derived from wind tunnel tests or from Computational Fluid Dynamics (CFD)

simulations (Bruno et al. 2023). Finally, Annex M is meant to link EN 1991-1-4 to the probabilistic requirements set by EN 1990.

3. PERSPECTIVES

The following main needs have emerged during the writing of the document.

There is the need for the definition of an advanced, standardised protocol for the assessment of extreme synoptic wind climate and of its implementation for the construction a European extreme synoptic wind map, as well as of defining non-synoptic wind hazard and more broadly of developing of a procedure for handling climate change when assessing wind actions on structures.

Concerning wind models, it seems that a better definition of standardized roughness classes is needed, together with the definition of enhanced orography models; non-synoptic wind models (thunderstorms in particular) would also be needed to be combined with the relevant hazard model.

The lack was felt of a homogeneous, probabilistically consistent set of aerodynamic coefficients, complying with the probabilistic requirements of EN 1990, together with the coverage of grey zones and guidance to the user on how to handle situations not covered by the code.

Finally, together with the procedures for the assessment of the characteristic value of wind actions, there is the need of calibrating the associated partial and combination factors, which are in the domain of EN 1990. It emerged that these depend at least on wind climate and on construction material, and in any case need an update based on more recent data allowing a better description of the uncertainty embedded in the definition of the characteristic value of the wind action.

REFERENCES

Bruno, L., Coste, N., Mannini, C., Mariotti, A., Patruno, L., Schito, P., Vairo, G., 2023. Codes and standards on computational wind engineering for structural design: State of art and recent trends. Wind and Structures 37(2), 133-151.

CEN, 2005. EN 1991-1-4. Eurocode 1: Actions on Structures – Part 1-4: General actions – Wind Action. European Committee for Standardization. Brussels.

CEN, 2006. EN 1993-3-1. Eurocode 3: Design of steel structures – Part 3-1: Towers, masts and chimneys – Towers and masts. European Committee for Standardization. Brussels.

CEN, 2022. EN 1990. Eurocode – Basis of structural and geotechnical design. European Committee for Standardization. Brussels.

CEN, 2024. prEN 1991-1-4. Eurocode 1: Actions on Structures – Part 1-4: General actions – Wind Action. European Committee for Standardization. Brussels.

Hansen S.H., Höffer R., Rees J., Ricciardelli F., Spehl P., 2019. Towards the second generation Eurocodes: evolution of EN 1991-1-4 Wind actions. Lecture notes in civil engineering. Proceedings of the XV Conference of the Italian Association for Wind Engineering, IN-VENTO 2018, 27, 350-364, Napoli, Italy.

Picozzi V., Ricciardelli F., Sørensen J.D., 2024. Calibration of wind action combination factors from experimental data. Proceedings of the XVII Conference of the Italian Association for Wind Engineering, IN-VENTO 2022, 461, 90-101, Milano, Italy.

Ricciardelli, F., 2023. prEN 1991-1-4:2021: the draft Second Generation Eurocode on wind actions on structures – A personal view. Wind and Structures 37(2), 79-94.

Accounting for the incomplete correlation of windward and leeward pressures in EN 1991-1-4

Frank Kemper[1], Richard Brand[2], Chris Geurts [3]

[1,2]RWTH, Center for Wind and Earthquake Engineering, Aachen, Germany, kemper@cwe.rwth-aachen.de
[3]TNO Mobility and Built Environment, Delft, The Netherlands, chris.geurts@tno.nl

SUMMARY:
The Eurocode on wind actions, EN 1991-1-4, defines pressure and force coefficients for the design and checking of civil engineering structures. To assess the stability of buildings, a factor is defined to account for the incomplete correlation of windward and leeward pressures. The application of this factor is limited with respect to slenderness, and is currently national choice. This paper addresses this factor, and its application is discussed based on measured data from wind tunnel experiments. The results indicate that the use of the correlation factor can be generally justified for low-rise buildings, as it effectively accounts for the pressure reduction in the core areas. However, special consideration must be given to the edge zones in the case of large facilities, where localized wind effects may result in higher net pressures that are not fully captured by the uniform application of the correlation factor.

Keywords: Wind Loads, Eurocode, High-rise buildings

1. INTRODUCTION

Wind-induced pressures on buildings are significant in structural design, requiring accurate methods to ensure safety and performance. The correlation between windward and leeward pressures is key in determining the overall wind load on a structure. EN 1991-1-4:2010 and its upcoming revision (prEN 1991-1-4:2024) provide guidance on managing this correlation in wind load calculations. These standards suggest applying pressure coefficients simultaneously on both windward and leeward walls (areas D and E), with adjustments based on a building's height-to-depth ratio (h/d). For slender buildings ($h/d \geq 5$), no reduction is applied, while for low-rise, wide buildings ($h/d \leq 1$), a reduction factor of 0.85 may be used. However, scientific validation for this recommendation is limited, and some countries, like Germany, exclude this correlation rule in their national annex. This paper aims to validate the correlation factor through wind tunnel studies on two low-rise buildings with $h/d < 1$, providing empirical data to support future revisions of the Eurocode and national annexes.

2. CORRELATED WIND PRESSURE ACCORDING TO EUROCODE

2.1. Correlation factor

According to EN 1991-1-4:2010 and prEN 1991-1-4:2024, the lack of correlation between windward and leeward wind pressures can be accounted for by applying a reduction factor based on the building's height-to-depth ratio (h/d). For buildings with a ratio $h/d \geq 5$, no reduction is

applied, and the resulting wind force should be multiplied by a factor of 1, indicating that full correlation is assumed. For low-rise buildings, where h/d ≤ 1, the resulting wind force may be reduced by multiplying by a factor of 0.85, reflecting a lower correlation between the pressures on opposite sides of the building. For buildings with intermediate height-to-depth ratios between 1 and 5, the appropriate reduction factor can be determined through linear interpolation. However, this factor is national choice, which may lead to different approaches in various countries.

2.2. Pressure coefficients

In combination with the provided pressure coefficients for vertical walls, the $c_{p,net}$ coefficients represent the net pressure difference between the windward and leeward sides of a building, defined as $c_{p,net} = c_{p,windward} - c_{p,leeward}$. This reflects the overall shear force acting on the building. The upcoming revision introduces global pressure coefficients aimed at simplifying the assessment of wind effects by reducing the number of pressure zones, particularly for walls and roofs parallel to the wind direction.

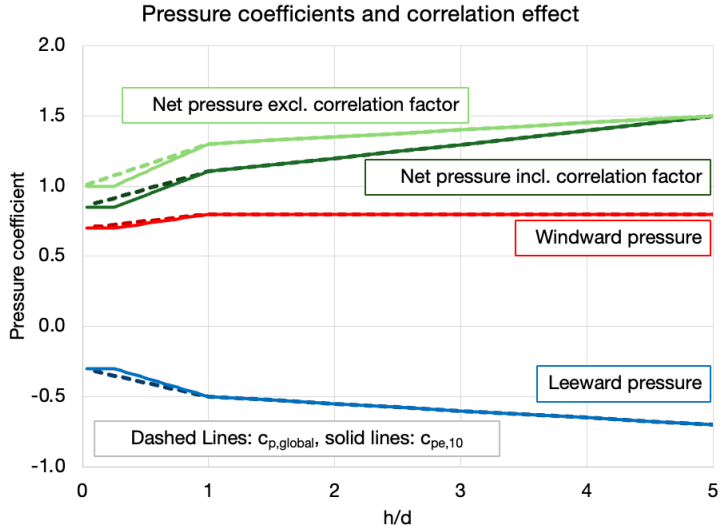


Figure 2. Pressure coefficients according to Eurocode and application of the proposed correlation factor

When comparing global pressure coefficients $c_{p,global}$ [prEN] to the more detailed coefficients $c_{pe,10}$[prEN, EN] for a tributary area of $A = 10m^2$, it becomes apparent that for buildings with h/d ≥ 1, the values of $c_{p,global}$ and $c_{pe,10}$ are identical. However, for buildings with h/d < 1, slight deviations can be observed, primarily due to the recommended interpolation scheme. The goal of the introduction of $c_{p,global}$ coefficients was not to reduce the numerical values of pressure coefficients themselves but to simplify the complexity of pressure zones, which becomes more relevant for surfaces such as walls and roofs that are parallel to the wind direction and not for the considered case. In Figure 2, we summarize both types of pressure coefficients and highlight the influence of the correlation factor towards the resulting net pressure $c_{p,net}$.

3. WIND TUNNEL STUDIES

3.1. Experimental set-up

For structures with a large ground plan, such as those currently being constructed e.g. in Germany

for car manufacturers and storage warehouses, the consideration of realistic wind pressure correlations is critical for accurate design. These “mega-facilities” present unique challenges due to their large dimensions and relatively low h/d ratios. The relevance of applying a reasonable correlation factor becomes even more pronounced in such cases, as neglecting the interaction between windward and leeward pressures could result in conservative or inaccurate wind load predictions.

In response to these challenges, wind tunnel investigations have been conducted for two models of such mega-facilities in a model scale of 1:250, which are shown in Figure 3 and dimensions in Table 3. These models represent h/d ratios between $0 < h/d \leq 0.25$, with model 1 having a ratio of $h/d = 0.035$ and model 2 with $h/d = 0.23$. Furthermore, models also differ in terms of their footprint, with model 2 d/b=1 being square and model 2 d/b=0.28 being more compact.

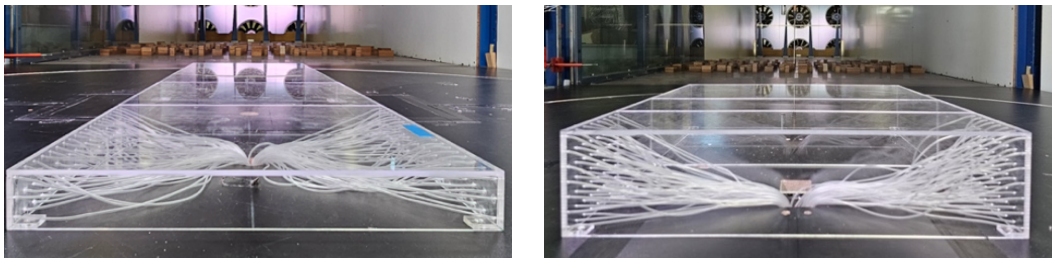


Figure 3. Wind tunnel models of two “mega-facilities”, left: model 1 with h/d=0.035, right: model 2 with h/d=0.23

The wind tunnel testing was conducted using a dense grid of pressure taps distributed along both opposing long sides of the building models. In total, 120 pressure taps were employed for model 1 and 116 taps for model 2. To capture the full range of wind directions and symmetry effects, the measurements were performed on a modular, interchangeable quarter of each building. Two test configurations were used: one with the quarter positioned at the outer edge of the building and the other with the quarter positioned in the inner core. Adhesive tape was used for the joints between the modules to ensure that there was no pressure loss. This approach ensured that all relevant wind flow scenarios were accounted for, with measurements taken for wind directions ranging from 0° to 358.75° in increments of 11.25°.

Table 3. Full-scale dimensions and aspect ratios of the investigated buildings

Modell	d [m]	b [m]	h [m]	d/b	h/d
Model 1	384	109	13.3	0.28	0.035
Model 2	135.9	135.9	31.0	1.0	0.228

3.2. Analysis of correlated pressure

The analysis methodology involved time integration and transient area-weighted averaging of the pressure data from both opposing walls, considering increasing tributary areas by gradually increasing the measurement points used for averaging. Results are presented based on the most unfavorable wind directions. The influence of the height on the displacement of the pressure resultant was also considered; the averaged pressures were slightly increased by 5.5% for Model 1 and 7.2% for Model 2 according to the actual cantilever support system which is typically used in industrial Halls to allow for comparable structural effects in the simplified application of a unique loading pattern.

3.3. Results

The wind tunnel investigations of the two large-scale structures with extreme height-to-depth ratios have yielded several critical insights regarding the correlation of wind pressures between windward and leeward sides. These findings are particularly important for refining the application of correlation factors in design standards [prEN, EN].

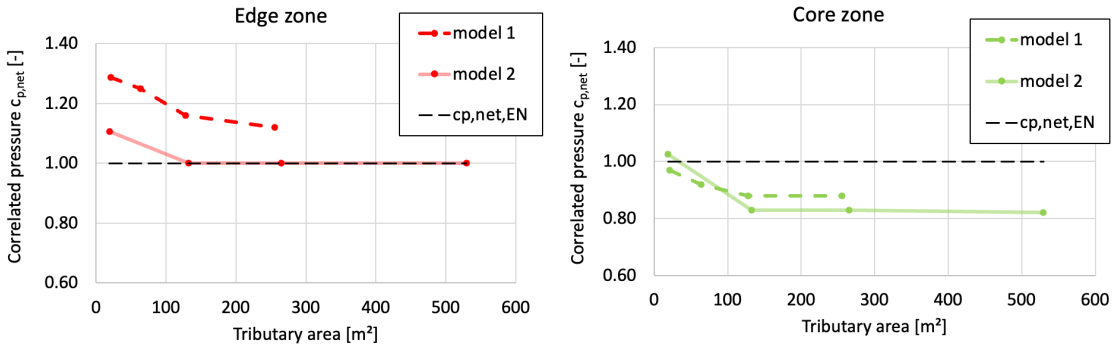


Figure 4. Results of the correlated windward and leeward pressure for both models, enveloping over all directions compared to $c_{p,net,EN}$ (without correlation factor). left: edge zone of the building, right: core zone

1. Significant reduction in pressure correlation in core areas: For both building models, wind loads in core areas showed a significant reduction due to pressure correlation, closely aligning with the proposed 0.85 factor. This confirms its suitability for low-rise buildings with similar height-to-depth ratios. Notably, when ignoring the height influence on the pressure resultant, both models yielded correlation factors below 0.85, suggesting a stronger correlation effect than current standards account for. The core area, covering 85% of the building length, benefits from reduced net wind forces, supporting the use of a correlation factor across large building areas and indicating potential for more efficient structural designs with less conservative wind load estimates.

2. Elevated $c_{\mathrm{p,net}}$ at building edges: Contrary to the core areas, building edges displayed $c_{\mathrm{p,net}}$ values equal to or exceeding those from EN 1991-1-4 without the correlation factor. This is likely due to overpressure on the windward side correlating with leeward edge separation in certain wind directions, causing localized increases in edge wind loads that a uniform correlation factor can't capture. The edge area with these higher pressures makes up only 7.5% of the building length, yet these results underscore the need to account for localized effects at edges, where wind loads may significantly exceed predictions based on average correlation factors.

4. CONCLUSIONS

The results of this analysis provide valuable insights into the application of pressure correlation factors for large, low-rise buildings. While the core areas of such buildings generally exhibit significant reductions in wind loads due to pressure correlation, validating the use of a factor close to 0.85, the edges of the buildings may experience elevated pressures that need to be carefully accounted for. These findings underscore the importance of distinguishing between core and edge areas when applying correlation factors in the structural design.

REFERENCES

EN 1991-1-4:2010 Eurocode 1: Actions on structures - Part 1-4: General actions - Wind actions
prEN 1991-1-4:2024 Eurocode 1: Actions on structures - Part 1-4: General actions - Wind actions

Computational wind engineering for structural design: the Annex K of the new Eurocode 1 part 1-4

Luca Bruno[1], Nicolas Coste[2], Claudio Mannini[3], Alessandro Mariotti[4], Luca Patruno[5], Paolo Schito[6], Giuseppe Vairo[7]

[1]*Politecnico di Torino, Turin, Italy, luca.bruno@polito.it*
[2]*Optiflow Company, Marseille, France, coste@optiflow.fr*
[3]*University of Florence, Florence, Italy, claudio.mannini@unifi.it*
[4]*University of Pisa, Pisa, Italy, alessandro.mariotti@unipi.it*
[5]*University of Bologna, Bologna, Italy, luca.patruno@unibo.it*
[6]*Politecnico di Milano, Milan, Italy, paolo.schito@polimi.it*
[7]*University of Roma Tor Vergata, Rome, Italy, vairo@ing.uniroma2.it*

SUMMARY:
This work hinges on the extensive work carried out by the members of the Special Interest Group on Computational Wind Engineering of the Italian Association for Wind Engineering (ANIV-CWE, www.aniv-iawe.org/aniv-cwe) for advising UNI CT021/SC1, which led to the drafting of the informative Annex K of the revised EN 1991-1-4. Such a work will be contextualized in the state of the art in Computational Wind Engineering (CWE), highlighting the different trends in research, engineering practice in structural design, and codification. Emphasis will be placed on the fundamental principles for CWE codification that guided the endeavor of the ANIV-CWE working group and that can be recognized in the Annex K draft document. The key concepts of class of problem, CWE Specialist, consistency of computational model components, and computational model validation will also carefully be addressed.

Keywords: Computational Wind Engineering, best practices, codes and standards

1. INTRODUCTION

The weight in research of Computational Wind Engineering (CWE) related to structural applications (but also to environmental applications) has rapidly increased in the last decades thanks to the exponential growth of computer power and the increasing availability of software and cloud computing (see, e.g., Bruno et al., 2023; Potsis et al., 2023; Y. Tamura and Van Phuc, 2015). For the same reasons, CWE has shown a great development in engineering practice too, though with some delay with respect to research. In particular, after a fairly long phase of skepticism, nowadays in what Roache (1997) called the "commercial CFD arena" it is not uncommon to read advertisings that, in a very arguable way, promise the easy use of some CFD/CWE software even without any expertise on CFD (Computational Fluid Dynamics) and wind engineering.

In this context, the codification of CWE for structural design has also evolved. As explained more extensively in Bruno et al. (2023), initially codes and standards prudentially did not mention CFD/CWE, and this had the effect to allow a sort of "CFD wild west", characterized by a completely unregulated use of CWE. Consequently, between 2005 and 2009, some standards in-

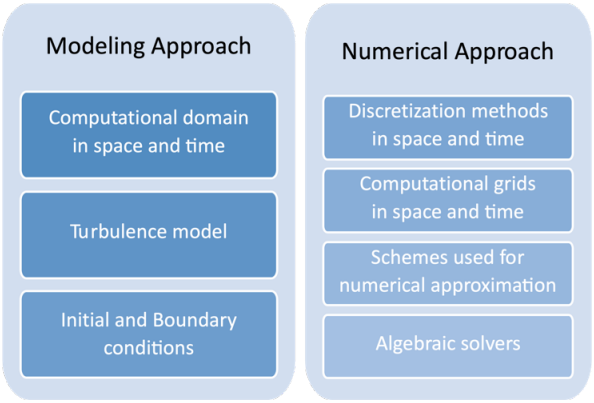


Figure 1. Components of a CFD/CWE model.

tervened, either by explicitly prohibiting the use of CFD for the wind-resistant design (such as the ISO 4354:2009) or by setting stringent prescriptions on the computational models and parameters to be used (such as AIJ-GWL 2005; see T. Tamura et al., 2008). Both approaches have drawbacks, since either they overlook the impressive advancements in research or they are destined to get old too fast due to the rapid evolution of CWE. In the light of that, the ANIV[1]-CWE Special Interest Group decided to follow a third path, a performance-based, informative approach, in its contribution first to the Annex T in the Italian recommendations CNR-DT 207-R1/2018, and more recently to the Annex K in PrEN 1991 1991-1-4:2021.

In the following, the fundamental principles and the general background of Annex K of the new Eurocode 1 part 1-4 are illustrated and discussed.

2. FUNDAMENTAL PRINCIPLES OF ANNEX K

In general, Annex K of the new Eurocode 1 part 1-4 is aimed at securing a correct and timely technology transfer between the CWE scientific community and the structural designers. The document has primarily been conceived to (i) allow structural designers to be aware of the fundamental principles of CWE; (ii) codify performance-based good practices for the use of CWE; (iii) warn designers against common misuses of CWE.

The document hinges on five fundamental principles, which are outlined here below (see Bruno et al., 2023 for more details).

1) CWE is not the same as CFD. Indeed, CWE blends concepts and methods of both CFD and wind engineering. Therefore, a CFD expert is not necessarily a CWE expert too, and specific guidelines for CWE are necessary.

2) A universal CWE model does not exist. Every model should reproduce with proper accuracy all the significant features of the physical phenomenon relevant to the application of interest. A schematic view of the main components of a CWE model is shown in Fig. 1, distinghing between those pertaining to the modeling approach and the numerical approach.

[1]Italian Association for Wind Engineering

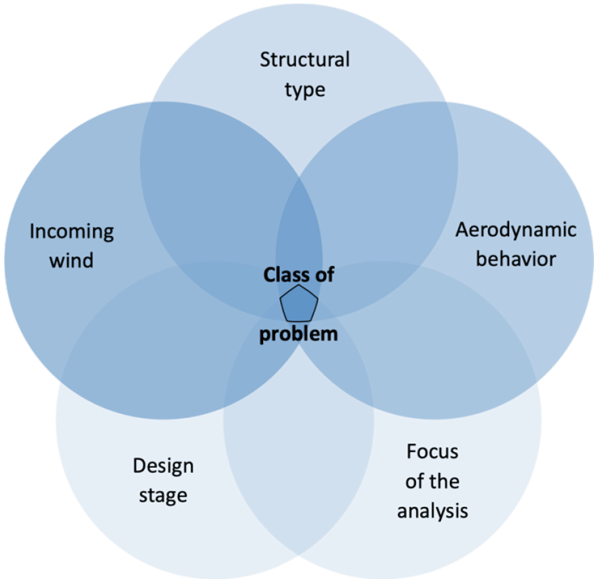


Figure 2. Design features contributing to the definition of a class of problem.

3) Pivotal role of the "class of problem". In view of point 2) above, the identification of the class of problem which the specific application belongs to is expected to represent the first and crucial step in a CWE analysis. As schematized in Fig. 2, the choice of the class of problem invokes a deep understanding of the physical background of the engineering application at hand, and even some qualitative predictions of the possible results of the analysis. Thus, this step clearly requires a solid expertise in both wind engineering and CFD.

4) Necessity of validation. In a similar way to other codes and standards about CWE, Annex K of the new Eurocode 1 part 1-4 requires that any computational model is validated against experiments or high-fidelity computational simulations selected from scientifically and technically qualified sources. Such a validation is mandatory for the class of problem to which the application belongs to, but it is not necessarily requested for every single application. In contrast, the use of a verified code is a necessary but not a sufficient condition for the reliability of a computational analysis of an engineering problem.

5) Distinction between the roles of Designer, CWE Specialist and Skilled Controller. The Annex hinges on the idea that interdisciplinary scientific and technical skills in both CFD and wind engineering, as well as long term professional experience are required to be in charge of CWE simulations. This means that the mere availability of CFD/CWE software and being familiar with its user-interface do not qualify for carrying out this task. The CWE Specialist is the person that fulfills these requirements, while the structural Designer usually does not have the specific competences required to play such a role. The Annex aims at allowing the structural Designer (or, more in general, the final customer of a CWE study) to dialogue and interact in an informed manner with the CWE Specialist. Finally, the document also envisages a third actor, that is a CWE Specialist without conflict of interest that can be entrusted by the customer to act as Skilled Controller to perform an independent control in particularly demanding design cases.

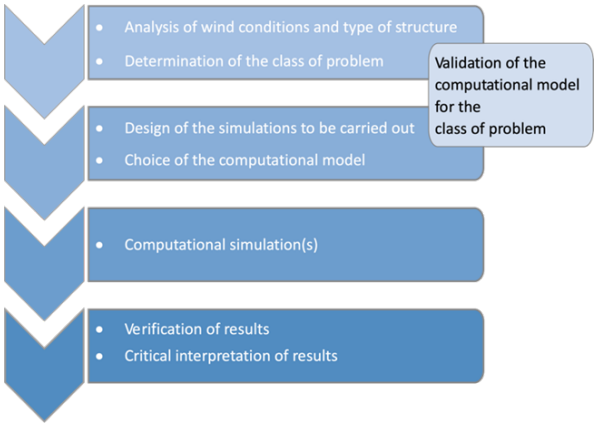


Figure 3. Recommended workflow of a CWE study.

Based on the fundamental principles outlined above, the workflow of a CWE study somehow implied by the Annex is schematized in Fig. 3.

3. CONCLUSIONS

In advising UNI CT021/SC1 for the drafting of Annex K of the new Eurocode 1 part 1-4, the ANIV-CWE Special Interest Group moved from the critical points risen by both an excess of prescriptive codification and an unconscious use of the rapidly evolving CWE techniques. Due to its informative nature, the document provides guidelines, mainly addressing Designers rather than CWE Specialists.

More information and discussion about the Annex and its background ideas will be reported in the conference presentation.

ACKNOWLEDGEMENTS

The activity outlined in this abstract was carried out under the umbrella of the Italian Association for Wind Engineering (ANIV), whose support is acknowledged. The authors warmly thank Davide Fransos and Andrea Lo Giudice, former members of the ANIV-CWE Group. The codification activity of the ANIV-CWE Group was strongly encouraged by Giovanni Solari, Franco Maceri and Francesco Ricciardelli: the authors gratefully acknowledge their stimuli.

REFERENCES

Bruno, L., Coste, N., Mannini, C., Mariotti, A., Patruno, L., Schito, P., and Vairo, G., 2023. Codes and standards on Computational Wind Engineering for structural design: State of art and recent trends. Wind and Structures 37, 133–151.

Potsis, T., Tominaga, Y., and Stathopoulos, T., 2023. Computational wind engineering: 30 years of research progress in building structures and environment. Journal of Wind Engineering and Industrial Aerodynamics 234, 105346.

Roache, P. J., 1997. Quantification of uncertainty in computational fluid dynamics. Annual Review of Fluid Mechanics 29, 123–160.

Tamura, T., Nozawa, K., and Kondo, K., 2008. AIJ guide for numerical prediction of wind loads on buildings. Journal of Wind Engineering and Industrial Aerodynamics 96, 1974–1984.

Tamura, Y. and Van Phuc, P., 2015. Development of CFD and applications: Monologue by a non-CFD-expert. Journal of Wind Engineering and Industrial Aerodynamics 144, 3–13.

Modernizing wind load standards for Ireland: A comparative analysis of first and second generation Eurocodes

Cunningham D.[1], MacReamoinn R.[2], Ramponi, R.[3], Keenahan, J.[4]

[1]*University College Dublin, Dublin, Ireland, david.cunningham2@ucdconnect.ie*
[2]*Arup, Dublin, Ireland, Reamonn.macreamoinn@arup.com*
[3]*Arup, Dublin, Ireland, Rubina.ramponi@arup.com*
[4]*University College Dublin, Dublin, Ireland, Jennifer.keenahan@ucd.ie*

SUMMARY: (10 pt)
This paper presents ongoing research examining the transition from first to second-generation Eurocodes (EN1991-1-4) for wind loading standards in Ireland. The study aims to evaluate the implications of proposed changes in wind loading calculations for typical Irish building structures, addressing previous criticisms of the first-generation Eurocodes regarding complexity, layout, and conservatism. The research methodology includes systematic evaluation of various building typologies, including industrial, residential, and commercial structures, to quantify the anticipated impact of revised calculation procedures for key parameters such as peak velocity pressure, structural factors, and pressure coefficients. The approach combines theoretical analysis with practical applications, utilizing automated modeling through Python-Robot Structural Analysis integration to assess potential effects on lateral stability system design. This methodology will enable comprehensive evaluation of both economic and environmental impacts of the code revisions. The research seeks to inform the National Standards Authority of Ireland (NSAI) regarding the suitability of the updated Eurocode for Irish construction, particularly focusing on the development of the new National Annex. Initial review has identified significant changes in calculation procedures and the introduction of new coefficients, which may influence the design of building structures across Ireland.

Keywords: wind loading, Eurocodes, calibration study.

1. INTRODUCTION

In anticipation of the implementation of the second-generation Eurocodes, this paper aims to analyse the changes made to the wind loading design code, EN1991-1-4. The project is focused on the expected impact of the wind loading changes on typical building structures in Ireland. Calibration studies have been conducted previously for the change in code of practice from the BS 6399-2 standard to the first-generation Eurocode, EN1991-1-4:2005. These calibration studies were useful in evaluating the differences in wind loading between the two codes and helped to inform the National Standards Authority of Ireland (NSAI) on suitable changes to be made to the European Standard during formulation of the Irish National Annex (NA). The goal of the research in this paper is to achieve a similar outcome by outlining the changes to the new draft Eurocode that are required to ensure a safe and economic standard for the country of Ireland.

Since the introduction of the first-generation Eurocodes in the early 2000s, the standards have received widespread criticism regarding their complexity, inconvenient layout and over-conservatism. EN1991-1-4 (wind actions on structures) is no exception, gaining notoriety for its difficulty to navigate for users. Calibration studies revealed issues in the calculation procedures for important parameters such as peak velocity pressure (qp). These were predominantly due to simplifications in the basic EN methods which led to both conservative and non-conservative results depending on the structure type and location. Implementing the Eurocode wind loading standard raised concerns regarding safety and economy for buildings in Ireland. As a result of this calibration study, the British and Irish National Annex made significant changes to the European standard code of practice to create a design code more alike to the previous standard, BS 6399-2.

With the upcoming introduction of the second generation EN codes, a new calibration study is required to determine its differences between the current Irish NA. Changes have been made to calculation procedures in the new code, each requiring a detailed analysis and comparison to the results achieved using the current code of practice. By considering typical building structures (see table 1.1) subject to wind loading derived from both the current and upcoming codes of practice, a detailed comparative analysis will be done, outlining areas of concern and improvement.

The results of this research project will allow the NSAI to assess the suitability of the updated codes for application to typical building structures in Ireland. Using the data from this project, informed decisions will be made possible regarding the suitability of particular methods, informative annexes and nationally determined parameters for inclusion in the new Irish National Annex.

2. METHODOLOGY

This research project is reliant on the identification of changes between the old and new codes of practice. A comparative study will be undertaken to identify key changes in code of practice which will form the basis of the analysis done in this project. This will be done for a variety of case studies as presented in Table 1.

Table 1. Typical Building Types to be Investigated.

Building Types	Geometric Variations			Structure Type
	Height		Plan Area	
	Number of Storeys	Storey-to-storey height		
Industrial Buildings	1	4m-15m	500 m^2 to 10,000m^2	Steel sway frame
	2-4	4.5m-6m		Braced steel frame
Residential	Low-rise: 1-3	3.15m	Medium: 600 m^2 to 1500m^2 Large: 1500 m^2 to 2500m^2	Rigid Diaphragms with Shear Walls
	Mid-rise: 4-10	3.15m	Medium: 600 m^2 to 1500m^2 Large: 1500 m^2 to 2500m^2	
	High-rise: 10-30	3.15m	Medium: 600 m^2 to 1500m^2 Large: 1500 m^2 to 2500m^2	
Commercial	Low-rise: 1-3	3.5m-4.5m	Small: 500 m^2 to 1000m^2 Medium: 1000 m^2 to 2500m^2 Large: 2500 m^2 to 5000m^2	Rigid Diaphragms with Shear Walls
	Mid-rise: 4-10	3.5m-4.5m	Small: 500 m^2 to 1000m^2 Medium: 1000 m^2 to 2500m^2 Large: 2500 m^2 to 5000m^2	

	High-rise: 10-30	3.5m-4.5m	Small: 500 m² to 1000m² Medium: 1000 m² to 2500m² Large: 2500 m² to 5000m²	

One of the goals of this research project is to provide a tangible impact of the changes in wind loading between the existing code, and the proposed new one. The previous wind load calibration study provided data and results regarding changes in wind load parameters such as pressure coefficients and wind speeds in isolation, without quantifying the effects of such changes on the actual design of the structure. Although these changes are of great importance to the structural engineer, other construction professionals are interested in the effect of these changes on the overall building. The aim is to contextualise any changes observed in wind loading parameters by providing tangible results relating to the final design of the lateral stability system of a structure through evaluation of its economic and environmental impact. For example, if a particular increase in wind load is observed for a braced frame structure, what effect will this have on the actual design of the laterally stabilising structure like bracing or shear walls?

Structures of varying function, material and geometry will be investigated. To achieve consistency in the analysis, design and comparison of performance of the lateral stability systems for these structures, the position and sizes of these systems need to be carefully chosen. By choosing the optimum location of such lateral stability systems for structures of differing geometry, a fair comparison can be made between the results obtained from the analysis and design these systems. To achieve this, algorithms for each building type will be used as a means of applying a consistent methodology for identifying optimum sizes and locations of lateral stability systems. For example, research by Ying Zhou & Mehmet E. Korkmaz (2013) provides detailed methodologies and optimisation algorithms for efficient placement of shear walls and bracing. Adeli and Zhang (1995) also provide algorithms to find optimal locations for lateral force-resisting systems in high rise buildings.

3. PRELIMINARY FINDINGS

A significant proportion of the new Eurocode has already been examined and fundamental changes or new inclusions have been identified. A sample of some of the important changes that will form the basis of this research include:

- Change in procedure for calculation of peak velocity pressure (q_p), structure factor (c_{sd}), turbulence intensity (I_u) for slender structures and windward wall external pressure coefficients (c_{pe}).
- Introduction of global pressure coefficients ($c_{pe,G}$) for evaluation of global wind effects on the foundations and lateral stability systems of buildings.
- Introduction of new procedures for determination of external pressure coefficients for irregularly shaped buildings, and additional guidance and assessment criteria for across and along-wind vibrations and aeroelastic phenomena such as galloping.

For each of the changes listed above, their effects will be quantified with respect to a series of chosen structure types of varying geometry and location. In the instance that a new inclusion in the updated Eurocode is being investigated, a comparison of the equivalent methodology that would have been conducted in absence of this additional guidance will be investigated. For

example, when examining the new procedures for irregularly shaped buildings, a comparison of a typical procedure implemented by a practicing engineer in absence of this guidance will be explored. From this analysis, a comparison between the two codes of practice will be made for values such as surface pressures, total base shear and overturning moment.

4. FURTHER WORK

The lateral stability system of each structure will be designed using the calculated wind loading values to illustrate the physical impact of the changes in wind loading magnitudes. This will be achieved through programmatic communication between Python and Robot Structural Analysis (Robot), a finite element analysis software commonly used in structural engineering practice in Ireland.

Robot has an extensive Application Programming Interface (API) through which one can communicate programmatically with the software. The API allows for almost any software functionality to be accessed through code, meaning that modelling of geometry, application of loads, structural analysis and extraction of results for design can all be automated. Python and Robot will be used to automate the modelling of geometry, application of wind loading and extraction of results for the various structures under investigation.

The Robot models created during the thesis will act as a reference point if future interrogation of the results generated from this project is required. As Robot is a commonly used software in structural engineering practice, this will increase the trustworthiness of the data generated in this project.

ACKNOWLEDGEMENTS

The authors wish to acknowledge seed funding provided by Construct Innovate in Ireland.

Along-wind dynamic response in Eurocode

Svend Ole Hansen [1], Marie Louise Pedersen[2], Robin G. Srouji[3], Nicolò Daniotti[4]

[1] *Svend Ole Hansen ApS, Copenhagen, Denmark, soh@sohansen.dk*
[2]*Svend Ole Hansen ApS, Copenhagen, Denmark, mlp@sohansen.dk*
[3]*Svend Ole Hansen ApS, Copenhagen, Denmark, rgs@sohansen.dk*
[4]*Svend Ole Hansen ApS, Copenhagen, Denmark, nid@sohansen.dk*

SUMMARY
The present abstract describes the calculation procedure for along-wind response of structures expected to be specified in the second-generation Eurocode on wind actions EN 1991-1-4, planned to be published in 2025. The current Eurocode provides two models deviating in the theoretical formulations, however without giving significant differences in the response calculated for most structures having mode shapes with constant sign. The two models are used to calculate the equivalent static wind loads using the structural factor being a product between a size effect factor and a dynamic factor, the latter taking the effect of resonant vibrations into account. The second generation of Eurocode on wind actions EN 1991-1-4 has specified a new model that is based on the most suitable features of the two models currently adopted. Furthermore, the same theoretical framework can be used to estimate the wind-induced loads of structures having modes with changing sign. An overview of the new model is provided in this abstract. The new model will be compared up against full-aeroelastic wind tunnel tests of cable-stayed bridges in their construction stage with maximum deck cantilevers.

Keywords: Eurocode, buffeting loads, equivalent static wind loads

1. BACKROUND

The current Eurocode EN1991-1-4 provides two models for calculating the buffeting response of structures having mode shapes with constant sign. The second generation of Eurocode on wind actions EN 1991-1-4, which is planned to be issued in 2025, includes a new codified model for calculating the along-wind dynamic response of structures. Among the different new features, the following may be outlined:

1. Aerodynamic admittance functions are included in a product format to model the correlation of surface pressures in each cross section and the correlation of the cross-sectional loads along the main axis of the structure.
2. Background and resonant response factors are calculated in a similar fashion with admittance functions using adequate non-dimensional size parameters.
3. For vertical structures such as tall buildings, the procedure allows for the calculation of both background and resonant response at different elevations above ground level.
4. Equivalent static wind loads can be estimated for structures having non-constant sign mode shapes.

The codified procedure covers structures for which only one dominant mode is significant for the wind-induced response. The mass per unit length is assumed to be constant in the portion of the

structure for which the modal deflection is significant.

2. ADMITTANCE FUNCTIONS

The admittance function describes the conversion of wind velocity power spectra to wind load power spectra. It is specified by the product between the cross-sectional admittance function and a span-wise admittance function based on the correlation of the incoming wind along the main axis of the structure, see Figure 1. The admittance function depends on the static influence line for background response and on the mode shape for resonant response.

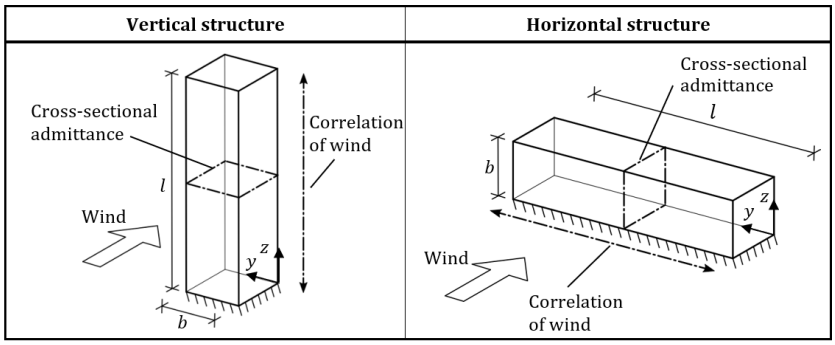


Figure 1. Cross-sectional admittance and correlation of wind where $l > b$.

The admittance functions for constant sign static influence lines and mode shapes are described via a basic reference case given by Equation (1) and shown in Figure 2:

$$\chi^2(\phi) = \chi_U^2(\phi) = \frac{2}{\phi^2} \cdot \left(\phi - 1 + e^{-\phi}\right) \tag{1}$$

where ϕ is a non-dimensional size parameter defined as the ratio between a structural dimension and a characteristic air flow dimension.

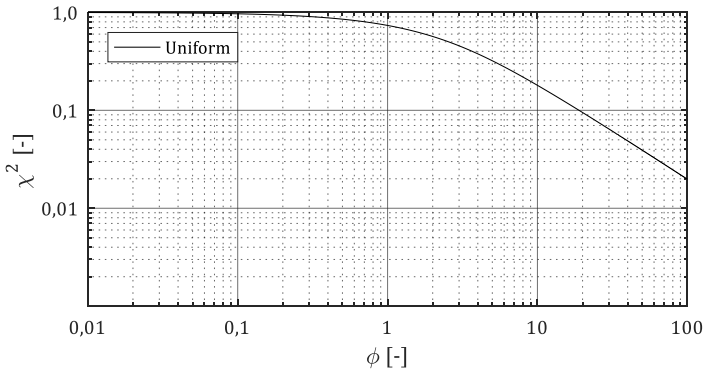


Figure 2. Admittance function for uniform static influence lines and mode shapes.

For background turbulence based on static influence lines, the air flow dimension is an integral length scale describing the flow correlations. For resonance turbulence based on mode shapes, the air flow dimension is a length scale corresponding to the natural frequency of the structure considered.

3. BACKGROUND AND RESONANCE RESPONSE FACTORS

The dynamic along-wind response of wind sensitive structures to wind turbulence consists of two

contributions: the background turbulence response and the resonant response. In the Eurocode format, they are modelled by the background response factor B^2 and resonance response factor R^2, respectively. Both factors, which are in principle two-dimensional, are calculated in a consistent way as a product between a cross-sectional admittance and a line-like admittance along the main axis of the structure. Background theory can be found in (Hoffmann et al., 2019).

The background response factor models the integrated effects on the response reduction due the lack of full correlation of surface pressures along the structure exposed to background turbulence. It is determined as follows:

$$B^2 = \chi_{\mathrm{U}}^2(\phi_{B,\mathrm{C}}) \cdot \chi^2(\phi_{B,\mathrm{L}}) \tag{2}$$

where $\chi_{\mathrm{U}}^2(\phi_{B,\mathrm{C}})$ and $\chi^2(\phi_{B,\mathrm{L}})$ are cross-sectional and span-wise admittance functions, respectively. They can be calculated using Equation (1) for modes with constant sign using prescribed non-dimensional background size parameters. For modes with changing sign, the span-wise admittance has a different expression, see Section 4.

The resonance response factor models turbulence in resonance with the considered vibration mode of the structure and is given by:

$$R^2 = \frac{\pi^2}{2\delta} S_{\mathrm{N},u}(n) \cdot \chi_{\mathrm{U}}^2(\phi_{R,\mathrm{C}}) \cdot \chi^2(\phi_{R,\mathrm{L}}) \tag{3}$$

where δ is the total logarithmic decrement of damping; $S_{\mathrm{N,u}}(n)$ is the non-dimensional power spectral density of the along-wind turbulence component evaluated at the reference elevation and at the natural frequency n; $\chi_{\mathrm{U}}^2(\phi_{R,\mathrm{C}})$ and $\chi^2(\phi_{R,\mathrm{L}})$ are cross-sectional and span-wise admittance functions, respectively. They can be calculated using Equation (1) for modes with constant sign using prescribed non-dimensional resonance size parameters. For modes with changing sign, the span-wise admittance has a different expression, see Section 4.

For vertical structures with constant sign mode shape cases with a single support, the resonance factor for responses at level $z = z_{up} > 0$ above the foundation may be determined as follows:

$$\frac{R_{z_{up}}^2}{R_{z_{up}=0}^2} = \left(\frac{1 - \frac{\zeta+2}{\zeta+1} \cdot \frac{z_{up}}{l} + \frac{1}{\zeta+1} \cdot \left(\frac{z_{up}}{l}\right)^{2+\zeta}}{\left(1 - \frac{z_{up}}{l}\right)^2} \right)^2 \quad \text{for } z_{up} < l, \tag{4}$$

$$\frac{R_{z_{up}}^2}{R_{z_{up}=0}^2} = K^2{}_{R,\mathrm{L}} \quad \text{for } z_{up} = l \tag{5}$$

where ζ is an exponent used to describe the fundamental mode shape $(z/l)^{\zeta}$ and $0 \le \zeta \le 2.50$; $K_{R,\mathrm{L}}$ is the load distribution factor for resonance turbulence computed as $K_{R,\mathrm{L}} = 1/2 \cdot (\zeta + 2)$.

4. NON-CONSTANT SIGN MODE SHAPES

For non-constant sign mode shapes, see Figure 3 as an example, the spatial and time-wise maximum amplitude of the fluctuating wind load is calculated as follows:

$$F_{\mathrm{w,f}} = 2 \cdot c_{\mathrm{f}} \cdot I_u(z_s) \cdot q_{\mathrm{m}}(z_s) \cdot b \cdot \sqrt{\left(k_{\mathrm{B}} \cdot K_{B,L} \cdot B\right)^2 + \left(k_{\mathrm{R}} \cdot K_{R,L} \cdot R\right)^2}\ , \tag{6}$$

where z_s is the reference height; c_f is the force coefficient; $I_u(z_s)$ is the along-wind turbulence intensity; q_m is the characteristic mean velocity pressure; b is crosswind height of the structure; k_B and k_R are peak factors for the background and resonance response, respectively; $K_{B,L}$ and $K_{R,L}$ are load distribution factors for background and resonance turbulence, respectively.

In the calculation of the background B^2 and resonance factors R^2, the span-wise admittance functions for mode shapes being cantilever are given by Equation (7) and shown in Figure 4:

$$\chi^2_{\mathrm{NC}}(\phi) = \frac{2}{3 \cdot \phi} - \frac{2}{\phi^2} + \frac{8}{\phi^4} - e^{-\phi} \cdot \left(\frac{2}{\phi^2} + \frac{8}{\phi^3} + \frac{8}{\phi^4}\right) \qquad \text{for cantilever} \tag{7}$$

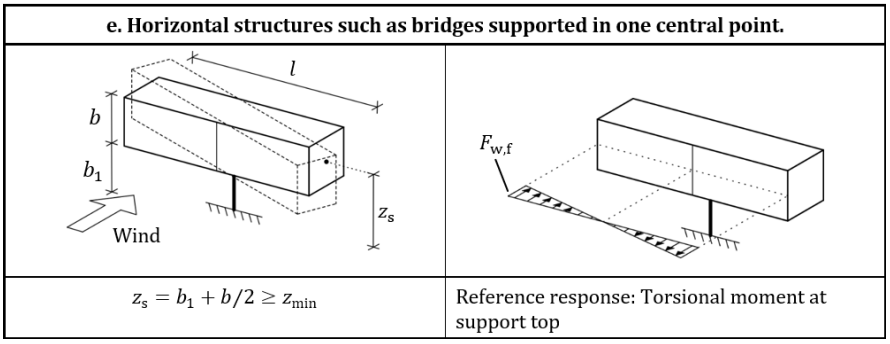


Figure 3. Structural dimensions and reference heights for structures where $l > b$. Non-constant sign mode shapes.

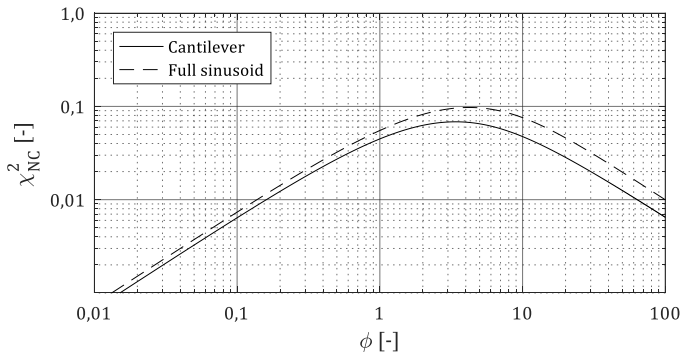


Figure 4. Span-wise admittance functions for non-constant mode shapes.

The presentation will provide a comparison between the codified procedure and wind tunnel tests on full-aeroelastic tests on cable-stay bridges during the construction stage with maximum deck cantilevers.

REFERENCES

Hoffmann, K., Pedersen, M. L., Hansen, S. O., 2019. Codified procedure for buffeting response of buildings and bridges. 15th International Conference on Wind Engineering (ICWE), Beijing, China.

Impact of climate change for blowing snow in Hokkaido assessed by a large ensemble dataset

Kuniyasu Sugawara [1,2], Masaru Inatsu[3], Yusuke Harada [1]

[1]*Civil Engineering Research Institute for Cold Region, Public Works Research Institute, Sapporo, Japan, sugawara-k@ceri.go.jp, harada-y@ceri.go.jp*
[2]*Graduate School of Science, Hokkaido University, Sapporo, Japan*
[3]*Faculty of Science and Center for Natural Hazards Research, Hokkaido University, Sapporo, Japan, inaz@sci.hokudai.ac.jp*

SUMMARY
This study evaluated the impact of climate change on the intensity of blowing-snow events across a wide probability spectrum including extreme events by a dynamically-downscaled meteorological dataset with a large number of ensembles called d4PDF. Focusing on the four sites in Hokkaido, the northernmost island of Japan, the hourly snow transport rate (STR; kg m^{-1} h^{-1}) was estimated as an index of the blowing-snow intensity. The bias-corrected historical experiment of d4PDF was found to be able to reproduce the STR distribution based on the AMeDAS observation data. The occurrence probability of severe blowing-snow events (STR exceeding 300 kg m^{-1} h^{-1}) exhibited non-uniform distribution. The +2-K future climate experiment using d4PDF data predicted that severe blowing-snow events would be suppressed. The frequency distribution of STR was the most shifted at a site along the Pacific coast.

Keywords: blowing snow, climate change, extreme event

1. INTRODUCTION

Blowing snow inhibits drivers' visibility and often causes snowdrifts on roads. It occurs not only during snowfall but also even in sunny weather if snow particles pump up from the snow surface. Hokkaido, the northernmost island of Japan, often experiences severe blowing snow and sometimes ends up with road closure (e.g., Inatsu et al. 2020).

A reduction in snowfall throughout the winter has been shown with global warming (e.g., Kawase et al. 2023). However, there are few publications on a future change focusing on blowing snow. One of the exceptions is Greaves et al. (2023), who assessed climate change effect on the severe blowing snow in Alaska, U.S.A., and Yukon, Canada. Based on two global climate model (GCM) simulations in 2006−2020 and 2081−2100, they suggested that severe blowing-snow events become less frequent but intensified. However, none of the studies quantitatively assessed blowing snow intensity directly. The purpose of this study is to assess the impact of climate change on the magnitude of the blowing-snow events across a wide probability spectrum including extreme events, by using a dynamically downscaled meteorological dataset with a large number of ensembles, the Database for Policy Decision Making for Future climate change (d4PDF; Mizuta et al. 2017; Fujita et al. 2019).

2. DATA AND METHOD

We used hourly data of 2-m air temperature, 10-m wind speed, and snowfall in 20-km resolution dynamical-downscaling d4PDF data covering Japan. The d4PDF contains the historical experiment (hereafter HIST run) and the +2-K future climate experiment (hereafter 2K run). The latter was almost equivalent to the 2040s in the RCP8.5 scenario. The number of ensemble members are 50 in the HIST run and 54 in the 2K run, each of which contains 60-year data.

We evaluated the intensity of blowing snow by the hourly snow transport rate (STR; kg m^{-1} h^{-1}). Following the previous studies, the hourly STR up to 7-m height Q_h is directly computed from the snowfall, 10-m wind speed, and surface air temperature (Takeuchi et al. 1986; Takechi et al. 2023). The STR greater than 300 kg m^{-1} h^{-1} has been shown to correspond to the hourly mean visibility of less than 50 m (Harada et al. 2023).

We also used the observational data at 22 sites of the Automated Meteorological Data Acquisition System (AMeDAS) in Hokkaido from the 2009/10 to 2018/19 winters. It should be noted that we focused on a winter season from November 1 to March 31 of the following year. In the calculation of STR in AMeDAS sites, the time difference in snow depth was regarded as precipitation of snow assuming that 1 cm of snow was equivalent to 1 mm of water. In addition, the wind speed was corrected to a 10-m height value by the logarithmic law for neutral air based on the anemometer height at AMeDAS sites. The roughness length was given as 1.5×10^{-4} m assuming a fresh snow surface (Oura et al. 1967). Considering the 10-winter's mean of the annual STR (Fig. 1), we targeted four AMeDAS sites of Haboro, Abashiri, Urakawa, and Iwamizawa in the analysis. The AMeDAS sites of Rumoi and Esashi were out of our scope because these two sites are located on headlands and docks, respectively.

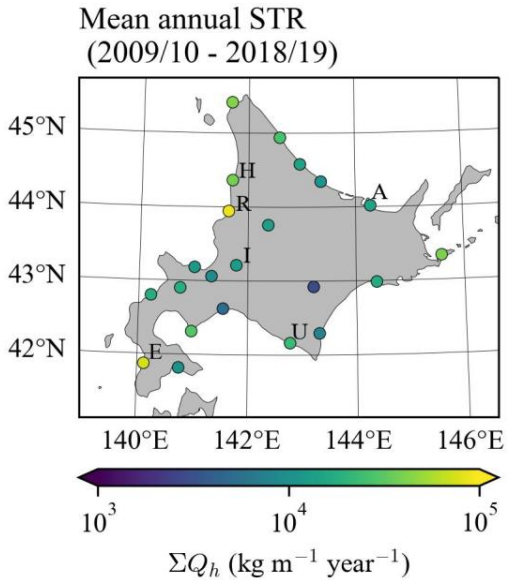


Figure 1. The mean annual STR of the AMeDAS observation points from 2009/10 to 2018/19 winters, as per the color reference in the bottom (kg m^{-1} h^{-1}). The letters H, A, U, I, R, and E respectively indicate the AMeDAS sites Haboro, Abashiri, Urakawa, Iwamizawa, Rumoi, and Esashi.

3. RESULT

Figure 2 shows the complementary cumulative frequency of the hourly STR at the target sites in Hokkaido (Fig. 1). The STR based on the AMeDAS data exhibited a similar frequency distribution to that based on the bias-corrected d4PDF data, except for the Haboro site (Fig. 2a). The hourly STR distribution has much spatial dependency: severe blowing snow with $Q_h > 300$ kg m^{-1} h^{-1} occurred approximately once per winter in Abashiri (Fig. 2b). The occurrence probability of such an event exceeded much more than once per winter in Haboro and Urakawa (Figs. 2a and 2c). In contrast, it is less frequent in Iwamizawa (Fig. 2d). As the STR generally decreased in response to global warming, the frequency distribution changed in a way that severe events became rarer. The STR frequency distribution was much shifted in Urakawa (Fig. 2c). The expected decrease in STR was up to 50% in Urakawa, whereas it was up to 20% at the other sites. It has been suggested that the suppression of severe blowing-snow events in Urakawa is related to a decrease in the duration of snow cover (Sugawara et al. 2024).

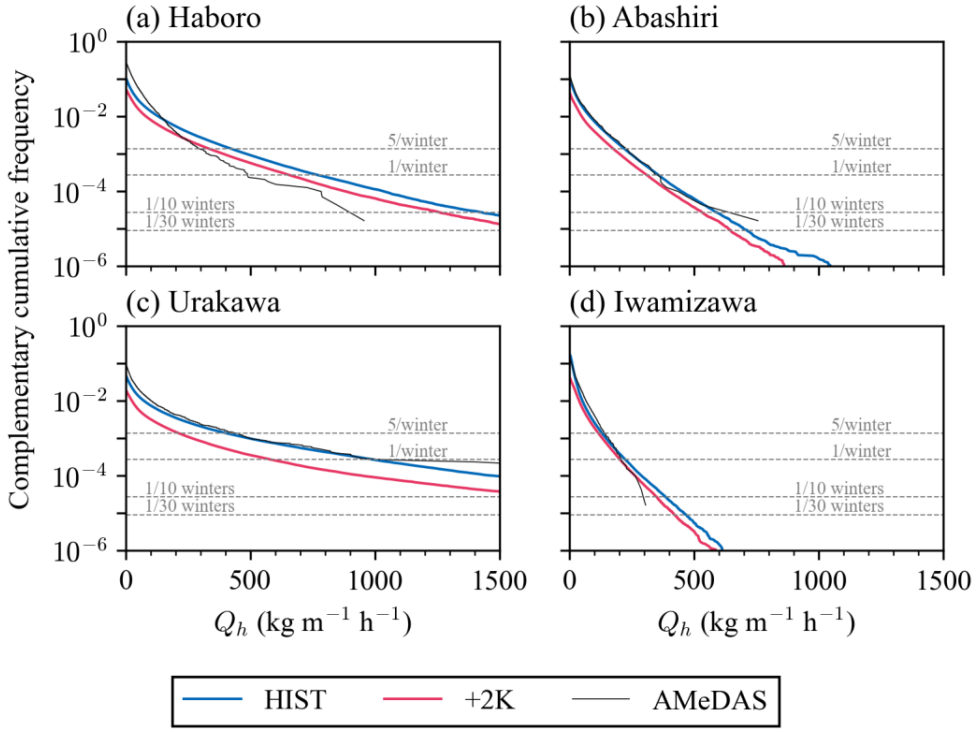


Figure 2. Complementary cumulative frequency of an hourly STR at (a) Haboro, (b) Abashiri, (c) Urakawa, and (d) Iwamizawa, plotted to the Cunnane plotting positions. Blue and red thick, and black thin lines denote the HIST run, 2K run, and AMeDAS, respectively. The gray dotted horizontal lines from top to bottom indicate the return periods of five times per winter, once per winter, once per 10 winters, and once per 30 winters.

ACKNOWLEDGEMENTS

We would like to thank Dr. Seika Tanji for her valuable comments on our study. This study is supported by JPMXD0722680734 of Ministry of Education, Sports, Culture, Science and Technology (MEXT) of Japan. MI is supported by the Environment Research and Technology Development Fund JPMEERF20232003 of the

Environmental Restoration and Conservation Agency of Japan. This study used d4PDF products produced with the Earth Simulator of Japan Agency for Marine-Earth Science and Technology jointly with science program of SOUSEI, TOUGOU, and SI-CAT of MEXT.

REFERENCES

Fujita, M., and co-authors, 2019. Precipitation changes in a climate with 2-K surface warming from large ensemble simulations using 60-km global and 20-km regional atmospheric models. Geophysical Research Letters 46, 435–442.

Greaves, H. E., N. T. Boelman, T. J. Brinkman, G. E. Liston, L. R. Prugh, and A. K. Reinking, 2023. Simulating future climate change impacts on snow- and ice-related driving hazards in Arctic-boreal regions. Environmental Research Letters 18, 025006

Harada, Y., S. Omiya, H. Takechi, and A. Nishimura, 2023. Investigation of evaluation for severe snowstorm and snowfall events in the snowy cold region of Japan, Part 1. Journal of Snow Engineering of Japan, 39, 11–27 (in Japanese with English abstract).

Inatsu, M., S. Tanji, and Y. Sato, 2020. Toward predicting expressway closures due to blowing snow events. Cold Regions Science and Technology 177, 103–123.

Kawase, H., and co-authors, 2023. Historical regional climate changes in Japan in winter as assessed by a 5-km regional climate model with a land surface process. Progress in Earth and Planetary Science 10.

Mizuta, R., and co-authors, 2017. Over 5,000 years of ensemble future climate simulations by 60-km global and 20-km regional atmospheric models. Bulletin of American Meteorological Society 98, 1383–1398.

Oura, H., D. Kobayashi, and S. Kobayashi, 1967. Characters of the Wind-speed Profile during Drifting Snow. I. Low temperature science. Series A, Physical sciences 25, 73–88 (Available online at: http://hdl.handle.net/2115/18062, accessed 10 October 2024, in Japanese with English abstract).

Sugawara, K., M. Inatsu, and Y. Harada, 2024. Climate change assessment on blowing snow in Hokkaido using a large ensemble dataset. Scientific Online Letters on the Atmosphere 20, 217–222.

Takechi, H., S. Omiya, T. Matsushima, Y. Harada, A. Nishimura, and T. Kameda, 2023: Comparison of blowing-snow amount based on conventional empirical formulae with new observation (2) – based on observations during blowing snow in Ishikari. Summaries of JSSI and JSSE Joint Conference on Snow and Ice Research - 2023 in Koriyama, 78 (in Japanese).

Takeuchi, M., K. Ishimoto, T. Nohara, and Y. Fukuzawa, 1986. Dynamic threshold wind speed for suspension. Proceedings of the annual meeting of the Japanese Society of Snow and Ice, 252 (in Japanese).

CFD simulation of aeolian sand erosion and deposition around a bluff body

Zitao Jiang[1], Yoshihide Tominaga[2], Xin Zhang[3]

[1]*Niigata Institute of Technology, Kashiwazaki City, Japan, jiang_zitao@niit.ac.jp*
[2]*Niigata Institute of Technology, Kashiwazaki City, Japan, tominaga@abe.niit.ac.jp*
[3]*Kochi University, Kochi City, Japan, xin.zhang@kochi-u.ac.jp*

SUMMARY:
Aeolian sand transport, accompanied by erosion and deposition, is of great relevance for built environment in costal and desert region. This paper investigates the sand movement around a rectangular bluff body by computational fluid dynamics (CFD). Two sand transport prediction methods were compared. In the previous studies, the sand surface height change was predicted by directly using the friction velocity, however, it neglects the sand deposition. To take the sand deposition into consideration, a new method uses the divergence of sand transport flux to estimate the sand surface height change rate. The performance of two methods are compared using CFD. Both methods predict sand erosion at the front corner. Method 1 entirely neglects the sand deposition while Method 2 overestimates the sand deposition area.

Keywords: CFD, Aeolian sand transport

1. INTRODUCTION

The built environment of coastal and desert cities is frequently affected by the adverse impacts of aeolian sand transport, encompassing both erosion and deposition processes. Modelling aeolian sand transport plays a crucial role in developing effective mitigation strategies to manage unwanted sand movement, thereby improving the quality and sustainability of the built environment.

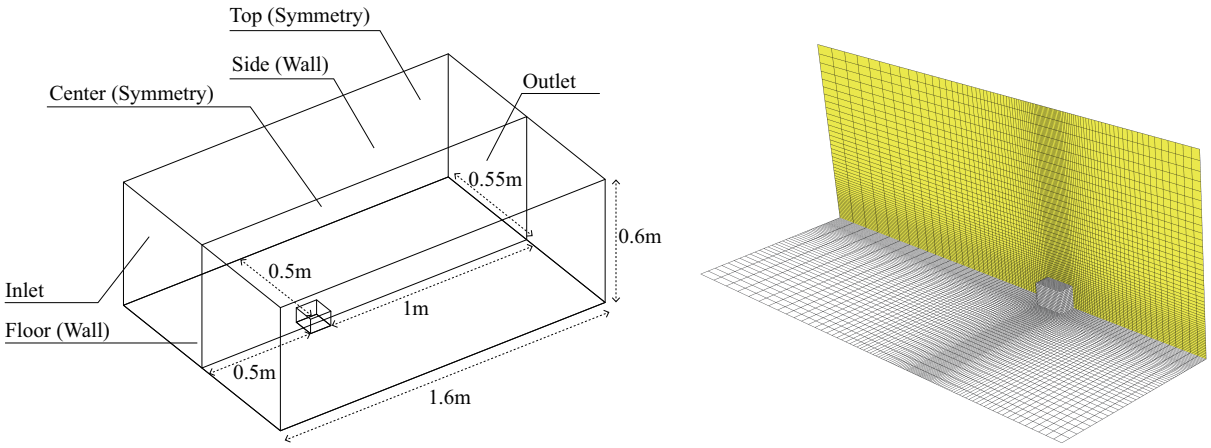
Aeolian sand transport has been explored through field measurements (Poppema et al., 2022), wind tunnel experiments (Tominaga, Okaze, et al., 2018), and numerical simulations (Pourteimouri et al., 2023). However, the complexity of environmental parameters and boundary conditions often renders field measurements impractical for parametric studies. In wind tunnel experiments, maintaining similarity laws for sand dynamics presents particular challenges, limiting the generalizability of conclusions from reduced-scale models (Raffaele, Beeck, et al., 2021; Raffaele, Glabeke, et al., 2023). As a result, carefully validated computational simulations offer significant potential for investigating the wind-driven sand transport process. Although several models of sand transport have been proposed, their integration into numerical simulations remains insufficiently explored and discussed in the literature.

This study employs Computational Fluid Dynamics (CFD) to investigate aeolian sand transport around a simple surface-mounted obstacle. The structure of this paper is as follows: Section 2 presents the numerical settings and two sand sediment models, Section 3 analyses the simulation results, and Section 4 summarizes the key findings of the study.

2. NUMERICAL SETTINGS

2.1. Computational settings

The CFD in this study intends to reproduce the experimental settings reported by Tominaga et al. (Tominaga and Zhang, 2024) in an atmospheric boundary layer wind tunnel at the Niigata Institute of Technology, Kashiwazaki, Japan. In the experiment, the floor was covered by a layer of 30mm deep sand, and the original dimension of the target obstacle was 0.1 (height) x 0.1 (width) x 0.1 (length) m^3. In the CFD, the height of the obstacle was set to 0.07 m to represent the obstacle height above the sand surface. The computational domain is 0.6 (height) $\times$ 0.55 (width) $\times$ 1.6 (length) m^3 as show in Fig. 1, the centre plane is set as symmetry boundary condition to reduce the computational resources. The upstream and downstream distance were set to 5H and 10H according to the AIJ guidelines for CFD to wind environment around buildings(Tominaga, Mochida, et al., 2008).



(a) Computation domain (b) Grid layout

Figure 1. Computational domain and grid layout.

The inlet wind profile measured in the wind tunnel experiment follows a power law with an exponent of 0.14, and the reference velocity and the reference height (100 mm from the sand surface) without the obstacle was 6.5 m/s. The standard $k-\varepsilon$ model was selected for the turbulence model with standard wall function.

2.2. Sand sediment transport model

Two sand transport model was considered in the present study. The difference between two methods lie in the treatment of height change. In the previous study (Tominaga, Okaze, et al., 2018), the sand surface changes was predicted by sand transport flux based on friction velocity (Method 1). Method 1 does not take the sand suspension into consideration. The equation proposed by Kawamura was used to predict the sand transport rate [kg/m $\cdot$ s] (Kawamura, 1951):

$$|\vec{q}| = C_1 \frac{\rho_a}{g}(|\vec{u_*}| - u_{*t})(|\vec{u_*}| + u_{*t})^2 \tag{1}$$

$$|\vec{q}| = 0 \qquad u_* \leq u_{*t} \tag{2}$$

where C_1 is the model constant = 2.78 [-], the fluid density ρ_a= 1.29 [kg/m^3], g is the gravitational acceleration [m/s^2], u_* is the friction velocity [m/s], the threshold velocity u_{*t} = 0.24 [m/s]. The

sand surface change rate $\Delta z/\Delta t$ can be calculated by the following equation:

$$\frac{\Delta z}{\Delta t} = \frac{|\vec{q}|}{\rho_s \cdot h_s} \tag{3}$$

where the sand density ρ_s= 1590 [kg/m^3], h_s in the present study is the height of the first cell centre to the sand surface, which is consistent with Tominaga's research (Tominaga, Okaze, et al., 2018).

In Method 2, the bed height change is based on the divergence of sand transport flux $\nabla\vec{q}$. The sand sediment flux is proposed by Nickling et al. (Nickling and Neuman, 2009) based on Bagnold's equation (Bagnold, 1937) calculated by Eq. (4).

$$\vec{q} = C_2 \frac{\rho_a}{g}\sqrt{\frac{d}{D}}(|\vec{u_*}| - u_{*t})^3 \frac{\vec{u_*}}{|\vec{u_*}|} \tag{4}$$

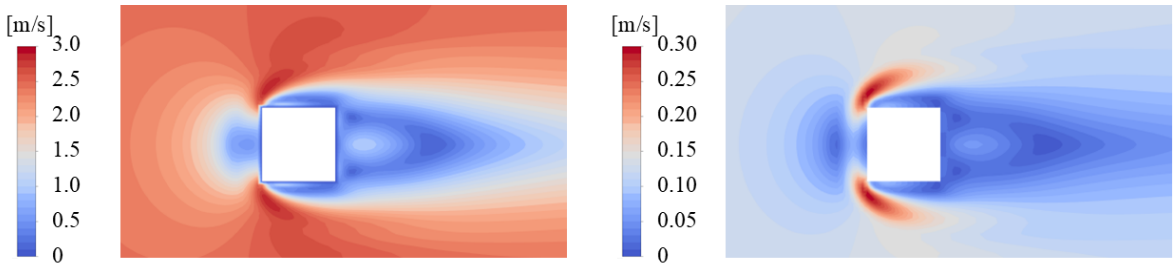
where the model constant C_2 =1.80 [-]. The sand bed level change was then calculated by the Exner equation (Yalin, 1972) according to Eq. (5)

$$\frac{\Delta z}{\Delta t} = -\frac{\nabla \cdot \vec{q}}{\rho_s(1-n)} \tag{5}$$

where the sediment porosity n=0.40 [-]. It should be noted that all the constants in both Method 1 and Method 2 should be further tuned in future studies.

3. RESULTS

Fig. 2 shows the velocity magnitude and friction velocity at the height of first cell centre (2.5mm). The largest friction velocity can be observed at the shear layer at frontal corner and lateral sides of the obstacle.



(a) Velocity magnitude contour (b) Friction velocity contour

Figure 2. (a) The velocity magnitude at the height of first cell centre; (b) The friction velocity at the height of first cell centre.

Fig. 3 compares sand erosion/deposition rate predicted by Method 1 and Method 2, respectively. Method 1 gave good prediction of erosion region while the deposition is entirely neglected. Method 2 predicted limited erosion region at the frontal corner while overestimating the deposition region area.



(a) Experiment after 5 minutes (b) Method 1 erosion rate (c) Method 2 erosion/deposition rate

Figure 3. (a) The sand surface photo after 5 mins in wind tunnel experiment; (b) Sand erosion rate ($\Delta z/\Delta t$) predicted by Method 1; (c) Sand erosion/deposition rate ($\Delta z/\Delta t$) predicted by Method 2.

4. CONCLUSION

A CFD was performed to compare the difference of two different aeolian sand transport models. The comparison between numerical analysis of sand surface evolution using dynamic mesh and experiment results will be presented in the final presentation.

ACKNOWLEDGEMENTS

This work was supported by Grant-in-Aid for JSPS Fellows, JSPS KAKENHI under grant numbers 24KJ1581, 20H02315 and 22K18850.

REFERENCES

Bagnold, R. A., 1937. The transport of sand by wind. The Geographical Journal 89, 409–438.

Kawamura, R., 1951. Study on sand movement by wind. Report 5, 95–112.

Nickling, W. G. and Neuman, C. M., 2009. Aeolian sediment transport. Springer, pp. 517–555.

Poppema, D. W., Wijnberg, K. M., Mulder, J. P., and Hulscher, S. J., 2022. Deposition patterns around buildings at the beach: effects of building spacing and orientation. Geomorphology 401, 108114.

Pourteimouri, P., Campmans, G., Wijnberg, K., and Hulscher, S., 2023. Modelling the influence of beach building pole heights on aeolian morphology and downwind sediment transport. Geomorphology 436, 108791.

Raffaele, L., Beeck, J. van, and Bruno, L., 2021. Wind-sand tunnel testing of surface-mounted obstacles: Similarity requirements and a case study on a sand mitigation measure. Journal of Wind Engineering and Industrial Aerodynamics 214, 104653.

Raffaele, L., Glabeke, G., Beeck, J. van, et al., 2023. Wind-sand tunnel experiment on the windblown sand transport and sedimentation over a two-dimensional sinusoidal hill. Wind Struct 36, 75–90.

Tominaga, Y., Mochida, A., Yoshie, R., Kataoka, H., Nozu, T., Yoshikawa, M., and Shirasawa, T., 2008. AIJ guidelines for practical applications of CFD to pedestrian wind environment around buildings. Journal of wind engineering and industrial aerodynamics 96, 1749–1761.

Tominaga, Y., Okaze, T., and Mochida, A., 2018. Wind tunnel experiment and CFD analysis of sand erosion/deposition due to wind around an obstacle. Journal of Wind Engineering and Industrial Aerodynamics 182, 262–271.

Tominaga, Y. and Zhang, X., Aug. 2024. Wind tunnel experiment of sand surface deformation around obstacle with simple shape. Proceedings of 9th International Colloquium on Bluff Body Aerodynamics and Applications. University of Birmingham, Birmingham, UK.

Yalin, M., 1972. *Mechanics of sediment transport*.

Optimalization of PV plants in snow rich areas

Thomas K. Thiis [1], Arnkell J. Petersen [1,2], Jan Potac[2], Matthias Henkies[3,4], Iver Frimannslund [1]

[1]*Norwegian University of Life Science, Norway, Thomas.thiis@nmbu.no*
[2]*Multiconsult Norge AS, Norway*
[3]*The University Centre in Svalbard, Norway*
[4]*Norwegian University of Science and Technology, Norway*

SUMMARY:
Snow accumulation on photovoltaic (PV) panels can significantly impact electricity production in regions prone to heavy snowfall. In this study, we investigate the effects of snowdrifts and optimize the design and orientation of PV panels to mitigate snow-related losses. We utilize computational fluid dynamics (CFD) simulations to assess wind flow and snow accumulation around PV panels in the current setup, validating the simulation results against measured data. Additionally, electricity production is simulated both with and without snowdrifts, and losses due to snow accumulation are quantified. An optimization of panel orientation and design is performed, focusing on minimizing snow accumulation, and enhancing energy yield. A final analysis of the results is used to find the best compromise between snow mitigation and electricity production efficiency.

Keywords: Snowdrifts, Photovoltaics, Arctic

1. INTRODUCTION

The efficiency of photovoltaic (PV) systems is highly dependent on environmental factors, including snow accumulation in regions with harsh winter conditions. Snow covering the PV panels can block sunlight, reduce output, and lead to significant losses in energy production (Pawluk et al. 2019). Snow can also increase albedo and thus the yield of the PV panels (Hayibo et al. 2022). Previous studies have indicated that optimizing the design and orientation of PV panels can reduce snow accumulation and enhance overall efficiency (Frimannslund et al. 2022), but these methods have not been fully explored in realistic field conditions. This paper investigates the effect of wind and snowdrifts on PV systems and proposes design optimizations to reduce energy losses caused by snow accumulation in one specific case. Using advanced simulation techniques validated against experimental data, we quantify the impact of snowdrifts on energy production and identify potential strategies to mitigate these losses through design adjustments.

2. METHODS

2.1. Simulation of Wind and Snow Accumulation

To study the impact of wind flow and snow accumulation, we conducted a series of computational fluid dynamics (CFD) simulations in which PV panels were modeled under varying wind conditions. The primary objective of these simulations was to assess how snowdrifts form around

PV panels and how the current orientation of panels affects snow buildup, and the method previously proposed by Thiis (2016) was used.

Wind data for the snow accumulation season 2023/2024 were obtained from the nearby weather station Isfjord Radio (frost.no, 2024). The wind rose in Figure 1 shows that the prevailing wind direction during snow drifting conditions (i.e. wind speed (FF) > 5 m/s) is from northeast and partially south.

2.2. Validation with Measured Data

To ensure the accuracy of our CFD simulations, we collected real-world data on snow accumulation around PV panels under similar environmental conditions. The snow drifts were measured by using photogrammetry taken from a low flying UAV. Together with meteorological data this provided the necessary inputs for comparison and validation of simulation results.

2.3. Electricity Production Simulations

Electricity productions were simulated under three conditions; 1. Without snowdrifts in the current configuration, 2. With simulated snowdrifts for the current configuration to assess the energy losses due to snow buildup and 3. with the orientation optimized to avoid snowdrifts.

Electricity production was simulated using the workflow described in Petersen & Frimannslund (2024), whereby bifacial PV production is simulated based on raytracing, considering all major components of production losses in the system.

3. RESULTS

3.1. Snow Accumulation and Wind Flow

Figure 1 shows measured snow depth around the PV panels. The measured snow pattern corresponds to the prevailing northeast wind. The major snow drifts were formed downwind the first two PV panels rows and in the vicinity of the panel ends facing the approaching wind. There is also significant snow accumulation upwind the first row, and between the rows.

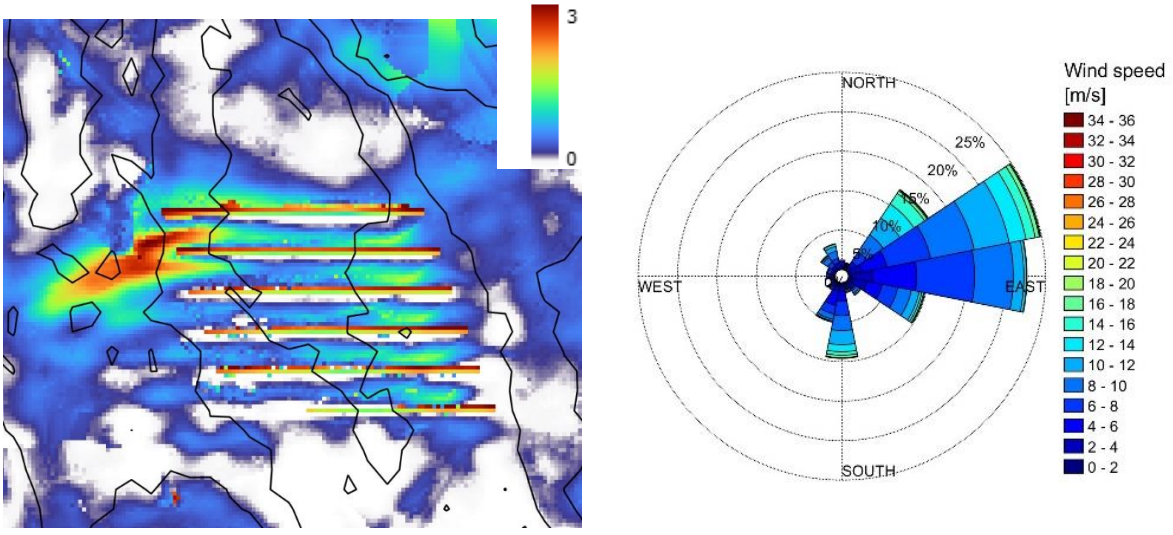


Figure 1 Measured snow depth distribution around the PV panels 10. April 2024 and wind rose for the site.

The results from the CFD simulations, displayed in Figure 2 a) revealed distinct patterns of snow accumulation based on wind direction and panel geometry. A significant snow buildup occurred between the panel rows blocking substantial portions of the PV surface.

The validation process indicated good agreement between simulated and measured snow patterns. The results from the simulation with wind direction parallel to the PV panels, Figure 2 b) shows considerably lower snow drifts.

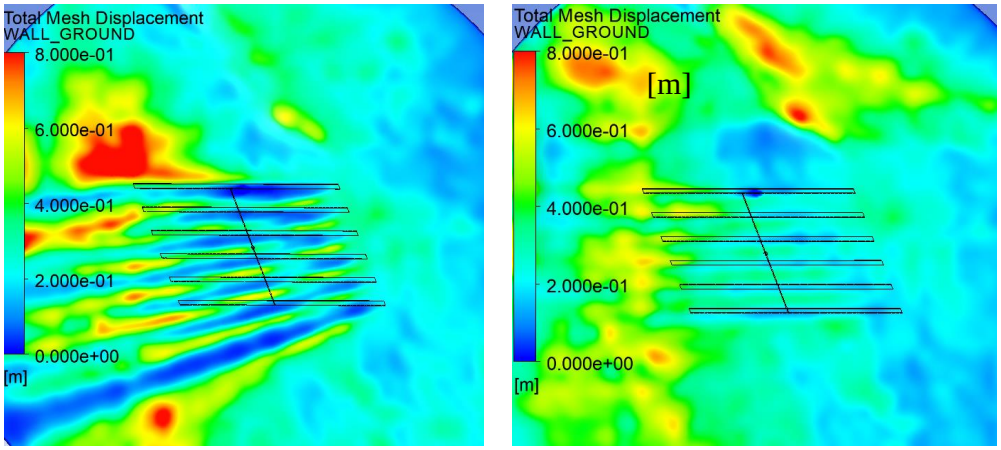


Figure 2 Simulated snow depth distribution around the PV panels for wind direction 70° and 90°.

3.2. Impact on Electricity Production

Simulated electricity production with snowdrifts showed substantial energy losses compared to the snow-free scenario. Figure 3 shows yearly PV production, after accounting for snow drifts as well as the loss of production caused by snow drifts. In particular, the most affected PV panels were those located in rows where wind-sheltering effects caused by adjacent panels allowed more snow to accumulate. The impact of local peaks in snow losses at the first and second row can influence the yield of the electrically connected panels due to the non-uniformity of the irradiance (*mismatch losses*). This effect is not captured in the simulations, indicating that the total snow losses are underestimated.

Panels at the downwind edges of the power plant were less affected by snow buildup. The albedo in the simulations was set to 0.2 and 0.7 for may-nov and dec-apr, respectively. The efficiency of the PV panels was 21 % and the temperature coefficient of PMAX of 0.34%/°C. The bifaciality factor of 70 % accounts for the production on the back side of the panels. The static efficiency with regards to array, inverter and soiling losses was set to 88 %.

3.3 Optimization of Orientation and Design

The design configuration optimized to reduce snowdrifts is oriented 20 towards east from due south the give a more parallel wind direction to the rows. The impact of the change in orientation in yield is not shown here, but will be included in the full article.

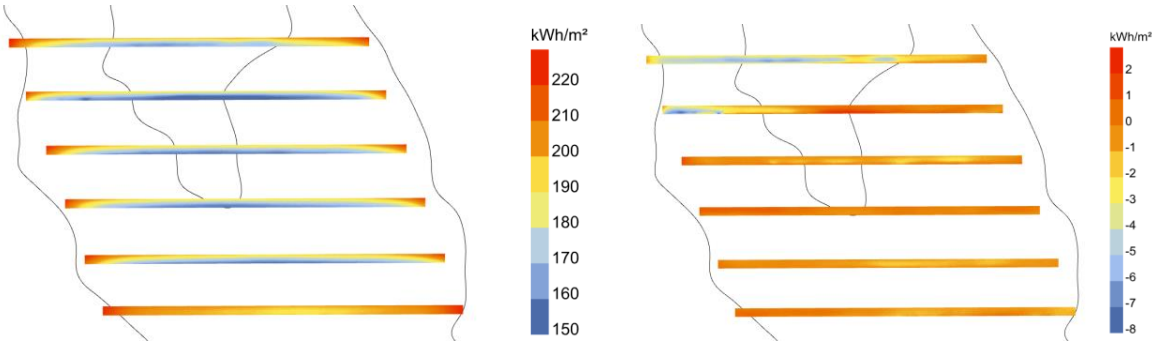


Figure 3 Yearly PV production, after accounting for snow drifts as well as difference in production with and without snow drifts.

4. DISCUSSION

The optimization of PV panel orientation based on wind direction showed promise in reducing snow buildup. However, there is a trade-off between orienting panels to shed snow and aligning them for optimal solar irradiance. Our simulations indicated that an optimal compromise involves a slight rotational adjustments to align with prevailing winds. This is of course dependent on local climate i.e., the wind direction in relation to the direction of the solar radiation.

5. CONCLUSIONS

This study highlights the impact of snow accumulation on PV system performance and presents optimized design strategies to mitigate energy losses due to snowdrifts. By simulating wind flow and snow accumulation, and validating these results with measured data, we were able to provide actionable insights for improving PV panel layouts in snow-prone regions. Optimizing PV systems for snow conditions involves a careful balance between snow optimization and maximizing solar exposure. These findings provide a framework for improving the performance of PV installations in cold climates.

ACKNOWLEDGEMENTS

The authors are deeply grateful for the assistance from Store Norske during the field measurements in April 2024. The fieldwork was also supported by the Research Council of Norway grant nr. 350277.

REFERENCES

Frimannslund, I., Thiis, T., Ferreira, A. D. & Thorud, B. (2022). Impact of solar power plant design parameters on snowdrift accumulation and energy yield. *Cold Regions Science and Technology*, 201: 103613. doi: https://doi.org/10.1016/j.coldregions.2022.103613.

Frost (2024). https://frost.met.no.

Hayibo, K. S., Petsiuk, A., Mayville, P., Brown, L. & Pearce, J. M. (2022). Monofacial vs bifacial solar photovoltaic systems in snowy environments. *Renewable Energy*, 193: 657-668. doi: https://doi.org/10.1016/j.renene.2022.05.050.

Petersen, A., Frimannslund, I. (2024). A Fast and Accurate Raytracing Approach for Assessing Photovoltaic Performance of Monoand Bifacial Panels in Complex Irradiance Conditions. *E3S Web of Conferences* 562, 05001 https://doi.org/10.1051/e3sconf/202456205001

Pawluk, R., Chen, Y. & She, Y. (2019). Photovoltaic electricity generation loss due to snow – A literature review on influence factors, estimation, and mitigation. *Renewable and Sustainable Energy Reviews*, 107: 171-182. https://doi.org/10.1016/j.rser.2018.12.031

Thiis, T.K., (2016). Use of numerical simulations of snow drift in planning of infrastructure – A case study from Northern Norway. International Conference on Snow Engineering 2016. https://cstb.hal.science/hal-01426073/file/ICSE2016_Proceedings_v2.pdf

Considerations in replicating In-cloud Ice Accretion on Power Lines in Climatic Wind Tunnel Testing

Francesca Lupi [1], Erick Ulloa Jimenez [2],
Lubomir Matejicka [3], Norbert Hoelscher [1], Holger Koss [3,4]

[1]*Niemann Ingenieure GbR, Bochum, Germany, Lupi@Niemann-Ing.de*
[2]*Amprion GmbH, Dortmund, Germany*
[3]*Force Technology, Lyngby, Denmark*
[4]*Technical University of Denmark (DTU), Lyngby, Denmark*

SUMMARY:
The paper discusses aspects in the physical replication of in-cloud icing on an overhead power line in climatic wind tunnel tests and the resulting ice accretion under different environmental conditions. In-cloud icing occurs in clouds of supercooled water droplets that remain liquid at a temperature below 0°C. The supercooled droplets are transported by the wind and freeze upon impact on an object. Depending on air temperature, rime or glaze accretions may form. The rate of growth is proportional to the liquid content in the cloud per unit time on the exposed surface. However, not all particles in the approaching flow will eventually hit the power line. Smaller particles are deflected by the flow around the conductor. The aim of this research study is to explore the validity of standard approaches under more extreme boundary conditions and to expand their applicability. The emphasis on test subject variability rather than one aspect focus, provided a better understanding of the multi-physical nature of in-cloud icing on power line conductors. The variation of test condition comprises pretensioned conductors on fixed and rotating support at different air temperatures, liquid water contents, surface temperature, and wind direction.

Keywords: Icing Process, Transmission Lines, Climatic Wind Tunnel Tests

1. INTRODUCTION

In-cloud icing is characterised by clouds of supercooled water droplets that remain liquid at a temperature below 0°C. They are transported by the wind and freeze upon impact on an object exposed to a temperature below freezing (Farzaneth, 2008). According to the Makkonen model (Makkonen, 2010), the rate of ice growth is directly proportional to the number of particles hitting the object per unit time. This depends on the liquid water content (LWC, measured in g/m^3), the wind speed and the impact area. However, not all particles of the incoming flow approaching the power line will eventually impinging on the conductor since smaller particles are carried around the conductor by the displaced and accelerated airflow. The Makkonen model (Eq.1) accounts for this effect with an empirical factor, α_1, the so-called "collision efficiency". Other parameters influencing the ice accretion is the "sticking efficiency", α_2, accounting for particles bouncing off the body's surface after initial contact, and the "formation efficiency", α_3, considering amongst other thermodynamic effects preventing the solidification of the water droplet to ice and eventually shedding from the body back into the flow (run-off). In Eq.1 dM/dt is the mass growth, V the mean airspeed, and A the along-wind projected area of the exposed object

$$dM/dt = \alpha_1\alpha_2\alpha_3 \cdot LWC \cdot V \cdot A \quad (1)$$

For rime ice accretion, parametric models like the Makkonen equation or the ISO 12494, assume that all impinging water droplets freeze solid hence transforming into dry rime ice. Consequently, the accumulation process of the ice layer is not influenced or reduced by water particles bouncing off ($\alpha_2 = 1$) or never transforming partially or completely into solid ice ($\alpha_3 = 1$). The here presented study is part of a research project on risk assessment and modelling of atmospheric icing of high-voltage transmission lines (Jiminez, 2025) addressing following aspects and questions:

- Applicability of linear parametric models to glaze ice
- Is the linearity assumption valid for extreme boundary conditions?
- When does glaze ice start (transition to rime ice)?
- How is the formation of ice influenced by the conductor temperature?
- How does the rotation of the conductor influence the ice layer build-up?
- Influence of wind angle to power conductor on ice accumulation process.
- variability of ice density and ice layer structure.

With more questions than wind tunnel time available to find all the answers, it was decided to conduct a three-week exploratory test campaign to establish at least indicative correlations in the multi-physical process. The test setup was designed for broad variability, allowing a high degree of freedom to adapt or change the study focus in response to findings and discussions. The experiments were conducted on original samples of two conductor types and on a more generic aluminum tube for thermodynamic testing.

2. EXPERIMENTS IN CLIMATIC WIND TUNNEL

Laboratory experiments on ice accretion processes on power lines are carried out in the climatic wind tunnel at Force Technology in Denmark. The following parameters are varied in the experiments: liquid water content (LWC), air temperature (T), wind speed (V). Other variations include mechanical boundary conditions (free, fixed, rotating cylinder), wind direction, sample (conductors of different types and diameters, smooth tube), surface temperature.



Figure 1. *Left:* Wind tunnel set-up of the power line conductor with endplates and two shorter power lines downstream. *Middle:* close-up of rime ice. *Right:* close-up of glaze ice with icicles. (LWC = 2.4 g/m^3, V = 5 m/s, D = 22.43 mm, T = -10°C for rime, -2°C for glaze)

Figure 1 (left) shows a picture of the wind tunnel set-up. The specimen in the foreground is a conductor section mounted on the main test frame with force balances and rotation mechanism. Two shorter conductor segments placed downstream are not equipped with instruments, but allow studies of icing structure and mass growth under different wind directions. Two conductor types with overall diameters of 22.43 mm and 32.46 mm were tested.

Figure 1 (middle) is a typical rime ice accretion, which was obtained after 80 minutes for LWC = 2.4 g/m^3, V = 5 m/s, D = 22.43 mm and T = -10°C. For relatively high LWC, the ice layer shows a distinct structure of two weakly connected growth zones above and below the stagnation area. However, measuring the mass shows that the assumption of linearity is still valid (Figure 2, left). The image of the ice layer cross section to the right in Figure 2 illustrates the linearity and the invariance of the accumulation pattern during the accretion process. This accretion formation is typical for high LWC (see e.g., Lynch & Khodadoust, 2001) and differs from the more uniform characteristic reported in Koss (2012) for LWC = 0.4 g/m^3.

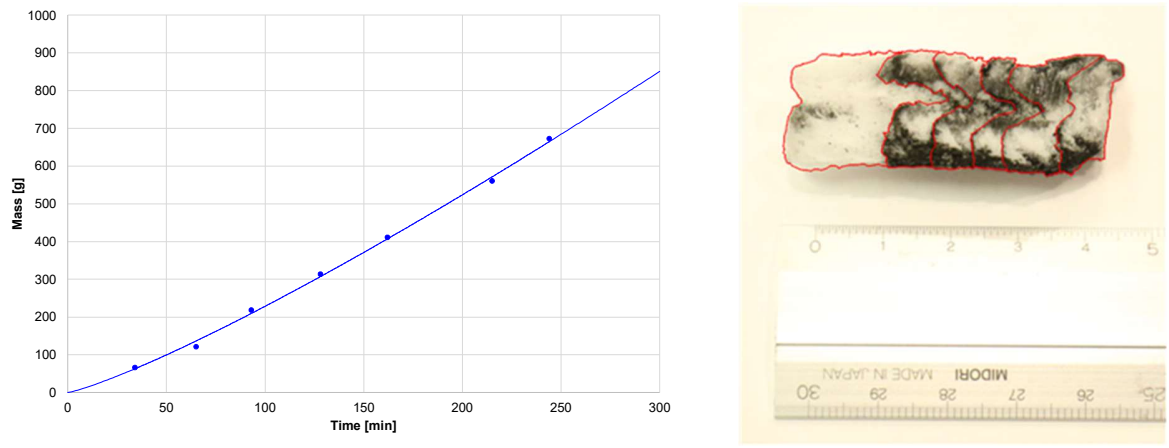


Figure 2. Masses of accreted rime ice in the experiments with a round wire D = 22.43 mm (LWC = 1.6 g/m^3, V = 5 m/s, D = 22.43 mm, T = -10°C)

Figure 1 (right) shows glaze ice. In this study, glaze is obtained by adjusting the air temperature to T = -2°C. At this condition, a large part of the impinging water droplets remain liquid forming a run-off. With increasing LWC or airspeed, the run-off may lead to the formation of icicles as typically observed in freezing rain. The coefficient α_2 can be still considered equal to unity under the assumption that all the impinging particles are supercooled but remain liquid after impact on the conductor. The build-up coefficient α_3 is less than 1 for glaze ice due to the run-off. However, under glaze ice condition, the icicles contribute to the total mass due to their own weight and partially compensate for the mass flux due to the run-off. At some point, the icicles grow to a size initiating an accretion process in their own right, yielding to an underestimation of the accreted mass by using Eq.1. One way of including the formation of icicles as accretion objects is to gradually increase the impact area A. Further results regarding the experimental estimation of the collision efficiency under different environmental conditions, the effect of conductor rotation, the effect of the surface temperature and the effect of wind direction will be discussed in the final contribution.

3. CONCLUSIONS AND OUTLOOK

Rime and glaze accretion in in-cloud conditions is tested in the climatic wind tunnel on prototype samples of two types of power line conductors. The observations and measurements of the ice growths are compared to the Makkonen model for both rime and glaze ice identifying the extent to which linearity can be assumed.

All wind tunnel tests are performed with LWC $\geq$ 1.6 g/m^3, which exceeds the typical values assumed for low level clouds. Exact values for low-altitude clouds or fog are sparse. For this reason, the robustness of available assessment models is tested at extreme conditions. Furthermore, increased levels of water droplets in the air allows forcing the effect of wind direction on the accretion process and hence to understand the correlation between driving parameters.

Apart from ice mass growth on "cold" conductors, the influence of conductor temperature on the onset of ice formation of the surface was tested through artificial heating of a generic test specimen.

The exploratory character of the study allows a more evidence-based estimation of effects in the outer corners of the multi-physical process. In this respect, the overall aims of the study are:

- Experimental prove of theoretical predictions especially for ice formation at or right below 0°C.
- Obtaining information not provided in literature hence expanding the basis for a parametric description of the icing process.
- Contrasting of effects and phenomenon correlation in a multi-physical process.

Future work will expand the findings from the exploratory tests to standard conditions focused on the primary effects relevant for a probability-based assessment of ice loading on overhead power lines.

ACKNOWLEDGEMENTS

This wind tunnel investigation was made possible through the kind support of Amprion GmbH. The authors deeply acknowledge this valuable contribution to the study.

REFERENCES

Farzaneh Masoud. Atmospheric Icing of Power Networks. Ed. Springer, 2008.

ISO 12494:2001. Atmospheric icing of structures

Jiminez E.U., Steevens S., Hoelscher N., Diburg S., 2025. Enhanced atmospheric Icing Modelling of High-Voltage Transmission Lines. Submitted to 9th European African Conference on Wind Engineering, Trondheim, Norway

Jimenez E.U., Lupi F., Hoelscher N., Diburg S., Bouchet J.P., Gauducheau B., Batmalle T., Delpech P., Flamand O., 2025. Wet Snow Accretion on Transmission Lines in Climatic Wind Tunnel. Submitted to 9th European African Conference on Wind Engineering, Trondheim, Norway

Koss H.H., Gjelstrup H., Georgakis C.T.
Experimental study of ice accretion on circular cylinders at moderate low temperatures. J. Wind Eng. Ind. Aerodyn. 104–106 (2012) 540–546

Lynch Frank T, Khodadoust Abdollah, Effects of ice accretions on aircraft aerodynamics, Progress in Aerospace Sciences, Volume 37, Issue 8, 2001, Pages 669-767, ISSN 0376-0421, https://doi.org/10.1016/S0376-0421(01)00018-5.

Makkonen Lasse, Wichura Bodo, 2010, Simulating wet snow loads on power line cables by a simple model, Cold Regions Science and Technology 61, 73–81.

Field Observations of Snowdrift Formation Process Under Blowing Snow Using a Portable LiDAR Device

Tsubasa Okaze [1], Hirofumi Niiya [2], Satoshi Omiya [3],
Sojiro Sunako [4], Takahiro Tanabe [5], Kouichi Nishimiura [6,7]

[1]*Institute of Science Tokyo, Yokohama, Japan, okaze.t.f356@m.isct.ac.jp*
[2]*Niigata University, Niigata, niiya@gs.niigata-u.ac.jp*
[3]*Civil Engineering Research Institute for Cold Region, Sapporo, Japan, somiya@ceri.go.jp*
[4]*Snow and Ice Research Center, NIED, Nagaoka, Japan, s_sunako667@bosai.go.jp*
[5]*Snow and Ice Research Center, NIED, Sinjo, Japan, tnabe@bosai.go.jp*
[6]*Professor Emeritus, Nagoya University, Nagoya, Japan, knishi99@gmail.com*
[7]*Yukiken Snow-Eaters, Sapporo, Japan, nishimura@snow-eaters.com*

SUMMARY:
In this study, we applied a portable Light Detection and Ranging (LiDAR) device to capture the snowdrift distribution under blowing snow. We first measured the snowdrift around a modelled fence installed on a snow field. The snow depth obtained by the LiDAR device agreed well with results obtained using a unmanned aerial vehicle combined with the Structure from Motion photogrammetry method. Subsequently, we analyzed the time-varying snow depth during a blowing snow event. In addition, we demonstrated LiDAR-based measurements of snow cornice on a ridge.

Keywords: Snowdrift, LiDAR, Field Observation

1. INTRODUCTION

Heavy snowfall along the coastline of the Sea of Japan, particularly in the Hokkaido and Tohoku regions, often leads to the formation of snowdrifts and snow cornices as well as reduced visibility due to blowing snow. We recently conducted tower-based observations of blowing snow in snowfields in eastern Hokkaido to obtain snow-drift flux time-series and examined the impact on visibility reduction (Kawashima et al., 2022). Snowdrifts and snow cornices form when snow particles transported by the wind deposited in wind-protected areas. Snowdrift fences are often installed along roadsides in the windward direction to prevent snowdrift formation and maintain visibility. Snow fence performance is significantly affected by the shape and growth of the snowdrift that forms around it. Unmanned aerial vehicles (UAVs) combined with the Structure from Motion (SfM) photogrammetry method were used to capture the snowdrift distribution. However, UAVs can only be used under mild winds during daytime and cannot adequately capture the snowdrift formation process during intense blowing snow or during night-time. In this study, we aimed to capture the shape of the snowdrift distribution and its development around a modelled solid fence during a blowing snow event using a small portable Light Detection and Ranging (LiDAR) device. The LiDAR-based results were compared with the SfM-based results, and the snowdrift formation process was analyzed. In addition, we demonstrated the use of LiDAR-based measurements for capturing the development of snow cornice in a mountainous area.

2. OUTLINE OF OBSERVATIONS

Snowdrift observations were conducted at a blowing snow observation site constructed by the Cold Regions Research Institute on the grounds of the Kushiro Area Mashu Tourism and Culture Center. The vertical distributions of wind velocity and snow-drift flux were measured at the observation tower using an ultrasonic anemometer (Young, CYG-81000) and a snow particle counter (Snowtech Niigata, SPC-95 or SPC-S7), respectively. For details on monitoring setup, we refer to Masuzawa et al. (2021). We analyzed the snowdrift formation process during a continuous blowing snow event that occurred on January 9, 2022, from 9:00 to 17:00. A temporal fence model was installed as a blue sheet-covered section (7.5 m in length at a height of 1 m) near the observation tower on January 7, i.e., two days before the blowing snow event. The fence was approximately perpendicular to the prevailing wind direction in winter at the site. The snowdrift shape was captured at hourly intervals using a small LiDAR device (Horizon, Livox) and the Livox Viewer software. Each LiDAR sampling period was set to 10 s. The LiDAR device, measuring 115 mm in length, 77 mm in width, and 84 mm in height and weighting 1,180 g, covered a field of view of 81.7° horizontally and 25.1° vertically, with the maximum data acquisition rate being 240,000 points/s. Additionally, we captured the shape of the snow surface before and after the blowing snow event, i.e. on January 7 and 10, using UAV–SfM. The UAV (DJI, Phantom 4 Pro+) images were processed using SfM (Agisoft, Metashape) to produce a Digital Surface Model (DSM).

3. RESULTS AND DISCUSSION

Figure 1 shows the 10-min mean wind speed at a height of 1 m measured at the observation tower. The wind speed began to increase on January 9 at around 5:00 and became approximately constant from 6:00 to 18:00 along the prevailing wind direction in winter, i.e., north-northwesterly, with evident intermittent low-level blowing snow. Figure 2 shows the snow surface elevation around the fence after the blowing snow on January 10, captured using (a) UAV–SfM and (b) LiDAR measurements. To exclude blowing snow particles from the LiDAR measurement analysis, low-intensity reflection points were removed from the point-cloud data obtained using LiDAR. The UAV–SfM result shows a snowdrift formation with a peak depth of 30 cm located 1.5 m windward of the fence with a range from 1 to 4 m. Although the LiDAR device did not capture data behind objects or outside its field of view, the DSM constructed based on the LiDAR device agreed well with the distribution obtained using UAV–SfM. The size and location of the snowdrift that formed on the windward side of the fence were accurately caputured. Figure 3 shows the time-dependent distribution of the snow depth along the normal direction passing through the center of the fence. The snow depth change was more pronounced on the windward side, extending up to approximately 4 m from the fence, with the peak position gradually shifting closer to the fence. Snow depth changes downwind of the fence were minimal, with only a slight increase observed approximately 1 m downwind of the fence. According to Tabler (1994), snowdrift formation around solid fences occurs in three primary stages. The initial stage, which we were able to capture, involves snowdrift formation windward of the fence, with the peak increasing to approximately the height of the stagnation point of the fence before transitioning to the downwind stage. After 15:00, only the snow depth between the peak and the fence continued to increase. Kobayashi (1972) proposed an empirical equation for the snow transport rate Q [g/ms], which is the mass of snow across an unit width per unit time, as a function of the mean wind speed at a height of 1 m U_{1m} [m/s]:

$$Q = 0.03U_{1m}^3 \quad (1)$$

By substituting the 10-min mean wind speed obtained from the tower observations into Eq.(1), we obtain the mean snow transport rate. Subsequently, by integrating over the previous hour, we obtain the cumulative snow transport rate per hour. Conversely, the hourly increase of the snowdrift amount can be calculated based on the cross-sectional snow depth change from the LiDAR measurements and the assumed snow density. Eventually, the snow trapping efficiency of the fence can be estimated by calculating the ratio of the change of the snowdrift amount captured by LiDAR device to the hourly cumulative snow transport rate. Figure 4 shows the cumulative snowdrift amount, snow transport rate, and estimated hourly trapping efficiency. The trapping efficiency remained at approximately 50% until 15:00, while it decreased sharply after 16:00. The timing of this decrease of the trapping efficiency coincided with the point where snow depth changes upwind of the peak snow drift position became negligible.

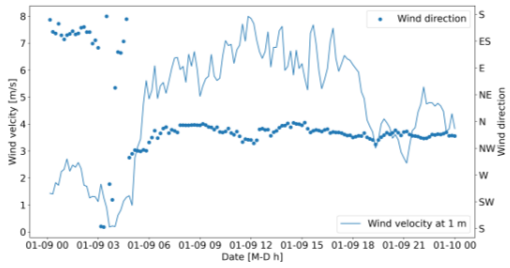


Fig. 1 10-min mean wind velocity at a height of1m.

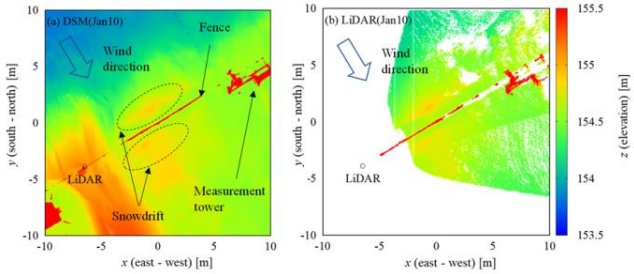


Fig. 2 Snow surface elevation. (a) UAV–SfM; (b) LiDAR.

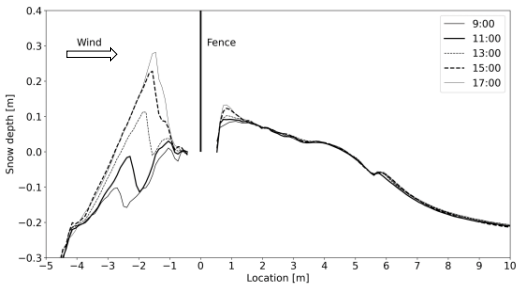


Fig. 3 Snow depth along with center of fence.

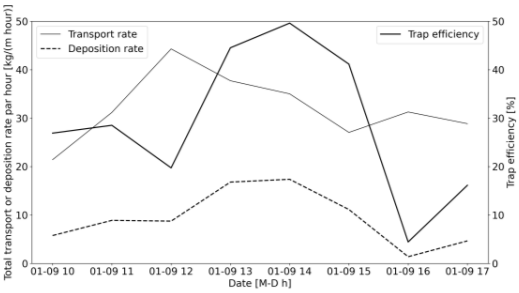


Fig. 4 Hourly change of trapping efficiency.

4. SNOW CORNICE DEVELOPMENT APPLICATION

In the previous section, the LiDAR-based snow drift observations were validated against the results obtained using UAV–SfM and manually measured snow depths. This section describes an observation campaign conducted in the backcountry area within the ski area of the Niseko Annupuri Mountain, Japan, on January 24-25, 2023, during which LiDAR-based observations were applied for monitoring snow cornice development. The LiDAR device (Avia, Livox) was connected via an Ethernet cable to a Raspberry Pi 4 Model B running Ubuntu 18.04, and point cloud data were acquired using the Livox SDK. A time-lapse camera was set up near the LiDAR device to capture images at 10-min intervals within the device's field of view. Both the LiDAR device and the Raspberry Pi were operated for two days using a portable power resource. Figure 5 shows a snow cornice at a ridge of the Niseko Annupuri Mountain on January 25 at 14:00. The observed wind direction aligns with the flow from left to right in the photograph. A steep slope is shown from the center to the right of the photograph, where a cornice is formed near the steep transition. Figure 6 illustrates the shape of the snow cornice formed on the near side of Figure 5 as

captured by the LiDAR device. Figure 7 shows the changes of the surface height time-series for a cross-section located 48 m from the LiDAR device as shown in Figure 6. The heights in Figure 7 are relative to the height of the LiDAR device. This indicates that although the surface heights on the windward and leeward sides of the surface height did not change, cornice growth was measured between 18:00 and 21:00. The overhanging on January 25 at 0:00 was well captured.

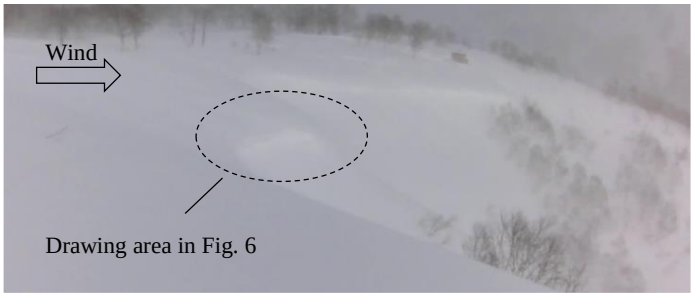


Fig. 5 photo of observed snow cornice taken on January 25, 2023, at 14:20.

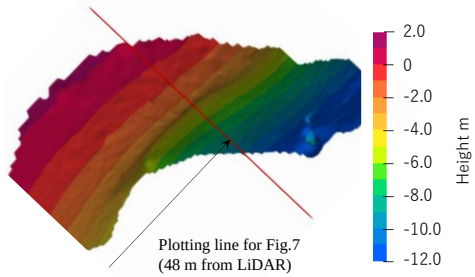


Fig. 6 Top view of elevation.

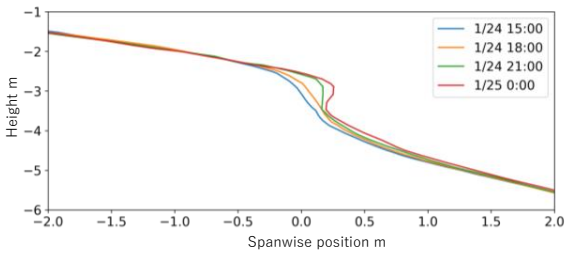


Fig.7 Cross-section of snow depth.

5. CONCLUDING REMARKS

We applied a portable LiDAR device to capture the snowdrift development process around a fence and a ridge during a blowing snow event. Future observations should focus on additional phases in which snowdrifts form behind the fence, fences with varying degrees of porosity, and the accumulation of different snow cornices.

ACKNOWLEDGEMENTS

This work was supported by JSPS KAKENHI (grant numbers 24K01037, 21H04601, and 20H01983) and the Environment Research and Technology Development Fund JPMEERF20232003 of the Environmental Restoration and Conservation Agency provided by the Ministry of the Environment of Japan.

REFERENCES

Kawashima, R., Omiya, S., Niiya, H., Nishimura, K., Okaze, T., 2022. Analysis of fluctuation of visibility distribution for increased snow-drift flux due to turbulent fluctuation under blowing snow without snowfall. Wind Eng. Res. 27, 48–57.

Kobayashi, D., 1972. Studies of Snow Transport in Low-Level Drifting Snow. Contrib. from Inst. Low Temp. Sci. A24, 1–58.

Masuzawa, S., Omiya, S., Okaze, T., Niiya, H., 2021. Elucidations of vertical structures of blowing snow with snowfall. J. Japanese Soc. Snow Ice 83, 259–273.

Tabler, R.D., 1994. Design Guidelines for the Control of Blowing and Drifting Snow.

The aerodynamic impact of overtaking manoeuvres on platooning vehicles

David Soper [1], Samuel Marshall[1], Mark Sterling[2] and Stefanie Gillmeier[3]

[1]*School of Engineering, University of Birmingham, Birmingham, UK, d.soper@bham.ac.uk*
[2]*Faculty of Science and Engineering, Manchester Metropolitan University, Manchester, UK*
[3]*Eindhoven University of Technology, Building Physics and Services, Department of the Built Environment, The Netherlands*

SUMMARY:
This paper presents a study of the aerodynamical forces and moments encountered by a close-proximity platoon of Heavy Goods Vehicles (HGVs) undergoing overtaking manoeuvres. From a series of wind tunnel experiments and moving model experiments, evidence is presented of a complex relationship between the drag and side force coefficients of the platoon, contrasting with an equivalent single lorry. This includes the potential of interactions akin to hysteresis. The benefits of these interactions on both the individual lorries and the platoon as a whole are discussed and explained, demonstrating the advantages/disadvantages of platooning techniques. Furthermore, the unsteady forces on a single overtaken lorry are considered for both the static and moving case.

Keywords: Aerodynamics, platoons, wind tunnel experiments, moving model experiments, HGVs.

1. INTRODUCTION

It is commonplace to see lorries in groups of two or more on motorways and in motorsport, slipstreaming is a well-known technique for overtaking. When bluff vehicles travel in close-proximity, the reduction in air pressure in the wake of an upwind vehicle reduces the pressure on the front of the downwind vehicle, tending to reduce drag. As such, driving in the wake of a vehicle may lead to improved fuel efficiency or electric vehicle range, with benefits in terms of cost reductions and CO_2 emissions. This phenomenon is of further interest given recent advances in connected and autonomous vehicles (CAVs). Several CAVs communicating with each other, can travel in close-proximity, safely and at high speed, in what is known as a 'platoon' formation. It has been estimated that well-programmed CAVs could reduce road accidents by 90% and that the optimisation of driving could cut emissions by 60% (S. Le Vine et al., 2015). It has been predicted that CAVs will be travelling alongside traditional vehicles in the next ten years, with mainstream consumer adoption by 2030 and CAVs as the primary means of transport by 2050. However, current public perception suggests that early adopters of this technology are likely to be haulage industry, specifically for heavy goods vehicles (HGVs).

Aerodynamic research has been conducted on platoons over the years, with primary focus on drag reduction techniques. However, before platooning can be introduced as a fully feasible commercial approach, real-world conditions must be investigated, especially regarding the safety of other road users and pedestrians. It is vital to explore the aerodynamic forces on a platoon of HGVs

undergoing an overtaking manoeuvre to ascertain any stability concerns or potential drag penalties (Le Good et al., 2018). This research aims to develop greater understanding of the aerodynamic flows and force loading encountered by a platoon of HGVs. The focus in this paper is on an experimental study of the aerodynamic impacts of overtaking manoeuvres in a platoon.

2. METHODOLOGY

The first set of experiments for this study were conducted in the atmospheric boundary layer wind tunnel at the Eindhoven University of Technology in the Netherlands, as shown in Figure 1.

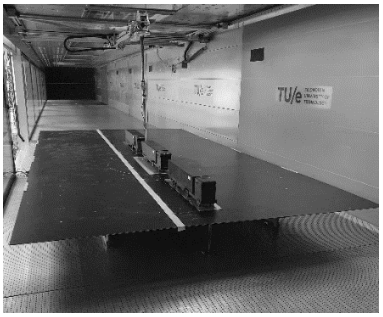


Figure 1. Platoon of three HGVs on a splitter plate inside the atmospheric boundary layer wind tunnel.

The wind tunnel is a closed-circuit type, with cross-sectional dimensions of 3 m x 2 m. For this study three models, based on the DAF XF HGV, were installed on a splitter plate. These models were 3D printed out of polylactic acid at 1:20th scale. Each model was ~825 mm in length, ~125 mm wide and ~190 mm high. The gap between models was chosen as 300 mm (the equivalent of 6 m at full-scale), as proposed by UK Government policy design requirement for close-proximity platoons (National Highways, 2022). For force and moment measurements, the middle vehicle was attached to a six component Interface force balance with a sampling frequency of 10 Hz. Tunnel flow velocity (~25 m/s) was measured via a TFI Cobra probe at a frequency of 1 kHz.

Experiments were also conducted at the University of Birmingham TRansient Aerodynamic INvestigation (TRAIN) rig moving model test facility. In these experiments five models were positioned in the platoon, overtaking a single model, with speeds 22.5 m/s and 12 m/s respectively. The models were fitted with surface pressure monitoring systems and run over a suspended ground plane, with a firing chassis onto which the models were mounted moving beneath this surface.

For the analysis of the data generated, the three aerodynamic force coefficients (Drag (D), Side (S) and lift (L)) were defined as follows:

$$C_i = \frac{F_i}{0.5\rho A_f U_{ref}^2} \qquad (i = D, S, L) \qquad (1)$$

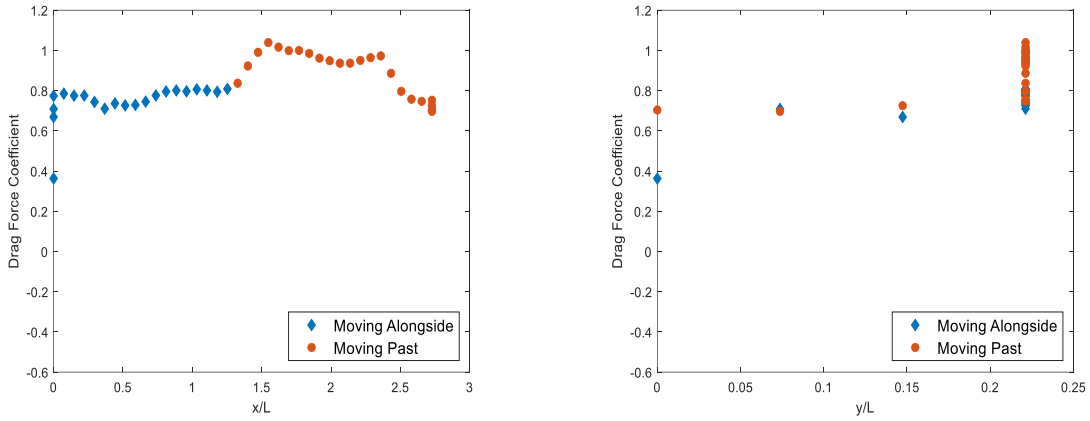
where C_i is the respective force coefficient, F_i is the respective force, ρ is the density of air, A_f is the projected area of the front of the lorry and U_{ref} is the effective lorry speed. Similarly, the moment coefficients were derived as follows:

$$C_{ii} = \frac{M_{ii}}{0.5\rho A h U_{ref}^2} \qquad (ii = xy, xz, yx) \qquad (2)$$

where M represents the respective moment in the *xy*, *xz* or *yz* plane, and *h* is the height of the lorry above the splitter plate.

3. RESULTS

Figure 2 shows the variation in drag force for a single vehicle moving out of alignment from a platoon and overtaking the vehicle in front, before moving back into alignment with the other vehicles in the platoon. As observed in Figure 3a, there is initially a large increase in drag force once the central middle moves out of alignment (x/L=0). In Figure 2b, a small movement in y/L leads to an immediate and significant drag response – when the HGV has moved ~0.5 vehicle width, the drag force coefficient roughly doubles in strength. This is believed to be due to vortex separation in the wake of the leading vehicle causing the flow to be directed into the partially-exposed central vehicle, so that the entire frontal area of the HGV will be subjected to the full flow speed, as if the lead vehicle was not blocking the flow at all. Figure 2a demonstrates that the drag on the central vehicle is reasonably uniform over the manoeuvre, with a peak when as the overtaking vehicle front draws level with the rear of the lead vehicle. It can also be noted that the drag force does not return to the original value after the manoeuvre is completed, due to the increased drag in the vehicle's new position at the front of the platoon.



(a) (b)

Figure 2. Drag force loading during overtaking: a.) streamwise motion, b.) lateral motion.

Expanding this to consider the wider effects within the platoon, the moving model tests can be used to integrate surface pressures to calculate forces across each vehicle within the platoon. As an example, Table 1 gives drag coefficient measurements calculated from surface pressure measurements of a platoon of five HGVs moving in a uniform (non-overtaking) configuration. It can be observed that the drag value of the second moving vehicle (HGV 2) is much lower than the lead vehicle and this trend continues to fall until the fourth vehicle (HGV4) in the platoon, whereby the drag value stabilises.

Table 1. Drag coefficients for each vehicle in moving platoon model.

	HGV 1	HGV 2	HGV 3	HGV 4	HGV 5
Drag Coefficient	0.6896	0.1954	0.1730	0.1587	0.1565

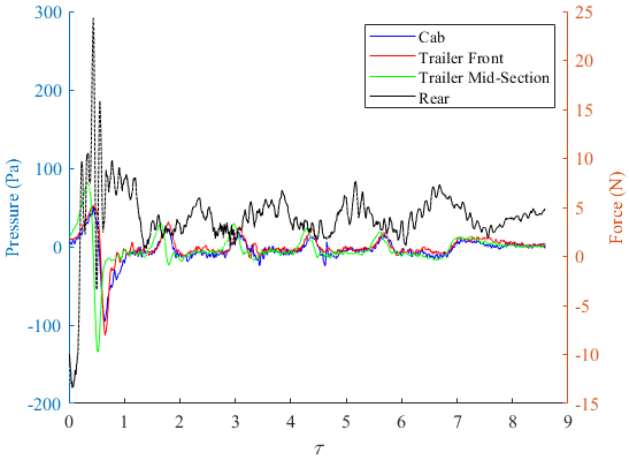


Figure 3. Surface pressure and side force loading measuring on a single static HGV during a platoon overtaking manoeuvre.

Figure 3 shows the variation in surface pressure and forces for a single vehicle being overtaken by a platoon of vehicles during the moving model tests. Here the x-axis τ is normalised by the vehicle length. It can be observed from the surface pressure trace that each vehicle of the platoon passing by can be clearly observed with a peak in pressure for each passing vehicle visible on the rear face, but also other faces. Further analysis for the presentation will also consider the case where the single vehicle is also moving.

4. CONCLUSIONS

The preliminary results presented here are drawn from a wider study on HGV platoons. These initial findings include useful information regarding the aerodynamical forces and moments acting upon a platoon undergoing an overtaking manoeuvre. It can be seen that the complex interaction of overlapping wake structures can cause changes in aerodynamic forces, which may potentially lead to driving instabilities. This point will be important to consider for the development of CAV computational systems and their ability to adapt effectively to on-road driving conditions.

ACKNOWLEDGEMENTS

The authors wish to acknowledge the Engineering and Physical Sciences Research Council (EPSRC) for funding this research. *This work is also part of the transnational access project "ERIES – THE AERODYNAMICS OF PLATOONING AND OVERTAKING VEHICLES", supported by the Engineering Research Infrastructures for European Synergies (ERIES) project (www.eries.eu), which has received funding from the European Union's Horizon Europe Framework Programme under Grant Agreement No. 101058684*

REFERENCES

Baker, C., Johnson, T., Flynn, D., Hemida, H., Quinn, A., Soper, D., & Sterling, M. (2019). *Train aerodynamics: fundamentals and applications.* Butterworth-Heinemann.

He, M., Huo, S., Hemida, H., Soper, D., Sterling, M., & Baker, C. (2022). The Flow Around a Lorry Platoon Subject to a Crosswind—a Detached Eddy Simulation. *Frontiers in Future Transportation*, *3*, 901204.

Le Good, G., Resnick, M., Boardman, P., & Clough, B. (2018). *Effects on the aerodynamic characteristics of vehicles in longitudinal proximity due to changes in style* (No. 2018-37-0018). SAE Technical Paper.

S. Le Vine, A. Zolfaghari and J. Polak. *Autonomous cars: The tension between occupant experience and intersection capacity*, Transport. Res. Part C: Emerging Tech., 52:1-14, 2015.

National Highways (2022). *HelmUK advanced platooning trials - final report.* National Highways. https://nationalhighways.co.uk/media/l43fgudu/helmuk-final-report.pdf.

Pollutant re-introduction investigation for occupational risk reduction (PRIORR)

Romain Guichard [1], Anjali Krishnan Radhakrishnan Jayakumari [2], Stefanie Gillmeier [2], Ali Bahloul [3]

[1]*Institut National de Recherche et de Sécurité, Vandœuvre-lès-Nancy, France, romain.guichard@inrs.fr*
[2]*Eindhoven University of Technology, Eindhoven, the Netherlands, a.k.radhakrishnan.jayakumari@tue.nl; s.g.gillmeier@tue.nl*
[3]*Institut de Recherche Robert-Sauvé en Santé et en Sécurité du Travail, Montréal, Canada, ali.bahloul@irsst.qc.ca*

SUMMARY:
Examples of possible pollution transfer from one room to another via outdoor air are numerous: emissions of gas and fine particles from ventilated enclosures of research facilities on a campus, downdraft of smoke from the chimneys of a production site toward office buildings, re-introduction of rooftop emissions through the ventilation system within the same building, etc. Instances of chronic pollution transfer exist according to field feedback, but are rarely reported in the literature, likely due to the lack of predictability of outdoor pollutant dispersion. The pollutant transfer is generally noticeable *a posteriori* in cases of odour pollution or abnormal occurrences of symptoms or illnesses. In this ongoing research project, we propose the setup of an experimental benchmark that will provide insights into the dynamics of pollutant dispersion in and around a building. It is based on reduced-scale wind tunnel measurements using a passive tracer gas. The building under study is equipped with a mechanical ventilation system, subjected to atmospheric wind conditions and exhaust pollutant generation. The results can be used as validation database for computational fluid dynamics (CFD) simulations to predict and mitigate possible occupational exposure to pollutants.

Keywords: wind-tunnel experiments, pollutant dispersion and re-introduction, mechanical ventilation

1. INTRODUCTION

Pollutant dispersion from one building to another has been widely studied by Computational Fluid Dynamics (CFD) simulations (Bahloul et al., 2014; Blocken et al., 2013; Gousseau et al., 2011; Tominaga and Stathopoulos, 2013; Wang and McNamara, 2006) and by wind tunnel or full-scale experiments (Ahmad et al., 2005; Hajra et al., 2013; Liu et al., 2010; Stathopoulos et al., 2014). Without question, it is crucial to understand the dynamics of airborne pollutants to prevent workers exposure to these pollutants. This topic is particularly important on campuses that combine office and training rooms with laboratories or industrial activities because exhausted pollutants from *e.g.*, laboratories might disperse into the ventilation system of surrounding buildings, thereby posing a risk to workers in *e.g.*, offices. It is also possible that pollutants are re-introduced into the building of their origin, as illustrated in Figure 1, which is even more difficult to prevent because it requires real-time monitoring of infiltration rates and ventilation air inlets.

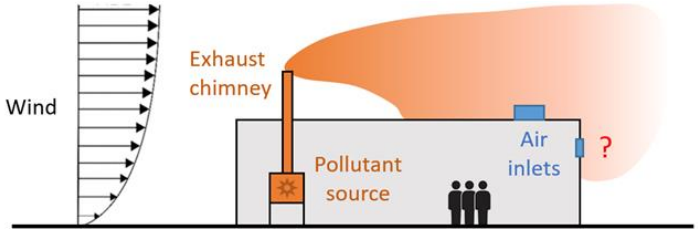


Figure 1. Illustration of pollutant re-introduction within a building.

Full-scale measurements might not be appropriate to study such phenomenon because it is impossible to control some boundary conditions (e.g. wind conditions, temperature, humidity). On this subject, the CFD technique can significantly help to investigate specific scenarios under well-controlled conditions, perform parametric studies and, when validated, provide practical recommendations for existing or future buildings. However, while the Reynolds-averaged Navier-Stokes (RANS) approach - most used but less accurate - can be based on extensive best practice guideline documents, for the large eddy simulations (LES) approach - computational demanding but more accurate - best practices are still largely missing, which is considered as serious limitation for high-quality LES in wind engineering (Blocken, 2018). There are also very few wind tunnel studies treating the interactions between external wind conditions and internal mechanical ventilation system, exclusive for nuclear safety (Le Dez et al., 2021; Le Roux et al., 2013, 2012), and there is no wind tunnel experiment quantifying the effects of wind on the possible re-introduction of pollutants through the mechanical ventilation system. The lack of such experimental studies may be attributed to the required multi-physics approach, coupling and scaling the atmospheric boundary layer (ABL) wind and the internal mechanical ventilation system, and unitizing a gas tracing system composed of mass flow controllers and a fast gas analyser.

Main goal of the PRIORR project is to provide the scientific community and all stakeholders with an innovative experimental benchmark aimed at quantifying the pollutant re-introduction into a building equipped with a mechanical ventilation system. This project is a first step to manage the combination of wind, mechanical ventilation, and pollutant dispersion in an ABL wind tunnel.

2. EXPERIMENTAL SETUP AND METHODOLOGY

A reduced-scale model equipped with a mechanical ventilation system on which external and internal pressure measurements can be conducted was designed by Jayakumari et al. (2024). That model has been tested under neutral ABL wind conditions to investigate external pressures, internal pressures, and airflow rates. It serves as base model for this study. The model utilized for this study is additionally equipped with a controlled pollutant source. To link findings from this study to previous measurements conducted on the same building model (Jayakumari et al., 2024, 2023), the atmospheric approach flow conditions are similar to the ones used by Jayakumari et al. (2023). To provide results for various experimental configurations and to avoiding symmetries with respect to the approaching wind direction, the stack is not located on the roof's centre and ventilation inlets will not be uniformly distributed on the building facade. Hence each tested wind direction will represent a new and specific configuration of the whole benchmark. Figure 2 shows a picture of the wind tunnel setup used by Jayakumari et al. (2024) and contains descriptive additions that are implemented for this study. The building model designed for this study is

manufactured at a geometrical scale of 1:40 and includes an artificial ventilation system that is driven by a single negative pressure unit located at the end of an extractor pipe underneath the wind tunnel, 40 ventilation air inlets and 6 leakage holes to account for air infiltration. This simulates a single-flow mechanical ventilation system, which is commonly used in buildings.

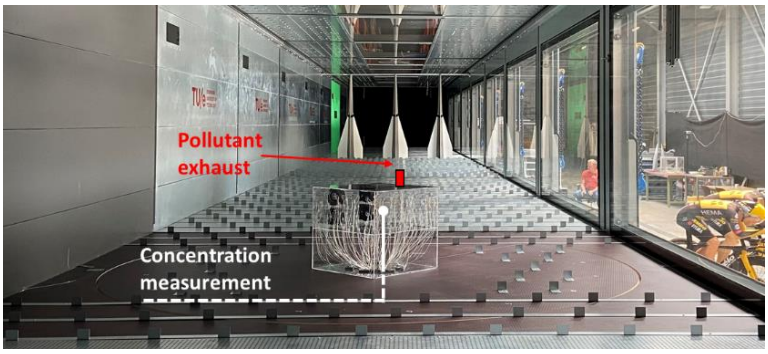


Figure 2. Picture of the reduced-scale building model and the ABL wind tunnel setup.

The building model has been scaled down based on airflow and pressure similarities based on the methodology of Jayakumari et al. (2024). The main characteristics of full-scale conditions and corresponding reduced-scale parameters are summarised in Table 1.

Table 1 Main characteristics of full-scale and reduced-scale conditions.

Parameter	Full-scale	Reduced-scale
L: Building side length	18 m	0.45 m
D: Stack diameter	0.2 m	0.005 m
H: Stack length	1 m	0.025 m
Stack location on building roof	6 m from edges on a roof corner	0.15 m from edges on a roof corner
U: Wind velocity @ building height	4.45 m/s and 6.5 m/s	6.3 m/s and 9.2 m/s
U_e: Exhaust velocity	7.5 m/s	10.61 m/s
Released volume flow rate	848,230 l/h	750 l/h

As passive tracer gas, ethylene is released, mixed with synthetic air. With a density of 1.16 kg/m^3 at 20°C and 1 bar, the density of ethylene is comparable to the density of air under the same atmospheric conditions. Fast-flame ionization detectors (Fast-FID) are used to measure the background concentration and pollution concentrations inside the building model. For the latter the Fast-FID sensor is mounted on a three-axis traverse system inside the wind tunnel, entering the building model through small openings in the roof that are sealed when not used. Measurements are carried out for 12 wind directions. For all wind directions, pollutant concentrations are measured in the extractor pipe to determine (1) the duration until steady state is reached and (2) to assess the average percentage of pollutant concentrations re-introduced. Results will be expressed by means of a percentage of exhausted pollutants re-introduced.

3. EXPECTED OUTCOMES

Results from the described measurement campaign will be presented in detail. It is to be expected that pollutant concentrations inside the building model show a heterogeneous distribution in space

and time. Findings are also expected to depend strongly on the approaching wind direction and velocity. A limitation of the study is that results are expected to be specific for the building geometry and design (including the mechanical ventilation characteristics), stack location and chosen approach flow characteristics, Nevertheless, findings are expected to prove valuable insights in the complex flow characteristics responsible for pollutant re-introduction.

ACKNOWLEDGEMENTS

This work is part of the transnational access project "ERIES – PRIORR", supported by the Engineering Research Infrastructures for European Synergies (ERIES) project (www.eries.eu), which has received funding from the European Union's Horizon Europe Framework Programme under Grant Agreement No. 101058684. This is ERIES publication number C35.

REFERENCES

Ahmad, K., Khare, M., Chaudhry, K.K., 2005. Wind tunnel simulation studies on dispersion at urban street canyons and intersections—a review. Journal of Wind Engineering and Industrial Aerodynamics 93, 697–717. https://doi.org/10.1016/j.jweia.2005.04.002

Bahloul, A., Stathopoulos, T., Chavez, M., Hajra, B., 2014. The Effect of Upstream and Downstream Buildings on Dispersion of Effluents: A Computational Fluid Dynamics (CFD) Approach. IRSST Report R-849.

Blocken, B., 2018. LES over RANS in building simulation for outdoor and indoor applications: A foregone conclusion? Build. Simul. 11, 821–870. https://doi.org/10.1007/s12273-018-0459-3

Blocken, B., Tominaga, Y., Stathopoulos, T., 2013. CFD simulation of micro-scale pollutant dispersion in the built environment. Building and Environment 64, 225–230. https://doi.org/10.1016/j.buildenv.2013.01.001

Gousseau, P., Blocken, B., Stathopoulos, T., van Heijst, G.J.F., 2011. CFD simulation of near-field pollutant dispersion on a high-resolution grid: A case study by LES and RANS for a building group in downtown Montreal. Atmospheric Environment 45, 428–438. https://doi.org/10.1016/j.atmosenv.2010.09.065

Hajra, B., Stathopoulos, T., Bahloul, A., 2013. A wind tunnel study of the effects of adjacent buildings on near-field pollutant dispersion from rooftop emissions in an urban environment. Journal of Wind Engineering and Industrial Aerodynamics 119, 133–145. https://doi.org/10.1016/j.jweia.2013.05.003

Jayakumari, A.K.R., Gillmeier, S., Ricci, A., Guichard, R., Blocken, B., 2023. Scaling effects on experimentally obtained pressures on an idealized building: Possible implications towards asbestos containment. Journal of Wind Engineering and Industrial Aerodynamics 239, 105442. https://doi.org/10.1016/j.jweia.2023.105442

Jayakumari, A.K.R., Guichard, R., Ricci, A., Gillmeier, S., Blocken, B., 2024. Towards an improved wind effect assessment for asbestos abatement: A methodology for reduced-scale experiments. Journal of Environmental Management 370, 122698. https://doi.org/10.1016/j.jenvman.2024.122698

Le Dez, T., Richard, J., Inard, C., Le Roux, N., Demouge, F., Faure, X., Ricciardi, L., 2021. Reduced-scale study of the coupling between thermal and wind effects on the ventilation systems of nuclear facilities. International Journal of Ventilation 20, 1–19. https://doi.org/10.1080/14733315.2019.1693135

Le Roux, N., Faure, X., Inard, C., Soares, S., Ricciardi, L., 2013. Reduced-scale study of transient flows inside mechanically ventilated buildings subjected to wind and internal overpressure effects. Building and Environment 62, 18–32. https://doi.org/10.1016/j.buildenv.2013.01.011

Le Roux, N., Faure, X., Inard, C., Soares, S., Ricciardi, L., 2012. Reduced-scale study of wind influence on mean airflows inside buildings equipped with ventilation systems. Building and Environment 58, 231–244. https://doi.org/10.1016/j.buildenv.2012.07.007

Liu, X.P., Niu, J.L., Kwok, K.C.S., Wang, J.H., Li, B.Z., 2010. Investigation of indoor air pollutant dispersion and cross-contamination around a typical high-rise residential building: Wind tunnel tests. Building and Environment 45, 1769–1778. https://doi.org/10.1016/j.buildenv.2010.02.003

Stathopoulos, T., Hajra, B., Chavez, M., Bahloul, A., 2014. A Wind Tunnel Study of the Effect of Adjacent Buildings on Near-Field Pollutant Dispersion from Rooftop Emissions (No. R-848). IRSST.

Tominaga, Y., Stathopoulos, T., 2013. CFD simulation of near-field pollutant dispersion in the urban environment: A review of current modeling techniques. Atmospheric Environment 79, 716–730. https://doi.org/10.1016/j.atmosenv.2013.07.028

Wang, X., McNamara, K.F., 2006. Evaluation of CFD Simulation using RANS Turbulence Models for Building Effects on Pollutant Dispersion. Environ Fluid Mech 6, 181–202. https://doi.org/10.1007/s10652-005-5656-9

Vortex shedding of circular cylinders mounted on a rolling support at different Reynolds number regimes

Alessio Torrielli[1], Andrea Orlando[2], Andi Xhelaj[3], Alessandro Giusti[4], Olivier Flamand[5]

[1]*Siemens Gamesa Renewable Energy A/S, Brande, Denmark,* *alessio.torrielli.ext@siemensgamesa.com*
[2]*Department of Civil, Chemical and Environmental Engineering, University of Genoa, Italy,* *andrea.orlando@edu.unige.it*
[3]*Department of Civil, Chemical and Environmental Engineering, University of Genoa, Italy,* *andi.xhelaj@edu.unige.it*
[4]*Siemens Gamesa Renewable Energy A/S, Brande, Denmark,* *alessandro.giusti@siemensgamesa.com*
[5]*Centre Scientifique et Technique du Bâtiment, Nantes, France,* *olivier.flamand@cstb.fr*

SUMMARY:
An offshore wind turbine is typically installed by special vessels, which carry the wind turbine components from the harbor to the offshore site. Such an installation process includes the sea transport of towers standing vertically on the deck of vessel without rotor nacelle assembly. Towers are therefore subjected to wind actions and vessel movements induced by waves and navigation. As far as the authors know, no research has been done on the possibility to develop resonant phenomena associated with wind-structure interaction, like vortex induced vibrations, on slender tower-like structures in navigation. This paper focuses on vortex shedding of circular cylinders mounted on a moving support, rolling as an installation vessel during sea transport. The problem is tackled by means of wind tunnel tests at high Reynolds number regime on cylinders equipped with eight rings of pressures taps, distributed along the height, and an accelerometer at the top. The development of vortex shedding is identified for different Reynolds numbers from about 2.6×10^5 to about 1.7×10^6. A detailed analysis of the standard deviation of the lift coefficients at different heights together with insights on the Strouhal number are presented.

Keywords: vortex shedding, rolling support, high Reynolds number regime

1. INTRODUCTION

Offshore wind turbines are typically installed through a peculiar process, which starts in the so called pre-assembly harbor, where the components (blades, nacelles and tower sections) are prepared for the load out onto the installation vessel, and continues in the sea till the final assembly of the turbine on the offshore foundation. Towers without rotor-nacelle assembly are usually erected at the harbor quayside to minimize the duration of offshore operations, which are one of the main cost drivers of the offshore wind energy industry. Depending on the length and mass of the tower sections and the capabilities of harbor and cranes, besides other possible environmental constraints as the free height for navigation under bridges, towers can be totally erected (full tower) or partially erected (split tower) at the harbor. Towers are then transported vertically on the installation vessel, which is a special vessel equipped with crane and legs for jack-up (see Fig. 1), in different group



Figure 1. Installation vessel (jack-up) in the North Sea during the installation of Borkum Riffgat wind farm (©Siemens Gamesa Renewable Energy).

arrangements (generally from one to six towers). Wind-structure interaction of isolated and groups of towers at small center-to-center distance recently captured the attention of researchers with focus on both aerodynamic coefficients (e.g., Mannini et al., 2023, Mannini et al., 2024, Torrielli and Giusti, 2023) and vortex shedding response (e.g., Kurniawati et al., 2024, Livanos et al., 2024, Ellingsen, 2021). These studies reflect the conditions of towers standing on a fixed foundation, as at the quayside or on a jack-up vessel, but they do not address sea transport, where towers are also subjected to the movement of the vessel deck induced by waves and navigation. This paper aims to start filling this gap with an experimental investigation of vortex shedding on finite-length circular cylinders at different Reynolds number regimes in case of fixed and rolling support.

2. TEST SETUP

The study is tackled by wind tunnel tests carried out at the Centre Scientifique et Technique du Bâtiment (CSTB), Jules Verne facility. The modeled cylinders have a geometry equivalent to a split tower. By contrast, the modeling of a full tower would have required either a taller wind tunnel or a smaller diameter, with the consequent reduction of the Reynolds number. The test model consists of a parallel sided cylinder of about 3.20 m in height and 0.36 m in diameter, mounted on a titling table (see Fig. 2) placed on the floor of the wind tunnel. The titling table is meant to apply to the cylinder the motion given by the rolling of the installation vessel, to study the influence of such a source of interaction with vortex shedding. Three different tilting scenarios are investigated, namely fixed tilting table, 1.04 Hz rolling frequency and 1.40 Hz rolling frequency. A wind tunnel blockage ratio of about 8.7% is estimated, considering a 6 m x 5 m working section. Along with the 200 pressure taps distributed on 8 rings, the cylinder is equipped with a 2D accelerometer mounted at the top of the cylinder. The dominant frequency of flexural vibrations of the cylinder, corresponding to a major spike of the power spectrum of the acceleration, is estimated to range between 5.7 Hz and 7.0 Hz. The lower and upper bound are respectively associated with the scenario of small vibrations, namely fixed tilting table and low flow velocity, and large vibrations, i.e., 1.4 Hz rolling frequency and high flow velocity. The non-negligible variability of the frequency of flexural vibration is likely due to the connection of the cylinder to

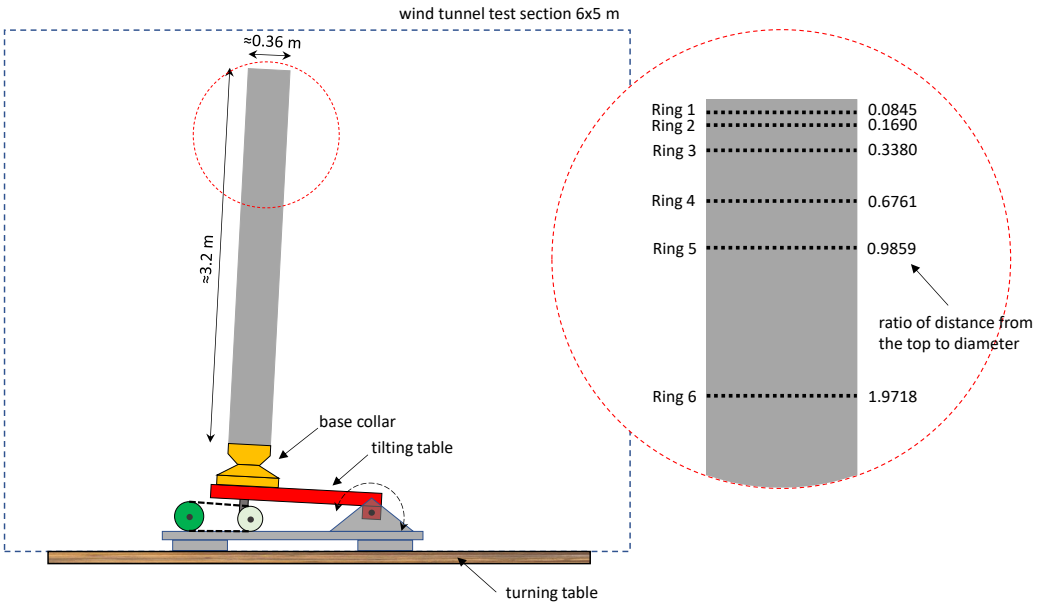


Figure 2. Wind tunnel test setup.

the base collar. The corresponding reduced frequencies are marked in Fig. 3 by vertical dashed lines with different colors. Their variability is related to the variability of the dominant frequency and a slight change of the flow velocity from test to test. For more details on the test program see also Giusti et al., 2025.

3. RESULTS

The preliminary results presented in this abstract are based on a direct post-process of the data from wind tunnel tests without applying any correction to missing or anomalous measurements. The focus is on the measurements got for Rings 2, 4 and 6, whose distance from the top of the cylinder is shown in Fig. 2. The power spectral density (PSD) of the lift coefficient at different heights of the cylinder and for different Reynolds numbers, shown in Fig. 3, suggests some preliminary observations. It is apparent that the rolling of the support does not significantly affect vortex shedding at high Reynolds numbers as it does for Reynolds numbers smaller than about 10^6. Moreover, the rings closer to the top seem less affected by the rolling.

4. CONCLUSIONS

The rolling of the support mainly affects the shape of the PSD of the lift coefficient and its energy content distribution at low Reynolds number regime, whereas at Reynolds numbers greater than 10^6 the differences are limited. This outcome, if confirmed by the ongoing post-process, would permit to decouple the vortex shedding response from the response associated with the vessel motion and to extend the classical and well-established models of vortex shedding of cylinders on a fixed foundation to the case of offshore wind turbine towers in navigation. Still to be clarified if the movement of the support affects the motion-induced forces rising from resonant phenomena like vortex induced vibrations. More insights will be presented at the conference.

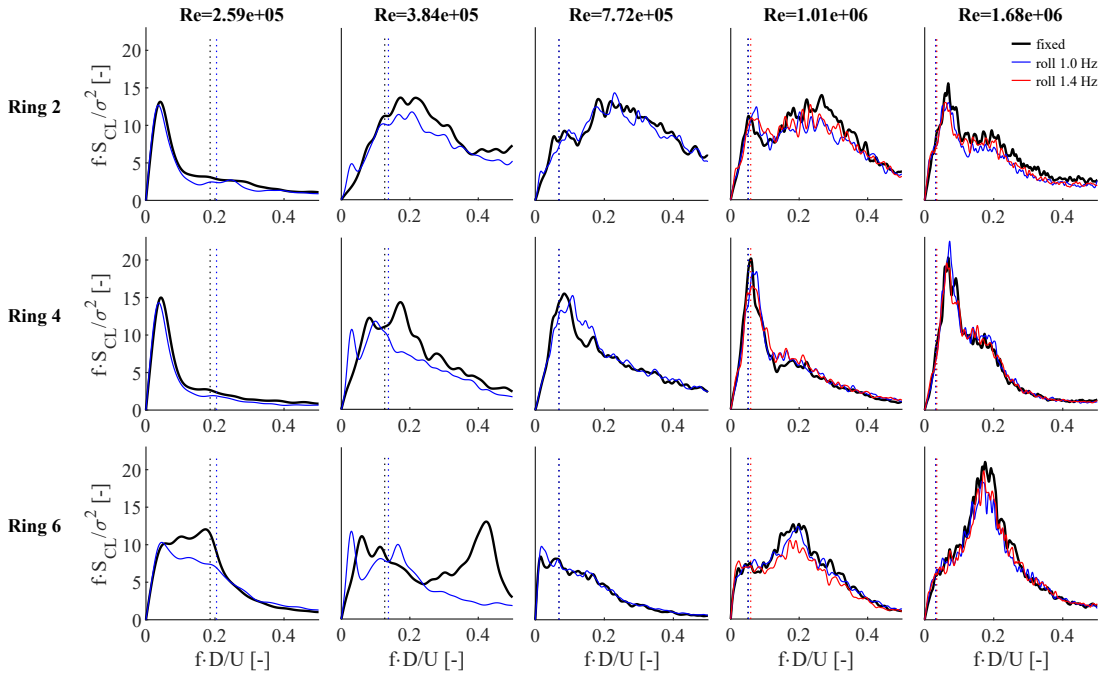


Figure 3. Power spectral density of the lift coefficient at different heights and for different Reynolds numbers. The vertical dashed lines mark the cylinder natural frequency of vibration estimated via acceleration measurements.

ACKNOWLEDGEMENTS

This work is part of the transnational access project "ERIES – VORSEA", supported by the Engineering Research Infrastructures for European Synergies (ERIES) project (www.eries.eu), which has received funding from the European Union's Horizon Europe Framework Programme under Grant Agreement No. 101058684. This is ERIES publication number C28.

REFERENCES

Ellingsen, Ø. M., 2021. Vortex-induced vibrations on industrial chimneys. École doctorale de l'Institut Polytechnique de Paris (EDIPP).

Giusti, A., Xhelaj, A., Orlando, A., Torrielli, A., and Flamand, O., 2025. Wind tunnel investigation of aerodynamic loads of circular cylinders from subcritical to supercritical Reynolds number regime. Proceedings of the 9th European-African Conference on Wind Engineering (EACWE 2025). Trondheim, Norway (extended abstract).

Kurniawati, I., Lupi, F., Seidel, M., Niemann, H.-J., and Höffer, R., 2024. Vortex shedding load on a full-scale wind turbine tower at transcritical Reynolds numbers. Journal of Wind Engineering and Industrial Aerodynamics 252, 105821.

Livanos, D., Kurniawati, I., Seidel, M., Daamen, J., Wenneker, F., Lupi, F., and Höffer, R., 2024. An enhanced analytical calculation model based on sectional calculation using a 3D contour map of aerodynamic damping for vortex induced vibrations of wind turbine towers. Wind and Structures 38, 445–459.

Mannini, C., Massai, T., Giachetti, A., and Giusti, A., 2023. Aerodynamic loads on groups of offshore wind turbine towers stored on quaysides during the pre-assembly phase. Journal of Wind Engineering and Industrial Aerodynamics 242, 105569.

— 2024. Aerodynamic loads on wind turbine towers arranged in groups with and without helical strakes. Proceedings of the XVII Conference of the Italian Association for Wind Engineering – IN-VENTO 2022. Milan, Italy, 260–269.

Torrielli, A. and Giusti, A., 2023. Uncertainties in the response of tower-like structures to wind gust buffeting. Journal of Wind Engineering and Industrial Aerodynamics 236, 105404.

Experimental evaluation of wind effects on non-standard shapes and structures

Anoop Kodakkal[1], Rodrigo Castedo-Hernandez[2], Guillermo Martinez-Lopez[2,3], Ann-Kathrin Goldbach[2], Kai-Uwe Bletzinger[2], Kimberly Adamek[4], Tibebu Birhane[4], Girma Bitsuamlak[4]

[1]*Lehrstuhl für Statik und Dynamik, Technische Universtität München, Munich, Germany,* *anoop.kodakkal@tum.de*
[2]*Lehrstuhl für Statik und Dynamik, Technische Universtität München, Munich, Germany*
[3]*Universitat Politècnica de València, Valencia, Spain*
[4]*WindEEE Research Institute, Western University, London, Ontario, Canada*

SUMMARY:
A comprehensive experimental study on wind effects on doubly curved structures was conducted at the WindEEE Dome, Western University, Canada. The research involved testing various doubly curved geometries that are common in membrane design, including hyperbolic paraboloid (hypar), ridge valley, arch-supported, cone, and umbrella shapes. Additionally, cone configurations were tested in both a single row of three (1x3) and a group of nine (3x3). All models were scaled to 1:25 and exposed to atmospheric boundary layer (ABL) flow with angles of attack ranging from 0° to 180° in 10° increments, along with an additional test at 45°. The hypar geometry was also subjected to two characteristic flow scenarios: tornado and downburst. In total, around 200 tests were conducted, providing valuable insights into the aerodynamic behavior of doubly curved structures under wind loads. A selection of notable and representative pressure results are presented here. The experimental tests were conducted as part of the Engineering Research Infrastructure for European Synergies (ERIES) project. This study offers crucial information for designing and analyzing such structures under wind loads in engineering applications.

Keywords: Wind tunnel, Membrane structures, Hypar, windeee

1. INTRODUCTION

The contribution focuses on recent experimental studies conducted at the WindEEE Dome, Western University, Canada, to standardize pressure maps for doubly curved membrane roofs. The project targets freestanding structures, which are commonly used to cover public spaces or leisure venues. This investigation is inspired by several iconic examples of freestanding canopies, including the Olympic Stadium Roof in Munich (1972, cable net), and the umbrellas in the Haram Plaza in Medina (2010, deployable membranes), as illustrated in Fig. 1.

Existing norms and standards offer only limited guidance for load assessments of such geometries. Typical forms can be seen in cable net structures and membrane canopies, where the geometry is mechanically defined by the level of prestress. The structures are considered rigid in this study. Wind loading patterns on these structures are typically based on rough estimates in engineering practice, with only a small number of specialized projects benefiting from detailed wind tunnel experiments or numerical simulations.

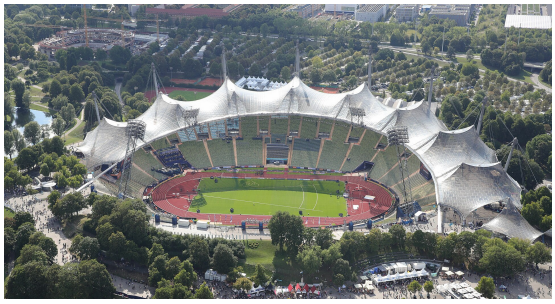




Figure 1. Iconic double-curved freestanding canopies: Olympic Stadium Roof in Munich (1972, left, SBP), Haram Plaza in Medina (2010, right, SL-Rasch)

The present study investigates five shapes — hypar, ridge valley, arch-supported, cone, and umbrella, as illustrated in Fig. 2 (Goldbach, 2021)—identified as representative by the TensiNet workgroup. These shapes were specifically emphasized in the 2015 Round Robin 3 (RR3) call (TensiNet, 2015) and its subsequent findings (Colliers et al., 2016). The study aims to generate high-resolution pressure maps, providing the mean and standard deviation of the relevant coefficients, which can be used by engineers and scientists in similar design scenarios. Various group configurations are tested in the wind tunnel under atmospheric boundary layer conditions. Additionally, the hypar geometry is examined not only under atmospheric boundary layer flow but also under non-synoptic wind scenarios, including tornadoes and downbursts.

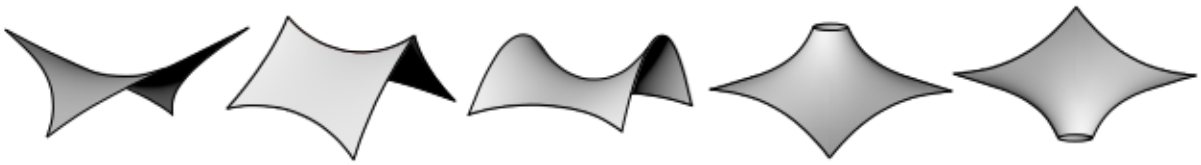


Figure 2. Shapes used for the current study, hyperbolic paraboloid (hypar), ridge valley, arch-supported, cone, and umbrella shapes from left to right.

The study focuses on presenting experimental results of wind tunnels for the five geometries investigated: hypar, ridge valley, arch-supported, cone, and umbrella shapes. These results provide high-resolution pressure maps and key aerodynamic coefficients for use in design and analysis.

2. METHODOLOGY

The atmospheric boundary layer (ABL), downburst, tornado characterization, and interaction with the structure tests detailed in this research were conducted at the WindEEE Dome. Located at Western University in London, Ontario, the WindEEE Dome has the unique capability to simulate boundary layer, shear, downburst, and tornadic-like wind flows. Fig. 3 presents an overview of the various test configurations conducted. The geometric and scaling details of the test specimen are shown in Fig. 4

ABL flows were tested to create an accurate simulation environment for evaluating the membrane structure models. Tests were conducted under both low-speed and high-speed configurations. Each

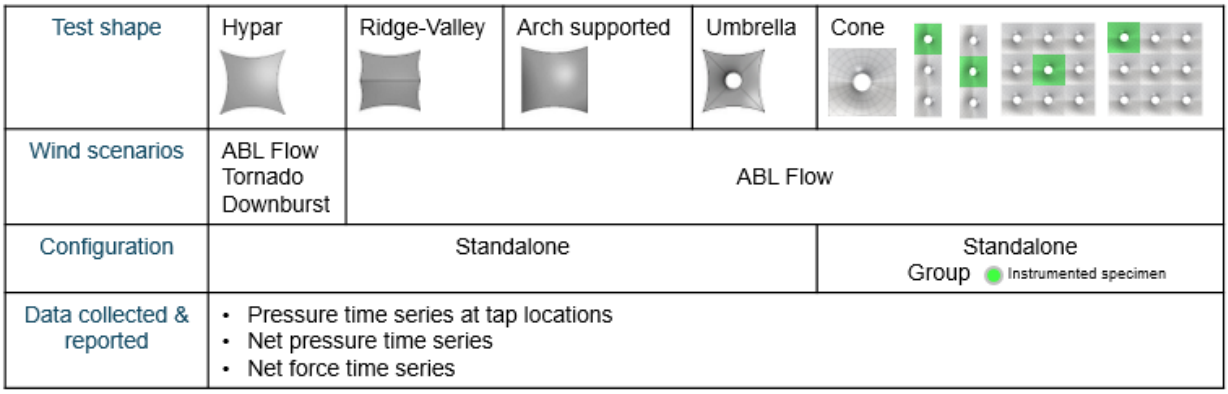


Figure 3. Details of the testing scenarios

setup incorporated various turbulence generation techniques, including roughness elements, spires, trips, and fan speed variations, to capture a range of flow conditions.

For the downburst characterization, 3-D velocity measurements were taken radially around the bell mouth, where the downburst-like flow was generated by the sudden release of pressure, creating an impinging jet. For the tornadic flows, low-speed configurations were used, incorporating various turbulence generation methods and fan speed variations. A precise simulation environment suited to the model scale and installation conditions is developed.

Tornadic flows were conducted to ensure accurate testing of membrane structure models, considering the model scale, size, and installation region. The tests were performed under low-speed conditions, using various turbulence generation methods, including roughness elements, spires, trips, and fan speed adjustments, to capture a range of flow behaviors across different configurations.



Figure 4. Details of the geometry of test specimen

All models are 1 cm thick with a 0.8cm cavity in between for pressure tubing. All models were tested every 10° between 0 and 180° plus a 45° angle of attack. The data were collected and analyzed.

3. RESULTS

This section focuses on presenting surface pressures on the tested hyper geometry. The pressure distribution shows how the flow affects the structure. Since these are membrane structures, the bottom and top pressures are summed up. The pressure taps are placed one on top of the other. A positive pressure indicates a pressure towards the top. Fig. 5 shows the pressure distribution of hypar for 3 three different angles of attack.

The H and L indicate the high and low points of the hypar geometry. The dots indicate the pressure tap locations and the arrows indicate wind direction. We map the point values to the 3D surface, which is shown in Fig. 5.

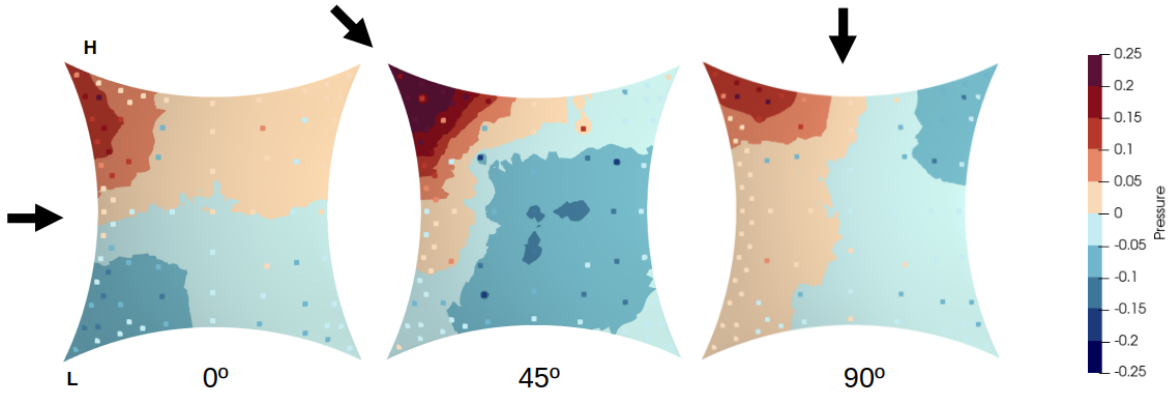


Figure 5. Mean of total pressure for hypar geometry for multiple directions of incoming wind. The H and L indicate the high and low points of the geometry. The bottom and top pressures are summed up with an inverted sign to obtain the total pressure.

4. CONCLUSIONS AND OUTLOOK

An experimental testing campaign is being conducted to analyze wind loads on some of the most common doubly curved shapes used in membrane design. The objective is to develop pressure coefficient maps to aid in the planning and design of these structures, contributing to further standardization. Additionally, a CFD campaign is planned to complement the experimental results and contribute to an open database for non-standard shapes and their wind pressure distributions.

ACKNOWLEDGEMENTS

This work is supported by the Engineering Research Infrastructures For European Synergies (ERIES) project (www.eries.eu), which has received funding from the European Union's Horizon Europe Framework Programme under Grant Agreement No. 101058684.

REFERENCES

Colliers, J., Mollaert, M., Vierendeels, J., and De Laet, L., 2016. Collating wind data for doubly-curved shapes of tensioned surface structures (Round Robin Exercise 3). Proceedings of International Symposium on "Novel structural skins - Improving sustainability and efficiency through new structural textile materials and designs".

Goldbach, A.-K., 2021. The CAD-integrated design cycle for structural membranes. phdthesis, School of Engineering and Design, Technical University of Munich.

Wet Snow Accretion on Transmission Lines in Climatic Wind Tunnel

Erick Ulloa Jimenez [1], Francesca Lupi [2], Norbert Hoelscher [2], Susanne Diburg [2], Jean Paul Bouchet [3], Bruno Gauducheau[3], Thomas Batmalle [3], Philippe Delpech [3], Olivier Flamand [3]

[1]*Amprion GmbH, Dortmund, Germany*
[2]*Niemann Ingenieure GbR, Bochum, Germany, Lupi@Niemann-Ing.de*
[3]*Centre Scientifique et Technique du Bâtiment (CSTB), Nantes, France*

SUMMARY
The investigation is concerned with ice loads on transmission lines caused by wet snow accretion. In addition to in-cloud icing and freezing rain, the phenomenon of wet snow accretion is particularly unfavourable for transmission lines due to the relatively high probability of occurrence at altitudes above 600 m and the significant ice loads. For high and exposed locations, ice loads play a crucial role in structural calculations. A probabilistic approach is typically used for structural analysis, which requires an extreme value distribution function for ice loads. Ice loads are simulated using empirical models based on weather parameters such as wind speed, air temperature and relative humidity. In order to improve the accuracy of existing ice load models, experiments have been carried out in the "Jules Verne" climatic wind tunnel at the CSTB Nantes facility in France. The aim is to study the iced loads caused by wet snow accretion for different snow characteristics. The liquid water ratio of snow particles plays the key role in determining whether the resulting ice accretion is lighter and drier or, conversely, heavier and wetter. The study also examines the effects of wind direction and conductor rotation on the mass of ice accretion.

Keywords: Ice loads, Transmission Lines, Climatic Wind Tunnel Tests

1. INTRODUCTION

The physical principle for calculating ice accretion is based on the Makkonen model. The Makkonen model defines the basic equation for ice accretion described in the International Organisation for Standardisation (ISO) for icing of structures. It expresses the rate of change of the ice mass accumulated on the exposed object, e.g., a cable, as a function of the air mass concentration of the impinging particles, the velocity of the particles with respect to the object and the effective cross-sectional area of the object. Empirical factors less than unity based on weather parameters reduce the icing rate from its maximum potential value. These factors are the collision efficiency α_1, the adhesion efficiency α_2 and the accretion efficiency α_3. α_1 is the fraction of particles that hit the object with respect to the flowing particles, α_2 is the fraction of particles that stick on the object without bouncing, while α_3 is the fraction of particles that freeze on the object and contribute to ice accretion.

There are three types of icing: in-cloud icing, freezing rain and wet snow accretion. The Makkonen model for wet snow accretion has been revisited by Nygaard (see Nygaard et al. (2013) and Ducloux&Nygaard (2014)), with particular effort in the determination of the sticking efficiency

for wet snow. Whereas in-cloud icing and freezing rain are caused by supercooled water droplets that remain liquid at temperatures below 0°C, wet snowflakes are a mixture of ice granules, liquid water and air bubbles. Snow adhesion is strongly dependent on the liquid water ratio, i.e. the ratio of the mass of the liquid part to the total mass of the snowflake. The liquid water ratio determines the quality of snow and its capacity to accumulate, considering that perfectly dry snow (LWR=0) will result to any accretion.
The paper presents the results of experiments carried out in the CSTB climatic wind tunnel on a 1:1 model of a real power line. The experiments are carried out by varying the snow quality in the wind tunnel by changing the air temperature. The torsional stiffness of the power line specimen and the wind direction are also considered.

2. EXPERIMENTS IN CLIMATIC WIND TUNNEL

Wet-snow accretions on a conductor specimen are simulated in the CSTB climatic wind tunnel ("Thermal" circuit). This climatic wind tunnel can reproduce different weather conditions: the temperature can be adjusted from -32°C to +55°C and the 1 MW fan allows the wind speed to reach 40 m/s. The test area of the thermal unit is 21m long, 10m wide and 7m high. The thermal wind tunnel is equipped with a snow gun system. For this experiment, the snow gun is placed 10 m before the testing position. Artificial snow is produced by mixing water and air at high pressure (6 to 10 bar). After mixing, the two-phase flow is expelled at high speed (80 to 100 m/s) through an orifice. The water particles (small droplets with a MVD of 250 microns) are injected into the air stream at a temperature close to +1°C. The particles begin to freeze as soon as they encounter the cold air stream.
The wind tunnel tests are carried out at a constant wind speed of 10 m/s by varying the air temperature. The air temperature range investigated in the experiments varies between -10°C and -2°C. The air temperature chosen for each experiment influences the freezing process of the flying particles. After the initial supercooled phase, in which the flying particles are still liquid, they gradually freeze during their flight. This is known as the freezing phase. During this stage, the amount of water inside the snow particle varies as a function of air temperature, flight path length and wind speed. Therefore, by conducting each test at a constant wind speed and with the snow gun at the same distance from the conductor, the air temperature is the only parameter that determines the quality of the snow. This is then directly related to the liquid water ratio. As a result, drier and lighter, or wetter and heavier ice accretions are observed in the temperature range tested during the experiments.

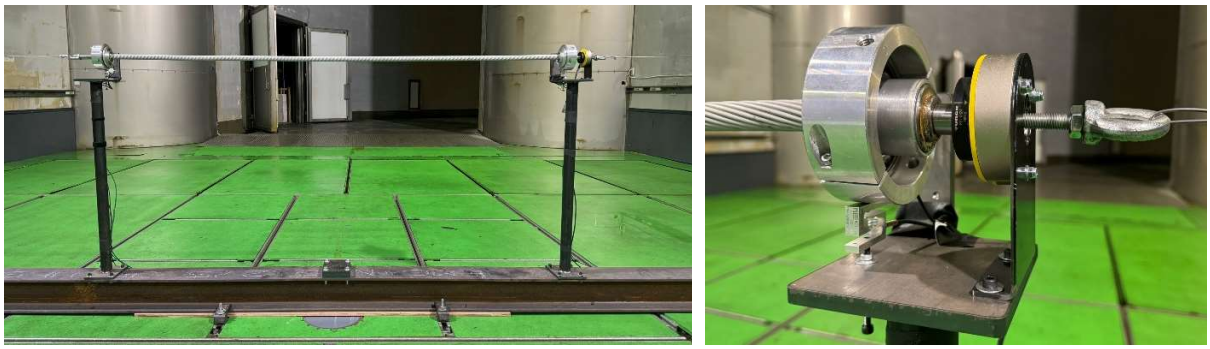


Figure 1. Test bench for the wind tunnel tests

A 2 m section of a real power line (d = 22.43 mm) is suspended and prestressed in the wind tunnel using the test bench shown in Figure 1. The power line is equipped with force sensors at its ends to measure horizontal and vertical forces. Figure 2 shows the variability of ice accretion and hence ice loads for different snow qualities, from very wet snow (almost freezing rain) to very dry snow.



Figure 2. Different types of accretion for different snow quality, from very wet to dry (1-hour exposure)

The torsional stiffness of the transmission line is another important parameter that strongly affects the ice loads. The following configurations are tested in the wind tunnel

- Conductor fixed at both ends (see Figure 2)
- Freely rotating conductor, with torsional stiffness corresponding to a real 400m span, reproduced by a taught piano wire of relevant diameter and length."

The experiments have shown that in a free rotation configuration, the progressive accumulation of snow on the windward face of the specimen leads to a linear evolution over time of the rotation angle. There was no experimental evidence that the process would eventually stop. The ice accretion grows cylindrically around the conductor, instead of having a streamlined shape on the windward side as in the case of the fixed conductor. As a result, the impact area of the conductor increases with time and the resulting ice load is much higher than the ice load on the non-rotating conductor. Finally, selected experiments are repeated for a wind direction yawed relative to the conductor axis. With regard to probabilistic modelling of ice loads on transmission lines, the inclusion of wind direction variability is important to calculate realistic ice loads.
Experimental results will be presented at the conference.

3. CONCLUSIONS AND OUTLOOK

Wet snow accretion is one of the dominant ice formation mechanisms affecting overhead power lines, particularly in high and exposed locations. These environmental conditions make it necessary to take ice loads into account in structural calculations, where such loads often play a critical role. A probabilistic approach is typically used for structural analysis, which requires an extreme value distribution function for ice loads (Jiminez et al., 2025, Lupi et al., 2025).
In order to develop realistic calculations of ice loads, experiments were carried out in the climatic wind tunnel at the CSTB. Firstly, the results emphasise the effect of snow quality, i.e. the liquid-water ratio of the snow particles, on the type of accretion and the ice loads. Second, the axial rotation of a conductor, due to its relatively low torsional stiffness, can result in much higher ice loads. Thirdly, the variability of the wind direction with respect to the conductor axis can be considered as a favourable effect to be included in the ice load modelling for realistic ice load calculations.

ACKNOWLEDGEMENTS

This work is part of the transnational access project "WiST", supported by the Engineering Research Infrastructures for European Synergies (ERIES) project (www.eries.eu), which has received funding from the European Union's Horizon Europe Framework Programme under Grant Agreement No. 101058684. This is ERIES publication number C49.

The authors also extend their gratitude to Amprion GmbH for the kind support in the investigation.

REFERENCES

Farzaneh M. 2008, Atmospheric Icing of Power Networks, Springer.

Ducloux H. and Nygaard B. E. 50-year return-period wet-snow load estimation based on weather station data for overhead line design in France. Nat. Hazards Earth Syst. Sci., 14, 3031–3041, 2014

Jiminez E.U., Steevens S., Hoelscher N., Diburg S., 2025. Enhanced atmospheric Icing Modelling of High-Voltage Transmission Lines. Submitted to 9th European African Conference on Wind Engineering, Trondheim, Norway

Lupi F., Jimenez E.U., Matejicka L., Hoelscher N., Koss H., 2025. Considerations in replicating In-cloud Ice Accretion on Power Lines in Climatic Wind Tunnel Testing. Submitted to 9th European African Conference on Wind Engineering, Trondheim, Norway

Makkonen Lasse, Wichura Bodo, 2010, Simulating wet snow loads on power line cables by a simple model, Cold Regions Science and Technology 61, 73–81.

Matejicka Lubomir, Delpech Philippe, Georgakis Christos T., Flamand Olivier, 2024, An experimental investigation of ice and snow shedding from bridge cables with and without surface modifications, Cold Regions Science and Technology, Volume 220, 2024, 104148, ISSN 0165-232X, https://doi.org/10.1016/j.coldregions.2024.104148.

Vigano A, Modélisation numérique et expérimentale des phénomènes de givrage par accrétion de neige collante. ISAE-ENSMA École Nationale Supérieure de Mécanique et d'Aérotechnique, 2012. France. NNT: 2012ESMA0026.

Vigano A. & Delpech, Philippe & Aguinaga, Sylvain & Guffond, D. & Jacques, Boree, 2013. Wind tunnel assessment of atmospheric icing and wet snow accretions on structures. 6th European and African Conference on Wind Engineering (EACWE), Cambridge 2013.

Nygaard B.E.K., Agustsston H., Somfalvi-Toth K., Modeling Wet Snow Accretion on Power Lines: Improvements to Previous Methods Using 50 Years of Observations. Vol. 52, Journal of Applied Meteorology and Climatology, 2013.

Wind impacts on vertiport design

Mohammad Amir Neshat[1], Edoardo Ruffini[1], Stefano Torre[1], Giuseppe Piccardo[1], Maria Pia Repetto[1], Yana Gorbachova[2], Dario Milani[2]

[1]*Department of Civil, Chemical and Environmental Engineering, DICCA, Polytechnic School, University of Genova, Genova, Italy, mohammadamir.neshat@edu.unige.it*
[2]*DM-AirTech GmbH, Ottenser Hauptstraße 2-6, Hamburg, Germany*

SUMMARY:
The integration of Vertical Take-off and Landing (VTOL) vehicles in Urban Air Mobility (UAM) presents new challenges, particularly in the design and planning of vertiports. As urban landscapes continue to evolve, the ability to accurately assess and mitigate wind-related risks will be essential for the successful implementation of UAM infrastructures. The objective of this study is to evaluate the influence of wind conditions on vertiport operations, providing critical insights to support infrastructure planning and safety. Wind variability in urban environments, influenced by buildings and urban geometries, can significantly impact VTOL operations. Unlike conventional aircraft, VTOLs are more sensitive to aerodynamic disturbances during vertical manoeuvres. Therefore, Thorough wind studies are paramount, not only to ensure that vertiports are located in areas where wind conditions do not jeopardise safety but also to provide essential insights for optimising vertiport design to enhance performance.
The goal of this research is to develop reliable datasets that quantify wind flow patterns and turbulence at candidate vertiport locations, both in urban environments and isolated conditions. This will be achieved through a combination of experimental field studies and computational simulations across various configurations of the urban vertiport concept. The current research aims to establish a benchmarking framework for the validation of Computational Fluid Dynamics (CFD) simulations to support vertiport design and optimization processes.

Keywords: Vertiport design, Wind tunnel testing, CFD simulations

1. MOTIVATION

Vertical Take-Off and Landing (VTOL) vehicles are poised to play a crucial role in the evolution of urban air mobility (UAM), offering the potential to alleviate traffic congestion and enhance transportation efficiency in densely populated areas. As their adoption increases, understanding the impact of wind actions on the planning and design of vertiports becomes essential, both in urban settings and sub-urban or rural environments, to ensure safety, performance, and integration into the existing infrastructure.

The primary concerns surrounding vertiports revolve around three critical factors: visibility, availability, and the safety of VTOL operations. These elements are essential for ensuring that travel is not only safe but also efficient and seamless. To tackle the first two factors, studies by (Jeong et al., 2024; Lim and Hwang, 2019; Thipphavong et al., 2018 and Taye et al., 2024) have delved into the trajectories of VTOL vehicles, aiming to pinpoint optimal planning frameworks. Nevertheless, in terms of safety, the location and design of vertiports are paramount. The rapid development of UAM underscores the necessity for a focused experimental investigation into the wind and turbulence effects on vertiport operations. As projected investments in UAM

infrastructure reach $32 billion by 2040, understanding the aerodynamic conditions that influence the performance and safety of VTOL vehicles is critical. Despite significant regulatory advancements from bodies such as the European Union Aviation Safety Agency (EASA, 2022) and the Federal Aviation Administration (FAA), there remains a notable lack of empirical data specifically addressing how local meteorological conditions impact vertiport siting and design.

Recent research, including studies by (Bernyk et al., 2023), has started to shed light on the aerodynamic challenges posed by vertiport design, particularly focusing on how rooftop edge configurations impact airflow. Using Particle Image Velocimetry (PIV) measurements, these investigations also consider various design modifications aimed at improving vertiport performance. Additionally, CFD studies have employed Large Eddy Simulation (LES) methods, combined with Spectral Proper Orthogonal Decomposition (SPOD) post-processing, as demonstrated by (Maleki et al., 2024), to capture the unsteady flow characteristics around vertiports. Despite these advancements, a substantial gap persists in the literature concerning the aerodynamic performance of vertiports. Site selection and turbulence characterization pose distinct challenges compared to traditional studies on pedestrian wind comfort and wind-induced forces on buildings. The complexities associated with locating and designing vertiports are primarily centered on accurately modeling wind properties and turbulence in the Final Approach and Take-Off area (FATO). Additionally, while there are synergies with existing industrial maturity issues, it is crucial to address these new challenges directly to enable the industry to make informed decisions. This is especially important given the implications for the operation of aerial vehicles in urban environments, directly impacting the safety of citizens. In urban areas, wind-induced conditions become increasingly complex due to the intricate nature of the urban flow field. Thus, PIV measurements can provide valuable insights into how air flows around vertiports in different locations, with the potential to enhance urban weather forecasting and enable near-real-time predictions of three-dimensional turbulent flow patterns along various flight paths. These insights can be crucial for optimizing the safety and performance of VTOL vehicles.

This study is part of the ERIES Horizon Project WonV1 and aims to address a critical gap in the field by examining how wind effects and aerodynamic considerations can influence vertiport locations. By providing valuable insights into the ongoing discourse on UAM, this research will help establish essential design parameters. Furthermore, the comparison of vertiports in urban settings versus those in open, unobstructed areas is expected to yield important insights into their vulnerability to upstream airflow and the influence of surrounding architectural features. By exploring different environmental and vertiport concepts, this research aims to establish the first standardized dataset for CFD model validation. First, it will support vertiport siting, design, and optimization processes, followed by the development of formal design guidelines to standardize safety and performance criteria in this emerging field of mobility.

2. PROJECT PHASES

The project aims to establish essential design and operational parameters for vertiport siting and construction across diverse environments, with a primary focus on assessing wind and aerodynamic impacts. The research is structured in two key phases, each centered on critical milestones that contribute to a comprehensive understanding of vertiport siting and design within the framework of UAM.

In Phase 1, a city model at a scale of 1:600 (Figure 1a) has been constructed to measure in the wind tunnel the effect atmospheric boundary layer (ABL) from the prevailing wind directions. The city of Los Angeles has been selected for this study, as it represents a pivotal location for the initial rollout of UAM infrastructure. Using a multi-hole Cobra probe, precise flow measurements are taken from eight directions at a single wind speed. Data is collected at multiple points: 10 vertical measurements at the tops of four specific buildings, and 10 horizontal measurements between the buildings (Figure 1b). The post-processing of this data have been integrated in the CFD model, with the objective of calibrating the numerical model to identify wind characteristics that are critical for vertiport design and safety.

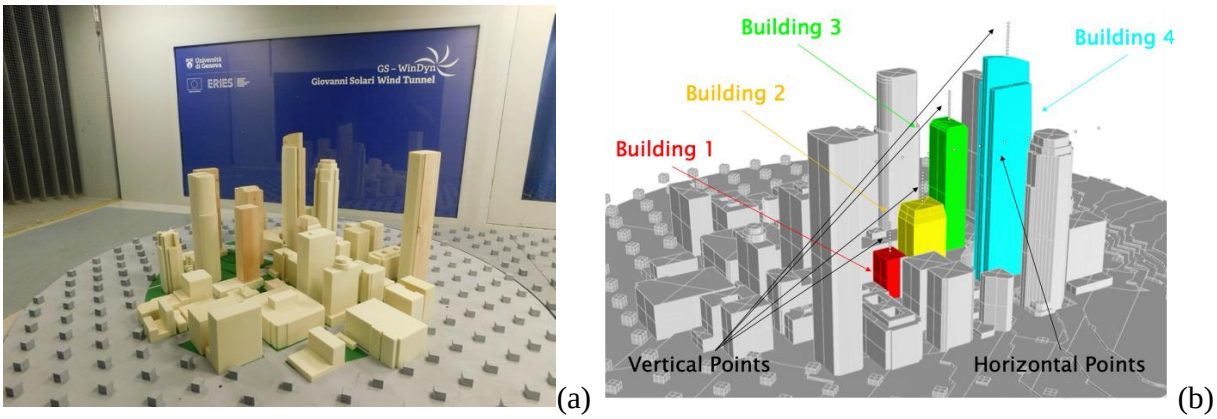
Phase 2 is currently underway, with a targeted completion date by the end of 2024. This phase involves the analysis of two distinct vertiport environments and corresponding design concepts: an Urban Vertiport, situated atop buildings within a dense urban setting, and a Surface Vertiport, positioned in an isolated area near the sea.
For the Urban Vertiport, the tests initiated in Phase 1 will be expanded to a larger scale (1:300-400), focusing on a detailed segment of the urban area studied previously. Multiple configurations will be analyzed, including a free-flow condition and one shielded by surrounding buildings configuration. Both Cobra probes and PIV technology will be employed to conduct high-resolution, non-intrusive measurements of complex flow patterns and velocities. PIV, known for its accuracy and precision in capturing intricate flow dynamics (e.g., Dantec Dynamics, 2022), will appear essential for identifying the aerodynamics that most influence vertiport performance.
For the Surface Vertiport, an area at ground level near the coast has been selected to analyze two distinct wind configurations—sea and land winds—each with unique wind profiles and characteristics. Detailed flow studies in this area will also employ PIV technology, supplemented by Cobra probes where necessary, to capture the variations in wind behavior that are crucial for understanding vertiport performance in open environments.

3. ON-GOING WORK

Preliminary results from Phase 1 indicate that the complex airflow patterns around building rooftops define important challenges for the safe operation of VTOL aircraft. Key factors impacting vertiport safety are the upstream wind velocity and turbulence intensity, both of which vary significantly with wind conditions and the configuration of surrounding buildings. Notably, flow separation in the wake of tall structures emerges as a critical aerodynamic concern, as it generates unstable wind patterns and increased turbulence, elevating risks during take-off and landing.

Building on these findings, Phase 2 will focus on establishing precise design and operational parameters, informed by infrastructure and operational requirements. Infrastructure considerations will encompass aspects such as vertiport capacity, layout, passenger zones (retail, check-in, gates, waiting areas), and, most critically, the sizing, shape, and positioning of the FATO area, both architecturally and structurally. Operational requirements, including optimal landing and take-off trajectories and approach angles, will guide the final engineering designs. The primary aim of Phase 2 is to develop guidelines that support the design for an optimized vertiport configuration, specifically focused on the reduction of wind impacts on the FATO area. The final output will not only establish a robust structural framework but also ensure that vertiport designs are well-

equipped to mitigate aerodynamic challenges, enhancing overall safety and reliability for VTOL operations.



(a) (b)

Figure 1. Phase 1 of the research project WonV1 focused on downtown Los Angeles: (a) wind tunnel model at a scale of 1:600; (b) schematic representation highlighting the flow measurement points.

ACKNOWLEDGEMENTS

This work is supported by the Engineering Research Infrastructures for European Synergies (ERIES) project (www.eries.eu), which has received funding from the European Union's Horizon Europe Framework Programme under Grant Agreement No. 101058684. This is ERIES publication number XXX.

REFERENCES

Bernyk, A., Mantri, V., and Sutherland, F., 2023. Aerodynamic Investigation of Vertiport Design for Air Taxis. AIAA 2023-76534, AIAA Regional Student Conferences.

Dantec Dynamics, 2022. Measurement Principles of PIV. https://www.dantecdynamics.com/solutions-applications/solutions/fluid-mechanics/particle image-velocimetry-piv/measurement-principles-of-piv/.

EASA, 2022. Vertiports – Prototype Technical Specifications for the Design of VFR Vertiports for Operation with Manned VTOL-Capable Aircraft Certified in the Enhanced Category (PTS-VPT-DSN). European Union Aviation Safety Agency (EASA), Cologne, Germany.

Jeong, T., Hong, Y., Lom, D., and Yee, K., 2024. Landing Trajectory Analysis of eVTOL aircraft for Urban Air Mobility Considering Vortex Ring State. AIAA 2024-2503, AIAA SCITECH 2024 Forum, January 8-12, 2024. Orlando, FL.

Lim, E., and Hwang, H., 2019. The Selection of Vertiport Location for On-Demand Mobility and Its Application to Seoul Metro Area. International Journal of Aeronautical and Space Sciences 20, 260–272.

Maleki, A., Ahmed, B., Singh, S., and Golubev, V.V., 2024. High-Fidelity Analysis of Unsteady Flow Characteristics Around Vertiport Model. AIAA 2024-2550, AIAA SCITECH 2024 Forum, January 8-12, 2024. Orlando, FL.

Taye, A.G., Valenti, R., Rajhans, A., Mavrommati, A., Mosterman, P.J., and Wei, P., 2024. Safe and Scalable Real-Time Trajectory Planning Framework for Urban Air Mobility. Journal of Aerospace Information Systems 21(8), 641–650.

Thipphavong, D.P., Apaza, R., Barmore, B. et al., 2018. Urban Air Mobility Airspace Integration Concepts and Considerations. Aviation Technology, Integration, and Operations Conference, June 25-29, 2018. Atlanta, Georgia.

CLIMATHUNDERR: A first attempt to combine impinging jet and gravity current techniques to simulate downburst winds at large scale

Federico Canepa [1], Anthony Guibert [2], Andi Xhelaj [1], Josip Zuzul [1], Djordje Romanic [3], Alessio Ricci [4], Horia Hangan [5], Olivier Flamand [2], Jean-Paul Bouchet [2], Philippe Delpech [2], Massimiliano Burlando [1]

[1]*University of Genoa, Genoa, Italy, federico.canepa@unige.it – andi.xhelaj@edu.unige.it – josip.zuzul@edu.unige.it – massimiliano.burlando@unige.it*
[2]*Centre Scientifique et Technique du Bâtiment (CSTB), Nantes, France, anthony.guibert@cstb.fr – olivier.flamand@cstb.fr – jeanpaul.bouchet@cstb.fr – philippe.delpech@cstb.fr*
[3]*McGill University, Montreal, Canada, djordje.romanic@mcgill.ca*
[4]*University School for Advanced Studies (IUSS) Pavia, Pavia, Italy, alessio.ricci@iusspavia.it*
[5]*Ontario Tech University, Oshawa, Canada, horia.hangan@ontariotechu.ca*

SUMMARY:
Thunderstorm downbursts are surface winds that can be very strong and dangerous for the natural and built environment. The CLIMATHUNDERR—CLIMAtic investigation of THUNDERstorm winds—project, funded by the European Union, examined a combined effect of large-scale gravity currents and impinging jets at the Jules Verne Climatic Wind Tunnel, in France, to study flow field and dynamics of thunderstorm outflows. Velocity measurements were captured using Large-Scale Particle Image Velocimetry (LS-PIV), while thermocouples were used to measure radial and vertical temperature profiles. To investigate how topography influences downburst behaviour, tests were also conducted on a scaled model of the Polcevera Valley in the Municipality of Genoa, Italy, examining the impact of complex terrain on downburst outflow geometries and velocities, particularly related to temperature effects.
This project brought together an interdisciplinary team with expertise from atmospheric physics and meteorology to experimental and numerical fluid dynamics, as well as civil and mechanical engineering. The data will be thoroughly documented in a data paper and made openly available to the public by the time of the conference.

Keywords: downburst, LS-PIV, temperature effects

1. INTRODUCTION

The study of thunderstorm downbursts has gained increasing attention over the last years also due to climate change impacts. Warm, humid air rises and condenses into a cumulonimbus cloud, then sinks as cold, dense air (downdraft), creating symmetrical vortices. Upon reaching the ground, the primary vortex (PV) drives the horizontal outflow which can cause severe damages. Recording downbursts in nature is highly challenging due to their complex, small-scale temporal and spatial structures. Nevertheless, there is an increasing need to better understand this phenomenon and develop accurate models to assess its impact on both natural ecosystems and built environments. Wind simulators are effective tools for studying downbursts in controlled conditions, and two primary simulation methods have emerged: (i) the impinging jet (IJ) method (Canepa et al., 2022;

Sengupta and Sarkar, 2008; Xu and Hangan, 2008), which generates downbursts using mechanically forced air, and (ii) the gravity current (GC) method (Simpson, 1969; Lundgren et al., 1992), which relies on the buoyancy generated from the natural density difference between a cold jet and the surrounding warmer air. While the GC method more accurately represents thermodynamic instabilities in the atmosphere prone to downbursts, its velocity and scale limitations often make the IJ method more suitable for wind engineering studies.

The project CLIMATHUNDERR, funded by the European Union's Engineering Research Infrastructures for European Synergies (ERIES) program, sought to extend the GC method's applicability to larger scales by combining it with the IJ approach and focusing on the role of thermal effects on downburst dynamics. An experimental campaign was conducted at the Jules Verne Climatic Wind Tunnel (JVCWT) of the Centre Scientifique et Technique du Bâtiment (CSTB) in Nantes, France. LS-PIV and thermocouples were used to measure velocity and temperature fields, respectively. In addition to bare floor of the wind tunnel, a 1:2000 reduced-scale model of the complex orography of the Polcevera Valley in the Genoa municipality, Italy, was tested to examine how topography and channelling influence flow dynamics and temperature profiles in the outflow.

2. EXPERIMENTAL SETUP

The thermal circuit of the JVCWT has a 25-m long rectangular test section (10 m × 7 m). To simulate the downburst downdraft, an 8 m³ impinging jet plenum (IJP) was manufactured and installed at 3 m above the chamber floor, with a bottom circular nozzle (D = 1 m) opening directly into the testing chamber. An air conditioning system cooled the air inside the IJP to as low as 5°-10°C. Different temperature differentials (ΔT) between the IJP and the chamber air were reproduced to investigate the buoyant effects on downburst dynamics. To manage the initial conditions and ensure repeatability of the start of the experiment, a piston was introduced to control the jet speed at the nozzle exit, representing the pure contribution of the IJ. Two piston velocities (0.15 and 0.25 m s^{-1}) were used, resulting in mechanical vertical jet velocities of 0.80 and 1.30 m s^{-1} at the nozzle exit. The final jet velocity (w) is a combination of the mechanical jet velocity (w_{IJ}) from the piston and the buoyant contribution (w_{GC}) from ΔT.

LS-PIV was used to measure flow velocity, using Helium-Filled Soap Bubbles (HFSB) injected into the IJP prior to jet release. Cameras were positioned along one side of the test chamber to capture image data of the downburst downdraft and outflow within a vertical plane. The first camera, with a 2.5 × 2.5 m² field of view (FOV) and 7 Hz acquisition frequency, was replaced after malfunctioning by a second camera with a larger 3.2 × 2.5 m² FOV and 12 Hz acquisition rate. For 12 configurations, a visualization of the downburst illuminated by two white light LED bars was recorded by a video camera (Figure 1). A total of 24 thermocouples were used to monitor the ΔT between the IJP and chamber, as well as to measure temperature profiles throughout the flow field and surface temperatures on the reduced-scale orography model. A total of 56 experiments were conducted. The initial 39 experiments were performed without the topography model to study the fundamental characteristics of the downburst flow under varying thermal conditions. Experiments 40 to 56 included the orography model to investigate how complex terrain influences downburst dynamics and temperature distributions.

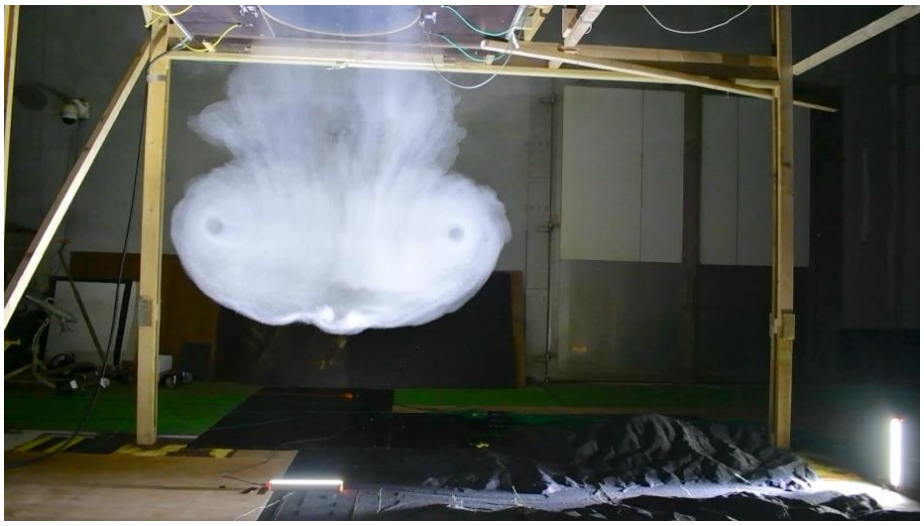


Figure 1. Flow visualization of the downburst jet approaching the ground and the orography model, captured at a temperature differential of ΔT = 0°, and a mechanical jet velocity of w_{IJ} = 0.80 m s^{-1}.

2.1. Flow investigation

The first set of 39 experiments examined the impact of different temperature differentials (ΔT = 0°, 10°, and 20 °C) on the downburst downdraft and its horizontal outflow. The FOV origin was fixed at the jet touchdown center, allowing for observation of the downburst evolution across different radial positions ($0 < r/D < 2.5$ or 3.2, based on the camera's FOV) and heights ($0 < z/D < 2.5$). Thermocouples were arranged along vertical profiles at specific radial distances in the outflow region to capture temperature variations within the flow. The results can be applied to any radial direction from the jet touchdown due to the assumption of radial symmetry.

2.2. Downburst flows on the orography model

The second phase of the study investigated the interaction between downburst flows (ΔT = 0° and 20° C) and complex terrain by introducing the scaled model (1:2000) of the Polcevera Valley in Genoa, Italy. The digital-milled Expanded Polystyrene (EPS) model (3.5 m × 2 m) represented an area of 7 km × 4 km in Genoa, extending from the port to the inland hills and mountains. To simulate different impact scenarios, the jet touchdown center was adjusted to two distinct positions relative to the model. The PIV FOV focused on the same outflow region along the valley (Figure 2a). Thermocouples were placed on the model's surface to analyse how channelling effects within the valley and ridge formations influenced temperature profiles during the downburst.

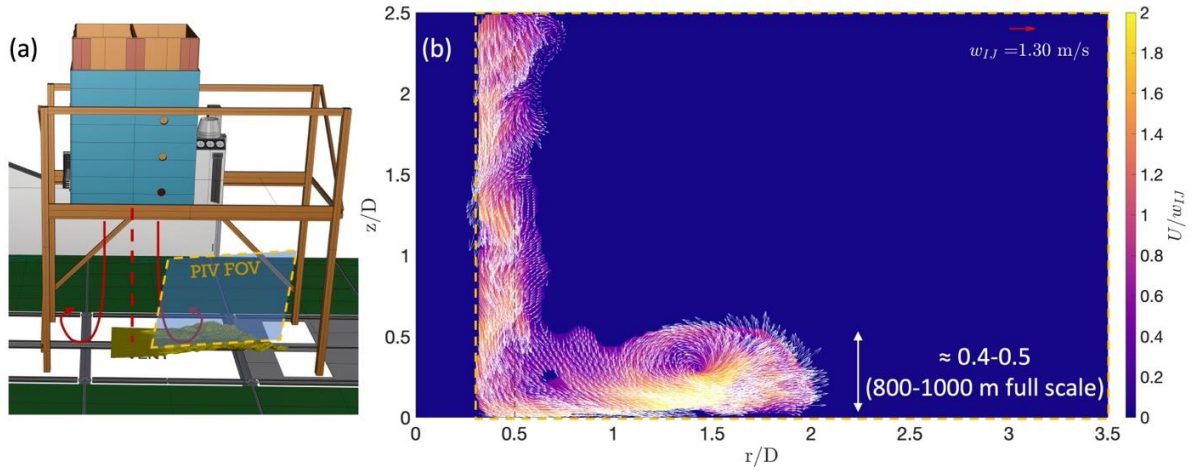


Figure 2. (a) Schematics of the experimental setup with 1:2000 scaled model installed in position 1. (b) Corresponding velocity field obtained from LS-PIV measurements and estimation of PV dimension.

3. DATABASE USE AND CONCLUSIONS

This study marks the first attempt to combine the impinging jet (IJ) and gravity current (GC) techniques to simulate the thermal effects on downburst winds at large geometric scales. The resulting database will be made publicly available in open-access form, with full details provided in a forthcoming data paper. This resource will enable researchers to conduct comprehensive analyses of the role of temperature in downburst flows and refine numerical and analytical models of these storm systems, contributing to the advancement and revision of design codes.

A separate paper presented at this conference will delve into the findings of the experimental campaign, highlighting the impact of different temperature differentials on the reproduced downburst jet velocities and geometries, as well as their interaction with a suburban canopy.

ACKNOWLEDGEMENTS

This work is part of the transnational access project "ERIES – CLIMATHUNDERR", supported by the Engineering Research Infrastructures for European Synergies (ERIES) project (www.eries.eu), which has received funding from the European Union's Horizon Europe Framework Programme under Grant Agreement No. 101058684. This is ERIES publication number C25. F. Canepa acknowledges the support of the RETURN Extended Partnership and received funding from the European Union Next-Generation EU (National Recovery and Resilience Plan—NRRP, Mission 4, Component 2, Investment 1.3—D.D. 1243 2/8/2022, PE0000005).

REFERENCES

Canepa, F., Burlando, M., Romanic, D., Solari, G., Hangan, H., 2022. Downburst-like experimental impinging jet measurements at the WindEEE Dome. Nature Scientific Data 9, 243. https://doi.org/10.1038/s41597-022-01342-1

Lundgren, T.S., Yao, J., Mansour, N.N., 1992. Microburst modelling and scaling. Journal of Fluid Mechanics 239, 461. https://doi.org/10.1017/S002211209200449X

Sengupta, A., Sarkar, P.P., 2008. Experimental measurement and numerical simulation of an impinging jet with application to thunderstorm microburst winds. Journal of Wind Engineering and Industrial Aerodynamics 96, 345–365. https://doi.org/10.1016/j.jweia.2007.09.001

Simpson, J.E., 1969. A comparison between laboratory and atmospheric density currents. Quarterly Journal of the Royal Meteorological Society 95, 758–765. https://doi.org/10.1002/qj.49709540609

Xu, Z., Hangan, H., 2008. Scale, boundary and inlet condition effects on impinging jets. Journal of Wind Engineering and Industrial Aerodynamics 96, 2383–2402. https://doi.org/10.1016/j.jweia.2008.04.002

ERIES-SOLAR: The assessment of downburst actions on solar panels at the WindEEE Dome

Antonio J. Álvarez [1], Felix Nieto [1], Petar Škvorc[2], Hrvoje Kozmar [2], Jeroen van Beeck [3], Tibebu Birhane [4], Kimberley Adamek [4], Girma Bitsuamlak [4]

[1]*CITEEC – University of A Coruña, A Coruña, Spain, antonio.jose.alvarez@udc.es*
[1]*CITEEC – University of A Coruña, A Coruña, Spain, felix.nieto@udc.es*
[2]*Faculty of Mechanical Engineering and Naval Architecture, University of Zagreb, Zagreb, Croatia, petar.skvorc@fsb.unizg.hr*
[2]*Faculty of Mechanical Engineering and Naval Architecture, University of Zagreb, Zagreb, Croatia, hrvoje.kozmar@fsb.hr*
[3] *von Karman Institute for Fluid Dynamics, Waterloo, Belgium, jeroen.vanbeeck@vki.ac.be*
[4] *WindEEE – Western University, London, Canada, tbirhane@uwo.ca*
[4] *WindEEE – Western University, London, Canada, kadamek2@uwo.ca*
[4] *WindEEE – Western University, London, Canada, gbitsuam@uwo.ca*

SUMMARY:
The focus of the ERIES-SOLAR project is on experimental modelling of non-synoptic wind loads on solar panels. In this study, the results of downburst-induced surface pressure on a six-row array of solar panel models designed at the 1:20 length scale, along with the downburst wind profiling, are presented. The complete set of pressure tests, which are currently underway, is to be reported at the conference.

Keywords: ERIES, WindEEE Dome, downburst, solar panels, pressure test.

1. INTRODUCTION

The project "Non-synoptic wind loads on solar panels (ERIES-SOLAR)" focuses on non-synoptic wind actions on solar panels using the world-class experimental facilities at WindEEE (London, ON, Canada). It is known that non-synoptic wind affects engineering structures differently than the ABL flows (Hangan and Kareem, 2021). The present study focuses on downbursts. The Transnational User Group awarded with the research grant is comprised of researchers from three European institutions, i.e., University of Zagreb (Croatia), von Karman Institute for Fluid Dynamics (Belgium) and University of A Coruña (Spain). Here we introduce the results of the wind-tunnel testing campaign conducted at the WindEEE Dome. The results of the experiments will be postprocessed in the forthcoming period and reported at the conference.

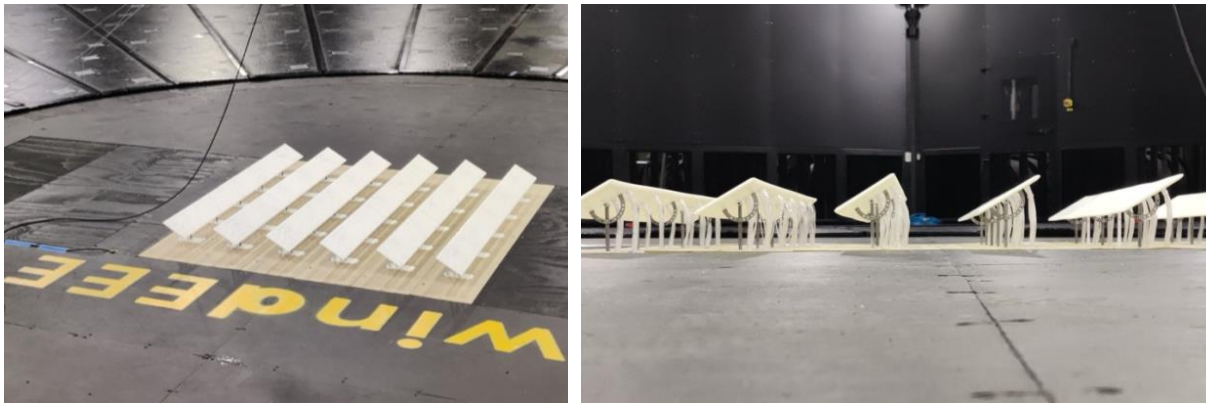
Downbursts associated with thunderstorm episodes may cause high-speed winds near the ground and they are still not well characterized from the perspective of structural design, Žužul et al. (2024). This type of action is not considered by structural codes for general building design. Solar panels are relatively flexible and prone to adverse effects due to wind actions likely to exhibit

interference effects between the rows. The analysis of the downburst effects on solar panels is of particular interest for practical applications to minimize wind-induced failures and collapse and to develop respective recommendations for international standards and codes.

2. EXPERIMENTAL SETUP

The WindEEE Dome facility is a closed-circuit flow-modeling facility with hexagonal geometry. It is capable of generating scaled downburst flows by releasing pressurized air from the upper plenum, thus creating a jet stream that impinges on the bottom surface. This jet can be combined with background boundary-layer type flow.

The test specimen consists of a six-row array model designed at the simulation length scale of 1:20. Each row is 1.05 m long and has a chord width of 0.10 m at the fixed-tilt angle of 30º, with ground clearance of 0.05 m. The rows are spaced such that the ground coverage ratio is 0.5 yielding a 1.2 m wide array model. Each row consists of 12 x 4 pressure taps equally distributed at the upper and bottom surfaces. Thus, the array is instrumented with 576 pressure taps (8 x 12 x 6), requiring about 18 (576/32) scanners each with 32 pressure ports. Photographs of the solar-panel model in the test chamber are provided in Figure 1.



a) b)

Figure 1. Six row array of PV panels, a) general view, and b) lateral view, including tube bundles.

3. DOWNBURST FLOW CHARACTERIZATION

Downburst wind profiling was performed using a rake of Cobra probes. Three positions are considered for the fixed bell mouth location (relative to the centre of the test chamber), i.e., r = 2.2 m, r = 1.9 m and r = 1.5 m with θ = 0º. The Cobra probes rake is placed at various positions, thus enabling the study to be performed on the effects of the relative location of the model and the impinging jet centre, and the orientation of the model relative to the radial outflow direction. For each test run case, the velocity at each probe was sampled at 1.25 kHz over a period of 30 s.

Time histories of the radial velocity for one of the wind profiling tests are provided in Figure 2 for the Cobra rake position r = 1.35 m and θ = 25º. The “ramp-up”, the “plateau” and the “dissipation” zones are apparent in the time histories, and in some cases the peaks associated with the ring vortices can be identified.

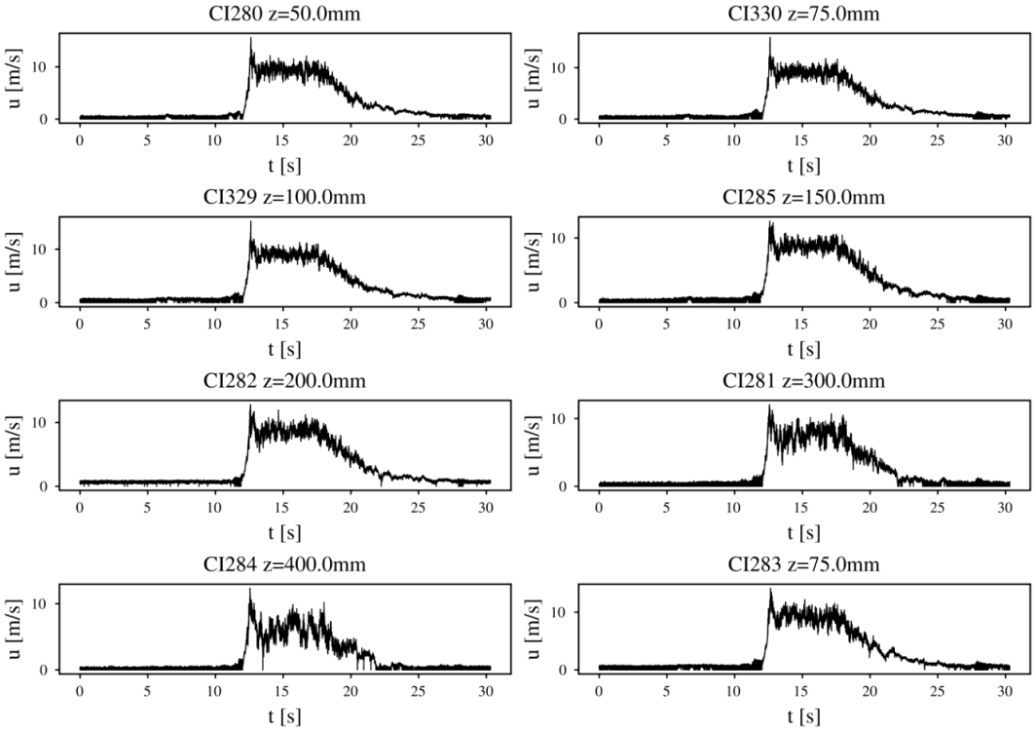
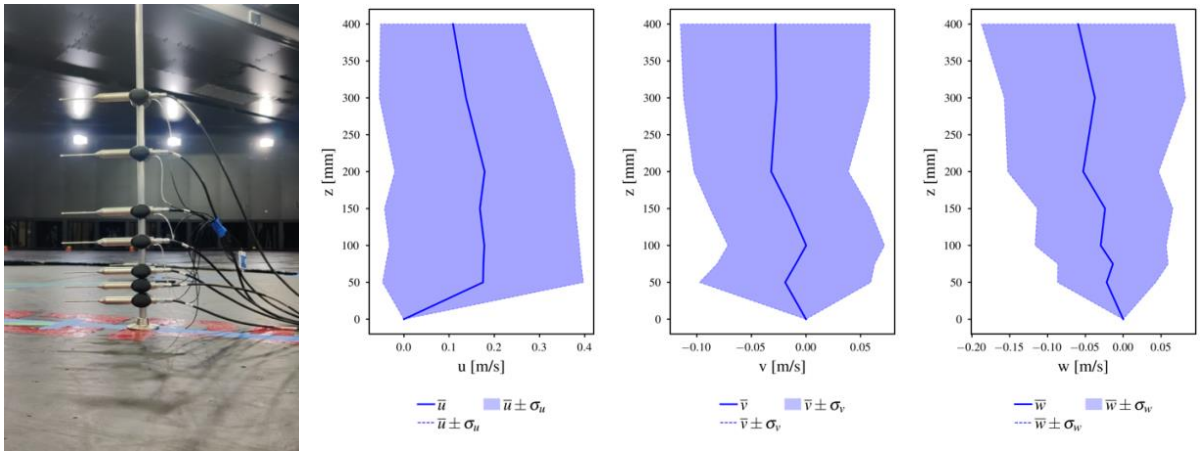


Figure 2. Radial velocity components recorded using Cobra probes at seven heights in the range from 0.05 m to 0.4 m).

In Figure 3, images of the Cobra probes rake and the vertical profiles corresponding to the three velocity components reported in Figure 2 are provided.



a) b) c) d)

Figure 3. Velocity profiles in the vertical direction, a) Cobra rake, b) radial component, c) tangential component and d) vertical component.

4. PRELIMINARY TESTS

The pressure model configuration M02 is tested under the action of downburst-like outflow winds. For each test run case, the surface pressure at each tap is sampled at 500 Hz over a period of at least 15 s during the strong gust duration. Each measurement is repeated 8 times to allow an ensemble averaging of the pressure time history. In Figure 4, the time histories of wind speed magnitude upstream of the array and pressure at one location on the top surface of one panel in the last row of the array are reported for the straight wind at 180º azimuth and downburst at 235º azimuth.

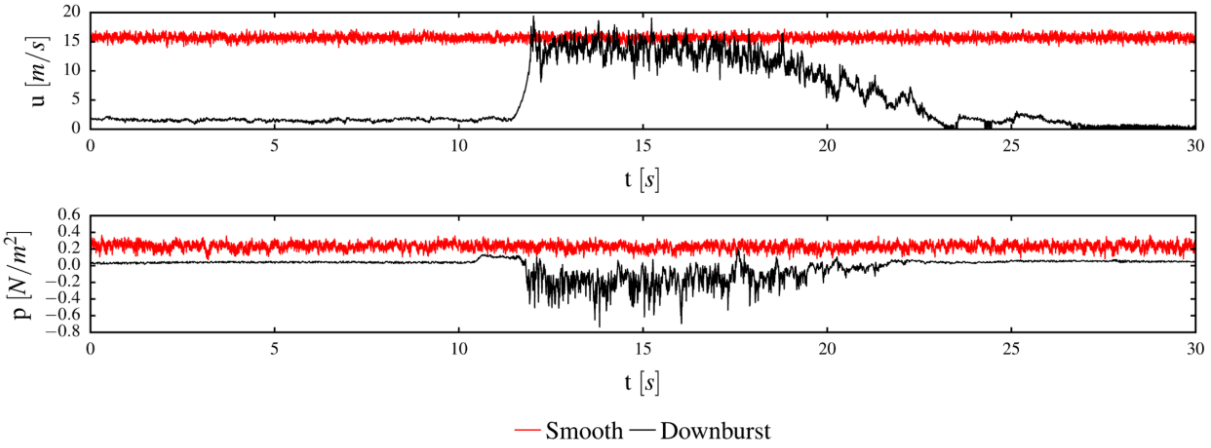


Figure 4. An example of the pressure time history at the same probe location for various flow conditions.

5. CONCLUDING REMARKS

The ERIES program has enabled research collaboration of the University of Zagreb, the von Karman Institute for Fluid Dynamics, the University of A Coruña and the WindEEE Research Institute at the Western University. The experimental campaign presented in this study addresses downburst wind actions on solar panels. A better characterization of this phenomenon is expected to improve design guidelines regarding the safety and feasibility of solar farms.

ACKNOWLEDGEMENTS

This work is part of the transnational access project "ERIES – SOLAR", supported by the Engineering Research Infrastructures for European Synergies (ERIES) project (www.eries.eu), which has received funding from the European Union's Horizon Europe Framework Programme under Grant Agreement No. 101058684. This is ERIES publication number C26. The support of the technical and administrative staff at the WindEEE Dome is greatly appreciated. This work was supported by the Croatian Science Foundation under the project number HRZZ-IP-2022-10-9434. The research grant for postdoctoral research stays awarded to Antonio J. Álvarez, funded by the University of A Coruña, is acknowledged.

REFERENCES

Hangan H., Kareem A., 2021. The Oxford Handbook of Non-Synoptic Wind Storms. Oxford University Press.

Žužul, J., Ricci, A., Burlando, M., Blocken, B., Solari, G., 2024. Vortex dynamics and radial outflow velocity evolution in downburst-like winds. Computers & Fluids, 283, 106393.

ERIES-TLTB: Thunderstorm Loading on Tall Buildings

Camila Aldereguía Sánchez [1,2], Stefano Torre [3], Anna Bagnara [3], Federica Tubino [1], Maria Pia Repetto [1]

[1]*University of Genoa, Genoa, Italy, camila.aldereguasnchez@edu.unige.it, federica.tubino@unige.it, repetto@dicat.unige.it*
[2]*Technological University of Havana Jose A. Echevarría, Havana, Cuba*
[3]*NOVA Fluid Mechanics Ltd, London, United Kingdom, stefano.torre@novafluidmechanics.com, anna@novafluidmechanics.com*

SUMMARY:
Tall buildings are very sensitive to wind-induced excitation. The wind loading on any type of structure is currently analyzed by the classical methodology for synoptic events, however, in many parts of the world, thunderstorms tend to dominate the local wind climate. Thunderstorm-downbursts differ from synoptic events due to their nose-shaped mean wind speed profile and non-stationary behavior over short intervals (10 minutes to 1 hour). Wind tunnel testing is an effective method for analyzing wind effects on structures. However, simulating thunderstorms in traditional facilities requires specialized equipment. Disregarding the non-stationary characteristics of thunderstorm outflows, ERIES-TLTB Project focuses on the wind-induced effects on tall buildings caused by thunderstorms and synoptic events, focusing on the impact of the variation of the mean wind profile. Experimental tests have been conducted using high-frequency force balance and pressure integration techniques on different tall building models. A comparison of the wind-induced loads and pressure coefficient distribution is provided for both types of events.

Keywords: tall buildings, thunderstorms, wind tunnel tests.

1. INTRODUCTION

Wind loading on structures is currently derived using the cyclone model for synoptic events, however, in many parts of the world, thunderstorms tend to dominate the local wind climate. Several investigations (Canepa et al. 2020; Solari 2020) have confirmed the different characteristics between these events such as the mean wind speed profile and non-stationary nature; therefore, a different analysis is required. In the case of tall buildings, the consideration of a logarithmic mean wind speed profile as established in the standards, could provide an overestimation of wind actions compared to that arising from downburst profiles, characterized by a maximum velocity close to the ground. The effect of thunderstorm downbursts on structures has been studied through full-scale measurements, experimental tests, and numerical simulation. Wind tunnel testing is a reliable method for assessing wind loads and structural motions, offering detailed insights into their actions and responses. Experimental downburst modeling can either replicate entire events or focus solely on their outflows (Aboutabikh et al. 2019; Canepa et al. 2022). The latter is a more practical and cost-effective approach, commonly used in Atmospheric Boundary Layer Wind Tunnel (ABLWT). Aldereguía Sánchez et al. (2023) proposed the use of a passive device to simulate thunderstorm mean wind speed profiles. However, this device is not able to reproduce the non-stationary characteristics of the incoming flow, limiting its application to

studying the mean wind speed profile effect on structures.

This study, conducted within the ERIES project Thunderstorm Loading on Tall Buildings (TLTB), aims to conduct experimental tests in a classic BLWT in order to evaluate thunderstorm mean wind speed profile effects on tall buildings. The study involves testing two tall building models using two techniques: High-Frequency Force Balance (HFFB) and High-Frequency Pressure Integration (HFPI). The measured quantities from each test will be analyzed, and the mean and peak base wind loads will be provided to determine the global effects of downbursts and to compare them with those induced by synoptic winds. From the HFPI measurements, pressure and load distribution on individual floors will be analyzed to understand how wind pressures vary along the height of the building, providing insights into localized effects. Additionally, wind-induced accelerations at several locations will be assessed and checked against comfort criteria to determine whether the building's response under thunderstorm conditions meets acceptable standards for occupant comfort.

2. WIND TUNNEL STUDIES

The experiments were conducted at the Giovanni Solari Wind Tunnel (GS WT) at the University of Genoa. The mean wind speed profiles of thunderstorms replicated in this work are taken from a previous study by Aldereguía Sánchez et al. (2023), based on the Wood and Kwok (1998) model. Different flow conditions are considered including variations of the nose height (z_m) and turbulence intensity levels during thunderstorm winds. Figure 1 presents the mean wind speed and turbulence intensity profiles for one of the group of profiles considered. In this particular case, a full-scale $z_m = 100\ m$ is assumed in conjunction with turbulence intensity levels within a range of approximately 15%. For comparison with classical synoptic events, the mean wind speed and turbulence intensity profiles with a roughness length (z_0) of 0.05 m are also simulated based on the expressions established in EN1991-1-4 (2004). The analysis is performed using a normalization that aligns with practical design standards, where design wind speeds are conventionally referenced at 10 meters ($\overline{U}_{10m}$). Thus, this analysis adopts the mean wind speed profile of each event with the same velocity at 10 meters above the ground.

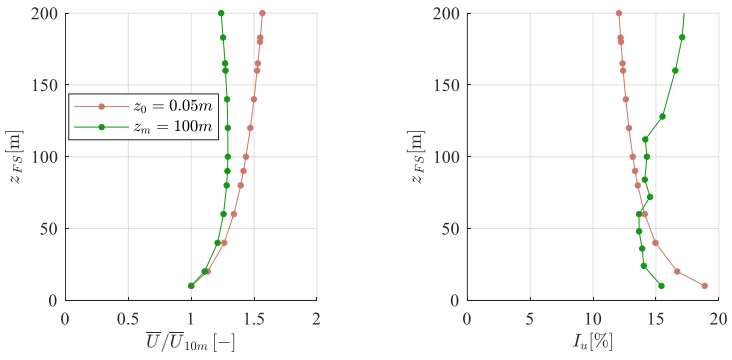


Figure 1. a) Mean wind speed profiles normalized with respect to the mean wind speed at 10 meters, b) Turbulence intensity profiles.

The initial stage of the project involves tests to derive wind loads based on HFFB and HFPI

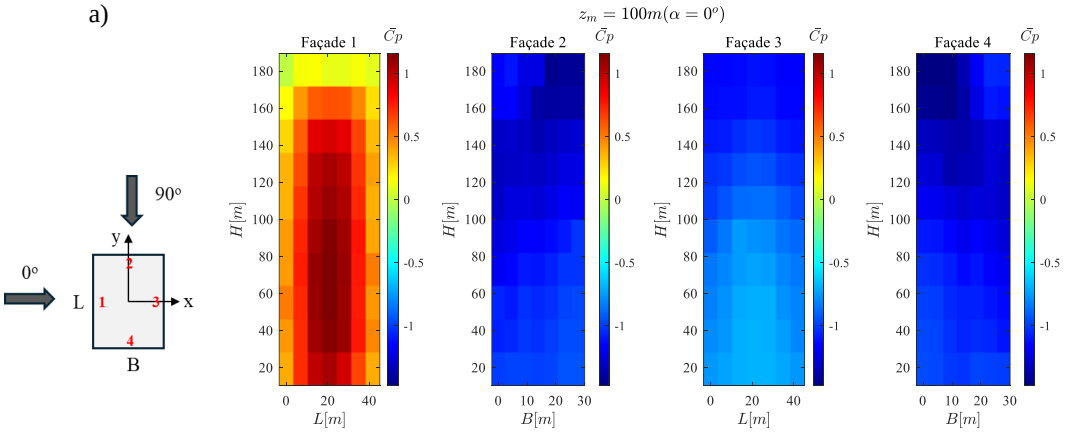
techniques on the benchmark building, CAARC, under different flow conditions such as those presented in Figure 1. This building is chosen as a good representation of typical tall buildings being currently built in the world. A model scale of 1:400 is adopted, and all tests are performed in isolation to accurately capture the key differences between the two weather phenomena. In addition, a 200 m tall building, called here as Project X, will be also tested in the context of its surroundings using the HFPI technique on a model scale of 1:300. For this analysis, design wind speeds obtained from statistical analysis of the recorded wind data in the area will be used with the corresponding mean wind speed profile.

3. PRELIMINARY RESULTS

During the HFFB tests the fluctuating base loads in terms of shear forces, bending moments, and torque for 19 wind directions (10˚ increments), while for HFPI tests, the time histories of the fluctuating pressures acting on external surface are measured. Depending on the acquisition of the tests different results will be provided, in terms of base wind loads, floor-by-floor loads, pressure coefficients acting on the façades for 0˚ and 90˚, and accelerations at several locations.

At a first step, the base wind loads obtained from HFFB and HFPI measurements on the CAARC building have been compared and a good agreement for all wind directions has been found. Then, analyses of pressure distributions have been carried out. As an example, Figure 2 illustrates the mean pressure coefficient distribution for wind coming from 0˚ obtained from the HFPI tests carried out at the GS WT. The results show that mean pressure coefficients for thunderstorms are comparable to those of synoptic winds at around 80 meters in height, while at the highest levels, synoptic winds provide values that are about 30% higher. This can be directly linked to the mean wind speed profile shape and the consideration of the same wind speed at 10 meters. Regarding negative mean pressure coefficients, the distribution is similar for both events, where synoptic values are about 5% greater than those of thunderstorm winds.

a)



b)

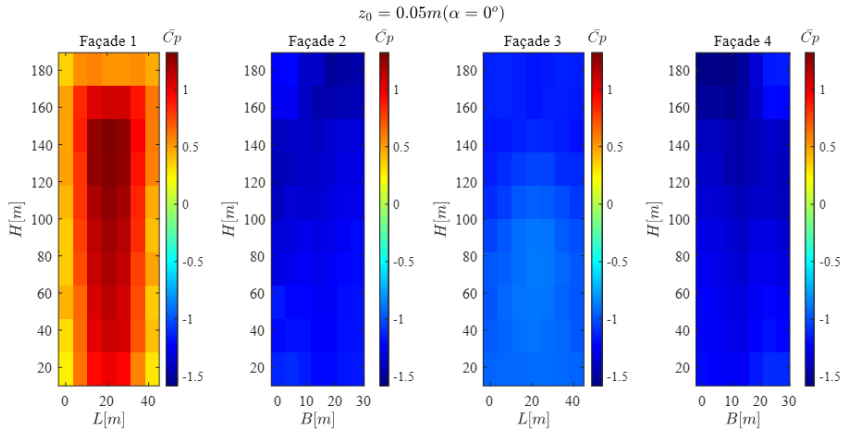


Figure 2. Mean pressure coefficients a) Thunderstorm profile (z_m=100 m), b) ABL profile (z_0=0.05m).

4. CONCLUSIONS

For the specific case study presented here, it was observed that if the analysis is performed using the same design wind speed at 10 meters, the worst-case scenario of the wind loads and response will be provided for synoptic. However, the project results confirm that for some other particular cases thunderstorms should not be negligible, especially if their turbulences have higher magnitudes and mean wind velocity averaged along the height is comparable to those of synoptic winds.

ACKNOWLEDGEMENTS

This work is part of the transnational access project "TLTB", supported by the Engineering Research Infrastructures for European Synergies (ERIES) project (www.eries.eu), which has received funding from the European Union's Horizon Europe Framework Programme under Grant Agreement No. 101058684. This is ERIES publication number C42.

REFERENCES

Aboutabikh, Ghazal, Chen, Elgamal, & Aboshosha, 2019. Designing a blade-system to generate downburst outflows at boundary layer wind tunnel. Journal of Wind Engineering & Industrial Aerodynamics 186, 23. doi:https://doi.org/10.1016/j.jweia.2019.01.005

Aldereguía Sánchez, Tubino, Bagnara, & Piccardo, 2023. Experimental simulation of thunderstorm profiles in an Atmospheric Boundary Layer Wind Tunnel. Applied Science 13, 8064. doi:10.3390/app13148064

Canepa, Burlando, Romanic, Solari, & Hangan, 2022. Experimental investigation of the near-surface flow dynamics in downburst-like impinging jets. Environmental Fluid Mechanics 22, 921-954. doi:https://doi.org/10.1007/s10652-022-09870-5

Canepa, Burlando, & Solari, 2020. Vertical profile characteristics of thunderstorm outflows. Journal of Wind Engineering & Industrial Aerodynamics 206. doi:https://doi.org/10.1016/j.jweia.2020.104332

European Committee for Standardization. (2004). Eurocode 1: Actions on structures - Part 1-4: General actions - Wind actions (EN 1991-1-4). CEN

Solari, 2020. Thunderstorm Downbursts and Wind Loading of Structures: Progress and Prospect. Frontiers in Built Environment. doi:https://doi.org/10.3389/fbuil.2020.00063

Wood, & Kwok. (1998). *An empirically derived estimate for the mean velocity profile of a thunderstorm downburst.* Paper presented at the Proceedings of the 7th Australian Wind Engineering Society Workshop, Auckland.

Evaluation of aerodynamic coefficients on a lattice structure by experimental wind tunnel tests

Bruno Clavelo[1,3], Kristof Maes[1], Patricia Martín[3], Vivian Elena[3], Federica Tubino[2], Giuseppe Piccardo[2], Maria Pía Repetto[2], Geert Lombaert[1]

[1]*KU Leuven, Department of Civil Engineering, Leuven, Belgium,* *brunojorge.claveloelena@kuleuven.be*

[2]*UNIGE, Department of Civil, Chemical and Environmental Engineering, Genova, Italy,* *federica.tubino@unige.it*

[3]*CUJAE, Department of Civil Engineering, Havana, Cuba, vivian@civil.cujae.edu.cu*

ABSTRACT:
Antenna masts are highly susceptible to dynamic wind loads and the presence of ancillaries has been documented to significantly affect the forces experienced by the mast. This paper describes the experimental campaign conducted to determine the drag, lift, and moment coefficients of an operating antenna mast. Wind tunnel tests have been performed on a scaled three-dimensional model of the mast under smooth and turbulent flow conditions and five different configurations of ancillaries are considered, based on the predominant patterns observed. For each configuration, the aerodynamic coefficients are obtained for angles of attack ranging from 0° to 360°. Drag, lift, and moment forces are measured using two six-dimensional force balances connected to the ends of the model, and the downstream three-component velocities are acquired using a Cobra probe mounted on a vertical stiff mast. The tests conducted enable the characterization of the force coefficients, highlighting certain differences compared to the values specified in codes and guidelines for similar cross-sections.

Keywords: aerodynamic coefficients, wind tunnel test, antenna mast

1. INTRODUCTION

The reliable estimation of the wind forces acting on structures is crucial to improve the current understanding of their structural response mechanisms and reduce the risk of failure. This is particularly relevant in the case of slender, flexible structures such as antenna masts, which are highly sensitive to dynamic wind loads, resulting in numerous collapses due to strong wind phenomena (Elena Parnás et al., 2015). Recent research at KU Leuven focuses on applying model-based system inversion techniques as an alternative to estimate wind loads on tall guyed masts. These techniques integrate measured response data with dynamic structural models to estimate the forces acting on the structure. A valuable set of full-scale response data and wind flow measurements has been acquired on an operating 80-m-tall mast, but accurate estimation of the aerodynamic coefficients is vital to establish a reliable reference model for the wind loads. Current design codes offer simplified methods to estimate such coefficients but often fail to account for intricate ancillary layouts and complex geometries (Carril et al., 2003; Tapia-Hernández and Cervantes-Castillo, 2018). Overall, wind tunnel tests (Calotescu et al., 2021; Martín et al., 2019; Yang and Niu, 2022) remain one of the most reliable methods for accurately determining aerodynamic coefficients for lattice structures. This study presents a recent experimental campaign conducted as part

of the ERIES Horizon Project at the Giovanni Solari Wind Tunnel Facility at the University of Genoa (GS-WinDyn, 2024). The objective was to characterize the aerodynamic coefficients of the aforementioned mast.

2. METHODS

The tests are performed using a carbon-fiber scaled sectional model of the 80-meter-tall antenna mast, with a triangular lattice cross-section. A 1:10 scale is chosen to ensure both model stiffness and manageable blockage ratios within the wind tunnel's test section, resulting in a sectional model of length $h = 1680$ mm and width $b = 160$ mm. The model is fitted with both linear ancillaries (ladders, power supply and feeder cables) and discrete ancillaries (UHF, VHF III, and VHF Dipole antenna systems), representing the most common configurations observed in the mast. The linear ancillaries are recreated using 3D-printed carbon fiber, whereas the discrete ancillaries, attached at the mid-section of the model, are replicated using a combination of carbon fiber, high-density foam and aluminium components. Fig. 1 shows the test setup and mounting system for the test models. Drag force, lift force, and moments are measured using two Kistler 9257B six-dimensional force balances mounted at each end of the model (Fig. 1b). To analyse downstream wind flow characteristics, a Cobra probe is positioned to capture three-component velocity data, allowing a detailed investigation of wake turbulence. Inlet wind velocities are monitored with a Pitot tube, and stepper motors are used to rotate the model, capturing a full range of wind attack angles from 0° to 360°. Data are recorded at each angle of attack α for 60 seconds at a 400 Hz sampling rate. Experiments were conducted under both smooth flow (turbulence intensity < 0.2%) and turbulent flow conditions (turbulence intensity ∼7-8%) by using a passive grid device. Table 1 summarizes the main characteristics of the tests performed.

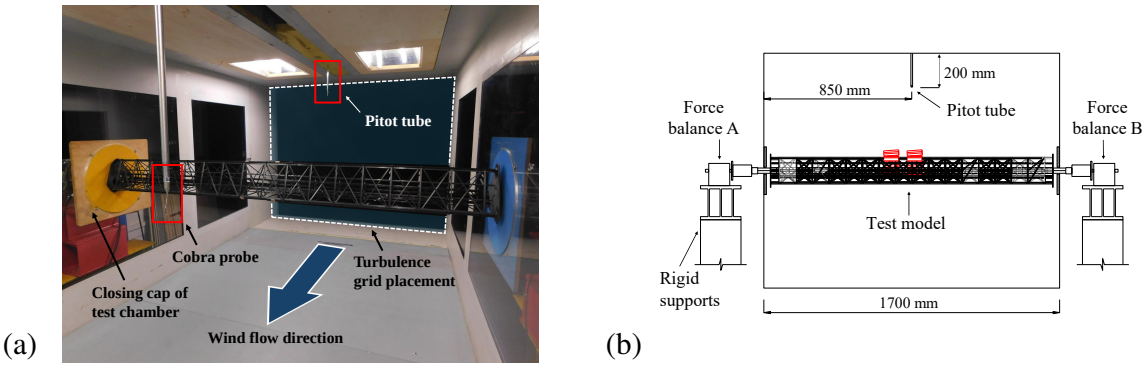


Figure 1. (a) Test setup layout and (b) schematic view of the test section and mounting system.

Table 1. Setup characteristics.

Setup	Test model	Flow type	U [m/s]	Angles of attack [°]	
				Basic	Additional
1	Bare	Smooth	15.2	0 : 10 : 360	5, 15, 25, 35, 85, 95, 115
2	Linear	Smooth	15.2	0 : 10 : 360	5, 15, 115, 195, 205, 315, 325
3	Linear	Turbulent	11.1	0 : 30 : 330	[-]
4	Linear + UHF	Smooth	15.2	0 : 10 : 360	5, 15, 115, 155, 195, 205, 325
5	Linear + VHF III	Smooth	15.2	0 : 10 : 360	5, 15, 115, 185, 195, 198, 202
6	Linear + VHF Dipole	Smooth	15.3	0 : 10 : 360	5, 15, 115, 195, 205

The drag, lift and moment coefficients are respectively computed as follows:

$$C_{\mathrm{D}} = \frac{2\bar{D}}{\rho \bar{U}^2 A_{\mathrm{s}}}; \quad C_{\mathrm{L}} = \frac{2\bar{L}}{\rho \bar{U}^2 A_{\mathrm{s}}}; \quad C_{\mathrm{M}} = \frac{2\bar{M}}{\rho \bar{U}^2 A_{\mathrm{s}} b}; \tag{1}$$

where ρ is the air density; $\bar{D}$, $\bar{L}$ and $\bar{M}$ are the mean values of the drag force, lift force and moment, respectively; $\bar{U}$ is the reference mean wind velocity; and b is the reference dimension of the model, in this case taken as the model width, equal to 0.16 m. The coefficients are normalized with respect to the solid area A_{s} for an angle of attack $\alpha = 0°$, taken as the total projected area of the structural elements and ancillaries located in the windward face. To account for blockage effects, the application of a correction factor (ESDU, 1980) is suggested when blockage ratios exceed 5%. The complete dataset, including processed aerodynamic coefficients and raw force measurements, will be made available shortly via an open-access repository.

3. RESULTS

Fig. 2 presents the aerodynamic coefficients obtained using Eq. (1). The drag coefficients obtained for the bare model are the lowest, while configurations including UHF and VHF antennas with linear ancillaries show a marked increase, with values peaking at up to 45% higher than those of the bare structure. Drag coefficients vary significantly with the angle of attack, particularly at 60°, where marked discrepancies between measured and standardised values are evidenced. The experimental data reveals a peak in drag coefficient around this angle, contrary to the standard design codes, which predict lower values. These results confirm previous experimental results (Fundora Sautié et al., 2020) and indicate that the geometry of double-angle leg members influences drag, highlighting the differences between experimental data and design code values for complex cross-sections.

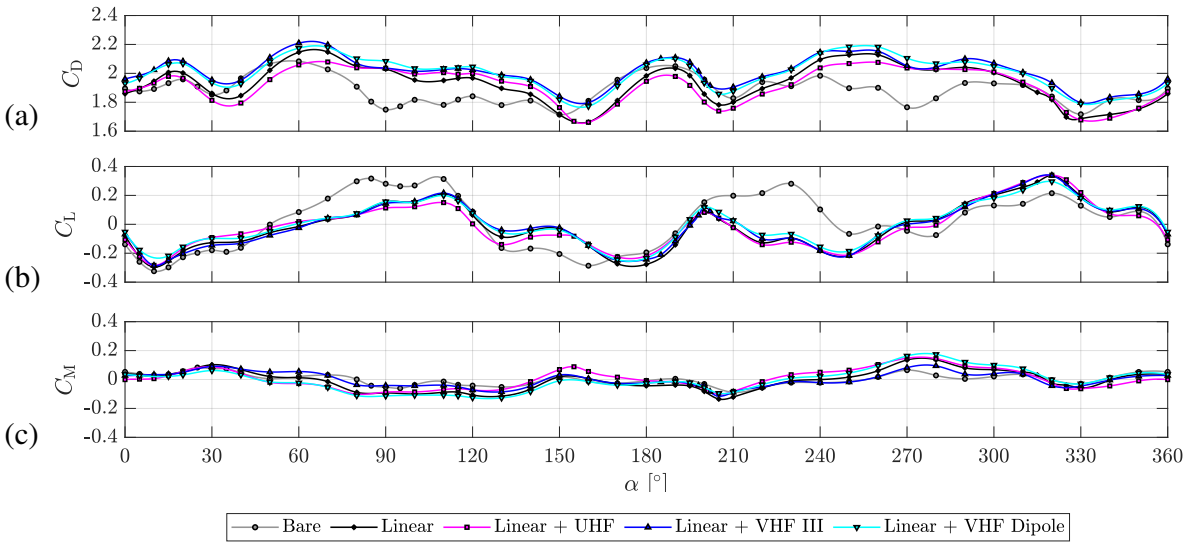


Figure 2. Aerodynamic coefficients: (a) drag C_{D}, (b) lift C_{L}, and (c) moment C_{M}, as a function of the angle of attack α (markers), with a third order cubic spline interpolation (solid line) superimposed.

Lift and moment coefficients remain close to zero across most configurations and angles of attack, aligning with the quasi-symmetric layout of the lattice. The study also finds substantial variation

in the drag resistance across different configurations, with drag resistance consistently increasing with the addition of ancillaries, as shown in Table 2.

Table 2. Drag resistance ($C_D \cdot A_s$) in m^2 for different test configurations.

α	**Bare**	**Linear**	**Linear + UHF**	**Linear + VHF III**	**Linear + Dipole**
0°	0.16	0.19 (20.1)*	0.21 (30.9)	0.22 (34.9)	0.21 (33.1)
60°	0.18	0.22 (26.1)	0.23 (30.9)	0.25 (38.3)	0.24 (36.4)
120°	0.16	0.21 (30.8)	0.23 (43.8)	0.22 (43.4)	0.23 (45.1)

*: number in parentheses indicates the percentage difference with respect to the bare structure.

4. FINAL REMARKS

This study presents a comprehensive dataset of aerodynamic coefficients for an antenna mast under varying ancillary configurations and flow conditions. The data are preliminarily validated by comparison with international codes and experimental studies available in the literature. The findings underscore the need for more nuanced design practices in the telecommunications industry. The dataset generated serves as a valuable resource for future research and structural engineering applications. Potential for reuse is observed in several applications, including comparison with experimental data obtained from other wind tunnel tests, validation of analytical and numerical CFD models with similar characteristics and estimation of wind loads due to ancillaries. Lastly, the validation of model-based system inversion techniques using accurate force coefficients holds promise for real-time wind load estimation on tall guyed masts, facilitating more resilient designs under dynamic loading conditions.

ACKNOWLEDGEMENTS

This work is part of the transnational access project “ERIES – EOLIC", supported by the Engineering Research Infrastructures for European Synergies (ERIES) project (www.eries.eu), which has received funding from the European Union’s Horizon Europe Framework Programme under Grant Agreement No. 101058684. This is ERIES publication number C32. The authors would also like to acknowledge the contributions and technical assistance provided by Ph.D. Stefano Torre and the technical team at the Giovanni Solari wind tunnel facility.

REFERENCES

Calotescu, I., Torre, S., Freda, A., and Solari, G., 2021. Wind tunnel testing of telecommunication lattice towers equipped with ancillaries. Engineering Structures 241, 112526.

Carril, C. F., Isyumov, N., and Brasil, R., 2003. Experimental study of the wind forces on rectangular latticed communication towers with antennas. Journal of Wind Engineering and Industrial Aerodynamics 91, 1007–1022.

Elena Parnás, V., Fernández Lorenzo, I., and Martín Rodríguez, P., 2015. Structural failure on telecommunication guyed mast under extreme winds. Proceedings of Proceedings of the 14th International Conference on Wind Engineering. Porto Alegre, Brazil.

ESDU, 1980. Blockage corrections for bluff bodies in confined flows. Engineering Sciences Data Unit, London.

Fundora Sautié, N., Camaño Schettini, E. B., Loredo Souza, A. M., and Parnás, V. E., 2020. Coeficientes de forma en sección compuesta con ensayos en túnel de viento. Ingeniería Hidráulica y Ambiental 41, 85–99.

Martín, P., Elena, V. B., Fernández, I., and Loredo-Souza, A. M., 2019. Drag coefficients of lattice towers with VHF antennas on wind tunnel. Revista Tecnica De La Facultad De Ingenieria Universidad Del Zulia 42, 118–125.

Tapia-Hernández, E. and Cervantes-Castillo, J. A., 2018. Influence of the Drag Coefficient on Communication Towers. International Journal of Civil Engineering 16, 499–511.

GS-WinDyn, 2024. *Giovanni Solari Wind Tunnel official website*.

Yang, F. and Niu, H., 2022. Wind tunnel tests on wind loads acting on steel tubular transmission towers under skewed wind. Wind and Structures 35, 93–108.

Vortex-induced vibrations of the flexible bridge cable model

Arsenii Trush [1], Stanislav Pospíšil [1], Olivier Flamand [2], Armando Carusone [2]

[1] *Institute of Theoretical and Applied Mechanics of the Czech Academy of Sciences, Prague, Czech Republic, trush@itam.cas.cz, pospisil@itam.cas.cz*
[2] *Centre Scientifique et Technique du Bâtiment, Nantes, France, olivier.flamand@cstb.fr*

SUMMARY:
The study aims to study vortex-induced vibrations of bridge cables under controlled laboratory conditions using advanced flexible aeroelastic models. The design of the models assumes the closest possible representation of the real shape of the cables, including the characteristic shape of cables covered with glaze ice, the ability to fine-tune natural frequencies for testing the realistic Reynolds number range, as well as ensuring the 3-dimensional nature of cable-wind interactions as observed during field vibrations. Flexible cable model consisting of a supporting core in the form of a small-diameter steel cable, and a shell consisting of alternating small sections made using 3D printing from rigid and flexible plastics.

Keywords: wind tunnel, bridge cable, vortex shedding, icing, Strouhal number

1. INTRODUCTION

Support cables are an effective structural element that, with a minimum area and weight, provide maximum load-bearing capacity. Moreover, due to their low natural frequencies and relative lightness, they are vulnerable to various types Wind Induced Vibrations (WIV), such as Vortex-Induced Vibrations (VIV), Galloping, Rain and Wind induced vibrations (RWIV), buffeting, etc,. The increase in instrumental recording capabilities and data acquisition storage during monitoring in recent years has illuminated some features of real-life cable vibration cases that are not covered by existing mathematical models and building code design procedures (Daniotti et.al., 2021; Kim et al., 2022; Denoël and Andrianne, 2017). Obtaining data in controlled conditions of real and virtual wind tunnels allows us to fill the gaps due to instrumental, physical capabilities and time limitations. In recent years, significant efforts have been devoted to the experimental research of vibrations on yawed bridge cables. Rigid models with elastic fastening at the ends, which facilitate surface modifications, equipment placement, and dynamic parameter configuration (Liu et al., 2021; Mannini et al., 2017; Chen et al., 2022; Lupi et al., 2018). Despite their advantages, these models do not fully capture the 3-dimensional nature of cable-wind interactions during field vibrations. Flexible cable models with steel rope core and adjacent to it foam filler with a top layer smooth plastic sheath allow, with reasonable tension values, to achieve cable natural frequencies close to real ones in laboratory conditions and allows the study of high and multimode VIV and RWIV in wind tunnel corresponding to those in real ABL (Chen et al., 2010; Gao et al., 2019). Another approach is to use small rigid segments attached to a steel rope core in such a way that the ability to bend within the gaps between the segments is maintained. In (Jafari and Sarkar, 2020; Matsumoto et al., 2020) to maintain length correlation continuity of flow along the cable the plastic

tape and rubber/paper membranes were used to close the gaps. The present proposal is to use a flexible cable model consisting of a supporting core in the form of a small-diameter steel cable, and a shell consisting of alternating small sections made using 3D printing from rigid and flexible plastic. In this way, it is possible to achieve a wide range of adjustments of natural frequencies, and reproduction of any desired shape, incl. and ice deposits while maintaining rigidity and cross-sectional shape even at high wind speed, model flexibility and 3D response.

2. EXPERIMENTAL SETUP

2.1. Models for aeroelsatic testing

The stiff parts of models were made using FEM technology with foaming filament LW-PLA by colorFABB. This gives the weight reduction by 45%. The flexible parts were produced by SLA technology with Formlabs Silicone 40A resin. The next models were tested: circular cylinder, used as reference model; and iced cable model, see Fig.1. The length of models will be 4.4 m, the diameter D = 0.11 m (for a circular part in the case of the iced cable model).



Figure 1. 3D printed smooth and iced cable models segments with fitted flexible silicone parts.

1. Stand for aeroelastic testing

Due to the expected size of the model and place needed space for placing fastening and tensioning equipment, main tests are carried out in CSTB Jules Verne climatic wind tunnel in Nantes. To provide orientation (setting of the yaw angle) and pre-tension the cable, a testing stand has been developed, see Fig.2. The stand consists of two parts, each of them has beam (1), console (2), mechanical tensioners (3-4), transportation brackets (5) and 2 sets of flat Plexiglas screens. The base plates are fastened to existing framing channels (6) on the turn table. Stand has mechanical threaded tensioners on both sides: on one side, the tensioner provides tension on the cable (3), ensuring structural integrity of the main (vertical and horizontal) eigenmodes and allows to achieve the required frequency. On the opposite side of the stand is tensioner (4) for strings are which are responsible for the torsional rigidity of the model and the corresponding eigenmodes.

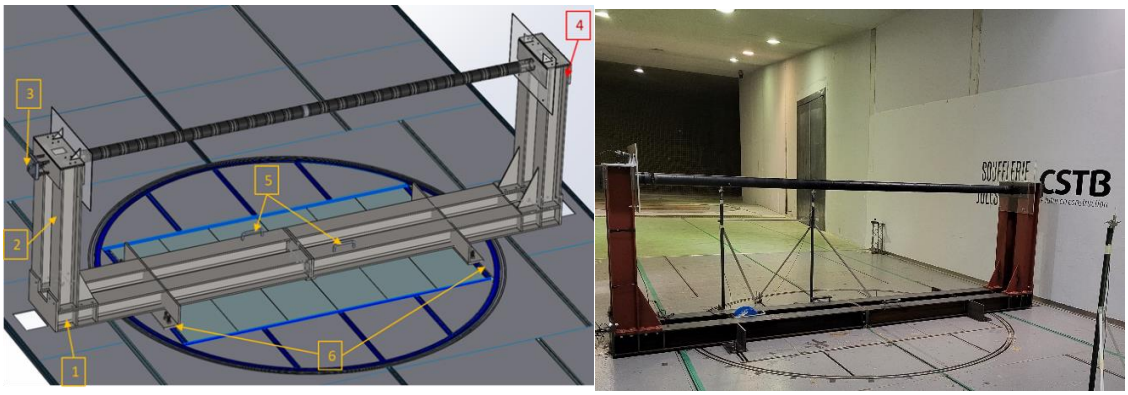


Figure 2. CAD model and installed stand with in CSTB Jules Verne Climatic Wind Tunnel.

3. WIND TUNNEL TESTS

Preliminary tests were carried out on a short 1.83 m long model in a domestic wind tunnel. The model was positioned vertically, with a ring-to-hook tensioner at the bottom part, see Fig.3. The yellow dashed line parallel to the model axis shows the undeformed state of the model (without vibrations - on the left). The red dashed line shows the deformed state of the model: with the first mode of VIV in the centre and the second mode on the right. Two tensions of the model corresponding to 5 and 10 Hz were tested. During the tests obtained values of Strouhal Number for the 1st and 2nd modes for both tensions were close to the data from the tests with rigid models, despite non-ideal turbulence characteristics and high blocking ratio. Moreover, the ratio of the Strouhal numbers of the smooth and iced models was maintained (10-30% higher depending on the angle of attack).

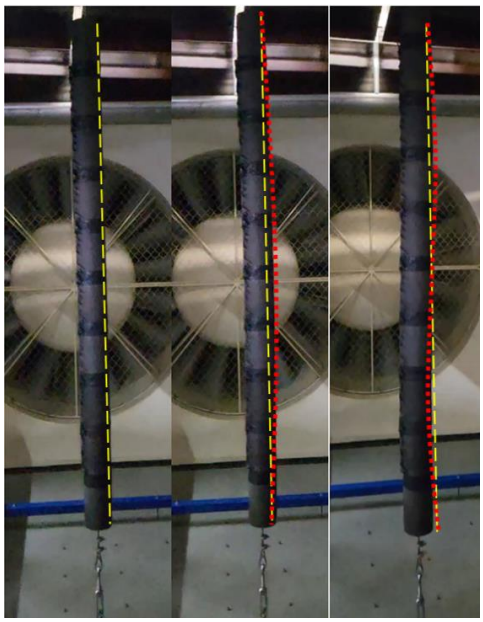


Figure 3. 3D printed smooth and iced cable models segments with fitted flexible silicone parts

More extensive tests were conducted in CSTB Jules Verne Climatic Wind Tunnel. The dynamic response at two yaw angles (0 and 15°) were investigated. In total it was tested 4 configurations:

smooth model and asymmetrical iced model (3 angles of attack on the ice "rib"). All configurations will be tested in tunnel with in flow with the low free stream turbulence about I_u=1.3%. The frequency of first natural mode supposed to be tuned at frequencies f = 5 and 10 Hz. The measurement of the response was carried out in the range of velocity 2-20 m/s. The Storuhal frequency was measured in the wake using two Cobra probes. For the reference smooth model were obtained 4 eigenmodes of vibrations. Using an exciter, the values of structural and aerodynamic damping were obtained from decay.

3. CONCLUSIONS

Present study deals with WIV of bridge cables under controlled laboratory conditions using advanced flexible aeroelastic models produced with additive technologies. The design of the models assumes the closest possible representation of the real shape of the cables, including the characteristic shape of cables covered with glaze ice as well as ensuring the 3-dimensional nature of cable-wind interactions. A stand that allows adjusting the yaw angle and the natural frequency of the model was built. Tests have shown the concept to be viable with low damping and amplitudes large enough to be measured with low relative error. The conducted research will serve as a reference for future research of more complex mechanisms of aeroelastic instabilities.

ACKNOWLEDGEMENTS

This work is part of the transnational access project "ERIES – FLAMBeRG", supported by the Engineering Research Infrastructures for European Synergies (ERIES) project (www.eries.eu), which has received funding from the European Union's Horizon Europe Framework Programme under Grant Agreement No. 101058684. This is ERIES publication number C34.

REFERENCES

Chen, C., Mannini, C., Bartoli, G., Thiele, K., 2022. Wake oscillator modeling the combined instability of vortex induced vibration and galloping for a 2:1 rectangular cylinder. Journal of Fluids and Structures 110.

Chen, W., Zheng, Z., Li, M., 2010 Multi-mode vortex-induced vibration of slender cable experiencing shear flow. Procedia Engineering 4, 145-152.

Daniotti, N., Bogunović Jakobsen, J., Snæbjörnsson, J., Cheynet, E., Wang, J., 2021. Observations of bridge stay cable vibrations in dry and wet conditions: A case study. Journal of Sound and Vibration 503.

Denoël, V., Andrianne, T., 2017. Real-scale observations of vortex induced vibrations of stay-cables in the boundary layer. Procedia Engineering 199, 3109-3114.

Gao, D., Chen, W.L., Zhang, R.T., Huang, Y.W., Li, H.,2019. Multi-modal vortex- and rain–wind- induced vibrations of an inclined flexible cable. Mechanical Systems and Signal Processing 118, 245-258.

Jafari, M., Sarkar, P., 2020. Wind-induced response characteristics of a yawed and inclined cable in ABL wind: Experimental- and numerical-model based study. Engineering Structures 214.

Kim, S., Kim, S., Kim, H., 2022. High-mode vortex-induced vibration of stay cables: monitoring, cause investigation, and mitigation. Journal of Sound and Vibration 524.

Liu, Z., Shen, J., Li, S., Chen, Z., Ou, Q., Xin, D., 2021. Experimental study on high-mode vortex-induced vibration of stay cable and its aerodynamic countermeasures. Journal of Fluids and Structures 100.

Lupi, F., Niemann, H.J., Höffer, R., 2018. Aerodynamic damping model in vortex-induced vibrations for wind engineering applications. Journal of Wind Engineering and Industrial Aerodynamics 174, 281-295.

Mannini, C., Massai, T., Marra, A.M., Bartoli, G., 2017. Interference of Vortex-Induced Vibration and Galloping: Experiments and Mathematical Modelling. Procedia Engineering 199, 3133-3138.

Matsumoto, M., Daito, Y., Kanamura, T., Shigemura, Y., Sakuma, S., Ishizaki, H., 1998. Wind-induced vibration of cables of cable-stayed bridges. Journal of Wind Engineering and Industrial Aerodynamics 74–76, 1015-1027.

Rain-wind induced vibration of stay cables: several recommendations for wind tunnel testing

Vitor Diniz Pinto [1,2], Christos T. Georgakis[1], Allan Larsen [2], Cristoforo Demartino[3], Werner Brand [4], Jasna B. Jakobsen[5], Francesco Ricciardelli[6], Don Bergman[2], Robert Soltys[7]

[1]*Aarhus University, Aarhus, Denmark, vdpi@cae.au.dk, cg@cae.au.dk*
[2]*COWI A/S, Lyngby, Denmark, vdpi@cowi.com, aln@cowi.com, dwb@cowi.com*
[3]*Roma Tre University, Roma, Italy, cristoforo.demartino@uniroma3.it*
[4]*DYWIDAG, Munich, Germany, werner.brand@dywidag.com*
[5]*University of Stavanger, Stavanger, Norway, jasna.b.jakobsen@uis.no*[1]
[6]*Università della Campania, Aversa, Italy, friccia@unicampania.it*
[7]*KI Rådgivende Ingeniører ApS, Copenhagen, Denmark, rso@ki.dk*

SUMMARY:
This study addresses challenges in wind tunnel testing of rain-wind induced vibration (RWIV) of stay cables. It provides several recommendations for future researchers focusing on ensuring successful RWIV test campaigns, and standardizing parameters and reporting to facilitate result comparisons. The recommendations are based on comprehensive test campaigns conducted at FORCE Technology in September 2024, and at CSTB in November 2024.

Keywords: stay cable vibration, rain-wind induced vibration, wind tunnel testing.

1. INTRODUCTION

Rain-wind induced vibrations (RWIV) account for the majority of recorded cases of stay cable vibrations (Gimsing and Georgakis, 2012). The interaction between wind flow, cable inclination and yaw angle, rain intensity, and rivulet position and motion make this type of vibration difficult to model theoretically. Thus, wind tunnel investigations are essential to increase understanding of the excitation mechanism (D'Auteuil et al., 2023; Flamand, 1995; Larose and Smitt, 1999). Georgakis and Matejicka (2021) recommended a standardized approach to testing bridge cables, including RWIV tests. The current work expands on several of those recommendations.

In 2024, RWIV wind tunnel test campaigns were conducted at FORCE Technology, Lyngby Denmark (Pinto et al., 2025) and Centre Scientifique et Technique du Bâtiment (CSTB), Nantes, France. Based on the experience gained from these campaigns, this work aims to highlight critical aspects that can be challenging to achieve and might be overlooked. The resulting recommendations focus on standardizing parameters and reporting to facilitate easier comparison of work conducted by different researchers using different wind tunnel facilities.

2. WETTABILITY

Wettability is crucial for a successful RWIV wind tunnel test. Cables often experience RWIV after years of service when the HDPE sheathing has been spoiled, scratched, and worn due to dust, saline deposits, acid rain, and UV exposure (Larose and Smitt, 1999). Measurement of a water contact angle, defined in Figure 1, is recommended for future tests to ensure reproducibility, and the result should be part of the report.

Figure 1 compares RWIV test results with and without Gohsenol treatment, showing significant dependence on wettability on the rate at which the response increases and the maximum amplitude.

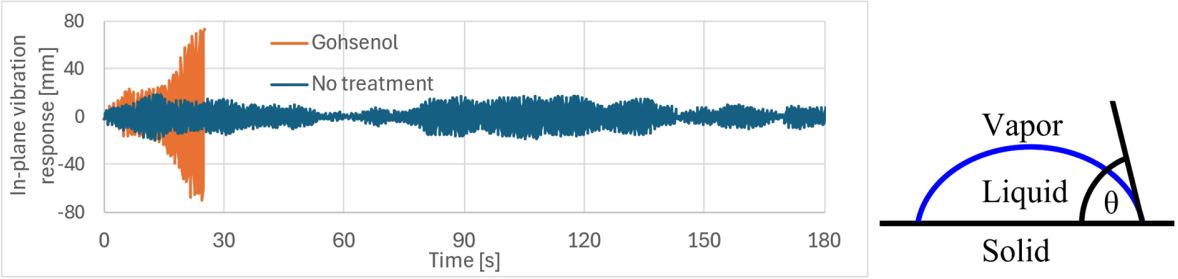


Figure 1. (Left) Example of wettability's influence on response. Inclination angle $\alpha = 25°$, yaw angle $\beta = 60°$, where $\beta = 0$ is wind parallel to the cable's horizontal projection. (Right) Contact angle definition (David et al. 2010).

Periodic wettability verification is essential if treatments are applied, as some may wear off faster than others. Based on the authors' experience, Gohsenol tends to wash off from the cable. Dry graphite lubricant is more resilient to water and wind; however, it is not resilient to physical contact. Thus, touching the sample after application should be avoided. Note that these constitute qualitative observations and are thus not based on any scientifically measured values.

3. WATER SPRAY SYSTEM

The spray system provides the rain simulation to the section model of the stay cable. An appropriate water flow rate and an even distribution of the water along the model are fundamental for the water rivulet to be sustainable. Within the two of the RWIV test campaigns conducted in 2024, several nozzle distributions were tested, and they are discussed below.

One large nozzle (similar to a fire hose) with high pressure and flow in the middle of the cross section of the wind tunnel; medium nozzles (similar to fire sprinklers) spaced every 1.0 m to 1.5 m; and a series of small nozzles (similar to misty sprinkler used in gardening) spaced at 20 cm to 50 cm intervals were tested. The last solution is recommended because it does not rely as much on the water pressure and wind velocity to distribute the water on the model, since the spacing between the nozzles is reduced. The series of nozzles can be attached to a thin wire at the same inclination and yaw as the model, to ensure even distribution of the water, and the wire and hose could be placed around 1 meter from the model in the wind flow's direction. The wire and hose should be of small diameter, otherwise they might create vortices or alter the oncoming flow, such that they can change the response of the model. The possibility of spray system flow interference should be tested by conducting dry tests with the spray system in place, i.e. with no rain.

4. DYNAMICS OF THE MODEL

Torsion motion of the cable model should be avoided, as it can induce unrealistic vibrations similar to the plunge and torsion 2-degree-of-freedom (2DOF) theoretical models for ice galloping discussed in the literature (Blevins, 1994). Large in-plane vibrations coupled with torsional response were observed in a 1DOF system (in-plane vibration only) when the out-of-plane motion was suppressed by short drag wires (see Figure 2). Torsion motion was suppressed when drag wires became longer.

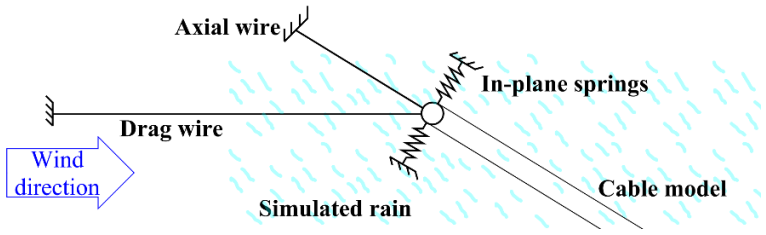


Figure 2. Sketch of the top of a cable model showing drag wire and axial wire.

Restraining the axial motion of the model ensures that the model does not move axially. On tests where there was no restraint, the cable had an undesirable axial motion (similar to a pendulum) which does not correspond to the prototype cable motion. Additionally, no significant vibrations were observed, possibly because this motion disrupted the necessary oscillation of the rivulet. However, when the axial motion was restricted, vibrations occurred. Therefore, based on the authors' findings, restraining the axial motion of the model is recommended. Long axial wires can be used for that purpose (see Figure 2).

5. CALIBRATION TEST

A calibration test can provide researchers with assurance that their system is operating correctly. Achieving a required damping to suppress the vibration seen in the wind tunnel, in the form of Scruton number (Sc), for a plain cable model (without helical fillet, rings, indentations, or other surface modifications) that approaches the recommended design value of $Sc = 10$ (PTI, 2018; Kumarasena, 2007) could serve as a benchmark. Pinto et al., (2025) describes a methodology for estimating required damping value from RWIV tests.

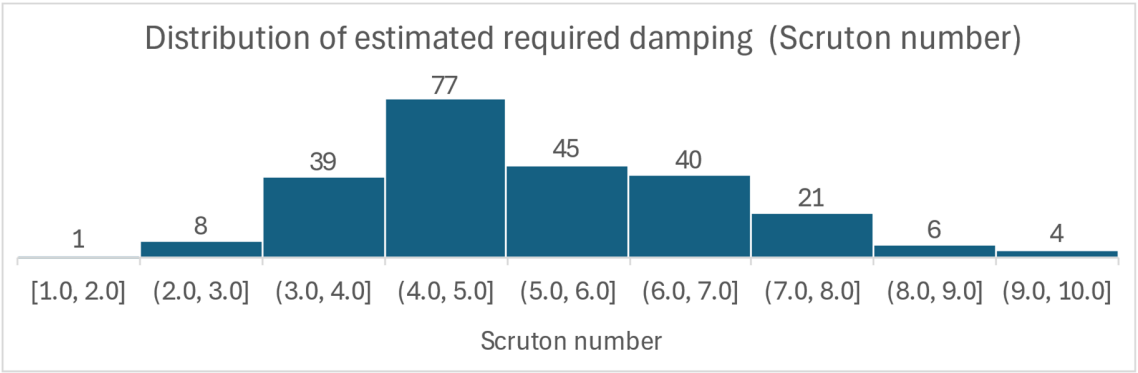


Figure 3. Distribution of estimated required damping to suppress RWIV (Pinto et al., 2025)

Figure 3 shows all RWIV tests results, from the tests described in Pinto et al., (2025), that have

achieved at least $\pm 80\ mm$ vibration amplitude ($160\ mm$ peak-to-peak). Main parameters of the tests are: model diameter $D = 160\ mm$, yaw angle $\beta = 60°$, inclination $\alpha = 25°$, wind velocities $U = 9, 10$ or $11\ m/s$. Assuming a Gumbel distribution, Table 1 shows the probability of achieving target Scruton number estimations. If $Sc = 7$ is the target of the calibration tests, it is not expected to take more than 23 tests to observe the target damping demand, if the system is working properly. Note that the convention is $\beta = 0$ means wind parallel to the cable's horizontal projection. Refer to Pinto et al., (2025) for a detailed description of the tests.

Table 1 Probability and Sample Size Requirements for Achieving Target Scruton Numbers

Target Scruton number	Probability of occurrence	Number of samples for 95% chance of occurrence
6	25.7%	11
7	12.4%	23
8	5.7%	52
9	2.6%	116

5. CONCLUSION

Several aspects of wind tunnel testing of RWIV are discussed. Recommendations for wettability, spray system, dynamics of the model, and calibration testing are presented. Following these recommendations can help achieve successful replication of RWIV and standardize comparisons across different wind tunnel facilities and test campaigns.

ACKNOWLEDGEMENTS

This work is part of the transnational access project "ERIES – RW-CASUMO", supported by the Engineering Research Infrastructures for European Synergies (ERIES) project (www.eries.eu), which has received funding from the European Union's Horizon Europe Framework Programme under Grant Agreement No. 101058684. This is ERIES publication number C31. This project has also received research funds from COWIfonden and Innovation Fund Denmark.

REFERENCES

Blevins, R.D., 1994. Flow-induced Vibration. Van Nostrand Reinhold, New York, USA.

D'Auteuil, A., McTavish, S., Raeesi, A., Larose, G., 2023. An investigation of rain-wind induced vibration on stay cables in a novel range of operating conditions. Journal of Wind Engineering and Industrial Aerodynamics 242 (2023): 105581.

David, R., Neumann, A.W., Zuo, Y., 2010. Applied surface thermodynamics. 2nd ed. CRC Press, Boca Raton, USA.

Flamand, O., 1995. Rain-wind induced vibration of cables. Journal of Wind Engineering and Industrial Aerodynamics 57 (2-3), 353 – 362.

Georgakis, C. T., Koss, H. H., Ricciardelli, F., Sep 2009. Design specifications for a novel climatic wind tunnel for the testing of structural cables. In: 8th International Symposium on Cable Dynamics, Paris, France. pp. 333–340.

Georgakis, C. T., Matejicka, L., 2021. Wind tunnel testing of bridge cables–recommendations towards a standardised approach. In: ISDAC 2021–Second International Symposium on the Dynamics and Aerodynamics of Cables. 2021.

Gimsing, N. J. and Georgakis, C. T., 2012. Cable supported bridges concept and design. 3rd ed. John Wiley & Sons, New York, USA.

Kumarasena, S., Jones, N. P., Irwin, P., Taylor, P., 2007. Wind-Induced vibration of stay cables. United States. Federal Highway Administration.

Larose, G., Smitt, L. W., Jun 1999. Rain/wind induced vibrations of parallel stay cables. In: Proceedings of the IABSE Conference, Cable-Stayed Bridges-Past, Present and Future, Malmo, Sweden.

Pinto, V.D., Georgakis, C.T., Larsen, A., Demartino, C., Bergman, D., 2025. Effects of Frequency Ratio and Damping on Rain-Wind Induced Vibration of Stay Cables: A preliminary evaluation. In: Proceedings of the IABSE Symposium, Tokyo, Japan.

PTI (Post-Tensioning Institute), 2018. Recommendations for stay cable design, testing and installation. Post-Tensioning Institute Committee on Cable-Stayed Bridges.

Costal Urban-BOundary Layer Dynamics (CU-BOLD)

Djordje Romanic [1], Alessio Ricci[2], Masoud Moeini[1], Priyadarshi Maurya[2], Massimiliano Burlando[3]

[1]*McGill University, Montreal, Quebec, Canada, djordje.romanic@mcgill.ca; masoud.moeini@mail.mcgill.ca*
[2] *University School for Advanced Studies (IUSS) Pavia, Pavia, Italy, alessio.ricci@iusspavia.it; priyadarshi.maurya@iusspavia.it*
[3]*University of Genoa, Genoa, Italy, massimiliano.burlando@unige.it*

SUMMARY:
As urbanization continues to rise, with 56% of the global population now living in cities, and 40% residing near coastal areas, understanding coastal urban boundary layer (CUBL) microclimates is crucial for enhancing the resilience of urban environments. The complexity of the urban boundary layer (UBL), especially its interaction with the marine atmosphere, presents challenges for accurate characterization. Using Doppler lidar technology, previous studies have explored wind conditions and turbulence in coastal areas. This study proposes utilizing a WindCube 400S pulsed Doppler lidar in Genoa's port to analyze CUBLs and test hypotheses on wind profiles and coastal urban heat islands, with the aim of improving urban resilience.
Keywords: coastal wind, urban boundary layer, lidar, resilience

1. INTRODUCTION

Approximately 56% of world's population lives in cities and the positive trend of urbanization is expected to continue (World Bank, 2024). Furthermore, the population density within 100 km of the coast is roughly twice the global average, with about 40% of the world's population living close to the coast (UNEP, 2023). Therefore, quantitative assessment of costal urban boundary layer (CUBL) microclimates is crucial for improving the sustainability and resilience of these urban environments. The UBL has a complex three-dimensional structure making it difficult to describe precisely in many circumstances (Rotach et al., 2005; see Figure 1). The lowest atmospheric layer inside the UBL is the urban canopy layer that stretches from the ground to approximately the average height of urban elements. Here, the wind flow is directly influenced by the geometry, orientation, porosity as well as other micro-scale characteristics of small-local roughness elements. The urban canopy layer is part of the so-called roughness sublayer, whose height and dynamics depend on the height and spatial distribution of roughness elements. While variable, the roughness sublayer height is usually between 2 and 5 times the height of the urban canopy layer (Raupach et al., 1991). In roughness sublayer, wind flow is spatially dependent, and turbulence is generally nonhomogeneous. The inertial sublayer, which is often well-defined in a rural ABL, is a blending layer between the roughness sublayer and mixed layer. In the UBL, the dynamics of inertial sublayer follow the theoretical concepts of the Monin-Obukhov similarity theory (Stull, 1998). While turbulence in the inertial sublayer is more homogeneous than in the roughness sublayer, the applicability of the Monin-Obukhov theory and the depth of internal sublayer are not properly

understood given the lack of high-resolution measurements and complex wind fields above urban fabrics. Moreover, less is known about the mixed layer due to the insufficient amount of meteorological measurements of wind, temperature, and humidity profiles above urban areas.

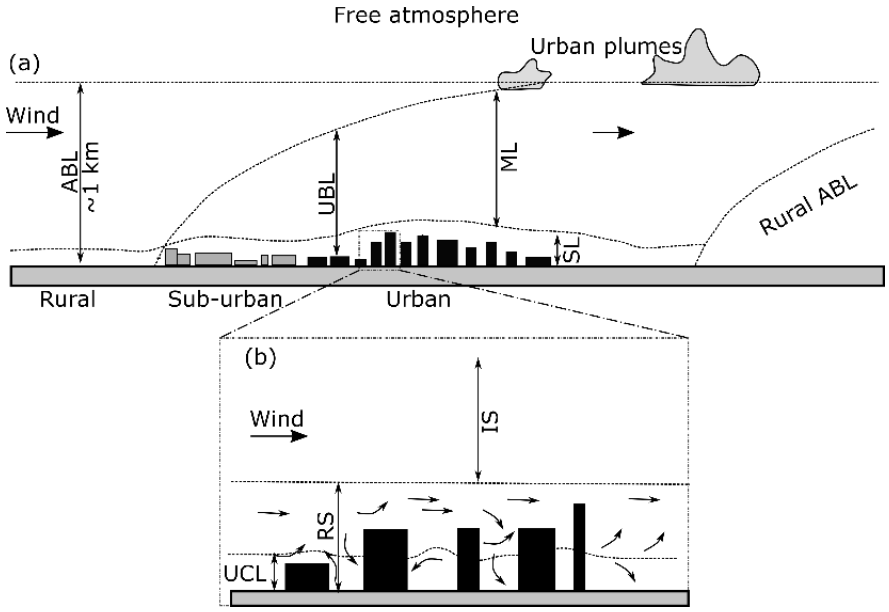


Figure 1. Idealized structure of the classical UBL based on Oke (1987). Mixed layer (ML); surface layer (SL); inertial sublayer (IS); roughness sublayer (RS); urban canopy layer (UCL).

A Doppler lidar utilizes the frequency shift of a transmitted electromagnetic signal and its backscatter from air particles to estimate the mean motion of the air. Further processing of backscatter and velocity data can provide insight into the turbulent characteristics of the atmosphere. Burlando et al. (2020) used the WindCube 400S Doppler lidar to investigate kinematics of a downburst outflow over the coastal region of Genoa during the collapse of the Morandi Bridge on 14 August 2018, which was only ~2.5 km away from the coastline. Shu et al. (2020) used a Doppler lidar at an offshore platform in Hong Kong to characterize the wind veer profiles up to a height of 180 m above sea level. They observed that the maximum wind veer angle was negatively correlated with mean wind speed. Tuononen et al. (2017) used a Doppler lidar on an island in the Finnish outer archipelago in the Baltic Sea to study the occurrence and characteristics of low-level jets and their diurnal and seasonal variations over two years of measurements. An abrupt change in surface roughness can also trigger the development of low-level jets at a coastline when the wind flows from rougher land to smooth sea—such jets are referred to as frictional–Coriolis–buoyancy jets (Orr et al., 2005). Vakkari et al. (2015) utilized Doppler lidar measurements from coastal locations in Limassol, Cyprus during summer, and Loviisa, Finland during winter. They determined the mixing layer height based on a velocity variance in low elevation-angle conical scans. Ricci et al. (2019) used the WindCube lidar profiler to detect marine boundary layer wind conditions approaching Livorno, Italy. The lidar marine boundary layer wind was then used as boundary condition in the computational fluid dynamics simulations to predict the urban canopy layer development through and over the port and city of Livorno, Italy. Li et al. (2024) analyzed costal wind Geno using a short-range lidar wind profiler.

While the progress made in the research discussed in the previous section and other studies is impressive and demonstrates the feasibility of lidar measurements in investigation of the UBL,

more comprehensive measurements of CUBLs and their interaction with the nearby marine atmosphere are needed. The present study therefore proposes the analysis of CUBLs using the WindCube 400S pulsed Doppler lidar installed in the Port of Genoa. The following research hypotheses shall be tested:

- Hypothesis 1: Vertical profiles of mean wind and turbulence characteristics in the CUBL different, at a level of statistical significance, from the profiles over the marine ABL. The difference is quantifiable and can be measured using a Doppler lidar.
- Hypothesis 2: Coastal urban heat island (UHI) exist under certain synoptic-scale conditions, and this dynamics can be quantified using a Doppler lidar for wind and circulation measurements, and local weather stations for air temperature measurements.

4. METHODOLOGY

We propose a scanning pattern in Figure 2a to estimate vertical profiles of wind properties over three downtown urban position ($\alpha = 75°$, 85° and 95°). Moreover, the line-of-sight at the azimuth angles $\alpha = 85°$ and 95° provide Doppler scans over marine environments (first approximately 10 and 8 km, respectively) and urban environments (the last segments of the scans). This setup enables direct comparison between urban and marine wind profiles along the same range-height indicator scan. The line-of-sight along $\alpha = 100°$ and $\alpha = 105°$ represent the scans along the coastline and over sea, respectively. The proposed scanning pattern is suitable for land and sea breeze wind directions as well as the along-coast wind directions. We also propose a plain position indicator scan at fixed elevation angles (2.5°, 5° and 7.5°) to characterize the wind field at nearly horizontal surfaces. The UBL height is about 1 km above the surface, and the surface layer is approximately the first 10% of the urban boundary layer. Given the challenges to assess a priori which of the proposed scanning pattern is the best choice for the proposed project, we plan to initiate this research by testing the suitability of different scanning patterns for the retrieval of wind velocity and UHI wind conditions.

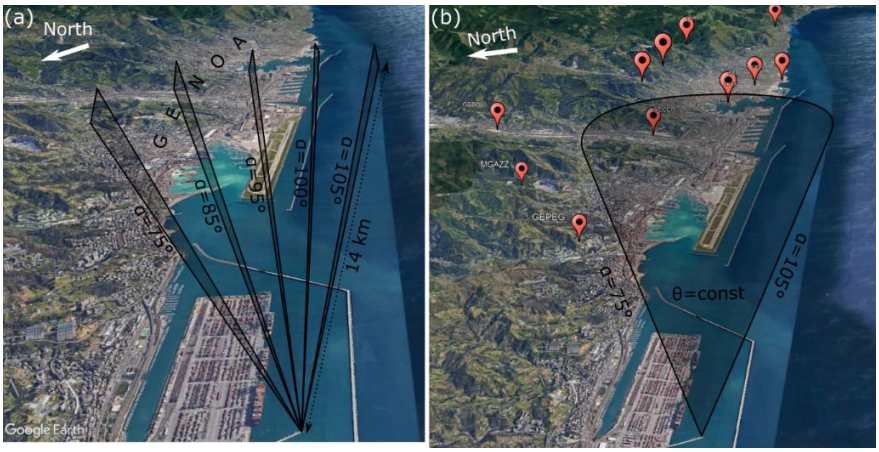


Figure 2. (a) Examples of five RHI lidar scans over urban, coastal, and marine regions of Genoa. The azimuth angles (α) of each scan are indicated in the figure. (b) Example of a PPI scan (θ=const) and the position of local weather stations (red symbols) in and around Genoa. Map source: Google Earth Pro®.

7. PRELIMINARY RESULTS AND FUTURE RESERCH

Figure 3 shows a velocity record measured by WindCube 400S in Genoa lidar during June 2021. We plan to acquire similar velocity measurements during the months of June, July and August 2025. Moreover, preliminary measurements of CUBL over Genoa for selected time periods during November 2024 and April 2025 will be conducted, analyzed and presented at the conference.

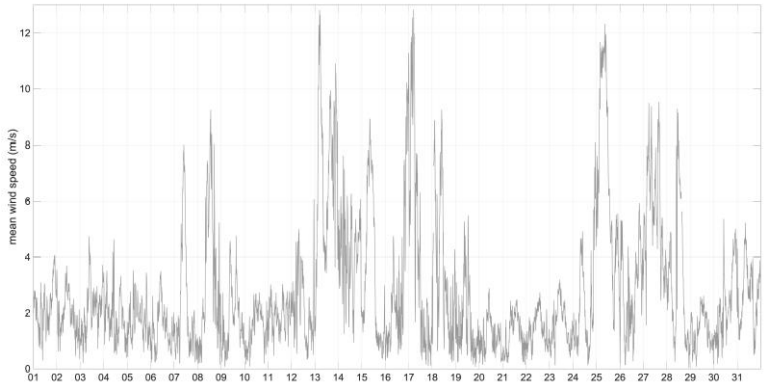


Figure 3. An example of WindCube 400S Doppler lidar measurements showing a time series of mean wind speed at 40 m above sea level for the month of June 2021.

REFERENCES

The World Bank. Urban Development Overview. World Bank 2024. https://www.worldbank.org/en/topic/urbandevelopment/overview (accessed March 4, 2024).

UNEP. Ocean, Seas and Coasts. UNEP - UN Environment Programme 2023. http://www.unep.org/topics/ocean-seas-and-coasts (accessed March 4, 2024).

Rotach MW, Vogt R, Bernhofer C, Batchvarova E, Christen A, Clappier A, et al. BUBBLE – an Urban Boundary Layer Meteorology Project. Theor Appl Climatol 2005;81:231–61. https://doi.org/10.1007/s00704-004-0117-9.

Raupach MR, Antonia RA, Rajagopalan S. Rough-wall turbulent boundary layers. Appl Mech Rev 1991;44:1–25. https://doi.org/10.1115/1.3119492.

Stull RB. An Introduction to Boundary Layer Meteorology. Springer Netherlands; 1988. https://doi.org/10.1007/978-94-009-3027-8.

Oke TR. Boundary Layer Climates. Psychology Press; 1987.

Burlando M, Romanic D, Boni G, Lagasio M, Parodi A. Investigation of the weather conditions during the collapse of the Morandi bridge in Genoa on 14 August 2018 using field observations and WRF model. Atmosphere 2020;11:724. https://doi.org/10.3390/atmos11070724.

Shu Z, Li Q, He Y, Chan PW. Investigation of Marine Wind Veer Characteristics Using Wind Lidar Measurements. Atmosphere 2020;11:1178. https://doi.org/10.3390/atmos11111178.

Tuononen M, O'Connor EJ, Sinclair VA, Vakkari V. Low-Level Jets over Utö, Finland, Based on Doppler Lidar Observations. Journal of Applied Meteorology and Climatology 2017;56:2577–94. https://doi.org/10.1175/JAMC-D-16-0411.1.

Orr A, Hunt J, Capon R, Sommeria J, Cresswell D, Owinoh A. Coriolis effects on wind jets and cloudiness along coasts. Weather 2005;60:291–9. https://doi.org/10.1256/wea.219.04.

Vakkari V, O'Connor EJ, Nisantzi A, Mamouri RE, Hadjimitsis DG. Low-level mixing height detection in coastal locations with a scanning Doppler lidar. Atmospheric Measurement Techniques 2015;8:1875–85. https://doi.org/10.5194/amt-8-1875-2015.

Ricci A, Burlando M, Repetto MP, Blocken B. Simulation of urban boundary and canopy layer flows in port areas induced by different marine boundary layer inflow conditions. Science of The Total Environment 2019;670:876–92. https://doi.org/10.1016/j.scitotenv.2019.03.230.

Li N, Dyer-Hawes Q, Romanic D, Burlando M. Investigation of coastal winds and turbulence characteristics using Doppler lidar. Journal of Geophysical Research: Atmospheres 2024: https://doi.org/10.1029/2024JD041429.

The ERIES BOLT Project: Behavior of Telecommunication Lattice Towers to Thunderstorms Winds

Ileana Calotescu[1], Costin-Ioan Coșoiu [2], Horia Hangan[3], Kim Adamek[4], Tibebu Birhane[5], Girma Bitsuamlak[6]

[1,2]*Technical University of Civil Engineering Bucharest, Bucharest, Romania,*
ileana.calotescu@utcb.ro[1], costinioan.cosoiu@utcb.ro[2]
[3]*Ontario Tech University, Oshawa, ON, Canada, Horia.Hangan@ontariotechu.ca*
[4,5,6] *WindEEE Research Facilities, Western University, London, ON, Canada,*
kadamek2@uwo.ca[4], birhane@uwo.ca[5] and gbitsuam@uwo.ca[6]

SUMMARY:
This paper introduces the ERIES-BOLT project (Engineering Research Infrastructures for European Synergies – Behavior of Telecommunication Lattice Towers (TLT) to Thunderstorms Winds). The main objective of the project is to investigate the behaviour of telecommunication lattice towers to thunderstorm winds by means of non-synoptic wind tunnel testing and field measurements. Two follow up objectives are: (1) to augment knowledge in thunderstorm wind research by simulating realistic atmospheric boundary layer (ABL) and thunderstorm events in the WindEEE research facility; (2) to improve the design of TLT to ABL and thunderstorm winds by conducting wind tunnel tests on aeroelastic and static models of two towers. Herein, the resulting database is presented including wind field characterization tests and aeroelastic tests on two lattice towers models of 90 m and 50 m heights as well as aerodynamic tests on the sectional model of the 50 m lattice tower.

Keywords: WindEEE, downburst, aeroelastic wind tunnel test, force balance, sectional test, lattice tower

1. INTRODUCTION

Research on thunderstorms and their effect on structures dates back to one of the earliest field programs carried out by Fujita in 1978 and subsequently in 1982 (Fujita, 1985) followed by other monitoring campaigns (Choi, 2004; Lombardo, 2014) the most recent one being the THUNDERR project (Solari et. al, 2020) conducted at Genova University, Italy. The ERIES-BOLT project aims at closing the knowledge gap between the wind field monitoring of real structures and wind tunnel testing by simulating real ABL and thunderstorm events measured in Sânnicolau Mare, Romania (Calotescu and Repetto, 2022) in the Wind Energy, Environment, Engineering (WindEEE) research facilities.

The WindEEE Dome is a unique 3D wind testing chamber that can generate both synoptic and non-synoptic storm systems (e.g. tornadoes, downbursts and gusts), (Hangan, 2014). WindEEE's unique capabilities and years of development of various complex flows such as tornado (Refan et. al, 2014), downburst (Romanic et al., 2019), full/large-scale synoptic winds (Birhane et. al, 2020) have attracted and benefitted users worldwide, leading to major advancements in the fields. The facility has enabled various studies by users on characterization of downburst both with (Romanic

and Hangan, 2020) and without (Junayed et. al, 2019) prevailing atmospheric boundary layer flows on both aerodynamic (Jubayer et. al, 2019) and aeroelastic models (Elawady et. al, 2017).

Three tests were conducted within the ERIES-BOLT project, namely (1) wind field characterization, (2) aeroelastic tests of the models corresponding to two TLTs of 90 m (T90) and 50 m (T50) heights and (3) aerodynamic tests on sectional models of the top of the 50 m tower.

2. WIND FIELD CHARACTERIZATION

This WindEEE testing was divided into 4 tests including the development of the ABL (Atmospheric Boundary Layer), downburst, downburst with ABL, and tripped downburst (to adjust height of max velocity). Cobra probes were used to measure wind velocity and turbulence.

The 60-fan wall of the WindEEE test chamber was used to generate various ABL flows. Cobra probes were placed at heights of 50, 100, 150, 200, 300, 400, 500, 600, 700, 800, and 900 mm from the ground. The downbursts-like flows (DLF) are generated by releasing the flow from a pressurised plenum above the testing chamber through a bell mouth with variable aperture. A stand of 11 TFI cobra probes was placed at various radial locations relative to the centre of the DLF.

Figure 1 shows the cobra probe stand (Fig. 1a) and the ABL profile (Fig. 1b) for profile ID CC2049 (ABL uniform 80%, 1.2 m spires, no trip, no roughness).

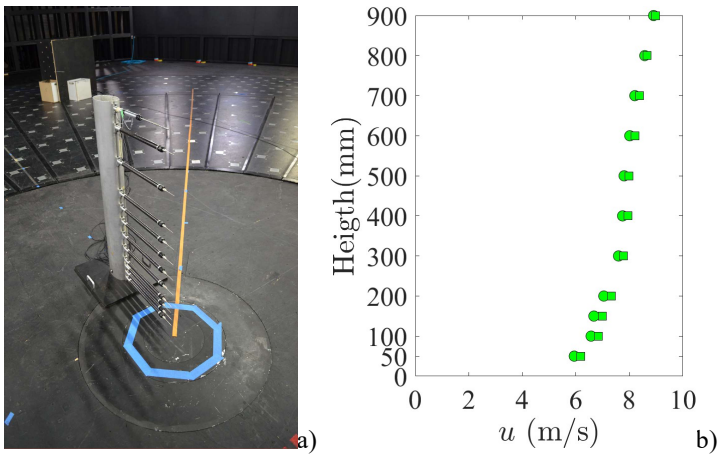


Figure 1. (a) cobra probes stand and (b) ABL profile development (CC2049- uniform flow 80%, 1.2 m spires)

3. AEROELASTIC TESTS OF LATTICE TOWERS

This specimen includes two triangular lattice towers of different heights (50 m and 90 m) built to a scale of 1:100 (0.5 m and 0.9 m at model scale). The models were made from a mixture of stainless-steel rods for the spines and bracing elements while the joints were made from 3D printed PolyJet material. Both towers were tested under ABL, downburst, and downburst with ABL configurations. The models were instrumented on a force balance to measure 6 base loading components including F_x, F_y, F_z, M_x, M_y, and M_z. Two 3-component accelerometers were placed on bracing components, one was near the middle and one at the top for each tower. In addition, a cobra probe was located at various positions to act as a flow reference during each flow type.

Figure 2 shows the aeroelastic model of tower T50 (Fig. 1a) and radial wind speed and corresponding acceleration at the top of the model for an aeroelastic test at radial position r/D=1.0 and angle of attack θ=0 (profile ID CC-1004 - Downburst, BD = 3.2m, UVFD = 40%).

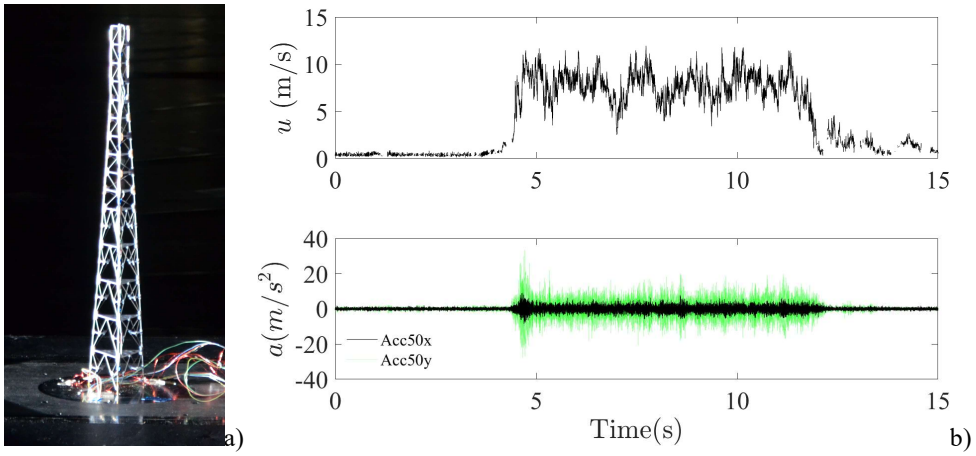


Figure 2. (a) 50 tower aeroelastic model in testing chamber and (b) aeroelastic test at radial position r/D=1.0 and angle of attack θ=0: radial wind speed (top) and acceleration (bottom)

4. AERODYNAMIC TESTS

This specimen includes a 1m tall section of the top of the 50 m tower at a scale of 1:10. It is constructed of brass, steel, 3D printed nylon, PolyJet 3-D printed material, and steel screws. The antennas, railing and central ladder are all removable. The three tests included the structure with just a base plate, the structure with both a base plate and a top plate, and the structure with ancillaries with just a base plate. The models were instrumented on a force balance to measure 6 base loading components including F_x, F_y, F_z, M_x, M_y, and M_z. In addition, a cobra probe was used as a flow reference during each flow type. All the models were tested in ABL winds.

Figure 3 shows the sectional model of tower T 50, the wind speed and corresponding forces. The *x* direction is aligned with a face of the tower while the *y* direction is perpendicular to the face.

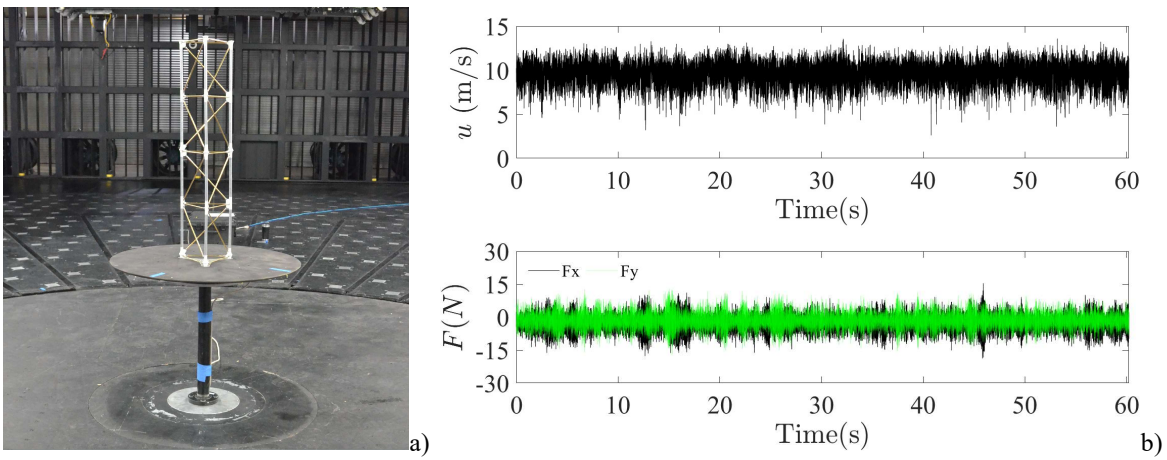


Figure 3. (a) 50 tower sectional model in testing chamber and (b) wind speed (top) and forces (bottom)

5. CONCLUSIONS

This paper presents the database of wind tunnel test measurements acquired within the ERIES-BOLT project. It includes winds field characterization tests (ABL, downburst, downburst with ABL, and tripped profiles), aeroelastic tests on the models of two lattice towers of 90 m and 50 m heights and aerodynamic tests on the sectional model of the 50 m lattice tower.

ACKNOWLEDGEMENTS

This work is part of the transnational access project "ERIES – BOLT", supported by the Engineering Research Infrastructures for European Synergies (ERIES) project (www.eries.eu), which has received funding from the European Union's Horizon Europe Framework Programme under Grant Agreement No. 101058684. This is ERIES publication number C38.

REFERENCES

Birhane, T. H., Bitsuamlak, G. T., Kahsay, M. T., Awol, A. D., 2020. Air-Permeability Factor for Wind Loads on Loose-Laid Pavers on Flat Roofs. Journal of Structural Engineering, 146(8), 04020151.

Calotescu, I., Repetto, M.P., 2022. Monitoring of thunderstorm activity in Sânnicolau Mare, Romania. The 8th European-African Conference on Wind Engineering, Bucharest, Romania, September 20-23, 2022.

Choi, E.C.C., 2004. Field measurement and experimental study of wind speed profile during thunderstorms. Journal of Wind Engineering and Industrial Aerodynamics 92, 275–290.

Elawady, A., Aboshosha, H., El Damatty, A., Bitsuamlak, G., Hangan, H., Elatar, A., 2017. Aero-elastic testing of multi-spanned transmission line subjected to downbursts. Journal of Wind Engineering and Industrial Aerodynamics, 169, 194-216.

Fujita, T.T., 1985. The Downburst Microburst and Macroburst Report of Projects NIMROD and JAWS.

Hangan, H., 2014. The Wind Engineering Energy and Environment (WindEEE) Dome at Western University, Canada", Wind Engineers, JAWE, 39(4):350-351

Jubayer, C., Romanic, D*., Hangan H. 2019 Aerodynamic loading of a typical low rise building for an experimental stationary and non-Gaussian impinging jet, Wind & Structures, 28(5): 315-329

Junayed, C., Jubayer, C., Parvu, D., Romanic, D., Hangan, H., 2019. Flow field dynamics of large-scale experimentally produced downburst flows. Journal of Wind Engineering and Industrial Aerodynamics, 188, 61-79.

Lombardo, F.T., Smith, D.A., Schroeder, J.L., Mehta, K.C., 2014. Thunderstorm characteristics of importance to wind engineering. Journal of Wind Engineering and Industrial Aerodynamics 125, 121–132.

Refan, M., Hangan, H., and Wurman, J., 2014. Reproducing tornadoes in laboratory using proper scaling. JWEIA, 135, 136-148.

Romanic, D., LoTufo, J., Hangan, H. 2019**,** Transient behavior in impinging jets in crossflow with application to downburst flows", Journal of Wind Engineering and Industrial Aerodynamics, 184: 209-227.

Romanic, D., Hangan, H., 2020. Experimental investigation of the interaction between near-surface atmospheric boundary layer winds and downburst outflows. Journal of Wind Engineering and Industrial Aerodynamics, 205, 104323.

Solari, G., Burlando, M., & Repetto, M.P., 2020. Detection, simulation, modelling and loading of thunderstorm outflows to design wind-safer and cost-efficient structures. Journal of Wind Engineering and Industrial Aerodynamics 200, 104142.

Data-driven Monte Carlo simulations of tornado-like-vortex-induced loads on low-rise buildings

Gabriel Narancio[1], Han Ping Hong[1], Horia Hangan[1]

[1]*Western University, London, Canada, enaranci@uwo.ca*

SUMMARY:
A data-driven method was developed to stochastically simulate pressure fields induced by tornado-like vortices (TLVs) on buildings. The method defines local pressure coefficients and decomposes these coefficients into slow- and fast-varying components. To calculate the local pressure coefficients, virtual local reference velocity and pressure values are determined, minimizing differences between instantaneous TLV pressure coefficients and mean atmospheric boundary layer (ABL) coefficients in the least squares sense. The slow component is derived using a spectral low-pass filter, capturing effects of TLV translation and wandering, while the fast component captures turbulence and coherent vortex effects. The slow component is simulated via a static transformation method and the discrete orthonormal Stockwell transform (DOST), and the fast component is simulated with a modified IAAFT method. These components are then combined to generate surrogates of the overall pressure time histories. The performance of the method was tested by calculating extreme value distributions at specific pressure taps, yielding promising results.

Keywords: Tornado-induced loads, Monte Carlo simulation

1. INTRODUCTION

Assessing tornado-induced loads is a challenging task. Physical simulations and computational fluid dynamics (CFD) have been used to analyze tornado-like vortices (TLVs) and evaluate their impact on structures. Tornado vortex generators (TVGs) are commonly used to produce TLVs as proxies for real tornado flow. However, these simulations involve scaling numerous parameters, making a fully probabilistic approach intractable. Furthermore, even with a fixed set of parameters, many experimental repetitions are needed to obtain statistically reliable load estimations (Chen et al., 2023). Thus, efficient methods are needed to maximize the utility of limited measurement data and reduce physical simulation costs. One solution is developing surrogate models calibrated based on these measurements to generate new artificial realizations of experiments. Such models have been used in wind engineering to create synthetic wind time series for Monte Carlo simulations (Carassale and Solari, 2006; Gurley et al., 1996; Hong et al., 2021).

This paper proposes a data-driven, two-layer surrogate model to simulate multi-variate pressure time histories induced by TLVs on model buildings. The model uses a local formulation of pressure coefficients based on those obtained from an ABL test on the same building model. It decomposes the pressure coefficients into slow- and fast-varying components, simulated independently. A static transformation combined with the discrete orthonormal Stockwell transform (DOST) is used to simulate the slow-varying component, while a modified algorithm from Borgnat et al., 2012 simulates the fast-varying part (see also Cui and Hong, 2021). The method shows promising results when applied to determining pressure extreme value distributions (EVD).

2. EXPERIMENTAL SETUP

Two experiments were conducted in the WindEEE Dome at Western University. Pressures were measured on the surface of a 1:150 scaled model of a community formed by 8 instrumented low-rise residential buildings and 22 proximity buildings while it interacted with an atmospheric boundary layer (ABL) with a roughness length $z_0 = 3.6 \cdot 10^{-5}$m and friction velocity $u_\tau = 0.38$m/s for 16 directions $\varphi_k = 0^o, 22.5^o, 45^o, \ldots, 337.5^o$ from north, corresponding to directions N, NNE, NE, ..., NNW. Mean pressure coefficients $\overline{C}_{p,ABL}$ were calculated for these directions using the velocity and pressure measured at 10 cm height within the undisturbed flow as references. The values at intermediate directions with a resolution of one degree are interpolated using an Akima method. In the second test, pressures on the surface of the buildings were measured as various TLVs passed close to the community. In this paper we use the pressure time histories measured while a TLV with swirl ratio S = 1.03 (Refan and Hangan, 2018) moved over the community with a translation velocity $V_T \approx 0.1$m/s. This experiment was repeated eight times (runs). For simplicity in the presentation we simulated the pressure at only three pressure taps on the surface of House 5, i.e. taps 1218, 1315, and 1316, as shown in Figure 1.

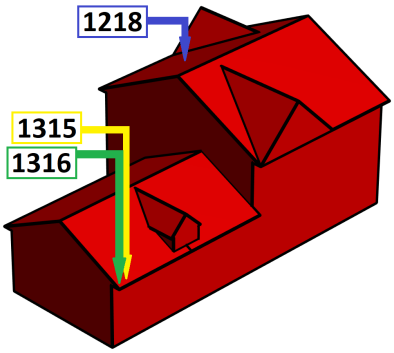


Figure 1. House 5 and pressure taps 1218, 1315, and 1316

3. PROCEDURE

3.1. Local pressure and velocity

At each instant, the correlation between the instantaneous pressure $C_{p,i,TLV}$ measured at all taps on the surface of the building and the corresponding mean pressure coefficients $\overline{C}_{p,i,ABL}$ at all directions are calculated. The direction where the maximum correlation occurs φ is identified, and virtual local pressure p_{local} and velocity V_{local} are defined such that $C_{p,i,TLV} \approx \overline{C}_{p,i,ABL}$ in the least squares sense. Moving mean values of the local pressure $\hat{p}_{local}(t)$ and velocity $\hat{V}_{local}(t)$ are calculated.

3.2. Decomposition of pressure coefficients

Local pressure coefficients at tap i can be expressed as

$$C_{p,i,local}(t) = \frac{p_i(t) - \hat{p}_{local}(t)}{\frac{1}{2}\rho \hat{V}^2_{local}(t)} \tag{1}$$

The pressure time history $p_i(t)$ at pressure tap i can be decomposed into "slow" $\overline{p}_i$ and "fast" $\tilde{p}_i$ fluctuating components as $p_i(t) = \overline{p}_i(t) + \tilde{p}_i(t)$, where the slow fluctuating component is determined by applying a low-pass filter with a cut-off frequency such that the slow component captures

the effect of the translation and wandering of the vortex, and the fast fluctuating component is defined as $\tilde{p}(t) = p(t) - \overline{p}_i(t)$. Then

$$C_{p,i,local}(t) = \frac{\overline{p}_i(t) - \hat{p}_{local}(t)}{\frac{1}{2}\rho\hat{V}^2_{local}(t)} + \frac{\tilde{p}_i(t)}{\frac{1}{2}\rho\hat{V}^2_{local}(t)} \tag{2}$$

Finally, defining the first and second terms in the right-hand side of Equation 2 as "slow" $\overline{C}_{p,i,local}$ and "fast" $\tilde{C}_{p,i,local}$ pressure coefficients, we have $C_{p,i,local}(t) = \overline{C}_{p,i,local}(t) + \tilde{C}_{p,i,local}(t)$.

3.3. Simulation of the slow component

The simulation of $\overline{C}_{p,i,local}(t)$ starts with the estimation of the conditional probability distribution function $F_{i,t}(x) = P\left[\overline{C}_{p,i,local} < x|t\right]$. This is done by estimating the first four moments of $F_{i,t}$ as a function of time and fitting a Pearson distribution at each instant. Then, a static transformation is performed as $y_i(t) = \Phi^{-1}\left[F_{i,t}\left(\overline{C}_{p,i,local}(t)\right)\right]$. Subsequently, the DOST coefficients are calculated for all y_i and the phase shuffled uniformly such that the phase difference between the corresponding coefficients for different y_i are kept equal. Using the inverse DOST, new y_i^{SIM} series are generated. Finally, the inverse static transformation $\overline{C}^{SIM}_{p,i,local}(t) = F^{-1}_{i,t}\left[\Phi\left(y_i^{SIM}(t)\right)\right]$ is applied.

3.4. Simulation of the fast component

For the simulation of the fast component, the marginal distributions are fitted to Pearson distributions and series of values from the fitted distributions are randomly generated along with uniformly distributed phase angles. Then, the DOST coefficients are calculated and the same phase added to the original phases by using the modified IAAFT method mentioned earlier. Once the new coefficient are calculated, new series are found using the inverse DOST. Now the series are sorted and substituted by the sorted Pearson generated values. The process is repeated until convergence is achieved.

4. RESULTS

Figures 2a, 2b, and 2c show in black the eight measured pressure time histories for taps 1218, 1315, and 1316, and in blue, 2000 simulations of the pressure at the same pressure taps. Figures 2d, 2e, and 2f present scatter plots of the pressure at the same taps, again black are measurements and blue are simulations. Finally, Figures 2g, 2h, and 2i show the empirical EVD estimated from simulations in blue and in black the empirical EVD obtained from measurements.

5. CONCLUSIONS

The method accurately predicts the EVD of the pressure at tap 1218 but underestimates it at taps 1315 and 1316. Tap 1218 is positioned at the center of the roof, while taps 1315 and 1316 are located near a roof corner. The similar EVD behavior at taps 1315 and 1316 is consistent, as both taps are positioned in close proximity. This underestimation may be due to the complexity of pressure behavior at roof corners, the limited data set—only 8 runs—used to fit the model, and the non-sycronized phase shift in the adopted IAAFT method. Given these factors, the results remain promising.

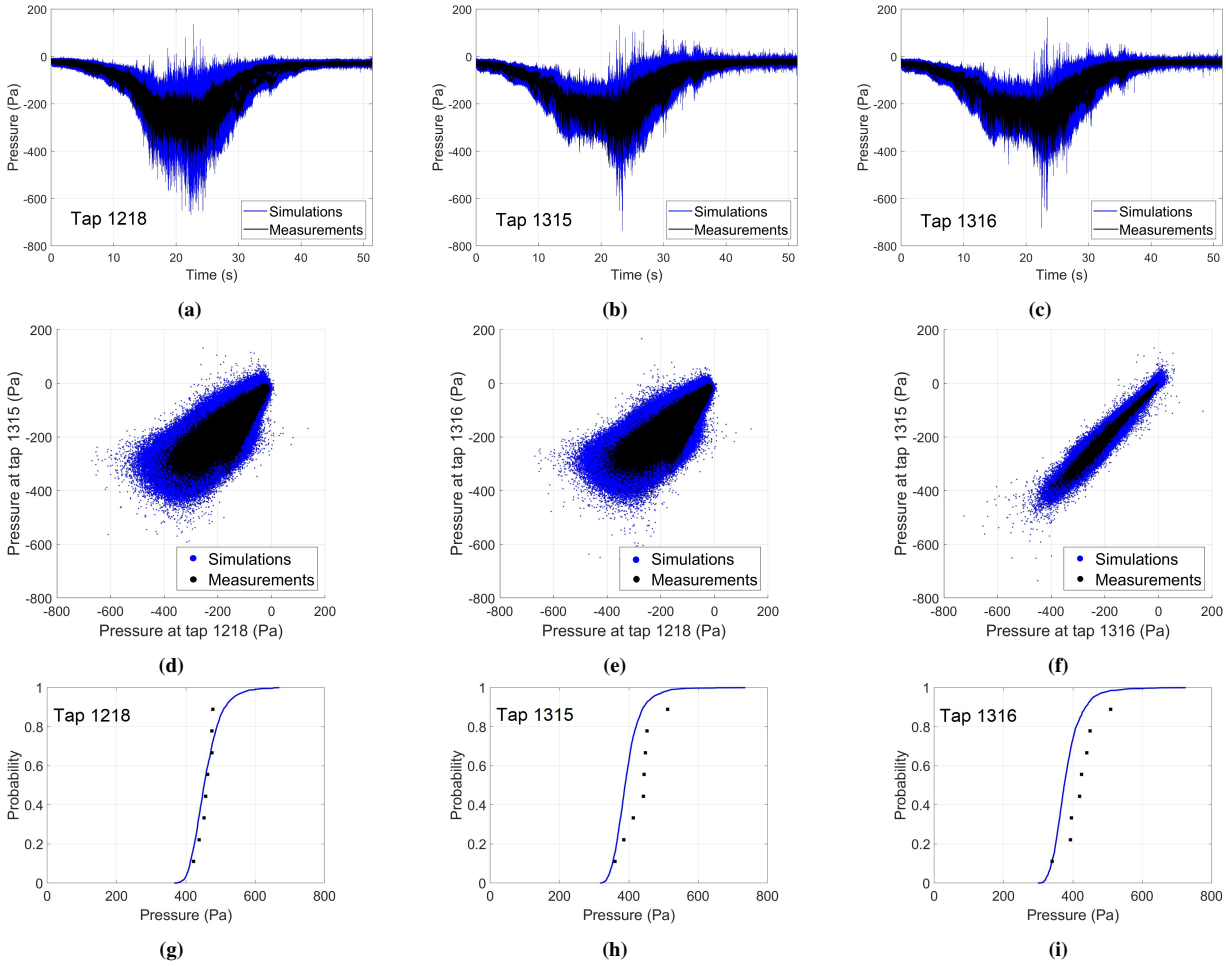


Figure 2. (a), (b), and (c) show the pressure time histories measured (black) and simulated (blue) at taps 1218, 1315, and 1316 respectively. (d), (e), and (f) present scatter plots between the pressures at taps 1218-1315, 1218-1316, and 1316-1315, measured in black and simulated in blue. (g), (h), and (i), show the empirically estimated EVD obtained from the measurements in black and in blue the one obtained from the 2000 simulations.

REFERENCES

Borgnat, P., Abry, P., and Flandrin, P., 2012. Using surrogates and optimal transport for synthesis of stationary multivariate series with prescribed covariance function and non-Gaussian joint-distribution. Proceedings of 2012 IEEE International Conference on Acoustics, Speech and Signal Processing (ICASSP). IEEE, 3729–3732.

Carassale, L. and Solari, G., 2006. Monte Carlo simulation of wind velocity fields on complex structures. Journal of Wind Engineering and Industrial Aerodynamics 94, 323–339.

Chen, Q., Tang, Z., Wu, X., Zuo, D., and James, D., 2023. Laboratory study of tornado-like loading on a low-rise building model. Journal of Wind Engineering and Industrial Aerodynamics 238, 105443.

Cui, X. and Hong, H., 2021. Simulating nonstationary and non-Gaussian vector ground motions with time-and frequency-dependent lagged coherence. Earthquake Engineering & Structural Dynamics 50, 2421–2441.

Gurley, K. R., Kareem, A., and Tognarelli, M. A., 1996. Simulation of a class of non-normal random processes. International journal of non-linear mechanics 31, 601–617.

Hong, H., Cui, X., and Xiao, M., 2021. Modelling and simulating thunderstorm/downburst winds using S-transform and discrete orthonormal S-transform. Journal of Wind Engineering and Industrial Aerodynamics 212, 104598.

Refan, M. and Hangan, H., 2018. Near surface experimental exploration of tornado vortices. Journal of Wind Engineering and Industrial Aerodynamics 175, 120–135.

Numerical simulation of the flow around a sectional model of a lattice tower

Costin-Ioan Coșoiu [1], Ileana Calotescu[2], Kim Adamek[3], Tibebu Birhane[4], Girma Bitsuamlak[5]

[1,2]*Technical University of Civil Engineering Bucharest, Bucharest, Romania,*
costinioan.cosoiu@utcb.ro[1], ileana.calotescu@utcb.ro[2]
[3,4,5] *WindEEE Research Facilities, Western University, London, ON, Canada,*
kadamek2@uwo.ca[3], birhane@uwo.ca[4] and gbitsuam@uwo.ca[5]

SUMMARY:
This study investigates the aerodynamic behavior of a sectional model of a 50 m telecommunication lattice tower through a combination of experimental wind tunnel testing and CFD numerical simulations. The experimental measurements were conducted at the WindEEE Dome on the 1:10 scaled model of the top section of a 50 m tower. The model was placed on a 6-component force balance and was tested under three setups: (1) model with a base plate, (2) model with both a base plate and a top plate, and (3) model equipped with ancillaries with just a base plate. In this paper, only the second setup is investigated. The computational domain and boundary conditions for the numerical simulations were chosen to align closely with the experimental setup, ensuring accurate replication of the flow. The numerical simulations were performed using Ansys Fluent and employed a hybrid poly-hex mesh with approximately 13.2 million cells. The *k-ω* SST turbulence model was used to better capture flow separations due to the tower's complex geometry.

Keywords: WindEEE, telecommunication lattice tower, wind tunnel testing, CFD simulations

1. INTRODUCTION

Free-standing lattice towers are used worldwide in telecommunications, energy production, power transmission, meteorological measurements and so on. Due to their slenderness and relatively low mass, they are sensitive to wind loading. The design of telecommunication lattice towers for wind loading involves the evaluation of force coefficients, which may be evaluated using procedures available in codes of practice (Eurocode 3, 2006). Although such procedures are straightforward to apply for simple tower configurations, in more complex cases, when towers are equipped with various configurations of antennas, they do not always provide the expected results (Szafran, 2015).

Wind tunnel testing has been extensively used to investigate the influence of ancillaries on the force coefficients of lattice towers (Martin et al., 2015; Calotescu et al., 2020). However, such experiments are time-consuming, expensive and not easily available. CFD simulations may represent a proper alternative to wind tunnel testing provided the results are validated (Allegrini et al., 2018).
The paper presents numerical CFD simulations that reproduce an experimental study of the flow

on a sectional model of a telecommunication lattice tower performed in a controlled laboratory environment. The experimental study is part of the ERIES-BOLT (Engineering Research Infrastructures for European Synergies – Behavior of Telecommunication Lattice Towers to Thunderstorms Winds) project, a complex work that aims at investigating the behaviour of telecommunication lattice towers to thunderstorm winds by means of non-synoptic wind tunnel testing and field measurements.

2. THE ERIES-BOLT PROJECT

A vast campaign of wind tunnel tests was conducted at the WindEEE (Wind Energy, Environment, Engineering) Dome at Western University, Canada within the ERIES-BOLT project. The dataset includes: (1) wind field characterization tests, (2) aeroelastic tests and (3) aerodynamic tests. The wind field characterization measurements were divided into 4 tests, including the development of the ABL (Atmospheric Boundary Layer), downburst, downburst with ABL, and downburst with radial trip profiles. The aeroelastic tests were performed on the models of two triangular lattice towers of different heights (50 m and 90 m) built to a scale of 1:100. Finally, the aerodynamic tests were performed on the sectional model of the top of the 50 m tower at a scale of 1:10. The model was constructed of brass, steel, 3D printed nylon, PolyJet 3-D printed material, and steel screws. The antennas, railing, and central ladder are all removable. Three setups were considered: (1) model with a base plate, (2) model with both a base plate and a top plate, and (3) model equipped with ancillaries with just a base plate. All the sectional models were tested in ABL flows.

3. AERODYNAMIC TESTS

This section presents the wind tunnel test performed on the sectional model with both a base plate and a top plate (setup 2 as described in Section 2). The model was mounted on a rig made up of a 12.7 cm diameter steel pipe and a wooden base plate. The reference system of the aerodynamic balance was aligned so that, for an angle of attack $\theta = 0^o$, the X-axis of the force balance is aligned with the flow main direction, as seen in Figure 1a. The top plate is installed 5 mm over the model, encouraging 2-D flow properties in ABL flow to mimic aerodynamic properties seen in horizontal testing in traditional wind tunnels. Figure 1b shows the lateral view of the model. Figure 1c shows the time variation of the velocity components (u, v, and w) and F_x and F_y forces during for testing 0^o angle of attack. The force coefficients resulting are $C_{F_x} = 1.84$ and $C_{F_y} = 0.024$.

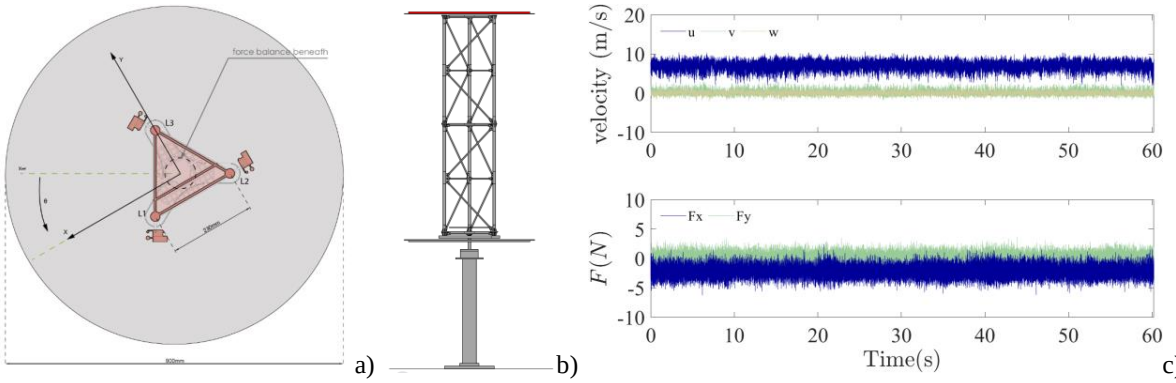
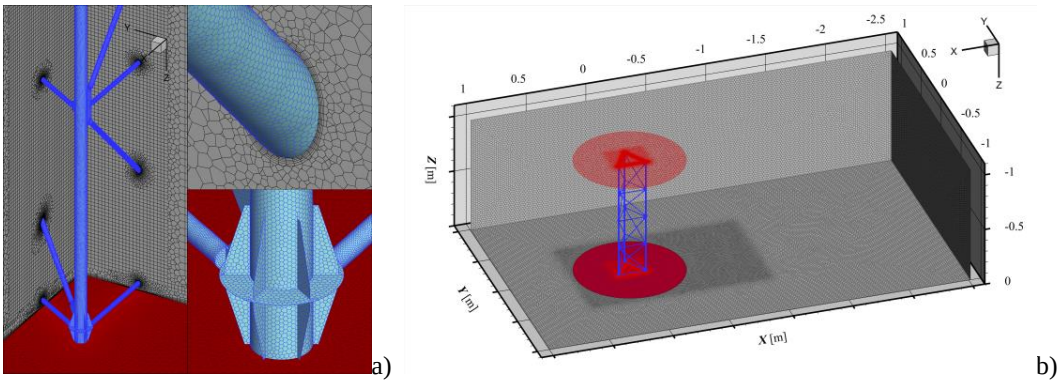


Figure 1. (a) reference system, (b) lateral view of the model and (c) velocity components (u, v, and w) (top) and F_x and F_y forces (bottom) for 0^o angle of attack

4. CFD SIMULATIONS

The fluid volume chosen for the simulations is represented by a brick with dimensions 3.5H × 2H × 1H (Length × Width × Height), where H represents the height of the experimental model between the rig's base and top plates. All plane elements were modeled as zero-thickness surfaces, and any details related to bolt assembly or welding traces were eliminated. The grid was discretized in Ansys Fluent Meshing and had approximately 13.2 million cells, the actual total number of cells depending on the angle of attack. The mesh was a hybrid poly-hex one. The minimum dimension of the characteristic cell length was equal to $0.5\times10^{-3}H$. The growth on the model surface was governed by curvature and proximity size functions with a maximum cell size of $10^{-3}H$ and a cell growth of 10%. The fine details of the model implied that for the curvature size function, a polygon with 40 sides was considered to model a full circle, while for the proximity size function, to model the gaps between adjacent surfaces, 4 cells were imposed. Around the model, a BOI (Body of Influence) size function with a characteristic length of $5\times10^{-3}H$ was imposed. Another BOI size function with a maximum characteristic length of $10^{-2}H$ was set to model the near wake and the upwind flow near the experimental model. The maximum cell characteristic length in the mesh was equal to $2\times10^{-2}H$ mm. To model the flow near the wall surfaces, 5 layers of prismatic cells were grown starting from the solid surfaces of the tower and the circular plates, considering a 1.2 growth rate and an aspect-ratio-based first layer characteristic length equal to 10. Figure 2a shows some details of the discretization grids, while Figure 2b presents a general view of the fluid domain with the boundary conditions and details of the mesh distribution at the outer boundaries of the mesh.



a) b)

Figure 2. (a) details of the discretization grids and (b) the fluid domain

The numerical simulations were performed using the CFD expert software Ansys Fluent. Considering the uniform flow experimented in laboratory conditions, the time was stationary. Due to the low wind speed and isothermal conditions, a pressure-based solver was chosen. A coupled algorithm was selected to couple the pressure and velocity fields for faster convergence. For all variables, second discretization schemes were set up. A RANS approach was chosen to simulate the turbulent flow using the k-ω SST turbulence model. This was imposed by the large separations that occur in the wake of the flow, which is better predicted by this numerical investigation method, considering the constraints of an isotropic hypothesis for turbulence. At the inlet of the fluid domain, a constant velocity was imposed, with a magnitude equal to the average value of the u-velocity component acquired during the experimental tests ($u_\infty = 7.09$ m/s). Considering that the average values of the v and w velocity components were 0, the flow direction was considered aligned with the X-axis, and the y and z components were neglected. The turbulence intensity computed from the experimental signal was imposed (TI=14.61%) and the turbulent length scale (L_t=0.23 m) was used to simulate the turbulence at the velocity inlet. A static pressure of 0 gauge

scale was set up at the outlet. The other four surfaces that materialize the outer boundaries of the fluid domain were considered as moving walls with the same velocity as those set up at the fluid domain inlet. On the base and top plates, a no-slip condition was imposed, the same as for all solid surfaces that describe the solid surfaces of the tower section.

Figure 3 shows the contours of pressure coefficients C_p on the lateral surface of the telecommunication tower sectional model. The force coefficients resulting from CFD simulations are $C_{F_x}^{CFD} = 1.39$ and $C_{F_y}^{CFD} = 0.054$.

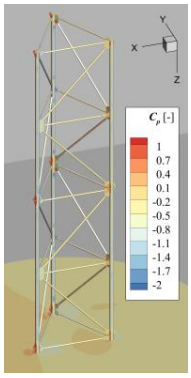


Figure 3. Contours of pressure coefficients C_p

5. CONCLUSIONS

In this study, the aerodynamic behavior of a sectional model of a 50 m telecommunication lattice tower was investigated through a combination of experimental wind tunnel testing and CFD numerical simulations. For this case and angle of attack, the numerical simulation underpredicts the results given by the experimental set-up. Future studies will include an in-depth analysis of the differences between experimental and simulated force coefficients.

ACKNOWLEDGEMENTS

This work is part of the transnational access project "ERIES – BOLT", supported by the Engineering Research Infrastructures for European Synergies (ERIES) project (www.eries.eu), which has received funding from the European Union's Horizon Europe Framework Programme under Grant Agreement No. 101058684. This is ERIES publication number C40.

REFERENCES

Allegrini, J., Maesschalck, J., Alessi, G., Glabeke, G., Christophe, J., van Beeck, J., 2018. Porous and geometry-resolved CFD modelling of a lattice transmission tower validated by drag force and flow field measurements. Eng Struct 168, 462–472.

Calotescu, I., Torre, S., Freda, A., Solari, G., 2021. Wind tunnel testing of telecommunication lattice towers equipped with ancillaries. Eng Struct 241, 112526.

Eurocode 3 – Design of Steel Structures - Part 3-1: Towers, masts and chimneys – Towers and Masts. European Committee for Standardization. Brussels: 2008.

Martín P, Elena VB, Loredo-Souza AM, Camaño EB., 2016. Experimental study of the effects of dish antennas on the wind loading of telecommunication towers. Journal of Wind Engineering and Industrial Aerodynamics 2016;149:40–7.

Szafran J., 2015. Analytical determination of aerodynamic resistance of the skeletal telecommunication towers. Structure and Environment, Kielce University of Technology, 7:5–14.

Does tornado vortex wandering really exist?

Aleksander Pistol [1], Mark Sterling [2], Mike Jesson [3], Girma Bitsuamlak [4], Fred L. Haan [5], Tibebu Birhane [6], Yealemnegus Waktola [7], Gregory A. Kopp [8]

[1]*Manchester Metropolitan University, Manchester, UK, a.pistol@mmu.ac.uk*
[2]*Manchester Metropolitan University, Manchester, UK, m.sterling@mmu.ac.uk*
[3]*University of Birmingham, Birmingham, UK, m.a.jesson@bham.ac.uk*
[4]*University of Western Ontario, London, ON, Canada, gbitsuam@uwo.ca*
[5]*Calvin University, Grand Rapids, MI, USA, flh2@calvin.edu*
[6]*University of Western Ontario, London, ON, Canada, tbirhane@uwo.ca*
[7]*University of Western Ontario, London, ON, Canada, ywaktola@uwo.ca*
[8]*University of Western Ontario, London, ON, Canada, gakopp@uwo.ca*

SUMMARY:
An extensive research campaign has been carried out through the ERIES framework to investigate tornado wind field interaction with low-rise buildings. The measurements were performed at the WindEEE Research Institute in London, Ontario. The goals of the campaign were to examine the tornado velocity and pressure field in a region close to the ground and to use this data to examine the structure of the tornado. The experiments outlined in this paper relate to a stationary tornado, i.e., a tornado with zero translation speed. The paper focuses on the wandering of the stationary tornado vortex, i.e. a seemingly random oscillating movement of the vortex centre. Results from ground pressure measurements are investigated in search of a pattern in this movement and its potential sources.

Keywords: tornado, vortex wandering, transient wind

1. INTRODUCTION

Although considerable research has been undertaken within the last decade related to tornadoes and the corresponding wind-induced forces arising from such phenomena (Baker and Sterling, 2018; Kopp and Wu, 2020), numerous gaps in our knowledge still exist. Whilst research has developed at a pace, in some cases, the enthusiasm of the community to make progress has resulted in several basic issues being overlooked (Baker and Sterling, 2019), and results being interpreted beyond what would normally be considered suitable or reliable. If this continues, then we run the risk of either inefficient structural design due to this lack of a true understanding of the underlying physics, with too much embedded carbon due to over-engineering or fundamentally unsafe designs.

This paper focuses on the issue of 'tornado wandering' – an oscillating movement of the vortex core, with a variable amplitude resulting from its vorticity and the background turbulence (Ashton et al., 2019; Iungo et al., 2009). This phenomenon complicates the tornado data analysis as it distorts the time-averaged vortex velocity field. Despite occurring in all physical simulations of tornadoes, only limited attempts have been made to properly examine and quantify this issue. Snow and Lund (1997) estimated that errors of up to 50% of the maximum

tangential velocity and 46% of the core radius resulting from wandering of an experimentally simulated Rankine-combined vortex can occur. Gillmeier et al. (2017) used proper orthogonal decomposition to decouple the influence of vortex wandering from the main flow field and estimate its relative effect for tornado-like vortices with different swirl ratios.

2. EXPERIMENTAL SETUP

The methodology and results presented in this paper are based on ground pressure measurements from a physical simulation of a stationary vortex at the Wind Engineering, Energy, and Environment (WindEEE) Dome (University of Western Ontario, Canada). The dimensions of the table where the measurements were conducted and the locations of the pressure taps on the ground are shown in Fig. 1. The standard distance between the majority of the taps was 90 mm. The sampling rate was 500 Hz and for the purpose of this analysis, a measuring time of 30 s is considered.

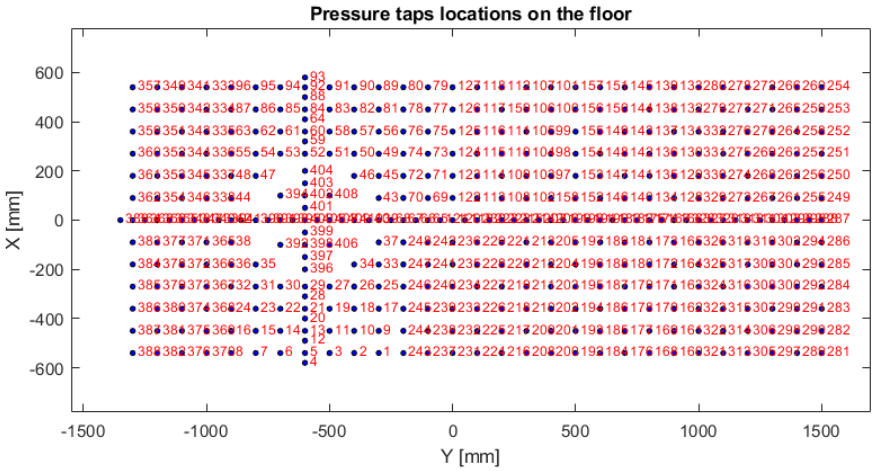


Figure 1. Pressure taps locations on the wind tunnel floor.

3. METHODOLOGY AND INITIAL RESULTS

The proposed methodology is presented below, along with some initial results to visualise the steps and outcomes of the method. Fig. 2a shows a multivariate probability density distribution of the identified locations of the centre of the vortex throughout the experiment along the X and Y coordinates. These locations were initially identified as the absolute pressure minima at each time step. Despite the restrictions in the spatial resolution of the measurements (due to the distance between the pressure taps) that influence the smoothness of this distribution, a bell shape can be clearly identified, suggesting that it can be approximated as Gaussian. To aid in mitigating the limited spatial resolution of the measurements, the ground pressures were spatially interpolated for a grid of 10 × 10 mm and then time-averaged for different periods ($\Delta T = 0.01$ s, 0.05 s and 0.25 s) to filter out any high-frequency outliers that may be attributed to smaller-scale secondary vortices (Fig. 2b).

The locations of pressure minima for each time step were found for the refined (interpolated) mesh and different averaging periods noted above. An example corresponding to $\Delta T = 0.25$ s is

shown in Fig. 2c. While a spiralling pattern can be discerned, there are still noticeable artifacts (discontinuities) resulting from the limited spatial resolution of the data. The resulting 'path' of the vortex centre was then smoothened by fitting a curve as another form of spatial refinement and the results, for each of the averaging periods, are shown in Fig. 3a and suggest that when viewed in 3D, the vortex wandering trend is analogous to a helix. The 'helices' produced for the two higher averaging periods are very similar, however, the one corresponding to $\Delta T = 0.01$ s shows a greater degree of variation – possibly suggesting the existence of high-frequency secondary vortices close to the vortex centre which remain despite the applied filter.

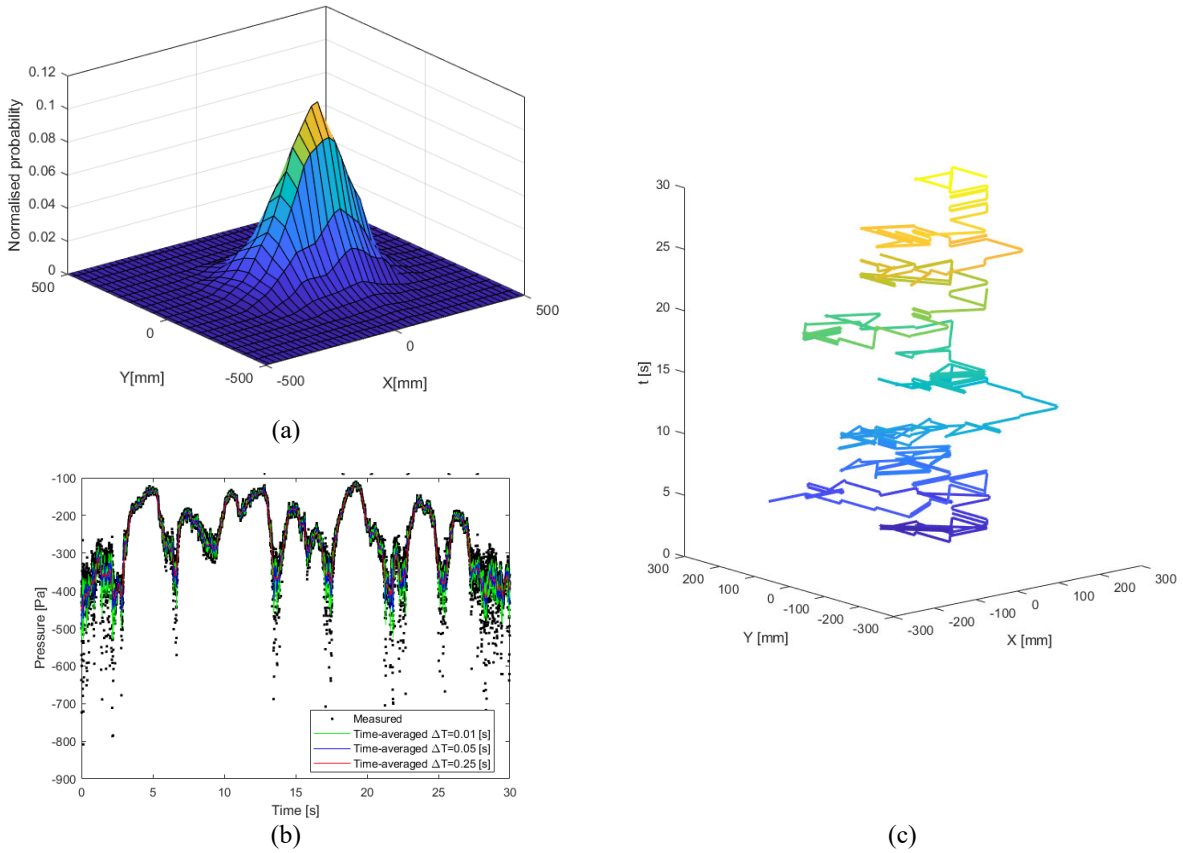


Figure 2. Normalised probability distribution of the location of the vortex centre over time (a), pressure time series over different averaging periods (b) and identified vortex centre coordinates for $\Delta T = 0.25$ s.

Several looping patterns that are repeating in the analysed time period can be distinguished in Fig. 3a. In an attempt to understand this further, an empirical mode decomposition (EMD) was undertaken for the results corresponding to $\Delta T = 0.25$ s. Fig. 3b shows the results of this decomposition for the first three intrinsic mode functions (IMFs), which were sufficient to obtain a mono-component signal (with zero crossings) from the interpolated data, and the residual. It seems that each of these modes may be driving the vortex wandering at different frequencies and over different radii. The results in Fig. 3b should be interpreted with care, as there are several factors that might affect them. For example, the limited spatial resolution of the pressure taps arrangement might result in a more ordered pattern across the measurement time than what happens in reality. Furthermore, the artificial grid refinement and interpolation of the measured

data are expected to aid in mitigating this issue, although its full extent requires further investigations.

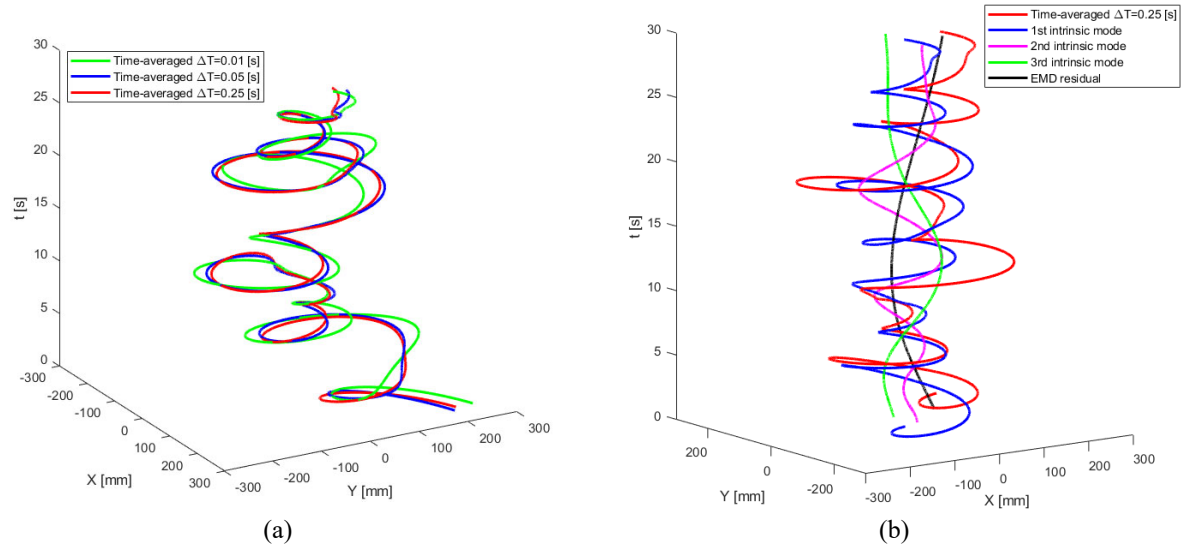


Figure 3. Smoothened coordinates of the vortex centre over time (a) and empirical mode decomposition of the vortex centre locations time series at $\Delta T = 0.25$ s (b).

4. CONCLUSIONS

The results presented in this paper provide a new insight into vortex wandering and suggest that an underlying mechanism may exist which might be possible to explain. However, it is acknowledged that the research is still in its infancy and further analysis is required.

ACKNOWLEDGEMENTS

This work is part of the transnational access project "ERIES-TNG", supported by the Engineering Research Infrastructures for European Synergies (ERIES) project (www.eries.eu), which has received funding from the European Union's Horizon Europe Framework Programme under Grant Agreement No. 101058684. This is ERIES publication number C43.

REFERENCES

Ashton, R., Refan, M., Iungo, G. V. and Hangan, H., 2019. Wandering corrections from PIV measurements of tornado-like vortices. Journal of Wind Engineering and Industrial Aerodynamics 189, 163-172.

Baker, C. J. and Sterling, M., 2018. A conceptual model for wind and debris impact loading of structures due to tornadoes. Journal of Wind Engineering and Industrial Aerodynamics 175, 283-291.

Baker, C. J. and Sterling, M., 2019. Are Tornado Vortex Generators fit for purpose? Journal of Wind Engineering and Industrial Aerodynamics 190, 287-292.

Gillmeier, S., Sterling, M., Baker, C. J. and Hemida, H., 2017. An analysis of non-stationary processes in tornado-like vortices. Physmod 2017 – Intl. Workshop on Physical Modelling of Flow and Dispersion Phenomena, 4-9.

Iungo, G. V., Skinner, P. and Buresti, G., 2009. Correction of wandering smoothing effects on static measurements of a wing-tip vortex. Experiments in Fluids 46, 435-452.

Kopp, G. A. and Wu, C.-H., 2020. A framework to compare wind loads on low-rise buildings in tornadoes and atmospheric boundary layers. Journal of Wind Engineering and Industrial Aerodynamics 204, 104269.

Snow, J. T. and Lund, D. E., 1997. Considerations in Exploring Laboratory Tornadolike Vortices with a Laser Doppler Velocimeter. Journal of Atmospheric and Oceanic Technology 14, 412-426.

Effects of the inflow turbulence on the force and pressure characteristics of a three-dimensional square cylinder by LES

Yoshiyuki Ono [1], Hiroto Kataoka [2]

[1]*Technogy Research Institute, Obayashi Corporation, Kiyose-shi Tokyo, Japan, ono.yoshiyuki@obayashi.co.jp*
[2]*Freelance (Former Technogy Research Institute, Obayashi Corporation), kataoka-hiroto-bs@alumni.osaka-u.ac.jp*

SUMMARY:
This paper examines the impact of oncoming flow turbulence characteristics on the application of CFD to wind-resistant design. LES analysis is performed on the flow around a three-dimensional square cylinder under various inflow turbulence conditions. Based on the computed results, the influence of inflow characteristics on the wind pressure and force of the square cylinder is investigated. The findings reveal that variations in the low-frequency fluctuations of the inflow turbulence lead to differences in the wind pressure and force characteristics, with local wind forces near the base of the cylinder increasing depending on the oncoming flow characteristics.

Keywords: LES, inflow turbulence, wind force characteristics

1. INTRODUCTION

When evaluating wind loads on buildings using CFD, it is crucial to select appropriate computational methods and conditions, and to verify the accuracy of the results by comparing them with reliable wind tunnel experiments and similar benchmarks in advance, utilizing suitable inflow turbulence. The *Guidebook of Recommendations for Loads on Buildings: Wind-induced Response and Load Estimations / Practical Guide of CFD for Wind-Resistant Design* (referred to hereafter as the *CFD Guide*), published by the Architectural Institute of Japan, outlines the computational methods and conditions for evaluating wind loads with CFD, as well as methods for assessing accuracy. One such method is a benchmark test of a three-dimensional square cylinder, as described in the *CFD Guide*. However, recent studies (Tambara et al.) report significant variations in wind pressure and wind force coefficients within both wind tunnel experiments and computational results. It has been suggested that one of the causes for these discrepancies is the influence of oncoming flow turbulence.

In this paper, LES analysis of the flow around a three-dimensional square cylinder is conducted to clarify the effects of oncoming flow turbulence on the wind pressure and force characteristics. The computations are performed using the same methods and conditions but with different inflow turbulence types, and the effects of these variations on the computed results are discussed.

2. COMPUTATIONAL METHOD AND COMPUTATIONAL MODEL

The governing equations for the present computations are the incompressible Navier-Stokes equations and the continuity equation. The computational algorithm is based on the fractional step method, with time integration using the Crank-Nicholson method. Spatial derivatives are

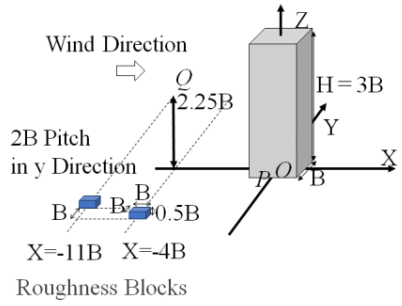


Figure 1. Computational model

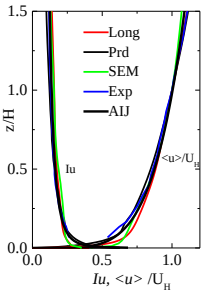


Figure 2. Velocity profile of the generated inflow turbulence

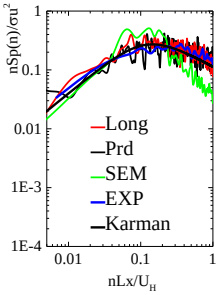


Figure 3. Power spectral densities

computed using a second-order accurate central difference scheme, with a small numerical dissipation added to suppress oscillations.

The computational model is a square cylinder with an aspect ratio (*H*/*B*, *H*: height, *B*: Breadth) of 3, as shown in Fig. 1. The computational grid consists of seven different mesh types, with a resolution of B/100 on the cylinder surface. The computational domain and resolution fully comply with the guidelines in the CFD Guide. The total number of grid points is approximately 13 million. The evaluation time is equivalent to about 50 minutes of actual time.

3. INFLOW TURBULENCE

Table 1. Generating methods of inflow turbulence in the present computations

Case name	Generating method
Long	Reproduction of wind tunnel testing equipment by LES with a long-fetch region
Prd	LES using quasi periodic condition (Lund et al.,1998) followed by a fetch over roughness
SEM	a synthetic-eddy method (Jarrin et al. ,2009) followed by a fetch over surface roughness

The inflow turbulence is generated using three different methods, based on Category III flat terrain from the AIJ Recommendations for Loads on Buildings. Table 1 summarizes the inflow turbulence generation methods used in the present computations. The vertical profiles of mean velocities and turbulence intensities, along with the wind tunnel experiment results, are shown in Fig. 2. The mean velocities approximately match in each case, except near the bottom surface, and the turbulence intensities are also similar across cases. Fig. 3 compares the distribution of power spectral densities at the height of the square cylinder. The Long and Prd cases, generated purely through LES analysis, closely follow the Karman-type distribution, while the SEM case, created using statistical methods, shows lower power in the high-frequency region. This may be due to the insufficient fetch length when inflow turbulence that does not satisfy the governing equations is used as the inflow boundary condition in the SEM case. These inflow turbulence profiles are applied as boundary conditions, and the present LES method is used to simulate the flow around a three-dimensional square cylinder. Additionally, to examine the effect of upstream surface roughness on the wind pressure and force characteristics of the square cylinder, computations are performed for all three types of inflow turbulence in two scenarios: one with the upwind region (with the inflow boundary at about x = -16B) as a smooth surface (referred to as the "without RB"

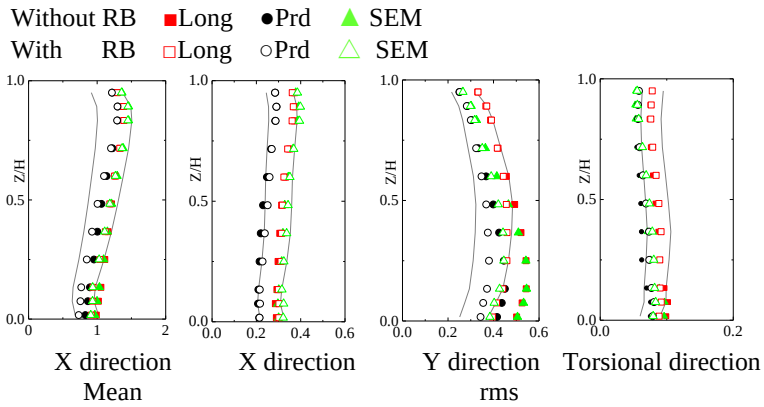


Figure 4. Layer wind force coefficients
The curves show the tolerance range of CFD guide.
The tolerances are set to account for variations in experimental results.

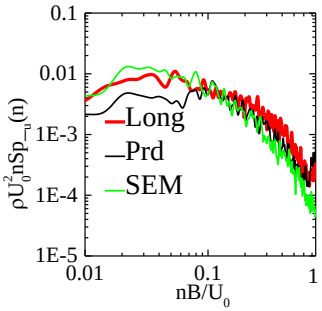


Figure 5. Power spectral densities of velocity fluctuations at x=-4B, z=2.25B

case) and one with two rows of roughness blocks set along the lines shown in Fig. 1 (referred to as the "with RB" case).

4. COMPUTATIONAL RESULTS

Fig. 4 compares the computed vertical distributions of local wind force coefficients, including the tolerance range outlined in the CFD Guide. The wind force coefficients are non-dimensionalized using the width of the square cylinder, B, and the wind velocity, U_H, at the height of the square cylinder. In this computation, the same methods and conditions are applied, so any differences in the results are attributed to the characteristics of the inflow turbulence. Regarding the X and torsional directions, the effect of the presence or absence of roughness blocks (RB) is minimal for each type of inflow turbulence. Examining the fluctuating components reveals variations in the distributions related to the inflow turbulence characteristics; the Long and SEM cases tend to exhibit larger values at each height compared to the Prd case. Fig. 5 presents the distribution of power spectral densities of the fluctuating velocities at the windward point Q (z = 2.25B, x = -4B), as shown in Fig. 1. The Long case demonstrates greater overall power, while the SEM case exhibits slightly less power in the high-frequency component but more in the low-frequency component. Thus, the increase in fluctuations of the local wind forces may be linked to the large-scale fluctuations in the approaching flow.

Here, focusing on the tolerance range specified in the CFD Guide, the results for the X and torsional directions in all cases fall within this range. In contrast, the local wind force coefficients in the Y direction remain within the tolerance range for the cases with roughness blocks (RB). However, in all cases without RB, these coefficients increase from the center height to the bottom of the square cylinder, with the Long and SEM cases significantly exceeding the tolerance range.

Fig. 6 displays the vertical profiles of velocities at the windward position (X/B = -2.35) for the six types of oncoming flow turbulence. In the cases without roughness blocks (RB), there is a recovery of mean velocity near the bottom surface. Additionally, the fluctuating components decrease over a wide range from the bottom surface to near the center height of the square cylinder in the without RB case.

Therefore, it is presumed that the characteristics of the approaching flow are the cause of the increased fluctuating characteristics of the local wind forces in the Y direction near the bottom of the square cylinder. Interestingly, the fluctuation component in the X direction was not significantly affected. It is known that an inverted conical vortex is locally generated near the

bottom of the leading edge on the side face when flow interacts with a three-dimensional square cylinder (Okuda and Taniike, 1993). This conical vortex is generated periodically in association with fluctuations in the wake. However, if the area of negative pressure generation is localized, its effect on the local wind force coefficient is considered to be minimal.

Fig. 7 illustrates the distribution of cross-correlation coefficients of pressure fluctuations on the side when point P on the lower part of the leading edge is used as the reference point. In the cases with roughness blocks (RB), the correlation values increase locally from point P diagonally upward. In contrast, in the cases without RB, high correlation is observed over a wide range, from the bottom of the leading edge to near the central height of the square cylinder. Therefore, the increase in the fluctuating local wind force coefficients in the Y direction for the cases without RB is thought to result from heightened periodic fluctuations of the conical vortex generated at the bottom, which are associated with an increase in mean velocities and a decrease in fluctuations of the approaching flow.

Based on the above, when evaluating the validity of pressure and wind force coefficients acting on a building computed using CFD, it is crucial to confirm the characteristics of the inflow turbulence at the target building location prior to the computations. Additionally, since the results vary depending on the inflow turbulence characteristics, the tolerance range of variation must be considered in the validation process.

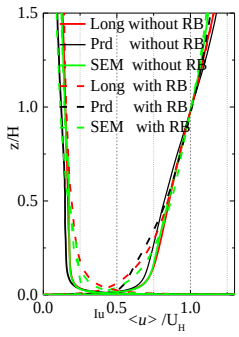


Figure 6. Streamwise Velocity profiles at X/B=-2.35

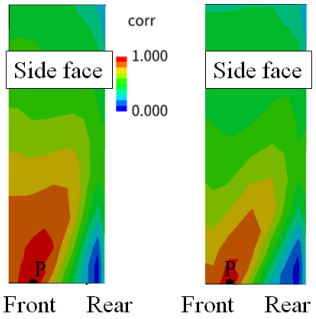


Figure 7. Distribution of cross-correlation coefficients of pressure fluctuations (SEM case)

5. CONCLUSIONS

The LES analysis was conducted using three different types of inflow turbulence to clarify the effects of inflow turbulence on the force characteristics of a three-dimensional square cylinder. The results indicate that the wind force coefficient varies depending on the low-frequency fluctuation components of the inflow turbulence, although they remain within the tolerance range specified in the CFD Guide. Additionally, the effect of the upwind conditions of the square cylinder was investigated. In cases where no roughness blocks were present in the upwind region, the local wind force coefficient in the Y direction increased, exceeding the tolerance range set by the CFD Guide. This is thought to be related to an increase in the periodic fluctuations of the conical vortex near the bottom of the square cylinder, which is associated with the recovery of the oncoming flow.

REFERENCES

Architectural Institute of Japan, 2017. Guidebook of recommendations for loads on buildings 2 –Wind-induced response and load estimation /Practical guide of CFD for wind resistance design-.

Okuda, T., Taniike, Y.,1993. Conical vortices over side face of a three-dimensional square prism. J. Ind. Aerodyn., Vol. 50, pp. 163-172.

Tambara, C., Ono, Y., Iida, Y. & Tamura, T.,2018. Study on characteristics of local suction and evaluation of peak wind pressure coefficients of a three-dimensional square cylinder based on les high-resolution computations. In Proceedings of 25th National Symposium on Wind Engineering, 2018, pp. 229–234.

Application of lattice Boltzmann method-based large-eddy simulation in flow around an isolated building

Mengtao Han [1], Hideki Kikumoto [2], Ryozo Ooka [3]

[1]*Huazhong University of Science and Technology, Wuhan, China, hanmt@hust.edu.cn*
[2]*The University of Tokyo, Tokyo, Japan, kkmt@iis.u-tokyo.ac.jp*
[3] *The University of Tokyo, Tokyo, Japan, ooka@iis.u-tokyo.ac.jp*

SUMMARY:
This study implements lattice Boltzmann method-based large eddy simulation (LBM-LES) in a high turbulent flow around an isolated building to investigate its simulation accuracy and computational cost in the outdoor CFD field. We first discuss the impacts of LBM simulation parameters on results accuracies, such as grid resolutions, sub-grid scale models, wall boundary conditions, discrete-velocity schemes, and relaxation time schemes. We also introduced the wall-function bounce boundary for LBM, incorporating the wall-function model and improving the near-wall accuracy. Subsequently, we concluded a set of recommended LBM-LES parameters for outdoor wind simulations. At last, simulation accuracy and results cost are compared between finite volume method-based LES and LBM-LES.

Keywords: lattice Boltzmann method, large-eddy simulation, parametric study, wall-function bounce, computational cost

1. INSTRUCTIONS

The lattice Boltzmann method (LBM) has been applied to outdoor turbulent flows during the last decade. LBM-based large-eddy simulation (LBM-LES) can solve the high turbulent flow without dealing with the Poisson equation. This advantage lets LBM-LES compute much faster than the finite volume method-based LES (FVM-LES). LBM shows more potential in high-speed LES simulations for complex and large-scale outdoor flows owing to its considerably simpler algorithm and the simplicity of boundary condition implementation. This study implements LBM-LES simulations of the flow around an isolated building to discuss the impacts of LBM simulation parameters on results accuracy. A set of recommended LBM-LES parameters for outdoor wind simulations is then concluded by introducing a developed wall boundary condition. This study also compares LBM-LES with FVM-LES in results accuracy and computational cost.

2. OUTLINE OF LBM-BASED LES

Based on the lattice Boltzmann equation (Eq. (1)), LBM simulates the fluid motion process by assuming a collection of colliding particles and stream behavior for their distribution functions. Here, Δt represents discrete time, $\boldsymbol{e}_i$ is the particles' speed in the i-direction, $f_i(\boldsymbol{r},t)$ is the distribution function for particles moving in the i-direction.

$$f_i(\boldsymbol{r}+\boldsymbol{e_i}\Delta t, t+\Delta t) - f_i(\boldsymbol{r},t) = \boldsymbol{\Omega}[f_i(\boldsymbol{r},t)] \quad (1)$$

$\boldsymbol{\Omega}[f_i(\boldsymbol{r},t)]$ is the collision function, for which the Bhatnagar-Gross-Krook (BGK) scheme (Eq. (2a), Bhatnagar et al., 1954) and multi-relaxation time (MRT) scheme (Eq. (2b), d'Humieres et al., 2002) are the most popular models. $f_i^{\mathrm{eq}}(\boldsymbol{r},t)$ is the equilibrium function of $f_i(\boldsymbol{r},t)$, τ is the relaxation time, $\boldsymbol{M}$ is a matrix structured for transforming distribution functions into moments,

$\boldsymbol{M^{-1}}$ is the inverse of the matrix $\boldsymbol{M}$, and $\boldsymbol{S}$ is the relaxation coefficient diagonal matrix.

$$\boldsymbol{\Omega}[f_i(\boldsymbol{r},t)] = -\frac{1}{\tau}[f_i(\boldsymbol{r},t) - f_i^{\mathrm{eq}}(\boldsymbol{r},t)] \quad (2a) \qquad \boldsymbol{\Omega}[f_i(\boldsymbol{r},t)] = -\boldsymbol{M^{-1}SM}[f_i(\boldsymbol{r},t) - f_i^{\mathrm{eq}}(\boldsymbol{r},t)] \quad (2b)$$

As Eq. (3a), the total viscosity ν_{total} is comprised of molecular viscosity ν and sub-grid scale (SGS) viscosity ν_{SGS} in LES. For LBM, one can use any popular SGS model to obtain ν_{SGS} and total relaxation time τ_{total} by Eq. (3b), in which e_s is the particles' sound speed. τ_{total} can replace τ in Eq. (2a) or corresponding τ in matrix $\boldsymbol{S}$ in Eq. (2b) to perform LBM-LES.

$$\nu_{\mathrm{total}} = \nu + \nu_{\mathrm{SGS}} \quad (3a) \qquad \nu_{total} = {e_s}^2(\tau_{\mathrm{total}} - 0.5)\Delta t \quad (3b)$$

3. OUTLINE OF LBM-LES SIMULATED FLOW AROUND AN ISOLATED BUILDING

A benchmark case of a flow field around a building with a scale ratio of 2*b*:*b*:*b* (height:width: depth) placed within a turbulent boundary layer was implemented. This case was provided in the CFD guidebook of the Architectural Institute of Japan (AIJ, 2016). Table 1 and Fig. 1 illustrate the simulation conditions and analysis domain for LBM-LES and FVM-LES (hereinafter abbreviated to LBM and FVM). The Reynolds number based on b (building width = 0.16 m) and U_{ref} (inflow velocity at $z = b$; 3.824 m/s) was approximately 40800. The detailed measurement reported (Meng, T., Hibi, 1998) was employed. Results were normalized using b and U_{ref}.

Table 1. Simulation conditions and case settings

Item	LBM-LES	FVM-LES
SGS model	Smagorinsky (c_k= 0.12) / WALE SGS model	
domain	21.5 *b* (*x*) × 13.75 *b* (*y*) × 11.25 *b* (*z*)	
period	Preparatory: 1 min, average: 1 min	
Inlet B.C.	Inflow turbulence data obtained from LES of urban boundary layer flow in a wind tunnel	
Outlet B.C.	Gradient-zero	
Wall B.C.	bounce-back / wall-function bounce (WFB)	wall function
Case settings	Grid resolution: *b*/8, *b*/16, *b*/32 (*b*/8 for FVM) SGS model: Smagorinsky, WALE Relaxation time scheme: BGK, MRT Discrete velocity scheme: D3Q9, D3Q27 Wall boundary: bounce-back, WFB	

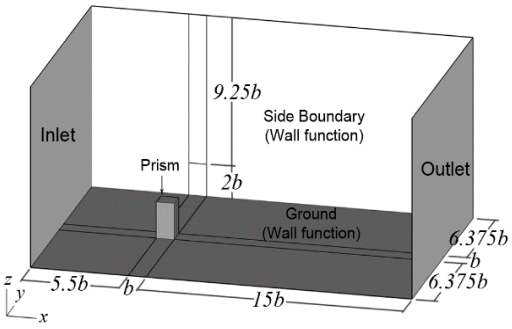


Figure 1. Analysis domain

4. SIMULATION RESULTS AND DISCUSSION ON LBM-LES PARAMETERS

4.1. Grid resolutions and SGS model

Grid independence analysis is a very preliminary but essential task. We go through three grid resolutions. Bounce-back boudnary is employed for all solid wall boundaries. MRT and D3Q19 schemes, and the WALE SGS model are utilized. Fig. 2 depicts the time-averaged velocity for the three grid resolutions within the near-ground horizontal section. (Han et al., 2020). The velocity is underestimated at almost all points in b/8. b/16 and b/32 show sufficient accuracy in this study.

In addition to the grid resolution, the choice of the SGS model is another fundamental issue. Fig. 3 takes b/16+MRT+D3Q19 as an example to explore3 explores the influence of the Smagorinsky model and WALE model, which is more prevalent in the field of the built environment in recent years., based on *b*/16+MRT+D3Q19. Results demonstrate that the difference between the two SGS models is very slight for the difference between the two SGS models is very slight for the time-averaged velocity. In comparison, WALE improves the turbulent kinetic energy (TKE) accuracy to a certain extent in the areas with higher turbulence intensity near the ground, such as the impinging and stripping region on the lateral side of the building.

4.2. Relaxation time scheme and discrete velocity scheme

This section discusses the effects of relaxation time schemes (SRT or MRT) and discrete velocity schemes (D3Q19 or D3Q27) on result accuracy. Fig. 4 shows the time-averaged velocity at the vertical section. SRT causes pronounced spatial oscillations near the roof, while MRT diminishes the oscillations. Nevertheless, MRT only shows a minor improvement in the accuracy of the results compared to SRT. D3Q27 does not reduce the oscillations but overestimates the near-roof velocity.

4.3. Wall boundary condition: bounce-back versus wall-function bounce

According to previous results, more significant errors are produced at near-ground regions when near-wall grids are coarse. This is partly due to the standard bounce-back (BB) boundary limitations, which correspond to the no-slip boundary and cannot catch the accurate shear drag. We proposed a wall-function bounce (WFB) boundary (Han et al., 20232021a, 2021b), which improves BB and incorporates a wall-function model. Fig. 5 shows the near-wall velocity by BB and WFB under different grid resolutions. BB underestimates the averaged velocity using coarse grids (*b*/8), and the underestimation is more significant in the high-speed regions. Meanwhile, WFB compensates for the underestimation in all areas. The WFB's compensation decreases with the improvement of grid resolutions and finally approaches similar to BB at *b*/32. However, in some key areas, when using grid resolutions of *b*/8, discrepancies between WFB and experimental data are observed, whereas the WFB with *b*/16 and *b* /32 agrees well with the experimental data.

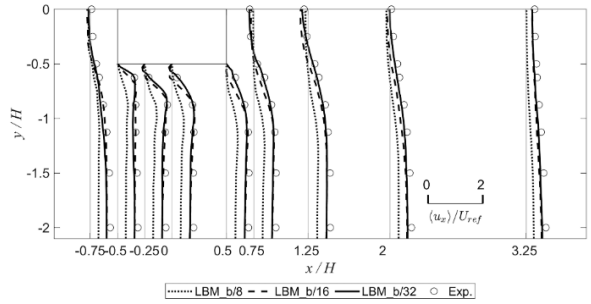


Figure 2. Near-ground $\langle u_z \rangle$ of various grid resolutions

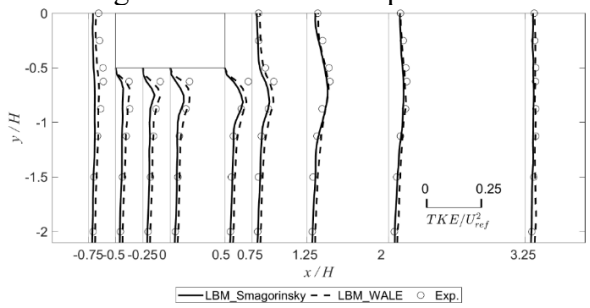


Figure 3. Near-ground TKE of various SGS models

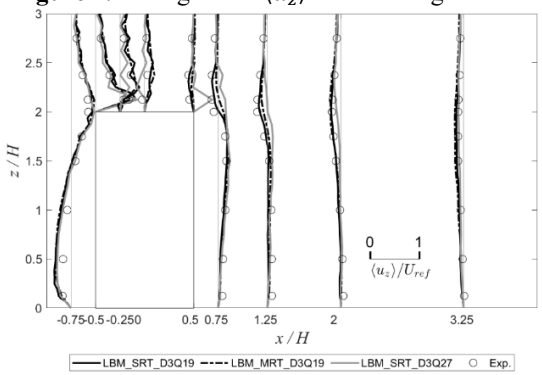


Figure 4. $\langle u_z \rangle$ of various relaxation time schemes and discrete velocity schemes at vertical section

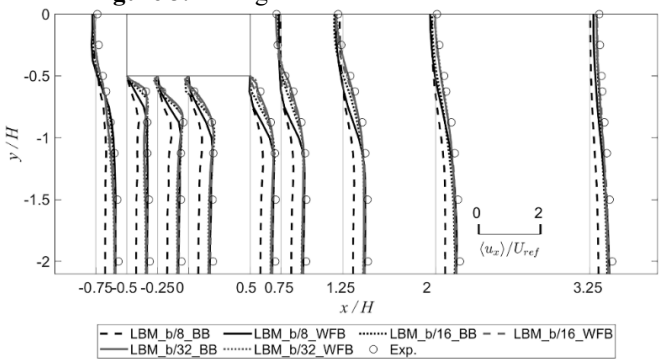


Figure 5. Near-ground $\langle u_z \rangle$ of various relaxation time schemes and discrete velocity schemes

5. COMPARISON BETWEEN LBM-LES AND FVM-LES IN RESULTS ACCURACY AND COMPUTATIONAL COST

LBM with "*b*/8 or *b*/16+WALE+MRT+D3Q19" yielded the best accuracy and thus is compared with FVM_*b*/8 using Mean error (ME, Eq. (4), Han et al., 2023). Here, $\Phi_{\mathrm{LBM\ or\ FVM}(i)}$ represents LBM or FVM-simulated quantity at point *i*, while $\Phi_{\mathrm{EXP}(i)}$ is the corresponding experimental value. *N* is the total number of measurement points. A smaller ME indicates a smaller difference

between simulation and experiment and higher simulation accuracy. Fig. 6 shows ME of the averaged and fluctuating velocities. LBM's ME decreased with the increase in grid resolution, and the ME of LBM_*b*/16BB is generally at the same level as FVM_*b*/8. This indicates that LBM using default BB wall boundary requires higher grid resolution to obtain comparable accuracy with FVM in the outdoor wind simulation (LBM requires half the grid length of the FVM in this study). In contrast, ME of LBM_*b*/8WFB significantly declines and is comparable to FVM_*b*/8, indicating that WFB can effectively improve LBM's accuracy to that of FVM with the same grid resolution.

$$\mathrm{ME} = \frac{1}{N}\sum_{i=1}^{N}\left|\Phi_{\mathrm{LBM\ or\ FVM}(i)} - \Phi_{\mathrm{EXP}(i)}\right| \tag{4}$$

Fig. 7 shows the parallel computing performance of LBM_*b*/8WFB and FVM_*b*/8. The computational time ratio (CTR) is about 14-17, indicating that the computational time of FVM is about 14-17 times that of LBM when using the same CPU cores. Parallel computing efficiency (PCE, = single-core / multi-core computational time) of both FVM and LBM increases with CPUs; FVM's PCE is about 6-13, while LBM's PCE can reach 15-25. This implies that the parallel computation performance of LBM is more outstanding than FVM, and the improvement of the parallel computation performance of LBM is more evident with the increase of core numbers.

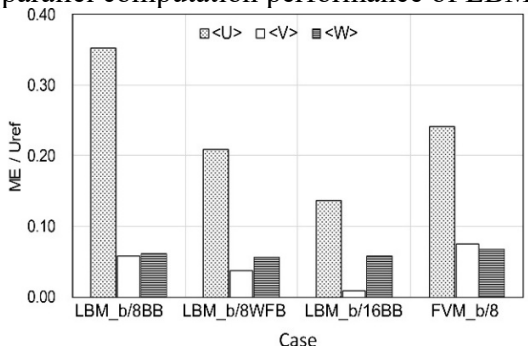


Figure 6. ME of LBM_*b*/8, *b*/16 and FVM_*b*/8 for BB and WFB

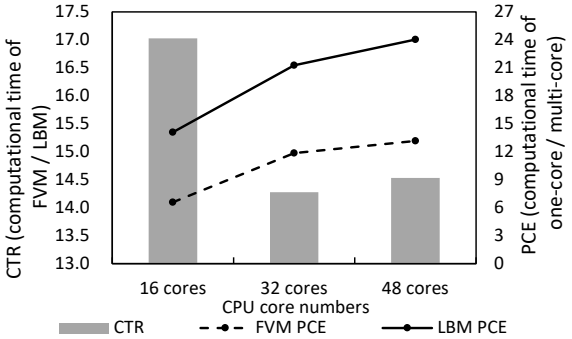


Figure 7. Parallel computational performance (LBM_*b*/8WFBvs.FVM_*b*/8)

56. CONCLUSIONS

This study conducted LBM-LES to the flow field around an isolated building and discussed the impact of LBM simulation parameters on result accuracies. We concluded a set of recommended parameters for outdoor wind LBM simulation, with which LBM can reach the same accuracy level as FVM: *b*/8 for grid resolutions with WFB for wall boundary, WALE SGS model, MRT for relaxation time scheme, and D3Q19 for discrete velocity scheme. LBM shows ten times the computational speed of FVM and more significant parallel computation performances than FVM.

ACKNOWLEDGEMENTS

This research was supported by the National Natural Science Foundation of China (Project No. 52208059).

REFERENCES

AIJ, 2016. AIJ Benchmarks for Validation of CFD Simulations Applied to Pedestrian Wind Environment around Buildings Architectural Institute of Japan.

Bhatnagar, P.L., Gross, E.P., Krook, M., 1954. A model for collision processes in gases. I. Small amplitude processes in charged and neutral one-component systems. Phys. Rev. 94, 511–525.

D'Humières, D., Ginzburg, I., Krafczyk, M., Lallemand, P., Luo, L.S., 2002. Multiple-relaxation-time lattice Boltzmann models in three dimensions. Philos. Trans. R. Soc. A Math. Phys. Eng. Sci. 360, 437–451.

Han, M., Ooka, R., 2023. Large-Eddy Simulation Based on the Lattice Boltzmann Method for Built Environment Problems. Springer Nature Singapore, Singapore.

Meng, Y., Hibi, K., 1998. Turbulent measurments of the flow field around a high-rise building. Wind Eng. JAWE 1998, 55–64.

CFD analysis of louvre blade designs on rooftop for enhancing wind energy potential

Yu-Hsuan Juan [1,2*], Wan-Yi Chen [1,2], Ting-Yu Wei [1]

[1] *Department of Mechanical Engineering, National Taipei University of Technology, Taipei, Taiwan, yhjuan@ntut.edu.tw*
[2] *Research Center of Energy Conservation for New Generation of Residential, Commercial, and Industrial Sectors, National Taipei University of Technology, Taipei, Taiwan, t113669010@ntut.org.tw*

SUMMARY:
This paper investigates the improvement of the potential of urban wind energy by incorporating with various louvre blade designs on building rooftops. As wind energy plays a crucial role in reducing carbon emissions and supporting energy sustainability, optimizing its use on rooftops through the integration of wind turbines and solar canopies offers a promising approach for sustainable urban development. The study focuses on using CFD to analyze louvre blade designs, specifically the placement and quantity, on a single high-rise building. The results identified the best locations for wind turbines and highlighted the potential for increased energy generation. These researches contribute to the growing knowledge on the integration of renewable energy in urban environments and provide practical solutions for Net-Zero construction and urban sustainability.

Keywords: Urban Wind Energy, Computational Fluid Dynamics, Louvre Blade Designs

1. INTRODUCTION

In recent years, rooftops in urban areas have evolved from merely serving as building coverings to becoming potential sites for renewable energy generation, particularly given the limited and complex available space in cities. We draw inspiration from the PowerNEST design, which combines efficient wind capture mechanisms with solar power systems, developed by IBIS Power in the Netherlands to investigate urban wind energy potential. This design can effectively improve wind speed and power (Patankar et al., 2016). Therefore, this research aims to explore the potential and practical benefits of louvre blade designs in further enhancing urban wind energy capabilities.

2. METHODOLOGY

This research explores the airflow distribution for various cases of louvre blades installed between the rooftop and the canopy on the windward side by using ANSYS Fluent® 19.2. The length (L) and width (W) of the canopy are both 20 m with a thickness of 0.2 m, positioned 6 m above the rooftop of a single full-scale building whose dimensions is $20 \times 20 \times 40$ m^3, as presented in Fig. 1(a). Fig. 1(b) shows that the main louvre blade thickness (D_W, D_H) is 0.2 m and the length of the louvre blades at the windward side (D_L) is 2 m. The study scenarios detailing the setting direction and arrangements of louvre blades are displayed in Table 1.

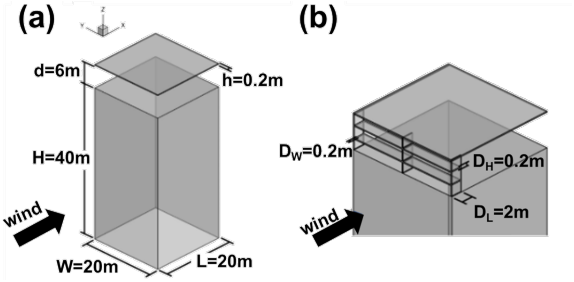


Figure 1. (a) Building with the canopy and (b) louvre blade configurations in cases

Table 1. List of Cases.

Case Name	Arrangements of louvre blades	Amounts of louvre blades
Case[Ref]	-	-
Case[H1]	Horizontal	1
Case[H2]	Horizontal	2
Case[H3]	Horizontal	3
Case[V1]	Vertical	1
Case[V2]	Vertical	2
Case[V3]	Vertical	3

Fig. 2 illustrates the schematic diagram of the boundary conditions set in the CFD calculation domain, measuring 840 m in length, 420 m in width, and 240 m in height. The distance from the inlet boundary to the windward side of the building and the side boundaries of the y-z plane from the building cluster are set at 5 times the height of the buildings (H). Furthermore, the distance to the upper boundary is defined as 6H, while the outlet from the buildings is set at 15H. These parameters are designed to prevent recirculation phenomena that can lead to iteration divergence as airflow interacts with the buildings. Based on turbulence model validation, the results indicated that the Reynolds Stress Model (RSM) provided the closest predictions to wind tunnel experimental data. Therefore, the RSM model was selected for simulation in this study.

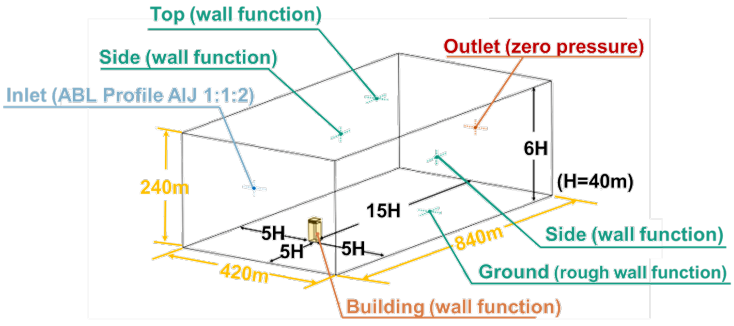


Figure 2. Computational domain and boundary conditions for CFD simulations

3. RESULTS & DISCUSSIONS

In the study, the predicted I_{ref} and wind power density (PD) values are utilized as key parameters to assess the wind energy potential. The formula of I_{ref} (IEC, 2013) and PD (Juan et al., 2022) are calculated as:

$$I_{ref} = \frac{TI}{0.75+\frac{5.6}{V}} \quad (1)$$

$$PD = \frac{1}{2}\rho V^3 \quad (2)$$

where *TI* stands for Turbulence intensity, V denotes the air velocity in three axial directions, and ρ signifies the air density (=1.225 kg/m^3). Based on the IEC 61400-2 standard (IEC, 2013) established by the International Electricity Commission, there is a reference I_{ref} limit for each wind turbine. Thus, I_{ref} of 0.16 is set as the threshold of the acceptable turbulence level in this paper.

3.1. Impact of Horizontal Louvre Blades on Rooftop

Contour plots of the dimensionless power density for cases with different amounts of horizontal louvre blades as presented in Fig. 3. In the vertical cross-section, Case H1 with a single horizontal blade shows a high wind power density of 2.2 at Y/H=0.0625. With two (Case H2) and three horizontal blades (Case H3), the wind energy density increases to 2.6 within the range of X/H=-0.25 to -0.2, representing a 7.8% enhancement. While the I_{ref} values are not below the 16% standard in the height range of Z/H=1 to 1.06, the high wind energy density areas indicated suitability for installing micro wind turbines. In addition, the analysis reveals that Case H3 significantly reduces the area of excessive turbulence from 43.85% to 35.64% compared to Case Ref. Based on the power density distribution, Case H3 achieves a 40% increase to 2.52, while Case H2 further boosts wind power density to 2.8, representing a 55% total improvement over Case Ref.

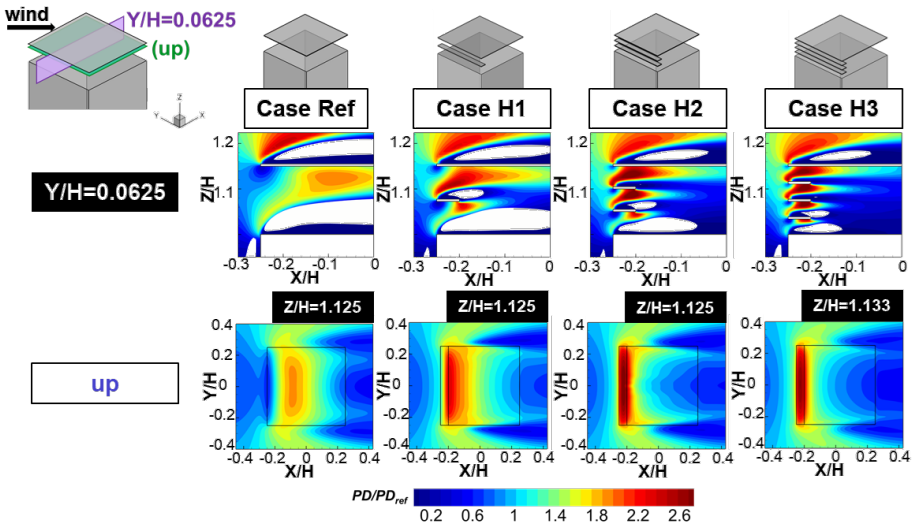


Figure 3. Contour plots of the dimensionless power density in vertical and horizontal planes for cases with different amounts of horizontal louvre blades (white areas indicate regions with unacceptable turbulence).

3.2. Impact of Vertical Louvre Blades on Rooftop

Fig. 4 demonstrates the predicted dimensionless power density in contours. In the vertical cross-section analysis, all cases with vertical louvre blades show non-compliance with turbulence standards within the height range of Z/H=1 to 1.08 at Y/H=0.0625. However, Case V3 displays uniform and stable wind power density above this height, highlighting the potential to enhance the stability of wind power resources. In the upper cross-section, Case V1 with a single vertical deflector blade exhibits the best performance, showing a larger area with a wind energy density of 1.9 (a 20% improvement) in the range of X/H = -0.175 to -0.025. However, Case V3 does not

significantly improve wind power density behind the blades, indicating that adding more blades did not necessarily enhance the effect.

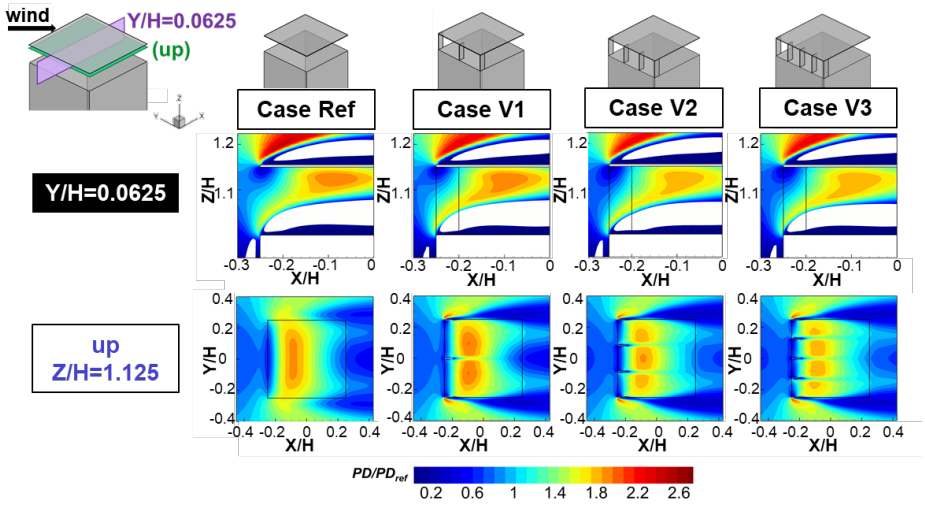


Figure 4. Contour plots of the dimensionless power density in vertical and horizontal planes for cases with different amounts of vertical louvre blades (white areas indicate regions with unacceptable turbulence).

4. CONCLUSIONS

The study examines the impact of various louvre blade arrangements and quantities on wind *PD* and I_{ref} above a single building. For louvre blade arrangements, vertical louvre blades increase wind power density by up to 21.5% behind the blades and horizontal louvre blades improve wind power density between the blades by up to 35% compared to Case Ref. Regarding the number of louvre blades, horizontal configurations show a decrease in wind power density behind the blades. In vertical configurations, Case V1 increases wind power density by up to 25.3%. The results highlight optimal louvre blade designs for enhancing urban wind energy generation. A future study will investigate the wind energy potential when the building is embedded between surrounding structures, assessing the impact of wake interference and altered wind flow patterns on energy harvesting efficiency.

ACKNOWLEDGEMENTS

The authors appreciate the financial support from National Science and Technology Council, Taiwan under grant number NSTC 113-2628-E-027-001. The authors also appreciate the financially supported by the "Research Center of Energy Conservation for New Generation of Residential, Commercial, and Industrial Sectors" from The Featured Areas Research Center Program within the framework of the Higher Education Sprout Project as well as the "Sustainable City Integrated Green Technology Interdisciplinary Talent Cultivation" from The Institution of Higher Education STEM Fields and Women Researcher Cultivation Subsidy Program by the Ministry of Education in Taiwan.

REFERENCES

IEC., 2013. Wind Turbines Part 2: Design Requirements for Small Wind Turbines. IEC 61400-2.

Juan, Y.-H., Rezaeiha, A., Montazeri, H., Blocken, B., Wen, C.-Y., & Yang, A.-S., 2022. CFD assessment of wind energy potential for generic high-rise buildings in close proximity: Impact of building arrangement and height. Applied Energy, 321, 119328.

Patankar, B., Tyagi, R., Kiss, D., & Suma, A. B., 2016. Evaluation of an Integrated Roof Wind Energy System for urban environments. Journal of Physics: Conference Series, 753(10), 102007.

Quality control of CFD analysis of virus-laden droplet transmission in indoor environments

Xuelin Zhang [1], Xiaodan Fan [1], A. U. Weerasuriya [2]

[1]*School of Atmospheric Sciences, Sun Yat-sen University, Southern Marine Science and Engineering Guangdong Laboratory, Zhuhai, China, zhangxlin25@mail.sysu.edu.cn*
[2]*Department of Construction and Quality Management, School of Science and Technology, Hong Kong Metropolitan University, Ho Man Tin, Hong Kong, China, auw@connect.ust.hk*

SUMMARY:
Computational Fluid Dynamics (CFD) simulation has emerged as the main technique for simulating the paths of indoor droplets and assessing the infection risk. The accuracy of CFD simulation is highly influenced by numerical parameters. This study investigates the effects of mesh configurations, manikin models, droplet size distributions, thermal boundary conditions, and droplet-droplet interaction on droplet dispersion through CFD simulations. The results suggest that Polyhexcore grids with prism layers at a first layer height of 1 mm exhibit small simulation errors and short computation times, making them an optimal choice. The simplified human model is not recommended since it alters droplet dispersion pathways and deposition distribution on occupant surfaces. The simplified droplet size distribution highly underestimates droplet deposition fraction on the occupants. Compared to uniform temperature on body surfaces, the method of heat fluxes enhances the thermal plume around the occupants, increasing the number of suspended droplets, but has a small impact on the deposition on occupants. Droplet-droplet interactions have little effect on the dispersion and distribution.

Keywords: Droplet dispersion, Numerical parameters, droplet-droplet interaction

1. INTRODUCTION

CFD simulation has been widely used for simulating droplet dispersion. Several computation parameters, such as mesh configuration, manikin model, droplet size distribution, thermal boundary conditions, and droplet-droplet interaction, can affect the accuracy of droplet dispersion simulations. Various settings and values have been used for these parameters without having a universal agreement among CFD modelers. This study is the first step towards establishing the best practice guidelines for CFD simulation of droplet dispersion to ensure accuracy and generality. To this end, this study investigates the effects of different settings of these parameters on droplet dispersion and distribution.

2. METHODOLOGY

We selected a fever clinic room as a typical indoor environment, which includes one doctor and one patient. Fig. 1(a) illustrates the main structure and layout of the room. The distance between them is 1.1 m, and both exhale droplets at a speed of 2.3 m/s, which is consistent with the experiments conducted by (Zhou et al., 2021). The surface temperature of the human body is set as 304 K. To validate our results, we compared wind speed at the inlet centerline and droplet

concentration 0.6m in front of the doctor from both simulations and the experiment, with errors below 5% (Fig. 1(c)).

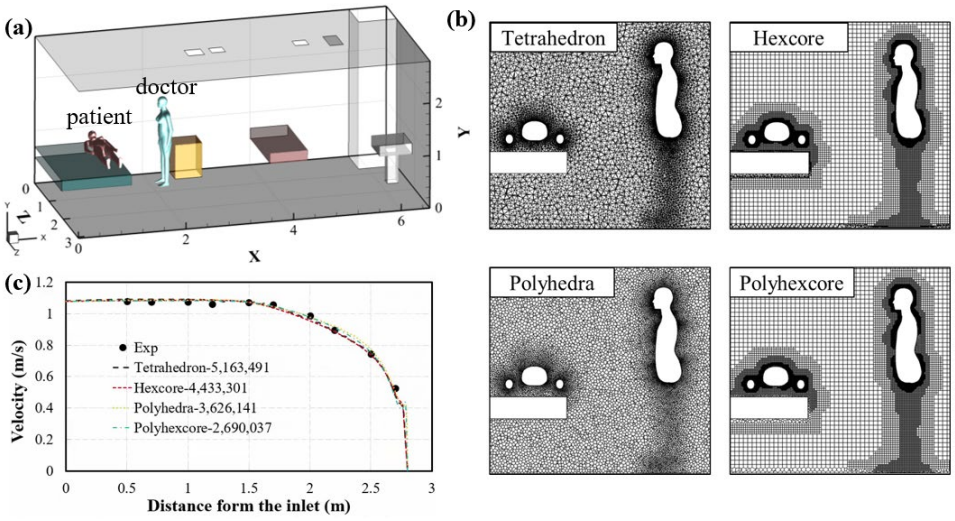


Figure 1. (a) The main structure of the fever clinic, (b) four types of mesh, and (c) Air velocity of experiment and simulation results.

3. RESULTS AND DISCUSSION

3.1. Effects of mesh types and resolutions

In the first step, we compared the simulation accuracy of four different grid configurations (Tetrahedron, Hexcore, Polyhedra, and Polyhexcore cells). Table 1 shows the average relative error of air velocity and droplet concentration between the simulation and experimental data. Except for the Hexcore grid, the wind speed errors for the other three grids were all under 3%. Besides, the Polyhedra grid requires the longest simulation time among them. Therefore, the Polyhexcore mesh was recommended for its lower relative error in predicting air velocity and droplet concentration, as well as its reduced computational time. We further evaluate the impacts of near-human grid resolutions on the accuracy of the simulation. Prism layers with three different first layer heights (0.2 mm, 1 mm, and 5 mm) were generated on the body surfaces, resulting in relative errors in droplet concentration of 1.76%, 2.54%, and 4.05%. To save computational resources, Polyhexcore grids with a first layer height of 1 mm ($y+ < 5$) were used.

Table 1. The relative error and computing time of four types of mesh.

Type of mesh	Numbers of cells	Relative error between CFD and Exp		Relative computing time
		Air velocity	Droplet concentration	
Tetrahedron	5.16 million	2.54 %	3.12 %	1
Hexcore	4.43 million	4.33 %	-	0.92
Polyhedra	3.63 million	1.92 %	-	1.85
Polyhexcore	2.69 million	2.11 %	3.31 %	0.78

3.2. Effects of manikin model simplification

In this section, we selected two human models: 3D-scanned realistic models and simplified cylindrical models (Fig. 2(a)). The droplet dispersion study commonly used the latter to save grid

resources. However, as shown in Fig. 2, compared to the 3D-scanned human model, the simplified model exhibits a stronger upward dispersion of exhaled droplets, leading to greater deposition on the ceiling or escape through the outlet. Additionally, changes in the dispersion trajectories of exhaled droplets from both individuals resulted in a 1.09% decrease in deposition on the simplified patient's arm, while deposition on the head increased by 0.79%. Therefore, we recommend using 3D-scanned models for indoor environment simulations whenever feasible.

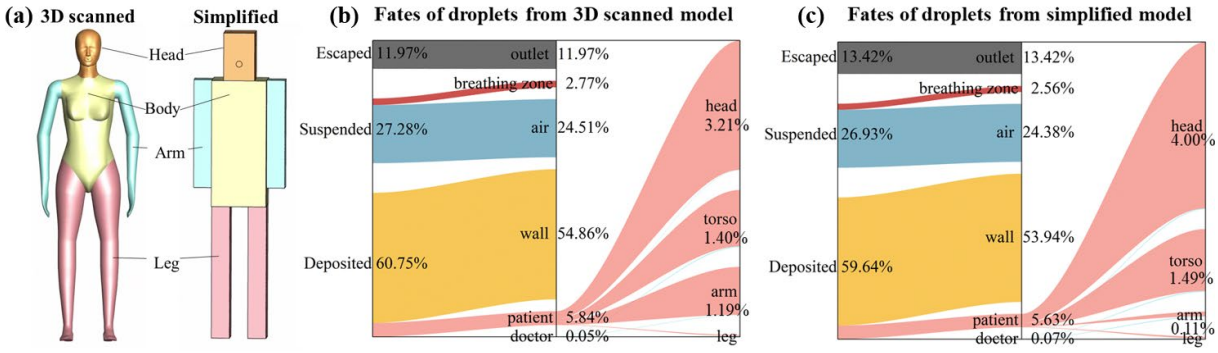


Figure 2. (a) The schematic diagrams of two human body models, and the distribution of droplets released from the (b) 3D-scanned model and (c) simplified model.

3.3. Effects of droplet size distribution

We further analyzed droplet dispersion under two different size distributions. The first distribution is based on speaking droplet size data measured by (Chao et al., 2009), with sizes ranging from 3 to 375 μm. The second is a simplified distribution, where the occupants release five equal quantities of droplets with sizes of 1, 10, 20, 50, and 100 μm. In both cases, the total number of droplets released is the same. As shown in Fig. 3(a), droplets smaller than 20 μm primarily remained suspended in the air, while droplets with sizes of 50 μm and 100 μm were mainly affected by gravity and settled downward. In the realistic droplet size distribution, more droplets in the 20-50 μm range were suspended in the breathing zone. Fig. 3(b) compared the droplet distribution for both cases, showing that the simplified size distribution significantly underestimates the deposition on the patient's body surface by 5.41%.

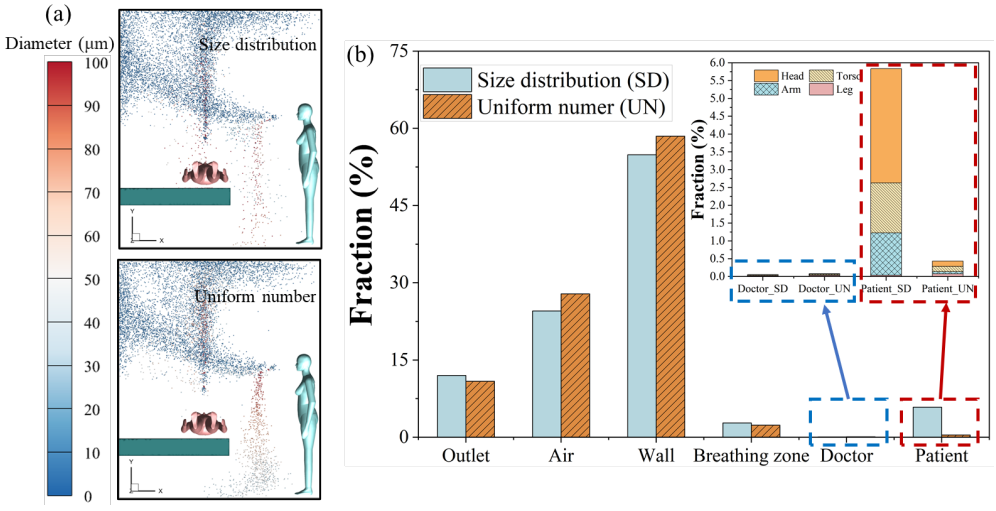


Figure 3. (a) Dispersion of droplets with real size distribution and uniform number in five size classes, and (b) distribution of exhaled droplets.

3.4. Effects of thermal boundary conditions and droplet-droplet interaction

In indoor environments with low airflow velocities, the flow patterns are often influenced by the thermal plumes from the human body. Previous studies typically employed two approaches to set the thermal boundary conditions on the human surface: (1) a uniform temperature across all surfaces, and (2) different heat fluxes for various body segments based on the temperature and heat transfer coefficient between the body and the environment (de Dear et al., 1997). We compared the effects of these two settings on droplet dispersion and found that using heat fluxes enhanced the upward thermal plumes around the human body, causing droplets on the patient's left side to disperse more upward. As a result, fewer droplets settled on the ground, while more escaped through the exit. However, since the thermal plume could not influence the strong exhaled airflow near the occupants, the difference in droplet deposition on the body surface was minimal in both cases. In addition to thermal boundary conditions, droplet-droplet interactions such as collisions, breakup, and coalescence also affect droplet dispersion pathways and concentration distributions. Previous studies suggested that the low Weber number and low concentration of respiratory droplets minimize the impact of such interactions; however, no quantitative comparisons have been conducted. To address this, we applied stochastic collision modelling and the Taylor Analogy Breakup model to account for collisions, breakup, and coalescence between droplets. The results showed that, aside from a 0.5% reduction in suspended droplets within the breathing zone, the overall droplet distribution remained largely consistent.

4. CONCLUSIONS

This study examined the influence of mesh configurations, manikin models, droplet size distributions, thermal boundary conditions, and droplet-droplet interaction on the droplet transmission pattern and distribution. The results suggest that Polyhexcore grid with prism layers at a first layer height of 1 mm exhibits low simulation errors and short computation times. The simplified human model alters droplet dispersion pathways and deposition distribution on the body surface. The simplified particle size distribution underestimates droplet deposition on the patient by 5.41%. When compared to the uniform temperature, heat flux thermal boundary conditions strengthen the thermal plume around the body, increasing the number of suspended droplets but having minimal effect on droplet deposition on human body surfaces. Droplet-droplet interactions have little effect on the dispersion pattern.

ACKNOWLEDGEMENTS

This study is partly supported by the National Natural Science Foundation of China (No. 42175180, No. 42475185) and the Innovation Group Project of Southern Marine Science and Engineering Guangdong Laboratory (No. 311020001).

REFERENCES

Zhou, Y., and Ji, S., 2021. Experimental and numerical study on the transport of droplet aerosols generated by occupants in a fever clinic. Building and environment, 187, 107402.

Chao, C. Y. H., Wan, M. P., Morawska, L., Johnson, G. R., Ristovski, Z. D., Hargreaves, M., ... & Katoshevski, D., 2009. Characterization of expiration air jets and droplet size distributions immediately at the mouth opening. Journal of aerosol science, 40(2), 122-133.

De Dear, R. J., Arens, E., Hui, Z., & Oguro, M., 1997. Convective and radiative heat transfer coefficients for individual human body segments. International journal of biometeorology, 40, 141-156.

Numerical study of wind effects on moored container ships in harbour environments

Andrea P. C. Bresciani, Matilde Fiore, Thomas Arnoult, Julien Christophe, Gertjan Glabeke, Jeroen van Beeck

Environmental and Applied Fluid Dynamics Department - von Karman Institute for Fluid Dynamics, Sint-Genesius-Rode, Belgium, andrea.bresciani@vki.ac.be

SUMMARY:
The increasing size of ultra-large container ships has led to a rise in incidents involving moored vessels breaking free in high-wind conditions, highlighting the need for more accurate wind load predictions. This paper presents a numerical analysis of moored container ships, validating the results with experimental data from wind tunnel tests conducted at the von Karman Institute. Steady Reynolds-Averaged Navier-Stokes (RANS) simulations with a k-ε turbulence model are used to replicate the experimental setup. The focus is on the pressure distribution over the ship's surface in response to varying wind directions. The study explores the effect of different environmental conditions, including open sea, empty quay, and quay with stacked containers or tanks. Future work will extend the analysis to full-scale ships and investigate the impact of non-standard wind profiles, such as high-shear and swirl flows.

Keywords: Moored container ships, Wind loads, Numerical simulations

1. INTRODUCTION

The increase in the size of modern ultra-large container ships has led to increased windage and air drafts. This, combined with local wind effects (Ricci, Janssen, et al., 2020) and severe extreme events, has contributed to incidents of moored vessels breaking loose in strong wind conditions (SAFETY4SEA, 2019). Traditional wind load calculations for, e.g., the sizing on mooring lines are based on empirical laws and scaling factors obtained from wind tunnel measurements on ships that no longer represent modern vessels (Van Zwijnsvoorde et al., 2019). Hence, improved prediction tools are crucial to ensure the safety of mooring procedures (Ricci, Vasaturo, et al., 2023).

The experiments conducted by the von Karman Institute (VKI) and presented in the companion abstract (Arnoult et al., 2024) address this issue with an extensive measurement campaign with a reduced scale container ship model and in controlled laboratory conditions. In the present work, the same issue is addressed from a numerical perspective: the numerical simulations are first validated against the experimental data and, then, extended to full-scale. Finally, the effect of non-standard wind profiles including high-shear and swirl is investigated.

As in the experimental campaign, four environments are considered: open sea, empty quay, quay with stacked containers, and quay with tanks. In this abstract, the validation for the open sea case is presented.

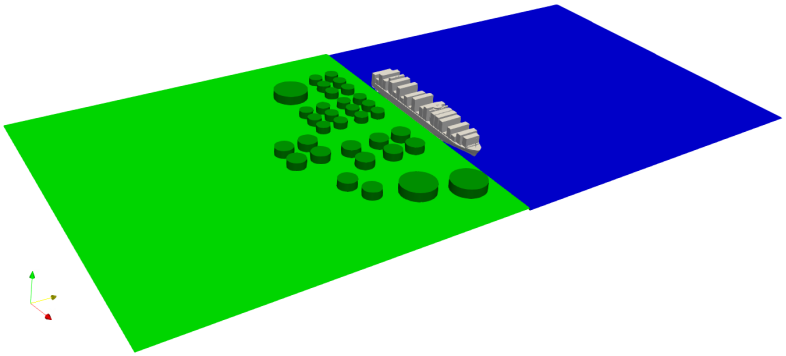


Figure 1. Computational domain considered for the reduced-scale simulations.

2. METHODOLOGY

Steady Reynolds-Averaged Navier–Stokes (RANS) simulations with the k-ε turbulence model are employed. The computational domain for the validation of numerical simulations replicates the experimental setup in the wind tunnel (Arnoult et al., 2024). The length of the test section considered is 6 m. At the inlet, an atmospheric boundary layer profile is imposed and it has been verified that it closely replicates the measured boundary layer in the wind tunnel. Slip wall boundary conditions are applied to the side and upper walls, while a zero-gradient pressure outlet is imposed at the outflow. Figure 1 shows the geometry simulated for the environment with the tanks. The simulations have been performed using OpenFOAM v9.

A mesh convergence study has been carried out for the open sea case (isolated ship). Forces and moments are computed for three different meshes with approximately 0.4, 1, and 1.6 million elements. Negligible differences are observed between the two more refined meshes and hence, the intermediate mesh with 1 milion elements is used in the following.

3. PRELIMINARY RESULTS AND FUTURE PERSPECTIVES

In this abstract, we focus on the pressure coefficient measured on the ship's surface for 36 wind directions and a reference velocity of 10 m/s. The measurements from 72 pressure probes are compared with the numerical results. Figure 2(a-b) show the pressure coefficient for two representative probes demonstrating the good agreement between measurements and numerics. A slight underestimation of the peaks is noticed in the numerical results and confirmed by fig. 2(c) which shows the comparison for the 72 probes and 36 wind directions.

Streamlines and pressure contours are shown in fig. 3 for a transversal wind (angle of attack AoA $=$ 0). The results for the other environments (empty quay, quay with tanks, and quay with stacked containers) will be presented at the conference with an additional analysis for non-standard wind profiles.

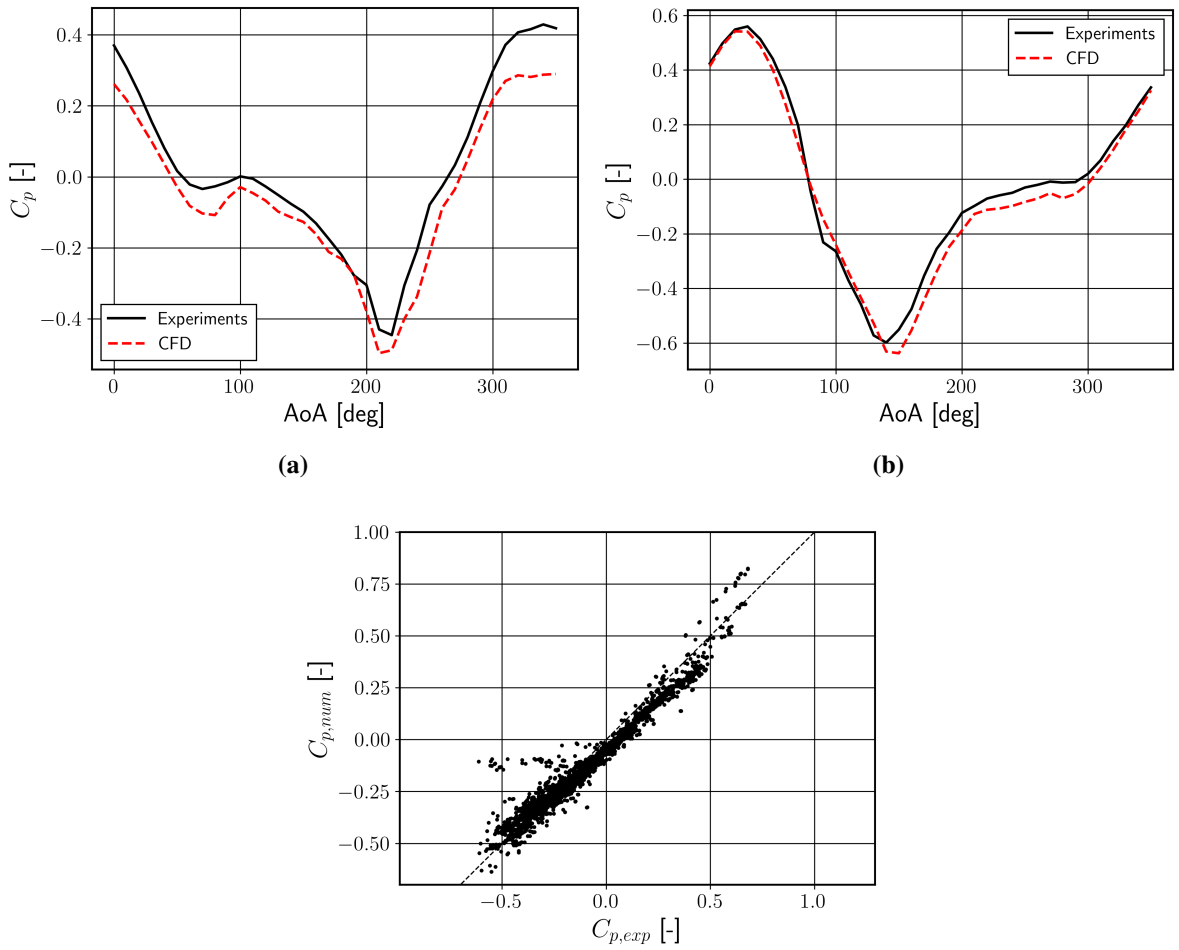


Figure 2. (a) Pressure coefficient as a function of the wind direction for two probes and (b) for 72 probes and 36 wind directions.

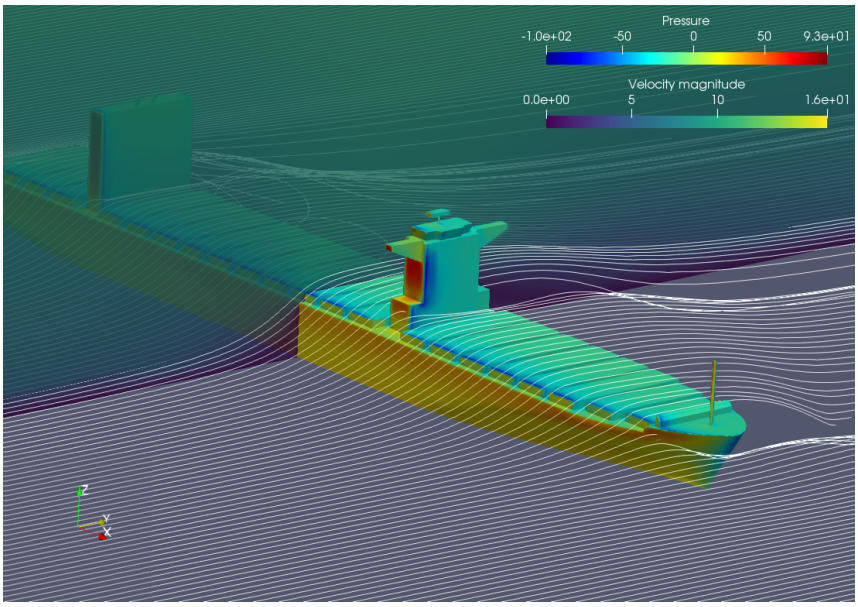


Figure 3. Streamlines and pressure contours for transversal wind.

ACKNOWLEDGEMENTS

This work was made possible by the financial support of VLAIO for the Everblue project (HBC.2022.0663).

REFERENCES

Arnoult, T., Glabeke, G., Donatini, L., and Beeck, J. van, 2024. Experimental analysis of wind effects on moored container ships in harbour environments. Proceedings of Submitted to EACWE, 2024.

Ricci, A., Janssen, W., Van Wijhe, H., and Blocken, B., Oct. 2020. CFD simulation of wind forces on ships in ports: Case study for the Rotterdam Cruise Terminal. en. Journal of Wind Engineering and Industrial Aerodynamics 205, 104315.

Ricci, A., Vasaturo, R., and Blocken, B., Mar. 2023. An integrated tool to improve the safety of seaports and waterways under strong wind conditions. en. Journal of Wind Engineering and Industrial Aerodynamics 234, 105327.

SAFETY4SEA, Dec. 3, 2019. Case study: Mooring line failure onboard. SAFETY4SEA.

Van Zwijnsvoorde, T., Donatini, L., Van Hoydonck, W., and Lataire, E., Oct. 17, 2019. Wind modeling for large container vessels: A critical review of the calculation proce dure. International Journal of Transport Development and Integration 3, 369–381.

Speeding Up Wind Load Predictions on Cargo Ships through Multi-Fidelity Modeling

Matilde Fiore[1], Miguel Alfonso Mendez[1], Jeroen van Beeck[1]

[1]*Environmental and Applied Fluid Dynamics Department - von Karman Institute for Fluid Dynamics, Sint-Genesius-Rode, Belgium matilde.fiore@vki.ac.be*

SUMMARY:

Modern container ships face higher wind loads due to increased windage areas, making accurate predictions essential for mooring design. Existing models, tailored for older ships, lack accuracy and ignore nearby structures. This study presents a multi-fidelity model leveraging heterogeneous data-sources to improve wind load estimations. A surrogate model for fore/aft wind coefficient based on recursive co-kriging was developed using an empirical correlation and a CFD model as data-sources. An active subspace analysis guided the input selection, and the design space was explored with sequential sampling. Initial results show superior accuracy of the multi-fidelity approach compared to the single-fidelity one.

Keywords: wind loads, surrogate modeling, multi-fidelity

1. INTRODUCTION

Nowadays, modern container ships are subject to higher wind loads due to increased windage areas and air draft of the vessels, making accurate wind load estimation critical for designing effective mooring systems. Correlations developed in recent decades (Isherwood, 1972), are no longer reliable for current designs as they were based on earlier, smaller vessels and do not consider the impact of nearby structures. To address these limitations, this study proposes a data-driven, multi-fidelity modeling approach that leverages and harmonises data from experiments, CFD simulations, and empirical models, allowing for more accurate and cost-effective predictions.

In this work, we present a proof of concept of multi-fidelity surrogate modelling for predicting wind loads on cargo ships. The surrogate model considers the ship used in a recent experimental campaign (Arnoult et al., 2025), and tested for various angles of attack and cargo configurations. For this preliminary modeling, only two data-sources are considered: an empirical correlation (Isherwood, 1972), and a CFD model developed in OpenFoam. The training of the surrogate model is performed through a sequential sampling algorithm that explores the parameter space at both fidelity levels based on the highest local uncertainties. Preliminary results indicate that the multi-fidelity surrogate achieves a very good accuracy using only a limited number of high-fidelity samples, significantly outperforming the single-fidelity approach with the same number of samples.

2. EMPIRICAL CORRELATION

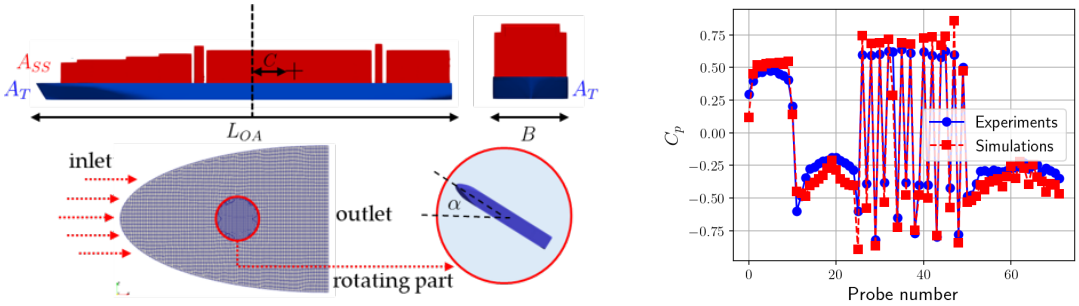
The correlation developed by Isherwood (Isherwood, 1972) expresses the fore/aft (C_x) and lateral (C_y) wind loads coefficients and the yawing moment coefficient (C_N) as functions of the angle of attack α and a set of geometrical parameters of the ship:

$$C_i = f\left(\frac{A_L}{L_{OA}}, \frac{A_T}{B}, \frac{L_{OA}}{B}, \frac{S}{L_{OA}}, \frac{C}{L_{OA}}, M, \frac{A_{SS}}{A_L}, \alpha\right), \tag{1}$$

in which A_L is the ship lateral projected area, A_T the transveral area,A_{SS} the area of the superstructures, L_{OA} is the overall length, B is the beam, S is the perimeter of the lateral projection, C the distance from the bow of the centroid of the lateral projected area, M is the number of dinstict groups in the cargo load and α is the angle of attack (see Figure 1).

3. CFD MODEL

The CFD model is based on a simplified representation of the ship's geometry presented in the complementary experimental investigation (Arnoult et al., 2025). Specifically, the gaps between the containers are modelled as porous regions with the Darcy-Forchheimer law, whose coefficients were determined from preliminary CFD simulations. The mesh, depicted in Figure 1, consists of two distinct parts that can rotate relative to each other, allowing the simulation of various angles of attack. Figure 1 shows the good comparison between numerical results and experimental data for the pressure coefficient C_p.



(a) (b)

Figure 1. Ship geometry and computational domain (a) and comparison between experimental and numerical coefficients of pressure (C_p) at different probe locations for $\alpha = 90.0$. (b)

4. MULTI-FIDELITY SURROGATE MODEL

For the modelling of the fore/aft wind load coefficient C_x with heterogeneous data we use the recursive formulation of co-kriging (Le Gratiet, 2013):

$$z_t(x) = \rho_{t-1} z_{t-1}(x) + \delta_t(x) \tag{2}$$

in which $z_t(x)$ is the model prediction at the fidelity level t, ρ_{t-1} is the correlation coefficient with the previous fidelity level and $\delta_t(x)$ is the Gaussian process (GP) based surrogate model (Williams and Rasmussen, 1995) trained at the fidelity level t. Conditioning the recursive GPs over the set

of multi-fidelity training data allows to estimate the expected C_x and the uncertainties σ_{δ_t} at each fidelity level.

The training process with the two data-sources is schematized in Figure 2. First, the multi-fidelity GP is trained with an initial design of experiments. Then, a wide ensemble of feasible configurations is used to query an acquisition function $\phi(x,t)$ that selects the next configuration to investigate. In this study, $\phi(x,t)$ is a function of the integral mean squared error obtained propagating the uncertainties $\sigma_{\delta_t}(x)$ through all the previous fidelity levels. Depending on the fidelity level t selected, the new sample is investigated either with the correlation or the CFD model.

The vector **x** of the input parameters contains only 4 out of the 10 parameters indicated by eq. (1), i.e. α, A_{SS}/A_L, C/L_{OA} and M. This subset of most sensitive parameters was determined with the analysis of the Active Subspace (Liu and Yan, 2012) of the correlation introduced by eq.(1).

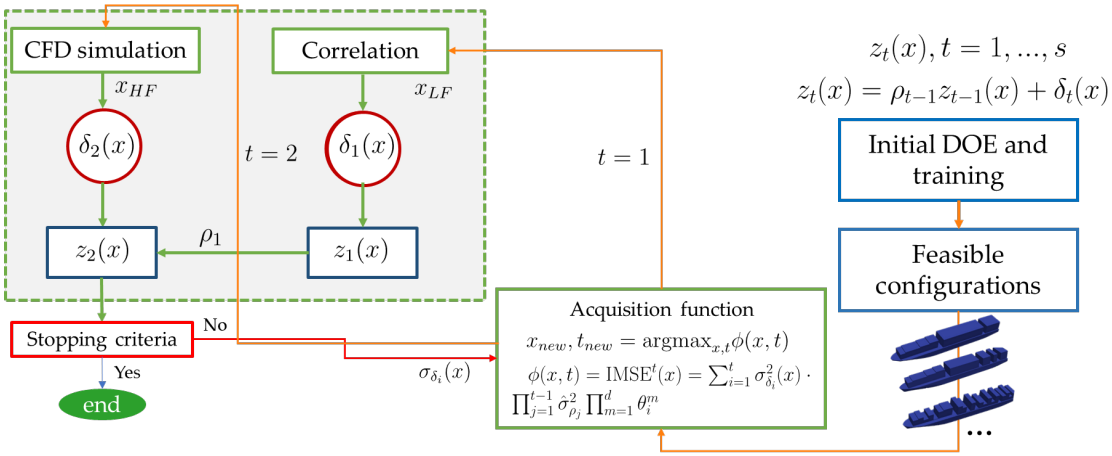


Figure 2. Schematics of the learning algorithm applied to train the multi-fidelity GP with the sequential filling of the parameter space.

5. RESULTS

The sequential sampling algorithm ran 20 iterations, over which the CFD solver was executed only 5 times, while the remaining samples were generated by the correlation. Figure 3 shows the configurations sampled by the algorithm and simulated using CFD.

Figure 4 (left) presents the predictions of the multi-fidelity GP for a specific configuration excluded from the training set. The highest fidelity level $z_2(x)$ accurately predicts the CFD data across the full range of angles of attack. On the right-hand side, figure 4 compares the predictions of a single-fidelity surrogate trained solely with the highest fidelity samples (CFD). This comparison highlights that, with the same number of high-fidelity samples, the multi-fidelity model is significantly more accurate, with a narrower uncertainty range. This demonstrates that the algorithm effectively leverages the correlation between data sources, resulting in enhanced accuracy.

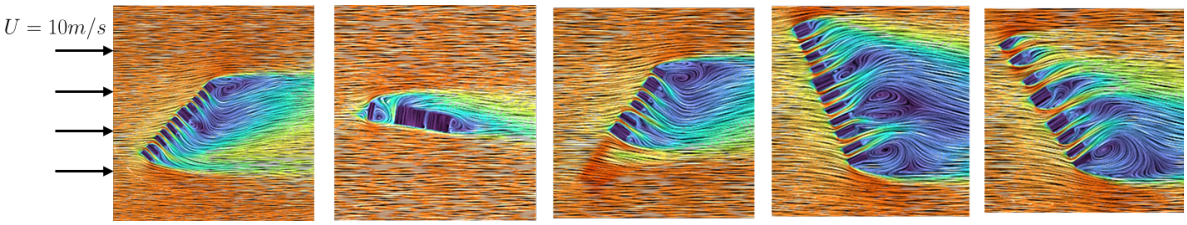


Figure 3. Configurations explored with CFD by the sequential sampling algorithm.

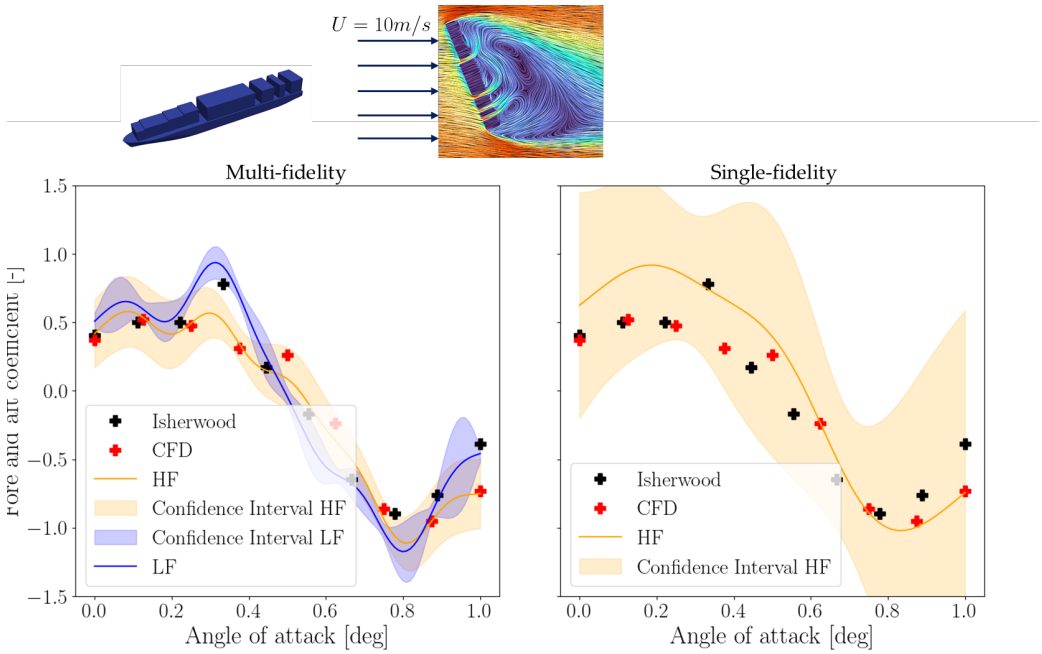


Figure 4. Predictions of C_x by the surrogate models for an unseen charge configuration. The predictions of the multi-fidelity model are presented on the left-hand side. On the right-hand side, the predictions of the single-fidelity counterpart trained with the same high-fidelity samples.

ACKNOWLEDGEMENTS

This work was made possible by the financial support of VLAIO for the Everblue project (HBC.2022.0663). The authors kindly acknowledge Luca Donatini for providing the CAD of the cargo ship.

REFERENCES

Arnoult, T., Glabeke, G., Donatini, L., and Beeck, J. van, 2025. "Experimental Analysis of Wind Effects on Moored Container Ships in Harbour Environments". Extended Abstract, EACWE 2025 Conference. Accepted for presentation at EACWE 2025 Conference.

Isherwood, R. M., 1972. Wind Resistance of Merchant Ships. Transactions of the Royal Institution of Naval Architects 114, 327–338.

Le Gratiet, L., 2013. Multi-fidelity Gaussian process regression for computer experiments. phdthesis, Université Paris-Diderot-Paris VII.

Liu, G. and Yan, S., 2012. Active subspace: Toward scalable low-rank learning. Neural computation 24, 3371–3394.

Williams, C. and Rasmussen, C., 1995. Gaussian processes for regression. Advances in neural information processing systems 8.

The importance of details during the development of CFD simulations: an example in sports aerodynamics

Fabio Malizia[1,2], Bert Blocken[1,2]

[1]*Heriot-Watt University, Edinburgh, United Kingdom, f.malizia@hw.ac.uk*
[2]*KU Leuven, Leuven, Belgium*

SUMMARY:
The development of a CFD simulation includes several stages, among which the creation of a computational geometry, grid sensitivity analysis and validation with experiments are of fundamental importance. Despite their importance, these steps are often rushed to proceed with the study related to the research question. This causes a possible deterioration in the accuracy of simulations and affects the confidence in the results. This paper shows how small details, often overlooked, can have a non-negligible impact on the results of CFD simulations and wind tunnel (WT) tests in sports aerodynamics, with main reference to cycling wheels. First, it is shown how a few mm difference in tire thickness can significantly change the results of CFD simulations and WT tests. Second, the impact of yaw angle is discussed, as well as the reason why grid sensitivities should be performed not only at zero degrees yaw angle. Finally, two WT tests on the "same" wheels are analysed through CFD simulations and the results discussed to see how both tests can be correct despite the large difference in drag results, up to 37%. This study aims to make aerodynamicists aware of the importance of small details in both CFD simulations and WT tests.

Keywords: CFD, guidelines, sport

1. INTRODUCTION

Best practice guidelines on how to perform aerodynamic simulations and measurements are available in many fields, from outdoor flows in urban environments (Blocken, 2015; Franke et al., 2007; Ricci, 2024) to cycling (Brownlie, 2019; Malizia et al., 2019; van Druenen and Blocken, 2024). Cycling aerodynamics requires accurate simulations and wind tunnel (WT) tests because aerodynamics causes a power loss of up to 90% when a cyclist rides at high speed and on flat terrain (Grappe et al., 1997). Moreover, races are not infrequently decided by time differences of fractions of a second. These small differences, together with the large impact of aerodynamics in cycling, mean that even small aerodynamic improvements can change the outcome of a race.

If small aerodynamic improvements are desired, we should be sure that our methodologies are able to capture them. Effort should be put into the early stages of the simulation or test development, which are usually rushed to get to work on the research question, especially in industry. The aim of the present study is to investigate how small details can be crucial in both performing accurate and reliable CFD simulations and increasing confidence in the WT tests used for CFD validation. First, the sensitivity of aerodynamic drag on a cycling wheel to changes in geometry is discussed, with a focus on tire width. Second, the effect of yaw angle is analysed from two different points of view: as a possible source of error in WT tests, i.e. in the results used for CFD validation, and

as an additional condition that should be analysed during the grid sensitivity analysis. Finally, it is shown how CFD simulations helped to understand how two WT tests on the "same" wheels could provide different but correct results at the same time.

2. SENSITIVITY TO GEOMETRY MODIFICATIONS

A cycling wheel is made of a tire, a rim and a hub. The rim and the hub are connected by either numerous thin spokes (spoked wheel), a few large spokes (tri-, four-, five-spoke wheel) or plates (disc wheels). Rear wheels also include a cassette with several gears. CFD simulations have shown that at 0° yaw angle, the tire alone can be responsible of ~50% of the wheel aerodynamic drag in a disc wheel (Malizia and Blocken, 2023) and the combined tire and rim can be responsible of ~60% of the total drag of a spoked wheel (Malizia and Blocken, 2020a). Therefore, the tire shape and size (Fig. 1a) can be considered a critical factor when trying to optimize the cycling wheel.

The tire-width to rim-width ratio (T/W) is a critical parameter in the wheel design, where an only 1% wider tire can already cause a 3.4% drag area increase for the wheel (Crane and Morton, 2018). In addition, the same tire fits differently on different wheels, making it difficult to estimate the tire width from the nominal width. This significantly complicates the CFD validation because the tire width is only provided through the nominal width (Tew and Sayers, 1999), if provided at all (Greenwell et al., 1995). Therefore, different tire shapes and sizes should be simulated to find the best agreement with the WT tests. The CFD simulations of a disc wheel inside a domain reproducing the WT shape from Greenwell et al. (1995) showed a similar qualitative behaviour for the aerodynamic drag of the same wheel with different tires but with absolute values different by 7% at 0° yaw angle to 21% at 8° yaw angle (Fig. 1b). Fig. 1c shows that using different wheel-tire combination for a spoked wheel, results change significantly, with wider tires increasing the wind-averaged drag. A reason is that the tire-rim interaction becomes very important at large yaw angles because it can trigger the laminar-to-turbulent boundary layer transition, delaying the flow separation (stall) even by 8° yaw angle and reducing drag even by 33% (Jux et al., 2023).

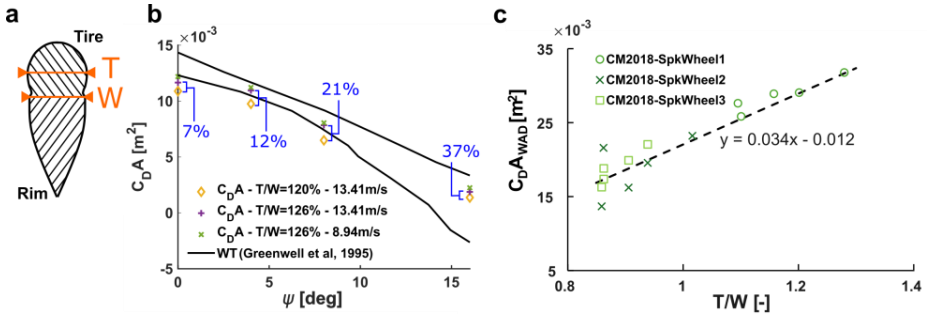


Figure 1. a) Tire width (T) and rim width (W); b) CFD validation for a disc wheel (Malizia and Blocken, 2023); c) wind averaged drag area (C_DA) against T/W for a stationary spoked wheel (Crane and Morton, 2018).

3. SENSITIVITY TO YAW ANGLE

The performance of cycling wheels is often investigated in crosswind conditions (Greenwell et al., 1995; Jux et al., 2023; Malizia and Blocken, 2020b). The drag has a large sensitivity to the yaw angle, with possible drag reduction thanks to the so called "sail effect", i.e. lift generation on the wheel that reduces the axial drag, but also sharp drag increases when the wheel stalls and the flow

separates from it (Jux et al., 2023). For example, Jux et al. (2023) measured a drag variation from about -50% to about +10% at 10° yaw angle compared to drag at 0° yaw angle for a spoked wheel, Malizia and Blocken (2020b) computed a drag increase of about 30-40% for a spoked wheel (with wide tire) at 10° yaw angle, and Malizia and Blocken (2023) computed a drag reduction of about 60 to 80% for a disc wheel at 8° yaw angle. The large sensitivity to yaw angle might create issues during WT tests, where the accuracy in the wheel alignment is critical to avoid erroneous measurements, as reported in Zdravkovich (1992), where a 10% difference in drag was reported when repeating the test with the same wheel, due to wheels misalignment of about 2°. The wheel alignment causes less problems in CFD, where the wheel is usually placed inside a cylindrical interface that allows to set any yaw angle. However, the wheel aerodynamics is different at different yaw angles, and this influences the grid sensitivity.

In cycling, the grid sensitivity is often limited to a yaw angle of 0°. Fig. 2c shows the results of the grid sensitivity study for a rear disc wheel (Malizia and Blocken, 2023) using a RANS approach. The grid sizes are 3.6, 11.9 and 19.6 M cells for the coarse, medium-1 and fine grid, respectively (Fig. 2a,b). Drag differences are less than 1% for both coarse and medium grids, providing (erroneous) confidence in the results. By repeating the same analysis at 10° yaw angle (Fig. 2c), the drag difference with the fine grid becomes -29.9% and -7.8% for the coarse grid and medium-1 grid respectively. A new medium grid was then created (medium-2), with local refinement on the tire, because the tire causes the largest drag in a wheel (46% at 0°) and is an area where flow can separate. The medium-2 grid had 12.6 million cells (+6% compared to the original medium-1 grid) and reduced the drag difference between fine and medium grids from -7.8% to -2.3%.

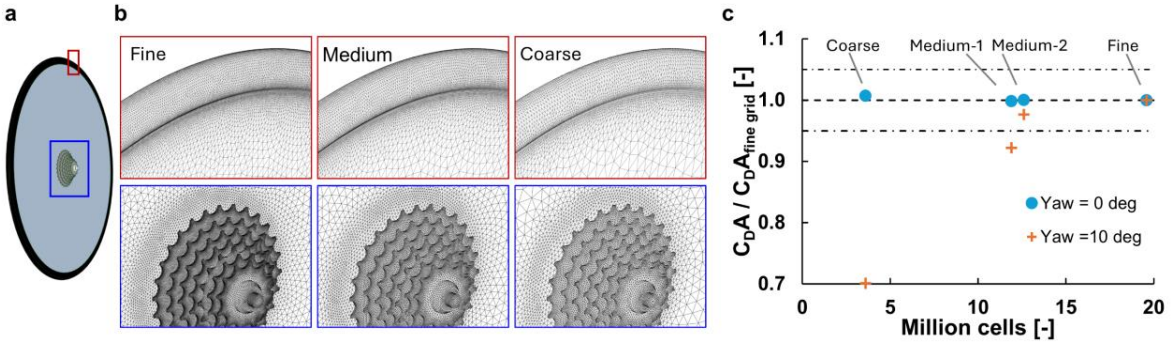


Figure 2. a) Rear disc wheel; b) close-up views to the grid on tire and gears; c) grid sensitivity analysis at 0° (•) and 10° yaw angle (+), results are expressed as a ratio of the drag area to the drag area with the fine grid.

4. WIND TUNNEL RESULTS FROM LITERATURE

During the CFD validation stage, results are compared to those from WT tests. However, it is not uncommon for two different WT campaigns to provide seemingly contradictory results. For example, two studies tested the same spoked and tri-spoke wheel's models (Greenwell et al., 1995; Tew and Sayers, 1999). The drag at 0° yaw angle was 37% and 16% different for the spoked and tri-spoke wheel, respectively. This raises the question how this drag difference could be explained.

The reasons why the WT measurements were different but correct at the same time could be explained from the results obtained by means of CFD simulations for a spoked wheel (Malizia et al., 2019; Malizia and Blocken, 2020a). First, the tested wheel model was the same (Campagnolo

Shamal) but the type of wheel was different, rear wheel (Greenwell et al., 1995) vs. front wheel in (Tew and Sayers, 1999). The rear wheel included a 7-gears cassette, which was responsible of 12% of the total drag (Malizia and Blocken, 2020a). Second, the type of WT used was different, a closed test-section (2.13 m × 1.52 m) in (Greenwell et al., 1995) and an open test-section in (Tew and Sayers, 1999). Including the WT in the simulation was found to add about 3% drag (Malizia et al., 2019; Malizia and Blocken, 2020a). The remaining drag difference can be explained by the different tires used in the tests. Their impact was explained in Section 2.2, where it was reported a 3.4% (wind-averaged) drag area increase for 1% wider tire (Crane and Morton, 2018): using a 21 mm wide tire rather than a 20 mm wide tire, could even cause 17% drag difference.

5. CONCLUSIONS

This extended abstract showed how details can lead to significant differences in the results obtained in CFD simulations and WT tests in cycling aerodynamics. Small geometrical differences can cause significant drag differences, also posing challenges for test reproducibility. It is known that yaw angles affect the aerodynamics of a body, but it has been shown that it should be considered when performing the grid sensitivity analysis. Moreover, care must be taken when reproducing WT tests during the CFD validation, as it is important to validate the computed physics rather than trying to reproduce the exact result of the WT test, as this could be the consequence of measurements influenced by small details not described in the test report.

REFERENCES

Blocken, B., 2015. Computational Fluid Dynamics for urban physics: Importance, scales, possibilities, limitations and ten tips and tricks towards accurate and reliable simulations. Build Environ 91, 219–245.

Brownlie, L.W., 2019. Wind Tunnels: Design Considerations in Wind Tunnel Testing of Cyclists, in: Pallis, J.M., McNitt-Gray, J.L., Hung, G.K. (Eds.), Biomechanical Principles and Applications in Sports. Springer, Cham, pp.

Crane, R., Morton, C., 2018. Drag and side force analysis on bicycle wheel-tire combinations. Journal of Fluids Engineering, Transactions of the ASME 140, 1–8.

Franke, J., Hellsten, A., Schlünzen, H., Carissimo, B., 2007. Best practice guideline for the CFD simulation of flows in the urban environment, COST action 732.

Grappe, F., Candau, R., Belli, A., Rouillon, J.D., 1997. Aerodynamic drag in field cycling. Ergonomics 40,1299-1311.

Greenwell, D.I., Wood, N.J., Bridge, E.K.L., Addy, R.J., 1995. Aerodynamic characteristics of low-drag bicycle wheels. The Aeronautical Journal 99, 109–120.

Jux, C., Sciacchitano, A., Scarano, F., 2023. Tire dependence for the aerodynamics of yawed bicycle wheels. Journal of Wind Engineering and Industrial Aerodynamics 233.

Malizia, F., Blocken, B., 2020a. CFD simulations of an isolated cycling spoked wheel: impact of the ground and wheel/ground contact modeling. Eur J Mech B Fluids 82, 21–38.

Malizia, F., Blocken, B., 2020b. CFD simulations of an isolated cycling spoked wheel: the impact of wheel/ground contact modeling in crosswind conditions. European Journal of Mechanics, B/Fluids 84, 487–495.

Malizia, F., Blocken, B., 2023. Impact of Disc Wheel Geometry on Aerodynamic Performance: A Computational Fluid Dynamics Investigation. Journal of Fluids Engineering, Transactions of the ASME 145, 1–13.

Malizia, F., Montazeri, H., Blocken, B., 2019. CFD simulations of spoked wheel aerodynamics in cycling: Impact of computational parameters. Journal of Wind Engineering and Industrial Aerodynamics 194.

Ricci, A., 2024. Review of OpenFOAM applications in the computational wind engineering: from wind environment to wind structural engineering. Meccanica.

Tew, G.S., Sayers, A.T., 1999. Aerodynamics of yawed racing cycle wheels. Journal of Wind Engineering and Industrial Aerodynamics 82, 209–222.

van Druenen, T., Blocken, B., 2024. CFD simulations of cyclist aerodynamics: Impact of computational parameters. Journal of Wind Engineering and Industrial Aerodynamics 249.

Zdravkovich, M.M., 1992. Aerodynamics of bicycle wheel and frame. Journal of Wind Engineering and Industrial Aerodynamics 40, 55–70.

Recommendations on practical applications of turbulence inflow for large eddy simulation in wind engineering

Bowen Yan [1], Yangjin Yuan[1], Qingshan Yang [1*], Jiawei Wan[2]

[1] *Key Laboratory of New Technology for Construction of Cities in Mountain Area (Ministry of Education), School of Civil Engineering, Chongqing University, Chongqing, China*
[2] *China Energy Science and Technology Research Institute Co. Ltd., China*
**Corresponding author: qshyang@cqu.edu.cn*

SUMMARY:
The synthetic random Fourier method is widely used as an inflow turbulence generation method in large eddy simulation (LES) to replicate an atmospheric boundary layer (ABL) wind field. However, the generated turbulence inflow is incompatible with the Navier-Stokes (N-S) equation, leading to the inconsistency of the wind characteristics with the intended targets along the computational domain. To address this issue, a synthetic turbulence velocity forcing method that directly exerts the artificially synthesized turbulent field on the grid centre of the selected cells is recommended in this study. The turbulent field data is imported into the computational domain with pre-described turbulence features to generate an ABL flow. Comparison studies of different appending methods indicate that the self-sustainability of the wind profiles simulated with the proposed method is much improved compared with the traditional methods. Moreover, the wind velocity and turbulence intensity profiles and the power spectra and probability density functions of the simulated velocity can all be appropriately reproduced within the proposed method based on RFG-based methods. Additionally, the proposed method exhibits computational efficiency and can be applied as a turbulence-appending technique for LES in wind engineering applications.

Keywords: Turbulence inflow, Synthetic turbulence velocity forcing method, Large-eddy simulation, forcing method

1. INTRODUCTION

The attenuation of the turbulence flow along with the computational domain during the spatially developing turbulence simulations is evolving to be a concerning issue (Zhang et al., 2022). The ignorance of this problem might lead to considerable discrepancy from practical situations in LES. Great efforts have been focused on turbulence inflow generation together with various correction methods in the past decades, the main challenge remains how to append the specific turbulence field into the computational domain to ensure correct propagation of the turbulent fluctuations within the computational domain. In this paper, different turbulence inflow appending methods are discussed to examine their effect on horizontal homogeneity in the computational domain. Furthermore, a procedure able to efficiently append the turbulence flow developed from precursor simulation into the primary computational domain is presented.

2. TRADITIONAL APPENDING METHODS FOR THE GENERATED TURBULENCE

To expound the appending methods of turbulence flow more straightforward, the computational domain is virtually divided into subdomains A and B in the streamwise direction, as illustrated in Fig.1. The semi-discrete momentum equation and continuity equation in the interior

computational domain can be expressed as Eq. (1-2).

$$\frac{d\boldsymbol{u}(t)}{dt}=\left(\boldsymbol{K}+\boldsymbol{N}(\boldsymbol{u},\boldsymbol{u}_b)\right)\boldsymbol{u}(t)\text{-}\boldsymbol{G}\boldsymbol{p}\ (t)+\boldsymbol{f}(t,\boldsymbol{u}_b)=\boldsymbol{M}\boldsymbol{u}(t)\text{-}\boldsymbol{G}\boldsymbol{p}\ (t)+\boldsymbol{f}(t) \tag{1}$$

$$\boldsymbol{D}\boldsymbol{u}(t)=\boldsymbol{r}(t) \tag{2}$$

Herein, $\boldsymbol{u}(t)$ and $\boldsymbol{p}(t)$ denote vectors storing the spatially discretized velocity and pressure fields to be solved; $\boldsymbol{u}_b(t)$ is a vector comprising the discrete velocities specified at inlet boundaries; $\boldsymbol{K}$ and $\boldsymbol{N}$ are the matrix representation of the linear and non-linear coefficients resulting from the spatial discretization of the convection and diffusion terms; $\boldsymbol{f}(t,\ \boldsymbol{u}_b)$ is a vector collecting forcing terms induced by $\boldsymbol{u}_b$ and other sources. The coefficient matrix $\boldsymbol{M}$, $\boldsymbol{G}$, and $\boldsymbol{D}$ contains the interaction of subdomains A and B, thus the equations can be disassembled into Eq. (3-4), with $\boldsymbol{u}=[\boldsymbol{u}_A\ \boldsymbol{u}_B]$ and $\boldsymbol{p}=[\boldsymbol{p}_A\ \boldsymbol{p}_B]$. The variables in the equations are stored in the cell center.

$$\frac{d}{dt}\begin{bmatrix}\boldsymbol{u}_A\\ \boldsymbol{u}_B\end{bmatrix}=\begin{bmatrix}\boldsymbol{M}_{AA} & \boldsymbol{M}_{AB}\\ \boldsymbol{M}_{BA} & \boldsymbol{M}_{BB}\end{bmatrix}\begin{bmatrix}\boldsymbol{u}_A\\ \boldsymbol{u}_B\end{bmatrix}+\begin{bmatrix}\boldsymbol{G}_{AA} & \boldsymbol{G}_{AB}\\ \boldsymbol{G}_{BA} & \boldsymbol{G}_{BB}\end{bmatrix}\begin{bmatrix}\boldsymbol{p}_A\\ \boldsymbol{p}_B\end{bmatrix}+\begin{bmatrix}\boldsymbol{f}_A\\ \boldsymbol{f}_B\end{bmatrix} \tag{3}$$

$$\begin{bmatrix}\boldsymbol{D}_{AA} & \boldsymbol{D}_{AB}\\ \boldsymbol{D}_{BA} & \boldsymbol{D}_{BB}\end{bmatrix}\begin{bmatrix}\boldsymbol{u}_A\\ \boldsymbol{u}_B\end{bmatrix}=\begin{bmatrix}\boldsymbol{r}_A\\ \boldsymbol{r}_B\end{bmatrix} \tag{4}$$

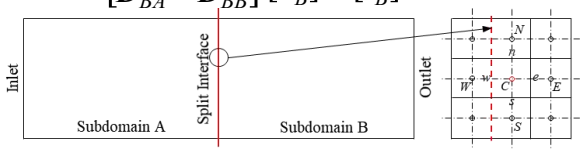
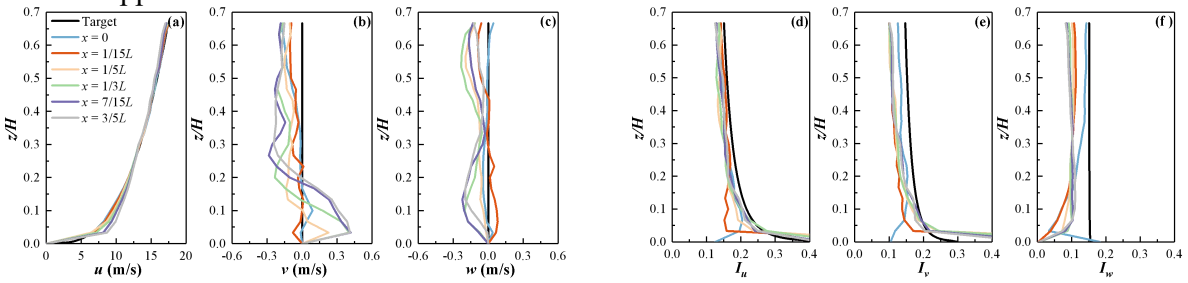


Fig. 1 Sketch diagram of computational segmentation

To append the synthetic turbulent velocity field $\boldsymbol{u}_s(\boldsymbol{x},t)$ into a computation domain, the most straightforward approach is to specify the time-varying $\boldsymbol{u}_b$ according to $\boldsymbol{u}_s$, which is a widely used method (e.g., Aboshosha et al., 2015) named method A in this study. The self-sustainability of the fluctuating wind fields along the streamwise direction is studied, as presented in Fig. 2. The vertical profiles of mean wind velocity and turbulence intensity at x = 0-3/5L and y=1/2B are plotted. The turbulence intensity is reduced along the computational domain, with the maximum relative error up to 13.7%, 27.4%, and 36% for I_u, I_v, and I_w, respectively, as shown in Fig. 2 (b). This phenomenon indicates that the synthetic turbulence cannot well propagate along the computational domain based on method A. The decay of turbulence along the computational domain might cause considerable deviation of the numerical results in practical applications.



(a) Wind velocity profiles (b) Turbulence intensity profiles

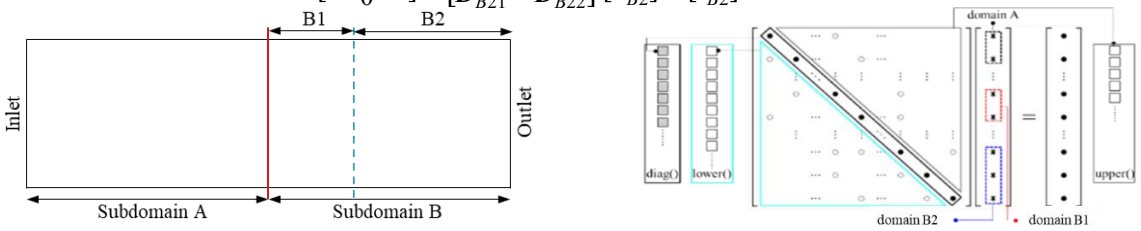
Fig. 2 Wind profiles along with the computational domain for method A

3. RECOMMENDED METHODS

To address the problem in method A, a new appending method (i.e., Method B) is proposed. In this method, subdomain B is further split into two parts (as illustrated in Fig. 3(a)). The semi-discrete NS equation in subdomains B1 and B2 can be further rewritten as Eq. (5-6).

$$\frac{d}{dt}\begin{bmatrix}\boldsymbol{u}_{B1}\\ \boldsymbol{u}_{B2}\end{bmatrix}=\begin{bmatrix}\boldsymbol{M}_{B11} & \boldsymbol{M}_{B12}\\ \boldsymbol{M}_{B21} & \boldsymbol{M}_{B22}\end{bmatrix}\begin{bmatrix}\boldsymbol{u}_{B1}\\ \boldsymbol{u}_{B2}\end{bmatrix}+\begin{bmatrix}\boldsymbol{G}_{B11} & \boldsymbol{G}_{B12}\\ \boldsymbol{G}_{B21} & \boldsymbol{G}_{B22}\end{bmatrix}\begin{bmatrix}\boldsymbol{p}_{B1}\\ \boldsymbol{p}_{B2}\end{bmatrix}+\begin{bmatrix}\boldsymbol{f}_{B1}\\ \boldsymbol{f}_{B2}\end{bmatrix}+\begin{bmatrix}\boldsymbol{M}_{B1A}\boldsymbol{u}_A\\ 0\end{bmatrix}+\begin{bmatrix}\boldsymbol{G}_{B1A}\boldsymbol{p}_A\\ 0\end{bmatrix} \tag{5}$$

$$\begin{bmatrix}\boldsymbol{D}_{B1A}\boldsymbol{u}_A\\ 0\end{bmatrix}+\begin{bmatrix}\boldsymbol{D}_{B11} & \boldsymbol{D}_{B12}\\ \boldsymbol{D}_{B21} & \boldsymbol{D}_{B22}\end{bmatrix}\begin{bmatrix}\boldsymbol{u}_{B1}\\ \boldsymbol{u}_{B2}\end{bmatrix}=\begin{bmatrix}\boldsymbol{r}_{B1}\\ \boldsymbol{r}_{B2}\end{bmatrix} \tag{6}$$



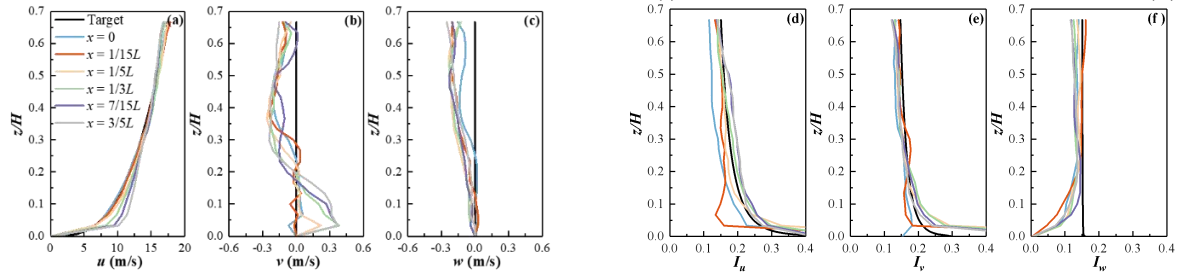
(a) Sketch diagram of computational segmentation (b) Sketch diagram of the discrete NS equation

Fig. 3 The diagram of the proposed inflow appending methods

For the implementation of Method B, the solver in OpenFOAM needs to be revised to adapt to the specified requirement of Method B. To improve the simplicity and convenience of the implementation of Method B, Method C is also derived from the expression described in Eq. (7-8). In this method, the terms related to the effect of subdomain A on subdomain B, such as $\boldsymbol{M}_{BA}\boldsymbol{u}_A$, $\boldsymbol{G}_{BA}\boldsymbol{p}_A$, and $\boldsymbol{D}_{BA}\boldsymbol{u}_A$, are directly specified. Fig.4 presents the wind velocity and turbulence intensity profiles along the computational domain by using method C. It can be found the turbulence attenuation along the computational domain is significantly reduced by applying the proposed method C. The relative errors of the transverse and vertical turbulence intensity are below 9.5% and 18.5%, although significant deviation of the turbulence intensity can be observed at the lower height due to the effect of the wall boundary condition.

$$\frac{d\boldsymbol{u}_B}{dt}=\boldsymbol{M}_{BA}\boldsymbol{u}_A+\boldsymbol{M}_{BB}\boldsymbol{u}_B+\boldsymbol{G}_{BA}\boldsymbol{p}_A+\boldsymbol{G}_{BB}\boldsymbol{p}_B+\boldsymbol{f}_A(t) \tag{7}$$

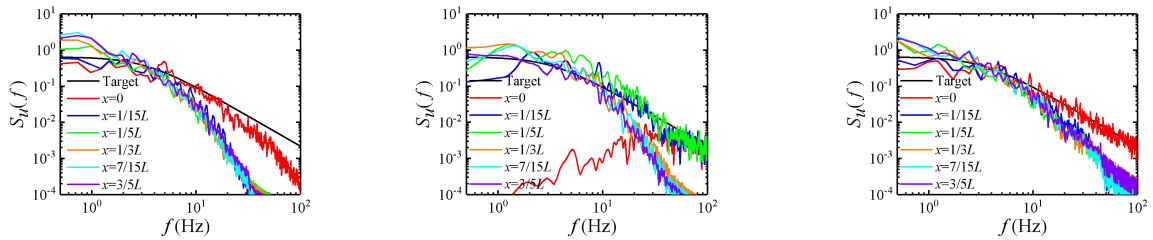
$$\boldsymbol{D}_{BA}\boldsymbol{u}_A+\boldsymbol{D}_{BB}\boldsymbol{u}_B=\boldsymbol{r}_B(t) \tag{8}$$



(a) Wind velocity profiles (b) turbulence intensity profiles

Fig. 4 The diagram of the proposed inflow appending methods

For all the appending methods, the spectra obtained at x=0 slightly deviate from the target von Karman spectrum. It can be observed that the attenuation slope of the PSDs in the case of the method A is much steeper than those in method C, which is a further indication of the improvement of homogeneity of the fluctuating wind velocity along the computational domain for method C.



(a) Method A (b) Method B (c) Method C

Fig. 5 Evolution of the power spectral density of the fluctuating velocity at z = 0.12H m in longitudinal direction for different appending methods

The simulated pressure fluctuations at (x= [0-L], y= 1/2B, z= 0.17H, 0.5H, and 0.83H) are presented in Fig. 6. The divergence-free correction method proposed by Kim et al (2013) is used during the application of the traditional and proposed methods. Near the inlet surface, the pressure fluctuations in methods B and C are significantly reduced compared with method A. At x>0.2L, the pressure fluctuations for different appending methods are below 0.2, which indicates that the effects of fluctuating pressure along the computational domain on the numerical results are limited. In addition, the contours of instantaneous longitudinal wind velocity at a same time instant are exhibited in Fig. 7. It can be observed that the vorticity energy generated near the inlet patch is significantly amplified compared with method A. For methods B and C, the vortex energy at the downwind region is much improved compared with that in method A.

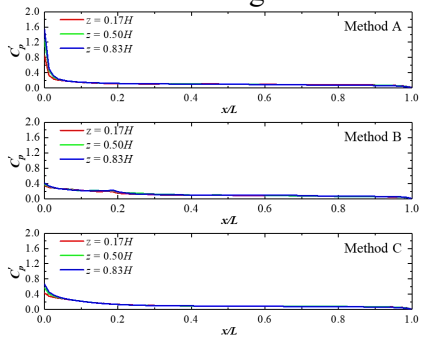


Fig. 6 Fluctuating pressure coefficients along the computational domain

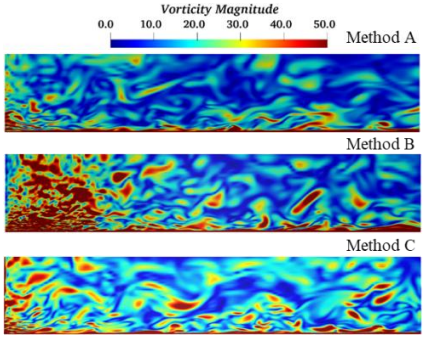


Fig. 7 Instantaneous vorticity contour of the flow at the vertical plane y =1/2B

4. CONCLUSIONS

In the present study, the problem of the traditional turbulence inflow appending method is discussed. A new turbulence field appending method is recommended for LES to generate ABL turbulence flow with target turbulence characteristics. The effect of the appending methods of the synthetic turbulence flow on the self-sustainability of the wind fields is compared in detail. The comparison studies manifest that the proposed method can not only improve the self-sustainability of the generated turbulence characteristic but also reduce the computational cost. The main characteristics and advantages of the proposed method are summarized as follows:

(1) Compared with traditional methods, the consistency of the mean velocity profiles, turbulence intensity profiles, and turbulence length scales with the targets is much improved for the proposed method. In addition, the decay of the longitudinal and transverse velocity spectra for the proposed method in the high-frequency range tends to be more gentle.

(2) For the proposed method, the self-sustainability of the wind fields is also improved compared with the traditional method, while the computational duration of the simulations is increased by 2384.0% compared with the proposed method when the same parallel computational strategies are applied.

REFERENCES

Zhang, Y.X., Cao, S.Y., Cao, J.X., 2022. An improved consistent inflow turbulence generator for LES evaluation of wind effects on buildings. Build. Environ. 223, 109459.

Aboshosha, H., Elshaer, A., Bitsuamlak, G.T., El Damatty, A., 2015. Consistent inflow turbulence generator for LES evaluation of wind-induced responses for tall buildings. J. Wind Eng. Ind. Aerod. 142, 198–216.

Kim, Y., Castro, I.P., Xie, Z.-T., 2013. Divergence-free turbulence inflow conditions for large-eddy simulations with incompressible flow solvers. Comput. Fluids 84, 56–68.

Complementary use of CFD simulations and wind tunnel tests in the built environment

Yoshihide Tominaga [1], Zitao Jiang [2]

[1] *Niigata Institute of Technology, Kashiwazaki, Japan, tominaga@abe.niit.ac.jp*
[2] *Niigata Institute of Technology, Kashiwazaki, Japan, jiang_zitao@niit.ac.jp*

SUMMARY:
It was expected that computational fluid dynamics (CFD) simulations in wind engineering (i.e., a numerical wind tunnel) would completely replace conventional wind tunnel testing. However, this has not been realized due to the high complexity of the considered flow fields. The current consensus is that CFD simulations are complementary to wind tunnel testing. This paper outlines the current status and challenges of combining CFD simulations and wind tunnel tests in wind engineering. There are four possible approaches for combining these methods: (1) the use of wind tunnel test results for the validation of CFD results, (2) the use of wind tunnel test results for improving CFD models, (3) the use of complementary scales and resolutions in the two methods, and (4) the use of CFD results for the development of more efficient and sophisticated wind tunnel tests. It is important to understand the characteristics of each method and to use the two methods in a complementary manner.

Keywords: Computational fluid dynamics (CFD), Wind tunnel test, Complementary testing

1. INTRODUCTION

Wind-related problems in the built environment range from structural problems, such as wind loads and wind vibrations acting on buildings, to environmental problems, such as the pedestrian wind environment and the dispersion of heat and pollutants in and around buildings. Since the 1940s, wind tunnel tests (and sometimes water tunnel tests) using scaled models have been conducted to investigate these problems (Cermak, 1975). Since the 1980s, computational fluid dynamics (CFD) simulations have also been used to investigate these problems (Murakami, 1990; Stathopoulos, 1997; Blocken, 2014; Tominaga, 2024).

It was expected that CFD simulations in wind engineering (i.e., a numerical wind tunnel) would replace traditional wind tunnel testing. However, this has not been realized due to the complexity of the considered flow fields (Castro and Graham, 1999; Stathopoulos, 2002; Tominaga, 2024). The current consensus is that CFD simulations are complementary to wind tunnel testing (Meroney, 2016).

This paper outlines the current status and challenges of combining CFD simulations and wind tunnel tests in the built environment.

2. COMPLEMENTARY USE OF CFD SIMULATIONS AND WIND TUNNEL TESTS

In this paper, four approaches of combining CFD simulations and wind tunnel tests are

considered. In the first approach, wind tunnel test results are used for CFD validation. This is the most common approach. In the second approach, wind tunnel tests are used to improve CFD models and increase their accuracy. This validation provides some feedback on CFD methods and models. In the third approach, complementary scales and resolutions are used in the two methods. CFD simulations can analyze flow fields on small scales; however, when the resolution is extended to scales that include the surroundings and terrain, the computational load becomes large. On the other hand, it is difficult to examine meteorological effects, including thermal effects, on a wide range of scales in a wind tunnel. These scale gaps can be eliminated by the combination of CFD simulations and wind tunnel tests. In the fourth approach, CFD simulations are used to improve the efficiency and sophistication of wind tunnel tests. In the next section, the above four approaches are explained using specific examples.

3. CASE STUDIES OF COMPLEMENTARY USE

3.1. Use of wind tunnel test results for validation of CFD results

Because of the large scale and spatio-temporal variability of flows in the built environment, it is generally difficult to measure real-world phenomena in a statistically meaningful way, so experiments using atmospheric boundary layer wind tunnels and scale models are often used as representative real-world phenomena for validation. In the built environment, the target for validation is often a flow around a single or multiple buildings with simple shapes, such as a rectangle. Buildings with complex shapes similar to actual buildings are considered in some cases.

The wind tunnel experiment databases currently available on the Internet are summarized in Table 1. The experimental database provided by the Architectural Institute of Japan (AIJ) is available on the Internet and has been widely used (Architectural Institute of Japan, 2016), along with the guidelines for the application of CFD to a pedestrian wind environment (Tominaga et al., 2008). For CFD validation, the experimental database must clearly state the boundary conditions and the uncertainty of the measurements.

Table 1. Databases of wind tunnel experiments for CFD validation available on the Internet

Database	Website
AIJ Validation Benchmark Tests	https://www.aij.or.jp/%20jpn/publish/cfdguide/index_e.htm
Cost 732 Model	https://cloud.uni-hamburg.de/s/sN5n9rN4Kit6wQY
Heavy gas dispersion	https://www.fdr.uni-hamburg.de/record/11779
COST ES1006	https://cloud.uni-hamburg.de/s/aoP9Don4dpbMg4r (Michelstadt) https://cloud.uni-hamburg.de/s/52yfanLaQ23oaGJ (CUTE)
CEDVAL-LES	https://cloud.uni-hamburg.de/s/bjNeP9GpH36mKKk
CEDVAL	https://cloud.uni-hamburg.de/s/LfSYD8qS2MH2wct
TPU Outdoor Air Pollution Database	https://www.wind.arch.t-kougei.ac.jp/info_center/pollution/pollution.html
CODASC	https://www.umweltaerodynamik.de/bilder-originale/CODA/CODASC.html
DAPPLE Datasets	https://admlc.com/datasets/
TPU Aerodynamic Database	https://wind.arch.t-kougei.ac.jp/system/eng/contents/code/tpu
NIST Aerodynamic Database	https://www.nist.gov/el/materials-and-structural-systems-division-73100/nist-

	aerodynamic-database
BUBBLE	https://www.mcr.unibas.ch/dolueg2/projects/campaigns/BUBBLE/textpages/ov_frameset.en.htm

3.2. Use of wind tunnel test results for improving CFD models

Although many numerical parameters and closure coefficients appear in CFD models, most of them are optimized for relatively simple flow fields such as boundary layer and channel flows. Their application to complex flow fields such as those in the built environment has long been a challenge. Shirzadi et al. proposed a systematic calibration method for improv the accuracy of urban airflow simulations using CFD models based on Reynolds-averaged Navier-Stokes (RANS) (Shirzadi et al., 2020). The calibration process used wind tunnel test results to define validation metrics, which were then used as the objective function of a stochastic optimization solver to obtain optimal values of closure coefficients for the RANS model. These optimal values were applied to three different urban airflow case studies and were found to provide significant improvements over existing coefficients implemented in commercial CFD codes.

3.3. Complementing different scales and resolutions in each method

Jubayer and Hangan proposed a method of combining CFD simulations with a wider computational domain of 65 km^2 and height differences on complex terrain and physical experiments using a wind tunnel system (WindEEE) that can vary the profile of the approaching flow by 60 multi-fans (Jubayer and Hangan, 2018). The method of determining the inflow profile by CFD simulations and applying the results in a wind tunnel experiment was demonstrated.

3.4. Use of CFD to make wind tunnel tests more efficient and sophisticated

Moonen et al. used CFD to assist in the design and evaluation of wind tunnels (Moonen et al., 2006, 2007). They performed CFD simulations that reproduced the entire closed-circuit wind tunnel, rather than just the measurement section, and showed that the average wind speed in the wind tunnel could be reproduced with an accuracy of within 10%. Their studies demonstrated that the information obtained in CFD simulations is useful for determining the pressure drop and flow rate in a wind tunnel, as well as the optimal locations of measurement points.

4. CONCLUSION

This paper outlined the current status and challenges of the complementary use of CFD simulations and wind tunnel tests in the built environment. There are four possible combination approaches: (1) the use of wind tunnel test results for the validation of CFD, (2) the use of wind tunnel tests for improving CFD models, (3) the use of complementary scales and resolutions in the two methods, and (4) the use of CFD to make wind tunnel tests more efficient and sophisticated. It is important to understand the characteristics of each method and to use the two methods in a complementary manner.

REFERENCES

Architectural Institute of Japan, 2016. AIJ Benchmarks for Validation of CFD Simulations Applied to Pedestrian Wind Environment around Building. Architectural Institute of Japan, Tokyo, Japan.

Blocken, B., 2014. 50 years of computational wind engineering: Past, present and future. Journal of Wind Engineering and Industrial Aerodynamics 129, 69–102. https://doi.org/10.1016/j.jweia.2014.03.008

Castro, I.P., Graham, J.M.R., 1999. Numerical wind engineering: the way ahead? Proc. Instn Civ. Engrs Structs & Bldgs 134, 275–277.

Cermak, J.E., 1975. Applications of fluid mechanics to wind engineering - A freeman scholar lecture. Journal of Fluids Engineering 97.

Jubayer, C.M., Hangan, H., 2018. A hybrid approach for evaluating wind fl ow over a complex terrain. Journal of Wind Engineering & Industrial Aerodynamics 175, 65–76. https://doi.org/10.1016/j.jweia.2018.01.037

Meroney, R.N., 2016. Ten questions concerning hybrid computational/physical model simulation of wind flow in the built environment. Building and Environment 96, 12–21. https://doi.org/10.1016/j.buildenv.2015.11.005

Moonen, P., Blocken, B., Carmeliet, J., 2007. Indicators for the evaluation of wind tunnel test section flow quality and application to a numerical closed-circuit wind tunnel. Journal of Wind Engineering and Industrial Aerodynamics 95, 1289–1314. https://doi.org/10.1016/j.jweia.2007.02.027

Moonen, P., Blocken, B., Roels, S., Carmeliet, J., 2006. Numerical modeling of the flow conditions in a closed-circuit low-speed wind tunnel. Journal of Wind Engineering and Industrial Aerodynamics 94, 699–723. https://doi.org/10.1016/j.jweia.2006.02.001

Murakami, S., 1990. Computational wind engineering. Journal of Wind Engineering and Industrial Aerodynamics 36, 517–538.

Shirzadi, M., Mirzaei, P.A., Tominaga, Y., 2020. RANS model calibration using stochastic optimization for accuracy improvement of urban airflow CFD modeling. Journal of Building Engineering 32, 101756. https://doi.org/10.1016/j.jobe.2020.101756

Stathopoulos, T., 2002. The numerical wind tunnel for industrial aerodynamics-Real or virtual in the new millennium? Wind and Structures 5, 193–208.

Stathopoulos, T., 1997. Computational wind engineering: Past achievements and future challenges. Journal of Wind Engineering and Industrial Aerodynamics 67 & 68, 509–532.

Tominaga, Y., 2024. CFD simulations of turbulent flow and dispersion in built environment : A perspective review. Journal of Wind Engineering & Industrial Aerodynamics 249, 105741. https://doi.org/10.1016/j.jweia.2024.105741

Tominaga, Y., Mochida, A., Yoshie, R., Kataoka, H., Nozu, T., Yoshikawa, M., Shirasawa, T., 2008. AIJ guidelines for practical applications of CFD to pedestrian wind environment around buildings. Journal of Wind Engineering and Industrial Aerodynamics 96, 1749–1761. https://doi.org/10.1016/j.jweia.2008.02.058

Linkage between spatial resolution and accuracy in 3D LES: three examples in bluff body aerodynamics

Félix Nieto [1], Antonio J. Álvarez [2], Kenny C.S. Kwok[3], Luca Patruno [4]

[1]*CITEEC – University of A Coruña, A Coruña, Spain, felix.nieto@udc.es;*
[2]*CITEEC – University of A Coruña, A Coruña, Spain, antonio.jose.alvarez@udc.es*
[3]*The University of Sydney, Sydney, Australia, kenny.kwok@sydney.edu*
[4]*University of Bologna, Bologna, Italy, luca.patruno@unibo.it*

SUMMARY:
Three examples of 3D LES simulations considering different spatial discretization resolutions and typologies are presented: a circular cylinder, a 3:2 rectangular prism at 12º AoA and a 4:1 rectangular prism under VIV. The impact of the mesh density, especially in the spanwise dimension, is shown to play a major role in the ability of the model to match the experimental results used for validation.

Keywords: CFD, 3D LES, turbulence, circular cylinder, 3:2 rectangular prism.

1. INTRODUCTION

The CFD (Computational Fluid Dynamics) modelling of the complex interplay between the free stream flow and a bluff body is full of challenges and uncertainties. It is well known that the mesh, that is the spatial discretization of the flow domain, may play a pivotal role in the ability of the simulation to reproduce correctly the phenomena of interest. There are several studies addressing this, such as Bruno and Oberto (2022), Bruno et al. (2012), among several others. In this contribution, three different cases adopting a 3D LES approach are presented for bluff bodies in smooth flow: a circular cylinder, a 3:2 rectangular prism at 12º angle of attack (AoA) and a 4:1 rectangular prism under VIV (vortex-induced vibration). For the three cases, it is emphasised how the mesh density and typology, and the spanwise mesh resolution impact the numerical results and the ability to accurately match the experimental references selected for validation.

2. GRID SIZING BASED ON THE TARGETED CUT-OFF FREQUENCY IN THE TURBULENT ENERGY SPECTRUM

In scale-resolved turbulence models such as LES, the ratio of the modeled vs resolved turbulent energy depends on the grid size, as the Navier-Stokes equations are spatially filtered. It is of interest to stablish beforehand the mesh size capable of resolving the targeted energy spectrum above a certain threshold, such as the 80% suggested in Pope (2004). The procedure proposed herein is based on the work of Geleta and Bitsuamlak (2022), using the cut-off velocity scale for isotropic turbulence v_c proposed by Sagaut (2006), as the cornerstone of the proposed approach:

$$v_c = \sqrt{\kappa_c E(\kappa_c)}, \tag{1}$$

where κ_c (κ_c=ω_c/U=$2\pi n_c/U$, with ω_c the circular frequency and n_c the one in Hz) is the cutoff wave number and $E(\kappa_c)$ is the energy spectrum based on the wavenumber related to κ_c.

Invoking Taylor's frozen hypothesis:

$$E(\kappa) = \frac{U}{4\pi}[S_u(n) + S_v(n) + S_w(n)] = \frac{U}{4\pi}S(n), \tag{2}$$

where S_u, S_v and S_w are the PSDs of the longitudinal, transversal and vertical wind components.

After appropriate manipulation, the expression for calculating the mesh size is obtained as shown in Eq. (3):

$$\delta_c = \sqrt{\frac{S(n_c)}{2n_c}} \tag{3}$$

In this application, the von Karman spectra have been used for the estimation of the cutoff frequency, and hence, the mesh element size.

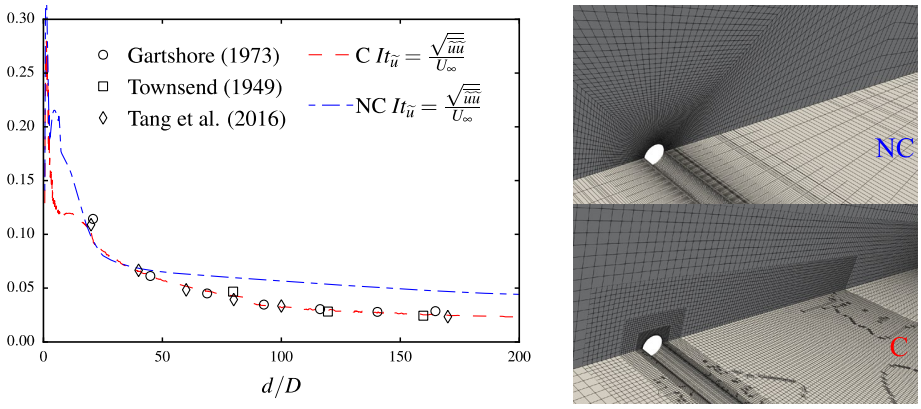
3. CASE 1: TURBULENCE INTENSITY IN THE WAKE OF A CIRCULAR CYLINDER

The authors have recently proposed the CFD implementation of the Small-Scale Rod-Induced Turbulence Method, SSRITM (Alvarez et al., 2023) as proposed in Gartshore (1973) for the analysis of aerodynamic responses under free stream turbulence. A key aspect of this approach is the correct reproduction of the turbulent characteristics in the wake of the upstream rod (circular cylinder) generating the turbulent flow. In Table 1, the characteristics of two different high-resolution meshes, one featuring non-conformal cells (NC) and the other featuring conformal ones (C), generated for an isolated rod of aspect ratio 48 are summarized. It can be noticed that the conformal mesh has a higher density in the spanwise direction and a lower height in the first layer attached to the circular cylinder, resulting in a higher number of overall elements in the grid.

Table 1. Circular cylinder mesh characteristics (D is the diameter of the cylinder, h_1 is the height of the first layer, h_{bl} is the height of the boundary layer mesh, δz is the spanwise discretization and T^* is the clock time per core and simulated second).

Mesh type	#elements	h_1/D	h_{bl}/D	n_{bl}	$\delta z/D$	T^*(s)
NC	2090368	1.205×10^{-3}	1.095×10^{-2}	6	1.380×10^{-2}	614
C	3776680	5.012×10^{-4}	1.027×10^{-2}	7	3.906×10^{-3}	670

In Figure 1, the longitudinal turbulence intensity profile along the wake centreline is provided for the two different mesh typologies at Re_D=11916. It can be seen that the conformal mesh produces a more accurate decay in the turbulent intensity profile. As the grid sizes increase in the non-conformal mesh, the resolved portion of the turbulent energy spectrum decreases, impacting the ability of the simulation to accurately reproduce the turbulent content in the wake.



a) b)

Figure 1. a) Along wind turbulent intensity in the wake centreline of the rod for conformal (C) and non-conformal (NC) meshes (D is the diameter of the rod and d is the distance downstream the rod), b) mesh details.

4. CASE 2: 3:2 RECTANGULAR PRISM AERODYNAMIC RESPONSE AT 12º AOA

Rectangular prisms with small width to depth ratios present a critical angle of attack, corresponding to the reattachment of the flow on the top or bottom sides of the prism partially facing the incoming flow, showing irregular vortex shedding (Carassale et al., 2014). For a ratio 3:2 rectangular prism, this critical angle of incidence is identified at an AoA α= 9º (Mannini et al., 2018). The numerical modelling of the aerodynamic response at an AoA higher than the critical is remarkably challenging. In Table 2, the characteristics of one non-conformal and another conformal mesh for the 3:2 rectangular prism are presented for reference. In Table 3, the time-averaged and fluctuating force coefficients along with the Strouhal number for the two meshes are provided along with the wind tunnel equivalent data at Re_H=143000. In can be noticed how the conformal mesh matches more accurately the experimental values adopted as reference.

Table 2. 3:2 rectangular prism mesh characteristics (H is the depth of the prism, h_1 is the height of the first layer, h_{bl} is the height of the boundary layer mesh and δz is the spanwise discretization and T^* is the clock time per core and simulated second).

3:2 Prism	#elements	h_1/H	h_{bl}/H	n_{bl}	$\delta z/H$	T^*(s)
NC	1487680	1.343×10^{-3}	4.752×10^{-2}	6	1.111×10^{-1}	76
C	1984368	4.700×10^{-4}	1.866×10^{-2}	9	3.125×10^{-2}	141

Table 3. 3:2 rectangular prism time-averaged and fluctuating force coefficients and Strouhal number.

3:2 Prism	$\overline{C_d}$	$\overline{C_l}$	$\overline{C_m}$	$\widetilde{C_d}$	$\widetilde{C_l}$	$\widetilde{C_m}$	St
NC	1.469	-0.716	0.188	0.122	0.318	0.032	0.138
C	1.697	-0.396	0.203	0.180	0.500	0.035	0.136
Mannini et al (2016, 2018)	1.681	-0.468			0.545		0.134

5. CASE 3: VIV OF A 4:1 RECTANGULAR PRISM

In Álvarez et al. (2019), a sensitivity study considering three different mesh resolutions for the vortex-induced vibration (VIV) response of a 4:1 ratio rectangular cylinder was reported. The study showed that for extrusion-generated grids the resolution in the spanwise direction played a

critical role in the ability of the 3D LES model to accurately replicate the range of VIV-prone reduced velocities and the peak oscillation response. In Table 4, a summary of the mesh characteristics along with the VIV response is reported for reference, showing the improved alignment with the experimental reference for C04, doubling the number of spanwise cells.

Table 4. Reduced velocity VIV range and peak response oscillation amplitude.

Method	Mesh	$\frac{\delta_z}{H}$	#cells vertical plane	#cells spanwise direction	total #cells	VIV range $U/(f_0 H)$	RMS (y/H)
3D LES	C03	0.1668	95462	24	2291088	(6.5, 11)	0.048
3D LES	C04	0.083	95462	48	4582176	(6.5, 10)	0.038
3D LES	C05	0.083	146953	48	7053744	(6.5, 10)	0.030
Exp. (Marra et al., 2011)						(6.2, 9.25)	0.032

6. CONCLUSIONS

In the context of 3D LES simulations, the review of the three cases considered herein has shed some light on the need for a high density spanwise discretization, of at least the 10% of the depth of the bluff body. Furthermore, the definition of the grid sizing based on the targeted percentage of the resolved turbulent energy spectrum offers a feasible balance between accuracy and computational demands.

ACKNOWLEDGEMENTS

This work has been supported by grant TED2021-132243B-I00 funded by MICIU/AEI/10.13039/501100011033 and by "European Union NextGenerationEU/PRTR. Funding has also been obtained from the Galician Regional Government through action ED431C 2021/33. The HPC resources at the Galician Supercomputing Centre (CESGA) have been used for the numerical simulations.

REFERENCES

Alvarez, A.J., Nieto, F., Nguyen, D.T., Owen, J.S. and Hernández, S., 2019. 3D LES simulations of a static and vertically free-to-oscillate 4:1 rectangular cylinder: Effects of grid resolution. J. Wind Eng. Ind. Aerodyn., 192, pp: 31-44.

Alvarez, A.J., Nieto, F., Kwok, K.C.S., Hernandez, S., 2023. A simplified CFD approach for bluff-body aerodynamics under small scale free stream turbulent flow. J. Wind Eng. Ind. Aerodyn., 241, 105500.

Bruno, L., Oberto, D., 2022. Effects of cell quality in grid boundary layer on the simulated flow around a square cylinder. Comput. Fluids, 238, 105351.

Bruno, L., Coste, N., Fransos, D., 2012. Simulated flow around a rectangular 5:1 cylinder: Spanwise discretisation effects and emerging flow features. J. Wind Eng. Ind. Aerodyn.. 104-106, pp: 203-215

Carassale, L. Freda, F., Marrè-Brunenghi, M., 2014. Experimental investigation on the aerodynamic behavior of square cylinders with rounded corners. Journal of Fluids and Structures, 44, pp:195-204.

Gartshore, I.S., 1973. The Effects of the Free Stream Turbulence on the Drag of Rectangular Two-Dimensional Prisms. University of Western Ontario, Canada. Technical report BLWT-4-T3.

Geleta, T. N., Bitsuamlak, G. T., 2022. Validation metrics and turbulence frequency limits for LES-based wind load evaluation for low-rise buildings. J. Wind Eng. Ind. Aerodyn., 231, 105210.

Marra, A.M., Mannini, C., Bartoli, G., 2011. Van der Pool-type equation for modeling vortex-induced oscillations of bridge decks. J. Wind Eng. Ind. Aerodyn., 147, pp: 776-785.

Mannini C., Marra, A.M., Massai, T., Bartoli, G., 2016. Interference of vortex-induced vibration and transverse galloping for a rectangular cylinder. J. Fluids Struct., 66, pp: 403-423.

Mannini, C., Massai, T., Marra, A.M., 2018. Unsteady galloping of a rectangular cylinder in turbulent flow. Journal of Wind Engineering and Industrial Aerodynamics, 173, pp: 210-226.

Pope, S.B., 2004. Ten questions concerning the large-eddy simulation of turbulent flows. New J. Phys. 6, 35.

Sagaut, P., 2006. Large Eddy Simulation for incompressible flows. An introduction, Third ed. Springer, Verlag, Berlin, Heidelberg, Germany.

LES for solar tracker wind loads: A benchmark experiment and validation study

Tsigereda G. Eshete[1,2], Tsinuel N. Geleta[1,3], Girma T. Bitsuamlak[1,4]

[1]*Western University, London, Ontario, Canada,*
[2]*teshete@uwo.ca*, [3]*tgeleta@uwo.ca*, [4]*gbitsuam@uwo.ca*

SUMMARY:
Severe weather and wind-induced damage are major drivers of utility-scale Photo-Voltaic (PV) system failures. Although Computational Fluid Dynamics (CFD) is proving to be a viable alternative to wind tunnels for wind load evaluation, its practical industry application has been limited due to the lack of standardized guidelines. This study is the second phase of a larger project focused on Large-Eddy Simulation (LES) benchmark validation for ground-mounted solar panels. It builds on the first phase by exploring solar tracker arrays in various configurations, incorporating new benchmark experiments and LES of key cases. The new boundary layer wind tunnel (BLWT) experiments provided high-quality wind field and aerodynamic data for 7 isolated and 35 SAT array configurations. Preliminary comparisons between LES and BLWT show excellent agreement in the wind field and aerodynamics. The study discusses details of the validation process and the effect of different parameters on solar tracker aerodynamics. The impact of auxiliary supports in wind tunnel experiments and best practices for obtaining reliable wind loads for solar arrays are also discussed.

Keywords: CFD, LES, Wind tunnel, Ground-mounted solar panels, Single-axis solar trackers, Wind loading

1. INTRODUCTION

Single-axis solar trackers (SATs) dominate utility-scale solar installation globally, comprising 94% of installations in the US in 2022 (Bolinger et al., 2023). Extreme weather and wind pose significant risk, being primary causes of utility-scale photovoltaic (PV) system failures. The aerodynamic characterization of SATs is complex due to their variable shapes, dynamic sensitivity, and low ground clearance. While quasi-static design procedures and code provisions for ground-mounted solar panels (GMSPs) account for dynamic effects, aeroelasticity and aeroelastic instability mechanisms remain active research areas.

Several studies (Bitsuamlak et al., 2010; Jubayer and Hangan, 2016) highlight the use and advantages of CFD for assessing wind loads on solar panels. Current research leverages large eddy simulation (LES) to examine unsteady behavior and peak aerodynamic loads, often validated with wind tunnel tests. However, standardizing CFD for wind load evaluation remains a challenge, underscoring the need for comprehensive benchmark WT tests and CFD-based guidelines.

This study builds on an LES benchmark validation campaign (Eshete et al., 2024) conducted on an isolated GMSP. The current study extends it with new benchmark wind tunnel tests and LES validation of select cases on a wide range of SAT arrays. Configurations exhibiting higher

aerodynamic loads were replicated in the LES for both validation and deeper insights into the flow mechanisms driving these loads. The study leverages the complementary strengths of WT tests and CFD simulations for a comprehensive analysis of solar tracker aerodynamics.

2. LES FOR SOLAR TRACKER WIND LOADS

A single-axis solar tracker array with nine rows is modeled using wind tunnel testing and large eddy simulation. Figure 1 shows the relevant geometric parameters of the aerodynamic model in BLWT and LES. A description of the target experiment and LES setup follows.

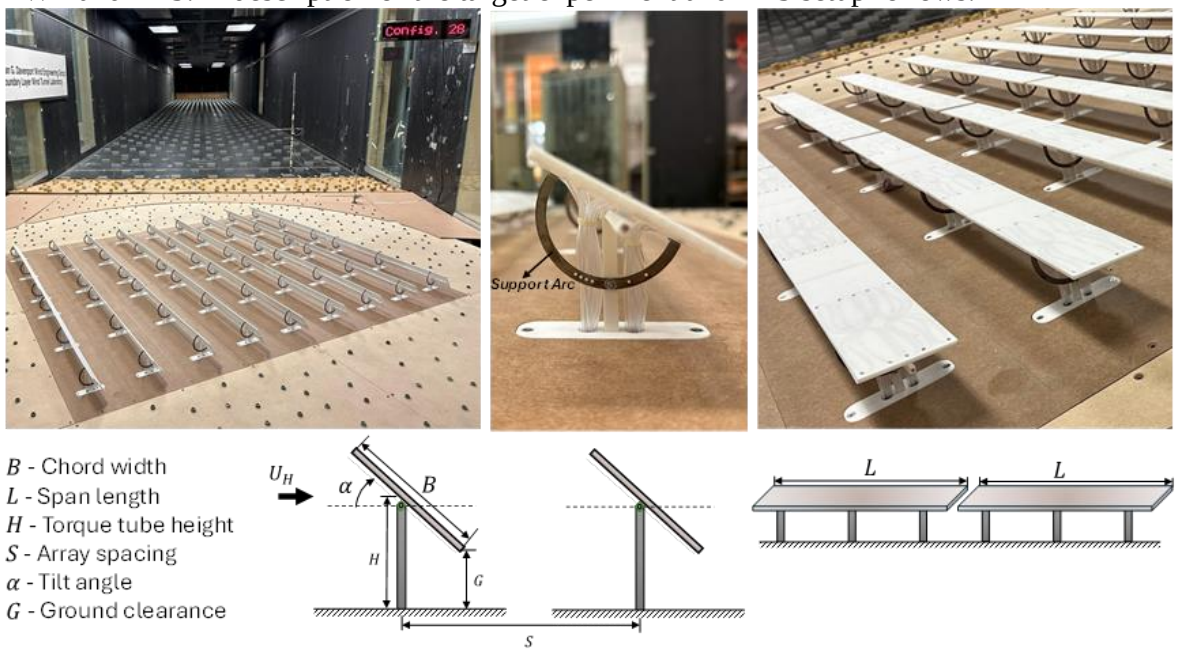


Figure 1. Standard configurations of the SAT array in wind tunnel and relevant geometric parameters

2.1. Benchmark wind tunnel experiment

Thirty-five array configurations were tested at Western University's BLWT Laboratory to generate a comprehensive dataset for LES validation. Table 1 details the test matrix. Configurations were varied by adjusting the tilt angle (0°- 60°), height (1.5-1.71 m), ground coverage ratio (0.35-0.41), and terrain (E2 & E3). The two boundary layer wind profiles 'E2' and 'E3' targeted nominal open terrain with aerodynamic roughness lengths $z_0 = 0.03$ and $z_0 = 0.05$ in full-scale. Pressure measurements were conducted at a tunnel speed of around 60 ft/s (18m/s) with the wind direction varying from 0° to 180° at 10° intervals. The aerodynamic model was designed per (ASCE, 2021) guideline, with additional provisions to minimize interference from instrumentation and auxiliary supports.

Table 1. Geometric details of the benchmark SAT array configurations. Lengths are at full scale in meters.

Configurations	B	L	α	S	H	G	Exposure
1 - 7	2.0	21.3		5.7	1.5	0.57	E2
8 - 14	2.0	21.3	0°, 5°, 10°,	5.7	1.5	0.57	E3
15 - 21	2.0	21.3	15°, 30°,	4.89	1.5	0.57	E2
22 - 28	2.0	21.3	45°& 60°	4.89	1.71	0.78	E2
29 - 35	2.0	21.3		5.7	1.71	0.78	E2

2.2. LES setup

The LES model replicates the wind tunnel setup, including the auxiliary supports, pressure tap distribution, and tube bundles beneath the panels. Figure 2 illustrates the computational domain and grid discretization scheme with the array in the 0° wind direction. Wind flows from left to right. Grid size and solver time-step are designed using equation (7) from (Eshete et al., 2024) to resolve turbulence up to a reduced frequency of 1 ($n_c B/U_H \geq 1$). The solver time-step is set at $0.0003s$, with further details on solver configuration available in (Eshete et al., 2024).

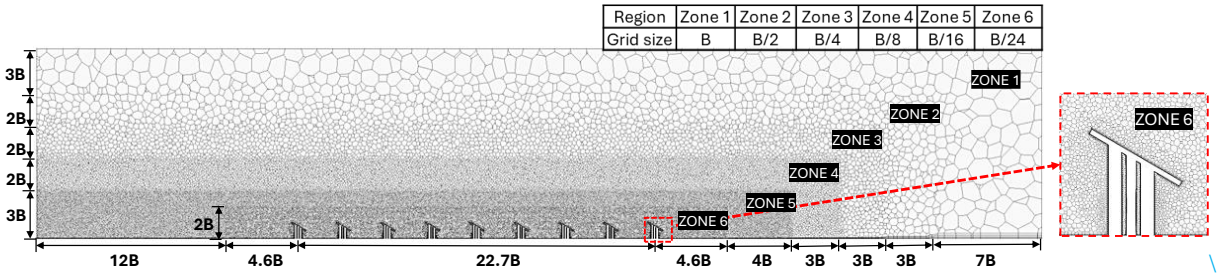


Figure 2. Computational domain and grid discretization

3. RESULTS AND DISCUSSION

LES validation typically involves three main steps: inflow generation, empty domain simulation, and main domain simulation. In the first step, target flow conditions are replicated using the selected inflow generation method and validated against BLWT data. The empty domain simulation outputs validate the incident flow, while the main domain simulation is used for aerodynamic loading validation. Accurate modelling of the incident wind field is essential in both WT and LES for proper aerodynamic pressure evaluation. Wind field validation is within 10% error margin for longitudinal velocity components at the reference height (U_H, $I_U(H)$ and ${}^{x}L_U(H)$). For brevity, only aerodynamic validation and related error margins are presented below.

Figure 3 displays the local pressure validation for one of the configurations replicated in LES, *SA_T30S190H50E2_AOA000SP*. This configuration represents a standard tracker with 30° tilt-angle, 1.5 m torque tube height and a ground coverage ratio of 0.35. The 0°-wind direction aligns with the "Nose Up into Wind" stow strategy. Figure 3(a) illustrates the peak pressure coefficients on the upper surface, demonstrating strong agreement between LES and wind tunnel results. Figure 3(b) presents a quantitative comparison of mean ($\bar{C}_P$), standard deviation (σ_{C_P}), and peak ($\hat{C}_P$) pressure coefficients across all pressure taps. While LES slightly underestimates peak C_P on the upper surface, it overestimates it on the lower surface. The scatter plot for all taps remains within the ±15% error margin, with the largest discrepancies observed in σ_{C_P} on the lower surface. The differences are possibly linked to space and time discretization sizes and physical imperfections of the WT model. Preliminary comparison shows that the auxiliary supports, i.e., tubing and other geometric details unique to the wind tunnel model, had minimal impact on the measured pressure coefficient for this configuration in straight wind direction. The percentage root mean square error (PRMSE) between LES and WT for all cases is below 20%. The full paper will further discuss validation details, the impact of parameters such as wind direction, tilt angle, and height, and the influence of auxiliary supports in wind tunnel studies of solar arrays.

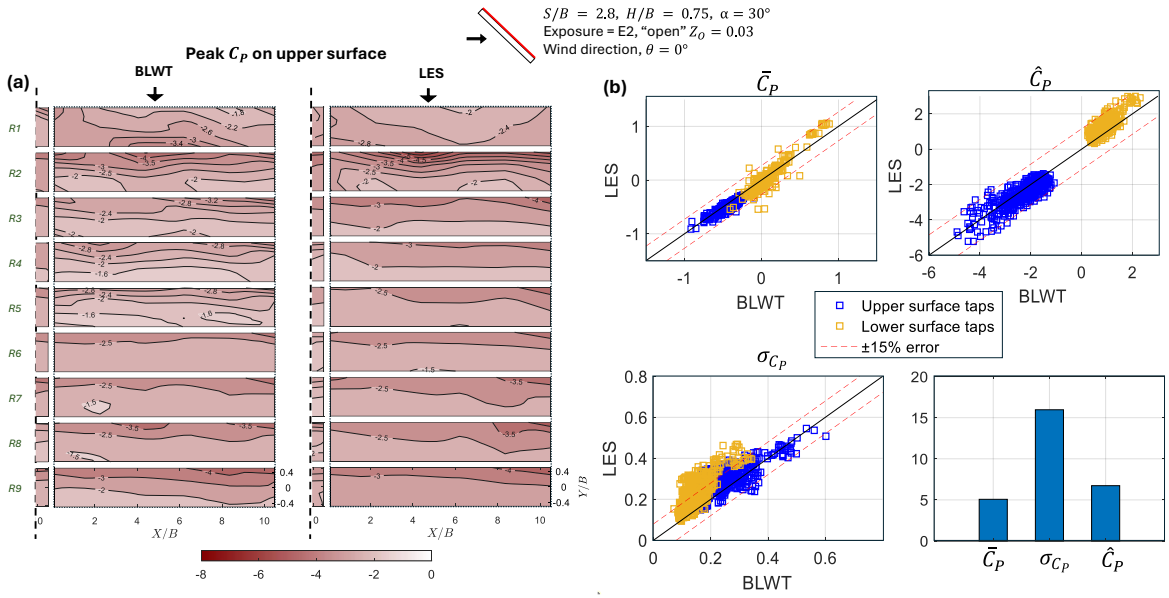


Figure 3. Local surface pressure validation (a) contour and (b) scatter plot for *SA_T30S190H50E2_AOA000SP*

4. CONCLUSIONS

A comprehensive benchmark wind tunnel dataset of wind field and aerodynamic data has been gathered for 7 isolated and 35 array configurations, primarily for CFD validation. The computational modeling framework and LES-based workflow, initially developed for an isolated GMSP, have been extended to this experimental dataset. Preliminary results indicate that the relative error in local pressure between BLWT and LES remains within 15%. The study demonstrated that with due attention to the detailed validation requirements, LES can produce a reasonably accurate wind load for solar tracker arrays.

ACKNOWLEDGEMENTS

The authors would like to thank Kimberley Adamek, Dan Ndhabihayimana, Fatma Abdul Hameed, and Leul T. Negate for their invaluable support during the experimental testing of the SAT array.

REFERENCES

ASCE, 2021. Wind tunnel testing for buildings and other structures ASCE/SEI 49-21, ASCE Standard. https://doi.org/10.1061/9780784415740

Bitsuamlak, G.T., Dagnew, A.K., Erwin, J., 2010. Evaluation of wind loads on solar panel modules using CFD. The Fifth International Symposium on Computational Wind Engineering 1–8.

Bolinger, M., Seel, J., Kemp, J.M., Warner, C., Katta, A., Robson, D., 2023. Utility-Scale Solar, 2023 Edition: Empirical Trends in Deployment, Technology, Cost, Performance, PPA Pricing, and Value in the United States 1–65.

Eshete, T.G., Geleta, T.N., Bitsuamlak, G.T., 2024. Towards benchmark validation of LES for ground-mounted solar panel wind loads. Journal of Wind Engineering and Industrial Aerodynamics 253, 105843. https://doi.org/https://doi.org/10.1016/j.jweia.2024.105843

Jubayer, C.M., Hangan, H., 2016. A numerical approach to the investigation of wind loading on an array of ground mounted solar photovoltaic (PV) panels. Journal of Wind Engineering and Industrial Aerodynamics 153, 60–70. https://doi.org/10.1016/j.jweia.2016.03.009

Challenges and developments in CFD modeling of urban microclimate at neighborhood scale

Aytaç Kubilay [1], Dominique Derome [2], Jan Carmeliet [3]

[1]*ETH Zurich, Zurich, Switzerland, akubilay@ethz.ch*
[2]*Université de Sherbrooke, Sherbrooke, Canada, Dominique.Derome@USherbrooke.ca*
[3]*ETH Zurich, Zurich, Switzerland, cajan@ethz.ch*

SUMMARY:
Numerical simulations of urban microclimate at neighborhood scale resolve a spectrum of physical processes. Such modeling is quite powerful to predict outdoor thermal comfort and the impact of heat mitigation measures and can provide valuable input for urban designers. However, no best-practice guidelines exist that englobe all aspects necessary for running urban microclimate simulations. This study provides an overview of important aspects to be considered such as boundary conditions, coupling between physical phenomena, numerical modeling and appropriate level of detail for vegetation and buildings using case studies. Coupled multiscale simulations are performed during heat wave conditions in urban neighborhoods showing different characteristics in three cities in Switzerland. Differences in outcomes are observed among the neighborhoods due to variations in building morphology and density, vegetation cover, street orientation, ventilation paths, and pavement and façade materials, among other variables. Challenges faced when obtaining necessary input data and interpreting the results are discussed.

Keywords: urban microclimate, outdoor thermal comfort, CFD modeling

1. INTRODUCTION

The combination of heatwaves with the urban heat island (UHI) effect can lead to very strong heat stress levels. As a result, many cities look for potential ways to help mitigate heat stress, including the use of vegetation and temporary shading devices, utilization of ventilation corridors, promotion of cool surfaces, use of water, etc. Numerical modeling of outdoor thermal comfort and potential heat mitigation measures involves taking into account several physical processes. These include the modeling of local wind-flow dynamics due to urban morphology, transport of heat and moisture in the air and in urban materials, wind resistance and evapotranspirative cooling due to vegetation, solar radiation entrapment and local shading, long-wave radiation exchange between urban surfaces and the sky, and may extend to anthropic heat sources and more.

Accurate assessment of mitigation measures and of their impacts requires high-resolution models that resolve the aforementioned physical processes. In addition, numerical simulations of urban microclimate at neighborhood scale often require a multiscale approach. For example, regional and city-wide conditions impact the overall flow patterns, while, at the same time, dynamic storage of heat and moisture at the scale of urban materials has a direct impact on the thermal conditions at pedestrian level. One significant challenge faced is the rather limited availability of guidelines or best practices on the modeling of these physical processes and on the coupling of various scales.

As a result, vastly different approaches are observed in the literature, making it difficult to interpret results and compare outcomes from different models.

In a first attempt to decipher generic methodological approaches that could be transposed into guidelines, this study focuses on the choices made in numerical settings, such as computational domain, numerical grid and boundary conditions, and in modeling approaches, such as the handling of urban trees and the level of detail for vegetation and buildings. These issues are presented and discussed through examples from case studies performed in different neighborhoods. A quantification of the respective impacts of different parameters delineates a path for generic guidelines

2. METHODOLOGY

A multiscale numerical approach is performed to model the urban climate with one-way coupling (Kubilay et al., 2020). At mesoscale, cities and their surroundings are modeled with a domain size around 50 km. This is performed by nested meteorological weather prediction models like WRF (Weather Research and Forecast Model) or COSMO (Consortium for Small-scale Modeling)(Strebel et al., 2024). At microscale, urban neighborhoods are modeled with a domain size around 1-2 km. This is performed using a solver developed by the authors, urbanMicroclimateFoam (2024), which is based on OpenFOAM libraries. The solver employs consecutive calculations of air flow with steady Reynolds-averaged Navier-Stokes (RANS), coupled with an unsteady heat and moisture (HAM) transport model for dynamic storage in urban materials. The long-wave and the reflected short-wave radiative exchanges are calculated with view factors using a radiosity approach with multiple reflections. Direct solar irradiation is modeled with ray casting to capture shading. The HAM model provides surface values of temperature and humidity as boundary conditions for the computational fluid dynamics (CFD) model. It requires the radiative, convective and latent heat fluxes calculated by the CFD model at coupled boundaries.

Foliage of trees are modeled as porous zones in the CFD domain with a non-zero leaf area density (LAD), which provide shading and modify wind flow. Source/sink terms are determined within these porous zones for momentum, heat, moisture. Heat balance on a leaf is determined based on the sensible, radiative and latent heat fluxes. Grass-covered surfaces are modeled with a leaf area index (LAI) and the radiative exchange between the grass and the underlying soil is modeled.

As for the lateral boundary conditions of the CFD domain, it is common to apply wind velocity and temperature profiles obtained from meteorological stations. Here, the local conditions obtained through the mesoscale simulations are applied to drive the flow in the microscale simulation using blending zones near the lateral boundaries. This allows for local changes in wind direction to be considered, e.g. rotation within the domain, compared to a fixed inlet/outlet flow.

3. RESULTS

Fig. 1 shows the results obtained for a case study in a part of the neighborhood of Altstetten in Zurich during a heat wave of three days. As the alignment of buildings and local wind direction can directly influence wind-flow patterns, the area of explicitly resolved buildings should be large

enough to prevent any artificial wind channeling due to missing upstream buildings. Grid sensitivity analysis can provide indications of numerical errors due to discretization. However, the large number of coupled models involved can complicate the analysis. For example, surface refinement may influence radiative exchange, which can then influence the flow field. Therefore, the same grid refinement is recommended to be used for each scenario to be solved, e.g. without and with trees.

Results show a large impact of parameters, such as tree size, LAD, time of day and air temperature, on transpirative cooling provided by urban trees. An example is given in Fig. 1b and 1c, which indicate that transpiration rate per leaf area is the highest for LAD = 0.5 m^2/m^3, while trees with high LAD show overall more transpiration and, as a result, lead to a lower leaf temperature on average. Such dependency of results on the imposed value of LAD lead to an uncertainty in interpreting results. This causes a difficulty compounded by appropriately selecting LAD for each specific tree, considering also that LAD is not constant throughout the year and not uniform within tree foliage. Furthermore, many numerical studies do not report how the transpiration rate is calculated. Trees can regulate their transpiration rate by controlling the openings on their leaves called stomata. Stomatal resistance is a function of plant species, solar radiation, vapor pressure deficit (relative humidity) in the air and available soil moisture content, causing additional uncertainty in results.

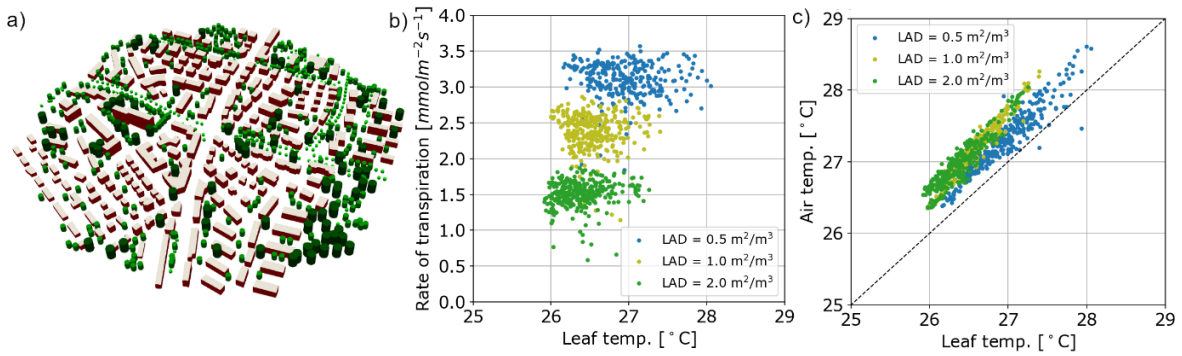


Figure 1. a) Modeled buildings and trees in Altstetten, Zurich. b) Volume-averaged values within the foliage of trees of rate of transpiration per leaf area and c) air temperature against leaf temperature at 12:00 CEST on July 29th, 2018. Each marker indicates a different tree.

Recently, we proposed two methodological improvements. First, Rodriguez et al. (2024) propose a polyhedron shape called rhombicuboctahedron (RBC) to represent tree foliage as it provides simplicity and flexibility to capture a large variety of foliage while retaining accuracy. In contrast, commonly-used shapes such as cubic or spherical representations can lead to discrepancies. Second, Nevers et al. (2024) investigate the modeling of lift-up buildings with a raised ground floor, which are common in typical neighborhoods in Singapore. A porous approach is proposed that improves the results in comparison to simplifications such as completely removing the columns on the raised ground floor.

Once the simulations are complete, the results are post-processed to evaluate the outdoor thermal comfort. Universal thermal climate index (UTCI) represents the human thermal sensation using an equivalent temperature considering the influence of long-wave radiation from surfaces and solar

radiation on a person, humidity and air speed in addition to the air temperature. Fig. 2 shows the UTCI patterns in three neighborhoods in Switzerland during the same heat wave. While the shading effect, through mean radiant temperature, seems to be the dominant parameter, the local impact of flow field is also visible. Therefore, choices mentioned above, e.g. wind-flow boundary conditions, tree dimensions and LAD, may influence the UTCI distribution and the predicted impact of potential mitigation measures.

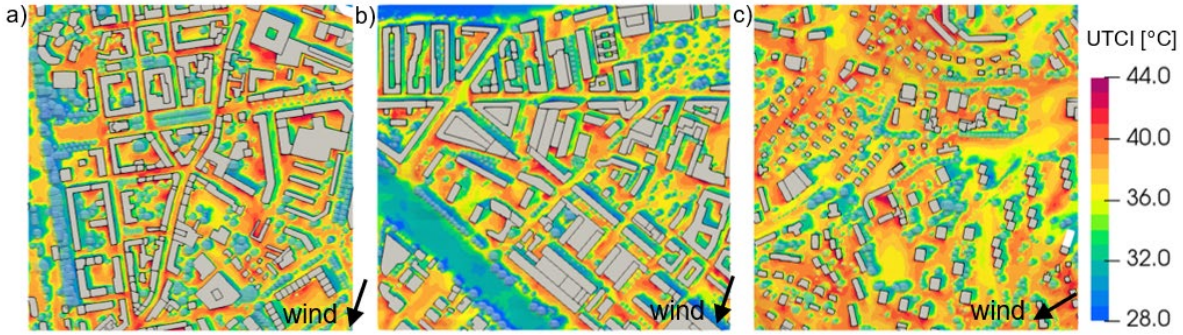


Figure 2. UTCI at 2 m height on June 24th, 2019, at 16:00 CEST in a) Carouge, Geneva, b) Jonction, Geneva and c) Schoenberg, Fribourg.

4. CONCLUSION

Recent examples of numerical simulations of microclimate at neighborhood scale show the strength of such modeling to predict outdoor thermal comfort and evaluate the impact of heat mitigation measures. These models resolve coupled physical processes at local scale which depend on a large number of input parameters. This study provides an overview of various challenges experienced during recent case studies performed in neighborhoods showing different characteristics, challenges, not yet considered by available best-practice guidelines. Further improvement to unify existing approaches or at least to streamline them is acutely needed, as otherwise it is difficult to compare and interpret results from different studies.

ACKNOWLEDGEMENTS

The authors would like to thank the financial support of project SWICE (Sustainable Wellbeing for the Individual and the Collectivity in the Energy Transition) within the funding pro-gramme SWEET of the Swiss Federal Office of Energy.

REFERENCES

Kubilay, A., Allegrini, J., Strebel, D., Zhao, Y., Derome, D., Carmeliet, J., 2020. Advancement in Urban Climate Modelling at Local Scale: Urban Heat Island Mitigation and Building Cooling Demand. Atmosphere 11, 1313.

Nevers, C., Kubilay, A., Carmeliet, J., Derome, D., 2024. CFD simulation of the wind flow under lift-up buildings using a porous approach. Build. Environ. 263, 111867.

Rodriguez, A., Lecigne, B., Wood, S., Carmeliet, J., Kubilay, A., Derome, D., 2024. Optimal representation of tree foliage for local urban climate modeling. Sustain. Cities Soc. 115, 105857.

Strebel, D., Derome, D., Kubilay, A., Carmeliet, J., 2024. Improved mesoscopic meteorological modeling of the urban climate for building physics applications. J. Build. Phys. 17442591241266553.

urbanMicroclimateFoam - An open-source solver for coupled physical processes modeling urban microclimate based on OpenFOAM [WWW Document], 2024. URL https://gitlab.ethz.ch/openfoam-cbp/solvers/urbanmicroclimatefoam (accessed 1.14.23).

Reflecting on the wind direction effects: how many degrees are enough?

Clara García-Sánchez[1] and Akshay Patil[1]

[1] *3D Geoinformation Research Group, Delft University of Technology, Delft, the Netherlands,*
C.Garcia-Sanchez@tudelft.nl

SUMMARY:
Urban flows are sensitive to a large set of input parameters such as wind speed, wind direction, stratification, and inflow turbulence, to list a few. Past studies have shown that wind direction is one of the most relevant parameters, determining where wakes with increased turbulence may appear or local zones acceleration may occur due to the morphological alignment with the wind direction. Although best practice guidelines recommend between 12 and 16 wind directions to evaluate pedestrian wind comfort, differences in urban flow predictions can be seen even with only a few degrees of difference within the input. This work explores the sensitivity of urban flow characteristics to wind direction by running a limited set of 25 wind directions (specifically 90°-115°) for the well-known Mock Urban Setting Test (MUST) experiment. We compute statistics using different samples and show how the results vary depending on the number of angles sampled for the average. The aim is to raise awareness about the sensitivity of the wind incidence angular resolution and its connection with the underlying urban morphology.

Keywords: computational fluid dynamics, urban flows, wind direction, morphology

1. INTRODUCTION

Urban flow simulations have been acquiring an increasing interest in the past decades (Blocken, 2015), driven by the the increased extreme meteorological events and the boundary layer response as a consequence. Thus, designing cities that consider the meteorological boundary conditions (García-Sánchez and Gorlé, 2018), aiming at maximizing cooling during heat waves and ensuring pedestrian wind comfort, can have a large impact in the future. One of the main parameters defining how the flow looks within a urban scenario is the wind direction (García-Sánchez, Philips, et al., 2014), affecting outdoor wind flows and indoor ventilation (Van Hooff and Blocken, 2010). Generally, current best practice guidelines recommended simulating between 12 and 16 different wind directions to ensure a good representation on an annual basis for pedestrian wind comfort (Yoshie et al., 2007). However, other studies have recently suggested that this number needs to be increased to 24 for higher accuracy or even 36 for cases where safety might be a concern (Hågbo and Giljarhus, 2024). Within this work, we set up a framework to analyze the impact of wind direction on urban wind flows and to understand the correlation between flow direction and urban morphology within our results. Our final goal is to understand the relation between these two fields to determine if there is a path to limit the number of wind directions, while ensuring predictability, and how much we can reduce the number of runs depending on the area of interest and the city's layout.

2. TEST CASE

We considered the Mock Urban Setting Test (MUST) experiment, a large outdoor field experiment that monitored atmospheric dispersion and wind flow. In addition to the real-scale campaign, further experiments included wind tunnel experiments. The data is publicly available under request (Biltoft, 2001; Yee and Biltoft, 2004). Although the campaign measured dispersion, within this work the analysis only focuses on wind fields.

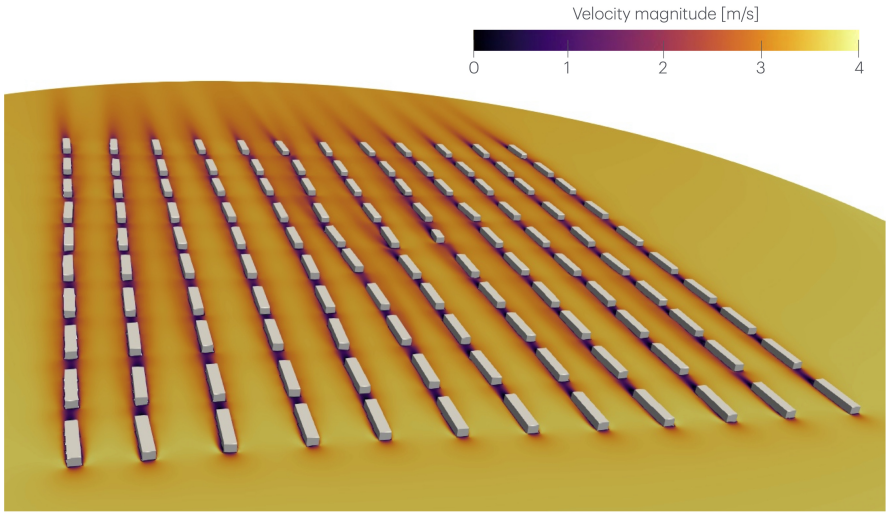


Figure 1. MUST buildings layout with a velocity magnitude contour plot at pedestrian height.

The idea of using this test case scenario is that most of the geometry is similar since the experiment included 119 shipment containers with the same shape (12.2m long, 2.54m high, and 2.42m wide) and 1 VIP van with a form that differs widely from the containers around the center of the domain. As figure 1 shows, the containers were placed on a grid of 10 by 12, and although not all containers were placed at the same distance from each other, due to measurement constraints, their position was well recorded and reproduced for the numerical simulations.

3. CFD SETUP

We use the open-source C^{++} libraries OpenFOAM, version 7, to solve the Reynolds-Averaged Navier-Stokes equations with the standard k-ε turbulence model (Jasak et al., 2007) and a roughness wall function for the terrain (Parente et al., 2011). The equations are solved in the steady state using a neutral atmospheric boundary layer assumption. Boundary conditions are defined based on best practice guidelines, guaranteeing at least 15H from inflow and outlet since a circular domain is used (Franke et al., 2011).

4. PRELIMINARY RESULTS

To process the results, we compute statistics based on average velocity magnitude fields at 1.75 m height, which we assume it corresponds to a typical pedestrian height. To compute this we use a diverse set of wind directions, including 1°, 2°, 5° and 10° resolution. We assume every wind direction is equally probable, considering an ideal uniform wind direction distribution where all

bins weight the same at the inflow. The velocity magnitude averaged at 1° resolutions is considered as the best possible results, and therefore our *reference case*.

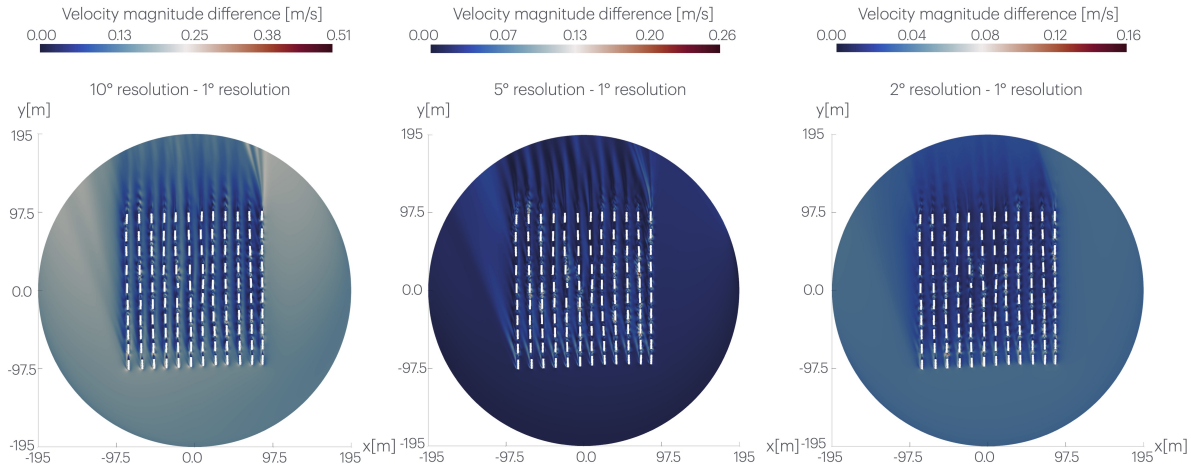


Figure 2. Velocity magnitude differences with the *reference case* (1°) at pedestrian height (1.75m): from left to right, using an angular wind incidence of (10°, 5°, 2°).

Figure 2 shows three contour plots with the differences in averaged velocity magnitude between the reference case and the averages performed at 10°, 5° and 2° resolutions. As it can be observed the differences decrease as we progress with finer angular resolution, reducing the maximum difference values between the cases. In all cases differences tend to peak between the building structures, as it can be also seen for the 2° resolution case. In larger degree resolution averages (5° and 10°), larger differences overall the domain can also be observed.

5. CONCLUSION & FUTURE WORK

As the results show, the number of wind directions considered to perform velocity magnitude averages will impact the results. The question here is, how much would that impact be, and is there a relation to the underlying building morphology? and if so, can we use that knowledge to determine which wind directions are best to run for each specific area?

To start addressing these questions, our future work envisions two further lines of research: first, extending our current analysis to all possible wind directions, including also an input wind direction probability more aligned with reality, and second, extrapolating the results into more realistic urban environments, where every geometry differs from each other and, therefore, different conclusions regarding morphology might be needed.

ACKNOWLEDGEMENTS

The authors acknowledge the use of computational resources of the DelftBlue supercomputer, provided by Delft High Performance Computing Centre (https://www.tudelft.nl/dhpc).

REFERENCES

Biltoft, C. A., 2001. Customer report for mock urban setting test. DPG Document, 160–000.

Blocken, B., 2015. Computational Fluid Dynamics for urban physics: Importance, scales, possibilities, limitations and ten tips and tricks towards accurate and reliable simulations. Building and Environment 91, 219–245.

Franke, J., Hellsten, A., Schlunzen, K. H., and Carissimo, B., 2011. The COST 732 Best Practice Guideline for CFD simulation of flows in the urban environment: a summary. International Journal of Environment and Pollution 44, 419–427.

García-Sánchez, C. and Gorlé, C., 2018. Uncertainty quantification for microscale CFD simulations based on input from mesoscale codes. Journal of Wind Engineering and Industrial Aerodynamics 176, 87–97.

García-Sánchez, C., Philips, D., and Gorlé, C., 2014. Quantifying inflow uncertainties for CFD simulations of the flow in downtown Oklahoma City. Building and environment 78, 118–129.

Hågbo, T.-O. and Giljarhus, K. E. T., 2024. Sensitivity of urban morphology and the number of CFD simulated wind directions on pedestrian wind comfort and safety assessments. Building and Environment 253, 111310.

Jasak, H., Jemcov, A., Tukovic, Z., et al., 2007. OpenFOAM: A C++ library for complex physics simulations. Proceedings of International workshop on coupled methods in numerical dynamics. Vol. 1000. Dubrovnik, Croatia), 1–20.

Parente, A., Gorlé, C., Beeck, J. van, and Benocci, C., 2011. A comprehensive modelling approach for the neutral atmospheric boundary layer: consistent inflow conditions, wall function and turbulence model. Boundary-layer meteorology 140, 411–428.

Van Hooff, T. and Blocken, B., 2010. On the effect of wind direction and urban surroundings on natural ventilation of a large semi-enclosed stadium. Computers & Fluids 39, 1146–1155.

Yee, E. and Biltoft, C. A., 2004. Concentration fluctuation measurements in a plume dispersing through a regular array of obstacles. Boundary-Layer Meteorology 111, 363–415.

Yoshie, R., Mochida, A., Tominaga, Y., Kataoka, H., Harimoto, K., Nozu, T., and Shirasawa, T., 2007. Cooperative project for CFD prediction of pedestrian wind environment in the Architectural Institute of Japan. Journal of wind engineering and industrial aerodynamics 95, 1551–1578.

Recommendations for CFD best practice guidelines and requirements for wind loads on buildings

Tsinuel N. Geleta [1], Girma T. Bitsuamlak [2]

[1]*Western University, London, Canada, tgeleta@uwo.ca*
[2]*Western University, London, Canada, gbitsuam@uwo.ca*

SUMMARY:
This study proposes best practice guidelines for using Computational Fluid Dynamics (CFD) in predicting wind loads on buildings, aiming to address the lack of standardized procedures that limit CFD's use in structural design. While existing CFD guidelines focus on non-transient methods like RANS, this paper emphasizes transient approaches such as Large-Eddy Simulation (LES) for more accurate wind load predictions. A detailed table outlines essential CFD parameters and requirements to improve alignment between simulation results and real-world conditions. The study also introduces a structured workflow with key validation steps, enhancing prediction reliability. Future research needs include mesh optimization, uncertainty quantification, and advanced turbulence models to position CFD as a reliable alternative to wind tunnel testing for structural applications.

Keywords: Computational fluid dynamics (CFD), Large-Eddy Simulation (LES), wind loads, best practice guidelines

1. INTRODUCTION

The main barrier to broader CFD adoption in structural wind load design is the lack of specific best practice guidelines. Although transient CFD methods have historically been costly, advancements like machine learning and GPU processing are reducing these expenses. Existing CFD guidelines in wind engineering (Franke et al., 2007, Blocken, 2015) focus mainly on RANS methods, which lack transient capabilities, and the only recognized standard for CFD wind loading is from the Architectural Institute of Japan (Tamura, 2008), creating a gap in standard procedures for critical applications. This study aims to fill that gap by offering guidelines specifically for CFD wind load simulations on buildings, addressing the complexities of wind load modeling and ways to reduce discrepancies between CFD results and target data.

2. RECOMMENDED WIND LOADING REQUIREMENTS FOR CFD

The wind loading requirements for CFD in Table 1 are based on essential physical principles to ensure accurate wind load predictions on structures. Closely aligning with ASCE/SEI, (2021) guidelines, they emphasize a rigorous, principle-driven approach rather than reliance on computational tools alone. This study reaffirms existing standards and introduces additional factors specific to CFD wind load assessments, proposing classifications for different structural types (e.g., flexible vs. rigid, low-rise vs. tall buildings) to tailor validation protocols. Table 1 outlines key CFD parameters for wind load evaluation, covering flow field simulations and load assessments to improve prediction accuracy and structural safety in wind engineering.

Table 1. Wind loading requirements and corresponding CFD parameters for components and cladding loads.

Physical parameter	Controlling CFD parameter	Requirements
Peak wind load	Turbulence modeling approach (i.e., RANS, LES, DNS, etc.)	• The CFD method must be transient to estimate the peak wind load reliably.
Flow field extents	Inflow, Computational domain (CD) size, mesh in the approach flow region	• Shall cover the region between the inlet and the building and
Reynolds no., Re	Viscosity, scales (velocity and length)	• $Re \geq 11{,}000$ †
Jensen number, L_b/z_0	Inflow, Near-ground boundary layer modeling (NGBLM)	• $\left(\frac{L_b}{z_0}\right)_m = \left(\frac{L_b}{z_0}\right)_p$ within a factor of 3 for ABL or partial ABL †
Surface Reynolds number, Re_τ	Inflow, NGBLM, viscosity	• $Re_\tau = \frac{u_* z_0}{\nu} \geq 2.5$ †
Turbulence intensity, I_u, I_v, I_w	Inflow, NGBLM, and mesh size in the approach flow region (δ^{AF})	• All components shall correspond to the velocity profile (i.e., z_0) †
Integral length scales, ${}^xL_u, {}^xL_v, {}^xL_w$	Inflow, computational domain size, duration	• All components shall correspond to the velocity profile (i.e., z_0) for $0.6L_b \leq z \leq L_b$ and $\left(\frac{{}^xL_u}{L_b}\right)_m = \left(\frac{{}^xL_u}{L_b}\right)_p$ or $\left(\frac{{}^xL_u}{L_b}\right)_m \geq 3$ †
Spectra, S_{uu}, S_{vv}, S_{ww}	Inflow, NGBLM, δ^{AF}	• All components shall correspond to the velocity profile (i.e., z_0) for $0.6L_b \leq z \leq L_b$ †
Small-scale turbulence	Inflow; LES filter (mesh) size, $\delta^{AF} = \sqrt{\frac{\pi}{n_c}F(n_c)}$, $F(n_c) = \sum S_{ii}(n_c)$, $n_c = \frac{f_{mk}U_H}{L_b}$ (Geleta and Bitsuamlak, 2022); time discretization; and CFL number	• The spectra shall match that of the target up to a reduced frequency. – $f_{mk} = 2$ – 2nd or higher-order time discretization – The mean CFL number shall be less than 1
Duration, T	Duration of simulation after the initial transient stage.	• $T \geq 500I$, where I is the integral time scale at the critical height for the load †
Spurious pressure	Inflow, level of spatial and temporal interpolation	• The inflow must be divergence-free $\nabla \cdot \vec{u} = 0$. • The spurious pressure at the building location shall be minimal.
Blockage	Computational domain size	• Shall be $< 5\%$, or it needs to be justified †
Local pressure coefficient, C_p	All the parameters controlling the flow field, local mesh, near-wall treatment on the building, SGS model, numerical schemes	• The flow field and aerodynamic load shall be validated in tandem. – The flow field must be validated with L_b, relevant for the load. – The mean, standard deviation, peak, skewness, and kurtosis of point (local) C_p shall match those of the target.
Area-averaged load	All the above parameters and local mesh resolution.	• The area-averaged peak load at various averaging areas shall match that of the target.
Integrated global loads	All the above parameters and local mesh resolution.	• The temporal statistics (mean, std., peak etc.) and spectra of the desired quantity (e.g., base shear and moment, etc.) shall agree with those of the target. • Multi-point statistics of wind field and in the order of the characteristic building dimension also needs validation
Structural response	All the above parameters and local mesh resolution.	• The temporal statistics (mean, std. etc.), especially peak response (e.g., displacement, acceleration, etc.) shall agree with those of the target.

† Adopted from ASCE 49-21 (ASCE/SEI, 2021)

3. RECOMMENDED CFD WORKFLOW FOR WIND LOAD EVALUATION

The simulation of wind load on structures involves a series of stages designed to ensure accuracy and reliability using methods like LES or DES. The process begins with defining the target flow field and selecting a verified CFD method, as shown in Figure 1. After classifying the wind loading problem, general settings—such as geometry, boundary conditions, and an empty domain mesh—are established. Next, the simulation is divided into two primary stages: an initial empty domain simulation to establish basic flow parameters, followed by the main domain simulation, which incorporates building-specific details. At each stage, a key aspect is validating results against requirements outlined in Section 2 to confirm they meet acceptable standards. If results fail validation, adjustments to mesh design, boundary conditions, numerical schemes, or turbulence models are made iteratively. Ultimately, the process concludes by either reporting wind loads or documenting validation details, providing a standardized approach for CFD simulations in wind loading applications.

4. FUTURE RESEARCH NEEDS

To advance the development of Computational Fluid Dynamics (CFD) guidelines for wind loading applications, future research should focus on several key areas. First, there is a need for refined criteria and detailed guidance on mesh design in different regions of the computational domain to optimize accuracy and efficiency in simulations. Second, uncertainty quantification for CFD should be emphasized, providing acceptable error margins to enhance the reliability of results. Third, research should explore the integration of advanced turbulence models that better capture complex flow patterns around structures, including the effects of boundary layer development and separation. Additionally, the development of benchmark experiments with consensus across several sources and the uncertainty margins of the data will be essential for validating CFD approaches and ensuring consistency in results. Lastly, validation studies against experimental data and real-world scenarios must be prioritized to ensure that CFD predictions align closely with observed wind loading conditions.

5. SUMMARY AND CONCLUSION

This study outlines requirements for CFD simulation of generalized wind loading, aligning with existing wind tunnel guidelines. The recommendations are divided into two parts: *recommended requirements*, which establish largely universal standards comparable to those for wind tunnels, and a *recommended workflow*, offering one approach to meeting these standards in LES, among other transient CFD methods. Research needs are also proposed to further refine and expand these guidelines. Key CFD parameters influencing requirements and specific recommendations for their application are highlighted.

ACKNOWLEDGEMENTS

We appreciate the HPC resources provided by the Digital Research Alliance of Canada and SHARCNET.

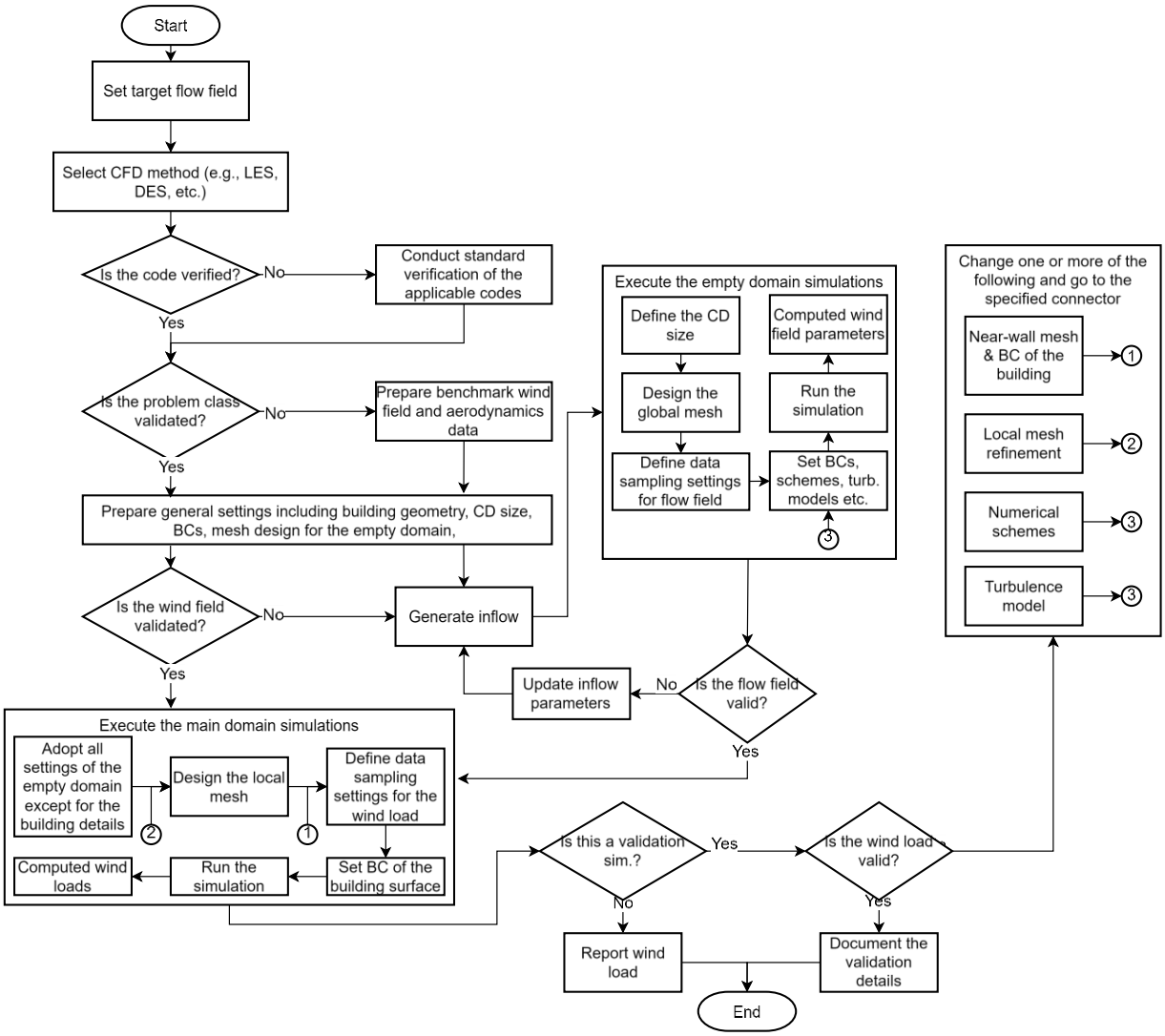


Figure 1. Recommended CFD workflow for wind load evaluation.

REFERENCES

ASCE/SEI, 2021. Wind tunnel testing for buildings and other structures ASCE/SEI 49-21, ASCE standard. American Society of Civil Engineers, Reston, VA, USA. https://doi.org/10.1061/9780784415740

Blocken, B., 2015. Computational Fluid Dynamics for urban physics: Importance, scales, possibilities, limitations and ten tips and tricks towards accurate and reliable simulations. Build. Environ. 91, 219–245. https://doi.org/10.1016/j.buildenv.2015.02.015

Franke, J., Hellsten, A., Schlünzen, H., Carissimo, B. (Eds.), 2007. Best practice guideline for the CFD simulation of flows in the urban environment, COST Action 732. Hamburg, Germany.

Geleta, T.N., Bitsuamlak, G.T., 2022. Validation metrics and turbulence frequency limits for LES-based wind load evaluation for low-rise buildings. J. Wind Eng. Ind. Aerodyn. 231, 105210. https://doi.org/10.1016/j.jweia.2022.105210

Tamura, T., 2008. Towards practical use of LES in wind engineering. J. Wind Eng. Ind. Aerodyn. 96, 1451–1471. https://doi.org/10.1016/j.jweia.2008.02.034

Implementing surface roughness in OpenFOAM using the CORINE database for mesoscale CFD simulations

Alessio Ricci [1], Massimiliano Burlando [2]

[1] *University School for Advanced Studies (IUSS), Pavia, Italy, alessio.ricci@iusspavia.it*
[2] *University of Genoa, Genoa, Italy, massimiliano.burlando@unige.it*

SUMMARY:
The rapid explosion of computation capacities of the last decades led to a massive use of Computational Fluid Dynamics (CFD) technique for simulation of wind fields at the mesoscale. Temporal and spatial mesoscales, typically simulated with forecast models (FM), have quickly become the focus of investigation for wind engineers and practitioners involved in various civil and wind engineering applications. The definition of surface roughness, along with other CFD settings, is essential for accurately modeling atmospheric winds over a mesoscale. In CFD studies, aerial views from Google Maps/Earth are commonly used in conjunction with international standards/codes to define and assign the aerodynamic roughness length (z_0) to specific zones by patches. However, accurately identifying the land cover and corresponding z_0 of mesoscale domains is time consuming and challenging. Nevertheless, methods widely used in atmospheric science for mapping surface roughness in FM can be leveraged to enhance mesoscale CFD studies. This was the goal of this study, which proposes a procedure integrating the CORINE land cover database with the opensource OpenFOAM tool to define and simulate an atmospheric boundary layer (ABL) wind on a complex meso-γ scale environment. Preliminary CFD results on the complex topography of Genoa region are provided here.

Keywords: surface roughness, CORINE land cover, OpenFOAM tool

1. INTRODUCTION

The rapid increase in computation capacity has enabled the widespread of CFD methods, typically adopted for building-scale simulations (e.g. ≤ 1 km), to conduct large-scale atmospheric boundary layer (ABL) simulations (e.g. ≤ 20 km) in complex topographies including hills and mountainous as well as built environments. As a result, the temporal and spatial mesoscales usually simulated by physicists with forecast models (FM) have quickly become the focus of investigation for wind engineers and practitioners who use the CFD for different civil engineering applications (e.g. Blocken, 2014; Ricci, 2024). According to the American Meteorological Society's Glossary of Meteorology and Orlanski (1975), the mesoscale is defined as the 2–2000 km scale sub-classified in meso-α, meso-β, meso-γ scales referring to horizontal scales of 200-2000 km, 20-200 km and 2-20 km, respectively. Horizonal scales smaller than 2 km, where most of the wind engineering phenomena occur, are classified as microscale. This indicates that the CFD has been widely used to investigate physical phenomena related to wind that typically occur at larger scales than the microscale. The definition of surface roughness, along with other CFD settings, is essential for accurately modeling atmospheric winds at the mesoscale. In CFD studies, aerial views from Google Maps/Earth are commonly used in conjunction with international standards/codes to define and assign the aerodynamic roughness length (z_0) to specific zones by patches. While the accurate definition of land cover and corresponding z_0 can be quite straightforward in case of small

environments (a few km^2), this step can be very time consuming and characterized by high degree of uncertainty for mesoscale domains, where a large number of patches (and z_0) should be defined and assigned. Given that the mesoscale is more usual of FMs, well-known methods used in atmospheric science for mapping surface roughness can be leveraged to enhance mesoscale CFD studies. This is the goal of this study, which proposes an automatic procedure that integrates the CORINE land cover database (Wyatt et al., 1988) with the OpenFOAM tool to define and simulate an atmospheric boundary layer (ABL) wind on a complex meso-γ scale environment. It is worth noticing that, in CFD studies the surface roughness patches can be defined in two ways irrespective of the land cover source: (1) during the geometry generation (prior to construct the grid), using Boolean operations between the geometries of the environment and the patches from CORINE land cover source; (2) during the grid generation, using specific `utilities` of the opensource OpenFOAM tool. While both strategies have their advantages and disadvantages, the strategy (2) was innovatively adopted here to allow greater flexibility in accommodating variations of roughness patches after the computational grid was generated. This project is only one stage of a wide research framework that proposes a fully opensource automated geometry and grid generation procedure tailored for CFD simulations of wind flow over large-scale domains (see Žužul et al., 2024).

2. METHODOLOGY

Following the strategy (2), in this study the roughness patches are defined through the CORINE land cover database on the complex topography of Genoa region (Figure 1). The selected area has dimensions of 18.5 (width) x 25.5 (length) x 4.0 (height) km^3.

The procedure is organized in six steps. In step 1, the topography is extracted from the public NASA Shuttle Radar Topography Mission (SRTM) repository (NASA JPL, 2013). The SRTM database provides access to terrain elevation data, allowing users to retrieve point clouds for a specific area of interest (Figure 1). It can be done interactively or in a programming language (e.g. Matlab) by specifying the latitude and longitude range. Then, the point clouds can be converted into the surface triangulation, namely the stereolithography (STL) as shown in Figure 1. In step 2, the CORINE land cover database is imported in QGIS, each land cover type is selected one by one and the corresponding bi-dimensional patches are extracted and saved in text files containing the patches' borders in the chosen coordinate system. Then, text files are imported in OpenSCAD and the patches are converted into three-dimensional volumes that will intersect the topography. Volumes are finally saved as STL files. In Step 3, the basic grid is generated in OpenFOAM using the `blockMesh` dictionary. Here, the basic grid size and growth rate of control volumes are defined by the users, based on their expertise on mesoscale CFD simulations, in an empty domain with the same dimensions of the selected area of interest. Note that, the grid size defined at this step may have implications on the roughness patches resolution defined in the next steps. In Step 4, the STL of the selected area is imported in OpenFOAM for grid generation to be executed with `snappyHexMesh` dictionary or the `Cf-Mesh` tool. For this study, high-quality hex-dominant cells are created in the domain and further refined near the topography and water surface, to better catch the wind flow behavior on the different roughness patches. In Step 5, the STL roughness volumes created in Step 2 are transferred to the computational grid (constructed in Step 4) by using the `topoSet` and `createPatch` dictionary of OpenFOAM. It is important to stress that, the grid-size resolution defined in Step 4 can heavily affect the roughness patch resolution, as discussed in Section 3.

In Step 6, the z_0 value of each roughness patch can be defined in `0/nut` once converted into the corresponding equivalent sand-grain roughness height (k_s).
In this study, the steady-state Reynolds-averaged Navier-Stokes (RANS) approach is used in combination to the realizable k-ε turbulence model to simulate a neutrally stratified ABL wind approaching the area of interest from South (Figure 1). The second-order discretization schemes are used for the convective and viscous terms of the governing equations. The SIMPLE algorithm is adopted to couple pressure and velocity fields.

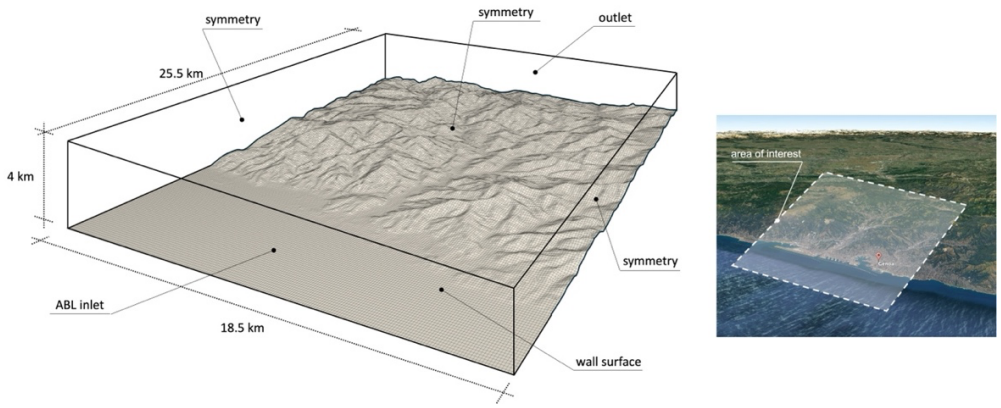


Figure 1. Computational domain and STL topography generated from the NASA SRTM repository with the indication of dimensions and boundary conditions. The selected area is also indicated on the aerial view of Liguria region from Google Earth.

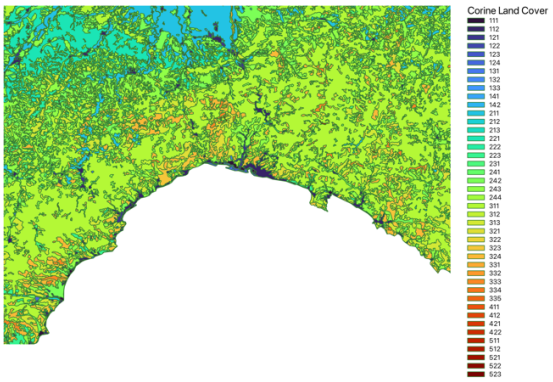


Figure 1. CORINE land cover database over the area under investigation. Numbers correspond to different land cover types.

3. RESULTS AND CONCLUDING REMARKS

In this section, the results of a sensitivity study related to the impact of grid-size resolution on the roughness patch resolution is discussed. An example on two "non-bordering roughness patches" from CORINE database is provided here. Four computational grids (i.e. *cases 1-4*) with a different grid-size resolution are generated, with a total cell count of $6.35e^{+5}$ for *case 1*, $2.87e^{+6}$ for *case 2*, $9.56e^{+6}$ for *case 3*, $1.14e^{+7}$ for *case 4* (Figure 3). Increasing the grid-size resolution particularly near the ground and water surfaces can lead to a better definition of roughness patches. It can be observed that in case of a coarse grid resolution (e.g. *case 1*) near the wall, the two originally non-bordering roughness patches imported from CORINE database are heavily bordering after the grid generation. The denser the grid becomes the less the borders of the two patches touch (e.g. *cases*

2-3). The optimum is achieved in *case 4*, where the two patches are not bordering each other and almost perfectly aligning with the two original CORINE patches. This mismatching (i.e. bordering zones) between the CORINE and new created CFD roughness patches can extend from few hundred meters (e.g. *case 1*) to few tens of meters (e.g. *case 3*), with direct implications on the local-scale and large-scale wind flow field. Additional CFD results concerning this procedure will be discussed in the oral presentation.

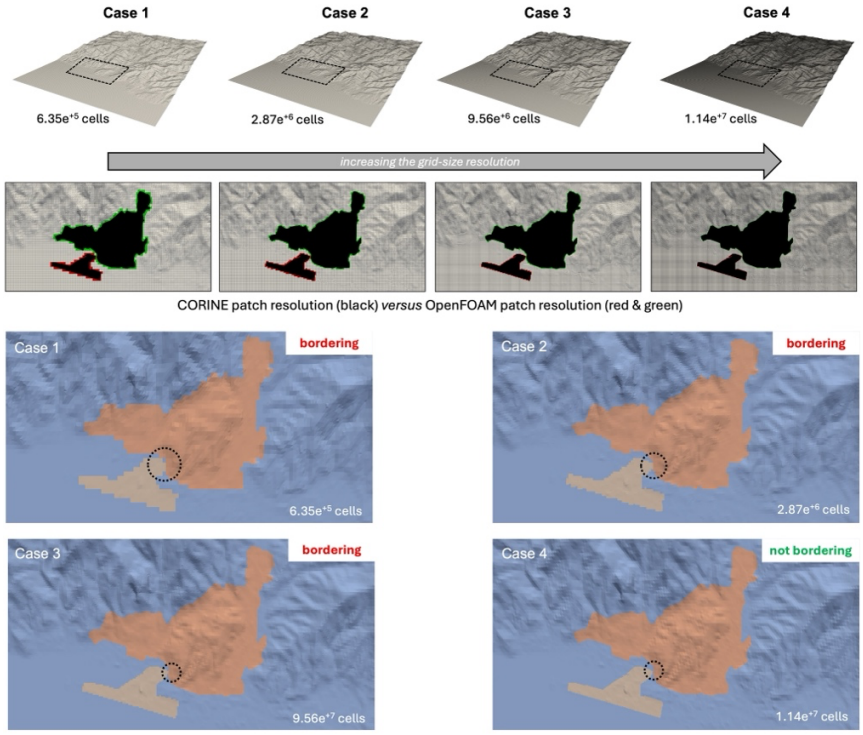


Figure 3. Sensitivity analysis on the impact of grid-size resolution on the roughness patch resolution.

ACKNOWLEDGEMENTS

This study was partially funded by ADAPTNOW Project – "ADAPTation Capacity Strengthening for Highly Affected and Exposed Territories in the Alps NOW" (Grant No. ASP0100048). ADAPTNOW is co-financed by the European Regional Development Fund through the Interreg Alpine Space Programme.

REFERENCES

Blocken, B., 2014. 50 years of computational wind engineering: past, present and future. Journal of Wind Engineering and Industrial Aerodynamics 129, 69–102.

NASA JPL, 2013. NASA Shuttle Radar Topography Mission Global 1 arc second. distributed by NASA EOSDIS Land Processes Distributed Active Archive Center. https://doi.org/10.5067/MEaSU REs/SRTM/SRTMG L1.003

Orlanski, I., 1975. A rational subdivision of scales for atmospheric process, Bulletin of the American Meteorological Society 56, 527–530.

Ricci, A., 2024. Review of OpenFOAM applications in the computational wind engineering: from wind environment to wind structural engineering. Meccanica. https://doi.org/10.1007/s11012-024-01826-x

Žužul, J., Ricci, A., Burlando, M., 2024. An automated geometry generation procedure for CWE applications in OpenFOAM: the case study of a thunderstorm downburst moving over Genoa city. Meccanica. https://doi.org/10.1007/s11012-024-01816-z

Wyatt, B., Briggs, D., Mounsey, H. CORINE: CORINE: An information system on the state of the environment in the European Community. Database for Global Science, Taylor & Francis, London (1988), pp. 378-396.

Some observations on LES vs RANS in predicting pedestrian wind comfort

Knut Erik Teigen Giljarhus[1,2] and Usman Shaukat[1]

[1]*University of Stavanger, Stavanger, Norway, knut.e.giljarhus@uis.no*
[2]*NablaFlow, Stavanger, Norway*

SUMMARY:
In the computational fluids dynamics (CFD) simulation of wind flow, Large Eddy Simulation (LES) offers a more accurate representation of turbulence compared to Reynolds-Averaged Navier-Stokes (RANS) models by resolving larger turbulent structures directly. However, LES requires greater computational resources due to its finer resolution and time-dependent nature. One of the applications of CFD where RANS is often considered to have satisfactory accuracy is in the prediction of pedestrian wind comfort. In this work, we provide examples on how the increased accuracy of LES compared to RANS for pedestrian wind comfort can be important in certain situations. This has potential implications for the development of guidelines for simulations.

Keywords: RANS, LES, Pedestrian wind comfort

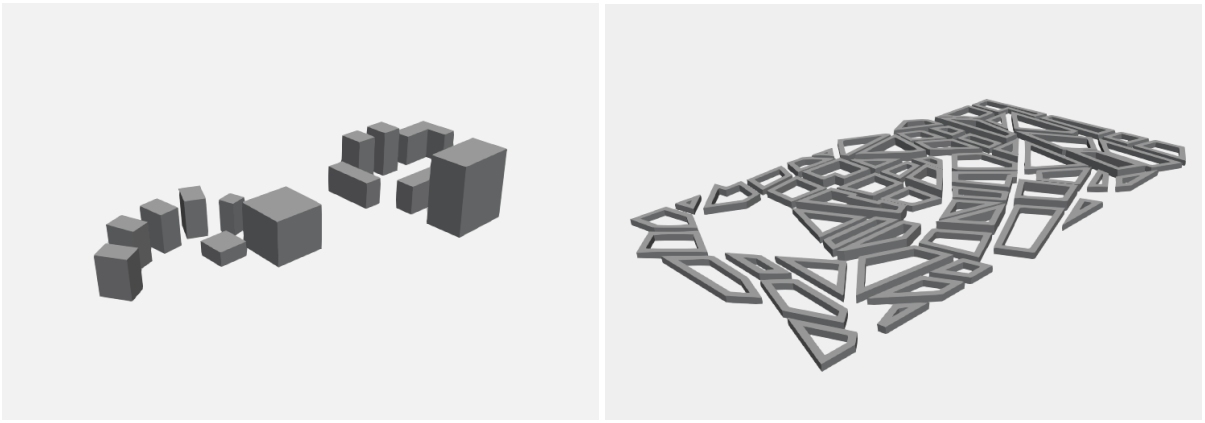
1. INTRODUCTION

In an early study on turbulent flow over obstacles, Ferziger (1990) stated that *"if it turns out that LES can be done on very coarse grids, it will be one of the few times that nature has been kind to us with regard to turbulent flows."* In recent reviews on pedestrian-level wind (Blocken, 2014, 2018; Blocken et al., 2016; Tominaga, 2024) this statement was extrapolated to argue that pedestrian-level wind comfort is one of the few topics in wind engineering where nature is kind to us concerning turbulent flows. This argument is built on studies showing that Reynolds-Averaged Navier-Stokes (RANS) simulations can capture the high-speed regions of the flow near the ground in a satisfactory manner. However, in pedestrian wind comfort analyses the low-speed regions can also be of importance, as they are often used for e.g. planning outdoor seating areas. Also, if guidelines state that RANS simulations are appropriate to evaluate wind comfort, these simulations may also be used outside its intended scope, e.g. for evaluating regions outside of the pedestrian level. This work provides some observations on the accuracy of RANS using comparisons against LES simulations and experiments.

2. METHODS

2.1. Geometries

Fig. 1 shows the two geometries considered in this work. Case A represents a representative Norwegian building site in a low-building-density residential area, with building heights ranging from 12 m to 65 m. Case B is the Michelstadt test case, used for extensive wind tunnel testing of wind and gas dispersion, representing an idealized low-rise Central-European urban environ-



(a) Case A: Building cluster **(b)** Case B: Michelstadt geometry

Figure 1. A graphical depiction of the setup

ment (Bastigkeit, 2011). Here, building heights range between 15 m and 24 m.

2.2. Simulation setup

The simulations were performed in OpenFOAM v2212, with grids generated using snappyHexMesh. The grid resolution was based on a recent LES study of the Case B geometry (Shaukat and Giljarhus, 2024). The grid had a horizontal cell size of 1.4 m in the region of interest, and the first cell center was placed at 0.2 m above ground level with a subsequent stretch factor in the vertical direction of 1.04.

The RANS simulations used the realizable k-epsilon turbulence model. A convergence criterion of 1e-4 for pressure and 1e-5 for velocity was used, which for the current case resulted in approximately 2000 iterations with the SIMPLEC algorithm. For case A, a neutral logarithmic boundary layer profile with roughness $z_0 = 0.3$ was applied at the inlet. For case B, the experimental profile was used.

The LES simulations used the default Smagorinsky model. For the inlet, a synthetic eddy method was used to generate an ABL with the same mean properties as the RANS simulations (Patruno and Ricci, 2017). The time integration was performed using a second-order method for 22.5 flow-throughs through the domain based on the reference velocity, and the fields were averaged over half the period. The time step was adapted to maintain a Courant number of approximately 0.5 throughout the simulation. The convective terms were treated with a blended method using 95 % centered scheme and 5 % second-ordered upwind scheme.

3. RESULTS

3.1. Case A - Building cluster

Figs. 2a and 2b compare the velocity magnitude at pedestrian level (2 m above ground). The overall flow pattern is similar in the two methods. However, there is a clear trend that the LES simulation has a higher turbulent mixing, resulting in higher velocities and less pronounced wakes behind the buildings.

Fig. 2c compares the velocity magnitude in the vertical plane between two buildings. It is evident that the larger mixing of the LES model results in an accelerated flow over this building and increased velocities on the roof. If RANS simulations were used to plan e.g. a roof terrace on this building, it could lead to unintended high winds and reduced comfort .

3.2. Case B - Michelstadt

Figs. 2d and 2e compare the RANS simulations and the LES simulations against wind tunnel experiments, respectively. The measurements were taken in the street canyons at heights of 2 m, 9 m, and 18 m, in the region shown in Fig. 2f. In the scatter plots there is a clear trend that the LES simulations have good agreement in the entire range. For the RANS simulations, there are larger deviations, especially for the lower velocities, but also in general for the 2 m level. This is further elucidated in Fig. 2f, which compares the axial velocity component in the measurement region. Again, the RANS simulations predict the overall flow pattern well, but especially in the mixing layers between high- and low-velocity regions there are deviations that lead to high local differences in velocity.

4. CONCLUSIONS

This work compared RANS and LES simulations for pedestrian-level wind in two test cases. While good overall agreement in the flow patterns were found, there are also important local differences. Although it appears that RANS can be used to understand the overall flow field, care should be taken when using the results in detailed planning. Additionally, it was shown that the reduced mixing in wakes causes underpredicted velocity fields in RANS simulations.

It is challenging to extrapolate results from simplified benchmarks to more complex urban environments, hence a continued effort on benchmark studies is recommended. Additionally, turbulence modelling is only one of many uncertainties in a wind engineering study. Other uncertainties such as building geometries, vegetation, inlet wind profiles etc, are also important to acknowledge.

REFERENCES

Bastigkeit, I., 2011. Erzeugung von Validierungsdaten für wirbelauflösende mikroskalige Strömungs-und Ausbreitungsmodelle. phdthesis, Staats-und Universitätsbibliothek Hamburg Carl von Ossietzky.

Blocken, B., 2014. 50 years of computational wind engineering: past, present and future. Journal of Wind Engineering and Industrial Aerodynamics 129, 69–102.

— 2018. LES over RANS in building simulation for outdoor and indoor applications: A foregone conclusion? Proceedings of Building Simulation. Vol. 11. Springer, 821–870.

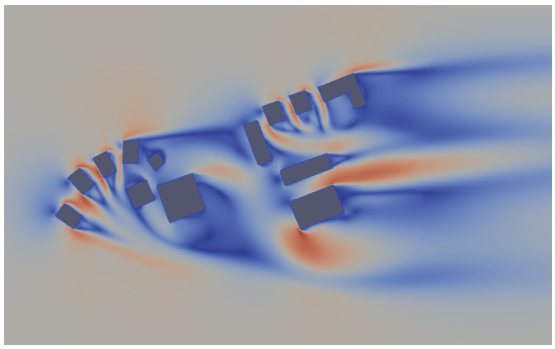
Blocken, B., Stathopoulos, T., and Van Beeck, J., 2016. Pedestrian-level wind conditions around buildings: Review of wind-tunnel and CFD techniques and their accuracy for wind comfort assessment. Building and Environment 100, 50–81.

Ferziger, J. H., 1990. Approaches to turbulent flow computation: applications to flow over obstacles. Journal of Wind Engineering and Industrial Aerodynamics 35, 1–19.

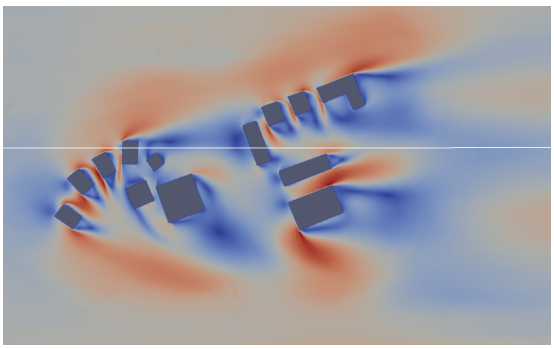
Patruno, L. and Ricci, M., 2017. On the generation of synthetic divergence-free homogeneous anisotropic turbulence. Computer Methods in Applied Mechanics and Engineering 315, 396–417.

Shaukat, U. and Giljarhus, K. E. T., 2024. "Validation of Large Eddy Simulations in Urban Wind Studies Using a New Overall Area Metric".

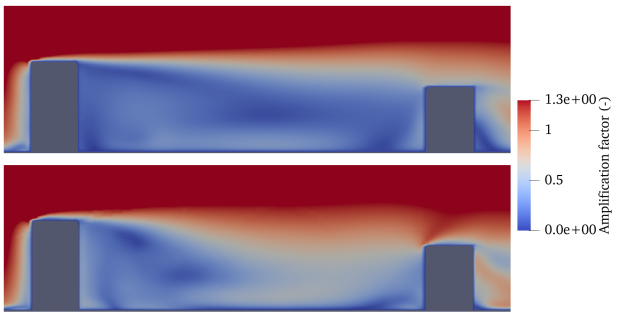
Tominaga, Y., 2024. CFD simulations of turbulent flow and dispersion in built environment: A perspective review. Journal of Wind Engineering and Industrial Aerodynamics 249, 105741.



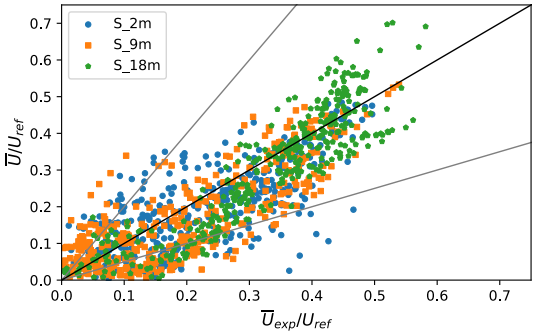
(a) Case A, RANS - horizontal slice at 2 m



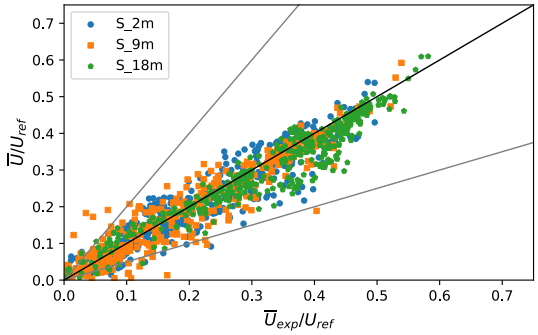
(b) Case A, LES- horizontal slice at 2 m



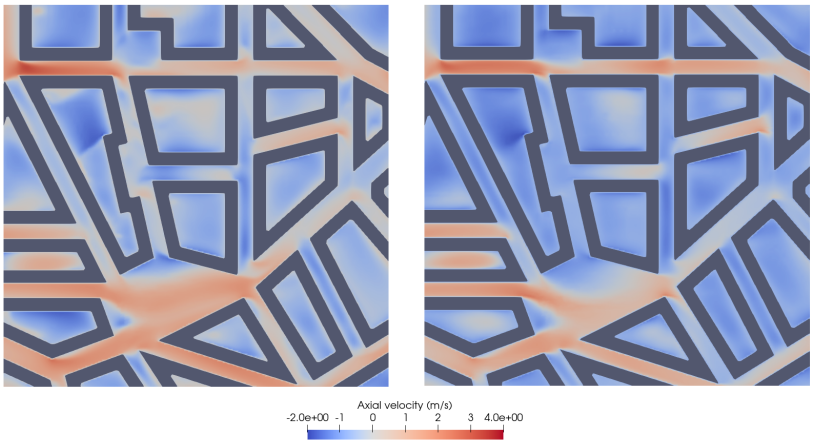
(c) Case A. Vertical slice (at position indicated by white line in (b)) comparing RANS (top) and LES (bottom).



(d) Case B, scatter plot for RANS vs experiment



(e) Case B, scatter plot for LES vs experiment



(f) Case B, axial velocity in center region for RANS (left) and LES (right).

Figure 2. Comparisons of LES and RANS simulations for Case A and Case B.

Automatic 3D geometry reconstruction of a large-scale city on complex topography for CFD simulations

Josip Žužul [1], Alessio Ricci [2], Massimiliano Burlando [1]

[1] *University of Genoa, Genoa, Italy, josip.zuzul@edu.unige.it – massimiliano.burlando@unige.it*
[2] *University School for Advanced Studies IUSS, Pavia, Italy, alessio.ricci@iusspavia.it*

SUMMARY:
Investigation of urban physics and wind engineering topics is nowadays closely linked with the reconstruction of mesoscale environments in the perspective of being studied by means of Computational Fluid Dynamics (CFD) simulations. Analyzing widely studied topics in the field, such as pollutant dispersion, pedestrian wind comfort, urban heat islands, and wind loading, requires first creating a digital twin of the analyzed area. Given the complexity of realistic, large-scale areas, creating a digital twin generally becomes a challenge – often making it problematic to conduct the intended analysis. This study aims to underline the recommendations to creating the digital twin summarized based on a user experience of creating a digital twin for a large-scale area around the city of Genoa (Italy) with about 600,000 inhabitants. In particular, this study will present the suggestions for required geometry simplification steps – both for terrain and buildings – to obtain effective and successful automatic mesh generation for the application of CFD in the field of wind engineering. Lastly, this study will demonstrate the application of the suggested digital twin generation pipeline on the case study of a wind flow in the urban canopy of the city of Genoa.

Keywords: digital twin, complex environment, CFD simulations

1. INTRODUCTION

Over the years, the CFD simulations of larger (mesoscale) environments have become a standard practice for investigating urban physics and wind engineering topics, which include — but are not limited to — pedestrian wind comfort, pollutant dispersion, urban heat islands, and wind loading. In such studies what is typically done is modeling of complex natural and built environments in an attempt of creating a digital twin. However, the efficient digital twin creation, especially for the built environment covering large-scale area is a challenging task which attracted the increased interest among researchers in the recent years (e.g. Alemayehu and Bitsuamlak, 2022; Pađen et al., 2022; Žužul et al., 2024). Despite that, a precise set of guidelines to accurate digital twin and mesh generation in complex environments is still missing. Such digital twin models are usually represented by diverse land covers such as hills and mountains, various water-type surfaces and vegetations. Although the terrain topography introduces significant degree of complexity, it is actually the shape and level of detail of the built infrastructure whose treatment plays a crucial role in the success of the digital twin generation procedure. The importance of certain geometrical details varies depending on the scale and focus of the problem in such a way that details critical for some applications may be entirely irrelevant for others. Consequently, it is common to apply a level of geometrical simplification to streamline automatic geometry reconstruction for large cities – especially as a clean, simplified representation is essential and key to successful mesh generation.

However, the applied level of geometrical simplifications have to be carefully studied before deciding on how much of simplification to adopt, as it can substantially influence the resultant flow field (Ricci et al., 2017). Despite advancements, computational resource limitations still remain a challenge, making geometrical simplifications increasingly necessary as considered city areas grow, since higher imposed levels of detail of geometry lead to larger computational mesh sizes. Ultimately, users should find a balance between level of detail and simplification to efficiently manage large-scale cases while always keeping in mind the overall goal of the analysis.

The most important considerations, recommendations and a step-by-step framework to automating a digital twin creation for CFD simulations in the wind engineering field will be discussed in this study. In particular, this study will also showcase a framework for automatic 3D geometry reconstruction of the large-scale city of Genoa in Italy — a coastal Mediterranean city of about 600,000 inhabitants, situated between the sea to the south and mountains to the north. The constructed digital twin will finally be used for CFD simulations of atmospheric wind flows.

2. GEOMETRY PREPARATION

The framework to digital twin creation starts with the considerations in geometry preparation. The procedure suggested in this study is to treat separately the built infrastructure with respect to the terrain topography. These preparation steps would therefore be in line with the approach of the City4CFD tool developed by Pađen et al. (2022). In that perspective, the user should first retrieve the data describing the terrain topography of the area of interests and pre-process it accordingly. This often involves surface smoothing to eliminate possible outliers due to measurement uncertainties. In this study, the area of the large-scale city of Genoa (Italy) with a total area of 37 x 18 km^2 was considered, and the underlying high-resolution digital terrain model dataset of 1 m resolution was smoothed by using a 50 x 50 m^2 moving window. Depending on the target domain topography at the boundary, this operation alone may not be sufficient for conducting successful CFD simulations due to irregular topography at the initial boundary. To address this issue, an additional step (artificial buffering) was introduced, extending the original terrain topography at the initial boundary outward to ensure smooth terrain transition from the farfield elevation (*i.e.* set to sea surface height z of 0 m). In this approach, buffering is split and follows the: (*i*) inner buffer, and (*ii*) outer buffer strategy like the method proposed by Žužul et al. (2024). However, here, instead of linear interpolation, the inner buffer region assumes smooth terrain surface by solving the Laplace equation, while the outer buffer maintains a fixed far-field elevation of 0 meters. The prepared terrain data is exported as the point cloud for final operations.

Buildings' infrastructure data was made available in the GeoJSON file format, where each building was represented by a polygon with specific height. Given a complex and irregular shape of buildings in the Mediterranean coast, constructing buildings out of the box was not possible. Therefore a set of simplification operations were conducted. Firstly, all buildings having a height smaller than 5 meters, and having a roof area of less than 25 square meters were explicitly removed. Second, the Ramer – Douglas – Peucker algorithm for shape simplification was adopted to reduce the number of points describing each building (Douglas and Peucker, 1973). Finally, the buildings which are considered "too close one to the other" (*i.e.* within 2 m distance) were merged to avoid having very small gaps and narrow passages between buildings. By removing possibilities of having small gaps, the simplified polygons representing buildings were eventually converted into a stereolithography (STL) file by using the open-source software OpenSCAD (2024). The

entire process of terrain and building preparation is fully automatized by an in-house python code. The representation of the prepared geometry tailored for CFD simulations of large-scale cities is presented in Fig. 1.

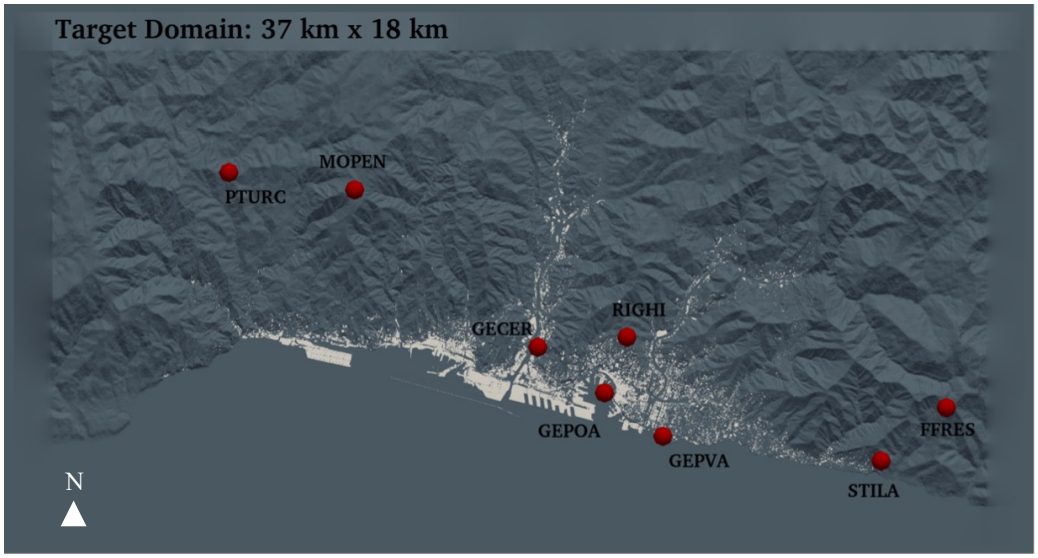


Figure 1. Target complex domain of 37 *x* 18 km^2 area around Genoa city (with artificial buffer at the outer boundary), and reconstructed buildings' infrastructure. Red dots refer to the meteorological stations recording data that will be used for hazard wind maps generation.

3. DIGITAL TWIN CREATION FOR CFD APPLICATIONS

Prepared terrain point cloud and buildings in STL file were finally passed through the essential ingredient of the digital twin creation pipeline - domain reconstruction in City4CFD tool which sorts out possibly remaining issues in terms of improper triangulation and buildings-terrain connectivity (Pađen et al., 2022). By using constructed computational domain boundaries, creating a computational mesh for a digital twin is no longer an issue. Computational mesh was created in `cfMesh`, an automatic mesh generation library available within the framework of `OpenFOAM`.

4. RESULTS

Steady Reynolds-averaged Navier-Stokes (RANS) simulations were performed for 12 different wind directions (*i.e.* α = 0°, 30°, 60°, 90°, …, 300° and 330°), under a neutrally stratified atmospheric boundary layer (ABL) wind. The aerodynamic roughness length (z_0) was defined for the water surface ($z_{0,sea}$ = 0.0002 m), the rural area ($z_{0,rural}$ = 0.4 m) and the urban area ($z_{0,urban}$ = 0.8 m), respectively. Fig. 2 highlights the comparison between the constructed computational mesh (Fig. 2a) and the large-scale complex area of Genoa city (Fig. 2b), while also showcasing the realistic wind velocity contours with the superimposed vectors in the horizontal plane at z = 30 m above sea level, at the domain sector at the western part of Genoa for a wind direction α = 210° (Fig. 2c and Fig. 2d).

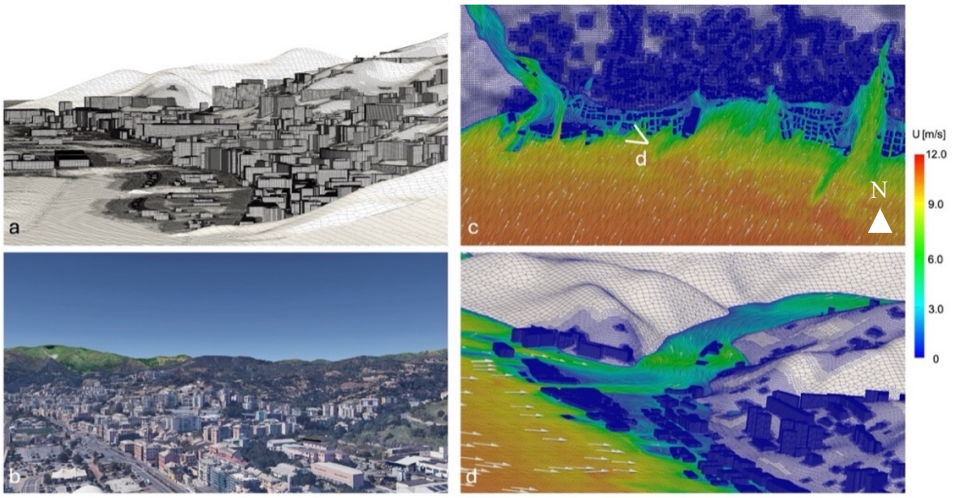


Figure 2. Comparison of computational mesh with the large-scale complex environment of Genoa (a-b); computational grid with superimposed wind velocity contours made at z = 30 m above the sea level (c-d).

5. CONCLUSIONS AND PROSPECTS

This study aims to highlight the experience gathered from the ongoing research on automatizing the geometry preparation to facilitate the digital twin and mesh generation procedure for cases involving large-scale city areas in complex topographies. Such cases commonly involve balancing several aspects and it was found that geometry simplification plays a crucial role for successful domain reconstruction. Leveraging these simplifications methods, automatic mesh generator `cfMesh` available in `OpenFOAM` has proven to be a reliable tool in constructing meshes for wind engineering applications. By streamlining these processes, this framework aims to enhance the feasibility and efficiency of conducting large-scale simulations, paving the way for more accurate and accessible modeling in urban physics and wind engineering.

ACKNOWLEDGEMENTS

This study was funded by ADAPTNOW Project—"ADAPTation Capacity Strengthening for Highly Affected and Exposed Territories in the Alps NOW" (Grant No. ASP0100048). ADAPTNOW is co-financed by the European Regional Development Fund through the Interreg Alpine Space programme. The authors also acknowledge the support of the Municipality of Genoa (Italy) in providing the relevant datasets used in the framework of this research study. The authors acknowledge the support of the Italian supercomputing center CINECA for providing access to their High-Performance Computing (HPC) facilities needed to carry out the research presented in this paper.

REFERENCES

Alemayehu, T.F. and Bitsuamlak, G.T., 2022. Autonomous urban topology generation for urban flow modelling. Sustainable Cities and Society, 87, 104181.

Douglas, D.H. and Peucker, T.K., 1973. Algorithms for the reduction of the number of points required to represent a digitized line or its caricature. The Canadian Cartographer 10(2), 112–122.

OpenSCAD, 2024. The Programmers Solid 3D CAD Modeller. https://openscad.org.

Pađen, I., García-Sánchez, C., and Ledoux, H., 2022. Towards Automatic Reconstruction of 3D City Models Tailored for Urban Flow Simulations. Frontiers in Built Environment, 8.

Ricci, A., Kalkman, I., Blocken, B., Burlando, M., Freda, A., and Repetto, M. P., 2017. Local-scale forcing effects on wind flows in an urban environment: Impact of geometrical simplifications. Journal of Wind Engineering and Industrial Aerodynamics, 170, 238- 255.

Žužul, J., Ricci, A., and Burlando, M., 2024. An automated geometry generation procedure for CWE applications in OpenFOAM: the case study of a thunderstorm downburst moving over Genoa city. Meccanica.

Uncertainties by surface roughness specification in RANS CFD simulations of wind flow in urban areas

Bert Blocken [1, 2]

[1]*Heriot-Watt University, Edinburgh, Scotland, United Kingdom, b.blocken@hw.ac.uk*
[2]*KU Leuven, Leuven, Belgium, bert.blocken@kuleuven.be*

SUMMARY:
This paper provides some views on the uncertainties that can be caused by the complex activity of surface roughness specification in RANS CFD simulations of wind flow in urban areas. This includes the aerodynamic roughness length for the inlet profiles, the roughness of the upstream part of the computational domain and the roughness of the ground surface in between the explicitly modelled buildings and constructions. A pedestrian-level wind comfort study for a small built-up area is performed and repeated using different types of roughness. It is shown that choosing a roughness length that is one class off in the Davenport-Wieringa roughness classification for the inlet profiles and the upstream part of the domain can easily change the wind comfort judgement from "moderate" to "poor", or vice versa, and might be decisive for granting a building permit. Concerning the ground roughness in between the explicitly modelled buildings however, this choice is clearly associated with a much lower uncertainty.

Keywords: surface roughness, complex terrain, urban area, computational fluid dynamics, uncertainty

1. INTRODUCTION

In CFD simulations in urban physics and wind engineering, a large number of choices have to be carefully made by the user of the CFD code. In this paper, the focus is on the terrain roughness boundary conditions, which constitute a well-known difficulty and potentially large source of uncertainty in CFD simulations. An approach for the specification of terrain roughness is provided, and the consequences of less careful terrain roughness specification are illustrated for the case study of pedestrian-level wind (PLW) comfort in a actual built-up area.

2. K_S VERSUS Z_0 ROUGHNESS SPECIFICATION

Generally a distinction is made between the two types of roughness specification (Blocken et al. 2007): using aerodynamic roughness length z_0 or equivalent sand-grain roughness height k_S. The concept of aerodynamic roughness length z_0 is typically associated with large-scale terrain roughness. The concept of equivalent sand-grain roughness length k_S on the other hand rather refers to small-scale surface roughness. It is due to Nikuradse (1933) who investigated flow in roughened pipes and channels where the roughness was applied by sandgrains. Because many CFD codes were initially developed for mechanical engineering applications and flow in machinery in which the small-scale roughness is relevant, many of the wall functions in these codes include roughness modifications based on k_S. A well-known example are the standard wall functions by Launder and Spalding (1974) and their roughness modification by Cebeci and Bradshaw (1977), which were and still are present in the commercial CFD codes ANSYS/Fluent, CFX and in the non-commercial CFD code OpenFOAM. Blocken et al. (2007) derived the exact relationship

between z_0 and k_S for several codes based on first-order matching between ABL mean velocity profiles and wall functions, yielding, for ANSYS/Fluent and OpenFOAM: $k_S = 9.973 z_0 / C_S$ where C_S is the roughness constant. For ANSYS-CFX, the relationship is $k_S = 29.6 z_0$. Figure 1 depicts a computational domain with explicitly modelled buildings in the centre region. A distinction is made between five spatial areas for roughness specification:

1. Area 1: upstream of the domain. This is a large-scale roughness, termed $z_{0,1}$. It can be estimated based on land-use maps in combination with a roughness classification such as that by Davenport updated by Wieringa (1992).
2. Area 2: inside the domain, upstream of the explicitly modeled buildings. The value of $z_{0,2}$ of this area should be estimated using the Davenport-Wieringa roughness classification.
3. Area 3: inside the computational domain representing the ground surface amidst the explicitly modelled buildings and other obstacles. This area typically contains small-scale topographic features that are not modelled explicitly, such as sidewalks, benches, fences, trees, hedges, etc. These should be implicitly modelled as an increased surface roughness $z_{0,3}$ or $k_{S,3}$.
4. Area 4: surfaces of the explicitly modeled buildings (facades, roofs) and structures inside the domain, which can be characterized by an equivalent sand-grain roughness height $k_{S,4}$.
5. Area 5: inside the computational domain, downstream of the explicitly modeled buildings. The aerodynamic roughness length $z_{0,5}$ of this area can again be estimated using the Davenport-Wieringa roughness classification.

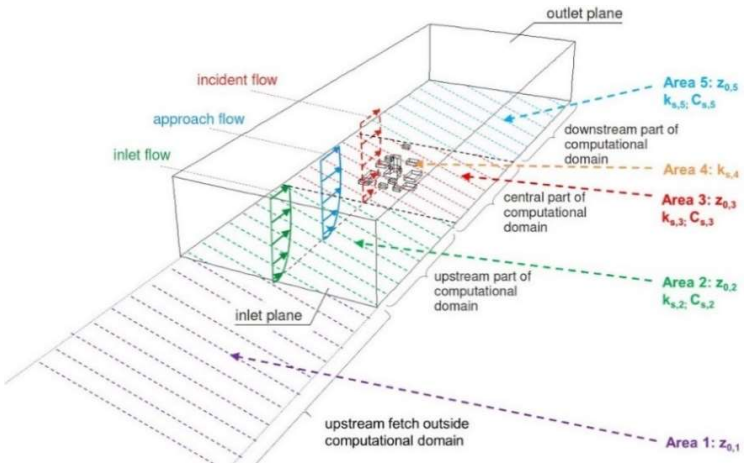


Figure 1. Schematic representation of a computational domain with five spatial areas for which roughness should be specified. Area 1 is situated outside the domain, while areas 2, 3, 4 and 5 are situated inside the domain.

3. CASE STUDY

The case study is a pedestrian wind comfort study focused on the Johan Cruijff ArenA football stadium in Amsterdam, the Netherlands (Blocken and Persoon 2009). Figure 2a shows the stadium, Figure 2b the target locations, i.e. pedestrian deck and streets and squares around the stadium, and Figure 2c depicts the surrounding buildings, where configuration A only includes the buildings in grey and configuration B includes all buildings, including the newly planned developments in white. The purpose of the study is to determine the wind comfort at the target locations for configurations A and B, using the Dutch Wind Nuisance Standard (NEN 2006). High-resolution computational grids were created with about 2.8 million cells. The boundary conditions were the vertical profiles of mean velocity and turbulence quantities for ABL neutral stratification, using

the upstream estimates for $z_{0,1}$ as shown in Figure 3. The simulations were performed with the 3D steady Reynolds-averaged Navier-Stokes (RANS) equations closed by the realizable k-ε model. The surface roughness in the domain was implemented by the sandgrain-based roughness modification by Cebeci and Bradshaw (1977) in the standard wall functions by Launder and Spalding (1974). The values of $z_{0,2}$ were taken identical to $z_{0,1}$, and the conversion to $k_{S,2}$ was done using $k_S = 9.973 z_0 / C_S$. For $k_{S,3}$ and $C_{S,3}$, 0.6 m and 0.5 were used. A successful validation study with full-scale measurements of mean wind speed on the deck was performed (see Blocken and Persoon 2009). The wind comfort was evaluated using the Dutch Standard NEN 8100 (NEN 2006), the comfort criterium is shown in Figure 3 (right). In the present paper, the focus is on the differences in wind comfort assessment introduced when using different values for $z_{0,2}$ (or $k_{S,2}$) and $z_{0,3}$ (or $k_{S,3}$).

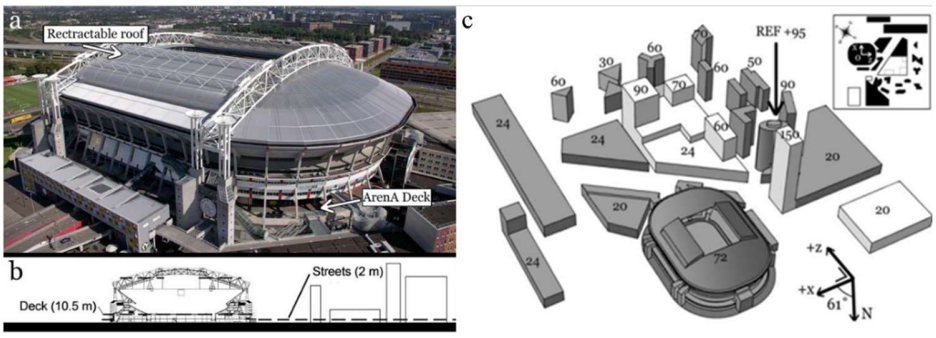
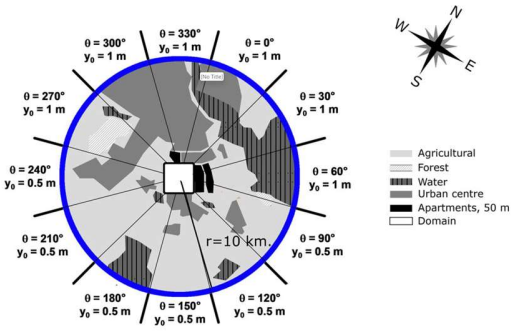


Figure 2. (a) Photo of Johan Cruijff ArenA; (b) Vertical cross-section showing the target areas; (c) ArenA and surrounding buildings with indication of building heights. The arrow points to the roof of the ABN Amro tower building, at which the reference wind speed U_{ref} is measured.



$P(U_{THR}>5$ m/s) (in % hours per year)	Grade	Activity		
		Traversing	Strolling	Sitting
Wind comfort				
<2.5	A	Good	Good	Good
2.5–5.0	B	Good	Good	Moderate
5.0–10	C	Good	Moderate	Poor
10–20	D	Moderate	Poor	Poor
>20	E	Poor	Poor	Poor

Figure 3. Left: Estimates of $z_{0,1}$; Right: Comfort criterium in the Dutch Wind Nuisance Standard.

4. ROUGHNESS SENSITIVITY STUDY

In the first part of the sensitivity study, the impact of changed $z_{0,3}$ (or $k_{S,3}$) is evaluated. Figure 4a shows two lines at 1.75 m height along which the results are evaluated. Figure 4b,c compare the wind speed ratio $U/U_{ref,num}$ where the denominator is the computed mean wind speed on the top of a 10 m mast situated at the roof of the nearby ABN-Amro tower building. Figure 4d shows the three sets of (k_S, C_S) values that are used. Large differences are only found for the first part of line CD and in a peak towards the end of this line. It appears that for the positions inside the cluster of buildings, the differences are very small. On the stadium deck, all differences are smaller than 4%. In the second part of the sensitivity study, the impact of changed $z_{0,2}$ is tested. Figure 5a compares

the exceedance probability P of the 5 m/s threshold at the deck as obtained using the more advanced procedure in NPR 6097 (NEN 2006b) versus that obtained using the simplified procedure by Simiu and Scanlan (), where the latter uses the values from Figure 3a. Figure 5b and c show the same, but here the values for the simplified procedure are taken one class lower and one class higher, respectively, than in Figure 3a. Clearly, the differences in P are very large, up to 4% in exceedance probability, which can be enough to change the outcome of the wind comfort study.

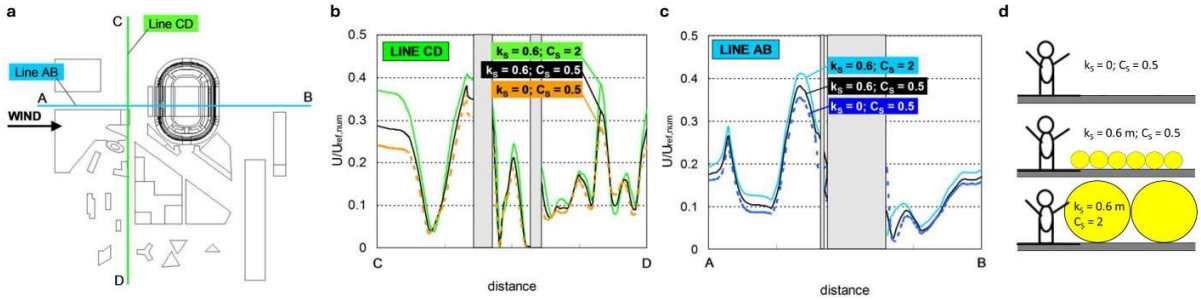


Figure 4. (a) Definitions of lines AB and CD at pedestrian level; (b) Wind speed ratio along line CD and (c) line AB; (d) Values of k_S and C_S used for sensitivity study.

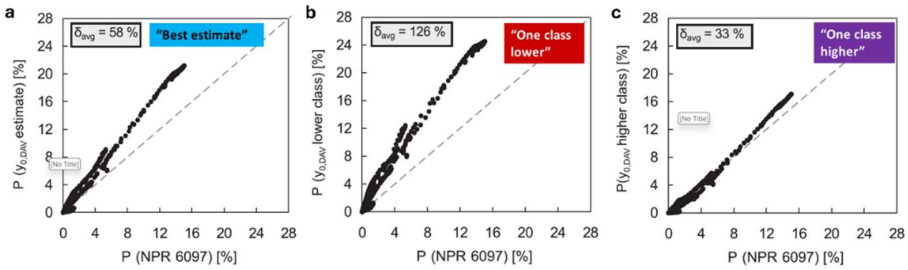


Figure 5. Discomfort exceedance probabilities: (a) Using NPR "best estimate"; (b) One class lower in roughness classification; (c) One class higher in roughness classification.

7. CONCLUSIONS

The ground roughness in between the explicitly modelled buildings contributed only to a fairly low uncertainty in pedestrian-level mean wind speed. However, a roughness length that is one class off in the Davenport-Wieringa roughness classification for the inlet profiles and the upstream part of the domain can easily change the wind comfort judgement from "moderate" to "poor", or vice versa, even on the elevated stadium deck.

REFERENCES

Blocken B, Stathopoulos T, Carmeliet J. 2007. CFD simulation of the atmospheric boundary layer: wall function problems. Atmospheric Environment 41(2): 238-252.

Cebeci T, Bradshaw P. 1977. Momentum transfer in boundary layers. Hemisphere Publishing Corporation, New York.

Launder BE, Spalding DB. 1974. The numerical computation of turbulent flows, Computer Methods in Applied Mechanics and Engineering 3:269-289.

NEN 2006a.Wind comfort and wind danger in the built environment, NEN8100 (in Dutch); Dutch Standard.

NEN 2006b. Application of mean hourly wind speed statistics for the Netherlands, NPR 6097. Practice Guideline.

Nikuradse J. 1933. Strömungsgesetze in rauhen Rohren. Forschg. Arb. Ing.-Wes. No. 361.

Simiu E, Scanlan RH. 1986. Wind Effects on Structures. 2nd Ed. Wiley, NewYork.

Wieringa J. 1992. Updating the Davenport roughness classification. J Wind Eng Ind Aerodyn 41-44, 357-368.

An inflow turbulence over rough terrain generated with a digital filter method

Tsubasa Okaze [1], Akashi Mochida [2]

[1] *Institute of Science Tokyo, Yokohama, Japan, okaze.t.f356@m.isct.ac.jp*
[2] *Professor emeritus, Tohoku University, Sendai, Japan, akashi.mochida.d1@tohoku.ac.jp*

SUMMARY:
Recent advancements in computational capabilities have enabled the widespread application of large-eddy simulation (LES) for urban wind environment assessments. To perform accurate LES, it is essential to generate inflow turbulence that reproduces the atmospheric boundary layer characteristics corresponding to windward terrain roughness. This study aims to develop an inflow turbulence dataset satisfying the turbulence statistics over suburban terrain situation. Using a two-dimensional digital filter method, artificial turbulence data were generated to satisfy the desired mean wind speed, turbulence intensity, and integral length scale of turbulence. The generated dataset was used as inflow boundary conditions for LES over rough terrain. LES was performed using OpenFOAM with the standard Smagorinsky subgrid scale turbulence model. The results demonstrated that the incident flow turbulence retained its statistical properties defined at inflow boundary, including spectral features, over significant downstream distances. The coherent turbulent structures reconstructed near the inlet evolved smoothly, maintaining their dominant scales throughout the domain. Future research will extend this approach to LES around buildings, with plans to release the dataset for broader applications in urban wind environment studies.

Keywords: Large-eddy simulation, Integral scales, AIJ roughness category

1. INTRODUCTION

In recent years, with advancements in computational capabilities, the application of large-eddy simulation (LES) for urban wind environment assessments, such as pedestrian wind environment, is becoming increasingly feasible (Tominaga, 2024). To perform appropriate LESs, it is essential to generate inflow turbulence that simulates atmospheric boundary layers in accordance with the characteristics of surface roughness on the windward side of the focus area. The methods for generating inflow turbulent wind can be classified into two types: 1) methods that directly obtain fluctuating wind through precursor simulations with (quasi-)periodic boundary conditions or by reproducing windward features of buildings, and 2) methods that artificially generate using random numbers to satisfy prescribed turbulent statistics. In wind tunnel experiments for assessing urban wind environments, spires and roughness blocks are strategically arranged to reproduce atmospheric boundary layer flow corresponding to desired windward terrain roughness. Similarly, in LES, inflow turbulent is often generated to satisfy the turbulence statistics over the specified terrain. However, in methods that rely on periodic boundary conditions (type 1) are limited in their ability to reproduce low-frequency components of wind velocity due to the finite length of the computational domain. This constraint poses challenges in accurately reproduce to the low-frequency components related to the integral length scales recommended by guidelines or design codes.

In this study, the digital filtering method proposed by Xie and Castro (2008) classified into type 2, which is capable of specifying the integral length and time scales of turbulence, was employed to artificially establish inflow turbulence dataset. Using this method, wind velocity fluctuations were generated to satisfy not only mean wind speed and turbulence intensity but also the integral scales, which relate to the dominant scales of turbulent fluctuations by setting the turbulence length scale as specified parameters. Furthermore, LES of incident flow over a rough terrain utilizing the generated inflow turbulence was demonstrated as a priori test.

2. INFLOW GENRATION METHOD

In this study, the components of instantaneous wind velocity, time-averaged components and fluctuating components are denoted as u_i, $\overline{u_i}$, and u_i', respectively. Here, the subscript i = 1,2 and 3 corresponds to steamwise, lateral and vertical components of wind velocity. The fluctuating can be decomposed using lower triangular matrix of Cholesky decomposition of Reynolds stress matrix a_{ij} as:

$$u_i' = a_{ij}\Psi_j, \tag{1}$$

where, Ψ_j are variables satisfying mean value 0 and variance 1. Unless Ψ_j satisfies the mentioned conditions, the variances and covariances calculated from the generated wind velocity fluctuation satisfy the matrix of Reynolds stresses on which the lower triangular matrix is calculated from. To impose prescribed integral time and length scales, a digital filter method proposed by Xie and Castro (2008) was applied. In this method, the turbulence statistics to be specified are the six components of Reynolds stress, the integrated time and length scale of turbulence in addition to mean wind velocity profile. The prescribed values were imposed by following The Recommendations for Loads on Buildings by the Architectural Institute of Japan (AIJ) (AIJ, 2019) respectively suggests the mean wind velocity $\langle u(z)\rangle$ (m/s), turbulence intensity in the streamwise component $I(z)$ (-), and longitudinal integral length scale in streamwise component L_{ux} (m) of atmospheric boundary layer on roughness terrains as

$$\langle u(z)\rangle = \langle u_{ref}\rangle \left(\frac{z}{z_{Ref}}\right)^{\alpha}, \tag{2}$$

$$I(z) = \frac{\langle u'u'\rangle}{\langle u(z)\rangle^2} = 0.1\left(\frac{z}{z_G}\right)^{-0.05-\alpha}, \tag{3}$$

$$L_{ux} = 100\left(\frac{z}{30}\right)^{0.5}, \tag{4}$$

where, $\langle u_{ref}\rangle$ is the mean wind velocity at a reference height z_{Ref}, α is a power low index for desired roughness category, and z_G is a height related to the atmospheric boundary layer height. The streamwise component of Reynolds stress $\langle u'u'\rangle$ was rewritten using eqs. (2) and (3). The normal stresses in the lateral and vertical components can be assumed to be half of the streamwise component. The Reynolds stress $\langle u'w'\rangle$ can be derived based on the assumption of local equilibrium for the transport equation of turbulence kinetic energy in the k-ε model:

$$\langle u'w'\rangle = -0.5C_\mu k, \tag{4}$$

where, k is turbulence kinetic energy and C_μ is empirical constant 0.09. All other Reynolds stresses can be set to zero. At the inflow boundary, the transverse length scale in lateral or vertical directions should be considered as the length scale for the streamwise wind velocity component. In this study, the transverse length scale in the streamwise component assumed to be one-third of the longitudinal length scale defined in eq (4):

$$L_{uy} = \frac{1}{3}L_{ux}. \tag{6}$$

The length scales for all other components were set with the same value. For the integral time scales, Taylor's hypothesis of frozen turbulence was applied. The time scales for all wind velocity components were calculated as

$$T_u = T_v = T_w = \frac{L_{ux}}{\langle u(z) \rangle}. \quad (7)$$

3. A PRIOLI TEST

3.1. Outline of calculation

We demonstrated LES for incident flow over rough terrain with an artificially generated inflow turbulence. The calculation domain was set to 5.0×1.0×1.0 km. The streamwise direction was extended approximately ten times the boundary layer height. A uniform grid spacing of 10 was utilized. The LES was performed using OpenFOAM v2006 with the standard Smagorinsky turbulence model (Smagorinsky, 1963). The Smagorinsky constant was set to 0.10. The second-order linear interpolation was used to discretize convection terms. The inflow turbulence obeys the profile over the roughness category III in the AIJ recommendations (AIJ, 2019) with $\alpha = 0.2$ and $z_G = 550$ m. The category III involves suburban, wooded terrain, area with low-rise buildings or with scattered tall buildings (4 to 9 floors) areas. The reference wind velocity was set as $\langle u_{ref} \rangle = 10$ m/s at $z_{ref} = z_R$. A z_0-type logarithmic law was applied to the ground surface, using a roughness length of z_0 = 1.5 m, which approximately reproduces the mean wind velocity profile over the roughness category III. The periodic boundary condition was applied to both lateral boundaries. The slip condition was applied to top boundary and convective outflow condition was applied to the outlet boundary. The time series of the inflow turbulence was stored after discarding the first 30 min of generated dataset. The LES was performed for 120 min after 20 min spin-up.

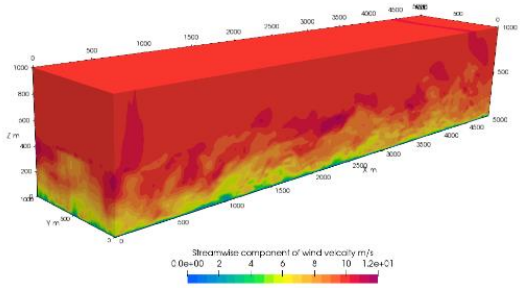
3.2. Results

The vertical profiles of generated inflow turbulence for the mean wind velocity, turbulence intensity and Reynolds stresses corresponded well with the desired values. In addition, its power spectra demonstrated good agreement with the von Kármán spectrum, including desired peak frequency related to the integral time scale (not shown here). Figure 1 illustrates the instantaneous streamwise and vertical component of wind velocity, and the isosurface of the second invariant of gradient of wind velocity tensor in the calculation domain. For the streamwise component, the large-scale fluctuations smoothly flowed to the downward. On the other hand, the vertical component, the large fluctuations were also observed near the inlet up to x = 1.0 km. Then, , a high-frequency components with a spatial scale of approximately half that near the inlet gradually began to be observed up to x = 2.0 km. Consequently, the high-frequency fluctuations were maintained downwind from x = 2.0 km or later. As shown in Figure 1(c), laterally stretched structures appeared immediately behind the inlet. This might be the effects that the all integral time scale assumed to be same in this study. Around x = 500 m, large clustered structures can be seen. Then, the stretched structure in streamwise direction appeared around x = 1.0 km. Finally, the similar-scale coherent-structures stretched in streamwise became dominant and maintained in downwind from x = 2.0 km. Detailed discussion will be made in the conference.

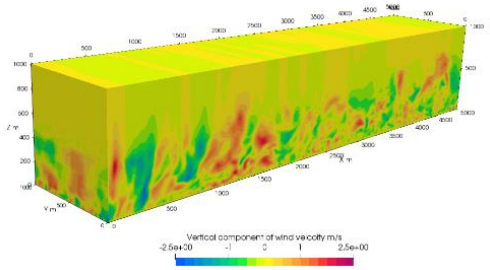
7. CONCLUSIONS

An inflow turbulence dataset conforming to the turbulence statistics specified for roughness category III corresponding to suburban area in the Recommendations for Loads on Buildings by

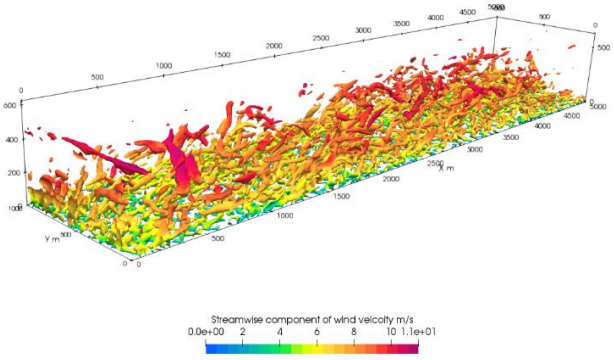
the Architectural Institute of Japan (AIJ, 2019) was developed for use as inflow boundary conditions in LES. This dataset was generated using a two-dimensional digital filter method (Xie and Castro, 2008) and accurately reproduced the prescribed mean wind speed, turbulence intensity, and integral length scale of turbulence. LES over rough terrain, utilizing this dataset, demonstrated that the incident flow retained statistical properties of the inflow turbulence over substantial downstream distances, after the reconstruction of turbulent coherent structures near the inlet. Future efforts will focus on extending this approach to LES around buildings, with plans to release the raw dataset of inflow turbulence to support broader applications in urban wind environment studies.



(a) Streamwise component of wind velocity.



(b) Vertical component of wind velocity.



(c) Isosurface of second invariant of gradient of wind velocity tensor.

Figure 1. Instantaneous quantities at the last calculation step.

ACKNOWLEDGEMENTS

This work was supported by JSPS KAKENHI (grant numbers 24K01037) and the Environment Research and Technology Development Fund JPMEERF20232003 of the Environmental Restoration and Conservation Agency provided by the Ministry of the Environment of Japan

REFERENCES

AIJ, 2019. AIJ Recommendations for Loads on Buildings (2015) Architectural Institute of Japan.

OpenFOAM. ln https://www.openfoam.com.

Smagorinsky, J., 1963. GENERAL CIRCULATION EXPERIMENTS WITH THE PRIMITIVE EQUATIONS. Mon. Weather Rev. 91, 99–164.

Tominaga, Y., 2024. CFD simulations of turbulent flow and dispersion in built environment: A perspective review. J. Wind Eng. Ind. Aerodyn. 249, 105741.

Xie, Z.-T., Castro, I.P., 2008. Efficient Generation of Inflow Conditions for Large Eddy Simulation of Street-Scale Flows. Flow, Turbul. Combust. 81, 449–470.

CFD simulation for urban canyon flow under surface heating: wall-resolved versus wall-modeled Large Eddy Simulation

Pu GONG [1], Weiheng LIANG [1], Xing ZHENG [1]

[1]*Department of Architecture and Civil Engineering, City University of Hong Kong, Hong Kong SAR, China, xzehng@city.edu.hk*

SUMMARY:
Large Eddy Simulation (LES) has been widely used to investigate urban airflow and heat removal processes. Due to the high computational costs associated with implicit filtering in LES, wall-modelled (WM) LES is often preferred over wall-resolved (WR) LES. However, the effectiveness of LES-WM for canyon flow under surface heating has not been thoroughly explored. This study assesses the performance of both WMLES and WRLES for reproducing the flow and temperature fields in a street canyon model with surface heating in a wind tunnel. Three computational grids with different resolutions, i.e., n/δ = 40, 10, and 2.5 are generated. WRLES is conducted with the grid with n/δ=40, and WRLES is conducted for all three grids. WRLES and WMLES with n/δ = 40 and n/δ = 10 demonstrate good agreement with the experiment, in terms of velocity, turbulent kinetic energy, and air temperature. In contrast, the WMLES simulation at n/δ = 2.5 significantly underpredict the turbulent kinetic energy and overpredict the air temperature near the heated wall.

Keywords: CFD guideline, Best practice recommendations, Large-eddy simulation; Buoyancy flow

1. INSTRUCTION

Understanding the airflow patterns and dissipation of heat from building surfaces is critical for addressing urban heat islands, which exacerbate energy consumption, public health risks, and thermal comfort issues in cities. Large Eddy Simulation (LES) is commonly used to examine the aerodynamics and heat removal from the building surfaces. Due to the high computational costs associated with implicit filtering in LES for flows at relatively high Reynolds numbers, (WM) LES is often preferred over wall-resolved (WR) LES (Chew et al. 2018, Iousef et al. 2023). However, the effectiveness of WMLES for such applications has not been thoroughly explored. Therefore, this study assesses the performance of both WMLES and WRLES for reproducing the flow and temperature fields within a street canyon model with surface heating in a wind tunnel.

2. METHODOLOGY

2.1. Description of the wind tunnel experiment

The wind tunnel experiment conducted at the University of Surrey examined the effects of local heating on flow dynamics in a street canyon (Marucci and Carpentieri 2019). Each of the building models that form the street canyon measures 0.166 m in height (H), 0.166 m in width, and 2.490 m in length. Electric heating mats were utilized to achieve local heating to the windward and leeward walls. Velocity measurements were performed using a two-component laser-Doppler anemometer. Air temperatures were measured using a calibrated fast-response cold-wire probe. The reference wind speed (U_{ref} = 0.65 m/s) was recorded upstream of the canyon model. In the

experiment, different heating conditions were examined. The present validation study takes the condition of windward wall heating under a neutral boundary layer.

2.2. COMPUTATIONAL SETTING AND PARAMETERS

The LES simulations are performed with OpenFOAM-v2012. The computational domain and boundary conditions follow the setups in the wind tunnel. Synthetic turbulence at the inlet is generated using the digital filter method (Xie and Castro 2008), which modifies the inlet velocity profiles by incorporating the Reynolds stress tensor, length scale, and white noise. As shown in Fig 1., three computational grids with different resolutions are generated, i.e., n/δ = 40, 10, and 2.5. Note that n represents the number of cells used to discretize the turbulence boundary layer thickness $\delta = H/2$ (Mukha et al. 2019). Only the grid n/δ = 40 is used for the WRLES. WMLES is conducted using the three computational grids. All WMLES simulations employ Spalding's law (Spalding and others 1961), which is valid for the wall region of $0 \leq y^+ \leq 350$:

$$y^+ = u^+ + e^{-\kappa B}\left[e^{-\kappa u^+} - 1 - \kappa u^+ - \frac{1}{2}(\kappa u^+)^2 - \frac{1}{6}(\kappa u^+)^3\right]$$

After the simulation reaches statistical steadiness, the sampling is taken from 81 seconds following (Qin et al. 2024).

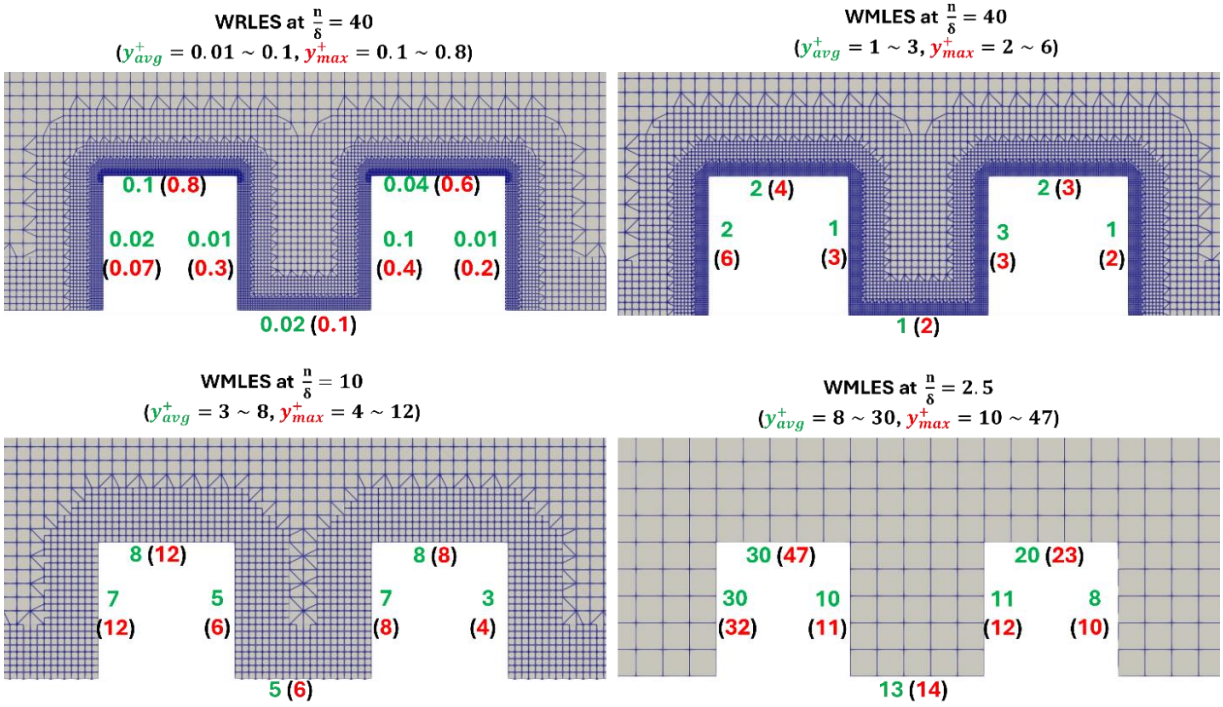


Figure 1. Area-averaged y⁺ values (y^+_{avg}, numbers in **green** color), area-maximum y⁺ values (y^+_{max}, numbers in **red** color), and the grid configurations of WRLES simulation at n/δ=40 and WMLES simulations at n/δ=40, 10, and 2.5 for the street canyon with the heated windward wall.

3. RESULTS

At a grid resolution of $n/\delta = 40$, WRLES simulation shows a y^+_{avg} ranging from 0.01-0.1, and y^+_{max} ranging from 0.1 to 0.8. These y^+ values indicate an adequate resolution of the boundary layer. All three WMLES simulations demonstrate y^+ values ranging from 0 to 350, indicating

that the grid resolution is suitable for modeling turbulence in the boundary layer. It should be noted that WRLES simulation at $n/\delta = 40$ and WMLES simulation at $n/\delta = 40$ yield different y^+ values, probably due to different predictions for the velocity close to the wall.

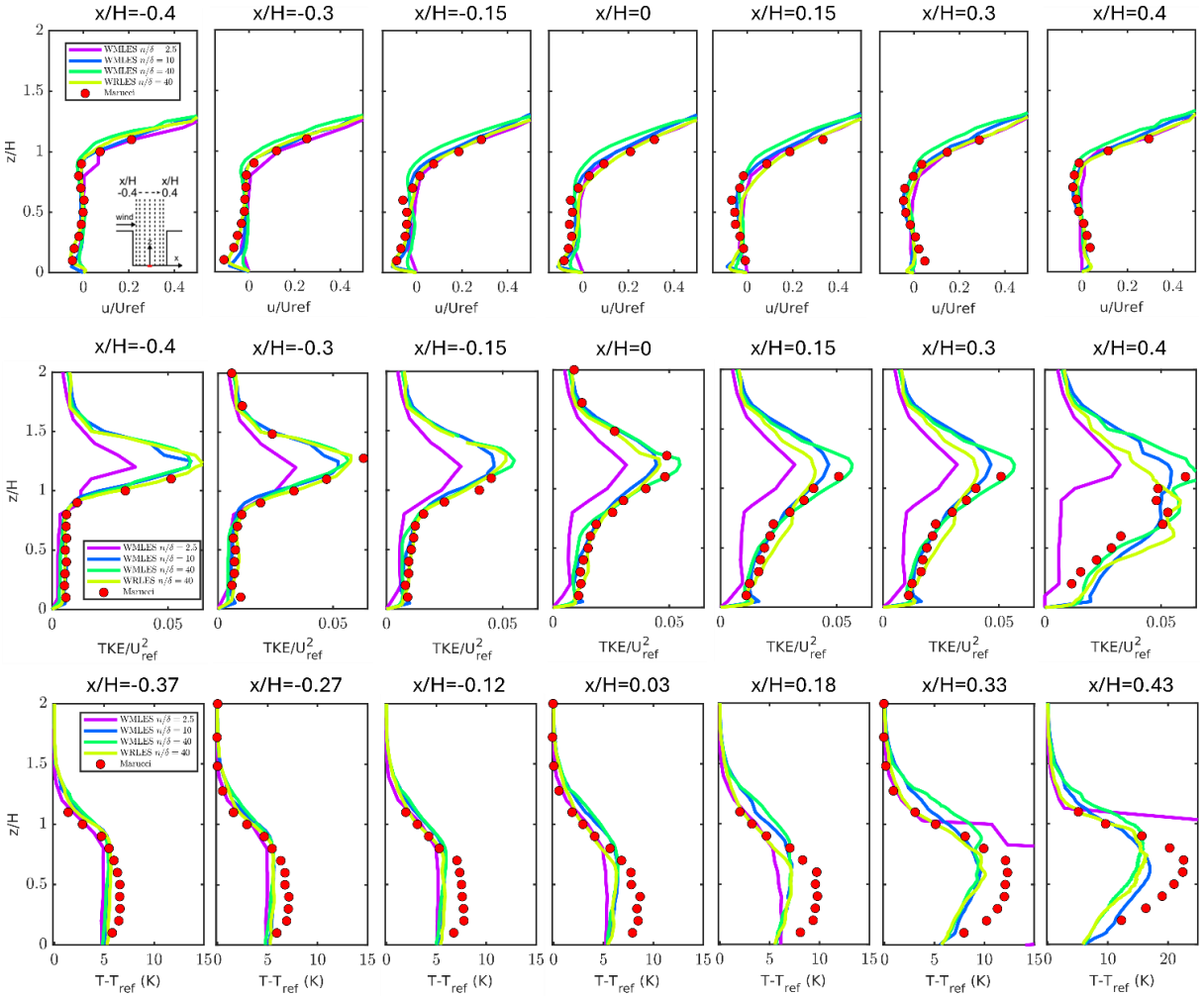


Figure 2. Comparison of the vertical profiles of (top) normalized streamwise velocity, (mid) normalized turbulence kinetic energy, and (bottom) relative temperature (T-T_{ref}) at different x values in the center section (y=0) between the wind tunnel experiment, WRLES simulation with n/δ =40 and WMLES simulations with n/δ =40, 10 and 2.5 replicating this experiment for a street canyon with heated windward wall

For the vertical profiles of the normalized streamwise velocity (see the top row in Fig. 2), WRLES simulation with n/δ = 40 and WMLES simulation with n/δ = 40 and n/δ = 10 demonstrates good agreement with the experiment. In contrast, the WMLES simulation at n/δ = 2.5 does not capture the flow in the anti-stream direction at ground level (0 < z/H < 0.2) at some locations, e.g., x/H = -0.15 or x/H = 0. For the vertical profiles of the normalized turbulence kinetic energy (see the middle row in Fig. 2), WRLES with n/δ = 40 and WMLES with n/δ = 40 and n/δ = 10 maintain consistency with the experiment by accurately capturing the TKE in the shear layer above the canyon within the range 1 < z/H < 1.5. In contrast, WMLES simulation with n/δ = 2.5 underpredicts the TKE in this region. For the vertical profiles of the relative temperature, the WRLES simulation with n/δ = 40 and the WMLES simulations with n/δ = 40 and n/δ = 10 captures the shape of the profile, with an underprediction of less than 3K within the height range

of 0.3<z/H<0.6. However, WMLES with n/δ = 2.5 significantly overpredict air temperature near the heated wall, given that the big cell occupied the near wall region.

ACKNOWLEDGEMENTS

Xing Zheng acknowledges a grant from City University of Hong Kong (Project No. (9610684)) for partially supporting the research in this paper and Beijng PARATERA Tech CO., Ltd. for providing HPC resources that have contributed to the results reported in this paper.

REFERENCES

Chew, L. W., Glicksman, L. R., and Norford, L. K. (2018), "Buoyant flows in street canyons: Comparison of RANS and LES at reduced and full scales," *Building and Environment*, 146, 77–87.

Marucci, D., and Carpentieri, M. (2019), "Effect of local and upwind stratification on flow and dispersion inside and above a bi-dimensional street canyon," *Building and Environment*, 156, 74–88.

Mukha, T., Rezaeiravesh, S., and Liefvendahl, M. (2019), "A library for wall-modelled large-eddy simulation based on OpenFOAM technology," *Computer Physics Communications*, 239, 204–224.

Qin, P., Ricci, A., and Blocken, B. (2024), "On the accuracy of idealized sources in CFD simulations of pollutant dispersion in an urban street canyon," *Building and Environment*, 265.

Spalding, D. B., and others (1961), "A single formula for the law of the wall," *Journal of Applied mechanics*, 28, 455–458.

Xie, Z. T., and Castro, I. P. (2008), "Efficient generation of inflow conditions for large eddy simulation of street-scale flows," *Flow, Turbulence and Combustion*, 81, 449–470.

A framework to assess the risk of windthrow in Irish forests.

Emmanuel Chukwudi Ekeoma [1,3], Mark Sterling [2], Nicole Metje [1], John Spink [4], Niall Farrelly [5], Owen Fenton[3]

[1]*University of Birmingham, Birmingham, UK*
[2] *Faculty of Science and Engineering, Manchester Metropolitan University, Manchester, UK*
[3] *Teagasc, Crops, Environment and Land-Use Programme, Johnstown Castle, Ireland*
[4] *Teagasc, Crops Research Centre, Oak Park, Carlow, Ireland*
[5] *Teagasc, Forestry Development Department, Mellows Centre, Athenry, Galway, Ireland*

SUMMARY
Wind-induced tree failure (windthrow) impacts the forested regions' ecological balance and economic stability. Current predictive models often lack the precision needed to forecast a forest's windthrow vulnerability due to limitations in accounting for the tree dynamic behaviour and soil properties. This paper describes a framework which integrates remote sensing and geotechnical data with a dynamic tree stability model into an earth observation framework for a more realistic windthrow risk assessment. An example of elements of this framework is applied to a forest in Northern England. The final version of this framework will also allow for the simulation of various forest management scenarios and their potential impact on windthrow vulnerability. This approach has the potential to markedly reduce economic losses through enhanced predictive accuracy and optimised forest management practices.

Keywords: Windthrow, tree failure, forest stability, GIS.

1. BACKGROUND

Windthrow is the most significant natural disturbance that affects the stability and functioning of trees in both tropical and temperate climate. This phenomenon has ecological, social, and economic implications. For example, the Lothar and Martin storms of 1999 which impacted Europe resulted in the loss of about 240 million m^3 of timber and the death of 140 people (Ekeoma et al., 2024); in Ireland fifty percent of the entire annual harvest was lost in 1974 largely due to windthrow (Keane and Sheridan, 2004), whilst in 2014 storm Darwin destroyed 8,000 ha of forest (McInereny et al., 2016).

Existing studies on the application of remote sensing technologies in windthrow typically focus on post-event analysis, utilising satellite imagery, aerial photography, airborne laser scanning (ALS) and synthetic aperture radar (SAR) data to map the extent of the damage. Although remote sensing data can be used in detecting windthrow, they may not effectively predict future vulnerabilities as they are inherently retrospective and lack insights into the mechanisms controlling tree stability. To predict windthrow risks, remote sensing data are integrated with either empirical or hybrid-mechanistic windthrow models (Gardiner et al., 2008). The hybrid-mechanistic models (HWIND and ForestGALES) are more generalisable as they account for some

underlying factors controlling tree stability. However, their inability to account for the dynamic swaying of the tree and soil characteristics, two factors which have been found to significantly contribute to tree stability (Ekeoma et al., 2024), limits their usage. The dynamic response of trees during wind loading can lead to soil failure which in turn increases the tree's response and reduces the maximum overturning moment the tree can withstand. Thus, tree failure is a complex area with several inter-dependencies often leading to non-linear responses.

This paper outlines a framework which has the potential to incorporate a dynamic windthrow model with remote sensing data for a more realistic prediction of windthrow. The windthrow risk assessment framework will be built using open-source geospatial tools. The key features and improvements of this framework are: (i) a model which accounts for the dynamic response of the tree, (ii) the inclusion of detailed soil parameters enabling soil stability to be accounted for (iii) the incorporation of remote sensing techniques which reduces the need and time spent in field assessments and (iv) the ability to represent several different harvesting and management scenarios.

2. GIS-BASED DYNAMIC WINDTHROW PREDICTION FRAMEWORK

The windthrow framework (Fig. 1) integrates LiDAR cloud point, landcover maps, soil, meteorological and tree growth datasets into a coherent, spatiotemporal dataset for windthrow assessment in forest stands. The LiDAR cloud point data are processed into the Digital Surface Model (DSM) and Digital Terrian Model (DTM) which is then used to determine the tree height, canopy, density, and ground elevation.

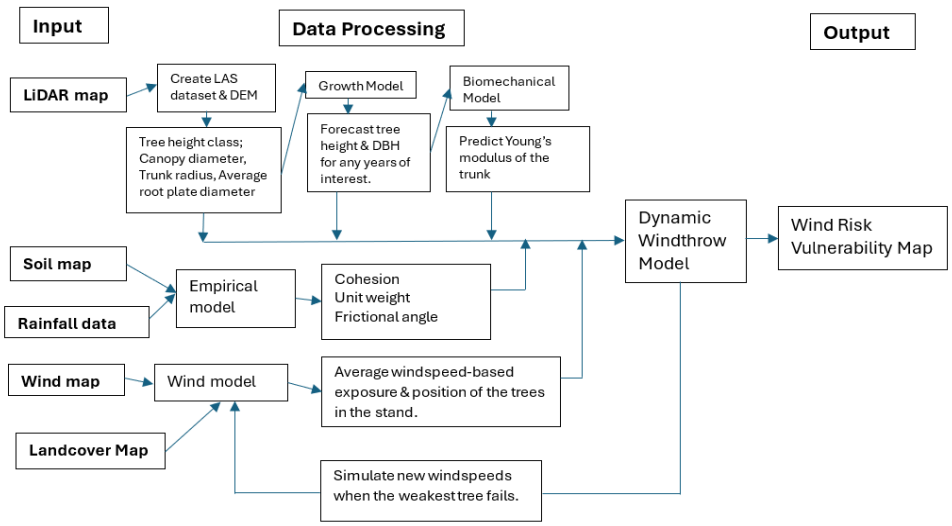


Figure 1. A casual representation of the framework of the windthrow prediction framework.

Historic wind speed and direction data across Ireland are collected from the Irish Meteorological Service which has approximately 25 measurement locations. This data is interpolated for any given forest location in Ireland based on the topography and roughness of the area as indicated in the Landcover maps. Soil maps are collected from Irish soil information system (Teagasc, 2024). However, the resolution of the soil data is very coarse; therefore, additional field assessment is performed to obtain a range of geotechnical properties (cohesion, unit weight, frictional angle) of different soil types. The cokriging method will be used to stochastically interpolate daily

precipitation measurements (Adhikary et al., 2017), which are crucial for assessing reductions in soil strength due to moisture variations. To enhance the capacity of the framework to predict the future range of vulnerability of the forest stands to windthrow, growth models for Stika spruce in Ireland are included (Lekwadi et al., 2012). These parameters feed into a windthrow model, discussed in the subsequent section.

3. WINDTHROW MODEL

A similar approach to Mansour et al. (2024) was adopted, which assumes that the failure mechanism of tree root-plate is analogous to a shallow foundation subjected to vertical (V), horizontal, and moment (M) loads. Mansour et al. (2024) used a 3D failure envelope for suction caisson foundations proposed by Villalobos et al. (2009). However, this requires several shape parameters which have only been validated for offshore foundations subjected to rotation and tensile loads. Therefore, the 3D failure envelope by Murff (1994) was adopted, which required fewer (unknown) shape factors (Equation 1).

$$\left(\frac{V}{V_o}\right)^2 + \left(\left(\frac{H}{H_o}\right)^2 + \left(\frac{M}{M_o}\right)^2\right)^{0.5} = 1 \qquad (1)$$

where V, H and M denote the vertical forces horizontal, forces and rotating moment acting on three tree and soil respectively while the subscript o denotes the ultimate capacities of these forces/moments. If it is assumed that the tree fails purely due to the moment and horizontal loads contributed by the wind, then V = 0. Therefore, tree failure occurs when equation (2) is greater than 1.

$$\left(\frac{H}{H_o}\right)^2 + \left(\frac{M}{M_o}\right)^2 = 1 \qquad (2)$$

Presently, the H and M loads were determined based on the mean wind induced drag force. In the next phase of this project, the time varying wind induced forces and dynamic response of the tree/soil will be taken into account. The vertical and horizontal capacities of the tree were determined using the bearing capacity equations given in Terzaghi (1943) and empirical relationships between tree height, crown width, and diameter at breast height (DBH) (Paul et al., 1988; Mansour et al., 2024).

4. PRELIMINARY RESULT

To demonstrate the potential of the framework a section of Kielder Forest Northumberland England has been chosen (55.2344° N, 2.5791° W). The tree heights and locations are obtained from DTM and DSM data (Department from Environment Food & Rural Affairs, 2024). In this example, the soil is assumed to be purely cohesive, with unit weight 18 kN/m³ and cohesion 5 kN/m², and the wind speed is taken as 20 m/s. In reality these values will fluctuate but for the purpose of the example they are considered reasonable. Fig. 2 shows the risk map of the forest-based on these conditions. Tree characteristics (heights and DBH) and soil parameters were found to play a significant role in determining the overall risk. This could explain why the trees in northeast section which were generally taller and had a higher risk of failure compared to other sections. Although the current version of our model extensively accounts for soil properties, factors such as wind direction, topography, and rainfall data have not yet been included. It is hypothesized that incorporating these additional environmental factors would lead to a more accurate and

comprehensive prediction of windthrow risk, particularly in complex terrain and variable climatic conditions.



Figure 2. Risk map for a portion of Kielder Forest, Northumberland England, given a 20m/s.

5. FUTURE MODELLING AND FIELDWORK

To further extend the existing model, the following activities are planned within the next 2 years to advance the development of the windthrow risk framework:

- Conducting field surveys to measure tree height, crown dimensions, and DBH using LiDAR (with a resolution of 2 meters) and traditional surveying techniques.
- Develop a mathematical model integrating soil geotechnical properties and tree dynamic responses for windthrow risk prediction.
- Development of the tree wind risk framework to allow for the simulation of different forest management strategies and potential impacts of climate change on wind patterns.
- The framework will be validated using historic windthrow data obtained from the recent storm Eowyn that occurred in Ireland on 24th January 2025.

ACKNOWLEDGEMENT

The authors would like to thank the Teagasc Walsh Scholarship Programme (Ref: 2022006) and the University of Birmingham for their support in making this research possible.

SELECTED REFERENCES

Adhikary, S. K., Muttil, N. and Yilmaz, A. G., 2017. Cokriging for enhanced spatial interpolation of rainfall in two Australian catchments. Hydrological processes, 31(12), 2143-2161.

Department for Environment Food & Rural Affairs 2004. Defra survey data download. Available at: https://environment.data.gov.uk/survey (Accessed: 10/10/2024).

Ekeoma, E. C., Sterling M., Metje N., Spink J., Farrelly. N. and Fenton O. 2024. Unearthing current knowledge gaps in our understanding of tree stability: review and bibliometric analysis. Forests, 15(3):513..

Lekwadi, S. O., Nemesova, A., Lynch, T., Phillips, H., Hunter, A. and Mac Siúrtáin M. 2012. Site classification and growth models for Sitka spruce plantations in Ireland. Forest Ecology and Management, 283, 56-65.

Mansour, M., Newson, T. and Peterson, C.J. 2024. Windthrow resistance of trees: geotechnical engineering approach. Trees, 38(3), 1-19.

Murff, J. D. 1994. Limit analysis of multi-footing foundation systems. Proceedings of computer methods and advanced geomechanics, Morgantown, 233-244.

Teagasc 2024 Irish soil information system. Available at: https://www.teagasc.ie/environment/soil/irish-soil-information-system/ (Accessed: 10/10/2024).

Wind vulnerability of industrial facilities equipment

Nahuel Bonfante [1], Jean-Paul Pinelli [2]

[1]*Florida Institute of Technology, Melbourne, US, nbonfante2023@my.fit.edu*
[2] *Florida Institute of Technology, Melbourne, US, pinelli@fit.edu*

SUMMARY:
The authors, with support from the Wind Hazard and Infrastructure Performance Center (WHIP-C), are developing wind vulnerability models for refineries. These facilities cover large areas with varying wind conditions and infrastructure types, such as tanks, pipe racks, and power stations. The goal is to standardize the methodology for assessing wind vulnerability, addressing inconsistencies in current approaches.

The methodology decomposes a refinery into subsystems, each representing different equipment types like tanks or pipe racks. For each subsystem, a conventional risk model is applied, following the principle "one site, one hazard, one vulnerability." These models are then combined based on intercorrelations between subsystems, using a “LEGO” approach that allows flexible integration of equipment vulnerabilities into an aggregated model.

Vulnerability matrices and curves are key to this method. Each matrix quantifies damage probabilities at various hazard intensities, while vulnerability curves plot expected damage against hazard intensity. By focusing on tanks and pipe racks, the study defines taxonomies and characterizes their vulnerabilities.

Preliminary results include mapping 48 processes and 71 product flows from a refinery's Process Flow Diagram (PFD), aiding in the evaluation of overall system vulnerability. Further findings, including vulnerabilities, shall be presented at the conference.

Keywords: Wind Vulnerability, Refinery, Risk Model, Equipment Classification, Industrial Networks.

1. MOTIVATION

The authors, with the support of the Wind Hazard and Infrastructure Performance Center (WHIP-C), are developing wind vulnerability models for large industrial facilities, such as refinery plants. These, and other industrial plants, are key elements of regional and country wide economies. Damage to these plants can have serious consequences for economic prosperity, as well as for human safety and wellbeing, and the environment, through the potential for natech incidents (technological incidents triggered by a natural hazard).

2. METHODS

This research presents numerous challenges, as these facilities are spread over vast areas that can exhibit significant variations in wind speeds, surface friction, topography, and other factors. Moreover, the infrastructure components of these facilities can vary greatly, including power stations, pipe racks, tanks, warehouses, cranes, towers, and more.

The authors decompose a refinery into several subsystems corresponding to its different

equipment. for which conventional risk models can be applied: one site, one hazard, one vulnerability. These models will then be combined (though not necessarily added) based on the intercorrelations between the subsystems. In this so-called "LEGO" approach, typical vulnerability equipment can be plugged in and interconnected, much like LEGO blocks, to produce an aggregated wind vulnerability model for the entire system.

The primary focus of this research lies in the development of wind vulnerability matrices and curves for refinery equipment and structures, which serve to quantify and assess the susceptibility to wind-induced damage. The columns of a vulnerability matrix are probability density functions (pdf) of damage conditional on different hazard intensity intervals (each column represents a different intensity interval). The vulnerability curve plots the expected damage for each column pdf as a function of hazard intensity. Vulnerability matrices and curves are commonly used to estimate potential economic losses by correlating hazard intensity with a specific loss metric.

The most vulnerable equipment, and therefore the focus of our study, are the tanks and pipe-racks, The study starts with detailed taxonomies of tanks and pipe-racks within refineries, which translate into the characterization of different classes for each type of equipment. The taxonomies also inform the nomenclature that identifies each class of equipment for which we define a vulnerability model. By characterizing all equipment into different classes based on their corresponding taxonomies and having established the vulnerabilities of each equipment class, we will achieve a comprehensive understanding of the vulnerability of the equipment in the refinery.

A refinery Process Flow Diagram (PFD), as shown in Figure 1, is an essential documentation for its operation. The PFD illustrates all the processes, each of which involves one or more equipment, and each equipment has its own taxonomy, and for which we have already defined vulnerability based on their type and class. What is particularly interesting is that it also shows the interconnections between these processes. This allows us to define a workflow, understanding the equipment involved and the vulnerabilities associated with each equipment, as well as the overall vulnerability of each process flow within the refinery. By weighting and interconnecting the vulnerabilities of each flow, we can determine the overall vulnerability of the refinery.

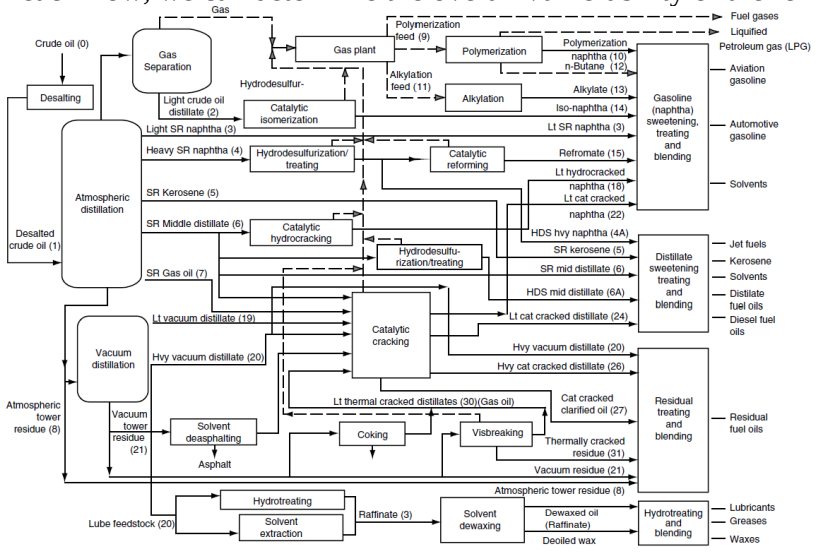


Figure 1. Schematic overview of a refinery. From OSHA (Occupational Safety and Health Administration) from USA, Technical Manual, Section IV, Chapter2, Petroleum Refining Processes.

3. RESULTS

A typical refinery PFD, as defined by the USA Occupational Safety and Health Administration (OSHA), was used to identify and map 48 key processes and 71 unique product flows. Processes were categorized by equipment type, and tanks and pipe-racks were classified into distinct categories (see Figure 2). A new nomenclature captures the taxonomy of the equipment related to wind vulnerability. Vulnerability curves for various tank types and pipe-racks, which are essential to refinery operations, are currently under development and shall be presented at the conference.

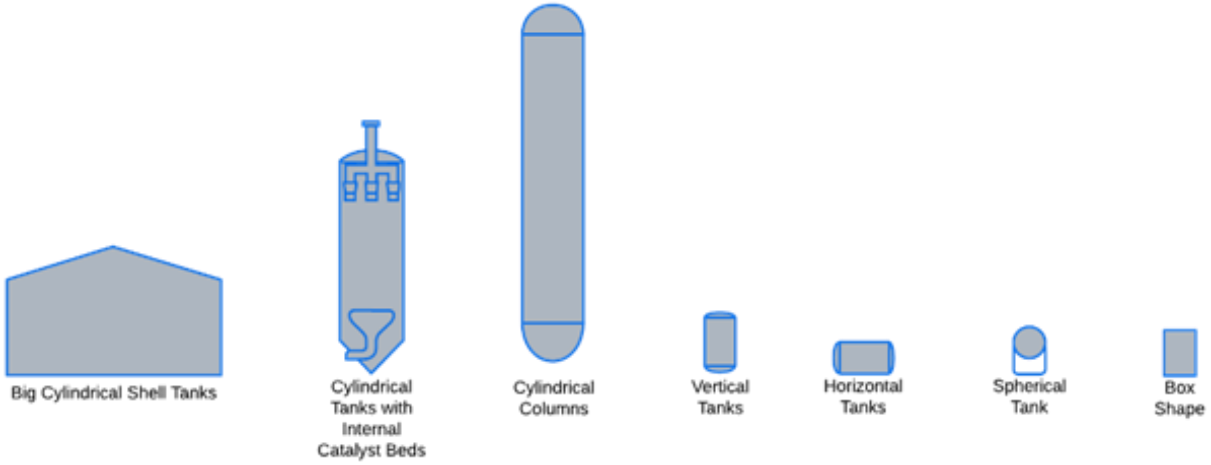


Figure 2. Tank Classification.

4. CONCLUSIONS

This research will provide a standardized approach to wind vulnerability modelling for refineries and large industrial facilities. By systematically classifying and characterizing equipment and processes, this work sets the foundation for more accurate and unbiased assessments of wind-induced damage. Results will be presented at the conference, including the mapping of crude oil process flows, equipment vulnerability, and a fully developed nomenclature. Future work will refine these models and address the issues of network vulnerability, validation and uncertainty quantification.

5. ACKNOWLEDGMENTS

The authors would like to thank the Wind Hazard and Infrastructure Performance Center (WHIP-C) for their support.

6. REFERENCES

Bailey, J. R., & Levitan, M. L. (2008). Lessons learned and mitigation options for hurricanes. Process Safety Progress, 27(1), 41–47. https://doi.org/10.1002/prs.10218

Barto, J., & Gardoni, P. (2021). Wind shielding in refining and petrochemical facilities. Journal of Wind Engineering and Industrial Aerodynamics, 214. https://doi.org/10.1016/j.jweia.2021.104676

Bernier, C., & Padgett, J. E. (2019a). Buckling of aboveground storage tanks subjected to storm surge and wave loads. Engineering Structures, 197. https://doi.org/10.1016/j.engstruct.2019.109388

Bernier, C., & Padgett, J. E. (2019b). Fragility and risk assessment of aboveground storage tanks subjected to concurrent surge, wave, and wind loads. Reliability Engineering and System Safety, 191. https://doi.org/10.1016/j.ress.2019.106571

Bernier, C., & Padgett, J. E. (2020). Fragility Assessment of Floating Roof Storage Tanks during Severe Rainfall Events. Journal of Performance of Constructed Facilities, 34(6). https://doi.org/10.1061/(asce)cf.1943-5509.0001505

Cruz, A. M., Steinberg, L. J., & Luna, R. (2001). Identifying hurricane-Induce hazardous material release scenarios in a petroleum refinery.

Godoy, L. A., & Asce, M. (2007). Performance of Storage Tanks in Oil Facilities Damaged by Hurricanes Katrina and Rita. Journal of Performance of Constructed Facilities. https://doi.org/10.1061/ASCE0887-3828200721:6441

Liu, X., Levitan, M., & Nikitopoulos, D. (2008). Wind tunnel tests for mean drag and lift coefficients on multiple circular cylinders arranged in-line. Journal of Wind Engineering and Industrial Aerodynamics, 96(6–7), 831–839. https://doi.org/10.1016/j.jweia.2007.06.011

Mileti, D., & Henry, A. J. (1999). Disasters by Design: A Reassessment of Natural Hazards in the United State. In Natural Hazards.

Misuri, A., Casson Moreno, V., Quddus, N., & Cozzani, V. (2019). Lessons learnt from the impact of hurricane Harvey on the chemical and process industry. Reliability Engineering and System Safety, 190. https://doi.org/10.1016/j.ress.2019.106521

Olivar, O. J. R., Mayorga, S. Z., Giraldo, F. M., Sánchez-Silva, M., Pinelli, J. P., & Salzano, E. (2020). The effects of extreme winds on atmospheric storage tanks. Reliability Engineering and System Safety, 195. https://doi.org/10.1016/j.ress.2019.106686

Omidvar, B. (2023). Instruments vulnerability wind vulnerability and resilience. In Crises in Oil, Gas and Petrochemical Industries: Loss Prevention and Disaster Management (pp. 29–48). Elsevier. https://doi.org/10.1016/B978-0-323-95163-0.00018-9

Ramírez, O. J., Mesa, A. M., Zuluaga, S., Muñoz, F., Sánchez-Silva, M., & Salzano, E. (2019). Fragility curves of storage tanks impacted by strong winds. Chemical Engineering Transactions, 77, 91–96. https://doi.org/10.3303/CET1977016

Rossi, L., Casson Moreno, V., & Landucci, G. (2022). Vulnerability Wind vulnerability assessment of process pipelines affected by flood events. Reliability Engineering and System Safety, 219. https://doi.org/10.1016/j.ress.2021.108261

Salzano, E., Basco, A., Busini, V., Cozzani, V., Marzo, E., Rota, R., & Spadoni, G. (2013). Public awareness promoting new or emerging risks: Industrial accidents triggered by natural hazards (NaTech). Journal of Risk Research, 16(3–4), 469–485. https://doi.org/10.1080/13669877.2012.729529

Sengul, H., Santella, N., Steinberg, L. J., & Cruz, A. M. (2012). Analysis of hazardous material releases due to natural hazards in the United States. Disasters, 36(4), 723–743. https://doi.org/10.1111/j.1467-7717.2012.01272.x

Stedman, D., & Vojjala, R. (2023). ComponentEquipment-based Vulnerability Wind vulnerability of Large Facilities.

Wong, S., Sepaha, A., Swamy, N., Amoroso, S. D., & Naqvi, D. (2012). Wind Loads On Non-Building Structures Using ASCE 7-10.

Observed wind characteristics causing property damage during severe misoscale thunderstorm events in a temperate coastal region

M.J. Glanville

CPP, Sydney, Australia, mglanville@cppwind.com

SUMMARY:
Wind characteristics and recurrence intervals of severe misoscale microburst outflow and tornadic events on the NSW coast of Australia have been estimated based on meteorological records, media reports and examined property damage following storms with reference to the Enhanced Fujita Scale. Terrain and buoyancy were observed to play a primary role in the outer spread of microburst outflows behaving as a thin jet of chilled, dense, rain-laden air skimming over the interfacial layer of terrain roughness with minimal turbulence mixing at ground level. An ocean born category of tornado hazard impacting the NSW coastal fringe is identified with intensity at high recurrence intervals applicable to essential facilities design. Findings are evaluated in the context of existing Australian and U.S. wind codes.

Keywords: Severe Misoscale Thunderstorm, Microburst, Tornado, Coastal

1. INTRODUCTION

Thunderstorm downbursts are a dominant extreme wind type for ultimate limit state design return periods in temperate coastal regions of southeast Australia (Holmes 2019), yet further codification work is required to improve multipliers for velocity profiles and topography in downburst events. Downbursts, especially misoscale microbursts and tornadic events, are usually missed by spatially separated anemometer stations. An understanding can instead be obtained indirectly by observing property damage following storms. This paper provides a summary of surveyed property damage caused by severe misoscale microburst and tornadic events with reference to the Enhanced Fujita Scale (EF-Scale) focusing on the NSW coast over the past few decades. Geo-marked photographic records of observed damage are used to assist with mapping each event, and reference is also made to available meteorological records, witness accounts, media reports and video footage.

2. COASTAL MICROBURSTS

Table 1 provides a summary of atmospheric conditions associated with three recent microburst events that were surveyed for property damage by the author, and which occurred near the NSW coast at Lismore, Mascot and the Northern Beaches of Sydney (Glanville and Moir, 2023). Key atmospheric ingredients for severe thunderstorms to form are warm atmospheric air temperatures with high moisture content, rising unstable air and a lifting mechanism. Varying levels of each were found in the surveyed microburst events noting their proximity to a bay, river and lagoons. Lifting mechanisms for each were cold fronts and large atmospheric instability is noted at Mascot.

Table 1. Surveyed microburst events.

Date	Event, near BoM AWS	Max damage	Atmospheric stability, TT, LI	Pre/Post atmospheric conditions at nearest BoM AWS. 1 min mean wind speed, direction, temp, RH, local time
27/12/2024	Mascot, ID:066037	EF1	Large instability, 52, -5.8°C	7.7ms^{-1}, 317°, 34.1°C, 35% @16:35 / 14.4ms^{-1}, 163°, 26.1°C, 65% @17:05(southerly cold front)
08/12/2024	Lismore, ID:058214	EF1	Marginal stability, 41, -3.3°C	6.2ms^{-1}, 172°, 33.7°C, 59% @17:15 / 28.8ms^{-1}, 174°, 23.1°C, 87% @17:26(southerly cold front)
19/12/2021	N Beaches, ID:066059	EF2	Marginal stability, 50, -2.6°C	13.4ms^{-1}, 286°, 30.5°C, 40% @15:21 / 7.9ms^{-1}, 267°, 20.1°C, 74% @15:31(westerly cold front)
Other recent EF1 up to EF2 coastal events in NSW include The Entrance 9th Dec 2023 and Port Macquarie 3rd Feb 2023. Turramurra downburst 21st Jan 1991 storm swathe was inspected producing up to EF3 damage.				

The Lismore microburst was captured in the time lapse of Fig. 1(L) from the viewing location shown in Fig. 1(C). EF-Scale rated damage without reference to wind speed (Womble, 2009) is overlayed on topographic contours in Fig. 1(C), with larger colour coded arrows providing an indication of local wind direction deduced from fallen trees. The microburst shaft commenced over Wilsons River with initial outflow passing directly over the Bureau of Meteorology (BoM) Lismore Airport Automatic Weather Station (AWS) which recorded a gust wind speed of 35 ms^{-1} (Fig. 1(R)); corresponding to an average recurrence interval R of 13.5 years (Standards Australia, 2021). A nose shape vertical velocity profile associated with the initial outflow is seen to the right of the top photographs in Fig. 1(L). A propagating outflow tip of cold and heavy rain laden air then continues northward in the lower photographs, appearing analogous to a thin sheet of water flowing over a beach swash zone which could be modelled as a dam break flow onto a frictionless bed. Video footage from within the outflow on the airport apron confirms minimal turbulence mixing at ground level (https://www.abc.net.au/news/2024-12-09/lismore-storm/104700932).

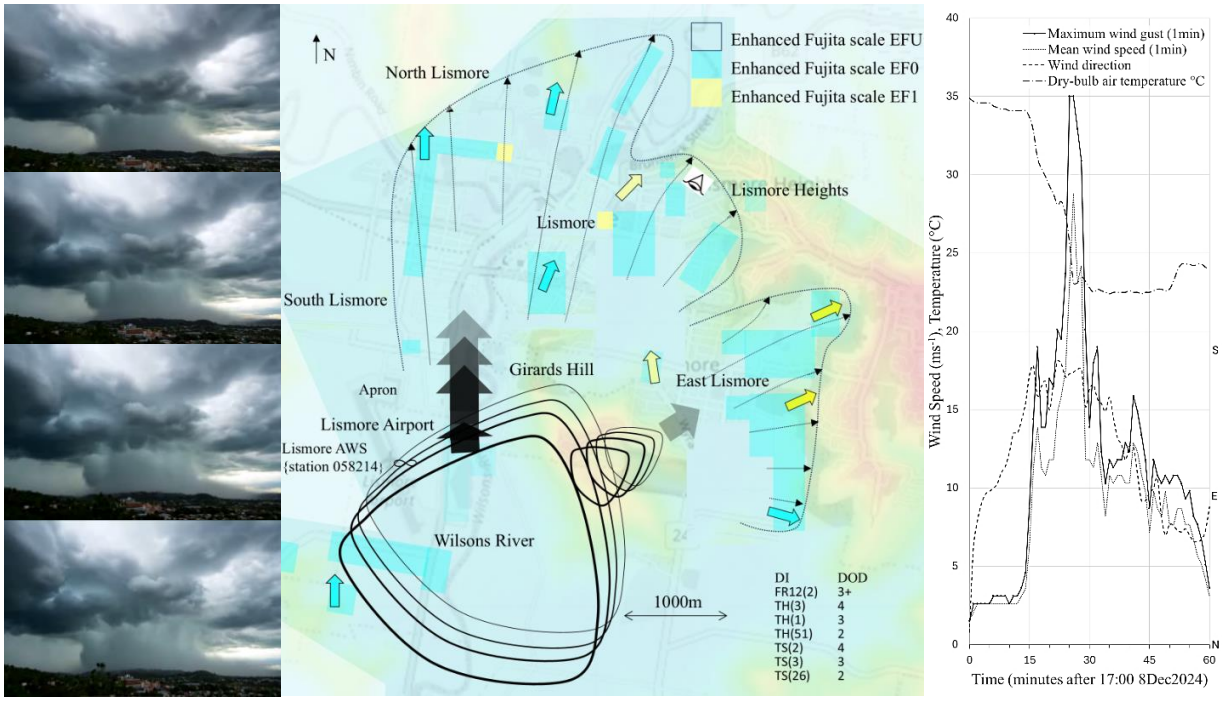


Figure 1. Lismore microburst filmed from Lismore Heights by *Force of Nature Photography* (L), Lismore terrain map (10-170m) with EF-scale damage ratings and storm path overlays (C), Lismore Airport AWS readings (R).

Buoyancy and terrain were observed to play a primary role in the spread of the cold heavy outflows for the events listed in Table 1. In Lismore, dense outflow moving up the Lismore Heights valley walls was slowed by gravity until it ceased at a run-up limit around 60 m above tarmac level. Similar run-up heights and damage were observed in the Mascot and Northern Beaches events.

Observed damage and video evidence of the Northern Beaches event supports a localised jet nature to the outflow with minimal turbulence mixing at ground level (Fig. 2). Evidence was found of thin ribbons of cold dense jet outflow skimming over building rooftops and the interfacial layer of ground roughness. The greatest observed building damage (up to EF2) was to roofs protruding into the jet stream or at ground level at the downstream end of long open corridors where outflow could gain momentum. Swath damage in Fig. 2 extended over a narrow plan area, and a similar ribbon of higher damage extending beyond the main outflow sheet was also found in the Mascot event. Further code modifications to downdraft profiles (Standards Australia, 2016) may consider the observed jet flow nature of outflows with finite dimensions and their interaction with local topography and the built environment contributing to the highest design wind speeds.

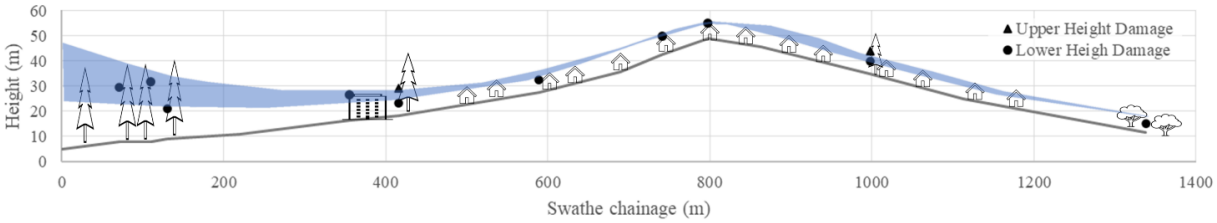


Figure 2. Outflow vertical section over a Northern Beaches headland estimated from damage survey.

3. COASTAL TORNADOES

A simplified tornado hazard probability model by (Thom, 1963) uses geometrical probability to determine the probability of a tornado striking a point per year within a defined area *P(s)*:

$$P(s) = \frac{\bar{a}n}{A} \quad (1)$$

Where $\bar{a}$ is the mean damage path area and *n* is the mean number of tornadoes per year assumed to be uniformly distributed in a region of area *A*. Tornadoes occur across the Australian continent but with reduced strike probability farther inland (Allen, 2021) and with most damage limited to EF1 (http://www.bom.gov.au/australia/stormarchive/). An historical review of recorded tornado days between 1805 and 1989 by (Evesson, 1970) and (Griffiths et al, 1993) suggests a Tornado strike rate *n* of the order 10 per year across the whole NSW state area A_{state}, giving a small strike probability over the state in the order 10^{-6} per year.

Fair-weather waterspouts occur regularly off the NSW coastline and usually cause limited EFU to EF1 damage if they reach shore. Supercell thunderstorms can form tornadic waterspouts and upon reaching landfall cause extensive property damage as occurred at Lennox Head (Glanville and Quinn, 2010) and Kurnell (Glanville et al, 2016), which recorded the strongest wind gust ever measured by the BoM in NSW at 59 ms^{-1}. Noteworthy at each event was the circular spread of damage debris. Table 2 identifies a category of ocean born tornadoes that caused extensive ≥EF2 damage along the NSW coastal fringe over the last 30 years. Table 2 includes the maximum distance each damage swathe penetrated inland perpendicular to the shoreline. Most are within 2000 m, used to define the width of a proposed coastal strip area A_{coast} following the length of the NSW shoreline (shortened to 600 km to exclude unpopulated locations).

Table 2. Known coastal tornadoes causing extensive ≥EF2 damage on the NSW coast since 1995.

Date	Event	Damage	Swathe mean width within A_{coast}	Swathe area within A_{coast}	Max swathe distance inland
16/04/1995	Merimbula/Pambula**	EF3/EF2	100 m	525,000 m^2	1,800 m
03/06/2010	Lennox Head*	EF2	50 m	35,000 m^2	350 m
23/02/2013	Seven Mile Beach***	EF2	110 m	200,000 m^2	15,000 m
23/02/2013	Kiama**,***	EF2	100 m	60,000 m^2	4,000 m
16/12/2015	Kurnell*	EF2	225 m	546,000 m^2	2,000 m
Earlier ≥EF2 coastal events at Port Macquarie 1962&1985 and Bulahdelah 1970. EF1 coastal events at La Perouse 2006, The Entrance 2009, Red Rock 2011, Jamberoo 2013, Palmers Island 2016 & Green Point 2024.					

*Damage survey during clean-up, witnesses & media review **Damage survey post-event, witnesses & media review, ***Louis (2018)

Swathe mean damage path areas within A_{coast} are used to calculate a tornado strike probability resulting in ≥EF2 damage to be in the order 10^{-4} per year. This was found to align with the American standard ASCE/SEI 7-22 tornado hazard for critical infrastructure with high recurrence intervals in the most prone U.S. regions. Tornadoes are known to occur as associated discrete events and cluster within years following Polya distributions as observed between 2010 and 2015.

4. CONCLUSIONS

Wind characteristics and recurrence intervals of severe misoscale microburst outflows and tornadic events at NSW coastal locations have been examined based in part on observed property damage. Terrain and buoyancy appear to play a primary role in the outer spread of microburst outflows behaving as a thin jet of chilled, dense, rain-laden air skimming above terrain roughness with minimal turbulence mixing at ground level. An ocean born category of tornado hazard impacting the NSW coastal fringe is identified with intensity at high recurrence intervals applicable to essential facilities design. Findings have been evaluated in the context of existing wind codes.

REFERENCES

Allen, J. T., Allen, E. R., Richter, H., and Lepore, C., 2021. Australian tornadoes in 2013: implications for climatology and forecasting. American Meteorological Society 149, 1211-1232.

American Society of Civil Engineers, 2022, Minimum Design Loads and Associated Criteria for Buildings and Other Structures, ASCE/SEI 7-22.

Evesson, D. T., 1970. Tornado occurrences in New South Wales. Australian Meteorological Magazine 17, 143–165.

Glanville, M. J., and Moir, N. A., 2023. A coastal microburst wind damage survey and observations. Proceedings of 21st Australasian Wind Engineering Society Workshop, 2-3 Feb. 2023, Bicentennial Park, Sydney, Australia.

Glanville, M. J., and Quinn, J. P., 2010. Waterspout damage at Lennox Head. Proceedings of 14th Australasian Wind Engineering Society Workshop, 5-6 Aug. 2010, Geoscience Australia, Canberra, Australia.

Glanville, M. J., Rohr, C. J., and Holmes, J. D., 2016. Tornadic waterspout impacts on coastal Australia. Proceedings 18th Australasian Wind Engineering Society Workshop, 6-8 July. 2016, McLaren Vale, South Australia, Australia.

Griffiths, D.J., Colquhoun, J. R., Batt, K. L., and Casinader, T. R., 1993. Severe thunderstorms in New South Wales: climatology and means of assessing the impact of climate change. Climatic Change, 25, 369–388.

Holmes, J. D., 2019. Extreme wind prediction – the Australian experience. Proceedings of the XV Conference of the Italian Association for Wind Engineering (IN VENTO 2018), 365–375.

Louis, S. A., 2018. A warm-front triggered nocturnal tornado outbreak near Kiama, NSW, Australia. Journal of Southern Hemisphere Earth Systems Science 68, 147–164.

Standards Australia, 2016. Australian/New Zealand Standard, Overhead line design (AS/NZS7000:2016).

Standards Australia, 2021. Australian/New Zealand Standard, Structural Design Actions, Part 2: Wind Actions (AS/NZS1170Pt.2:2021).

Thom, H., 1963. Tornado probabilities. Monthly Weather Review 91, 730-736.

Womble, J. A., Smith, D. A., Mehta K. C., and McDonald J. R., 2009. The enhanced Fujita scale: for use beyond tornadoes? Forensic Engineering Congress 2009, Copyright ASCE.

A novel framework to assess multiscale wind hazard on structures and infrastructures: an application to Italy

Lorenzo Raffaele[1,5], Luca Bruno[2,5], Elisabetta Colucci[3,5], Nicolas Coste[4]

[1]*Politecnico di Torino, Torino, Italy, lorenzo.raffaele@polito.it*
[2]*Politecnico di Torino, Torino, Italy, luca.bruno@polito.it*
[3]*Politecnico di Torino, Torino, Italy, elisabetta.colucci@polito.it*
[4]*Optiflow Company, Marseille, France, coste@optiflow.fr*
[5]*GeoWindy R&D group, geowindy@polito.it*

SUMMARY:
Synoptic extreme winds are typically represented at a macroscale resolution (hundreds of kilometers) using time series data from land-based anemometric stations. The evaluation of design wind speed for construction sites is typically entrusted to the designer, based on the so-called return criterion. However, several critical issues impact the traditional map-and-return method, including the sparse and uneven distribution of anemometric stations, uncertainties related to their setup, measurement inaccuracies, the subjective assessment of exposure roughness, and inconsistencies across national wind standards. This study aims to explore an alternative methodology by directly evaluating wind hazards at a meso-γ scale resolution (approximately 2 kilometers) and, eventually, micro-β scale resolution (approximately 100 meters) surrounding construction sites. The proposed approach utilizes data from a weather forecast computational model, its reanalysis by means of assimilated remote sensing observations, and its downscaling. The resulting wind maps across Italy are rigorously compared with measurements from 21 stations. Errors across models are analyzed for both current and extreme wind speeds over various return periods. Finally, a framework to assess multiscale wind hazard on structures and infrastructures is proposed.

Keywords: wind hazard, multiscale, computational approach

1. INTRODUCTION

In the practice, the design wind speed is commonly determined through wind speed maps. The well-known return criterion was formalized by Ballio et al., 1999 and it is traditionally adopted in Italy through the standards in force (DM 17-01-2018, 2018; EN 1991-1-4:2005, 2005). The return criterion relies on the accurate mapping of the basic wind speed v_b, i.e. the characteristic 10-min average wind speed at 10 m above the ground in open field terrain, to evaluate the mean wind speed v_m, defined as a function of the local site conditions (Fig. 1b). The mapping of v_b was conceived by Ballio et al., 1999 on the basis of wind speed v anemometric measurements resulting from a total of 69 stations distributed over the Italian territory (Fig. 1a). The resulting horizontal resolution of the stations used to define the national design wind speed map $L_{stat,IT}$ is then equal to 69.4 km on average. Wind speeds were corrected (v_c) by filtering and adjusting unreliable data, and transformed (v_t) to homogenize the time averaging period and local site conditions, in order to get 10-min averaged wind speeds measured at $z = 10$ m, over flat, uniformly open terrain conditions with roughness $z_{0,ref} = 0.05$ m. Wind maps resulted form the definition of the reference wind speed $v_{ref,0}$ as the value of v_t with mean return period $T_R = 50$ years, the clustering of $v_{ref,0}$

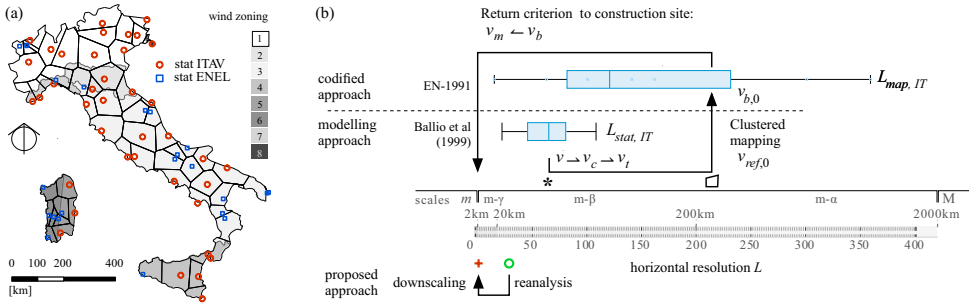


Figure 1. Voronoi discretization of Italian land based on 69 ITAV and ENEL stations together with current codified wind map (a). Comparative workflow between the return criterion and the proposed approach (b).

into nine geographical zones, and the definition of the basic wind speed at sea level $v_{b,0}$ for each zone. As a result, the transition from v to $v_{b,0}$ inevitably implied the coarsening of the horizontal resolution of the wind speed map $L_{map,IT}$, leading to an average value approximately equal to 170 km and widely uneven over the Italian land.

Recently, other approaches have been implemented to map wind speed in several scientific fields. Climate reanalysis data from numerical weather prediction models (Hersbach, Bell, et al., 2020) are widely adopted in wind energy, agriculture, water resources, insurance, and very recently in Wind Engineering, specifically along transmission lines (Yang et al., 2022). Climate reanalyses combine past observations with models to generate consistent time series of multiple climate variables. Furthermore, they enables a high spatial resolution with respect to codified extreme wind maps in Wind Engineering, the continuous update, and datasets available worldwide, avoiding conflicts of the national wind maps at boundaries.

This study aims to evaluate if reanalysis models (ERA5, Hersbach, Bell, et al., 2020), eventually coupled with deterministic (ERA5-Land, Muñoz-Sabater, Dutra, et al., 2021), dynamical (VHR-REA_IT, Raffa, Reder, et al., 2021) or steady Computational Wind Engineering (RANS, Castorrini et al., 2021) downscaling approaches, can be suited to map extreme winds, and which are the advantages compared to in-force codified wind maps.

2. MODELLING APPROACHES

In the following, reanalysis modelling approaches tested in this study are briefly reviewed by focusing on the main variables of interest. Their space and time resolutions are given in Fig. 2 by referring to the scales of the atmospheric processes.

ERA5 is the fifth generation reanalysis developed by the European Centre for Medium-Range Weather Forecasts (ECMWF). It provides hourly estimates for a large amount of atmospheric, ocean wave and land surface variables, wind components at 10 m included. Observations used as input for reanalysis in ERA5 come from satellite instruments and conventional data (Hersbach, Bell, et al., 2020). With regard to wind velocity at 10 m, measurements made near the sea surface on ships and drifting/moored buoys are retained only, while observations at land airport weather stations are limited to surface pressure. It follows that the comparison between records at land anemometric stations and reanalysis is not trivial and directly driven by assimilation.

ERA5-Land (ERA5L, in the following) is a reiteration of the land component of the ERA5 climate reanalysis at an enhanced horizontal resolution, using ERA5 atmospheric variables as input

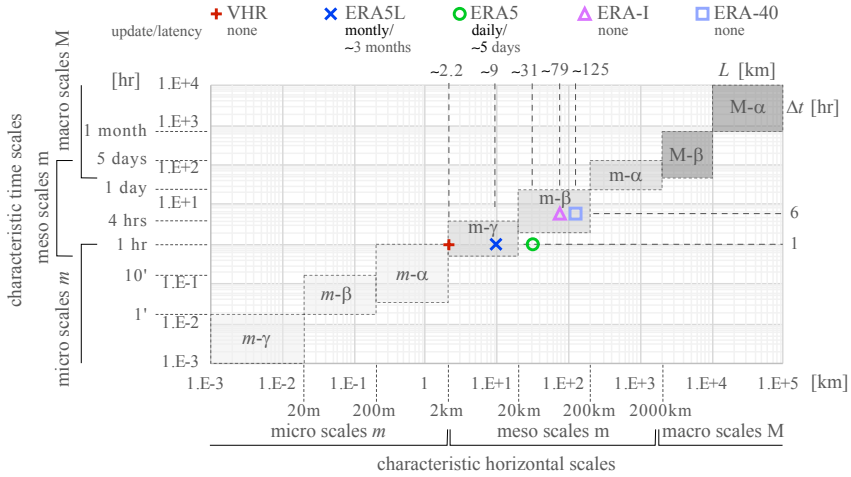


Figure 2. Space and time scales of the atmospheric processes, and synopsis of mean horizontal and time resolutions of ERA-40, ERA-Interim (ERA-I), ERA5, ERA5-Land (ERA5L), VHR-REA_IT (VHR).

(Muñoz-Sabater, Dutra, et al., 2021). In particular, wind speed has purely been deterministically interpolated to the ERA5L grid via a linear interpolation method.
VHR-REA_IT (VHR, in the following) is obtained by dynamical downscaling of ERA5 climate reanalysis to the lower bound of the meso-γ scale, also called convection-permitting scale (horizontal resolution lower than 4 km), over the domain covering Italy. The dynamical downscaling is carried out with the regional climate model COSMO-CLM with the module TERRA-URB to model urban environment (Raffa, Reder, et al., 2021). Such a dynamical downscaling allows to explicitly resolve atmospheric deep convection, responsible for the formation of synoptic-scale storm systems, and to improve the modelling of wind systems dominated by fine-scale topography (Prein, Langhans, et al., 2015).

3. PRELIMINARY RESULTS

The VHR-based meso-scale Italian wind map of the extreme wind speeds for a 50-year return period is shown in Fig. 3(a) in terms of filled isocontours. The drafting of each map involved the statistical processing of about 163.5 billion wind speed data at 444,000 cells, i.e. about 160,000 times the data available 33 year ago. To better appreciate the horizontal resolution of the Italian map and its mesoscale features, a closeup isocontour view of the zone surrounding the Adige and Sarca valleys is shown in Fig. 3(b). The spatial resolution of VHR massively enriches the description of the extreme wind speeds with respect to the current design wind speed zoning. The highest wind speed magnitudes take place over (i) water bodies, i.e. sea and lakes, due to the low roughness; and (ii) mountain ridges, due to the strong orographic effects directly accounted for.
In the light of the above, obtained results over the Italian Country will be critically discussed with respect to anemometric records and standards in force.

ACKNOWLEDGEMENTS

This study was carried out within the RETURN Extended Partnership and received funding from the European Union Next-GenerationEU (National Recovery and Resilience Plan – NRRP, Mission 4, Component 2, Investment 1.3 –

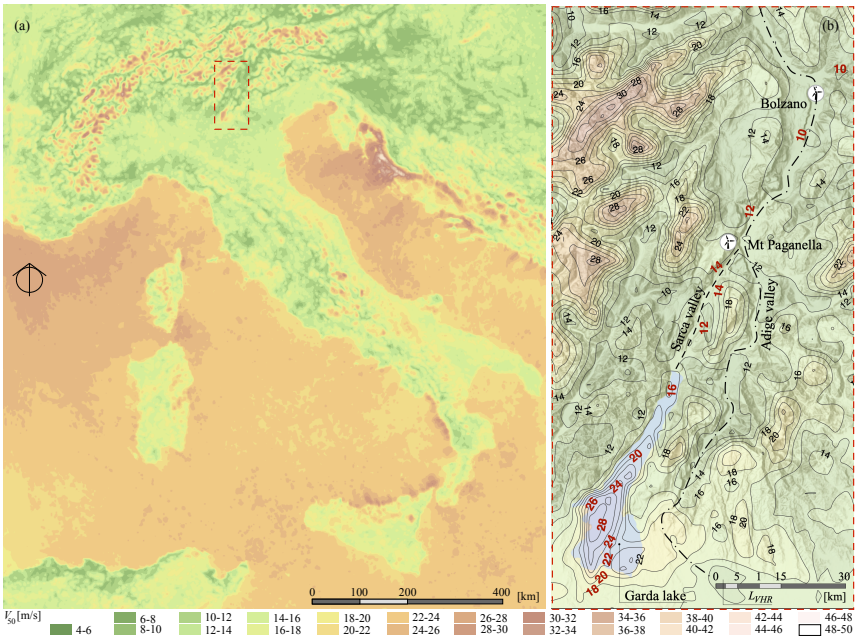


Figure 3. Map of the extreme wind speed V_{50} with return period $T_R = 50$ (a). Closeup view of the map around the zone surrounding the Adige and Sarca valleys, from Bolzano to the Garda lake (b).

D.D. 1243 2/8/2022, PE0000005) – SPOKE TS 2. This study was jointly developed in the framework of the research project PROtection Technologies from Eolian Events for Coastal Territories (PROTEECT, http://www.proteect.polito.it/) within the Ministerial Decree no. 1062/2021 and received funding from the FSE REACT-EU - PON Ricerca e Innovazione 2014-2020. This manuscript reflects only the authors' views and opinions, neither the European Union nor the European Commission can be considered responsible for them.

REFERENCES

Ballio, G., Lagomarsino, S., Piccardo, G., and Solari, G., 1999. Probabilistic analysis of Italian extreme winds: Reference velocity and return criterion. Wind and Structures 2, 51–68.

Castorrini, A., Gentile, S., Gentili, E., and Bonfiglioli, A., 2021. Increasing spatial resolution of wind resource prediction using NWP and RANS simulation. Journal of Wind Engineering and Industrial Aerodynamics 210, 104499.

DM 17-01-2018, 2018. *Technical Standards for Construction - update DM January 17, 2018*. Standard. Ministry of Infrastructures and Transport, Rome, Italy.

EN 1991-1-4:2005, 2005. *Eurocode 1 – Actions on structures – Part 1- 4: General actions – Wind actions*. Standard. European Committee for Standardization (CEN), Brussels, Belgium.

Hersbach, H., Bell, B., et al., 2020. The ERA5 global reanalysis. Quarterly Journal of the Royal Meteorological Society 146, 1999–2049.

Muñoz-Sabater, J., Dutra, E., et al., 2021. ERA5-Land: A state-of-the-art global reanalysis dataset for land applications. Earth System Science Data 13, 4349–4383.

Prein, A., Langhans, W., et al., 2015. A review on regional convection-permitting climate modeling: Demonstrations, prospects, and challenges. Reviews of Geophysics 53, 323–361.

Raffa, M., Reder, A., et al., 2021. VHR-REA_IT Dataset: Very High Resolution Dynamical Downscaling of ERA5 Reanalysis over Italy by COSMO-CLM. Data 6.

Yang, S., Chouinard, L. E., and Langlois, S., 2022. Hourly wind data for aeolian vibration analysis of overhead transmission line conductors. Journal of Wind Engineering and Industrial Aerodynamics 230.

Stow regime considerations for single axis tracker solar structures

Mike Gibbons [1], Zachary Taylor [2], Julia Veerman [3], David Horrocks [4]

[1] *Rowan Williams Davies & Irwin, Inc. (RWDI), Thunder Bay, Canada, mike.gibbons@rwdi.com*
[2] *Rowan Williams Davies & Irwin, Inc. (RWDI), Guelph, Canada, zachary.taylor@rwdi.com*
[3] *Rowan Williams Davies & Irwin, Inc. (RWDI), Vancouver, Canada, julia.veerman@rwdi.com*
[4] *Rowan Williams Davies & Irwin, Inc. (RWDI), Calgary, Canada, david.horrocks@rwdi.com*

SUMMARY:
A single-axis tracker (SAT) is more sensitive to wind loads when in 'tracking' mode than when in stow position. Most SATs utilize a stow regime to avoid exposing the array to elevated wind speeds when in 'tracking' mode. Depending on stow regime and tracking manufacturer, this transfer into stow may take on the order of 10 to 20 minutes. Therefore, an analysis has been undertaken to characterize the wind speed 'ramp rate' at various international locations to inform a risk-based assessment of stow strategy. The 'ramp rate' is defined as the rate at which wind speeds can increase in a particular project location, measured as m/s/minute. It has been found that the magnitude of the ramp rate depends on the type of extreme wind event (e.g., thunderstorm or synoptic system), the amount of time it takes for the array to get to stow position, and the magnitude of the initial wind speed. Ramp rates have been calculated based on available historical data to aid in the characterization of the adequacy of a stow regime in a risk-based framework. To date, no publicly available research exists on this topic.
Keywords: extreme value analysis, solar PV structures, active mitigation

1. INTRODUCTION

Due to their relatively light weight and flexible design, ground mounted photovoltaic (PV) solar structures are known to be very sensitive to wind loads and effects. There are two main types of ground mounted PV solar structures - fixed tilt designs and sun-tracking designs. Sun-tracking designs take various forms, but the predominate design form is known as a single-axis tracker (SAT). SAT designs track the sun from east to west to maximize power production. A typical SAT design consists of vertical posts which connect the structure to the ground, and torque tubes connected to the vertical posts, running in the parallel to the ground in the north-south direction. The torque tube is driven by a mechanical device that allows it to rotate and is connected to purlins, which connect the torque tube to the PV modules.

There are two primary modes for a SAT: tracking and stow position. SATs are more sensitive to wind loads and effects when in tracking mode than when in stow position. Most SATs utilize a stow regime, to avoid exposing the array to elevated wind speeds at more vulnerable tilt angles when in tracking mode. This stow position is an active measure and is used by designers to decrease the magnitude of wind loads that need to be considered in design and to increase the resilience of the structure. Depending on stow regime and tracker manufacturer, this transfer into stow may take on the order of 10 to 20 minutes. Therefore, an analysis has been undertaken to

characterize the wind speed 'ramp rate' at several locations internationally as this is an important consideration in the specification of a stow regime. The 'ramp rate' is defined as the rate at which wind speeds can increase in a particular project location, measured as m/s/minute.

The magnitude of the ramp rate depends on the type of extreme wind event (e.g., thunderstorm, synoptic system or tropical cyclone), the amount of time it takes for the array to get to stow position and the magnitude of the initial wind speed. Ramp rates have been calculated based on available historical and modelled data to aid in the characterization of the adequacy of a stow regime in a risk-based framework.

1.1. Datasets

Historically, long term and publicly accessible meteorological datasets recorded at airports and climate stations are available with an hourly or near-hourly (e.g. 3-hour, 30-minute) time interval between recordings. More recently, public datasets have become available that provide a continuous sample of wind speed and are publicly accessible. Two examples are the TD6405 dataset in the United States (NCEI, 2006), and One-Minute Data Holdings from the Australia Bureau of Meteorology. These high temporal resolution datasets have been leveraged in several wind engineering studies (Gibbons et al, 2015, Cook 2022, Chen and Lombardo 2020). The data availability of these datasets generally begins in the late 1990s/early 2000s, which means there is approximately 25 to 30 years of data available. This is advantageous, as they offer a suitable period of record to perform a statistical analysis.

Other privately held datasets with one-minute interval data are available; however, they have not been used within this study due to use restrictions of the datasets and a generally shorter period of record.

2. ANALYSIS

The 1-minute interval data has been obtained from several locations which are subject both thunderstorm and synoptic wind climates. Ramp rates have been determined according to the following method:

- The maximum daily gust wind speeds were obtained for each day;
- Days with maximum gust wind speeds greater than 10 m/s were identified. For each maximum gust wind speed exceeding 10 m/s the preceding 15 minutes prior to the maxima were obtained;
- The change in wind speed to the maximum wind speed event was calculated for 1, 2, 3, 4, 5, 10, and 15 minutes before the high wind speed event;
- An extreme value analysis, assuming a Fisher-Tippett Type 1 distribution, was conducted on the change in wind speed to estimate the mean recurrence interval with each change.

To account for fluctuations in minute-by-minute wind speed measurements, the analysis was conducted on a rolling maximum wind speed (within a 15-minute period). The use of the rolling maximum wind speed rather than the instantaneous wind speed ensures that momentary drops in wind speed are not included within the ramp rate calculation.

An example set of results for a thunderstorm climate is shown in Table 1 with mean recurrence interval of 1, 5, 10, 25, 50, and 100 years.

Table 1. Example gust wind speed ramp rates in a thunderstorm climate, with gust wind speeds measured in m/s/min.

Mean Recurrence Interval (Year)	Minutes Prior to Peak of Event				
	1	2	5	10	15
1	12	7	3	2	1
5	17	10	4	2	1
10	19	11	4	2	2
25	22	12	5	3	2
50	24	13	5	3	2
100	26	14	6	3	2

This information can be used by designers to assess the level of risk associated with stow regimes for SATs. A stow regime can be characterized according to:

A) The time it takes to get to the stow position
B) The maximum survival speed or design wind speed for the system when not in stow position
C) The trigger wind speed that initiates the process for the array to go to the stow position

Based on the values for A, B and C as defined above, the risk that B is exceeded can be calculated according to:

$$\frac{dV}{dt} = \frac{B-C}{A} \tag{1}$$

where *dV/dt* is ramp rate and is a function of mean recurrence interval and the time it takes to get to stow position. If a targeted hazard tolerance is known, Eq. (1) can be rearranged to determine an appropriate value for trigger wind speed (C) or the impact of decreasing the amount of time it takes to get to the stow position (A). This also serves as a framework for evaluating competing SAT designs during the procurement phase of a project.

7. CONCLUSIONS

To date, the 'ramp rate', defined as the rate at which wind speeds can increase over a given amount of time, has be ill-defined in the literature, but it is of significant importance to the design of SATs. The current study presents a framework for characterizing ramp rate in a risk-based framework. The presentation and full paper will present ramp rates for several locations in synoptically and thunderstorm governed wind climates.

REFERENCES

Chen, G. and Lombardo, F.T., 2020. An automated classification method of thunderstorm and non-thunderstorm wind data based on a convolutional neural network. *Journal of Wind Engineering and Industrial Aerodynamics*, *207*, p.104407.

Cook, N.J., 2022. Curating the TD6405 database of 1-min interval wind observations across the USA for use in Wind Engineering studies. Journal of Wind Engineering and Industrial Aerodynamics, 224, p.104961.

Gibbons, M., Sifton, V., Kilpatrick, J., Hussain, S. and McNamara, K., 2015. Effect of selective sampling of wind speeds on parent and extreme distributions. 14th International Conference on Wind Engineering.

NCEI, 2006. Data Documentation for Data Set 6405 (DSI-6405). National Centers for Environmental Information.

Integrated Risk Assessment of Tree-Induced and Wind-Induced Damage to Low-Rise Buildings in Hurricane Scenarios

Mohammad Bakhshandeh[1], Jean-Paul Pinelli[2], Amal Elawady[3], Haitham A. Ibrahim[3], and Fahim Ahmed[3]

[1]*Florida Institute of Technology, Melbourne, FL 32901, USA, mbakhshandeh2023@my.fit.edu*
[2]*Florida Institute of Technology, Melbourne, FL 32901, USA, pinelli@fit.edu*
[3]*Florida International University, Miami, FL 33174, USA, aelawady@fiiu.edu*

SUMMARY:
Windstorms are a significant hazard that can severely damage buildings, especially in areas with dense tree cover. Strong winds can break trees, which may fall on nearby structures. This risk is even higher in urban and suburban areas, where trees are often located close to buildings, increasing the chance of damage during hurricanes. This study presents a vulnerability model that evaluates the risk of tree-induced damage to low-rise buildings by incorporating factors such as tree species, densities, and wind conditions to simulate potential damage across different scenarios. In addition to assessing structural damage, the model also considers interior and content damage, offering a more comprehensive evaluation of total losses. Once tree-induced damage is calculated, it is combined with wind-induced damage in the Florida Public Hurricane Loss Model (FPHLM) to provide a comprehensive estimate of overall hurricane-related losses, including exterior, interior, and content damage.
Keywords: Vulnerability modeling, risk assessment, wind-induced damage, tree-induced damage, Monte Carlo simulations, Florida Public Hurricane Loss Model (FPHLM)

1 METHODOLOGY

The team developed a vulnerability model using a scenario-based approach to assess the potential damage to different building classes caused by wind-induced tree falls. The output are vulnerability curves that give mean damage ratios against wind speeds for different tree densities and species. Below are the key steps in the methodology:

1.1 Tree Fragility Curves

Fragility curves for seven tree species: oak live, oak water, mahogany, pine shortleaf, loblolly pine, American sweet gum, and slash pine, yield the probability of tree failure under varying wind speed. (Ahmed, F.et al. 2022)

1.2 Tree impact energy model

Tree impact energy during blowdowns is calculated by estimating the potential energy of the tree's trunk and crown using parameters like Diameter at Breast Height (DBH) and tree height, assuming it falls due to gravity. Larger DBH leads to higher impact energy, which correlates with greater structural damage upon impact (FEMA, 2022).

1.3 **Damage Function**

Limited data, based on incomplete tests conducted at Clemson University in the 1990's (FEMA 2022), relate qualitatively damage states (DS) for timber and masonry walls to the impact energy from falling trees (Tables 1&2).

Table 1. One and two-story Timber building damage states due to impact energy in HAZUS

Damage State #		1	2	3	4	5	6	7	8
One-Story Wood	Impact Energy (foot-pound) (1)	250	2,000	5,600	6,400	8,800			
	Example Tree Height (2) (feet)	30.0	46.9	57.5	59.0	62.6			
	Damage State Description	Surface damage	Roof deck crack	Top-plates rupture	One-Fourth Cut into wall	Cut through wall			
Two-Story Wood	Impact Energy (foot-pound)	250	2,000	5,600	6,400	8,800	14,400	15,200	17,600

Table 2. One and two-story Masonry building damage states due to impact energy in HAZUS

Damage State #		1	2	3	4	5	6	7	8
	Example Tree Height (feet)	32.0	50.2	61.3	62.8	66.6	72.5	73.3	75.2
	Damage State Description	Surface damage	Roof deck crack	Top-plates rupture	One-Fourth Cut into upper wall	Cut through upper wall	Floor-plates rupture	One-Fourth Cut into lower wall	Cut through lower wall
One-Story Masonry	Impact Energy (foot-pound)	250	2,000	11,000	13,000	19,000			
	Example Tree Height (feet)	30.0	46.9	65.2	67.2	72.0			
	Damage State	Surface damage	Roof deck crack	Bond-beam rupture	¼ Cut into wall	Cut through wall			
Two-Story Masonry	Impact Energy (foot-pound)	250	2,000	11,000	13,000	19,000	30,000	32,000	38,000

The authors transformed the wall DS from Tables 1&2 into quantitative overall building damage ratios for each estimate of impact energy, based on engineering judgment. Polynomial damage functions were then fitted to the ensemble of pairs of (impact energy, and damage ratio) to model the relationship between the impact energy of a falling tree and the resulting overall damage to the building for both weak-strength timber and masonry buildings (see Figure 1). Further research shall validate these preliminary curves and expand to the case of medium- and high-strength buildings.

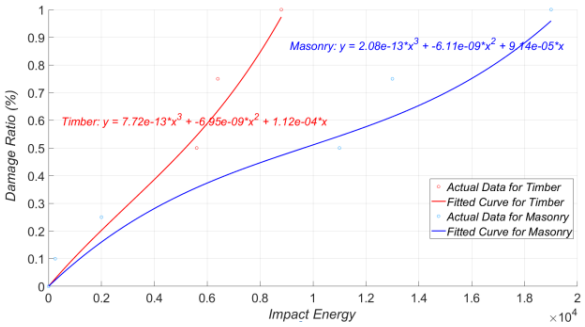


Figure 1. Building Damage Functions for Timber and Masonry 1-story Building

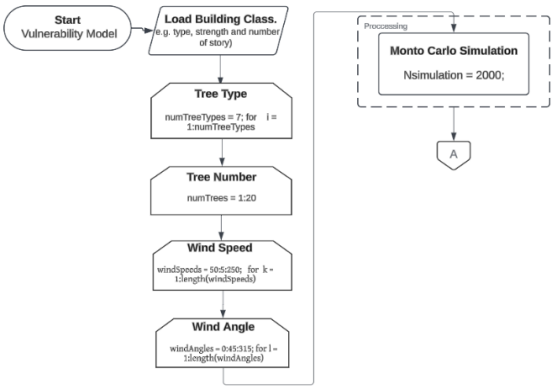


Figure 2: Vulnerability Flowchart for tree-induced damage to buildings – Define Scenarios

1.4 **Scenario-Based Approach for Tree-Induced Damage:**

A scenario-based approach assesses wind-induced tree damage on various building classes with varying structural strengths and materials (weak, medium, and strong), and different height (1-story and 2-story buildings). For each scenario, tree quantity ranges from 1 to 20, in one tree increment. Wind speed ranges from 22.4 to 111.8 -m/s in 2.24 m/s increments at a height of 10 meters, with wind directions spanning from 0° to 360° in 45° increments. Figure 2 presents a flowchart which is part of the vulnerability model illustrating the scenario definition for tree-induced damage to buildings, and serves as input for the Monte Carlo simulation

1.5 **Monte Carlo Simulations:**

For a given building class, for each combination of tree species, tree quantity, wind speed, and direction, 2000 Monte Carlo simulations are conducted. In each simulation, tree locations and crown diameters are randomized. The model then determines if trees fall and calculates the accumulated impact energy from all the trees that strike the building. This energy is used to estimate the building's damage ratio. The simulations result in damage vectors, for each combination of wind speed and direction, where each row corresponds to the output of an individual simulation. The vectors for the different wind directions, given a wind speed can be combined.

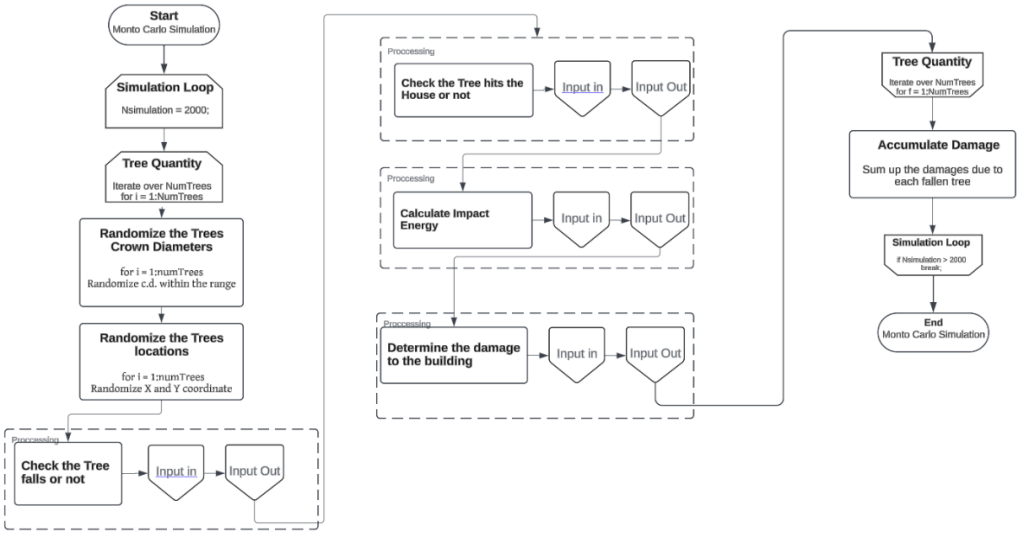


Figure 2: Vulnerability model for tree-induced damage to buildings- MC simulations: Random variables

1.6 **Tree damage vulnerability matrices and curves**

The results of the simulation model are presented as a damage matrix, where each row corresponds to the output of an individual simulation. The columns of the matrix represent three-second gust wind speeds. Aggregated damage ratios are used to develop a vulnerability matrix, where each cell represents the conditional probability of a specific building damage ratio, given a particular wind speed interval. Then the vulnerability curves are simply the mean values of the probability mass functions as a function of wind speed. Also, weighted vulnerability matrices can be derived by combined the vulnerability matrices for different combinations of species (e.g. deciduous vs. coniferous), and different tree density levels (e.g. low, medium, or high).

Furthermore, a structured nomenclature has been developed, to provide a standardized way to reference and distinguish between different scenarios, variables, and outputs (such as tree species, building types, and density levels) across simulations, facilitating easier interpretation, reproducibility, and collaboration in the research.

1.7 **Estimation of Interior and Content Damage**

We do not have data on damage to buildings due to falling trees, which makes estimating interior and contents damage challenging, but several options exist. The current adopted approach considers an overall building damage function (Figure 1), which projects the total damage to the building, including both exterior and interior components. Another semi-engineering option is to

separate the estimates of exterior and interior damage. The model can project envelope breaches to the walls and floors due to the tree impact, which can lead to water ingress and subsequent interior and contents damage. But this presupposes a component-based model. In the absence of such a model, an alternative option would be to derive statistics that would relate envelope breaches to interior and contents damage and evaluate statistically the possible interior and contents damage. These options are currently under evaluation, and they will be discussed at the conference.

1.8 **Integration of Tree-induced and Wind-Induced Vulnerability Models**

The Florida Public Hurricane Loss Model (FPHLM) is a tool for estimating insured losses in the state of Florida (FPHLM, 2023; Pinelli et al., 2020) The tree-induced building damage vulnerability model described above is combined with the wind-induced building damage vulnerability model of the FPHLM. Tentatively, this integration uses the following formula:

$$\text{Total Damage} = \text{Wind Damage} + \text{Tree Damage} - (\text{Wind Damage} \times \text{Tree Damage}) \quad (1)$$

This formula is provided to combine the two independent damage estimates while accounting for potential overlap, ensuring that the same damage is not counted twice. The main advantage of this approach is indeed its simplicity.

2 **CONCLUSION:**

This is a work in progress. The authors have generated a preliminary library of tree-induced building damage vulnerability matrices and curves. The next step involves validating and calibrating the model using reconnaissance data from previous hurricanes, followed by combining tree and wind models in the FPHLM. At the conference, the authors will present and compare these vulnerability curves, and they will show the impact of combining tree- and wind-induced damage estimates on overall portfolio loss projections in tree-covered areas.

ACKNOWLEDGEMENTS

The National Science Foundation supports the Wind Hazard and Infrastructure Performance Center (WHIP-C) through grant No. 1841523, and the WHIP-C's Industrial Advisory Board endorsed this work through grant No. WHIP2022_05. The opinions, conclusions, and results presented in this document are solely those of the authors and do not necessarily represent the views of the NSF or the WHIP-C.

REFERENCES

Ahmed, F., Ibrahim, H. A., Elawady, A., and Pinelli J. P. (2022). Evaluating Probability of Failure of Urban Trees Under Extreme Wind Event. In the 14th Americas Conference on Wind Engineering (14th ACWE) , Lubbock, Texas | May 17-19, 2022

FEMA (2022). Hazus Flood Model Technical Manual, Federal Emergency Management Agency, Mitigation Division, Washington, D.C., 2022.

Florida Public Hurricane Loss Model. (2023). Florida Public Hurricane Loss Model Technical Document https://fchlpm.sbafla.com/media/ghll1ufp/2023_03_11_fphlm_2022_submission_document-1.pdf

Pinelli, JP., Da Cruz, J., Gurley, K. et al. Uncertainty Reduction Through Data Management in the Development, Validation, Calibration, and Operation of a Hurricane Vulnerability Model. Int J Disaster Risk Sci 11, 790–806 (2020). https://doi.org/10.1007/s13753-020-00316-4

Effects of climate change on future winds and wind engineering practice in the UK

Rubina Ramponi[1], David Hankin[2], Anna Bagnara [3], Daniel Hackett [4], Stefano Cammelli [5]

[1]*Arup, Dublin, Ireland, rubina.ramponi@arup.com*
[2]*NOVA Fluid Mechanics Ltd, Teddington, UK, david@novafluidmechanics.com*
[3]*NOVA Fluid Mechanics Ltd, Teddington, UK, anna@novafluidmechanics.com*
[4]*RWDI, Milton Keynes, UK, dan.hackett@rwdi.com*
[5]*WSP UK, London, UK, stefano.cammelli@wsp.com*

SUMMARY:
Climate change represents one of the most critical global challenges, posing significant threats to the built environment. While it is evident that the climate is changing, the projected variation in frequency and intensity of different weather events (temperature, rainfall, wind, etc.) over time is not always clear. This is particularly true for wind, and investigations of both the global and local future trends are still a very active area of research. Part of the complexity in outlining future wind projections lies in the limited availability of historical data for many localised extreme wind events and the challenges in their representation using the relatively coarse temporal and spatial resolution of the climate models.
A better understanding of the climate change impact on local winds, however, is key for wind engineers to re-assess some of the baseline assumptions underpinning current practice and contribute to adaptation more effectively. The UK Wind Engineering Society has established a 'Future Winds' working group in response to this emerging need. This paper presents the initial findings of the working group, including a literature review and some practical implications for wind loading and pedestrian comfort.

Keywords: Climate Change, Future winds

1. INTRODUCTION

Climate Change represents one of the most critical global challenges and it is largely driven by anthropogenic activities, particularly rising concentration of greenhouse gasses like carbon dioxide (CO2) from industrial emissions, transportation, agriculture, etc. Since the middle of the 20th century, the near-surface air layer over both continent and oceans has experienced significant warming. Over the last decade, the effects of climate change have become increasingly apparent through more frequent temperature extremes, continuous sea level rise and extreme precipitation in various regions. It is expected that these changes will continue into the foreseeable future, with potentially severe consequences on the built environment.

While it is evident that the overall global climate is changing, there are varying degrees of certainty regarding the rate of change in the frequency and intensity of different climate events, especially at the local scale. For example, there is broad consensus around future trends for temperature and

rainfall, but future winds are still considered very much uncertain and an active area of research. One reason for these uncertainties lies in the difficulty of analyzing and projecting different types of wind (synoptic winds, hurricanes/typhoons, thunderstorms, tornadoes, etc.). These winds have different drivers, characteristics and magnitude. Among others, thunderstorms and tornadoes are very localized in space and time. These events have been difficult to capture from surface weather stations and are hard to reproduce in numerical models. The latest IPCC Report (2021) emphasises the uncertainties related to the coarse spatial and temporal resolution of the climate models to capture strong, localised wind events (IPCC, 2021) and their limitations in resolving convective processes, especially related with the cloud formation and the release of latent heat (IPCC, 2021). When looking at climate projections for the UK, the current general consensus is that the mean wind speeds are expected to decrease, while extreme wind speeds (both from extra tropical cyclones and thunderstorms) are expected to increase both in frequency and intensity (Bagnara et al. 2024).

A better understanding of the impact of climate change on the local and regional wind conditions is key for practitioners to incorporate climate change considerations into design. Current wind engineering practice relies heavily on historical data, for example to describe the correlation between wind speeds and return periods and to derive values that are used for wind loading. While these methods are well-established, they are implicitly based on the assumption that past climate trends will remain applicable in the future, at least within the expected life of the buildings currently being designed. Considering the predictions that have been made about the potential impacts of anthropogenic climate change, especially in relation to the magnitude and frequency of extreme weather events, we should accept the possibility that methodologies based solely on the past climate may no longer be accurate (Bagnara et al. 2024).

The UK Wind Engineering Society has formed a 'Future Winds' working group to review key information on the climate change projections of wind events in the UK and to assist local practitioners towards adapting the wind engineering practice to climate change. This paper will provide a summary of the literature review and outline the next steps of the working group in terms of implications for wind loading and pedestrian comfort.

REFERENCES

Bagnara, A., Hackett, D., Hankin, D., Cammelli, S., 2024, Future winds: a review of the likely impacts of anthropogenic climate change on wind engineering in the UK. Available at: https://eprints.soton.ac.uk/493313/1/09_Hankin.pdf (Accessed 14th November 2024).

Intergovernmental Panel on Climate Change, 2021. Climate Change 2021: The Physical Science Basis. Contribution of Working Group I to the Sixth Assessment Report of the Intergovernmental Panel on Climate Change. Cambridge University Press, Cambridge, United Kingdom. doi:10.1017/9781009157896.

Met Office, 2021. Recent trends and future projections of UK storm activity. Available at: https://www.metoffice.gov.uk/research/news/2021/recent-trends-and-future-projections-of-uk-storm-activity (Accessed 25th July 2024).

Investigating the impacts of urban microclimate on energy consumption of residential high-rise buildings

Wenbing Liu [1], Xuelin Zhang [1], A. U. Weerasuriya [2]

[1] *School of Atmospheric Sciences, Sun Yat-sen University, Zhuhai, PR China, liuwb53@mail2.sysu.edu.cn, zhangxlin25@mail.sysu.edu.cn*
[2]*Hong Kong Metropolitan University, Ho Man Tin, Hong Kong, auweeras@hkmu.edu.hk*

SUMMARY:
Urban microclimate can significantly affect building energy consumption. However, most studies used weather data from rural meteorological stations to estimate building energy consumption, ignoring urban microclimate conditions. This study developed a coupled computational fluid dynamic (CFD) and building energy simulation (BES) workflow using urban microclimate data as boundary conditions. The microclimate data were generated from an urban weather generator (UWG) and CFD simulations. It was found that UWG's inability to simulate wind speed reduction resulted in significant variations in building energy consumption. Furthermore, building arrangements were found to be the most influencing factor in urban microclimate. For example, the staggered building arrangement caused a 1.58 K temperature increase and a 1.04 m/s wind speed reduction around buildings. Overall, a 5.7% to 9.5% underestimation of building energy consumption resulted from the omission of urban microclimate from building energy simulations.

Keywords: Urban microclimate, building energy simulation, CFD simulation, high-rise building

1. INTRODUCTION

Urban morphology modifies microclimate parameters, such as wind speed, solar radiation, and relative humidity, which all affect buildings' thermal performance and energy consumption (Shareef, 2021). In particular, urban ventilation can significantly influence building energy consumption by controlling convection heat transfer from building surfaces and natural ventilation. However, most building energy simulations (BES) are based on the typical meteorological year (TMY) weather data, ignoring urban microclimate. TMY weather data based on the observations from meteorological stations in rural and relatively open sites does not represent the environmental conditions in high-density city centers (Singh & Sharston, 2022). A solution is to couple Computational Fluid Dynamics (CFD) simulations with BES to incorporate the impact of urban microclimate on building energy consumption.

A coupled CFD-BES workflow can fix another shortcoming of most BES, which usually assesses the energy consumption of stand-alone buildings, ignoring the impact of adjacent buildings. The surrounding buildings dynamically modify metrological parameters around buildings. Therefore, accurate BES requires unsteady simulations with time-dependent boundary conditions instead of steady-state simulations with constant boundary conditions (Xu et al. 2024). This study developed a CFD-BES workflow, which used boundary conditions based on CFD simulations to demonstrate the impact of microclimate on the energy consumption of a building cluster.

2. METHODOLOGY

Fig. 1 shows the CFD-BSE workflow of the current study to estimate the energy consumption of a building cluster in Guangzhou, China. In the first step, five geometric models of the residential high-rise buildings were generated using the Grasshopper plugin embedded in Rhino software (Fig. 2). The building form and layout were based on common designs of high-rise residential building groups in a Local Climate Zone (LCZ) 1in Guangzhou, China. In the second step, the in-situ meteorological data was used as boundary conditions for the Urban Weather Generator (UWG) and CFD simulations to predict microclimate conditions. The boundary conditions for a 24-hour-long transient CFD were hourly wind speed, air temperature, and solar radiation. Moreover, anthropogenic heat emissions, such as heat emissions from air conditioners, were also considered for CFD simulations. In the third step, BES was conducted using the Honeybee Grasshopper plugin with EnergyPlus as the BES engine. For BES, input parameters, such as window-to-wall ratio and building materials properties, were set according to the government building codes (Chinese Standard, 2021). This study compared the estimated building energy consumption using site data (BC-1), UWG (BC-2), and CFD simulations (BC-3) to analyze the impact of microclimate on the energy consumption of various building clusters.

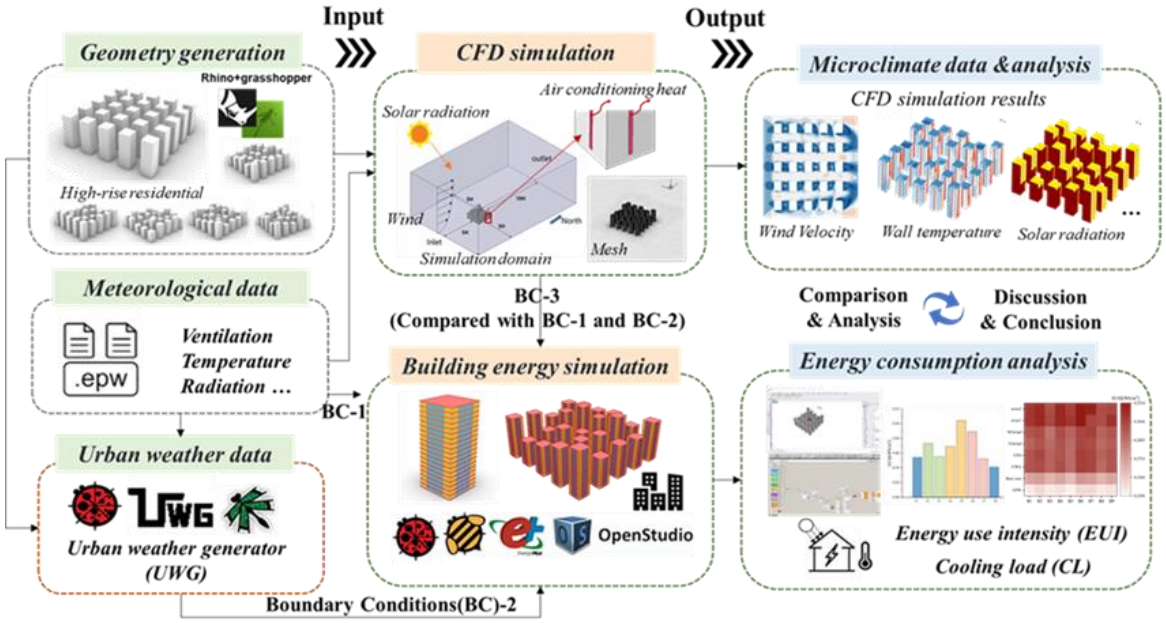


Figure 1. Schematic workflow of the study

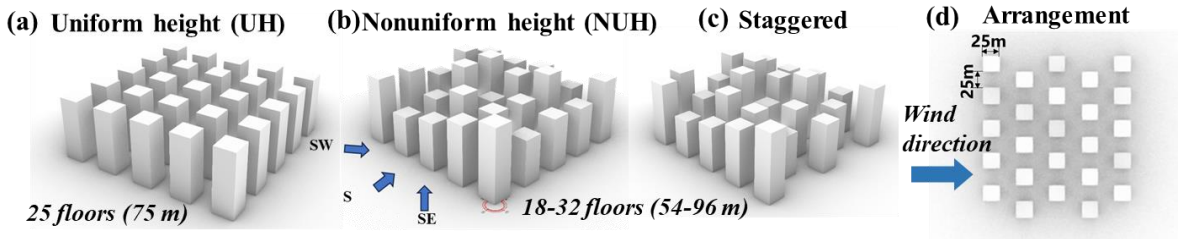


Figure 2. Geometric building models of this study: (a) uniform height (UH), (b) nonuniform height (NUH), (c)Staggered building arrangements, and (d) Plan view of staggered building arrangement

3. RESULTS AND DISCUSSION

3.1. Comparison of weather data

Fig. 3 compares the in-situ meteorological data of a suburban site with the weather data generated by UWG and microclimate data from CFD simulations. Throughout the day, UWG and CFD simulations predicted significantly higher air temperature at a 2 m height than suburban site data. The average temperature simulated by UWG and CFD was 1.6 K and 1.1-1.6 K higher than the in-situ data. The CFD simulation results indicated the highest temperature increase at noon, whereas the UWG demonstrated the largest temperature rise at night.

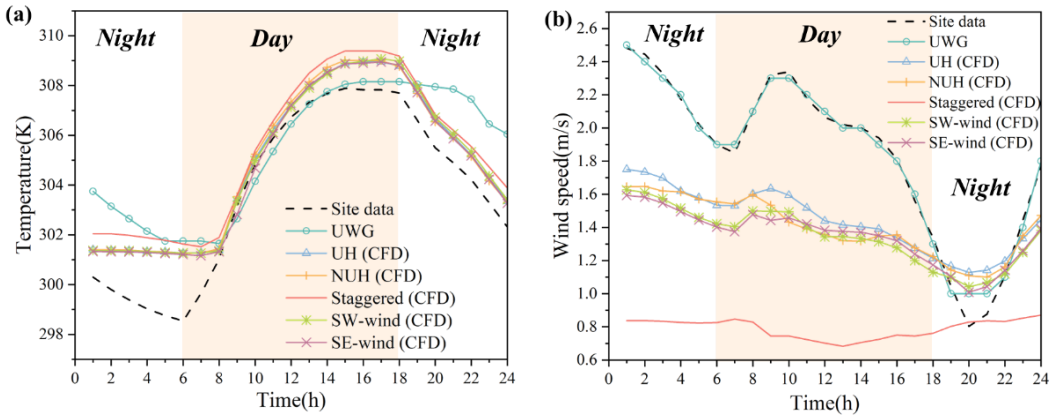


Figure 3. (a) Air temperature at 2 m height and (b) wind speed at 10 m (the reference weather station).

Fig. 3b shows wind speeds at the 10 m height from suburban site data, July 24, 2022. In general, all building clusters reduced the wind speed in the neighborhoods. In particular, wind speeds within the staggered buildings had the lowest wind speeds, probably due to the largest obstruction to wind flow between buildings. Low wind speeds deterred efficient heat removal from buildings, resulting in the highest air temperatures in the staggered building arrangement. The wind direction and the uniform building height had a minimal influence on the temperature and wind speed in the building clusters. When the wind speed of suburban sites is lower than 1 m/s at night (8 p.m.), the thermal effect caused by heat storage in the ground and walls can lead to an increase in wind speed around the buildings in urban. UWG did not explicitly simulate buildings and thus could not account for the effects of buildings on the microclimate. As a result, the wind speed predicted by the UWG closely aligned with the input suburban site data and was significantly higher than the simulation results obtained from CFD.

3.2. Energy consumption of building clusters

Fig. 4 shows the estimated energy use intensity (EUI) using different weather data inputs. Based on the comprehensive CFD results, the microclimate boundary conditions for the nine central buildings (B1-B9) were individually adjusted for energy consumption calculations (Fig. 4a). Overall, EUI calculated using the simulation cases (UWG and CFD) was significantly higher than that estimated using in-situ measurements. Among the five CFD cases, the staggered building arrangement had the highest energy consumption due to lower wind speeds and higher air temperature. Fig. 4b shows the EUI distribution of nine building clusters. The uniform-height buildings had similar energy consumption. The difference in EUI between nine central buildings was less than 0.006 kWh/m^2 (Fig. 4a). The average EUI of nine central buildings in the case of uniform (0.685 kWh/m^2) and nonuniform height (0.682 kWh/m^2) was similar, while the EUI

difference between nonuniform hight buildings was up to 0.04 kWh/m^2, which was much higher than that of uniform height. This indicates that the substantial impact of variations in building height on the dissimilar energy consumption of buildings. For example, the energy consumption calculated by UWG input data was 8.9% higher than that directly input by site data, and the EUI calculated by CFD microenvironment data input was 5.7%-9.5% higher (Fig. 4b).

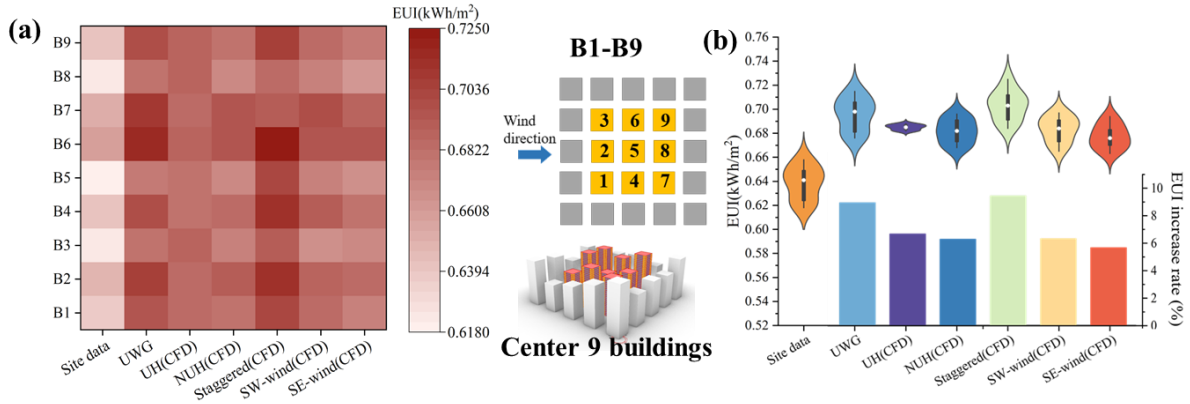


Figure 4. (a) Energy use intensity (EUI) of 9 center buildings, (b) violin plots of EUI and EUI increase rate

4. CONCLUDING REMARKS

The results of this study suggest a significant impact of urban microclimate on building energy consumption. The urban microclimate was influenced by building morphology and external meteorological factors, such as wind speed, air temperature, and anthropogenic heat emission. The boundary conditions based on suburban site data can lead to a 5.7% to 9.5% underestimation of energy consumption. This study found a shortcoming of the boundary conditions developed using UWG because of its inability to account for the reduction in wind speed around buildings. This is particularly important for differently arranged buildings, whose settings significantly influence the surrounding microclimate and building energy consumption. Moreover, this study found that the non-uniformity of building height can significantly influence the unevenness of energy consumption across buildings. Our analytical workflow and model account for microclimate factors, offering a reliable direction for improving energy consumption predictions

ACKNOWLEDGEMENTS

This study is partly supported by the National Natural Science Foundation of China (No. 42175180, 42475185, and 21EAA00654). The CFD simulations of this research were conducted on the Tianhe II supercomputer at the National Supercomputer Center, Guangzhou, P. R. China.

REFERENCES

Chinese Standard. 2021. General code for energy efficiency and renewable energy application in buildings. GB 55015-2021. Ministry of Housing and Urban-Rural Development of the People's Republic of China

Shareef, S., 2021. The impact of urban morphology and building's height diversity on energy consumption at urban scale. The case study of Dubai. Building and Environment, 194, Article 107675.

Singh, M., & Sharston, R., 2022. Quantifying the dualistic nature of urban heat Island effect (UHI) on building energy consumption. Energy and Buildings, 255, Article 111649.

Xu, F., Zhang, J., & Gao, Z., 2024. A case study of the effect of building surface cool and super cool materials on residential neighbourhood energy consumption in Nanjing. Renewable and Sustainable Energy Reviews, 189, 114027.

Reducing the double corner effect in orthogonal building layout to improve pedestrian wind comfort

Hakan Baş

İzmir Katip Çelebi University, İzmir, Turkiye, hakan.bas@ikcu.edu.tr

SUMMARY:
Large buildings exposed to open winds are at risk of pedestrian wind discomfort. This study aims to mitigate wind speed amplification between orthogonal buildings exposed to open winds. Three idealized building arrays were created based on two morphological parameters: building height and number of building rows. Computational fluid dynamics simulations of the building arrays were conducted and validated through wind tunnel experiments. The single-row building array with a height of 2H (H_1=10 m) resulted in a 57% increase in wind speed. In contrast, the optimal combinations of H_2/H_1 (7H/2H) and H_3/H_2 (10H/7H) in the three-row building array led to a maximum 15% increase in wind speed and a 42% improvement in pedestrian wind comfort.

Keywords: pedestrian wind comfort, orthogonal building layout, computational fluid dynamics (CFD)

1. INTRODUCTION

Large buildings can increase wind speed and create uncomfortable conditions for pedestrians. Similarly, coastal urban areas are often exposed to strong winds from the open sea. When strong winds pass through narrow streets between two perpendicular buildings, their speed can increase significantly due to the *venturi* and *double corner effect*. As a result, special attention is needed in the design of coastal buildings to ensure pedestrian comfort and enhance urban quality of life.

Numerous studies have been conducted to identify optimal building geometries for enhancing pedestrian wind comfort. Mittal et al. (2019) investigated modifying building corners to minimize wind speed amplification. The size of streets and buildings are other geometric factors that impact wind comfort. Blocken et al. (2007) examined the influence of different street widths on wind speed amplification, while Reiter (2010) studied the effect of building dimensions (height and width) on wind speed amplification between two parallel buildings. Bas et al. (2022) investigated the impact of shifted building configurations, along with specific building and street parameters, to reduce the intensity of wind speed amplification in coastal streets.

This study aims to reduce wind speed amplification between orthogonal buildings. This can be achieved by reducing the pressure difference between the windward and leeward sides of the buildings. The strategy involves directing the wind to the leeward side of the buildings (negative pressure area). Such a directing effect can be accomplished by gradually increasing the height of the buildings towards the rear with a parametric approach. Minimizing wind speed amplification in orthogonal building layouts in coastal urban areas can be helpful for architects, city planners, and urban policymakers in creating comfortable urban open spaces.

2. METHOD

This study uses a methodology that integrates the CFD method with the parametric approach. STAR-CCM+ was used as the CFD code and validated by wind tunnel experiments.

2.1. Geometric description of idealized building arrays

Three idealized building arrays (BA1, BA2, and BA3) were created for the study. BA1 is the baseline array, consisting of a single row of buildings. The width and length of each building are 20 m and 15 m, respectively, as shown in Fig. 1. The tested building heights range from 2H (10 m) to 12H (60 m). BA2 is derived from BA1 by adding a second row of buildings. The height of the first-row buildings (H_1) is constant at 10 m, while the second-row buildings (H_2) vary from 10 m to 60 m in 5 m increments. BA3 is created from BA2 by adding a third row of buildings. In BA3, the height of the buildings gradually rises from the first row (A1) to the third (A3). The height of the first-row buildings (H_1) is 10 m (constant). The height of the third-row buildings is greater than the second-row buildings and varies from 10 m to 60 m, with an increment of 5 m.

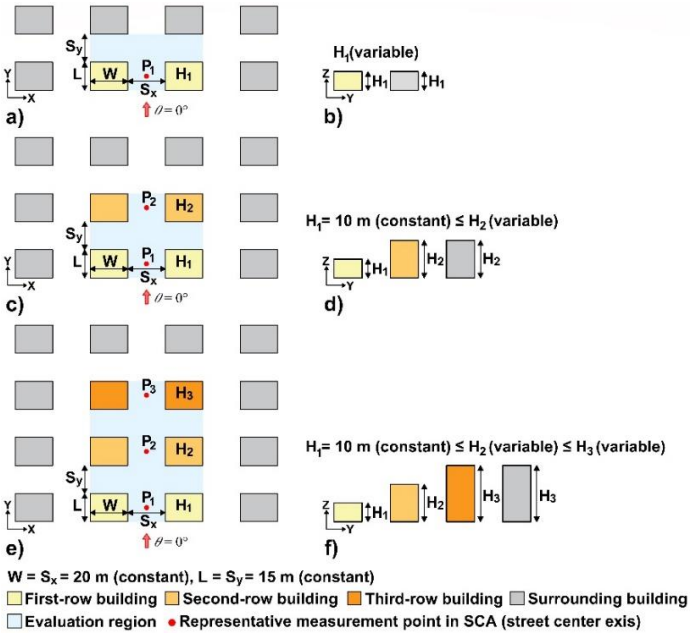


Figure 1. Geometric description and views of the building array alternatives; (a) plan view of BA1 (b) section view of BA1 (c) plan view of BA2 (d) section view of BA2 (e) plan view of BA3 (f) section view of BA3.

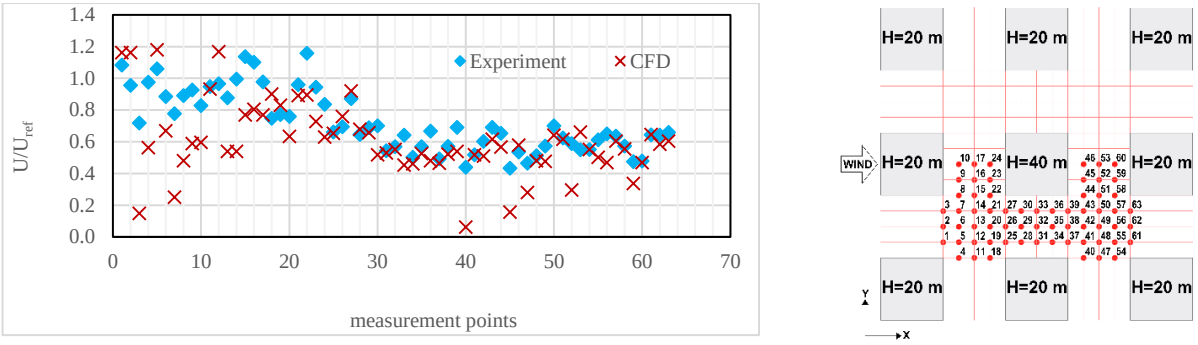
To accurately predict the maximum wind speed, measurement points were placed on the street centre axis (SCA) at a pedestrian level of 2 meters in the evaluation region. These measurement points are representative of the maximum wind speed. The maximum wind speed at or around these measurement points will be considered based on the simulation results. This can be achieved using the CFD method, which allows for visualization of the entire flow field.

2.2. CFD Validation

The sub-case (Case 2H) of Test Case C, provided by the Working Group of the Architectural Institute of Japan (AIJ, 2016), was utilized for CFD validation. The sub-case comprises a 3 × 3 × 3 layout of blocks with uniform height (20 m) and a street width of 20 m. The central building has a height of 40 m. The wind speed values are normalized to the reference wind speed using the

wind speed ratio formula: WSR = U/U_{ref}, where U is the mean wind speed at the measurement point, and U_{ref} is the inlet mean wind speed (z = 2 m). The size of the computational domain and the boundary conditions were determined based on the recommendations of Franke et al. (2007).

The turbulent wind flow pattern was obtained by solving the 3-dimensional steady Reynolds-averaged Navier Stokes (RANS) equations with the Reynolds Stress Model (RSM). Grid independence was achieved when a grid cell size of 1.25 m or smaller (1 m) was used. Fig. 2a compares CFD and experimental wind speed ratios. The overall per cent error (%) was 20.3% in 63 measurement points (Fig. 2b).



a) **b)**

Figure 2. Wind speed ratios in experiment and CFD (a); Plan view of the measurement points (b)

3. RESULTS

The maximum wind speed ratios (WSR) in three building arrays were calculated. Fig. 3 displays the WSR (U/U_{ref}) by building height (H_1) in BA1. Maximum WSR (U/U_{ref}) range from 1.57 and 2.07. Parametrically, as the H_1 increases, U/U_{ref} gradually increases on P1.

In BA2, when the H_2/H_1 ratio is increased, U/U_{ref} in P1 decreases, confirming the strategy's positive effect of increasing the height of the second-row buildings to the first-row buildings. However, U/U_{ref} increases in P2. When the H_2/H_1 ratio is 6 (12H/2H), U/U_{ref} is 1.15 in P1 and 1.60 in P2. The optimal condition, with the lowest U/U_{ref} in P1 at 1.24 and P2 at 1.20, is achieved when the H_2/H_1 ratio is 7H/2H.

In BA3, when the H_2/H_1 ratios are increased, U/U_{ref} in P1 decreases. In contrast, increasing the H_2/H_1 and H_3/H_2 ratios increases U/U_{ref} in P2 and P3. When the H_2/H_1 is above 3 (6H/2H), U/U_{ref} never exceeds 1.25 in P1, P2 and P3. Additionally, when the H_2/H_1 is above 3.5 (7H/2H), U/U_{ref} never exceeds 1.2. The optimal wind comfort conditions are achieved when the H_2/H_1 is 7H/2H and H_3/H_2 is 10H/7H, where the U/U_{ref} value never exceeds 1.15.

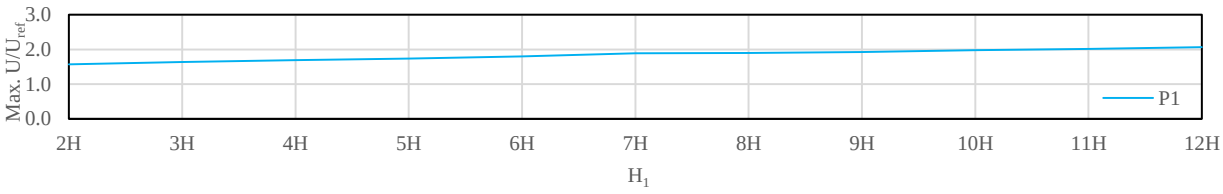


Figure 3. Maximum wind speed ratios (U/U_{ref}) by H_1 in P1.

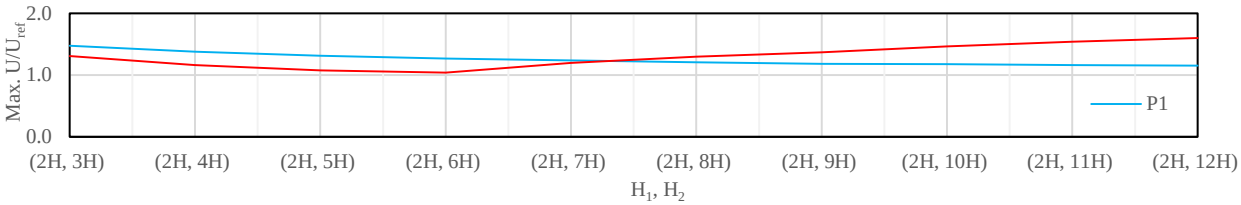


Figure 4. Maximum wind speed ratios (U/U_{ref}) by H_1 and H_2 in P1 and P2.

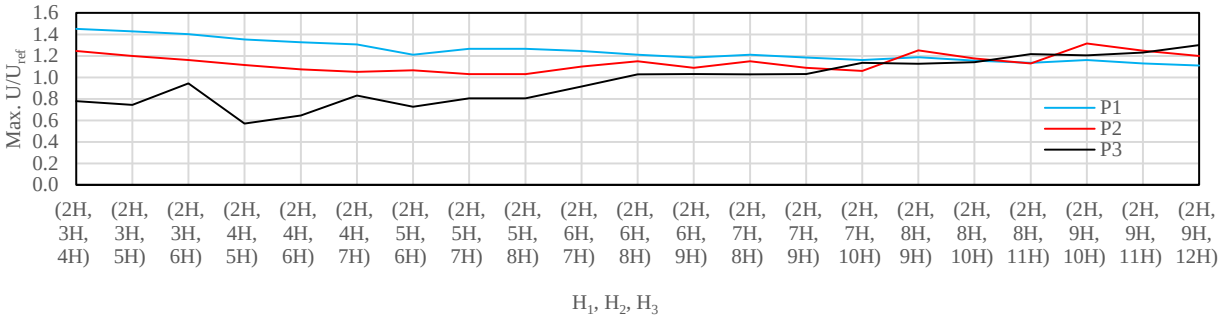


Figure 5. Maximum wind speed ratios (U/U_{ref}) by H_1, H_2 and H_3 in P1, P2 and P3.

4. CONCLUSION

This study presents the design of three idealized, orthogonal building arrays (single-row, double-row, and three-row) to mitigate wind speed amplification and investigate how building height and the number of building rows affect pedestrian wind comfort with computational fluid dynamics (CFD) simulations. The results indicate that the first-row building array with uniform-height buildings 2H (10 m) increases the wind speed by 57%. However, gradually increasing the building heights from the first row to the third redirects the wind to the leeward side of the buildings, reducing the pressure difference between the windward and leeward sides and thus reducing wind speed amplification. In the three-row building array, if the ratio of the second-row height to the first-row height (H_2/H_1) is above 3 (6H/2H), wind speed amplification never exceeds 25%. Furthermore, if the ratio is above 3.5 (7H/2H), wind speed amplification never exceeds 20%. The optimal combination of ratios (7H/2H for H_2/H_1 and 10H/7H for H_3/H_2) results in a maximum wind speed amplification of 15% and improves pedestrian wind comfort by 42%.

REFERENCES

Architectural Institute of Japan, 2016. AIJ Benchmarks for Validation of CFD Simulations Applied to Pedestrian Wind Environment Around Buildings. Tokyo: Architectural Institute of Japan.

Bas. H, Dogrusoy, I.T. and Reiter, S., 2022. Wind adaptive urban seafront buildings design for improving urban ventilation and pedestrian wind comfort in Mediterranean climate. International Journal of Global Warming 28(3), 239–259.

Blocken, B. Carmeliet, J. and Stathopoulos, T., 2007. CFD evaluation of wind speed conditions in passages between parallel buildings—effect of wall-function roughness modifications for the atmospheric boundary layer flow. Journal of Wind Engineering and Industrial Aerodynamics 95(9-11), 941–962.

Johansson, E. and Yahia, M.W., 2020. Wind comfort and solar access in a coastal development in Malmo¨, Sweden. Urban Climate 33, 100645.

Mittal, H. Sharma, A. and Gairola, A. 2019. Numerical simulation of pedestrian level wind flow around buildings: Effect of corner modification and orientation. Journal of Building Engineering 22, 314–326.

Reiter, S. 2010. Assessing wind comfort in urban planning. Environment and Planning B Planning and Design 37(5), 857–873.

Predicting probability distributions of pedestrian-level wind speeds in realistic urban environments using mean and standard deviation

Wei Wang [1], Naoki Ikegaya [2]

[1,2]*Faculty of Engineering Sciences, Kyushu University, Fukuoka, Japan;*
wang.wei.530@m.kyushu-u.ac.jp, ikegaya.naoki@kyudai.jp

SUMMARY:
Understanding the probabilistic characteristics of urban wind environments is crucial. Previous studies have often used the Gaussian distribution, based on mean and standard deviation, to evaluate gusty winds. While these parameters are often sufficient, recent studies highlight the importance of higher-order moments, such as skewness, in capturing non-Gaussian characteristics. To balance simplicity and accuracy, this paper models the probability density function (PDF) using four distributions: Gaussian, Lognormal, Weibull, and Gamma, with parameters derived from mean and standard deviation using the method of moments. Using LES results from a realistic urban case, the Gamma distribution provided the best global fit for PDFs, followed by the Weibull. The Lognormal and Gaussian distributions were less effective, with Gaussian showing the largest errors due to its symmetric shape. For extreme wind speed quantiles (1% exceedance probability), Weibull and Gamma outperformed the others, while Gaussian and Lognormal exhibited larger errors. Overall, the Gamma distribution was the most reliable for modeling both PDFs and extreme wind quantiles. This study offers valuable insights into wind speed modeling and serves as a foundation for improving statistical models.

Keywords: urban wind environment, probability distribution, large-eddy simulation

1. INSTRUCTION

Understanding gusty wind features in urban area is important for the wind-resistant design and wind environment assessment. Based on the assumption that wind speed follows a Gaussian stationary process, (Davenport, 1964) developed a theoretical equation for the peak factor in determining gusty wind. However, it has been observed that non-Gaussian characteristics in wind speed PDFs can negatively affect the accuracy of peak factor estimates. (Kareem and Zhao, 1994) addressed this issue by proposing a moment-based Hermite transformation method that incorporates skewness and kurtosis, allowing for a more accurate representation of non-Gaussian processes in peak factor estimation. Furthermore, to model the non-Gaussian PDFs of wind speed, (Wang et al., 2022) applied the Gram–Charlier Series (GCS), which incorporates higher-order statistics like skewness and kurtosis. However, both the moment-based Hermite transformation method and the GCS method are expansions of the standard Gaussian distribution. These approaches still inherit some of the mathematical constraints of the Gaussian distribution. Furthermore, while incorporating higher-order statistics can improve modeling accuracy, it also

increases the complexity of statistical modeling, making practical applications more challenging due to the added computational and analytical demands.

This study aims to assess the accuracy of several distribution functions (Gaussian, Weibull, Lognormal, and Gamma distributions) in modeling the PDF of urban wind speed, potentially offering a more suitable foundation for statistical models than the traditional Gaussian distribution. The input parameters for modeling the PDFs in this evaluation are the mean and standard deviation, determined using the method of moments, as these two statistics are commonly used and readily available in many cases.

2. METHODOLOGY

The LES results of the real urban layout in Niigata City, Japan, subjected to a west wind condition based on Case-E from the AIJ benchmark cases (AIJ, 2020) was analyzed in this study. The PDF, mean and standard deviation of the Gaussian, Weibull, Lognormal and Gamma distributions are listed in **Table 1**. Here, θ_1 and θ_2 represent the distribution parameters, and $\Gamma(z) = \int_0^\infty x^{z-1}e^{-x}dx$ represents the gamma function.

Table 1. Theoretical equations of each distribution function

	PDF	μ	σ
Gaussian	$f(x) = \frac{1}{\sqrt{2\pi\theta_2^2}}\exp\left[-\frac{(x-\theta_1)^2}{2\theta_2^2}\right]$	θ_1	θ_2
Weibull	$f(x) = \frac{\theta_2}{\theta_1}\left(\frac{x}{\theta_1}\right)^{\theta_2-1}\exp\left(-\left(\frac{x}{\theta_1}\right)^{\theta_2}\right)$	$\theta_1\Gamma\left(1+\frac{1}{\theta_2}\right)$	$\theta_1\left[\Gamma\left(1+\frac{2}{\theta_2}\right)-\Gamma^2\left(1+\frac{1}{\theta_2}\right)\right]^{\frac{1}{2}}$
Lognormal	$f(x) = \frac{1}{x\sqrt{2\pi\theta_2^2}}\exp\left[-\frac{(\ln(x)-\theta_1)^2}{2\theta_2^2}\right]$	$\exp\left(\theta_1+\frac{\theta_2^2}{2}\right)$	$\exp\left(\theta_1+\frac{\theta_2^2}{2}\right)[\exp(\theta_2^2)-1]^{\frac{1}{2}}$
Gamma	$f(x) = \frac{1}{\Gamma(\theta_2)\theta_1^{\theta_2}}x^{\theta_2-1}\exp\left(-\frac{x}{\theta_1}\right)$	$\theta_1\theta_2$	$\theta_1\theta_2^{\frac{1}{2}}$

In this study, the estimated distribution parameters $(\widehat{\theta_1}, \widehat{\theta_2})$ for all distribution functions, derived using the method of moments, are determined by Eq. (1) based on the differential evolution algorithm. Here, $\mu(\theta_1, \theta_2)$ and $\sigma(\theta_1, \theta_2)$ represent the theoretical mean and standard deviation of each distribution, while $\hat{\mu}$ and $\hat{\sigma}$ are the sample mean and standard deviation (i.e., from the LES results).

$$\widehat{\theta_1}, \widehat{\theta_2} = \text{argmin}((\mu-\hat{\mu})^2 + (\sigma-\hat{\sigma})^2) \quad (1)$$

The validation metrics used in this study include the root mean square error (RMSE=$\left[\frac{1}{N}\sum_{i=1}^{N}(E_i - T_i)^2\right]^{0.5}$), and relative error (RE=$\frac{E_i-T_i}{T_i}$). Here, T_i represents the true value (from LES), and E_i is the estimated value (from the distribution functions). Both T_i and E_i can refer to either the PDF or quantile values.

3. DISCUSSION

Figure 2 presents the RMSE of the PDFs, comparing the PDFs obtained from the LES results with those estimated from the distribution parameters. It is evident that the Gaussian distribution exhibits the highest maximum RMSE. This large error is likely due to the inherent constraint of the Gaussian's symmetric bell-shaped PDF, which may not accurately capture the asymmetry in the wind speed data. The Lognormal distribution also shows relatively high maximum and median RMSE values compared to the other distributions. In contrast, both the Weibull and Gamma distributions demonstrate significantly lower RMSE values, suggesting better alignment with the LES results. Among these, the Gamma distribution stands out as the most accurate, exhibiting the lowest RMSE values in terms of both maximum and median, making it the most effective at modeling the wind speed data for the current realistic urban case.

Figure 3 presents the RE of the wind speed quantile with an exceedance probability of 1% for each distribution. It is evident that the REs for the Gaussian and Lognormal distributions are significantly higher than those of the other distributions. In contrast, the Weibull and Gamma distributions exhibit much lower REs, demonstrating greater accuracy. Additionally, the Gaussian and Weibull distributions tend to underestimate $s_{1\%}$, while the Lognormal and Gamma distributions tend to overestimate this value, due to their respective mathematical constrains.

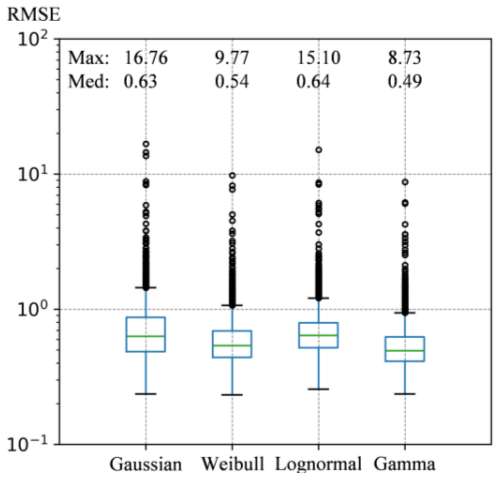


Figure 2. Box plot of the RMSE for the PDF of each distribution function. The maximum and median of RMSEs for each distribution are indicated on the plot.

4. CONCLUSION

In this study, we analyzed the probability density functions (PDFs) and quantiles of the wind speed at the pedestrian level of a realistic urban case using four distribution functions: Gaussian, Lognormal, Weibull, and Gamma. The LES results for Niigata City, Japan, were used in the statistical analysis. Distribution parameters for all functions were determined using the method of moments, based on mean and standard deviation.

Among all the distribution functions, the Gamma distribution showed the best global fit of wind speed PDFs, followed by the Weibull distribution. The Lognormal and Gaussian distributions performed relatively worse, with the Gaussian distribution exhibiting larger errors due to its constrained, symmetric bell-shaped PDF. The Weibull and Gamma distributions consistently

provided higher accuracy when estimating wind speed quantiles, especially for extreme wind speeds (e.g., $s_{1\%}$). Their performance was notably better than the Gaussian and Lognormal distributions, which showed significantly higher errors in some regions.

ACKNOWLEDGEMENTS

This study was partially supported by a Grant-in-Aid for Scientific Research from JSPS KAKENHI (Grant Nos. 23K26263, 23K17789, 23K13454); the FOREST program from JST (Grant No. JPMJFR205O).

REFERENCES

AIJ, 2020. Guidebook for CFD Predictions of Urban Wind Environment.

Davenport, A.G., 1964. Note on the Distribution of the Largest Value of a Random Function With Application To Gust Loading. Proceedings of the Institution of Civil Engineers. 28, 187–196.

Kareem, A., Zhao, J., 1994. Analysis of non-gaussian surge response of tension leg platforms under wind loads. Journal of Offshore Mechanics and Arctic Engineering. 116, 137–144.

Wang, W., Seta, K., Ikegaya, N., 2022. Modelling probability density functions based on the Gram–Charlier series with higher-order statistics: Theoretical derivation and application. Journal of Wind Engineering and Industrial Aerodynamics. 231, 105227.

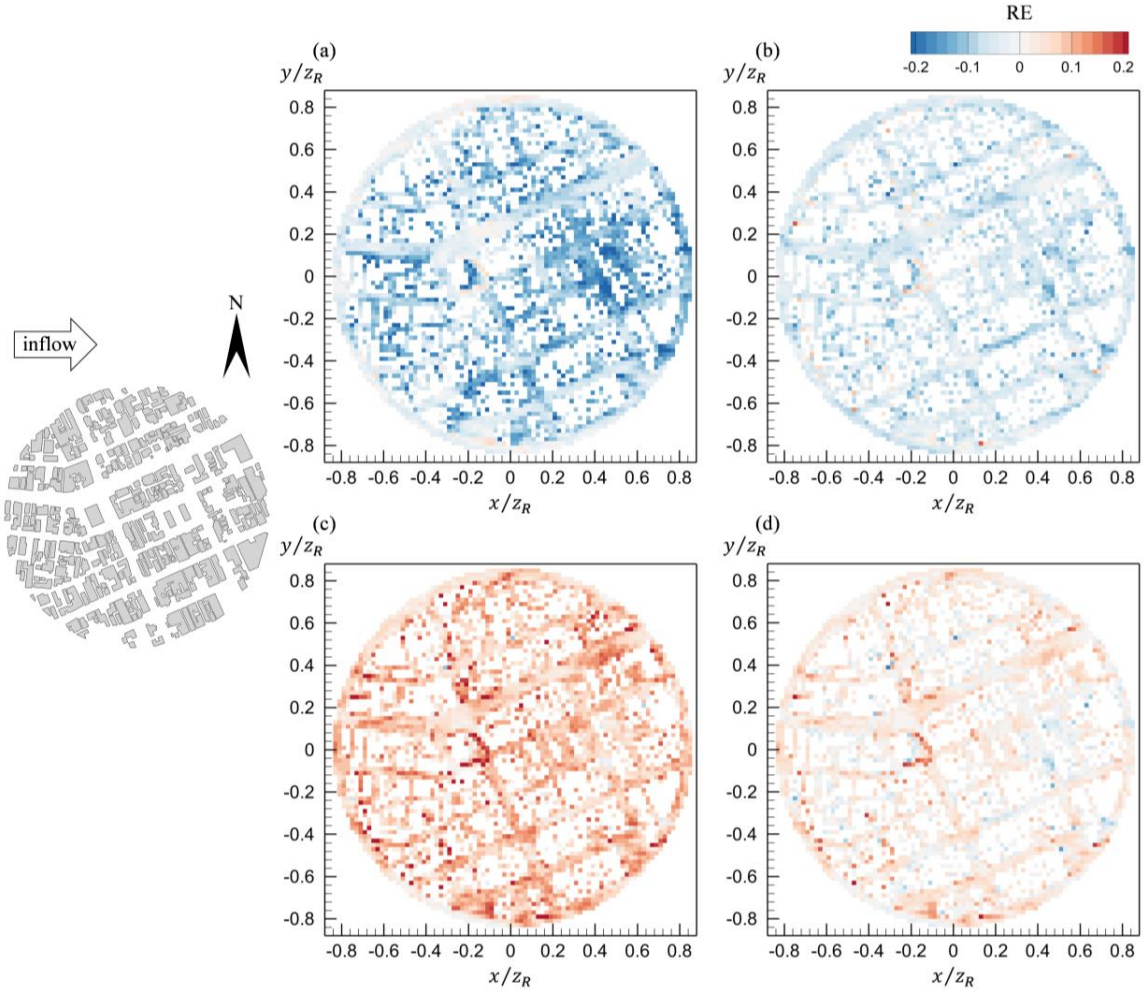


Figure 3. RE of the wind speed quantile with exceedance probability as 1%. (a–d) Gaussian, Weibull, Lognormal, Gamma distributions, respectively. The building layout is shown on the left.

Wind microclimate studies in the UK: subtleties, discrepancies and on-going challenges

Stefano Cammelli [1], Andrew Nicoli [2]

[1] *WSP UK Ltd., London, UK, stefano.cammelli@wsp.com*
[2] *WSP UK Ltd., London, UK, andrew.nicoli@wsp.com*

SUMMARY
Quantifying the aerodynamic effects within the urban fabric of a city is an important step in the assessment of the pedestrian level wind conditions. Urban landscapes can in fact create intricate wind microclimates featuring three-dimensional turbulent flow conditions that have the potential to significantly impact both pedestrian comfort and safety. In addition to the average wind speed, 'gusts' play a pivotal role in describing pedestrian level wind conditions. Computationally, gust wind speeds are typically estimated using summary statistics obtained from steady-state RANS simulations. This approach tends to disregard the complex and unsteady nature of urban flow dynamics and this, in the authors' experience, has the potential to compromise the accuracy of the numerical predictions. The aim of this extended abstract is to examine how pedestrian level wind studies in the UK have evolved in recent times, highlighting nuances, inconsistencies and current challenges; and to reflect - with the support of a case study, on the computational challenges associate with urban flow simulations, particularly within the canopy region.

Keywords: wind microclimate, boundary layer wind tunnel testing, computational wind engineering.

1. INTRODUCTION

For new developments in the UK, planners expect thorough wind microclimate considerations from the outset of a project, not only through a comprehensive and rigorous wind assessment but also by showcasing built-in design strategies that mitigate or even eliminate unacceptable impacts (Cammelli and Stanfield, 2017). In the UK, until approximately 2018, most of the pre-planning wind microclimate studies were supported by boundary layer wind tunnel tests which, on average, relied on 60 to 90 surface-mounted probes with measurements typically taken for 16 wind directions. Back then, there were no prescriptive guidelines in the UK for the execution of such studies. At the time this extended abstract is written, wind microclimate studies are supported by boundary layer wind tunnel tests and / or by computer simulations. The average number of probes used in physical testing has nowadays at least doubled with measurements now typically taken for 36 wind directions as standard. Also, several guidelines on the provision of wind microclimate assessments have been / are currently being published in various cities across the country.

2. LEGISLATION, POLICY AND GUIDELINES IN THE UK

There is no legislation in the UK directly relating to 'wind microclimate'. At national level, the 'National Planning Policy Framework' (2023) does not contain national planning policies directly relating to the topic of 'wind microclimate' and the 'National Design Guide' (2021) only states

that *"Proposals for tall buildings […] require special consideration. This includes […] environmental impacts, such as sunlight, daylight, overshadowing and wind"*. From a regional planning policy standpoint, the 'Sustainable Design and Construction Supplementary Planning Guidance' (2014) published by the Greater London Authority is more specific, as it states that *"Large buildings have the ability to alter their local environment and affect the microclimate. For example, […] particularly tall buildings […] can influence how wind travels across a Site, potentially making it unpleasant at ground level or limiting the potential to naturally ventilate buildings"*. From a local planning policy perspective, documents such as the 'City of London - Local Plan' (2015) and the 'Manchester's Local Development Framework - Core Strategy Development Plan Document' (2012) (as an example) make strong reference to 'wind' and 'microclimate': the former states that *"[...] all developments [...] to be of a high standard of design and to avoid harm to the townscape and public realm, by ensuring that [...] the design and materials avoid unacceptable wind impacts at street level [...]"*, whilst the latter states that *"Tall buildings [...] can also have an impact on the local micro-climatic conditions, for example, by creating wind tunnels"*. Other relevant documents include the 'Wind Microclimate Guidelines - For Developments in the City of London' (2019) and the 'Draft Wind & Micro-climate Toolkit for Leeds' (2021) which provide general guidelines for wind microclimate studies required as part of the planning applications of new development proposals; provide a recommended approach for wind microclimate studies; set general technical requirements; specify requirements for both Computational Fluid Dynamics [CFD] and boundary layer wind tunnel studies; and outline recommendations for the presentation of results and reporting.

3. A CASE STUDY

The authors of this extended abstract recently assessed the pedestrian level wind conditions for a site in Aldgate, an area of the City of London to the east of the "City Cluster". The average building height in Aldgate is around 30m to 50m - a range of heights for which the 'Wind Microclimate Guidelines - For Developments in the City of London' (2019) recommend that either CFD simulations or boundary layer wind tunnel tests are conducted. As such, a comparison between these two approaches was carried out.

Figure 1a) presents a comparison of the wind comfort across the area of interest for the winter months obtained using steady-state Reynolds Averaged Navier-Stokes [RANS] simulations (contoured data) against results obtained using boundary layer wind tunnel testing (discrete dots). Both computer simulations and experiments were conducted for 36 wind directions. The wind statistics as well as the 'City Lawson' criteria of the 'Wind Microclimate Guidelines - For Developments in the City of London' (2019) were used. Within the non-scale-resolving simulations, gust wind speeds were estimated using a peak factor, g, of 3.5 - whereas in the boundary layer wind tunnel tests the gust wind speeds were evaluated as the 99th percentile of the 3-second moving averaged data (Lawson and Penwarden, 1975). The results obtained from the RANS simulations are significantly calmer than the ones derived experimentally, with large proportions of the area of interest predicting wind conditions at street level suitable for 'frequent sitting' whereas the results from the boundary layer wind tunnel tests indicate wind conditions generally only suitable for 'standing', i.e. on average two categories worse. Also shown in Figure 1b) is the variability of the peak factor, g, across the area of interest for a wind direction of 270° (i.e. westerly winds), derived from scale-resolving Detached Eddy Simulations [DES] via the 99th

percentile approach.

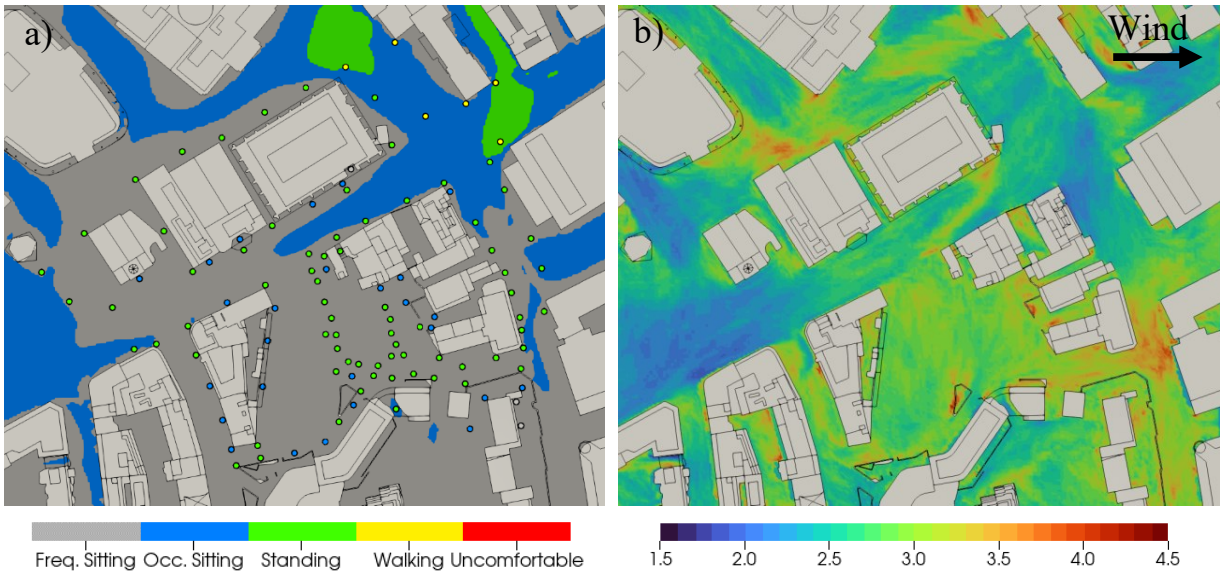


Figure 1. a) Wind comfort across the area of interest obtained from RANS simulations (contoured data) and from boundary layer wind tunnel testing (discrete dots); **b)** Contour of the peak factor derived from scale-resolving DES for a wind direction of 270° (i.e., westerly winds).

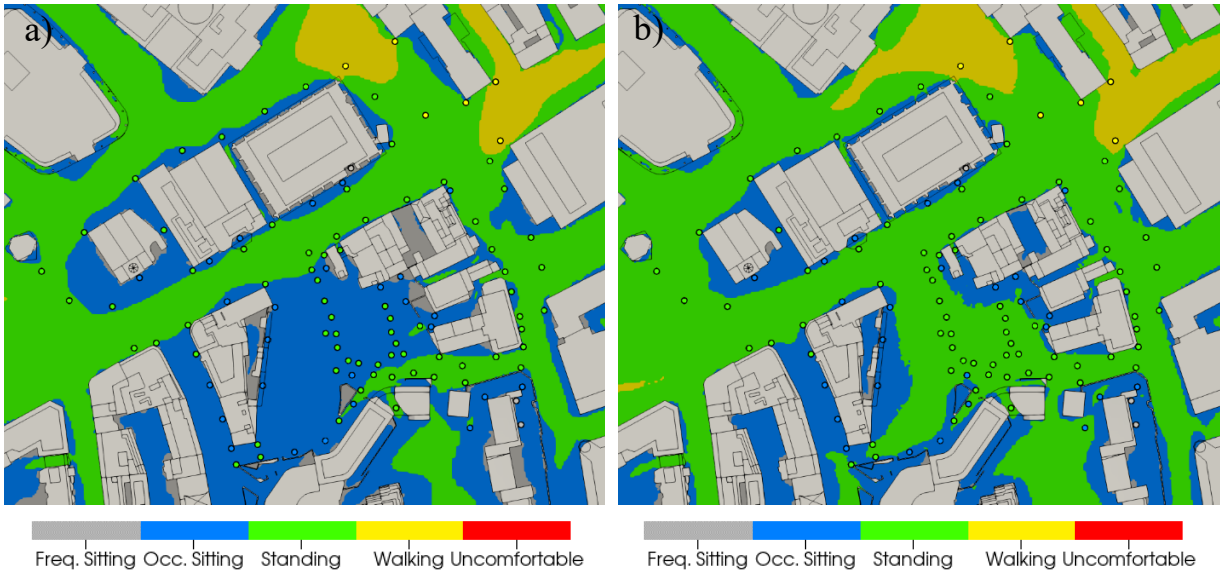


Figure 2. a) Wind comfort across the area of interest obtained from boundary layer wind tunnel testing (discrete dots) compared against results obtained using RANS simulations in conjunction with a wind tunnel-based gust model; **b)** Results obtained using RANS simulations in conjunction with a DES-based gust model.

Figure 2 presents a comparison of the wind comfort across the area of interest for the winter months

obtained using boundary layer wind tunnel testing (discrete dots) against results obtained using RANS simulations in conjunction with a gust model developed either through a) linear regression [LR] that uses the less spatially resolved experimental data (36 wind directions) or b) a random forest [RF] regressor applied to the output of more granular DES (12 wind directions). Both RANS simulations and experiments were conducted for 36 wind directions.

4. CONCLUDING REMARKS

The results presented within the case study of this extended abstract have shown that, despite the improvements made in the last 6 years in the UK wind microclimate consultancy business, a degree of variability in the output of such studies remains. An initiative of the UK Wind Engineering Society [WES] (https://www.windengineering.org.uk) has recently been launched to shed further light on this matter (Vita et al., 2024). Also, a joint working group of the Chartered Institution of Building Services Engineers [CIBSE] Resilient Cities Group and WES, is currently working on a 'national' guideline for wind microclimate studies. Despite these on-going efforts, some unanswered questions about wind microclimate studies remain: in the computational wind engineering space, did we get ahead of ourselves? Has the 'entry barrier' to wind engineering consultancy simply become too low? Does the industry need a 'chartership' status for wind engineering practitioners to be introduced to safeguard this field?

REFERENCES

Cammelli, S., Stanfield, R., 2017. Meeting the Challenges of Planning Policy for Wind Microclimate of High-rise Developments in London. Procedia Engineering, Volume 198, 43-51.

City of London, 2015. Local Plan. https://www.cityoflondon.gov.uk/assets/Services-Environment/planning-local-plan-adopted-2015.pdf (accessed 15.10.24).

City of London (2019). Wind Microclimate Guidelines - For Developments in the City of London. https://www.cityoflondon.gov.uk/assets/Services-Environment/wind-microclimate-guidelines.pdf (accessed 15.10.24).

Greater London Authority, 2014. Sustainable Design and Construction - Supplementary Planning Guidance. https://www.london.gov.uk/sites/default/files/gla_migrate_files_destination/Sustainable%20Design%20%26%20Construction%20SPG.pdf (accessed 15.10.24).

Lawson, T. V., Penwarden, A. D., 1975. The Effects of Wind on People in the Vicinity of Buildings. Proceedings of the Fourth International Conference on Wind Effects on Buildings and Structures, Cambridge University Press, Heathrow, 605-622.

Leeds City Council, 2021. Draft Wind & Micro-climate Toolkit for Leeds. https://www.leeds.gov.uk/docs/Draft%20wind%20and%20microclimate%20toolkit.pdf (accessed 15.10.24).

Manchester City Council, 2012. Manchester's Local Development Framework - Core Strategy Development Plan Document. https://www.manchester.gov.uk/info/200074/planning/1562/about_the_local_development_framework_ldf (accessed 15.10.24).

Ministry of Housing, Communities & Local Government, 2021. National Design Guide - Planning practice Guidance for beautiful, enduring and successful places. https://assets.publishing.service.gov.uk/media/602cef1d8fa8f5038595091b/National_design_guide.pdf (accessed 15.10.24).

Ministry of Housing, Communities & Local Government, 2023. National Planning Policy Framework. https://assets.publishing.service.gov.uk/media/669a25e9a3c2a28abb50d2b4/NPPF_December_2023.pdf (accessed 15.10.24).

Vita, G., et al., 2024. Introducing BeStPLW: A Benchmark Study on Pedestrian Level Winds. Proceedings of the 14th UK Conference on Wind Engineering, 4-6 Sept. 2024. Southampton, UK.

Comprehensive study of pedestrian wind comfort in large city centre

Agnieszka Kocoń [1,2]

[1]*Czestochowa University of Technology, Częstochowa, Poland, agnieszka.kocon@pcz.pl*
[2]*Cracow University of Technology, Cracow, Poland, agnieszka.kocon@pk.edu.pl*

SUMMARY:
This paper presents the results of an extensive campaign comprising field measurements, surveys with local population and wind tunnel tests aimed at making the first step towards establishing regulations concerning pedestrian wind comfort in Poland. Pedestrian wind comfort was assessed according to two different types of comfort criteria applied currently in Europe basing on wind tunnel tests results. The assessment was compared with the results of research surveys concerning the sensation of wind comfort by pedestrians in the city centre of Warsaw taking into account meteorological parameters prevailing during the measurements. These investigations resulted in determination of initial threshold wind speed for different types of pedestrian activities. The results provide current data concerning pedestrian wind comfort in areas with high-rise buildings.

Keywords: urban planning, wind tunnel tests, environmental impact on people

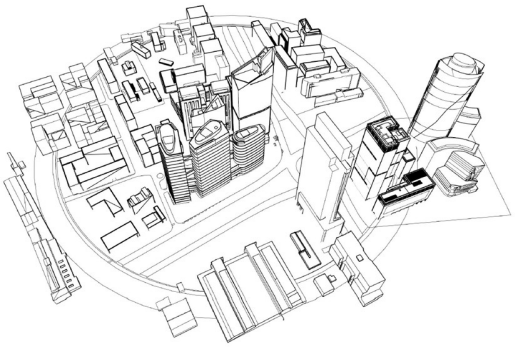
1. INTRODUCTION

Due to the growing density of high-rise buildings in urban areas, the problem of pedestrian wind comfort grow the attention through the last years. Up to now many researchers elaborated different comfort criteria that may be used to evaluate pedestrian wind comfort. The choice of the comfort criteria set is crucial because wind comfort assessment can differ substantially when using different of them (Janssen et al., 2013). The main reason of these differences is that pedestrian wind comfort criteria should be determined locally: for a specific region with similar wind conditions and for the general population with similar characteristics related to the sensation of wind discomfort.
This paper presents a local analysis of pedestrian wind comfort around the complex of high-rise buildings located in the city centre of Warsaw in Poland. Results obtained in this research campaign may be the first step to determine pedestrian wind comfort criteria for Poland because up to now, there is no data available on this issue.

2. METHODOLOGY

The research was conducted in two phases: field studies and wind tunnel tests. During first phase the surveys concerning individual feeling of people about pedestrian wind comfort in a few areas were conducted. Meanwhile, wind speed and air temperature were measured at the site. The second phase were wind tunnel tests where the model of the subject region of Warsaw was analyzed using two different wind comfort criteria. The location was chosen as Warsaw is densely developed and there was a notable deterioration of wind comfort conditions signalized in this particular area.

a)



b)

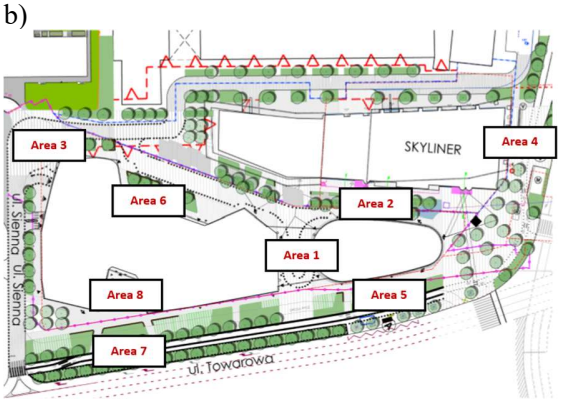


Figure 1. Measurement location: 3D view (a), areas analyzed in the research campaign (b).

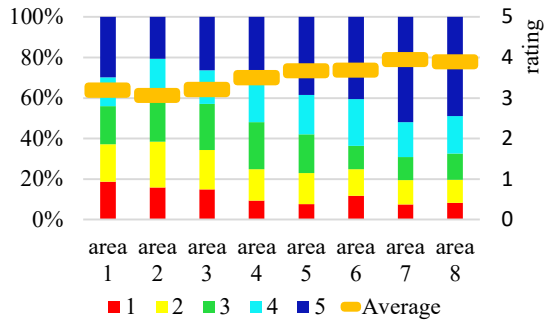
Field measurements were carried out in eight areas illustrated in Fig.1 differing with respect to prevailing wind conditions and the type of usual pedestrian activity. The interviewers asked pedestrians about the frequency of attending the area and their feeling of wind comfort (on the day of measurement and usually in this area). The total number of surveys was 3 200, with the rate 45% of women and 55% of men responses. Concurrently to the surveys, the measurements of weather parameters using HWS1000 Handheld Weather Station took place. The field measurements were conducted during daylight for 10 days throughout different seasons.

Wind tunnel tests were conducted at the boundary layer wind tunnel of the Wind Engineering Laboratory at the Cracow University of Technology. The closest surroundings of the analyzed high-rise buildings in a radius of 300 m were re-created in the scale of 1:300. Measurements were carried out for IVth terrain category according to (PN-EN, 2008) for twelve wind directions, with a 30° angle increment. Wind speed at the pedestrian level was measured in 16 points using biaxial hot-wire anemometers.

3. RESULTS

The results of field surveys concerning the assessment of wind comfort by pedestrians are presented in two separate charts in Fig. 2 concerning the rating of Today's Wind Comfort (TWC) and Usually Prevailing Wind Comfort (UPWC). The results of all the surveys from 10 days of field measurements are cumulated in these charts, taking into account the percentage of each answer of respondents (rating in the range of 1 to 5, where 1 is the worst wind comfort, 5 – is the highest wind comfort).

a)



b)

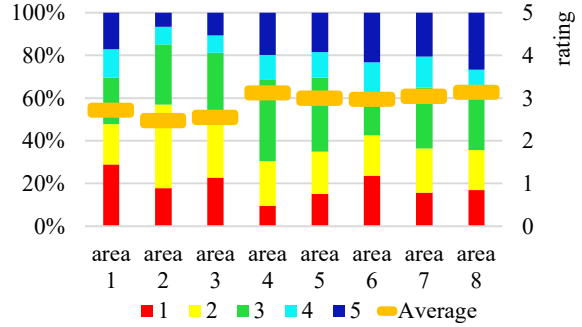


Figure 2. The assessment of pedestrian wind comfort according to field surveys: today wind comfort (a), wind comfort prevailing usually (b).

The results for the TWC assessment are significantly different from the results obtained for the UPWC assessment. Results show that people are able to distinguish between wind conditions that they experience during one day and wind conditions that they experience usually in a given area.

Wind tunnel tests allowed to assess pedestrian wind comfort using two previously established wind comfort criteria sets: NEN 8100 criteria (NEN, 2006) and Lawson criteria (Lawson, 1980). To compare the results of wind tunnel tests with the results of field surveys, the ratings between 1 and 5 were adopted to the type of pedestrian activity (5 – for sitting long/ dinning outside, 2 – for sitting short/ sitting, 3 – for walking leisurely/ standing or walking, 2 – for walking fast/ business walking, 1 – for uncomfortable wind conditions). Figure 3 compares the results of wind tunnel tests and field surveys concerning UPWC in each of the areas.

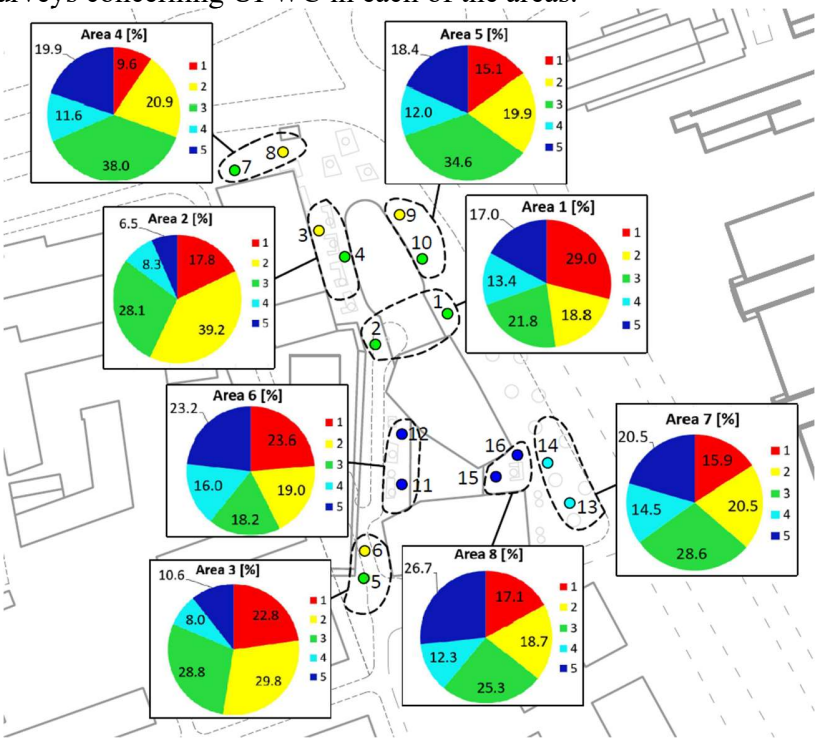


Figure 3. Results of field surveys (pie chart) and wind tunnel tests (colored dots) using NEN 8100 criteria.

To compare both types of results, fields surveys were analyzed taking into account: dominant rating (the rating which was most commonly indicated by respondents) and the majority rating (the majority of respondents rated wind comfort at that value or above). It seems that the applied wind comfort criteria slightly overestimate pedestrian wind comfort; however, the results of wind tunnel tests and field surveys are in quite good agreement. The comparison provides important information that threshold values proposed in NEN 8100 and in Lawson criteria may be suitable for the social profile of people and local weather conditions in the analyzed region. However, a modification is required to provide information about wind conditions experienced by the majority of people in this region.

Basing on the results the procedure of calculation threshold wind speed was proposed. This procedure takes into account wind speed at the measurement site as well as people assessment of

wind comfort in specific area. Figure 4 presents the resulting threshold wind speeds obtained for different ratings marked K1–K5 in the charts for two different types of activities generally distinguished in the tested area: sitting and walking.

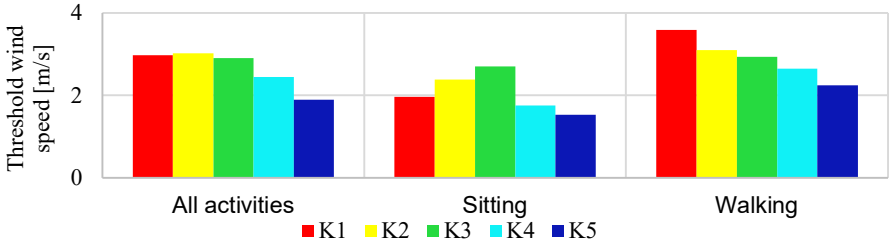


Figure 4. Threshold wind speed values for different types of activities with respect to wind comfort rating.

Generally, higher threshold wind speeds are observed for lower ratings and lower threshold wind speeds are observed for higher ratings, which was expected as the higher wind speed, the worse the experience of wind conditions. Quite surprisingly, a different trend is presented in the chart for sitting, which may be explained by different expectations with regard to wind conditions than people who walk through as well as it might be a result of bias or misunderstanding the question by some respondents. The threshold wind speeds for sitting are lower than for walking for all the ratings. It also confirms that people have different expectations of wind conditions depending on the type of activity, which is already included in most of the wind comfort criteria.

4. CONCLUSIONS

This paper presents a novel insight on how people experience wind conditions in the city centre with high-rise buildings and gives useful conclusions on the development of wind comfort criteria:

- The wind comfort criteria based on a fixed threshold wind speed with different limits of exceeding probability can be interpreted easily by people.
- The wind comfort criteria should take into account unsteady wind speed of lower value than assumed in the wind comfort criteria included in this paper. The effect of people vulnerability on unsteady winds is even more pronounced in the city centers, characterized by high turbulence, where both local wind speed and wind direction change frequently.
- The results of the tests presented in this paper are promising and may be the first step to initialize a larger campaign with the goal of providing pedestrian wind comfort criteria in Poland.

ACKNOWLEDGEMENTS

This research was funded in whole by the National Science Centre, Poland under Grant No. 2023/07/X/ST8/00571. For the purpose of Open Access, the authors have applied a CC-BY public copyright license to any Author Accepted Manuscript (AAM) version arising from this submission.

REFERENCES

Janssen, W.D. , Blocken, B., and van Hooff, T., 2013. Pedestrian wind comfort around buildings: Comparison of wind comfort criteria based on whole-flow field data for a complex case study. Building and Environment 59, 547-562.

Lawson, T., 1980. Wind Effects on Buildings. Applied Science Publishers LTD, Londyn.

NEN, 2006. Wind comfort and wind danger in the built environment. NEN 8100 (in Dutch) Dutch standard.

PN-EN 1991-1-4, 2008. Actions on structures. General actions. Wind actions.

Urban ventilation dynamics assessment of opening geometry and vertical configuration in permeable buildings

Ying-ming Su [1], Yu-cheng Fang [2]

[1] *Department of Architecture, National Taipei University of Technology, Taiwan, R.O.C, ymsu@ntut.edu.tw*
[2] *Department of Architecture, National Taipei University of Technology, Taiwan, R.O.C, charlesfang19@gmail.com*

SUMMARY:
High-density building clusters create "Wall Effect" that obstructs urban airflow due to their height and width. Research indicates that permeable building designs can effectively enhance urban ventilation. Study uses CFD simulations on 3x3 idealized city to examine two permeable building heights: 50m (L) and 100m (H), analysing the effects of two opening geometries long rectangular (r, R) and short rectangular (s, S) at various heights (0m, 15m, 30m, 60m) on the urban wind environment. Results indicate that in the 50m buildings lower opening heights significantly improve ventilation at pedestrian level of opening platform and street canyon. Specifically, case Lr0 achieved a highest wind speed of 0.912 m/s, resulting in a 147% increase in street canyon wind flow compared to non-permeable case. Conversely, wind speed of Ls0 at test point p6 in the rear street canyon significantly decreased to 0.127 m/s, which is 0.2% lower than the non-permeable scenarios, which could exacerbate weak-wind zones and pollutant retention. For 100m high-rise buildings, the highest wind speed (HS60) reached 0.736 m/s, contributing to enhance urban airflow, although its effect on pedestrian-level ventilation was weaker than the 50m modeling. The wind speed difference between HS60 and HR60 configurations was +6.74%, favoring HS60 over HR60.

Keywords: Permeable Building, Opening Geometry, Wall Effect

1. INTRODUCTION

Urbanization is leading to a growing trend of populations residing in high-density cities (Ritchie et al., 2024). By 2050, urban center is expected to house approximately 68% of the global population, revealing an increasingly close connection between urbanization and environmental degradation (United Nations Environment Programme, 2019). In many countries, panel buildings, characterized by large, broad, and tall single-directional forms, are often located in areas with proximity to ports or scenic views. However, these designs commonly contribute to low sunlight exposure, poor ventilation, urban canopy pollutant retention, and the urban heat island effect. Thus, the term "Wall Effect" carries negative implications (Hong Kong Institute of Real Estate Administration).Permeable building designs are becoming more prevalent worldwide, incorporating ventilation corridors and open layers to enhance wind flow and improve urban ventilation (Chen, 2015; Tsai, 2022). Studies have shown that building porosity, density, and type significantly impact urban ventilation and air quality (Sha et al., 2018; An et al., 2019). Zhang et al. (2023) highlighted the benefits of ground-level permeability, noting that as ground-level porosity increases, differences in the mean ventilation rate (MVR) between various opening locations decrease. For the same porosity, the MVR is higher with openings in the middle and on

both sides, while it is lowest when positioned opposite to the building. Hong Kong's Sustainable Building Design Guidelines APP-152 established quantifiable standards for controlling building porosity and site ventilation areas (Yuan and Ng, 2012; Hong Kong Planning Department, 2016). Using computational fluid dynamics (CFD), the study simulates a central building in a 3x3 idealized city scenarios to explore how different opening geometries and heights in permeable building designs affect urban air flow environments, providing quantitative data for analysing microclimate changes in urban areas.

2. METHODOLOGY

The study modeling references 3x3 idealized city layout cases following Nazarian & Kleissl (2016), with street block unit dimensions based on the typical block sizes in Taipei City (100m in length by 50m in width; Ministry of the Interior, 2008). Using Rhinoceros 6 and ANSYS Fluent software, a 3D urban model was developed for subsequent calculations and simulation analyses. Two building height configurations were designed: 50m (L) and 100m (H) high-rise building. Building permeability was assessed based on the method used by the Hong Kong Planning Department, where the permeable area of each evaluation layer is set to 100% * 1/3P, setting two opening geometries with aspect ratios of 1:4 (long rectangular, r and R) and 1:1.5 (short rectangular, s and S). For the 50m buildings, three opening heights (0m, 15m, 30m) were tested, while the 100m buildings were tested with four opening heights (0m, 15m, 30m, 60m), resulting in total of 16 simulated scenarios including a baseline with non-permeable case. Measurement points were located at pedestrian level within the front row canyon (p1-p3) and the rear row canyon (p4-p6) for wind-thermal environment analysis. Based on idealized units and relevant guidelines, three primary variables were explored: opening geometry, opening height, and building height variations. The study design and configurations are illustrated in Figure 1.

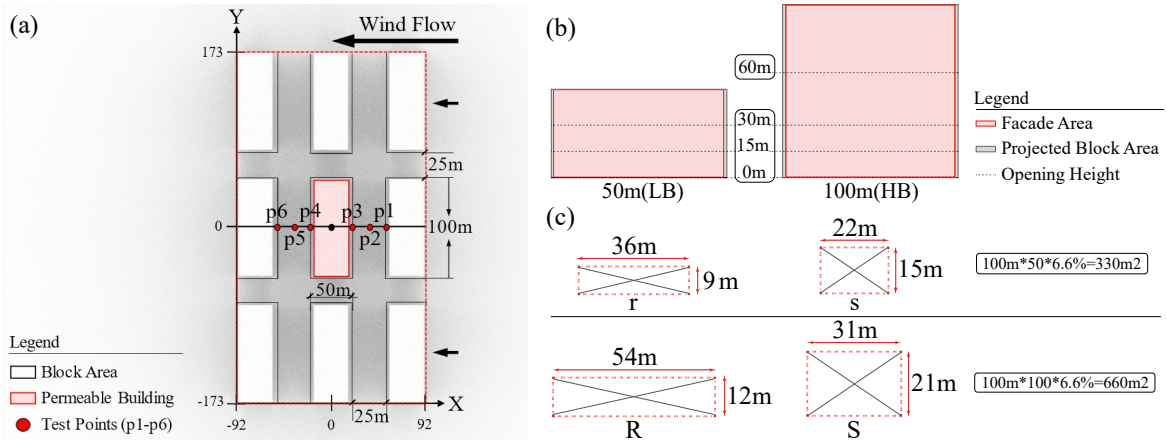


Figure 1. (a) Idealized city and test point locations, (b) Opening height variations, (c) Opening size instructions

3. RESULTS AND DISCUSSION

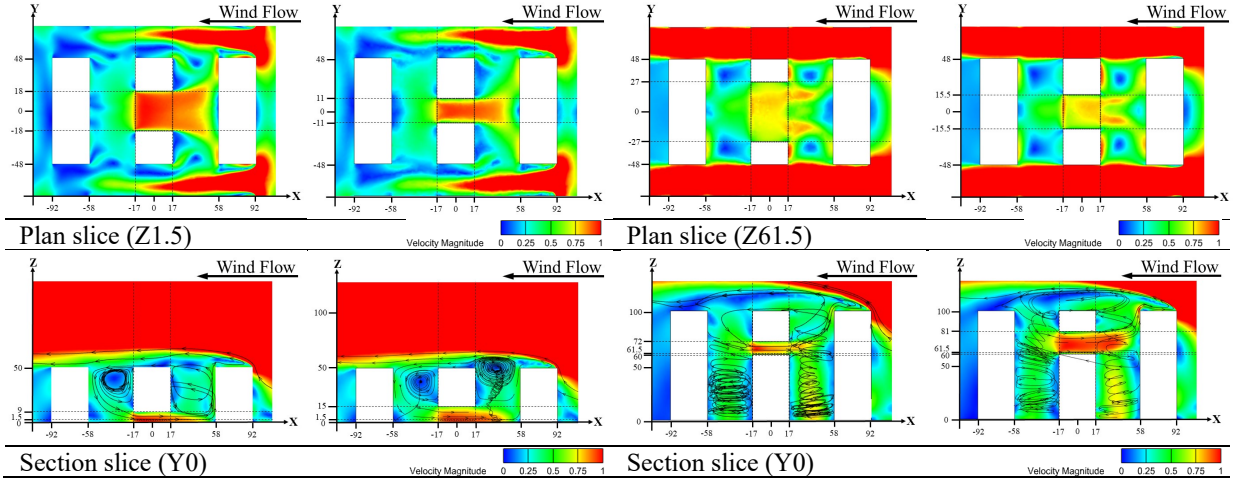
3.1 Wind Speed Analysis

3.1.1 Ventilation effects at pedestrian level for permeable platform at different building heights

50m buildings (L): among the opening configurations, the internal average wind speed is lowest for Ls30 (0.308 m/s) and highest for Lr0 (0.912 m/s), showing a difference of 196%. In the 50m building scenarios, the overall wind speed decreases as the opening height increases. Both opening geometries exhibit optimal wind speed at the ground-level openings, with the long

rectangular bottom opening (Lr0) showing a slightly higher wind speed than the short rectangular bottom opening (Ls0) by 0.082 m/s (+9.8%), as shown in Table 1(a).In the 100m high-rise buildings (H): case HS0 opening has the lowest average wind speed (0.501 m/s), while the HS60 opening reaches the highest (0.736 m/s). In the 100m building scenarios, wind speed performance improves with increased opening height. For opening heights of 0m, 15m, and 30m, the long rectangular openings (R) outperform the short rectangular openings (S). However, at 60m, the short rectangular opening has a slightly higher wind speed than the long rectangular one by 0.017 m/s, as presented in Table 1(b).

Table 1. Comparison of ventilation performance at pedestrian level (1.5m) for openings.

(a) Simulation of ground-level openings wind speed for different opening geometries in 50m building scenario.		(b) Simulation of upper-level openings wind speed for different opening geometries in 100m building scenario.	
Lr0	Ls0	HR60	HS60
			

3.1.2 Wind speed at pedestrian Level (1.5m) in urban street canyons

In the 50m building scenarios (L): In the case of ground-level permeability, shielding effect redirects airflow toward the rear street canyon, creating recirculating flow and an acceleration effect as air flows back into the openings. This leads to enhanced wind speed in the front street canyon, where both Lr0 and Ls0 show significantly higher wind speeds compared to LB. Wind speed in rear street canyon gradually decreases as distance from the permeable building increases, with Ls0 experiencing a severe wind speed reduction to 0.127m/s at p6, slightly lower by 0.033m/s than the non-permeable scenario. This further amplifies low-wind areas prone to pollutant accumulation in the central low-speed turbulence, thus reducing pollutant dispersion at pedestrian level. Variations in permeability configuration at ground level affect pedestrian-level ventilation across the street canyon; overall wind speed for other points increases significantly by 0.378m/s (+134%) compared to non-permeable buildings, contributing to improved pedestrian height airflow and microclimate.In the 100m high-rise building scenarios (H): For HR60, airflow rebounds off the rear structure, creating vortices in the front street canyon after passing through the openings, with wind speed generally decreasing with height. The longer rectangular opening exhibits more pronounced lateral airflow dispersion from side urban canopy, causing the most significant wind speed reduction at p3 (-0.201m/s). All other points show superior wind speeds to the non-permeable scenario as illustrated in Figure 2. HS60 demonstrates a slightly better overall street canyon wind speed than HR60 by 6.74%.

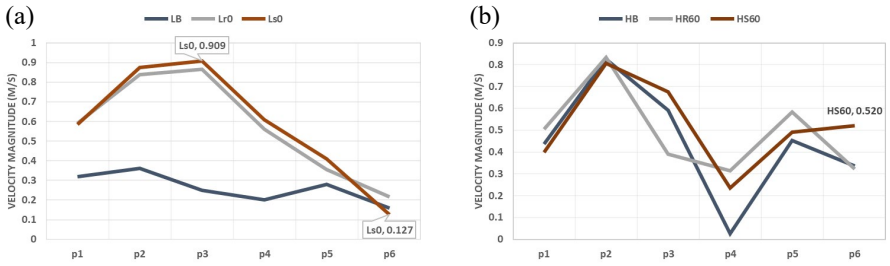


Figure 2. (a) Wind velocity of urban street canyons (Z=1.5m): LB vs. Lr0, Ls0 and (b) HB vs. HR60, HS60

4. CONCLUSIONS

4.1 At the pedestrian-level platform of Lr0 shows superior wind compared to Ls0, with effect being more pronounced in the 50m building scenarios than 100m building scenarios.

CFD simulation results indicates that ground-level permeable configuration effectively mitigates the urban heat island effect in the 50m building. The average wind speed at the Lr0 opening platform is the highest 0.912m/s. In 100m building scenarios, the high-level permeable configuration shows the greatest ventilation microclimate enhancement.

4.2 Lr0 offers the highest microclimate improvement for pedestrian-level (1.5m) areas within the street canyon, and the 100m building scenarios have relatively lower impact.

In 50m building scenarios, the optimal configurations in terms of wind speed at the opening, Lr0 and Ls0, show that Lr0 produces the highest wind speeds in front-row street canyon as it approaches the opening: p1 (0.59 m/s), p2 (0.84 m/s), and p3 (0.867 m/s). In the rear street canyon, wind speed gradually decreases with distance from the permeable building: p4 (0.559 m/s), p5 (0.355 m/s), and p6 (0.217 m/s). The wind speed trend for Lr0 is more stable than for Ls0, resulting in a significant improvement of 147% in the front street canyon and 76% in the rear compared to the non-permeable case. With its optimal performance in both internal openings and street canyon wind conditions, the ground-level long rectangular permeable geometry demonstrates the greatest benefit for urban ventilation enhancement at the pedestrian level.

4.3 Vertical configuration of the openings has a more significant influence than opening geometry. In 50m building scenarios, lower opening heights result in higher wind speeds.

The air flow variations between opening height and geometry are more pronounced in the 50m building scenarios compared to the 100m high-rise building cases. When the opening geometry is the same, wind speed variations are more significantly influenced by changes of the opening height, particularly at heights of 0m and 15m (Lr0 and Lr15 differ by 0.367 m/s; Ls0 and Ls15 differ by 0.438 m/s). As the opening height remains the same, the wind speed variation due to geometry of opening is less pronounced.

ACKNOWLEDGEMENTS

This study is particularly grateful for the funding support from the Ministry of Science and Technology project (Project No.: NSTC 113-2221-E-027-025).

REFERENCES

An, K., Wong, S.-M., & Fung, J. C.-H. (2019). Exploration of sustainable building morphologies for effective passive pollutant dispersion within compact urban environments. Building and Environment, 148, 508-523.

Li, Y., & Chen, L. (2020). Study on the influence of voids on high-rise building on the wind environment. Building Simulation, 13(2), 419-438.

Yuan, C., & Ng, E. (2012). Building porosity for better urban ventilation in high-density cities – A computational parametric study. Building and Environment, 50, 176-189.

Fast short-term forecasting of wind field using meteorological reanalysis data and near-surface observations

Xiang Wang [1], Hongyuan Jia[2], Chaoyi Hu[3], Keisuke Naoka[4], Hideki Kikumoto[5]

[1]The University of Tokyo, 4-6-1 Komaba, Meguro-Ku, Tokyo, 153-8505, wx7229@iis.u-tokyo.ac.jp
[2] The University of Tokyo, 4-6-1 Komaba, Meguro-Ku, Tokyo, 153-8505, jhy@iis.u-tokyo.ac.jp
[3] The University of Tokyo, 4-6-1 Komaba, Meguro-Ku, Tokyo, 153-8505, hu-cy123@iis.u-tokyo.ac.jp
[4]Sustainable System Research Laboratory, CRIEPI, 1646 Abiko, Abiko-shi, Chiba, nakao@criepi.denken.or.jp
[5]The University of Tokyo, 4-6-1 Komaba, Meguro-Ku, Tokyo, 153-8505, kkmt@iis.u-tokyo.ac.jp

SUMMARY:
The near-surface meteorological observation network has been developed worldwide to provide real-time local observations, but upper-level urban wind speed observation is still challenging. The development of high-resolution meteorological analysis data provides complementary data for urban wind fields. However, high-precision meteorological data requires observation data assimilation to correct the accumulated bias in weather forecast models, which means that meteorological analysis data are released with a delay. Therefore, this study attempts to monitor or forecast urban wind fields by fusing meteorological near-surface observations and high-resolution local objective reanalysis data. In this study, we use linear stochastic estimation (LSE) and multiple-time-delay LSE to monitor or forecast urban wind fields using meteorological observation. The results show correlation coefficient between predicted wind fields and validation is above 0.8 for 3 lead hours and 0.7 for 6 lead hours. MLSE within a 6-hour delay has relatively better results.

Keywords: urban wind forecast, meteorological reanalysis data, linear stochastic estimate

1. INSTRUCTIONS

The wind velocity in the urban boundary layer plays a crucial role in influencing heat transfer, water vapor, air pollution, and other flux variables. The gradient wind in the urban areas shows spatial inhomogeneity owing to complex urban morphology, which differs from the homogeneous underlying surfaces in rural areas. Accurate urban microclimate simulations require reliable boundaries or initial conditions generally provided by urban meteorological observation stations (Tominaga et al., 2008). The near-surface meteorological observation system has been developed in cities worldwide, continuously supplying valuable observation data for urban climate assessment and weather forecasting. However, conducting time-continuous upper-level wind speed monitoring at multiple meteorological supersite observatories in urban areas is challenging due to the expensive construction and maintenance costs (Lam et al., 2023). The development of local-scale meteorological models and data assimilation techniques has promoted the generation

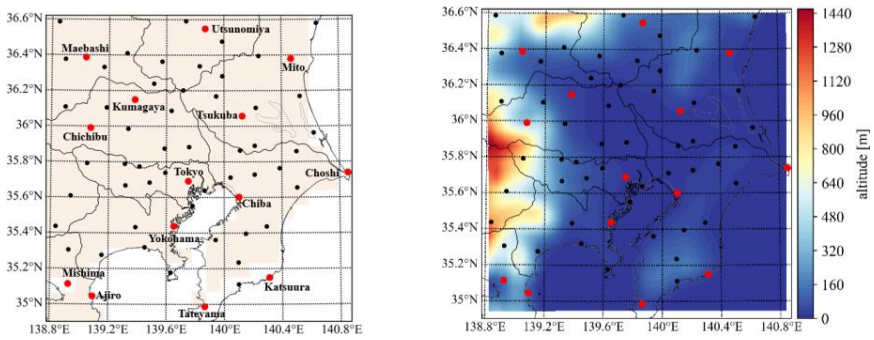
of high-resolution and high-precision meteorological reanalysis data, which provides complementary data for assessing wind speeds above urban areas. The forecast of meteorological elements typically runs numerical weather prediction (NWP) models using current reanalysis data as initial conditions, simulating the future state of the atmosphere. Due to the high complexity of these models, this process requires substantial computational resources to ensure timely forecasts. The development of machine learning also offers an alternative efficient method for short-term forecasting. This study attempts to employ a combination of Proper Orthogonal Decomposition (POD) and Multiple-time-delay Linear Stochastic Estimation (MLSE) methods to achieve short-term hourly resolution predictions of urban wind fields.

2. METHOD AND DATA USAGE

2.1. Data using

Local objective analysis (LA) data, developed by the local forecast model of the Japan Meteorological Agency (JMA), work as meteorological reanalysis data, which can provide 5-km resolution data on wind velocity, temperature, relative humidity, and geopotential height at several pressure levels (from 1000 to 100 hPa and 10 m above ground), with a horizontal spatial resolution of 5 km and an hourly temporal resolution (JMA, 2024). The Automated Meteorological Data Acquisition System (AMeDAS) meteorological observation network with approximately 20-km resolution, has been providing long-term observation data for many urban regions in Japan.

LA and AMeDAS data from 2018 to 2022 are used as meteorological high-resolution reanalysis data and observations, respectively, to validate the proposed method. LA data at 10 m, 1000 hPa (about 120 m a.s.l.), and 975 hPa (about 340 m a.s.l.) are selected as a training dataset. The meteorological elements including wind velocity (U and V components corresponding to the west-east and south-north directions, respectively), air temperature (AT), vapor pressure (VP) at three levels, and sea level pressure (SLP) are considered in the proposed forecast model. The meteorological data in the Tokyo area are selected as a study case, as shown in Figure 1. The accuracy of the proposed model is verified using LA data from January to September 2023, while the accuracy of LA data has been confirmed in previous studies (Wang et al., 2023, 2024).



(a) Locations of observatories (b) Terrain altitude

Figure 1 Locations of AMeDAS meteorological observations and DLS urban observations in the Tokyo area. (Red sites indicate the main observatories with wind speed and direction, air temperature, vapor pressure, relative humidity, and mean sea level pressure; black sites indicate the observatories only with wind speed, direction, and air temperature).

2.2. Proper Orthogonal Decomposition with Linear Stochastic Estimation

POD is a method of data feature extraction by decomposing data into multiple feature modes and corresponding energy coefficients. POD has been discussed in detail by previous studies (Wang et al., 2024; Berkhooz et al., 1993). The U, V, AT, and VP at three levels, along with SLP of LA data are used to extract meteorological spatial structure described by a series of POD modes. Projecting instantaneous meteorological data on the POD modes obtains temporal coefficients that describe the dynamic change of meteorological data.

MLSE estimates an unknown event based on one or a series of known information with multiple delay times by linear relationships among events (Durgesh and Naughton, 2010). In this study, MLSE is used to estimate the POD temporal coefficients for the forecasts at 1-hour, 3-hour, 6-hour, 9-hour, and 12-hour lead time, using surface-level observations as input data via building multiple dependent forecast models. The MLSE model considers five cases with delays of 1, 3, 6, 12, and 24 hours. When delay time equals zero, MLSE degrades to LSE, which is used as the baseline. The correlation coefficient (R) and root mean square error (RMSE) are used as metrics to quantify the performance of forecast models.

3. RESULT

For brevity, this section presents only the comparison at a height of 10 m. Figure 2 shows the R and RMSE between forecasted wind speed and LA data at 10 m. Each point indicates the spatially averaged metric over the study area. In LSE, the metrics at zero represent the baseline that monitors wind fields based on current observations. MLSE within a 6-hour delay shows a relatively better forecast than that beyond 12 hours. This phenomenon is partly attributed to the autocorrelation and cross-correlation functions of wind speed in the study area show an approximately linear decay trend within 6 hours as the delay time increases (Wang et al., 2024). When predicting the 3-hour future wind speed, the distribution of metrics at 10 m above the ground for the MLSE-6 case is shown in Figure 3. The areas with higher altitudes have relatively lower R. There are similar results at the other two pressure levels.

4. CONCLUSION

In this study, we use hourly-resolution near-surface meteorological observations to predict urban wind fields. The correlation coefficient between the predicted wind speed and the validation data is above 0.8 for 3 lead hours and 0.7 for 6 lead hours at 10 m. The MLSE within a 6-hour delay provides a more accurate forecast than the MLSE with longer delay times.

ACKNOWLEDGEMENTS

A part of this work was supported by the Japan Society for the Promotion of Science KAKENHI Grant Number 20H02308, 22K04448, and 24KJ0777.

REFERENCES

Berkhooz, G., Holmes, P., and Lumley, J. L., 1993. “The Proper Orthogonal Decomposition in the analysis of Turbulent Flows”, Annual Review of Fluid Mechanics, Vol. 25, Annual Reviews Inc., pp. 539-575.

Durgesh, V., Naughton, J.W., 2010. “Multi-time-delay LSE-POD complementary approach applied to unsteady high-Reynolds-number near wake flow”. Exp Fluids 49, 571–583.

JMA, 2024. Meteorological observation statistical indicators agency. Japan Meteorological Agency.

Lam et al., 2023. “Learning skillful medium-range global weather forecasting”. Science 382, 1416-1421.

Tominaga et al., 2008. “AIJ guidelines for practical applications of CFD to pedestrian wind environment around buildings”, Journal of Wind Engineering and Industrial Aerodynamics 96, 1749–1761.
Wang, X., Hu, C., Kikumoto, H., Jia, H., Nakao, K. & Ooka, R., 2024. “Data extension of high-resolution wind speed database by fusing meteorological observation and local objective analysis data with POD–LSE”. Journal of Wind Engineering and Industrial Aerodynamics 252, 105812.
Wang, X., Kikumoto, H., Jia, H., Lin, C., Nakao, K., 2023. “Investigation of spatial variability in power law index of wind profiles above the urban area around Tokyo Bay based on local objective analysis data”. Journal of Wind Engineering and Industrial Aerodynamics, 240, 105471.

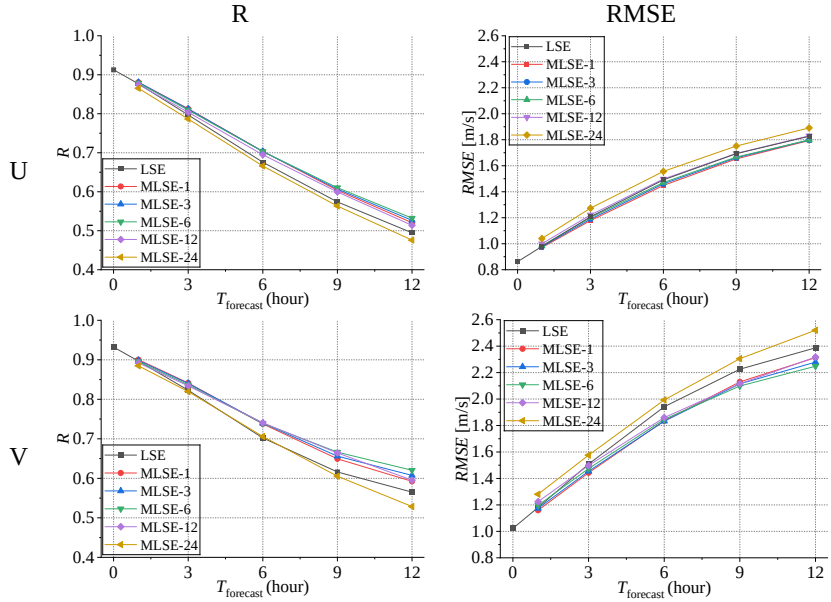


Figure 2 Spatially averaged metrics for multiple forecast times over study areas at 10 m above ground (the number in legend is the delay time considered in that method; T_{forecast} is lead time)

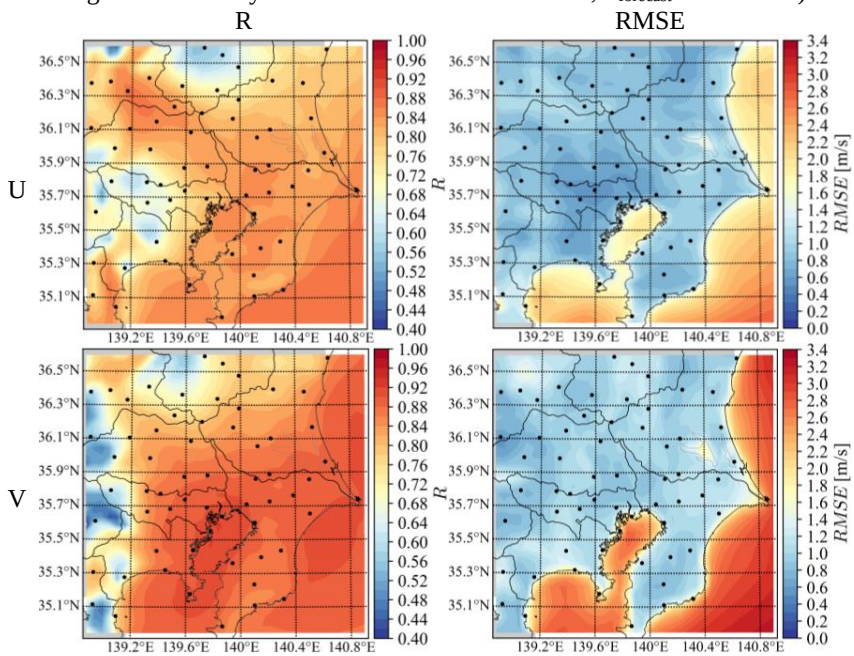


Figure 3 Metrics comparing forecasted wind velocity with LA data at 3-hour lead time on 10 m above the ground for MLSE-6 case (Black points show the locations of meteorological observatories)

Urban planning at Nyhavna using CFD

Ken-Robert G. Jakobsen [1], Jacob Hudtwalcker [1], Tore Andreas Helgedagsrud[1], Ralph Bertram [2], Sara Falbe Hansen[3]

[1]*Dr.techn. Olav Olsen AS, Oslo, Norway, firmapost@olavolsen.no*
[2]*Topic:Architecture and Design, Oslo, Norway, rb@topicark.no*
[3]*Cobe, Copenhagen, Denmark, saha@cobe.dk*

SUMMARY
This study utilizes computational fluid dynamics (CFD) simulations to assess wind comfort levels at Nyhavna in Trondheim, Norway, based on Lawson's wind comfort criteria. As a waterfront area being developed from industry to an urban downtown district, Nyhavna is influenced by unique wind patterns that affect pedestrian comfort and urban usability. The present work provides critical insights for the architects and urban planners with design recommendations to improve wind comfort wherever needed.

Computational fluid dynamics, Wind comfort, Urban planning

1. INTRODUCTION

Under Nyhavna Utvikling, the area called Nyhavna in Trondheim will be transformed from industry and port operations to a sustainable downtown district available for everyone, and the so-called ”Transittkaia” is first out and is now ready to be sent to detailed zoning plans. As part of the winning team for the development of Transittkaia under the leadership of the Danish architecture firm Cobe, Dr. techn. Olav Olsen AS (OO) has been engaged to assist with design tasks in areas such as structural engineering, geotechnics, climate adaptation and environmental geology. This also includes wind comfort studies where the aim of the work has been to document the comfort situation for the architects' planning proposal, including two different solutions for a specific commercial building located at the south end of the planning area, as well as provide input for possible mitigation measures wherever necessary.

The wind study was planned and carried out to ensure a high degree of details in the results enabling in depth investigations of both overall wind comfort levels as well as local effects at ground level in the planning area, including sensitivity studies for the building designs. The local climate analysis must follow the zoning plan at Nyhavna and measures to improve the microclimate on the ground floor must be accounted for in the detailed plans and secured in regulations.

2. WIND COMFORT

Wind comfort is based on numerical concepts to describe how people perceive different wind conditions, at varying levels of activity. Evaluation of wind comfort for pedestrians in an urban area is based on three main parameters:

- **Historical wind data (from wind measurements)**
- **Local wind conditions (CFD calculations)**
- **Specific comfort criteria (e.g. Lawsons).**

The local wind speed must be related to statistics of the local weather station. We then determine the probability of the local wind speed exceeding given thresholds defined by the comfort criteria, at a height 1.5 meters above ground level.

There are several methods to quantify wind comfort. Here we use the industry standard Lawson's LDDC criteria for wind comfort (Lawson, 1978). As shown in Table 1, comfort is assessed by categories and defined as acceptable if the limit values occur less than 5% of the time. This then provides acceptable speeds for different activities. In the event of exceedance, mitigating measures should be explored.

Table 1. Comfort levels in Lawson LDDC.

	Category	Wind speed	Probability	Activity
	1	4.0 m/s	< 5 %	Sit for a long time
	2	6.0 m/s	< 5 %	Sit for a while
	3	8.0 m/s	< 5 %	Stand still, stroll
	4	10.0 m/s	< 5 %	Go
	5	10.0 m/s	> 5 %	Uncomfortable

Wind comfort is usually defined based on either mean wind speed or a so-called equivalent wind gust speed (GEM), where the latter includes the effect of 3-second wind gusts and will consequently be the more conservative method of the two. In this report, the GEM speed is found through the standard deviation (σ) of the measured wind speeds from a representative measuring station located at Brattøra close to Nyhavna (www.portwind.no).

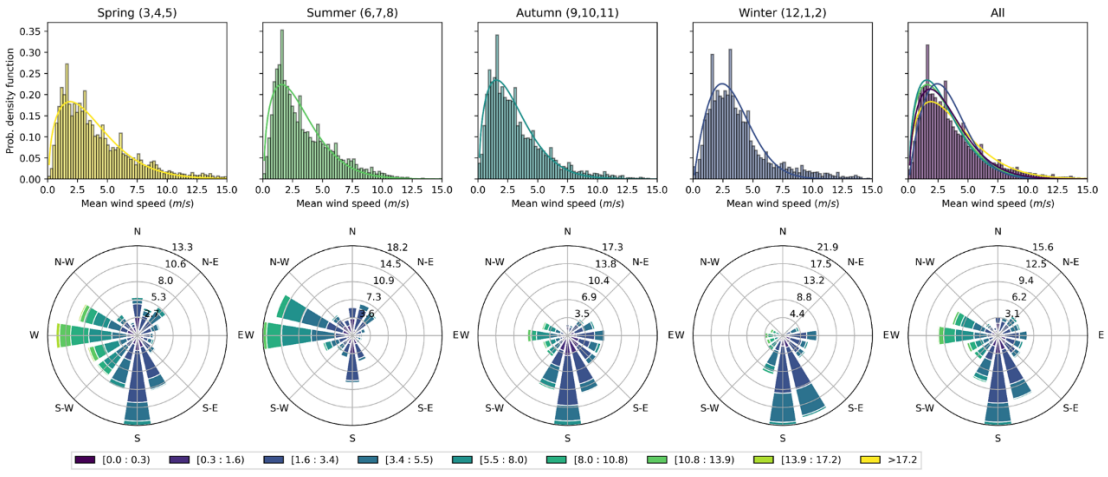


Figure 1. Wind statistics Nyhavna.

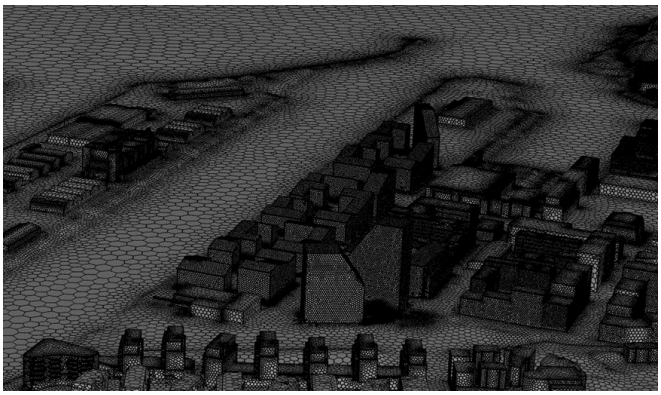


Figure 2. Computational mesh Alternative 2.

3. NUMERICAL METHOD

3D steady-state CFD analyses are used to establish the local wind conditions at Transittkaia at Nyhavna in Trondheim. The simulations are performed with the commercial program ANSYS Fluent and the cloud solution ANSYS Cloud is used for extra computing power. Turbulence modelling is handled with the industry standard SST k-ω model. This is a RANS (Reynolds Averaged Navier-Stokes) model which is based on a time averaging of the Navier-Stokes equations. A circular computational domain consisting of the relevant planning area with existing buildings and terrain/topography has been established at a radius of approx. 1.2 km from the area of interest, so that any shadow and/or amplification effects from surrounding buildings and topography are properly accounted for. To enhance the development of the wind field approaching the area of interest, a log-law velocity profile suitable for urban areas is applied at the inlet boundary combined with a medium turbulence intensity. A zero-pressure condition is utilized at the outlets, including the top horizontal boundary. Simulations at 16 different wind directions are performed for each case, and, finally, the results are combined with the with the wind statistics and relevant comfort criteria as omni-plots. A large degree of automation has been applied in every step from CAD modelling in ANSYS SpaceClaim to model setup in ANSYS Fluent to post-processing in ParaView, which is an open-source data post-processing software (Paraview, 2024). Figure 2 shows an outtake of the computational mesh for Alt. 2 consisting of about 6 million cells. Refinements have been made towards the buildings and terrain, including inflation layers.

4. RESULTS

Examples results are shown in Figure 3 as one LDDC wind comfort map (left) and one figure showing detailed flow patterns (right) for Nyhavna (Alt. 2 only). The wind comfort maps are provided for all directions throughout the year (omni-plot) and the vector plot shows a combination of the three most prominent directions from the west scaled for the most likely wind speed throughout the year equal to 2 m/s, as found from the wind statistics in Figure 1. The present work also includes the extraction of wind comfort and flow details for focus areas such as Doratorget and around specific commercial buildings, but this is not shown here. As the assignment spans several engineering disciplines in-house at OO, the results have also been used to extract wind loads on a selection of the new buildings as input to geotechnics to check the buildings' requirements for resistance against overturning moments.

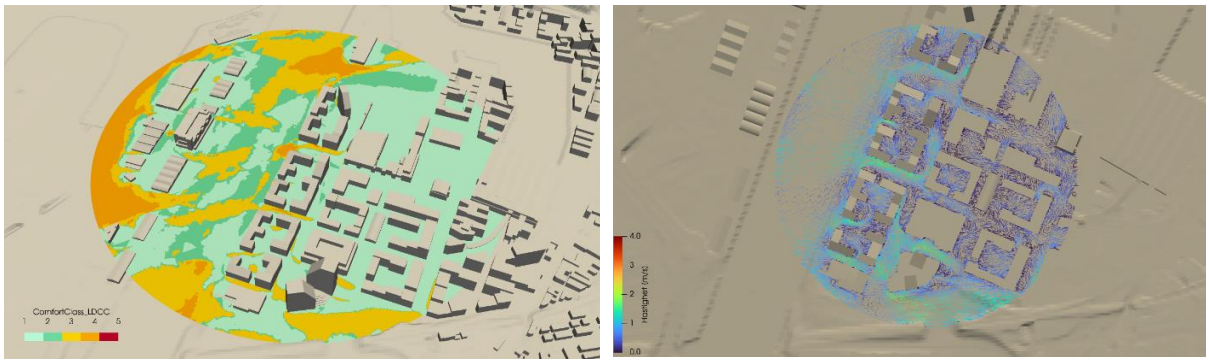


Figure 3. Left: LDDC wind comfort map, right: vector plot for wind from west.

6. CONCLUSIONS AND DISCUSSION

A wind comfort study has been carried out for two different planning proposals as part of the development of Transittkaia at Nyhavna in Trondheim, under the management of the Danish architecture firm Cobe. The results were evaluated against Lawson's criteria, which classify wind conditions into various comfort levels for outdoor spaces. The CFD model combines openly available terrain data, building models received from the architect and local historical wind data. From this wind comfort maps covering the planning area are generated.

The results show that the wind conditions in general at Transittkaia are good at ground level, where most of the planning area is placed in Class 1, but that there are also some areas in Class 2 and 3. Smaller areas indicate Class 4, but this is considered to be of insignificant extent. This means, however, that standing and walking activities are acceptable throughout the area, and mostly sitting (Class 2). In some recreational areas, mitigation measures such as strategic planting are planned to meet the extra strict requirements for wind comfort that are set there (frequent stays and sitting). At Transittkaia it is mainly winds from the west and west-north-west that provide the basis for the highest classes. The wind is strongest from the south, but here the planning area is protected from existing buildings and terrain.

By integrating CFD analysis into urban planning, this research underscores the significance of ensuring optimal outdoor comfort in urban developments, ultimately enhancing the liveability and usability of public spaces in Nyhavna.

ACKNOWLEDGEMENTS

We would like to thank Cobe and Topic for a great collaboration so far, and to Nyhavna Utvikling who has given the winning team this opportunity.

REFERENCES

Davenport, A. G., 1968. The dependence of wind loads on meteorological parameters. Proceedings of Proceedings International Research Seminar “Wind effects on buildings and structures", 11-15 Sept. 1967. Ottawa, Canada, 19–82.

Lawson, T. V. (1978). The wind content of the built environment. Journal of Wind Engineering and Industrial Aerodynamics, 3(2-3), 93-105.

Ayachit, U., The ParaView Guide: A Parallel Visualization Application, Kitware, 2015, ISBN 9781930934306

Characterising the velocity field in the pedestrian zone under the influence of landscaping elements.

Jeremy Sacco[1], Daniel Micallef[1], Sudarshan Babu[1], Simon P. Borg[1], Christopher Micallef[2]

[1]*University of Malta: Department of Environmental Design, Msida, Malta*
[2]*University of Malta: Department of Mechanical Engineering, Msida, Malta*

SUMMARY:
An investigation utilising windtunnel-based PIV and RANS-based CFD to model airflow within the pedestrian zones as influenced by landscaping elements

Keywords: CFD, PIV, pedestrian urban canyon flows

1. INTRODUCTION AND LITERATURE SUMMARY

The characteristics of urban canyons and the airflow patterns that tend to develop in such areas have long been studied and established (Hunter et al., 1990; Oke, 1987). Such flow patterns are of paramount importance for understanding many urban environmental processes such as pedestrian comfort and safety(Blocken, Janssen, et al., 2012), pollutant transport(Abhijith and Gokhale, 2015), building and infrastructure erosion(Tang et al., 2004), etc. This study uses the same idealized geometry approach used by other studies, to investigate the airflow around roadside landscaping elements. Landscaping elements in general are progressively becoming more popular in urban settings for both aesthetic reasons and for secondary functional reasons such as shading, windbreaks, pollution control and crash barriers. These elements will be modelled as solid walls with porous vegetative sections using both a windtunnel setting and a CFD simulation. Focus will be given in particular to the pedestrian zones assumed to be on the sides between the elements and the walls. Multiple cases are explored with varying features like vegetation volume and segmentation while also comparing them to an empty canyon case.

2. METHODOLOGY AND TEST CASES

The setup for the investigation comes in two parts: the CFD simulation and the windtunnel testing. The CFD simulations were set up to run a steadystate RANS simulation using a SST $k-\omega$ turbulence model in OpenFOAM(Weller et al., 1998) . The mesh geometries were constructed to resemble the windtunnel test section with some run-up and hind length for the flow to develop and exit with minimal interference. Force source terms modelling a plant canopy with drag coefficient $C_D = 0.2$ and Leaf Area Density $LAD = 4.731$ /m were applied to regions where vegetative elements would be. These values are dynamically similar to sparse shrubs which are $C_D = 0.2$ and $LAD = 0.333$/m (Buccolieri et al., 2018; Santiago et al., 2017). On the other hand, the windtunnel

facilities available in the Fluids Laboratory at the Department of Mechanical Engineering at the University of Malta has a square test section of sides 15" (0.381 m) and a flow-wise length of 23" (0.5842 m) that permits a maximum freestream flow velocity of 30 m/s. To circumvent the resolution loss of having to build such a small model for investigation as would be required for dynamic similarity, the windtunnel itself was modified to have a box protruding from the test section such that the tunnel itself forms the canyon geometry. The resulting canyon has a square aspect ratio with sides 23" (0.5842 m), a streetwise length of 15" (0.381 m) and a newly measured freestream velocity of 28.65 m/s. The landscaping element models were constructed of different blocks of dimensions $0.035 \times 0.035 \times 0.126$ m which is intended to be dynamically similar to $0.5 \times 0.5 \times 1.79$ m. Nylon rigged frames were used to approximate the vegetative element, having $C_D \approx 0.2$ and $LAD \approx 4.731$ /m as shown in Figure 1. The flow imaging was done using Stereo Particle Image Velocimetry (SPIV) with the imaging regions being the leeward and windward pedestrian zones.

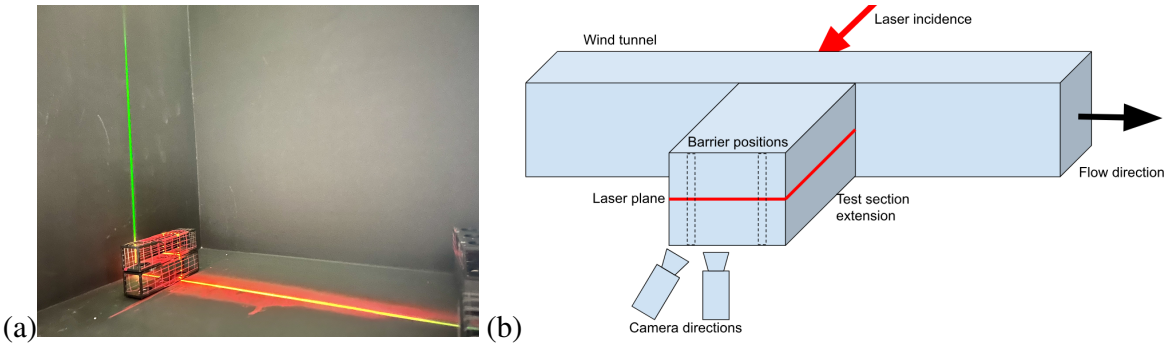


Figure 1. The model of the barrier placed in the wind tunnel as in the experiments. **(a)** The laser showing the field-of-view plane of the PIV setup. **(b)** A simplified illustration of the windtunnel setup showing the protruded test section extension, the cameras capturing the canyon flow from below and the laser plane intersecting the canyon and the models cross-sectionally (0.29 m above the base of the test section).

The cases tested were designed to represent an empty canyon (case 0), continuous landscaping elements that are one a solid base with vegetation on top (case 1), and an all vegetation variant that is segmented rather than continuous (case 2). The summary of the exact dimensions of the elements used is given in Table 1 whereas Figure 2(a) shows the segmentation configuration of the landscaping elements. The PIV images for each case were constructed as the ensemble flow field of 130 instantaneous PIV images to obtain a picture that better corresponds to the result computed by the steadystate RANS simulations. The comparison between the CFD and SPIV was made based on contour plots of the test-sections and the probe lines as indicated in Figure 2 (b).

Table 1. A table detailing all the cases tested along with their configurations denoted in terms of number of blocks being stacked. The "Segmentation" column denotes what is described in Figure 2

Case Number	Solid Height (mm)	Porous Height (mm)	Segmentation (blocks)	
0	0	0	0	Empty case
1	35	35	3	Continuous solid + vegetation
2	0	70	2	Segmented vegetation

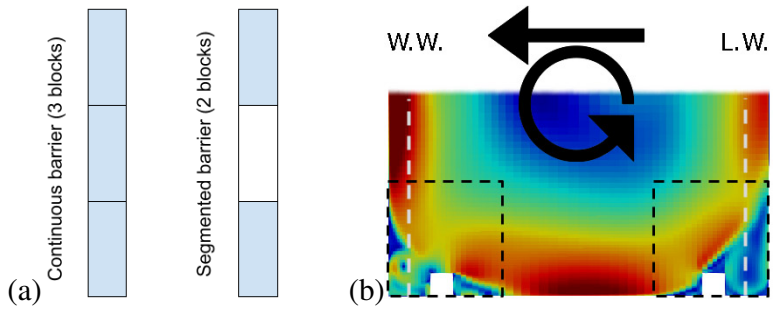


Figure 2. (a) a top view explaining the segmentation configurations of the landscaping element setups. The number of blocks used in the setup of each case is outlined in the "Segmentation" column in Table 1. **(b)** An example contour plot of the velocity magnitude from the simulation of case 1 at a cross-section equivalent to that of the laser plane in the windtunnel. The arrows above the contour indicate the freestream direction and the circulation within the canyon. The white vertical broken lines are indications of where the the probe lines are located for comparison with the PIV contour and the black broken lines show the window of the PIV test section.

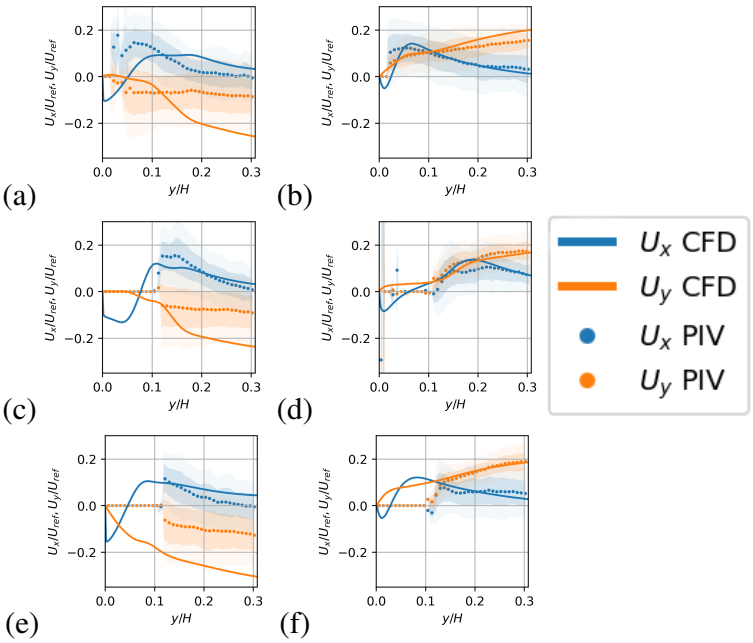


Figure 3. The contour plots for the probe lines showing the normalised U_x/U_{ref} and U_y/U_{ref} components for the PIV measurements (scatter) and the CFD simulation (line) along the normalised height. H and U_{ref} are the canyon height and the freestream velocity respectively. The **a,c,e** plots are the windward probes and the **b,d,f** are the leeward plots, with the rows from top down being case 0, case 1 and case 2 respectively. The 0 velocity region at low y/H is due to the parallax obstruction of the landscaping element. The error bands are the standard deviations of the PIV data.

3. RESULTS

Figure 3 compares the U_x and U_y components and shows there are reasonable agreements between all the cases with the exception of the windward y-component as seen from the probe-line plots in Figure 3. This systematic discrepancy is a consequence of the windtunnel's divergent inlet resulting in more ram air hitting the windward side of the canyon rather than traversing smoothly along the freestream. It can be noted that the maximum x-velocity shifts to a higher height as a direct result of the solid part in case 1 acting like a baffle while being a more subtle effect on the all-

vegetation, segmented construction of case 2. Focusing on the contour plots shown in Figure 4, it is clear that the leeward side experiences decreased 2D velocity magnitude within the pedestrian zone while the windward side experiences increased velocities. As would be expected, solid segments induce more defined secondary vortices within the pedestrian zones while vegetative elements induce a turbulent wake. The leeward side also experiences an amplified effect since the incident airflow would have already been influenced by the structure on the windward side. While being more subtle, the segmented vegetation barrier promoted a turbulent wake behind it with lower velocities. Results can be seen under different perspectives. Considering pedestrian comfort as a starting point using accepted criteria such as the Lawson criteria, the wind speeds formed would be dynamically similar to very comfortable for both walking and sitting. Turbulence intensity, while being above the 20% criterion within the regions of interest(Blocken, Stathopoulos, et al., 2016), the flow velocity causing it isn't enough to make turbulence effects noticeable. The vegetation barrier being segmented also has the feature of providing gaps where the pedestrians can access the street with greater convenience which come as a trade off from more consistent wind comfort benefits. Further cases will be investigated in order to look for further features that will both generalise aspects of landscaping elements and to find more promising options available.

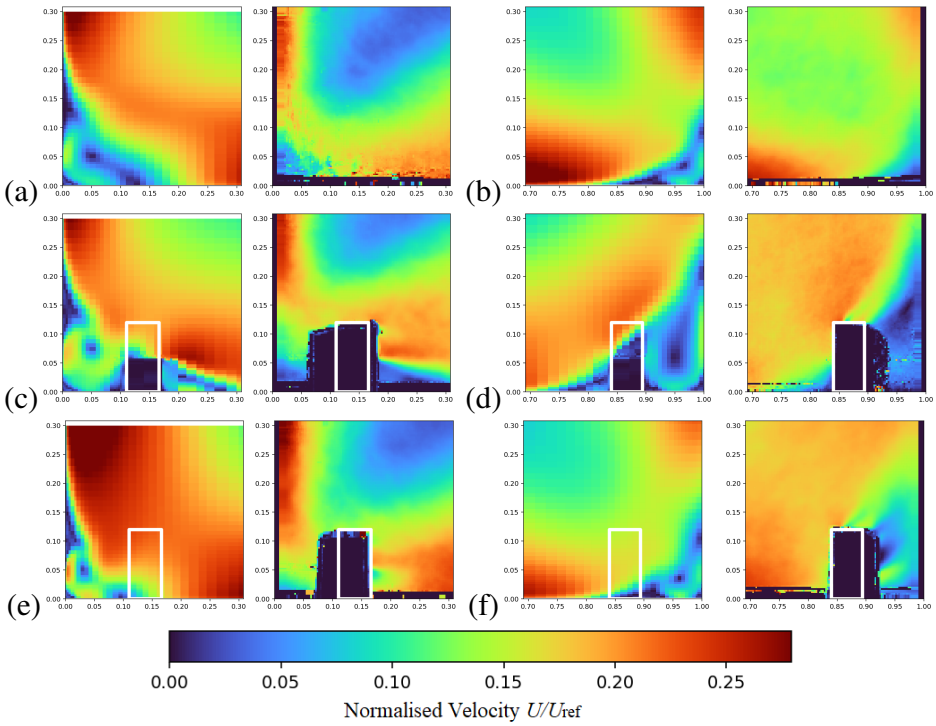


Figure 4. The resulting contour plots comparing the CFD and the PIV data. **a,c,e** are the windward contours and **b,d,f** are the leeward contours. From top to bottom the rows are case 0, case 1 and case 2. Each image has the CFD result on the left and the PIV result on the right. The vertical and horizontal axes are the normalised coordinates y/H and x/H. H and U_{ref} are the canyon height and the freestream velocity respectively.

4. DISCUSSION AND CONCLUSION

The following main conclusions can be drawn from this study:

- Landscaping elements effect airflow patterns differently with solid elements causing flow accelerations over the barrier
- Airflow velocities increase on the windward side and decrease on the leeward side, particularly within pedestrian zones. This underscores the need for urban planners to consider different landscaping elements on both leeward and windward sides.
- The solid part of the landscaping element induces more defined secondary vortices, affecting pedestrian comfort. Vegetative elements, meanwhile, create a turbulent wake that may have important implications to air quality in pedestrian zones.

REFERENCES

Abhijith, K. and Gokhale, S., 2015. Passive control potentials of trees and on-street parked cars in reduction of air pollution exposure in urban street canyons. Environmental Pollution 204, 99–108.

Blocken, B., Janssen, W., and van Hooff, T., 2012. CFD simulation for pedestrian wind comfort and wind safety in urban areas: General decision framework and case study for the Eindhoven University campus. Environmental Modelling and Software 30, 15–34.

Blocken, B., Stathopoulos, T., and van Beeck, J., 2016. Pedestrian-level wind conditions around buildings: Review of wind-tunnel and CFD techniques and their accuracy for wind comfort assessment. Building and Environment 100, 50–81.

Buccolieri, R., Santiago, J.-L., Rivas, E., and Sanchez, B., 2018. Review on urban tree modelling in CFD simulations: Aerodynamic, deposition and thermal effects. Urban Forestry and Urban Greening 31, 212–220.

Hunter, L., Watson, I., and Johnson, G., 1990. Modelling air flow regimes in urban canyons. Energy and Buildings 15, 315–324.

Oke, T., 1987. Boundary Layer Climates. Routledge.

Santiago, J.-L., Martilli, A., and Martin, F., Mar. 2017. On Dry Deposition Modelling of Atmospheric Pollutants on Vegetation at the Microscale: Application to the Impact of Street Vegetation on Air Quality. Boundary-Layer Meteorology 162, 451–474.

Tang, W., Davidson, C. I., Finger, S., and Vance, K., 2004. Erosion of limestone building surfaces caused by wind-driven rain: 1. Field measurements. Atmospheric Environment 38, 5589–5599.

Weller, H., Tabor, G., Jasak, H., and Fureby, C., Nov. 1998. A Tensorial Approach to Computational Continuum Mechanics Using Object Orientated Techniques. Computers in Physics 12, 620–631.

POD study of Bristol CFD simulations with different levels of detail

Álvaro Manzano Sevillano[1], Clara García-Sánchez[2], Soledad Le Clainche Martínez[3], Dani Fernández Comesaña[4]

[1]*Universidad Politécnica de Madrid, Arnhem, Netherlands, alvaro.manzano@alumnos.upm.es*
[2]*TU Delft, Delft, Netherlands, C.Garcia-Sanchez@tudelft.nl*
[3]*Universidad Politécnica de Madrid, Madrid, Spain, soledad.leclainche@upm.es*
[4]*Microflown Technologies, Arnhem, Netherlands, fernandez@microflown.com*

SUMMARY:
A multi-LOD RANS study of Bristol containing an urban circular area of 500m of radius with a marked unequal terrain has been performed. A total of 3 cases, with LOD 1.2, 1.3 and 2.2 buildings, have been simulated with OpenFOAM and posteriorly a POD study will be applied to understand the consistency of the modes.

Keywords: Urban CFD, Bristol, POD

1. MOTIVATIONS

Computational fluid dynamics (CFD) microscale modelling of urban areas has been studied in the literature for different configurations, ranging from ideal to realistic geometries, and with or without validation (Toparlar et al., 2017). As the trend of increasing data availability continues, in the present the same reality can be represented with different realistic models, underlining the need for consequent studies on the possibilities.

Level of detail has been increasingly regarded in literature as an important geometry classifying factor given the impact it can have in calculations. LOD categories can vary (Biljecki et al., 2016), but the detail in elements such as facades and roof shape remains a decisive factor for buildings in urban CFD studies (García-Sánchez et al., 2021); with additional elements such as trees starting also to be considered (Fu et al., 2024).

Even if LOD is confirmed to be a factor in urban studies, established pattern extracting techniques such as proper-orthogonal decomposition (POD) have only been used in urban settings for simple two-block buildings (Lazpita et al., 2022) (Martinez-Sanchez et al., 2023) and in big areas (Liu et al., 2023), not for different LODs studies or much less in big areas.

The city of Bristol has been chosen for its particular terrain distribution, with numerous elevated areas 50m high surrounding the urban area. The distribution of the terrain is especially complicated as the highest building of 98m, according to COST 732 guidelines (Franke et al., 2011), requires a surrounding buffer length 15 times that height in a circular geometry, causing the need to include an area close to the boundary in which are both the highest terrain area and a valley.

2. METHODS

Geometry reconstruction of the circular 500m radius urban region was performed using an automated tool called City4CFD (Pađen et al., 2022), and using as input vector (Ordnance Survey, 2023) (Ordnance Survey, 2024) and point cloud (Environment Agency, 2019) UK public data.

Automatic reconstruction tools has facilitated the annexion of hundreds of buildings to the uneven terrain would require a significant amount of time. Thanks to the CFD purpose of the tool not only the resulting domain of 1830m of radius and 740m of height contains a 500m of radius urban area, but it also has patches to set different vegetation and water aerodynamic roughness.

As the public information contained the heights and areas of terrain, buildings. and vegetation and water areas; but it wasn't accurate enough or missed a small number of high buildings, some features as towers were added manually to better caracterize the geometry.

The resulting geometries were then meshed with OpenFOAM's snappyHexMesh tool and a mesh study was performed afterwards with a second order scheme with simpleFoam solver.

3. PRELIMINARY RESULTS

Preliminary results consist in the reconstruction of the urban area of Bristol and its terrain, containing patches for the vegetation and water as can be seen in Fig. 1 and Fig. 2; as well as a potential 140 million cells mesh in Fig. 3 and Fig. 4 with refinement close to the surfaces.

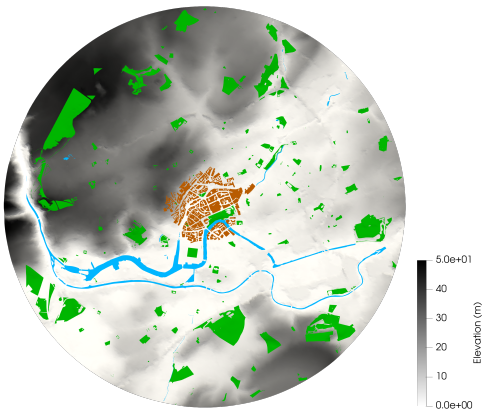


Figure 1. Vertical view of Bristol domain, with the valley and highest area in the west side. © Environment Agency copyright and/or database right 2019. All rights reserved.

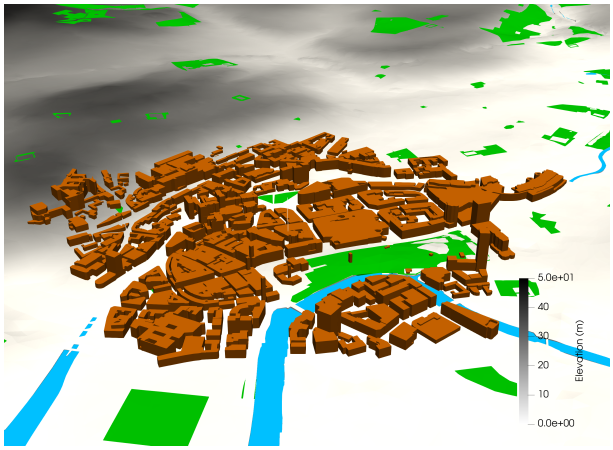


Figure 2. Resulting LOD 1.3 geometry of Bristol containing the highest building and the city center. © Environment Agency copyright and/or database right 2019. All rights reserved.

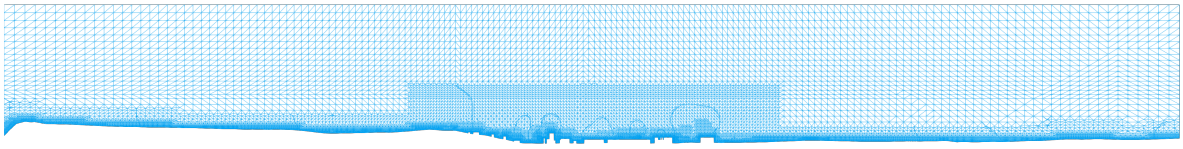


Figure 3. Mesh generated with snappyHexMesh © Environment Agency copyright and/or database right 2019. All rights reserved.

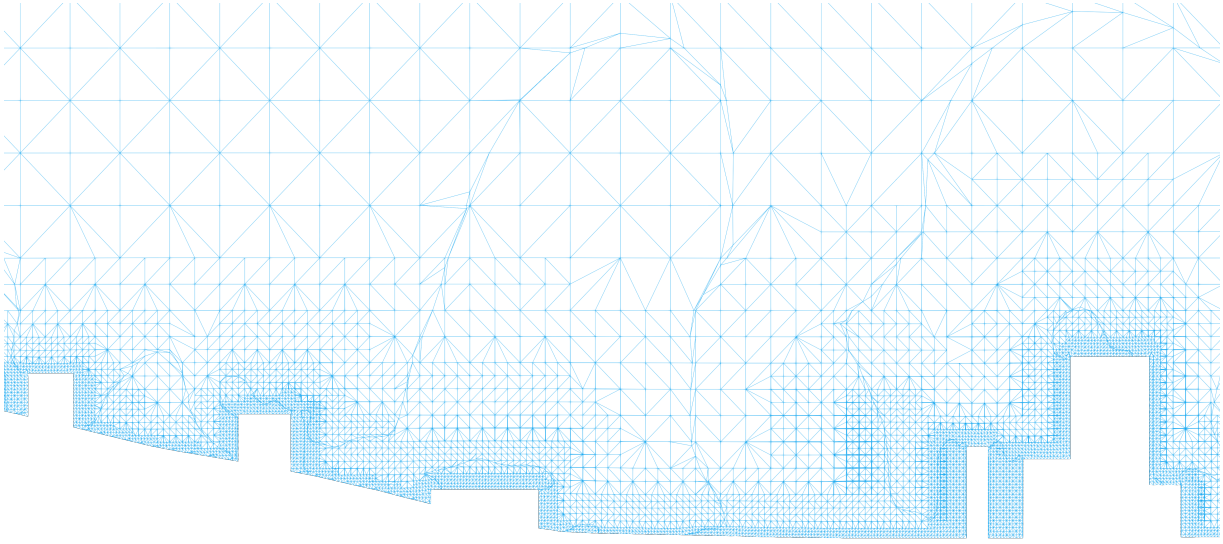


Figure 4. Mesh generated with snappyHexMesh © Environment Agency copyright and/or database right 2019. All rights reserved.

4. CONCLUSIONS AND FUTURE WORK

Bristol geometry was reconstructed using public vector and point cloud data, resulting in a domain characterized by its terrain height difference and an urban nucleus with 500m of radius.

The automatic method employed, City4CFD, facilites the automated reconstruction of 3 different building LODs from the same input data, allowing a posterior CFD simulation and comparison using OpenFOAM.

Finally, the POD method will be applied on the different geometries, each consisting on a different building LOD, due to its potential capabilities to analyze the flow.

ACKNOWLEDGEMENTS

This project has received funding from the European Union's Horizon Europe research and innovation programme under grant agreement No 101072559.

The authors gratefully acknowledge the Universidad Politécnica de Madrid (www.upm.es) for providing computing resources on Magerit Supercomputer.

Contains OS data © Crown copyright [OS OpenData] [2024].

Contains OS data © Crown copyright [OS Open Greenspace] [2024].

© Environment Agency copyright and/or database right 2019. All rights reserved.

REFERENCES

Biljecki, F., Ledoux, H., and J., S., 2016. An improved LOD specification for 3D building models. Computers, Environment and Urban Systems 59, 25–37.

Environment Agency, 2019. *LIDAR Time Stamped Point Cloud*. Retrieved 2023-05-01, Open Government Licence v3.0.

Franke, J., Hellsten, A., Schlünzen, H., and Carissimo, B., 2011. The COST 732 Best Practice Guideline for CFD simulation of flows in the urban environment: A summary. International Journal of Environment and Pollution (IJEP) 44 (1-4), 419–427.

Fu, R., Pađen, I., and García-Sánchez, C., Feb. 2024. Should we care about the level of detail in trees when running urban microscale simulations? Sustainable Cities and Society 101, 105143.

García-Sánchez, C., S., V., I., P., and J., S., 2021. The impact of level of detail in 3D city models for CFD-based wind flow simulations. The International Archives of the Photogrammetry, Remote Sensing and Spatial Information Sciences XLVI-4/W4-2021, 67–72.

Lazpita, E., Martínez-Sánchez, A., Corrochano, A., Hoyas, S., Le Clainche, S., and Vinuesa, R., May 2022. On the generation and destruction mechanisms of arch vortices in urban fluid flows. Physics of Fluids 34 (5).

Liu, Y., Liu, C. H., G.P., B., and Chao, C. Y. H., Feb. 2023. Proper orthogonal decomposition of large-eddy simulation data over real urban morphology. Sustainable Cities and Society (SCS) 89.

Martinez-Sanchez, A., Lazpita, E., Corrochano, A., Le Clainche, S., Hoyas, S., and Vinuesa, R., Apr. 2023. Data-driven assessment of arch vortices in simplified urban flows. International Journal of Heat and Fluid Flow 100, 109101.

Ordnance Survey, 2023. *OS OpenMap – Local*. Retrieved 2023-05-01, Open Government Licence v3.0.

— 2024. *OS Open Greenspace*. Retrieved 2023-05-01, Open Government Licence v3.0.

Pađen, I., García-Sánchez, C., and H., L., Aug. 2022. Towards automatic reconstruction of 3D city models tailored for urban flow simulations. Frontiers in Built Environment 8.

Toparlar, Y., B., B., Maiheu, B., and Van Heijst, G. J. F., 2017. A review on the CFD analysis of urban microclimate. Renewable and Sustainable Energy Reviews 80, 1613–1640.

Method for Visualizing Wind Corridors Using Persistent Homology

Yuta Honda [1], Shumpei Fujii [2], Tsubasa Okaze [3]

[1]*Institute of Science Tokyo, Yokohama, Japan, honda.y.5138@m.isct.ac.jp*
[2]*Obayashi Corporation, Japan, shun.skua@gmail.com*
[3]*Institute of Science Tokyo, Yokohama, Japan, okaze.t.f356@m.isct.ac.jp*

SUMMARY:
This study proposes a method for visualizing wind corridors by applying persistent homology (PH) to analyze three-dimensional (3D) flow-field data within urban areas. The approach consists of three key steps: 1) The 3D wind speed ratio, which compares local wind speed to its surrounding context, is calculated using two different space filters applied to wind speed data derived from a computational fluid dynamics (CFD) simulation for urban areas. 2) PH is then applied to the 3D wind speed ratio to generate a two-dimensional persistence diagram (PD), providing insights into the characteristics of regions with high wind velocity within the flow field. 3) Finally, regions with long lifetimes in the PD are visualized as wind corridors. In the proposed method, we assumed that the high wind speed ratio regions corresponded to the regions in which the wind flowed smoothly. In addition, we applied the proposed method to a CFD simulation focusing on the waterfront area of Tokyo.

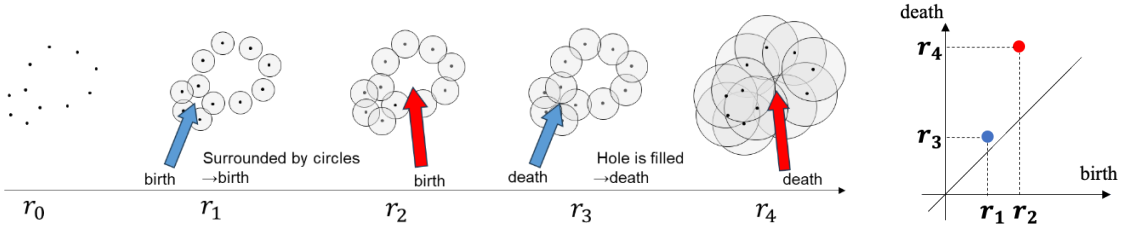
Key Words: Wind corridor, Persistent homology, Persistence diagram

1. INTRODUCTION

The concept of the “wind corridor” has attracted attention in many cities since its introduction in the urban planning of Stuttgart, Germany, around 1990. It was first proposed as a strategy to channel cold air drainage from mountainous slopes into the city center of Stuttgart to mitigate air pollution (Klimaatlas Region Stuttgart, 2008). In Germany, a climate atlas called “Klimaatlas” was developed to reduce thermal stress in summer and air pollution in winter (VDI, 1997; Mayer et al., 1994). Several major cities facing the ocean have introduced sea breezes to mitigate the heat island effect. Wind corridors are qualitatively interpreted as spatially continuous open spaces. However, the methodology for visualizing the morphology of these corridors depends on the guidelines and recommendations of the city, and no universally accepted quantitative method has yet been established. Persistent homology (PH) (Zomorodian et al., 2024) is classified as a topological data analysis method and excels at describing data structures. It has been used in diverse applications, such as the structural analysis in materials science (Hong et al., 2019) and the identification and tracking of low-pressure systems (Inatsu et al., 2017). PH has been widely applied to visualize characteristic structures in complex datasets. In this study, we propose a novel method for visualizing wind corridors by applying PH to a three-dimensional (3D) flow field within urban areas using computational fluid dynamics (CFD). We further demonstrate the applicability of this approach by presenting a case study involving the coastal area of Tokyo. The results illustrate the potential of PH as a tool for quantitatively and systematically analyzing urban wind corridors.

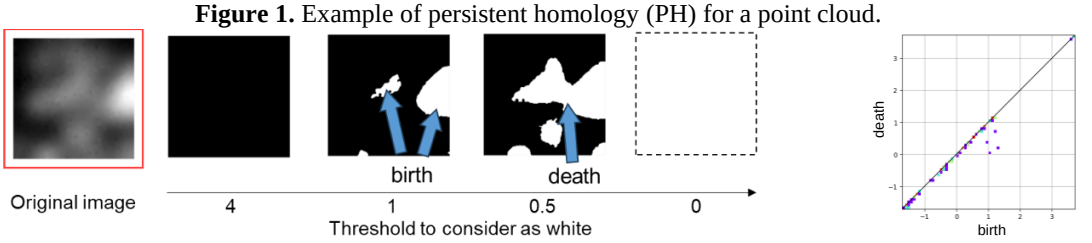
2. OVERVIEW OF PERSISTENT HOMOLOGY

PH is a relatively novel mathematical method that allows for the quantitative investigation of the shape and size of "data" by focusing on the "holes" within it and effectively capturing multiscale topological features. Figure 1 illustrates an example of the application of PH to a point cloud. The radius of the circle centered at each point gradually increases via filtration. The appearance and disappearance of holes enclosed by circles are then recorded using the radius. In Figure 1, holes appear at radii r_1 and r_2 and disappear at r_3 and r_4. A persistence diagram (PD) is a scatter plot in which the radius of the circle at the time the hole is created is plotted on the horizontal axis as the birth time, and the radius at the time the hole disappears is plotted on the vertical axis as the death time. Here, the difference between the two times (death time - birth time) is called the lifetime. Longer lifetimes tend to represent larger data structures. The red point (r_2, r_4) in Figure 1(2) is farther from the diagonal and has a longer lifetime than the blue point (r_1, r_3), indicating a larger "hole" in the structure. In this study, we applied the concept of PH to data with continuous signal values, as discussed by Obayashi et al. (2022), in a 3D flow field. Figure 2 depicts an example of PH applied to continuous grayscale values in a two-dimensional pixel image. By incrementally changing the threshold value considered as "white" in the grayscale image, a PD is constructed to quantitatively analyze the structural features of data. In this approach, the threshold at which white regions first emerge represents the "birth time," whereas the threshold at which these regions merge denotes the "death time." In the PD shown in Figure 2(2), the point located toward the lower right indicates a longer lifetime, similar to the PH for the point cloud, corresponding to a larger-scale structure in the image.



(1) Filtration (2) Persistence diagram

Figure 1. Example of persistent homology (PH) for a point cloud.



(1) Filtration (2) Persistence diagram

Figure 2. Example of PH for a grayscale two-dimensional image

3. CFD SIMULATION

A CFD simulation was performed to obtain a detailed 3D flow field within an urban environment. Shinagawa District, a coastal area in Tokyo characterized by a high density of high-rise buildings, was selected as the study area (Figure 3). The size of the calculation domain was set to 4200 × 5600 × 600 m. The urban morphology was reproduced utilizing Project PLATEAU data provided by the Ministry of Land, Infrastructure, Transport and Tourism of Japan. The building geometries

were simplified by arranging them in a 10-meter cubic grid, as illustrated in Figure 3(3). The calculation domain was discretized using a polyhedral mesh. The minimum mesh size near the buildings was 2 m, while the maximum mesh size was set to 8 m, with an expansion ratio of 1.1. The total number of meshes was 4.25 million. A steady-state simulation using the Reynolds-Averaged Navier–Stokes (RANS) equation model was conducted using OpenFOAM-v2006 (OpenFOAM). The standard k-ε model was applied as the turbulence model. A second-order upwind scheme was used to discretize the convection terms. The mean wind velocity profile at the inflow boundary obeyed the power law with an index of 0.27. To reproduce the sea breeze from Tokyo Bay during the summer, the wind direction and speed were set to SES and 5.1 m/s, respectively, at 44 m at the inflow boundary, as suggested by the Tokyo Metropolitan Government (TMG) in the "Guidelines for Promoting Environmentally Friendly Urban Development around Shinagawa and Tamachi Stations."

Figure 4 shows the horizontal mean wind velocity 50 m above the ground using CFD. Wake regions behind high-rise buildings appeared in the area between the Shinagawa and Tamachi Stations. On the west side of Shinagawa Station, regions of high wind speeds greater than 5.0 m/s, extending downstream, are illustrated. A relatively large open space can also be found roughly halfway between Shinagawa and Tamachi stations. Figure 5 shows the wind corridors drawn by TMG in the guidelines. According to the guidelines, the wind corridors were primarily defined based on the criterion that "A relatively large and unified region with mean wind speeds at 50 m high of approximately 4.0 m/s or higher extending downwind." However, it is difficult to quantitatively consider how large and unified regions are and their applicability to other cities for specific conditions of a threshold wind speed of 4.0 m/s and an evaluation height of 50 m. Therefore, we applied a novel PH-based method to 3D CFD data to visualize wind corridors.

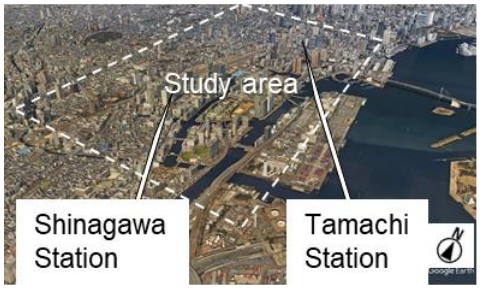


Figure 3. Bird's-eye view of study area.

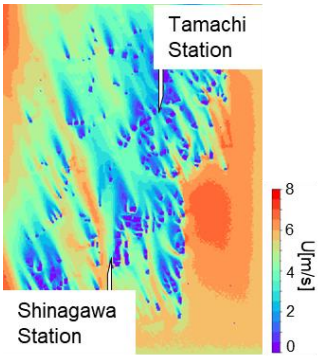


Figure 4. Wind speed distribution at a height of 50 m above the ground.

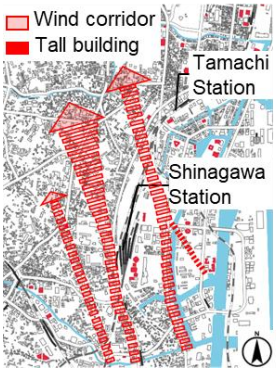


Figure 5. Wind corridors drawn by the TMG.

4. VISUALIZATION OF WIND CORRIDORS USING PERSISTENT HOMOLOGY

Wind corridors are essentially corridors which winds flow. The corridors are considered to be continuous regions where the wind speed is not smaller than the wind speed of the surroundings. To express this quantitatively, we first introduced the ratio of the wind speed near the evaluation point to the spatially averaged wind speed of the surroundings. Two different spatial filter sizes were utilized: a local filter, which is a narrower-space filter used to calculate the local average wind speed near the evaluation point, and a global filter, which is a wider-space filter used to calculate the average wind speed of the surroundings. To perform spatial filtering, the CFD results obtained in the previous section were interpolated on grid points at 5-meter intervals. Figure 6

shows a PD with a global filter of 400 × 400 × 10 m and a local filter of 200 × 200 × 10 m. Structures with a long lifetime between death times of approximately 1.0 and 1.2 were analyzed. Figure 7 illustrates the visualized structures of long lifetime (lifetime > 0.45) points shown in Figure 6. The two large long structures expanded more than 2000 m along the wind direction around Shinagawa Station, visualized with the PH in this study, and roughly corresponded to the wind corridors drawn by the TMG shown in Figure 5. Additionally, large structures over Tamachi Station, which did not appear in the TMG map, were visualized.

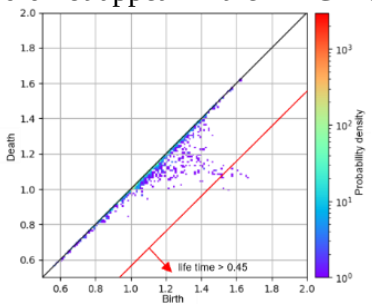


Figure 6. Persistence diagram (PD) with global and local filters (400 × 400 × 10 m and 200 × 200 × 10 m, respectively).

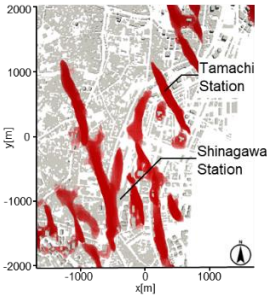


Figure 7. Visualized structure (lifetime ＞ 0.45).

5. CONCLUSIONS

We proposed a wind corridor visualization method that applies PH to the wind speed ratio and applied it to the CFD analysis results for a coastal area in central Tokyo. In addition, the larger structures with peak lifetimes in the PD appeared in the region where the death time, a value corresponding to the wind speed ratio, was approximately 1.0–1.2. This feature may be closely related to the spatial structure of the wind corridor, and it can be inferred to be related to the structure of wind corridors in other cities, although further investigation of the relationship between global and local filter sizes and visualized structure scales is needed. In the future, we plan to study its applicability to various urban morphologies.

REFERENCES

Klimaatlas Region Stuttgart (2008) https://www.stadtklima-stuttgart.de/index.php?klima_klimaatlas_region

VDI. 1997, VDI-Guideline 3787, Part 1, Environmental Meteorology-Climate and Air Pollution Maps for Cities and Regions, VDI, Berlin.

Zomorodian, A, Carlsson, G., 8 June 2024. Computing persistent homology. SCG '04: Proceedings of the twentieth annual symposium on Computational geometry, 347-356

Mayer, H., Beckröge, W. u. Matzarakis, A., 1994: Bestimmung von stadtklimarelevanten Luftleitbahnen, UVP-report 5/94, S. 265-268.

Hong, S, Kim, D., 19 August 2019. Medium-range order in amorphous ices revealed by persistent homology. Journal of Physics: Condensed Matter, Volume 31, Number 45,

Inatsu, M, Kato, H, Katsuyama, Y, Hiraoka, Y, Obayashi, I., A Cyclone Identification Algorithm with Persistent Homology and Merge-Tree. Sci Online Lett Atmos. 2017; 13:214-218. doi:10.2151/sola.2017-039

Tokyo Metropolitan Government: Guidelines for Promoting Environmentally Friendly Urban Development around Shinagawa and Tamachi Stations, https://www.toshiseibi.metro.tokyo.lg.jp/seisaku/guideline2020/index.html, Accessed: May 27, 2024 (In Japanese)

Obayashi, I, Nakamura, T, Hiraoka, Y., 2022 Persistent Homology Analysis for Materials Research and Persistent Homology Software: HomCloud. J. Phys. Soc. Jpn. 91

OpenFOAM, https://www.openfoam.com/ Accessed: November 29, 2024

Ministry of Land, Infrastructure, Transport and Tourism of Japan, https://www.mlit.go.jp/plateau/ Accessed: November 29, 2024 (In Japanese)

Windbreak effects of Igune as traditional homestead trees in a clustered settlement at Osaki Koudo, Japan

Kento Minami [1], Eito Mizuta [2], Chinatsu Yonezawa [3], Tsubasa Okaze [4]

[1]*Shinshu University, Nagano, Japan, minami@shinshu-u.ac.jp*
[2]*Institute of Science Tokyo, Yokohama, Japan, mizuta.e.26db@m.isct.ac.jp*
[3]*Tohoku University, Sendai, Japan, chinatsu.yonezawa.e7@tohoku.ac.jp*
[4]*Institute of Science Tokyo, Yokohama, Japan, okaze.t.f356@m.isct.ac.jp*

SUMMARY:
Traditional homestead trees, maintained as groups of trees with diverse functions, play a critical role in protecting residential areas from environmental conditions such as strong winds and solar radiation. This study used large-eddy simulations (LESs) to assess the windbreak effects of Igune and its flow field characteristics, focusing on a clustered settlement in Osaki Koudo, Miyagi Prefecture, Japan. The simulations compared two scenarios: one from 2010, before the cutting of Igune, and another from 2020, after part of Igune had been cut down. LES results revealed that multiple rows of Igune, arranged perpendicularly to the prevailing wind direction, formed an extensive low wind speed zone within the settlement. This configuration reduced the mean wind speed by approximately half throughout the settlement and by up to one-third on the downwind side. Despite the reduction in the number of trees, the spacing between the remaining Igune is sufficient to sustain the windbreak effect, comparable to that observed in 2010.

Keywords: Large-eddy simulation, Homestead trees, Windbreak effects

1. INTRODUCTION

Traditional homestead trees, which are groups of trees, have been maintained with various functions to protect residential areas from adverse environmental conditions, such as strong wind and solar radiation. In Osaki Koudo, located in northern Miyagi Prefecture, Japan (Fig. 1(1)), tree clusters, known as Igune, still exist in approximately 40% of local households. We recently conducted field observations and large-eddy simulations (LESs) in a scattered settlement area (Fig. 1 (2)) to analyze their windbreak effects (Minami et al., 2022a). Osaki Koudo also features clustered settlements (Fig. 1 (3)), where Igune are arranged in multiple rows perpendicular to the



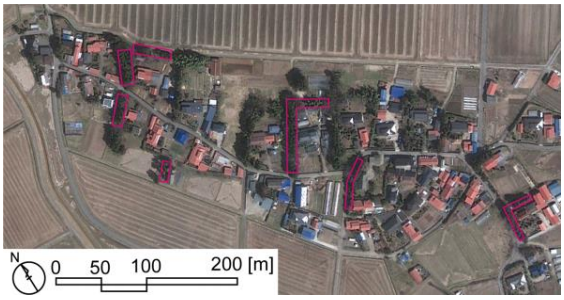
(1) Location of Osaki Koudo. (2) Scattered settlement. (3) Clustered settlement.

Figure 1. Outline of Osaki Koudo and Igune.

prevailing wind direction. To preserve Igune as shared resource within these clustered settlements, it is essential to clarify the combined and widespread effects of wind speed reduction provided by the Igune rows. This study quantified the windbreak effects of Igune in clustered settlements using LESs. Conditions from 2010, before Igune was partially cut down, and from 2022, after several trees in part of Igune were cut down, were simulated.

2. CHARACTERISTICS OF IGUNE ON THE SUBJECT SITE

The subject site, selected by the Osaki City office, represents an area where well-maintained Igune have remained within the settlement. The settlement's length extends approximately 550 m, and as of March 2024, 140 people lived in 42 households. Although parts of Igune, primarily tall trees, have been cut down in certain areas, many Igune still exist on the west-northwest side, which is the prevailing wind direction during winter. Each residential site measures approximately 50–70 m, with Igune planted along the northern and western boundaries. Thus, this layout forms multiple rows of Igune perpendicular to the prevailing wind direction in the settlement (Fig. 2). Traditionally, Igune consists of shrubs and tall trees, with Bambuseae (shrubs) and Cryptomeria japonica (tall trees) being the most commonly used species (Fig. 3). The height of the shrubs and tall trees ranges from 9–16 m, whereas the height of the shrubs alone ranges from 3–6 m. As shown in Fig. 2, several trees within the settlement were cut down by 2022.



Google Earth. Image © 2024 Maxar Technologies

Figure 2. Aerial view as of April 2010.
(Red enclosures represent trees cut down by 2022.)



Figure 3. Comparison of Igune.

3. INVESITGATION OF WINDBREAK EFFECTS OF IGUNE USING LES

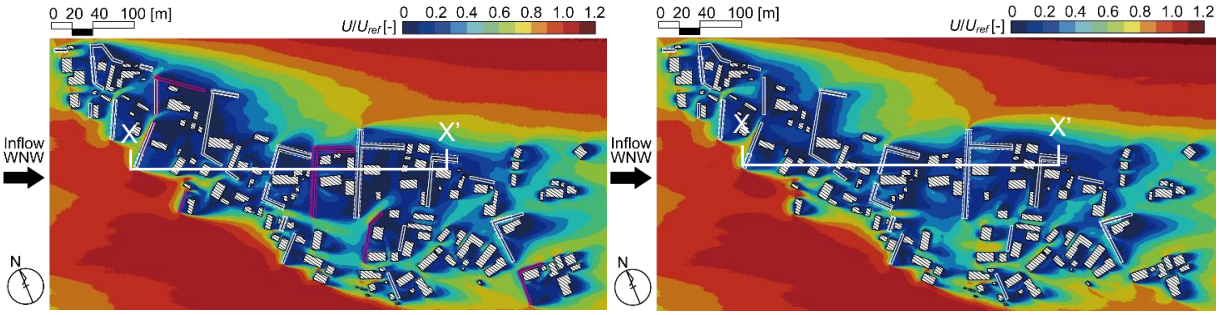
3.1. Numerical settings

The open-source computational fluid dynamics (CFD) code, OpenFOAM-v2006 (ESI Group, 2023), was used for the LESs. Two simulations were performed: one replicating the current distribution of Igune as of December 2022 and the other simulating the previous situation as of April 2010, before trees were cut down. The shapes of the houses and Igune in 2022 were reproduced using a 3D-CAD constructed from a digital surface model and derived from unmanned aerial vehicle photographs of 723 locations on December 12, 2022. In 2010, in addition to the houses and Igune in 2022, shrubs and tall trees were added by confirming their top view in an aerial photograph from Google Earth Pro. The heights of the added shrubs and tall trees were set to the same height as that of the adjacent Igune in 2022. The computational domain was 400 m × 950 m × 100 m. The total mesh number was approximately 4.2 million with polyhedral meshes. The standard Smagorinsky model (Smagorinsky, 1963) with a Smagorinsky constant of 0.12 was

used as the subgrid-scale turbulence model. In the Igune area, a drag force term based on the vegetation canopy model was added to the filtered Navier–Stokes equations (Minami et al., 2022b). The parameters were set to replicate the drag force acting on the leaves following the current situation: C_f = 0.5 and the leaf area density: a = 6.0 m^2/m^3 (Kamiyama et al., 2004) for the shrubs, and C_f = 0.5 and a = 0.5 m^2/m^3 (Nakai et al., 2009) for the tall trees. The wind direction was set to west-northwest, which is the prevailing wind direction during winter. Other numerical settings were applied as described in a previous study (Minami et al., 2023).

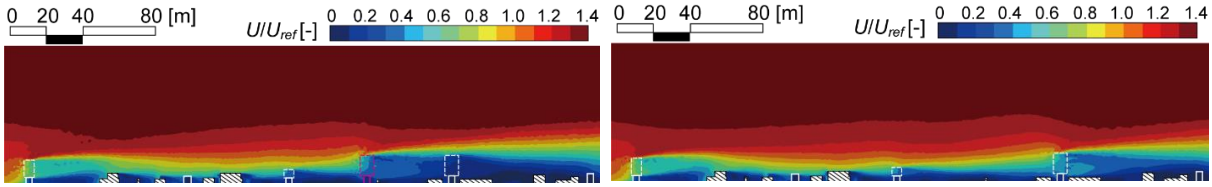
3.2. Result

The wind speed was normalized to the mean wind speed at the reference point U_{ref} located approximately 120 m west of the settlement. The mean wind speed in the 2022 simulation closely matched field observations measured for a 10-min mean wind speed at 35 points of pedestrian height within the settlement by Minami et al. (2024) (not shown here). Fig. 4 shows the horizontal distribution of the mean wind speed at a height of 1.5 m, i.e., the pedestrian height. The white lines represent the cross-section of shrubs, white dotted lines represent the locations of tall trees, and red lines in Fig. 4(1) denote the areas where Igune was removed by 2022. In 2010 (Fig. 4(1)), the mean wind speed was < 0.5 across the entire settlement, indicating that the mean wind speed within the settlement was reduced to approximately half of that outside the settlement. In the northern area of the settlement on the downwind side, where rows of Igune trees are planted, the mean wind speed was approximately 0.3. In 2022, as shown in Fig. 4(2), the mean wind speed remained at 0.3 the northern area, suggesting that the removal of some trees had minimal impact. However, in the southern part of the settlement, where Igune tend to be shorter, the mean wind speed exceeded 0.6. The mean wind speed distribution in the X–X' vertical section is shown in Fig. 5, with results in 2010 closely comparable to those from 2022. At pedestrian height, the low wind speed region was continuously distributed. Furthermore, strong winds separated at the top of the Igune on the



(1) 2010 (Before Igune was cut down). (2) 2022 (Cutting of Igune in progress).

Figure 4. Horizontal distribution of mean wind speed at 1.5 m height.



(1) 2010. (2) 2022.

Figure 5. Mean wind speed in the X–X' vertical section.

windward side weakened as they passed through the Igune on the leeward side.

The windbreak effects of a single Igune row occurred at approximately 10 times the height of the Igune in the downwind direction (Minami et al., 2022a). Even after the spacing of Igune was altered by cutting in 2022, the windbreak effect persisted, as the spacing remained within 10 times the height of the Igune. This observation indicates that the impact on wind speed was minimal. The tall trees (Cryptomeria japonica) and shrubs (Bambuseae) of Igune were cut and replanted, considering their use as building materials. Igune may have been planted at intervals shorter than the low wind speed region formed by individual rows of Igune to maintain calm wind conditions within the settlement during repeated planting processes.

4. CONCLUSIONS

LESs were conducted to investigate the windbreak effects of Igune and the characteristics of the flow field within a clustered settlement in Osaki Koudo, Miyagi Prefecture, Japan, replicating scenarios before the Igune was cut down. Multiple rows of Igune were placed perpendicularly in the prevailing wind direction, forming a wide low wind speed region within the settlement. The mean wind speed was reduced to approximately half of that outside the settlement. Even after the Igune was partially cut down within the settlement, the spacing between the Igune remained within the range to maintain continuous windbreak effects. Consequently, the windbreak effects after the partial removal of Igune were largely comparable to those before the reduction.

ACKNOWLEDGEMENTS

The authors are grateful to the Osaki City office and the owners of the Igune for the observation. This research was supported by JSPS KAKENHI (Grant number 24K08965, 24K22994).

REFERENCES

ESI Group. OpenFOAM. ln https://www.openfoam.com, Accessed January 31, 2023.

Geospatial Information Authority of Japan. GSI Maps. ln https://maps.gsi.go.jp, Accessed January 31, 2023. (in Japanese).

Kamiyama, K., Ohashi, M., and Narita, K., 2004. Wind tunnel experiments on drag coefficient of trees with the leaf area density as a reference area. J. Environ. Eng., AIJ, No.578, 71–77. (in Japanese).

Nakai, Y., Hosoi, F., and Omasa, K., 2009. Estimation of Leaf Area Density of Zelkova Trees Using Airborne and Portable Scanning Lidar Systems. Eco-Engineering, No.21(1), 9–14. (in Japanese).

Minami, K., Mizuta, E., Yonezawa, C., and Okaze, T., 2024. Influence of a group of Igune rows orthogonal to prevailing wind direction on windbreak effects within a rural village. Wind Engineering Research, No.28, 120–128. (in Japanese).

Minami, K., Mizuta, E., Yonezawa, C., and Okaze, T., 2023. Wind velocity reduction with Igune as traditional homestead trees in Osaki Koudo, Japan. Proceedings of 16th International Conference on Wind Engineering, TS-27-678.

Minami, K., Yonezawa, C., and Okaze, T., 2022a. A Study of Effects of Wind Speed Reduction by “Igune” as Homestead Trees around Rural House in Osaki Koudo based on Large-Eddy Simulation. J. JASS, No.38, 37–42. (in Japanese).

Minami, K., Yonezawa, C., and Okaze, T., 2022b. Applicability of a plant canopy model in large-eddy simulation with a 0-equation model considering only drag force term for pedestrian wind environments. Wind Engineering Research, No.27, 19–27. (in Japanese).

Smagorinsky, J., 1963. General circulation experiments with the primitive equations. Monthly Weather Review, Vol. 91, 99–164.

SAMURAI-S: A novel drone-mounted sonic anemometer for turbulence analysis

Mauro Ghirardelli[1], Stephan T. Kral[1,2], Etienne Cheynet[1], Joachim Reuder[1,2]

[1]*Geophysical Institute and Bergen Offshore Wind Centre, University of Bergen, 5020 Bergen, Norway etienne.cheynet@uib.no*

[2]*Geophysical Institute, University of Bergen, and Bjerknes Centre for Climate Research, 5020 Bergen, Norway*

SUMMARY:
The study introduces the SAMURAI-S, a new system that combines a research-grade 3D sonic anemometer with a multi-rotor drone in a sling load arrangement to enhance the flexibility of wind measurements beyond the constraints of fixed-position mast observations. The SAMURAI-S system measures three-dimensional turbulence while the drone hovers, offering greater manoeuvrability and positional precision compared to traditional setups. The effectiveness of the system was assessed through flight tests ranging from 10 to 28 minutes, during which turbulence measurements were taken at 30 and 60 metres altitude and compared against data collected by sonic anemometers on a met-mast. Findings reveal that the SAMURAI-S provides data quality on par with stationary systems for horizontal wind measurements but tends to slightly overestimate vertical turbulence, with a wind speed-dependent constant relative error. This system could mark a significant improvement in atmospheric measurement techniques and wind engineering.

Keywords: atmospheric turbulence, drone, atmospheric measurement technique

1. INTRODUCTION

Since the 1960s, mast and tower-based sonic anemometry have been the standard for high-frequency turbulence measurements in atmospheric boundary layer (ABL) research and wind engineering. However, tower-based measurements have major limitations, emphasizing the need for more flexible approaches in flow measurement techniques. For example, the study of turbulence for offshore wind turbine design would require the erection of multiple 300-metre masts close to each other, which is impractical. Scanning Doppler wind lidars can be used with limited success (Cheynet et al., 2021). Similarly, met-masts have limited applicability to study turbulence in Norwegian fjords for bridge design (Midjiyawa et al., 2021). Fixed-wing uncrewed aerial vehicles (UAVs) have been used to extend the range of turbulence-related measurements, but their inability to hover or move very slowly restricts their ability to sample data in situations that require stationary point measurements. More recently, rotary-blade UAVs offer a more suitable sensor platform for localised and stationary measurements (Abichandani et al., 2020; Prudden et al., 2018).

Recent studies have explored atmospheric flow measurement methods using drone dynamics and miniaturised sonic anemometers. However, limitations in sampling frequency and 3D flow measurement capabilities prevent a rigorous analysis of turbulence. To address these issues, this study introduces SAMURAI-S, an innovative airborne measurement system with potential applications in wind engineering, atmospheric science, and wind energy. SAMURAI-S features a drone

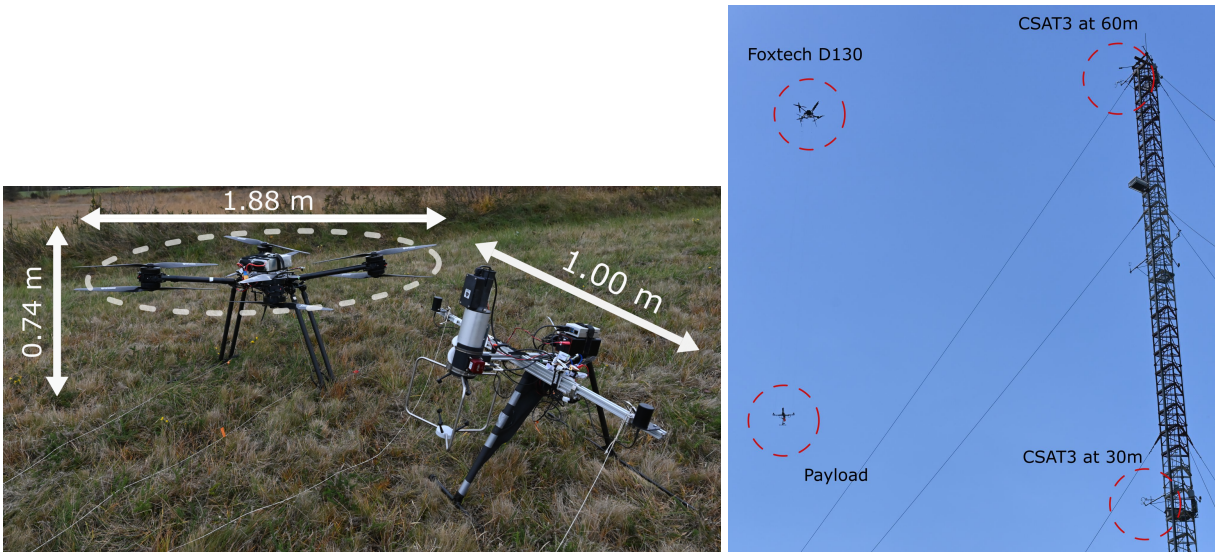


Figure 1. Left panel: close-up of the SAMURAI-S system with the anemometer in the foreground and the octocopter in the background. Right panel: SAMURAI-S hovering side-by-side with the reference mast. The two CSAT sonic anemometers are mounted at 30 m and 60 m above the ground, oriented towards 218.0° and 230.5°, respectively.

equipped with a 3D research-grade ultrasonic anemometer suspended 18 metres below a rotary-wing UAV. This setup is designed to overcome the limitations of previous UAV configurations for flow measurements.

2. THE SAMURAI-S SYSTEM

The SAMURAI-S system (fig. 1) includes a rotary-blade UAV using a drone-mounted 3D sonic anemometer. The Foxtech D130 octocopter was chosen for its ability to lift the 4 kg payload, including the sonic anemometer, inertial navigation system (INS), batteries, data logger, and mounting frame. This setup allows for up to 30 minutes of flight time. The sonic anemometer was mounted 18 metres below the drone to avoid propeller-induced flow (PIF) distortion (Ghirardelli et al., 2023) using a novel sling load configuration. The payload includes the RM Young 81000 sonic anemometer and the SBG Elipse-D INS, with a Raspberry Pi 4 data logger. Also, a triangular wind vane was used to aid the alignment of the sensor with the mean wind vector.

3. METHODS

The study compares outputs from the drone-mounted sonic anemometer (SAMURAI-S) with data from two Campbell Scientific CSAT3 sonic anemometers installed at 30 m and 60 m on a mast serving as reference points. During the validation period, SAMURAI-S conducted ten hovering flights at the corresponding altitudes of 30 m and 60 m, ensuring proximity to the mast. The drone-mounted sonic anemometer data were first corrected for the dynamic motion of the payload using INS records. The corrected data were afterwards synchronised with those from the mast-mounted sonic anemometer using the cross-correlation function between the two signals. The double rotation method was applied to correct static tilt angle errors. This method align the velocity vectors with the mean streamlines. This technique consists of two sequential rotations: first, aligning the

mean wind direction with the x-axis, and second, rotating around the new z-axis to set the mean vertical velocity to zero. Here, x represents the along-wind direction, y the cross-wind direction, and z the vertical direction normal to the surface. Finally, the analysis of turbulence characteristics was performed on the linearly detrended data. This included calculating the Reynolds stress tensor, auto and cross-power spectral densities (PSD and CPSD) of the velocity and temperature fluctuations. The spectral comparisons in this study also rely on the blunt and pointed spectral models (Olesen et al., 1984; Tieleman, 1995) to examine whether the velocity spectra conform to the $-5/3$ power law in the inertial subrange.

4. RESULTS

The notation introduced hereinafter includes velocity components u (streamwise), v (cross-stream), and w (vertical), respectively. Key statistical metrics used are the mean wind speed ($\overline{u}$) and standard deviations (σ_u, σ_v, σ_w). The power spectral densities (PSD) for each velocity component are denoted S_u, S_v, and S_w, and are expressed as a function of the frequency f.

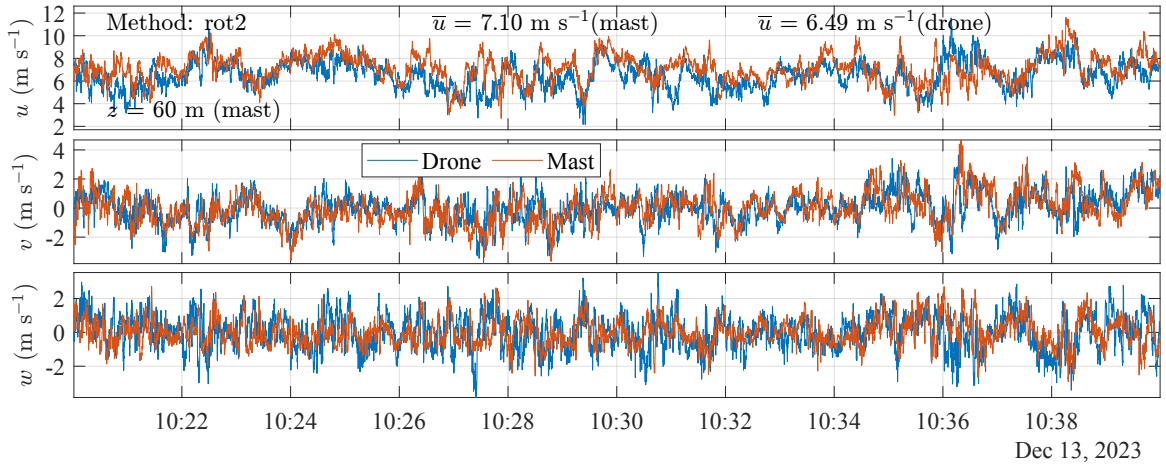


Figure 2. Velocity time series from the drone flights where the SAMURAI-S anemometer is located near the sonic mast-mounted sonic anemometer at 60 m above the ground. The record starts at 10:20:00 on the 2023-12-13.

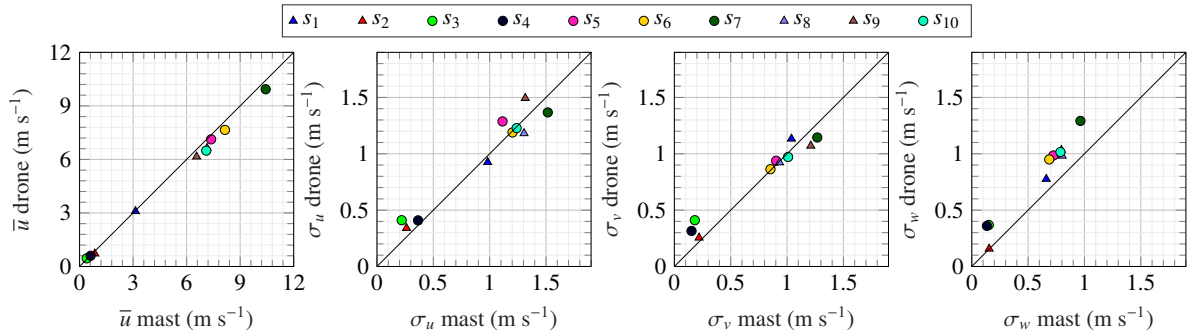


Figure 3. Comparison of mean wind speed ($\overline{u}$) and standard deviations (σ_u, σ_v, σ_w) between mast-mounted and drone-mounted sonic anemometers, based on 10 samples collected in 2023. Circle markers represent measurements from the mast at 30 m above the surface, while triangle markers denote measurements at 60 m.

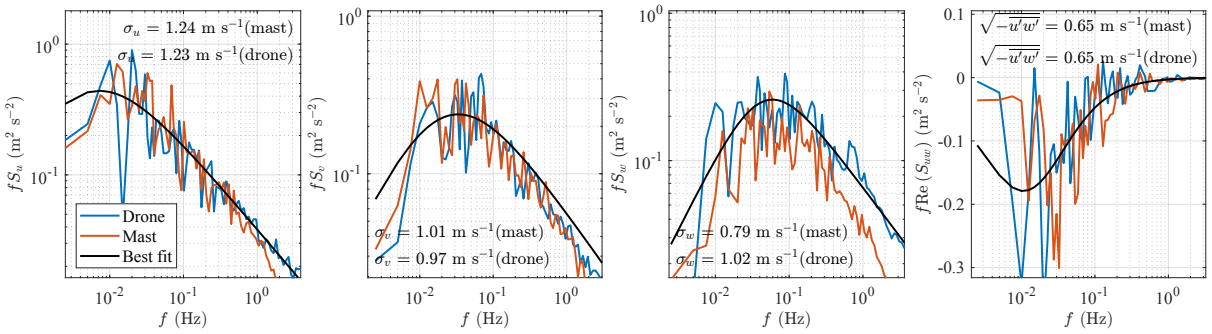


Figure 4. Wind velocity power spectral density estimates for both the drone-mounted and the mast-mounted anemometers at a height of 60 m above the ground for samples s_{10} recorded on the 2023-12-13 at 10:20:00. The black line refers to the blunt model (for S_u, S_v, and S_{uw}) or pointed model (for S_w) fitted to the flying anemometer data.

Figure 2 presents time series of the velocity components u, v, and w for one of the ten samples collected. A good agreement is observed for the two horizontal components. However, the vertical component shows a slightly noisier signal, maybe due to the larger tilt angle of the mast-mounted anemometer at moderate wind speed. Such deviations are visible in fig. 3 for σ_w. Nevertheless, an overall excellent agreement is observed between the selected turbulence statistics from the mast-mounted and drone-mounted sensors. The PSD and cross-PSD (CPSD) of the velocity components for the sample studied at 10:20:00 on 2023-12-13 are displayed in fig. 4. The excellent agreement for the PSD of the u and v components is reflected by the S_u and S_v spectra, indicating the ability of the drone-mounted anemometer to accurately record the horizontal velocity fluctuations across a wide range of frequencies. The S_w spectra are larger at both low and high frequencies in the drone-mounted data, echoing the larger values observed in fig. 3 for the vertical component. Notably, the cross-PSD is properly captured by the drone-mounted sonic anemometer, highlighting the potential of this setup to study the Reynolds stress tensor and the dynamic atmospheric stability.

5. CONCLUSIONS

This study demonstrates the use of a 3D sonic anemometer mounted 18 m beneath a drone to measure turbulence, offering an innovative alternative to traditional mast-mounted sensors. The introduction of a dynamic motion compensation algorithm enhanced measurement accuracy by adjusting for the drone's motion and tilt. Comparative analyses with mast-mounted sonic anemometer data showed that drone-mounted anemometers yield a high potential for detailed turbulence measurements. Although some overestimations were noted in vertical wind fluctuations, these findings underscore the potential of drone-based systems in atmospheric science, warranting further exploration under varied conditions. Alternative application of these systems in wind engineering applications such as bridges, high-rise buildings, and wind turbine design suggests that drone-based measurement could lead to significant breakthroughs in atmospheric research.

ACKNOWLEDGEMENTS

This research is funded by the Marie Sklodowska Curie Innovation Training Network Train2Wind (H2020-MSCA-ITN-2019, Grant number 861291). The MOSAI project is funded by French ANR (Agence Nationale de la Recherche) and uses measurements acquired at ACTRIS (Aerosol, Clouds and Trace Gases Research Infrastructure) and ICOS

(Integrated Carbon Observation System) instrumented sites. AERIS data centre is in charge of the data distribution and of the website of the MOSAI project. (https://mosai.aeris-data.fr). We want to thank Tor Olav Kristensen for supporting the initial phase of this project. We also extend our sincere gratitude to everyone involved in the MOSAI campaign, whose help has been invaluable in the success of this study.

REFERENCES

Abichandani, P., Lobo, D., Ford, G., Bucci, D., and Kam, M., 2020. Wind Measurement and Simulation Techniques in Multi-Rotor Small Unmanned Aerial Vehicles. IEEE Access 8, 54910–54927.

Cheynet, E., Flügge, M., Reuder, J., Jakobsen, J. B., Heggelund, Y., Svardal, B., Saavedra Garfias, P., Obhrai, C., Daniotti, N., Berge, J., et al., 2021. The COTUR project: remote sensing of offshore turbulence for wind energy application. Atmospheric Measurement Techniques 14, 6137–6157.

Ghirardelli, M., Kral, S. T., Müller, N. C., Hann, R., Cheynet, E., and Reuder, J., 2023. Flow Structure around a Multicopter Drone: A Computational Fluid Dynamics Analysis for Sensor Placement Considerations. Drones 7, 467.

Midjiyawa, Z., Cheynet, E., Reuder, J., Ágústsson, H., and Kvamsdal, T., 2021. Potential and challenges of wind measurements using met-masts in complex topography for bridge design: Part II–Spectral flow characteristics. Journal of Wind Engineering and Industrial Aerodynamics 211, 104585.

Olesen, H. R., Larsen, S. E., and Højstrup, J., 1984. Modelling velocity spectra in the lower part of the planetary boundary layer. Boundary-Layer Meteorology 29, 285–312.

Prudden, S., Fisher, A., Marino, M., Mohamed, A., Watkins, S., and Wild, G., 2018. Measuring wind with small unmanned aircraft systems. Journal of Wind Engineering and Industrial Aerodynamics 176, 197–210.

Tieleman, H. W., 1995. Universality of velocity spectra. Journal of Wind Engineering and Industrial Aerodynamics 56, 55–69.

Comparative analysis of gust factor for offshore monsoon, tropical cyclone, and thunderstorm winds

Yu-Cheng Xue [1], Jun-Yi He [1], Pak-Wai Chan [2], Qiu-Sheng Li [1,*]

[1]*Dept. of Architecture and Civil Engineering, City University of Hong Kong, Kowloon, Hong Kong, yuchenxue5-c@my.cityu.edu.hk, junyihe3@cityu.edu.hk, bcqsli@cityu.edu.hk*
[2]*Hong Kong Observatory, Kowloon, Hong Kong, pwchan@hko.gov.hk*

SUMMARY
Offshore wind resources have been receiving significant attention over the past few decades. This study presents a comparative study of gust factors for different types of extreme wind events, including monsoon, tropical cyclone, and thunderstorm winds, on the basis of a 16-year wind dataset collected from three offshore meteorological stations in Hong Kong. The variation of the gust factor with wind speed and gust duration, along with a comparison with existing prediction models, are thoroughly analyzed. The outcome of this study aims to provide useful references for the wind-resistant design of offshore structures and make a contribution to a better understanding of atmospheric boundary layer characteristics.

Keywords: Extreme wind events, Gust factor, Offshore meteorological station

1. INTRODUCTION

As fossil fuels are consumed, the growing importance of renewable energy is being recognized, with offshore wind power leading the market due to ample turbine space and abundant wind resources (He et al., 2020). However, wind turbines also endure the strong dynamic forces generated by offshore turbulent wind fields while harnessing wind energy. Therefore, a comprehensive analysis of gust wind is crucial for structural safety of wind turbines located in offshore areas. A variety of studies were carried out based on wind data collected from onshore meteorological stations, bridges, and observational towers. However, few studies have been conducted to analyze the offshore gust factor due to the challenges of obtaining offshore wind datasets. With regard to this issue, this work utilizes a 16-year wind dataset collected from three offshore meteorological stations in Hong Kong to investigate the characteristics of gust factors for monsoon, tropical cyclone, and thunderstorm winds.

2. OBSERVATION SITES AND DATA SOURCES

As shown in Figure 1, Waglan Island (WGL; 22.18°N, 114.30°E) is located in the southeast of Hong Kong, adjacent to the Western Pacific Ocean, with no obstructions around it and the nearest island, Sung Kung Island, being 1.2 km away. Cheung Chau Island (CCH; 22.21°N, 114.03°E) is in the South China Sea, situated 10 km southwest of Hong Kong Island and 2 km southeast of Lantau Island. Wailingding Island (WLD; 22.11°N, 114.02°E) is located southeast of Guangdong, China, 50.9 km west of Zhuhai and approximately 64.8 km north of Shenzhen. Elevations of the

anemometers installed on the three offshore islands are 82.7 m, 98.4 m, and 43.0 m above mean sea level, respectively.

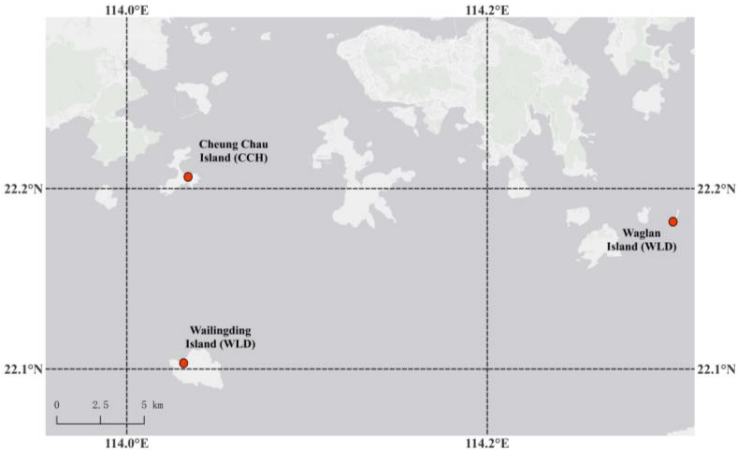


Figure 1. Locations of WGL, CCH, and WLD offshore meteorological stations.

The dataset used in this paper includes 1-min, 10-min, and 1-hour average wind speed (U_{60}, U_{600}, and U_{3600}) and direction (θ_{60}, θ_{600}, and θ_{3600}) from three automatic offshore weather stations distributed across the South China Sea, as well as the 3-s gust wind during these three time periods ($U_{3,60}$, $U_{3,600}$, and $U_{3,3600}$). Only monsoon, tropical cyclone, and thunderstorm wind data with warning signals above level three, as issued by the Hong Kong Observatory (HKO), are considered for gust factor analysis. Additionally, to avoid the influence of overlapping occurrences of these weather conditions, periods with overlapping warnings are excluded from the analysis.

3. RESULTS

Only the analysis results for the WGL station are presented herein. As shown in Figure 2 and Table 1, the variation in gust factors with wind speed is not significant within the strong wind region (U_{600}>10m/s), and the Generalized extreme value distribution (GEV) model more effectively describes the gust factor distribution of the three extreme wind events compared to the Lognormal model. Moreover, this work conducts a comparable study of the observed gust factor and expected mean gust factor based on the estimation method proposed by Vickery and Skerlj (2005). For over-water terrain, the roughness length (z_0) cannot be estimated visually, Large and Pond (1981) and Donelan (2004) proposed the following Equations (1) to (3), respectively, to compute the roughness length. Comparison results are shown in sub-figures (a), (b), and (c) in Figure 2. Rose plot of the gust factor is shown in Figure 3. Additionally, fitting results for the variation of gust factor with gust duration are shown in Figure 4, indicating a linear correlation for monsoon and tropical cyclone winds, but this correlation is less evident for thunderstorm winds.

$$z_0 = \frac{10}{\exp\left(\frac{\kappa}{C_d}\right)}$$, κ refers to the von Karman constant, which is assumed to be 0.4 (1)

$$C_d = \begin{cases} 0.0012 & U_T(10) \le 11m/s \\ (0.49 + 0.065U_T(10) \times 0.001) & U_T(10) \ge 11m/s \end{cases}$$ (2)

$$C_d = \begin{cases} 0.0006 & U_T(10) \le 5m/s \\ (0.25 + 0.065U_T(10) \times 0.001) & 5 < U_T(10) \le 33m/s \\ 0.0024 & U_T(10) \ge 33m/s \end{cases} \quad (3)$$

where C_d is the drag coefficient, $U_T(10)$ refers to mean wind speed at 10m.

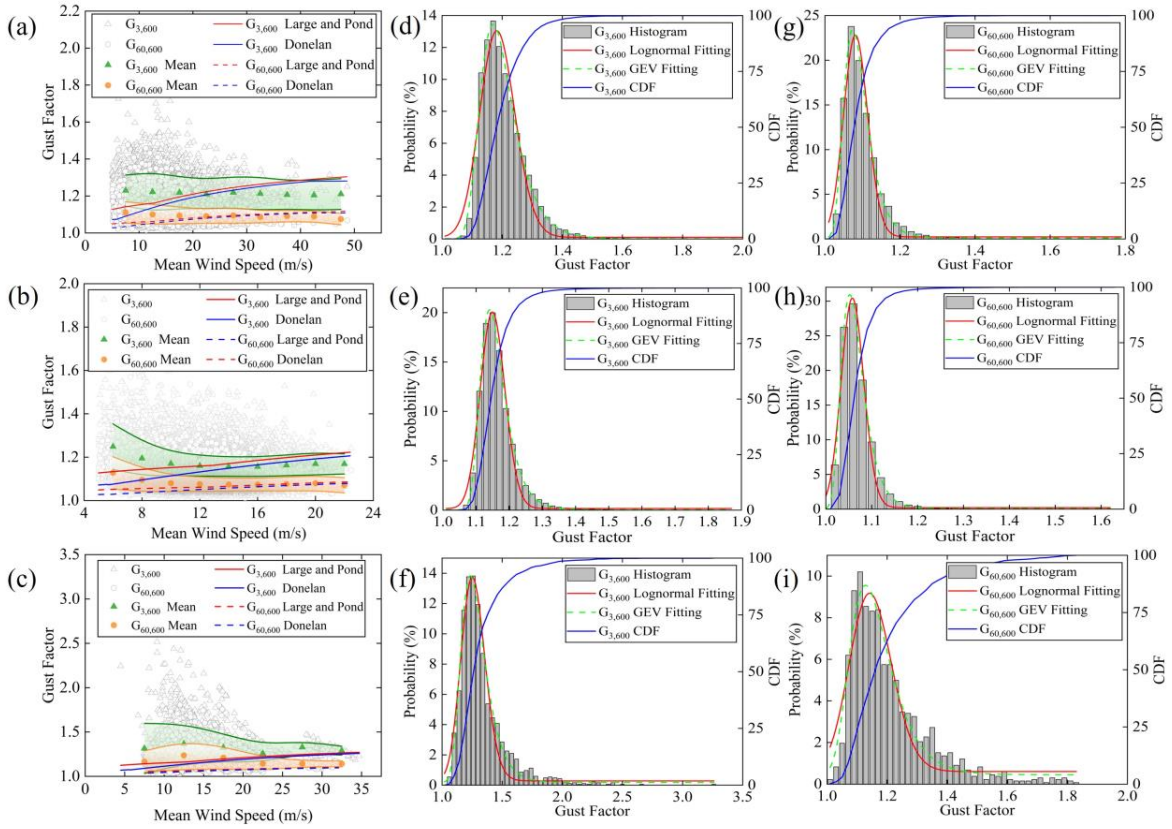


Figure 2. Gust factors for WGL station during tropical cyclone (a), (d), and (g), monsoon (b), (e), and (h), and thunderstorm (c), (f), and (i). The shaded area refers to the mean value ± 1.5 standard deviation.

Table 1. Statistics of $G_{3,600}$ and $G_{60,600}$ for monsoon, tropical cyclone, and thunderstorm winds.

	Monsoon	Tropical cyclone	Thunderstorm
Mean	1.16 (1.08)	1.21 (1.10)	1.33 (1.21)
Max	1.87 (1.63)	2.03 (1.97)	3.25 (1.83)
Min	1.05 (1.01)	1.06 (1.01)	1.06 (1.01)
GEV Fitting R^2	0.99 (0.99)	0.99 (0.99)	0.98 (0.96)
Lognormal Fitting R^2	0.98 (0.97)	0.97 (0.96)	0.96 (0.89)

Note: Values in the brackets refer to $G_{60,600}$

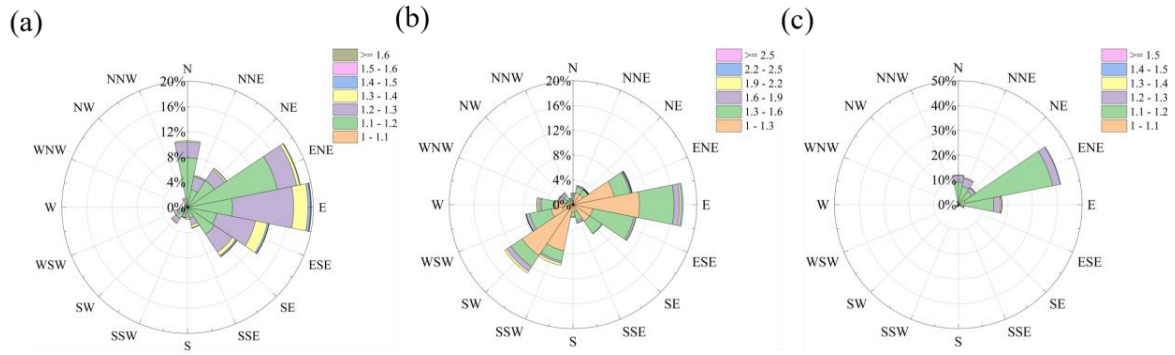


Figure 3. Rose plot of gust factor for (a) tropical cylone, (b) monsoon, and (c) thunderstorm.

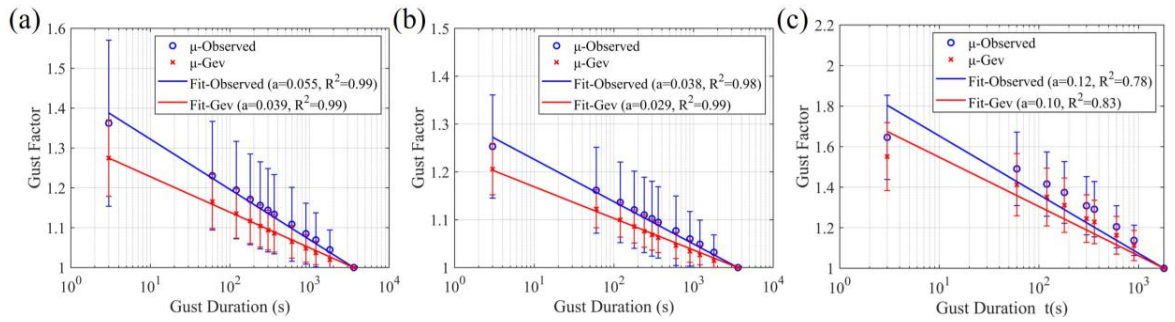


Figure 4. Variation of gust factor and gust duration for (a) tropical cylone, (b) monsoon, and (c) thunderstorm.

7. CONCLUSIONS

This study conducted a comparative analysis of gust factors over open-water terrain during monsoon, tropical cyclone, and thunderstorm events. The results show that the GEV distribution model provides a better fit for gust factor distribution compared to the lognormal distribution model. Gust factors for thunderstorms are significantly higher than those for monsoons and tropical cyclones. Additionally, previous prediction models perform well in estimating gust factors for monsoons and tropical cyclones but tend to underestimate gust factors during thunderstorms.

ACKNOWLEDGEMENTS

The work described in this paper was fully supported by grants from the Science, Technology and Innovation Commission of Shenzhen Municipality (Project No: JCYJ20220818101201003), and the Research Grants Council, University Grants Committee, Hong Kong (Project No: RIF: R1006-23 and GRF: CityU 11213523, CityU 11206922).

REFERENCES

Donelan, M.A., 2004. On the limiting aerodynamic roughness of the ocean in very strong winds. Geophysical Research Letters 31, L18306.

He, J.Y., Chan, P.W., Li, Q.S., Lee, C.W., 2020. Spatiotemporal analysis of offshore wind field characteristics and energy potential in Hong Kong. Energy 201, 117622.

Large, W.G., Pond, S., 1981. Open ocean momentum flux measurements in moderate to strong winds. Journal of Physical Oceanography 11, 324-336.

Vickery, P.J., Skerlj, P.F., 2005. Hurricane gust factors revisited. Journal of Structural Engineering 131, 825-832.

Vortex-induced force estimation in long-span bridges using latent force model

Shengyi Xu[1], Øyvind Wiig Petersen[2], Genshen Fang[3], Ole Øiseth[4], Yaojun Ge[5]

[1]*Shanghai Fengxian Development Group Co., Ltd, Shanghai, China, xushengyichn@outlook.com*
[2]*Norwegian University of Science and Technology, Trondheim, Norway, oyvind.w.petersen@ntnu.no*
[3]*Tongji University, Shanghai, China, 2222tjfgs@tongji.edu.cn*
[4]*Norwegian University of Science and Technology, Trondheim, Norway, ole.oiseth@ntnu.no*
[3]*Tongji University, Shanghai, China, yaojunge@tongji.edu.cn*

SUMMARY:
Quantifying vortex-induced forces is crucial to understanding vortex-induced vibration (VIV) in long-span bridges, but it is not feasible to measure directly on structures in situ. Existing structural health monitoring systems, which rely on accelerometers, only capture structural responses at discrete points. This study employs common Bayesian filters (a Kalman filter and an RTSS smoother) with acceleration output data to estimate vortex-induced forces. This research introduces a Gaussian process exponential-periodic latent force model (EP-LFM), informing the Bayesian filters about the cyclic nature of the loading. A 1650 m long suspension bridge is introduced as a case study for its sensitivity to VIV. The analysis revealed that the estimates of vortex-induced forces are stable and do not accumulate errors, clearly distinguishing between buffeting and VIV responses across multiple modes. The results indicated that the suggested framework can be seamlessly integrated into the online monitoring system for VIV, eliminating the need for extensive hyperparameter tuning for each VIV event.

Keywords: Force identification, Exponential-periodic latent force model, Vortex-induced vibration

1. INTRODUCTION

Vortex-induced vibration (VIV) is a self-excited vibration with finite amplitude that typically occurs in long-span bridges at low wind speeds (Wu and Kareem, 2012). If VIV persists for a long period of time and has a relatively large amplitude, it can cause fatigue damage, discomfort to drivers, and even frighten the bridge users. Quantification of the vortex-induced force on the bridge deck is usually achieved through wind tunnel tests or simplified numerical simulations. Although wind tunnels provide a controlled environment for studying aerodynamic phenomena of VIV, the translation of these findings to full-scale structures remains challenging. The scale effects and differences in environmental conditions can lead to discrepancies in the VIV performance (Fenerci et al., 2023). Thus, inverse identification of vortex-induced forces on long-span bridges through data obtained from health monitoring systems could lead to a better understanding of full-scale VIV for real wind field conditions, despite the challenges in direct measurement and the limitations of available sensors. Over the last decade, the Kalman filter has attracted considerable interest, leading to its adaptation for state and force estimation in output-only scenarios (Lourens et al., 2012). This study aims to explore the use of Gaussian processes with an exponential-periodic latent force model (EP-LFM) tailored for identifying vortex-induced forces.

2. IDENTIFICATION TECHNIQUES

The response data of in-situ structures do not only contain the vortex-induced vibration of a single mode, but also include multimodal stochastic components. Therefore, the forces acting on the structure are conceptualized as comprising two distinct sources: the vortex-induced force and the buffeting force. The structure's response can be approximated by the contribution of multiple modes, expressed as $\boldsymbol{r}(t) \approx \boldsymbol{\Phi}\boldsymbol{z}(t)$. The modal equation of motion can be written as:

$$\ddot{\boldsymbol{z}}(t) + 2\boldsymbol{\Xi}_{\text{sys}}\boldsymbol{\Omega}\dot{\boldsymbol{z}}(t) + \boldsymbol{\Omega}^2\boldsymbol{z}(t) = \mathrm{S}_{\text{VIV}} \cdot p_{\text{VIV}}(t) + \boldsymbol{p}_{\text{buff}}(t) \tag{1}$$

where $\boldsymbol{\Xi}_{\text{sys}}$, and $\boldsymbol{\Omega} \in \mathbb{R}^{\mathrm{n_m} \times \mathrm{n_m}}$, represent the modal damping ratio and frequency matrices associated with the structural properties, respectively. In the modally reduced model it assumed that the vortex-induced force targets mainly the single VIV mode, while the other modes are mainly excited by the modal buffeting loads $\boldsymbol{p}_{\text{buff}}(t) = \boldsymbol{\Phi}^{\mathrm{T}}\boldsymbol{f}_{\text{buff}}(t)$. Therefore, $\mathrm{S}_{\text{VIV}} \in \mathbb{R}^{\mathrm{n_m}}$ is binary matrix that selects the targeted VIV mode, and $p_{\text{VIV}}(t) = \boldsymbol{\Phi}_{\text{VIV}}{}^{\mathrm{T}}\boldsymbol{f}_{\text{VIV}}(t)$ is the modal vortex-induced force. $\boldsymbol{\Phi}^{\text{VIV}} \in \mathbb{R}^{\mathrm{nDOF}}$ and $\boldsymbol{\Phi} \in \mathbb{R}^{\mathrm{nDOF} \times \mathrm{n_m}}$ specify mode shapes.

Introducing the modal state vector $\mathbf{x}(t) = [\mathbf{z}(t)^{\mathrm{T}}\,\dot{\mathbf{z}}(t)^{\mathrm{T}}]^{\mathrm{T}} \in \mathbb{R}^{2\mathrm{n_m}}$, the system equation is converted into state-space form:

$$\dot{\mathbf{x}}(t) = \mathbf{A}_{\mathrm{c}}\mathbf{x}(t) + \mathbf{B}_{\mathrm{c}}^{\text{VIV}}p_{\text{VIV}}(t) + \mathbf{B}_{\mathrm{c}}^{\text{buff}}\mathbf{p}_{\text{buff}}(t), \mathbf{A}_{\mathrm{c}} = \begin{bmatrix} \mathbf{0} & \mathbf{I} \\ \Omega^2 & 2\boldsymbol{\Xi}_{\text{sys}}\boldsymbol{\Omega} \end{bmatrix}, \mathbf{B}_{\mathrm{c}}^{\text{VIV}} = \begin{bmatrix} \mathbf{0} \\ \mathbf{S}_{\text{VIV}} \end{bmatrix}, \mathbf{B}_{\mathrm{c}}^{\text{buff}} = \begin{bmatrix} \mathbf{0} \\ \mathbf{I} \end{bmatrix} \tag{2}$$

The vortex-induced force is treated as a realization of a Gaussian process with a specifically designed kernel. Within the scope of this application, a kernel encoding both periodicity and a fading temporal correlation emerges as a suitable choice for representing the vortex-induced force. We refer to this as the exponential-periodic latent force model (EP-LFM) and relte it to the following stochastic differential equation model:

$$\dot{\mathbf{s}}(t) = \mathbf{F}_{\mathrm{c}}\mathbf{s}(t) + \mathbf{L}_{\mathrm{c}}\mathbf{w}(t), p_{\text{VIV}}(t) = \mathbf{H}_{\mathrm{c}}\mathbf{s}(t) \tag{3}$$

where the matrices are given by:

$$\mathbf{F}_{\mathrm{c}} = \begin{bmatrix} -\lambda & -\omega_0 \\ \omega_0 & -\lambda \end{bmatrix}, \quad \mathbf{L}_{\mathrm{c}} = \begin{bmatrix} 1 & 0 \\ 0 & 1 \end{bmatrix}, \quad \mathbf{H}_{\mathrm{c}} = \begin{bmatrix} 1 & 0 \end{bmatrix} \tag{4}$$

and $\mathbf{s}(t) \in \mathbb{R}^2$ is the latent state variable which is driven bt the Gaussian white noise $\mathbf{w}(t) \in \mathbb{R}^2$ with a diagonal covariance matrix given by

$$\mathbf{Q}_{w,\mathrm{c}} = \sigma_w^2\mathbf{I}, \quad \sigma_w^2 = \sigma_{\text{VIV}}^2 \cdot 2\lambda \tag{5}$$

The augmented format of the state-space model is found by combining the dynamic system in Eq. 2 with the EP-LFM in Eq. 3:

$$\begin{bmatrix} \dot{\mathbf{x}}(t) \\ \dot{\mathbf{s}}(t) \end{bmatrix} = \begin{bmatrix} \mathbf{A}_{\mathrm{c}} & \mathbf{B}_{\mathrm{c}}^{\text{VIV}}\mathbf{H}_{\mathrm{c}} \\ \mathbf{0} & \mathbf{F}_{\mathrm{c}} \end{bmatrix} \begin{bmatrix} \mathbf{x}(t) \\ \mathbf{s}(t) \end{bmatrix} + \begin{bmatrix} \mathbf{B}_{\mathrm{c}}^{\text{buff}}\mathbf{p}_{\text{buff}}(t) \\ \mathbf{L}_{\mathrm{c}}\mathbf{w}(t) \end{bmatrix} \tag{6}$$

The acceleration output vector $\mathbf{y}(t)$ is written as:

$$\begin{aligned}\mathbf{y}(t) &= \mathbf{G}_{\mathrm{c}}\mathbf{x}(t) + \mathbf{J}_{\mathrm{c}}^{\mathrm{VIV}} p_{\mathrm{VIV}}(t) + \mathbf{J}_{\mathrm{c}}^{\mathrm{buff}}\mathbf{p}_{\mathrm{buff}}(t) + \mathbf{v}(t) \\ &= \begin{bmatrix}\mathbf{G}_{\mathrm{c}} & \mathbf{J}_{\mathrm{c}}^{\mathrm{VIV}}\mathbf{H}_{\mathrm{c}}\end{bmatrix}\begin{bmatrix}\mathbf{x}(t) \\ \mathbf{s}(t)\end{bmatrix} + \mathbf{J}_{\mathrm{c}}^{\mathrm{buff}}\mathbf{p}_{\mathrm{buff}}(t) + \mathbf{v}(t)\end{aligned} \tag{7}$$

where the following matrices are defined:

$$\mathbf{G}_{\mathrm{c}} = \begin{bmatrix}-\mathbf{S}_{\mathrm{a}}\Phi\Omega^2 & -\mathbf{S}_{\mathrm{a}}\Phi 2\Xi_{\mathrm{sys}}\Omega\end{bmatrix}, \mathbf{J}_{\mathrm{c}}^{\mathrm{buff}} = \left[\mathbf{S}_{\mathrm{a}}\Phi\right], \quad \mathbf{J}_{\mathrm{c}}^{\mathrm{VIV}} = \begin{bmatrix}\mathbf{S}_{\mathrm{a}}\Phi^{\mathrm{VIV}}\end{bmatrix} \tag{8}$$

Both the state and measurement equations can be simplified by introducing the augmented state vector $\mathbf{z}(t) = [\mathbf{x}^{\mathrm{T}}(t)\,\mathbf{s}^{\mathrm{T}}(t)]^{\mathrm{T}}$, and the augmented matrices $\mathbf{A}_{\mathrm{ac}} = \begin{bmatrix}\mathbf{A}_{\mathrm{c}} & \mathbf{B}_{\mathrm{c}}^{\mathrm{VIV}}\mathbf{H}_{\mathrm{c}} \\ \mathbf{0} & \mathbf{F}_{\mathrm{c}}\end{bmatrix}$, and $\mathbf{G}_{\mathrm{c}} = \begin{bmatrix}\mathbf{G}_{\mathrm{ac}} & \mathbf{J}_{\mathrm{c}}^{\mathrm{VIV}}\mathbf{H}_{\mathrm{c}}\end{bmatrix}$.

$$\dot{\mathbf{x}}_{\mathrm{c}}^{\mathrm{a}}(t) = \mathbf{F}_{\mathrm{ac}}\mathbf{x}_{\mathrm{c}}^{\mathrm{a}}(t) + \mathbf{w}_{\mathrm{c}}^{\mathrm{a}}(t), \mathbf{y}(t) = \mathbf{G}_{\mathrm{ac}}\mathbf{x}_{\mathrm{c}}^{\mathrm{a}}(t) + \mathbf{v}_{\mathrm{c}}^{\mathrm{a}}(t) \tag{9}$$

The augmented equations can be converted into their discrete-time counterparts:

$$\mathbf{x}_{k+1}^{\mathrm{a}} = \mathbf{F}_{\mathrm{ad}}\mathbf{x}_k^{\mathrm{a}} + \mathbf{w}_k^{\mathrm{a}}, \mathbf{y}_k = \mathbf{G}_{\mathrm{ad}}\mathbf{x}_k^{\mathrm{a}} + \mathbf{v}_k^{\mathrm{a}} \tag{10}$$

where, $\mathbf{F}_{\mathrm{ad}} = e^{\mathbf{F}_{\mathrm{ac}}\Delta t}$, $\mathbf{G}_{\mathrm{ad}} = \mathbf{G}_{\mathrm{ac}}$, $\mathbf{J}_{\mathrm{d}}^{\mathrm{buff}} = \mathbf{J}_{\mathrm{c}}^{\mathrm{buff}}$, $\mathbf{w}_k^{\mathrm{a}} = \begin{bmatrix}\mathbf{B}_{\mathrm{d}}^{\mathrm{buff}}\mathbf{p}_k^{\mathrm{buff}} \\ \mathbf{L}_{\mathrm{d}}\mathbf{w}_k\end{bmatrix}$

Through the application of a Kalman filter followed by a backward Rauch-Tung-Striebel (RTS) smoother, this state-space representation is utilized to estimate the augmented state vector $\hat{\mathbf{x}}_k^{\mathrm{a}}$, subsequently deriving the modal state estimate $\hat{\mathbf{z}}_k$ and the vortex-induced force estimate $\hat{\mathbf{p}}_k^{\mathrm{VIV}} = \mathbf{H}_{\mathrm{d}}\hat{\mathbf{s}}_k$.

3. IDENTIFICATION RESULTS

After selecting two sets of different EP-LFM hyperparameters, the vortex-induced forces were estimated using the Kalman filter and the RTS smoother as depicted in Figure 1 (a) and (b). These estimations reveal that both EP-LFMs produce comparable force estimates. Additionally, for comparison, the estimated force obtained by the frequency domain deconvolution method is illustrated in Figure 1 (c). The comparison highlights a consistent overall trend between the estimates from the Kalman filter and those from the frequency domain deconvolution method, as illustrated in Figure 1 (d). However, the results from the latter method do not appear as smooth. This is attributed to the EP-LFM acting as a prior, influencing the evolution of the force dynamics. As VIV invariably coexists with buffeting for real bridge scenarios, the EP-LFM is capable of enhancing the smoothness of the estimated force, thereby mitigating the components of the buffeting force. Additionally, the identification process is an online procedure, and the hyperparameters are not necessarily tuned for each VIV event.

4. CONCLUSIONS

This study has proposed a methodology for identifying the vortex-induced forces using measured acceleration data. The results indicated that utilizing the Gaussian Process Exponential-Periodic Latent Force Model (EP-LFM) for estimating vortex-induced forces enables the integration of prior knowledge about the unknown forces, thereby reconstructing the system's actual dynamic behavior more accurately.

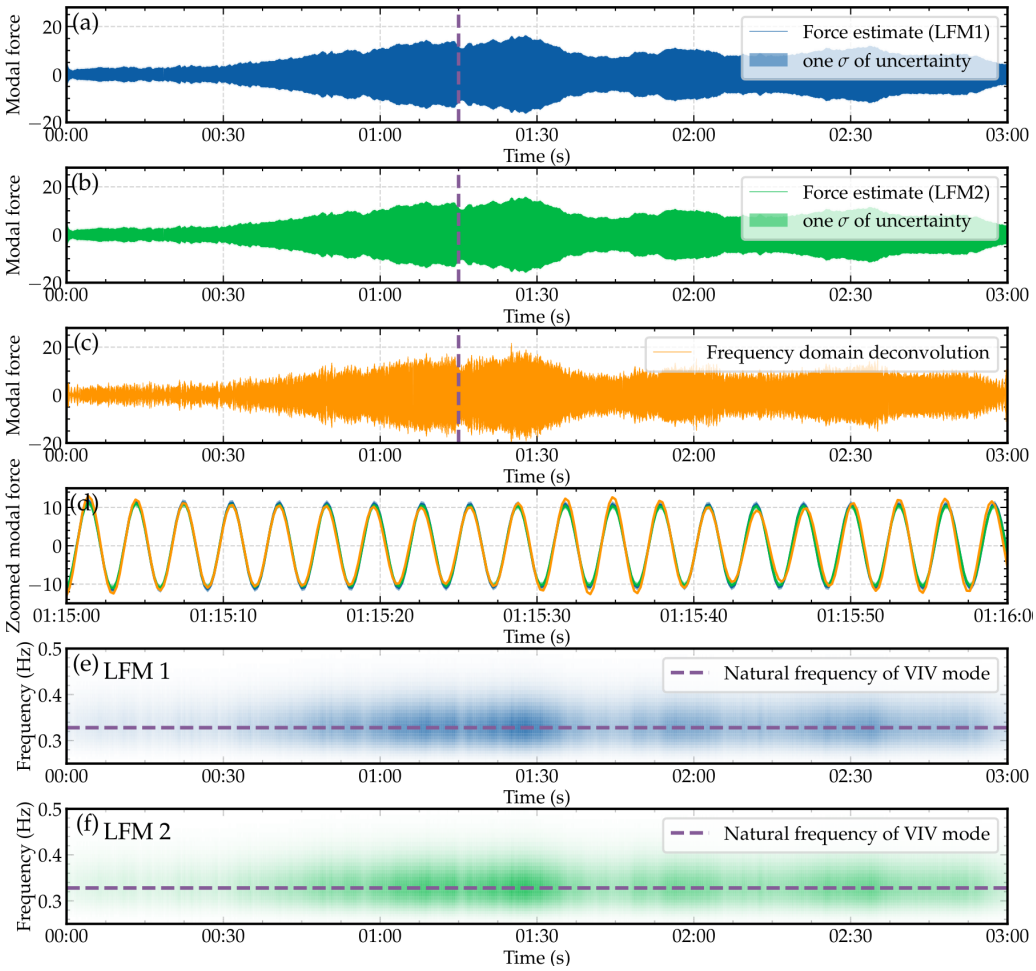


Figure 1. Estimation of vortex-induced forces and characteristics in time and frequency domains. (a) force estimation with LFM1; (b) force estimation with LFM2; (c) force estimation with frequency domain deconvolution; (d) detailed comparison of forces from (a), (b), and (c); (e) instantaneous frequency analysis of force estimation with LFM1; (f) instantaneous frequency analysis of force estimation with LFM2.

ACKNOWLEDGEMENTS

The authors gratefully acknowledge the support of the National Natural Science Foundation of China (52108469, 52278520), Young Elite Scientists Sponsorship Program by CAST (2023QNRC001), the Chenguang Program of Shanghai Education Development Foundation and Shanghai Municipal Education Commission (22CGA21), the Fundamental Research Funds for the Central Universities (22120220577).

REFERENCES

Fenerci, A., Lystad, T. M., and Øiseth, O., Nov. 2023. Full-Scale Monitored Wind and Response Characteristics of a Suspension Bridge Compared with Wind Tunnel Investigations at the Design Stage. Journal of Wind Engineering and Industrial Aerodynamics 242, 105583.

Lourens, E., Reynders, E., De Roeck, G., Degrande, G., and Lombaert, G., Feb. 2012. An Augmented Kalman Filter for Force Identification in Structural Dynamics. Mechanical Systems and Signal Processing 27, 446–460.

Wu, T. and Kareem, A., Dec. 2012. An Overview of Vortex-Induced Vibration (VIV) of Bridge Decks. Frontiers of Structural and Civil Engineering 6, 335–347.

Drone swarm wind measurements within the shear layer of a nominally cuboid building

Sebastian Kean [1], Matthew Marino [1], Simon Watkins [1], Abdulghani Mohamed [1]

[1]*RMIT University, Melbourne, Australia, sebastian.kean@rmit.edu.au*

SUMMARY:
In this paper, a data set of multi-point simultaneous airborne wind measurements recorded atop of a 43m nominally cuboid building is presented. A brief description of the drone and measurement system is presented as well of a breakdown of the environment in which the data was collected. Static masts are expensive and limiting with respect to their placement, and recent advances in drone technology has enabled new possibilities for collecting novel wind data sets. It is expected that this will provide insights for a variety of applications including urban air mobility concepts, CFD validation and wind energy extraction.

Keywords: drone, building shear layer, wind measurement, turbulence, swarm

1. INTRODUCTION AND MOTIVATION

Urban environments represent some of the most chaotic and difficult to replicate atmospheric wind conditions due to the high levels of turbulence present. Although these environments are well studied with respect to the static and dynamic loadings on buildings and infrastructure, gaps exist regarding short time and length scales. These higher frequency phenomena are of particular interest to Urban Air Mobility concepts, that expect to have semi or fully autonomous aircraft operating in and around urban infrastructure. These future air vehicles vary in scale from small package delivery drones to crewed air taxis, often featuring hybrid fixed wing configurations and unconventional propulsion systems. Previous studies utilizing combinations of CFD and experimental measurements(Mohamed, Abdulghani et al. 2023; Thompson et al. 2011) anticipate that shear regions around the roofs and corners of buildings are likely to present large disturbances under strong wind conditions. Therefore, to begin understanding the limitations of these aircraft, we must first understand the environment they need to operate within.

Drone based wind measurements provide many advantages over conventional mast measurements. They can be easily positioned and reconfigured, as well as reaching locations that may not be possible using masts, such as the flow conditions outside of the influence of the building. They can also measure the incoming wind flow along a moving path, such as a takeoff or landing trajectory, to study how the turbulence would be perceived by an aircraft. Doing this with laterally separated drones could be used to represent the aircraft's span, examining the velocity correlations most relevant to the aircraft size(Thompson et al. 2011).

2. DRONE AND MEASUREMENT SYSTEM

Four drones have been constructed, each with a custom designed 4-hole pressure probe. The drones were designed to operate in highly turbulent environments, whist providing as stable as

possible measurement platform. Custom ground control software has also been developed to enable synchronized formation flights, useful for collecting spanwise and horizontal point measurements. This swarming system has been successfully used to measure atmospheric boundary layer profiles. Further details on the design of the drones and validation of the system can be found in(Kean et al. 2024).

The probes are designed with a prismoid head after the commercially available cobra probes. and were calibrated in the aeronautical wind tunnel at RMIT in nominally laminar flow (Ti = 0.007) on a specially designed calibration rig. This produces functions that can resolve the dynamic pressures recorded at the tip into a 3D air speed vector. The flow definitions chosen for calibration are outlined in (Sitaram & Treaster 1985). By synchronizing the 3D airspeed measurements with the attitude and motion of the aircraft, it can be converted in a 3D wind vector in an Earth centric co-ordinate system. Alternatively, the airspeed vector can be used directly to represent the flow conditions an aircraft would perceive if it were to travel along the same trajectory. Figure 1 depicts the absolute accuracy of the pitch and yaw angles against the incoming airspeed vector. This was calculated by rotating the probe through all pitch and yaw angles in a wind tunnel and finding the difference between the set angle and the measured angle.

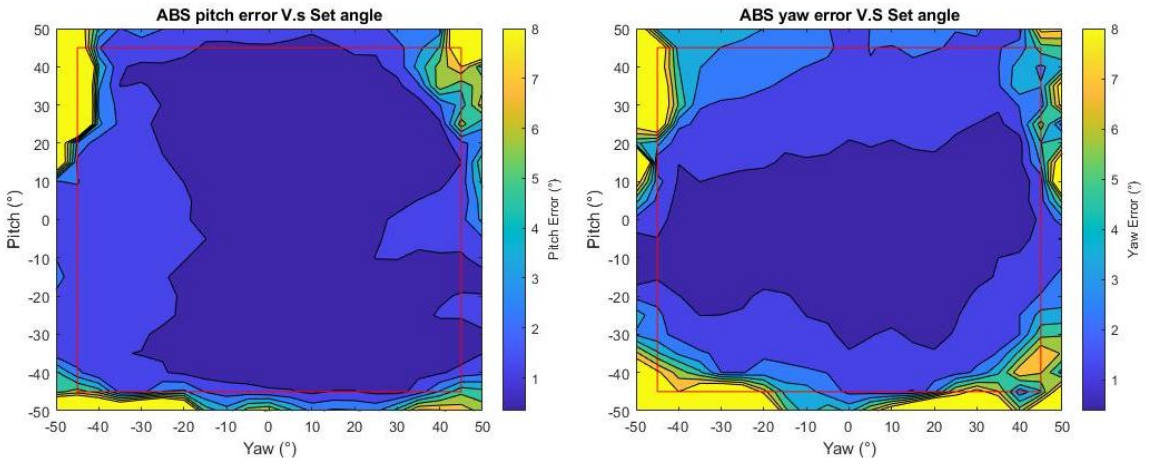


Figure 1. (Left) Absolute pitch error of the probe V.S set angle position. (Right) Absolute yaw error of the probe V.S set angle position.

3. METHOD

A sequence of flights is planned to examine the development of the shear layer over the roof of the building in strong wind conditions. This will include slow forward flight through the shear layer at varying heights from the roof (preliminary results shown in Section 4), examining the 3D flow with respect to the leading edge of the building. It is expected that two drones can be flown side by side in this space to collect spanwise wind data. During these experiments, another drone will be kept in a stationary hover upwind of the building. This will be used as a reference to compare the wind flow outside the influence of the structure. These flight experiments are part of a larger body of work at RMIT studying the flow structures around building 201 using a delayed detached Large Eddy CFD simulation(Mohamed, A. et al. 2015) and a range of experimental measurements in both $1/100^{th}$ model scale and full-scale. A description of the model-scale and full-scale experimental measurements are given in separate papers submitted to EACWE25.



Figure 2. (Left) Building 201 flight path and wind direction and upstream drone location. (Right) North face of the building. Leading edge shown in red

4. PRELIMINARY RESULTS

The following preliminary results were recorded on a test flight during a single of strong northerly winds. The reference drone recorded an average wind speed of 12.6 m/s with instantaneous maximums of 18 m/s at 53m above the ground. Within the overspeed region, this resulted an average velocity of 15.3 m/s and instantaneous velocities exceeding 21 m/s. A single drone was flown in forward flight through the shear layer at heights above the roof varying from 3m to 8m. The drone started from ~20m behind the leading edge of the building and flew just in front of the leading edge as shown in Figure 2. This was repeated 8 times sequentially over a period of 12 minutes. The probe was recording pressure samples at 1000Hz, which were post processed into velocity data, subtracting the kinematics of the drone. Finally, the results were normalized for comparison against a CFD model(Mohamed, A. et al. 2015), using an equivalent reference velocity calculated from the same logarithmic boundary layer profile used to initialize the simulation. Reference velocities were 3m/s and 5m/s at 10m altitude for the CFD and real data respectively.

Figure 2 shows the normalised wind speed as the vehicle transitions through the shear layer to just in front of the building. The transition through the shear layer is dependent on the height of vehicle above the roof, showing reasonable agreement with the simulation, however, the magnitude of the transition is consistently larger than the simulation predicts. Measurement 6 indicates an almost instantaneous increase in velocity far exceeding the CFD predictions and other measurement data. Correlations with the upstream reference drone indicate this may be the result of a momentary increase in wind speed.

Figure 4 depicts the vertical velocity component and shows extremely large fluctuations within the recirculation zone. As the 4-hole probe has a 90° cone of acceptance, in highly directional flows wind measurements outside of this cone produce large instantaneous fluctuations that do not accurately represent the true flow direction. This is a limitation of the 4-hole probe system, and this data can be detected and removed, however it is useful to indicate the highly directional nature of the flow. The measured vertical velocity shows significant variation with respect to the CFD data, likely a result of the turbulence already present in the atmosphere, which can be

observed using the upstream reference drone. Although an updraft is present in front of the leading edge, it is generally smaller in magnitude than CFD suggests. Further analysis is being undertaken, including filtering the measured data for a better comparison to the CFD model.

5. CONCLUSION

Using just these two small data sets, a picture of how the building affects atmospheric flows can begin to be developed. By expanding upon this data set, as well as conducting the other planned flight experiments (see Section 3), its thought that comparisons can be drawn with CFD and scale model data sets, to better understand the flow though the separated regions atop a building.

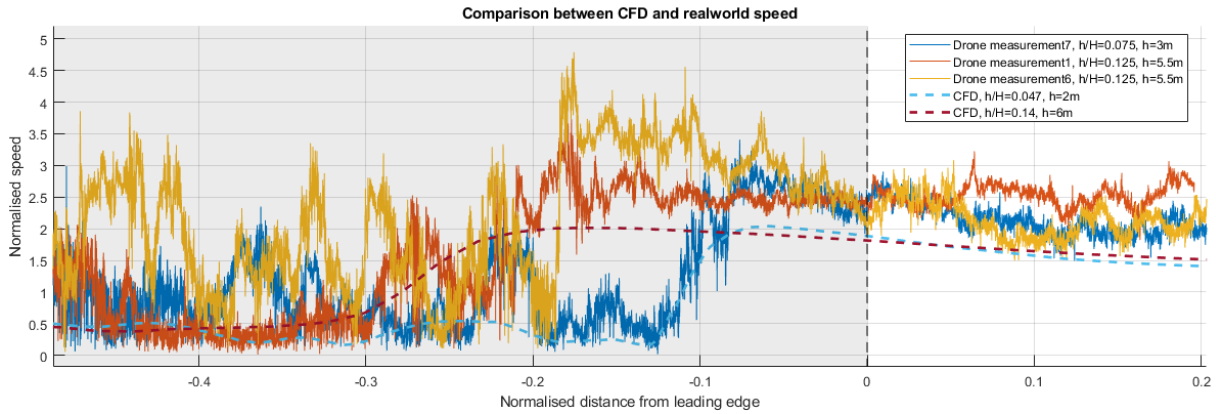


Figure 3. Comparison of normalised wind speeds between drone measurements and CFD model.

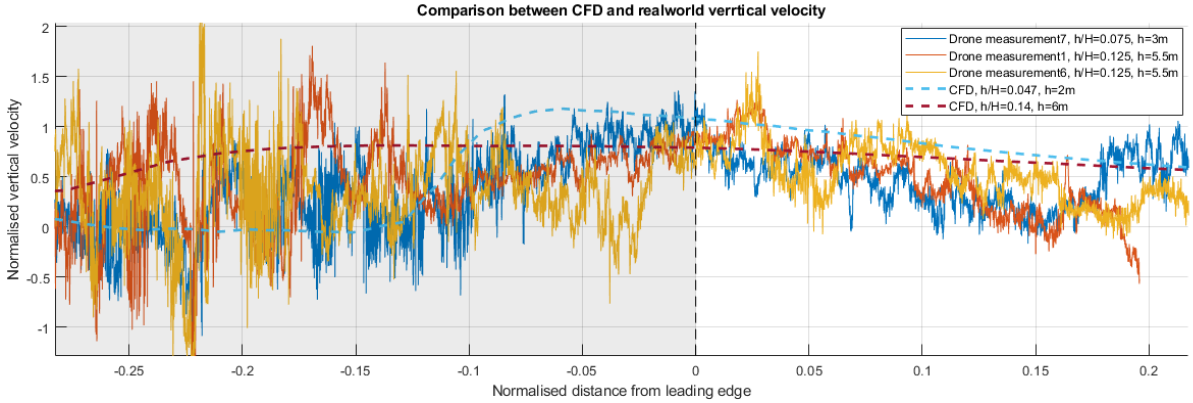


Figure 4. Comparison of vertical velocity between drone measurements and CFD model

REFERENCES

Kean, S, Marino, M, Watkins, S & Mohamed, A 2024, 'Swarm based airborne wind measurement', *International Micro Air Vehicles, Conference*, vol 15, pp. 156--162.

Mohamed, A, Carrese, R, Fletcher, DF & Watkins, S 2015, 'Scale-resolving simulation to predict the updraught regions over buildings for MAV orographic lift soaring', *Journal of wind engineering and industrial aerodynamics*, vol. 140, pp. 34-48.

Mohamed, A, Marino, M, Watkins, S, Jaworski, J & Jones, A 2023, 'Gusts Encountered by Flying Vehicles in Proximity to Buildings', *Drones (Basel)*, vol. 7, no. 1, p. 22.

Sitaram, N & Treaster, AL 1985, 'A Simplified Method of Using Four-Hole Probes to Measure Three-Dimensional Flow Fields', *Journal of fluids engineering*, vol. 107, no. 1, pp. 31-35.

Thompson, M, Watkins, S, White, C & Holmes, J 2011, 'Span-wise wind fluctuations in open terrain as applicable to small flying craft', *Aeronautical journal*, vol. 115, no. 1173, pp. 693-701.

Outdoor Particle-Tracking Velocimetry of Wind Above a Full-Scale Nominally Cuboid Building

Finn Sutherland[1], Simon Watkins[2], Matthew Marino[3], Abdulghani Mohamed[4]

RMIT University, Melbourne, Australia
s3369733@student.rmit.edu.au

SUMMARY:
This study demonstrates outdoor particle tracking velocimetry (PTV) as a viable method for mapping wind around buildings and similar structures and discusses some tips and recommendations for performing this type of PTV. Here 2D PTV is used to map a section of the wind velocity field above a full-scale building, using bubbles as tracer particles and a standard digital SLR camera to record footage. The study also demonstrates a drone-mounted camera as a viable method of capturing footage for 2D PTV, which allows greater flexibility with camera positioning and the field of view. An even background appears to be beneficial for outdoor PTV, and it is the authors opinion that direct sunlight is beneficial and cloud cover will usually hinder this type of PTV.

Keywords: PTV, wind, buildings

1. INTRODUCTION, MOTIVATION AND OBJECTIVES

The velocity field around the top of buildings is a relatively understudied part of wind engineering but is now the focus of those working in areas of urban aviation operations as they are starting to encroach into what was, until now, a no fly zone. Measurement techniques typically consist of discrete point measurements, often with temporal spacing, e.g. (Frost et al., 1977; Lim et al., 2016; Watkins et al., 2013; White et al., 2012), and while this is often fine for standard wind measurements in open areas where the time-averaged gradients are small, multiple measurement points are needed to capture the highly sheared flow field around buildings and inform the perturbations that aircraft using rooftop landing pads will be exposed to (Mohamed et al., 2014; Watkins et al., 2010).

Scale wind-tunnel PIV and PTV experiments are powerful tools for studying wind flow around buildings, as they can give the full velocity field in a plane or volume. The size and speed restrictions imposed by wind-tunnel facilities and PIV and PTV systems severely limit the achievable Reynolds number though, limiting the validity of data about the wind conditions that aircraft will be exposed to when using rooftop landing pads. Here we conduct PTV around a full-scale building, providing a real-world flow mapping of wind above a building.

2. THE BUILDING, SETUP AND PTV EQUIPMENT

The building in question is a roughly-cuboid 43m high building on RMIT University's campus in Bundoora, Melbourne, Australia. It is isolated from other structures of a similar height and surrounded by suburban terrain, so should be exposed to a canonical suburban atmospheric boundary layer. Weather conditions at the time were a 7km/h northerly wind (according to weather station measurements 7km to the South-East) and it was clear and sunny. Flow tracking was done using 10 bubble guns (**Figure 3**) mounted on a mast erected out in front of the building and recording footage of the bubbles. Two methods of recording footage were tried, the first was a tripod-mounted DSLR camera, while the second used a drone for recording footage. **Figure 2** shows the location of the bubble-gun mast and tripod-mounted camera, the camera was 7m from the bubble stream and the drone was about 15m from the bubble stream out of view of the photo. The drone was a DJI Spark and the DSLR camera was a Cannon 80D camera body with a 18mm lens. Both cameras recorded video at 30fps at 1920x1080 resolution and used a 1/8000s exposure. The DSLR camera had an f/22 aperture and 100 ISO setting, aperture and ISO for the drone camera are unknown.



Figure 1. RMIT University B201 LHS view from south-east showing terrain RHS view from north



Figure 2. Building rooftop showing bubble generator and position of fixed camera (drone camera was out of view).



Figure 3. Bubble guns used for seeding the flow.

Point measurements of wind velocity were taken in the bubble stream for validation of the PTV results, using two Cobra probes (multi-hole pressure probes). The Cobra probes were positioned in the shear layer, 6m back from and 3.4m above the upwind edge of the building.

3. RESULTS

Figure 4 shows the time-averaged and instantaneous wind speed results from the tripod-mounted camera and drone respectively, overlaid on a cross-section of the building. The drone recording was taken at a different time to the recording taken with the fixed camera, so the wind speed is different between the two recordings. It should also be noted that bubble dispersal effectively thickened the plane that is tracked, which will lead to some lateral spatial averaging and introduce error into the calculated bubble velocities due to the distance of the bubbles from the camera changing.

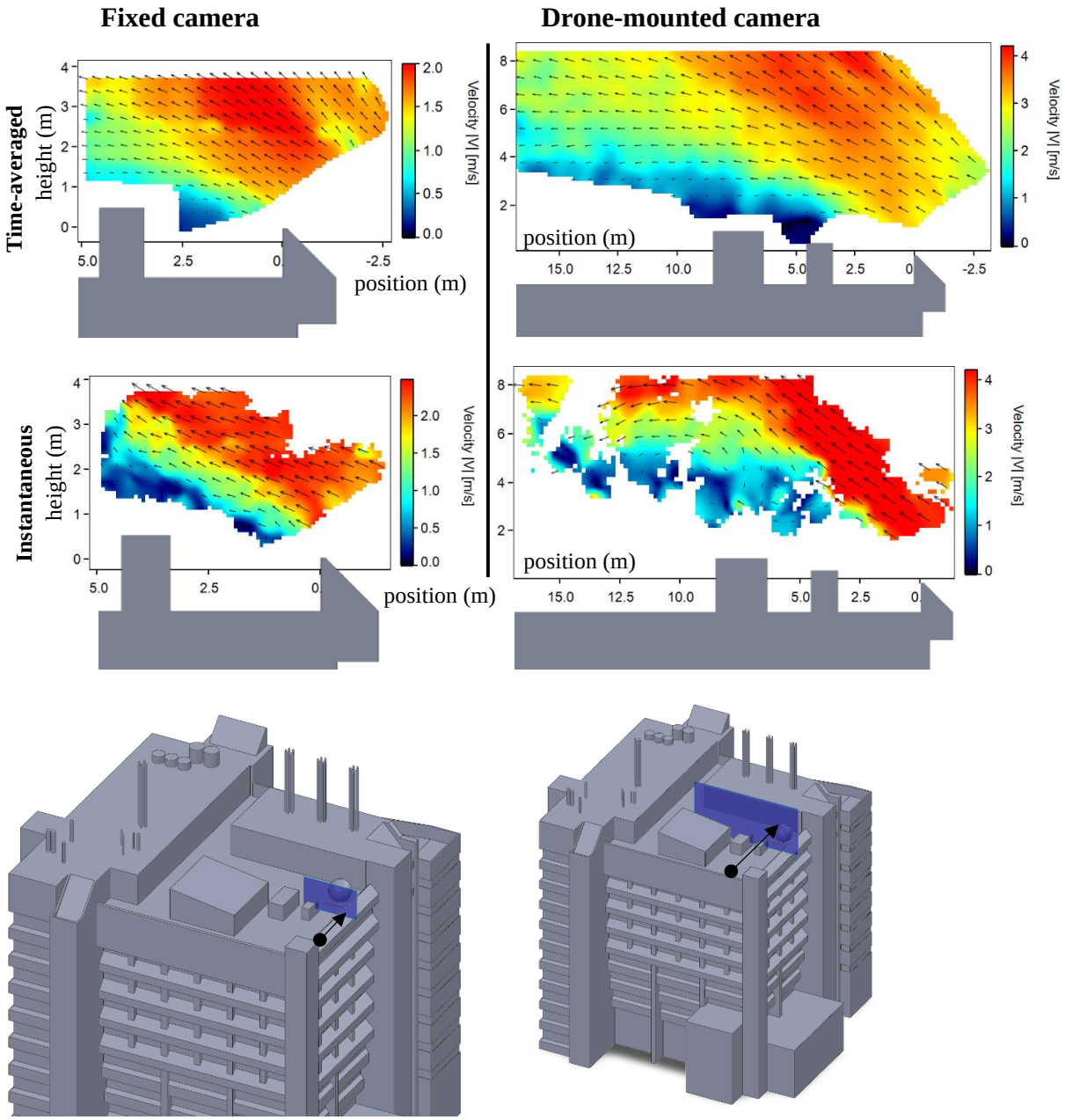


Figure 4. Time-averaged (top) and instantaneous (bottom) wind speed from the fixed camera (left) and drone-mounted camera (right), and isometric view of the building showing measurement plane for the two cameras, and camera positions (black dot).

4. DISCUSSION

The PTV results captured the sheared flow in the shear layer coming off the upwind edge of the building. The instantaneous results appear to capture turbulent eddies in the shear layer, but a comparison with reliable measurements is needed to determine how well the method is capturing these transients. Recording footage from the drone gave more flexibility with positioning than using the tripod-mounted camera, allowing shooting from beyond the extents of the building which allows a larger field of view and reduces error introduced by bubble dispersal. Pre-processing the footage to correct for the drone's movement was necessary though.

Having a shaded/dark background is beneficial, so tracking was good in areas with the shaded brick wall as the background. Tracking against the sky was more challenging but still possible, although a clear sky is desirable as there would probably not be enough contrast against cloud or with the sun behind clouds. Tracking with uneven background intensity (i.e. the ground, other objects) was most challenging, as sharp changes in brightness are much more difficult to filter out in pre-processing. It should be noted that there was substantial camera movement during these recordings though, (>1 pixel) even after manipulating the images to correct for this movement, uneven backgrounds will probably cause less interference with less camera movement.

5. CONCLUDING REMARKS

Here we have demonstrated outdoor full-scale particle-tracking velocimetry as a viable technique, including around structures like buildings, however validation of the results is required before confirming it as a valid method of mapping or tracking wind. We also demonstrated that using drone-based footage for 2D particle-tracking velocimetry is viable, giving much greater flexibility with the field of view and camera positioning than conventional camera mountings. Future research will focus on the extraction of turbulence statistics and spectra, as well as their implications for aircraft landing on buildings. Comparisons to other experimental and CFD results for the same building will be drawn as part of on-going work. This will enhance our understanding of the conditions and control inputs that autonomous aircraft landing on top of building will encounter as well as providing data to validate (or otherwise) CFD simulations.

REFERENCES

Frost, W., Shahabi, A. M., Institute, U. o. T. S., Aeronautics, U. S. N., Administration, S., & Center, G. C. M. S. F. (1977). *A Field Study of Wind Over a Simulated Block Building*. National Aeronautics and Space Administration. https://books.google.com.au/books?id=MVtR0q_mfHUC

Lim, K. E. W., Watkins, S., Clothier, R., Ladani, R., Mohamed, A., & Palmer, J. L. (2016). Full-scale flow measurement on a tall building with a continuous-wave Doppler Lidar anemometer. *Journal of wind engineering and industrial aerodynamics*, *154*, 69-75. https://doi.org/10.1016/j.jweia.2016.04.007

Mohamed, A., Watkins, S., Clothier, R., & Abdulrahim, M. (2014). Influence of Turbulence on MAV Roll Perturbations. *International journal of micro air vehicles*, *6*(3), 175-190. https://doi.org/10.1260/1756-8293.6.3.175

Watkins, S., Lim, E. W., & Ladani, R. (2013). *The velocity field around the top of a tall building; model-scale and full-scale measurements*. International Association for Wind Engineering.

Watkins, S., Thompson, M., Loxton, B., & Abdulrahim, M. (2010). On Low Altitude Flight through the Atmospheric Boundary Layer. *International journal of micro air vehicles*, *2*(2), 55-68. https://doi.org/10.1260/1756-8293.2.2.55

White, C., Lim, E. W., Watkins, S., Mohamed, A., & Thompson, M. (2012). A feasibility study of micro air vehicles soaring tall buildings. *Journal of wind engineering and industrial aerodynamics*, *103*, 41-49. https://doi.org/10.1016/j.jweia.2012.02.012

RMIT Classification: Trusted

The Flow Field over a Cuboid Building: Full-Scale and Model-Scale Comparison

Finn Sutherland [1], Simon Watkins[1], Abdulghani Mohamed[1] and Matt Marino[1]

[1]*RMIT University, Melbourne, Australia, s3369733@student,rmit.edu.au*

SUMMARY
Cobra probe measurements of the velocity fluctuations over the roof of a nominally cuboid building are presented in both full-scale and in a 1/100th scale wind-tunnel replication for locations in, above and below the shear layer. Generally reasonable agreement was found, but for locations in and above the shear layer the full-size turbulence intensities were greater than in the model scale, whereas below the shear layer (in the full separated flow region over the roof) this trend was reversed. Further work and analysis will be presented in the full paper.

Keywords: velocity, turbulence, roof, building, full-scale, model-scale, spectra, drone, delivery, Cobra, PTV

1 INTRODUCTION, MOTIVATION AND OBJECTIVES

The velocity field around the top of buildings is a relatively understudied part of wind engineering but is now of interest as autonomous aircraft are starting to encroach into cities. Aircraft can vary in size from 0.3 m to 30 m with the smaller craft used to deliver packages, food etc. (e.g. pizza delivery) and the larger air taxis planned to deliver passengers. There are several challenges associated with this new and growing part of aviation, including keeping a steady position or flight trajectory. The focus of this paper is the wind field over the roof of a building. The most challenging aspects of the flow field, from the perspective of a flying or hovering craft are thought to be the separated flow above the roof and from shear layers separating from the upstream face of the building which can provide a strong perturbation to flying craft (Mohamed et. al., 2023).

The building studied is part of RMIT Bundoora Campus and is subject to a suburban residential atmospheric boundary layer (ABL). The flow has been the focus of a delayed detached Large Eddy CFD simulation (Mohamed et. al., 2015) and a range of experimental measurements in both 1/100th model scale and full-scale. Cobra-probe measurements and particle tracking velocimetry (PTV) have been done at both 100th-scale and full scale, and recently flying Cobra-probe measurements have been taken at full scale. A description of the flying Cobra probe system and details of the PTV are given in separate papers submitted to EACWE25.

These measurements and simulations allow a comparison to be made between full-size velocity measurements, wind-tunnel measurements and CFD. The objective of this paper is to compare and contrast the results from scale wind-tunnel tests with the full-scale measurements, particularly the temporal variations in time and space which challenge the steadiness of craft and how well model-scale experiments can accurately predict these temporal variations.

RMIT Classification: Trusted

2 THE BUILDING, INSTRUMENTATION AND MODEL-SCALE REPLICATION

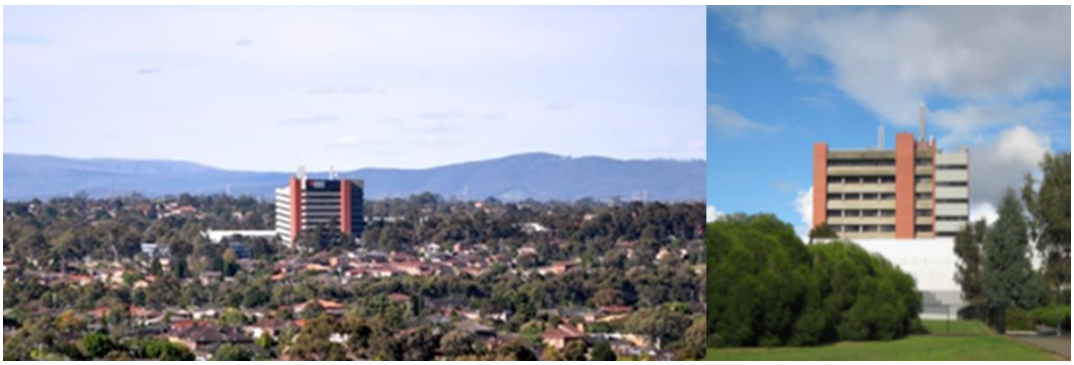


Figure 1. RMIT University B201 LHS view from south showing terrain RHS view from north

All results were related to a nominally northerly wind and were taken above the roof line with some data taken forward of the building (upstream) mainly using Cobra-probe mounted drones.

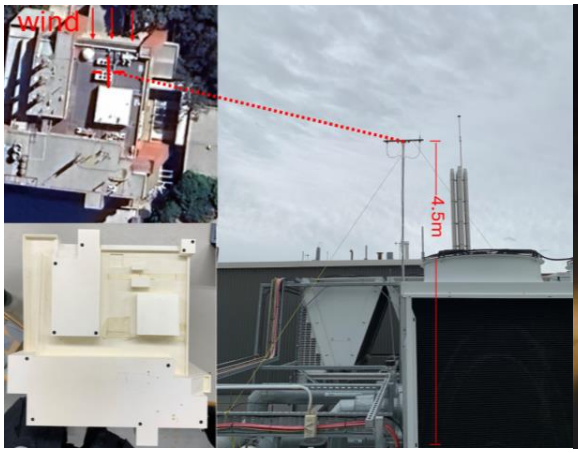


Figure 2. Roof with location of Cobra probes



Figure 3. 1/100th rapid-prototyped replica in RMIT Industrial Wind Tunnel

Cobra probes were used to measure the fluctuating velocities, both outdoor and in the tunnel. These provide a 90-degree cone of acceptance and can resolve the velocity fluctuations in the three orthogonal directions at frequencies up to 2000Hz, an example time-history trace of wind velocity is shown in Figure 4. In the outdoor measurements two cobra probes were positioned on the mast laterally separated by 450 mm (Figure 2) and were simultaneously sampled at 150Hz. In the tunnel (Figure 3) one was used (with an automated traversing system), set to the default sampling rate of 2000Hz. A replicated suburban ABL was generated in the tunnel and a good replication of mean velocity profile and turbulence intensities (u,v,w, again measured with the Cobra probes with no buildings present) resulted.

RMIT Classification: Trusted

3 RESULTS AND DISCUSSION

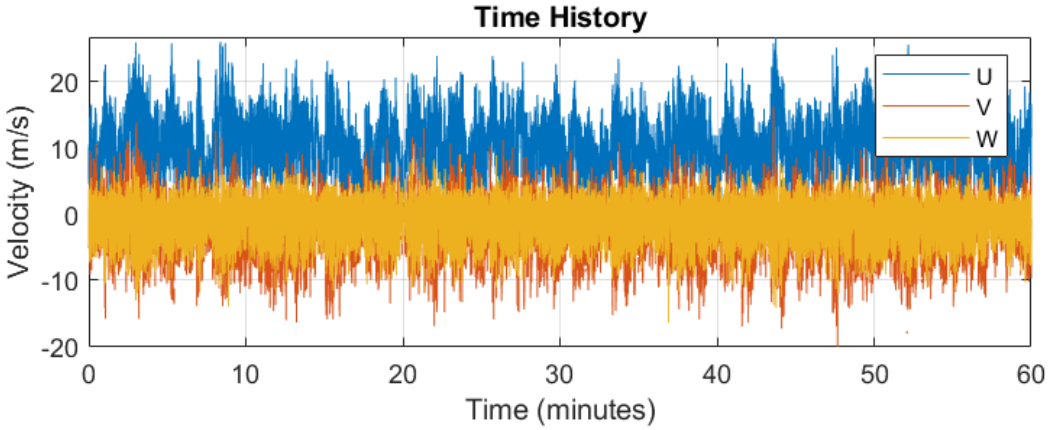


Figure 4. Typical time-history trace of wind velocity components over the sampling period (full-scale measurement shown here).

Table 1. Turbulence intensities measured below, in, and above shear layer above full-scale building (blue) and 100th-scale model (red).

Turbulence Intensities	Below shear layer	In shear layer	Above shear layer
Full-scale	0.364	0.262	0.201
100th-scale	0.424	0.214	0.141

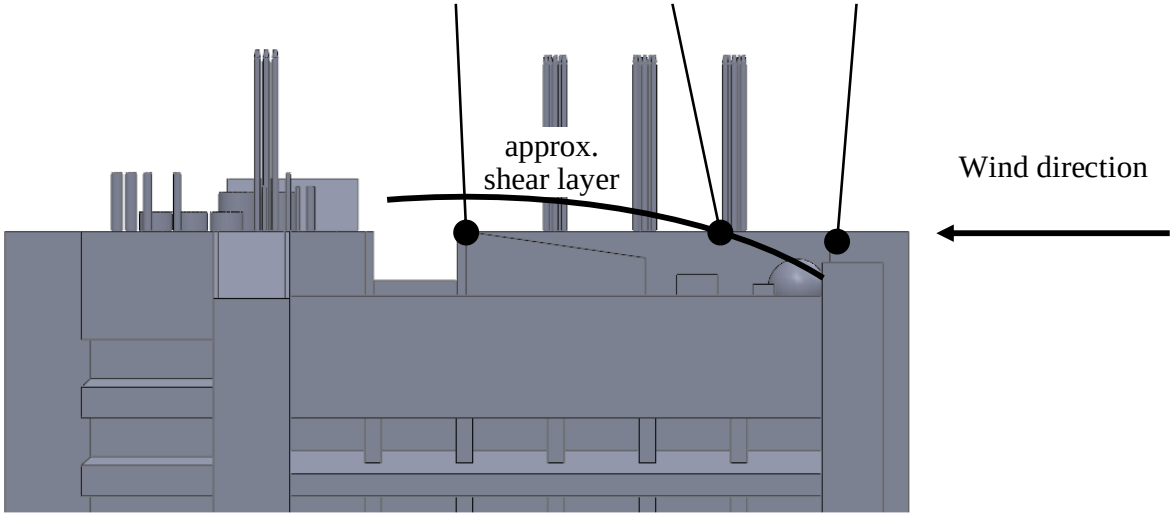


Figure 5. Sideview of building showing Cobra-probe positions and the approximate time-averaged shear layer.

RMIT Classification: Trusted

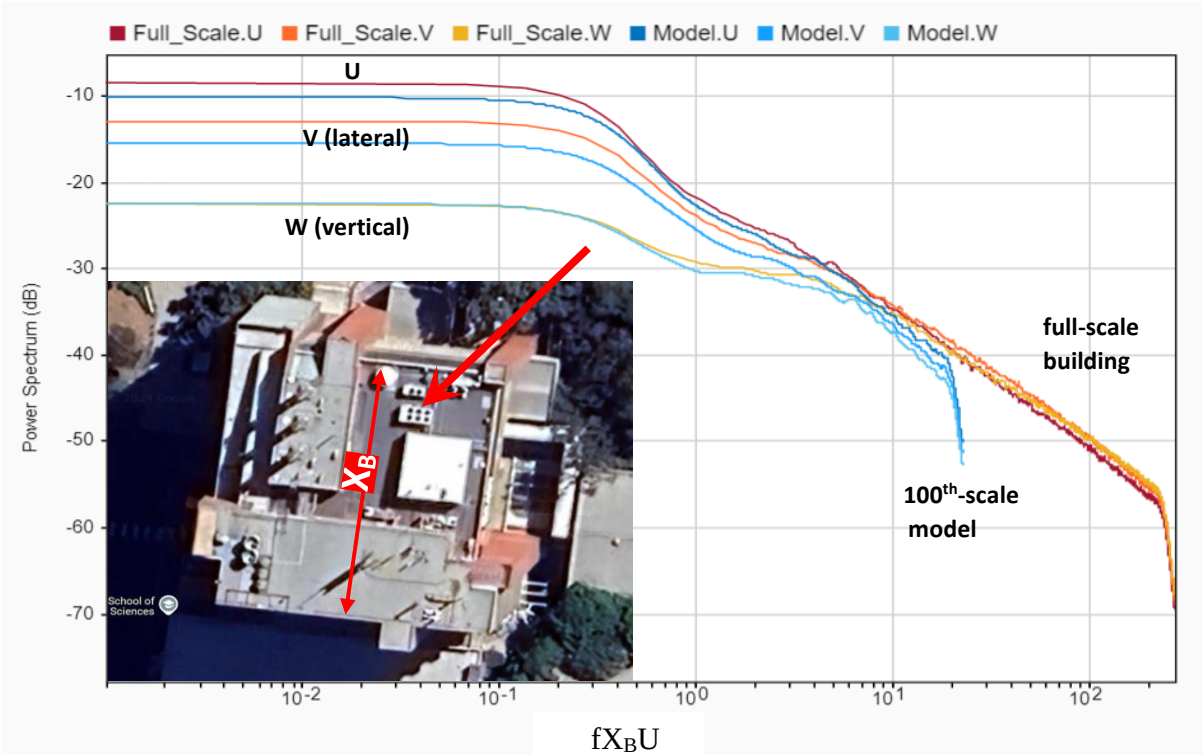


Figure 6. Power spectrum of velocity components in the shear layer above the full-scale building and 100th-scale model.

There are some differences between the full-size and model-scale turbulence intensities in Figure 5, with most of these differences in the lateral and along-wind components in the lower frequency parts of the spectra (Figure 6). However the wind speed measured outdoors (over one hour) was very steady and removal of the low-frequency trends did little in removing the discrepancy, but more data processing is on-going to attempt to further understand the reasons between the outdoor and model-scale results and to draw comparison with the CFD data.

5 REFERENCES

Kean, S, Marino, M, Watkins, S & Mohamed, A 2024, 'Swarm based airborne wind measurement', vol., pp. 156--162.

Mohamed, A, Carrese, R, Fletcher, DF & Watkins, S 2015, 'Scale-resolving simulation to predict the updraught regions over buildings for MAV orographic lift soaring', Journal of wind engineering and industrial aerodynamics, vol. 140, pp. 34-48.

Mohamed, A, Marino, M, Watkins, S, Jaworski, J & Jones, A 2023, 'Gusts Encountered by Flying Vehicles in Proximity to Buildings', Drones (Basel), vol. 7, no. 1, p. 22.

OBJ

Aerodynamic forces on novel tetra-shaped solar panels mounted on flat roof: first insights from field measurements

Anjali Radhakrishnan Jayakumari [1], Stefanie Gillmeier[1]

[1]*Eindhoven University of Technology, Eindhoven, the Netherlands,*
a.k.radhakrishnan.jayakumari@tue.nl - s.g.gillemeier@tue.nl

SUMMARY:
The increasing demand for clean energy necessitates innovations in renewable energy technologies to enhance both performance and cost efficiency. A novel lightweight tetra-shaped solar panel has been developed. This study examines the aerodynamic performance of this design through a field measurement campaign. A 4x4 configuration of tetra-shaped panels was installed on the flat roof of a high-rise building to analyse the aerodynamic lift forces acting on the panels under varying wind conditions. Wind speed and direction at the location, along with the resulting pressures on the upper and lower surfaces of the panels, were measured simultaneously to assess the resulting lift forces. The first results indicate that the innovative tetra design seems to exhibit relatively low average lift forces across various wind speeds and directions, while peak lift forces increase with wind speed.

Keywords: aerodynamic lift, flat roof-mounted solar panel, wind effects

1. INTRODUCTION

Solar photovoltaic (PV) panels have gained significant popularity as a renewable energy solution due to their versatility in generating power for both individual households and larger-scale solar farms (REN21, 2021). To further reduce installation costs for roof-mounted solar panels, a novel tetra-shaped design has been developed jointly with the company Solarge using lightweight polymer composite materials. This innovative design has been compared to conventional flat and dual-tilted solar panels through wind tunnel tests and computational fluid dynamics simulations (Jayakumari et al., 2024) for ground-mounted scenarios. Analyzing the aerodynamic performance for roof-mounted scenarios is essential, as the aerodynamic forces are influenced by the complex flow field created by vortices from roof-edge separations and turbulence in the atmospheric boundary layer (Kopp et al., 2012). This paper presents field measurement results for an array of tetra-shaped solar panels installed on the flat roof of a tall building at Eindhoven University of Technology (the Netherlands) at 15.5 m height, offering valuable first insights into real-world aerodynamic performance.

2. METHODOLOGY

A 4x4 configuration of tetra-shaped solar panels is installed on the southwest corner of the flat building roof, at a height of 15.5 meters. The panels are positioned close to each other, with a gap of 0.01 m between them. The tetra-shaped panel features a 3-dimensional design with a tilt angle (φ) of 12.5° in four directions and an opening at the center, as illustrated in Figure 1a. The panel measures 2.1 m in length and width, with a height of 0.23 m and the central opening has a dimension of 0.38 x 0.38 m^2. Side covers are attached to the panel, ensuring they touch the roof surface and prevent any wind flow underneath the panel through the sides. Two of the four solar panels (labeled A and B in Figures 1a-b) are equipped with pressure sensors -16 sensors on the top surface and 16 on the bottom surface (Figure 1b – odd numbers correspond to sensors on bottom surface and even numbers correspond to sensors on the top surface). A 64-channel Scanivalve MPS4264 pressure transducer is used for pressure measurements. The transducer is connected to the sensors via 8 m long urethane tubing. To account for any phase and amplitude distortion resulting from the longer pressure tubes, tubing transfer functions are acquired using the methodology proposed by Irwin et al. (1979) and corrections are applied to the raw time series before data analysis. Pressure data is recorded at 10 Hz and saved in 1-hour batches. The static reference pressure (P_0), measured in a shielded box located on the roof near the solar panels, accounts for atmospheric variations in static pressure. The pressure recorded at each of the 16 sensors is compensated for the P_0. At the end of each hour, the pressure hoses are flushed with Nitrogen to prevent blockages before the next recording. The aerodynamic lift force (F_L) on each panel is calculated from the pressure difference measured across the panel surfaces. For this, each panel is divided into 16 sub-surfaces assuming uniform pressure distribution, and total lift force is determined using the following Eq. (1):

$$F_L = \sum A_n \Delta P_n \cos\varphi \tag{1}$$

where, n - index corresponding to a subsurface, n = 1,2,...,16, A_n is the area of a sub-surface, ΔP_n is the net pressure across the sub-surface and φ is the tilt of the panel surface with respect to a horizontal plane. To simultaneously monitor the wind conditions, an anemometer is also installed on a higher roof of the same building at 70 m height (Figures 1c-d). A 3-axis ultrasonic anemometer (WindMaster, Gill Instruments Ltd.) is used for velocity measurements. The anemometer recorded all three velocity components at 10 Hz, enabling the calculation of wind speed and direction.

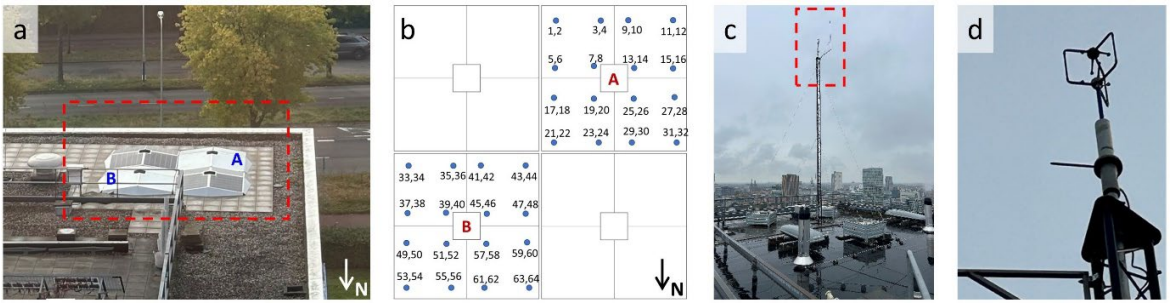


Figure 1. (a) Solar panels installed on the roof at 15.5 m height; (b) pressure sensor locations on the top and bottom panel surfaces; and (c,d) the anemometer installed on the roof at 70 m height.

3. RESULTS

The pressure and wind characteristics are monitored for over six months, however for brevity, this abstract focuses on the analysis of two relevant one-hour intervals – one-hour of a relatively higher wind speed and one-hour of a relatively lower wind speed. Figure 2a-b shows the resulting wind speed and the directionality for the chosen period of relatively higher wind speed. The average wind speed is 10 m/s with the highest wind speed recorded of 21.7 m/s at 70 m height. The prevailing wind direction for the period is south-west. Figure 3 shows the time series of the lift experienced by the panels for this period. The average lift force ($F_{L,mean}$) is -0.3 N for panel A and 1.5 N for panel B. The minimum and maximum instantaneous lift $F_{L,min}$ and $F_{L,max}$ recorded for panel A are -27.3 N and 20 N, respectively. For panel B, the $F_{L,min}$ and $F_{L,max}$ are -11.9 N and 27.1 N, respectively. Negative/positive forces imply an upward/downward suction force on the panel. Table 1 shows the comparison of the results from the lower and higher wind speed scenarios. From there it can be observed that the lift forces increase with increased wind speed. However, for the considered wind speed and directions, the tetra panel design is aerodynamically efficient, with minimal F_L on average for both panels, irrespective of the wind conditions. This efficiency is likely due to the central opening, which promotes a more balanced pressure distribution between the top and bottom surfaces, effectively reducing F_L. Additionally, the close positioning of the panels, along with the side covers that prevent airflow beneath the panels, further contributes to this reduction in F_L.

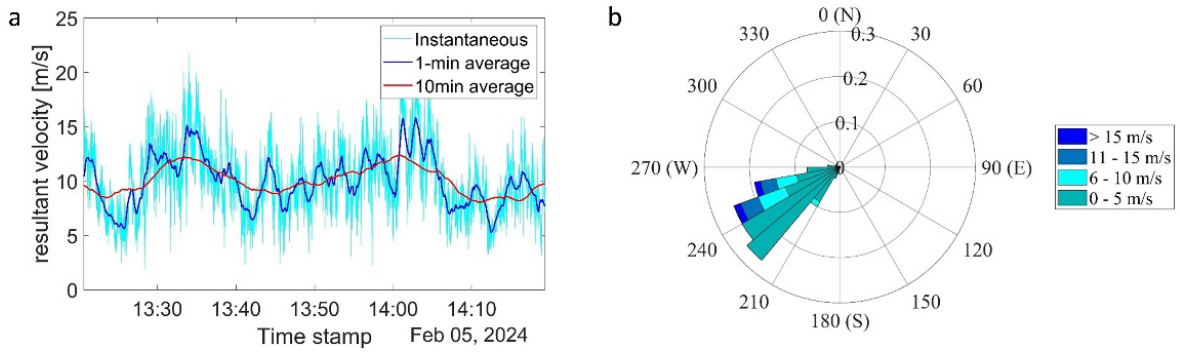


Figure 2. (a) Wind speed for a duration of 1 hour; and (b) Wind rose showing the wind directionality and speed for the period.

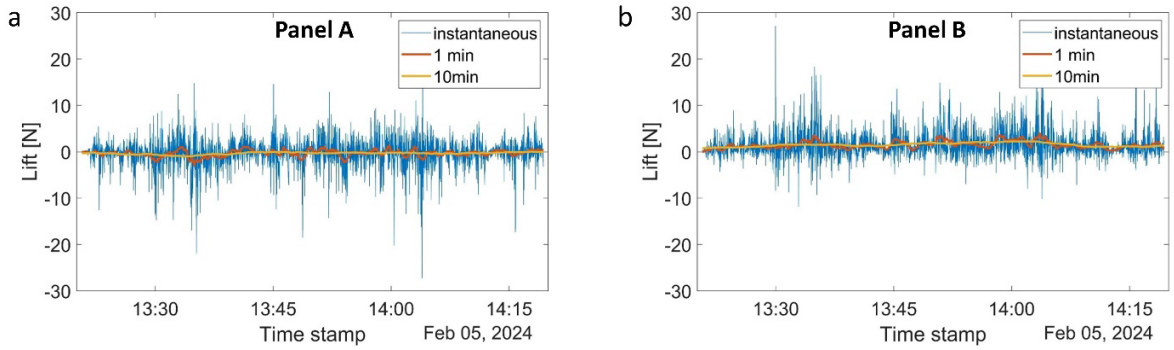


Figure 3. Time series of the lift force (F_L) for the higher wind speed scenario on (a) panel A and (b) panel B.

Table 1. Wind characteristics and the lift forces on the panels for the two wind speed scenarios.

	Higher wind speed scenario		Lower wind speed scenario	
	Panel A	Panel B	Panel A	Panel B
Mean wind speed [m/s]	10		3.62	
Wind directionality	Southwest		East-southeast	
$F_{L,mean\ [N]}$	-0.3	1.5	-0.2	0.2
$F_{L,min\ [N]}$	-27.3	-11.9	-1.4	-0.3
$F_{L,max\ [N]}$	20.0	27.1	0.3	1.5

7. CONCLUSIONS

The arrangement of 4x4 tetra-shaped solar panels installed on the flat roof of a high-rise building is analysed under two distinct wind conditions. It is observed that instantaneous lift forces varied significantly with changes in wind speed and direction. The maximum and minimum lift (or downward) force increases with increasing wind speeds. On average, the panel experiences minimal lift forces for the wind speeds and directions analysed, likely due to pressure equalization facilitated by the central opening between the top and bottom surfaces, the close positioning of the panels, and the inclusion of side covers. Additional measurements will be carried out to further investigate the central opening's potential role in reducing lift forces. It should be noted that these findings are specific to the analysed scenarios, including building and roof configurations, orientation with respect to wind direction, wind-building interactions, panel orientation on the roof, and wind characteristics.

ACKNOWLEDGEMENTS

The authors thank the Netherlands Enterprise Agency (Rijksdienst voor Ondernemend Nederland), section Missiegedreven Onderzoek, Ontwikkeling en Innovatie (MOOI), for their financial support for this project and the solar panel company Solarge for the excellent collaboration and support throughout this project. The authors also appreciate the contributions of the consortium partners SolarFields Nederland B.V., Elro Dakbedekking Zuid B.V., and Rombouts Kunststof Techniek Tholen, for the successful collaboration.

REFERENCES

Irwin, H.P.A.H., Cooper, K.R., Girard, R., 1979. Correction of distortion effects caused by tubing systems in measurements of fluctuating pressures. Journal of Wind Engineering and Industrial Aerodynamics 5, 93–107, 93–107.

Jayakumari, A.K.R., Ricci, A., Gillmeier, S., 2024. Assessment of aerodynamic force coefficients on different solar panels by LES simulations. Proceedings of 9th International Colloquium on Bluff Body Aerodynamics and Applications, 29 July – 2 August 2024. Birmingham, UK.

Kopp, G.A., Farquhar, S., Morrison, M.J., 2012. Aerodynamic mechanisms for wind loads on tilted, roof-mounted, solar arrays. Journal of Wind Engineering and Industrial Aerodynamics 111, 40–52.

REN21, 2021. Renewables 2021 Global Status Report. REN21 Secretariat, Paris, France. ISBN 978-3-948393-03-8.

Wind conditions monitoring for solar collector array design: the case of Nevada Solar One

Yuanchen Wan[1], Etienne Cheynet[1], Yan Li[2], Ulrike Egerer[3]

[1]*Geophysical Institute and Bergen Offshore Wind Centre, University of Bergen, Bergen, Norway, yuanchen.wan@uib.no; etienne.cheynet@uib.no*
[2]*Department of Mathematics, University of Bergen, Bergen, Norway*
[3]*National Renewable Energy Laboratory (NREL), USA*

SUMMARY: This work examines the wind conditions near a concentrated solar power plant based on full-scale field measurements. The study aims to provide novel insights into the mean and turbulence characteristics of the wind flows, which are necessary to improve the wind-resistant design of solar energy facilities. The turbulence intensity and roughness length were estimated for wind directions ranging from 180° to 360°, with 270° indicating undisturbed wind perpendicular to the trough rows. The sector-averaged upstream roughness length was estimated to range from 0.1 to 0.18 m, leading to turbulence intensity of 29% at 5 m above the ground for the along-wind component. Monin-Obukhov similarity theory is found to apply well to the momentum flux in the lowest 7.5 m above the ground, except for moderately and strongly stable flows. Spectral analysis reveals deviations from the Simiu and Scanlan turbulence model used in wind engineering at low frequencies.

Keywords: roughness length,turbulence intensity,power spectra

1. INTRODUCTION

Parabolic troughs are widely used in solar thermal energy plants, accounting for more than 80% of the concentrating solar power (Zhang et al., 2020). These devices use thin mirrors with a parabolic shape, making them highly sensitive to wind loads. High turbulence intensity is experienced by the mirrors due to their proximity to the ground. Also, the temperature difference between day and night creates a strong diurnal cycle of turbulence (Sutherland et al., 2016). This work aims to assess the wind conditions at Nevada Solar One (NSO) based on full-scale measured data (Egerer et al., 2024) performed by National Renewable Energy Laboratory (NREL). The results of this study will provide a foundation for improving the wind-resistant design of solar systems.

2. BACKGROUND AND METHOD

Following Monin-Obukhov similarity theory (MOST, Kaimal (1994)), the dimensionless wind shear can be expressed as a function of $\zeta = z/L$ (eq. (1)), where z is the height and L is the Obukhov length:

$$\phi_m = (1+16|\zeta|)^{-1/4} \text{ for } -2 \leq \zeta \leq 0 \text{ and } \phi_m = 1+5\zeta \text{ for } 0 \leq \zeta \leq 1. \quad (1)$$

where ϕ_m represents the dimensionless vertical wind shear of u, ζ represents the dimensionless stability parameter.

The power spectral density of the three wind velocity components are compared to the the spectral velocity model by Simiu and Scanlan (1996), defined as:

$$\frac{nS_u(n)}{u_*^2} = \frac{200f_r}{(1+50f_r)^{5/3}}, \text{ and } \frac{nS_v(n)}{u_*^2} = \frac{15f_r}{(1+9.5f_r)^{5/3}} \text{ and } \frac{nS_w(n)}{u_*^2} = \frac{3.36f_r}{(1+10f_r^{5/3})} \quad (2)$$

where n is the frequency, S_u, S_v and S_w are the power spectra of u, v and w wind components (the u is the longitudinal component from west to east, v is the lateral component from south to north and the w is the vertical velocity component), $f_r = nz/\overline{u}$ represents the reduced frequency and u_* is the friction velocity.

NSO is located at 35.8°N, 114.983°E, at an elevation of 540 meters in a hilly desert area. The left panel of figure 1 shows the topographic map of NSO. The inflow wind data was measured at heights of 7 m, 5 m and 3.5 m using 3D sonic anemometers and all anemometer were calibrated in accredited wind tunnel or by the manufacturer. It was recorded from October 2021 to June 2023 at a frequency of 20 Hz. This paper focuses on inflow data with wind directions from 180° to 360°, avoiding the direct wake of parabolic trough arrays (the red patch in figure 1).

The right panel of figure 1 shows the distribution of the stability parameter ζ as a function of the mean wind speed. This distribution shows that when the wind speed at 5 m is larger than 5 m s^{-1} the atmosphere can be considered as near-neutral 80% of the time.

3. RESULTS

Figure 2 shows the roughness length (left panel) and the associated turbulence intensity (right panel) estimated by the sonic anemometer at 5 m above the surface. The roughness length was calculated by fitting the logarithmic wind speed profile to the measured wind profile and friction velocity under near-neutral conditions (Panofsky and Dutton, 1984). In total, 18 different inflow

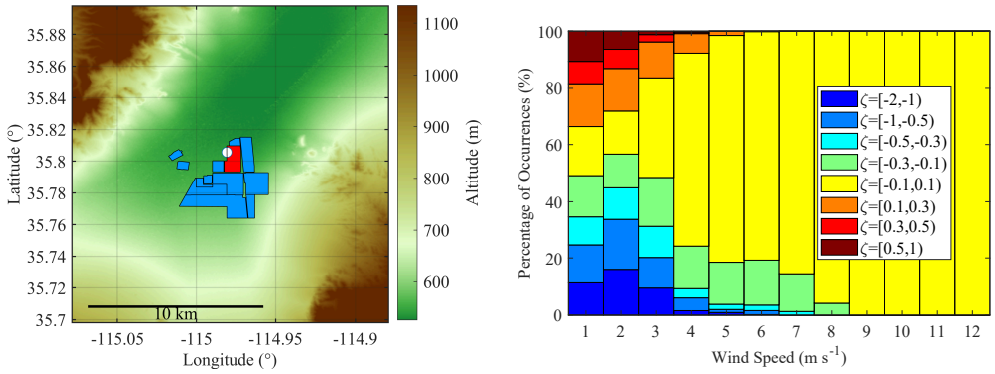


Figure 1. Left panel: Topography around NSO, where the white circle denotes the location of the inflow mast; the red and blue patches represent the area of interest and photovoltaic solar plants, respectively. The right panel shows the dynamic atmospheric stability ζ estimated at 5 m above the surface against the mean wind speed.

directions, ranging from 180° to 360°, were selected to assess the dependence of the roughness length on the wind sector. The average roughness length in the western direction is 0.18 m, while the minimum value is 0.02 m in the northern direction. Comparison with the topography map in Figure 1 suggests that the maximum roughness length is due to the leeside of the mountain at 320°. For westerly winds, the roughness length is around 0.177 m, likely increased by buildings upstream of the mast. The estimated roughness length reflects the topography of the site, characterized by small bushes and sparse vegetation (Wieringa, 1986).

The dimensionless vertical wind shear, ranging from 240° to 360°,is shown in figure 3 at the three different heights. Overall, the measurements agree well with MOST, except for $\zeta > 0.3$. This suggests that MOST can be applied in our case at heights below 10 m above the surface, except under moderately and strongly stratified atmosphere.

Figure 3 compares the power spectral densities of three wind components from 240° to 360° with the Simiu and Scanlan model (SSM) (Simiu and Scanlan, 1996). The curves indicate that the inertial subrange is well represented by the SSM, though some aliasing or flow distortion is noticeable at $f_r > 8$. For frequencies below $f_r < 0.1$, the S_u and S_v spectra deviate from the SSM. This is likely due to the measurements being taken in the eddy-surface layer, where surface-induced eddy distortion causes a broad, flattened spectral peak (Hunt and Morrison, 2000). These results suggest that a modified spectral model may be needed to accurately describe turbulence near the surface.

4. CONCLUSION

This work examined the near-surface wind conditions at the NSO parabolic troughs power plant, based on publicly available full-scale datasets (Egerer et al., 2024). For westerly wind representing upstream wind conditions, the roughness length at NSO was estimated to range from 0.10 to 0.18 m, consistent with a roughness length for low vegetations. MOST is found to be appropriate for the momentum flux equation, except under moderately and strongly stable stratification conditions.

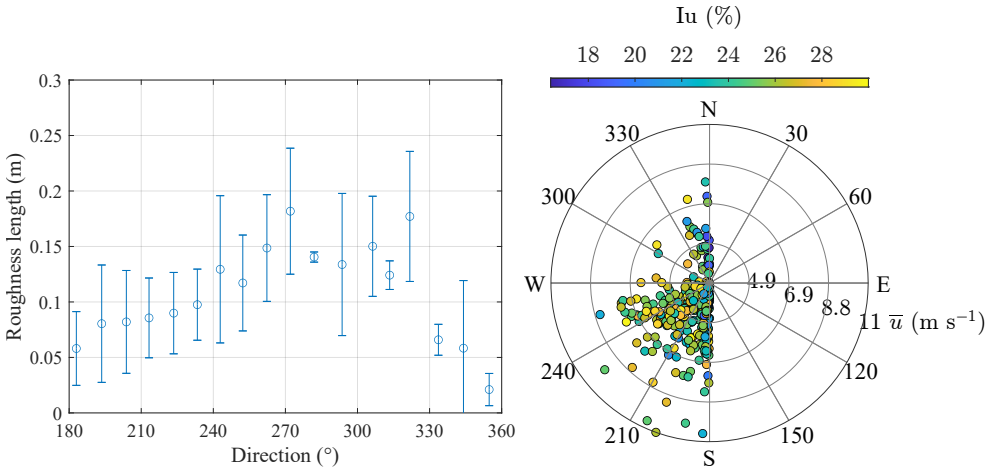


Figure 2. Left panel: Roughness length against the inflow directions. The errorbar represents two standard deviations. Right panel: Along-wind turbulence intensity recorded by the sonic anemometer at 5 m above the surface.(637 samples collected from 2022-01-01 to 2023-04-01)

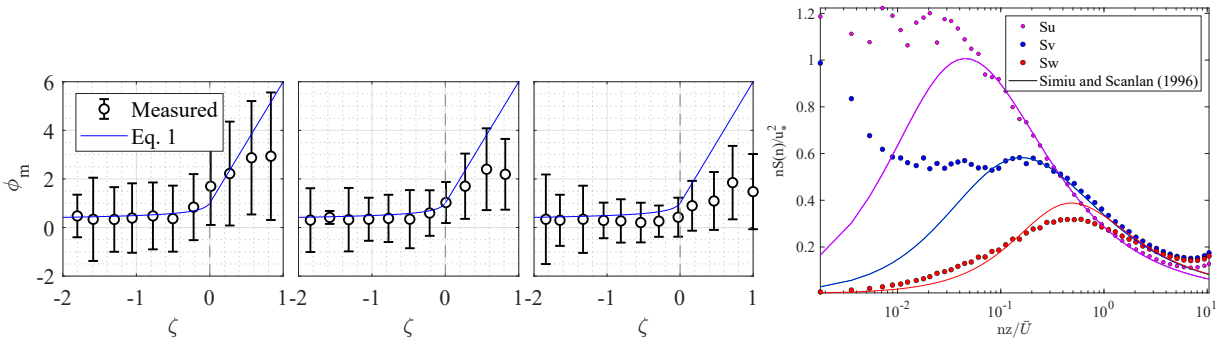


Figure 3. Left panel: Non-dimensional wind shear as a function of atmospheric stability parameter ζ at 3.5 m (left panel), 5 m (middle panel) and 7 m (right panel).(2840 samples each panel collected from 2022-01-01 to 2023-04-01);Right panel: Ensemble-averaged power spectral density of the three velocity components estimated at 5 m above the ground (174 samples collected from 2022-01-01 to 2023-04-01)

The SSM for the velocity spectra generally works well, but it shows discrepancies at frequencies below 0.05 Hz. It cannot well capture the blocking by the ground that distorts large eddies. This suggests that modifications to SSM in the low frequency range are needed to accurately represent near-surface spectral turbulence in a semi-arid region.

Acknowledgement. This work was authored in part by the National Renewable Energy Laboratory, operated by Alliance for Sustainable Energy, LLC, for the U.S. Department of Energy (DOE) under Contract No. DE-AC36-08GO28308. Funding provided by U.S. Department of Energy Office of Energy Efficiency and Renewable Energy Solar Energy Technologies Office. The views expressed in the article do not necessarily represent the views of the DOE or the U.S. Government. The U.S. Government retains and the publisher, by accepting the article for publication, acknowledges that the U.S. Government retains a nonexclusive, paid-up, irrevocable, worldwide license to publish or reproduce the published form of this work, or allow others to do so, for U.S. Government purposes.

REFERENCES

Egerer, U., Dana, S., Jager, D., Xia, G., Stanislawski, B. J., and Yellapantula, S., 2024. Wind and structural loads data measured on parabolic trough solar collectors at an operational power plant. Scientific Data 11, 98.

Hunt, J. C. and Morrison, J. F., 2000. Eddy structure in turbulent boundary layers. European Journal of Mechanics-B/Fluids 19, 673–694.

Kaimal, J., 1994. Atmospheric Boundary Layer Flows: Their Structure and Measurement. Vol. 289. Oxford University Press.

Panofsky, H. A. and Dutton, J. A., 1984. Atmospheric turbulence. Models and methods for engineering applications. New York: Wiley.

Simiu, E. and Scanlan, R. H., 1996. Wind effects on structures: fundamentals and applications to design. Vol. 688. John Wiley New York.

Sutherland, G., Marié, L., Reverdin, G., Christensen, K. H., Broström, G., and Ward, B., 2016. Enhanced turbulence associated with the diurnal jet in the ocean surface boundary layer. Journal of Physical Oceanography 46, 3051–3067.

Wieringa, J., 1986. Roughness-dependent geographical interpolation of surface wind speed averages. Quarterly Journal of the Royal Meteorological Society 112, 867–889.

Zhang, Z., Sun, J., Wang, L., and Wei, J. J., 2020. Multiphysics-coupled study of wind load effects on optical performance of parabolic trough collector. Solar Energy 207, 1078–1087.

Studying wind-induced vibration of traffic signal structures: Health monitoring and vibration mitigation

Partha Sarkar [1], Nayan Tiwari [2], Alice Alipour [3]

[1]*Professor, Iowa State University, Ames, Iowa, USA, ppsarkar@iastate.edu*
[2]*Graduate Research Assistant, Iowa State University, Ames, Iowa, USA, nayandt@iastate.edu*
[3]*Associate Professor, Iowa State University, Ames, Iowa, USA, alipour@iastate.edu*

SUMMARY:
The vulnerability of traffic signal structures to wind loading has become increasingly evident, particularly at the pole-to-arm connection, where significant stress accumulates due to the heavy weight and low mechanical damping of the mast arm. In this study, a traffic signal structure with three units of vertical lights was selected for long-term health monitoring, to assess its wind-induced dynamic behaviour using accelerometers and strain gauges. A time-domain numerical method is employed to simulate the wind-induced response of this structure, where the aerodynamic properties of the mast arm, pole, and signal light units were used as obtained from the wind tunnel tests. The simulated responses will be validated with the full-scale measurement responses, yielding essential insights into the aerodynamic performance of these structures under varying wind conditions while assessing the robustness and efficacy of the proposed approach. To mitigate the wind-induced vibrations and potential fatigue failures of these structures, a design modification of the signal light unit is proposed. This study presents a comprehensive strategy for enhancing the structural integrity and resiliency of traffic signal structures and thereby improving their overall reliability and reducing their maintenance costs.

Keywords: Traffic signal structure, Wind-tunnel tests, Wind-induced vibration, Full-scale measurements.

1. INTRODUCTION

Traffic signal structures are critical components of urban infrastructure, ensuring the safe and efficient movement of vehicles, passengers, and goods on highways across the United States. These structures, typically consist of a mast arm, pole, and signal light units, and are subjected to various environmental loads, with wind-induced vibrations being one of the most significant concerns. Due to their slender and flexible design, traffic signal structures are particularly vulnerable to dynamic wind effects, leading to fatigue-induced failures at the mast arm-to-pole connection. This vulnerability can result in serviceability issues and, in extreme cases, structural failure. Several instances of such failures have been documented, emphasizing the need for improved predictive models and mitigation strategies (Wu et al., 2000). Previous studies have largely focused on observational data concerning the impact of wind-induced vibrations on traffic signal structures (Tsai and Alipour, 2021; Wieghaus et al., 2014; Zuo and Letchford, 2010). However, predicting the dynamic response of these structures to wind remains challenging due to the complex interaction between the aerodynamic forces and the structure's flexibility. This is compounded by the variability of wind conditions and the dynamic behaviour of these structures.

To address this gap, a cantilevered traffic signal structure with three vertical signal lights was installed in Ames, Iowa, for long-term health monitoring. While most existing research has

focused on cantilevered traffic signal structures with horizontal signal lights, traffic signal structures with vertical signal lights, which are also widely used, remain understudied. The structure is instrumented to collect real-time data on critical performance metrics, including acceleration and strain, providing a benchmark for validating the proposed time-domain model with real-world behaviour. Improvements are made to a previously developed time-domain method (Jafari et al., 2019) to simulate the aerodynamic loads and responses of traffic signal structures under varying wind conditions. The influence of the taper in mast arm on wind loads and the vertical signal light unit configuration on the across-wind and along-wind responses are considered by identifying the key aerodynamic parameters in the wind tunnel. These insights will form the basis for predictive modelling and the development of vibration mitigation strategies. Additionally, a modified signal light will be designed using wind-tunnel experimental results aimed at reducing wind-induced vibrations. This modified signal light will be installed thereafter on the full-scale structure, and field measurements will be compared with those from the original configuration. This comparison will help determine the effectiveness of the proposed mitigation strategy in reducing vibrations and enhancing structural durability under wind loads.

2. EXPERIMENTAL SETUP

2.1. Wind Tunnel Tests

In this study, experiments were conducted in the aerodynamic test section of the AABL (Aerodynamic/Atmospheric Boundary Layer) Wind and Gust Tunnel at Iowa State University (ISU). The mast arm and signal light models were chosen to ensure that the wind tunnel blockage ratio remained below 5% for all test scenarios (Simiu and Scanlan, 1996). Limited two-dimensional aerodynamic characteristics of the signal light model were obtained from a previous study (Jafari et al. 2019). Lift and drag coefficients, along with flutter derivatives, were evaluated for multiple yaw angles, addressing the limitation of the prior study that considered a single yaw angle. For the tapered mast arm, section model testing determined its aerodynamic performance. The drag and lift coefficients, along with the Strouhal number, were measured at different yaw angles using a static test setup. Aerodynamic damping and stiffness parameters for self-excited and vortex-induced vibrations were extracted at low to moderate wind speeds using a dynamic setup (Fig. 1). Special consideration was given to capture the correlation of aerodynamic loads along the mast arm, which will be incorporated in time-domain method. With all aerodynamic parameters obtained, the tip response and induced stresses of the traffic signal structure can be calculated in both vertical and lateral directions using the generalized coordinate technique.

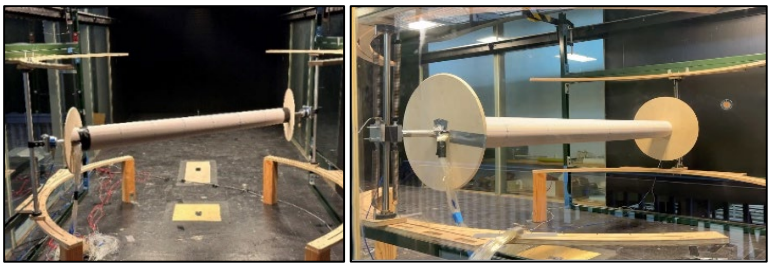
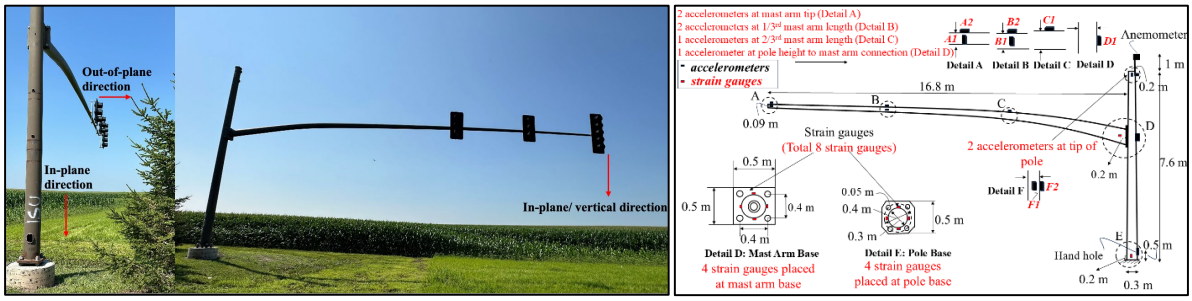


Figure 1. Static (left) and dynamic (right) wind-tunnel set-ups for mast arm experiments.

2.2. Field Measurements

A signal light structure was installed in the field, as part of an ISU Facility, to study its wind-

induced behaviour through long-term monitoring (Fig. 2). This structure consists of a 7.6 m vertical pole, a 16.8 m mast arm, and three vertical traffic lights attached to the mast arm with a 3.5 m gap between each signal light. The diameter taper rate is 0.011 m/m for the pole and the mast arm. The three vertical traffic lights include one 5-unit traffic light (2.0 m height, 0.6 m width) at the tip of the mast arm and two 3-unit traffic lights (1.3 m height, 0.6 m width). Sensors including eight accelerometers, eight strain gauges, and an anemometer were installed on the traffic signal structure to monitor its wind-induced motion and record wind data. The acceleration data was collected along two principal directions, namely the in-plane and out-of-plane axes as shown in Fig. 2 (a). To ensure accurate monitoring of wind-induced acceleration responses, three locations on the mast-arm and two locations on the vertical pole were selected (Fig. 2 (b)). Given the wind frequency and natural frequency of the structure, a sampling rate of 20 Hz was selected for data collection and analysis. A data acquisition device was used to record data from all the sensors and store it on an external memory card on the device.

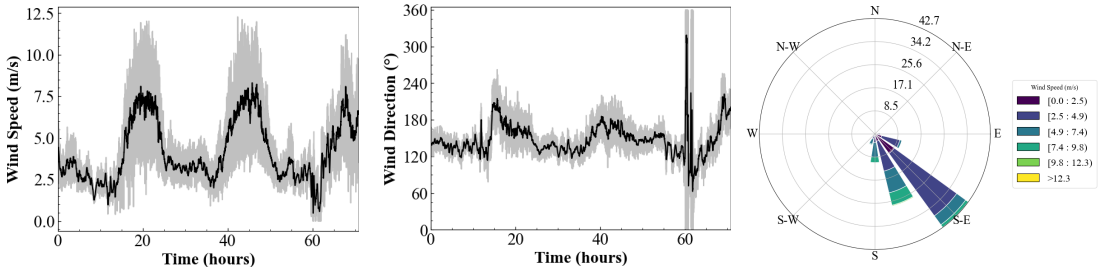


(a) (b)

Figure 2. (a) Installed signal light structure at ISU facility and (b) Instrumentation plan of the installed structure.

3. PRELIMINARY RESULTS

In this section, preliminary results from full-scale measurements collected over a 70-hour period are presented to provide an early indication of the dynamic behavior of the traffic signal structure under real-world wind conditions. To address this, a strategic arrangement was designed to enhance the structure's stability against dynamic wind patterns, exposing it to a wider range of wind directions. Figs. 3 (a) and (b) show the wind speed and wind direction time histories recorded by the anemometer. The wind rose diagram in Fig. 3 (c) indicates that, during the recording period, the predominant wind direction was from the southeast.

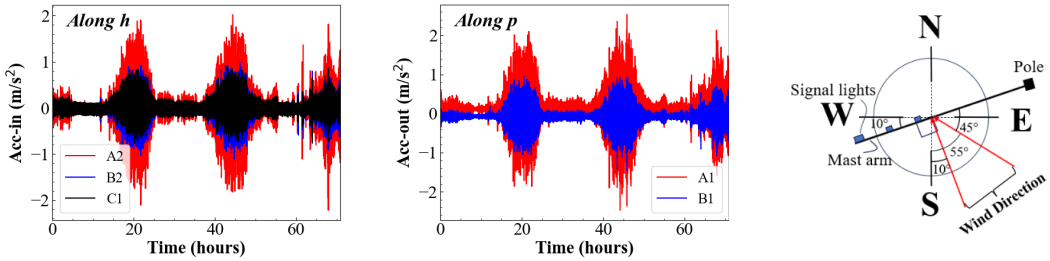


(a) (b) (c)

Figure 3. (a) Wind speed and (b) wind-direction time-histories; (c) Wind-rose diagram.

Figs. 4 (a) and (b) show the acceleration time histories along the in-plane and out-of-plane

directions, respectively. In Figs. 4 (a) and (b), A1 and A2 represent the location of accelerometers at the mast-arm tip, B1 and B2 at one-third of the mast-arm length from the tip, and C1 at two-thirds of the length (refer Fig. 2). Fig. 4 (c) shows the alignment of the mast arm relative to the prevailing wind direction, set at 10° counterclockwise with respect to the west. Previous studies have shown that large-amplitude vibrations tend to occur when the predominant wind direction is 45°, with the wind approaching from behind the signals (Jafari et al., 2019). Although these preliminary results provide valuable early insights into the structure's in-plane and out-of-plane accelerations, long-term monitoring is necessary to develop a more comprehensive understanding of its response to varying wind conditions. This extended observation will be conducted with both the original and modified signal light designs to assess the effectiveness of the mitigation strategy.



(a) (b) (c)

Figure 4. Acceleration responses in (a) in-plane and (b) out-of-plane directions; (c) Alignment of mast-arm.

7. CONCLUSIONS: FINAL CHECKS AND SUBMISSION

This research provides a comprehensive investigation of the wind-induced vibration problem of traffic signal structures using both wind tunnel tests and full-scale monitoring. By analysing real-time acceleration data and simulating responses with a time-domain numerical model, the study offers insights into the aerodynamic behaviour and fatigue risks of these structures. Proposed design modifications, based on wind-tunnel results, aim to reduce vibrations and improve structural resilience, offering practical solutions for enhancing durability, minimizing service disruptions, and lowering maintenance costs in urban infrastructure. Long-term monitoring will further validate the effectiveness of the mitigation strategies.

ACKNOWLEDGEMENTS

The authors gratefully acknowledge National Cooperative Highway Research Program (NCHRP) Innovations Deserving Exploratory Analysis (IDEA), project number NCHRP IDEA 241 for supporting this research.

REFERENCES

Jafari, M., Sarkar, P.P. and Alipour, A.A., 2019. A numerical simulation method in time domain to study wind-induced excitation of traffic signal structures and its mitigation. Journal of Wind Engineering and Industrial Aerodynamics, 193, p.103965.

Simiu, E. and Scanlan, R.H., 1996. Wind effects on structures: fundamentals and applications to design (Vol. 688). New York: John Wiley.

Tsai, L.W. and Alipour, A., 2021. Studying the wind-induced vibrations of a traffic signal structure through long term health monitoring. Engineering Structures, 247, p.112837.

Wieghaus, K.T., Hurlebaus, S., Mander, J.B. and Fry, G.T., 2014. Wind-induced traffic signal structure response: Experiments and reduction via helical arm strakes. Engineering structures, 76, pp.245-254.

Wu J, Chen G, Barker MG. Wind-induced stresses on traffic signal mast arms: case studies. 2000.

Zuo, D. and Letchford, C.W., 2010. Wind-induced vibration of a traffic-signal-support structure with cantilevered tapered circular mast arm. Engineering Structures, 32(10), pp.3171-3179.

Offshore vertical wind shear WRF simulation in Atlantic Ocean coast location.

Victor Silveira[1], Ignacio Franco[2], Alejandro Gutiérrez[3]

[1]*IMFIA FING UdelaR, Montevideo, Uruguay, vsilveira@fing.edu.uy*
[2]*IMFIA FING UdelaR, Montevideo, Uruguay, ifranco@fing.edu.uy*
[3]*IMFIA FING UdelaR, Montevideo, Uruguay, aguti@fing.edu.uy*

SUMMARY:
The present study assessed the performance of WRF simulations in comparison with observational wind data at multiple heights from coastal location of La Paloma, Uruguay, focusing on wind blowing from the Atlantic Ocean. We compare WRF outputs to observational data for 2017. The analysis focuses on wind shear characteristics across seasonal conditions. Results show that WRF model present higher correlations in wind velocity during Autumn-Winter seasons in comparison with Spring and Summer. WRF diurnal cycle of vertical wind shear show a similar pattern in comparison with observational data, with lower dispersion both WRF and observational data, during daytime. Future work will focus on extending the dataset and asses local topology effects in the region close to the met mast

Keywords: Offshore Winds, WRF, Met mast meassurements

1. INTRODUCTION

The estimation of offshore wind energy potential presents particular complexities compared to its onshore counterpart. The availability of on-site wind speed measurements is more limited, which has led to the development of various techniques aimed at accurate estimation. In particular, (Carreno-Madinabeitia et al., 2021) use re-analysis data to estimate it for the Iberian Peninsula, while (Aboobacker et al., 2021), (Samal, 2021), and (Ahmad et al., 2022) also incorporate coastal tower measurements for Qatar, India, and Pakistan, respectively (Carreno-Madinabeitia et al., 2021), (Aboobacker et al., 2021), (Samal, 2021), (Ahmad et al., 2022). (Carvalho et al., 2014), (Lima et al., 2015), and (Chancham et al., 2017) use mesoscale models with re-analysis data, mast measurements, and buoys to characterize offshore wind potential in the Iberian Peninsula, Brazil, and the Gulf of Thailand, respectively (Carvalho et al., 2014), (Lima et al., 2015), (Chancham et al., 2017). There are records of prior local efforts, particularly related to the installation of measurement stations and the characterization of coastal turbulent flow (Franco et al., 2019). Local records also exist for the evaluation of atmospheric stability regimes for the first 100 meters of height in coastal areas of Uruguay (Gutiérrez and Fovell, 2018). (Silveira and Gutiérrez, 2023) presents cases of WRF simulations in coastal areas, comparing the performance of the vertical profile at height, and representing a first approach to the problem of simulating offshore wind speed fields in Uruguay. Building on this foundation, the present work focuses on analyzing wind speed and direction data from a coastal met mast and comparing it with WRF-simulated data for 2017. This study aims to evaluate the WRF model's accuracy in reproducing wind conditions at different heights and over various seasons, providing valuable insights for future offshore wind energy development in Uruguay.

2. OBSERVATIONAL WIND DATA, TOWER LOCATION

The met mast is located in the Atlantic Ocean coast (La Paloma). The chosen met mast is on a strategic position, as depicted in figure 1a. The tower have three three-dimensional 32-Hz ultrasonic WindMaster Pro anemometers (Gill Instruments Ltd., UK) mounted at 16.4, 45.4 and 71.4 meters above sea level (ASL), figure 1b, shows the tower and sonic anemometers. Each anemometer is installed at 3.5 m from the tower to reduce the effect of the tower wake. The installation adhered to standard (*IEC 61400-12* 2022) on both cases.



(a) La Paloma's met mast position



(b) Met mast description

Regarding previous studies on the area, (Franco et al., 2019) found that the lower anemometer is influenced by an internal boundary layer when the wind comes from the shore. This work also presents a drag coefficient as a function of the wind direction, which is lower and constant over the directions around 55^o and 235^o. Only data corresponding of wind blowing from selected directions coming from the Atlantic Ocean are included in the present analysis.

We consider mean hourly data from 01/01/2027 to 31/12/2017. Due to communication errors with the measuring system, only 68.9% of the hourly data is available for this study.

3. WRF SIMULATION DESCRIPTION

Our WRF simulations used version 4.3 simulation domain. It is composed of a 74 × 98 grid with a 12 km resolution, Lambert projection. The center of the domain is located at the coordinates 34.305^oS and 56.146^oW. Geographical static data with the highest resolution available from (WPS-V4, 2024) were employed. These simulations aimed to obtain hourly horizontal wind at the same levels as the met mast anemometers over the period 01/01/2017 to 31/12/2017. All the parametrization employed on the simulation, are the same used in (Gutiérrez and Fovell, 2018).

For comparison with measured data, an ocean node located at 20km from the shore (coordinates 34.79^oS and 54.01^oW) is selected. Vertical discretization were implemented with first three eta levels, ranging about 10, 50 and 120 meter. Two interpolation methods were employed. First one is a simple linear interpolation. The second one, consist in adjusting a logarithmic function between the two closer eta levels, if the wind speed has a positive shear, otherwise is a linear interpolation.

4. DATA ANALYSIS

For the analysis, we have select 24-hour (day) event with continuous wind blowing from the Atlantic Ocean, in those cases (days) shear were computed with WRF simulation and observational data. As an example, figure 2 presents 24-hour events, including high and low wind scenarios in particular days: 17/09/2017 and 07/02/2017 for the Spring - Summer seasons, and 17/04/2017 and 01/06/2017 Autumn - Winter seasons. The figure shows a comparison between observational data and WRF simulations for 45.4m and 71.4m levels.

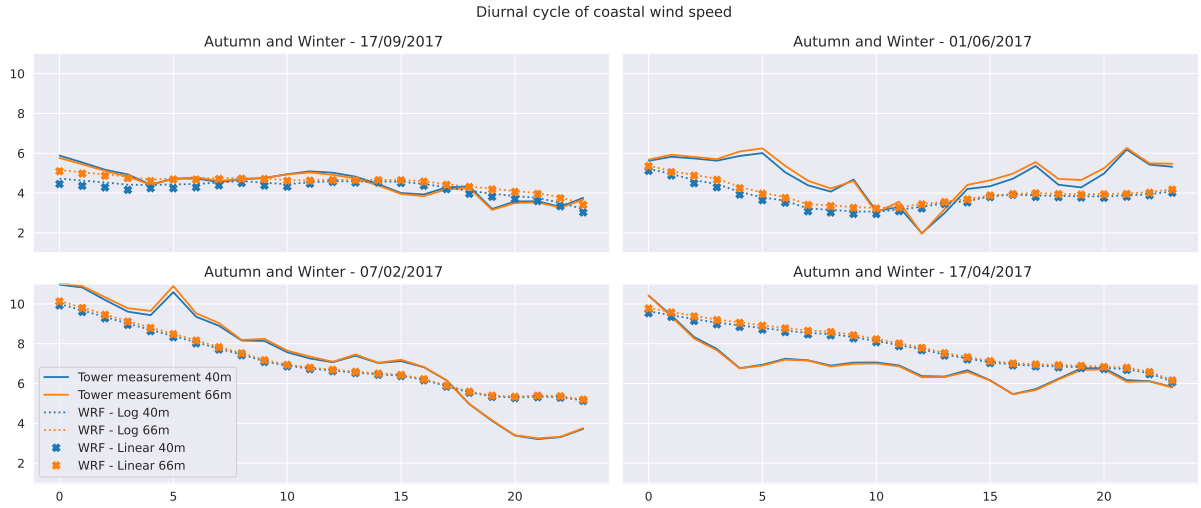


Figure 2. Diurnal cycle of hourly mean velocity for low and high wind events

Considering the full dataset for the period 01/01/2017 to 31/12/2017, the available data that comply to the 24-hour event criteria were 12 days over Spring - Summer seasons, and 10 days for Autumn - Winter seasons. Wind shear is computed for the observed data as well as for simulated data. The results are presented in a box plot on figure 3.

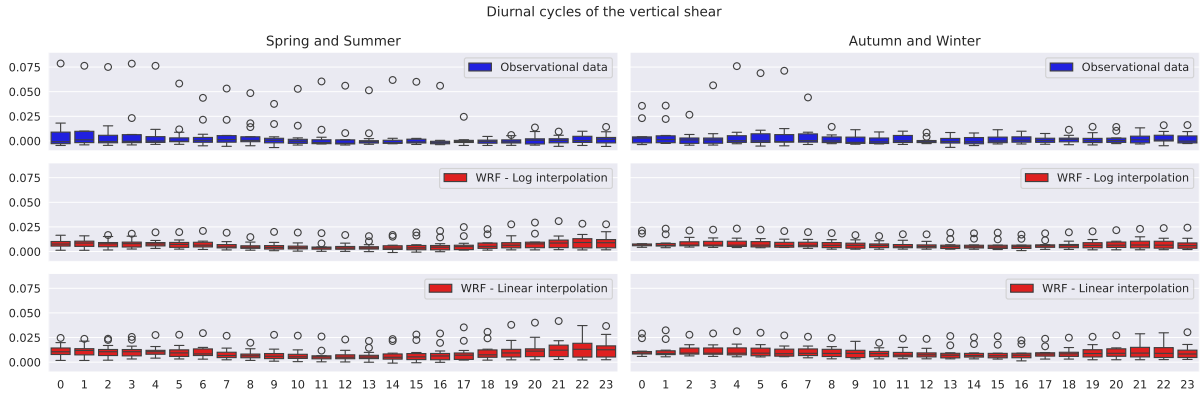


Figure 3. Box plot of diurnal cycle of vertical wind shear computed for WRF and observational data

Results are presented in table 1, where is observed high correlation during Autumn and Winter in comparison with Spring - Summer seasons, for both analyzed heights. The correlation between

observed and simulated wind directions were also evaluated, giving a value of 68.9% using the circular correlation method presented by (Jammalamadaka and Sengupta, 2001). Following work will include longer datasets to perform the comparison, as well as correlations and error estimators.

Table 1. Correlation values between observed and simulated diurnal cycles

	Spring - Summer		Autumn - Winter	
	Log	Linear	Log	Linear
45.4m height	0.692	0.697	0.831	0.831
71.m height	0.720	0.723	0.835	0.834

5. CONCLUSIONS:

The present study assessed the performance of WRF simulations in comparison with observational wind data from coastal location of La Paloma, Uruguay, focusing on wind blowing from the Atlantic Ocean.

WRF model present higher correlations in wind velocity during Autumn-Winter seasons in comparison with Spring and Summer. WRF diurnal cycle of vertical wind shear show a similar pattern in comparison with observational data, with lower dispersion both WRF and observational data, during day time. Future work will focus on extending the dataset and asses local topology effects in the region close to the met mast.

REFERENCES

Aboobacker, V. M., Shanas, P. R., Veerasingam, S., Al-Ansari, E. M. A. S., Sadooni, F. N., and Vethamony, P., 2021. Long-Term Assessment of Onshore and Offshore Wind Energy Potentials of Qatar. Energies 14.

Ahmad, S., Abdullah, M., Kanwal, A., Rehman Tahir, Z. ul, Saeed, U. B., Manzoor, F., Atif, M., and Abbas, S., 2022. Offshore wind resource assessment using reanalysis data. Wind Engineering 46, 1173–1186.

Carreno-Madinabeitia, S., Ibarra-Berastegi, G., Sáenz, J., and Ulazia, A., 2021. Long-term changes in offshore wind power density and wind turbine capacity factor in the Iberian Peninsula (1900–2010). Energy 226, 120364.

Carvalho, D., Rocha, A., Gómez-Gesteira, M., and Silva Santos, C., 2014. Offshore wind energy resource simulation forced by different reanalyses: Comparison with observed data in the Iberian Peninsula. Applied Energy 134, 57–64.

Chancham, C., Waewsak, J., and Gagnon, Y., 2017. Offshore wind resource assessment and wind power plant optimization in the Gulf of Thailand. Energy 139, 706–731.

Franco, I., Gutierrez, A., and Cataldo, J., 2019. Effects of the Surface and Atmospheric Stability on the Integral Length Scale at a Coastal Site. Boundary-Layer Meteorology 172, 317–332.

Gutiérrez, A. and Fovell, R. G., 2018. A new gust parameterization for weather prediction models. Journal of Wind Engineering and Industrial Aerodynamics 177, 45–59.

IEC 61400-12, Sept. 5, 2022. Wind turbines - Part 12: Power performance measurements of electricity-producing wind turbines. International Electrotechnical Commission (IEC).

Jammalamadaka, S. and Sengupta, A., 2001. Topics in Circular Statistics. Series on multivariate analysis. World Scientific.

Lima, D. K., Leão, R. P., dos Santos, A. C., de Melo, F. D., Couto, V. M., de Noronha, A. W., and Oliveira, D. S., 2015. Estimating the offshore wind resources of the State of Ceará in Brazil. Renewable Energy 83, 203–221.

Samal, R. K., 2021. Assessment of wind energy potential using reanalysis data: A comparison with mast measurements. Journal of Cleaner Production 313, 127933.

Silveira, V. and Gutiérrez, A., 2023. Evaluating the Accuracy of WRF Simulations for Vertical Wind Profiles at Coastal Locations: A Comparison of Measurement Data and PBL Schemes. Proceedings of 16th International Conference on Wind Engineering. ICWE16.

WPS-V4, 2024. *WPS V4 Geographical Static Data Downloads Page*. Accessed: 2024-10-15. URL: https://www2.mmm.ucar.edu/wrf/users/download/get_sources_wps_geog.html.

A dataset for studying the impact of heat waves on the built environment in a humid continental climate

Miguel Martin[1], Clara Garcia-Sanchez[1], Jantien Stoter[1], Mario Berges[2]

[1]*Department of Urbanism, Faculty of Architecture and the Built Environment, Delft University of Technology, Delft, Netherlands, urbanism-bk@tudelft.nl*
[2]*Department of Civil and Environmental Engineering, Carnegie Mellon University, Pittsburgh, United States, cee-business@andrew.cmu.edu*

SUMMARY:

This paper presents a field experimental network designed to collect data on the outdoor built environment during a heat wave in a humid continental climate. The network comprised four weather stations and one infrared camera, installed on a university campus in Pittsburgh, United States. The data can be utilized to investigate the vulnerability of buildings to heat waves, the influence of urban overheating on human behavior and traffic patterns, and the dynamics of wind flow within street canyons. Before analysis, thermal images from the infrared camera must be validated against measurements from a contact surface sensor.

Keywords: Urban overheating, infrared thermography, weather data, outdoor built environment, continental climate

1. INTRODUCTION

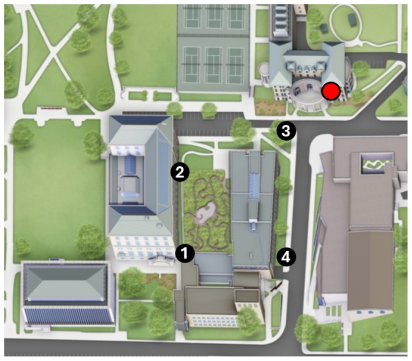
Since the Industrial Revolution of the 18th century, a large portion of the world's population has moved from rural to urban areas. According to the United Nations, two-thirds of the world's population is projected to live in urban areas by 2050 (Srivastava, 2009). This important agglomeration of the world's population in cities has implications for the built environments. To accommodate such a large population on limited land, taller buildings and larger roads are necessary for housing and transportation. High building density, extensive paved surfaces, and lack of vegetation contribute to urban overheating. In many parts of the world, this climatic hazard has emerged as a major threat to urban sustainability, prompting governments to prioritize mitigation efforts (Santamouris, 2020).

In other regions, however, authorities have not prioritized addressing urban overheating. For instance, in the Northern United States, urban overheating is often viewed as a phenomenon that can enhance outdoor and indoor thermal comfort during winter months (Lowe, 2016). With the current trend of global warming and its impact on urban climates, these regions are beginning to take urban overheating more seriously, especially during heat waves. Indeed, these regions are highly vulnerable to heat waves, as their buildings are not designed to withstand extreme heat. Despite the potential public health risks of urban overheating, limited data is available to study the built environment's response to heat waves in these regions.

To advance the study of built environments during heat waves in continental climates, this paper presents a dataset collected during a field experiment conducted between July 29 and September 21, 2024, on a university campus in Pittsburgh, United States. The dataset includes weather data collected from four locations on campus and thermal images captured from the fourth floor of a building. It enables the observation of buildings, traffic, pedestrians, and wind flow during an extreme heat event, opening up several research opportunities.

2. METHODOLOGY

Between July 29 and September 21, 2024, four Davis Vantage weather stations and one FLIR A50 infrared camera were operating on a university campus in Pittsburgh, United States, to collect information on the outdoor built environment during a heat wave (see Figure 1). Weather stations were mounted 2 meters above the ground on a metal pole, secured by a drilled hole. They were powered by solar panels and backup batteries. They remotely sent measurements of temperature, relative humidity, wind speed, wind direction, and rainfall every five minutes to a cloud platform. In contrast, the infrared camera was directly connected to a laptop to store thermal images in a hard drive. Thermal images were collected from the 4th floor of a building (i.e., 30 meters above the ground) at a frequency of 1 Hz.



Devices	Specification			
Weather stations	**Parameter**	**Range**	**Accuracy**	**Resolution**
	Temperature	-40 ... +150 °F	± 1 °F	0.1 °F
	Humidity	0 ... 100 %	± 3 %	0.1 %
	Wind speed	2 ... 180 mph	± 2 mph	0.1 mph
	Wind direction	0 ... 360°	± 3°	0.1°
	Rain fall	0 ... 199.99"	4%	0.01"
Infrared camera	**Feature**		**Value**	
	Field of view		95° (W) x 74° (H)	
	Image resolution		464 (W) x 348 (H)	
	Accuracy		± 2 °C or ± 2% of reading	
	Operating temperature range		-20 ... +50 °C	
	Storage temperature range		-20 ... +175 °C	
	Spectral range		7.5 ... 14 μm	
	Image format		16-bit	

Figure 1. Field experimental setup and instrument specifications

Because the infrared camera was positioned behind an open window, the radiometric values $\widehat{U}_{ij}$ (in Volts) captured by the receptor at pixel ij can be formulated as:

$$\widehat{U}_{ij} = \frac{1}{\varepsilon_{ij}\tau_{out}} U_{ij} - \frac{1-\varepsilon_{ij}}{\varepsilon_{ij}} U_{sky} - \frac{1-\tau_{out}}{\varepsilon_{ij}\tau_{out}} U_{out} \tag{1}$$

where U_{ij} (in Volts) is the true radiometric value of the observed object at pixel ij, ε_{ij} (0-1) the emissivity of the object, U_{sky} (in Volts) and U_{out} (in Volts) the radiometric value associated to the sky temperature T_{sky} (in K) and outdoor air temperature T_{out} (in K), respectively, and τ_{out} (0-1) the outdoor air transmissivity.

3. RESEARCH OPPORTUNITIES

The data collected during the field experiment can be used to explore the following research opportunities:

- Air and land surface temperature measurements are valuable for assessing the exposure of the built environment to heat waves. By incorporating information about occupant demographics, such as age, gender, socioeconomic status, and ethnicity, thermal images could be used to develop a heat wave vulnerability index for individual buildings.
- Thermal images were captured at a high frequency. They can thus be used to observe pedestrian and vehicular traffic patterns during both day and night. Given that thermal images were collected during a heat wave, they can be used to study the impact of urban overheating on traffic and human behavior.
- In addition to air temperature and humidity, weather stations measured wind speed and direction. These measurements can be valuable for validating CFD simulations of wind flow in street canyons.

4. CONCLUSIONS

This paper described a field experimental campaign conducted between July 29 and September 21, 2024, on a university campus in Pittsburgh, United States. During the field experimental campaign, valuable information was collected using four weather stations and one infrared camera to study the impact of heat waves on the outdoor built environment in a humid continental climate. These studies could explore building vulnerability to heat waves, the impact of urban overheating on traffic and human behavior, and the validation of CFD models for wind flow.

To ensure the accuracy of these studies, the surface temperature derived from thermal images should be validated against measurements from contact surface sensors. Measurements made by an infrared camera are influenced by internal parameters, which can vary between experimental environments. These parameters must be calibrated before using the derived surface temperatures for analysis.

ACKNOWLEDGEMENTS

This research has received funding from the European Union's Horizon research and innovation programme under the Marie Sklodowska-Curie grant agreement No 101059484.

REFERENCES

Lowe, S. A., 2016. An energy and mortality impact assessment of the urban heat island in the US. Environmental Impact Assessment Review 56, 139–144.

Santamouris, M., 2020. Recent progress on urban overheating and heat island research. Integrated assessment of the energy, environmental, vulnerability and health impact. Synergies with the global climate change. Energy and Buildings 207, 109482.

Srivastava, K., 2009. *Urbanization and mental health*.

Field Observations of Buffeting Loads on a Suspension Bridge Girder

Nicolò Daniotti [1,2], Jasna B. Jakobsen [2], Jonas Snæbjörnsson [3,2], Etienne Chyenet[4]

[1] *Svend Ole Hansen Ap, Copenhagen, Denmark, nid@sohansen.dk*
[2]*University of Stavanger, Stavanger, Norway, Jasna.b.jakobsen@uis.no*
[3]*Reykjavik University, Reykjavík, Iceland, jonasthor@ru.is*
[4]*University of Bergen, Etienne.Cheynet@uib.no*

SUMMARY:
The presented work deals with buffeting wind loads on a suspension bridge girder. The load generation mechanism and the resulting cross-sectional and span-wise forces are studied based on wind surface pressures recorded by a tailored pressure measurement system installed on the closed-box girder. The pressure recordings are complemented by continuous monitoring of the inflow conditions by a set of 3D sonic anemometers. The two data sources allow for a thorough investigation of the incoming flow "distortion" during the passage around the bridge deck, e.g. in terms of the surface pressure time series, their statistical moments and (cross-)spectral content. Emphasis is placed on the resultant cross-sectional forces in the vertical and horizontal direction and the overturning moment. Their spectral content and coherence for several span-wise separations are investigated as a function of the corresponding properties of the incoming turbulence. The study provides unique estimates of the spatiotemporal characteristics of the forces, including the force-length scales, as a function of the length scales of natural turbulence.

Keywords: suspension bridge, surface pressures, buffeting forces

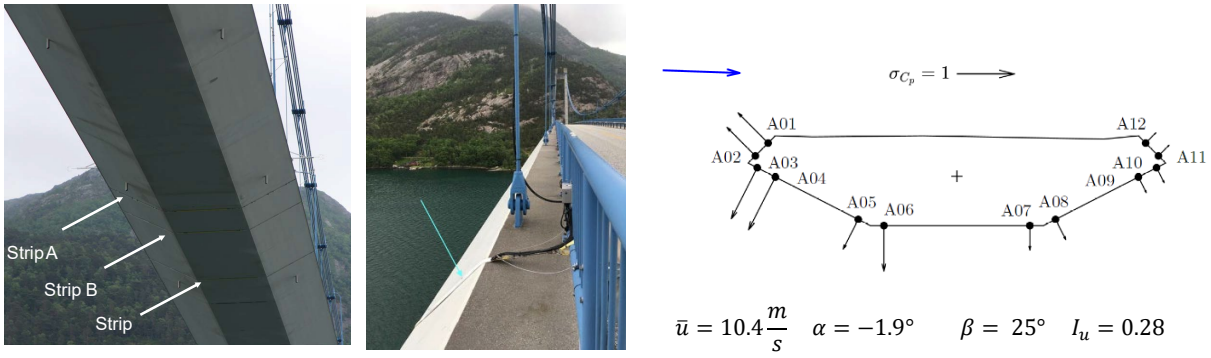
1. BACKGROUND

Long-span bridges are susceptible to various types of wind excitation, including forces due to atmospheric turbulence and so-called buffeting loading. Extreme buffeting load action is dealt with in the Ultimate Limit State design (ULS) of long-span bridges. The buffeting loads on bridge girders have traditionally been investigated with section models in wind tunnels simulating the natural turbulence (Larose, 2003). The wind tunnel tests have documented the turbulence-girder interaction along and across the main flow path. However, the results are associated with uncertainties related to the simplified representation of the natural turbulence in a wind tunnel environment, which has size limitations while maintaining a suitable scaling of a bridge girder model. This research gap can only be addressed by full-scale field studies. In the present work, the buffeting load action is examined in a measurement setup that combines on-site turbulence monitoring with wind-induced pressure measurements on the surface of a suspension bridge girder.

2. MEASUREMENT SYSTEM

The field measurements were conducted on the Lysefjord Bridge, a suspension bridge with a main span of 446 m and a 12.3 m wide, 2.7 m tall steel box girder. The monitoring system on the bridge

has been in operation since 2013 (Snæbjörnsson, 2017). The current instrumentation consists of eleven 3D sonic anemometers, a weather station, eight accelerometers, a satellite-based displacement sensor and a pressure measurement system that was added in 2021. The pressure taps are placed on three strips that are stretched between the railings on each side of the bridge, as shown in Fig.1a) and b). Each strip accommodates twelve pressure taps, 6 mm in diameter, distributed as shown in Fig.1c). The system is described in detail in (Daniotti, 2022).



(a) (b) (c)

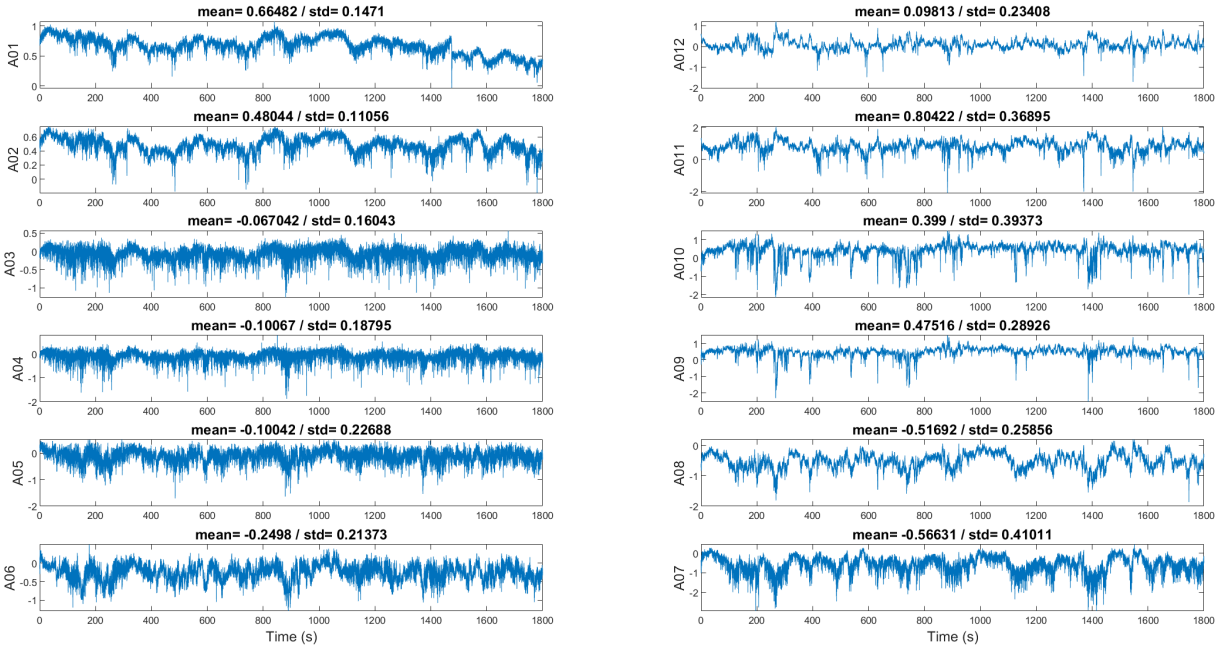
Figure 1. (a) and (b) Strips with pressure taps and (c) Standard deviations of surface pressures recorded on strip A on 06.08.2021, 18:30-19:30, wind from north-east.

3. SURFACE PRESSURES AND BUFFETING LOAD CHARACTERISTICS

Fig.1 illustrates standard deviations of surface pressure for a selected case of north-easterly wind with a high along-wind turbulence level of 28%. The yaw (β) and inclination (α) angles are given in the figure.

For south-westerly wind of a higher magnitude but considerably lower turbulence intensity, the time series of surface pressure coefficients are displayed in Fig. 2. The overall pressure variation is similar across the pressure taps, governed by the incoming flow conditions. While the upstream pressure taps on the upper inclined part of the box (A12 and A11) closely resemble the incoming velocity fluctuations, more frequent bursts of negative pressure are present on the lower inclined surface for taps A10 to A08. Past the lower upstream corner, at A07, the pressures are similar to those at A08 but now include a higher frequency component related to the flow separation and a vortex shedding process, which is apparent in the signals at taps A05 to A03.

The integrated effect of the surface pressures, in terms of the vertical and horizontal force and the overturning moment on strip A, for the case illustrated in Fig. 1c) is presented in Fig. 3. The absence of the pressure data for the upper bridge girder surface is compensated for through analysis of a corresponding pressure data collected in a similar measurement campaign on Gjemnessund bridge (Andersen, 2021), which allowed a comparison between a complete set of pressure data and a reduced set of data corresponding to the setup on the Lysefjord bridge.



$\bar{u} = 14.3\ m/s \qquad I_u = 11\% \qquad \bar{w} = 1.16\ m/s \qquad I_w = 7\% \qquad \beta = 25°$

Figure 2. (a) Surface pressures time-series recorded on 23.02.2022, wind from the southwest.

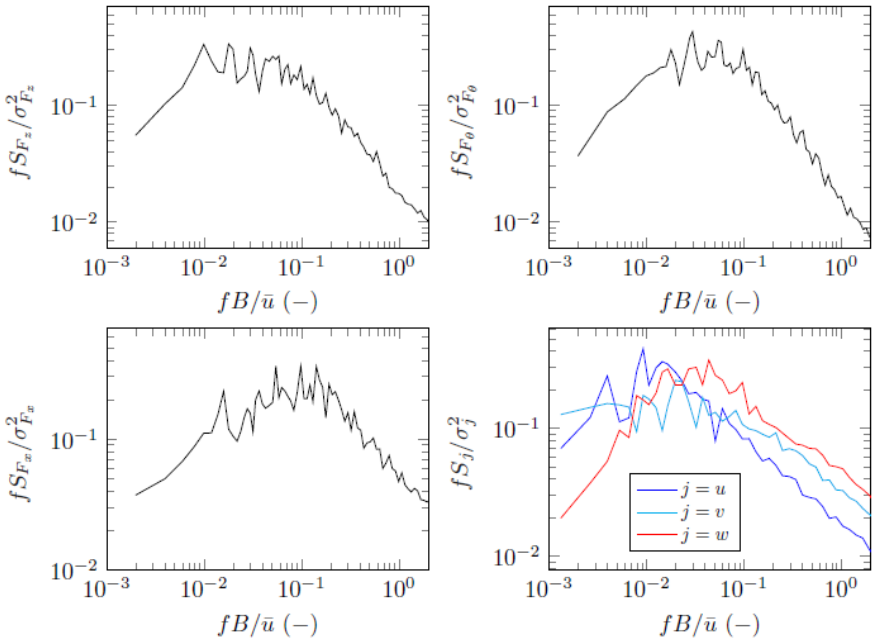


Figure 3. Normalised power spectral densities of vertical force (top left panel), overturning moment (top right panel), horizontal force (bottom left panel) at chord A, and incoming turbulence components; full-scale data from 06.08.2021, 8:30 to 19:30 UTC.

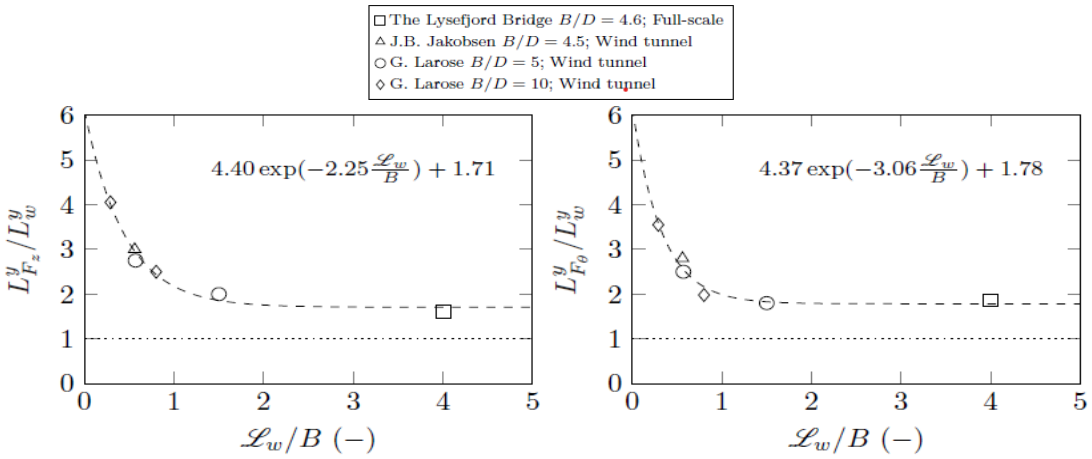


Figure 4. The span-wise length scale of vertical force and overturning moment relative to the scale of vertical turbulence as a function of the normalised along-wind length scale of vertical turbulence, data for 06.08.2021, 8:30 to 19:30 UTC.

In Fig.4, the span-wise extent of the buffeting load is presented in terms of the length scales of the vertical force and the overturning moment in relation to the length scale of the vertical turbulence. The result indicates a lower level of "deformation" of wind gusts compared to the selected wind tunnel results, included in Fig. 4, that are based on smaller turbulence length scales relative to the deck width (Larose, 2003).

4. CONCLUSIONS

This paper presents a field study of the generation of buffeting wind load on a suspension bridge girder. The buffeting load is studied by combining the rich data set from eleven sonic anemometers installed on the bridge with surface pressure measurement records. The latter is acquired on thirty-six pressure taps fitted to three strips stretched between the deck railings. The surface pressure data capture the combined effect of the incoming flow fluctuations, adapted to the bridge surface, as well as the vortex shedding process which intensity depends on the levels of the approaching flow turbulence. In the case studied, the span-wise length scales of both the vertical buffeting force and the overturning moment are estimated to be twice the value of the length scale for the vertical turbulence. This supports the hypothesis of a more limited "deformation" caused by wind gusts along- and across the girder in a natural flow, compared to the conditions commonly investigated in wind tunnels, with smaller turbulence length scales relative to the size of the structure.

REFERENCES

Andersen, M. S., 2021. Operational fluid modal analysis of full-scale pressure and wake flow measurements on the Gjemnessund Bridge. Engineering Structures 249, 113295.

Daniotti, N., 2022. Bridge deck aerodynamics: A case study in full-scale. Ph. D. thesis, University of Stavanger.

Larose, G. L., 2003. The spatial distribution of unsteady loading due to gusts on bridge decks. Journal of Wind Engineering and Industrial Aerodynamics 91(12-15), 1431–1443.

Snæbjörnsson, J., J. Jakobsen, E. Cheynet, and J. Wang, 2017. Full-scale monitoring of wind and suspension bridge response. In IOP Conference Series: Materials Science and Engineering, Volume 276, pp. 012007. IOP Publishing.

Urban flow observations using lidars on a university campus

Jónas Thor Snæbjörnsson [1,2], Jasna B. Jakobsen-[1],

[1]*University of Stavanger, Stavanger, Norway, Jasna.b.jakobsen@uis.no*
[2]*Reykjavik University, Reykjavík, Iceland, jonasthor@ru.is*

SUMMARY:
The study presents wind flow measurements at the University of Stavanger campus using two continuous-wave nacelle lidars and a vertical continuous-wave profiler, which are installed on building roofs. The installation aims to gain experience with the instruments while also investigating the urban wind conditions on campus. The analysis emphasises data from the horizontal lidars, which provide fifty radial wind speeds along a scanning circle as well as the wind speed, turbulence intensity and yaw angle at the centre of the scanning circle. The horizontal lidars are set up to capture both the approaching wind and the wake flow. The study highlights the potential of remote wind sensing for monitoring urban wind while demonstrating the significant variability in the local urban flow. Recordings from the fifty scanning points along the scanning circle can effectively capture the non-uniform urban flow. Combined with data from the vertical profiler, the flow observations represent a valuable resource for validating numerical models of urban flow.

Keywords: wind, urban flow, lidars.

1. INTRODUCTION

Wind field characterisation in an urban environment is challenging due to the complexity of the flow. Urban flow characterisation traditionally relies on numerical simulations and experimental investigations at a reduced scale, sometimes combined with single-point observational data (Sattar et al., 2018). A combination of ground-based vertical profiler and horizontal lidars promises complementary information on the complex interactions between the built environment and the atmosphere (Filioglou et al., 2022).

This study examines data acquired by two nacelle lidars and one profiler located on building roofs at the campus of the University of Stavanger (UiS). The goal is to gain experience using these instruments while investigating the urban environment's impact on the flow. For a selected event, wind speed observations from the different instruments are compared in terms of mean flow and turbulence parameters, including surface roughness, turbulence intensity, along-wind spectra, and a reduced Reynolds stress tensor (Voigt et al., 2024).

2. INSTRUMENTATION

Instruments from ZX Lidars are currently used for remote wind sensing on the university campus. Two continuous-wave nacelle lidars (ZXTM), are installed on the roof of the 16 m tall Kjølv Egeland's (KE) building located at the northwest end of the campus (Fig 1). Additionally, a vertical continuous-wave profiler (ZX300) is positioned 4 meters above ground on the roof of Ivar

Langen's (IL) building (Fig. 1). Each of these three instruments is equipped with a met station, which includes a 2-D sonic anemometer that measures both horizontal wind speed and direction.

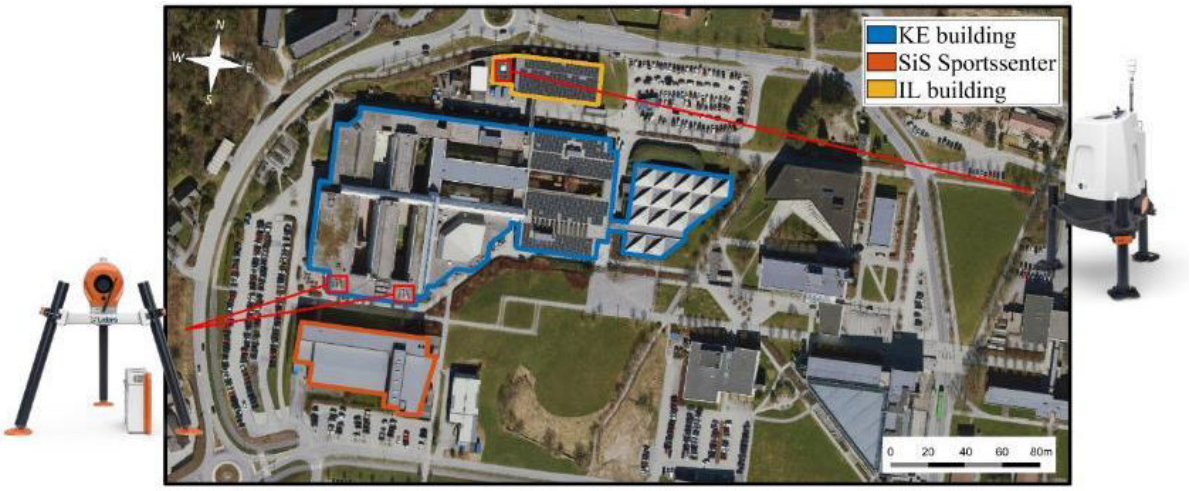


Figure 1. Lidar locations at the northwest end of the University of Stavanger campus (Vogt et al., 2024).

All three lidars scan along a conical surface with a half cone opening angle of 15°, providing fifty recordings along the circle in one second. The vertical profiler records data at 11 selected heights, from 10 m to 300 m, with a sampling rate of about 0.06 Hz at each height. The radial velocity observations at each height are processed internally and presented as estimates of wind direction, along wind speed, and vertical wind speed. The two nacelle lidars are aligned along the building side towards west and east, respectively, and are tilted upward at an inclination angle of 5°. They are set to measure at a 40 m distance from their location, resulting in a scanning circle with a radius of 10.7 m. Each of the fifty observation points along the circle is revisited approximately once every second. The sampling volume at a 40 m distance is 2 m (FWHM).

3. RESULTS

The observed wind climate on the UiS campus is illustrated using data from October 31, 2024, for the hours between 14:00 and 24:00. During this period, the incoming westerly wind was stable with a velocity in the range of 6 m/s to 8 m/s, and suitably aligned with the view of the lidars, ensuring good data availability.

The vertical wind profiler on the IL building's roof provides information on the along wind speed, the wind direction, the vertical wind speed, and the turbulence intensity at each measurement level. Fig. 2 shows the averages for these quantities for the 10-hour observation period. The wind direction is unstable at the lower levels (14 m to 42 m) but linearly changing from 210° at 54 m height to 216° at 300 m height. The mean wind velocity goes from 5 m/s at 14 m height above ground to 18.5 m/s at 300 m height. The mean wind velocity follows approx. an exponential profile with a power of 0.25. A logarithmic profile was also fitted to the data, and the surface roughness length was between 1.7 m and 3 m, depending on which data points were included or excluded. This is a considerably higher surface roughness length than the authors expected for this location. The vertical wind speed is negative at levels below 75 m but linearly increases from 0 to 0.35 m/s

at 300 m height. The turbulence intensity above the 50 m level is ~10% and follows a traditional pattern with height. Below 50 m, the turbulence is high, indicating the flow disturbance caused by nearby buildings and vegetation.

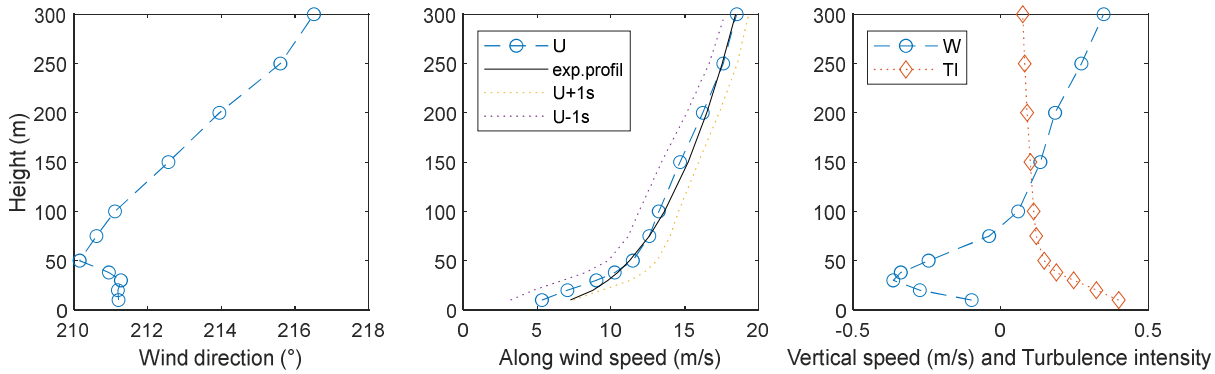


Figure 2. Mean along wind speed (U), vertical wind speed (W) and turbulence intensity (TI) on Oct. 31, 2024, between 14:00 and 24:00.

Fig. 3 shows the wind velocity and turbulence levels observed by the two horizontal lidars on the roof of the KE building, as well as data from the reference sonic anemometers on top of the lidar units. Following the incoming wind from the west, we have recordings of its velocity at 40 m in front of the building, at the top edge of the windward side of the building, at the top edge of the leeward side of the building and then 40 m behind the building in its wake area. It should be noted that lidar data is from the centre of the scanning circle, which is ~19.5 m above the ground due to the ~5° tilting of the lidar. The route of the flow is reflected in Fig. 3, as we see that 40 m in front of the building, the wind speed ranges from 6 m/s to 8 m/s while the wind speed is somewhat lower at 2 m above the edges of the building, and then in the wake, 40 m behind the building, the mean wind speed is less than half of the incoming one.

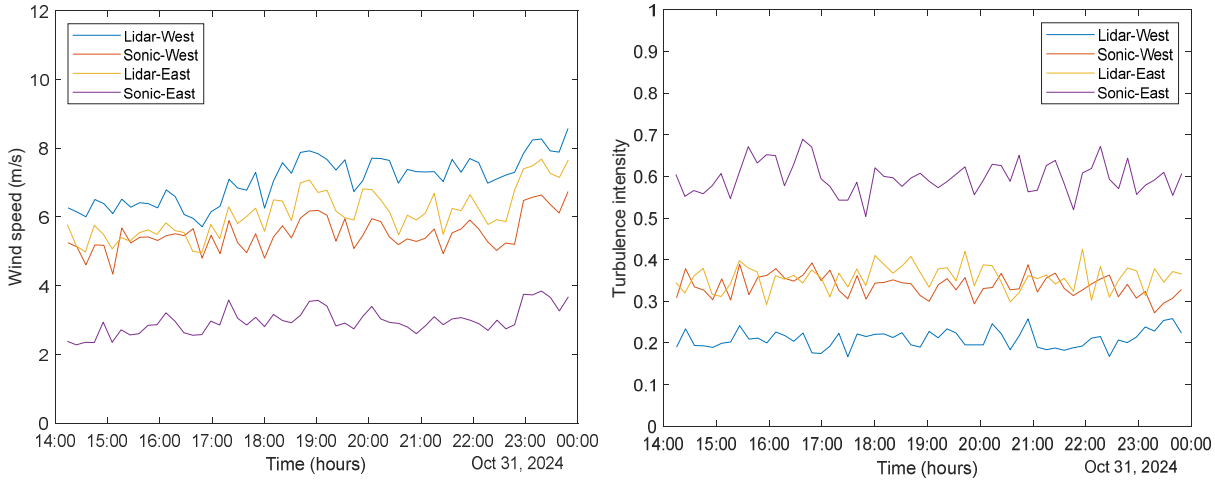


Figure 3. 10-minute mean along wind velocities (left panel) and turbulence intensities (right panel), shown for the flow approaching the building (Lidar-West), above the building (Sonics) and in the wake (Lidar-East).

The turbulence intensity shown in Fig. 3 (left panel) displays the opposite trend, being around 0.2 in the incoming flow, around 0.35 above the building edges and then 0.6 in the wake, or three times the turbulence level of the incoming flow. The different turbulence characteristics at these four monitoring locations are also reflected in the spectral density of the respective data. The spectra are presented as unitless autoregressive power spectral density estimates using Burg's method. The frequency axis is normalised with the along wind turbulence length scale, L_u, and the 10-minute mean wind speed, U. The classical Von Karman-Harris turbulence spectrum is also plotted for reference. As can be seen, all the measured spectra are affected by the local surrounding terrain to a certain degree, particularly the spectrum of the wake flow. The turbulence spectral density from the sonics above the edge of the roof shows increased energy above a normalised frequency of 1, indicating the local effects of the building on the flow.

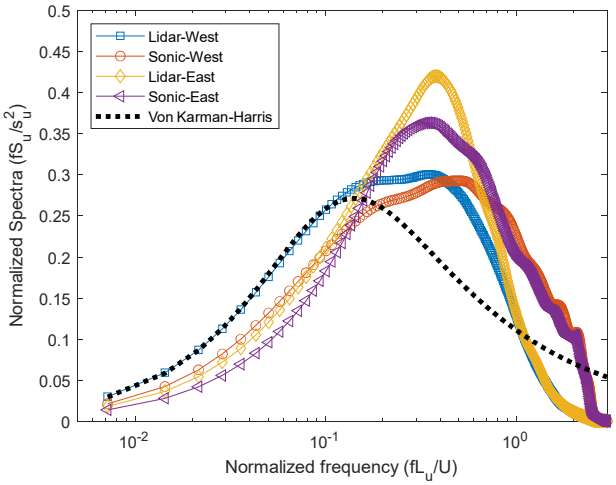


Figure 4. Normalised power spectral density of flow approaching the building (Lidar-West), above the building (Sonics) and in the wake (Lidar-East).

4. CONCLUSION

The study demonstrates the overall potential of remote wind sensing for wind monitoring in an urban environment. The buildings and the local terrain induce significant variability of the local wind flow, making measurements over small observation volumes essential to capture the flow field. In the present case, the wind lidar instruments are found to capture the non-uniform flow in the monitored regions around the buildings realistically. Combining the information from the horizontal lidars and the vertical wind profiler provides a valuable data source for validating related numerical urban flow models.

REFERENCES

Filioglou M. et al., 2022. Evaluating modelled winds over an urban area using ground-based Doppler lidar observations Meteor. Appl. 29 e2052.

Sattar, A.M.A., Elhakeem, M., Gerges, B.N. et al., 2018. Wind-Induced Air-Flow Patterns in an Urban Setting: Observations and Numerical Modeling. Pure Appl. Geophys. **175**, 3051–3068. https://doi.org/10.1007/s00024-018-1846-5.

Vogt, L., et al 2024 J. Phys.: Conf. Ser. 2875 012017. https://doi.org/10.1088/1742-6596/2875/1/012017.

ZXLidars: https://www.zxlidars.com/

Hazard Maps of Typhoon-induced Wind, Wave and Surge along Southeast China

Xiaonong Hu [1], Genshen Fang[1], Yaojun Ge [1]

[1] *State Key Lab of Disaster Reduction in Civil Engineering, Tongji University, Shanghai, China, 2210016@tongji.edu.cn*

SUMMARY:
The southeastern coastal region of China frequently faces typhoon attacks, posing significant threats to its ever-growing infrastructure. Quantifying multiple typhoon-induced hazards in terms of wind, wave, and surge would provide valuable data to support structural design, risk assessments, and disaster mitigation. This study simulated the evolution of wave and surge driven by typhoon wind fields using the SWAN + ADCIRC coupling model, generating extreme samples of wind speed, significant wave height, and surge height. Trivariate joint probability distributions were established at six typical coastal stations (Hong Kong, Xiamen, Fuzhou, Wenzhou, Zhoushan, and Shanghai) based on optimal copula functions. Using the environmental contour method, appropriate combinations of design environmental loads were analysed for a specific return period. The results revealed a reasonable combination type for the 100-year design period, which selects a variable group corresponding to the maximum value of the dominant variable on the environmental surface. The finding was further extended to the entire computational area to develop hazard maps covering the Southeast Sea area. The hazard maps show that the design values of significant wave height increase with distance from the coast. In contrast, the spatial distribution of surge presents the opposite pattern.

Keywords: typhoon-induced hazards, joint probability distribution, hazard map

1. MOTIVATION

Strong typhoon winds are among the most destructive disaster factors, causing significant damage to infrastructures annually in Southeast China. The transport of typhoons over the ocean generates huge waves and storm surges, posing a severe threat to structural safety. To determine a reasonable combination, joint analysis of multiple environmental hazards has received significant attention in recent years. However, most of these studies have focused on several specific sites rather than on the entire sea region. Significant discrepancies exist among the analysed results from different locations, indicating that findings at one site may not be applicable to engineering projects at other locations. Furthermore, while many related studies have analysed the correlations between two types of hazards, few have conducted three-dimensional correlation analyses of winds, waves, and surges. Consequently, it is essential to explore the correlations among typhoon-induced winds, waves, and surges and to develop joint hazard maps for the sea area along Southeast China. Considering the aforementioned points, this study aims to: (i) establish trivariate joint probability distributions of typhoon-induced wind speed, significant wave height, and surge height; (ii) discuss methodologies for determining reasonable combinations of multiple environmental loads; (iii) develop corresponding hazard maps for the typhoon-prone southeastern coastal regions of China.

2. CONSTRUCTION OF THE COUPLING MODEL

As shown in Fig. 1 (a), the computation domain is mainly located in southeast China sea, with a range from 105 °E to 126 °E and from 15 °N to 33 °N. Considering the balance of computation efficiency and accuracy, the unstructured mesh size near the coast and islands is 500 m and the maximum size in the open sea is 20 km. Simulated historical typhoon events are selected from a period of 36 years (1987-2022). This study takes six stations (Hongkong, Xiamen, Fuzhou, Wenzhou, Zhoushan and Shanghai) along the coast as reference points. At each station, a radius of 300 km is adopted to determine the specific influencing area. A typhoon whose track intersects this area is considered influential. In total, 196 typhoons are selected for study (see Fig. 1 (b)).

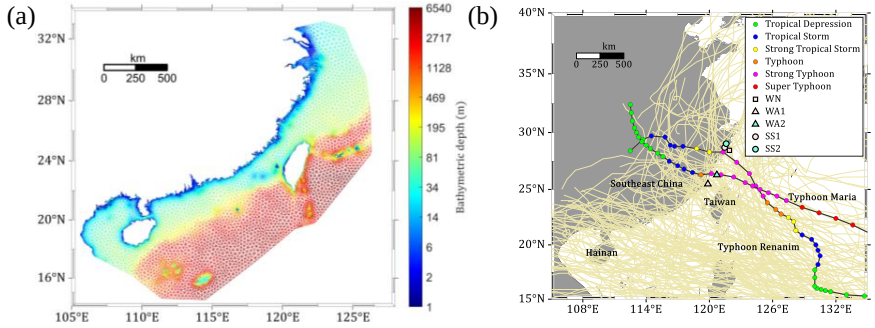


Figure 1. The coupling model for wave and surge evolution.

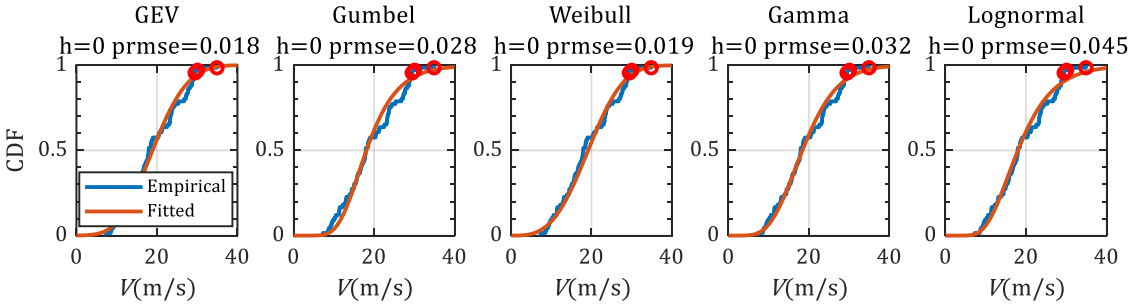


Figure 2. Marginal distribution.

3. JOINT PROBABILITY ANALYSIS

Five probability distributions including generalized extreme value (GEV), Gumbel, Weibull, Lognormal and Gamma, are applied to fit each group of samples for the three random variables (the wind speed V, the significant wave height H_s and the surge height S). The result of Kolmogorov-Smirnov (K-S) test and the goodness of fit at the distribution tail are utilized to choose the optimal distribution. In Fig. 2, for the samples of wind speed at Fuzhou station, all models pass the K-S test while the GEV distribution presents the best performance at the distribution tail, which is important for the estimation of extreme quantiles.

With the marginal distribution, the copula functions can be employed to determine the joint distribution of two variables. For m-dimensional distribution function F, with continuous marginal distributions $F(x_i)$ $(i = 1,2,\cdots,m)$, there exists a copula function that is expressed as:

$$F(x_1, x_2, \cdots, x_m) = C(F_1(x_1), F_2(x_2), \cdots, F_m(x_m)) \quad (1)$$

in which $F(\cdot)$ is the joint CDF of n-dimensional vector $[x_1, x_2, \cdots, x_m]$, and $C(\cdot)$ is the copula function that describes the dependence of the multi-variables. Three copula functions (Clayton, Gumbel, and Frank) are adopted for the bivariate joint distribution. To extend two-dimensional copula functions to high dimensions, the nested method can be utilized. As shown in Fig. 3 (a), after using the second bivariate copula function C_2 to connect the marginal distribution u and v, the first bivariate copula function C_1 will be utilized to connect C_2 and another marginal distribution w. As a result, characteristics of the trivariate joint distribution can be described by C_1 and C_2. It should be noted that u and v are always the group with the highest correlation among all two-variable groups of the three variables. In Fig. 3 (b) and (c), taking samples at Fuzhou station as an example, the Akaike information criterion statistic is introduced here to evaluate the goodness of fit between original samples and the constructed joint distribution. Results show that the Frank copula has the best performance among the three copula functions for both C_1 and C_2.

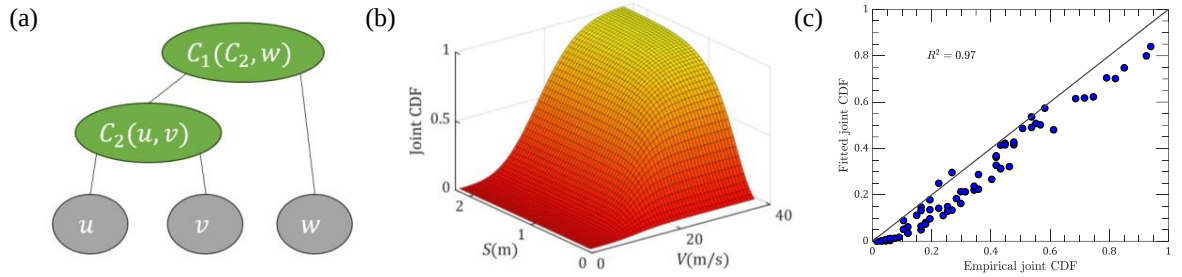


Figure 3. Joint distribution ((a) the nested method; (b) C_2 (Wind-Surge); (c) Fitting effect of C_1).

4. COMBINATION AND HAZARD MAPS OF WIND, WAVE, AND SURGE

The method of environmental contour based on IFORM provides load combination with consideration of structural reliability. The relationship between the return period T_β and the structural reliability index β can be described using Eq. (2). For the trivariate case, β is the radius of the sphere constructed by three independent standard-normally distributed variables U_1, U_2, and U_3. The IFORM method based on Rosenblatt transformation can match variables (U_1, U_2, and U_3) in the standard normal space and environmental variables (X_1, X_2, and X_3) as Eq. (3) (Rosenblatt, 1952; Valamanesh et al., 2015). In this study, environmental variables consist of V, H_s, and S. Thus, the three-dimensional environmental surface can be obtained in physical space, which representing the extreme environmental conditions under a certain return period.

$$T_\beta = 1/[N * (1 - \Phi(\beta))] \quad (2)$$

$$U_1{}^2 + U_2{}^2 + U_3{}^2 = \beta^2 \quad (3a)$$

$$\Phi(U_1) = F_1(x_1) \quad (3b)$$

$$\Phi(U_2) = F_{2|1}(x_2|X_1 = x_1) \quad (3c)$$

$$\Phi(U_3) = F_{3|1,2}(x_3|X_1 = x_1, X_2 = x_2) \quad (3d)$$

With environmental surfaces, a group of variable values can be selected as the design values. Two methods are used in this study. One method is to choose the point on the surface with the highest joint PDF value, indicating that this group of values is most likely to occur. In the other method, the dominant variable takes the maximum value on the sphere, while the other two variables take

the corresponding values. In most cases, combination values with the highest PDF values are relatively low, potentially leading to safety concerns. In contrast, the results with the maximum dominant variable value are more reasonable, avoiding the underestimation of environmental loads. The values of the secondary variables also fall within appropriate ranges. Therefore, the second method is recommended for determining environmental load combinations.

The nodal results in the computation domain are analysed to obtain hazard maps. Considering that the boundary can affect the accuracy of simulation results, nodes within 60km from the boundary are excluded to eliminate such influence. As shown in Fig. 4, high wind speed values consistently occur in specific sea areas, including the region close to Wenzhou, the area between Xiamen and Hongkong, and the area near Hongkong. Geographical patterns exist in the wave and surge hazard maps. Design values of significant wave height increase with the distance to the coast. The decreasing water depth and the presence of offshore islands and reefs lead to wave energy dissipation, wave underdevelopment, and wave breaking. Notably, H_s values near Xiamen and Fuzhou are generally lower than those in the nearby ocean due to the shelter from the large island. In contrast, the spatial distribution of surges presents an opposite pattern: surge design values decline with increasing offshore distance. The decreasing water depth and complex nearshore topography cause tidal reflection and interference, resulting in greater storm surge amplitudes.

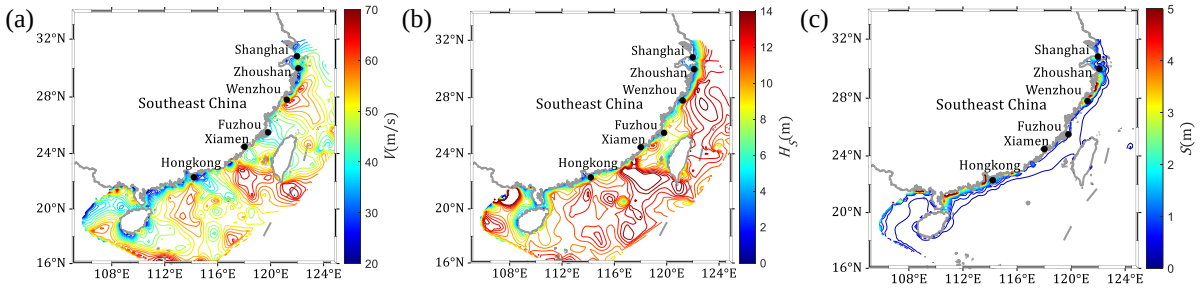


Figure 4. Hazard maps ((a) V-dominated, V; (b) H_s-dominated, H_s; (c) S-dominated, S).

5. CONCLUSIONS

By constructing the SWAN+ADCIRC coupling model and performing numerical simulations during 196 typhoons, extreme samples of typhoon-induced winds, waves, and surges are extracted and utilized to establish multivariate joint probability distributions. Employing the environment contour method, this study evaluates different combinations of multiple environmental variables. Furthermore, hazard maps are developed to reflect environmental risk along Southeast China.

ACKNOWLEDGEMENTS

The authors acknowledge the support of the National Natural Science Foundation of China (52108469, 52278520).

REFERENCES

Rosenblatt, M., 1952. Remarks on a multivariate transformation. Annals of Mathematical Statistics 23(3), 470−472.

Valamanesh, V., Myers, A. T., Arwade, S. R., 2015. Multivariate analysis of extreme metocean conditions for offshore wind turbines. Structural Safety 55, 60–69.

Scaling of a full-scale thunderstorm for laboratory simulations

Ileana Calotescu [1], Horia Hangan [2]

[1]*Technical University of Civil Engineering Bucharest, Bucharest, Romania, ileana.calotescu@utcb.ro*
[2]*OntarioTech University, Oshawa, Canada, Horia.Hangan@ontariotechu.ca*

SUMMARY:
In this paper, a full-scale velocity record is used to test a scaling methodology proposed in literature for laboratory simulations of thunderstorm events. The record was measured by a wind and structural monitoring system installed on a 50 m tall telecommunication lattice tower located in Afumați, Romania. The system comprises an ultrasonic anemometer, a triaxial accelerometer, three strain gauges and four video surveillance cameras. This paper demonstrates the applicability of the scaling methodology for particular thunderstorm events. Moreover, the geometric scales ranges are discussed to emphasize the possibility to simulate both wind and structural characteristics corresponding to real thunderstorms.

Keywords: thunderstorms, downburst scaling, full-scale wind measurements, wind tunnel testing.

1. INTRODUCTION

Research on thunderstorms has been developed over the last decades around the world in an effort to identify their characteristics needed for engineering design of structures (Fujita, 1990; Solari et al., 2015). Field measurements and experimental investigations are complementary tools used in the field of wind engineering to understand the features of thunderstorm downburst as well as their effect on structures. One of the challenges associated with combining these tools is scaling of real events in relation with laboratory simulations.

In this paper, the velocity record corresponding to a real thunderstorm event is used to test a scaling methodology proposed in literature by Romanic et. al (2020) in order to emphasize its applicability and limitations. The record was measured in Afumați, Romania on May 7th 2024 (Calotescu and Bîtcă, 2024) by a wind and structural monitoring system installed on a 50 m tall telecommunication lattice tower. The full-scale record is compared to downburst-like measurements (Canepa et. al, 2022) obtained in the Wind Engineering, Energy and Environment (WindEEE) Dome (Hangan, 2014) at Western University, Canada.

2. SCALING METHODOLOGY

The velocity decomposition associated to both real and simulated thunderstorm records may be expressed as (Solari at. al, 2015, Romanic et. al, 2020):

$$v_s(t_s) = \overline{v}_s(t_s) + v'_s(t_s) = \overline{v}_{\max,s}\gamma_s(t_s)\left[1 + \overline{I}_{v,s}\mu_s(t_s)\tilde{v}'_s(t_s)\right] \quad (1)$$

where the subscript s is either m (model, i.e. physical simulation in the wind chamber) or p (prototype, i.e. real event in the atmosphere), $t_s \in [0, \Delta T_s]$, ΔT_s is the length of either m or p velocity

records, $\overline{v}_s$ is the slowly-varying mean speed, v'_s is the residual turbulent fluctuation, $\tilde{v}'_s$ is the reduced turbulent fluctuation and γ and μ are two non-dimensional ratios expressed as:

$$\gamma_s\left(t_s\right)=\overline{v}_s\left(t_s\right)/\overline{v}_{\max,s} \text{ and } \mu_s\left(t_s\right)=I_{v,s}\left(t_s\right)/\overline{I}_{v,s} \tag{2}$$

where $\overline{v}_{\max,s}$ is the maximum value of $\overline{v}_s\left(t_s\right)$ and $\overline{I}_{v,s}$ is the average value of $I_{v,s}\left(t_s\right)$.

Considering a couple of *m* and *p* events, the velocity scale is defined as (Romanic et. al, 2020):

$$\Lambda_v\left(T_m\right)=\frac{v_p\left(t_p\right)}{v_m\left(t_m\right)}=M_v\left(T_m\right)\cdot F_v\left(T_m\right) \tag{3}$$

where M_v represents the scaling between mean flows and F_v represents the scaling of the fluctuating part of the two velocity records expressed as:

$$M_v\left(T_m\right)=\frac{\overline{v}_{\max,p}\gamma_p\left(t_p\right)}{\overline{v}_{\max,m}\gamma_m\left(t_m\right)} \text{ and } F_v\left(T_m\right)=\frac{1+\overline{I}_{v,p}\mu_p\left(t_p\right)\tilde{v}'_p\left(t_p\right)}{1+\overline{I}_{v,m}\mu_m\left(t_m\right)\tilde{v}'_m\left(t_s\right)} \tag{4}$$

where T_m represents the averaging period for the *m* events, while for the *p* events the averaging window is considered T_p = 30 s (Solari et. al, 2015).

Assuming that the proper moving average period $T_{m,p}$ for the fluctuating part of the flow is the same as for the mean flow, the time scale may be defined based on the number of readings (k_s) and the frequency of acquisition (f_s) of the instrument as:

$$\Lambda_{T,P}\left(T_{m,p}\right)=\frac{f_{a,m}}{f_{a,p}}\frac{k_p}{k_{m,P}} \tag{5}$$

where $T_{m,p}$ is the properly selected averaging window for *m* events which leads to similar shapes of $\gamma_m\left(t_m\right)$ and $\gamma_p\left(t_p\right)$ functions.

Finally, the proper length scale between the mean flows of the *m* and *p* events is calculated as:

$$\Lambda_{L,P}=M_{v,P}\cdot\Lambda_{T,P} \tag{6}$$

3. SCALING OF THE FULL-SCALE THUNERSTORM

On May 7th 2024, the anemometer measured an instantaneous peak wind speed of 20.3 m/s around 16:17 UTC+2 (Coordinated Universal Time). The total duration of the event was less than 10 minutes, the ramp-up and ramp-down being visible in a 5 minutes interval.

The scaling of this real event is done based on the methodology described in Section 2 and the results are compared with downburst-like measurements obtained in the WindEEE Dome (Canepa et. al, 2022). Some limitations regarding the length scale are worth considering. As the cross-sections of the tower elements are quite small (circular members with diameters between 51 and 146 mm), a length scale $\Lambda_{L,P}\leq 100$ would lead to a proper scaled geometrical model of the tower. The question then arises if there exists a proper *m* record measured in the WindEEE Dome for which, given an imposed length scale, proper velocity and time scales could be found to accurately represent the May 7th 2024 event.

Figure 1 shows the decomposition of the real thunderstorm measured record on May 7th 2024 (*p* event) and the corresponding the record (*m* event) simulated in the WindEEE Dome which led to good similarities between $\gamma_m(t_m)$ and $\gamma_p(t_p)$ functions (Fig. 2). For this, a 5 min interval centered on the peak wind speed was selected for the *p* event while for the simulated *m* event, an interval of 2 seconds provided the best match between the γ functions.

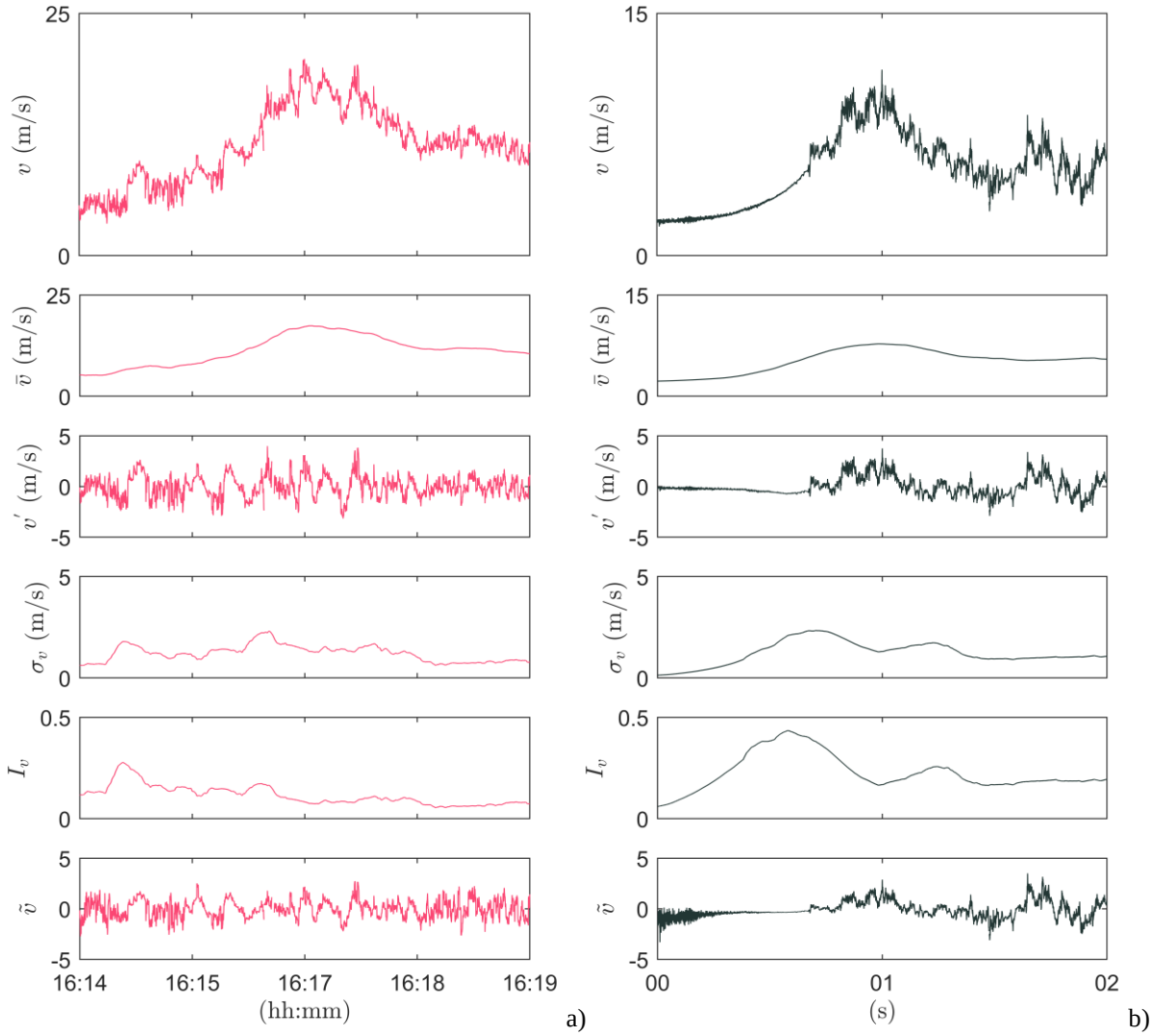


Figure 1. Decomposed wind velocity of the (a) May 7th 2024 event (*p* event) and (b) a downburst-like record (*m* event) simulated in the WindEEE Dome

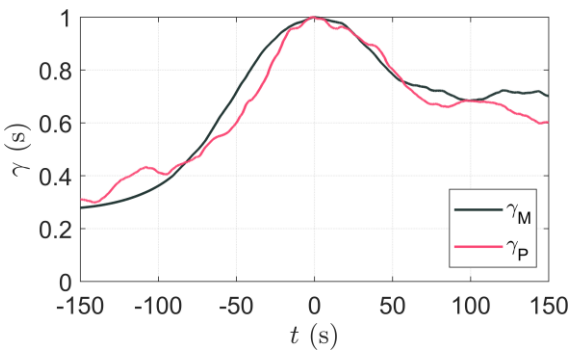


Figure 2. Comparison of γ functions for the *p* event and the *m* event

The proper moving average period which led to good similarities between the γ functions of the *p* and *m* events resulted $T_{m,P}$=0.6. Considering the sampling frequencies of the instruments (10 Hz for the anemometer and 2500 Hz for the cobra probes) the time scale resulted as $\Lambda_{T,P}$ = 50. Therefore the full scale equivalent $T_{m,P}$=30 s used to evaluate the time scale is in the range of time scales indicated by Holmes et al.(2008) and Solari et al (2015). The scaling between mean flows (M_v) and the fluctuating parts of the two velocity records (F_v) together with the overall velocity and length scales are shown in Figure 3. These results were obtained for a *m* event measured at radial position r/D=0.8 and cobra probe height z=50 cm where, *r* represents the radial distance from the jet centerline while D is the jet diameter as defined by Canepa et. al (2022).

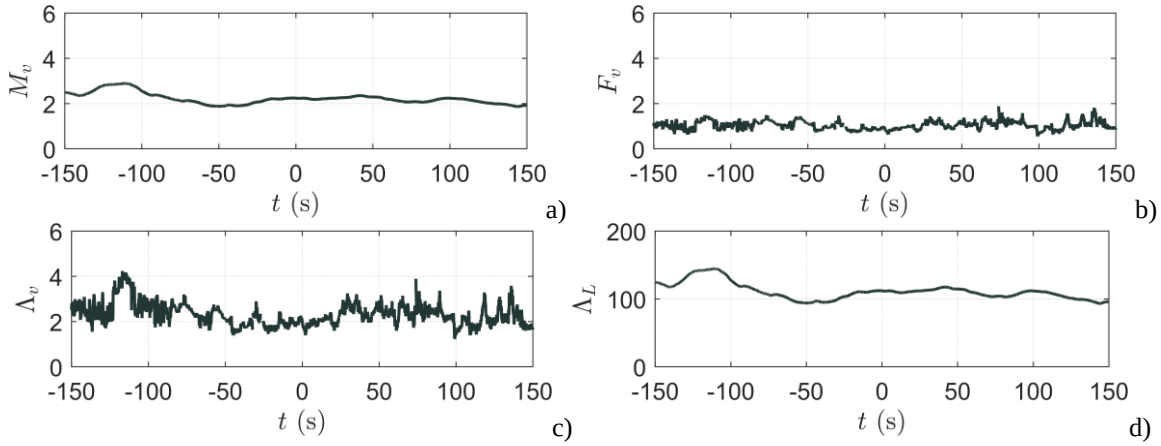


Figure 3. (a) Mean velocity scale, (b) fluctuating velocity scale, (c) overall velocity scale and (d) length scale

4. CONCLUSIONS

This paper presents an applicative study for the validation of a scaling methodology proposed in literature for full-scale thunderstorms in wind simulators. A real thunderstorm measured in Afumați, Romania, is compared to simulated downburst-like records measured in the WindEEE Dome. A particular attention is given to the choice of length scales which would allow for proper modelling of the tower for possible simulations of both wind and structural characteristics.

ACKNOWLEDGEMENTS

The work performed by the first author was supported by a National Research Grants of the UTCB, project number $GnacC_{2023}^{ARUT}$ -UTCB-06.

REFERENCES

Calotescu, I., Bîtcă, D., 2024. Characteristics of a thunderstorm downburst measured near Bucharest, Romania. ERCOFTAC SIG41 Symposium on "Fluid-Structure Interaction in complex systems": from aero to astro Thermopylae/Kamena Vourla and joint with Hypati Observatory, Greece, August 2024, 20-21.

Canepa, F., Burlando, M., Romanic D., Solari G. and Hangan H., 2022. Downburst-like experimental impinging jet measurements at the WindEEE Dome, Sci Data 9, 243.

Fujita, T., 1990. Downbursts: meteorological features and wind field characteristics. Journal of Wind Engineering and Industrial Aerodynamics, 36, 75-86.

Hangan, H., 2014. The Wind Engineering Energy and Environment (WindEEE) Dome at Western University. Canada. Wind Eng. JAWE 39, 350–351.

Holmes, J.D., Hangan, H., Schroeder, J.L., Letchford, C.W. and Orwig, K.D. 2008. A forensic study of the Lubock-Reese downdraft of 2002, Wind and Structures, 11(2): 137-152.

Romanic, D., Nicolini, E., Hangan, H., Burlando M., 2020. A novel approach to scaling experimentally produced downburst-like impinjing jet outflows. Journal of Wind Engineering and Industrial Aerodynamics 196, 104025.

Solari, G., Burlando, M., De Gaetano, P., Repetto, M.P., 2015. Characteristics of thunderstorms relevant to the wind loading of structures. Wind and Structures, An International Journal 20, 763–791.

Extreme gust trees damage in Montevideo city, operational alarm forecast with WRF ensemble simulation.

Alejandro Gutiérrez[1], Mariana Molinari[2], German Vazquez[3], Sofia Orteli[4], Victor Silveira[5]

[1]*IMFIA FING UdelaR, Montevideo, Uruguay, aguti@fing.edu.uy*
[2]*IMFIA FING UdelaR, Montevideo, Uruguay, mmolinari@fing.edu.uy*
[3]*IMFIA FING UdelaR, Montevideo, Uruguay, gvazquez@fing.edu.uy*
[4]*IMFIA FING UdelaR, Montevideo, Uruguay, sofiao@fing.edu.uy*
[5]*IMFIA FING UdelaR, Montevideo, Uruguay, vsilveira@fing.edu.uy*

SUMMARY:
This study analyzes meteorological events linked to tree damage in Montevideo City, based on historical data from 2014 to 2022. The data comprises records of emergency tree maintenance works documented by the Montevideo City Hall. The primary objective is to identify critical meteorological factors and develop an operational forecasting model capable of generating real-time alerts for extreme wind events, utilizing WRF (Weather Research and Forecasting) ensembles. Key thresholds for maximum daily wind speed, wind gusts, and precipitation were determined during the analysis. The findings indicate that tree damage typically occurs under the following conditions: Accumulated precipitation exceeding 20 mm over the preceding 7 days, Maximum daily mean wind speeds at 10 m above ground level surpassing 5 m/s, and Maximum daily wind gusts exceeding 15 m/s. These thresholds provide a foundation for operational forecasting of tree damage and improving urban resilience to extreme weather events.

Keywords: extreme wind and gust, trees damage, forecast

1. INTRODUCTION

Montevideo, the capital of Uruguay, is situated in the mid-latitudes of South America. Its geographic location exposes the region to rapid meteorological changes driven by the interaction of cold air masses from the poles and warm air masses from the tropics. These frontal encounters frequently lead to precipitation and storms, which can develop within hours. Extreme convective storm events often result in significant damage to structures and infrastructure across the country (Durañona et al., 2019). Previous studies have contributed to understanding wind dynamics in the region. For instance, Gutiérrez and Fovell, 2018 developed a gust model for 100 meters above ground level using data from measurement towers in Uruguay. Later, Gutiérrez, Porrini, et al., 2020 evaluated the model's performance specifically for convective storms. Building on these foundations, this study analyzes meteorological events associated with tree damage in Montevideo City, utilizing historical data from 2014 to 2022. The data comprises records of emergency tree maintenance works documented by the Montevideo City Hall. Additionally, an operational forecasting system was implemented, with WRF (Weather Research and Forecasting) ensemble numerical simulations to generate real-time alerts for extreme wind events.

1.1. Methodology

Extreme wind events associated with tree damage were classified by region within the city and by tree species. All types of damage were recorded, including tree falls and branch breakage. The primary objective of this study is to identify critical factors and develop an operational forecasting model capable of generating real-time alerts for extreme wind events, utilizing WRF (Weather Research and Forecasting) ensemble simulations. To characterize the meteorological events, observational data from three INUMET (Uruguayan National Institute of Meteorology) stations were analyzed. The dataset included daily accumulated precipitation, average wind speed, and maximum wind speed (gusts). The analysis revealed that tree damage typically occurs under the following threshold conditions: Accumulated precipitation over the preceding 7 days exceeding 20 mm, Maximum daily mean wind speed at 10 m above ground level surpassing 5 m/s, and Maximum daily wind gusts exceeding 15 m/s. Gusts were identified as a critical parameter for detecting extreme wind events. Tree damage associated with extreme winds was found to occur more frequently during the summer months. Notably, the most representative tree species in Montevideo, Fraxinus and Melia azedarach, typically shed their leaves during the winter. The mechanical interaction of extreme winds with leafless trees is considered a key factor in the reduced frequency of tree damage and related maintenance work recorded between March and September. To support the forecasting model, WRF simulations from 2014 to 2022 were conducted on a 12 km grid. These simulations aimed to refine the prediction of average wind speed and develop an accurate gust model for extreme wind events.

2. ANALYSIS

Meteorological events associated with tree damage in Montevideo City were analyzed using data from 2014 to 2022. The dataset comprised records of emergency tree maintenance works documented by the Montevideo City Hall. Figure 1 illustrates the analysis for the year 2018. The following data are plotted: Daily precipitation (black line), Maximum mean wind velocity (blue line), Maximum wind gust (blue dot), Maintenance emergency tree works (red dot), Intensive maintenance emergency tree works (yellow dot), and Extreme meteorological events identified by the analysis (green square) and registered by the Montevideo City Hall (yellow square). Figure 2 (middle panel) displays images of tree damage in Montevideo City caused by an extreme wind event. Figure 3 presents the Gust Factor ($GF = \frac{Gust}{MeanWindVelocityWRF}$) model developed for three locations during the training period, along with a histogram illustrating the model's performance during the validation period.

2.1. Operational Alarm

An operational forecasting system was implemented using 30 members of GFS-WRF ensemble numerical simulations. Figure 4 illustrates the gust forecast for a simulation initialized on 11 October 2024 for the Prado location in Montevideo City. The operational alarm system functions as follows: when forecasted conditions exceed thresholds, an automatic email alert is sent to the Montevideo City Hall's Tree Management Team.

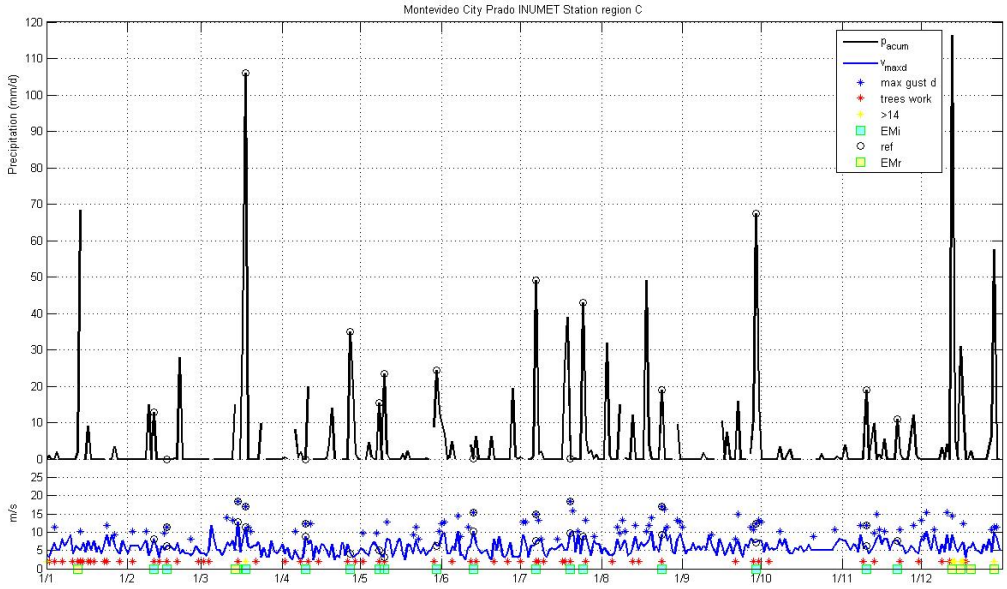


Figure 1. Analysis of extreme meteorological event during 2018 in region C of Montevideo city. Black is plotted precipitation, blue line maximum mean velocity, blue dot maximum gust, red dot maintenance emergency tree works, yellow dot intensive maintenance emergency tree works, green and yellow square extreme meteorological event identified by the analysis a registered by the Hall respectively



Figure 2. Trees with different damages in Montevideo City, during an extreme meteorological event.

3. CONCLUSIONS

Extreme weather events causing tree damage are frequently associated with wind gusts exceeding 10 m/s, while critical events typically involve gusts surpassing 15 m/s. Analysis of precipitation patterns revealed that in all events associated with damage—particularly critical events—there were high frequencies of accumulated precipitation ranging between 20 mm and 60 mm over the two days preceding the event and the day of the event itself (i.e., a three-day accumulation). For critical events, precipitation patterns over a seven-day period were found to be particularly relevant, with accumulated precipitation generally exceeding 20 mm. A Gust Factor model was developed

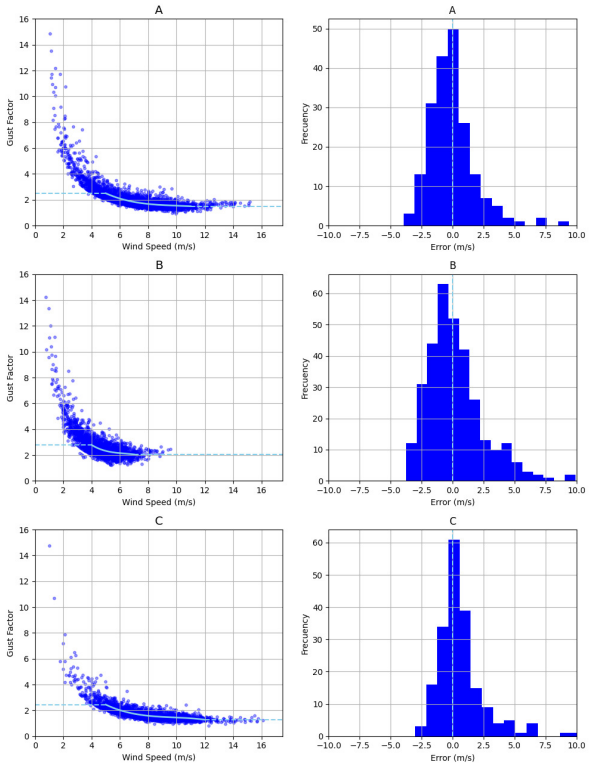


Figure 3. Gust Factor model developed for three locations, and histogram during validation.

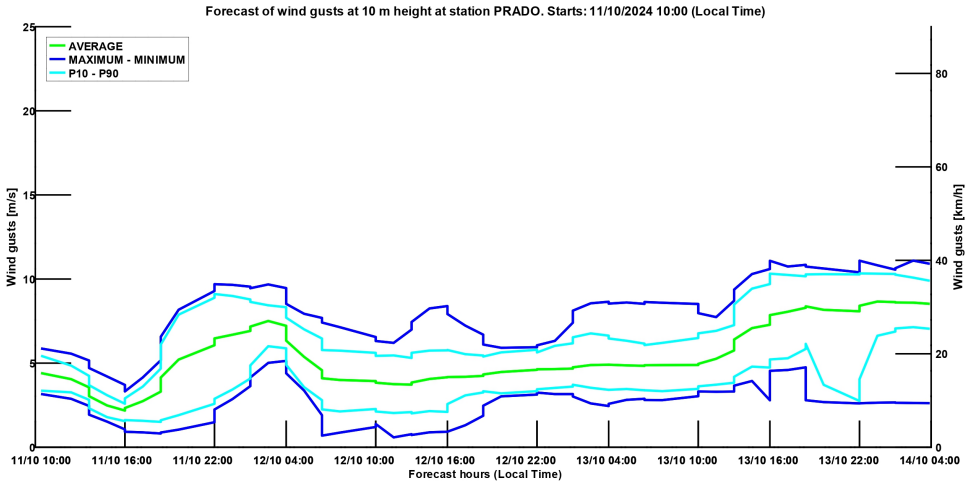


Figure 4. Operational gust forecast 30 members of GFS-WRF ensembles numerical simulation initialized on 11 October.

and trained using WRF (Weather Research and Forecasting) simulations for three observational data stations. Additionally, an operational alarm forecasting system, based on WRF ensemble simulations, was implemented. This system automatically sends email alerts to the Montevideo City Hall's Tree Management Team when threshold conditions are forecasted. The performance

of this system will be further analyzed during the Southern Hemisphere summer of 2024–2025.

ACKNOWLEDGEMENTS

Alfonso Arcos - IMM and CSIC IMM I+D "Pronóstico operativo de tormentas severas sistema automatizado de alarmas por mail".

REFERENCES

Durañona, V., Marchesoni, E., and Sallés, R., 2019. A first characterization of high winds that affect the energy distribution system of Uruguay and their related effects. Journal of Wind Engineering and Industrial Aerodynamics 184, 128–138.

Gutiérrez, A. and Fovell, R. G., 2018. A new gust parameterization for weather prediction models. Journal of Wind Engineering and Industrial Aerodynamics 177, 45–59.

Gutiérrez, A., Porrini, C., and Fovell, R. G., 2020. Combination of wind gust models in convective events. Journal of Wind Engineering and Industrial Aerodynamics 199, 104118.

Torsional instabilities of single-axis solar trackers: a benchmark for wind tunnel testing

Carlos Rodríguez-Casado [1], Eduardo Blanco Marigorta [2], Sebastian Franchini Longhi [3], Juan A. Cárdenas-Rondón [4], Antonio Navarro-Manso [5]

[1] *Energy Department, University of Oviedo, Gijón, Spain, rodriguezccarlos@uniovi.es*
[2] *Energy Department, University of Oviedo, Gijón, Spain, eblanco@uniovi.es*
[3] *Universidad Politécnica de Madrid. Instituto Universitario de Microgravedad "Ignacio Da Riva" (IDR/UPM), Plaza Cardenal Cisneros, 3, Madrid, 28040, Spain, s.franchini@upm.es*
[4] *Universidad Politécnica de Madrid. Instituto Universitario de Microgravedad "Ignacio Da Riva" (IDR/UPM), Plaza Cardenal Cisneros, 3, Madrid, 28040, Spain, ja.cardenas@upm.es*
[5] *Energy Department, University of Oviedo, Gijón, Spain, navarroantonio@uniovi.es*

SUMMARY:
The wind-induced torsional oscillation of single-axis solar trackers is a complex phenomenon involving multiple fluid-structure interaction effects, such as torsional galloping, divergence, 1DOF flutter, vortex-induced vibration, and buffeting. The greatest risk of structural damage arises from torsional aeroelastic instability, which occurs when wind speed surpasses a critical threshold. Current engineering guidelines lack reliable criteria to ensure safe operating conditions, making individual wind tunnel testing necessary for each case. Due to limited and inconsistent data in existing research, there is a growing need for an established benchmark to facilitate comparisons and validate methodologies across different studies. This study presents a solar tracker model with both torsional and bending aeroelastic characteristics designed for wind tunnel testing, and includes specifications for geometry, mounting, experimental methods, and a criterion for determining critical wind speeds. Solar tracker units constructed following this model were tested at two wind tunnels—Polytechnic University of Madrid and University of Oviedo—and the measurements show strong agreement. The results presented include stability maps, a comparison with existing literature, and an analysis of the observed phenomena.

Keywords: aeroelastic model, Stability Diagram, critical velocity

1. MOTIVATION

The rapid growth of solar energy and demand for cost-effective photovoltaic systems have spurred the development of single-axis solar trackers (SAT), which rotate to follow the sun and maximize energy capture. However, narrowing torque tubes and larger panel arrays has increased SAT vulnerability to aeroelastic instabilities (Martínez-García et al., 2021; Taylor et al., 2024). These aerodynamic phenomena (Rohr et al., 2015) can cause severe structural damage if not adequately addressed (Valentín et al., 2022).

Despite long-standing research on aeroelasticity in various structures, SAT-specific challenges render traditional design standards insufficient. The complex fluid-structure interactions complicate instability predictions (Enshaei et al., 2023). Furthermore, the lack of standardized wind tunnel testing for assessing SAT aeroelastic performance has resulted in scattered and inconsistent data. While static wind tunnel testing has been useful for evaluating wind loads, it does not capture critical dynamic responses like torsional divergence and flutter, essential for

optimizing SAT performance in real-world conditions (Strobel and Banks, 2014). Numerical simulations, such as Computational Fluid Dynamics (CFD), require experimental validation to ensure accuracy (Taylor and Browne, 2020).

To address these challenges, a standardized wind tunnel testing approach for SATs is crucial to provide reliable data for design and research. Developing a comprehensive benchmark model, based on a full 3D aeroelastic replica of a SAT, is vital for studying critical wind speeds and effects like turbulence, wind direction, and row interference. Establishing this benchmark will aid in validating computational models, enhancing reproducibility across research facilities, and supporting industry standardization (Browne et al., 2020; Cheruku et al., 2020).

The benchmark model tested at the Polytechnic University of Madrid and the University of Oviedo has produced detailed stability maps and critical velocity criteria for torsional aeroelastic instability (Rodríguez-Casado et al., 2024), including comparisons with sectional 2D wind tunnel tests (Cárdenas -Rondón et al., 2023). Ultimately, this work will improve SAT durability, establish better design practices, and enhance solar energy infrastructure resilience worldwide (Taylor et al., 2024).

2. METHODS

The prototype for this study is a reference Single-Axis Solar Tracker, characterized by a central pillar (driver) and two wings consisting of two independent vertical rows of panels, totaling 96 panels (2.4 m x 1.2 m each). The overall length is 57.6 m, with a torque tube made of steel supported by six pillars. The structure's natural frequencies, primarily dictated by the torque tube's torsional stiffness and the rotational inertia of the panels and supports, have been calculated, resulting in a natural torsional frequency of 0.90 Hz.



Figure 1. Benchmark scale model undergoing torsional instability in the wind tunnel.

To explore aeroelastic instability, a half-scale model (1/30) was constructed (made of PLA 3D printed), featuring a length of 960 mm and a torque tube made of brass and aluminum. The model's design retains similarity in key structural coefficients, including torsional stiffness and rotational inertia, detailed by dimensional analysis. The configuration allows only rotational motion while preventing vertical or horizontal movements. The experimental setup includes adjustable components to facilitate tilt adjustments and minimize friction, ensuring effective wind tunnel testing (see Fig. 1). Table 1 below shows the main characteristics of both prototype and benchmark scale model:

Table 1. Prototype and scale model characteristics.

GENERAL DATA	SYMBOL	PROTOTYPE	SCALE MODEL
Length	L	28.8 m	0.960 m
Chord	b	4.8 m	0.160 m
Aspect Ratio	AR	12	12
Height	H	3.0 m	0.100 m
Torque tube (TT) diameter	D	0.200 m	0.005 m
Torque tube (TT) thickness	e	0.004 m	0.0005 m
Clearance (distance panel to TT)	h_p	0.24 m	0.008 m
Torsional stiffness	K_T	$6.64 \cdot 10^4$ N·m	1.51 N·m
Natural frequency, torque tube torsion	f_T	5.65 rad/s	131.03 rad/s
Mass	M	2592 kg	0.099 kg
Inertia	I_R	$5.14 \cdot 10^3$ kg·m^2	$2.17 \cdot 10^{-4}$ kg·m^2
Flexural stiffness	EI	$2.30 \cdot 10^5$ N·m^2	0.17 N·m^2

3. RESULTS

Fig. 2 summarizes part of the results of the study:

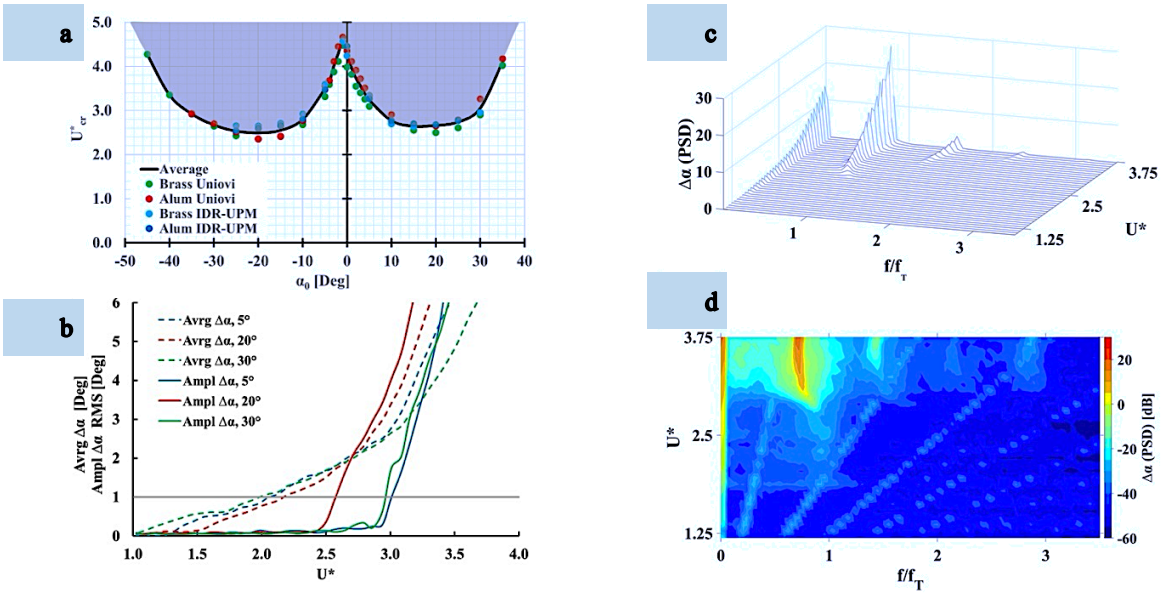


Figure 2. a) Stability Diagram, b) RMS and rotation for several tilt angles, c) Power spectra density (PSD) of the angle signal for different reduced velocities (tilt angle +20º), d) Contours of PSD corresponding to c).

The Stability Diagram of the tracker is depicted, in terms of reduced variables. The critical velocity of the onset of the stability is measured by means of the moment in the driver and the angular rotation of the free end of the tracker. Furthermore, a comparison with other studies is pointed out.

4. CONCLUSIONS

This study presents a Benchmark model for single-axis photovoltaic solar trackers, focusing on 3D aeroelastic behavior to replicate commercial trackers' geometry and structural dynamics. Designed for wind-structure interaction research, the model reproduces aeroelastic torsional instability in a wind tunnel setting, with carefully defined dimensions and construction details,

including natural frequencies and non-dimensional bending coefficients. Testing took place in two wind tunnels: at the Polytechnic University of Madrid (IDR-UPM) and the University of Oviedo (UniOvi). The single-row configuration was subjected to low turbulence, uniform crossflow, enabling the identification of critical wind speeds for torsional instability across various tracker tilt angles. Both facilities produced consistent stability diagrams mapping reduced critical velocities against tracker tilt, highlighting stable regions essential for safe PV plant operation.

The stability analysis further examined tilt angle limits, asymmetry, and vibration amplitudes, revealing vortex-induced vibrations at sub-critical wind speeds. Evaluating the tracker's position within a row and turbulence effects showed both similarities and significant discrepancies with existing literature on sectional and 3D models, underscoring the need for a standardized validation framework. The proposed Benchmark model aims to establish this standard, providing a reliable reference for future studies in tracker aeroelasticity. Its implementation will enhance design optimization, ensure safer operational limits under wind loading, and contribute to cost savings in solar PV plant construction and maintenance.

ACKNOWLEDGEMENTS

This work is part of the project TED2021-130541B-C21 funded by MCIN/AEI/10.13039/501100011033, the European Union "NextGenerationEU"/PRTR and project PID2022-137630OB-C21 financed by MCIN/AEI /10.13039/501100011033/FEDER, UE.

REFERENCES

Browne, M.T.L., Taylor, Z.J., Li, S., Gamble, S., 2020. A wind load design method for ground-mounted multi-row solar arrays based on a compilation of wind tunnel experiments. Journal of Wind Engineering and Industrial Aerodynamics 205. https://doi.org/10.1016/j.jweia.2020.104294

Cárdenas-Rondón, J.A., Ogueta-Gutiérrez, M., Franchini, S., Manzanares-Bercial, R., 2023. Stability analysis of two-dimensional flat solar trackers using aerodynamic derivatives at different heights above ground. Journal of Wind Engineering and Industrial Aerodynamics 243. https://doi.org/10.1016/j.jweia.2023.105606

Cheruku, S., Browne, M.T.L., Eng, M., Eng, P., Asce, M., 2020. Utility-Scale Photovoltaic Power Plants: Analysis and Design. Structure Magazine 32–35.

Enshaei, P., Chowdhury, J., Sauder, H., Banks, D., 2023. Wind Tunnel Testing of Torsional Instability in Single-Axis Solar Trackers: Summary of Methodologies and Results, in: 21st Australasian Wind Engineering Society Workshop. pp. 1–6.

Martínez-García, E., Blanco-Marigorta, E., Parrondo Gayo, J., Navarro-Manso, A., 2021. Influence of inertia and aspect ratio on the torsional galloping of single-axis solar trackers. Engineering Structures 243. https://doi.org/10.1016/j.engstruct.2021.112682

Rohr, C., Bourke, P.A., Banks, D., 2015. Torsional Instability of Single-Axis Solar Tracking Systems, in: 14th International Conference on Wind Engineering.

Rodríguez-Casado, C. et al., 2024. Experimental Benchmark for the 3D wind tunnel testing of torsional aeroelastic instabilities in single-axis solar trackers. Journal of Wind Engineering and Industrial Aerodynamics 253. https://doi.org/10.1016/J.JWEIA.2024.105838.

Strobel, K., Banks, D., 2014. Effects of vortex shedding in arrays of long inclined flat plates and ramifications for ground-mounted photovoltaic arrays. Journal of Wind Engineering and Industrial Aerodynamics 133, 146–149. https://doi.org/10.1016/j.jweia.2014.06.013

Taylor, Z.J., Browne, M.T.L., 2020. Hybrid pressure integration and buffeting analysis for multi-row wind loading in an array of single-axis trackers. Journal of Wind Engineering and Industrial Aerodynamics 197. https://doi.org/10.1016/j.jweia.2019.104056

Taylor, Z.J., Feero, M.A., Browne, M.T.L., 2024. Aeroelastic instability mechanisms of single-axis solar trackers. Journal of Wind Engineering and Industrial Aerodynamics 244. https://doi.org/10.1016/j.jweia.2023.105626

Valentín, D., Valero, C., Egusquiza, M., Presas, A., Egusquiza, E., 2022. Failure investigation of a solar tracker due to wind-induced torsional galloping induced torsional galloping. Engineering Failure Analysis 135. https://doi.org/10.1016/j.engfailanal.2022.106137

Reconstructing thunderstorm wind speed time series from observed damage

Djordje Romanic [1]

[1]*Department of Atmospheric and Oceanic Sciences, McGill University, Montreal, Quebec, Canada, djordje.romanic@mcgill.,ca*

SUMMARY:
Strong winds are a major cause of structural damage during thunderstorms, with post-disaster reports estimating wind gusts through engineering analysis of the damage. However, high-frequency anemometer data is rarely available near damaged sites. This study addresses what an anemometer would have recorded if installed at the damage location by introducing two models for reconstructing wind speed time series. The first model uses a simple analytical equation to relate the estimated gust that caused damage to the mean wind and instantaneous peak gust. The second employs constrained stochastic simulations based on turbulent wind spectra.

Keywords: thunderstorm, wind damage, analytical model.

1. INTRODUCTION

Strong winds are a leading cause of structural damage during thunderstorms. Following severe thunderstorm events, specialized agencies and research groups routinely produce post-disaster damage assessment reports in many regions around the globe. When structural damage is attributed to high winds, these assessments estimate the characteristic wind gusts through wind engineering analysis of the damage.

Since high-frequency anemometer measurements are rarely available near the site of observed damage, this research addresses the following question: What would an anemometer record during the storm if it had been installed at the damage location? To address this question, we introduce two models for reconstructing thunderstorm wind speed time series. The first is a simple analytical equation that provides a closed-form solution, linking the estimated wind gust to the mean wind speed and instantaneous peak during the storm. The second model employs constrained stochastic simulations, using the power spectral density of turbulent winds to generate a wind record statistically indistinguishable from actual measurements. The models are validated against measured thunderstorm winds and used to recreate wind speed records from damage observations.

2. MODELS DEVELOPMENT

Time series of instantaneous thunderstorm wind speeds $v(t)$ at a location of the observed wind damage can be expressed as:

$$v(t) = \bar{v}(t) + v'(t) \quad (1)$$

where t is the time, $\bar{v}(t)$ is the slowly varying mean speed evaluated using a 30-s averaging window (values between approximately 20 s and 60 are deemed appropriate) and $v'(t)$ is the residual turbulence fluctuations. Further, $v'(t)$ in Eq. (1) can be expressed as (Romanic et al. 2020):

$$v'(t) = \sigma_v(t)\tilde{v}'(t) \tag{2}$$

where $\sigma_v(t)$ is the slowly varying standard deviation and $\tilde{v}'(t)$ is the reduced residual fluctuations. Then, inserting Eq. (2) into Eq. (1) yields:

$$v(t) = \bar{v}(t)[1 + \bar{I}\tilde{v}'(t)] \tag{3}$$

where

$$\bar{I} \equiv \frac{\sigma_v(t)}{\bar{v}(t)} \tag{4}$$

is the mean turbulence intensity.

The slowly varying mean wind speed is modelled as (Le and Caracoglia, 2016):

$$\bar{v}(t) = \begin{cases} \bar{v}_A + \frac{\bar{v}_M - \bar{v}_A}{2}\left(\cos\left(\frac{2\pi t}{T}\right) + 1\right), & |t| < \frac{T}{2}, \\ \bar{v}_A, & |t| \geq \frac{T}{2}. \end{cases} \tag{5}$$

where $\bar{v}_A$ is the mean atmospheric boundary layer wind speed prior to the storm, $\bar{v}_M = \max_{|t|<T/2} \bar{v}(t)$ the maximum of the slowly varying wind speed, which is unknown at this point, and T is the windstorm duration.

The deterministic model assumes sinusoidal fluctuations superimposed on the slowly varying mean flow (Fujita 1971):

$$\tilde{v}'(t) = \cos\left(\frac{2\pi t}{p}\right) \tag{6}$$

where p is the period of the sinusoidal gust.

From the definition of the fastest characteristic-path damaging wind (Fujita, 1971), v_D, we write:

$$D = v_D\tau \tag{7}$$

where τ is the time in which the fastest characteristic-path wind traverses the characteristic path D at a rate of v_D (Figure 1). v_D is the wind gust that caused structural damage and is based on the engineering analysis of the observed damage.

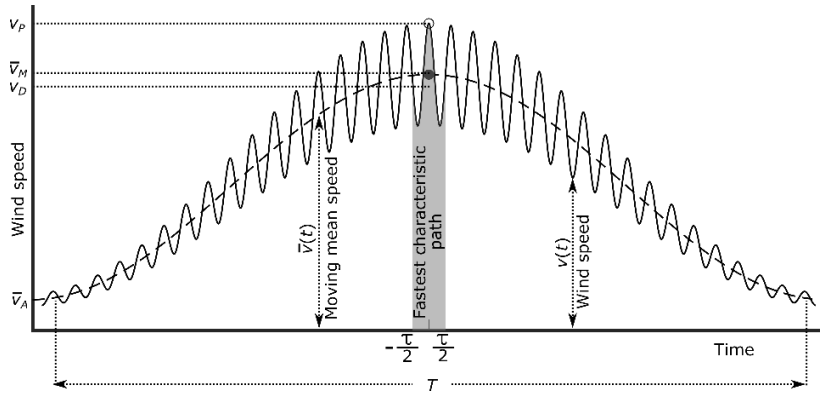


Figure 1. Time variation of a simplified thunderstorm wind speed record. The mean thunderstorm wind and fluctuations are represented by sinusoidal variation of periods T and p, respectively.

From Eq. (7) and Figure 1, one can also write:

$$D = \int_{-\frac{\tau}{2}}^{\frac{\tau}{2}} v(\zeta) d\zeta \tag{8}$$

where ζ is a dummy variable for time integration. Inserting Eqs. (5) and (6) into Eq, (3), and then solving the integral in Eq. (8) yields, after some mathematical manipulation, the following expression (Romanic 2024):

$$\bar{v}_M = \bar{v}_A + \frac{D - \frac{\bar{v}_A D}{v_D} - \frac{\bar{v}_A \bar{I} p}{\pi} \sin\left(\frac{\pi D}{v_D p}\right)}{\frac{T}{2\pi}\sin\left(\frac{\pi D}{v_D T}\right) + \frac{\bar{I} p}{2\pi}\sin\left(\frac{\pi D}{v_D p}\right) + \frac{pT\bar{I}}{4\pi}\left(\frac{\sin\left(\pi D \frac{T+p}{v_D pT}\right)}{T+p} + \frac{\sin\left(\pi D \frac{T-p}{v_D pT}\right)}{T-p}\right) + \frac{D}{2v_D}} \tag{9}$$

This result presents the first closed-form solution to determine the maximum value of the slowly varying wind speed during thunderstorm passage using the damage assessment information (v_D).

The constrained stochastic model follows the work of Bierbooms (2004). Instead of deterministic turbulence fluctuations in Eq. (6), we use their stochastic representation through Fourier series:

$$\tilde{v}'(t) = \sum_{k=1}^{K} a_k \cos(\omega_k t) + b_k \sin(\omega_k t) \tag{10}$$

where a_k and b_k are the Fourier coefficients that are mutually uncorrelated and have zero mean and unit standard deviation. However, instead of an entirely random velocity record that would be generated by Eq. (10), our aim is to generate a stochastic record with deterministic wind gust, say A, associated with the observed damage at the time $t = t_0$ (e.g., in the present case, $t_0 = 0$). This requirement corresponds to the following constraints:

$$\tilde{v}'(t_0) = A \tag{11}$$
$$\tilde{v}'(t_0) = 0 \tag{12}$$

Inserting these constraints into Eq. (10) and through numerous mathematical manipulations that involve linear algebra and the theory of conditional sampling (Bierbooms, 2004), one can

demonstrate that a constrained stochastic simulation of turbulent fluctuations, $\tilde{v}_c'(t)$, is modelled as:

$$\tilde{v}_c'(t) = \tilde{v}'(t) + \big(A - \tilde{v}'(t_0)\big) r(t - t_0) + \frac{\dot{\tilde{v}}'(t_0)\dot{r}(t-t_0)}{\lambda^2} \tag{13}$$

where $r(t)$ is the normalized autocorrelation function and λ^2 is the normalized second order spectral moment. Finally, the desired value of the constrained, A, can be calculated from the results of the deterministic model:

$$A = \frac{1}{\bar{I}} \left(\frac{v_P}{\bar{v}_M} - 1 \right) \tag{14}$$

where the instantaneous peak velocity is:

$$v_P = \bar{v}_M (1 + \bar{I}) \tag{15}$$

3. RESULTS AND CONCLUSIONS

An example of a 1-hour long wind speed record with thunderstorm duration of 15 min and assumed 5-s gust v_P = 38 m s^{-1} is presented in Figure 2. This velocity time series is generated at an arbitrary height of 50 m above ground level, which falls within the height range of many structures. In practical applications of the model, this assumed 5-s gust would be the estimated wind gust that caused the observed damage to the structure. More examples are provided in Romanic (2024).

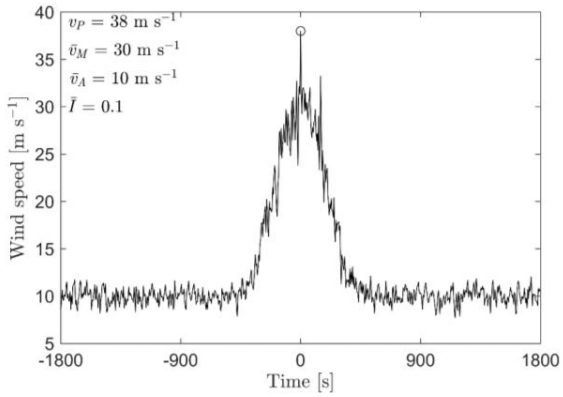


Figure 2. 1 hour of generated wind data at 50 m above ground with the thunderstorm duration of 15 min and timestep of 5 s. The circle at t = 0 is the prescribed (constrain) value of v_P.

REFERENCES

Bierbooms W. 2004. A gust model for wind turbine design. JSME International Journal Series B Fluids and Thermal Engineering, 47, 378-386.

Fujita T. 1971. Proposed characterization of tornadoes and hurricanes by area and intensity. SMRP Research Paper No. 91, p. 42.

Le T-H., and Caracoglia L. 2016. Modeling vortex-shedding effects for the stochastic response of tall buildings in non-synoptic winds. Journal of Fluids and Structures 61, 461-491.

Romanic D. 2024. Deterministic and constrained stochastic models of thunderstorm winds. Journal of Wind Engineering and Industrial Aerodynamics, 253.

Romanic D., Nicolini E., Hangan H., Burlando M., and Solari G. 2020. A novel approach to scaling experimentally produced downburst-like impinging jet outflows. Journal of Wind Engineering and Industrial Aerodynamics. 196.

Experimental investigation of building openings effect on internal and external pressures induced by tornadic flows

Shirin Barkhordari[1], Elena Dragomirescu[1], Matthieu Hancock-LeFebour[1]

[1]*University of Ottawa, Ottawa, Canada, sbark090@uottawa.ca*
[1]*University of Ottawa, Ottawa, Canada, elndrag@uottawa.ca*
[1]*University of Ottawa, Ottawa, Canada, mhank046@uottawa.ca*

SUMMARY:
The current study investigated the impact of openings, such as broken windows and doors, of a two-floors residential building model, on internal and external pressures experimentally induced by tornadic flows. A pressure taps model scaled 1:100 was tested in the Wind-induced Damage Simulator (WDS) under tornadic flows of 800 RPM and 2000 RPM fan speeds representing varying tornado intensities. Internal and external pressures were recorded across critical wall points and floors of the model with two configurations: a closed model without openings and a model with 5 openings to assess the impact of broken windows and main door during a tornadic extreme event, on the internal and external pressure distributions. The results revealed that the closed model experienced higher external suction on wind-facing surfaces, while the model with openings recorded reduced external pressure, due to a partial pressure equalization. However, for the model with openings, increased pressure fluctuation was measured on the separator plate between the two floors and near the connection points, thus indicating a need for reinforcement and tornado ties adoption at these critical locations.

Keywords: Experimental simulation of tornadic flows, Tornado induced internal pressure, Building pressure taps models

1. INTRODUCTION

Recently, numerous studies have focused on simulating tornado-like vortices in laboratory, such as the VorTECH simulator at Texas Tech (Chen et al., 2023), WindEEEDome at Western Ontario University (Refan and Hangan, 2018) and the tornado simulators at the Iowa State University (Case et al., 2011) and Missouri University, and they all agreed that there are a new set of parameters required to characterized the tornadic flows, quite different than the conventional wind tunnel ones. The swirl ratio S, the radial Reynolds number Re_r, tangential velocity the internal aspect ratio a, were defined.

A breadth of research has been reported on scaled models of low-rise residential buildings (Wang et al., 2018; Santos et al., 2021; Williams and Dragomirescu, 2022; Case et al., 2018; Haan et al., 2008; etc.), however only a few studies have investigated the variation of internal pressure caused by openings in the building, to account for potential breach of windows and doors during extreme tornado events. The presence of openings in walls can significantly affect a building's internal pressure during tornadoes, due to the additional pressure associated with tornadoes. Various studies have investigated the dynamics of external and internal pressures in tornado vortex scenarios. For instance, Sarkar and Kikitsu (2009) found that internal pressures are influenced by

the extent of natural leakage and the position of the openings. Thampi et al. (2011) showed that internal pressures depend on both porosity and the location of openings, indicating that different configurations can lead to varying modes of failure. Sabareesh et al. (2013) measured internal pressures and noted that a building with a central opening had significantly higher internal pressure coefficients compared to one with multiple small leaks when positioned within the vortex core, although this trend reversed outside the core. These findings underscore the need for further research to understand the wind pressures acting on low-rise buildings in tornado-like conditions, as existing knowledge is still limited, highlighting the importance of this area for developing safer wind-resistant designs (Wang et al., 2018; Roueche, 202).

2. EXPERIMENTAL SETUP AND TESTED MODELS

The Wind-induced Damage Simulator (WDS) at the University of Ottawa is an experimental facility consisting of a steel chamber designed to simulate extreme wind conditions, including tornadoes, hurricanes and impinging jets. The chamber, of 3.6 m x 3.6 m and 3.0 m height, is reinforced along the outside walls, to withstand up to 30 kPa of uniform pressure and features multiple circular inlets along the base of the walls, allowing airflows to enter the chamber for creating a range of experimental setups. An industrial blower is connected to the ceiling of the chamber and extracts the wind flows, generating wind speeds of up to 40 m/s inside the chamber and wind speeds up to 90 m/s with one inlet open, which is comparable to Category 4 hurricane conditions. When tornadic flows are simulated, 4 inlets situated in the corner of the chamber are used, and when the fan functions at 800 RPM, a vortex is formed in the middle of the chamber, with wind speeds of 19.15 m/s, while for 200 RPM, wind speeds of up to 31.06 m/s are obtained. Two 1:100 scale house models were tested in the WDS at four different fan speeds: 800, 1000, 1500, and 2000 RPM, to determine tornado-induced pressures. A total of 68 pressure taps were distributed across walls, as well as a separator plate between floors to capture pressure data. These taps were connected to DSA3217 pressure scanners, which recorded measurements at 400 Hz. The dimensions of the scaled models of two-story buildings were selected according to the dimensions outlined by Case et al. (2011), conducted at Iowa State University. Both models include a separator plate between the floors, allowing for a comprehensive analysis of pressure variations between the first and second floors compartments, while only one model features 5 openings on the front wall, at the location of the first-floor windows and door, and the second-floor windows, thus facilitating a comparative investigation of the effects of openings on the internal and external pressures. The models have the following dimensions width 98 mm, length 146 mm, roof pitch, 15.6 deg and the roof ridge height is 124 mm, and were placed 10 cm away from the center of the WDS testing chamber WDS doors, as previous research has shown this area to be where wind speed is strongest. The models were tested at four different wind speeds: 800 RPM (8.98 m/s), 1000 RPM (11.20 m/s), 1500 RPM (16.83 m/s), and 2000 RPM (22.44 m/s). The experiment was conducted in two stages: in the first stage, pressure taps were attached to the walls, and in the second stage, they were moved to the separator plate and front wall. The peak pressure values obtained during these tests were used to calculate the maximum pressure coefficients, C_{p_max} for each of the 68 taps. Wind velocity parameters in the WDS were measured using a 12-hole Omniprobe sensor to capture the tornado-induced tangential wind velocities. The Omniprobe was positioned to measure tangential velocities at 5 cm intervals from the centre of the simulated tornado and the velocity conversion and calculation was done using the Aeroflow 2 software. Figure 2 a) illustrates the radial profiles of the tangential velocity for various heights, compared to a radial profile of the

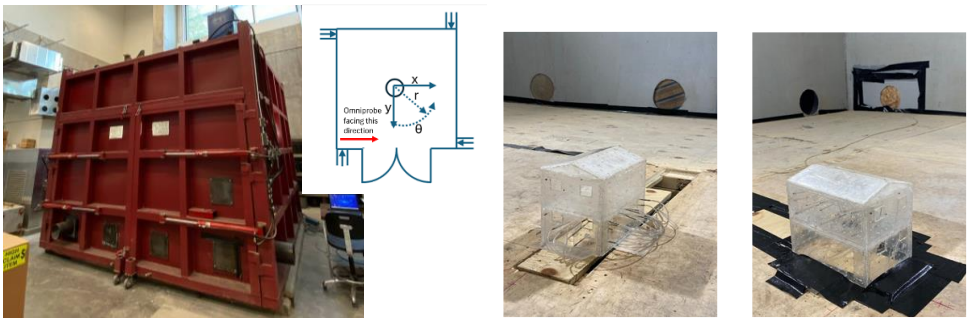


Figure 1. a) Wind Damage Simulator (WDS) Facility b) Building model with openings.

modified Rankine model, at different RPMs for nondimensional WDS heights, z/zmax of 0.14, 0.43 and 1. The contour plot of the tangential velocity shows a clear vortex core in yellow (Fig. 2b)), with rapidly decreasing velocity in the center and slowly decreasing velocity beyond the core. The core seems to be decreasing in size along the height, which possibly hints at a conical shape for the tornadic flow simulated, however the vortex at up to 20 cm above the ground is important for the testing conditions as the tested models are 124 mm in height.

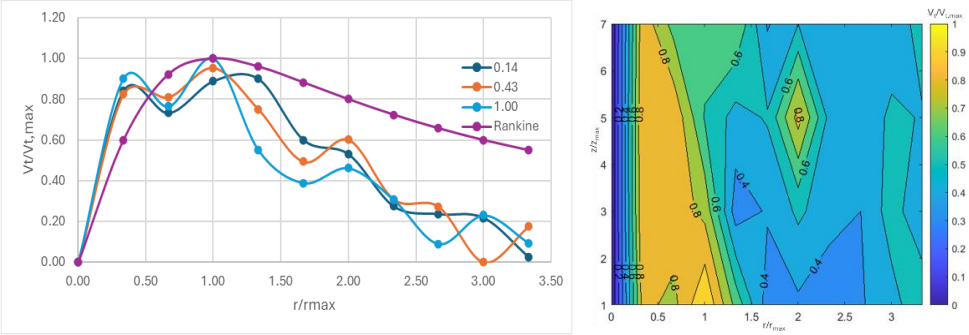


Figure 2. a) Radial profiles of the tangential velocity (800 RPM) b) Tangential velocity distribution (2000 RPM).

3. PRESSURE COEFFICIENTS FOR THE MODEL WITH OPENINGS

The results for the model with openings showed that the external pressure coefficients were almost double on the corner side of the walls, but for other regions they were in the same range, thus leading to pressure equalization. When looking at the first-floor vs second floor pressures, it was noticed that the internal pressure on the second-floor walls was higher than the internal pressure on the first-floor walls, especially for high RPMs of 1500 and 2000. This trend was noticed for the external pressure as well, as it can be noticed in Figure 3 a) and b), which shows the external and internal pressure coefficients for the left wall, where the first floor Cp is represented by full lines and the second floor Cp is represented with interrupted lines. Pressure coefficients for the front wall, where the openings are located, were higher on the first-floor region, when compared with the second-floor. When average pressure coefficients are determined for all walls, it was noticed that the internal Cp decreases gradually with the increase of wind speed, however a drastic decrease is registered for the external pressure for high RPMs of 1500 and 2000. It is also worth mentioning that for the model without openings, the average coefficients were very similar, except for the 1500 and 2000 RPMs, where external suction for the model with openings was higher.

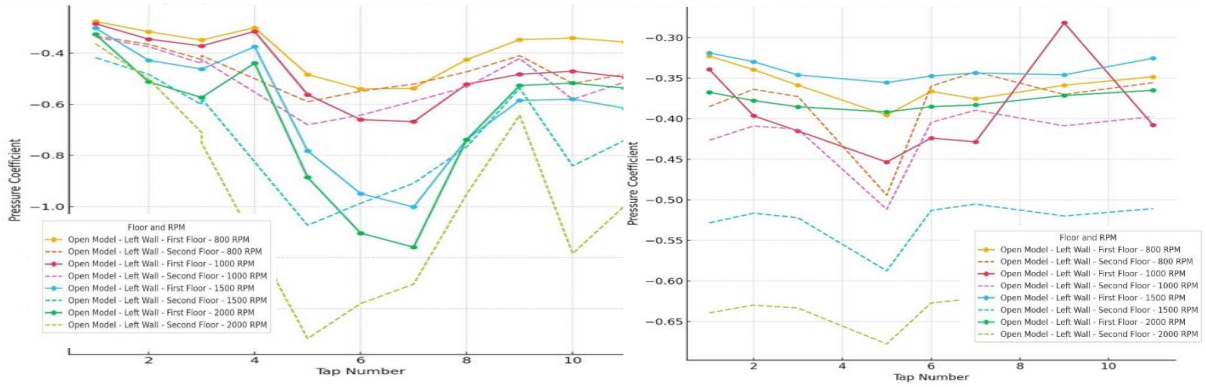


Figure 3. Pressure coefficients on the left wall a) External pressure coefficients b) Internal pressure coefficients

4. CONCLUSIONS

The experimental investigation of the tornadic flows on low-rise building models showed that the presence of openings on the front wall has increased the external pressure coefficients, particularly for high RPM conditions that simulate strong tornadic winds. In general, the outside walls registered higher suction, when compared with the inside walls (internal pressure). Also, the corner of the left wall, connecting to the front fall, exhibited notable pressure differences, with internal pressures slightly exceeding external ones at lower RPMs but shifting to greater external suction at higher RPMs. This trend suggests that the mid-wall section may be vulnerable to high wind loads. For the right wall, the same corner connecting to the front wall also shows variable pressure differentials, with minor positive values at lower RPMs that become negative as RPM increases, indicating increased external suction. These sections may need reinforcement to manage wind forces effectively.

REFERENCES

Chen, Q., Tang, Z., Wu, X., Zuo, D., & James, D. 2023. Laboratory study of tornado-like loading on a low-rise building model. Journal of Wind Engineering and Industrial Aerodynamics, 238, 105443.

Case, P., Sarkar, P., & Sritharan, S. 2014. Aerodynamic Loads on Low-Rise Buildings Under Tornado-Like Vortex Flows. Journal of Wind Engineering and Industrial Aerodynamics 133. 124-134.

Haan, F. L., Balaramudu, V., & Sarkar, P. P. 2008. Tornado-induced wind loads on a low-rise building. Journal of Structural Engineering, 134(1), 64-73.

Refan, M., and Hangan, H. 2018. Tornado-Induced Loads on Low-Rise Buildings: The Influence of Building Dimensions and Swirl Ratio. Journal of Wind Engineering and Industrial Aerodynamics, 175, 287-297.

Roueche, D. B., Prevatt, D. O., & Haan, F. L. 2020. Tornado-induced and straight-line wind loads on a low-rise building with consideration of internal pressure. Frontiers in Built Environment, 6, 18.

Sabareesh, G. R., Matsui, M., and Tamura, Y. 2013. Characteristics of internal pressures and net local roof wind forces on a building exposed to a tornado-like vortex. J. Wind Eng. Ind. Aerodyn., 112, 52–57.

Santos, R., Almeida, J. P., & Rojas, A. 2021. Effects of roof geometry on tornado-induced structural actions of a low-rise building. Engineering Structures, 226, Article 111367. https://doi.org/10.1016/j.engstruct.2020.111367.

Sarkar, P. P., and Kikitsu, H. 2009. Experimental studies on internal pressure and debris strike for improved tornado induced loads of low-rise buildings. Proc., 41st U.S.-Japan Panel on Wind and Seismic Effects, Tsukuba, Japan.

Thampi, S., Verma, M. K., Agnihotri, N., & Kumar, A. 2011. Simulation of tornado-induced pressures on buildings using CFD. Journal of Wind and Structures, 14(3), 253-274.

Williams J. and Dragomirescu E. 2022. Tornado-induced pressures on residential buildings. 14th Americas Conference on Wind Engineering (ACWE'14). Lubbock. USA.

Maximum dynamic response of a monitored structure subjected to thunderstorm outflows: comparison between closed-form solutions and full-scale data

Luca Roncallo[1], Federica Tubino[2], Mekdes Tadesse Mengistu[3], Maria Pia Repetto[4]

[1]*University of Genoa, Genoa, Italy, luca.roncallo@edu.unige.it*
[2]*University of Genoa, Genoa, Italy, mekdestadesse.mengistu@edu.unige.it*
[3]*University of Genoa, Genoa, Italy, federica.tubino@unige.it*
[4]*University of Genoa, Genoa, Italy, repetto@dicca.unige.it*

SUMMARY:
This study aims to carry out a comparison between the recorded maximum dynamic response of a full-scale monitored slender vertical structure subjected to the impact of a thunderstorm downbursts and the one estimated through closed-form solutions implemented within the thunderstorm gust response factor (TGRF) technique. The structure is a steel lighting pole equipped with an ultrasonic anemometer, strain gauges and accelerometers. Starting from the strains recorded during a thunderstorm event, the wind speed time history of the corresponding displacement at the top of the pole is reconstructed and its maximum value is compared with the one estimated through the TGRF. The parameters required for the application of the TGRF are extracted from the time history recorded by the anemometer and a nose-shaped mean wind profile is assumed. To account for the uncertainties on the structure and wind speed parameters, suitable range of variations for each parameter are defined and the interval of variation of the maximum response is estimated. The comparison between the recorded maximum response and the interval of variation estimated through the TGRF shows a satisfying agreement.

Keywords: Dynamic response, Full-scale monitoring, Thunderstorm outflows

1. INTRODUCTION

Thunderstorm outflows, together with extra-tropical cyclones, shape the wind climate in Europe, often producing wind gusts that exceed those associated with synoptic-scale events. However, while engineers have a unified approach available for designing structures to withstand wind gusts associated with synoptic events, no such approach exists yet for the design of structures against thunderstorm outflows. Indeed, various methods have been proposed for predicting the equivalent wind loading and the maximum dynamic response of structures exposed to thunderstorms, aiming to achieve a safer and more cost-effective structural design (e.g., Kwon and Kareem, 2019; Solari, 2016; Roncallo and Tubino, 2023a). Among these methods, the Thunderstorm Gust Response Factor (TGRF), in its closed-form formulation (Roncallo and Tubino, 2023a), has proven to be a valuable tool, demonstrating good agreement with time-domain solutions derived from full-scale thunderstorm records. However, a more robust validation can be achieved by comparing the dynamic response of full-scale monitored structures during thunderstorm outflows. In this context, the GS-WinDyn research group at the University of Genoa has collected extensive data from a

monitored lighting pole located at the port of La Spezia on the Tyrrhenian Sea (Mengistu et al., 2023). Using the collected monitoring data, this study aims to compare the maximum response recorded by the monitoring system with the predictions made using the TGRF, thereby evaluating its accuracy for a full-scale structure. Due to uncertainties in the dynamic and aerodynamic properties of the structure, as well as wind speed profile, a range of variation for each parameter is defined, allowing for the estimation of an interval of variation for the maximum response.

2. ANALYTICAL FRAMEWORK

The monitored slender structure is schematized as a cantilever beam along the vertical coordinate z ($z = 0$ m at the ground) and its dynamic response is considered to be dominated by the first mode of vibration ψ_1. The maximum dynamic response to a thunderstorm outflow at its top $z = H$, it can be expressed as (Roncallo, Gimondo, et al., 2023):

$$x_{max} = G_x \bar{x}_{max} \tag{1}$$

where G_x is the gust response factor, $\bar{x}_{max} = \rho \bar{v}^2_{max}(h) c_D a_1 / 2 m_1 (2\pi n_1)^2$ is the maximum value of the mean response; h is the anemometer height assumed as reference; m_1 is the first modal mass; n_1 is the first modal frequency; c_D is the drag coefficient (assumed constant with the height) and a_1 is given by:

$$a_1 = \int_0^H \alpha^2(z) b(z) \psi_1(z)\, dz \tag{2}$$

where b is the width of the structure and α the vertical profile of the mean wind speed profile, for which the model by Wood and Kwok (1998) is assumed:

$$\alpha(z) = \left(\frac{z}{h}\right)^{1/6} \left(\frac{1 - erf[0.7 z/z^*]}{1 - erf[0.7 h/z^*]}\right) \tag{3}$$

with $z^* = 6 z_m$ and z_m the height of the tip of the nose-shape profile. The gust response factor in Eq. (1) takes the form (Roncallo and Tubino, 2023a):

$$G_x = 1 + I_v g_x (\nu_x T_{eq}) \sqrt{B^2 + R^2} \mathscr{C} \tag{4}$$

where I_v is the turbulence intensity evaluated at the equivalent height $z_e = 0.6H$; g_x is the Davenport peak factor; ν_x is the expected frequency of the response; T_{eq} is the equivalent period; $\mathscr{C}$ is the non-dimensional equivalent standard deviation and B and R are the background and resonance factor respectively (Solari, 1993). The closed-form solutions for T_{eq} and $\mathscr{C}$ read (Roncallo and Tubino, 2023a):

$$\mathscr{C}^2 = \frac{\gamma^{*20}\left(\frac{T_{max}}{T_{r,0}} - 1\right) + \left(\Lambda^5 - \frac{5}{2}\Lambda^4\Phi + \frac{10}{3}\Lambda^3\Phi^2 - \frac{5}{2}\Lambda^2\Phi^3 + \Lambda\Phi^4 - \frac{1}{6}\Phi^5\right)}{\gamma^{*16}\left(\frac{T_{max}}{T_{r,0}} - 1\right) + \left(\Lambda^4 - 2\Lambda^3\Phi + 2\Lambda^2\Phi^2 - \Lambda\Phi^3 + \frac{1}{5}\Phi^4\right)} \tag{5}$$

$$T_{eq} = \frac{\gamma^{*16}(T_{max} - T_{r,0}) + T_{r,0}\left(\Lambda^4 - 2\Lambda^3\Phi + 2\Lambda^2\Phi^2 - \Lambda\Phi^3 + \frac{1}{5}\Phi^4\right)}{[\mathscr{C}^2]^4} \tag{6}$$

where γ^* is a measure of the intensity of the background wind; $T_{max} = 600$ s, $\Lambda = \Phi + \gamma^{*4}$ and $\Phi = \beta(1-\gamma^{*4})$; being $\beta = 1/[1+1/4\xi n_1 T]$, with T the duration of the intense phase of the outflow; $T_{r,0} = (T_1 + T_N)$ with $T_1 = T/2$ and:

$$T_N = \begin{cases} T_2, & T_2 <= T_{max}/2 \\ T_{max}/2, & T_2 > T_{max}/2 \end{cases}, \qquad T_2 = T_1[1+1/(2\xi n_1 T)] \tag{7}$$

3. FULL-SCALE WIND AND STRUCTURAL RESPONSE MONITORING

The structure case study is a tapered steel lighting pole with height $H = 16.6$ m and a polygonal hollow cross-section of width 528 mm at the base and 254 mm at the top. The pole is equipped with an anemometer for the measurement of the wind speed, located at $h = 21.7$ m, accelerometers, located at 10.5 and 16.6 m, and strain gauges, located at 0.5 and 1.5 m, for the structural response detection (Mengistu et al., 2023). The sampling frequencies are 10 Hz for the anemometer, 100 Hz for the strain gauges, and 200 Hz for the accelerometers. The dynamical properties of the structure are calculated using operational modal analysis techniques starting from the full-scale measurements. The first mode of vibration is found to be bending mode at a frequency of $n_1 = 0.75$ Hz while the estimation of the structural damping ξ has shown some uncertainties, varying between 0.5% and 1.5% as reported in (Mengistu et al., 2023). A thunderstorm event recorded by the anemometer located on the structure is selected for the study. Having no information on the vertical profile of the mean wind speed α (Eq. (3)), a range between 25 m and 100 m is considered for the parameter z_m. The drag coefficient showed dependency on the angle of attack, thus a range between 0.8 and 2.3 is estimated coherently with the angle of attack of the wind speed, according to the wind tunnel tests carried out by Orlando et al. (2023). In order to account for the uncertainties on the parameters ξ, c_D and z_m, these quantities are treated as interval variables (Santoro et al., 2021), considering as lower bound and upper bound the extremes values of their respective range of values. The midpoint of each interval is referred to as nominal value. In this framework, the maximum response is also characterized with an interval nature.

4. RESULTS

The maximum displacement at the top of the structure estimated through Eq. (1) is compared with the registered maximum displacement, starting from the strain registrations during the event considered. In order to calculate the gust response factor in Eq. (4), the parameters γ^* and T, as well as the turbulence intensity and integral length scale, are extracted from the recorded wind speed. Specifically, the parameters of the slowly-varying mean wind speed γ^* and T are directly estimated from the modulating function of the mean wind speed employing a fitting procedure using the cosine model proposed in Roncallo and Tubino (2023b). In Fig. 1 the comparison between the recorded dynamic response and the estimated maximum response is plotted, fixing the nominal value of the drag coefficient $c_D = 1.55$ and the height of the nose-shaped profile $z_m = 62.5$m. It can be observed that the range of the maximum response estimated includes the recorded peak. In particular, the upper bound gives an accurate estimate while the nominal value and lower bound show some underestimations. The results obtained by varying the parameters c_D and z_m are omitted for sake of conciseness, however it is observed that they are also influenced by the parameters uncertainties.

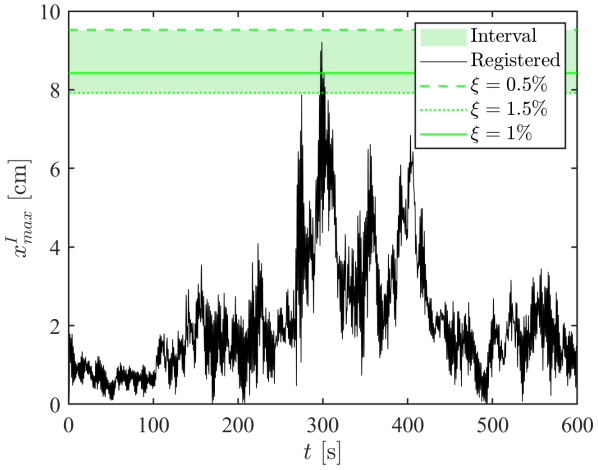


Figure 1. Comparison between the recorded and the estimated maximum response: $c_D = 1.55$, $z_m = 62.5$m.

5. CONCLUSIONS

The study showed that the proposed closed-form solution gives a good estimate of the maximum dynamic response recorded. However, the uncertainties on the parameters cannot be neglected since they have a significant impact on the results.

ACKNOWLEDGEMENTS

This research is funded by the European Research Council (ERC) under the European Union's Horizon 2020 research and innovation program (grant agreement No. 741273) for the project THUNDERR - Detection, simulation, modelling and loading of thunderstorm outflows to design wind-safer and cost-efficient structures - supported by an Advanced Grant 2016.

REFERENCES

Kwon, D. K. and Kareem, A., 2019. Towards codification of thunderstorm/downburst using gust front factor: Model-based and data-driven perspectives. Engineering Structures 199, 109608.

Mengistu, M. T., Orlando, A., and Repetto, M. P., 2023. Wind and structural response monitoring of a lighting pole for the study of downburst effects on structures. Journal of Wind Engineering and Industrial Aerodynamics 240, 105447.

Orlando, A., Pagnini, L., and Pia Repetto, M., 2023. Wind tunnel tests of a hexadecagonal cylinder with imperfections and ancillaries: aerodynamic characterization and technical discussion. Engineering Structures 274, 115114.

Roncallo, L., Gimondo, M., and Tubino, F., 2023. Dynamic Response of Slender Vertical Structures Subjected to Thunderstorm Outflows. Applied Sciences 13, 11440.

Roncallo, L. and Tubino, F., 2023a. Thunderstorm gust response factor: A closed-form solution. Journal of Wind Engineering and Industrial Aerodynamics 240, 105487.

— 2023b. Thunderstorm Gust Response Factor: general tendencies and sensitivity analysis. Journal of Wind Engineering and Industrial Aerodynamics 236, 105376.

Santoro, R., Sofi, A., and Tubino, F., 2021. Serviceability Assessment of Footbridges Via Improved Interval Analysis. ASCE-ASME Journal of Risk and Uncertainty in Engineering Systems Part B: Mechanical Engineering 7, 20906.

Solari, G., 1993. Gust buffeting II. Dynamic alongwind response. Journal of Structural Engineering 119, 383–398.

Solari, G., 2016. Thunderstorm response spectrum technique: Theory and applications. Eng. Struct. 108, 28–46.

Wood, G. S. and Kwok, K. C. S., 1998. An empirically derived estimate for the mean velocity profile of a thunderstorm downburst. Proceedings of 7th Australian Wind Engineering Society Workshop. Auckland, Australia.

Large-eddy simulation of downburst wind interaction with a mid-rise building

Mohammad Hadavi [1], Djordje Romanic [1], Alessio Ricci [2]

[1]*McGill University, Montreal, Canada, mohammad.hadavi@mail.mcgill.ca, djordje.romanic@mcgill.ca*
[2]*University School for Advanced Studies (IUSS), Pavia, Italy, alessio.ricci@iusspavia.it*

SUMMARY
Downbursts are intense downdrafts that produce powerful outflows of wind, causing localized yet severe damage to structures. Despite their destructive potential, their impact on buildings is relatively underexplored. This study investigates how downburst-induced winds affect a standard mid-rise building, focusing on wind flow patterns and vortical structures. Validation was conducted with only an atmospheric boundary layer (ABL) wind on a benchmark building. This was followed by an analysis combining the ABL and an impinging jet on the same building (without validation). The large-eddy simulations reveal distinct wind maxima at the pedestrian level, both in front of and behind the building, where wind speeds reach about four times those in the ABL-only scenario. A region of high-velocity forms near the ground between the stagnation point and the windward façade of the building. This poses significant wind safety concerns. Above the roof, horizontal wind speeds reach almost twice the ABL. Further analyses using the Q-criterion highlight organized vortical structures and notable vortex shedding near the building, leading to complex wind loading. These interactions generate fluctuating forces that can impact building resilience. Understanding these dynamic behaviours is critical for designing buildings that can endure extreme weather events such as downbursts.

Keywords: Downburst, LES, mid-rise building

1. INTRODUCTION

Downbursts are intense downdrafts of negatively buoyant air that descend rapidly from thunderstorm clouds, striking the earth's surface. Upon impact, these downdrafts spread out horizontally, producing powerful outflows of wind that can be highly localized yet extremely destructive. The resulting winds can reach speeds comparable to those found in tornadoes, creating significant risks to human safety and causing extensive damage to both built structures and natural landscapes. Despite their destructive potential, downbursts have received relatively less attention than other extreme wind events, such as tornadoes and hurricanes, when it comes to their impact on buildings. Understanding how downburst outflows interact with buildings is crucial for enhancing design standards and increasing resilience to these events. This research study investigates the interaction between downburst-induced winds and an isolated benchmark building, with a focus on transient wind flow patterns and vortical structures.

2. METHODOLOGY

This research comprises two stages. Stage 1: Perform large-eddy simulations (LES) of atmospheric boundary layer (ABL) wind acting solely on an isolated building for validation purposes. Stage 2:

Conduct LES of the same building subjected to both ABL wind and downburst outflow.

A benchmark building from the Architectural Institute of Japan database is selected (Meng and Hibi, 1998), with a length and width of b = 0.08 m and a height of 2b = 0.16 m (Fig. 1a). Real downburst events are driven by density gradient, while an impinging jet can closely replicate the observed wind flow in these events through dynamic forcing. The impinging jet method is widely recognized in the wind engineering community (Romanic and Hangan, 2020). Therefore, a jet with a height and diameter of 12.5b = 1 m and a downdraft centerline velocity (w_{jet}) of 10 m s^{-1} is used to replicate the downburst-like flow. The computational domain follows guidelines, with distances from the building of 40b to the inlet, 60b to the outlet, 30b to the sides, and 16b to the top. The building is positioned at x/D = 1 from the jet center, where the peak velocity of the outflow is expected to occur. The LES approach in combination with the Smagorinsky model is used to capture the complex turbulent flow dynamics.

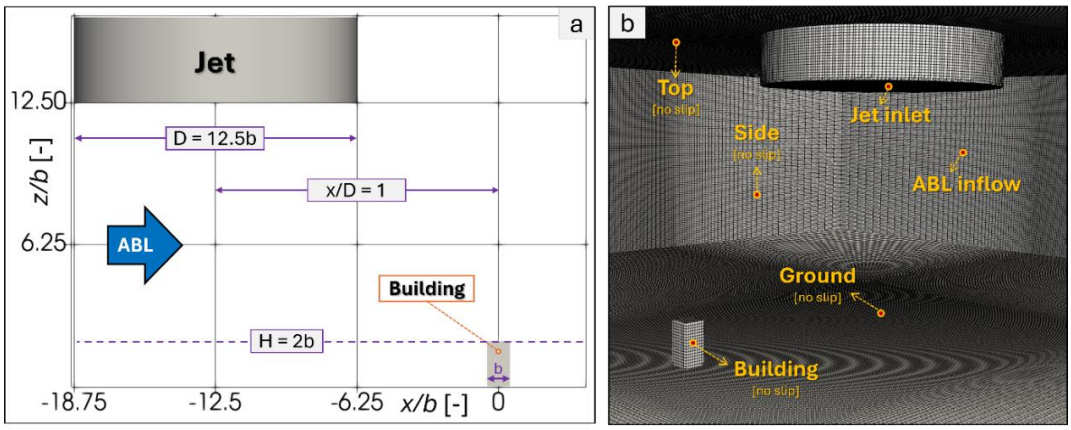


Figure 1. a) Schematic of a part of the computational domain including the building and jet. b) Computational grid around the building and jet, with an indication of boundary conditions.

In the target region around the building and jet, a uniform cell size of 0.01 m is applied, with a stretching ratio kept below 1.05 throughout the domain (Fig. 1b). The average non-dimensional distance from the building's surfaces (y^+) is kept above 30 during the post-impingement phase while this is around 1 in the touchdown region (bottom surface) dominated by stagnation region. Spalding's universal law of the wall for smooth surfaces is used to model the near-surface flow. The Courant–Friedrichs–Lewy number is maintained below 0.5, with an average value under 0.1 across the simulation. Additionally, the ratio of resolved turbulent kinetic energy to total kinetic energy remains above 80%, ensuring the capture of most of the turbulent flow structures. While not included in this abstract due to the space limitation, the LES results of an isolated jet were also validated against Kim and Hangan (2007).

3. RESULTS

3.1. LES validation of ABL wind

As shown in Fig. 2, the LES results for ABL wind closely matches wind tunnel measurements. The average normalized root mean square error values are 0.03, 0.18, and 0.25 for the results in

front of, above, and in the leeward façade of the building, respectively. These values emphasize the superior accuracy of LES over Reynolds-averaged Navier-Stokes approach (Hadavi and Pasdarshahri, 2020) in capturing key flow dynamics, including flow separation, vortex shedding, and wake development.

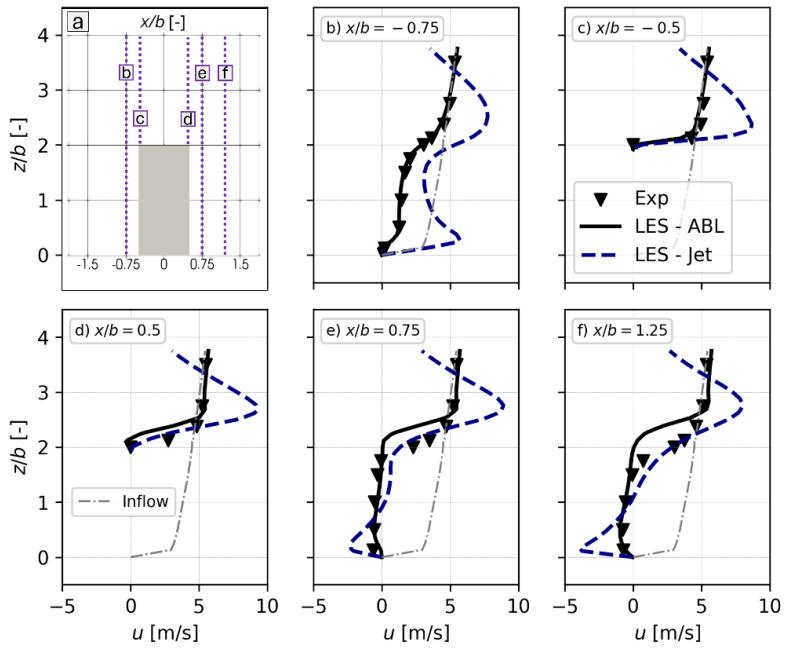


Figure 2. a) Building geometry, showing the five measurement locations marked by dashed purple lines. b-f) Comparison of experimental and LES results for ABL-only scenario, as well as LES results for ABL-downburst scenario, at the jet centerline across five vertical lines around the building: x/b = -0.75, -0.5, 0.5, 0.75, and 1.25. LES results are averaged over a 5-second period following the initial transition period.

3.2. Downburst-like outflow

Figure 2 also shows the results associated with the downburst outflow in the presence of the background ABL wind. In front of the building, two peaks are evident in the horizontal velocity (Fig. 2b). The first occurs at the pedestrian level ($z \cong 0.3$b), where the wind speed reaches about four times the ABL-only scenario. A region of high velocity ($\geq w_{\text{jet}}$) with a height of ~b forms near the ground between the stagnation point and the windward façade of the building. This region persists throughout the impingement and is pushed toward the building by the ABL flow (refer to the attached animation on the last page), leading to the first peak. This can notably impact wind safety near the building. The second peak occurs above the roof level and is less intense than the first one.

Above the building (Fig. 2c-d), horizontal wind speeds reach up twice the ABL-only case, then decrease to values even lower than the inflow. This is due to turbulence generated from jet-ABL-building interactions. Behind the building (Fig. 2e-f), similar nose-shape profiles appear at both the pedestrian and roof levels. The pedestrian-level wind peak is in the $-x$ direction due to flow separation and the recirculating wake, which intensifies further away from the building as the wake develops (Fig. 2f). On the other hand, the roof-level peak is more prominent closer to the building (Fig. 2e). The rest of the profiles resemble the ABL-only scenario.

To investigate the vortical structures, the Q-criterion (Jeong and Hussain, 1995) is used to quantify the relative strength of localized flow rotation by computing the second invariant of the velocity gradient tensor (Fig. 3). Positive values indicate vortex cores (strain-dominated regions), while negative values highlight rotation-dominated regions. Three dimensionless timesteps are considered: a) the moment of jet release, b) just after jet impingement, and c) after the jet interacts with the ground/building for some time. At τ = 61.8, the primary vortices are in their descending phase (Fig. 3a). Both vortices exhibit organized structures with distinct vortex cores and rotation-dominated regions at the boundaries with the surrounding air (Žužul et al., 2024). By τ = 63.1 (Fig. 3b), the interaction between the ABL, downburst outflow, and the building generate larger and more complex vortices on the jet's right side. Trailing ring vortices form by τ = 92.4 (Fig. 3c) on the left side of the touchdown. An intense rotation-dominated region develops near the windward façade of the building, with significant vortex shedding from the building edges. Downstream, the flow is densely populated with vortices, indicating intense mixing and turbulence. The presence of pronounced vortices near the building could lead to fluctuating loads on the surfaces. This highly unsteady vortex formation can result in both uplift and lateral forces, increasing the complexity of the wind loads experienced by the structure. Understanding these interactions is critical for designing buildings capable of withstanding extreme events like downbursts.

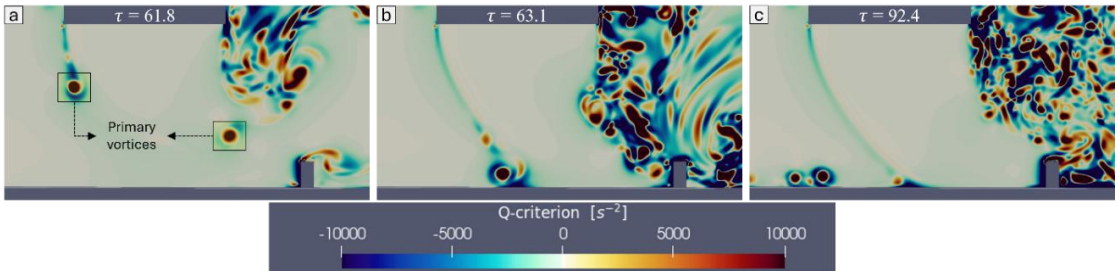


Figure 3. Contours of Q-criterion at the jet centerline (y = 0) for three dimensionless time steps: a) τ = 61.8, b) τ = 63.1, and c) τ = 92.4, qualitatively representing phases of jet release, jet impingement, and post-impingement, respectively. The ABL wind flows from left to right.

REFERENCES

Hadavi, M. and Pasdarshahri, H., 2020. Quantifying impacts of wind speed and urban neighborhood layout on the infiltration rate of residential buildings. Sustainable Cities and Society 53, 101887.

Jeong, J., and Hussain, F., 1995. On the identification of a vortex. Journal of Fluid Mechanics 285, 69–94.

Kim, J. and Hangan, H., 2007. Numerical simulations of impinging jets with application to downbursts. Journal of Wind Engineering and Industrial Aerodynamics 95(4), 279–298.

Meng, Y., Hibi, K., 1998. Turbulent measurements of the flow field around a high-rise building. Journal of Wind Engineering, Japan Association for Wind Engineering 76, 55–64.

Romanic, D., and Hangan, H., 2020. Experimental investigation of the interaction between near-surface atmospheric boundary layer winds and downburst outflows. Journal of Wind Engineering and Industrial Aerodynamics 205, 104323.

Žužul, J., Ricci, A., Burlando, M., Blocken, B. and Solari, G., 2024. Vortex dynamics and radial outflow velocity evolution in downburst-like winds. Computers & Fluids 283, 106393.

For further visualization of the ABL-downburst-building interactions, refer to the following animation:
Animation link

Simulation of high-translation-speed tornado-like vortex effects on building aerodynamics through a rapid traversing system

Stefano Brusco [1], Adrian Costache [2], Timothy J. Acosta [1], Gregory A. Kopp [1,3]

[1] *Faculty of Engineering, Western University, London, Ontario, Canada, sbrusco@uwo.ca*
[2] *WindEEE Research Institute, Western University, London, Ontario, Canada*
[3] *Canadian Severe Storms Laboratory, Western University, London, Ontario, Canada*

SUMMARY:
This paper documents the development of a rapid traversing system for the WindEEE Dome that was designed in order to examine the transient aerodynamics of buildings in tornadoes. A moving section of the floor was constructed, with a 12.8 m track, which spanned from one side to the other of the chamber. The track allows the movement of a cart and of an elliptical aluminum baseplate through the action of a servo-motor and of a system of chains. The results of a first experimental campaign that was conducted with the new system are proposed. The baseplate was instrumented with pressure taps, and a pressure model of a low-rise building was installed on top of it. Several nominally identical repeats were carried out, with the system translating from one side to the other of a spatially stationary tornado-vortex for two different translational speed (~1.5 m/s and ~4 m/s). Static tests were carried out as well, and the comparison with the moving cases in terms of pressure distributions and force coefficients is discussed.

Keywords: Tornadoes, Experimental techniques, Building aerodynamics.

1. INTRODUCTION

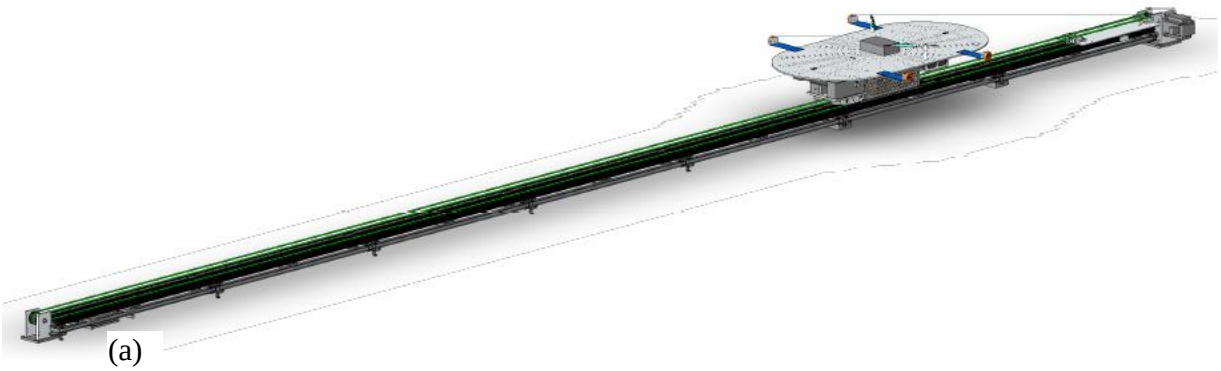
The WindEEE Dome at the University of Western Ontario is the largest simulator for tornado and downburst-like flows in the world. It is characterized by a hexagonal wind testing chamber, which is 25 m in diameter and 4 m in height. Six fans are present in the upper chamber, which generate the necessary updraft for the generation of tornadic-like flows in the lower chamber. The required swirl is provided by periphery vanes that are inclined at a given angle. The two chambers are connected through the presence of a bell-mouth. Other generic details may be found in Refan and Hangan (2018).

At the WindEEE Dome, the translating nature of the tornado-like flows may be simulated by moving the bell-mouth through a relatively slow-moving system (Kopp and Wu, 2020; Brusco and Kopp, 2024). On the other hand, an adequate simulation of the translation speed is important, as it alters the instantaneous wind direction, the local wind speed and acceleration (Haan et al., 2024). This has also been confirmed by recent experimental investigations (e.g., Chen et al., 2023), which pointed out how a different level of translation speed is reflected on the characteristics of the loads experienced by low-rise buildings. Therefore, a new rapid traversing system was conceived for the WindEEE Dome. This was accomplished by realizing a moving section of the floor. The system was consequently employed to study the effects induced by different levels of translation speed on

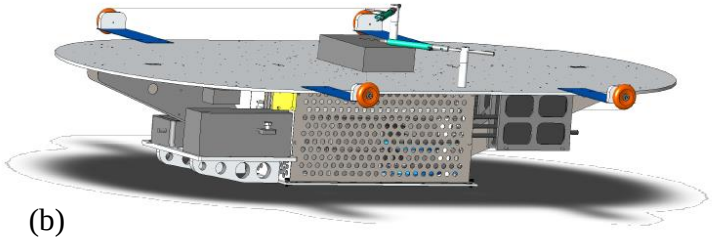
the aerodynamics of a low-rise building. Section 2 describes the design of the apparatus. Section 3 documents preliminary measurements gathered during the experimental campaign and draws future perspectives.

2. DESIGN OF THE MOVING-FLOOR MEASUREMENT SYSTEM

The realization of the system was possible through the installation of a 12.8 m track (Figure 1a) within the test chamber of the WindEEE Dome. This was possible through the removal of two circular sector-sections of the WindEEE floor. An aluminum cart slides on top of the track through a system of chains that is connected to a plate bolted to its bottom. An elliptical aluminum baseplate (with a size of 2.05 m and 1.10 m) is secured on top of the cart, constituting the moving floor. The cart is sized to host and protect the instrumentation that is required for the test measurement. For the experimentation described in Section 3, the instrumentation consisted of the pressure system, the Digital-Acquisition System of Cobra Probes, the laptop that controlled the acquisitions, laser displacements and accelerometers to monitor the position of the cart in time, as well as the batteries powering the entire apparatus. Figure 1b shows a close-up of the cart and of the baseplate. The cart moves on the track through the action of a servo-motor, which was placed at one end of the path, that was calibrated to move the entire system at different translational speeds.



(a)



(b)

Figure 1. Apparatus to realize the rapid traversing system: (a) full length track and moving floor; (b) close-up on the cart and baseplate.

3. EXPERIMENTAL CAMPAIGN AND PRELIMINARY RESULTS

The baseplate is instrumented with 226 pressure taps placed along radial lines converging to its center; their presence allows the estimation of the surface pressure field induced by the tornado-like flows and its fitting with mathematical formulations (e.g., Baker and Sterling, 2018). A 1:50 scale pressure model of the Texas Tech University (TTU) Wind Engineering Research Field Laboratory (WERFL) was installed on its surface (Figure 2a). The building has plan dimensions of 183 mm x 275 mm, with an eave height, *H*, of 78 mm. This is equipped with 204 pressure taps, nearly uniformly distributed among walls and roof. The long side of the building was installed perpendicularly to the direction of translation. Two Cobra-Probes were installed in its proximity (Figures 1b, 2b), with the aim of assessing local wind velocities. Cobra probes and pressure measurements were simultaneously acquired with the laser displacement and accelerometers.

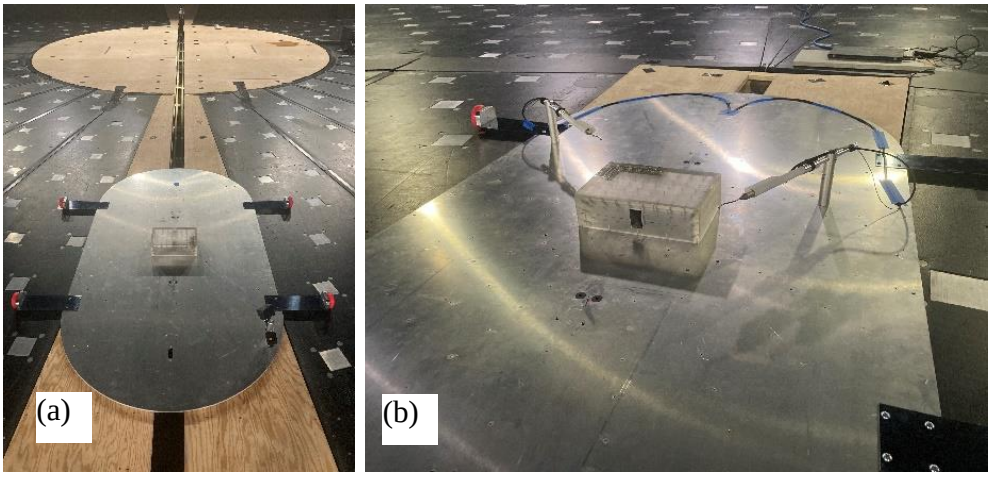


Figure 2. WindEEE Dome set-up for the experimental campaign: (a) baseplate and TTU building; (b) close-up on the TTU building and the two Cobra-Probes in its proximity.

The system was translated within spatially stationary tornado-like flows characterized by a swirl ratio, S, equal to 0.76, and a nominal radio, r_0, equal to 400 mm. The tornado core diameter was approximately three times larger than the largest plan dimension of the building. Nominally identical repeats were conducted at different translating speed (U_t) (30 for U_t ~1.5 m/s and 60 for U_t~4 m/s), with the bell-mouth fixed 320 mm aside. Figure 3 shows the 60 aligned time-history of a pressure tap on the roof of the building acquired for the maximum translating velocity. On top of them, a black thick line indicates the corresponding translational velocity of the system, whose ordinate is indicated on the right side of the graph. It is noted that the pressure drop, associated with the interaction between tornado-like flows and building, occurs while the translational velocity is almost stationary.

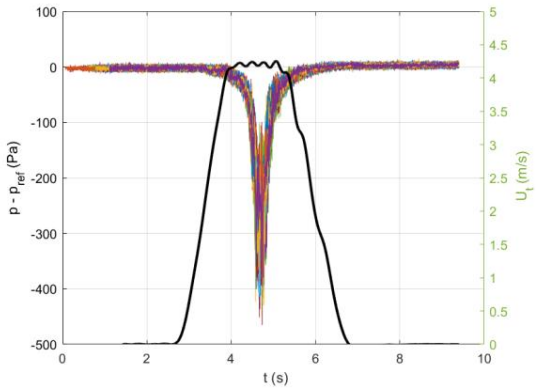


Figure 3. Aligned time-histories of a pressure tap of the roof of the TTU building for the 60 nominally identical repeats conducted at the maximum translation speed (indicated with a black thick signal, whose ordinate is on the right-side of the graph).

Static tests (1-min acquisitions) were carried out as well for specific positions of the system. The final paper will examine the effects induced by transient aerodynamics on the pressure distributions of the building and the relevant overall force coefficients. To do this, the separation between the effects induced by the static gradient of pressure associated with the tornado-like flows and those associated by building aerodynamics will be performed (e.g., Kopp and Wu, 2020). Also comparisons with results obtained by using the traditional slow-moving bell-mouth will be included in the final paper.

ACKNOWLEDGEMENTS

The Authors gratefully acknowledge the contribution of University Marchine Services at the University of Western Ontario for assisting with the design of the apparatus and its assembly. The contribution of Ian J. Vinkenvleugel is particularly acknowledged. The Authors are also thankful to the WindEEE staff (Maksim Faronov, Mark Parker, Tristan Cormier) for the technical support before and during the experimental campaign. Finally, they thank Eugen J. Porter and Trent Steensma from the Electronics Shop at Western, and Jake W. Slusarczyk for the support in designing and calibrating the servo-motor. This work was partially funded by ImpactWX.

REFERENCES

Brusco, S., Kopp, G.A., 2024. Streamline curvature effects generated by tornado-like flows on the aerodynamics of low-rise structures, J. Wind Eng. and Ind. Aerodyn. 253, 105865.

Baker, C.J., Sterling, M., 2018. A conceptual model for wind and debris impact loading of structures due to tornadoes. J. Wind Eng. Ind. Aerod. 175, 283–291.

Chen, Q., Tang, Z., Wu, X., Zuo, D., James, J., 2023. Laboratory study of tornado-like loading on a low-rise building model. Journal of Wind Engineering and Industrial Aerodynamics 238, 105443.

Haan Jr., F. L., Wang, J., Sterling, M., Kopp, G. A., 2024. Experimentally estimating wind load coefficients for tornadoes – An alternative perspective, Journal of Wind Engineering and Industrial Aerodynamics 251 105811.

Kopp, G. A., Wu, C.H., 2020. A framework to compare wind loads on low-rise buildings in tornadoes and atmospheric boundary layers, J. Wind Eng. and Ind. Aerodyn. 204, 104269.

Refan, M. and Hangan, H., 2018. Near surface experimental exploration of tornado vortices. Journal of Wind Engineering and Industrial Aerodynamics 175, 120–135.

Comprehensive Framework for Scaling and Analyzing Downburst-like Outflows in Wind Tunnels— methodology and case study

Mohamed Eissa [1], Amal Elawady [2,3]

[1]*Civil and Environmental Engineering, Florida International University, Miami, Florida, USA; meiss002@fiu.edu*
[2]*Civil and Environmental Engineering, Florida International University, Miami, Florida, USA; aelawady@fiu.edu*
[3]*Extreme Events Institute, Florida International University, Miami, Florida, USA*

SUMMARY:
The temporal transient nature of downburst winds causes additional complexity to the scaling process of any field wind event compared to synoptic winds. This is particularly even more tangled when a simultaneous simulation of the downburst-structure experiment is targeted. The simultaneous scaling of both the structural properties and the main characteristics of downbursts poses a challenge mainly due to the limited facility size, the limited instrumentation capabilities, and the random nature of downbursts where every event is unique. The available scaling methodologies preserve only the main characteristics of the full-scale events in the time domain and, in many cases, compromise similarities in the frequency domain. To address this issue, a generalized framework that couples both flows' time and frequency features in obtaining the proper scaling parameters has been developed. For the sake of simplicity, we employ the classical moving mean method in our proposed framework. Consequently, this necessitates finding a suitable answer to a pressing question: "What is the appropriate time-averaging window to be incorporated into the classical moving mean method to derive the time-varying mean in which the subjectivity of the classical method can be minimized?". This framework enables researchers and wind tunnel technicians to have an enhanced level of consistency and robustness in scaling and analyzing transient wind events and performing a comparison with different studies. A case study utilizing the proposed framework is presented in this study.

Keywords: downburst, non-stationary process, wind tunnel, scaling methodology, aerodynamic testing, time and frequency domain.

1. INTRODUCTION AND MOTIVATION

A downburst is a small-scale cold air column generated by thunderstorm clouds that rapidly descends toward the ground surface, causing severe outwards wind laterally. Downbursts come in two forms: microbursts and macrobursts, which differ in size but have the same characteristics. There are also wet downbursts, accompanied by heavy precipitation at the surface, and dry downbursts, which occur with little to no precipitation. Although downbursts are shorter in duration compared to large-scale weather events like hurricanes, they can cause significant damage to both aviation and ground properties in the affected areas. As a result, there have been many initiatives to collect field measurements to better interpret the physical characteristics of this intricate phenomenon (Dodge et al. 1986; Fujita 1979; McCarthy, Wilson, and Fujita 1982; Solari, Giovanni et al. 2015; Wolfson, DiStefano, and Forman 1987). However, the literature findings are insufficient to study the structural response during extreme downburst winds. Therefore, it is

crucial to thoroughly investigate the effects of downburst (DB) winds on different types of structures— from a structural standpoint. This motivated researchers, over the past few decades, to experimentally simulate downburst alike-wind in conventional wind tunnels by adopting different simulation approaches such as the wall jet approach (e.g., Lin et al. 2007), the impinging jet approach (e.g., Junayed et al. 2019), and the buoyancy-driven flow approach (e.g., Alahyari and Longmire 1995). To be physically well-presented, these simulations require developing a scaling method, considering the transient nature of downburst outflows. In the context of the available literature, it has been proven that the proper decomposition approach of highly transient wind phenomena (e.g., downbursts) lacks consensus in the wind community (Le and Caracoglia 2018). Many approaches are posed to derive the transient mean, resulting in different results and, subsequently, inconsistencies in scaling procedures. To that end, the wind-induced structural analysis is reliant on, firstly, *an appropriate derivation of the mean and fluctuation components* and, secondly, *a proper scaling methodology to ensure that the structure is fully immersed in the flow*.

The study by Junayed et al. 2019 utilizes the traditional scaling method through which the time scale is the ratio between the full- and model-scale's time-averaging window (T_{avg}), while the velocity scale is calculated by taking the ratio between the maximum slowly-varying means of both full- and model-scale— the same method for synoptic winds. Despite the simplicity of this method, the velocity scale can be spurious due to random turbulence fluctuations in the flow and/or sampling errors in the field data acquisition. In contrast, the study by Romanic et al. 2020 advances the traditional method by utilizing the entire time series of both flows to determine the velocity scale instead of two velocity values. This method effectively compares the standardized moving mean records of both flows in the time domain to determine the time-averaging window that provides the proper scaling between them, thereby portraying their similarity along the full-scale event period. It's important to highlight that this method only assesses the footprint similarity of both downburst outflows in the time domain. Furthermore, it does not examine the effectiveness of the chosen time-averaging window in distinguishing between the low-frequency components (slowly varying mean) and the high-frequency component (residual fluctuations part). The latter method can be improved by incorporating the similarities between both flows in the frequency domain to ensure a heightened level of similarity. It is important to note that encountering two contradicting times (i.e., Tavg and event duration) will be addressed in the proposed framework by fixing one time to guide the other. Also, one can derive the velocity scale by assuming the time-varying mean ratio, which is limited by the simulated profile height that determines the length scale. These interconnected parameters are not adequately addressed in many studies, mainly when we simulate a field event. *Therefore, this is the first attempt to establish a generalized framework for scaling and analyzing downburst winds in a way that considers the similarity in both frequency and time domain between full- and model-scale flows while avoiding discrepancies between scaling parameters.*

2. POTENTIAL CONTRIBUTIONS

- Utilize available metrics in the literature and propose new metrics to assess time-averaging window compatibility. This is a step forward in minimizing the subjectivity of the moving mean method while preserving its simplicity and straightforwardness.
- Develop a generalized framework for scaling full-scale downburst events by achieving a

heightened level of similarity between full- and model-scale in both time and frequency domains.

3. CASE STUDY

The WOW is an open-jet full-scale and large-scale testing facility simulating hurricane winds, reaching a maximum sustained test section wind speed of 70 m/s (157 mph). The wall-jet technique is adopted to create the outflow region of the downdraft, resulting in the typical nose-shaped downburst vertical profile and the main features, including the transient wind speed time histories and the formation of the main rolling vortex. To accomplish this, an external mechanical apparatus has been designed to be affixed to the outlet of the flow management box, as illustrated in Figure 1. Aerodynamic testing of a large-scale transmission tower model with a geometric scaling of 1:50 has been conducted. The prototype transmission tower is a vertical self-supported delta lattice tower with a base of 13m (42.8ft) wide and 13m (42.8ft) in length. The tower's height is 60m (196ft), as illustrated in Figure 2. Experiments presented in this paper were conducted at the NSF-NHERI Wall of Wind (WOW) Experimental Facility (EF). Additionally, the study aims to analyze how altering the ratio between the distance of the model (X) and the diameter of the simulated DB (D) event affects the estimation of the drag coefficient for sectional models. It also seeks to explore the interplay between the location of the sectional models concerning the wind profile and the drag coefficient.

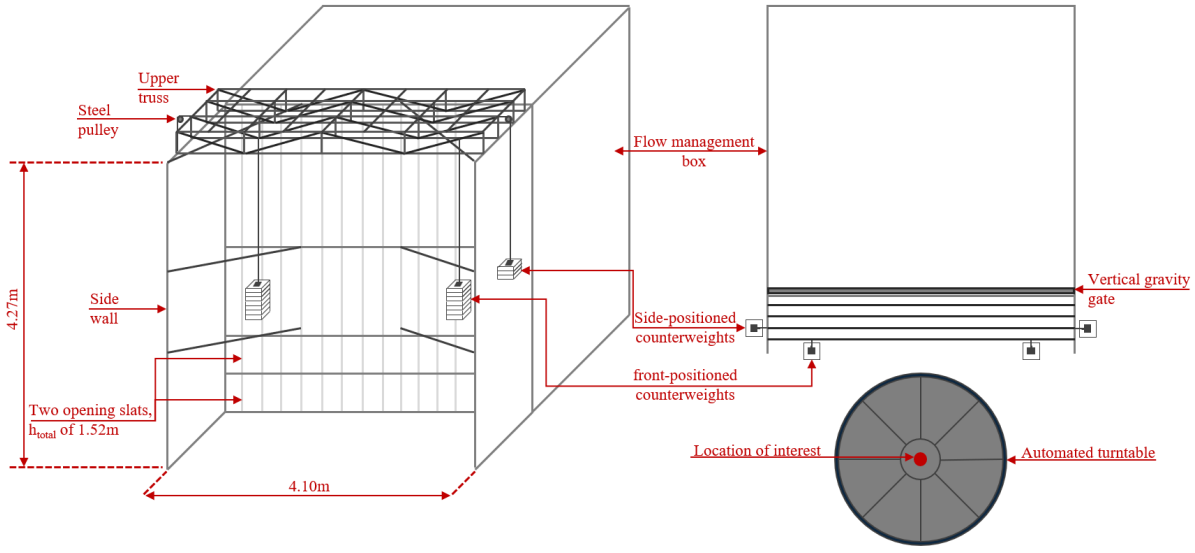


Figure 1. Schematics of the downburst apparatus attached to the flow management box. (a) 3D-view of the apparatus, and (b) the plan view of the test section. Side-positioned counterweights control the opening slats' movement, while the front-positioned counterweights manage the vertical gravity gate.

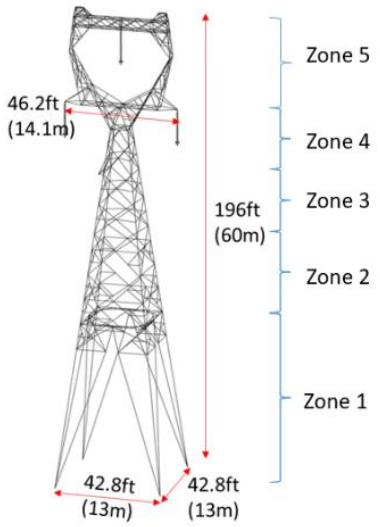


Figure 2. Prototype model of the 196ft Self-supported lattice tower, indicating the zones.

ACKNOWLEDGEMENTS

This paper is based upon work sponsored by the National Science Foundation (NSF) award numbers CMMI 1762968 and CMMI 2146277. The opinions, findings, conclusions, or recommendations expressed in this article are solely those of the authors and do not represent the opinions of the funding agencies.

REFERENCES

Alahyari, Abbas, and Ellen K. Longmire. 1995. "Dynamics of Experimentally Simulated Microbursts." AIAA Journal 33(11):2128–36. doi: 10.2514/3.12957.

Dodge, James, James Arnold, Gregory Wilson, James Evans, and Ted Fujita. 1986. "The Cooperative Huntsville Meteorological Experiment (COHMEX)." Bulletin of the American Meteorological Society 67(4):417–19.

Fujita, Tetsuya Theodore. 1979. "Objectives, Operation, and Results of Project NIMROD." Preprints, Eleventh Conference on Severe Local Storms, Kansas City, American Meteorological Society, Boston 259–66. doi: http://hdl.handle.net/10605/261973.

Junayed, Chowdhury, Chowdhury Jubayer, Dan Parvu, Djordje Romanic, and Horia Hangan. 2019. "Flow Field Dynamics of Large-Scale Experimentally Produced Downburst Flows." Journal of Wind Engineering and Industrial Aerodynamics 188:61–79. doi: 10.1016/j.jweia.2019.02.008.

Le, Viet, and Luca Caracoglia. 2018. "Computationally Efficient Stochastic Approach for the Fragility Analysis of Vertical Structures Subjected to Thunderstorm Downburst Winds." Engineering Structures 165:152–69. doi: 10.1016/j.engstruct.2018.03.007.

Lin, William, Leigh Orf, Eric Savory, and C. Novacco. 2007. "Proposed Large-Scale Modelling of the Transient Features of a Downburst Outflow." Wind and Structures 10. doi: 10.12989/was.2007.10.4.315.

McCarthy, John, James W. Wilson, and T. Theodore Fujita. 1982. "The Joint Airport Weather Studies Project." Bulletin of the American Meteorological Society 63(1):15–22. doi: 10.1175/1520-0477(1982)063<0015:TJAWSP>2.0.CO;2.

Romanic, Djordje, Edoardo Nicolini, Horia Hangan, Massimiliano Burlando, and Giovanni Solari. 2020. "A Novel Approach to Scaling Experimentally Produced Downburst-like Impinging Jet Outflows." Journal of Wind Engineering and Industrial Aerodynamics 196:104025. doi: 10.1016/j.jweia.2019.104025.

Solari, Giovanni, Burlando, Massimiliano, De Gaetano, Patrizia, and Repetto, Maria Pia. 2015. "Characteristics of Thunderstorms Relevant to the Wind Loading of Structures." Wind and Structures 20(6):763–91. doi: 10.12989/WAS.2015.20.6.763.

Wolfson, M. M., J. T. DiStefano, and B. E. Forman. 1987. "The FLOWS (FAA-Lincoln Laboratory Operational Weather Studies) Automatic Weather Station Network in Operation." Massachusetts Institute of Technology, Lincoln Laboratory.

3D wind field retrieval within the thunderstorm cloud that occurred on September 23, 2023 in Piedmont (Italy)

Priya Kumari [1], Massimiliano Burlando [1], Renzo Bechini [2], Djordje Romanic [3], Alessandro Battaglia [4]

[1]*University of Genoa, Genoa, Italy, priya.kumari@edu.unige.it massimiliano.burlando@unige.it*
[2]*Regional Agency for Environmental Protection of Piedmont, Turin, Italy, renzbech@arpa.piemonte.it*
[3]*McGill University, Montreal, QC, Canada, djordje.romanic@mcgill.ca*
[4]*Polytechnic of Turin, Turin, Italy, alessandro.battaglia@polito.it*

SUMMARY
Windstorms in Europe present a major risk, accounting for over 70% of damage and casualties from natural disasters, primarily driven by mid-latitude extratropical cyclones, Medicanes, and thunderstorm outflows. This study focuses on the investigation of the three-dimensional structure and dynamics of thunderstorm clouds in Northern Italy. It aims to analyze the whole three-dimensional wind field and its evolution within thunderstorm clouds which contribute to downburst formation at the ground. This goal is achieved by utilizing historical thunderstorm events along with radar and lidar observational data. A field campaign is ongoing in Piedmont using two Doppler radars and one scanning lidar to detect and measure radial velocities inside thunderstorm clouds. The PyDDA algorithm, which is based on a 3Dvar technique for data assimilation, is used to retrieve the 3D components of the entire wind field. Here, a thunderstorm event that occurred on September 23, 2023 is briefly analyzed and some preliminary results are presented. At the conference, this event will be presented in greater detail focusing on the 3D reconstruction of updraft(s) and downdraft(s) that develop within cumulonimbus clouds, and thunderstorm outflows at the ground.

Keywords: Thunderstorm outflows, Meteorological radar and lidar, PyDDA 3D wind field retrieval

1. INTRODUCTION

Wind impacts society, infrastructure, and agriculture both positively and negatively. Windstorms can cause significant damage, like uproot trees, damage crops (Gardiner et al., 2016), and compromise critical infrastructure (Klawa and Ulbrich, 2003). In Europe, windstorms pose a significant risk, accounting for over 70% of damage and casualties from natural disasters, largely fueled by mid extra-tropical cyclones and thunderstorm outflows (Ulbrich et al., 2013). Despite extensive research on tropical cyclones since the 1920s, studies on localized thunderstorms and their outflows are less developed. There is a concerning lack of models to assess the effects of thunderstorm outflows on infrastructure, particularly given the increasing influence of climate change on severe weather phenomena.

The introduction of Doppler radar technology in the 1950s revolutionized meteorological research, significantly enhancing our ability to detect thunderstorms and tornadoes (Barratt and Browne, 1953; Brown and Lewis, 2005). This study aims to investigate the three-dimensional structure and

dynamics of thunderstorm clouds and their impacts on the Earth's surface using Doppler radars and lidars, focusing on Northern Italy, which is a region prone to strong convective activity throughout the year.

Scanning radars/lidars represent the most effective means of acquiring three-dimensional wind volumes during severe thunderstorms. However, the process of retrieving three-dimensional winds from radar/lidar measurements is complex. Unlike direct wind measurements, these systems capture the velocity of scatterers along the emitted beam, necessitating additional information to reconstruct the complete wind field. This typically involves incorporating physical constraints, such as the conservation of mass, or utilizing supplementary data from sources like model reanalyses, wind profilers, and rawinsondes. In this study, we utilize the Pythonic Direct Data Assimilation (PyDDA) package for wind retrieval from scanning weather radars. This study is part of the PRIN Project, "WIND RISK: Thunderstorm Outflows Measurement and Modeling for Strong-WIND Nowcasting and RISK Mitigation" (Burlando et al., 2024).

2. MEASUREMENT CAMPAIGN

The study employs radar and lidar systems situated in the Piedmont region (i.e., Northwestern Italy) to monitor severe thunderstorms, utilizing two Doppler radars (one C-band and another X-band) and one lidar system strategically positioned for optimal coverage. Fig. 1 illustrates the geographical locations of these instruments, highlighting their critical role in capturing thunderstorm dynamics.

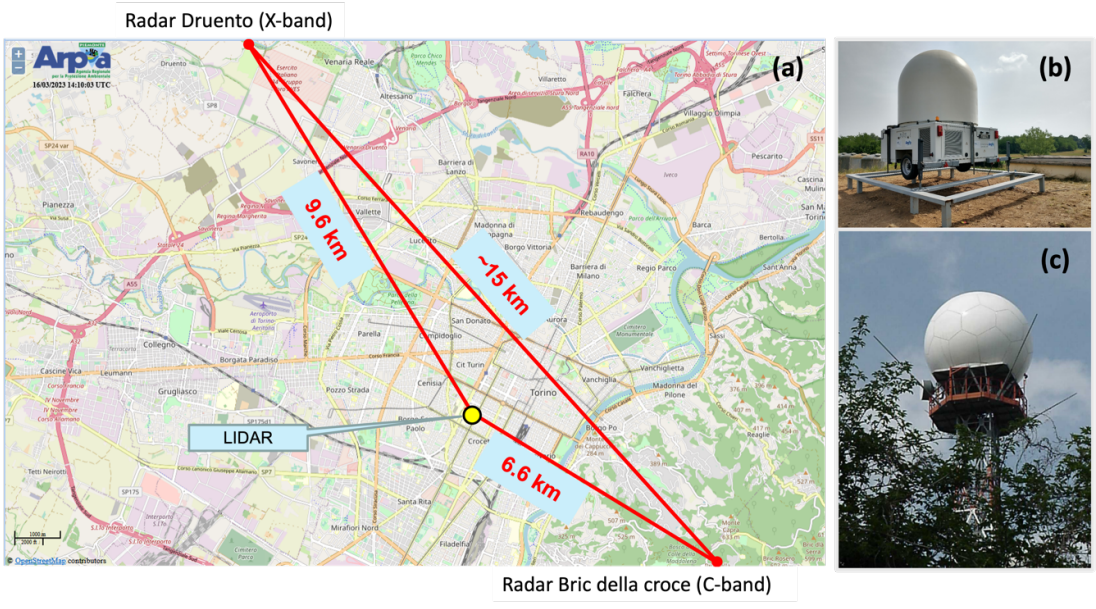


Figure 1. (a) Location of two radars and one Lidar in google map. (b) Druento radar and (c) Bric della croce radar.

The Bric della croce radar operates with a temporal sampling duration of 5 min and offers a spatial resolution of 340 m, enabling effective monitoring of weather patterns. In contrast, the Druento radar has a shorter temporal duration of 2.5 min and a spatial resolution of 150 m, allowing for finer detail in its measurements. Additionally, the Polytechnic of Turin contributes a lidar system,

enhancing the overall data collection capabilities. These advanced systems enable us to gather a wealth of co-located measurements from small atmospheric volumes, approximately 100 m in size. This abundance of data is expected to facilitate the optimization of processing algorithms, particularly for estimating signal attenuation and precipitation intensity, significantly improving our ability to analyze and understand thunderstorm behavior in the region.

3. WIND RETRIEVAL METHODOLOGY

To reconstruct three-dimensional wind fields from thunderstorm clouds, we employ the PyDDA algorithm (Shapiro et al., 2009; Potvin et al., 2012). This technique integrates dual Doppler radar observations into wind retrieval, allowing for in-depth analyses of the internal dynamic of thunderstorms. Additionally, the integration of the two radars measurements is enhanced by the inclusion of a scanning lidar, which effectively addresses the blind spots of the radars close to the ground, thereby improving the continuity and accuracy of the wind field data all within the thunderstorm cloud and beneath it.

The wind retrieval process in PyDDA employs the three-dimensional variational (3DVAR) technique, aiming to find the wind vector field that minimizes a specified cost function. This cost function is composed of several components, each representing different observational or physical constraints, like mass conservation.

4. PRELIMINARY RESULTS

A severe thunderstorm was reported around 4:30 UTC (i.e., 6:30 am local time) on September 23, 2023 over Druento and nearby areas. Preliminary results presented in Fig. 2 and 3 show the reflectivity and radial velocity, respectively, from three different radar sweeps taken simultaneously. High reflectivity values exceeding 30 dBZ and velocities above 5 m/s were observed, confirming that the radar successfully captured the thunderstorm echoes. We are currently using the PyDDA algorithm to analyze in detail the wind components associated with this storm.

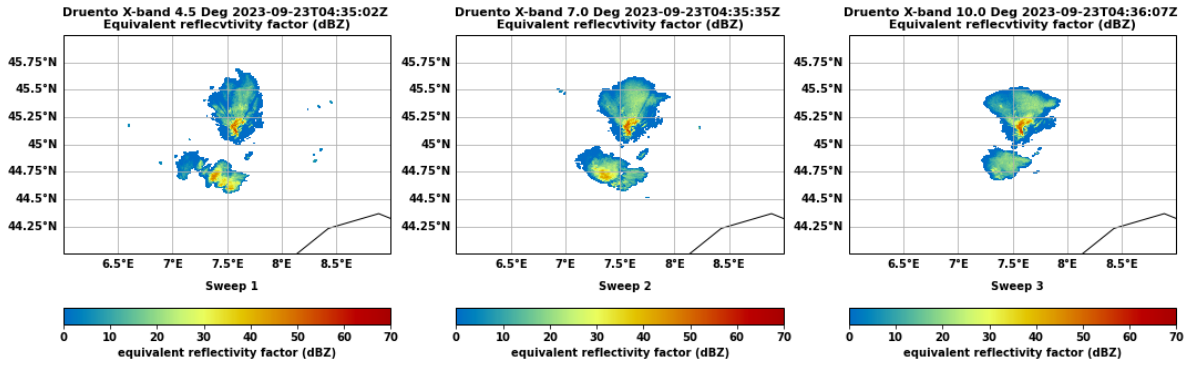


Figure 2. Contour plot of the reflectivity of Druento radar at 4:30 am on September 23, 2023. Sweep 1, 2 and 3 correspond to elevations equal to 4.5°, 7°, and 10°, respectively.

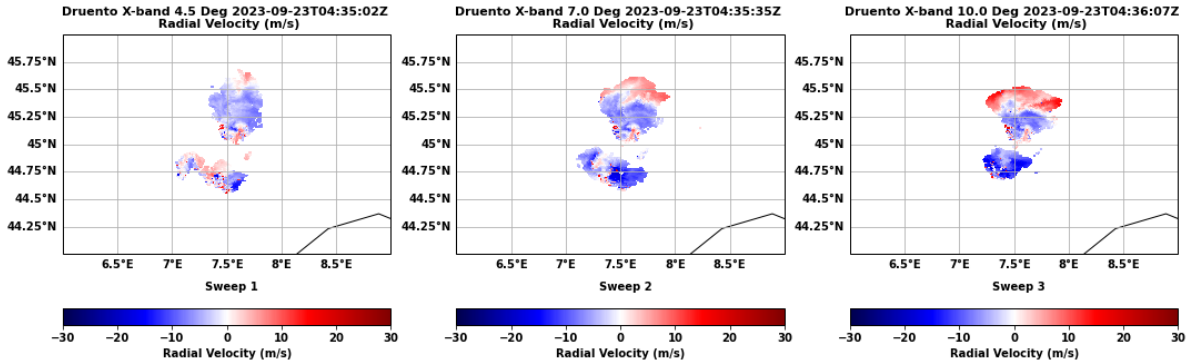


Figure 3. Same as Fig. 2, but contours of radial velocity.

5. CONCLUSIONS

This analysis seeks to uncover the relationships between environmental conditions and the formation of downbursts and gust fronts. By examining historical thunderstorm events alongside surface meteorological data, we will delve into the cloud dynamics of severe weather phenomena, with special focus on the surface wind fields characteristic of interest in the wind engineering field. Further analyses and results of this event will be presented at the conference.

ACKNOWLEDGEMENTS

This research is funded by the European Union – Next Generation EU for the Project – WIND RISK "Thunderstorm Outflows Measurement and Modeling for Strong-WIND Nowcasting and RISK Mitigation" (Grant no. 2022NPKCLX, CUP D53D23004790006).

REFERENCES

Barratt, P., and Browne, I.C., 1953. A new method of measuring vertical air currents. Quarterly Journal of the Royal Meteorological Society 79, 550.

Brown, R. A., and Lewis, J. M., 2005. PATH TO NEXRAD: Doppler radar development at the National Severe Storms Laboratory. Bull. Amer. Meteor. Soc. 86, 1459–1470. DOI: https://doi.org/10.1175/BAMS-86-10-1459

Burlando, M., Miglietta, M. M., Avolio, E., Bechini, R., Cassola, F., De Martin, F., Lagasio, M., Milelli, M., Parodi, A., Romanic, D., 2024. The –WIND RISK project: nowcast and simulation of thunderstorm outflows. Bull. Of Atmos. Sci. & Technol. 5:15. DOI: https://doi.org/10.1007/s42865-024-00079-6

Gardiner, B., Berry, P., Moulia, B., 2016. Review: Wind impacts on plant growth, mechanics and damage. Plant Sci. 245, 94-118. DOI: 10.1016/j.plantsci.2016.01.006

Klawa, M., and Ulbrich, U., 2003. A model for the estimation of storm losses and the identification of severe winter storms in Germany. Natural Hazards and Earth System Sciences 3(6), 725-732.

Potvin, C.K., Shapiro, A., and Xue, M., 2012. Impact of a vertical vorticity constraint in variational dual-Doppler wind analysis: Tests with Real and Simulated Supercell Data. J. Atmos. Oceanic Technol. 29, 32–49, DOI: https://doi.org/10.1175/JTECH-D-11-00019.1

Shapiro, A., Potvin, C.K., and Gao, J., 2009. Use of a vertical vorticity equation in variational dual-Doppler wind analysis. J. Atmos. Oceanic Technol. 26, 2089–2106. DOI: https://doi.org/10.1175/2009JTECHA1256.1

Ulbrich, U., Leckebusch, G. C., and Donat, M. G., 2013. Windstorms, the most costly natural hazard in Europe. In Natural disasters and adaptation to climate change, Cambridge University Press, pp. 109-120.

Thermal effects on large-scale experimental downbursts

Federico Canepa [1], Anthony Guibert [2], Andi Xhelaj [1], Josip Zuzul [1], Djordje Romanic [3], Alessio Ricci [4], Horia Hangan [5], Olivier Flamand [2], Jean-Paul Bouchet [2], Philippe Delpech [2], Massimiliano Burlando [1]

[1]*University of Genoa, Genoa, Italy, federico.canepa@unige.it – andi.xhelaj@edu.unige.it – josip.zuzul@edu.unige.it – massimiliano.burlando@unige.it*
[2]*Centre Scientifique et Technique du Bâtiment (CSTB), Nantes, France, anthony.guibert@cstb.fr – olivier.flamand@cstb.fr – jeanpaul.bouchet@cstb.fr – philippe.delpech@cstb.fr*
[3]*McGill University, Montreal, Canada, djordje.romanic@mcgill.ca*
[4]*University School for Advanced Studies (IUSS) Pavia, Pavia, Italy, alessio.ricci@iusspavia.it*
[5]*Ontario Tech University, Oshawa, Canada, horia.hangan@ontariotechu.ca*

SUMMARY:
Thunderstorms are a major feature of European and other mid-latitude climates, producing severe weather events such as intense rainfall, hail, and strong winds. Downburst winds, a key phenomenon associated with thunderstorms, develop when cold air from a thunderstorm cloud descends to the ground, creating a potentially powerful horizontal outflow upon impact. The recent CLIMATHUNDERR project at the Jules Verne Climatic Wind Tunnel, in France, aimed to replicate downburst winds using combined impinging jet and gravity current techniques. By simulating thermal instability, this study recreated cold-air downdrafts and examined how varying temperature differences between the jet and surrounding air affect downburst dynamics. The experimental findings reveal how buoyancy-driven acceleration alters the flow's evolution, leading to asymmetric vortices and squashed vortex "eyes" near the ground during outflow, particularly in the primary vortex (PV) leading the downburst. Additionally, reduced-scale testing on a real, complex topography showed significant influences on temperature profiles and the development of the PV. The open-access database, detailed in a separate contribution at this conference, along with the related journal data paper, offers valuable insights into downburst behaviour, enhancing the understanding and forecasting of severe downbursts impacts in mid-latitude regions.

Keywords: downburst, large-scale gravity current, LS-PIV

1. INTRODUCTION

Downbursts are intense wind events driven by thermal instability between cold air within cumulonimbus cloud and warmer surrounding air. This instability initiates a downdraft of cold air that, upon reaching the ground, spreads horizontally in a nearly radial pattern. The short-lived, localized nature of downbursts makes it challenging to accurately characterize and model these events using full-scale data. Controlled simulations are therefore critical for understanding the flow physics and dynamics of thunderstorm winds. Despite advances in computational power and simulation techniques, numerical models still struggle to provide reliable data on flow turbulence and instability. For this reason, physical simulators are often preferred for studying extreme, non-stationary wind systems such as downbursts. Gravity current (GC) methods (e.g., Lundgren et al., 1992) use fluid density differences to mimic the thermal instabilities driving the downburst

downdraft. However, they are limited by their small geometric and velocity scales. In contrast, the impinging jet (IJ) technique (e.g., Canepa et al., 2022), while not capturing the thermal aspects, is often preferred for accurately reproducing downburst dynamics within the atmospheric boundary layer (ABL) and assessing their impact on natural and built environments near the ground.

The CLIMATHUNDERR—CLIMAtic investigation of THUNDERstorm winds—project, funded by the European Union under the Engineering Research Infrastructures for European Synergies (ERIES) program, combined GC and IJ techniques to simulate downbursts at the Jules Verne Climatic Wind Tunnel (JVCWT) of the Centre Scientifique et Technique du Bâtiment (CSTB) in Nantes, France. This approach enabled the first large-scale experimental simulation of thermal instabilities that drive downburst dynamics. The effects of varying temperature differentials, ΔT, between the jet and test chamber air were quantified in relation to the velocity and geometric structure of the downdraft and outflow. The reproduced downbursts were further simulated over a 1:2000 scale model of the Polcevera Valley in the Municipality of Genoa, Italy. Results show that complex terrain significantly alters vortex structures and temperature profiles along the valley.

2. EXPERIMENTAL SETUP

The thermal circuit of the Jules Verne Climatic Wind Tunnel (JVCWT) (Moonen et al., 2006) features a rectangular test section measuring 10 m (W) × 7 m (H) × 25 m (L). To simulate downbursts, an 8 m³ impinging jet plenum (IJP) was installed at a height of 3 m, equipped with a circular nozzle (D = 1 m) opening directly into the testing chamber. An air conditioning system cooled the IJP air to as low as 5°-10°C, allowing for the reproduction of different ΔT between the IJP and the wind tunnel (WT) test chamber ($\Delta T = T_{\mathrm{IJP}} - T_{\mathrm{WT}}$) to study the buoyant effects on downburst dynamics. A piston was incorporated to control the jet speed at the nozzle exit, ensuring repeatable initial conditions. Two imposed piston velocities of 0.15 m s^{-1} and 0.25 m s^{-1} resulted in mechanical vertical jet velocities at the nozzle exit of 0.80 m s^{-1} and 1.30 m s^{-1}, respectively. The combined contribution of mechanical jet velocity from the piston, w_{IJ}, and buoyant velocity from the thermal instability, w_{GC}, produced the overall downdraft velocity.

Large-Scale Particle Image Velocimetry (LS-PIV) was utilized to measure flow velocity, with Helium-Filled Soap Bubbles (HFSB) injected into the IJP prior to jet release. Two cameras were employed for image acquisition: the first had a 2.5 × 2.5 m² field of view (FOV) at 7 Hz, replaced by a second camera with a 3.2 × 2.5 m² FOV at 12 Hz after malfunctioning of the first camera. A total of 24 thermocouples monitored ΔT and temperature profiles along the downburst outflow and surface of the topography model.

A total of 56 experiments were conducted: the first 39 focused on varying ΔT values (0°, -10°, and -20°C) to observe downburst and outflow dynamics; experiments 40 to 56 included interactions with the 1:2000 scale model (i.e., 3.5 m × 2 m) of the Polcevera Valley in Genoa, Italy, examining how complex terrain influenced flow and temperature profiles during downbursts.

3. RESULTS

Significant differences are observed due to variations in the thermal instability imposed at the boundary between the IJP and the chamber air. Figure 1 presents the instantaneous velocity field at the time of maximum velocity for two experimental cases, one without temperature differential (ΔT = 0°, pure IJ case, Figure 1a) and the other with ΔT = -20° (IJ+GC case, Figure 1b). Both the velocity magnitudes and flow field geometry reveal notable differences between these cases. The

buoyant contribution in the IJ+GC setup substantially accelerates the downdraft and outflow, enhancing the ground-level vortex speed. This buoyancy-driven effect also alters the PV shape: in the IJ+GC case, the PV loses symmetry, becoming more compressed vertically near the ground and elongated radially compared to the pure IJ case. Both cases show maximum velocities very close to the ground (between 1 and 3 cm above the ground) and approximately at radial position r/D = 1.5, with the peak occurring at a slightly lower height and farther out in the IJ+GC case. The maximum wind speed in the IJ+GC case exceeds $3w_{\mathrm{IJ}}$.

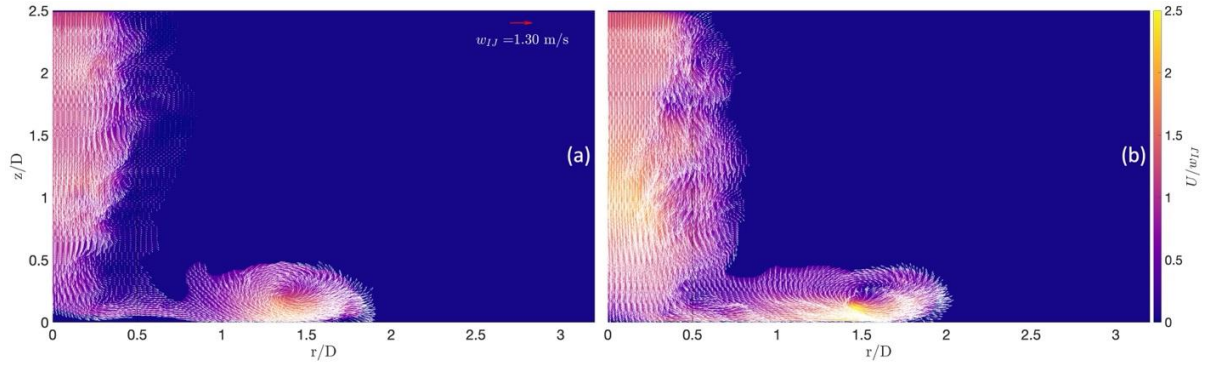


Figure 1. Instantaneous flow field captured at the time of maximum wind speed for w_{IJ} = 1.3 m s^{-1}. (a) pure IJ case (exp. #34), t = 6.58 s (after nozzle opening) and ΔT = 0 °C; (b) IJ+GC case (exp. #38), t = 5.00 s (after nozzle opening) and ΔT = -20 °C.

Figure 2 illustrates the timeseries of wind speed and temperature (the latter for the IJ+GC case only) and their vertical profiles at selected radial positions (r/D = 1.0, 1.5, 2.0, and 2.5) for the same experimental cases defined above. All experimental runs are synchronized to the opening of the nozzle (t = 0). The buoyant effect clearly convects faster both the downdraft and the ground-level outflow, leading to an earlier wind speed peak induced by the passage of the PV. Concurrently, thermocouples record a sudden temperature drop, indicating the presence of colder downdraft air carried by the PV propagation within the outflow. Following the jet dissipation, the temperature gradually returns to the ambient chamber level.

Wind speed maxima are consistently located near the ground, within a vertical height of z/D = 0.20, due to accelerated flow at the interface between the ground and the propagating PV. An important result of the overall "flow compression" for the IJ+GC case is that the maximum velocity is always larger and closer to the ground compared to the IJ case. At radial positions r/D = 1.5 and, partially, 1.0, wind speed remains roughly constant near the maximum, while more variability is observed at larger radial positions. Above this zone, velocity decreases with a more rapid drop-off in the IJ+GC case than in the pure IJ case. The temperature minimum is located at the ground level for r/D = 1.0, which approximately aligns with the PV landing location. This height increases with radial distance, possibly due to the PV elevating above the ground. At r/D = 2.5, the temperature profile becomes relatively uniform around the ambient chamber temperature due to the weakened outflow and increased mixing with surrounding air.

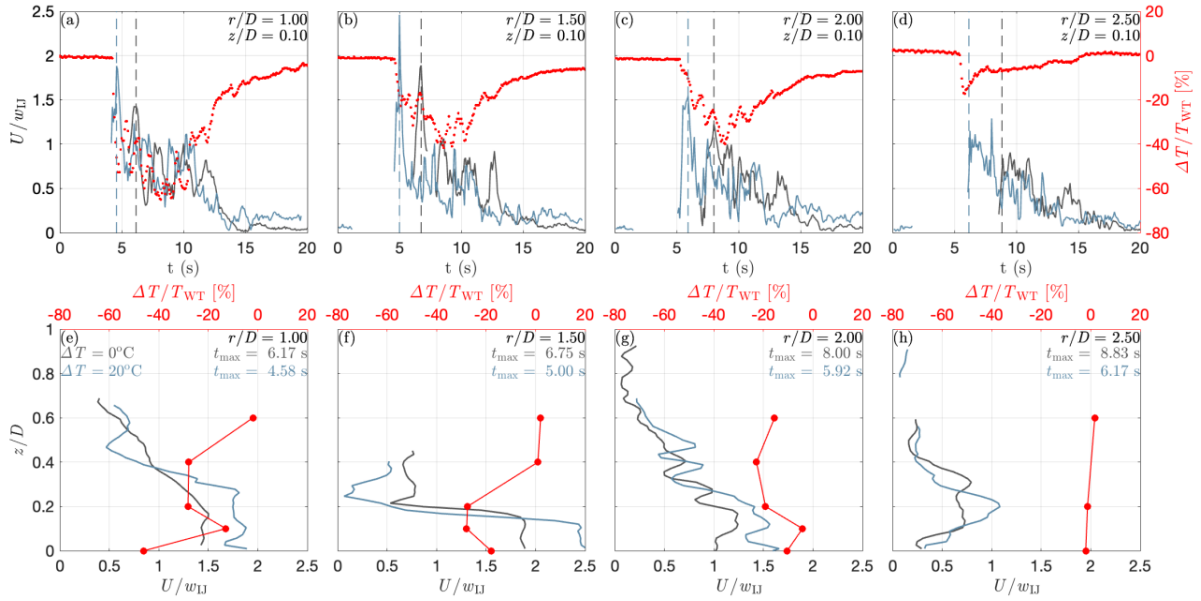


Figure 2. Wind speed and temperature for radial locations r/D = 1.0 (a,e), 1.5 (b,f), 2.0 (c,g), and 2.5 (d,h): (a-d) timeseries; (e-h) vertical profiles at the time of maximum wind speed (vertical dashed lines in a-d) (e-h). Grey and light blue colors refer to wind speed for pure IJ and IJ+GC cases, respectively. Red color refers to temperature records of the IJ+GC case. Wind speed timeseries are shown at z/D = 0.1 while temperature timeseries at z/D = 0. Temperature is shown as the percentage variation with respect to ambient (chamber) air.

3. CONCLUSIONS AND PROSPECTS

Preliminary analysis of the open-access database, containing velocity and temperature measurements obtained via LS-PIV and thermocouples, respectively, reveals a substantial impact of buoyancy on the dynamic and flow evolution of the simulated downburst wind and its associated vortex structures. The presentation will provide an in-depth examination of these flow dynamics, extending the discussion to the interactions between the simulated flows and the 1:2000 scaled complex terrain model. This analysis will explore topographic influences on flow velocity and temperature, offering insights into how terrain features affect downburst behaviour.

ACKNOWLEDGEMENTS

This work is part of the transnational access project "ERIES – CLIMATHUNDERR", supported by the Engineering Research Infrastructures for European Synergies (ERIES) project (www.eries.eu), which has received funding from the European Union's Horizon Europe Framework Programme under Grant Agreement No. 101058684. This is ERIES publication number C30. F. Canepa acknowledges the support of the RETURN Extended Partnership and received funding from the European Union Next-Generation EU (National Recovery and Resilience Plan—NRRP, Mission 4, Component 2, Investment 1.3—D.D. 1243 2/8/2022, PE0000005).

REFERENCES

Canepa, F., Burlando, M., Romanic, D., Solari, G., Hangan, H., 2022. Downburst-like experimental impinging jet measurements at the WindEEE Dome. Sci Data 9, 243. https://doi.org/10.1038/s41597-022-01342-1

Lundgren, T.S., Yao, J., Mansour, N.N., 1992. Microburst modelling and scaling. J. Fluid Mech. 239, 461. https://doi.org/10.1017/S002211209200449X

Moonen, P., Blocken, B., Roels, S., Carmeliet, J., 2006. Numerical modeling of the flow conditions in a closed-circuit low-speed wind tunnel. Journal of Wind Engineering and Industrial Aerodynamics 94, 699–723. https://doi.org/10.1016/j.jweia.2006.02.001

Challenges in simulating the wind field for full bridge buffeting response to non-synoptic winds

Maria Antonietta Pace[1], Filippo Calamelli[1], Tommaso Argentini[1]

[1]*Politecnico di Milano, Dept. of Mechanical Engineering, Milan, Italy,*
mariaantonietta.pace@polimi

SUMMARY:
Standard atmospheric wind simulations typically assume stationary processes with constant statistical properties over time. However, this assumption does not hold for extreme wind events, which exhibit significant low-frequency fluctuations in wind speed and angle of attack. Such characteristics can notably affect the buffeting response of bridges. This study introduces a methodology for creating a synthetic non-synoptic wind scenario based on full-scale monitoring data. The process begins with an analysis of the time-varying wind parameters, which are then used to simulate the event. Results indicate that conventional techniques for stationary events are not always applicable to extreme weather phenomena. Evaluating the spatial distribution of wind characteristics along the bridge deck, particularly in areas without anemometers, poses additional challenges. This generation methodology and a simulation of the aeroelastic response of a bridge case study will be presented at the conference, followed by a comparison of results with full-scale measurements.

Keywords: wind generation, non-synoptic winds, long-span bridges, spatial coherence.

1. INTRODUCTION

In the case of extreme events such as thunderstorms and downbursts, the assumption of stationary process with constant statistical properties is no longer valid. Indeed, these non-stationary phenomena, whose frequency has increased in recent years, are characterized by sudden and intense variations in wind speed and angle of attack. These characteristics can have a significant impact on the aeroelastic response of long span bridges (Calamelli et al., 2024) and therefore it is crucial to develop a numerical procedure capable of reliably generating non-synoptic wind events. This research proposes a methodology to numerically simulate a non-synoptic wind scenario, focusing on the possibility and limitations of performing this task starting from full scale monitored data. The ultimate goal of this work is to enhance the analysis of the aeroelastic response of long span bridges under non-synoptic events.

2. CHALLENGES IN NON-SYNOPTIC WIND FIELD SIMULATION

A primary challenge in the simulation of non-stationary events is the definition of the time-varying wind characteristics. This can be achieved using experimental data from monitoring campaigns carried out on numerous bridges around the world, which provide wind time histories recorded at a few locations along the deck. Instead of determining stationary parameters, as it is commonly done to generate standard synoptic winds, a time-varying evaluation is performed at each measurement point.

Another crucial aspect is the spatial definition of the wind characteristics along the bridge deck (i.e. wind speed longitudinal $U(t)$ and vertical $W(t)$ components, time-varying along-wind $I_u(t)$ and vertical $I_w(t)$ turbulence intensities, integral length scales ${}^{x}L_u(t)$ and turbulence spatial coherence $\gamma(t)$). Indeed, to generate a wind scenario suitable for simulating the dynamic response of the bridge, it is necessary to apply the wind input along the deck at regular intervals (approximately equal to the width of the bridge deck). Nevertheless, full-scale recordings are only available at a few positions along the deck. This requires careful consideration of the wind properties across the deck during extreme events.

3. SIMULATION PROCEDURE

Figure 1 illustrates the flowchart of the numerical simulation, where the initial phase focuses on the analysis of the experimental wind characteristics, which are used as input to numerically generate a non-synoptic wind field (e.g. using the method proposed by Li et al., 2023). Subsequently, the generated non-synoptic wind, along with the bridge aerodynamic properties, will be used to compute the aerodynamic forces which will be applied to a numerical model of the structure to simulate its aeroelastic response (phase 2 in the flowchart). For the specific case study of the Hardanger Bridge, the aerodynamic characteristics of the deck section will be determined through sectional model tests in the Polimi wind tunnel. To consider the nonlinearities of the aerodynamic forces induced by non-synoptic winds, the simulation will be performed using a rheological model able to capture these effects (Calamelli et al., 2024). Finally, the numerical results, in terms of deck displacements and accelerations, will then be compared with full-scale measurements carried out on the bridge (phase 3 in Figure 1).

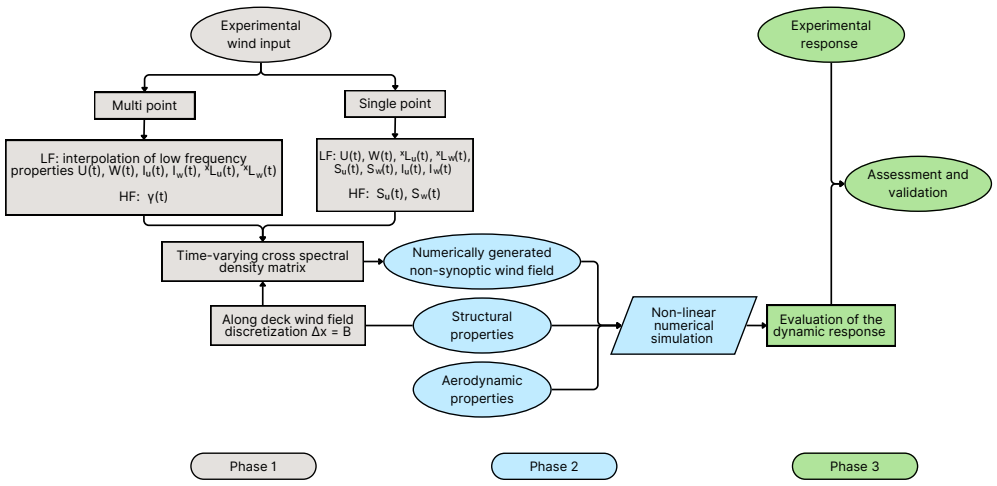


Figure 1. Flowchart of the methodology

4. PRELIMINARY RESULTS FOR NON-SYNOPTIC WIND ANALYSIS

As a first example, time-histories recorded in 2016 on the Hardanger Bridge during the storm "Tor" are selected (Fenerci and Øiseth, 2018). The analysis is performed by dividing the measured wind into a low-frequency (LF) and a high-frequency (HF) part. This division is made because the two parts of the signal are characterized by significantly different spatial and temporal properties.

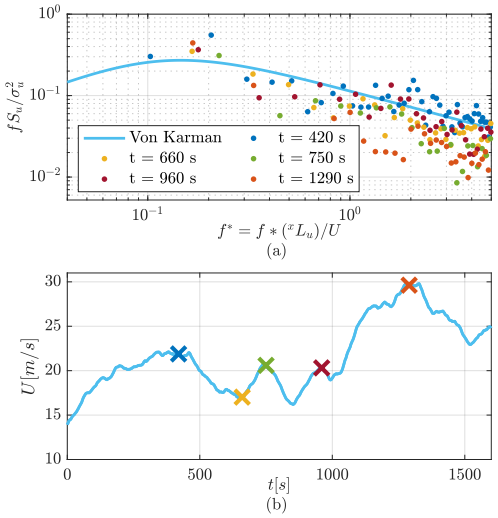


Figure 2. Experimental non-dimensional power spectral densities, for the anemometer A3 (Figure (a)), at different time instants (Figure (b)). The power spectral densities are fitted with non-dimensional Von Karman spectrum

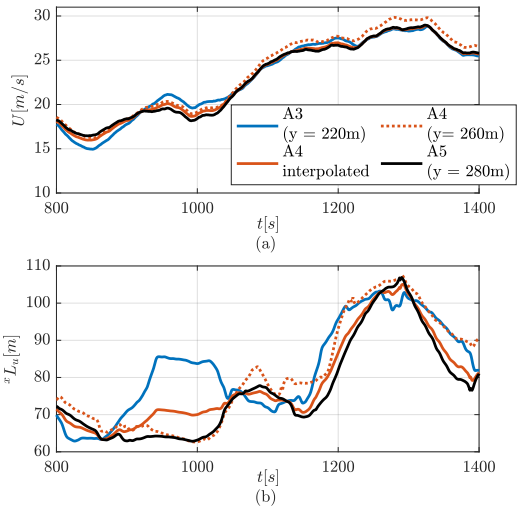


Figure 3. Figure (a): time varying wind velocity. y represent the position of the anemometer along the deck with respect to the anemometer A1 (refer to (Fenerci and Øiseth, 2018)). Figure (b): time varying integral length scale

4.1. Single-Point Analysis

Individual analysis of anemometers enables the determination of LF wind velocity evolution through low-pass filtering of recorded signals. LF wind properties are assessed using $100s$ moving windows, calculating mean values for longitudinal and vertical velocities within each window. The HF portion, representing non-synoptic event turbulence, is obtained by subtracting the LF part from the original signal. Turbulence intensities are then computed as the ratio of the standard deviation of HF components to corresponding LF means.

Integral length scales within each window are evaluated by fitting experimental power spectral densities to the Von Karman spectrum (Hu et al., 2013). Figure 2 shows five normalized experimental power spectral densities at different time instants, fitted against the Von Karman spectrum. The spectrum aligns better with points at $t = 420s$ and $t = 960s$, while discrepancies are more pronounced at other times. This variation underscores how wind turbulence spectral content can change over time during non-synoptic events.

4.2. Multi-Point Analysis

Simultaneous analysis of signals from multiple anemometers enables the assessment of wind characteristics at deck locations lacking direct measurements. Figure 3 illustrates the LF variation of the along-wind velocity and integral length scale for three anemometers on the Hardanger Bridge (A3, A4, and A5, as in (Fenerci and Øiseth, 2018)). Additionally, it shows the time histories at A4, positioned centrally, obtained by linear interpolation of A3 and A5 signals. This comparison evaluates how closely the linear interpolation approximates experimental values. For velocity, the interpolation offers an acceptable match to the measured scenario, but for integral length scales, discrepancies are more pronounced.

The HF wind spatial coherence over time can be assessed using two fixed, closely spaced anemome-

ters. For the considered time window, coherence functions γ_{uu} and γ_{ww}, related to the along-wind and vertical turbulence components, can be fitted using (Hansen and Krenk, 1999)'s formulation. Figure 4 exemplifies the evolution of the fitting constant C_{uy} for anemometers A4 and A5 ($\Delta y = 20m$). An oscillation around a mean value is noted, with increased C values corresponding to rapid changes in velocity.

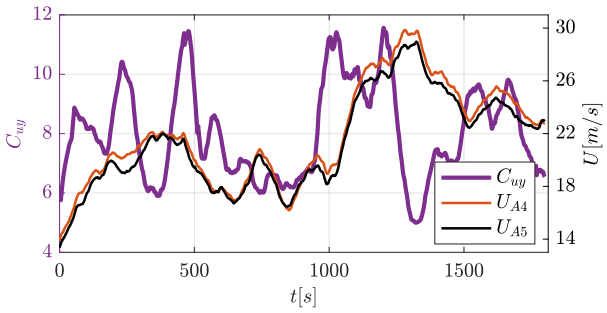


Figure 4. Time varying constant C_{uy} used in the exponential fitting of the coherence

5. CONCLUSIONS

This paper outlines a methodology to create a non-synoptic wind scenario based on full-scale measurements. Initially, extreme event characteristics, both low and high frequency, are analyzed using data from individual and multiple anemometers to assess spatial coherence. These findings feed the numerical generation of the non-synoptic wind field. The methodology and comparison of the numerically simulated response with actual measurements will be detailed at the conference. The study notes discrepancies between the Von Karman spectrum and experimental data during peak wind periods, and highlights issues with linear interpolation for estimating LF wind properties, especially for integral length scales. The fitting constant for turbulence coherence remains largely stable. The approach will be extended to other extreme events to identify common traits of non-synoptic wind behavior.

REFERENCES

Calamelli, F., Rossi, R., Argentini, T., Rocchi, D., and Diana, G., 2024. A nonlinear approach for the simulation of the buffeting response of long span bridges under non-synoptic storm winds. Journal of Wind Engineering and Industrial Aerodynamics 247, 105681.

Fenerci, A. and Øiseth, O., 2018. Strong wind characteristics and dynamic response of a long-span suspension bridge during a storm. Journal of Wind Engineering and Industrial Aerodynamics 172, 116–138.

Hansen, S. and Krenk, S., 1999. Dynamic along-wind response of simple structures. Journal of Wind Engineering and Industrial Aerodynamics 82, 147–171.

Hu, L., Xu, Y., and Huang, W., Dec. 2013. Typhoon-induced non-stationary buffeting response of long-span bridges in complex terrain. Engineering Structures 57.

Li, C., Chen, L., and Cao, L., 2023. High-efficiency simulation of nonstationary wind velocity using diagonal POD of decomposed time-frequency interpolation node spectrum matrices. Journal of Wind Engineering and Industrial Aerodynamics 233, 105314.

Identification of non-synoptic wind events from historical meteorological data

Adriana-Silviana Chitez [1], Ileana Calotescu [2]

[1]*Cardiff University, Cardiff, United Kingdom, chiteza@cardiff.ac.uk*
[2]*Technical University of Civil Engineering of Bucharest, Romania, ileana.calotescu@utcb.ro*

SUMMARY:
Climate change has the potential of increasing the recurrence of extreme wind events worldwide. The increasing severity and frequency of thunderstorms is becoming an important factor when it comes to estimate the total economic losses associated with extreme weather and building design codes should be further improved to fully take them into account for realistic load assessment. A straight-forwards separation algorithm was developed to classify wind data collected in Romania from 2013 to 2022 into two classes of records: (1) thunderstorm and (2) non-thunderstorm records. Maps that compare the distribution of these identified types of records with the current wind zonation map provided by the Romanian wind code (CR1-1-4, 2012) were created. The current algorithm determined that 267 out of 300 investigated 3-s gust speed records were meeting the thunderstorm event criteria.

Keywords: thunderstorm, wind speed mapping, wind loading code

1. INTRODUCTION

Codes of practice in the field of wind engineering play an important role in preventing the partial or total collapse of build environment. The methodologies that they provide focus on wind load assessment based on wind pressures and pressure coefficients such that the structural behaviour of wind-sensitive built environment can be realistically predicted, and casualties be avoided. Wind speed measurements are a paramount parameter to determine the external pressures applied on structures and usually are found in the form of wind speed maps developed using historical meteorological data. However, these maps have limitations since they are not able to differentiate between synoptic and non-synopic winds, which are caused by different physical phenomena. Therefore, from the numerical point of view, the synoptic and non-synopic winds are described by different statistical models.

In the last 30 years researchers manifested their interest to separate thunderstorm (T) from non-thunderstorm (NT) winds. The classification has been made by collecting and analysing high-frequency anemometric records, surface meteorological parameters, radar and satellite imagery and lightning observations (Twisdale and Vickery, 1992; Zhang et al., 2019). The automated classification approaches employed are complex methodologies that vary from statistics to pattern recognition and/or neural network by means of which visual frameworks are identified for the variation of thunderstorm gust velocities or other meteorological parameters such as temperature, atmospheric pressure, precipitations (Vallis et al., 2019; Chen and Lombardo, 2020; Cook, 2023).

In the endeavour to determine the regions of Romania impacted by downburst thunderstorm winds, a wind damage catalogue containing 228 reported events covering the timeframe 2013-2022 was published (Calotescu and Chitez, 2022). The purpose of this research was firstly to map the occurrence of strong wind episodes for future generation wind loading codes and secondly to assess their intensity in terms of destroying effects for inhabited and non-habited areas. To build the map, a separation between the T and NT historical wind data was performed using a statistical analysis-based methodology of the 3-s gust speed records measured by the Romanian National Meteorological Administration (Meteo Romania) in the day of the event (Calotescu et al., 2024). The selection of the analysed events was done post-factum, by mass-media crowdsourcing that targeted reported wind-induced damage.

2. METHODOLOGY

An extensive search in local and national online papers was performed through Google engine and both wind and hail-induced events found during the yearly thunderstorm season were collected. For the identified wind-related events the following information was catalogued: occurrence date, narrative, number of injuries and deaths, cause of damage (wind or hail) and type (structural and/or non-structural), wind velocities (10-min mean wind speed and 3-s gust speed), wind direction. The latter two wind-related parameters were obtained from the measurements taken at the nearby meteorological stations located within 100 km of the reported damage locations. The threshold wind speed value to consider an event as being caused by a possible thunderstorm was set to a minimum value of 15 m/s for the maximum 3-s gust speed. Thus, the database contained 300 daily wind velocity records to be investigated via the proposed separation methodology. The most affected region of the country in terms of number of events between 2013 1nd 2022 was the western region, with Timis County being the lead as it is illustrated in Fig. 1.

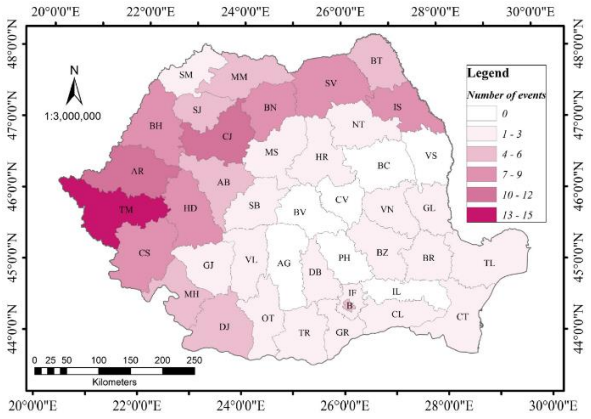


Figure 1. Distribution of extreme wind events in Romania (2013–2022).

The extreme wind events were classified in two generic families of records: thunderstorm and non-thunderstorm, taking into account a set of characteristics of hourly anemometric records. T-records exhibit a sudden increase in gust speeds (usually within an hour) followed by a decrease to approximately the pre peak gust vales. For NT-records the characteristic is a steadily increasing gust speed (for several hours) that gradually decreases in time.

In order to separate the extreme wind records, the variation pattern of the autocorrelation coefficient r_j given in Eq (1) was constructed and analyzed (Brett and Tuller, 1991):

$$r_j = \frac{K_j}{\sigma_V^2} \quad (1)$$

where j represents the lag, K_j is the autocovariance at lag j and σ_V^2 is the variance of the time series that consists of n observations of the 3-s gust speed records. A record was classified as a T-record if the difference between the zero-lag autocorrelation coefficient and the subsequent one was larger or equal to 0.1. Otherwise, a second condition was imposed, i.e. that the difference between the maximum gust speed and the preceding value be larger or equal to 5 m/s. Records not satisfying these conditions were classified as NT-records. Out of the available 300 records, there were 18 daily gust speed variations that did not fit any classification criteria. In this case a visual interpretation of the daily gust speed profile and expert judgement were used to categorize them. The validation of the separation algorithm was done analyzing the lightning activity recorded by Blitzortung.org network on the day of the event.

3. RESULTS

The above-described classification was used to compile the maps in Fig. 2 in which the distribution of thunderstorm and non-thunderstorm type records is overlapped with the zonation of Romania in terms of reference wind velocity pressure.

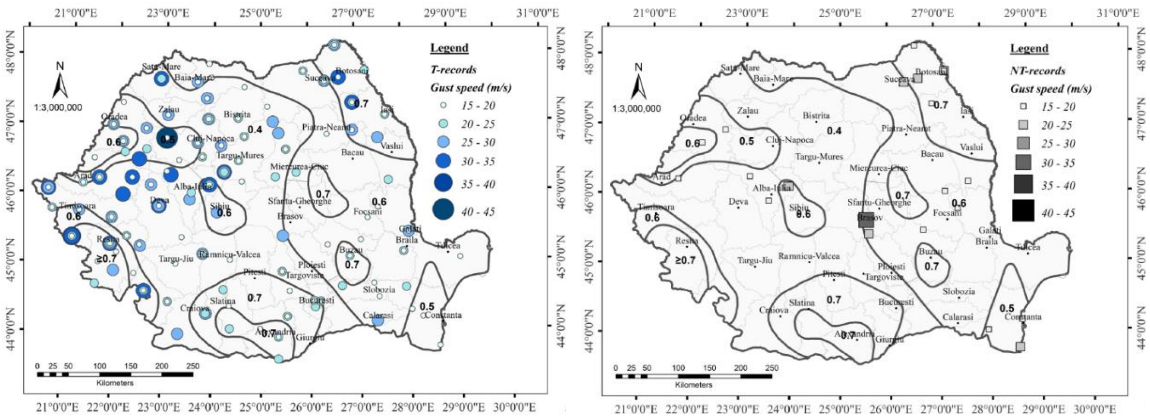


Figure 2. Maximum gust speeds of T-records (left) and NT-records (right); isolines correspond to the zonation of the reference gust velocity pressure in kPa, according to the Romanian wind code (CR1-1-4, 2012).

The maximum gust speed of all T-records was 40.9 m/s measured at Huedin meteorological station. According to the Romanian wind code (CR1-1-4, 2012), the reference wind velocity pressure corresponding to the 50 years Mean Return Interval (MRI) for this location is 0.5 kPa (reference wind velocity v_b = 28.28 m/s). Considering terrain category II (open terrain - areas with grass and/or isolated obstacles located at distances of at least 20 times the height of the obstacle) where met stations are typically located, the peak wind velocity evaluated based on the code yields v_p = 48.21 m/s which means that the gust speed represents approximately 84% of the code-recommended value. A similar approach was employed for the maximum gust speed of the NT-records (30.7 m/s measured at Brasov meteorological station) and it resulted that the gust speed measured represents approximately 58% of the code-recommended value. Fig. 3 illustrates the histograms between the ratios of maximum 3-s gust speeds (V_{max}) and the peak wind velocities

(v_p) for both T- and NT-records. The distributions show that there is a higher probability for the maximum annual gust speeds to correspond to thunderstorms rather than synoptic winds.

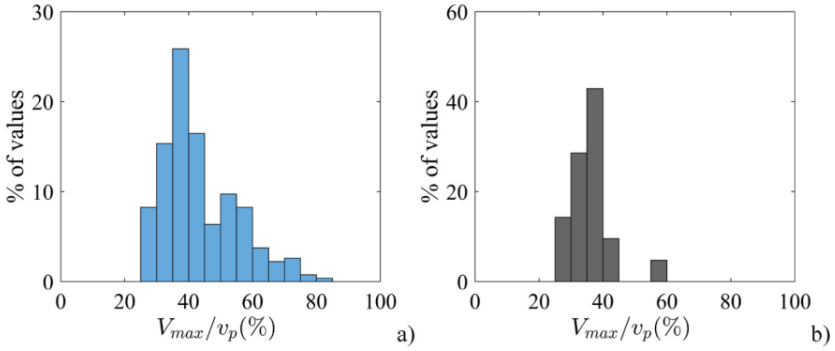


Figure 3. Histograms of V_{max}/v_p ratios for (a) T-records and (b) NT-records.

4. CONCLUSIONS:

A number of 155 wind-related damage events occurred in Romania between 2013 and 2022, especially in Banat (South-West) region. From the corresponding 3-s gust speed data a number of 267 records were classified as T-records, 21 were classified as NT-records and 12 records remained unclassified due to missing data. In approximately 10% of identified cases, the maximum gust speeds of T-records represented 60% to 84% of the code recommended values, while for NT-records this speed did not exceed 60% of the code prescribed magnitude.

ACKNOWLEDGEMENTS

The research presented herein was carried out under the "HAZCON" research grant, code UTCB-CDI-2022-014 financed according to the provisions of the Order of the Ministry of Education no. 3, 126/ 11.02.2022, published in the Official Gazette of Romania no. 179/23.02.2022. The authors also like to acknowledge the Romanian National Meteorological Administration (Meteo Romania) for providing the wind data used in this study.

REFERENCES

Brett, A.C., Tuller, S.E., 1991. The autocorrelation of hourly wind speed observations. Journal of Applied Meteorology and Climatology 30, 823–833.

Calotescu I. and Chitez A. S., 2022. Wind Damage Catalogue of Romania 2013-2022, Conspress, Bucuresti, Romania.

Calotescu I., Chitez A. S., Birsan M.-V., Micu D. and Dumitrescu A., 2024. Assessment of thunderstorm-prone areas in Romania based on wind damage occurrence and surface observation data. Journal of Wind Engineering 250, 105765, 1-18

Chen, G., Lombardo, F.T., 2020. An automated classification method of thunderstorm and non-thunderstorm wind data based on a convolutional neural network. Journal of Wind Engineering and Industrial Aerodynamics 207, 104407, 2-13.

Cook, N.J., 2023. Automated classification of gust events in the contiguous USA. Journal of Wind Engineering and Industrial Aerodynamics 234, 105330, 2-26.

CR1-1-4, 2012. Cod de proiectare. Evaluarea Acțiunii Vˆantului Asupra Construcțiilor, Indicativ CR1-1-4/2012, Monitorul Oficial Al Romˆaniei Nr 704bis/15.X.2012. Matrix Rom.

Twisdale L. A. and Vickery P. J., 1992. Research on thunderstorm wind design parameters. Journal of Wind Engineering and Industrial Aerodynamics 41, 545-556.

Vallis M. B., Loredo-Souza A. M., Ferreira V. and Nascimento E. de L., 2019. Classification and identification of synoptic and non-synoptic extreme wind events from surface observations in South America. Journal of Wind Engineering and Industrial Aerodynamics 193, 103963, 1-23.

Zhang S., Yang Q., Solari G., Li B. and Huang G., 2019. Characteristics of thunderstorm outflows in Beijing urban area. Journal of Wind Engineering and Industrial Aerodynamics 195, 104011, 1-18.

Combined use of mast and lidar measurements for improved mapping of the wind climate in complex topography

Hálfdán Ágústsson[1], Martin S. Grønsleth[1], Ola K. Eriksen[1]

[1]*Kjeller Vindteknikk, Norconsult Norge AS, Lillestrøm, Norway,*

SUMMARY: (10 pt)
Tall meteorological masts are still the de-facto choice of wind measurement platform for many crossing campaigns. However, the limitations they pose are particularly large in complex terrain and for long crossings. In complex terrain the measurements may not represent adequately the atmospheric flow a short distance from the masts; i.e. they may be sampling a very local flow which is decoupled from the atmospheric flow at nearby locations. Scanning and profiling wind lidars can be used to overcome parts of the limitations associated with masts, allowing for continuous or discrete measurements of the wind in a larger area or at distant locations where masts cannot be placed, i.e., further aloft, over water bodies or steep terrain. The downside with lidars are relatively high costs compared to masts, more complex operations and typically lower data availability. We discuss the combined the use of masts and lidar in a recent measurement campaign in western Norway, pertaining to the planned bridge crossing of the ~3 km wide Sulafjorden. The results show how the wind in complex orography can be mapped away from the masts, aloft and over the sea, giving more detailed and accurate data for use in estimating the relevant design parameters.

Keywords: tall wind masts, wind lidars, complex terrain.

1. INTRODUCTION

On the Norwegian west coast, several large bridges are being planned to replace ferries crossing the fjords. One of the most spectacular projects is the crossing of Sulafjorden, a wide and deep fjord surrounded by high mountains and characterized by very complex wind conditions. The proposed solutions include a suspension bridge in excess of 3 km, with bridge towers reaching approximately 400 m. As a comparison, Norway's longest suspension bridge, "Hardangerbrua", is 1380 m long. In addition, the bridge towers will stand out at a height of approximately 400 metres. The fjord is surrounded by mountains resulting in a complex wind climate.

The design and planning for such a long suspension bridge requires a careful mapping of the wind at the relevant site. The Norwegian Public Road Authority initiated a large and ambitious measurement campaign employing both masts and lidars, corroborated with long timeseries of atmospheric simulations at high spatial resolution.

We will discuss the combined the use of masts and lidar in the measurement campaign, showing how lidar technology can be used to map the wind field in complex orography away from mast locations, aloft and over the sea surface. The campaign and key results presented underline the potential of using lidars to enhance the value of mast data in complex terrain, giving a more

detailed and accurate description of the 3-dimensional structure of the wind climate than can be achieved with mast measurement data only.

2. MEASUREMENT SETUP

Four scanning lidars are used in the campaign as well a two vertical lidars. Two scanning lidars are located at each of the red dots in Figure 1. Together, the 4 scanning lidars work in pairs, forming 2 intersections at any location where wind measurements are required. By combining data from two lidar beams intersecting at exactly the same location, one can calculate the horizontal wind speed and direction at the intersection. The lidars started measuring in the autumn of 2018 and were dismantled in early 2024. The bulk of the time has been devoted to measurements at several locations at the middle of the fjord and at a quarter of the distance across the fjord, away from Kvitneset. This enables high frequency measurements of the horizontal wind speed and direction, enabling an analysis of both the mean wind as well as of the the turbulence conditions, including turbulent spectra.

Four masts were installed and operated in Sulafjorden, with two masts relevant for the planned suspension bridge, a 100 m tall mast at Kvitneset and a 75 m tall mast at Trælbodneset (Fig. 1). Measurements of the 3-dimensional wind were done with at 10 Hz temporal resolution at at 3-4 levels in each mast. Measurements start in late 2016 and were ended in April 2024. Mast data are described in Furevik et al. 2020 and available online.

A vertical lidar was placed at the top of a 100 m tall mast at Kvitneset. This extends the measurements to approximately 400 metres asl. Another vertical lidar (installed and operated by Fugro Oceanor AS) was installed on a buoy and located below one of the scanning lidar intersections. This adds a vertical velocity component to the measurements, as well as measurements at other vertical levels. The buoy was located at two different locations below the bridge deck during the campaign.

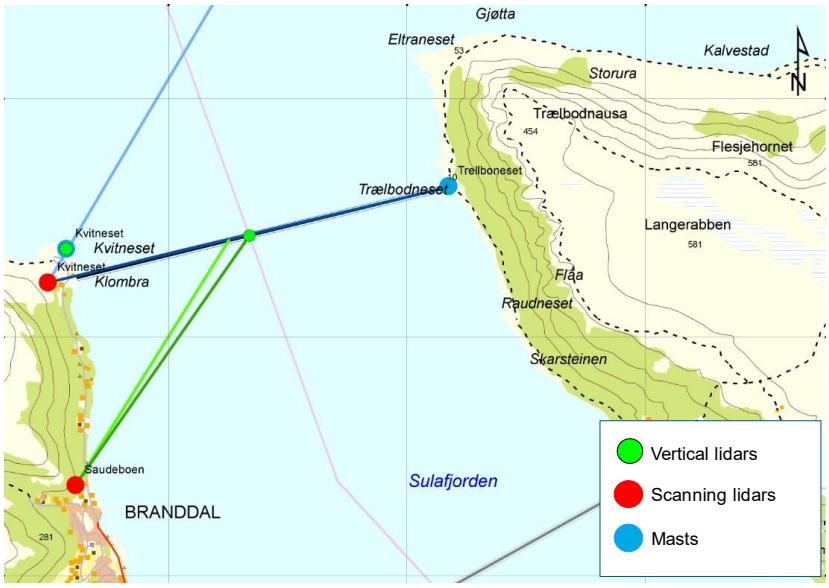


Figure 1. Locations of measurement platforms

The operation of the lidars was continuously monitored to ensure the quality of the measured data. This includes regularly verifying that the lidar beams are pointing exactly in the intended direction. This is done by pointing each lidar directly towards a fixed target, ideally a narrow and tall mast, which should always be found at the same azimuth and elevation of the lidar beam. In addition, the lidar measurements were validated against anemometer data at the Trælbodneset mast, with results for mean wind shown in Figure 2.

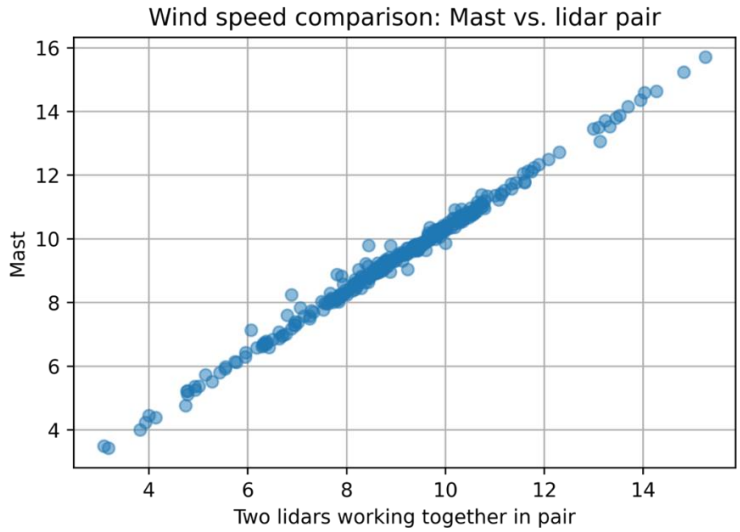


Figure 2. Example of the comparison of measurements of 10-minute mean wind in a mast and derived from scanning lidar observations.

3. SOME EXAMPLES OF RESULTS

Time series of measurements during storm situations reveal a complex structure, with large variations in wind strength at each of the masts and at the centre of the fjord. The location and strength of the wind maxima varies with the large-scale wind direction and small changes in direction may lead to differences of up to 10 m/s between the measurement platforms, as revealed in Figure 3.

A vertically measuring lidar was placed at the top of the 100 m tall Kvitneset mast, allowing for measuring the mean wind profile up to the top of the planned bridge towers at 400 m. With mast data only, the vertical wind profile would be estimated by the windshear from the ultrasonic measurements but the lidar reveals that the profile above the mast can be completely different from the expected. Effects from the complex terrain results in complex wind profile as shown in Figure 4, where the three lowest points, A, B and C are ultrasonic sensors in the met mast, while the rest of the points are measured by lidar.

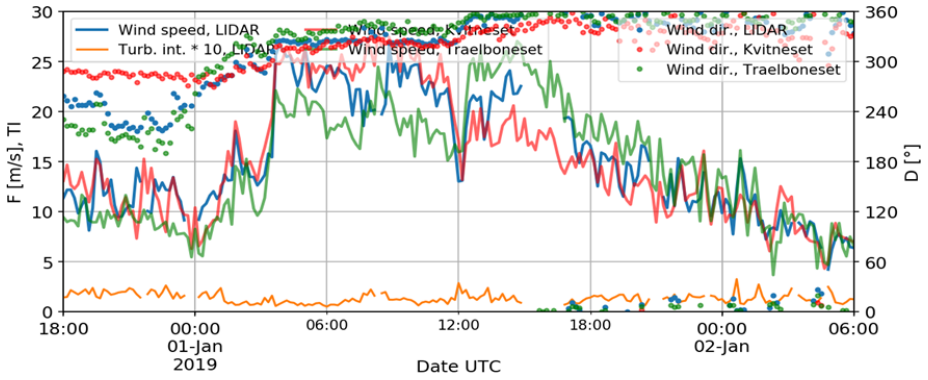


Figure 3. Observed 10-minute mean wind speed and direction, as well as turbulence intensity (scaled by 10), at the lidar point at height of the bridge deck at the fjord centre, as well as at the top sensors in the masts, during the storm of 1 January 2019.

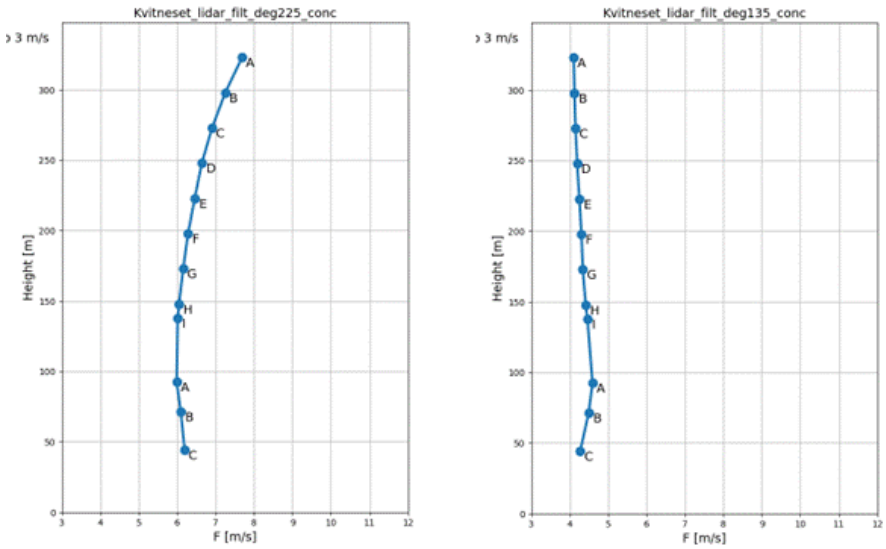


Figure 4. The mean vertical wind profile at Kvitneset for tow different wind directions. The three lowest points are measured by ultrasonic sensors in a met mast, and the rest of the points are measured by a lidar.

ACKNOWLEDGEMENTS

We acknowledge the contribution of Jørn Arve Hasselø at NPRA, who lead the fjord crossing project, together with Magne Gausen. The measurement campaign was financed by the Norwegian Public Roads Administration as part of the Coastal Highway E39 project in mid-Norway

REFERENCES

Furevik, B. R., Ágústsson, H., Borg, A. L., Midjiyawa, Z., Nyhammer, F., and Gausen, M.: Meteorological observations in tall masts for the mapping of atmospheric flow in Norwegian fjords, Earth Syst. Sci. Data, 12, 3621–3640, https://doi.org/10.5194/essd-12-3621-2020, 2020.

Dynamic response of the Hålogaland Bridge subject to non-stationary wind

Sebastian K. Hansen[1], Aksel Fenerci[2], Øyvind W. Petersen[1], Ole Øiseth[1]

[1]*NTNU, Trondheim, Norway, sebastian.k.hansen@ntnu.no*
[1,2]*Multiconsult, Oslo, Norway, aksel.fenerci@multiconsult.no*
[1] *oyvind.w.petersen@ntnu.no*
[1] *ole.oiseth@ntnu.no*

SUMMARY:
This study examines field measurements from a storm at the Hålogaland Bridge, using anemometer and accelerometer data to analyse the dynamic behaviour of the bridge under non-stationary wind. Peak gusts of 39.2 m/s led to significant lateral, vertical, and torsional responses. Findings reveal the bridge's sensitivity to such wind conditions and highlight the value of monitoring systems to improve structural resilience in extreme weather.

Keywords: Suspension bridge, Field measurements, Non-stationary

1. INTRODUCTION

As bridges become longer and longer they become more susceptible to wind which becomes the governing load. The wind velocity field is a stochastic process that usually is assumed to be stationary over a 10-minute period. However, that is not always the case, e.g. storms or thunderstorm downburst can exhibit strong non-stationary winds. Non-stationary wind can give rise to extreme response of suspension bridges as observed in recent years in the UK and Norway (Fenerci and Øiseth, 2018; Owen et al., 2020; Petersen, Øiseth, et al., 2020). This contribution presents field measurements, including anemometer and accelerometer data, from a suspension bridge during a storm that took place at the end of January 2024, aiming to get a better understanding of the wind-bridge dynamics of suspension bridges during non-stationary wind.

2. MONITORING SYSTEM AT THE HÅLOGALAND BRIDGE

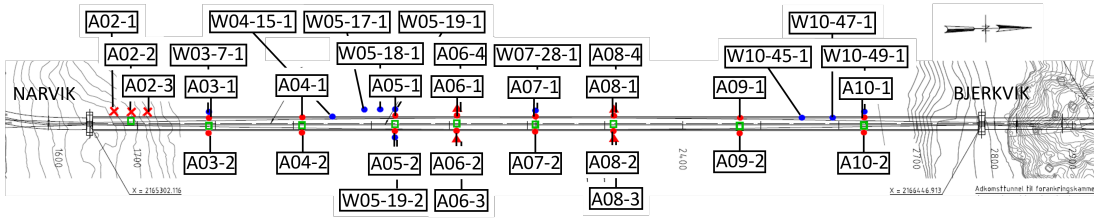


Figure 1. Sensor layout of accelerometers and anemometers at the Hålogaland Bridge.

The Hålogaland Bridge, with a main span of 1145 m, is the second longest suspension bridge in Norway and is located in Narvik. The bridge is equipped with temperature sensors, strain gauges,

3-axis piezoelectric (Dytran 3143D1) and 3-axis force balance (Geosig AC-73) accelerometers and 3-axis anemometers (Gill WindMaster Pro). Fig. 1 show the layout of accelerometers (A) and anemometers (W) along the main span of the Hålogaland Bridge, the force balance accelerometers are placed inside the girder and labelled as red dots. The anemometers are placed 8 m above the road. For more information regarding the monitoring system, see Petersen, Frøseth, et al. (2021).

3. STORM INGUNN

Ingunn was the name given to a storm that hit Norway at the end January 2024. It was a particularly large and strong storm, setting a new Norwegian record for highest observed 10-minute mean wind speed with 54.4 m/s, which corresponds to Category 3 on the Saffir-Simpson scale (Fagerlid et al., 2024). Storm Ingunn hit the Hålogaland Bridge around 01:00 29th January 2024 and lasted until the morning of the 31st January, Fig. 2 shows the wind measurements at the midspan. The figure shows the 3 s gust speed as well as the along-wind 10-minute moving mean wind speed. The highest gusts are in the first 24 hours of the storm. There are two prominent peaks, the first around 10:00 29th January and the second around 18:00 29th January. Both the gust and mean wind speed exhibit strong non-stationarity throughout the storm. The first peak gust speed was measured at 39.2 m/s and the 10-minute moving average at 32.2 m/s.

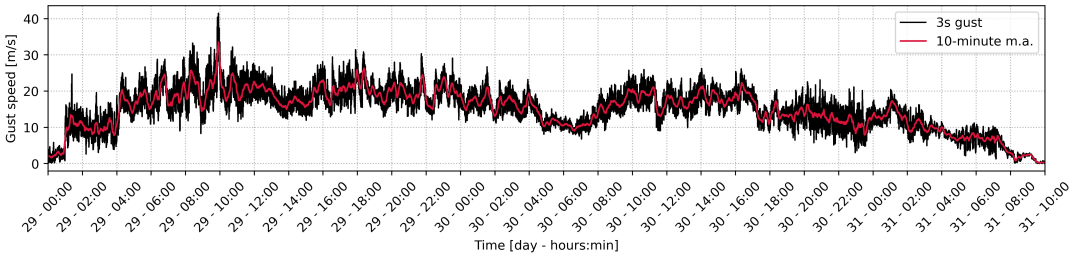


Figure 2. Gust wind speed with 10-minute moving mean speed (sensor W05-19-2).

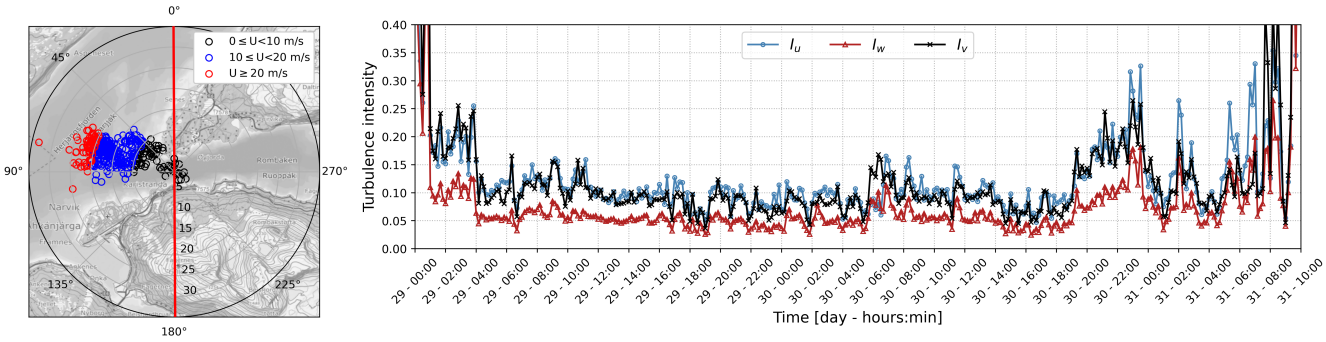


Figure 3. Left: Wind rose plot of 10-minute mean wind speed at sensor W05-19-2 (base map courtesy of ©Kartverket). Right: Turbulence intensity.

The left side of Fig. 3 show the wind rose plot of the 10-minute mean wind speed. It is seen that the wind direction throughout Storm Ingunn is consistently coming from the northwest-west. The right side of Fig. 3 show the along-wind (I_u), cross-wind (I_v) and vertical (I_w) turbulence intensities. The turbulence intensities are here the ratio of standard deviation of the turbulence components and

the mean wind speed over 10-minute intervals. In the first 24 hours of the storm I_u varies between 4 and 15 %, I_v varies between 3 and 16 % and I_w varies between 2.5 and 10 %, except for in the beginning of the storm where the turbulence intensities are higher where the wind embody sudden increases and decreases in velocity.

4. DYNAMIC RESPONSE

The horizontal (a_y), vertical (a_z) and torsional (a_θ) acceleration responses from A10 for the first half of the storm duration are shown in Fig. 4. The accelerometers are placed in pairs on either side of the girder to capture the torsional response. The horizontal and vertical acceleration are here the average of the pair. The acceleration signals are filtered with a low-pass filter with 1 Hz cut-off frequency as well as a linear de-trending for every 10-minute interval. A few prominent peaks are visible in the response time series around 29th 06:30, 08:30, 09:50 and 21:40. Looking at the wind speeds from Fig. 2 we see that the peak dynamic response corresponds with the times where there is a sudden increase and then decrease in the mean wind velocity.

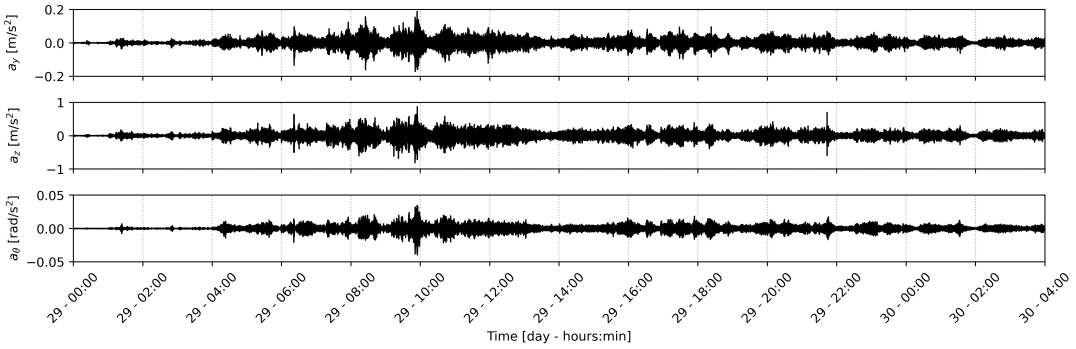


Figure 4. Accelerations measured from A10.

Fig. 5 show the 10-minute root mean square (RMS) of the lateral, vertical and torsional acceleration from all the available accelerometer pairs at the time of the recording, plotted against the 10-minute mean wind velocity (from anemometer W05-19-2). In the figure there is an outlier at the highest mean wind velocity that coincide with the peak accelerations in Fig. 4 and peak mean wind and gust speed in Fig. 2. Accelerometer pair A03 and A10 are placed an equal distance from the midspan of the bridge and the difference in their respective RMS values are relatively low.

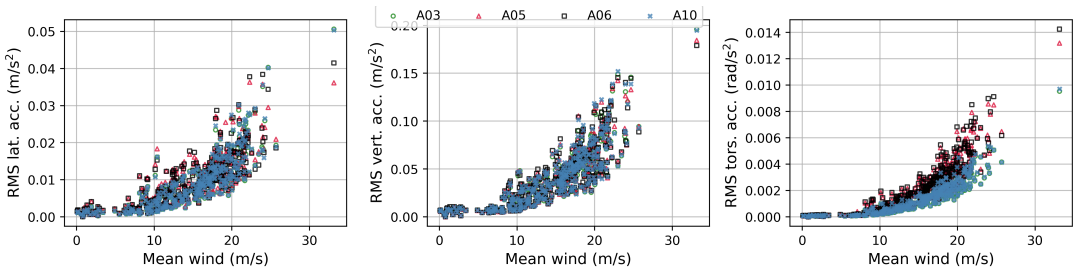


Figure 5. 10-minute RMS accelerations vs. mean wind speed (W05-19-2) comparison.

The horizontal (d_y), vertical (d_z) and torsional (d_θ) dynamic displacements are shown in Fig. 6.

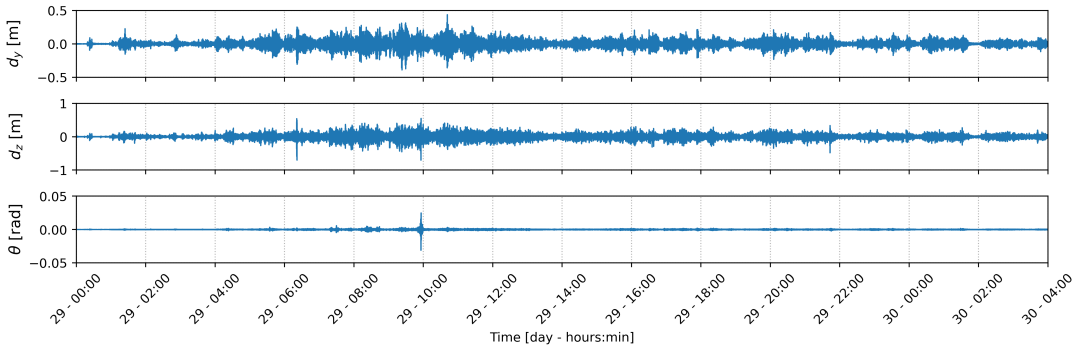


Figure 6. Integrated accelerations from accelerometer pair A10.

The dynamic displacements are obtained from double numerical integration of the accelerations from A10. From the dynamic displacements we see peak responses that coincides with the peak accelerations in Fig. 4. In addition, there is a peak horizontal displacement, around 29th 10:40, that was not as prominent in the acceleration response, but the same increase then decrease in the mean wind velocity can be seen at the time in Fig. 2.

5. CONCLUSIONS

This study highlights the vulnerability of long-span suspension bridges to strong and non-stationary winds, such as those recorded during Storm Ingunn at the Hålogaland Bridge. The largest recorded dynamic response occurred during a non-stationary increase in wind velocity. This implies that the response will be underestimated using stationary wind load models. Monitoring data is essential for understanding the importance of non-stationary wind events in bridge design.

ACKNOWLEDGEMENTS

This study is funded by the Norwegian Public Roads Administrations and the Norwegian University of Science and Technology. This funding is greatly appreciated.

REFERENCES

Fagerlid, G. O., Soldal, I. H., Mamen, J., Ristesund, E. W., and Velle, M., 2024. *Ekstremværet "Ingunn"; ekstremt kraftige vindkast i Trøndelag og Nordland 31. januar og 1. februar 2024.* Meteorlogisk institutt.

Fenerci, A. and Øiseth, O., 2018. Strong wind characteristics and dynamic response of a long-span suspension bridge during a storm. Journal of Wind Engineering and Industrial Aerodynamics 172, 116–138.

Owen, J. S., Nguyen, D. T., Meng, X., Psimoulis, P., and Xie, Y., 2020. An observation of non-stationary response to non-synoptic wind on the Forth Road Bridge. Journal of Wind Engineering and Industrial Aerodynamics 206, 104389.

Petersen, Ø. W., Frøseth, G. T., and Øiseth, O., 2021. Design and deployment of a monitoring system on a long-span suspension bridge. Proceedings of the International Conference on Structural Health Monitoring of Intelligent Infrastructure.

Petersen, Ø. W., Øiseth, O., and Lourens, E., 2020. Investigation of dynamic wind loads on a long-span suspension bridge identified from measured acceleration data. Journal of Wind Engineering and Industrial Aerodynamics 196, 104045.

Simulating a Downburst Turbulent Outflow Velocity Field on a Moving Vehicle

Andi Xhelaj [1], Massimiliano Burlando [1], Luisa Pagnini [1], Maria Pia Repetto [1]

[1]*University of Genoa, Genoa, Italy, andi.xhelaj@edu.unige.it - massimiliano.burlando@unige.it- luisa.pagnini@unige.it - maria.pia.repetto@unige.it*

SUMMARY:
Downbursts generate intense, non-stationary winds that pose significant risks to vehicles. Current research often overlooks this problem. This paper presents a method to simulate the wind velocity field experienced by a moving vehicle during a downburst. The approach involves modeling the slowly varying mean wind field, simulating turbulence as a non-stationary process, reconstructing the total wind field, and calculating the relative wind velocity encountered by the vehicle. Results demonstrate the model's effectiveness in simulating wind conditions impacting vehicles, providing essential data for assessing aerodynamic loads on vehicles under extreme downburst winds.

Keywords: downburst simulation, aerodynamic loads on vehicle, turbulent wind field.

1. INTRODUCTION

Downbursts are localized, intense downdrafts that, upon reaching the ground, spread out radially, creating high-velocity wind fields distinct from synoptic winds. These outflows generate intense, non-stationary winds that pose significant risks to road vehicles travelling through areas affected by peak wind intensities (see Fig. 1). Studies have reported a high incidence of vehicular accidents related to intense storm conditions (Baker and Reynolds, 1991). Zhang et al. (2018) demonstrated that sudden changes in wind intensity and direction can generate high-risk scenarios.

Despite these findings, most research on wind-induced vehicular accidents focuses on the stability of vehicles under generic synoptic wind conditions (e.g., Winkler et al., 2016), leaving a gap in understanding vehicle responses to downburst conditions.

This paper addresses this gap by presenting a fast and reliable procedure to simulate the wind velocity field caused by a downburst as experienced by a vehicle travelling through it. Specifically, the model adopts a four-step approach:

1. Mean Wind Field Modelling: The horizontal, slowly varying mean wind velocity field of a travelling downburst at a generic height z above the ground is modelled using established methods (Xhelaj et al., 2020).
2. Downburst Turbulent Field Simulation: The model simulates the downburst turbulence field, defined as a non-stationary, non-Gaussian, bi-variate, three-dimensional, partially coherent random process using the spectral representation method (Shinozuka and Deodatis, 1991). The properties of this process are characterized based on an extensive database of real-world downburst outflows obtained from anemometric and lidar measurements.
3. Reconstruction of the Turbulent Wind Velocity Field: The turbulent outflow wind velocity field is reconstructed by superimposing the turbulence components onto the slowly varying wind velocity field obtained in the previous steps.

4. Relative Wind Velocity Calculation: The time history of the relative wind velocity encountered by the moving vehicle is calculated as a function of the vehicle's motion within the simulation domain.

(a) (b) (c)



Figure 1. Severe wet downburst event on I-29 in southwest Iowa (June 11, 2018), causing the overturning of ten semi-tractor trailers due to extreme winds (35-40 m/s). Documented by Jon Davies: Davies Weather Blog.

2. METHODOLOGY

2.1. Mean wind field modelling

The analytical model developed by Xhelaj et al. (2020) is used to simulate the horizontal mean wind velocity generated by a travelling downburst. The horizontal slowly varying wind velocity at a generic height z above the ground is expressed as the vector summation of three independent components: the radial outflow component $\overline{\boldsymbol{V}}_r$, representing the radial wind velocity resulting from the downdraft impacting the ground and spreading outward; the storm motion component $\overline{\boldsymbol{V}}_s$, accounting for the translation of the downburst cell across the terrain characterized by its speed and direction; and the background Atmospheric Boundary Layer (ABL) component $\overline{\boldsymbol{V}}_{ABL}$, representing the ambient wind conditions present prior to or during the downburst event, considered constant throughout the simulation domain. The total slowly varying wind velocity at any point (X, Y) within the simulation domain at time t is obtained by vectorially adding these components:

$$\overline{\boldsymbol{V}}(X,Y,t) = \overline{\boldsymbol{V}}_r(X,Y,t) + \overline{\boldsymbol{V}}_s(X,Y,t) + \overline{\boldsymbol{V}}_{ABL} \tag{1}$$

2.2. Turbulence Modelling of Downburst Outflows

The turbulent fluctuations of downburst outflows are modelled using the directional decomposition technique (Zhang et al., 2019), where they are decomposed into a local longitudinal component u' and a local lateral component v' relative to the slowly varying wind direction $\bar{\beta}$ of $\overline{\boldsymbol{V}}$ in Eq. (1). The turbulent fluctuations are generated as:

$$\begin{aligned} u'(X,Y,t) &= \sigma_u(X,Y,t) \cdot \tilde{u}'(X,Y,t) = \bar{I}_u \cdot \bar{V}(X,Y,t) \cdot \tilde{u}'(X,Y,t) \\ v'(X,Y,t) &= \sigma_v(X,Y,t) \cdot \tilde{v}'(X,Y,t) = \bar{I}_v \cdot \bar{V}(X,Y,t) \cdot \tilde{v}'(X,Y,t) \end{aligned} \tag{2}$$

Here, σ_u and σ_v are the slowly varying standard deviations of the turbulent fluctuations in the local longitudinal and lateral directions, respectively. They are proportional to the magnitude of the slowly varying wind velocity $\bar{V}$ multiplied by the mean turbulence intensities $\bar{I}_u$ and $\bar{I}_v$, which are assumed constant throughout the simulation domain. The reduced turbulent fluctuations

$\tilde{u}'$ and $\tilde{v}'$ are dimensionless, zero-mean, unit-variance and assumed uncorrelated with each other. Each component is modelled as univariate, three-dimensional, partially coherent Gaussian stochastic wave, with its power spectral density and spatial coherence described by the Solari and Piccardo (2001) turbulence model. The reduced turbulent fluctuations are generated using Monte Carlo simulations via the spectral representation method (Shinozuka and Deodatis, 1991). Since the slowly varying wind direction $\bar{\beta}$ varies in space and time, the local turbulent fluctuations are transformed into the global X, Y coordinate system using:

$$\begin{aligned} V'_X(X,Y,t) &= u'(X,Y,t)\cdot\cos\bar{\beta}(X,Y,t) - v'(X,Y,t)\cdot\sin\bar{\beta}(X,Y,t) \\ V'_Y(X,Y,t) &= u'(X,Y,t)\cdot\sin\bar{\beta}(X,Y,t) + v'(X,Y,t)\cdot\cos\bar{\beta}(X,Y,t) \end{aligned} \tag{3}$$

2.3. Simulation of the Turbulent Wind Velocity Field and Relative Wind Velocity Calculation

The turbulent wind velocity field is reconstructed by superimposing the turbulent fluctuations onto the slowly varying wind velocity field obtained from the previous steps. The total wind velocity components at any point (X, Y) and time t are given by:

$$\begin{aligned} V_X(X,Y,t) &= \bar{V}_X(X,Y,t) + V'_X(X,Y,t) \\ V_Y(X,Y,t) &= \bar{V}_Y(X,Y,t) + V'_Y(X,Y,t) \end{aligned} \tag{4}$$

where $\bar{V}_X$ and $\bar{V}_Y$ are the slowly varying wind components from Eq. (1), while V'_X and V'_Y are the turbulent fluctuations from Eq. (3). The vehicle is assumed to move from an initial position in a straight line with constant speed V_{veh} and constant heading angle θ_{veh}, defined as the angle between the vehicle's direction of motion and the positive X-axis (East). The relative wind velocity components encountered by the vehicle are calculated by subtracting the vehicle's velocity components from the total wind velocity components at the vehicle's instantaneous position:

$$\begin{aligned} V_{rel,X}(t) &= V_X(X_v(t), Y_v(t), t) - V_{veh}\cdot\cos\theta_{veh} \\ V_{rel,Y}(t) &= V_Y(X_v(t), Y_v(t), t) - V_{veh}\cdot\sin\theta_{veh} \end{aligned} \tag{5}$$

Where $X_v(t)$ and $Y_v(t)$ are the vehicle's position at time t. From Eq. (5), the instantaneous magnitude $V_{rel}(t)$ and direction $\theta_{rel}(t)$ of the relative wind velocity experienced by the vehicle can be easily calculated. Note that subtracting the vehicle velocity is a vector operation: when the vehicle moves nearly opposite the wind direction, the velocity can effectively add in magnitude, causing wind speed to exceed the wind speed in the ground frame (i.e., in the absolute frame).

3. RESULTS AND CONCLUSIONS

Figure 2 presents a simulation of a downburst event and its influence on a moving vehicle. The simulation covers a 10,000 × 10,000 m^2 spatial domain with a 25 m grid resolution and runs from 0 to 600 seconds at a 10 Hz sampling frequency. Suitable key downburst parameters, including touchdown location, maximum radial speed, radial length scale, intensity, decay periods, storm motion, and direction, define the slowly varying wind field (Fig. 2a) and Eq. (1). The vehicle moves at a constant speed of 80 km/h (22.2 m/s) and a fixed heading of 55° from North (with North aligned along the Y-axis, following meteorological convention). An additional ABL wind of 5 m/s from 270° is included. Panel (b) displays the total (instantaneous) wind speed and the slowly varying wind speed at the vehicle's instantaneous location. Panel (c) shows the total and slowly varying wind direction at the vehicle position, aligned with meteorological convention. Panels (d) and (e) shows the relative wind speed and direction, respectively, as experienced by the

vehicle, considering both the instantaneous and slowly varying components. The latter information is essential for evaluating the aerodynamic loads and assessing the vehicle's dynamic response under extreme wind conditions. A methodology to identify hazardous crosswind scenarios for moving vehicles under extreme downburst conditions will be presented at the conference. The approach defines safety metrics (e.g., critical crosswind speeds, overturning risks) and systematically samples parameters of the downburst and vehicle motion. Preliminary optimization-based results will be presented.

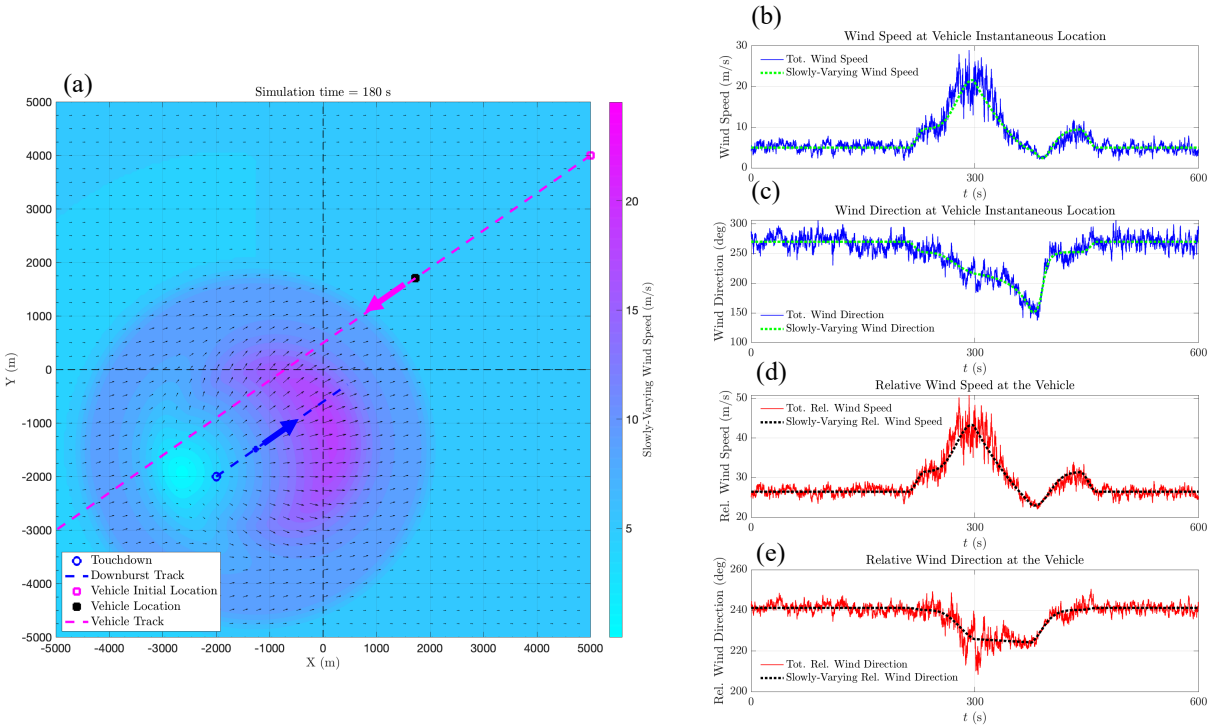


Figure 2. Downburst simulation impact on a moving vehicle: (a) Spatial slowly varying mean wind field with vehicle and downburst path; (b) Instantaneous and slowly varying wind speed at vehicle's instantaneous location; (c) Instantaneous and slowly varying wind direction at vehicle's instantaneous location; (d) Instantaneous and slowly varying relative wind speed experienced by the vehicle; (e) Instantaneous and slowly varying relative wind direction experienced by the vehicle.

ACKNOWLEDGEMENTS

This research was supported the Italian Ministry of University and Research (MUR), through the PRIN 2022 funded project 'CROSSwind stability of road vehicles under thunderSTORMs (CROSS-STORM)' (Grant Number 202284ZER9).

REFERENCES

Baker, C. J., and Reynolds, S., 1992. Wind-induced accidents of road vehicles. Accident Analysis and Prevention 24(6), 559–575.

Zhang, Z., Li, J., and Guo, W., 2018. Combined simulation of heavy truck stability under sudden and discontinuous direction change of crosswind with computational fluid dynamics and multi-body system vehicle dynamics software. Advances in Mechanical Engineering 10(7).

Winkler, N., Drugge, L., Stensson Trigell, A., and Efraimsson, G., 2016. Coupling aerodynamics to vehicle dynamics in transient crosswinds including a driver model. Computers & Fluids 138, 26–34.

Xhelaj, A., Burlando, M., and Solari, G., 2020. A general-purpose analytical model for reconstructing the thunderstorm outflows of travelling downbursts immersed in ABL flows. Journal of Wind Engineering and Industrial Aerodynamics 207, 104373.

Shinozuka, M., and Deodatis, G., 1991. Simulation of stochastic processes by spectral representation. Applied Mechanics Reviews 44(4), 191–204.

Zhang, S., Solari, G., Burlando, M., and Yang, Q., 2019. Directional decomposition and properties of thunderstorm outflows. Journal of Wind Engineering and Industrial Aerodynamics 189, 71–90.

Solari, G., and Piccardo, G., 2001. Probabilistic 3-D turbulence modeling for gust buffeting of structures. Probabilistic Engineering Mechanics 16(1), 73–86.

Climate Change and Structural Damage Sensitivity in Extreme Storm Events: The Case of Storm Anatol.

Johanne Kristine Haandbæk Øelund[1,2,3], Hans Holger Hundborg Koss[3], Jens Hesselbjerg Christensen[1], Rune Magnus Koktvedgaard Zeitzen[2], Henrik Vedel[2]

[1]*University of Copenhagen, Copenhagen, Denmark, johanne.oelund@nbi.ku.dk*
[2]*DMI, Copenhagen, Denmark*
[3]*DTU, Lyngby, Denmark*

SUMMARY:
Extratropical cyclones frequently affect Western Europe, and occasionally these systems intensify into severe windstorms capable of causing widespread damage. Over the past decade, windstorm-related losses in Europe have surpassed EUR 85 billion (European Environment Agency, 2024), underscoring their socio-economic impact. Despite the damage potential of these storms, significant uncertainties remain regarding their sensitivity to anthropogenic climate change — a factor essential for improving wind engineering and mitigation strategies. This study investigates the 1999 European windstorm that impacted Denmark, where recorded wind speeds reached an unprecedented 41.4 m/s with gusts exceeding 51.4 m/s, resulting in extensive structural and infrastructural damage. Using a pseudo-global warming framework, future warming scenarios are assessed on how might influence the intensity of such windstorms. These findings will contribute to understanding climate change impacts on extreme wind events, providing critical insights for designing resilient infrastructure and refining risk mitigation approaches in wind engineering across Europe.

Keywords: Storm, Climate change, Constructional damages

1. INTRODUCTION - THE STORM ANATOL

On December 3rd, 1999, Denmark was impacted by one of the most severe storms in its recorded history. As a low-pressure system rapidly deepened over the North Sea from 995 hPa to 958 hPa in 12 hours , driven by a powerful westerly jet stream, it crossed Denmark in the early evening, producing record-breaking wind speeds and widespread damage (Voldborg, 2000). The rapid pressure drop classified the storm as a potentially destructive phenomenon known as a "meteorological bomb" (Kettle, 2021). The storm generated a 10-minute average wind speed exceeding 41.4 m/s (causing the failure of anemometers), with gusts reaching 51.4 m/s onshore and up to 59.2 m/s offshore. The event led to massive damages in Denmark. The impact even extended to Sweden, where significant forest loss and nuclear reactor shutdowns occurred due to salt deposits (Cappelen et al., 2018; Mühlhausen and Sønderiis, 1999; Nielsen and Sass, 2003). Extreme events like these, though rare, highlight the importance of understanding storm risk within the context of global warming. While extreme precipitation is expected to intensify with warming, climate models do not consistently indicate an increase in extratropical storm intensity. The experimental design in this study follows a similar approach to that of Matte et al., 2022, applying a spatially uniform modification to simulate the effects of a warmer climate.

2. DAMAGES DONE BY ANATOL IN 1999.

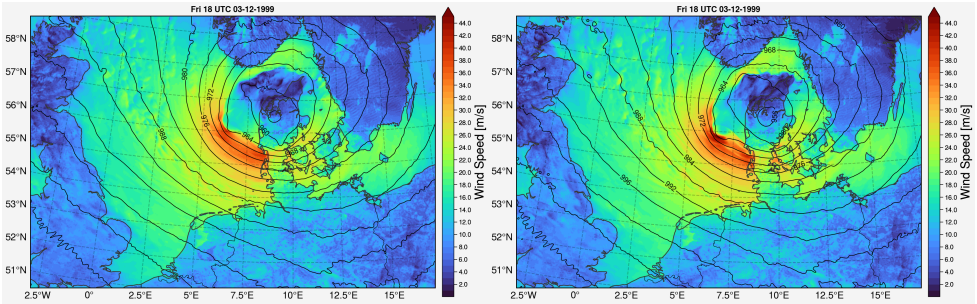
The storm had a profound impact on Danish society, causing widespread destruction valued at over 13 billion DKK (1999 value). Seven lives were lost, and more than 800 individuals required medical assistance from severe injuries. Extensive windthrow in Danish forests led to the loss of approximately 4 million cubic meters of timber. The storm brought transportation to a standstill, with all trains, ferries, and flights canceled, and bridges closed. Nearly 1,000 passengers were rescued from trains stranded in the Storebælt tunnel. Power lines were downed, resulting in over 200 fires, while countless homes, roofs, and other structures suffered damage, leading to significant property destruction, including numerous vehicles. One of the most notable incidents involved the collapse of a massive crane at the Lindø shipyard onto a vessel under construction, resulting in damages estimated at 200 million DKK. In total, more than 400,000 individual damages caused by the storm were reported (Cappelen et al., 2018; Kettle, 2021; Nielsen and Sass, 2003).

3. METHOD

This study explores how the December 1999 storm might have unfolded under modified climate conditions using the HARMONIE forecasting system (Bengtson et al., 2017) with a convection-permitting model (2 km resolution) and a pseudo-global warming approach (PGW, see (Matte et al., 2022)). By comparing the event's intensity in present-day, pre-industrial, and warmer scenarios, the study examines the influence of atmospheric warming on storm severity (Zeitzen et al., 2024). The simulation shows the event's evolution under modified climates, providing insights into how anthropogenic warming may influence the risks of severe storms in Northern Europe.

4. RESULTS

From the HARMONIE weather forcasting model runs were made with the perturbation of -1° C, +1° C, +2° C, +3° C and a control run. The storm hit the coast of Jutland at approximately 18.00. The wind speed and mean sea level pressure (MSLP) for 18.00 is shown in figure 1.



(a) Reference run **(b)** Model $+3°C$ perturbation

Figure 1. The wind speed and MSLP for the control run and $+3°C$ perturbation.

The storm's development is notably similar across the five model runs, and the 3∘ perturbation shows both higher wind and gust speeds throughout the storm's duration (gust plots not shown, but they exhibit a similar trend to mean wind).

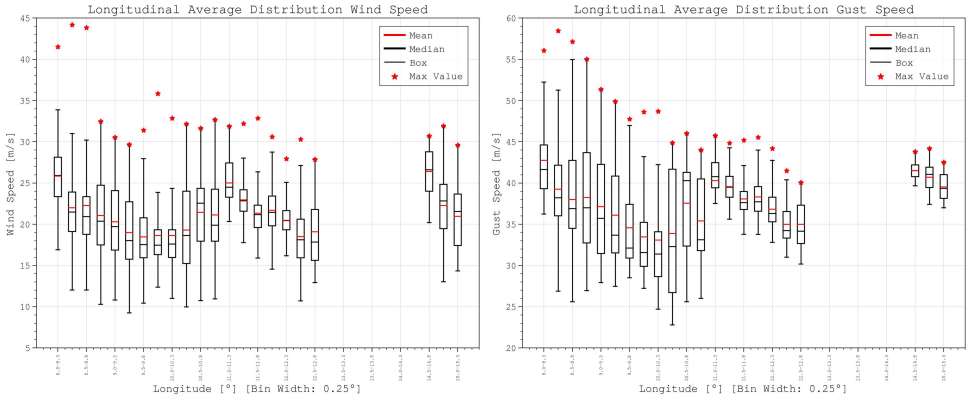
The maximum mean wind speed and gust values over Denmark are presented in table 1. All model

runs indicate wind speeds surpassing hurricane levels (> 32.6 m/s) with further analysis revealing both an increase in peak wind velocities and an extended duration during which parts of Denmark experience sustained winds above 24.5 m/s. Additionally, the percentage of land area exposed to high winds appears to increase. A similar pattern, though more pronounced, is evident in the gust analysis, where maximum gusts reach up to 60 m/s for a duration of one hour in the control run. In the warmer-world experiments, this threshold is exceeded, with a clear tendency for higher maximum gusts as the temperature increases across the experiments (Zeitzen et al., 2024).

Table 1. Maximum wind and gust velocities in the various runs.

	$-1°C$	Control run	$+1°C$	$+2°C$	$+3°C$
Wind [m/s]	44.5	44.2	45.9	45.7	46.7
Gust [m/s]	58.9	60.1	62.2	60.3	62.6

In addition to the increase in wind speed, the HARMONIE model also indicates a deeper minimum pressure for the low-pressure system under the $+3°C$ scenario, reaching 952 hPa. In contrast, the other model runs exhibited minimum pressures of approximately 954 hPa. According to (EUROCODE, 2015), the basic wind speed value, which should only be surpassed once in 50 years, in Denmark is set at 24 m/s across most regions, except within a marginal zone at the west coast of Jutland. In this zone, which includes areas within 25 km of the North Sea and Ringkøbing Fjord, the basic wind speed is 27 m/s at the coast, gradually decreasing to 24 m/s at the zone's inland boundary. In figure 2 this marginal zone is illustrated, with each bin representing approximately 16 km. The 10 m wind velocities in figure 2a shows a distinct drop in wind speed beyond approximately 30 km, while the gust figure 2b indicates a more gradual decline.



(a) Wind speed [m/s] - West to East

(b) Gust speed [m/s] - West to East

Figure 2. Cross-section of Denmark in $0.25° \sim 16$ km bins showing wind/gust distribution for the $+3°$C perturbation.

5. DISCUSSION

The results indicate that differences in simulated wind velocities over Denmark may be attributed to PGW. Beyond the evident increase in wind speeds, the findings suggest an extended duration of high wind events. Such changes could have significant implications for structural design, urban planning and infrastructure resilience, highlighting the need to consider these factors in city construction and adaptation strategies. Older generations of climate models have struggled to accurately represent extreme wind events due to limitations in spatial and temporal resolution. This has

led to the assumption that the risk of storms may not increase as a result of climate change(Spinoni et al., 2020). However, a study by Severino et al., 2024 indicates an intensification in future climate-related windstorm damage. Storms with a current return period of 100 years may, under future climate scenarios, occur as frequently as every 28 years.

6. CONCLUSION

The findings reveal a potential increase in wind speeds under warmer conditions, with implications for higher onshore wind risks and inland expansion of hurricane-level winds (>32.6 m/s), beyond observed patterns. Given the potential for future storms with even higher wind and gust speeds, the likelihood of more extensive structural damage is substantial. Furthermore, prognosing an increase of the mean wind speed of about 6%, the results indicate a review of the characteristic wind speeds given for coastal and remaining areas of Denmark.

The future impacts of extreme wind events can be mitigated through various measures, including the development and implementation of enhanced windstorm-resistant standards and building codes.

ACKNOWLEDGEMENTS

The author extend sincere gratitude to Henrik Feddersen at DMI for conducting the HARMONIE model runs, and to Niels Woetmann Nielsen for his valuable meteorological insights. Special thanks are also due to Rune Zeitzen for his assistance with plots and coding, which contributed significantly to the analysis, and to Jens Hesselbjerg Christensen and Henrik Vedel for the idea and design of the original experiments.

REFERENCES

Bengtson et al., 2017. The HARMONIE-AROME Model Configuration in the ALADINE-HIRLAM NWP System. Monthly Weather Review 145, 1919–1935.

Cappelen, J., Olufsen, S., Ribergaard, M. H., Nielsen, J. W., Schmith, T., and Hansen, N., 2018. *Decemberorkanen 1999*. https://www.dmi.dk/vejr-og-atmosfare/temaforside-decemberorkanen-1999.

EUROCODE, 2015. *Eurocode 1: Last på bygværker – Del 1-4: Generelle laster - Vindlast*.

European Environment Agency, 2024. *Annual economic losses caused by weather-and climate-related extreme events in the EU Member States*. (Visited on 11/14/2024).

Kettle, A. J., 2021. Storm Anatol over Europe in December 1999: impacts on societal and energy infrastructure. Advances in Geosciences 56, 141–153.

Matte, D., Christensen, J. H., Feddersen, H., Vedel, H., Nielsen, N. W., Pedersen, R. A., and Zeitzen, R. M. K., 2022. On the potentials and limitations of Attributing a Small-Scale Climate event. Geophysical Research Letters 49.

Mühlhausen, B. and Sønderiis, E., 1999. *Orkan over Danmark*.

Nielsen, N. W. and Sass, B. H., 2003. A numerical, high-resolution study of the life cycle of the severe storm over Denmark on 3 December 1999. Tellus A: Dynamic Meteorology and Oceanography 55A.

Severino, L. C., Kropf, C. M., Afargan-Gerstman, H., Fairless, C., Jan de Vries, A., Domeisen, D. I. V., and Bresch, D. N., 2024. Projections and uncertainties of winter windstorm damage in Europe in a changing climate. Natural hazards and Earth system science 24.

Spinoni, J., Giuseppe Formetta, G., Mentaschi, L., Forzieri, G., and Feyen, L., 2020. Global warming and windstorm impacts in the EU. European Commission.

Voldborg, H., 2000. Vredens julemåned. Vejret 82, 1–7.

Zeitzen, R. M. K., Christensen, J. H., Feddersen, H., Vedel, H., Nielsen, N. W., and Matte, D., 2024. The wind of change: A self-Consistent storyline of an Intense Extratropical Cyclone at Mesoscale-resolving resolution. Geophysical Research Letters.

Experimental modeling of gusty bora windstorms

Petar Škvorc[1], Hrvoje Kozmar[2], Branko Grisogono[3], Antonio J. Álvarez[4], Felix Nieto[5], Jeroen van Beeck[6], Tibebu Birhane[7], Girma Bitsuamlak[8]

[1,2]*Faculty of Mechanical Engineering and Naval Architecture, University of Zagreb, Zagreb, Croatia, petar.skvorc@fsb.unizg.hr[1], hrvoje.kozmar@ fsb.unizg.hr[2]*

[3]*Department of Geophysics, Faculty of Science, University of Zagreb, Zagreb, Croatia, branko.grisogono@gfz.hr*

[4,5]*CITEEC – University of A Coruña, A Coruña, Spain, antonio.jose.alvarez@udc.es[4], felix.nieto@udc.es[5]*

[6]*Von Karman Institute for Fluid Dynamics, Waterloo, Belgium, jeroen.vanbeeck@vki.ac.be[6]*

[7,8]*WindEEE – Western University, London, Canada, tbirhane@uwo.ca[7], gbitsuam@uwo.ca[8]*

SUMMARY:
Bora is a non-synoptic wind characterized by its strong gusts. It commonly occurs at the eastern Adriatic coast, but also in many other dynamically similar places around the world. This fact makes the findings regarding bora wind and its turbulence globally applicable. In the present study, experimental episodes of severe bora windstorms were created using three approaches, i.e., a) oscillating flow velocity was created to be similar with the bora velocity measurements in nature, b) the bora velocity time history measured on the meteorological mast in nature was simulated in the laboratory, c) straight horizontal flow was combined with the vertical downdraft (downburst) flow. The results strongly indicate the suitability of the WindEEE Dome for experimental modeling of straight gusty winds.

Keywords: Gusty bora wind; Experimental modeling; WindEEE Dome

1. INTRODUCTION

Bora wind is a non-synoptic wind at the eastern Adriatic coast, blowing from the mountain ranges towards the sea. It typically occurs in the geographic area ranging from Trieste, Italy, to Dubrovnik, Croatia, and even further south, e.g., Bajić (1988). This wind is usually chilly and generally dry, with extreme gustiness as its most notable features, Grisogono and Belušić (2009). While average wind velocities rarely exceed 20 m/s, gust wind velocity can be five times higher, Belušić et al. (2013). The wind velocity and direction can vary significantly. Bora is most common in winter, lasting from a few hours to several days, Jeromel et al. (2009), with pulsation periods typically ranging from 3 to 11 minutes, Belušić et al. (2007). Due to its high wind velocity, gustiness and unpredictable nature, bora is harmful to traffic, agriculture and infrastructure, with severe impact on energy structures such as wind turbines and solar panels.

The scope of the present study is to experimentally simulate non-synoptic bora winds in the WindEEE Dome facility at the Western University, London, Ontario, Canada. The unique capabilities of the WindEEE Dome are used in three ways to simulate complex flow characteristics of the bora wind. Some preliminary results are presented here, while extensive experiments are

still underway and to be presented at the conference.

2. WINDEEE DOME

Wind Engineering Energy and Environment (WindEEE) Dome at Western University is a unique experimental facility designed to simulate complex wind systems, such as tornadoes and downbursts. This laboratory is particularly useful given the fact that it is not possible to simulate complex non-synoptic winds in standard boundary-layer wind tunnels (BLWTs). The test section is a hexagonal shape with 25 m in diameter. It houses 100 fans in the vertical walls capable of creating flow velocities up to 25 m/s and six fans in the ceiling, Hangan (2014).

Above the test section, there is a hexagonal chamber with six more fans which can create positive or negative pressure in that chamber. This chamber is connected to the test section below with a bell-mouth, which is used to regulate the airflow between the chamber and the test section. This design allows for the control of flow characteristics, simulating various non-synoptic winds such as tornado and downburst. The WindEEE Dome can operate in two main modes, i.e., for a) straight synoptic winds, such as the atmospheric boundary layer (ABL), and b) non-synoptic winds. A photograph of the WindEEE Dome test section with contraction and surface roughness elements is shown in Figure 1.



Figure 1. WindEEE Dome test section with contraction and surface roughness elements

3. BORA WIND SIMULATION

Bora wind characteristics are simulated with a particular focus on its characteristic gustiness. Three experimental approaches were employed for this purpose:

1. **Generic flow**: Two flow velocities were selected (base and gust velocities) and alternated over a time record. This was performed by rapidly adjusting the fan rotations per minute (RPM), thus creating multiple transitions between the two flow velocities in each time record.
2. **Prototype simulation**: Velocity measurements taken at full-scale on a meteorological mast are replicated in the laboratory by adjusting the RPM of the fans.
3. **Concurrent straight flow and downburst**: Concurrent action of the quasi steady, turbulent straight flow and downburst.

A rake of seven Cobra probes at heights 0.050 m, 0.075 m, 0.100 m, 0.150 m, 0.200 m, 0.300 m,

and 0.400 m was used to measure the flow velocity. All measurements were performed at the 1.25 kHz sampling rate. The generic flow and prototype simulation tests were performed over 300 s, while the concurrent straight flow and downburst tests were carried out over a period of 30 s.

3.1. Generic flow

The longitudinal flow velocity was set to alternate between a base (low) velocity and a gust (high) velocity by rapidly adjusting the fan RPM. This approach, developed to simulate the gustiness of the bora wind, is like the approach in Kozmar et al. (2012, 2015). In the WindEEE Dome, 60 fans in the wall of the test chamber, all at the same RPM, are used for this purpose. The base velocity was ~5 m/s, corresponding to 20% of the fans' nominal RPM. Its duration is 10 s and then it rapidly increases to the gust velocity. The maximum fan acceleration was set at 5% per second of the nominal RPM. Each time record is 300 s long, with consistent base velocity and duration with various gust velocities and durations. Three gust velocities were studied (10 m/s, 15 m/s, and 20 m/s), with gust durations of 10 s, 20 s and 30 s. The recorded longitudinal velocity time history is shown in Figure 2.

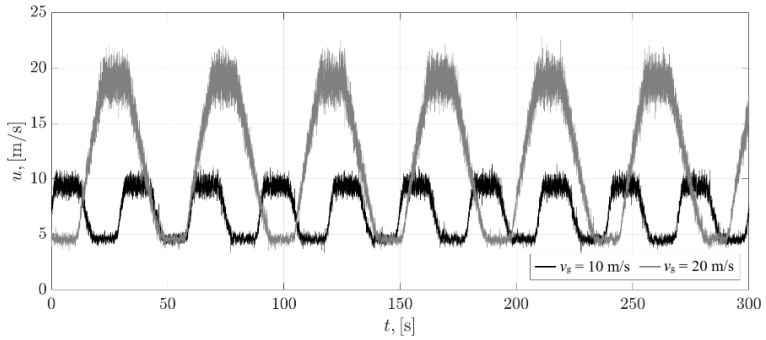


Figure 2. Velocity records for two gust velocities v_g = 10 m/s (black line) and v_g = 20 m/s (grey line) with gust duration t_g = 10 s.

3.2. Prototype simulation

The 300 s long velocity time record of bora, obtained on a meteorological mast, was used as an input to the fan RPM. Due to the extreme gustiness of bora wind in nature and the technical constraints of the fans in the WindEEE Dome, the field flow velocity was reduced to its half, thus yielding a downscaled laboratory simulation. The longitudinal flow velocity measured in the WindEEE Dome is presented in Figure 3; this is qualitatively similar to Figure 2b from the bora observation in Grisogono and Belušić (2009).

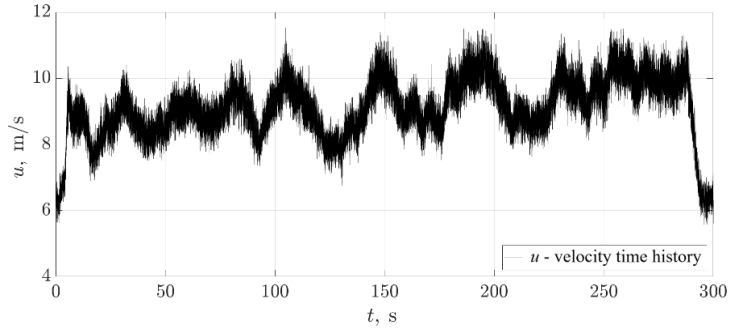


Figure 3. Flow velocity record of the simulated bora gusts

3.3. Concurrent straight flow and downburst

WindEEE Dome is a unique facility capable of simulating downburst winds. By positioning the bell-mouth of the WindEEE Dome and arranging the measurement equipment, the intense wind gusts typical for the bora wind can be simulated. Quasi steady horizontal turbulent flow is created as well. These two types of flow acting concurrently yield the base bora flow. Hence, these tests are currently underway and the respective results will be reported at the conference.

4. CONCLUSIONS

Three approaches to experimental modeling of gusty bora windstorms are developed in the WindEEE Dome facility, i.e., a) oscillating flow velocity was created to be similar to the bora wind velocity in nature, b) bora velocity time history recorded on the meteorological mast was simulated in the laboratory, c) straight horizontal flow was combined with the vertical downdraft (downburst) flow. The results indicate the applicability of the WindEEE Dome facility for experimental modeling of gusty windstorms. More importantly, these findings will strengthen the efforts regarding gusty wind effects on structures, which will allow for further improvements of international wind engineering standards and codes.

ACKNOWLEDGEMENTS

This work is part of the transnational access project "ERIES – SOLAR", supported by the Engineering Research Infrastructures for European Synergies (ERIES) project (www.eries.eu), which has received funding from the European Union's Horizon Europe Framework Programme under Grant Agreement No. 101058684. This is ERIES publication number C29. The support of the technical and administrative staff at WindEEE is greatly appreciated. This work was supported by the Croatian Science Foundation under the project number HRZZ-IP-2022-10-9434.

REFERENCES

Bajić, A., "The strongest Bora event during ALPEX SOP", *Rasprave-Papers*, **23**, 1-9 (1988)

Belušić, D., Hrastinski, M., Večenaj, Ž., Grisogono, B., "Wind regimes associated with a mountain gap at the northeastern Adriatic coast", *Journal of Applied Meteorology and Climatology*, **52**(9), 2089-2105, (2013)

Belušić, D., Žagar, M., Grisogono, B., "Numerical simulation of pulsations in the Bora wind", *Quarterly Journal of the Royal Meteorological Society*, **133**(627), 1371-1388, (2007)

Grisogono, B., Belušić, D., "A review of recent advances in understanding the meso- and micro-scale properties of the severe Bora wind", *Tellus*, **61**, 1-16, (2009)

Hangan, H., "The Wind Engineering Energy and Environment (WindEEE) Dome at Western University. Canada", *Wind Engineers JAWE* **39**, 350–351 (2014).

Jeromel, M., Malačič, V. and Rakovec, J., "Weibull distribution of Bora and sirocco winds in the northern Adriatic Sea", *Geofizika*, **26**(1), 85-100, (2009)

Kozmar, H., Butler, K., Kareem, A., "Transient cross-wind aerodynamic loads on a generic vehicle due to bora gusts", *Journal of Wind Engineering and Industrial Aerodynamics*, **111**, 73-84, (2012)

Kozmar, H., Butler, K., Kareem, A., "Downslope Gusty Wind Loading of Vehicles on Bridges", *Journal of Bridge Engineering*, 04015008, 1-11, (2015)

Equivalent Synoptic Wind: a tool for assessing non-synoptic wind effects on slender structures

Andrea Orlando [1], Luisa Pagnini [2], Maria Pia Repetto [3]

[1]*Polytechnic School, University of Genoa, Italy, andrea.orlando@edu.unige.it*
[2]*Polytechnic School, University of Genoa, Italy, luisa.pagnini@unige.it*
[3]*Polytechnic School, University of Genoa, Italy, repetto@dicca.unige.it*

SUMMARY:
Starting from an ongoing full-scale monitoring campaign over three steel towers, this paper introduces the concept of an Equivalent Synoptic Wind (ESW) as a tool to interpret and assess the non-synoptic wind-induced effects on slender structures. The dynamic response of the monitored structures is recorded by accelerometers and strain gauges; simultaneous measurements of the wind field are supplied by ultrasonic anemometers installed on top of the towers, providing the structural behaviour under different wind phenomena, namely extra-tropical cyclones, thunderstorms and gust fronts. For each measured non-synoptic record, an ESW is defined as the synoptic wind that produces the measured structural effect, obtained from a well-established calculation model. The statistical parameters of the ESW events (e.g., mean wind speed and turbulence properties) are presented and compared with real synoptic wind records.

Keywords: Non-synoptic wind, Structural Monitoring, Slender structures

1. INTRODUCTION

The European wind climate, like many regions worldwide, can be classified as a mixed climate—a climatologic condition where various wind phenomena coexist (Gomes and Vickery, 1978). Extra-tropical cyclones, typical of mid-latitude areas, generate synoptic winds, which exhibit stationary and Gaussian behavior over 10-minute to 1-hour intervals. Since Davenport's pioneering work in 1968, established methods have been developed to model synoptic wind fields and their effects on structures. Conversely, non-synoptic meteorological phenomena with limited spatial and temporal scales can produce very high wind speeds, characterized by rapid, non-stationary, and non-Gaussian fluctuations. Traditional analysis methods, such as the gust loading factor approach, may be inadequate for evaluating non-synoptic effects. Despite extensive research across several areas (e.g., Choi and Hidayat, 2002; Kwon and Kareem, 2013; Solari et al., 2020), understanding and modelling the effects of non-synoptic winds on structures remain challenging. It is still uncertain if non-synoptic events pose the most critical scenarios for structural safety, in terms of statistical distribution, aerodynamic behavior, and dynamic amplification.

Working in this field, the research group of the University of Genoa set a wide monitoring network to obtain robust full-scale measurements of wind velocity (Burlando et al., 2018) and structural response parameters (Orlando, 2021). In particular, the dynamic response of three steel towers (namely two lighting towers and a lattice tower) is currently monitored by accelerometers and strain gauges; simultaneous measurements of the wind field are supplied by ultrasonic

anemometers installed on top of the towers, providing the structural behavior under different wind phenomena. Using a separation algorithm (De Gaetano et al., 2014), the recorded data were categorized into three groups: (i) synoptic winds associated with extra-tropical cyclones, exhibiting stationary and Gaussian patterns; (ii) non-synoptic winds linked to thunderstorm outflows, showing non-stationary and non-Gaussian patterns; and (iii) intermediate events related to gust fronts, characterized by stationary but non-Gaussian patterns.

This paper introduces a new approach to analyze and compare wind-induced response across different wind phenomena by leveraging structural monitoring data. To achieve this, each full-scale record is associated with an Equivalent Synoptic Wind (ESW)—a synoptic wind that produces the structural effect measured by sensors during that record. ESW parameters are determined by reversely applying a calculation model for synoptic wind-induced response. For the lighting towers, a well-established analytical model of wind effects is used from literature (Solari and Pagnini, 1999); for the lattice tower, where a specific model is unavailable, an artificial neural network (ANN) is developed to predict structural effects under synoptic winds. The statistical parameters characterizing the ESW of non-synoptic records are presented and analyzed in comparison to those for actual synoptic records.

2. FULL-SCALE MONITORING AND DATASET

The monitored structures are two lighting towers, 16.6 m and 35 m high, respectively located in the Harbours of La Spezia and Genoa, Italy, and a 50 m high lattice tower installed in Sânnicolau Mare, Romania. Each structure is equipped with a monitoring system that includes wind speed and structural response sensors.

A three-axis ultrasonic anemometer, positioned at the top of each structure, records wind speed at a 10 Hz sampling rate. The structural response is recorded simultaneously at 100 Hz using biaxial accelerometers (placed at the top and mid-levels of the towers) and uniaxial strain gauges (installed at the base). Data from these sensors have been collected continuously over the past three years, with some intermittent gaps.

a) b) c)

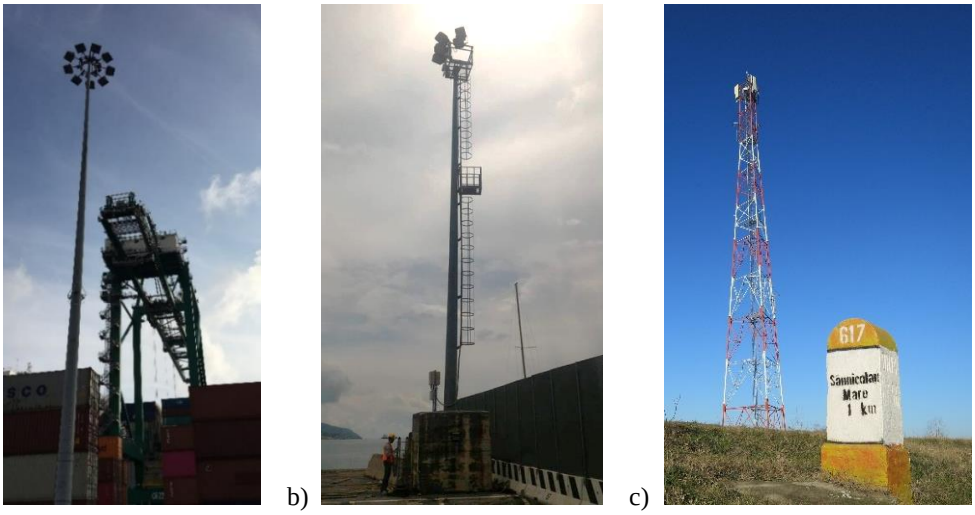


Figure 1. The monitored towers in Genoa (a), La Spezia (b) and Sânnicolau Mare (c).

Wind velocity records are analyzed to identify and distinguish synoptic extra-tropical cyclones, thunderstorm outflows, and intermediate events using a semi-automated approach (De Gaetano et al., 2014). High-intensity records, with peak wind velocities exceeding 15 m/s, are categorized into three corresponding datasets.

3. EQUIVALENT SYNOPTIC WIND CALCULATION

The Equivalent Synoptic Wind (ESW) is defined as the synoptic wind event that produces the structural effect (e.g., the maximum top displacement) detected by the real full-scale record. In order to define the ESW, a calculation model of the synoptic wind-induced response is required.

As regards the lighting towers, the analytical model proposed by Solari and Pagnini (1999) for the calculation of wind-induced effects on poles is adopted. The model has been validated in previous research (Orlando, 2021), comparing analytical predictions with full-scale records of synoptic wind-induced response. According to the formulation, assuming a classical synoptic wind field model and once the aerodynamic, modal and terrain parameters are defined, the structural effects depend only on the mean wind velocity, in turn governing the turbulence properties. Thus, a numerical procedure is established, able to retrieve those wind speed statistical parameters from the measured maximum displacement. The synoptic wind event characterized by the obtained mean wind speed and turbulence components is defined as the ESW.

In the case of the lattice tower, lacking a specific detailed calculation model, an ANN is developed to predict structural effects under synoptic winds. Simultaneous records of wind speed and structural response during synoptic events are used to train the algorithm. Once the algorithm's efficacy is validated, it is reversely used starting from non-synoptic response records to obtain the ESW parameters.

As an example, Figure 2 (a) shows a thunderstorm wind velocity record experienced by the lighting tower in La Spezia and the corresponding 10-min mean and standard deviation of the ESW event. Figure 2 (b) shows the thunderstorm-induced top displacement record and the corresponding maximum displacement adopted to retrieve the ESW parameters. It is worth noticing that the ESW,

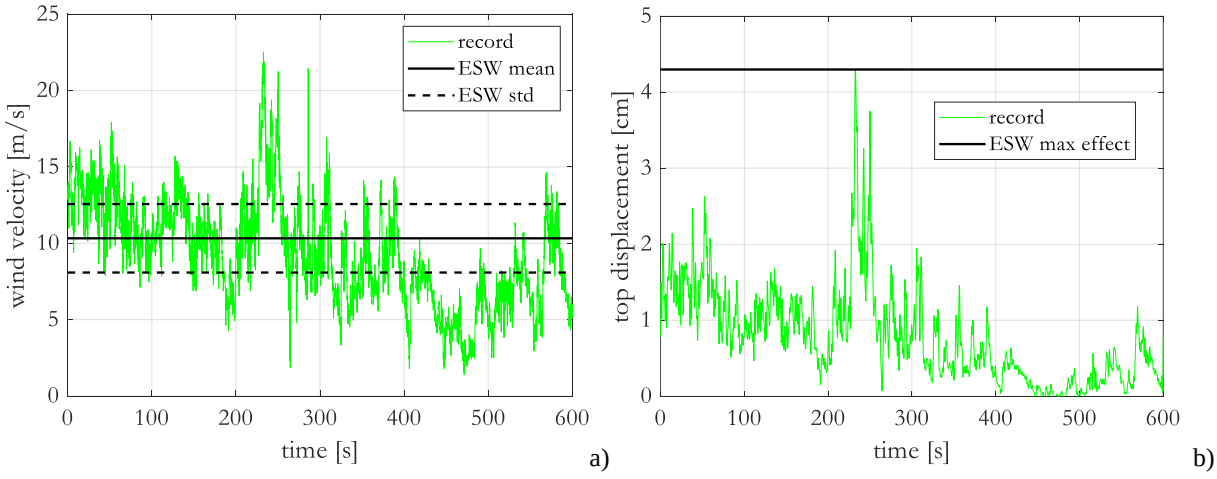


Figure 2. Thunderstorm recorded in La Spezia and relevant ESW (a); simultaneous displacement record (b).

evaluated for non-synoptic wind-induced response records, has no meteorological meaning, rather it is an engineering tool to trace back the non-synoptic structural effects to conventional well-known parameters.

Comparing the distribution of mean wind speeds associated with ESW events and synoptic events may offer a criterion for addressing non-synoptic winds through an equivalent design wind velocity. Applying this procedure starting from various response quantities—specifically, mean top displacement, maximum bottom stress, and mean bottom stress—could provide an indirect measure for assessing how non-synoptic winds induce different structural effects compared to synoptic winds.

4. CONCLUSIONS AND PERSPECTIVES

The final paper outlines the proposed algorithm used to define the ESW and presents the ESW events assessed from non-synoptic records available in the full-scale monitoring databases; it discusses the structural effects induced by each identified wind phenomenon and provides a statistical analysis of wind speed parameters for both ESW and observed synoptic events.

ACKNOWLEDGEMENTS

This research is funded by the European Union - NextGenerationEU and by the Ministry of University and Research (MUR), National Recovery and Resilience Plan (NRPP), Mission 4, Component 2, Investment 1.5, project "RAISE - Robotics and AI for Socio-economic Empowerment" (ECS00000035).

REFERENCES

Burlando, M., Zhang, S., and Solari, G., 2018. Monitoring, cataloguing, and weather scenarios of thunderstorm outflows in the northern Mediterranean. Natural Hazards and Earth System Sciences 18, 2309-2330.

Choi, E. C. C. and Hidayat, F. A., 2002. Gust factors for thunderstorm and non-thunderstorm winds. Journal of Wind Engineering and Industrial Aerodynamics 90, 1683-1696.

Davenport, A. G., 1968. The dependence of wind loads on meteorological parameters. Proceedings International Research Seminar “Wind effects on buildings and structures", 11-15 Sept. 1967. Ottawa, Canada, 19–82.

De Gaetano, P., Repetto, M. P., Repetto, T., and Solari, G., 2014. Separation and classification of extreme wind events from anemometric records. Journal of Wind Engineering and Industrial Aerodynamics 126, 132-143.

Gomes, L. and Vickery, B. J., 1978. Extreme wind speeds in mixed wind climates. Journal of Wind Engineering and Industrial Aerodynamics 2, 331-344.

Kwon, D. K. and Kareem, A., 2013. Generalized gust-front factor: A computational framework for wind load effects. Engineering Structures 48, 635-644.

Orlando, A., 2021. Full-scale monitoring of the wind-induced response of vertical slender structures, with fixed and rotating masses. Ph.D. Dissertation, University of Genoa, Genoa, Italy.

Solari, G., Burlando, M., and Repetto, M. P., 2020. Detection, simulation, modelling and loading of thunderstorm outflows to design wind-safer and cost-efficient structures. Journal of Wind Engineering and Industrial Aerodynamics 200, 104142.

Solari, G. and Pagnini, L. C., 1999. Gust buffeting and aeroelastic behaviour of poles and monotubular towers. Journal of Fluids and Structures 13, 877-905.

Experimental testing of bridge decks in downburst-like winds

Øyvind Wiig Petersen [1], Aksel Fenerci [1], Sebastian Knedahl Hansen [1], Ole Øiseth[1], Tibebu Birhane [2], and Girma Bitsuamlak [2]

[1]*Norwegian University of Science and Technology, Trondheim, Norway, ole.oiseth@ntnu.no, oyvind.w.petersen@ntnu.no, aksel.fenerci@ntnu.no, sebastian.k.hansen@ntnu.no*

[2]*WindEEE Research Institute, Western University of Ontario, London, Canada, tbirhane@uwo.ca, gbitsuam@uwo.ca*

SUMMARY:

The ERIES-AEROBURST project is centered on investigating the aerodynamics loads due to non-stationary downburst-like winds on long-span suspension bridges. A novel test campaign will be conducted in the WindEEE Dome using a 1:100 scaled section model of a single-deck suspension bridge. Awaiting experimental results, this contribution describes the experimental design and setup. Preliminary experimental results will be shown at the conference. The wind tunnel tests will include surface pressure measurements and free vibration tests under downbursts with and without boundary layer winds.

Keywords: downburst, suspension bridge, wind tunnel, WindEEE

1. INTRODUCTION

Loads from non-synoptic winds such as downbursts, characterized by their non-stationary and transient nature, challenge traditional aerodynamic models. Such loads are rarely considered in the wind-resistant design of long-span bridges. Yet, recent full-scale observations of monitored bridges in Norway [1] and the UK [2] have revealed substantial non-stationary dynamic responses of bridges. These findings call for an updated understanding of the significance of non-synoptic winds in the assessment of structural integrity under wind loads.

In this contribution, we present the ERIES-AEROBURST project, which aims to address the knowledge gap in understanding the aerodynamic and aeroelastic effects of transient, non-stationary downburst-like winds on long-span suspension bridges. The project adopts an experimental approach as a pilot study to evaluate the feasibility of testing bridge decks in facilities capable of physically simulating downburst winds. A comprehensive review of such facilities worldwide can be found in [3]. The proposed experiments will take place in the WindEEE Dome [4], a unique facility that replicates downburst outflows at reduced scale using an impinging jet mechanism. As the experiments are still in the planning stage, this contribution focuses on the experimental design and the anticipated outcomes, with initial results expected to be presented at the conference.

2. EXPERIMENTAL CAMPAIGN AT WINDEEE DOME

2.1. Test specimen and setup

The selected test specimen is a section model similar to the Hardanger Bridge, see Fig. 1. A few simplifications are made; the top surface is made flat. This bridge deck is chosen since the authors have monitored this bridge for a number of years [5], and strong non-stationary events have been observed in the monitoring data.

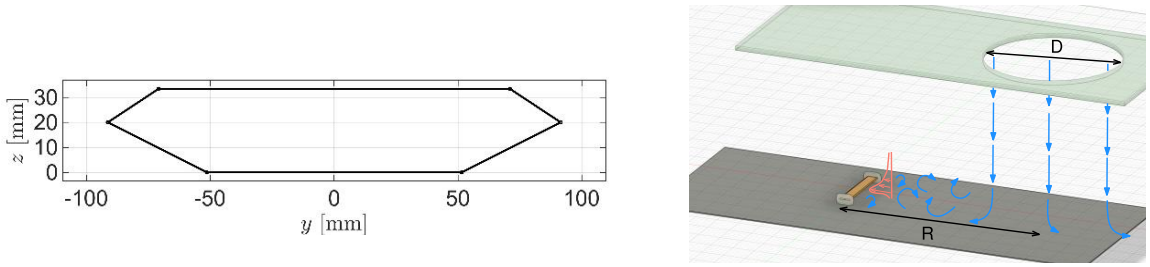


Figure 1. Left: shape of tested bridge deck; right: sketch of downburst test setup

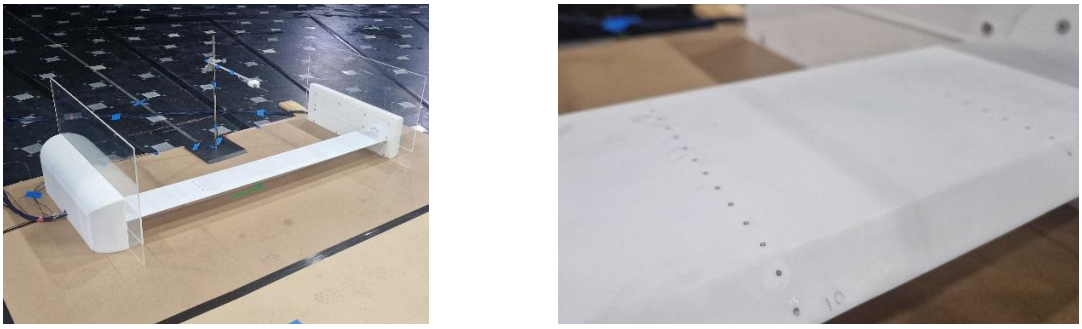


Figure 2. Left: fixed section model during the test; right: close-up of a strip of pressure taps on the model

Two section models are planned to be tested: (i) a fixed section model (Fig 2) and (ii) an elastically suspended section model (not shown here). The fixed section model will be equipped with pressure taps arranged as circumferential strips in several locations, see Fig. 2. A strip with finer resolution is located in the mid-length of the model for accurate integration of pressures. Other strips will also be added towards the two sides of the model to study the correlation of pressures in the span-wise direction. In addition, the measured pressures along the span can provide insights into the progression of the downburst front onto the bridge, as the outflow is expected to radially spread from the burst impact point, thus hitting the bridge center first, then span ends with a slight delay.

The elastically spring-suspended section model allows motion in drag (horizontal), lift (vertical), and pitch (torsional) directions to study the transient dynamics of the bridge. The forces on the section model will be measured using load cells. Cobra probes will be used to measure the wind speed and turbulence in several elevation levels and at several distances from the downburst impact point.

Table 1. Characteristic quantities targeted in the experiment

Quantity	Factor	Example	Prototype	Model
Length	λ_L=1/100	Deck width, B	18.3 m	18.3 cm
		Downdraft diameter, D	320 m	3.2 m
Mass per unit length	${\lambda_L}^2$	Bridge deck mass, m_z	12800 kg/m	1.28 kg/m
Rotational inertia per unit length	${\lambda_L}^4$	Bridge deck inertia, m_θ	426000 kg/m	0.00426 kg/m
Time (T)	λ_T=1/50	Downburst gust duration	100-200 s	2-4 s
Frequency (f)	$\lambda_f = 1/\lambda_T = 50$	Horizontal frequency	0.05 Hz	2.5 Hz
		Vertical frequency	0.14 Hz	7 Hz
		Torsional frequency	0.36 Hz	18 Hz
Wind velocity (U)	$\lambda_U = \lambda_f \lambda_L = 1/2$	Gust speed	0-30 m/s	0-15 m/s

2.2. Scaling

The introduction of scaling requires a balance between two primary objectives: (i) representing the physics at full-scale as accurately as possible and (ii) ensuring the practicality of model construction and experiment execution. An overview of the targeted design quantities is provided in Table 1. It is chosen to scale the bridge deck geometrically at 1:100, which allows the downdraft diameter in the WindEEE dome (3–4 meters) to simulate a full-scale downburst diameter of 300–400 meters. A smaller scale microburst is more desirable here, as it allows studying 3-dimensional effects of a downburst even using a section model of limited length.

The model will measure 1.5 meters in length, 18.3 cm in width, and 3.3 cm in height. For the elastically suspended model, the natural frequencies are tuned to match those of the prototype full-scale bridge (after scaling is introduced).

2.3. Planned tests and expected outcomes

The experiments will start by characterizing the downburst wind field using cobra probes, where spatial and temporal correlations will be important metrics. Next, the test program will include combinations of several test parameters:

Model configurations: (i) a section model which is fixed, focusing on surface pressures and(ii) an elastically suspended section model, focusing on the dynamic response to transient gusts and highly correlated wind loads.
Wind conditions: (i) isolated downburst winds to study the direct effects of non-stationary loading and (ii) downburst winds combined with a boundary layer flow, simulating real-world conditions where synoptic winds interact with downburst outflows.
Bridge positioning: The bridge model will be positioned at multiple radial distances from the downburst impact point and multiple vertical distances to explore the dependence on the proximity and elevation above ground.

The data will be processed to study the transient aerodynamic forces and moments acting on bridge decks, hypothesizing that these forces may deviate from those induced by synoptic winds. Tests where boundary layer wind and downbursts are combined will give insights into potential additive effects. From a design viewpoint, it is also likely that such a combination represents a

more adverse load condition for a suspension bridge than an isolated downburst.

Eventually, the study aims to bridge the gap between the predicted dynamical behavior based on experimental results and real-world observations of bridge responses from monitoring campaigns. The study will contribute to refining predictive models and advancing design methodologies for bridges subjected to non-stationary wind loading scenarios.

In accordance with the ERIES policy for openness and outreach, the experimental data (including metadata) will be made available at www.dataaccessportal.eu/.

7. CONCLUSIONS

This experimental study aims to advance the understanding of downburst-like winds and their impact on suspension bridges, addressing non-synoptic loading scenarios often overlooked in traditional bridge designs. Through extensive testing in the WindEEE Dome, the project seeks to provide experimental validation for analytical models and serve as a reference dataset for comparisons with full-scale bridge observations. The study anticipates contributing to engineering practices for considering non-synoptic wind effects, ensuring structural safety under extreme wind events.

ACKNOWLEDGEMENTS

This work is part of the transnational access project "ERIES-AEROBURST", supported by the Engineering Research Infrastructures for European Synergies (ERIES) project (www.eries.eu), which has received funding from the European Union's Horizon Europe Framework Programme under Grant Agreement No. 101058684. This is ERIES publication number C45.

REFERENCES

[1] A. Fenerci and O. Øiseth, "Strong wind characteristics and dynamic response of a long-span suspension bridge during a storm," *Journal of Wind Engineering and Industrial Aerodynamics,* vol. 172, p. 116–138, 2018.

[2] J. S. Owen, D. T. Nguyen, X. Meng, P. Psimoulis and Y. Xie, "An observation of non-stationary response to non-synoptic wind on the Forth Road Bridge," *Journal of Wind Engineering and Industrial Aerodynamics,* vol. 206, p. 104389, 2020.

[3] S. Li, R. A. Catarelli, B. M. Phillips, J. A. Bridge and K. R. Gurley, "Physical simulation of downburst winds for civil structures: A review," *Journal of Wind Engineering and Industrial Aerodynamics,* vol. 254, p. 105900, 2024.

[4] F. Canepa, M. Burlando, D. Romanic, G. Solari and H. Hangan, "Downburst-like experimental impinging jet measurements at the WindEEE Dome," *Scientific Data,* vol. 9, p. 243, 2022.

[5] A. Fenerci, K. A. Kvåle, Ø. W. Petersen, A. Rønnquist and O. Øiseth, "Dataset for long-term wind and acceleration monitoring of the Hardanger Bridge," *Journal of Structural Engineering,* vol. 147, 2021.